PROCEEDINGS OF THE FIFTEENTH INTERNATIONAL SYMPOSIUM ON ARTIFICIAL LIFE AND ROBOTICS

(AROB 15th'10)

Feb.4 - Feb.6, 2010
B-Con Plaza, Beppu, Oita, JAPAN

Editors: Masanori Sugisaka and Hiroshi Tanaka

Publisher: ALife Robotics Co., Ltd.
Publication Date: Jan. 15, 2010
ISBN 978-4-9902880-4-4

Program of The Fifteenth International Symposium on

ARTIFICIAL LIFE AND ROBOTICS

(AROB 15th '10)

Feb. 4 - Feb.6, 2010

B-Con Plaza, Beppu, Oita, Japan,

Editors: Masanori Sugisaka and Hiroshi Tanaka

THE SIXTEENTH INTERNATIONAL SYMPOSIUM ON ARTIFICIAL LIFE AND ROBOTICS (AROB 16th '11)

January 27-29, 2011, B-Con Plaza, Beppu, Oita, JAPAN

☐ I would like to participate in the symposium

☐ I intend to present a paper ENTITLED:

Last name .... First name ....

Title .... Position ....

Affiliation ....

Address ....

....

Tel: .... Fax: ....

E-mail: ....

All correspondence related to the symposium should be addressed to: AROB Secretariat

ALife Robotics Corporation Ltd.

301 Koopo Nagaoka 1385-1 Miyazaki, Oita 870-1133, JAPAN

TEL/FAX +81-97-594-0181

E-MAIL arobsecr@alife-robotics.co.jp

Home Page http://alife-robotics.co.jp/

PUBLICATION:

Accepted papers will be published in the Proceedings of AROB. Authors of high quality papers appearing in the Proceedings may be requested to resubmit their papers for the consideration for publication in a new international journal ARTIFICIAL LIFE AND ROBOTICS.

Map of Japan

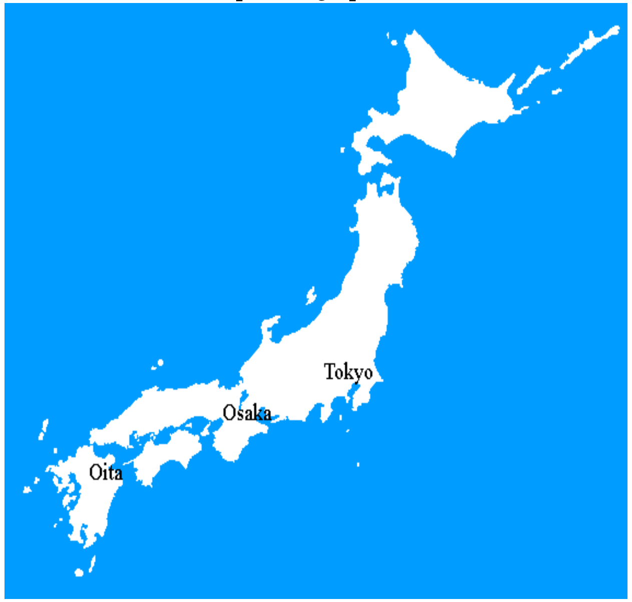

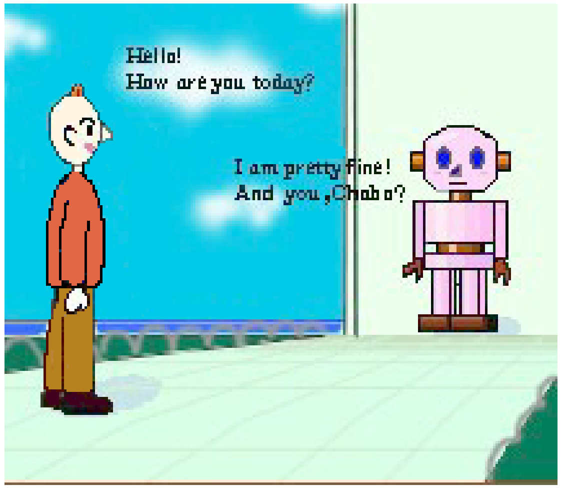

Call for Papers

THE SIXTEENTH INTERNATIONAL SYMPOSIUM ON ARTIFICIAL LIFE AND ROBOTICS (AROB 16th '11)

January 27-29, 2011

B-Con Plaza, Beppu, Oita, JAPAN

INTERNATIONAL ORGANIZING COMMITTEE of AROB

(Alife Robotics Corporation Ltd. and NBU)

THE SIXTEENTH INTERNATIONAL SYMPOSIUM
ON
ARTIFICIAL LIFE AND ROBOTICS
(AROB 16th '11)

ORGANIZED BY:
Organizing Committee of International Symposium on Artificial Life and Robotics (AROB)

CO-SPONSORED BY:
Santa Fe Institute (SFI, USA)
The Society of Instrument and Control Engineers (SICE, Japan)
The Robotics Society of Japan (RSJ, Japan)
The Institute of Electrical Engineers of Japan (IEEJ, Japan)
The Institute of Systems, Control and Information Engineers (ISCIE)
The Institute of Electronics, Information and Communication Engineers (IEICE)
The Institute of Electrical and Electronics Engineers, Inc. (IEEE Japan Council)
Japan Robot Association (JARA)
Institute of Control, Robotics and Systems (ICROS, Korea)
Chinese Association for Artificial Intelligence (CAAI, P. R. China)

ADVISORY COMMITTE CHAIRMAN
F. Harashima (Tokyo Metropolitan University, Japan)

GENERAL CHAIRMAN:
M. Sugisaka (Nippon Bunri University and ALife Robotics Co., Ltd., Japan)

PROGRAM CHAIRMAN
H. Tanaka (Tokyo Medical & Dental University, Japan)

VICE-CHAIRMAN:
J. L. Casti (Technical University of Vienna, Austria)
J. J. Lee (KAIST, Korea)
H. H. Lund(Technical University of Denmark, Denmark)
Y. Jia (Beihang University, P. R. China)

ADVISORY COMMITTEE:
T. Fukuda (Nagoya University, Japan)
F. Harashima (Tokyo Metropolitan University, Japan)
H. Kimura (RIKEN, Japan)
M. Tomizuka (University of California Berkeley, USA)

INTERNATIONAL ORGANIZING COMMITTEE：
H. Abbass (University of New South Wales, Australia)
K. Aihara (The University of Tokyo, Japan)
C. Barrett (Los Alamos National Laboratory, USA)
M. Bedau (Reed College, USA)
J. L. Casti (Technical University of Vienna,Austria)
M. Eaton (University of Limerick, Ireland)
J. M. Epstein (The Brookings Institution, USA)
T. Fukuda (Nagoya University, Japan)
A. Grzech (Wroclaw University of Technology, Poland)
H. Hashimoto (The University of Tokyo, Japan)
D. J. G. James(Coventry University, UK)
Y. Jia (Beihang University, P. R. China)
K. Kyuma (Mitsubishi Electric Corporation, Japan)
M. H. Lee (Pusan National University, Korea)
J. J. Lee (KAIST, Korea)
H. H. Lund(Technical University of Denmark, Denmark)
S. Rasmussen (Santa Fe Institute, USA)
T. S. Ray (University of Oklahoma, USA)
M. Sugisaka (Nippon Bunri University and ALife Robotics Co.,Ltd., Japan) (Chair)
C. Taylor (University of California-Los Angeles, USA)
W. R. Wells(University of Nevada-Las Vegas, USA)
J. Wang (Beijing Jiaotong University, P. R. China)
C. Zhang (Tsinghua University, P. R. China)
Y. G. Zhang (Academia Sinica, P. R. China)

INTERNATIONAL PROGRAM COMMITTEE:
K. Abe (Nihon University, Japan)
K. Aihara (The University of Tokyo, Japan) (Co-Chair)
T. Arita (Nagoya University, Japan)
M. Bedau (Reed College, USA)
R. Belew (University of California-San Diego, USA)
S- M. Chen (National Taiwan University of Science and Technology, Taiwan)
Y. I. Cho (The University of Suwon, Korea)
Y. Y. Fan (University of California-Davis, USA)
H. Hamdan (SUPELEC, France)
S. H. Han (Kyungnam University, Korea)
H. Hashimoto (The University of Tokyo, Japan)(Co-chair)
N. Homma (Tohoku University, Japan)
S. Ishikawa (Kyushu Institute of Technology, Japan)
T. Ito (Ube National College of Technology, Japan)
T. Iwamoto (Mitsubishi Electric Corporation, Advanced Technology R&D Center, Japan)
J. Johnson (The Open University, UK)
O. Katai (Kyoto University, Japan)
H. Kawamura (Hokkaido University, Japan)
M. Kono (University of Miyazaki, Japan)
S. Kumagai (Osaka University of Economics and Law, Japan)
K. Kurashige (Muroran Institute Technology, Japan)
J. M. Lee (Pusan National University, Korea)
H. H. Lee (Waseda University, Japan)
H. H. Lund (Technical University of Denmark, Denmark)
M. Nakamura (Saga University, Japan)
K. Nakano (The University of Electro-Communications, Japan)
K. Naitoh (Waseda University, Japan)
W. Nistico (University of Dortmund, Germany)
K. Ohnishi (Niigata University, Japan)
M. Okamoto (Kyushu University, Japan)
S. Omatu (Osaka Prefecture University, Japan)
H. Oogai (Waseda University, Japan)
M. Osano (Aizu University, Japan)
M. Oswald (Vienna University of Technology, Austria)
L. Pagliarini (Technical University of Denmark, Denmark)
R. Pfeifer (University of Zurich-Irchel, Switzerland)
T. S. Ray (University of Oklahoma, USA) (Co-Chair)
M. Rozailan (TaTi University College, Malaysia)
S. Sagara (Kyushu Institute of Technology, Japan)
P. Sapaty (National Academy of Sciences of Ukraine, Ukraine)
T. Sawaragi (Kyoto University, Japan)
T. Shibata (AIST, Japan)
K. Shimohara (Doshisha University, Japan)
K- B. Sim (Chung-Ang University, Korea)
K. Sugawara (Tohoku Gakuin University, Japan)
M. Sugisaka (Nippon Bunri University and ALife Robotics, Co., Ltd., Japan)
H. Suzuki (The University of Tokyo, Japan)
H. Tanaka (Tokyo Medical & Dental University, Japan) (Chair)
K. Uosaki (Fukui University of Technology, Japan)
H. Umeo (Osaka Electro-Communication University, Japan)
K. Watanabe (Okayama University, Japan)
H. Yanagimoto (Osaka Prefecture University, Japan)
Y. Yin (The Beijing University of Science and Technology, P. R. China)
M. Yokota (Fukuoka Institute of Technology, Japan)
T. Zhang (Tsinghua University, P. R. China)

LOCAL ARRANGEMENT COMMITTEE:
F. Dai (Tianjin University, P. R. China)
Z. Ibrahim (TaTi University College, Malaysia)
M. Rizon (King Saud University, Saudi Arabia)
S. Sagara (Kyushu Institute of Technology, Japan)
M. Sugisaka (ALife Robotics Co., Ltd, Japan) (Chair)
J. Wang (Beijing Jiaotong University, P. R. China)

HISTORY
This symposium was founded in 1996 by the support of Science and International Affairs Bureau, Ministry of Education, Culture, Sports, Science and Technology, Japanese Government. Since then, this symposium has been held every year at B-Con Plaza, Beppu, Oita, Japan except in Oita, Japan (AROB 5th '00) and in Tokyo, Japan (AROB 6th '01). The Fifteenth symposium will be held on February 4 –6, 2010, at B-Con Plaza, Beppu, Oita, Japan. This symposium invites you all to discuss development of new technologies concerning Artificial Life and Robotics based on simulation and hardware in the twenty first century.

OBJECTIVE
The objective of this symposium is the development of new technologies for artificial life and robotics which have been recently born in Japan and are expected to be applied in various fields. This symposium will discuss new results in the field of artificial life and robotics..

TOPICS:

Artificial brain research	Artificial intelligence
Artificial life	Artificial living
Artificial mind research	Bioinformatics
Bipedal robot	Brain science
Chaos	Cognitive science
Complexity	Computer graphics
Control techniques	DNA computing
Evolutionary computations	Fuzzy control
Genetic algorithms	Human-welfare robotics
Human-machine cooperative systems	Image Processing
Innovative computations	Intelligent control ＆modeling
Micromachines	
Micro-robot world cup soccer tournament	Mobile vehicles
	Molecular biology
Multi-agent systems	Nano-biology
Nano-robotics	Neural networks
Neurocomputing technologies and its application for hardware	Neurocomputers
	Pattern recognition
Robotics	Robust virtual engineering
Virtual reality	Visualization
Others	

DEADLINES:

September 1, 2010	Electronic submission of a 400-600 word long abstracts at our website
September 15, 2010	Notification of acceptance of papers**
October 1, 2010	Submission of final camera-ready papers

** Accepted papers are divided into two types.Oral presentation (4 pages) and poster presentation (2 pages)

CONFERENCE LANGUAGE: English

Artificial Life and Robotics

We invite you to publish your paper

in this journal full of inventive scientific findings and state-of-the art technologies.

Two types of papers from the world are

Ⅰ. Recommended papers presented at **the International Symposium on Artificial Life and Robotics (ISAROB),**

Ⅱ. Contributed papers.

Contribution fee :

4 pages or less **¥ 19,000 per page,**

extra pages **¥ 16,000 per page.**

(Pages are counted on single-line basis as they appear in the journal.)

Shipping Cost:

in Japan **¥ 700 per one issue,**

overseas **¥3,000 per one issue.**

We deliver every corresponding author (or sponsor) one copy of journal in which his/her paper is included. We would like to thank authors for their support in the form of contribution fee payable before publication, which funds the production of this journal contracted by Springer Japan.

Order:

1. **Price for co-authors: ¥ 5,000 per copy (for every co-author)**,
   If necessary, please order extra copies for co-authors to the Journal Office.

2. **Subscription fee: ¥ 20,000 per year**,

3. **Purchase price for single issue: ¥ 8,000 per issue**.

AROB Journal Office : joffice@alife-robotics.co.jp

Artificial Life and Robotics

Our Review System

For contributed papers,

1. Duration:

   Two months is our target time of the whole review process, however, we are trying our best to make it as short as possible.

2. Review results:

   Every contributed paper will be reviewed by three assigned reviewers with score ranging from 1 (highest mark) to 4 (lowest mark);

   1. publish with no revision,
   2. publish with minor revisions,
   3. possibly publish with revision and re-review,
   4. reject.

   Review results, a total score of the three evaluation scores, would be read as;.

3 or 4	:	accepted and to be published as it is,
4, 5, or 6	:	accepted and to be published after minor revisions,
7, 8, or 9	:	acceptable but subject to rewriting and re-review,
10, 11, or 12	:	rejected

For recommended papers,

The recommended papers are ones that the chair of each session reads before, during, and after the symposium that year and recommends to AROB Journal Office using the same evaluation score above. Therefore, the quality of recommended papers is apparent at the time of recommendation.

We express our heartfelt gratitude to chairs and reviewers of ISAROB for their support and sincere voluntary work without which this journal never exists.

AROB Journal Office : joffice@alife-robotics.co.jp

Intelligent Mobile Robot

Full Version

(Taro-1 and Trao-2)

Simplifed Version (Taro-A)

Fig.1 Full Version(Taro-1(right),Taro-2(left) and Simplified Vesion

Full Version

Feature:

1.Recognize the line and moves on or along the line
2. Recognizes the shape of objects
3. Can be controlled by voice(20 sentences, etc.)
4. Recognizes human faces (about 10 people)
5. Can be controlled by Internet and mobile phone (remote control)
Price:￥5,000,000($50,000)

Simplified Version (Taro-A)

Size and weight of robot is half of Figure1

Functions of full version 1.~4. are equipped

･Fundamental software based on Window and Linux is provided

･The robot is most suitable for R & D (Master and Doctor courses)

･Price(Only hardware from ¥2,300,000(=$23,000) with fundamental software

Spec. and style can be changed

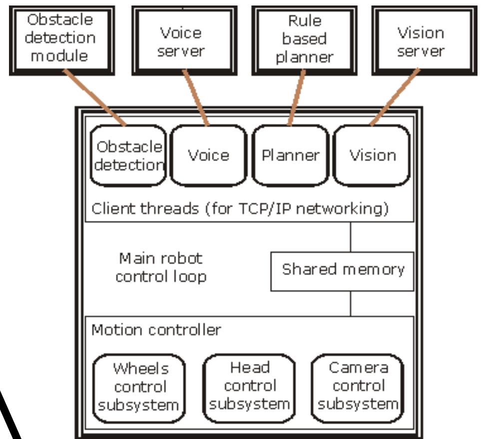

Fig.2 System block diagram

ALife Robotics Corporation Ltd.

Address: 301 Koopo Nagaoka, Miyazaki 1385-1, Oita, 870-1133, JAPAN

tel: 097—567—3088 fax: 097—594-0181 e-mail ms@alife-robotics.co.jp

URL http://alife-robotics.co.jp/

This is belong to Australian Defense Force Academy, Australia

Simplified Version of Intelligent mobile robot-Taro-A

Main Specification of Taro-A(Born from Taro)

・Weight: 28kg

・Height: 60(from floor:65cm), Width: 28cm, Depth: 40cm

・Robot behaviors can be controlled by voice

・Behaviors of the Simplified Version of Intelligent of Mobile Robot

1.The robot can understand meaning of human voice and can answer to human by robot voice . In addition, the robot can provide various information to human's requirements.

2. Human asks for robot. What is this by showing object to robot. The robot answers for it by voice. (Pattern recognition and understanding)

3. The robot can carry various things (Foods, Letters, Newspapers, Other heavy materials (approximately 25-30kg). The robot can turn around accurately by specified degree.

4. The robot can climb up on the sloop with 15-30 degrees.

5. The robot can teach child by answering questions from child in pleasant playing condition as private teacher.

6. The robot can teach English, Japanese, Chinese, any other languages to human.

・Size and weight : ½ of Full version of Intelligent Mobile Robot "Taro"

・We provide fundamental software for robot by Window or Linux

・Most suitable for research and development on mobile robot

・Most suitable for human being's partner

・Price (JPY 2,300,000=$23,000)

(*) Design and specification will be decided in consultation with customer

Correspondence: ALife Robotics Corporation Ltd.

〒870-1133 301 Koopo Nagaoka, 1385-1 Oaza Miyazaki, Oita, Japan

Tel: 81-97－567－3088, Fax: 81-97－594-0181, e-mail ms@alife-robotics.co.jp

URL http://alife-robotics.co.jp:81/

This is belong to Electro-Communication University, Tokyo, Japan

Delivery Record (From 2009)

1. ADFA, Australia
2. Electro-Communication Univ., Japan
3. KAIST, Korea
4. TATiUC, Malaysia
5. Others

ALife Robotics Corporation, Ltd.
Challenge for New Technologies in 21st Century
301 Koopo Nagaoka,1385-1 Oaza Miyazaki, Oita 870-1133, Japan
TEL:81-97-567-3088, FAX: 81-97-594-0181, E-MAIL: ms@alife-robotics.co.jp

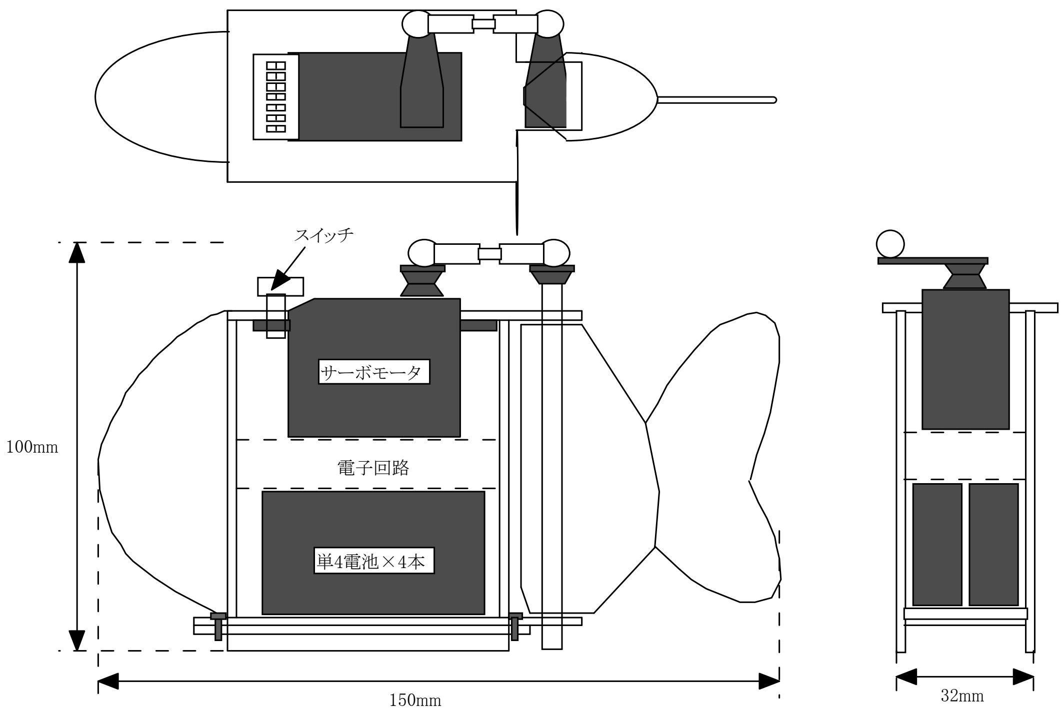

Fig.1 Fish Robot (Sizes)

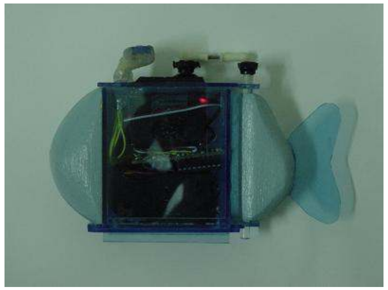

Fig.2 Picture of Fish Robot

Table 1 Functions of Fish Robot

Switch No.	Functions	Comments
1	ON,OFF of Power	
2	Right Turn	
3	Left Turn	
4	Change of Speeds	LOW, HIGH Mode
5	Change for Swing Angle of Caudal Fin	Change for 4 Steps
6		
7	Random Mode	

1.Hardware and Fundamental Software

2. PIC Writer

3.Text Book for Learning Control Techniques Based on PIC

are included.

OPTIONS:

C-MOS Camera, Remote Control Unit, Dorsal, Pectoral, Ventral Fins can be installed

THE FIFTEENTH INTERNATIONAL SYMPOSIUM ON ARTIFICIAL LIFE AND ROBOTICS

(AROB 15th '10)

ORGANIZED BY

Organizing Committee of International Symposium on Artificial Life and Robotics
(ALife Robotics Corporation Ltd. and Nippon Bunri University(NBU), Japan)

SPONSORED BY

Mitsubishi Electric Corporation Advanced Technology R&D Center
Oita Gas Co., Ltd.
ME System Co., Ltd.
SANWA SHURUI Co.,Ltd

CO-OPERATED BY

Santa Fe Institute (SFI, USA)
The Robotics Society of Japan (RSJ, Japan)
The Institute of Electrical Engineers of Japan (IEEJ, Japan)
Institute of Control, Robotics and Systems (ICROS, Korea)
Chinese Association for Artificial Intelligence (CAAI, P. R. China)
The Institute of Systems, Control and Information Engineers (ISCIE)
The Institute of Electronics, Information and Communication Engineers (IEICE)
The Institute of Electrical and Electronics Engineers, Inc. (IEEE Japan Council)
Japan Robot Association (JARA)
The Society of Instrument and Control Engineers (SICE, Japan)

SUPPORTED BY

Kyushu Bureau of Economy, Trade and Industry, Ministry of Economy, Trade and Industry
OITA PREFECTURE
Oita City
BEPPU CITY
Oita Chamber of Commerce and Industry
The Oita Prefectural Organization of the Industrial Groups
Kyodo News
JIJI PRESS
Oita Godo Shimbunsya
The Asahi shimbun
The Mainichi Newspaper Co., Ltd.
THE YOMIURI SHIMBUN SEIBUHONSHA
The Nishinippon Shimbun
THE NIKKAN KOGYO SHIMBUN, LTD
Japan Broadcasting Corporation Oita Station
Oita Broadcasting System
Television Oita System Corporation
Oita Asahi Broadcasting co., ltd.

ADVISORY COMMITTE CHAIRMAN

F. Harashima (Tokyo Denki University, Japan)

GENERAL CHAIRMAN

M. Sugisaka (Nippon Bunri University(NBU), Japan)

PROGRAM CHAIRMAN

H. Tanaka (Tokyo Medical & Dental University, Japan)

VICE-CHAIRMAN

J. L. Casti (Institute for Applied Systems Analysis, Austria)
J. J. Lee (KAIST, Korea)
H. H. Lund (Technical University of Denmark, Denmark)
Y. G. Zhang (Academia Sinica, P. R. China)

ADVISORY COMMITTEE

T. Fukuda (Nagoya University, Japan)
F. Harashima (Tokyo Denki University, Japan)
H. Kimura (RIKEN, Japan)
M. Tomizuka (University of California Berkeley, USA)

INTERNATIONAL ORGANIZING COMMITTEE

K. Aihara (The University of Tokyo, Japan)
C. Barrett (Los Alamos National Laboratory, USA)
M. Bedau (Reed College, USA)
J. L. Casti (Institute for Applied Systems Analysis and The Kenos Circle, Austria)
M. Eaton (University of Limerick, Ireland)
J. M. Epstein (The Brookings Institution, USA)
T. Fukuda (Nagoya University, Japan)
H. Hashimoto (The University of Tokyo, Japan)
D. J. G. James (Coventry University, UK)
K. Kyuma (Mitsubishi Electric Corporation, Japan)
J. J. Lee (KAIST, Korea)
M. H. Lee (Pusan National University, Korea)
S. Rasmussen (Santa Fe Institute, USA)
T. S. Ray (University of Oklahoma, USA)
M. Sugisaka (Nippon Bunri University(NBU), Japan) (Chairman)
C. Taylor (University of California-Los Angeles, USA)
W. R. Wells (University of Nevada-Las Vegas, USA)
Y. G. Zhang (Academia Sinica, P. R. China)

INTERNATIONAL PROGRAM COMMITTEE

K. Abe (Nihon University, Japan)
K. Aihara (The University of Tokyo, Japan) (Co-chairman)
T. Arita (Nagoya University, Japan)
M. Bedau (Reed College, USA)
R. Belew (University of California-San Diego, USA)
S. M. Chen (National Taiwan University of Science and Technology, Taiwan)
Y. I. Cho (The University of Suwon, Korea)
Y. Y. Fan (University of California-Davis, USA)
H. Hamdan (Spelec, France)
S. H. Han (Kyungnam University, Korea)
H. Hashimoto (The University of Tokyo, Japan) (Co-chairman)
N. Homma (Tohoku University, Japan)
S. Ishikawa (Kyushu Institute of Technology, Japan)
T. Ito (Ube National College of Technology, Japan)
T. Iwamoto (Mitsubishi Electric Corporation, Advanced Technology R&D Center, Japan)
J. Johnson (The Open University, UK)
O. Katai (Kyoto University, Japan)
H. Kawamura (Hokkaido University, Japan)
M. Kono (University of Miyazaki, Japan)
S. Kumagai (Osaka University of Economics and Law, Japan)
K. Kurashige (Muroran Institute of Technology, Japan)
J. M. Lee (Pusan National University, Korea)
H. H. Lee (Waseda University, Japan)
H. H. Lund (Technical University of Denmark, Denmark)
R. Mamat (TATi University College, Malaysia)
M. Nakamura (Saga University, Japan)
K. Nakano (The University of Electro-Communications, Japan)
K. Naitoh (Waseda University, Japan)
W. Nistico (University of Dortmund, Germany)
K. Ohnishi (Niigata University, Japan)
M. Okamoto (Kyushu University, Japan)
S. Omatu (Osaka Prefecture University, Japan)
H. Oogai (Waseda University, Japan)
M. Osano (Aizu University, Japan)
M. Oswald (Vienna University of Technology, Austria)
R. Pfeifer (University of Zurich-Irchel, Switzerland)
L. Pagliarini (Technical University of Denmark, Denmark)
T. S. Ray (University of Oklahoma, USA) (Co-chairman)
S. Sagara (Kyushu Institute of Technology, Japan)
P. Sapaty (National Academy of Sciences of Ukraine, Ukraine)
T. Sawaragi (Kyoto University, Japan)
T. Shibata (AIST, Japan)
K. Shimohara (Doshisha University, Japan)
K. Sugawara (Tohoku Gakuin University, Japan)
M. Sugisaka (Nippon Bunri University(NBU), Japan)
H. Suzuki (The University of Tokyo, Japan)
H. Tanaka (Tokyo Medical & Dental University, Japan) (Chairman)
M. Tanaka-Yamawaki (Tottori University, Japan)
K. Uosaki (Fukui University of Technology, Japan)
H. Umeo (Osaka Electro-Communication University, Japan)
K. Watanabe (Saga University, Japan)
T. Yamamoto (Tokushima College of Technology, Japan)

H. Yanagimoto (Osaka Prefecture University, Japan)
M. Yano (Tohoku University, Japan)
Y. Yin (The Beijing University of Science and Technology, P. R. China)
M. Yokota (Fukuoka Institute of Technology, Japan)

LOCAL ARRANGEMENT COMMITTEE

F. Dai (Matsue National College of Technology, Japan)
Z. Ibrahim (TATi University College, Malaysia)
M. Ito (Maizuru National College of Technology, Japan)
R. Mamat (TATI University College, Malaysia)
M. Rizon (King Saud University, Saudi Arabia)
S. Sagara (Kyushu Institute of Technology, Japan)
M. Sugisaka (Nippon Bunri University(NBU), Japan) (Chairman)
J. Wang (Alife Robotics Co., Ltd., Japan)
X. Wang (Niihama National College of Technology Japan)

HISTORY

This symposium was founded in 1996 by the support of Science and International Affairs Bureau, Ministry of Education, Culture, Sports, Science and Technology, Japanese Government. Since then, this symposium has been held every year at B-Con Plaza, Beppu, Oita, Japan except in Oita, Japan (AROB 5th '00) and in Tokyo, Japan (AROB 6th '01). The Fifteenth symposium will be held on 4– 6 February, 2010, at B-Con Plaza, Beppu, Oita, Japan. This symposium invites you all to discuss development of new technologies concerning Artificial Life and Robotics based on simulation and hardware in the twenty first century.

OBJECTIVE

The objective of this symposium is the development of new technologies for artificial life and robotics which have been recently born in Japan and are expected to be applied in various fields. This symposium will discuss new results in the field of artificial life and robotics.

GENERAL SESSION TOPICS

Artificial brain research
Artificial life & Brain science
Control & Techniques I
Evolutionary computations
Human-machine cooperative systems
Image processing II
Mobile vehicles I
Multi-agent systems
Robotics I
Robotics & Bipedal robot
Pattern recognition
Artificial intelligence
Chaos & Cognitive science
Control & Techniques II
Intelligent control & Modeling
Image processing I
Innovative computations
Mobile vehicles II
Neural networks
Robotics II
Robotics & Application
Virtual reality

ORGANIZED SESSION TOPICS

System sensing and control
Learning control and robotics
Control and automata
Soft robotics
Intelligent system and applications
Robot control
Intelligent systems
Artificial intelligent
Intelligent classification
Intuitive human-system interaction
Molecular computing
Bio-inspired theory and applications
Brain-like intelligence and biomedical applications
Artificial application & Artificial and green technology I
Machine learning and computer vision
MOT and interdisciplinary research
Analysis and implementation of nonlinear systems
Computer vision and robotics
Intelligent control and applications
Biomimetic machines and robots
Bio-symphony
Intelligent robots
Embracing complexity in natural intelligence
Intelligent signal processing
Special environment localization and navigation
Real time methods for structural change detection of ongoing time series date
Artificial application & Artificial and green technology II

COPYRIGHTS

Accepted papers will be published in the proceeding of AROB and some of high quality papers in the proceeding will be requested to re-submit their papers for the consideration of publication in an international journal ARTIFICIAL LIFE AND ROBOTICS. All correspondence related to the symposium should be addressed to AROB Secretariat.

AROB Secretariat
ALife Robotics Corporation Ltd.
301 Koopo Nagaoka 1385-1 Miyazaki, Oita 870-1133, JAPAN
TEL/FAX：+81-97-594-0181
E-MAIL：arobsecr@alife-robotics.co.jp
Home Page：http://alife-robotics.co.jp/

ADDRESS

Sadayoshi Suga
Bunri Gakuen Educational Foundation
Nippon Bunri University
Chairman/Chancellor

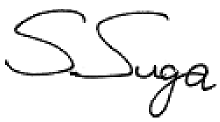

Sadayoshi Suga
Bunri Gakuen Educational Foundation
Nippon Bunri University
Chairman/Chancellor

It is my great pleasure to welcome you all to The Fifteenth International Symposium on Artificial Life and Robotics. I would like to offer my sincere thanks and respect to the many people who have helped make this yearly event possible.

In 2008, Nippon Bunri University invited Professor Sugisaka to lead the symposium's team, and with his help we have undertaken this new venture.

As well as being a great venue to meet specialists in many fields, I also feel it's an important platform for presenting research and giving Universities the opportunity to support such research.

As Chairman of this University, I feel great pleasure in working with such outstanding educators who have, on so many occasions, presented their research to the world.

It's my sincere wish that advances in Artificial Life and Robotics Research, in cooperation with the Medical Sciences, Information Systems and other technological fields will lead to improvements in all of our lives.

During your stay here in Beppu, please take time to enjoy the beautiful scenery, relaxing hot springs, and healthy Japanese cuisine that Oita Prefecture has to offer. It's my heartfelt hope that when you leave here, you do so with fresh enthusiasm and motivation.

MESSAGES

Fumio Harashima
Advisory Committe Chairman
(Professor, Tokyo Metropolitan University)

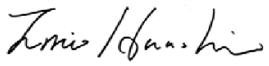

Fumio Harashima
Advisory Committee Chairman of AROB

The science and technology (S&T) on Artificial Life and Robotics was born in 1996, and it's been providing human being with happiness. This S & T is not only important but also necessary for people living in the world to maintain high quality of life. Research is heart and desire of human being and the S&T is going toward clarifying tool to achieve our objective.

I would like to congratulate researchers who work in the fields on Artificial Life and Robotics.

Masanori Sugisaka
General Chairman
(Professor, Nippon Bunri University and President, ALife Robotics Co., Ltd. , Japan)

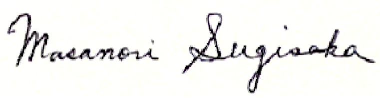

Masanori Sugisaka
General Chairman of AROB

It is my great honor to invite you all to the Fifteenth International Symposium on Artificial Life and Robotics (AROB 15th '10).

The symposium from the first (1996) to the Fourteenth (2009) were organized by Oita University, Nippon Bunri University(NBU), and ALife Robotics Corporation Ltd. under the sponsorship of the Science and Technology Policy Bureau, the Ministry of Education, Science, Sports, and Culture (Monbusho), presently, the Ministry of Education, Culture, Sports, Science, and Technology (Monkasho), Japanese Government, Japan Society for the Promotion of Science (JSPS), The Commemorative Organization for the Japan World Exposition ('70), Air Force Office of Scientific Research, Asian Office of Aerospace Research and Development (AFOSR/AOARD), USA. I would like to express my sincere thanks to not only Monkasho, JSPS, the Commemorative Organization for the Japan World Exposition ('70) but also Japanese companies for their repeated support.

This symposium is organized by International Organizing Committee of AROB and is co-operated by the Santa Fe Institute (USA), RSJ, IEEJ, ICASE (Now ICROS) (Korea), CAAI (P. R. China), ISCIE, IEICE, IEEE (Japan Council), JARA, and SICE.

The AROB symposium is growing up by absorbing many new knowledge and technologies into it. The future of the AROB symposium is brilliant from a point of view of yielding new technologies to human society in 21st century.

I hope that fruitful discussions and exchange of ideas between researchers during symposium will yield new merged technologies for happiness of human beings and, hence, AROB 15th '10 will facilitate the establishment of an international joint research institute on Artificial Life and Robotics in future.

Hiroshi Tanaka
Program Chairman
(Professor, Tokyo Medical and Dental University)

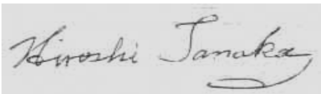

Hiroshi Tanaka
Program Chairman of AROB

On behalf of the program committee, it is my great pleasure and honor to invite you all to the Fifteenth International Symposium on Artificial Life and Robotics (AROB 15th 2010). This symposium is made possible owing to the cooperation of Nippon Bunri University and Santa Fe Institute. We are also debt to Japanese academic associations such as SICE, RSJ, and several private companies. I would like to express my sincere thanks to all of those who make this symposium possible.

As is needless to say, the Alife or biologically-inspired Robotics approach now attracts wide interests as a new paradigm of science and engineering. Taking an example in the field of bioscience, the accomplishment of HGP (Human Genome Project) and subsequent post-genomic comprehensive "Omics data" such as transcriptome, proteome and metabolome, bring about vast amount of bio-information. However, as a plenty of omics data becomes available, it becomes sincerely recognized that the framework by which these omics data can be understood to make a whole picture of life is critically necessary. Thus, in the post-genomic era, biologically-inspired systems approach like Alife is expected to give one of new alternative ideas to integrate this vast amount of bio-data.

This example shows the Alife approach is very promising and may exert a wide influence on the effort to develop a new paradigm for next generation of life science. We hope this symposium becomes a forum for exchange of the ideas of the attendants from various fields, including the life science field, who are interested in the future possibility of biologically-inspired computation and systems approach.

I am looking forward to meeting you in Beppu, Oita.

Ju-Jang Lee
Vice Chairman
(Professor, KAIST)

Ju-Jang Lee
Vice Chairman of AROB

The Fifteenth International Symposium on Artificial Life and Robotics (AROB) will be held in Beppu, Oita, Japan from Feb. 4th to 6th, 2010. This year's Symposium will be held amidst the high expectation of the increasingly important role of the new interdisciplinary paradigm of science and engineering represented by the field of artificial life and robotics that continuously attracts wide interests among scientist, researchers, and engineers around the globe.

Since the time of the very first AROB meeting in 1996, each year, distinguished researchers and technologists from around the world are looking forward to attending and meeting at AROB. AROB is becoming the annual excellent forum that represents a unique opportunity for the academic and industrial communities to meet and assess the latest developments in this fast growing artificial life and robotics field. AROB enables them to address new challenges, share solutions, discuss research directions for the future, exchange views and ideas, view the results of applied research, present and discuss the latest development of new technologies and relevant applications.

In addition, AROB offers the opportunity of hearing the opinions of well known leading experts in the field through the keynote sessions, provides the bases for regional and international collaborative research, and enables to foresee the future evolution of new scientific paradigms and theories contributed by the field of artificial life and robotics and associated research area. The twenty-first century will become the century of artificial life and intelligent machines in support of humankind and AROB is contributing through wide technical topics of interest that support this direction.

It is a great for me as the Vice Chairman of the 15th AROB 2010 to welcome everyone to this important event. Also, I would like to extend my special thanks to all authors and speakers for contributing their research works, the participants, and the organizing team of the 15th AROB.

Looking forward to meeting you at the 15th AROB in Beppu-Oita and wishing you all the best.

J. Casti
Vice Chairman
(Professor, International Institute for Applied Systems Analysis)

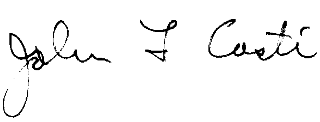

John Casti
Vice Chairman of AROB

Since its inception, the AROB has become the most important meeting in Asia each year for workers in the fields of artificial life and robotics. Many significant advances in these areas have been first discussed at the AROB, and it has served as a forum for building an international network of researchers exploring novel uses of computing for social needs. So as a member of the Scientific Committee of AROB since it began, I'm pleased to wish Professor Sugisaka and all participants another successful in the lovely surroundings of Beppu.

Y. G. Zhang
Vice Chairman
(Professor, Academia Sinica)

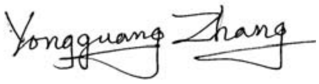

Y. G. Zhang
Vice Chairman of AROB

Dear all friends and all participants,

Here I would like to show my warm welcome to you all attending the Fifteenth International Symposium on Artificial Life and Robotics (AROB '10). As you know, this annual symposium was founded in 1996 by the support of Science and International Affairs Bureau, Ministry of Education, Science, Sports, and Culture (currently, Ministry of Education, Culture, Sports, Science and Technology) of Japan. Since then AROB is gradually become worldwide famous international symposium. Now AROB is already not an "academic baby", but "academic teenage", and AROB also owns an international journal, named the "Journal of Artificial Life and Robotics" published by Springer in decade.

The objective of AROB is aimed to develop new technologies for Artificial Life and Robotics which have been born recently. The important devotion of AROB is not only to pay attention to the development of theory on Artificial Life, but also expected to apply the principle to various fields, especially, the combination of both the Artificial Life and Robotics together. So far there are only few international symposiums or conference on artificial life, however, AROB is the only one that to explore the new generation of Robotics in far-sight with artificial life principle. In fact, some intelligent toys and intelligent systems have already been developed, although they have not completed knowledge construction and no evolution. Obviously, this is a very great and difficult career, and need continuous and consistent efforts of more and more scientists and engineers. In recent years, to our pleasure, many young professors and researchers join our team and bring significant outcomes of their work focusing on intelligent robots that we believe applies to the concepts of artificial life and artificial brain. We'd like to welcome and encourage more challenges like these for we are also devoting to the same target.

Beppu, the place of held most AROB symposium, is very charming city in Japan, she has variety of hot spring (jigoku), beautiful bay and colorful mountains. Her phantasmagoric visual change in various season attract many tourists. I hope all of you enjoy and appreciate her.

Finally, I would like to show my great thanks to all people who are working for this AROB 15th '10, including all staffs of AROB Secretariat at ALife Robotics Co., Ltd., and students, the successful holding of AROB symposium is dependent on the contributions of you all.

Henrik Hautop Lund
Vice Chairman
(Professor, Technical University of Denmark)

Henrik Hautop Lund
Vice Chairman of AROB

I am much honored to invite you to the Fifteenth International Symposium on Artificial Life and Robotics (AROB 15th '10). The international symposium marks its 15th anniversary after the being held each year since 1996, initially organized by Oita University and now being organized by Nippon Bunri University.

The symposium attracts an impressive range of researchers from all continents, who all share the vision of merging research based upon artificial life and robotics. The symposium is visionary in merging these two, science and engineering disciplines, and has become the most important forum for research into merging artificial life and robotics.

The research in artificial life and robotics is very important since it both brings us insight into ourselves as human beings and natural systems, and brings us new engineering solutions that may influence our lives. It is my hope that you will use this insight and opportunity to develop systems that help humankind in socially responsible ways.

I would like to take this opportunity to thank the general chairman of AROB, Prof. Masanori Sugisaka, for being so visionary 15 years ago to engage in creating and organizing this important annual event for our research community. It takes a lot of courage to be the first to create a novel interdisciplinary research field such as the one that comes from the merge between artificial life and robotics. Prof. Sugisaka has shown how being courageous enough to engage in the adventurous activities of merging two fields may lead to very fruitful research and to the lively research community that you are now part of with your participation in this international symposium.

I would also take this opportunity to thank Springer-Verlag for supporting this research community, and remind all participants of the Springer-Verlag Artificial Life and Robotics Journal. Hopefully, we will see numerous, high quality contributions to the journal as the outcome of this symposium and the research collaboration that may entail the symposium. Indeed, it is my hope that you will all engage in open and fruitful scientific discussions with your colleague researchers during the symposium, and that these discussions may open up for future research collaborations in order to bring new insight into artificial life and robotics to the community.

Plenary talker:

Professor
Shigeo Hirose

PT1 From dream to reality: Snake-like, spider-like robots

Shigeo Hirose

(Tokyo Institute of Technology, Japan)

Mother Nature is precious source of imagination to develop new type of robotic system. I will introduce the history of designing a series of snake-like robots, and discuss the design and control of amphibious snake-like robot ACM R-5 and rescue robot Souryu which can crawl into the debris after a big earthquake occurred. I also talk about spider-like walking robots, such as wheel-walking hybrid vehicle Roller Walker, quadruped wall-climbing robot Ninja, and 7 ton world largest walking robot for steep slope construction task.

Education:
- In 1971, B.E. degree in Mechanical Engineering from Yokohama National University, Japan
- In 1973, Master Degree from Dept of Control Engineering at Tokyo Institute of Technology, Japan
- In 1976, Doctor Degree from Dept of Control Engineering at Tokyo, Institute of Technology, Japan

Professional Training and Employment:
- 1976 – 1979 Research Associate, Tokyo Institute of Technology
- 1979 - 1992 Associate Professor, Tokyo Institute of Technology
- 1992 - Professor, Dept of Mechanical and Aerospace Engineering, Tokyo Institute of Technology

PT2 Extreme events in human society: The xevents observatory and simulator

John L. Casti

(International Institute for Applied Systems Analysis, Austria)

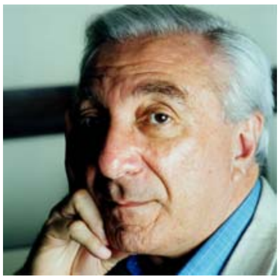

**Professor
John L. Casti**

In this plenary talk, I discuss extreme events (Xevents) created by humans, not nature. These include things like terrorist attacks, pandemics, political revolutions and financial system meltdowns. The talk explores the types of methodological tools needed to develop early-warning signals for such events—and what to do with such signals once they are obtained. We also present the outlines for a new research venture at IIASA, involving an Xevents "observatory" for development of methodology and an Xevents "simulator" to serve as a laboratory for both testing of tools, as well as identification of Xevents that have never before occurred.

Education:
- In 1969, M.S. degree in Mathematics from the University of Southern California, Los Angeles
- In 1970, Ph.D. Mathematics from the University of Southern California, Los Angeles

Professional Training and Employment:
- 1974--present, Research Scholar, Int'l Institute for Applied Systems Analysis, Vienna
- 1992-2002, Professor, Santa Fe Institute, Santa Fe, USA
- 2002-2005, Professor, Wissenschaftzentrum Wien, Vienna
- 2005-present, Director, The Kenos Circle, Vienna

PT3 Robomusic with modular playware

Kasper Falkenberg, Niels K. Bærendsen, Jacob Nielsen,
Carsten Jessen, Henlik Hautop Lund

(Technical University of Denmark, Denmark)

Professor
Henrik Hautop Lund

Playware is intelligent hardware and software that creates play and playful experiences for users of all ages. Playware research seeks to understand play dynamics and play forces in order to implement them in play tools. Playware is of course not the only type of products which can create play and motivate users to perform actions, but digital technology contains new and expanded possibilities, e.g. when developed with embodied artificial intelligence. Playware-tools are tools with a behaviour that initiates play force (e.g. a motion, in the case of sensorimotor play) via interaction. This is the basis for the play dynamic to emerge through which the users are brought into a state of playing. Embodied artificial intelligence can be used to design behaviours of the play tools, e.g. by providing means for creating adaptive play tools. The understanding of play dynamics can help guiding this design of behaviours to be used specifically to create playful and motivating tools for a variety of play interactions, well-knowing that there are both similarities and differences in the play dynamics of different users, environments and activities. Using a modular approach inspired by behavior-based robotics gives opportunity to create modular playware that allows any user to create activities in a flexible manner, regardless of the cognitive and physical abilities of the user. Indeed, the modular approach allows a generalization over users, environments and activities as well as a commercial possibility of mass-production for customization. For Human-Robot Interaction, when considering a modular approach, we are often interested in the interactivity and the opportunities for the human interaction, so instead of developing self-reconfigurable modular robotics, we may describe the above systems in terms of user-configurable modular robotics. In this talk, I will show numerous, specific examples of how such an approach of modular playware (in the form of modular interactive tiles and cubes) facilitates generalization over users, environments and activities in the fields of playgrounds, cardiac rehabilitation, stroke rehabilitation, elderly home care, autism therapy, dementia treatment, soccer training, dancing, music concerts, etc., and how the playful approach provides motivation for users to interact with the modular technological solutions in these fields. Videos will feature use in rehab, play, sport, music, and dance.

Education:
- M.Sc. degree in Computer Science from University of Aarhus, Denmark
- Ph.D. degree in Computer Systems Engineering from University of Southern Denmark

Professional Training and Employment:
- 1992-1993 and 1994-1995, Research Assistant, the National Research Council, Rome, Italy, University of
- 1996-1997, Research Associate (Post Doctor), Department of Artificial Intelligence,
  Edinburgh, UK
- 1997-2000, Head of LEGO Lab
- 1998-2000, Research Associate, Department of Computer Science, University of Aarhus, Denmark
- 2000-2008, Full Professor, the Maersk Mc-Kinney Moeller Institute, University of Southern Denmark
- 2003-2007, Member of the Danish Research Council
- 2008-present, Full Professor, the Center for Playware, Technical University of Denmark

Invited talker:

IT1 XML-based genetic programming framework: Design philosophy, implementation and applications

Associate Professor
Ivan Tanev

Ivan Tanev and Katsunori Shimohara
(Doshisha University, Japan)

We present the design philosophy, the implementation and various applications of XML-based genetic programming (GP) framework (XGP). The key feature of XGP is the distinct representation of genetic programs as DOM-parse trees featuring corresponding flat XML-text. XGP contributes to the achievement of (i) fast prototyping of GP by using the standard built-in API of DOM-parsers for manipulating the genetic programs, (ii) human-readability and modifiability of the genetic representations (iii) generic support for the representation of grammar of strongly-typed GP using W3C-standardized XML-schema; and (iv) inherent inter-machine migratability of the text-based genetic representation (i.e., the XML text) in the distributed implementations of GP.

Education:

- In 1987, M.S. degree in Computer Engineering (with honors) from Leningrad Institute of Electrical Engineering, Leningrad, Soviet Union
- In 1993, Ph.D. in Computer Engineering from Saint Petersburg State University of Electrical Engineering, Saint Petersburg, Russia
- In 2001, Dr.Eng in Computer Science and System Engineering from Muroran Institute of Technology, Muroran, Japan

Professional Training and Employment:

- 1987, Researcher, Space Research Institute, Bulgarian Academy of Sciences, Bulgaria
- 1988-1989, Researcher, Central Institute of Computer Engineering and Technology, Bulgaria
- 1994-1997, System Administrator, National Electricity Company, Bulgaria
- 2001-2002, Software Developer, Synthetic Planning Industry Co.Ltd., Japan
- 2002-2004, Senior Researcher, ATR Human Information Science Laboratories, Japan
- 2004-2006, Lecturer, Department of Information Systems Design, Doshisha University, Japan
- 2006-present, Associate Professor, Department of Information Systems Design, Doshisha University, Japan

Expert-Researcher
Jian-Qin Liu

IT2 Brain's doing in its resting-state: Default mode network as an inside story within the brain

Jian-Qin Liu[1] and Katsunori Shimohara[2]

([1]NICT, KARC, Japan)
([2]Doshisha University, Japan)

As a promising research field after the turn of the new century, *Default Mode Network* (abbreviated as DMN) of the brain shows the strong potential of a new breakthrough to neuroscience, which emphasizes the baseline of the brain's activities when brain is awake but without any external input signal to it. This study is highlighted recently and expected to provide keys to understanding the mental disorders such as Alzheimer's disease. This paper consists of following two sections. (1) A brief tutorial on the DMN is presented with necessary fundamental knowledge of neuroscience on brain. (2) A framework of network informatics for DMN is proposed based on network dynamics; models of information networks are discussed by bridging the gap between the level of regions and the level of neurons of the brain; major issues on analyzing the DMN by brain imaging technology are discussed as well. In a word, one of the inspirations from DMN is how spontaneous collective behavior is emerged within an autonomous system, which is crucial to systematically understand the brain's function and exploring new design principles of autonomous robotics to demonstrate complex life-like behaviors in engineering.

Education:

- In 1986, B.S. in Computer and Systems Science from Nankai University, China
- In 1992, M.S. in Automation Theory and Applications from Xi'an Jiaotong University, China
- In 1997, Ph.D. in Industrial Automation from Central South University of Technology, China
- In 2006, Dr. of Informatics from Kyoto University, Japan

Professional Training and Employment:

- 1986-1991, Assistant Lecturer, Institute of AI and Robotics, Department of Information and Control Engineering, Xi'an Jiaotong University
- 1992-1994, Lecturer, Institute of AI and Robotics, Department of Information and Control Engineering, Xi'an Jiaotong University
- 1994.09-1995.09, Guest Researcher, Information and Communication R & D Center, Ricoh Co. Ltd., Japan
- 1995-1999, Associate Professor, College of Information Engineering, Central South University of Technology
- 2000, Certificate of Professor, College of Information Engineering, Central South University
- 1999-2003.03, Researcher, Advanced Telecommunications Research Institute International (ATR), Japan
- 2003.04-2006.03, Senior Researcher, Advanced Telecommunications Research Institute International (ATR), Japan
- 2006.04-present, Expert Researcher, Kobe Advanced ICT Research Center (KARC), National Institute of Information and Communications Technology (NICT), Japan

IT3 Wearing the playware

Luigi Pagliarini[1,2] and Henrik Hautop Lund[1]

([1]Technical University of Denmark, Denmark)
([2]Academy of Fine Arts of Bari, Via Gobetti, Italy)

Professor
Luigi Pagliarini

In this conceptual paper, we describe and define the range of possible applications and the technical contours of a robotic system to be worn on the body for playful interactions. Earlier work on Modular Robotic Wearable, MRW, described how, by using modular robotics for creating wearable, it is possible to obtain a flexible wearable processing system, where freely inter-changeable input/output modules can be positioned on the body suit in accordance with the task at hand. Here, we drive the attention on early prototypes to show the potentialities of such an approach, and focus on depicting possible application in the electronic games domain. Indeed, the Modular Robotic Wearable is an example of modular playware, which can create playful interactions for many application domains, including electronic games.

Education:
- Master Degree in Experimental Neuropsychology

Professional Training and Employment:
An Artist, Art Curator, Psychologist, Multimedia and Software Designer, and a worldwide known as a theoretician and expert in (mainly Artistic) Robotics, A.I. and Artificial Life.
- Professor, Theories of Perception and Psychology of Shape and of Computer Art, the Academy of Fine Arts of Bari, Italy
- Associate Professor, Center for Payware, Technical University of Denmark
- Founder and Director, the Pescara Electronic Artists Meeting
- President, the Cultural Association Artificialia
- Art Director, Ecoteca
- Founder of RoboCup Junior and Member of its International Committee

TIME TABLE(2/4)

		RoomA	RoomB	RoomC	RoomD
2/3 (Wed)	13:00				
		Registration (Registration Desk)			
	17:00	Welcome Party (at Hotel ARTHUR)			
2/4 (Thur)	8:00	Registration (Registration Desk)			
	8:40	OS 19 (6) Chair M. Yokota	OS 20 (6) Chair J. M. Lee	GS 7 (6) Chair M. K. James	OS 25 (6) Chair D. H. Kim
	10:10	Coffee Break			
	10:30	Opening Ceremony (Room E) Chair J.Y. Shim			
	10:55	Plenary Talk (Room E) PT1 S. Hirose Chair J. J. Lee			
	11:45	Lunch			
	12:40	OS 16 (5) Chair Y. Ishida	GS 13 (5) Chair I. Zunaidi	OS 21 (5) Chair M. Oswald	GS 8 (5) Chair S.Y. Yi
	13:55	Coffee Break			
	14:15	OS 1 (7) Chair M. Uchida	OS 2 (7) Chair T. Ito	GS 2 (7) Chair T. Fuchida	OS 9 (6)+GS15-1 Chair J-T. Zou
	16:00				
	16:05	GS12 (6) Chair K-L. Su	OS 15 (6) Chair M. Rizon	OS 8 (6) Chair K-H. Hsia	GS 18 (6) Chair J.M. Lee
	17:35				

GS:General Session **OS:Organized Session** **PS:Poster Session** **PT:Plenary Talk** **IT: Invited Talk**

GS1 Artificial brain research
GS2 Artificial intelligence
GS3 Artificial life & Brain science
GS4 Chaos & Cognitive science
GS5 Control technique Ⅰ
GS6 Control technique Ⅱ
GS7 Evolutionary computations
GS8 Intelligent control & Modeling
GS9 Human-machine cooperative systems
GS10 Image Processing Ⅰ
GS11 Image Processing Ⅱ
GS12 Innovative computations
GS13 Mobile vehicles Ⅰ
GS14 Mobile vehicles Ⅱ
GS15 Multi-agent systems
GS16 Neural networks
GS17 Robotics Ⅰ
GS18 Robotics Ⅱ
GS19 Robotics & Bipedal robot
GS20 Robotics & Application
GS21 Pattern recognition
GS22 Virtual reality
OS1 System sensing and control
OS2 MOT and interdisciplinary research
OS3 Learning control and robotics
OS4 Analysis and implementation of nonlinear systems
OS5 Control and automata
OS6 Computer vision and robotics
OS7 Soft robotics
OS8 Intelligent control and applications
OS9 Intelligent system and application
OS10 Biomimetic machine and robots
OS11 Robot control
OS12 Bio-symphony
OS13 Intelligent systems
OS14 Intelligent robots
OS15 Artificial intelligent
OS16 Embracing complexity in natural intelligence
OS17 Intelligent classification
OS18 Intelligent signal processing
OS19 Intuitive human-system interaction
OS20 Special environment localization and navigation
OS21 Molecular computing
OS22 Brain-like intelligence and biomedical applications
OS23 Bio-inspired theory and application
OS24 Real time methods for structural change detection of ongoing time series data
OS25 Artificial application & Artificial and green technology Ⅰ
OS26 Artificial application & Artificial and green technology Ⅱ
OS27 Machine learning and computer vision

TIME TABLE(2/5)

	RoomA	RoomB	RoomC	RoomD	RoomE
2/5 (Fri) 8:00	Registration (Registration Desk)				
8:40	OS 17 (5) Chair S. Omatsu	OS 27 (3) Chair H. Hamdan will end at 9:25	GS 1 (5) Chair M. Obayashi		
9:55	Coffee Break				
10:15	Plenary Talk (Room E) PT2 J. Casti Chair Y.G. Zhang				
11:05	OS 7 (4) Chair K. Nakazono	GS 14 (4) Chair J. Wang	GS 21 (4) Chair K. Hashimoto	OS 11 (4) Chair Y-M. Jia	PS1 (4)
12:05	Lunch				
13:00	GS 3 (4) Chair M. Nakamura	GS 4 (4) Chair T. Shimada	OS 13 (4) Chair J. Y. Shim	Invited Talks session IT1 I. Tanev IT2 J-Q. Liu IT3 L. Pagliarini Chair K. Shimohara	PS2 (5)
14:00 14:05	OS 22 (6) Chair N. Homma	GS 20 (6) Chair S.H. Han	OS 18 (5) Chair S. Omatsu will end at 15:20		
15:35	Coffee Break				
15:55	Plenary Talk (Room E) PT3 H. Lund Chair H. Tanaka				
16:45	GS 11 (3) Chair C-N. Ko will end at 17:30	OS 3 (4) Chair H. H. Lee	GS 10 (4) Chair T. Matsubara	OS 14 (4) Chair J. J. Lee	
17:45 18:25 20:35	AROB Award Ceremony (Chair K. Naitoh) Banquet – Hotel Shiragiku (Chair J. M. Lee)...... Welcome Address H.Tanaka / M. Oswald/ Y-M.Jia / K.L. Su / L. Pagliarini				

GS:General Session **OS:Organized Session** **PS:Poster Session** **PT:Plenary Talk** **IT: Invited Talk**

GS1 Artificial brain research
GS2 Artificial intelligence
GS3 Artificial life & Brain science
GS4 Chaos & Cognitive science
GS5 Control technique Ⅰ
GS6 Control technique Ⅱ
GS7 Evolutionary computations
GS8 Intelligent control & Modeling
GS9 Human-machine cooperative systems
GS10 Image Processing Ⅰ
GS11 Image Processing Ⅱ
GS12 Innovative computations
GS13 Mobile vehicles Ⅰ
GS14 Mobile vehicles Ⅱ
GS15 Multi-agent systems
GS16 Neural networks
GS17 Robotics Ⅰ
GS18 Robotics Ⅱ
GS19 Robotics & Bipedal robot
GS20 Robotics & Application
GS21 Pattern recognition
GS22 Virtual reality
OS1 System sensing and control
OS2 MOT and interdisciplinary research
OS3 Learning control and robotics
OS4 Analysis and implementation of nonlinear systems
OS5 Control and automata
OS6 Computer vision and robotics
OS7 Soft robotics
OS8 Intelligent control and applications
OS9 Intelligent system and application
OS10 Biomimetic machine and robots
OS11 Robot control
OS12 Bio-symphony
OS13 Intelligent systems
OS14 Intelligent robots
OS15 Artificial intelligent
OS16 Embracing complexity in natural intelligence
OS17 Intelligent classification
OS18 Intelligent signal processing
OS19 Intuitive human-system interaction
OS20 Special environment localization and navigation
OS21 Molecular computing
OS22 Brain-like intelligence and biomedical applications
OS23 Bio-inspired theory and application
OS24 Real time methods for structural change detection of ongoing time series data
OS25 Artificial application & Artificial and green technology Ⅰ
OS26 Artificial application & Artificial and green technology Ⅱ
OS27 Machine learning and computer vision

TIME TABLE(2/6)

		RoomA	RoomB	RoomC	RoomD
2/6 (Sat)	8:00	Registration (Registration Desk)			
	8:40	OS 4 (5) Chair H. Suzuki will end at 9:55	OS 23 (6) Chair I. Yoshihara	OS 5 (6) Chair M. Kono	GS 22 (6) Chair T. Yamada
	10:10	Coffee Break			
	10:30	OS 24 (5) Chair T.Hattori	OS 12 (5) Chair K. Naitoh	OS 10 (5) Chair K. Watanabe	GS 9 (5) Chair A. Nakamura
	11:45	Lunch			
	12:40	GS 5 (4) Chair M. Oya will end at 13:40	GS 15 (4) GS15-1->OS9-7 Chair S.M. Yang will end at 13:40	GS 17 (5) Chair S. Sagara	GS 6 (3) Chair H. H. Lee will end at 13:25
	13:55	Coffee Break			
	14:15	GS 16 (7) Chair T. Kondo	GS 19 (7) Chair M. Zhao	OS 26 (6) Chair D. H. Kim will end at 15:45	OS 6 (6) Chair Y. Yoshitomi will end at 15:45
	16:00				

GS:General Session **OS:Organized Session** **PS:Poster Session** **PT:Plenary Talk** **IT: Invited Talk**

GS1 Artificial brain research
GS2 Artificial intelligence
GS3 Artificial life & Brain science
GS4 Chaos & Cognitive science
GS5 Control technique Ⅰ
GS6 Control technique Ⅱ
GS7 Evolutionary computations
GS8 Intelligent control & Modeling
GS9 Human-machine cooperative systems
GS10 Image Processing Ⅰ
GS11 Image Processing Ⅱ
GS12 Innovative computations
GS13 Mobile vehicles Ⅰ
GS14 Mobile vehicles Ⅱ
GS15 Multi-agent systems
GS16 Neural networks
GS17 Robotics Ⅰ
GS18 Robotics Ⅱ
GS19 Robotics & Bipedal robot
GS20 Robotics & Application
GS21 Pattern recognition
GS22 Virtual reality
OS1 System sensing and control
OS2 MOT and interdisciplinary research
OS3 Learning control and robotics
OS4 Analysis and implementation of nonlinear systems
OS5 Control and automata
OS6 Computer vision and robotics
OS7 Soft robotics
OS8 Intelligent control and applications
OS9 Intelligent system and application
OS10 Biomimetic machine and robots
OS11 Robot control
OS12 Bio-symphony
OS13 Intelligent systems
OS14 Intelligent robots
OS15 Artificial intelligent
OS16 Embracing complexity in natural intelligence
OS17 Intelligent classification
OS18 Intelligent signal processing
OS19 Intuitive human-system interaction
OS20 Special environment localization and navigation
OS21 Molecular computing
OS22 Brain-like intelligence and biomedical applications
OS23 Bio-inspired theory and application
OS24 Real time methods for structural change detection of ongoing time series data
OS25 Artificial application & Artificial and green technology Ⅰ
OS26 Artificial application & Artificial and green technology Ⅱ
OS27 Machine learning and computer vision

TECHNICAL PAPER INDEX

February 4 (Thursday)

Room E
10:55~11:45 Plenary Talk
Chair J. J. Lee (KAIST, Korea)

PT1 *From dream to reality: Snake-like, spider-like robots*
S. Hirose (Tokyo Institute of Technology, Japan)

February 5 (Friday)

Room E
10:15~11:05 Plenary Talk
Chair Y. G. Zhang (Academia Sinica, China)

PT2 *Extreme events in human society:The xevents observatory and simulator*
J. Casti (International Institute for Applied Systems Analysis, Austria)

15:55~16:45 Plenary Talk
Chair H. Tanaka (Tokyo Medical and Dental University, Japan)

PT3 *Robomusic with modular playware*
H. Lund (Technical University of Denmark, Denmark)

Room D
13:00~15:35 Invited Talks Session
Chair K. Shimohara(Doshisha University, Japan)

IT1 *XML-based genetic programming framework:Design philosophy, implementation and applications*
I. Tanev (Doshisha University, Japan)

IT2 *Brain's doing in its resting-state: Default mode network as an inside story within the brain*
J-Q. Liu (Doshisha University, Japan)

IT3 *Wearing the playware*
L. Pagliarini (Technical University of Denmark, Denmark)

February 4 (Thursday)

8:00~Registration

Room A

8:40~10:10 OS19 Intuitive human-system interaction
Chair: M. Yokota (Fukuoka Institute of Technology, Japan)
Co-Chair: T. Oka (Fukuoka Institute of Technology, Japan)

OS19-1 *Towards natural intelligence modeling as a formal system based on mental image directed semantic theory (Part 1)*
M. Yokota, H. Li, H. Quan, K. Sugita (Fukuoka Institute of Technology, Japan)
T. Oka (Nihon University, Japan)

OS19-2 *Towards natural intelligence modeling as a formal system based on mental image directed semantic theory (Part 2)*
M. Yokota, R. Zhao, T. Tometsuka, K. Sugita (Fukuoka Institute of Technology, Japan)
T. Oka (Nihon University, Japan)

OS19-3 *Commanding a humanoid to move objects in a multimodel language*
T. Oka (Nihon University, Japan)
M. Yokota, K. Sugita (Fukuoka Institute of Technology, Japan)

OS19-4 *Face detection and face authentication based on 3D face image*
H. Kamitomo, C. Lu (Fukuoka Institute of Technology, Japan)

OS19-5 *Stripes extraction technique of projection pattern for 3D shape measurement*
K. Sun, C. Lu (Fukuoka Institute of Technology, Japan)

OS19-6 *A software framework for universal multimedia access*
Y. Maeda, K. Sugita (Fukuoka Institute of Technology, Japan)
T. Oka (Nihon University, Japan)
M. Yokota (Fukuoka Institute of Technology, Japan)

12:40~13:55 OS16 Embracing complexity in natural intelligence
Chair: Y. Ishida (Toyohashi University of Technology, Japan)
Co-Chair: T. Okamoto (Kanagawa Institute of Technology, Japan)

OS16-1 *Evaluations for an immunity-based anomaly detection with dynamic updating of profiles*
T. Okamoto (Kanagawa Institute of Technology, Japan)
Y. Ishida (Toyohashi University of Technology, Japan)

OS16-2 *A secure routing scheme for mobile wireless sensor networks*
Y. Watanabe, Tong Tran Nhat Linh (Nagoya City University, Japan)

OS16-3 *Prediction of space weather by adaptive information processing*
M. Tokumitsu, Y. Ishida (Toyohashi University of Technology, Japan)
S. Watari (National Institute of Information and Communications Technology, Japan)
K. Kitamura (Tokuyama College of Technology, Japan)

OS16-4 *An adaptive sensor network for home intrusion detection by human behavior profiling*
M. Tokumitsu, M. Murakami, Y. Ishida (Toyohashi University of Technology, Japan)

OS16-5 *A network visualization of stable matching in stable marriage problem*
Y. Morizumi, T. Hayashi, Y. Ishida (Toyohashi University of Technology, Japan)

14:15~16:00 OS1 System sensing and control
Chair: M. Uchida (The University of Electro-Communications, Japan)
Co-Chair: T. Mizuno (Tokyo Polytechnic University, Japan)

OS1-1 *Broadband robust PWM power amplifier using approximate 2DOF digital control*
T. Nomura, H. Iwata, K. Higuchi, N. Nakano (The University of Electro-Communications, Japan)

OS1-2 *A consideration on immunity-based reinforcement learning with continuous states*
S. Hosokawa, K. Nakano (The University of Electro-Communications, Japan)

OS1-3 *Investigation of voluntary movements in auditory stimulated conditions by integrative measurement*
K. Saito, Y. I. Park, M. Uchida (The University of Electro-Communications, Japan)

OS1-4 *Swing analysis of body-parts motion accompanied by apparent movement*
Y. I. Park, K. Saito, M. Uchida (The University of Electro-Communications, Japan)

OS1-5 *EMG activity of force sensation evoked by vibration stimulation*
T. Mizuno, M. Sato, M. Kimura, Y. Kume (Tokyo Polytechnic University, Japan)

OS1-6 *Emotion spectrum analysis for daily repetitive mental workload*
A. Nozawa, K. Karita (Myojo University, Japan)

OS1-7 *Single-trial analysis of voice stimulus evoked potentials*
H. Tanaka, T. Matsuoka (Kogakuin University, Japan)

16:05~17:35 GS12 Innovative computations
Chair: K-L. Su (National Yunlin University of Science & Technology, Taiwan)

GS12-1 *Fast processing method for PIV using GPGPU*
K. Miyazaki, K. Kawasue (University of Miyazaki, Japan)

GS12-2 *Data envelopment analysis for evaluating Japanese universities*
K. Inoue, R. Gejima, S. Aoki (Osaka Prefecture University, Japan)

GS12-3 *Data envelopment analysis for supply chain*
A. Naito, R. Gejima, K. Inoue, S. Aoki, H. Tsuji (Osaka Prefecture University, Japan)

GS12-4 *On a Brownian cellular automaton implementing self-reproducing loop*
Koji Ono, T. Isokawa (University of Hyogo, Japan)
F. Peper (Nano ICT Group, Japan)
Jia Lee(ChongQing University, China)
A. Saitoh, N. Kamiura,N. Matsui (University of Hyogo, Japan)

GS12-5 *An application of self-reproducing loops to defect-tolerant computation on self-timed cellular automaton*
Koji Ono, T. Isokawa (University of Hyogo, Japan)
F. Peper (Nano ICT Group, Japan)
A. Saitoh, N. Kamiura,N. Matsui (University of Hyogo, Japan)

GS12-6 *Management of experience data for rapid adaptation to new policies based on bayesian significance evaluation*
Saifuddin Md. Tareeq (The Graduate University for Advanced Studies)
T. Inamura (National Institute of Informatics, Japan)

Room B

8:40~10:10 OS20 Special environment localization and navigation
Chair: J. M. Lee (Pusan National University, Korea)

OS20-1 *A robust control of mobile inverted pendulum using single accelerometer*
H.U. Ha, S.M. Ryu, J.M. Lee (Pusan National University, Korea)

OS20-2 *Localization of multiple robots in a wide workspace*
J.H. Park, W.S. Jang, J.M. Lee (Pusan National University, Korea)

OS20-3 *Pallet recognition and driving method for pallet-engaging of unmanned autonomous forklift*
J.J. Park, J.M. Kim, K.H. Jung, S.S. Kim, (Pusan National University, Korea)

OS20-4 *Monitoring the level in a large structure localization method*
J.M. Kim, H.J. Kim (Pusan National University, Korea)

OS20-5 *Performance improvement of outdoor localization using classified sensing points*
T.B. Kwon, J.B. Song, Y.J. Lee (Korea University, Korea)

OS20-6 *Collision detection of robot manipulator in cryogenic environment*
S.H. Lee, K.H. Yu, M.C. Lee (Pusan National University, Korea)

12:40~13:55 GS13 Mobile vehicles Ⅰ
Chair: I. Zunaidi (TATi University College, Malaysia)

GS13-1 *Trajectory tracking control of mobile robot moving along curved wall using imaginary wall*
S. Furuno, K. Yanagi (Kitakyushu National College of Technology, Japan),
M. Kobayashi (Kitakyushu Institute of Technology, Japan),
G. Hirano (Kinki University, Japan)

GS13-2 *Vision-based obstacle avoidance system for autonomous mobile robot in outdoor environment*
J.E. Jung, K.S. Lee, H.G. Park (Pusan National University, Korea)
Y.H. Koh (Futronic Co., Ltd., Korea)
M.H. Lee (Pusan National University, Korea)

GS13-3 *Cooperative localization by using knowledge of self-organized regularity*
M. Kubo, T. Matsubara, S. Shimizu, H. Sato (National Defense Academy, Japan)

GS13-4 *A collaborative localization tolerant to recognition error by double check particle exchange*
T. Matsubara, M. Kubo, Y. Murachi (National Defense Academy, Japan)

GS13-5 *Study on the route extraction based on the image processing*
J. Wang (Beijing Jiaotong University, China)
M. Sugisaka (Nippon Bunri University, Japan)

14:15~16:00 OS2 MOT and interdisciplinary research
Chair: T. Ito(Ube National College of Technology, Japan)
Co-Chair: S. Matsuno (Ube National College of Technology, Japan)

OS2-1 *Estimating stochastic volatility models of stock returns in Chinese markets*
S.Q. Lu, S. Xie (Fudan University, China)
T. Ito(Ube National College of Technology, Japan)

OS2-2 *An analysis of organizational behaviors in the Keiretsu of Mazda*
T. Ito, S. Tagawa (Ube National College of Technology, Japan)
M. Sakamoto(University of Miyazaki, Japan, Japan)
S.Q. Lu (Fudan University, China)

OS2-3 *An analysis of interactive influence in the Keiretsu of Mazda*
S. Matsuno, T. Ito (Ube National College of Technology, Japan)
Z. Xia (Wenzhou University, China)
M. Sakamoto(University of Miyazaki, Japan, Japan)

OS2-4 *The connection law and networks*
T. Ito (Ube National College of Technology, Japan)
Y. Ma (Wuhan University of Science and Engineering, China)
M. Sakamoto(Miyazaki University, Japan)

OS2-5 *Discovering the efficient organization structure: horizontal versus vertical*
S. Ikeda (University of Miyazaki, Japan)
T. Ito (Ube National College of Technology, Japan)
M. Sakamoto (University of Miyazaki, Japan)

OS2-6 *A centrality analysis of transaction relationship of Panasonic*
Y. S. Park (Ube National College of Technology, Japan)
Y. Chen (Kyushu International University, Japan)

OS2-7 *A study of accounting standard-setting using graph theory*
K. Ogata (University of Nagasaki, Japan)

16:05~17:35 OS15 Artificial intelligent
Chair: Mohamed Rizon (King Saud University, Saudi Arabia)
Co-Chair: Ali Selamat (Universiti Teknologi Malaysia, Malaysia)

OS15-1 *Fast shape matching and retrieval based on approximate dynamic space warping*
Naif Alajlan (King Saud University, Saudi Arabia)

OS15-2 *Prediction model of permeability from well logs using type-2 fuzzy logic systems*
Sunday Olusanya Olatunji, Ali Selamat (Universiti Teknologi Malaysia, Malaysia)
Abdul Azeez, Abdul Raheem (King Fahd University of Petroleum and Mineral, Saudi Arabia)

OS15-3 *Real-time iris detection*
Mohamed Rizon (King Saud University, Saudi Arabia)
Chai Tong Yuen (Universiti Tunku Abdul Rahman, Malaysia)
Ali S. AlMejrad (King Saud University, Saudi Arabia)

OS15-4 *Comparison of human emotion recognition through different set of EEG channels*
M. Murugappan (Universiti Malaysia Perlis, Malaysia)
M. Rizon (King Saud University, Saudi Arabia)
R. Nagarajan(Universiti Malaysia Perlis, Malaysia)
Ali S. AlMejrad (King Saud University, Saudi Arabia)
S. Yaacob (Universiti Malaysia Perlis, Malaysia)

OS15-5 *Design of intelligent system for speech monitoring and treatment of low and excessive vocal intensity*
Ali S. AlMejrad (King Saud University, Saudi Arabia)

OS15-6 *Modified relevance feedback for content based image retrieval using support vector machine*
Ali Selamat, Pei-Geok Lim (Universiti Teknologi Malaysia, Malaysia)

Room C

8:40~10:10 GS7 Evolutionary computations
Chair: M.K. James (Tokyo University of Information Sciences, Japan)

GS7-1 *Mixed constrained image filter design using particle swarm optimization*
Z. Bao, T. Watanabe (Waseda University, Japan)

GS7-2 *A reinforcement learning with switching controllers for continuous action space*
M. Nagayoshi (Niigata College of Nursing, Japan),
H. Murao, H. Tamaki (Kobe Univ., Japan)

GS7-3 *A framework for embodied evolution with pre-evaluation applied to a biped robot*
J. Nakai, T. Arita (Graduate School of Information Science, Nagoya University, Japan)

GS7-4 *Efficient flooding method for wireless sensor networks based on discrete particle swarm optimization computing multiple forwarding nodes sets*
J. Nagashima, A. Utani, H. Yamamoto (Tokyo City University, Japan)

GS7-5 *Fixed column primer for Boolean Matrix multiplication with DNA computing*
N.Rajaee, H.Aoyagi, O.Ono (Meiji University, Japan)

GS7-6 *Applying soft computing for remote sensing data composite algorithms*
Kenneth J. Mackin, T. Yamaguchi, J.G. Park, E. Nunohiro, K. Matsushita (Tokyo University of Information Sciences, Japan)
Y. Yanagisawa, M. Igarashi (Nihon University, Japan)

12:40~13:55 OS21 Molecular computing
Chair: M. Oswald (Vienna University of Technology, Hungary)
Co-Chair: Y. Suzuki (Nagaya University, Japan)

OS21-1 *P-system communications architectures configuration based on growing SOM*
A. Gutiérrez, S. Delgado, S. Gómez (Universidad Politécnica de Madrid, Spain)

OS21-*2 Hardware circuit for the application of evolution rules in a transition P-system.*
V. Martínez, S. Alonso, A. Gutiérrez (Universidad Politécnica de Madrid, Spain)

OS21-3 *Calculating maximal multisets by using RAM as support*
A. Arteta, F Arroyo, A. Goñi (Universidad Politécnica de Madrid, Spain)

OS21-4 *Investigation of the efficient protection from Influenza pandemic using CARMS*
Y. Suzuki (Nagoya University, Japan)
K. Tsunoda (Kobe University, Japan)
K. Shinya (Nagoya University, Japan)

OS21-5 *Organization levels in P systems*
M. Oswald (Vienna University of Technology, Hungary)

14:15~16:00 GS2 Artificial intelligence
Chair: T. Fuchida (Kagoshima University, Japan)

GS2-1 *Reinforcement learning using Voronoi space division*
Kathy Thi Aung, T. Fuchida (Kagoshima University, Japan)

GS2-2 *Machine learning approach to 9-dof robotic arm control*
S.Nishioka, S.Maeda (Kyoto University, Japan)
Y.Nakamura (Osaka University, Japan)
T.Ueno (Kyoto University, Japan)
H.Ishiguro (Osaka University, Japan)
S.Ishii (Kyoto University, Japan)

GS2-3 *Consideration on gesture recognition based on multilayer neural network by using input device of home gaming console*
I. Iimura, T. Fujiki (Prefectural University of Kumamoto, Japan)
H. Tsurusawa (Oita National College of Technology, Japan)
S. Nakayama (Kagoshima University, Japan)

GS2-4 *A learning Petri net model based on reinforcement learning*
L-B. Feng, M. Obayashi, T. Kuremoto, K. Kobayashi (Yamaguchi University, Japan)

GS2-5 *On detecting a human and its body direction from a video*
Y. Nakashima, J-K. Tan, S. Ishikawa, T. Morie (Kyushu Institute of Technology, Japan)

GS2-6 *Parallel computing method of extraction of frequent occurrence pattern of sea surface temperature from satellite data*
A. Niimi, T. Yamaguchi, O. Konishi (Future University-Hakodate, Japan)

GS2-7 *Cultural evolution of compositional language under multiple cognition of meanings*
R. Matoba, S. Sakamoto, T. Hashimoto (Japan Advanced Institute of Science and Technology, Japan)

16:05~17:35 OS8 Intelligent control and applications
Chair: K-H. Hsia (Far East University, Taiwan)
Co-Chair: C-C. Wang (Far East University, Taiwan)

OS8-1 *Production scheduling and process planning based on mixed-integer evolutionary algorithm*
Y-C. Lin, Y-C. Lin (WuFeng Institute of Technology, Taiwan)
K-L. Su (National Yunlin University of Science and Technology, Taiwan)

OS8-2 *Further study on camera position estimation from image by ANFIS*
S-F. Lien（National Yunlin University of Science and Technology, Taiwan）
K-H. Hsia (Far East University, Taiwan)
C-C. Wang (Chienkuo Technology University, Taiwan)
T-E Lee (National Yunlin University of Science and Technology, Taiwan)
J-P. Su (Overseas Chinese University, Taiwan)

OS8-3 *Gaussian radial basis function neural network controller of synchronous reluctance motor in electric motorcycle applications*
C-A. Chen (Automotive Research and Testing Center, Taiwan)
H-K. Chiang, W-B. Lin (National Yunlin University of Science and Technology, Taiwan)

OS8-4 *Implementation of robust complex extended Kalman filter with LabVIEW for detection in distorted signal*
W-B. Lin (Far East University, Taiwan)
H-K. Chiang (National Yunlin University of Science and Technology, Taiwan)
K-R. Shih (National Formosa University, Taiwan)
C-A. Chen (Automotive Research and Testing Center, Taiwan)

OS8-5 *Fuzzy PID control for an overhead crane using hybrid optimization approach*
C-N. Ko（Nan-Kai University of Technology, Taiwan）
C-C. Yang（Hsiuping Institute of Technology, Taiwan）
G-Y. Liu (Nan-Kai University of Technology, Taiwan)
K-L. Su (National Yunlin University of Science and Technology, Taiwan)

OS8-6 *Parameter estimation of chaotic systems by nonlinear time-varying evolution PSO method*
C-N. Ko, Y-Y. Fu, C-M. Lee (Nan-Kai University of Technology, Taiwan)
C-J. Wu (National Yunlin University of Science and Technology, Taiwan)

Room D

8:40~10:10 OS25 Artificial application & Artificial and green technology Ⅰ
Chair: Dong-Hwa Kim (Hanbat University, Korea)

OS25-1 *Spatial information of game for body interface using webcam*
Y. J. Lee (Jeonju University, Korea)

OS25-2 *A study on accurate time synchronization protocol with improved SNTP for smart AMR*
(withdrawal)
S.Y Oh, C.H. Lee (ADMOTECH Inc., Korea)

OS25-3 *Calculation of arm parameter for surface scanning with axis moment*
J.C. Jeong, H.C. Shin (University of Science & Technology, Korea)
D.D. Lee, C.H. Lee (ADMOTECH Inc., Korea)

OS25-4 *Development of interactive wireless AMR with distribution automation system*
C.H. Yoon, D.D. Lee, C.H. Lee (ADMOTECH Inc., Korea)

OS25-5 *Improved SNTP for accurate time synchronization in smart AMR systems*
S.Y. Oh, D.D. Lee, C.H. Lee (ADMOTECH Inc., Korea)

OS25-6 *Personal color decision system using fuzzy logic*
J.M. Oh, M.S. Hong, J.T. Kim, D.W. Lee, C.W. Son, G. Lee (Hannam University, Korea)

12:40~13:55 GS8 Intelligent control ＆ modeling
Chair: S.Y. Yi (Seoul National University of Technology, Korea**)**

GS8-1 *Evaluation of cycling posture considering the difference of saddle height with principal component analysis based on leg electromyography*
S. Matsumoto, T. Tokuyasu (Oita National College of Technology, Japan)
Koji Hirakoba (Kyushu Institute of Technology, Japan)
Keichi Ohba (Oita National College of Technology, Japan)

GS8-2 *A control system based on the fuzzy neural network for a robot joint*
H. Zhao (Shanghai Institute of Technology, China)
M. Sugisaka (Nippon Bunri University, Japan)

GS8-3 *Proposal of sensors for robot supporting to take medicines on time*
Y. Kitazono, X. Zheng, S. Nakashima, S. Yang, S. Serikawa (Kyushu Institute of Technology, Japan)

GS8-4 *Development and case study of trend analysis software based on FACT-Graph*
R. Saga (Kanagawa Institute of Technology, Japan)
H. Tsuji, T. Miyamoto (Osaka Prefecture University, Japan)
K. Tabata (Kanagawa Institute of Technology, Japan)

GS8-5 *Gait planning for a robot dog*
S.Y. Yi (Seoul National University of Technology, Korea)
D.S. Choi (DASA Corp., Korea)

14:15~16:00 OS9 Intelligent system and application
Chair: J-T. Zou (National Formosa University, Taiwan)
Co-Chair: K-L. Su (National Yunlin University of Science & Technology, Taiwan)

OS9-1 *The development of the omnidirectional home care mobile robot*
J-T. Zou (National Formosa University, Taiwan)
F-C. Chiang (WuFeng Institute of Technology, Taiwan)

OS9-2 *Path planning of the multiple mobile robot system*
S-V. Shiau, K-L. Su (National Yunlin University of Science & Technology, Taiwan)
C-C. Wang (Chienkuo Technology University, Taiwan)
J-H. Guo (National Yunlin University of Science & Technology, Taiwan)

OS9-3 *Multi-level multi-sensor based security system for intelligent home*
S-H Chia, K-L Su, S-V Shiau (National Yunlin University of Science & Technology, Taiwan)
T-L Chien (Wu-Feng Institute of Technology, Taiwan)

OS9-4 *Multisensor fusion based gas detection module*
J-H. Guo (NationalYunlin University of Science & Technology, Taiwan)
I-C. Chien (National Cenrral University, Taiwan)
K-L. Su, C-J. Wu (NationalYunlin University of Science & Technology, Taiwan)

OS9-5 *A fast parameters estimation for nonlinear multi-regressions based on choquet integral with quantum-behaved particle swarm optimization*
Y-M. Jau, C-J. Wu, J-T. Jeng (National Yunlin University of Science & Technology, Taiwan)

OS9-6 *Application of a remote image surveillance system in a robotic weapon*
C-C. Wang (Chienkuo Technology University, Taiwan)
K-H. Hsia(Far East University, Taiwan)
K-L. Su (National Yunlin University of Science & Technology, Taiwan)
Y-C. Hsieh, C-L. Lin (Chienkuo Technology University, Taiwan)

16:05~17:35 GS18 Robotics Ⅱ
Chair: J.M. Lee (Pusan National University, Korea)

GS18-1 *Human tracking with variable prediction steps based on Kullback-Leibler divergence*
N. Takemura, Y. Nakamura (Osaka University, Japan)
Y. Matsumoto（AIST, Japan）
H. Ishiguro (Osaka University, Japan)

GS18-2 *Optimal path planning with holonomic mobile robot using localization vision sensor*
D.S. Lee, C.S. Kim, S.Y. Kim, K.S. Lee, H.G. Park (Pusan National University, Korea)
Y.H. Koh (Futronic Co., Ltd., Korea)
M.H. Lee (Pusan National University, Korea)

GS18-3 *Efficient robotic memory controller for long-term planning*
Hassab Elgawi Osman (Tokyo Institute of Technology, Japan)

GS18-4 *Construction of the robot control system with use of pointing action and voice*
Y. Takenaka, N. Abe, Y. Tabuchi (Kyushu Institute of Technology, Japan)
H. Taki (Wakayama University, Japan)
Shoujie He (VuCOMP, USA)

GS18-5 *The water-tank test of novel underwater positioning system based on sensor networks*
Bin Fu, Lian Lian (Shanghai Jiao Tong University, China)
Zhang Feifei, M. Ito (Tokyo University of Marine Science and Technology, Japan)
Li Wen tao (Shanghai Jiao Tong University, China)

GS18-6 *Countering asymmetric situations with distributed artificial life and robotics approach*
Peter Sapaty (National Academy of Sciences, Ukraine)
M. Sugisaka (Nippon Bunri University, Japan)

February 5 (Friday)

8:00~ Registration

Room A

8:40~9:55 OS17 Intelligent classification
Chair: S. Omatu (Osaka Prefecture University, Japan)
Co-Chair: J. A. Dargham (University Malaysia Sabah, Malaysia)

OS17-1 *Intelligent classification of bills by neural networks*
S. Omatu, M. Yoshioka, H. Yanagimoto (Osaka Prefecture University, Japan)

OS17-2 *Signal separation by independent component analysis*
S. Omatu, M. Yoshioka, H. Yanagimoto (Osaka Prefecture University, Japan)

OS17-3 *The land cover estimation with ALOS satellite image using neural-network*
Y. Tsuchida, S. Omatu, M. Yoshioka (Osaka Prefecture University, Japan)

OS17-4 *The analysis of Japanese voice sound by using real-time spectral analysis*
H. Nakatsuji, S. Omatu (Osaka Prefecture University, Japan)

OS17-5 *Selection of parameters in design of real-time spectral analysis*
H. Nakatsuji, S Omatu (Osaka Prefecture University, Japan)

11:05~12:05 OS7 Soft robotics
Chair: Kunihiko Nakazono (University of the Ryukyus, Japan)

OS7-1 *GA simulation of evolution of the hierarchical module structure on gene networks*
S. Nakashima, K. Kurata (University of the Ryukyus, Japan)

OS7-2 *Swing-up control of the acrobot using genetic programming considering an actuator dynamics*
R. Fukushima, E. Uezato (University of the Ryukyus, Japan)

OS7-3 *Neurocontrol for a rotary crane system with disturbance*
K. Tamanoi, K. Nakazono (University of the Ryukyus, Japan)

OS7-4 *Particle swarm optimization with genetic recombination - A hybrid evolutionary algorithm*
S-C. Duong, H. Kinjo, E. Uezato (University of the Ryukyus, Japan)
T. Yamamoto (Tokushima Technology College, Japan)

13:00~14:00 GS3 Artificial life & Brain science
Chair: M. Nakamkura (Research Institute of Systems Control)

GS3-1 *Why we talk?: Altruism and multilevel selection in the origin of language*
K. Sugiura, T. Arita (Graduate School of Information Science, Nagoya University, Japan)

GS3-2 *A variety of competitive properties arises from STDP incorporating metaplastic regulation*
S. Kubota (Yamagata University, Japan)
J. Rubin (University of Pittsburgh, USA)
T. Kitajima (Yamagata University, Japan)
T. Nakamura (Yamagata University, Japan)

GS3-3 *Automatic estimation of light sleep level during short nap*
B. Wang (East China University of Science and Technology, China)
T. Sugi (Saga University, Japan)
X. Wang (East China University of Science and Technology, China)
Shuichiro Shirakawa (National Centre of Neurology and Psychiatry, Japan)
M. Nakamura (Research Institute of Systems Control, Japan)

GS3-4 *Evolving behavior sequences for a humanoid entertainment robot*
W-P. Lee, J-S. Jong, T-H. Yang (National Sun Yat-sen University, Taiwan)

14:05~15:35 OS22 Brain-like intelligence and biomedical applications
Chair: N. Homma (Tohoku University, Japan)
Co-Chair: N. Sugita (Tohoku University, Japan)

OS22-1 *A guess for natural neural activity and a suggestion on the modification of the ANN*
Y. G. Zhang (The Institute of Systems Science, China)
M. Sugisaka (Nippon Bunri University, Japan)

OS22-2 *Research on automatic text summary based on latent semantic indexing*
D. Ai, Y. Zheng, D. Zhang (University of Science and Technology of Beijing, China)

OS22-3 *Sensitivity improvement of automatic pulmonary nodules detection in chest X-ray CT images*
S. Shimoyama, N. Homma, T. Ishibashi, M. Yoshizawa (Tohoku University, Japan)

OS22-4 *A time variant seasonal ARIMA model for lung tumor motion prediction*
K. Ichiji, M. Sakai, N. Homma, Y. Takai, M. Yoshizawa (Tohoku University, Japan)

OS22-5 *Pulse transmission time based on temporal difference in the instantaneous phase between electrocardiogram and photoplethysmogram signals*
M. Murakoshi, M. Yoshizawa, N. Sugita, M. Abe, N. Homma, T. Yambe, S. Nitta (Tohoku University, Japan)

16:45~17:30 GS11 Image Processing Ⅱ
Chair: C-N. Ko (Nan-Kai University of Technology, Taiwan)

GS11-1 *Segmentation of artery areas on none-enhanced fresh blood imaging based on dot enhancement filter and 3-D region growing method*
A. Yamamoto, T. Nishizaki, H.S. Kim, J-K. Tan, S. Ishikawa (Kyushu Institute of Technology, Japan)

GS11-2 *Construction of a sense of force feedback and vision for micro-objects*
R.Uehara, E.Hayashi (Kyushu Institute of Technology, Japan)

GS11-3 *A real-time face detection and recognition system for mobile robot in the complex background*
S. Chen, T. Zhang, C. Zhang, Y. Cheng (Tsinghua University, China)

Room B

8:40~9:40 OS27 Machine learning and computer vision
Chair: H. Hamdan (SUPELEC, France)
Co-Chair: Khaled Al Mutib (King Saud University, Saudi Arabia)

OS27-1 *Biomimetic control architecture for robotic cooperative tasks*
N. Bizdoaca (University of Craiova, Romania)
H. Hamdan (SUPELEC, France)
D. Coman, A. Petrisor, E. Bizdoaca (University of Craiova, Romania)

OS27-2 *ANN dexterous robotics hand optimal control methodology grasping and manipulation forces optimization*
Ebrahim Matter al-Gallaf (University of Bahrain, Kingdom of Bahrain)
Khaled Al Mutib (King Saud University, Saudi Arabia)
Hani Hamdan (SUPELEC, France)

OS27-3 *Dense stereovision using mono-CCD color cameras*
Hachem Halawana (LAGIS, USTL)
Hani Hamdan (SUPELEC, France)

11:05~12:05 GS14 Mobile vehicles Ⅱ
Chair: J. Wang (Beijing Jiaotong University, China)

GS14-1 *Intelligent OkiKoSenPBX1 security patrol robot via network and map-based route planning*
Mbaïtiga Zacharie (Okinawa National College of Technology, Japan)

GS14-2 *Obstacle arrangement detection using multichannel ultrasonic sonar for indoor mobile robots*
K. Okuda, M. Miyake, H. Takai (Hiroshima City University, Japan)
K. Tachibana (Osaka Gakuin University, Japan)

GS14-3 *A collision avoidance achievement of vehicle warning system in intersection via DSRC*
C. W. Hsu, C. N. Liang, L. Y. Ke, H. Y. Huang, F. Y. Huang (Automotive Research & Testing Center, Taiwan)

GS14-4 *Autonomous navigation system using geographical feature elements information for navigation mapping system*
I. Zunaidi, M. Rozailan, MS Samsi (TATi University College, Malaysia)
N. Kato (Mie University, Japan)

13:00~14:00 GS4 Chaos & Cognitive science
Chair: T. Shimada (Meiji University, Japan)

GS4-1 *Visual attention model involving feature-based inhibition of return*
S. Hotta, S. Oba, S. Ishii (Kyoto University, Japan)

GS4-2 *Relation between impression of touch panels' coloration and operation*
M. Sakamoto, H. Suto, M. Sawai (Muroran Institute of Technology, Japan)

GS4-3 *An extension of a duffing oscillator and nonlinear energy harvesting* (withdrawal)
T. Shimada, T. Moriya, H. Uchiyama (Meiji University, Japan)

GS4-4 *Matrix diagonalization in the quantum anisotropic Kepler problem*
K. Kubo, T. Shimada (Meiji University, Japan)

14:05~15:35 GS20 Robotics & Application
Chair: S. H. Han (Kyungnam University, Korea)

GS20-1 *Variable step-size affine projection algorithm based on excess mean square error*
C.Hee Lee, P.G. Park (Pohang University of Science and Technology, Korea)

GS20-2 *Basic research on new underwater positioning technology based on machine vision*
B. Fu, W-T. Li, T. Ge, L. Lian, H. Zhang (Shanghai Jiao Tong University, China)

GS20-3 *Basic research on underwater laser ranging and speed-measuring*
B. Fu, H. Zhang, T. Ge, L. Lian, W-T. Li (Shanghai Jiao Tong University, China)

GS20-4 *Ultrasonic sensor based navigation for a mobile robot using fuzzy logic*
Nguyen Huu Cong (Kyungnam University, Korea)
Sung-Hyun Han (Kyungnam University, Korea)

GS20-5 *Robust real-time control of autonomous mobile robot by using ultrasonic and infrared sensors*
V-Q. Nguyen, S-B. Kyun, S.H. Han (Kyungnam University, Korea)

GS20-6 *Artificial life intelligent contour following industrial robot*
MS Samsi, I Zunaidi, N Nagarajan, Y Sazali , M Rozailan (TATi University College, Malaysia)

16:45~17:45 OS3 Learning control and robotics
Chair: H.H. Lee (Waseda University, Japan)
Co-Chair: H. Ogai (Waseda University, Japan)

OS3-1 *Real time traffic signal learning control using BPNN based on prediction for probabilistic distribution of standing vehicles*
C. Cui, J.S. Shin, H.H. Lee (Waseda University, Japan)

OS3-2 *Advanced pipe inspection robot using rotating probe*
K. Nishijima (Waseda University, Japan)
Y. Sun (Shanghai Jiao Tong University, China)
H. Ogai (Waseda University, Japan)
R.K. Srivastava, B. Bhattacharya (Indian Institute of Technology Kanpur, India)

OS3-3 *Quasi-ARX neural network and its application to adaptive control of nonlinear systems*
J. HU, L. Wang (Waseda University, Japan)

OS3-4 *Real-time generation of developed view for drain pipe based on web camera video*
Z. Wang, H. Ogai, S. Takeno (Waseda University, Japan)

Room C

8:40~9:55 GS1 Artificial brain research
Chair: M. Obayashi (Yamaguchi University, Japan)

GS1-1 *Revisited: Hebbian postulate under homeostatic plasticity*
S. Fernando, S. Matsuzaki, Y. Nakamura, A. Marasinghe (Nagaoka University of Technology, Japan)

GS1-2 *Memory capacity and information capacity of the sparsely encoded associative memory with replacing units*
R. Miyata (University of the Ryukyus, Japan)
S. Muta, K. Kurata (University of the Ryukyus, Japan)

GS1-3 *A study on Q-learning considering negative rewards*
T.Fuchida, Kathy T.A, A.Sakuragi (Kagoshima University, Japan)

GS1-4 *Intelligent agent construction using the attentive characteristic patterns of chaotic neural networks*
M.Obayashi, T.Kuremoto, K.Kobayashi (Yamaguchi University, Japan)

GS1-5 *An effective image transmission method in ZigBee System for intruder detection systems*
S.K. Hwang, S.G. Lee (Hannam University, Korea)

11:05~12:05 GS21 Pattern recognition
Chair: K Hashimoto (Osaka Prefecture University, Japan)

GS21-1 *A color-based particle filter for multiple objects tracking in outdoor environment*
B. Sugandi, H. Kim, J.K. Tan, S. Ishikawa (Kyushu Institute of Technology, Japan)

GS21-2 *A Study of dimension reduction of Gabor features from different facial expressions*
R. Samad, H. Sawada (Faculty of Engineering, Kagawa University, Japan)

GS21-3 *Interactive musical editing system to support human errors and offer personal preferences for an automatic piano*
- A method for searching for similar phrases using DP matching and for inferring performance expression with the best alignment of DP matching-
K. Koga, E. Hayashi (Kyusyu Institute of Technology, Japan)

GS21-4 *A Corpora-based detection of stylistic inconsistencies of text in the targeted subgenre*
K Hashimoto (Osaka Prefecture University, Japan)
K. Takeuchi, H. Ando (Osaka Electro-Communication University, Japan)

13:00 ~14:00 OS13 Intelligent systems
Chair: J. Y. Shim (Kangnam University, Korea)
Co-Chair: J. J. Lee (KAIST, Korea)

OS13-1 *Emotion inspired mechanism in the intelligent system*
J.Y. Shim (Kangnam University, Korea)

OS13-2 *Object recognition algorithm using vocabulary tree and pre-matching array*
H.Y. Seo, J.J. Lee (KAIST, Korea)

OS13-3 *Memory association and reaction by conditioning*
J.Y. Shim (Kangnam University, Korea)

OS13-4 *Application of neuro-fuzzy PID controller for post chlorine process*
H.H. Lee, C.M. Oh, J.J. Lee (KAIST, Korea)
A.K. Lee, D.H. Lee (Korea Water Resources Corporation, Korea)

14:05~15:20 OS18 Intelligent signal processing
Chair: Sigeru Omatu (Osaka Prefecture University, Japan)
Chair: Mohad Saberi Mohamad (Osaka Prefecture University, Japan)

OS18-1 *Face image make up system by using ε -filter*
M. Yoshioka, S. Omatu, H. Yanagimoto (Osaka Prefecture University, Japan)

OS18-2 *Image segmentation using probability density estimation*
K. Imaguma, M. Yoshioka, S. Omatu, H. Yanagimoto (Osaka Prefecture University, Japan)

OS18-3 *Particle swarm optimization with a modified sigmoid function for gene selection from gene expression data*
M.S. Mohamad, S. Omatu (Osaka Prefecture University, Japan)
S. Deris (Universiti Teknologi Malaysia, Malaysia)
M. Yoshioka (Osaka Prefecture University, Japan)

OS18-4 *Selecting informative gene for cancer classification by using particle swarm optimization*
M.S. Mohamad, S. Omatu (Osaka Prefecture University, Japan)
S. Deris (Universiti Teknologi Malaysia, Malaysia)
M. Yoshioka (Osaka Prefecture University, Japan)

OS18-5 *Radon transform for face recognition*
J. A. Dargham, A. Chekima, E. Moung (University Malaysia Sabah, Malaysia)
S. Omatu (Osaka Prefecture University, Japan)

16:45~17:45 GS10 Image Processing Ⅰ
Chair: T. Matsubara (National Defense Academy, Japan)

GS10-1 *A dynamically reconfigurable processor for the H.264/AVC image prediction*
Y. Hayakawa, A. Kanasugi (Tokyo Denki University, Japan)

GS10-2 *X-ray computed tomography using material-class modeling by MRF energy minimization*
W. Fukuda, S. Maeda, A. Kanemura, S. Ishii (Kyoto University, Japan)

GS10-3 *Implementation of TFT inspection system using the stream processor*
B.Y. Park, C.H. Lee, P.G. Park (Pohang University of Science and Technology, Korea)

GS10-4 *Study on the crack detection of bridges based on digital image processing*
J. Wang, G. Zhang, Mingcheng E (Beijing Jiaotong University, China)

Room D

11:05~12:05 OS11 Robot control
Chair: Y-M. Jia (Beihang University, China)
Co-Chair: J-P. Du (Beihang University, China)

OS11-1 *Adaptive image filtering for tracking control of robots*
D. Cao, Y-M. Jia (Beihang University, China)
J-P. Du (Beijing University of Posts and Telecommunications, China)

OS11-2 *Non-fragile control for trajectory tracking of mobile robot systems with time-delay*
N. Ni, Y-M. Jia (Beihang University, China)
J-P. Du (Beijing University of Posts and Telecommunications, China)

OS11-3 *Experimental comparison among three typical data-driven control algorithms*
S. Jin, Y. Li, Y. Zhu, J. Hao, Z. Hou (Beijing Jiaotong University, China)

OS11-4 *Adaptive identification and prediction control foe time delay nonlinear systems based on neural networks*
J. Na, X. Ren (Beijing Institute of Technology, China)

16:45~17:45 OS14 Intelligent robots
Chair: J. J. Lee (KAIST, Korea)
Co-Chair: Maki .K Habib (The American University in Cairo, Egypt)

OS14-1 *Behavior based autonomous navigation system for mobile robots*
M.K. Habib (The American University in Cairo, Egypt)

OS14-2 *The optical FBG contact force measurement system for the haptic feedback of minimal invasive surgery robot*
H.S. Song, J.W. Suh, Y.I. Yoo, J.J. Lee (KAIST, Korea)

OS14-3 *Impedance model force control using a neural network-based effective stiffness estimator*
F. Nagata, T. Mizobuchi (Tokyo University of Science Yamaguchi, Japan)
T. Hase, Z. Haga (R&D Center, Meiho Co. Ltd., Japan)
K. Watanabe (Okayama University, Japan)
M K. Habib (The American University in Cairo, Egypt)

OS14-4 *Fuzzy sliding mode control for under-actuated system with mismatched uncertainties*
S.Y. Shin, J.J. Lee (KAIST, Korea)

Room E

11:05~12:05 PS1 Poster session 1

PS1-1 *A study of embedded community network system in home automation*
C-L. Chen, P-Y. Chen (Nan Kai University of Technology, Taiwan)

PS1-2 *A novel coding method for genetic algorithms based on redundant binary number*
A. Murayama, A. Kanasugi (Tokyo Denki University, Japan)

PS1-3 *The optimal combination of dither matrix by using genetic algorithm*
T. Kato, K. Tanaka (Meiji University, Japan)

PS1-4 *Improved algorithm for solving the maximal CliqueProblem with DNA computing*
H. Aoyagi, N. Rajaee, O. Ono (Meiji University, Japan)

13:00~14:00 PS2 Poster session 2

PS2-1 *Difference of 3-back task performance due to three levels of arousal*
M.H. Choi, J.S. Choi (Konkuk University, Korea)
B.C. Min (Hanbat National University, Korea)
G.R. Tack, S.C. Chung (Konkuk University, Korea)

PS2-2 *Detection of human respiration based on measurement system of current generated by electro-static induction*
K. Kurita (Kochi National College of Technology, Japan)

PS2-3 *Authentication of the reconstructed image from computer-generated hologram: synthesized by complex Hadamard transform*
F. Inaba, N. Fujii, K. Tanaka (Meiji University, Japan)

PS2-4 *Feature extraction method using laser range finder for SLAM*
T.R. Kim, S.Y. Jung, J.M. Kim, S.S. Kim (Pusan National University, Korea)

PS2-5 *A case study of discussion classes in mathematics education (Research for the improvement of mathematics education)*
Hyang Joo Rhee (Duksung Womens University, Korea)

February 6 (Saturday)

8:00~ Registration

Room A

8:40~10:10 OS4 Analysis and implementation of nonlinear systems
Chair: H. Suzuki (The University of Tokyo, Japan)
Co-Chair: T. Kohno (The University of Tokyo, Japan)

OS4-1 *An Izhikevich type silicon neuron circuit*
Y. Nagamatsu, K. Aihara, T. Kohno (The University of Tokyo, Japan)

OS4-2 *A digital spiking silicon neural network*
T. Nakayama, Y. Katori, K. Aihara, T. Kohno (The University of Tokyo, Japan)

OS4-3 *Failure of pseudo-periodic surrogates*
M. Shiro, Y. Hirata, K. Aihara (The University of Tokyo, Japan)

OS4-4 *Estimation of excess entropy from spike trains*
H. Motoyoshi, Y. Katori, and H. Suzuki (The University of Tokyo, Japan)

OS4-5 *Synchronized brain activity changes related to perceptual alternations*
K. Iwayama (The University of Tokyo, Hokuriku Innovation Cluster for Health Science, Japan)
K. Takahashi (The University of Tokyo, JSPS Research Fellow, Japan)
K. Watanabe (The University of Tokyo, Hokuriku Innovation Cluster for Health Science, Japan)
Y. Hirata, K. Aihara, H. Suzuki (The University of Tokyo, Japan)

10:30~11:45 OS24 Real time methods for structural change detection of ongoing time series data
Chair: T. Hattori (Kagawa University, Japan)
Co-Chair: H. Kawano (NTT Advanced Technology, Japan)

OS24-1 *Structural change point detection by sequential probability ratio test and Chow test*
T. Hattori, K. Takeda (Kagawa University, Japan)
T. Izumi (Micro Technica Co.,Ltd, Japan)
H. Kawano (NTT Advanced Technology, Japan）

OS24-2 *Extended SPRT for structural change detection of time series based on multiple regression model*
T. Hattori, K. Takeda (Kagawa University, Japan)
T. Izumi (Micro Technica Co.,Ltd, Japan)
H. Kawano (NTT Advanced Technology, Japan）

OS24-3 *Application of SPRT to image data sequence for remote monitoring system*
K. Takeda, T. Hattori (Kagawa University, Japan)
T. Izumi (Micro Technica Co.,Ltd, Japan)
H. Kawano (NTT Advanced Technology, Japan）
S. Masuda (C Micro Co., Ltd., Japan)

OS24-4 *Early structural change detection as an optimal stopping problem (I)*
-Formulation using dynamic programming with action cost
T. Hattori, K. Takeda (Kagawa University, Japan)
T. Izumi (Micro Technica Co.,Ltd, Japan)
H. Kawano (NTT Advanced Technology, Japan）

OS24-5 *Early structural change detection as an optimal stopping problem (II)*
-Solution theorem and its proof using reduction to absurdity
H. Kawano (NTT Advanced Technology, Japan）
T. Hattori, K. Takeda (Kagawa University, Japan)
T. Izumi (Micro Technica Co.,Ltd, Japan)

12:40~13:40 GS5 Control technique Ⅰ
Chair: M. Oya (Kyushu Institute of Technology, Japan)

GS5-1 *Lateral control of an UCT(Unmanned Container Transporter) using ultrasonic satellite system and system identification* (withdrawal)
H.G. Park, S.M. Yoon 1, K.S. Lee, S.Y. Kim (Pusan National University, Korea)
M.H. Lee (Pusan National University, Korea)

GS5-2 *Autonomous load-balancing data transmission scheme to multiple sinks for long-term operation of wireless sensor networks*
K. Matsumoto, A. Utani, H. Yamamoto (Tokyo City University, Japan)

GS5-3 *Robust ride comfort control of vehicles without measurements of tire deflection*
K. Okumura (Department of Fukuoka Industrial Technology Center, Japan)
M. Oya (Kyushu Institute of Technology, Japan)
H. Wada (Shin-Nippon Nondestructive Inspection Co., Japan)

GS5-4 *Specification and real-time control of robotic manufacturing systems based on concurrent process modeling*
G. Yasuda (Nagasaki Institute of Applied Science, Japan)

14:15~16:00 GS16 Neural networks
Chair: T. Kondo (Tokushima University, Japan)

GS16-1 *Learning algorithm of the revised RBF network and its application to the media art system*
C. Kondo (Keio University, Japan)
T. Kondo (Tokushima University, Japan)

GS16-2 *Feedback GMDH-type neural network algorithm and its application to medical image analysis of cancer of the liver*
C. Kondo (Keio University, Japan)
T. Kondo (Tokushima University, Japan)

GS16-3 *Improvement of a neural network based motion generator with bimanual coordination for upper limb prosthesis*
E. Inohira, H. Yokoi (Kyushu Institute of Technology, Japan)

GS16-4 *Midpoint-validation algorithm for support vector machine classification*
H. Tamura, S. Yamashita, K. Tanno (University of Miyazaki, Japan)

GS16-5 *An analog-digital circuit for sound localization based on the biological auditory system*
T. Tomibe, K. Nishio (Tsuyama National College of Technology, Japan)

GS16-6 *Artificial neural networks paddy field classifier using spatiotemporal remote sensing data*
T. Yamaguchi, K. Kishida, E. Nunohiro, J.G. Park, Kenneth J. Mackin, K. Hara,
K. Matsushita, I. Harada (Tokyo University of Information Sciences, Japan)

GS16-7 *Transformation of neural network weight trajectories on 2D plane for learning type neural network direct controller*
T. Yamada (Ibaraki University, Japan)

Room B

8:40~10:10 OS23 Bio-inspired theory and application
Chair: I. Yoshihara (University of Miyazaki, Japan)
Co-Chair: M. Yasunaga (University of Tsukuba, Japan)

OS23-1 *Study upon cooperative optimization problem between two humans by mutual tracking*
Y. Hayashi (Tohoku Institute of Technology, Japan)
Y. Tamura (Tohoku Gakuin University, Japan)
F. Ishida (Toyama National College of Technology, Japan)
K. Sugawara (Tohoku Gakuin University, Japan)
Y. Sawada (Tohoku Institute of Technology, Japan)

OS23-2 *A study on the behavior of a few ant workers*
K. Sugawara, M. Yuki (Tohoku Gakuin University, Japan)
Y. Hayashi (Tohoku Institute of Technology, Japan)
T. Kikuchi, K. Tsuji (University of the Ryukyus, Japan)

OS23-3 *Estimation of average hitting time in genetic algorithms by Markov chain*
Q-L. Ma, Y-A. Zhang, M. Sakamoto, H. Furutani (University of Miyazaki, Japan)

OS23-4 *Quest for genetic information hidden behind disorder in DNA sequences*
Y. Koyama, K. Nishimuta, K. Yamamori, I. Yoshihara (University of Miyazaki, Japan)
M. Yasunaga (University of Tsukuba, Japan)

OS23-5 *Development of a novel crossover of hybrid genetic algorithms for large-scale traveling salesman problems*
M. Kuroda, K. Yamamori (University of Miyazaki, Japan)
M. Munetomo (Hokkaido University, Japan)
M. Yasunaga (University of Tsukuba, Japan)
I. Yoshihara (University of Miyazaki, Japan)

OS23-6 *Signal integrity improvement method and its robustness evaluation for VLSI and VLSI-packaging*
M. Ishiguro, H. Nakayama, Y. Shimauchi, N. Aibe, Y. Yamaguchi (University of Tsukuba, Japan)
I. Yoshihara (University of Miyazaki, Japan)
M. Yasunaga (University of Tsukuba, Japan)

10:30~11:45 OS12 Bio-symphony
Chair: K. Naitoh (Waseda University, Japan)
Co-Chair: T. Ohira (SONY CSL Inc., Japan)

OS12-1 *Onto-biology: clarifying also spatiotemporal structure*
K. Naitoh (Waseda University, Japan)

OS12-2 *Morphogenetic-cycle model: Clarifying several stages of embryo, brain, lung, and heart*
A. Suzuki, K Naitoh (Waseda University, Japan)

OS12-3 *Inner-asymmetry and outer-symmetry underlying life*
K. Ogata, K Naitoh (Waseda University, Japan)

OS12-4 *Entrainment of a circadian clock in vitro*
H. Ito (Ochanomizu University, Japan)
T. Yoshida, Y. Murayama, M. Nakajima, T. Kondo (Nagoya University, Japan)

OS12-5 *Delay, Noise and Resonance: Human balancing and temporal non-locality*
Toru Ohira (SONY CSL Inc., Japan)

12:40~13:55 GS15 Multi-agent systems
Chair: S.M. Yang (The University of Suwon, Korea)

GS15-1 *Robots' action control of autonomous decentralized FMS by remorse mind*
H. Yamamoto, K. Ikebuchi, T. Yamada (Gifu University, Japan) **(moved to OS9-7)**

GS15-2 *Improvement of a software estimate efficiency centered PSP practice support system using multiagent techniques*
D. Yamaguchi (Toin University of Yokohama, Japan)
A. Niimi (Future University-Hakodate, Japan)
M. Takahashi (Toin University of Yokohama, Japan)

GS15-3 *A communication protocol based on IR-Space division transceivers for mobile robots*
T. Abe, H. Takai (Hiroshima City University, Japan)
K. Tachibana (Osaka Gakuin University, Japan)

GS15-4 *Intelligent network surveillance system based on ontology*
S.M. Yang (The University of Suwon, Korea)

GS15-5 *A multi-agent-based approach for furniture arrangement*
S. Ono, T. Oshige, S. Nakayama (Kagoshima University, Japan)

14:15~16:00 GS19 Robotics & Bipedal robot
Chair: M. Zhao (Tsinghua University, P. R. China)

GS19-1 *Design of robotic arm's action to imitate the mechanism of an animal's consciousness*
T. Yamasaki, E. Hayashi (Kyushu Institute of Technology, Japan)

GS19-2 *Development of an autonomous-drive personal robot (Self-position correcting by door recognition)*
S. Matsuura, E. Hayashi (Kyusyu Institute of Technology, Japan)

GS19-3 *A user recognition system using a stemma camera*
S. Tanaka, E. Hayashi (Kyusyu Institute of Technology, Japan)

GS19-4 *Design of robotic behavior that imitates animal consciousnesss*
- Development of method for pursuing or escaping from an object -
K. Kurogi, E. Hayashi (Kyusyu Institute of Technology, Japan)

GS19-5 *Recognition and movement in artificial environment with bipedal robot*
N. Ohtsu, N. Abe, K. Tanaka, Y. Tabuchi (Kyusyu Institute of Technology, Japan)

GS19-6 *Estimation of other's sensor patterns based on motion imitation and communication -- Identification of symbolization strategy for sensor by comparative evaluation questions --*
K. Okuno (Sokendai, Japan)
T. Inamura (NII/Sokendai, Japan)

GS19-7 *A walking gait generation using stance-leg actuation*
X. Zhang, M. Zhao (Tsinghua University, P. R. China)

Room C

8:40~10:10 OS5 Control and automata
Chair: M. Kono (University of Miyazaki, Japan)
Co-Chair: M. Yokomichi (University of Miyazaki, Japan)

OS5-1 *Sampled-data models for affine nonlinear systems using a fractional-order hold and their zero dynamics*
M. Nishi, M. Ishitobi (Kumamoto University, Japan)

OS5-2 *Development of 6-DOF force feedback system with pneumatic parallel mechanism*
Y. Hitaka (Kitakyushu National College of Technology, Japan)
Yoshito, Tanaka, Yutaka Tanaka (Hosei University, Japan)
J. Ishii (Kitakyushu National College of Technology, Japan)

OS5-3 *A study of guaranteed cost control of the manipulator with passive revolute joint*
J. Hara, N. Takahashi, J. Kato, O. Sato, M. Kono (University of Miyazaki, Japan)

OS5-4 *Analysis of manipulator in consideration of relative motion between tray and object*
A. Sato (Miyakonojo National College of Technology, Japan)
O. Sato, N. Takahashi, A. Uekubo, M. Kono (University of Miyazaki, Japan)

OS5-5 *Parallel turing machines on four-dimensional input tapes*
T. Ito (Ube National College of Technology, Japan)
M. Sakamoto, A. Taniue, T. Matsukawa (University of Miyazaki, Japan)
Y. Uchida (Ube National College of Technology, Japan)
H. Furutani, Y. Ma, M. Kono (University of Miyazaki, Japan)

OS5-6 *Some properties of four-dimensional parallel turning machines*
Y. Uchida (Ube National College of Technology, Japan)
M. Sakamoto, A. Taniue, R. Katamune (University of Miyazaki, Japan)
T. Ito (Ube National College of Technology, Japan)
H. Furutani, M. Kono (University of Miyazaki, Japan)

10:30~11:45 OS10 Biomimetic machine and robots
Chair: K. Watanabe (Okayama University, Japan)
Co-Chair: K. Izumi (Saga University, Japan)

OS10-1 *Adaptation of robot perception on fuzzy linguistic information by evaluating vocal cues for controlling a robot manipulator*
A.G.B.P. Jayasekara (Saga University, Japan)
K. Watanabe (Okayama University, Japan)
K. Kiguchi, K. Izumi (Saga University, Japan)

OS10-2 *Stick-slip motion control for an orthogonal-type robot*
F. Nagata, T. Mizobuchi, S. Tani (Tokyo University of Science, Japan)
T. Hase, Z. Haga (R&D Center, Meiho Co. Ltd., Japan)
K. Watanabe (Okayama University, Japan)
M. K. Habib (American University in Cairo, Egypt)

OS10-3 *Modeling an autonomous underwater vehicle with four-thruster*
Zainah Md. Zain, K. Watanabe, T. Danjo (Okayama University, Japan)
K. Izumi (Saga University, Japan)
I. Nagai (Okayama University, Japan)

OS10-4 *The number of unscented transformations and the effect of noise estimates in an unscented kalman filtering problem*
Saifudin bin Razali, K. Watanabe, S. Maeyama (Okayama University, Japan)
K. Izumi (SagaUniversity, Japan)

OS10-5 *Research on movements in formation of multiple mobile robots*
T. Kato, K. Watanabe, S. Maeyama (Okayama University, Japan)

12:40~13:55 GS17 Robotics Ⅰ
Chair: S. Sagara (Kyushu Institute of Technology, Japan)

GS17-1 *Development of variable stiffness joint drive module and experimental results of joint angle control*
J. Kobayashi (Kyushu Institute of Technology, Japan)
K. Okumura, Y. Watanabe (FITC, Japan)
N. Suzuki (Mitsuwa, Japan)

GS17-*2 Digital RAC with disturbance observer for underwater vehicle-manipulator systems*
S. Sagara, T. Yatoh, T. Shimozawa (Kyushu Institute of Technology, Japan)

GS17-*3 Development of an autonomous-drive personal robot "An object recognition system using image processing and an LRS"*
Y. Kibe, E. Hayashi (K.I.T., Japan)

GS17-4 *Path planning algorithm using the values clustered by k-means*
W.S. Kang, S.H. Lee, B. Abibullaev, J.W.Kim, J.N. An (DGIST, Korea)

GS17-5 *Homing navigation with image matching approach*
J.W. Lee, D.E. Kim (Yonsei University, Korea)

14:15~15:45 OS26 Artificial application & Artificial and green technology Ⅱ
Chair: D.H. Kim (Hanbat National University, Korea)

OS26-1 *Online-based therapeutic services for individuals who are searching for new challenges in life*
J.H. Lim (Daegu cyber university, Korea)
H.W. Yoon (Gachon university of medicine and science, Korea)

OS26-2 *Multimodal context-awareness system for automated monitoring-control* **(withdrawal)**
S.D. Park, H.K. Chang, B.M. Jang, B.H. Kim, E.J. Choi (Hannam Univ., UBNC Co. Ltd, Korea)

OS26-3 *The design of GHG(Greenhouse Gas) reduction control system*
Y.S. Choi, S.K. Cha, K.J. Cheon, H.C. Kim (Comesta, Inc. Korea)

OS26-4 *Analysis of soil cement characteristics using recycled fine aggregates for landfill* **(withdrawal)**
Y.M. Kim (Hanbat National University, Korea)

OS26-5 *Design of LCL filter for renewable energy sources using bacterial foraging optimization*
D.H. Kim (Hanbat National University, Korea)
J.H. Cho (Chungbuk National University Korea)

OS26-6 *Semantic query processing based on SQL*
H.C. Lee, H.S. Hwang (WonKwang University, Korea)

Room D
8:40~10:10 GS22 Virtual reality
Chair: T. Yamada (Gifu University, Japan)

GS22-1 *Detection of volume data of aortic tissues based on three dimensional domain growing*
T. Tokuyasu, T. Shuto, K. Yufu (Oita National College of Technology, Japan)
N. Abe (Kyushu Institute of Technology, Japan)
S. Kanao, A. Marui (Kyoto University, Japan)
M. Komeda (Nagoya Heart Center, Japan)

GS22-2 *Autonomous walking with use of quadruped virtual robot*
K. Miyoshi, N. Abe, Y. Tabuchi (Kyusyu Institute of Technology, Japan)
H. Taki (Wakayama University, Japan)
Shoujie He (VuCOMP, USA)

GS22-3 *Construction of the head model for the operation simulation system targets the brain aneurysm*
T. Miyagi, N. Abe (Kyushu Institute of Technology, Japan)
Y. Kinoshita (Munakata Suikokai General Hospital, Japan)
T. Tokuyasu (Oita National College of Technology, Japan)
H. Taki (Wakayama University, Japan),
Shoujie He(VuCOMP, USA)

GS22-4 *The construction of remote communication system between haptic-devices*
Y. Uchida, N. Abe (Kyushu Institute of Technology, Japan)
Y. Kinoshita (Munakata Suikoukai General Hosputal, Japan)
H. Taki (Wakayama University, Japan)
T. Tokuyasu (Oita National College of Technology, Japan)
Shoujie He(Vu COMP,USA)

GS22-5 *Construction of virtual dense elastic object from medical image data and deformation with haptic device*
H. Takada, N. Abe (Kyushu Institute of Technology, Japan)
Y. Kinoshita (Munakata Suikokai General Hospital, Japan)
H. Taki (Wakayama University, Japan)
T. Tokuyasu (Oita National College of Technology, Japan),
Shoujie He (VuCOMP, USA)

GS22-6 *Stability analysis of 3D grasps by considering curvatures and torsions of contact geometry*
T. Yamada (Gifu University, Japan)
T. Taki (Nagoya Institute of Technology)
M. Yamada (Nagoya Institute of Technology)
Y. Funahashi (Chukyo University)
H. Yamamoto (Gifu Univesity)

10:30~11:45 GS9 Human-machine cooperative systems
Chair: A. Nakamura (AIST, Japan)

GS9-1 *Real time interpolation of haptic information using case base*
T. Toki, H. Taki, H. Miura, N. Matsuda, M. Soga (Wakayama University, Japan)
N. Abe (Kyushu Institute of Technology, Japan)

GS9-2 *Recovery technique from classified errors in skill-based manipulation*
A. Nakamura, Y. Kawai (AIST, Japan)

GS9-3 *Development of an inheritance assist system for experienced operation skill by using a haptic function of PHANToM*
T. Tokuyasu, K. Yufu, T. Shuto (Oita National College of Technology, Japan)
N. Abe (Kyushu Institute of Technology, Japan)
A. Marui (Kyoto University, Japan)

GS9-4 *Automatic detection of pedestrians from stereo camera images*
K. Inumaru, J-K Tan, S. Ishikawa (Kyushu Institute of Technology, Japan)
T. Morie (Kyushu Institute of Technology)

GS9-5 *Human behavior analysis with optical flow and median-filtered temporal motion segmentation method*
Md. Atiqur Rahman Ahad, J.K. Tan, H. Kim, S. Ishikawa (Kyushu Institute of Technology, Japan)

12:40~13:25 GS6 Control technique Ⅱ
Chair: H. H. Lee (Waseda University)

GS6-1 *A method using same light sensor for detecting multiple events on window in home intruding crime*
A. Yamawaki,T. Katakami,Y. Kitazono,S. Serikawa (Kyushu Institute of Technology, Fukuoka, Japan)

GS6-*2 A learning control of unused energy power generation*
S. Shikasho, J.S. Shin, C-Y. Cui, H.H. Lee (Waseda University, Japan)

GS6-*3 Design optimization of switched reluctance motor torque controller in electric vehicles*
Y. Zhu, D. Wang, G. Zhao, D. Yang, M. Xin (Harbin Institute of Technology, China)
T. Ito (Ube National College of Technology, Japan)

14:15~15:45 OS6 Computer vision and robotics
Chair: Y. Yoshitomi (Kyoto Prefectural University, Japan)
Co-Chair:O. Sato (Miyakonojo National College of Technology, Japan)

OS6-1 *An improvement of MSEPF for visual tracking*
Y. Nakagama , M. Yokomichi (Miyazaki University, Japan)

OS6-2 *A system for synchronizing nods of a CG character and a human using thermal Image processing and moving average model*
R. Kato, Y. Yoshitomi, T. Asada, M. Tabuse (Kyoto Prefectural University, Japan)

OS6-3 *Quadruped walking with parallel link legs*
T. Yaginuma, E. Shimizu, M. Ito (Tokyo University of Marine Science and Technology, Japan)
J. Tahara (Japan Agency for Marine-Earth Science and Technology, Japan)
T. Takesima (Tokyo University of Marine Science and Technology, Japan)

OS6-4 *Development of under water use humanoid robot*
Y. Li, E. Shimizu, M. Ito (Tokyo University of Marine Science and Technology, Japan)

OS6-5 *Improvement of underwater vehicle remote control environment with parallel link operation base*
K. Inabe, E. Shimizu, M. Ito (Tokyo University of Marine Science and Technology, Japan)
J. Tahara (Japan Agency for Marine-Earth Science and Technology, Japan)

OS6-6 *Spinning control of basketball with robot fingers*
Y. Ohtake, M. Ito, F. Zhang (Tokyo University of Marine Science and Technology, Japan)

From Dream to Reality: Snake-like, Spider-like Robots

Shigeo HIROSE, Makoto MORI, Ryuichi HODOSHIMA
Tokyo Institute of Technology, Tokyo, JAPAN,hirose@mes.titech.ac.jp

Abstract

In this paper, we introduce two types of robots started to develop from the inspiration of the motion of wild life and at the same time aiming at practical applications. One is a snake-like robot. Variable motion of the snake-like robots is introduced and demonstrated their motion by the constructed mechanical model ACM-R3. Another is spider-like walking robot. Design of the construction walking machine which can move around on the steep slope is discussed and demonstrated the feasibility of the concept by the constructing TITAN XI, seven ton quadruped waking machine.

1. Introduction

The acquisition of useful knowledge in engineering from studying living things is not necessarily easy. Movements and shapes, etc., of living things are determined by a large number of factors. To extract the contributions of desired factors from their large-scale system requires not only careful observations but also carefully planned experiments. Even should the contributions be clarified, direct engineering application is often difficult because the constitutive elements of living things such as the muscular and neural systems differ greatly from engineering elements which can be utilized by man. However, the biological inspiration is very variable and they sometimes visualize us brand new type of the machines.
In this paper, we introduce two types of robots started to develop from the inspiration of the motion of wild life and at the same time aiming at practical applications. One is a snake-like robot and another is spider-like walking robot.

2. Snake-like robot

2.1. Research on biomechanisms of snakes

We have been developing snake-like robot since 1972 as **Figure 1** and try to make the machine practical for many applications. We called the snake-like machine, having a slender code-like body with active bending function as "Active Cord Mechanism (ACM)". The feature of the ACM or snake-like machine is versatility. The body of snake can be an "arm" when it holding something by coiling the body around the object, it can be a "leg" when it makes creeping motion and it can be a "trunk" when it moves from brunch to brunch. It is surprising that the very simple slender body of the snake can be transferred to perform such versatile motions. The feature of the snake-like robots will be said as follows:

1. The snake can propel itself over very uneven, rough ground, or along winding paths by using its slender body,
2. It is adapted to moving over places where the surface is not firm, such as marshland or sand dunes, because it can distribute its weight over its whole body,

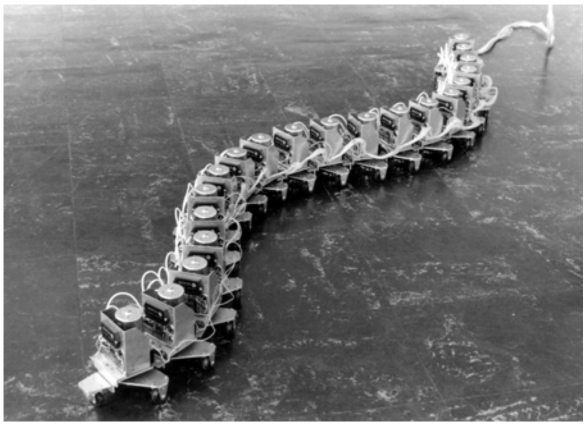

Figure 1: *ACM prototype model(1972)*

3. Because it normally propels itself in a kinematically stable posture, it is adapted to achieve stable movement on irregular terrain, such as spanning rifts or in trees.

These are the characteristics derived from the specific feature of the snake's slender and active body. When we regard the characteristics of the ACM from the engineering viewpoint, we can add following features:

4. Because its body is formed from compartmentalized sections, it has a high level of redundancy and can thus form a highly reliable

system. For example, once a section is broken, all we have to do is to separate the broken section and the rest of the system will work. We can separate the body into several independent sections, and they can perform different tasks individually if necessary. In short it has the feature of the essence of a decentralized system.

5. Between the joints make bending movements only, and endless rotational movements is not used. For this reason, improvements in airtightness are possible, and in addition, the fact that creeping propulsion movements are highly efficient in water offers the possibility of an amphibious mobile body.

From the above, we can think of the ACM's mode of movement as having the special characteristic of being well adapted to rough ground. From research on the ACM's movement function, we can anticipate the development of a new shape of 'off-the-road vehicle', that can propel over all types of natural and artificial environment on earth.

Until now, the engineering applications have been examined taking these functions as manipulator and locomotor's mechanism [1]. The engineering analysis was especially carried out on creeping propulsion by the snake. It was clear that the creeping propulsion was based on the ratio of friction between the trunk direction and the direction that is orthogonal to it by the course. It can be said that this is similar to skating, and it has been proposed as "glide propulsion". Such propulsion has been realized in the mechanical models ACM-III and ACM-R1 [2]. Moreover the next mechanical model ACM-R2 was meant to add a new degree of freedom in the pitch direction at each node, and to construct an ACM that realizes three-dimensional and various functions [3]. Snake-like robots are also studied around the world, such as Poly Bot (Mark Yim et al.) [4], Sewer Robot (K. –U. Scholl et al.) [5], GMD-SNAKE2 (Bernhard Klaassen et al.) [6], snake robot by Kevin J. Dowling [7] and so on[12][13].

Active Cord Mechanisms are useful for disaster relief such as searching for survivors of earthquakes through the debris of collapsed houses. With possibilities to approach these issues in mind, we developed the new Active Cord Mechanism "ACM-R3" (**Figure 2**) to be used easily by snake-like robotics researchers in several applications [8][10].

In this paper, the various move methods realized by 3-dimensional ACM are divided into three kinds, and are introduced. One is movement by which a Shift control system and one are generated by the Rolling control system, and another is generated by those compositions.

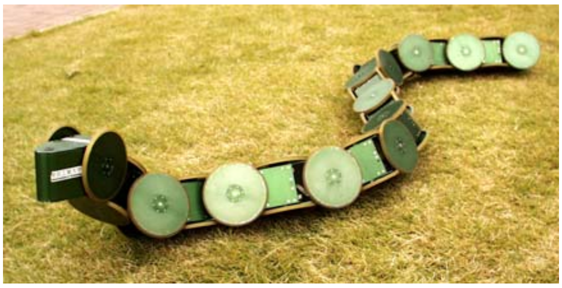

Figure 2: *ACM-R3-21 unit model*

2.2. Shift-control Category

2.2.1. Serpentine

Two-dimensional Serpentine Locomotion has already been realized (**Figure 3**). ACM-R3 can go ahead and backward according to the shape in the continuous curve of body (s-axis) by transiting an angle using only the yaw angle joints. It also can control its speed, and steer itself by adding a bias to the angle order.

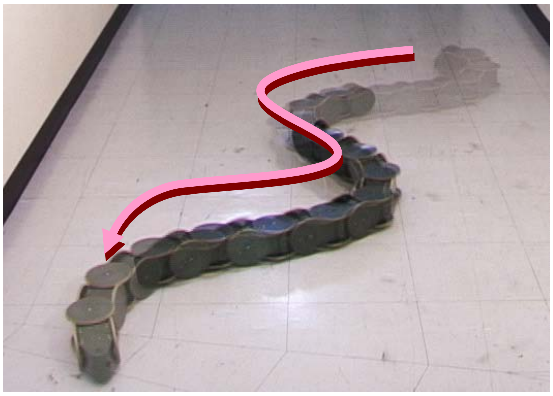

Figure 3: *Serpentine movement*

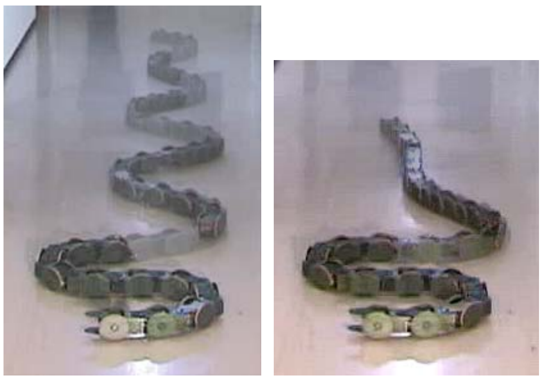

Figure 4: *change winding angle*

In this mode the winding angle alpha can be changed to the maximum of 97.4 degrees continuously. It can also be steered if the sum of bias angle and alpha angle is within the limit of 61.2 degrees for every joint. **Figure 4** shows ACM-R3 moving with the alpha angle changing continuously.

2.2.2. Sinus-Lifting

When a snake winds and progresses, it floats and oscillates both ends in the air, because they work as frictional resistance. We call this three-dimensional motion as Sinus-lifting [1]. This motion can be realized by the composition of the horizontal serpenoid curve around the yaw axis and the sagittal serpenoid curve from the bending angle around the pitch axis. The ratio of the wave length of serpenoid curves in the horizontal and the sagittal plane is 1:2.This body-shaped curve raises the body at the extremities and supports itself at the center of the horizontal serpenoid curve [9]. ACM-R3 realizes this motion as shown in **Figure 5**.

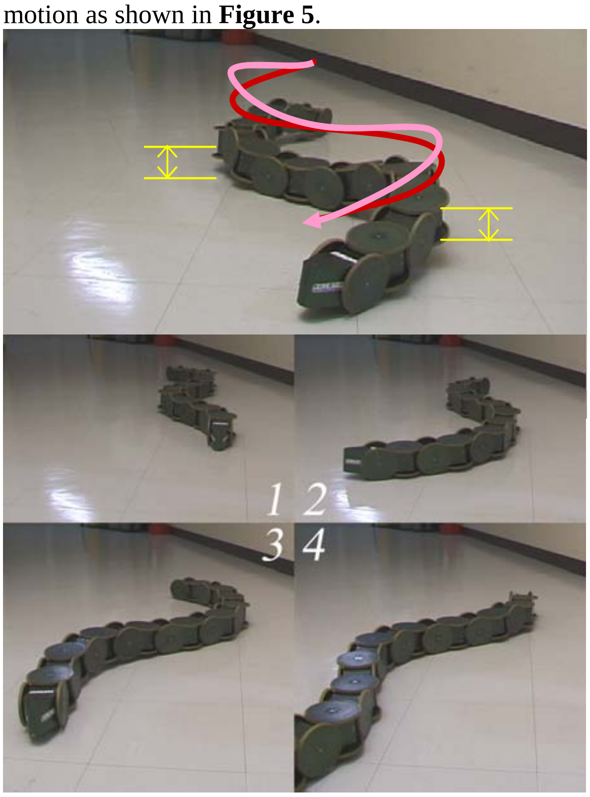

Figure 5: *Sinus-lifting*

The main advantages when performing this motion with a snake-like robot such as ACM-R3 are the following.
Firstly, in this method there are fewer units generating impelling force and touching the ground. This is especially effective when creeping on a slippery floor, so that wheels with a higher concentrated will not slip so easily.
In addition, when moving on a surface with high friction, dispersion of the model as a difference from a theoretical value causes binding force from the ground, and generates large resistance forces. If two-dimensional serpentine locomotion is carried out on such rough surfaces, large resistance occurs, and there are cases when the mechanism cannot move. By reducing the grounding portion sharply, these resistances can be minimized.

2.2.3. Pedal Wave

The locomotion of "pedal wave" without stretching also can be realized. A serpenoid curve is generated in the perpendicular direction of the s-axis, and it makes slow progress in the main direction by sending a wave, as shown in **Figure 6**, and **Figure 7**. However, only the grounding passive wheels are removed in order not to slip. It was also verified that it could steer by bending the joints of yaw axis.

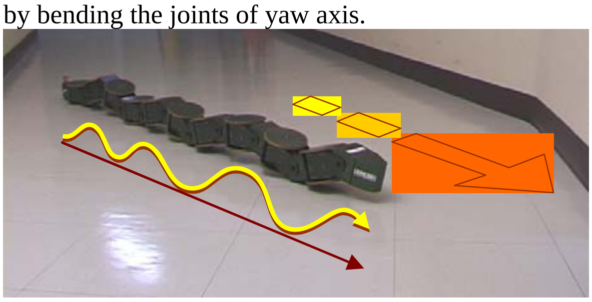

Figure 6: *Pedal Wave*

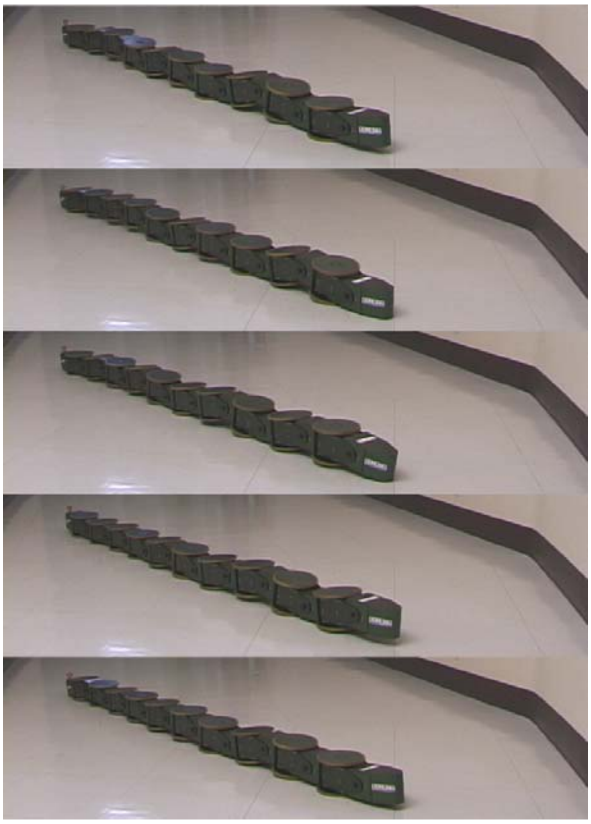

Figure 7: *Pedal Wave sequence*

2.2.4. Side-Winding

The snake which lives in a desert performs the Side-Winding locomotion as a method of moving. This locomotion carries the body to move for side direction by shift control. The projection form to a run plane is mostly in agreement with the usual serpentine promotion, so it can apply the control formula of serpentine locomotion about yaw axes control. On the other hand, it is necessary to adjust perpendicular direction so that it may ground for every cycle. To apply basic angle control of pitch axes to same cycle sine-curve makes this form.

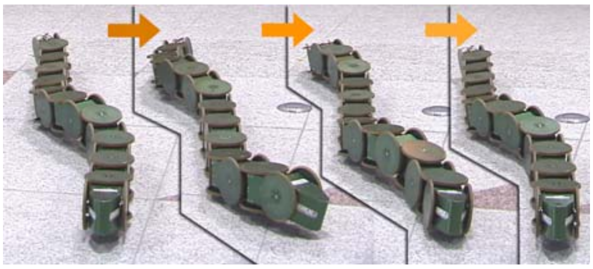

Figure 8: *Sinus-lifting*

In this locomotion with continuous sine-curve angle control, the body-line may ground with curve. Unless it generates the waveform of two or more cycles to whole length, it puts grounding mark only to one point and cannot carry out stable movement. Furthermore, it has the feature which is easy to cause rocking along with a grounding curved surface like the state of the Lateral-Rolling promotion under below-mentioned Sinus-Lifting locomotion.

The above problem affects a dispersion problem greatly in the system to which the number of paragraphs is restricted. Applying the waveform of about four cycles to the system can also realize Side-Winding. However, as a cycle is increased, promotion distance also becomes small and the influence of dispersion also becomes quite larger. If the intermittent state of straight line form is wedged whenever it generates Side-Winding by one cycle, it will become unnecessary to suppress rocking, and to become possible to stabilize and ground, and for the number of cycles to full length to be also two or more cycles. It checked that it could stabilize and move also with the system by this method.

Although the friction coefficient to sidewall was theoretically movable satisfactory even if it was uniformly high, also in the experiment which attached the passive wheel for glide promotion (also setting in the state with few friction coefficients of the direction of a trunk axis), it checked that the direction movement of the side was possible as **figure 8**.

2.2.5. Spiral Swimming Locomotion

Fundamentally, in shift control, since it promotes by crookedness, application can be done also to underwater movement. The ACM for underwater type "HELIX" is already developed, and it proved experimentally that underwater movement can be performed using the generation formula of the spiral form which is the special solution of a Side-Winding formula [11].

Figure 9: *Spiral locomotion(HELIX)*

2.3. Rolling-control Category

The snake-like robot makes its s-axis to be curved on the ground plane, rotates in a bending direction around the s-axis, and then rolls at the lateral direction.

2.3.1. Basically Lateral Rolling (arch type)

In conventional research, experiments are mainly conducted with simple circle forms in which the point of inflection does not exist. For an Active Cord Mechanisms that is able to bend along its s-axis, it is also possible to make a part of the body bended and to move in this way. This is an effective motion method for when some joints break down. There is little load

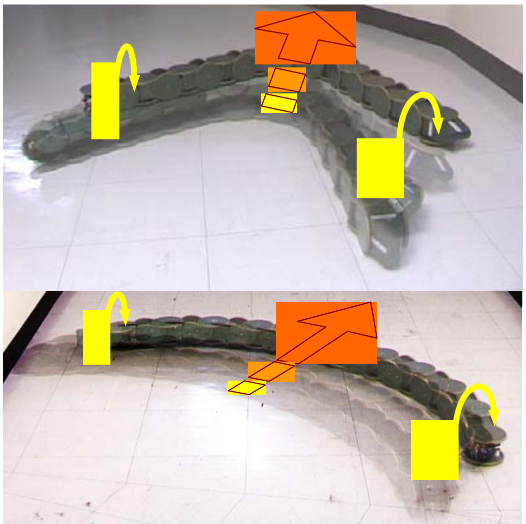

Figure 10: *Lateral Rolling*

in each joint, since the whole bended body is used. Both shapes have been realized by ACM-R3, as shown in **Figure 10**. Since the units rotate at right angles to the rotating direction of the passive wheels, they actually do not depend on attached wheels to perform this motion.

2.3.2. Lateral Rolling (winding type)

In the previous method, motion toward the inner side of the s-axis bended body is more stable than toward outside. For this reason, in movement on a slope, if an inner side is turned to the bottom of the slope, it can always perform stable movements. If bending angle is enlarged, its stability increases. However, rotating a straight body or a body bended in a single curvature are not the only options. It is possible to perform Lateral Rolling in the posture (in the shape "S" character) to which the point of inflection exists in the bended s-axis. When the general serpentine movement, which has one cycle assigned to the total length, is considered, the center of gravity is always located in the center position of the wave axis. Besides, in the waveform posture in any arbitrary phase generated in such state, experiments confirmed that Lateral Rolling movement to the direction of the side is possible, as shown in **Figure 11**. If it has only bending portion touched to a run plane steadily, it can advance with Lateral Rolling movement.

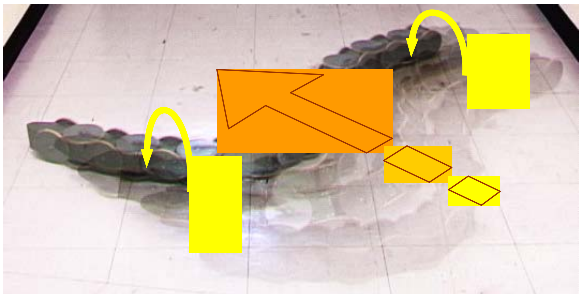

Figure 11: *S-character like Lateral Rolling*

2.3.3. Lateral-Walking

The above-mentioned Lateral-Rolling is movement produced with the posture relation of the curve and run side which a trunk axis should imitate by performing rotation centering on a space curve held. However, since it has limited width unlike a space curve, though the system is in not a curve but a straight line state, it has static stability. The grounding paragraph has the 43mm stable domain also for ACM-R3 used for the experiment in the main subject at the maximum in the trunk axis radius direction. If the center of gravity has been settled in a static stable margin domain to every angle of the circumference of a trunk axis, a trunk paragraph will begin static walking in the direction contrary to the advance direction of original Lateral-Rolling locomotion, without rotating to a run plane (**figure.12**). Suppose that this movement is called Lateral-Walking.

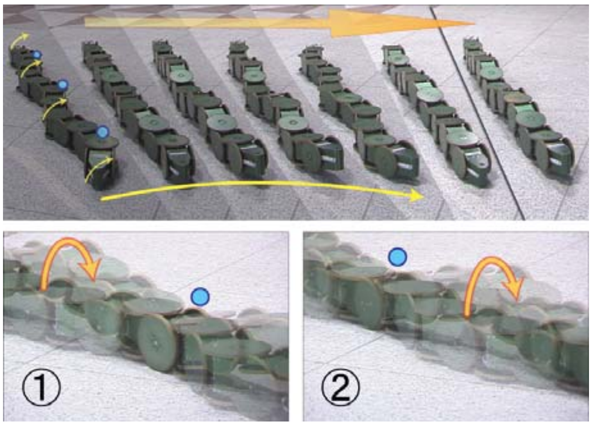

Figure 12: *Lateral Walking*

Unlike the usual Lateral-Rolling, the feature of this moving method is in what "grounding point keeps still" like Side-Winding promotion. In order that the above-mentioned Lateral-Rolling movement may progress with rotational movement to the ground like a wheel, it is needed to all the directions of the circumference of a trunk axis for grounding to be possible. Therefore, in a brittle run side like the sands, the trouble of the promotion accompanying decline in movement efficiency or run side collapse may happen.
Lateral-Walking does not almost have the posture change under movement, and a grounding portion is not accompanied by rotational movement, either. If it is the system which has grounding capability in the one direction of the circumference of a trunk axis, it is realizable promotion movement.
However, promotion speed becomes remarkably slow compared with the usual Lateral-Rolling. If both sides compare by movement of one cycle, although perimeter distance part promotion is possible at the maximum in Lateral-Rolling, it can promote only to stable domain width at the maximum in Lateral-Walking.

2.4. Mixture Category

2.4.1. Lean Serpentine

The posture of ACM-R3 in the above-mentioned "S" character-like Lateral Rolling is exactly the same as the posture in two-dimensional Serpentine locomotion. Therefore, it is possible to start Lateral Rolling operation from any position while in Serpentine form.
In addition, since ACM-R3 has all the body covered by passive wheels, the friction ratio required for glide propulsion can be obtained in the direction of s-axis to

every side. So, if ACM-R3 started performing Lateral Rolling from Serpentine movement, it means that Serpentine movement can be resumed by the mechanism at any time (even after rotating a certain angle), as shown in **Figure 13**.
Therefore, if "Serpentine Locomotion", which moves in the direction of s-axis, and "Lateral Rolling", which is propelled in the perpendicular direction of s-axis, are compounded, the new proposed method "Lean Serpentine (Serpentine Locomotion in Leaned Posture)" is realizable, as shown in **Figure 13**.

This locomotion differs from the usual Serpentine method in the fact that both pitch and yaw axes are coupled at an arbitrary rate. Although there is a difference in the effectiveness of this propulsion method, the great advantage is that omni-directional motion is possible. With this feature, ACM-R3 can also perform in narrow spaces.

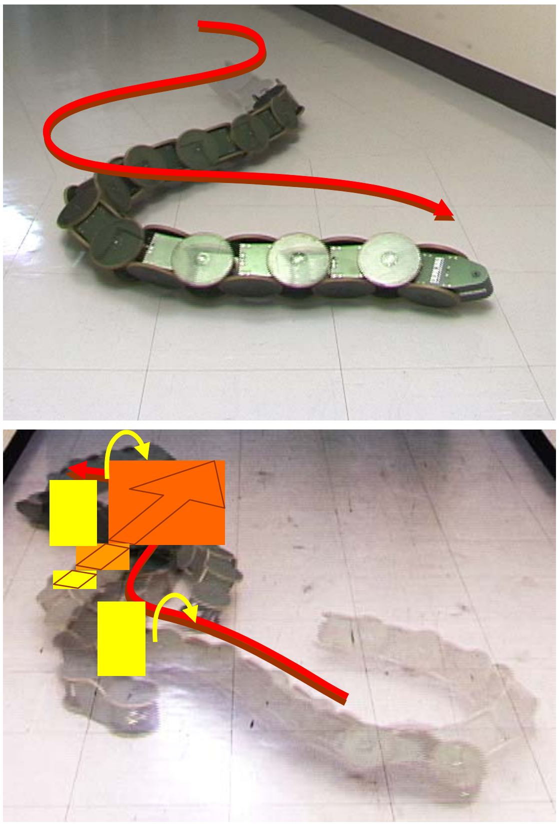

Figure 13: *Serpentine Locomotion in leaned*

2.4.2. Lean Sinus-Lifting

The same idea of Lean Serpentine is applied to Sinus-lifting. By combining Sinus-lifting and Lateral rolling, a new motion mode is obtained, called Lean Sinus-lifting (Sinus-lifting locomotion in leaning). In this method, the same effects of Lean Serpentine are obtained, such as omni-directional movement.(**Figure 14,15**).

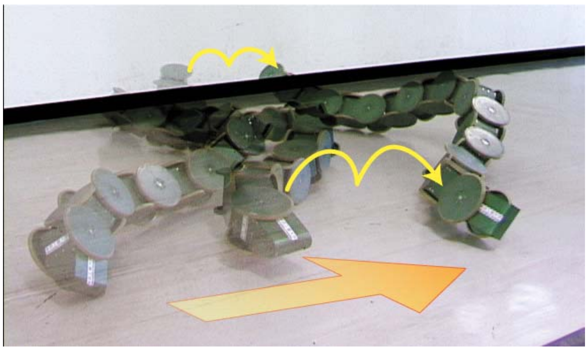

Figure 14: *Sinus-Lift Rolling*

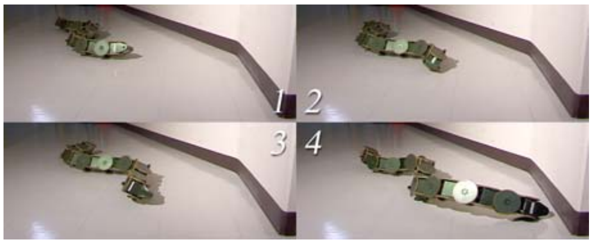

Figure 15: *Sinus-lifting in leaning*

2.4.3. Lift Rolling

If Sinus-Lifting posture is inverted, only the points of maximum amplitude touch the ground (**Figure 16**). This propulsion method can reduce useless friction, so that wheels are grounded in the state perpendicular to the advance direction and grounding points decrease on the whole. In other words, it gives an effect of moving on the ground similar to vehicles. (It can be realized without wheels around the body, though.)

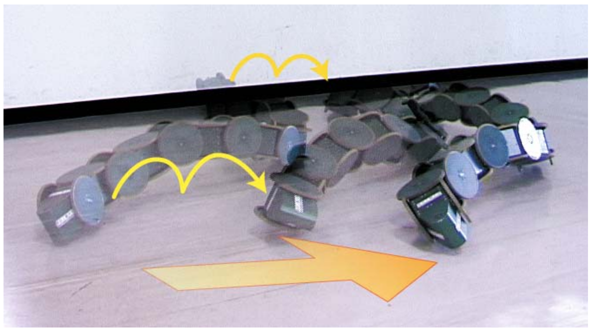

Figure 16: *Lift Rolling*

3. Spider-like robot

3.1. Research on walking machines

We have been working on walking machine research since 1976. In general, walking machines are not practical. Its mechanism usually weights too much because more numbers of actuators are required to drive system of the multi DOF legs than the wheeled or crawler vehicle and commercially available actuators are bulky and heavy. However, the foot of walking machines contacts the ground with discrete points and the contact points can be arbitrary selected according to the terrain condition, walking machines have such special characteristics:

1) Walking machines can move stably over a rugged terrain, and can pass over fragile objects on the ground without touching them.

2) Walking machines can change the direction of motion without slipping even if the sole contacts the ground with a large area.

3) The legs can be utilized not only for motion, but also rest. At standstill posture, the legs become outriggers to hold the upper body stable even on an uneven ground. The upper body can be actively driven while the feet are fixed to the ground.

In addition, the legs that are insect-type like a spider has the following characteristics:

4) It provides high stability during both walking and working, as the legs are sprawled.

5) It can provide a wide movable range for the legs on the ground, which facilitates terrain-adaptive walking.

So, by carefully selecting the applications, walking machines will be used in practical situations.

We believe that optimum numbers of the leg are four which is the minimum number for walking machines to walk statically stably. The number of the leg should be as small as possible because this reduces the number of the actuators, and total body weight decreases. So we have been mainly studying on mechanisms, gait control, sensor system of quadruped walking machines.

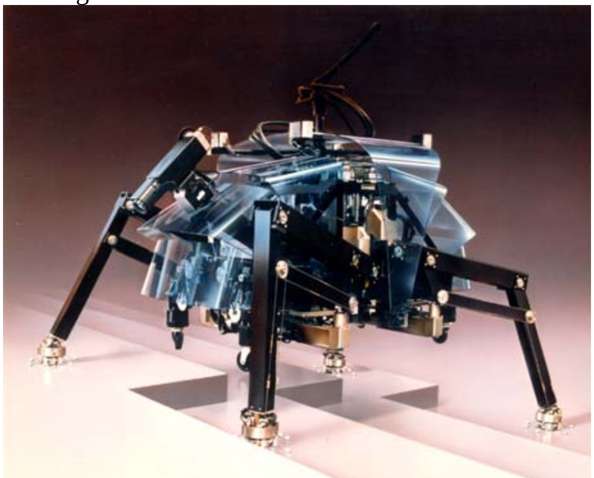

Figure 17: TITAN IV on staircase

A typical example of a quadruped walking machines, TITAN IV [14] is shown **Figure.17**. TITAN IV was exhibited at the science exhibition of Tsukuba in 1985.

It has made straight and turning walking on a stage with three steps for half a year (**Figure.17**). It has walked, in total, about 40 km. On sole of the feet are installed whisker sensors which identify the ground contact conditions and detects the obstacles such as the step of staircase. The body of the machine is maintained horizontal by using inclination sensors.

3.2. Walking machine for steep slope operation

We have been developing a quadruped walking robot for steep slope operation [15].

In Japan, many slopes are being reinforced in order to construct road or railway in sites surrounded by mountains. These slopes need to have concrete frames installed and anchor/rock bolts inserted, and these works are performed by man. However they are large-scale works and the conventional methods are inefficient and consume too much money and time. In addition, they are very dangerous because the workers may fall down. From this background, the automation of some steps is required.

Figure.18: Conventional mechanized construction method on slopes

Construction machines with wheels or crawlers that drill holes for inserting rock bolts have already been developed and this construction method is called "Non-scaffold construction method", as shown in the left picture of **Figure.18**. This construction method should be better than the conventional method, but these machines have difficulties in working on such an environment. The workspace of the wheeled machines is limited because of rugged terrain and crawler machines have possibilities of destroying concrete frames.

Taking a different approach, we have already pointed out the advantages of a quadruped walking robot supported by tethers for this kind of works, such as stable motion on rugged terrain and motion on the slope without damaging the obstacles [16].

So, we decided to develop a practical quadruped walking robot for steep slope operation, TITAN XI, which is intended for practical use, in order to improve existing construction methods.

TITAN XI shall perform the following three operations:

1. Transfer from the ground to the slope.
2. Walk on the slope with concrete frames and transport the drilling machine to the work site.

3. Control the posture of the drilling machine using the legs and perform drilling to install rock bolts.

The operation on slopes using TITAN XI shall be performed according to the following procedure, as shown in **Figure.19**.

1. Transported by the truck to the vicinity of the site.
2. Use auxiliary crawlers to descend from the truck and travel on the level terrain to get close to the slope.
3. Switch to walking when the robot is near the slope and transfer from the ground to the slope.
4. Walk on the slope to transport the drilling machine to the work site (mainly crossings of concrete frames).
5. Control the posture of the drilling machine using the legs and perform drilling.
6. Repeat 4 and 5.

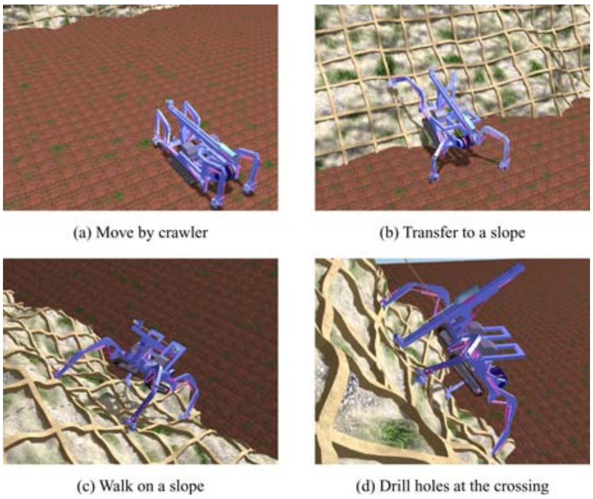

Figure.19: Construction steps

To perform such works, TITAN XI is composed mainly of the following mechanism elements (**Figure.20**):

1. A box-shaped body of 2.2×3.4×0.2 [m]
2. 4 legs of the same characteristics
3. Auxiliary traveling crawlers to travel on the level terrain
4. Two winches to rewind auxiliary tow wire
5. A drilling machine
6. An engine-lift to keep the engine in a horizontal position.
7.

Based on the discussion above, we manufactured a prototype of TITAN XI, as shown in **Figure.21**. The specifications are shown in **Table.1**.

Figure.21: TITAN XI

To confirm the performance of TITAN XI, we have conducted the basic experiment of walking (**Figure.22**), tether system (**Figure.23**).

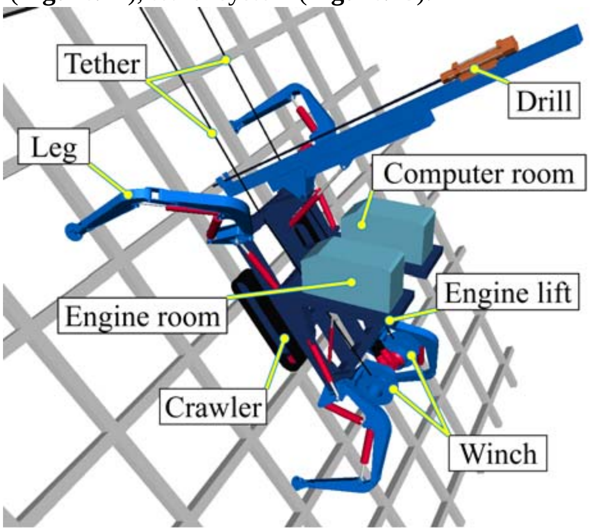

Figure.20: Concept of TITAN XI

Table.1: Specification of TITAN XI

Size [m]	4.8 x 5.0 x 2.0
Mass [kg]	7,000
Power [kW]	41.9

Figure.22: Snapshots of standard gait of TITAN XI.

Figure.23: Walking with tether on slope

As shown above, mechanism of TITAN XI was completed. However, there are still several technical challenges for practical application. They include:

1. Measure the slope and make the map using the optical system, and realize terrain-adaptive gait using the map information.
2. Travel from the level terrain to the slope.
3. Walk on the slope and transport the drilling machine to the work site (mainly crossings of concrete frames).
4. Control the posture of the drilling machine by using the multi DOFs legs and conduct drilling experiment.

We will examine these technical challenges soon and repeat experiments to build a machine for practical use.

4. Conclusion

We introduced two biologically inspired robots that we have developed. These robots will be used in wide application in the near future.

Snake-like robots can go in the narrow space like the interspaces of rock, rubble, pipes. So they will be used in rescue operation, or the inspection device inside the machines.

Spider-like robots can move on the rugged terrain like the rocky ground, construction site, staircases. So they will be used in off-road vehicle, robot for agriculture and forestly, vehicle for the construction works, and humanitarian demining robots.

Reference

[1] [1] Shigeo Hirose, Biologically Inspired Robots (Snake-like Locomotor and Manipulator), Oxford University Press, 1987.

[2] [2] G. Endo, K. Togawa, and S. Hirose, "Study on self-contained and Terrain Adaptive Active Cord Mechanism", Proc. of the IROS, pp1399-1405, 1999.

[3] [3] K. Togawa, M. Mori, and S. Hirose "Study on Three-dimensional Active Cord Mechanism: Development of ACM-R2", Proc. of the IROS, pp2242-2247, 2000.

[4] [4] Mark Yim et al. "PolyBot:a Modullar Reconfigurable Robot", Proc. of the ICRA, pp.514-520, 2000.

[5] [5] K.-U.Scholl et al. "Controlling a Multijoint Robot for Autonomous Sewer Inspection", Proc. of the ICRA, pp.1701-1706, 2000

[6] [6] Bernhard Klaassen et al. "GMD-SNAKE2:A Snake-Like Robot Driven by Wheels and a Method for Motion Control", Proc. of the ICRA, pp.3014-3019, 1999.

[7] [7] Kevin Dowling "Limbless Locomotion: Learning to Crawl", Proc. of the ICRA, pp.3001- 3006, 1999.

[8] [8] M.Mori, and S.Hirose "Development of Active Cord Mechanism ACM-R3 with Agile 3D mobility", Proc. of the IROS, pp1552-1557, 2001.

[9] [9] H. Ohno and S. Hirose, " Design of Slim Slime Robot and its Gait of Locomotion", Proc. of the IROS, pp707-715, 2001.

[10] [10] M.Mori, and S.Hirose "Three-dimensional serpentine motion and lateral rolling by Active Cord Mechanism ACM-R3", Proc. of the IROS, pp829-834, 2002.

[11] [11] T.Takayama, and S.Hirose "Amphibious 3D Active Cord Mechanism HELIX with Helical Swimming Motion", Proc. of the IROS, pp775-780, 2002.

[12] [12] T.Kamegawa, H,Matsuno, at el., "Development of the Sequentially Connected Multiple-unit Rescue Robot (KOHGA)", The 21nd Annual Conference of the Robotics Society of Japan, 2003, 1L14

[13] [13] R.Sasaki, S.Ma, K.Inoue, "Development of a 3-D Snake-like Robot based on 3-DOF Joints", The 21st Annual Conference of the Robotics Society of Japan, 2003, 1L12

[14] Shigeo Hirose, "A study of design and control of a quadruped walking vehicle," Int. J. Robotics Research, vol.3, no.2, pp.113-133, 1984.

[15] Ryuichi Hodoshima, Takahiro Doi, Yasushi Fukuda, Shigeo Hirose, "Development of TITAN XI: a QuadrupedWalking Robot to Work on Slopes - Design of system and mechanism," Proc. Int. Conf. on Intelligent Robots and Systems, Sendai, Japan, pp.792-797, 2004.

[16] Shigeo Hirose, Kan Yoneda and Hideyuki Tsukagoshi, "TITAN VII: Quadruped Walking and Manipulating Robot on a Steep Slope," Proc. Int. Conf. on Robotics and Automation, Albuquerque, New Mexico, pp.494-500, 1997

Extreme Events in Human Society: The Xevents Observatory and Simulator

John L. Casti
International Institute for Applied Systems Analysis
and
The Kenos Circle
Vienna, Austria

In this plenary talk, I discuss extreme events (Xevents) created by humans, not nature. These include things like terrorist attacks, pandemics, political revolutions and financial system meltdowns. The talk explores the types of methodological tools needed to develop early-warning signals for such events—and what to do with such signals once they are obtained. We also present the outlines for a new research venture at IIASA, involving an Xevents "observatory" for development of methodology and an Xevents "simulator" to serve as a laboratory for both testing of tools, as well as identification of Xevents that have never before occurred.

Keywords: Extreme events; agent-based simulation; extreme events methodology

1. Xevents in Nature and in Life

Consider the following events:

- A virulent strain of the avian virus jumps to humans in Hong Kong, sweeps across Asia, and ends up killing more than fifty million people.
- A magnitude 8 earthquake centered on the Ginza in Tokyo kills two million people outright, with property damage mounting into the trillions.
- Bees around the world begin dying off in massive numbers, interfering with pollination of plants worldwide, precipitating a global food shortage.
- An asteroid ten kilometers wide crashes into the Atlantic Ocean, setting off a tsunami that destroys all life on Earth.
- Iranian terrorists set off a nuclear weapon in Times Square during rush hour, leveling much of Manhattan, killing a half a million people, and permanently reducing New York City to rubble.
- A tanker car carrying chlorine derails in Rio de Janeiro, spilling its content and killing more than five million Cariocas.

This list could be carried on almost indefinitely. The point is that surprising events capable of killing millions, if not hundreds of millions, of humans happen. Moreover, even without huge loss of lives, capital stock is decimated, setting back development worldwide for decades. Not a single one of the items on the foregoing list is impossible. And, in fact, some of them like an asteroid impact or the spill of a deadly chemical have already happened—many times!

Each of these events is what has come to be called recently an "extreme" event, or *Xevent* for short. These are events generally seen as deadly surprises whose likelihood is difficult to estimate, and that can turn society upside-down in a few years, perhaps even minutes. Xevents come in both the "natural" and "human-caused" variety. The asteroid strike illustrates the former, while a terrorist-inspired nuclear blast serves nicely for the latter.

But what really qualifies as an Xevent, anyway? I don't think a consensus has emerged on the question. But two factors are certainly part of the answer: (1) an Xevent is rare, something outside everyday experience, and (2) the event is capable of causing massive destruction of human life and property. In regard to the first property, if sufficient data on the type of event exists to enable us to apply statistical tools to estimate the likelihood of an Xevent taking place, the distribution describing that likelihood will be one with what are termed "fat tails". The default gaussian distribution so beloved by probabilists and statisticians everywhere simply does not apply to measure how often such events are likely to occur. Xevents are a lot more frequent than the normal distribution would lead us to believe.

Evolutionary biologists and geophysicists have noted that many long-term processes are ultimately driven by the Xevents. For instance, the theory of "punctuated" equilibrium in evolutionary biology argues that most of the time evolution isn't doing much of anything. Then along comes an Xevent, such as the Cambrian explosion about 530 million years ago in which most major groups of complex animals appeared over about 70-80 million years, and the whole system is set off onto an entirely new trajectory. There is evidence suggesting that the same phenomenon applies in the human social domain, as well.

Generally speaking, when we use the term "extreme event" we think of something that's negative or damaging to society, as with the events mentioned above. But this bias stems mostly from the linguistic fact that in everyday speech the word "event" refers to an occurrence that's localized in space and time. In other words, it's something that takes a relatively short period of time and is confined to a limited spatial region. Hurricanes and tornadoes are good examples. They unfold over a few hours and generally affect a limited geographical area. With this interpretation of what's meant by an "event", it's not surprising that almost all Xevents are negative, in that they result in many deaths and/or do great property damage and they do it quickly. But if we abandon such a limited interpretation of what constitutes an event, things begin to look rather different.

The first point to note is that events have a characteristic *unfolding time* (UT), a period that measures the time between the start of the event and when it ends. For some events, like earthquakes, the UT might be just a few minutes or even seconds. For other types of events, such as a war, the UT is more likely to be measured in years. Moreover, events are not necessarily localized in space, either. Something like a financial crisis or a pandemic may well encompass the entire world.

When it comes to the effect of an event on society, we have what might be termed an *impact time* (IT) over which the event's effects can be felt. So, for instance, the IT of an asteroid strike may well be millennia, while the IT of a hurricane like Katrina is probably just a few years.

Putting these two notions together, consider the quantity

$$X = 1 - UT/(UT + IT)$$

This quantity is always between 0 and 1, which is convenient Here are a few examples to illustrate the basic idea of this measure:

- *A Force 5 Hurricane Striking Miami Beach*: Here the *X* is near 1, with a short UT and a much longer IT. So this is an Xevent.
- *A Force 5 Hurricane over the Caribbean Sea*: In this case, $X = 0$, t since the IT is zero (there is no societal impact, at all). Thus, it is not an Xevent, at all.
- *The Post-WWII German "Economic Miracle"*: This event *might* be an Xevent or not, depending on what you mean by the event versus its impact. Is the event the implementation of the Marshall Plan? If so, the UT is around 5 years, while the IT is probably about 25 years. So the $X = 5/6$, which would characterize this as a "moderate" Xevent.
- *The Development of Agriculture*: Best accounts would measure the UT as about 8,000 years ending around 2000bc. In this case, the IT is still taking place, 4,000 years later. Then *X* would then be around 1/3—and growing. I'd characterize this as a "mild" Xevent, one that's developing into a major one.

The last two examples are Xevents that are by no means negative or damaging, but just the opposite. Here we see why the conventional interpretation that an Xevent always refers to something negative is very misleading. If the UT is short, the overwhelming likelihood is that the impact on society will be destructive for the simple reason that it's a lot easier– and quicker–to tear something down than to build it up (2nd Law of Thermodynamics!). So if you insist that the term "event" refers to an action or occurrence very localized in time, you're virtually forced into regarding it as an Xevent that leads to death and destruction, not growth and better life quality.

Of course, there will be problems with almost any measure like *X* in the sense that examples can be cited when everyday common sense says one thing while the measure suggests something else. So I think *X* as defined above should be taken as a kind of 밿ule-of-thumb? a starting point for deeper consideration of any potential Xevent.

2. Fingerprints of Xevents

A careful examination of numerous natural and man-made Xevents turns up a few distinguishing fingerprints of such events. These include

- *Statistical*: If there exists sufficient data to employ extreme event statistics, the distributions for the occurrence and magnitude of an Xevent is generally from a family of probability distributions, like that *(stable) Levy or (stable) Paretian distribution*. These families include the familiar gaussian distribution as a very special case, as the gaussian is the *only* member of the family that has a finite variance. All other members display the fat tail property, which technically means they have an infinite variance. Many Xevents, though, are so rare that we have little, if any, data upon which to bring statistical procedures of any type to bear upon them.

We also note the ubiquity of *power-law* distributions in the world of Xevents. These distributions measure the relationship between the frequency of an event and its magnitude. For instance, an earthquake twice as large is four times as rare. If this pattern holds for earthquakes of all sizes, then the distribution is said to "scale". This means that there is no *typical* size of earthquake in the conventional sense of "size".

It's now known that the distributions of a wide variety of quantities seem to follow the power-law form, at least in their upper tail (Xevents). Scientific interest in power-law relations stems partly from the ease with which certain general classes of mechanisms generate them. The demonstration of a power-law relation in a collection of data can point to specific kinds of mechanisms that might underlie the phenomenon in question, and often suggests a deep connection with other, seemingly unrelated, systems

- *Dynamics:* Systems displaying Xevents live far from equilibrium. This means that system variability and collective effects from the components of the system in interaction are the most important determinants of the behavior of the system.
- *Evolutionary Processes:* As noted earlier, the Xevents shape the direction that the system's evolution takes. Small, incremental changes operate for long periods of time. Then, *wham*, an Xevent takes place and the whole system is shot off onto an entirely different course.
- *More Effect than Cause:* The commonalities of behavior of Xevent systems is focused more on the effect the events have on human life than on the specific cause that gives rise to the event. Deaths from the Xevent are large, financial losses are large, and environmental destruction is large.
- *The Mere Possibility of Disaster or Boom:* In the developing world, the very possibility of disasters, combined with the lack of social safety nets, limits risk taking in the society (i.e., lack of credit due to disaster risk) and appears to be a major contributor to poverty traps. On the other hand, in the developed countries, research and exploration of "possibility space" is likely to lead to new technological innovations that can be expected to lead to an Xevent-generated boom leading to "the next big thing".
- *Policy Response: Society typically* underestimates the chance of an Xevent, even those that are not so unlikely. For example, expenditures on disaster assistance involve investing far more in reacting to disasters than in taking steps to prevent them. Moreover, probabilistic tools are rarely used to support policy decisions involving Xevents.

3. Methodological Issues

Let's now consider a few conceptual issues that serve as a framework for a coherent research program on Xevents.

- ✓ *Anticipation:* Without a doubt, the single most important tool we could develop for dealing with Xevents would be a systematic procedure for early warning of a possible event. As the saying goes, "forewarned is forearmed", and to have a reliable, consistent procedure for anticipating major discontinuities like a financial meltdown or a crash of the Internet would be a huge step toward effectively addressing such crises.
- ✓ *Forecasting:* Some may argue that anticipation and forecasting are the same thing, for all practical purposes. But this is not the case. Anticipation deals with early warning of the *possibility* of an event occurring; forecasting has to do with claims that an event of a certain type and of a certain magnitude will take place at a certain place and time with a given *likelihood*. As noted earlier, the notion of likelihood is a slippery one, especially in the context of Xevents where we have little, or perhaps even no, actual data upon which to base any kind of standard probabilistic forecast. What we need here is more like a

"theory of surprise" than a theory of likelihood.

- ✓ *Trends:* The majority of people operating as "futurists" generally make the following type of forecast: "Tomorrow will be just like today except a little better or a little worse". In short, they are trend followers and simply extrapolate whatever the current trend is into the future. For such people, surprises never occur and trends never change. Strangely, this kind of trend following is almost always *right.* But it's also almost always useless as well, and you certainly shouldn't pay any money to a so-called futurist for this type of forecast. What you should be ready to pay for, though, is information about the *turning points*, those moments in time when the current trend is rolling over and beginning to change. That type of information is golden (and not fool's gold, either). Mathematically, such turning points are called "critical" points and there is a very well developed theory about them in the dynamical systems literature. Oddly, though, that theory has been very little employed for the kind of practical questions about Xevents that concern us here.
- ✓ *Modeling:* Traditional mathematical modeling a la physics will have to give way to what Stephen Wolfram has termed "a new kind of science". This is a science in which computer programs replace mathematical formalisms. The creation of an agent-based modeling (ABM) laboratory for testing hypotheses about Xevents is necessarily an important component of whatever form an Xevents initiative might take, since we require some type of "laboratory" to do controlled, repeatable experiments with systems that we cannot experiment with "in the wild".

To summarize, here's a telegraphic list of the types of methodological foci a possible Xevents research activity might comprise:

- Global catastrophes (including the human-caused variety)
- Early-warning/horizon-scanning systems
- Extreme risk analysis and management procedures
- Surprise, resilience and tipping points
- Methods of forecasting collective social events and behaviors
- Computer simulation and scenario construction as laboratories for studying Xevent
- Development of counterfactual thought experiments in social processes
- Tools for the analysis of the fragility of critical infrastructures

REFERENCES

1. May, R. S. Levin and G. Sugihara. "Ecology for Bankers." *Nature*, Vol. 451, 21 February 2008, 893-895. (Short, provocative report on a meeting organized by the US National Academy of Sciences and the New York Federal Reserve Bank to investigate systemic risk in the global financial system. The article suggests many analogies between ecosystems and financial systems that have yet to be fully explored.)
2. Newman, M., A.-L. Barabasi, and D. Watts, eds. *The Structure and Dynamics of Networks.* Princeton University Press, Princeton, NJ, 2006. (A collection of pivotal articles in network analysis, together with very interesting commentary by the editors.)
3. Albeverio, S, V. Jentsch, and H. Kantz, eds. *Extreme Events in Nature and Society.* Springer, Berlin, 2006.
4. Carlson, J. and J. Doyle. "Complexity and Robustness." *Proc. National Acad. Sci. USA*, Vol. 99, 19 February 2002, 2538-2545. (Overview of the theory of "Highly Optimized Tolerance (HOT)", a theoretical framework showing how networks can be highly structured internally, yet robust and fragile in their external behavior.)
5. Barabasi, A.-L. *Linked.* Perseus Books, Cambridge, MA, 2002. (Popular account of the multiyear odyssey leading to the discovery of the ubiquity of scale-free networks. Along the way, the author provides many insights into why networks are the way they are and not some other way.)

RoboMusic with Modular Playware

Kasper Falkenberg Niels K. Bærendsen Jacob Nielsen Carsten Jessen Henrik Hautop Lund*
Center for Playware, Technical University of Denmark, Kgs. Lyngby, Denmark
* hhl@playware.dtu.dk
www.playware.dk

Abstract
Based on the concepts of RoboMusic and Modular Playware, we developed a system composed of modular playware devices, which allow any user to perform music in a simple, interactive manner. The key features exploited from the Modular Playware approach are modularity, flexibility, and construction, immediate feedback to stimulate engagement, creative exploration of play activities, and in some cases activity design by end-users (e.g. DJ's). We exemplify the approach with the development of 11 rock genres and 6 pop music pieces for modular I-BLOCKS, which are exhibited and in daily use at the Rock Me exhibition and used at several international music events in Japan and USA. A key finding is that the professional music design is essential for the development of primitives in a musical behaviour-based system and this professional aesthetics is necessary for engaging the users in the activity of assembling and coordinating these 'professional' musical primitives. The paper describes, explores and discusses this concept.

Introduction

In recent developments, some research has focussed on the development of modular robotic devices that act as playware. We define *playware* as the use of technology to create the kind of leisure activities we normally label play, i.e. intelligent hardware and software that aims at producing play and playful experiences among users of all ages and of which e.g. computer games are a sub-genre [1, 2].

The aim of the research is to combine robotic systems, artificial intelligence and play culture to produce new products that can be used in play, sports, health, rehabilitation, music, architecture, art and learning. Here, we will focus on how we may be able to combine the modular playware approach [3] with the RoboMusic approach [4] in order to design novel, interactive music products that allow any user to perform and remix music with a professional sound quality.

Modular Playware

In response to the somewhat static nature of much related work, the Modular Playware design approach [3] was developed to lead to flexible, interactive play tools for both sensorimotor and constructive play activities as designed by the end-users themselves. It is our belief that the flexibility obtained through distributed and modular playware holds many advantages for developing engaging play as can be performed with music. The principles for the creation of flexible, modular play tools include the design of playware based upon modularity and flexibility, tangibility and immediate feedback to stimulate engagement, construction and physical movement, end-user activity design and inclusive games design.

In some playware research, for allowing any user to create activity, we find inspiration in *user-guided behaviour-based robotics* (e.g. [5, 6]). This approach was developed and applied to many robotic systems, such as manipulative robotic technologies, mobile and humanoid robots, in order to investigate how non-expert users could develop their own complex robot behaviours within very short time with no prior knowledge to the robot technology. The concept was initially explored with software components, e.g. for RoboCup Junior in 1998 [7], and later extended with hardware components through the robotic building block concept that allowed 'programming by building' [8], which, for instance, allow African school children and African hospitalised children with no a priori knowledge whatsoever about IT, robotics and technology to develop their own electronic artefacts [9, 10]. In the case with such a physical user-guided behaviour-based system, according to the definition [5, 6], each module needs to have a physical expression and should be able to process and communicate with its surrounding environment. The communication with the surrounding environment can be through communication to neighbouring robotic modules and/or through sensing or actuation. The modular system is constructed from many such modules.

We build on the belief that behaviour-based systems can include not only the coordination of primitive behaviours in terms of control units, but also include coordination of primitive behaviours in terms of physical control units. We can imagine a physical module expressing a primitive behaviour. Thereby, the physical organisation of primitive behaviours made by the user will (together with the interaction with the environment) decide the overall behaviour of the system. Hence, in a similar way to the control of robot behaviours by the coordination of primitive behaviours [11, 12], we can imagine the overall behaviour of a robotic artefact to emerge from the coordination of a number of physical robotic modules that each represents a primitive behaviour. Here, we will present such modules for music creation utilising the concept of RoboMusic, expanding the concept to allow music creation through physical construction with music behaviour primitives.

RoboMusic

RoboMusic defines a novel genre of music [4]. In RoboMusic, music is composed using robotic instruments, music is recorded based on playing robotic instruments, and concerts are performed with robotic instruments.

A robot is defined to be a programmable machine that by its interaction with the surrounding environment autonomously can perform a variety of tasks, and its behaviour is different from a computer program by the interaction with the environment through sensors and actuators. Hence, a robotic instrument is programmable instrument that by its interaction with the surrounding through sensors and actuators can be used for playing a variety of music. Through communication, robotic instruments can be used together to orchestra an ensemble. If left untouched by human (or environmental) interaction, the robotic instrument will behave with its own performance composed by the music artist. When a human or other environmental subject interacts with a robotic instrument, the instrument may change performance from its normal autonomous behaviour.

The artistic and technological challenge of the music artist is to compose baseline behaviour of the robotic instruments and compose the behavioural response to interaction by human musicians. The music artist is transformed from a composer of static music tunes to a developer of robot behaviours – behaviours that are expressed by the robotic system as music pieces. Music compositions are transformed from being static to become dynamic; music compositions are transformed from being static nodes to become robotic behaviours.

A RoboMusic concert is performed with robotic instruments, and changes the concept of live concerts by inviting the audience to interact with the band's instruments themselves and thereby guide the live performance of the music themselves. The audience is actively engaged in the performance of the music of their concert, and their interaction with the robotic instruments guides the robotic behaviour and thereby creates a unique live concert performance that change from concert to concert depending on the behaviour of the audience. Each RoboMusic concert is a unique live performance. The music artist has composed the baseline, and the audience is manipulating the robotic instruments to allow the robotic behaviour to change, and thereby the music tune to diverge. For the audience, the concert form has changed from passive listening to active participation in playing the concert.

In RoboMusic, the design challenge is to create primitive robotic behaviours and to coordinate these primitive behaviours in order for the music piece to emerge as the coordination of primitive behaviours. Thereby, a music composition emerge from the way the composer, musicians or audience interact with the robotic instruments that provide the primitive behaviours.

Each robotic instrument is used to trigger a particular primitive behaviour dependent on the interaction with the instrument(s). In RoboMusic, the primitive behaviours can be anything from a volume or a cut-off to a small sequence of tones. The music composer designs the way in which the primitive behaviours that are triggered should interact with each other.

Hence, as is the case when designing behaviour-based robots such as mobile robots (e.g. [11, 12]), the robot designer (in this case the music composer) designs the primitive behaviours and the coordination scheme. And, as is the case with *user-guided behaviour based robotics* [5, 6], if non-expert users (e.g. live concert audience) are supposed to manipulate and become creative with the systems, it is crucial that the designer (music composer) creates primitives on a fairly high abstraction level that allows the non-expert user to understand and have positive feedback from the human-robot interaction within a very short time frame.

For the first RoboMusic concert by Funkstar De Luxe in 2006, instruments used to play the music included interactive tiles that measure touch, rolling pins that measure rotational acceleration, and light&sound

cylinders that measure distance (of a person/hand). Such features as pressure, rotational acceleration and distance were used to trigger primitive behaviours which include variations in resonance, cut-off, volume and pan of musical tracks in the musical composition (see Figure 1 and 2 for the concert set-up).

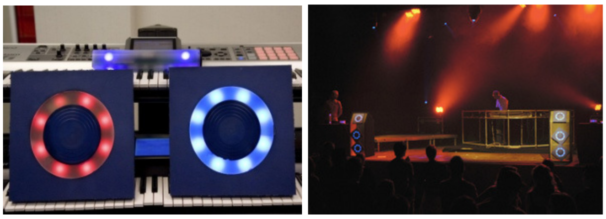

Figure 1. Left: Two Tiles and a RollingPin used as robotic instruments. Right: The RoboMusic live concert set-up, with Funkstar De Luxe and his control station in the center, and the robotic instruments on the left and right side of the stage.

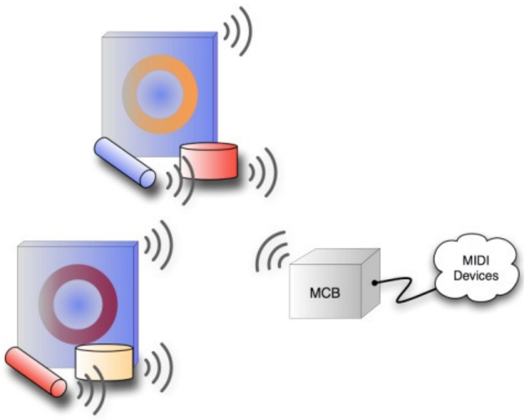

Figure 2. The concert set-up for RoboMusic. In a similar way, we developed the cubes to communicate to a MIDI Control Box (MCB) which is connected to MIDI Device, which in this case is a PC running Ableton Live.

Modular I-BLOCKS for RoboMusic

Using the modular building blocks, I-BLOCKS, as the technologic platform, we create a RoboMusic scenario where a user can experiment freely with music using a set of pre-composed looped musical pieces. The I-BLOCKS is our user-configurable modular robotic platform developed and tested through several prototype and application generations [10, 13, 14, 15]. For the RoboMusic application presented here, the user identifies the functionality and behaviour of the I-BLOCKS through musical feedback when rotating, attaching and detaching the I-BLOCKS (see Figure 3).

Figure 3. Children creating music with the cubic I-BLOCKS.

The current generation I-BLOCKS consists of cubic modules (see Figure 4) that can communicate with each other when physically connected. Each cube can communicate with up to four of its six possible neighbours and is fully self-contained with respect to power, connectors and processing. At the edges of the four communicating sides of a cube are four RGB LEDs, which can light up in many different colours. The I-BLOCKS communicate locally via infrared light, and can be internally expanded to support global wireless radio communication (XBEE) as well, in order to facilitate 'structure to structure' or 'structure to device' communication.

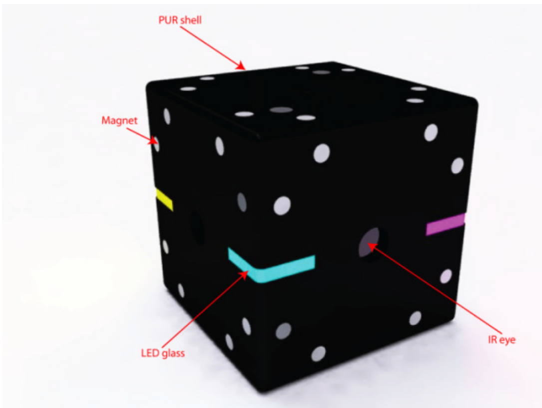

Figure 4. An explained visualization of the I-BLOCK.

Each I-BLOCK makes use of a 3D accelerometer to detect its orientation with respect to gravity. This makes it able to detect, for instance, which side is facing down.

The I-BLOCKS connect to each other's faces using magnets, allowing for uni-sex connection at 90-degree angles. At the electronic centre of each I-BLOCK is the Atmel ATMEGA1280 8-bit microcontroller, which takes care of all processing including peripheral device communications etc. The I-BLOCKS' hardware is encapsulated by black polyurethane (PUR) shell that has a soft rubber-like feel, with hard plastic plate lids in top and bottom in which charge plugs, programming connectors, sensors and actuators are integrated.

The I-BLOCKS are meant as a general platform for exploring physical programming – or "programming by building". The construction with I-BLOCKS results not only in the development of a physical structure, but also in the development of a functionality of that physical structure. This functionality or emergent behaviour is a product of user interaction, the sensor inputs, the actuator outputs, the communication and the processing of the individual I-BLOCKS [15].

Summary of the cubic I-BLOCKS:

- PUR (Polyurethane) Shell (9x9x9 cms)
- Magnetic connectors
- ATmega1280 microcontroller
- 4 communication channels (IR light)
- Opportunity for expansion, e.g. display, XBee or USB and various sensors.
- 4 RGB LEDs
- 3-axis accelerometer

The music created by the user is computed and played back on a PC, using the Ableton Live© music software as a playback unit responding to MIDI messages coming from the I-BLOCKS. In order to allow the I-BLOCKS to "talk MIDI" to a PC we designed and built a socalled "MIDI Box" that converts serial wireless data coming from an XBEE-enabled I-BLOCK into MIDI signals (see Figure 2 and 5). By using wireless technology we allow users to manipulate the I-BLOCKS freely just like conventional building blocks.

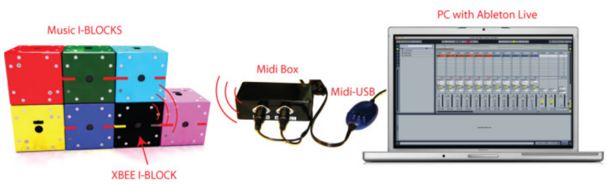

Figure 5. Music setup with I-BLOCKS, MIDI-box and PC.

The pieces of music that was made here were all constructed using these rules: There are five or six predefined instruments or groups of instruments, varying in type according to genre, and within each piece of music there are up to six variations per instrument type, and there can be an unspecified number of different instruments.

In this application each coloured I-BLOCK represents an instrument or group of instruments. The individual I-BLOCKS orientation - which side is facing down - determines the variation of that specific instrument. The I-BLOCK LEDs change colour depending on their orientation, in order to make it possible for the user to remember and activate specific variations.

The musical setup can be seen from Figure 5. Note the black XBEE-enabled I-BLOCK, which communicates wirelessly with the MIDI Box. When instrument blocks are connected to this, music starts playing depending on the actual I-BLOCK's colour and orientation. The music is loop-based, meaning that when active, each variation of each instrument is playing for a certain time and then repeating itself over and over until it is finally deactivated when the user removes the current instrument I-BLOCK from the structure or shifts its orientation.

Music development

In the development of the musical content we chose to make two overall categories of music:

1) Songs that are inspired by and which represent certain historic periods of popular music in order to give the user an insight into a specific style or genre of music.
2) Songs that are made by famous Danish artists and then modified to fit this concept allowing the user to "remix" these songs.

We made 11 different songs representing non-classical music from the 1950's (rockabilly rock 'n' roll) and up untill the 1990's (Grunge). These 11 styles of music are chosen from their ability to show various forms of musical expression both in regard to instrumental and vocal performance as well as in regard to composition, production and recording methods that were used through the last sixty years.

The musical content is composed, arranged and recorded following careful study and analysis of each musical style and its characteristics, making the songs fit into these characteristics as well as possible. We have tried to record each music piece in the same way as the corresponding musical style was originally recorded (e.g. Rockabilly is recorded in mono and with very few microphones in order to create that specific sound). When composing, recording and mixing the music, we have studied the original productions closely. For instance, we have strived to make our Reggae track sound like an original Bob Marley tune but with new melodies and lyrics.

These extraordinary efforts regarding the musical quality was done to ensure that the user experience to interact with music and not with technology. We see the technology used as a means that allows for the any user to gain access to music as a kind of "material", with which the user can mould directly in the authentic, timbral substance [16]. By the use of the modular playware concept contained in the I-BLOCKS, music becomes a physical, moldable object, much like modeling-wax – flexible and manageable in the hands of the user. Because music is so much more than a simple series of notes, the "material" that is put to the user's disposal consequently must comprise the elements, which make up the different musical styles. When manipulating the I-BLOCKS, the user is not altering notes, but all parts of the musical sounds as a musician is doing when playing. It is obvious, we believe, that the musical "material" is composed with the craftsmanship and aesthetical feeling of a skilled musician.

The second part (famous Danish pop songs) is characterized by a modern HiFi music production. The challenge in converting these songs into tracks usable in this musical setup has been to make new drum, guitar, bass, etc. tracks that fit the original tune and at the same time being so diverse and varied that it was possible for the user to create a remix that sounds different without being "untrue" to the original song. The creation of these tracks for allowing appropriate and aesthetical appealing combinations clearly demands professional remix skills.

Recording methods

To record and mix the music we use Logic Pro 8 (multitrack recording software). We record both "real" instruments such as drum, bass, guitars, keyboards and software instruments which emulate e.g. grand pianos, old analog synthesisers, drums etc. In order to recreate music from different periods of time in music history, it is extremely important that the musicians who record the tracks have a deeper understanding of the different styles, which has been build up over years by listening and consciously or unconsciously analyzing the tiny differences in feel and approach towards playing the music. This professional competency is crucial for making the small musical parts (primitives) fit well together (coordinate) to a musical piece of high quality in all the potential combinations.

All songs are made as relatively short loops (16-32 bars) that are made to go on and on until the user chooses to stop the song. In every song there are drums, basses, guitars, keyboards and vocals (there are exceptions for these groups of instruments if a specific style of music e.g. does not have guitars in it). At the end of the recording/mixing process all the files are imported into Ableton Live (version 8.0) – software that is specialized in handling loops. The I-BLOCKS control the tracks in Ableton Live.

Everything has to fit together

There are five I-BLOCKS representing five different instruments (drums, bass, guitar, keyboards and vocals) and one "master" blocks that works as an "on/off button". When the master is connected to one or more of the I-BLOCK instruments, they play a certain figure (melody/rhythm/chords/riff). Every I-BLOCK has six sides. Each side represents one figure. In order to choose another figure, the user simply turns the I-BLOCK. That means that every one of the 30 different tracks which each song has (5*6=30) has to fit each other in every possible combination, and at the same time every figure has to sound good and be interesting to the user if it plays alone. The key to this challenge was to make real quality recordings on every single track and create a certain role for every instrument-group in which one can create very distinguishable figures, which have an explicit response when changing figures. However, at the same time the figures should be created to not making the musical whole too "full" and unclear when all five cubes are on and playing. To make cube responses distinguishable, it also becomes very important to "clean up" excess frequencies, for example so the bottom part of the guitar does not interfere with the bass.

Tests

The RoboMusic concept may provide both a means for everyday users to develop their own musical pieces by coordinating the musical primitives, and a means for professional musicians to perform at concerts with physical, interactive musical objects. The two uses can even be combined by allowing the audience to interact with the musical primitives in professional live performances as interplay with the professional musician(s).

Everyday user play: RockMe

The above-mentioned 11 different songs in the historic category are implemented as the main part of the exhibition "Rock Me" at The Danish Rockmuseum, which is under construction in vicinity of the famous annual rock festival at Roskilde, Denmark, (Europe's oldest and largest rock festival). The exhibition consists of three music stations, two equipped with headphones to allow visitors to explore rock genres in groups of two (see Figure 6), and one equipped with loudspeakers and a stage where visitors can perform for each other.

The main finding from the first half year of the exhibition is that the I-BLOCKS music concept works very well for the visitors, who use them in a relatively short period. The concept is easily understood and grasped, because it is based on the principle of building blocks and because any change in the physical construction results in clear audible changes. In spite of the fact that the connection between building blocks and music is new and unknown to the visitors, they accept this new "material" and immediately start manipulating, building, and experimenting, which to us is an important proof of concept regarding modular playware and physical user interaction. Not surprisingly, the performance opportunity is mainly used by kids and young people, who come in groups, for instance school classes.

Figure 6. Visitors playing music with the cubic I-BLOCKS at the RockMe exhibition, Roskilde, Denmark.

Professional live performance

The cubic I-BLOCKS were used for live RoboMusic performances at a number of occasions. For DJ and dance music, we performed together with Funkstar De Luxe at the Winter Music Conference, Miami, March 2009, which is one of the world's largest DJ and dance music events [17]. For the opening of the RockMe exhibition, a famous Danish pop musician, Simon Kvamm of Nephew, and a famous Danish rap musician, L.O.C., performed a battling session where each of them performed each other's music using the cubes (see Figure 7). Also, live rock music performances were made during the robot festival RoboDays in Odense, Denmark, September 2009, and at Japan Robot Festival in Toyama, Japan, September 2009.

In all live performances, the professional musicians were able to utilise the RoboMusic concept in a natural way with the cubes to make an appropriate live performance. The RoboMusic performances would last only around 30 minutes, and thereby in some cases appear only as a part of a longer concert. The professional musicians seemed to receive a very positive response from the audience. Main challenges for the professional musicians were in all cases (i) to remember that cubes can only connect on four of the six sides (IR communication is only on four sides), (ii) the timing for attaching and detaching cubes at the exact beat timing, and (iii) to know/remember what musical effect results from turning a cube.

Figure 7. Professional pop musician, Simon Kvamm of the Danish pop music group Nephew, performing live with the I-BLOCKS in Roskilde, Denmark, July 2009.

Discussion and Conclusion

The challenge of understanding what musical effect results from interaction is general to the RoboMusic concept, and appears in both everyday user play and professional live performances. This challenge is particular clear with the I-BLOCK cubes, but also general to other RoboMusic instruments. Indeed, transparency of functionality is a general challenge for most tangible interface design, and part of a modular playware design [3]. The mapping between the physical affordances of the objects with the digital components (different kinds of output and feedback) is a design and technological challenge.

This challenge becomes particular evident with the RoboMusic concept in which the user combines three senses to understand the functionality: auditory, visual and touch. Here, the user has to match the visual sense to the auditory result. We believe that there is a lot to learn for tangible interface design from understanding such relationships between different sensory modalities and from understanding the cognitive challenges which are involved.

For the user interaction (e.g. in user-guided behaviour-based systems), the RoboMusic experiments also highlight the challenge of understanding how to design the primitives at the most appropriate granularity level. An interesting research topic appears to be to gain knowledge about whether the same granularity level of primitives is the most appropriate for all user groups, and how the granularity level relates to transparency of functionality. In the case of RoboMusic, it is further necessary to design the primitives (music components), so that the coordination is aesthetical appealing while at the same time the design provides the necessary freedom to the user to become creative. We find it essential to put focus on professional design of primitive behaviours and coordination of primitive behaviours for the specific application field (e.g. music, soccer, physiotherapy, cognitive rehabilitation). In this case of RoboMusic, this is done by the professional music composers who designs the musical tracks (primitives) and tries to ensure that the tracks can mix (coordinate) in an aesthetical appealing form (i.e. the music composer becomes a designer of primitive behaviours for a behaviour-based system [4].)

The RoboMusic concept is general to many different implementations of musical primitives, coordination mechanisms and designs of 'instruments'. Here, we exemplified with the cubic I-BLOCKS as an instance of modular playware for RoboMusic, and the cubic I-BLOCKS showed good potential in a number of informal tests. Whereas this paper by intention provides the general concept description of RoboMusic with modular playware, future publications will report on more formal testing with the cubic I-BLOCKS, and hopefully other researchers may utilise the general concept for investigating other implementations and experiments.

Acknowledgements

The following made valuable contribution to the concept development, experimental set-up and/or tests: Danish Rockmuseum, Poco Piu, Funkstar De Luxe, Center for Playware DTU/DPU.

References

[1] H. H. Lund and C. Jessen. Playware - Intelligent Technology for Childrens play. Technical Report 1, The Maersk Mc-Kinney Moller Institute, SDU, June 2005.

[2] H. H. Lund, T. Klitbo, and C. Jessen. Playware Technology for Physically Activating Play, *Artificial Life and Robotics Journal, 9:4,* 165-174, 2005.

[3] H. H. Lund, and P. Marti. Designing Modular Robotic Playware. In IEEE 18th International Workshop on Robot and Human Interactive Communication (Ro-Man 2009), IEEE Press, 115-121, 2009.

[4] H. H. Lund, and M. Ottesen. RoboMusic – A Behavior-Based Approach, *Artificial Life and Robotics Journal, 12: 1-2*, pp. 18-23, 2008.

[5] H. H. Lund. Modern Artificial Intelligence for Human-Robot Interaction. *Proceedings of the IEEE journal, 92:11*, 1821-1838, 2004

[6] H. H. Lund. *Robots at Play*. ISBN 978-87-992302-0-4, 160 pages, Odense, 2007.

[7] H. H. Lund and L. Pagliarini. RoboCup Jr. with LEGO Mindstorms. In Proceedings of Int. Conf. On Robotics and Automation (ICRA2000), IEEE Press, NJ, 2000.

[8] H. H. Lund, H. H. Intelligent Artefacts. In Sugisaka and Tanaka (eds.) Proceedings of 8th International Symposium on Artificial Life and Robotics, I11-I14, ISAROB, Oita, 2003.

[9] H. H. Lund, and P. Marti. Designing Manipulative Technologies for Children with Different Abilities. *Artificial Life and Robotics Journal, 9:4*, 175-187, 2005.

[10] J. Nielsen, and H. H. Lund. Contextualised Design of African I-BLOCKS, in H. H. Lund et al. (eds.) Proceedings of Fourth IEEE International Workshop on Technology for Education in Developing Countries. IEEE Press, 14-18, 2006.

[11] R. A. Brooks. A robust layered control system for a mobile robot. *IEEE Journal of Robotics and Automation, 2(1):*14--23, 1986.

[12] R. C. Arkin. *Behavior Based Robotics*, MIT Press, Cambridge MA, 1998.

[13] J. Nielsen, and H. H. Lund. Spiking neural building block robot with Hebbian learning, in Proceedings of IEEE International Conference on Intelligent Robots and Systems (IROS2003), 1363-1369, IEEE Press, 2003.

[14] J. Nielsen, and H. H. Lund. Modular robotics as a tool for education and entertainment, *Computers in Human Behavior, 24*, Elsevier, pp. 234-248, 2008.

[15] J. Nielsen, User Configurable Modular Robotics - Control and Use, Ph.D, University of Southern Denmark, Odense, 2008 (http://phd.jacobnielsen.net)

[16] N. K. Bærendsen, C. Jessen, and J. Nielsen. Music-Making and Musical Comprehension with Robotic Building Blocks. In Chang, M., Learning by Playing. Game-based Education System Design and Development. Springer-Verlag, 2009.

[17] Wikipedia – Winter Music Conference. http://en.wikipedia.org/wiki/Winter_Music_Conference (checked: 7/12/2009).

XML-based Genetic Programming Framework: Design Philosophy, Implementation and Applications

Ivan Tanev and Katsunori Shimohara

Department of Information Systems Design,
Faculty of Science and Engineering, Doshisha University,
1-3 Miyakodani, Tatara, Kyotanabe,Kyoto 610-0321, Japan

e-mail: {itanev, kshimoha}@mail.doshisha.ac.jp

Abstract

We present the design philosophy, the implementation and various applications of XML-based genetic programming (GP) framework (XGP). The key feature of XGP is the distinct representation of genetic programs as DOM-parse trees featuring corresponding flat XML-text. XGP contributes to the achievement of (i) fast prototyping of GP by using the standard built-in API of DOM-parsers for manipulating the genetic programs, (ii) human-readability and modifiability of the genetic representations (iii) generic support for the representation of grammar of strongly-typed GP using W3C-standardized XML-schema; and (iv) inherent inter-machine migratability of the text-based genetic representation (i.e., the XML text) in the distributed implementations of GP.

Keywords: genetic programming, strongly-typed genetic programming, genetic representation, XML, DOM.

1 Motivation

Developing controllers of mobile autonomous robots is often performed as a sequence of simulated off-line design (phylogenetic learning) of the robot's software model followed by on-line adaptation (ontogenetic learning) on the physical robot situated in real environment. Justification to incorporate off-line software simulation into the process of robots controller design comes from the facts that verification of robot behavior on physical robots is extremely time consuming and often dangerous for the robot and surrounding environment. These arguments in favor of software simulation of controller as a process, which precedes the physical design and online learning on real robot become even more relevant within the context of recently emerged trends in robotics such as investigating the social behavior, the role and value of communication in emergent coherence, cooperation and collaboration in the robots' societies situated in inherently competitive or cooperative environments. Simulating robot controllers as software agents and focusing on the model of their relevant features is viewed as a promising way to address the above mentioned shortcomings of direct verification of behavior on physical robots.

GP, which we propose as an approach for offline learning implies that the agent's code is automatically designed by computer system via simulated evolution employing selection and survival of the fittest in a way similar to the evolution of species in the nature. While for many tasks handcrafting the agent code can be seen as natural approach, it might be unfeasible for most of real-world problems due to their typically enormous complexity. Moreover, in many problems the challenge is to develop a solution, which is competitive or even better than human-designed one. Such a solution might be well beyond the abilities of human to handcraft it.

The software model of the evolvable robot's controller should fulfill the basic requirements of being adequate, fast running, and quickly developed. Considering the adequacy of the model as beyond the scope of this document, we intend to highlight the issues related to the efficiency of the system (in terms of reduced developing- and execution time) for evolving agent's behavior. The typically slow developing time of GP stems from the highly specific semantics of main attributes of GP (representation, initial population, genetic operations and fitness evaluation) and the lack of generic support to these attributes in 3G algorithmic languages and corresponding software engineering standards. *Developing time* of GP can be significantly reduced incorporating commodity-off-the-shelf software components and standards in software engineering of GP. The *runtime* of GP can be reduced as a cumulative result of reduced computational effort (the amount of individuals that should be processed in order to obtain a solution with specified probability) and increased computational performance (the amount of individuals evaluated per unit of time).

The *objective* of our research is to develop a genetic representation of the evolvable autonomous agents, which based on commodity-off-the-shelf software components and widely adopted industrial standards, would facilitate the achievement of easy and quick development phase of GP and would contribute to the achievement of better computational effort. The long-term aim is to employ such a representation in our research on the emergence and the survival value of social behavior and communication in multi-agent systems.

The remaining of the document is organized as follows. Section 2 introduces GP as algorithmic paradigm for offline learning of behavior of predator agents in predator-prey multi-agent systems (MAS). It also elaborates the proposed approach of representing evolvable agents (genetic programs) as DOM-parsing trees and discusses its design-time and runtime-related implications. Section 3 presents the result of verification of our approach on predator-prey pursuit problem. Conclusion is drawn in Section 4.

2 Approach

2.1 Algorithmic Paradigm

We consider a set of stimulus-response rules as a natural way to model the reactive behavior of autonomous agents which in general can be evolved using artificial neural networks, genetic algorithms, and GP. GP is a domain-independent problem solving approach in which a population of computer programs (individuals) is evolved to solve problems [2]. The simulated evolution in GP is based on the Darwinian principle of reproduction and survival of the fittest. In GP individuals are represented as parsing trees whose nodes are functions, variables or constants. The nodes that have sub-trees are non-terminals - they represent functions where the sub-trees represent the arguments to function of that node. Variables and constants are terminals – they take no arguments and they always are leaves in the parsing tree. The set of terminals for evolving agent's behavior in predator-prey MAS [3] includes the relevant stimuli such as perceptions (e.g. distance and visible angle to various objects in the world), its own state, etc.; and the response (actions) which the agent is able to perform. The most relevant functions (non-terminals) are the arithmetical and logical operators (>, <, =, +, - , etc.), and the `IF-THEN` function, establishing the relationship between certain stimulus and corresponding response. A sample stimulus-response rule is shown in Figure 1. It expresses a reactive behavior of turning to the bearing (angle) of the peer agent (`Peer_a`) plus `10` (degrees) as a result of stimulus of distance to that agent (`Peer_d`) being less than `20` (mm). A parsing tree of rule, depicted in Figure 1 is shown in Figure 2.

```
IF (Peer_d<20) THEN Turn(Peer_a+10)
```

Figure 1. Sample stimulus-response rule governing the agent behavior.

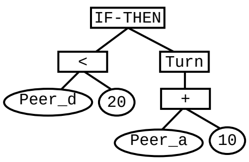

Figure 2. Sample stimulus-response rule represented as a parsing tree in GP.

Parsing-tree representation and its flat equivalents (LISP S-expression, postfix or prefix notations) are typically maintained and manipulated by GP-systems in a customized way. Therefore, an eventual tailoring of the available general purpose GP-systems for the task of evolving autonomous agents would be a time consuming approach. Design of GP-system from scratch would be (if not the only feasible) at least faster and more flexible way, providing that the implementation of main attributes of GP is based on widely adopted industrial standards and off-the-shelf technologies.

2.2 Genetic Representation

Inspired by flexibility and recently emerged widespread adoption of document object model (DOM) and extensible markup language (XML), we propose an approach of representing genetic program as a DOM-parsing tree featuring corresponding flat XML text. Our additional inspiration comes from the fact that despite of the reported use of DOM/XML for representing computer architectures, source codes, and agents' communication languages we are not aware about any attempts to employ this technology for representing evolvable structures such as genetic programs in generic, standard, and portable way. Our approach implies performing genetic operations on DOM-parsing tree using off-the shelf, platform- and language neutral DOM-parsers, and using XML-text representation as a format, feasible for migration among the computational nodes in eventual distributed GP.

The DOM-parsing tree of the sample rule considered earlier (Figure 1) looks in exactly the same way as parsing tree in canonical representation of genetic programs (Figure 2). However the flat representation of the rule is XML (Figure 3), rather than LISP S-expression.

```
<GP>
  <IF-THEN>
    <LE>
      <PERC>Peer_d</PERC>
      <PERC>20</PERC>
    </LE>
    <TURN>
      <PLUS>
        <PERC>Peer_a</PERC>
        <PERC>10</PERC>
      </PLUS>
    </TURN>
  </IF-THEN>
</GP>
```

Figure 3. XML representation of stimulus-response rule in GP.

2.3 Design-time Implications

In contrast to the typical approaches to manipulate parsing trees using custom code and representations, the proposed XML-based genetic programming (XGP) offers benefits of requiring *minimum programming efforts* and allowing developers to use the software platform, developing language, and/or programming paradigm which better fits the aims of concrete implementation of GP. These benefits are result of:

- Use of API of DOM-parsers: parsing tree of genetic program is manipulated using built-in API of DOM-parsers,
- Platform neutrality of parsers: DOM-parsers are available for virtually any of widely used software platforms (e.g., as Java classes), facilitating the portability of GP across different software platforms,
- Language neutrality of parsers: DOM-parsers are also available as language-neutral components (e.g. Microsoft COM), offering the same programming model of parsing trees regardless of the language employed to develop the code of GP that manipulates them, and
- Paradigm neutrality of parsers: DOM-parsers are available for programming paradigms, such as database stored procedures, web-client and web-server-side scripts, etc.

2.4 Run-time Implications

The potential strength of GP to automatically evolve a set of stimulus-response rules featuring arbitrary complexity without the need to a priory specify the extent of such complexity might imply an enormous computational effort caused by the need to discover a huge search space while looking for optimal solution to the problem. A well-known way to limit the search space, and consequently, to reduce the computational effort of GP is to impose a restriction on the syntax of evolved genetic programs based on their a priory known, domain specific semantics. The approach is known as strongly typed genetic programming (STGP) and its advantage over canonical GP in achieving better computational effort is well proven. Our objective is in XGP to realize a generic support of STGP.

Considering the same sample rule as shown in Figure 3, and multimodality of perception information, it is noticeable that all nodes (i.e. both the functions and their operands) are associated with *data types* such as distance (`Peer_d, 20`), angle (`Peer_a, 10`), Boolean (`Peer_d<20`), etc. An eventual arbitrary creation or modification of such genetic program semantically would make little sense: e.g. it is unfeasible to maintain a rule with stimulus-related part featuring arithmetical expression involving operands of different data types (e.g. distance, angle and Booleans) at least because physically they are of different dimensions. In addition, there is clear possibility in maintaining introns if such an expression compares perception variable with constant beyond the range of corresponding sensor (e.g. `Peer_d>1000`, in case that sensor range is `400`). Analogically, the semantics of action `Turn()` implies a parameter of corresponding data type - an angle. However data types are not explicitly specified in considered so far DOM/XML representation of genetic programs in XGP, and consequently, not evident for the routines that create and alter it. To address the issue, in XGP we explicitly introduced the notion of type (in a way similar to STGP) represented as XML-tag for all the entities the genetic programs are composed of. In addition, we established a set of rules (i.e. grammar) describing the allowed relationship between types in semantically meaningful genetic program. Routines that create and alter genetic programs (e.g. creation of initial population and mutation) refer to the type of entity they are going to currently alter and impose the corresponding constraints to the sub-tree structures or values being generated. In crossover only nodes (with corresponding sub-trees) of the same type can be swapped.

In XGP we represent the grammar of STGP as a *XML schema* [1][2], which is an official World Wide Web Consortium (W3C) recommended, standard way to define the relationship among the entities in XML-document (i.e. genetic program). Since the syntax of schema conforms to the XML-standard, the routines those create and alter the parsing tree of genetic program access the schema via API of DOM-parsers in a way, identical to the way of accessing DOM/XML-based representation of genetic program.

We developed a set of formal rules for translating a BNF-defined grammar of STGP into corresponding XML-schema. Without touching the details of such rules, we present the resulting fragment of XML-schema (Figure 4) that corresponds to stimulus-related part of sample rule illustrated in Figure 3. Notice the definition of the sensory abilities – the *morphology* of the agent: the kind of perception information (`Wall_d, Peer_d`) and the range of corresponding sensor (`0..400`). In a similar way XML schema defines the response abilities (actions) of the agents. Considering the communication as response for the speaker and stimulus for listener, the XML-schema offers a generic way to define the *communication abilities* of the agent. The section of XML-representation of strongly typed genetic program created applying the same fragment of XML schema is shown in Figure 5.

```
<xs:complexType name="IF-THEN"><xs:sequence>
  <xs:element name="COND-THEN" type="COND-THEN" />
  <xs:element name="THEN" type="THEN" />
</xs:sequence></xs:complexType>
<xs:complexType name="COND-THEN">
  <xs:choice>
  <xs:element name="COND_TDist" type="COND_TDist" />
  ...
</xs:choice></xs:complexType>
<xs:complexType name="COND_TDist">
  <xs:sequence>
  <xs:element name="VAR_TDist" type="VAR_TDist" />
  <xs:element name="OPER_TDist" type="OPER_TDist" />
  <xs:element name="CONST_TDist" type="CONST_TDist" />
</xs:sequence></xs:complexType>
<xs:simpleType name="VAR_TDist">
  <xs:restriction base="xs:string">
  <xs:enumeration value="Wall_d" />
  <xs:enumeration value="Peer_d" />
</xs:restriction></xs:simpleType>
<xs:simpleType name="OPER_TDist">
  <xs:restriction base="xs:string">
  <xs:enumeration value="GE" />
  <xs:enumeration value="LE" />
</xs:restriction></xs:simpleType>
<xs:simpleType name="CONST_TDist">
  <xs:restriction base="xs:integer">
  <xs:minInclusive value="0" />
  <xs:maxInclusive value="400" />
</xs:restriction></xs:simpleType>
```

Figure 4. XML schema of XGP, defining the grammar corresponding to the stimulus-related part of rule shown in Figure 1 and Figure 2.

```
<GP>
  <IF-THEN>
    <COND-THEN>
      <COND_TDist>
        <VAR_TDist>Peer_d</VAR_TDist>
        <OPER_TDist>LE</OPER_TDist>
        <CONST_TDist>20</CONST_TDist>
      </COND_TDist>
    </COND-THEN>
    <THEN>
    ...
    </THEN>
  </IF-THEN>
</GP>
```

Figure 5. XML-representation of strongly typed genetic program, created applying the fragment of XML schema shown in Figure 4.

3 Verification

In order to verify the feasibility of XGP and its design- and run-time implication we implemented a prototype of GP system for offline phylogenetic learning of agents in predator-prey pursuit problem. The problem comprises four predators (agents) whose goals are to capture a prey by surrounding it on all sides in a world (Figure 6) [3]. XGP runs on Windows OS system and employs Microsoft DOM parser – MSXML4.0. Considering the elaboration of the issues related to the emergence of surrounding behavior as irrelevant to the aims of this document and focusing on the verification of proposed approach as technology for representing genetic programs, we would like to summarize the result as follows:

- Developing the prototype of XGP is significantly alleviated by use of DOM-parser. We measured about few [men x days] of development efforts (without considering the development of user interface), and
- XML schema in XGP offers generic way to impose the semantics constraints of genetic programs represented as DOM-parsing trees. The resulting computational effort for considered instance of predator-prey problem is relatively low and is in order of several thousands evaluations of genetic programs.

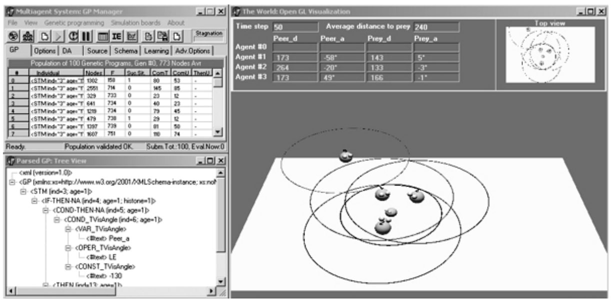

Figure 6. Snapshot of XML, employed for evolution of predator agents in predator-prey MAS

We observed similar design-, and run-rime implications of XGP, also applied for the evolution of snake-like robot (Figure 7) [4], Sony's Aibo quadruped robot (Figure 8), and computer-controlled scale car [5].

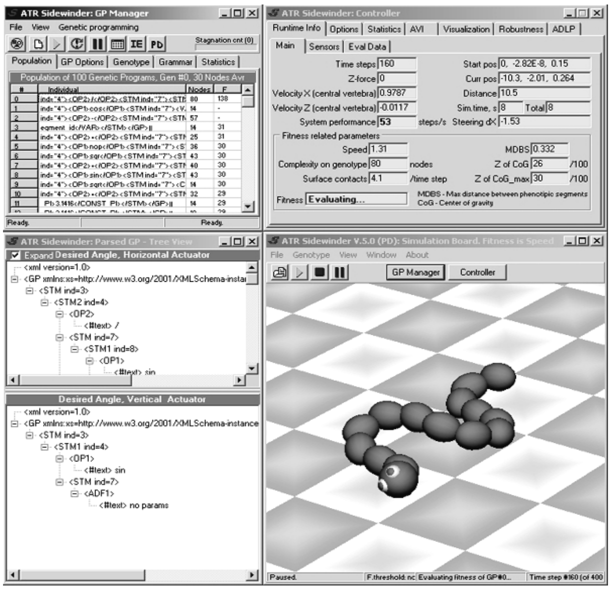

Figure 7. XGP applied for evolution of locomotion gaits of simulated snake-like robot.

4 Conclusion

We presented the result of our work on the role of genetic representation in facilitating quick design of efficiently running offline phylogenetic learning via GP. We proposed an XML-based genetic programming featuring a portable representation of evolvable agents (genetic programs) based on widely adopted DOM/XML standard. The manipulation of genetic programs implies the use of build-in API of off-the-shelf DOM-parsers. The approach features significant reduction of time consumption of usually slow process of software engineering of GP. In addition it offers a generic way to facilitate the reduction of computational effort via limitation of search space of GP by handling of only semantically correct genetic programs. Consistent with the concept of strongly typed GP, an approach of using W3C-recommended standard XML schema is developed as a generic way to represent and impose the grammar rules. The ideas laid in the foundation of the proposed approach are verified on the implementation of genetic programming for evolving social behavior of agents in predator prey pursuit problem. Due to the domain neutrality of GP, the approach can be applied for quick developing of efficiently running GP in various problem domains.

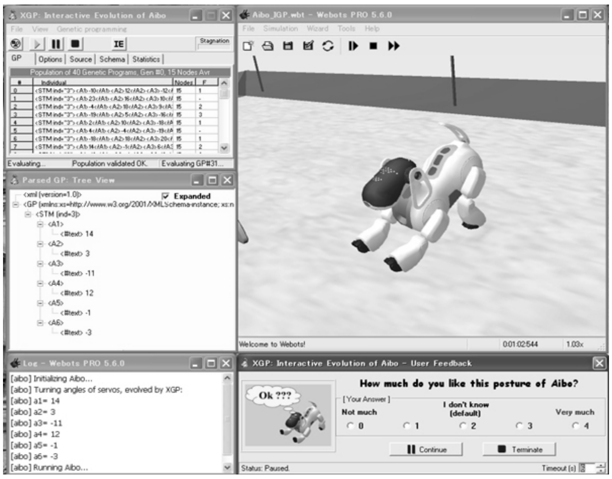

Figure 8. XGP applied for evolution of postures of the model of Sony's Aibo quadruped robot.

References

[1] D.Beech, M.Maloney, N.Mendelsohn, H. Thompson, XML Schema Part 1: Structures. W3C Recommendation, 2001. http://www.w3.org/TR/2001/REC-xmlschema-1-20010502/

[2] J.R.Koza, Genetic Programming: On the Programming of Computers by Means of Natural Selection, Cambridge, MA: MIT Press, 1992.

[3] I. Tanev, M. Brzozowski, and K. Shimohara, Evolution, Generality and Robustness of Emerged Social Behavior in Continuous Predators-prey Pursuit Problem, Genetic Programming and Evolvable Machines, Vol.6, Number 3, 2005, 301-318

[4] I. Tanev, T. Ray, and K. Shimohara, Exploring the Analogy in the Emergent Properties of Locomotion Gaits of Snakebot Adapted to Challenging Terrain and Partial Damage, Journal of ISCI, Vol.19, No.6, 2006, 220-232

[5] I. Tanev, and K. Shimohara, Evolution of Agent, Remotely Operating a Scale Model of a Car through a Latent Video Feedback, Journal of Intelligent Robotic Systems, No.52, Springer, 2008, 263-283

Brain's Doing in Its Resting-State: Default Mode Network as an Inside Story within the Brain

Jian-Qin Liu*and Katsunori Shimohara+

*Kobe Advanced ICT Research Center
National Institute of Information and Communications Technology,
588-2, Iwaoka, Nishi-ku, Kobe, Hyogo 651-2492, Japan
(Tel : 81-78-969-2227; Fax : 81-78-969-3928)
(Email address liu@nict.go.jp)

+Department of Information Systems Design,Faculty of Science and Engineering,
Doshisha University,
1-3 Tatara Miyakodani, Kyotanabe City, 610-0394 Japan
(Tel : 81-0774-65-6973; Fax : 81-0774-65-6801)
(Email address kshimoha@mail.doshisha.ac.jp)

Abstract: As a promising research field after the turn of the new century, Default Mode Network (abbreviated as DMN) of the brain shows the strong potential of a new breakthrough to neuroscience, which emphasizes the baseline of the brain's activities when the brain is awake but without any external input signal to it. This study is highlighted recently and expected to provide keys to understanding the mental disorders. This paper consists of following two sections: (1) A brief tutorial on the DMN is presented with necessary fundamental knowledge of neuroscience on the brain. (2) A framework of network informatics for DMN is proposed based on network dynamics; models of information networks are discussed by bridging the gap between the level of regions and the level of neurons of the brain; and major issues on analyzing the DMN by brain imaging technologies are discussed as well. In a word, one of the inspirations from DMN is how spontaneous collective behavior is emerged within an autonomous system, which is crucial to systematically understand the brain's function and exploring new design principles of autonomous robotics to demonstrate complex life-like behaviors in engineering.

Keywords: Default Mode Network, Neuroscience, Brain's Function**.**

I. INTRODUCTION

As one of most mysterious phenomena, the human's intelligence from the brain is always an important theme for sciences, in which the psychological aspect of the human's behaviors has a relative long history. With the advances in brain imaging technologies such as fMRI, MEG, PET, NIRS, EEG and others, nowadays the images constructed by the signals of the brain's activities with certain degree of the spatial and temporal resolution are obtained. Consequently, it becomes feasible to quantitatively analyze the informatics network mechanism for the brain's function.

It is well known that autonomy exists in the nervous systems such as autonomous sympathetic and parasympathetic nervous systems. In the artificial life community, the brain as a complex system is one of the kernel contents of the study on innovating new core design principles of autonomous robot systems inspired by artificial life, where the informatics network is expected to play an inevitable role.

II. BASIS OF NEUROSCIENCE

1. The Levels of Neuroscience

By means of neuroscience, the brain is studied at the cognitive, functional, (functionally-specified) sub-systems, cellular and molecular level in terms of reductionism. Here the sub-systems refer to those nervous systems such as sensory, motor and regulatory systems.

2. Quantitative Analysis of Neuron Interactions

The quantitative analysis of neuron activities can be carried out at the level of the regions of the brain and used as the reference for modeling the dynamics of the neurons and their interactions. Here one of the methods for modeling the dynamics of neuron activities is the nonlinear differential equations under the condition of the mean field theory. Column-centered model is an important method to bridge the gap between the regions and neurons and shows high efficiency in analyzing the dynamics mechanism of the signaling processes among interacted neurons. In order to understand how the interactions of neurons contribute to the dynamical behavior of the neural signaling leading to systematical modeling of nervous system, systematically modeling for computational neuroscience is necessary and imperative.

3. Integrating Dynamics and Signal Processing

By integrating the methodology of systems biology and principle of computational neuroscience, the neuron interaction mechanism can be inferred by using the correlation degree of the time series signals observed by brain imaging technologies. As an example of quantitative analysis on the above mentioned dynamical signaling process, blind identification is expected to be used to identify the structure the network that consists of the neurons where correlated signaling processes are based on the self-oscillation phenomenon. In order to systematically understanding the underlying dynamics of the interacted neuron activities, the methodology of complex science is helpful when the signaling network of the brain is modeled in terms of complex systems.

4. DMN as an Instance for Brain Science

Default Model Network (abbreviated as DMN) [1~5] is an instance of complex systems. Both in nature and in engineering, various types of complex systems have been observed. In order to explore new information processing paradigm to understand unknown mechanism in brains, it is necessary to know what the brain is doing when it has no input signals when the brain is modeled as a system. This status is the baseline of the brain, which plays an important role on observation and analysis of the brain in nonlinear dynamics. In the eyes of complex systems, DMN provides us important information on the baseline state of the brain, which is a promising field of neuroscience.

II. BASIS OF DEFAULT MODE NETWORK

1. Concept of DMN

Default Mode Network is a network of signals within the brain when the system of the brain has no input. In informatics DMN is formulated as graph in topology $G = <V, E>$ where V is the set of the vertexes and E is the set of the edges. The vertex refers to the location of the regions of the brain, which is known in anatomy. The value of the vertex refers to the signals obtained from brain imaging, e.g., fMRI. The edge refers to the relationship among the vertexes, i.e., the functionally connection and structural interaction among regions. Here, functional connection means that the regions cooperate for certain functions of the brain; structural interaction means that the signals of the nodes located at specific regions of the brain are included in a function in nonlinear dynamics so that some of these signals influence other signals or all of these influence each other. The weight of the edges can be assigned by the value of the functional connectivity measure between the two nodes linked by the edge.

DMN is active under the condition of the resting state of the brain. In order to describe the corresponding dynamics of DMN, a dynamical graph is given as follows: $G = <V, E, Q>$ where Q is a function to describe the dynamics of the signaling process for the variables corresponding to the vertexes. The general form of Q is given as follows:

$$
\begin{aligned}
d/dt\, X_1 &= f_1\,(X_1, X_2, \ldots, X_n)\\
d/dt\, X_2 &= f_2\,(X_1, X_2, \ldots, X_n)\\
&\ldots\\
d/dt\, X_n &= f_n\,(X_1, X_2, \ldots, X_n)
\end{aligned}
$$

where $X_1, X_2, \ldots, X_n$ are the variables that correspond to the vertexes, $f_1(.), f_2(.), \ldots, f_n(.)$ are the functions to describe the underlying dynamics. In computational neuroscience, one of the tasks is to identify these function based on the data of the variables. The information processing mechanism of DMN looks like the operating system of a computer or a network in metaphor. It is clear that the *dynamics* mechanism of DMN is one of the kernel topics in computational neuroscience.

2. Significance of DMN Study in Medicine

One of the direct applications of DMN research may be the medicine although there is still a long way to go, owing to the fact that DMN is related to the states of brains when diseases such as autism, schizophrenia and Alzheimer's disease occur [1].

3. DMN as a Topological Graph

In anatomy, the areas where DMN is located include: vMPFC – Ventral medial prefrontal cortex; PCC/Rsp – posterior cingulated/retosplenial cortex; IPL – Inferior parietal lobule; LTC – Lateral temporal cortex; dMPFC – dorsal medial prefrontal cortex; HF+ Hippocampal formation.

With the reference of the anatomical locations, a topological representation is summarized in [1], which is an undirected graph consisting of *the set of nodes* {IPL(R and L types of IPL), PCC/Rsp, vMPFC, dMPFC(negative), PHC(R,L types of PHC), HF (R and L types of HF), LTC (L and R types of LTC)} *and links* whose length is given according to the correlation measurement. Here dMPFC(negative) refers to that the signal of dMPFC is anti-correlated with the one of the medial temporal lobe subsystem [2]. This topological network shows an interesting feature – the structure of hubs in network structure and sub-systems in system structure.

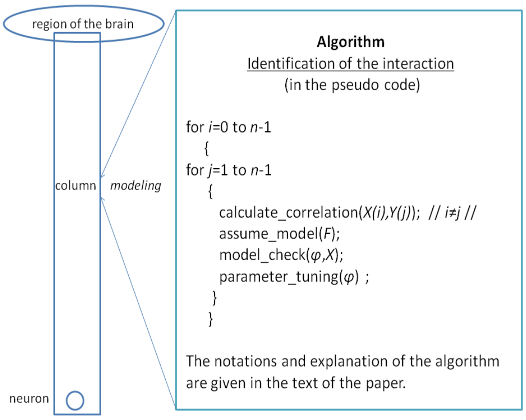

Fig. 1 The Identification Algorithm

III. NETWORK IFNORMATICS FOR DMN

1. Building Blocks of the DMN Dynamics

Multiple nodes and links for interaction among these nodes are the basis for networking. On the nonlinear dynamics, feedforward and feedback are two key factors. The node should be assigned with the signals constrained by nonlinear dynamics. The nonlinear dynamics here should be temporal and/or spatial. Considering an autonomous distributed (decentralized) system that consists of elements of information processing (e.g., agent in autonomous multi-agent systems), the local rules are defined and assigned to the elements, and no central control exists. The interaction among these autonomous components (elements) gives rise to the collective behavior, which reflects the emergence from the network with nonlinear dynamics.

2. The network informatics framework for DMN

The framework of network informatics for DMN is suggested as follows:

(1) The basic data structure for dynamical networks:

We can adopt the representation of dynamical networks as graph in topology and/or dynamical graph to describe the underlying network structure and corresponding dynamics mechanism for the signaling processes.

(2) Discrete Models:

Discrete mathematical models including automata are possible to describe the autonomy of the underlying network under the condition of the abstraction.

(3) Nonlinear Dynamics:

Considering the characteristics of the distributed system where each node is formalized by certain local rules and the interactions among these nodes give rise to the collective behaviors, a generalization of the entire network as a system is necessary. In principle, the ***Generalization*** takes the following form:

$$d/dt[\boldsymbol{X_i(t+1)}] = -\ \alpha\, \boldsymbol{X_i(t)} + \text{nonlinearity} + n\ (\text{noise}) \quad (1)$$

where i=0,1.,…, n-1 refers to the index of the node within the network. The study on the nonlinear dynamics aspect of DMN covers a broad scope from multiple disciplinary fields, e.g., stability and robustness are two issues to evaluate the performance of the system of DMN where the related parametric specificity is quantitatively analyzed. It will be also an interesting topic to investigate whether or not the chaos and/or bifurcation exist in DMN. In Fig.1, an identification algorithm is given in brief.

(4) Cognitive science aspect of the DMN

According to the relation between self-reference and DMN, the Bayesian model can be expected to model the function by using logical operation in computer science where the stochastic models and logic programming will be integrated.

(5) DMN-Inspired Routing for Computer Networks

Considering the dynamics mechanism of DMN and computer networks, a DMN-inspired routing algorithm for overlay networks in the field of computer networks is proposed as follows:

```
Algorithm (in the pseudo code)
  initialization ()
  WHILE NOT (V≠∅)
  // multiple path for multiple input and output //
   do
   {
   select (i,j)
   // select any two nodes i and j (i≠j) for a path from i
     to j //
   V ← V/{node(i),  node(j)}
   l = i
```

```
    WHILE NOT (node (j) is reached)
    {
    single_path_generation
    // start from node i //
    calculate_correlation (node(l),  node(l+1))
    // return {correlation (node(l),  node(l+1))} //
    neighbor_find(l,(correlation
(node(l),node(l+1))<Tc))
    // select node (l) with correlation (flow (node(l),
      node(l+1))
      that satisfies certain threshold //
    // return (node (l+1)) //
    path (l, l+1)
    weight_of_path (l,l+1) ← capacity (path (l, l+1))
   for l' = 0 to Ml-1
     // l' is the node in the set of V except i, j, l (l≠i)
       and l+1  //
     {
     weight of link (l, l')
     // set by Monte Carlo method //
     // l' ∉ path (l,l+1) //
     path_set' (l') ← path_set ∪ {path (l')}
     V' = V' ∪ {l'}
     }
     return (matrix (l,l')) // the size of the matrix is Ml
    ×Ml //
   path_set ← path_set ∪ path (l,l+1)
     l++
   }
   path_set' ← path_set ∪ path_set' (l')
   modeling_the_dynamics (V')
   // to estimate the signal of node (j) according to the
     path_set' //
  calcaulte_difference(correlation(path_set),correlation(
  path_set'))
// return diff(correlation(path_set), correlation(path_set'
  )) //
   diff_v ← diff (correlation(path_set),
     correlation(path_set'))
   if diff_v > Td
   {
   reconfigure()
     // the kernel operation is
          path_set ← path_set' //
   }
   routing_by_path (path_set)
}
```

Fig. 2 An algorithm of routing

Here the anti-correlated signal (time series) in DMN gives us the hint to select multiple routes that the related flows are with the complementary quantities. The total quantity of the traffic in the multiple routes is considered in this case. Normally in the transport layer, the knowledge of TCP dynamics can be used to design congestion window control and rate control. But in the case the existing route fails, the above-mentioned algorithm will be applied.

VI. CONCLUSION

The basis and the framework of DMN are presented in this paper, and a brief picture of DMN is made in the eyes of network informatics. As one of the examples of biologically inspired networking, a DMN-inspired routing algorithm is proposed, from which robustness is expected to be obtained.

ACKNOWLEDGEMENT

J.-Q. Liu sincerely thanks Satoru Miyauchi, Shigeyuki Kan and Takahiko Koike on brain science, Masayuki Murata, Naoki Wakamiya and Kenji Leibnitz on advanced network architecture, Haruhiko Nishimura and Teruya Yamanishi on nonlinear dynamics, Kazuhiro Oiwa on molecular biology.

REFERENCES

[1] Raichle ME et al. (2001), A default mode of brain function. Proc. Natl Acad. Sci. USA 98:676-682

[2] Buckner RL, et al. (2008), The brain's default network: anatomy, function, and relevance to disease. Ann. N. Y. Acad. Sci. 1124:1-38

[3] Fox MD and Raichle ME (2007), Spontaneous fluctuation in brain activity observed with functional magnetic resonance imaging, Nature Reviews Neuroscience 8: 700-711.

[4] Greicius MD, et al. (2004), Default-mode network activity distinguishes Alzheimer's disease from healthy aging: evidence from functional fMRI, Proc. Natl Acad. Sci. USA 101 (13): 4637-4642.

[5] Gusnard DA et al. (2001), Medial prefrontal cortex and self-referential mental activity: relation to a default mode of brain function, Proc. Natl Acad. Sci. USA 98 (7): 4259-4264.

Wearing the Playware

Luigi Pagliarini[1,2] Henrik Hautop Lund[1]

[1] Centre for Playware, Technical University of Denmark, 2800 Kgs. Lyngby, Denmark
[2] Academy of Fine Arts of Bari, Via Gobetti, 8. 70125 Bari, Italy

luigi@artificialia.com hhl@playware.dtu.dk
www.playware.dk

Abstract

In this conceptual paper, we describe and define the range of possible applications and the technical contours of a robotic system to be worn on the body for playful interactions. Earlier work on Modular Robotic Wearable, MRW, described how, by using modular robotics for creating wearable, it is possible to obtain a flexible wearable processing system, where freely inter-changeable input/output modules can be positioned on the body suit in accordance with the task at hand. Here, we drive the attention on early prototypes to show the potentialities of such an approach, and focus on depicting possible application in the electronic games domain. Indeed, the Modular Robotic Wearable is an example of modular playware, which can create playful interactions for many application domains, including electronic games.

Modular Robotic Wearable and Gaming

The Modular Robotic Wearable (MRW) technology [1] is an attempt to build a ubiquitous gaming interface strictly keeping in mind the early future of computer game design and game play. It considers the research and development of tangible narratives and live role-playing games, as well as interactive narrative experiences moving away from traditional media to fully embrace the physical surrounding. The MRW technology is designed for ubiquity, sensitivity, and tangibility, and it enhances electronic devices interfaces to bring them in a real-world/real-body context through the use of multiple sensors detecting posture, gesture, physical and body parameters, location, proximity, direction, etc.

The basic idea underlying the MRW systems is to move the games interaction out of the usual "push the button", "click here" or the "move the stick" routine, to reach a body-game interrelation experience which should be in part conscious and, in part, unconscious or automated. Therefore, the challenge is to design a general gaming interface that focuses on the player's body interaction with real world, and possibly a social environment. Indeed, we believe that the player can be easily identified as a specific and unique character/personality which can be measured, quantified, and formalized, through body actions and interactions, in order to play his/her specific/personalized role. (An example of categorization of players on playgrounds is provided in [2].)

Through the use of the MRW technology, a large set of games can be conceived as a body-to-body set-up, hence without any intervening external hardware or software. That is because once certain MRW modules are worn, they transform the user into a "physical agent" in the world as well as between other physical agents. Therefore, we can hypothesize any behavior based (e.g. flocking) or ambient related (i.e. physical parameter chasing) game.

Physical game interfaces

For decades, the arcade game industry has developed physical game interfaces. In the 1990's, Konami developed the BEMANI (BeatMania) series of music games (e.g. Physical DJ games) and Namco developed the famous Taiko no Tatsujin drum game, where the player has to physically hit the drum with two large drumsticks based upon the colored circles that appear on the graphical monitor encoded to follow the drum beat. This physical game structure was developed in a very similar form into numerous physical music interaction games such as GuitarFreaks, Guitar Hero, Drumania, Dance Dance Revolution, etc. Also, the arcade game industry developed physical game interfaces for shooter games (e.g. guns) and sports games (e.g. skies, sports cars). Such arcade game machines are typically expensive, with the cost in the order of 10.000 USD, but over the last decade, cheaper versions have penetrated into the consumer game market. Sony developed the Eye-toys with a camera detecting physical motions for creating a home use physical interaction to games, and also early examples include simple guns for shooter games and simple steering wheels for racing car games. Simple dancing mats were developed for Disney games and dancing games, and later electronic plastic guitars were made for Guitar Hero and similar music games duplicating the arcade games.

It is clear that Nintendo revolutionized the game console market with the launch of the Nintendo Wii, which has sold a volume of approximately 70 million. Wii's hand-held game controller embeds a 3-axis accelerometer and IR sensor to measure motion, using an infra-red light reference to calibrate the motion relative to a fixed source. With the Nintendo Wii, physical game interaction has positioned itself as a very important part of a large part of gaming.

In parallel to this development for home use of physical game interfaces, there has been a development of physical game interfaces for fitness and health, also known as exergames (exercise games). Numerous exergames are developed. The different kinds of sensory exercise bikes with interface to screen based games is a simple example (e.g. [3]), and numerous other physical exercise interfaces were developed for screen based games, e.g. Trazer and Dance Dance Revolution for health and fitness purposes. Also, Wii Fit was developed as a physical exergame interface to screen based games. However, many exergames are also developed to be stand alone physical games without graphical game interfaces on a screen, in order to facilitate the set-up and versatility of use. These physical exergame products include LightSpace, tWall, skywall, DigiWall, sportstrainer, Makoto, etc. In these cases, the set-up is fixed for the user. In contrast, as an exergame, Modular Robotic Tiles provide the opportunity to have a flexible set-up which can easily be set up by any user within a minute [4, 5].

Another category of physical game interfaces are technology enhanced playgrounds such as the Smart-Us from Lappset, and the ICON from KOMPAN. In these cases, playgrounds are enhanced with sensors, typically touch sensors, and the playgrounds will react dependent on the children's physical movements on the playground. Smart-Us is mainly screen based, so that the feedback on the physical interaction happens graphically on a screen, whereas ICON avoids the screen and provides sound and colored light feedback from items placed on the traditional playground equipment itself.

Also, physical user interfaces have been developed for mobile games. For instance Bleecker and Brinson [6] used a tablet PC and 3–axis orientation sensor to allow the players to observe the entire game scene by physically moving their bodies in a full 360 degree circle. Other handheld consoles with tilt sensors such as i-Phone and Nintendo Game Boy Advance are used for physical interactions to control screen based games (on the small handheld console screen). Further, augmented reality games, such as augmenting traditional toys with RFID tags (e.g. by Miglino et al. and numerous products on the market), may allow the toy object to react dependent on where the player physically move it (on top of RFID tag readers).

Other mobile games with physical body interaction include location based games, both on a small scale indoor with tracking systems using IR, cameras, etc., and on a larger scale outdoor using GPS and mobile phone signals. Outdoor location based games often demand the players to move around physically, e.g. in the city space, while having mobile phones or other handheld devices with small screens tracked through GPS signals. An example of a contextualized location based game, Visions of Sara, is developed by Ejsing-Duun and DJEEO [7]. The indoor systems are often bulky and demand the set-up of an infrastructure, careful calibration, etc. For instance, this is often the case when using camera-projector systems (e.g. [8]), though the camera-projector systems can provide for interesting physical interaction and displays such as the systems from Snibbe Interactive (e.g. exhibited at MoMa). A number of projects have made set-ups to track 3D gestures, and for instance Payne et. al. [9] tested how 3D gestures affect usability and "fun" for screen based game user interfaces.

The physical game interfaces may also provide social interaction over distance, where users interact physically at one location to manipulate signals (the game) at another location. For instance, Mueller et al. showed how physical ball game activities were transferred over distance to a user at another location as overlayed video conferencing [10]. Such haptic interfaces for social interaction over distance can take many forms. For instance, in 2001, the New York Hall of Science arranged a tug-of-war between two teams of children 13 miles apart from each.

When designing for a playful human physical interaction, it is of course important to consider what category of physical interaction is intended. For instance, some physical game interfaces may not withstand strong physical actions, whereas others may be designed for forceful, strong interactions with the body, such as required in many sports activities [11]. As a guideline for the design of interactive device(s), it is important to design the interactive device(s) with the physical activity and use in mind.

MRW Definition and Characteristics

Modular Robotic Wearable (MRW) was defined [1] as a robotic system composed of interactive robotic modules which are worn on the body.

- By wearable we intend that the system has to be worn on the body and interact with the body as part of the surrounding environment of the system.
- By a robotic module we intend an entity with a physical expression which is able to process and communicate with its surroundings. The communication can be directed towards neighbouring modules and/or via sensory input and actuation output to the surroundings (i.e. interactive robotic modules). A modular robotic system is constructed from many such robotic modules.

Modular Robotic Wearable combines the wearable with the modular robotics and exploits the intersection of this combination. This, in combination with the design guidelines for modular playware [12], provides an opportunity to obtain a flexible wearable processing system, where input/output modules (robotic modules) are freely interchangeable and freely can be positioned on the body suit in accordance with the task at hand. As with any modular robotic system, the design of the individual module is crucial for the performance of the modular robotic wearable. Design issues include attachment mechanism, communication method, size, form, material, and energy as well as the definition of processing, input and output capabilities. An example of MRW is presented with the Fatherboard (Fig. 1) [1, 13].

MRW advantages can be summarized as:

- lightweight, small physical device size;
- lightweight operating system which demands fewer resources;
- good battery life;
- near instant on/off;
- modular, both in configuration and run time use;
- distributed, so components can be worn all over the body for greater comfort;
- customizable;
- cable free, where possible

MRW aims to be a set of networked intelligent modules for the body-state, motion and feeling capture, in virtual and real realities. For example the enhancement powered by affect sensitive action/feeling can be easily applied to software like chats, e-games, iPhone, and etc. in order to reinforce and intensify own feelings, and reproduce and simulate the emotions felt by the partner (either virtual or real) during wired or wireless communication. Such an implemented system can considerably enhance emotionally immersive experience providing feelings of co-presence and intensifies our emotions through the senses. This is both for basic and complex emotion.

We are now experimenting with textile bands, and considering the use of different tools which might be applied to special body parts like fingers, eyes, etc. (see [1,13] for details). This is because we believe that e.g. a field like personalized long-term healthcare monitoring will become fundamental to improve medicine's capabilities for diagnosing and correctly treating diseases at an early stage, therefore the production of wearable wireless sensor networks for health monitoring such as those provided by the MRW system might be essential.

Indeed, a crucial role might be played by textile-based electronic sensors, especially if for monitoring and measuring healthcare parameters. These include ECG active electrodes; capacitance sensors for respiration monitoring; modular wireless sensor node system into several health monitoring clothing applications.

Figure 1. The Fatherboard – one of our first examples of a Modular Robotic Wearable (MRW), see [1, 13].

Interfacing MRW to games and play

Studying MRW may provide a fundamental understanding of how humans and autonomous machine agents can operate efficiently as teams to accomplish mission objectives and share in tasks in a way that the differing abilities of the humans and machines are used to best advantage. This sharing and interactions can happen with immersive 3D VR techniques, games, etc. on one side, and reactive physical material on the other side, e.g. augmented reality object (RFID) and special robots / automated machines that perform complex tasks with certain impact. In both cases, we can study the interaction as a play scenario.

For such studies, we can utilise one of the major advantages of MRW systems, namely the possibility to interface it with existing commercial devices like games and other products. When doing so, we must consider that a MWR device is both multifaceted and multi-modal, since it might serve a software with almost any kind of information coming from almost any part of the body. Being multi-connected to electronic artefacts means, besides controlling a large part of the physical-to-virtual representation of the body, to speed the dialog with any software and to, eventually, open to unconscious reactions. Thus enhancing the interfacing to a much higher level of human-machine interrelation and pushing the game to a much higher emotional level.

Once certain MRW modules are worn, they transform the user into a "physical agent" in the world, as well as a physical agent between other physical agents. Therefore, with MRW we can hypothesize any behavior based (e.g. flocking) or ambient related (i.e. physical parameter chasing) game.

MRW modules are realized in such a way that they can interact via wireless connection with both a specific hardware (e.g., Bluetooth, XBee) or amongst each other (e.g. Xbee). In this way, modules positioned on strategical places of the body, say the hands, the feet, the heart, and so on can communicate their *acceleration*, *3D position* and *state* to virtual/real companion/adversary both in software and real games extending the physical capabilities of the players. One interesting point of such a tool is that the modules, being in most cases plug-and-play and easily applicable can be replaced and substituted quickly or, vice-versa, can be switched from one player's costume to another player's costume, right away. This may increase the game(s) dynamic and favor the exchange of roles amongst players. In this sense, such modules can provide the player with an immediate feedback (e.g. through lights, vibrations and sounds) enhancing the personal experience to a personal and 'believable' level.

Further, since some modules are built in order to perceive and measure ambient circumstances and parameters (i.e. proximity, distance, temperature, humidity, light, etc.) they enlarge considerably the feeling of the player of being immerse into the world, and the idea of using the physical world as part of the game. Hence, such modules might result very significant when trying to conceive immersion and engagement in games and tend to arise the feeling of location-dependent actions/reaction. Being lightweight and wearable, MRW based games might easily be played everywhere – especially when not incorporating external devices.

Finally, some of the modules, e.g. for the Fatherboard (see Fig. 1 and [1, 13] for details), were conceived for aesthetic purposes (i.e. lights, sounds, etc.) and were thought as for being activated either by the *host agent* (i.e. the player wearing the specific module) and the *client agent* (i.e. the other player/s). Such a conception, besides increasing the elegance of the game and the aesthetic of interaction power of "seduction" of the games, sometimes raise them to a "magic" level -- it is the "magic" makes the difference when differentiating games and beautiful games. Despite of that, of course, such aesthetics-modules besides being for the "fantasy" might still be realistic and functional with the MRW approach.

Acknowledgements

The authors wish to thanks the sculptor Demian Battisti for his essential contribution in building the first prototypes and the Superavatar suit and mask. Also thanks to the Centre for Playware colleagues for discussions of the concept presented here.

References

[1]. L. Pagliarini, and H. H. Lund. "Modular Robotic Wearable" In Sugisaka and Takaga (eds.) Proceedings of 14th International Symposium on Artificial Life and Robotics (AROB'14), ISAROB, Oita, 2009.

[2]. A. Derakhshan, F. Hammer, H. H. Lund, Y. Demazeau, and L. Pagliarini. "Adapting Playgrounds using Multi-Agent Systems". In Proceedings of 9th Scandinavian Conference on Artificial Intelligence (SCAI 2006): 151-158, Helsinki, 2006.

[3]. H.-C. Lee , E.-S. Kim, I.-C. Kang and G.-T. Hur "A Study on the Functional Silver Game Contents and

Interface Technology", IJCSNS International Journal of Computer Science and Network Security, VOL.9 No.6, June 2009.

[4]. H. H. Lund, M. D. Pedersen, and R. Beck. "Modular Robotic Tiles – Experiments for Children with Autism". In *Proceedings of 13th International Symposium on Artificial Life and Robotics (AROB'13)*, ISAROB, Oita, 2008.

[5]. H. H. Lund "Modular Robotics for Playful Physiotherapy", in Proceedings of IEEE International Conference on Rehabilitation Robotics, IEEE Press, 571-575, 2009.

[6]. J. Bleecker and P. A. Brinson "Vis-à-vis: A physical user interface for mobile games", ACM. http://www.nearfuturelaboratory.com/files/papers/VisAVis_ShortPaper_ACM.pdf (checked 10/12/2009)

[7]. S. Ejsing-Duun: (checked 10/12/2009) http://pervasivegames.blogspot.com/2009/05/visions-of-sara-danish-title-saras.html

[8]. P. Song, S. Winkler, and J. Tedjokusumo "A Tangible Game Interface Using Projector-Camera Systems" J. Jacko (Ed.): Human-Computer Interaction, Part II, HCII 2007, LNCS 4551, Springer-Verlag Berlin Heidelberg, pp. 956–965, 2007.

[9]. J. Payne, P. Keir, J. Elgoyhen, M. McLundie, M. Naef, M. Horner, and P. Anderson. "Gameplay issues in the design of spatial 3D gestures for video games." CHI '06 extended abstracts on Human factors in computing systems, ACM Press, Montreal, Quebec, Canada, 2006.

[10]. F. Mueller, S. Agamanolis, R. Picard, "Exertion Interfaces: Sports over a Distance for Social Bonding and Fun" Proceedings of CHI 2003, ACM, 2003.

[11]. F. Mueller, S. Agamanolis, M. Gibbs, F. Vetere, "Remote Impact - Shadowboxing over a Distance" Proceedings of CHI 2008, ACM, 2008.

[12]. H. H. Lund, and P. Marti. "Designing Modular Robotic Playware". In IEEE 18th International Workshop on Robot and Human Interactive Communication (Ro-Man 2009), IEEE Press, 115-121, 2009.

[13]. *Fatherboard, The Superavatar* (checked 10/12/2009): http://www.artificialia.com/Fatherboard

The Fifteenth International Symposium on Artificial Life and Robotics 2010 (AROB 15th '10),
B-Con Plaza, Beppu,Oita, Japan, February 4-6, 2010

Towards natural intelligence modeling as a formal system based on Mental Image Directed Semantic Theory (Part 1)

Masao Yokota, Haosheng Li, Hailan Quan, Kaoru Sugita and Tetsushi Oka

Fukuoka Institute of Technology, 3-30-1 Wajiro-higashi, Higashi-ku, Fukuoka-shi, 811-0295, Japan
(Tel : 81-92-606-5897; Fax : 81-92-606-8923)
(yokota@fit.ac.jp)

Abstract: Yokota,M. has proposed his original semantic theory "Mental Image Directed Semantic Theory (MIDST)" and has been challenging to model natural intelligence as a formal system. This paper presents the fundamentals of the formal system and how to formalize mental operations and natural concepts within it.

Keywords: Natural intelligence, Mental image model, Natural language, Formal system.

I. INTRODUCTION

In order for facilitating intuitive and *coherent* human-robot interaction, it is essential to develop a systematically computable knowledge representation language (KRL) as well as representation-free technologies such as neural networks for processing unstructured sensory/motory data. This type of language is indispensable to knowledge-based processing such as understanding sensory events, planning appropriate actions and knowledgeable communication with ordinary people in natural language, and therefore it needs to have at least a good capability of representing spatiotemporal events that correspond to human/robotic sensations and actions in the real world. Yokota, M. has employed the formal language so called 'Mental-image Description Language (L_{md})' proposed in his original semantic theory 'Mental Image Directed Semantic Theory (MIDST)' [1]. This language has already been implemented on several types of computerized intelligent systems including IMAGES-M [2]. The most remarkable feature of L_{md} is its capability of formalizing spatiotemporal matter concepts grounded in human/robotic sensation while the other similar KRLs are designed to describe the logical relations among conceptual primitives represented by lexical tokens [3] with the risk of "predicate drift" [4].

Our final goal is to model natural intelligence as a formal system based on MIDST. A formal system is defined as a pair of a formal language and a deductive system consisting of the axioms and inference rules employed for theorem derivation. L_{md} is a formal language for many-sorted predicate logic with 5 types of terms specific to the mental image model. Therefore, the deductive system intended here is to be based on the deductive apparatus for predicate logic. This paper introduces the formal system and focuses on its fundamentals.

II. FORMAL SYSTEM BASED ON L_{md}

A formal system is defined as a pair of a formal language and a deductive system consisting of the axioms and inference rules employed for theorem derivation. L_{md} is a formal language for many-sorted predicate logic with 5 types of terms specific to the mental image model. Therefore, the deductive system intended here is to be based on the deductive apparatus for predicate logic.

1. Syntax of L_{md}

The symbols of L_{md} for the deductive system are listed as (i)-(ix) below. These symbols are possibly subscripted just like A_{01}, G_t, etc.

(i) logical connectives : ~, ∧, ∨, ⊃, ≡
(ii) quantifiers : ∀, ∃
(iii) auxiliary constants : ., (,)
(iv) sentence variables : χ
(v) predicate variables : ψ
(vi) individual variables
  a) matter variables : x, y, z
  b) attribute variables : a
  c) value variables : p, q, r, s, t
  d) pattern variables : g
  e) standard variables : k
(vii) sentence constants : N
(viii) predicate constants : L, =, ≠, >, < (and others to be introduced where needed)
(ix) individual constants
  a) matter constants : to be introduced where needed
  b) attribute constants : A, B
  c) value constants : to be introduced where needed
  d) pattern constants : G
  e) standard constants : K
(x) function constants : arithmetic operators such as +, -, etc. (and others to be introduced where needed)
(xi) meta-symbols : ⇔, →, ↔ (and others to be introduced where needed)
(xii) others: to be defined by the symbols above.

The system is a many-sorted predicate logic with five kinds of individuals employed for one special predicate constant '*L*' so called 'Atomic Locus'. Except this point, the syntactic rules and the theses of the system are the same as those of the conventional predicate logic.

The predicate 'L' is such a seven-place predicate that is given by expression (1).

$$L(\omega_1, \omega_2, \omega_3, \omega_4, \omega_5, \omega_6, \omega_7) \quad (1)$$

Expression (1) is a well-formed formula (i.e. wff) called 'Atomic locus formula' if and only if the conditions below are satisfied. A well-formed formula consisting of atomic formulas and logical connectives is called simply 'Locus formula'.

(a) w_1 is a matter term (variable or constant)
(b) w_2 is a matter term
(c) w_3 is a value or a matter term
(d) w_4 is a value or a matter term
(e) w_5 is an attribute term
(f) w_6 is a pattern term
(g) w_7 is a standard (or matter) term

2. Semantics of L_{md}

The domain-specificity in the syntax and semantics of L_{md} is exclusively related to atomic locus formulas and the essential part of its semantics is subject to their interpretation controlled by the family of domain-specific constants, namely, Attributes, Values, Patterns and Standards intended to correspond well with natural or artificial sensory systems.

So far, about 50 attributes (e.g. Color, Volume, Taste) related to the physical world have been extracted exclusively from Japanese and English words. The values for each attribute (e.g. Red, Small, Sour) are to be arranged so as to form a structure "Attribute Space", so called.

Correspondingly, six categories of standards (i.e. Rigid, Species, Proportional, Individual, Purposive and Declarative Standards) have been found that are assumed necessary for representing values of each attribute. In general, the attribute values represented by words (e.g. Dark, Large, Bitter) are relative to certain standards. These standards are to be utilized exclusively for coping with vagueness and controlling granularity of attribute values.

As for the pattern term, two constants have been hypothetically provided, that is, G_t (i.e. Temporal event) and G_s (Spatial event) indicating temporal and spatial change in an attribute, respectively.

III. DEFINED CONSTANTS

1. Tempological connective and Empty event

The deductive system employs 'tempo-logical connectives (TLCs)' with which to represent both temporal and logical relations between two loci over certain time-intervals. The definition of a tempo-logical connective C_i is given by **D1**, where t_i, c and C refer to one of ***purely*** temporal relations indexed by an integer 'i', a locus, and an ordinary binary logical connective such as the conjunction '$\wedge$', respectively. The suffix 'i' ($-6 \leq i \leq 6$) indicate 13 types of 1-D topological relation (i.e. 0: EQUALS; +1: MEETS; -1: MET-BY; +2: STARTS; -2: STARTED-BY; +3: DURING; -3: CONTAINS; +4: FINISHES; -4: FINISHED-BY; +5: BEFORE; -5: AFTER; +6: OVERLAPS; -6: OVERLAPPED-BY [5]). The TLCs used most frequently are 'SAND ($\wedge_0$)' and 'CAND ($\wedge_1$)', standing for 'Simultaneous AND' and 'Consecutive AND' and conventionally symbolized as 'Π' and '•', respectively.

D1. $\chi_1 \, C_i \, \chi_2 \Leftrightarrow (\chi_1 \, C \, \chi_2) \wedge \tau_i(\chi_1, \chi_2)$
where
$\tau_{-i}(\chi_2, \chi_1) \equiv \tau_i(\chi_1, \chi_2)$
$(\forall i \in \{0,\pm1,\pm2,\pm3,\pm4,\pm5,\pm6\})$

In order for explicit indication of ***absolute*** time elapsing, 'Empty Event' denoted by 'ε' is introduced as **D2** with the attribute 'Time Point (A_{34})' and the Standard of absolute time 'K_{Ta}', where $\boldsymbol{R}$ and D denote the total sets of real numbers and absolute time intervals, respectively. (Usually people can know only a certain ***relative*** time point by a clock that is seldom exact and that is to be denoted by another Standard in the L_{md}.) According to this scheme, the suppressed absolute time-interval $[t_a, t_b]$ of a locus χ can be indicated as (2).

D2. $\varepsilon([t_i,t_j]) \Leftrightarrow (\exists x,y,g) L(x,y,t_i,t_j,A_{34},g,K_{Ta})$
where
$[t_i,t_j] \in D = \{[t_1, t_2] \mid t_1 < t_2 \ (t_1, t_2 \in \boldsymbol{R})\}$

$$\chi \Pi \varepsilon([t_a,t_b]) \quad (2)$$

2. Mental Operations

People can transform their mental images in several ways such as mental rotation [6]. Here are introduced two kinds of such mental operations, namely, 'reversing' and 'duplicating'.

For example, people can easily imagine the reversal of an event just like 'rise' versus 'sink'. This mental operation is here denoted as a meta-function 'R' and recursively defined as **D3**, where χ_i stands for a perceptual locus. The reversed values p^R and q^R depend on the properties of the attribute values p and q.

D3. $(\chi_1 \bullet \chi_2)^R \Leftrightarrow \chi_2^R \bullet \chi_1^R$
$(\chi_1 \Pi \chi_2)^R \Leftrightarrow \chi_1^R \Pi \chi_2^R$
$L^R(x,y,p,q,a,g,k) \Leftrightarrow L(x,y,q^R,p^R,a,g,k)$

For another example, people can easily imagine the repetition of an event just like 'visit twice' versus 'visit once'. This operation is also a meta-function recursively defined as **D4**, where 'n' is an integer representing the frequency of a locus formula χ.

D4. $\chi^n \Leftrightarrow \chi \quad (n=1)$
$\chi^n \Leftrightarrow \chi \bullet \chi^{n-1} \quad (n>1)$

3. Natural Concepts

All the natural concepts of physical or metaphysical matters and their relations are to be defined in association with specific loci in specific attribute spaces formalized by the four types of individual constant stated above. These concepts can be introduced as non-logical constants, namely, predicate constants (e.g. carry, snow) or matter constants (e.g. Tokyo, Tom) and defined in context of locus formulas as follows.

A. Event Concepts

An event here, usually referred by a verb, preposition, adjective or so in natural language, is defined as a spatiotemporal relation among certain matters in the world, which is to be conceptualized as a generalization of a perceptual locus, namely, a combination of atomic loci articulated by tempological conjunctions (i.e. $\wedge_i$) with the abstraction operator 'λ'.

For example, the English verb concepts 'carry (=convey)' and 'shuttle' are to be defined as (3) and (4), respectively. In turn, the expression (5) is the definition of the English verb concept 'fetch'. This implies such a temporal event that 'x' goes for 'y' and then comes back with it. In the same way, the English verb concept 'hand' or 'receive' is defined equivalently as (6) or its abbreviation (7). These concepts can be graphically interpreted as Fig.1.

$$(\lambda x,y)\mathrm{carry}(x,y) \Leftrightarrow (\lambda x,y)\mathrm{convey}(x,y)$$
$$\Leftrightarrow (\lambda x,y)(\exists p,q,k)L(x,x,p,q,A_{12},G_t,k)$$
$$\Pi L(x,y,p,q,A_{12},G_t,k) \wedge x\neq y \wedge p\neq q \qquad (3)$$

$$(\lambda x)\mathrm{shuttle}(x) \Leftrightarrow (\lambda x)(\exists p,q,k)$$
$$(L(x,x,p,q,A_{12},G_t,k)$$
$$\bullet L^R(x,x,p,q,A_{12},G_t,k))^n \wedge p\neq q \wedge n\geq 1$$
$$\Leftrightarrow (\lambda x)(\exists p,q,k)$$
$$(L(x,x,p,q,A_{12},G_t,k)$$
$$\bullet L(x,x,q,p,A_{12},G_t,k))^n \wedge p\neq q \wedge n\geq 1 \qquad (4)$$

$$(\lambda x,y)\mathrm{fetch}(x,y) \Leftrightarrow (\lambda x,y)(\exists p_1,p_2,k)$$
$$L(x,x,p_1,p_2,\ A_{12},G_t,k)$$
$$\bullet(\underline{L(x,x,p_2,p_1,A_{12},G_t,k)}$$
$$\underline{\Pi L(x,y,p_2,p_1,\ A_{12},G_t,k)}) \wedge x\neq y \wedge p_1\neq p_2 \qquad (5)$$

$$(\lambda x,y,z)\mathrm{hand}(x,y,z)$$
$$\Leftrightarrow (\lambda x,y,z)\mathrm{receive}(z,y,x)$$
$$\Leftrightarrow (\lambda x,y,z)(\exists k)L(x,y,x,z,A_{12},G_t,k)$$
$$\Pi L(z,y,x,z,A_{12},G_t,k) \wedge x\neq y \wedge y\neq z \wedge z\neq x \qquad (6)$$
$$\Leftrightarrow (\lambda x,y,z)(\exists k)L(\{x,z\},y,x,z,A_{12},G_t,k)$$
$$\wedge x\neq y \wedge y\neq z \wedge z\neq x \qquad (7)$$

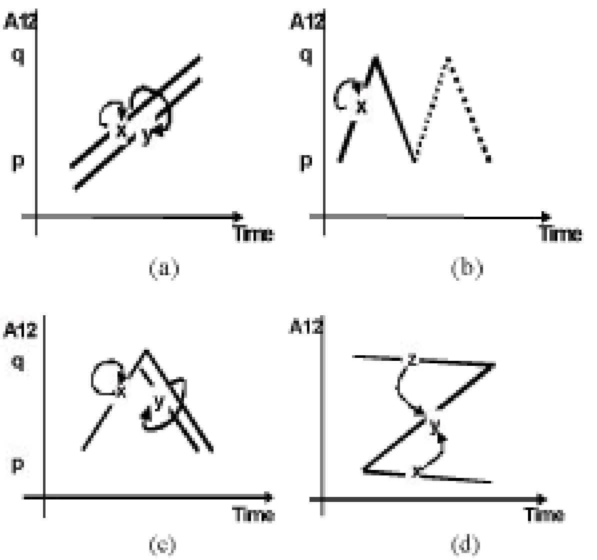

Fig.1. Pictorial interpretation of verb concepts: (a) 'carry', (b) 'shuttle', (c) 'fetch' and (d) 'hand/receive'.

Such locus formulas that correspond with natural event concepts are called 'Event Patterns' and about 40 kinds have been found concerning the attribute 'Physical Location (A_{12})', for example, *move, stay, start, stop, meet, separate, carry, return*, etc.

Employing TLCs, tempo-logical relationships between miscellaneous event concepts can be formulated without explicit indication of time intervals. For example, an event 'fetch(x,y)' is necessarily *finished by* an event 'carry(x,y)' as indicated by the underline at (5). This fact can be formulated as (8), where '$\supset_{-4}$' is the '*implication* ($\supset$)' furnished with the temporal relation '*finished-by* (τ_{-4})'. This kind of formula is not an axiom but a theorem deducible from the definitions of event concepts in the deductive system intended here.

$$(\forall x,y)(\mathrm{fetch}(x,y) \supset_{-4} \mathrm{carry}(x,y)) \qquad (8)$$

B .Matter Concepts

A matter, usually referred to by a noun in natural language, is to be conceptualized as a conjunction of the mental images of itself and its relations with others that in turn are to be reduced to certain loci in attribute spaces. In the formal system, a matter concept 'ψ' is defined in such a context as (9), where 'ψ^+' and 'ψ^{++}' are to represent the conceptual images of itself and its relations with others, respectively, and in turn to be reduced to atomic locus formulas of all the attributes.

$$(\lambda z)\psi(z) \Leftrightarrow (\lambda z)\psi^+(z) \wedge \psi^{++}(z) \qquad (9)$$

Whereas ψ(z) must be a total description of all the attributes, for simplicity here is to be given only its important part with the symbol '%' representing its abbreviated part. The part $\psi^+(z)$ is given as a combination of atomic locus formulas for the Attribute Carrier 'z' without any other specific matter involved unlike the other part $\psi^{++}(z)$. For example, the matter called 'ice' can be conceptualized as (10). This formula reads that ice is always equal to or less than 0°C cold, is always of no vitality and melts into water (or is something from that H_2O) changes into water)'. In turn, the matter 'snow' can be conceptualized as (11), reading 'Snow is powdered ice attracted from the sky by the earth'. The attributes 'A_{28}', 'A_{39}' and 'A_{41}' refer to 'Temperature', 'Vitality' and 'Quality', respectively. The special symbol '_', defined by (12), is a variable bound by an existential quantifier but does not refer to any specific matter or so in the context while '*' and 'ϕ' represent 'always' and 'no value (or matter)', respectively, defined by (13) and (14).

$$(\lambda x)\mathrm{ice}(y) \Leftrightarrow (\lambda x)\mathrm{ice}^+(z) \wedge \mathrm{ice}^{++}(x)$$
$$(\lambda x)\mathrm{ice}^+(x) \Leftrightarrow (\lambda x)((\exists p,q)L(\_,x,p,q,A_{28},G_t,\_)$$
$$\wedge p\leq 0^\circ C \wedge q\leq 0^\circ C)^* \wedge L^*(\phi,x,\phi,\phi,A_{39},G_t,\phi) \wedge \%$$
$$(\lambda x)\mathrm{ice}^{++}(x) \Leftrightarrow (\exists z,x_1)L(\_,z,x,x_1,A_{41},G_t,\_)$$
$$\wedge \mathrm{water}(x_1)\ (\wedge H_2O(z)) \wedge \% \qquad (10)$$

$$(\lambda x)\mathrm{snow}(x)$$
$$\Leftrightarrow (\lambda x)(\exists x_1)((L(\_,x,x_1,x_1,A_{41},G_t,\_)\Pi$$
$$L(\mathrm{Earth},x,\mathrm{Sky},\mathrm{Earth},A_{12},G_t,\_)) \qquad (11)$$
$$\wedge \mathrm{powder}(x_1) \wedge \mathrm{ice}(x_1) \wedge \%$$

$$L(\ldots,\omega_i,\_,\omega_j,\ldots)\Leftrightarrow(\exists\omega)L(\ldots,\omega_i,\omega,\omega_j,\ldots) \quad (12)$$

$$\chi^{*}\Leftrightarrow(\forall[p,q])\ \chi\ \Pi\ \varepsilon([p,q]) \quad (13)$$

$$L(\ldots,\omega_i,\phi,\omega_j,\ldots)\Leftrightarrow\sim(\exists p)L(\ldots,\omega_i,p,\omega_j,\ldots) \quad (14)$$

As easily understood, matter concepts include miscellaneous spatiotemporal relations (i.e. events) among matters usually referred by verbs, prepositions or so. Therefore, a matter concept is usually much more complicated than an event concept in definition. By the way, a noun originated or derived from a verb is to be conceptualized so as to include the verb concept. For example, the concept of 'conveyance' is to be introduced as (15).

$$(\lambda z)\mathrm{conveyance}(z) \Leftrightarrow(\lambda z)\mathrm{conveyance}^{+}(z)\wedge \mathrm{conveyance}^{++}(z)$$
$$(\lambda z)\ \mathrm{conveyance}^{+}(z) \Leftrightarrow(\lambda z)L^{*}(\phi,z,\phi,\phi,A_{32},G_t,\phi)\wedge \%$$
$$(\lambda z)\mathrm{conveyance}^{++}(z)\Leftrightarrow(\lambda z)(\exists x,y) L(\_,\{x,y\},z,z,A_{01},G_t,\_)\Pi \mathrm{convey}(x,y) \quad (15)$$

It is well known that people perceive more than reality, for example, 'Gestalt' so called in psychology. A psychological matter here is not a real matter but a product of human mental functions, including Gestalt and abstract matters such as 'society', 'information', etc. in a broad sense.

For example, Fig.2 concerns the perception of the formation of multiple objects, where FAO (Focus of Attention of Observer) runs along an imaginary object so called '*Imaginary Space Region (ISR)*'. This spatial event can be verbalized as S3 using the preposition 'between' and formulated as (16) or (17), corresponding also to such concepts as 'row', 'line-up', etc. Employing ISRs and the 9-intersection model [7] all the topological relations between two objects can be formulated in such expressions as (18) or (19) for S4, and (20) for S5, where '*In*', '*Cont*' and '*Dis*' are the values 'inside', 'contains' and 'disjoint' of the attribute 'Topology (A_{44})' with the standard '9-intersection model (K_{9IM})', respectively. Practically, these topological values are given as 3×3 matrices with each element equal to 0 or 1 and therefore, for example, '*In*' and '*Cont*' are transpositional matrices each other.

(S3) The square is between the triangle and the circle.

$$(\exists x_1,x_2,x_3,y,p,q)(L(\_,y,x_1,x_2,A_{12},G_s,\_)\Pi L(\_,y,p,p,A_{13},G_s,\_))\bullet(L(\_,y,x_2,x_3,A_{12},G_s,\_)\Pi L(\_,y,q,q,A_{13},G_s,\_))\wedge ISR(y)\wedge p=q \ \wedge\mathrm{triangle}(x_1)\wedge\mathrm{square}(x_2)\wedge\mathrm{circle}(x_3) \quad (16)$$

$$(\exists x_1,x_2,x_3,y,p)(L(\_,y,x_1,x_2,A_{12},G_s,\_)\bullet L(\_,y,x_2,x_3,A_{12},G_s,\_))\Pi L(\_,y,p,p,A_{13},G_s,\_)\wedge ISR(y)\wedge\mathrm{triangle}(x_1)\wedge\mathrm{square}(x_2)\wedge\mathrm{circle}(x_3) \quad (17)$$

(S4) Tom is in the room.

$$(\exists x,y)L(Tom,x,y,Tom,A_{12},G_s,\_)\Pi L(Tom,x,In,In,A_{44},G_t,K_{9IM}) \wedge ISR(x)\wedge \mathrm{room}(y) \quad (18)$$

$$(\exists x,y)L(Tom,x,Tom,y,A_{12},G_s,\_)\Pi L(Tom,x,Cont,Cont,A_{44},G_t,K_{9IM}) \wedge ISR(x)\wedge \mathrm{room}(y) \quad (19)$$

(S5) Tom exits the room.

$$(\exists x,y,p,q)L(Tom,Tom,p,q,A_{12},G_t,\_)\Pi L(Tom,x,y,Tom,A_{12},G_s,\_)\Pi L(Tom,x,In,Dis,A_{44},Gt,K_{9IM})\wedge ISR(x)\wedge \mathrm{room}(y)\wedge p\neq q \quad (20)$$

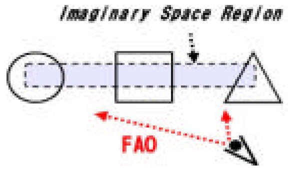

Fig.2. Row as spatial event.

IV. CONCLUSION

The fundamentals of the formal system were presented based on MIDST. The expressive power of the formal language L_{md} was demonstrated with linguistic or pictorial manifestations throughout this paper. Its most remarkable point in comparison with other KRLs resides in that it can provide natural concepts such as *carry*, *snow*, etc. with precise semantic definitions that are normalized by atomic locus formulas and visualized as loci in attribute spaces in both temporal and spatial extents (i.e. temporal and spatial events), which leads to good computability and intuitive readability of L_{md} expressions.

To be continued to another paper of ours [8] for this session.

REFERENCES

[1] Yokota M (2008), In Choi B (Ed.), Humanoid Robots, I-Tech Education and Publishing, 333-362

[2] Yokota M & Capi G (2005), Cross-media Operations between Text and Picture Based on Mental Image Directed Semantic Theory. WSEAS Trans. on Information Science and Applications, 10-2:1541-1550

[3] Dorr B & Bonnie J (1997), Large-Scale Dictionary Construction for Foreign Language Tutoring and Interlingual Machine Translation, *Machine Translation*, Vol.12, No.4, pp.271-322

[4] Lenat D (1996), CyC: A Large-Scale Investment in Knowledge Infrastructure, Communications of the ACM.

[5] Allen J F (1984), Towards a general theory of action and time. Artificial Intelligence, 23-2: 123-154

[6] Shepard R & Metzler J (1971), Mental rotation of three dimensional objects. Science, 171(972):701-3

[7] Egenhofer M (1991), Point-set topological spatial relations. Geographical Information Systems, 5-2, 161-174

[8] Yokota M et al (2010), Towards natural intelligence modeling as a formal system based on Mental Image Directed Semantic Theory (Part 2), Proc. of AROB2010, Beppu, Oita, Feb. 2010.

The Fifteenth International Symposium on Artificial Life and Robotics 2010 (AROB 15th '10),
B-Con Plaza, Beppu,Oita, Japan, February 4-6, 2010

Towards natural intelligence modeling as a formal system based on Mental Image Directed Semantic Theory (Part 2)

Masao Yokota, Taiki Tometsuka, Rong Zhao, Kaoru Sugita and Tetsushi Oka

Fukuoka Institute of Technology, 3-30-1 Wajiro-higashi, Higashi-ku, Fukuoka-shi, 811-0295, Japan
(Tel : 81-92-606-5897; Fax : 81-92-606-8923)
(yokota@fit.ac.jp)

Abstract: Yokota, M. has proposed his original semantic theory "Mental Image Directed Semantic Theory (MIDST)" and has been challenging to model natural intelligence as a formal system. This paper presents a brief sketch of the attempt on systematic representation and computation of subjective spatiotemporal knowledge based on certain hypotheses of mental image in human.

Keywords: Natural language, Multimedia understanding, Robotic sensation and action.

I. INTRODUCTION

Another paper of ours for this session [1] presents the fundamentals of the formal system for natural intelligence and how to formalize mental operations and natural concepts within it. The forma l system consists of the formal language L_{md} [1] and the deductive system. The latter is based on the deductive apparatus for predicate logic and is to be provided with postulates concerning human empirical knowledge of space and time as well. This paper focuses on systematic formalization of human empirical knowledge pieces of space and time as postulates for the deductive system and its application to natural language understanding (NLU) for spatiotemporal expressions.

II. PROVISION OF POSTULATES

The deductive system must be as well provided with knowledge pieces in order to solve certain problems in its world or task domain. Such knowledge pieces as called "postulates" here stand for human intuitive laws of the world and are to be treated as equivalents to axioms. Those presented below concern exclusively space and time in order for spatiotemporal language understanding.

1. Fundamental Properties of Locus

The postulates **P1** and **P2** state that <u>*a matter never has different values of an attribute with a standard at a time*</u>. These are called "Postulates of Identity in Assigned Values". **P1** is employed exclusively to detect semantic anomaly in such a sentence as "The red box is black" while **P2** is useful to detect event gaps in such a context as "Tom was in London yesterday and he is in Paris today."

The syntax of L_{md} allows Matter terms to appear at Values and Standard in order to represent their values in each place at the time and over the time-interval, respectively. This rule can be formulated as **P3** and **P4**. The postulate **P3** is to be utilized for such inference as "Mary went to Tom when he was in the garden. Therefore, Mary went to the (same) garden." while **P4** is for such inference as "Jim is taller than Tom. Tom is 2m tall. Therefore, Jim is taller than 2m."

P1. $L(x,y,p_1,q_1,a,g,k)\Pi L(z,y,p_2,q_2,a,g,k)$
$.\supset.\ p_1=p_2\wedge q_1=q_2$

P2. $L(x,y,p_1,q_1,a,g,k)\bullet L(z,y,p_2,q_2,a,g,k)$
$.\supset.\ q_1=p_2$

P3. $L(x_0,y,z_1,z_2,a,g,k)\Pi L(x_1,z_1,p_1,q_1,a,g,k)\Pi$
$L(x_2,z_2,p_2,q_2,a,g,k).\supset_0.L(x_0,y,p_1,q_2,a,g,k)$

P4. $L(x_0,y,p_1,p_2,a,g,z)\Pi L(x_1,z,q,q,a,g,k)$
$.\supset_0.L(x_0,y,p_1,p_2,a,g,q)$

It is quite subjective how to articulate a locus. For example, whether the point (t_2, q) in Fig.1-a is significant or not so as in Fig.1-b, more generally, locus articulation depends on the precisions or the granularities of these standards, which can be formulated as **P5** and **P6**, so called, '*Postulates of Arbitrariness in Locus Articulation*'.

P5. $(\forall p,q,r,k)(\exists k')L(y,x,p,q,a,g,k)\bullet L(y,x,q,r,a,g,k)$
$.\supset_0.L(y,x,p,r,a,g,k')\wedge k'\neq k$

P6. $(\forall p,r,k)(\exists q,k')L(y,x,p,r,a,g,k).\supset_0.$
$L(y,x,p,q,a,g,k')\bullet L(y,x,q,r,a,g,k')\wedge k'\neq k$

These postulates affect the process of conceptualization on a word based on its referents in the world and moreover they are very useful for spatiotemporal inference in such a context as "Tom flied from Tokyo to Nagoya and consecutively from Nagoya to Osaka. Therefore, he moved from Tokyo to Osaka" or "Tom moved from Tokyo to Osaka. Therefore, he passed somewhere (between the two places)".

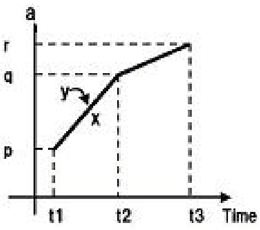

(a)

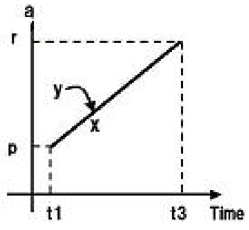

(b)

Fig.1. Arbitrariness in locus articulation due to standards: Standard k_1 (a) is finer than k_2 (b).

2. Perception of Time

A perceptual locus can be formulated with atomic locus formulas and temporal conjunctions such as SAND ($\wedge_0$ or Π) and CAND ($\wedge_1$ or $\bullet$). This is not necessarily the case for a conceptual locus corresponding to such a generalized mental image or knowledge piece. For example, people usually interpret the construction '*B* happens *before A* happens' as a general causality, namely, as 'If *A* happens, *B* happens *in advance*'. Whereas this should be formulated with logical connectives other than conjunctions also involved, **D1** [1] is exclusively for perceptual loci so far as it is because there is no interpreting a negated locus formula as a locus with ***a unique time-interval*** necessary to determine a unique temporal relation t_i.

Considering such a definition as '$A\supset B \Leftrightarrow \sim A\vee B$ $(.\equiv.\sim(A\wedge\sim B))$' in standard logic, it is not unnatural to assume the identity of a locus formula with its negative in absolute time-interval, that is, negation-freeness of absolute time passing under a locus referred to by its suppressed absolute time-interval. Therefore, in order to make **D1** valid also for conceptual loci, we introduce a meta-function *d* defined by **D5** and its related postulates **P7** and **P8** as follows, where *d* is to extract the ***suppressed*** absolute interval of a locus formula *c*.

D5. $\delta(\chi)=[t_a,t_b](\in D)$
where $\chi\Pi\varepsilon([t_a,t_b])$.

P7. $\delta(\sim\alpha)=\delta(\alpha)$
where *a* is an atomic locus formula.

P8. $\delta(\chi)=[t_{min}, t_{max}]$
where t_{min} and t_{max} are respectively the *minimum* and the *maximum* time-point included in the absolute time-intervals of the atomic locus formulas, either positive or negative, within *c*.

These postulates lead to **T1** (Theorem of absoluteness of time passing (or negation-freeness of absolute time passing)) below. This theorem can read that absolute time passes during an *objective* event whether it may be perceived *subjectively* as χ or as $\sim\chi$.

T1. $\delta(\sim c)=\delta(c)$

(Proof)

According to **P5** and **P6**, the time-interval of each atomic locus formula involved in *c* is negation-free and therefore so is for $[t_{min}, t_{max}]$ of $d(c)$. **[Q.E.D.]**

The counterpart of the contrapositive in standard logic (i.e. $A\supset B.\equiv.\sim B\supset\sim A$) is given as **T2** (Tempological Contrapositive) whose rough proof is as follows immediately below, where the left hand of ':' refers to the theses (e.g., **PL** is a subset of those in pure predicate logic) employed at the process indicated by the conventional meta-symbol '$\rightarrow$' or '$\leftrightarrow$' for entailment (left-to-right or bi-directional).

T2. $\chi_1\supset_i\chi_2.\equiv.\sim\chi_2\supset_{-i}\sim\chi_1$

(Proof)

D1: $\chi_1\supset_i\chi_2 \leftrightarrow (\chi_1\supset\chi_2)\wedge\tau_i(\chi_1,\chi_2)$

PL: $\leftrightarrow (\sim\chi_2\supset\sim\chi_1)\wedge\tau_i(\chi_1,\chi_2)$

T1: $\leftrightarrow (\sim\chi_2\supset\sim\chi_1)\wedge\tau_i(\sim\chi_1,\sim\chi_2)$

D1: $\leftrightarrow (\sim\chi_2\supset\sim\chi_1)\wedge\tau_{-i}(\sim\chi_2,\sim\chi_1)$

D1: $\leftrightarrow \sim\chi_2 \supset_{-i} \sim\chi_1$ **[Q.E.D.]**

Therefore, S1 and S2 are proved to be paraphrases each other by employing T2 while S3 and S4 are proved so by the definition of tempological conjunctions (i.e. $\wedge_i$).

(S1) It gets cloudy *before* it rains.
=If it rains, it gets cloudy *in advance*.
($\equiv$Raining$\supset_{-5}$ Getting_Cloudy)

(S2) It does not rain *after* it does not get cloudy.
=Unless it gets cloudy, it does not rain *later*.
($\equiv\sim$Getting_Cloudy $\supset_5$ ~Raining)

(S3) It got cloudy *before* it rained.
($\equiv$Raining$\wedge_{-5}$Getting_Cloudy)

(S4) It rained *after* it got cloudy.
($\equiv$Getting_Cloudy$\wedge_5$Raining)

3. Reversibility of Spatial Event

As already mentioned in [1], all loci in attribute spaces are assumed to correspond one to one with movements or, more generally, temporal events of the FAO. Therefore, the L_{md} expression of an event is compared to a movie film recorded through a floating camera because it is necessarily grounded in FAO's movement over the event. And this is why S5and S6 can refer to the same scene in spite of their appearances, where what 'sinks' or 'rises' is the FAO as illustrated in Fig.2 and whose conceptual descriptions are given as (1) and (2), respectively, where 'A_{13}', '$\uparrow$' and '$\downarrow$' refer to the attribute 'Direction' and its values 'upward' and 'downward', respectively.

(S5) The path sinks to the brook.

(S6) The path rises from the brook.

$$(\exists y,z,p)L(\_,y,p,z,A_{12},G_s,\_)\Pi\ L(\_,y,\downarrow,\downarrow,A_{13},G_s,\_)\wedge path(y)\wedge brook(z)\wedge z\neq p \quad (1)$$

$$(\exists y,z,p)L(\_,y,z,p,A12,G_s,\_)\Pi\ L(\_,y,\uparrow,\uparrow,A_{13},G_s,\_)\wedge path(y)\wedge brook(z)\wedge z\neq p \quad (2)$$

Such a fact is generalized as **P9** (*Postulate of Reversibility of Spatial Event (PRS)*), where χ_s and χ_s^R are a perceptual locus and its 'reversal' for a certain spatial event, respectively, and they are substitutable with each other because of the property of '$=_0$'. This postulate can be one of the principal inference rules belonging to people's common-sense knowledge about geography.

P9. $\chi_s^R .=_0 \chi_s$

This postulation is also valid for such a pair of S7 and S8 as interpreted approximately into (3) and (4), respectively. These pairs of conceptual descriptions are called equivalent in the PRS, and the paired sentences are treated as paraphrases each other.

(S7) Route A and Route B meet at the city.
(S8) Route A and Route B separate at the city.

$$(\exists p,y,q)L(\_,Route\_A,p,y,A_{12},G_s,\_)\Pi L(\_,Route\_B,q,y,A_{12},G_s,\_)\wedge city(y)\wedge p\neq q \quad (3)$$

$$(\exists p,y,q)L(\_,Route\_A,y,p,A_{12},G_s,\_)\Pi L(\_,Route\_B,y,q,A_{12},G_s,\_)\wedge city(y)\wedge p\neq q \quad (4)$$

Fig.2. Slope as spatial event.

4. Partiality of Matter

Any matter is assumed to consist of its parts in a structure (i.e. spatial event), which is generalized as **P10** (*Postulate of Partiality of Matter*) here. For example, Fig.3 shows that an ISR x_1 can be deemed as a complex of ISRs x_2 and x_3. This postulate, in cooperation with P9, is utilized for translating such a paradoxical sentence as "The Andes Mountains run north and south." into such a plausible interpretation as "One part of the Andes Mountains runs north (from somewhere) and the other part runs south".

P10. $L(y,x_1,p,q,a,G_s,k)\bullet L(y,x_1,q,r,a,G_s,k)$
$.=_0. L(y,x_2,p,q,a,G_s,k)\Pi L(y,x_3,q,r,a,G_s,k)$

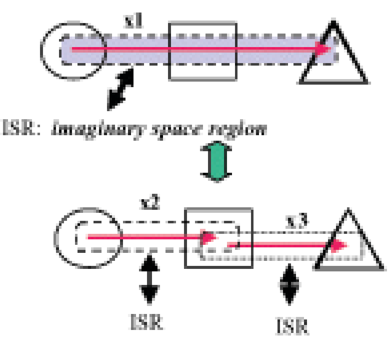

Fig.3. Partiality of ISR.

III. APPLICATION TO NLU

Our intelligent system IMAGES-M [1] can translate systematically natural language and L_{md} expression into each other by utilizing syntactic rules and word meaning descriptions of natural language.
A word meaning description M_w is given by (5) as a pair of 'Concept Part (C_p)' and 'Unification Part (U_p)'.

$$M_w \Leftrightarrow [C_p:U_p] \quad (5)$$

The C_p of a word W is a locus formula about properties and relations of the matters involved such as shapes, colors, functions, potentialities, etc while its U_p is a set of operations for unifying the C_ps of W's syntactic governors or dependents. For example, the meaning of the English verb 'carry' can be given by (6).

$$[(\exists x,y,p_1,p_2,k)L(x,x,p_1,p_2,A_{12},Gt,k)\Pi L(x,y,p_1,p_2,A_{12},Gt,k)\wedge x\neq y\wedge p_1\neq p_2:ARG(Dep.1,x); ARG(Dep.2,y);] \quad (6)$$

The U_p above consists of two operations to unify the first dependent (Dep.1) and the second dependent (Dep.2) of the current word with the variables x and y, respectively. Here, Dep.1 and Dep.2 are the 'subject' and the 'object' of 'carry', respectively. Therefore, the surface structure '*Mary carries a book*' is translated into the conceptual structure (7) via the surface dependency structure shown in Fig.4. This process is completely reversible.

$$(\exists y,p_1,p_2,k)L(Mary,Mary,p_1,p_2,A_{12},Gt,k)\Pi L(Mary,y,p_1,p_2,A_{12},Gt,k)\wedge Mary\neq y \wedge p_1\neq p_2\wedge book(y) \quad (7)$$

For another example, the meaning description of the English preposition 'through' is also given by (8).

$$[(\exists x,y,p_1,z,p_3,g,k,p_4,k_0)(\underline{L(x,y,p_1,z,A_{12},g,k)}\bullet L(x,y,z,p_3,A_{12},g,k))\Pi L(x,y,p_4,p_4,A_{13},g,k_0) \wedge p_1\neq z\wedge z\neq p_3:ARG(Dep.1,z); IF(Gov=Verb)\rightarrow PAT(Gov,(1,1)); IF(Gov=Noun)\rightarrow ARG(Gov,y);] \quad (8)$$

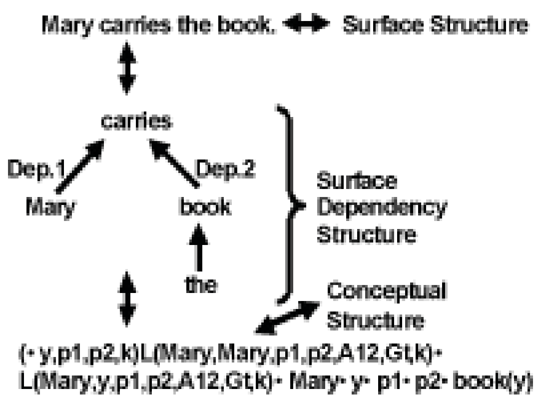

Fig.4. Mutual translation between text and L_{md}

The U_p above is for unifying the C_ps of the very word, its governor (Gov, a verb or a noun) and its dependent (Dep.1, a noun). The second argument (1,1) of the command PAT indicates the underlined part of (9) and in general (i,j) refers to the partial formu la covering from the ith to the jth atomic formula of the current C_p.

This part is the pattern common to both the C_ps to be unified. This is called 'Unification Handle (U_h)' and when missing, the C_ps are to be combined simply with '$\wedge$'. Therefore the sentences S9, S10 and S11 are interpreted as (9), (10) and (11), respectively. The underlined parts of these formulas are the results of PAT operations. The expression (12) is the C_p of the adjective 'long' implying 'there is some value greater than some standard of 'Length (A_{02})' which is often simplified as (12').

(S9) The train runs through the tunnel.

$$(\exists x,y,p_1,z,p_3,k,p_4,k_0)(\underline{L(x,y,p_1,z,A_{12},Gt,k)}\bullet L(x,y,z,p_3,A_{12},Gt,k))\Pi L(x,y,p_4,p_4,A_{13},Gt,k_0) \wedge p_1\neq z \wedge z\neq p_3 \wedge train(y) \wedge tunnel(z) \tag{9}$$

(S10) The path runs through the forest.

$$(\exists x,y,p_1,z,p_3,k,p_4,k_0)(\underline{L(x,y,p_1,z,A_{12},Gs,k)}\bullet L(x,y,z,p_3,A_{12},Gs,k))\Pi L(x,y,p_4,p_4,A_{13},Gs,k_0) \wedge p_1\neq z \wedge z\neq p_3 \wedge path(y) \wedge forest(z) \tag{10}$$

(S11) The path through the forest is long.

$$(\exists x,y,p_1,z,p_3,x_1,k,q,k_1,p_4,k_0)(L(x,y,p_1,z,A_{12},Gs,k)\bullet L(x,y,z,p_3,A_{12},Gs,k))\Pi L(x,y,p_4,p_4,A_{13},Gs,k_0) \wedge L(x_1,y,q,q,A_{02},Gt,k_1) \wedge p_1\neq z \wedge z\neq p_3 \wedge q>k_1 \wedge path(y) \wedge forest(z) \tag{11}$$

$$(\exists x_1,y_1,q,k_1)L(x_1,y_1,q,q,A_{02},Gt,k_1)\wedge q>k_1 \tag{12}$$

$$(\exists x_1,y_1,k_1)L(x_1,y_1,Long,Long,A_{02},Gt,k_1) \tag{12'}$$

For simplicity, we have recently employed such a format for text meaning representation as shown in Table 1, so called, 'Discourse Image Tree (DIT)'. This table represents the meaning of S12 where all the formulas are expressed in Polish notation. In general, the leaves of a DIT consist of atomic locus formulas, labeled as 'L_n', and connectives such as CANDs and SANDs. Table 2 shows the DIT for S13.

Table 1*. Discourse Image Tree of S12

Discourse Image	**D1=Ù S1S2**		
Sentence Image	**S1=C1**		**S2=C2**
Clause Image	**C1=P P1P2**		**C2=P3**
Phrase Image	**P1=L1**	**P2=L2**	**P3=L3**
Locus Image	**L1**	**L2**	**L3**
Causer	x	x	x1
Attr_Carrier	road	**P1**	it
IntVal	Tokyo	west	very. long
FinVal	Osaka	west	very. long
Attribute	A_{12}	A_{13}	A_{02}
Event Type	Gs	Gs	Gt
Standard	k	k_1	k_2

* $\mathbf{P_1}=(\exists x,y,k)L(x,y,Tokyo,Osaka,A_{12},Gs,k)\wedge road(y)$

$\mathbf{P_2}=(\exists x,k_1)L(x,\mathbf{P_1},west,west,A_{13},Gs,k_1)$

Table2. Discourse Image Tree of S13

D1=•S1S2					
S1=· C2C1					**S2=C3**
C1=P P P1P2P3				**C2=P4**	**C3=P5**
P1=P P L1L2		**P2=L3**	**P3=L4**	**P4=L5**	**P5=L6**
L1	**L2**	**L3**	**L4**	**L5**	**L6**
tom	tom	x_1	x_2	he	x_3
tom	book	book	**P1**	he	book
q_1	q_1	red	very.fast	q_2	?q
OSK	OSK	red	very.fast	TKY	?q
A_{12}	A_{12}	A_{32}	A_{16}	A_{12}	A_{12}
Gt	Gt	Gt	Gt	Gt	Gt
k_1	k_1	k_2	k_3	k_1	k_1

A DIT can realize hierarchical representation and computation of text meaning consisting of five levels of image: 1) Locus level image, 2) Phrase level image, 3) Clause level image, 4) Sentence level image and 5) Discourse level image and thereby can cope with higher-order meaning representation as shown just below Table 1.

(S12) The road runs west from Tokyo to Osaka. It is very long.

(S13) Tom carries the red book very fast to Osaka after he reaches Tokyo. Then, where is the book?

IV. CONCLUSION

Most of computations on $\boldsymbol{L_{md}}$ are simply for unifying (or identifying) atomic loci and for evaluating arithmetic expressions such as 'p=q', and therefore we believe that our formalismcan reduce the computational complexities of the traditional ones when applied to the same kinds of problems described here. Moreover, recent employment of DITs has enabled us to program in procedural languages and thereby remarkably reduced computational complexity for $\boldsymbol{L_{md}}$ expressions while the earlier version of IMAGES-M was programmed in PROLOG and therefore inefficient in computation. This advantage of ours comes from the meaning representation scheme normalized by atomic locus formulas, which has come to facilitate higher-order representation and computation as shown in Tables 1 and 2.

Our future work will include further elaboration of the deductive system, improvement of DIT processing algorithms and establishment of learning facilities for automatic acquisition of word concepts from sensory data and more powerful interfaces for human-system communication by natural language under real environments.

REFERENCES

[1] Yokota M et al (2010), Towards natural intelligence modeling as a formal system based on Mental Image Directed Semantic Theory (Part 1), Proc. of AROB2010, Beppu, Oita, Feb. 2010.

Commanding a humanoid to move objects in a multimodal language

T. Oka*, K. Sugita and M. Yokota

**Nihon University, 1-2-1 Izumicho, Narashino, Chiba, 275-8575 JAPAN*
Fukuoka Institute of Technology, 3-30-1Wajiro-higashi, Higashi-ku, Fukuoka, 811-0295 JAPAN
*(*Tel : 81-47-474-9693; Fax : 81-47-474-2669)*
(oka.tetsushi@nihon-u.ac.jp, sugita@fit.ac.jp, yokota@fit.ac.jp)

Abstract: This paper describes a study on a humanoid robot that moves objects on the requests of its users. The robot understands commands in a multimodal language which combines spoken messages and two types of hand gestures. All of the ten novice users directed the robot using gestures when they were asked to spontaneously direct the robot to move objects after learning the language for a short period of time. The success rate of multimodal commands was over 90 % and the users completed their tasks without trouble. They thought that gestures were more preferable than and as easy as verbal phrases to inform the robot action parameters such as direction, angle, step, width, and height. The results of the study show that the language is fairly easy for non-experts to learn and can be more effective for directing humanoids to move objects by sophisticating the language and our gesture detector.

Keywords: humanoid, multimodal, command language speech, gesture

I. INTRODUCTION

In recent years, various humanoid robots have been developed for the purpose of realizing robots which work for humans in homes, offices, hospitals, etc. Humanoids have advantages for a multi-purpose robot which helps people. As they look like humans and their structures are similar to us, it is easier for us to communicate with them and for them to work in our environments. On the other hand, because they have at least 15 degrees of freedom, it is difficult to operate them with a conventional interface device. Thus, humanoids in the future need certain autonomy and a new kind of intuitive user interface.

The authors have been developing a multimodal command language for home robot users which combines speech, gestures, body touches, and key press actions [1] and conducting studies on robots including humanoids [2] that can be directed in the language. The results of these studies show that the language can be useful for realizing cost-effective home-use robots for various purposes. This study focuses on combining speech and hand gestures in order to direct humanoids to move objects such as boxes and chairs.

II. MULTIMODAL LANGUAGE

The multimodal command language is based on the Japanese language and two types of hand gestures. It is a set of multimodal commands which consist of a spoken message and a hand gesture. The language is defined by a grammar for spoken messages and a set of gesture events, which enables Japanese speakers to command a humanoid in a fairly natural way to pick up and place objects such as boxes, take steps forward and backward, turn left and right, step aside, and push and pull chairs. Table 1 shows actions that can be commanded in the language.

The grammar for spoken messages defines a set of spoken commands including words to specify an action. Thus, one can command a humanoid robot by giving a spoken command without a gesture in the language.

A single hand waving gesture generates a gesture event containing three parameter values: *direction*, *amplitude*, and *count* values (see Table 2). Single hand gesture events substitute spoken phrases to convey action parameter values such as *step*, *direction*, and *angle* values in Table 1. For instance, a single hand movement to the right means “to the right” for action types *sidestep*, *turn*, and *slide*. Table 3 shows the mapping of the *amplitude* and *count* values of gesture events to the *step* and *angle* values of actions.

A both hand gesture event occurs when a user moves the hands simultaneously up and down. It contains two parameter values, *distance* and *count*, and conveys action parameter values, *width* and *height* (Tables 1 and 2). The *distance* value of a both hand gesture specifies the size of an object, *small*, *medium* (the distance between the shoulders of the robot itself), or *large*, to be picked up. The count of a both hand gesture conveys one of four *height* values: *the floor*, *the knees* (of the robot), *the table*, and *the hips*.

Table 4 shows how hand gestures substitute verbal phrases of spoken action commands and constitutes multimodal commands. As one may notice, multimodal commands include a word or phrase that specifies an action type and a gesture event for one or more action parameters. The commands can include verbal phrases for one or more action parameter values as well, which always override parameter values in gesture events.

Table 1. Actions to move objects

	Parameters	Examples
moveforward	*step*	*mf_3steps*
movebackward	*step*	*mb_2steps*
turn	*direction, angle*	*turn_l_30deg* *turn_r_much*
sidestep	*direction, step*	*sstep_r_2steps* *sstep_l_short*
pickup	*width, height*	*pu_30cm_20cm* *pu_small_table*
place	*height*	*place_table*
push/pull	*height* *step*	*push_h_2steps* *pull_l_3steps*
slide	*height* *step* *direction*	*slide_h_3steps_r*

Table 2. Gesture events

	Parameters	Examples
Single hand	*direction* *amplitude* *count*	*sh_l_long_3* *sh_r_short_2*
Both hand	*distance* *count*	*bh_me_4* *bh_short_2*

Table 3. Mapping of amplitude and count

amp. \ count	1	2	3
short	one step 15 deg.	4 steps 60 deg.	6 steps 90 deg.
long	two steps 30 deg.		

Table 4. Multimodal and spoken commands

Spoken command	Multimodal command
Take 3 steps!	sh_l_long_1 + Walk!
Pick the medium-size object from the table!	bh_medium_3 + Pick (that) up!
Turn right by 15 degrees!	sh_r_short_1 + Turn!
Place it on the floor!	bh_short_1 + Place it!
Slide that left at the height of your hips by 4 steps!	sh_l_short_2 + Slide it at the height of your hips!

III. USER EVALUATION METHOD

1. Simulated humanoid that moves objects

We developed a 23-DOF simulated humanoid robot (Fig. 1) using a humanoid model on Webots [3] robot simulator. The robot can execute action commands of our multimodal language (Table 1) to move boxes and chairs in simulated environments.

The humanoid can interpret multimodal commands using a multi-agent command understanding system [2] on top of OAA [4], which include an OpenCV based hand gesture detector using a web camera we developed by ourselves and a grammar based speech recognition system (Julius4.1.1) [5].

Fig.1. Simulated humanoid that moves objects

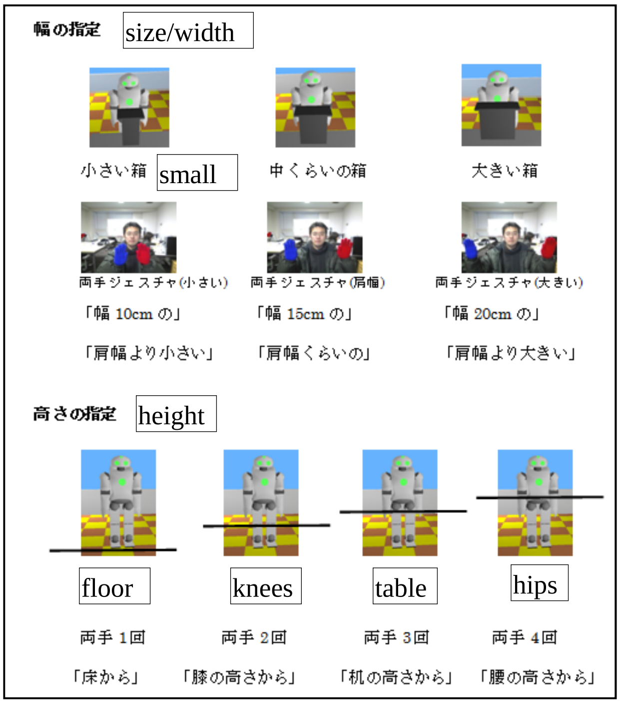

Fig.2. A page of the leaflet

2. User evaluation

Our humanoid robot was evaluated with ten students of Fukuoka Institute of Technology, who had never commanded our robot in the multimodal language.

At the beginning of each user evaluation session, we explained the user how to command the humanoid by speech alone using a leaflet illustrating spoken and multimodal commands (Fig. 2) within five minutes. Then, we demonstrated how to use gestures in the language and gave the user time to practice and learn to use them. Finally, we took ten minutes to teach the user multimodal commands combining gestures and speech.

After the demonstrations and practice, we gave the user the first task to estimate speech and gesture recognition rates and command success rates (Task1). The user read out 23 spoken commands printed in a sheet of paper, made 15 hand gestures as instructed, and gave 20 multimodal commands. The user had to use gestures given only spoken phrases specifying action parameter values in order to give the 20 multimodal commands. After this first task, the user was allowed to practice multimodal commands for ten minutes in order to learn to command the robot successfully without misrecognition and human errors. At this point, the user gave 13 spoken and 15 multimodal commands instructed in another sheet of paper in the same manner as Task1 (Task2).

The third task given to the user was to achieve three goals commanding the robot in the language:

1. Moving a medium-size box on a table down in a specified area on the floor
2. Move a box down to the floor (without information about its size and height)
3. Operate the robot following oral instructions

The user was allowed to consult the leaflet.

After Task3, the user was given the same task as Task1 to demonstrate how well commands and gestures by the user work. Finally, the user was asked how easy it was to specify action parameter values by speech and using hand gestures in 7 point scales from very difficult (1) to very easy (7).

IV. RESULTS

Tables 5-7 show speech recognition rates, gesture recognition rates, and command success rates, respectively, in each task. Gesture error rates for each action parameter in multimodal commands are shown in Table 8. The average ratings of the users about how easy to specify action parameters are shown in Table 9.

Eight of the ten users answered that they preferred multimodal commands to spoken commands. In fact, all of the commands given in Task3 were multimodal commands including both a hand gesture and a spoken message.

In Task3, all the users achieved each goal within three minutes. Six of them commanded the robot without consulting the leaflet. In total, 211 multimodal commands were given and there were two false alarms by the speech recognizer. Some single hand long gestures were misrecognized as the hand went out of the camera view.

Table 5. Speech recognition rates

	Task1	Task2	Task3	Task4
Spoken	92.2 %	88.5 %	-	96.9 %
Multimodal	97.5 %	98.7 %	96.7 %	99.0 %

Table 6. The Gesture recognition rates

	Task1	Task2	Task3	Task4
Gesture	95.2 %	-	-	98.0 %
Multimodal	93.0 %	98.0 %	93.4 %	99.0 %

Table 7. Command success rates

	Task1	Task2	Task3	Task4
Spoken	93.0 %	90.0 %	-	97.4 %
Multimodal	92.0 %	96.7 %	90.1 %	98.0 %

Table 8. Gesture error rates for action parameters

	Task1	Task2	Task3	Task4
direction	0.0 %	0.0 %	4.4 %	0.0 %
angle	2.5 %	3.3 %	5.5 %	0.0 %
step	10.0 %	0.0 %	10.7 %	1.4 %
width	8.0 %	2.5 %	3.1 %	0.0 %
height	0.0 %	1.7 %	1.5 %	1.1 %

Table 9. Average user ratings (7 point scale)

	Speech	Gesture
direction	6.3	6.5
angle	5.4	5.6
step	5.8	5.6
width	6.0	5.8
height	6.0	5.7

V. DISCUSSION

The multimodal language can be effective for the purpose of commanding humanoids to move objects by sophisticating the language and our gesture detector.

First, novice users were able to achieve given goals in Task3 without troubles. Secondly, over 90 % of the multimodal commands were successful (Table 7) in spite of the fact that some gestures were misrecognized when the hand went out of sight. Besides, the success rate of multimodal commands in Task4 was about 98%, which is higher than the success rate of spoken commands in the same task. The results of Task4 show that a novice user can successfully direct humanoids to move objects by speech and using gestures within a short period of time.

The speech recognition rates of multimodal commands are higher than the rates of spoken commands (Table 5) because most of spoken messages in multimodal commands include only a word or phrase to specify an action type. Novice users need a little practice commanding in the spoken language since some actions with two or three parameters are difficult even for Japanese speakers to command by speech alone. They also have to adapt to the speech recognizer, speak clearly, and use the microphone properly.

The results in Table 6 show that novice users can successfully use the two types of gestures with some practice. The recognition rates in Task4 imply that the users were better and better at using gestures. Some gestures were unsuccessful in Task3 probably because the users had to concentrate on looking at the humanoid on the computer screen and sometimes they failed to move their hands properly. The users had to move their hands a lot due to the limitations of our gesture detector. A better gesture detector using a stereo vision which can precisely detect subtle movements would make the language easier to learn.

Novice users need more experiences in order to successfully and quickly achieve goals in various situations as the success rate of multimodal commands in Task3 was lower than the rates of Task2 and Task4 (Table7) due to the lower recognition rates (Tables 5 and 6). In Task3, the users were not given printed words for action parameter values or action types; they had to find the right gestures for parameter values and the right words to inform the robot action types. In addition, some single hand gestures failed because the hand went out of the camera view.

Tables 8 and 9 indicate that it was slightly more difficult to specify *step* and *angle* values using single hand gestures than to specify values of the other parameters. There are some possible reasons for this. First, the mapping in Table 3 was not very natural and required the users some effort to learn it. Second, the long gestures were physically difficult and not very natural because they had to move their hand horizontally about 50cm; in Task3, long gestures failed for this reason. Designing a better mapping and allowing shorter gestures may help users. Another solution is allowing users to cue the robot using a simple gesture whenever they want to stop it.

VI. CONCLUSION

This paper described the results of a study on a humanoid robot that can be directed by its users in a multimodal language to moves objects. Ten novice users successfully directed the robot in multimodal commands to achieve given goals. The success rate of multimodal commands was over 90 % and the users thought that gestures were more preferable than and as easy as verbal phrases to inform the robot action parameters to move objects. The results of the study show that the language can be easier for non-experts to learn and effective for directing humanoids.

ACKNOWLEDGMENT

The authors would like to thank Toyokazu Abe and Kazuki Furihara for their kind help. This work was supported by KAKENHI Grant-in-Aid for Scientific Research (C) 19500171.

REFERENCES

[1] Oka T, Abe T, Sugita K, Yokota M (2009) RUNA: a multi-modal command language for home robot users. Journal on Artificial Life and Robotics 13-2:455-459

[2] Oka T, Abe T, Shimoji M, Nakamura T, Sugita K, Yokota M (2008) Directing humanoids in a multi-modal command language. The 17th International Symposium on Robot and Human Interactive Communication 580-585

[3] Michael O (2004) Cyberbotics Ltd – WebotsTM: Professional Mobile Robot Simulation. International Journal of Advanced Robotic Systems 1-1:39-42

[4] Cheyer A, Martin D (2001) The open agent architecture. Journal of Autonomous Agents and Multi-Agent Systems, 4-1/2:143-148

[5] Lee A, Kawahara A, Shikano K (2001) Julius --- an open source real-time large vocabulary recognition engine. The 7th European Conference on Speech Communication and Technology 1691-1694

Face Detection and Face Authentication Based on 3D Face Image

Hiroya Kamitomo and Cunwei Lu

Fukuoka Institute of Technology, 30-1 Wajirohigashi3-chome, Higashi-ku, Fukuoka
(Tel : 81-92-606-7395)
(bd09001@bene.fit.ac.jp)

Abstract: The technique of face authentication is needed which can be used also by cases, such as make-up face or illumination change. The past technique based on 2-D color image showed low authentication rate, in the case of a photography environmental variation or makeup. We proposed a technique of face authentication based on 3-D face image. In order to solve the above problem, we used the 3D image measurement technique to acquire 3D fac e image and used 3D face image to perform face recognition. In this paper, the 3-D face image measurements are explained. First, I explained the application to the direction detection of the 3-D face. after that. Finally, I explained the application to the 3-D face authentication for security or an access control.

Keywords: *3-d shape measurement, range image, face detection, face authentication*

I. INTRODUCTION

There is a variety of measurement techniques proposed so far. First, stereo vision technique, which is a method to calculate 3-D coordinates in accordance with the principle of the triangulation by way of taking a picture of the measurement object from plural directions with camera. But it is difficult for detection automation on the curved surface and the very confined edge on account of its necessity to detect the correspondence point from two or more images. Therefore, the method called pattern light projection [1] has been prevailing in the case of requirement to measure 3-D shapes in a high sensitivity. Aiming at the measurement object, the ability of decomposition should be improved for the addition of features actively by projecting the pattern light with some features from the projector. The method of Pattern projection has been classified fully into various techniques, depending on the variety of light. The space encoding pattern projection method [1] used stripes pattern of monochrome binary added a binary code to the measurement object with increasing the pitch of light and shade in time sequencing order. In a word, n bit of binary code are allocated in each area of the measurement object by the stripes pattern projection as often as n times. However, it is beyond handling dynamic scene for the time problem and the increase of times of pattern projection so as to do a high decomposition. The density inclination pattern projection method and the color pattern projection method are used multilevel intensity-modulated projection pattern [2]. Owing to the color distribution and reflectivity on the surface of the target object, a lot of projection angle information is obtained by single filming theoretically. The pattern feature after projection has been changed, which would result in the difficulty about the detection of steady projection angle information, and finally its reliability can't be secured.

We proposed the practicable 3-D image measurement system based on optimal intensity-modulation projection technique [3]. It is used as a technique for stabilizing multilevel intensity-modulated projection pattern stripes and extracting them. Stripes detection accuracy can be improved by optimally combining the order of stripes strength of the projected pattern with the strength difference between stripes to the maximum. Thus, for the measurement object that is hard to keep motionless, like human being, it is possible to attain a high-speed, highly accurate measurement by using 3-D image measurement system proposed here. In this text, I aimed to demonstrate the application example applied to the probable, man-machine interface and the security field because of its usage of practicable 3-D image measurement system.

II. 3-D SHAPE MEASUREMENT

A method of triangulation was the radical principle of 3-D image measurement based on the pattern light projection. The pattern light was projected from the projector to the measurement object, and it took a picture of the appearance from a different angle with the camera. Do as formula 1 to calculate the depth distance

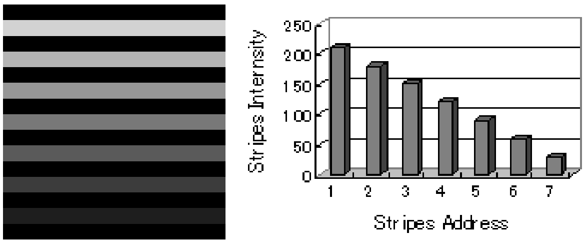

Fig.1. Intensity modulated pattern

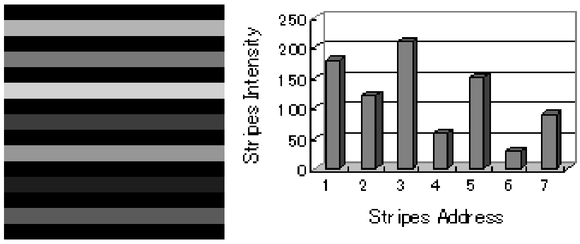

Fig.2. Optimal intensity modulated pattern

of measurement point from projection angle of pattern stripes and stripe coordinate on the observation image.

$$z = \frac{b}{\tan a + \tan b} \quad (1)$$

Here, z was a depth distance of the measurement point; b was a base length (the distance between source of light and the center of lens of camera); a was stripes projection angle; ß was an observation angle degree; b was known among these; ß was computable by stripes coordinates on the observation image.

When the strength modulation pattern light was used as shown in Fig 1, stripes projection angle could be calculated by a single piece of picture theoretically. However, influenced by the surface color of the measurement object and reflection, the intensity value of the projection stripes in the observation image changed and the correspondence to the projection angle collapsed. There was an optimum strength combination pattern light projection method to solve such a problem. It was a technique to optimize projection pattern and to seek for regulation of variations in intensity at a maximum about intensity difference of projection between adjacent stripes.

In a set of stripes addresses $\{1,2,\ldots,N\}$, when the intensity order of the address $p_i \in \{1,2,\ldots,N\}$, the projection light intensity of the stripes strength order was defined as the following magnitude correlations.

$$I_{\min} \le I_{p_1} \le I_{p_2} \le \cdots \le I_{p_N} \le I_{\max} \quad (2)$$

Here, I_{p_i} is the projection light intensity of stripe address, $I_{\min}$ and $I_{\max}$ are minimum value and maximum value of the projection light intensity respectively. The function was defined when the projection light intensity difference of the stripes strength distribution combination $(I_1, I_2, \ldots I_N)$ was at the maximum, evaluation function $d(I_1, I_2, \ldots I_N)$ was also at the maximum.

$$d(I_1, I_2, \ldots I_N) = \sum_{i=M+1}^{N} \sum_{j=1}^{M} k_j \left| I_i - I_{i-j} \right| \quad (3)$$

Here, kj was a weight factor. M was width of the filter on which evaluation function has been set. As the relation of formula 2, when $d(I_1, I_2, \ldots I_N)$ was at the maximum, $d(p_1, p_2, \ldots p_N)$ amounted to the same thing. Thus, it can be said that $d(p_1, p_2, \ldots p_N)$ seek combination $(p_1, p_2, \ldots p_N)$ at the maximum as its optimum combination. Projection pattern shown in Fig 2 was replaced by the stripes order of projection pattern in Fig 1. We knew that the strength difference between adjacent stripes has been increasing as graph. As a result, stripes projection angle should be computable accurately as long as the strength change rule was maintained even if the error margin was included in the detection of stripes projection light intensity.

III. APPLICATIONS

1. Face Detection

Face detection is to detect the direction that human is facing. As the computer can automatically do face detection, it can be used to find out something deserved to be paid attention to and to be under watch without looking the other way during travels. Man's face does movement by rotating from top to bottom of the neck right and left. Therefore, to understand the direction of the face accurately, 3-D information on the face is needed. This time, 3-D image of the face can be acquired by using 3-D shape measurement proposes it. 2-D color information and 3-D shape information are included in 3-D image. First of all, we extracted the face organs such as both eyes and noses by using 2-D color information, and then calculated the inclination angle in the frontal direction by using 3-D position relation of the face organs.

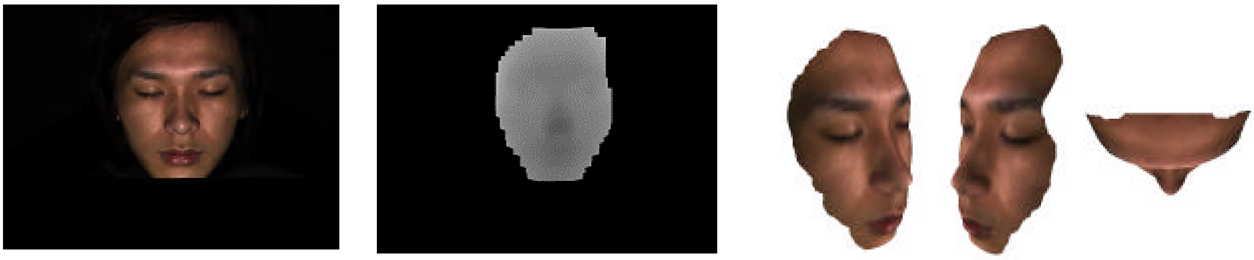

(a) Color image (b) Range image (c) 3DCG

Fig.3. 3D-shape measurement result

2. Face Authentication

2-D image was to take a picture of the object with the digital camera and record information on the shade, brightness, and vividness, etc. While 3-D image recorded information on a three-dimensional size, position, and shape what the object originally has, which was useful for the depth change and the curved surface inspection. That was difficult for 2-D image to analyze.

Face recognition used traditional 2-D image made it easy to come about misidentification as a result of influences like face position, expression, make-up, and lighting environment, etc. For the factors stated above, it can be expected that robust recognition should be practicable by using 3-D face image. Now, 3-D face image can be acquired by using 3-D image measurement system proposed here. It corresponded to the variation of face by generating the distance image vector from face on all sides by way of 3-D image and studying each person's range image through subspace method [4].

The range image sample for study was showed in the sets of the image vector. Here, m was a product of width and the height of the range image, n was the number of range image samples.

When L was projected to the partial space, the basis vector in which the error of mean square was minimized was calculated by the KL conversion. As an unknown range image vector was projected to the partial space, if it were a same person, the projection vector length should grow. Therefore, certification should be done by requesting the projection vector length to a partial space as a degree of similarity with the registration character.

IV. RESULTS AND DISCUSSION

Various objects were measured by using 3-D image measurement systems which was used the optimal intensity-modulation projection technique. Fig 3(a) was a color image of the measurement object taken with camera. Fig 3(b) was a range image expressed by light and shade from the projector. It was clear that 3-D coordinates were calculated in each pixel. Fig 3(c) was an expression of 3-D shape of the object with 3DCG. From the outcome of experiment, we have known that the measurement concerning 3-D shape of the target object can be done in a high sensitivity from the counting system that mounted the optimal intensity-modulation projection technique. Moreover, single-projection could shorten the processing time and the measurement to the dynamic object like human should be practicable. Comparing the size of a columnar object with the depth distance of the measurement result, measurement accuracy was evaluated, which resulted in about 0.3mm of the average error margin and 0.8mm or so of the maximum error margin.

The sample data used to experiment on face recognition was 3-D image of 15 subjects who acquired it by using 3-D shape measurement system. The direction of the face was changed from the front, the right, and upward. 3-D image of the frontal face was assumed to be registration data, and the range image for 125 kinds of faces was generated for the design of a partial space. Unknown input data was collated with the registration data 1 to 1, and the occurrence rate of similarity degree was calculated respectively in person among classes. Fig 4 showed the distribution of the frequencies of similarity degree. A large value was taken when it was a person himself, and if it were others, it should be taken a small value. The threshold to

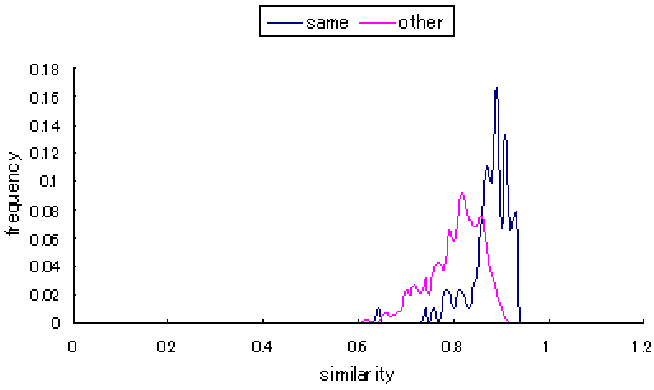

Fig.4. Frequency of similarity

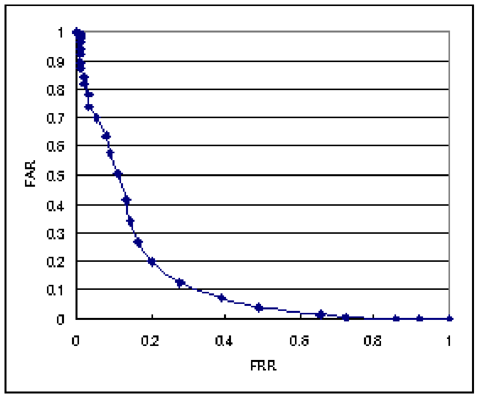

Fig.5. ROC curve

distinguish one person himself from the others was assumed to be a parameter, and misidentification certificate rate FRR and FAR were calculated respectively. The result was shown in ROC curve of Fig 5. From frequency distribution of similarity degree in Fig 4, the case that similarity degree in the others' group was high. It was thought that a common feature with others was extracted by designing a partial space, and the difference between one people himself with the others was vague. Moreover, because the change for the face of the learning pattern was set within 20 degrees in the turning angle, it was difficult to correspond to the change for a face.

However, because it had possibility of extracting the same feature among different people when the turning angle degree of the learning pattern was raised and the number of distance images was increased, it was necessary to improve the method of designing a partial space. It differed from the subspace method that used the color image as another cause, and personal characteristics were valued in the area where the depth change in the face surface shape was intense in the subspace method that used the range image. It was thought that personal characteristics had decreased on the other hand though the worry that ambient light and the make-up influenced disappeared because the range image is separated from the feature of color information based on the color strength difference like eyes, eyebrows, and the skins.

V. CONCLUSION

The practical use of 3-D image measurement was anticipated in the manufactory field. In my study, I aimed to introduce practical 3-D image measurement system with the use of possible and optimum strength modulation pattern light projection method to carry out a high-speed, high sensitivity measurement. Moreover, as an application of measurement system, with the use of face detection and recognition, I am looking forward to demonstrate the correspondence to 3-D movement so as to compensate something troublesome like make-up and lighting for 2-D image. In the present study, it proposed the technique for generating the regularized distance image from 3-D face measurement data as feature data used for the collation processing. As a result, because the feature data separated from color information on the face was obtained, the attestation technique for not receiving the influence of outside ambient light was able to be achieved. Moreover, an invariable attestation became a position variation with possible by the constant generation of the distance image of the size of the face that did not depend on the position of the measurement apparatus with the person and the face registration by the nose top coordinates of the range image. In the present study, the subspace method of the range image was applied to the problem of the change for the face of multiple degrees of freedom.

REFERENCES

[1] Batlle J, Mouaddib E, Salvi J (1998), Recent progress in coded structured light as a technique to solve the correspondence problem. Pattern Recognit 7:963-982
[2] Sato K, Inokuchi S (1985), Range Picture Input System Based on Space-Encoding (in Japanese). IEICE 3:369-375
[3] Lu C, Xiang L (2003), Optimal Intensity-Modulation Projection Technique for Three-Dimensional Shape Measurement (in Japanese). IEICE 23:4649-4657
[4] Oja E, Xiang L(1983), Subspace Methods of Pattern Recognition, Research Studies Press. England

The Fifteenth International Symposium on Artificial Life and Robotics 2010 (AROB 15th '10),
B-Con Plaza, Beppu,Oita, Japan, February 4-6, 2010

Stripes Extraction Technique of Projection Pattern for 3D Shape Measurement

Ke Sun and Cunwei Lu

Fukuoka Institute of Technology
(Tel : 81-92-606-3578; Fax : 81-92-606-0726)
(bd08001@bene.fit.ac.jp) and (lu@fit.ac.jp)

Abstract: **3D image measurement based on pattern light projection can be roughly classified into two groups, binarization type and non-binarization type, from projection pattern intensity and color distribution characteristic. Binarization type is a method of using binarizationalized projection and image, but there are some difficult problems such as the necessity to do the multi-projection so as to detect information of the projection patterns, much time spent on measurement manipulation as well as the correspondence to the move objects. Non-binarization type is a method of using the non-binarizationalized projection pattern, monochrome image or color image. The technique has been in great anticipation of practicability with the popularization of digital camera and projector recently with reason that it may get much more information with single projection through binarizationalized measurement and calculate the high sensitivity 3D information. But the technique is premised on the situation that it must get reflex pattern image with essential number of slit and intensity distribution, that is to say, the ideal observation pattern image so as to secure the sensitivity and accuracy of measurement. So, as for the target object without specification on the surface reflectance and distribution of surface color, the measurement would encounter several problems such as deficiency of the volume of information on the reflex projection patterns, uncertainty of the target measurement sensitivity as well as the troublesome of measurement manipulation. In order to solve the problems presented above, I propose Fast Fourier transform (FFT) technique on one initial observation image in my study. Furthermore, I strove for 3D image detection by using one initial observation image by single pattern light projection through merging the technique of monochrome projection-color analysis (MPCA) with the optimal intensity modulated projection (OIMP) together, which resulted in the high speed and high accuracy of 3D image observation.**

Keywords: **Pattern Projection, Frequency Domain, Monochrome-projection, Color-analysis.**

I. INTRODUCTION

Figure 1 showed the projection pattern used a measurement technique, saying, intensity modulation pattern projection measurement technique. Intensity modulation pattern projection technique was that adding the intensity modulation which had been made correspondence between stripes location information and the intensity information to projection patterns and doing 3D measurement by using their correspondence between the stripes intensity value of the projection pattern and the stripes intensity value of the observation pattern image. But taking discontinuance between stripes of the projection pattern into account, it's possible to make a steady measurement to resist noise with comparison to analogue technique such as the density inclination pattern etc. If the intensity modulation pattern with N pieces of stripes was projected and stripes address were to be detected from the observation pattern image correctly, the depth measurement sensitivity equivalent to slit optical projection as often as N times should be obtained by single measurement.

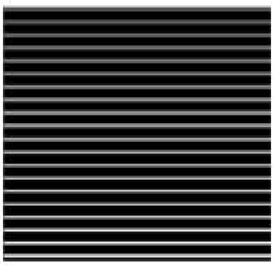

Fig.1. Intensity modulat ion pattern

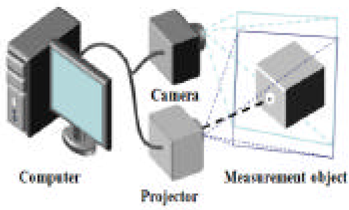

Fig.2. Pattern projection measurement system

The traditional intensity modulation pattern projection technique was chiefly projected to the grey intensity modulation pattern and utilized image analysis technique through grey scale input, but it has been proved to be difficult to obtain reflection pattern with necessary measurement range in the case of measuring objects with multiple color distribution. Owing to its necessity to correct slit pattern by taking more than 2 photos so as to get wide measurement image of the intensity range, the measurement was always costly and hard to deal with the moving object. In the present study, the observation pattern image with a wide and ideal stripes intensity distribution of the intensity range was automatically acquired by using the monochrome projection color analysis technology, furthermore, as to the synthesized observation pattern image, the influence of the measurement outcome due to the measurement condition, such as surface reflectance of the target object, was reduced by the Fourier transform in the frequency domain. Because of the possibility to detect stripes address by sharpening slit patterns, the problems mentioned above were solved, which would result in the reduction of the cost and improvement of the measurement accuracy.

II. ALGORITHM

Figure 2 was a composition of typical pattern projection measurement system. The projection pattern been output by the computer was projected to the measurement object from the projector, camera was used to take a picture of the projected pattern reflected to the measurement object as an observation pattern image, finally, the information stored in the camera was input to the computer. Next, the directions of the stripes of projection pattern were detected from the observation pattern image which had been input, and then 3D shape of the object was restored based on the principle of the triangulation. The following contained processing of each step was stated simply.

Step1: Projecting intensity modulation pattern to measurement object.

Step2: Taking a picture of the image and using it as the initial observation pattern image.

Step3 :Doing color analysis of the initial observation image and synthesizing the image for the measurement based on the color channel for the measurement. The color channel that reflection intensity value was stronger than the others was extracted every pixel from input image and used it as the channel for the measurement. The influence caused by other color components and the surface reflectance in the same part of the measurement object were reduced by synthesizing single channel image for calculation with a channel for the measurement of each pixel.

Step4: Extracting measurement object from the image for measurement and deleting the noise with threshold extraction method.

Step5: Confirming the influence of surface reflectance. If there were no influence, Step 6 should be omitted and jumped to step 7 directly.

Step6: Correcting the influence of the surface reflectance of the measurement object from the image for the measurement with the object of detecting stripes address in high accuracy and sharpening stripes pattern for the measurement. To reduce the influence on the measurement result according to the measurement condition of the surface reflectance etc. of this object, it proposed the Fourier transform technique of the image in the frequency domain in the present study. In the following Chapter 3, I described the technique and principle.

Step7 :Extracting slit pattern address in the light of a linear relation of each stripes intensity value from the corrected image for measurement because the intensity value of each stripes pattern was decided by majority according to the intensity value of each pixel of each stripes pattern.

Step8 :Calculating the 3D space world coordinates based on the detected stripes address. The calculation of three dimension shape by using the principle of the triangulation was omitted in this thesis.

III. PRINCIPLE AND METHOD

1. Problem of reflectivity reduction

About the intensity modulation pattern projection measurement, it was ideal that the relation between the intensity of the reflection pattern stripes obtained from the input image and a pattern stripes degree were a one-to-one correspondence in order to obtain three dimension shape with accuracy. However, the measurement object was multiple color distribution, and it was difficult to obtain such an ideal relation when it had reflectivity taken with a versatile digital camera. Generally, the gray projection pattern was projected to the measurement object with a variety of color distribution, information obtained from the reflection pattern image was only brightness, coordinates, color information on the measurement object decreased and the measurement range confused became narrow.

2. Space area correction method

For the projected pattern intensity $P(x, y)$, if pixel intensity $I(i, j)$ in the image was always (1), the correction method of traditional reflectivity should be ideal.

$$P(x,y):I(i,j)=1:1 \qquad (1)$$

Actually, Surface reflection element $O(x,y)$ of the object can be actually contained, and intensity of each pixel in the reflection pattern image that hit the object be shown as follows.

$$I_l(i,j)=P_n(x,y)\times O(x,y) \qquad (2)$$

At this time, because the surface reflection element had its influences in (2), stripes degree n of $P_n(x,y)$ can not be detected. Then, we projected projection pattern with uniform intensity $P_f(x,y)$ to the same measurement scene, the relation of (3) was obtained.

$$I_f(i,j)=P_f(x,y)\times O(x,y) \qquad (3)$$

The following relation was obtained from (2) and (3).

$$\frac{I_l(i,j)}{I_f(i,j)}=\frac{P_n(x,y)}{P_f(x,y)} \qquad (4)$$

That is to say, the image for the calculation with the projection light stripes intensity distribution and linear correspondence was obtained by the dividing calculation correction. With correction method, steady stripes pattern for measurement could be obtained, but confronting the fact, which meant its difficulty to deal with the moving object, furthermore, the necessity to have two pieces of observation image made the measurement cost expensive.

3. Frequency area correction method

Rather than delete surface reflectivity from each pixel, my study aimed to obtain measureable stripes pattern in the power spectrum within the frequency area of the whole image by using single observation image.

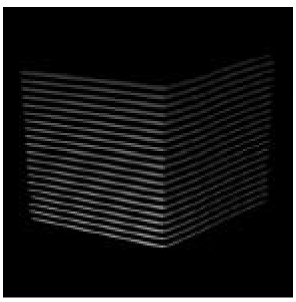

Fig.3. Synthesized measurement image

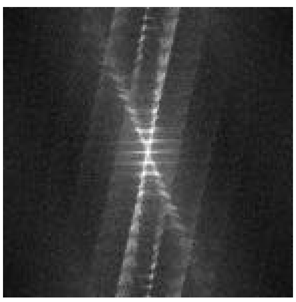

Fig.4. Power-spectrum of image for

Here, Figure 3 showed the synthesized image for measurement, while Figure 4 was power spectrum of the measurement image. According to Figure 3 and Figure 4, it was clear that a power spectrum image with a characteristic of the periodic light and shade pattern like the synthetic measurement image had the repetitive brightness edge. For instance, against the engine arranged in the vertical direction of the power spectrum image, it was composed in the horizontal direction on the original measurement image. If a strong edge existed for a power spectrum image's diagonal depending the length edge, to lean to the right, and to come, it should be comprehended to arrange stripes pattern in each edge and the direction (for left diagonal horizontal direction) in which it goes directly in an original measured imagery. But, when the patterns in all directions confused in the measurement image, the frequency image scattered everywhere, so the power spectrum was. At this time, it meant that the bright places and low frequency existed so many in the center of the power spectrum, in reverse, high patterns of the frequency existed in the far, direct component lied in the center.

The method of the present study was that extracting stripe pattern from the initial observation image, synthesizing the image for the measurement. And, stripes pattern was converted into a power spectrum image from this composited image, and then, stripe pattern was sharpened in the light of the extraction of the frequency of stripes pattern for the measurement in the power spectrum of the composite image, finally, measurement image reflectivity was corrected. The extraction method of stripes pattern was done by setting the threshold in a power spectrum image. In addition, when stripes pattern for the measurement was a curve, which made the edge of the corresponding power spectrum was not clear, the number of low frequencies was extracted by using the nether Butterworth filter another time as an auxiliary means after the power spectrum of stripes pattern was extracted from the threshold, stripes pattern was sharpened at last.

$$H(i,j)=\frac{1}{1.0+(\sqrt{2}-1)\,p^{\frac{1}{4}}} \qquad (5)$$

Here, $H(i,j)$ was coefficient of the filter, p was the distances from each pixel to the image center in a power spectrum image (The unit: pixel).

IV. OUTCOME OF AN EXPERIMENT

The experiment was done in the spaciousness environment where the lighting was erased. The experiment system was composed of the liquid crystal projector, the CCD color camera, and the computer, an ideal stripes number of the projection pattern was set to 20.

Fig.5. Measurement object measurement

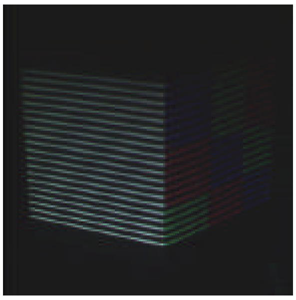

Fig.6. Initial image of observation pattern

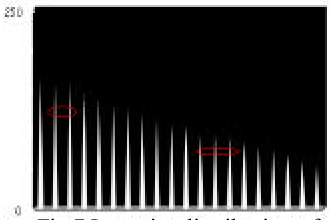

Fig.7 Intensity distribution of measurement composition

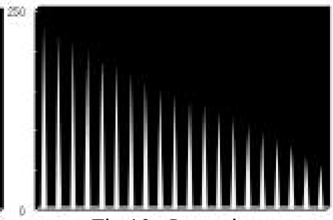

Fig.10. Intensity distribution of correcte

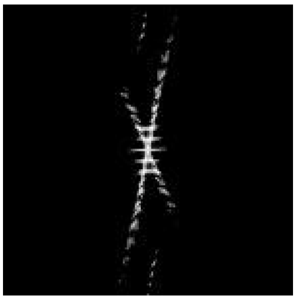

Fig.8. Extracted power-spectrum

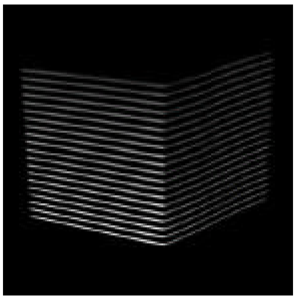

Fig.9. Corrected measurement image

Stripes pattern after the calibration of Figure 1 was projected from an algorithm above-mentioned Chapter 2 to the measurement object of Figure 5, it took a picture, and an initial image of Figure 6 was obtained. The measurement image of Figure 3 was compounded by using color analysis, because the intensity range of the measurement image which had been compounded became narrower on the one hand, the intensity distribution was not linear on the other, the accuracy of detecting stripes address was obtained. Figure 7 showed the intensity distribution of the composite image, we can find something influential came from the surface reflectance (Stripes enclosed in a red line were not linear, and the intensity range narrows down greatly, too). So as to decrease influence, we sought for the composite power spectrum image through Fourier transform (refer to Figure 4), extracted power spectrum of the stripes pattern in it, conversed to Fourier and did image correction. Figure 8 showed the image of a power spectrum of the extraction. Figure 9 showed the measurement image which had been corrected. Figure 10 showed the intensity distribution of measurement image which had been corrected. We have known that the stripes intensity distribution at this time was almost distributed in a linear target, intensity range became wider.

V. CONCLUSION

In the present study, it proposed three dimension measurement technique of the object with multiple color distribution by using Fourier transform technique from one initial observation image. According to the characteristic of the measurement system, the intensity modulation pattern calibrated was projected to the object with the multiple color distribution, and color information in the reflection pattern image filmed was analyzed, And then, the image for measurement was compounded, finally, the wide range intensity distribution stripes with projection pattern stripes degree and linear correspondence can be obtained by the intensity correction of the measurement image. Thus, it was possible to utilize effectively image information and resulted in a high efficiency and accurate measurement.

The further study of the validity concerning the technique proposed here in the case of the objects with multi-materials and its system practicability would be mentioned as the assignment in the future.

REFERENCES

[1] G. Cho and C. Lu: 3D Image Measurement for Object with Multiplex Color Information Analysis; *Proceedings of 9th Symposium on Sensing via image Information(SSII 03)*, pp.79-82(2003).

[2] G. Cho and C. Lu: Practical 3D Measurement System based on Projection Pattern Control Techniques; *IEEJ Trans. EIS*; Vol.127, No.4, pp561-567(2007).

[3] C. Lu and G. Cho: 3D Image Measurement by Combination of Monochrome-Projection Color-Analysis and OIMP Technique; *Transactions of The Institute of Systems, Control and Information Engineers*: Vol.17, No.6,pp.233-240(2006)

The Fifteenth International Symposium on Artificial Life and Robotics 2010 (AROB 15th '10),
B-Con Plaza, Beppu,Oita, Japan, February 4-6, 2010

A Software Framework for Universal Multimedia Access

Yusaku Maeda[1], Kaoru Sugita[2], Tetsushi Oka[3], Masao Yokota[2]

[1]*Graduate school of fukuoka institute of technology, 3-30-1, Wajiro-Higashi, Higashi-ku, Fukuoka, 811-0295, Japan*

[2]*Fukuoka institute of technology, 3-30-1, Wajiro-Higashi, Higashi-ku, Fukuoka, 811-0295, Japan*

[3] *Nihon University College of Industrial Technology, 1-2-1 Izumicho, Narashino-shi, Chiba 275-8575 Japan*

Tel : 81-92-606-4965; Fax : 81-92-606-4965

[1]*mgm08004@bene.fit.ac.jp*, [2]*{sugita, yokota}@fit.ac.jp*, [3]*oka.tetsushi@nihon-u.ac.jp*

Abstract: Recently, immense multimedia information has come to be exchanged on the Internet, where 3DCG, video, image, sound, and text are involved in various circumstances with terminal devices, networks and users different in their competences and performances. This fact may easily lead to 'digital divide' so called unless any special support is given to the weaker. We have already proposed a new concept of 'universal multimedia access' intended to narrow the digital divide by providing appropriate multimedia expressions according to users' (mental and physical) abilities, computer facilities, and network environments. In this paper, we discuss a software framework for our new concept and its implementation.

Keywords: Multimedia system, Switching functions, Monitoring functions, Multimedia transmission protocol.

I. INTRODUCTION

Recently, immense amount of multimedia information has come to be exchanged on the Internet, where 3DCG, video, image, sound, and text are involved in various circumstances with terminal devices and networks, and users different in their competences and performances. This fact may easily lead to the so-called 'digital divide' unless any special support is given to the weaker users.

A universal design concept is proposed to support handicapped people in their social activities [1]. In the computer science field, the universal web [2] has been proposed to develop this concept. However, this does not support changes in the contents, the media and the quality of service (QoS) function to use the devices and network environments to their full capacity. On the other hand, many studies on the QoS function have proposed optimizing the video quality for priorities areas at users' requests [3]. These studies focused on the performances of devices and network environments, but not on the users' abilities or equipments. Of course, there were also several studies on 'universal multimedia access (UMA)' but they could not narrow the digital divide because they concerned 'content switching' only [4].

In consideration of this fact, we have already proposed a new concept of UMA [5, 6] intended to narrow the digital divide by providing appropriate multimedia expressions according to users' (mental and physical) abilities, computer facilities and network environments. In this paper, we discuss a software framework for our new concept and its implementation.

II. UNIVERSAL MULTIMEDIA ACCESS

The digital divide is caused by the differences in users' personal competences, computer facilities, and network environments. Therefore, multimedia information is necessarily accompanied by the need to switch the user interface, the media and the QoS parameters, thus reflecting these differences. Here, we present a new approach to UMA for handicapped people to help them to use their devices and network environments to their full capacity. Our purpose is exclusively to develop a new mechanism for appropriately switching user interfaces, media and QoS parameters based on a concept such as that shown in Fig.1.

III. SWITCHING FUNCTIONS

UMA means to selectively provide three kinds of switching function (SF), namely, user interface switching (UIS), media switching (MS), and QoS switching (QS). Fig.2 shows these switching functions working as follows:

(SF1) UIS: switch to the user interfaces (UI) appropriate for users' competences and display devices,

(SF2) MS: switch to the media which is appropriate for users' competences, performances of terminal devices and networks,

(SF3) QS: control the media qualities so that they are appropriate for users' competences and terminal devices.

These functions are applied in ascending order (from SF1 to SF3) when starting to use multimedia information or in descending order when it is being used.

1. User Interface Switching

UIS sets up the following items.

(U1) A writing style which is appropriate for the users' language ability,

(U2) The UI type and annotation option which are appropriate for users' computer skill,

(U3) The media size, font size, number of media, and number of characters which are appropriate for the size of the display device.

In addition, the I/O function is reflected by the users' disability.

2. Media Switching

MS switches to the appropriate media according to predetermined priorities after determining usable media types and the QoS parameters. The numbers and types of media are selected by UIS. The media and their quality are limited by the performances both of terminal devices and networks. When MS could not continue to play a medium because of an overload of CPU or network, MS is switched to UIS to reduce this load.

3. QoS Switching

QS controls the media size and media rate with QoS parameters to measure the performances of both terminal devices and networks. The QoS parameter 'Size' means:

(S1) Video – Give priority to frame sizes

(S2) Audio – Give priority to sampling resolution and stereo sound

(S3) Image - Give priority to size of image

(S4) Text – Enlarge characters

The QoS parameter 'Rate' means:

(R1) Video – Give priority to frame rates

(R2) Audio – Give priority to sampling rates

(R3) Image - Give priority to display timing

(R4) Text – Take priority over any other medium

IV. Monitoring Functions

The SF is selectively provided by the management system and receives several types of message from 4 monitoring modules and the network interface (NI) as shown in Fig.3. These modules monitor the following items to send/receive event messages as shown in Tab.1.

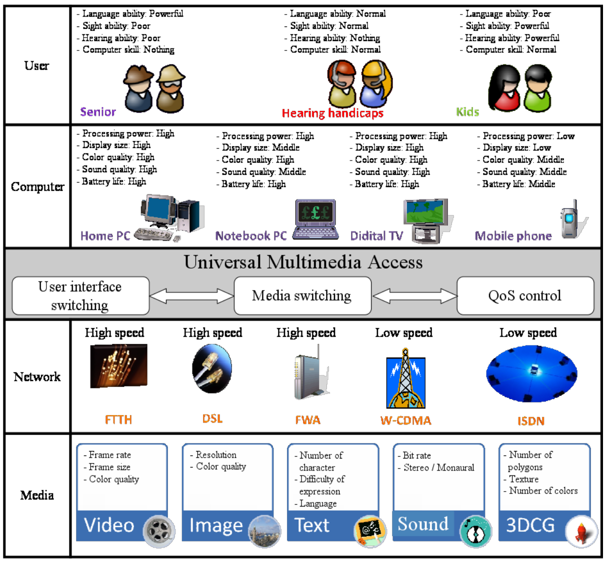

Fig.1. Universal multimedia access

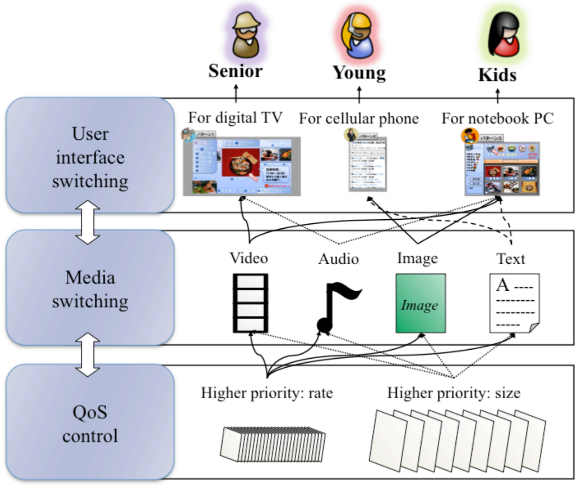

Fig. 2. Switching functions

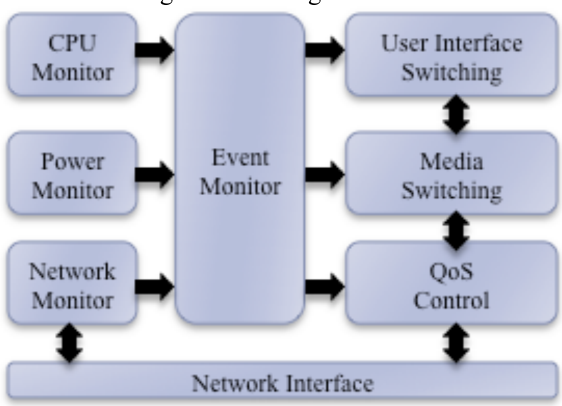

Fig. 3. Configuration of Management System

(M1) CPU Monitor: give the CPU load average to the Event Monitor for checking the CPU load factor.

(M2) Power Monitor: give the power consumption to the Event Monitor for reviewing the power resources.

(M3) Network Monitor: give a throughput to collect packet loss rates and the round trip time (RTT) using the real time transmission control protocol (RTCP).

(M4) Event Monitor: request to each SF according to the events from other monitoring modules and user's operations.

In addition, the QS receives the message and the media data from the NI.

V. Transmission Protocols

The management system keeps synchronizing a master media with some slave media as shown in Fig.4. These synchronizations are caused both within and among multimedia contents by the network time protocol (NTP) according to the common time line. A transmission protocol has 4 layers constructed on real time transmission protocol (RTP) and RTCP to use multimedia contents for supporting three types of SF and to keep these synchronizations. Figure 5 shows this transmission protocol and their layers to be achieved as follows:

(L1) Multimedia Transmission Protocol: media combination, inter-media synchronization,

(L2) Media Transmission Protocol: media exchange, intra-media synchronization,

(L3) Frame Transmission Protocol: frame rate control,

(L4) Packet Transmission Protocol: packet rate control, congestion control.

A multimedia contents is provided with a starting phase and a switching phase as shown in Fig.4 and Fig.5, respectively.

In the starting phase, the UIS is applied to UI according to the command 'Request(Action)' from the event monitor after receiving users' information and computer specification as shown in Fig.6. Also, the MS and the QS are performed to provide appropriate media and media qualities synchronized by the 'Request(...)' from the event monitor, respectively.

In the switching phase, each SF is performed according to user's request for parameter change 'Request(Change_**)' and media quality change 'Notice(Change)', a notification of overflow and underflow 'Notice(Over) from monitoring functions as shown in Fig.7. Also, each SF returns 'Accept(...)' or 'Refuse(...)' to apply these request.

Table. 1. Types of Event Message

Type of message	Type of information	Meaming
Report	User	User information
	Computer	Terminal information
	Network	Network information
Request	Content	Send the content data
	Action	Execute the request
	Change_**	Change to another request
	Kill	Stop the process
Accept	Accept to request 'Chage'	
Refuse	Refuse to request 'Change'	
Notice	Change_**	User's request for another threshold
	Over_**	Over flow or under flow to threshold
Display	Content	Display content
	Reply	Replay for notice 'Change_**'
Info	Information of any other event	

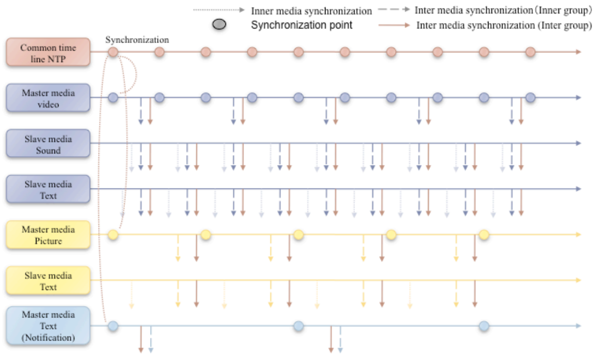

Fig. 4. Mechanism for multimedia synchronization

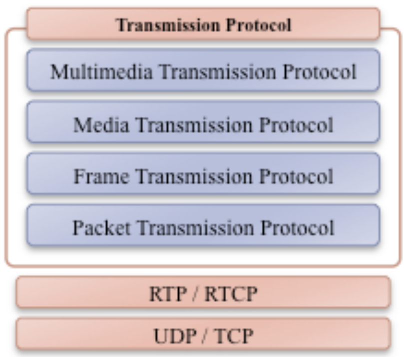

Fig. 5. Transmission protocol

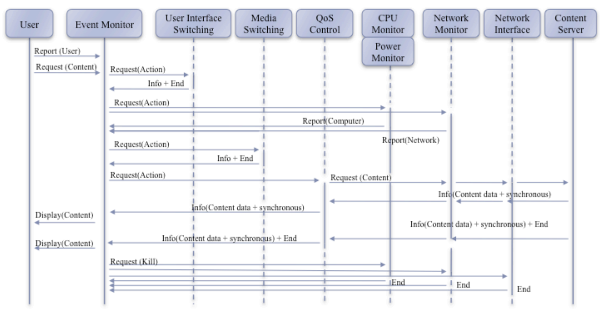

Fig. 6. Event sequence at starting phase

VI. Implementation

A prototype system has been developed as a client-server system in C++, Win32API and WinSock2, which supports a multi-thread to enable playing several remote media simultaneously. But, the current system hasn't supported the SF yet. The client software and the server software are configured such modules as shown in Fig.8 and Fig.9, respectively. A snapshot is the client software recommended for kids using notebook PCs as shown in Fig.10.

VII. CONCLUSION

In this paper, we discussed a software framework for our new concept and its implementation. Currently, we are implementing switching functions for providing appropriate multimedia expressions according to users' (mental and physical) abilities, computer facilities and network environments. In the future, we will evaluate our software framework, define rules for each switching function and develop a multimedia markup language for UMA.

REFERENCES

[1] Ronald L. Mace, Graeme J. Hardie, and Jaine P. Place (1991), Accessible Environments: Toward Universal Design, The Center for Universal Design, North Carolina State University, USA
[2] Kazuhiko Yamazaki (2001), Achievement of universal Web (1) (in Japanese). Design study research 48:330-331
[3] Mohan, R, Smith, J.R and Chung-Sheng Li (1999), Adapting multimedia Internet content universal access, IEEE Multimedia Transcations 1(1):104-114
[4] Fernando Pereira and Ian Burnett (2003), Universal Multimedia Experience for tomorrow, IEEE Signal Proccesing Magazine, IEEE 20(2): 63-73
[5] Y. Maeda, K. Sugita, T. Oka, and M. Yokota (2008), Proposal of a New Concept of Universal Multimedia Access, Proc. 13th International symposium on ARTIFICIAL LIFE AND ROBOTICS (AROB 13th '08), OS7-6.
[6] Y. Maeda, E. Tsujimura, K. Sugita, T. Oka, and M. Yokota (2009), Some consideration on user adaptive interface for universal multimedia access, Proc. 13th International symposium on ARTIFICIAL LIFE AND ROBOTICS (AROB 14th '09), OS13-5.

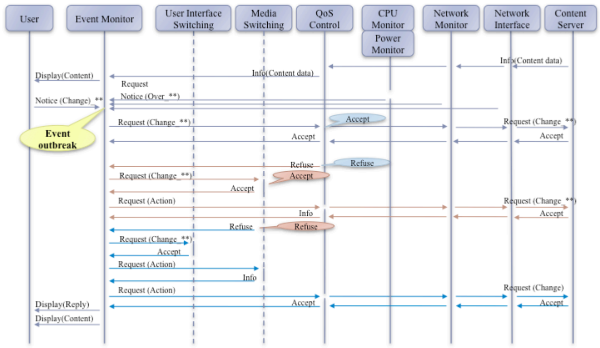

Fig. 7. Event sequence at switching phase

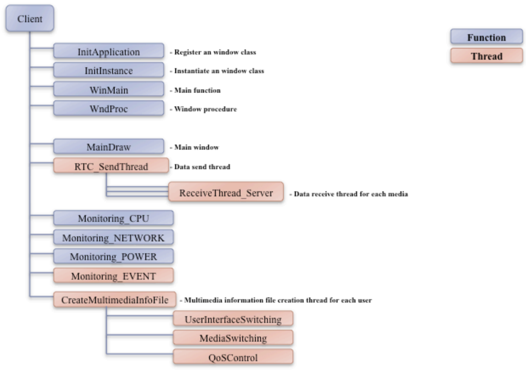

Fig. 8. Module configuration for client software

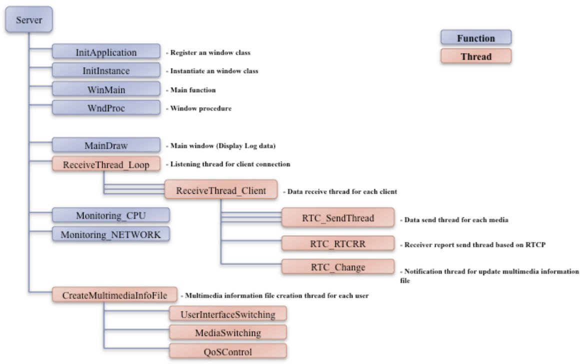

Fig. 9. Module configuration for server software

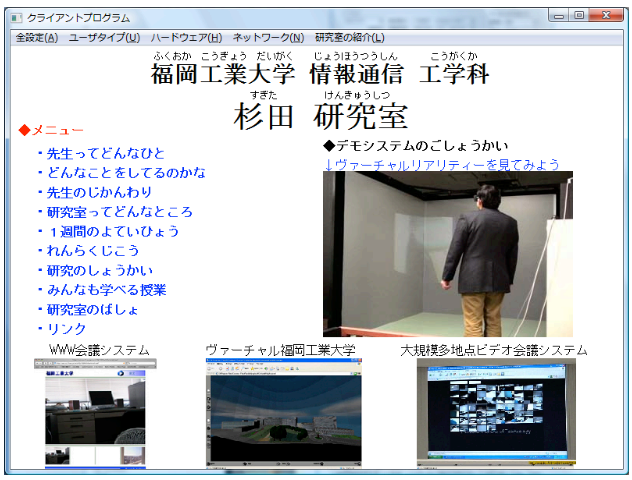

Fig. 10. Prototype system for kids using a notebook PC

Evaluations for an Immunity-Based Anomaly Detection with Dynamic Updating of Profiles

Takeshi Okamoto[1] and Yoshiteru Ishida[2]

[1] *Dept. of Information Network and Communication, Kanagawa Institute of Technology, 1030 Shimo-ogino, Atsugi, Kanagawa 243-0292, Japan*

[2] *Dept. of Knowledge-Based Information Engineering, Toyohashi University of Technology, Tempaku, Toyohashi , Aichi 441-8580, Japan*

Abstract: This paper presents evaluations of an immunity-based anomaly detection method with dynamic updating of profiles. Our experiments showed that the updating of both self and nonself profiles markedly decreased both the false alarm and missed alarm rates in masquerader detection. In computer worm detection, all the *random-scanning worms* and simulated *metaserver worm* examined were detected. The detection accuracy of the simulated *passive worm* was markedly improved.

Keywords: Immunity-based system, anomaly detection, computer worm, ROC, adaptation.

I. INTRODUCTION

Many anomaly detection methods [1] are restricted to the reference of a single user profile. One drawback of these methods is that many false alarms arise when valid users carry out new operations that they have never performed previously. To improve their detection accuracy, we have proposed a new immunity-based anomaly detection method with multiple agents based on the specificity and diversity of the immune system [2]. Our approach makes use of multiple profiles rather than a single profile, which leads to an improvement in detection accuracy.

In addition, we incorporated a new framework of dynamically updating of profiles with test sequences (i.e., not training sequences) into our immunity-based anomaly detection method. The updating of both self and nonself profiles markedly decreased both the false alarm and missed alarm rates in internal masquerader detection [3]. However, the detection accuracy of external masqueraders and computer worms was not evaluated.

In this paper, we made a slight change in profile construction to escape assignment overflow. In experiments, we evaluated the extent to which profile updating improved the detection accuracy of external masqueraders and computer worms.

II. RELATED WORKS

Artificial immune systems for computer security can be divided roughly into three types [4]: hybrid approaches combined with multiple conventional detection methods [5], approaches inspired by the mechanism of negative selection in the thymus [6], and approaches motivated by the danger theory [7].

Our system is related to those using the second approach. The difference in intrusion detection between our method and those reported previously is the reference information used for detection. Previous systems referred only to nonself information, while our method refers to both self and nonself information. This reference to self information contributes to a reduction in false alarms.

III. IMMUNITY-BASED ANOMALY DETECTION

1. Definitions of "self" and "nonself"

The heart of the immune system is the ability to distinguish between "self" (i.e., the body's own molecules, cells, and tissues) and "nonself" (i.e., foreign substances, such as viruses and bacteria). Similarly, operation sequences executed by a user on his/her own account are defined as "self," and all other sequences are defined as "nonself." For example, if one user executes commands on his/her own account, the command sequence is "self." If another user executes commands on someone else's account, the command sequence is "nonself." Such a user is defined as a masquerader or an intruder, regardless of whether the user's actions are malicious.

In an immunity-based anomaly detection system, operation sequences for each user in the training data belong absolutely to "self." The operation sequences are used to construct a profile for each user. The profile yields the probability that the operation sequence belongs to "self." Based on this probability, the system classifies the operation sequence as either belonging or not belonging to "self."

2. Generation of agents

An immune cell has a unique receptor with high affinity for specific antigens. Similarly, our immunity-based system generates a user-specific agent for every user, i.e., every account. An agent has a unique profile, representing the probability that the operation sequence is performed by the original user. The probability is expressed by a score, which is derived from the detection method, i.e., HMM, IPAM, the Bayes 1-step Markov method, etc. We chose the HMM method, because previous studies indicated that it performs well [2]. The parameters of the HMM are given by $\lambda = [\pi, A, B]$ and V, where π is the initial state distribution, A is the state-transition probability distribution, B is the operation probability distribution, and V is the operation table that assigns a unique number to each operation in training data composed of operation sequences obtained previously from each original user. The size of the operation table V is limited to M_{max} to avoid assignment overflow, where M_{max} is specified by a system administrator. The parameters π, A, B are estimated from the training data, as described [2]. The parameter V is determined by operations in training data.

The agent can compute the likelihood $P(O|\lambda)$ of the sequence O with the profile λ. The likelihood $P(O|\lambda)$ represents the probability that the sequence O was performed by the original user corresponding to the agent, i.e., the profile λ. The agent would compute a high likelihood, i.e., a high score, only for the sequences of the original user corresponding to the agent.

3. Adaptive discrimination of self and nonself

Our immunity-based system has a user-specific agent for every account. Each agent monitors operations on its own account until the length of the operation sequence reaches L, where L is specified by a system administrator. The agent of the account on which the length of the sequence reaches L is activated.

The activated agent shares the sequence with all the other agents. All agents compute their own score of the sequence. The activated agent computes the effective threshold, $Min + (Max - Min) \times Th$, where Min is the minimum score of all scores, Max is the maximum score of all scores, and Th is the percentage difference between Min and Max. Th is specified by a system administrator. The activated agent compares its own score, X, with the effective threshold, Y. If $X \geq Y$, the activated agent classifies the sequence as normal, i.e., self. Otherwise, the agent classifies the sequence as abnormal, i.e., nonself. Exceptionally, provided that X is equal to the computational minimum value of $P(O|\lambda)$, the sequence is regarded as abnormal. Conversely, the sequence is regarded as normal if X is equal to the computational maximum value of $P(O|\lambda)$.

If the activated agent classifies the sequence as self, it updates its own profile (i.e., a self profile). If not, the agent that computed the maximum score of all agents updates its own profile (i.e., a nonself profile) and the activated agent raises an alarm to a system administrator. These profiles are newly estimated from the sequence just examined and all the sequences trained previously. Note that the size of the operation table V is limited to M_{max} specified by a system administrator. Once the size of V reaches M_{max}, the least frequently used operation is replaced with a new one.

Finally, the activated agent returns to a normal state and continues to monitor operations on its own account.

IV. EXPERIMENTS AND DISCUSSIONS

1. Masquerader detection

As experimental data, we used network traffic captured from 12 users for about one month. These data are identical to those used in our previous study [8]. This experiment uses web traffic extracted from the data, as web traffic accounts for the majority of network traffic. The web traffic of each user contained more than 3,000 requests. The first 500 requests for each user are training data to allow construction of a profile. The next 1,000 requests are test data to evaluate the detection accuracy. The test for the sequence is performed every 100 requests. All the profiles that are to be updated are updated synchronously by incrementing the sequence number. Anomalous behavior is simulated by testing one user's request sequence against another user's profile.

The number of hidden states of the HMM is set to 1 due to the lowest computational cost and the best accuracy of other states [8]. The HMM parameter is equal to $\lambda = [1, 1, B]$, where B is equal to a relative frequency distribution of operations in training data.

The metrics of detection accuracy are based on the false alarm rate, i.e., false positive rate, and missed alarm rate, i.e., false negative rate. In general, there is a trade-off between the false alarm rate and the missed alarm rate. The relationship between these rates can be described visually by a receiver operating characteristic (ROC) curve, which is a parametric curve generated by

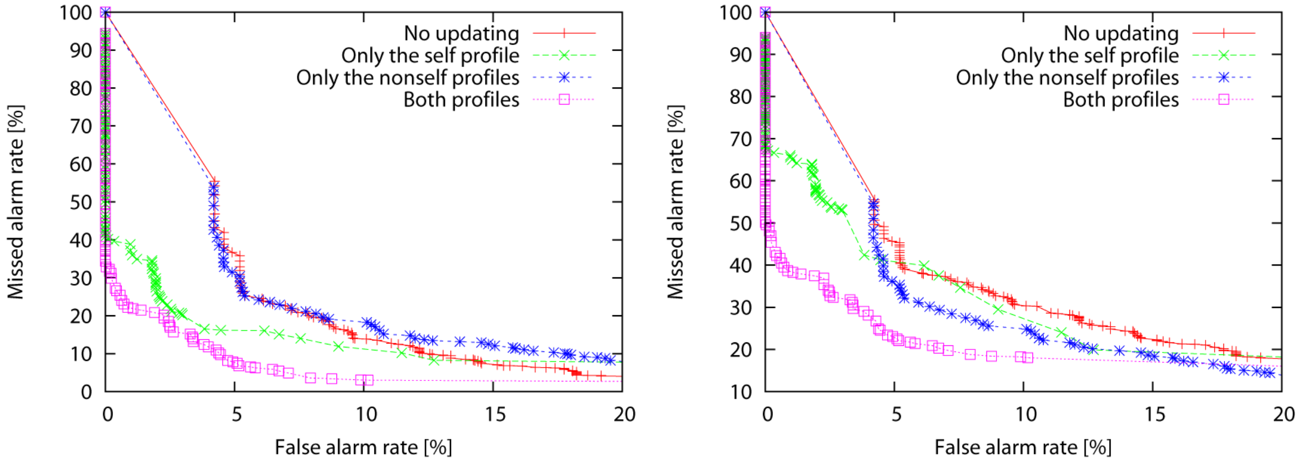

(a) Internal masquerader detection (b) External masquerader detection

Fig. 1. ROC curves of internal and external masquerader detection for the method without updating any profiles, with updating only the self profiles, with updating only the nonself profiles, and with updating both profiles.

varying the threshold Th from 0% to 100%, and computing these rates at each threshold Th. In this experiment, each ROC curve consists of 101 points for simplicity. Each point corresponds to one threshold from $Th = 0$ to $Th = 1.0$. In addition, the area under the ROC curve (AUC) is computed as a scalar measure for ROC analysis. The AUC enables quantitative comparison of multiple ROC curves. In this experiment, the AUC may be much larger than the exact AUC due to thinning out plots.

We evaluated the detection accuracy of the profile updating. Figure 1 shows ROC curves of internal and external masquerader detection for the method without updating any profiles, with updating only the self profiles, with updating only the nonself profiles, and with updating both profiles. In each ROC curve, 6 internal users were chosen randomly from among the total of 12 users, with all the others being the external users. Each point on the ROC curve is an average over 100 combinations. The statistics of the AUCs for 100 combinations of internal and external users were examined and the statistical significance of differences was analyzed by ANOVA with Dunnett's test for multiple comparisons.

In Figure 1(a), the method with updating both profiles indicated the best detection accuracy of all curves. The mean AUC of the method with updating both profiles was 0.026, which was significantly lower ($P < 0.001$) than that of the method without updating any profiles (0.072). This statistical significance seemed to be dependent mainly on the updating of the self profiles, as the updating of only the self profiles decreased the false alarm rate, whereas the updating of only the nonself profiles slightly increased the missed alarm rate. It should be noted that the updating of both profiles achieved a missed alarm rate of 34.37% without false alarms at the threshold 43.43%.

Similar to Figure 1(a), Figure 1(b) indicated that the method with updating both profiles outperformed all the other methods. The mean AUC of the method with updating both profiles was 0.108, significantly lower ($P < 0.001$) than that of the method without updating any profiles (0.150). This statistical significance is due to the updating of both the self and nonself profiles. The updating of the self profiles decreased the number of false alarms, and the updating of the nonself profiles decreased the number of missed alarms. It should be noted that the updating of both profiles achieved a missed alarm rate of 50.13% without false alarms at the threshold 43.43%.

2. Worm detection

Computer worms are divided into five types of target discovery: *random-scanning*, *hit-list*, *metaserver*, *topological*, and *passive worms* [9].

A. Random-scanning worms

We evaluated four random-scanning worms in the wild: `CodeRedv2`, `CodeRedII`, `Slammer`, and `Blaster`. These worms attempt to infect randomly selected computers. As with our previous study [8], there were no missed alarms without false alarms on any of the accounts for all the worms examined in all methods.

B. Hit-list worms

A *hit-list worm* attempts to infect computers of target lists pre-generated by an attacker or its author.

The hit-list includes IP addresses of vulnerable servers or always-connected IP addresses. All the methods seem to detect these worms if the hit-list does not include IP addresses of the operation table. Otherwise, for example, an attacker can randomly insert many IP addresses of popular websites into the hit-list at the expense of high-speed spreading. In that case, our method could not detect these worms because IP addresses of popular websites are likely to coincide with those of the operation table.

C. Metaserver worms

A *metaserver worm* obtains a target list from a metaserver that keeps a list of active servers and attempts to infect computers on these lists. The `Santy` worm is a *metaserver worm*, which attempts to propagate to IP addresses in the search results provided by Google™ (`www.google.com`).

All the methods detected the simulated *metaserver worm* [8] because these worms have difficulty guessing IP addresses on the operation table.

D. Topological worms

A *topological worm* obtains a target list from the devices of the infected computer. For example, the worm obtains targets from peer-to-peer software in an infected computer and attempts to infect all peers. This worm may escape all methods, because the traffic pattern of this worm may appear normal and the peers may be included in the operation table. An alternative method would be needed to prevent *topological worms* from spreading.

E. Passive worms

The *passive worm*, which either waits for target computers to visit or follows user's requests into target computers, is more difficult for an anomaly detection system to detect, because its behavior is similar to that of the user.

The evaluation results of a simulated *passive worm* [8] were almost the same as those in Fig. 1. The mean AUC of the method with updating both profiles was 0.029, which was significantly lower (P < 0.001) than that of the method without updating any profiles (0.121). The mean difference between the method with updating both profiles and without updating any profiles was larger than that of the internal masquerader detection. Briefly, profile updating markedly improved the detection accuracy of the simulated *passive worm*.

V. CONCLUSIONS

We have made a change in our immunity-based anomaly detection method to escape assignment overflow in the operation table, and we evaluated and discussed the extent to which profile updating improves the detection accuracy of external masqueraders and computer worms.

Experimentally, we showed that the updating of both profiles markedly decreased both the false alarm rate and the missed alarm rate in masquerader detection. In worm detection, all the *random-scanning worms* and the simulated *metaserver worm* examined were detected. The detection accuracy of the simulated *passive worm* was markedly improved. Detection of *topological worms* may require an alternative method to investigate inbound traffic in order to detect exploit codes and/or shellcodes.

ACKNOWLEDGEMENTS

This work was supported by Grant-in-Aid for Scientific Research (B) 19700072, 2009.

REFERENCES

[1] Schonlau M, DuMouchel W, Ju W, et al. (2001), Computer intrusion: Detecting masquerades, Statistical Science 16(1):58-74.

[2] Okamoto T, Ishida Y (2009), An Immunity-Based Anomaly Detection System with Sensor Agents, Sensors 9(11):9175-95.

[3] Okamoto T, Ishida Y (2008), Dynamic Updating of Profiles for an Immunity-Based Anomaly Detection System. LNAI 5179, pp. 456-64.

[4] Kim J, Bentley P, Aickelin U, et al. (2007), Immune system approaches to intrusion detection - a review, Natural computing 6(4):413-66.

[5] Kephart J (1994), A biologically inspired immune system for computers. Artificial Life IV, pp. 130-39.

[6] Forrest S, Hofmeyr S, Somayaji A, et al. (1996), A sense of self for unix processes. Proc. of the 1996 IEEE Symposium on Security and Privacy, pp. 120-28.

[7] Aickelin U, Cayzer S (2002), The danger theory and its application to artificial immune systems. Proc. of the 1st Int. Conf. on Artificial Immune Systems, pp. 141-48.

[8] Okamoto T, Ishida Y (2006), Towards an immunity-based anomaly detection system for network traffic. LNAI 4252, pp. 123-30.

[9] Weaver N, Paxson V, Staniford S, et al. (2003), A taxonomy of computer worms. Proc. of the 2003 ACM workshop on Rapid malcode, pp. 11-18.

A Secure Routing Scheme for Mobile Wireless Sensor Networks

Yuji Watanabe and Tong Tran Nhat Linh

Graduate School of Natural Sciences, Nagoya City University,
1 Yamanohata, Mizuho-cho, Mizuho-ku, Nagoya 467-8501 Japan
(Tel : 81-52-872-5037; Fax : 81-52-872-5037)
(yuji@nsc.nagoya-cu.ac.jp)

Abstract: Frequency-hopping (FH) is a well-known spread-spectrum method of transmitting radio signals by hopping frequency channels along a predefined hopping sequence known to both transmitter and receiver. Although FH is resistant to jamming by external malicious nodes which have no knowledge of the sequence, it is of no effect against at tacks by internal compromised nodes which know the sequence. In this paper, we propose a secure creation scheme of the hopping sequence for mobile wireless sensor networks. The proposed scheme is based on the idea of a statistical en-route filtering (SEF). SEF exploits collective decision-making by multiple detecting nodes in the de nse deployment of large sensor networks. We evaluate the performance of our scheme thorough simulations.

Keywords: Mobile wireless sensor networks, Frequency-hopping, Hopping sequence, Statistical en-route filtering**.**

I. INTRODUCTION

Wireless sensor networks (WSNs) have lately drawn considerable attention because of the popularization of sensors that are smaller, cheaper, and intelligent [1]. These sensors are equipped with one or more sensors, a processor, memory and a power supply. They can also communicate with each other to form network with wireless interfaces. WSNs have many applications such as environment monitoring and target tracking. A type of WSN is a mobile wireless sensor network where sensor nodes have the ability to move such as robots. For example, researches on mobile WSNs are Robomote [2], Emulab [3] and ZebraNet [4]. Challenges in mobile WSNs include deployment, localization, self-organization, navigation, coverage, and energy maintenance. A difference between static and mobile WSNs is routing, that is, dynamic routing is used in a mobile WSN unlike a static WSN using fixed routing or flooding.

The issue of security in WSNs must be addressed because WSNs may be deployed in potentially adverse or hostile environment. Adversaries can inject jamming which may cause not only false alarms but also the depletion of the limited energy of sensor nodes. Frequency-hopping (FH) is a well-known spread-spectrum method of transmitting radio signals by rapidly changing the frequency channel, using a predefined hopping sequence known to both transmitter and receiver [5, 6]. Although FH is resistant to jamming by external malicious nodes which have no knowledge of the sequence, it is of no effect against attacks by internal compromised nodes which know the sequence. Since the computation and storage constraints of low-end sensor nodes make complex cryptography-based mechanisms for hopping sequence creation infeasible, it is necessary to create the sequence securely and simply.

In this paper, we propose a secure creation scheme of the hopping sequence for mobile wireless sensor networks. The proposed scheme is based on the idea of a statistical en-route filtering (SEF) [7]. In SEF, assuming that the same event can be detected by multiple nodes, forwarding nodes along the way to base station can statistically detect false reports en-route. SEF has achieved the early detection of false data reports with low computation and communication overhead. We evaluate the performance of our scheme thorough simulations.

The rest of the paper is organized as follows: In Section II, we describe the frequency-hopping and the statistical en-route filtering in detail. Section III presents our secure creation scheme of the hopping sequence for mobile wireless sensor networks. In Section IV, we evaluate the performance of our scheme thorough simulations. Section V concludes the paper.

II. RELATED WORKS

1. Frequency-hopping (FH) [5, 6]

FH is the periodic changing of the frequency channel of a transmitted radio signal according to a predefined hopping sequence (pattern) known to both transmitter and receiver. FH is highly resistant to narrowband interference and intercept compared with a fixed-frequency transmission. FH is actually used for IEEE 802.11-1997 and Bluetooth [8, 9].

In FH, hopping occurs over a frequency band which includes M frequency channels. Figure 1 illustrates the example of frequency-hopping sequence with 16 frequency channels. The time interval between hops is called the slot. The number of frequency channels for IEEE 802.11 and Bluetooth in the 2.4 GHz ISM frequency band is 14 and 79, respectively.

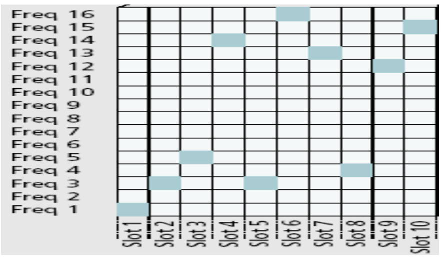

Fig.1. Example of frequency-hopping sequence

Normally the procedure of FH is as follows:

1. The transmitter sends a request via a predefined frequency channel.
2. The receiver sends a number, known as a seed.
3. The transmitter uses the seed as a variable in a predefined algorithm, which calculates the hopping sequence that must be used.
4. The transmitter sends a synchronization signal via the first frequency in the calculated sequence, thus acknowledging to the receiver it has correctly calculated the sequence.
5. The communication begins at the same point in time, and both the transmitter and the receiver change their frequencies along the sequence.

The sequence must be created securely and simply.

2. Statistical en-route filtering (SEF) [7]

SEF can probabilistically filter out false reports en-route. SEF exploits collective decision-making by multiple detecting nodes and collective false detection by multiple forwarding nodes in the dense deployment of large sensor networks.

SEF consists of three major components: 1) key assignment and report generation, 2) en-route filtering, and 3) base station verification. The process of key assignment and report generation is as follows:

1. The base station (sink) maintains a global key pool of N keys $\{K_i, 0 \le i \le N-1\}$, divided into n non-overlapping partitions. Each partition has m keys.
2. Before each sensor node is deployed, it stores randomly chosen k (k < m) keys from a randomly selected partition in the key pool.
3. When an event appears, multiple surrounding nodes can detect the event and a cluster head (center-of-stimulus node) is elected to generate the event report. Note that SEF assume that the same event can be detected by multiple nodes.
4. Each of the detecting nodes generates a keyed message authentication code (MAC) M_i using the event report (for example, the location, the time, and the type of event) and randomly selected K_i, one of its k stored keys.
5. The cluster head collects all the MACs from detecting nodes and attaches randomly chosen T MACs to the report. This set of multiple MACs acts as the proof that the report is legitimate.

In en-route filtering, when the cluster head forwards the event report with multiple MACs toward the base station, intermediate forwarding nodes verify the correctness of the MACs probabilistically and drop those with forged MACs en-route.

Due to the statistical nature of the detection mechanism, a few bogus reports with invalid MACs may escape en-route filtering and reach the base station. In base station verification, the base station further verifies the correctness of each MAC and eliminates false reports that elude en-route filtering.

III. PROPOSED SCHEME

We propose a secure creation scheme of the hopping sequence based on the SEF for mobile WSNs. The basic idea is to use multiple MACs generated by detecting nodes as a seed of the hopping sequence. In addition, although original SEF is applied for static WSNs, mobile WSNs require dynamic routing to search and find pathways to the base station. Therefore, in the proposed scheme, SEF is carried out in routing phase. Step 4 and 5 in the process of key assignment and report generation is changed as follows:

4'. Each of the detecting nodes generates a keyed MAC M_i using only the time of detection and randomly selected K_i. The total event report can be securely sent using FH after routing phase.

5'. The cluster head collects all the MACs from detecting nodes and attaches randomly chosen T MACs and the time of detection to RREQ

(Route Request) packet. The cluster head broadcasts RREQ packets to find route to the base station.

En-route filtering and base station verification, which function in the same way as original SEF, are carried out for the MACs in RREQ packets. After the base station verification, when the RREQ packet has valid MACs, the following process is additionally performed:

1. The base station sends RREP (Route Reply) packet back to the cluster head along the found route.
2. The cluster head and the intermediate forwarding nodes which can receive the RREP packet calculate the hopping sequence using the valid MACs as the seed in a predefined algorithm.
3. Both the transmitter and the receiver change their frequencies along the sequence, and the total event report is securely sent to the base station.

Figure 2 illustrates our secure creation scheme of the hopping sequence based on the SEF for mobile WSNs.

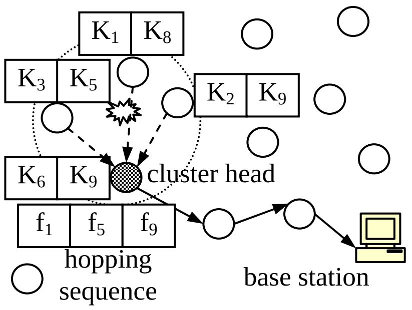

Fig.2. Secure creation scheme of the hopping sequence based on the SEF for mobile WSNs.

IV. SIMULATION RESULTS

We evaluate the performance of our scheme using network simulator NS2 [10]. We use a field size of 1000mX1000m, where 50 normal nodes and 1 malicious node are randomly located. Each node can move according to random waypoint model [11] with the speed randomly selected from 1m/s to 10m/s. In simulations, there are 5 event reports which must be sent to the base station by normal cluster heads. The speed of the packet is 4 packets per second, and the size of the packet is 512 bytes.

Like original SEF, we use a global key pool of 1000 keys, divided into 10 partitions, with 100 keys in each partition. Each node has 50 keys. Since the malicious node generates only incomplete multiple MACs using the time of false detection and its 50 stored keys, it send a forged event report to the base station along a invalid hopping sequence calculated by the incomplete MACs. As to the other simulation conditions, the maximum number of frequency channels is 14 like IEEE 802.11 in the 2.4 GHz ISM frequency band, and dynamic source routing (DSR) [12] is applied for mobile WSNs.

Figure 3 shows the packet delivery rate of event reports from normal cluster heads and the malicious node changing the number of frequency channels. The results of 1 channel correspond to the case without FH. When FH is not used, 97% packets of event reports from normal cluster heads can reach the base station, and 96% packets of the forged report from the malicious node can also reach. However, as the number of frequency channels increases, although the packet delivery rate from normal cluster heads slightly decreases, the delivery rate from the malicious node dramatically drops down. When the number of frequency channels is 14, only 13% packets of the forged report from the malicious node can reach.

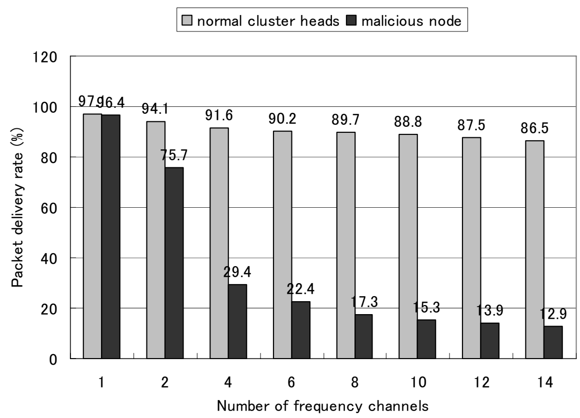

Fig.3. Simulation Results

V. CONCLUSION

This paper proposed a secure creation scheme of the hopping sequence for mobile wireless sensor networks based on the statistical en-route filtering. The effectiveness of our scheme is demonstrated thorough simulations.

REFERENCES

[1] Yick J, Mukherjee B, Ghosal D (2008), Wireless sensor network survey. Computer Networks 52:2292-2330

[2] Sibley GT, Rahimi MH, and Sukhatme GS (2002), Robomote: A Tiny Mobile Robot Platform for Large-Scale Ad-hoc Sensor Networks. Proceedings of the IEEE International Conference on Robotics and Automation. Washington DC

[3] Johnson D, Stack T, Fish R, Flickinger DM, Stoller L, Ricci R, Lepreau J (2006), Mobile Emulab: a robotic wireless and sensor network testbed. IEEE INFOCOM

[4] Zhang P, Sadler CM, Lyon SA, Martonosi M (2004), Hardware design experiences in ZebraNet. Proceedings of the SenSys'04, Baltimore, MD

[5] Torrieri D (2005), Principles of spread-spectrum communication systems. Boston: Springer

[6] Wikipedia, http://en.wikipedia.org/wiki/Frequency-hopping_spread_spectrum

[7] Ye F, Luo H, Lu S and Zhang L (2005), Statistical En-Route Filtering of Injected False Data in Sensor Networks. IEEE Journal on Selected Areas in Communications, 23(4):839-850

[8] IEEE 802.11, The Working Group Setting the Standards for WLANs, http://www.ieee802.org/11/

[9] Bluetooth.com, http://www.bluetooth.com/

[10] Ns2, http://www.isi.edu/nsnam/

[11] Camp T, Boleng J and Davies V (2002), A Survey of Mobility Models for Ad Hoc Network Research. Wireless Communications and Mobile Computing, 2(5):483-502

[12] Johnson DB, Maltz DA (1996), Dynamic source routing, in: T. Imielinski, H.F. Korth (Eds.), Ad Hoc Wireless Networks Mobile Computing 353

Prediction of Space Weather by Adaptive Information Processing

Masahiro Tokumitsu[1], Yoshiteru Ishida[1], Shinichi Watari[2] and Kentarou Kitamura[3]

[1]*Department of Knowledge-Based Information Engineering,*
Toyohashi University of Technology, Tempaku, Toyohashi 441-8580, Japan
(Tel : +81-53-244-6895; Fax : +81-53-244-6873)
(tokumitsu@sys.tutkie.tut.ac.jp)

[2]*Applied Electromagnetic Research Center, National Institute of Information and Communications Technology,*
4-2-1 Nukuikitamachi, Koganei, Tokyo, 184-8795, Japan

[3]*Department of Mechanical and Electrical Engineering, Tokuyama College of Technology,*
Gakuendai, Shuna, Yamaguchi, 745-8585, Japan

Abstract: Space weather can be predicted using data from satellites. For example, condition of high-energy electron is vital in providing warnings to spacecraft operations. We investigate an adaptive predictor based on intelligent information processing. Adaptive and learning performances have been focused in the investigation. The predictor can forecast the conditions of high-energy electrons. The predictor was tested with the normal and abnormal test data. Our model succeeded in forecasting the high-energy electron flux 24 hours ahead.

Keywords: sensor network, adaptive information processing, space weather, dynamic relational network.

I. Introduction

Satellites are important social infrastructures. There are high-energy electrons at Geostationary Earth Orbit (GEO). High-energy electrons penetrate circuits and cables deeply and cause deep dielectric charging. There are reports that the spacecrafts anomalies at GEO are associated with enhancement in high-energy electron fluxes. For example, the Intelsat K spacecraft at GEO lost altitude control due to the failure of the momentum wheel control circuitry on January 20, 1994. The analysis of specialists revealed that the spacecraft anomaly occurred due to dielectric charging by the high-intensity and long-duration enhancement of high-energy electrons [1].

The enhancement of high-energy electron fluxes is known to be correlated with solar activities such as Coronal Mass Ejection (CME) (Fig.1) and coronal hole. Fig.2 shows that variation of electron flux in association with solar wind speed (V) and north-south component of interplanetary magnetic filed (B_z). The electron fluxes vary in two phases: initial-to-main phase and recovery phase of geomagnetic storms. During the initial-to-main phase, high-energy electron fluxes rapidly decrease; and after this phase, the fluxes increase significantly. The problem is that higher level of fluxes causes the irreparable damage to the instruments on satellites in the recovery phase of geomagnetic storms.

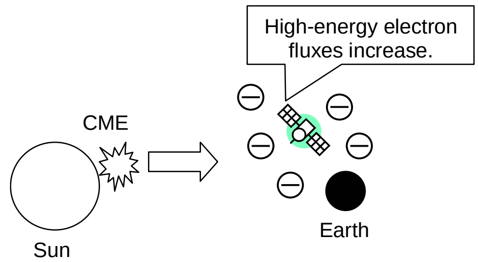

Fig.1 Schematic illustration of relationship between CME and spacecraft.

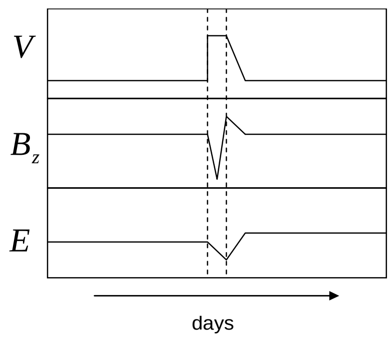

Fig.2 Schematic plot of parameters correlated with CME. The V, Bz and E are corresponded to the solar wind speed, the south-north component of interplanetary magnetic field and high-energy electron fluxes.

The dynamics on variations of high-energy electrons are under investigation [2]. Many studies have reported that the enhancement of high-energy electron is correlated with the high-speed solar wind [3]. Furthermore, the north-south component of the interplanetary magnetic field (IMF) is also known to be another important parameter of the flux enhancement.

Many predictors for high-energy electron fluxes at GEO have been proposed [5, 6]. Those studies have developed predictors that could forecast the predicted the fluxes real. The motivation for developing the predictor is to protect spacecrafts from the deep dielectric charging.

Earlier studies have tried to involve the relationships between high-energy electrons and solar wind parameters to the predictors. In space weather, the huge data for several or decades years are used for forecasting the space environment. The forecast could be done based on profiles of observed data. This paper tries to construct and evaluate a dynamic relational network [7] for anomaly prediction of high-energy electron fluxes. The network could predict whether high-energy electron fluxes attain to the alert level after 24 hours.

II. Profiling of Space Environment Data

2.1 Profiling High-energy Electron Fluxes and Solar Wind Data

We focus on profiling on the activities of high-energy electrons and solar wind. Profiling can be used to extract features of the sensor data [6]. We make the profiles of the relationships among the observed data. Those data involves normal and abnormal data. We define that normal and abnormal data of high-energy electrons are corresponded to the alert and quiet level flux respectively. In this paper, the alert level follows criteria of alerts of Space Weather Prediction Center (NOAA) [9]. The normal data is determined using the solar wind speed and north-south component of IMF when the high-energy electron fluxes are quiet level. In other cases, those data are defined as abnormal. We create the profiles of the normal data from only daily variations of high-energy electron fluxes that not involve coronal hole and CME event data.

2.2 Profiling Time Series Data by Vector Autoregressive Models

The satellites observe the space environment using their sensors. The data are sent to ground station and then stored into databases. The high-energy electron fluxes and the solar wind data are represented in a style with physical values. We can obtain them as time series data from the databases.

We create the profiles from the observed data with a statistical method. As the model for the time series analysis, we use the vector autoregressive models. In the VAR model, not only its own past values but also those of related variables are involved. Let $x(t)$ and $y(t)$ be explained variables; $x(t-1)$,…, $x(t-m)$; $y(t-1)$,…, $y(t-m)$ be explaining variables; and a_1 ,…, a_m ; b_1 ,…, b_m ; c_1 , …, c_m ; d_1, …, d_m be autoregressive coefficients. The VAR model of order m is expressed as follows:

$$x(t) = \underline{\sum_{i=1}^{m} a_i x(t-m) + \sum_{i=1}^{m} b_i y(t-m)} + \varepsilon_x$$

$$y(t) = \underline{\sum_{i=1}^{m} c_i x(t-m) + \sum_{i=1}^{m} d_i y(t-m)} + \varepsilon_y$$

The underlined parts $(x'(t), y'(t))$ represent predicted values while are the residual errors. In offline training, we estimate the autoregressive coefficients by the Levinson's algorithm. The profile is created by estimating the coefficients from couple of observed data. The order of the VAR model is determined by using the values of AIC (Akaike Information Criterion) of the models. We determine the order of the model from the models that the AIC value is the highest.

III. Dynamic Relational Network for Anomaly Prediction of High-energy Electron Fluxes

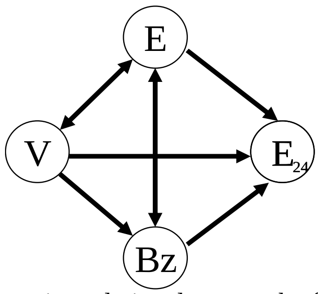

Fig.3 Dynamic relational network for anomaly prediction on high-energy electron fluxes.

This paper tries to predict the alert level flux of high-energy electrons using dynamic relational network. The dynamic relational network is consisted of sensors and arcs. The sensors of the network diagnose each other by evaluating target's sensor data. The credibility of sensors will change dynamically as the diagnosis proceeds, and then the network will adapt to the changes of the environment.

We build the dynamic relational network as black and white model [7] using real three sensors and one virtual sensor (Fig.3). The real sensors are the high-energy electron fluxes (E), the solar wind speed (V) and the north-south component of IMF (B_z). The virtual sensor is high-energy electron fluxes 24 hours ahead (E_{24}). The virtual sensor will be diagnosed from other sensors. The network will detect anomaly when the credibility of the electrons flux after 24 hours is less than the alarm threshold. For estimating the electron fluxes, we regard the current flux data as the future flux data because we cannot obtain them.

The arcs are corresponded to the profiles. The diagnosis of each sensor is done by calculating error $p(t)$ between the actual value and predicted value. The sensor diagnose the target sensor as abnormal when $p(t)$ deviates the threshold θ. The threshold θ is defined as $\theta = n\delta$ where the n and δ are the deviation coefficient and standard deviation of observed data respectively.

IV. Tests and Evaluations

4.1 Data source

We use one hour averaged data of the solar-wind and the high-energy electron flux at GEO. The solar wind data observed by the Advanced Composition Explorer (ACE) satellite are obtained from the OMNI-2 database [8] in the National Space Science Data Center (NSSDC), the National Aeronautics and Space Administration/Goddard Space Flight Center.

The electron flux data observed by the GOES satellite are obtained from the National Geophysical Data Center (NGDC), and the National Oceanic and Atmospheric Administration (NOAA). We obtain both data during the period from January 1, 1998 to December 31, 2006, thus eight years in total.

4.2 Data Handling

The data observed by the satellites could include the missing data due to the instruments troubles by the space weather events and/or various reasons for the operations. We regard the data as missing where the interval of the missing exceeds two hours. The missing data are interpolated if the observation down time is less than three hours. We exclude the missing data in training and simulations.

4.3 Methods and Evaluations

We evaluate the dynamic relational network based on the test results. The network is tested by inputting the

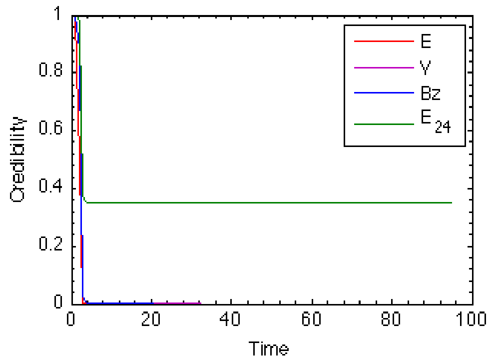

Fig.4 Time evolution of credibility when dynamic relational network tests abnormal data involving CME event. The deviation coefficient is 0.06. The threshold of anomaly detection is 0.5.

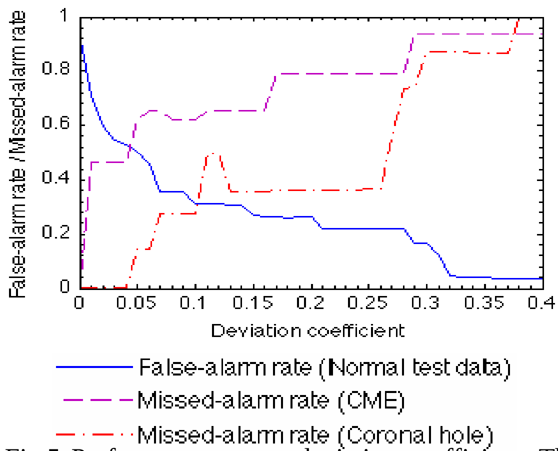

Fig.5 Performance versus deviation coefficient. The deviation coefficient varies from 0 to 0.4. The threshold is 0.5 in this test. The threshold of anomaly detection is 0.5.

test data. The test data are consisted of normal and abnormal data. The normal test data only involves the data where high-energy electron fluxes are the alert level. On the other hand, the abnormal test data involves the data where the flux is the quiet level. The abnormal test data contain the data on coronal hole and CME events. We prepare 20 test cases as normal test data and 7 test cases on coronal hole and CME events (14 cases in total) as abnormal test data. For the abnormal test cases, we choose the test cases from the event list [3]. The period of the test data is about 5 days. The period of the test data is different due to the conditions of the space environment. The performance of anomaly prediction is evaluated by calculating false-alarm rate and missed-alarm rate. We evaluate the test result in each step whether the anomaly prediction succeeds.

4.4 Test Results

Fig.4 shows a diagnosis result of the dynamic relational network for the abnormal data involving CME event.

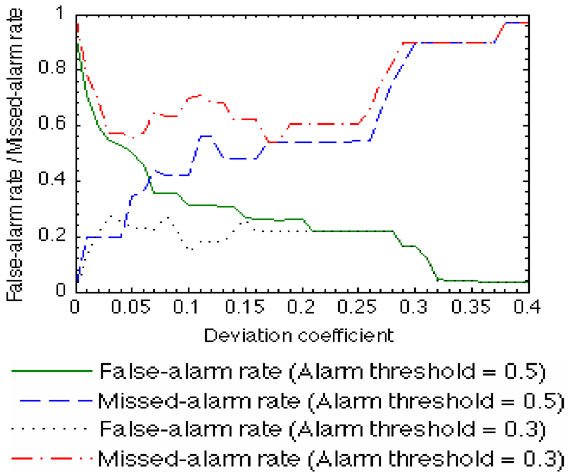

Fig.6 Performance versus deviation coefficient when the alarm threshold is compared with 0.3 and 0.5. The deviation coefficient varies from 0 to 0.4.

The CME happens when the test starts in this test case. The credibility of high-energy electron flux 24 hours ahead is diagnosed as anomaly. The anomaly prediction is successful in this test case.

Fig.5 shows the performance trade-off when the deviation coefficient varies. The false-alarm decreases as the deviation coefficient increases while the missed-alarm rate rises. The performance of the dynamic relational network shows the trade-off on the deviation coefficient.

Fig.6 shows the performance when the alarm threshold is changed. The missed-alarm rate increases when the deviation coefficient is 0.3. On the other hand, the false-alarm rate is kept low level. The dynamic relational network would predict successfully if both parameters are adjusted appropriately.

V. Discussions

We have investigated the performance of the dynamic relational network for the anomaly prediction on high-energy electron fluxes. The diagnosis of the network is done in online and therefore the credibility will change dynamically [6]. Our model differs from the neural network predictors [4, 5] in that it could adapt to the dynamic environment. However, the adaptation of the network is influenced by the tuning parameters [6]. For the tests, the deviation coefficient and the alarm threshold are used as tuning parameters of the network.

The performance of the network changes according to the deviation coefficient. The performances also changes according to the alarm threshold. Each parameter of the networks should be controlled appropriately to achieve the performance requirement in order to protect the satellites from dielectric charging. For future works, we need to evaluate the network using the profiles created from only abnormal data.

VI. Conclusions

We constructed a dynamic relational network for anomaly prediction on high-energy electron fluxes. The network could predict the alert level flux. Furthermore, we investigated the trade-off of the performances in order to manage the performance.

Acknowledgments. This work was supported by The Global COE Program "Frontiers of Intelligent Sensing", from the ministry of Education, Culture, Sports, Science and Technology.

REFERENCES

[1] D.N. Baker, Satellite Anomalies due to Space Storms, In I.A. Daglis, ed., *Space Storms and Space Weather Hazards*, pp. 285–311, 2001

[2] M.W. Liemohn, A.A. Chan, Unraveling the Causes of Radiation Belt Enhancements, *EOS Transactions*, 88, pp. 425–426, 2007

[3] R. Kataoka, Y. Miyoshi, Flux Enhancement of Radiation Belt Electrons during Geomagnetic Storms Driven by Coronal Mass Ejections and Corotating Interaction Regions, *Space Weather*, 4, S09004, 2004

[4] M. Fukata, S. Taguchi, T.Okuzawa, T. Obara, Neural network prediction of relativistic electrons at geosynchronous orbit during the storm recovery phase: effects of recurring substorms, *Annales Geophysicae*, 20, pp. 947–951, 2002

[5] M. Tokumitsu, Y. Ishida, S. Watari and K. Kitamura, Adaptive Forecasting of High-Energy Electron Flux at Geostationary Orbit Using ADALINE Neural Network, *Lecture Notes in Computer Science*, LNCS5712, pp. 797-804, 2009

[6] Y. Ishida and M. Tokumitsu, Adaptive Sensing Based on Profiles for Sensor Systems, *Sensors*, 2009, http://www.mdpi.com/1424-8220/9/11/8422

[7] Y. Ishida, Designing an Immunity-Based Sensor Network for Sensor-Based Diagnosis of Automobile Engines, *Lecture Notes in Computer Science*, LNCS 4252, 2006

[8] J.H. King, N.E. Papitashvili, Solar wind spatial scales in and comparisons of hourly Wind and ACE plasma and magnetic field data, *J. Geophys. Res. (Space Physics)*, 110(A9), A02104, 2005

[9] Space Weather Prediction Center, the National Oceanic and Atmospheric Administration (NOAA), http://www.swpc.noaa.gov/alerts/description.html

An Adaptive Sensor Network for Home Intrusion Detection by Human Activity Profiling

Masahiro Tokumitsu, Masashi Murakami and Yoshiteru Ishida

Department of Knowledge-Based Information Engineering,
Toyohashi University of Technology, Tempaku, Toyohashi 441-8580, Japan
(Tel : +81-53-244-6895; Fax : +81-53-244-6873)
(ishida@tutkie.tut.ac.jp)

Abstract: An adaptive sensor network for home intrusion detection has been proposed. The sensor network combines a profile-based anomaly detection and an adaptive information processing based on Hidden Markov Models (HMM) that allows the system to train and tune the profiles automatically. The trade-off between miss-alarm and false-alarm has been experimentally studied. Several types of hypothetical intrusion have been tested and successfully detected. However, hypothetical anomalies supposing a fall down of a resident due to sudden illness have been difficult to detect.

Keywords: sensor network, adaptive information processing, human activity profile, home intrusion detection.

I. Introduction

On the one hand sensor technology has been developed and many sensors are available to detect several quantities in the environment. These sensors range from the ones with low-cost but low resolution to the expensive ones with high precision. One the other hand, recent rapid progress on the wireless technology and information network allows aggregating and organizing many sensors distributed in a space of the environment [1]. The space ranges from a small one within a room to a large-scale covering an entire buildings and production plants.

With the advent of both low energy-consuming sensors and networking technology, sensor networks have been attracting attention [2]. What is required is synthesizing large-scale data collected from the sensor network to the meaningful information in real time. We have studied a design framework for an adaptive sensor network based on the immune systems analogy [3]. However, here we focus on another sensor network involving the Hidden Markov Model (HMM) (e.g., [4]) to attain an adaptive system while using the similar framework of profiling the human behavior.

Even when restricted to statistical methods, there have been many methods such as Support Vector Machine (SVM) [5]. For human activity monitoring, sensors can be mounted to the body [6]. We have focused on the adaptability that allows the sensor network (installed in a room) adapt to the environment.

Section 2 explains the intrusion detection based on profiling. Section 3 presents how the profiles are constructed and used for detection. Section 4 presents the experimental results. Section 5 discusses performance analysis comparing two experimental data acquired from the two homes.

II. Adaptive Intrusion Detection based on Profiling

2.1 Profiling Human Activity and Anomaly Detection

Profiling on agents has been widely studied and used even restricted to human. When restricted to human, DNA profiling may be most popular to find and identify evidences and to narrow down the scope of suspects in the criminal acts such as murder.

Here, we focus on the profiling on human activity and behavior in their daily life, particularly in their homes. Profiles of the residents are used to detect anomaly in their daily life such as housebreaking by an intruder, fall down and lost mobility due to sudden illness (e.g., heart attack), and long absence due to prowl caused by an illness (e.g., Alzheimer disease). In this paper, we deal with the first two: the housebreaking and the fall down.

2.2 Profiling Time Series Data by Hidden Markov Models

The sensor network monitors usual resident's behavior, extracts normal activities, and updates the normal activity profile. A deviation from the profile can be used as an evidence of anomaly. In this note, we use a collection of parameters of the HMM as a profile (Fig.

1). The HMM is suited for a task of handling time series data such as speech recognition and gesture recognition systems [7]. Since the HMM assumes that states are not directly observable, the parameters include output probabilities and initial distribution of probabilities, other than state transition probabilities. These parameters are estimated from the data monitored by the sensors.

The data of the first few days (up to five days) sampled from the sensors monitoring the resident's activity in his/her home are used for estimating the parameters, and the collection of the parameters is regarded as the profile of the resident to identify his/her normal life in the home. We call the period of few days a training period and the data collected in these days a training data. After the training period, the detection will be carried out by calculating a likelihood that the current data are within the range expected from the normal life, testing against the profile of a normal life (Fig.1).

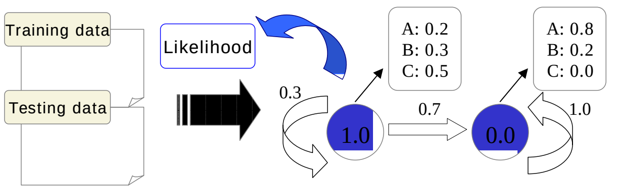

Fig. 1. Anomaly Detection by HMM parameters as profiles.

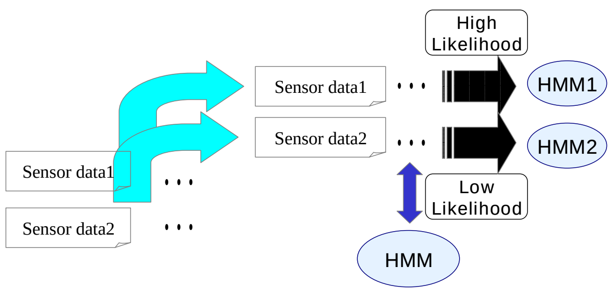

Fig. 2. Generating process of HMM profiles..

III. Sensor Network for Home Intrusion Detection

3.1 A Framework for Home Intrusion Detection by Sensor Networks

In our detection framework, we used multiple HMMs (Fig. 2) even for a single resident for detection accuracy, since even one man can have multiple patterns of activities. In a detection mode, a likelihood is calculated from the current monitoring data and the HMM to judge whether the current activities are within the expectation. If all the likelihoods calculated from corresponding HMMs are not greater than the predetermined thresholds, then anomaly will be concluded. These thresholds are acquired in a training phase.

Tuning of the thresholds plays a critical role in setting alarms, since any alarming systems are under a trade-off between miss-alarm and false-alarm. Too high thresholds turn out to be too many false-alarms, while too low thresholds lead to too many miss-alarms.

3.2 Processing of Sensor Data for Hidden Markov Models

Sensor data are sampled from the Infra-Red (IR) sensors installed to a room in a home as shown in Fig. 3. The detection system processes the data obtained through a sensor net interface.

Sensor data must be coded to input sequence of symbols for HMM. In the experiment, sensor data are sampled and transformed to 1 (reacted, or ON) / 0 (not reacted, or OFF) sequence of four bits (Fig. 4) in every five seconds. One minute collection of the 1/0 data is coded into one symbol sequence (Fig. 4).

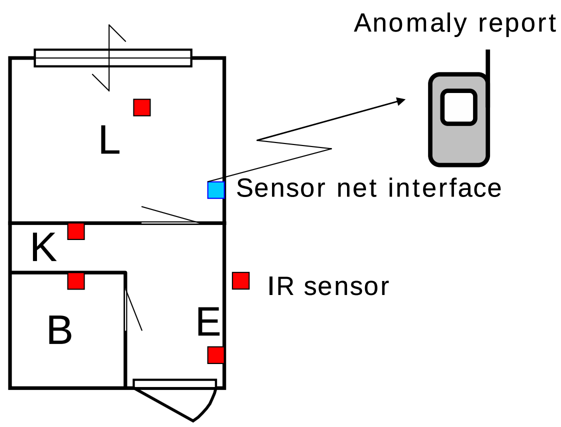

Fig. 3. Layout of sensors in a room for the experiment.

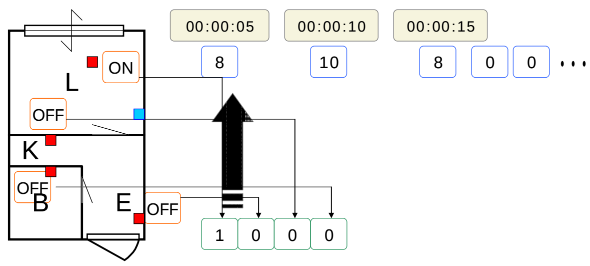

Fig. 4. Sensor Data Coding for HMM.

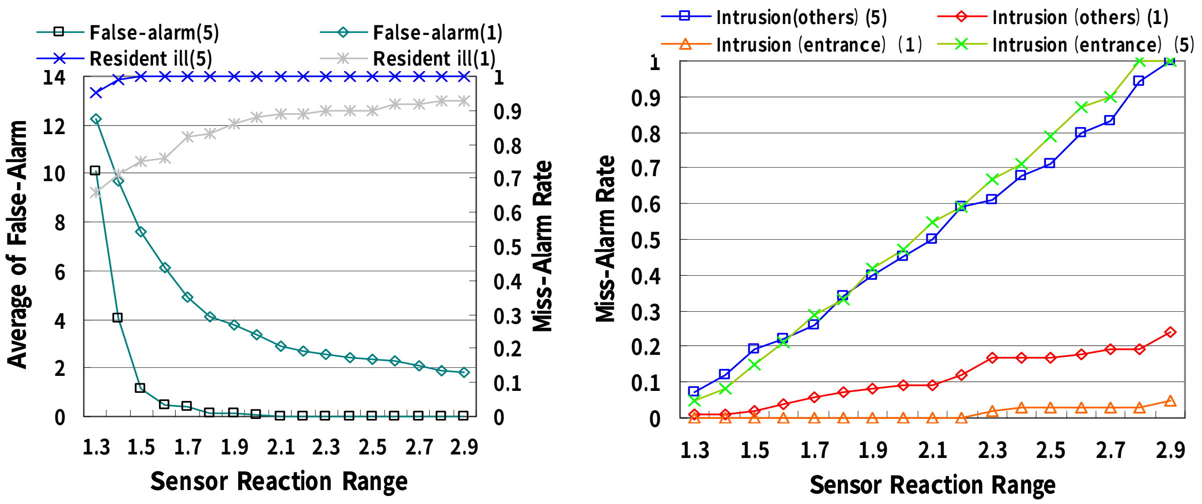

Fig.5. Average of False-Alarms (left) and Miss-Alarm Rate (right) when Sensor Sensitivity is varied in a home A. The number in parenthesis indicates the number of days used for the training of the system.

IV. Experiments and Performance Analysis

4.1 A Framework for Home Intrusion Detection by Sensor Networks

The sensor networks have been installed to a room in a home. Sensor layout in one room was shown in Fig. 3. Activities of a resident are monitored for three months. Since the actual anomaly would not happen, virtual anomalies have been set for performance analysis of the system. The following three types of anomalies are presented to the system:

1) Housebreaking from the entrance,

2) Housebreaking from other than the entrance (e.g., from the window), and

3) Resident falls down due to sudden illness.

4.2 Performance Analysis on the Adaptive Sensor Network

Among the monitored data, up to five days are used as learning data to train the HMM. The rest of data are used to test the performance in detection. The number of false-alarms (i.e., the system gave to alarm even when anomaly did not occur) in a day (Fig. 5 left) as well as the rate of miss-alarms (i.e., the system failed to alarm even when anomaly actually occurs) (Fig. 5 left) are plotted with the reactive range on which the sensitivity depends varied.

When the detection sensitivity decreases by lowering the thresholds for each HMM, the number of false-alarms decreased (Fig. 5 left) while the miss-alarm rate increased (Fig. 5 right). As expected, this trade-off holds for two data sets from two different homes. The events of resident fall down are difficult to detect. Indeed, missalarm rate for the resident fall down is higher than that for housebreaking.

V. Discussions

We have conducted the above experiments for two homes whose floor plan differs (Fig. 6) to compare the performances and to make performance analysis in more detail. That is, we want to investigate and narrow down the factors that affect the performance.

Fig. 7 shows the plots of average of false-alarms and miss-alarm rate for both homes. It can be first observed that the performance of the system for both homes is similar, even though the floor plan and hence the sensor layout differs from each other. This means that the adaptability of the system offered an adaptation to the sensor layout as long as the number of sensors and coverage to the room are adequately set. In this experiments also, the number of IR sensors are equal (four) and at least one IR sensor is installed to each room: living (L), kitchen (K), bedroom (B), and the entrance (E).

Again, the events of resident fall down are difficult to detect in both experiments. Since the events of resident fall down occurs in the middle of some normal activities, it may be difficult to discriminate them from normal activities in the coded profiles. It would be expected if the activities were monitored more frequently by sampling the data from the sensors in less than five minutes; the miss-alarm rate would be

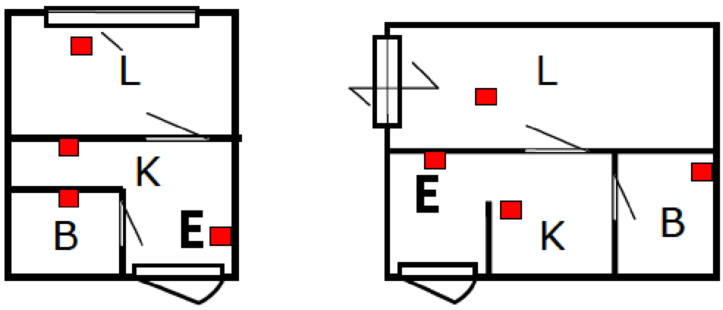

Fig.6. The IR sensor layout in the room of the home A (left) and B (right) for the experiment. The living (L), kitchen (K), bedroom (B), and the entrance (E) are shown.

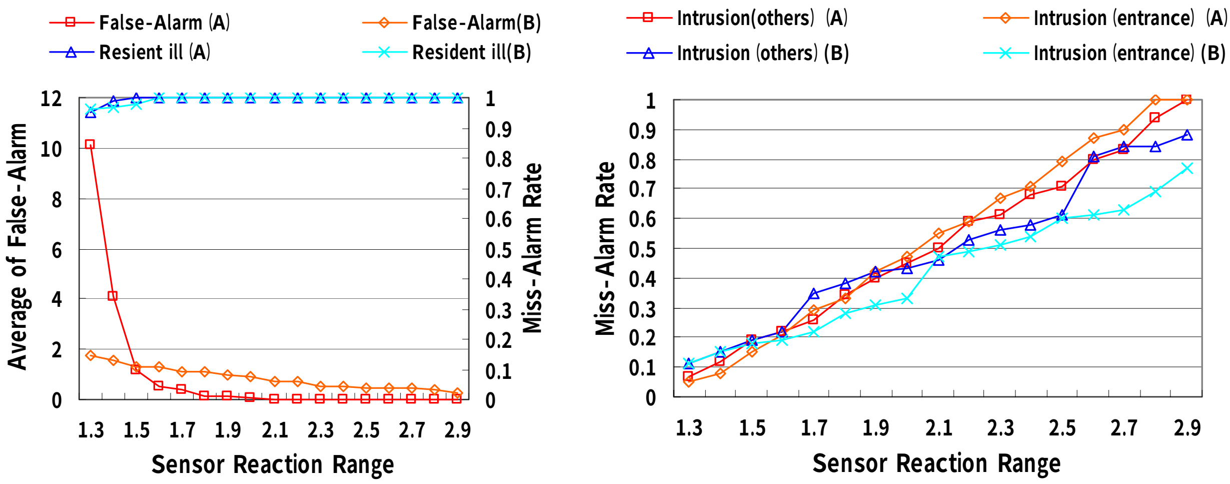

Fig.7. Average of False-Alarms (left) and Miss-Alarm Rate (right) of two homes A and B when Sensor Sensitivity is varied. A and B in the legend indicate the data from the home A and B, respectively.

improved. As a future work, the sampling time should be adapted to the environment.

VI. Conclusion

Experiments demonstrated that anomaly detection based on adaptive updates of resident's normal behaviors allows not only detection anomaly in the behaviors but also adaptation of the system to the environment. Here, the environment includes dynamic and diverse patterns of abnormal and normal behavior, dynamic but periodic life pattern. Reflecting the periodic conditions in short-terms such as hours and in longterms such as months and seasons to the profiles would improve the performance of detection success rate.

Acknowledgments. This work was supported by The Global COE Program "Frontiers of Intelligent Sensing", from the ministry of Education, Culture, Sports, Science and Technology. This work was also supported in part by Grants-in-Aid from Toyohashi University of Technology and CASIO Science Promotion Foundation.

REFERENCES

[1] Culler, D.E., Mulder, H.: Smart Sensors to Network the World, *Scientific American*, June (2004)

[2] Culler, D.E., et. al.: Overview of Sensor Networks, *IEEE Computer, Special Issue in Sensor Networks*, Aug (2004)

[3] Ishida, Y.: *Immunity-Based Systems: A Design Perspective*. Springer (2004)

[4] Rabiner, L.R.: A tutorial on Hidden Markov Models and selected applications in speech recognition". Proceedings of the IEEE 77-2 (1989) 257-286

[5] Preece, S.J. et al: Activity identification using body-mounted sensors—a review of classification techniques, *Physiol. Meas*. 30 (2009) R1-R33

[6] Jie Yin; Qiang Yang; Pan, J.J.: Sensor-Based Abnormal Human-Activity Detection, *IEEE Transactions on Knowledge and Data Engineering*, 20-8 (2008) 1082 – 1090

[7] Wilson, A.D., Bobick, A.F.: Parametric Hidden Markov Models for Gesture Recognition. IEEE Transaction Pattern analysis and machine intelligence, 21-9 (1999) 884-900

The Fifteenth International Symposium on Artificial Life and Robotics 2010 (AROB 15th '10),
B-Con Plaza, Beppu,Oita, Japan, February 4-6, 2010

A Network Visualization of Stable Matching in Stable Marriage Problem

Yoshihisa Morizumi, Tatsuya Hayashi and Yoshiteru Ishida

Department of Knowledge-Based Information Engineering,
Toyohashi University of Technology, Tempaku, Toyohashi 441-8580, Japan
(Tel : +81-53-244-6895; Fax : +81-53-244-6873)
(ishida@tutkie.tut.ac.jp)

Abstract: The Stable Marriage Problem (SMP) seeks matching between *n* women and *n* men satisfying a stability, which could otherwise lead to divorce and extramarital affairs. We have introduced a network consisting of nodes representing matching and links between nodes which attains each other by exchanging a partner between two pairs. For visualization, the network is depicted with nodes layouted involving several coordinates such as either women's or men's or both satisfactions. With the network visualization, regularity and symmetry can be made conspicuous in specific instances of SMP such as Latin SMP.

Keywords: network visualization, stable marriage problem, stable matching, Latin square, matching network**.**

I. Introduction

Since the landmark work of Gale and Sharpley [1], stable marriage problem has been studied extensively in several communities such as discrete mathematics, algorithm, operations research, and economics. Not only theoretical work but practical applications of heuristics had been implemented in the real assignment problem of intern to the hospitals without minding the theoretical results [2].

Knuth conjectured that any stable matching may be attained by matching blocking pairs by exchanging partners [3], however, the counterexample had been presented by Tamura [4]. This fact would suggest that the network visualization of the assignment problems including the stable marriage problem might not only clarify the problems themselves but give an insight of the solutions such as symmetries and stabilities embedded in the solution spaces, hence allowing decision making by an authority or by individuals easier.

On the other hand, network visualization demonstrated its power by visualizing large-scale networks such as computer networks, power grids, social networks, etc as well as complex networks such as genetic networks, cell networks, and metabolic networks. Graph drawing algorithms have been studied extensively to draw these large-scale and complex networks (e.g. [5]).

The visualization of network connecting all the nodes corresponding to matching solutions including stable matching would enhance understanding the structure of the solution network such as existence of specific cycles. It would also enhance understanding several solutions such as man-optimal (hence woman-pessimal) and woman-optimal (hence man-pessimal) and other ones between them in the distributive lattice [3] where the partial order between matchings is defined as every woman (man) in a matching is as satisfied with the partner as with the partner in the lower ordered matching. The network visualization may be implemented in several distinct ways depending on the aspect to be visualized using different coordinates measuring man's (woman's) satisfaction and total satisfaction.

The stable marriage problem has been studied by networks ranging from some-what direct expression of bipartite graph to a sophisticated expression of marriage graph [6]. The network of solutions also has been studied by means of the network such as a distributive lattice. We also express the matching by a network with several distinct coordinate-systems. The network visualization of instances of SMP reveals several similarity, regularities and symmetries among instances, which have not been recognized otherwise. One of the notable symmetries is the degeneration of the net-work, where degenerated network is defined by multiple nodes and edges are placed in the common coordinate in the coordinate system.

Section 2 presents stable marriage problems with the definition of stability. Section 3 defines the network whose nodes are matchings and edges partner-exchange. Section 4 explains the coordinates where nodes (matchings) are placed. Section 5 presents several examples of SMP with a regular structure whose matching networks are visualized.

II. Stable Marriage Problem and Stable Matching

The Stable Marriage Problem (SMP) assumes n women and n men each of them has an ordered preference list (or a ranking) without tie to the opposite sex. As in the example shown in Fig. 1, the men m_2 has an ordered preference list (w_3, w_2, w_1, w_4) or a ranking (3, 2, 1, 4), which means m_2 likes w_3 best, and he prefers w_3 to w_2, w_2 to w_1, and w_1 to w_4. One could say that there is an injection (one to one, but not necessarily onto) mapping from a set of women (men) to an element of permutation group of size n such as shown in the ranking by each person (Fig. 1).

Under the above assumptions, SMP seeks for the complete matching between n women and n men (a bijection from n women to n men), which satisfies stability. The stability requires the concept of blocking pair. Two pairs (m_i, w_p) and (m_j, w_q) are blocked by the pair (m_i, w_q) if m_i, prefers w_q to w_p and w_q prefers m_i to m_j, as illustrated in Fig. 2. A complete matching without being blocked is called *stable* matching.

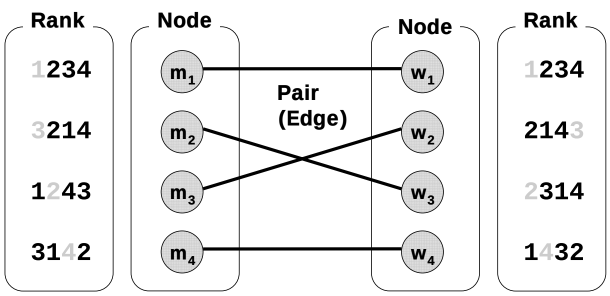

Fig. 1. An illustration of Stable Marriage Problem with size 4.

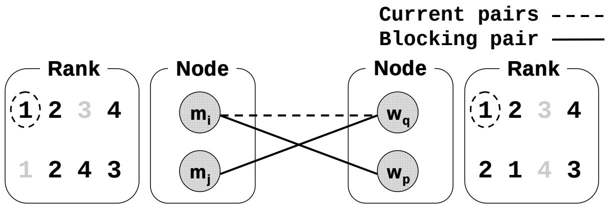

Fig. 2. An illustration of blocking pair.

III. A Network of Matching Solutions

Although instances of men's preference and women's preference can be expressed by networks, we will rather express matching solutions on networks. In the network, each node expresses matching and an edge between two nodes indicates that the matching corresponding the node can be realized by exchanging partners in two pairs of another node linked (Fig. 3). With two sets of n men and n women above, let us consider the following two matchings M_1, M_2:

$$M_1 = \{(m_1,w_1),(m_2,w_3),(m_3,w_2),(m_4,w_4)\}$$
$$M_2 = \{(m_1,w_1),(m_2,w_3),(m_3,w_4),(m_4,w_2)\}$$

The matching M_2 can be attained by exchanging the partners in two pairs: (m_3,w_2), and (m_4,w_4) in the matching M_1, thus two nodes corresponding these two matchings are linked in the network. We will call the network complete when the network includes all possible matchings as nodes and all possible partner-exchange as links.

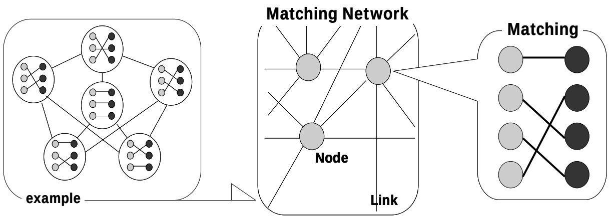

Fig. 3. An example of a matching network with size 3. Bipartite graph indicating each matching is shown inside each node for illustrative purpose.

IV. Coordinates for Network Visualization

Motivation for visualizing matching solutions as a network is to bring regularities and symmetries into daylight of visual perception, which are unseen otherwise. To this end, selection of appropriate coordinates (and its scale) is of great importance. Here, we will use simple and natural coordinates. For example, men's satisfaction P_m is defined as follows:

$$P_m = \sum (n+1-R_{mi})$$

where n is the size of the stable marriage problem and R_{mi} is the man m_i's rank (an integer ranging from 1 to n where 1 means the most favorite) to the current partner in the matching M. Women's satisfaction P_w is similarly defined with R_{wp} the woman w_p's rank to the partner in the matching. These two coordinates may be expressed by one coordinate $P_{mw}= P_m - P_w$ which means men's satisfaction relative to women's satisfaction. Although this P_{mw} is an asymmetric one, the following *E energy* is a symmetric coordinate reflecting both men and women's satisfaction symmetrically.

$$E = \sum (n+1-R_{mi})(n+1-R_{wp})$$

where the summation is taken over all the pair m_i and w_p in the matching M.

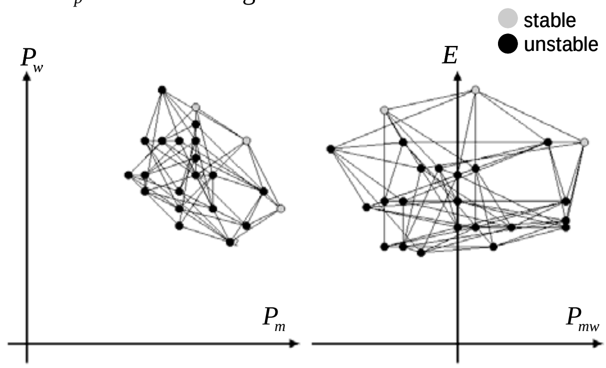

Fig. 4. Network visualization of an instance of SMP with size 4. Left: two coordinates of men's satisfaction P_m and women's satisfaction P_w are used. Right: symmetric coordinate E and asymmetric coordinate P_{mw} are used.

When P_w and P_m are used as two axes (Fig. 4 left), as the points are placed toward more upper-right, the better the solution for either women or men or both. This is similar to indifference curves plotting utility (satisfaction) in microeconomic theory, and to the receiver operating characteristic (ROC) curves in detection theory. Stable solutions are placed on the curve, since they will most often satisfy either women, men or both.

When E and P_{mw} are used as two axes (Fig. 4 right), the points placed higher the better for both women and men, more right the better for men, and more left the better for women. They are upward convex, similarly to the P_w - P_m curve.

It should be noted that the curves include unstable solutions as in Fig. 4, although stable solutions are often included in the curve. Of course, there are exceptions, for it is known that stable matching may not be obtained with any local (local in the sense that individual rank or paired ranks are aggregated) measure such as P_w, P_m, P_{mw} and E. Stable matching nodes are placed at the highest location in E coordinates, and of course there are exceptions too with the same reason.

V. Specific Instances of Stable Marriage Problem

When we visualize matching network of SMP instances with specific structure, some regularities and symmetries will be observed. Latin SMP [7], for example, defines instances where each person's rank to the person in the opposite sex and the rank from the person to the original person add to a constant n+1. Than is,

$$R_{mi,wp} + R_{wp,mi} = n + 1$$

where $R_{mi,wp}$ is the man m_i's rank to the the woman w_p. This equation means a rather strange constraint that the higher a person ranked to persons in the opposite sex, the lower being ranked by them.

Preference structure of SMP may be expressed by a preference matrix $\{ a_{ij} \}$ where the element in i^{-th} row and j^{-th} column a_{ij} is defined to be $R_{mi,wj}$ / $R_{wj,mi}$. For the Latin SMP with size 4, the preference matrix is as follows:

1/4, 2/3, 3/2, 4/1
2/3, 1/4, 4/1, 3/2
3/2, 4/1, 1/4, 2/3
4/1, 3/2, 2/3, 1/4.

For this Latin SMP with size 4, the matching networks are visualized in Fig. 5, where coordinates are drawn in the same manner as in Fig. 4. Regularity and symmetry of the stable matching solutions in the network is made conspicuous. The degeneracy is obvious in P_m - P_w coordinate, for every nodes are stable, and unstable ones are masked by the stable ones. From the definition of the Latin SMP, the preference structure should be symmetric for women and men. This fact is evidently reflected in both figures with P_m - P_w coordinate (Fig. 5 left) and with P_{mw} – E coordinate (Fig. 5 right).

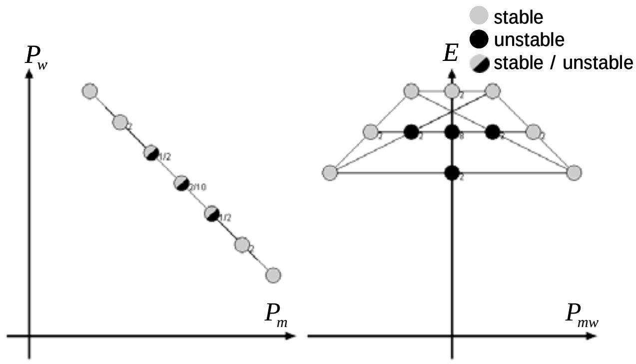

Fig. 5. Network visualization of a Latin SMP with size 4. Left: two coordinates of men's satisfaction P_m and women's satisfaction P_w are used. Stable matchings are shown by squares, while unstable ones by circles in the left to avoid masking when overlapped. Right: symmetric coordinate E and asymmetric coordinate P_{mw} are used.

The followings are three preference matrices of SMP of size 4 with regularities:

1/2,2/3,3/4,4/1	1/3,2/2,3/1,4/4	1/3,2/2,3/1,4/4
2/3,1/2,4/1,3/4	2/4,1/1,4/2,3/3	2/2,1/3,4/4,3/1
3/4,4/1,1/2,2/3	3/1,4/4,1/3,2/2	3/1,4/4,1/3,2/2
4/1,3/4,2/3,1/2	4/2,3/3,2/4,1/1	4/4,3/1,2/2,1/3.

These three preference matrices are obtained by fixing the men's rank to women but shifting and rotating the women's rank to men in several ways in the Latin SMP above. These three SMPs with the above preference matrices (left, middle, right) are visualized in Fig. 6 (above, middle, below, respectively).

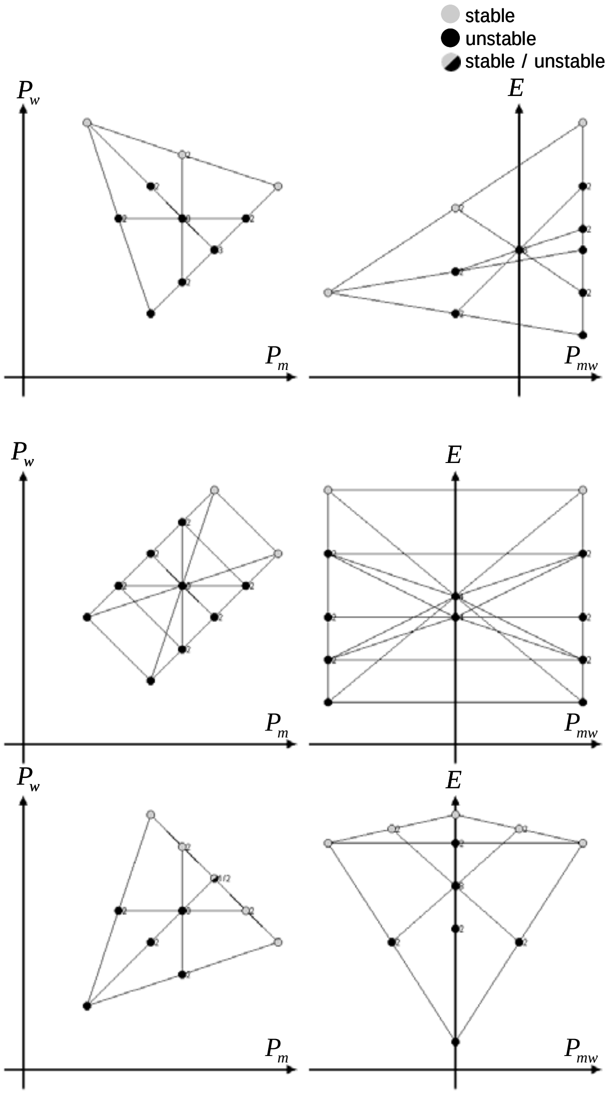

Fig. 6. Network visualization of three instances of SMP with regular structures. Left: two coordinates of men's satisfaction P_m and women's satisfaction P_w are used. Right: symmetric coordinate E and asymmetric coordinate P_{mw} are used.

It can be observed that the first SMP (Fig. 6 above) and the last SMP (Fig. 6 below) share the similar preference structure such as isomorphic with 90 degree anti-clock wise rotation in P_m - P_w coordinate, however, the last SMP is symmetric for men and women while the first one is not as observed with P_{mw} – E coordinate. The symmetry for women and men can be observed for the middle SMP, too. With the preference matrices alone, these facts may not be as obvious as seen in the network visualization.

VI. Summary

The preference structures are involved in the two matrices: preference from women to men; and that from men to women. Although the preference structure itself can directly be expressed by a weighted bipartite graph or stable marriage graph, the matchings are expressed by the matching network whose nodes are matchings and edges partner-exchange. By visualizing the network with adequate nodes layout in the coordinate, the space composed by matching (including stable ones) will be understood geometrically.

As we have glimpsed, symmetry in the preference structure will be understood from the viewpoint of symmetry in the graph visualizing the matching network with an adequate coordinate for the nodes layout.

Acknowledgments. This work was supported by Toyohashi University of Technology.

REFERENCES

[1] D. Gale and L.S. Shapley, College admissions and the stability of marriage, *American Mathematical Monthly*, 69:9-15, 1962

[2] D. Gusfield and R.W. Irving, *The Stable Marriage Problem: Structure and Algorithm*, MIT Press, London, 1989

[3] D.E. Knuth, *Stable marriage and its relation to other combinatorial problems: An intro-duction to the mathematical analysis of algorithms*, CRM Proceedings & Lecture Notes, Vol. 10, 1997

[4] A. Tamura, Transformation from Arbitrary Matchings to Stable Matchings, *J. of Combi-natorial Theory*, Series A 62: 310-323, 1993.

[5] G.D. Battista, P. Eades, R. Tamassia, I.G. Tollis (1998), *Graph Drawing: Algorithms for the Visualization of Graphs*, Prentice Hall

[6] M. Balinski and G. Ratier, Of stable marriages and graphs, and strategy and polytopes. SIAM Review 39 (1997) 575 – 604.

[7] A.T. Benjamin, C. Converse, H.A. Krieger, How do I marry thee? Let me count the ways, *Discrete Applied Mathematics*, 1995

Broadband Robust PWM Power Amplifier Using Approximate 2DOF Digital Control

Takahiro NOMURA[1], Hiroshi IWATA[1], Kohji HIGUCHI[1], Kazushi NAKANO[1]
[1]The University of Electro-Communications, 1-5-1 Chofu-ga-oka, Chofu, Tokyo 182-8585
email:nomura@francis.ee.uec.ac.jp, higuchi@ee.uec.ac.jp

Abstract

Lately, it is required that the bandwidth of PWM power amplifier is extended. For example, it is in application of the testing power supply of a low ferquency immunity examination, or a class-D ampllifier. In this paper, we show that the bandwidth of PWM power amplifier can be extended by using an Approximate 2DOF Digital Controller. This controller is implemented on a DSP. It is demonstrated from experiments that the bandwidth can be made wider with this controller.

1 Introduction

A PWM power amplifier used as a power supply or amplifier has good power conversion efficiency, small size and lightweight, it is widely used for common apparatus. We apply the PWM power amplifier to an AC power supply apparatus. The AC power supply apparatus output the same AC as the commercial power supply. Since, in the commercial power supply, the voltage may fall and the waveform may not be a precise sine-wave or the noise may be mixed, the AC power supply apparatus is used as a AC regulated power supply. Especially it is needed when performing precise electric measurement etc. And it has a function of frequency conversion or voltage conversion, so it is used when testing and producing of the goods of a foreign country, or when the same power supply specification as the one of a foreign country must be supplied. Furthermore, it is used as the power supply for a low frequency wave immunity test. The low frequency wave immunity test examines whether the electronic devices operate normally in abnormal conditions, such as a fall of voltage and an instantaneous breaking off. Therefore, the AC power supply apparatus in which the transient response characteristics does not deteriorate for the various load characteristics from capacitivity to inductivity is needed. In the low frequency wave immunity test, it is necessary to make various waveforms, such as breaking off wave etc. which have rapid changes. Therefore, it is required that the bandwidth of PWM power amplifier must be very wide in order to follow at high speed to a reference imuunity test signal without overshooting. We proposed[1, 2] previously the different methods from the other methodsd[3, 4] for designing a robust digital controller for PWM power amplifiers which can attain those demands. This method used the idea of an apprximate 2-Degree-of-Freedom(2DOF) sytem. However, the bandwidth is not so wide and is about 2[kHz]. It is necessary to extend the bandwidth to deal with various problems. In this paper we show that the bandwidth can be extended using the approximate 2DOF digital controller by getting more high sampling and switching frequency. This digital controller is actually realized by using a DSP. Some experiments show that the controller can extend the bandwidth.

2 PWM power amplifier

The power amplifier as shown in **Fig.1** is being manufactured. The triangular wave double carrier system is adopted as a PWM switching signal generating part. A power amplification part is a full-bridge type chopper circuit, and the voltage of direct-current power-supply E is 30[V]. The LC circuit is a filter for removing carrier and switching noises. The values of LC circuit are $L_0 = 20[\mu\text{H}]$ and $C_0 = 2.16[\mu\text{F}]$. If the frequency of control signal u is smaller enough than that of the carrier, the state equation of the DC-DC converter at a resistive load in Fig.1 except for the controller in DSP can be expressed from the state equalizing method as follows :

$$\begin{cases} \dot{x} = A_c x + B_c u \\ y = Cx \end{cases} \tag{1}$$

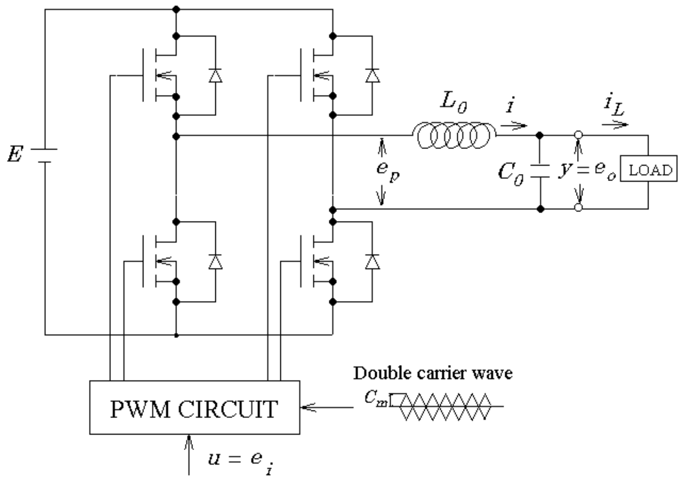

Figure 1: PWM power amplifier

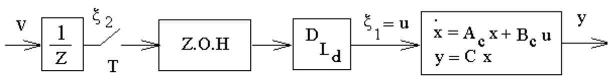

Figure 2: Controlled object with input dead time $L_d(\leq T)$

where

$$x = \begin{bmatrix} e_o \\ i \end{bmatrix} \quad A_c = \begin{bmatrix} -\frac{1}{C_0 R_L} & \frac{1}{C_0} \\ -\frac{1}{L_0} & -\frac{R_0}{L_0} \end{bmatrix} \quad B_c = \begin{bmatrix} 0 \\ \frac{K_p}{L_0} \end{bmatrix}$$

$$C = \begin{bmatrix} 1 & 0 \end{bmatrix} \quad u = e_i \quad y = e_0 \quad K_p = -\frac{E}{C_m}$$

and R_0 is the total resistance of coil and ON resistance of FET, etc., and the value is $0.015[\Omega]$. When realizing a digital controller by a DSP, a delay time exists between the starting time of the sampling operation and the outputting time of the control signal due to the calculation and AD/DA conversion times. This delay time is considered to be equivalent to the input dead time which exists in the controlled object as shown in **Fig.2**. Then the state equation of the system in Fig.2 is expressed as follows :

$$\begin{cases} x_{dw}(k+1) = A_{dw} x_{dw}(k) + B_{dw} v(k) \\ y(k) = C_{dw} x_{dw}(k) \end{cases} \quad (2)$$

where

$$x_{dw}(k) = \begin{bmatrix} x_d(k) \\ \xi_2(k) \end{bmatrix} \quad x_d(k) = \begin{bmatrix} x(k) \\ \xi_1(k) \end{bmatrix}$$

$$A_{dw} = \begin{bmatrix} A_d & B_d \\ 0 & 0 \end{bmatrix} \quad B_{dw}(k) = \begin{bmatrix} 0 \\ 1 \end{bmatrix}$$

$$A_d = \begin{bmatrix} e^{A_c T} & e^{A_c(T-L_d)} \int_0^{L_d} e^{A_c \tau} B_c d\tau \\ 0 & 0 \end{bmatrix}$$

$$B_d = \begin{bmatrix} \int_0^{T-L_d} e^{A_c \tau} B_c d\tau \\ 1 \end{bmatrix}$$

$$C_{dw} = \begin{bmatrix} C_d & 0 \end{bmatrix} \quad C_d = \begin{bmatrix} C & 0 \end{bmatrix} \quad \xi_1(k) = u(k)$$

Now, the power amplifier with the following specifications 1-3 is designed and manufactured by constituting digital control systems to the PWM power amplifier (controlled object) at no load.

1. The band-width of control systems is higher than 20[kHz] to each load , i.e., no load, resistance load, capacitive load, parallel load with resistance and capacitive load and inductive load. The value of such loads is restricted to a certain range.
2. Against all the loads of spec.1, an over-shoot is not allowable in a step response.
3. The specs. 1 and 2 are satisfied also to change of the direct-current power supply of $\pm 10\%$.

The load change for the controlled object and the direct-current power supply change are considered as parameter changes in eq.(2). The parameter changes can be transformed to equivalent disturbances q_v and q_y as shown in **Fig.3**. Moreover, if the saturation in the input arises or the input frequency is not so small in comparison with the carrier frequency, the controlled object will be regarded as a class of nonlinear systems. Such characteristics changes can be also transformed to equivalent disturbances as shown in Fig.3. Therefore, what is necessary is just to constitute the control systems whose the pulse transfer functions from equivalent disturbances q_v and q_y to the output y become as small as possible in their amplitudes, in order to robustize or suppress the influence of these parameter changes, i.e., load change, and direct-current power-supply change. In the next section, an easy designing method which makes it possible to suppress the influence of such disturbances with the target characteristics held will be presented.

3 Design of approximate 2DOF digital controller

First, the transfer function between the reference input r and the output y is specified as follows :
$W_{ry}(z)$

$$= \frac{(1+H_1)(1+H_2)(1+H_3)(z-n_1)(z-n_2)(z+H_4)}{(1-n_1)(1-n_2)(z+H_1)(z+H_2)(z+H_3)(z+H_4)} \quad (3)$$

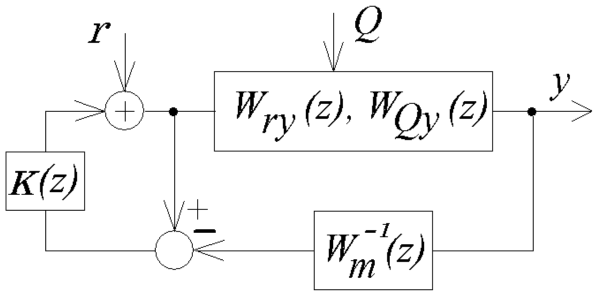

Figure 3: System reconstituted with inverse system and filter

where, n_1 and n_2 are the zeros for the discrete-time control object (2). It shall be specified that the relation of H_1 and H_2, H_3 becomes $|H_1| \gg |Re(H_2)|$, $|H_1| \gg |Re(H_3)|$. Then $W_{ry}(z)$ can be approximated to the following first-order model:

$$W_{ry}(z) \approx W_m(z) = \frac{1+H_1}{z+H_1} \tag{4}$$

This target characteristics $W_{ry}(z) \approx W_m(z)$ is specified so that it satisfies the specs.3 and 4.

Applying a state feedback and a feedforward

$$v = -Fx^* + GH_4r \quad x^* = [y \;\; x_2 \;\; \xi_1 \;\; \xi_2]^T \tag{5}$$

$$\xi_1(k+1) = Gr \tag{6}$$

to the discrete-time controlled object (2), we determine $F = [F(1,1) \quad F(1,2) \quad F(1,3) \quad F(1,4]$ and G so that $W_{ry}(z)$ becomes eq.(3). If equivalent conversion is carried out at the system which does not use current feedback directly, the control system of only voltage feedback will be obtained. The transfer function $W_{Qy}(z)$ between this equivalent disturbance $Q = [q_v \;\; q_y]^T$ and the output y of the model matching system desfined as

$$W_{Qy}(z) \;\; = \;\; \left[\; W_{q_v y}(z) \quad W_{q_y y}(z) \; \right] \tag{7}$$

The system added the inverse system and the filter to the system in Fig.3 is constituted as shown in **Fig.4**. In Fig.4, the transfer function $K(z)$ becomes

$$K(z) \;\; = \;\; \frac{k_z}{z-1+k_z} \tag{8}$$

The transfer functions between $r-y$ and $Q-y$ of the system in Fig.4 are given by

$$y \;\; = \;\; \frac{1+H_1}{z+H_1}\frac{z-1+k_z}{z-1+k_zW_s(z)}W_s(z)r \tag{9}$$

$$y \;\; = \;\; \frac{z-1}{z-1+k_z}\frac{z-1+k_z}{z-1+k_zW_s(z)}W_{Qy}(z)Q \tag{10}$$

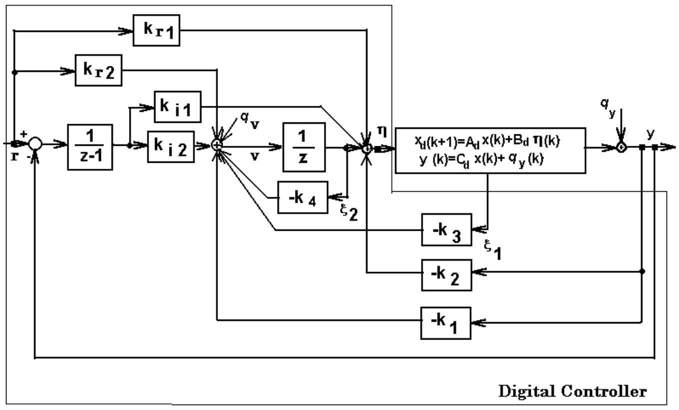

Figure 4: Approximate 2DOF digital integral type control system

where

$$W_s(z) = \frac{(1-H_2)(1+H_3)(z-n_1)(z-n_2)}{(z-H_2)(z+H_3)(1-n_1)(1-n_2)} \tag{11}$$

Here, if $W_s(z) \approx 1$, then Eqs.(9) and (10) become, respectively,

$$y \;\; \approx \;\; \frac{1+H_1}{z+H_1}r \tag{12}$$

$$y \;\; \approx \;\; \frac{z-1}{z-1+k_z}W_{Qy}(z)Q \tag{13}$$

From eqs.(12) and (13), it turns out that the characteristics from r to y can be specified with H_1, and the characteristics from Q to y can be independently specified with k_z. That is, the system in Fig.4 is an approximate 2DOF, and its sensitivity against disturbance becomes lower with the increase of k_z.

If an equivalent conversion of the controller in Fig.4 is carried out, the approximate 2DOF digital integral-type control systems will be obtained as shown in **Fig.5**. In Fig.5, the parameters of the controller are as follows :

$$\begin{aligned} k_1 &= F(1,1+F(1,2)FF(1,1)+((-F(1,4) \\ &\quad -F(1,2)FF(1,4))(-F(1,2)/FF(1,2))) \\ &\quad +(GH_4+GF_z)(k_z/(1+H_2)) \\ k_2 &= F(1,2)/FF(1,2)+G(k_z/(1+H_2)) \\ k_3 &= F(1,3)+F(1,2)(FF(1,3)) \quad k_4 = -F_z \\ k_{i1} &= Gk_z \quad k_{i2} = (GH_4+GFz)k_z \\ k_{r1} &= G \quad k_{r2} = GH_4+GF_z \end{aligned} \tag{14}$$

where

$$FF(1,1) = -A_d(1,1)/A_d(1,2)$$

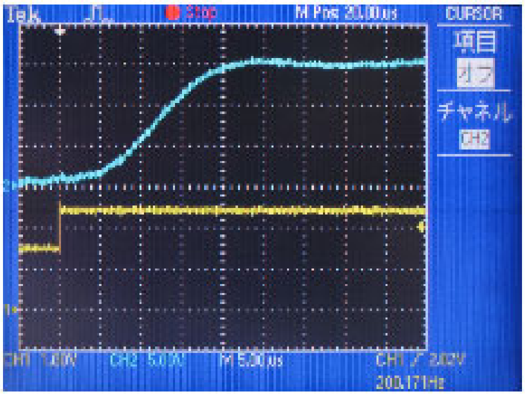

Figure 5: Experimental step response of the output voltage (the upper side : output 5[V/div], the lower side : input 1[V/div], time : 10[μs/div])

$$FF(1,2) = A_d(1,2)$$
$$FF(1,3) = -A_d(1,3)/A_d(1,2)$$
$$FF(1,4) = -B_d(1,1)/A_d(1,2)$$
$$F_z = -F(1,4) - F(1,2)FF(1,4)$$

4 Experimental studies

DSP TMS320LF2801 is used for the digital controller. The sampling frequency is set at 555[kHz] and the design parameters H_1, H_2, H_3 and H_4 are specified as

$$\begin{aligned} H_1 &= -0.825 \quad H_2 = -0.33 - 0.35i \quad H_3 = -0.33 + 0.35i \\ H_4 &= -0.68 \quad k_z = 0.145 \end{aligned} \tag{15}$$

Then the parameters of controller become as

$$\begin{aligned} k_1 &= -1.4068 \quad k_2 = 2.0296 \quad k_3 = 0.21572 \\ k_4 &= -0.34143 \quad k_{i1} = 0.16316 \quad k_{i2} = -0.05524 \end{aligned} \tag{16}$$

Then experimental result of a step response at no load is shown in **Fig.6**. Here, sine-wave are inputted into the control system with the sampling period $T = 1.8[\mu s]$, and the frequency band width were verified as shown in **Fig.7**. This figure shows that the bandwidth is about 20[kHz] because the output voltage has fallen by about 3 dB at the input frequency 20[kHz]. It turns out that at no load the specification is satisfied.

5 Conclusion

In this paper, it has shown that the bandwidth the PWM power amplifier can be extended using the approximate 2DOF digital controller by getting more

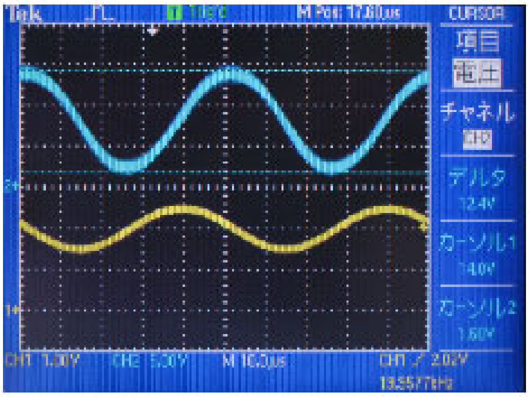

Figure 6: Experimemtal output voltage when the reference input is sine-wave of 20[kHz] (the upper side : output 5[V/div], the lower side : input 1[V/div], time : 10[μs/div])

high sampling and switching frequency. The digital controller was equipmented in DSP, amd it checked by experiment that the sufficient frequency characteristics could be acquired. The bandwidth is about 20[kHz]. As a result, it can use as the examination power supply for many kinds of immunity tests. A future subject is deciding the ranges of all loads and it is checking whether other specifications being satisfied. Furthermore, in order to use for more application, for example the class-D amplifier for audio, it is necessary to acquire more broadband characteristics.

References

[1] K. Higuchi,K. Nakano, K. Araki and F. Chino, "NEW ROBUST CONTROL OF PWM POWER AMPIFIER," IFAC 15th Triennial World Congress(CD-ROM)(2002.7).

[2] K. Higuchi, K. Nakano, T.Kajikawa, E.Takegami, S.Tomioka, K.Watanabe, "Robust Control of DC-DC Converter by High-Order Approximate 2-Degree-of-Freedom Digital Controller", *IEEE IECON'2004*, (CD-ROM), 2004.

[3] L. Guo, J. Y. Hung, and R. M. Nelms, "Digital controller Design for Buck and Boost Converters Using Root Locus", *IEEE IECON'2003*, 1864/1869 (2003).

[4] H. Guo, Y. Shiroishi and O. Ichinokura, "Digital PI Controller for High Frequency Switch*IEEE INTELEC'03*, 536/541 (2003).

A Consideration on Immunity-based Reinforcement Learning in a Continuous State Space Environment

Shu Hosokawa, Kazushi Nakano

Dept. of Electronic Eng., The University of Electro-Communications
1-5-1 Chofu-ga-oka, Chofu, Tokyo 182-8585, Japan
(Tel : 81-42-443-5190; Fax : 81-42-443-5183)
(hosokawa@francis.ee.uec.ac.jp, nakano@ee.uec.ac.jp)

Abstract: Many reinforcement learning methods have been studied on the assumption that state is discretized and environment size is pre-determined. However, an operating environment may have a continuous state and its size may not be known in advance such as in robot navigation and control. When applying these methods to the environment described above, we may need a large amount of time for learning or fail to learn. In this study, we improve our previous immunity-based reinforcement learning method to work in continuous state space environment. Since our method selects an action based on the distance between the present state and the memorized action, environment information (e.g. environment size) is not required in advance. The validity of our method is demonstrated through simulations for a swing-up control of an inverted pendulum.

Keywords: Reinforcement learning, Continuous state space, Adaptive immune system

1 Introduction

The Immunity-based reinforcement learning method is built based on the adaptive immune system [1]. This learning method is superior to traditional methods[2][3] in learning speed regardless of the initial and reward values. But, since this approach has an assumption that it works well in a discrete state space environment, it is likely to fail to learn or decrease convergence speed in learning when applied to a continuous state space environment. Even if it learns successfully, it requires a lot of computer memory. For a continuous state space environment, there exist a method based on a combination of discrete learning methods[4], Actor-Critic[5], etc. However, these methods require in advance to set a probabilistic model and/or the number of divisions according to the environmental dimension.

In this study, we improve our previous immunity-based reinforcement learning method so as to extend it applicable to the continuous state space. For this, we reconsider the mechanism of the adaptive immune system, and re-model such kind of learning mechanism. The adaptive immune system can acquire immunity by ingesting pathogens in advance that are similar to other pathogens, such as in vaccinations. Previous learning methods have been used to select an action by using only the information that states memorizing past actions perfectly coincide with sensor observations. Focusing on this point, we take into account the fitness of memorized states and sensor observations, and make use of the fitness and the reward gained from the environment for action selection. The validity of the proposed method is demonstrated through simulations for the swing-up control of the inverted pendulum.

2 Adaptive Immunity-based Reinforcement Learning

This section explains how to eliminate pathogens that invade an human body, and introduce the immunity-based reinforcement learning algorithm to correspond with the above model.

2.1 Summary of adaptive immunity

Figure 1 shows a relationship between cells in adaptive immunity. The pathogen is called antigen. The antigen is captured and recognized by the antigen presenting cell. The antigen presenting cells include B cells, macrophage, etc. The information of the antigen is presented to T cells. The T cells which the information is presented release the cytokines, and send the signal to the B cells for activation. The activated B cells then produce the antibody to neutralize the antigen. Therefore, the invaded antigen can be eliminated. The T cells playing the above role are called Helper T cells (Th cells). The relationship of B cells - antigens and B cells - Th cells is specific. Generally, T cells and B cells die after eliminating the antigen. But, some activated T cells and B cells have a long lifetime, circulate throughout in the body and survive as memory cells. As a result, the adaptive immunity becomes able to respond quickly and eliminate effectively the same type of antigen.

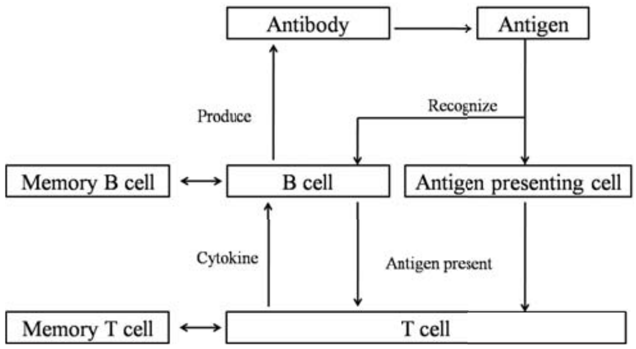

Figure 1: Adaptive immunity

2.2 Action selection algorithm

First of all, the set of all the states where the agent can exist is defined as S. The agent state is defined as $s_i(\in S)$. Th cells memorize state s_i, action a_k, and cytokine signal w_k. In addition, B cells that perform actions a_k is expressed as B_k. The state of B_k activated by antigens, is expressed as m_k. B_k became activated ($m_k = 1$) if the information matches the antigen, otherwise ($m_k = 0$). Action selection is performed based on the values of m_k and w_k by selecting B cells. B cells are selected to execute the action of antibody $A(s_i, k)$ that describes the current state s_i and actions are generated.

An algorithm for B cell selection using the Th database is presented as follows:

1. The agent exists in s_i, Th database releases a cytokine signal $w_k(s_i)$ according to the state. On the other side, B cells present the degree of stimulation m_k according to the current state.

2. After calculating $v_k = m_k \times w_k(s_i)$, a B cell is selected through the roulette selection using v_k of the selection probability for B_k.

3. Antibody $Ab(s_i, k)$ is produced by B_k. The antibody has the parameter called concentration which means the antibody's lifetime. When the antibody is produced, its concentration is set to 1 ($Ab(s_i, k) = 1$). If the same antibody has already been produced, or if the same B cell has already been selected in the past same state, a new antibody is not produced, and the existing antibody's concentration is reset to 1.

4. The concentrations of other antibodies produced in the past are updated with the following equation:

$$A_b \leftarrow \beta \times A_b \tag{1}$$

where $\beta(0 < \beta < 1)$ is the discount rate.

By performing the above process, the agent decides the B cell to be selected.

2.3 Update of Th database

When the agent receives a reward from its environment after it executed an action, the Th database is updated. This means that each $w_k(s_i)$ is updated as

$$w_k(s_i) \leftarrow w_k(s_i) + \alpha(r_k(s_i) - w_k(s_i)) \tag{2}$$

$$r_k(s_i) = \begin{cases} A_b(s_i, k) \times R & : A_b(s_i, k) \text{ produced} \\ 0 & : \text{otherwise} \end{cases} \tag{3}$$

where R is the reward which the agent receives from its environment, and $\alpha(0 < \alpha < 1)$ is the learning rate. This update formula is performed for all w. After updating, all antibodies are erased.

The agent becomes able to select an appropriate rule for its environment by repeating the learning with the above process of rule selection.

3 Immunity-based Reinforcement Learning in a Continuous State Space Environment

This section discusses how to improve the immunity-based reinforcement learning to work in a continuous state space environment. Traditional reinforcement learning methods used cytokine w_k of Th cell with coincidence of the memorized states and sensor observations for computing $v(k)$ in action selection. However, there is almost no matching of the memorized states and sensor observations in a real continuous state space.

In the actual adaptive immune system, Th cells do not recognize the whole individual antigen. Th cells change with their activities based on the fitness of a part of the original antigen degraded by antigen-presenting cells[6]. Th cells are activated when antigens are presented with the degree of similarity with their own receptors, and release cytokine signals to B cells. Focusing on this mechanism, we make use of the distance between the present and the memorized states for the activity of Th cells. The cytokine signal and the activity of Th cells are used for action selection.

The following is presented as a modification of the immunity-based reinforcement learning algorithm. Th cell is generated as a cell which records the continuous state ($\boldsymbol{\xi} = [\xi_1, \xi_2 \cdots, \xi_n]$), action ($a$) and evaluation value which is explained below. Here, only a special Th cell (Th_0) which outputs the same cytokine signal to all states and actions is generated. First, set the initial value of the evaluation to this cell. Next, give the following formula to calculate the activity of the current state ($\boldsymbol{\xi}'$) and the memorized state $\boldsymbol{\xi}^j$:

$$L(Th_j, a_k) = \begin{cases} \gamma \sum_{p=1}^{n} |\xi'_p - \xi^j_p| & a_k \text{ memorized} \\ \infty & \text{otherwise} \end{cases} \tag{4}$$

Eq.(4) is the Manhattan distance, which is defined as the sum of the distances of all dimensions. γ is a gain parameter given as a positive value. The larger value of γ, the smaller number of cells. This corresponds exactly with fine discretization of a continuous state space. A cytokine is obtained which outputs Th cell by calculating the values of the activity and the evaluation.

$$w_k = \sum_{j=0}^{N} \frac{W_j}{\exp(L(Th_j, a_k))} \tag{5}$$

where N is the total number of Th cells and W_j is the evaluation value memorized in j-th Th (Th_j).

Our action selection algorithm with considering a continuous state space is given as follows:

1. The agent exists in $\boldsymbol{\xi}$, then B Cells present the degree of stimulation m_k according to current state.

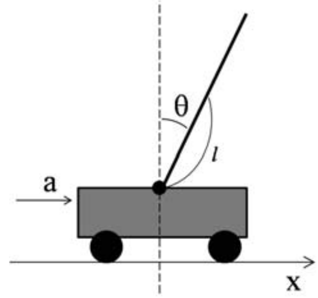

Figure 2: Swing-up of inverted pendulum

2. Th cell cytokine output(w_k) is calculated by using Eq (5).
3. A B cell is selected through the roulette selection with v_k as the selection probability for B_k after calculating $v_k = m_k \times w_k$.
4. Antibody $Ab(s_i, k)$ is produced by B_k. The antibody has the concentration which means the antibody's lifetime. When the antibody is produced, its concentration is set to 1 ($Ab(s_i, k) = 1$). If the same antibody has already been produced or the same B cell has already been selected in the past same state, a new antibody is not produced, and the existing antibody's concentration is reset to 1.
5. The concentrations of other antibodies produced in the past are updated with Eq.(1).

When the agent receives a reward from its environment, W_j is updated as follows:

1. Th cell is generated from the antibody's information. After setting the following evaluation, we erase the antibody information:

$$W_j = A_b(\boldsymbol{\xi}, k) \times R \tag{6}$$

2. All the evaluation values of Th cells are updated as

$$W_j \leftarrow W_j(1 - \alpha) \tag{7}$$

4 Simulation Results

This section shows simulation results of our proposed method applying to the swing up control of the inverted pendulum(Fig.2). The motion equation of the inverted pendulum is described by

$$(M+m)\ddot{x} + ml\cos\theta\ddot{\theta} + D_x\dot{x} + ml\sin\theta\dot{\theta} = a \tag{8}$$
$$-ml\cos\theta\ddot{x} + I\ddot{\theta} + D_\theta\dot{\theta} - mgl\sin\theta = 0 \tag{9}$$

Table 1: Initial state and target state

Parameter	Initial state	Target state
x	0	don't care
$\dot{x}$	0	0 ± 0.5
θ	π	0 ± 0.5
$\dot{\theta}$	0	0 ± 0.2

where, M is the mass of the truck, m is the weight of the pendulum, l is the length of the pendulum to the center of gravity, D_x is the friction on the truck, D_θ is the friction of the pendulum rotation, I is the moment on the rotation of the pendulum. In this simulation, we perform a learning of the swig-up control of the inverted pendulum through selections of $a \in A = [-10, 0, 10]$ (action list). The control task is to swing up the pendulum from its natural pendant position ($\theta = \pi$) and stabilize it in the inverted position ($\theta = 0$) under the assumption that all the physical parameters are unknown.

Table 1 shows the initial state and target state. The states $x, \dot{x}, \theta$ and $\dot{\theta}$ are inputted to the learning module, whose values are observed with the uniform random values (± 0.1) added. If we can reach the target, we give the reward of 10 and end one episode. The truck motion is limited on the range of $-10 \leq x \leq 10$. If going out of the range, the truck should be stopped ($\dot{x} = 0$). Also, if we could not reach the target even after 5000 steps, we restart to learn from the next episode without any reward. Figure 3 shows the results by using the proposed reinforcement learning method.

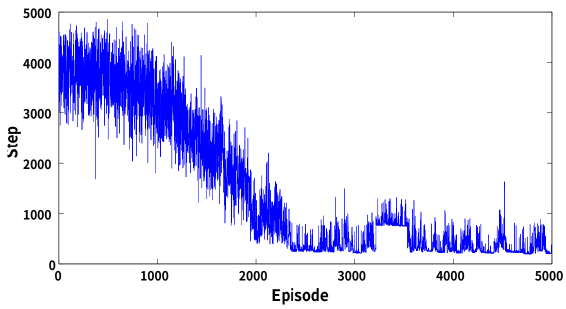

Figure 3: Result of swing-up control

Our method can acquire a swing-up control action even in an observation noise case. The discrete state - reinforcement learning method could not acquire any swing-up -.

5 Conclusions

We improved the immunity-based reinforcement learning method in order to extend it applicable to a continuous state space environment. Also the method was verified by simulations for a swing-up control of an inverted pendulum. As a result, our proposed method was able to perform a learning even in the continuous state space environment.

In our future works, we should handle negative rewards (penalty). However, our proposed method using a roulette selection for action selection, cannot handle negative evaluation values. We need to develop a new reward function or a new method for action selection where the negative reward can be used for stabilizing control.

References

[1] J. Ito, K. Nakano, K. Sakurama and S. Hosokawa: "Adaptive immunity based reinforcement learning", Artificial Life and Robotics, **13**, 1, pp.188–193 (2008).

[2] C. J. C. H. Watkins and P. Dayan: "Technical note: q-learning", Mach. Learn., **8**, 3-4, pp.279–292 (1992).

[3] J. J. Grefenstette: "Credit assignment in rule discovery systems based on genetic algorithms", Readings in Machine Learning (Eds. by J. W. Shavlik and T. G. Dietterich), Kaufmann, San Mateo, CA, pp.524–534 (1988).

[4] T. Matsui, N. Inuzuka and H. Seki: "Profit sharing with linear function approximation", The 16th Annual Conference of Japanese Society for Artificial Intelligence, pp.2D3–03 (2002) (in Japanese).

[5] H. Kimura and S. Kobayashi: "An analysis of actor-critic algorithms using eligibility traces : Reinforcement learning with imperfect value functions", Journal of Japanese Society for Artificial Intelligence, **15**, 2, pp.267–275 (2000) (in Japanese).

[6] S. Kakiuchi, K. Ikebuchi, K. Ota, Y. Kobayashi, R. Simosato and Z. Mizuguchi (Eds.): "Immunology handbook", Ohm sha (2006) (in Japanese).

Investigation of Voluntary Movements in Auditory Stimulated Conditions by Integrative Measurement

Kazuya Saito*, Young-il Park* and Masafumi Uchida**

**The Graduate School of Electro-Communications, The University of Electro-Communications*
***The Department of Electronic Engineering, The University of Electro-Communications*
1-5-1, Chofugaoka, Chofu, Tokyo, Japan
(Tel: 81-42-443-5173 Fax: 81-42-443-5173)
(E-mail: sait@zidane.ee.uec.ac.jp)

Abstract: In general, voluntary movements can easily change from trial to trial. The reasons why are not clearly understood. We used an integrative biological information measurement and analysis system that we previously proposed to measure biological information during voluntary movements, especially handwriting, under auditory stimulation, and we considered the relationship between changes in voluntary movement and stimulation. Our findings will be applicable to rehabilitation, functional electrical stimulation, bio-feedback, and voluntary movement correction.

***Keywords*: EMG, EEG, Handwritten Characters, Auditory Stimulation**

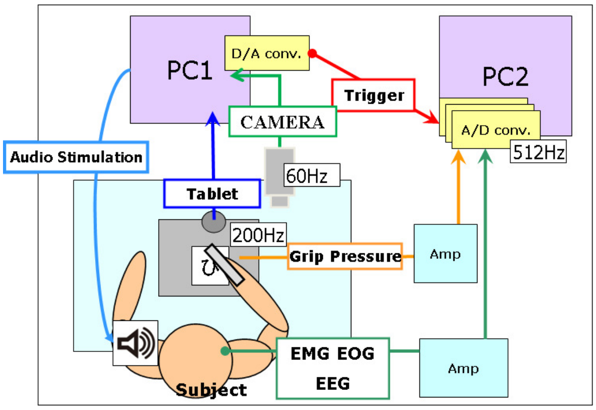

Fig. 1. Measurement system.

I. INTRODUCTION

Recently, studies on handwriting have been reported in many fields [1] [2]; however, there have been few studies examining character deformation [3]. In our earlier studies, we considered the relations between biological information, the shapes of handwritten characters, and their variations. We also developed an integrative measurement system for measuring and analyzing biological information and character shapes [4]. We used the same system in the present study reported here. The purpose of this study was to investigate the underlying relationships between stimulation and character deformation under auditory stimulation conditions, based on biological information, such as EMGs, EEGs and so on.

Ordinarily, handwriting is affected by various stimuli. During the handwriting process, we first receive stimulation from the external environment via our sensory organs, such as the eyes, ears, skin and so on. Then, when the stimulation reaches our brain via nerve conduction, our brain cannot continue the writing process with precision. As a result the handwriting is deformed.

The findings of this study are expected to find applications in functional electrical stimulation (FES), biofeedback, and so on. Biofeedback involves reporting invisible internal information of the body in a recognizable way, which usually means visually or aurally.

II. MEASUREMENT SYSTEM

Fig. 1 shows the measurement system developed in our earlier studies. It consists of five components: (1) a tablet, (2) three pressure sensors, (3) EMG, EOG, and EEG measurement systems, (4) a tracking system, and (5) an auditory stimulation presentation system. The sampling frequencies were different in each system. Therefore, an interpolating method was used to make the sampling rates conform to each other. In detail, biological information and grip pressure were acquired via the same A/D converter, whose sampling frequency was 512 Hz. The tablet's sampling frequency was limited to 200 Hz, and the camera's was limited to 60 Hz.

1. Character recognition system

The character recognition system used a tablet (WACOM Intuos 3 PTZ-930) for handwritten character recognition. The tablet could measure the location (X,Y) of the tip of a pen, the writing pressure, and the elevation and azimuth angles. The tablet was controlled by software, which also controlled the camera and the D/A converter for outputting a trigger signal for

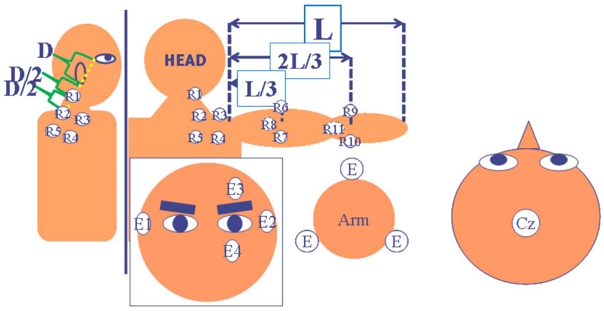

Fig. 2. EMG, EOG and EEG channels.

synchronization. The sampling frequency of the tablet was 200 Hz.

2. Pen grip pressure measurement system

The grip pressure was measured with three pressure sensors (Nitta Corporation: FlexiForce), placed on the pen to correspond to the thumb, the index finger, and the middle finger. The pressure measurement system was connected to the A/D converter on PC2, and the sampling frequency depended on the A/D converter, which was set to 512 Hz.

3. EMG EOG and EEG measurement system

In our early study, the number and positions of the EMG, EOG, and EEG measurement channels were defined as shown in Fig. 2. The number of EMG channels was 24, the number of EOG channels was 2, and the number of EEG channels was 1.

The sampling conditions are shown in Tables 1 and 2. A common sampling frequency of 512 Hz was used for the EMG, EOG, and EEG channels.

Table 1. EMG and EOG sampling conditions. (HFF: high frequency filter; LFF: low frequency filter)

HFF	30 Hz
LFF	1.5 Hz
Sense	50 μV
Ham Filter	50 Hz

Table 2. EEG sampling conditions.

HFF	50 Hz
LFF	0.01 Hz
Sense	50 μV
Ham filter	50 Hz

4. Real-time tracking system

The tracking system consisted of a CCD camera (Library Corp.: GE60) and software (based on Library Corp.: Radish SDK) to control the camera and provide a

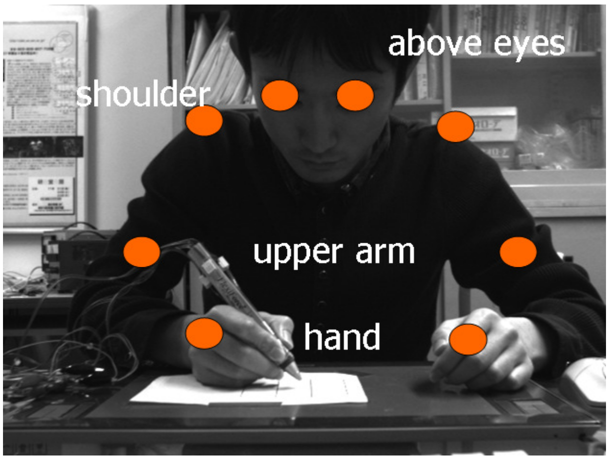

Fig. 3. Tracking points.

tracking function for tracking eight points, as shown in Fig. 3. The tracking points were the hands, upper arms, shoulders, and areas above the eyes, on both the left and right sides. The tracking results were recorded on PC1 as coordinate data (X, Y) with a trigger signal issued when the pen touched or was released from the tablet. The sampling frequency of 60 Hz was limited by the camera.

5. Stimulus Presentation System

Subjects were presented auditory stimulation, a 1000 Hz 50 ms-long tone, through noise-canceling headphones (Maxell: HP-NC22.OH-BK) from PC2. The headphones cancelled noise from 60 to 520 Hz, with a suppression level of about 22 dB down at 200 Hz.

6. Data Synchronization

All systems were synchronized by experimental software designed to control the tablet, the camera, and the D/A converter and to save the collected data. Data collected by the tablet was the character shapes (X,Y), writing pressure, and elevation and azimuth angles. The number of tracking points was limited to eight, and each data item had two dimensions. This software generated a trigger signal when the tablet detected a pen touch/release. The signal was +5 V when the pen touched and +2.5 V when the pen was released.

III. ANALYSIS

1. Classification

Before analysis, the measured data were classified into three groups: Group 1, just before the stimulated trial; Group 2, during the stimulated trial; and Group 3, just after the stimulated trial.

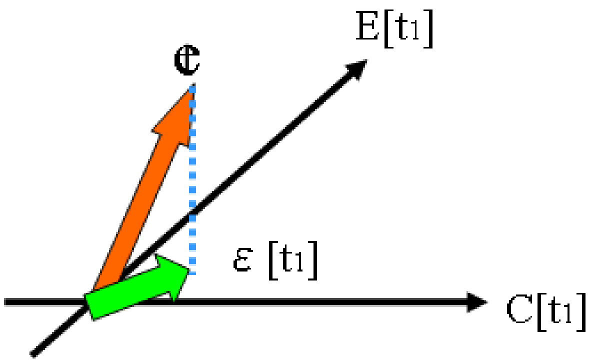

Fig. 4. Eigenvector Projection for $^{(i)}C_m$ - $^{(k)}E_m$, at t1.

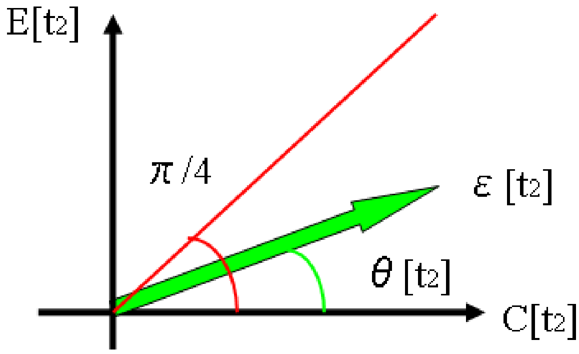

Fig. 5. Argument of the projected vector on C_m - E_m dimension, at t2.

2. Evaluation Processes

The evaluation method adopted in this study was based mainly on principal component analysis (PCA), which was developed in our earlier study. The evaluation process used in this study is described below.

First, preprocessing was executed. The EEG result was frequency analyzed to calculate the alpha wave, the beta wave, and the evoked wave that consisted of 1–30 Hz EEG. Then the original EEG data were replaced by the two sets of frequency-analyzed data. Next, measured character shapes were normalized based on their centers of gravity, and all data were normalized to 500 Hz for every trial. Three-dimensional spline interpolation, a well-known method, was used for upsampling.

Second, the measured and preprocessed data were defined as matrixes $^{(i)}C_m$ and $^{(k)}E_m$, where $i=(1,2), k=(1,2,\ldots,50)$, and m means the number of characters. Matrix C contained the character coordinates (X, Y), and matrix E contained 30 channels of biological information, 3 channels of data collected by the tablet, except for character coordinates, and 8 channels of X and Y tracking coordinates.

Third, $^{(i)}C_m$ and $^{(k)}E_m$ were used for PCA for each i and k. There were 100 patterns of the matrixes. By extracting only the first principal component from all the measured data, high correlation of the body position and character deformation was estimated with an evaluation function, P, defined as follows:

$$^{(i)(k)}P_n[t] = \left| ^{(i)(k)}\varepsilon_q[t] \right| \times \left| 1 - \frac{\frac{\pi}{4} - {}^{(i)(k)}\theta_q[t]}{\frac{\pi}{4}} \right| \quad (1)$$

where i is the number of dimensions indicating the character location (X, Y), k is the number of measured channels, and q is the number of principal components. The term $\varepsilon_q[t]$ is the eigenvector $e_q[i,k]$ of the q-th principal component projected on the character information – other information dimension (C – E dimension). Therefore, if θ is $\pi/4$, the position of the body has a high correlation with the changes in the character shapes. $^{(i)(k)}P_n[t]$ exists over a range of 0 to 1. $^{(i)(k)}P_n[t]$ is a time-series evaluated value that indicates the correlation between changes in character shapes and each EMG channel. In detail, changes in the EMG indicate that a muscle moved. Therefore, the higher $^{(i)(k)}P_n[t]$, the higher the correlation between the channel and changes in character shapes.

Fourth, $^{(i)(k)}P_n[t]$, the evaluated value, for Group 1 and Group 2 were compared based on the coefficients of correlation. In detail, areas (periods) before and after the stimulated point for Groups 1 and 2 were compared. The area 400 ms before the stimulation was defined as area X, and the area 400 ms after the stimulation started was defined as area Y. If the character shapes were changed in response to the stimulation, the values of the coefficients should have changed after the stimulation, that is, area Y.

Therefore, two rules, Rule A and Rule B, were defined for evaluating the coefficients. For Rule A, the coefficient of correlation was Cx<-0.4, Cx>0.4 and -0.2<Cy<0.2. This corresponds to deformation caused by the stimulation. On the other hand, for Rule B, the coefficient of correlation was -0.2<Cx<0.2, and Cy<-0.4, and Cy>0.4. In other words, the changes in character shapes and biological information were small before the stimulation, whereas larger changes appeared after the stimulation. This is called the correction effect. In this study, because none of the channels satisfied rule B, only rule A was considered.

IV. EXPERIMENT

Subjects were required to write 20 *hiragana* (Japanese syllabary) characters "ひ" in about 1 second per character, and this was defined as one session. The auditory stimulation was presented randomly with a probability of 10%, and the experiment was conducted until the number of stimulated trials reached 90. To measure clear EEG signals, the experiment was performed in the afternoon, at least 2 hours after the subject's last meal. Three subjects participated in this study. The total number of measured and analyzed channels was 49: 24 EMGs, 1 EEG, 2 EEGs, 3 grip pressures, writing pressure, elevation and azimuth angles, and 8 tracking points.

V. RESULTS

Table 3 shows the channels that satisfied Rule A for the three subjects. In this study, we focused on biological information. Therefore, data for Subject 3 was rejected because channel 43, the horizontal axis tracked by the camera, was not a biological channel.

Table 3. Channels that satisfied Rule A.

Subjects	Channels
Subject 1	25,28,30,32,33
Subject 2	3,22,30,41,43,46,49
Subject 3	43

Channels 25 and 30 on Subjects 1 and 3, and Channels 22 and 30 on Subject 2 were biological information channels. Channel 30 was the alpha wave, which was a common channel. Channel 25 was horizontal EOG, Channel 3 was the right neck, and Channel 22 was the left forearm. Fig. 6 shows the time-series variation of Channel 25 (EOG) for Subject 1, for a period from 200 to 1000 ms, where the stimulation was presented at 600 ms. Group 1 is non-stimulated trials, and Group 2 is stimulated trials. As shown in Fig. 6, the average amplitude of Group 2 was lower than that of Group 1, showing that the horizontal movement of the eyes of Subject 1 were reduced.

VI. CONCLUSION

The aims of this study were to investigate handwriting changes caused by auditory stimulation using an integrated measurement system and to examine the possibility of correcting changes in voluntary movements by using stimulation. Although the first aim was achieved, the second was not adequately achieved

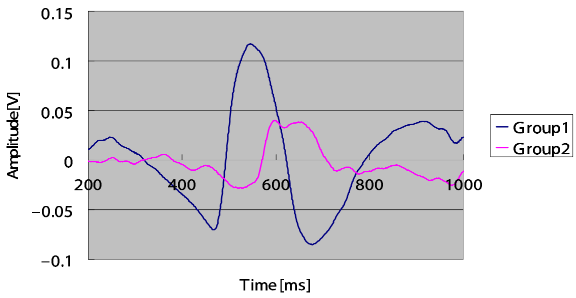

Fig. 6. Horizontal EOG of Groups 1 and 2 for Subject 1.

because none of the measured data channels satisfied Rule B, that is, the correction effect.

VII. FUTURE TASKS

In this study, we investigated the relations between character shapes and auditory stimulation in three subjects. However, we were not able to observe a correction effect induced by the stimulation. Our future work will involve experiments under other stimulation conditions and with more subjects.

ACKNOWLEDGMENT

A part of this study was supported by the HAYAO NAKAYAMA Foundation for Science & Technology and Culture and Grant-in-Aid for Scientific Research (Basis Research (C), Assignment Number: 21500511).

REFERENCES

[1] K. Odaka, "Handwriting analysis and measurement system," The Papers of Technical Meeting on Instrumentation and Measurement, IEE Japan, IM-06-40, 2006. (in Japanese)

[2] M. Nishizawa and M. Uchida, "Transformation analysis of handwritten character by using multi-channnel measurement of surface EMGs," The Papers of Technical Meeting on Instrumentation and Measurement, IEE Japan, IM-06-39, 2006. (in Japanese)

[3] A. Ishida, S. Hirokawa, S. Miyazaki and T. Hayashi, "Biomechanics of Human Movement," Corona Publishing Co., pp. 41-71, March 2003 (in Japanese).

[4] M. Nishizawa, M. Uchida, K. Odaka and Y. Kimura, "Integrative Measurement System of Handwriting Process," 22nd SICE International Symposium on Biological and Physiological Engineering, January 13-14, 2007, Harbin, China pp.191-194

Swing Analysis of Body-parts Motion Accompanied by Apparent Movement

Young-il Park*, Kazuya Saito* and Masafumi Uchida**

**The Graduate School of Electro-communications, The University of Electro-communications,*

***The Department of Electronic Engineering, The University of Electro-communications,*

1-5-1 Chofu-ga-oka Chofu-shi, Tokyo, Japan

(Tel: +81-42-4435-5173; Fax: +81-42-4435-5173)
(park01@zidane.ee.uec.ac.jp)

Abstract: In this research, we examined the tactile sense for sensory substitution in people who have lost a certain sense. We considered use of apparent movement to communicate something via the tactile sense. It is necessary to measure the apparent movement objectively and quantitatively because apparent movement is normally a subjective thing. We extracted swing motion, a vital reaction characteristic accompanied by the apparent movement, using an EMG. We presented individual stimuli and performed a t-test with a combination of the presented stimuli. From the t-test results, the difference in vital reaction characteristic for each combination of presented stimuli was not small. The result presented here was obtained using only one subject; it will be necessary to increase the number of subjects in future.
Keywords: EMG, Apparent Movement, Tactile stimuli, Tactile sense**.**

I. INTRODUCTION

People depend on various senses in life. However, some people may have lost a certain sense due to congenital or postnatal handicaps. The lost sense can often be made up for with another sense, a concept known as *sensory substitution*. Examples of this include sign language, which the hearing impaired use, or Braille, which the visually impaired use. One human sense system is the tactile sense, which is a cutaneous sense that lies scattered over the whole body, allowing us to sense pain, warmth and so on. Complete loss of the tactile sense over the whole body is rare, although there are sometimes obstacles in a partial sense; nevertheless, it an efficient sense organ for sensory substitution.

Tactile displays have been developed as a sensory substitution for the visual sense and acoustic sense. Most of them involve placing many tactile stimulation elements in an array, and the main topic of study has been how to realize high-density implementations [1][2][3]. However, if the information to be conveyed can be transmitted adequately by limited tactile stimuli, high-density arrays of tactile stimulation elements are not necessary [4][5][6]. In addition, if the portability, convenience, maintainability, and cost of these information presentation devices could be improved, there is a possibility that tactile displays will grow as new means of transmitting information.

With the tactile sense, there is an illusion called *apparent movement*. Apparent movement is a phenomenon whereby, when tactile stimuli are presented at two points on the body with an appropriate time delay between the two stimuli, a person feels as if the sensation due to the presented stimuli moves between the two points. In advanced studies of apparent movement, a basic characteristic, such as the frequency characteristic, of the apparent movement has been examined [7][8][9]. Many of these studies have focused on how to evaluate a subjective quantity corresponding to the perceived apparent movement. It is also important to examine the origin of the apparent movement from a physiological viewpoint.

In this study, we examined a method to measure apparent movement objectively and quantitatively with a simple operation. We focused on the swinging motion occurring when apparent movement was perceived in the stimulated body part. We developed a method to measure the swinging motion of this body part based on the skin surface line electric potential from electromyography (EMG) and examined its effectiveness experimentally.

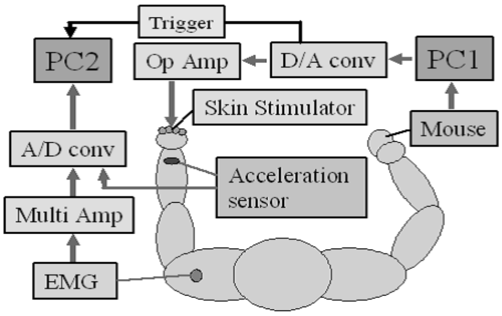

Fig. 1 System setup.

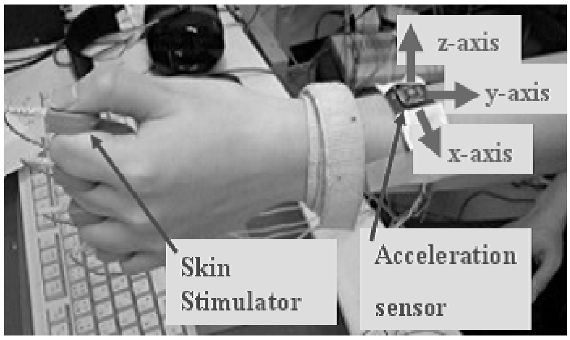

Fig. 3 Placement of vibration elements and acceleration sensor.

II. EXPERIMENTAL METHOD

1. Experimental system

Figure 1 shows the setup of the experimental system. A personal computer (PC1) recorded on its hard disk drive (HDD) the tactile stimulus generated to produce apparent movement and the subject's response when they recognized the apparent movement (the subject is directed to click a mouse attached to PC1). The output waveform (amplitude 5 V) generated with the digital-to-analog (DA) board of PC1 (Interface Co., PCI-3310) was amplified to about three times with an op-amp to serve as a vibration stimulus applied with a vibration generator. The data recorded in PC1 were the type of presented stimulus, whether or not a mouse click occurred, and the time from presenting the stimulus to the mouse click.

Electromyography (EMG) amplified with a living body amplifier (Digitex Lab. Co., Ltd., MA1132US) was recorded on the HDD of personal computer (PC2) through an analog-to-digital (AD) board (Interface Co., PCI-3176). The two computers were synchronized by sending a trigger signal from PC1 to PC2.

2. Presented stimuli

The four rectangular waves (amplitude 5 V) shown in Fig. 2 were output from PC1 through the DA board and were amplified by a factor of three with the op-amp, and the vibration stimuli were generated with the vibration generator.

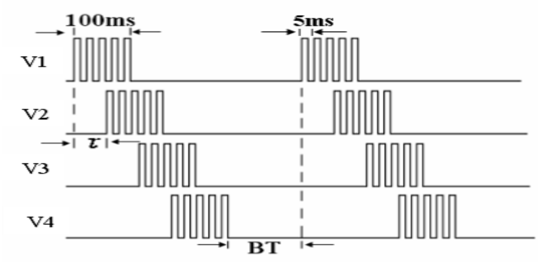

Fig. 2 Presented stimulus.

The period of the presented stimulus was 5 ms, the vibration duration was 100 ms, and the time difference τ was used as a parameter, as shown in Fig. 3. The relation to the perceived apparent movement was examined in this experiment.

3. Experimental method

The subject was asked to sit still with his/her eyes shut, and wearing noise-canceling headphones. The vibration generator used was Skin Stimulator manufactured by Audio Logical Engineering Co. The subject held four Skin Stimulators between the knuckle joints of adjacent fingers and between the index finger knuckle and the tip of his/her thumb, and extended his/her arm forward, where he/she held it in position, as shown in Fig. 3.

In PC1, the time difference τ was set at random, and the stimulus was presented to the subject as a vibration lasting for $3t$+100 ms. The subject clicked the mouse connected to PC1 only when the apparent motion was recognized. The time from the end of the presented stimulus until the mouse click is called *click time*.

The procedure described above constituted a single trial.

4. EMG measurement

The subject extended his/her arm, on the side where the stimulus was presented, forward horizontally and held it in position. Therefore, any shaking of the arm induced by the apparent movement is expected to be observed as a peculiar change in the EMG around the shoulder.

Eight electrodes were placed around the shoulder, and EMG was measured with a total of 14 channels, as shown in Fig. 4.

The electrode fixing points were as follows. The length L below is assumed to be the standard length from the corner of the eye to the base of the earlobe. Electrode 1 was placed at a distance L on the extension

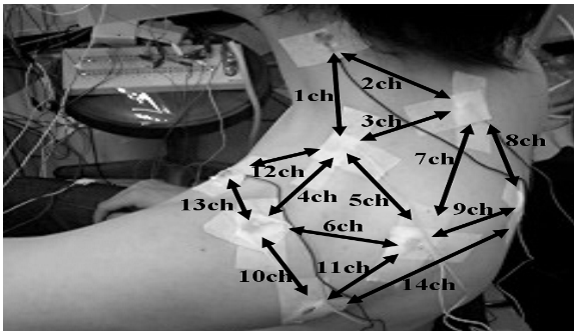

Fig. 4. Placement of the electrodes

line from the base of the earlobe. On a straight line connecting a certain shoulder peak, Electrode 2 was placed a distance L from Electrode 1, and Electrode 3 was placed at a distance $2L$. Electrodes 4 to 8 were placed based on Electrodes 1 to 3 so that the length formed an equilateral triangle with sides of length L, as shown in Fig. 4.

III. PSYCHOPHYSICAL MEASUREMENTS

1. Analysis method

The level of subjectivity corresponding to the perceived apparent movement was evaluated based on the mouse click data recorded in PC1. The ratio of subjects who recognized a stimulus when the time difference τ = 0, 20, 40, …, 160 ms (nine values in total) was calculated; this value is called the *recognition rate*.

If the recognition rate was found for each presented stimulus, the time difference τ at which the subjects recognized the apparent movement can be captured from a psychophysical viewpoint. One set consisted of 300 trials, and a total of eight sets were conducted, allowing sufficient rest in between. Therefore, there were a total of 2400 trials in the experiment. Because the presented stimulus was selected from the nine available types at random, each stimulus will be presented in about 270 trials on average.

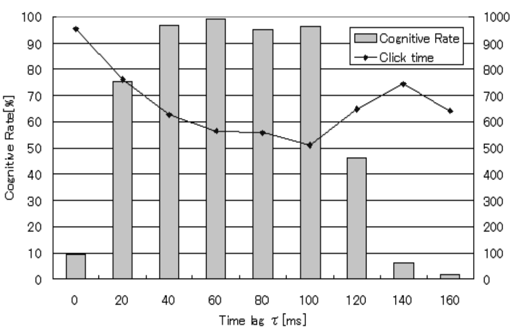

Fig. 5 Result of psychophysical measurements.

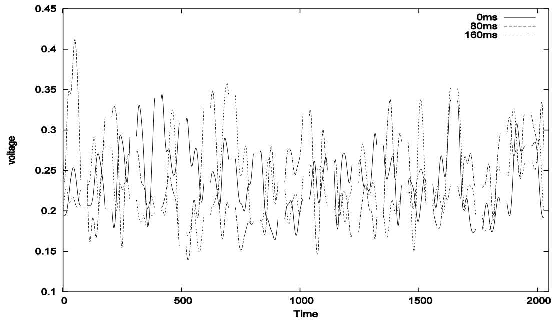

Fig. 6 Average envelope curves.

2. Measurement results

The results of the psychophysical measurements are presented in Figure 5, which shows the recognition rates for the time differences τ.

When the time difference τ was 40–100 ms, the recognition rate became 90 % or more, showing that the apparent movement was easily recognized. For the time differences 0 ms, 140 ms, and 160 ms, the recognition rate was less than 10 %, indicating that the presented stimulus was seldom recognized as an apparent movement. Note that the time difference of 0 ms showed a recognition rate of about 10 %, even though this time difference is incapable of causing any apparent movement. This is thought to be because this experiment is limited to only the downward direction of the apparent movement, and the subject was informed of this fact beforehand. For a similar reason, for the time difference of 20 ms, there is a possibility of showing a higher value than the original recognition rate. A negative correlation was seen between the recognition rate and the click time. The calculated correlation coefficient was -0.66.

IV. EMG MEASUREMENT

1. EMG Preprocessing

EMG measures the muscle electric potential ${}^{ch}_{s}x^{tr}[t]$ (*ch* is the channel number, 1,2,…,14; *tr* is the trial frequency, 1,2,…,300; and s is the set frequency, 1,2,…,8; and t is the time from the end of the presented stimulus) for a period of 2000 ms from the end of the presented stimulus at a sampling frequency of 1024 Hz. Each muscle electric potential was subjected to preprocessing to square the waveform envelope.

2. EMG analysis

Figure 6 shows examples of average envelope curves for three kinds of presented stimuli, ${}^{ch}_{s}x^{tr}[t]$.

A wave-like difference can be observed between the different kinds of stimuli, but it is difficult to find each

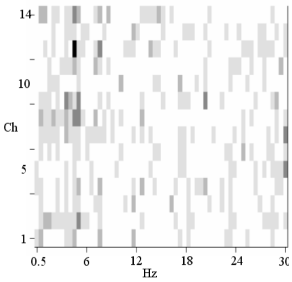

Fig. 7 T^{0}_{80}

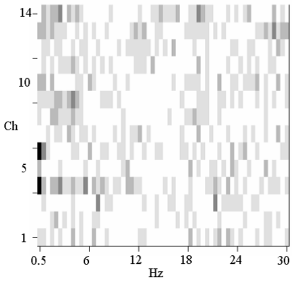

Fig. 8 T^{0}_{160}

characteristic at this step. The characteristic was extracted by frequency analysis. A Fast Fourier transform (FFT) was performed on each trial ${}^{ch}_{s}x^{tr}[t]$; a total of 60 frequency elements for f =0.5–30 Hz were extracted. As results, ${}^{ch}_{s}x^{tr}[t]$ are shown by matrix ${}_{s}P^{tr}$ containing 14 ch × 60 elements. Each procession element and each mean value of classified $\overline{{}_{s}P^{tr}\big|_{\tau=0}}$, $\overline{{}_{s}P^{tr}\big|_{\tau=20}}$, …, $\overline{{}_{s}P^{tr}\big|_{\tau=160}}$ is assumed to be $\overline{{}_{s}P^{tr}\big|_{\tau=0}}$, $\overline{{}_{s}P^{tr}\big|_{\tau=20}}$, …, $\overline{{}_{s}P^{tr}\big|_{\tau=160}}$ in the case of τ in each set. We performed a T-test of $\overline{{}_{s}P^{tr}\big|_{\tau=\tau 1}}$ and $\overline{{}_{s}P^{tr}\big|_{\tau=\tau 2}}$, which gave a P-value (significant difference) of 5 %, when assuming τ_1, τ_2 = 0, 20, …, and 160 ms. We defined matrix $T^{\tau_1}_{\tau_2}$ as the sum (over s)of matrix ${}_{s}D^{\tau_2}_{\tau_1}$, where each matrix element was 1 when the P-value was above 5 % and 0 when the P-value was below 5 %:

$$T^{\tau_2}_{\tau_1} = \sum_{s}^{8} {}_{s}D^{\tau_2}_{\tau_1} \qquad (1)$$

For example, Figs. 7 and 8 show the results for τ_1 = 0 ms and τ_2 = 80 ms and 160 ms. The values of the procession element are shown by shading (light = low, dark = high). There were many sets with a P-value was above 5%, as shown by the thick black regions.

3. Cluster analysis

T^{0}_{20}, …, T^{0}_{160} each consisted of 840 elements in a 14 × 60 matrix. These 840 elements were subjected to cluster analysis. Figure 9 shows the obtained dendrogram. A cluster was formed with high uniting levels T^{0}_{20}, € 46 T^{0}_{100} and T^{0}_{120}, € 46 T^{0}_{160}. Agreement with the psychophysical measurements (Fig. 5) was confirmed from the results of the cluster analysis.

V. CONCLUSIONS

In this paper, we examined a body part that was stimulated, causing apparent movement, with subsequent shaking of the stimulated body part when apparent movement under a specific experimental environment was recognized. We proposed a method of

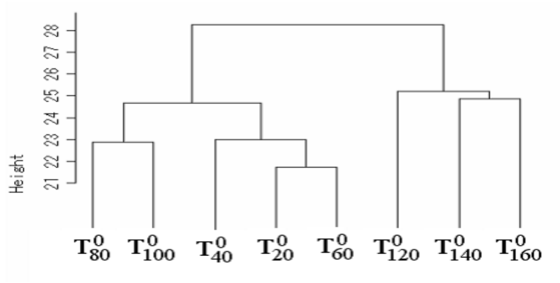

Fig. 9 Results of cluster analysis.

measuring the shaking of this body site using the EMG potential of a muscle near the skin surface.

From the results of cluster analysis, agreement was seen with the psychophysical EMG measurements, suggesting a relation between the apparent motion and the EMG measurements.

ACKNOLEDGMENTS

This work was supported in part by a Grant-in-Aid for Scientific Research (C) (No.21500511).

REFERENCES

[1] C. Domenici and D. Derossi: "A stress-component-selective tactile sensor array", *Sensors Actuators,* Vol. 13, pp. 97-100 (1992)

[2]B.L. Gray and R.S. Fearing: "A surface micro-machined micro-tactile sensor array", *IEEE Int. Conf Rob. and Auto.*, Vol. 1, pp. 1-6(1996)

[3] D. Pawuk, C. Buskirk, J. Killebrew, S. Hsiao, and K. johnson: "Control and pattern specification for a high density tactile array", *IMECE Proc. of the ASME Dyn. Sys. and Control Div.*, Vol. 64, pp. 97-102 (1998)

[4] M. Uchida, H. Tanaka, H. Ide, and S. Yokoyama: "A Tactile Display by 16 kinds of modulated wave vibration Used Only One PZT Vibrator", *T. IEE Japan*, Vol. 120-C, No. 6, pp. 825-830 (2006) (in japanese)

[5] T. Shiozaki, M. Uchida, H. Tanaka A. Nozawa, and H. Ide: "The Evaluation of Cognition to the Modulated Vibration Stimulus by ERP", *T. IEE Japan*, Vol. 122-C, No. 9, pp. 1567-1572 (2002-9) (in Japanese)

[6] M. Uchida, A. Nozawa, and H. Ide: "Difference Evaluation to Modulated Vibration Stimuli by Using Single Trial Waveform of ERP", *IEEJ Trans. EIS*, Vol. 124, No. 1, pp. 73-78 (2004-1) (in Japanese)

[7] J.H. Kirman: "Tactile apparent movement: The effects of interstimulus onset interval and stimulus ", *Perception & Psychophysics*, Vol. 15, pp. 1-6 (1974)

[8] J.H. Kirman: "Tactile apparent movement: The effects of number of stimulators", *J. Experimental Psychology*, Vol. 103, pp. 1175-1180 (1974)

[9] J.H. Kirman: "Tactile apparent movement: The effects of shape and type of motion", *Perception & Psychophysics*, Vol. 34, pp. 96-102 (1983)

EMG Activitiy of Force Sensation Evoked by Vibration Stimulation

Tota Mizuno, Mitsuaki Sato, Mizuo Kimura and Yuichiro Kume

Tokyo polytechnic university, 1583 Iiyama, Atsugi, Kanagawa 243-0297 Japan
(Tel : +81-46-242-9508; Fax : +81-46-242-9508)
(mizuno@mega.t-kougei.ac.jp)

Abstract: Force display devices used under virtual environments are desired to be small and simple not to restrict users' movements and comforts. Force sensations of fingers are evoked when vibro-tactile stimulation is applied onto the fingertips. This phenomenon is expected to be used for a simple and small force display, since the users wear only tiny vibrators on their fingertips. The aim of this study is to clarify the relationship between the force sensations by vibro-tactile stimulation and the activities of electromyogram (EMG) of fingers. As a result, it is shown that EMGs of extensor indicis and extensor digitorum are more active than those of other finger muscles, and that the force sensations of index fingers in extendor direction are perceived. The vibration stimulates extensor muscles more effectively.

Keywords: force sensation, vibration, fingertip, EMG, muscle spindle.

I. INTRODUCTION

Force displays and feedbacks are needed in order to handle objects effectively under virtual environments. A number of force display devices have been developed with various methods. Some of them have been available commercially. Most of these devices employ desk /floor grounded or exoskeleton structures using arms or wires for force transmission. As the display areas are expanded, the whole sizes of force display devices have to be enlarged. However, large displays restrict portability and convenience. From this view point, force display devices are desired small and simple. If the mechanisms and configurations of force displays became small and simple, a number of new applications, such as a hand-held electronic game device, could be developed. Some studies have been conducted to develop small and simple force displays. For examples, electrical stimulation directly to muscles has been studied to elicit force sensation [1], and a hand-held force device using angular momentum change with flywheels has been proposed [2].

We have been studying force sensations of a fingertip evoked by vibro-tactile stimulation [3]. Figure 1 show that force sensation of a finger is evoked in the direction of extending, when vibro-tactile stimulation is applied onto the fingertip. The forces are felt with only a tiny vibrator, and the finger feels resistance (antiforce) in the direction of extending. This phenomenon is expected to be used for a new force display. In our

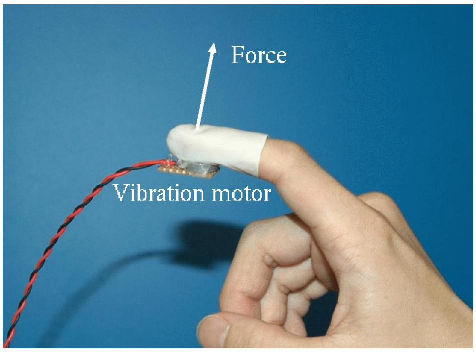

Fig.1. Experimental system

previous studies, the force sensations were psychophysically investigated with a vibration motor stimulating a fingertip. The strengths of the force sensations were measured as vibration intensities were changed. In addition, the sensitivities of force sensations are affected by arm and finger postures and with each finger were examined. It was found that forces can be perceived with vibration over thresholds of vibration intensity, that the sensitivities are affected by the arm and finger postures, and that the sensitivities are different among five fingers.

Although the force sensations were psychophysically measured, the activities of muscles were still unknown. When the forces are felt, finger muscles are expect to work by vibration stimulation. In this study, when force sensations of fingers are evoked by vibrotactile stimulation onto fingertips, the activities of the

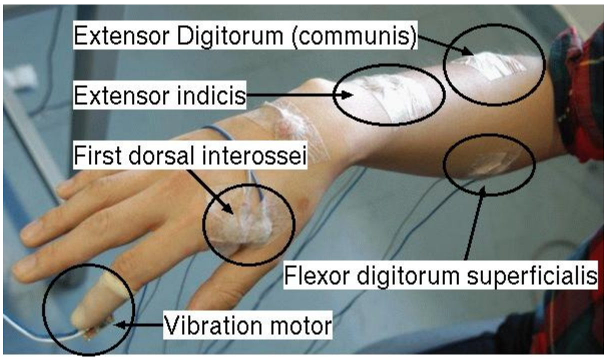

Fig.2. Electrodes to measure EMG.

finger muscles were examined by electromyogram (EMG).

II. MEASUREMENTS

From our previous studies, when a tip part beyond distal interphalangeal (DIP) joint of a finger is stimulated, force sensation is felt. In addition, the sensitivity of force sensation of forefinger is higher than those of other fingers. Therefore, the fingertip of palm side of forefinger was stimulated in these experiments. A simple device including a fingerstall and a pancake-type vibration motor was used for the stimulation. Figure 1 shows this device. The vibration motor used in this study includes a DC coreless motor and an eccentric weight, which are used in cellular phones commercially. This simple structure allows user's free postures and movements, and stable contact between the skin of the fingertip and the vibration motor. The stimulation intensities were measured in terms of acceleration with a piezo-accelerometer attached to the motor. The stimulation intensities on the skin surface are a little different from those of the motor. As applied voltage to the motor increases, the stimulation intensity increases almost linearly, and the vibration frequency changes from 50 to 100[Hz].

Since the stimulation part was fingertip of forefinger in this study, surface electrodes to measure EMGs were placed on muscles moving the forefinger. Figure.2 shows the setup points of these electrodes. These muscles were "extensor digitorum (communis)", "flexor digitorum superficialis", "extensor indicis", and "first dorsal interossei". The EMGs were measured with DEGITEX LAB Co., Ltd., Polymate II AP216. Seven healthy adult subjects were used. They were male and 21-25 years old.

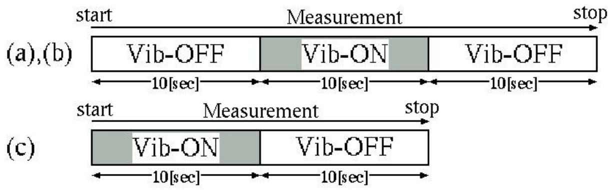

Fig.3. Experimental protocol

The EMGs were rectified and integrated every 0.1 s. In the psychophysical experiments in our previous study, the sensitivity of the force sensation is higher when the whole arm floats in the air. (Afterward this posture assume basic posture) In the experiments mentioned here, a subject wore the vibration device with the basic posture, and EMGs were measured when the subject posed and moved the finger with the following three posture and movement patterns: (a) flexion, (b) extension, (c) movement and vibration was on and off. Figure3 shows the measurement protocol.

(a) Vibration stimulation in finger flexion state was given every 10s. The duration of EMG measurement was 30 s (Vibration OFF / ON / OFF)

(b) Vibration stimulation in finger extension state was given every 10s. The duration of EMG measurement was 30 s (Vibration OFF / ON / OFF)

(c) A finger was moved voluntarily. The index finger was flexed and extended slowly for 10s. The subject repeated these movements twice for 20s. Vibration stimulation continued for 10s from the beginning. The EMG was measured for 20 s.

The rates of change were calculated with comparing the EMG of the vibration ON state with that of OFF state by the following methods: At first, EMGs were averaged every 10 s of each section. Next, the decline rates before and after vibration OFF and ON in (a) and (b) were calculated respectively. A rate of change was assumed the average of rate of decline before and after. In (c), a rate of change assumed a rate of decline of OFF after ON. A rate of decline shows in the following equation:

$$\text{A rate of decline} = (\text{Vib OFF}/\text{Vib ON}) \times 100$$

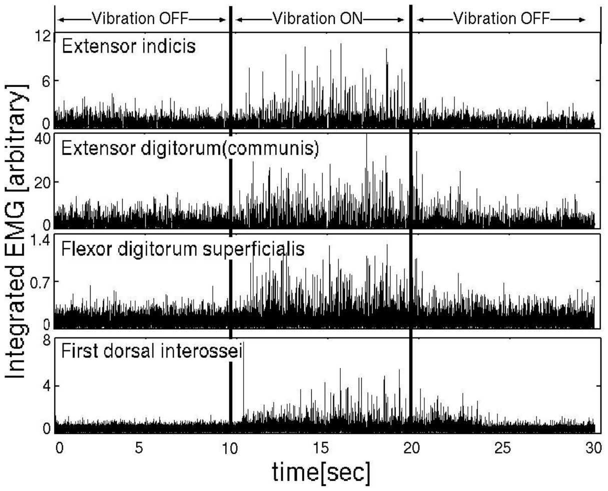

Fig.4. The EMG of the finger in the flexion state

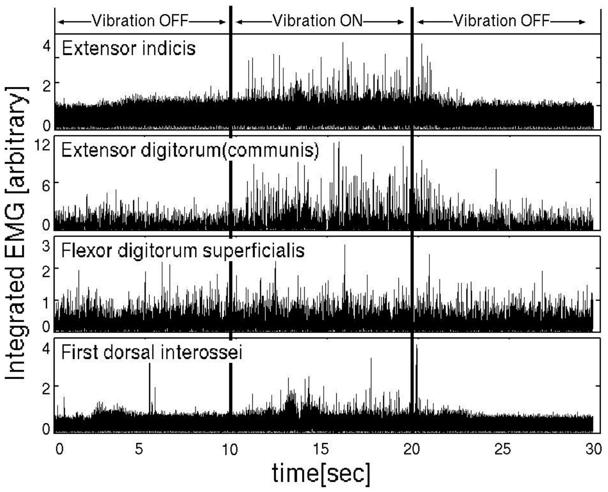

Fig.5. The EMG of the finger in the extension state

III. RESULTS

1. The EMG of the finger in the flexion state

Figure 4 shows an example of the EMG activities of Figure 4 shows an example of the EMG activities of the finger in the flexion state. The EMG activities of "extensor digitorum (communis)" and "extensor indicis" increase clearly during vibration. Table 1 shows the average change rates of all the subjects. The average values of "extensor digitorum (communis)" and "extensor indicis" are larger, and those values of "first dorsal interossei" are smaller.

2. The EMG of the finger in the extension state

Figure 5 shows an example of the EMG activities of the finger in the extension state. The EMG activities of "extensor digitorum (communis)" and "extensor indicis" increase clearly during vibration in the same mannor as those in Figure 4. In addition, the EMG activities of "flexor digitorum suerficialis" and "first

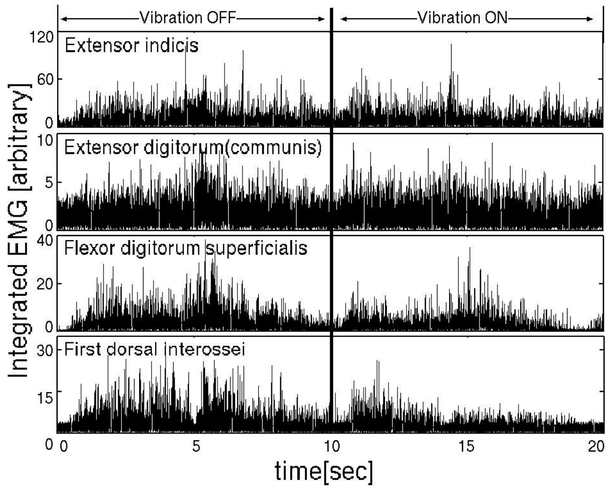

Fig.6. The EMG in the movement condition

Table 1. Average and SD of a rate of change

muscle	Flexion (SD)[%]	Extension(SD)[%]	Movement(SD)[%]
Extensor indicis	83.3(7.5)	82.9 (15.2)	83.0 (13.0)
Extensor digitorum (communis)	81.3(13.9)	85.5 (11.1)	81.9 (14.1)
Flexor digitorum superficialis	98.6(3.1)	95.1 (9.5)	88.4 (14.1)
First dorsal interossei	94.7(4.9)	86.8 (18.3)	88.2 (8.0)

dorsal interossei" increase a little, too. Table 1 shows, the EMG activities of "extensor digitorum (communis)" and "extensor indicis" are larger than those of "first dorsa interossei", similarly as shown in Result 1.

3. EMG of the finger in the movement condition

Figure 6 shows an example of the EMG activities with slow finger movements. The figure shows a change of EMG activities by the vibration stimulation cannot be observed during finger movements. Table 1 shows that the average of the change rates of extensor digitorum (communis) and extensor indicis are large. Those of flexor digitorum superficialis and first dorsal interossei" are also larger, but not so large as those of extensor digitorum (communis) and extensor indicis. The EMG activities are higher during the finger movement in the experimental condition(c) than those in the stationary conditions, (a) and (b).

From these results, vibration stimulation to a fingertip affects extensor muscles more effectively than flexor muscles. After confirming the normal distribution and the dispersion of the data, the two factor analyses of variance was performed in terms of the rate of change (Flexion - Extension - Movement state×Each EMG). The main effect of the rate of change is accepted ($F_{3,21}$ =

5.68, $p < 0.05$). In addition, multiple comparison tests (Scheffe's procedure) were performed. As a result, "extensor indicis" versus "flexor digitorum suerficialis" and "extensor digitorum (communis)" versus "flexor digitorum suerficialis" are accepted in four kinds of EMG ($p < 0.05$).

From these results, the EMGs with vibration stimulation to a fingertip are more active than those without vibration. In addition, it is supposed that the vibration stimulation affects extensor muscles more effectively. Consequently, it is considered that the force sensation felt in flexion direction is produced with some physiological mechanisms.

IV. CONCLUSION

It has already been known that a muscle contraction and an illusion of a joint angle are caused with a muscle spindle excited by vibration given onto the skin surface [4][5]. From our experiments, it is guessed that muscle spindles are stimulated by vibration propagating through a finger extensor tendon from a fingertip, and that force sensation is induced with extensor muscle contraction. When the fingers flex, the extensor contract, and it causes resistance (anti-force) in the direction of extending. It is conjectured that efforts against extensor muscle contraction to maintain the joint angle of a finger produce the force sensation.

V. SUMMARY

In this study, when force sensations of fingers are evoked by vibro-tactile stimulation onto fingertips, the activities of the finger muscles were examined by EMG. The results indicate that the EMG activities are observed with force sensation evoked vibration stimulation, and that some physiological mechanisms are expected. If this phenomenon is used, a new and simple force display device will be developed.

However, the users feel not only forces but also vibration. If a user grasps a vibrating virtual object, it will be acceptable. But, the vibration can be a disadvantage as an interface device for general applications.

To develop practical force display devices and applications, further studies shall be conducted to elucidate the perceptual properties of the force sensation and to develop potential applications.

VI. ACKNOWLEDGEMENT

This study was supported by "High-Tech Research Center" Project for Private Universities: matching fund subsidy from the Ministry of Education, Culture, Sports, Science and Technology (2005-2009).

REFERENCES

[1] Kinya Fuhita: Bio-Interface using electrical stimulus, Journal of Human Interface Society, Vol.6, No. 1, pp. 39-42, 2004 (in Japanese).

[2] Norio Nakamura, Yukio Fukui: Trend of a touch technical development of portable sense information and communication, Journal of the Society of Biomechanisms Vol. 31, No. 2, pp.90-94, 2007 (in Japanese) .

[3] Hidenori Kuribayashi, Kaori Iijima and Yuichiro Kume: Force Sensation Induced by Vibro-tactile Stimulation, proceedings of the 13th Annual Conference, pp.150-151, 2008 (in Japanese) .

[4] Tadashi Ohyama, Shogo Imai, Tenji Wake: sense - perception psychological handbook, Saishinsyobo, 150-151, 2008 (in Japanese).

[5] G.M. Goodwin, et al.: The contribution of muscle afferents to kinesthesia shown by vibration-induced illusions of movement and by the effect of paralyzing joint afferents, Brain, vol.95, pp.705-748, 1972.

[6] Yoshiaki Iwamura: Touch, Neuropsychology, Igakusyoin, 2005 (in Japanese).

[7] Robert F.Schimidt, translated by Y.Iwamura, A.Sato, S.Matsuura, H.Sakata, J.Toyota, T.Ono: Sense physiology, Kinpodo , 1989 (in Japanese)

[8] Dictionary of cognitive science, Japanese Cognitive Science Society pp208,2003 (in Japanese)

Emotion Spectrum Analysis for Daily Repetitive Mental Workload

Akio Nozawa and Keita Karita

Graduate School of Meisei University
(Tel: 81-42-591-5895; Fax: 81-42-591-5895)
(lily@biel.ee.meisei-u.ac.jp)

Abstract: In this study, a mental workload for daily mental arithmetic training was objectively evaluated by physiological indices using the emotion spectrum analysis for the group with daily mental arithmetic training. Physiological measurement on mental arithmetic task was conducted once a week for subject. Physiological indices measured were alpha-wave power spectrum, beta-wave power spectrum, Fmθ-wave power spectrum, variation in nasal skin temperature and high frequency component of heart rate variability. And depressive tendency for the mental arithmetic task was measured as psychophysical index by using POMS (Brief Form), and time duration for the mental arithmetic task was also measured as performance index. Correlation between physiological indices, psychological index, performance index, and emotion spectrum analysis was analyzed in relation of mental workload.

Keywords: Mental workload, Emotional spectrum analysis, Physiological measurement, Mental arithmetic task

I. INTRODUCTION

In ubiquitous society in the future, the opportunity to use the telecommunication equipment by various scenes in daily life will increase. However, a benefit of ubiquitous society as "obtaining information anywhere anytime" may cause the risk in "using information and communication machinery for anywhere anytime." For example, with informatization in an automobile, causation with operation of information technology devices in the automobile and the accident has been pointed out. On the other hand, the driver's physiology psychology has been measurement from a safe viewpoint for the prevention of the car accident [1-5]. Mental activity is called mental work (MW), and a load given by MW is called Mental Workload (MWL). The continuance of excessive MW increases MWL, which will become the factor of a human error and health problems. For example, where high accuracy and safety are demanded, the worker is forced to have the strain for a long time. MWL increases while working like this and the incidence of a human error increases. The method of measuring MWL has been researched from the viewpoint of a human factor in the field where risk management like the aerospace field etc. is demanded [6-7].

In general, MWL is evaluated by the performance indices, the subjective psychology indices, and the physiology indices. Objective and quantitative evaluation in the real time are possible, and the evaluation method based on physiology indices has the advantage in detection of the reaction under the unconsciousness.

MWL does not merely depend on the objective degree of difficulty of the MW task. It is analogized by the experienced fact that MWL is related to a task performance, motivation, habituation, proficiency and so on. However, the personal attribute of MWL which evaluated quantitative with physiology indices are not investigated. From the viewpoint of stress management, serial assessment for the effect in physiology indices for daily MWL is the issue, which is the essential for the development of the technique of quantizing the MWL by physiological indices. Objective assessment of physiology indices have been studied about the influence of repetition of MW task proficiency by Fmθ-wave [8]. On the other hand, the examination about the change of emotion about the repetition of the MW task has not been studied. Emotional Spectrum Analysis (ESA) is emotion estimation method by the physiology indices, which is Electroencephalograms (EEG). The ESA calculates four independent emotion vectors from coefficients of correlation between EEG signals measured by scalp electrode, which express the state of the brain and the state of mind [9]. In this study, EEG was focused as the physiology index, and MWL evaluated by psychophysiological index which was ESA derived from EEG measurement was serially assessed. The MW task was mental arithmetic task, which is Hundred Cell Calculation Method (MAT). The subjects trained MAT everyday routinely and psychophysiology measurement experiment for MAT performance was

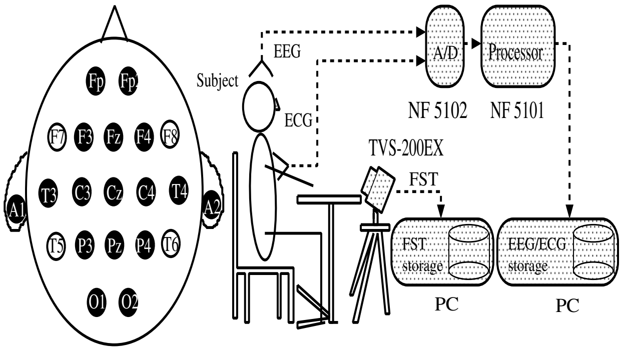

Fig.1. Measurement system and EEG electrode arrangement.

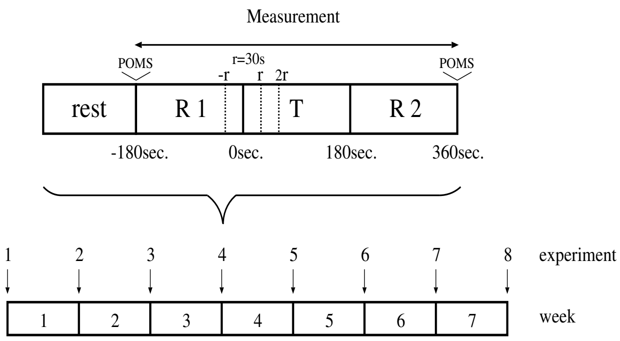

Fig. 2. Experiment protocol

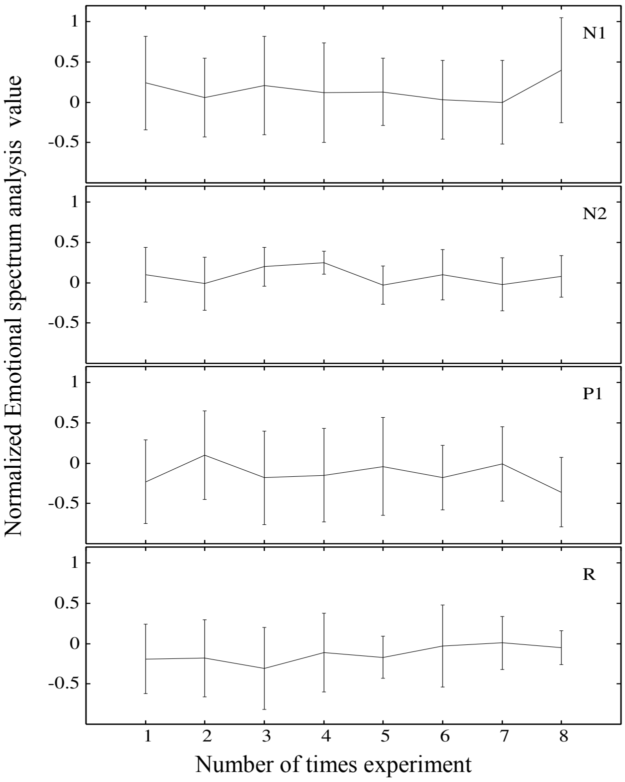

Fig. 3. Variations of emotional spectrum in experiments.

conducted once daily. The physiology index is α-wave β-wave and θ-wave of electroencephalogram (EEG), nasal skin temperature (NST), and high frequency ingredient (HF) of the electrocardiogram (ECG). In addition, Japanese edition of POMS in short form (POMS) was measured as the psychology index. The performance index was task-elapsed time of MAT.

II. EXPERIMENTAL

Experimental equipment setup and electrode arrangement for scalp EEG are shown in figure 1. Experiments were executed in a measurement booth divided with partition walls of 1.8m in height. An infrared thermograph system (TVS-200EX, AVIONICS) was installed 0.7m in front of subject. Facial skin thermograms were created with 1s sampling periods. Image resolution of thermograms was 320×240 pixels, and room temperature was set at 26±1.0 degrees Celsius. a seated position in a resting. An electrode headpiece (Pasteless Electrode Helmet, Brain Function Laboratory) and set of headphones were placed on the subject. EEG was recorded at a sampling frequency of 200 Hz using a biological amplifier/sampler (5102 EEG HEAD BOX, NF Electronic Instruments) and digital signal processor unit (5101 PROCESSOR BOX, NF Electronic Instruments). Electrodes used for scalp for scalp EEG were Fp1, Fp2, F3, F4, P3, P4, O1, O2, T3, T4, C3, C4, Fz and Pz, based on the international 10-20 method, and a reference electrode was A1 and A2. Electrodes used for ECG were put on the superior margin of the sternum and cardiac apex based on a modified Lead NASA in order to reduce artifacts of EEG from ECG. A common ground electrode for both EEG and ECG was put on Cz.

The protocol for the experiment is shown in figure 2. Subjects were eight 20- to 23-year-old healthy men. Subjects were well informed about the experiments and the objective of this study before participation experiments. In this study, The MAT was Hundred Cell Calculation Method of the multiplication. The experiment was performed for seven weeks and subjects trained MAT once a day at home. Psychophysiology measurement of the MAT performance was conducted once a week. The day of experiment could be before or after the day scheduled. The measurement was not begun until the subject had been in the room for at least 15 minutes to habituate to the room temperature. The measurement consisted of 3 periods time series, which

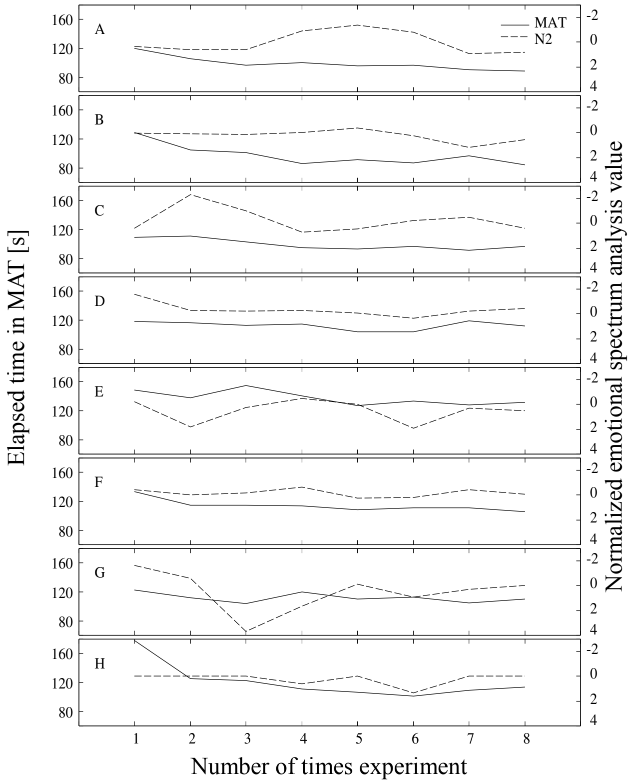

Fig. 4. Relationship between MAT and N2.

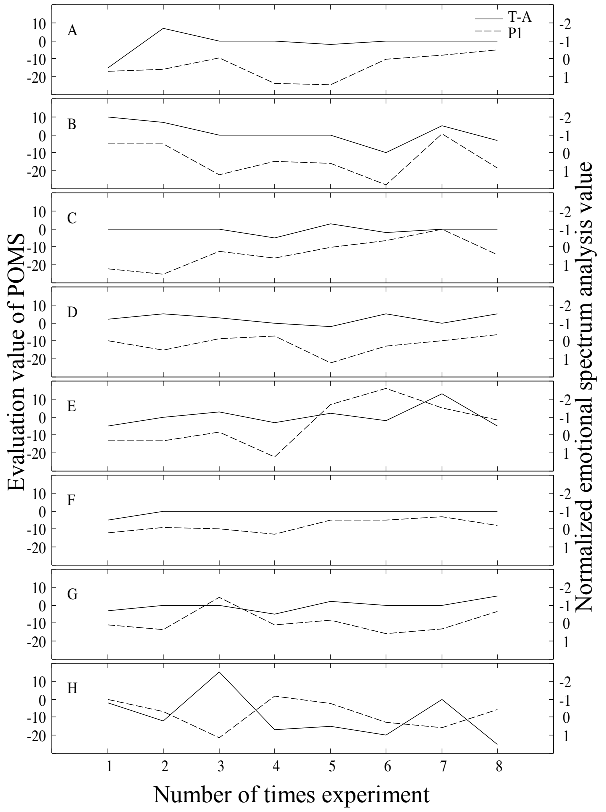

Fig. 5. Relationship between T-A and P1.

were 3-min eye-closed resting period (period R1), 3-min eye-opened period under controlled stimulation of the MW task (period T), and 3-min eye-closed resting period (period R2). Japanese edition of POMS(in short form) was measured before and after the measurement as a psychology index of the trend of dejection for the MAT task. POMS had 30 questions used to evaluate a trend of dejection and could measure the state of temporary feelings. The experiment was conducted during the day except within 2 hours after eating.

III. RESULTS AND DISCUSSION

In this study, correlation of time of performance index, psychology index and physiology index was analyzed. The θ-wave, α-wave and β-wave power spectrum of EEG, the high frequency component of heart rate variability (HF) of ECG and NST time series were extracted from analyze of measured physiological data. The θ-wave, α-wave and β-wave show total brain activity. HF represents parasympathetic nervous system activity. Decreasing NST time series indicates sympathetic nervous system's activation. HF time series was calculated as follows. A source R-wave interval time series was extracted from ECG time series by using threshold processing. Temporally equidistant R-wave intervals (HRV) were derived by resampling process in frequency of 20 Hz after cubic spline interpolation. The power spectrum time series of HRV was calculated every 1s by fast Fourier transformation (FFT) using 512 data points at a sampling frequency of 20 Hz. Finally, HF time series was created as a summation of discrete frequency components in power spectrum time series of HRV, in which the frequency range of HF was 0.15 Hz to 0.4 Hz.

θ-wave, α-wave and β-wave time series were calculated as follows. The power spectrum time series of averaged EEG lead from O1 and O2. And it calculated every 5s by FFT using 1024 data points at a sampling frequency of 200 Hz. θ-wave was defined as frequency components of the EEG in frequency range of 5 Hz to 8 Hz, 8 Hz to 13 Hz defined of α-wave, and that of 13 Hz to 20 Hz defined of β-wave. The q-wave, a-wave and b-wave power spectrum time series were created as a summation of frequency components in each frequency range.

NST time series was calculated as follows. Thermal images of nasal region were extracted from facial skin thermograms (FST) time series by using template matching method, which the template was a partial image sampled from the first FST image. Then, NST time series was created as a cascade of spatial average temperature for pixels in each thermal image of nasal region.

Figure 3 shows variation of average emotion vectors between period R1 and period R2 of subjects.

Emotion vector was normalized against the temporal average of entire interval. The error bars here represent standard deviation. In the figure, N2 (stress), N1 (sad), P1 (pleasant) and R (relax) represent emotion vector respectively. There is no statistical significant difference (by Friedman test). A correlation analysis of emotion vectors and other indices was performed. Figure 4 shows relationship between the elapsed time of MAT performance and emotion vector N2 (stress). Negative correlation is provided in seven subjects. This figure shows that N2 (stress) increases while the elapsed time of MAT is shortened. It is considered that subjects had acquired proficiency in MAT and might get bored and annoyed with MAT. Figure 5 shows the relationship between POMS (T-A) and emotion vector P1 (sad). Negative correlation was provided in eight subjects, where correlation coefficients were from -0.32 to -0.88. The figure indicates that emotion vector P1 (sad) rises while POMS (T-A) declines. Estimated 'sad' feeling by the emotion vector agrees with a psychology index and shows that emotion vector is effective in estimation for repetitive MWL.

VI. CONCLUSION

In this study, perform an MW task repetitive to evaluate the effectiveness of the ESA of repetitive MWL and evaluated it with physiology index psychology index and performance index temporal. As a result, in repetitive MWL, the effectiveness of the ESA was shown.

REFERENCES

[1]Y. Nishio and M. Suzuki: "Evaluation of Human Arousal Levels through Physiological Responses," OMRON TECHNICS, Vol. 38, No. 2, pp. 184–190 (1998)
[2]S. Kumakura, T. Hara and Y. Goi: "Predicting Changes in Drivers' Drowsiness Level During Prolonged Driving: Etractinglong blinks from EOG data," Transaction of Society of Automotive Engineers of Japan, Vol. 29, No. 1, pp.155–159 (1998)
[3]T. Asao, J. Ishimura, T. Wada and K. Tsukamoto: "Influence of Conversational Contents on Driving Behaviors," Transaction of Society of Automotive Engineers of Japan, Vol. 35, No. 2, pp. 205–210 (2004)
[4]W. Wierwille and L. Tijerina: "An analysis of driving accednt narratives as a means of determining problems," Z Verkehrssicherheit, Vol. 41, No. 4, pp. 164–168 (1995)
[5]T. Ishida and T. Matsuura: "Mobile Communication in Transport, The Effect of Cellular Phone Use on Driving Performance,"IATSS Res (Int Assoc Traffic Saf Sci),Vol. 25, No.2, pp.6–14(2001)
[6]G. Reid and T. T. Nygren: "The Subjective Work-load Assessment Technique: A scaling procedure for measuring mental workload," Human Mental Workload, pp. 185–218 (1988)
[7]S. G. Hart and L. E. Staveland: "Development of NASATLX (Task Load Index): Results of empirical and theoretical research,"Human Mental Workload, pp. 139–183 (1988)
[8]S. J. Laukka, et al: "Frontal midline theta related to learning in a simulated driving task," Biological Psychology, Vol. pp. 313-320 (1995)
[9] T. Musha: "Estimation of Emotional State by EEG and its Limitation", Journal of the Japan Society of Mechanical Engineers, Vol. 105, No. 1006, pp.610-611 (2002)

Single-trial analysis of voice stimulus evoked potentials

Hisaya Tanaka and Takashi Matsuoka
Dept. of Information Design, Kogakuin University
1-12-24 Nishi-shinjuku, Shinjuku-ku, Tokyo, JAPAN 163-8677
(Tel : 81-3-3340-0890; Fax : 8-3-3348-3486)
(hisaya@cc.kogakuin.ac.jp)

Abstract: We are developing BCI for event-related potentials (P300) using speech stimulus in the Japanese language based on the need investigation of ALS patients. In the past, we studied the single-trial analysis of P300 with a 4Hz low-pass filter in order to improve the entry speed of BCI. However, the problem was low detection accuracy, i.e., approximately 30-80%. In this paper, we reviewed the application of independent component analysis (ICA) in order to improve the accuracy of single-trial analysis of P300. As a result, the detection ratio improved from 54.2% for the traditional 4Hz low-pass filter to 90.9% in the choice of one between two. Furthermore in the offline experiment, the detection ratio of P300 response to each sound of "a, i, u, e and o" improved in the task to choose one among five with synthetic speech stimulus. The maximum detection ratio was 94.7%, and the detection ratio per sound improved from 47.0% to 85.1%.

Keywords: Single-trial analysis, ERP, ICA, Brain-Computer Interface, EEGLAB

I. INTRODUCTION

The Brain-Computer Interface (BCI) is the communication interface to enter characters, etc. by utilizing brain waves or brain blood flow volume. Based on the need investigation of ALS patients, we are developing BCI for event-related potentials (P300) using speech stimulus in the Japanese language [1]－[4]. With the BCI, it is possible to assign five phonological systems specific to the Japanese language (e.g. a-i-u-e-o, a-ka-sa-ta-na and ha-ma-ya-ra-wa) and enter hiragana characters by their combinations, if differences of five stimulus sounds by a user can be understood and differentiated (task to choose one among five). In the past, single-trial analysis of P300 with a 4Hz low-pass filter has been studied in order to improve the entry speed of BCI. However, the problem was the low detection ratio, i.e., 30-80%. In this paper, we reviewed application of independent component analysis (ICA) in order to improve the accuracy of the single-trial analysis of P300.

II. Odd-ball TASK WITH VISUAL STIMULUS

1. Experiment procedure

The target stimulus response as well as non-target stimulus response (original waveform) to visual stimulus was recorded in accordance with the odd-ball paradigm. The visual stimulus was specified as black and white lattice patterns (checkered patterns) (Figure 1). The target stimulus was specified as 16x16 lattices where the length of each side is 48mm, and non-target stimulus as 64x64 lattices where the length of each side is 12mm. The subjects were in a resting and sitting position, and the point of view was fixed in the center of the stimulus visual field. The subjects were four males at the ages of 22-24 (Y.G, T.K, T.M and T.T, respectively). With seven electrodes of FZ, CZ, PZ, C3, C4, P3 and P4 under the international 10-20 system, Ag-AgCl skin electrodes were placed. The ground electrode was placed between FP1 and FP2, and the reference electrode was placed on the metapophysis behind the earlobe. EEGLAB of University of California at San Diego (UCSD) was used for the ICA analysis software [5]. The standard to determine P300 induction is 21.0μV or higher voltage around 500ms latency, derived from averaging results. The waveform in Figure 2 is obtained when the 4Hz low-pass filter is applied. P300 with the voltage 17.5μV was successfully interpreted at 590ms latency at the exploring electrode PZ. However, the ocular potential due to blinking is mixed around 300ms latency, and it is difficult to interpret at other exploring electrodes. On the other hand, when ICA is applied, brain waves are analyzed and generated in the order of highly-independent signals. In Figure 3, independent components (IC) are indicated in the order from 1 to 7, and P300 with the voltage 18.0μV at 595ms latency was successfully interpreted at the second IC. When interpreted for all trials (150 times), the P300 component is generated at the 1st and 2nd IC at the proportion of 90% or more in the case of ICA.

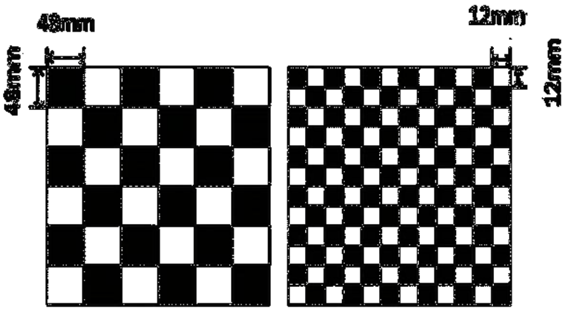

Target Stimulus Non-Target stimulus
Fig.1. Screen of visual stimulus

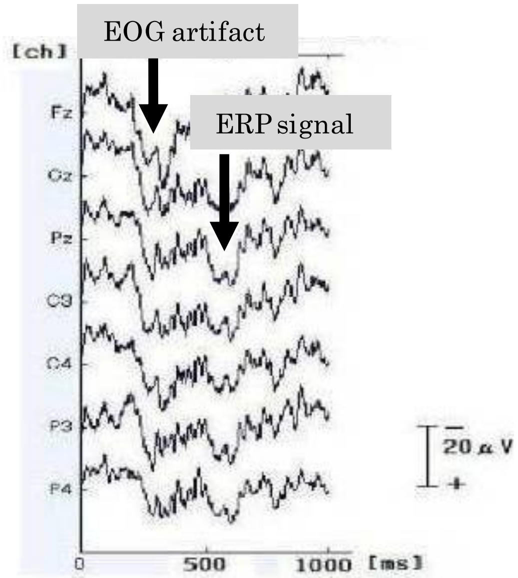

Fig.2. Analysis with low-pass filter of 4Hz (Sub. Y.G)

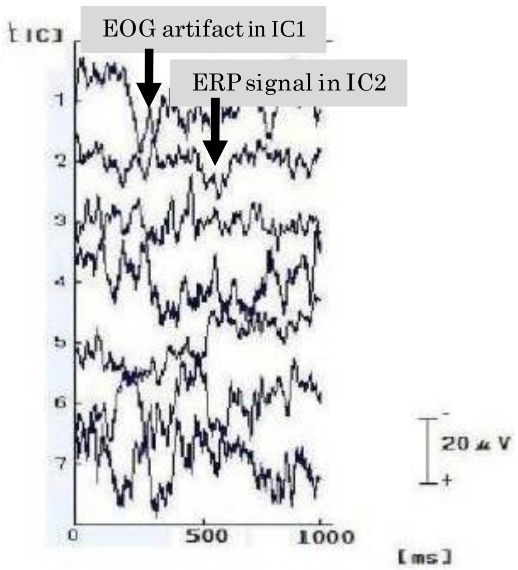

Fig.3. Analysis with ICA (Sub. Y.G)

2. Analysis by signal detection theory

Based on the above conditions, the proportions of Hits, Misses, False Alarms and Correct Rejections in the signal detection theory were calculated along with the frequency filter and ICA. The analysis results for the subject Y.G are indicated in Table 1. When the results are compared in the 30 trials, Hits (the proportion of correct detection of target stimulus response) is 97% for ICA and 47% for the frequency filter, and Correct Rejections (the proportion of correct detection of non-target stimulus) also increased from 83% to 93%. On the other hand, Misses (the proportion of erroneous detection of target stimulus) decreased from 53% to 3%, and False Alarms (the proportion of erroneous detection of non-target stimulus) decreased from 17% to 7%. In regards to other subjects T.K, T.M and T.T, Hits increased from 27% to 60%, from 13% to 83% and from 3% to 53%, and the proportion of Misses decreased from 73% to 40%, from 87% to 17% and from 97% to 47%, respectively, indicating improvement of P300 detection ratio with ICA.

Table 1. Detection ratio of event-related potentials P300 (Sub. Y.G)
[4Hz low-pass filter (traditional) →ICA (proposed)]

	Detection	
	Target (P300)	Non-Target
Target Stimulus	47%→97% (Hits)	53%→3% (Misses)
Non-target stimulus	17%→7% (False Alarms)	83%→93% (Correct Rejections)

Next, the power of 4Hz low-pass filter and ICA was compared by obtaining $\hat{d}'$ in the 30 trials for each of target stimulus and non-target stimulus, in order to compare the detection capability. $\hat{d}'$ is obtained with the following formula, by using the values for Hits and False Alarms. h and f are values for Hits and False Alarms, respectively, and Z(p) is the value corresponding to normal Gaussian distribution.

$$\hat{d}' = Z(h) - Z(f) \qquad (1)$$

As a result, $\hat{d}'$ was between 0.87 and 3.36 for the subject Y.G, between 2.14 and 1.53 for the subject T.K, between 0.87 and 1.36 for the subject T.T, and between 1.75 and 3.01 for the subject T.M. $\hat{d}'$ decreased in the case of the subject T.K., while the power of ICA was significant for other subjects. In accordance with these results, it is found that the P300 component can be successfully detected with one-time or a few measurement(s) by using ICA.

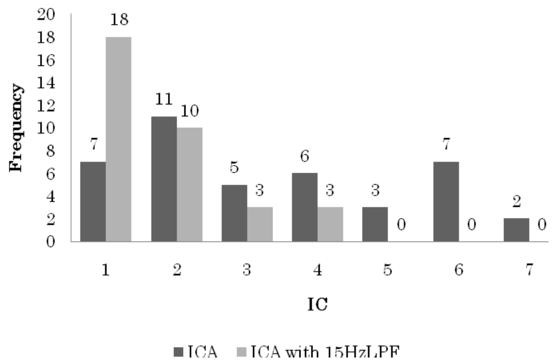

Fig.4. IC where P300 were detected and the detection frequency (Sub. Y.G)

3. Combination of low-pass filter and ICA

Although the P300 component can be separated just by applying ICA, the number of IC where P300 is observed is different every time, and system design is difficult upon considering automatic detection. Since IC is determined by signal strength, signals with higher independence than P300 component might be at work, e.g. voluntary brain waves and electromyogram which increase by thinking. Therefore, the 15Hz low-pass filter was applied before ICA, in order to eliminate them. The results for the subject Y.G. are indicated in Figure 4. Compared with the case of ICA analysis only, the P300 component was successfully observed at IC1 and 2 at the proportion of 90% when combined with the 15Hz low-pass filter.

III. CHOICE AMONG FIVE THINGS WITH SPEECH STIMULUS

Next, the experiment on the assumption of incorporating ICA into the BCI system [1] was conducted offline. This BCI system is the sound-control character entry system, and using the method to choose one among five, with one sound among "a, i, u, e and o" as the target stimulus; therefore the difficulty in detecting the P300 component is higher than the odd-ball paradigm (choose one between two). Application of the traditional filter and ICA in this BCI system was analyzed by independent evaluation based on t-test, and reliability was compared.

1. Experiment procedure

The diagram for Japanese voice presentation type BCI is indicated in Figure 5. Brain waves are induced with the unipolar induction method with the earlobe as the reference electrode using skin electrodes, and amplified to the bioamplifier (Digitex Lab BA1104-E). They are then incorporated into the notebook PC (DELL Inspiron) through the A/D board (National Instruments DAQ Card 6024E). The sound is generated from the speaker by utilizing PC's sound output function (sound board). It is also generated on the PC monitor from the VGA output, in order to confirm the screen and characters entered. The software part of BCI was developed with LabVIEW 7.1 from National Instruments. Functions of brain wave measurement control, filtering, statistic processing, and speech stimulus were programmed.

Five kinds of stimulus of "a, i, u, e and o" were used as the stimulus method. They were set to appear randomly and at the probability of 20%. Thus, approximately 20 times of stimulus is given per sound. One sound was chosen among the five sounds as the target stimulus, and five trials were conducted. Stimulus with the five sounds had three patterns: synthetic sound, live voice of a male and female. The odd-ball task by pure sound (2KHz and 1KHz) was also given for comparison. The subject was one 22-year-old male.

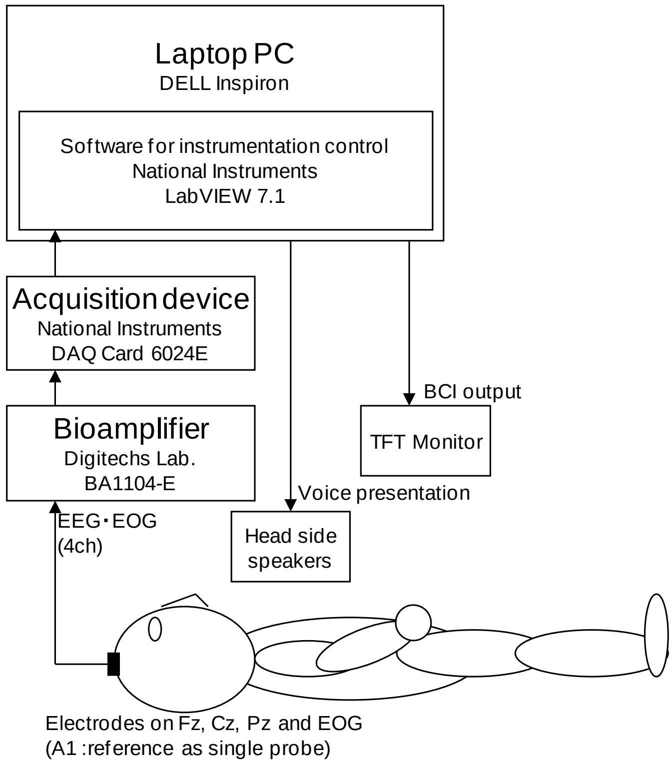

Fig.5. Japanese voice presentation type BCI

Table 2. Comparison of communication reliability in the speech stimulus type (choose one among five style) BCI system (synthetic sound)

	Synthetic sound	a	i	u	e	o
Reliability [%]	Filter (traditional)	53.1	30.7	24.6	96.0	30.7
	ICA (Proposed)	83.6	83.6	72.0	94.7	91.5

2. Results

In regards to the odd-ball task, the ratio was 90.9% for ICA, the proposed method, and 54.2% for the 4Hz low-pass filter, the traditional method, when P300's analyzed section at the time of latency was from 200ms to 500ms. This indicates that the detection method with ICA also has higher detection capacity than that with the filter in the case of odd-ball task for sound stimulus as well. Although the evaluation method is different, ICA's effectiveness supports the experiment results in Chapter 2. Meanwhile, the average reliability at three points of FZ, CZ and PZ is used in regards to reliability of the frequency filter.

Next in regards to the task to choose one among five by sound, the P300's analyzed section at the time of latency was exhaustively investigated by sound by 100ms unit. First of all, the detection ratio improved to 83.6% for ICA compared with 53.1% for the traditional filter in the section from 100ms to 300ms for "a." In the same way, it improved from 30.7% to 83.6% in the section from 200ms to 400ms for "i," from 24.6% to 72.0% in the section from 100ms to 400ms for "u," from 96.0% to 94.7% in the section from 400ms to

1000ms for "e" and from 30.7% to 91.5% in the section from 100ms to 300ms for "o" (Table 2).

In regards to the live voice of a male, the detection ratio improved from 58.1% to 82.0% in the section from 200ms to 700ms for "a," from 28.0% to 0.0% in the section from 300ms to 500ms for "i," from 59.1% to 87.9% in the section from 300ms to 600ms for "u," from 31.3% to 0.0% in the section from 300ms to 700ms for "e" and from 59.5% to 89.6% in the section from 300ms to 700ms for "o."

In regards to the live voice of a female, the detection ratio improved from 32.1% to 95.1% in the section from 200ms to 600ms for "a," from 59.6% and 93.4% in the section from 100ms to 900ms for "i," from 93.9% and 96.4% in the section from 100ms to 800ms for "u," from 30.2% to 0.0% in the section from 300ms to 700ms for "e" and from 31.7% to 93.3% in the section from 100ms to 400ms for "o."

While the detection ratio for "e" decreased in the case of synthetic sound, it was higher than 94.7% for ICA; therefore practical problems in BCI are unlikely to occur. The detection ratio per sound improved from 47.0% to 85.1% on average. As a result, it was found that the detection ratio of P300 with single trial is improved with ICA. On the other hand, the detection ratio is 0% in the case of "i" and "e" for live voice of a male and "o" for live voice of a female, and practical problems are likely to occur. This is considered to be the individual differences in the relationship between the ease-to-hear sounds and P300 response. Therefore, it is necessary for users of BCI to select and use sounds easier to hear in advance.

IV. RESULTS

In this paper, we studied the unidirectional analysis with ICA, in order to improve the detection ratio of P300 in Japanese voice presentation type BCI. As a result, the detection ratio improved from 54.2% for the traditional 4Hz low-pass filter to 90.9%, in the choice of one between two. In the task to choose one among five with synthetic speech stimulus, the detection ratio of P300 response to each sound of "a, i, u, e and o" improved as well, while it was the offline experiment. The maximum detection ratio was 94.7%, and the detection ratio per sound improved from 47.0% to 85.1%. We plan to install ICA onto the Japanese voice presentation type BCI in the future.

ACKNOWLEDGEMENTS

We would like to extend our sincere appreciation to Mr. Takenobu Inoue of the National Rehabilitation Center for Persons with Disabilities, Mr. Yuya Otowa of the University of Tokyo, Faculty of Engineering, Department of Engineering Synthesis, and Mr. Tomohiro Madarame of the University of Tokyo, School of Engineering, Department of Engineering Synthesis for their cooperation on this study, as well as to those who cooperated in the experiment. This study was partially subsidized by the Scientific Research Fund for Young Scientists (B)20700437 of the Ministry of Education, Culture, Sports, Science and Technology.

REFERENCES

[1] Hisaya Tanaka, Takenobu Inoue (2009), The Development of a Brain Computer Interface for Amyotrophic Lateral Sclerosis Patients (in Japanese), Research Bulletin, National Rehabilitation Center for Persons with Disabilities, vol.20:11-23

[2] Takenobu Inoue, Hisaya Tanaka, Akira Toyohara, Motoki Shino, Minoru Kamata (2008), Development of communication device using aural stimulation origin event-related potential (in Japanese), Biomechanism, Vol.19.

[3] Tomohiro Madarame, Hisaya Tanaka, Takenobu Inoue, Minoru Kamata, Motoki Shino (2008), The Development of a Brain Computer Interface Device for Amyotrophic Lateral Sclerosis Patients, Proceedings of IEEE System Man and Cybernetics (SMC2008) 2401-2406

[4] Yuya Otowa, Misato Nihei, Motoki Shino, Takenobu Inoue, Hisaya Tanaka, Minoru Kamata (2009), Brain activity detection technique to Japanese voice stimulation for BCI (in Japanese), Rehabilitation engineering conference

[5] EEGLAB, Swartz Center for Computational Neuroscience, http://sccn.ucsd.edu/

Fast processing method for PIV using GPGPU

Koji Miyazaki and Kikuhito Kawasue

University of Miyazaki, 1-1 Gakuen Kibanadai-Nishi, Miyazaki 889-2192, Japan
(Email: ng3804u@student.miyazaki-u.ac.jp)

Abstract: In the present study, the ability to apply general purpose computation on graphics processing units (GPGPUs) to particle image velocimetry (PIV) is confirmed, and the processing speed of the PIV is accelerated by GPGPUs. Our code is based on the direct cross-correlation method, where one of the PIV algorithms is rewritten for GPGPU computing using the CUDA tool kit. The results of a performance test indicate that GPU computing for PIV demonstrated an excellent acceleration rate of more than 100 times greater than CPU computing while maintaining acceptable precision.

Keywords: GPGPU, CUDA, PIV, Parallel computing, Image processing

I. INTRODUCTION

In our research, the processing speed of particle image velocimetry (PIV) was accelerated by general-purpose computation on graphics processing units (GPGPUs), which has been considered as a new acceleration technique for computing. Computations using GPGPUs use the graphics processing unit (GPU) on a graphics card for not only image processing but also general purposes such as numerical simulation [1]. The acceleration of processing using GPGPUs has been attempted for various numerical simulations, such as computational fluid dynamics and medical image processing [1]-[4]. However, reports on the application of GPGPUs to PIV are rare. Therefore, we applied GPGPU to PIV, which is an image-based measurement method, and evaluated the resulting performance. The computational errors related to GPGPUs should be also examined. Since most GPUs do not have double-precision arithmetic units, the results of computing on GPUs for application to PIV may have problems related to precision. Therefore, the results of the PIV analysis obtained using a GPGPU were compared to those obtained using a CPU.

Particle image velocimetry is a useful tool in the study of transient fluid flow phenomena [5][6]. The velocity vectors of a fluid are obtained by measuring the translational displacement of tracer particle during a short time interval without interfering with the flow. In general, the direct cross-correlation (DCC) method, which is a PIV algorithm, offers improved accuracy as compared with the FTT-based cross-correlation method. However, the DCC method requires several process iterations, unlike the FTT-based cross-correlation method. In the case of actual analysis, as the size of the analysis region becomes larger, the processing time increases, often reaching several minutes. Since this is problematic in the case of practical application, the processing speed using the DCC method should be accelerated. In the DCC method, in order to determine the displacement of a small region, cross-correlations between the interrogation region and several candidate regions must be calculated, and the associated processing comprises the majority of the calculation costs for the whole process. The calculation of all of the cross correlations was parallelized and accelerated using a GPGPU with CUDA, which is one of the software development environments for GPGPUs used in the present study. CUDA is freely distributed by NVIDA and extends the C language for use with the GPU, which has an excellent architecture for parallelism. As a result of a performance test, computing on the GPU for application to PIV exhibits an excellent acceleration rate of more than 100 times greater than CPU computing. In this case, approximately 95% of the entire process was executed on the GPU.

II. GPGPU

1. GPU hardware architecture

Figure 1 describes the architecture of the NVIDIA GeForce GTX 275 GPU used in this study, and Table 1 lists its hardware specifications. The GPU chipset of the GeForce GTX 275 is the GT200, which can operate in graphics mode or parallel computing mode. In GPGPU computing, the parallel computing mode is used. In graphics processing mode, the GPU architecture consists of ten texture processing clusters, and, in parallel computing mode, the GPU architecture consists of ten thread processing clusters. Here, TPC stands for texture processing cluster in graphics processing mode and thread processing cluster in parallel computing mode. Each TPC is made up of three streaming multiprocessors (SMs), each of which contains eight streaming processors (SPs), which are either processor cores or thread processors. The total number of SMs on the GT200 GPU is thirty. Unlike the general CPU architectures, the GPU can perform zero-cost hardware-based context switching, i.e., the GPU can immediately switch to another thread process, and it supports over thirty thousand concurrent threads in hardware (see Table 1). However, the maximum number of concurrent threads depends on environmental variables such as the executed kernel size (program size) in the GPU. Although double-precision arithmetic units have been implemented in the GT200 GPU, only one unit is implemented per SM and thirty units are implemented per GPU. Therefore, the performance of the double-precision arithmetic may be poor.

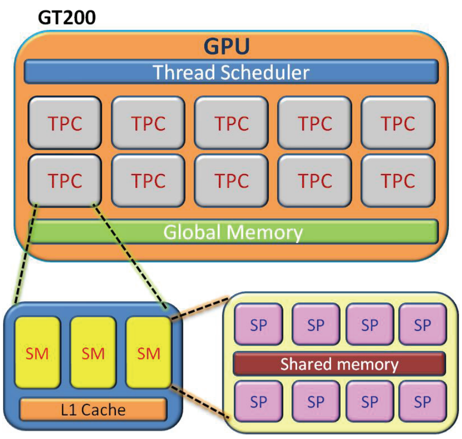

Fig. 1 NVIDIA GeForce GTX 275 GPU architecture in parallel computing mode

Table 1 NVIDIA GeForce GTX 275 hardware specifications

Texture processor clusters (TPCs)	10
Streaming multiprocessors (SMs) per TPC	3
Super function units (SFUs) per SM	2
Streaming processors (SPs) per SM	8
Total SPs (Cores)	240
Maximum concurrent threads per SM	1,024
Total maximum concurrent threads	30,720
Double-precision arithmetic units per SM	1
Peak floating point performance GFLOPS	933
Global memory size	869 MB
Shared memory per SM	16 KB
Registers per SM	16,384 registers

2. Software development environment for GPGPU

Cg is a conventional software development tool kit for GPU application software. Because the Cg is the specifically designed programming tool kit for computer graphics, it is not suitable for the development of GPGPU application software. However, recently, software development environments, such as CUDA and OpenCL, which consist of a complier, libraries, and useful tools for GPGPUs have been made freely available. CUDA is a C language development environment for NVIDA CUDA-enabled GPUs but OpenCL can be used for both NVIDA and ATI GPUs, which support the OpenCL architecture. In the present study, we used CUDA as the development tool of the program code for GPGPU computing.

III. PIV ALGORITHM

1. Direct cross-correlation (DCC) method

In PIV, the velocity information is estimated using two consecutive images detected by a camera. Figure 2 shows an example of standard PIV consecutive images [7], and illustrates the procedure of the direct cross-correlation method. In order to extract the velocity at each location, a normalized cross-correlation coefficient between the location (x, y) in the first image and the location ($x+dx$, $y+dy$) in the second image is defined as follows:

$$R_{fg}(dx,dy)=\frac{\sum_{i=1}^{N}\sum_{j=1}^{N}\{f(x_i,y_j)-f_m\}\{g(x_i+dx,y_j+dy)-g_m\}}{\sqrt{\sum_{i=1}^{N}\sum_{j=1}^{N}\{f(x_i,y_j)-f_m\}^2\sum_{i=1}^{N}\sum_{j=1}^{N}\{g(x_i+dx,y_j+dy)-g_m\}^2}} \quad (1)$$

where $f(x,y)$ and $g(x,y)$ are the intensities at location (x,y) in the first image and the second image, respectively, and N denotes the size of a side of the interrogation region, which is determined considering the concentration of tracer particles and the maximum velocity of the flow. This cross-correlation coefficient is used to estimate the translational displacements of tracer particles between two consecutive images. The displacement at location (x,y) between two images is estimated as follows. First, the values of the above cross-correlation coefficient are calculated between location (x,y) in the first field and the possible point $(x+dx,x+dy)$ in the second field. Second, the dx and dy values of the displacement are changed, and the cross-correlation coefficient is recalculated. By repeating this procedure, the best estimate of the translational displacement of the tracer particles is determined as the pair (dx,dy) that maximizes the correlation coefficient. The global velocity profile of the flow can be obtained by repeating the above computation at every location. Figure 3 shows a flow chart of the DCC method.

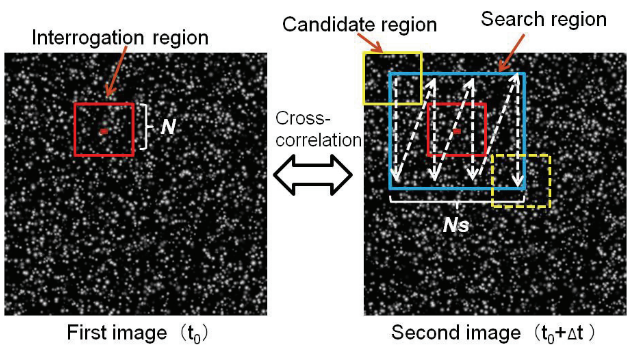

Fig. 2 Overview of the procedure of the DCC method

2. Amount of computations in the DCC method

In Fig. 2, Ns denotes the size of one side of the search region. In order to obtain one velocity vector in the DCC method, the correlation coefficient is calculated $Ns \times Ns$ times. When Ns = 33 and the number of locations required in order to determine the velocity vectors is 256, the number of calculations per location reaches 1,089, and the calculation is performed a total of 278,784 times during processing. Table 2 shows an example of the increase in the number of calculations. As *Ns* increases, the required calculation amount increases extremely (proportional to $Ns \times Ns$). In the DCC method, the computational cost required to calculate all of the cross-correlation coefficients between the interrogation region and all of the candidate regions in the search region is enormous. In the case of our code for the DCC PIV, the processing time required to calculate the cross-correlation coefficients accounts for approximately 99% of the total processing time. Since the cost is expected to be substantially reduced and the processing speed is accelerated by parallelizing the calculation process, the associated part of our code based on the DCC algorithm was rewritten to the GPGPU computing code using the CUDA tool kit. A flow chart of the parallelized DCC method using GPGPU is shown in Fig. 4.

IV. PERFORMANCE TESTS

1. Testing conditions

Tables 3 and 4 show, respectively, the testing environments and test cases used to evaluate the performance of the GPU computing for PIV. In Cases 1 through 5, the search region size was varied as indicated in Table 4, and the total number of cases is 15. Cases 1 through 4 were performed to confirm the acceleration rate of GPGPU over conventional CPU computing, and Case 5 was tested in order to evaluate the performance of the new double-precision arithmetic implemented on the GT200 GPU. The CPU computing and GPU computing were performed with double precision and single precision, respectively, except in Case 5.

Table 2 Example of the increase in the number of calculations

Locations	*Ns*	Calculations per location ($Ns \times Ns$)	Total calculations ($Ns \times Ns \times$ *locations*)
256	33	1,089	278,784
256	65	4,225	1,081,600
256	97	9,409	2,408,704

Table 3 Hardware testing environments

Environment	Env. 1	Env. 2
CPU	Phenom 9750	Core i7 920
Memory	4 GB	6 GB
GPU	GeForce GTX275	GeForce GTX275

Table 4 Lists of test cases

Case	Env.	Computing	Precision	Search region size ($Ns \times Ns$)
1	Env. 1	CPU	double	1,089 (33×33), 4,225 (65×65), 9,409 (97×97)
2	Env. 1	GPU	single	
3	Env. 2	CPU	double	
4	Env. 2	GPU	single	
5	Env. 2	GPU	double	

2. Results of the performance tests

Figure 5 and 6 show the elapsed times for the above test cases. Here, the elapsed time indicates the time just for the process execution after the process was created. In cases of processing by only the CPU (Cases 1 and 3), the elapsed time increases linearly with the search region size, whereas in cases of processing by the GPGPU (Cases 2 and 4), the elapsed time increases only slightly. On the other hand, the difference in the results for the GPGPU computing between the Phenom CPU and Core i7 CPU suggests that the performance of the GPGPU depends not only on the GPU architecture but also on the CPU or system architecture. The results for Case 5 indicate that double-floating-point

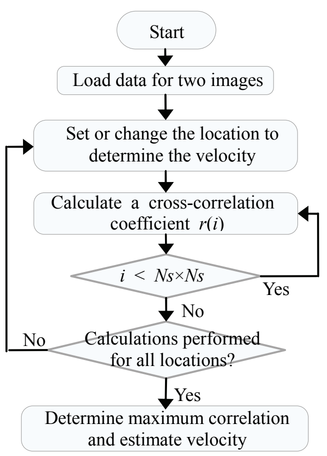

Fig. 3 Flow chart of the DCC method for CPU computing

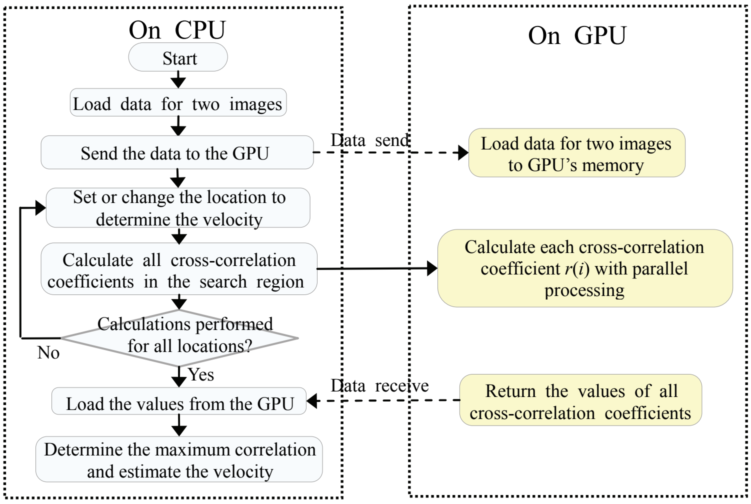

Fig. 4 Flow chart of the parallelized DCC method for GPU computing

calculation requires greater processing time than the single-floating-point calculation, because the number of double-precision arithmetic units of the GPU is not sufficient to execute a large number of parallel threads. Figure 7 shows the fractions of the elapsed time used for CPU and GPU processing. The CPU processing time includes the data translation time between the host memory and the GPU memory. Although there is a difference related to the search region size, approximately 95% of the elapsed time was used for GPU processing. Figure 8 shows the acceleration rates of the GPU computing over CPU-only computing, where rates of over 100 times and about 80 times can be seen for the Phenom CPU and the Core i7 CPU, respectively.

In the present study, the computing results for PIV based on the DCC method for all cases were exactly the same. In the case of the PIV analysis, the computational error caused by the floating point calculation is not a significant problem. This indicates that the precision of the processing on GPU for the PIV is adequate.

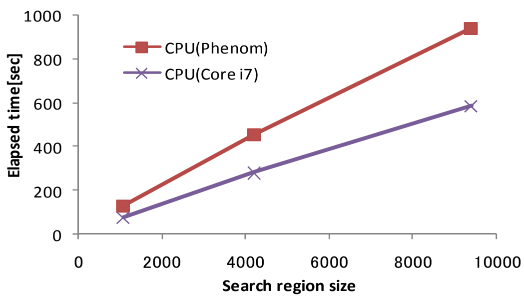

Fig. 5 Elapsed times for Cases 1 and 3

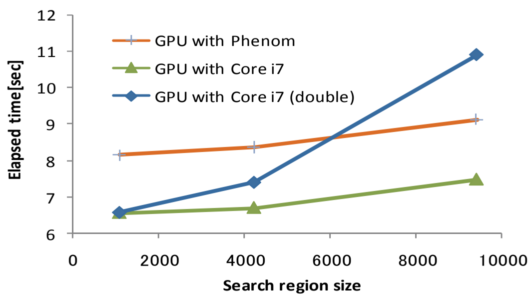

Fig. 6 Elapsed times for Cases 2, 4 and 5

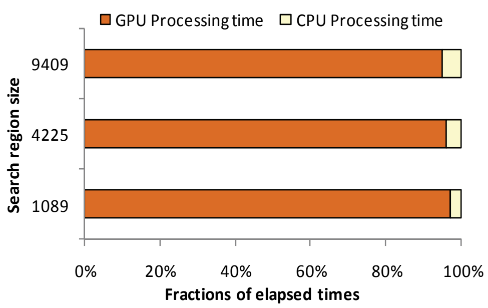

Fig. 7 Fractions of the elapsed time used for CPU and GPU processing for Case 4

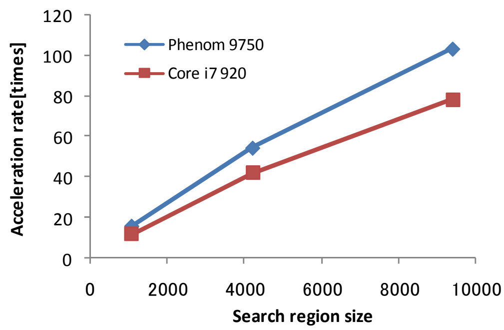

Fig. 8 Relationship between acceleration rate and search region size for GPGPU and CPU computing

V. CONCLUSION

A very high acceleration rate was obtained and the processing ability was improved by the use of a GPGPU. The performance of GPU computing depended not only on the GPU but also on the system architecture. Single-floating-point calculation precision was found to be sufficient for PIV analysis. These results indicate that the application of GPGPU to PIV is highly effective.

REFERENCES

[1] John D. Owens, David Luebke, Naga Govindaraju, et al. (2007), A Survey of General-Purpose Computation on Graphics Hardware, Computer Graphics Forum. Vol. 26, Issue 1, pp. 80-113

[2] John E. Stone, James C. Phillips, Peter L. Freddolino, et al. (2007), Accelerating molecular modeling applications with graphics processors, Journal of Computational Chemistry, Vol.28, pp. 2618-2640

[3] T. Aoki (2009), CFD Applications Fully Accelerated by GPU (in Japanese). Journal of Information Processing Society of Japan, Vol.50, Issue 2, pp.107-115

[4] F. Ino, J. Gomita, Y. Kawasaki and K. Hagihara (2006), A GPGPU approach for accelerating 2-D/3-D rigid registration of medical images. In Parallel and Distributed Processing and Applications (ISPA), LNCS, vol.4330, pp.939–950

[5] T.S. Wung and F.G.Tseng (1992), A color-coded particle tracking velocimetry with applications to natural convection, Vol.13, Experiments in Fluids, pp.217-223

[6] Y.A.Hassan and R.E.Canaan (1991), Full-field bubbly flow velocity measurements using a multi frame particle tracking technique, Vol.12, Experiments in Fluids, pp.49-60

[7] K. Okamoto, S. Nishio, T. Saga and T. Kobayashi (1997), Standard Images for Particle Imaging Velocimetry, Proc. PIV-Fukui'97

Data envelopment analysis for evaluating Japanese Universities

Kazushige Inoue[1], Ryota Gejima[1] and Shingo Aoki[1]

[1]Osaka Prefecture University, 1-1 Gakuencho Naka-ku Sakai Osaka
(Tel : 81-72-254-9353; Fax : 81-72-254-9915)
({ inoue@mis., gejima@mis., aoki@}cs.osakafu-u.ac.jp)

Abstract: In order to evaluate universities from various aspects, this study proposes method by utilizing DEA (Data Envelopment Analysis). The management of universities is complex and necessary to find out strength and weakness to be better educational institute. In this sense, DEA contributes for evaluation since it can show efficiency of universities based on multiple viewpoints. However, when the number of evaluated universities is increased, result of evaluation among universities is similar. Therefore, it is difficult to understand the specific points each university has. So this study proposes method for developed evaluation by ramifying DMU to some viewpoints. The utility and effectiveness of the proposed method are shown by numerical experiments.

Keywords: Data Envelopment Analysis, Linear Programming, Many-sided Evaluation, Decision Making Support.

I. INTRODUCTION

Recently the number of students who take entrance examination to university is decreasing due to declining birth rate in Japan. Moreover, public universities were reformed to be independent administrative organizations. Therefore, every university needs to consider the evaluation from the side of society in order to be attractive educational institute. In this sense, each university should evaluate themselves to understand the characteristics such as strength or weakness. Then better management policy can be prepared based on the valuable analysis. However, evaluation for universities is not often carried out. Even if there are evaluations, most of cases do not have the aspects from other universities [1]. That is why this study analyzes each university based on the characteristics by utilizing DEA (Data Envelopment Analysis).

DEA is a method for analyzing management efficiency of DMU (Decision Making Unit). The applicable field of DEA is now expanding such as policy evaluation, data mining, or so. The characteristics of DEA are as follows: (1) evaluate efficiency by multiple input and output data of DMU. (2) evaluate advantage aspects as much as possible by assigning variable weight to each elements of input and output. However, a lot of DMUs are evaluated as efficient if the number of input and output is large excessively compared with the number of evaluated DMUs. Thus analyst can not get informative knowledge from evaluation.

So this study proposes DEA method for many-sided evaluation to solve the above problem. Then the power of the proposed method is examined by applying data of Japanese universities.

II. DATA ENVELOPMENT ANALYSIS

1. Outline of DEA

DEA was proposed by A. Charnes et al. in 1978 as a method for management analysis. The applicable field of DEA is wide such as data mining or prospect of bankruptcy [2].

DEA regards each DMU as production function that produces output by input. Then the efficiency of DMU is calculated compared with other DMUs relatively. There are two characteristics DEA has; (1) weights are assigned to each input and output data and virtual input and output are generated. These weights are not fix but variable so that each DMU can employ suitable weight to be evaluated better. (2) common index for evaluation is shown as efficiency value. The efficient DMU gets efficiency value as one. On the other hand, inefficient DMU gets efficiency value less than one.

Assuming that there are *n* DMUs and each DMU is characterized by *m* input and *s* output. Then the DMU_K has input expressed as $x_{1k},\ldots,x_{mk}$ and output expressed as $y_{1k},\ldots,y_{sk}$. Here the efficiency value is shown by calculating following linear programming [2].

$$
\begin{aligned}
\max\ & \sum_{r=1}^{s} u_r y_{rk} \\
\text{s.t.}\ & \sum_{i=1}^{m} v_i x_{ik} = 1 \\
& -\sum_{i=1}^{m} v_i x_{ij} + \sum_{r=1}^{s} u_r y_{rj} \le 0 \quad (j=1,\ldots,n) \\
& v_i \ge 0 \quad (i=1,\ldots,m) \\
& u_r \ge 0 \quad (r=1,\ldots,s)
\end{aligned}
\tag{1}
$$

Above formula signifies that weights are assigned to input of DMU_K to make it as one. Then DEA controls the efficiency value of other DMUs does not exceed over one based on the weights for DMU_K. Objective function has the role for maximizing output of remarkable DMU. Moreover, it is possible to analyze strong points of each DMU by weights. That is because input and output are considered in evaluation when the weights have value.

2. Mathematical problem

The problem is generated when the number of input and output elements are large compared with the number of DMUs. In DEA, the number of evaluation criteria is creased if the number of input & output elements is increased. Therefore, more DMUs are evaluated as the state of efficient than usual. Moreover, at least one advantage of input or output elements makes that DMU efficient. That is why the elements which do not have advantages are not emphasized so that more zero weights are assigned to more input and output. Thus excessive number of input and output lead the following two problems: (1) evaluation does not make sense because of many efficient DMUs. (2) many-sided evaluation can not be achieved due to many zero weights. To deal with these problems, there is a restriction for selecting input and output. Assuming that *m* input elements, *s* output elements and *n* DMUs, n should be satisfied with restriction of $n \geq \max\{m \times s, 3 \times (m+s)\}$. However, there are many cases that many-sided evaluation is carried out based on many input and output like evaluation for universities.

III. PROPOSED METHOD

This paper proposes the framework for many-sided evaluation without regard to the number of input, output and DMUs. This framework makes layered structure based on evaluation perspective and assigns input and output elements to each node that is perspective. Then input and output of upper layer include those of lower layer. It is possible to evaluate based on each perspective by calculating efficiency value of each node.

This chapter explains the proposition for making layered structure. Then the procedure of making layered structure is shown. Finally the example concerning comparison between DMUs is shown.

1. Hierarchization of DMU

There are *n* evaluated DMUs. And they have *m* input elements and *s* output elements. Here input elements are $X=(X_1,...,X_m)$ and expressed as $X_i=(x_{i1},...,x_{in})$. So X_i indicates i input group of all DMUs. Equally, $Y=(Y_1,...,Y_s)$, $Y_r=(y_{r1},...,y_{rn})$ are defined. The efficiency value of DMU_K shown as θ_K is calculated by (1) formula. Moreover, efficiency value is calculated based on possible production set S formed by input and output.

Next it is necessary to consider the case that specific input and output are utilized for analysis. New input and output groups are selected and they are denoted as $X'=\{X' \in X, X' \neq \phi\}$, $Y'=\{Y' \in Y, Y' \neq \phi\}$. Then the efficiency value of DMU_K shown as θ'_K based on this data set (X',Y') is calculated by (1) formula. It means this efficiency value is calculated based on possible production set S'. Thus $S' \in S$ is satisfied and two different efficiency values θ_K, θ'_K are followed inequality $\theta_K \geq \theta'_K$. The efficiency value of selected data is less than that of original data.

2. Relationship between nodes

The proposed method hierarchizes by resolving the evaluation perspective and assigns input and output elements to each node. In this time, input and output of upper layer have to include those of lower layer. Then analysis is carried out in each node. Thanks to the proposition in previous section, the efficiency value of lower layer never exceeds that of upper layer. Therefore, it is possible to treat the efficiency value of each node evenly since efficiency signifies the state of each DMU by unified way. Thus inefficient DMU as a whole never be the state of efficient in some node. And the reason for decline about efficiency is revealed. For example, which parts of node affect to the efficiency badly or how degree the specific DMU influences the efficiency. It is possible to analyze these kinds of knowledge from all perspective analyst prepares.

Moreover, comparison of the efficiency value among different nodes reveals the reason for the efficiency. For example, DMU in certain layer has efficiency value as one, and DMU in lower has also the same one. In this case, the node in lower layer strongly supports to upper node and its efficiency. On the contrary, if DMU in lower layer has efficiency value as 0.1, this node is factor to restrain the efficiency of upper node. Then new weight is developed to compare with linked nodes. Assuming that the DMU_K's efficiency value of β node in α layer is expressed as $\theta_K^{\alpha\_\beta}$ and the efficiency value of γ node in $\alpha+1$ layer is expressed as $\theta_K^{\alpha+1\_\beta}$. The new weight is calculated as follow:

$$w_{\gamma}^{\alpha,\alpha+1} = \frac{\theta_K^{\alpha+1\_\beta}}{\theta_K^{\alpha\_\gamma}} \tag{2}$$

The new weight is ration between layers and range is $0 < w^{\alpha,\alpha+1} \leq 1$. This weight signifies the importance of lower layer for supporting the efficiency of upper layer. In this sense, lower node is necessary factor for upper node to have higher efficiency if weight between them is one. On the contrary, lower node is weak perspective for upper one if the weight between them is few.

IV. NUMERICAL EXPERIMENTS

1. Data set and evaluation criteria

The experiments are carried out by using date of Japanese thirty-one universities. Then the proposed method constructs three layers and eight nodes. The practical figure of layered structure is shown in Fig.1.

As you can see in Fig.1., analyst is able to observe the evaluation from multiple aspects. Firstly, the efficiency is calculated based on each node. Next we would like to examine the evaluation of universities by gathering those kinds of experimental results.

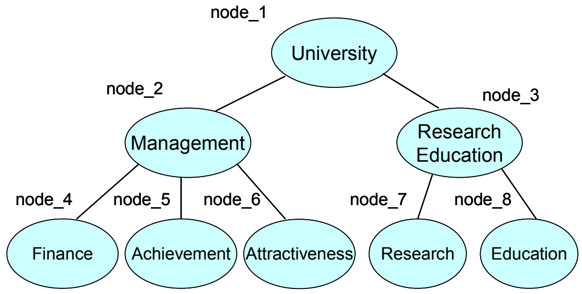

Fig.1. Layered structure

The experimental data consist of multiple elements and are divided to input data and output data as follows:
Input: 1. Number of faculty, 2. number of worker, 3. education and research expense, 4. Grant-in aid for management, 5. General and administrative expenses, 6. Profit of donation.
Output: 1. Maximum deviation, 2. Number of paper, 3. Number of graduate student, 4. Number of undergraduate student, 5. Number of books, 6. Grant-in-aid for scientific research, 7. Contract research funds, 8. Profit of business.

The general evaluation for universities is shown as node_1 in upper layer. It means that the efficiency value is the same as traditional DEA method and higher efficiency value is regarded as more efficient state. On the other hand, five nodes in lower layer are ramified functionally from general evaluation. Therefore, point of view concerning these five nodes is mentioned with showing input and output in each node. Here elements in each node are denoted by number shown in above paragraph.

<node_1> University
Input: 1～6 Output: 1～8
<node_2> Management
Input: 2, 4, 5, 6 Output: 1, 3, 4, 8
<node_3> Research and Education
Input: 1, 3 Output: 2, 3, 4, 6, 7
<node_4> Finance Input: 4, 5, 6 Output: 8

The efficiency value in this node signifies how much university can get profit with possible funds that are input. To assume two types of high efficient DMUs is reasonable. (i) DMU which has larger profit than that of other DMUs. (ii) DMU which has smaller possible investment to the profit.

<node_5> Achievement Input: 2, 4, 5, 6 Output: 1

The efficiency value in this node signifies how high university has deviation with possible funds and human resources. Thanks to this value, it is possible to examine how much DMUs invest funds to certain deviation. DMU which is higher efficiency operates by fewer funds. On the other hand, DMU which is lower efficiency invest funds excessively for their management.

<node_6> Attractiveness Input: 2, 4, 5,6 Output: 3,4

The efficiency value in this node signifies how many university gather students with possible funds and human resources. DMU which is higher efficiency has high attractiveness. On the other hand, DMU which is lower efficiency has less attractiveness and need to improve the situation. For example, they can increase the number of students.

<node_7> Research
Input: 1, 3 Output: 3, 4

The efficiency value in this node signifies how many university get external funds or accomplishments of research. DMU which is higher efficiency does research admitted by outside.

<node_8> Education
Input: 1, 3 Output: 2, 6, 7

The efficiency value in this node signifies how much university invests funds and human resources to education for students. DMU which is higher efficiency operates by fewer resources. On the other hand, DMU which is lower efficiency operates by much funds and resources. Higher efficiency value is suitable for the side of university and lower efficiency value is favorable for the side of student.

2. Result

The experimental results are shown in Table 1. For instance, DMU_No. 2 has efficiency value as one based on "University" (node_1) and has it as 0.234 based on "Achievement" (node_5).

3. Discussion

(i) Comparison of the traditional and proposed method

The traditional method shows the efficiency value based on only "University" (node_1). In contract, the proposed method ramifies nodes so that there are eight nodes, namely eight efficiency value for one DMU.

Firstly, "University" (node_1) is remarkable. There are twenty-one DMUs which have efficiency value as one shown in Table. 1. Therefore, it is difficult to decide superiority or inferiority. This is one of the problems of DEA, or more specifically, relationship between the number of DMUs and that of input and output. Some of the same efficiency values exist when the number of input and output is large compared with that of DMUs.

The new seven nodes that the proposed method produces are notable. There are no DMUs which have efficiency value as one in all nodes. (the proposed method has characteristic as follow: the efficiency value of certain node never exceed that of upper node. Thus it is possible to restrain the number of DMU which has same efficiency value in all nodes in case of other data set.)

This result means that the proposed method can find some difference compared with the traditional method which is difficult to show superiority or inferiority regarding each DMU.

For example, the efficiency values of DMU_No.1 and DMU_No. 2 are one based on "University" (node_1) that is traditional way so that there is no difference. However, DMU_No. 1 is superior based on "Management" (node_2) and DMU_No. 2 is superior based on "Research and Education" (node_3). This is the difference of characteristic.

(ii) Analysis of strength or weakness for each university

Visualization concerning DMU_No. 28 is shown in Fig.1. in order to emphasize effectiveness of the proposed method. The name of node and efficiency value is shown on each node. The value shown in the link between nodes is weight. If this weight is less than one, lower node represents weakness compared with upper node. For example, the efficiency value based on "University" (node_1) is one. Then weight of "University"-"Management" is one and that of "University"-"Research and Education" is 0.648. Therefore, this DMU has room for improvement in the field of "Research and Education".

Then analysis about DMU_No. 28 is done by utilizing these weights. This DMU has high efficiency in the area of "Management" (left section in Fig.1.). Especially, "Achievement" gets higher value though the average in that node is . From these result, this DMU has strength regarding "Management", especially "Achievement" or "Attractiveness".

Then the efficiency value based on "Research and Education" (right section in Fig.1.) is less efficiency. Especially, "Research and Education" is lowest efficiency as 0.649. the weight of "Research and Education"-"Research" is also lowest value as and this is just bottleneck.

As a result, the proposed method is able to analyze which section is strength or weakness for each DMU by examining weights and efficiency values.

Table 1-(a). Efficiency value based on each node

DMU	Node				
	University (node_1)	Management (node_2)	Finance (node_4)	Achievement (node_5)	Attractiveness (node_6)
No. 1	1	1	0.494	0.234	1
No. 2	1	0.959	0.334	0.124	0.959
No. 3	1	0.950	0.413	0.183	0.950
No. 4	1	0.919	0.670	0.396	0.917
No. 5	1	0.900	0.393	0.230	0.900
No. 6	1	0.787	0.313	0.191	0.787
No. 7	0.958	0.776	0.316	0.159	0.776
No. 8	1	1	0.715	0.500	1
No. 9	1	0.940	0.467	0.314	0.940
No. 10	0.970	0.927	0.655	0.449	0.927
No. 11	1	1	0.473	0.275	1
No. 12	1	0.776	0.651	0.519	0.776
No. 13	1	0.959	0.674	0.240	0.959
No. 14	1	0.771	0.591	0.521	0.771
No. 15	0.802	0.672	0.603	0.607	0.671
No. 16	1	0.710	0.631	0.557	0.710
No. 17	1	1	0.977	0.953	1
No. 18	0.884	0.748	0.091	0.551	0.741
No. 19	0.876	0.658	0.617	0.658	0.612
No. 20	0.932	0.695	0.684	0.669	0.618
No. 21	0.945	0.609	0.583	0.602	0.598
No. 22	0.966	0.666	0.576	0.651	0.562
No. 23	1	1	1	1	1
No. 24	1	1	1	1	1
No. 25	1	1	0.964	0.813	1
No. 26	0.989	0.548	0.076	0.548	0.485
No. 27	0.982	0.805	0.666	0.805	0.662
No. 28	1	1	0.946	1	1
No. 29	1	0.721	0.438	0.496	0.721
No. 30	1	0.577	0.454	0.577	0.512
No. 31	1	0.679	0.489	0.679	0.515

Table 1-(b). Efficiency value based on each node

DMU	Node			
	University (node_1)	Research & Education (node_3)	Research (node_7)	Education (node_8)
No. 1	1	0.892	0.833	0.801
No. 2	1	1	1	0.996
No. 3	1	1	1	1
No. 4	1	1	1	0.955
No. 5	1	1	1	0.912
No. 6	1	1	0.967	1
No. 7	0.958	0.925	0.873	0.884
No. 8	1	1	1	1
No. 9	1	0.903	0.753	0.903
No. 10	0.970	0.900	0.658	0.886
No. 11	1	0.892	0.684	0.883
No. 12	1	1	0.914	1
No. 13	1	1	1	0.993
No. 14	1	1	0.904	1
No. 15	0.802	0.787	0.643	0.744
No. 16	1	0.967	0.899	0.917
No. 17	1	1	0.937	1
No. 18	0.884	0.820	0.735	0.766
No. 19	0.876	0.779	0.504	0.733
No. 20	0.932	0.802	0.448	0.779
No. 21	0.945	0.851	0.585	0.830
No. 22	0.966	0.838	0.805	0.674
No. 23	1	1	0.577	1
No. 24	1	1	0.550	1
No. 25	1	1	0.470	1
No. 26	0.989	0.875	0.618	0.850
No. 27	0.982	0.866	0.591	0.836
No. 28	1	0.649	0.446	0.632
No. 29	1	0.929	0.904	0.889
No. 30	1	0.924	0.865	0.759
No. 31	1	0.809	0.549	0.780

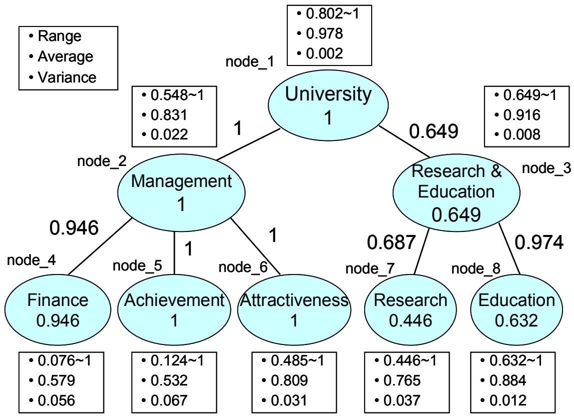

Fig.2. Visualization of DMU_No. 28

V. CONCLUSION

Though the traditional method sometimes can not find the superiority or inferiority, the proposed method solves such problem. It ramifies the DMU to multiple nodes that is viewpoint and shows the efficiency based on each node. Therefore, characteristics (strength or weakness) of each DMU can be revealed by efficiency value and weights between nodes. The proposed method works well for evaluation of universities and effectiveness is confirmed through the numerical experiments.

REFERENCES

[1] Shimizu T (2008), Universities ranking 2009. The Asahi Shimbun Company.

[2] Charnes, A., Cooper, W. W. and Rhodes, E. L. (1999), Measuring the Efficiency of Decision Making Units. European Journal of Operational Research, Vol. 2, pp. 429--444.

The Fifteenth International Symposium on Artificial Life and Robotics 2010 (AROB 15th '10),
B-Con Plaza, Beppu,Oita, Japan, February 4-6, 2010

Data envelopment analysis for supply chain

Akio Naito[1], Ryota Gejima[1], Kazushige Inoue[1], Shingo Aoki[1] and Hiroshi Tsuji[1]

[1]*Osaka Prefecture University, 1-1 Gakuencho Naka-ku Sakai Osaka*
(Tel : 81-72-254-9353; Fax : 81-72-254-9915)
({naitou@mis., gejima@mis., inoue@mis., aoki@, tsuji@}cs.osakafu-u.ac.jp)

Abstract: DEA (Data Envelopment Analysis) is a method for evaluating management efficiency of DMU (Decision Making Unit). This paper proposes DEA model for supply chain management. Traditional study focuses on selection of partners and construction of supply chain. Therefore, this study would like to consider how to optimize supply chain itself for maximizing benefit by DEA. In addition, the significant matter is that supply chains sometimes have the unbalanced business processes. It means some particular DMUs on supply chain have superiority and keep the efficiency excessively. That is why the rest DMUs on supply chain need to operate in unfavorable condition. As a result, their operations affect to whole efficiency on supply chain badly. Thus, the proposed method introduces adjustment variable to calculate optimum operation as a supply chain. The utility and effectiveness of the proposed method are shown by numerical experiments.

Keywords: Data Envelopment Analysis, Linear Programming, Supply Chain Management, Decision Making Support**.**

I. INTRODUCTION

DEA (Data Envelopment Analysis) is a method for analyzing management efficiency of DMU (Decision Making Unit). This method assumes production activity of DMU as transformation process by focusing on the input and output data. Then the efficiency of the transformation is evaluated by efficiency value shown as θ. DEA introduces benchmarking method for measuring efficiency value. And the efficiency value of each DMU is calculated by relative comparison to DMU set which is under competition. DEA enables analysts to know the strength (or weakness) among the DMUs in same field or industry. In recent study, the model for supply chain is developing in order to extend applicability of DEA since consideration for collaboration among DMUs in different field or industry is needed [1]. This traditional study utilizes the aspect of evaluation method comes from DEA and proposes the way for choosing beneficial partners to construct supply chain effectively. Therefore, this paper complements the previous study through discussion how to optimize the supply chain after choosing the partners.

So this study proposes the method for optimizing the production activity on supply chain by adjusting input and output data. Then it is possible to regard the collaboration among multiple DMUs as continuous activity under the DEA analysis. Here it is defined that optimization is improvement of efficiency value on supply chain (collaborated DMUs).

II. PROBLEM SETTING

1. Supply chain

This study assumes that five different production activities (A~E) form one business and the network is constructed shown in Fig.1. Production activities of A and B in upper chain operate procurement of raw materials and its processing. Then processed goods are manufactured into the products in activity of C. Finally activities of D and E distribute the products to consumers. The study hereafter is expanded based on this business flow.

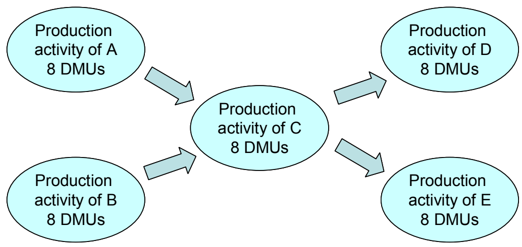

Fig.1. Supply Chain

There are multiple DMUs on each production activity and they are competitive. In case of manufacturing regarding automobile, products are manufactured from iron and electrical parts. Then consumers get the products through dealers or trade company.

2. Argument for applicability of DEA

Definition for input and output elements on each production activity are shown in Fig.2. Production activity of A has two inputs and one output, that of B has one input and two outputs, that of C has two inputs and one output, that of D has two inputs and one output, and that of E has one input and two outputs. The eight supply chains that have the same elements are prepared in order to carry out relative comparison.

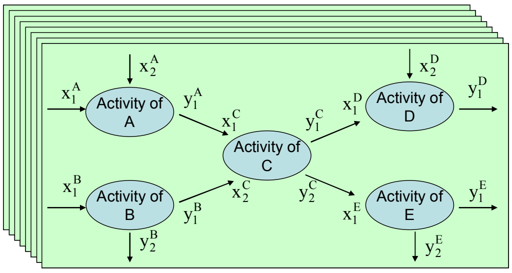

Fig.2. Elements of input and output

The definitions and conditions in this study are summarized as follows.

Condition 1:

There are seven competitors in each production activity (A~E) and their performances are evaluated individually based on their own production activity. Therefore, evaluation concerning one supply chain is judged by summation of five different efficiency values.

Condition 2:

The four arrows connecting between production activities shown in Fig. 2 signify the possible adjustment parts. So that analyst can adjust the amount of input and output. For instance, output y_1^A on production activity of A and input x_1^C on production activity of B are possible to be adjusted. And they have relationship that input x_1^C is decreased if output y_1^A is restricted.

III. DEA AS AN EVALUATION METHOD

Though DEA has various models, this study employs RAM model [2]. This model is able to deal with surplus of input and lack of output together and show the improvement for ideal management states. Thus RAM model is suitable for our study since it can consider adjustment between DMUs on supply chains. RAM model is defined by following formula (1).

$$\begin{aligned}
\max\quad & 1-\frac{1}{m+s}\left\{\sum_{i=1}^{m}\frac{d_{xi}}{R_{xi}}+\sum_{r=1}^{s}\frac{d_{yr}}{R_{yr}}\right\}\\
\text{s.t.}\quad & \sum_{j=1}^{n}x_{ij}\lambda_j+d_{xi}=x_{ik}\quad(i=1,2,\cdots,m)\\
& \sum_{j=1}^{n}y_{rj}\lambda_j-d_{yr}=y_{rk}\quad(r=1,2,\cdots,s)\qquad\qquad(1)\\
& \sum_{j=1}^{n}\lambda_j=1\\
& \lambda_j\ge 0\ (j=1,2,\cdots,n),\ d_{xi}\ge 0\ (i=1,2,\cdots,m)\\
& d_{yr}\ge 0\ (r=1,2,\cdots,s)
\end{aligned}$$

There are *n* evaluated DMUs. And they have *m* input elements and *s* output elements. Then maximization to objective function (surplus of input and lack of output) is carried out. That is to say, objective function indicates how far remarkable DMU is performing compared with efficient state. Moreover, scales of the data are controlled by Rx and Ry that are maximum value of input and output.

DMU is the state of efficient if all slacks are zero in RAM model. On the other hand, DMU is the states of inefficient if one or more slacks have value.

IV. DEA MODEL FOR ADJUSTING INPUT AND OUTPUT

1. Proposed model

This study defines the characters as follows in order to extend the RAM model to the proposed model.

- The number of supply chain: p
- The number of production activity: q

Then more detail definitions are set for production activity of h on k supply chain.

- The number of input element: m_h
- The number of output element: s_h
- The variable signifies the degree of reference to each DMU: λ_j^h $(j=1,2,\ldots,p)$
- The input and output data of DMU_k: (x_{ik}^h, x_{rk}^h)
- The variable signifies the slack of input element i: $d_{x_{ik}^h}$
- The variable signifies the slack of output element r: $d_{y_{rk}^h}$
- The adjustment variable of input element i: $I^+_{x_{ik}^h}, I^-_{x_{ik}^h}$
- The adjustment variable of output element r: $O^+_{y_{rk}^h}, O^-_{y_{rk}^h}$

The proposed method calculates efficiency of k supply chain by applying following formula (2).

$$\begin{aligned}
\max\quad & \sum_{h=1}^{q}\left\{1-\frac{1}{m_h+s_h}\left(\sum_{i=1}^{m_h}\frac{d_{x_{ik}^h}}{R_{x_{ik}^h}}+\sum_{r=1}^{s_h}\frac{d_{y_{rk}^h}}{R_{y_{rk}^h}}\right)\right\}\\
\text{s.t.}\quad & \sum_{j=1}^{p}x_{ij}^h\lambda_j^h+d_{x_{ik}^h}+I^+_{x_{ik}^h}-I^-_{x_{ik}^h}=x_{ik}^h\\
& (i=1,2,\ldots,m_h;\ h=1,2,\ldots,q)\\
& \sum_{j=1}^{p}y_{rj}^h\lambda_j^h-d_{y_{rk}^h}+O^+_{y_{rk}^h}-O^-_{y_{rk}^h}=y_{rk}^h\\
& (r=1,2,\ldots,s_h;\ h=1,2,\ldots,q)\\
& \sum_{j=1}^{p}\lambda_j^h=1\qquad(h=1,2,\ldots,q)\qquad\qquad(2)\\
& \lambda_j^h\ge 0\qquad(j=1,2,\ldots,p;\ h=1,2,\ldots,q)\\
& d_{x_{ik}^h}\ge 0\qquad(i=1,2,\ldots,m_h;\ h=1,2,\ldots,q)\\
& d_{y_{rk}^h}\ge 0\qquad(r=1,2,\ldots,s_h;\ h=1,2,\ldots,q)\\
& I^+_{x_{ik}^h},\ I^-_{x_{ik}^h}\ge 0\qquad(i=1,2,\ldots,m_h;\ h=1,2,\ldots,q)\\
& O^+_{y_{rk}^h}, O^-_{y_{rk}^h}\ge 0\qquad(r=1,2,\ldots,s_h;\ h=1,2,\ldots,q)
\end{aligned}$$

The objective function in formula (2) indicates total efficiency of q DMUs form k supply chain.

2. Explanation of the proposed method

The proposed method analyzes improvement of efficiency as whole production activity by introducing adjustment variables between activities. However, this method can not obtain optimum solution without restriction concerning adjustment variables.

Then the proposed method assumes that adjustment variables $O^+_{y^h_{rk}} - O^-_{y^h_{rk}}$, $I^+_{x^{h+1}_{ik}} - I^-_{x^h_{ik}}$ are equal if output y^h_{rj} (production activity of h) is equal to input x^{h+1}_{ij} (production activity of h+1). Thus input of following production activity increases when previous output is increased. Therefore, it is possible to consider optimum input and output.

Moreover, the calculated adjustment variables can show direction for higher efficiency. For instance, the input about production activity of h should be decreased in case of $I^+_{x^{h+1}_{ik}} > 0$. On the other hand, the input should be increased in case of $I^-_{x^h_{ik}} < 0$ to optimize the efficiency of supply chain.

V. NUMERICAL EXPERIMENTS

1. Experimental conditions and data

There are two experiments in order to examine the utility of the proposed method which introduces adjustment variables for input and output. The first experiment is the case of introduction of adjustment variables and the second one is case of non-introduction of those variables. The experimental conditions are as follows to apply the proposed (2) formula to the supply chain model shown in the second chapter.

<Common condition in both experiments>

$p=8$, $q=5$, $m_1=2$, $s_1=1$, $m_2=1$, $s_2=2$, $m_3=2$, $s_3=2$, $m_4=2$, $s_4=1$, $m_5=1$, $s_5=2$

<Condition in experiment 1>

$I^+_{x^C_{1k}} - I^-_{x^C_{1k}} = O^+_{y^A_{1k}} - O^-_{y^A_{1k}}$, $I^+_{x^C_{2k}} - I^-_{x^C_{2k}} = O^+_{y^B_{1k}} - O^-_{y^B_{1k}}$,

$I^+_{x^D_{2k}} - I^-_{x^D_{2k}} = O^+_{y^C_{1k}} - O^-_{y^C_{1k}}$, $I^+_{x^E_{1k}} - I^-_{x^E_{1k}} = O^+_{y^C_{2k}} - O^-_{y^C_{2k}}$,

Other adjustment variables are equal to zero.

<Condition in experiment 2>

All adjustment variables ($I^+_{x^h_{ik}}, I^-_{x^h_{ik}}, O^+_{y^h_{rk}}, O^-_{y^h_{rk}}$) are equal to zero.

Experimental data are shown in Table 1.

Table 1-(a). Experimental data (supply chain 1~4)

Production activity	Input and Output	Supply chain 1	2	3	4
A	x_1^A	144	229	102	261
	x_2^A	50	100	98	177
	y_1^A	205	250	184	203
B	x_1^B	52	59	63	61
	y_1^B	110	186	124	93
	y_2^B	210	209	200	13
C	$x_1^C (=y_1^A)$	205	250	184	203
	$x_1^C (=y_1^B)$	110	186	124	93
	y_1^C	76	96	44	111
	y_2^C	144	80	83	61
D	x_1^D	148	126	101	36
	$x_2^D (=y_1^C)$	76	96	44	111
	y_1^D	195	92	199	207
E	$x_1^E (=y_2^C)$	144	80	83	61
	y_1^E	18	204	76	195
	y_2^E	176	129	133	182

Table 1-(b). Experimental data (supply chain 5~8)

Production activity	Input and Output	Supply chain 5	6	7	8
A	x_1^A	77	203	244	56
	x_2^A	131	106	58	164
	y_1^A	132	88	126	242
B	x_1^B	108	71	49	72
	y_1^B	177	144	41	61
	y_2^B	224	190	67	266
C	$x_1^C (=y_1^A)$	132	88	126	242
	$x_1^C (=y_1^B)$	177	144	41	61
	y_1^C	156	185	62	50
	y_2^C	173	218	88	107
D	x_1^D	94	13	105	101
	$x_2^D (=y_1^C)$	156	185	62	50
	y_1^D	186	33	200	153
E	$x_1^E (=y_2^C)$	173	218	88	107
	y_1^E	37	57	282	224
	y_2^E	187	175	78	90

Characteristics of experimental data are summarized. First of all, the structure of experimental data are revealed by looking at the result of non- adjustment (experiment 2). According to the Table 2., first, third, fifth, and eighth supply chains have efficiency value as one in production activity of A. And other supply chains are the state of inefficient (efficiency value is less than one). Especially, sixth supply chain has less efficiency that is 0.66. This supply chain has large input and less output compared with third supply chain. This is clearly proven by their input and output data that are $x_1^A=203$, $x_2^A=106$, $y_1^A=88$ (sixth supply chain) and $x_1^A=102$, $x_2^A=98$, $y_1^A=184$ (third supply chain). The results reflect productivity regarding each production activity well.

Next supply chains themselves are remarkable. In the first supply chain, production activities of A and B have efficiency value as one and the other production activities have efficiency value less than one. Therefore, upper activities (procurement or its processing) are the state of efficient and lower activities (manufacturing or distribution) are that of inefficient in this supply chain.

On the other hand, fourth supply chain is the opposite situation. Moreover, there is no case that all production activities (A~E) are the state of efficient in the prepared supply chains. That is why experimental data generate supply chains that have unbalanced production activities.

2. Experimental Result

The results regarding the efficiency value are as shown in Table 2.

Table 2-(a). Efficiency value (supply chain 1~3)

Production activity	Supply chain					
	1		2		3	
	Adjustment	—	Adjustment	—	Adjustment	—
A	1	1	1	0.80	1	1
B	1	1	1	1	0.98	0.87
C	0.90	0.77	0.83	0.50	0.85	0.63
D	0.53	0.67	0.48	0.65	0.71	1
E	0.57	0.57	0.69	0.90	0.53	0.74
Total	4.00	4.01	4.00	3.85	4.07	4.24

Table 2-(b). Efficiency value (supply chain 4~6)

Production activity	Supply chain					
	4		5		6	
	Adjustment	—	Adjustment	—	Adjustment	—
A	0.61	0.61	1	1	0.82	0.66
B	0.75	0.58	0.86	1	0.94	0.86
C	0.83	0.78	0.94	0.82	0.83	1
D	0.87	1	0.70	0.75	1	1
E	0.76	1	0.93	1	0.58	0.58
Total	3.82	3.97	4.43	4.57	4.17	4.1

Table 2-(c). Efficiency value (supply chain 7, 8)

Production activity	Supply chain			
	7		8	
	Adjustment	—	Adjustment	—
A	0.86	0.75	1	1
B	1	1	1	1
C	0.92	1	0.88	0.82
D	0.95	0.95	0.83	0.91
E	1	1	0.83	0.84
Total	4.73	4.7	4.54	4.57

3. Discussion

The power of adjustment variable is considered by the result in Table 2. Though production activities of A and B are the state of inefficient (A: 0.66, B: 0.86) with non-adjustment in sixth supply chain, the efficiency values are improved (A: 0.82, B: 0.94) with adjustment. However, efficiency value in production activity of C is decreased from 1.0 to 0.83. As a result, whole efficiency shown as total efficiency value is increased 4.1 to 4.17. It is revealed that introduction of adjustment variables works effectively. The result of slacks and adjustment variables is shown in Table 3. to explain the effect of the proposed method.

The values of slacks in Table 3. indicate surplus of input and lack of output and larger values mean less efficiency. Then output y_{23}^B in production activity of A and input x_{13}^C in production activity of C are remarkable. That is because the lack regarding y_{23}^B is decreased from 0.47 to 0 with adjustment. On the other hand, surplus regarding x_{13}^C is increased from 0 to 0.47. This is the situation that production activity of C receives the inefficient burden from that of A.

The adjustment variables work well in sixth supply chain since all five efficiency values are increased. However, some total efficiency value are decreased like eighth supply chain. The reason is that objective function of the proposed method might not be proper for the prepared supply chain network. Moreover, production activity of C plays an important role for optimization since it has four adjustment variables. Then total efficiency value of supply chains which have efficiency value as one with non-adjustment is increased by the proposed method. It means production activity of C has a function for receiving the burden from other activities when it is the state of efficient.

Table 3. Slacks and adjustment variables on sixth supply chain

Production activity	Input and Output	Slack		Adjustment variable
		adjustment	—	
A	x_{13}^A	0.23	0.23	—
	x_{23}^A	0.32	0.32	—
	y_{13}^A	0	0.47	−0.47
Efficiency value		0.82	0.66	
B	x_{13}^B	0.11	0.11	—
	y_{13}^B	0	0.23	−0.23
	y_{23}^B	0.07	0.07	—
Efficiency value		0.94	0.86	
C	x_{13}^C	0.47	0.00	−0.47
	x_{23}^C	0.23	0	−0.23
	y_{13}^C	0	0.00	0.00
	y_{23}^C	0	0.00	0.00
Efficiency value		0.83	1	
D	x_{13}^D	0.00	0	—
	x_{23}^D	0.00	0	0.00
	y_{13}^D	0.00	0	—
Efficiency value		1	1	
E	x_{13}^E	0.72	0.72	0.00
	y_{13}^E	0.49	0.49	—
	y_{23}^E	0.04	0.04	—
Efficiency value		0.58	0.58	

VI. CONCLUSION

This study has proposed DEA model which introduces adjustment variables in order to improve whole efficiency on supply chain. According to the numerical experiments, adjustment variables contribute for supply chain management since some of the supply chains get better efficiency. Moreover, the key DMU which softens and receives unbalanced operation is revealed. This benefit indicates the practical possibility of DEA for applying supply chain management more.

REFERENCES

[1] Srinivas T, Baker, R. C. (2002), A multi-phase mathematical programming approach for effective supply chain design. European Journal of Operational Research, Vol. 141, pp. 544-558.

[2] Cooper, W. W, Park, K. S., and Paster, J. T. (1999), RAM: A Range Adjusted Measure of Inefficiency for Use with Additive Models and Relations to Other Models and Measures in DEA. Journal of Productivity Analysis, Vol. 11, pp. 5-42.

On a Brownian Cellular Automaton Implementing Self-Reproducing Loop

Koji Ono†, Teijiro Isokawa†, Ferdinand Peper‡†, Jia Lee*,
Ayumu Saitoh†, Naotake Kamiura†, and Nobuyuki Matsui†

†Graduate School of Engineering, University of Hyogo, Japan
‡Nano ICT Group, National Institute of Information and Communications Technology, Japan
*College of Computer Science, ChongQing University, ChongQing, China

Abstract

An implementation of Self-Reproducing Loops (SRL) on Brownian Cellular Automata (BCA) is proposed in this paper. BCA are asynchronous cellular automata in which certain local configurations propagate randomly in the cellular space, resembling Brownian motion. In the proposed SRL, the signals in the loops and the loop heads can move backward and forward because of the Brownian nature of BCA, thus making it possible to avoid collisions of loop heads.

1. Introduction

A Self-Reproducing Loop (SRL) is a simple structure that is capable of reproducing itself on a Cellular Automaton (CA). Originated by Langton [1], these loops have been extensively studied (e.g. see [2]). They commonly contain structural information that is used in two ways: *interpreted*, as instructions to be executed to construct their offspring, and *uninterpreted*, as data to be copied to the offspring. This resembles the situation in natural systems, such as DNA molecules, which contain genetic information of natural organisms.

SRLs are usually implemented on synchronous cellular automata, that is, all the cells in the cellular space are updated at the same time by a central clock. Synchronous updating enables us to construct SRLs and to analyze their dynamic behavior easily, but, nature is asynchronous: this type of updating scheme has hardly been observed in natural systems. So, if an SRL is treated as an organism in an artificial living system, the behavior of the SRL or of each cell in the cellular space could be driven in an asynchronous manner.

Various models of SRLs working on asynchronous cellular automata have been proposed. Nehaniv showed an implementation of Langton's loop on Asynchronous Cellular Automata (ACA) [3]. This CA is updated by a so-called *marching-soldier scheme*, in which each cell is locally synchronized among its neighboring cells by exchanging information about which cell precedes which in time, but this is not efficient, both in reproduction speed as in the number of states required in cells. Lee et al. constructed a self-reproducing loop on ACA [4] where the reproduction process is conducted sequentially, i.e., one parent loop can produce only one daughter loop. This SRL cannot treat situations in which the construction head of the loop collides with other loop structures. Takada et al. proposed an SRL on Self-Timed Cellular Automata (a type of ACA) in which the SRL is capable of collision detection [5]; however, a significant number of transition rules is required to realize this capability.

In this paper, we propose a scheme to implement an SRL based on Brownian Cellular Automata (BCA). BCA are ACA in which certain local configurations, like signals, propagate randomly in the cellular space, resembling Brownian motion [6]. By exploiting the randomness inherent in BCA in an active way in computation, this model has been proven to be computational universal, i.e., any Turing machine can be simulated on it.

The challenge in this research is that it requires the construction of a self-reproducing mechanism that works flawless even in the presence of asynchronous and random processes, which are hardly found in conventional CA-based SRLs but do have a distinct place in many biological organisms. The proposed SRL includes a self-inspection mechanism: before producing a daughter loop, the mechanism inspects the shape of the mother loop to base the construction on. Therefore, it is capable of self-reproducing a great variety of loop shapes in the cellular space. Though—due to the asynchronous timing—collisions of loop heads may occur when daughter loops are created in the same region, loop heads can move backward and forward because of the Brownian nature of BCA, thus preventing deadlocks these collisions would otherwise give rise to.

2. Brownian Cellular Automaton

A BCA [6] is a two-dimensional asynchronous CA of identical cells, each of which can assume one of a finite number of states at a time. Cells undergo transitions in accordance with transition rules that operate on each cell and its direct four neighbors, shown in Fig. 1. The rules are of a type called Von Neumann neighborhood aggregate rules. In a

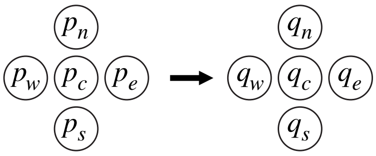

Fig. 1 Transition on BCA

BCA, transitions of the cells occur at random times, independent of each other. Furthermore, it is assumed that neighboring cells of the cells being in transition never undergo transitions at the same time to prevent a situation in which such cells simultaneously write different states into the same location.

We assume that the transition rules are rotational symmetric, i.e., one transition rule has four rotated analogues. Consequently, when we represent the transition in Fig. 1 as

$$(p_c, p_n, p_e, p_s, p_w) \rightarrow (q_c, q_n, q_e, q_s, q_w), \qquad (1)$$

the following three rules also exist:

$$\begin{aligned}(p_c, p_e, p_s, p_w, p_n) &\rightarrow (q_c, q_e, q_s, q_w, q_n)\\ (p_c, p_s, p_w, p_n, p_e) &\rightarrow (q_c, q_s, q_w, q_n, q_e)\\ (p_c, p_w, p_n, p_e, p_s) &\rightarrow (q_c, q_w, q_n, q_e, q_s)\end{aligned}$$

3. Self-Reproducing Loop based on a Brownian Cellular Automaton

An SRL implemented on BCA in this paper is subject to the following conditions: (1) The loop lacks a protective layer (i.e. unsheathed) and contains only one signal, which is different from Langton's loop, and (2) The loop shape is linear, so it should be a loop and not contain T-junctions in its simplest form, and one T-junction will only occur in a loop at the base of where construction starts. Apart from these conditions, an SRL may have an arbitrary shape. A state of a cell can be in one of the 12 states shown in Fig. 2 and the functions of the states are listed in Fig. 3. The transition rules used are not shown in this paper due to the limitation of page space[1].

The basic element of the loop is a *path*, which is used for transmitting signals. The path lacks a protective layer (i.e. it is unsheathed). An *arm head* attached to the tip of a path operates upon receiving a signal and may create a new path. Figure 4 shows a path and an arm head.

The SRLs in this paper are of a type called *shape-encoding* or *self-inspection* [4, 5, 7], which differs from the original (Langton's) loop where the SRL already contains its construction signals. The SRL contains only one signal and the reproduction procedure is initiated by this signal, followed by several other phases. First the structure of the mother loop is scanned, after which construction signals are created based on the scanned information, and this is followed by the construction of a daughter's loop structure. Finally, the umbilical cord between the loops of a mother and her daughter is cut.

[1] see http://www.eng.u-hyogo.ac.jp/eecs/eecs12/arob10/srlonbca/

Symbol	"Blank"	✣	●	▲	▼	□	◇	◆	✛	○	■	✚
State	0	1	2	3	4	5	6	7	8	9	a	b

Fig. 2 The symbols used to represent the states of a cell

State	Symbol	Function
1	✣	Path.
2	●	Advance the head straight ahead.
3	▲	Advance the head leftwards.
4	▼	Advance the head rightwards.
6 - 7	◇ ◆	Trace and encode the shape.
7	◆	Arm head.
7 - 5	◆ □	Collision detection.
8	✛	Separate a child loop from a parent loop.
9	○	Find next corner and create an arm.
a	■	Padding put on the joint of the arm.
b	✚	Finalize construction.

Fig. 3 States listed with their functions

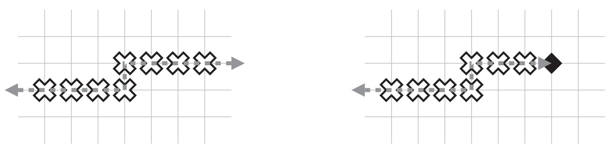

(a) (b)

Fig. 4 (a) path and (b) arm head

The reproduction process is initiated by the signal initially in the loop. This signal can travel bidirectionally in the loop and when it arrives at what would be a left corner of the loop if the signal would travel counterclockwise, this creates an arm head at the front of the arm. This signal also creates a *scanning signal* at its left for scanning the structure of the loop and a *terminator* at its back, which is used for its eventual destruction. The process is shown in Fig. 5, whereby the numbers above/below arrows between the consecutive configurations show the transition rule that is applied.

Most of the self-reproducing process in this SRL is bi-directional, i.e., each process can be traced backward by applying an appropriate transition rule. The only exception concerns the cutting of the umbilical cord.

A scanning signal is bi-directional, i.e., it travels both

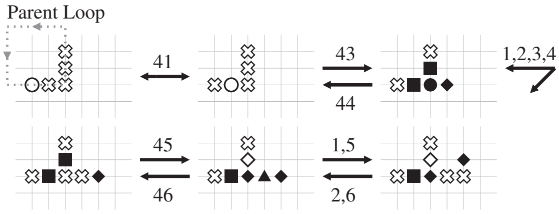

Fig. 5 The start of the self-reproduction process

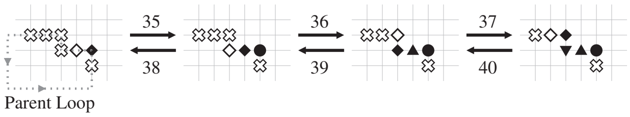

Fig. 6 Process for encoding the structure of the loop

clockwise and counterclockwise in a loop. When this signal moves counterclockwise in one cell, it produces one of three kinds of signals (states 2, 3, and 4) corresponding to the structure of the loop at the location of the scanning signal (see Fig. 6). These signals are *constructing signals*, which also travel in the loop without surpassing other signals and which are used for operating the arm head. A scanning signal can move clockwise in a loop, but this will only be allowed to occur when the scanning signal is at the directly neighboring cell of a construction signal, causing this construction signal to vanish. Moving the scanning signal in one cell clockwise and counterclockwise causes a construction signal being consumed and produced, respectively, so construction signals for a new loop will always correctly reflect the information describing the loop structure.

A construction signal in the state 2, 3, or 4, respectively, creates a new path that is an extension forward, to the left, or to the right of the arm head. Figure 7 shows the process of extending a path by construction signals processed at the arm head.

While the construction signals produced in the mother loop are processed at the arm head, a daughter loop is constructed next of the mother loop, whereby the daughter's shape is the mirror image of the mother's shape relative to the umbilical cord. The final stage of the self-reproduction process consists of cutting the umbilical cord. Figure 8 shows the cutting process. These transitions are irreversible.

Figure 9 shows an example of a cellular space that contains several SRLs. Starting from one initial loop, the loop reproduces itself, thus forming its direct neighbors. Unlike conventional SRLs, the Brownian version occasionally struggles to move forward through the process due to its randomized motion, but on the other hand it is asynchronous like many processes in biological organisms, and

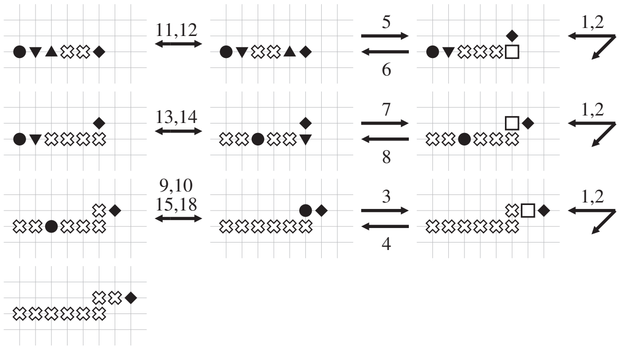

Fig. 7 Extending a path by the construction signals

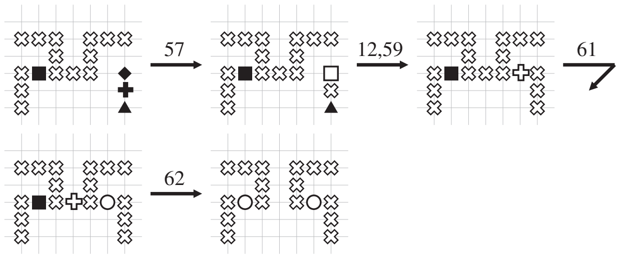

Fig. 8 Cutting process between two loops

deadlocks can be resolved in a natural way.

An example of the resolution of deadlocks is shown in Fig. 10, in which an arm head of one loop collides with the path of another loop. When the collision is detected at the arm head, the arm head stops and no longer accepts any construction signals. The remaining construction signals, which cannot be processed at the arm head, will eventually return to the scanning signal and vanish, thus completing the withdrawal of the loop. After the withdrawal process finishes, the reproduction process starts at another corner of the loop.

4. Conclusions and Discussion

The SRL in this paper can be implemented on a BCA of which cells have 12 states. The number of transition rules is 62, and based on these rules, self-reproduction with asynchronous timing of cells is possible, including the scanning of the loop structure and the avoidance of deadlocks among loops.

The reproduction speed of the SRLs in this paper is not high, due to the fluctuations of signals in the loops, i.e., their movement backward and forward. In the computation by BCA in [6], a configuration called *ratchet* is introduced that prevents signals from moving backward. As a result, the speed of the computation can be accelerated significantly. The introduction of a ratchet-like configuration

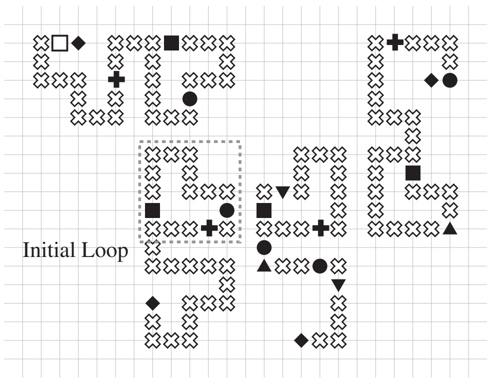

Fig. 9 Self-reproduction of loops

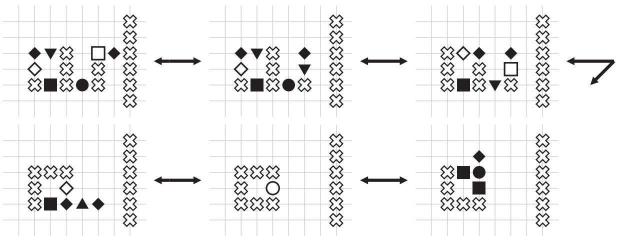

Fig. 10 Arm head colliding with the path of another loop

into the presented SRLs will be an interesting future challenge, because it needs to be applied such that deadlocks are avoided.

References

[1] C. G. Langton. Self-reproduction in cellular automata. *Physica D*, 10:135–144, 1984.

[2] J. A. Reggia, S. L. Armentrout, H-H. Chou, and Y. Peng. Simple systems that exhibit self-directed replication. *Science*, 259(5099):1282–1287, 1993.

[3] C. L. Nehaniv. Self-reproduction in asynchronous cellular automata. In *Proc. NASA/DoD Conf. on Evolvable Hardware*, pages 201–209, 2002.

[4] J. Lee, S. Adachi, and F. Peper. Reliable self-replicating machines in asynchronous cellular automata. In *IEICE General Conference*, 2005.

[5] Y. Takada, T. Isokawa, F. Peper, and N. Matsui. Asynchronous self-reproducing loops with arbitration capability. *Physica D*, 227:26–35, 2007.

[6] J. Lee and F. Peper. Efficient computation in brownian cellular automata. In *Proc. of 4th International Workshop on Natural Computing*, pages 47–56, 2009.

[7] J. Ibáñez, D. Anabitarte, I. Azpeitia, O. Barrera, A. Barrutieta, H. Blanco, and F. Echarte. Self-inspection based reproduction in cellular automata. In *Advances in Artificial Life, Third European Conference on Artificial Life (ECAL95)*, volume 929 of *LNCS*, pages 564–576, 1995.

The Fifteenth International Symposium on Artificial Life and Robotics 2010 (AROB 15th '10),
B-Con Plaza, Beppu,Oita, Japan, February 4-6, 2010

An Application of Self-Reproducing Loops to Defect-Tolerant Computation on Self-Timed Cellular Automaton

Tadashi Kunieda[1], Teijiro Isokawa[1*], Ferdinand Peper[2,1],
Ayumu Saitoh[1], Naotake Kamiura[1], Nobuyuki Matsui[1]

[1] Division of Computer Engineering, Graduate School of Engineering,
University of Hyogo, 2167 Shosha, Himeji, 671-2280, Japan.
[2] Nano ICT Group, National Institute of Information and Communications Technology, Japan
[*] Corresponding author, E-mail: **isokawa@eng.u-hyogo.ac.jp**

***Abstract*:** For the realization of nanocomputers it will be important to have built-in defect-tolerance, which is the ability to overcome the unreliability caused by defective components. This paper explores defect-tolerance for nanocomputers based on Self-Reproducing Loops, in which each of the loops in the system acts as a computational element, supporting the propagation of signals along transmission wires and their processing in logic elements. The loop-based design facilitates the adaptation to defects through the expansion of wires such as to prevent them from being blocked by defects. The proposed system is implemented on an asynchronously timed Cellular Automaton.

1 Introduction

Cellular Automata (CA) attract increasing attention as architectures for computers with nanometer-scale devices (nano-computers), because their regular structures and local connectivity offer much potential for manufacturing based on molecular self-assembly [1]. An obstacle to the realization of nanocomputers is the reduced reliability of nanometer-scale devices as compared to their VLSI counterparts, due to fabrication defects. Discarding chips with only a small amount of defects, however, will be inefficient for the imperfect manufacturing processes expected for molecular self-assembly.

For this reason, alternative approaches to defect-tolerance need consideration. There have been several studies on defect-tolerance in Self-Timed CA (STCA) [1], which is a type of asynchronous CA [2]. The resulting models, however, tend to suffer from a large overhead in terms of the number of transition rules required to implement defect-tolerance (95% of all rules), while computation itself requires only few rules.

This paper proposes an STCA model with defect-tolerant capability that is based on Self-Reproducing Loops (SRLs) [3]. Computation on the STCA is realized by embedding so-called [illegible] [4] on the cell space, whereby wires, crossovers of wires, and logic elements are implemented in terms of SRLs.

2 Preliminaries

Self-Timed Cellular Automaton (STCA) [1] is a two-dimensional asynchronous CA of identical cells, each of which has a state that is partitioned into four parts

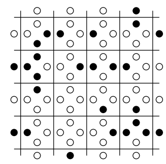

Fig. 1 Example of self-timed cellular space

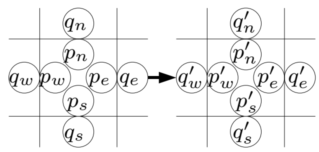

Fig. 2 Rule based on transition function f

in one-to-one correspondence with neighboring cells. If each partition of a cell state consists of 1 bit, the resulting 4 bits of the cell encode 16 states, and the cellular space is an array like in Fig. 1, where a filled circle denotes a 1-bit, and a open circle a 0-bit. Each cell undergoes transitions in accordance with a transition function f that operates on the four partitions p_n, p_e, p_s, p_w of the cell and on the nearest partition of each of its four neighbors q_n, q_e, q_s, q_w (Fig. 2), whereby a state symbol to which a prime is attached denotes the new state of a partition after update. Dummy transitions are not included in the transition function, so we assume that the left-hand side of Fig. 2 differs from the right-hand side. The transition rules of an STCA are rotation-symmetric, so each of the rules has four rotated analogues. In an STCA, transitions of the cells occur at random times, independent of each other. It is assumed that neighboring cells never undergo transitions simultaneously to prevent a situation in which such cells write different values in shared bits at the same time.

Computational elements needed in the model to ensure computational universality are [4]: a signal, a wire (possibly equipped with branching wires), a crossover of

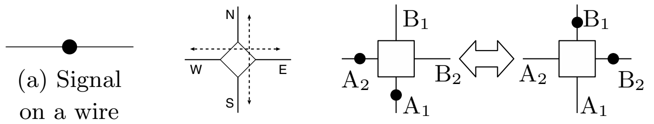

(a) Signal on a wire (b) Crossover (c) Conservative Join

Fig. 3 Computational Elements

wires and a delay insensitive logic element, called Conservative Join(CJoin).

A signal can travel along a wire, like in Fig. 3(a). A crossover element (Fig. 3(b)) accepts a signal at port N (or S) and produces an output signal from port S (or N, resp.). In a similar way, the ports W and E are connected to each other.

A CJoin is a two-input two-output logic element with four input/output wires A_1, A_2, B_1, B_2. Two signals from A_1 and A_2 (or B_1 and B_2 ,resp.) result in output signals from B_1 and B_2 (or A_1 and A_2, resp.) (see Fig. 3(c)) Both of the two input signals are necessary for the operation of a CJoin to take place.

Self-Reproducing Loops (SRLs) used in this paper work asynchronously and independently from each other; they are equipped with capabilities of shape-encoding and collision detection, like in [5]. Each SRL contains one "[illegible]" that circulates clockwise in the loop. This signal is used for reproducing the loop, detecting defect neighboring loops, conducting computation, and expanding a transmission wire. The reproduction process starts when the loop signal arrives at a corner of the loop; here is where an arm starts to grow. An arm head will appear at the front of the arm, and if the cellular space in front of the arm head is not occupied by other loops, the loop signal will circulate in the loop to extract signals encoding the shape of the loop. These signals are processed at the arm head, resulting in a newly created loop structure. Due to asynchronously timing of the reproduction process in the loops, sometimes the arm head collides with other loops. In this case, the arm head withdraws itself and self-destructs, while the encoded signals remaining in the loop are deleted. The signal in the loop then starts again to scan the loop.

3 Implementing computational elements by Self-Reproducing Loops

3.1 Loops and Signals

The SRLs constructed in the model are connected to each other through a network structure in which individual SRLs exchange information via connections called [illegible] (Fig. 4). Each loop has one signal circulating

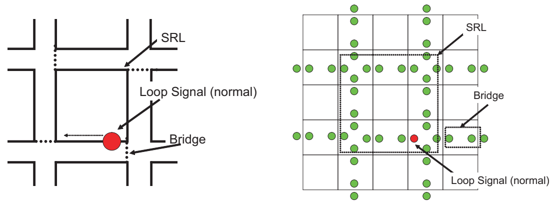

(a) (b)

Fig. 4 (a) Loop connected to neighboring loops via bridges. (b) Implementation of Loop with Bridges on STCA.

clockwise in it, and when a signal arrives at a Bridge, the signal tries to interact with a signal in the neighboring loop at the other side of the Bridge. A signal in a loop can assume one out of a total of four states. At its default, a signal has state [illegible], indicating that no information is present. To encode information in a signal we use the other three signal states, which we call [illegible]. The first of these is state [illegible], which is used as a general-purpose information carrier. The second and third of the computational states are [illegible] and [illegible]. Signals in these states are designed with the functionality of logic elements or crossovers of wires in mind. Signals in two loops interact with each other if one signal happens to be at one side of a Bridge and at the same time the other signal is at the other side. The basic interactions of signals in different states are as follows:

- If a signal in state [illegible] meets with a signal in state [illegible] ($i = 0, 1, 2$), then the states of the signals are exchanged.
- If two signals in state [illegible] meet each other, then one signal changes its state to [illegible] and the other to [illegible].
- If a signal in state [illegible] meets with a signal in state [illegible], then both signals will change their states to [illegible].

3.2 Wires and Membranes

Loops form a homogeneous space at which signals interact with each other, but in order to conduct useful computations, a structure should be imposed on this space. Wires are formed on the space of SRLs through defining [illegible] cells, which separate the inside of wires from their outsides. Sheath cells assume one of three states $\{+, -, =\}$. In its basic form, a wire has $+$ cells at one side and $-$ cells at its other side (Fig 5). A wire is able to dynamically expand when it has insufficient capacity for its signals, for example due to the presence

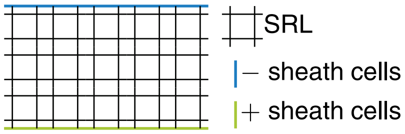

Fig. 5 Wire based on SRLs

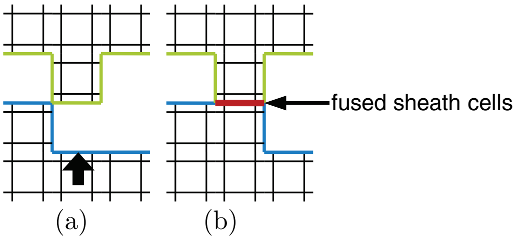

Fig. 6 Two wires getting in contact by expanding

of an SRL with a defect in it. Such a defect is detected through the failure of the SRL to circulate its signal through it. This failure will render the SRL incapable to react to external signals, which in turn will trigger the production of expansion signals emanating from the SRL. Expansion signals will push the sheath cells of the wire towards the outside, thus creating additional room for signals to pass through. Expansion may continue up to the point that the + sheath of one wire gets in contact with the − sheath of an adjacent wire, and in this case the + sheath and − sheath are fused at their contact areas, resulting in a sheath in state = (Fig. 6).

Another element imposing structure on a homogeneous space of SRLs is a so-called [illegible]. Signals in neighboring loops but separated by a membrane have interactions that are more complicated than the interactions described in section 3.1 between the signals in adjacent SRLs. The effects that membranes have on signals and their states appear as if the signals pass through the membranes, whereby the signals change their states. There are three types of membrane: a-membranes, b-membranes, and c-membranes. Fig. 7 shows the interactions of signals through membranes. An a-membrane is used to pass a [illegible] signal in one direction when the signal at the other side of the membrane is in state [illegible] (see Fig. 7(a)). One possible use for an a-membrane is as a ratchet for [illegible] signals. The other membranes also let signals pass through, and in the process change signal states in specific ways (Fig. 7(b) and 7(c)). However, these membranes differ from a-membranes by being reversible.

3.3 Logic Elements

Logic elements are constructed by combining membranes in appropriate ways. Fig. 8(a) shows the construction of a crossover element. When a [illegible] signal arrives at the port 'N', it passes through the b membrane and results in a [illegible] signal inside the crossover element (see Fig. 7(b)). This signal will eventually pass through the membrane at the element's 'S' port, thereby changing its state back to [illegible]. Passing a signal from port 'W' to 'E' or back works in the same way, except that the intermediate state of the signal inside the crossover element will be [illegible].

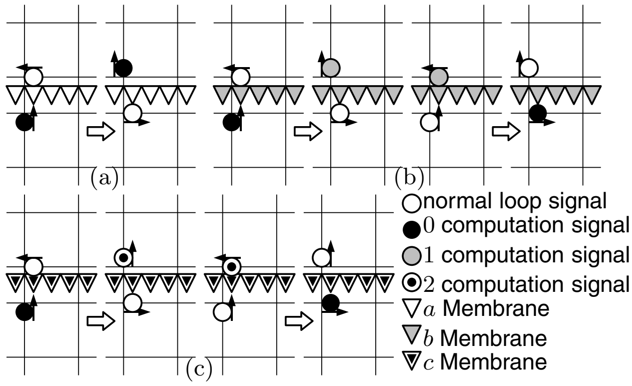

Fig. 7 Signal moving through membranes.

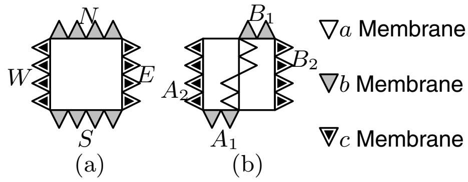

Fig. 8 Logic elements constructed by membranes. (a) Crossover and (b) Conservative Join

The construction of the Conservative Join is shown in Fig. 8(b). When each of the ports 'A_1' and 'A_2' receives a [illegible] signal, the signals are transformed into a [illegible] signal and a [illegible] signal, respectively, after passing through the membranes of 'A_1' and 'A_2'. Once the signals are in the left chamber of the Conservative Join, they are unable to pass through the membrane in the center, unless they react with each other. As a result of the reaction of a [illegible] signal with a [illegible] signal, we get two [illegible] signals in the left chamber, and only then these signals can pass through the center membrane to the right chamber. Once in the right chamber, the two [illegible] signals may return to the left chamber via the center membrane. However, they also have the choice to stay in the right chamber and recombine into one [illegible] signal and one [illegible] signal, which can only leave the right chamber via the membranes of port 'B1' and port 'B2' respectiveley, thereby outputting one [illegible] signal at each of these ports.

Table 1 Symbols encoding the states of cell partitions

0	1	2	3	4	5	6	7	8
	○	●	◍	🟦	□	🟩	🟥	■

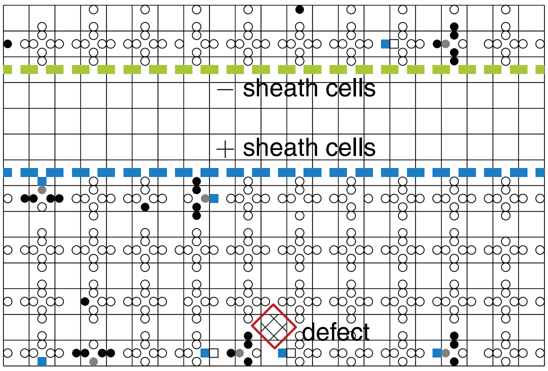

(a) Wire with defect in it at center bottom

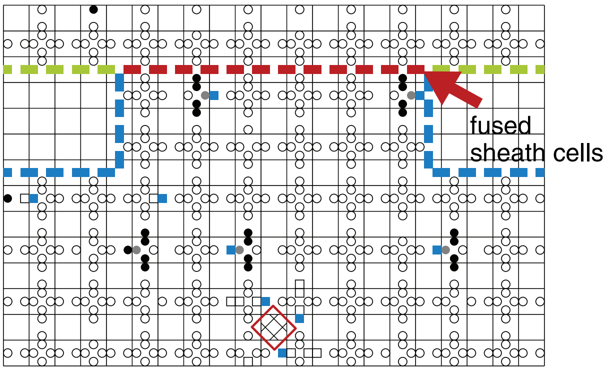

(b) Wire after expansion primed by the defect

Fig. 9 Wire configuration on an STCA

4 STCA implementations

Implementations of components described in the previous section are presented in this section. In the underlying STCA model, each cell partition can be in one of the 9 states indicated by the symbols shown in Table 1.

Fig. 9(a) shows two transmission wires implemented on the STCA, where the lower wire contains one defective SRL. As a result of expansion signals arriving at + sheath cells above the defect, the transmission wire expands up to the point that both wires get in contact with each other, after which the cells at the boundaries change their states to '=' (Fig. 9(b)). The STCA implementations of the crossover element and the Conservative Join are shown in Fig. 10.

5 Conclusions and Discussion

We have presented a computational model based on SRLs. The ability of SRLs to exchange signals in all directions fits well with the fluctuation-based nature of the underlying Brownian circuit model. The proposed model is robust to defects on account of the redundancy inherent in the use of multiple SRLs and in the expandability of wires. The proposed system is implemented on a 9^4 state-STCA with 362 transition rules. Simulations have shown the model to work correctly.

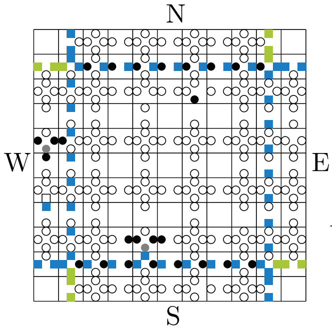

(a) Crossover

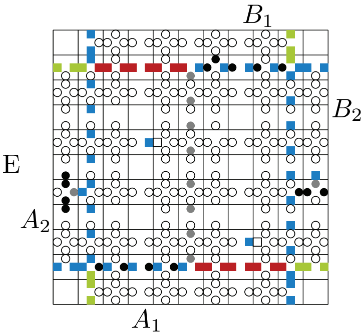

(b) Conservative Join

Fig. 10 STCA implementations of logic elements

References

[1] F. Peper, J. Lee, S. Adachi, and S. Mashiko. Laying out circuits on asynchronous cellular arrays: a step towards feasible nanocomputers? [illegible], 14:469–485, 2003.

[2] T. Kunieda, T. Isokawa, F. Peper, A. Saitoh, N. Kamiura, and N. Matsui. Reconfiguring Circuits Around Defects in Self-Timed Cellular Automata. In [illegible], pages 200–209, 2008.

[3] C. G. Langton. Self-reproduction in cellular automata. [illegible], 10:135–144, 1984.

[4] J. Lee and F. Peper. On brownian cellular automata. In [illegible], pages 278–291, UK, 2008. Luniver Press.

[5] Y. Takada, T. Isokawa, F. Peper, and N. Matsui. Asynchronous self-reproducing loops with arbitration capability. [illegible], 227:26–35, 2007.

The Fifteenth International Symposium on Artificial Life and Robotics 2010 (AROB 15th '10),
B-Con Plaza, Beppu,Oita, Japan, February 4-6, 2010

Management of Experience Data for Rapid Adaptation to New Policies based on Bayesian Significance Evaluation

Saifuddin Md. Tareeq and Tetsunari Inamura
The Graduate University for Advanced Studies, National Institute of Informatics, Japan
smtareeq@nii.ac.jp;inamura@nii.ac.jp

Abstract

This paper shows a rapid learning method of behavior policy for mobile robots teleoperated by an operator. Rapid policy adaptation cannot be achieved when data from every process cycle is used for learning because important and meaningful data are not differentiated with other data. We propose a method to solve the problem by selecting significant data for the learning based on change in degree of confidence of the behavior decision. A small change in the degree of confidence can be regarded as reflecting insignificant data for learning, so that data can be discarded. Accordingly the system can avoid having to store too much experience data and the robot can adapt rapidly to changes in the user's policy. In this paper we discuss the experimental result of an experiment in which user policy changes between 'avoid' and 'approach' on a mobile robot.

Keywords: Bayesian Network, Rapid Adaptation, Degree of Confidence

1 Introduction

One of the important abilities for personal service robots which act in real environment with human beings is to learn and acquire novel behavior strategy according to observation of users' behavior. To learn the behavior strategy, conventional methods observes sets of sensor input and command output, extracts meaningful relation between the sensor and commands using statistical methods. But the performance of the learning strongly depends on the quality of the dataset of sensor and command. When the dataset included important and meaningful experience data, the learning would be a success; however it is difficult to obtain sophisticated experience dataset for human-robot interaction in real world, because the robots basically stores the dataset in every process cycle. For example, when a user kept operating same command in same situation, the statistical learning procedure tends to output the frequent command even though the sensor is not the frequent but rare. To select the rare command for rare sensor, the system should ignore insignificant frequent dataset to avoid bad learning quality. In this paper, we propose a technique to manage experience dataset with evaluation of significance of the dataset based on a concept of change in degree of confidence for behavior decision. A small change can be regarded as an insignificant data for learning, so that data will be discarded. Accordingly, the system can avoid having to store too frequent experience data.

Conventional methods like window [1][2] based adaptation require background investigation of the domain to find a suitable window, dual model [3][4] based methods uses separate model for short term and long term learning but are unsuitable for rapid adaptation with long term model, interaction [5][6][7] based methods does not deal with adaptation with user policy but only with acquiring user policy.

Bayesian network is suitable to represent policy, because sensor and command can be represented even though the observation of the user is not well conducted and also it can output a degree of belief for behavior decision based on observation of sensor as evidence. Conventional simple belief calculation based on frequency of the dataset causes the problem that the system tends to output the most frequent command even though sensor input for rare situation is given, when the dataset observed continuously during the human-robot interaction. The problem arises because the prior probability is calculated using the numbers of observations. This factor also causes another problem that the robot cannot adapt rapidly to changeable policies of the user. We adopt Dirichlet distribution to evaluate the significance of data. The Dirichlet distribution represents not only event probability among several propositions, but also degree of confidence for the output probability just referring a set of number of observation for the propositions. The system calculates the degree of confidence before and after the current observation. The change in the two degrees of confidence can be regarded as the importance of the observation to the learning process.

2 Bayesian Network and Significance Evaluation

2.1 Bayesian network

A Bayesian network is a directed acyclic graph consists of parent nodes representing causes and child nodes representing effects as shown in Fig. 1. Each node has a propositions assigned to it which might have several values. The activation of a proposition is represented probabilistically, and as a result, each node has a stochastic variable. Specifically, sensor information in the robot, the behavior that the robot is to perform, and the content provided by a person are assigned to a node. The relationship among nodes is described using conditional probabilities with stochastic variables.

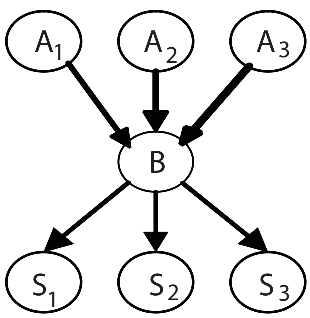

Figure 1: A Bayesian network

Let us denote a stochastic variable for a particular node B with the propositional symbols $b_1, b_2, \ldots, b_m$ by $B = \{b_1, b_2, \ldots, b_m\}$. The set of parent nodes connected from above to this node is $\mathbf{A} = \{A_1, A_2, \ldots, A_k\}$, and the space consisting of a combination of each value for the stochastic variables is $\mathbf{a}_1, \mathbf{a}_2, \ldots, \mathbf{a}_l$. The reasoning can be expressed

$$Bel\left(B\right) = \beta\lambda\left(B\right)\pi\left(B\right), \tag{1}$$

where $\lambda(B)$ represent the current strength of diagnostic support contributed by the children of B given by $\prod_i \lambda_i(B)$, $\pi(B)$ represent the current strength of the causal support contributed by the parents of B and β is the coefficient for normalization. Elements of $Bel(B)$ indicate the plausibility for each proposition of the behavior node. One of the advantages of Bayesian networks is that a robot can evaluate the vagueness of a behavior decision, and this leads it to ask questions and give suggestions to users [5]. For example, the robot should ask the user to confirm the behavior decision when the elements of $Bel(B)$ are almost equal.

2.2 Conventional Method

Suppose that B represent a behavior node and it does not have any parent nodes $\mathbf{A}$ in Fig. 1 and $\mathbf{S}$ represent sensor nodes. The robot observes the human's behavior b_j and gathers the sensor information $\mathbf{d}_i$ at the same moment. Let $\mathbf{v}[t]\epsilon\{\mathbf{d}_1, \mathbf{d}_2, \ldots, \mathbf{d}_n\}$ be the observation of the sensor at time t. Let $o[t]\epsilon\{b_1, b_2, \ldots, b_m\}$ be the observation of the user's behavior at time t. The sensor observation vector is written as $\mathbf{V}[t] = \{\mathbf{v}[1], \mathbf{v}[2], \ldots, \mathbf{v}[t]\}$ and user instruction vector as $\mathbf{O}[t] = \{o[1], o[2], \ldots, o[t]\}$. Then, we can define data as $\mathbf{D}[t] = \{\mathbf{V}[t], \mathbf{O}[t]\}$. Let N be the number of observed data, N_j the number of observations of behavior b_j, and n_{ij} the number of observation of data when d_i is observed with b_j. One of the simplest calculations based on the observation is

$$P\left(\mathbf{d}_i|b_j\right) = P\left(S = \mathbf{d}_i|B = b_j\right) = \frac{n_{ij}}{N_j}, \tag{2}$$

$$P\left(b_j\right) = \frac{N_j}{N}, \tag{3}$$

A problem arises with this simple calculation when the data $\mathbf{D}[t]$ is continuously input during the observation. Suppose that the propositions of behavior b_1 and b_2 are set in the behavior node. When a rare but important operation b_2 is observed even though N_2 is smaller than N_1 the prior probability $P(B = b_2)$ is close to 0 while $P(B = b_1)$ is close to 1. The problem arises because the prior probability is calculated using the numbers of observations. We propose an approach in which the important observation is selected on basis of the change in the degree of confidence. When the change in confidence in two consecutive time steps is small, this situation is regarded as familiar; the experience data is considered insignificant to be discarded. In contrast, when the robot detect a large change in confidence in two consecutive time steps, this situation is considered unfamiliar; the experience data is considered significant to be accepted. The next section discusses an algorithm to distinguish the above two cases.

2.3 Proposed method

We use a Dirichlet distribution to evaluate the significance of data based on changes in the degree of confidence. A m-directional Dirichlet distribution for $x = \{x_1, x_2, \ldots, x_m\}$, is given by

$$f_d\left(\mathbf{x}; \alpha_1, \ldots, \alpha_m\right) = \frac{1}{Z}\prod_k x_k^{\alpha_{k-1}}, \tag{4}$$

where,

$$Z = \frac{\prod_{k-1}^{m} \Gamma(\alpha_k)}{\Gamma\left(\sum_{k-1}^{m} \alpha_k\right)}, \tag{5}$$

is a normalization factor, Γ is the gamma function and the parameters α_m are assumed to be positive. The Dirichlet distribution parameters are expressed in terms of observations of different behaviors for example $\alpha_1 = 1 + N_1$. The system increases one Dirichlet parameter α_1 by observing behavior b_1. When α_1 becomes larger than the other Dirichlet parameters, the peak of the distribution moves within a small area at the end of corresponding variable as shown in Fig. 2.

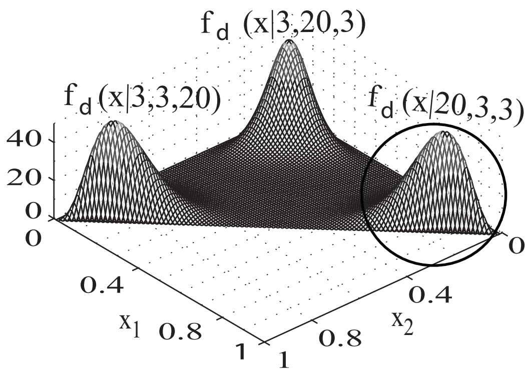

Figure 2: Dirichlet density functions with peak moved to the corresponding parameter

The system calculates the degree of confidence before and after the current observation. Confidence at time t is calculated as

$$C_t = \int_{\Delta} f_d\left(\mathbf{x}; \alpha^t\right) d\mathbf{x}, \tag{6}$$

where $f_d\left(\mathbf{x}; \alpha^t\right)$ is the Dirichlet distribution at time t and Δ represents area of integration where the peak of the distribution is moved like the area inside the circle in Fig. 2. The change in the two degrees of confidence can be regarded as the importance of the observation to the learning process. To evaluate the significance of the observation data, the criteria

$$E = C_t - C_{t-1}, \tag{7}$$

is calculated. Data $\{\mathbf{V}_i[t], \mathbf{O}_i[t]\}$ are accepted when $E \geq \theta$, and data are discarded when $E < \theta$. θ should be set according to required rapidness of the learning because significance of data can be controlled with θ. For example, an application with a very high input frequency will likely have a different threshold (a lower one) from one with a very low input frequency (relatively higher) for adapting to the user's new preference. For rapid adaptation, the area and threshold should be empirically determined by experimentation.

3 Experiment and Result

3.1 Experimental Setup

We developed a teaching and learning system in a virtual environment that incorporated our concept. The environment, as shown in Fig. 3 was prepared using webot real-time simulation software. The environment had an enclosed area of 8 [m]× 8 [m]. A static square obstacle whose size was 1 [m]× 1 [m] was placed inside the area. The user interface consisted of a lever joystick and the user controlled the robot by using it. We taught two policies to the robot, avoid and approach, in the field. In the experiment, we used a Bayesian network consists of eight distance sensor nodes and a behavior node as in Fig. 4.

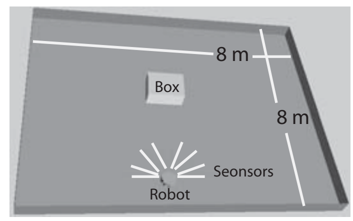

Figure 3: Virtual experimental environment

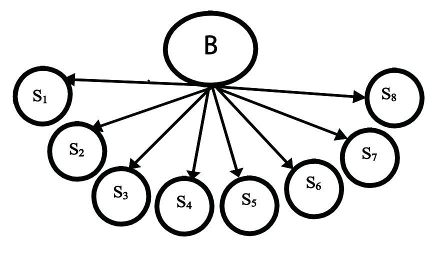

Figure 4: A Bayesian network used in the experiment

The robot model had eight front laser distance sensors (S_i,$i = 1, 2, \ldots, 8$) mounted on the front to measure the distance to obstacles along a horizontal line parallel to the floor. Joystick inputs were translated into discrete instructions by using a predetermined threshold. We found [8] that area of integration was inversely proportional and threshold value was directly proportional to the time required reach the discarding criteria respectively. Therefore we set the area of integration to the maximum non-overlapping area and the threshold to 1.0×10^{-6}.

The user can teleoperate the robot at any time and halt operation temporarily for changing robot orientation in the virtual environment. When user do not operate the robot, it operates automatically with it's own degree of confidence for behavior node. Previously we have shown that our algorithm can adapt to the user preference rapidly [8]. In that paper we have shown that robot adapted to user preference like go forward, turns left or turn right. In this experimental setup user policy correspond to robot behavior, avoids and approach. Avoid policy is accomplished by going forward when there is no obstacle and turning left when there is an obstacle. Approach policy is accomplished by going forward when there is no obstacle and approaching the obstacle when there is one.

3.2 Experimental Results

The user first taught avoid policy twice. The user then changed the policy and approached the obstacle. Fig. 5 shows the changes in probability of degree of confidence during teleoperation. When the user changed the policy from avoid to approach around step 250 the system could override the previous policy just after step 300 and the robot could rapidly adapted to the new policy.

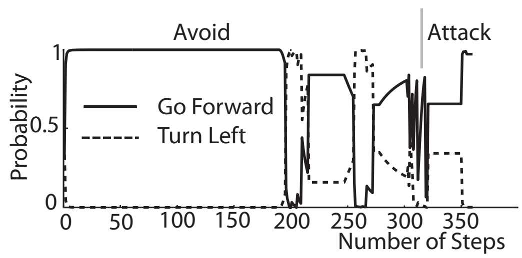

Figure 5: Probability of behavior during policy adaptation

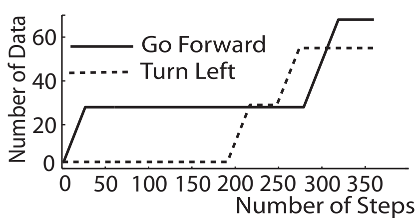

Figure 6: Number of data in the secondary database during policy adaptation

Fig. 6 shows the number of data evaluated as significant and kept in secondary database. The number of data in the secondary database is increased until the change in the degree of confidence was low for any user behavior. Flat part represents when data is evaluated as insignificant and discarded or the robot operate automatically. Here we observe that data is kept for one go forward and two turn left behavior for avoid policy. And when policy is changed the system accepted data for approach and overridden policy around after steps 300.

4 Conclusions

Experimental results show that proposed method can adapt to user's policy change based on significance evaluation using change in degree of confidence. The novel point of the method is that the policy adaption depends on the number of selected significant data rather than enormous amount of observed data. Currently, significance evaluation is done on the behavior node. We are considering significance evaluation for each sensor proposition of every sensor node. This will ensure that only significant sensor observation will be used for learning and that will make our system more robust.

References

[1] Widmer G. and Kubat M., *Learning in the Presence of Concept Drift and Hidden Contexts* in Machine Learning, **23**, 69-101, 1996.

[2] Klinkenberg R., *Learning Drifting Concepts: Example selection vs. Example weighting* in Intelligent Data Analysis, Special Issue on Incremental Learning Systems Capable of Dealing with Concept Drift, **8**(3), 281-300, 2004.

[3] Billsus D. and Pazzani M. J., *User Modeling for Adaptive News Access* in User Modeling and User-Adapted Interaction, **10**, 147-180, 2000.

[4] Chiu P. and Webb G., *Using Decision tree for Agent Modeling; Improving Prediction Performance* in User Modeling and User-Adapted Interaction, **8**, 131-152, 1998.

[5] T. Inamura, M. Inaba and H. Inoue, *PEXIS: Probabilistic Experience Representation Based Adaptive Interaction System for Personal Robots* in Systems and Computers in Japan, **35**(6), 98-109, 2004.

[6] T. Inamura, M. Inaba and H. Inoue, *User Adaptation of Human-Robot Interaction Model based on Bayesian Network and Introspection of Interaction Experience* in Proc. of Int'l Conf. on Intelligent Robots and Systems (IROS 2000), 2139-2144, 2000.

[7] M. Nicolescu and M. Mataric, *Learning and interacting in human-robot domains* in IEEE Transactions on System in Man and Cybernetics-Part A: Systems and Humans, **31**(5), 419-430, 2001.

[8] Tareeq S. M. and Inamura T., *A sample discarding strategy for rapid adaptation to new situation for Bayesian behavior learning* in Proceedings of the IEEE International Conference on Robotics and Biomemtics, 1950-1955, 2008.

A robust control of mobile inverted pendulum using single accelerometer

Hyunuk Ha, Sungmin Ryu, Jangmyung Lee (Dept. of Electrical engineering, Pusan National University, Korea)

(Tel : +82-51-510-1696; Fax : +82-51-514-1693)
(hhook@pusan.ac.kr, smryu@pusan.ac.kr, jmlee@pusan.ac.kr)

Abstract: This paper proposes a single accelerometer sensor control algorithm to mobile inverted pendulum(MIP), generally called 'Segway', and evaluates the performance of this system comparing to the conventional ones. The commercialized 'Prototype Segway-PT' is initially considered as a next-generation transport vehicle. However, this robot is operated by three gyroscopes and two accelerometers to control the posture and speed, and it requires the complex signal processing for fusing the two sets of data. As the result of this, the growth rate of market size of 'Segway' is slow because of its high price mainly. In this paper, the MIP is operated by a single accelerometer to simplify the control system to lower the price. Low pass filter is one of the good sensors to reducing the variation of an accelerometer, but it has time delay. This time delay disturbs real-time control. Like this, other various algorithms are used for this system, but each one has their own weak points. So this paper proposes a new accelerometer filtering method, median filter and EKF. Median filter is used to image processing to reject impulse elements like 'salt & pepper noise'. As the major performance evaluation parameter for the accelerometer, the high-frequency to low frequency ratio from FFT(Fast Fourier Transform) and PSD(Power Spectral Density) are used. Effectiveness of the proposed algorithms has been verified and demonstrated through the simulations using matlab and real experiments for a MIP.

Keywords: Segway, Mobile inverted pendulum, accelerometer, performance evaluation, filter

I. Introduction

The mobile inverted pendulum(MIP), generally called 'Segway' is invented by Dean Kamen in 2001 for commercial use[1]. At that time, 'Segway' is considered as next-generation transportation. Conventional transportation method by that time guaranteed the stability along the pitch direction by the position of the wheels which is placed at the front and the rear, but the wheels of the 'Segway' is placed by the side of the robot body[2]. The 'Segway-PT' use five gyroscopes and two tilt sensors to sensing the angle of robot body's slope. By the two kinds of sensor information, robot can real-time calculate the alternation of COG(Center Of Gravity), then moving from the combined information of the knob, which determine the direction, and the angle calculated as above sequences.

Commercialized 'Segway' use sensor fusion of multiple gyroscopes and tilt sensors, 'Segway' is relatively experience to be a next-generation transporter. The MIP is well researched for partial feedback linearization method[3] and iterative impulsive control[4], and so on. But these researches is biased to control algorithm fields, and this is initially assume that multiple sensor fusion algorithm. These factors make 'Segway' is lack of sociality, nevertheless it has a strong advantage like unnecessariness of a special skill like bicycle.

This paper proposed a new single accelerometer filtering algorithm to control MIP. Median filter, popularly used in image processing, and EKF(Extended Kalman filter) was used to reduce the fluctuation noise of the accelerometer signal.

This paper is consist of six-sections including introduction. In section 2, the shortcoming of LPF(Low Pass Filter) for the accelerometer, a time delay caused by time constant and lack of robustness, and theoretical back ground of signal processing of accelerometer, median filter and EKF as mentioned above, is stated. Section 3 shows the simulation and experimental results. Section 4 describes the performance evaluation by spectrum analysis using FFT(Fast Fourier Transform) and PSD(Power Spectral Density). In section 5, experimental environment and simulation tool, fda-tool(A filter design and analysis GUI tool) of provided by matlab, was described, and compare conventional block diagram of MIP and proposed one. In section 6, detail conclusion is described by quantitative analysis based on section 5, verified simulations and real experimental results.

II. Single accelerometer filtering algorithm

Conventional MIP control method is sensor fusion of multiple gyroscopes and tilt sensors for reliable angle information. Gyroscope is robust for the external disturbance by the structural characteristics. But generally, gyroscope has many demerits, 1. Truncation error caused by limited sampling period or limited bits for resolution of A/D converter. 2. Non-linearity of conversion factor by the temperature. 3. Feasible modeling error caused by G-sensitivity. 4. The gap of angular velocity information mean and 0(integrate infinitely and this unbiased information lead to accumulate of angle signal), generally called bias drift[3]. This gyroscope error signal is accumulated as time goes on. By this reasons, commercialized 'Segway' use sensor fusion algorithm to estimate angle. For another sensor, tilt sensor is weak for the external disturbances so if there exist disturbances over the fixed threshold, the robot operates as a hardware amplifier, so sometimes it's diverging. The most common filtering method for reducing this variation is LPF. But LPF has its own time delay caused by time constant, essentially exist during designing a LPF. This time delay makes MIP hard to real-time control, so LPF has some restrictions to apply for single accelerometer signal processing. Figure 1 illustrates the shortcoming of LPF for mobile inverted pendulum.

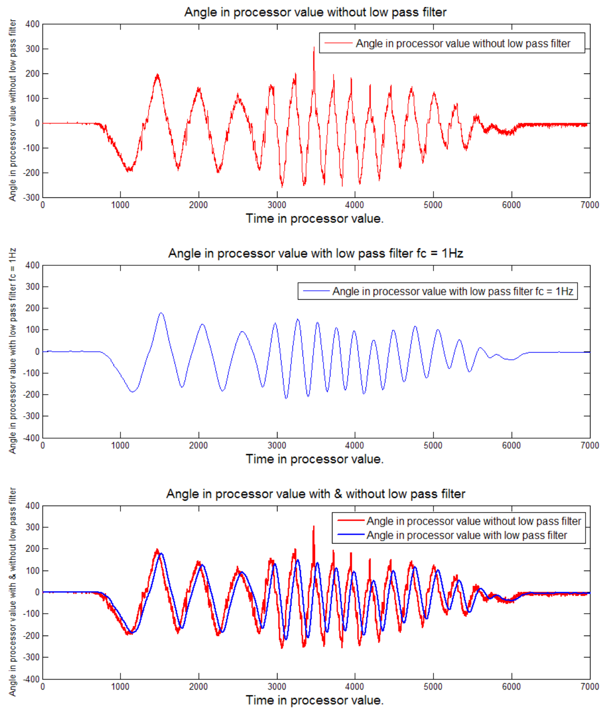

Fig. 1. Shortcoming of low pass filter for mobile inverted pendulum

Figure 1.a. shows the accelerometer signal without filter. It has many variations having high frequency. Figure 1.b. displays the accelerometer signal after 10th order LPF. Figure 1.c. illustrates both signal stated above. After LPF signal doesn't have high frequency information but has time delay comparing with original signal. So LPF is not suitable for real-time controller like MIP.

This paper proposed a new real-time accelerometer noise & variation reduction algorithm, median filter and EKF, one of the most effective adaptive filter. The theoretical back ground of these two method is described next section.

2.1. Median filter

Median filter is well known as a most effective filter to removing AWGN widely distributed in frequency domain, especially removing 'salt & pepper noise' which has impulsive noise in image processing. The window of median filter can be adjusted as various formulations. But the accelerometer signal is real-time one dimensional signal, so set up a horizontal window. Median filter algorithm as stated above is simply realized as figure 2.

```
For cnt1=0,… N1          // N1 is variable window size
    For cnt2=cnt1+1,… N1 +1
        If  ( accelerometer[cnt1] > accelerometer [cnt2] )
            temporary value   =  accelerometer[cnt1];
            accelerometer[cnt1] =  accelerometer[cnt2];
            accelerometer[cnt2] =  temporary value;
        End if
    End for
End for
```

Fig. 2. Median filter algorithm

Figure 3 illustrates the results for median filter applied to single accelerometer.

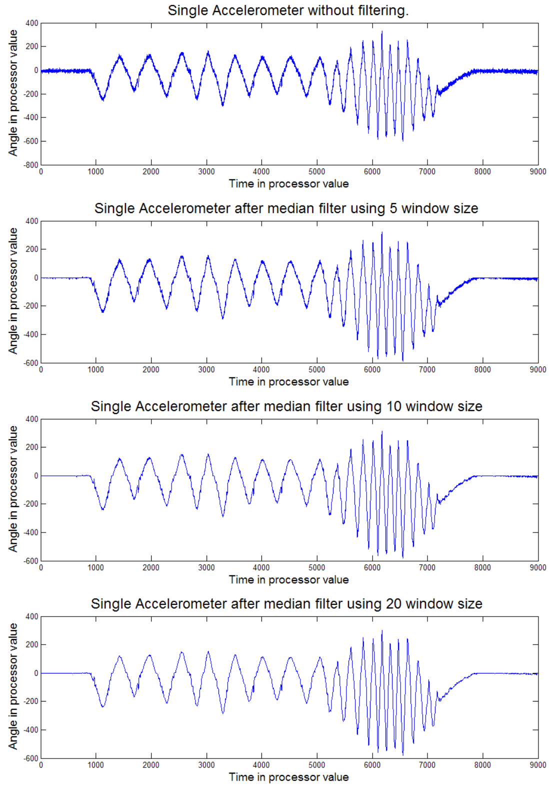

Fig. 3. Results of median filtering for the various window size(0,5,10,20).

2.2. EKF(Extended Kalman Filter)

EKF is described below in equation 1. EKF is consist of time update process and state update process iteratively, during these sequences, if the system is not deterministic, but noise is Gaussian distributed, then this algorithm can find local optimal solution(s).

Time update equation(predict)

$$\hat{x}_k^- = f(x_{k-1}, u_k, 0) \quad (1.a)$$

$$P_k^- = A_k P_{k-1} A_k^T + W_k Q_{k-1} W_k^T \quad (1.b)$$

Measurement update equation(correct)

$$K_k = P_k^- H_k^T (H_k P_k^- H_k^T + V_k R V_k^T)^{-1} \quad (1.c)$$

$$\hat{x}_k = x_k^- + K_k (z_k - H(x_k^-, 0)) \quad (1.d)$$

$$P_k = (I - K_k H_k) P_k^- \quad (1.e)$$

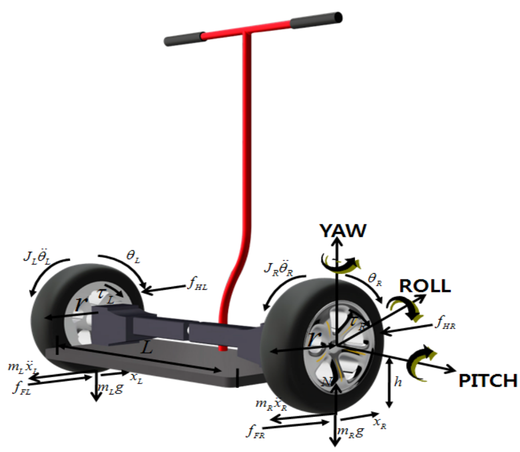

Figure. 4. Modeling of mobile inverted pendulum for EKF.

III. Experimental results

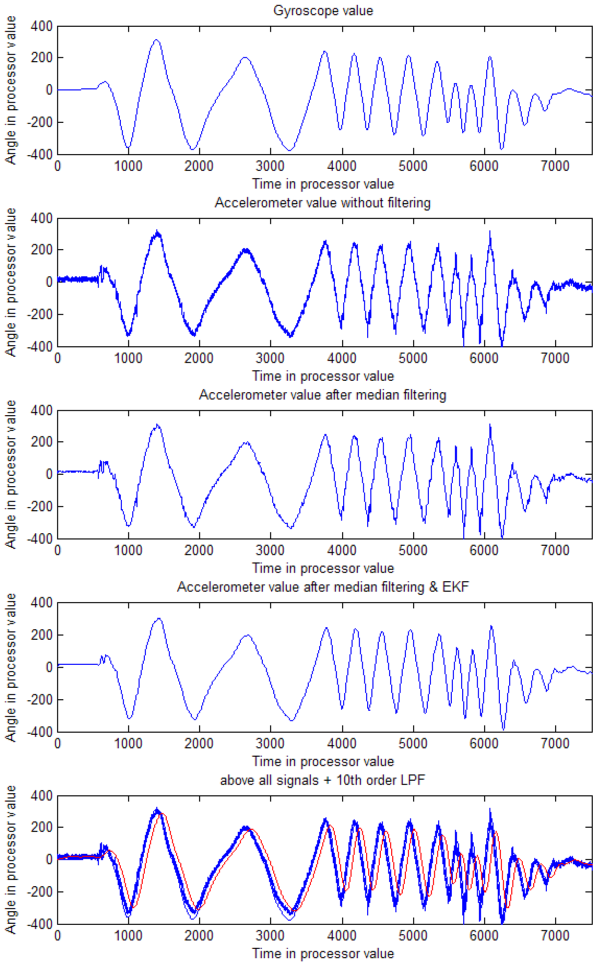

Fig. 5.a. Compensated gyroscope signal. Fig. 5.b. Accelerometer signal without filtering. Fig. 5.c. Accelerometer signal after median filter only(Window size = 20). Fig. 5.d. Accelerometer signal after median filter and EKF. Fig. 5.e. Above 4 signals and 10^{th} order LPF signal which have some time delay.

Figure 5 shows the experimental results for proposed algorithm and LPF. Figure 5.a. shows the compensated gyroscope signal. It's smooth and considered as reference when performance evaluation. Figure 5.b. shows raw accelerometer signal has many variation and weak for external disturbances. Figure 5.c. illustrates accelerometer signal after median filtering, high frequency, impulsive noise, is removed out. Figure 5.d. displays an accelerometer signal after median filter and EKF, which is similar with reference, compensated gyroscope signal. Figure 5.e. shows above 4 signals and LPF signal. Above 4 signal has almost same except for variation, but 10^{th} LPF signal(red line) has time delay caused by time constant.

IV. Performance evaluation

4.1. Spectrum analysis using PSD(Power Spectral Density)

In this paper, performance evaluation parameter is selected as spectrum analysis using FFT and PSD. Figure 6 illustrates the PSD of accelerometer signals applied various window size(0,5,10,20) of median filter.

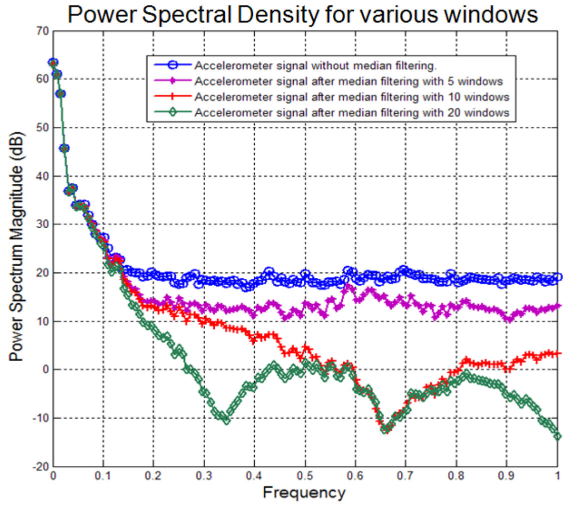

Figure 6. PSD of various window size of median filter.

4.2. Spectrum analysis using FFT(Fast Fourier Transform)

In figure 7, FFT signal of raw accelerometer signal, median filtered signal, and median filter and EKF signal are shown, respectively.

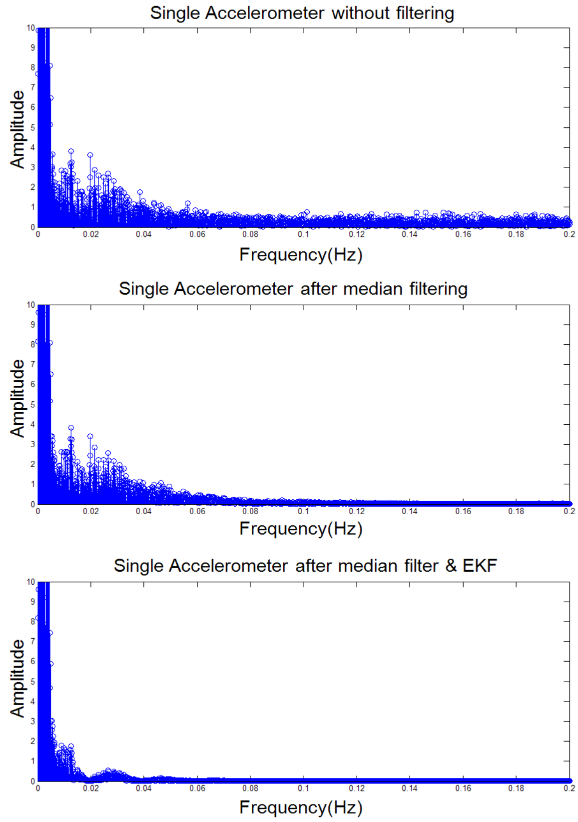

Fig. 7.a. FFT signal of without filtering. Fig. 7.b. FFT signal of median filtering with 20 window size. Fig. 7.c. FFT signal of median filter & EKF.

V. Simulation & Experiment

4.1. Mobile inverted pendulum block diagram

Conventional operating block diagram when using only PID controller is illustrated in figure 8.

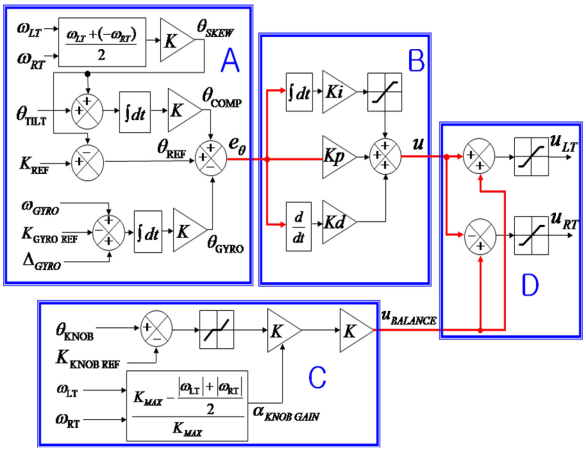

Fig. 8. Conventional operating algorithm of MIP.

A block of figure 8 is sensor fusion, between gyroscope and accelerometer, algorithm using 'kalman filter'. DC information of gyroscope signal is rejected and integrated to calculate gyroscope angle. And accelerometer is used for compensatin the accumulated drift error of gyroscope signal. In figure 10, proposed block diagram is shown. A-block is replaced with median filter and EKF.

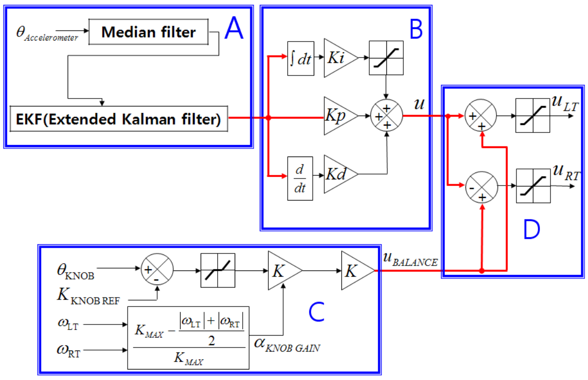

Fig. 9. Proposed operating algorithm of mobile inverted pendulum using single accelerometer.

VI. Conclusion

Conventional mobile inverted pendulum uses sensor fusion algorithm between multiple gyroscopes and accelerometers to calculate real-time angle. Single gyroscope control has accumulated drift error, and this cause divergence in future, as stated in section 2. And single accelerometer has a fatal shortcoming, weak for external disturbances. This paper proposed a new accelerometer filtering algorithm, median filter and EKF(Extended Kalman filter), and verify through simulations using matlab and real experiment. 'Segway' must cost reduce to be a next-generation transporter. For this aspect, single accelerometer filtering algorithm is essential for 'Segway'. Research on single accelerometer filtering algorithm for cost reduction and sensor fusion for performance improvement must be progressed concurrently. Future research topic on mobile inverted pendulum is, 1. Optimal controller design for a single accelerometer. 2. Study on predictive control method to reduce the response time and robust for the disturbances. 3. Cooperation control between mobile inverted pendulum and humanoid robot shown in figure 10, and so on. And performance evaluation method to be added is, Cross-correlation algorithm and RLMS(Recursive Least Mean Square) to calculate the difference between compensated gyroscope signal, as we think reference, and single accelerometer signal applied proposed algorithm.

Fig. 10. Cooperation control scheme between MIP and humanoid robot.

Acknowledgement

This work was supported (in part) by Ministry of Knowledge Economy under Human Resources Development Program for Convergence Robot Specialists.

REFERENCES

[1] http://www.segway.com/

[2] F. Grasser, A. D'Arrigo, S. Colombi "JOE: a mobile, inverted pendulum", *IEEE Transactions on industrial electronics,* vol.49, no.1, pp.107-114, Mar. 2002.

[3] Li Liang-qun, Ji Hong-bing,Luo Jun-hui "The iterated extended kalman particle filter", *in ISCIT,* vol.2, no.1, pp.1213–1216, Oct. 2005.

[4] K. Pathak, J. Franch, and S. K. Agrawal, "Velocity and position control of a wheeled inverted pendulum by partial feedback linearization", *IEEE Transactions on Robotics and Automation,* vol.21, no.3, pp.505–513, Jun. 2005.

Localization of multiple robots in a wide workspace

J.H. Park, W.S. Jang and J.M. Lee

Dept. of Electrical engineering, Pusan National University, Korea
(Tel : +82-51-510-1696; Fax :+82-51-514-1693)
(jae-hyun@pusan.ac.kr, masura0727@pusan.ac.kr, jmlee@pusan.ac.kr)

Abstract: This paper proposes a localization method for the multiple robots navigation in a multi-block workspace. Indoor localization schemes using ultrasonic sensors have been widely studied due to its cheap price and high accuracy. However, ultrasonic sensors have some shortages of short transmission range and interferences with other ultrasonic signals. In order to use multiple robots in wide workspace concurrently, it is necessary to resolve the interference problem among the multiple robots. This paper introduces an indoor localization system for concurrent multiple robots in a wide service area which is divided into multi-block for the reliable sensor operation. A beacon scheduling algorithm is developed to avoid the signal interferences and to achieve efficient localization with high accuracy and short sampling time.

Keywords: Localization, Multiple robots, Multi-block, Beacon scheduling, Block recognition.

I. INTRODUCTION

In order to perform the commands of humans, robots have to know their own positions and target position. For that reason, localization is one of the problems which are basic and important in robotics. Ultrasonic based localization is susceptible to environmental noises from their propagation characteristics and has decay phenomena when it is transmitted over a long distance. However, it has been widely used in the indoor environments since it is cheap, easy to be controlled and has high accuracy and repeatability. To use it in a wide area, multi-block consisted by a number of beacons is mainly used [1]. However, multiple robots localization in multi-block has some problems which are ultrasonic signal interferences and determination of sequence calling beacons [2]. This paper proposes efficient multi-block division for multiple robot localization in a wide area using Master/Slave robot division for beacon arbitration of robots and beacon scheduling algorithm for calling beacon without interference in ultrasonic signal with short sampling time.

II. MULTIPLE ROBOTS LOCALIZATION

1. **Problems Definition**

If there are more than two mobile robots in a same workspace, where consists of three or four beacons, they separately call different beacons for localization concurrently. And then all selected beacons send out ultrasonic signals at once. At this time, mobile robots cannot recognize which beacons send out a useful signal from beacon themselves called since TOF of ultrasonic from beacons is different and the robots recognizes a threshold value of the first arrival signal. Therefore, the robots do not know their own real positions due to measurement of wrong distance.

2. Master/Slave Robot

Only one robot is designated as the master robot and the other robots are designated as the slave robots. Master robot has a mission to call the specified beacon only and Slave robots respectively receive the ultrasonic signal from a specified beacon calling the master robot. The master robot considers max transmission time of ultrasonic because the arrival times of ultrasonic signal are different according to positions of the robots.

III. BEACON SCHEDULING

1. Beacon Scheduling

For localization without signal interference in a multi-block workspace which is divided in a detectable range, a round robin schedule is one of the simple methods. However, the round robin schedule is not suitable in a real time localization system which updates each position of robots in a fast period due to increasing a time to call all beacons as increasing the number of beacons. For that reason, efficient beacon scheduling algorithm needs to obtain the fast period for localization in a multi-block workspace. This paper proposes a new beacon scheduling algorithm applied a color code scheduling algorithm.

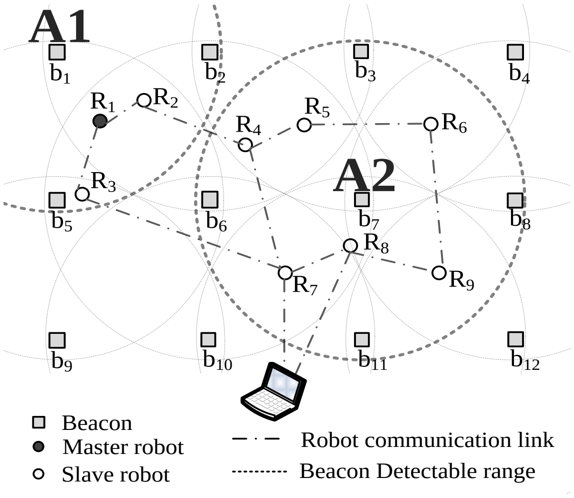

Fig.1. Basic structure of multiple robot localization in a multi-block workspace

2. Color Code Scheduling

Color code scheduling is the method that concurrently calls beacons without collision among signals based on the idea that ultrasonic signal does not collide out of their interference range. Color code scheduling is divided into three steps which are conflict graph, graph coloring and scheduling [2]. The first step is to draw a conflict graph considering beacon's position and ultrasonic interference range from the beacon. For example, b1 beacon in Fig. 2 is connected with b2, b5, b6 and b9 beacons with edge in Fig. 2-(a) because of overlapping the interference ranges shown in Fig. 1. With conflict graph about all beacons, the second step is to assign a color code to each beacon such that any two beacons with a conflict edge cannot have the same color. This paper uses a Welsh-Powell algorithm [4] to find the coloring solution with the chromatin number. Figure 2-(b) shows graph coloring with conflict graph in Fig. 2-(a). Finally, the third step is to make a color code schedule which is designated by different color codes in Fig 2-(c).

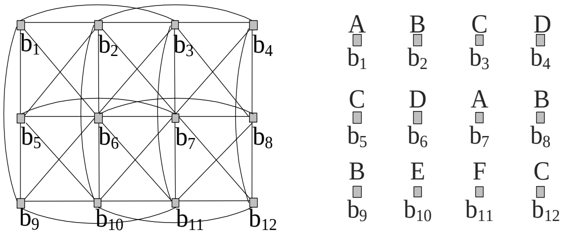

(a) Conflict graph (b) Graph coloring

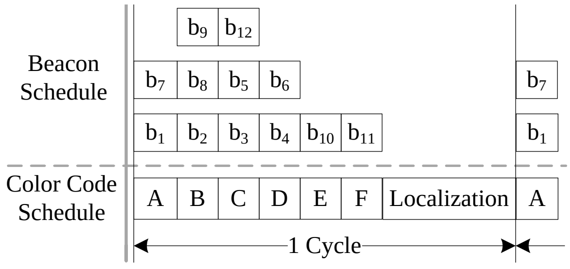

(c) Color code schedule

Fig.2. Color code beacon scheduling

3. New Color Code Beacon Scheduling

The conventional color code scheduling is able to concurrently call two beacons which never overlap the interference ranges. But, in case of ultrasonic localization system using threshold value, ultrasonic signal from the closed beacon always arrives firstly. In a multi-block workspace, therefore, some cases that are able to concurrently call beacons which overlap the interference ranges exist. For example in Fig. 3, a b1 beacon belong to block 1 overlaps the interference range of a b3 and b6 belong to block 2 only not to block 1. If b1 and b2 beacons concurrently call, R1 robot existed in the interference range of them always receives the ultrasonic signal from a b1 firstly. Hence, concurrently calling them will be possible. Considering the abovementioned problems, algorithm to draw a new conflict graph represents in Fig. 4.

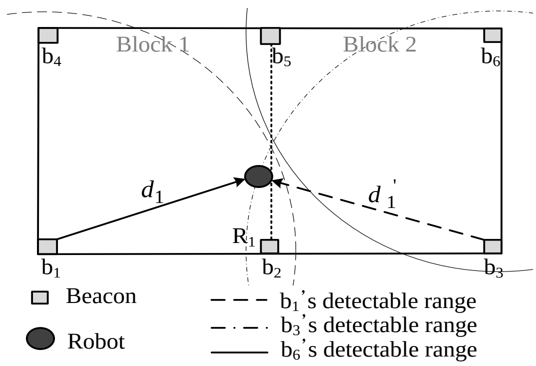

Fig.3. New conflict graph algorithm

```
Input : Coverage of each beacon C(bi) ( 1<= I <= Nb)
Output : conflict graph CG(Vb, E)
For each beacon i = 0, …, Nb
    For beacon i+1,…, Nb
        If ((C(bi) ∩ C(bi+1)) > 0)
            If(beacon ID(bi+1)∈ block of beacon bi Block(bi)
              && C(bi+1) != diagonal C(bi))
                CG[i][i+1] = 1;   // conflict
            else
                CG[i][i+1] = 0;
```



```
            End if
        else
            CG[i][i+1] = 0;
        End if
    End for
End for
```

Fig.4. New conflict graph algorithm

Figure 5 shows new color code beacons scheduling allows some interference with the position and the interference range of all beacons shown in Fig. 1.

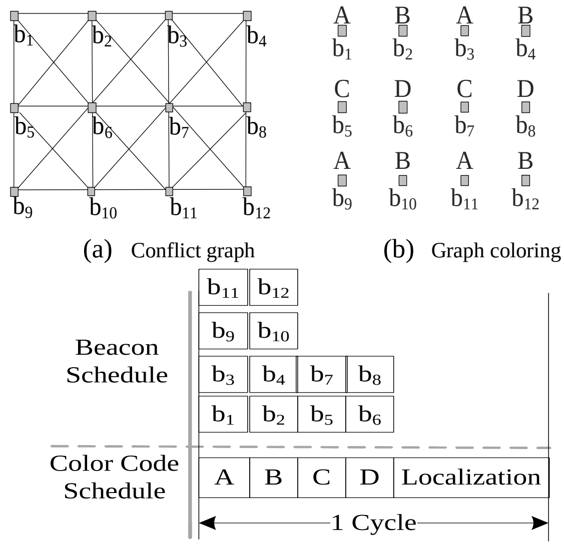

(a) Conflict graph (b) Graph coloring

(c) Color code schedule

Fig.5. New color code beacon scheduling

IV.BLOCK RECOGNITION

Existing block recognition method[1] for using new color code beacon scheduling can sometimes make problems that the robot estimates a wrong position shown in the Fig. 6. In case of color codes B and D, each range is overlapped, but it is assumed that it is possible to call them at the same time. When a robot is at P_{n-1} in block 1, it will receive the US signal from the b1 beacon firstly than b3 beacon if a beacon of color code B is called, and the robot will receive the US signals from b1 and b3 beacons at nearly same time if it moves to the boundary of a block, P_n. In case of existing methods, if the mobile robot is moving out of the boundary of block 1, it may recognize block 2 by using its own position. However, the mobile robot will be localized by using the position information of beacons in block 1 and $d_i', (i=1,2,3,4)$, the same distance value with $d_i, (i=1,2,3,4)$ measured by P_{n+1} if the beacon scheduling algorithm suggested in this paper is used, because it can receive a signal from b3 beacon but it cannot recognize block 2 when it is moving from P_n to P_{n+1}. Hence, it will not measure P_{n+1} but P_{n+1}' which is wrong position of the robot. To solve this problem, this paper presents a new block recognition algorithm using a previous position value and a predicted position value obtained by motion characteristics of the robot at the boundary of blocks.

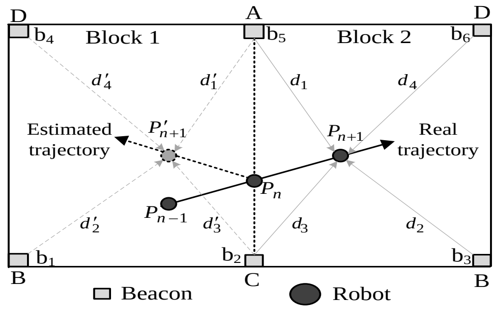

Fig.6. Error location estimation of mobile robot due to fault of block recognition

1. **Estimating the position of a robot**

Theoretically, it is possible to calculate them which are the angular velocity of the mobile robot, r_ω, the driving distance of the mobile robot, d and the rotation radius, R if the information of two past position $P_{n-1} = [x_{n-1}\ y_{n-1}\ \theta_{n-1}]^T$, $P_n = [x_n\ y_n\ \theta_n]^T$ are known [3]. Based upon the motion-continuity property, the state of the mobile robot at time $n+1$, $P_{n+1} = [x_{n+1}\ y_{n+1}\ \theta_{n+1}]^T$ can be predicted as [15]

$$\hat{x}_{n+1} = x_n + R\{\sin(\theta_n + \Delta\theta) - \sin(\theta_{n+1})\}, \quad (1\text{-a})$$

$$\hat{y}_{n+1} = y_n + R\{\cos(\theta_n + \Delta\theta) - \cos(\theta_{n+1})\}, \quad (1\text{-b})$$

$$\hat{\theta}_{n+1} = \theta_n + \Delta\theta. \quad (1\text{-c})$$

This predicted location is used for the recognizing blocks.

2. **Block recognition by using the predicted location**

If the mobile robot is approaching near the boundary between block 1 and block 2(±10cm, considering the maximum error of iGS), it is able to calculate two new position coordinates of location $P_{block\ 1}$ and $P_{block\ 2}$ by using beacon information of each block and then, a new position coordinates is going to be a minimum value which is obtained between the predicted location, $\hat{P}_{n+1}$ from 2 previous locations and the measured location, $P_{block\ 1}$, $P_{block\ 2}$. If the robot goes through a beacon b6 in Fig. 1, it will be possible to recognize a new block by comparing between four beacons coordinates from four blocks and predicted coordinates.

V. EXPERIMENTS

For algorithm verification, four-block were built by 9 beacons with one master robot and two slave robots. Error comparative analysis method was used between the encoder trajectory and iGS moving trajectory of mobile robot.

Fig. 7 & 8 illustrate moving trajectory of three mobile robots in one workspace consists of several blocks and the estimated error for each robot, respectively. The average error of three mobile robots is 22.12mm and the maximum error is 67.62mm, which is accurate enough to apply to most of the mobile robot navigations using beacon scheduling algorithm and block recognition algorithm.

VI. CONCLUSION

Although ultrasonic localization system is not feasible for localization of multiple robots in multi-block environment because of attenuation and interference among ultrasonic sensors, it is widely used for indoor localization systems since it is cheap and easy to be controlled and also it has high accuracy and repeatability. This paper proposes a new color code beacon scheduling algorithm for the arbitration among robots. A new block recognition algorithm based on motion characteristics of the mobile robot is also proposed in this paper for recognition of block boundary when the mobile robot is moving freely in the multi-block environment. And also for the efficient localization of multiple robots, the master and slave concept is introduced to govern the localization process synchronously. The efficiency of localization algorithms proposed in this paper is verified through the real experiments for multiple robots' localization in a multi-block workspace. Through this research, the base of the localization-based services is established since this localization scheme is robust against increase of the number of robots and the size of indoor environments.

ACKNOWLEDGMENT

This work was supported by the IT R&D program of MKE/ITA. [2008-S033-01, Development of Global Seamless Localization Sensor]

REFERENCES

[1] D.G. Seo, J.M. Lee, "Localization Algorithm for a mobile robot using iGS," Proceedings of the 17th World Congress The International Federation of Automatic Control, Jul. 6 - 11, 2008.

[2] M.Y. Nam, Al-Sabbagh, J. E. Kim, M.K. Yoon, C.G. Lee, E. Y. Ha, "A Real-Time Ubiquitous System for Assisted Living : Combined Scheduling of Sensing and Communication for Real-Time Tracking," IEEE TRANSACTIONS ON COMPUTERS, vol. 57, no.6, Jun. 2008.

[3] S.S. Han, H.S. Lim, J.M. Lee, "An Efficient Localization Scheme for a Differential-Driving Mobile Robot Based on RFID System," IEEE TRANSACTIONS ON INDUSTRIAL ELECTRONICS, vol. 54, pp. 1-8, Dec. 2007.

[4] D. J. A. Welsh and M. B. Powell, "An upper bound for the chromatic number of a graph and its application to timetabling problems", Computer Journal, vol. 10, pp. 85-86, 1967.

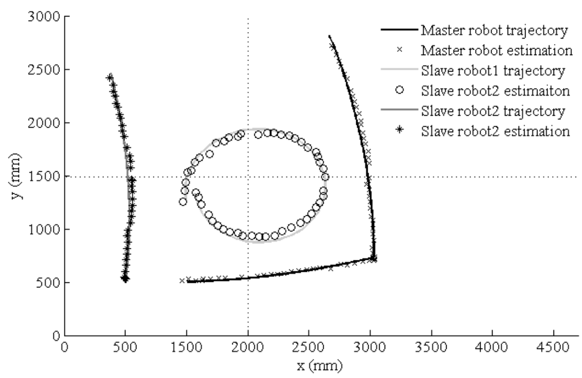

Fig.7. Trajectory of three robots in four-block

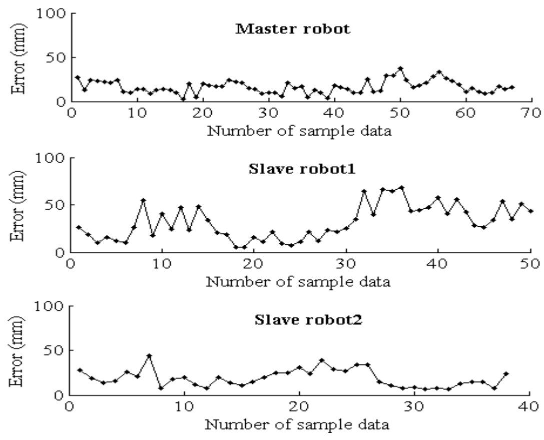

Fig.8. Estimated position error according to the number of sampled data

Pallet Recognition and Driving Method for Pallet- engaging of Unmanned Autonomous Forklift

Jungje Park, Jungmin Kim, Kyunghoon Jung, and Sungshin Kim

School of Electrical Engineering, Pusan National University,
Jangjeon-dong, Geumjeong-gu, Busan, 609-735, Republic of Korea
(Tel : 82-51-510-2367; Fax : 82-51-513-0212)
(Email : {parkjj, kjm16, hooraring, sskim}@pusan.ac.kr)

Abstract: This paper present error minimization using angular histogram for engaging pallet of forklift AGV(autonomous guided vehicle). Existing pallet recognition methods using LRF(laser range finder) have used various linearization methods for error minimization of LRF. However, to apply forklift AGV which need near real-time control, those methods need large amount of operation. Hence we studied error minimization of LRF using angular histogram to search suited linearization for forklift AGV. For experiment, we attach LRF on forklift AGV that we made ourselves, and recognize pallet. In result, we verified that average recognized angle error of pallet is within 1.2° when pallet is placed on far at 2m, 3m from forklift AGV.

Keywords: forklift, AGV, pallet, engaging, LRF, angular histogram

I. INTRODUCTION

In the modern industrial technology, it is importance to production administration so that AGV is actively developed. As a result, it was made huge profits in the cost and time. Especially, the forklift AGV could be used multipurpose, so it is studying popular [1-3].

First, for development of the forklift AGV, the development of autonomous vehicle needs to recognize location of vehicle accurately. Therefore, for localization of vehicle, SLAM(simultaneous localization and mapping), GPS, Laser Navigation System are studying actively.

The forklift needs to engage a pallet through the accurate pallet recognition for automation of the loading and unloading. Therefore, we must know the accurate angle and position for development of forklift. At this time, the forklift AGV need to recognize the accurate angle as well as position for put safely in the hole of pallet. Existing methods for pallet recognition are mainly using stereo vision camera[4,5]. However, the accuracy of methods using camera changes by brightness, the position of camera or environmental condition. So, we think that it's not suitable for the forklift AGV. Therefore, this paper present pallet recognition using LRF(laser range finder) that is less influenced of environmental condition.

This paper is divided into four sections. Section 2 proposes the methods of pallet recognition and section 3 introduces some experimental results for proving proposed methods. Finally, section 4 is conclusions and our future research.

II. PALLET RECOGNITION

We can know position and height of a pallet when a pallet is placed on the rack in work space. But, position and angle of a pallet are changed during repeatedly works. If the forklift AGV recognizes only position of a pallet without angle, it causes any problem. Therefore, the accurate pallet recognition is necessary to solve this problem.

In this paper, we used LRF(URG-04lx) for a pallet recognition. URG-04lx scans every 0.36° between 0° and 240° range and can measure maximum 4 meters. After we set up LRF at the front of fork as shown in Fig. 1., we studied recognition of a pallet.

Fig.1. LRF is set up at forklift AGV

Because shape of the pallet is rectangle, the forklift AGV can recognize the position and angle of a pallet by detecting at the front line of a pallet. Results of LRF scanning a pallet are shown in Fig.2. We are possible to extract region of pallet because of knowing location of the rack.

In the result of LRF scanning, scan data is included noises as shown in Fig.2-(b). So, we needed to reduce noise. In this paper, we proposed angular histogram method for reducing noise. Angular histogram calculate angle of between two points about all points and count every 10°. And then, the forklift AGV recognizes a pallet using both end points of maximal frequency that result of angular histogram.

step 1. Scanning using LRF
step 2. Sampling range of pallet
step 3. Reducing noise using angular histogram
step 4. Detecting at the front line of pallet
step 5. Calculating range of pallet using both end points

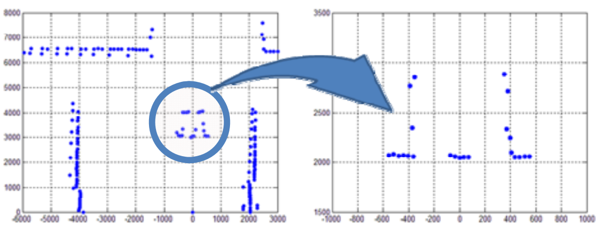

(a) Result of scanning (b) Sampled pallet
Fig.2. Result of LRF scanning

III. EXPERIMENTS

1. Experimental environment

We tested the pallet recognition using the actual forklift AGV for verifying performance. Present position of the forklift AGV were possible to calculate online by localization system. We set up LRF between forks as mentioned in section 2. For engaging pallets, we assumed that forklift AGV has at target point as far 2m from a pallet. This distance(2m) is considered a fork size and the minimum curve radius. If angle of a pallet is between -10° and 10° based the forklift AGV, it is able to insert forks in a pallet by forward driving. In the other case, forklift AGV need to drive back and drive forward to engage pallet. We tested pallet recognition about 0°, 5° and 10° when a pallet is placed on far at 2m and 3m.

2. Experimental Result

The experiment of pallet recognition is repeated 20 times, and average angle of recognized pallet is shown in Table 1. We could show that recognized angle at 2m is more precise than at 3m. The reason is that LRF is more precise as close. The best results at 3m are shown in Fig.3 and recognized angles of pallet are -0.75°, 4.39° and 8.97°. Similarly, results at 2m are shown in Fig.4 and recognized angles of pallet are 0.41°, 4.98° and 9.69°. Because experimental result is that the average error angle is calculated within 1.2°, this error doesn't influence pallet engaging and doesn't occur any problem. We confirmed that the proposed method effectively reduced noises of LRF and is possible to apply to the forklift AGV for pallet recognition based on experimental result.

Table 1. Experimental result of pallet recognition

	3m			2m		
	0°	5°	10°	0°	5°	10°
avg.	-1.22	3.73	8.32	-0.98	4.45	8.97
RMSE	1.22	1.27	1.68	0.98	0.55	1.03

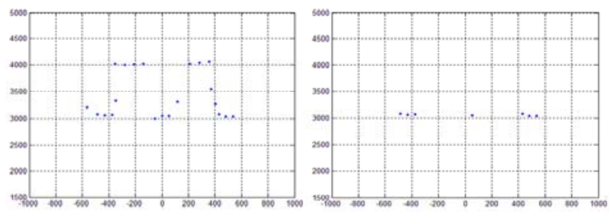

(a) 3m, 0°

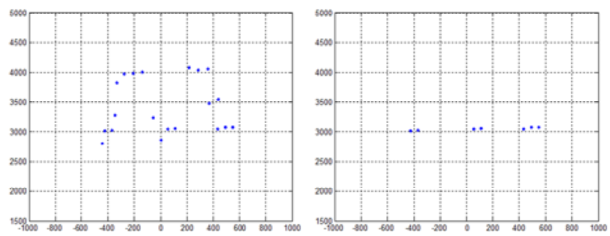

(b) 3m, 5°

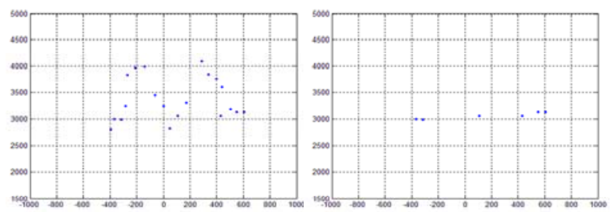

(c) 3m, 10°
Fig.3. Pallet recognition result (far 3m from LRF)

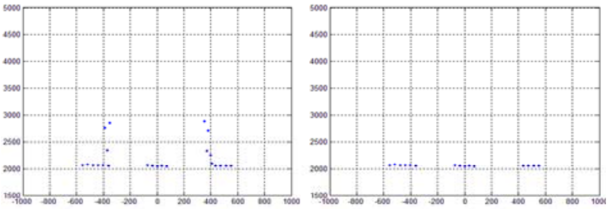

(a) 2m, 0°

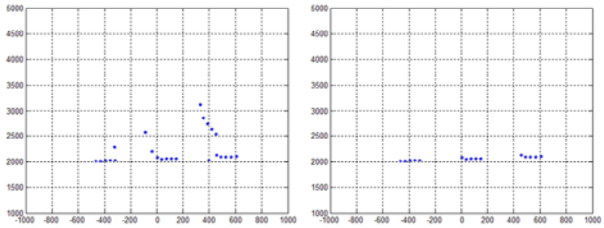

(b) 2m, 5°

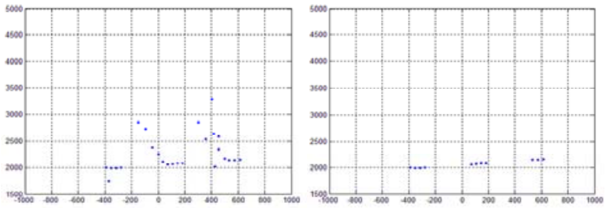

(c) 2m, 10°

Fig.4. Pallet recognition result (far 2m from LRF)

IV. CONCLUSION

This paper proposed pallet recognition and noise reduction for engaging a pallet. We used angular histogram to reduce noise of LRF data and tested proposed method by installing LRF at the actual forklift AGV. Experiment was performed repeatedly 20 times about 0°, 5° and 10° when a pallet is placed on fat at 2m, 3m. The average error of angle is calculated -1.22°, 3.73°, 8.32° at 3m, and it is calculated -0.98°, 4.45°, 8.97° at 2m. This error rates doesn't affect for engaging a pallet. Therefore, we verified the proposed pallet recognition has enough accuracy and is applicable forklift AGV.

Acknowledgment This work was supported (Pusan National University Specialized Environment Navigation/ Localization robot technology research center) by Ministry of Knowledge Economy under Human Resources Development Program for Convergence Robot Specialists.

REFERENCES

[1] Schulze, L. Wullner, A.(2006), The Approach of Automated Guided Vehicle Systems. Service Operations and Logistics and Informatics. 522-527
[2] Tuan Le-Anh, M.B.M. De Koster(2006), A review of design and control of automated guided vehicle systems. European Journal of Operational Research. 171. Issue 1:1-23
[3] Jungje Park, Taeryong Jeon, Jungmin Kim and Sungshin Kim(2009), Fuzzy Inference System for Autonomous Navigation on Forklift AGV. International Conference on Ubiquitous Robots and Ambient Intelligence. 7-9
[4] Seelinger, M. Yoder, J.-D.(2005), Automatic Pallet Engagment by a Vision Guided Forklift. International Conference on Robotics and Automation. 4068-4073
[5] Byun S., Minhwan Kim(2008), Real-Time Positioning and Orienting of Pallets Based on Monocular Vision. International Conference on Tools with Artificial Intelligence. 2:505 – 508

Monitoring the Level in a Large Structure Localization Method

Jong-Min Kim, Dong-Sul Shin, and Hee-Je Kim*

School of Electrical Engineering, Pusan National University,
Jangjeon-dong, Geumjeong-gu, Busan, 609-735, Republic of Korea
(Tel : 82-51-510-2770; Fax : 82-51-513-0212)
(Email: heeje@pusan.ac.kr)

Abstract: In many manufacturing processes and robotic applications, localizing geometric structure is very important and useful. Localizing a large structure on the sea is a challenging process as sensory information. The purpose of this paper is to create a new localization method for large structures by using laser beam. In this paper, we propose a new method of large structure localization. This method is mainly based on using inexpensive PC included a LD, a PD, and a real time data transmission (RTDT) system to acquire precise measurements.

Keywords: Localization, localizing geometric structure, laser beam sensor, real time data transmission, RTDT

I. INTRODUCTION

In many manufacturing processes and robotic applications, localizing geometric structure is very important and useful. Localization of a general structure has been studied in many papers [1-4]. In the construction industry, large objects are normally measured directly using tapes and plummets. However, LD and PD with wireless communication capacity eliminate the burden of direct contact to the object. This eliminates the risk to operators who previously had to move around a large dangerous structure. This approach also gives more precise data to the level measurement, and is more productive. In addition, it creates a retrievable digital record on to the PC database (Microsoft Excel).

In order for this method to be accepted generally it must be inexpensive and accessible to people with no knowledge of laser measurements. This method is mainly based on using inexpensive PC included a LD, a PD, and a real time data transmission (RTDT) system to verify the precise level measurement. We have applied this method to monitor the correct level of a large structure on the near sea. As the result, it is possible to detect the height of a large structure with only minor errors.

II. EXPERIMENTS

1. Description of the laser measurement system

Fig. 1(a) shows the schematic diagram of our monitoring system for measuring the correct height of a large
structure. The rotating laser system on the floor emits the red beam at 635*mm* in wavelength and 2mm in diameter. The receiver catches the laser beam, and the real time data is transferred to monitoring room by the RS-422 communication or Bluetooth, then it is displayed on the LCD. The specifications of laser transmitter are as follows. Automatic control range of angle: ±5˚, rotating speed : 50~ 300*rpm*, accuracy : ±20″

The diameter of beam from laser sensor is about 2*mm*. In 5*mm* interval, two sensors are located, and then it becomes possible to detect the size of laser beam in the near region. The size of laser point gets larger as it goes further. Therefore many receiving sensors installed on PCB could detect the laser beam. At that moment, the output signal from the laser beam is transmitted to the input of microprocessor. Fig. 1(b) shows the enlarged beam spot in the far away region. In this case, the microprocessor read the signal from center of the enlarged laser beam. Therefore, it could be possible to detect the correct level even though the larger beam size in a long distance.

Fig. 2(a) shows the driving circuits of receiving sensor. The photo sensor perceives the signal from the rotating laser beam, at that moment, the obtained TTL

* Corresponding author. Tel.:+82-51-510-2770; Fax: +82-51-513-0212
E-mail address: heeje@pusan.ac.kr (H.-J. Kim)

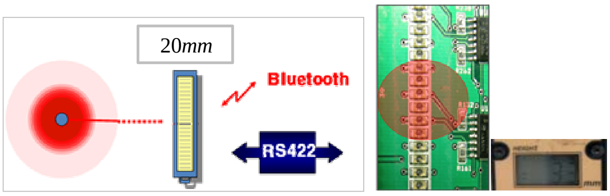

signal is transmitted to the microprocessor. Only constant frequency is transmitted by using band-pass filter circuit, while the scattering light is cut off. Up and down frequency near the constant frequency is ignored by the programming techniques. Therefore, it is designed to perceive signal of rotating laser beam. Fig. 2(b) shows Fig.1. The schematic diagram of monitoring system, and the enlarged beam spot in the far away region

the waveforms which come out from the receiving sensor. The upper yellow waveform is obtained from the amplifier, and the lower blue waveform is obtained from the ending part of Fig. 2(a). This is also the input signal for microprocessor. Fig. 3 shows the transmitting circuit of RS-422 and Bluetooth which sends the retrievable perceiving signal to PC through the communication systems. It is possible to send signal selectively with wireless or not.

Fig. 4 shows real time data transmission (RTDT) module. It consists of three parts which are the laser beam sensors, RTDT board, and the PC monitoring system. The RTDT module has 10 channels which deal with accumulated data in real time communications with RS-232. At this moment, each sensor has its own numbering and the height is displayed on the PC monitor with numbering. In case of wireless, each signal is transmitted by the Bluetooth module.

Each signal from laser beam sensors is read on the PC monitor in a real time. And the change of accumulated data is displayed with graphs on the PC monitor. The difference between previous and current data is also displayed. All the data is stored in Excel file according to the elapsed time. Fig. 5 shows the example of experimental arrangement. The location of installed sensors is shown in this figure. There are more than 3 laser sensor poles in P-line and S-line. These sensors perceive the beam spot from the rotating laser on ground, the perceived data is transmitted to the PC monitor in real time. Up-down balance is sustained by comparing with the reference level. The location of NEAR and FAR sensors perceive the barge level which is right or left.

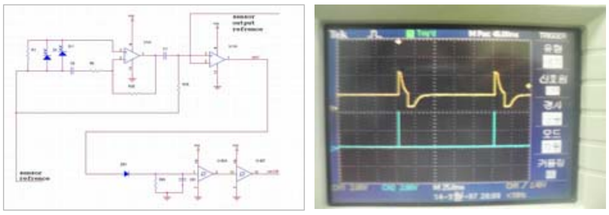

Fig.2. The driving circuits of receiving sensor, and the waveforms which come out from the receiving sensor

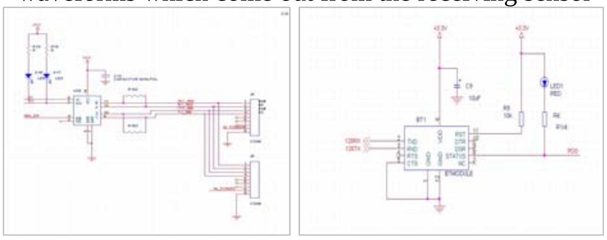

Fig.3. The transmitting circuit of RS-422

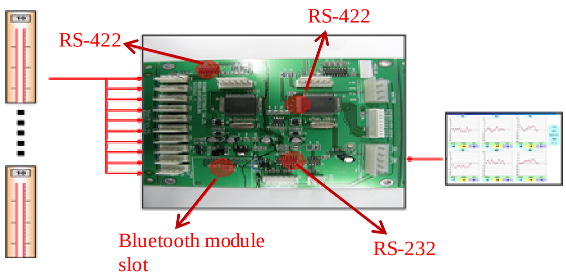

Fig.4. The real time data transmission (RTDT) module

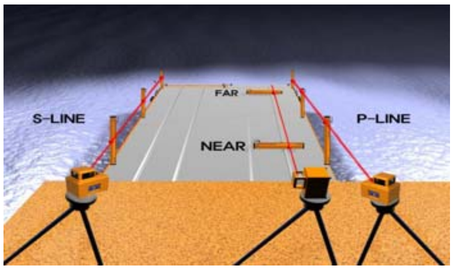

Fig.5. The example of experimental arrangement

III. CONCLUSIONS

In this work, we try to attempt the real time localization by using inexpensive PC included a LD, a PD, and a real time data transmission (RTDT) system to verify the precise level measurement. We attempt this method to monitor the correct level of a large structure on the sea. As the result, it is possible to detect the height of a large structure with a small error.

REFERENCES

[1] Z.X. Li, J.B. Gou, Y.X. Chou (1998), Geometric algorithms for workpiece localization, IEEE Trans. on

Robotics Autom. 14(6):864-878
[2] J. Hong, X. Tan (1990), Method and apparatus for determining position and orientation of mechanical objects, US patent No. 5208763
[3] M.C. Lu, W.Y. Wang, C.Y. Chu (2005), Optical based distance measuring system (ODTS), The 8th International Conference on Automation Technology, 282-283
[4] L. Koessler, et. al (2007), Spatial localization of EEG electrodes, Clinical Neurophysiology, 37:97-102

Performance Improvement of Outdoor Localization Using Elevation Moment of Inertia (EMOI)

Tae-Bum Kwon, Jae-Bok Song* and Yong-Ju Lee

Korea University, Seoul, Korea.
(Tel : 82-2-3290-3363; Fax : 82-2-3290-3757)
(artistkwon@gmail.com, jbsong@korea.ac.kr, yongju_lee@korea.ac.kr)

Abstract: This research proposes a novel approach to outdoor localization based on map matching. The main map for localization is an elevation map which is a grid map with elevation information on each cell. This research presents an elevation moment of inertia (EMOI) which represents the distribution of elevation around a robot in the elevation map. A robot continues to build a local elevation map using a laser sensor and calculates its EMOI. This EMOI is then compared with the EMOIs for all cells of the given reference elevation map to find a robot pose with respect to the reference map. The experimental results of particle filter-based localization show that the proposed EMOI-based approach can be successfully used for outdoor localization with an elevation map.

Keywords: Outdoor Localization, Monte Carlo Localization, Elevation Map.

I. INTRODUCTION

Localization is one of the most important techniques for mobile robot navigation in the indoor and outdoor environments, and various types of maps such as a grid map, elevation map, topological map, and so on, can be exploited for localization. A 2D grid map is the efficient and sufficient map when a robot navigates in the indoor environment with a range sensor. In this case, the motion of a robot can be expressed by 3 degrees of freedom (x, y, θ) in 2D space. However, outdoor navigation usually requires the estimation of 6 DOF motion (x, y, z, roll ψ, pitch θ, yaw φ) in 3D space, and therefore the environment should be represented by a 3D map for localization.

An elevation map is the most popular map to represent 3D outdoor environment. In this map, the environment is regularly divided into small cells, say, 0.1m*0.1m, and each cell has height information. An accurate elevation map can be generated using the airplane mapping system equipped with both a GPS/INS for localization and a lidar sensor for range data acquisition. This type of map is suitable for large outdoor environment and used as a main map for special applications such as military robots. In this research, an elevation map is used as a main map for localization.

Research in city modeling using DSM (digital surface map) has been conducted in Fruh [1]. DSM is used as a reference elevation map and a vehicle pose with respect to the DSM is estimated through the MCL (Monte Carlo localization) method. The range data obtained by a laser scanner is compared with that predicted from the DSM to estimate a vehicle pose. The path generated by MCL is very accurate without error accumulation even after traveling more than 10km because it estimates a pose with respect to the reference map. However, it takes very long to generate the path because of high computational complexity.

The concept of moment of inertia is widely exploited in various fields. 2D/3D object recognition is an example to use the moment of inertia in Laga [2] and Ohbuchi [3]. The characteristics of various 3D objects are defined according to the surface moment of inertia which represents the distribution of surface about three principal axes. By comparing the moment of inertia of the unknown model with those of the known models in the database, the most similar model could be found.

This research proposes the elevation moment of inertia (EMOI) which is used for matching of elevation maps to find a robot pose with respect to the pre-given elevation map. The EMOI quantifies the distribution of elevation using the concept of moment of inertia. Then the similarity between the reference map and the locally built map is evaluated using the EMOI. A particle filter is used for localization, and the probability of each particle is updated using the results of similarity comparison. Since probability update based on EMOI is simple and fast, the robot pose can be found globally without knowledge of the initial position in the large outdoor environment.

The Fifteenth International Symposium on Artificial Life and Robotics 2010 (AROB 15th '10),
B-Con Plaza, Beppu,Oita, Japan, February 4-6, 2010

II. ELEVATION MAP BUILDING

Figure 1 shows the experimental setup consisting of a Pioneer 3AT mobile robot and a SICK laser scanner. This laser scanner senses the environment within 32 m and is tilted from -45° to 45° by a DC motor. The absolute roll and pitch angles of a robot are sensed by the IMU (inertial measurement unit), and the yaw angle and small motion increments are sensed by both the wheel encoder and IMU. Combining these data allows the estimation of the 6 DOF motion in the global coordinate frame in Lacrois [4].

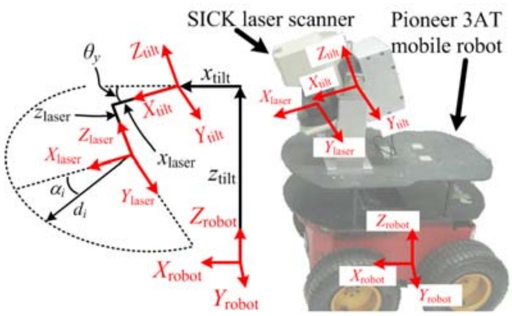

Fig. 1. Experimental setup and local coordinate frames.

An obstacle is sensed by a tilted laser scanner, and its elevation can be calculated based on a 6 DOF robot pose. The elevation of each cell is updated when it is sensed as follows.

$$e_t(i,j) = \begin{cases} z_t(i,j), & \text{if } z_t(i,j) > e_{t-1}(i,j) \\ e_{t-1}(i,j), & \text{otherwise.} \end{cases} \quad (1)$$

where $e_t(i,j)$ is the elevation of cell (i,j) at time t, and $z_t(i,j)$ is the sensed elevation of cell (i,j). If the newly sensed elevation of cell (i,j) is higher than the previous elevation, the elevation of cell (i,j) is replaced by this new elevation. This is a simple and common method for building of an elevation map. Figure 2 shows an example of the environment under consideration and its elevation map.

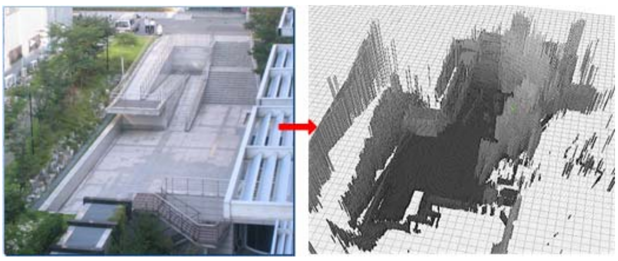

Fig. 2. Example of elevation map.

III. ELEVATION MOMENT OF INERTIA

The elevation and distance are the most important information when the elevation map is adopted as a model for the environment. These two properties, therefore, should be combined to design a new feature for elevation map matching. In this research, we propose an elevation moment of inertia. It means the distribution of elevation along the distance from a certain position of interest, as shown in Fig. 3. EMOI is calculated using the elevation values of all cells within a circular region of radius R. The EMOI calculation is not affected by the orientation of a robot, which makes the matching process simple and fast. The reference elevation of an elevation map is not fixed. For example, the elevation can be calculated with respect to a sea level, start position, and so on. Therefore, the difference in elevation, Δe, from the center of the region is exploited, and the EMOI is defined as follows.

$$\mathrm{EMOI}(x,y) = \int r^2 de, \ \text{for } r \le R \quad (2)$$

where (x,y) represents the center of the region at which the EMOI is calculated, r is the distance from the center to a certain cell of which the elevation difference is Δe, and R represents the radius of the region of interest. In this research, (2) is implemented in a real elevation map as follows.

$$\begin{aligned} \mathrm{EMOI}(i,j) &= \frac{1}{n}\sum_{k=1}^{n} r_k{}^2 \Delta e_k \\ &= \frac{1}{n}\sum_{p=i-R'}^{i+R'}\sum_{q=j-R'}^{j+R'} [(p-i)^2+(q-j)^2][e(p,q)-e(i,j)], \quad (3) \\ &\text{for } \sqrt{(p-i)^2+(q-j)^2} < R' \end{aligned}$$

where (i,j) represents the cell at which the EMOI is calculated, $e(i,j)$ is the elevation of cell (i,j) updated by (1), and n is the number of cells within the circular region of interest. R' is the radius of the region expressed in the unit of grids. For example, if the size of a cell is 0.1 m * 0.1 m, then 10 cells exist along a distance of 1m, and thus R' is a rounded value of (10*R). The term $\sqrt{(p-i)^2+(q-j)^2}$ is the distance from cell (i,j) to cell (p,q) and if this distance is less than R', cell (p,q) is within the region of interest and it is used for EMOI calculation. If the cell size is changed, the number of cells used for EMOI calculation is also changed and it affects the EMOI values. To eliminate this effect, the result is averaged by division of n.

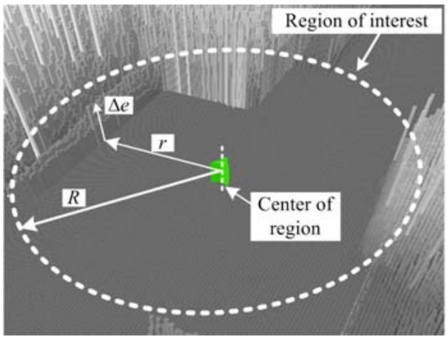

Fig. 3. Concept of elevation moment of inertia (EMOI)

Figure 4(a) shows the elevation map of the experimental environment of 90 m * 70 m in size. Figure 4(b), (c), and (d) represent EMOIs of all cells with several values of R. The size of a cell is 0.1 m * 0.1 m and the resolution of elevation is 0.1m. A high EMOI means that the distribution of elevation within the region of interest changes substantially and is not uniform. If the reference elevation map is given for localization, the EMOIs of all cells can be calculated in advance, as shown in Fig. 4, and it makes the matching process very fast.

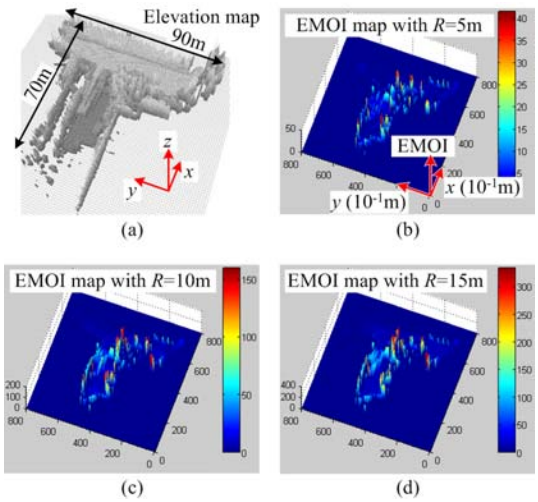

Fig. 4. EMOI calculated from all grids of elevation map with R = 5, 10, 15 m.

IV. EXPERIMENTAL RESULTS IN OUTDOOR LOCALIZATION

A particle filter is used for localization in this research. A particle filter is one of the popular Bayesian filters that can track the distribution of probability using a set of particles. At each time step, the probabilities of particles are updated using a motion model and a sensor model, and then the particles are re-sampled. The state, a robot pose in this case, is represented by the weighted sum of all particles. More detail on particle filter-based localization can be referred to Thrun [5].

In this research, the EMOI is used as an observation. To calculate the EMOI using sensor data, the local elevation map is generated as shown in Fig. 5 by the mapping method described in Section 2. As a robot continues to move around, it senses the environment more and more. Suppose a robot moves forward about 5 m. Then a circular region with a radius of 5 m around a robot can be mapped sufficiently. The EMOI with R = 5, therefore, can be calculated from this local elevation map, and the probabilities of particles are updated using a sensor model. Then, the local elevation map is erased and a new elevation map is built again to calculate the EMOI at a different location. If the value of R for EMOI calculation is small, an update by a sensor model is frequently executed. However, the EMOI of cells may be almost uniform in some environments because the region of interest for the EMOI is small and only a few obstacles may be within that region. If R for EMOI calculation is large, many obstacles are considered in calculating the EMOI, but an update by EMOI is executed less frequently. Therefore, different values of R can be exploited according to the environmental characteristics.

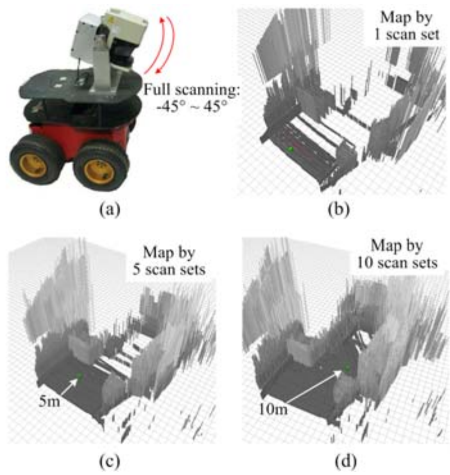

Fig. 5. Building of local elevation map with different scan sets.

Figure 6 shows the experimental results of particle filter-based localization using the EMOI. The outdoor environment is 70 m * 90 m in size and 20,000 particles are used to find a robot pose globally with respect to the reference map. The EMOI is computed for R = 5 m and thus the probabilities of all particles are updated about every 5 m. During localization, a robot moves at a speed of 0.3 m/s and all processes run in real-time on a Dual Core 1.7 GHz notebook. Figure 7 shows the number of particles and standard deviation of particle positions as a function of travel distance. Though a robot pose is estimated by correct particles in Fig. 6(e) and (f), they converge and diverge slightly depending on the nearby environment.

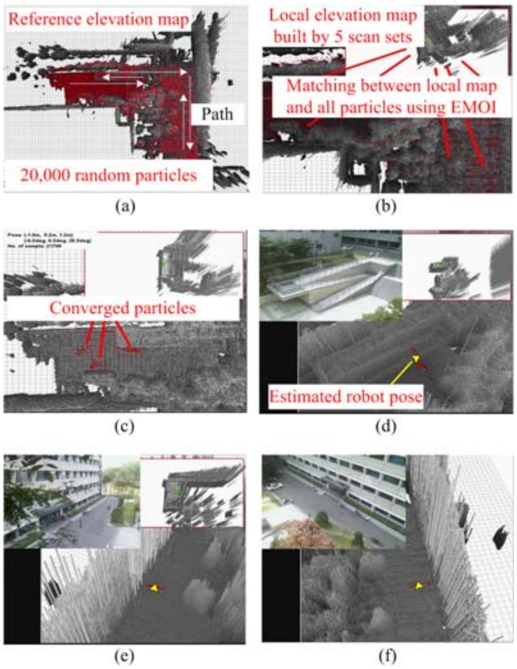

Fig. 6. Experimental results of particle filter-based localization using EMOI in outdoor environment.

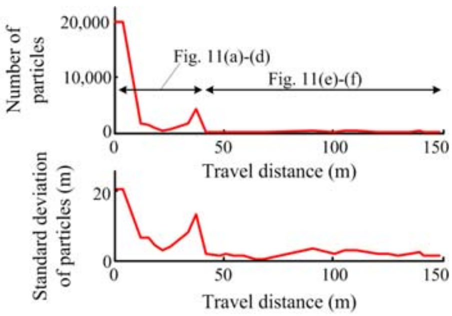

Fig. 7. Number of particles and standard deviation of particle positions.

V. CONCLUSION

This paper describes a localization scheme with an elevation map in the outdoor environment. To find a robot pose, a local map built by the range sensor is compared with the entire reference elevation map. To this end, a new feature for elevation map matching was proposed based on the concept of moment of inertia. The characteristics and performance of the proposed feature, EMOI, were verified by a series of experiments. From this research, the following conclusions have been drawn.

1. The proposed EMOI applies the concept of moment of inertia to elevation map matching. Each position has its own EMOI, and the EMOI can be exploited as a feature for finding a position.
2. The probabilities of all particles in the particle filter can be updated by the EMOI, and a robot pose can be estimated in real time during movement in the large outdoor environment.

The EMOI is a scalar value and the whole distribution of elevation in a certain region is compressed into this scalar value. It can make local tracking inaccurate as well as simple and fast. The local peak near the travel distance of 40 m in Fig. 7 occurred because of this situation. This is a weak point of this proposed localization scheme using EMOI, and the research on improving the performance of local tracking is under way.

ACKNOWLEDGMENT

Authors are gratefully acknowledging the financial support by Agency for Defense Development and by UTRC (Unmanned Technology Research Center), Korea Advanced Institute of Science and Technology.

REFERENCES

[1] C. Fruh and A. Zakhor (2004), An Automated Method for Large-Scale Ground-based City Model Acquisition. Int. Journal of Computer Vision 60: 5-24
[2] H. Laga, H. Takahasi and M. Nakajima (2006), Spherical Wavelet Descriptors for Content-based 3D Model Retrieval. International Conference on Shape Modeling and Applications: 75-85
[3] R. Ohbuchi, T. Otagiri, M. Ibato and T. Takei (2002), Shape-Similarity Search of Three-Dimensional Models Using Parameterized Statistics. 10th Pacific Conference on Computer Graphics and Applications (PG'02): 265-274
[4] S. Lacrois, A. Mallet, D. Bonnafous, G. Bauzil, S. Fleury, and M. Herrb (2002), Autonomous rover navigation on unknown terrains: functions and integration. Int. Jour. of Robotics Research 21: 913-942
[5] S. Thrun, W. Burgard and D. Fox (2005), Probabilistic Robotics. The MIT Press, Cambridge.

Collision Detection of Robot Manipulator in Cryogenic Environments

Seung-Heui Lee, Ki-Ho Yu and Min Cheol Lee

Research Institute of Mechanical Technology, Pusan National University,
San 30, Jangjeon2-Dong, GeumJeong-Gu, Busan, Korea
(Tel : 82-51-510-3081; Fax : 82-51-512-9835; Email address : youneye@pusan.ac.kr)
Dept. of Intelligent Mechanical Engineering, Pusan National University,
San 30, Jangjeon2-Dong, GeumJeong-Gu, Busan, Korea
(Tel : 82-51-510-3081; Fax : 82-51-512-9835; Email address : yukiho1118@pusan.ac.kr)
School of Mechanical Engineering, Pusan National University,
San 30, Jangjeon2-Dong, GeumJeong-Gu, Busan, Korea
(Tel : 82-51-510-2439; Fax : 82-51-512-9835; Email address :mclee@pusan.ac.kr)

Abstract: This paper studies a method how a robot can detect collision between the canister on the end-effector of a robot and a pin of a slot in a rack of the vessel during operating the manipulator of an automatic cryogenic storing vessel which can improve a ratio of survival of a cord blood. The cord blood is kept in liquid nitrogen in the cryogenic vessel. The integrated robot control system for storing a cord blood is developed, which is based on mechanism of SCARA robot. The robot manipulator consists of four axes. To overcome difficulty in detecting collision between canister and the pin of the slot in cryogenic circumstances around -196°C, a collision detection algorithm for the robot manipulator is proposed. To improve performance of the integrated system, the proposed algorithm for the collision avoidance is applied to the end effecter of the robot manipulator.

Keywords: Motion control, Collision detection, Robot manipulator, Cryogenic

I. INTRODUCTION

Many researchers recently have studied to extract adult stem cells from umbilical cord blood and to implant embryonic stem in the body for improvement of human life [1], [2], [3]. The cord blood is used to usefully cure disease such as cancer. Therefore a storing vessel of the cord blood in cryogenic environment is important to keep a ratio of survival of the cell. Storing vessel is divided manual type and automatic type. The ratio of survival is higher than manual type. Because of the ratio of survival, the automatic type is developed and has been operated even if the price of an automatic storing vessel type is 10 times higher than the one of a manual type. In addition, because the work of picking the cord blood up by hand outside is frequent, the ratio of survival is low due to sudden temperature change. We have been developed the automatic type previous study [4]. A collision is occurred in previous study. This study is proposed the algorithm of collision avoidance in cryogenic environment. Because of an electronic sensor can not apply to the environment of liquid nitrogen. This study is accomplished that the method how a robot manipulator can detect collision between the canister and the end effecter of robot manipulator.

II. DESIGN OF ROBOT

The storing cord blood system consists of cryogenic vessel, robot manipulator, and control PC. Fig. 1 shows inner space of storing vessel's layer and the canister. Each layer consists of 7 rings. The ring consists of three racks. An outer rack has 270 ea slot pin. Middle rack has 149 ea slot pin. Inner rack has 71 ea slot pin. The numbers of total slot pin are 3,430 ea. When storing the cord blood, liquid nitrogen is filled up the top of the ring. The material of the ring and the canister is a stainless steel. A ratio of contraction in z-axis is bigger than x-y plane. Therefore we consider the contraction for a direction of z-axis. So we propose the collision avoidance algorithm for robot manipulator based on collision detection algorithm using the position of z-axis.

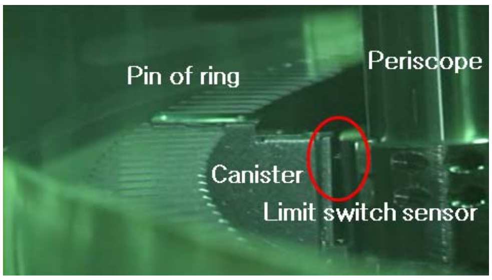

Fig.1. Pins of ring in rack and canister

Fig. 2 shows the block diagram of robot manipulator based on mechanism of SCARA robot [5], [6]. The link of manipulators are consists of d_1, l_2, d_2, l_3, d_3, and l_4. The parameter of d_1 is height of storing vessel. The value of l_2 add to l_3 is a radius of major lid. The parameter of l_3 is a radius of minor lid. But the storing vessel should be a sealed structure because of liquid nitrogen is vaporization gas in the normal temperature. Therefore, major lid and minor lid are designed using the structure of the robot manipulator instead of upper cover. Table 1 is D-H parameter of the robot manipulators. Transformation matrixes are as formula (1). The material of the cryogenic vessel and the robot manipulators were made of a stainless steel.

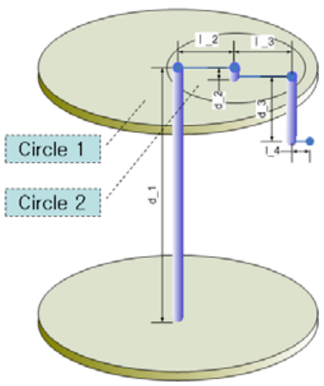

Fig.2. Block diagram of manipulator for SCARA

Table 1. D-H parameter of robot manipulator

Θ	d	α	a
θ1	d_1	0	0
Θ2	0	0	l_2
Θ3	-d_3	0	l_3
0	0	0	l_4

$$A_1=\begin{bmatrix}\cos\theta_1 & -\sin\theta_1 & 0 & 0\\ \sin\theta_1 & \cos\theta_1 & 0 & 0\\ 0 & 0 & 1 & d\_1\\ 0 & 0 & 0 & 1\end{bmatrix} A_2=\begin{bmatrix}\cos\theta_2 & -\sin\theta_2 & 0 & l\_2\cdot\cos\theta_2\\ \sin\theta_2 & \cos\theta_2 & 0 & l\_2\cdot\sin\theta_2\\ 0 & 0 & 1 & 0\\ 0 & 0 & 0 & 1\end{bmatrix}$$

$$A_3=\begin{bmatrix}\cos\theta_3 & -\sin\theta_3 & 0 & l\_3\cdot\cos\theta_3\\ \sin\theta_3 & \cos\theta_3 & 0 & l\_3\cdot\sin\theta_3\\ 0 & 0 & 1 & -d\_3\\ 0 & 0 & 0 & 1\end{bmatrix} A_4=\begin{bmatrix}1 & 0 & 0 & l\_4\\ 0 & 1 & 0 & 0\\ 0 & 0 & 1 & 0\\ 0 & 0 & 0 & 1\end{bmatrix} \qquad (1)$$

$$^0A_4=\begin{bmatrix}\cos(\theta_1+\theta_2+\theta_3) & -\sin(\theta_1+\theta_2+\theta_3) & 0 & (l\_3+l\_4)\cdot\cos(\theta_1+\theta_2+\theta_3)+l\_2\cdot\cos(\theta_1+\theta_2)\\ \sin(\theta_1+\theta_2+\theta_3) & \cos(\theta_1+\theta_2+\theta_3) & 0 & (l\_3+l\_4)\cdot\sin(\theta_1+\theta_2+\theta_3)+l\_2\cdot\sin(\theta_1+\theta_2)\\ 0 & 0 & 1 & d\_1-d\_3\\ 0 & 0 & 0 & 1\end{bmatrix}$$

III. SIMULATION

The robot manipulator consists of four axes. Each axis consists of a rotation of a major lid, a rotation of a minor lid, a rotation of periscope and a linear motion of periscope. Fig. 3 shows the rotation direction of each axis. Motions of manipulators have three patterns for storing. One is rotation motion by major lid and periscope. Another is linear motion by combination of three axes. The other is linear motion of z-axis by ball screw.

Fig. 4 shows a simulation of dynamics using OpenGL program. We know a position of the canister in the storing vessel by the simulation. Fig. 5 shows forward kinematic analysis and inverse kinematic analysis using MATLAB program. Parameters of an existing product were used for the simulation [7].

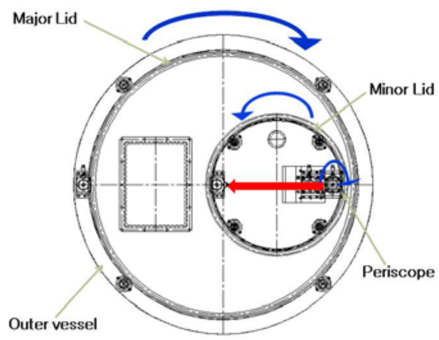

Fig.3. A rotation direction of each axes

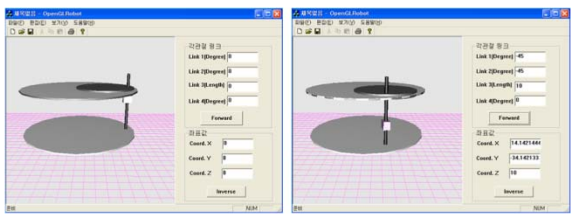

Fig.4. Visual C++ program of OpenGL simulation

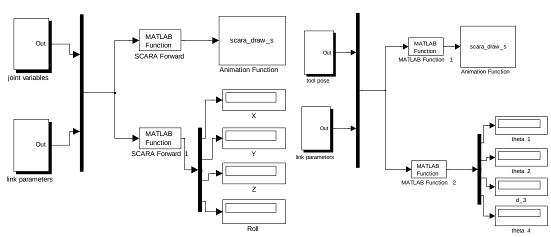

Fig.5. Block diagram of MATLAB simulation

IV. COLLISION DETECTION ALGORITHM

Fig. 6 shows block diagram of a direction for storing canister. If collision state is occurred, a contact of the limit switch sensor is closed. Fig. 7 shows procedure of a canister for storing procedure. We defined safety area for the robot manipulator. A rotation motion moved by major lid for search a correct ring of address pin. The collision detection algorithm was used for a linear motion by combination of three axes.

Fig. 8 shows a view of the canister and the pin of the slot in the rack. The ratio of contraction as the direction of z-axis is bigger than the x-y plane in cryogenic environment. Therefore we consider the control of manipulator for the direction of z-axis. So we propose the collision avoidance algorithm for robot manipulator based on collision detection algorithm using the position of z-axis. We used two parameters that are length of linear move for the x-y plane and the status of limit switch contact in the end effecter of the hook. Fig. 9 shows each case of the canister position. Case 1 is normal operation. The collision detection is case 2 and case 3. Case 4 is failure canister for storing in rack pin.

The relationship of each case is
- Case1 : Normal linear motion and open contact s/w
- Case2 : Short linear motion and close contact s/w
- Case3 : Short linear motion and close contact s/w
- Case4 : Open contact s/w and open contact s/w

Fig. 10 shows a flowchart of collision detection algorithm. The signal of the limit switch sensor and the position value of AC servo motor's encoder are used. Each manipulator of servo motor is controlled by using MMC board on the control PC. I/O port of MMC board gets a signal of input for contact of limit switch sensor.

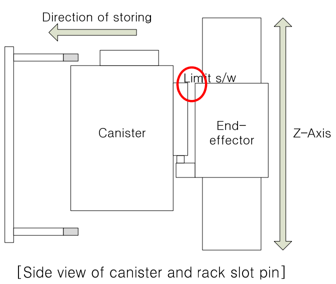

Fig.6. Block diagram of direction for storing

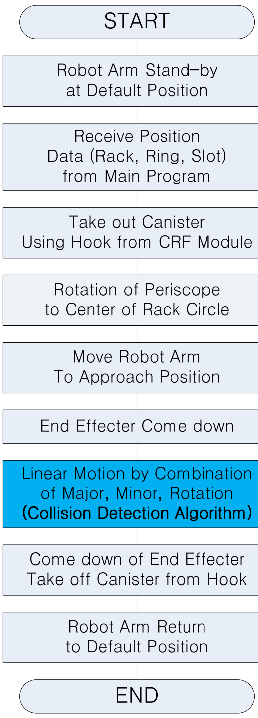

Fig.7. Procedure of a canister for storing

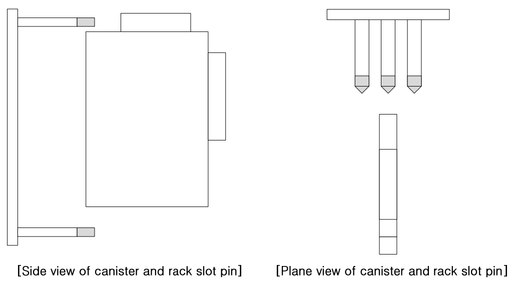

Fig.8. View of the canister and rack slot pin

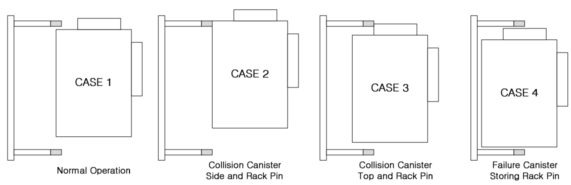

Fig.9. Each cases of the canister position

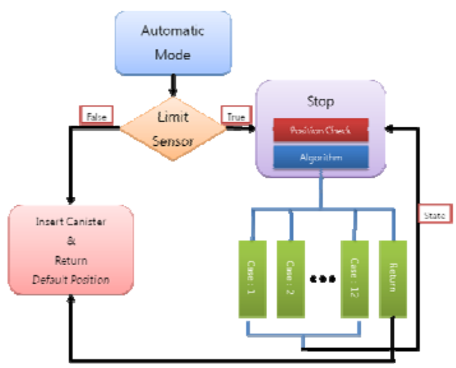

Fig.10. Collision detection algorithm

V. CONCLUSION

The cryogenic vessel of containing liquid nitrogen for the storing of the cord blood in the canister is needed to precision control. We defined the position of the canister by analyzing of kinematics. The ratio of contraction in liquid nitrogen is bigger than in the air. It is too difficult to measure using visual or other electronic sensors in cryogenic environments. To overcome difficulty to detect collision between the canister and the pin of the slot in the rack of the vessel, the limit switch sensor was designed the hook of the end effecter for robot manipulator. If the canister of the cord blood to enter with abnormal location for storing, the algorithm for the collision avoidance can be modified in the normal location by operating of the limit switch sensor. The canister of the cord blood can be store in the normal position by using this collision detection method.

ACKNOWLEDGEMENT

This work was supported (in part Pusan National University Specialized Field Navigation/Localization Technology Research Center) by Ministry of Knowledge Economy under Human Resources Development Program for Convergence Robot Specialists.

REFERENCES

[1] R. Bornstein, A. I. Flores, M. A. Montalban, M. J. Del Rey, J. De La Serna and F. Gilsanz (2005), A modified cord blood collection method achieves sufficient cell levels for transplantation in most adult patients, Stem Cells, Vol. 23, no. 1, pp. 324-334

[2] K. Z. Tang and K. K. Tan (2006), Development of an automated umbilical cord blood collection system, Artificial Cells Blood Substitutes and Biotechnology, Vol. 34, no. 1, pp. 75-88

[3] K. K. Tan, K. Z. Tang and S. Huang (2007), Devices for umbilical cord blood collection, Recent Patents on Engineering, Vol. 1, no. 1, pp. 89-94

[4] S. H. Lee, Y. Y. Park, D. Y. Jeong and M. C. Lee (2008), Robot Manipulator Design for Storing Cord Blood in Cryogenic Environments, KSPE 2008 Autumn Conference, pp. 183-198

[5] K. Son, M. C. Lee, J. M. Lee, S. H. Han, M. H. Lee and S. K. Kim (1997), Real-Time Evaluation of an Off-Line Programming System for SCARA Robot, Proc. of 2nd Asian Control Conference, Vol. I, pp. 89-92, July

[6] J. M. Lee, M. C. Lee, K. Son, M. H. Lee and S. H. Han (1998), Implementation of a Robust Dynamic Control for SCARA Robot, KSME International Journal, Vol. 12, No. 6 pp. 1104-1115, June

[7] BioArchive System, Automated Liquid Nitrogen Storage System Service and Maintenance Manual, Thermo Genesis Corp.

Trajectory Tracking Control of Mobile Robot Moving along Curved Wall Using Imaginary Wall

Seiji FURUNO*, Minoru KOBAYASHI**, Kouhei YANAGI* and Go HIRANO***

*Kitakyushu National College of Technology
Tel : 81-93-964-7261; E-mail : furuno@kct.ac.jp
**Kyushu Institute of Technology
***Kinki University

Abstract: In this study, a trajectory tracking control method of a mobile robot moving along curved wall is proposed. To move along curved wall, we use imaginary wall that is generated by distance between the mobile robot and the wall the trajectory tracking control method consists of three control methods. The first one is a method that controls the mobile robot to move along a wall maintained constant. The second one is a method that controls the mobile robot to move along a wall in case of the wall direction changes. The third one is obstacle avoidance on a path. We developed a mobile robot which has two-driven wheels and the laser range finder to confirm the proposed method.

Keywords: Mobile Robot, Trajectory Tracking Control, Wall, Obstacle, Laser Range Finder.

I. INTRODUCTION

In recent year, differential type mobile robots have been applied in not only a factory but also a hospital and an office. For examples, a security robot for security patrols in a building, a cleaning robot and an information robot that works at a shop and an airport are developed. To move these robots autonomously, it is necessary to determine its own position and orientation. Dead-reckoning by using an internal sensor such as a rotary encoder and an external sensor such as a vision sensor are used so as to determine the position and orientation of the mobile robot. Many studies on the dead-reckoning of the mobile robot have been proposed. A position estimation method of a wheeled mobile robot by integrating the informations in an odometric dead reckoning and a laser navigation system (*e.g.*, [1]), a method of mobile robot localization on a Topological-Geometrical map which permits inaccurate description (*e.g.*, [2]) are reported. But measurement errors of the position and orientation of the mobile robot increase as the distance covered increases in the localization method using the dead-reckoning.

On the other hand, a motion control method for the mobile robot using an external sensor is studied. Sensor-based navigation used a target direction sensor for the mobile robot among unknown obstacles in work space (*e.g.*, [3]), long distance outdoor navigation of the autonomous mobile robot along a curbstone (e.g., [4]) are reported.

When the autonomous mobile robot moves the long distance, it often moves along the target such as the guide tapes, wall and curbs. Kojima et al [5] proposed a hierarchical vehicle control system of the mobile robot along the wall. Their control system consists of a desired signal generator of wheel velocities using two laser displacement sensors and a wheel velocity controller.

II. Development of Mobile Robot with Two Independently Drive Wheels

1. System construction

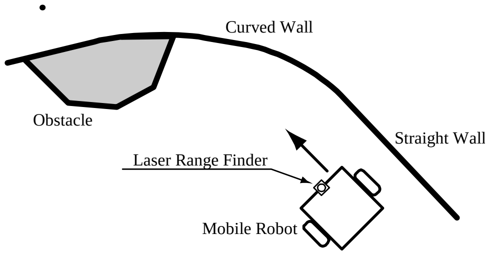

Fig.1 Mobile robot moving along wall and avoiding obstacle

We develop a mobile robot has two independently driven wheels shown in Fig.2 (a). The mobile robot has one laser range finder in the front of the body, two driving wheels on both sides and two non-driving wheels in the front and in the rear. The system construction of the mobile robot is shown in Fig.2 (b). A DC servomotor with a reduction gear and a rotary encoder actuates the driving wheel using a belt pulley. The mobile robot is controlled by a notebook computer. The DC motor which actuates the wheel is controlled by a DA converter and a motor driver. A signal of a rotary encoder is measured by a counter board and sent to the notebook computer. An angular velocity of wheel is detected by numerical differentiation of signal of the rotary encoder.

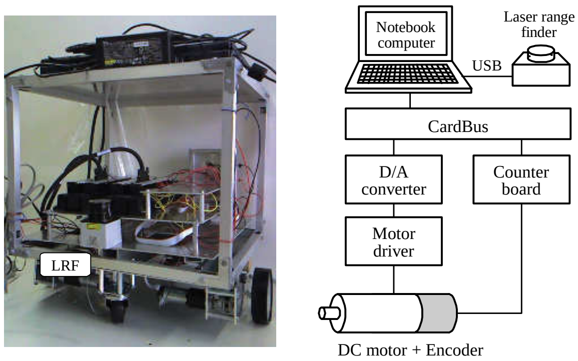

(a) Mobile robot (b) System construction

Fig.2 Mobile robot and system construction

2. Laser Range Finder

Figure 3 illustrates the 2-dimensinal laser range finder which was made by Hokuyo Automatic Co, Ltd... This sensor features compactness, lightweight, high precision and low power consumption, and provides the wide scan angle with high resolution, which is very important for environment recognition by mobile robots (*e.g.*, [6]).

Fig.3 Laser range finder "URG-04LX"

III. Wall Tracking Method for Mobile Robot using LRF

To move the autonomous mobile robot along the wall require maintaining a distance between the mobile robot and the wall constant, measuring a changing direction of the wall and avoiding obstacles on a path. In this study, the wall tracking control method for the mobile robot follows some rules as below conditions.

- The distance between the mobile robot and the wall is maintained constant.
- The mobile robot moves along a curved wall and a changing direction of the wall.
- The mobile robot avoids obstacles.

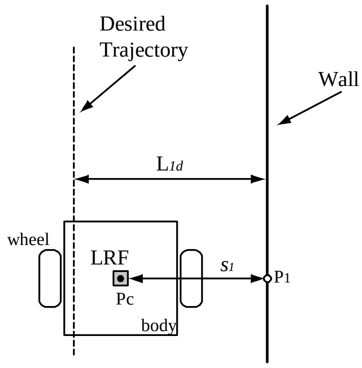

Fig.4 Relationship between mobile robot and wall

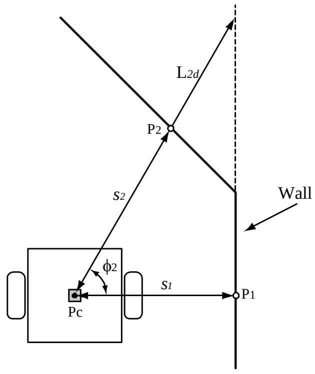

Fig.5 Calculation of the changing direction of wall

1 . Control Method to Maintain the Distance between Mobile Robot and Wall Constant

Figure 4 shows a coordinate of the mobile robot and the wall. The LRF is mounted on the center of gravity of the mobile robot. The LRF can measure a precise distance to a target. A maximum scanning angle range is 270[degrees] and a resolution of the angle range is 0.36[degrees]. In this subsection, only a distance to a perpendicular direction to the forward direction is used. The distance to the perpendicular direction is s_1 and a point of intersection between s_1 and the wall is P1. Here a desired distance between the center of gravity of the mobile robot and the wall is L_{1d}, a deviation to maintain the distance between the robot and the wall is written as follows.

$$\delta = s_1 - L_{1d} \tag{1}$$

Next, the wall is not necessarily straight. It is difficult for the mobile robot to track not straight wall by eq. (1). Then to estimate the changing direction of the wall, a distance s_2 that inclines by ϕ_2 relative to the s_1 is measured. Assuming that the wall continues in parallel to the forward direction of the mobile robot as shown in the dotted line in Fig.5, a distance to the wall in the direction of s_2 is expressed as following equation.

$$L_{2d} = \frac{s_2}{\cos\phi_2} \quad (2)$$

If $s_2 < L_{2d}$, the changing direction of the wall is as shown in solid line in Fig.5. When a point of intersection between s_2 and the wall is defined to be P2, an imaginary wall that connects P1 with P2 is generated as shown in Fig.6. An angle of inclination of the imaginary wall ϕ is express as following equation.

$$\phi = \tan^{-1}\left(\frac{s_1 - s_2\cos\phi_2}{s_2\sin\phi_2}\right) \quad (3)$$

To move the mobile robot track the wall, control objectives are to bring δ and ϕ to 0. In case of the mobile robot with two independently driven wheels, δ and ϕ is able to bring to 0 by controlling the angular velocity. Let Δt be a frequency of sensing, a desired angular velocity of the mobile robot to move along the wall ω^{ref} is written as follow.

$$\omega^{ref} = \omega(t) - (K_\phi\phi + K_\delta\delta)\Delta t \quad (4)$$

Let v^{ref} be a desired forward velocity, desired angular velocity of right and left wheels ω_r^{ref}, ω_l^{ref} is expressed as follows.

$$\begin{pmatrix} \omega_r^{ref} \\ \omega_l^{ref} \end{pmatrix} = \begin{pmatrix} \frac{1}{R_w} & \frac{T}{2R_w} \\ \frac{1}{R_w} & -\frac{T}{2R_w} \end{pmatrix} \begin{pmatrix} v^{ref} \\ \omega^{ref} \end{pmatrix} \quad (5)$$

If the inclination of the wall changes as shown in Fig.6 ($s_2 > L_{2d}$), the angle of inclination of the imaginary wall cannot be calculated. In that case, the mobile robot can move along the wall shown in Fig.6 by setting ϕ to 0.

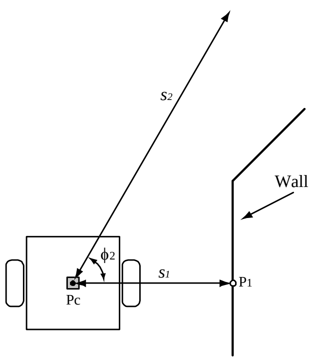

Fig.6 Relationship between mobile robot and wall

2. Obstacle Avoidance

It is difficult to avoid the obstacle and dead-end in the method of subsection III.1. Then, to avoid the obstacle and the dead-end as shown in Fig.7, a distance of forward direction s_3 is measured by the LRF. Let L_{3d} be a minimum allowed distance between the mobile robot and the forward object. If $s_3 < L_{3d}$, the mobile robot turns until $s_3 > \alpha L_{3d}$. α is safety rate.

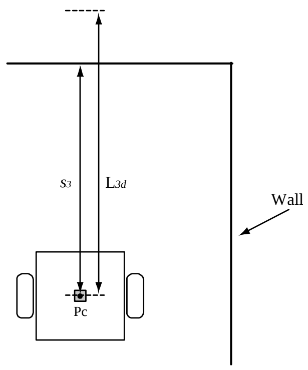

Fig.7 Obstacle and dead-end avoidance

3. Tracking Control

The mobile robot can move along the wall and avoid the obstacle and the dead-end by using the proposed method. But it is difficult to satisfy the tracking control, the obstacle avoidance and dead-end avoidance simultaneously. Then in this study, we introduce the concept of the order of priority into the tracking control method. Here, we place the first priority is given to obstacle and dead-end avoidance, the second priority is given to tracking control moving along wall. The algorithm of the proposed method is shown as follows.

STEP 1: The distance to a perpendicular direction to the forward direction s_1, the distance s_2 that inclines by ϕ_2 relative to the s_1 and the distance of forward direction s_3 are measured by the LRF.

STEP 2: If $s_3 < L_{3d}$, the mobile robot turn until $s_3 > \alpha L_{3d}$ then return to STEP 1. If $s_3 > L_{3d}$, go to STEP 3.

STEP 3: From eq.(2), \$$L_{2d}$ is calculated. If $s_2 < L_{2d}$, the angle of inclination of the imaginary wall is calculated from eq.(3). If $s_2 > L_{2d}$, ϕ is set to 0. From eq.(1), δ is calculated.

STEP 4: From eq.(4), the desired angular velocity of the mobile robot ω^{ref} is calculated, the desired angular velocity of the right and left wheels ω_r^{ref} and ω_l^{ref} are calculated by eq.(5).

IV. Experiments

To verify the efficiency of proposed method, this section shows two experiments result. In first experiment, one obstacle is placed on the path. In second experiment, the path is dead end.

1. Experiment 1

Figure 8 shows the experimental environment composed of the obstacle, the straight line wall and the curved wall. A size of the obstacle is 0.5[m] x 0.5[m] and the other parameters are as follows; v^{ref} = 0.2[m/sec], L_{1d} = 0.5[m], L_{3d} = 0.6[m], Δt = 0.1[sec], t_f = 26.0[sec]. From Fig.8, the mobile robot is able to move along the wall and to avoid the obstacle. After the obstacle avoidance, the mobile robot moves toward the straight wall then follows again along the straight and curved one.

2. Experiment 2

Figure 9 shows the experimental environment composed of the obstacle, the straight line wall, the curved wall and the dead end. Parameters are as follows; v^{ref} = 0.2[m/sec], L_{1d} = 0.5[m], L_{3d} = 0.6[m], Δt = 0.1[sec], t_f = 37.0[sec]. Fig.8 the mobile robot moves along the wall and avoids the obstacle. Therefore, the efficiency of the proposed method is confirmed.

V. Conclusion

In this paper, we discussed the tracking control method for the mobile robot moving along the wall. This method consists of maintaining the distance between the mobile robot and the wall constant, estimating the changing direction of the wall and tracking it with avoiding the obstacle and the dead-end. To track the wall efficiently, we introduce the concept of the order of priority into the tracking control method. Finally, we demonstrate the effectiveness of proposed method in actual environments.

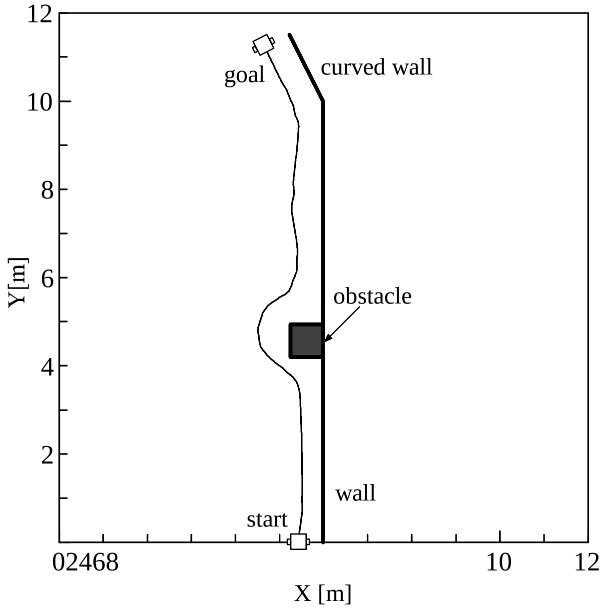

Fig.8 Experimental environment and resultant path in experiment 1

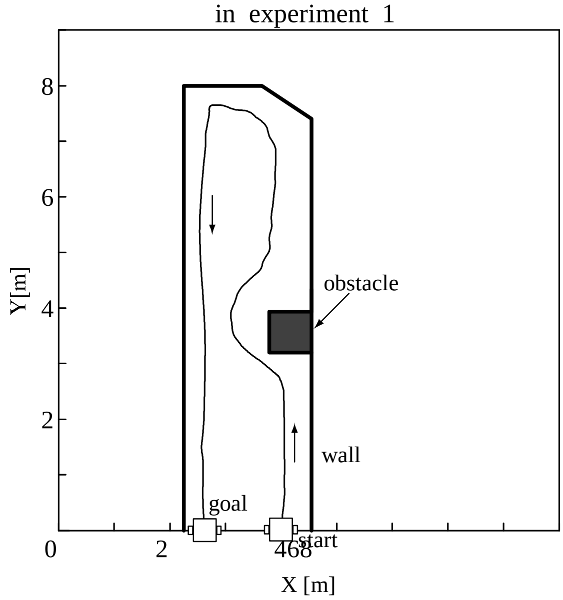

Fig.9 Experimental environment and resultant path in experiment 2

REFERENCES

[1] M. Hashimoto, F. Oba, Y. Fujikawa et al (1993), Position Estimation Method for Wheeled Mobile Robot by Integrating Laser Navigation and Dead Reckoning Systems (in Japanese), J. of the Robotics Society of Japan, 11(7): 1028-1038.
[2]M. Tomono and S. Yuta (2002), Mobile Robot Locali zation on a Map with Large Inaccuracy (in Japanese), J. of the Robotics Society of Japan, 20(4): 75-86.
[3]M. Yamamoto, N. Ushimi and A. Mohri (1999), Development of Sensor-Based Navigation for Mobile Robots Using Target Direction Sensor (in Japanese), J. of Robotics and Mechatronics, 11(1): 39-44 [4]T. Shimizu, A. Ohya and S. Yuta (2004), Curb based Outdoor Navigation of Autonomous Mobile Robot (in Japanese), Proc. of ROBOMEC 2004: 29-30
[5]H. Kojima, H. Matsumura, T. Ito et al, Trajectory Tracking Control of Mobile Robot along Wall (in Japanese), Transaction of the Japan Society of Mechanical Engineers. C 67(658): 1890-1896
[6]H. Kawata, A. Ohya, S. Yuta, et al (2005), Development of ultra-small lightweight optimal range sensor system, Proc. of IEEE/RSJ Int. Conference on Intelligent Robots and Systems 2005: 3277-3282

Vision-based Obstacle Avoidance System for Autonomous Mobile Robot in Outdoor Environment.

Ji Eun Jung*, Kil Soo Lee*, Hyung Gyu Park*, Yung Ho Koh**, Man Hyung Lee*
**Graduate School of Mechanical Engineering, Pusan National University*
***Futronic Co,. Ltd*

Abstract: In this paper, we propose the obstacle avoidance system on based vision sensor for an autonomous mobile robot. For real-time turn angle correction, we obtain the state equation of a mobile robot from input-output continuous data. Each individual image pixel is classified as belonging either to an obstacle or non-obstacle based on its color property (HSI color model). HSI color model is less sensitive to illumination changes than RGB color model. Using some conditions and the voting system, we choose the path area, the navigation point, and the turn angle. This method uses a single color camera.

Keywords: Vision system, Autonomous mobile, obstacle avoidance.

I. INTRODUCTION

As to vision-based approaches to obstacle detection, they basically can be divided into three classes. In the first class, obstacles are extracted directly from 2D images. Only one camera and only the image in the current navigation cycle are used, with certain a priori knowledge and predefined assumptions being considered. In the second class of approaches, motion information obtained from a sequence of images are utilized to detect obstacles. The most popular approaches in this class are based on optical flow. In the third class of approaches, obstacles are detected using stereo-vision techniques.[1]

Although the first class in general takes less computing time and has better detection results than the second and the third classes, in fact, it does not really detect obstacles because obstacles are extracted directly from the 2D image. Shadows on roads may also be regarded as obstacles in this class of approaches. On the contrary, in the second and the third classes, 3D computer vision techniques are used to really judge whether object on roads are obstacles, although more computing time is required in these two classes than the first class

In this paper, we propose an intelligent approach to obstacle guidance in outdoor environments using a single color camera.

We use subspace system identification algorithms, calculate a state-space model form input-output measurements of system. As the state-space model, we predict the real wheel angle of robot. By the combination of wheel angle and velocity, prediction of location can be computed.

Various color information on roads is used in this paper to extract path and obstacle. For this, the HSI color model is chosen, which is less sensitive to intensity than RGB color model. To judge whether a pixel is an obstacle or not, the histogram of the front trapezoid is compared with one of the input image. The process to vote the possible area as path, the path area is extracted. We select the navigation point, turn angle from the path area.

The remainder of the paper is organized as follows. In section 2, subspace system identification algorithms are introduced. In section 3, the details of the proposed vision-based obstacle detection method is described. The descriptions of the obstacle avoidance method are included in section 4. Experimental studies from simulation in section 5 and conclusion are presented in section 6, respectively. The paper ends with reference.

II. Subspace System Identification

1. State-space model

Subspace identification algorithms calculate a state-space model from input-output measurements of a linear system of the form

$$x_{k+1} = Ax_k + Bu_k + w_k \quad (1)$$
$$y_k = Cx_k + Du_k + v_k \quad (2)$$

where $u_k \in R^m$ and $y_k \in R^l$ are the given measured input and output sequences of the multivariable system with m inputs and l outputs. The consecutive states $x_k \in R^n$ are unknown, as are the (real) system matrices A, B, C and D of appropriate dimensions. The sequences $w_k \in R^l$ and $v_k \in R^m$ represent so-called process and observation noises, respectively. The noise w_k and v_k are both assumed to be stationary white Gaussian processes with zero-mean and covariance matrices:

$$E\left[\begin{pmatrix} w_p \\ v_p \end{pmatrix}\begin{pmatrix} w_q^T & v_q^T \end{pmatrix}\right] = \begin{bmatrix} Q & S \\ S^T & R \end{bmatrix}\delta_{pq} \geq 0 \tag{3}$$

Where $\delta(\cdot)$ is the Kronecker delta function.

$$\begin{bmatrix} \hat{A} & \hat{B} \\ \hat{C} & \hat{D} \end{bmatrix} = \min_{A,B,C,D} \left\| \begin{bmatrix} \hat{x}_{i+1} & \cdots & \hat{x}_{i+j} \\ y_i & \cdots & y_{i+j-1} \end{bmatrix} - \begin{bmatrix} A & B \\ C & D \end{bmatrix}\begin{bmatrix} \hat{x}_i & \cdots & \hat{x}_{i+j-1} \\ u_i & \cdots & u_{i+j-1} \end{bmatrix} \right\|_F^2 \tag{4}$$

Where $\|\cdot\|_F$ denotes the Frobenius-norm of a matrix[2].

Formidable as it may seem, subspace algorithms manage to identify the order of the system n (the number of difference equations needed to model the data appropriately) and to calculate the matrices A, B, C, D, Q, R and S.[3]

A least squares problem to obtain the state space matrices solve Eq. (5).

$$\begin{pmatrix} X_{i+1} \\ Y_{i|i} \end{pmatrix} = \begin{pmatrix} A & B \\ C & D \end{pmatrix}\begin{pmatrix} X_i \\ U_{i|i} \end{pmatrix} \tag{5}$$

Where $U_{i|i}$, $Y_{i|i}$ are block Hankel matrices with only one block row of inputs respectively outputs, namely $U_{i|i} = \begin{pmatrix} u_i & u_{i+1} & \cdots & u_{i+j-1} \end{pmatrix}$ and similarly for $Y_{i|i}$. This set of equations can be solved. As there is no noise, it is consistent.

2. Modeling of robot

The system input is steering wheel angle and output is vehicle's yaw. Fig. 1 represents the input signal and Fig. 2 represents the output signal.

We use the Visual C++ for data acquisition and use MATLAB toolbox for data processing. By relation of input data and output data, we solve the discrete-time state equation.

Fig. 3 represents the estimation of system model using the discrete-time state equation.

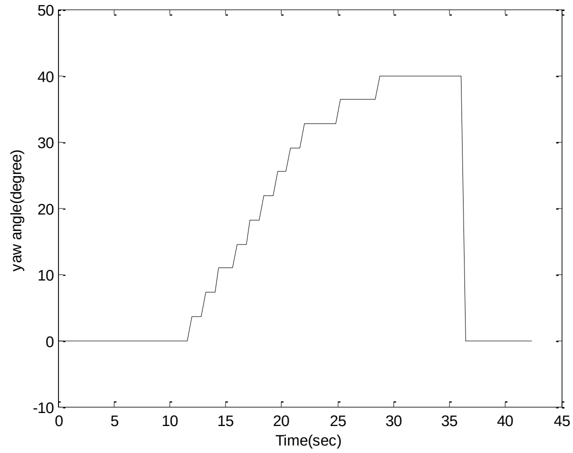

Fig.1 Input data(Steering wheeling angle)

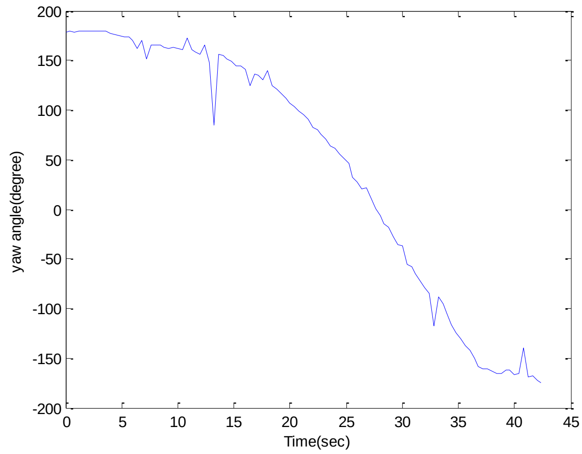

Fig.2 Output data(yaw angle)

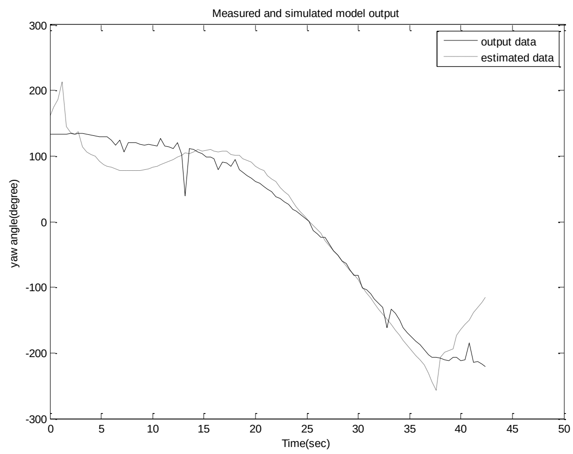

Fig.3 Performance of subspace identification

The discrete-time state equations in sampling time T=0.01sec is the following (Eq.6).

$$A = \begin{bmatrix} 0.016214 & 0.17667 & -0.74701 \\ 0.12678 & 1.3821 & -4.8858 \\ 0.42002 & 5.1668 & -11.208 \end{bmatrix}$$
$$B = \begin{bmatrix} 0.000086638 \\ 0.0085629 \\ 0.0027416 \end{bmatrix} \quad (6)$$
$$C = \begin{bmatrix} -1062.4 & 2.8312 & -44.839 \end{bmatrix}$$
$$D = 0$$

III. Obstacle detection method

The simplified version of our appearance-based obstacle detection method consists of the following four steps:

i) Filter color input image.
ii) Transformation into HSI color space.
iii) Histogramming of reference area.
iv) Calculation the back project of the histogram.

In the first step, the 320×260 color input image is filtered with a 5×5 Gaussian filter to reduce the level of noise.

In the second step, the filtered RGB values are transformed into the HIS (hue, saturation, and intensity) color space. Because color information is very noisy at low intensity, we only assign valid values to hue and saturation of the corresponding intensity is above a minimum value. Similarly, because hue is meaningless at low saturation, hue is only assigned a valid value if the corresponding saturation is above another minimum value. An appealing attribute of the HSI model is that it separates the color information into an intensity and a color component. As a result, the hue and saturation band are less sensitive to illumination changes than the intensity band.

In third step, a trapezoidal area in front of the mobile robot is used for reference. The valid hue and intensity values of the pixels inside the trapezoidal reference area are histogrammed into two one-dimensional histograms, one for hue and one for intensity. Histograms are well suited for this application, as they naturally represent multi-model distributions. In addition, histograms require very little memory and can be computed in little time.[4]

In the fourth step, the backprojection of histogram puts the value of the histogram bin, corresponding to the tuple in the output image, for each tuple of pixels at the same position of all input single-channel images (hue channel, intensity channel). In terms of statistics, the value of each output image pixel is the probability of the observed tuple given the distribution (histogram). The backprojection of hue and intensity histograms are united by OR operation.

A pixel is classified as an obstacle if the value of pixel is above the threshold in backprojection image. In the current experiment, the threshold is set to 100.

a) b)

Fig.4 a) Input color image with trapezoidal reference area b) output image

IV. Obstacle avoidance method

The software of the obstacle avoidance algorithm uses two queues: a candidate queue and a reference queue. From the central line, we search a trapezoidal area. A trapezoid area is stored in the candidate queue if the two following conditions are satisfied:

i) The sum of the value at the inner pixel is below the intensity threshold.
ii) The angle δ of the nonparallel side and the longer parallel side is bigger than 45 degree.

If a trapezoid is satisfied condition of the candidate queue, all pixel of current trapezoid gain weight at dimension of trapezoid. After trapezoid retrieval is over, a pixel is classified a reference queue if the weight of pixel is above the voting threshold.

The reference queue is chosen to path area. The center point of the top horizon line is selected as the navigation point. After the navigation point is chosen, the turn angle θ is calculated to be

$$\theta = \tan^{-1}\left(\frac{u_0 - \frac{u}{2}}{v_0}\right) \tag{7}$$

Where NP: (u_0, v_0) is the navigation point, u, v are width and height of image, respectively.

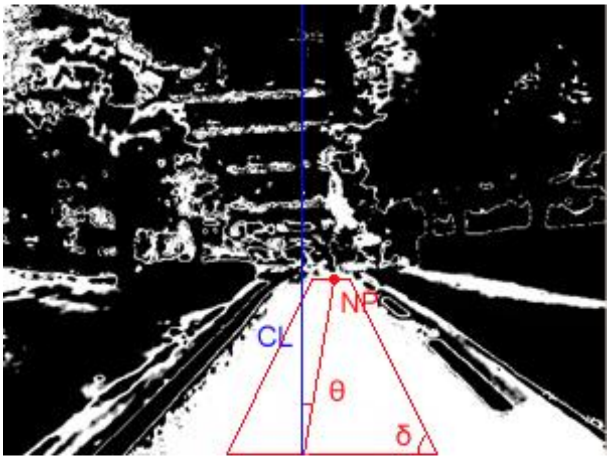

Fig.5 Illustration of how the candidate queue is chosen.

The turn angle θ inputs Eq. (6) and gets the predicted output data (the yaw angle of mobile robot) by system state equation. Until the error of current angle and destination angle is less than the past error, the turn angle input four times. In the current experiment, the intensity threshold is set to 5000.

V. EXPERIMENT

Fig. 6 shows some images and their results in several complex road environments. Fig 6 (a) shows a road image that include one red color area, which is candidate queue. NP_1 (the naviga-tion point) is set to be central and avoid lane that exist left side of image.

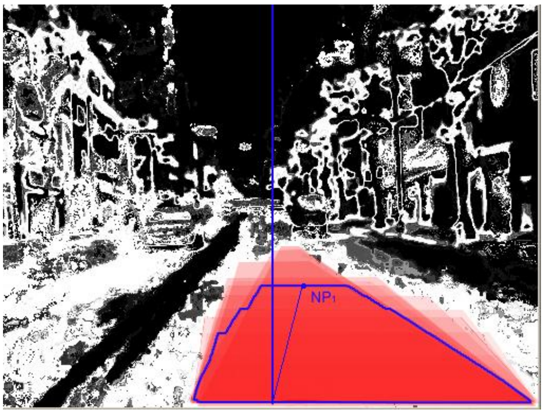

Fig.6 Experimental result

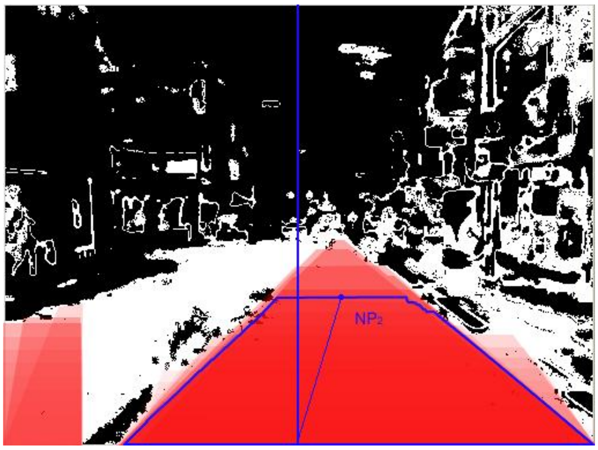

Fig.7 Experimental result

The pixel of blue line zone has over weight than weight threshold. As shown Fig.7, candidate queues of the left side are being dropped, because pixel's weight is below the threshold. As a result, the right navigation point can be calculated successfully.

VI. CONCLUSION

This paper presented a method for obstacle detection and avoidance with a single color camera. The method performs in real-time and provides the path area, the navigation point, and the turn angle. Using the system state equation, the turn angle is closed to the destination yaw angle gradually. The system can be trained and has performed well in outdoor environments.

REFERENCES

[1] Kuang-Hsiung C, Wen-Hsiang T, "Vision-based obstacle detection and avoidance for autonomous land vehicle navigation in outdoor roads," *Automation in Construction*, Vol. 10, pp. 1-25(2000)

[2] Seong Man Yoon, Seong Taek Hwang, and Jae Heon Ryu and Man Hyung Lee, "System Identification and Controller Design for Lateral Control of an Unmanned Vehicle", *The Thirteenth International Symposium on Artificial Life and Robotics* 2008(AROB 13th '08), 2008

[3] J. Poshtan and H. Mojallali, "Subspace system identification," *Iranian Journal of Electrical & Electronic Engineering*, Vol. 1, No. 1, pp. 11-17, January 2005.

[4] I. Ulrich and I. Nourbakhsh, "Appearance-Based Obstacle Detection with Monocular Color Vision," *Proceedings of the AAAI National Conference on Artificial Intelligence*, July/August 2000

Cooperative Localization by using Knowledge of Self-organized Regularity

Masao KUBO, Takashi MATSUBARA, Satoshi SHIMIZU, Hiroshi SATO

Computer Science, National Defense Academy of Japan, Yokosuka, Japan
(Tel : 81-46-841-3810; Fax : 81-46-844-5911)
(Email address {masaok, matubara, g53247, hsato}@nda.ac.jp)

Abstract: In this paper, a new localization approach for a team of robots which utilize emergent properties of their formation is proposed. At times, some of such a synchronized behavior generates spin-off effects that include geometric patterns on them. Therefore, it seems to be a reasonable question whether it is possible to utilize the pattern. Firstly, the authors discuss Takayama's control strategy which is proposed for target enclosure formation, which is a typical formation for Robocup. Then they propose a simple and useful expansion of Monte Carlo localization to utilize the emergent pattern of this formation. The proposed algorithms are confirmed by a series of computer simulations.

Keywords: Distributed Robots, Swarm Intelligence, Particle Filter

I. INTRODUCTION

Localization is an important issue for mobile robotics. It requires to integrate a set of observed data captured by different sensors. Bayesian approach is one of the major approaches which sets up probabilistic mathematical framework. Particle Filter is a non-parametric probabilistic Bayesian approach which is adequate for non Gaussian distribution of particles. However, it needs larger amount of computational resources than others. Generally, localization accuracy is depended on robot's behavior and task so on. Therefore, when a robot cannot manage sufficient computational resource for its localization by itself multi robot cooperation seems to be a hopeful direction. However, current multi robot cooperation for localization methods indicates poor scalability.

In this paper, we discuss a new multi robot localization approach which complements this weakness. We assume that robots already know their collective behavior which are emerged while they are at work. Collective behavior is a bottom-up phenomena, for example, *Mexican wave*. Generally, the phenomena is more stable, the larger the group size is. Therefore, it can be possible to make a new cooperative localization approach by using this property which works well when the group size is large. In this paper, we show an good example and formulate its ability.

This paper is composed as follows. Firstly, we explain Takayama's target enclosure scheme which is adopted as their work to generate collective behavior. Also Monte Carlo Localization is explained which is the algorithm to estimate a robot's position. Then, a new multi robot localization algorithm is proposed. Then, the results of a series of computer simulation verify this idea. As a result, the proposed algorithm can use target as a new landmark with $1/\sqrt{n}$ times small variance.

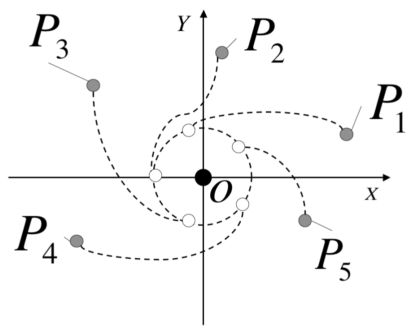

Fig.1. Takayama's Target Enclosure: dynamics

II. COOPERATIVE LOCALIZATION

2.1. Particle Filter(MCL)

A bunch of sensor fusion methods are introduced. Multisensor fusion method based on particle filter is called as MCL(Monte Carlo Localization).

MCL is an implementation of Bayes Filter which a set of particles are used for representing probability distribution. Let's suppose current time is t. The set of particle at t is

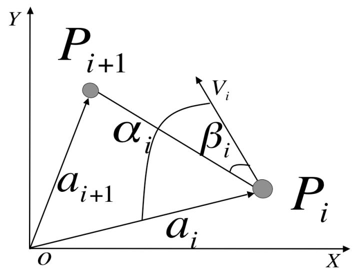

Fig.2. Takayama's Target Enclosure: rules

$$\chi_t := x_t^{[1]}, x_t^{[2]}, \ldots, x_t^{[M]} \qquad (1).$$

Each particle represents a hypothesis about state of its robot. Here, a hypothesis means robot's position and direction in 2D space, namely (x, y, θ).

The a set of particle is updated by the step. A single update procedure is composed the following 3 sub procedures.

Step1) sampling

The new particle set $x_t^{[m]}$ is generated by the last particle set $x_{t-1}^{[m]}$ and the control signal at t u_t. We supposed that each robot has crawler so that $x_t^{[m]}$ is calculated by [2] and $u_t = (v, \omega)$. The set of new particles are called as $\bar{\chi}_t$

Step2) Evaluation

In this step each particle of $\bar{\chi}_t$ is evaluated. The likelihood of each particle $w_t^{[m]}$ is calculated. Let's suppose there are J landmarks on map L, which location is known. The $w_t^{[m]}$ is calculated by the probability $p(z_t | x_t^{[m]}, L_j)$ of observing $z_t = (r, \phi)$ about j-th landmark $L_j \, (1 \le j \le J)$ when it locates $x_t^{[m]}$ as follows.

$$w_t^{[m]} * = prob(r - \hat{r}) \cdot prob(\phi - \hat{\phi}) \qquad (2)$$

where $(\hat{r}, \hat{\phi})$ is the true valu of j-th landmark L_j and *prob* indicates a error function.

Step3) Resampling

The new set of particle χ_t is generated by $\bar{\chi}_t$ We adopt roulette selection. The selection probability of m-th particle is $w_t^{[m]}$.

2.2. Particle Filter(MCL)

A bunch of sensor fusion methods based on Bayesian approach are introduced [1]. Relative distance[3], rendezvous probability[4] transmitted are utilized for new evaluation criteria of equation (2). [5] proposes a camera system which uses transmitted particle for new candidates. It works well but all of these previous works supposed that each robot can identify all other robots. It makes serious problems when robots move fast and when they work in closed order. Basically, larger number of robots there are in a team, it makes harder to recognize a particular teammate.

III. THE PROPOSED ALGORITHM

3.1. Collective Behavior and Bottom Up Properties

By the above summary the following idea comes up naturally. If some properties which get more reliable as increase of the number of robots are utilized, the robots can expect more accurate localization by using equation(2). Generally speaking, collective phenomena is occurred when many objects interact, for example, jam, Mexican wave. As known well, it is more difficult to emerge such character when the number of people in stadium is small so that this collective phenomena seems to be a good candidate for the robust property for localization of dense robots. For this purpose, we assume the following. Normally, these phenomena occur by chance and it is not intentional act. However, in this paper, we suppose that all of robots agree that they take some action to generate such collective pattern. More over, all of them know the bottom up pattern before hand.

3.2. Target Enclosure Behavior

In this paper, target enclosure behavior proposed by takayama [6] is adopted in exemplification of this new multi robot localization framework. Takayama proposes interesting simple rule for target enclosure in 2D plane. Let's suppose that n nonholonomic robots try to enclose a target at origin (see Fig.1). These robots are numbered counterclockwise. They propose the following control method.

$$v_i = f\beta_i \qquad (3)$$

$$\omega_i = v_i / \bar{r} - k \cos \alpha_i \qquad (4)$$

The P_i , v_i and ω_i denote i-th robot , its control speed v_i, and angular velocity respectively. This rule uses 2 angle information, α_i, β_i(see Fig.2) and relative distance to the target. $k, f > 0$ are gain parameters. According this rule, the robots form a circle path around the target(see Fig.3).

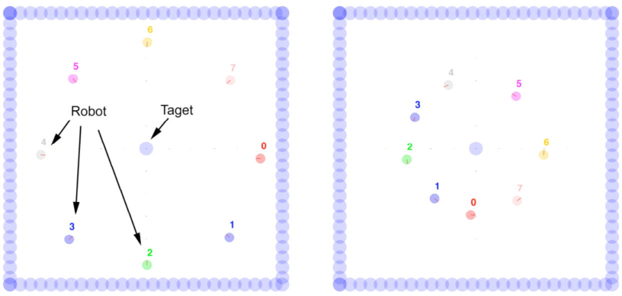

Fig.3 a scene of the target enclosure behavior. (i) An initial state (ii) A convergence state

Therefore, the following characteristics could be observable when this circular formation succeeds.

(E1) the relative distance to the target should be kept $\bar{r}$.

(E2) the relative angle α_i to the target should be kept $\pi/2$(by tangent line theorem).
(E3) the relative angle to its neighborhood should be equalized.

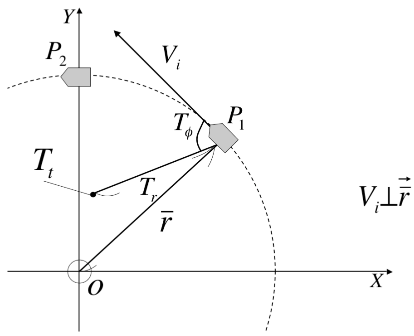

Fig.4. The proposed algorithm

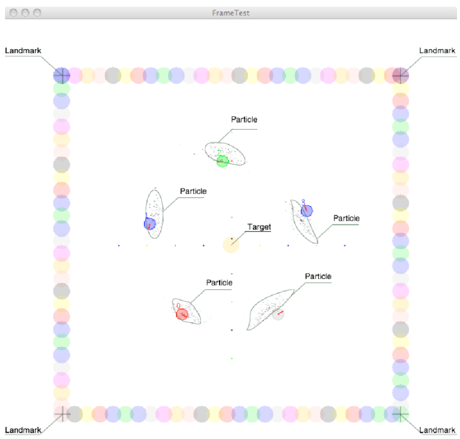

Fig.5. The simulation environment

3.3. Proposed algorithm

By these 3 information, the localization algorithm is proposed(Fig.4). This algorithm composes of 3 stages. Firstly, each robot P_i deduces its position $\overline{xi_t}$ by average of its own particles $xi_t^{[m]}$. Next, by transmitting the deduced position each other, the position of target T_t is estimated by averaging the set of position of them, namely $T_t = 1/n \Sigma \overline{xi_t}$.

At the third step, in MCL, the particle $x_t^{[m]}$ is evaluated by this information about the target and its observation z_t more than the landmark information L_j.

$$w_t^{[m]} = prob(T_r - \bar{r}) \cdot prob(T_\phi - \pi/2) \cdot prob(r - \hat{r}) \cdot prob(\phi - \hat{\phi}) \quad (5)$$

$$T_r = \sqrt{(T_x - x)^2 + (T_y - y)^2} \quad (6)$$

$$T_\phi = atan2(T_y - y, T_x - x) - \theta \quad (7)$$

where T_t is the distance to the target when P_i locates at $x_t^{[m]}$, and T_ϕ indicates the angle to the target T_t when P_i is at $x_t^{[m]}$.

IV. EXPERIMENTS

4.1. Accuracy of the target position

Our algorithm consists of 3 steps, and the first 2 steps estimates the target location by averaging of all of robots position. Firstly, the results of estimation of the target location are shown(Table.3.2).

We build the simulation (see Fig.5). Each robot is simplified as a 40cm diameter cylinder. The 12m x 12m rectangle field is surrounded by the same shape objects as wall. There are 4 landmarks at each corner of this field. At the center of the field, the target is set. The $\bar{r}$ sets 3m. All sensors installed at a robot contains realistic nose. Any measure of the distance suffers Gaussian nose with variance of 1m $N(0,1.0)$, on the other hand, $N(0,0.01rad)$ Gaussian noise comes to be mixed in any measure of angle.

Fig.6 shows the error of the estimation of target location by the proposed method (blue) and the error of the estimation by an isolated robot (red). The x axis means the time progress (step). Table 1 shows the statistic of the result.

Fig.6 says that the proposed method can estimate the target location more accurate than that of a single robot. Additionally, this method can provide the good quality information immediately on starting to enclose the target.

The estimation of target location is average of members' location. Therefore, the improvement seems to be getting large as the increase of the number of robots. Let's suppose that the standard deviation of error of distance to one of landmark is σ_L. Also σ_X and σ_T denote the standard deviation of error of localization of a robot and estimation of the target, respectively. An isolated robot uses landmarks only to estimate its position so that

$$\sigma_X = \sigma_L \quad (8)$$

If each of the above estimation is independent, $\sigma_T{}^2$ can be written as follows,

$$\sigma_T{}^2 = \frac{1}{n} \Sigma \sigma_X{}^2 \quad (9).$$

Then, we get

$$\sigma_T = \sigma_X / \sqrt{n} \quad (10)$$

Therefore, we can conclude that the proposed method can provide a $1/\sqrt{n}$ time more stable target location estimation than that by a single isolated robot.

Table 1 shows the results of that by a single robot (left column), by 5 robots team(the center column), and 8 robots team (the right column). σ_T of single robot is 0.5004. On the other hand, σ_T of 5 robots team and 8robots team are 0.2323 and 0.1836 respectively. These results about the improvement fit the above discussion because $1/\sqrt{5}$ =0.4472 ≒ 0.4642=(0.2323/0.5004) and $1/\sqrt{8}$ =0.3535 ≒ 0.3669=(0.1836 /0.5004)

Therefore, the proposed algorithm in n robots can estimate the target location with $\sigma_L/\sqrt{n}$ deviation.

4.2. Accuracy of Proposed localization Algorithm

Finally, we show the total performance of the proposed method. $\bar{r}$ =3m. A simulation runs 3000 steps. Table 2 shows the statistics of the robot's location estimation error of the last 2000 steps. The left column indicates localization error by a single isolated robot. The center and the right column mean that by 5 robots team and by 8 robots team, respectively. The 5 robots team can get better estimation (0.2618 m) than that of a single robot.(0.3356 m) Moreover, the 8 robots team can get more better estimation than that of 5 robots team.

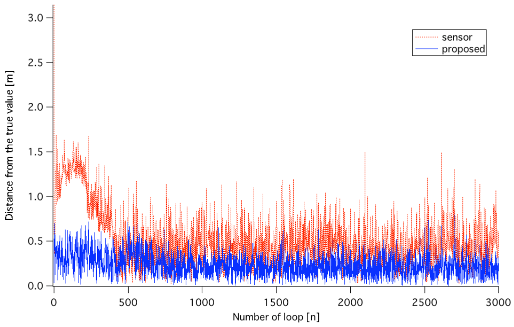

Fig.6. The error of the estimation of the target location by the proposed method.

Table 1. The statistics of the estimation error of the target location by the proposed method.

(meter)	estimation by an isolated robot	the proposed by 5 robot team	the proposed by 8 robot team
error average	0.5004	0.2323	0.1836
deviation of error	0.311	0.124	0.111
distribution of error	0.097154	0.015556	0.012502
the number of samples	3000	3000	3000
the worst error	3.1432	0.7945	0.9241
the best estimation	0.0243	0.0011	0.0023

Table 2. The statistics of the estimation error of robot location.

(meter)	an isolated robot	the proposed(5 robots)	the proposed(8 robots)
error average	0.3356	0.2618	0.2574
deviation of error	0.021274	0.021094	0.023420
the worst error	0.9005	0.9856	1.0394
the best estimation	0.0069	0.0023	0.0053

V. CONCLUSION

In this paper, we proposed a new multi robot localization approach by using collective behavior which are emerged while they are at work. The results of a series of computer simulation based on Takayama's target enclosure scheme verify this idea. Then this cooperative localization approach by using this bottom-up property which works well. Especially, the proposed algorithm can use target as a new landmark with $1/\sqrt{n}$ times small variance. Therefore, we hope that this framework could complement the low scalability of traditional multi robot cooperative localization.

REFERENCES

1)Bolic, M., Djuric, P.M., Sangjin Hong, Resampling algo-rithms and architectures for distributed particle filters,IEEE Transactions on Signal Processing, Volume 53, Issue 7, pp 2442- 2450(2005)

2) Endo, Nagatani, Yoshida, improvement of Dead-Reckoning Accuracy of Crawler-Type Mobile Robot by Considering its Slippage , the 24-th conference proceedings of the robotics society of japan,2G17 （CDROM） (2006-09)(2006)

3) Sebastian Thrun, Wolfram Burgard, Dieter Fox, Probabilistic Robotics (Intelligent Robotics and Autonomous Agents), MIT press(2007)

4) Mark Coats, "Distributed Particle Filter for Sensor Networks", IPSN2003, Springer, pp.99-107 (2004).

5)Misu, Matsui, Naemura, Fujii, and Yagi, Distributed Cooperative Particle Filter for Sensor Network : An Application to Multi-View Soccer Ball Tracking, Technical report of IEICE. HIP,106(540),pp.11-16 20070215 (2007)

6)Takayama, Yamamoto, Takimoto, Distributed For mation Control of a Nonholonomic Multi-agent Syst em for Target-enclosing Operations, The 9-th confe rence of SICE System Integration Division SY0015/ 08/0000 , pp.679-680(2008)

A Collaborative Localization Tolerant to Recognition Error by Double Check Particle Exchange

Takashi Matsubara, Masao Kubo, and Yusuke Murachi

National Defense Academy, 1-10-20 Hashirimizu, Yokosuka, Kanagawa, Japan
(Tel : 81-468-41-3810; Fax : 81-468-44-5911)
(Email matubara@nda.ac.jp)

Abstract: Statistical algorithms for collaborative multi-robot localization have been proposed using particle filter. In these algorithms, with synchronizing each robot's belief or exchanging particle of robots each other, fast and accurate localizations are attained. These algorithms assume correctness of recognition of other robots, and influence of recognition error is not discussed. However, if the recognition of other robots is wrong, a large amount of error in localization may occur. This paper explains this problem. Furthermore, an algorithm for collaborative multi-robots localization is proposed to cope with this problem. In the proposed algorithm, particles in a robot are sent to other robots according to measurement result in the sending robot, at the same time, some particles remain in the sending robot. Received particles from other robots are evaluated using measurement result in the receiving robot. The proposed method is tolerant to recognition error by remaining particles and twice evaluations of exchanging particles in sending robot and receiving robot, and if there is no recognition error, the proposed method increases accuracy of estimation by these twice evaluations. These properties of the proposed method are argued mathematically. Simulation results show that mistakes of recognition of other robots does not cause serious problem in the proposed method.

Keywords: Multi-Robot Localization, Particle Filter, Localization, Collaborative Multi-Robot System

I. INTRODUCTION

Localization of mobile robot using sensors is considered to be one of the most important problems in mobile robotics, and probabilistic methods have been proposed [1]. Probabilistic methods are expected to be robust for sensor noise or some inappropriate sensor information. The Kalman filter and Monte Carlo Localization (MCL) are widely used for probabilistic localization [1]. These are based on Markov localization [2],[3],[4],[5]. MCL uses particle filter that consists of possible positions of a robot [6],[7],[8].

In a multi-robot system, each robot can recognize other robots as mobile landmarks for localization and know relative positions of other robots by using sensors, and each robot can know the estimation results of locations in other robots by communication. In this situation, the accuracy of localization may increase and the calculation time may decrease by collaborating information of robots. For example, there are such collaborative methods by using geometrical group configuration of robots. Nakamura et al.[9] propose a localization method for mobile robots using geometrical constraints of observed robots and landmarks in the environment. Also, Kurazume et al. propose CPS (Cooperative Positioning System) [10]. In CPS, robots are divided into two groups, and while robots in one group are moving, robots in another group are stationary as landmarks.

On the other hand, there are methods by unifying localizations of robots. In these methods, first, each robot localizes own position independently without information of other robots, and then localization information of robots are exchanged and unified. Using Kalman filter, Bahr et al. [11] propose a method for cooperative localization. This method combines multiple estimations. In general, Kalman filter assumes the distribution of noise to be Gaussian. In particle filter, there are few assumptions about distribution of noise. In this paper, robot localization problem using particle filter is discussed.

Fox et al.[12],[13] propose a method for collaborative multi-robot localization using particle filter. In this method, each robot's belief is synchronized whenever one robot detects another. With this collaboration, faster calculation and higher accuracy of localization is obtained. Gasparri et al. [14] propose another method, in which particles and sensor information are exchanged if these weights exceed a threshold.

In these probabilistic collaborative multi-localization algorithms using particle filter, recognition of other robots is assumed to be correct, and influence of recognition error of other robot is not discussed. However, recognition of other robots is difficult in some cases. For example, in a case that a robot recognizes other robot using laser range sensors and shapes of robots are similar, it is difficult to distinguish robots. This may cause a serious problem for localization. This paper discusses this problem.

To cope with this problem, a new algorithm for probabilistic collaborative multi-robot localization is proposed. In the proposed algorithm, particles in a robot are sent to other robots according to measurement result in the sending robot, at the same time, some particles remain in the sending robot. Received particles from other robots are evaluated using measurement result in the receiving robot. With remaining particle, localization results are expected to be tolerant to recognition error of other robot, and with twice evaluation of exchanging particles in sending robot and receiving robot, high accuracy is expected. These properties of the proposed method are argued mathematically and confirmed by simulation in this paper.

II. OUTLINE OF SOME CONVENTIONAL ALGORITHMS FOR COLLABORATIVE MULTI-ROBOT LOCALIZATION

First, the outline of MCL without collaboration is presented [1]. Here, the only one robot is considered. MCL is a probabilistic method and uses particle filter to represent the probability of location of robot that is called belief. Belief is the probability $bel(\mathbf{x}_t) = p(\mathbf{x}_t \mid \mathbf{u}_t, \mathbf{z}_t)$, where $\mathbf{x}_t$ is the location of robot at the time t and $\mathbf{x}_t = (x_t, y_t, \theta_t)$. $\mathbf{u}_t$ is input data such as behavior of robot, and $\mathbf{z}_t$ is measurement data by sensors of robot. Precisely, there are two types of belief, that is, prior belief and posterior belief. $bel(\mathbf{x}_t)$ means posterior belief and prior belief is denoted by $bel^-(\mathbf{x}_t)$.

Particle filter represents above probability distributions by particles. Current set X_t of particles is obtained as follows. For each particle $\mathbf{x}_{t-1}^{(k)} \in X_{t-1}$ $(1 \le k \le M)$, another set X_t^- of particles is made according to the motion model $p(\mathbf{x}_t \mid \mathbf{u}_t, \mathbf{x}_{t-1}^{(k)})$. X_t^- represents prior belief $bel^-(\mathbf{x}_t)$, expressed by $X_t^- \approx bel^-(\mathbf{x}_t)$. For each $\overline{\mathbf{x}}_t^{(k)} \in X_t^-$ $(1 \le k \le M)$, a weight $w_t^{(k)} = p(\mathbf{z}_t \mid \overline{\mathbf{x}}_t^{(k)})$ is calculated according to measurement model $p(\mathbf{z}_t \mid \mathbf{x}_t)$.

Finally, M particles are selected randomly from X_t^- with probability proportional to its weight, and X_t consists of these M particles with $X_t \approx p(\mathbf{x}_t \mid \mathbf{u}_t, \mathbf{z}_t)$.

Fox et al. [13] have expanded algorithms for multi-robot by using this MCL. They denote N is the number of robots, d_i is the data gathered by robot i and $\mathbf{x}_n$ is the location of robot n. d_i consists of odometry measurements, environmental measurements and detections by robot i. When robot j recognizes other robot i, information about the location of robot i relative to robot j is sent to robot i from robot j, and $bel(\mathbf{x}_{i,t})$ is calculated as below.

$$\begin{aligned} bel(\mathbf{x}_{i,t}) &= p(\mathbf{x}_{i,t} \mid d_{i,t}) p(\mathbf{x}_{i,t} \mid d_{j,t}) \\ &= p(\mathbf{x}_{i,t} \mid d_{i,t}) \int p(\mathbf{x}_{i,t} \mid \mathbf{x}_{j,t}, r_{j,t}) p(\mathbf{x}_{j,t} \mid d_{j,t-1}) d\mathbf{x}_{j,t}, \end{aligned} \quad (1)$$

where $r_{j,t}$ is a detection variable showing relative position of robot i from robot j.

Gasparri et al. have proposed another algorithm for collaborative multi-robot localization [14]. Particles in each robot are exchanged if these weights exceed some threshold, under the assumption that recognitions of robots are correct.

III. THE PROBLEM OF RECOGNITION ERROR OF OTHER ROBOTS

The conventional collaborative multi-robot localization methods assume that recognition of a robot from other robot is correct. That is, the robot number of robot i is recognized as i correctly from robot j. In a multi-robot system, many robots with the same shape are used. In that case, recognition of a robot from other robot is difficult. In the case that initial positions of all robots are known, a robot can recognize other robots by tracing positions of other robots successively using laser sensors of the robot. However, if other two robots are very near, these robots cannot be distinguished by the robot and recognition of other robots may fail.

In the method proposed by Fox et al., probabilities of localizations of robots are collected and multiplied and the probability of localization of a robot is obtained as (1). However, if recognition of a robot from another robot is wrong, collected probability from wrong recognized robot may be very small and the probability of localization of a robot is also very small. In (1), if robot i' is recognized as robot i incorrectly, $bel(\mathbf{x}_{i,t}) = p(\mathbf{x}_{i,t} \mid d_{i,t}) p(\mathbf{x}_{i',t} \mid d_{j,t})$ and this may become very small.

In the case that the recognized robot location is far from the correct robot location, the probability of localization may be almost zero. In this case, the probability of location cannot be calculated correctly and estimated location of a robot may be very far from the correct location and this causes a serious problem.

In the case that the recognized robot location is near to the correct robot location, the estimation error of location is not very large. However, as the distance between the correct robot location and the wrong recognized robot is larger, the estimation error of location becomes large.

IV. THE PROPOSED ALGORITHM

To cope with the problem described in the previous section, a new algorithm for collaborative multi-root localization is required. Recently the accuracy of laser range sensor is very high, therefore we assume that there is no error about measurements for relative position from a robot to another robot. Additionally, we assume that there is no communication delay between robots. In the proposed algorithm, particles of robots are exchanged. Some particles are selected according to their weights determined by perception using sensors. Selected particle are sent to another robot and weights of these particles are evaluated again by using sensors of another robot. These particles are evaluated twice at sending robot and receiving robot. Some particles remain in the sending robot. If detection of another robot is wrong, weight of received particle is very small, and detection error is not harmful for localization by using remained particles. If detection of another robot is correct, weight of particle is evaluated in two robots, and improvement of accuracy of localization is expected.

The number of robots is assumed to be N. Robot has a set of M particles $X_{i,t} = \{\mathbf{x}_{i,t}^{(1)}, \mathbf{x}_{i,t}^{(2)}, \ldots, \mathbf{x}_{i,t}^{(M)}\}$ at the time t which represents $bel(\mathbf{x}_{i,t}) = p(\mathbf{x}_{i,t} \mid \mathbf{u}_{i,t}, \mathbf{z}_{i,t})$, where $\mathbf{x}_{i,t} = (x_i, y_i, \theta_i)$.

In the same way, $X_{i,t}^{-} = \{\overline{\mathbf{x}}_{i,t}^{(1)}, \overline{\mathbf{x}}_{i,t}^{(2)}, \ldots, \overline{\mathbf{x}}_{i,t}^{(M)}\}$ represents $bel^{-}(\mathbf{x}_{i,t})$, that is, $X_{i,t}^{-} \approx bel^{-}(\mathbf{x}_{i,t})$. A weight of $\overline{\mathbf{x}}_{i,t}^{(k)}$ is denoted by $w_{i,t}^{(k)}$, that is, $w_{i,t}^{(k)} = p(\mathbf{z}_{i,t} \mid \overline{\mathbf{x}}_{i,t}^{(k)})$.

The relative position of robot j from robot i can be represented as $\mathbf{s}_{ij} = (x_{ij}, y_{ij}, \theta_{ij})$, and ideally $\mathbf{x}_j = \mathbf{x}_i + \mathbf{s}_{ij}$. In this paper, $\mathbf{s}_{ij}$ is assumed to be correct and $p(\mathbf{x}_j \mid \mathbf{x}_i, \mathbf{s}_{ij})$ is assumed to be Dirac delta function, then

$$p(\mathbf{x}_j \mid \mathbf{u}_i, \mathbf{z}_i, \mathbf{s}_{ij}) = \int \delta(\mathbf{x}_j - (\mathbf{x}_i + \mathbf{s}_{ij}))\, p(\mathbf{x}_i \mid \mathbf{u}_i, \mathbf{z}_i)\, d\mathbf{x}_i = p(\mathbf{x}_j - \mathbf{s}_{ij} \mid \mathbf{u}_i, \mathbf{z}_i). \quad (2)$$

In robot i, $(1-p_0)M/(N-1)$ particles $(0 < p_0 < 1)$ are selected from $X_{i,t}^{-}$ according to their weights. These particles are considered to represent $p(\mathbf{x}_{i,t} \mid \mathbf{u}_{i,t}, \mathbf{z}_{i,t})$. For each selected particle $\overline{\mathbf{x}}_{i,t}^{(k)}$, $\hat{\mathbf{x}}_{j,t}^{(k)} = \overline{\mathbf{x}}_{i,t}^{(k)} + \mathbf{s}_{ij,t}$ is calculated. The set $\hat{X}_{ij,t}$ of these $\hat{\mathbf{x}}_{j,t}^{(k)}$ represents $p(\mathbf{x}_{j,t} \mid \mathbf{u}_{i,t}, \mathbf{z}_{i,t}, \mathbf{s}_{ij,t})$. Then $\hat{X}_{ij,t}$ is sent to robot j from robot i. In the same way, robot i receives a set $\hat{X}_{ji,t}$ of particles from robot j. The number of received particles in robot i is $(1-p_0)M$. Whereas a set R_i of $p_0 M$ particles remains in robot i, which are selected from $X_{i,t}^{-}$ according to their weight.

In robot i, a weight for each received particle is calculated according to the measurement model. Particles remained in i and received particles are collected as the disjoint union : $X_{i,t} = R_i \cup \bigcup_{j \neq i} \hat{X}_{ji,t}$.

M particles are resampled from $X_{i,t}$ according to its weight, and $\tilde{X}_{i,t}$ is produced. $\tilde{X}_{i,t}$ represents current position of robot i.

Probabilistic property of the proposed method will be discussed mathematically. In probabilistic expression,

$$\tilde{X}_{i,t} \approx \eta[p_0 \cdot p(\mathbf{x}_{i,t} \mid \mathbf{u}_{i,t}, \mathbf{z}_{i,t}) + \frac{1-p_0}{N-1} \sum_{j \neq i} p(\mathbf{x}_{i,t} \mid \mathbf{u}_{i,t}, \mathbf{z}_{i,t})\, p(\mathbf{x}_{i,t} \mid \mathbf{u}_{j,t}, \mathbf{z}_{j,t}, \mathbf{s}_{ji,t})], \quad (3)$$

where η is the normalization coefficient for probability distribution.

When abilities of sensors of robots are almost the same and relative position of robots j's from robot i are estimated correctly, the second term of (3) have smaller standard deviation than that of the first term of the equation and the estimation of position of robot i is expected to be more accurate than the original estimation.

For example, $p(\mathbf{x}_{i,t} \mid \mathbf{u}_{i,t}, \mathbf{z}_{i,t})$ and $p(\mathbf{x}_{i,t} \mid \mathbf{u}_{j,t}, \mathbf{z}_{j,t}, \mathbf{s}_{ji,t})$ are assumed to be normal distribution with mean value being true value $\hat{\mathbf{x}}_{i,t} = (\hat{x}_i, \hat{y}_i, \hat{\theta}_i)$ for the location of robot i.

$$p(\mathbf{x}_{i,t} \mid \mathbf{u}_{i,t}, \mathbf{z}_{i,t}) = \eta \exp\left[-\tfrac{1}{2}(\mathbf{x}_{i,t} - \hat{\mathbf{x}}_{i,t})\Sigma_i^{-1}(\mathbf{x}_{i,t} - \hat{\mathbf{x}}_{i,t})^T\right], \quad (4)$$

where η is normalization coefficient and Σ_i is the covariance matrix assumed to be a diagonal matrix $\Sigma_i = diag\{\sigma_i^2, \sigma_i^2, \mu_i^2\}$ with diagonal elements $\sigma_i^2, \sigma_i^2, \mu_i^2$, and

$$p(\mathbf{x}_{i,t} \mid \mathbf{u}_{j,t}, \mathbf{z}_{j,t}, \mathbf{s}_{ji,t}) = \eta \exp\left[-\tfrac{1}{2}(\mathbf{x}_{i,t} - \hat{\mathbf{x}}_{i,t})\Sigma_{ji}^{-1}(\mathbf{x}_{i,t} - \hat{\mathbf{x}}_{i,t})^T\right], \quad (5)$$

where η is another normalization coefficient and Σ_{ji} is the covariance matrix assumed to be $\Sigma_{ji} = diag\{\sigma_{ji}^2, \sigma_{ji}^2, \mu_{ji}^2\}$.

Then, $p(\mathbf{x}_{i,t} \mid \mathbf{u}_{i,t}, \mathbf{z}_{i,t})\, p(\mathbf{x}_{i,t} \mid \mathbf{u}_{j,t}, \mathbf{z}_{j,t}, \mathbf{s}_{ji,t}) = \eta \exp\left[-\tfrac{1}{2}\left((\mathbf{x}_{i,t} - \hat{\mathbf{x}}_{i,t})(\Sigma_i^{-1} + \Sigma_{ji}^{-1})(\mathbf{x}_{i,t} - \hat{\mathbf{x}}_{i,t})^T\right)\right]$ and the covariance matrix is $(\Sigma_i^{-1} + \Sigma_{ji}^{-1})^{-1} = diag\{(\sigma_i^{-2} + \sigma_{ji}^{-2})^{-1}, (\sigma_i^{-2} + \sigma_{ji}^{-2})^{-1}, (\mu_i^{-2} + \mu_{ji}^{-2})^{-1}\}$. Since $(\sigma_i^{-2} + \sigma_{ji}^{-2})^{-1} < \sigma_i^2$, the standard deviation of the second term of (3) becomes smaller than that of the first term, and the localization is expected to be more accurate. Especially when $\sigma_i \approx \sigma_{ij}$ and $\mu_i \approx \mu_{ij}$, standard deviation becomes $(\sigma_i^{-2} + \sigma_{ji}^{-2})^{-1/2} \approx \sigma_i / \sqrt{2}$.

Now the problem of the previous section is discussed in the proposed algorithm. Robot i detects another robot j by using sensor. We consider the case that robot j is recognized incorrectly as robot j'.

Proposed method works well under these conditions. If there is a recognition error of robot as above, the corresponding summand in the second term of (3) becomes $p(\mathbf{x}_{i,t} \mid \mathbf{u}_{i,t}, \mathbf{z}_{i,t}) p(\mathbf{x}_{i,t} \mid \mathbf{u}_{j,t}, \mathbf{z}_{j,t}, \mathbf{s}_{j'i,t})$ and may be very small. Then, remaining parts of the equation (in the case all recognitions are wrong, only the first term $p(\mathbf{x}_{i,t} \mid \mathbf{u}_{i,t}, \mathbf{z}_{i,t})$) are not small and correct estimation is done from the remaining part. This can be seen as below. $p(\mathbf{x}_{i,t} \mid \mathbf{u}_{i,t}, \mathbf{z}_{i,t})$ and $p(\mathbf{x}_{i,t} \mid \mathbf{u}_{j,t}, \mathbf{z}_{j,t}, \mathbf{s}_{j'i,t})$ are assumed to be normal distributions as above (4),(5). But in this case, from (2), $p(\mathbf{x}_{i,t} \mid \mathbf{u}_{j,t}, \mathbf{z}_{j,t}, \mathbf{s}_{j'i,t}) = p(\mathbf{x}_i - \mathbf{s}_{j'i} \mid \mathbf{u}_j, \mathbf{z}_j) = \eta \exp[-\frac{1}{2}(\mathbf{x}_{i,t} - \hat{\mathbf{x}}_{ijj',t}) \Sigma_{ji}^{-1} (\mathbf{x}_{i,t} - \hat{\mathbf{x}}_{ijj',t})^T]$, where $\hat{\mathbf{x}}_{ijj',t} = \hat{\mathbf{x}}_{i,t} - (\hat{\mathbf{x}}_{j,t} - \hat{\mathbf{x}}_{j',t}) = (\hat{x}_{ijj'}, \hat{y}_{ijj'}, \hat{\theta}_{ijj'})$. If $\Sigma_{ji} \approx \Sigma_i$, and Σ_i is assumed as above,

$$
\begin{aligned}
& p(\mathbf{x}_{i,t} \mid \mathbf{u}_{i,t}, \mathbf{z}_{i,t}) p(\mathbf{x}_{i,t} \mid \mathbf{u}_{j,t}, \mathbf{z}_{j,t}, \mathbf{s}_{j'i,t}) \approx \\
& \eta \exp\left[-\tfrac{1}{2}\{((x_i - \hat{x}_i)^2 + (x_i - \hat{x}_{ijj'})^2)\sigma_i^{-2} + ((y_i - \hat{y}_i)^2 + \right. \\
& (y_i - \hat{y}_{ijj'})^2)\sigma_i^{-2} + ((\theta_i - \hat{\theta}_i)^2 + (\theta_i - \hat{\theta}_{ijj'})^2)\mu_i^{-2}\}] \\
& \le \eta \exp[-\tfrac{1}{4}\{(\hat{x}_{j'} - \hat{x}_j)^2 \sigma_i^{-2} + (\hat{y}_{j'} - \hat{y}_j)^2 \sigma_i^{-2} + (\hat{\theta}_{j'} - \hat{\theta}_j)^2 \mu_i^{-2}\}].
\end{aligned}
$$

The last inequality is obtained from the inequality $(a^2 + b^2) \ge \frac{1}{2}(a - b)^2$ for arbitrary real numbers a, b.

In the case that wrong recognized robot j' is apart from robot j, $(\hat{x}_{j'} - \hat{x}_j)^2$, $(\hat{y}_{j'} - \hat{y}_j)^2$ becomes very large, hence $p(\mathbf{x}_{i,t} \mid \mathbf{u}_{i,t}, \mathbf{z}_{i,t}) p(\mathbf{x}_{i,t} \mid \mathbf{u}_{j,t}, \mathbf{z}_{j,t}, \mathbf{s}_{j'i,t})$ becomes very small.

V. SIMULATION

The effectiveness of the proposed method is confirmed in this section by computer simulation. Each robot knows the precise locations of landmarks and makes a map of the field. Behaviors of each robot are assumed to be two : straight moving and pivoting (rotation in place). One of these two behaviors is selected randomly in each time. In this experiment, five robots are used.

The comparison result of the proposed method and conventional MCL without collaboration is shown in Fig. 1. The horizontal axis shows the number of particles and the vertical axis shows the estimation error between estimated location and true location. In this simulation, there assumes to be no recognition error of robots, and $p_0 = 0.85$. Simulations are executed with 150 trials. Lines without markers show the results of conventional estimation. Lines with markers show the results of the proposed method.

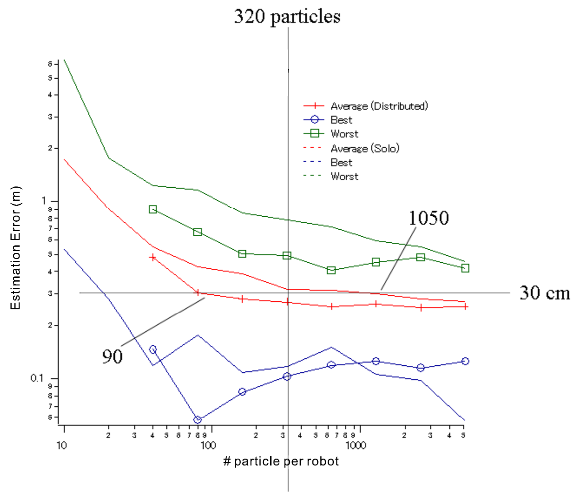

Fig.1. Estimation error and number of particles

Average of estimation error of the proposed method is better than that of conventional method. The proposed method needs less number of particles than conventional method for attaining the same average of estimation error. For example, seeing the horizontal line of estimation error 30cm, the number of particles required for attaining the average of estimation error less than 30cm is approximately 90 in the proposed method. However, that number is approximately 1050 in the conventional method.

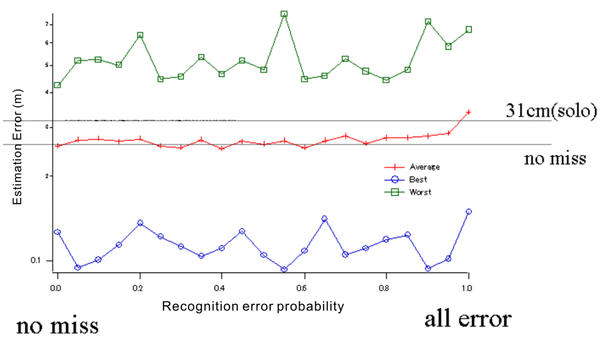

Fig.2. Estimation error and recognition error

The relation of estimation error and recognition error probability is shown in Fig. 2. The number of particles is 320 and $p_0 = 0.85$ as before, and the number of trials is 150. The recognition error probability is varied between 0.0 and 1.0. As an implementation of recognition error of other robots at robot i in the simulation, a wrong robot j' is selected randomly except robot i and the correct robot

j. Particles for exchange are sent to robot j' instead of robot j.

In Fig. 2, vertical axis shows estimation error and horizontal axis shows recognition error probability. The horizontal line with 31cm shows the estimation error of conventional MCL without collaboration in the case that the number of particles is 320.

When there is no recognition error of robots, the average of estimation error is 25cm and minimum among all recognition error probability. When all recognitions of robots are wrong, the average of estimation error is 34cm and maximum. Even if recognition error probability is 95%, estimation error of the proposed method is better than that of conventional MCL without collaboration. This result shows that the proposed method improves estimation error of localization by collaboration, unless recognition error probability is almost 100%.

These simulation results confirm the effectiveness of proposed method under the condition of existence of recognition error of robots.

VI. CONCLUSION

In this paper, the problem of recognition error of robots in localization of multi-robots has been discussed. The discussion has shown that if the recognition of other robots is wrong, a large amount of error in localization may occur. Then, a new algorithm for collaborative multi-robot localization using particle filter has been proposed to cope with this problem. In the proposed method, particles in a robot are sent to other robots according to measurement result in the sending robot, at the same time, some particles remain in the sending robot. Received particles from other robots are evaluated by using measurement result in the receiving robot. The proposed method copes with recognition error by remaining particles in sending robot, and increases accuracy of estimation by twice evaluation of exchanging particles in sending robot and receiving robot.

By simulations, estimation errors of localization of the proposed method and conventional MCL without collaboration have been compared. From the simulation with recognition error, even if there are many recognition errors, estimation error of the proposed method is better than that of conventional MCL without collaboration. From the simulation without recognition error, the accuracy of localization of the proposed method is better than that of the conventional method, if the numbers of particles are the same. In addition, the proposed method needs less number of particles than the conventional method for attaining the same accuracy of estimation, and this shows that the execution time of the proposed method can be faster than the conventional method with the same estimation error.

From these results, the proposed method is tolerant to recognition error and accurate for multi-robot localization.

REFERENCES

[1] S. Thrun, W. Burgard and D. Fox (2005), Probabilistic Robotics, MIT
[2] R. Simmons and S. Koenig (1995), Probabilistic Robot Navigation in Partially Observable Environments, Proc. IJCAI
[3] A. R. Cassandra et al. (1996), Acting under Uncertainty: Discrete Bayesian Models for Mobile-Robot Navigation, Proc. IROS
[4] W. Burgard et al. (1996), Estimating the Absolute Position of a Mobile Robot Using Position Probability Grids, Proc. AAAI, 2, pp.896-901
[5] D. Fox, W. Burgard and S. Thrun (1999), Markov Localization for Mobile Robots in Dynamic Environments, Journal of Artificial Intelligence Research, Vol. 11, pp.391-427.
[6] F. Dellaert et al. (1996), Monte Carlo Localization for Mobile Robots, Proc. ICRA
[7] D. Fox, W. Burgard and S. Thrun (1999), Monte Carlo localization: Efficient Position Estimation for Mobile Robots, Proc. AAAI
[8] S. Thrun et al. (2001), Robust Monte Carlo Localization for Mobile Robots, Artificial Intelligence, Vol. 128, pp.99-141
[9] T. Nakamura et al. (2003), Self-Localization Method for Mobile Robots Using Multiple Omnidirectional Vision sensors, Journal of the Robotics Society of Japan, Vol. 21, No.1, pp.109-117
[10] R. Kurazume, S. Nagata and S. Hirose (1994), Cooperative Positioning with Multiple Robots, Proc. ICRA, Vol. 2, pp.1250-1257
[11] A. Bahr, M. R. Walter and J. J. Leonard (2009), Consistent Cooperative Localization, Proc. ICRA, pp.3415-3422
[12] D. Fox et al. (1999), Collaborative Multi-Robot Localization, Lecture Note in Computer Science, Vol. 1701/1999, pp.255-266
[13] D. Fox et al. (2000), A Probabilistic Approach to Collaborative Multi-Robot Localization, Autonomous Robots, Vol. 8, Issue 3, pp.325-344.
[14] A. Gassparri et al. (2008), A Fast Conjunctive Resampling Particle Filter for Collaborative Multi-Robot Localization, Proc. AAMAS

Study on the Route Extraction Based on the Image Processing

Jiwu Wang[1] Masanori Sugisaka[2]

Department of Mechanical Engineering, Beijing Jiaotong University, Beijing, China[1]
Department of Mechanical and Electrical Engineerin, Nippon Bunri University, Oita, Japan[2]
Email: jwwang@bjtu.edu.cn, ms@alife-robotics.co.jpT

Abstract: In the application of a mobile robot, we generally pay more attention on the navigation. In this paper, we study the visual based navigation for a mobile robot. We assume that we set the moving trace with some simple marks. Based on the image processing, the robot can extract the moving trace and realize self-location. At the same time, combing with some logic algorithms, the robot can reach the target point. Here, we try to find how to extract the visual signal from the simple continuous landmarks.

Keywords: Image processing, Navigation, Mobile robot.

I. INTRODUCTION

Navigation is the important part to develop a mobile robot. After we complete the development of the fundamental functions, such as the basic motor control etc. We will consider how to make the robot reach specified target. Till now, many solutions have been developed for the navigation. Considering the reliability and repeatability, we pay more attention on the visual navigation.

For the visual navigation, the robot uses the visual signal to control navigation. The robot captured the images with the CCD camera. By special image processing technique, the target signal is extracted. That means the target signal is important for the visual based navigation. But it is not easily to extract the target signal under any environments based on present image processing techniques. This is because the background is always changed when the robot is moving. Sometimes, some objects similar to the target will appear in the background. The robot will make mistakes if the algorithms are not robust enough. Moreover, the lighting conditions are changed as the robot moves. Most of important, some landmarks will be missed if the robot move at different speed. In view of those problems, there are many things to be studied before the robot can realize reliable visual based navigations.

In this paper, we pay more attention on the route extraction. We assume that we set the moving trace with some simple marks based on our requirements. The route works like the continuous landmarks. By the image processing, the moving trace will be extracted and the robot can realize self-location. Moreover, it will also know the moving target. We will introduce how to extract the guideline from the common guideline settings. And we will also introduce how to mark the cross points, the horizontal line and vertical line. After the robot obtain those information, combined with some logic algorithms, we hope the robot can realize self-location under some simple environments settings.

II. ROUTE PLANNING

For the navigation, it is necessary to perform route planning first. In real applications, generally we will meet following route planning.

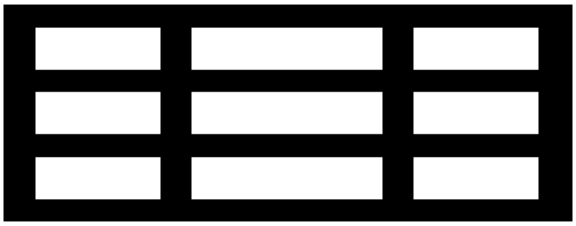

Figure 1 Route format sample 1

In format sample 1, we only set the route simply. It is also the common setting for general applications. In this case, the robot has to recognize the crossing point automatically.

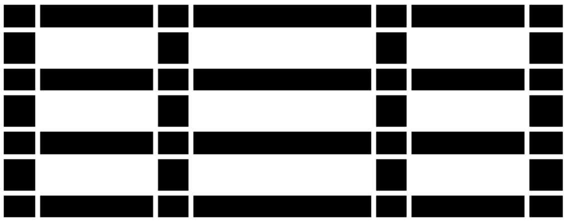

Figure 2 Route format sample 2

In format sample 2, the crossing points are intentionally separated from the vertical line and horizontal line.

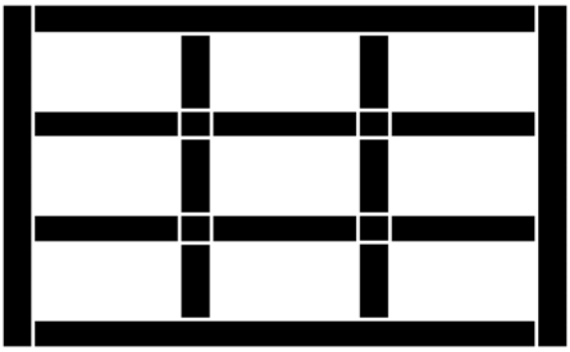

Figure 3 Route format sample 3

In the format 3, it is a little different from sample 2. Here only the internal crossing points are considered.

In the real applications, we will design various routes based on the requirements. But for the robot, it is necessary to separate the vertical line, the horizontal line and the crossing points. After the robot obtains those information, combining some sign landmarks, the robot will gradually realize the self location.

Considering the geometric information of the route, we can separate the vertical line, horizontal line and crossing points. The results are shown as followings.

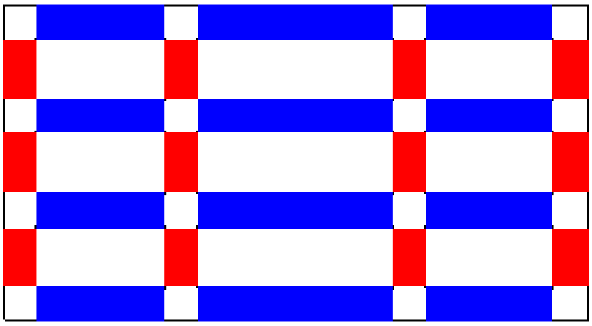

Figure 4 The result of the sample 1

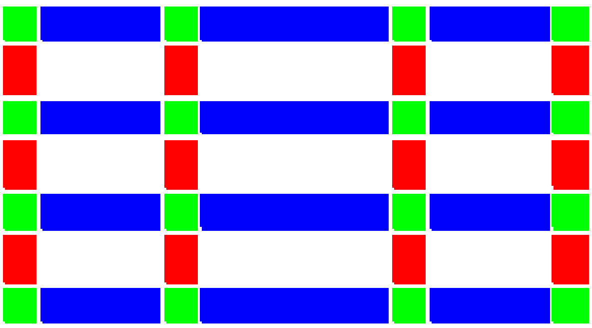

Figure 5 The result of the sample 2

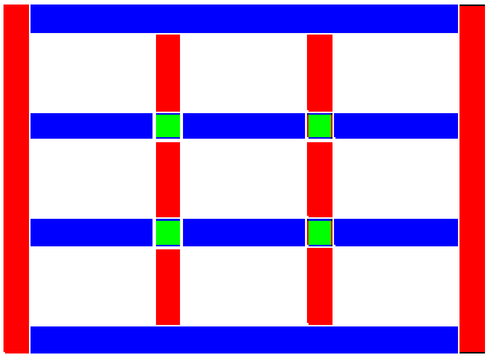

Figure 6 The result of the sample 3

In this process, we mark the vertical line, horizontal line and crossing point of different formats with different color.

III. EXPERIMENTS

The structure of our mobile robot is shown in figure 7.

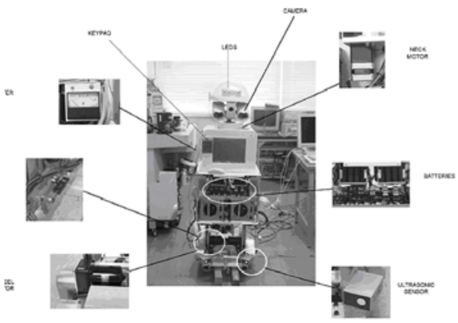

Figure 7 The structure illustration of the mobile robot

In the navigation development of our mobile robot, we only use the visual signal to control the robot to reach the specified target. The navigation route is set with the continuous landmarks.

Till now artificial landmarks of red/yellow circle, triangle, cross and guideline were developed. Under normal lighting conditions, these landmarks can be recognized accurately. But under poor lighting or strong reflection conditions, because there were not enough pixels that can be extracted from the image taken by the CCD video camera, sometimes these landmarks can be detected but not be recognized. Figure 8 is the illustration of the red landmarks of triangle and cross that were recognized in recognition experiments.

In real cases, it is normal that the characters of the sign landmarks can not be all extracted because various reasons, such as lighting, hiding, the interval of the camera to take the picture etc. It is necessary to use compound sensors or compound image processing techniques for some important sign landmarks.

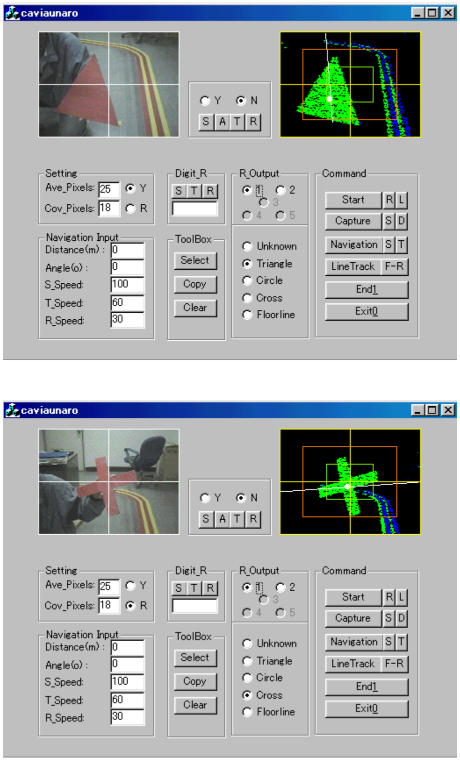

Figure 8 The recognition illustration of some landmarks

In order to find the guideline in any intervals when the robot is moving, the moving speed should be controlled based on the curvature of the guideline. Because of the camera frame rate (NTSC 30fps) and time constants of the motors (20-30ms, experimentally determined from non-load step response), the cycle time for our control loop was impossible to be extended. The robot will miss some landmarks or the guideline if the robot moves at high speed when there is the curvature change of the guideline or the locations of the landmarks does not correspond the intervals effectively. In the practical applications, such cases can not be avoided. In order to make the response in real time, the speed of the robot was controlled based on the curvature of the guideline. The robot can move at high speed when it moves along the straight guideline. Otherwise, it will move at low speed. Figure 9 is the illustration of self-location for the robot when it is moving. One is the case of straight guideline, and another is the robot will move along the curve line. The position and direction of the robot relative to the guideline were calculated in the real time.

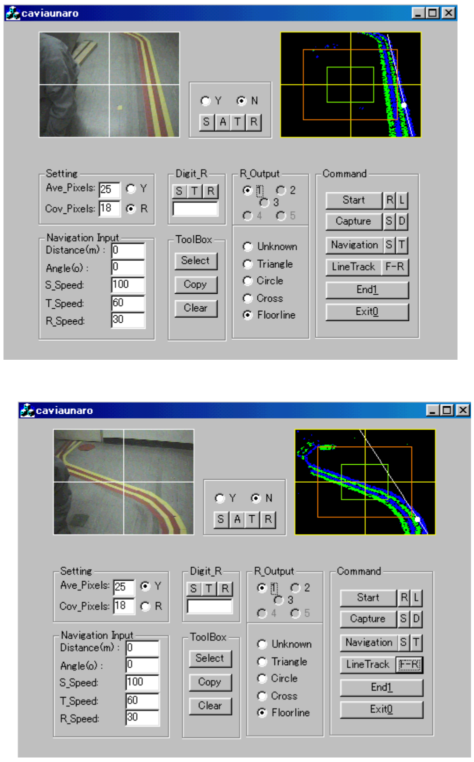

Figure 9 The illustration of the self-location in the visual servo control

IV. CONCLUSION

In this paper, we try to study how to control the mobile robot with the visual signal. It is possible to extract the general map setting based on the image processing technique. By the image processing, the robot can realize the self location. Moreover, the robot will also separate the vertical line, the horizontal line and the crossing points. Finally, we test the navigation of our mobile robot with the visual signal.

REFERENCES

[1] M.Sugisaka, Wang Xin and J. Lee, "Artificial brain f or a mobile vehicle", Applied mathematics and computa tion, Vol. 111, 2000.
[2] Jiwu Wang, M.Sugisaka, "Study on a color based target detection technique", Proc. of the seventh Int. Symp. On artificial life and robotics (AROB 7th'02), Beppu, Oita, Japan. 16-18 January, 2002.
[3] Cathy-Ann Radix, Andrey Loukianov, Masanori Sugisaka, "Evaluating motion on the alife robot prototype", Proceedings of the 32nd ISR (International Symposium on Robotics), 19-21 April 2001.
[4] Ulrich Nehmzow, Carl Owen, "Robot navigation in the real world: experiments with Manchester's Fortytwo in unmodified, large environments", Robotics and autonomous systems, Vol. 33, 2000.

[5] F.El-Khaly, M.A.Sid-Ahmed, "Machine recognition of optically captured machine printed Arabic text", Pattern recognition, vol. 23, No. 11, 1990.
[6] Alireza Khotanzad, Yaw Hua Hong, "Rotation invariant image recognition using feature selected via a systematic method", Pattern recognition, Vol. 23, No. 10, 1990.
[7] S.O.Belkasim, M.Shridhar and M.Ahmadi, "Pattern recognition with moment invariants: a comparative study and new results", Pattern recognition, Vol. 24, No. 12, 1991.
[8] Jiwu Wang, M.Sugisaka, "Improve digit recognition capability of backpropagation neural networks by Enhancing image preprocessing technique", Proceedings of International Conference on Control, Automation and Systems, Cheju University, Jeju, Korea, October 17-21, 2001.
[9] Jiwu Wang, M.Sugisaka, "Study on calibration of stereo cameras for a mobile robot prototype", Proc. of the seventh Int. Symp. On artificial life and robotics (AROB 7th'02), Beppu, Oita, Japan. 16-18 January, 2002.
[10] Seth Hutchinson, Gregory D.Hager, Peter I.Corke, "A tutorial on visual servo control", IEEE Transactions on Robotics and Automation, Vol. 12, No. 5, October 1996.
[11] Peter I.Corke, Malcolm C.Good, "Dynamic effects un visual closed-loop systems", IEEE Transactions on Robotics and Automation, Vol. 12, No. 5, October 1996.

Estimating Stochastic Volatility Models of Stock Returns in Chinese Markets

Shu Quan Lu[1*], Shiyu Xie[1], and Takao Ito[2]

1 School of Economics, Fudan University, Shanghai, China
(lushuquan2000@yahoo.com, syxie@fudan.edu.cn)
2 Dept. of Business Administration, Ube National College of Technology, Yamaguchi, Japan
(Tel : 81-836-35-7115; Fax : 81-836-35-7115)
(ito@ube-k.ac.jp)

Abstract: Volatility plays a key role for microstructure issues in the study of financial market. Stochastic Volatility (SV) models have been applied to the behavior study of financial variables. Two stock markets exist in China: Shanghai Stock exchange and Shenzhen Stock exchange. As emerging stock markets, investors are increasingly concerned about volatilities of these two stock markets. We introduce briefly how to estimate SV models using Markov chain Monte Carlo (MCMC) method. In order to do full and comprehensive analyses of the volatilities of stock returns, we estimate SV models using most of the historical data and different data frequencies of the two Chinese markets. We find that estimated values of volatility parameters are very high for all data frequencies. It suggests that stock returns are extremely volatile even at long term intervals in Chinese markets.

Keywords: MCMC Method, Volatility, Stock returns, Chinese markets.

I. INTRODUCTION

Volatility plays a key role for financial market microstructure issue. This gives rise to strong interest in volatility model which describes the evolution of conditional variance of the time-series variable.

There are essentially two types of models for describing the dynamics of volatility. One is GARCH model, and the other is SV models.

GARCH model considers only one source of uncertainty, but SV model introduces the additional innovation to the conditional variance equation so that they are much more flexible than ARCH or GARCH models [1].

There are two stock markets in China: Shanghai Stock exchange and Shenzhen Stock exchange. Many want to know Chinese stock markets' volatility.

In this paper, we primarily apply SV models to describe the behavior of volatility for different frequencies data for Chinese stock returns. In order to compare the results form SV models with other models, we also estimate stock returns' volatility with GARCH models.

The first contribution is that our analyses almost cover all historical data of Chinese stock markets, providing a full description about volatility. The second contribution of this paper is that we set and estimate SV models for different data frequencies, so we give very comprehensive analyses for the behaviors of volatilities of stock returns.

The rest of the paper is outlined as follows. In section 2, we introduce the basic principle and framework of SV models. Section 3 applies SV models, together with GARCH models, to analysis of Chinese stock returns, and then provides and discusses the estimated results. A final section concludes.

II. SV MODELS

1. The structure of volatility and GARCH model

Before discussing how to estimate SV models, we briefly introduce the structure of a volatility and GARCH model. The structure of a volatility model can be described as

$$x_t = \mu_t(\theta) + \varepsilon_t \tag{1}$$

$$\varepsilon_t = \sigma_t(\theta) z_t \tag{2}$$

In (1), the return x_t at time *t* is decomposed into a residual term ε_t and a conditional mean $\mu_t(\theta)$ According (2), the residual term ε_t has volatility conditional on information set available at time *t*-1, denoted σ_t. θ is the vector of unknown parameters. The variable z_t will be assumed to follow some distribution with mean 0 and variance 1.

The conditional variance of a GARCH is

$$\sigma_t^2 = \alpha_0 + \sum_{i=1}^{p} \alpha_i \sigma_{t-i}^2 + \sum_{j=1}^{q} \beta_j \varepsilon_{t-j}^2 \tag{3}$$

For this model to be well defined and the conditional variance to be positive, the parameters must satisfy the following constraints:

$\alpha_0 > 0$,

$\alpha_i \geq 0$,

$i = 1, \cdots, p$,

$\beta_j \geq 0$, and

$j = 1, \cdots, q$.

2. Stochastic volatility

Jacquier, Polson, and Rossi consider a model where the log σ_t^2 follows an AR (1) process with the error term v_t of volatility σ_t^2 [2, 3].

$$x_t = \mu_t + \varepsilon_t \qquad (4)$$

$$\varepsilon_t = \sigma_t z_t \qquad (5)$$

$$\ln \sigma_t^2 = \alpha_0 + \alpha_1 \ln \sigma_{t-1}^2 + \sigma_v v_t \qquad (6)$$

3. Estimating SV models: MCMC method

SV model is not estimated directly by Maximum Likelihood method because the process σ_t^2 is an unobservable variable. In this paper, we model stochastic volatility using MCMC method.

Tsay gives great details to work for the above described with Gibbs sampling approach [4].

III. STOCHASTIC VOLATILITY MODELS OF STOCK RETURNS IN CHINESE MARKETS: EMPIRICAL ANALYSIS

1. Data

As authoritative statistical indicators widely adopted by domestic and overseas investors in measuring the performance of Chinese stock markets, many indices are compiled and published by Shanghai and Shenzhen stock exchanges. We choose the composite index of Shanghai stock exchange spanning the period from Dec 31, 1991 through Sep 30, 2009, and the component index of Shenzhen exchange, spanning the period from Jan 3, 1994 through Sep 30, 2009[1].

For the observed sequence, *t = 1*, ……, *T*, we let X_1 to be the last composite index of Shanghai stock exchange and X_2 to be the last component index of Shenzhen stock exchange. Then, we let Y_1 to be the returns of the composite index and Y_2 to be the returns of the component index. Y_1 and Y_2 are defined as follows.

$$Y_{1t} = \ln(X_{1t} / X_{1t-1}) \qquad (7)$$

$$Y_{2t} = \ln(X_{2t} / X_{2t-1}) \qquad (8)$$

In order to examine the features of stock indexes' returns for different frequencies, we consider three frequencies: daily returns, monthly returns, and quarterly returns. Denote that Y_{1t}^d, Y_{1t}^m, and Y_{1t}^q are Shanghai composite indexes' daily log returns, monthly log returns, and quarterly log returns, respectively. Denote that Y_{2t}^d, Y_{2t}^m, and Y_{2t}^q are Shenzhen component indexes' daily log returns, monthly log returns, and quarterly log returns, respectively. Each log return is measured in percent.

2. Estimating GARCH models

In contrast to SV models' results, we estimate GARCH models for log returns using Maximum Likelihood method.

For parsimony, we let mean equation equal to constant, hence, volatility model is

$$\sigma_t^2 = \alpha_0^G + \alpha_1^G \sigma_{t-1}^2 + \beta^G \varepsilon_{t-1}^2 \qquad (9)$$

There are estimated values of α_1^G in Table 1.

Table 1. Estimating GARCH Models

α_1^G		
Y_{1t}^d	Y_{1t}^m	Y_{1t}^q
0.788	0.517	0.696
Y_{2t}^d	Y_{2t}^m	Y_{2t}^q
0.891	0.702	0.838

In Table 1, all estimates of volatility parameter, α_1^G, for different frequencies of two stock markets are statistically significant; in fact, their significant levels are all below 1%. The volatility parameter α_1^G measures the persistence of volatility, namely, volatility clustering. This suggests that volatility of log returns is strongly serially correlated; in other words, this means that a large (positive or negative) return tends to be followed by another large (positive or negative) return.

[1] Data is retrieved on Oct 20, 2009, from http://vip.stock.finance.sina.com.cn/.

3. Estimating SV models

Consider SV models,

$$\ln \sigma_t^2 = \alpha_0^{SV} + \alpha_1^{SV} \ln \sigma_{t-1}^2 + \sigma_v^{SV} v_t \qquad (10)$$

We run the Gibbs sampling for 10000 iterations for daily log returns, but for 2000 iterations for monthly log returns and quarterly log returns because of their small sample size relative to daily log returns. We discard results of the first 100 iterations in order to make remaining samples independent.

Table 2. Estimating SV Models

	α_1^{SV}	
Y_{1t}^d	Y_{1t}^m	Y_{1t}^q
0.903	0.891	0.891
Y_{2t}^d	Y_{2t}^m	Y_{2t}^q
0.889	0.857	0.889

According our estimating, SV models provide improvements in model fitting relative to GARCH models since most of parameters are statistically significant. (Here we do not present the t-statistics of GARCH and SV models for parsimony.) From Table 2, we see that all estimated values of persistent parameters α_1^{SV} are larger than estimated values α_1^G, the persistent parameters for GARCH models. This shows that in the case of SV models, the persistence of volatilities is high, relative to the case of GARCH models. In addition to high persistence in volatilities, there are almost identical estimated values of α_1^{SV} for different frequencies in SV models, while estimated values of α_1^G for monthly log returns are apparently smaller than estimated values for other frequencies in GARCH models.

4. Discussion

Table 2 shows that log returns are extremely volatile for Chinese stock markets even with a long time interval.

Lu, Ito, and Voges indicate that stock returns of Shenzhen component index exhibit long memory processes [5]. Lu and Ito find that there is a two-way feedback between Chinese two stock markets by using the expectational model to trace the response of a stock market to the other stock market [6]. These studies could suggest that high volatilities of stock markets could give rise to long memory or strong two-way feedback for stock market. Moreover, Lu and Ito have showed Chinese many macroeconomic series seem to turn out to be unstable [7]. Hence, this suggests that macro-economic instability could cause the stock market to be extremely volatile.

IV. CONCLUSION

Volatility is very important issue for studying the behavior of stock markets. There are two stock markets in China: Shanghai Stock exchange and Shenzhen Stock exchange. As emerging stock markets, investors are increasingly concerned about volatilities of the two stock markets.

We estimate SV and GARCH models of Chinese stock markets' returns in this paper.

According to our empirical analyses for Chinese stock markets, we show that SV models provide improvements in model fitting relative to GARCH models since most of parameters are statistically significant. Furthermore, for all data frequencies of Chinese stock markets, we find that estimated values of volatility parameters are very high for all frequencies' data. This implies that log returns are extremely volatile even with a long time interval in Chinese stock markets.

REFERENCES

[1] Bollerslev T., (1986), Generalized Autoregressive Conditional Heteroskedasticity, *Journal of Econometrics* 31, 307-27.

[2]Jacquier E., Polson N. G.., and Rossi P. E., (1993), Priors and Models for Multivariate Stochastic Volatility, *unpublished manuscript, University of Chicago*, Graduate School of Business.

[3]Jacquier E., Polson N. G.., and Rossi P. E., (1994), Bayesian Analysis of Stochastic Volatility Models, *Journal of Business & Economic Statistics*, October, Vol. 12, No. 4, 69-87.

[4]Tsay R. S, (2005), *Analysis of Financial Time Series*, 2nd edition, New York: John Wiley & Sons.

[5]Lu S. Q. and Ito T., (2008), Structural Breaks and Time-varying Parameter: A Survey with Application, *Innovation and Knowledge Management in Business Globalization, Theory & Practice: The 10th International Business Information Management Association Conference, Malaysia*, 422-428.

[6]Lu S. Q., and Ito T., (2009), An Empirical Investigation of Chinese Stock Markets with Feed-back Models, *The 11th International Business Information Management Association Conference: Innovation and Knowledge Management in Twin Track Economies: Challenges & Solutions, Egypt*, 257-262.

[7]Lu S. Q., Ito T., and Voges K., (2008), An Analysis of Long Memory in the SSE's Component Index, *The 9th International Business Information Management Association Conference: Information Management in Modern Organizations: Trends & Challenge, Morocco*, 924-929.

---

* Shu Quan Lu is also affiliated to School of Business, Shandong University in Weihai now.

The Fifteenth International Symposium on Artificial Life and Robotics 2010 (AROB 15th '10),
B-Con Plaza, Beppu,Oita, Japan, February 4-6, 2010

An Analysis of Organizational Behaviors in the Keiretsu of Mazda

Shinya Tagawa[1], Takao Ito[1], Makoto Sakamoto[2], and Shu Quan Lu[3]

1 Dept. of Business Administration, Ube National College of Technology, Yamaguchi, Japan
(Tel : 81-836-35-7115; Fax : 81-836-35-7115)
(ito@ube-k.ac.jp, tagawa@ube-k.ac.jp)
2 Dept. of Computer Science and Systems Engineering, University of Miyazaki, Miyazaki, Japan
(Tel : 81-985-58-7392; Fax : 81-985-58-7392)
(sakamoto@cs.miyazaki-u.ac.jp)
3 School of Economics, Fudan University, Shanghai, China
(lushuquan2000@yahoo.com)

Abstract: The limit cycle is one of the effective tools to analyze organizational behaviors. The authors discuss the background of this research, and explain the outline of the limit cycle. The organizational behavior and velocity history of all companies in the keiretsu of Mazda, Kansai Yokokai, are measured in this paper. Imasen Electric Industrial Co., Ltd, Hi-lex Corporation, and Tokai Corporation are excluded because of lack of data. The organizational behaviors of all suppliers are divided into four patterns using new approach of the limit cycle, and the velocity history are measured in this paper. The authors concluded this paper by indicating the weak point of the limit cycle.

Keywords: Organizational pattern, Limit cycle, Velocity history, Chaos, Keiretsu, Mazda**.**

I. INTRODUCTION

One of the essential issues in corporate management is how to analyze the organizational behaviors. All of statistical techniques are linear model. But most of the organizational bahaviors can be explained better by nonlinear model, because they are not linear. The main contribution of this paper is that the organiaitonal behavior is successfully divided into four different patterns using the limit cycle, and the velocity history of these companies have been measured. The managerial implication of the organizational behaviors and their velocity history are discussed. In this paper, the authors expalin the basic information of Yokokai, and measure the limit cycles and velocity history of all listed companies in the keiretsu of Mazda, Kansai Yokokai. In Section 2, the authors introduce a brief background of this research. The details of the limit cycle will be explained and all of the companies in the Kansai Yokokai have been measured in section 3. In section 4, the authors discuss the results. The authors summarize this paper in section 5.

II. BACKGROUND

New findings in physics and biology have discovered some examples of the chaos [1]. An original index developed in hydrology for the practical matter of determining optimum dam sizing for the Nile river's volatile rain and drought conditions has been published in 1951 [2]. It is a typical nonlinear index and directly related to fractal dimension. In 1992, Tsuda I. et al found a chaotic pulsation in a finger's capillary vessels in normal subjects and psychiatric patients, as well as cardiac chaos [3]. Generally, Chaos would be described as disorder state. But most of the recent findings showed us that chaos is driven by deterministic nonlinear processes, such as hydraulic flow and astronomical phenomena.

Priesmeyer H. R. and Baik K. proposed a new method to discover the pattern of chaos in 1989 [4]. They noticed that organization have characteristic limit cycle like the human heart. Furthermore, Ito T. and Sakamoto M. successfully clarified the relationship between economic development and the velocity history of the typical companies in Japan using the limit cycle [5].

III. MEASUREMENT

1. Data collection

In order to discover the pattern of the organizational behaviors, the authors collected the data from the keiretsu of Mazda. Like other keiretsu organization, there are three groups of suppliers, Kanto Yokokai, Kansai Yokokai and Nishinihon Yokokai. Kansai Yokokai is one of the most important groups in the keiretsu of Mazda. There are totally 26 listed companies in Kansai Yokokai. The authors focus their analysis on 23 listed companies of Kansai Yokokai, all companies except Imasen Electric Industrial Co., Ltd, Hi-lex Corporation, and Tokai Corporation because of lack of data[i].

2. Results

The authors measured the limited cycle and velocity history of all these companies using a computer program. Fig. 1 and Fig. 2 show the result of limit cycle and its velocity of the selected companies respectively.

IV. DISCUSSIONS AND IMPLICATIONS

In complex systems theory, a set of states, invariant under the dynamics, towards which neighboring states in a given basin of attraction asymptotically approach in the course of dynamic evolution, is called attractor. According to Priesmeyer, there are 4 patterns of chaos in the limit cycle. They can be expressed as Fig. 3 [6].

Compared Fig. 1 with Fig. 2, these companies can be divided into five parts. Sumitomo Electric Industries, Ltd., NTN Corporation, Bando Chemical Industries, Ltd., and Suminoe Textile Co., Ltd. can be considered as Period Two, because these limit cycles are very similar with straight lines. Aisan Industry Co., Ltd. and Chuo Spring Co., Ltd. can be regarded as Period Four. The limit cycles of these companies look like butterfly. And Ashimori Industry Co., Ltd., Exedy Corporation, Owari Precise Products Co., Ltd., Kawashima Selkon Textiles Co., Ltd., Seiren Co., Ltd., Daido Steel Co., Ltd., Daido Metal Co., Ltd., Tsubakimoto Chain Company, Denso Corporation, Tokai Rubber Industries, Ltd., NGK Spark Plug Co., Ltd., Matsushita Electric Industrial Co., Ltd. and Mitsuboshi Belting Ltd. can be divided into the group of Period Eight. The limit cycles of these companies look like chaos.

Part of these companies is no equivalent for Fig. 3. For example, Toyoda Gosei Co., Ltd. can be regarded as behavior pattern between period One and Two. And Aichi Steel Corporation, ShinMaywa Industries, Ltd., and Sumitomo Metal Industries, Ltd. can be considered as a group between Period Four and Eight. (See Table 1)

Toyoda Gosei Co., Ltd. is a wholly-owned subsidiary of Toyota. Its capital reaches 28 billion Japanese Yen. It experiences an annual oscillation that reflects proportional changes in performance. And Aichi Steel Corporation and Sumitomo Metal Industries, Ltd. produce specialty steel, forged products, electronic and magnetic parts, and rail automotive and machinery parts such as wheels and break disks, Tubes and pipes. ShinMaywa Industries, Ltd. is engaged in producing special purpose trucks, vacuum systems, automotive wire processing machines, environment systems. These companies are slightly different with other parts-maker. This difference may be considered as the reason why these companies differ from other companies.

In order to understand the difference between Period Four and Eight, two typical companies such as Denso Corporation and Aisan Industry Co., Ltd. should be considered. Denso Corporation falls within the group of period eight with high-order chaos and unpredictable pattern. Priesmeyer once indicated that "Period 8 limit cycles are common in business. The result from turbulent external environments and management decisions made without knowledge of the structural patterns of change that bind the organization." [6, p.35]. Denso Corporation is one of the important subsidiaries of the keiretsu of Toyota, separated from Toyota Motor Co., Ltd in 1949. Denso Corporation provides its products to not only Mazda, but also Toyota, Honda Motor Co., Ltd, Suzuki Motor Corporation and other automakers. Contrarily, Aisan Industry Co., Ltd. is also one of subsidiaries of Toyota. Compared Aisan Industry Co., Ltd. with Denso Corporation, the dependence from Toyota is very clear. This may be the reason why the behavior of Aisan differs from Denso Corporation.

From Fig. 3, it is easy to find the same change in velocity history for Toyoda Gosei Co., Ltd. and Aisan Industry Co., Ltd. because they are both subsidiaries of Toyota. Basically, it is easy to find the same change of the velocity in the same group.

The difference between these two companies can be expressed as follows. The first is the scale. The sales and ordinary profit of Denso Corporation reaches 22,929 billion Japanese Yen and 2,021 billion Japanese Yen in 2006 while those of Aisan Industry Co., Ltd. are 121 billion Japanese Yen and 6 billion Japanese Yen[ii].

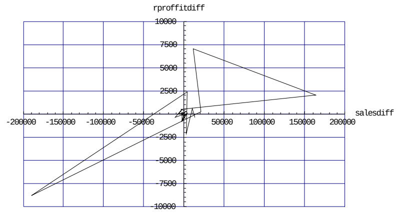

Aisan Industry Co., Ltd.

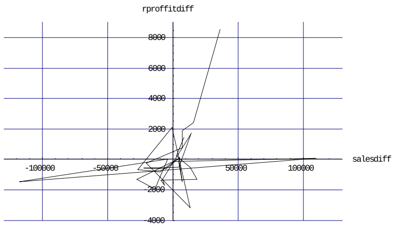

Aichi Steel Corporation

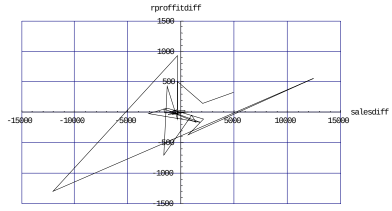

Ashimori Industry Co., Ltd.

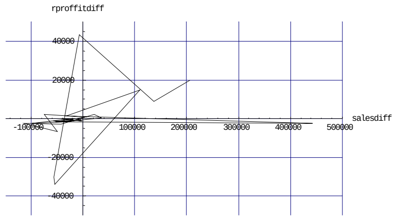

Sumitomo Electric Industries, Ltd.

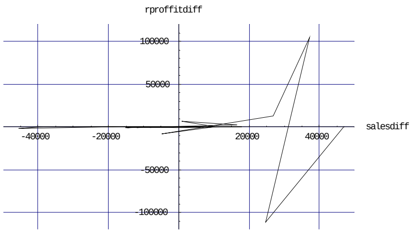

Toyoda Gosei Co., Ltd.

Fig.1 The limited cycle of selected companies in Yokokai.

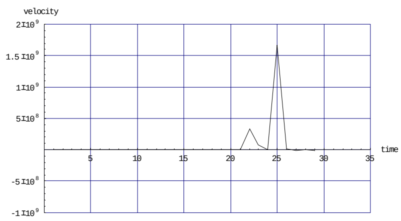

Aisan Industry Co., Ltd.

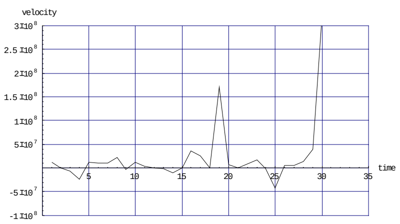

Aichi Steel Corporation

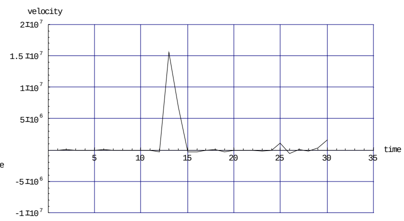

Ashimori Industry Co., Ltd.

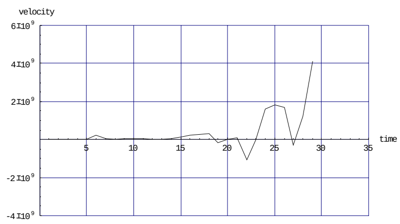

Sumitomo Electric Industries, Ltd.

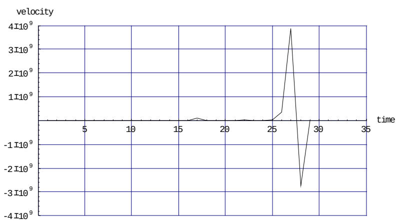

Toyoda Gosei Co., Ltd.

Fig.2 The velocity history of selected companies in Yokokai.

Table 1. Classification of all companies in Kansai Yokokai

Period	Companies
Period One	None
Between Period One and Two	Toyoda Gosei Co., Ltd.
Period Two	Sumitomo Electric Industries, Ltd. , NTN Corporation , Bando Chemical Industries, Ltd., and Suminoe Textile Co., Ltd.
Between Period Two and Four	None
Period Four	Aisan Industry Co., Ltd. and Chuo Spring Co., Ltd.
Between Period Four and Eight	Aichi Steel Corporation , ShinMaywa Industries, Ltd. , and Sumitomo Metal Industries, Ltd.
Period Eight	Ashimori Industry Co., Ltd. , Exedy Corporation , Owari Precise Products Co., Ltd., Kawashima Selkon Textiles Co., Ltd., Seiren Co., Ltd., Daido Steel Co., Ltd., Daido Metal Co., Ltd., Tsubakimoto Chain Company , Denso Corporation , Tokai Rubber Industries, Ltd. , NGK Spark Plug Co., Ltd. , Matsushita Electric Industrial Co., Ltd. and Mitsuboshi Belting Ltd.

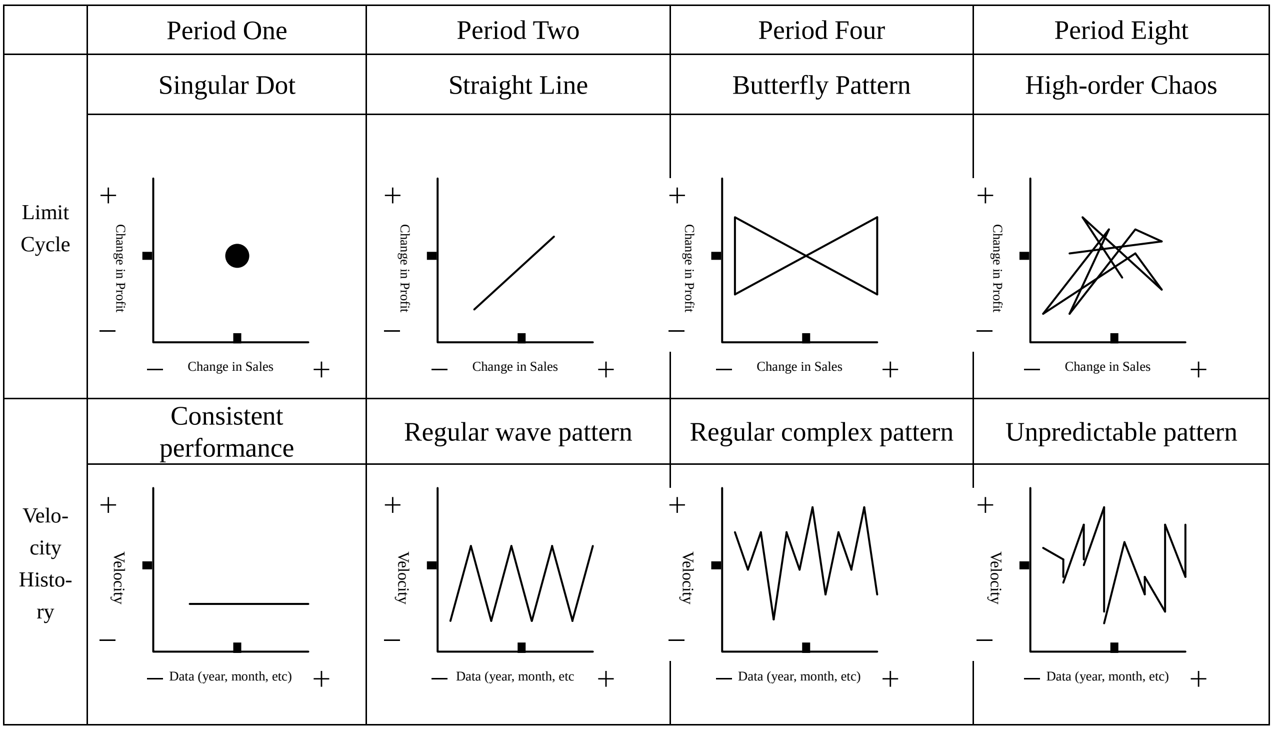

Fig. 3. Limit cycles and its velocity of each period.

The second is the dependence from Toyota. Denso Corporation has a chaotic pattern because it deals with many automakers rather than Aisan Industry Co., Ltd. Compare with Denso Corporation, Aisan Industry Co., Ltd. is one of the subsidiaries under the direct control of Toyota. The difference of scale and independence may be considered as the important factors to determine the different patterns of organizational behavior.

VI. CONCLUSION

The authors measured limit cycle and its velocity using limit cycle theory, and found that difference of scale and independence may determine different organizational behaviors. One of the weak points of limit cycle theory is that it will be very hard to recognize the difference behaviors among the same group, such as Period Eight. Much more measurement is required. To better understand the pattern of different organizational behaviors, much more researches should be developed.

ACKNOWLEDGEMENT

This research was partially supported by the Ministry of Education, Science, Sports and Culture, Grant-in-Aid for Exploratory Research, 21510171, 2009.

REFERENCES

[1]Moon F. C. (1987) *Chaotic Vibrations: An Introduction for Applied Scientists and Engineers*, pp.3, John Wiley & Sons.

[2]Hurst H. E. (1951) Long-term storage capacity of reserviors, *Transaction of the American Society of Civil Engineers*, 116, pp.770-808.

[3]Tsuda I., Tahara T., and Iwanaga H. (1992) Chaotic Pulsation in Human Capillary Vessels and its Dependence on Mental and Physical Conditions, *International Journal of Bifurcation and Chaos*, Vol.2, No.2, pp.313-324, World Scientific Publishing Company.

[4]Priesmeyer H. R., Kibok Baik (1989) Discovering the Patterns of Chaos, *Planning Review*, pp.14-21 and pp.46-47, November/ December 1989.

[5]Ito T. and Sakamoto M.(2007) A Consideration on Limit Cycle Theory, *The papers of Technical Meetings on Information Systems*, IS-07-10～15, pp. 19-23, The Institute of Electrical Engineers of Japan(Japanese Edition).

[6]Priesmeyer H. R. (1992) Organizations and Chaos: Defining the Methods and Management, pp.28-36, Greenwood Publishing Group, Inc.

---

[i] The authors collected data of Imasen and Hi-lex Corporation from 1996 to 2006, Tokai Corporation from 1988 to 2006 respectively. These data is not s ufficient for analyzing these companies with Limit Cycle theory.

[ii] Webpage of Denso Corporation and Aisan, Industry Co., Ltd., retrieved on 12 November, 2007, from http://www.aisan-ind.co.jp/ company/data.htm and http://www.denso.co.jp/ja/aboutdenso/company/

The Fifteenth International Symposium on Artificial Life and Robotics 2010 (AROB 15th '10),
B-Con Plaza, Beppu,Oita, Japan, February 4-6, 2010

An Analysis of Interactive Influence in the Keiretsu of Mazda

Seigo Matsuno[1], Takao Ito[1], Zengyu Xia[2], and Makoto Sakamoto[3]

1 Dept. of Business Administration, Ube National College of Technology, Yamaguchi, Japan
(Tel : 81-836-35-7115; Fax : 81-836-35-7115)
(matsuno@ube-k.ac.jp, ito@ube-k.ac.jp)
2 School of Management, Wenzhou University, Zhejiang, China
(xiazengyu2003@163.com)
3 Dept. of Computer Science and Systems Engineering, University of Miyazaki, Japan
(Tel : 81-985-58-7392; Fax : 81-985-58-7392)
(sakamoto@cs.miyazaki-u.ac.jp)

Abstract: One of the most important issues in corporate management is to find those companies that have higher influence and strength their reciprocal relationship with them. A set of companies with interlocking business relationships is known as a Keiretsu in Japan. In this paper we use the influence analysis tool DEMATEL (DEcision MAking Trial and Evaluation Laboratory), to measure one kind of reciprocal relationship, the influence, of each company in the keiretsu of Mazda Yokokai from the viewpoints of transactions and cross-shareholdings. Furthermore, we calculate the centrality index of each company, and then analyze the relationship between centrality index and influence in order to identify the determinants of the influence. The results of this research are used to identify some characteristics of the effective relationships between Mazda and its suppliers.

Keywords: Influence, Relationship, Cross-shareholdings, Transactions, DEMATEL, Mazda**.**

I. INTRODUCTION

A keiretsu is a set of companies with specific interlocking business relationships. These relationships include not only friendship and workflow, but also cross-company transactions and cross-shareholdings among automobile manufacturers and companies supplying their parts in the Japanese automobile manufacturing industry. A keiretsu can be considered as a type of network organization based upon the viewpoint of network theory.

The main contributions of this paper are to identify the important issue of determining the board of network, and to measure the influence of the keiretsu of Mazda using one kind of analytical tool DEMATEL (DEcision MAking Trial and Evaluation Laboratory). And then we measure the quantitative influence of each company in the keiretsu of Mazda Yokokai, and hence discover the effective relationships between the automobile manufacturers and their suppliers.

This paper is organized as follows. In Section 2, we briefly review some previous studies of relationships. Section 3 introduces and applies the DEMATEL measurement technique, showing the result of the influence of each firm in the keiretsu of Mazda. An analysis and discussion of the implications of the measurement results are presented in Section 4. Finally, in Section 5 we conclude by a summary of this paper and discuss opportunities for future research.

II. BACKGROUND

Many kinds of reciprocal relationships such as friend relationship and workflow relationship will be considered as the important factors for designing an effective strategy. As an effective approach, qualitative analysis is considered as one of the most important studies of the relationship [1, 2]. Recently, quantitative approach is becoming more and more important analytical tool due to the advances in computer technology. Dyer H. J. analyzed the relationship among firms based on distances between their locations and the frequency of face-to-face communication among engineers in the automobile industry [3, 4]. Furthermore, inter-organizational relationships in keiretsu have been analyzed with quantitative analysis tools such as centrality analysis. Fukuoka et al. reported a new trend in relationships between firms in the keiretsu of Nissan from the viewpoint of network organization [5].

One kind of reciprocal relationship is the level of influence between firms. An important strategy in the field of corporate management is to find those firms that have higher influence and strength their reciprocal relationship with them. Measuring this level of influence helps to identify effective relationships between firms. However, there are only a few empirical studies that analyze the influence, one of the most important reciprocal relationships between the firms in the keiretsu.

III. MEASUREMENT

Influence is defined as one of the powers to directly and indirectly control or affect the actions of other persons or things. In the social sciences, influence derives from an interpersonal relationship, and most research into influence is based on a psychological approach. Fontela E. and Gabus A. developed a mathematical model for visualizing the structure of complicated causal relationships with matrixes or digraphs, called DEMATEL, which is an abbreviation for DEcision MAking Trial and Evaluation Laboratory [6]. This model distinguishes the cause and effects between individual firms and identifies the structure presenting these two groups separately. DEMATEL model has been successfully applied in many fields.

As a new analytical tool, DEMATEL can be considered as an approach to find not only direct relations but also indirect relations in a group. In this paper, DEMATEL model is used to measure the influence of the direct and/or indirect power of each firm within the keiretsu of Mazda Yokokai, based on the principle "Friends of my friend are my friends".

1. Outline of DEMATEL and data collection

A brief overview of the mathematical basis of DEMATEL is as follows.

In a social network composed of n actors, the binary relation between each actor and the strength of this binary relation can be identified. Based upon the structure of this pattern of reciprocal relationships, an $n \times n$ adjacent matrix A^* can be obtained. The first step in the analysis is to normalize this matrix by multiplying each element of A^* by λ, the largest row sum of A^*. The normalized matrix $A = \lambda A^*$ is therefore obtained. The (i, j) element of a_{ij} of this matrix denotes the level of direct influence from actor i to actor j.

The reachable matrix, denoted by A^x, refers to the fact that actor i can reach actor j through the number of steps x. For instance, A^2 means that actor i can reach actor j through 2 steps. Therefore, A^x measures the indirect influence from actor i to actor j. All of the levels of indirect influence can be summarized as follows, which we refer to as the indirect matrix.

$$A^f = A^2 + A^3 + \cdots + A^n = A^2 (I - A)^{-1} \qquad (1)$$

The total influence matrix, which includes both the direct and indirect influence matrix, can therefore be expressed as follows.

$$T = A + A^f = A + A^2 + A^3 + \cdots + A^n = A(I - A)^{-1} \qquad (2)$$

In order to measure the influence among Yokokai, data showing the transactions and cross-shareholdings in the keiretsu of Mazda Yokokai were collected from the publications of the Japan Auto Parts Industries Association and Automotive Parts Publishing Company [7]. Yokokai is the suppliers' association of Mazda. It is composed of three groups categorized by the geographic location, namely, Kanto Yokokai, Kansai Yokokai, and Nishinihon Yokokai.

The relationships between the firms in each category were identified through graph modeling. A tie shows the presence or absence of transactions or cross-shareholdings between each pair of firms. We collected directed and weighted data to measure the influence of each firm. The network of transactions in Yokokai is shown in Fig. 1.

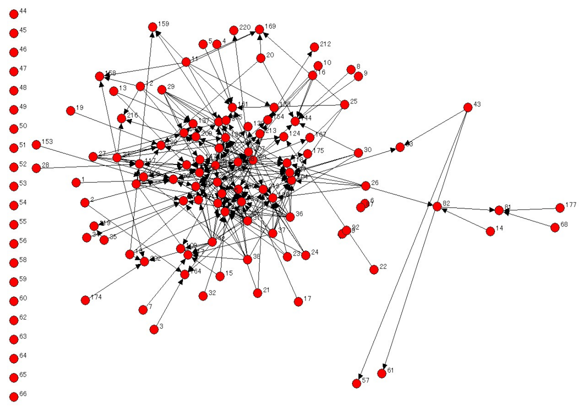

Fig.1. Graph of transaction relationship in Yokokai in 2003-04.

2. Influence measurement

We developed a computer program and calculated the influence of each firm in Yokokai. The result of the influence of transactions is shown in Fig. 2.

In order to find the firms with high influence to Mazda in Yokokai, we also calculated the detailed influence between Mazda and all other suppliers. The transactional influence from Mazda to all other suppliers and the influence of cross-shareholdings from all other suppliers is zero respectively because Mazda does not supply any parts to other suppliers in the network of transaction, and no any suppliers invest to Mazda. Fig. 3 shows the details of the influence of cross-shareholdings from Mazda to other suppliers and the transactional influence from all other suppliers.

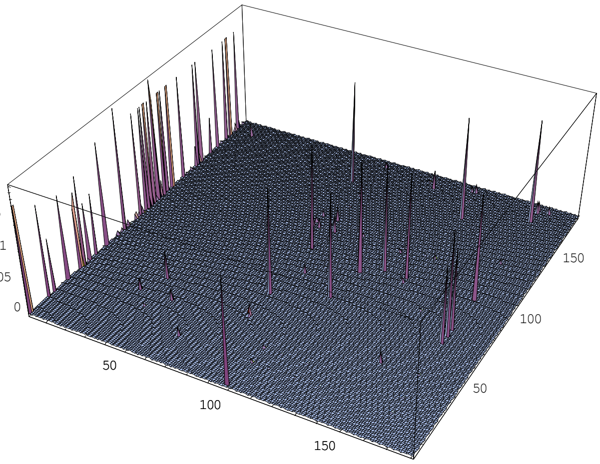

Fig.2. The results of the influence of transactions in Yokokai.

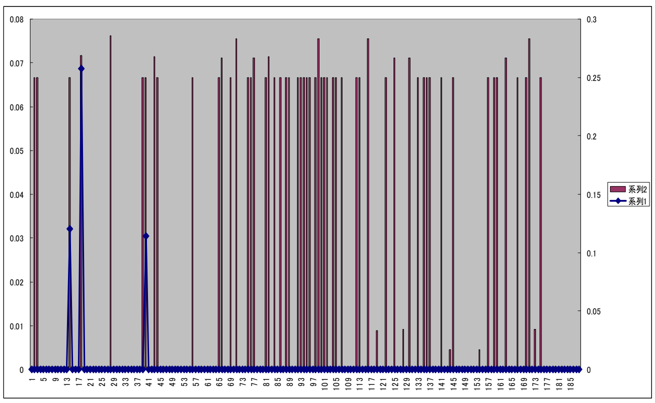

Fig.3. Influences of transactions from other suppliers to Mazda (bar graph) and cross-shareholdings from Mazda to other suppliers (line graph).

Fig. 3 shows the influence of transactions from other suppliers to Mazda and the influence of cross shareholdings from Mazda to other suppliers in detail. The total influence from other suppliers reaches 3.85. This shows Mazda received many parts from suppliers. The top five firms are Sumino Kogyo Co., Ltd. (0.076), NOK Corporation (0.075), NSK Ltd. (0.075), Marui Industrial Co., Ltd. (0.075), and Hanshin Electric Co., Ltd. (0.075).

The influence of cross-shareholdings was calculated using the same method. The influence from Mazda to other three suppliers, Kurashiki Kako Co., Ltd., Keylex Corporation, and Japan Climate System Corporation, are high. These three firms also have higher influence of transaction to Mazda. The rank of these firms is 6, 14 and 14 respectively. This result shows that there are correlation between investments and transactions.

IV. ANALYSIS AND IMPLICATIONS

The finding that the more investment that Mazda makes in its supplier firms the more transactions Mazda will have with them is not an unexpected result. Two questions can now be asked. The first is "How strong is this relationship between level of investment and number of transactions?" The second is "what kind of relationship between the influence and centrality?" To answer these two questions, we calculated centrality index of all these firms, and analyzed the correlation coefficients between transaction and cross share-holdings. The details of centrality index are described in Ito et al. [8]. The results of this analysis are shown in Table 1.

In Table 1, Influence A means actor i directly influences actor j, and Influence B means actor i is influenced from actor j. This shows that two correlations, that between influence B of transactions and influence A of cross-shareholdings, and that between influence A of transactions and influence B of cross-shareholdings, were significant ($P < 0.01$). The correlation ratios were 0.678 and 0.399 respectively, which shows that a strong relationship exists between the level of transactions and cross-shareholdings. In other words, the statement that "the more a firm invests in a supplier, the more the firm receives parts from that supplier" is valid. The reciprocal finding that "the higher level of investment that a firm accepts, the more parts that firm will supply" is also valid.

V. CONCLUSION

In this paper, the influence of each firm was measured in order to investigate the pattern of relationships in the keiretsu of Mazda. The study found that the influence of cross-shareholdings in other firms is closely related to the influence of the transactions between them. This means that the higher influence of cross-shareholdings has a strong impact on the influence of transactions. The implication of this finding for the automobile manufacturer Mazda is that an important strategy for them is to find those firms that have higher influence in the keiretsu and strengthen their reciprocal relationship with them.

One limitation of the paper is that the data of transactions and cross-shareholdings in this analysis are restricted to one fiscal year. Data from more years would be required in order to more completely study the trend of these identified influences through time series analysis.

Table 1. Matrix of correlation coefficient between transaction and cross-shareholdings.

		Cross-shareholdings		Transaction	
		Influence A	Influence B	Influence A	Influence B
Cross-shareholdings	Influence A	1.000	0.030	0.039	0.678**
		-	0.687	0.604	0.000
		181	181	181	181
	Influence B		1.000	0.399**	-0.033
			-	0.000	0.660
			181	181	181
Transaction	Influence A			1.000	-0.036
				-	0.633
				181	181
	Influence B				1.000
					-
					181

**$P < 0.01$.

In addition, the form of influence investigated in this study is only one aspect of the reciprocal relationship between an automobile manufacturer and its suppliers. Further quantitative research, such as the use of capacity analysis between two actors and clique analysis of the network structure, will be undertaken in the future, to attempt to capture the complexity of the relationships in the keiretsu of Mazda.

ACKNOWLEDGEMENT

This research was partially supported by the Ministry of Education, Culture, Sports, Science and Technology, Grant-in-Aid for Exploratory Research, 21510171, 2009 and by Japan Society for the Promotion of Science, Grant-in-Aid for Scientific Research (C) 20530332, 2009.

REFERENCES

[1]Hakansson H and Waluszewski A (2002), *Managing Technological Development: IKEA, the Environment and Technology*, Routledge

[2]Lincoln R L and Gerlach M L (2004), *Japan's Network Economy Structure, Persistence, and Change*, Cambridge University Press

[3]Dyer H J (1994), "Dedicated Assets: Japan's Manufacturing Edge," *Harvard Business Review*, November-December, 174-178

[4]Dyer H J (1996), "Specialized Supplier Networks as a Source of Competitive Advantage: Evidence from the Auto Industry," *Strategic Management Journal*, vol. 17, 271-291

[5]Fukuoka S, Ito T, Passerini K, and Sakamoto M (2006), "An Analysis between Transaction and Cross Shareholdings in the Keiretsu of Nissan," *Managing Information in the Digital Economy Issues & Solutions*, IBIMA International Conference, Bonn, Germany, 163-169

[6]Fontela E and Gabus A (1976), "Current Perceptions of the World Problematique," in Churchman C W and Mason R O, *World Modeling: a Dialogue*, North-Holland Publishing Company and American-Elsevier, 81-88, Retrieved October 4th, 2006, from http://home page.sunrise.ch/mysunrise/agabus/eff'endi/dematel/ dematel.html

[7]JAPIA & APPC (2005), *Japanese Automotive Parts Industry* (in Japanese), Automotive Parts Publishing Company

[8]Ito T, Passerini K, and Sakamoto M (2008), "Structure Analysis of Keiretsu of Toyota," in Putnik G D and Cunha M M (Ed.), *Encyclopedia of Network and Virtual Organizations*, Ideas Group Publishing

The Connection Law and Networks

Takao Ito[1], Chris Medlin[2], Yuchao Ma[3], and Sakamoto Makoto[4]

1 Dept. of Business Administration, Ube National College of Technology, Yamaguchi, Japan
(Tel : 81-836-35-7115; Fax : 81-836-35-7115)
(ito@ube-k.ac.jp, matsuno@ube-k.ac.jp)
2 Business School, The University of Adelaide, Australia
(Tel : 61-8-8303-7351; Fax : 61-8-8303-4843)
(chris.medlin@adelaide.edu.au)
3 College of Economics and Management, Wuhan University of Science and Engineering, Wuhan, China,
(ma_yuchao2002@sina.com)
4 Dept. of Computer Science and Systems Engineering, University of Miyazaki,
(Tel : 81-985-58-7392; Fax : 81-985-58-7392)
(sakamoto@cs.miyazaki-u.ac.jp)

Abstract: Cooperation is one of the most important factors in organizations. Unsolved issues of cooperation are still left although many researches have been published. One is the mechanism of cooperation. In Barnard's book, He analyzed the principle of cooperation, but he did not explain the mechanism of cooperation because he considered the ability of each individual to be equal. We believe Barnard's idea to be incorrect; therefore, we will discuss this issue and try to understand network organization using mathematical model to prove our point. Furthermore, we attempt to simulate a percolation model of network organization, and to discover the connection law under the condition that the abilities of all individuals are not equal. Discovering the connection law of cooperation is vital because it will take on more significance in the age of Information Technology than ever before.

Keywords: *connection law, network organization, mechanism of cooperation, percolation, simulation.*

I. INTRODUCTION

Many different groups are formed by individuals and subgroups. These groups face their different situations when they deal with various social activities. One type of the different groups is an organization such as an enterprise and/or a firm. Cooperation is one of the most important factors in organizations. Some unsolved issues of cooperation are still left. One of them is the mechanism of cooperation.

In this paper we review the relevant literature of network analysis and discuss the issue of cooperative mechanism. The main contributions of this paper is that we discover the connection law under the condition of the abilities of all individual's are not equal in network organization using computer simulation with percolation model.

The rest of this paper is organized as follows. In the next section, we review some background and previous literature of the cooperation theories. In section 3, we focus on computer simulation with an invasion percolation model, and we explain the connection law in network organization. The final section contains concluding remarks.

II. BACKGROUND

An organization, especially a corporate organization like an enterprise, would not only vary with the structure of the organization, but also with the cooperative relationship with other firms and the fluctuation of the economic situation. Needless to say, cooperation is one of the most important factors determining the success or failure of a corporate organization. Cooperation is meaningful not only for the participants of the organization, but also for the management of the organization itself to discover the mechanism of cooperation.

The market is controlled by the relationships between business entities under the principle of competition. The relation between demand and supply is adjusted and the effective allocation of managerial resources can be realized through the mechanism of market price. On the other hand, the internal process of vertical integration in under the control of authority in traditional organizations. Organizations generate a participant consciousness and a belonging sense of memberships, and create a trust value.

Network organizations realize both the merit of the market and the organization and maintain the relationship among autonomous business entities under the utilization of common managerial resources. A network organization is a form which differs from the form of an organization and market, and it is considered as a form located at the middle between market and organization, so it is called a moderate organization.

Network organization could be considered as one of the cooperative systems. Network organizations provide a higher degree of responsiveness to change that cannot be obtained within hierarchical organizational structures [1]. Cooperation plays an important role in network organization. For instance, personal contacts play key roles in obtaining information about job opportunity [2, 3]. The relationships among the firms in network organization are analyzed. The relationship between corporate performance and the structure of network such as centrality and network size are also measured [4-6].

Most of the recent researchers focused on the relationship among firms and the structure of network organizations. But they do not take mechanism of cooperation, one of the most important issues into consideration in their research.

III. CONNECTION LAW

Invasion percolation model is one kind of complex theories [7]. Invasion percolation model will be executed in this paper to uncover the mechanism of connection in business activities.

1. Connection by individuals

In order to uncover the mechanism of connection, percolation model and hypothesis are executed as below.

Suppose that the percolation model will be executed in a two-dimensional square lattice system. And the following steps will be executed in our percolation model.

Step1. Each individual and/or business entity could be considered as a node in percolation model. Each one has its own ability of *p*. The starting node exists and its optional ability is p. The range of p is from 0 to 1.

Step2. Neighbor node of the starting node means von Neumann neighborhood with random number of p hereby.

Step3. Sort the ability of each neighbor node of the starting node and compare the ability of the starting node with the abilities of each neighbor node.

Step4. Put the node whose value of p is the smallest one in the neighbor nodes into the cluster of starting node if there is any node whose value of p is smaller than the starting node. And then new neighbor nodes will be formed.

Step5. Execute the sequence from step 3 to step 4 repeatedly until *n* if there exists the node whose p is less than starting node in the cluster of new neighbor node until the p of all neighbor nodes is larger than the starting node.

From these steps mentioned above, we can image that business entities, as the starting node, do their business activities repeatedly and expand their scale gradually depending upon the ability of the starting node. The business entity could be explained as the autonomous individual or autonomous company.

The relationship between ability (influence) of the starting node and the average of cluster caused from the repeated activities of the starting node with computer simulation can be illustrated as Fig. 1 and Fig. 2.

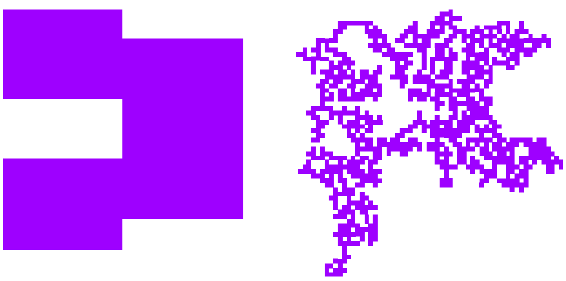

[n=1000, p=0.2] [n=1000, p=0.8]

Fig.1. Simulation results of percolation model

Cluster curve of the starting node could be divided into three parts in Figure 2.

The first is the group of node whose abilities are all smaller than 0.40. And the increasing ranges of the average of cluster, as the speed of incorporate is very small. And the second is the group of node whose abilities are from 0.40 to 0.68, and its increasing range is obviously large one. And the third is the group of node whose abilities are over 0.68, and it shows the same trend as the first one.

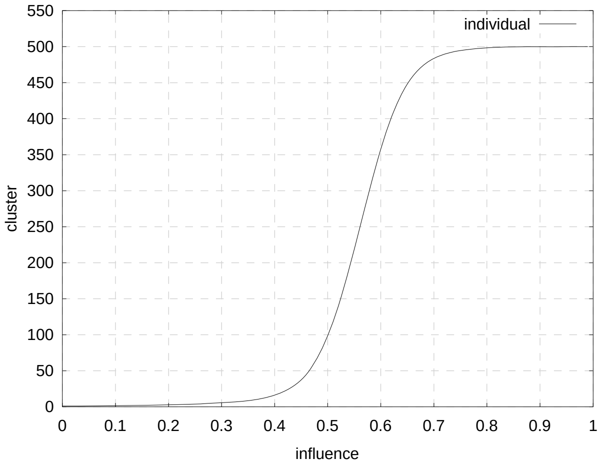

Fig.2. Relationship between Individual influence and cluster

Some conclusions will be drawn as follows.

1. If the ability of each node is smaller than 0.4, the gap among each node is very small even if there are big difference between them.

2. If the ability of each node is lager than 0.40, the gap of each node is very remarkable even if there are very small differences.

3. If the ability of each node is larger than 0.68, the gap of each node is very small again even if there are some difference between them.

The ability hereby can be considered the influence such as transaction power and the R&D of new products in the case of enterprise. Other influences, for instance, capital power, sales power and the power of market share also will be included. Therefore, the result of competition will be reversed at any time if the market share is less than 40 percent. In the case that the market shares are larger than 40 percent, the power will be remarkable even if the difference between them is only 1 percent. It means the competition is under an uncertain situation. At last, if the market share is larger than 68 percent, the power becomes a very small one again. It could be explained that this is an uncertain situation, but in fact it is impossible that the market share of two companies are both over 50 percent.

2. Connection by new clusters

The computer simulation mentioned above is executed under the condition of each node whose ability does not grow with the increase of the number of node in new cluster. In other words, the ability of new cluster is equivalent to the ability of the starting node. It is a constant variable. Such phenomenon is only seen in small enterprises. The ability of new cluster will grow with the increase of the number of node in new cluster in many business cases.

One typical example of competitions is the competition between Sony and the JVC. It is a competition of the network organization, but not as an individual organization. The ability of the network organization will be improved with the expansion of new cluster. Therefore, the ability of p will grow when the number of nodes increases in new cluster. In other words, it is better to consider the ability of new cluster instead of the starting node.

It is necessary to revise program mentioned in previous section in this paper from this viewpoint. The result of new computer simulation is shown in Figure 3 and Fig. 4.

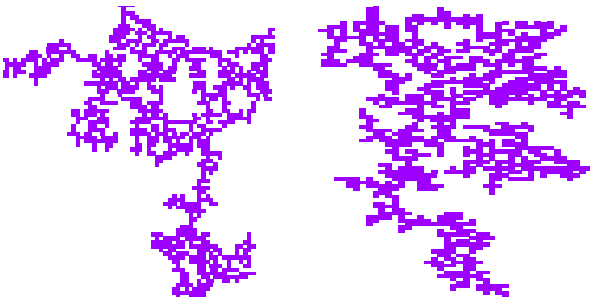

[n=1000, p=0.2] [n=1000, p=0.8]

Fig.3. Simulation results of the revised percolation model

Figure 4 shows the tendency which the ability of new cluster grows depending upon the ability of new cluster formed with other nodes. The tendency stops at the ability of 0.76 of new cluster. It means that business entities with small ability have a greater advantage to organize a network organization. In network organization a small enterprise will obtain a larger merit.

A gap between individual and the new cluster formed with other nodes is illustrated in Figure 5.

Gap between individual and the new cluster formed with other nodes grows remarkably with the ability increasing of other nodes, and stops at 0.43 of the ability. The gap will continue to grow slowly when the ability of an individual is larger than 0.43, and stop at 0.78 with the ability increasing of an individual. Therefore, in comparing with an individual, the new cluster formed with other nodes under 0.43 will get a bigger effect of connection. It is necessary to connect with other individuals for these entities when their abilities are

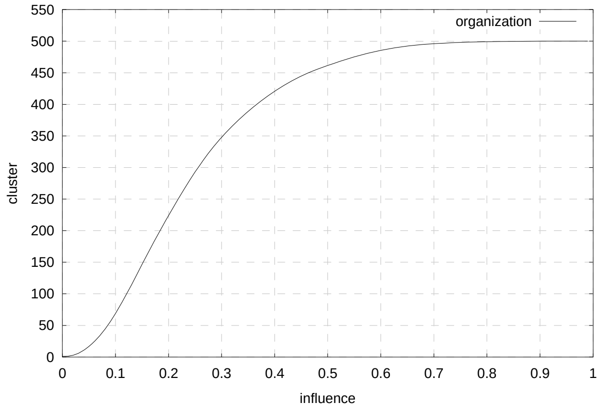

Fig.4. Relationships between the ability of new cluster and the effect of connection

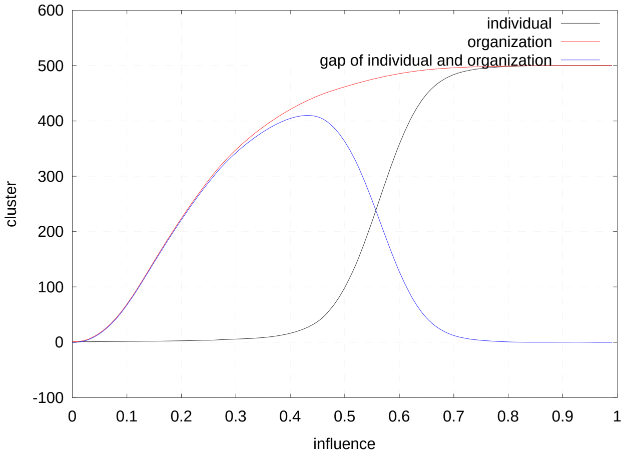

Fig.5. Gaps between the Ability of Individual and the New Cluster

under 0.43 and it is not necessary to connect with other individuals when their abilities are over 0.78 because the connect effect will be small.

The author called it the connection law in this paper. The connection law means entities such as individuals and/or companies need to connect with each other when their abilities are small than 43 percent in order to get much more advantages and benefits from cooperation. The advantages and benefits will be very small if their abilities are larger than 78 percent. This result shows us the principle of the connection and helps us to understand how to cooperate with each.

IV. CONCLUSION

As the mechanism of cooperation to determine the economy of connection, the connection law in an organization has been uncovered in this paper under the consumption that the ability of each individual is not equal.

The next research is to measure the ability (such as influence or power) of the individual and the ability of the individual organized by network, and uncovers the relationship between ability of business entity and corporate performance based on this conclusion.

ACKNOWLEDGEMENT

This research was partially supported by the Ministry of Education, Science, Sports and Culture, Grant-in-Aid for Exploratory Research, 21510171, 2009.

REFERENCES

[1]Achrol R. S. & Kotler P. (1999). Marketing in the Network Economy, *Journal of Marketing*, 63 (4), 146-164.
[2]Granovetter M. (1995). Getting a Job: A Study of Contacts and Careers, 2nd edition,University of Chicago Press, Chicago.
[3]Arrow K. J. & Borzekowski R. (2004). Limited Network Connections and the Distribution of Wages, Retrieved February 5, 2009, from http://www.federalreserve.gov/pubs/feds/2004/200441/200441pap.pdf.
[4]Ito T. & Sakamoto M. (2005) Importance Analysis of Firm in the Keiretsu of Toyota, in Mehdi Khosrow-Pour (Ed.), *Managing Modern Organizations with Information Technology* 930-933, Ideas Group Publishing.
[5]Fukuoka S., Ito T., Passerini K., & Sakamoto M. (2006). An Analysis between Transaction and Cross Shareholdings in the Keiretsu of Nissan, in Khalid S. Soliman (Ed.), *Managing Information in Digital Economy*, 163-169, IBIMA.
[6]Ito T., Passerini K., & Sakamoto M. (2008). Structure Analysis of Keiretsu of Toyota, in Putnik G. D. & Cunha M. M. (Ed.), *Encyclopedia of Network and Virtual Organizations*, Ideas Group Publishing.
[7]Gaylord R. J. & Wellin P.R. (1997). *Computer Simulations with MATHEMATICA Explorations in Complex Physical and Biological Systems*, Springer-Verlag Telos.

The Fifteenth International Symposium on Artificial Life and Robotics 2010 (AROB 15th '10),
B-Con Plaza, Beppu,Oita, Japan, February 4-6, 2010

Discovering the Efficient Organization Structure: Horizontal versus Vertical

Satoshi IKEDA[1] Takao ITO[2] Makoto SAKAMOTO[1]

[1] Department of computer Science and Systems Engineering, University of Miyazaki, Miyazaki 889-2192, Japan, {bisu,sakamoto}@cs.miyazaki-u.ac.jp

[2] Department of Business Administration, Ube National College of Technology, Ube 755-8555, Japan, ito@ube-k.ac.jp

Abstract: Structure analysis is one of the most important issues in corporate management. Pyramid structure, as one of the well-known vertical structure, plays an important part in the corporate organization. Most structures of the traditional organizations such as functional structure and divisional structure are vertical. Recently, due to the development of Information Technology, a new horizontal structure, instead of the vertical one, has been drawn considerable attention. In this paper, we reviewed the efficient organization structure, and found that there are two efficient structures: vertical structure and horizontal structure, depending on the different abilities of each member in any organizations with the comprehensive evaluation measurement. The line structure of vertical organization is efficient when the ability of all members is small. While the ability of all members is large, the star structure of horizontal organization will be efficient. Therefore, this paper provides a theoretical perspective to prove the efficient organization structures and their required conditions.

keywords: vertical structure, horizontal structure, efficient, comprehensive evaluation measurement.

1 Introduction

Organization structure is one of the important factors to determine organizational performance. It means the formal system of task and communication that control, coordinates, and motivates employees in order to achieve organization's goal. Most structures of the conventional organizations, such as functional structure and divisional structure, are vertical. They generally refer to the formal, prescribed hierarchy of authority, or administrative structure. Recently organizational structure has been changed from vertical to horizontal due to the development of informational technology. Most of the empirical studies showed that horizontal structure more effective [1, 2, 3].

The question is what kind of structures is an efficient? And what kind of conditions is required for an efficient structure. The main contribution of this paper is to answer this question, and clarify the relationship between the efficient structures and their condition. And based upon our result, we will discuss the implication.

2 Notations

Suppose that $G = (V(G), E(G))$ is a graph. Through this paper, a graph is always finite, undirected and simple with order $n = |V(G)| (n \geq 2)$ and size $m = |E(G)|$.

For U is any set of vertices, $G - U$ is obtained from G deleting all the vertices in $V(G) \cap U$ and their incident edges. If $U = \{v\}$ is Singleton, we write $G - v$ rather than $G - \{v\}$. As above, $G - \{e\}$ and $G + \{e\}$ are abbreviated to $G - e$ and $G + e$ for $e \in E(G)$.

For $u \in V(G)$, by $N(u) = \{v \mid \{u, v\} \in E(G)\}$, we denote the set of vertices adjacent to u, and call $\deg(u) = \sharp N(u)$ the degree of $u \in V(G)$. We refer to a path in $G = (V(G), E(G))$, by the sequence of its vertices, writing,

$$G(x_0, x_k) = x_0 x_1 \cdots x_k$$

for $x_i \in V(G) (i = 0, 1, \cdots, k)$ and $x_j x_{j+1} \in E(G)$ $(j = 0, 1, \cdots, k-1)$, where x_i are all distinct, and calling $G(x_0, x_k)$ a path from x_0 to x_k in G. And the number of edges of path is its length; above path $G(x_0, x_k)$ has length k.

Assume that $P = x_0 x_1 \cdots x_{k-1}$ is a path and $k \geq 3$, then

$$C \equiv P + x_{k-1} x_0$$

is called a cycle. On the other hand, an acyclic graph, one not containing any cycles, is called a forest. A connected forest is called a tree. Thus, a forest is a graph whose components are tree. Sometimes we consider one vertex of a tree as special, then such vertex is called the root of this tree. While the vertices of degree 1 in a tree but the root of the tree, are its leaves. A tree graph T with fixed root r is written by T_r and then the set of T_r's leaves is written by $L(T_r)$. That is,

$$L(T_r) = \{v \in E(T_r) | \deg(v) = 1,\ v \neq r\}.$$

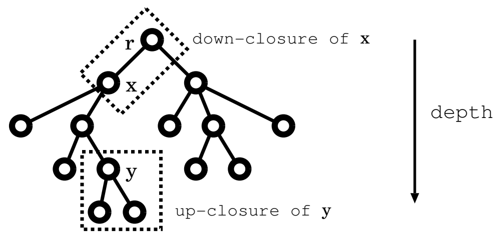

Fig. 1: $x \prec y$ in T_r, down-closure of x, and up-closure of y.

Writing $x \preceq y$ for $x \in T_r(r, y)$, then defines a partial ordering on $V(T_r)$, the tree-order associated with T_r. This ordering will be considered as the expression 'depth': if $x \prec y$, we say x lies below y in T_r, see Fig.1. We call

$$\lceil x \rceil \equiv \{v \in V(T_r) | v \preceq x\}$$

and

$$\lfloor y \rfloor \equiv \{v \in V(T_r) | v \succeq y\}$$

the down-closure of x and the up-closure of y in T_r. Note that the root r is the least element, and that the leaves of T_r are its maximal elements in this partial order.

Suppose that $\Sigma = \{\sigma_1, \sigma_2, \cdots, \sigma_n\} (n \geq 2)$ and $\mathcal{A} (\sharp\mathcal{A} \geq 1)$ are finite sets. For a given Σ, we call $(\Sigma, \{\phi_i\}_{i \in \mathcal{A}})$ an evaluation system, if

$$\phi_i : \Sigma \to \mathbf{R}^+ \equiv \{x \in \mathbf{R} \mid x > 0\} \quad \text{for } i \in \mathcal{A}.$$

We call $\phi_i(\sigma)$ the personal ability of $\sigma \in \Sigma$ with respect to $i \in \mathcal{A}$.

For a given $(\Sigma, \{\phi_i\}_{i \in \mathcal{A}})$, let T_r be a tree graph with $V(T_r) = \Sigma$. Then we shall evaluate the rooted tree T_r by

$$\Phi(T_r) = \sum_{i \in \mathcal{A}} \sum_{l \in L(T_r)} \prod_{v \in T_r(r,l)} \phi_i(v). \tag{2.1}$$

We call $\Phi(T_r)$ the ability value of T_r with respect to the evaluation system $(\Sigma, \{\phi_i\}_{i \in \mathcal{A}})$. Our purpose is to find the most efficient organization structure tree which maximize its ability value for a given $(\Sigma, \{\phi_i\}_{i \in \mathcal{A}})$.

Through this paper, we shall substitute (Σ, ϕ) for $(\Sigma, \{\phi\})$ if $\sharp\mathcal{A} = 1$. Since $\sharp A$ means the number of evaluation measures, thus $\sharp\mathcal{A} = 1$ indicates that its number is one. This paper should treat only this special case. Then we have the following.

Lemma 1 *Suppose that T_r is an efficient tree for a given (Σ, ϕ). Then we see that $x \prec y$ implies $\phi(x) \geq \phi(y)$.*

Proof of lemma 1 For a given (Σ, ϕ), let T_r be an efficient tree. Assume that $\phi(x) < \phi(y)$ holds for some $x, y \in \Sigma$ with $x \prec y$ in T_r. And that T'_r is the tree by interchanging x and y in T_r. Then we get

$$\begin{aligned} &\Phi(T'_r) - \Phi(T_r) \\ = &\left(\frac{\phi(y)}{\phi(x)} - 1\right) \sum_{\substack{l \in L(T_r) \\ l \succeq x,\ y \notin T_r(r,l)}} \prod_{v \in T_r(r,l)} \phi(v) > 0. \end{aligned}$$

This contradicts that T_r is an efficient tree for (Σ, ϕ). Thus we get $\phi(x) \geq \phi(y)$ if $x \prec y$ in T_r. $\square$

Lemma 1 suggests that our efficient trees are suitable for a hierarchical model of the group Σ whose personal abilities are given by $\{\phi(\sigma)\}_{\sigma \in \Sigma}$, when the number of evaluation measures is only one. In this article, we shall show that our efficient trees must be the following three types under our special setting of $\sharp\mathcal{A} = 1$.

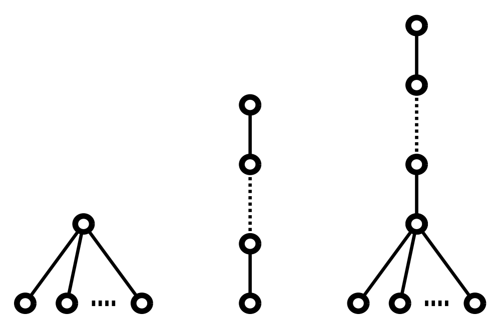

Fig. 2: Three types of our efficient trees when $\sharp\mathcal{A} = 1$.

Actually, two or more evaluation measures exist, so the overall evaluation value of the organization should obtain the expression (2.1). Thus, there might be the most efficient tree besides the types in Fig.2. For example, let us set $\Sigma = \{1,\ 2,\ 3,\ 4\}$, and put

$$\phi_1(1) = \phi_1(2) = 3, \qquad \phi_1(3) = \phi_1(4) = 1/2,$$
$$\phi_2(1) = \phi_2(2) = 1/2, \qquad \phi_2(3) = \phi_2(4) = 3.$$

Then we get an efficient tree for $(\Sigma, \{\phi_i\}_{i=1,2})$ as follows.

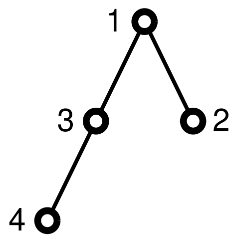

Fig. 3: An efficient tree for $(\Sigma, \{\phi_i\}_{i=1,2})$.

3 Results for $\sharp\mathcal{A} = 1$

In this section, we shall discuss a structure of an efficient tree for a given (Σ, ϕ). Without loss of generality, we may assume that

$$\phi(\sigma_1) \geq \phi(\sigma_2) \geq \cdots \geq \phi(\sigma_n) \qquad (3.1)$$

for $\Sigma = \{\sigma_1, \sigma_2, \cdots, \sigma_n\}$. Firstly, we shall examine what kind of situation would be better if organization structure tree branch off. For a given $(\{\sigma_1, \cdots, \sigma_n\}, \phi)(n \geq 3)$, let us $\{\sigma_{\pi(1)}, \cdots, \sigma_{\pi(n)}\}$ be a permutation of $\{\sigma_1, \cdots, \sigma_n\}$ satisfying with

$$\begin{gathered} \sigma_{\pi(1)} = \sigma_1, \\ \phi(\sigma_{\pi(2)}) \geq \phi(\sigma_{\pi(3)}) \geq \cdots \geq \phi(\sigma_{\pi(l)}), \\ \phi(\sigma_{\pi(l+1)}) \geq \phi(\sigma_{\pi(l+2)}) \geq \cdots \geq \phi(\sigma_{\pi(n)}) \end{gathered}$$

and $2 \leq l \leq n-1$. Let us set two organization structure trees T_{σ_1} and T'_{σ_1} as shown in Fig.4.

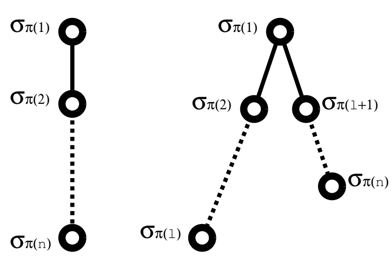

(a) T_{σ_1} (b) T'_{σ_1}

Fig. 4: Two organization structure trees T_{σ_1} and T'_{σ_1} for (Σ, ϕ)

Then, we see that

$$\begin{aligned} &\Phi(T_{\sigma_1}) - \Phi(T'_{\sigma_1}) \\ = \;& \phi(\sigma_1) \left(\prod_{i=2}^{l} \phi(\sigma_{\pi(i)}) \prod_{i=l+1}^{n} \phi(\sigma_{\pi(i)}) \right. \\ & \left. - \prod_{i=2}^{l} \phi(\sigma_{\pi(i)}) - \prod_{i=l+1}^{n} \phi(\sigma_{\pi(i)}) \right). \end{aligned}$$

Therefore we have the following lemma.

Lemma 2 *Under the assumption (3.1), for T_{σ_1} and T'_{σ_1} in Fig.4, we get*

$$\Phi(T_{\sigma_1}) - \Phi(T'_{\sigma_1}) \begin{cases} \geq 0 & \textit{if} \;\; \phi(\sigma_n) \geq 2 \\ \leq 0 & \textit{if} \;\; \phi(\sigma_2) \leq 1. \end{cases}$$

By using lemma 2 repeatedly, we obtain the following conclusions.

Theorem 1 *Under assumption (3.1), we have the followings.*

(a) If $\phi(\sigma_n) \geq 2$ holds. Then we see that an efficient graph is the path graph $\sigma_1\sigma_2\cdots\sigma_n$ in Fig.5.

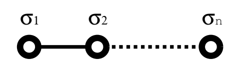

Fig. 5: T_{σ_1} as a path graph.

(b) If $\phi(\sigma_2) \leq 1$ holds. Then we see that an efficient graph is the star graph with center σ_1 in Fig.6.

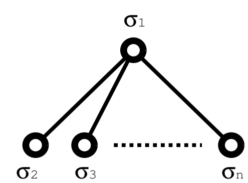

Fig. 6: T_{σ_1} as a star graph.

The typical form of the efficient tree is a path graph or star graph which appeared in Theorem 1. In general, we can show that the form of the efficient tree becomes the form which seems to have put these two figures together, when $\sharp\mathcal{A} = 1$.

For a given (Σ, ϕ) and its organization structure tree T_r, let us define

$$\begin{aligned} D_3(T_r) = \{\sigma \in \Sigma |\, & \deg(\sigma) \geq 3 \text{ if } \sigma \neq r, \\ & \deg(\sigma) \geq 2 \text{ if } \sigma = r\}. \end{aligned}$$

Theorem 2 *Assume that T_r is an efficient tree for a given (Σ, ϕ). Then we see the followings.*

(a) $\sharp D_3(T_r)$ is equal to 0 or 1.

(b) Putting $D_3(T_r) = \{x\}$ when $\sharp D_3(T_r) = 1$. Then $\{\sigma \in \Sigma \mid \sigma \succ x \text{ in } T_r\} = L(T_r)$ holds.

The general form of the most efficient tree which theorem 2 insists on, is shown in Fig.7. It is obvious that the upper-half is a path graph, and the lower-half is the star graph.

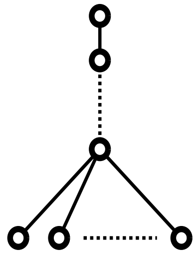

Fig. 7: General form of the efficient tree.

Proof of theorem 2 Assume that $\sharp D_3(T_r) \geq 2$. Then we can find $x, y \in D_3(T_r)$ satisfying with $x \prec y$ and $x, y \in T_r(r, l)$ for some $l \in L(T_r)$. If $\Phi(T_r(r,x)) < \Phi(T_r(r,y))$, put

$$T'_r = T_r - x\sigma + y\sigma$$

for some $\sigma \in N(x)$ with $\sigma \succ x$ and $\sigma \notin T_r(x,y)$. Then we see that

$$\begin{aligned} & \Phi(T'_r) - \Phi(T_r) \\ = & \Big(\Phi(T_r(r,y)) \\ & \qquad -\Phi(T_r(r,x))\Big)\Phi(\lceil\sigma\rceil) > 0. \end{aligned} \quad (3.2)$$

Since T_r is the efficient tree under the assumption of theorem, (3.2) implies contradiction.

Next, if $\Phi(T_r(r,x)) \geq \Phi(T_r(r,y))$, put

$$T'_r = T_r + \bigcup_{\sigma \in N(y),\ \sigma \succ y} (x\sigma - y\sigma)\,.$$

Then we see that

$$\begin{aligned} \Phi(T'_r) - \Phi(T_r) = \Phi(T_r(r,x)) + \\ \Big(\Phi(T_r(r,x)) - \Phi(T_r(r,y))\Big)\Phi(\lceil y\rceil)/\phi(y) > 0 \end{aligned}$$

which implies contradiction. Therefore, we get (a) of theorem 2, by reduction to absurdity.

From the discussion mentioned above, we see that $\sharp D_3(T_r)$ is equal to 0 or 1. To prove (b) of theorem 2, thus, we have only to think about the case of $\sharp D_3 = 1$ in Fig.8.

Put $D_3(T_r) = \{x\}$. Assume that there exist $y \succ x$ with $y \notin L(T_r)$. If $\phi(y) > 1$, put

$$T'_r = T_r + \bigcup_{\sigma \in N(x),\ \sigma \succ x,\ \sigma \neq y} (y\sigma - x\sigma)\,.$$

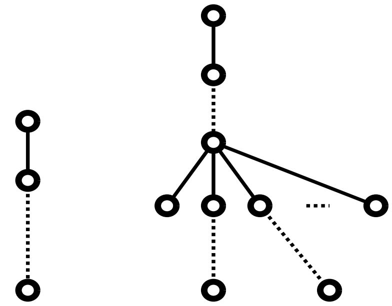

(a) $\sharp D_3 = 0$ (b) $\sharp D_3 = 1$

Fig. 8: Two kind of possible form

Then we see that

$$\begin{aligned} \Phi(T'_r) - \Phi(T_r) = \Phi(T_r(r,x))(\phi(y) - 1) \\ \times \sum_{\sigma \in N(x),\ \sigma \succ x,\ \sigma \neq y} \Phi(\lceil\sigma\rceil) > 0, \end{aligned}$$

which implies contradiction. Next, if $\phi(y) \leq 1$, put

$$T'_r = T_r - y\sigma + x\sigma,$$

for $\sigma \in N(y)$ with $\sigma \succ y$. Then we see that

$$\begin{aligned} & \Phi(T'_r) - \Phi(T_r) \\ = & \Phi(T_r(r,x))\frac{1-\phi(y)}{\phi(y)}\Phi(\lceil y\rceil)\Phi(T_r(r,y)) > 0 \end{aligned}$$

which implies contradiction. Therefore, we get (b) of theorem 2, by reduction to absurdity. □

Acknowledgment : This research was partially supported by the Ministry of Education, Science, Sports and Culture, Grant-in-Aid for Exploratory Research, 21510171, 2009.

References

[1] Alvesson Mats(1989/1990), A Flat Pyramid: A Symbolic Processing of Organizational Structure, International Studies of Management and Organization, 19-4,5-23

[2] Krackhardt David and Jeffrey R. Hanson(1993), Informal Networks: The company Behind the Chart, Harvard Business review,71-4,104-111

[3] Reinhard Diestel(2000), Graph Theory(Third Edition),Springer

A Centrality Analysis of Transaction Relationship in Panasonic

Yousin Park[1] and Yunju Chen[2]

1 Dept. of Business Administration, Ube National College of Technology, Yamaguchi, Japan
(Tel : 81-836-35-5028; Fax : 81-836-35-5028)
(ecventure@ube-k.ac.jp)
2 Faculty of Economics, Kyushu International University, Kitakyushu City, Japan
(Tel :81-93-671-8971)
(shellyfight@yahoo.co.jp)

The strategy called Value Creation 21 had been undertaken by Panasonic in 2001. This strategy gave strong impact on the transaction relationship of Panasonic. Therefore, it is one of the important issues to analyze how transaction network of Panasonic has been changed during the period of Value Creation 21. In order to make transaction relationship visible and countable, we introduce graph theory and measure centrality index from viewpoints of degree, closeness, and betweenness, using the collected data in 2002 and 2005. The findings of this paper are as follows. First, the number of firms included in transaction network of Panasonic in 2005 is less than that in 2002. Second, not only the degree but also the closeness and betweenness of all firms in Panasonic Group and their suppliers decreased in 2005 compared that of 2002. Third, though the in-degree of Panasonic is decreased, the relative importance of Panasonic in network is increased. Fourth, the divisions of Components/Devices, and Digital AVC Network in Panasonic group are ranked higher than other firms in transaction network of Panasonic. Fifth, the out-degree of suppliers decreased in 2005 compared that of 2002. Based on these findings, we finally concluded how Panasonic arranged its transaction relationship during turnaround.

***Keywords*: Centrality Analysis, the Transaction Relationship, Panasonic, Turnaround**

I. INTRODUCTION

In recent years, companies have been suffering from unexpected change of global market, technological innovation, hypercompetition, etc. These unfavorable phenomena have made companies in financial deficits and low profits. In order to successfully cope with these problems, company managers are surely interested in learning how to escape from these situations and reconfiguring their competitiveness, which it is called turnaround. So far many researchers have studied the various factors of crises and strategies/methods of turnarounds. However, the general theory of turnaround has not been established yet. In this paper, the definition of turnaround refers to a situation that companies recover their performance while they suffer serious profit decline, business crisis etc. [1, 2].

Regarding to the turnaround, a company has to carry out not only the internal reform, but also inter-firm reform. For example, it will be necessary that company have to change the transaction relationship between itself and its suppliers. We have observed such kind of transaction relationship change of Panasonic and its suppliers after turnaround. How company arranges its transaction relationships during turnaround is our interest.

II. BACKGROUND

Panasonic had many problems at the end of 1990s. Panasonic faced two serious problems were: first, Panasonic have not fallen a drastic decline of net profit and its rate has been at a very low level for several years. Second, there is an overlap of resources between the Panasonic, divisions and affiliations. For instance, two companies of the Panasonic Group: Matsushita AVC and Matsushita Kotobuki have made the same products of audios, videos, video cameras. Though their middle managers had recognized such an overlap of the resources and cannibalization, they could not solve these problems for long times.

In order to solve these problems, Panasonic unveiled in “Value Creation 21” plan that the principal was “Deconstruct and Create” in 2001. The concept of the plan was based on a Super Manufacturing Company business model, which placed top priority on providing customer-oriented services and creating value for customers through the development and supply of tailored systems, equipment and components and devices.

As the principle presented, the core elements of the plan contained 1) structural reforms with an emphasis on profitability and efficiency improvements, which were referred to deconstruction strategies, and 2) the creation of a new growth strategies [3, 4]. Itami pointed out that these strategies were implemented to reform a wide range of functions and business areas such as employment, business structure, marketing, accounting, supply chain management etc. What Panasonic concerned was to build a unified platform to take full competitive advantage of its combined group-wide strengths. Based on the platform, Panasonic selected and focused its businesses on certain domains.

Because this project gave strong impact on the transaction relationship of Panasonic, we introduce centrality analysis to make transaction relationship changed after enterprise's turnaround visible and countable, in order to provide precise insight to turnaround analysis [5, 6].

III. HYPOTHESIS

According to the strategies of "domain company" and building black-box technologies, the importance of Components/Devices and Digital Network domain of Panasonic Group will be enhanced. Thus, Hypothesis 1 was set as follows.

Hypothesis 1: The Components & Devices and Digital Network domain of Panasonic Group will be more important than the situation before turnaround.

The strategy of building black-box technologies will bring the change of transaction relationships between Panasonic Group and its suppliers. It is hypothesized.

Hypothesis 2: The degree of Panasonic suppliers will be more decreased than before turnaround.

IV. RESEARCH METHOD

1. Data

In this paper, we use centrality analysis as the methodology based on graph theory. Centrality is one of the well known index in this field. Freeman proposed three distinct conceptions of centrality: degree, betweenness and closeness [7, 8].

The data on transactions relationship of Panasonic was collected from IRC's *The Actual Situation of Panasonic Group* [9].These data shows the situation before and after "Value Creation 21" reform. We use the item "Main purchaser" and define data as 1 if Panasonic Group companies have transaction with other companies, otherwise 0. Next, we input the data into matrix table. Finally, the data was analyzed by the software UCINET 6.0.Table 1 is the list of transaction relationship of Panasonic. Panasonic transaction network consists of Panasonic, Panasonic affiliated firms, their suppliers.

Table 1 The list of transaction network of Panasonic in 2002 and in 2005

2002 year			2005 year		
Number	Class	Firms	Number	Class	Firms
1-59 (59)	Panasonic Group	Panasonic, Matsushita Electric Works etc.	1-65 (65)	Panasonic Group	Panasonic, Matsushita Electric Works etc.
60-640 (581)	Panasonic suppliers	KOA, Kyosha, TAMURA, Shimoda, etc.	66-625 (569)	Panasonic suppliers	Alps Electric, Kyosera, Seiko Instruments, etc.

2. Analysis

Figure 1 is the transaction networks of Panasonic in 2002 and that of Panasonic in 2005. When two transaction networks are compared, it revealed five points of differences.

First, the number of firms included in transaction network of Panasonic in 2005 is less than that in 2003. The number of firms included in transaction network of Panasonic in 2003 was 536 companies and that in 2005 was 385 companies. It means that 184 companies had been isolated nodes and they had lost transaction relationship with Panasonic and Panasonic Group.

Second, not only the in-degree but also the closeness and betweenness of all firms in Panasonic Group decreased in 2005 compared that of 2002. Although Panasonic had transactions with 445 suppliers in 2002, the number of transactions with suppliers dropped to 197 in 2005 (See Figure 2).

Third, the relative importance of Panasonic in network was enhanced although the degree of it decreased. As mentioned above, Panasonic had transactions with 197 suppliers in 2005, but Panasonic had much more supplier than Panasonic affiliated firms.

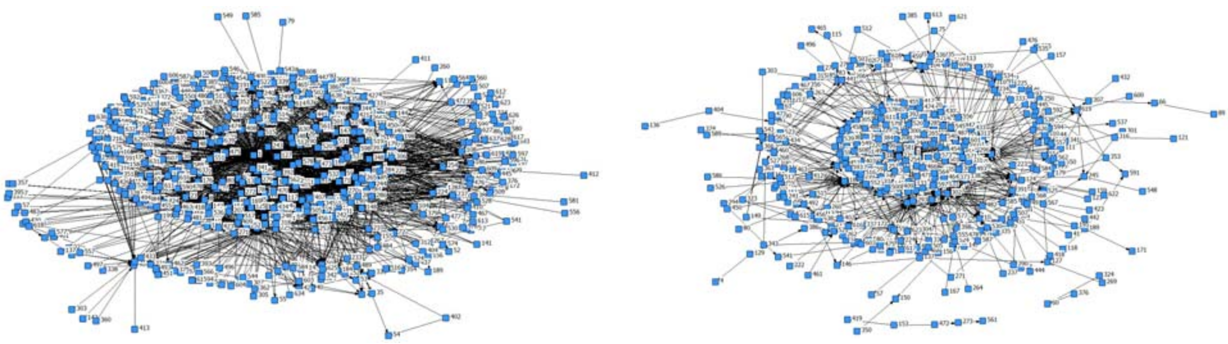

Figure 1 The transaction Network of Panasonic in 2002(left) and that of Panasonic in 2005(right)

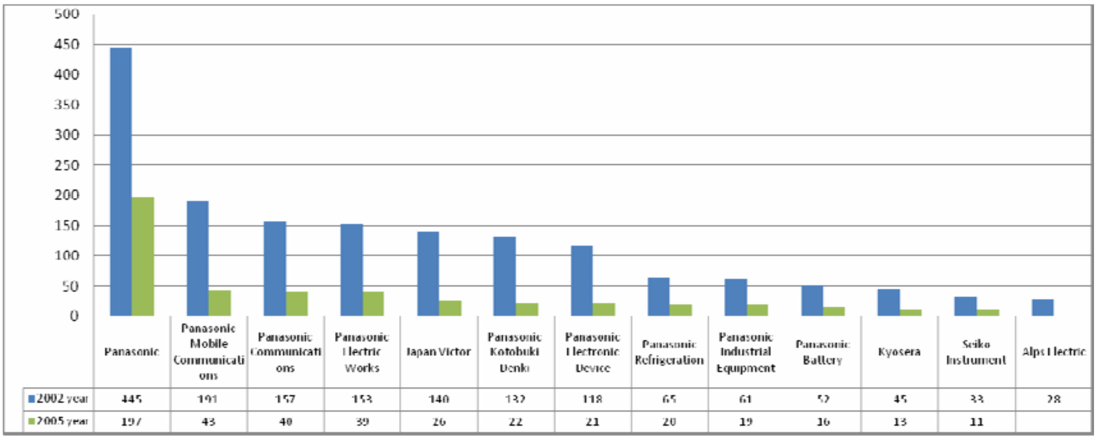

Figure 2 The top 10 in-degree firms of Panasonic transaction network in 2002 and in 2005

Table 2 The top 10 out-degree firms of Panasonic transaction network in 2002 and 2005

2002 year			2005 year		
Node	Firms	Out-degree	Node	Firms	Out-degree
71	Koa Corp.	28	302	Sony Chemical & Information Device Corp.	11
228	Kyosha Co., Ltd.	21	12	Sansha Eletric Manufacturing Co., Ltd.	11
94	Tamura Corp.	18	155	Okaya Electric Industries Co., Ltd.	8
225	Shimoda Kougyo Co., Ltd.	18	493	Hitachi Metals, Ltd.	8
318	Taiyo Stainless Spring Co., Ltd.	17	482	Hamamatsu Photonics K. K.	7
187	Nippon Mektron, Ltd.	17	506	Priken Corp.	7
125	Daishinku Corp.	16	138	Enplas Corp.	6
511	Echo Electric Co., Ltd.	15	447	Optical Coatings Japan	6
222	Eta Electric Industry Co., Ltd.	14	133	SDK Corp.	6
231	Ishizuka Electronics Corp.	14	131	Echo Electric Co., Ltd.	6

Fourth, from the figure 2, we can see that affiliated firms related to Component &Devices and Digital AVC Networks in Panasonic group are ranked higher than other firms in transaction network of Panasonic. Especially, Panasonic Mobile Communications, Panasonic Communications and Panasonic Electronic Device occupied higher ranking in 2005.

Fifth, the out-degree of suppliers decreased in 2005 compared that of 2002. Main suppliers changed from the components to material/commodity manufactures (See table 2).

V. DISCUSSION

From the result of analysis, it is showed that the importance of affiliated firms of Component & Devices and Digital AVC network in the group increased and the number of firms included in transaction network decreased. Therefore, Hypothesis 1 is supported. In addition, the out-degree of Panasonic's suppliers will be decreased after the turnaround, and the spices of suppliers shifted from components to material/commodity manufactures. We can say Hypothesis 2 is also supported.

Based on the findings above, the change of Panasonic's transaction network can show how Panasonic form its technology platform. Figure 3 is the image of how Panasonic arranged it transaction network to construct its technology platform during the "Value Creation 21" reform.

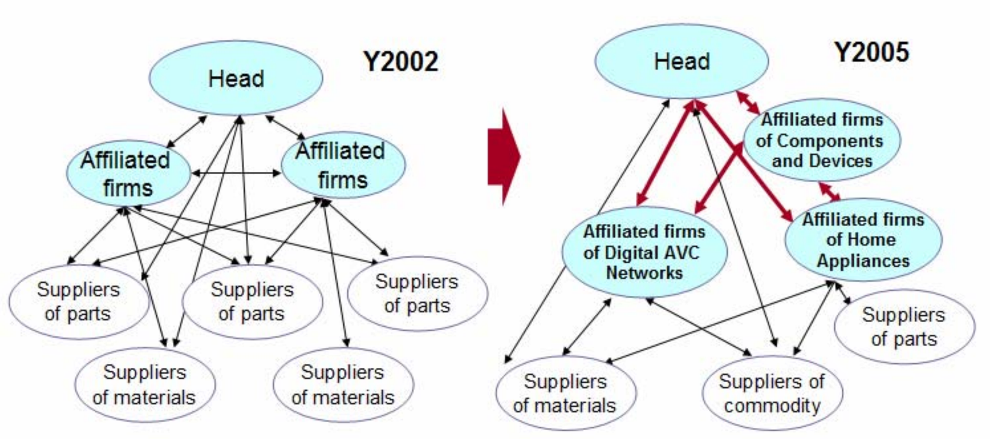

Figure 3 The change of Panasonic transaction network

By reducing the number of transactions, Panasonic reduced purchase cost and centralized transactions to some important affiliated firms such as Panasonic Mobile Communications, Panasonic Communications and Panasonic Electronic Device in 2002. It means that Panasonic Group shares important resources only inside the group and prevents a technology spillover from the group.

VI. CONCLUSION AND FUTURE WORKS

We calculated the centrality of transaction network of Panasonic, and found the change of transaction relationship of Panasonic after turnaround. By introducing the centrality analysis to make the result of turnaround visible and countable, the turnaround results are consistent with the objectives of business structural reform strategies. Also, we can finally explain how Panasonic managed its transaction relationships to form its technology platform, and conclude how Panasonic arranged its transaction relationship during turnaround. In the near future, we plan to figure out how the profit of companies in network (not only Panasonic group but also its suppliers) changed after turnaround [10, 11].

ACKNOWLEDGMENTS

This research was supported by the Grants-in-Aid for Scientific Research <KAKENHI> Scientific Research (B) 21330095, Grant-in-Aid for Young Scientists (B) 21730335. The authors would like to thank the support.

REFERENCE

[1] Imura, N. & Chen, Y.J., (2008), "Corporate Recovery in Asia: The Japanese and Taiwanese Perspective", *Proceedings for 21th Annual Conference,* Association of Japanese Business Studies.

[2] Chen, Y.J. et al., (2009), "The Reconfiguration of Competitiveness through Turnaround Process in Taiwan: The Case Study of Acer/Wistron", *KIU Journal of Economics & Business Studies*, 15 (2&3), pp. 1-30.

[3] Matsushita Electric Industrial Co., Ltd., *Annual Report,* 2001 edition.

[4] Itami, H., (2007), *The Management innovation of Matsushita*, Yuhikaku.

[5] Chen, Y.J. & Park, Y.S., （2009）, "How to Analyze Corporate Turnarounds: The Application of Social Network Analysis in Panasonic Group's Case", *KIU Journal of Economics & Business Studies*, 16 (1), pp. 25-49.

[6] Ito, T. (2004), "Quantitative analysis of a firm's relationship in the Keiretsu of Toyota group," *Proceedings of the 2004 Information Resources Management Association,* Innovations through Information Technology, pp. 1078-1079.

[7] Freeman, L.C. (1977) "A Set of Measures of Centrality Based on Betweenness", *Sociometry*, 40, 1, pp. 35-41.

[8] Freeman, L.C. (1978/79) "Centrality in Social Networks Conceptual Clarification", *Social Networks*, 1, pp. 215-239.

[9] IRC, *The Actual Situation of Panasonic Group*, 2003 & 2006 edition.

[10] Ito, T. (2002), *Network organization and information* (in Japanese), Hakuto Shobo

[11] Ito.T., Fukuda, K., Passerini, K., and Sakamoto, S. (2008), "Centrality analysis in the Keiretsu of Mazda," *Proceedings of the 9th International Business Information Management Association*, International Conference on Information Management in Modern Organizations, pp. 504-510.

The Fifteenth International Symposium on Artificial Life and Robotics 2010 (AROB 15th '10),
B-Con Plaza, Beppu,Oita, Japan, February 4-6, 2010

A Study of Accounting Standard-Setting using Graph Theory

Kensuke Ogata
University of Nagasaki, 123 Kawashimo-cho, Sasebo, Nagasaki Prefecture, 858-8580, Japan
(Tel: 81-956-47-6831; Fax: 81-956-47-6831)
(Email: ogata@sun.ac.jp)

Abstract: Accounting standards settings are subject to political activities by preparers or companies. Despite of strong objections from preparers of financial statements, the FASB set the conceptual and user-oriented accounting standards on business combinations. The aim of this paper is to clarify who or what kinds of groups played central roles in, using graph theory. These analyses using voice data and data produced from voting behaviors in the board meetings reveals that the centrality of preparer (group) is low, and ones of academician (group) and user (group) are high in this project. This result may indicate that what blows hole in the powers of preparers in the FASB exists.

Keywords: accounting standard-setting, graph theory, centrality, FASB, business combinations

I. INTRODUCTION

The numbers in financial statements effect the decision making of the users of financial statements, and change the distribution of wealth and the allocation of resources in a whole society. The changes or creations of accounting standards or regulations sometimes make profits of companies fall, and make positions in corporate financings worse. To avoid unfavorable results and gain favorable results, companies and other stakeholders will intervene accounting standard settings. Therefore, the standards setting processes are subject to political activities, as we have seen in cases in history (Horngren [1], Zeff [2], Kelly-Newton [3], Wolk, et al. [4]).

In setting the accounting standards, the setters such as the International Accounting Standards Board (IASB) and the Financial Accounting Standards Board (FASB) usually proceed with setting conceptual-based and user-oriented accounting standards, because they have responsibilities for protecting users and conceptual framework which they should follow in the setting standards. When the standards make unfavorable results for companies or preparers of the financial statements that are regulated by the setters, they wish to prevent setting standards. Therefore, the conflict between preparers of the financial statements and users of these statements often has occurred.

When such conflicts occurred, how have the setters set the accounting standards? Or, what kinds of group in the setters played important roles? This paper focuses on the internal structures of the setter, or the relationships of members in the setter, and aims to clarify the above second question using the centrality concept in the graph theory. To achieve this purpose, this paper covers the FASB's Business Combinations Project, Phase II. Because this project prominently occurred the conflict between preparers and users.

II. OUTLINE OF THE FASB'S BUSINESS COMBINATIONS PROJECT

The main purposes of the project were to provide for the consistent application of the purchase method or the acquisition method, and to set a single high-quality global accounting standard. For accomplishing such purposes, the FASB proposed the provisions which had three features. The first feature is to establish measuring fair values as the measurement principle. All assets and liabilities that are recognized in a business combination, including identifiable assets acquired and liabilities assumed, and noncontrolling interests, should be measured by fair values. The second feature is the application of the full goodwill method, which is derived from the above proposition. Finally, the third feature is to classify noncontrolling interests into the equity section. As a result of the classification, the transactions between controlling interests and noncontrolling interests would be viewed as equity transactions (FASB [5] [6]). These propositions are based on the economic unit concept, which was described as one of the conceptual basis for consolidated financial statements in the FASB's Discussion Memorandum (FASB [7]). Thus, it is thought that the boards set the standard which is weighted in favor of conceptual thinking.

These propositions may make companies some harmful effects. The full goodwill method needs to estimate fair value of the noncontrolling interests. Usually, as the fair values of the interests will be much higher than the carrying amounts, the amounts of goodwill will be incremental. It means that if the impairment losses of the goodwill occur, the losses are much bigger than applying the original method and exert enormous influences to profits of companies (Dennis [8]). And, because of the difficulties of estimating fair values, preparation costs of financial statements increase through rising auditing fees (IASB [9]). In fact, nearly all the preparers that responded to the board and most of participants in business roundtable meetings heavily criticized these propositions.

Throughout 2006 to 2007, the FASB redeliberated the issues, which were raised by the respondents and the participants, in the board meetings. As a result of the redeliberations, in December 2007, the FASB issued final statements, SFAS141(R) and SFAS160 (FASB [10] [11]). Despite of receiving heavy critiques, the FASB decided on almost the same provisions as originally planned.

III. THE CENTRALITY CONCEPTS IN GRAPH THEORY

Graph theory seeks to model relationships in the network to depict the network structure. The most basic feature of graph theory is quantified by considering the relations measured among the actors in a network. Methods using in network analysis provide descriptions of structural properties of actors, subgroups of actors, or groups. Another feature of graph theory is to describe the network structure using a graph. A graph is expressed for the network relationships using nodes and edges. Nodes refer to the actors or the organizations, and edges to the linkage between them (Wasserman and Faust [12]).

A main concern of graph theory is generally to make clear the centrality of the network. It is important that we know who is central, who is a leader within the network, and who influences the network most heavily. However, centrality is equivocal. Therefore, graph theory has some indicators useful for studying the centrality of the network, for example, degree centrality, closeness centrality, betweenness centrality, and so on (Wasserman and Faust [12], Scott [13], Hanneman and Riddle [14], Knoke and Yang [15]).

Degree centrality supposes that actors who have more ties to other actors have advantaged positions. Degree centrality measures the extent to which a node (actor) connects to all other nodes in the network.

$$C_D(n_i) = \frac{\sum_j n_{ij}}{g-1} \tag{1}$$

where n_{ij} means the node in the network, normalized actor degree centrality measure, $C_D(n_i)$, divides an actor i's degree centrality score by the maximum number of possible connections with the $g-1$ other actors.

Closeness centrality supposes that the closer an actor reaches to all others within the organization, the more important the actor becomes. Closeness centrality measures how near a node is to the other nodes in the network.

$$C_C(n_i) = \frac{g-1}{\sum_{j=1}^{g} d(n_i, n_j)} (i \neq j) \tag{2}$$

where $d(n_i, n_j)$ means the distance between node i and node j that is the another in the network. The closeness centrality measure is computed as the inverse of the sum of the geodesic distances of the both and multiplying by $g-1$ in order to normalize.

Betweenness centrality supposes that an actor who becomes a mediator among actors becomes the source of power. Betweenness centrality measures the extent to which other actors lie on the geodesic path between pairs of nodes in the network.

$$C_B(n_i) = \frac{\sum_{j<k} [g_{jk}(n_i)/g_{jk}]}{(g-1)(g-2)/2} \tag{3}$$

where g_{jk} means the number of geodesic paths between the two nodes j and k, and $g_{jk}(n_i)$ is the number of geodesics between the j and k that contain node i. Then, dividing $g_{jk}(n_i)$ by g_{jk} measures the proportion of geodesic paths connecting j and k in which node i is involved. The betweenness centrality measure is computed by summing the portions and then dividing the sums by the theoretical value, $\frac{(g-1)(g-2)}{2}$, in order to normalize.

IV. RESEARCH QUESTIONS AND RESEARCH DATA

Research Questions

The accounting standard setters usually are comprised of the members who have various backgrounds such as preparers, users, auditors, and academicians, in order to acquire the legitimacy of the organizations from the constituents. In those days when the FASB addressed the business combination project, the board was composed with seven members; three CPAs, two preparers, one user, and one academician (Miller and Redding [16]).

In considering facts described in section II, it is anticipated that, in setting the standards, the power in the FASB lay not on the preparer's side, but on the user's and academician's side. Thus, research questions in this paper are that:

(1) Are the centralities of the preparer's side relative low? And,

(2) Are the centralities of the user's and academician's side relative high?

Using Data

To testify the above questions, this paper uses two data sets. Both sets are extracted from the 28 minute records which have been released on the FASB's website (from October 30, 2002 to April 27, 2005), before issuing the propositions on June 30, 2005. One data set is data extracted from the voices among members in the board meetings. The aim of using this data set is to specify what kinds of group have influential powers in the network. Table 1 shows the counts of voices on the basis of member to member in matrix style.

Table 1 Voice Data

	Herz	Batavick	Crooch	Foster	Schieneman	Schipper	Seidman	Trott	Wulff	Young
Herz	–	10	10	3	15	16	15	36	12	0
Batavick	10	–	8	0	6	10	9	28	0	1
Crooch	10	8	–	3	8	13	10	31	6	3
Foster	3	0	3	–	3	4	0	7	10	0
Schieneman	15	6	8	3	–	12	13	30	9	0
Schipper	16	10	13	4	12	–	19	45	9	0
Seidman	15	9	10	0	13	19	–	28	0	1
Trott	36	28	31	7	30	45	28	–	16	2
Wulff	12	0	6	10	9	9	0	16	–	0
Young	0	1	3	0	0	0	1	2	0	–

Another set is data extracted from voting behaviors in the meetings. The FASB voted 113 times during the term. The aim of using this data set is to confirm the similarities among the members and to specify what kinds of group dominant in the decision making in the network. This data set is made from the data on each actor's voting behaviors using an affiliate analysis in UCINET VI (Borgatti, et al. [17]). Table 2 shows the analytical result, that is, the homogeneities of voting behaviors on the basis of member to member in matrix style.

Table 2 Data on Homogeneities of Voting Behaviors

	Herz	Batavick	Crooch	Foster	Schieneman	Schipper	Seidman	Trott	Wulff	Young
Herz	113	74	87	12	92	99	84	92	16	7
Batavick	74	80	62	0	63	68	73	67	0	7
Crooch	87	62	103	18	76	89	69	84	14	9
Foster	12	0	18	24	10	16	0	16	8	0
Schieneman	92	63	76	10	104	82	69	79	18	0
Schipper	99	68	89	16	82	113	78	100	16	7
Seidman	84	73	69	0	69	78	88	73	0	7
Trott	92	67	84	16	79	100	73	108	12	7
Wulff	16	0	14	8	18	16	0	12	24	0
Young	7	7	9	0	0	7	7	7	0	9

In addition, Table 3 shows the list of FASB members from the beginning of the project (June, 2001) to issuance of the propositions. In this table, Time 1 is the beginning of the project. Time 2 is the starting point for disclosing minutes on the FASB's website. Time 3 is when Seidman succeeded Wulff. Time 4 is when Batavick succeeded Foster, and Time 5 is the point when Young succeeded Schieneman.

Table 3 List of FASB members in the Business Combinations Project

Time 1 (Jun-01)	Time2 (Oct-02)	Time 3 (Jul-03)	Time 4 (Aug-03)	Time5 (Jan-05)
Jenkins (CPA), chairman	Herz (CPA), chairman	Herz (CPA), chairman	Herz (CPA), chairman	Herz (CPA), chairman
Crooch (CPA)	Crooch (CPA)	Crooch (CPA)	Crooch (CPA)	Crooch (CPA)
Trott (CPA)	Trott (CPA)	Trott (CPA)	Trott (CPA)	Trott (CPA)
Foster (Non-Financial)	Foster (Non-Financial)	Foster (Non-Financial)	Batavick (Non-Financial)	Batavick (Non-Financial)
Larson (Financial)	Wulff (Non-Financial)	Seidman (Consultant)	Seidman (Consultant)	Seidman (Consultant)
Cope (Analyst)	Schieneman (Analyst)	Schieneman (Analyst)	Schieneman (Analyst)	Young (Analyst)
Mueller (Academic)	Schipper (Academic)	Schipper (Academic)	Schipper (Academic)	Schipper (Academic)

(shaded parts means the succeeding member)

V. RESULTS AND DISCUSSIONS

Results of Centralities Based on the Voice Data

This paper analyses two data sets from the perspective of above three centralities using UCINET VI. Table 4 presents the results of multiple centrality analysis based on the data of Table 1. Table 4 reveals that the centralities of Trott (CPA) and Crooch (CPA) are very high, and those of Herz (CPA), Schieneman (user), and Schipper (academician) are relatively high. And, Figure 1 shows the graph based on the result of centralities using NetDraw (Borgatti [18]). Thus, in terms of the centrality based on the voices in the network, it is clearly seen that CPAs might be at the centre of the board meetings with support from academician and user.

Table 4 Results of Multiple Centrality Analysis based on Voice Data

Normalized Centrality Measures

	Degree	Closeness	Betweenness
Herz	88.889	90.000	2.222
Batavick	77.778	81.818	2.083
Crooch	100.000	100.000	7.083
Foster	66.667	75.000	0.000
Schieneman	88.889	90.000	2.222
Schipper	88.889	90.000	2.222
Seidman	77.778	81.818	2.083
Trott	100.000	100.000	7.083
Wulff	66.667	75.000	0.000
Young	44.444	64.286	0.000

Descriptive Statistics for Each Measure

	Degree	Closeness	Betweenness
Mean	80.000	84.792	2.500
Std Dev	16.330	10.835	2.477
Sum	800.000	847.922	25.000
Variance	266.667	117.390	6.134
SSQ	66666.664	73071.086	123.843
MCSSQ	2666.667	1173.898	61.343
Euc Norm	258.199	270.317	11.128
Minimum	44.444	64.286	0.000
Maximum	100.000	100.000	7.083

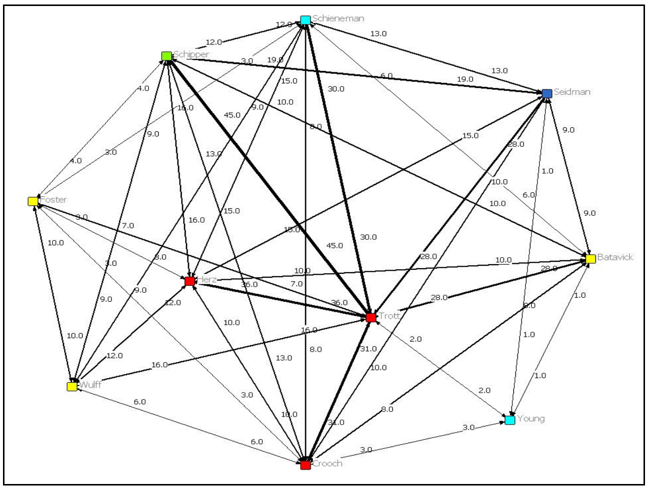

Figure 1 The Graph Based on the Centrality Analysis (prepared with NetDraw)

Results of Centralities Based on Data of Voting Behaviors

Table 5 presents the results of multiple centrality analyses based on the data in Table 2. These analyses include three centralities, like above analysis. Table 5 reveals that, for all three indicators of centralities, the centralities of Herz, Crooch, Schipper, and Trott are very high, and those of Schieneman are relatively high. In terms of the centrality based on the homogeneity of voting behaviors, it is clearly seen that CPAs and academician might be at the centre of the board meetings with support from user.

Table 5 Results of Multiple Centrality Analysis based on Voting Behavior Data

Normalized Centrality Measures

	Degree	Closeness	Betweenness
Herz	100.000	100.000	4.074
Batavick	77.778	81.818	0.463
Crooch	100.000	100.000	4.074
Foster	66.667	75.000	0.000
Schieneman	88.889	90.000	2.222
Schipper	100.000	100.000	4.074
Seidman	77.778	81.818	0.463
Trott	100.000	100.000	4.074
Wulff	66.667	75.000	0.000
Young	66.667	75.000	0.000

Descriptive Statistics for Each Measure

	Degree	Closeness	Betweenness
Mean	84.444	87.864	1.944
Std Dev	14.229	10.785	1.843
Sum	844.444	878.636	19.444
Variance	202.469	116.324	3.395
SSQ	73333.328	78363.430	71.759
MCSSQ	2024.692	1163.244	33.951
Euc Norm	270.801	279.935	8.471
Minimum	66.667	75.000	0.000
Maximum	100.000	100.000	4.074

An Additional Test

Above analyses are performed on the basis of the individual-level data. Members of the FASB are different from the points of starting career as a member. As there are some variances on numbers of participating in the board meetings, of voices, and of votes among members in certain project, the centrality analyses based on the individual-level have limits to some extent.

Thus, this paper performs the core/periphery analysis based on the data of group-level as an additional test to verify the above results. This analysis seeks to identify a set of actors who have a high-density of ties among themselves (the core) by sharing many events in common, and another set of actors who have a very low-density of ties among themselves (the periphery) by having few events in common (Hanneman and Riddle [14]). This analysis divides both the rows and the columns into two classes. One of the blocks on the main diagonal is a high-density block; the other block on the main diagonal is a low-density block.

Data using in this analysis is the group-level data on homogeneity of voting behaviors to which transforms data shown in Table 2 from the individual-level. This analysis divided the FASB's members by seven groups according as backgrounds of the members. Table 6 shows the result of this analysis. It is clearly seen that one CPA group (Herz), Academician group (Schipper), and User group (Schieneman/Young) lie on the core, in contrast, two CPAs (Crooch, Trott) and two Preparer groups (Foster/Batavick, Wulff/Seidman) lie on the periphery. Similar to other indicators, this result also shows that Academician group and User group play important roles at the FASB's decision-making processes.

Table 6 Result of Core/Periphery Analysis based on Group-Level Data

Blocked Adjacency Matrix

	CPA(Her)	Academician(Sch)	User(Sch/You)	Preparer(Fos/Bat)	CPA(Cro)	Preparer(Wul/Sei)	CPA(Tro)
CPA(Her)	113	99	99	86	87	100	92
Academician(Sch)	99	113	89	84	89	94	100
User(Sch/You)	99	89	113	80	85	94	86
Preparer(Fos/Bat)	86	84	80	104	80	81	83
CPA(Cro)	87	89	85	80	103	83	84
Preparer(Wul/Sei)	100	94	94	81	83	112	85
CPA(Tro)	92	100	86	83	84	85	108

Density Matrix

	1	2
1	95.667	89.750
2	89.750	82.667

Discussions

From what has been discussed above, it seems that an accounting standard on business combinations might be developed under the network structure, in which CPAs, academician, and user are central and core positions, in contrast, preparers are periphery positions. The results are consistent with facts surrounding the standard, which might be proposed a conceptual and user-oriented standard and might be criticized heavily from preparers. Therefore, it seems that the standard was needed, not for the preparers, but for the users.

VI. CONCLUSION

Above discussions may indicate that what blows hole in the powers of preparers or companies in the FASB exists. That is, in the circumstances where the board faces the accounting standard-setting competition with the IASB, the FASB may strengthen links with user's group in order to acquire a competitive advantage. To clarify this point, it is necessary to broaden research subjects and to perform cross-sectional and time-series analyses.

Significances of this research using graph theory are to testify the accounting standard-settings from the perspective of network structure with quantified data analyses. Especially, this paper may test the validity of intuitional results with these analyses. Although it is necessary to elaborate research methods, in this regard, it is thought that this paper made a kind of contribution.

REFERENCES

[1] Horngren CT (1973), The Marketing of Accounting Standards, The Journal of Accountancy, 136(4): 61-66.
[2] Zeff SA (1978), The Rise of "Economic Consequences", The Journal of Accountancy, 146(6): 56-63.
[3] Kelly-Newton L (1980), Accounting Policy Formulation: The Role of Corporate Management, Addison-Wesley Publishing Company, Inc.
[4] Wolk HI, Dodd JL Tearney MJ (2004), Accounting Theory, Conceptual Issues in a Political and Economic Environment, 6th edition, Thomson South-Western.
[5] FASB (2005), Business Combinations, a replacement of FASB Statement No.141 (Exposure Draft), FASB.
[6] FASB (2005), Consolidated Financial Statements, Including Accounting and Reporting of Noncontrolling Interests in Subsidiaries, a replacement of ARB No.51 (Exposure Draft), FASB.
[7] FASB (1991), An Analysis of Issues Related to Consolidation Policy and Procedures (Discussion Memorandum), FASB.
[8] Dennis D (2008), The Process Towards Convergence Continues, Accountancy Ireland, 40(2): 18-21.
[9] IASB (2008), Business Combinations Phase Ⅱ, Project Summary, Feedback and Effect Analysis, IASB.
[10] FASB (2008), Business Combinations (Statement of Financial Accounting Standards No.141, revised), FASB.
[11] FASB (2008), Noncontrolling Interests in Consolidated Financial Statements, an amendment of ARB No.51 (Statement of Financial Accounting Standards No.160), FASB.
[12] Wasserman S, Faust K (1994), Social Network Analysis: Methods and Applications, Cambridge University Press.
[13] Scott J (2000), Social Network Analysis, a handbook, 2nd edition, SAGE Publications, Ltd.
[14] Hanneman B, Riddle M (2005), Introduction to Social Network Methods, University of California, Riverside, CA, (published in digital form at http://faculty.ucr.edu/~hanneman/).
[15] Knoke D, Yang S (2008), Social Network Analysis, 2nd edition, Sage Publications.
[16] Miller PBW, Redding R (1986), The FASB: The People, the Process, and the Politics, Richard D. Irwin, Inc.
[17] Borgatti SP, Everett MG, Freeman LC (2002), Ucinet for Windows: Software for Social Network Analysis, Harvard, MA: Analytic Technologies.
[18] Borgatti SP (2002), Netdraw Network Visualization, Harvard, MA: Analytic Technologies.

Fast Shape Matching and Retrieval Based on Approximate Dynamic Space Warping

Naif Alajlan

Advanced Lab for Intelligent Systems Research
Department of Computer Engineering
King Saud University, P.O.Box 51178, Riyadh 11543, Kingdom of Saudi Arabia
(najlan@ksu.edu.sa)

Abstract: Dynamic space warping (DSW) has emerged as a very effective tool for matching shapes. However, a central computational difficulty associated with DSW arises when a boundary's starting point (or rotation angle) is unknown. In this paper, the HopDSW algorithm is proposed to speed up the starting point computation. Rather than performing an exhaustive search for the correct starting point as in classical approaches, the proposed algorithm operates in a coarse-to-fine manner. The coarse search is global and uses a hopping step to exclude points from the search. Then, the search is refined in the neighborhood of the solution of the coarse search. A criterion that governs selecting the hopping step parameter is given, which reduces the number of starting point computations by an order. For shape representation, triangle area signature (TAS) is computed from triangles formed by the boundary points. Experimental results on the MPEG-7 CE-1 database of 1400 shapes show that the proposed algorithm returns the solution of the exhaustive search with a high degree of accuracy and a considerable reduction in the number of computations.

Keywords: - Shape matching, Shape retrieval, Approximate dynamic space warping, Dynamic programming.

I. INTRODUCTION

Shape is an important visual information that is traditionally used in many automated tasks such as industrial visual inspection [10], trademark registration [8], and content-based image description and retrieval [13]. Over the last decade, the adaption of dynamic time warping (DTW) for two-dimensional shape matching and retrieval has received considerable interest. This trend is mainly motivated by the high effectiveness of the DTW algorithm in achieving intuitive correspondences between the boundary points of two shapes being matched. Most (if not all) shape matching techniques reported in the literature that achieved the highest retrieval rates are based on Dynamic Programming (DP). However, the main limitation of DP-based shape matching techniques is the high computational complexity, which is the main focus of this work. Other issues related to shape matching such as robustness to noise and partial occlusion are beyond the scope of this paper.

Unlike the Euclidean and other vector-based distances, which provide a one-to-one alignment between points of two sequences, a nonlinear alignment can be achieved via the DTW algorithm, as shown in Fig. 1. Note that the Euclidean distance maps rigidly each boundary point in shape *A* to its counterpart in shape *B*. On the other hand, nonlinear alignment is possible using the DTW algorithm where one point in shape *A* can be matched to one or more points in shape *B*. Such alignment compensates for nonrigid deformations that occur in shape images in practice such as articulation and partial occlusion. The DTW algorithm finds the optimal (least cost) warp path that aligns the points of two boundaries. This warp path is constrained to be bounded (i.e., starts and ends by aligning the end points of the two sequences), monotonically increasing, and continuous. These constraints ensure that every point in the two boundaries is used in the warp path, a more intuitive alignment is obtained, and an efficient recursive implementation of the algorithm is possible.

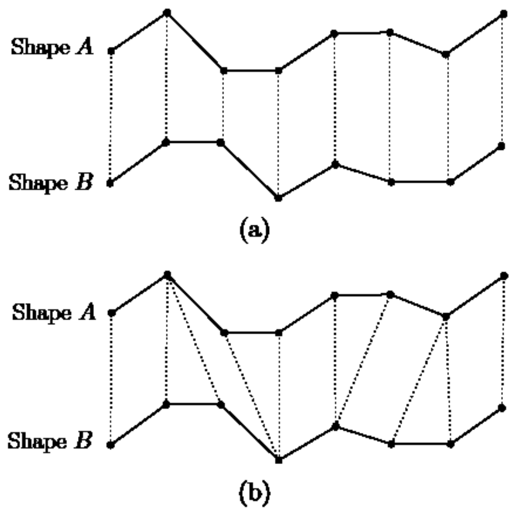

Fig. 1. An illustration of aligning the boundary points of two shapes *A* and *B* using (a) the Euclidean distance and (b) the DTW algorithm.

The basic DTW algorithm has quadratic time complexity since all pairwise distances between the points of two sequences have to be computed. For closed boundaries and rotation-dependent shape representations, where the starting point is unknown, the time complexity becomes cubic, since the basic DTW algorithm has to be executed for every possible starting point. Several approximations were proposed to reduce the computations as described in Section 2. In this paper, an approximate DSW algorithm, HopDSW, is proposed to speed up the basic DSW algorithm for planar shape matching and retrieval. Rather than searching all possible starting points for the optimal solution, only the points that most likely correspond to the optimal solution are searched in a coarse-to-fine fashion. The proposed approximate DSW algorithm works in two stages: coarse and refined. The coarse search for the minimum-cost starting point uses a constant-step hopping to avoid local minima solutions. Then, a refinement search in close proximity around the minimum-distance points returned by the coarse stage is performed. Our experiments show that selecting only the best point from the coarse search is sufficient to obtain a highly accurate solution. The proposed approach is applied to the triangle area representation (TAR) [3], which is sensitive to the starting point selection or shape rotation, as the shape signature. Experiments are conducted on the widely used MPEG-7 CE-1 shape database.

The rest of the paper is organized as follows. Section 2 reviews the related work in the literature. Then, Section 3 explains the proposed algorithm in more details. Experimental results are presented in Section 4 and, finally, Section 5 concludes the work of this paper.

II. RELATED WORK

The matching of one-dimensional sequences using dynamic programming was originated by the speech recognition community [5, 7, 18], where an optimal alignment between elements of two sequences is searched via DTW. Over the past decade, many researchers have applied DTW in the shape matching problem [1, 4, 12, 14]. This trend is mainly motivated by the desirable property of DTW in achieving nonrigid and more intuitive alignments. A particular computational difficulty occurs in matching shapes using DTW when the shape signature is sensitive to the starting point selection or the rotation angle. In [1, 3], a greedy search for the minimum-cost alignment is performed by executing the basic DTW algorithm for every possible starting point.

Several approximations were proposed from the speech recognition community to speed up the DTW algorithm. One of the most well-known approaches is the Sakoe-Chiba band [18], which imposes a constraint on the computation of the cost matrix to be limited within a fixed-width diagonal band. This band, besides reducing the computations, prevents matching farther points, which results in more meaningful alignments. For speech recognition, the Sakoe-Chiba band is set to approximately 10% of the sequence length. However, it is found that this choice is not suitable for the shape matching [1, 3] and the data mining applications [16], where the band width is set to less than 5%. This can be regarded to the fact that silence is allowed in speech, which requires longer warping.

Another class of approximate DTW methods is to reduce the size of the data representation itself and, thus, reducing the number of elements in the cost matrix. In [19], the DTW algorithm is applied to speech sequences at multiple sampling rates or resolutions, starting at the lowest resolution, and at each resolution level, the solution from the lower level is used to reduce the search space and obtain a more accurate solution.

Keogh et. al. proposed an iterative approach to the rotation invariance of the DTW algorithm [9]. Their method is based on discarding unnecessary computations of the DTW algorithm at starting points where the distance exceeds a predefined threshold. More specifically, lower and upper sequences are computed from a group of stored sequences, which results in an envelope or wedge. When a query sequence is presented, it is first compared to that wedge and the resulted distance is guaranteed to be less than or equal to the distance between the query and any member of the wedge's group; therefore, allowing early abandoning. However, when the area of the wedge is large, its distance to the query becomes very small and early abandoning is most likely not possible. To overcome this difficulty, the stored sequences, which may represent the same sequence at different starting points, are grouped based on their similarity to constitute multiple wedges. The authors reported impressive results where the main DTW is greatly sped-up. This method needs a parameter for optimal partitioning of the stored sequences in order to obtain thinner wedges.

III. THE PROPOSED APPROACH

In the following, we give a detailed description of the HopDSW, which is an algorithm that speeds up the basic DSW algorithm when the shape representation is not rotation invariant (or sensitive to the starting point selection). The proposed algorithm does not need parameter tuning and works for any rotation-variant shape representation that can be matched using the DSW algorithm. We first describe the triangle area signature (TAS) that is used for shape representation.

1. Triangle Area Signature (TAS)

The TAS is based on the area of the triangles formed by the points on the shape boundary, which has been used by many researchers as the basis for shape representations [6, 17]. In fact, the TAS is an abstracted version of the triangle area representation described in [3], which is considered as one of the most efficient boundary-based shape representations in the literature so far. The TAS is computed for an arbitrary closed boundary as described in the following.

Given a binary image containing a single shape, the boundary is extracted using the bug-following technique [15]. Then, each boundary point is represented by its x and y coordinates and separated parameterized boundary sequences x_n and y_n are obtained and re-sampled to N equidistant points. The curvature of the boundary point (x_n, y_n) is measured as:

$$TA(n,t_s)=\frac{1}{2}[x_n(y_{n+t_s}-y_{n-t_s})+x_{n+t_s}(y_{n-t_s}-y_n)+x_{n-t_s}(y_n-y_{n+t_s})] \quad (1)$$

where $TA(n,t_s)$ is the triangle area of point $n \in \langle 1,N \rangle$ at scale (or triangle side length) $t_s \in \langle 1,T_s \rangle$, (x_{n-t_s}, y_{n-t_s}), (x_n, y_n), and (x_{n+t_s}, y_{n+t_s}) are three consecutive boundary points. When the boundary is traversed in counter clock-wise direction, positive, negative and zero values of TA mean convex, concave and straight-line points, respectively. Fig. 2 demonstrates these three types of the triangle areas. The triangles at the edge points are formed by considering the periodicity of the closed boundary. Fig. 2 also shows the complete TA signature for the hammer shape when $t_s = 1$. By Increasing the length of the triangle sides, i.e., considering farther points, the function of eq. (1) represents longer variations along the boundary.

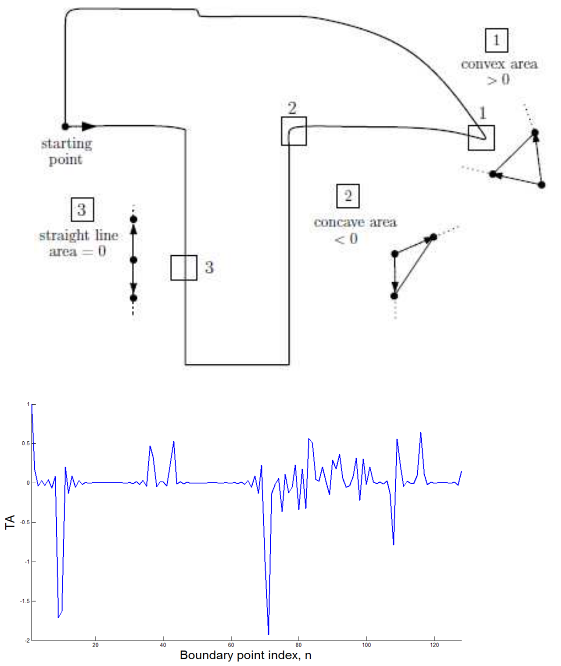

Fig. 2. Three different types of the triangle area values and the TA signature when $t_s = 1$ for the hammer shape.

For shape matching, there is a need to for normalizing eq. (1) to prevent the domination of large scales, which have large triangle areas. For this purpose, the signature is normalized locally at each scale or triangle side length:

$$TAN\,(n,t_s) = \frac{TA\,(n,t_s)}{\max\limits_{1 \le n \le N} TA\,(n,t_s)} \tag{2}$$

Where $TAN\,(n,t_s)$ is a normalized version of $TA\,(n,t_s)$. Note that the triangle area exhibits an odd symmetry with respect to the triangle side length, where the center point is $N/2$ when N is even and does not exist when N is odd. Therefore, the number of scales (T_s) considered in this paper is equal to the floor value of $(N-1)/2$. Finally, the TAS is computed as:

$$TAS\,(n) = \frac{1}{T_s}\sum_{t_s=1}^{T_s} TAN\,(n,t_s) \tag{3}$$

2. The HopDSW algorithm

The HopDSW algorithm is concerned with solving the rotation invariance or the starting point problem for boundary-based shape matching using the basic DSW. It should be noted that this algorithm works for any one-dimensional sequence, representing shapes, that is sensitive to the starting point selection. Instead of executing the basic DSW for all possible starting points, only points that most likely correspond to the minimum-cost solution are searched in a two-stage manner. In the following, a more detailed description of the proposed algorithm is given.

A pseudo code of the HopDSW algorithm is given in Algorithm 1. The algorithm accepts as inputs $TAS_A(n)$ and $TAS_B(n)$ of shapes A and B, where $n \in \langle 1, N \rangle$, and a hopping step $h_s \ge 1$. The hopping step controls the number of boundary points being skipped during the coarse search of the optimum starting point and the criterion for selecting h_s is discussed in the remainder of this section. In the coarse stage, a group of candidate starting points, with each consecutive pair is separated by $h_s - 1$ points, are executed using the basic DSW algorithm of Algorithm 2. Therefore, the number of these points equals $\lceil N / h_s \rceil$, where $\lceil\ \rceil$ is the ceiling function. The boundary point k that yields the minimum distance is passed to the fine stage where the search is resumed within the surrounding points up $h_s - 1$ points in each direction. Therefore, the number of starting points executed in this stage is $2(h_s - 1)$.

The basic DSW algorithm is described in the pseudo code of Algorithm 2. This algorithm starts by initializing a distance matrix, D_T, whose dimensions equal the lengths of the two sequences being matched. The Sakoe-Chiba band [18] of width w is used to restrict the warp path to remain within the w-width diagonal of D_T. Such restriction is useful in both reducing the number of computations and preventing the matching of farther points, which achieves more meaningful alignments. The distance d between two boundary points A_i and B_j is defined as:

$$d\,(A_i, B_j) = \left| TAS_A(i) - TAS_B(j) \right| \tag{4}$$

The elements of the first row and column of D_T that lie within the w-width diagonal band are computed as the distances of the corresponding points. Then, the rest of the w-width diagonal elements are computed as:

$$D_T\,(i,j) = d\,(A_i, B_j) + \min \begin{cases} D_T\,(i-1, j) \\ D_T\,(i-1, j-1) \\ D_T\,(i, j-1) \end{cases} \tag{5}$$

The distance between shapes A and B is taken as the value of $D_T\,(N, N)$, which corresponds to the least cost path between their TAS according to the selected starting point. To account for the shape flipping transformation, it is sufficient to flip one signature and repeat the algorithm. An illustrative example of the HopDSW search mechanism for the optimum starting point is shown in Fig. 3. The classic DSW includes all possible starting points in a greedy search as shown in panel (a) of the figure. Finding the optimum starting point, $n = 18$ in this example, is guaranteed; however, the basic DSW algorithm is executed 128 times. On the other hand, the coarse search of the HopDSW algorithm uses a hopping step $h_s = 8$ and returns $n = 17$ as the minimum distance point, as shown in panel (b). Then, the refinement stage, shown in panel (c), searches in points surrounding $n = 17$ and returns the optimal point, which is $n = 18$. Only 30 executions of the basic DSW algorithm are required by the HopDSW algorithm in this example. Our experiments have shown that the solution returned by this algorithm is the optimum with a high degree of accuracy. Besides, in many applications such as shape retrieval, an approximate solution is sufficient.

Algorithm 1: Approximate DSW (main algorithm):
dist = HopDSW(TAS$_A$, TAS$_B$, h$_s$)

Notation:

TAS_A and TAS_B are TAS of shapes *A* and *B*, respectively.
N is the number of boundary points for each shape.
h_s is the hopping step.

1: $TAS_A \leftarrow [TAS_A\ TAS_A\ TAS_A]$ {to allow cyclic shifting}
2: $dist \leftarrow \infty$
{coarse search}
3: **for** $i = 1$ to $\lceil N/h_s \rceil$ **do**
4: $c \leftarrow (i - 1) \times h_s + 1 + N$
5: $d \leftarrow BasicDSW(TAS_A(c : c{+}N{-}1), TAS_B)$
6: **if** $d < dist$ **then**
7: $dist \leftarrow d$
8: $k \leftarrow c$
9: **end if**
10: **end for**
{fine search}
11: **for** $i = k - h_s{+}1$ to $k + h_s{-}1$ **do**
12: $d \leftarrow BasicDSW(TAS_A(i : i + N{-}1), TAS_B)$
13: **if** $d < dist$ **then**
14: $dist \leftarrow d$
15: **end if**
16: **end for**
17: Flip TAS_A and repeat steps 3 to 16
18: **return** *dist*

Algorithm 2: *d = BasicDSW(TAS$_A$, TAS$_B$)*

Notation:

w is the width of the Sakoe-Chiba band. For N = 128, w is set to 3.
D_T is an $N \times N$ distance matrix initialized as:

$$D_T(i,j) = \begin{cases} 0 & \max(1, i - w + 1) \le j \\ & \le \min(N, i + w - 1) \\ \infty & otherwise \end{cases}$$

1: **for** $i = 1$ to w **do**
2: $D_T(i,1) \leftarrow |\, TAS_A(i) \text{- } TAS_B(1)|$
3: $D_T(1,i) \leftarrow |\, TAS_A(1) \text{- } TAS_B(i)|$
4: **end for**
5: **for** $i = 1$ to N **do**
6: **for** $j = max(1,i{-}w{+}1)$ to $min(N,i{+}w{-}1)$ **do**
7: $p \leftarrow min[D_T(i{-}1\ ,\ j)\ D_T(i{-}1\ ,j{-}1)\ D_T(i\ ,j{-}1)]$
8: $D_T(i\ ,\ j) \leftarrow |\, TAS_A(i) \text{- } TAS_B(j)| + p$
9: **end for**
10: **end for**
11: **return** $d \leftarrow D_T(N,N)$

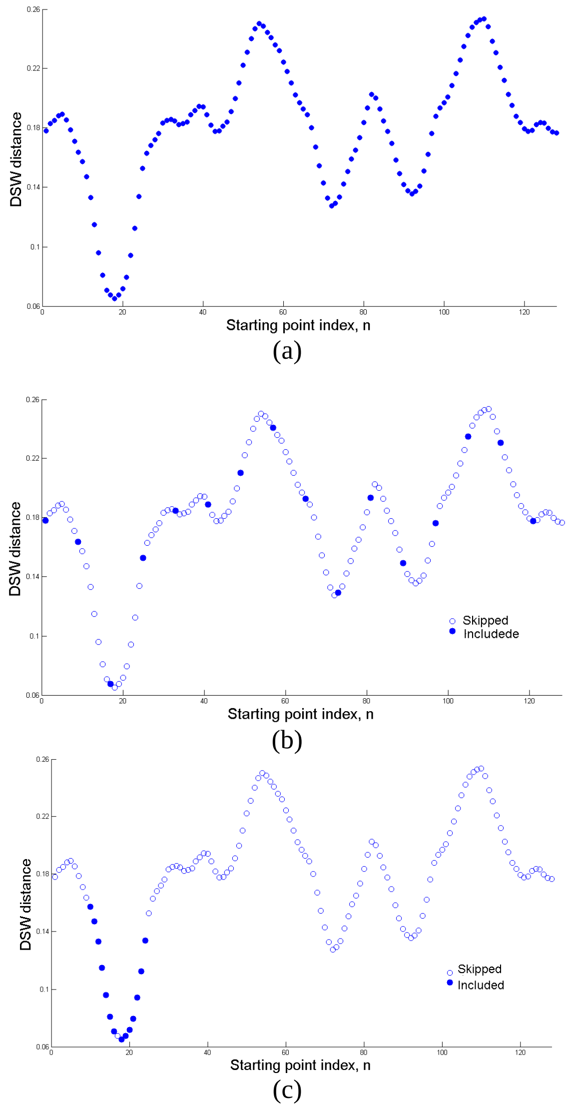

Fig. 3. The DSW distance versus the starting point of two MPEG-7 shapes returned by (a) the classic DSW algorithm, and (b) the coarse and (c) the fine stages of the HopDSW algorithm.

The selection of the hopping step parameter h_s is critical to the performance of the HopDSW algorithm. Let $F(h_s)$ represents the number of starting points executed by the HopDSW algorithm at a given h_s. Then, F is given by:

$$F(h_s) = \left\lceil \frac{N}{h_s} \right\rceil + 2(h_s - 1) \qquad (6)$$

where $h_s \in \langle 1, \lfloor N/2 \rfloor - 1 \rangle$, and $\lceil\ \rceil$ and $\lfloor\ \rfloor$ are the ceiling and floor functions, respectively. As h_s increases, the number of starting points executed during the coarse search decreases and that of the fine search increases, represented by the second term of eq. (6). Note that the function of F is upper-bounded by N (when $h_s = 1$) and $h_s \geq \lfloor N/2 \rfloor$ is not considered since the value of F will exceed N in this case, which means unnecessary repetition of some starting points. Note also that the function of eq. (6) has a single minimum since the first and second terms are inversely monotonic. In this paper, h_s is chosen such that F is minimized. However, it is very difficult to analytically differentiate eq. (6) because the ceiling function is not continuous. Therefore, the minimum is computed numerically.

IV. RESULTS AND DISCUSSIONS

In this section, an empirical evaluation of our algorithm is presented. Two main tests were conducted. In the first, the effect of the hopping step h_s on the accuracy of the distance computation is investigated. The second test includes the shape retrieval application.

The well-known MPEG-7 CE-shape-1 database [11], which consists of 1400 images semantically classified into 70 classes with 20 shapes per class, is used here. This database contains a mixture of natural and artificial objects under various rigid and non-rigid deformations. In the following, the boundary of each shape is extracted and re-sampled to 128 equidistant points. Then, the TAS of each shape is computed according to eq. (3). To ensure availability, all datasets and algorithms used in this evaluation are placed online [2]. The codes are written using the Matlab © (version 7.0) software.

1. Accuracy of HopDSW

The aim of this experiment is to test the accuracy of the HopDSW algorithm. For this purpose, each shape is matched with all other shapes in the database using the HopDSW algorithm, which results in $K(K+1)/2$ distances, where K is the number of shapes in the database. These distances are compared with those obtained using the classic DSW algorithm. Fig. 4 shows the accuracy of the HopDSW algorithm as the number of shapes, K, increases. Note that in this case the number of distance computations ranges from about 5000 (for $K = 100$) to about a million (for $K = 1400$). In this figure, h_s is set to 8 according to eq. (6). Although the number of distance computations increased by more than two orders, there is no significant change in the accuracy, which suggests that the proposed algorithm has the ability to scale-up with the size of the shape database.

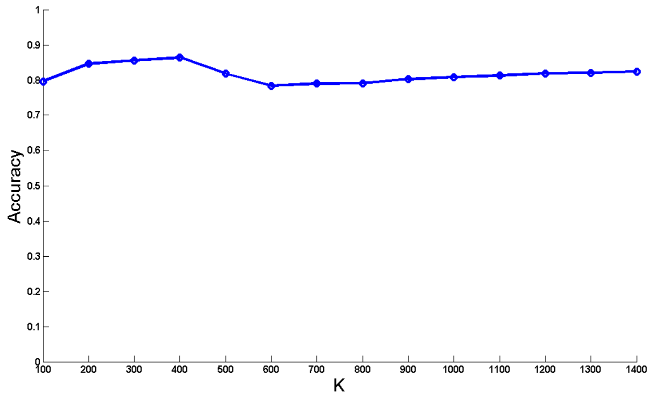

Fig. 4. The accuracy of the HopDSW algorithm, with h_s=8, versus the number of shapes, K, using the MPEG-7 CE-1 database. Note that there are $K(K+1)/2$ distance computations at each point.

To illustrate the role of the hopping step parameter, Fig. 5 depicts the accuracy of the HopDSW algorithm at different values of h_s. Interestingly, the accuracy at h_s=8, which corresponds to the minimum number of starting point executions as given by eq. (6), is higher than other larger values of h_s, although these values include more starting points in the distance computation. The reason can be regarded to the fact that the additional starting points in the latter case come in favour of the local search for the optimum solution, which is represented by the second term in eq. (6). Whereas the former case more points are included in the global search represented by the first term of the same equation. This suggests that the choice of the parameter h_s that minimizes eq. (6) achieves a good balance for searching both globally and locally for the optimum solution.

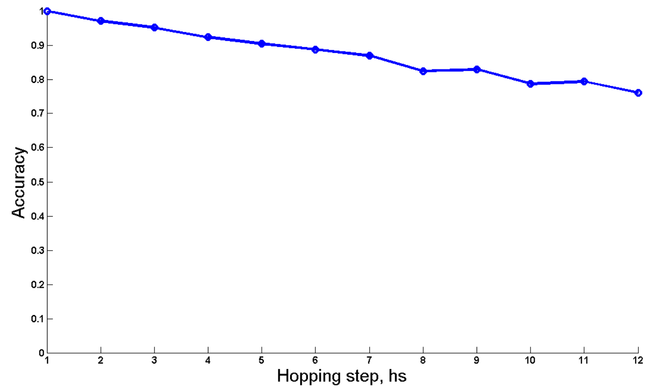

Fig. 5. The accuracy of the HopDSW algorithm versus the hopping step, h_s, using all 1400 shapes of the MPEG-7 CE-1 database.

2. Shape retrieval test

In shape retrieval, the aim is to acquire a ranked list of shapes according to their similarity with a query shape presented by a user. Therefore, obtaining an exact value of the distance is not a critical issue since approximate solutions are usually sufficient. It should also be emphasized that the work presented in this paper is not intended to enhance the effectiveness of shape retrieval, but rather, to reduce the number of starting point computations. However, shape retrieval results are reported here to demonstrate the trade-off between speed and accuracy of the proposed algorithm.

The MPEG-7 CE-1 part B test is conducted for both Algorithms. In this test, each of the 1400 shapes is considered as a query and the remaining shapes are ranked according to their similarity with the query. Then, the number of correct matches are counted among the first 40 retrieved shapes. The final precision is the average of all individual shape precisions. Table 1 shows the performance of the HopDSW algorithm at different values of h_s. It is obvious that the drop in the precision due to the hopping step is marginal. This suggests that the approximate distance returned by the HopDSW algorithm is either equal or very close to the exact distance returned by classic DSW algorithm ($h_s = 1$).

Table 1. The results of the MPEG-7 CE-shape-1 part B test using the HopDSW algorithm.

h_s	1	2	3	4	5	6
Precision	77.96	77.95	77.95	77.86	77.90	77.89
h_s	7	8	9	10	11	12
Precision	77.95	77.81	77.89	77.69	77.80	77.58

V. CONLCLUDING REMARKS

In this paper, a shape matching algorithm that approximates the DSW distance for arbitrary starting points is introduced. The algorithm performs a global search via hopping to locate a minimum-distance point followed by a local, refined search around the located point. The proposed algorithm achieves reduction by an order of the number of starting points as compared with the greedy search. Besides, experimental tests show that the proposed algorithm achieves a high degree of accuracy. This suggests that the basins of attraction for the minimum-cost starting point are quite large; therefore, there is no need to try every possible starting point. A desirable property of this algorithm is that it doesn't require any parameter setting by the user.

REFERENCES

[1] Adamek T and O'Connor N (2004), A multiscale representation method for nonrigid shapes with a single closed contour, IEEE Trans. on Circuits and Systems for Video Tech, 14(5):742–753.

[2] Alajlan N (2008), http://faculty.ksu.edu.sa/naifajlan/pages/activities.aspx.

[3] Alajlan N, Elrube I, Kamel MS, and Freeman H (2007), Shape retrieval using triangle-area representation and dynamic space warping, Pattern Recognition, 40:1911–1920.

[4] Bartolini I, Ciaccia P, and Patella M (2005), Warp: accurate retrieval of shapes using phase of fourier descriptors and time warping distance, IEEE Trans. Pattern Analysis and Machine Intelligence, 27(1):142–147.

[5] Deller J, Hansen J, and Proakis J (1999), Discrete-Time Processing of Speech Signals. Wiley-IEEE Press; Reprint edition.

[6] Ip HHS and Shen DG (1998), An affine-invariant active contour model (ai-snake) for model-based segmentation. Image and Vision Computing, 16(2):135–146.

[7] Itakura F (1975), Minimum prediction residual principle applied to speech recognition, IEEE Trans. Acoustics Speech Signal Process, 23:52-72.

[8] Jain AK and Vailaya A (1998), Shape-based retrieval: A case study with trademark image databases, Pattern Recognition, 31(9):1369–1390.

[9] Keogh E, Wei L, Xi X, Lee SH, and Vlachos M (2006), LB_Keogh supports exact indexing of shapes under rotation invariance with arbitrary representations and distance measures, In Proceedings of the 32nd international conference on very large data bases, pages 882–893.

[10] Kunttu I and Lepisto L (2007), Shape-based retrieval of industrial surface defects using angular radius fourier descriptor, IET Image Processing, 1(2):231–236.

[11] Latecki LJ, Lakamper R, and Eckhardt U (2000), Shape descriptors for non-rigid shapes with a single closed contour, In IEEE Conf. on Computer Vision and Pattern Recognition, pages 424–429.

[12] Ling H and Jacobs D (2005), Using the inner distance for classification of articulated shapes, In IEEE International Conference on Computer Vision and Pattern Recognition, 2: 719–726.

[13] Pentland A, Picard R, and Sclaroff S (1996), Photobook: content-based manipulation of image databases, International Journal of Computer Vision, 18(3):233–254.

[14] Petrakis EGM, Diplaros A, and Milios E (2002), Matching and retrieval of distorted and occluded shapes using dynamic programming, IEEE Trans. on Pattern Analysis and Machine Intelligence, 24(11):1501–1516.

[15] Pratt WK (1991), Digital Image Processing, John Wiley and sons Inc, second edition.

[16] Ratanamahatana C and Keogh E (2005), Three myths about dynamic time warping data mining, In International Conference on Data Mining, pages 506–510.

[17] Roh K and Kweon I (1998), 2-D object recognition using invariant contour descriptor and projective refinement, Pattern Recognition, 31(4):441–445.

[18] Sakoe H and Chiba S (1978), Dynamic programming algorithm optimization for spoken word recognition, IEEE Trans. Acoustics, Speech, and Signal Processing, 26:43–49.

[19] Salvador S and Chan P (2004), FastDTW: Toward accurate dynamic time warping in linear time and space, In KDD Workshop on Mining Temporal and Sequential Data, pages 70–80.

Prediction Model of Permeability From Well logs Using Type-2 Fuzzy Logic Systems

Sunday Olusanya Olatunji
(s.o.olatunji@gmail.com,
oluolatunji.aadam@gmail.com)
Intelligent Software Engineering Laboratory, Faculty of Computer Science & Information Systems, Universiti Teknologi Malaysia, 81310 UTM Skudai, Johor, Malaysia

Ali Selamat
(aselamat@utm.my)
Intelligent Software Engineering Laboratory, Faculty of Computer Science & Information Systems, Universiti Teknologi Malaysia, 81310 UTM Skudai, Johor, Malaysia

Abdul Azeez Abdul Raheem
(toazeez@gmail.com)
Centre for Petroleum and Minerals, The Research Institute, King Fahd University of Petroleum and Mineral, Dhahran 31261, Kingdom of Saudi Arabia

Abstract: In this paper, the viability and capability of using Type-2 Fuzzy Logic Systems as a novel approach for predicting permeability from Well Logs has been investigated and implemented. Type-2 fuzzy logic is powerful in handling uncertainties, including uncertainties in measurements and data used to calibrate the parameters. In the formulation used, the value of a membership function corresponding to a particular permeability value is no longer a crisp value; rather, it is associated with a range of values that can be characterized by a function that reflects the level of uncertainty. In this way, the model will be able to adequately account for all forms of uncertainties associated with predicting permeability from well log data, where uncertainties are very high and the need for stable results are highly desirable. Comparative studies have been carried out to compare the performance of the proposed framework with those earlier used methods, using real industrial reservoir data. Empirical results from simulation show that Type-2 FLS approach outperforms others in general and particularly in the area of stability and ability to handle data in uncertain situations, which are the common characteristics of well logs data. Another unique advantage of the newly proposed model is its ability to generate, in addition to the normal target forecast, prediction intervals as its by-products without extra computational cost.

Keywords: Permeability estimation, Well logs, Type-2 fuzzy logic systems, reservoir characterization, Support Vector Machines, Feedforward Neural Networks

I. INTRODUCTION

Permeability is one of the most important of reservoir properties, and their prediction has been one of the fundamental challenges to petroleum engineers and researchers [1]. Accurate knowledge of Permeability property is required to determine the amount of oil or gas present in reservoirs, the amount that can be recovered, the flow rate of oil or gas, the forecast of future production, design of production facilities, and for the overall reservoir management and development requires accurate knowledge of permeability [1, 2]. Permeability, or flow capacity, is the ability of porous rock to transmit fluid [3]. Although a rock may be very porous, it is not necessarily very permeable. Permeability is the ease with which fluid is transmitted through a rock's pore space**.** It is a measure of how interconnected the individual pore spaces are in a rock or sediment.

The recent success of applying artificial neural networks (ANN) to solve various engineering problems has drawn the attention to its potential applications in the petroleum industry. Thus, an alternative approach to the parametric modeling approach is the application of artificial neural networks (ANNs). In attempt to resolve problems associated with the parametric approach, the standard artificial neural networks (ANNs) have been used to provide better prediction models [13-16]. These works yielded a significant prediction improvement in the oil and gas industries. See [17-24] for further works carried out in this direction. However, the technique still suffers from several drawbacks. These shortcomings include the trial-and-error approach of ANN, the need to guess its architectural parameters in advance, such as, number and size of hidden layers and the type of transfer function(s) for neurons in the various layers. Moreover, the training algorithm parameters were determined based on guessing initial random weights, learning rate, and momentum. Although acceptable results may be obtained with effort, it is obvious that potentially superior models can be overlooked. Most importantly, ANN suffers from instability in its predictions and it is unable to model uncertainties, which characterize well logs in particular.

Researchers in both machine learning and data mining communities did their best to address and overcome these problems of ANN. As a result, several variants of ANN and other methods like support vector machines (SVM) and functional networks (FN) have been proposed and used [4, 12, 24], yet each has its limitations that still call for further research of this nature, particularly their inability to handle uncertainties and the need to ensure stability in permeability predictions. Recently, Type-2 Fuzzy Logic Inference Systems have been proposed as new intelligence frameworks for both prediction and classification to handle all forms of uncertainties [26-29]. Type-2 fuzzy logic is powerful in handling uncertainties, including uncertainties in measurements and data used to calibrate the parameters. It has since featured in a wide range of medical, business and engineering applications, often with promising and stable results [30-36]. Therefore, bearing in mind the fact that there is uncertainty in reservoir characteristics and well log data, it becomes clear that the best way to tackle this problem of uncertainty is to make use of type-2 fuzzy logic; which is an approach that has been specifically invented to deal with all forms of uncertainty [26] that is inherent in our day to day natural encounters and mode of reasoning. Thus the significance of type-2 fuzzy logic based prediction model, hereby proposed, cannot be overemphasized.

The main objectives of this study are (1) to investigate the feasibility of type-2 FLS in forecasting permeability; (2) to develop a new intelligence framework, based on type-2 FLS, for predicting permeability from well logs using real industrial well log data; (3) to investigate how various earlier commonly used standard neural network, support vector machines and functional networks compare in their performance in predicting permeability of carbonate reservoirs; and (iv) to explore how type-2 FLS framework can generate prediction intervals, permeability, effortlessly as its by-product.

II THE PROPOSED TYPE-2 FUZZY LOGIC SYSTEM INTELLIGENCE FRAMEWORK

In this work, type-2 fuzzy logic framework is presented and utilized for predicting permeability from well log data based on distinct real-world industrial data. The goal is to completely specify the FLSs using the training data, which is a unique characteristic of adaptive fuzzy systems. Type-2 Adaptive Fuzzy Inference Systems (ANFIS) is an adaptive network that learns the membership functions and fuzzy rules, from data, in a fuzzy system based on type 2 fuzzy sets, see [26, 37] for details. “Type-2 fuzzy sets are fuzzy sets whose grades of membership are, them-selves, fuzzy. They are intuitively appealing because grades of membership can never be obtained precisely in practical situations” [38]. The fuzzifier takes the well log input parameters values as inputs. The output of the fuzzifier is the fuzzified measurements which will be the input to the inference engine. The resultant of the inference engine is type-2 fuzzy output sets which can be reduced to type-1 fuzzy set by the type reducer. This type reduced fuzzy set in this model is an interval set which gives the predicted external attribute measurement as a possible range of values. The defuzzifier calculates the average of this interval set to produce the predicted crisp external attribute measurement (which is the permeability values).

1. Initializing the Framework

To initialize the framework, we need to define the components of a typical type-2 fuzzy logic system from the perspective of permeability model. In this work, we initialized FLS from the numerical dataset. In this model, we have the antecedents and consequents: (1) internal attributes are the antecedents, which in this case are the well log variables, (2) external attribute is the consequent which is the permeability value to be predicted in this case. To initialize the framework, we make use of training data set created from the available measurement data. The proposed model required that the antecedent and consequent membership functions be considered as type-2 Gaussian with uncertain mean (m) and the input membership functions will be type-2 Gaussian with uncertain standard deviation (σ) as shown below.

$$\mu_A(x) = \exp\left[-\frac{1}{2}\left(\frac{x-m}{\sigma}\right)^2\right] \quad m \in [m_1, m_2]$$

Corresponding to each value of m, there will be a different membership curve as shown in figure 5.

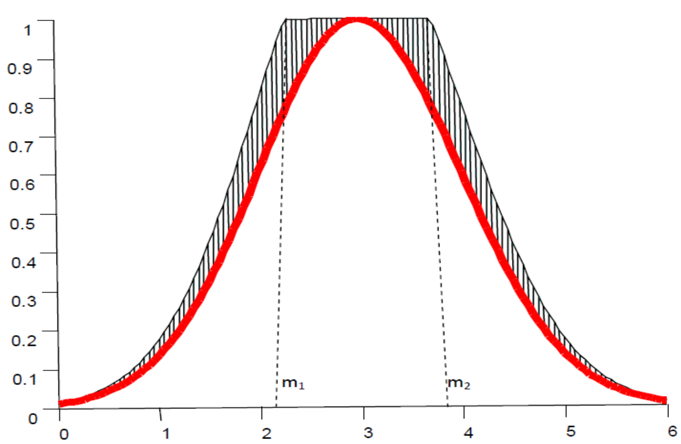

FIGURE 1: Foot print of uncertainty (FOU) for Gaussian primary membership function with uncertain mean.

$$\mu_A(x) = \exp\left[-\frac{1}{2}\left(\frac{x-m}{\sigma}\right)^2\right] \quad \sigma \in [\sigma_1, \sigma_2]$$

Corresponding to each value of σ, there will be a different membership curve as shown in figure below.

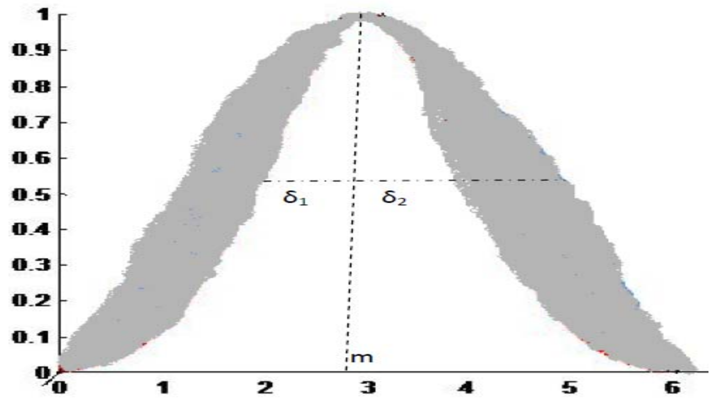

FIGURE 2: Foot print of uncertainty (FOU) for Gaussian primary membership function with uncertain standard deviation.

The uniform shading for the foot print of uncertainties (FOU), in the two figures above, again denotes interval sets for the secondary membership function and represents the entire interval type-2 fuzzy set $\mu_{\tilde{A}}(x,u)$.

Sample rule for the framework looks like;

$$R^i : IF\ x_1\ is\ F_1^i\ and\ x_2\ is\ F_2^i ...and\ x_P\ is\ F_P^2\ THEN\ y_i\ is\ G^i$$

From the above rules, for the consequent part, R^i represent the i[th] type-2 fuzzy rule for the i[th] sample, F_1^i is a fuzzy set whose membership function is centered at the 1[st] attribute of the i[th] sample. For the consequent part, G^i is a fuzzy set whose membership function is centered at target output y of i[th] sample.

For a further detail explanation of various ways to initialize and train type-2 FLS, see [26].

2. Training the Model with Adaptive Type-2 Fuzzy Learning Process

After initializing the FLS, part of the available dataset will be used as training data. It will contain the input-output pair where the inputs are independent variables and the output is the target attribute. Our training procedure follow strictly type-2 fuzzy logic standard, details of which can be found in [26, 29]. Figure 3 depicts the proposed type-2 adaptive fuzzy inference system network. The network depicted has a number of parameters to be learnt. Firstly there are parameters for the membership grades of the antecedent type 2 fuzzy sets in layer 1. Layer 3 has the consequent type 2 fuzzy sets and there are parameters to be learnt there as well. Since the output of the network is numeric this can be compared with the expected output from a teacher (i.e. supervised learning) and back propagation used to feed the error back to adjust the parameters in the nodes. For illustration purposes, the method for two inputs is discussed but this is extendable. GR and RT are vectors representing well log inputs (Gamma Rays and Resistivity respectively) that might have different representations for different type 2 fuzzy sets while Perm denote the final permeability output from the system.

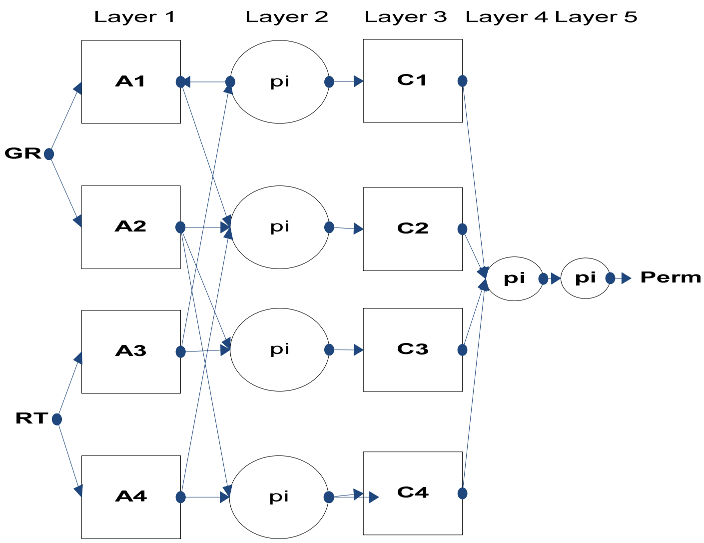

FIGURE 3: A type-2 adaptive neuro-fuzzy inference system network.

The grades in type-2 sets are actually fuzzy numbers, that is, rather than a membership grade being crisp in [0, 1] it's a fuzzy number in [0,1] where the width of the set indicates the uncertainty attached to the number. For a two input, one output model there can be four fuzzy rules as follow:

IF GR is A1 and RT is B1 THEN Z is C1
IF GR is A1 and RT is B2 THEN Z is C2
IF GR is A2 and RT is B1 THEN Z is C3
IF GR is A2 and RT is B2 THEN Z is C4,

where A1, A2, B1, B2, C1, C2, C3, C4, are type 2 fuzzy sets. The network in figure 3 describes the type-2 fuzzy system encoded in the rules above. A square node indicates an adaptive node with modifiable parameters whereas a circle indicates a fixed node that simply performs a function.

III EMPIRICAL WORK, DISCUSSION AND COMPARATIVE STUDIES

In order to carry out empirical study, two distinct real-industrial databases (Well-W1 with 356 data points and Well-W2 with 478 data points) were acquired having well log inputs parameters that include Wire line logs from these wells included CT (electrical conductivity), DRHO (density), DT (sonic travel time), MSFL (Micro spherically Focused Log), NPHI (Neutron porosity), PHIT (total porosity), RHOB (bulk density), RT (Resistivity), and SWT (water saturation). One important additional benefit of type-2 FLS worth mentioning at this point is that, compared with earlier used models, the proposed type-2 FLS will generate not only the permeability predictions, but also prediction intervals effortlessly as its by-product. It achieved this through its type-reduction process that generates the intervals as the by-product. See,[26], for further details. A sample permeability prediction intervals generated in this work is shown in figure 4. This, indeed, is another great contribution of this work.

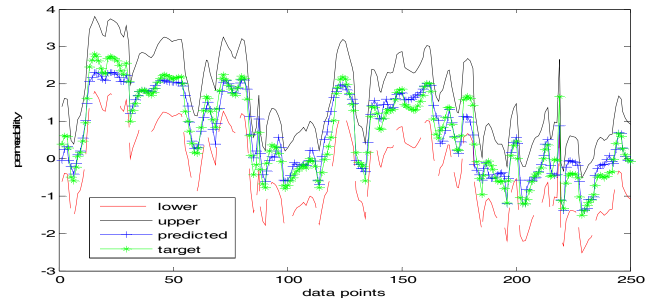

Figure 4: Permeability prediction intervals based on Type-2 FLS

IV CONCLUSION AND RECOMMENDATION

In this study, two distinct industrial data set were made used of in investigating the feasibility, performance, and accuracy of the proposed type-2 FLS based modeling scheme as a new framework for predicting the permeability from well log. A new computational intelligence modeling scheme, based on the type-2 fuzzy logic system has been investigated, developed and implemented, as predictive solution, that takes care of all forms of uncertainties, for predicting permeability from well logs. Validation of the framework is done using real industrial well log data. In-depth comparative studies have been carried out between this new framework and the standard neural networks, support vector machines and functional network. Empirical results from simulations show that the proposed model outperformed all the compared models in all fronts. Based on the published literature to date, it can be said here that, for the first time in the history of permeability predictions, this work has presented a Type-2 FLS based model that will generate not only the target permeability forecast but also prediction intervals without effortlessly. As a form of future work recommendations, it is suggested that other models like that of porosity, history matching, lithofacies and other reservoir engineering properties could be built using this framework. Also more dataset could be considered while investigating the effect of absence or presence of preprocessing techniques.

REFERENCES

[1] Balan, B., Mohaghegh, S., and Ameri, S.: 'State-of-the-Art in permeability determination from well log data: part I-A comparative study, model development '. Proc. SPE Eastern Regional Conference and Exhibition, West Virginia1995 pp. Pages

[2] Balan, B., Mohaghegh, S., and Ameri, S.: 'State-Of-The-Art in Permeability Determination From Well Log Data: Part 2-Verifiable, Accurate Permeability Predictions, the Touchstone of All Models'. Proc. SPE Eastern Regional Conference and Exhibition, West Virginia, USA, September 18-20 1995 pp. Pages

[3] Ahmed, U., Crary, S.F., and Coates, G.R.: 'Permeability Estimation: The Various Sources and Their Interrelationships', Journal of Petroleum Technology, 1991

[4] Lim, J.S., and Kim, J.: 'Reservoir porosity and permeability estimation from well logs using fuzzy logic and neural networks'. Proc. The Society of Petroleum Engineering (SPE), Asia Pacific Oil and Gas Conference and Exhibition, Perth, Australia2004 pp. Pages

[5] Archie, G.E.: 'The Electrical Resistivity Log as an Aid in Determining Some Reservoir Characteristics', Trans., AIME, 1942, 146, (1), pp. 54-62

[6] Tixier, M.P.: 'Evaluation of Permeability From Electric-Log Resistivity Gradients', Oil & Gas Journal, 1949, (June), pp. 111-113

[7] Wyllie, M.R.J., and Rose, W.D.: 'Some Theoretical Considerations Related to the Quantitative Evaluation of the Physical Characteristics of Reservoir Rock from Electric Log Data', Trans., AIME, 1950, 189

[8] Pirson, S.J.: 'Handbook of Well Log Analysis' (Englewood Cliffs, N.J., Prentice-Hall, Inc., 1963. 1963)

[9] Timur, A.: 'An Investigation of Permeability, Porosity, and Residual Water Saturation Relationship for Sandstone Reservoirs', The Log Analyst, 1968, 9, (4), pp. 8-21

[10] Coates, G.R., and Dumanoir, J.L.: 'A New Approach to Improved Log-Derived Permeability', The Log Analyst, 1974

[11] Wendt, W.A., Sakurai, S., and Nelson, P.H.: 'Permeability Prediction From Well Logs Using Multiple Regression' (Academic Press, 1986. 1986)

[12] El-Sebakhy, A.E., Abdulraheem, A., Ahmed, M., Al-Majed, A., Raharja, P., Azzedin, F., and Sheltami, T.: 'Functional Network as a Novel Approach for Prediction of Permeability in a Carbonate Reservoir'. Proc. SPE Conference, Bahrain2007 pp. Pages

[13] Baldwin, J.L., Bateman, A.R.M., and Wheatley, C.L.: 'Application of neural network to the problem of mineral identification from well logs', The Log Analyst, 1990, 3, pp. 279-293

[14] Chang, H.C., Kopaska-Merkel, D.C., Chen, H.C., and Durrans, S.R.: 'Lithofacies identification using multiple adaptive resonance theory neural networks and group decision expert system', Computers and Geosciences, Elsevier, 2000, 26, (5), pp. 591-601

[15] Mohaghegh, S., Arefi, R., Ameri, S., and Rose, D.: 'Design and development of an artificial neural network for estimation of permeability'. Proc. Society of Petroleum Engineers1994 pp. Pages

[16] Mohaghegh, S., Arefi, R., Ameri, S., and Nutter, R.: 'Petroleum Reservoir Characterization with the Aid of Artificial Neural Networks', Journal of Petroleum Science & Engineering, 1996, 16, pp. 263-274

[17] Mohaghegh, S., McVey, D., Ameri, S., and Aminian, K.: 'Predicting Well Simulation Results in a Gas Storage Field in the Absence of Reservoir Data, Using Neural Networks'. Proc. Society of Petroleum Engineering, September 1995 pp. Pages

[18] Osborne, D.A.: 'Permeability Estimation Using a Neural Network: A Case Study from The Roberts Unit, Wasson Field, Yoakum County, Texas', AAPG South West Section Transactions, 1992, pp. 125-132

[19] Wiener, J.: 'Predicting Carbonate Permeability from Wire line Logs Using a Back-Propagation Neural Network', CM2.1, Society of Exploration Geophysicists, Expanded Abstracts with Biographies, Technical Program, 1991, 1

[20] Wong, K.W., and Gedeon, T.D.: 'A modular signal processing model for permeability prediction in petroleum reservoir: Neural Networks for Signal Processing'. Proc. 2000 IEEE Signal Processing Society Workshop2000 pp. Pages

[21] Wong, P.M., Henderson, D.H., and Brooks, L.J.: 'Permeability Determination using Neural Networks in the Ravva Field, Offshore India', SPE Reservoir Evaluation and Engineering, 1998, 1, pp. 99-104

[22] Raiche, A.A.: 'pattern recognition approach to geophysical inversion using neural nets', Geophysical Journal International, 1991, 105, pp. 629-648

[23] El-Sebakhy, E.A., Sheltami, T.R., Al-Bukhitan, S.Y., Shabaan, Y.M., P., R.I., and Y., K.: 'Support vector machines framework for predicting PVT properties of crude oil systems'. Proc. The 15th Middle East Oil Show, Society of Petroleum Engineering (SPE) Bahrain2007 pp. Pages

[24] El-Sebakhy, A.E.: 'Forecasting PVT properties of crude oil systems based on support vector machines modeling scheme', Journal of Petroleum Science and Engineering, 2009, 64, (1-4), pp. 25-34

[25] Ali, K.I., Mohammadreza, R., and Seyed, A.M.: 'A fuzzy logic approach for estimation of permeability and rock type from conventional well log data: an example from the Kangan reservoir in the Iran Offshore Gas Field', Journal of Geophysics Engineering, 2006, pp. 356–369

[26] Mendel, J.M.: 'Uncertain Rule-Based Fuzzy Logic Systems: Introduction and New Directions' (Prentice-Hall, 2001. 2001)

[27] Liang, Q., and Mendel, J.M.: 'Interval type-2 fuzzy logic systems: Theory and design', IEEE Transactions Fuzzy Systems, 2000, 8, pp. 535.550

[28] Mendel, J.M.: 'Fuzzy Sets for Words: A New Beginning'. Proc. The IEEE conference on Fuzzy Systems2003 pp. Pages

[29] Mendel, J.M., and John, R.I.B.: 'Type-2 Fuzzy Sets Made Simple,' IEEE Transactions On Fuzzy Systems, 2002, 10, (2)

[30] Zarandi, M.H.F., Rezaee, B., Turksen, I.B., and Neshat, E.: 'A Type-2 Fuzzy Rule-Based Expert System Model for Stock Price Analysis', Expert Systems with Applications, 2007

[31] Dongrui, W., and Mendel, J.M.: 'A vector similarity measure for linguistic approximation: Interval type-2 and type-1 fuzzy sets', Information Sciences, 2008, 178, pp. 381-402

[32] Liang, Q., and Mendel, J.M.: 'Equalization of Non-linear Time-Varying Channels Using Type-2 Fuzzy Adaptive Filters', IEEE Trans. on Fuzzy Systems, 2000, 8, pp. 551-563

[33] Liang, Q., and Mendel, J.M.: 'Overcoming Time-Varying Co-channel Interference Using Type-2 Fuzzy Adaptive Filters', IEEE Trans. on Circuits and Systems, 2000

[34] Liang, Q., Karnik, N.N., and Mendel, J.M.: 'Connection Admission Control in ATM Networks Using Survey-Based Type-2 Fuzzy Logic Systems: Applications and Reviews', IEEE Trans. on Systems, Man and Cybernetics: Part C, 2000, 30, pp. 329-339

[35] Mashinchi, M.R., and Ali Selamat: 'Constructing a Customer's Satisfactory Evaluator System Using GA-based Fuzzy Artificial Neural Networks', World Applied Sciences Journal, 2008, 5, (4), pp. 432-440

[36] Mashinchi, M.R., and Ali Selamat: 'An Improvement of Genetic-based Learning Method for Fuzzy Artificial Neural Networks', Applied Soft Computing, Elsvier Science, 2009

[37] Cox, E.: 'Adaptive Fuzzy Systems', IEEE Spectrum, 1993

[38] Dubois, D., and Prade, H.: 'Fuzzy Sets and Systems: Theory and Applications' (Academic Press, 1982. 1982)

[39] Zadeh, L.A.: 'The Concept of a Linguistic Variable and its Application to Approximate Reasoning - I', Information Sciences, 1975, 8, pp. 199-249.

Real-Time Iris Detection

[1]Mohamed Rizon, [2]Chai Tong Yuen, [1]Ali AlMejrad and [3]Naif Alajlan

[1]Department of Biomedical Technology, King Saud University
P.O. Box 10219, Riyadh 11433, Kingdom of Saudi Arabia
[2]Department of Mechatronic & Biomedical Engineering
Universiti Tunku Abdul Rahman (UTAR),
Jalan Genting Kelang, Setapak 53300, Kuala Lumpur, Malaysia
[3]Advanced Lab for Intelligent Systems Research
Department of Computer Engineering
King Saud University, P.O.Box 51178, Riyadh 11543, Kingdom of Saudi Arabia
(mjuhari@ksu.edu.sa)

***Abstract**:* A real-time algorithm to automatically detect human face and irises from color images has been developed. Haar cascade-based algorithm has been applied for simple and fast face detection. The face image is then converted into grayscale image. Three types of image processing techniques have been tested respectively to study its effect on the performance of iris detection algorithm. Then, iris candidates are extracted from the valley of the face region. The iris candidates are paired up and the cost of each possible pairing is computed by a combination of mathematical models. The pairing with the lowest cost is considered as iris. The algorithm has been tested by quality images from Logitech camera and noisy images from Voxx CCD camera. The proposed algorithm has achieved a success rate of 83.60% for iris detection in an open office environment.

***Keywords**:* - Face detection, Iris detection, Illumination normalization, Face recognition

I. INTRODUCTION

In past ten years, face recognition has attracted substantial attention from various disciplines and experienced a tremendous growth in researches. Nowadays, face recognition has been widely applied in security system, surveillance, identity verification and other purposes. Automatic face and facial features detections are vital for face recognition development. Humans are good at face identification but it is never an easy task for a computer to recognize human faces automatically. Automatic real-time face detection systems continue to gain substantial attention in the field of face recognition. Two of such systems have been developed based on still-image [1, 28, 29] and video sequences [30] achieving detection rate of 90% and 99% respectively. These systems used YCbCr or RGB color space in the effort to detect face region. No significant efforts have been reported in dealing with variabilities such as lighting, facial expressions and head tilts.

Generally, face recognition is categorized into holistic method and feature-based method. The holistic approach [3, 4] treats a face as a two dimensional pattern of intensity variation. The feature-based approach [2, 13, 14] recognizes a face using the geometrical measurements [6, 8] taken among facial features. Many methods have been proposed to locate eyes [8, 32], mouth [4, 5], and face region [3, 7] in an image. Popularity of using template matching [2, 3] features detection has been shown at the earlier stage of feature-based research. However, template matching and eigenspace methods require large number of templates for varying poses and face normalization for variation of size and orientation.

Vertical and horizontal projections have been combined with template matching [2, 3], gabor transformation [22], genetic algorithm [7] and the Smallest Univalue Segment Assimilating Nucleus (SUSAN) [14]. SUSAN algorithm has emerged as a simple and accurate method for corner detection either in grayscale image [15, 16] or color image [17, 18, 19]. Anyhow, integral projection might not robust enough to tackle the illumination changes.

In the most recent researches, Adaboost [23] is used to search through the entire face region to get all possible combinations of features based on maximum likelihood. A new facial features localization system has been developed based on Gaussian Mixture Model (GMM) to locate the regions of eyes [24] but it is not fully automated. Most of the studies have been done under controlled environment. Conditions such as beard, moustache, head orientation, hairstyle and facial expressions have been excluded from the face databases used in researches [6, 8, 13, 14, 17, 18, 19].

The aim of this research is to improve the performance of face and iris detection in real-time environment. The proposed algorithm will first locate the face region by using Haar Cascade face detector. Then, illumination normalization is applied to reduce the effect of lighting variation. After that, iris candidates are extracted from the valleys of the face region using feature template and separability filtering. Iris candidates are determined by the total costs computed from Hough Transform, seperability and intensity information. Finally, the pair of irises will be determined by the total costs and matching correlation in a mathematical approach.

II. FACE LOCALIZATION

There are two databases with images captured by using Voxx CCD box camera (Database A) and Logitech Quickcam Pro9000 (Database B) in office environment. Logitech camera has 2.0 megapixels of resolution while Voxx camera has high resolution

480TVL. Both of the cameras have different build qualities and specifications.

In this experiment, OpenCV Haar Cascade based face detector [25] has been used for real-time detection instead of the skin-color based face detector [29]. This is because the RGB color based face detection tends to be affected easily by the lighting variation and complex background in the office. The images of each employee are captured during the face verification process to open their lockers. The images are collected during office hours and no constraint has been set besides facing the camera for verification purpose. Eq. (1) is the main function being used in face detection.

$$cvHaarDetectObjects(a,b,c,d,e,f,g) \tag{1}$$

where (a=image; b=cascade; c=memory storage; d=scale factor; e=min. neighbors; f=flags; g=min. size). The parameters d, e, f, g have been set as 1.1, 3, CV_HAAR_FIND _BIGGEST_OBJECT and 65×65 in this experiment.

III. ILLUMINATION NORMALIZATION

This section describes the chosen image processing technique which is similar to the method proposed by Xiaoyang Tan and Bill Triggs [27] before implementing the iris detection algorithm. It incorporates a series of steps to counter the effects of illumination variations, local shadowing and highlights while preserving the originality of the visual appearance. The first step of this algorithm is gamma correction which is a nonlinear gray-level transformation that replaces gray-level I with I^{γ}, where $\gamma \in [0,1]$ is a user-defined parameter. This can enhance the local dynamic range of the image in dark region while compressing it in bright regions.

. In order to recover object-level information independent of illumination, a power law with the exponent γ in the range of [0, 0.5] is a good compromise to this problem. Difference of Gaussian (DoG) Filtering can be used to reduce the aliasing and noise. The inner Gaussian is typically set to $\sigma_0 \leq 1$ pixel while the outer one might have σ_1 of 2-4 pixels, depending on the spatial frequency at which low frequency information becomes misleading rather than informative. $\sigma_0 = 1.0$ and $\sigma_2 = 2.0$ are used as default setting. Then, two stages of processes as shown in Eq. (2) have been proposed:

$$I(x,y) \leftarrow \frac{I(x,y)}{\left(mean\left(\left|I(x',y')\right|^{a}\right)\right)^{1/a}}$$
$$I(x,y) \leftarrow \frac{I(x,y)}{\left(mean\left(\min\left(\tau,\left|I(x',y')\right|\right)^{a}\right)\right)^{1/a}} \tag{2}$$

Here, α is a strongly compressive exponent that reduces influence of large values, τ is a threshold used to truncate large values after the first phase of normalization and the mean is over the unmasked part of the image. $\alpha = 0.1$ and $\tau = 10$ are used in this experiment. Finally, a nonlinear function is being used to compress over-large values to reduce the influence of those extreme values on subsequent stages of processing. The hyperbolic tangent has been used $I(x,y) \leftarrow \tau \tanh(I(x,y)/\tau)$, thus limiting I to the range $(-\tau,\tau)$.

This algorithm has been tested on its robustness under various lighting conditions. From Fig. 1, the normalized images have shown similarity in terms of illumination distribution even though the input images are taken under different lighting conditions. Besides, LogAbout [26] and histogram equalization have been compared with the proposed normalization method to evaluate the performance of iris detection based on the processed images.

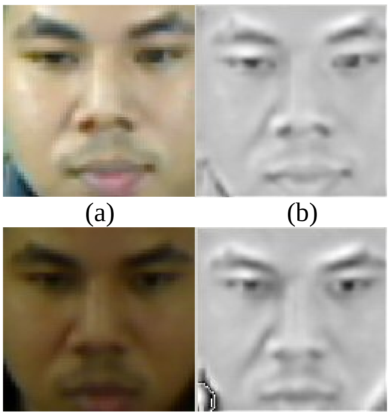

Fig. 1. (a) and (c) are input images; (b) and (d) are the respective output images after illumination normalization

IV. IRIS DETECTION ALGORITHM

The proposed algorithm will first apply grayscale conversion on the input image followed by grayscale closing [12]. Then, illumination normalization and light spot deletion are applied to remove the reflection of lighting on the irises. This can be done by replacing the center pixel of a mask by the smallest intensity value of the pixels within the mask. Histogram equalization [29], LogAbout and illumination normalization have been tested and compared in this experiment to reduce the effect of lighting variation.

1. Valley extraction

After the illumination normalization, valley extraction as shown in Eq. (3) has been carried out. Each pixel (x,y) in the face region:

$$V(x,y) = G(x,y) - I(x,y) \tag{3}$$

where $G(x,y)$ and $I(x,y)$ denote the value obtained from grayscale closing and intensity value. Region which consists of pixels (x, y) such that $V(x, y)$ is greater than or equal to a threshold value are determined to be valleys.

2. Selection of iris candidates

In irises selection, this algorithm performs similar method as proposed in [29]. First, it computes the costs $C(x, y)$ for all pixels in the valleys and selects m pixels according to non-increasing order that give the local maxima of $C(x, y)$ as the iris candidate locations.

$$C(x, y) = C_1(x, y) + C_2(x, y) \tag{4}$$

Where $C_1(x, y)$ is the mean crossing of the row and column pixels and $C_2(x, y)$ is the intensity difference between the center part and the boundary part of a square region. An eye template as shown in Fig. 2 is placed at each candidate location and measures the separability [10] between the two regions R_1 and R_2 given by:

$$\eta = B/A \tag{5}$$

Where $A = \sum_{i=1}^{N} (I(x_i, y_i) - \overline{P}_m)^2$,

$B = n_1(\overline{P}_1 - \overline{P}_m)^2 + n_2(\overline{P}_2 - \overline{P}_m)^2$,

$n_k (k = 1,2)$: number of pixels in R_k,

$N = n_1 + n_2$,

$\overline{P_k}$ (k = 1,2): average intensity in R_k,

$\overline{P_m}$: average intensity in the union of R_1 and R_2,

$I(x_i, y_i)$: the intensity values of pixels (x_i, y_i) in the union of R_1 and R_2.

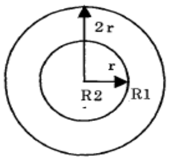

Fig. 2. An eye template to detect blob

Next, it applies Canny edge detector [11] to the face region and measures the fitness of those iris candidates to the edge image using Hough Transform [21]. The vote calculated from Hough Transform is defined as $C_1(i)$. Given an iris candidate $B_i = (x_i, y_i, r_i)$, measures the fitness of iris candidates to the intensity image by placing two templates similar as Fig. 2. Compute the separabilities $\eta_{23}(i)$, $\eta_{24}(i)$, $\eta_{25}(i)$ and $\eta_{26}(i)$ using Eq. (5) for $C_2(i)$ and $C_3(i)$. $C_4(i)$ is the ratio of average intensity of each iris candidate over average intensity of all the candidates. Then the cost for each iris candidate is calculated as below:

$$C(i) = C_1(i) + C_2(i) + C_3(i) + C_4(i) \tag{6}$$

Where $C_1(i) = \dfrac{V_{max}}{V(i)}$

$$C_2(i) = \frac{|\eta_{23}(i) - \eta_{24}(i)|}{\eta_{23}(i) + \eta_{24}(i)}$$

$$C_3(i) = \frac{|\eta_{25}(i) - \eta_{26}(i)|}{\eta_{25}(i) + \eta_{26}(i)}$$

$$C_4(i) = \frac{U(i)}{U_{av}}$$

where $V(i)$ is the vote for B_i given by Hough transform; V_{max}, the maximum of $V(i)$ over all iris candidates; $U(i)$ is the average intensity inside B_i and U_{av} is the average of $U(i)$ over all iris candidates. Finally, computes the cost for each pair of iris candidates B_i and B_j:

$$F(i, j) = t\{C(i) + C(j)\} + (1 - t)/R(i, j) \tag{7}$$

Where $C(i)$ and $C(j)$ are costs computed by Eq. (6). $R(i, j)$ is the normalized cross-correlation value computed between eye template and the input image. The eye template used in this experiment is shown in Fig. 3 t is the weight to adjust two terms of the cost. The lowest cost $F(i, j)$ is selected as the pair of irises as shown in Fig. 5.

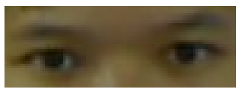

Fig. 3. The eye template used for computation of $R(i, j)$

V. RESULT AND DISCUSSION

Experiments have been done to evaluate the real time performance of the proposed iris detection algorithm with histogram equalization, LogAbout and illumination Normalization. A total of 109 and 122 images captured by Voxx and Logitech cameras are collected for this experiment under office environment. One image from Voxx camera and three images from Logitech camera have been eliminated from the databases since one of the iris is not appeared in the images. This research intends to make the system user-friendly whereby users have not been limited in wearing spectacles, type of clothes, hairstyles, facial expressions, multiple faces and background. Here, Database A represents the images captured by Voxx camera while Database B represents the images captured by Logitech camera.

From Table 1, histogram equalization, LogAbout and illumination normalization scored 38.53%, 54.13% and 68.81% respectively for database A for success detection. The success rates of iris detection for database B are 62.30% (histogram equalization), 71.31% (LogAbout) and 83.60% (illumination normalization). Thus, Illumination normalization has achieved the highest iris detection rate in both databases at real-time followed by LogAbout and histogram equalization. This means the images processed by illumination normalization have better contrast and stability when dealing with lighting variation. However, all of the processing techniques do not show outstanding results when dealing with database A which are noisier and blur images.

Table 1. Iris detection rates for different image processing techniques for Database A and Database B

Processing Technique	Database A (%)	Database B (%)
Histogram Equalization	38.53	62.30
LogAbout	54.13	71.31
Illumination Normalization	68.81	83.60

The proposed processing technique has improved the performance of iris detection more than 30% (Database A) and 21% (Database B) compared to the histogram equalization which was proposed in previous research. Although the improvement rate for Database A is greater but the overall success rate is still considered low for all the tested processing methods with the highest detection rate of 68.81%. Anyhow, illumination normalization outperforms LogAbout to nearly 15% when processing the low quality and noisy images from Database A.

Successful iris detections from both databases are shown in Fig. 4. This has covered a variety of lighting conditions, genders, backgrounds, spectacles, expressions and hairstyles. The improved iris detection algorithm has shown its robustness through this experiment especially when facing issues such as complex backgrounds and multiple faces. However, there are also some failures reported. The examples of the fail detection are shown in Fig. 5. Most of the subjects in those fail detections are wearing spectacles. The proposed algorithm has not been successful when dealing with certain types of spectacles which have some levels of lens reflectance when expose to lighting. This explains why there are also successful iris detections for the same subjects under different lighting conditions.

By studying the fail cases, frame of a spectacle can cause the iris detection algorithm to fail in some situations. This tends to happen when the subject wears the spectacle slightly lower than its normal position. The upper frame will block or appear at the same line as the irises horizontally. This has confused the proposed algorithm in making the correct decision especially when the color of the frame is black which has similar intensity values with the iris. Besides, spectacle with low transparency affects the visibility of iris. This becomes worse in darker lighting condition, low quality image and the subject has some distances from the camera. Another possibility that can cause fail detection is the appearance of irises.

Some facial expressions of the subjects have caused the eyes to be nearly closed and indirectly causing the irises not visible enough for detection. One of the failure case in Fig. 5 shows that the thick moustache of a subject under such lighting condition might confuse the detection algorithm. Solutions in terms of mathematical model or rules need to be set to differentiate the features which have similar intensity value as irises. The integration of illumination normalization into the iris detection algorithm replacing histogram equalization has improved the performance of the proposed algorithm in real-time. Besides, the ability of this algorithm to deal with the appearance of spectacles has been increased.

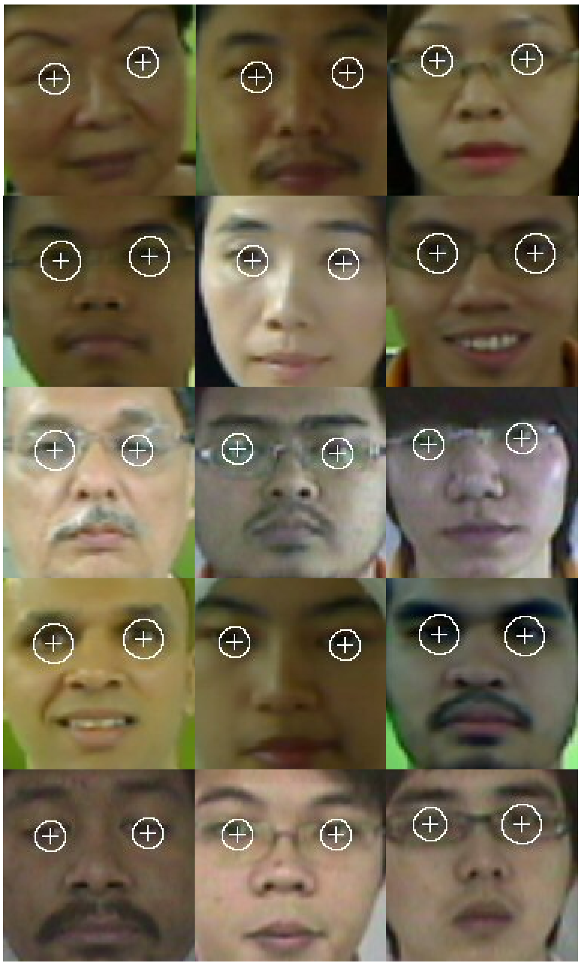

Fig. 4. Successful iris detections

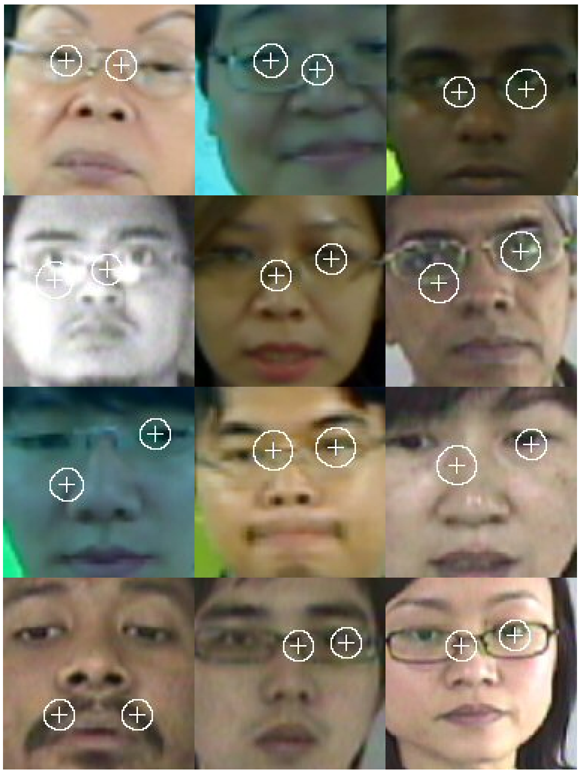

Fig. 5. Fail iris detections

VI. CONCLUSION

The experimental result has proven that the performance of the iris detection algorithm can be improved more tan 30% by applying a better image processing technique. Illumination normalization has proven its ability to cope with lighting variation under office environment. The proposed iris detection algorithm has achieved a success rate of 83.60% in a user-friendly real-time environment. Through this experiment, the algorithm has shown its robustness when tested with subjects wearing different kind of spectacles. In future, the iris detection algorithm needs to be enhanced in order to perform better under conditions like lens reflectance, facial expressions, disruption of moustache and excessive lighting. Finally, official online databases will be used to benchmark and evaluate the performance of the proposed algorithm in near future.

REFERENCES

[1] Tsuyoshi K and Mohamed R (2003), Iris detection using intensity and edge information, Pattern Recognition 36:549-562.

[2] Brunelli R and Poggio T (1993), Face recognition: features versus templates, IEEE Trans. Pattern Anal. Mach. Intell. 15 (10):1042-1052.

[3] Beymer DJ (1994), Face recognition under varying pose, Proceedings of IEEE Conference on Computer Vision and Pattern Recognition, Seattle, Washington:756-761.

[4] Li CM, Li YS, Zhuang QD and Xiao ZZ (2004), The face localization and regional features extraction, Proceedings of the Third International Conference on Machine Learning and Cybernetics, Shanghai: 26-29.

[5] Karin S and Ioannis P (1998), A novel method for automatic face segmentation, facial feature extraction and tracking, Signal Processing: Image Communication 12:263-281.

[6] Selin B, Bulut MM and Volkan A (2002), Projection based method for segmentation of human face and its evaluation, Pattern Recognition Letters 23:1623-1629.

[7] Wong KW, Lam KM and Siu WC (2001), An efficient algorithm for human face detection and facial feature extraction under different conditions, Pattern Recognition 34.

[8] Ryu YS and Oh SY (2001), Automatic extraction of eye and mouth fields from a face image using eigenfeatures and multilayer perceptrons, Pattern Recognition 34:2459-2466.

[9] Lin CH and Wu JL (1999), Automatic facial feature extraction by genetic algorithms, IEEE Trans. Image Process. 8 (6):834-845.

[10] Fukui K and Yamaguchi O (1997), Facial feature point extraction method based on combination of shape extraction and pattern matching, Trans. IEICE Japan J80-D-II (8):2170-2177.

[11] Canny J (1986), A computational approach to edge detection, IEEE Trans. Pattern Anal. Mach. Intell. 8 (6):679-698.

[12] Sternberg SR (1986), Grayscale morphology, Computer Vision Graphics Image Process. 35:333-355.

[13] Hua G, Guangda S and Cheng D (2003), Feature points extraction from faces, Image and Vision Computing NZ, Palmerston North.

[14] Yu S, Kun H, Zhou J, Liu Z and Kui L (2004), Multi-resolution feature extraction in human face, Proceedings of International Conference on Information Acquisition.

[15] Stephen MS and Michael BJ (1997), SUSAN – A new approach to low level image processin, International Journal of Computer Vision 23(1):45-78.

[16] Mauricio H and Geovanni M, Facial feature extraction based on the Smallest Univalue Segment Assimilating Nucleus (SUSAN) algorithm, Image Processing and Computer Vision Research Lab (IPCV-LAB), Escuela de Ingenieria Electrica, Universidad de Costa Rica.

[17] Yulu Q, Goenawan B and Nuanwan S (1998), Finding the estimated position of facial features on the human face using intensity computation, IEEE Asia-Pacific Conference (APCCAS):579-582.

[18] Vladimir V (2002), Face and facial feature tracking for natural human-computer interface, International Conference Graphicon, Nizhny Novgorod, Russia.

[19] Jie Y and Alex W (1996), A real-time face tracker, Application of Computer Vision, WACV'96:142-147.

[20] Martinez AM and Benaventa R (1998), The AR face database, CVC Technical Report, No.24.

[21] Tsuyoshi K, Daisuke H, Mohamed R, Detection of eyes from human faces by hough transform and separability filter, Department of Computer Science and Intelligence Systems, Oita University, Oita, Japan:870-1192.

[22] Zhao Y, Shen X and Georganas ND (2008), Combining integral projection and gabor transformation for automatic facial feature detection and extraction, Proceedings of IEEE

International Workshop on Haptic Audio Visual Environment and their Applications:103-107.
[23] Erukhimov V and Lee KC (2008), A bottom-up framework for robust facial feature detection, Proceedings of 8th International on Automatic Face and Gesture Recognition:1-5.
[24] Kumatani K, Ekenel HK, Gao H, Rainer S, Aytul E (2008), Multi-stream gaussian mixture model based facial feature localization, Proceedings of Signal Processing, Communications and Applications Conference:1-4.
[25] Viola P and Jones MJ (2004), Robust real-time face detection, International Journal of Computer Vision 57(2):137-154.
[26] Liu H, Gao W, Miao J and Li J (2002), A novel method to compensate variety of illumination in face detection, Joint Conference on Information Sciences:692-695.
[27] Tan X and Bill T (2007), Enhanced local texture feature sets for face recognition under difficult lighting conditions, IEEE International Workshop on Analysis and Modelling of Faces and Gestures:235-249.
[28] Chew WJ, Ang LM and Seng KP (2008), Automatic model based face feature detection system, Proceedings of International Symposium on Information Technology:1-6.
[29] Chai TY, Mohamed R, Woo SS and M Sugisaka (2008), Automated detection of face and facial features, The 7th WSEAS Int. Conference on Signal Processing, Robotics and Automation, University of Cambridge, United Kingdom:230-234.
[30] Balasubramaniam M, Palanivel S, and Ramalingam V (2008), Real time face and mouth Recognition using radial basis function neural networks, Expert Systems with Applications:1-8.

Comparison of Human Emotion Classification through different set of EEG channels

M. Murugappan[1], Mohamed Rizon[2], R. Nagarajan[1], Ali S. AlMejrad[2] and S. Yaacob[1]

[1] *School of Mechatronics Engineering, Universiti Malaysia Perlis*
02600, Kangar, Perlis, Malaysia
[2]*Department of Biomedical Technology, King Saud University*
P.O. Box 10219, Riyadh 11433, Kingdom of Saudi Arabia
(mjuhari@ksu.edu.sa)

Abstract**:** Assessing human emotional state through EEG is one of key research area in developing intelligent man-machine interfaces. EEG signals are collected using 64 channels from 20 subjects in the age group of 21~39 years for determining discrete emotions. An audio-visual induction based protocol has been designed for evoking the discrete emotions (happy, surprise, fear, disgust, neutral). The raw EEG signals are preprocessed through Surface Laplacian filtering method and decomposed into five different EEG frequency bands using Wavelet Transform. The main objective of this present work is to develop the emotion recognition system with lesser number of channels. Therefore, we have compared the efficacy of original set of channels (64 channels) with reduced set of channels (24 channels), which is proposed by the earlier work based on localization of brain region for assessing emotions. In our work, "db4" wavelet function is used to derive a new set of statistical features based on frequency band power for classifying the emotions. In this work, KNN outperforms LDA by offering the average classification accuracy of 79.783 % for 24 channels and 82.898 % for 62 channels. Finally we present the average classification accuracy and individual classification accuracy of two different classifiers for justifying the performance of our emotion recognition system.

Keywords*:* - Human emotion, EEG signals, Wave transform, Features extraction

1. INTRODUCTION

The estimation of emotional changes from electroencephalogram (EEG) signals has recently gained attention among BCI and Human Computer Interaction (HCI) researchers for developing the BCI/HCI devices. Traditional Human Machine Interaction (HMI) is normally based on passive instruments such as keyboards, mouse, etc. Emotion is one of the most important features of humans. Without the ability of emotions processing, computers and robots cannot communicate with human in natural way. It is therefore expected that computers and robots should process emotion and interact with human users in a natural way. In recent years, research efforts in Human Computer Interaction (HCI) are focused on the means to empower computers to understand human emotions. Although limited in number compared with the efforts being made towards intention-translation means, some researchers are trying to realize man-machine interfaces with an emotion understanding capability. Most of them are focused on facial expression recognition and speech signal analysis [1, 2]. Another possible approach for emotion recognition is physiological signal analysis. We believe that this is a more natural means of emotions recognition, in that the influence of emotion on facial expression or speech can be suppressed relatively easily, and emotional status is inherently reflected in the activity of nervous system. The traditional tools for the investigation of human emotional status are based on the recording and statistical analysis of physiological signals from the both central and autonomic nervous systems. Several approaches have been reported by different researchers on finding the correlation between the emotional changes and EEG signals [3-5]. The past works on emotion recognition using EEG signals is reported in [6]. One of the major limitations on this area of research is "curse of dimensionality". The dimensionality of the data vectors extracted from the EEG data needs to be reduced because for most classification algorithms it is very difficult to reliably estimate the parameters of a classifier in high dimensions when only few training examples are available.

In our work, we have used audio-visual stimuli (video clips) for evoking five different emotions such as disgust, happy, fear, surprise and neutral. The new statistical features based on power have been derived using wavelet transforms over three different frequency bands (alpha, beta and gamma). These numerical features are classified using two different linear classifiers namely K Nearest Neighbor (KNN) and Linear Discriminant Analysis (LDA). The main objective of this work to compare the efficacy of discrete emotion classification of original set of channels (62 channels) and reduced set of channels (24 channels) which is proposed in [4] based on localizing brain activity in EEG signal for different emotions. The required EEG data for this reduced number of channels are derived from the EEG data of original set of channels for classifying emotions. Finally, we have compared the classification rate of discrete emotions on two different channel combinations over three frequency bands by combining wavelet features and linear classifiers. Figure 1 shows the human emotion recognition system using EEG.

The rest of this paper is organized as follows. In Section II, we summarize the research methodology by elucidating the data acquisition process, preprocessing, feature extraction using wavelet transform, and classification of emotions by linear classifiers. Section III illustrates the overview of the results and discussion of this present work, and conclusions are given in Section IV.

2. MATERIALS AND EXPERIMETAL DESIGN

2.1 EEG Data Acquisition

This section describes the acquisition of EEG signals for emotion stimulation experiments. From our earlier experiment, we found that audio-visual stimulus is superior in evoking the discrete emotions than visual stimulus method [7]. Hence, we have used an audio-visual induction based protocol for eliciting the discrete emotions in this present work. The structural flow of emotion recognition using EEG signals is shown in Figure 2. A pilot panel study is conducted on 25 university students to select any 5 video clips (trials) for each emotion from 115 emotional video clips including from the international standard emotional clips (www.stanford.edu).

The selection of video clips is based on self assessment questionnaires mentioned in [8]. The subjects who have undergone for this panel study does not take part in the data collection experiment. The audio-visual stimulus protocol for Trial 1 of our experiment is shown in Figure. 3. From Trial 2 to Trial 5, the orders of the emotional video clips are changed in a random manner. X1 to X5 denote time periods of selected video clips. The time duration of video clips vary from one another.

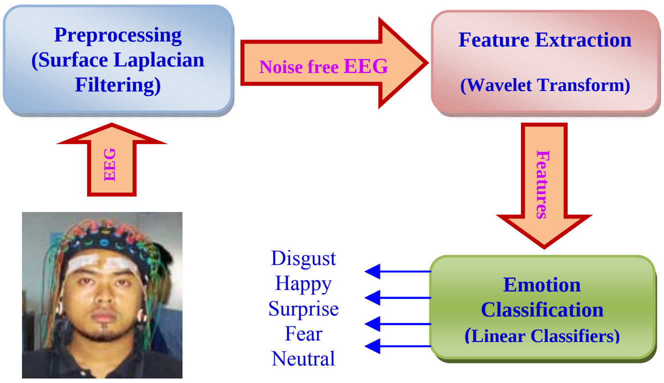

Figure 1. Emotion Recognition system overview

The selection of video clips is based on self assessment questionnaires mentioned in [8]. The subjects who have undergone for this panel study does not take part in the data collection experiment. The audio-visual stimulus protocol for Trial 1 of our experiment is shown in Figure. 2. From Trial 2 to Trial 5, the orders of the emotional video clips are changed in a random manner. X1 to X5 denote time periods of selected video clips. The time duration of video clips vary from one another. Three females and seventeen males in the age group of 21~39 years were employed as subjects in our experiment. Once the consent forms were filled-up, the subjects were given a simple introduction about the research work and stages of experiment. The recording of EEG signal has been done through Nervus EEG, USA with 64 channel electrodes at a sampling frequency of 256 Hz and band-pass filtered between 0.05 Hz and 70 Hz. Totally, we have used 62 active electrodes, one each for reference (AFz) and ground (Oz). All the electrodes are placed over the entire scalp using International standard 10-10 system. The impedance of the electrodes is kept below 5 kΩ.

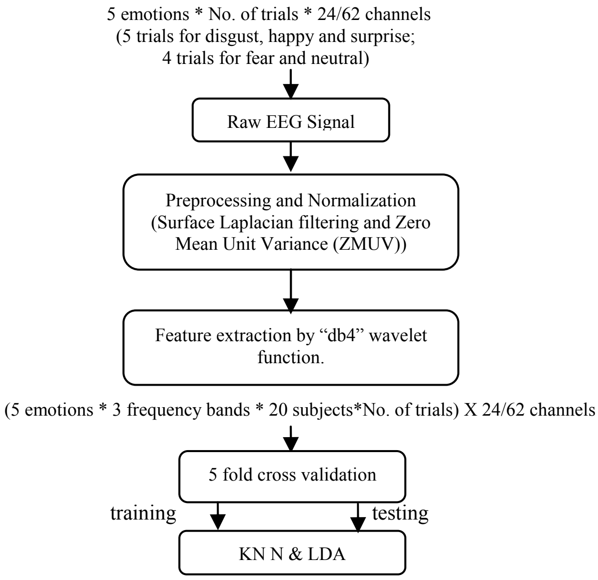

Figure 2. Systematic procedure of our work on emotion recognition using reduced set of EEG channels

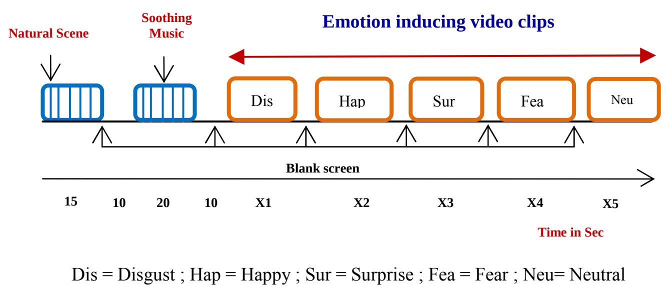

Figure 3. EEG data acquisition protocol using audio-visual stimulus

Between each emotional video clips, under self assessment section, the subjects were informed to answer the emotions they have experienced [8]. Finally, 5 trials for disgust, happy and surprise emotions and 4 trials for fear and neutral emotions are considered for further analysis.

2.2 Preprocessing

EEG signals recorded over various positions on the scalp are usually contaminated with noises (due to power line and external interferences) and artifacts (Ocular (Electroocculogram), Muscular (Electromyogram), Vascular (Electrocardiogram) and Gloss kinetic artifacts). The complete removal of artifacts will also remove some of the useful information of EEG signals. This is one of the reasons why considerable experience is required to interpret EEGs clinically [9, 10]. A couple of methods are available in the literature to avoid artifacts in EEG recordings. However, removing artifacts entirely is impossible in the existing data acquisition process.

In this work, we used Surface Laplacian (SL) filter for removing the noises and artifacts. The SL filter is used to emphasize the electric activities that are spatially close to a recording electrode, filtering out those that might have an origin outside the skull. In addition, it also attenuates the EEG activity which is common to all the involved channels in order to improve the spatial resolution of the recorded signal. The neural activities generated by the brain, however, contain various spatial frequencies. Potentially useful information from the middle frequencies may be filtered out by the analytical Laplacian filters. Hence, the signal "pattern" derived from SL filters is similar to "spatial distribution of source in the head".

The mathematical modeling of Surface Laplacian filter is given as

$$X_{new}(t) = X(t) - \frac{1}{N}\sum_{i=1}^{N} X_i(t) \tag{1}$$

where X_{new} : filtered signal ; X(t) : raw signal ;
N: number of neighbor electrodes

2.3 Feature Extraction

There are two important aspects of feature extraction: (a) extracting the features using the most salient EEG channels (b) extracting the features only from the selected EEG channels. In the emotion recognition research using EEG signals, the non-parametric method of feature extraction based on multi-resolution analysis of Wavelet Transform (WT) is quite new. The joint time-frequency resolution obtained by WT makes it as a good candidate for the extraction of details as well as approximations of the signal which cannot be obtained either by Fast Fourier Transform (FFT) or by Short Time Fourier Transform (STFT) [11, 12].

The non-stationary nature of EEG signals is to expand them onto basis functions created by expanding, contracting and shifting a single prototype function ($\Psi_{a,b}$, the mother wavelet), specifically selected for the signal under consideration

The mother wavelet function $\Psi_{a,b}$ (t) is given as

$$\psi_{a,b}(t) = \frac{1}{\sqrt{a}}\psi\left(\frac{t-b}{a}\right) \tag{2}$$

where a, b ∈ R, a>0, and R is the wavelet space. Parameters 'a' and 'b' are the scaling factor and shifting factor respectively. The only limitation for choosing a prototype function as mother wavelet is to satisfy the admissibility condition (Eqn. 3),

$$C_\psi = \int_{-\infty}^{\infty} \frac{|\Psi(\omega)|^2}{\omega} d\omega < \infty \tag{3}$$

where ψ (ω) is the Fourier transform of $\psi_{a,b}$ (t).

The time-frequency representation is performed by repeatedly filtering the signal with a pair of filters that cut the frequency domain in the middle. Specifically, the discrete wavelet transform decomposes the signal into an approximation coefficients (CA) and detailed coefficients (CD). The approximation coefficient is subsequently divided into new approximation and detailed coefficients. This process is carried out iteratively producing a set of approximation coefficients and detail coefficients at different levels or scales [13].

In this work, the multi-resolution analysis of "db4" wavelet function is used for decomposing the EEG signals into three different frequency bands (alpha, beta, and gamma). This wavelet function "db4" has been chosen due to their near optimal time-frequency localization properties. Moreover, the waveforms of "db4" are similar to the waveforms to be detected in the EEG signal. Therefore, extraction of EEG signals features are more likely to be successful [14]. In Table (1), A5, D5, D4, D3, and D2 represents the five EEG frequency bands. In order to analyze the characteristic natures of different EEG patterns, we propose a new set of statistical features based on power called: *Recoursing Power Efficiency* (RPE), *Logarithmic Recoursing Power Efficiency* (LRPE), and *Absolute Logarithmic Recoursing Power Efficiency* (ALRPE) for classifying the discrete emotions (Eqn 5 to Eqn 7). These features are derived from the three frequency bands of EEG. Table 1 also presents the bandwidth and the frequencies corresponding to different levels of decomposition for "db4" wavelet function with a sampling frequency f_s=256 Hz [13].

Table 1 Decomposition of EEG signals into different frequency bands with a sampling frequency of 256 Hz

Frequency Range	Decomposition Level	Frequency Bands	Frequency Bandwidth (Hz)
0 - 4	A5	Theta	4
4 – 8	D5	Delta	4
8 – 14	D4	Alpha	8
14 – 32	D3	Beta	16
32 – 64	D2	Gama	32
64 - 128	D1	Noises	64

A : Approximation coefficients D: Detail coefficients

$$P_{total-3B} = P_{alpha} + P_{beta} + P_{gamma} \tag{4}$$

$$RPE_{gamma} = \frac{P_{gamma}}{P_{total-3B}} \tag{5}$$

$$LRPE_{gamma} = \log_{10}\left|\frac{P_{gamma}}{P_{total-3B}}\right| \tag{6}$$

$$ALRPE_{gamma} = abs\left(\log_{10}\left|\frac{P_{gamma}}{P_{total-3B}}\right|\right) \tag{7}$$

2.4 Classification

In this work, we used two simple linear classifiers such as Linear Discriminant Analysis (LDA) and K Nearest Neighbor (KNN) for classifying the discrete emotions. Among these two classifiers, LDA provides extremely fast evaluations of unknown inputs performed by distance calculations between a new sample and mean of training data samples in each class weighed by their covariance matrices. A linear discriminant analysis tries to find an optimal hyperplane to separate five classes (here, disgust, happy, surprise, fear and neutral emotions).

In addition, KNN is also a simple and intuitive method of classifier used by many researchers typically for classifying the signals and images. This classifier makes a decision on comparing a new labeled sample (testing data) with the baseline data (training data). In general, for a given unlabeled time series X, the KNN rule finds the K "closest" (neighborhood) labeled time series in the training data set and assigns X to the class that appears most frequently in the neighborhood of k time series. There are two main schemes or decision rules in KNN algorithm, that is, similarity voting scheme and majority voting scheme [15]. In our work, we used the majority voting for classifying the unlabeled data. It means that, a class (category) gets one vote, for each instance, of that class in a set of K neighborhood samples. Then, the new data sample is classified to the class with the highest amount of votes. This majority voting is more commonly used because it is less sensitive to outliers.

Besides the training and testing samples, LDA does not require any external parameter for classifying the discrete emotions. However, in KNN, we need to specify the value of "K" closest neighbor for emotions classification. In this experiment, we try different "K" values ranging from 1 to 6. This value of "k" which gives a maximum classification performance among the other values of K is considered for emotion classification.

3. RESULTS AND DISCUSSIONS

Among all twenty subjects, we sample and preprocess the total of 460 EEG epochs from five discrete emotions. The number of data points in each epoch depends on the time duration of video clips. In our experiment; the time duration of video clips vary from one another. The next stage is to train the KNN classifier with a best value of K while LDA classifier directly works for classifying the emotions. The classification ability of a statistical feature set can be measured through classification accuracy by averaging five times over a 5 fold cross-validation. The basic stages of 5 fold cross-validation includes: (a) total number of samples are divided into 5 disjoint sets (b) 4 sets are used for training and 1 set is used for testing (c) repeat stage (b) for five times and each time the data set is permuted differently. From Table 2, we found that, KNN gives higher average classification accuracy than LDA on all different channels sets. The maximum classification accuracy of 79.78 % and 64.92 % is obtained using Logarithmic Recoursing Power Efficiency (LRPE) feature among the three newly proposed statistical features in KNN and LDA respectively.

Among the two different channel combinations, the statistical feature (LRPE) on the original set of channels gives maximum average classification accuracy over reduced set of channels. Here, the LRPE feature measures the frequency band power variations over different emotional EEG data. And so, each emotional EEG signals have its own frequency band power variation characteristics and it can be easily found out by using the LRPE feature. Table 3 shows the individual emotions classification rate of three different statistical features over two different liner classifiers. Table 4 shows the average classification rate of emotions on original set of channels using LRPE feature on KNN and LDA [16]. From Table 3 and Table 4, we found that, the 24 channel EEG data gives the maximum individual classification rate in disgust, happy and fear emotions compared to 62 channels respectively. In addition, 62 channels EEG data performs well on achieving higher classification rate on neutral and surprise emotions than 24 channels. Therefore, the region of brain which is covered by a set of 24 channels will able to detect the three emotions (disgust, happy and fear) with higher classification rate over 62 channels. In a similar way, the original set of channels gives a maximum classification rate on neutral and surprise emotions over reduced set of channels. Over all the feature analysis, the EEG data on disgust and neutral data gives a classification rate nearly 90 % over other features. This accuracy of classification shows the potentiality of the audio-visual stimuli for evoking the emotion. In addition, the classification rates of two channels are nearly equal or we can say that, minimum in difference. However, this equivalent classification rate with lesser number of channels is more suited for the development of real-time emotion recognition system. Since, it reduces the computational complexity, physical burden to the subjects and time required for placing electrodes. All the programming was done in Matlab environment on a desktop computer with AMD Athlon dual core processor 2 GHz with 2 GB of random access memory.

Table 2: Comparison average classification rate of statistical features on KNN and LDA

Classifier	RPE		LRPE		ALRPE	
	24 Channels	62 Channels	24 Channels	62 Channels	24 Channels	62 Channels
KNN	**79.42**	**82.61**	**79.78**	**82.89**	**79.21**	**81.74**
LDA	64.71	76.88	64.92	75.58	67.24	75.72

Table 3: Subset of discrete emotion classification rate of three statistical features on KNN and LDA

Classifiers	KNN	LDA	KNN	LDA	KNN	LDA	KNN	LDA	KNN	LDA
Feature	Disgust		Happy		Surprise		Fear		Neutral	
RPE	90	78.33	75	31.66	76.67	68.33	**78.916**	58.33	93.75	68.75
LRPE	88.33	**91.67**	**80**	36.67	76.67	70	70.83	45.83	89.58	64.58
ALRPE	88.33	91.67	75	38.33	75	71.67	77.08	70.83	85.41	77.08

Table 4: Subsets of discrete emotion classification rate of 62 channels EEG data using KNN and LDA

Classifier	Feature	Disgust	Happy	Surprise	Fear	Neutral
KNN	LRPE	**91.67**	78.33	73.33	75	**95.83**
LDA	LRPE	90	65	**80**	66.67	95.83

3 CONCLUSIONS

This work addresses the classifiability of human emotions using reduced set of EEG channels. The results presented in this paper indicate that the multi-resolution analysis based newly proposed features works well with the context of discrete emotion classification. The experimental result on the performance of KNN is very encouraging. These results represent a possibility of determining the emotional changes of human mind through EEG signals. In addition, these results also confirm our hypothesis that it is possible to differentiate and classify the human emotions the linear and non-linear features. The results of this study provide a framework of methodology that can be used to elucidate the dynamical mechanism of human emotional changes underlying the brain structure. In addition, the results can be extended to the development of online emotion recognition system.

4 ACKNOWLEDGEMENT

This work is financially supported by the two grants by Ministry of Science and Technology Innovation (MOSTI), Malaysia. Grant Code: 9005-00002 & 9005-00020.

REFERENCES

[1] Bung H, and Furui S, "Automatic Recognition and understanding of spoken languages- a first step toward natural human machine communication", *Proceedings of IEEE*, vol. 88, issue. 8, pp, 1142-1165, 2000.

[2] Cowie R, Douglas E, Tsapatsoulis N, Votsis G, Kollias G, Fellenz W and Taylor J G, "Emotion Recognition in human-computer interaction", *IEEE Signal Processing*, pp, 3773-3776, 2001.

[3] Kim K.H, Band S.W., and Kim S.B, "Emotion Recognition System using short-term monitoring of physiological signals", *Proceedings on Medical & Biological Engineering & Computing*, vol. 42, pp, 419-427, 2004.

[4] Chanel, G., Karim, A.A. and Pun, T, "Valence-arousal evaluation using physiological signals in an emotion recall paradigm", *Lecturer Notes in Computer Science*, Springer, pp, 530 – 537, 2007.

[5] Kazuhiko, T, "Remarks on emotion recognition from bio-potential signals", *2nd International Conference on Autonomous Robots and Agents*, New Zealand, pp, 186–191, 2004.

[6] M.Murugappan, M Rizon, R.Nagarajan and S Yaacob, "Inferring of Human Emotion States using Multichannel EEG", International Journal of Soft Computing and Applications (IJSCA), EURO Journals, United Kingdom. (Accepted)

[7] M.Murugappan, M Rizon, R.Nagarajan, and S Yaacob, "An Investigation on visual and audiovisual stimulus based emotion recognition using EEG", *Transactions on Medical Engineering and Informatics*, vol. 1, no 3, pp, 342-356, 2009.

[8] M.Murugappan, M Rizon, R.Nagarajan, S Yaacob, D Hazry, and I Zunaidi, "Time-Frequency Analysis of EEG Signals for Human Emotion Detection", *IFMBE Proceedings*, no. 21, pp, 262-265, 2008, Springer Book chapter.

[9] Jung T, "Removing Electroencephalographic Artifacts by Blind Source Separation", *Journal of Psychophysiology*, vol. 37, no. 2, pp, 163-178, 2000.

[10] Gott P. S, Hughes E. C., and Whipple, "Voluntary Control of Two Lateralized Conscious States: Validation by Electrical and Behavioral Studies", *Journal of Neuropsychological*, vol. 22, pp, 65-72, 1984.

[11] Mallat S. G, "A Theory for Multi-Resolution Signal Decomposition: The Wavelet Representation", *IEEE Transactions on Pattern Analysis and Machine Intelligence*, vol. 11, no 7, pp, 674–693, 1989.

[12] Merzagora A.C, Bunce S, Izzetoglu M., and Onaral B Wavelet Analysis for EEG Feature Extraction in Deceptive Detection. *IEEE Proceedings on EBMS*, pp, 2434-2437, 2006.

[13] Chethan P and Cox M, "Frequency Characteristics of Wavelets", *IEEE Transactions on Power Delivery*, vol. 17, no. 3, pp, 800-804, 2002.

[14] Charles W.A. and Zlatko, S, "Classification of EEG signals from four subjects during five mental tasks", *IEEE Proceedings on Engineering Application in Neural Networks*, pp.407–414, 1997.

[15] Wanpracha A C, Ya-ju Fan, and Rajesh C S, "On the Time Series K-Nearest Neighbor Classification of Abnormal Brain Activity", *IEEE Transactions on Systems, Man and Cybernetics – Part A:Systems and Humans* , vol. 37, no. 6, pp, 1005-1016, 2007.

[16] M.Murugappan, R.Nagarajan, and S Yaacob, "Frequency Band Selection for Assessing Human Emotions from EEG using Modified Power based Wavelet Features", *Journal of Computer Science and Technology*, Springer. (Under Review).

Design of intelligent system for speech monitoring and treatment of low and excessive vocal intensity

Ali S. AlMejrad

Department of Biomedical Technology, King Saud University
P.O. Box 10219, Riyadh 11433, Kingdom of Saudi Arabia
(amejrad@ksu.edu.sa)

Abstract: Number of people and especially children suffer from speech problems such as too low or often excessive vocal intensity which is one of the behavioral problems that may be encountered in people with intellectual disability. Also it may happen due to the aggressive behaviors which produce disturbance which is rejected by others. The persons with this behavior may often be unaware of their problems. To limit these negative outcomes an intelligent system has been designed for monitoring, to provide a patient with information about speech intensity outside the clinic and for controlling of the treatment of excessive and low vocal intensity without the need to the continuous therapeutic follow-up in speech pathology clinic. The use of the intelligent system proves to be an effective due to the many features of this system. The technical design considerations, the system features and system evaluation will be discussed.

Keywords: - intelligent system, speech monitoring, vocal intensity

I. INTRODUCTION

There are common vocal cords disorders include vocal cord nodules, vocal cord polyps, contact ulcers, laryngitis, vocal cord tumors, vocal cord paresis in addition to vocal loading [1]. Speech impairments such as low or reduced vocal intensity which present in patient with Parkinson's disease is generally been classified as a dysarthria which refers to motor defects of speech resulting from lesions of the nervous system [2, 3]. Others have described this symptom as inadequate volume, soft voice, and weak voice. Many parkinsonian patients thus have problems normally regulating the volume of their speech. However, if instructed to speak louder, the patient can regulate the speaking volume but unfortunately such improvement generally is not long-term one. On the other side, excessive vocal intensity due to speaking loudly in addition to the vocal abuse and misuse may result in vocal cord pathologies such as vocal nodules. This pathology occurs in more than 50% of children with voice disorders [4, 5]. This pathology is one of the behavioral problems that may be encountered in people with intellectual disability [6]. Also it may happen due to the aggressive behaviors which produce disturbance which is rejected by others.

Usually the persons with the above behaviors may often be unaware of their problems, so intervention program is required to limit these negative outcomes. Speech monitoring is necessory in the first instance in addition to the use of biofeedback training. Biofeedback is that technology which can learn to exercise some control over a physiological process if information related to that process immediately available. Compared to the simple verbal prompting by therapist such as (" you are speaking too low or too loudly") which failed to regulate their speech the use of biofeedback instead is more effective. Zicker et el. used feedback instrument for speech therapy with Parkinson's disease patients [7]. This system is a general-purpose feedback training device which is based on the microcomputer and some additional hardware interfaces of 1 kg weight. Prosek et al. and Schliesser use the biofeedback training employing electromyography (EMG) to voice disorders [8, 9]. McGillivray et al. developed a biofeedback analog device to reduce excessive vocal intensity and treat a case of a child with soft nodules on her vocal cords by interrupt her conversation with a loud tone when her speech exceeded an intensity level determined by the therapist [10]. This device is simple and has limited functions of only tone. The use of a portable auditory-feedback and vibratory-feedback devices was used by Lancioni [11, 12] for reducing excessive vocal loudness in persons with mental retardation and a deaf woman [13].

To limit these negative outcomes an intelligent system has been proposed for speech monitoring, to provide a patient with information about speech intensity outside the clinic and for controlling of the treatment of both excessive and low vocal intensity without the need to the continuous therapeutic follow-up in speech pathology clinic. The intelligent system which will be based on microcontroller technology will be an effective due to the many features of this system such as portability and wearily due to its small size, ease of programmability, patient alert, automatic tracking of up normal occasions during therapeutic sessions. The technical design considerations, the system features and system evaluation will be discussed.

II. MATERIALS AND METHODS

Hardware: The proposed intelligent speech monitoring system in this work consists of many components including: transducer, amplifiers, filters, rectifier, unity gain buffer, comparators, and integrator in addition to a low-cost microcontroller; auditory and vibratory feedback. Capacitors and headers were added to the circuit design and operational amplifiers were selected to make the system battery operated as shown in Figure 1.

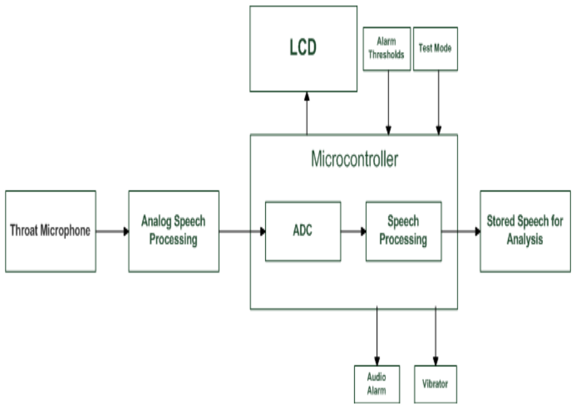

Figure 1. Block diagram of the intelligent speech monitoring system

The objective of the analog circuitry is to take the speech signal coming from the microphone, band pass filter it, amplify it, and make every output value positive [14]. The analog signal conditioning consists of filter to eliminate unwanted noise, main Amplifier with an adjustable gain to make the signal bigger, rectifier to turn negative signal values to positive (absolute value) and integrator to evaluate voice intensity over a set time period and determines whether or not alarm triggers. As a test only two comparators are used to compare input (speech) with specific threshold(s). The most important issue was determining the values for the corner frequency of the filter. A low pass filter with a 500 Hz corner frequency was considered because this frequency was low enough to include the volume or intensity aspects of the voice. It would cut off the high frequencies that are associated with pitch, quality, or uniqueness of a particular speech. Since the typical values expected were on the order of 10 mV and the circuitry components needed to work with volts, the gain of the amplifier was designed to be 100. The operational amplifier is selected based on its minimal operating voltage requirement due to

Speech signals from a throat microphone is sampled and passed through analog circuitry to filter, amplify and rectify the speech signal to convert it into appropriate and useable input for the analog-to-digital converter (A/D) as shown in Figure 2.

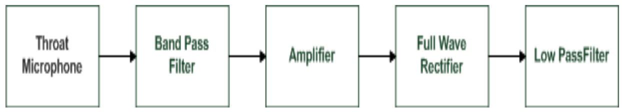

Figure 2. Block diagram of the Analog speech signal processing

Limited space permitted for batteries. The LM358 was selected because it required only 3V operating voltage. It was necessary that the signal prior to the integrator be rectified in order to prevent the negative and positive values from equaling zero. The integrator is designed using a setup resembling a low pass filter to allow the signal logarithmically to serve the intended purpose. For test only two separate analog comparators are used to properly compare the input values to the set thresholds.

After conditioning the speech signal using analog circuitary it passes through the microcontroller 8-bit A/D converter to digitize the speech signal for processing and performing speech intensity level calculations on the sampled speech signal using microcontroller based system (PIC16F877A from Microchip Technology Inc.). The feedback consisting of an audio alarm (a beeb sound) and a vibrator (a vibrating motor of weight of 2.5 g from Korea Partner IND. CO.. LTD.) are used and controlled by the microcontroller. The purpose of the feedback device is to warn the patient when his or her speech intensity had gone below or above the specified threshold specified by therapist. With a minimal amount of feedback, the patient would be notified that vocal changes and regulation of speech were needed to be made. It is believed that tactile feedback devices are more appropriate to use in this case than non-tactile devices. Therefore, a vibrating motor, similar to those used in commercial pagers, is used. The pager is selected because of its smallest size, most rigid, mounting capability and cost. The pager could be worn on the waist that gives off enough vibration to alert the user that changes in the speech volume need to be made.

Finally, the microcontroller is programmed to process the speech data gathered and to determine when feedback to the patient is necessary.

Software: a usable algorithm, a step-by-step problem-solving procedure, has been written with C and encoded into assembly program that the microcontroller can read and run as shown in the flow chart below (Figure 3).

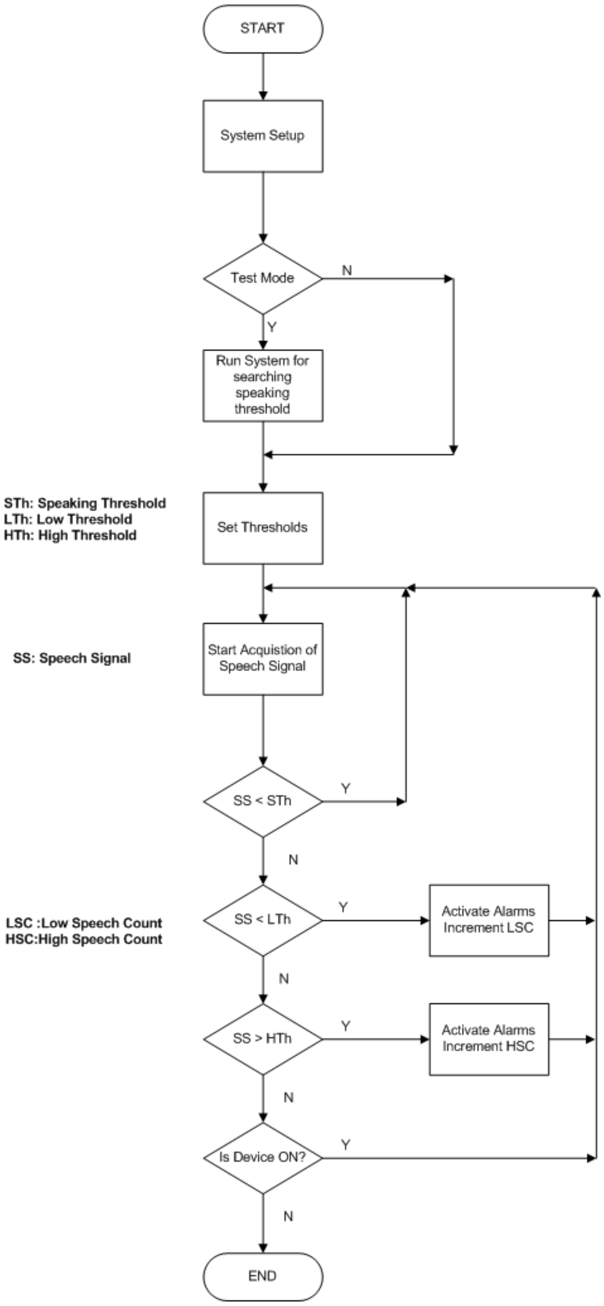

Figure 3. Speech processing of vocal intensity and biofeedback activation flowchart

The microcontroller receives one input signal and can send one output signal. This input is a steady varying voltage signal, which is representative of the patient's speech intensity. This speech signal is then converted from an analog signal (measured in volts) to a digital signal (in binary) using A/D. The lower or louder the patient speaks, the lower or greater the intensity measured by the microcontroller. The microcontroller then utilizes the algorithm to process the inputted data derived by the voltage signal and decides whether or not feedback should be sent to the patient. Feedback of an audio and vibration alarms is the result of the patient speaking too softly or loudly for an extended period of time, which at this time is assumed to be one-half second.

The speech processing algorithm required by the microcontroller of the speech feedback device needed to be flexible and accurate [15]. This means the device could be configured to each patient's needs in order to minimize the amount of false feedback given to the patient. The algorithm implemented in this design aims to meet these criteria. In order to avoid giving false responses, the user must, before using the device, sample the background noise level by pushing a button on the device that activates the test mode. While in the test mode, the intensity of the current ambient noise is determined, which determines a minimum speaking threshold-equivalent to the intensity measurement at which the user is not speaking. In other words, when the noise intensity measured by the device is less than this minimum threshold, the user is not speaking and all readings below this intensity are disregarded. Only those measurements in which the speech intensity is above the speaking threshold are used for further processing.

An alarm threshold, preset by a speech therapist, based on the patient's requirements is determined and programmed into the device prior to use. This alarm threshold is the intensity level the patient needs to speak above or below. An integrator and counter have been used in order to determine when the device must send feedback to the user. During times in which the user is not speaking, the counter is held constant, while speaking below the threshold, the counter is decreased by one, and while speaking above the threshold; the counter is increased by one. When the user's speech intensity falls below the low alarm threshold for duration of time that allows the counter to reach the preset alarm threshold, a signal is sent to the feedback device that alerts the patient that they must speak with greater intensity. The same process is repeated when the user's speech intensity exceeds the high alarm threshold for duration of time that allows the counter to reach the preset alarm threshold, a signal is sent to the feedback device that alerts the patient that they must speak with lower intensity The counter is reset after every two seconds to be reevaluated during testing time frame in which the microcontroller is inputting the patient's speech intensity.

At first, the code will determine a speaking threshold when the button is pushed. It will try to get the maximum intensity of the background noise over a range of time. The speaking threshold is then set around 80 mV above this maximum value as the speaking threshold. In addition to that, the speaking threshold is made to be at max of a certain value. This is for anticipating if there is a sudden and very high intensity noise, which is unusual.

After that, it will start processing the signal received. If the signal received is below the speaking threshold, it will repeat taking another value of signal before it try to compare it with the appropriate speech alarm thresholds. Each signal value obtained will be stored in the additional RAM. Further more, if the speech signal value is below or above the appropriate speech alarm threshold, it will increase a counter. On the other hand, when it is normal, it will decrease the counter. If the counter is beyond a certain limit, it will set the alarm to be high. The method that we are using to fill the addresses in the memory is called first in first out (FIFO). In this way the memory is filled and refilled circularly thus reusing the allocated memory addresses. After processing and storing the first set of samples, it will loop back to process and store another set. The data replaced by a new value will be read and compared to the alarm appropriate speech threshold to update the counter of alarm into a value which the counter should be at, if the data is not there. Then, it will take another sample to define the new set and then determine whether to set the alarm or not. This loop repeats until the person turns off the device.

III. TESTING AND RESULTS

In this study a complete simulation for evaluation was performed. To test the system that should work in theory, an initial prototype was created using a breadboard to evaluate the connections to each unit of the system. Each stage of the intelligent system was implemented, tested and calibrated separately. The processing stage using the programmable microcontroller was simulated firstly using different levels of speech intensity of speech-like signals. Secondly it was tested by different normal subjects who were asked to speak by reading many statements for few minutes using different levels of speech intensity and test to speak softly or loudly a few seconds and check if the biofeedback activates the audio and the vibrator alarms attached to the patient. To make accurate tests a sound level meter above the speech monitoring system was used to monitor the volume of sounds and speech intensity to adjust the biofeedback to be activated when low or excessive speech intensity. In addition to that two comparators are used to compare input (speech) with specific threshold(s) for test only. After calibration, the system was tested for various levels of speech intensity and in each test the system was successful.

IV. CONCLUSION AND FURTHER WORK

The proposed intelligent speech monitoring system developed as a prototype achieved the requirement of this work such as the portability, programmability and low power consumption. Our intelligent speech monitoring system performed satisfactorily as a prototype system for monitoring, to provide a patient with information about speech intensity outside the clinic and for controlling of the treatment of excessive and low vocal intensity without the need to the continuous therapeutic follow-up in speech pathology clinic. The system is able to collect speech intensity signals through a throat microphone and able to discriminate between speech and silence and is only active when the subject is speaking. The device activities an alarm and vibration as a biofeedback to the subject whenever the speech intensity falls below or exceeds above an adjustable thresholds for a preset time interval. The system is able to record and count up normal occasions and display them in real-time.

The system can be enhanced by additional memory to store information concerning time dependent data of the user's speech intensity when alarms occurred. Following use, this data could then be downloaded to a personal computer (PC) where it can be analyzed by a speech therapist. This additional information would allow not only real time feedback, but also the speech therapist could use it to monitor the patient's progress and make changes to the therapy program if it is necessary.

Clinical evaluations of the developed system based on specific procedures using different patients who have speech disorders such as Parkinson's disease and patients suffering from the problem of excessive speech are required to test its feasibility to be used as monitoring and therapeutic device.

ACKNOWLEDGEMENT

This work is supported by the grant from Applied Medical Research Center, the Deanship of Scientific Research, King Saud University. Grant Code: PS/39/26

REFRENCES

[1] Greene, M., Lesley M., (2001), *the* Voice and its Disorders, John Wiley & Sons; 6th Edition.
[2] de Swart BJ, Willemse SC, Maassen BA, Horstink MW, (2003), Improvement of voicing in patients with Parkinson's disease by speech therapy, Neurology. 60(3):498-500.
[3] Spielman J, Ramig LO, Mahler L, Halpern A,

Gavin WJ., (2007), Effects of an extended version of the lee silverman voice treatment on voice and speech in Parkinson's disease, Am J Speech Lang Pathol.;16(2):95-107.
[4] Hooper CR., (2004), Treatment of voice disorders in children, Lang Speech Hear Serv Sch.; 35(4):320-6.
[5] Wilson, D., 1987, Voice problems of children, Williams and Wilkins Co., pp. 33-35.
[6] Lancioni GE, van Houten K, ten Hoopen G., (1997), Reducing excessive vocal loudness in persons with mental retardation through the use of a portable auditory-feedback device, J Behav Ther Exp Psychiatry.;28(2):123-8.
[7] Zicker JE, Tompkins WJ, Rubow RT, Abbs JH, (1980), A portable microprocessor-based biofeedback training device, IEEE Trans Biomed Eng.;27(9):509-15.
[8] Prosek, R, Montgomery, A. Walden, B., and Schwartz, D., (1978), EMG biofeedback in the treatment of hyperfunctional voice disorders, J. Speech Hear. Disorders, XLIII, pp. 282-294.
[9] Schliesser, H., (1987), EMG biofeedback as a function of voice-quality change, J. Percept. Motor Skills, 64, pp. 719-724.
[10] McGillivray R, Proctor-Williams K, McLister B., (1994), Simple biofeedback device to reduce excessive vocal intensity, Med Biol Eng Comput.; 32(3):348-50.
[11] Lancioni GE, Brouwer JA, Markus S., (1995), A portable visual-feedback device for reducing excessive vocal loudness in persons with mental retardation, Percept Mot Skills;81(3 Pt 1):851-7.
[12] Lancioni GE, Markus S., and Behrendt, M. (1998), A portable vibratory-feedback device for reducing excessive vocal loudness: A case study, Behavioural and Cognitive Psychotherapy, 26, 371-376.
[13] Lancioni GE, Markus S, (1999), a deaf woman learning to control her excessive vocal loudness through a portable feedback system, Percept Mot Skills.; 88(3 Pt 2):1347-9.
[14] Webster, J., (1997), Medical Instrumentation Application and Design, 3rd Edition, Wiley.
[15] Rainer, L. and Schafer, R., (1978), Digital processing of speech signals, Englewood Cliffs, NJ, PH.

Modified Relevance Feedback for Content Based Image Retrieval Using Support Machine

Pei-Geok Lim
(anggie@gmail.com)
Intelligent Software Engineering Laboratory,
Faculty of Computer Science & Information Systems,
Universiti Teknologi Malaysia,
81310 UTM Skudai, Johor, Malaysia

Ali Selamat
(aselamat@utm.my)
Intelligent Software Engineering Laboratory,
Faculty of Computer Science & Information Systems,
Universiti Teknologi Malaysia,
81310 UTM Skudai, Johor, Malaysia

Abstract: The rapid growth of the computer technologies and the advent of World Wide Web have increased the amount and the complexity of multimedia information. Content-based image retrieval (CBIR) system has been developed as an efficient image retrieval tool whereby user can provide their query to the system to allow it to retrieve the user's desired image from image database. However, the traditional relevance feedback of CBIR has some limitations that decrease the performance of the CBIR system that are the imbalance of training set problem, classification problem, limited information from user problem, and insufficient training set problem. Therefore, in this paper we propose a modified relevant feedback method to support the user query and user profiles based on the weight ranking of the image retrieved. The Support Vector Machine (SVM) has been used to support the learning process in order to reduce the semantic gap between user and the CBIR system. From the experiments, the proposed learning method has enabled the users to improve their search results based on the precision and accuracy.

Keywords: Image Retrieval, Content-based Image Retrieval (CBIR), Relevance Feedback, and Support Vector Machines (SVM).

I. INTRODUCTION

Images are considered as the prime media type to be used to retrieve hidden information within data. In general, an image retrieval system is a computer system for browsing, searching, and retrieving images from a large digital image database. Early trends witnessed image retrieval utilizing some method of adding metadata such as captioning, keywords, or descriptions to the images [1] so that retrieval can be performed over the annotation words. The issue of subjectivity of human perception here means that the perception of different persons or the same person for the same image may vary under different circumstances [2]. Beside the human subjectivity issue, similarity is another issue that is highly focused on in CBIR. This issue has affected the retrieved results based on the similarities of pure visual features that are not necessarily perceptual and semantically meaningful. In addition, each type of visual feature tends to capture only one aspect of the image property and it is usually hard for a user to specify clearly how different aspects are combined [3]. Hence, there are semantic gaps between the low-level features and the high level query in the CBIR system. The semantic gap expresses the discrepancy between the low-level features that can be readily extracted from the images and the descriptions that are meaningful for the users. To solve these problems, an interactive relevance feedback which involves the interaction between human and system was introduced. Relevance feedback is a supervised active learning technique which uses the positive and negative examples feedback from the users to improve system performance. For a given query, the system first retrieves a list of ranked images according to a predefined similarity metrics. Then, the user marks the retrieved images as relevant (positive examples) or not relevant (negative examples) to the query. The system will refine the retrieved results based on the feedback and present a new list of images to the user. This process will go through several iterations until the user is satisfied with the retrieved result.

II. RELATED WORKS

The traditional CBIR relevance feedback techniques include query refinement [2] and re-weighting [4]. However, both techniques did not deliver satisfying performances for CBIR due to several issues. The most important issue in relevance feedback is how to incorporate positive and negative examples to refine the query and/or to adjust the similarity measure [5]. On the other hand, classification is another issue that needs to be considered by the CBIR domain. However, classification problem occurred in relevance feedback for CBIR when the learning problem regarding the positive samples (relevant images) and the negative samples (irrelevant images) are presented as two difference groups [6]. In this situation, it becomes difficult to retrieve the positive images which may disperse in the feature space; as a result, it is difficult to retrieve them directly based on low-level feature similarity whether they are refined or not [7]. Thus, a classifier or statistical learning technology is needed in order to identify these groups into positive and negative examples in the feature space [5]. During the feature similarity measure part, it will find the similar texture region based on the query image from the set of images in the database. A similarity comparison within the texture feature of query image and the database images will be conducted in this part. At the end of this part, the images that are over certain predefine similarity index threshold will be retrieved into the relevance feedback part for classification purposes. After the feature similarity part, a set of possible images will be retrieved by the system and sent to the user. The user will determine and mark the images as relevant or irrelevant in the relevance feedback part. The selected images that are marked by the users will be considered as relevant images and treated as input for support vector machine for adaptive learning purpose. This process will be repeated iteratively until the user is satisfied with the feedback images that are retrieved by the system. Finally the preferences of the user will be captured and acknowledged by the system. The system will automatically retrieve the relevant images based on the user's query.

III. TEXTURE EXTRACTION METHOD

After obtaining the user's query, the query image will go through a pre-processing process. In the pre-processing process, the image will be resized to 24 x 24 dimensions. The purpose of resizing is to help reduce the computations and complexity. This will also cause some of the information being lost after the image has been resized. After that, the image will be transformed into a gray scale image. After the pre-processing process is completed, the texture feature will be extracted from the gray scale image. Each vector in the texture feature represents the index of each pixel in the image. Each obtained decimal magnitude of pixel will be thresholded with an identified fixed threshold value. In this case, the threshold value is set at 100. A binary texture vector will be obtained after the thresholding process.

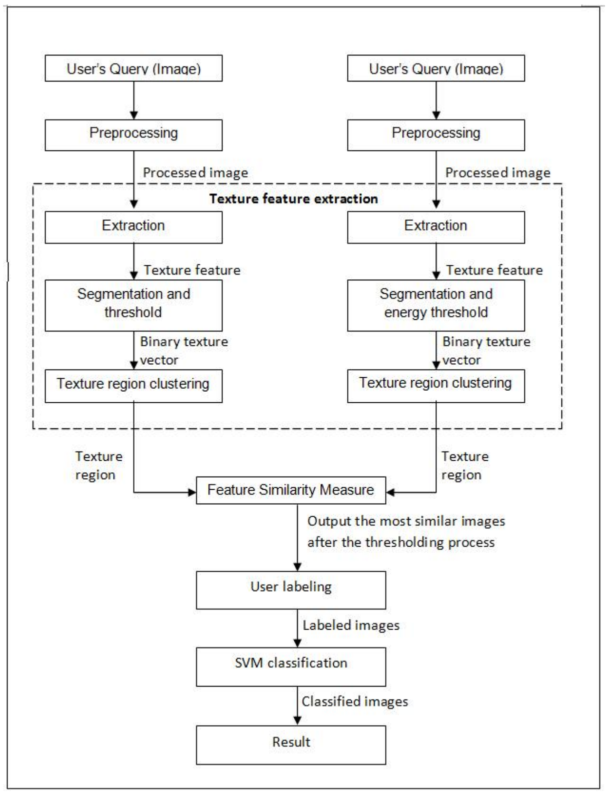

Fig. 1: Methodology of the CBIR by using SVM.

Equation (1) shows how the binary texture vector will be obtained from the gray scale image.

$$b_k[m,n] = \begin{cases} 1 & if \quad y_i[m,n] \geq \mathrm{T}_k \\ 0 & otherwise \end{cases} \qquad (1)$$

where $b_k[m,n]$ = binary value of each pixel with m and n coordinate

$y_k[m,n]$ = texture feature vector of each pixel with m and n coordinate

T_k = threshold

Texture segmentation is the process by which the image is split into different regions of homogeneous texture. By using the binary feature set that is obtained after thresholding process, the texture segmentation will take place to segment the binary feature set to some significant texture set with lower dimension. This segmentation mechanism can help to reduce the computational burden and at the same time produce some significant texture feature set. Therefore, some of the insignificant texture vector or regions will be eliminated. In this project, the segmentation mechanism uses the threshold method which the segmented area will be output as binary one if that area contains 50% of binary one. Otherwise, the segmented area will be output as zero if it contains less than the threshold value.

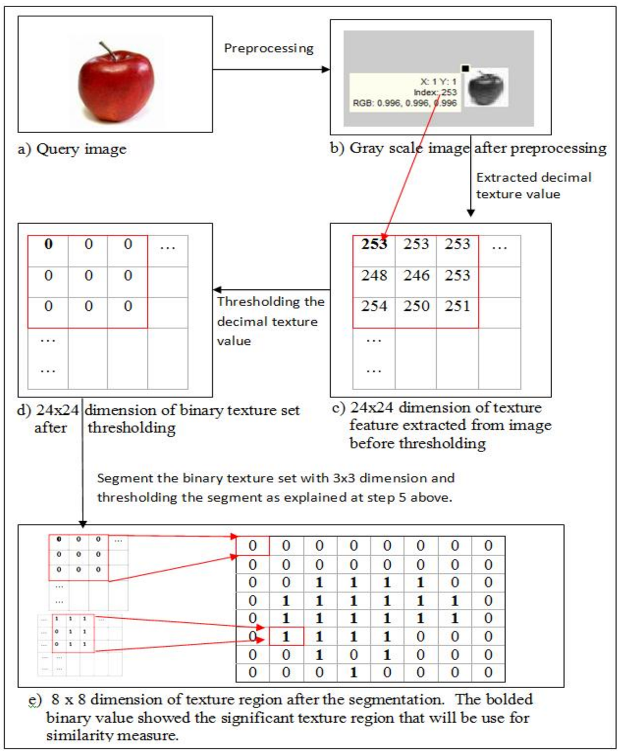

Fig. 2: The texture feature extraction mechanism.

1. FEATURE SIMILARITY MEASURE

The feature similarity measure will compare the similarity percentage between the texture regions of two images. Therefore, the similarity percentage shows how similar an image is from the image database to the query image. As a result, an output list that shows the similarity percentage to an input query will be obtained as shown in Figure 1. From the output list, the image which has the similarity percentage more than 40% will be retrieved for the user to mark, as shown in Figure 2.

2. SVM BASED RELEVANCE FEEDBACK

As we know, the relevance feedback process involves the interaction between human and the system, and this process will go through several iterations until the user is satisfied with the output images. In our experiment, relevance feedback process is aimed to evaluate the accuracy of CBIR system with the usage of the SVM classifier and without using of SVM classifier. A list of retrieved images from the feature similarity measurement will be given to the user. User will mark the images that are relevant to the query images. The unmarked images among these retrieved images will be considered as irrelevant images. Both relevant and irrelevant retrieved images will be used as training samples in classification process. Support Vector Machine (SVM) is used to learn the pattern of the relevant and irrelevant images within the training samples and classify the unlabeled images within the image database. In the end, the images from the image database were being classified as relevant or irrelevant images to the query image by the classifier. The new ranked list of similar images according to the result of the SVM will be retrieved in the next iteration of relevance feedback process.

Table 1: Type of dataset that use for experiment

Dataset	Category	Size
Dataset 1 (30 Samples)	Fruits	10
	Natural Scene	10
	Building	10
	Total	**30**
Dataset 2 (60 Samples)	Fruits	20
	Natural Scene	20
	Building	20
	Total	**60**
Dataset 3 (90 Samples)	Fruits	30
	Natural Scene	30
	Building	30
	Total	**90**

IV. EXPERIMENTAL RESULTS

In this study, the experiment uses three types of image dataset which are dataset 1, dataset 2, and dataset 3. Each dataset consists of three data categories which are fruits, natural scene, and building, as shown in Table 1. The main purpose of these dataset is to evaluate the performance of texture feature extraction. The results of this experiment will be evaluated using the accuracy rate measurement as shown in Eq. (2). In this experiment, the accuracy rate is calculated as the percentage of the images being identified as relevant or irrelevant image correctly by the system and human over the total of images in the database.

Accuracy Rate =

$$\frac{\textit{Total retrieved images that correctly identified as relevant or irrelevant images}}{\textit{Total image samples}} \quad (2)$$

Table 2: Similarity measurement for image database of dataset 1.

Category	Fruits	Natural Scene	Building
Comparison Result	0.47826	0.34783	0
	0.3913	0.65217	0.52174
	0.47826	0.26087	0.086957
	0.56522	0.17391	0
	0.21739	0.34783	0.34783
	0	0.30435	0.17391
	1	0.13043	0.043478
	0	0.73913	0.043478
	0.21739	0.17391	0.86957
	0.78261	0.26087	0.3913
Possibly retrieval by system	5	2	2

V. RESULT AND DISCUSSION

The experiments were conducted using the dataset that are shown in Table 1. The experiments were conducted under two different approaches which are relevance feedback without SVM and relevance feedback with SVM. We conducted the first experiment using relevance feedback without SVM. After the texture feature extraction process, the query images and database images would go through the feature similarity measurement. The percentage of texture region similarity within query images and database images would be measured. Images that were over a certain predefine similarity index threshold would be retrieved by the system for the user to do the user labelling process (relevance feedback process). In this experiment, we predefined the similarity threshold as 0.5. The images database with over 0.5 similarity index would be retrieved by the system and sent for the user to label them. Table 2 shows the similarity measurement result using dataset 1 (30 image samples). We found that there were 5 fruits images, 2 natural scene images, and 2 building images that were considered similar and retrieved by the systems respectively, as shown in Figure 3. This retrieval result is evaluated using the accuracy formula. Similar experiments had been conducted using two other dataset which are dataset 2 (60 image samples) and dataset 3 (90 image samples). Figure 5 shows the comparison of the accuracy measurement for the approach of relevance feedback with SVM and without SVM, using different size of dataset which are 30, 60 and 90 image samples.

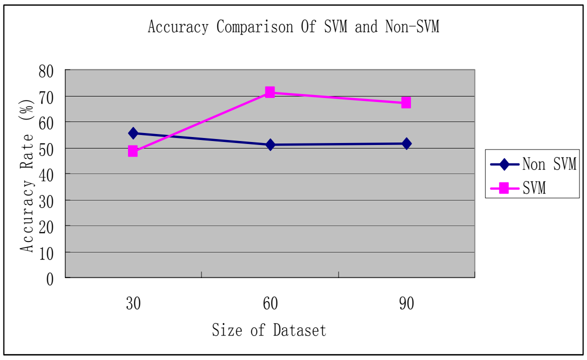

Fig. 3: Comparison of accuracy measurement for non-SVM and SVM according to different size of dataset.

We notice that for the relevance feedback without the SVM approach, the accuracy rate decreases as the size of dataset increases. This experiment result illustrates that the system could not perform adaptive learning and even insufficient (pls insert insufficient for what) especially when the number of images expanded. Meanwhile, on the average, the system also does not achieve a satisfactory performance with results lower than 60 percent accuracy rate. The experiment results illustrate that a better relevance feedback technique is necessary in order to improve the CBIR performance.

VI. CONCLUSIONS

In this paper, we propose a relevance feedback using the SVM learning method to retrieve images according to user's preferences. This proposed method has been used to support the learning process in order to reduce the semantic gap between the user and the CBIR system. The results of experiments have shown the improvement of the search result based on the precision and accuracy.

ACKNOWLEDGEMENTS

This work is supported by the Ministry of Science & Technology and Innovation (MOSTI), Malaysia and Research Management Center, University of Technology Malaysia (UTM) under the Vot 79200.

REFERENCES

[1] F. Long, H. Zhang and D. F. David. "Multimedia Information Retrieval and Management- Technological Fundamentals and Applications, chapter Fundamentals of Content-Based Image Retrieval," Springer, 2003.

[2] Y. Rui, T. S. Huang, M. Ortega, and S. Methrotra. "Relevance feedback: A power tool in interactive content-based image retrieval," *IEEE Trans. On Circuits and Systems for Video Techonology*, 8(5), 644-655, 1998.

[3] D.H. Kim, J.W. Song, J.H. Lee and B.G. Choi, "Support Vector Machine Learning for region-based image retrieval with Relevance Feedback," *ETRI Journal. Volume 29, Number 5*, October 2007.

[4] Y.Rui and T.S.Huang. "A novel relevance feedback techniques in Image retrieval," *In: Proc. 7th ACM Conf. on Multimedia, pp. 67–70*, 1999.

[5] D.C. Tao, X.O. Tang, X.L. Li, X.D. Wu, "Asymmetric Bagging and Random Space for Support Vector Machines-Based Relevance Feedback in Image Retrieval," *IEEE Trans. Pattern Analysis and Machine Intelligence*, vol.28, n07, July 2006.

[6] T. Qin, X.D. Zhang, T.Y. Liu, D.S. Wang, W.Y. Ma, H.J. Zhang. "An active feedback framework for image retrieval," *Pattern Recognition Letters*, *Volume 29*, *Issue 5*, *Pages 637-6461*, April 2008

[7] P. Hong, Q. Tian, T.S. Huang. "Incorporate support vector machines to content-based image retrieval with relevance feedback," *Image processing, 2000. Proceedings. 2000 International Conference on Volume 3, Page: 750-753 vol.3*, 10-12 Sept. 2000.

The Fifteenth International Symposium on Artificial Life and Robotics 2010 (AROB 15th '10),
B-Con Plaza, Beppu,Oita, Japan, February 4-6, 2010

Mixed Constrained Image Filter Design Using Particle Swarm Optimization

Zhiguo Bao and Takahiro Watanabe

Graduate School of Information Production and Systems, Waseda University
Kitakyushu-shi, Japan
(Email: baozhiguo@moegi.waseda.jp)

Abstract: This paper describes evolutionary image filter design for noise reduction using particle swarm optimization (PSO), where mixed constraints on the circuit complexity, power and signal delay are optimized. First, the evaluating values about correctness, complexity, power and signal delay are introduced to the fitness function. Then PSO autonomously synthesizes a filter. To verify the validity of our method, an image filter for noise reduction is synthesized. The performance of resultant filter by PSO is similar to that of Genetic Algorithm (GA), but the running time of PSO is 10% shorter than that of GA.

Keywords: PSO, Evolutionary Design, Image Filter.

I. INTRODUCTION

The idea of evolutionary hardware design was introduced at the beginning of 1990s in papers [1, 2], and it is usually defined as an approach in which the Genetic Algorithm (GA) is utilized to search for a suitable configuration of a reconfigurable device in order to meet a given specification.

The image filter design problem is often approached by means of evolutionary design techniques. In addition to an optimization of filter coefficients (for example, [3]), evolutionary approaches are applied to find a complete structure of image filters. In [4], Gaussian noise filters were evolved using a variant of Cartesian Genetic Programming in which target filters were composed of simple digital components, such as logic gates, adders and comparators. Later, image filters for other types of noise and edge detectors were evolved using the same technique [5]. But they did not discuss any circuit constraints such as complexity, power consumption and signal delay, while we proposed mixed constrained design optimization using GA for some combinational circuits [6, 7]. The proposed method could synthesize good circuits about complexity, power and signal delay, but it took the large running time for GA process. As another optimization method, particle swarm optimization (PSO) [8, 9, 10] was proposed and evaluated, and it is promising to find a good solution in shorter time, compared to GA.

This paper applies PSO to mixed constrained image filter design for noise reduction, shown in Fig. 1. The circuit complexity, power and signal delay which are caused by both logic gates and wires, are optimized. In this design, first, the evaluating value about correctness, complexity, power and signal delay are introduced to the fitness function. Then PSO autonomously synthesizes an image filter which is simpler and has better performance than the conventional design. To verify the validity of our method, an image filter for reducing noise is experimentally synthesized.

The organization of this paper is as follows: a brief overview of PSO is described in the next section. Section III describes design optimization for an image filter using PSO. Section IV shows the experimental results. Finally, Sect. V concludes this paper.

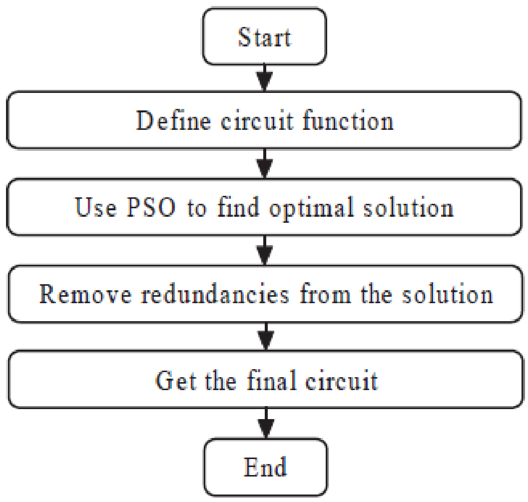

Fig. 1. The overview of our method

II. Particle swarm optimization

Particle swarm optimization (PSO) is an algorithm model on swarm intelligence that finds a solution to an optimization problem in a search space, shown in Fig. 2.

In PSO, a particle represents a candidate solution to the problem. Each particle is treated as a point in the *D*-dimensional problem space. The *i*-th particle is represented as $X_i = (x_{i1}, x_{i2}, \dots, x_{iD})$. The best previous position (the position giving the best fitness value) of the *i*-th particle is recorded and represented as $P_i = (p_{i1}, p_{i2}, \dots, p_{iD})$. The index of the best particle among all the particles in the population is represented by the symbol *g*. The rate of the position change (velocity) for particle *i* is represented as $V_i = (v_{i1}, v_{i2}, \dots, v_{iD})$. The particle is updated according to the following equations:

$$v_{id}^{(t+1)} = w \times v_{id} + c_1 \times rand() \times (p_{id} - x_{id}^{(t)}) + c_2 \times Rand() \times (p_{gd} - x_{id}^{(t)}). \quad (1)$$

$$x_{id}^{(t+1)} = x_{id}^{(t)} + v_{id}^{(t+1)}. \quad (2)$$

where,
$0 <= i <= (n-1)$, $1 <= d <= D$.
n : number of particles in a group.
D : number of members in a particle.
t: pointer of iterations (generations).
w : inertia weight factor.
c1, c2 : acceleration constant.
rand(), Rand(): uniform random value in the range [0,1].
$v_{id}^{(t)}$: velocity of particle *i* at iteration *t*, $V_d^{\min} \le v_{id}^{(t)} \le V_d^{\max}$.
$x_i^{(t)}$: current position of particle *i* at iteration *t*.

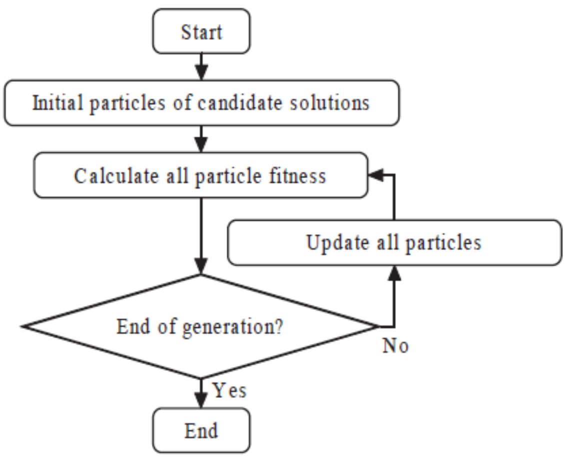

Fig. 2. The evolutionary process of PSO

The inertia weight factor *w* is employed to control the impact of the previous history of velocities on the current velocity, thereby influencing the trade-off between global (wide-ranging) and local (fine-grained) exploration abilities of the "flying points". A larger inertia weight facilitates global exploration (searching new areas), while a smaller inertia weight tends to facilitate local exploration to free tune the current search area. Suitable selection of the inertia weight provides a balance between global and local exploration abilities and thus requires lesser iterations on average to find the optimum. Good values of *w* are usually slightly less than 1 [10]. It could be randomly initialized for each particle. Or a high value of *w* at the beginning of the run facilitates global search, while a small *w* tends to localize the search.

c_1 and c_2 are constants that say how much the particle is directed towards good positions. They represent a "cognitive" and a "social" component, respectively, in that they affect how much the particle's personal best and the global best (respectively) influence its movement. Usually we take $c_1 = c_2 = 2$ [10].

III. Image filter design using PSO

PSO is applied to search good solutions to optimize the image filter design.

The target image filter is to provide identical functional behavior with less complexity, less power and less signal delay.

1. Image filter

Every image operator is considered as a digital circuit with nine 8-bit inputs and a single 8-bit output, which processes gray-scaled (8-bit/pixel) images.

As shown in Fig. 3, every pixel value of the filtered image is calculated using a corresponding pixel and its eight neighbors in the processed image [5].

2. Reconfigurable processing array for image filter

Similarly to [11], the reconfigurable image filter is implemented as a Virtual Reconfigurable Circuits (VRC) (Fig. 4). As a new pixel value is calculated using nine pixels, the VRC has got nine 8-bit inputs and a single 8-bit output. The VRC consists of two-input CLBs (Configurable Logic Blocks in FPGA) placed in a 4*4 array. Any input of each CLB may be connected to either a primary circuit input or the output of a CLB in the preceding column. Any CLB can be programmed to implement one of the functions given in Table 1 [5]. All these functions operate with 8-bit operands and produce 8-bit results. Table 1 also gives value of complexity (FC), power (FP) and signal delay (SD) for each function in a CLB.

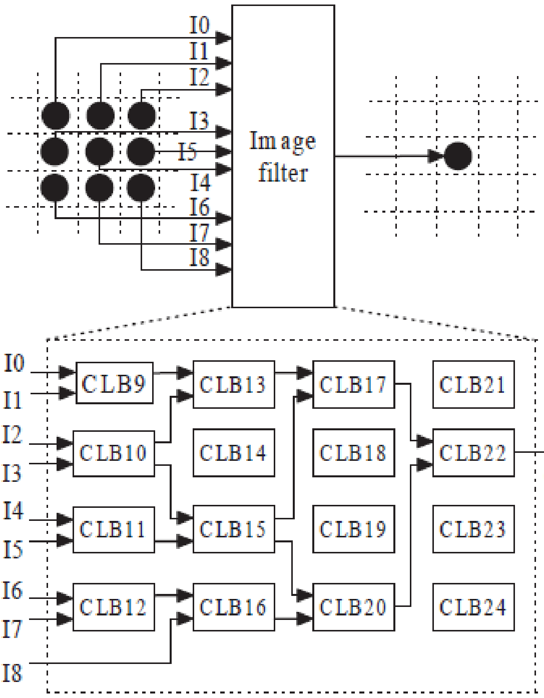

Fig. 3. A candidate image filter

In Fig. 4, there are position of inputs and output of each logic block. Therefore, we add values of wire about complexity, power and signal delay in Table 1.

3. Genetic encoding

The chromosome (particle) is a string of integers where each three continuous integers constitute a logic block. Each triplet in the chromosome encodes the two inputs and the function type of a logic block, respectively, such as:

(*Input_1*, *Input_2*, *Function type*).

A typical chromosome then can be a sequence of triplets [6, 7], such as:

$(IN_1^1, IN_2^1, F_{type}^1) \ldots (IN_1^i, IN_2^i, F_{type}^i) \ldots$

Here, IN_1^i and IN_2^i mean positions of the corresponding signal. F_{type}^i means *Function_type*. For primary input from I_0 to I_8, the range of IN^i is $(0 <= IN^i <= 8)$. For input from output of a logic block CLB_m, that is, CLB_9 to CLB_{24} in Fig. 4, $IN^i = m$. Function in a CLB is defined as shown in Table 1.

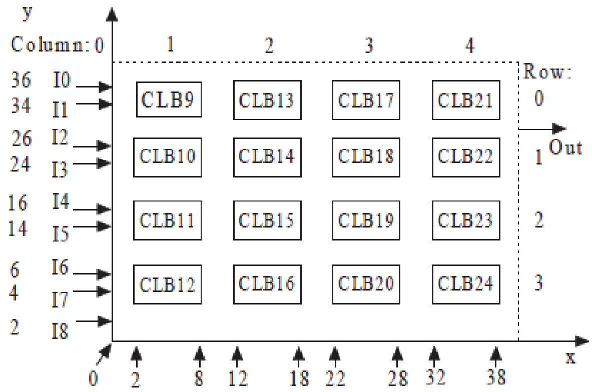

Fig. 4. A reconfigurable processing array

Table 1. Functions implements in a CLB

ID	Function	Description	FC	FP	SD
0	255	Constant	8	8	1
1	x	Identity	16	16	2
2	$255 - x$	Inversion	24	24	3
3	$x \vee y$	Bitwise OR	32	32	3
4	$\overline{x} \vee y$	Bitwise $\overline{x}$ OR y	40	40	4
5	$x \wedge y$	Bitwise AND	32	32	3
6	$not(x \wedge y)$	Bitwise NAND	40	40	4
7	$x \oplus y$	Bitwise XOR	64	64	4
8	$x \gg 1$	Right shift by 1	15	15	2
9	$x \gg 2$	Right shift by 2	14	14	2
10	$(x \ll 4) \vee (y \gg 4)$	Swap	16	16	2
11	$x + y$	+ (addition)	358	358	18
12	$x +^s y$	+ with saturation	367	367	19
13	$(x + y) \gg 1$	Average	350	350	18
14	$max(x, y)$	Maximum	240	240	16
15	$min(x, y)$	Minimum	240	240	16
-	(wire)	(wire)	16	16	2

FC: function complexity.
FP: function power.
SD: signal delay.

4. Fitness function

The pixels of corrupted image c_i are used as inputs of VRC. Pixels of filtered image f_i are generated, which are compared to the pixels of original image o_i.

The design objective is to minimize the difference between the filtered image and the original image. The image size is *nc*nr* pixels, but only the area of *(nc-2)*(nr-2)* pixels is considered, because the pixel values at the borders are ignored, and thus remain unfiltered. The fitness value of a candidate filter is obtained as follows:

(1) the VRC is configured using a candidate chromosome

(2) the created circuit is used to produce pixel values in the image f_i and

(3) the fitness value is calculated as

$$Fitness = (-1) \times (F_1 \times \beta + F_2). \qquad (3)$$

Where, F_1 and F_2 are defined as follows and β is the weight on F_1.

$$F_1 = \sum_{i=1}^{nc-2} \sum_{j=1}^{nr-2} (|fi(i,j) - oi(i,j)|). \qquad (4)$$

Where,
nc: the number of columns of the pixels in the image.
nr: the number of rows of the pixels in the image.
$f_i(i; j)$: the pixel (i, j) in filtered image f_i, the value range is [0,255].
$o_i(i ; j)$: the pixel (i, j) in original image o_i, the value range is [0,255].

$$F_2 = SD \times \alpha_{sd} + Pg \times \alpha_{pg} + Cg \times \alpha_{cg} + Pw \times \alpha_{pw} + Cw \times \alpha_{cw}. \qquad (5)$$

Where,
SD: signal delay of a circuit individual, determined by a critical path.
α_{sd}: the weight on signal delay in F_2.
Pg: power of logic blocks in a circuit, calculated by summation of all logic block's power.
α_{pg}: the weight on power of logic blocks in F_2.
Cg: complexity of logic blocks in a circuit, calculated by summation of all logic block's complexity.
α_{cg}: the weight on complexity of logic blocks in F_2.
Pw: power of all wires in a circuit, calculated by summation of all wire's power.
α_{pw}: the weight on power of wires in F_2.
Cw: complexity of wires in a circuit, calculated by summation of all wire's complexity.
α_{cw}: the weight on complexity of wires in F_2.

The priority of evaluating values in Eq. (3) is: $F_1 > F_2$. In this experiment, β is set to $0.1*10^9$. The priority of evaluating values in Eq. (5) is: $SD > Pg > Cg > Pw > Cw$. In this experiment, α_{sd} is set to $0.1*10^6$, α_{pg} is set to $1*10^3$, α_{cg} is set to $0.1*10^3$, α_{pw} is set to 10, and α_{cw} is set to 1. All α's and β are empirically assigned in our experiment.

IV. Experimental results

Table 2 shows the parameters of the evolution of PSO used in this experiment. Some preliminary experiments were performed in advance to decide parameters suitable for our experiment.

The proposed method was implemented in Eclipse SDK 3.1.1 with jre 1.6.0; and tested on a PC with Inter(R) Core(TM) 2 CPU at 2.67 GHz and 2.0 GB RAM.

Table 2. Conditions for evolution

Number of Generation : 100.
Population Size : 600.
Inertia weight factor w : [0.4, 1.0]. Limit of change in velocity of each member in an individual: $V_d^{max} = 0.5 * P_d^{max}, V_d^{min} = -0.5 * P_d^{max}$. Acceleration constant : c1 = 2, c2 = 2.

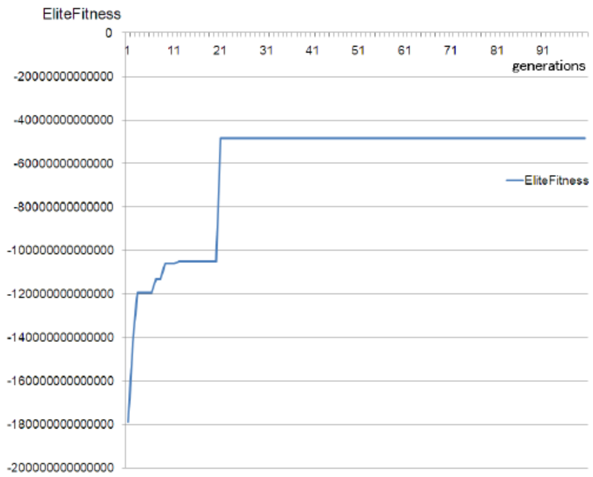

Fig. 5. Elite fitness of PSO (Y-axis) vs. the number of generations (X-axis)

The image filter is evolved for a 512*512 Lena image corrupted by 5% salt-and-pepper noise, shown in Fig. 7.

Fig. 5 shows the elite fitness of PSO with w = 0:9 vs. the number of generations during the image filter evolution. The elite fitness is increasing during evaluation time.

Table 3 shows the results of PSO with different w. For each PSO, we use results over 10 independent trials. "max" means the best elite fitness value from 10 trials; "average" means the average fitness value of 10 individuals; "time" means the average running time (minutes) of one trial. The larger the fitness is, the better the image filter is. The less the ratio is, the better the image filter is.

From the results, we can see that PSO (0.9) produces better solutions than others, from the point of the best elite fitness.

An example of chromosome by PSO (0.9) with fitness -48550809287267 is as follows:

(0, 0, 0)(1, 7, 15)(3, 5, 14)(8, 5, 15)(0, 0, 0)
(0, 0, 0)(0, 0, 0)(11, 12, 14)(0, 0, 0)(0, 0, 0)(0, 0, 0)
(4, 16, 15)(10, 20, 14)(0, 0, 0)(0, 0, 0)(0, 0, 0)

Table 3: Fitness values of PSO with different w, and GA.

Item	Max		Average		Running time	
	Fitness	Ratio	Fitness	Ratio	Time(m)	Ratio
$PSO(0.4)$	-80005207479684	1.65	-99745634920892	1.11	42.80	0.99
$PSO(0.5)$	-80535402393364	1.66	-94873624466988	1.06	43.60	1.01
$PSO(0.6)$	-79181905512328	1.63	-97375325953839	1.09	43.20	0.99
$PSO(0.7)$	-56076103257304	1.15	-94746895485425	1.06	42.60	0.98
$PSO(0.8)$	-57981907477527	1.19	-91487054845692	1.02	41.70	0.96
$PSO(0.9)$	-48550809287267	1.00	-89652125806386	1.00	43.00	1.00
$PSO(1.0)$	-85478004803230	1.76	-102629344653216	1.14	40.00	0.92
$PSO(w1)$	-82558108959223	1.70	-93726626111394	1.05	42.80	0.99
$PSO(w2)$	-63176503079148	1.30	-91741585167119	1.02	42.00	0.97
GA	-47595302921595	0.98	-64678393342856	0.72	49.70	1.10

$PSO(w)$: PSO with $w = 0.4, 0.5, 0.6, 0.7, 0.8, 0.9, 1.0$.
$PSO(w1)$: PSO with $w = 1.0 - 0.6 * generation/generation\_size$.
$PSO(w2)$: PSO with $w = 0.4 + 0.6 * random()$.
GA: Number of Generation, Population Size is same to that of PSO; Elite Size = 10, Crossover Probability (Pc) = 0.3, Mutation Probability (Pm) = 0.1, (ref. [7]).

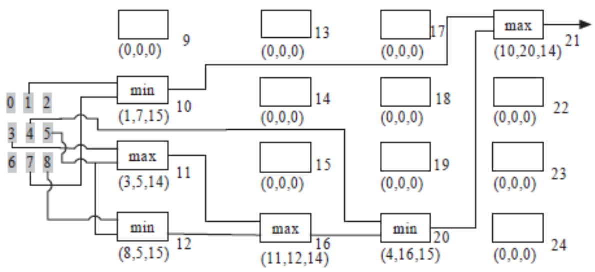

Fig. 6. The optimized image filter by PSO (0.9)

The graphical representation of this chromosome is shown in Fig. 6.

As the image is relatively large, we can assume that the evolved filter is general. The filter is able to remove the same type of noise also from other images. The image filter was evolved using Lena image and tested on other images.

Fig. 7, 8 and 9 show the input images with 5% salt-and-pepper noise, the Mean difference per pixel (MDPP) value of these images are 6.42, 6.29 and 6.35, respectively. Fig. 10, 11 and 12 show the output images by the image filter in Fig. 6, the MDPP value of these images are 1.87, 2.37 and 2.51, respectively. Obviously, this image filter could reduce noise for all cases.

V. Conclusions

This paper proposed the use of PSO (Particle Swarm Optimization) for mixed constrained image filter design for noise reduction. The complexity, power and signal delay both of the CLBs (Configurable Logic Blocks) and wires are considered. An image filter for removing noise is experimentally synthesized using PSO, to verify the validity of our method. By evolution, quality of the optimized image filter by PSO (0.9) is almost same as that of GA, but the running time of PSO is 10% shorter than that of GA.

Acknowledgements

This research was supported by the "Ambient SoC Global COE Program of Waseda University" of the Ministry of Education, Culture, Sports, Science and Technology (MEXT), Japan and partially by the Intellectual Cluster project of MEXT, Japan and the Core Research for Evolutional Science and Technology (CREST) of Japan Science and Technology Agency (JST).

REFERENCES

[1] T. Higuchi, T. Niwa, T. Tanaka, et al. (1993), "Evolving hardware with genetic learning: a first step towards building a Darwin machine," Proc. the Second International Conference on Simulated Adaptive Behaviour, MIT Press, pp. 417-424.
[2] H. de Garis (1993), "Evolvable hardware: Genetic programming of a Darwin machine," Proc. International Conference on Artificial Neural Networks and Genetic Algorithms, Innsbruck, Austria, Springer.

Figure 7: The input image (Lena) with noise, (MDPP: 6.42).

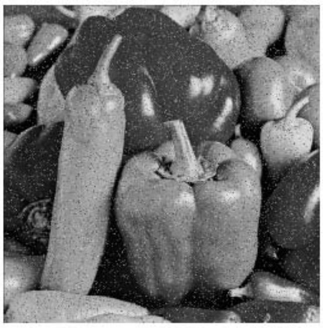

Figure 8: The input image (Peppers) with noise, (MDPP: 6.29).

Figure 9: The input image (Goldhill) with noise, (MDPP: 6.35).

Figure 10: The output image (Lena), (MDPP: 1.87).

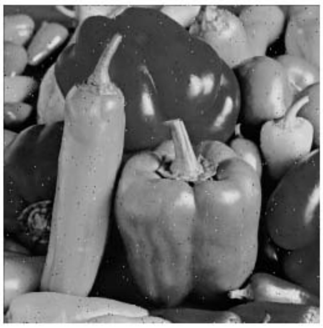

Figure 11: The output image (Peppers), (MDPP: 2.37).

Figure 12: The output image (Goldhill), (MDPP: 2.51).

[3] J. Dumoulin, J. Foster, J. Frenzel, et al. (2000), "Special Purpose Image Convolution with Evolvable Hardware," Real-World Applications of Evolutionary Computing, vol. 1803 of LNCS, Springer, 2000, pp. 111-125.
[4] L. Sekanina (2002), "Image Filter Design with Evolvable Hardware," Applications of Evolutionary Computing, (the 4th Workshop on Evolutionary Computation in Image Analysis and Signal Processing, EvoIASP 2002), vol. 2279 of LNCS, Springer, 2002, pp. 255-266.
[5] Z. Vasicek and L. Sekanina (2007), "Evaluation of a New Platform for Image Filter Evolution," Proc. the Second NASA/ESA Conference on Adaptive Hardware and Systems, 2007 (AHS 2007), Aug. 2007, pp. 577-586.
[6] Z. Bao and T. Watanabe (2009), "A Novel Genetic Algorithm with Cell Crossover for Circuit Design Optimization," Proc. IEEE International Symposium on Circuits and Systems 2009 (ISCAS 2009), Taipei, Taiwan, May 2009, pp. 2982-2985.
[7] Z. Bao and T. Watanabe (2009), "Evolutionary Design for Image Filter using Genetic Algorithm," Proc. IEEE TENCON 2009, Singapore, Nov. 2009, (accepted).
[8] J. Kennedy and R. Eberhart (1995), "Particle swarm optimization," Proc. IEEE International Conference on Neural Networks, Vol. 4, 1995, pp. 1942-1948.
[9] Russell C. Eberhart and Yuhui Shi (1998), "Comparison between genetic algorithms and particle swarm optimization," Evolutionary Programming VII, Lecture Notes in Computer Science, Springer, Volume 1447, 1998, pp. 611 - 616.
[10] Jacob Robinson and Yahya Rahmat-Samii (2004), "Particle swarm optimization in electromagnetic," IEEE Transactions on Antennas and Propagation, Volume 52, Issue 2, Feb. 2004, pp. 397 - 407.
[11] T. Martinek and L. Sekanina (2005), "An Evolvable Image Filter: Experimental Evaluation of a Complete Hardware Implementation in FPGA," Evolvable Systems: From Biology to Hardware, vol. 3637 of LNCS, Springer, 2005, pp. 76-85.

A Reinforcement Learning with Switching Controllers for Continuous Action Space

Masato Nagayoshi[a], Hajime Murao[b], and Hisashi Tamaki[c]

[a] Niigata College of Nursing, 240, Shinnan, Joetsu 943-0147, Japan
nagayosi@niigata-cn.ac.jp

[b] Faculty of Cross-Cultural Studies, Kobe Univ. 1-2-1, Tsurukabuto, Nada-ku, Kobe 657-8501, Japan
murao@i.cla.kobe-u.ac.jp

[c] Graduate School of Engineering, Kobe University, Rokko-dai, Nada-ku, Kobe 657-8501, Japan
tamaki@al.cs.kobe-u.ac.jp

Abstract

Reinforcement Learning (RL) attracts much attention as a technique of realizing computational intelligence such as adaptive and autonomous decentralized systems. In general, however, it is not easy to put RL into practical use. This difficulty includes a problem of designing a suitable action space of an agent, i.e., satisfying two requirements in trade-off: (i) to keep the characteristics (or structure) of an original search space as much as possible in order to seek strategies that lie close to the optimal, and (ii) to reduce the search space as much as possible in order to expedite the learning process.

In order to design a suitable action space adaptively, in this paper, we propose a RL model with switching controllers based on Q-learning and Actor-Critic to mimic a process of an infant's motor development in which gross motor skills develop before fine motor skills. Then, a method for switching controllers is constructed by introducing and referring to the "entropy". Further, through computational experiments by using a path planning problem with continuous action space, the validity and the potential of the proposed method have been confirmed.

1 Introduction

In recent years, artificial systems have become extremely complicated and enlarged. The conventional way, in which systems are controlled in a top-down manner mainly by humans, is facing up to the difficulties of not only optimality but also adaptability and flexibility. As one of the solutions to this issue, the development of an autonomously adaptive system has been ongoing. Engineers and researchers are paying more attention to Reinforcement Learning (RL)[1] as a key technique of realizing autonomous systems. In general, however, it is not easy to put RL into practical use. Such issues as satisfying the requirement of learning speed, resolving the perceptual aliasing problem, and designing reasonable state and action spaces of an agent, etc. must be resolved. Our approach mainly deals with the problem of designing the action space. By designing a suitable action space adaptively, it can be expected that the other two problems will be resolved simultaneously. Here, the problem of designing the action space involves the following two requirements: (i) to keep the characteristics (or structure) of an original search space as much as possible in order to seek strategies that lie close to the optimal, and (ii) to reduce the search space as much as possible in order to expedite the learning process. These requirements are, in general, in conflict.

In order to design a suitable action space adaptively, in this paper, we propose a RL model with switching controllers based on Q-learning and Actor-Critic to mimic a process of an infant's motor development in which gross motor skills develop before fine motor skills. Here, the controller based on Q-learning acquires gross motor skills, and the other controller based on Actor-Critic acquires fine motor skills. Then, a method for switching controllers, i.e., adjusting the search space adaptively, is constructed by introducing and referring to the "entropy" which is defined on action selection probability distributions in a state. Some models which combine Q-learning and Actor-Critic have been proposed so far [3, 4]. However, none of the existing models aim to mimic the process of the infant's motor development, nor do they function to switch from Q-learning to Actor-Critic depending on the state, nor is the action selected by Q-learning performed directly.

Through some computational experiments by using a path planning problem, the proposed method is compared with an Actor-Critic method and three Q-learning methods that divide the action space evenly into 4, 8, and 16 spaces.

2 Typical Reinforcement Learning Methods

2.1 Q-learning

Q-learning works by calculating the Quality of a state-action combination, namely Q-value, that gives the expected utility of performing a given action in a given state. By performing an action $a \in \mathcal{A}_{\mathrm{Q}}$, where $\mathcal{A}_{\mathrm{Q}} \subset \mathcal{A}$ is the set of available actions in Q-learning and $\mathcal{A}$ is the action space of the agent, the agent can move from state to state. Each state provides the agent a reward r.

The Q-value is updated according to the following formula, when the agent is provided the reward:

$$Q(s(t\text{-}1)\ a(t\text{-}1)) \leftarrow Q(s(t\text{-}1)\ a(t\text{-}1)) + {}_{\mathrm{Q}}\ r(t\text{-}1) + \gamma \max_{b \in \mathcal{A}_{\mathrm{Q}}} Q(s(t)\ b) \quad Q(s(t\text{-}1)\ a(t\text{-}1)) \quad (1)$$

where $Q(s(t\text{-}1)\ a(t\text{-}1))$ is the Q-value for the state and the action at the time step t-1, ${}_{\mathrm{Q}} \in [0\ 1]$ is the learning rate of Q-learning, $\gamma \in [0\ 1]$ is the discount factor.

The agent selects an action according to the stochastic policy, $(a|s)$, which based on the Q-value. $(a|s)$ specifies probabilities for taking each action a in each state s. Boltzmann selection, which is one of the typical action-selection methods, is used in this research. Therefore, the policy $(a|s)$ is calculated as follows:

$$(a|s) = \frac{\exp(Q(s\ a)\quad)}{\sum_{b \in \mathcal{A}} \exp(Q(s\ b)\quad)} \quad (2)$$

where is a positive parameter labeled the temperature.

2.2 Actor-Critic

Actor-Critic methods have a separate memory structure to explicitly represent the policy independent of the value function. The policy structure is called "Actor", which selects actions, and the estimated value function is called "Critic", which criticizes the actions made by the Actor. The Critic is a state-value function. After each action selection, the Critic evaluates the new state to determine whether things have gone better or worse than expected. That evaluation is TD-error:

$$(t\text{-}1) = r(t\text{-}1) + \gamma V(s(t)) \quad V(s(t\text{-}1)) \quad (3)$$

where $V(s)$ is the state Value. This TD-error can be used to evaluate the action just selected. If $(t\text{-}1)$ is positive, it suggests that the tendency to select $a(t\text{-}1)$ should be strengthened for the future, whereas if $(t\text{-}1)$ is negative, it suggests the tendency should be weakened.

Then, $V(s(t\text{-}1))$ is updated according to Eq. (4) in the Critic, based on this $(t\text{-}1)$. In parallel, it is updated for the stochastic policy, $(a|s)$, in the Actor.

$$V(s(t\text{-}1)) \leftarrow V(s(t\text{-}1)) + {}_{\mathrm{C}}\ (t\text{-}1) \quad (4)$$

where ${}_{\mathrm{C}} \in [0\ 1]$ is the learning rate of the Critic.

It is typical for the normal distribution to be used, shown in Eq. (5), as the stochastic policy in the Actor, when Actor-Critic is applied to a continuous action space[2]. In this case, both the mean (s) and the standard error of the mean $\sigma(s)$ about the normal distribution are calculated using TD-error $(t\text{-}1)$ in the Actor, as Eq. (6),(7).

$$(a|s) = \frac{1}{\sigma(s)\sqrt{2}} \exp(\frac{(a \quad (s))^2}{2\sigma(s)^2}) \quad (5)$$

$$(s(t\text{-}1)) \leftarrow (s(t\text{-}1)) + \quad (t\text{-}1)(a(t\text{-}1) \quad (s(t\text{-}1))) \quad (6)$$

$$\sigma(s(t\text{-}1)) \leftarrow \sigma(s(t\text{-}1)) + {}_{\sigma}\ (t\text{-}1)((a(t\text{-}1) \quad (s(t\text{-}1)))^2 \quad \sigma(s(t\text{-}1))^2) \quad (7)$$

where $\in [0\ 1]$ ${}_{\sigma} \in [0\ 1]$ are the learning rate of the mean and the standard error of the mean respectively. Here, if Eq. (7) is used directly, the standard error could be 0 or a negative value. So, it is necessary for the setting of the standard error to be creative to specify the range, etc.

3 A Switching Reinforcement Learning from Q-learning to Actor-Critic

3.1 Outline of a Computational Model

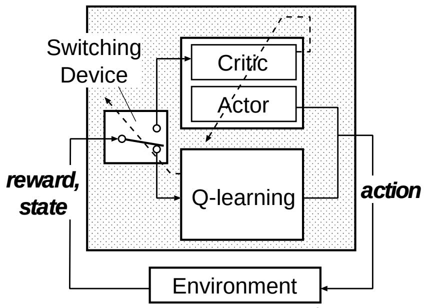

Figure 1: Proposed switching reinforcement learning model.

In this section, we propose a RL model with switching controllers based on Q-learning and Actor-Critic to mimic a process of an infant's motor development.

The proposed model is constructed by two learning controllers and a switching device, as shown in Fig. 1.

Then, the following procedure is conducted to mimic a process of an infant's motor development in which gross motor skills develop before fine motor skills.

1. The controller based on Q-learning (hereafter called "QL controller") estimates the Q-values for each typical action pre-designed by humans. The actions selected by the QL controller correspond to gross motor skills.
2. After "sufficient learning" has been achieved in a state s, the learning controller for the state s is switched from Q-learning to Actor-Critic, as will be described in detail below.
3. The controller based on Actor-Critic (hereafter called "AC controller") adjusts actions continuously. The actions selected by the AC controller correspond to fine motor skills.

It can be expected that the proposed model 1) demonstrates a good performance with regard to the ultimately obtained control rule, because it can adjust actions continuously unlike models using only a QL controller. 2) has a better performance in the early stages of learning than the model using only an AC controller do by switching from the QL controller, where the possible actions are limited beforehand. 3) reduces a designer's load and responsibilities in designing the action space of the QL controller, because the AC controller adjusts actions after switching the controller.

3.2 A Method to Switch Controllers

A variety of methods to switch from the QL controller to the AC controller can be considered. In this paper, we propose a switching method referring to the "entropy", which is defined on action selection probability distributions in a state, and the number of learning opportunities in the state.

The entropy of action selection probability distributions using Boltzmann selection in a state, $H(s)$, is defined by

$$H(s) = \quad (1 \quad \log|\boldsymbol{\mathcal{A}}_{\mathrm{Q}}|) \sum_{a \in \boldsymbol{\mathcal{A}}_{\mathrm{Q}}} \quad (a|s) \log \quad (a|s) \tag{8}$$

where $|\boldsymbol{\mathcal{A}}_{\mathrm{Q}}|$ is the number of available actions of the QL controller.

The switching method treats this entropy $H(s)$ as an index of sufficiency for the number of learning opportunities in the state.

The controller is switched to Actor-Critic, if the following formula is satisfied:

$$H(s) < \theta_{\mathrm{H}} \tag{9}$$

In prior studies, Ito at el.[5] have referred to the entropy as the residual entropy, and used the average of the residual entropies when switching from the coarse-graining state space to the fine-graining one. In our early studies[6, 7], we have used the entropy as an index of a correctness of state aggregation when adjusting the aggregation size of s.

In parallel, the controller is also switched to Actor-Critic, if the following formula regarding the number of learning opportunities in s, $L(s)$, is satisfied:

$$L(s) > \theta_{\mathrm{L}} \tag{10}$$

where θ_{L} is set at a sufficiently big number. This is used because the entropy can not be small after the controller learned a sufficient number of times, if the state space is designed too coarse-graining[6, 7].

When switching controllers, the following procedure is conducted:
i) the state value of the Critic,$V(s)$, is initialized by

$$V(s) = \max_{a \in \boldsymbol{\mathcal{A}}_{\mathrm{Q}}} Q(s \ \ a) \tag{11}$$

ii) the normal probability distribution used by the Actor is calculated by

$$(s) = \arg\max_{a \in \boldsymbol{\mathcal{A}}_{\mathrm{Q}}} Q(s \ \ a) \tag{12}$$

$$\sigma(s) = |\boldsymbol{\mathcal{A}}| \ \ (6 \cdot |\boldsymbol{\mathcal{A}}_{\mathrm{Q}}|) \tag{13}$$

where $|\boldsymbol{\mathcal{A}}|$ is a size of the action space of the AC controller. Here, Eq. (13) is presupposed to be designed such that the action space of the QL controller is divided evenly.

4 Computational Example

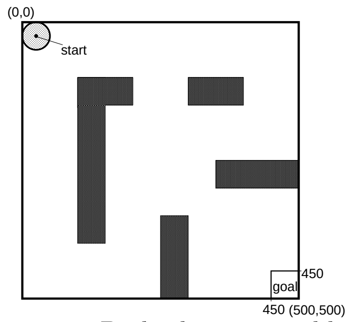

Figure 2: Path planning problem.

The proposed method is applied to a so-called "path planning problem" where an agent is navigated from a start point to a goal area in a continuous space as shown in Fig. 2. Here, the agent has a circular shape (diameter = 50[mm]), and the continuous space

Table 1: Parameters for Experiments.

Method	Parameter	Value
A, Q4, Q8, and Q16	Q	0 1
A and AC	C σ	0 1
all	γ	0 9
A, Q4, Q8, and Q16		0 1
A	θ_H	0 3
A	θ_L	10000

is 500[mm] 500[mm] bounded by the external wall with internal walls as shown in black. The agent can observe the center position of the agent: (x_A y_A) as the input, and move 25[mm] in a direction, i.e., decide the direction: θ_A as the output.

The positive reinforcement signal $r_t = 10$ (reward) is given to the agent only when the center of the agent arrives at the goal area and the reinforcement signal $r_t = 0$ at any other steps. The period from when the agent is located at the start point to when the agent is given a reward, labeled as 1 episode, is repeated.

After dividing the state space evenly into 20 20 spaces, the proposed method (hereafter called "method A") is compared with an Actor-Critic method (hereafter called "method AC") and three Q-learning methods that divide the action space evenly into 4, 8, and 16 spaces (hereafter called "method Q4", "method Q8", and "method Q16" respectively).

All initial values of the state and standard errors are set at 0.0 and 1.0 respectively, and all initial means are set to randomize within a range of [0 1 1 0] for the method AC. Then, all initial Q-values are set at 5.0 as the optimistic initial values[1] for Q-learning methods. Here, the initial values and the maximum limit of $\sigma(x)$ are set so that $\pm 3\sigma$ becomes the size of the action space: 2 .

Computer experiments have been done with parameters as shown in Table 1. Here, θ_H was set referring to about 0.312: the maximal value of the entropy when the highest selection probability for one action is 0.9, θ_L was set in consideration of the enough big number.

The number of average steps required to accomplish the task was observed during learning over 20 simulations with various methods as described in Fig. 3.

Learning speed and obtained control rule: It can be confirmed from Fig. 3 that, 1) method A and Q4 have good performances with regard to the learning speed, 2) method A has good performance as well as method AC with regard to the obtained control rule, 3) any proper control rule by method Q4, Q8, and Q16 couldn't be obtained.

Therefore, we have confirmed that method A demonstrates better performance than any other method on the path planning problem with the continuous action space.

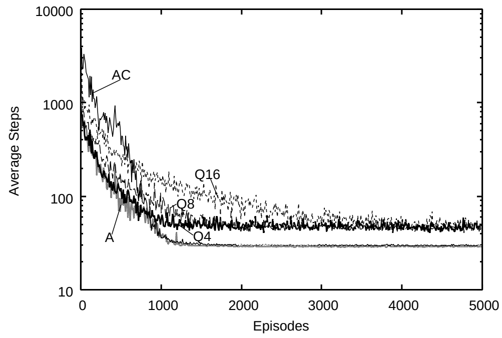

Figure 3: Required steps.

5 Conclusion

In order to design the suitable action space adaptively, we propose in this paper the RL model with switching controllers based on Q-learning and Actor-Critic, and the method for switching controllers referring to the "entropy". Then, through some computational experiments by using the path planning problem with continuous action space, the validity and the potential of the proposed method have been confirmed.

Our future projects include: 1) to apply more complicated problems, 2) to investigate multi-step models for mimicking the process of the infant's motor development, 3) to mimic the process of an infant's perceptual development, etc.

Acknowledgment

This work was supported in part by a Grant-in-Aid for Young Scientists (B), (No. 21700258), from MEXT, Japan.

References

[1] R.S. Sutton and A.G. Barto: Reinforcement Learning, A Bradford Book, MIT Press (1998).

[2] H. Kimura and S. Kobayashi: An Analysis of Actor-Critic Algorithms using Eligibility Traces: Reinforcement Learning with Imperfect Value Functions, *JSAI Jour.*, **15**(2), 267-275 (2000)(in Japanese).

[3] J. Morimoto and K. Doya: Acquisition of stand-up behavior by a real robot using hierarchical reinforcement learning, *Robotics and Autonomous System*, **36**, 37-51 (2001).

[4] K. Shibata, T. Nishino, and Y. Okabe: Active Perception Learning System Based on Actor-Q Architecture, *T. IEICE Japan*, **J84-D-II**(9), 2121-2130 (2001) (in Japanese).

[5] A. Ito and M. Kanabuchi: Speeding up Multi-Agent Reinforcement Learning by Coarse-Graining of Perception - Hunter Game as an Example -, *T. IEICE Japan*, **J84-D-I**(3), 285-293 (2001) (in Japanese).

[6] M. Nagayoshi, H. Murao, and H. Tamaki: A State Space Filter for Reinforcement Learning, *Proc. AROB 11th'06*, 615-618(GS1-3) (2006).

[7] M. Nagayoshi, H. Murao, and H. Tamaki: A State Space Filter for Reinforcement Learning in POMDPs - Application to a Continuous State Space -, *Proc. of the SICE-ICSE International Joint Conference 2006*, 6037-6042(SE18-4) (2006).

The Fifteenth International Symposium on Artificial Life and Robotics 2010 (AROB 15th '10),
B-Con Plaza, Beppu,Oita, Japan, February 4-6, 2010

A Framework for Embodied Evolution with Pre-evaluation Applied to a Biped Robot

Junichi Nakai Takaya Arita
Graduate School of Information Science, Nagoya University
Furo-cho, Chikusa-ku, Nagoya 464-8601, Japan
E-mail: nakai@alife.cs.is.nagoya-u.ac.jp, arita@nagoya-u.jp

Abstract: "Embodied evolution (EE)" is a methodology in evolutionary robotics, in which, without simulations on a host computer, real robots evolve on the basis of the interactions with actual environment. However, we had to accept robot behavior with low fitness especially in the early generations when adopting EE. This paper introduced pre-evaluation into the EE framework for a biped robot in order to restrain robot behavior of which fitness is estimated to be low, especially, falling down to the ground. We provide a comparative discussion on the conventional simulate-and-transfer method, the original EE method and the proposed one in terms of calculation time, cost of fitness evaluation and cost of simulation or modeling based on the evaluation experiments. We believe that the EE framework with pre-evaluation is applicable to a wide variety of optimization tasks in which the cost or risk of fitness evaluation is not negligible.

Keywords: evolutionary robotics, embodied evolution, biped robot, coevolution, genetic algorithm

1 Introduction

Evolutionary robotics is a challenging technique for creation of autonomous robots based on the Darwinian principle of natural selection [1]. In the conventional evolutionary robotics, the "simulate-and-transfer" method has been adopted, in which a controller is developed using an evolutionary algorithm on a host computer and then the solution is transferred to a physical robot. However, some issues are increasingly problematic for the method: performance of evolved behavior tends to be less than expected owing to the gap between simulation and the real world. Also, it is necessary to model the environment every time when a new task is given.

Pollack et al. proposed "embodied evolution (EE)" for solving these issues, in which real robots evolve based on the interactions with actual environment without simulation on a host computer [2]. Usui and Arita extended the framework by providing each robot with an evolving population of virtual individuals in order to reduce the dependence of the number of the robots and of the frequency of encounter with other robots on the speed of evolution [3]. However, these studies brought in new issues. We have to accept robot behavior with low fitness especially in the early generations. Also, evaluation based on robot behavior needs longer convergence time in general.

This paper introduces pre-evaluation into the EE framework so as to restrain robot behavior whose fitness is estimated to be low and evaluates the proposed architecture that is applied to a humanoid robot. The mechanism for pre-evaluation is introduced as a coevolutionary system in the proposed architecture. In other words, both the robot behavior and evaluation of the robot behavior evolve while interacting with each other. We expect introduction of pre-evaluation to decrease the number of falls in the early stage of evolution of biped-walking.

2 Framework

Fig. 1 shows the framework for Embodied Evolution with pre-evaluation. A set of information specifying the robot controller (Controller Genome, CG) and its fitness value evaluated by robot behavior (Fr) or estimated by pre-evaluation (Fp) are coupled and stored as an individual in the Controller Pool (CP). A new individual is generated by selecting (copying) two CGs from the CP based on the roulette wheel selection, and then uniform crossover and mutation are operated. The new CG is then coupled with an Environment Genome (EG) on which genetic operators have also been performed similarly and put into the genome queue. Pre-evaluation of a CG is done using its coupled EG before the robotic evaluation in the real world. In case the pre-evaluation value is less than a threshold described below, it skips robotic evaluation and returns to the CP coupled with the pre-evaluation value. Otherwise, robotic evaluation is conducted and returns to the CP coupled with the fitness value. This study does not consider transmission of individuals among robots, although migrations of CGs among robots are allowed in the framework.

EG, which is a set of information specifying the environment in pre-evaluation, is also coupled with its fitness value and stored into the Environment Pool (EP). The fitness of an EP is the agreement rate between the fitness value by robotic behavior and the estimated value by pre-evaluation. The design of the evolutionary system for pre-evaluation depends on the requirements of users. If knowledge about the robot and the task are not built-in at all, then the evolutionary system corresponds to genetic programming that constructs a function of a EG specifying the fitness value of it. On the other hand, if most possible information is built-in, then it corresponds to a kind of parameter tuning. There are important trade-offs here, which will be investigated thoroughly in later sections.

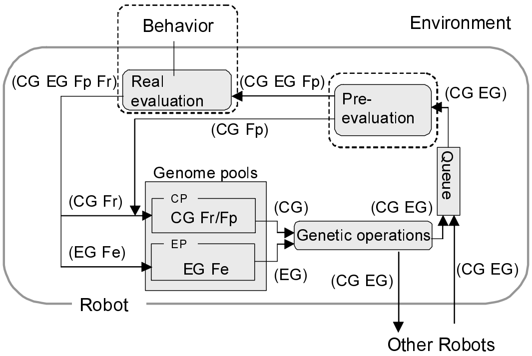

(a) The proposed architecture.

(1) Selection of a pair of CG and EG based on Fr, Fp, Fe
(2) Uniform crossover and mutation on the pair
(3) Pre-evaluation of the CG using EG (Fp is obtained)
(4) If Fp is less than T then go to (8)
(5) Robotic evaluation of CG (Fr is obtained)
(6) CG accompanied with Fr returns to CP
(7) Computation of Fe from Fp and Fr
(8) EG accompanied with Fe returns to EP
(9) Go to (1)

(b) The loop of the architecture.

CG: Controller Genome
EG: Environment Genome
CP: Controller Pool
EP: Environment Pool
Fr: Fitness of the CG based on robotic evaluation
Fp: Fitness of the CG based on pre-evaluation
Fe: The tness of EP (Agreement rate between Fr and Fp)
T: Threshold value for bypassing the robotic evaluation

Figure 1: A framework for embodied evolution with pre-evaluation.

3 Implementation

We compared the original EE method with the one with pre-evaluation. We adopted two methods for pre-evaluation: A pre-defined function with parameters is optimized (PE1) and a neural network is optimized (PE2) both by evolution. The latter has a larger search space of pre-evaluation. We used a humanoid robot with two four-degree-of-freedom arms and two six-degree-of-freedom legs (HRP-2m Choromet), and biped walking was evolved. Walking distance was measured by using built-in power sensors and used as a fitness value.

Fig. 2 shows walking pattern for the biped robot. N was the walk count constituting one trial (walking pattern). The trajectory of legs was generated by a cosine function. $a(0 \leq a \leq 0\ 05)[m]$ represents the length of the movement of the center of gravity by inclining the legs to the left or right, $c(0 \leq c \leq 0\ 05)[m]$ represents the length of the movement of the

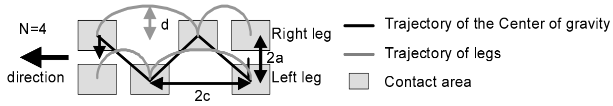

Figure 2: The following sequence constitutes a trial ($N = 4$): 1) Both legs are parallel with half-sitting (state 0), 2) Move center of gravity to the left by inclining the legs, 3) Move right leg to the front (action 1), 4) Move center of gravity to the right-front by inclining the legs (action 2), 5) Move left leg to the front, 6) Move center of gravity to the left-front by inclining the legs, 7) (action 1), 8) (action 2), 9) Move left leg to the front , 10) (state 0).

center of gravity by moving the legs to the front, and $d(0 \leq d \leq 0\ 02)[m]$ represents the height to which legs are raised. Each CG is composed of these three parameters.

F_r was calculated as follows: $F_r = c\sum_{i=1}^{N} Z_i$, where Z_i was the value output from the built-in power sensors.

When adopting PE1, the pre-evaluation value was calculated as follows:

$$F_p = crP_a^{a_1} P_c^{c_1} P_d^{d_1} \quad (1)$$

$$P_a = a'(a \quad a_2)^2 + 1 \quad (2)$$

$$a' = \begin{cases} 1 \ a_2^2 & (a_2 \quad a_{max} \ 2) \\ 1 \ (a_{max} \quad a_2)^2 & (a_2 < a_{max} \ 2) \end{cases} \quad (3)$$

$$P_c = c'(c \quad c_2)^2 + 1 \quad (4)$$

$$c' = \begin{cases} 1 \ c_2^2 & (c_2 \quad c_{max} \ 2) \\ 1 \ (c_{max} \quad c_2)^2 & (c_2 < c_{max} \ 2) \end{cases} \quad (5)$$

$$P_d = d'(d \quad d_2)^2 + 1 \quad (6)$$

$$d' = \begin{cases} 1 \ d_2^2 & (d_2 \quad d_{max} \ 2) \\ 1 \ (d_{max} \quad d_2)^2 & (d_2 < d_{max} \ 2) \end{cases} \quad (7)$$

in which a_1, a_2, c_1, c_2, d_1, d_2, and r were the genes in EG with initial values of 3, 0.03, 3, 0.05, 3, 0.015, and 18000, respectively, and the upper limits of a, c and d are represented as a_{max}, c_{max} and d_{max}, respectively. This function represents a fitness landscape in which when each value moves from the optimal value, the function value decreases rapidly (which corresponds to the increase in the number of falling down). The mutation rate was set to 0.3.

When adopting PE2, the neural network for identifying the fitness function that evaluates each EG was defined as follows:

$$y_j = sig(\sum_{i=1}^{3} x_i w_{i+3(j \quad 1)} \quad \theta_j) \quad (8)$$

$$z = sig(\sum_{i=1}^{4} y_i w_{i+12} \quad \theta_5) \quad (9)$$

$$sig(x) = \frac{1}{1 + exp(\quad x)} \quad (10)$$

$\theta_1 \sim \theta_5$ were the thresholds of the neurons. The input of the neural network was $x_1 = a \ a_{max}$, $x_2 = c \ c_{max}$ and $x_3 = d \ d_{max}$, respectively and the output

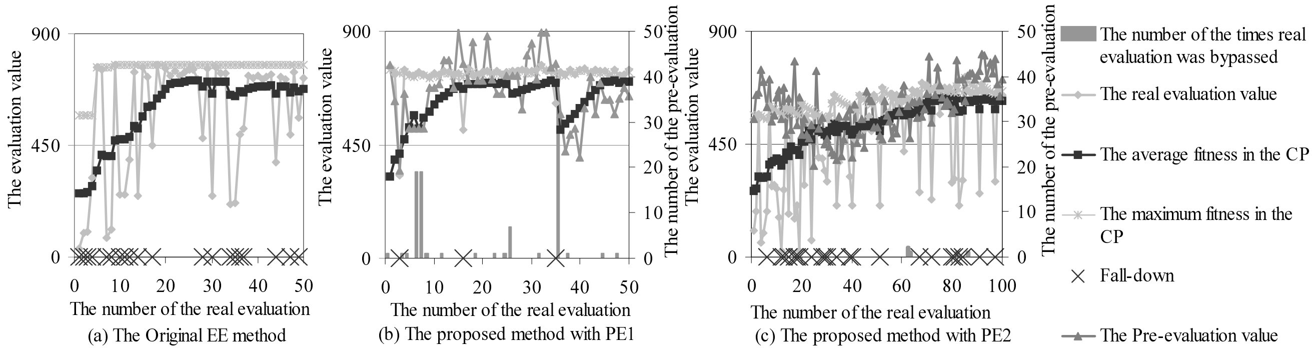

Figure 3: The index values of CG.

of it, pre-evaluation value, was $F_p = z \quad 10^3$. EG was composed of 21 weights of the neural network ($w_1 \sim w_{16}$). The initial values were set at random in the range of -1.0 to 1.0. This mutation rate was set to $0\ 7 \quad 0\ 4 \cdot \frac{\sum_{i=1}^{P} F_{ei}}{P}$ which changed according to the average value of the fitness of EG. P was the size of CP and EP.

The fitness of each EG was defined as the agreement rate between the real evaluation value and the pre-evaluation value: $F_e = \begin{cases} \frac{F_p}{F_r}(F_r \quad F_p) \\ \frac{F_r}{F_p}(F_r < F_p) \end{cases}$.

T was the threshold calculated as the average CG value times the average EG value: $T = \frac{(\sum_{i=1}^{P} F_{ri})(\sum_{i=1}^{P} F_{ei})}{P2}$. In case the pre-evaluation value was below the threshold, CG skipped the evaluation based on robot behavior and returned to CP. Some kind of deterioration was introduced in such a way that the fitness of individuals in both CP and EP decreases by $w = 1\%$ every when CG or EG returns to their pool.

4 Evaluation

We evaluated the proposed architecture applied to a biped robot, in which one of the two methods was adopted for pre-evaluation as described in the previous section: function optimization (PE1) or neural network optimization (PE2) both by coevolution. We compared them with the original EE method. In addition, we evaluated the simulate-and-transfer method for comparison. The size of CP and EP was 10. The number of initial individuals was 10 in each of CP and EP. The mutation rate was set to 0.3, and N was set to 4. $\theta_1 \sim \theta_5$ were set to 0.

Fig. 3 shows the transition of fitness in CG, real evaluation values, pre-evaluation values and the times of pre-evaluations in the case of EE (a), PE1 (b), or PE2 (c). Also, x-marks in the graph indicate the real evaluations in which the robot fell down to the ground, and in case of PE1 and PE2 each bar graph indicates the number of the times the real evaluation was bypassed according to the low pre-evaluation values.

It is shown that the average fitness in PE1 increased more rapidly in the early evaluations than the one in the EE, while the one in the PE2 increased less rapidly than the one in the EE. We observe the same tendency with the transitions of the real evaluation value, although they fluctuated significantly. The good performance of PE1 was attained by bypassing the real evaluation of the individuals whose pre-evaluation was low. However, in case of PE2, the evolution of EG is harder than the one in case of PE1, and therefore the speed of the evolution of CG was reduced.

We see that the number of falls was significantly decreased by introducing pre-evaluation in case of PE1, especially in the early evaluations (approximately from 10 to 2 in the first 20 real evaluations). This was attained also by pre-evaluation without real evaluation, which happened 25 times during the first 20 real evaluations. In case of PE2, introduction of pre-evaluation reduced the total number of falls, but the effect was far less than in case of PE1.

The pre-evaluation values moved roughly in accordance with the real evaluation values. This means the coevolution had been successfully applied in the architecture. However, they tended to be a bit larger than the real evaluation values. This is due to the unique property of the evolution of EG. There are two kinds of selection pressure. The explicit one is to increase the fitness, in other words, by definition, to decrease the difference between the real evaluation value and the pre-evaluation value. The implicit pressure is to increase the pre-evaluation value because the EG does not return to the EP when the pre-evaluation value is smaller than the threshold and thus the EG bypasses the real evaluation (Fig. 1).

Fig. 4 shows the transitions of the average and maximum fitness in EP and the fitness of EG in case of PE1 (a) and PE2 (b). Their values were relatively large even in the early stages and fluctuated significantly even in later stages. This is because the fitness of EG is not defined absolutely but relatively as the difference between the real and the pre-evaluation values.

We further evaluated a kind of the simulate-and-transfer method, in which the same simulation frame-

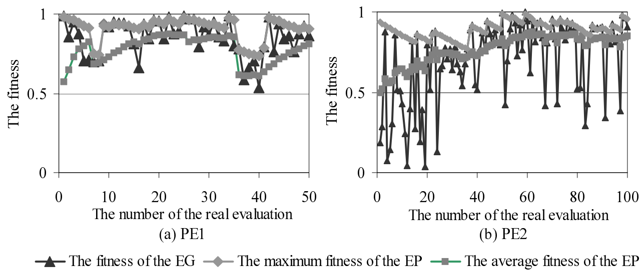

Figure 4: The fitness of EG.

work as the EE method was used except that the robotic evaluation was replaced by simulation carried out using the robotic platform OpenHRP. Table 1 shows the all of the evolved individuals (CGs) in CP after 50 evaluations. The first column shows the fitness in simulation environment. Each CG was then transferred into the robot and evaluated. The second column shows the fitness based on robotic behavior, and the third column shows whether the robot fell down to the ground or not in robotic evaluation. It is shown that nine out of ten individuals suffered from the decreased fitness caused by falling in real world. This result shows a typical gap between simulation and real world ("reality gap").

Table 1: Reality gap between simulation and real world.

Fitness (simulation)	830	814	806	797	781	769	766	751	743	735
Fitness (robotic behavior)	167	141	149	149	135	149	752	182	166	166
Falling down (With: ×, without: ○)	×	×	×	×	×	×	○	×	×	×

5 Conclusions

We introduced pre-evaluation into the embodied evolution (EE) framework for a biped robot in order to restrain robot behavior of which fitness contribution is estimated to be low, specifically falling down to the ground. We believe that the EE framework with pre-evaluation is applicable to a wide variety of optimization tasks by evolution in which the cost or risk of fitness evaluation is not negligible. We adopted two methods for pre-evaluator construction: PE1 and PE2. We comparatively evaluated the proposed architecture based on one of these two methods, the original EE, and a conventional simulate-and-transfer method.

Table 2 summarizes the characteristics of these methods based on the results of the evaluation experiments in terms of reality gap, calculation time, the cost for evaluation in real world (e.g. the risk of robot falling), and the cost of modeling or simulation. Each evaluation result is represented by the size of a circle or the thickness of a line in the table.

Table 2: The comparison between proposed method and other two methods.

	Original EE	EE with Pre-evaluation prior implementation of pre-evaluator (Min → Max)		Sim. & Trans.
		Min	Max	
Reality Gap	▪	▪		○
Calculation Time	○	○	∘	∘
Real Evaluation Cost	○	○	∘	∘
Simlulation/modeling Cost	∘	∘	○	○

The design of the evolutionary system for pre-evaluation depends on the requirements of users as described in Section 2. If we implement the evolutionary system for pre-evaluation to the utmost extent before evolution, the framework will become equal to the system with simulate-and-transfer except for the robotic evaluation of fitness. Generation of the pre-evaluator by PE1 corresponds to function optimization by evolution, and the architecture is close to the one in case of simulate-and-transfer. On the other hand, if we let the evolution generate the system for pre-evaluation to the utmost extent, each evaluation result will get closer to the case with EE. However, in this case the search space via evolution will get larger and thus the good solutions might be difficult to be obtained, as we observed the decrease in performance in case of PE2. The most important thing in implementing the proposed architecture is to consider the tradeoffs shown in this table.

Humans evaluate the behavior in advance using their internal models of the world before they actually do it. At the same time, receiving the feedback from the real world, they build and refine their internal models. It might be interesting to investigate the parallelism between the evolution of human intelligence and the evolution in the proposed architecture.

References

[1] Nolfi S, Floreano D (2000), [illegible], MIT Press.

[2] Watson R A, Ficici S G, Pollack J B (2002), Embodied Evolution: Distributing an Evolutionary Algorithm in a Population of Robots, [illegible], 39(1): 1-18.

[3] Usui Y, Arita T (2003), Situated and Embodied Evolution in Collective Evolutionary Robotics, [illegible], 212-215.

[4] Watson R A, Ficici S G, Pollack J B (1999), Embodied Evolution: Embodying an Evolutionary Algorithm in a Population of Robots, [illegible], 335-342.

The Fifteenth International Symposium on Artificial Life and Robotics 2010 (AROB 15th '10),
B-Con Plaza, Beppu,Oita, Japan, February 4-6, 2010

Efficient Flooding Method for Wireless Sensor Networks Based on Discrete Particle Swarm Optimization Computing Multiple Forwarding Nodes Sets

Junya Nagashima†, Akihide Utani‡, and Hisao Yamamoto‡

†*Graduate School of Engineering, Tokyo City University*
‡*Faculty of Knowledge Engineering, Tokyo City University*
1-28-1, Tamazutsumi, Setagaya, Tokyo 158-8557, Japan
{autani; yamahisa}@tcu.ac.jp

Abstract: In wireless sensor networks, flooding is required for the dissemination of queries and event announcements. The original flooding causes the overlap problems. In the original flooding, each sensor node receiving a broadcast message forwards it to its neighbors, resulting in a lot of collisions and duplicate messages. For dense wireless sensor networks, the impact caused by the original flooding may be overwhelming. The original flooding may result in the reduced network lifetime. Therefore, the selecting method of forwarding nodes for the dissemination of queries and event announcements is needed to prolong the lifetime of wireless sensor networks. This paper proposes a new efficient flooding method using discrete particle swarm optimization for the long-term operation of wireless sensor networks. We evaluate the proposed method using computer simulations. In simulation experiments, the performance of the proposed method is compared with those of the existing ones to verify its effectiveness.

Keywords: Query Dissemination, Efficient Flooding, Particle Swarm Optimization, Wireless Sensor Networks.

I. INTRODUCTION

A wireless sensor network, which is a key network to realize ubiquitous information environments, has attracted a significant amount of interest from many researchers [1]. In wireless sensor networks, hundreds or thousands of micro-sensor nodes, which are compact and inexpensive, are placed in a large-scale observation area and sensor information of each node is gathered to a sink node by inter-node wireless multi-hop communication. Each sensor node consists of a sensing function to measure the status (temperature, humidity, motion, etc.) of an observation point or object, a limited function on information processing, and a simplified wireless communication function, and generally operates on a resource of a limited power-supply capacity such as a battery. The suppression of communication loads is generally required for the long-term operation of wireless sensor networks.

In wireless sensor networks, flooding is required for the dissemination of queries and event announcements. The original flooding causes the overlap problems. In the original flooding, each sensor node receiving a broadcast message forwards it to its neighbors, resulting in a lot of collisions and duplicate messages. For dense wireless sensor networks, the impact caused by the original flooding may be overwhelming. The original flooding may result in the reduced network lifetime. Therefore, the selecting method of forwarding nodes for the dissemination of queries and event announcements is needed to prolong the lifetime of wireless sensor networks. The methods of [2-4] have been proposed in the existing studies to resolve or improve the overlap problems of the original flooding in disseminating queries or event data in a wireless sensor network. However, the gossiping of [2] may result in some nodes not receiving queries or event data. The existing methods of [3,4] can disseminate queries or event data to the whole nodes in a wireless sensor network, but can not select a most efficient and optimum forwarding nodes set for the dissemination.

This paper proposes a new efficient flooding method using discrete particle swarm optimization for the long-term operation of wireless sensor networks. The rest of this paper is organized as follows. In Section II, the proposed method is described. In Section III, the results of simulation experiments are reported, and the effectiveness of the proposed method is demonstrated by comparing the performance of it with those of the existing ones. Finally, the paper closes with conclusions and ideas for further research in Section IV.

II. PROPOSED METHOD

In this paper, a new efficient flooding method using Discrete Particle Swarm Optimization (DPSO), which detects not only an optimum forwarding nodes set but also multiple forwarding nodes sets, is proposed. By disseminating queries or event data over switching the selected forwarding nodes sets, the lifetime of wireless sensor networks can be extended. In this section, the

PSO method is first outlined. Then, the proposed method based on DPSO is described.

1. Particle Swarm Optimization

The PSO method belongs to the category of swarm intelligence methods. It was developed and first introduced as a stochastic optimization algorithm [5]. Currently, the PSO method is intensively researched because it is superior to the other algorithms on many difficult optimization problems [6-10]. The ideas that underlie the PSO method are inspired not by the evolutionary mechanisms encountered in natural selection, but rather by the social behavior of flocking organisms, such as swarms of birds and fish schools. The PSO method is a population-based algorithm that exploits a population of individuals to probe promising regions of the search space. In this context, the population is called a *swarm* and the individuals are called *particles*. In the PSO method, a multidimensional solution space by sharing information between a swarm of particles is efficiently searched. The algorithm is simple and allows unconditional application to various optimization problems.

Assume an n-dimensional search space S, and a swarm consisting of N particles. Each particle (The i th particle) has a position vector

$$\boldsymbol{x}_i = (x_{i1}, x_{i2}, \ldots, x_{in})^{\mathsf{T}} \in S,$$

and the velocity vector

$$\boldsymbol{v}_i = (v_{i1}, v_{i2}, \ldots, v_{in})^{\mathsf{T}} \in S,$$

where the subscript i ($i = 1, \ldots, N$) represents the particle's index. In addition, each particle retains the position vector $\boldsymbol{pbest}_i$ of the best evaluation value found by the particle in the search process and the evaluation value $f(\boldsymbol{pbest}_i)$, and also the position vector $\boldsymbol{gbest}$ of the best evaluation value among all particles and the evaluation value $f(\boldsymbol{gbest})$ as information shared in the swarm in the search process.

In the PSO method, each particle produces a new velocity vector $\boldsymbol{v}_i^{k+1}$ by linearly coupling the best solution [$\boldsymbol{pbest}_i^k$] found by the particle in the past, the best solution [$\boldsymbol{gbest}^k$] shared in the swarm, and the previous velocity vector $\boldsymbol{v}_i^k$ and moves to the next position $\boldsymbol{x}_i^{k+1}$, where the superscript k indicates the number of search iterations. At the k+1 search, the velocity vector $\boldsymbol{v}_i^{k+1}$ and the position vector $\boldsymbol{x}_i^{k+1}$ of the i th particle is updated by the following equations:

$$\begin{aligned}\boldsymbol{v}_i^{k+1} &= \omega \cdot \boldsymbol{v}_i^k + c_1 \cdot r_1 \cdot (\boldsymbol{pbest}_i^k - \boldsymbol{x}_i^k) \\ &\quad + c_2 \cdot r_2 \cdot (\boldsymbol{gbest}^k - \boldsymbol{x}_i^k) \\ \boldsymbol{x}_i^{k+1} &= \boldsymbol{x}_i^k + \boldsymbol{v}_i^{k+1}\end{aligned} \qquad (1)$$

where r_1 and r_2 are random numbers, uniformly distributed within the interval [0,1]. ω is a parameter called the *inertia weight*, and c_1, c_2 are positive constants, referred to as *cognitive* and *social* parameters, respectively. The settings of ω, c_1, c_2 of the terms affect the performance of the PSO method. An alternative version of the PSO method is denoted in [7].

2. Proposed Method Based on DPSO

The DPSO method, which is a discrete binary version of the PSO method, is a promising method proposed for combination optimization problems, where the search process of the DPSO method complies with that of the PSO method [11]. In the DPSO method, each element of the position vector is transformed in {0,1} according to the following rule:

$$\begin{aligned}&\text{if } \rho < sig(v_{id}^{k+1}) \quad \text{then} \quad x_{id}^{k+1} = 1; \\ &\qquad\qquad\qquad\qquad\; \text{else} \quad x_{id}^{k+1} = 0\end{aligned} \qquad (2)$$

$$sig(v_{id}^{k+1}) = \frac{1}{1 + \exp(-v_{id}^{k+1})} \qquad (3)$$

where ρ is a quasirandom number selected from a uniform distribution in [0,1].

In this study, a general wireless sensor network consisting of static sensor nodes placed in an object area is assumed. At the initial stage of the network, the sink node set requests the topology information from every sensor node by broadcasting a Topology Discovery Message (TDM) to the network by using the original flooding. Each sensor node receiving the TDM sends a Topology Response Message (TRM) with the local topology information of the sensor node, such as the number of neighbor nodes and the list of neighbor node IDs, to the sink node. The sink node constructs the network topology information from the gathered TRMs. The proposed method searches multiple forwarding nodes sets based on the constructed network topology information.

By the repetitive searches based on the DSPO method, multiple forwarding nodes sets are computed. In order to detect different forwarding nodes sets, the following rule corresponding to the above (2) is introduced:

$$\begin{aligned}&\text{if } \rho < sig(v_{id}^{k+1}) \times s_r \quad \text{then} \quad x_{id}^{k+1} = 1; \\ &\qquad\qquad\qquad\qquad\qquad\; \text{else} \quad x_{id}^{k+1} = 0\end{aligned} \qquad (4)$$

where s_r is a constant determined in the interval [0,1], named the *suppression* parameter.

In the first search, the *suppression* parameter (s_r) is set to 1.0 and the search by the ordinary DPSO method is executed. On and after the second search, multiple forwarding nodes sets can be effectively computed by the *suppression* parameter (s_r) set in (0,1). In case that s_r is set to 0.0, perfectly different multiple forwarding nodes sets can be searched.

To detect the optimum forwarding nodes set for disseminating queries or event data to the whole nodes in a network, the objective function is set as follows:

$$\max. \quad f(n_{forward}, n_{receive}) = \frac{s^{-(n_{total} - n_{receive})}}{n_{forward}} \qquad (5)$$

where $n_{receive}$ and $n_{forward}$ represent the number of nodes receiving data and the number of forwarding nodes selected, respectively. n_{total} is the number of the whole nodes in a network.

III. EXPERIMENTAL RESULTS

Through the experiments, the performance of the proposed method is investigated to verify its effectiveness. The conditions of simulation and the values on DPSO parameters, which were used in the experiments performed, are shown in Table 1, where the selected values on DPSO parameters are considered proper default values and they are used in the relevant literature on the DPSO method. In Figure 1, an optimum forwarding nodes set is shown, where static sensor nodes are randomly arranged in the set experimental area.

Table1. Conditions of simulations and settings on DPSO parameters

Simulation size	$100m \times 100m$
The number of sensor nodes	73
Range of radio wave	$25m$
The number of particle	30
Cognitive parameter c_1	2.1
Social parameter c_2	0.8
Inertia weight ω	1.0

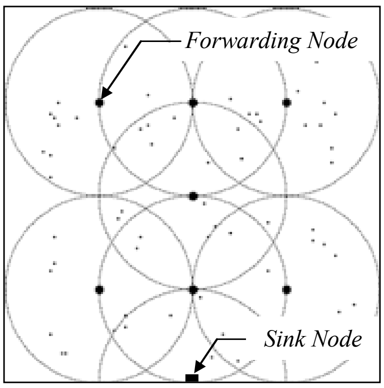

Fig.1. Simulation model

In the experimental results reported, the proposed method is evaluated through the comparison with the existing ones of [3,4] and based on Genetic Algorithm. On the method based on Genetic Algorithm, the parameter settings that were used in [4] and produced good results in a preliminary investigation were adopted for the comparison with the proposed method.

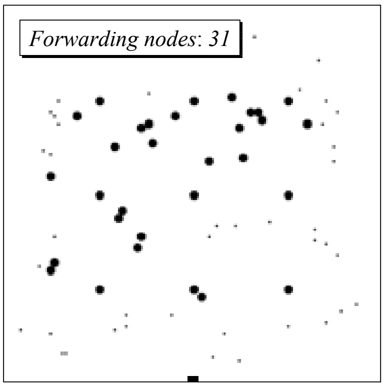

(a) Results by the method of [3]

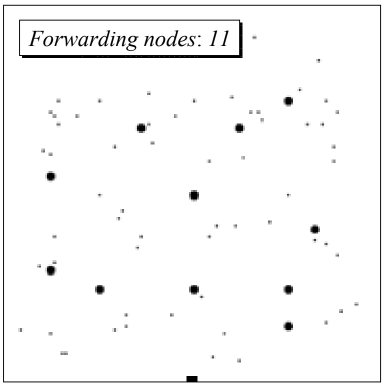

(b) Results by the method of [4]

Fig.2. Forwarding nodes set computed by using the methods of [3,4]

Table2. The number of selected forwarding nodes

	Greedy	*IUA*	*GA*	*Proposal*
The number of selected forwarding nodes	31	11	11	7

In Figure 2, a forwarding nodes set computed by using the methods of [3,4] is shown. The number of forwarding nodes selected by each method is reported in Table 2. In this table, two methods of [3] and [4] are denoted as *Greedy* and *IUA*, respectively. The method based on Genetic Algorithm is denoted as *GA*. The result on the proposed method is that obtained by the first search. From the results of Figure 2 and table 2, it is confirmed that the existing methods can not detect an optimum forwarding nodes set.

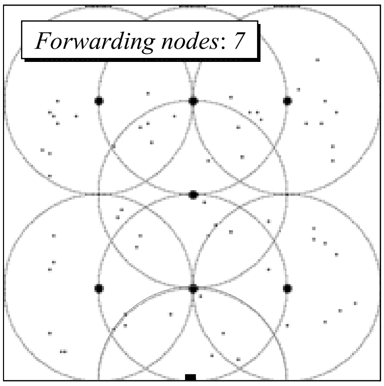

(a) The first search

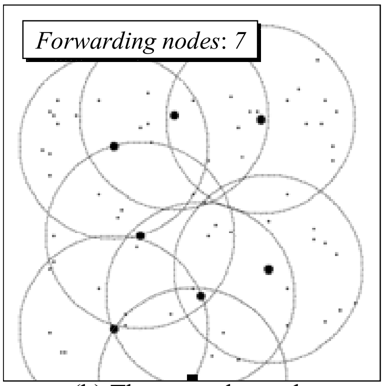

(b) The second search

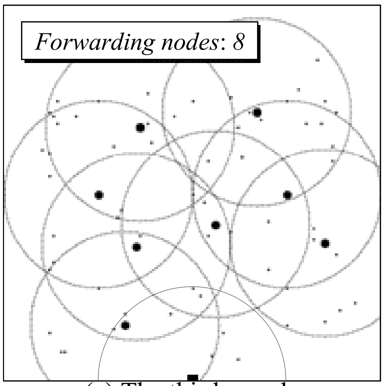

(c) The third search

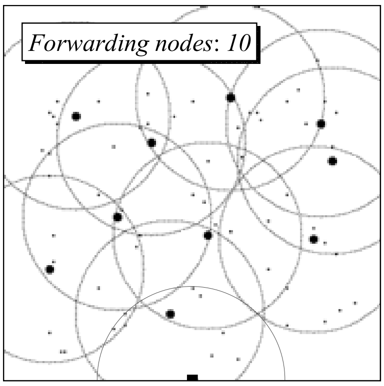

(d) The fourth search

Fig.3. Forwarding nodes computed by the proposal

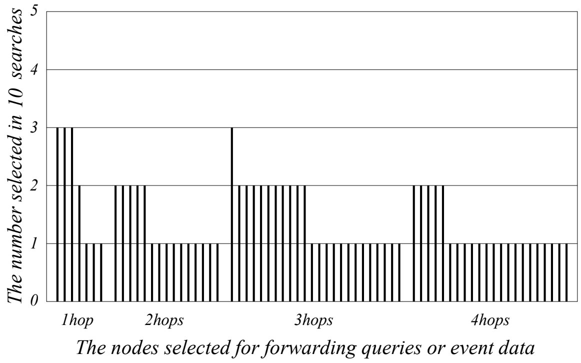

(a) $s_r = 0.2$

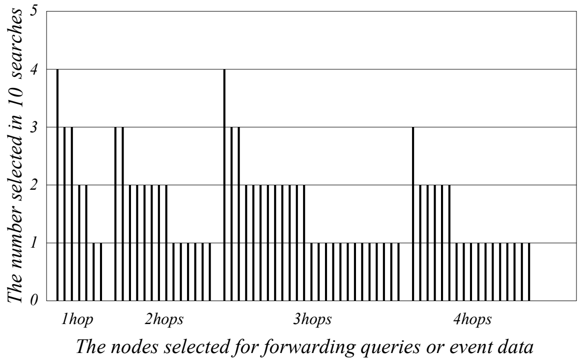

(b) $s_r = 0.4$

Fig.4. The number selected as forwarding nodes in a total of 10 searches

Forwarding nodes sets computed by using the proposed method are illustrated in Figure 3. On the result of Figure 3, the *suppression* parameter (s_r) is set to 0.0. By the proposed method, perfectly different four forwarding nodes sets that include two optimum forwarding nodes sets are detected. The proposed method is a promising one selecting forwarding nodes for the dissemination of queries and event announcements. In Figure 4, the number selected in a total of 10 searches of the nodes selected for forwarding queries or event data by the proposed method are shown. From the result of Figure 4, it is considered that the nodes selected as forwarding ones are limited to some ones as the set value of the *suppression* parameter (s_r) is great.

IV. CONCLUSIONS

In this paper, a new efficient flooding method using discrete particle swarm optimization for the long-term operation of wireless sensor networks, which computes multiple forwarding nodes sets for disseminating queries and event announcements to the whole nodes in a wireless sensor network, has been proposed. Experimental results indicate that the proposed method has the development potential as an efficient flooding method for wireless sensor networks. In future studies, we want to execute the detailed evaluation on the parameter added to the proposed method, and on various network sizes and node density.

REFERENCES

[1] Akyildiz I, Su W, Sankarasubramaniam Y, and Cayirci E (2002), Wireless sensor networks: A survey. Computer Networks Journal 38(4):393-422

[2] Lin MJ, Marzullo K, and Masini S (2000), Gossip versus deterministic flooding: Low message overhead and high reliability for broadcasting on small networks. DISC, pp.253-267

[3] Adjih C, Jacquet P, and Viennot L (2002), Computing connected dominated sets with multipoint relays. Technical Report 4597, INRIA:1-16

[4] Nagashima J, Utani A, and Yamamoto H (2009), A study on efficient flooding in wireless sensor networks. IEICE Technical Report 108(443):49-52

[5] Kennedy J and Eberhart RC (1995), Particle swarm optimization. Proc. IEEE Int. Conf. on Neural Networks, pp.1942-1948

[6] Eberhart RC and Shi Y (2001), Tracking and optimizing dynamic systems with particle swarms. Proc. 2001 IEEE Congr. Evolutionary Computation, pp.94-100

[7] Clerc M and Kennedy J (2002), The particle swarm-explosion, stability, and convergence in a multidimensional complex space. IEEE Trans. Evol. Comput. 6(1): 58-73

[8] Shen M and Tsai Y (2008), CPW-fed monopole antenna characterized by using particle swarm optimization incorporating decomposed objective functions. Int. J. Innovative Computing, Information and Control 4(8): 1897-1919

[9] Zhang Q, Zhang R, and Wang B (2009), DNA sequence sets design by particle swarm optimization algorithm. Int. J. Innovative Computing, Information and Control 5(8):2249-2255

[10] Kumamoto A, Utani A, and Yamamoto H (2009), Advanced particle swarm optimization for computing plural acceptable solutions. Int. J. Innovative Computing, Information and Control 5(11) (to appear)

[11] Kennedy J and Eberhart RC (1997), A discrete binary version of the particle swarm algorithm. Proc. IEEE Int. Conf. on Systems, Man and Cybernetics, pp.4104-4108

The Fifteenth International Symposium on Artificial Life and Robotics 2010 (AROB 15th '10),
B-Con Plaza, Beppu,Oita, Japan, February 4-6, 2010

Fixed Column Primer for Boolean Matrix Multiplication with DNA Computing

N. Rajaee [1], H. Aoyagi[1] and O. Ono [1]

[1]*Institute of Applied DNA Computing, Meiji University*
1-1-1 Higashimita, Tamaku, Kawasaki, Kanagawa, 214-8571 Japan
[1] (nrajaee, ce77002 ,ono)@isc.meiji.ac.jp

Abstract: In our previous work, we implemented an in vitro Boolean matrix multiplication with DNA computing. However, with the increase in the problem size, we realize the material consumption and experimental work required to compute the problem with DNA increases drastically. Thus in this paper, we modify our previous algorithm to reduce the material consumption and the labour intensiveness of the computation.

Keywords: DNA Computing, Boolean Matrix Multiplication, Parallel Overlap Assembly

I. INTRODUCTION

Using DNA for computation has gathered interest in many fields of application due to its massive parallel processing capability. With high density and low energy dispersion, DNA can compute up to 10^{14} maximum operation per second in a single test tube [1]. Such characteristics of DNA computing made it an alternative for solving NP hard problems which require brute force in traditional computing. However, several drawbacks of DNA computing became obvious after its implementation in laboratory works – one of which is the exponential growth of DNA volume required to solve a problem according to its problem size.

In our previous work, we represented the matrix multiplication problem as a directed graph problem and synthesize DNA oligonucleotides to represent the vertices and edges in the graph. However, it shows that for a larger N×N Boolean matrix multiplication with DNA, the volume of the DNA increases and the number of experimental work becomes tedious and impractical to be considered as a viable technology [2,3]. Thus, in this paper we propose a strategy to reduce the experimental protocols and the material consumption for solving a larger set of Boolean matrix multiplication with DNA computing by using a fixed primer to represent the whole set of row indicators for the product matrix.

II. BOOLEAN MATRIX MULTIPLICATION

Boolean matrix multiplication is a fundamental operation that is used in many scientific areas of research such as linear algebra, signal processing, digital control and graph theory.

Consider a binary matrix Y with dimension $m \times n$. Matrix $Y=A\cdot B$ can be represented as a product of two matrices A and B with dimensions $m \times k$ and $k \times n$ respectively. Two Boolean matrices and its product can further be represented by a graph problem [Kim]. The row indicators for the first matrix A and the product matrix Y are represented as initial vertices; the column indicators for the second matrix B and the product matrix Y are represented as terminal vertices; and the column indicators for the first matrix A and the row indicators for the second matrix B are represented as intermediate vertices. For all elements of value 1 in the matrices A and B, a directed edge is drawn for the corresponding initial vertex-intermediate vertex or intermediate vertex-terminal vertex intersections. Elements of value 1 in the product matrix Y is determined by the existence of a "path" which is a continuous linkage of directed edges from an initial vertex to a terminal vertex.

III. COMPUTING BOOLEAN MATRICES WITH DNA

In our previous work, we implemented a Boolean matrix multiplication problem with DNA computing. Let two Boolean matrices A and B and its multiplication product Y, be represented by a graph problem G. We implemented the matrix multiplication problem with a 5 step algorithm:

(Step1) Sequence designs for V and E in G.
(Step2) Generate an initial pool.
(Step3) Determine Primers for Filtering.

(Step 4) Remove unwanted strands/Mass Copying.
(Step 5) Identify strands.

Basic bio-molecular tools used for the computation are briefly discussed as follows:
Parallel Overlap Assembly (POA) is used to generate an initial pool containing all possible solutions to the problem. *Polymerase Chain Reaction* (PCR) is a technique which uses a pair of DNA sequences known as "primers" to signal the start point and end point for a specific DNA sequence for mass amplification. *Gel electrophoresis* is used to identify the results.

We generate randomly unique single stranded DNA sequences to represent all vertices in graph *G*. The DNA sequences for directed edges are designed to be connector strands from an initial vertex to an intermediate vertex or from an intermediate vertex to a terminal vertex. The primers for filtering are determined from the row and column indicators for the product matrix Y to amplify only "path" strands during the mass copying. The elements in the product matrix are represented by test tubes containing primer combinations for each row and column. The value of the elements in the product matrix is identified from the constructed solution "paths" viewed in the gel electrophoresis process which yield highlighted bands for amplified "path" strands.

Computation of Boolean matrix multiplication with DNA normally requires an $m + n$ number of primers to be used as row and column indicators in the product matrix; and an m x n number of test tubes to represent all the elements in the product matrix. Thus, for a 10 ×10 product matrix, a total of 20 primers are used to represent the row and column indicators; and a 100 test tubes are needed to represent all elements in the product matrix.

	a – j									
A1	1	0	0	0	0	0	0	0	0	0
A2	0	0	0	1	0	0	1	0	0	0
A3	0	0	0	0	0	0	0	0	1	0
A4	0	1	0	0	0	0	0	0	0	0
A5	0	0	0	0	0	1	0	0	0	0
A6	0	0	0	0	0	0	0	1	0	0
A7	0	0	0	0	1	0	0	0	0	0
A8	0	0	1	0	0	0	0	0	0	0
A9	0	0	0	0	0	0	0	0	0	1
A10	0	0	0	1	0	0	0	0	0	0

X

	B1 – B10									
a	0	0	0	0	0	0	0	0	0	1
b	0	1	0	0	0	0	0	0	0	0
c	0	0	1	0	0	0	0	0	0	0
d	1	0	0	0	0	0	0	0	0	0
e	0	0	0	0	0	0	0	0	1	0
f	0	0	0	0	0	0	0	1	0	0
g	0	0	0	1	0	0	0	0	0	0
h	0	0	0	0	0	1	0	0	0	0
i	0	0	0	0	1	0	0	0	0	0
j	0	0	0	0	0	0	1	0	0	0

=

	B1	B2	B3	B4	B5	B6	B7	B8	B9	B10
A1	0	0	0	0	0	0	0	0	0	1
A2	1	0	0	1	0	0	0	0	0	0
A3	0	0	0	0	1	0	0	0	0	0
A4	0	1	0	0	0	0	0	0	0	0
A5	0	0	0	0	0	0	0	1	0	0
A6	0	0	0	0	0	1	0	0	0	0
A7	0	0	0	0	0	0	0	0	1	0
A8	0	0	1	0	0	0	0	0	0	0
A9	0	0	0	0	0	0	1	0	0	0
A10	1	0	0	0	0	0	0	0	0	0

Fig. 1 Two 10 x 10 matrices and its product

IV. FIXED COLUMN PRIMER

We consider a matrix problem in Figure 1. The main concept of a fixed column primer is to represent the whole set of row indicators with a fixed starting strand sequence. Instead of *10* different primer sequences as row indicators, the whole column for initial vertices is represented by one common primer sequence ($m = 1$). The individual rows are distinguished from each other by manipulating the different lengths for each initial vertex, to allow each element in the product matrix arrive at different path lengths, respective to only the corresponding row.

	(10-mer)		(20-mer)	(20-mer) B1	B2	B3	B4	B5	B6	B7	B8	B9	B10
A1	A	10	a	0	0	0	0	0	0	0	0	0	60
A2	A	20	b	70	0	0	70	0	0	0	0	0	0
A3	A	30	c	0	0	0	0	80	0	0	0	0	0
A4	A	40	d	0	90	0	0	0	0	0	0	0	0
A5	A	50	e	0	0	0	0	0	0	0	100	0	0
A6	A	60	f	0	0	0	0	0	110	0	0	0	0
A7	A	70	g	0	0	0	0	0	0	0	0	120	0
A8	A	80	h	0	0	130	0	0	0	0	0	0	0
A9	A	90	i	0	0	0	0	0	0	140	0	0	0
A10	A	100	j	150	0	0	0	0	0	0	0	0	0

Fig. 2 Fixed Column Primer for Initial Vertices

Figure 2 shows all strands for the initial vertices sharing a common 10-mer fixed column primer sequence A. Each row indicator is then varied in their lengths to retain their separate row distinctiveness. With a fixed column primer, only an $m + n$ primer and n test tubes are necessary to compute the Boolean matrix multiplication. In this case, primers required for row indicators in Figure 2 is an $m = 1$ and for column indicators is $n = 10$. This drastically reduces the total number of primers to $m + n = 11$. Since the fixed column primer is shared by the row indicators and the detection of path is dependent on the number of primer combinations, elements in the product matrix can be verified with only 1 x n test tubes. Hence, a total of only 10 test tubes are sufficient. This drastically reduces the experimental steps needed to identify the elements in the product matrix.

The elements in the product matrix are verified by DNA sequence lengths in each column. An element in a product matrix is defined by its total length:

Total Length (path) = *fixed column primer*
\+ *additional sequence for initial vertex*
\+ *intermediate vertex*
\+ *terminal vertex*

V. DESIGN AND SYNTHESIS

We implemented a (3x3) x (3x3) Boolean matrix multiplication as in Figure 3 with a fixed column primer.

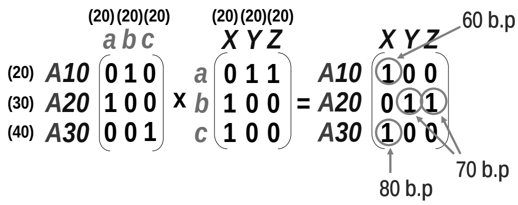

Fig. 3 (3x3) x (3x3) Boolean Matrix Multiplication

A 10-mer DNA sequence "`tccccgttcc`" is embedded in all three initial vertex sequences A10, A20, A30. Additional unique sequences are constructed to distinguish the vertices with varied lengths of 20-mer, 30-mer and 40-mer respectively. Intermediate vertices and terminal vertices are set at 20-mer each.

A*-10** ***TCCCCGTTCC **tattcgccta (20 mer)**
A*-20** ***TCCCCGTTCC **acctcggttaaggaagtacg (30 mer)**
A*-30** ***TCCCCGTTCC **ccctcttttaagcaagtaatgtactatgcg (40 mer)**

Fig. 4 Fixed column primer sequences for Initial Vertices

The DNA sequences for all vertices are shown in Table I and the DNA sequences for the edges are shown in Table II.

TABLE I
DNA SEQUENCES FOR VERTICES WITH FIXED COLUMN

Vertex	DNA Sequence (5' – 3')	Length (mer)
A10	tccccgttcctattcgccta	20
A20	tccccgttccacctcggttaaggaagtacg	30
A30	tccccgttccccctcttttaagcaagtaatgtactatgcg	40
a	tcaagcatcgggtcgcaact	20
b	cctatccacggcttggggtc	20
B1	ccaacgagggtgtattccgc	20
B2	ctcagtgccgaaccttgcct	20
B3	aggacatacagaggcgggca	20

TABLE II
DNA SEQUENCES FOR DIRECTED EDGES

Edges	DNA Sequence (5' – 3')	Length (mer)
A10a	cgatgcttgataggcgaata	20
A20b	cgtggataggcgtacttcct	20
A30a	cgatgcttgacgcatagtac	20
aB1	ccctcgttggagttgcgacc	20
bB2	cggcactgaggaccccaagc	20
bB3	tgtatgtcctgaccccaagc	20

VI. EXPERIMENT

All synthesized DNA sequences for vertices and edges are poured together into a single T0. Parallel Overlap Assembly method is used to generate an initial pool containing all possible solution to the problem. The initial pool generation is performed in a solution containing 67.5µl ddH20 (Maxim Biotech), 1µl for every DNA strand (oligo) (Proligo Primers & Probes), 10µl of dNTP (TOYOBO, Japan), 10µl KOD dash buffer (TOYOBO, Japan) and 0.5µl KOD dash (TOYOBO, Japan). The solution is run for 25 cycles with the first stage of 90ºC for 30 seconds, second stage of 55ºC for 30 seconds and third stage of 74ºC for 10 seconds per cycle. At the end of the POA cycles, the strands for "paths" are formed.

PCR is conducted for all test tubes in Table III, each containing 13.875µl ddH20 (Maxim Biotech), 1µl of template DNA from POA process, 2.5µl of dNTP (TOYOBO, Japan), 2.5µl KOD dash buffer (TOYOBO, Japan) and 0.125µl KOD dash (TOYOBO, Japan) and 2.5 µl of each primer combination. The solutions are spun for 13000 rpm in 25 ºC for 5 minutes before running them for 25 cycles with the first stage of 90ºC for 30 seconds, second stage of 55ºC for 30 seconds and third stage of 74ºC for 10 seconds per cycle.

VII. RESULTS AND DISCUSSIONS

The experimental results are shown in Figure 4.

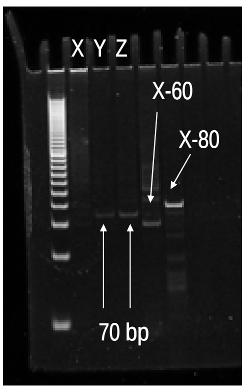

Paths:

A10 → b → X = 60 b.p.
(20) (20) (20)

A20 → a → Y = 70 b.p.
(30) (20) (20)

A20 → a → Z = 70 b.p.
(30) (20) (20)

A30 → c → X = 80 b.p.
(40) (20) (20)

Fig. 4 Results from Gel Electrophoresis

The lanes for each test tube representing the columns X, Y and Z show the read-outputs for the Boolean matrix computation. From the results, lanes for column Y and Z yield 70 b.p. highlighted bands which are consistent with our predicted outcomes. However, the lane for column X is devoid of such highlighted band. We conduct a second PCR to confirm whether the predicted 60 b.p. and 80 b.p. length paths exist for the column X and the results are successful. Both lanes for X-60 and X-80 yield highlighted bands.

The primer A has no problem identifying and amplifying all strands with the defined starting sequences. However, the non-existence of highlighted bands for 60 b.p and 80 b.p in lane X when the paths of 60 b.p and 80 b.p actually exist indicates a problem in Step 4. While the mass amplification works successfully for identification of one type of path strand in a tube (Y and Z), it was less successful in amplifying more than one path in a tube (X).

Another problem with using the fixed column primer algorithm is the restriction of length for initial vertex sequence strands. While in theory, the length of the initial vertex sequence is varied to retain the rows distinctiveness, in actual there is a practical limit to the length of vertex sequence for effective construction of path. Generated DNA sequence strands longer than 80 b.p immediately increase in its melting temperature with some strands having ≥ 100°C. This will cause a problem in the processes employed to implement Step2 and Step4 which have three temperature stages. Vast differences in melting temperatures between the shorter and longer strands will cause the strands with higher melting temperature to not anneal when the shorter strands with lower melting temperature do. Similarly, the shorter strands with lower melting temperature will not denature when the longer strands do which leads to mishybridizations and incomplete paths.

Proper design of oligonucleotides is important for a successful implementation in DNA computing. Hybridizations between DNA molecules work as an information carrier that executes the computation. Therefore, mishybridizations such as based mismatches, shifted hybridizations, and hairpin formations can lead to fatal errors during the implementation steps. While both careful encoding and external reaction conditions such as salt and temperature can be adjusted to minimize errors, some mishybridizations are due to occur as the implementation of DNA computing is a wet-lab process than is unstable. Therefore, realistic precautions and problem anticipation must be taken into account while designing the sequences for computation.

VIII. CONCLUSIONS

We proposed a fixed column primer to reduce the material consumption and experimental works for computing Boolean matrix multiplication with DNA computing. The results successfully yield predicted outcomes of constructed path but the extraction process is less effective.

ACKNOWLEDGEMENT

The first author would like to thank University Malaysia Sarawak and Ministry of Higher Education Malaysia for supporting the study leave.

REFERENCES

[1] R. Deaton, M. Garzon, J. Rose, D.R Franceschetti and S.E Stevens Jr, "DNA Computing: A Review", Funfamenta Informaticae, IOS Press, Vol 30, pp. 23-41, 1997
[2] N. Rajaee, Y. Kon, K. Yabe and O. Ono, Matrix multiplication with DNA based computing: a comparison study between hybridization-ligation and parallel overlap assembly, Proc. of the 4th IEEE International Conference on Natural Computation, Jinan, China, pp. 527-530, 2008.
[3] K.H Zimmerman, Efficient DNA sticker algorithm for NP-complete graph problems, Computer Physics Communications 144, pp. 297-309, 2002.
[4] L. Adleman, "Molecular computation of solutions to combinatorial problems," Science, vol. 266, 1994, pp. 1021-1024.
[5] Martyn Amos, Theoretical and Experimental DNA Computation, Natural Computing Series, Springer, 2004
[6] N. Rajaee, Y. Kon, K. Yabe and O. Ono, Matrix multiplication with DNA based computing: a comparison study between hybridization-ligation and parallel overlap assembly, Proc. of the 4th IEEE International Conference on Natural Computation, Jinan, China, pp. 527-530, 2008.
[7] R. Agrawal, F. Gustavson and M. Zubair, A high-performance matrix multiplication algorithm on a distributed memory parallel computer using overlapped communication, IBM Journal of Research and Development, vol 38, no. 6, pp 673-681, 1994.
[8] P. D. Kaplan, D.S. Thaler and A. Libchaber, Parallel overlap assembly of paths through a directed graph, Preliminary Proc. of the 3rd DIMACS Workshop on DNA based computers, Philadelphia PA, pp. 127-141、1997.
[9] R. Bakar, J. Watada and W. Pedrycz, A proximity approach to DNA based clustering analysis, International Journal of Innovative Computing, Information and Control, vol. 4, no. 5, pp. 1203-1212, 2008.

The Fifteenth International Symposium on Artificial Life and Robotics 2010 (AROB 15th '10),
B-Con Plaza, Beppu,Oita, Japan, February 4-6, 2010

Applying Soft Computing for Remote Sensing Data Composite Algorithms

Kenneth J. Mackin[1], Takashi Yamaguchi[1], Jong Geol Park[2], Eiji Nunohiro[1], Kotaro Matsushita[2], Yukio Yanagisawa[3], and Masao Igarashi[3]

[1]*Department of Information Systems, Tokyo University of Information Sciences*
4-1 Onaridai, Wakaba-ku, Chiba, Japan
(Tel : 81-43-236-1329; Fax : 81-43-236-1329)
(mackin@rsch.tuis.ac.jp)
[2]*Department of Environmental Information, Tokyo University of Information Sciences*
4-1 Onaridai, Wakaba-ku, Chiba, Japan
[3]*College of Bioresource Sciences, Nihon University*
1866 Kameino, Fujisawa, Kanagawa 252-8510, Japan

Abstract: Remote sensing of the earth surface using satellite mounted sensor data is one of the most important methods for global environmental monitoring today. However, when using satellite sensor data, clouds in the atmosphere can interfere with the remote sensing, and specific land points may not be correctly monitored on a given day. In order to overcome this problem, a common workaround is to use multiple day composite data. Multiple day composite data uses several consecutive days' remote sensing data, and picks the most accurate data within the temporal dataset for the same land point. This allows creating a more complete dataset by patching together data uninterfered with clouds during a specified time period, to create a clearer, more usable dataset. In this paper, we propose applying soft computing, namely fuzzy logic, in order to select the clearest data in the temporal interval for the composite data. Moderate resolution remote sensing data of areas in Japan were used for evaluation, and results were compared with previous composite methods.

Keywords: remote sensing, composite algorithm, MODIS, fuzzy logic

I. INTRODUCTION

Remote sensing of the earth surface using satellite mounted sensor data is one of the most important methods for global environmental monitoring today. For example, changes in land surface use can be monitored using remote sensing data. By monitoring the changes of vegetation coverage, the amount of carbon held in vegetation and how much is released into the atmosphere can be calculated.

However, when using satellite sensor data, clouds in the atmosphere can interfere with the remote sensing, and specific land points may not be correctly monitored on a given day (Fig.1). In order to overcome this problem, a common workaround is to use multiple day composite data. Multiple day composite data uses several consecutive days' remote sensing data, and picks the most accurate data within the temporal dataset for the same land point (Fig.2). This allows creating a more complete dataset by patching together data uninterfered with clouds during a specified time period, to create a clearer, more usable dataset.

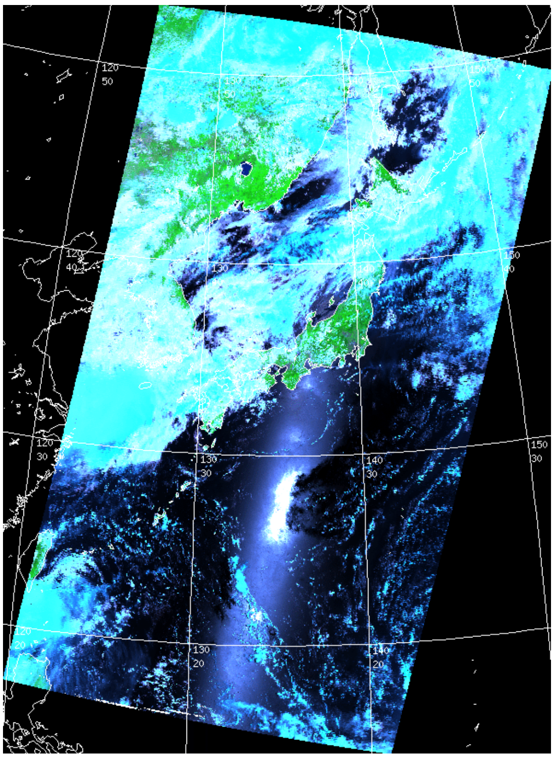

Fig.1. 1 pass of MODIS data with cloud interference

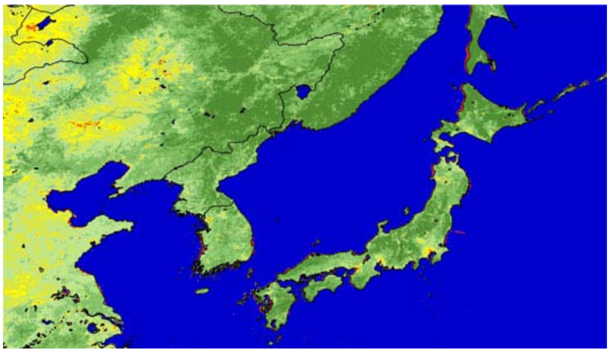

Fig.2. Monthly composite data

There have been many data composite algorithms proposed, and different methods have their merits and demerits, but all methods require tuning of parameters to achieve best accuracy for a specific region. In this paper, we propose applying a soft computing approach, namely fuzzy logic[3], in order to facilitate tuning of the data composite algorithm in order to achieve the best accuracy for a specific region. Moderate resolution remote sensing data of areas in Japan were used for evaluation, and results were compared with previous composite methods.

II. SATELLITE DATA

With the increased interest in monitoring the global ecological changes, the demand for satellite remote sensing has increased. NASA-centered international Earth Observing System project has launched many satellites to monitor the earth for scientific purposes, including Terra and Aqua.

A key instrument aboard the Terra and Aqua satellites is MODIS (Moderate Resolution Imaging Spectroradiometer). Terra's orbit around the Earth is timed so that it passes from north to south across the equator in the morning, while Aqua passes south to north over the equator in the afternoon. Terra MODIS and Aqua MODIS enable the viewing of the entire Earth's surface every 1 to 2 days. MODIS captures data in 36 spectral bands, or groups of wavelengths. Moderate resolution remote sensing allows the quantifying of land surface type and extent, which can be used to monitor changes in land cover and land use for extended periods of time. This data is used to monitor and understand global dynamics and processes occurring on the land, oceans, and lower atmosphere.

For this paper, we used MODIS data collected at Tokyo University of Information Sciences (TUIS), Japan. TUIS receives satellite MODIS data over eastern Asia, and provides this data for open research use.

III. COMPOSITE ALGORITHM

There have been many different satellite data composite algorithms proposed [1][2], and each method have different merits depending on the target usage. Different composite methods include 1) MVC (maximum value composition) using maximum NDVI (normalized difference vegetation index), 2) MVC using maximum temperature reflectance, 3) minimum scan angle with high NDVI, 4) minimum scan angle with high NDVI and temperature reflectance, 5) minimum blue reflectance with high NDVI.

In this research, we use MODIS sensors satellite data for evaluation of the composite algorithms.

The MODIS data is a raster format image file where each pixel of the image is the reflectance value of a specific bandwidth for the location. MODIS sensor data contains 36 different bands, including visible red (band 1), near infra-red (band 2). MODIS has sensors in 3 different spatial resolutions, $250m^2$ resolution (band 1-2), $500m^2$ resolution (band 3-7), $1km^2$ resolution (band 8-36), so each pixel data will be the average reflectance value for the location in the specified spatial resolution.

NDVI is a standard vegetation index defined by the following equation,

$$NDVI = \frac{NIR - R}{NIR + R} \tag{1}$$

where R is band 1 (visible red) reflectance value, and NIR is band 2 (near infra red) reflectance value for the given location.

NDVI reflects the growth of vegetation, so for a given temporal interval the value is not expected to change drastically. It is also known that NDVI values become lower when clouds in the atmosphere interfere with the reflection. MVC with NDVI takes into account these 2 assumptions, and selects the highest NDVI value within a set temporal interval for the same location, to pick the best cloud-free data for the location within the temporal interval.

To create a 10-day composite image, assuming there is 1 MODIS reading every day for a total of 10 files, the maximum NDVI value is selected from the 10 different MODIS readings for the exact same location. The maximum NDVI marks the best cloud-free data for the temporal interval for the location, and the reading is copied to the composite image file for the same location. The reflective values of each of the different bands for the same location and day are also copied to the respective composite image files for each band. This is repeated for every location (pixel) in the MODIS NDVI image file to create a composite image for the specified temporal interval.

IV. PROPOSED METHOD

The composition method using minimum blue criterion from among high NDVI values is also widely used. This method is based on the observation that visible blue wavelengths are highly sensible to atmospheric interference, and the blue reflectance values increase with rise in atmospheric interference. Therefore, the clearest days should have the lowest blue reflectance readings. This method first selects a set of candidate readings with high NDVI values, and then selects the reading with the lowest blue value from among the candidates. The candidates are selected for example by selecting NDVI values within 80% range of the maximum NDVI for the temporal interval.

In this research we propose applying soft computing approach, namely fuzzy logic[3], in order to create a composition method which can be more easily tuned for specific regions.

In this paper we take the minimum blue criterion as the initial model. In the standard rule-based minimum blue criterion, there is a crisp criterion of high NDVI candidates (e.g. 80% of maximum NDVI) and crisp criterion of lowest blue value from among the candidate. In this standard crisp rule-based method, a very low blue value with 79% NDVI value will be discarded. Similarly, even if the maximum NDVI value has second lowest blue value, the maximum NDVI value will be discarded.

We extend the blue criterion composition algorithm by defining a fuzzy set of high NDVI values, and a fuzzy set of low blue values, and selecting the best value from the combined fuzzy set of high NDVI and low blue using fuzzy logic.

We set the fuzzy set N as the set of readings with high NDVI values and fuzzy set B as the set of readings with low blue values, defined by the membership function m_N and m_B on total space X and Y of NDVI and blue readings, respectively.

$$N = \int_X m_N / x \qquad x \in X \tag{2}$$

$$B = \int_Y m_B / y \qquad y \in Y \tag{3}$$

$$m_N : X \rightarrow [0,1] \tag{4}$$

$$m_B : Y \rightarrow [0,1] \tag{5}$$

The membership value or grade $m_N(x)$, $m_B(y)$ for reading x and y is similarly defined as below.

$$m_N(x) \in [0,1] \tag{6}$$

$$m_B(y) \in [0,1] \tag{7}$$

From fuzzy logic, the fuzzy set of readings with high NDVI values and low blue values are defined as the fuzzy intersection of set N and B, and given as below.

$$\begin{aligned} N \cap B \Leftrightarrow m_{N \cap B}(x,y) \\ = m_N(x) \wedge m_B(y) \\ = \min\{m_N(x), m_B(y)\} \end{aligned} \tag{8}$$

By defining an appropriate membership function for fuzzy set N and B, the reading with best value can be calculated as the reading with the highest grade in $N \cap B$.

For this experiment, the membership grade for $m_N(x)$ and $m_B(x)$ was defined as below.

$$m_N(x) = \begin{cases} \dfrac{(x - T_N)}{(x_{MAXN} - T_N)}, & x \geq T_N \\ 0, & x < T_N \end{cases} \tag{9}$$

$$m_B(y) = \begin{cases} \dfrac{(T_B - y)}{(T_B - y_{MINB})}, & y \leq T_B \\ 0, & y > T_B \end{cases} \tag{10}$$

x_{MAXN} is the maximum NDVI value, y_{MINB} is the minimum blue value, T_N is the threshold value for large NDVI candidates, T_B is the threshold value for low blue candidates.

V. RESULTS AND CONCLUSION

The proposed method was applied to create a monthly composite data for July 2001 over regions in Japan. This was compared with composite data for the same temporal interval and region using MVC with maximum NDVI. The proposed method was able to remove clouds successfully, and the final composite result was very close to that of standard MVC using maximum NDVI.

In this paper, an extension to minimum-blue criterion composition method for remote sensing data was proposed. The proposed method applies fuzzy set theory and fuzzy logic to facilitate parameter tuning, as well as produce a composite method allowing a more flexible selection of data for the composite image.

For future works, we need to closely examine the differences of output between the proposed method and standard method, and evaluate the effectiveness and accuracy of the proposed method.

VI. ACKNOWLEDGMENTS

This research was supported by the Research project of Tokyo University of Information Sciences for the sustainable development of economic and social structure dependent on the environment in eastern Asia.

REFERENCES

[1] Takeuchi W, Yasuoka Y (2003), Comparison of composite algorithm for South East Asia using MODIS data (in Japanese). Proceeding of Annual Conference of Japan Society of Photogrammetory and Remote Sensing, 2003/6, Tokyo, Japan

[2] van Leeuwen W. J. D., Huete A. R., Laing T. W. (1999), MODIS Vegetation Index Compositing Approach: A Prototype with AVHRR Data, Remote Sens. Environ. 69:264–280

[3] Zadeh L. A. (1965), Fuzzy sets, Informat. Control 8 (3): 338–353

[4] National Aeronautics and Space Adminstration (NASA), MODIS Web, http://modis.gsfc.nasa.gov/

P-System Communications Architectures Configuration based on Growing Self-Organizing Maps

Abraham Gutiérrez, Soledad Delgado, Sandra Gómez

Natural Computing Group - Universidad Politécnica de Madrid
Carretera de Valencia Km. 7, Madrid - 28031, Spain
{abraham,sole,sgomez}@eui.upm.es

Abstract. The different viable architectures that implement P-Systems (membrane systems) over distributed cluster of processors have a major drawback: the distribution of these architectures in a balanced tree of processors that can minimize external communications and maximize the parallelism grade. For a given P-System and K processors, there exists a great volume of possible distributions of membranes over these. In a recent paper the feasibility of using Self-Organizing Neural Networks (SONN) with growing capability to help in the selection process of a distribution for a given P-System has been demonstrated, although the nature of two-dimensional patterns used in the study limited the possibility of defining more flexible degrees of communication, making more difficult to locate the best distribution. In this paper the capacity of Growing Cell Structure (GCS) model of projecting high-dimensional spaces in bi-dimensional graphs is explored.

Keywords: Natural Computation, SONN Networks, GCS Networks.

I. INTRODUCTION

P-Systems, introduced by Păun [1], are a class of distributed, massively parallel and non-deterministic systems. This model has become, during last years, a powerful framework for developing new ideas in theoretical computation and connecting the Biology with Computer Science. Possibilities offered by P-Systems for solving NP-problems, in lineal time and of course lineal resources, have made researchers concentrate their work towards HW and SW implementations of this new computational model.

Nowadays, it is possible to find different viable architectures that implements P-Systems in a distributed cluster of processors [2]. These proposed architectures have reached a certain compromise between the massively parallelism character of the system and evolution step times. These architectures are based in the distribution of several membranes in each processor, the use of proxies to control the communication between membranes and mainly, the suitable distribution of the architecture in a balanced tree of processors. All this facts allows obtaining a better evolution step time than in others suggested architectures congested quickly by the network collisions when the number of membranes grows. The main problem in these architectures is to find the proper distribution of the membranes between processors and the definition of a network topology that minimizes communication between processors without reducing the system parallelization.

In a previous paper [3], we suggest the use of Self-Organizing Neural Networks (SONN) with growing capability, based in Fritzke work [5], to help in the search and selection of the balanced distribution for a given P-system, with the purpose of obtaining as a final objective the reduction of the run times of each step of evolution in a P-System, although the nature of two-dimensional patterns used in the study limited the possibility of defining more flexible degrees of communication, making more difficult to locate the best distribution. In this paper the capacity of Growing Cell Structure (GCS) model of projecting high-dimensional spaces in bi-dimensional graphs is explored. Specifically, we propose a more flexible definition of the internal and external communications degrees that occur in the processors, which basically needs the use of vectors with a dimension greater than two. In this case, it is necessary to work with the concept of topographic maps of the output layer of the GCS network to generate two-dimensional graphics that can be used to explore the high-dimensional input space. The proposed experiments have presented the opportunity of evaluating what kind of information about membrane-processor-communication is most appropriate in finding the best distribution when using the vector projections provided by the GCS network.

II. P SYSTEM COMMUNICATION ARCHITECTURES

The viable architectures that implements P-Systems in a distributed cluster of processors are based on the following:

Membranes distribution: In each processor, K membranes are located that will evolve, at worst, sequentially. The value of K is determined by the relation between the number of membranes M and processors P, where $K \geq 1$. The benefit obtained is that the number of the external communications decreases. The total number of communications splits in two classes: a group of internal communications for pairs of membranes located in the same processor (the run time to carry out the internal communications will be negligible) and another group of external communications to interchange information among pairs of membranes located in different processors.

Proxy for processor: When a membrane wants to communicate with another one located at a different processor, the first one uses a proxy (programs or device located in the processor that carries out an action in representation of another), instead of doing it directly. This intermediate element located between the bus and the membranes concentrates and reduces the information that must be reported.

Tree topology of processors: The benefit obtained with the tree topology of processor is that it minimizes the total number of external communications made as the proxies interchange information only with its direct predecessor and its direct successors, and therefore the total number of external communications for P processors in each evolution step is 2(P − 1).

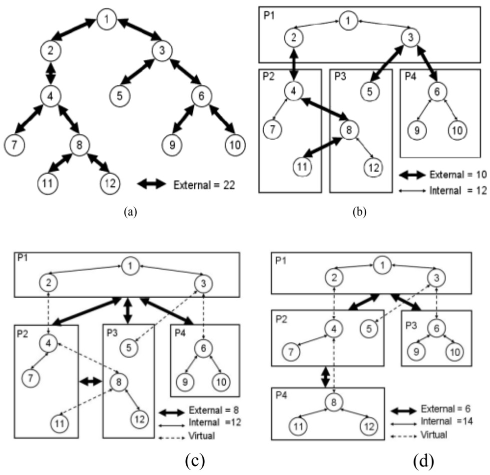

Fig.1. (a) P-System communications. (b) Communications with membranes distribution (c) Communications with a proxy for processor. (d) Communications using a tree topology

III. FRITZKE'S GROWING CELL STRUCTURES (GCS)

Self-Organizing Map (SOM) is an artificial neural network model with competitive and unsupervised training. SOM network has two main characteristics: it makes possible obtaining a simplified model of the training data (normally high-dimensional) and it has the capacity to project them on a two dimensional map that shows the existing relations among them. In 1982, Kohonen [4] proposed first model of SOM, where the complete network structure had to be specified in advance and remained static during all the training process. In 1994, B. Fritzke [5] proposed a SOM model called Growing Cell Structure (GCS) where this static structure limitation was eliminated.

GCS is a two-layer architecture network. Neurons located at the input layer are fully connected with those in the output one. These connections have associated a weight, w_{ij}, where i identify the input neuron and j the output one. There exist as many input neurons as dimension has the input vectors. Neurons in the output layer have neighbor connections between them presenting a topology formed by groups of basic k-dimensional hyper-tetrahedrons structures. In order to facilitate the visualization of the output layer, in this work a value of k=2 has been used.

Every output c unit has an n-dimensional synaptic vector $w_c = (w_{1c}, \ldots, w_{nc})$ associated. This vector can be seen as the position of c in the input vector space. Each time a new input pattern $e = (e1, \ldots, en)$ is processed, only one output neuron is activated, called the *best matching unit (bmu)*, that is the one with the synaptic vector that matches best with the input pattern. Formally:

$$S_{bmu} = \arg\min \|e - w_c\| \tag{1}$$

Thereby ‖ ·‖ denotes the Euclidean vector norm. By this the input vector space is partitioned into a set of regions, each consisting of the locations having a common nearest synaptic vector. This way, the set of all synaptic vectors of the output layer can be seen as a simplified model of the input vector space.

The training phase in GCS network adapts synaptic vectors looking for that each output neuron represents a group of similar input patterns. At the beginning of the training phase the output layer of the network has only three neurons interconnected via neighbor relations (k=2). During the training process a set of input patterns is presented to the network iteratively. In each adaptation step an input pattern is processed, the *bmu* is calculated and its synaptic vector and its topological neighbor's synaptic vectors are modified using equations 2 and 3 respectively (where $\varepsilon_b > \varepsilon_n$).

$$\Delta w_{bmu} = \varepsilon_b (e - w_{bmu}) \tag{2}$$

$$\Delta w_c = \varepsilon_n (e - w_c) \quad (\text{for all } c \text{ neigbor of } bmu) \tag{3}$$

After a fixed number of adaptation steps a new output unit is inserted and is connected to other cells in such a way that the triangular groups of neighbor units are guaranteed. Periodically superfluous neurons are removed in order to obtain better results when input space consists of several separate regions of positive probability density. A constant threshold, η, is used to eliminate those neurons with probability density below this value. The removal process ensures the triangular architecture of the output layer, but the output neighbor mesh can results broken in several sub-meshes. In this work the modification of the GCS training algorithm proposed in [6] has been used in order to achieve a better interpretation of the removal parameters.

In a trained network the output layer map can be seen as a projection of the input vector space in a bi-dimensional plane that exhibits the relations of the input patterns. Printing the output layer map, called topographic map, data inherent knowledge can be discovered. As it has been exposed previously, when k=2 architecture factor is used, the GCS output layer is organized in groups of interconnected triangles. In spite of bi-dimensional nature of these meshes, it is not obvious how to embed this structure into the plane. In this paper the projection technique exposed in [7] has been used to generate the topographic map. Using this methodology, traditional Kohonen visualization methods can be implemented using GCS networks. The following GCS visualization methods have been used: distance map, Unified map (U-map), distance addition map, and component planes [7].

IV. EXPERIMENTS AND RESULTS

Several experiments have been carried out to validate GCS networks as a tool to help in discovering the best membrane distribution over a set of processor in a concrete P-System. In particular, thirty P-System models generally used in the literature of P-System have been employed in this study. Several membrane distributions between a concrete number of processors (calculated using eq. 5) have been generated for every P-System, observing how the resulting communications of the distribution affect to the parallelization grade. A great volume of GCS networks have trained using this information with the intention of visualize the output layer and establish the optimal distribution, which will be the one that balances the degrees of external communications and parallelization.

The minimal execution time of a complete P-System [2] is expressed in the formula:

$$T_{\min} = 2\sqrt{2\,M\,T_{apl}\,T_{com}} - 2T_{com}. \qquad (4)$$

Where T_{apl} is the maximum time used by the slowest membrane in applying its rules, T_{com} is the maximum time used by the slowest membrane for communication, and M is the number of membranes. The optimal number of processors that minimizes the execution time of a complete P-System is calculated by:

$$P_{opt} = \sqrt{\frac{M\,T_{apl}}{2T_{com}}}. \qquad (5)$$

For each P-System three families of data have been generated. The first consists of one vector for membrane-processor-distribution, where each one maintains the degree of internal and external communications that generates one specific membrane in a concrete processor for one of the combinations. In this case vectors are bi-dimensional, and for a particular combination there exists as many vectors as membranes has the P-System. In this first family of data each vector is labeled with a string that identifies i membrane, j processor, and k combination ($M_iP_jC_k$). In the second group of data a vector by combination has been generated, whose dimension corresponds with the double of existing membranes. For each membrane the degrees of internal and external communications are included in the corresponding vector. In this case each pattern is labeled only with the k combination that represents (C_k). Finally, the third group of data consists of a vector for processor-distribution, which includes six components that maintain different levels (high, medium and low) of internal and external communication obtained using fuzzy logic. Each vector is labeled to identify the j processor and the k combination (P_jC_k).

The goal we seek training a GCS network with any of these three groups of data is to obtain an arrangement of the vectors that allows us to analyze graphically, using topographic maps, the volume of internal and external communications that take place for each combination, been able to determine the best that balances the degree of parallelization and external communications. After the training phase the output units of the GCS network can be labeled with the union of the tags of all those input patterns that fall inside its Voronoi region. For space reasons this section only shows some of the experiments and results obtained for a particular P-System (Fig. 1a) which consists of 12 membranes. Fifteen feasible combinations, which fulfill the condition of tree topology of processors, of 12 membranes have been generated for 4 processors (the optimal number calculated by eq. 6). The volume of communications produced by membranes is not homogeneous. Using the 15 combinations three families of data previously described have been created. For the first group, each pair of internal-external communication of a membrane forms a vector (altogether there are 180 vectors). For the second group there are 15 vectors of 24 dimensions. Finally, the last family of data has been generated using fuzzy logic values to define 15 vectors of 6 dimensions for each processor.

Using these three sets of data several GCS networks have been trained. The common learning parameters used in all the experiments are: LEAE insertion criterion, ε_b = 0.06 (*bmu* adaptation rate), ε_n = 0.002 (*bmu* neighbor adaptation rate), λ=1 epoch (number of iterations to insert a new unit). The only varying factor involving experiments is related with the concluding condition of the training process, fulfilled when the output layer gets a specific number of output units or when at least an explicit number of isolated clusters of output units are obtained. For the first, a removal threshold μ = 0 has been used, and for the last a value of μ=0.0006.

Figure 2 shows the scattergram of a GCS network, trained with the first group of bi-dimensional data (concluded when at least 6 isolated clusters of output units are obtained), where the position of each output unit is determined by the two components of its synaptic vector (lines between points represents the output layer neighbor connections). X-axis coordinates indicates the internal degree of communications and Y-axis the external one. We have grouped the neurons into three classes: bad (from 1 to 11), medium (from 14 to 18) and good (from 19 to 28). Within each of these three groups we have ordered neurons from highest to lowest level of external communication and for those with a similar value, from highest to lowest level of internal communication. Based on this information has been determined that the best distribution is the C13, that contains 1 bad neuron, 4 medium neurons and 7 good neurons. Moreover, this distribution has one of the best ratios of communication.

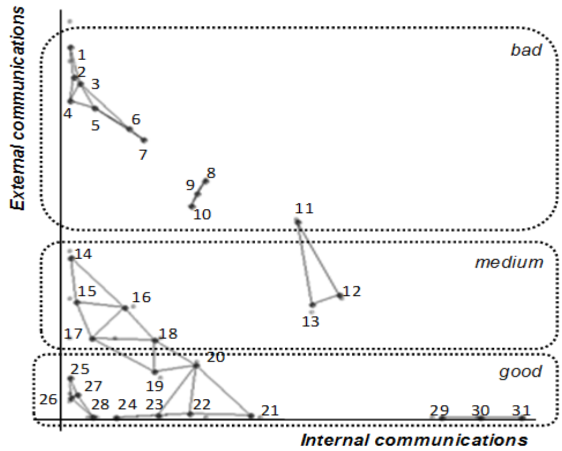

Fig.2. Scattergram of the GCS network trained with bi-dimensional patterns. Points represent neurons and lines between them neighbor connections.

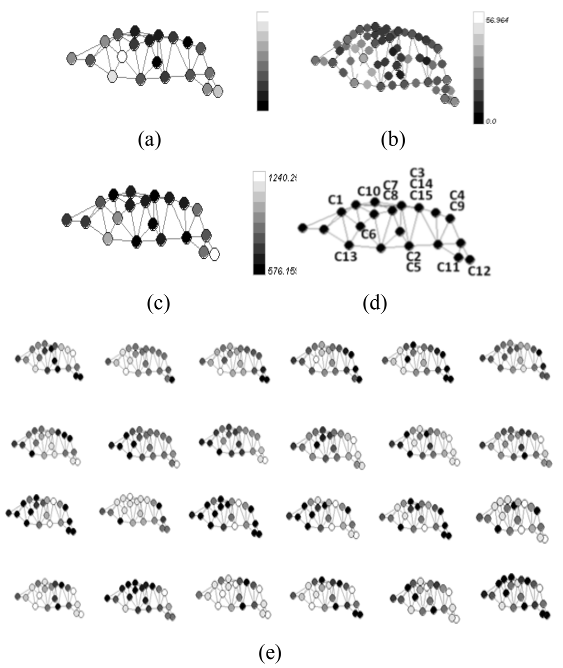

Fig.3. GCS network trained with 24-dimensional vectors. a) Distance map. b) U-map. c) Distance addition map. d) Labeled topographic map. e) Component planes.

Figure 3 includes some of the topographic maps of the GCS network trained with the 24-dimensional data. In this experiment, the learning concluding condition was determined when the output layer got 20 output units. Distance map, U-map, Distance addition map and labeled topographic map show certain grade of clustering associated with the patterns C2, C3, C5, C7, C8, C10, C14 and C15, C11 with C12, C4 with C9, and finally, C1, C6 and C13 seems to be isolated. Component planes in the first and second rows show the internal and external communications associated to the membranes 1 to 12 from left to right, respectively, where black color represents low values. The high dimension of the vectors make no easy to find the combination that better minimizes the degree of external and internal communications. The C13 combination that results the better one in the previous experiment, continues showing good characteristics, although the C1 or C6 is perhaps better.

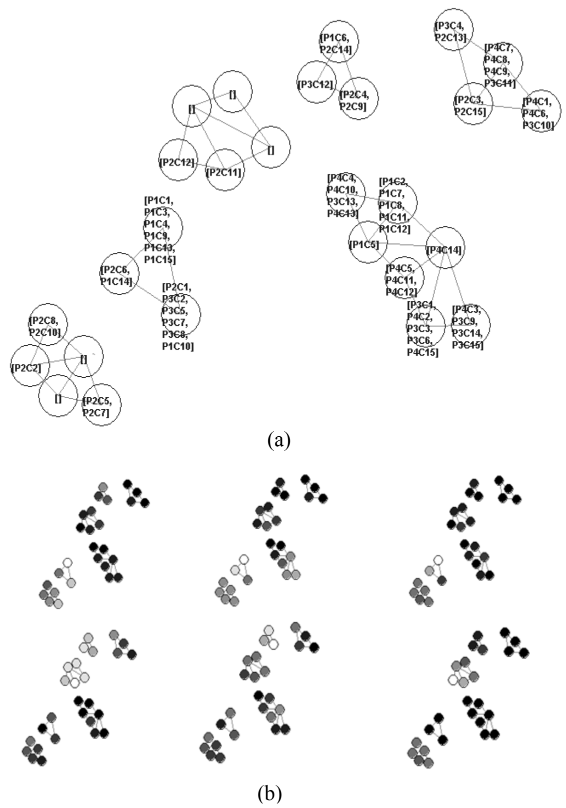

Fig.4. GCS network trained with 6-dimensional vectors. a) Labeled topographic map. b) Component planes.

Finally, Figure 4 shows the information of the GCS network trained with the third set of data (concluded when at least 6 isolated clusters of output units are obtained). In this network only 6 component planes exist, simplifying its visual analysis. Component planes in the first row show the high, medium and low internal communications and the high, medium and low external communication appear in the second one, where black color represents low values. The two clusters in the upper left are the worst external communications high, medium and low show (although the grades for internal communications are good). The two clusters below on the left offer good levels of external communications, but they have the worst internal communications levels. The two remaining clusters get the best ratios by minimizing both types of communications. Each of the 15 combinations consists of 4 patterns (one per processor). The combination that has more patterns in the two best clusters is the C13 again (it has 3 out of 4).

With the first set of data the problem that arises in searching the best distribution is the dispersion of the vectors that compose a concrete combination of membranes by processor. Although this example is relatively simple, with only 12 membranes, it lets patent the complication to determine which the best distribution is. With respect to the second data set, although it solves the previous problem because there only exists a single vector by combination, the high dimension of the input space makes difficult the component plane analysis. The third data set raises a commitment between the first two sets, presenting so many vectors by combination as processors exist. The volume of processors is not usually high, because it would increase the volume of external communications, making easy to find in the graphs all the patterns associated to a concrete combination. On the other hand, the dimension of these vectors facilitates the analysis of the component planes.

V. CONCLUSIONS

GCS networks have demonstrated to be a useful tool to P-System in the searching of membrane balanced distributions. Although the example that has been used to document the methodology has a small volume of membranes, the feature of simplified model associated to GCS networks allows working with high volumes of membranes where the distribution possibilities go off.

The analysis of the information of a GCS network could be automated for feeding a system of automatic membrane distribution over processors. In particular, this tool is being adapted to be used in the distributed system of membranes based on microcontrollers exposed in [8][9].

The experiments have showed that the input patterns family that better display a P-System communication information is the third, where for a given combination four patterns are generated to describe a fuzzy characterization of the internal and external communications produced in a particular processor for a specific combination.

VI. REFERENCES

[1] Gh.Păun (1998), Computing with membranes. Journal of Computer and System Sciences, 61 (2000), and Turku Center for Computer Science-TUCS Report nº 208.
[2] A. Tejedor, L. Fernandez, F. Arroyo, et al (2007), An architecture for attacking the bottleneck communication in P Systems. LNCS, ISSN 1433-5298, Artificial Life and Robotics vol. 12, Springer Japan, pp. 236-240.
[3] A. Gutiérrez, S. Delgado y L. Fernandez (2009), Suitability of Using Self-Organizing Neural Networks in Configuring P-System Communications Architectures, LNCS vol. 5507, ICONIP 2008, Part II, Springer-Verlag Berlin Heidelberg, pp. 437–444.
[4] T. Kohonen (1982), Self-Organized Formation of Topologically Correct Feature Maps. Biological Cybernetics, Vol. 4359--69.
[5] B. Fritzke (1994), Growing Cell Structures – A Self-organizing network for Unsupervised and Supervised learning. Neural Networks, Vol. 7, no.1. 1441--60.
[6] S. Delgado, C. Gonzalo, E. Martinez and A. Arquero (2004), Improvement of Self-Organizing Maps with Growing Capability for Goodness Evaluation of Multispectral Training Patterns. Geoscience and Remote Sensing Symposium, IEEE International. Vol. 1, 564-567.
[7] S. Delgado, C. Gonzalo, E. Martinez and A. Arquero (2007), Visualizing High-Dimensional Input Data with Growing Self-Organizing Maps. LNCS, vol. 4507, Springer, Berlin, 580-587.
[8] A. Gutierrez, L. Fernández, F. Arroyo, et al (2008), Hardware and Software Architecture for Implementing Membrane Systems: A Case of Study to Transition P Systems. LNCS, Springer, Berlin, DNA Computing 211-220.
[9] A. Gutierrez, L. Fernández, F. Arroyo, et al (2008), Suitability of Using Microcontrollers in Implementing new P System Communications Architectures. LNCS, ISSN 1433-5298, Artificial Life and Robotics vol. 13, Springer Japan, pp. 102-106.

Hardware Circuit for the Application of Evolution Rules in a Transition P-System

Víctor Martínez, Santiago Alonso, Abraham Gutiérrez

Natural Computing Group - Universidad Politécnica de Madrid – Madrid
(Tel : +34-91-336-7901; Fax : +34-91-336-7893)
({victormh, salonso, abraham}@eui.upm.es)

Abstract: P systems or Membrane Computing are a type of systems based on biological membranes. Transition P systems perform computation through transition between two consecutive configurations. One transition is obtained by applying the evolution rules, which are in each region of the system in a non-deterministic maximally parallel manner. This paper is part of an investigation line which objective is to implement a hardware system that evolves as it does a transition P system. To achieve this objective, it has been carried out a division of this generic system in several stages. The first stage was to determine active rules in a determined configuration for the membrane. The second stage is developed by obtaining the part of the system that is in charge of the application of the active rules. In fact, the circuit obtained in this article counts the number of times that the active rules are applied. In first place, the initial specifications are defined in order to outline the synthesis of the circuit of active rules application. Later on, the design and synthesis of the circuit will be shown, as well as the operation tests, required to present the experimental results obtained.

Keywords: Bioinformatics, Membrane Computing, Robotics, Digital Systems.

I. INTRODUCTION

Membrane Computing or P Systems are computation systems based on the biomolecular processes of living cells [1]. These systems perform a computation through transition between two consecutive configurations by using evolution rules present in each region. If the system reaches a configuration in which there are no applicable rules at any membrane, it is said that the system reaches a halting configuration and, hence, the computation is successful.

This article is a part of a project to obtain a hardware system able to simulate P systems evolution. This generic system has been divided into several stages. The first stage develops a FPGA circuit able to determine active rules in a determined configuration for the membrane [2] y [3]. In this document, the second stage is developed: a circuit for the application of the active rules obtained in the first stage. In general, the application of the active evolution rules for a region of an evolution P system is a repetitive process that may be implemented following different algorithms. A previous study [4] of the possible positive and negative aspects each one of these application methods, allows us to obtain different circuits or systems that differ complexity level and expense of resources.

The first process to obtain the rules that can be used in a certain evolution step consists on obtaining the active rules. From the active rules, we select in a non-deterministic manner, all the rules that will be applied in parallel in each one of the regions. The rules also proceed in parallel to the transformation of the regions contents and of the own structure of the system sending objects and, in their case, dissolving membranes. After the communication and modification of the structure of membranes of P system has taken place, the system has evolved from a configuration to another. The process of application evolution rules in a membrane region is illustrated in the following sequence of steps:

1. Once the system is initialized, the process starts up with the loading of the active rules register R obtained by means of the selection active rules circuit.
2. In each iteration, one of the active rules r_i will be applied. This rule is aleatorily obtained.
3. The application of the selected rule r_i consists on the subtraction for the initial multiset ω, of the elements values from the rule antecedent. In turn, we will increase 1 time the particular accountant that counts the number of times that the rule has been applied.

4. With the new multiset *ω'* obtained it is loaded again in the register *R*, the new set of active rules. Every time that the group of active rules is upgraded, the finish of the process is controlled. The stop condition is obtained when the number of active rules is zero. Therefore, while the cardinal of *R* is bigger than zero, it executes a new iteration of the application process again.

II. HARDWARE CIRCUIT FOR APPLICATION RULES

A first option to obtain the application of the active rules consists on the use of an iterative algorithm of application of the active rules group. In each step of the algorithm, one active rule is choosing in an aleatory way, until draining all the possible applications. This process "*step by step*" may be considered as the most immediate and easy to implement, and the Hardware Circuit for Application Rules presented implements the different processes from this algorithm. The ultimate circuit is obtained from the assembly of the different Functional Units created, along with the control sequential logic. The sequential logic determines the evolution of the internal steps that must take place inside the system until reaching the condition of shutdown. This condition will occur when the active rules register is empty. On a simplified way, the main functional units will be those that implement each one of the steps of the used algorithm, this is:

1. To obtain the active rules: $R \leftarrow ActiveRule$
2. To choose a single rule randomly: $r_i \leftarrow Aleatory(R)$
3. To update the objects multiset: $\omega' \leftarrow (\omega - (Antecedent(r_i)))$
4. To count the rules implicated: $counts(1, r_i)$

The functional unit that obtains the active rules consists of a designed, developed and displayed circuit in [3]. In order to update the objects multiset ω, it must be decreased as many times as the values of the antecedent objects of the rule that is being applied indicate. For it, we address the memory with the position of the rule to be applied, and a functional unit of multisets subtraction will obtain the value of the new updated multiset ω. The subtraction multisets functional unit must make the subtraction of each pair of elements mi from each one of the registers that represent the multiset values.

The sequential controller circuit is in charge of sequential activation of different units functional, as well as control of condition of shutdown, that determines the evolution of the internal steps that must cross the system. The sequence of events that must activate the sequential controller generates 4 states. The account continues of cyclical form until the condition of shutdown is reached, that will deactivate the accountant. In the state 0 is loaded objects multiset register *ω* present, and is calculated the active rules. In the state 1 is loaded *ActiveRules* register and obtained one active rule randomly. In the state 2 is loaded *1 Active Aleatory Rule* register, and is calculated the values of the new objects multiset and the increase of the accountant of applied rules. Finally, in the state 3 is loaded *ω'* and *AppliedRule* registers.

The operation of the obtained circuit is based on the following process: once the circuit is initialized, with the load of the initial objects multiset register and the ROM memory with the evolution rules, the circuit operation under the supervision of the sequential controller begins, which will cross the different states from the system.

The Fig. 1 shows the detailed scheme of the designed circuit for the rules application. The condition of shutdown of the circuit by means of a function AND that detects when there is no rule to apply; and in this case, disables the sequential controller. The size of the different elements: registers, memory, connections, etc. it has been chosen based on the characteristics of the practical case that will be developed.

III. EXPERIMENTAL RESULTS

Next we will present the complete process of obtaining the rules to apply on a concrete example of a transition P-system region. This will allow us to illustrate the operation of the developed model, as well as to show the tests to make. The definition, according to formal annotation, of the membrane system used is in the expressions and diagram with its structure of regions:

$\Pi = (V,\mu,\omega_1,...\omega_4, (R_1,\rho_1),...,(R_4,\rho_4),4)$

$V = \{a,b,c,d,e\}$

$\mu = [_1[_2[_3]_3]_2[_4]_4]_1$

$\omega_1 = aac$

$R_1 = \{r_1: c \rightarrow (c,in_4), r_2: c \rightarrow (b,in_4), r_3: a \rightarrow (a,in_2)b, r_4: dd \rightarrow (a,in_4)\}$

$\rho_1 = \{ r_1 > r_3, \quad r_2 > r_3\}$

The circuit to be carried out obtains the region 1 rules to apply. The region 1 input values will be the objects multiset ω_1, the group of rules R_1, the priority relationships among rules ρ_1 and the inner adjacent regions number (two regions in this case). The number of objects V is 5 with decimal multiplicity (0 - 9), therefore, we will need 4 bits to represents each object. And so, a word representing the multiplicity of the 5 objects will occupy 20 bits. The rules group is formed by 4 rules which will be stored in the device memory. Each of the 4 rules will be coded with 64 bits. This is, 20 bits for the antecedent, 20 bits for each consequent of the two inner interior regions, plus 4 remaining bits used to code the priorities mask of each rule with regard to the other ones. The rules are stored, therefore, in a ROM 4x64 bits memory [3].

Like previous step, is due to initialize the system with the load of the initial objects multiset register: *w_a[3..0] = 2(decimal), w_c[3..0] = 1(decimal), w_b, w_d, w_e = 0;* the inner regions existence indication bits *In1 = 1 (Region 1 Exists), In2 = 1 (Region 2 Exists)* and ROM memory with the evolution rules.

Next they are described with detail the states which the system goes through until completing the first cycle of sequence of states:

<u>Cycle 1 of sequence of states</u>: In state 0 the registry ω_i with the present objects multiset is loaded and the process of calculation of active rules begins. In state 1 the active rules register $a_1, a_2, a_3, a_4=(1,1,0,0)$ is validated, and the calculation of *1 Aleatory Active Rule* is qualified. State 2 been validate the load of the *1 Random Active Rule* register $r_1, r_2, r_3, r_4=(1,0,0,0)$ for example, select the information in memory of the rule that allows to update the values of the present multiset $\omega' \leftarrow (\omega - (Antecedent(r_0)))$, and it is increased the accountant of applied rules. State 3 the load of the registry $\omega' = aac - c = aa$ is validated, and the registry applied rules: $ar_1, ar_2, ar_3, ar_4=(1,0,0,0)$.

<u>Cycle 2 of sequence of states</u>: In state 0 the registry ω_i with the present objects multiset is loaded *w_a = 2, w_b, w_c, w_d, w_e = 0;* and the process of calculation of active rules begins. In state 1 is validated the active rules register $a_1, a_2, a_3, a_4=(0,0,1,0)$ and the calculation of *1 Aleatory Active Rule* is qualified. State 2 the load of the *1 Random Active Rule* register $r_1, r_2, r_3, r_4=(0,0,1,0)$ is validated. State 3 is validated the load of the registry $\omega' = aa - a = a$, and the registry applied rules: $ar_1,ar_2,ar_3,ar_4=(1,0,1,0)$.

<u>Cycle 3 of sequence of states</u>: In state 0 the registry ω_i with the present objects multiset is loaded *w_a = 1, w_b, w_c, w_d, w_e = 0;* and the process of calculation of active rules begins. In state 1 the active rules register $a_1, a_2, a_3, a_4=(0,0,1,0)$ is validated, and the calculation of *1 Aleatory Active Rule* is qualified. State 2 the load of the *1 Random Active Rule* register $r_1, r_2, r_3, r_4=(0,0,1,0)$ is validated. State 3 are validated the load of the registry $\omega' = a - a = 0$ and the registry applied rules: $ar_1,ar_2,ar_3,ar_4=(1,0,2,0)$.

As we can verify, after 3 complete system evolution cycles, the process stops because the condition of shutdown is reached. The obtained result corresponds with the awaited one: rule 1 must be applied 1 time, and rule 3 must be applied 2 times. The Fig. 2 shows the chronogram that illustrates the sequence of states of the system.

IV. FIGURES

Fig.1. Scheme of the designed circuit.

Fig. 2. Chronogram that illustrates the sequence of states of the system

V. CONCLUSION

This article presents a way to obtain a circuit capable to obtain the rules inside the P-system membrane that must be applied. The operation and verification of the obtained circuit is shown with a practical case of membrane system. We can verify like, from an initial P system configuration, and based on the external conditions, a satisfactory final result is reached.

The synchronization between the different functional units that compose the system is controlled by the sequential controller. It will be necessary to fit the clock cycles so that the circuit reaches the stable results within each cycle. The obtained circuit behavior is based on the evolution rules stored in memory and the inputs, which correspond with the values of the region state. If the conditions of the region change, the circuit modifies its outputs being adjusted to the new values. This feature is of a supreme importance in order to integrate this circuit as a module that works cooperatively together with other circuits.

This circuit comprises of a complete system that allows implementing the operation and evolution of a transition P system. The following step in this line will be to obtain the way of communication of objects between regions, which allows building each evolution step.

REFERENCES

[1] Gh. Păun, Computing with Membranes, Journal of Computer and System Sciences, 61 (2000), 108-143, and Turku Center of Computer Science-TUCS Report No 208, 1998.
[2] Víctor J. Martínez, L.Fernández, F.Arroyo, A. Gutiérrez. A Hw Circuit for the Application of Active Rules in a Transition P-System Region. Fourth International Conference Information Research and Applications I.TECH 2006. Varna(Bulgaria). Del 20 al 25 de Junio de 2006.
[3] Víctor Martínez, Abraham Gutiérrez, Luis Fernando de Mingo. Circuit FPGA for Active Rules Selection in a Transition P System Region. ICONIP 2008 - 15th International Conference on Neural Information Processing of the Asia-Pacific Neural Network Assembly. Auckland, New Zealand November 25-28, 2008 Lecture Notes in Computer Science ICONIP 2008, Part II, LNCS 5507
[4] L.Fernández, F.Arroyo, J.Castellanos, J.A.Tejedor, I.García, New Algorithms for Application of Evolution Rules based on Applicability Benchmarks, BIOCOMP06 International Conference on Bioinformatics and Computational Biology, Las Vegas (USA), july, 2006.

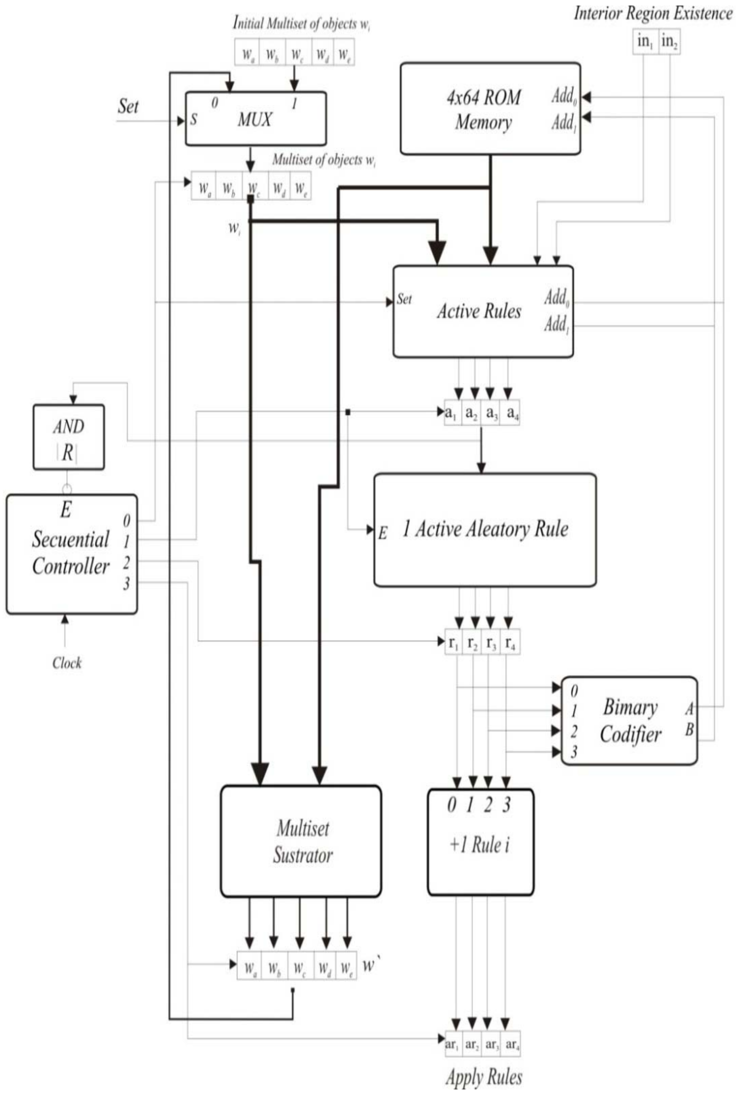

Fig. 1

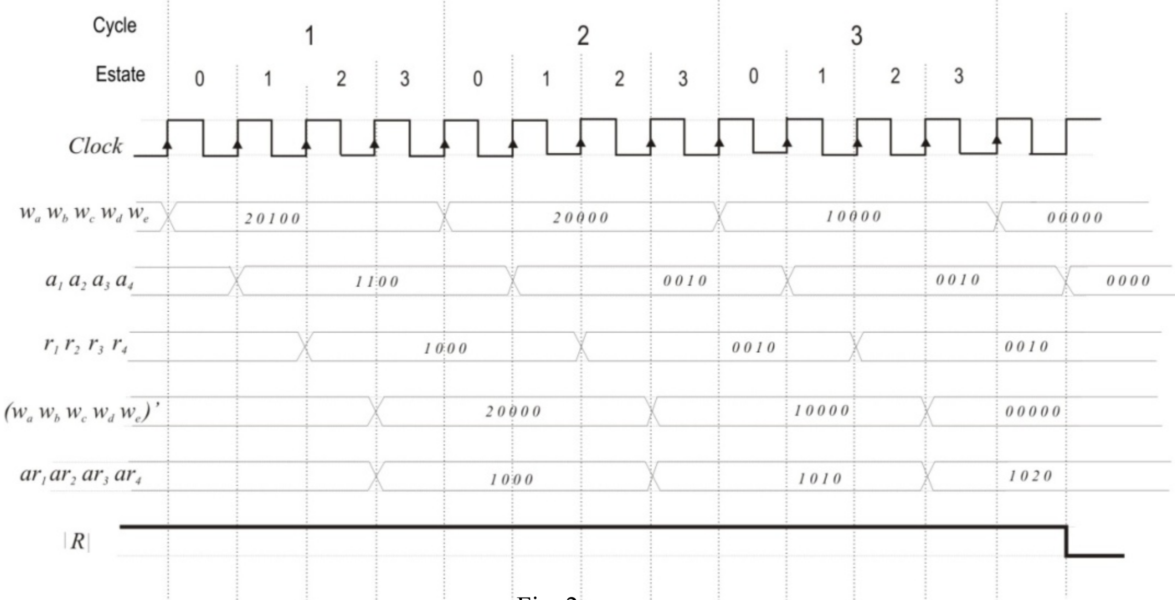

Fig. 2

The Fifteenth International Symposium on Artificial Life and Robotics 2010 (AROB 15th '10),
B-Con Plaza, Beppu,Oita, Japan, February 4-6, 2010

Calculating maximal multisets of objects by using RAM as support

Alberto Arteta, Fernando Arroyo, Ángel Goñi

Natural computing group (UPM)
Ctra. de Valencia, Km. 7
28031 - MADRID
Phone.: 913367903-04

aarteta@eui.upm.es , farroyo@eui.upm.es, agmoreno@gcn.upm.es

***Abstract*:** Within the membrane computing research field, there are many papers about software simulations and a few about hardware implementations. In both cases, algorithms are implemented. These algorithms implement membrane systems in software and hardware that try to take advantages of maximal parallelism. P-systems are parallel and non deterministic systems which simulate membranes behavior when processing information.
This paper describes the evolution rules application process and it presents software techniques for calculating maximal multisets on every evolutionary step. These techniques improve the best performance achieved when applying evolution rules over multisets of objects.

Keywords: P-systems, Parallel systems, Natural Computing, evolution rules application, structure.

I. INTRODUCTION

Membrane computing is a parallel and distributed computational model based on the membrane structure of living cells [1]. P-systems are the structures that reproduce the information processing occurring in living cells. Nowadays, it can be found that several P Systems simulators are much elaborated" [2].At this point, there is a problem with the parallelism synthesized in [2] by: "parallelism -a dream of computer science, a common sense in biology". This is the reason why, Păun avoids "to plainly saying that we have 'implementations of P systems', because of the inherent non-determinism and the maximal parallelism of the basic model, features which cannot be implemented, at least in principle, on the usual electronic computer. […]

There are several uses of the p-systems. P-systems can be used to increase performance when dealing with known problems; for example, the *knapsack problem* [3].

II. WORK RESSUME

We are going to define concepts regarding membrane computing as , p-systems, multisets of objects, multiplicities, etc; then we will describe the evolution rules application phase. After this, we will create a *n-dimensional structure* throughout an application that establishes a link between the *initial multisets*, and the number of times that each *evolution rule* should be applied in order to obtain a maximal *multiset*. The number of entries this structure has will be determined by a prefixed value called *"benchmark"* .Finally, some conclusions will be established. These conclusions will be the result of doing a study in detail throughout the entire work presented here.

III. DEFINITIONS

Definition 3.1 Transition P Systems

A Transition P System of degree n, n > 1 is a construct
$=$ [illegible]

Where: V is an alphabet; its elements are called objects; μ is a membrane structure of degree n, with membranes and regions labeled in a one-to-one manner with elements in a given set ; we always use labels 1,2,..,n;

$\omega_i\ 1 \le i \le n$, are strings from V^* representing multisets over V associated with the regions 1,2,..,n of μ

$R_i\ 1 \le i \le n$, are finite set of evolution rules over V associated with the regions 1,2,..,n of μ;

ρ_i is a partial order over $R_i\ 1 \le i \le n$, specifying a priority relation among rules of R_i . An evolution rule is a pair (u,v) which we will usually write in the form $u \to v$ where u is a string over V and v=v' or v=v' δ where v' is a string over $(V \times \{here, out\}) \cup (V \times \{in_j\ 1 \le j \le n\})$, and δ is a special symbol not in. The length of u is called the radius of the rule $u \to v$ i_o is a number between 1 and n which specifies the output membrane of Π

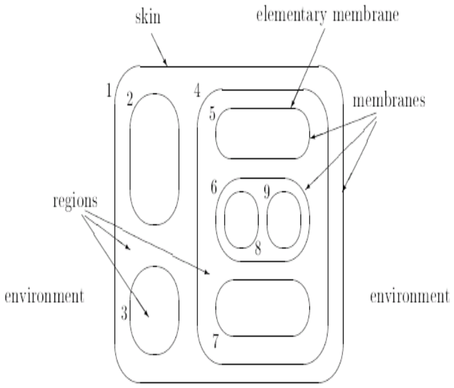

Fig 1 P-system structure

Definition 3.2 *Multiset of objects*

Let *U* be a finite and not empty set of objects and *N* the set of natural numbers. A *multiset of objects* is defined as a mapping:

$$M: U \longrightarrow N$$
$$a_i \longrightarrow u_i$$

Where a_i is an object and u_i its multiplicity. Here are some representations:

$$M = \{(a_1)(a_2)(a_3)\} = \{a_1^{u_1} a_2^{u_2} \ldots a_n^{u_n}\}$$

Note: *Initial Multiset* is the multiset existing within a given region in where no application of evolution rules has occurred yet.

Definition 3.3

Evolution rule with objects in *U* and targets in *T* is defined by $r = (m, c, \delta)$ where $m \in M(U), c \in M(UxT)$ *and* $\delta \in \{$*to dissolve, not to dissolve*$\}$

From now on *'c'* will be referred a s the consequent of the evolution rule *'r'*

Note The *set of evolution rules* with *objects* in *U* and targets in *T* is represented by *R (U, T)*.

Definition 3.4 *Multiplicity of an object in a multiset of objects M (U)*

Let $a_i \in U$ be an object and let $m \in M(U)$ be a multiset of objects. The multiplicity of an object is defined over a multiset of objects such as:

$$|\ |_{a_i} : U \times M(U) \rightarrow N$$
$$(a_i, m) \rightarrow |m|_{a_i} = n \mid M(a_i) = n$$

Definition 3.4.1 *Multiplicity of an object in an evolution rule r*

Let $a_i \in U$ be an object and let $R(U,T)$ be a multiset of evolution rules. Let $r = (m, c, \delta) \in R(U,T)$ where [illegible]

The multiplicity of an object is defined over an evolution rules such as:

$$|\ |_{a_i} : U \times R(U,T) \rightarrow N$$
$$(a_i, r) \rightarrow |r|_{a_i} = n \mid M(a_i) = n$$

Let C_i be the *consequent* of *the evolution rule* r_i. Thus, the representation of the evolution rules is:

$$r_1 : a_1^{u_{11}} a_2^{u_{12}} \ldots a_n^{u_{1n}} \longrightarrow C_1$$
$$r_2 : a_1^{u_{21}} a_2^{u_{22}} \ldots a_n^{u_{2n}} \longrightarrow C_2$$
$$\ldots \longrightarrow \ldots$$
$$r_m : a_1^{u_{m1}} a_2^{u_{m2}} \ldots a_n^{u_{mn}} \longrightarrow C_m$$

P-systems evolve, which makes it change upon time; therefore it is a dynamic system. Every time that there is a change on the p-system we will say that the p-system is in a new transition. The step from one transition to another one will be referred to as an evolutionary step, and the set of all evolutionary steps will be named computation. Processes within the p-system will be acting in a maximally parallel and non-deterministic manner. (Similar to the way the living cells process and combine information).

We will say that the computation has been successful if:

- The halt status is reached.
- No more evolution rules can be applied.
- Skin membrane still exists after the computation finishes.

Evolution rule application phase

This phase is the one that has been implemented f ollowing different techniques. In every region withi n a p-system, the evolution rules application phase is described as follows:

Rules application to a multiset of object in a region is a transforming process of information which has input, output and conditions for making the transfor mation.

Given a region within a p-system, let U= $\{a_i \mid 1 \le i \le n\}$ be the alphabet of objects, *m* a multiset of objects over U and R(U,T) a multiset of evolution rules with antecedents in U and targets in T.

- The input in the region is the initial multiset *m*
- The output is a maximal multiset *m'*
- The transformations have been made based on the application of the evolution rules over *m* until *m'* is obtained.

Application of evolution rules in each region of P systems involves subtracting objects from the initial multiset by using rules antecedents. Rules used are chosen in a non-deterministic manner. This phase ends when no rule is applicable anymore. The trans formation only needs rules antecedents as the conse quents are part of the communication phase.

Observation.

Let $k_i \in N$ be the number of times that the rule r_i is applied. Therefore, the number of symbols a_j which have been consumed after applying the evolution rules a specific number of times will be:

$$\sum_{i=1}^{m} k_i \cdot u_{ij}$$

Definition 3.5 ***Maximal Multisets***

We say m is a maximal multiset when not anymore evolution rules can be applied to it.

Observation

Given a region R and alphabet of objects U, and R (U, T) set of evolution rules over U and targets in T.

$$r_1 : a_1^{u_{11}} a_2^{u_{12}} .. a_n^{u_{1n}} \rightarrow C_1$$

$$\ldots \qquad \rightarrow \ldots.$$

$$r_m : a_1^{u_{m1}} a_2^{u_{m2}} .. a_n^{u_{mn}} \rightarrow C_m$$

Maximal multiset is that one that complies with:

$$\prod_{l=1}^{n}\left[\bigcup_{i=1}^{n}\left(u_{li} \ne \sum_{j=1}^{m} k_j \cdot u_{lj}\right) \ne u_{li}\right] \quad [4]$$

Within a given membrane, *Let U=* $\{a_i \mid i=1,..n\}$ be a set of objects. *Let T be* a set of targets. *Let* $\omega = a_1 a_2 .. a_n$ *be a multiset of objects and let* u_i *be the multiplicity of* a_i. *Let R(U,T) be a multiset of evolution rules with objects in U and targets in T.* Let *m* be the number of evolution rules within *R(U,T).* Let k_i be the number of times that the rule $r_i \in R(U,T)$ is applied. We define:

$$\varphi : N^m \rightarrow N^n$$

$$(k_1, k_2, .., k_m) \rightarrow (u_1, u_2, .., u_n)$$

"m" is the number of the evolution rules within R(U,T), "n" is the number of symbols within the given membrane.

$$\varphi(k_1, k_2, .., k_m,) \equiv \begin{pmatrix} u_{11} & u_{21} & \ldots u_{m1} \\ u_{12} & u_{22} & \ldots u_{m2} \\ \ldots & \ldots & \ldots \\ u_{1n} & u_{2n} & \ldots u_{mn} \end{pmatrix} \begin{pmatrix} k_1 \\ k_2 \\ \ldots \\ k_m \end{pmatrix} = \begin{pmatrix} u_1 \\ u_2 \\ \ldots \\ u_n \end{pmatrix}$$

Based on definition we are interested on

$$\{k = (k_1, k_2, .., k_m) \in N^m \,/\, \varphi_1(k) = u = (u_1, u_2, .., u_n)\}$$

and $\prod_{l=1}^{n}\left[\bigcup_{i=1}^{n}\left(u_{li} \ne \sum_{j=1}^{m} k_j \cdot u_{lj}\right) \ne u_{li}\right]$ [4].

We know that there might be more than one value "k". We are just interested on one value 'k' that complies with $\varphi_1(k) = x$. This is possible as the set $K = \{k = (k_1, k_2, .., k_m) \in N^m / \varphi_1(k) = x\}$ is always included in a feasible region [4]. This feasible region is an area which contains the set *K*. There are several methods to select one element of *K* within a feasible region. These methods are studied on [4].

Because any of these methods always returns a value, we can state that this is possible. It is stated in the *algorithm for Application of Evolution Rules based on linear Diophantine equations.* [4]

IV. Building the Structure L.

Within a region, let *U=* $\{a_i \mid i = 1,..n\}$ be a *multiset of objects and let R (U, T) be* a multiset of evolution rules. *Given the set* {$k_i \in N$ *the number of times that the evolution rule* r_i *is applied over the initial multiset},* *The values we are seeking are:* $k = (k_1, k_2, .., k_m) \in N^m$ For any element, $u = (u_1, u_2, .., u_n) \in N^n$, we store the value $k = (k_1, k_2, .., k_m) \in N^m \,/\, \varphi_1(k) = u$. Thus, $L[(u_1, u_2, .., u_n)] = k_1 k_2 .. k_m$

If the position $(u_1, u_2, .., u_n)$ of the structure already has information, then we do not store anything. Each entry of the structure contains the values: $k_1 .,.. k_m$. These values will indicate the number of times that an evolution rule should be applied to an initial multiset in order to obtain an extinguished multiset. The number of objects determines the coordinates of a given position in the structure; thus, as the number of objects increases so it does the dimension of the structure; i.e. working with an alphabet *V* of 2 symbols V= (a_1, a_2) means that our structure is two-dimensional. The numbers of entries existing in the structure depends on the dimension, (number of symbols of our alphabet) and the benchmark of every object. This benchmark is a value associated to every object of our alphabet. The benchmark fixes a limit for the multiplicity of the objects existing in our alphabet. In order to make the structure useful, we need to fix reasonably high benchmarks. Our structure does not store information about the values that are higher that the prefixed benchmarks.

V. The algorithm

The algorithm searches on the structure that has been previously built. The multiplicities of a given initial multiset are provided as input for the algorithm.
During compilation time the structure is build and stored in memory. During the execution time, *the algorithm just searches in the structure L the position* $(u_1, u_2, .., u_n)$

```
u_1,u_2,..,u_n ← Multiplicity(m)
BEGIN
output(L(u_1,u_2,..,u_n))
END
REPLACE(L(u_1,u_2,..,u_n))
```

$(u_1, u_2, .., u_n)$ *is the input value corresponding to the multiplicities of the initial multiset m.. After the output is given, another value (if it exists)*
$k' = (k'_1, k'_2, .., k'_m) \in N^m \,/\, \varphi_1(k') = u$
replaces the entry $(u_1, u_2, .., u_n)$. That way we assure that every time we execute the algorithm for the same input, we obtain a different output

VI. Conclusions

This work contributes with a new technique in finding maximal multisets from initial multisets. The technique offers a complement to be used by the traditional algorithms which calculate extinguished multisets. These algorithms find the extinguished multisets after applying a certain number of evolution rules a certain number of times. The technique presents the idea of going "backwards" from the initial multisets to the number of times that each rule should be applied. This process automatically obtains the times that each rule should be applied and no extra calculation is necessary. From there, calculating the extinguished multisets is immediate.
,In order to generalize this technique, a deeper analysis would be necessary to estimate the memory needed when certain rules are provided. This study will focus on four factors when building the structures:

- Number of evolution rules
- Applicability Benchmark of an evolution rule
- Number of symbols
- Benchmark associated to the symbols.

Within the researching area: "*membranes computing",* this work proves that not only using parallelism is beneficial in terms of performance but also memory is really helpful under certain conditions. In this case, a proper utilization of memory let us build a structure which will reside in the physical and/or the virtual memory.

VII References

[1]. Gh. Păun, "Computing with Membranes", Journal of Computer and System Sciences, 61(2000), and Turku Center of Computer Science-TUCS Report nº 208, 1998.
[2]. Gh. Păun, "Membrane computing. Basic ideas, results, applications", Pre-Proceedings of First International
Workshop on Theory and Application of P Systems, Timisoara (Romania), pp. 1-8, September , 2005.
[3]. Lingian Pan, Carlos Martin-Vide
"Solving multidimensional 0-1 knapsack problem by P systems with input and active membranesl"
Journal of Parallel and Distributed Computing
Volume 65 , Issue 12 (December 2005)
[4]. A. Arteta, L.Fernandez, J.Gil "Algorithm for Application of Evolution Rules based on linear diophantine equations" Synasc 2008
Timisoara Romania September 2008.

Investigation of the efficient protection from Influenza pandemic using CARMS

Kenji Tsunoda[1], Kyoko Shinya[2] and Yasuhiro Suzuki[1]

[1]Graduate School of Information Science, Nagoya University, Furocho Chikusa Nagoya City, 464-8603 JAPAN
,[2]International Center for Medical Research and Treatment, Kobe University,
7-5-1 Kusunoki-cho, Chuo-ku, Kobe 650-0017 Japan
(Tel : 81-52-7894783; Fax : 81-52-789-4783)
(Email;ysuzuki@is.nagoya-u.ac.jp)

Abstract:The new influenza A virus,H1N1-pdm, is spreading out all over the world including Japan.Since almost all the people are non-immunized for this new influenza virus, it spreads all over the world quickly. Currently, we have two options for the disease prevention, i.e. vaccination and antiviral drags. And among them, vaccination is the best way for mass protection. However current system of vaccine production has limitation for production number and preparation time. To understand "the most efficient mass protection", we simulate the influenza spreading by using the Cellular Abstract Rewriting System on Multusets, CARMS**.**

Keywords: Influenza, pandemic, CARMS

I. INTRODUCTION

The new pandemic influenza virus, H1N1-pdm, is efficiently spreading out all over the world, because almost all the people in the world do not have antibody against this new influenza virus. Vaccination is a biological tool for acquisition of immunity to a particular disease. For the mass protection from influenza virus infection, vaccine has been developed and used. Vaccinated host's immune system can recognize the influenza virus as foreign material then destroy and "remember" it. The immunized host can be more resistant to the pathogen, because they easily and quickly exclude the virus after the exposure. Therefore a vaccinated person can reduce morbidity risk when the person contacts with infected persons. As a logical consequence, vaccination can decrease the chance of contact between contagious and susceptive persons. Vaccination creates "buffer" between infected and non-infected persons and therefore prevents epidemic.

However, as current problem, vaccine production takes long time; even when a new strain of influenza virus with epidemic potential is identified and isolated; it will take approximately five to six month for the first supplies of approved vaccine to become available. And once a new vaccine has been approved, the vaccine production process typically takes between 6 and 9 months.

Effectiveness of influenza vaccine to prevent infection is not perfect; there are multiple reasons behind in vaccine efficacy, the most common of which are the declining immunological function and frailty associated with advanced age [2],[4],[5].

It is no wonder that vaccination is the most effective method for preventing influenza virus infection, but we should consider that effectiveness of vaccine is not perfect, so even if all citizens have been vaccinated, we cannot prevent infection completely. And since it takes time to create and produce vaccines, it is not easy to deliver vaccines to all citizens quickly [3],[4].

In this study we investigate the effectiveness of strategies of prevention of pandemics;

i. how many persons should be vaccinated?
ii. how high effectiveness rates of vaccines are required?,
iii. how effective is we take the priority for inoculation?

II. Method

We model the influenza infection process by using the cellular automata of Abstract Rewriting System on Multisets, CARMS..

ARMS [6] was proposed in 1996 as an abstract model of chemical reactions, *Artificial Chemistry* (AC), in the context of the Artificial Life. An ARMSis a construct Gamma Γ=(A,w,R), where A is an alphabet, w is a multiset present in the initialconfiguration of the system, and R is the set of multiset rewriting rules. Let A be an *alphabet* (a finite set of abstract symbols). A *multiset* over A is a mapping M: A→**N**, where **N** is the set of natural numbers; 0, 1, 2,…. For each $a_i \in A$, $M(a_i)$ is the *multiplicity* of a_i in M, we also denote $M(a_i)$ as $[a_i]$. We denote by $A^\#$ the set of all multisets over A,with the empty multiset, emptyset, defined by emptyset (a)=0 $\forall$ a $\in$A.

A multiset M: A→**N**, for A={a_1,…, a_n} is represented by the state vector w = ($M(a_1)$, $M(a_2)$, …, $M(a_n)$), w. The union of two multisets M_1, M_2: A →o **N** is the addition of vectors w_1 and w_2 that represent the multisets M_1, M_2, respectively. If $M_1(a) \leq M_2(a)$ for all a $\in$ A, then we say that multiset $M_1$is included in multiset M_2 and we write $M_1 \subseteq M_2$.A *reaction rule r* over A can be defined as a couple of multisets, (s_u), with $s_u \in A^\#$. A set of reaction rules is expressed as R. A rule r = (s, u) is also represented as r = s→u. Given a multiset w$\subseteq$ s, the application of a rule r=s→u to the multiset w produces a multiset w' such that w' = w - s + u.

In order to simulate pattern formation, we compose cellular automataby using the ARMS and call it Cellular Automata of Abstract Rewriting System on Multisets (CARMS) [2]. An n dimensional ARMS is called nD-CARMS. A periodic boundary condition is assumed. In the 2D-CARMS which we used, each molecule has three attributes: position in a field (2 dimensional spaces, 500 x 500), velocity and the condition of health. The condition of health is represented by following three states; health, infected and cured (vaccinated).

In the initial state, each molecule is located randomly in the field and is given a random speed, v=1.0~2.0, and a random angle, Θ=0~2π. The size of an molecule is 12 in diameter. And the periodic boundary condition has been taken. Each molecule updates velocity (speed and angle) at the every collision, while an molecule does not collide, its velocity and angle do not change. When a health molecule collides with an infected molecule , its condition of health is changed to "infected"; while other types of collisions do not change the condition of health. An infected molecule changes the condition of health from "infected" to "vaccinated" after 200 time steps from when it has been collided with an "infected" molecule . In the initial state of every simulation, we set the number of infected molecule is one.

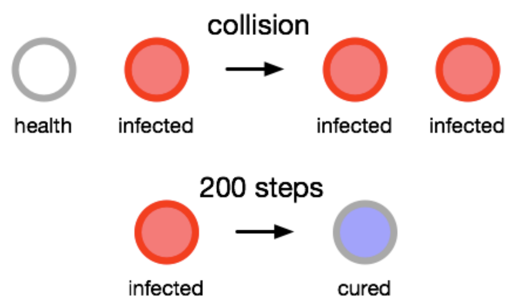

Fig.1 Reaction rules of molecule s actions

II. Experiments

Experiment1: how many parsons should be vaccinated?;

We set the *p* for immunization rate for vaccines of a group, where we assume that the vaccine efficacy rate is 100% so every person gains anti-body by an inoculation. We increase *p* from 0.1 to 0.9 by 0.1 and examine the temporal development of the number of infected persons, the number of step until the termination epidemic and the number of not infected persons until the epidemic terminates.

Experiment2: how high effectiveness rates of vaccines are required?

In order to express the effectiveness rate of a vaccine, we set the threshold value for applying reaction rules; in case an molecule has a low effective vaccine then the molecule will be infected when it will collide infected molecule s few times, where the threshold value, Θ set to small, and the reaction rule of "health + infected → infected, infected" (Fig.1 upper) will not be fired within Θ times of collisions with infected molecule s, while in case the effectiveness is high, Θ is set to large and the reaction rule will not be applied within many times of collisions . We examine the change of temporal development of the number of infected persons, when Θ is 1, 2, 5 and 10.

Experiment3: how effective if we take the priority for inoculation?

We simulate the case when we take priority of inoculating for high risk of infection possessed molecule s. In order to express the degree of the risk of infection, we use the velocity of moving of an molecule ; when the velocity is slow then the molecule will not collide against many infected molecule s so the probability of infection will be low, while the velocity is fast then the molecule will collide against many infected molecule s and the probability of infection will be high. We classify molecule s into three groups with according to its risk of infection as low, middle and high. In this experiment, the total number of molecule s is 300 and they are classified into three groups equally (100 molecule s each). We examine the case when the all molecule s in one of these groups take priority for inoculation and the change of temporal development of the number of infected persons are examined.

III. Results

All of the results of simulations are the average of 100 trials.

Experiment 1

When the immunization rate for vaccines *p* = 50%, the peak of the number of infected molecule s was suppressed around 75% low compared to the case when *p* = 0%; however, the duration of epidemic was prolonged and all molecule s is infected, after all (Fig.2).

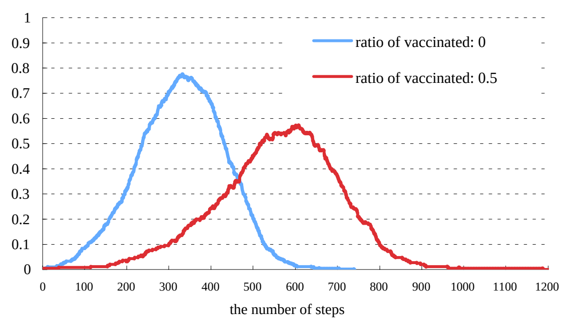

Fig.2 temporal development of the number of infected molecule , where the blue line illustrates the case when *p* = 0% and the red line illustrates when *p* = 50%.

The average rate of the number of not infected and infected molecule s until the epidemic terminates (we will denote this rate as γ) increased exponentially when p = 0.8; so when p is equal or larger than 0.8 almost no one was infected. In such cases, infected molecule s were likely to be disappeared until 200 simulation steps so the value of γ increased rapidly; when p = 0.8 and 0.9, the number of cases when no epidemic emerges was 25 and 42 for 100 times of trials of simulations (Fig.3).

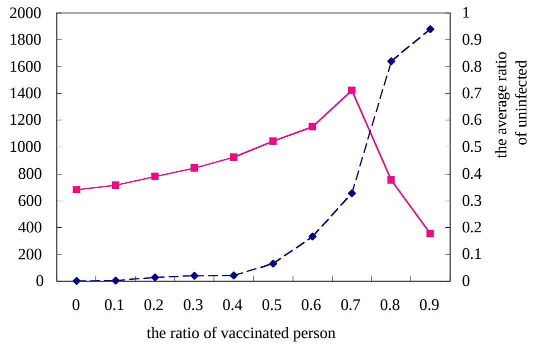

Fig.3 the immunization rate for vaccines p and the average of the number of not infected molecule s until epidemic terminates.

Experiment 2

We examined temporal development of the number of infected molecule s when the effectiveness rate of vaccinated, Θ is 1, 2, 5 and 10. When Θ = 5, the peak of the number of infected molecule s were largely suppressed, compared to the case when Θ= 1 or 2. When Θ=1, 2, and 5, the ratio of the number of infected molecule s for the total number of molecule s were 0.88, 0.78 and 0.48, respectively. And when Θ= 10, no epidemic emerges and infections were terminated (Fig.4).

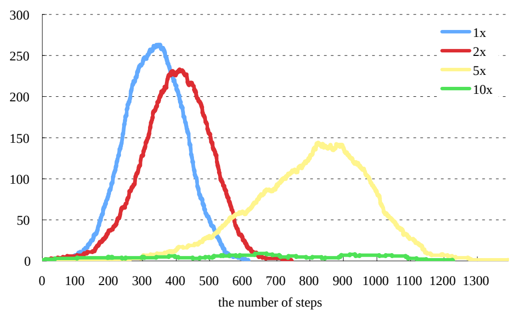

Fig. 4 temporal development of the number of infected molecule s, where blue line illustrates the case when Θ=1, red line, Θ=3, yellow line, Θ=5 and green line, Θ=10.

Experiment 3

When only the low risk infection molecule s were vaccinated, the ratio of the number of infected molecule s at the peak of epidemic is 0.83 (=165/200), it was lesser than the case when no molecule was vaccinated (276/300 = 0.92). When only the middle risk infection molecule s were vaccinated, the number of infected molecule s at the peak was 0.75 (150/200), while only the high risk molecule s were vaccinated, the number of infected molecule at the peak was 0.45 (=89/200) (Fig.5).

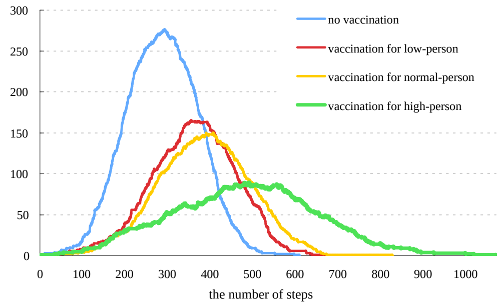

Fig.5 temporal development of the number of infected molecule s when the priority for vaccination is taken; where the red line illustrates when low risk infection molecule s are vaccinated, the yellow line, middle risk molecule s are vaccinated and the green line, high risk molecule s are vaccinated (the blue line illustrates the case when no molecule is vaccinated).

IV. Discussion

It is no wonder that vaccination is effective method for preventing infection; throughout simulations it has shown that vaccination creates "buffer" between infected and non-infected persons and prevents epidemic.

The result of experiment 1 shows that vaccination suppresses the number of infected molecule s at the peak of pandemic; it is important for controlling the pandemic, because the high peak of the infected people's number causes break down of social and medical structures. However, the result of experiments shows that large scale vaccination (more than 80% in the experiment) will be required for preventing pandemic, otherwise vaccination cannot completely prevent spreading of the infection and it will be smoldering until almost all the persons are infected, even if it can suppress the peak number of infected persons during pandemic.

It has been reported that effectiveness of influenza vaccine to protect form the infection is not perfect; because of the declining immunological function and frailty associated with advanced age [1]. However the result of experiment 2 shows that even if the quality of vaccine is not perfectly good, it can prevent the pandemic.

The result of experiment 3 indicates that the priority for vaccination for high risk infection molecule s, such as medical experts, will be effective for preventing epidemic. Hence, in case we cannot take large scale vaccination, we can suppress the pandemic by the priority for vaccination; this policy has been proposed by the Ministry of Health and Welfare of Japan and this result supports its effectiveness.

In this study, we modeled temporal development of the number of infected / non-infected persons; to expand this simple model including diffusions in the space [1] is our future work.

References

[1] Ferguson NM, Cummings DA, Cauchemez S, Fraser C, Riley S, Meeyai A, Iamsirithaworn S, Burke DS. Strategies for containing an emerging influenza pandemic in Southeast Asia. Nature. 2005 Sep 8;437(7056):209-14. Epub 2005 Aug 3.

[2] M.Umeki and Y. SuzukiA simple method for simulating chemical reactions, Computing and Informatics,Vol. 27, no. 3+ (2008), p. 529-550.

[3] Shingo Iwami, Takafumi Suzuki, Yasuhiro Takeuchi, Paradox of Vaccination: Is Vaccination Really Effective against Avian Flu Epidemics?, PLoS ONE , Volume 4 (3): e4915, 2009.

[4] Shweta Bansal1, Babak Pourbohloul2, Lauren Ancel Meye, A Comparative Analysis of Influenza Vaccination Programs, PLoS MEDICINE vol3. Issue 10, 1816-1825, 2006.

[5] Simonsen, L., Taylor, R.J., Viboud, C., Miller, M.A., & Jackson, L.A. (2007). Mortality benefits of influenza vaccination in elderly people: An ongoing controversy. The Lancet Infectious Diseases, 7, 658-666.

[6] Yasuhiro Suzuki, Shusaku Tsumoto, Hiroshi Tanaka, Analysis of cycles in symbolic chemical system based on Abstract Rewriting System on Multisets, Alife V, 521-529, 1996, MIT press.

Organization Levels in P Systems

Marion OSWALD
Computer and Automation Research Institute
Hungarian Academy of Sciences
Budapest, Hungary
marion@sztaki.hu

Abstract

We discuss different (structural) organization forms of a formal model of computation that is abstracted from the structure and functioning of living cells: P systems, introduced in 1998 by Gh. Păun. After a brief review of some of the main classes of P systems, having an underlying tree or graph structure, we present some indications that suggest to use a more general hierarchical structure. We highlight some examples and point out further applications where this broader approach could be useful.

1 Introduction

Membrane Computing has become a vivid and active research front in the past eleven years. (For an introduction to the field see [13], a complete bibliography can be found at [19]).

P systems (also called membrane systems) have originally been defined by Gh. Păun [12] as a computing model in the following sense. In a hierarchical membrane structure (that can also be represented as a tree), objects evolve according to so-called evolution rules. Starting from an initial configuration of the system, a computation is performed by applying the rules in a nondeterministic, maximally parallel way until the system eventually halts.

Dating back only a decade, many interesting aspects have already been investigated, e.g., the computational power of different variants, normal forms, the solution of NP-complete problems in polynomial or even linear time, etc., see for instance [14].

Although, as stated in [12], the original intention of P systems was not to model the cell, but to abstract from its structure and function to obtain a computing device, we can observe a recent trend in the area towards modeling biological phenomena in this versatile framework.

While the underlying structure of the original P system is a tree, where membranes can be nested, and hence be represented by a Venn diagram (but without intersecting sets), a more general structure has been taken into account a short time later: tissue P systems, having an underlying (arbitrary) graph structure. Only recently, an even more general (i.e., hypergraph) structure was taken into account.

Without going into formal details, we here give an outline of the structural concepts employed in membrane computing so far and point out possible extensions.

After some preliminaries about graph concepts and P systems in general, we briefly review recent variants that take into account a more general organization form in section 3. Some possible extension to a more general model are discussed in section 4, some notes on possible applications conclude the paper.

2 Preliminaries

2.1 (Hyper)Graphs

A *graph* G is a pair (V, E), where V is a non-empty set of nodes and E is a set of edges $e = (v_1, v_2)$, $v_1, v_2 \in V$. A *path* in G is a sequence of vertices of the form $v_0, v_1, ..., v_n$ such that $(v_i, v_{i+1}) \in E$ for $i = 0, ..., n-1$. In a closed path (also called *cycle*), $v_0 = v_n$. We call a graph G *connected* if there is a path between any two distinct vertices. A graph is a *tree* if and only if for every pair of distinct vertices v_1, v_2 there is exactly one path from v_1 to v_2. In other words, a tree is a connected graph without cycles.

While in graphs, edges are between two nodes, in a more general graph, a so-called *hypergraph*, edges are between sets of nodes (that may also intersect). The edges in a hypergraph are also called *hyperedges*.

Following [3], a hypergraph is defined as follows.

Let $V = \{v_1, v_2, ..., v_n\}$ be a finite set. A hypergraph on V is a family $H = \{E_1, E_2, ..., E_n\}$ of subsets of such that

- $E_i \neq \emptyset$, $1 \leq i \leq m$ and
- $\cup_{i=1}^{m} E_i = X$.

The notion of hypergraph can even be more generalized by having hyperedges pointing to hyperedges, thereby inducing a hierarchy, that then corresponds to a so called *directed acyclic graph* (or *dag*, for short). An example is shown in figure 1.

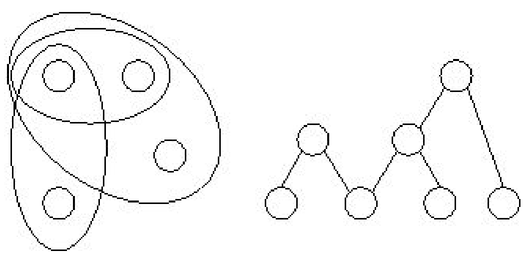

Figure 1: hypergraph and associated dag

For more details we refer to any textbook in the area, e.g. to [5].

2.2 P Systems

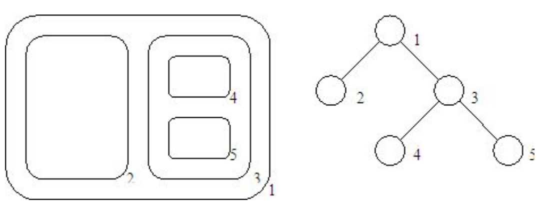

Figure 2: membrane structure and associated tree

P systems are computing devices abstracted from cell functioning and are based on the notion of a *membrane structure*. A membrane structure consists of membranes hierarchically embedded in the outermost skin membrane; every membrane encloses a region possibly containing other membranes; the region outside the skin membrane is called outer region or environment. A membrane structure can be graphically represented by a Venn diagram without intersecting sets, so that any two sets are either disjoint or one set is a subset of the other one. Since the membranes in such a structure (usually labelled in a one-to-one manner) are hierarchically arranged, it can also be represented by a tree (an example for a membrane structure and its associated tree is shown in figure 2). On the other hand, it can also be described by a string of correctly matching parentheses (e.g., the membrane structure from figure 2 corresponds to the string $[_1 [_2\,]_2\, [_3\, [_4\,]_4\, [_5\,]_5]_3\,]_1$).

In the membranes, *multisets of objects* can be placed, which evolve according to given *evolution rules*. Depending on the model, these rules can be applied in parallel across all membranes or in a rather sequential manner. Usually, the rules to be applied are non-deterministically chosen (i.e., if an object can evolve according to more than one evolution rule at the same time, any one is chosen). A configuration can be illustrated by putting the objects and rules in the corresponding compartments of the membrane structure. In this way, a computing device is obtained in the following sense: Starting from an initial configuration (given by the membrane structure, the distribution of the objects, as well as evolution rules), the system evolves by passing from one configuration to another one, thereby performing a computation, see [13] for motivations and examples.

Many variants of P systems have been investigated since their introduction, by varying various ingredients (the nature of the objects, evolution rules, derivation modes, etc.) We refer the interested reader e.g. to [14] for more details.

3 Higher Organization Levels in P Systems

P systems with an underlying tree structure (as originally defined) offer the possibility of hierarchical organization: one of the main feature of membrane systems and their biological motivation is that it can also bee seen as having more layers of abstraction, e.g., atoms-molecules-cells-tissues-organs-organisms, etc.

However, the exhibited hierarchical organization is limited because on one hand, a tree is rather restrictive (in that it can only have one root node), and on the other hand, the nodes cannot overlap (i.e., the membranes are nested but do not intersect). Yet just this overlap could be extremely interesting. On one hand, it is naturally plausible (e.g., several signaling and/or metabolic networks may overlap, like for example the Wnt signaling pathway that plays a role in embryogenesis and cancer, see [7]) and it might well be used in an algorithmic way as well (see section 5).

Taking a more general (arbitrary) graph structure, the above mentioned restriction is partly overcome, but at the price of loosing the hierarchical information.

Yet in the last few years, more general forms of (structural) organization came to existence also in membrane computing, we give a few examples in chronological order:

- **Quorum sensing P systems** were introduced in 2005, and can in fact be considered the first ones that took this the mentioned overlap into account, although not explicitly. In [2], the authors model colonies of bacteria by means of Quorum sensing P systems, where each bacterium acts in its specific environment, and the different environments can overlap.
- **Multigraphical Membrane Systems**, introduced by Obtułowicz in 2007 [11] present a visual formalism that is based on multigraphs (i.e., graphs that can have multiple edges, but the edges cannot overlap).
- **Modularisation** is taken into account by Romero-Campero et al. [15], [16]. By means of Stochastic P systems, the authors investigate a very particular variant for a specific model, taking into account 3 levels: the molecular, the cell, and the colony level.
- **Hyperdag P Systems** were only recently introduced by Nicolescu et al. [10] as P systems with an underlying generalized multiset-based hypergraph (i.e., dag) structure, thereby also introducing rules for enhanced inter-level communication ("go-sibling", see [10]).

While in [2], [15], and [16], the focus is on biological modelling, the investigations in [10] are of a more general kind, even proposing a new planar representation of hyperdag P systems. While this definitely has its merits in some areas, it also has limitations when it e.g. comes to biological modelling, where the visualization is of great importance. Hypergraphs might not be the best choice due to its difficulty of being drawn as a pictorial representation. Yet a closely related concept called metagraphs (introduced by Basu and Blanning [1]) seems to be a better choice in this respect. Metagraphs support nodes, edges and even subnetworks contained and nested within a scalable structure, where the nodes can also overlap. Easy transitions between different levels of resolution are supported, called "semantic zooming" (see [8]), a concept that is already adopted by some software tools (e.g., VisANT, see [20]).

4 Towards a more general structural approach

As already stated in the previous sections, it might well be useful to think of P systems having an underlying generalized hypergraph or directed acyclic graph structure. From a theoretical point of view, it is obvious that the system under consideration does not loose its computational power if only the structure is changed in this way (since a hypergraph is more general than a graph, i.e., each graph is a hypergraph, in which the cardinality of each hyperedge is exactly two.)

Yet from the modeling perspective, (and not only concerning computer networks, as explored in [10]), it offers a new opportunity to include more complex system behavior (as e.g. argued by Mesarovic and Sreenath [9] in terms of "complex "systems biology). In this respect, in addition to the more general organization levels, many possible extensions could facilitate the accuracy of the model.

Like in the category theory framework of memory evolutive systems as explored in [6] (also see [18]), one could incorporate different timescales for the levels (as, e.g., reactions at an atomic level happen faster than those on the molecular level.)

On the other hand, and especially when the system becomes more complex, we could include some regulation mechanism.

For example, we could introduce regulators that have a certain "radius" (i.e., be responsible for some elements, e.g., for a certain number of nodes in one level). Now if a regulator observes a specific pattern, then it can induce an action in the corresponding cells, like e.g. changing the ruleset of a cell.

If we look at the evolution of the system, it is also natural to not only let the symbols evolve in the course of time, but also the underlying structure. Some parts of the system might grow, while others could (structurally) reorganize themselves or even die.

This idea is not new in the area of membrane computing (so-called P systems with active membranes have already been introduced in 2001, originally mainly used to solve NP-complete problems in polynomial, sometimes even linear time), but in this more general framework of course needs some adaptations to capture also the possible overlap of the cells, i.e., the nodes in the hypergraph (e.g., we could consider rules like $[_i a]_i [_j b]_j \rightarrow [_i c [_j d]_i e]_j$ to account for this). The structural change could be induced by rules (e.g., in the sense of [4]), or be incited by the regulators.

While all the above mentioned extensions can be defined (i.e., incorporated in a formal definition) in a straightforward way, a big challenge remains in defining concepts that allow for emergence, a central concept of complex systems.

5 Conclusion

We discussed different structural organization forms of P systems, highlighting the usefulness of a more general underlying structure, i.e., (generalized) hypergraphs that might enrich especially the modelling of hierarchical systems (biological, social, ecological, cultural systems, etc.).

On the other hand, it seems also to be worthwhile to explore the proposed systems for their algorithmic capabilities. Many computations comprise a common set of known interaction and computation patterns. One particular example are overlapping subproblems (i.e., subproblems that are reused several times). Problems that have this property are often solved by dynamic programming techniques more efficiently than with other methods. Yet very often complex data dependencies occur and complicate parallelization. Investigations concerning the practicability of P systems (with an underlying hypergraph structure) in this respect are currently performed by the author (focusing on so-called nonserial polyadic dynamic programming, like e.g., matrix chain multiplication and RNA secondary structure prediction).

Acknowledgements We gratefully acknowledge interesting and fruitful discussions with E. Csuhaj-Varjú, T. Roska and Gy. Vaszil.

References

[1] A. Basu, R.W. Blanning, A. Shtub: Metagraphs in Hierarchical Modeling. Management Science 43 (5) 1997, 623–639.

[2] F. Bernardini, M. Gheorghe, N. Krasnogor: Quorum sensing P systems. Theoretical Computer Science 371 (2007) 20—33.

[3] C. Berge: *Hypergraphs*. North-Holland Mathematical Library, Amsterdam, 1998.

[4] E. Csuhaj-Varjú, A. Di Nola, Gh. Păun, M. J. Pérez-Jiménez, Gy. Vaszil: Editing Configurations of P Systems. Fundamenta Informaticae 82 (1-2), 2008, 29–46.

[5] R. Diestel: *Graph Theory*. 3rd edition, Graduate Texts in Mathematics 173, Springer, Heidelberg, 2005.

[6] A.C. Ehresmann, J.-P. Vanbremeersch: *Memory Evolutive Systems; Hierarchy, Emergence, Cognition* (Studies in Multidisciplinarity). Elsevier Science, 2007.

[7] H. A. Kestler, M. Kühl: From individual Wnt pathways towards a Wnt signalling network. Phil. Trans. R. Soc. B 363 (1495) 2008, 1333–1347.

[8] Z. Hu, J. Mellor, J. Wu, M. Kanehisa, J. M. Stuart, C. DeLisi: Towards zoomable multidimensional maps of the cell. Nature Biotechnology 25 (5) 2007, 547–554.

[9] M. Mesarovic, S.N. Sreenath: Beyond the flat earth perspective in systems biology. Biological Theory 1 (1) 2006, 33-34.

[10] R. Nicolescu, M.J. Dinneen, Y.-B. Kim: Structured Modelling with Hyperdag P Systems: Part A. in: M. A. Martínez-del-Amor, E. F. Orejuela-Pinedo, Gh. Păun, I. Pérez-Hurtado, A. Riscos-Núñez (Eds.): Seventh Brainstorming Week on Membrane Computing, Sevilla, February 2-6, 2009, Volume II, 85 – 108.

[11] A. Obtułowicz: Multigraphical Membrane Systems: a Visual Formalism for Modeling Complex Systems in Biology and Evolving Neural Networks. In: G. Eleftherakis, P. Kefalas, Gh. Păun (Eds.): Proceedings of the 8th InternationalWorkshop on Membrane Computing (WMC8), SEERC 2007, 509–512.

[12] Gh. Păun: Computing with Membranes. Journal of Computer and System Sciences 61, 1 (2000), 108–143.

[13] Gh. Păun: Computing with Membranes: An Introduction. Springer, Berlin, 2002.

[14] Gh. Păun, G. Rozenberg, A. Salomaa (eds.): *The Oxford Handbook on Membrane Computing*. Oxford University Press, to appear.

[15] F. J. Romero-Campero, J. Twycross, M. Bennett, M. Càmara, and N. Krasnogor: Modular Assembly of Cell Systems Biology Models Using P Systems. Int. J. Found. Comput. Sci. 20(3) 2009, 427–442.

[16] F. J. Romero-Campero, J. Twycross, H. Cao, J. Blakes, and N. Krasnogor: A Multiscale Modelling Framework Based On P Systems. In: D.W. Corne, P. Frisco, Gh. Păun, G. Rozenberg, A. Salomaa (Eds.): Membrane Computing. 9th InternationalWorkshop, WMC 2008 Edinburgh, UK, July 28-31, 2008, 63-77.

[17] E. Van Hensbergen, C. Forsyth, J. McKie, R. Minnich: Holistic aggregate resource environment. ACM SIGOPS Operating Systems Review 42 (1) 2008, 85–91.

[18] The MES Web Page, `http://pagesperso-orange.fr/vbm-ehr/`

[19] The P Systems Web Page, `http://ppage.psystems.eu`

[20] The VisANT Web Page, `http://visant.bu.edu/`

Reinforcement Learning Using Voronoi Space Division

KATHY THI AUNG	Takayasu FUCHIDA

kathythiaung@gmail.com	fuchida@ibe.kagoshima-u.ac.jp

Information and Computer Science Department, Engineering Faculty, Kagoshima University, Kagoshima, Japan
(Tel: 81-99-285-8453; Fax: 81-99-285-8464)

Abstract: This research is concerned with the study method of the robot and program. It deals with the reinfo rcement learning and has gradually become one of the most active research areas in machine learning, artificia l intelligence and neural network research [3]. Using the Voronoi diagram for space division of reinforcement learning creates a new Voronoi region which permits an arbitrary point in the plane. This paper constructs a new
method for space division by a Voronoi diagram and shows some results in four-dimensional spaces.

Keywords: Reinforcement Learning, Q-Learning, Q Element, Voronoi Diagram, VQE

I. INTRODUCTION

Q-learning is preserved in the table, it has the value of each action in a certain state as action value (Q value) and it is called Q table [4] but the size of Q table will increase rapidly by Curse of dimensionality when continuous is treated by Q table and it is not realistic.

Curse of dimensionality means if the dimension number of state space increases, the state also increases exponentially when state space is divided like lattice and the learning speed decreases dramatically. [4]

II. PREVIOUS STUDIES IN THE FIELD

We introduced table element (QE) that dynamically gives the Q value to the state action pair. It is difficult to update of adaptive QE hand it to the state space because of it makes the shape of QE into a rectangular QE. The problem area of adaptive QE is difficult to add, divide and integrate. To solve this problem, we propose VQE using the concept of Voronoi division.

III. PURPOSE

The focus of this study is Voronoi diagrams for space partition creates Voronoi regions where Voronoi Q-value Elements (VQE) are to be located in the continuous state space and it has been proposed for solving the waste of spaces.

The present paper proposes applying a Voronoi division for the continuous state space satisfying the above conditions. Concerning with these region, a Voronoi diagram are defined.

IV. RESEARCH METHODS

1. Reinforcement Learning

Reinforcement learning (RL) is one of the most important learning methods for machine learning and is learning by interacting with an environment. [1] In a reinforcement learning paradigm, a system called agent repeatedly observes the current state of its environment, and then select an action and performs an action. The environment changes the state by the agent's behavior and returns the reward. The agent transits the next state and takes the reward. And then learns based on the reward and updates by its own action policy. [1] Figure 6 shows the fundamental standard feature of framework for RL.

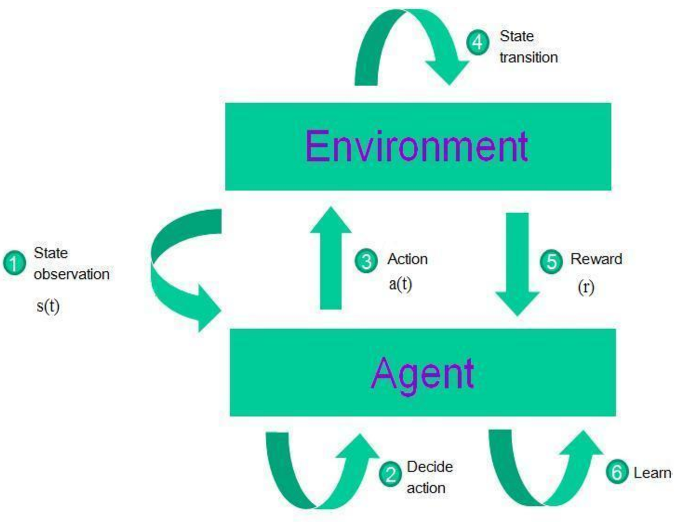

Fig.1. Reinforcement Learning

A. Q-learning

Q-learning is one of the typical techniques of reinforcement learning (RL) and has been applied in this study [1]. The Q-function is used to predict the discounted cumulative reinforcement (also called Q value) for each state-action pair (*s*, *a*) given that the agent is in that state and executes that action because of the agent learns a mapping from states and actions to their Q values. We can estimate the Q values using this method because an action can be chosen just by taking the one with the maximum Q value for the current state.

At each step state (*s*), choose the action (*a*) which maximizes the function $Q(s_t, a_t)$ where Q is the estimated utility function that it tells us how good an action is given a certain state and execute it. And then it receive immediate reward (*r*) and observe the new state (s_{t+1}). $Q(s_t, a_t)$ is immediate reward for making an action and best utility (*Q*) for the resulting state.

The Q-function can update in the following way after looking farther ahead:

$$Q(s_t, a_t) = Q(s_t, a_t) + \alpha(r + \gamma \max_a Q(s_{t+1}, a) - Q(s_t, a_t))$$

This equation means if the Q value of next state is higher than the current Q value, it depreciate the current Q value. On the other hand, if low, upgrade the current Q value.

Where γ is a discount factor and α is the learning rate. $Q(s_t, a_t)$ is time(*t*), state(*s*), action(*a*) of Q value.

B. Voronoi Diagram (VD)

Voronoi diagram (VD) has the property that for each site (clicked with the mouse) every point in the region around that site is closer to that site than to any of the other sites. [2] Generally, Voronoi like partitions. It can be used to preserve spatial relationships. [2] But if space is metric space, where distance between a pair of points can be defined but if space is as set of dimensions that are not related spatial. In dimension, constructing the Voronoi diagram (VD) is no longer the method of choice for finding the closest pair, due to its exponentially increasing size but it introduced for finding the nearest neighbors of a point in expected time. So it can solve the all nearest neighbor problem for each point and can find the shortest paths. The graphic of VD is illustrated in figure 2, where the color areas indicate the Voronoi diagram belong the black point and the black point are the mother point arranged in space.

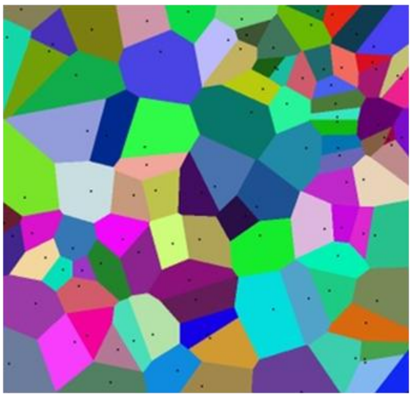

Fig.2. Voronoi Diagram

2. Voronoi Space Division of State Space

A. Division methods of Q-learning

The normal Q-learning is suit for the discrete space but it is difficult to treat the continuous state space. So when we treat such continuous cases, it needs to divide the space into a lot of smaller discrete regions. Using the normal Q-learning in continuous state space, the state space is divided like lattice but the lattice like division possibly generates the waste spaces. So when we divide the normal Q learning in continuous state space by lattice method, it is evenly arranged the Q value in all over the space and if the dimension increases, the number of state also increases by exponentially.

B. VQE (Voronoi Q-value Elements)

Learning evaluates the necessary state in details but the unnecessary part of state make up as a method of roughly so it suggested to use the area of division technique that is called Voronoi diagram (fig2) and it partitioned which arbitrary point is nearest compared with mother points arranged on a space.

In the case of the input point enters within more than one of the region, the input point and each of VQE of the distance are refer to VQE of the most shortest distance. And then, act the action learn using that of Q value. According to the Voronoi division, the overlapping area within the range of VQE is divided finely. In figure 3, the old areas are used as Voronoi division. The red circles are created as VQE when the input enters in such a place.

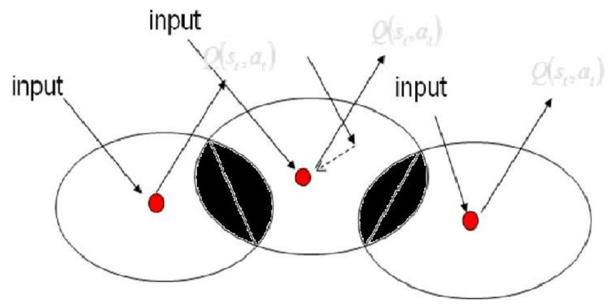

Fig3. Shape of VQE

C. Division Method of VQE

The division method of VQE is arranged by VQE in mostly at the place that a lot of points of VQE.

V. EXPERIMENT

1. 4-D Model of VQE

Figure 4 is the shape of continuous state space of VQE in 4 dimensional spaces. The content of simulation is as follows: the control action of agent is three types of forward, left rotation and right rotation. The input states of four values are the distance from the agent to the reward area1, reward area2 and the angles between the agent and those two areas.

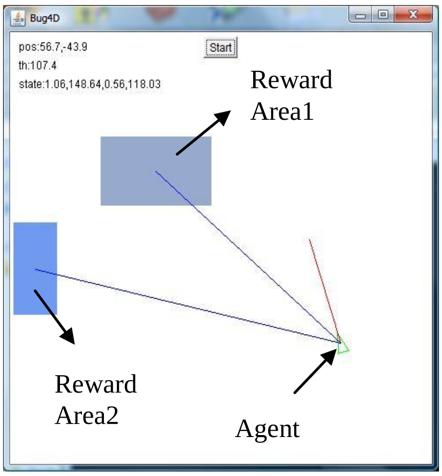

Fig.4. 4-D Model of VQE

2. Comparison of Q table and VQE

Figure 5 shows the number of rewards on the amount of one millions times over one time in four dimensional space of Q table and Voronoi Q value elements (VQE) with the constant radius when the number of state are same.

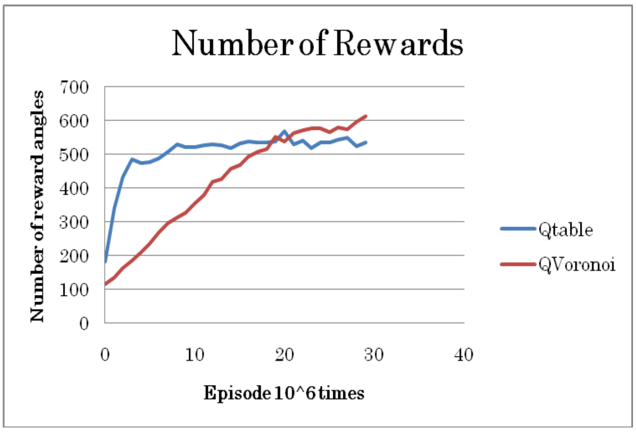

Fig.5. Q table and VQE of Reward Numbers

VI. CONCLUSION

By adopting the concept of the Voronoi diagram, VQE is constructed when the inputs are entered partially in the entire space. This method effectively simulates four dimensional spaces. Compared with the previous method on Q table and VQE, VQE is good performance. But it uses much more memory time and execution time than Q table. In order to increase the computational speed, we used the MD tree method. It is noted that, for with the constant radius of VQE.

Given the result of this study, it has been acknowledged that the VQE was suitable in higher dimension for the space division of RL with continuous state space and it was able to be confirmed that the number of elements was related to convergence time of study and a final amount of acquisition reward in VQE.

Advantages of Voronoi Space Division

It has three points. Firstly, if we use the rectangular Q elements (QE), they have the overlapping area, but when we use the Voronoi division, it does not have the unnaturalness of overlapping within the range of VQE. Secondly, when data are deleted, other data can supplement the space in the erased part. The last point is, it becomes easy to integrate.

FURTHER STUDIES

Firstly, it is necessary to adjust the number of elements of VQE. It is because the influence is whether to reach standing up and the optimum solution for study by the number of VQE. So I intend to make without the radius of VQE and VQE of movement, division and integration.

Secondly, needs to find another best way to decide which VQE is closed to the input vector by using Delaunay triangulation.

Finally, will corresponds the executed of four dimensions to a high level dimensions.

REFERENCES

[1] Richard S. Sutton and Andrew .G. Barto, Reinfo rcement Learning: An Introduction Cambridge, MA: MIT Press, 1998.
[2] Nobuyuki TANIGUCHI, Chuichi ARAKAWA and Toshio, KOBAYASHI, Construction of a Flow-Simulating Method with Finite Volume Based on a Voronoi Diagram.
[3] Peter Dayan, Christopher JCH Watkins, Reinforcement Learning
[4] Yuta HOKAMURO and Takayasu FUCHIDA, Research of Reinforcement Learning in Continuous State Space (in Japanese), 2008, Kyushu Conference, IEICE (The Institute of Electronic, Information and Communication Engineers), 09-1A-10.

A machine learning approach to 9-DOF robotic arm control

†S. Nishioka, †S. Maeda, ‡Y. Nakamura, †T. Ueno, ‡H. Ishiguro and †S. Ishii

†Graduate School of Informatics Kyoto University
†(Tel : +81-774-38-3938; Fax : +81-774-38-3941)
†Email :{nishioka-s, ichi, tsuyos-u, ishii}@sys.i.kyoto-u.ac.jp
‡Graduate School of Engineering Science, Osaka University
‡(Tel : +81-6-6879-7970; Fax : +81-6-6850-6360)
‡Email :{nakamura@is, ishiguro@}.sys.es.osaka-u.ac.jp

Abstract: In this study, we propose a new control strategy for a arm robot system which has 9-DOF actuated by McKibben artificial muscles. Since the dynamics of the McKibben actuators are complex due to the dependence on the internal pneumatic pressure, it is difficult to control the robot by solving the inverse kinematics according to the motion equations in real-time computing. Also, the state of each link of the arm cannot be determined uniquely from the position of the hand due to the ill-posedness in the arm posture. To resolve these difficulties, we introduce a notion of imitation, that is, 1) a human tutor taught the robot several patterns of exemplary trajectories by moving the robotic arm directly, so that the robot's forward model can learn how the robot dynamics follow those exemplary trajectories. Then, 2) the exemplary trajectories are pursued by a controller that has learned the relationship between the control signal and the consecutive arm states before and after the control signal is applied during the free control phase prior to the real-time control.
Keywords: Motion Planning, Inverse Kinematics, Robotics, Artificial Muscle

I. Introduction

In recent years, studies of robots using artificial muscles have been actively carried out, because of naturalness of produced motions. McKibben artificial muscle is one of such artificial muscles, which is actuated by pneumatic power. The McKibben actuator is drawing an interest because it realizes flexible motions like human muscles and of light weight and reasonable cost [1].

The improvement in the servo system of the McKibben actuator, which has been brought by the recent large computation power, contributes to extending the application field of the McKibben actuator [1]. However, several inherent difficulties in the McKibben actuator hinder further practical use. One difficulty comes from the variation in the control valve; it causes large individual deviations in the degree of expansion and shrinkage of the actuator. Second, it does not necessarily emit the same control torque for a specific control input because its tension is dependent on the internal air pressure of the actuator, that is, there is an internal state. Moreover, when there are multiple actuators, they could physically interfere with each other. Therefore, the development of the control method that resolves these difficulties has been desired in order to allow the McKibben actuators to be used more in practical situations.

In this study, we propose a machine-learning approach to controlling a 9-DOF human-like robotic arm with 26 McKibben actuators, so that it follows the exemplary trajectories taught by a human tutor in advance. In particular, we aim to control the robot to reproduce handshake gesture. To realize natural movements, we do not set a rigid target trajectory, but let the controller perform a real-time motion planning in a flexible manner to the robot state. The motion planning is done by a forward model implemented as a Gaussian Process (GP) regressor [2], so that the generated trajectory resembles one of the exemplary trajectories. The generation of control signals to pursue the target trajectory is realized by an inverse model implemented as a Normalized Gaussian network (NGnet) [3], which learns the relationship between the control signal and the consecutive arm states before and after the control signal is applied during the free control phase. A statistical combination of these two models is expected to allow us to avoid the difficulty in solving the complex motion equations of the 9-DOF robot arm system actuated by McKibben actuators and to realize human-like natural movements.

II. Systems

1. Robotic Arm

Figure 1 shows the appearance of the robot arm system we used in this study, which imitates the human right arm. It has five joints and six links which are connected to and controlled by 26 McKibben actuators. A McKibben actuator is able to generate a contractile force axially when compressed air is put it in.

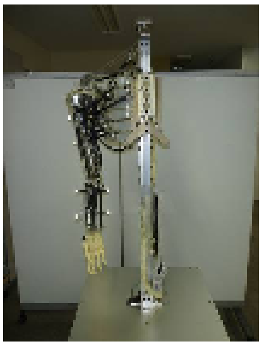

Fig.1. Appearance of the robotic arm

2. Observations and Control

The 3-D arm positions are monitored by a motion capture device (MAC3D system, Motion Analysis Corporation) with the sampling frequency of 200 Hz. Ten markers are attached so that the motion capture device can monitor all the positions of the 9 links. Since each marker position is represented as a three-dimensional vector, the state vector s_t that indicates all the positions of the ten markers becomes a 30-dimensional vector at each time t. During the imitation phase, in which a human tutor directly manipulates the robot arm like a handshake, exemplary trajectories of the manipulated robot arm, D, are also monitored by the motion capture device.

In addition to the link positions, the internal air pressure of each McKibben actuator is monitored. Since there are 26 McKibben actuators, the internal air pressure of all the actuators at time t are represented by a 26-dimensional vector P_t.

The robotic arm is controlled by a servo system; for each McKibben actuator, the target air pressure P_{gt} is provided as the control signal and the servo system works to realize the target pressure instantaneously.

III. Controlling method

After the robot controller has been trained based on the set of exemplary trajectories, D, the robot arm is controlled in real time by sequentially estimating the target air pressure P_{gt} at time *t*, given the current state s_t, the previous state s_{t-1}, and the current internal state P_t. This estimation is done by

$$\begin{aligned} & p(P_{gt} \mid P_t, s_t, s_{t-1}, D) \\ & = \int p(P_{gt} \mid P_t, s_t, s_{t+1}) p(s_{t+1} \mid s_t, s_{t-1}, D) ds_{t+1} \\ & \approx p(P_{gt} \mid P_t, s_t, \hat{s}_{t+1}) \end{aligned} \quad (1)$$

where $\hat{s}_{t+1} = \arg\max_{s_{t+1}} p(s_{t+1} \mid s_t, s_{t-1}, D)$. To solve the integral in the second line of eq. (1), the 'forward' model $p(s_{t+1} \mid s_t, s_{t-1}, D)$ is approximated by a Dirac's delta function $\delta(s_{t+1} - \hat{s}_{t+1})$ whose center is the MAP estimate of the forward model. Although the probabilistic distribution can provide rich information to the controller, it is assumed in this study that the controller emits the simplest mode signal, $\hat{P}_{gt} = \arg\max_{P_{gt}} p(P_{gt} \mid P_t, s_t, \hat{s}_{t-1}, D)$. Then, our task is to identify the two probability distributions, the 'inverse' model $p(P_{gt} \mid P_t, s_t, s_{t+1})$, and the forward model $p(s_{t+1} \mid s_t, s_{t-1}, D)$, through the training.

1. Gaussian Process (GP)

In the imitation phase, the forward model $p(s_{t+1} \mid s_t, s_{t-1}, D)$ is identified based on the exemplary trajectories D. We assume that in the forward model, each dimensionality (each marker position) is independent, i.e., $p(s_{t+1} \mid s_t, s_{t-1}, D)$ is factorized as $p(s_{t+1} \mid s_t, s_{t-1}, D) = \prod_i p(s_{t+1,i} \mid s_t, s_{t-1}, D)$ where $s_{t+1,i}$ is the *i*th element of s_{t+1}. Each constituent model $p(s_{t+1,i} \mid s_t, s_{t-1}, D)$ is represented by a non-parametric probabilistic model, Gaussian Process (GP) regressor [2].

Let $\mathbf{x}$ and y denote an input vector and an output from a GP regressor, respectively; $\mathbf{x}$ is a concatenation of the state vectors s_t and s_{t-1}, and y is a certain element of s_{t+1}. Using these notations, GP estimates $p(y \mid \mathbf{x}, D)$ as $p(y \mid \mathbf{x}, D) = N(y \mid m(\mathbf{x}; D), \sigma^2(\mathbf{x}; D))$, where $N(\cdot \mid m, \sigma^2)$ denotes a Gaussian distribution with mean m and variance σ^2.

When there are T series of input and output, $\mathbf{u} = \{\mathbf{u}_1, \cdots, \mathbf{u}_T\}$ and $\mathbf{v} = \{v_1, \cdots, v_T\}$, respectively, where $\mathbf{u}_i = [s_{t'}, s_{t'-1}]$ and $\mathbf{v}_i = s_{t'+1}$ in the set of exemplary trajectories D, the mean and the variance are given by $m(\mathbf{x}; D) = \mathbf{k}^T C^{-1} \mathbf{v}$ and $\sigma^2(\mathbf{x}; D) = c - \mathbf{k}^T C^{-1} \mathbf{k}$, respectively. Here, $\mathbf{k}$ is a T-dimensional vector whose *i*th element is $k(\mathbf{u}_i, \mathbf{x})$, and C is a *T*-by-*T* matrix whose *(m,n)* element is $k(\mathbf{u}_m, \mathbf{u}_n) + \beta^{-1}\delta_{mn}$. Also, $c = k(\mathbf{x}, \mathbf{x}) + \beta^{-1}$. $k(\cdot,\cdot)$ is called the kernel function, and in this study, we used a Gaussian kernel:

$$k(\mathbf{x}_m, \mathbf{x}_n) = \theta_1 \exp\left\{ -\frac{\theta_2}{2} \| \mathbf{x}_m - \mathbf{x}_n \|^2 \right\}.$$

The parameters θ_1, θ_2 and β are determined heuristically.

The GP-based forward model is expected to reproduce a trajectory similar to one of the exemplary trajectories D; this generalization capability is due to the smooth kernel function $k(\cdot,\cdot)$. It is also noted that in this imitation scheme, each trajectory to be imitated is realized by the target robot system rather than a human demonstrator. Then, each exemplary trajectory is consistent with the kinematics of the robot system.

2. Normalized Gaussian Network (NGnet)

The inverse model $p(P_{gt} \mid P_t, s_t, s_{t+1})$ is used to solve the inverse kinematics of the target robot system, that is, to output an appropriate control signal P_{gt}, given the current state s_t, the current internal state P_t, and the target next state s_{t+1}. The inverse model is represented by NGnet [3], a probabilistic model-based regressor. Although the inverse kinematics are often ill-posed, especially when the robot's DOF is large, this difficulty can be avoided by learning probabilistic relationship between the control signal and the consecutive robot states before and after the control signal is applied. Specifically, $p(P_{gt} \mid P_t, s_t, s_{t+1})$ is given by

$$p(P_{gt} \mid P_t, s_t, \hat{s}_{t+1}) = \sum_{k=1}^{M} w_k N(P_{gt} \mid W_K x_t + c_k, \Sigma_k) \tag{2}$$

where x_t denotes a concatenation of vectors P_t, s_t, and $\hat{s}_{t+1}$, and $w_k = \dfrac{g_k N(x_t \mid \mu_k, Q_k)}{\sum_{k'=1}^{M} g_{k'} N(x_t \mid \mu_{k'}, Q_{k'})}$.

During the free control phase (see below), the parameters $W_k, s_k, \Sigma_k, g_k, \mu_k$, and Q_k are estimated by variational Bayes (VB) estimation method [3]; though the VB method obtains the posterior distribution of the parameters, we just used their means in eq. (2). The NGnet divides the input space softly into sub-regions by means of Gaussian-based soft clustering, and linearly represents the relationship between the input and the output in each local sub-region, so that the final output is integrated such linear relationship like eq. (2). Since the relationship between the control input and the current and next states of the robotic arm should be nonlinear but is expected to be smooth within each local sub-region, the locally linear model like NGnet seems appropriate to well approximate such a moderate nonlinear relationship

IV. Experiment

1. Detailed experimental condition

1-1. Dimensionality reduction

Since the robotic arm system used in this study has 9 DOF and 26 McKibben actuators, a naïve control strategy could suffer from a curse of dimensionality. To reduce the redundant dimensions efficiently, we performed the dimensionality reduction in advance [4][5]. In particular, we used principal component analysis (PCA). Figure 2 shows the cumulative contribution rate against the number of PC dimensions when the robotic arm was randomly controlled. In this study, the state s_t is reduced to a four-dimensional vector s'_t, so that the cumulative contribution rate is 0.997.

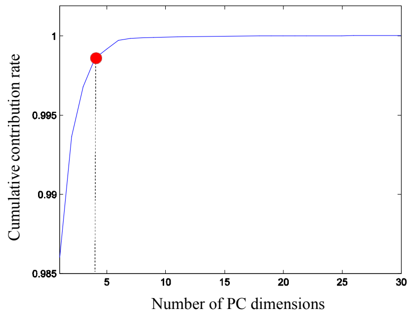

Fig.2. Dimensionality reduction by PCA

To avoid the extra complexity in controlling the robotic arm, only two McKibben actuators out of 26 McKibben actuators were controlled dynamically; the target air pressures of these two actuators were estimated by NGnet, and those of the rest of the McKibben actuators were fixed so that they maintain some stiffness. The two dynamically-controlled McKibben actuators were chosen heuristically after confirming they can lift the hand of the robotic arm up and down. The internal air pressure P_t is also reduced to such a two-dimensional vector that represents the internal air pressures of the two dynamically-controlled actuators.

1-2. Imitation phase

The exemplary trajectories were generated by moving the robotic arm manually by a human tutor. The tutor manipulated the robotic arm like handshake gesture. The exemplary trajectories consisted of 250 time points in total, including about 12 handshake motions, each of which had an approximately same period. Figure 3 shows a picture when the human tutor directly manipulated the robotic arm so that it imitates the handshake gesture.

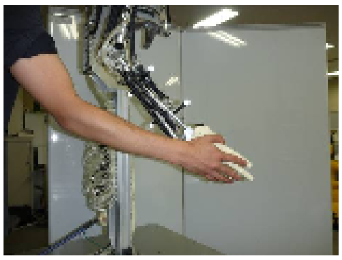

Fig.3. Human teaches the robot

1-3. Free control phase

In the free control phase, two periodic target air pressures were given to the two dynamically-controlled McKibben actuators. Each target air pressure was generated by a single sin function, but the periodicities of these sin functions were made to be different with each other so that they did not synchronize and the wide variety of the states was realized. 40,000 data points were collected at the sampling frequency of 200Hz, and used to train the inverse model (NGnet).

To determine the number of components of the NGnet, M in eq. (2), we performed "Ten-fold cross validation" [6]. Figure 4 shows the result. Since the cross-validation error decreases as M increases for these M values, we set $M = 30$; note that the computation cost becomes too much if the number of components is larger than 30.

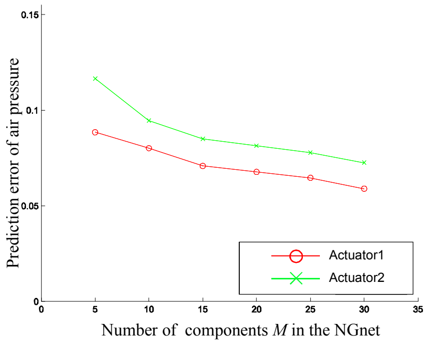

Fig.4. Ten-fold cross-validation

Figure 5 depicts the information flow of our contr ol system.

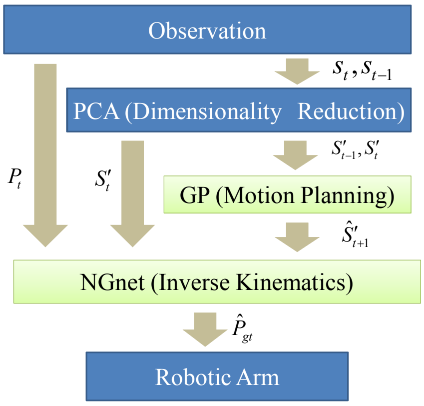

Fig.5. Information flow in our scheme

2. Results of the experiment

Figures 6 and 7 show the trajectories of the first and the second principal components of the states, respectively, when the trained robotic arm reproduces the handshake motions in the real-time control. The blue line is an exemplary trajectory, and the red and green lines are the trajectories realized by our control system before and after the training, respectively.

As can be seen in the figure, the robotic arm successfully reproduced a smooth and periodic trajectory after the training. In accordance with the figure, we visually confirmed the robotic arm performed a natural handshake gesture.

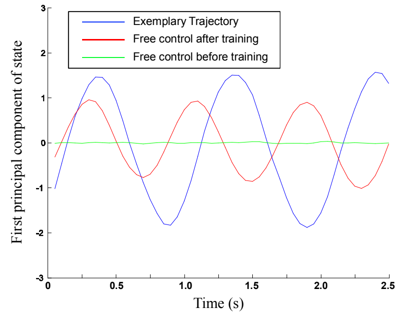

Fig.6. Trajectory of the first PC

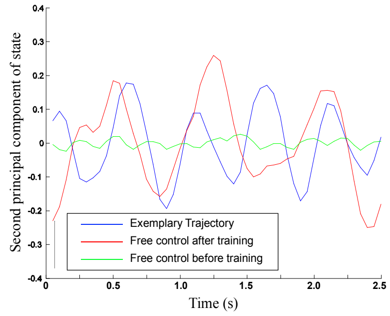

Fig. 7 . Trajectory of the second PC

Ⅶ. Conclusion

In this study, we propose to employ machine learning-based regressors to perform a real-time motion planning and to solve the inverse kinematics of the robot. The real-time motion planning (forward model) enabled the robotic arm to reproduce a natural handshake gesture as the human tutor taught and the learning of the inverse kinematics (inverse model) enabled real-time computing of the control input. It is expected that the proposed framework is applicable to other robots, and to perform other motions, since our framework is not task-specific but general enough.

Reference

[1] Noritsugu T (1997), Pneumatic Actuators (in Japanese). J. Robot. Soc. Japan, 15:355-359
[2] Rasumssen CE, Williams CKI (2006), Gaussian Processes for Machine Learning, MIT Press
[3] Yoshimoto J, Ishii S, Sato M (2003), Normalized Gaussian Network Based on Variational Bayes Inference and Hierarchical Model Selection (in Japanese), SICE J. Cont., Meas., and Syst. Int., 39(5):503-512
[4] Bishop CM (2006), Pattern Recognition and Machine Learning, Springer
[5] Calinon S, Guenter F, Billard A (1995), On Learning, Representing and Generalizing a Task in a Humanoid Robot, Complexity, 1:12-1
[6] Kohavi R (1995), A Study of Cross-Validation and Bootstrap for Accuracy Estimation and Model Selection. in Proc. Int. Joint Conf. Artificial Intelligence, 2:1137-1143

The Fifteenth International Symposium on Artificial Life and Robotics 2010 (AROB 15th '10),
B-Con Plaza, Beppu,Oita, Japan, February 4-6, 2010

Consideration on Gesture Recognition Based on Multilayer Neural Network by Using Input Device of Home Gaming Console

Ichiro Iimura Takuroh Fujiki Hidenobu Tsurusawa† Shigeru Nakayama‡

[illegible]
iiimura, g0530214 @pu-kumamoto.ac.jp

† [illegible]
htsuru30@oita-ct.ac.jp

‡ [illegible]
shignaka@ibe.kagoshima-u.ac.jp

***Abstract*:** We consider that the human intention and feelings conspicuously appear at the force added to a body rather than the positions of hands in the gesture that is nonverbal communication. In this paper, we have tried gesture recognition based on multilayer neural network by using acceleration sensor because the force to act during motion can be detected by acceleration. From the experimental result, we have proven that our gesture recognition method can recognize the gesture patterns such as numerical characters and graphic symbols. As an input device in this study, we used the Wii remote attached to the home gaming console Wii instead of a special device. Furthermore, we have obtained high recognition rate in the case of not only specific performers but also unspecified performers by using the permutation of the simple normalized acceleration for input values of multilayer neural network. Therefore, we could develop versatile gesture recognition engine.

***Keywords*:** Gesture recognition, Neural network, Input device, Home gaming console, Wii remote

I. INTRODUCTION

Recently, the operation mode of computers has diversified in the mobile environments, information appliances and so on, from miniaturization and high performance. Computers are fusing to our real world. Therefore, a study of new user interface technology becomes popular to realize that a human operates a machine naturally. In the communication of intention and feelings between humans, it is generally said that nonverbal means by the physical media such as gesture or hand-gesture, [illegible], is one of the important communication as well as verbal means by words [1, 2]. If a machine/computer can understand this gesture, it can become the natural and intuitive new input means.

In conventional studies, Sawada et al [3]. proposed gesture recognition methods using acceleration data or features patterns of acceleration and developed their practical systems. In particular, three-axes acceleration sensor have been built into some of the recent mobile phones, and the input by intuitive operation that uses it is also possible. As the studies of Sawada et al. about the gesture recognition using acceleration after Reference [3], they progressed their studies to the application to the sign-language recognition [4] and the data retrieval by gesture [5].

In this study, we have accepted the consideration of Sawada et al [3]. in which the human intention and feelings conspicuously appear at the force added to a body rather than the positions of hands in the gesture that is nonverbal communication. We have tried gesture recognition based on multilayer neural network by using acceleration sensor because the force to act during motion can be detected by acceleration. In the acceleration measurement, we used the Wii remote attached to the home gaming console Wii of Nintendo Co., Ltd. as an input device instead of a special device. Wii remote is equipped with Bluetooth, a three-axes acceleration sensor, and a CMOS sensor detecting infrared rays. In this study, we decided the adoption of the Wii remote as an input device, because of both the convenience of the no-cabling by using Bluetooth and the easiness of getting acceleration by using the three-axes acceleration sensor. The development language we used was Java language and used WiiRemoteJ 1.5 for controlling the Wii remote that is an input device. Besides, as applications to the entertainment, we are plan to study the recognition of flag signaling, the estimate of emotion [6, 7], and the development of application systems such as the instruction of a dance or an exercise. These studies is based on biological motion data [8] of the human movement which we get with three-axes acceleration sensor. Therefore, this study deserves a preliminary experiment.

II. KINETIC FEATURE QUANTITY FOR GESTURE RECOGNITION

We show the appearance of the input device, which we used for an acceleration measurement in this study, in Figs. 1(a), 1(b) and 1(c). Among x, y and z axial acceleration $a_x(t)$, $a_y(t)$ and $a_z(t)$ measured with this input device, we adopted the acceleration of x and z axis directions, which we showed in

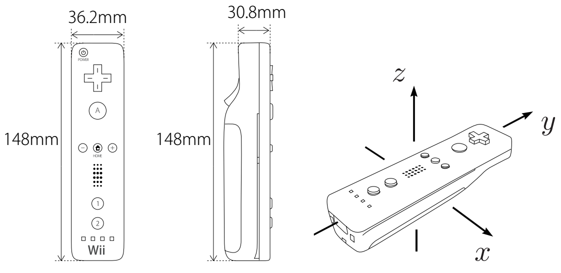

(a) Top (b) Side (c) Perspective

(d) Front (e) Diagonal

Figure 1: Input device with three-axes acceleration sensor and directions of two axes in which acceleration is measured.

Figs. 1(d) and 1(e), as kinetic feature quantity and used them for gesture recognition. In addition, the start and end of the gesture were judged from pressing Ⓐ-button of the input device shown in Fig. 1. Furthermore, as for the time and the force intensity of one gesture, it is thought that the individual variation occurs by presenters. Therefore, in this study, we normalized the number of acceleration data per one axis, e.g. $a_x(t)$ or $a_z(t)$, and the value of acceleration per one axis to N_a and the range of [0 1], respectively. We used the permutation which simply connected the normalized acceleration of the directions of x and z axes in the recognition experiment described later.

As an example, we show the transitions of the normalized acceleration in the directions of x and z axes in Fig. 2, concerning numerical character "2" and graphic symbol "☆" of two examinees A and B. In these figures, a solid line and a dotted line are the transitions of the x axial and z axial normalized acceleration, respectively. The number of each axial normalized data, N_a, is 50. Figs. 2(a) and 2(b) show the acceleration transitions of the gesture "2" in the different examinees. We can confirm that these transitions tend to be almost similar when we compare these transitions. We can confirm a similar tendency in Figs. 2(c) and 2(d), too. However, the acceleration transitions are clearly different in different gestures of a same examinee. From these results, we have considered that the recognizing gestures by the simple acceleration transitions is possible.

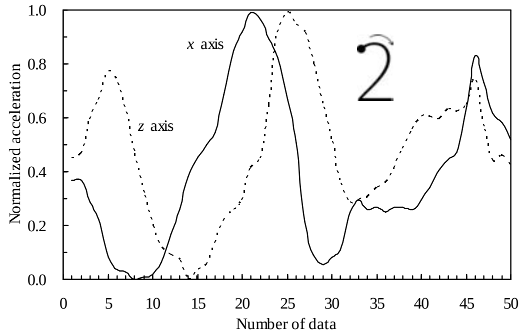

(a) "2" (Examinee A)

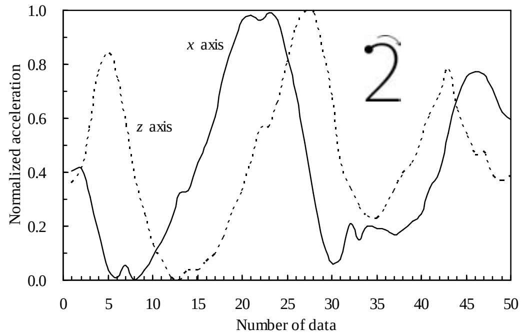

(b) "2" (Examinee B)

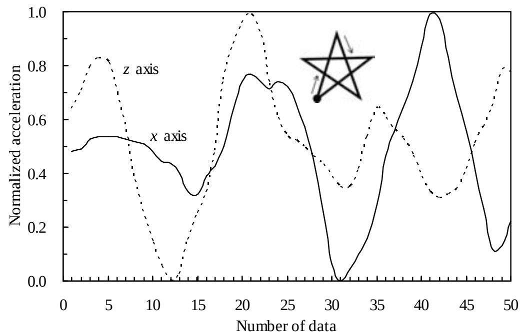

(c) "☆" (Examinee A)

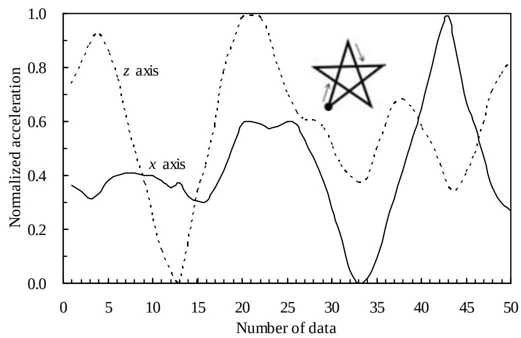

(d) "☆" (Examinee B)

Figure 2: Transitions of the normalized acceleration in the directions of x and z axes.

III. GESTURE RECOGNITION

1. Recognition experiment

Neural Network (NN) is one of the information processing mechanisms which modelled the structure

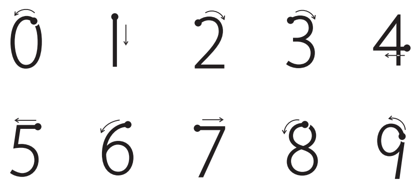

(a) Ten numerical-character-gesture patterns

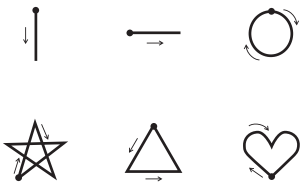

(b) Seven graphic-symbol-gesture patterns

Figure 3: Gesture patterns used in the experiment.

of the nerve cell in the human brain. In this study, we adopted hierarchical NN of the three layers, whose usefulness has been confirmed by applications to the problems such as the pattern recognition, for recognizing gesture patterns. In addition, we used Back-Propagation (BP) method [9], which is the supervised learning method, for learning.

We used the ten numerical-character-gesture patterns and the seven graphic-symbol-gesture patterns shown in Fig. 3 for the recognition experiment of this study. We constructed two NNs for the numerical-character-gesture patterns and the graphic-symbol-gesture patterns, and separately experimented in the two kinds of gesture patterns. As described in Section II, the data of one pattern to use in the recognition experiment was the permutation which simply connected the normalized acceleration of the directions of x and z axes. N_a of each axis was 50. The data used in the experiment was collected from 20 examinees, and we got ten samples per one gesture pattern. Here, we randomly divided 20 examinees into two groups, Group A and Group B, in which each group consists of ten examinees. The collected data was classified as follows according to a use.

DL The data was gotten from ten examinees who belonged to Group A.

DR $^{+}$ The data was gotten from ten examinees who belonged to Group A again besides data for learning, DL.

DR $^{-}$ The data was gotten from ten examinees who belonged to Group B.

We used DL for learning of NN, and used DR^{+} and DR for recognition experiment.

The NN we constructed consists of the input layer of 100 units and the hidden layer of 150 units. As for the output layer, we had one unit correspond to one gesture pattern. That is, we decided the number of units in the output layer to ten units and seven units for recognizing the numerical-character-gesture patterns and the graphic-symbol-gesture patterns, respectively. The parameter values for learning by BP method are desided by the pretest. As a result, the learning rate was 0 25 and the stabilization constant , which determines the effect of past weight changes on the current direction of movement in weight space, was 0 5 [1]. The at-end condition for learning by NN was when the squared-sum of the error between output value of the output layer and teacher signal became less than 1 8 10 ^{3}.

2. Experimental result and consideration

We constructed the NN for recognizing the numerical-character-gesture patterns by using DL of the numerical-character-gesture patterns. In the same way, we constructed the another NN for recognizing the graphic-symbol-gesture patterns by using DL of the graphic-symbol-gesture patterns, too. We experimented on recognizing gesture patterns by using each NN we constructed. The recognition results concerning the numerical-character-gesture patterns and the graphic-symbol-gesture patterns are shown in Figs. 4(a) and 4(b), respectively. In both figures, the axis of abscissas is each gesture pattern, and the axis of ordinates is recognition rate [%]. Because we gotten ten samples per one pattern from one examinee, the recognition rate concerning DR^{+} and DR is 100% if the NN we constructed succeeds in recognition for 100 samples (= 10[samples examinee] 10[examinees]) per one pattern.

From these experimental results, we have confirmed that the recognition rate of DR^{+} was almost 100%. We have confirmed that the recognition rate of DR was satisfactory performance, too. That is, we have obtained high recognition rate in the case of not only specific performers but also unspecified performers in spite of using the permutation of the simple normalized acceleration for input values of NN.

IV. COMPARISON WITH CONVENTIONAL STUDIES

In order to confirm the effectiveness of the gesture recognition engine constructed in this study, we compared the proposed method with the conventional study of Sawada et al [3]. related to the gesture recognition. Table 1 shows the comparison result of the recognition rate concerning examinees whose data was not learned. Sawada et al. dealt with ten gesture patterns in Reference [3], but we dealt with seven gesture patterns except three patterns as shown in Fig. 3(b) because the specific motion of these three patterns was not clear in Reference [3].

In the conventional method [3], Sawada et al. recognized the gestures by pattern matching. In other words, we cannot simply compare the recognition performance because the conventional method is different from the proposed method in the recognition

[1] As for the details about the learning rate and the stabilization constant , please refer to Reference [9].

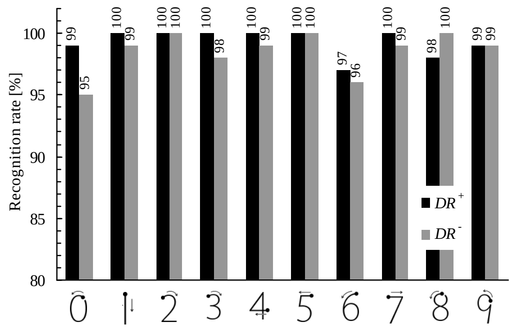

(a) Numerical-character gestures

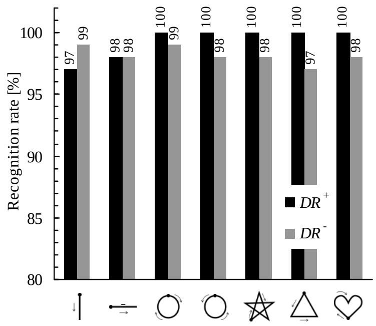

(b) Graphic-symbol gestures

Figure 4: Recognition rate [%] in terms of ten numerical-character-gesture and seven graphic-symbol-gesture patterns.

Table 1: Comparison of recognition rate [%] in terms of seven graphic-symbol-gesture patterns.

Gesture patterns	Conventional method	Proposed method (DR)
↓	100.0	99.0
	100.0	98.0
↻	100.0	99.0
↺	80.0	98.0
☆	100.0	98.0
△	80.0	97.0
♡	100.0	98.0
Average	94.3	98.1

method. However, in ↺ and △ which were misrecognized by the conventional method because of gesture patterns with similar kinetic feature quantity, the proposed method have shown high recognition rate as well as other gesture patterns. Furthermore, the proposed method has not shown the decrease of recognition rate in specific gestures. As for the average recognition rate in seven patterns, the proposed method is about 98.1%, whereas the conventional method is about 94.3%. In addition, the recognition rate of each pattern in the proposed method is the result of 100 samples by 10 examinees, whereas the recognition rate of each pattern shown in Reference [3] is the result of only ten samples by one examinee. From these analysis, we have confirmed the higher recognition stability of the proposed method compared with the conventional method.

V. CONCLUSIONS

In this study, we have tried gesture recognition based on multilayer neural network by using acceleration sensor because the force to act during motion can be detected by acceleration. From the experimental result, we have proven that our gesture recognition method can recognize the gesture patterns such as numerical symbols and graphic symbols. As an input device in this study, we used Wii remote attached to the home gaming console Wii instead of a special device. Furthermore, we have obtained high recognition rate in the case of not only specific performers but also unspecified performers by using the permutation of the simple normalized acceleration for input values of multilayer neural network. Therefore, we could develop versatile gesture recognition engine. In the near future, we are plan to try the recognition of more complicated gestures by using acceleration of three axes, though the acceleration of only two axes was used in this study, and to study the human-emotion estimate.

References

[1] Kurokawa, T. (1994), Nonverbal interface (in Japanese). Ohmsha

[2] Kanayama, N. (1983), Sekai 20-kakoku non babaru jiten (in Japanese). Kenkyusha

[3] Sawada, H. and Hashimoto, S. (1996), Gesture recognition using acceleration sensor and its application for musical performance control (in Japanese). IEICE Trans. Fundamentals J79-A(2):452–459

[4] Sawada, H., Hashimoto, S. and Matsushima, T. (1998), A study of gesture recognition based on motion and hand figure primitives and its application to sign language recognition (in Japanese). IPSJ Journal 39(5):1325–1333

[5] Notsu, T., Hashimoto, S. and Sawada, H. (2002), Multi-modal sign language database and its retrieval by gesture inputs (in Japanese). Trans. HIS 4(1):51–58

[6] Ishii, M. and Maruta, H. (2005), Percept of emotion from biological motion (in Japanese). IEICE Technical Report 105(165):123–126

[7] Maruta, H. and Ishii, M. (2006), Feature extraction with ICA for human-emotion discrimination from biological motion data (in Japanese). IEICE Technical Report 105(534):135–139

[8] Johansson, G. (1973), Visual perception of biological motion and a model for its analysis. Perception & Psychophysics 14:201–211

[9] Rumelhart, D.E., Hinton, G.E. and Williams, R.J. (1986), Learning internal representations by error propagation. Parallel Distributed Processing, vol. 1, MIT Press, pp. 318–362

A Learning Petri Net Model Based on Reinforcement Learning

Liang-Bing Feng, Masanao Obayashi, Takashi Kuremoto and Kunikazu Kobayashi

Graduate School of Science and Engineering, Yamaguchi University, 2-16-1 Tokiwadai, Ube, Yamaguchi, Japan

(Tel : 81-836-85-9518; Fax : 81-836-85-9501)
(n007we, m.obayas,wu,koba@yamaguchi-u.ac.jp)

Abstract: In this paper, a hybrid intelligent control system – Learning Petri Net (LPN) that combines the Petri net and reinforcement learning is presented. LPN is expanded High-level Time Petri nets, in which some transition's input arc weight function and transition delay time have a value item which records the reward from environment. Based on interaction with environment, LPN can adjust the arc weight function and transition delay time when it's modeling system is running. The arc weight function and transition delay time learning algorithm is based on Q-learning – a kind of Reinforcement Learning (RL). Finally, for the purpose of certification of the effectiveness of our proposed Learning Petri net, it is used to model a discrete event dynamic control system – Sony AIBO learning control system as an example. The result of the experiment shows this method is correct and effective.

Keywords: Petri Net, Reinforcement Learning, Discrete event dynamic system.

I. INTRODUCTION

Petri nets combine a well defined mathematical theory with a graphical representation of the dynamic behavior of systems. The theoretic aspect of Petri nets allows precise modeling and analysis of system behavior, while the graphical representation of Petri nets enable visualization of the modeled system state changes [1]. So, Petri net is widely used to model various dynamic systems. But the Petri net doesn't have the learning capability, all the parameters which describe the system characteristic need to be set individually and empirically when dynamic system is modeled. Recently, there are some researches for making the Petri net has learning capability. In paper [2], the global variables are used to record all state of colored Petri net when it is running. The global variables are optimized and colored Petri net is updated according to these global variables. Here, colored Petri net is only a tool of learning. A learning Petri net model which combines Petri net with neural network is proposed in [3]. This learning Petri net model can realize an input-output mapping through Petri net's weight function is adjusted just like an artificial neural network. And this learning method was applied to nonlinear system control. Paper [4] created a Time Interval Petri net for modeling real-time decision making. It makes the Petri net have learning capability through converting arc's type, adding a record to an output arc operator table. Based on these researches, a learning Petri net model based on reinforcement learning is proposed in this paper.

The rest of this paper is organized as followed. Section 2 gives the definition of LPN and illustrates the learning algorithm of LPN. Section 3 describes the application to discrete event dynamic system control and gives the simulation result. Finally, Section 4 summarizes the paper and discusses some directions for future work.

II. THE LEARNING PETRI NET AND LEARNING ALGORITHM

Learning Petri nets is Petri nets which have learning capability.

1. Definition of Learning Petri net

Learning Petri net is constructed based on High-Level Time Petri Net (HLTPN).

Definition 1: HLTPN has a structure $HLTPN = (NG, C, W, DT, M_0)$ [5], where

(i). $NG = (P, T, F)$ is called net graph with P that is a finite set of nodes, called Places. $ID: P \rightarrow N$ is a function marking P, $N = (1,2,\ldots)$ is the set of natural number. Using $P_1, P_2, \ldots, P_n$ represents the elements of P and n is the cardinality of set P;

T is a finite set of nodes, called Transitions, which disjoint from P, $P \cap T = \varnothing$; $ID: T \rightarrow N$ is a function marking T. Using $T_1, T_2, \ldots, T_m$ represents the elements of T, m is the cardinality of set T;

$F \subseteq (P \times T) \cup (T \times P)$ is a finite set of directional arcs, known as the flow relation;

(ii). C is a finite and non-empty color set for describing difference type data;

(iii). W: $F \rightarrow C$ is a weight function on F. If $F \subseteq (P \times T)$, the weight function W is W_{in} that decides which colored Token can go through the arc and enable T fire. This color tokens will be consumed when transition is fired. If $F \subseteq (T \times P)$, the weight function W is W_{out} that decides which colored Token will be generated by T and be input to P.

(iv). DT: $T \rightarrow N$ is a delay time function of a transition which has a *Time* delay for an enable transition fired.

(v). M_0: $P \rightarrow \text{U}_{p \in P} \mu C(p)$ such that $\forall p \in P$, $M_0(p) \in \mu C(p)$ is the initial marking function which associates a multi-set of tokens of correct type with each place.

Now, we give the definition of LPN.

Definition 2: Learning Petri Net has a structure, *LPN= (HLTPN, VW, VT)*, where

(i). *HLTPN=* (*NG, C, W, DT,* M_0) is a High-Level Time Petri Net.

(ii). *VW* (the value of weight function): $W_{in} \rightarrow R$, is a function marking on W_{in}. A $F \subseteq (P \times T)$ has several W_{in} and every W_{in} has a reward value $R \in$real number.

(ii). *VT* (the value of delay time): $DT \rightarrow R$, is a function marking on *DT.* A transition has several *DT* and every *DT* has a reward value $R \in$real number.

Using LPN, a mapping of input-output Token is gotten. For example, we construct a LPN which is showed in Fig. 1. Colored Tokens C_{ij} $(i=1;j=1,2\ldots n)$ are input to P_1 by T_{input}. There are n weight functions $W(<C_{ij}>, VW_{Cij,i,j})$ on a same $F_{i,j}$. Token C_{ij} obeys weight functions $W(<C_{ij}>, VW_{Cij,i,j})$ that is decided by the value $VW_{Cij,i,j}$. After Token C_{ij} passed through arc $F_{i,j}$ $(i=1;j=1,2\ldots n)$, $T_{i,j}(i=1;\ j=\ 1,2\ \ldots n)$ fires and generates Tokens $C_{ij}(i=2;j=1,2\ldots n)$ in P_2. After P_2 has color Token $C_{ij}(i=2;j=1,2\ldots n)$, $T_{i,j}(i=2;\ j=\ 1,2\ \ldots n)$ fires and different colored Token $C_{ij}(i=3;j=1,2\ldots n)$ is generated. Then, a reward will be gotten from environment according to whether it accords with system rule that C_{3j} generated by C_{1j}. These rewards are propagated to every $VW_{Cij,i,j}$ using algorithm 1.

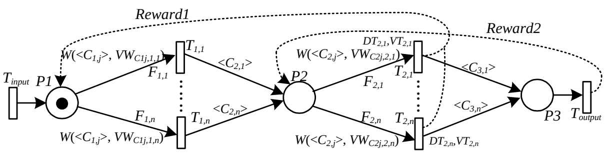

Fig.1. A Learning Petri Net.

Using LPN to model a dynamic system, the system state is modeled as Petri net place and the system state change is modeled as transition. Several characteristics parameters of system state and action can be expressed by Token number and color, arc weight function, transition delay time, and so on. When the system is modeled, some characteristics are unknown. So, these characteristics are set randomly and are gotten gradually and appropriately when the system runs. So, we use Learning Petri net to learn the system condition from real-time situation.

2. Learning algorithm of Learning Petri net

In Learning Petri net, RL is used to learn the *VM* and *VT* through interacting with environment. RL could learn the optimal policy of the dynamic system through environment state observation and improve its behavior through trial and error with the environment. RL agent senses the environment and takes actions. It receives numeric award and punishments from some reward function. The agent learns to choose actions to maximize a long term sum or average of the future reward it will receive [6].

In this paper, the arc weight function and transition delay time learning algorithm are based on Q-learning – a kind of RL. In arc weight function learning algorithm, $VW_{Cij,i,j}$ is randomly set firstly. So, the weight function on the arc is arbitrary. When the system runs, we use formula (1) to update $VW_{Cij,i,j}$.

$$VW_{Cij,i,j} = VW_{Cij,i,jj} + \alpha\,[r + \gamma\overline{(VW_{ci+1j,i+1,j})} - VW_{Cij,i,j}], \quad (1)$$

where, (i). α is the step-size, γ is discount rate.

(ii). r is reward which $W(<C_{ij}>, VW_{Cij,i,j})$ gets when $T_{i,j}$ is fired by $<C_{ij}>$. Here, because environment only gives system reward at last step, so a feedback learning method is used. If $W(<C_{ij}>, VW_{Cij,i,j})$ through $T_{i,j}$ generated Token $<C_{i+1,j}>$ and $W(<C_{i+1j}>, VW_{Ci+1j,i+1,j})$ through $T_{i+1,j}$ generated Token $<C_{i+2,j}>$, $VW_{Ci+1j,i+1,j}$ gets an update value. And this value is feedback as $W(<C_{ij}>, VW_{Cij,i,j})$ next time reward r.

(iii). $\overline{(VW_{ci+1j,i+1,j})}$ is calculated from all $W(<C_{i+1j}>, VW_{Ci+1j,i+1,j})$ feedback value as formula (2).

$$\overline{(VW_{ci+1j,i+1,j})}_{t} = \gamma\overline{(VW_{ci+1j,i+1,j})}_{t-1} + r_t, \quad (2)$$

where t is time for that $<C_{i+1j}>$ is generated by $W(<C_{ij}>, VW_{Cij,i,j})$.

In the transition delay time learning algorithm, the reward can learn immediately. $VT_{i,j}$ can be updated using formula (3).

$$VT_{i,j} = VT_{i,j} + \alpha\,[r + \gamma\overline{R} - VT_{i,j}], \quad (3)$$

where, r is reward that an action get after it acted. $\overline{R}$ is average of all the reward. α is the step-size, γ is discount rate.

Now, we found the algorithm of Learning Petri net which is listed in Table 1.

Table 1. Learning Algorithm for Learning Petri Net

Algorithm 1 Weight function learning algorithm

Step 1. Initialization: Set all VW_{ij} and r of all input arc's weight function to zero.

Step 2. Initialize learning Petri net. i.e. make the Petri net state as M_0.

Repeat i) and ii) until system becomes end state.

i) When a place gets a colored Token C_{ij}, there is a choice that which arc weight function is obeyed if the functions include this Token. This choice is according to selection policy which is ε greedy (ε is set according to execution environment by user, usually $0<\varepsilon<<1$).

A: Select the function which has the biggest $VW_{cij,i,j}$ at probability $1-\varepsilon$;

B: Select the function randomly at probability ε.

ii)The transition which the function correlates is fired and reward is observed. Adjust the weight function value using $VW_{Cij,i,j} = VW_{Cij,i,jj} + a[r+\gamma(VW_{ci+1j,i+1,j}) - VW_{Cij,i,j}]$. At the same time, $a[r+\gamma(VW_{ci+1j,i+1,j}) - VW_{Cij,i,j}]$ is fed back to weight function with generate C_{ij} as its reward for next time.

Algorithm 2 Delay time learning algorithm

Step 1. Initialization: Set all VT_{ij} of transition to zero.

Step 2. Initialize learning Petri net. i.e. make the Petri net state as M_0.

Repeat i) and ii) until system becomes end state.

i) When a transition is fired, choose a delay time using selection policy which is ε greedy (ε is set according to execution environment by user, usually $0<\varepsilon<<1$).

A: Select delay time which has the biggest VT_{ij} of service at probability $1-\varepsilon$;

B: Select the function randomly at probability ε.

ii) After transition fires and reward is observed, the weight function value is adjusted using $VT_{i,j}= VT_{i,j}+ a[r+\gamma\bar{R} - VT_{i,j}]$.

III. APPLICATION TO DISCRETE EVENT DYNAMIC SYSTEM CONTROL

In this section, we will apply the LPN to control a discrete event dynamic system.

1. Discrete event dynamic system and AIBO voice command recognition system

A discrete event dynamic system is a discrete-state, event-driven system of which the state evolution depends entirely on the occurrence of asynchronous discrete events over time [7]. Petri nets have been used to model various kinds of dynamic event-driven systems like computers networks, communication systems, and so on. In this paper, it is used to model Sony AIBO learning control system for the purpose of certification of the effectiveness of our proposed Learning Petri net.

AIBO (Artificial Intelligence roBOt) is a type of robotic pets designed and manufactured by Sony. AIBO is able to execute different actions, such as go ahead, move back, sit down, stand up and cry, and so on. And it can "listen" voice via microphone. A command and control system will be constructed for making AIBO understand several human voice commands by Japanese and English and take corresponding action.

The simulation system is developed on Sony AIBO's OPEN-R (Open Architecture for Entertainment Robot) [8]. The architecture of simulation system is showed in Fig. 2. Because there are English and Japanese voice commands for same AIBO action, the partnerships of voice and action are established in part (4). The lasted time of an AIBO action is learning in part (5). After an AIBO action finished, the rewards for action and action lasted time correctness are given by that different AIBO's sensors are touched.

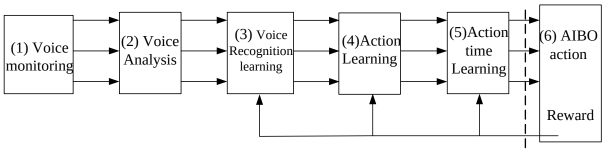

Fig.2 The system architecture of voice command recognition

2. Learning Petri net model for AIBO voice command recognition system

In the Learning Petri net model for AIBO voice command recognition system, AIBO action change, action time are modeled as transition, transition delay, respectively. The human voice command is modeled by different color Token. The LPN model is showed in Fig. 3. The meaning of every transition is listed below:

T_{input} change voice signal as colored Token which describe the voice characteristic.

T_{11}, T_{12} and T_{13} can analyze the voice signal. T_1 generates 35 different Token $VL_1 \ldots VL_{35}$ according to the voice length. T_2 generates 8 different Token $E2_1 \ldots E2_8$ according to the front twenty voice sample energy characteristic. T_3 generates 8 different Token $E4_1 \ldots E4_8$ according to the front forty voice sample energy characteristic [9]. These three types Token are compounded into a compound Token $<VL_l> + <VE2_m> + <VE4_n>$ in P_2 [10].

T_{2j} generates the different voice Token. The input arc's weight function is $((<VL_l>+<VE_{2m}>+ <VE_{4n}>)$,

$VW_{Vlmn,2j}$) and the output arc's weight function is different voice Token. And voice Token will generate different action Token through T_{3j}.

When $P_4 - P_8$ has Token, AIBO's action will last. T_{4j} takes Token out from $P_4 - P_8$, and makes corresponding AIBO action terminates. T_{4j} has a delay time DT_{4i}, and every DT_{4i} has a value VT_{4i}. Transition adopts which delay time DT_{4i} according to VT_{4i}.

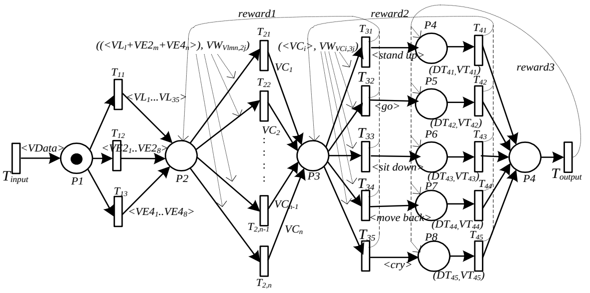

Fig. 3 The LPN model of voice command recognition

3. The results of simulation

When the system begins running, it can't recognize the voice commands. A voice command comes and it is changed into a compound Token in P_2. This compound Token will randomly generate a voice Token and puts into P_3. This voice Token randomly arouses an action Token. A reward for action correctness is gotten, then, VW and VT are updated. For example, a compound colored Token ($<VL_l> + <VE_{2m}> + <VE_{4n}>$) fired T_{21} and colored Token VC_1 is put into P_3. VC_1 fires T_{32} and AIBO acts "go". A reward is gotten according to correctness of action. $VW_{VC1,32}$ is updated by this reward and $VW_{VC1,32}$ updated value is fed back to P_2 as next time reward value of ($<VL_l> + <VE_{2m}> + <VE_{4n}>$) fired T_{21}. After an action finished, a reward for correctness of action time is gotten and VT is updated.

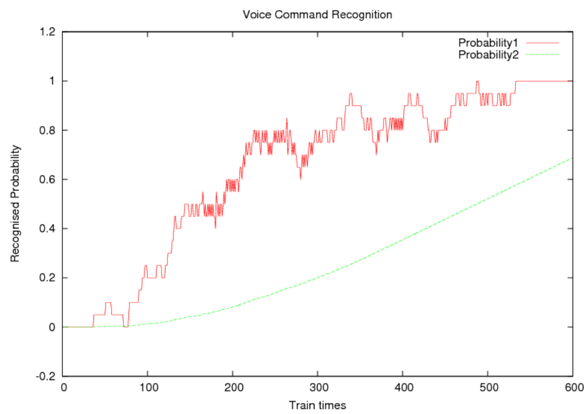

Fig. 4 Relation of training times and recognition probability

Fig. 4 shows the relation of training times and voice command recognition probability. Probability 1 shows the successful probability of recently 20 times training. Probability 2 shows the successful probability of total training times. From the result of simulation, we get that Learning Petri net is correct and effective using the AIBO voice command control system.

IV. CONCLUSION

In this paper, we proposed a hybrid intelligent control system – Learning Petri Net (LPN) that combines the Petri net and reinforcement learning. The definition of LPN is given and the learning algorithm is constructed. For the purpose of certification of the effectiveness of our proposed Learning Petri net, it is used to model Sony AIBO learning control system as an example. The result of the experiment shows this method is correct and effective.

We plan to use reinforcement learning algorithm to adjust other parameter of Petri net and extend our work to model other dynamic system in the future.

REFERENCES

[1]J. Wang (2007), Petri nets for dynamic event-driven system modeling. Handbook of Dynamic System Modeling, Ed: Paul Fishwick, CRC Press: 1-17
[2]V. Baranaushas, K. Sarkauskas (2006), Colored Petri Nets-Tool for control system Learning. Electronics and Electrical Engineering, 4(68):41-46
[3]Hirasawa K., Ohbayashi M., Sakai S, Hu J (1998), Learning Petri network and its application to nonlinear system control. IEEE Transactions on systems, man and cybernetics. Part B: Cybernetics, 28(6):781-789
[4]Vadim B., David C. W. (2005), Machine Learning for Time Interval Petri Nets. In Australian Joint Conference on Artificial Intelligence, Springer-Verlag: 959-965
[5]Guangming C., Minghong L., Xianghu W. (2006), The Definition of Extended High-level Time Petri Nets. Journal of Computer Science, 2(2):127-143
[6]R. S. Sutton, A. G. Batto (1998), Reinforcement learning: An Introduction. The MIT Press. Cambridge, Massachusetts, USA
[7]B. Hrúz, M.C. Zhou (2007), Modeling and Control of Discrete-event Dynamic Systems: with Petri Nets and Other Tools. Springer Press, London, UK
[8]OPEN-R programming group (2004), OPEN-R programming introduction. Sony corporation, Japan
[9]Frederick JelinekR (1999), Statistical Methods for Speech. The MIT Press. Cambridge, Massachusetts, USA
[10]H.S.Yan,J.Jian (1999), Agile concurrent engineering. Integrated Manufacturing Systems, 10(2): 103-113

The Fifteenth International Symposium on Artificial Life and Robotics 2010 (AROB 15th '10),
B-Con Plaza, Beppu,Oita, Japan, February 4-6, 2010

On Detecting a Human and Its Body Direction from a Video

Yuuki Nakashima, Joo Kooi Tan, Seiji Ishikawa, Takashi Morie
Department of Mechanical and Control Engineering
Kyushu Institute of Technology
Sensuicho 1-1, Tobata, Kitakyushu 804-8550, Japan
E-mail: {nakashima, etheltan, ishikawa}@ss10.cntl.kyutech.ac.jp, morie@brain.kyutech.ac.jp

Abstract: This paper describes a novel technique for detecting a human and its body direction using HOG feature. The HOG feature is a well-known feature for the judgment of a human. But normally it contains the background feature, which gives negative influence on the judgment. This paper proposes the employment of the HOG feature based on a human model. The feature is also employed for detecting human body direction. Experimental results show effectiveness of the proposed technique compared to the conventional one.

Keywords: HOG, human models, body direction, SVM

1. Introduction

Recently, car vision technologies have been paid much attention in the field of ITS (Intelligent Transport System), aiming at reducing traffic accidents to a large extent. Various techniques for detecting cars, car lanes, traffic signs, etc., have been developed by the employment of a PC with high specification and cheap digital cameras. In particular, techniques for automatic detection of pedestrians or humans have been studied enthusiastically.

Although human detection from outdoor scenes is one of the difficult problems in computer vision because of a variety of clothes, occlusion, illumination change, image resolution, etc., a robust human detection algorithm has been reported recently. The HOG feature proposed by Dalal and Triggs [1] is a well known feature for representing and recognizing a human image. But, in its original algorithm, it includes an unnecessary part of the image such as the background. It is not conceivable that the background feature contributes to high recognition rate of a human image. Zhu et al. [2] employ the HOG feature based on variable block size, but they also include the background in the feature.

In this paper, we propose a method of detecting a human and its body direction employing the HOG feature based on a human model. The reason for detecting body orientation is to predict his/her sudden step into a road. The present method differs from other existent methods in that (i) the HOG feature is calculated referring to a human model and therefore it does not include the background in a given image, and that (ii) human body direction is also recognized by the HOG feature based on the human models which represent respective body directions. To the best of our knowledge, the HOG feature has been employed to date only for detecting a human and not for recognizing its body direction. The proposed method is described in the following and the performance of the method is shown by the experiments employing real outdoor scenes.

2. Detecting a human

2.1 The HOG feature

The HOG (Histograms of Oriented Gradients) feature [1] is based on image gradients vectors. An image is separated into non-overlapping cells containing 5×5 pixels. Gradients are calculated at each pixel on the cell and the histogram on the orientation of the calculated gradients is made with the cell. These cells are collected into a block containing 3×3 cells and all the nine histograms are normalized on the block. This block is defined at every cell: Namely, the blocks overlap spatially. Finally, all the blocks containing the normalized histograms are collected into a single vector. This is the HOG feature of an image. As is understood from the above procedure, the background image is inevitably included in the HOG feature.

2. 2 A human model

The main idea of the proposed method is to calculate the HOG feature on a human model instead of calculating it on the whole image. A human model is created in the following way.

1: The intensity of gradient is calculated of all the images in an image database.
2: The average values of the intensity of the gradient are calculated at every pixel on the images and a normalized average gradient intensity image is produced.
3: An edge image is produced from the average gradient intensity image.
4: A silhouette image is created from the average gradient intensity image and a skeleton image is made from the silhouette image.
5: Finally a human model image is yielded by performing logical OR operation between the edge image obtained at step 3 and the skeleton image obtained at step 4.

The flowchart of the above steps is given in **Fig. 1**. Examples of the images at each step of the above procedure are depicted in **Fig. 2**.

2. 3 A feature vector

Using the human model, the method calculates the HOG feature as shown in **Fig. 3**. The histograms are made only at the points specified on the human model. We set a cell (5×5 pixels) at each white pixel on a human model. A gradient orientation histogram $\boldsymbol{a}_i = (a_{ij})$ is made at the ith cell (i=1,2,…,N; j=1,2,…,9). These histograms are collected into a single vector $\hat{\boldsymbol{v}}$ of the form

$$\hat{\boldsymbol{v}} = (\boldsymbol{a}_1, \boldsymbol{a}_2, ..., \boldsymbol{a}_N) \equiv (a_{ij}) \quad (i = 1,2,...,N;\ j = 1,2,...,9). \tag{1}$$

Vector $\hat{\boldsymbol{v}}$ is normalized into vector $\boldsymbol{v}$ of the form

$$\boldsymbol{v} = (v_1, v_2, ..., v_{9N}) \tag{2a}$$

by

$$v_k = \frac{a_{ij}}{\sqrt{\|\hat{\boldsymbol{v}}\|^2 + \varepsilon^2}},\ k = 9(i-1) + j \tag{2b}$$

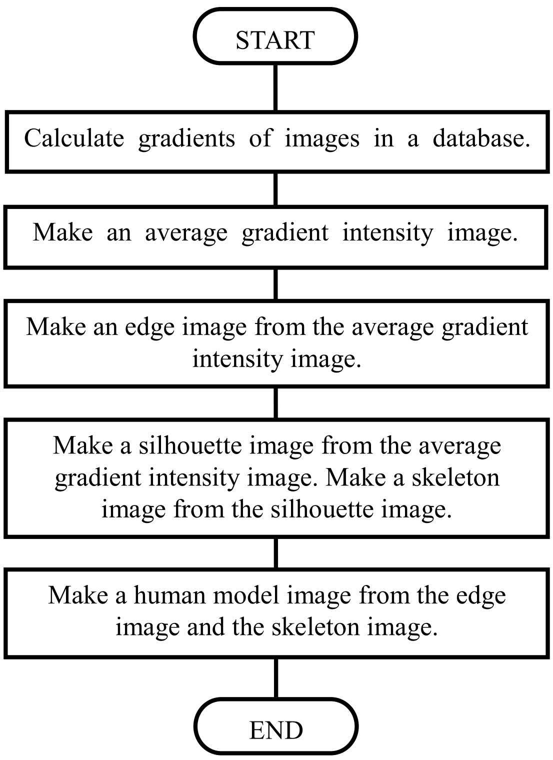

Fig.1. Flow chart of making a human model.

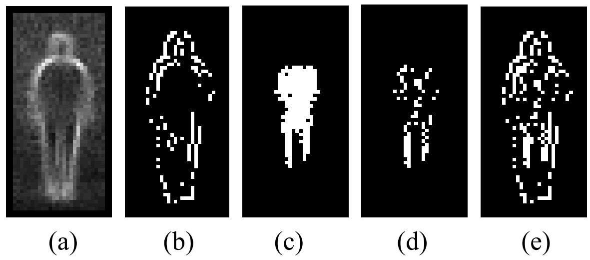

Fig. 2. Images obtained at each step of the procedure: (a) An average gradient intensity image, (b) an edge image, (c) a silhouette image, (d) a skeleton image, and (e) a human model image.

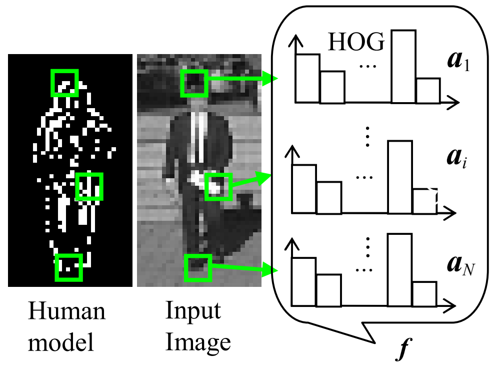

Fig. 3. Histogram creation employing a human model.

The vector $\boldsymbol{v}$ of Eq. (2) finally represents the given image based on the human model. The proposed method employs this vector for the judgment of human or non-human images. It is noted that the present method does not employ a block introduced in [1]. Instead, the cells scattered and overlapped on an image according to the human model are collected into a single feature vector $\boldsymbol{v}$.

A database is prepared for the development of a recognition system. The database contains a number of human images as positive data and a number of images without a human as negative data. The feature vectors of Eq. (2) are calculated from these images to define a non-linear SVM in the feature space. Human image recognition is then performed employing the SVM.

3. Detecting human body direction

The proposed method is applied to detecting human body direction. The direction is roughly separated into front(F), right(R) and left(L), and three human models are defined, respectively. In the first step of the detection, three SVM classifiers are generated and used:

They are based on one vs. rest method, i.e., left or others, front or others, and right or others. If not decided, it proceeds to the second step where two SVM classifiers are generated and used based on one vs. one method, i.e., left or front, and front or right. The judgment scheme is given in **Fig. 4**.

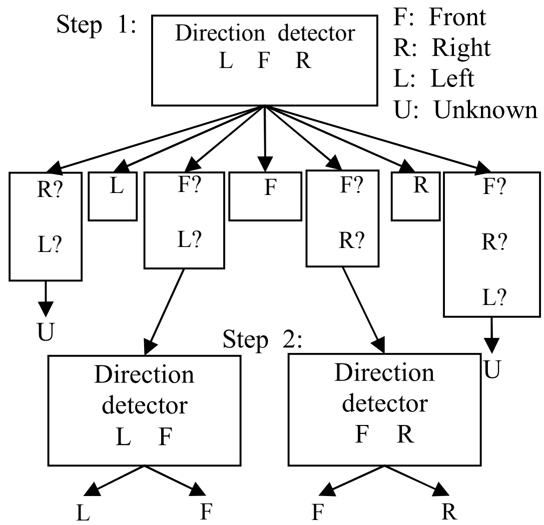

Fig. 4. Judgment of body direction.

4. Experimental results

4. 1 Detecting a human

We use 1602 human images as positive training dataset and 3235 images without a human as negative training dataset. For validation, we employ a dataset containing 1000 human images and the images without a human. The image size is 30 × 60 pixels. The employed human model is illustrated in **Fig. 5a**. Some learning images and test images are shown in Fig. 5b and Fig. 5c.

The proposed method is compared with the conventional method [1] in order to evaluate its performance. The result is provided by DET (Detection Error Trade-off) curves as shown in **Fig. 6**. When the true negative rate is 0.5[%], the false positive rate is 7.5[%] by the proposed method, whereas it is 19.1[%] by the conventional method. Thus the false positive rate has decreased by 11.6[%] in the proposed method compared to the conventional one. The computation time was 29.1 [msec/window] in the proposed method, whereas it was 54.4[msec/window] in the conventional one.

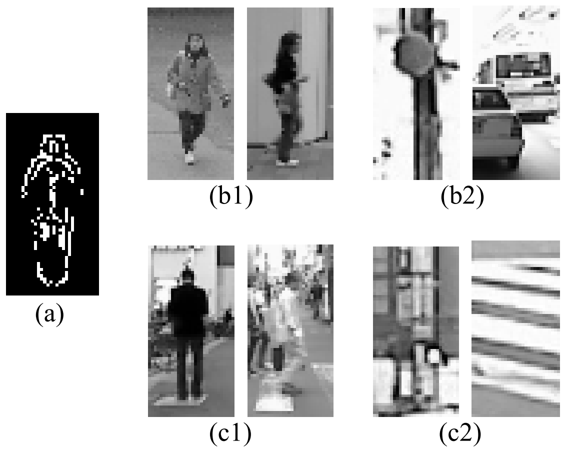

Fig. 5. Employed human model and some of the learning images and test images: (a) Human model; (b) Learning images, (c) test images; (1) human images, (2) images without a human.

4. 2 Detecting human body direction

In this experiment, 217 images with each direction are used as learning data. As for validation, we use 2 datasets. Dataset 1 contains 200 images with each direction captured in a specified environment (no occlusion and human natural standing posture). On the other hand, dataset 2 is a set of images taken in a real environment. It also contains 200 images with each direction. The proposed method is compared its performance with the conventional method [1]. The result of recognition (the rate of correct detection of body direction) is given in **Table 1**. The computation time was 26.7 [msec/image] in the proposed method, whereas it was 60.6[msec/image] in the conventional one.

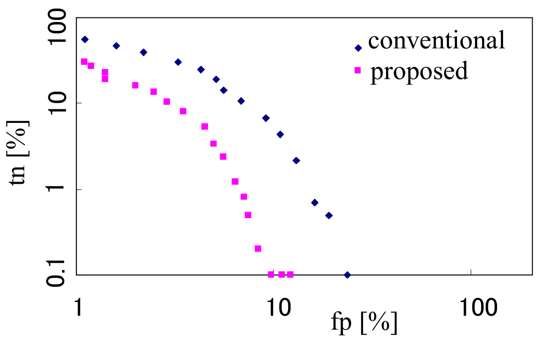

Fig. 6. The DET curve of the proposed method and the conventional method.

Table 1. Recognition rate (%)

method	Dataset	success	error	unknown
conventional	1	67.8	8.2	24.0
	2	56.0	22.3	21.7
proposed	1	94.2	1.0	4.8
	2	79.0	15.3	5.7

5. Discussion

We have proposed a method of detecting a human and its body direction employing the HOG feature [1]. The novelty of the present paper is that the HOG feature is calculated on a human model in the proposed method, unlike other reported techniques in which the HOG feature is calculated in a cell that spreads all over a given image. Since HOG features calculated in the background of an image may not contribute much in human recognition, the proposed method can discard the undesired background effect to a large extent. In the original literature [1], three by three adjacent cells are collected into a single block and the block is chosen one after another on the image so that they may have enough mutual overlap. This overlap among blocks is realized by the overlap among cells in the present method. After all, the feature vector defined by Eq. (2) keeps the HOG features only within and on the border of a human figure.

Another novelty of the present paper is that the HOG feature is employed in detecting human body direction. The proposed method detects not only a human facing front but also a human facing sideways by the employment of respective human models. It is well known that the HOG feature is a strong and robust feature for recognizing a human in an arbitrary environment. Extending the recognition technique employing the HOG feature to detecting human body direction may have application to car vision, where a person should be predicted who might step or run into a road out of a side walk.

The experimental results show effectiveness of the proposed method. We understand that undesired background effect has decreased to a certain extent, as the HOG feature was calculated based on a human model. However, not all HOG features may be necessary for the detection. We have a plan to select effective feature locations, which may result in better performance of the proposed method.

6. Conclusions

A method was proposed for detecting a human and its body direction employing the HOG features based on a human model. Performance of the method was satisfactory. Refinement of the human model by selecting effective feature locations remains for further study.

Acknowledgement

This work was partly supported by a grant of Knowledge Cluster Initiative implemented by Ministry of Education, Culture, Sports, Science and Technology (MEXT).

References

[1] N. Dalal, B. Triggs: "Histograms of oriented gradients for human detection", Proc. IEEE Conf. on Computer Vision & Pattern Recognition, 886-893, 2005.
[2] Q. Zhu, et al.: "Fast human detection using a cascade of histograms of oriented gradients", Proc. IEEE Conf. on Computer Vision & Pattern Recognition, 2006.

The Fifteenth International Symposium on Artificial Life and Robotics 2010 (AROB 15th '10),
B-Con Plaza, Beppu,Oita, Japan, February 4-6, 2010

Parallel Computing Method of Extraction of Frequent Occurrence Pattern of Sea Surface Temperature from Satellite Data

Ayahiko Niimi
Department of Media Architecture
Future University-Hakodate
116-2 Kamedanakano-cho, Hakodate-shi,
Hokkaido 041-8655, JAPAN

Takehiro Yamaguchi
Graduate School of Systems Information Sciences
Future University-Hakodate
116-2 Kamedanakano-cho, Hakodate-shi,
Hokkaido 041-8655, JAPAN

Osamu Konishi
Department of Complex Systems
Future University-Hakodate
116-2 Kamedanakano-cho, Hakodate-shi,
Hokkaido 041-8655, JAPAN

Abstract

In this paper, we propose the method for finding the frequent occurrence patterns and the frequent occurrence time-series change patterns from the observational data of the weather-monitoring satellite. The observational data of the weather-monitoring satellite is temporal and spatial large-scale data. Various use like the forecast of marine resources is thought by analyzing the satellite data. However, there is a problem of the calculation cost to analyze a large amount of data. Then, we propose to use the parallel computation when the frequent occurrence pattern and the frequent occurrence time series change pattern are extracted in this paper.

Keyword:

distributed processing, clustering, frequent occurrence pattern extraction, satellite data, data stream

1 Introduction

In recently network society, the development of information processing technique enables us to collect and utilize massive amount of data, and the data mining is technology of discovery new knowledge and patterns in those data has been paid attention. But those data are changing from moment to moment, and have become new type large scale data. Record of financial and distributional transactions, telecommunications records and network access logs are typical examples, and those data are called data stream. By data stream, it is that the conditions temporally-changed massive amount of data record are generated, cumulative and consumed are looked on as flow of data (stream). In the real world, the requirement that whenever we need information, we want to elicit from those large scale data stream has been growing. At first glance data mining seems to be effective, but data stream has following dynamic properties:

1. massive amount of data are
2. coming over high-speed stream
3. temporally-changing
4. continue to arrive permanently,

and there is a limitation applied data stream to data mining intending static data. Data mining to efficiently deal in large scale data stream, therefore data stream mining technology has been developed [1, 2, 3, 4, 5, 6, 7].

Data from the satellite is a data stream. The satellite data is used for various usages. For instance, the land-cover classification and the forecast that uses the satellite data are researched [8], and the marine information analysis is done [9, 10, 11, 12, 13]. However, the satellite data had been handled up to now as static data. Therefore, there was a problem of taking the computing time to analyze a large amount of data.

In this paper, we propose the method solved by using distributed processing.

In this paper, we propose the method for finding the frequent occurrence patterns and the frequent occurrence time-series change patterns from the observational data of the weather-monitoring satellite. The observational data of the weather-monitoring satellite is temporal and spatial large-scale data. Various use like the forecast of marine resources is thought by analyzing the satellite data. However, there is a problem of the calculation cost to analyze a large amount of data. Then, we propose to use the parallel computation when the frequent occurrence pattern and the frequent occurrence time series change pattern are extracted in this paper.

Our proposal method is the following. First of all, to extract the frequent occurrence pattern from the satellite data, necessary marine information is acquired by using the filter from the satellite data. Next, the extracted marine data are applied clustering to marge similar data, and labeled. As a result, similar data are brought together for data with a spatial extension. The labeling data are re-clustering to the data group, and re-labeled with according to the degree of similarity between labels. As a result, similar data is brought together for data with a time extension. Finally, the frequent event are extracted as the frequent occurrence pattern from the labeling data. Moreover, the frequent occurrence of the time series pattern can be extracted as rules by catching the change in the labeling data group. However, it takes the computing time to analyze long-term data. Therefore, we propose to shorten the computing time by the parallel computation of clustering and the frequent occurrence of the time series pattern rule extraction by dividing data and integrating the results. As for clustering and the frequent occurrence of the time series change pattern extraction, the parallel computation is possible by divide data. The more shorten computing time can be expected by division degree, because each algorithm never influences in the parallel calculate.

In this paper, each algorithm examined whether making to the parallel was possible. Because clustering and extracting of change pattern can be applied parallel computing, we cnstructed the system with clustering of marine information and the extraction of the change pattern. In this paper, the frequent occurrence pattern and the frequent occurrence of the time series change pattern of the sea surface temperature have been extracted by using the data of the sea surface temperature with the weather-monitoring satellite for the verification. The extraction result was compared with an existing technique, and shortening at the computing time was confirmed.

2 Details of Satellite Data

We acquired the data of Meteorological Satellite Center as satellite data. We used the observation monthly report of Meteorological Satellite Center to experiment [14]. The observation monthly report can be obtained with CD-ROM. These CD-ROMs contain the Monthly Report of observation data derived from MTSAT-1R and the polar orbital meteorological satellite NOAA. This Monthly Report contains image data observed by the following 4 channels and processed satellite product data from the observation data. 4 channels are IR:Infrared(10.3–11.3μm), VS:Visible(0.55–0.90μm), WV:Water Vapor(6.5–7.0μm) and SW:3.8 micron image(3.5–4.0μm).

In the problem of forecasting the hot spot of marine products using the satellite data, the sea surface temperature, the chlorophyl, and the flow of the ocean, etc. are often targeted. Because only the data of the sea surface temperature is included in the observational data, sea surface temperature was used to experiment.

Ten-day mean Sea Surface Temperature (SST) consists of grid points arrayed every one degree latitude and longitude covering the area from 50 degrees North to 50 degrees South and 90 degrees East to 170 degrees West. SST is derived from brightness temperatures of infrared split-window channels (IR1 and IR2) and satellite zenith angle using multiple regression equation. In the table, SSTs are expressed in 0.1 degree centigrade by integer form (multiplied by 10) of three digits, e.g., 12.3 degree centigrade is expressed as 123. The marks "/" and "." show "land" and "no valid data" respectively. SST data are provided by text data in tabular form generated in Meteorological Satellite Center. These data are recorded in ASCII code and HTML format.

We use data from 2009-March to 2009-May, because the regression equation for Sea Surface Temperature is updated on March 1, 2009.

3 The Proposed Method

In this paper, we propose the method for finding the frequent occurrence patterns and the frequent occurrence time-series change patterns from the observational data of the weather-monitoring satellite.

Fig. 1 shows a flowchart of the proposed system.

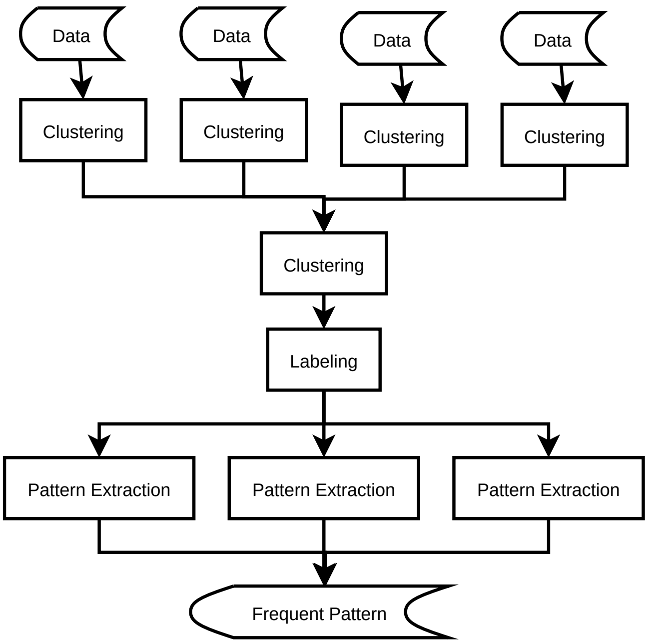

Figure 1: Frowchart of proposed system

The flow of the algorithm is shown below.

1. First of all, to extract the frequent occurrence pattern from the satellite data, necessary marine information is acquired by using the filter from the satellite data.
2. Next, the extracted marine data are applied clustering to marge similar data, and labeled.
3. The labeling data are re-clustering to the data group, and re-labeled with according to the degree of similarity between labels.
4. Finally, the frequent event are extracted as the frequent occurrence pattern from the labeling data.

In first clustering, similar data are brought together for data with a spatial extension. In second clustering, similar data is brought together for data with a time extension. Moreover, the frequent occurrence of the time series pattern can be extracted as rules by catching the change in the labeling data group. However, it takes the computing time to analyze long-term data. Therefore, we propose to shorten the computing time by the parallel computation of clustering and the frequent occurrence of the time series pattern rule extraction by dividing data and integrating the results. As for clustering and the frequent occurrence of the time series change pattern extraction, the parallel computation is possible by divide data. The more shorten computing time can be expected by division degree, because each algorithm never influences in the parallel calculate.

In this paper, each algorithm examined whether making to the parallel was possible. Because clustering and extracting of change pattern can be applied parallel computing, we cnstructed the system with clustering of marine information and the extraction of the change pattern.

4 Experiments

In this paper, the frequent occurrence pattern and the frequent occurrence of the time series change pattern of the sea surface temperature have been extracted by using the data of the sea surface temperature with the weather-monitoring satellite for the verification.

The data used by the experiment is the sea surface temperature of the observation monthly report of Meteorological Satellite Center. We use linear interpolation with the data at time before and after for the missing value. The input data used 9 attributes in which the data of 8 neighborhood are added to data of a certain point. We already described detailed data in section 2.

We use InTrigger platform of the information explosion project [15]. InTrigger is a distributed platform for information technology research for Information Explosion Era. It is a cluster of clusters distributed across Japan.

In the experiment, we applied the first clustering, and it was confirmed to be able to shorten the computing time by the proposal technique.

5 Conclusions

In this paper, we propose the method for finding the frequent occurrence patterns and the frequent occurrence time-series change patterns from the observational data of the weather-monitoring satellite. The observational data of the weather-monitoring satellite is temporal and spatial large-scale data. Various use like the forecast of marine resources is thought by analyzing the satellite data. However, there is a problem of the calculation cost to analyze a large amount of data. Then, we propose to use the parallel computation when the frequent occurrence pattern and the frequent occurrence time series change pattern are extracted in this paper.

It is scheduled to conduct the evaluation experiment of the entire system including second-clustering and pattern extraction, and to experiment to data that contains the density of the chlorophyl in the future.

References

[1] Martin H. C. L., Zhang, N., Anil, K. J.: Nonlinear Manifold Learning For Data Stream, In Proc. SIAM International Conference for Data Mining, pp.34–44 (2004).

[2] Jain, A., Zhang, Z., Chang, E. Y.: Adaptive nonlinear clustering in data streams, CIKM '06: Proceedings of the 15th ACM international conference on Information and knowledge management, Arlington, Virginia, USA, pp.122–131 (2006).

[3] Graf, H. P., Cosatto, E., Bottou, L., Durdanovic, I., Vapnik, V.: Parallel support vector machines: The cascade svm, In Advances in Neural Information Processing Systems, pp.521–528 (2005).

[4] Zhang, Y., Jin, X.: An Automatic Construction and Organization Strategy for Ensemble Learning on Data Streams, SIGMOD Record, Vol.35, No.3, pp.28–33 (2006).

[5] Wang, H., Fan W., Yu, P.S., Han, J.: Mining Concept-Drifting Data Streams Using Ensemble Classifiers, SIGKDD'03, pp.226–235 (2003).

[6] Yamaguchi, T., Niimi, A.: Community Graph Sequence with Sequence Data of Network Structured Data, 5th International Workshop on Computational Intelligence & Applications (IWCIA2009), Hiroshima, Japan, pp.196–201 (2009).

[7] Minegishi, T., Ise, M., Niimi, A., Konishi, O.: Extension of Decision Tree Algorithm for Stream Data Mining Using Real Data, 5th International Workshop on Computational Intelligence & Applications (IWCIA2009), Hiroshima, Japan, pp.208–212 (2009).

[8] Yamaguchi, T., Noguchi, Y., Ichimura, T., Mackin, K.J.: Applying Cluster Ensemble to Adaptive Tree Structured Clustering, 5th International Workshop on Computational Intelligence & Applications (IWCIA2009), Hiroshima, Japan, pp.186–191 (2009).

[9] Mustapha, M. A., Saitoh, S.: Observations of sea ice interannual varitions and spring bloom occurrences at the Japanese scallop farming area in the Okhotsk Sea using satellite imageries, Estuarine, Coastal and Shelf Science, 77, pp.577–588 (2008).

[10] Zainuddin, M., Kiyofuji, H., Saitoh, K., Saitoh, S.: Using multi-sensor satellite remote sensing and catch data to detect ocean hot spots for albacore (Thunnus alalunga) in the northwestern North Pacific, Deep-Sea Research II, 53, pp.419–431 (2006).

[11] Iida, T., Saitoh, S.: Temporal and spatial variability of chlorophyll concentrations in the Bering Sea using empirical orthogonal function (EOF) analysis of remote sensing data, Deep-Sea Research II, 54, pp.2657–2671 (2007).

[12] Radiarta, I N., Saitoh, S.: Satellite-derived measurements of spatial and temporal chlorophyll-a variability in Funka Bay, southwestern Hokkaido, Japan, Estuarine, Coastal and Shelf Science, 79, pp.400–408 (2008).

[13] Zainuddin, M., Saitoh, K., Saitoh, S.: Albacore (Thunnus alalunga) fishing ground in relation to oceanographic conditions in the western North Pacific Occean using remotely sensed satellite data, Fisheries Oceanography, Vol.17, No.2, pp.61–73 (2008).

[14] Meteorological Satellite Center Monthly Report, Meteorological Satellite Center.

[15] InTrigger, https://www.intrigger.jp/wiki/index.php /InTrigger

The Fifteenth International Symposium on Artificial Life and Robotics 2010 (AROB 15th '10),
B-Con Plaza, Beppu,Oita, Japan, February 4-6, 2010

Cultural Evolution of Compositional Language under Multiple Cognition of Meanings

R. Matoba[*1], S. Sakamoto[*1] and T. Hashimoto[*2]

**1 School of Information Science,*
**2 School of Knowledge Science,*
Japan Advanced Institute of Science and Technology,
1-1, Asahidai, Nomi, Ishikawa, 923-1292, Japan
(Tel : +81-0761-51-1372; Fax :+ 81-0761-51-1149)
{r-matoba, s0710202, hash}@jaist.ac.jp

Abstract: In the actual world, we often happen to meet a state which contains several meanings. In this paper, we call this phenomenon *multiple cognition of meanings*. Under an environment of multiple cognition, language needs to distinguish ``A do B'' from ``B is done by A'' to represent speaker's intension, even a state change which is pointed these two sentences are the same state change. Solving this matter, most present existing languages have functions such as case marking, agreement of person and number, or word order, etc. Here, one question is popped up, which is where these functions come from. Thinking of this question, we employed Iterated Learning Model which represents evolution of compositional language, and built state change and multiple cognition into this model. Simulating with our model, we speculated an influence of multiple cognition on evolution of compositional language.

Keywords: Cultural Evolution, Compositionality, Multiple Cognition, Iterated Learning Model

1. Introduction

In the actual world, we encounter a situation which contains several meanings frequently. For example, if there exist two objects, object A and object B separately on a table, and somebody puts object A on top of object B, then we can describe this action in different expressions such as ``object A is put on object B", or ``object B is put under object A", even the way the state has changed is the same. In this paper, we use a term *multiple cognition* as one uttered situation which contains several possible meanings, like above example. To represent speaker's intention precisely, existing languages have grammatical features such as agreement of number, person, and gender, case marking, or word order, and so on. Taking advantages of these features, language users are able to discriminate subject and object of a sentence, i.e., preventing influence of multiple cognition. As long as a person communicates with a person, there are possibilities to happen multiple cognition, but it is hard to assume that grammatical features for preventing influence of multiple cognition had existed from origin of language. Hence, these features might have been generated in the course of language evolution.

In this paper, we employed the Iterated Learning Model (ILM, hereafter) by Kirby[1] which is one of models of cultural evolution represents evolution of compositional language from holistic language, and built state change and multiple cognition into ILM. Through the computer simulation using our model, we speculated an influence of multiple cognition on evolution of compositional language.

2. ILM with State Change

2.1. Briefing Kirby's Model

Our study is based on the ILM by Kirby[1], who introduced the notions of *compositionality* and *recursion* as fundamental features of grammar, and showed that they made it possible for a human to acquire compositional language. Also, he adopted the idea of two different domains of language[2,3,4], namely, I-language and E-language; I-language is the internal language corresponding to speaker's intention or meaning, while E-language is the external language, that is, utterances. In his model, a parent is a speaker agent and her infant is a listener agent. The speaker agent gives the listener agent a pair of a string of symbols as an utterance (E-language), and a predicate-argument structure (PAS) as its meaning (I-language). A number of utterances would form compositional grammar rules in listener's mind, through learning process. This process is iterated generation by generation, and finally, a certain generation would acquire a compact, limited number of grammar rules. We include a meaning inference using a state change into this process. We implement agents with state change in a virtual world, and make them learn a grammar by computer simulation.

In our model, we changed two points of Kirby's model, which are (i) taking away the transmittance of meanings between the parent and the infant, and (ii) giving a state change which contains more than one meaning.

2.1.1 Utterance Rule of Kirby's Model

According to Kirby's model, we show a pair of I-language and E-language as follows.

S/eat(john, apple) → `eatjohnapple` (1)

Where a speaker's intention is a PAS *eat(john, apple)* and its utterance becomes `eatjohnapple'; the symbol `*S*' stands for that they belong to the category Sentence. Thus, as far as a listener is given an utterance paired with its meaning (PAS), the listener can understand the speaker's intention precisely at all times. However, compared to the actual situation, it seems a very strong assumption. In our model, we loosen this assumption and build state change instead of meaning share into this model. This means that the listener agent receives utterances without meanings, to show the influence of multiple cognition of meanings.

2.1.2 Rule Subsumption

chunk This operation takes pairs of rules and looks for the least-general generalization. For example, if there are two rules below,

S/read(john, book) → `ivnre` (2)
S/read(mary, book) → `ivnho` (3)

then, after operation chunk, the two rules above become

S/read(x, book) → `inv N/x` (4)
N/john → `re` (5)
N/mary → `ho` (6)

merge If two rules have the same meanings and strings, replace their nonterminal symbols for one common symbol. For example, if given rules below,

S/read(x, book) → `ivn A/x` (7)
A/john → `re` (8)
A/mary → `ho` (9)
S/eat(x, apple) → `apr B/x` (10)
B/john → `re` (11)

then, after operation merge, the rules above become

S/read(x, book) → `ivn A/x` (12)
A/john → `re` (13)
A/mary → `ho` (14)
S/eat(x, apple) → `apr A/x` (15)

replace If a rule is embeddable in another rule, replace the latter for a compositional rule with variables. For example, if given two rules below,

S/read(pete, book) → `ivnwqi` (16)
B/pete → `wqi` (17)

then, after operation replace, the rules above become

S/read(x, book) → `ivn B/x` (18)
B/pete → `wqi` (19)

2.2. State, State Change, Action of Predicates

The difference point between Kirby's model and our model is that the listener cannot always get a meaning of an utterance precisely, i.e., in Kirby's model, the listener always gets a pair of the utterance and its meaning (PAS). Instead of getting the meaning of the utterance, the listener gets the utterance and a state change which corresponds to the utterance, and uses them for his learning.

In our representation, the state which agents pay attention to is constructed by five connected boxes, and two or three boxes out of five are filled with numbers, from one to five. See figure 1.

	1		5	

Fig.1. State representation

The state change is represented as a change of numbers and a change of places which numbers are filled with. The agent's language of our model is constructed five kinds of predicates and five kinds of arguments like Kirby's model. The arguments are numbers from one to five, and the predicates are `step', `gather', `swap', `put', and `sub'. In our model, each predicate has an operation to change a state. The followings are the definitions of each predicate. Hereafter, we call a state which is not operated yet `before state', and a state which is operated by the parent `after state'.

step(x, y)
Condition: Before state contains x and y, and there is at least one box between x and y.
Operation: move x to y one box. If the box next to x is filled with a number, swap the number and x.
gather(x, y)
Condition: Before state contains x and y, and there is at

least one box next to y.
Operation: move x next to y.
swap(x, y)
Condition: Before state contains x.
Operation: If before state contains y, swap a position of x and y. If before state does not contain y, swap x and y, and x disappears from after state.
put(x, y)
Condition: Before state contains x, and does not contain y, also there is at least one box next to x.
Operation: add y next to x.
sub(x, y)
Condition: Before state contains x, and x > y, also does not contain x-y.
Operation: Subtract y from x (rename x to x-y).

3. What is Multiple Cognition of Our Model?

To represent multiple cognition, i.e., several meanings for one situation, the operations performed by the parent are designed to overlap its action deliberately. Figure 2 indicates multiple cognition of `step(2, 4)', `step(2, 5)', and `gather(2, 5)'.

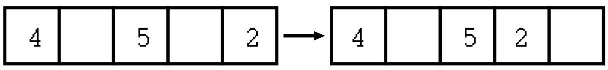

Fig.2. Example of multiple cognition
step(2, 4) – step(2, 5) – gather(2, 5)

III. Experimented Procedure

The simulation implements these processes:
1. The speaker tries to produce utterances which will form input to the listener. This process repeats number of times (depends on the experimenter: in our experiment, it is limited to 50 times, which is the same as Kirby's experiment).
(a) The speaker is given a before state and an operation (meaning) chosen randomly from a meaning space.
(b) The speaker executes the operation, and makes an after state.
(c) If the speaker is able to generate strings as an utterance for that operation using her grammar, she makes it. Otherwise, she invents strings randomly, and if the need arises, she uses this invented rule again.
(d)The listener infers the operation (meaning) of the strings (utterance). If he can figure out the operation of strings, uses a pair of the operation (meaning) and the strings (utterance) to his learning. If there exists several candidates of operation, choose them randomly. If he cannot figure out the operation of the strings, then he adapts one operation randomely.
2. The speaker's grammar is logged, and she is deleted from the simulation
3. The listener becomes the new speaker, and a new listener with an empty grammar knowledge is added to the simulation.

IV. Experiment and Result

In this section, we show the procedure and the result of our experiment. The purpose of the experiment is to demonstrate acquisition of compositional language under environment of multiple cognition. To evaluate the accomplishment of the learning, we investigate expressivity in the following definition, as well as the number of grammar rules.

Definition (Expressivity)
Expressivity is the ratio of the utterable meanings against the whole meaning space.

The experiment was carried out until the 100th generation. In fact, we have carried out until the 1000th generation; however, both of expressivity and the number of rules converged until the 100th generation, and thus we discuss the result derived by the 100th generation.

2. Experiment 2: Learning without Meaning of Utterance

In this experiment, the listener does not get a meaning of an utterance, and infers the meaning from the utterance and a state change. Different from Kirby's model, incomprehensible utterances are given at the tail of the 50 utterances, e.g., in case of 20 %, the first 40 sentences are given paired with PAS as training data while the rest 10 utterances are meaningless. This is because inference of the listener must be evoked after a certain accumulation of grammar knowledge. Namely, the listener could consider that the intention of the speaker was not clear but referring back to the previous knowledge the listener could partially guess what the speaker had said. Figure 3 and Figure 4, the results of the average of 100 trials, show that the expressivity and the number of rules at the rate of the inference rate are set from 0% to 100 %.

The results of this experiment show that while the inference rate is low, i.e., the listener can get many training data from the speaker, the expressivity of the grammar indicates high value, and the number of rules is small. Namely, the listener acquires compositional language. On the other hand, the more inference rate

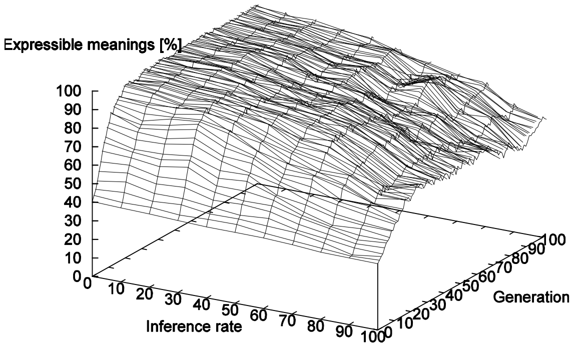

Fig.3. The movement of the expressivity per generation with inference.

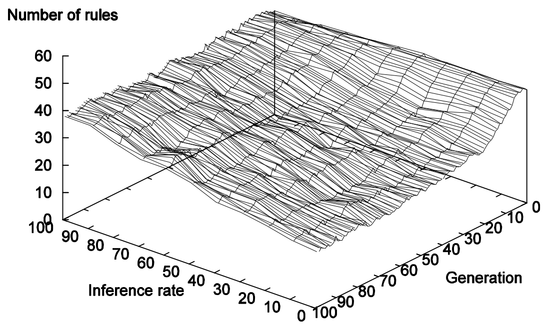

Fig.4. The movement of the number of rules per generation with inference.

increases, the more the expressivity decreases and the number of rules increases. The possible reason is that the complement of meanings by inference is incomplete, the listener acquires rules which were originally not included in the speaker's grammars, so the listener cannot generalize such rules well. Also, the mechanism to avoid multiple cognition of our model is only the training data from the speaker, so increase of inference rate leads low expressivity and large number of rules. Table 1 shows the acquired grammar of the listener in the convergence generation while inference rate is 8 %, and table 2 shows the result of the inference rate is 50 %. Obviously, we can observe many polysemous words in table 2.

V. Conclusion and Future Work

In this paper, we investigated the influence of multiple cognition to the development of compositional

Table 1. Sample grammar of convergence generation. Inference rate is 8 %.

S/p(x, y) → j A/x g A/y D/p inrgh	
A/1 → h	*D/gather* → k
A/2 → i	*D/put* → la
A/3 → m	*D/step* → gnnag
A/4 → ji	*D/sub* → nke
A/5 → f	*D/swap* → kr

Table 2. Sample grammar of convergence generation. Inference rate is 50 %.

S/p(x, y) → A/x e C/p oc A/y	
S/p(x, y) → A/y e C/p poc A/x	
A/1 → q	*D/gather* → v
A/2 → q	*D/put* → czc
A/3 → q	*D/step* → v
A/4 → q	*D/sub* → v
A/5 → cr	*D/swap* → v

language with Iterated Learning Model. As the result of our experiment, without training data from the speaker, the listener could not avoid the influence of multiple cognition. The result of ILM strongly responds to learning algorithm, so instead of just following Kirby's model, we need to improve learning algorithm of our model. In our present model, if a need to choose one meaning from several meanings arises, the listener chooses randomly. In the near future, using weighted selection, we will improve this random selecting method to a method with directional characteristics for selecting one meaning. Also, we are planning to employ prefix or suffix to the arguments of predicate of language in our model to avoid multiple cognition.

REFERENCES

[1] Kirby, S. (2002), Learning, bottlenecks and the evolution of recursive syntax. In: Linguistic Evolution through Language Acquisition. Cambridge University Press.
[2] Kirby, S. (1999), Function, Selection and Innateness: The Emergence of Language Universals. Oxford: Oxford University Press.
[3] Chomsky, N. (1986), Knowledge of Language. Praeger, New York.
[4] Hurford, J. (1987), Language and Number: The Emergence of a Cognitive System. Blackwell, Oxford.

Production Scheduling Based on Mixed-Integer Evolutionary Algorithm

Yung-Chin Lin[a,b], Yung-Chien Lin[a], Kuo-Lan Su[b]

[a]*Department of Electrical Engineering, WuFeng Institute of Technology, Chiayi, Taiwan*
[b]*Department of Electrical Engineering, National Yunlin University of Science & Technology, Yunlin, Taiwan*
e-mail: {yclin@mail.wfc.edu.tw; chien-lin@mail.wfc.edu.tw; sukl@yuntech.edu.tw}

Abstract: Production scheduling is one of the most important decision-making problems in the manufacturing industry. The problem is complex due to coupling with combinatorial property and constrained requirements. To describe production scheduling, a mixed-integer nonlinear programming (MINLP) model is developed to formulate this decision-making problem. On the other hand, in order to effectively make an optimal decision, a mixed-integer evolutionary algorithm is proposed to solve this MINLP problem. Finally, an experimental example is used to test the algorithm. The experimental results demonstrate the proposed algorithm can effectively handle the production scheduling problem.

Keywords: production scheduling, mixed-integer nonlinear programming, evolutionary algorithm**.**

I. Introduction

In a batch manufacturing system, production scheduling is one of the most important decision-making problems. In such a manufacturing system, batch operations (e.g. batch drying, batch distillation, batch reactors, etc.) are often used to produce multiple products that are similar in nature. When products are similar in nature, they need identical processing steps and the same series of processing units. Therefore, in order to maximize productivity in the shortest possible time, the optimal process scheduling is crucial in such a sequential processing decision problem.

Due to the coupling with combinatorial property and conflict constraints, this decision-making problems is complex and difficult to solve. In order to describe this decision-making problem, we develop a mixed-integer nonlinear programming (MINLP) model, based on Karimi's models [1], to formulate this production scheduling problem. In the MINLP model, continuous variables are used to describe the interactive relationships (e.g. mass balances, energy balances, physical phenomena, etc.), and integer variables are used to represent the existence of processes and the operational status of the processing units. Owing to the combinatorial property of production-strategy selection together with conflict constraints, the MINLP model presents complex characteristics such as multimodality, large dimensionality, strong nonlinearity, nonconvexity, and nondifferentiability. As a result, it is difficult to find the globally optimal solution.

Evolutionary algorithms (EAs) [2], [3] are defined as a class of stochastic search and optimization methods that begin a population of randomly generated solutions and evolve towards an optimal solution by repeatedly applying a set of genetic operations. Due to their ability to escape from the local optimal solutions, EAs have been demonstrated a promising candidate for solving complex optimization problems, including the constrained optimization problems. For optimization problems with complicated constraints, Michalewicz and Schoenauer [4] surveyed and compared several constraint-handling techniques used in EAs. Of these techniques, the penalty function method is one of the most popularly used techniques to handle the constraints. In this method, the fitness function including a penalty function, i.e. the squared or absolute constraint violation term, is used to reject infeasible solutions. However, these penalty function methods have a fatal weakness when the penalty parameters are large. For example, if the penalty parameters are large, the penalty function tends to be ill-conditioned near the boundary of feasible domain. Thus it may lead to a local solution or an infeasible solution. In this paper, to effectively solve mixed-integer constrained optimization problems (or MINLP problems), a mixed-integer evolutionary algorithm based on Lagrange method is developed for solving the MINLP problems as production scheduling problems.

In this paper, we not only formulate two MINLP models to describe the production scheduling problems, but also propose a mixed-integer evolutionary algorithm to handle them. The proposed algorithm has been successfully applied to a number of mixed-integer optimization problems [5], [6]. Finally, a production scheduling problem presented by Karimi [1] is employed to test the performance of the proposed method. The computational results demonstrate that the proposed method performs much better than the penalty method.

II. MINLP Formulation for Production Scheduling

Karimi [1] proposed a mixed-integer linear programming (MILP) model to formulate the production scheduling problem. In the following, we will describe this problem for details, and then propose a complete and explicit MINLP model to handle the production scheduling problem.

In this paper, we investigate a problem of scheduling N products across an M-stage serial processing plant with a single unit per stage. The configuration of this multiproduct batch plant is shown in Figure 1. In this batch plant, no storage (buffer) is available between the processing units. Therefore, if a product finishes processing on a unit and the downstream unit is not free (i.e. still processing a previous product), then the completed product must be held in the unit until the downstream unit becomes free. In this multiproduct plant, all products pass through the series of M units and the processing conditions are known *a priori* for all the products (i.e., the processing time t_{kj} of the product P_k on unit j is specified). Based on these specified processing conditions, the objective of the scheduling problem is to obtain the order in which the batches should be produced so as to maximize the productivity of the process, i.e., to minimize the makespan (the total time required to produce all the batches).

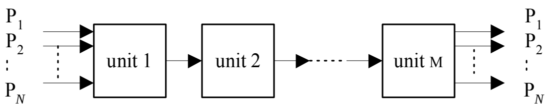

Fig.1. Configuration of batch plants.

Firstly, let C_{ij} denote the time at which the ith product in the production sequence leaves unit j. Hence, C_{NM} is the makespan of the given product sequence. To compute C_{ij}, consider the time-space relation of neighborhood stages and successive products. The completion time of the ith product in the sequence on unit j is simply the time at which unit j starts processing the ith product plus its processing time p_{ij}. But unit j cannot start processing the ith product until it has processed the previously (i-1)th product, or until the ith product has been processed by the upstream unit (j-1), as shown in Figure 2. We therefore have the following recurrence relations except for unit 1:

$$C_{ij} = \max\left[C_{(i-1)j}, C_{i(j-1)}\right] + p_{ij} \qquad (1)$$

$$\text{for } i = 1,\ldots,N;\ j = 2,\ldots,M$$

For unit 1, the completion times for each product can be obtained as follows:

$$C_{i1} = \max\left[C_{(i-1)1}, C_{(i-2)2}\right] + p_{i1}, \quad \text{for } i = 1,\ldots,N \qquad (2)$$

Note that $C_{ij} = 0$ for $i \le 0$ or $j \le 0$.

To order the production sequence of products, a set of binary variables are introduced as follows:

$$Y_{ki} = \begin{cases} 1, & \text{if product } \mathrm{P}_k \text{ is at position } i \\ & \text{in the production sequence} \\ 0, & \text{otherwise} \end{cases} \qquad (3)$$

for $k = 1,\ldots,N;\ i = 1,\ldots,N$

For example, $Y_{32} = 1$ means that product P_3 is the second in the production sequence, and $Y_{32} = 0$ means that it is not in the second position. Based on the significance of Y_{ki}, we obtain the following two sets of equality constraints.

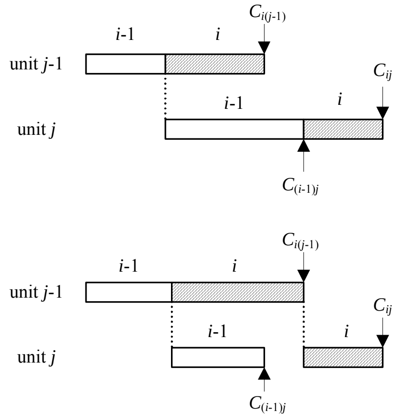

Figure 2. The time-space relation of C_{ij}, $C_{i(j-1)}$ and $C_{(i-1)j}$.

The first set of constraints ensures that a product is assigned to one and only one position in the processing sequence:

$$\sum_{i=1}^{N} Y_{ki} = 1 \quad k = 1,\ldots,N \qquad (4)$$

The second set of constraints ensures that a position in the sequence is assigned to one and only one product:

$$\sum_{k=1}^{N} Y_{ki} = 1, \quad i = 1,\ldots,N \qquad (5)$$

Let t_{kj} denote the processing time for product P_k on unit j. Now we must utilize a given set of Y_{ki} and t_{kj} to determine the processing time p_{ij} of the ith product in the production sequence on unit j. If product P_k in the sequence position i, then p_{ij} must be t_{kj}. On the other hand, we know that if product P_k in the sequence position i, then $Y_{ki} = 1$ and $Y_{k1} = Y_{k2} = \cdots = Y_{k(i-1)} = Y_{k(i+1)} = \cdots = Y_{kN} = 0$. Therefore, the processing time p_{ij} can be represented as:

$$p_{ij} = Y_{1i}t_{1j} + Y_{2i}t_{2j} + \cdots + Y_{Ni}t_{Nj}$$

$$\text{for } i = 1,\ldots,N;\ j = 1,\ldots,M \qquad (6)$$

Replacing (1) and (2) by (6), so we have:

$$C_{ij} = \max\left[C_{(i-1)j}, C_{i(j-1)}\right] + \sum_{k=1}^{N} Y_{ki}t_{kj}$$

$$\text{for } i = 1,\ldots,N;\ j = 2,\ldots,M \qquad (7)$$

$$C_{i1} = \max\left[C_{(i-1)1}, C_{(i-2)2}\right] + \sum_{k=1}^{N} Y_{ki}t_{k1} \quad \text{for } i = 1,\ldots,N \qquad (8)$$

Since the criterion is to minimize the makespan, the scheduling problem can be formulated as a MINLP problem as follows:

$$\min C_{NM} \qquad (9)$$

subject to Eqs. (4), (5), (7) and (8)

III. Mixed-Integer Evolutionary Algorithm

Let us consider a mixed-integer nonlinear constrained optimization problem as follows:

$$\min_{\mathbf{x},\mathbf{y}} f(\mathbf{x},\mathbf{y}) \tag{10}$$

subject to
$$h_j(\mathbf{x},\mathbf{y}) = 0,\ j = 1,\ldots,m_e \tag{11}$$
$$g_j(\mathbf{x},\mathbf{y}) \le 0,\ j = 1,\ldots,m_i \tag{12}$$

where $\mathbf{x}$ represents an n_C-dimensional vector of continuous variables, $\mathbf{y}$ is a n_I-dimensional vector of integer variables, and $h_j(\mathbf{x},\mathbf{y})$ and $g_j(\mathbf{x},\mathbf{y})$ stand for the equality and inequality constraints. To abbreviate these expressions, a compact notation $\mathbf{z} = (\mathbf{x},\mathbf{y})$ is used in the following discussions, and the problem is referred to as primal problem.

The Lagrange function corresponding to the primal problem is defined by

$$L(\mathbf{z},\lambda,\mu) = f(\mathbf{z}) + \sum_{k=1}^{m_e} \lambda_k h_k(\mathbf{z}) + \sum_{k=1}^{m_i} \mu_k g_k(\mathbf{z}) \tag{13}$$

where λ_k and μ_k are the Lagrange multipliers. The exterior penalty term can be used to define the new objective function, termed the augmented Lagrange function, as

$$L_a(\mathbf{z},\nu,\upsilon) = f(\mathbf{z}) + \sum_{k=1}^{m_e} \alpha_k \left\{ [h_k(\mathbf{z}) + \nu_k]^2 - \nu_k^2 \right\} + \sum_{k=1}^{m_i} \beta_k \left\{ \langle g_k(\mathbf{z}) + \upsilon_k \rangle_+^2 - \upsilon_k^2 \right\} \tag{14}$$

where α_k and β_k are positive penalty parameters, the bracket operation is denoted as $\langle g \rangle_+ = \max\{g,0\}$, and the corresponding Lagrange multipliers $\nu = (\nu_1,\ldots,\nu_{m_e})$ and $\upsilon = (\upsilon_1,\ldots,\upsilon_{m_i}) \ge \mathbf{0}$ are defined as $\lambda_k = 2\alpha_k \nu_k$ and $\mu_k = 2\beta_k \upsilon_k$.

In nonlinear programming, the Kuhn-Tucker optimality conditions are used to solve constrained optimization problems. The Kuhn-Tucker optimality conditions are suitable only for differentiable and convex problems. Unfortunately, the mixed-integer constrained optimization problems are just non-differentiable. However, the saddle point theorem [7] can provide sufficient conditions for solving constrained optimization problems without any differentiability or convexity requirements. It states that, if a point is a saddle point of the augmented Lagrange function associated with the primal problem, then the point is the solution of the primal problem. Accordingly, in this paper the saddle point theorem is used to solve mixed-integer constrained optimization problems.

The saddle point can be obtained by minimizing $L_a(\mathbf{z},\nu^*,\upsilon^*)$ with the optimal Lagrange multipliers (ν^*,υ^*) as a fixed parameter vector. However, the difficulty of this minimization is that it requires the knowledge of (ν^*,υ^*) previously. In general, the optimal values of Lagrange multipliers are unknown *a priori*. The duality theorem [7] can be employed to overcome this difficulty.

According to the duality theorem, we can construct an evolutionary max-min algorithm to solve mixed-integer constrained optimization problems. The evolutionary min-max algorithm (MIHDE-AMM) includes two phases as stated in Table 1. In the first phase (step 2 in Table 1), a mixed-integer evolutionary algorithm, called MIHDE [6], is used to minimize the augmented Lagrange function with multipliers fixed. In the second phase (step 3 in Table 1), the Lagrange multipliers are updated to ascend the value of the dual function toward obtaining maximization of the dual problem.

Table 1. Evolutionary max-min algorithm for mixed-integer constrained optimization problems.

Step 1. Set initial iteration: $l = 0$. Set initial multipliers: $\nu_k^l = 0$ for $k = 1,\ldots,m_e$, $\upsilon_k^l = 0$ for $k = 1,\ldots,m_i$. Set penalty parameters: $\alpha_k > 0$ for $k = 1,\ldots,m_e$, $\beta_k > 0$ for $k = 1,\ldots,m_i$.

Step 2. Use MIHDE to solve $L_a(\mathbf{z},\mathbf{v}^l,\boldsymbol{\upsilon}^l)$. Let $\mathbf{z}_b^l = (\mathbf{x}^l,\mathbf{y}^l)_b$ be a minimum solution to the function $L_a(\mathbf{z},\mathbf{v}^l,\boldsymbol{\upsilon}^l)$.

Step 3. Update the multipliers as follows:
$$\nu_k^{l+1} = h_k(\mathbf{z}_b^l) + \nu_k^l$$
$$\upsilon_k^{l+1} = \langle g_k(\mathbf{z}_b^l) + \upsilon_k^l \rangle_+$$

Step 4. Update α_k and β_k, if necessary.

Step 5. If the maximum iteration is reached, stop. Otherwise, let $l = l + 1$ and repeat Steps 2 to 4.

As far as the evolutionary computation is concerned, the evolutionary max-min procedure may increase many function evaluations and affect the convergence rate. However, in order to find the exact solution, it is necessary and inevitable unless using other special approaches, e.g., sequential quadratic programming (SQP) [8], to continuously update the Lagrange multipliers. Unfortunately, SQP is not applicable for the non-differentiable mixed-integer constrained optimization problems. The update of the Lagrange multipliers is based on the exact or approximate minimum of the augmented Lagrange function with multipliers fixed. As presented by Arora *et al.* [8], an exact or approximate minimum is necessary in order to ensure proper shift of the Lagrange function towards the required solution. With a rough minimum, the shift of the Lagrange function may be far away from the required solution leading to obtain a nonexistent dual function so that the duality theorem shall be disobeyed.

IV. Experimental Example

An example in Karimi [1] is given here to test the performance of the MIHDE-AMM algorithm. The MIHDE with penalty function method (MIHDE-PFM) is used to be compared.

In this example, we consider a three-unit, four-product production scheduling problem. Therefore, the MINLP problem with 8 equality constraints includes one real variable and 16 integer variables. Table 2 shows the data of processing times as discussed in Karimi [1]. Karimi obtained the minimum makespan of 34.8 hrs. In this example, we use the minimum value as a stopping criterion to check how much iteration for MIHDE-AMM reaching to this global solution. The product sequence of 1-3-4-2 with a makespan of 34.8 hrs, and the optimal completion times are shown in Figure 3.

Table 2. Processing times (h) of products.

Products	units		
	1	2	3
1	3.5	4.3	8.7
2	4.0	5.5	3.5
3	3.5	7.5	6.0
4	12.0	3.5	8.0

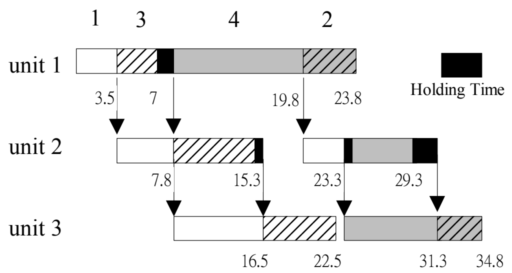

Figure 3. Optimal completion times for four products.

For comparison, The penalty function method (MIHDE-PFM) is also applied to solve the production scheduling problem. Table 3 shows that the computational results for MIHDE-AMM and MIHDE-PFM with penalty parameters of 1, 10^3 and 10^6. For penalty parameters of 10^3 and 10^6, both two algorithms can find the same optimal solution. However, the feasible solution are not obtained by MIHDE-PFM with penalty parameters of 1 because some inequality constraints are violated. Conversely, the MIHDE-AMM can obtain the same optimal solution using the penalty parameters of 1. This result demonstrates that the MIHDE-AMM outperforms the MIHDE-PFM.

IV. Conclusions

In this paper, a mixed-integer nonlinear programming (MINLP) model is developed to formulate the production scheduling problem. In order to effectively find the optimal solution, a mixed-integer evolutionary algorithm is proposed to solve this MINLP problem. From computational results, we can find that better results are obtained in comparison with the penalty function method. This demonstrates that the algorithm can effectively handle the decision-making problem of production scheduling.

Table 3. Comparison of the MIHDE-AMM and MIHDE-PFM for various penalty parameters, α_k, $k = 1,\ldots,8$.

Item	MIHDE-AMM			MIHDE-PFM		
	$\alpha_k=1$	$\alpha_k=10^3$	$\alpha_k=10^6$	$\alpha_k=1$	$\alpha_k=10^3$	$\alpha_k=10^6$
$f(\mathbf{z})$	34.8	34.8	34.8	8.0†	34.8	34.8
$h_1(\mathbf{z})$	0.0	0.0	0.0	-1.0‡	0.0	0.0
$h_2(\mathbf{z})$	0.0	0.0	0.0	-1.0‡	0.0	0.0
$h_3(\mathbf{z})$	0.0	0.0	0.0	-1.0‡	0.0	0.0
$h_4(\mathbf{z})$	0.0	0.0	0.0	-1.0‡	0.0	0.0
$h_5(\mathbf{z})$	0.0	0.0	0.0	-1.0‡	0.0	0.0
$h_6(\mathbf{z})$	0.0	0.0	0.0	-1.0‡	0.0	0.0
$h_7(\mathbf{z})$	0.0	0.0	0.0	-1.0‡	0.0	0.0
$h_8(\mathbf{z})$	0.0	0.0	0.0	-1.0‡	0.0	0.0
TFC	21905	663	663	NTR	663	663

NTR: The global solution is not to reach.
†: The solution is infeasible.
‡: The constraint is violated.

References

[1] I. A. Karimi, "Multiproduct Batch Plant Scheduling in CACHE," Chemical Engineering Optimization Models with GAMS, vol. 6

[2] Z. Michalewicz, "Genetic Algorithm + Data Structure = Evolution Programs," Springer-Verlag, 1994.

[3] T. Back, D. Fogel, and Z. Michalewicz, *Handbook of Evolutionary Computation*. New York: Oxford Univ. Press, 1997.

[4] Z. Michalewicz, Z. and M. Schoenauer, "Evolutionary Algorithms for Constrained Parameter Optimization Problems," *Evolutionary Computation*, vol. 4, no. 1, pp. 1-32, 1996.

[5] Y. C. Lin, K. S. Hwang, and F. S. Wang, "An evolutionary Lagrange method for mixed-integer constrained optimization problems," *Engineering Optimization*, vol. 35, no. 3, pp. 267-284, 2003.

[6] Y. C. Lin, K. S. Hwang, and F. S. Wang, "A mixed-coding scheme of evolutionary algorithms to solve mixed-integer nonlinear programming problems," *Computers & Mathematics with applications*, vol. 47, pp. 1295-1307, 2004.

[7] D.A. Wismer and R. Chattergy, *Introduction to Nonlinear Optimization*. Elsevier North-Holland, 1978.

[8] J. S. Arora, A. I. Chahande, and J. K. Paeng, "Multiplier methods for engineering optimization," *Int. J. Numerical Methods in Engineering*, vol. 32, pp. 1485-1525, 1991.

Further Study on Camera Position Estimation from Image by ANFIS

Shao-Fan Lien [1], Kuo-Hsien Hsia [2], Chun-Chieh Wang [3], Ting-En Lee [4] and Juhng-Perng Su [5]

[1,4]Graduate School of Engineering Science & Technology (Doctoral Program)
National Yunlin University of Science & Technology
No. 123, University Road, Section 3, Douliou, Yunlin 64002, Taiwan, R.O.C.
(E-mail: g9510801@yuntech.edu.tw[1], E-mail: g9310808@yuntech.edu.tw[4])
[2]Department of Management Information System, Far East University
No. 49, Chung Hua Rd., Hsin-Shih. Tainan County 744, Taiwan, R.O.C.
(Tel : 886-6-597-9566#7008; Fax : 886-6-597-7010)
(E-mail: khhsia@cc.feu.edu.tw)
[3]Department of Electronic Engineering, Chienkuo Technology University
No. 1, Chieh Shou N. Rd., Changhua City, Taiwan, R.O.C.
(E-mail: jasonccw@ctu.edu.tw)
[5]Department of Electrical Engineering, National Yunlin University of Science & Technology
No. 123, University Road, Section 3, Douliou, Yunlin 64002, Taiwan, R.O.C.
[5]Department of Information Technology, Overseas Chinese University
No. 100, Ciao Kwang Rd., Taichung 40721, Taiwan, R.O.C.
(E-mail: sujp@yuntech.edu.tw)

Abstract: It is clear that different images will be obtained when one takes pictures with different camera positions. One can easily determine the characteristics of the captured image by projective geometry. However, it is hard to estimate the camera position only from an image. Machine learning methods are very useful for the nonlinear relation identifying. In this research, released situations of the images comparing to the earlier works are considered. An adaptive neuro-fuzzy inference system (ANFIS) network design is deployed and used for camera position estimating in this paper. From the experimental results, it is evidently that the proposed method can estimate the center of the camera correctly and effectively.

Keywords: ANFIS, Image feature extraction, Camera position estimation, Projective geometry.

I. INTRODUCTION

The 3D scenery and the pictured 2D image which could be related by projective geometry. However, the relationship is nonlinear and highly complicated. Adaptive neuro-fuzzy inference system (ANFIS) is provided for finding out this relationship, and that may be a possible way to building the relationship.

Consider a circular target in the 3D scenery, and the center of the circular target is projected to the centerline of a 2D image, the circle in the 3D scenery will be projected to a deformed circle in the 2D image. By projective geometry, the features of the deformed circle can be obtained from the diameter of the circular target, the distance between the camera center and the target center, and the variation angle of the camera. By this relation, it is possible to estimate the position of the camera from some features of the deformed circle and the circular target. However, the relationship between these features and the position of the camera is more complicated then previous research. In [1][2], an algorithm was developed for solving the problem under the condition that the target center must be at the center of image. However, it is not general enough for the applications of security systems [3] and aerial photography [4]. Thus we try to release the restriction and to solve this problem in this paper.

ANFIS is used for learning the mapping relation between the 3D world and the 2D image in this paper. The data pre-processing procedure [5] is provided to speed up the learning efficiency of the ANFIS. The experimental results show that the camera positions could be estimated quickly and accurately by the image features. Details are illustrated in the following contents.

II. PROJECTIVE TRANSFORMATION OF THE IMAGE

When we take pictures by camera, a point in the 3D space is projected to 2D image through the camera center, and different positions of camera center will result different projections of the point [6]. Consider the captured image. It is the projection of a circular target in the 3D space. A circular target will result in a deformed circle in the captured image. One can always trim the camera so that the crossover point of the axes of the deformed circle, called the 'center' of the deformed circle, is located on the vertical line crossing the center of the image, as shown in Figure 1. Obviously, this 'center' is the projection of the center of the circular target.

From Figures 1 and 2, one can choose five quantities to form the following features:

1. "$Ratio_{project} = h/k$" is dependent on the pitch angle of the camera.
2. "$Ratio_{height} = \bar{r}/d$" is dependent on the distance between the camera and the image center in the 3D world.
3. "$Ratio_{angle} = h/\bar{r}$" is dependent on both the pitch angle of the camera and the distance between the camera and the image center in the 3D world.
4. "$Ratio_{position} = k/Q$" is dependent on the target position.

The relationships of these parameters could be calculated by trigonometric relations and projective geometry. The relationships are shown in Figures 2 (a), (b) and (c). From above, the algorithm to find these ratios could be written as in Algorithm 1.

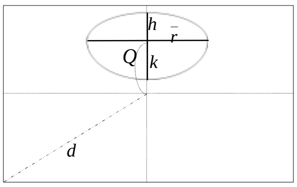

Figure 1. Projected image of a circular target.

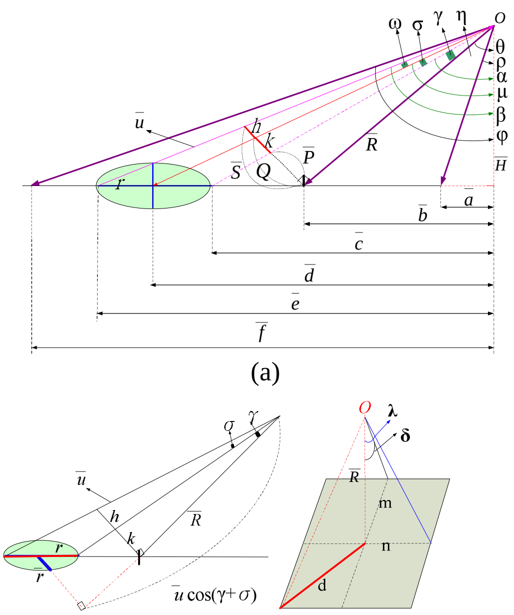

(a)

(b) (c)

Figure 2. Relationship between the circular target and the projection: (a) Features of the circular target projection. (b) Feature $\bar{r}$ of the circular target projection. (c) Half visual angles.

Algorithm 1: Algorithm for finding the ratios.

Find the geometry projection of the **Perspective target**.

Procedure Perspective_target (***Ratio**$_{project}$*, ***Ratio**$_{height}$*, ***Ratio**$_{angle}$*, ***Ratio**$_{position}$*)

"MinRtm: The lowest boundary of the target moving range in image."
"MaxRtm: The highest boundary of the target moving range in image."
"r: The radius of target."
"λ : The half vertical visual angle of camera."
"δ : The half horizontal visual angle of camera."
"R: The distance between the camera and the image center in the 3D world."
"θ : The pitch angle of the camera."
"The remainder definitions of parameters are shown in Figure 2. "

r=2.6, λ =27, δ =36
for R=20:1:300
for θ =-62:1:62
{

$\bar{H} = \sin\theta * \bar{R}$,
$\bar{a} = \sin\rho * \bar{H}$, $\bar{b} = \cos\theta * \bar{R}$,
$\rho = \theta - \eta$, $\varphi = \theta + \eta$
$\bar{f} = \tan\varphi * \bar{H}$, $\bar{d} = \bar{f} - 2r$,
MinRtm= $(\bar{b} - \bar{a} - r)$
MaxRtm= $(\bar{f} - r - \bar{b})$

for Range = MinRtm: 1: MaxRtm
{

$\bar{e} = \bar{b} + Range$,
$\mu = \tan^{-1}(\frac{\bar{e}}{\bar{H}})$, $\alpha = \tan^{-1}(\frac{\bar{d}}{\bar{H}})$
$\omega = \varphi - \mu$, $\sigma = \mu - \alpha$, $\gamma = \alpha - \theta$
$\bar{P} = \tan\gamma * \bar{R}$, $Q = \tan(\gamma + \sigma) * \bar{R}$,
$\bar{S} = \tan(\gamma + \sigma + \omega) * \bar{R}$
$k = Q - \bar{P}$, $h = \bar{S} - Q$, $\bar{u} = \sqrt{(\bar{e})^2 - (\bar{H})^2}$
$\bar{v} = \tan\lambda * \bar{u}$, $m = \tan\lambda * \bar{R}$,
$n = \tan\delta * \bar{R}$
$d = \sqrt{m^2 + n^2}$, $\bar{r} = \frac{\bar{R} * r}{\bar{u}\cos(\gamma + \sigma)}$
$Ratio_{project} = h/k$, $Ratio_{height} = \bar{r}/d$,
$Ratio_{angle} = h/\bar{r}$, $Ratio_{position} = k/Q$
}
}

III. FEATURE EXTRACTION AND IMAGE PROCESSING

In this paper, the features of image are $Ratio_{project}$, $Ratio_{height}$, $Ratio_{angle}$ and $Ratio_{position}$. The procedure for feature extraction and image processing is illustrated in Figure 3.

Thresholding and filtering are proposed for target segmentation in this procedure. The binary image could be get by thresholding, and that will be more easily for analyzing and computing [7] [8]. The range of the basic rectangle [7] is defined by the minimum rectangle containing the object. The definitions of the major axis and the minor axis are the longer edge and the shorter edge of the rectangle, respectively.

In this case, refer to Figure 1, the length of the major axis is equal to $\bar{r}+\bar{r}$, and the length of the minor axis is equal to h + k.

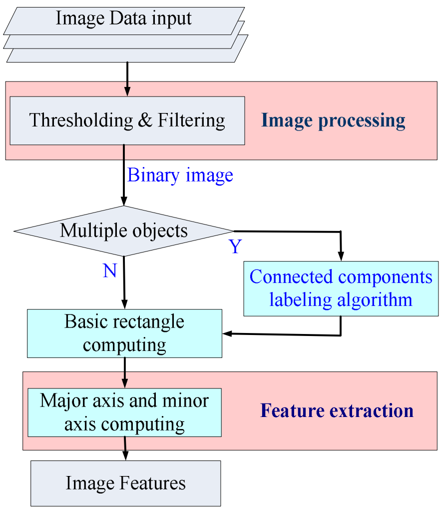

Figure 3. Procedure for feature extraction.

IV. DATA PRE-PROCESSING AND ANFIS TRAINING

In this paper, the ANFIS [5][9] is provided for replace the highly complicated relationship between a circular target in the 3D scenery and its projective transformation. The training data is constructed by Algorithm 1. The amount of the data is so huge that the training time is intolerably long. The data pre-processing procedure, illustrated in Figure 4, is proposed to speed up the training. There are two parts in this method, which are data segmentation and data classification. In the first part, the data are segmented into several stages for reducing the huge data base, are called "*Data stage_1~k*". In the second part, the "*Data stage_i*" is classified as four inputs related to Q, θ and $\bar{R}$, respectively. For further data classification, each class of data are sorted out the high correlated data and low correlated data for ANFIS training.

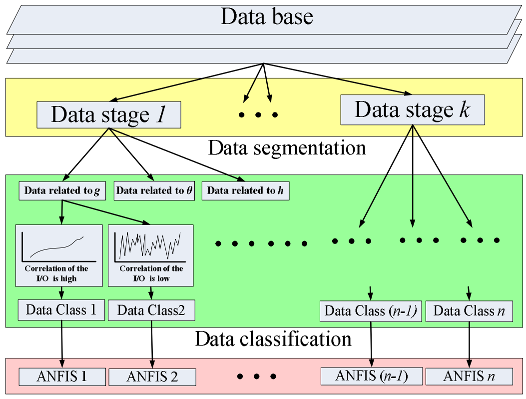

Figure 4. The data pre-processing procedure.

The ANFIS is trained with the highly correlated data, which will result in defining fewer fuzzy sets on the input data. This idea can save a lot of time for training, and the resulting ANFIS will have more precise estimation.

V. EXPERIMRNTAL RESULTS

Consider the case that the radius of the circular target in 3D world is 2.6 cm, the angle θ is varied from -62° to 62°, and the distance R is varied from 20 cm to 300 cm. The training data is generated by geometry computing. By the data pre-procession procedure, the data base is classed into the smaller and simpler stages for ANFIS training. Consequently, the numbers of the ANFIS are increased with the data stages. For this example, the data stage of "*height 126~130cm*" is selected for demonstrating the ANFIS training results.

There are three ANFIS's used for estimating Q, θ and R. The input data for these ANFIS's are $Ratio_{project}$, $Ratio_{height}$, $Ratio_{angle}$ and $Ratio_{position}$. The ANFIS training results are shown in Figures 5 (a), (b) and (c), and the resulting RMSE (root mean squared error) of Q, R and θ are 0.641, 0.124 and 0.365, respectively. The numbers of fuzzy sets on the inputs for each ANFIS are summarized in Table 1. Take the first row of Table 1 as an example, the ANFIS input $Ratio_{position}$ and ANFIS output Q has the highly correlation, therefore the number of fuzzy sets for $Ratio_{position}$ is 4; on the contrary, the number of fuzzy sets for other inputs are larger than 4. All the membership functions of the input fuzzy sets are in the shape of Gaussian.

Consider the image shown in Figure 6(a). The size of this image is 160*120 pixels. Figure 6(b) is the binary image of it, and Figure 6(c) shows the basic rectangle of the target. The length of the major axis is 29.6583 and that of the minor axis is 21.8644. In Figure 6(c), its features are extracted by image processing algorithm. The extracted features will be the input of ANFIS for the camera position estimation. For this case, the image features were extracted and that were shown in Table 2. The result of camera position estimation by ANFIS is shown in Table 3. From Table 3, it is shown that the camera position could be estimated from a real image by the proposed procedure.

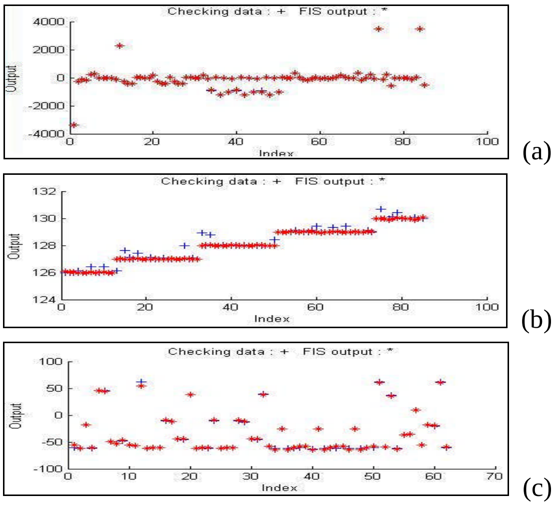

Figure 5. ANFIS checking results. (a) the distance Q (b) the distance R (c) the angle θ

Table 1. Numbers of fuzzy sets on inputs for each ANFIS

Input / ANFIS	$Ratio_{project}$	$Ratio_{height}$	$Ratio_{angle}$	$Ratio_{position}$
for Q	8	8	8	4
for R	8	4	8	8
for θ	4	8	8	8

(a) (b) (c)

Figure 6. Image of the reference object. (a) Image input (b) Binary image (c) Basic rectangle of image

Table 2. Image features of Figure 6(a).

Features	$Ratio_{project}$	$Ratio_{height}$	$Ratio_{angle}$	$Ratio_{position}$
Ratios	1.1092	1.0247	8.9016	0.0817

Table 3. Estimated results of Figure 6(a).

	Q (cm)	R (cm)	θ (°)
ANFIS Output	2.34	36.87	41.89
Camera position	2.5	37	42
Error	0.16	0.13	0.11

VI. CONCLUSION

In this paper, the restriction in [2] that the 'center' of the deformed circle, which is the projection of the circular target, has to be located at the center of the captured image has been released to be located at the vertical line crossing the center of the image. The proposed algorithm could estimate the camera position under this condition. The released condition caused the huge amount of training data. The data pre-processing procedure was introduced on the training process for ANFIS to speed up training. Experimental results show that this can simplify the ANFIS learning and reduce the learning time.

From the experimental results, we use the image feature extraction algorithm to find out the available features of the object as ANFIS inputs. The algorithm could extract the features of object precisely, and the obtained ANFIS also can estimate camera position effectively. It shows that the complicated mapping and highly nonlinear image projective transformations could be replaced by ANFIS.

REFERENCES

[1] K. H. Hsia, S. F. Lien, C. C. Wang, T. N. Lee and J. P. Su (2009), "Camera position estimation from image by neural network," ICIC Express Letters (EI). Vol.3, No.4, pp. 1161-1166.
[2] K.H. Hsia, S.F. Lien, C.C. Wang and J. P. Su (2009), "Camera position estimation from image by ANFIS," Fourth International Conference on Innovative Computing, Information and Control (ICICIC 2009).
[3] K. Sage and S. Young (1999), "Security applications of computer vision," Aerospace and Electronic Systems Magazine, IEEE, pp. 19-29.
[4] J.A. Franco, M. Moctezuma, and F. Parmiggiani (2002), "A fusion-based segmentation algorithm for high-resolution panchromatic aerial photography," Proc. International Geoscience and Remote Sensing Symposium, IEEE, vol. 6, pp. 3396-3398.
[5] M. T. Hagan, H.B. Demuth and M. Beale (2004), Neural Network Design, Thomson.
[6] R. Hartley and A. Zisserman (2003), Multiple View Geometry in computer vision, Cambridge University Press.
[7] L.G. Shapiro and G. C. Stockman (2001), Computer Vision, Prentice Hill.
[8] M. Nixon and A. Aguado (2008), Feature Extraction & Image Processing, Amsterdam Academic, Boston.
[9] A.D. KulKarni (2001), Computer Vision and Fuzzy-Neural systems, Upper Saddle River, Prentice Hall.

Gaussian Radial Basis Function Neural Network Controller of Synchronous Reluctance Motor in Electric Motorcycle Applications

Chien-An Chen[1], Huann-Keng Chiang[2] and Wen-Bin Lin[3]
[1] *Electronic Vehicle and System Verification Group R & D Division, Automotive Research and Testing Center, Changhua 50544, Taiwan*
[2] *Department of Electrical Engineering, National Yunlin University of Science & Technology, Taiwan*
[3] *Graduate School of Engineering Science & Technology, National Yunlin University of Science & Technology, Taiwan*
Fax :+886-5-5312065
E-mail: chianghk@yuntech.edu.tw

Abstract: In this paper, a sliding mode control (SMC) design based on Gaussian radial basis function neural network (GRBFNN) is proposed for the synchronous reluctance motor (SynRM) system in electrical motorcycle applications. The conventional sliding mode control is assumed that the upper lumped boundary of parameter variations and external disturbances is known and the sign function is used. It causes high frequency chattering and high gain phenomenon. In order to avoid above drawback, the proposed method utilizes the Lyapunov stability method and the steep descent rule to guarantee the convergence asymptotically and reduce the magnitude of the chattering or avoid the chattering. Finally, numerical simulations are shown to illustrate the good performance of our controller design.

Keywords: Sliding mode control, Radial basis function neural network, Synchronous reluctance motor, Electric m otorcycle, Lyapunov stability method.

I. INTRODUCTION

In recent years, the discussion of environmental protection such as reducing air pollution and to avoid gasoline depletion, some countries require their automotive industries to develop electric vehicles in place of gasoline-powered automobiles gradually [1,2]. In Asia, motorcycles are much more widespread than automobiles for individual transportation, so we attention on the development and research of electric motorcycles. SynRM [3,4] has been a renewed interesting research subject, due to the rotor circuit of the SynRM is opened such that the flux linkage of SynRM is directly proportional to the stator currents.

The fast and error-free dynamic response is a primary topic in control systems. Recently, many researches have focused on designing the electric motors. The parameters of electric motors may be changed in working circumstances. Therefore, the robust control technology can be solved in parameter variations and external disturbances.

One of the famous methods about robust control of the parameter variations system is the so-called variable structure control [5,6] in modern control theories. The sliding mode control has been proven as an effective and robust control technology to overcome the uncertainties when the upper lumped uncertainty boundary of the systems is known.

The GRBFNN control1er is an effective method when the systems mathematical model is unknown, or known with uncertainties. It is a three-layer feedforward neural network structure [7] which has the nonlinear transformation of Gaussian basis function in the hidden layer and output layer is the linear combination of hidden layer responses.

According to the RBFNN advantages, we proposed the SMC design based on GRBFNN concept of SynRM system. The GRBFNN doesn't use the signum function control element hence this system reduces chattering phenomenon and has the response smoother.

II. MOTORCYCLE MODEL

The model of the electric motorcycle propulsion system is shown in Figure 1. This model describe is based on the principles of mechanics and aerodynamics. The load torque of motorcycle is shown in Figure 2, it is composed of F_r, F_a and F_g. The total load of the motorcycle is given by

$$F = F_r + F_a + F_g \quad (1)$$

where the F_r, F_a and F_g are rolling resistance, aerodynamic drag and grading resistance, respectively. They are the function of rotational speed as follows.

$$F_r = MgC_r \cos\theta \quad \text{: rolling resistance}$$

$$F_a = \frac{1}{2}\rho C_d A_f v^2 \quad \text{: aerodynamic drag}$$

$$F_g = Mg\sin\theta \quad \text{: grading resistance}$$

where, ρ is the air density, C_d is the aerodynamic drag coefficient, A_f is the orthographic projection area which is composed of the driver and the travel direction of the vehicle, v is the linear speed of the motorcycle, M is the mass of the motorcycle, g is the gravitational constant, C_r is the rolling resistance coefficient, θ is the grade angle. The linear speed v

is proportional to the rotor speed of SynRM as

$$v = \frac{R_t}{i_o}\omega_r \tag{2}$$

where R_t is the radius of the tire, i_o is the total ratio between the motor shaft and the differential axle of the vehicle, respectively. Hence, the total load torque is represented as follows.

$$\begin{aligned} T_L &= \frac{R_t}{i_o}(F_r + F_g + F_a) \\ &= \frac{R_t}{i_o}(MgC_r \cos\theta + Mg\sin\theta + \frac{1}{2}\rho C_d A_f v^2) \end{aligned} \tag{3}$$

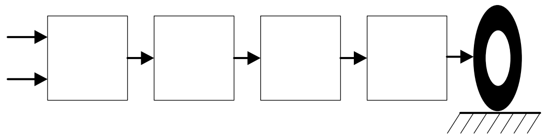

Fig. 1. Configuration of the electric motorcycle propulsion system.

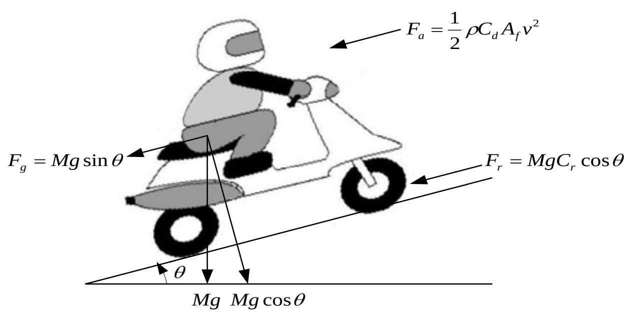

Fig. 2. Elementary forces acting on the motorcycle.

III. MODELING OF THE SYNRM

The model of the SynRM is shown in Figure 3. The d-q equivalent voltage equations of the SynRM with the synchronously rotating rotor reference frame are represented as

$$V_{ds} = R_s i_{ds} + L_{ds}\frac{di_{ds}}{dt} - \omega_r L_{qs} i_{qs} \tag{4}$$

$$V_{qs} = R_s i_{qs} + L_{qs}\frac{di_{qs}}{dt} + \omega_r L_{ds} i_{ds} \tag{5}$$

where the V_{ds} and V_{qs} are direct and quadrature axis terminal voltages, respectively. The i_{ds} and i_{qs} are, respectively, direct axis and quadrature axis terminal currents or the torque producing current. The L_{ds} and L_{qs} are the direct and quadrature axis magnetizing inductances, respectively. The R_s is the stator resistance and ω_r is the speed of the rotor.

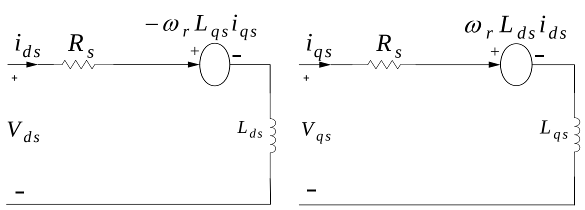

Fig. 3. The model of synchronous reluctance motor

The corresponding electromagnetic torque T_e and motor dynamic equation are given as following

$$T_e = \frac{3}{2}P(L_{ds} - L_{qs})i_{ds}i_{qs} \tag{6}$$

$$T_e - T_L = J\frac{d\omega_r}{dt} + B\omega_r \tag{7}$$

where P, T_L, J and B are the pair of poles, the torque load, the inertia moment of rotor and the viscous friction coefficient, respectively. If both i_{ds} and i_{qs} are suitable selected values, we can control the electromagnetic torque in (6) and (7) to satisfy the torque of load and the speed command.

A comparative study of different control methods of the SynRM was done by Betz et. al. [3]. We adopt the maximum torque control (MTC) strategy [4].

IV. SLIDING MODE CONTROL (SMC)

We can rewrite the motor dynamic equation of (7) as follows:

$$\begin{aligned} \dot{\omega}_r &= (-\frac{B_m}{J_m})\omega_r + (\frac{1}{J_m})(T_e - T_L) \\ &= a\omega_r + b(T_e - T_L) \\ &= a_o\omega_r + b_o(u(t) + f) \end{aligned} \tag{8}$$

where

$$a \equiv -\frac{B_m}{J_m} = a_o + \Delta a\,; \qquad b \equiv \frac{1}{J_m} = b_o + \Delta b$$

$$u \equiv T_e\,; \qquad f \equiv \frac{1}{b_o}(\Delta a\omega_r + \Delta b u(t) - bT_L)$$

$$J_m \equiv J_{mo} + \Delta J_m\,; \qquad B_m \equiv B_{mo} + \Delta B_m$$

The subscript index "o" indicates nominal system value; "Δ" symbol expresses uncertainty, and f is the lump uncertainty. Defining the velocity error $e(t) = \omega_{ref} - \omega_r$, ω_{ref} is the velocity command.

The sliding function is defined as

$$S = e(t) + c\int_0^t e(\tau)d\tau,\ c > 0 \tag{9}$$

The input control $u(t)$ (the electromagnetic torque T_e) can be defined

$$u(t) = u_{eq}(t) + u_n(t) \tag{10}$$

To satisfy equivalent control concept $\dot{S}(e) = 0$, we get

$$\dot{S} = (\dot{\omega}_{ref} - a_o\omega_r - b_o u_{eq} + ce) - b_o(u_n + f) \tag{11}$$

We set

$$u_{eq} = \frac{1}{b_o}(\dot{\omega}_{ref} - a_o\omega_r + ce) \tag{12}$$

To satisfy the sliding condition $S(e)\dot{S}(e) < 0$, we have

$$S\dot{S} = -S[b_o(u_n + f)] \tag{13}$$

Let $|f| \le K$, the uncertain nonlinear switching control input can be defined as

$$u_n = K sign(S) \tag{14}$$

where

$$sign(\upsilon) = \frac{\upsilon}{|\upsilon|}$$

Hence, the sliding condition $S(e)\dot{S}(e) < 0$ can be guaranteed. To avoid the chattering phenomenon, the $sign(\cdot)$ is replaced by saturation function $sat(\cdot)$. Therefore, u_n becomes

$$u_{nM} = Ksat(S) \qquad \textbf{(15)}$$

This method has a steady state error.

V. SLIDING MODE CONTROLLER BASED ON GRBFNN

In real world, the physical systems always have certain nonlinear and various uncertainties. The error back propagation NN has the disadvantages of slower learning speed and local minimal convergence. Hence, we use the GRBFNN to solve these problems and develop a model-free controller structure based on GRBFNN. The structure of the SMC based on GRBFNN model is shown in Fig. 4. The RBFNN model has j receptive field units. We select the Gaussian function $\varphi_j(S) = \exp\left(-\left(S-c_j\right)^2/(2b_j^{\,2})\right)$ as the receptive field units, where S is the sliding surface function and c_j, b_j are the spread factor and central position of the Gaussian function, respectively. j is the number of hidden layer neurons. The output u of the RBFNN is the sum of weights which the output can be described as

$$u = \sum_{j=1}^{5} w_j \varphi_j(S) \qquad \textbf{(14)}$$

$$\varphi_j(S) = \exp\left(-\frac{\left(S-c_j\right)^2}{2b_j^{\,2}}\right), \quad j = 1,\cdots,5 \qquad \textbf{(15)}$$

where

$$\theta = \left[\varphi_1(S), \varphi_2(S), \cdots, \varphi_5(S)\right]^T, \quad W = [w_1, w_2, \cdots, w_5]^T$$

$$c_1 = \frac{2000\pi}{6}, c_2 = \frac{2000\pi}{12}, c_3 = 0, c_4 = -\frac{2000\pi}{12}, c_5 = -\frac{2000\pi}{6}$$

$$b_1 = b_2 = b_3 = b_4 = b_5 = 500\pi/6$$

According the SMC reaching condition $S\dot{S} < 0$, the adaptive rules of this structure derive from the steep descent method to minimize the value of the performance index $S\dot{S}$ with the weight w_j as follows:

$$\dot{w}_j = -\eta\frac{\partial S\dot{S}}{\partial w_j} = -\eta\frac{\partial S\dot{S}}{\partial u}\frac{\partial u}{\partial w_j} \qquad \textbf{(16)}$$
$$= \eta \cdot S \cdot b_o \cdot \varphi_j(S)$$

where η is the learning rate.

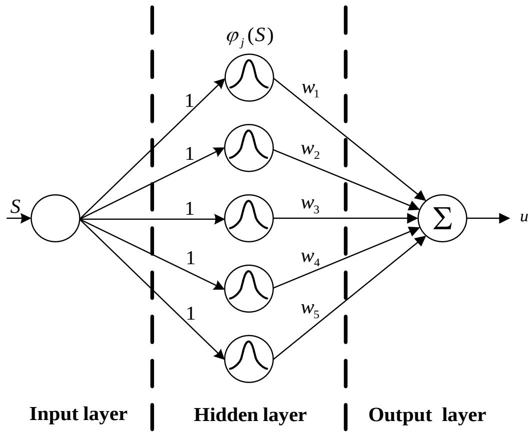

Fig. 4. The structure of the RBFNN model

VI. NUMERICAL SIMULATION RESULTS

System parameters for the motor and the motorcycle are setting as shown in Table 1 and 2, respectively, and the proposed controller parameters are in Table 3. The sampling period of control rules is set as 0.3 $m$sec . To investigate the effectiveness of the proposed controllers, two conditions are provided in the numerical simulation, In Fig. 5, the response under grade angle $\theta = 0^\circ$ is depicted. In Fig. 6, shows the same speed control command under grade angle $\theta = 5^\circ$ is presented. From Fig. 5 and 6, the proposed controller has good velocity performance.

Table 1. The parameters of SynRM

$R_s = 4.2\Omega$	$P = 1$
$L_{ds} = 0.328$ H ($f = 60$Hz)	$L_{qs} = 0.181$ H ($f = 60$Hz)
$J_{mo} = 0.00076\ kg\text{-}m^2$	$B_{mo} = 0.00012\ Nt\text{-}m/rad/sec$

Table 2. The parameters of motorcycle

$R_t = 0.2m$	$i_o = 8$	$\rho = 1.2\, kg/m^3$
$A_f = 1m^2$	$C_d = 0.4$	$C_r = 0.015$
$M = 30kg$	$g = 9.81m/\sec^2$	

Table 3. The parameters of proposed controller

$c = 6$	$\eta = 0.0086$

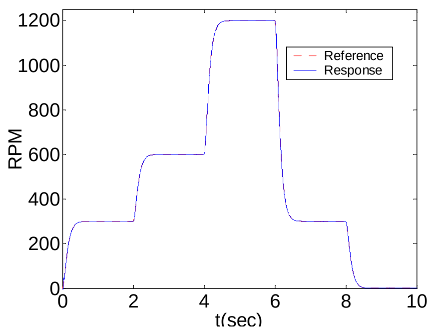

(a)

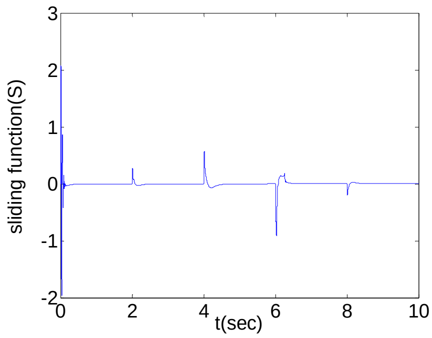

(b)

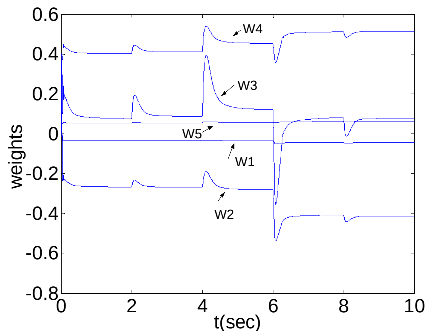

(c)

Fig. 5. simulation results of the SMC based on RBFNN under grade angle $\theta = 0^{\circ}$ (a) rotor velocity (b) sliding function (c) weights

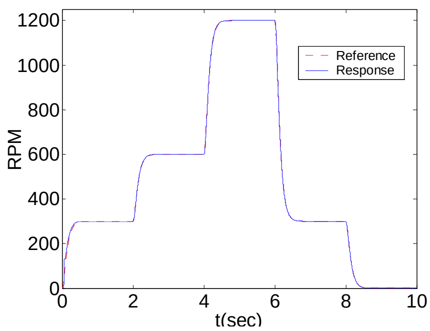

(a)

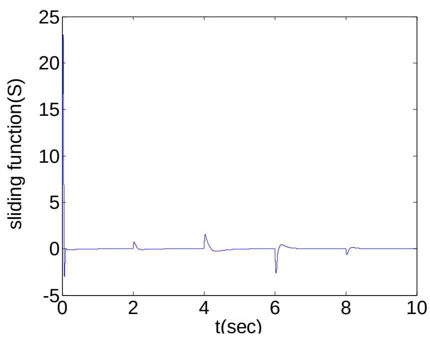

(b)

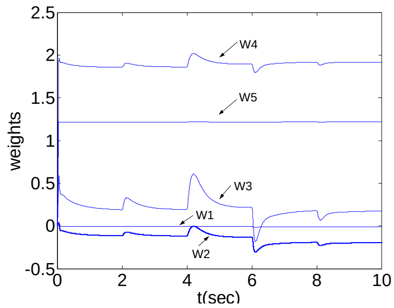

(c)

Fig. 6. simulation results of the SMC based on RBFNN under grade angle $\theta = 5^{\circ}$ (a) rotor velocity (b) sliding function (c) weights

VII. CONCLUSION

A SynRM of the electric motorcycle using the sliding mode control based on GRBFNN is proposed in this paper. It derives from the steep descent method to minimize the value of the performance index $S\dot{S}$. Hence, the chattering problem can be minimized with the proposed control and has the better smooth response. Finally, we employ the numerical simulation results to validate the proposed method.

ACKNOWLEDGMENT

This work is supported by the National Science Council in Taiwan, Republic of China, through grant NSC98-2221-E-224-070.

REFERENCES

[1] Chan CC, and Chau KT (1997), An overview of power electronics in electric vehicles. IEEE Transactions on Industrial Electronics 29(1):3-13
[2] Unnewehr LE and Nasar SA (1982), Electric Vehicle Technology. Wiley & Sons
[3] Betz RE, Lagerquist R and Jovanovic M (1993), Control of synchronous reluctance machines. IEEE Transactions on Industry Applications 29:1110-1121
[4] Chen CA, Chiang HK and Lin BR (2008), The novel adaptive sliding mode position control for synchronous reluctance motor drive. Journal of the Chinese Society of Mechanical Engineers 29(3):241-247
[5] Chiang HK and Tseng CH (2004), Design and implementation of a grey sliding mode controller for synchronous reluctance motor drive. Control Engineering Practice 12(2):155-163
[6] Chiang HK and Tseng CH (2004), Integral variable structure controller with grey prediction for synchronous reluctance motor drive. IEE Proceedings-Electric Power Applications 151(3):349-358
[7] Huang SJ, Huang KS and Chiou KC (2003), Development and Application of a Novel Radial Basis Function Sliding Mode Controller. Mechatronics 13: 313-329

Implementation of Robust Complex Extended Kalman Filter with LabVIEW for Detection in Distorted Signal

Wen-Bin Lin[1], Huann-Keng Chiang[2], Kuang-Rong Shih[3] and Chien-An Chen[4]
[1] *Department of Optoelectronic Engineering, Far East University, Tainan 74448 ,Taiwan*
[2] *Department of Electrical Engineering, National Yunlin University of Science & Technology, Taiwan*
[3] *Department of Electrical Engineering, National Formosa University, Yunlin 63208, Taiwan*
[4] *Electronic Vehicle and System Verification Group R & D Division, Automotive Research and Testing Center, Changhua 50544, Taiwan*

Fax :+886-5-5312065
E-mail: lawrence@cc.feu.edu.tw

Abstract: This paper presents the PC-based LabVIEW as a software to develop the algorithm of the robust complex extended Kalman filter (RCEKF) for detection of the parameters of voltage signal in power systems. The hardware of this paper is to take sample-and-hold card and DAQ (Data Acquisition) card for extracting the datum from the outside system to the PC, and the program compute the amplitude, frequency, and phase of the voltage signal with RCEKF. For validating the performance of RCEKF in this paper, the voltage signal from function generator is applied to check the feasibility of algorithm firstly, and then this application was also used in the TPC (Taiwan Power Company) secondary substation in Sijhou, Taiwan.

Keywords: Complex Kalman filter, robust algorithm, voltage distorted signal, LabVIEW.

I. INTRODUCTION

The parameters of voltage signal include amplitude, phase angle, and frequency. The accuracy of estimation parameter is a very important issue for the application of power system. From the literature review [1,2], the using state variable types of the extended Kalman filter are real type and complex type in the application of signals estimation generally. But the former method in practical application, if signal is out of order, it will result in the value of estimated value. The pitch of measured value and estimated value will increase gradually through tracking time. In order to develop the drawbacks as above, therefore, the complex extended Kalman filter was proposed [3], and was applied in the estimation of voltage distortion signal parameter. The complex extended Kalman filter is considered only on the linear part of equation during filtering process. When the parameter is unnormal, sometimes the nonlinear will take a great influence.

According to literature review [4], if there is a unusual signal in the system, the variation quantity will result the errors between the estimated value and the optimal value. This condition will cause the variable state which does not attach the optimal solution, and it can not estimate the parameter exactly.

In order to solve this problem as above, the paper [4] proposed a robust calculation method in the model of extended Kalman filter. Thus, it can be a state estimation application of power system. This effect is pretty good by simulating verify. But the robust calculation method is composed by exponential function in innate character. It is $\exp\left(-\left|y_k - H\tilde{x}_k\right|\right)$. The application meaning is that the more difference between measured value and estimated value is, the less effect on estimation filtering is. This paper is proposed this robust calculation approach of complex extended Kalman filter in signal estimation to improve performance. The application of signal estimation is only applied on the simulation stage in literature review [3-14]. But these approaches are seldom applied in practical measurement. Thus, each algorithm does not have practical verification in practical task.

The LabVIEW [15-20] by PC-based is often applied in power system. Thus, this paper is used the graphic control software of LabVIEW to finish the program of robust complex extended Kalman filter. This program is used practical measurement as follows. Firstly, it is given the sine wave by function generator. Secondly, it is given the voltage signal of Sijhou secondary sub-station in Changhua county of TPC. From the above items, it can verify algorithm practicality in practical measurement. This paper is organized as follows. Section 1 is given a brief introduction. Section 2 is described the models and algorithms of this paper proposed robust complex Kalman filter. Section 3 is stated the used practical measurement to verify the algorithm of Section 2 proposed. Finally, we draw some specific available conclusions in this algorithm for this paper and its research direction in the future in section 4.

II. THE MATHEMATICS OF ROBUST COMPLEX EXTENDED KALMAN FILTER

Step 1:

Input time-changing signals measurement value y_k, the initial value of state variable $\hat{x}_0$, the initial value of error covariance P_0, and the measured value of error covariance R_0.

Step 2:

Begin to track at time k=0.

Step 3:

State estimates $\tilde{x}_k = \mathbf{A}\tilde{x}_{k-1}$ (1)

Step 4:

$$F_k = \frac{\partial(Ax_k)}{\partial x_k} \quad (2)$$

$$M_{k+1|k} = F_k P_{k|k} F_k^{*T} \quad (3)$$

Step 5:

Measurement error covariance

$$R_k = W_k^{-1} \quad (4)$$

$$W_k = W_k e^{-|y_k - H\hat{x}_{k-1}|} \quad (5)$$

Where, $e^{-|y_k - H\hat{x}_{k-1}|}$ is the Robust exponential function of complex style.

If it is real style, the Robust exponential function is $e^{-|y_k - h(\hat{x}_{k-1})|}$.

Step 6:

The Calculation of Kalman is shown as follows.

$$K_k = P_k H^{*T}\left[HP_k H^{*T} + R_k\right]^{-1} \quad (6)$$

Step 7:

State filtering

$$\hat{x}_k = \tilde{x}_{k-1} + K_k\left(y_k - H\tilde{x}_{k-1}\right) \quad (7)$$

Then, renews the P_k.

Step 8:

To judge time value k, we have to depend on if it is larger setting time or not. If it is less than this value, then it is progressed to trace next time point. If it is larger than this value, then it is ended this tracking.

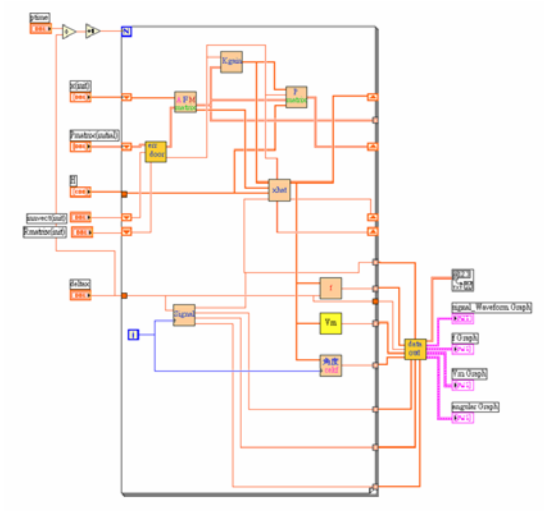

Fig. 1. The program equation of Robust Complex Extended Kalman filter.

Robust Complex Extended Kalman filter is by means of W_k of step 5 to control the Kalman Gain value. Thus, it can restrain un-exact measurement value or the parameter unusual changed to the effect of total estimation procedure. When some unusual measurement occurs, it is presented that measurement value y_k has the significant change. But the prediction of state variable hasn't detected the unusual measurement value. And it is mistaken the calculation of measurement value function which is under normal condition. Thus, when the measurement value happens to distort, the absolute value of Innovation Vector will increase. This outcome will result in the value of exponential function to reduce. Thus, it can assist to decrease the weight value. It can reduce the effect of distortion measurement value for estimation. Fig. 1 as shown is applied the software LabVIEW edited the equation of Robust Complex Extended Kalman filter.

III. NUMERICAL SIMULATION & RESULT

This paper is applied the program of Robust Complex Extended Kalman filter on LabVIEW base. It is verified practical measurement for three situations as follows. Firstly, it is given the sine wave by function generator. Secondly, it is given the voltage signal of Sijhou secondary sub-station in Changhua county of TPC. The function generator supplies the sine wave form signal in the first condition. This signal can alter the magnitude of amplitude and frequency. This paper proposed test signal frequency is 60Hz, and its amplitude is 1V sine wave form signal. It is modulated parameter by the knob of function generator. The voltage signal measurement of Sijhou secondary sub-station is at Changhua county of TPC in condition (2). Now, different application results of signals measurement are depicted as follows.

Fig. 2. The wave form of function generator by oscilloscope display.

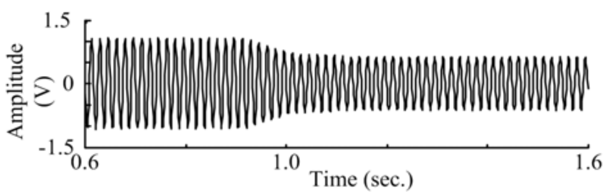

Fig. 3. The signal wave form of function generator displayed from 0.6 second to 1.6 second.

Situation 1: The measurement that function generator supplies the sine wave form signal

a.Signal amplitude change

Fig. 2 shows that function generator supplies the sine wave form. The frequency of this signal is 59.99Hz, and the amplitude is 1.05V. Its amplitude is 0.625V from 0.97 second to 1.1 second after variation. Fig.3 shows that function generator supplies the sine wave form from 0.6 second to 1.6 second. Fig. 4 shows the amplitude estimation diagram of this paper proposed method. The value of amplitude estimation is 1.041V at 0.6 second before variation. Its relative error is 0.86%. The estimation value is 0.624V at 1.8 second. Its relative error is 0.16%. Its response time of estimation is 0.7 second.

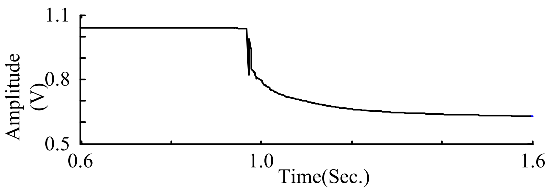

Fig. 4. The amplitude estimation diagram of this paper proposed method.

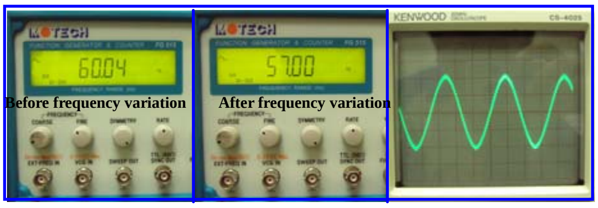

Fig. 5. The wave form of function generator by oscilloscope display.

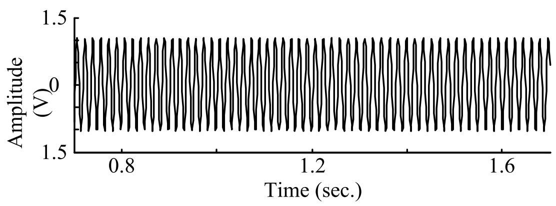

Fig. 6. The signal wave form of function generator measured from 0.7 second to 1.7 second.

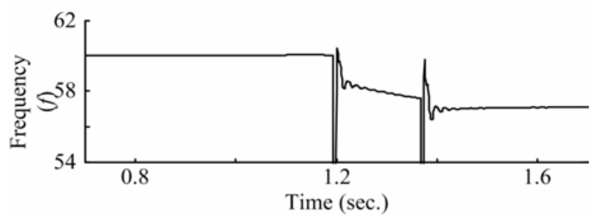

Fig. 7. The frequency estimation diagram of this paper proposed method.

b.Signal frequency change

Fig. 5 shows that function generator supplies the sine wave form. The frequency of this signal is 60.04Hz, and the amplitude is 1.05V. Its frequency variation is from 1.19 second to 1.40 second. Fig.6 shows that function generator supplies the sine wave form from 0.7 second to 1.7 second. Fig. 7 shows the frequency estimation diagram of this paper proposed method. The frequency estimation happens to oscillation suddenly during frequency changes, then it will trace to the signal frequency. The frequency estimation value is 60.032Hz at 1 second before frequency variation in Fig.7. Its value is closed to the value of Fig.6. Fig.6 displays the value 60.04Hz of function generator frequency. The relative error is 0.13% between Fig.7 and Fig.6. After frequency variation, the frequency estimation value is 57.06Hz at 1.6 second. The signal frequency of function generator is 57Hz at 1.6 second. Therefore, there is a 0.06Hz error at 1.6 second.

Situation 2: The voltage signal measurement of Sijhou secondary sub-station at Changhua county of TPC

We take a practical measurement of Sijhou secondary sub-station at Changhua county of TPC. We measured the 11.4kV BUS (Single Phase 66KV) voltage signal at the substation by means of PT (6600/115V) converting. The measured point is shown as Fig.8. Fig. 9, Fig.10 and Fig.11 are the estimation diagrams of one phase frequency, amplitude, and phase angle individual. The estimation value of frequency is 60.21Hz. The estimation value of amplitude is 160.2V. The voltage scale shown in oscilloscope is that, the amplitude is 160V after converting. Both the estimation value and the oscilloscope display value are very similar. The estimation value of phase angle is approximately -129.5°.

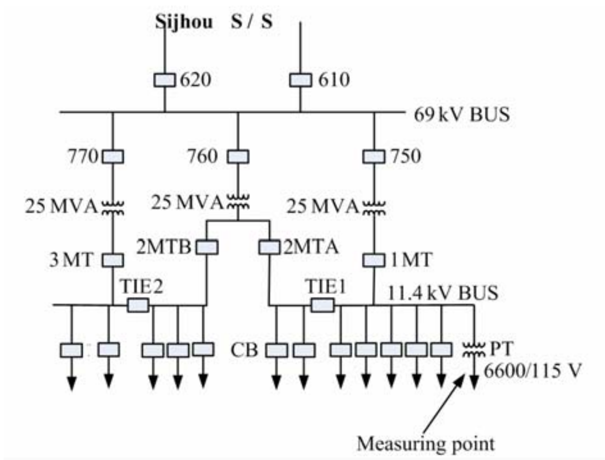

Fig. 8. The single line diagram of Sijhou secondary substation.

IV. CONCLUSIONS

It only takes the simulation of software verse signal parameter in past literature review. This paper proposes LabVIEW the software edited by means of the program of Robust Complex Extended Kalman filter. We can get state variable of system to trace the estimation parameters-amplitude, frequency, and phase angle. Thus, we can accomplish to detect if the signal is in distortion or not. We can prove the feasibility of structure that can trace the signal parameter by means of measuring the sine wave form of function generator through the practical measuring Sijhou secondary sub-station at Changhua county of TPC.

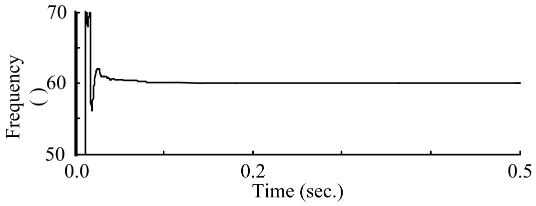

Fig. 9. The frequency estimation diagram of this paper proposed method.

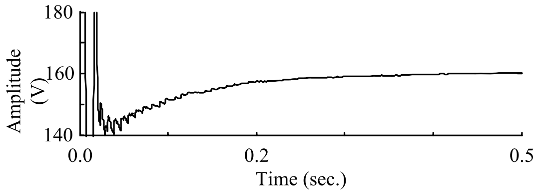

Fig. 10. The amplitude estimation diagram of this paper proposed method.

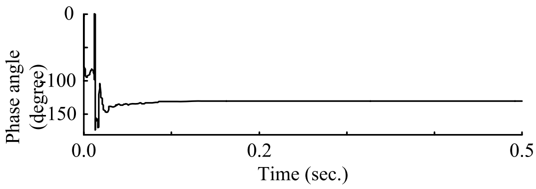

Fig. 11. The phase angle estimation diagram of this paper proposed method.

ACKNOWLEDGMENT

This work is supported by the National Science Council in Taiwan, Republic of China, through grant NSC98-2221-E- 224-070.

REFERENCES

[1] Tadeusz L. and Jacek R. (1977), Real-Time Determination of Power System Frequency, IEEE Transactions on Instrumentation and Measurement, 46(4), 877-881

[2] Nishiyama K. (1997), A Nonlinear Filter for Estimating A Sinusoidal Signal and Its Parameters in White Noise: On The Case of A Single Sinusoid, IEEE Transactions on Signal Processing, 45, 970-981

[3] Dash P. K., Panda R. K. and Panda G. (2000), An Extended Complex Kalman Filter for Frequency Measurement of Distorted Signals, IEEE Transactions on Instrumentation and Measurement, 49(4), 746-753

[4] Huang S. J. and Shih K. R. (2002), Dynamic State-Estimation Scheme Including Nonlinear Measurement-Function Considerations, IEE Proceedings-Generation, Transmission and Distribution, 149(6), 673-678

[5] Ferreira I. M. and Maciel Barbosa F. P. (1994), A Square Root Filter Algorithm for Dynamic State Estimation of Electric Power Systems, Electrotechnical Conference, 3, 877-880.

[6] Xia Q., Rao M., Ying Y., Shen S.X. and Sun Y. (1992), A New State Estimation Algorithm-Adaptive Fading Kalman Filter, IEEE Proceedings of the 31st Conference on Decision and Control, 1216-1211

[7] Hargrave P. J. (1989), "A Tutorial Introduction to Kalman Filtering," IEE Colloquium on Kalman Filter: Introduction, Application and Future Developments, 1-6

[8] Mandal J. K., Sinha A. K. and Roy L. (1995), Incorporating Nonlinearities of Measurement Function in Power System Dynamic State Estimation, IEE Proceedings-Generation, Transmission and Distribution, 142(3), 289-296

[9] Irving M. R. and Macqueen C. N. (1998), Robust Algorithm for Load Estimation in Distribution Networks, IEE Proceedings-Generation, Transmission and Distribution, 145(5), 499-504

[10] Beides H. M. and Heydt G. T. (1991), Dynamic State Estimation of Power System Harmonics Using Kalman Filter Methodology, IEEE Transactions on Power Delivery, 6, 1663-1670

[11] Durgaprasad G. and Thakur S. S. (1998), Roust Dynamic State Estimation of Power System Based on M-Estimation and Realistic Modeling of System Dynamics, IEEE Transactions on Power Systems, 13(4), 1331-1336

[12] Liu Y. Z. and Chen S. (2001), A Wavelet Based Model for On-Line Tracking of Power System Harmonics Using Kalman Filtering , IEEE Power Engineering Society Summer Meeting, 2, 1237-1242

[13] Routray A., Pradhan A. K. and Rao K. P. (2002), A Novel Kalman Filter for Frequency Estimation of Distorted Signals in Power Systems, IEEE Transactions on Instrumentation and Measurement, 51(3), 469-479

[14] Dash P. K., Pradhan A. K., Panda G. (1999), Frequency Estimation of Distorted Power System Signals Using Extended Complex Kalman Filter, IEEE Transactions on Power Delivery, 14(3), 761-766

[15] Johnson G. W., Richard J. (2001), LabVIEW Graphical Programming Practical Applications Ininstrumentation and Control, 3rd ed, McGraw-Hill, New York

[16] Johnson G. W. (1998), LabVIEW Power Programming, McGraw-Hill, New York.

[17] Jamal R., and Pichlik H. (1999), LabVIEW Applications and Solutions, Upper Saddle River, NJ: Prentice Hall PTR

[18] National Instruments (2003), LabVIEW Measurements Manual, National Instruments.

[19] National Instruments (1994), SC-2040 User Manual, National Instruments

[20] National Instruments (1998), DAQ PCI-6023E/6024E/6025E User Manual, National Instruments

Fuzzy PID Control for an Overhead Crane Using Hybrid Optimization Approach

Chia-Nan Ko[1], Chi-Ching Yang[2], Guan-Yu Liu[3], and Kuo-Lan Su[4]
Department of Automation Engineering, Nan-Kai University of Technology
Tasotun, Nantou 542, Taiwan

[1]*Department of Automation Engineering, Nan-Kai University of Technology*
Tasotun, Nantou 542, Taiwan
[2]*Department of Electrical Engineering, Hsiuping Institute of Technology*
Dali, Taichung 542, Taiwan
[3]*Department of Electronic Engineering, Nan-Kai University of Technology*
Tasotun, Nantou 542, Taiwan
[4]*Department of Electrical Engineering, National Yunlin University of Science and Technology*
Douliou, Yunlin 640, Taiwan
(email: [1]*t105@nkut.edu.tw* ; [2]*ccyang@mail.hit.edu.tw* ; [3]*guanyu@nkut.edu.tw* ; [4]*sukl@yuntech.edu.tw*)

Abstract: In this paper, a hybrid optimization approach is proposed to design fuzzy PID controllers for asymptotical stabilization of a three-dimensional overhead crane. In the proposed method, a fuzzy PID controller is expressed in terms of fuzzy rules, in which the input variables are the error signals and their derivatives, while the output variables are the PID gains. In this manner, the PID gains are adaptive and the fuzzy PID controller has more flexibility and capability than the conventional ones with fixed gains. To tune the fuzzy PID controller simultaneously, a hybrid optimization procedure integrating genetic algorithm (GA) and particle swarm optimization (PSO) method is proposed. The simulation results illustrate that the proposed controller can effectively perform the asymptotical stability of the prototype overhead crane.

Keywords: Three-dimensional overhead crane, particle swarm optimization, genetic algorithm, fuzzy PID control, hybrid optimization

I. INTRODUCTION

Overhead cranes are widely used in industry for transportation systems. However, the overhead cranes have several problems. Such that load swing usually degrades work efficiency and sometimes causes load damages and even safety accidents in the worst cases. Therefore, some researchers have endeavored to control the load swing [1-8]. However, the control of overhead cranes is not a simple task since the overhead cranes have fewer control inputs than degrees of freedom. Recently, many methods have been proposed for the design of controllers. Most industrial processes nowadays are still controlled by PID controllers [9-12]. However, a conventional PID controller may have poor control performance for nonlinear and/or complex systems that have no precise mathematical models. The main disadvantage is that they usually lack in flexibility and capability.

Fuzzy controllers provide reasonable and effective alternatives for conventional controllers. Many researchers attempted to combine conventional PID controllers with fuzzy logic [13,14]. Despite the significant improvement of these fuzzy PID controllers over their classical counterparts, it should be noted that they still have disadvantages. Furthermore, for nonlinear multivariable systems, how to reduce the number of fuzzy rules is unsolved.

Several evolutionary algorithms have been proposed recently to search for optimal PID controllers. Among them, genetic algorithm (GA) has received great attention and particle swarm optimization (PSO) method has been successfully applied to various fields [15,16]. In this paper, a hybrid optimization approach integrating GA and PSO will be adopted to perform the fuzzy PID control. In this manner, the proposed method is fully capable of creating a fuzzy PID controller and eliminates the need for human expertise information in the design process. To show the flexibility and capability of the proposed method, an overhead crane is adopted as an illustrative example. From the simulation results, one can find that the designed fuzzy PID controller guarantees not only prompt damping of load swing but also accurate control of crane positions.

II. FUZZY PID CONTROLLERS

In the proposed fuzzy PID controller, the input variables of the fuzzy rules are the error signals and their derivatives, while the output variables are the PID gains. The fuzzy PID control rules are expressed as

$$\text{If } e_1 \text{ is } X_1^i \text{ and } \dot{e}_1 \text{ is } X_2^j \text{ and } e_2 \text{ is } X_3^k \text{ and } \dot{e}_2 \text{ is } X_4^l,$$
$$\text{then } K_{P1} = Y_{P1}^{ijkl}, K_{I1} = Y_{I1}^{ijkl}, \cdots, K_{D2} = Y_{D2}^{ijkl}$$
$$\text{for } 1 \le i \le n_1,\ 1 \le j \le n_2,\ 1 \le k \le n_3,\ 1 \le l \le n_4 \quad (1)$$

where e_1, e_2 and $\dot{e}_1$, $\dot{e}_2$ are the error signals and their derivatives, $X_1^i, X_2^j, X_3^k, X_4^l$ are the membership functions of e_1, $\dot{e}_1$, e_2, and $\dot{e}_2$, $K_{P1}, K_{I1}, \cdots, K_{D2}$ are the PID gains, $Y_{P1}^{ijkl}, Y_{I1}^{ijkl}, \cdots, Y_{D2}^{ijkl}$ are real numbers, n_1, n_2, n_3, and n_4 denote the numbers of input membership functions, respectively.

The membership functions of an FLC are usually parametric functions such as triangular functions, trapezoidal functions, Gaussian functions, and singletons. Though the proposed method is equally applicable to all these kinds of membership functions, asymmetric Gaussian ones are used as the antecedent fuzzy sets in this paper. This means that input membership functions are represented as

$$X_k^{m_k}(x_k) = \begin{cases} \exp\left[-\left(\dfrac{x_k - \rho_k^{m_k}}{\sigma_{kl}^{m_k}}\right)^2\right] & \text{if } x_k \le \rho_k^{m_k} \\ \exp\left[-\left(\dfrac{x_k - \rho_k^{m_k}}{\sigma_{kr}^{m_k}}\right)^2\right] & \text{if } x_k > \rho_k^{m_k} \end{cases} \quad \text{for } k = 1, 2, \cdots, 4,$$

$$1 \le m_1 \le n_1, 1 \le m_2 \le n_2, 1 \le m_3 \le n_3, 1 \le m_4 \le n_4 \quad (2)$$

where x_k represents the input linguistic variables, $\rho_k^{m_k}$, $\sigma_{kl}^{m_k}$, and $\sigma_{kr}^{m_k}$ denote the values of the centers, the left widths, and the right widths of the input membership functions, respectively. For the output membership functions, singleton sets are adopted. In the defuzzification process, Wang [17] used the center of gravity method to determine the output crisp values. Then, if the PID control law is used and the control signal is determined as

$$\begin{aligned} u(t) &= K_{P1}e_1(t) + K_{I1}\int e_1(t)dt + K_{D1}\dot{e}_1(t) \\ &+K_{P2}e_2(t) + K_{I2}\int e_2(t)dt + K_{D2}\dot{e}_2(t) \end{aligned} \quad (3)$$

From the above description, one can find that the gains of the fuzzy PID controller are adaptive such that the controller should have more flexibility and capability than the conventional ones. However, it is very difficult, if not impossible, to determine the parameters directly. Therefore, a novel method integrating PSO and GA is proposed to search for the optimal values of these parameters simultaneously.

III. A SIMULATION EXAMPLE

1. Dynamic of An Overhead Crane

In practice, load swing is suppressed as much as possible for safety considerations. This study considers this practical case of small load swing around the stable equilibrium. Then, for the generalized coordinates x, θ_X y, and θ_Y, in Fig. 1 the following linearized dynamic model [5] can be derived:

$$(M_X + m)\ddot{x} + mL\ddot{\theta}_X = F_X - D_X\dot{x} \quad (4)$$

$$\ddot{x} + L\ddot{\theta}_X + g\theta_X = 0 \quad (5)$$

$$(M_Y + m)\ddot{y} + mL\ddot{\theta}_Y = F_Y - D_Y\dot{y} \quad (6)$$

$$\ddot{y} + L\ddot{\theta}_Y + g\theta_Y = 0 \quad (7)$$

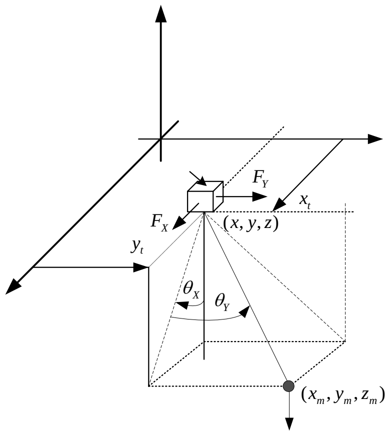

Fig. 1. Coordinate systems of an overhead crane.

where m is the load mass; L is the rope length; M_X and M_Y are the *x* and *y* components of the crane mass including the moment of inertia of the gear train and motors, respectively; D_X and D_Y denote the viscous damping coefficients of the crane in the *x* and *y* directions, respectively; F_X and F_Y are the force inputs to the crane in the x and y directions, respectively; g denotes the gravitational acceleration.

2. GA-PSO tuning Fuzzy PID Controller

In the overhead crane, the desired value of $x(t)$ and $\theta(t)$ are denoted by x_d and θ_d. If the PID control law is employed, then the input-output relation of the crane system is expressed as

$$\begin{aligned} \tau(t) &= k_{P1}e_1(t) + k_{I1}\int e_1(t)dt + k_{D1}\dot{e}_1(t) \\ &+k_{P2}e_2(t) + k_{I2}\int e_2(t)dt + k_{D2}\dot{e}_2(t) \end{aligned} \quad (8)$$

where $e_1(t) = x(t) - x_d$, $e_2(t) = \theta(t) - \theta_d$, $\dot{e}_1(t) = \dot{x}(t) - \dot{x}_d$, and $\dot{e}_2(t) = \dot{\theta}(t) - \dot{\theta}_d$.

3. Fitness

In designing the fuzzy PID controller, the primary goal is to drive an overhead crane system from the given initial state to the desired final state. However, if the number of fuzzy rules is large, then heavy computation burden and huge memory requirement are inevitable. Therefore, the primary goal and the way to reduce the number of fuzzy rules should be taken into account simultaneously in defining the fitness function. This means that two performance criteria are chosen as follows:

$$f = \frac{1}{[(1+\sum_{i=1}^{n_1} p_i)\cdot(1+\sum_{j=1}^{n_2} p_j)\cdot(1+\sum_{k=1}^{n_3} p_k)\cdot(1+\sum_{l=1}^{n_4} p_l)]^2} + \frac{1}{\int t[e_1^2(t) + e_2^2(t)]dt} \quad (9)$$

where p_i, p_j, p_k, and p_l, are the binary elements to indicate which ones of the membership functions are activated. From the definition (9), the fitness value can be calculated to evaluate the performance of the fuzzy PID controller and a higher fitness value denotes a better performance.

IV. INTEGRATION OF PSO AND GA

PSO is a population-based stochastic searching technique developed by Kennedy and Eberhart [18]. It is similar to the GA in that it begins with a random population matrix and searches for the optima by updating generations.

1. Particle Representations

Before applying the novel auto-tuning method, how to encode the parameters must be introduced firstly. In the proposed method, a mixed coding method is used, in which n_1, n_2, n_3, and n_4 are encoded as binary numbers and $\rho_k^{m_k}$, $\sigma_{kl}^{m_k}$, $\sigma_{kr}^{m_k}$, Y_{P1}^{ijkl}, Y_{I1}^{ijkl}, Y_{D1}^{ijkl}, Y_{P2}^{ijkl}, Y_{I2}^{ijkl}, Y_{D2}^{ijkl} are encoded as real numbers. This means that the positions of particles are represented as

$$\boldsymbol{P} = [\boldsymbol{p}_{binary}\ \ \boldsymbol{p}_{real}] \tag{10}$$

The particle $\boldsymbol{p}_{binary}$ contains binary variables taking the value of one or zero. The elements of $\boldsymbol{p}_{binary}$ are used to indicate which ones of the membership functions are activated. As for the real particles $\boldsymbol{p}_{real}$, the elements of $\boldsymbol{p}_{real}$ are used to represent the values of $\rho_k^{m_k}$, $\sigma_{kl}^{m_k}$, $\sigma_{kr}^{m_k}$, Y_{P1}^{ijkl}, Y_{I1}^{ijkl}, Y_{D1}^{ijkl}, Y_{P2}^{ijkl}, Y_{I2}^{ijkl}, and Y_{D2}^{ijkl}.

2. Evolutionary Algorithms

In evolutionary strategies, the real particles $\boldsymbol{p}_{real}$ will employ the PSO method. As for binary particles $\boldsymbol{p}_{binary}$, it will adopt the GA because of their nature and simplicity. In PSO method, the particles update their velocities and positions based on the local best and global best solutions [19]. In the evolutionary procedure, the inertia weight, the cognitive parameter, and the social parameter are linearly adaptable over the evolutionary procedure [19]. In the proposed GA-based method for binary particles, one cut-point crossover operator and single-point mutation operator will be employed [20].

V. SIMULATION RESULTS

The parameters of the overhead crane system shown as Fig. 1 are chosen as [2]

$$M_X = 1440\ kg,\ D_X = 480\ N \cdot s/m$$
$$M_Y = 110\ kg,\ D_Y = 40\ N \cdot s/m$$
$$m = 10\ kg,\ L = 1\ m,\ g = 9.8\ m/s^2$$

and the constraints shown as

$$-4800\ \text{N} \le F_X \le 4800\ \text{N},\ -200\ \text{N} \le F_Y \le 200\ \text{N}$$
$$-\pi/12\ \text{rad/s} \le \theta \le \pi/12\ \text{rad/s}$$
$$-\pi/6\ \text{rad/s} \le \dot{\theta} \le \pi/6\ \text{rad/s}$$
$$0\ m \le x \le 5.5\ m,\quad 0\ m \le y \le 3.5\ m$$
$$-0.5\ m/s \le \dot{x} \le 0.5\ m/s,\ -2\ m/s^2 \le \ddot{x} \le 2\ m/s^2$$
$$-0.3\ m/s \le \dot{y} \le 0.3\ m/s,\ -1.5\ m/s^2 \le \ddot{y} \le 1.5\ m/s^2$$

The initial state and the desired final state of the overhead crane are $(x, y, \theta) = (1, 1, \pi/18)$ and $(x, y, \theta) = (0, 0, 0)$. In the proposed algorithm, the population size, the maximal iteration number, the crossover rate, and mutation rate are chosen to be 40, 2000, 0.8, and 0.2, respectively. Moreover, it is assumed that the values of n_1, n_2, n_3, and n_4 are all chosen as five, and the singletons of the output linguistic variables are all chosen as real numbers. According to the procedure of the GA-PSO algorithm, the minimal fuzzy rules and the optimal membership functions of the input linguistic variables are determined. Moreover, the optimal values of $\boldsymbol{p}_{binary}$ and $\boldsymbol{p}_{real}$ can be determined. The former is found to be [00101010010101010010] and it means that only the membership functions X_1^3, X_1^5, X_2^2, X_2^5, X_3^2, X_3^4, X_4^1, and X_4^4 are activated. Meanwhile, this also means that there are 16 ($= 2 \times 2 \times 2 \times 2$) fuzzy rules in the fuzzy PID controller. Since the number of fuzzy rules is reduced from 625 ($= 5^4$) to 16, the computation burden in implementation of this fuzzy PID controller will also be reduced significantly.

The simulation results shown as Fig. 2 through Fig. 5 illustrate that the proposed fuzzy PID controller can effectively complete the asymptotical stability of the prototype overhead crane.

VI. CONCLUSION

In fuzzy PID tuning techniques, the parameters of fuzzy sets and PID gains are difficult to obtain the optimal values for stabilizing an overhead crane. In this paper, we present a hybrid optimization approach integrating GA and PSO to design a fuzzy PID controller to asymptotically stabilize the prototype overhead crane.

ACKNOWLEDGMENT

This work was supported in part by the National Science Council, Taiwan, R.O.C., under grant NSC 98-2221-E-252-004.

REFERENCES

[1] Yu J, Lewis FL, Huang T (1995), Nonlinear feedback control of a gantry crane. Proc of American Control Conf, pp. 4310-4315
[2] Lee HH (1998), Modeling and control of a three-dimensional overhead crane. J of Dyn Systs, Meas, and Control 120: 471-476
[3] Singhose W, Porter L, Kenison M, Kriikku E (2000), Effects of hoisting on the input shaping control of gantry cranes. Control Eng Pract 8:1159-1165

[4] Moustafa KAF, Ebeid AM (1988), Nonlinear modeling and control of overhead crane load sway. J of Dyn Syst, Meas, and Control 110:266-271

[5] Cho SK, Lee HH (2002), A fuzzy-logic antiswing controller for three-dimensional overhea cranes, ISA Trans 41:235-243

[6] Hua YJ, Shine YK (2007), Adaptive coupling control for overhead crane systems. Mechatronics 17:143-152

[7] Chang CY (2007), Adaptive fuzzy controller of the overhead cranes with nonlinear disturbance. IEEE Trans on Ind Inform 3(2):164-172

[8] Park MS, Chwa DY, Hong SK (2008), Antisway tracking control of overhead cranes with system uncertainty and actuator nonlinearity using an adaptive fuzzy sliding-mode control. IEEE Trans on Ind Electronics 55(11):3972-3984

[9] Keel LH, Rego JI, Bhattacharyya SP (2003), A new approach to digital PID controller design. IEEE Trans on Automatic Control 48(4):687-692

[10] Cervantes I, Garrido R, Jose AR, et al (2004), Vision-based PID control of planar robots. IEEE Trans on Mechatronics 9(1):132-136

[11] Whidborne JF, Istepanian RSH (2001), Genetic algorithm approach to designing finite-precision controller structures, IEE Proc of Control Theory Applications 148(5):377-382

[12] Lin L, Jan HY, Shieh NC (2003), GA-based multiobjective PID control for a linear brushless dc motor. IEEE Trans on Mechatronics 8(1):56-65

[13] Tao CW, Taur JS (2005), Robust fuzzy control for a plant with fuzzy linear model. IEEE Trans on Fuzzy Syst 13(1):30-41

[14] Wu CJ, Liu GY, Cheng MY, et al (2002), A neural-network-based method for fuzzy parameter tuning of PID controllers. J of the Chin Inst of Eng 25(3): 265-276

[15] Gaing ZL (2004), A particle swarm optimization approach for optimum design of PID controller in AVR system. IEEE Trans on Energy Conversion 19(2): 384-391

[16] Habib SJ, Al-kazemi BS (2005), Comparative study between the internal behavior of GA and PSO through problem-specific distance functions. The 2005 IEEE Congress on Evolutionary Computation, pp. 2190-2195

[17] Wang LX (1997), A Course in Fuzzy Systems and Control. Prentice-Hall, New Jersey

[18] Kennedy J, Eberhart R (1995), Particle swarm optimization. Proc of the IEEE Int Conf on Neural Networks, pp. 1942-1948

[19] Ratnaweera A, Halgamuge SK, Watson C (2004), Self-organizing hierarchical particle swarm optimizer with time-varying acceleration coefficients. IEEE Trans on Evolutionary Comput 8(3):240-255

[20] Haupt RL, Haupt SE (2004), Practical Genetic Algorithms, 2nd edition. John Wiley & Sons, New York

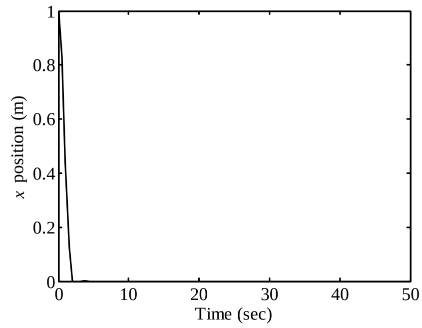

Fig. 2. Plot of x-position $x(t)$ for the overhead crane using the proposed fuzzy PID controller.

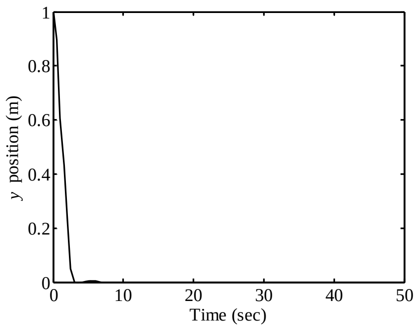

Fig. 3. Plot of y-position $y(t)$ for the overhead crane using the proposed fuzzy PID controller.

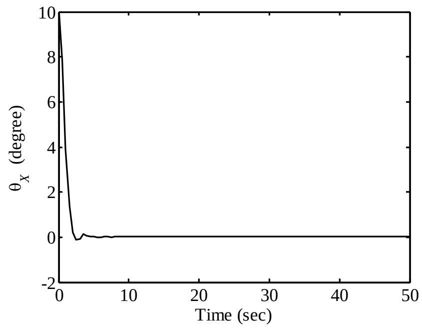

Fig. 4. Plot of X-angle $\theta_X(t)$ of the overhead crane using the proposed fuzzy PID controller.

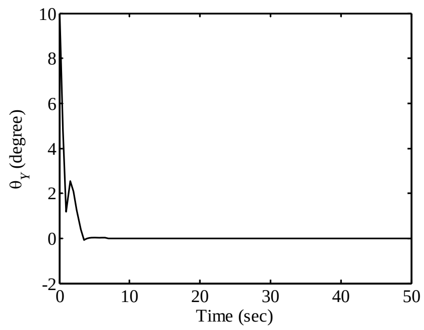

Fig. 5. Plot of Y-angle $\theta_Y(t)$ of the overhead crane using the proposed fuzzy PID controller.

Parameter Estimation of Chaotic Systems by Nonlinear Time-Varying Evolution PSO Method

Chia-Nan Ko[1], Yu-Yi Fu[2], Cheng-Ming Lee[3], and Chia-Ju Wu[4]

[1,2]*Department of Automation Engineering, Nan-Kai University of Technology*
Tasotun, Nantou 542, Taiwan
[3]*Department of Computer and Communication Engineering, Nan-Kai University of Technology*
Tasotun, Nantou 542, Taiwan
[4]*Department of Electrical Engineering, National Yunlin University of Science and Technology*
Douliou, Yunlin 640, Taiwan
(*E-mail:* [1]t105@nkut.edu.tw; [2] t098@nkut.edu.tw; [3] t104@nkut.edu.tw; [4] wucj@yuntech.edu.tw)

Abstract: An important issue in nonlinear science is parameter estimation for Lorenz chaotic system. Much attention has attracted increasing interests for the identification in various research fields, which could be essentially formulated as a multi-dimensional optimization problem. A novel evolutionary computation algorithm, nonlinear time-varying evolution particle swarm optimization (NTVEPSO) is employed to estimate the parameters. In the NTVEPSO method, the nonlinear time-varying evolution functions are determined by using matrix experiments with an orthogonal array, in which a minimal number of experiments would have an effect that approximates the full factorial experiments. The NTVEPSO method and other PSO methods are then applied to identify of Lorenz chaotic system. Numerical simulation and the comparisons demonstrate the feasibility and the superiority of the proposed NTVEPSO method.

Keywords: Particle swarm optimization, nonlinear time-varying evolution, chaotic system, Lorenz chaotic system.

I. INTRODUCTION

Synchronization and control of chaotic systems have been investigated intensely in various fields during recent years[1–3]. Many of the proposed approaches only work under the assumption that the parameters of chaotic systems are known in advance. In real world, the parameters may be difficult to determine due to the complexity of chaotic systems. Therefore, parameter estimation for chaotic systems has become a hot topic in the past decade[4–9]. Recently, some evolutionary computation algorithms have been successfully applied to real world optimization problems. Several researchers have introduced the evolutionary-based methods into parameter estimation for chaotic systems[10–13].

Particle swarm optimization (PSO) has evolved recently as an important branch of stochastic techniques to explore the search space for optimization[14]. Nowadays, PSO has been developed to be real competitors with other well-established techniques for evolutionary-based optimization methods[15-17]. In this paper, parameter estimation for chaotic systems is formulated as a multi-dimensional optimization problem, and a nonlinear time-varying evolution PSO (NTVEPSO) approach is employed to solve the problem. Numerical simulation based on Lorenz system and comparisons with results obtained by several existed PSO methods verify the feasibility and the validity of the NTVEPSO approach.

II. PROBLEM FORMULATION

Considering the following n-dimensional chaotic system:

$$\dot{\boldsymbol{X}} = F(\boldsymbol{X}, \boldsymbol{X}_0, \boldsymbol{Q}_0) \tag{1}$$

where $\boldsymbol{X} \in R^n$ denotes the state vector, $\boldsymbol{X}_0$ denotes the initial state, and $\boldsymbol{Q}_0$ is a set of original parameters.

When estimating the parameters, suppose the structure of the system is known in advance, and thus the estimated system can be described as follows:

$$\dot{\hat{\boldsymbol{X}}} = F(\boldsymbol{X}, \boldsymbol{X}_0, \boldsymbol{Q}) \tag{2}$$

where $\dot{\hat{\boldsymbol{X}}} \in R^n$ denotes the state vector, and $\boldsymbol{Q}$ is a set of estimated parameters. Therefore, the problem of parameter estimation can be formulated as the following optimization problem:

$$\text{Min} \quad J = \frac{1}{M}\sum_{K=1}^{M} \left\| \boldsymbol{X}_K - \hat{\boldsymbol{X}}_K \right\|^2 \tag{3}$$

where M denotes the length of data used for parameter estimation, $\boldsymbol{X}_K$ and $\hat{\boldsymbol{X}}_K$, $K = 1, 2, \ldots, M$, denote state vectors of the original and the estimated systems at time K, respectively.

Obviously, the parameter estimation for chaotic systems is a multi-dimensional continuous optimization problem, where the decision vector is $\boldsymbol{Q}$ and the optimization goal is to minimize J. The principle of parameter estimation for chaotic systems in sense of optimization can be illustrated with Fig. 1.

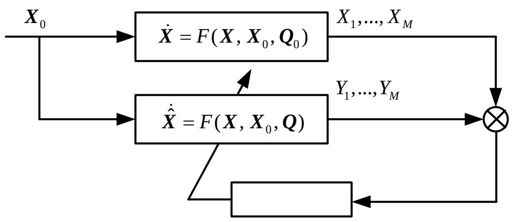

Fig. 1 The parameter estimation scheme for chaotic systems

Due to the unstable dynamic behavior of chaotic systems, the parameters are not easy to obtain. In addition, there are often multiple variables in the problem and multiple local optima in the landscape of *J*, so traditional optimization methods are easy to trap in local optima and it is difficult to achieve the global optimal parameters.

III. NONLINEAR TIME-VARYING EVOLUTION PSO APPROACH

1. Review of some PSO methods

Particle swarm optimization, first introduced by Kennedy and Eberhart[14], is based on observations of the social behavior of animals, such as bird flocking, fish schooling and the swarm theory. PSO is initialized with a population of random solutions. Each individual (called a particle) is assigned with a random velocity and evolves according to the flying experiences of its own and companions. The particles then fly through hyperspace and approach the global optimum. In PSO algorithm, each particle keeps track of its own position and velocity in the problem space. At each iteration, the new positions and velocities of the particles are updated using the following two equations:

$$P_i(k+1) = P_i(k) + V_i(k+1) \quad \text{for} \quad i = 1,\ 2, \cdots,\ m \tag{4}$$

$$\begin{aligned} V_i(k+1) &= V_i(k) + c_1 \cdot r_1 \cdot (P_i^l(k) - P_i(k)) \\ &\quad + c_2 \cdot r_2 \cdot (P^g - P_i(k)) \end{aligned} \tag{5}$$

where m is the number of particles in a population, k is the number of current iteration, c_1 and c_2 are acceleration coefficients, r_1 and r_2 are random numbers between 0 and 1, $P_i(k)$, $P_i^l(k)$, and $V_i(k)$ are the position, the local best, and the velocity of *i*th particle at iteration k, P^g is the global best of all particles.

Several researchers have put much effort to improve the original version of PSO since the introduction of the PSO method in 1995[14]. Shi and Eberhart[18] used a linearly varying inertia weight over iterations. The mathematical representations of this PSO method are given as shown in (4) and

$$\begin{aligned} V_i(k+1) &= \omega(k) \cdot V_i(k) + c_1 \cdot r_1 \cdot (P_i^l(k) - P_i(k)) \\ &\quad + c_2 \cdot r_2 \cdot (P^g - P_i(k)) \quad \text{for} \quad i = 1,\ 2, \cdots,\ m \end{aligned} \tag{6}$$

where the acceleration coefficients c_1 and c_2 are fixed, r_1 and r_2 are two random numbers. The inertia weight starts with a high value $\omega_{\max}$ and linearly decreases to $\omega_{\min}$ at the maximal number of iterations. From hereafter, this PSO algorithm will be referred to as the time-varying inertia weight factor method (TVIWPSO).

Eberhart and Shi[19] found that the TVIWPSO method is not very effective in tracking dynamic systems. Considering the dynamic nature of real-world applications, they proposed a random inertia weight factor to track dynamic systems. In their method, the representations are the same as those in the TVIWPSO method except that the inertia weight factor changes randomly. In the rest of this paper, this algorithm will be referred to as the RANDWPSO method.

An automation strategy for the PSO with time-varying acceleration coefficients was proposed[20]. The objective is to enhance the global search in the early part of the optimization and to encourage the particles to converge toward the global optimum at the end of the search. In their method, the representations are the same as those in the TVIWPSO method except that the acceleration coefficients change according to linear time-varying evolution. From hereafter, this algorithm will be referred to as the TVACPSO method.

A time-varying nonlinear function modulated inertia weight adaptation was proposed by Chatterjee and Siarry[21]. In this method, the acceleration coefficients are also fixed. However, the inertia weight starts with a high value $\omega_{\max}$ and nonlinearly decreases to $\omega_{\min}$ at the maximal number of iterations. This means that the representations are the same as those in the TVIWPSO method except that the inertia weight factor changes according to

$$\omega(k) = \omega_{\min} + \left(\frac{iter_{\max} - iter}{iter_{\max}} \right)^{\alpha} \cdot (\omega_{\max} - \omega_{\min}) \tag{7}$$

where $iter_{\max}$ is the maximal number of iterations and $iter$ is the current number of iterations.

2. PSO-NTVE method based on orthogonal arrays

In this section, based on the concept presented[20,21], an NTVEPSO method is proposed. In the proposed PSO method, the inertia weight is given as described in (7). The cognitive parameter c_1 starts with a high value $c_{1\max}$ and nonlinearly decreases to $c_{1\min}$. Meanwhile, the social parameter c_2 starts with a low value $c_{2\min}$ and nonlinearly increases to $c_{2\max}$. This means that the mathematical expressions are given as shown in (4), (7), and

$$\begin{aligned} V_i(k+1) &= \omega(k) \cdot V_i(k) + c_1(k) \cdot r_1 \cdot (P_i^l(k) - P_i(k)) \\ &\quad + c_2(k) \cdot r_2 \cdot (P^g - P_i(k)) \quad \text{for} \quad i = 1,\ 2, \cdots,\ m \end{aligned} \tag{8}$$

$$c_1(k) = c_{1\min} + \left(\frac{iter_{\max} - iter}{iter_{\max}} \right)^{\beta} \cdot (c_{1\max} - c_{1\min}) \qquad (9)$$

$$c_2(k) = c_{2\max} + \left(\frac{iter_{\max} - iter}{iter_{\max}} \right)^{\gamma} \cdot (c_{2\min} - c_{2\max}) \qquad (10)$$

where α, β, and γ are constant coefficients.

The proposed PSO method will encourage particles to wander through the entire search space, instead of clustering around a local optimum, during early iterations of the optimization. On the other hand, the algorithm will expedite convergence toward the global optimum during latter iterations. In this manner, the optimal solution should be obtained in a computation-efficient way.

To determine the optimal combination of α, β, and γ, all combinations must be tested. An $L_{25}(5^6)$ is an orthogonal array that can deal with at most six variables in five possible values with 25 experiments[22,23]. Instead of 5^3 possible combinations, one only needs to perform 25 experiments to determine the optimal combination of α, β, and γ.

IV. SIMULATION RESULTS

Lorenz system, a typical chaotic system[10–12], is adopted as an example in this paper. The mathematical description of Lorenz system is described as follows:

$$\begin{cases} \dot{x}_1 = a(x_2 - x_1) \\ \dot{x}_2 = bx_1 - x_1x_3 - x_2 \\ \dot{x}_3 = x_1x_2 - cx_3 \end{cases} \qquad (11)$$

where $a = 10, b = 28, c = 8/3$ are the original parameters.

In our simulation, the original Lorenz system firstly evolves freely from a random initial state. Then successive M states ($M = 300$) of both the original system and the estimated system are used to calculate J. The searching ranges are set as follows: $9 \le a \le 11,\ 20 \le b \le 30,$ and $2 \le c \le 3$. In the Lorenz system (11), three-dimensional parameter are unknown and need to be estimated.

In the simulation for PSO methods, the population size and the maximal iteration number are chosen to be 40 and 100, respectively. Moreover, the particles in PSO methods are all chosen as real numbers in the ranges of a, b, and c in (11). Several parameters in the PSO simulation must be specified first. In the employed PSO methods, the values of $\omega_{\max}$, $\omega_{\min}$, $c_{1\max}$, $c_{1\min}$, $c_{2\max}$, and $c_{2\min}$ in (7), (9), and (10) are set to 0.9, 0.2, 2.5, 0.5, 2.5, and 0.5, respectively. These values are determined based on Ratnaweera et al.[20]. In the orthogonal-array-based NTVEPSO, first, assume that α, β, and γ in (7), (9), and (10) are all within the set $\{0.5, 1, 1.5, 2, 2.5\}$. The values of α, β, and γ are 0.5, 1.5, and 1.5 determined by 25 experiments of orthogonal arrays.

The statistical results obtained by PSO methods are shown in Table 1, in which each algorithm is implemented after 20 times independently. From the results, it is clear that the best, the average, and the worst results obtained by NTVEPSO are better than those obtained by the other PSO methods.

V. CONCLUSION

Parameter estimation for chaotic systems was formulated as a multi-dimensional optimization problem in this paper. A novel orthogonal-array-based evolutionary algorithm, NTVEPSO, was applied to solve such an issue. Numerical simulation and comparisons based on Lorenz system demonstrated the effectiveness and efficiency of NTVEPSO. The future work is to apply PSO for other chaotic systems and to develop more effective and adaptive PSO based approaches.

ACKNOWLEDGMENT

This work was supported in part by the National Science Council, Taiwan, R.O.C., under grant NSC 98-2221-E-252-004.

REFERENCES

[1] Lu Z, Shieh LS, Chen GR (2003), On robust control of uncertain chaotic systems: a sliding-mode synthesis via chaotic optimization. Chaos, Solitons & Fractals 18(4):819-27

[2] Yang SS, Duan CK (1998), Generalized synchronization in chaotic systems. Chaos, Solitons & Fractals 9(10):1703-1707

[3] Elabbasy EM, Agiza HN, El-Dessoky MM (2005), Global synchronization criterion and adaptive synchronization for new chaotic system. Chaos, Solitons & Fractals 23(4):1299-309

Table 1 Statistical results of different approaches for three-dimensional parameter estimation (14) after 20 times.

PSO method	Average result				Best result				Worst result			
	a	b	c	J	a	b	c	J	a	b	c	J
PSO-TVIW	10.3311	27.7707	2.9425	5.6777	10.0237	28.0430	2.6532	0.0291	10.1359	24.6792	2.000	40.6330
PSO-RANDW	10.3960	27.3898	2.9023	9.7032	10.1720	27.9128	2.6704	0.2364	10.7252	24.8650	2.3745	30.7412
PSO-TVAC	10.5719	27.6857	2.9089	6.2706	10.0798	27.8970	2.6804	0.0677	10.6266	24.0630	2.000	45.9042
PSO-NTVE	10.5804	27.7521	2.9406	**5.4474**	9.9803	28.0279	2.6636	**0.0083**	10.7770	25.0512	2.0000	43.6542

[4] Saha P, Banerjee S, Chowdhury AR (2004), Chaos, signal communication and parameter estimation. Phys Lett A 326(1-2):133-139
[5] Alvarez G, Montoya F, Romera M, Pastor G (2003), Cryptanalysis of an ergodic chaotic cipher. Phys Lett A 311(2-3):172-179
[6] Wu XG, Hu HP, Zhang BL (2004), Parameter estimation only from the symbolic sequences generated by chaos system. Chaos, Solitons & Fractals 22(2):359-366
[7] Xu DL, Lu FF (2005), An approach of parameter estimation for non-synchronous systems. Chaos, Solitons & Fractals 25(2):361-366
[8] Fostin HB, Woafo P (2005), Adaptive synchronization of a modified and uncertain chaotic van der Pol–Duffing oscillator based on parameter identification. Chaos, Solitons & Fractals 24:1363-1371
[9] Gu M, Kalaba RE, Taylor GA (1996), Obtaining initial parameter estimates for chaotic dynamical systems using linear associative memories. Appl Math Comput 76:143-59
[10] Guerra FA, Coelho LS (2008), Multi-step ahead nonlinear identification of Lorenz's chaotic system using radial basis neural network with learning by clustering and particle swarm optimization. Chaos, Solitons & Fractals 35:967-979
[11] Dai D, Ma XK, Li FC, You Y (2002), An approach of parameter estimation for a chaotic system based on genetic algorithm. Acta Phys Sinica 11:2459-2462
[12] He Q, Wang L, Liu B (2007), Parameter estimation for chaotic systems by particle swarm optimization. Chaos, Solitons & Fractals 34:654-661
[13] Liu B, Wang L, Jin YH, Tang F, Huang DX (2006), Directing orbits of chaotic systems by particle swarm optimization. Chaos, Solitons & Fractals 29:454-61
[14] Kennedy J, Eberhart R (1995), Particle swarm optimization. Proc of the IEEE Int Conf on Neural Networks, pp. 1942-1948
[15] Gaing ZL (2004), A particle swarm optimization approach for optimum design of PID controller in AVR system. IEEE Trans on Energy Conversion 19(2):384-391
[16] Boeringer DW, Werner DH (2004), Particle swarm optimization versus genetic algorithms for phased array synthesis. IEEE Trans on Antennas and Propagation 52(3):771-779
[17] Elbeltagi E, Hegazy T, Grierson D (2005), Comparison among five evolutionary-based optimization algorithms. Advanced Eng Inform 19(1):43-53
[18] Shi Y, Eberhart RC (1998), A modified particle swarm optimizer. Proc of the IEEE Int Conf on Evolutionary Comput, pp. 69-73
[19] Eberhart RC, Shi Y (2001), Tracking and optimizing dynamic systems with particle swarms. Proc of the IEEE Int Congress on Evolutionary Comput, pp. 94-100
[20] Ratnaweera A, Halgamuge SK, Watson HC (2004), Self-organizing hierarchical particle swarm optimizer with time-varying acceleration coefficients. IEEE Trans on Evolutionary Comput 8(3):240-255
[21] Chatterjee A, Siarry P (2006), Nonlinear inertia weight variation for dynamic adaptation in particle swarm optimization. Computers and Operations Research 33:859-871
[22] Montgomery DC (1991), Design and Analysis of Experiments, third edition. Wiley, New York
[23] Hicks CR (1993), Fundamental Concepts in the Design of Experiments, fourth edition. Saunders College, Texas

Spatial Information of Game for Body Interface Using Webcam

Young Jae Lee

Dept. of Multimedia, Jeonju University, Jeonju City, Korea

(Tel. : 82-63-220-2936; Fax : 82-63-220-3071)
(leeyj@jj.ac.kr)

Abstract: In this paper, we propose an efficient game spatial division and analysis algorithm that gives special information for collision avoidance of game objects and natural interface. We divide into 9 parts of game space and part 4, 5, 6 are divided into 2 more detail parts for check the enemy position and movement information of gamer. And we calculate optimal path for collide avoidance of the enemy. To evaluate the method, we implemented a motion based game that consists of a webcam, a player, an enemy, and we obtained some valid results of our method for the collision avoidance and interesting interactions. The results demonstrated that the proposed approach is robust. If movement information is in front of enemy, then the enemy waits or turns back and finds the place and runs to avoid attack. This algorithm can be used basic development of effective body interface and level control for motion based game.

Keywords: game spatial division, collision avoidance, optimal path, motion based game

I. INTRODUCTION

Game is highly-concentrated on culture & information technology in the digital entertainment industry and is to lead the 21st century in the field of cultural contents industry. Currently, the game industry is undergoing rapid growth, helped by the ever-developing computer and internet technology. The game industry is showing infinite potentials as the new growth engine for the economy and employment generator because of the internet-driven individualized cultural atmosphere and computer-focused entertainment trend. In particular, motion-based games and technology-integrated games, which use various game technologies and computer vision techniques, are emerging as the new trend[1-7]. Motion-based game is the kind of game in which the gamer gets engrossed in the game with maximized sense of reality through interaction and it has been designed to track the changes in the gamer's responses. It is not like other games in which only eyes and hands are used to do the game. In the motion-based game, on the other hand, the user fully expresses the gestures of the characters in the game with his or her own body[2-7]. Most of the games developed for PC use are designed to use only limited array of hardware, such as keyboard, mouse and joystick, which puts limits on the space used and also lessens the sense of reality. Developing motion-based games, is not simple since it requires hardware development as well as software, unlike in the case of conventional PC games. Motion-based games consist of arcade-motion games in a big game room, consol-motion game using game-controller with motion features and PC motion-based games[3]. PC motion-based games lag behind consol or arcade games in game reality or other effects because of less-developed game graphics or feedback systems. But the advantages of PC motion-based games are wide availability and relatively cheap game production cost[1-4]. Therefore, this paper seeks to suggest effective collision avoidance in an effort to develop sensory functional game for entertaining exercise. To realize the algorithm, virtual space division method is used to suggest and verify the collision avoidance methodology. For this purpose, the sensory functional game(first-person action game) which is composed of web camera, gamer and enemy character, has been made and proposed algorithm undergoes the verification process through experiments.

II. Motion-based Game

Fig. 1. is the diagram of the motion based serious game (first-person action game) in which the gamer can gain scores as well as getting the benefit of working out,

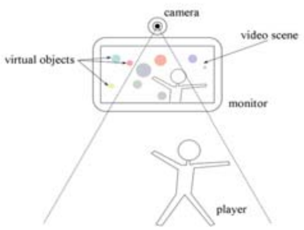

Fig. 1. Configuration of motion based game

by attacking the virtual object appearing on the monitor according to the game scenario. The enemy character, which is the virtual object is VH:Virtual Horse[8]. The game space has been designed to make the visual zone wide enough and to bring the workout effect for the gamer through the use of hands, arms, head, torso and so on. The movement information has been used as the attacking data so the collision led to scoring, through which the levels of difficulty and actions could be controlled.

1. Game collision event

In this paper, the most commonly used "quadrangle collision" has been used to detect the collision.

1.1 Quadrangle collision

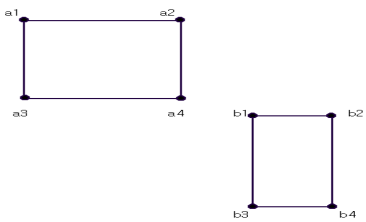

Fig. 2. Collision detection using quadrangle

Quadrangle has four feature points(Fig.2) and each has x and y coordinates. So the values of each coordinate can be used to identify the collision of quadrangles. For example, if we say the a4 coordinate is (x4,y4) and b1 coordinate is (x1',y1') the collision has not happened if the condition satisfies either (x1'>x4 || y1'> y4) or (x1>x4' || y1 > y4') when the a1 coordinate is (x1,y1) and the b4 coordinate is (x4',y4').

III . COLLISION AVOIDANCE

Color and action information enables the cognition of the necessary parts in the game space. But in games in which real-time interface is required, calculation for cognition can lower the speed of frame rate and therefore hamper the real-time interaction. To increase the movements of the gamer and to be able to use the movements information of shoulder and torso(as well as skin areas on the hands and the face) for attack data, this paper extracts the information for actions by using the visual information frame by frame and tries to analyze the action information and game space to realize the collision avoidance by sensing the action information and by controlling the movements of the virtual object.

1. Proposed algorithm

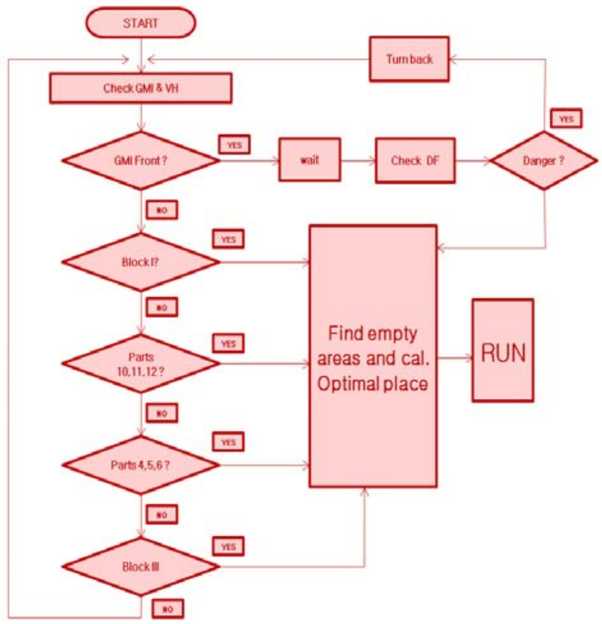

Fig. 3. Flowchart of the proposed algorithm

First of all, the space information for the game has been segmented from area 1 to area 12. Information for each area has been acquired after dissecting the areas, into 1-3(Block I), 4-7(Block II including 10, 11,12), and 7-9(Block III). After the analysis of the gamer's movement information in each area, it is compared with the current positional information of the enemy for the calculation of the optimal position course in the four directions where the enemy character could move. Block I is the uppermost area which only the hands of the gamer can touch and therefore highly secure. In Block II, we can get information on hands, arms and the head. Block III gives the information on body, hands and arms. So we have to consider it when generating the path for collision avoidance. For example, in Block I, area 1 has the longest gamer's movement path than area 1 or area 3 and it is relatively advantageous if the movement goes to area 1 when the gamer's movements are in 5,6,8,9 in the area 4. When VH is in area 1 and the movement information is in area 3,5,6, and 8, VH does the standing leaps to calculate the optimal path. If the area 3 or the area 5 is empty, the next movement is calculated after movement to the area 3 and 5. In this way, area information is identified and analyzed to realize the effective collision avoidance. (Refer to Fig. 3.) Fig. 3 shows the finding optimal path algorithm for collision avoidance of VH.

2. Division of the game space

(a) spatial division (b) position of hand

Fig. 4. Game spatial division

The area 4, 5, and 6(Block II) have the most hand movements and especially the area 5 has the most head movement information. Areas 4, 5, 6 are divided into 2 more detail areas 10, 11, 12 for check the enemy position and movement information of gamer. Area 7, 8 and 9(Block III) can have torso and hand movements at the same time. Area 1, 2 and 3(Block I) are where only hands can go and could be classified as the area of less movement information.

V. Experiment

Various game situations between the enemy character(VH, horse) and the gamer have been experimented by using the proposed algorithm. The upper visual of the gamer visual in the experiment is color and the lower visual is gray and the resulting visual has been applied the threshold value in the case of specific movement. Since the time gap from frame to frame is different from game to game, the division has been applied such as t1 frame, t2 frame and etc

1. Experiment 1

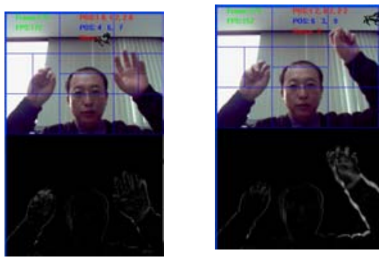

(a)t1 framae image (b)t2 frame image

Fig. 5. Image of Experiment I

VH is moving in the area 2 and the movement information is in area 10, 12, and 7. But the movement information in the next frame suddenly changes to area 3.(Fig. 5.(a)) VH waits in its position to identify the movement information because its current movement and the gamer's hand movement are in the same area. In the next frame VH identifies the movement information in which the gamer's left hand moves to area 3 and accelerates to move to area 3.(Fig. 5.(b)) In Experiment 1, VH effectively avoids collision with the gamer's hand by using the proposed algorithm When the movement information exists in the front part of the same direction, VH can do the standing jumps in its position while keeping getting the movement information, thus realizing more pleasurable and effective collision avoidance.

2. Experiment II

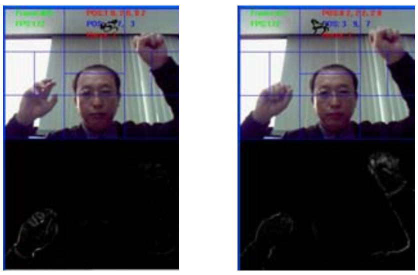

(a)t1 frame image (b)t2 frame image

Fig. 6. Image of Experiment II

VH is moving in the area 2 and the movement information is in area 10, 12, 7 and 9(Fig. 6.(a)). But the movement information changes getting upwards to area 3 in the next frame(Fig. 6.(b)). VH waits in its position to identify the movement information like experiment I because its current movement and the gamer's hand movement is getting dangerous. In the next frame VH identifies the movement information in which the gamer's left hand moves to area 3 and turns back to area 1. In Experiment II, VH has no room to avoid collision with the gamer's hand and turns back to safe area 1 by using the proposed algorithm. When the movement information exists continuously in the front part of the same direction, VH can do the standing jumps or turning back in its position, thus realizing effective collision avoidance and natural interaction.

VI. CONCLUSION

Motion-based games are different from conventiona l games in that the gamer can enjoy the game with whole body instead of with mere hands and eyes and they are getting established as the new trend in the field.

To produce the motion based serious game, the paper divides and analyzes the movement are of the gamer, extracts the movement information through visual information of each frame and suggests the algorithm which can control the effective movement paths for the virtual object which is the enemy character. For verification, the motion based serious game(first-person action game) has been made and experiments have been done by changing the movement information which includes the current position of the VH and the gamer position. The experiments have verified the validity of the proposed algorithm. Especially, when the movement information and the movement information of the VH are in the same direction, the VH can do the standing jumps while keeping getting the movement information to find the next path or turning back, realizing interesting interactions with the gamer. In addition, through rapid raising and horizontal acceleration of the VH, the gamer has been induced to move more. The proposed algorithm could be used as the basic materials for producing the motion base serious games using webcam.

REFERENCES

[1] Youngjae Lee, Daeho Lee, Sang-Bong Yi, "Motion Baesd Serious Game Using Spatial Information of Game Web-cam", Marine Information Paper Collection Book 13, No.9, 2009,pp1795-1802

[2] Youngjae Lee, Daeho Lee, "Feature map for detecting collision in motion-based game by using web camera", Marine Information Paper Collection Book 12, No.4, 2008, pp620-626

[3] Sumi Jee, Study on increasing sense of reality in motion-based game, Gwangun University, 2006, Thesis for Master's Degree

[4] Daeho Lee, Youngjae Lee, Estimation of collision response between virtual and arbitrary-shaped real objects, IEICE Electronics Express, Vol.5 No.17, 2008, pp.678-682

[5] Jiyoung Park, Kichan Kim, Jungwoo Park, Junho Lee, "Motion-based boxing game based on computer vision technology", Research Paper Collection, Sungkyungwan University(science and technology section), Book 53. No. 2, 2002, pp.35-51

[5] Kang,Wonhyung, Handheld Augmented Reality Game System Using Dynamic Environment, KAIST, 2007, mater thesis

[6] Haerin Kim, Hejung Jang, Sungho Park, "Research on tangible inferface design in motion-based game", 2004 HCI Academic Seminar Paper Collection Book 2, 2004, pp413-419

[7] Samha Choi, Kyungshik Kim, Sungjun Yoon, "Analysis of motion-system application in online games" Korea Game Society. Thesis Collection. Book 4, No. 2, 2004, pp1-8

[8] Kim,SangHyun, Windows API , Ganamsa, 2004

Calculation of Arm Parameter for Surface Scanning with Axis Moment

Jae-Chan Jeong
University of Science and Technology, 113 Science Street, Yusong-Gu, Daejon 305-333, South Korea
(Tel : 82-42-860-6116; Fax : 82-42-860-6790)
E-mail : channij@gmail.com
Dong-Doo Lee, Chang-Hwa Lee
ADMOTECH Inc., 1320 Gwanpyung-Dong Yusong-Gu, Dagjon 305-509, South Korea
(Tel : 82-42-936-1353; Fax : 82-42-936-1350)
E-mail : {ddlee, chlee}@admotech.com

Abstract : In this paper proposed about the system for measuring the diffusion of the electric wave in 3D space. The end-effecter having the Pan-tilt joint in the cartesian coordinate system robot was set up and it comprised of the robotic arm of 5 degree of freedoms. In an end-effecter, the sensor measuring the diffusion of the electric wave was set up.
In the cartesian coordinate system robotic section, it was comprised of the stepping motor. And the Servo Motor was used to an end-effecter.

Keywords : robot arm, electric wave

I. INTRODUCTION

In order to measures the diffusion shape of the electric wave, therefore, the elaborate position control of a sensor the electric wave measuring sensor has to measure repetitively on the determined location is necessary. In this paper, we propose the robotic arm for measuring the electric wave diffusion shape. However, a complexity and cost of a system are enhanced if the electric wave is diffused, it tries to measure by all directions, it takes precedence to measure in the limited domain.[1][2]

II. ROBOT ARM BASIC STRUCTURE

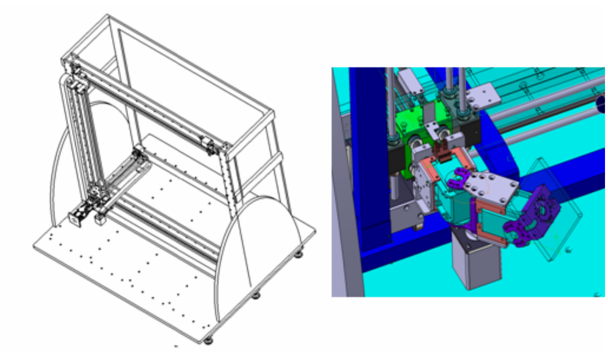

Fig.1. The configuration diagram of the robotic arm.

Fig.1 shows to be composed of the cartesian coordinate system robotic arm part and end-effector part. The cartesian coordinate system robotic arm part had 3 degree of freedoms. And it designed to operate with the stepping motor. An end-effector part has 2 degree of freedoms of Pan-tilt. And by using the Serve Motor, it is driven. Each physical spec is as follows. The robotic arm can move ± 400mm to the x-axis and ± 200mm to the y-axis and ± 400mm to the z-axis. In the Pan joint, the length to the tilt joint is 78mm. And the length to a sensor has 100m in the tilt joint.

III. CALCURATION OF ARM PARAMETER

The necessary parameter of the robotic arm for measuring the diffusion of the electric wave is the X,Y,Z value of the cartesian coordinates robot arm and The pan angle and tilt angle of the pan-tilt joint are needed.

In order to calculating each parameter, firstly the sender location is determined. The point for measuring the electric wave should be determined. A sender location assumes an origin in order to be simple. Each coordinates is moved after all calculations are completed.

First, the length to the pan-tilt joint is defined in a sensor as a l1. The length to a pan-joint is defined in a tilt-joint as a l2.

$$Pe = P + l_1 \times \frac{P}{|P|} \tag{1}$$

(1) The direction of Pe and P is the same . And the size of Pe is a l1.

$$\mathrm{Pan\_angle} = \mathrm{acos}\left(\frac{P_y \times Y_{axis}}{|P_y| \times |Y_{axis}|}\right) \tag{2}$$

$$\mathrm{Tilt\_angle} = \mathrm{acos}\left(\frac{P_z \times Z_{axis}}{|P_y| \times |Y_{axis}|}\right) \tag{3}$$

The Pan angle can calculate as the interval angle between the Py (projection with Y-axis P) and the Y-axis. And it can calculate the Tilt angle with the interval angle between the Pz (projection with Z-axis P) and the Z-axis.

$$\mathrm{Pe2} = [0\ l_2\ 0\ 1] \times \mathrm{Rot}(Z,\alpha) \times T(\mathrm{Pe}) \tag{4}$$

$$\mathrm{Rot}(Z,\alpha) = \begin{bmatrix} C(\alpha) & -S(\alpha) & 0 & 0 \\ S(\alpha) & C(\alpha) & 0 & 0 \\ 0 & 0 & 1 & 0 \\ 0 & 0 & 0 & 1 \end{bmatrix} \tag{5}$$

$$T(P) = \begin{bmatrix} 1 & 0 & 0 & P_x \\ 0 & 1 & 0 & P_y \\ 0 & 0 & 1 & P_z \\ 0 & 0 & 0 & 1 \end{bmatrix} \tag{6}$$

By substituting calculated Pe and the Pan angle for (4) and using a ratation and parallel movement about the Z-axis, Pe2 is calculated.[4]

$$\mathrm{Pe3} = [0\ l_3\ 0\ 1] \times T(\mathrm{Pe2}) \tag{7}$$

Pe3 can calculate through Pe2.

Finally, P, Pe, Pe2, and Pe3 are obtained after the transformation matrix defined in (6) is used in order to move as a sender given location.

IV. SIMULATION

By using Matlab, it simulated in order to verify whether it operated normally with the proposed numerical formula or not.

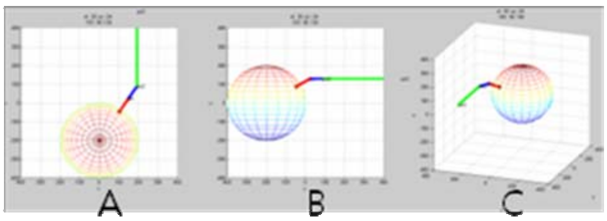

Fig.2. Matlab Simulation

The center of a globe is the transmission unit of the electric wave. An end-effect can confirm the features pointing to the center of a globe.

.

VI. CONCLUSION

In this paper, 5 frees for measuring the diffusion of the electric wave were proposed about the method calculating the parameter of the joint of the robotic arm. We used a rotation and translation transform in order to calculate each joint. The task implementing HW of the robotic arm was not concluded and it simulated through a matlab but it outputted visually to calculate the parameter of the joint. It confirmed to operate normally. Presently, it remains as the subject of front to confirm whether it normallies operate by applying the parameter calculated to the implemented robotic arm or not.

REFERENCES

[1] Nicolescu, G. (2000), Multilanguage Design of a Robot Arm Controller: Case Study. WVLSI'00.P29

[2] Zhang, S., Huang, P.S. (2006), High-resolution, real-time three-dimensional shape measurement. Optical Engineering, 45 (12), art. no. 123601

[3] Pauly, M., Mitra, N.J., Giesen, J., Gross, M., Guibas, L.J.(2005) Example-Based 3D Scan Completion. Proc. Eurographics symposium on Geometry processing, p. 23.

[4] Saeed B. Niku (2002), Introduction to Robotics Analysis, System, Applications

Development of Interactive Wireless AMR with Distribution Automation System

Chang-Hwan Yoon, Dong-Doo Lee, Chang-Hwa Lee

ADMOTECH Inc, 1320 Gwanpyung-Dong Yusong-Gu, Dagjon 305-509, South Korea
(Tel : +82-42-936-1353; Fax :+82-42-936-1350)
E-mail : {chyoon, ddlee, chlee}@admotech.com

Abstract : Recently WSN has become one of the most interesting ubiquitous networking technologies and its application for the AMR is rapidly growing. To introduce this concept, interactive wireless automatic meter reading node integrated with distribution automation system has been developed in the ADMOTECH Inc.. In our developed system, wireless communication is based on IEEE 802.15.4 and half duplexer interactivity is implemented. Our prototype can handle up to 75 AMR nodes and can be easily extended to larger scale for interactive meter reading application. This paper presents the conceptual structure of system layout and shows details of physical hardware, communication protocols and UI. Furthermore, our system is capable of measure, record various data - such as energy consumption, power factor and additional parameters - and control electric load operation.

Keywords : AMR, Interactive, Automation.

I. INTRODUCTION

Traditionally, the electricity meters are installed on consumer's premises and the consumption information is collected by meter-readers on their fortnightly or monthly visits to the premises. This method of gauging electricity consumption has the following disadvantages:[1]

(i) Sometimes the meters are installed inside people's homes and, if the consumer is not at home, the meter-reader cannot record the fortnightly or monthly consumption and then the utilities' company has to resort to considering the average bill-amount of the previous months as an indicator of the likely consumption for the current month. This results in burden for both consumer and the electricity supply company. May be the consumer has not utilized similar amount of electricity in the current month as in the previous months for reasons such as, holidaying elsewhere or being in the hospital, etc. during the month, and sending him a bill for a larger amount based on his history of electricity consumption may result in his/her financial hardship. This method of billing is also not suitable for the electricity supply company because it gives inaccurate account of the overall electricity consumption in the consumer's area and may ultimately result in errors in future planning by the company.

(ii) Hiring of a number of meter-readers by utilities' companies and providing means of transportation to them is an expensive burden on the companies' budgets. Moreover, these visits of the meter readers to consumers' premises generate pollution in the air which has negative impact on the environment and the greenhouse effect.

(iii) Dissatisfaction of some customers who consider meter-readers' entrance to their homes as some sort of invasion of their privacy. This is especially applicable in countries, like Oman, where during the day most men are outside of their homes earning a living and only women are at home doing the housework.

In order to overcome these disadvantages of the traditional meter reading system, efforts are underway around the world to automate meter reading and to provide comprehensive information to the consumer for efficient use of the utilities[2,3,4].

This paper is organized as follows: In Section II, detailed design of 3-phase Electric power meter module has been presented. This is followed by IEEE 802.15.4 wireless interface and its implementation explained in Section III. Distribution Automation System are given in Section IV which are followed by conclusion in Section V.

II. 3-PHASE ENERGY MEASURING

The block-diagram of a 3 phase meter developed is shown in Fig. 1. The meter can be used in a 3 or 4 wires system and is capable of performing the following measurements.

. Apparent energy (kVA) . Active energy (kWHr)

. Power factor (0-1.0) . Phase voltages (Vrms)

. Phase currents (Arms) . Reactive energy (kVarHr)

The line voltages and line currents are sensed and properly scaled by voltage dividers and current transformers to within the operating ranges (2V approximately) of the measurement unit. These scaled voltages and currents are then sampled by the energy measuring circuit which performs 16-bits Delta-Sigma A/D conversion and calculates all energy

Such a 16-bits digitization resolution of voltages and currents in the energy measuring circuit gives the meter an accuracy of class 0.5 that guarantees less than 0.5% error – as shown in figure 2 (the calibration setup) - through a wide range of voltage, current and power factor. These data are then read from the energy measuring circuit by the embedded-processor(EPU) which also performs appropriate energy collection, updates real-time clock, displays the energy data on an LCD panel and controls two communication devices, i.e. IEEE 802.15.4 standard PHY chip.

This meter also has a battery back-up system using a CR-2032 type 1.5V coin cell. When there is a power failure, the brown-out detector unit in the EPU will automatically inform the EPU to shut down all units except the time keeper and store all important energy data in the battery back-up Flash RAM. During this time, the EPU is put into sleep mode and the total current consumed from the back-up system is kept minimum at 800nA or less.

III. THE ZIGBEE RF HARDWARE

In our prototype design, we adopt the IEEE 802.15.4 standard compliant transceiver CC2520 from Texas Instruments. CC2520 provided IEEE802.15.4 PHY hardware for 2.4GHz/Zigbee.

The CC2520 also includes digital RSSI/LQI (Receive Signal Strength Indicator/Link Quality Indication) support and 12-bit ADC (Analog-to-Digital Converter) with up to eight inputs and configurable resolution.

Powerful USARTs with support for several serial protocols. Combined with the Zigbee protocol stack (Z-Stack) supported from TI. 2520EM board is used to develop the initial state proto-type system.

The data gathering/collection approach may be carried out on a cluster-based, tree constructive based network.

The selection of appropriate network organization depends on the physical location of AMR nodes and the data features. In addition, distributed data compression and aggregation method may be implemented to improve the efficiency of data gathering.

The software is developed using IAR Embedded Workbench EW430 based on TI's Z-stack.

The ZigBee RF hardware in this system has the following features:

- Operating frequency : 2.4GHz, ISM band
- Antenna : mono-pole, chip type (selectable)
- Transmit power : 0dBm ±3 dB
- Receiver Sensitivity : -92 dBm
- Coverage(Radius) : 30m (indoor), 100m (outdoor)
- Maximum Data Rate : 250 kbps
- Internal packet memory : 127 Bytes
- Data interface : SPI for Energy Circuit, serial to DM
- Serial data rate :1200-115200 bps
- Channels : 16 Direct Sequence channel
- Addressing Options : PAN ID, Channel and Addresses

It is natural to set the data packet format in the communication channel according to ANSI C12.18 regulation since this is already used for the optical reading. Hence the same application layer used in the infrared system is also implemented for the RF system. Each data packet consists of the following fields.

IV. DISTRIBUTION AUTOMATION SYSTEM

Distribution automation system(DAS) is PC based AMR data management automation platform. [Fig. 4]

This system consists of developing layer for which both development and execution is enabled as well as execution layer for which only execution is enabled.

Each layer type has at least 75 point products based on the number of the real AMR nodes. Designed as the open system architecture, it can not only satisfy various special needs of users, but also provide system interfaces with other software systems. Features of the open system architecture of DAS considered in its design include OLE automation, ODBC, VB script, OCX, etc.

User programs operable inside DAS can be created using script language. User can apply various functions without special training since VB script language is supported. With the use of the internal functions of DAS in addition to the general functions provided by VB Script, whole systems can be controlled in more various ways.

Using ODBC, DAS can be freely connected to various general purpose DB servers. Since standard Structured Query Language is supported, all DB applications including record inquiry, modify, add, and delete functions can be implemented.

DAS can be connected various networks such as RS232C/422, LAN and wireless communication and it supports the standard protocol such as OPC and MODBUS. Therefore DAS can communicate with most PLCs. [Fig. 5]

Table 1 illustrates the summarized our system specifications

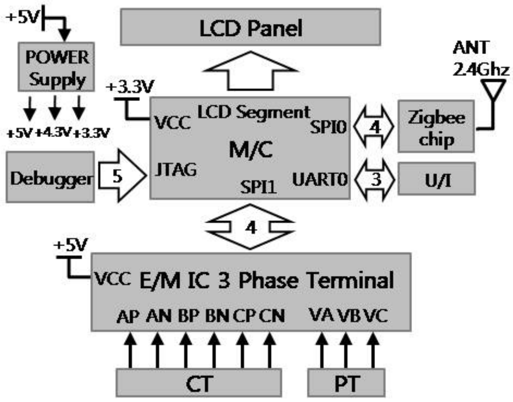

[Fig. 1] The internal hardware architecture of the AMR

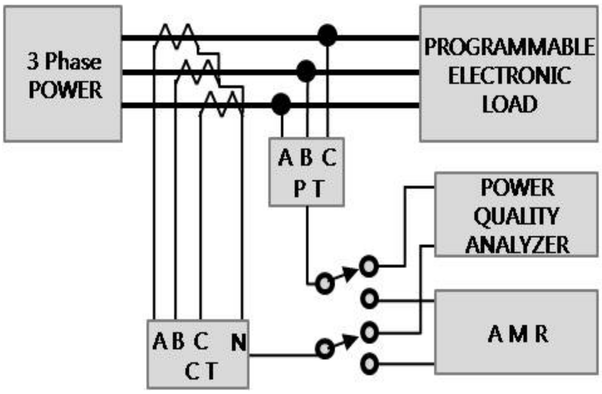

[Fig. 2] Block diagram of calibration setup.

[Fig. 3] Precision analysis based on commercial equipment.

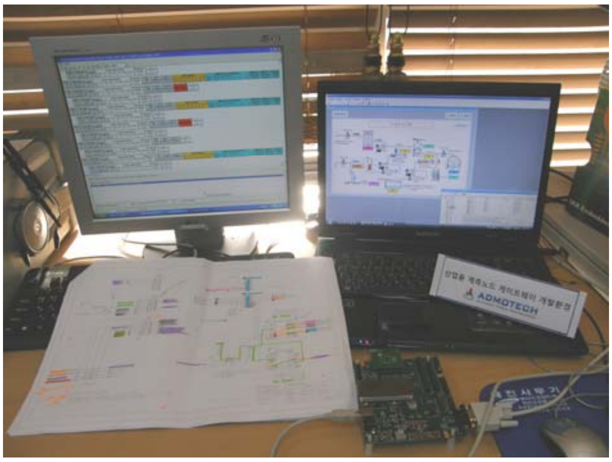

[Fig. 4] Developing layer environment of DAS.

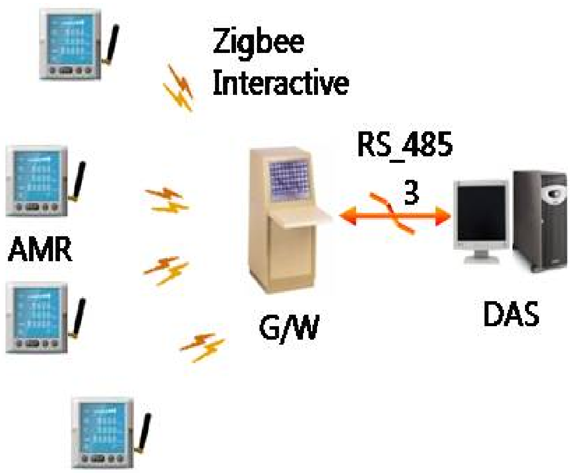

[Fig. 5] Block-diagram of interactive wireless AMR

[Fig. 6]. A 1 day energy profile plot

<Table 1> Specifications of wireless AMR

Item		AMR
Wire connection		3P3W or 3P4W
Network		ZigBee wireless Network.
Electric parameters		V, A, W, Var, VA, PF, Hz, WH, etc.
Conversion Rate		1 / sec.
CT, PT Ratio		1 ~ 9999
Power Supply		AC 110~220V, 50/60Hz
Input	Current	0 ~ 100A or external CT
	Voltage	0 ~ 600V
	Frequency	45~65 Hz
Communication		RS232 or RS-485 and Zigbee

V. CONCLUSION

A prototype interactive wireless 3- phase AMR with a ZigBee 2.4GHz RF unit and DAS is developed. This system will be suitable for an industrial plant as it can measure and accumulate active energy, reactive energy, apparent energy. Its distinctive feature is the ability to interactively communicate with a remote management DAS server using 2.4GHz band IEEE 802.15.4 standard wireless media.

ACKNOWLEDGEMENTS

The work developed in this paper has been supported by the DAEDEOK INNOPLIS ("R&D Hub Cluster project").

REFERENCES

[1] Tariq Jamil, "Design and Implementation of a Wireless Automatic Meter Reading System" *Proceedings of the World Congress on Engineering 2008 Vol I,* WCE 2008, July 2 - 4, 2008, London, U.K.

[2] T. Whittaker, "Final word," *IET Control and Automation*, Vol. 18, No. 3, June/July 2007, p. 48.

[3] M. Venables, "Smart meters make smart consumers," *IET Engineering and Technology*, Vol. 2, No. 4, April 2007, p.23.

[4] C. Brasek, "Urban utilities warm up to the idea of wireless meter reading," *The IEE Computing and Control Engineering*, Vol. 15, No. 6, December/January 2004/05, pp. 10-14.

Improved SNTP for Accurate Time Synchronization in Smart AMR systems

Se-Young Oh, Dong-Doo Lee, Chang-Hwa Lee

ADMOTECH Inc, 1320 Gwanpyung-Dong Yusong-Gu, Dagjon 305-509, South Korea
(Tel : 82-42-936-1353; Fax : 82-42-936-1350)
E-mail : {syoh, ddlee, chlee}@admotech.com

Abstract : In distributed sensor network such as distributed AMR system, accurate time synchronization is necessary to assure the concurrence of event timing for measured data. There are NTP(Network Time Protocol) and SNTP (Simple Network Time Protocol), RBS (Reference Broadcast Synchronization), TPSN (Time synchronization Protocol for Sensor Networks) in time synchronization for distributed network systems.

In this paper, we suggested improved SNTP using precise meta data exchange and agile interrupt handling techniques and showed that our method has accuracy of sub-millisecond compared to conventional SNTP with accuracy of few second from the time synchronization performance analysis results.

Keywords : Time Synchronization, SNTP

I. INTRODUCTION

As in distributed sensor network such as distributed AMR systems, accurate time synchronization is necessary to assure the concurrence of event timing for measured data.

There are two main purposes of time synchronization.

The first purpose is to ensure that events occur on time, in the correct sequence. Therefore, synchronization is necessary to start scheduled events and to register their occurrence. Many activities in commerce, banking, financial, business, transport, medicine, services, as a few examples, may need to guarantee that tasks are timely scheduled, and concurrent and cooperating processes interoperate correctly. The second purpose is tracing, that is, retrieving information concerning past events, whenever is necessary, regarding when the events occurred and in what sequence. This task is possible only if accurate timestamps of each event are available.

In this paper, we suggested improved SNTP using precise meta data exchange and agile interrupt handling techniques and showed that our method has accuracy of sub- millisecond compared to conventional SNTP with accuracy of few second from the time synchronization performance analysis results.

II. OVERVIEW[2]

All network time synchronization methods rely on some sort of message exchange between nodes.

Non-determinism in the network dynamics makes the synchronization task challenging in many systems.

When a node in the network generates a timestamp to send to another node for synchronization, the packet carrying the timestamp will face a variable amount of delay until it reaches and is decoded at its intended receiver. This delay prevents the receiver from exactly comparing the local clocks of the two nodes and accurately synchronizing to the sender node. We can basically decompose the sources of error in network time synchronization methods into basic components:

☐ Send Time: This is the time spent to construct a message at the sender. It includes the overhead of operating system, and the time to transfer the message to the network interface for transmission.

☐ Access Time: Each packet faces some delay at the MAC layer before actual transmission. The sources of this delay depend on the MAC scheme used, but some typical reasons for delay are waiting for the channel to be idle or waiting for the TDMA slot for transmission.

☐ Propagation Time: This is the time spent in propagation of the message between the network interfaces of the sender and the receiver.

☐ Receive Time: This is the time needed for the network interface of the receiver to receive the message and transfer it to the host.

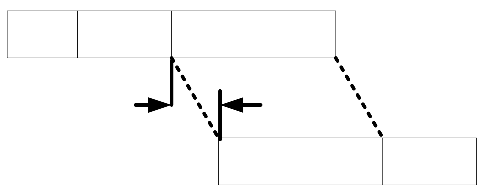

[Fig. 1]. Message delivery delay

a. The Need For Synchronization in Sensor Networks

There are several reasons for addressing the synchronization problem in sensor networks.

First, sensor nodes need to coordinate their operations and collaborate to achieve a complex sensing task. Data fusion is an example of such coordination in which data collected at different nodes are aggregated into a meaningful result. For example, in a vehicle tracking application, sensor nodes report the location and time that they sense the vehicle to a sink node which in turn combines these information to estimate the location and velocity of the vehicle. Clearly, if the sensor nodes lack a common timescale (i.e., they are not synchronized) the estimate will be inaccurate.

Second, synchronization can be used by power saving schemes to increase network lifetime. For example, sensors may sleep at appropriate times, and wake up when necessary. When using power-saving modes, the nodes should sleep and wake-up at coordinated times, such that the radio receiver of a node is not turned off when there is some data directed to it. This requires a precise timing between sensor nodes.

b. Reference Broadcast Synchronization (RBS)

Reference Broadcast Synchronization (RBS) [3], where their simple yet novel idea is to use a "third party" for synchronization, their scheme synchronizes a set of receivers with one another.

In RBS scheme, nodes send reference beacons to their neighbors. A reference beacon does not include a timestamp, but instead, its time of arrival is used by receiving nodes as a reference point for comparing clocks.

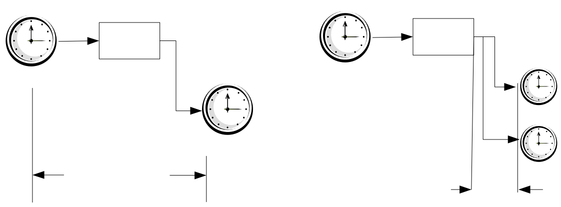

[Fig. 2] Comparison of conventional method to RBS

The authors argue that, by removing the sender's non-determinism from the critical path [Fig. 2], RBS achieves much better precision compared to traditional synchronization methods that use two-way message exchanges between synchronizing nodes. As the sender's non-determinism has no effect on RBS precision, the only sources of error can be the non-determinism in propagation time and receive time. The authors claim that a single broadcast will propagate to all receivers at essentially the same time, and hence the propagation error is negligible. This is especially true when the radio ranges are relatively small, as is the case for sensor networks. So they only account for the receive time errors when analyzing accuracy of their model.

In the simplest form of RBS, a node broadcasts a single pulse to two receivers. The receivers, upon receiving the pulse, exchange their receiving times of the pulse, and try to estimate their relative phase offsets. This basic RBS scheme can be extended in two ways:

1) allowing synchronization between n receivers by a single pulse, where *n* may be larger than two,

2) increasing the number of reference pulses to achieve higher precision. The authors show by simulation that 30 reference broadcasts (for a single synchronization in time) can improve the precision from 11 μs to 1.6 μs

c. Timing-Sync Protocol for Sensor Networks (TPSN)

Timing-Sync Protocol for Sensor Networks (TPSN) [4] works in two phases: level discovery phase" and synchronization phase". The aim of the first phase is to create a hierarchical topology in the network, where each node is assigned a level. Only one node is assigned level 0, called the root node. In the second phase, a node of level i synchronizes to a node of level $i-1$. At the end of the synchronization phase, all nodes are synchronized to the root node and the network-wide synchronization is achieved.

Consider a two-way message exchange between nodes A and B as shown in [Fig.3]. Node A initiates the synchronization by sending a synchronization pulse packet at $T1$ (according to its local clock). This packet includes A's level number, and the value $T1$.

B receives this packet (according to its local clock) at $T2 = T1 + \Delta + d$, where Δ is the relative clock drift between the nodes, and d is the propagation delay of the pulse. B responds at time $T3$ with an acknowledge-ment packet, which includes the level number of B and the values $T1$, $T2$, and $T3$. Then, node A can calculate the clock drift and propagation delay as below, and synchronize itself to B.

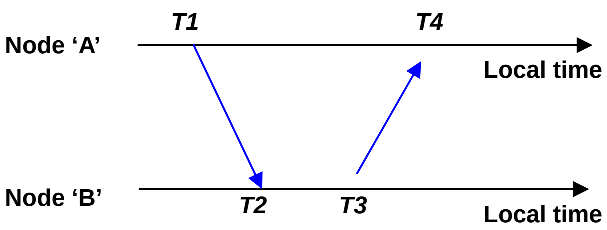

[Fig. 3] Two way message exchange between a pair of nodes

$$\Delta = \frac{(T2 - T1) - (T4 - T3)}{2}; \qquad \text{Eq. 1.}$$

$$d = \frac{(T2 - T1) + (T4 - T3)}{2}; \qquad \text{Eq. 2.}$$

The synchronization phase is initiated by the root node's time sync packet. On receiving this packet, level 1 nodes initiate a two-way message exchange with the root. Before initiating the message exchange, each node waits for some random time, in order to minimize collisions on the wireless channel. Once they get back a reply from the root node, they adjust their clocks to the root node. Level 2 nodes, overhearing some level 1 node's communication with the root, initiate a two-way message exchange with a level 1 node, again after waiting for some random time to ensure that level 1 nodes have completed their synchronization. This procedure eventually gets all nodes synchronized to the root node. TPSN is implemented on Berkeley's Mica architecture, and makes use of time-stamping packets at the MAC layer in order to reduce uncertainty at sender. Ganeriwal et.al. claim that TPSN achieves two times better precision than RBS. They state that the precision of 6.5 μs .

d. Requirements on the Synchronization Schemes for Sensor Networks

There are trade off between the requirements of an efficient synchronization solution (e.g., precision versus energy efficiency), thus a single scheme may not satisfy them altogether.

□ Energy Efficiency : As with all of the protocols designed for sensor networks, synchronization schemes should take into account the limited energy resources contained in sensor nodes.

□ Scalability - Most sensor network applications need deployment of a large number of sensor nodes. A synchronization scheme should scale well with increasing number of nodes and/or high density in the network.

□ Precision - The need for precision, or accuracy, may vary significantly depending on the specific application and the purpose of synchronization. For some applications, even a simple ordering of events and messages may suffice whereas for some others, the requirement for synchronization accuracy may be on the order of a few μs .

□ Cost and Size - Wireless sensor nodes are very small and inexpensive devices. Therefore, as noted earlier, attaching a relatively large or expensive hardware on a small, cheap device is not a logical option for synchronizing sensor nodes. The synchronization method for sensor networks should be developed with limited cost and size issues in mind.

III. CONFICURATION

In Smart AMR system we would like to assure the concurrence of event timing for measured data within milliseconds. Concerning the trade-off no hardware and bandwidth added to basic PHY.

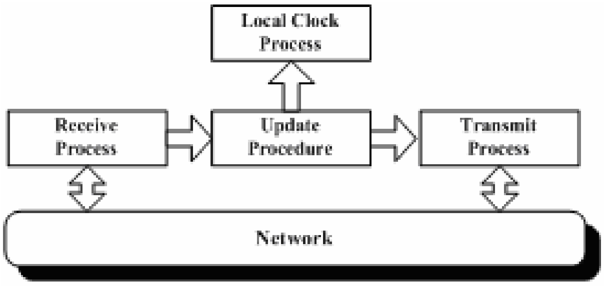

[Fig 4] Implementation Model

Followings are major component consist of our system configuration.

- Two-way time transfer algorithm
- One millisecond counting RTC
- Agile interrupt handler
- Simple moving average digital filter

The moving average is the most common digital filter to understand and use. In spite of its simplicity, the moving average filter is optimal for a common task: reducing random noise while retaining a sharp step response. This makes it the premier filter for time domain encoded signals.

As the name implies, the moving average filter operates by averaging a number of points from the input signal to produce each point in the output signal. In equation form, this is written:

$$y[i] = \frac{1}{M} \sum_{j=0}^{M-1} x[i+j] \qquad \text{Eq. 3.}$$

Where $x[]$ is the input signal, $y[]$ is the output signal, and M is the number of points in the average.

IV. ANALYSIS

[Fig. 5] shows the effect of how this works reduce timing fluctuation. The signal colored yellow is timing raw data. The other color's plots show moving averaged result, the smoothing action of the moving average filter decreases the amount of the random time variance. The amount of noise reduction is equal to the square-root of the number of points in the average. For example, a 100 point moving average filter reduces the noise by a factor of 10.

[Fig. 6] and [Fig. 7] show probability density function for simple moving average and square weighted moving average respectively.

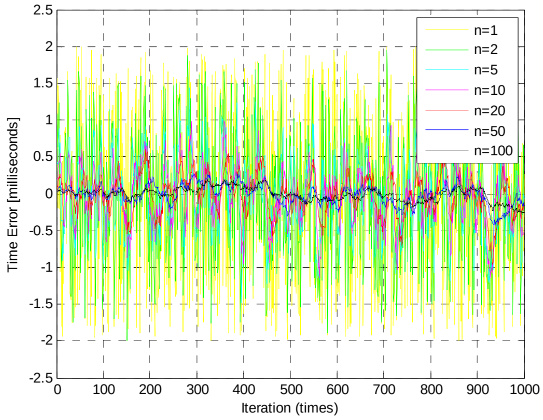

[Fig. 5] Time Synchronization error smoothing characteristics for variable average numbers.

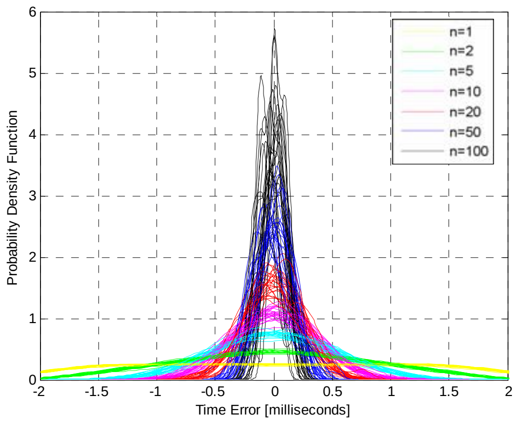

[Fig. 6] Probability density function for simple moving average

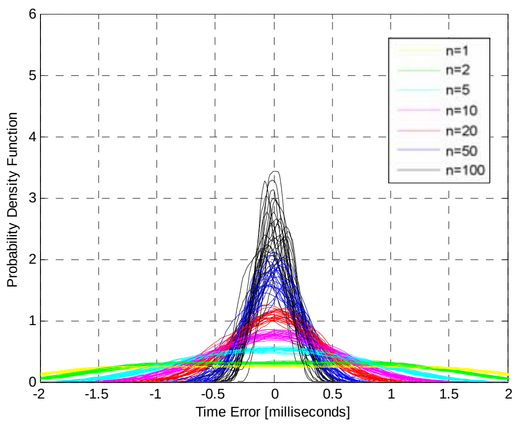

[Fig. 7] Probability density function for square weighted moving average

V. CONCLUSION

There are trade off between the requirements (eg. Energy Efficiency, Precision, Cost and Size). We constructed improved SNTP using precise meta data exchange and agile interrupt handling techniques with simple moving averaging algorithm. It shows 0.48 millisecond jittering performance is obtained with 100 points in the average.

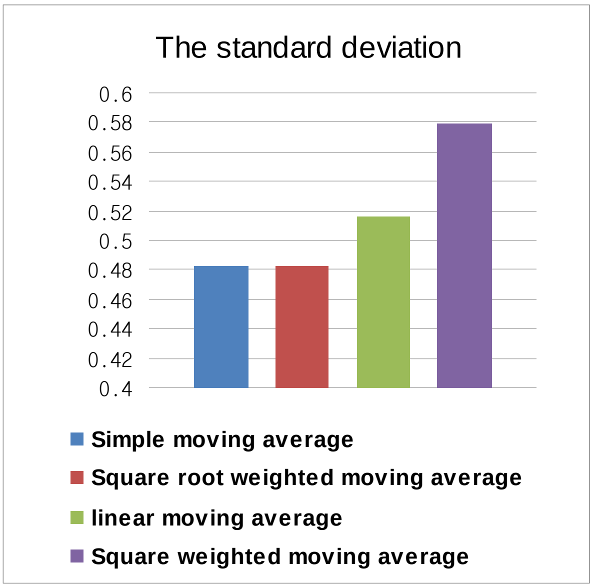

[Fig. 8] Jittering Characteristics
Standard deviation vs. averaging algorithm

ACKNOWLEDGEMENTS

The Work developed in this paper has been supported by the DAEDEOK INNOPLIS ("R&D Hub Cluster project").

REFERENCES

[1] Cristina D. Murta, Pedro R. Torres-Jr., "Characterizing Quality of Time and Topology in a Time Synchronization Network"

[2] Fikret Sivrikaya et. al., "Time Synchronization in Sensor Networks: A Survey" IEEE In Network, IEEE, Vol. 18, No. 4. (2004), pp. 45-50.

[3] J. Elson, L. Girod, D. Estrin, \Fine-Grained Time Synchronization using Reference Broadcasts", Proceedings of the Fifth Symposium on Operating Systems Design and Implementation (OSDI 2002), Boston, MA, December 2002.

[4] S. Ganeriwal, Ram Kumar, M. Srivastava, \Timing Sync Protocol for Sensor Networks", ACM SenSys, Los Angeles, November 2003.

[5] D. Mills, Simple Network Time Protocol (SNTP) Version 4 for IPv4, IPv6 and OSI, University of Delaware, 1996

[6] Steven W. Smith, "The Scientist and Engineer's Guide to Digital Signal Processing" Second Edition, California Technical Publishing, San Diego, 1999, *pp 277-279*

Personal Color Decision System Using Fuzzy Logic [1]

JungMin Oh, Min-Seok Hong, Jin-Taek Kim, Do-Won Lee,
Choul-Woong Son, Geuk Lee
Dept.of Computer Engineering, Hannam University, Korea
E-mail : mindein@hotmail.com, ycy824@gmail.com, kkotda@gmail.com,
skyinfriends@gmail.com, sincleo@nate.com, leegeuk@hnu.kr

Abstract

This paper, which is based on the research in the personal color diagnosis system, uses the fuzzy logic. We propose the method which constructs more systematic color selection system using personal color database and fuzzy logic. This paper will refer to this system as FPCS (Fuzzy logic Personal Color System). The FPCS program proposed in this study is able to produce rapid and accurate results without the complex processes of existing color diagnosis therefore it is convenient and can save time and money.

Keywords: Personal Color System , Fuzzy Logic

1. Introduction

The color diagnosis system that is currently being used universally mainly uses the draping method of using color diagnosis fabric which is done by a trained color analyst along with a basic questionnaire.

However, because the basis of diagnosis has not yet been unified and the diagnosis is done based on the subjective view or unclear data of the person conducting the diagnosis, the probability of an incorrect analysis is significant.

When season color type is decided based on improper analysis, its feasibility test also becomes difficult, decreasing reliability of the decision and its accuracy.

This study, as a way for improving such problems, aims to present a more accurate and specific color diagnosis rules through a test applying the Fuzzy logic based on data gathered from the first questionnaire program. In addition, increase of objective objectivity was also intended by analyzing and certifying the designed and realized program.

1.2. Scope of study

This study computed the membership degree of RGB values for each body color of individuals and used objective data as its basis by defining the fuzzy membership function whose style used in this study was a non parametric estimation method using the nearest neighbor algorithm.

The validity of FPCS was secured through a validation test by a professional, which in this study was the χ^2 test.

2. Related Studies

2.1. personal color

The personal color system as the study of systematization already from the West Europe long time ago, was introduced in Japan since about 20 years[1].But In our country, recently the research to be advanced by some specialists, is tendency of revitalization with supplying in rapid pace as the interest of multitude is concentrated.

Johannes Itten, the professor, and the scholar of the color of the Bauhaus, as the synthetic moulding school in Germany, has found that the preference color of the students is related to their unique color, namely, the color of skin, hair, eyes etc. as their own, and paid attention to the relationship between the appearance and the subjective view of chromatic in 1928, It is becoming known as the beginning of color analysis[2].

Our human body show each different skin color like some people are yellow, another are more red than the others, and some people are darker than the others etc. for effect of 3 kinds of pigments like carotene, the hemoglobin and the melanin[3].

The personal color is decided with proper color which

[1] This work was supported by a grant from Security Engineering Research Center of Ministry of Knowledge Economy & supported by second stage of the Brain Korea21 project.

individual keeps, namely, the color of skin, hair, eyes, etc. among those 3 elements, the skin color became the most important element. (Table1. 1 explains the point of reference like this).

The personal color is made by the 4 seasonal color analysis as the spring, summer, autumn, winter which is harmonized with each personal proper body color after diagnoses the proper color which individuals were born, especially it classifies 4 seasonal color types with dividing color of skin, hair, eyes.

All of colors could be divided with cold color and warm color, the basic background color of pattern of spring, autumn is yellow and gold color as warm color, it has the feeling of movement, clearness, deepness, elegant, and the basic background color of pattern of summer, winter is blue, black color, and it has the images of soft, thickness, romanticism, clearness, urban, dynamic image [3].

The skin color of the human being is accomplished with 3 kinds of pigments, namely, melanin, hemoglobin, and carotene, generally the black race has more melanin, the white race has more hemoglobin, and the yellow race has more carotene contents compared to the other pigments, and the thing that the each skin color is shown differently though same race is the result following to the component ratio of these 3 kinds of pigments[4].

Our skin could be divided in 2 types largely, as warm type skin of ivory, yellow, copper color, and gold and cool type skin of white, pink, red, and blue[5].

Cool color means the color which includes white, blue, black in every color.

Especially the color which includes white and blue is called summer type color, and the color which includes blue and black is called winter type color.

Warm color is the color which includes yellow and gold in every color. Especially the color which yellow is basic background color, is called spring type color, and yellow and gold become a basic background color that is called autumn color. [5].

(Table1. Cool class color & warm class color)

Colors of cool class	Colors of warm class
The bright skin which with color is lingering	Bright yellowish skin
The middle tone skin which is canescent color	Yellowish skin of middle tone
The skin which is little bit red and canescent.	Yellowish skin which red tint is lingering.
The dark tone skin which is canescent	Yellowish skin which brown color is lingering.
Uran, cold, sharp image	Warm, healthy, familiar image

Because of the skin color of spring type people is yellowish, transparent and thin, it's the type which the spots like freckle could be appeared in the face easily. The eyes color is yellowish, the hair wears the light brown color. The image of the spring person is bright and vivid so there are many style which looks younger than age and cute. .

The skin color of summer type person is white and green light goes round or the pink light circles round, and does not burn well in the sun and to be red. The eyes color is the soft brown, the hair is the brown which wears gray and is a dry lackluster type. The image of summer type is somewhat cold, romantic and feminine.

The skin color of autumn type person is yellowish, lackluster and white-livered. It's easy to be burn in the sun, the face color changes to brown easily. The hair is lackluster dark brown, eyes color is umber which gives peaceful and fluffy. The image of the autumn person is warm and soft which gives intimate and comfortable feeling, it has natural and classic image

The skin color of the winter type person is cold and pale, the eyes and hair color is deep gray-brown or black so it's contrasted with white skin and gives polished image. The image of the winter person is cold and intense, keeps the intellectual impression.

2.2 Use of Personal Color

When the 4 season color image classification approach is observed, it is closely related to color image scale [6].

The 4 season image classification and color image scale classification have very similar in their logical connection.

Their only different characteristic is the difference in the concept of warm colors and cool colors. The color image scale classifies red tones as warm colors and blue tones as cool colors, and in contrast, the 4 season colors view all colors to have warm shades and cool shades.

In other words, in the color red, there is a warm red to which a yellow shade is added and a cool red to which a white tone is added. The same applies also for blue tones.

2.3 Images and harmonious colors of the 4 season type

• Spring type: Bright and cute

Representative colors of spring give off a warm feeling with yellow hues added in all colors.

Spring colors are clear and soft, and they are groups with high level of brightness and chroma, and include a broad range of colors.

(Fig.1 harmonious colors of the Spring type)

•Summer Type: Bright and elegant

All summer colors include blue and white colors. They give off a soft and cool feel, and include ranges of pink tones and pastel tones that do not clash. Types of colors are also somewhat diverse.

(Fig.2 harmonious colors of the Summer type)

•Autumn Type: Deep autumn tones

All autumn colors have yellow tones in them and therefore give off a warm feeling.

They are not glossy or shiny, and clothes that display the quality of the fabric project depth. .

There are many ranges of brown tones. They include golden yellow, and colors of fields, autumn forests, and autumnal tints.

(Fig.3 harmonious colors of the autumn type)

• Winter type: Classy and urban

Colors that represent winter are mostly blue tones and are colors that stand out with clarity. They include lemon yellow, blue green, indigo, deep blue, black, and wine.

(Fig.4 harmonious colors of the winter type)

2.4. Fuzzy Theory

Fuzzy is the theory which could appear fuzzy intellection of human being that couldn't divide with only dichotomy in the computer with mathematical function, as compared with the logic circuits of computer moves by the absolute standard like 0 and 1, this theory is the method which let the computer executes the thought, studying, self-development, etc. that the intelligence of the human being could do [7-8].

3. Fuzzy Logic Design

3.1 Data Collection

This system aims to statistically formulate a fuzzy logic based on data gathered from specialists.

In order to gather the necessary data, first questionnaire was conducted with 212 subjects in the age bracket of 20 - 50 years over 2 months, from August to September of 2008.

A total of 212 data were collected and the male to female ratio was 62 male respondents to 150 female respondents.

Of the gathered information, skin, hair, and eye colors were used and the diagnosis program was designed based on this collected data by determining the preference order of the 4 seasons (order by season).

3.2 Questionnaire

The program for the questionnaire was designed to determine the 4 ranks by selecting 1. basic characteristics, 2. skin factor check, 3. color mix.

3.3. Fuzzy Logic Design

The fuzzy function was defined by computing the membership degree of RGB value for each of skin, hair, and eye colors that determine the 4 season type and based on this, a fuzzy based personal color system was formulated and a more scientific and systematic color diagnosis method was presented. Determining season type

● **Season Type**

When skin, hair, and eye colors are each unique colors, the season type is predetermined.

Ex) when skin=(255, 233, 204), hair=(180, 154, 102), eye=(126, 93, 50), season type is "Spring"

A total of 9 dimensions are expressed by expressing three dimensionally(RGB) the color feature space for identification of season type with three colors.

Season types were marked as "Spring", "Summer", "Autumn", and "Winter."

$$Y : C \rightarrow t \quad C \in [0..255]^9 \quad t \in T = \{S, M, A, W\}$$

When physical colors of a specific person are skin =(255, 233, 204), hair=(180, 154, 102), and eye=(126, 93, 50), the fuzzy function determines the season type for the applicable physical colors as "Spring".

· ● **Calculation of Distance from Season Type**

The distance in feature space between colors of the predetermined season type and color in question is computed.

At this time, if more than two season types are predetermined, the distance to the nearest season type is defied as the applicable season type distance.

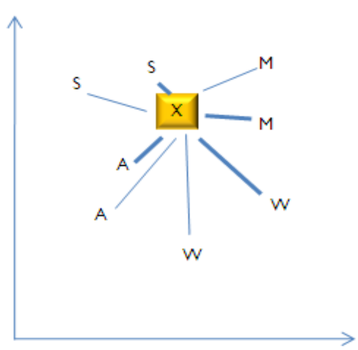

(Fig. 8 . Distance from Season Type)

$$D_T(x) = \min_{\{c_t^i | t=T\} \in C} dist(x, c_t^i)$$

Distance between (x) in question and applicable season(T)

Physical color of (x) in question

Physical color applicable to season in question among collected data

$dist(x, c_t^i)$ c_t^i: distance between one () among collected data and a specific physical color (x). It is defined as Weighted Euclidean Distance between the two points within the 9 dimensional feature space that express physical colors.

c_t^1 c_t^{212} c: Sum of all gathered data. When 212 data are collected, it will have a total of 212 elements from to .

$\{c_t^i | t = t^*\} \equiv C_{t^*}$ t^*: Partial sum containing data applicable to a specific season() among collected data (C). For example, when =S, among the collected data, those that responded "spring" as color preference are expressed.

$D_{t'}(x)$: Distance between physical color (x) of the person whose season type is to be diagnosed and the applicable season (t). For calculating the distance, Weighted Euclidean distances between physical color (x) and each data collected for applicable season in the feature space were computed and distance with the nearest neighbor was used.

$$dist(x, c_t^i) = \sqrt{\sum_{m=\{Skin,Hair,Eye\}} \left(\alpha_m \sum_{n=\{R,G,B\}} (x(m,n) - c_t^i(m,n))^2 \right)}$$

Physical area (Skin, hair, eye).

α_m α_{skin} α_{hair} α_{eye}: Weight by physical color. By determining the weight skin(), hair(), eye(), the weight each physical color takes up when determining the distance can be controlled differently.

$x(m,n)$ $c_t^i(m,n)$ c_t^i, : Among the specific physical color (x) and collected data, one color() signifies one dimension among each of the colors that is expressed in 9 dimensions (three color types and three RGB).

m signifies the type (among 3) of physical color, and n signifies one of RGB (among 3).

● Estimating Season Type for Query Color

Fuzzy membership function was designed by using the logic that the closer the distance between query color and season type sample in feature space, the higher the degree of membership will be.

Fuzzy membership function was used by fixing the reciprocal of distance with each season type as the sum of all reciprocals.

Also, a coefficient (α) that controls sensitivity was used to decrease the risk of the fuzzy membership function placing weight on a single specific sample.

$$p(t^* \mid C) = \frac{\left(\dfrac{1}{D_{t^*}(C)}\right)^{\alpha}}{\sum_{t \in T}\left(\dfrac{1}{D_t(C)}\right)^{\alpha}}$$

$p(t^*|x)t^*$: A fuzzy membership function for a single season type () for a specific physical color (x) of the individuals. Fuzzy membership function was used by expressing the reciprocal of the distance between each season type as the sum of all reciprocals.

Also, a coefficient () that controls sensitivity was used to decrease the risk of the fuzzy membership function placing weight on a single specific sample.

4. Experiment and Results Analysis

4.1 FPCS test

Fuzzy function style used in this test is the non parametric estimation using the nearest neighbor algorithm.

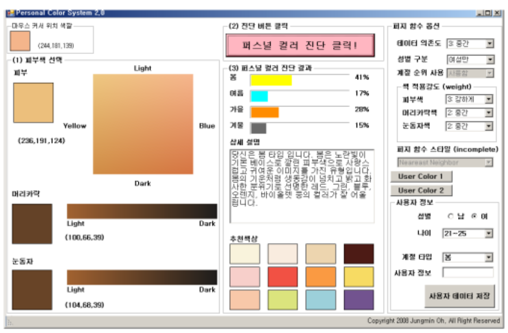

(Fig. 5. FPCS Simulation)

4.2. FPCS Results Analysis

Based on the logic that personal color elements, which are colors of the individual, are determined by skin, eye, and hair colors the following experiment was conducted in order to verify that skin color has discrimination in determining the color mix of the 4 season type by comparing those that were diagnosed by the FPCS system and the three elements that were diagnosed using their eyes.

For FPCS system test analysis, Leave-one-out Cross-Validation technique was used[9].

This is a verification method of using each collected sample in the training set with the exception of the applicable sample.

The result of analysis using this method revealed that when distribution of skin color by 4 season types is observed, skin color distribution is grouped uniformly based on the person's season type as seen below.

(Table 3.Skin color distribution by season type)

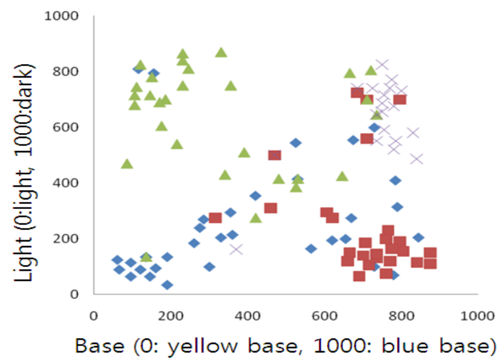

The horizontal axis signifies the base color, and the vertical axis signifies brightness.

(Table 4. Accuracy of season type diagnosis)

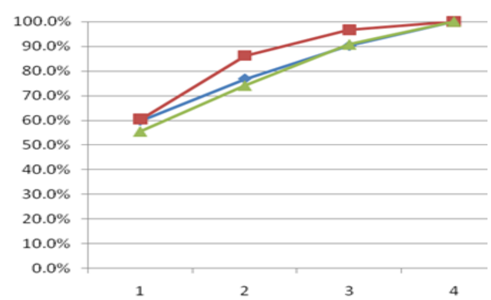

When these season type color mix decision results are observed, rank 1 season type percentiles were 60.3% for the specialist 1, 55.6% for the specialist 2, and 59.8% when all data were used.

Also, when cases upto rank 2 are observed, the percentiles were 82.6% for the specialist 1, 74.1% for the specialist 2, and 76.8% when all data were used.

(Table 5 Season type diagnosis result)

Data / Rank	Use of All (112)	Specialist group 1 (54)	Specialist Group 2 (58)
1	59.8%	60.3%	55.6%
2	76.8%	86.2%	74.1%

3	90.2%	96.6%	90.7%
4	100%	100%	100%

When above results are examined, it experimently verifies that skin color has discrimination in determining the season type color mix.

4.3. Comparison of existing method and FPCS

The result of analysis using this method revealed that when distribution of skin color by 4 season types is observed, skin color distribution is grouped uniformly based on the person's season type as seen below. When the FPCS proposed in this study and existing color diagnosis system are compared and analyzed, existing personal color diagnosis system has low functionality, affordability, originality, and reliability, but familiarity between the person conducting the diagnosis and one receiving the diagnosis is high.

In contrast, FPCS of this study has high functionality, affordability, originality, and reliability, but it is difficult to expect familiarity between the program and the user.

When the FPCS proposed in this study and existing color diagnosis system are compared and analyzed, existing personal color diagnosis system has low functionality, affordability, originality, and reliability, but familiarity between the person conducting the diagnosis and one receiving the diagnosis is high.

In contrast, FPCS of this study has high functionality, affordability, originality, and reliability, but it is difficult to expect familiarity between the program and the user.

5. Conclusion and Future Study Objective

The FPCS program proposed in this study is able to produce rapid and accurate results without the complex processes of existing color diagnosis therefore it is convenient and can save time and money.

Also, it can not only be used by specialists but also by anyone for basis personal color self diagnosis.

If additional study is conducted, database of sufficient size is built through testing, and based on it, further studies are accomplished, a more effective development of diagnosis system can be anticipated.

Reference

[1] Sumie Matsuura, Transition of Personal Color System in Japan. Journal of Korean Society for Clothing Industry Vol 5. No6. 2004

[2] Myung- Sook Han, "A Study on the personal color selection factors and the satisfaction - Centered on the colors for hair and make-up –,"Journal of the Korean Society of Clothing Industry, Vol 4. No4. pp369-375, 2002

[3] Hee Seon Oh, "A Study on Personal Color in Relation with Well-matched Color and Preferred Color" Journal of Fashion Business, Vol 3. No2. pp.31-36, 1992

[4] Mi Ran Kim, Kwuy Young Lee, "A Proposal for the Personal Color Analysis Method Using KOSCOTE." Journal of the Korean Society of Cosmetology, Vol 13. No3. pp.907-914, 2007

[5] RenaeK Nnapp, Living In Color, Lighthouse publishing Group, Inc, 1998

[6] Park Hwa Sun, <Personal Color Types of College Students and Image Evaluation of Color of Apparel>, Kyungpook National University, Doctoral Thesis p.4, 2000

[7] Lee Geon Chang, 《Fuzzy Loging》, Kyung moon Publishers, Inc., 2007

[8] Lee Gwang Hyeong, Oh Gil Rok, 《Fuzzy logic and application》, Hongreung Science Publishing Company, 2005

[9] Lee Wei Suk, Im Yong Bin, Seong Nae Gyeong, So Byeong Su, 《Statistics Initiation》 Kyungmoon Publishers, Inc., 1997

Evaluation of Cycling Posture Considering the Difference of Saddle Height with Principal Component Analysis Based on Leg Electromyography

Shimpei Matsumoto*, Tatsushi Tokuyasu*, Koji Hirakoba** and Keichi Ohba*

*Oita National College of Technology, 1666 Maki, Oita-city, Oita, Japan
Tel/FAX : 81-97-552-7421, E-mail: smatsu@oita-ct.ac.jp
**Kyushu Institute of Technology, 680-4 Kawazu, Iizuka-city, Fukuoka, Japan

Abstract: The popularity of cycling sports is gradually increasing along with the growing awareness of environmental issues including the people who are not professionally trained and riding on a bicycle for only their physical fitness and holiday's recreation. Many types of bicycles have been developed and have been widely used in our daily life, and these bicycles have various size of frame for user's physical size based on positions, saddle and handle. However there is lack of concern about the importance of bicycle position. This paper quantitatively evaluates the muscular activities during bicycle exercise. The raw electromyographic (EMG) data is converted to power spectrum data by Fast Fourier Translation (FFT), and then it is analyzed by using on-line usage of principal component analysis (PCA). For our fundamental study, we have restricted the freedom degrees about bicycle's position to one, the saddle height and have employed binding shoes in order to fix the pedals of bicycle and the bottoms of rider's feet. As the result of our experiments, the scheme of predict for necessary operation to make saddle height get up the best saddle height of the subject could be derived.

***Keywords*: Bicycle exercise, EMG, FFT, PCA, Saddle height**

I. INTRODUCTION

In competitive cycling, setting the proper position is extremely important for both performance and injury prevention. The position of bicycle is determined by the settings of saddle and handle. It has already reported that the performance in cycling is affected by various factors, including aerobic and anaerobic capacity, muscular strength and endurance, and body composition [1]. The bicycle position might involve the performance of cycling exercise deeply, because it dominates a basic riding posture and pedaling form. However, the determination standard of bicycle position has not been established and now it is empirically given by user's riding experience. Within our inquiry, there are few researches investigating on the effects of bicycle sittings for performance on the basis of biological information.

This paper aims to establish an evaluation method to search an effective saddle height based on rider's individual physical properties. This paper assumes that the leg muscles are relatively and evenly activated near the rider's best saddle height, so focuses on leg muscular activities during cycling exercise. As measuring objects, this paper selects five leg muscles, lateral vastus (LV), medial vastus (MV), biceps femoris (BS), medial triceps surae (MTS), and lateral triceps surae (LTS), which are thought to be important muscles for cycling exercise. A good position might vary according to each individual's physical description even with similar size and appearance, because their physical features such as the length of body parts and joint flexibility are definitely not the same. If it becomes possible to optimally fit the bicycle position against rider's physical features before riding, we would be able to obtain comfortable cycling life and exercise efficiency with less physical burden. Moreover, if it becomes possible to easily make the optimal settings of bicycle for users, we can use bicycle more effectively and healthfully.

Many researchers have provided a review of the pedaling technique using an EMG approach, and have shown how the pattern of muscle activation during pedaling can be analyzed in terms of muscle activity level and muscle activation timing. This paper firstly constructs an automatic saddle height control system consisting of a computer running on .NET environment, an instrument device of high sensitive amplifier processing EMG, and an available fixed cycle trainer. Then we establish an evaluation method as criterion for rider's pedaling performance with one skillful cyclist. Muscular activations during pedaling exercise of skilled riders are more stable and suitable for evaluate pedaling performance than inexperienced riders. For the same subject, we measure his leg electromyography data during pedaling exercise, and apply both of FFT and PCA to the data. Some experimental results show that our proposal techniques have a possibility to seek the most suitable saddle height of bicycle form rider's physical properties.

II. RELATED WORKS

The saddle height is defined as the greatest distance from saddle surface to the center of the upper pedal surface in a straight line along saddle pillar and crank [1]. To find an efficient saddle height based on biological reaction, Hamley and Thomas [2] concluded by using oxygen consumption that the most efficient saddle height is 109% of symphysis pubis height (inseam), and other studies including the effort of [3] also confirmed that this method provides optimum aerobic power. Holmes recommended using 109% of inseam for eliciting high performance, and using 25-35 knee angles for injury prevention [4]. Peveler et al. compared a saddle height of 109% of inseam with 25-35 knee angle from the viewpoint of anaerobic power production by using a 30s Wingate test, and showed that using the 25-35 knee angle produces better results than 109 % of inseam [5]. Some studies have shown power decreasing at lower saddle heights, but knee angle was not used [2, 3, 6]. Houtz et al. correlated EMG to exercise on a stationary bicycle with accompanying expertise of joint range studies, and evaluated the efficacy of some of the clinical methods with 3 Subjects, healthy young adult women and experienced bicycle riders [7]. They showed that saddle height does not influence timing of the muscle activity but the exercise is performed with less effort with higher saddle height. Jorge et al. denoted that muscle activity levels bear an inverse relationship to saddle height. Specifically muscular activity bears a complex relationship with saddle height, and quadriceps activity level decreases with higher saddle height. They also showed that muscular activity levels of the quadriceps are influenced by the type of shoes worn, and muscular activity levels increase with soft sole shoes as opposed to cycling shoes with cleats and toeclips [8]. From above mentioned efforts, it is clarified that EMG activity patterns are not strongly related to pedaling conditions, such as load, saddle height and shoe type. The level of muscle activity, however, is significantly affected by pedaling conditions. Ericson quantified the pedaling load induced in the lower limb joints and muscles during bicycle exercise, and studied how these loads changed with adjustments of the bicycle, workload, pedaling rate, saddle height, pedal foot position [9]. He showed that an increased saddle height caused an increase in activity of the gluteus medius, medial hamstring, and gastrocnemius muscles, but the other muscles were not significantly changed due to changes of saddle height.

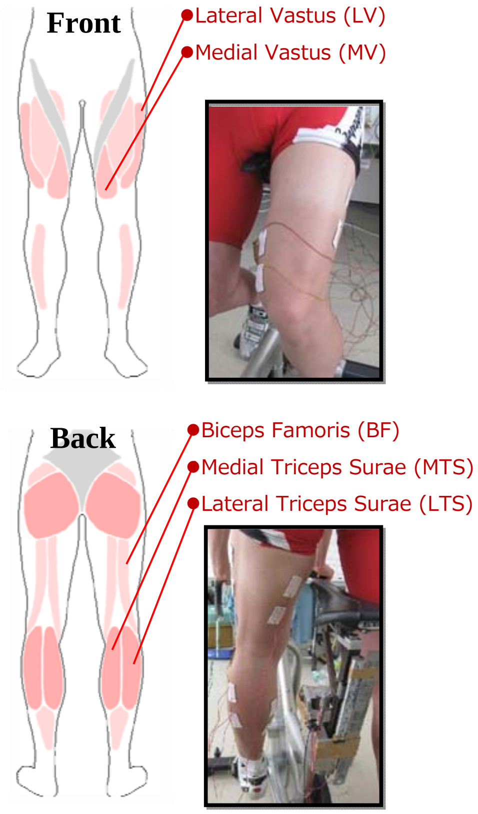

Fig.1. Measuring muscles

III. METHOD AND EXPERIMENTS

1. Definition of criterion

In order to establish a criterion to evaluate subject's pedaling performance, this paper has employed leg electromyographic signals, where five electrodes are patched on the surface of subject's leg as shown in Fig. 1; LV, MV, BS, MTS and LTS. These electromyographic signals are measured at 1000 Hz sampling rate. We assume that these muscles work better in pedaling exercise and these muscular activities can be easily detected by using EMG. Majority of professional cyclists pedal at 90 rpm or greater while riding on a flat road [10], so the electromyography data is measured in pedaling exercise at 90 rpm.

To process raw electromyographic signals, this paper derives power spectrum through FFT, where Hann window function is applied to 64 EMG. In order to evaluate a total amount of power spectrum per one revolution of pedaling, the averaged power spectrum value for 10 per spectrum values is derived, and then used as muscular activity data in this paper. Power spectrum contains some electric noises through entire frequency band, so that we use only the peak value of the averaged power spectrum data as the amount of activity of muscles per unit time during pedaling.

After three times calculation of the muscular activity, PCA is applied to the data obtained. This paper adopts 1st and 2nd principal component (PC) because it is clarified that the total amount of their contribution rate usually exceeds over 84% from the experimental results several times already confirmed by our previous efforts. In order to evaluate the changes of muscular activities in response to the changes of saddle height, we have built an on-line usage algorithm of PCA shown in Fig.2. The saddle height control system can continuously operate PCA processing consisting of data before and after the change of saddle height. The values plotted at PCA score are displayed with different color and shape according to the saddle height, so we can relatively compare plots, i.e., the difference in distribution of two saddle heights as shown in Fig.3. Fig.3 shows the distribution of 1st and 2nd PC scores which is an example of experimental result consisting of two saddle heights, 650mm and 660mm. The difference of distribution and mean value can be found from Fig.3.

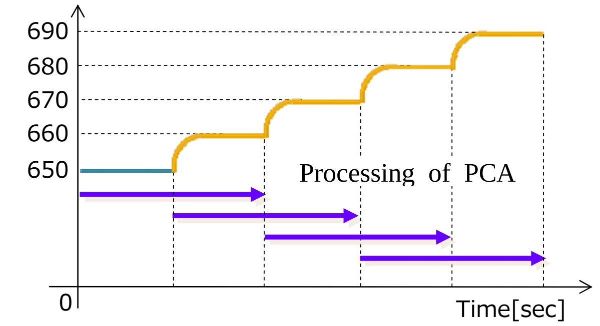

Fig.2. On-line usage of PCA

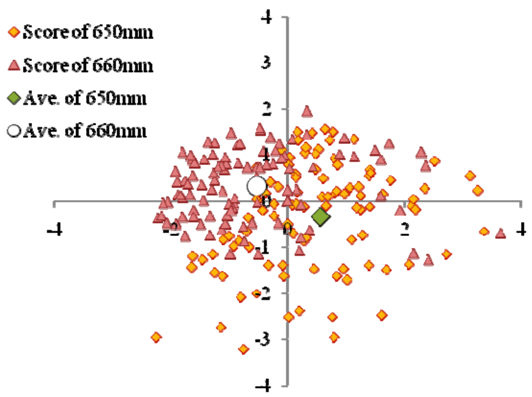

Fig.3. Distribution of 1st and 2nd PC scores

2. Experiment

In order to verify the proposed evaluation method using FFT, PCA, and these on-line usage, verification experiments are implemented under the following conditions. The subject is a cyclist, who is the coauthor and has over ten years cycling careers with various road race experiences as Japanese semiprofessional cyclist. Firstly the subject rides on the fixed cycle trainer and sets the handle and saddle height to match his racing bicycle geometry. The subject has felt that his best saddle height is 670.0mm, so this paper performs experiments on the changes of muscle activity at 20mm above or below 670mm, 650-690mm as shown in Fig.2. After patching electrodes on the surface of subject's leg, pedaling exercise begins. The subject firstly pedals on the settings at 650mm, and after 100 calculations of muscle activity, the saddle height rises 10mm. To avoid the effects of fatigue onto electromyographic signals, adequate rests are taken between experiments. For these results, as already shown in Fig.3, we focused on the relative positional relationship between the averaged PC score before and after the change of saddle height.

IV. RESULTS AND DISCUSSION

The proposed optimization method for the rider's individual most suitable saddle height of a bicycle is based on measuring muscular activities that we had measured. The saddle height derived from the method might bring out certainly rider's muscular strength but there were no concerns about riding comfort. Relationships between each muscle's activities and variance are shown in Fig.4. From Fig.4, this paper can find the saddle height of 660mm minimizes the total number of muscular activities. Considering the dynamic theory of bicycle exercise, law of conservation of momentum can be applied to the relation between rider's physical loads and bicycle's work load. Therefore, the exercise of that the saddle height setting is 660mm stimulated other non-measured muscles. It was impossible to quantitatively and rigorous setting of workload, however the workload were sufficiently low for the subject and shakiness of upper body of the subject were not recognized. Because our multi-high sensitive amplifier can measure 8 channels' signal of EMG at the same time, so gluteus maximus muscle, latissimus dorsi muscle, and musculus trapezius are added as the measure to be measured. If we will include concerns about muscles throughout whole body, then the proper setting of workload of the bicycle corresponding to rider's physical strength. VO2 max, maximal oxygen consumption, is one of the evaluation standard against not only cyclist but also athletes of other endurance sports. An analysis device for expired gas tells us subject's oxygen uptake during cycling exercise in which the workload increases gradually. Adequate load will be derived noninvasively from the measurement of oxygen uptake and VO2 max.

According to the physiologist coauthor, muscle is composed of two different type's muscle fiber. They are fast muscle fiber and slow muscle fiber, and their use rate change corresponding to the workload. We are considering embedding the use rate between fast and slow muscle fibers into PCA analysis. It is assumed that rate of change of muscular fiber use is different due to individual physical characteristics and pedaling skill, and so on. And it has some relations with total contribution ratio of eigenvector calculated in one of processes of PCA.

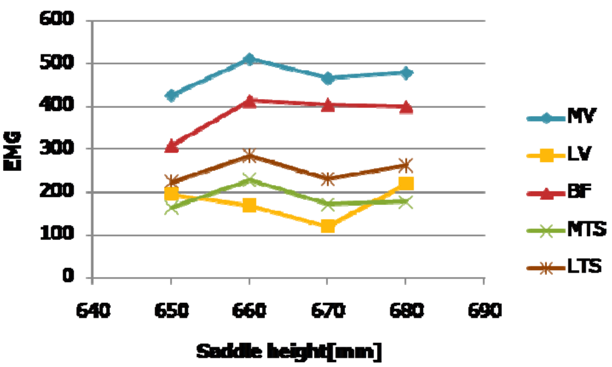

Fig.4. Differences of muscular activity for saddle height

V. CONCLUSION

This paper assumed that an efficient saddle height enables leg muscles to induce well-balanced action while pedaling. When the saddle is controlled to favorable height after changing higher saddle height, the averaged PC score after changing relatively moved in the first quadrant of coordinate system. Therefore this paper considered that to seek the best saddle height is equal to seek the saddle height to move the average value to the direction of first quadrant on PC score sheet.

The amount of each muscle used by pedaling exercise is different, so electromyographic signals increase depending on the muscle mass. Then this paper employed the use of a correlation matrix in PCA in order to evaluate the muscular activity evenly not influenced by the muscle mass. The feature of correlation matrix is to analyze based on considering the relationship between all values of muscles activity.

The saddle height control system calculates a power spectrum data every 64[msec] and derives muscular activity every 640[msec] in order to consider the muscular fatigue with dynamic change during measurement. It can be found that Wavelet analysis method is better suited for the consideration of the muscular fatigue, because time domain information can be taken account. Then we will use Wavelet transform to evaluate the effects of muscular fatigue.

The decision of saddle height depends on ambiguous human sensibility. By the basis of this concept we will determine to apply Fuzzy logic as a way to seek an effective optimal saddle height.

REFERENCES

[1] E. Burk and A. Pruitt (1996), Body positioning for cycling, High-Tech Cycling (ed. E. Burk and Human Kinetics): 79-99

[2] E. Hamley and V. Thomas (1967), Physiological and postural factors in the calibration of the bicycle ergometer, Journal of Physiology, 191: 55-57

[3] K. Nordeen-Snyder (1977), The effect of bicycle seat height variation upon oxygen consumption and lower limb kinematics, Medicine and Science in Sports and Exercise, 9(2): 113-117

[4] J. Holmes, A. Pruitt and N. Whalen (1994), Lower extremity overuse in Bicycling, Clinics in Sports Medicine, 13(1):187-203

[5] W. Peveler, J. Pounders and P. Bishop (2007). Effect of Saddle Height on Anaerobic Power Production in Cycling, Journal of Strength & Conditioning Research, 21(4): 1023-1027

[6] P. Shennum and A. deVries (1976), The effect of saddle height on oxygen consumption during bicycle ergometer work, Medicine and Science in Sports and Exercise, 8(2): 119-121

[7] S. Houtz and F. Fischer (1959), An analysis ofmuscle action and joint excursion during exercise on a stationary bicycle, The Journal Of Bone And Joint Surgery, American Volume.41-A(1): 123-131.

[8] M. Jorge and M. Hull (1986), Analysis of EMG measurements during bicycle pedaling. Journal of Biomechanics, 19(9): 683-694.

[9] M. Ericson (1986), On the biomechanics of cycling. A study of joint and muscle load during exercise on the bicycle ergometer. Scandinavian Journal Of Rehabilitation Medicine, Supplement, 16: 1-43

[10] A. Lucia, J. Hoyos and J. Chicharro (2001), Preferred pedaling cadence in professional cycling, Medicine and Science in Sports and Exercise, 33(8): 1361-1366

The Fifteenth International Symposium on Artificial Life and Robotics 2010 (AROB 15th '10),
B-Con Plaza, Beppu,Oita, Japan, February 4-6, 2010

A control system based on the fuzzy neural network for a robot joint

Huailin Zhao[1](zhao_huailin@yahoo.com) Masanori Sugisaka[2]

[1]School of Mechanical and Automation Engineering, Shanghai Institute of Technology, China

[2]Mec. & Ele. Course, Nippon Bunri University, Japan

Abstract: To the robot joint actuated by two McKibben muscles, a new model is supposed, and a control algorithm based on fuzzy CMAC is designed. The new model of the robot joint supposes that there are two independent inputs so that the stiffness control of the robot joint becomes possible. The control algorithm based on both fuzzy logic and CMAC is designed. The fuzzy logic fuzzifys the relationships among the blocks of CMAC so that the performance of the CMAC is improved. At last the simulation is done.

Key word: robot joint, control algorithm, fuzzy CMAC.

1 Introduction

We have done some study on the intelligent control algorithm for the robot joint actuated by a pair of Mckibben muscles[1]. The study aimed only at the joint posture. In another word, the study mainly concerned the angle of the robot joint. But the stiffness of the robot joint is important too in practice. Based on human feeling, to the same joint and the same joint angle, the stiffness can be different. For example, the stiffness should be different when the load changes if the joint wants to keep the same joint angle. So both the angle and the stiffness of the robot joint are important.

In the previous study, we used the robot joint model as Fig.1. Based on the model, the pressure changes of the two Mckibben muscles are related with each other. The pressures of the two Mckibben muscles will change at the same time. In this way we can only control the joint angle. The stiffness of the robot joint can't be adjusted, because the pressures of the two Mckibben muscles can't be adjusted independently. In this study, we improve the control algorithm based on the previous research which only emphasized the joint angle. In the position control, when the joint angle is changed from one value to another one, not only the joint angle should be got to the required value, but also the joint stiffness may be adjusted too. In this study, a special adjusting algorithm of the pressures of the two Mckibben muscles is designed. In the new algorithm, the pressures of the two Mckibben muscles can changes independently and a special constraint condition limits their pressure changes of the two Mckibben muscles when the robot joint works.

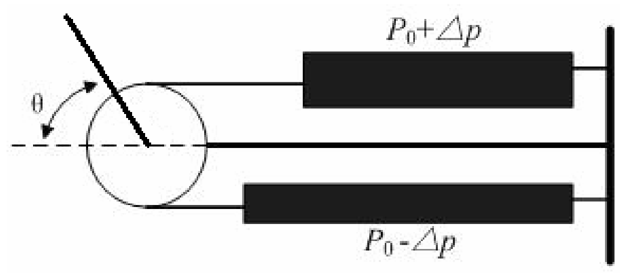

Fig.1 The old model

2 The robot joint actuated by McKibben muscles

In this study, a new robot joint model is designed which is shown in Fig.2. The structure is as a little same as the old one. But the pressures of the two Mckibben muscles change in different way. Both P_1 and P_2 change independently. Based on this model, the angle and the stiffness of the robot joint can be controlled independently.

When the robot joint working, the two Mckiben muscles will be input by two gas pressures P_1 and P_2 which are independent, and they will output pulling forces F_1 and F_2 independently. We use formula (1) to calculate the static forces[2]:

$$F = c_1 P \tfrac{b^2}{4\pi n^2}\{3[(1-c_2 R_c)\tfrac{L}{b}]^2 - 1\} \quad (1)$$

This is a revised force model based on experiments. Where, P is the pressure of the Mckibben muscle, R_c is its contraction rate, L is its current length, b is the length of the fiber in its outer layer, n is the number of winding turns of a single fiber, and c_1 and c_2 are two constants decided by the experiments.

Then we establish the dynamic model as the following:

$$M = J\frac{d^2\omega}{dt^2} \tag{2}$$

$$M = M_s - M_v \tag{3}$$

$$M_s = R(F_1 - F_2) \tag{4}$$

$$M_v = c(P_1 + P_2)\frac{d\omega}{dt} \tag{5}$$

Where, M is the total moment of the robot joint, M_s is its static moment, M_v the moment item related with joint viscous damping, J is the rotation inertia, R is the radius of the joint cylinder, and c is the viscous damping factor.

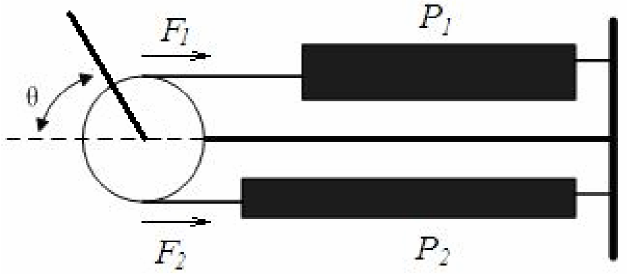

(a)

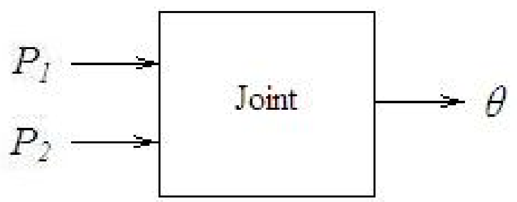

(b)

Fig.2 The new model of the robot Joint

3 The control system based on the fuzzy neural networks

In previous studies, we designed the control algorithms based on the neural networks, which including the pure CMAC network and the compound control algorithm based on both CMAC and PID. To those algorithms, there are some problems not resolved. One problem is that the pure neural network controller is not absolutely reliable. Another one is referred to the compound control algorithm. The compound controller consists of a CMAC controller and a PID controller which are parallel to each other. The problem is that we must determine the PID parameters before the controller working. The previous study concluded that the PID parameter values should be within a proper field. So we must try the PID parameters before the control system begins to work. And there is a risk that the compound control system may fail if the robot joint or its load changes too much. Summarizing the above analysis, we design a new control algorithm based on both fuzzy logic and CMAC networks, shown in Fig.3. This algorithm can solve the two problems at the same time.

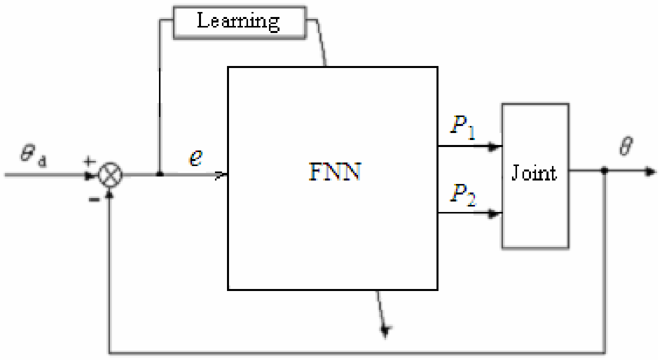

Fig.3 The fuzzy neural network control system

In Fig.3, θ_d is the desired angle of the robot joint, θ is the real angle, e is the difference between θ_d and θ, and FNN is the controller.

To a same robot joint angle, there are numberless pairs of P_1 and P_2 corresponding to it. So here we add a constraint to them, which is the formula (6).

$$(\Delta P_1)^2 + (\Delta P_2)^2 = \min \tag{6}$$

Where, ΔP_1 and ΔP_2 are the changes of P_1 and P_2 respectively.

The structure of the fuzzy neural network controller is shown in Fig.4.

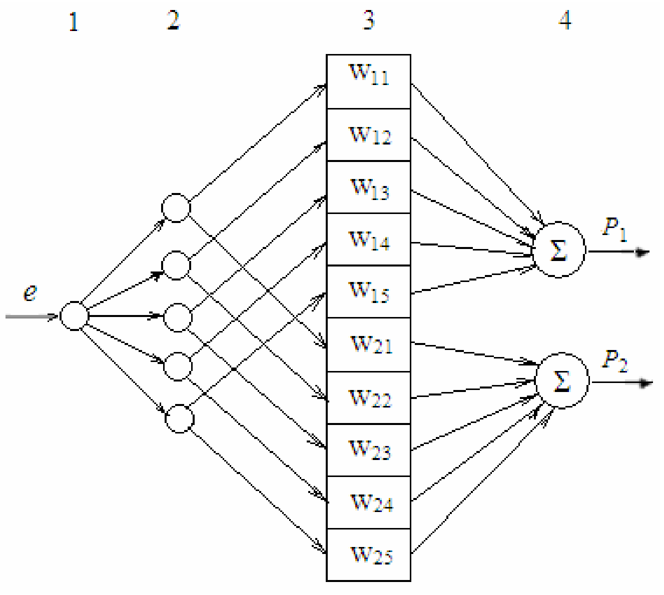

Fig.4 The fuzzy neural network controller

In Fig.4, we divide the controller into 4 layers. Layer 1 introduces the input of the controller. Its output and input has the relationship as formula (7).

$$O^{(1)} = I^{(1)} = e \qquad (7)$$

Where, $O^{(1)}$ and $I^{(1)}$ are respectively the output and input of the layer 1.

In layer 2, the input of the controller is fuzzified. Here we divide the whole input space into 5 blocks and define 5 Gaussian functions as the membership functions of the 5 blocks:

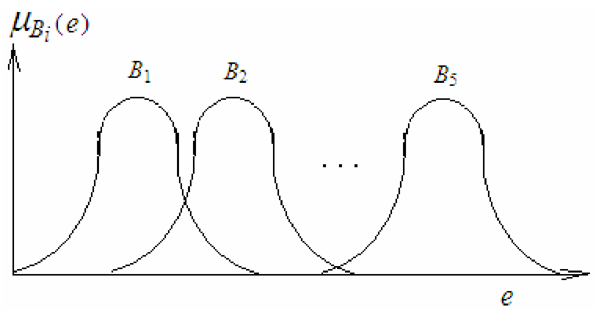

Fig.5 The Gaussian functions and their distribution

$$\mu_{B_i}(e) = e^{-(\frac{e-\sigma_i}{\upsilon_i})^2} \qquad \text{(i=1,2,3,4,5)} \qquad (8)$$

Therefore, the relationship between the input and the output in layer 2 should be:

$$O_i^{(2)} = I_i^{(2)} = \mu_{B_i}(e) \qquad \text{(i=1,2,3,4,5)} \qquad (9)$$

In the layer 3, the output of the layer 2 activates the associative intensity in the associative units, and the output is calculated by the formula (8).

$$O_{ji}^{(3)} = O_i^{(2)} \times w_{ji} = \mu_{B_i}(e) \times w_{ji}$$

$$\text{(i=1,2,3,4,5,} \quad \text{j=1,2)} \qquad (10)$$

The layer 4 sums the outputs of the associative units and then calculates the output of the controller. The calculation is the formula (11).

$$P_j^{(4)} = \sum_{i=1}^{5} O_{ji}^{(3)} = \sum_{i=1}^{5}(O_i^{(2)} \times w_{ji}) = \sum_{i=1}^{5}(\mu_{B_i}(e) \times w_{ji})$$

$$\text{(i=1,2,3,4,5,} \quad \text{j=1,2)} \qquad (11)$$

4 The leaning algorithm of the fuzzy CMAC controller

The learning of the controller should include the associative intensity w_{ji}, central value σ_i and width υ_i of the Gaussian function parameters. Here we suppose P_d and P are the desired and real outputs of the controller, and define the objective function of the error as the formula (12). And the network learns by δ algorithm[3].

$$E = \tfrac{1}{2}(P_d - P)^2 \qquad (12)$$

$$\Delta w_{ji}(k) = -\eta_1 \tfrac{\partial E}{\partial w_{ji}} = -\eta_1 \tfrac{\partial E}{\partial P} \bullet \tfrac{\partial P}{\partial w_{ji}} = \eta_1 (P_d - P) O_i^{(2)}$$

$$\text{(i=1,2,3,4,5,} \quad \text{j=1,2)} \qquad (13)$$

$$\Delta \sigma_i(k) = -\eta_2 \sum_{i=1}^{5} [\tfrac{\partial E}{\partial P} \bullet \tfrac{\partial P}{\partial O_i^{(2)}} \bullet \tfrac{\partial O_i^{(2)}}{\partial \sigma_i}]$$

$$= 2\eta_2 (P_d - P) \sum_{i=1}^{5} [O_{ji}^{(3)} \bullet \tfrac{e-\sigma_i}{\upsilon_i^2}]$$

$$\text{(i=1,2,3,4,5,} \quad \text{j=1,2)} \qquad (14)$$

$$\Delta\upsilon_i(k) = -\eta_3 \sum_{i=1}^{5} [\frac{\partial E}{\partial P} \bullet \frac{\partial P}{\partial O_i^{(2)}} \bullet \frac{\partial O_i^{(2)}}{\partial \upsilon_i}]$$

$$= 2\eta_3(P_d - P)\sum_{i=1}^{5}[O_{ji}^{(3)} \bullet \frac{(e-\sigma_i)^2}{\upsilon_i^3}]$$

(i=1,2,3,4,5, j=1,2) (15)

Where, η_1, η_2 and η_3 are the learning rates, and each of them should belong to (0,1). Therefore the three parameters should be calculated as

$$w_{ji}(k+1) = w_{ji}(k) + \Delta w_{ji}(k)$$

(i=1,2,3,4,5, j=1,2) (16)

$$\sigma_i(k+1) = \sigma_i(k) + \Delta\sigma_i(k)$$

(i=1,2,3,4,5) (17)

$$\upsilon_i(k+1) = \upsilon_i(k) + \Delta\upsilon_i(k)$$

(i=1,2,3,4,5) (18)

5 Simulation

Based on both the model of the robot joint and the control algorithm, we simulate the control system by MATLAB. There is no load, the initial conditions are that both $\theta(0)$ and $\omega(0)$ are zero. The desired track of the robot joint $\theta_d(t)$=sin($2\pi t$). The sampling time is 0.001 second. And we add a disturbance item to the joint which is M_d=sin($10\pi t$).

The simulation results are shown in Fig.6, which indicates that the control system is stable and it can resist the outer disturbance.

6 Conclusion

To the nonlinear system like the robot joint actuated by the McKibben muscles, a new model with two inputs and one output is supposed. The changes of the pressures of the two Mckibben muscles are independent. It is possible to realize the stiffness control based on the model. The control algorithm based on Both fuzzy logic and CMAC is designed. The simulation shows that the control algorithm is effective and the control system is stable. The control system can resist the outer disturbance too.

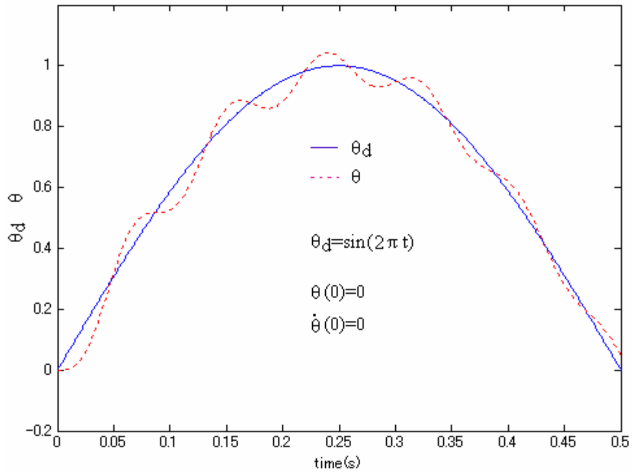

(a) The tracking lines

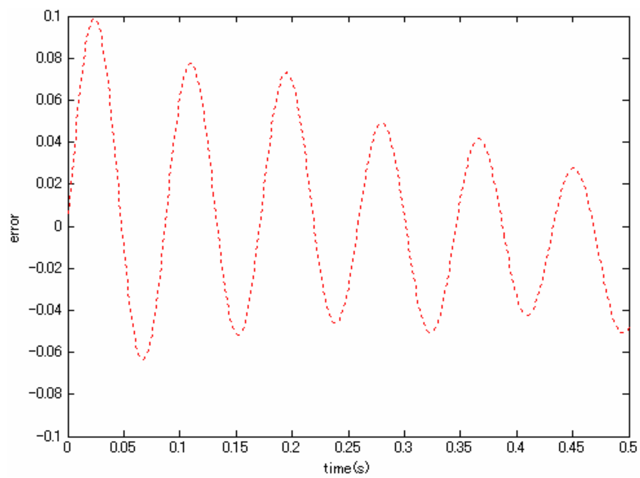

(b) The tracking error

Fig.6 Tracking and error of the control system

Acknowledgement

This study is supported by the project from Shanghai Institute of Technology, China (YJ2008-12).

Reference:

[1] Huailin Zhao, Masanori Sugisaka, Simulation study of CMAC control for the robot joint actuated by McKibben muscles, Applied Mathematics and Computation, 203(2008), pp457-462

[2] Huailin Zhao, Masanori Sugisaka, A Model of the Mckibben muscle actuator based on experiments, Systems science, Vol. 34(2008), No. 2, pp83 - 88

[3] Yaonan Wang, Intelligent control engineering for robots, Beijing: Science Publishing House, 2004

The Fifteenth International Symposium on Artificial Life and Robotics 2010 (AROB 15th '10),
B-Con Plaza, Beppu,Oita, Japan, February 4-6, 2010

Proposal of Sensors for Robot Supporting to Take Medicines on Time

Yuhki Kitazono, Xianglan Zheng, Shota Nakashima, Shiyuan Yang, Seiichi Serikawa

Kyushu Institute of Technology, 1-1 Sensui-cho, Tobata-ku, Kitakyushu-shi, Fukuoka 804-8550, Japan
(Tel : 81-93-884-3282; Fax : 81-93-884-3015)
(kitazono@boss.ecs.kyutech.ac.jp)

Abstract: Patients sometimes forget to take medicine. It may make recovery of patients slow down. In this study, we propose a new robot supporting to take medicines on time using medicine sensors and a chewing sensor. When medicines are put into medicine sensor, the electric capacity of the medicine sensor will be changed. According to the value of capacity of the sensor, this robot can easily judge whether medicines are in the medicine box or not. The chewing sensor is made up of an ear wearing device and a unit which consists of a photodiode and an infrared LED. The infrared rays from the infrared LED irradiate a mandible. Using reflected light received by the photodiode, the chewing sensor can judge whether foods have been taken or not. By using the medicine sensors and the chewing sensor, the robot can bring the user medicines on time and have following function. If medicines are not taken at time to take medicines, the robot announces to the user. In case of medicines taken before meals, the robot warns the user to take medicines if the user is chewing before taking medicines.

Keywords: Robot supporting to take medicines, Medicine sensor, Electric capacity, Chewing sensor.

I. INTRODUCTION

According to National Livelihood Survey 2008, the ratio of the patients to Japanese people was 0.3336[1]. If medicines are prescribed for most of patients, over 30 percent of Japanese take medicines. However, over 60 percent of the patients forget to take medicines on time[2]. If patients do not take medicines on time, the effect of medicines is not enough. In addition, it may make the state of illness worse. For this reason, methods to prevent forgetting to take medicines are necessary and helpful to patients[3]. There are several kinds of systems that announce the time of taking medicines to a patient[4]~[6]. However, these systems cannot accurately judge whether a patient takes medicines or not, and cannot judge that the patient takes medicine before meals or after meals. Many chewing sensors are used to detect that, but most of them are uncomfortable in direct contact type. There is also non contact-type using an infrared sensor, but it needs to be fixed on glasses and needs to be adjusted[7]. Thus, the solution of these problems is needed. In addition, a robot that brings medicines is more useful for patients of bedridden than the systems only of the announcement.

Therefore, a robot supporting to take medicines on time is proposed. In this paper, new medicine sensor and chewing sensor for the robot are developed. Regardless of size and shape of medicines, the robot can accurately judge whether medicines have been taken out or not from the medicine sensors. The robot can also accurately judge whether a user is chewing or not by the chewing sensor. By using the medicine sensors and the chewing sensor, the robot can bring medicines to a user and announce to take medicines on time.

II. ROBOT SUPPORTING TO TAKE MEDICINES ON TIME

A robot supporting to take medicines on time is structured as shown in Fig.1 (a). The picture of the experimental robot is shown in Fig.1 (b) and (c). A unit for person judges whether a user is chewing or not from a chewing sensor, and transmits the result to the robot. The robot judges whether medicines have been taken out or not from medicine sensors. If medicines are not taken at time to take medicines, the robot announces to the user. In case of medicines taken before meals, the robot warns the user to take medicines if the user is chewing before taking medicines.

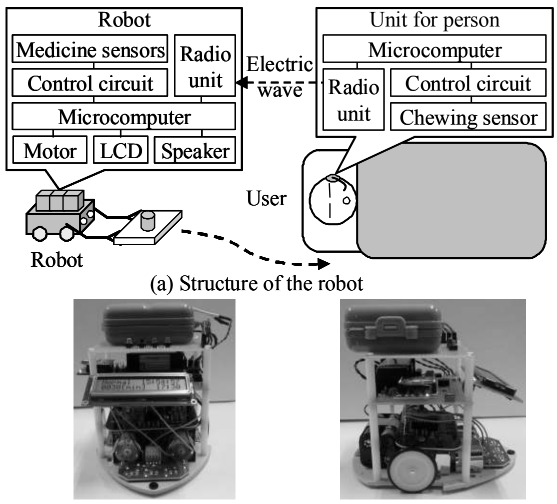

(a) Structure of the robot

(b) Front view of the robot (c) Side view of the robot

Fig.1. Robot supporting to take medicines

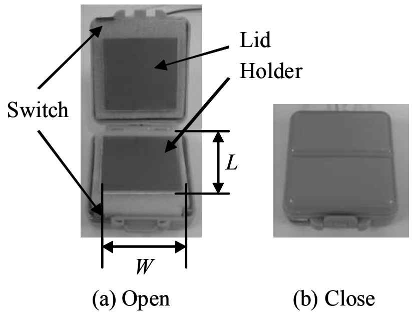

Fig.2. Picture of medicine sensor

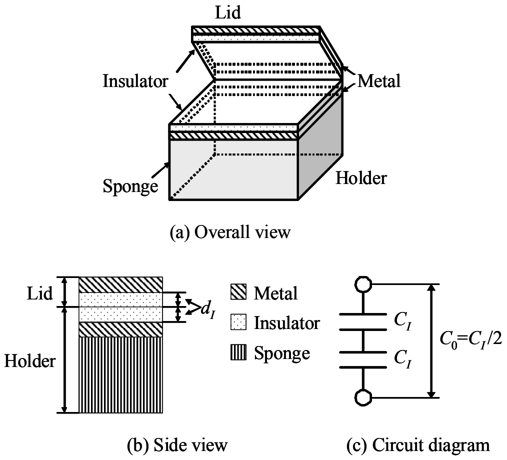

Fig.3. Structure of inside of sensor box in case of no medicine

1. Medicine Sensor

The picture of medicine sensor and the structure of sensor box are shown in Fig.2, 3 and 4. Two pieces of metals are set on the inside of the lid and the holder, and insulators are put on the metals. A sponge is set between the metal and the bottom of the holder. This is used instead of spring. When there is no medicine in the sensor, the distance between the metal of the holder and that of the lid is $2d_I$ (Refer to Fig.3 (b)). The circuit diagram is shown in Fig.3 (c). The electric capacity of each insulator is assumed C_I. The combined electric capacity is C_0 (=C_I /2). When there is a medicine in the sensor (Refer to Fig.4 (a)), the distance between the metal of the holder and that of the lid is $2d_I$+d_M (Refer to Fig.4 (b)). The circuit diagram becomes Fig.4 (c). The electric capacities of medicine and air between the insulator of the holder and that of the lid are assumed C_M and C_A. The electric capacity of each insulator in part of air is assumed C_{IA}. The combined electric capacities of C_a, C_m and C_1 are as shown in Fig.4 (c). These are represented as followings.

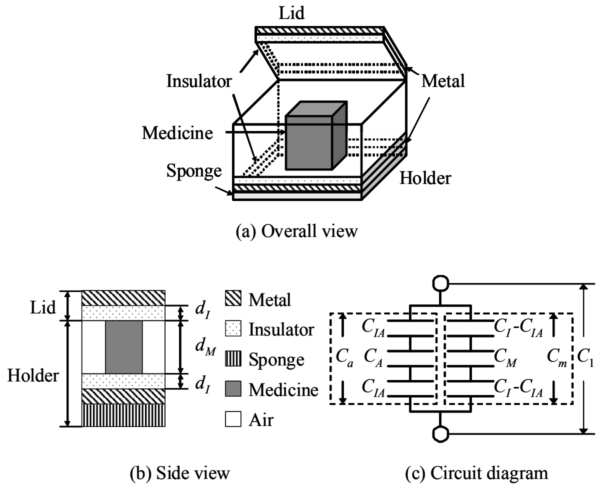

Fig.4. Structure of inside of sensor box in case of medicine

$$C_a = \frac{1}{1/C_{IA} + 1/C_{IA} + 1/C_A} = \frac{C_{IA}}{2 + C_{IA}/C_A} < \frac{C_{IA}}{2} \quad (1)$$

$$C_m = \frac{C_I - C_{IA}}{2 + \left(C_I - C_{IA}\right)/C_M} < \frac{C_I - C_{IA}}{2} \quad (2)$$

$$C_1 = C_a + C_m < \frac{C_{IA}}{2} + \frac{C_I - C_{IA}}{2} = \frac{C_I}{2} = C_0 \quad (3)$$

Then C_1 is lower than C_0 if C_M and C_A take a limited positive value. When there is a medicine in the sensor, the electric capacity of the sensor becomes low. Therefore, it can be judged whether medicines are in the sensor or not by measuring the electric capacity of the sensor.

In order to avoid misjudging, a switch is set below lid of the sensor as shown in Fig.2. When the lid is opened, it may be misjudged because of the change of capacity of the sensor. The switch signal is used to stop the judgment while the lid opens.

In this robot, when there are medicines in a sensor, the capacity of the sensor is low. The robot judges whether medicine sensors contain medicines or not when all lids have been closed.

2. Chewing Sensor

The proposed chewing sensor is shown in Fig.5 (a). It is made up of an ear wearing device and a unit which consists of a photodiode and an infrared LED. The sensor worn on one ear needs to be fixed about 1 [cm] away from a mandible as shown in Fig.5 (b). The modulated (10 [kHz]) infrared rays from the infrared LED irradiate the mandible. The reflected light is received by the photodiode. Then, the signal goes through the circuit which consists of amplifiers and a band-pass filter. The microcomputer judges whether chewing or not by the output of the circuit.

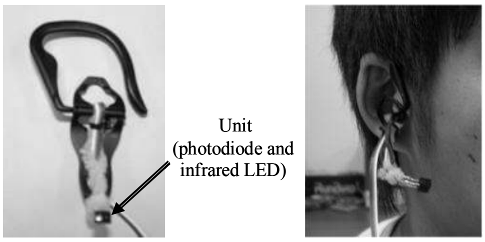

(a) Picture of the sensor (b) Wearing the sensor

Fig.5. Chewing sensor

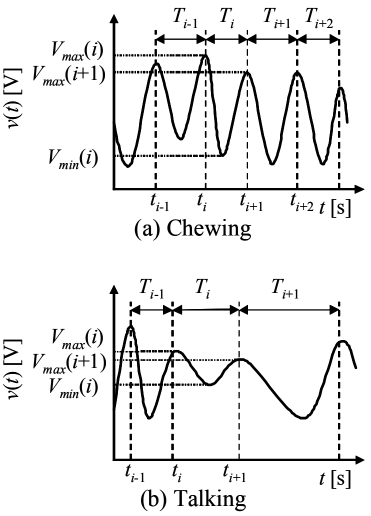

Fig.6. Shape of waves of chewing and talking

Talking and chewing can be distinguished from the shape of waves of the output as shown in Fig.6. In case of chewing, a similar shape of waves is repeated because of the similar movements of the mandible. However, in case of talking, the shape of waves is irregular. Using correlation of waves, it can be judged whether chewing or not. In addition, people normally chew 0.5~3 times in one second. Therefore, if the waves satisfy the following Eq. (4), (5), (6) and (7), it is assumed that they are "correlation waves".

$$\frac{V_{max}(i)+V_{max}(i+1)}{2}-V_{min}(i) \geqq V_{th} \quad (4)$$

$$|T_{i+1}-T_i| \leqq 0.3[\mathrm{s}] \quad (5)$$

$$R_i = \frac{\sum_{t=0}^{T} v(t_{i-1}+t)v(t_i+t)}{\sqrt{\sum_{t=0}^{T} v^2(t_{i-1}+t)}\sqrt{\sum_{t=0}^{T} v^2(t_i+t)}} \geqq 0.97 \quad (6)$$

$$T=\min(T_{i-1},T_i)$$

$$0.3[\mathrm{s}] \leqq T_i \leqq 2.0[\mathrm{s}] \quad (7)$$

A local maximum voltage and the following local minimum voltage are assumed $V_{max}(i)$ and $V_{min}(i)$ respectively as shown in Fig.6. The next local maximum voltage is assumed $V_{max}(i+1)$. The time from $V_{max}(i)$ to $V_{max}(i+1)$ is T_i, the time from $V_{max}(i+1)$ to $V_{max}(i+2)$ is T_{i+1}. Regularized cross correlation function from T_i to T_{i+1} is R_i. V_{th} is the threshold voltage. In this experiment, it is set 100 [mV]. If the correlation waves continually occur over 5 times, it is considered as chewing.

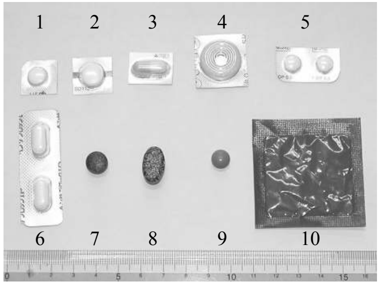

Fig.7. Medicines used in the experiment

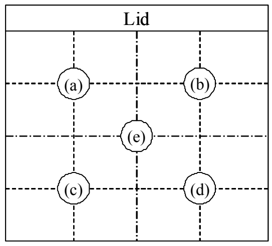

Fig.8. Positions of medicine in the sensor

III. EXPERIMENTS

1. Experiments of Medicine Sensor

In the part of experiments for medicine sensor, the metals with the area of 36 [cm^2] (W = 6 [cm], L = 6 [cm]) and the insulators (Glass-epoxy, Relative Permittivity: 4.5~5.2[8]) with thickness (d_I) of 1.6 [mm] are used. The sensor shown in Fig.2 is used in the experiments.

The variance of the output voltages of the sensor is confirmed for determine the threshold voltage (V_m) to judge whether medicines are in the sensor or not when medicine is put into the sensor as follows.

A.Influence of the Position of Medicine

In this experiment, the influence of position of medicine in the sensor on output voltage of the sensor is confirmed. The output voltage of the sensor is measured when the medicine (Refer to Fig.7, No.1) is put into the sensor. Five places where medicine is put (Refer to Fig.8, positions (a)~(e)) are tried. It is tried 10 times for each condition. The output voltages at each position and the output voltage in case of no medicine in the sensor are shown in Fig.9.

B.Influence of type of Medicine

In this experiment, the influence of type of medicine on capacity of the sensor is confirmed. The capacity of the sensor is measured when the medicine is put in the

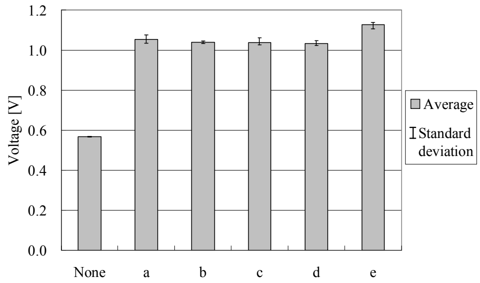

Fig.9. Influence of position of medicine on output voltage of medicine sensor

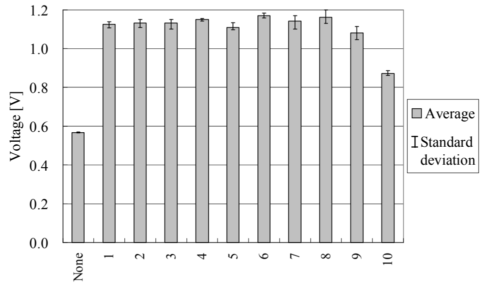

Fig.10. Influence of type of medicine on output voltage of medicine sensor

sensor. Ten types of medicines with different sizes and shapes are used 10 times for each of them as shown in Fig.7. A medicine is placed at the position of center as shown in Fig.8 (e). The result is shown in Fig.10.

If the output voltage is higher than V_m, it is assumed that medicines are in the medicine sensor. The recognition rate of 100 [%] is obtained when V_m is in the range of 0.57~0.86 [V]. Therefore, V_m is decided 0.70 [V]. It can accurately judge whether the user have taken medicines or not.

2. Experiments of Chewing Sensor

In the next part of experiments, chewing sensor shown in Fig.5 is used. Ten people (a~j) do the experiments of talking and chewing, and every people does those 3 times. As the result shown in figure 11, in case of chewing, continuous correlation waves are over 8 times. In case of talking, those are not over 3 times. Therefore, the recognition rate is 100 [%]. It can accurately judge whether the user is chewing or not.

3. Operation Check of the Robot

In this experiment, operation check of the robot is performed. Experimental conditions are three cases as followings. (1) User takes medicines on time. (2) User does not take medicines on time. (3) In case of medicines taken before meals, user is chewing before taking medicines. It is tried 10 times for each condition. As the result, the robot did nothing in the condition of (1). In the condition of (2), the robot brought the user medicines, and announced user to take medicines. In the condition of (3), the robot brought the user medicines, and warned user to take medicines before having foods. Thus, it was confirmed that the robot correctly brought, announced and warned.

IV. CONCLUSIONS

A robot supporting to take medicines on time is proposed in this study, and a medicine sensor and a

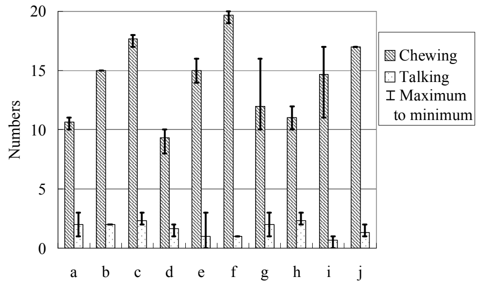

Fig.11. Numbers of continuous correlation waves relating to chewing

chewing sensor are developed. The robot can bring the user medicines on time. If medicines are not taken at time to take medicines, the robot announces to the user. In case of medicines taken before the meals, the robot warns the user to take medicines if the user is chewing before taking medicines.

REFERENCES

[1] http://www.mhlw.go.jp/toukei/saikin/hw/k-tyosa/k-tyosa07/3-2.html

[2] N. Kutsuma, K. Yamaura, M. Nakayama, M. Namiki, K. Akiba, S. Kimura, H. Ueda, S. Numajiri, D. Kobayashi, and Y. Morimoto, "Practice for Promoting Proper Use of Reusing the Leftover Medicine in the Outpatients of the Chronic Disease", Journal of the Pharmaceutical Society of Japan, Vol.124, No.6, pp.355-364 (2004)

[3] A. Yamanaka, "Why We Often Forget to Take Medicine? : Perspective Memory Error", Journal of Business Administration, Vol.3, No.3-4, pp.127-130 (2006)

[4] "Management System of Taking Medicines", Nikkei Healthcare 21, No.6, pp.97-100 (2006)

[5] H. Uemura and T. Arai, "Containers for Medicines, Japanese Published Patent", P2002-291840A (2002)

[6] T. Kobayashi, "Medicine Container, Japanese Published Patent, P2002-291844A (2002)

[7] K. Obata, T. Saeki, and Y. Tadokoro, "No Contact-type Chewing Number Counting Equipment Using Infrared Sensor", Transactions of SICE, Vol.38, No.9, pp.747-752 (2002)

[8] http://yamaden-sensor.jp/technology/table.html

The Fifteenth International Symposium on Artificial Life and Robotics 2010 (AROB 15th '10),
B-Con Plaza, Beppu,Oita, Japan, February 4-6, 2010

Development and Case Study of Trend Analysis Software Based on FACT-Graph

Ryosuke Saga[1], Hiroshi Tsuji[2], Takao Miyamoto[2], and Kuniaki Tabata[1].

[1]*Kanagawa Institute of Technology, 1030 Shimo-ogino, Atsugi, Kanagawa, Japan*
[2]*Osaka Prefecture University, 1-1 Gakuencho, Nakaku, Sakai, Osaka, Japan*
(Tel : 81-46-291-3235; Fax : 81-46-242-8490)
({saga,tabata}@ic.kanagawa-it.ac.jp, tsuji@cs.osakafu-u.ac.jp, aki@center.osakafu-u.ac.jp)

***Abstract*:** This paper proposes text mining software to analyze FACT-Graph and describes case study by using the software. FACT-Graph is a trend graph which visualizes what kinds of topics exist and shows the change of trend in time-series text data. However, FACT-Graph itself does not have enough environments to analyze trend although it provides the clue for trend. In order to resolve the problem, we develop the software called Loopo. This software provides the functions of adding the consideration of analyst as the keywords and operating FACT-Graph itself such as moving, adding, and clearing nodes. Also, the system allows analysts to refer information source, keyword information, and network information in order to analyze and consider FACT-Graph. In a case study about criminal trend using the title of articles of newspaper between 1987 and 2007, we confirm the usability of this software.

***Keywords*:** Trend Analysis, FACT-Graph, Text Mining,, Text Mining System

I. INTRODUCTION

Recently, the usage of text data on web page has been promoted on the back of fast networks and large volume storage. Text mining has been developed to use this text data. Text mining uses unstructured and voluminous text data and discovers new usage knowledge. Text mining methods are used for keyword extractions, summarizations, and visualizations [1]-[4].

This paper focuses on the trend analysis that uses time-series text data and several text mining methods [5]. In many cases of trend analysis, terms and topics in text data (i.e. *bag-of-words*) are used. Consequentially, analysts who analyze trends need to find out what are the terms that receive a lot of attention in a certain time period. To identify and summarize trends, Saga et al. have developed a trend visualization method called *FACT-Graph* [6]. FACT-Graph classifies terms on the basis of their importance and the relationships between them. FACT-Graph visualizes how these two elements change as time elapses. Fig. 1 shows the visualized information as a co-occurrence graph, and an analyst speculates about the trends from this graph.

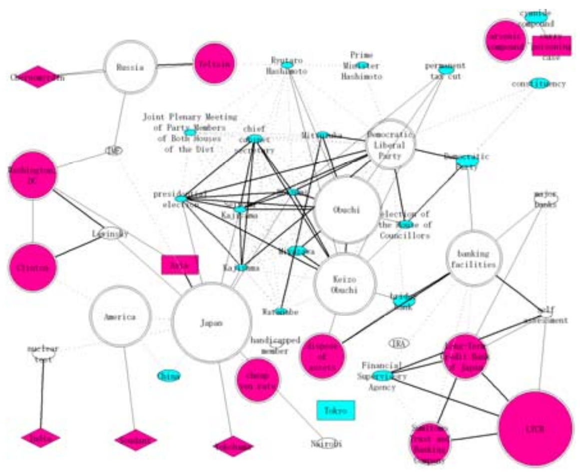

Fig.1. FACT-Graph

However, text mining based on human-centric actions is currently receiving much attention [7]. This text mining emphasizes the centrality of analyst interactivity in knowledge discovery processes. It repeats the processes in which an analyst considers the text mining results, reflects the considerations in the result, and analyzes again. For human-centric text mining operations, text mining necessitates the system-based support that aims to show the evidences and reflects the analyst's intentions.

This paper describes text mining software called *Loopo* that extend FACT-Graph as human-centric text mining. Loopo provides information on the processes of analyzing terms, networks, and evidences for trends analysis to identify trends.

The rest of this paper is organized as follows; Section 2 introduces FACT-Graph. Section 3 describes Loopo in detail. Section 4 details a case study about crime trends in Japan using newspaper articles. Finally, Section 5 concludes our papers.

II. FACT-Graph

FACT-Graph visualizes the change of keywords trend and relationships between terms over two time periods (Fig. 1). The usefulness of FACT-Graph has been discussed in several previous studies [6][8].

FACT-Graph is shown using nodes and links. FACT-Graph embeds the change in a keyword's class transition and co-occurrence in nodes and edges. The keyword's class transition, which is one of the essential elements of FACT-Graph, is based on class transition analysis that separates keywords into four classes based on term frequency (TF) and document frequency (DF) [9]. The result of the analysis shows the transition of keywords between two time-periods shown in Table 1. For example, if a term belongs to Class A in a certain time period and moves into Class D in the next time period, then the trend regarding that term is referred to as "fadeout". FACT-Graph identifies these trends by the node's color. For example, red color shows fashionable, blue color shows unfashionable and white shows unchanged in FACT-Graph

Additionally, a FACT-Graph visualizes keywords and relationships between keywords by using co-occurrence information. As a result, useful keywords can be obtained from their relationship with other keywords, even though that keyword does not seem to be important at a glance, and the analyst can extract such keywords by using FACT-Graph. Moreover, from the result of the class-transition analysis, the analyst can comprehend trends in keywords and in topics (consisting of several keywords) by FACT-Graph.

The steps for generating FACT-Graph are as

Table 1. Class transition and keyword trends

		After			
		A	B	C	D
Before	A	Hot	Cooling	Bipolar	Fade
	B	Common	Universal	-	Fade
	C	Broaden	-	Locally Active	Fade
	D	New	Widely New	Locally New	Negligible

follows:

1. Separate time-series text data in accordance with the analysis periods
2. Extract keywords in each period by morphological analysis and TF-IDF algorithm
3. Carry out class transition analysis and extract co-occurrence relations.
4. Visualize keywords and relations.

A FACT-Graph is composed of three factors: time, keywords, and a co-occurrence network. The analyst of a FACT-Graph configures several parameters related to these factors such as analysis period, keyword filtering, and threshold of co-occurrence.

III. Loopo

Loopo is software made to extend FACT-Graph as a human-centric text mining system. Loopo enable users to analyze FACT-Graph efficiently by improving the analysis process of FACT-Graph. In order to improve the analysis process, Loopo aims to repeat user input such as parameters' setting and reflection onto FACT-Graph and output such as smoothly generating FACT-Graph and information references.

Fig. 2 is a screenshot of how Loopo draws FACT-

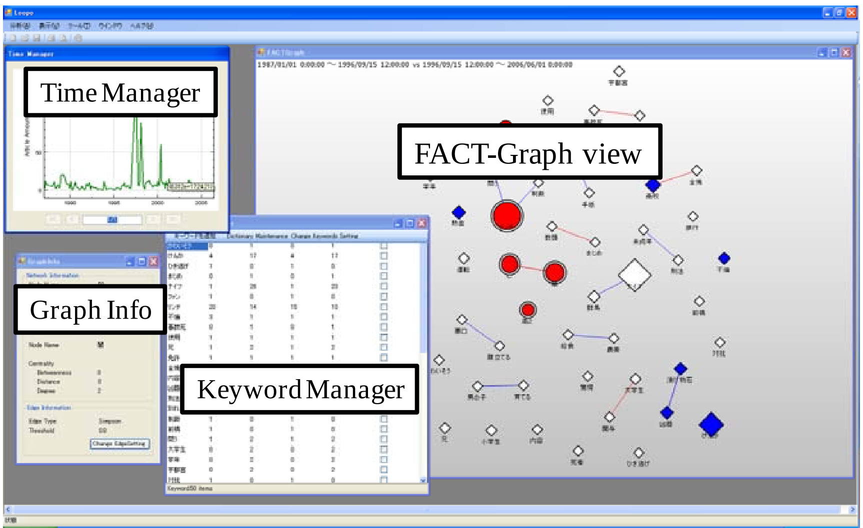

Fig.2. Loopo

Graph from certain text data. Loopo consists of four windows: "FACT-Graph View," which shows and operates the FACT-Graph itself; "Keyword Manager," which manages keywords; "Time Manager," which manages information and parameters concerning analysis periods; and "GraphInfo," which shows and manages parameters concerning the network of the FACT-Graph. User can configure the parameters to generate FACT-Graph via these windows.

The analysis by Loopo starts with the import of time-series text data. From the data, Loopo makes visualization at the same time as generating FACT-Graph. Loopo renders FACT-Graph dynamic so a user can moves keywords via FACT-Graph View to facilitate visualization. Also, the user can add terms that are deselected by the parameter to FACT-Graph and removes unnecessary keywords from the graph.

A. FACT-Graph View

FACT-Graph View shows the analysis results for the text data which is imported to Loopo as FACT-Graph. The analyst can move, clear and fix keywords for trend analysis easily via the window. For example, the "fixing keyword" function is used to fix the locations of noteworthy keywords between multiple analysis periods. The analyst can therefore browse through remarkable keywords and their related keywords over the periods at ease. FACT-Graph View also allows the analyst to refer to original text data from remarkable keywords and helps them to comprehend macro/micro trends.

B. Time Manager

It is important to configure time period for time-series analysis. Usually, the number of articles is shown as a clue of setting of time periods. By displaying the trend in article volume as a chart, Time Manager helps the analyst configure the parameter concerning analysis period. The window indicates how the time periods are divided up for analyzing a FACT-Graph (which is output according to the time periods). Time Manager also has a function for setting time periods forward or backward. With this function, the analyst can view a series of FACT-Graphs via FACT-Graph View along with the change of time period.

C. Keyword Manager

Keyword Manager is the window for listing and managing the keywords currently shown in a FACT-Graph. The analyst can add and delete keywords, and refer to the original text data from a keyword via Keyword Manager or FACT-Graph View. As a result, the window can reflect the analyst's awareness in FACT-Graph. The analyst can also configure the parameter, such as thresholds, concerning keyword extraction.

D. Graph Info

One of the measures for identifying whether a FACT-Graph is meaningful is network information such as network size and density. GraphInfo shows the network information about FACT-Graph. GraphInfo shows network size, density, and the type of links as an overview of a FACT-Graph. It also shows several centralities such as betweenness centrality and closeness centrality when analyst selects a node of interest via FACT-Graph View [11][12]. Moreover, GraphInfo allows the analyst to change co-occurrence type and thresholds of co-occurrence.

IV. CASE STUDY

A. Environment

This section describes a case study to confirm the usability of Loopo. In this case study, we use article titles from Japanese newspaper between 1987 and 2007, and we try to analyze crime trends. The detailed data is shown in Table 2. In this analysis, we use the keywords the TF-IDF weight of which contains the top 30 in each time period, and we adopt Simpson coefficient for co-occurrence. We also adopt more than 0 as thresholds of keyword and co-occurrence because articles titles are generally abbreviated sentences.

Table 2. Basic information of analysis data

The number of articles		2971
Analysis Span		1987-2007
Co-occurrence Type		Simpson
Parameters	Keywords	30
	Thresholds(TF, DF)	0
	Thresholds (Co-occurence)	0

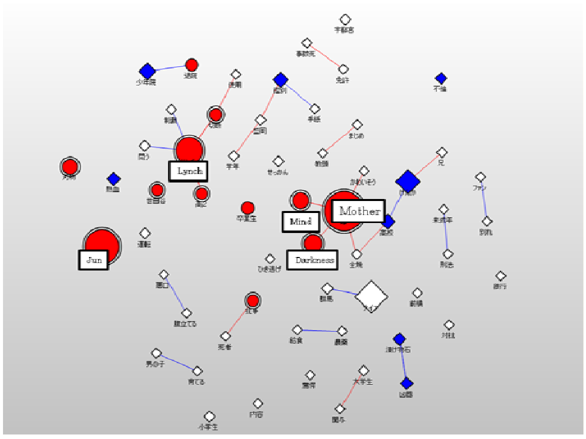

Fig.3. FACT-Graph between 1987 and 2007

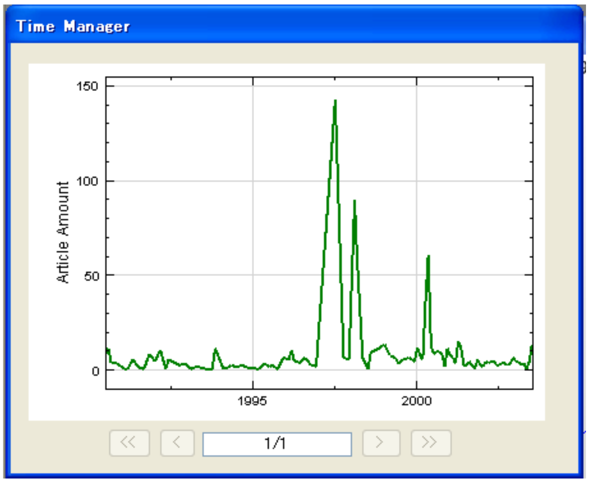

Fig.5. Time Manager in Case Study

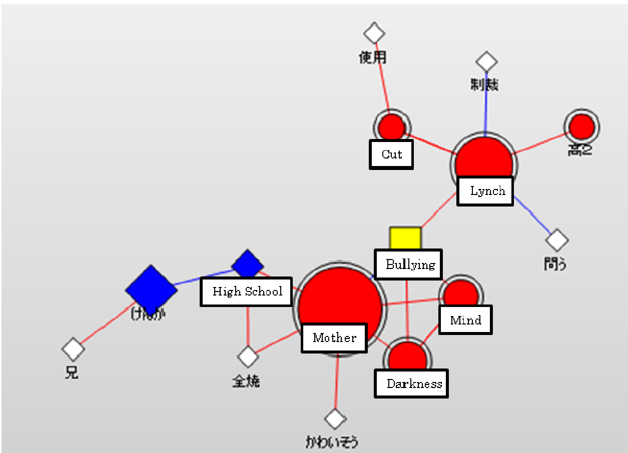

Fig.4. FACT-Graph added the keyword "Bullying"

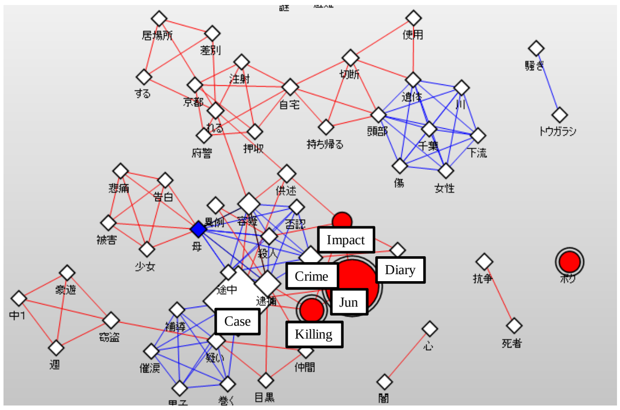

Fig.6. FACT-Graph
between November 1996 and October 1997

B. Analysis Result

At first, we separated entire text data into two parts, that is, the period from 1987 to 1997 and the period from 1997 to 2007, and then generated FACT-Graph. The result is shown in Fig. 3. FACT-Graph visualizes a fashionable keyword as a red node. Therefore we could obtain the several fashionable keywords such as "Mother", "Lynch", "Mind", and "Darkness" from the figure. Then By using the function of Loopo, we could found that "Mind" and "Darkness" were used frequently as one phrase "Darkness of Mind" and the phrase did not appear in before period.

Simultaneously, we noticed that "Bullying" which was not in FACT-Graph appeared with "Darkness of Mind" frequently. Here, we added the "Bullying" via the Keyword Manager in Loopo. The result is shown in Fig. 4. From the result, "Bullying" appeared as a bridge between two topics. Also the betweenness from GraphInfo is highest among other keywords, so "Bullying" was possibly important over 20 years of crimes.

Next, we focused on the two peaks of the number of articles between November 1996 and May 1998 because Time Manager indicated that the number of articles increased twice suddenly in this period (Fig. 5). Fig. 6 visualizes the FACT-Graph for the first peak around 1997. In this figure, "Jun", a male name that also appears in Fig. 3, is most fashionable keyword. On the other hand, the FACT-Graph in the second peak around 1998 shows Fig. 7(a). However, there are so many unnecessary keywords such as "Related" and "Reports" that it is difficult to analyze trends. Therefore, by using Loopo, we removed these keywords by referring to the original information source, so we can retain the important keywords in Fig. 7(b). From the processed figure, we found that teenage crimes and information on particular criminals are focused on in these periods.

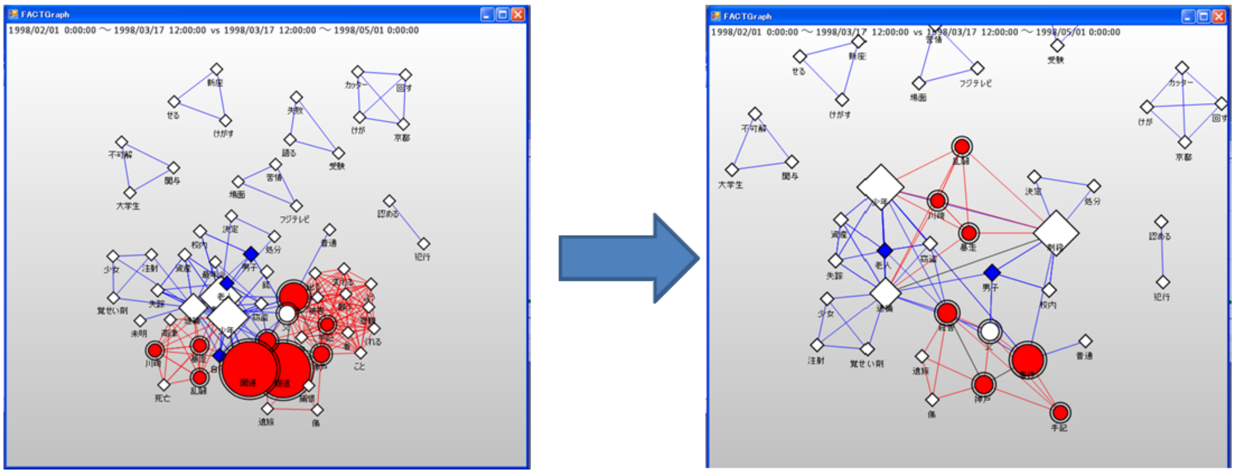

(a) Output FACT-Graph (b) After removing unnecessary keyword

Fig.7. FACT-Graph between October 1997 and October 1998

V. CONCLUSION

This paper proposes text mining software to analyze FACT-Graph and describes case study by using the software. FACT-Graph is a trend graph which visualizes what kinds of topics exist and shows the change of trend in time-series text data. However, FACT-Graph itself does not have enough environments to analyze trend.

In order to resolve the problem, we develop Loopo which provides the functions of adding the consideration of analyst as the keywords and operating FACT-Graph itself such as moving, adding, and removing nodes. Also, the system allows analysts to refer information source, keyword information, and network information in order to analyze and consider FACT-Graph. In a case study about criminal trend using the title of articles of newspaper between 1987 and 2007, we confirm the usability of this software.

REFERENCES

[1] Salton G (1989), Automatic Text Processing. Addison-Wesley Publishing Company
[2] Harman D (1992), Ranking algorithms, in Information Retrieval, chapter 14. Prentice Hall
[3] Yamanishi K, Li H (2002), Mining Open Answers in Questionnaire Data. IEEE Intelligent Systems 17(5):58-64
[4] Feldman R, Aumann Y, Zilberstein A and Ben-Yamada Y (1998), Trend graphs: Visualizing the evolution of concept relationships in large document collections. Second European Symposium on Principles of Data Mining and Knowledge Discovery (PKDD 1998):38-46
[5] Havre S, Hetzler B and Nowell L (2002), ThemeRiver(TM): In search of trends, patterns, relationships. IEEE Trans Visualization Computer Graphics8:9-20
[6] Saga R, Terachi M and Tsuji H (2009), FACT-Graph: Trend Visualization by Frequency and Co-occurrence. IEEJ transactions on electronics, information and systems 129(3):545-552
[7] Brachman R, Anand T (1996), The Process of Knowledge Discovery in Databases: A Human CenteredApproach. A KDDM, AAAI/MIT Press:37-58
[8] Saga R, Terachi M, Sheng Z and Tsuji H(2008), FACT-Graph: Trend Visualization by Frequency and Co-occurrence. in Lecture Notes on Artificial Intelligence (LNAI 5243: Ed by A. Dengel et al.(Eds)). Springer-Verlag Berlin Heidelberg:308-315
[9] Terachi M, Saga R and Tsuji H (2006), Trends Recognition in Journal Papers by Text Mining. Systems. Man & Cybernetics (IEEE/SMC 2006):4784-4789
[10] Ozaki N and Ohsawa Y (2003), Polaris: An Integrated Data Miner for Chance Discovery. Proceedings of Workshop of Chance Discovery and Its Human Computer Interaction Conference(HCI2003), Crete, Greece
[11] Matsuo Y, Ohsawa Y and Ishizuka M (2002), Keyword Exraction using Small World Structure in a Document. Transactions of Information Processing Society of Japan 43(6):1825-1833
[12] Freeman L C (1979), Centrality in social networks: Conceptual clarification. Social Networks 1(3):215-239

The Fifteenth International Symposium on Artificial Life and Robotics 2010 (AROB 15th '10),
B-Con Plaza, Beppu,Oita, Japan, February 4-6, 2010

Gait Planning for a Robot Dog

*Sooyeong Yi and **Daesung Choi

*Dept. of Electrical Engineering, Seoul National University of Technology, Korea
**DASAROBOT, Korea
(*Tel : 82-2-970-6407; Fax : 82-2-978-2754 **Tel : 82-32-329-5551; Fax:82-32-329-5558)
(*suylee@snut.ac.kr, **hawk@dasarobot.com)

Abstract: This paper proposes a gait control algorithm for a commercial quadruped robot pet developed by Dasarobot Co., Korea. Reliable motion and online characteristics are the key requisites for the motion planning algorithm of a commercialized robot. Centroid body sway ensures walking stability to achieve reliability of the proposed gait. By using ground coordinate representation, it is possible to integrate several online gaits to realize a compact and efficient gait planning algorithm. Experimental results are presented to verify the proposed gait planning and control.

Keywords: Quadruped; Robot pet; Gait planning; Initial posture

I. INTRODUCTION

Small-sized robot pets have gained increasing attention for their high industrial potential in recent years. The robot dog AIBO was developed by Sony, Japan, in 1998, and the similar i-Cybie was launched by Silverlit/Tiger Electronics, USA, in 2000 [1]. Recently, DASAROBOT in Korea produced the commercialized robot dog Genibo in 2008 [2]. In contrast to conventional fixed-body industrial robots, robot dogs have the unique feature of quadruped locomotion as well as intelligence and emotion. Thus, smooth and natural walking has an important impact on robot dog behavior.

Quadruped gait control had been studied for several decades. There are two methods for gait design: systematic planning and incremental learning. Gait design by planning is a means of online trajectory generation based on mathematical analysis. Song addressed the well-known static walking stability of the static wave gait in [3], and several gaits such as the crawl gait [4], crab gait, and spin gait have been studied [5][6]. On the other hand, the learning method connects several basic motion behaviors through repetitive trial-and-error to construct a gait [7]. For basic motion behaviors, the tip trajectory for a swinging leg, body sway motion for stable walking, shoulder height, stance, etc. are set, and a genetic evolution algorithm searches and evaluates the connected parameters of motion behaviors to generate the appropriate walking motion. Incremental learning is basically an offline scheme since it requires extra processes to search and optimize the basic motion behaviors. The optimization search process consumes considerable time. Moreover, it is difficult to change gait parameters such as the gait period, duty factor, stride, etc., since a different gait motion needs another learning process; this makes the learning method difficult to apply to commercialized robots.

The main aim of this study is to implement an online gait control algorithm for the commercialized quadruped robot pet Genibo. For commercial purposes, gait planning should be compact and portable for an embedded controller and satisfactory performance of gait motion should be guaranteed. To realize real-time capability, the proposed gait control algorithm is based on constructive planning rather than incremental learning. Most hitherto developed quadruped gait control algorithms were for research purposes, not commercial purposes.

II. KINEMATIC STRUCTURE

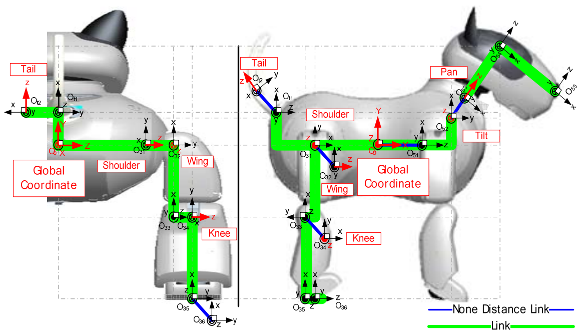

Fig. 1 Kinematic structure

The quadruped pet robot Genibo is 193 mm in height and 1.5 kg in weight. Each leg has 2 DOF (degrees of freedom) at the shoulder joint and 1 DOF at the knee joint. The robot has 2 DOF for the pan and tilt joints on its neck and one tail joint. The total number of joints is 16. The kinematic structure of the robot and the coordinate frame assignment at each joint according to D-H (Denavit-Hartenberg) conventions are shown in Fig. 1. By using an analytic approach, it is possible to derive the inverse kinematics solution (1) of the foot coordinate O_{16} with respect to the shoulder coordinate O_{11} :

$$\theta_i = f_i(F_x, F_y, F_z, d, a, \alpha), \quad i = 1,2,3 \tag{1}$$

where $\mathbf{F} = [F_x, F_y, F_z]^t$ denotes the foot position vector in the shoulder coordinates and d , a , and α are the link parameters for D-H representation.

III. GAIT PLANNING

1. Gait integration

The leg motion for a gait can be represented by (i) moving coordinates on a robot body, i.e. body coordinates; and (ii) reference coordinates fixed on the ground, i.e. ground coordinates. For body coordinates, the foot positions of all supporting legs move in the opposite direction of the body motion. However, for ground coordinate representation, the foot positions of the supporting legs are fixed onto the ground regardless of body motion. It is easy to integrate various gaits-such as forward, backward, spin, crab, etc.-into ground coordinate representation since the fixed foot positions of the supporting legs are common to all gait types. Easy integration implies memory reduction and compact implementation in small embedded controllers.

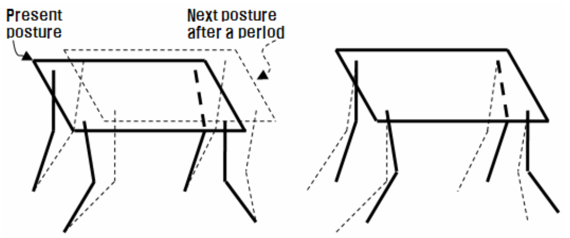

(a) Ground coordinates (b) Body coordinates

Fig. 2 Representation in the ground and the body coordinates

Since the inverse kinematics solution in Section 2 was described with respect to the shoulder coordinates T_s, the leg motion represented in the ground coordinates should be transformed into the shoulder coordinates as in (2).

$$ft_w = T_{wb} \cdot T_{bs} \cdot ft_s \quad \equiv \quad ft_s = T_{bs}^{-1} \cdot T_{wb}^{-1} \cdot ft_w \qquad (2)$$

where ft_w and ft_s are foot positions for the ground and shoulder coordinates. This coordinate transformation is illustrated in Fig. 3, where T_w, T_b, and T_s denote the ground, body, and shoulder coordinates. T_{wb}, T_{bs}, and T_{st} imply the ground-to-body, body-to-shoulder, and shoulder-to-foot transformations, respectively.

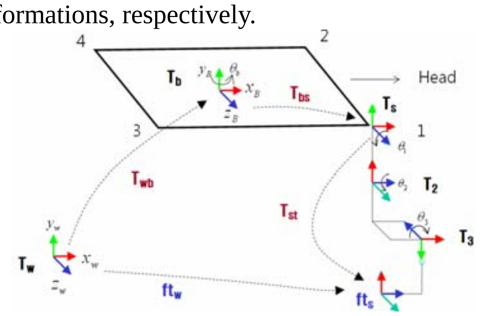

Fig. 3 Coordinate transformation

2. Gait planning

Quadruped walking is a state transition process between three-leg and four-leg support states. A gait diagram of the well-known standard wave gait [3] was modified as shown in Fig. 4 to allow a long enough time interval for all four-leg support states, so that a landing foot has firm ground contact to maintain a stable stance.

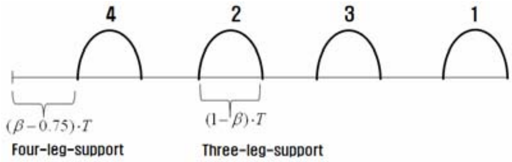

Fig. 4 Gait diagram

In Fig. 4, $\beta(>0.75)$ denotes the duty factor, time ratio between the support interval to a walking period. Here, the 4-2-3-1 swing sequence is assumed from several possible leg sequences.

Under this framework, gait planning determines the body trajectory and the next foothold of each leg for each gait period. According to a given walking distance λ and heading angle change ϕ, the body trajectory in ground coordinates can be described as

$$T_w^b(h) = T_w^b(0) \cdot \begin{bmatrix} \cos(h\phi) & 0 & -\sin(h\phi) & h\lambda\cos(\phi) \\ 0 & 1 & 0 & 0 \\ \sin(h\phi) & 0 & \cos(h\phi) & -h\lambda\sin(\phi) \\ 0 & 0 & 0 & 1 \end{bmatrix} \qquad (3)$$

where $T_w^b(0)$ implies the initial body coordinates and $h = \frac{t}{T}$, $0 \le h \le 1$ denotes the normalized time for a gait period T. Here, the robot is assumed to keep its body balance during walking.

One possible condition for foothold design is to maintain the robot posture after a gait period. With this condition, it is relatively easy to determine the next footholds as illustrated in Fig. 5, where all swing legs contribute the same amount of body motion for a period.

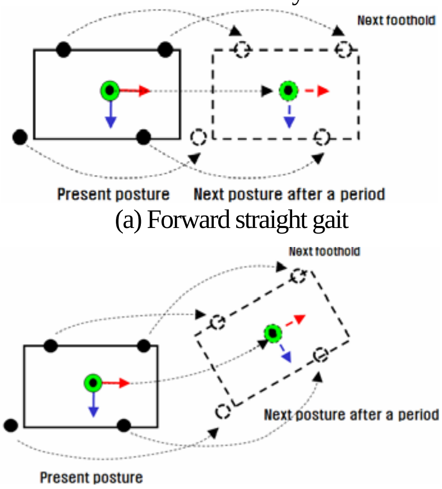

(a) Forward straight gait

(b) Turning gait

Fig. 5 Body trajectories and next footholds of several gaits

3. Body sway for stable walking

Due to an unbalanced body weight and reaction force from a swing leg, the quadruped robot could fall down while walking. In order to ensure walking stability, the body should sway towards a stable position inside the support polygon. The most stable position is the centroid of the support polygon [8]. In this study, body sway moves the body center to the centroid of the upcoming support polygon at each four-leg-support state in advance. The body sway motion could conflict with walking commands. For example, when the walking command is the forward gait, body sway moves the body center backwards while a front leg swings. In this case, the front leg is liable to violate the admissible kinematic range. Weighting factors compromise body sway to the admissible kinematic range as shown below:

$$v_x = \mu_x \cdot (c_x - p_x)/\tau$$
$$v_z = \mu_z \cdot (c_z - p_z)/\tau \qquad (4)$$

where v denotes body velocity, μ implies the weighting factor, τ is the time interval for the four-leg support state, and c and p represent the centroid and body center respectively. Here, the weighting factors can be determined empirically.

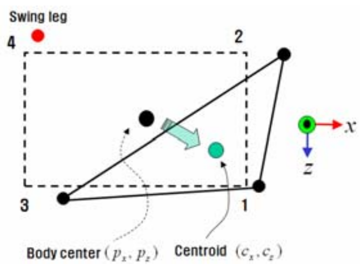

Fig. 6 Centroid body sway

4. Initial posture

In general, a quadruped robot places all feet at the same positions on the ground in the shoulder coordinates at first. Since each leg starts swinging at mutually different time instants, as in the gait diagram shown in Fig. 7, the swing ranges of all legs are different, and the length of a stride is limited by the admissible kinematic range, as illustrated in Fig. 7 (a). It is possible to produce a longer stride by a proper initial posture that places each foot as shown in Fig. 7 (b), which makes the swing ranges of all legs even in the shoulder coordinates. According to the gait diagram in Fig. 4, feet positions of the proper initial posture for the forward straight gait can be described in the shoulder coordinates as follows:

$$\text{First swing leg}: \quad ft_s^x = -\left(\frac{1}{2} - \frac{\beta - 0.75}{\beta}\right) \cdot \lambda$$
$$\text{Second swing leg}: \quad ft_s^x = -\left(\frac{1}{2} - \frac{\beta - 0.5}{\beta}\right) \cdot \lambda \qquad (5)$$
$$\text{Third swing leg}: \quad ft_s^x = \left(\frac{\beta - 0.25}{\beta} - \frac{1}{2}\right) \cdot \lambda$$
$$\text{Fourth swing leg}: \quad ft_s^x = \frac{1}{2} \cdot \lambda$$

where λ is the stride and ft_s^x denotes x axis of foot position in the shoulder coordinates.

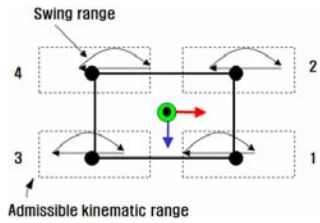

(a) Without initial gait posture

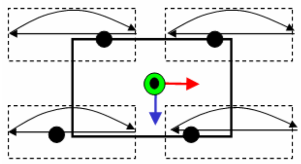

(b) With initial gait posture

Fig. 7 Work range of tip position

IV. EXPERIMENTS

1. Effect of the initial posture

As described in Section 3.4, it is possible to maximize the stride through a proper initial posture, which makes the swing range of the legs even with respect to the origin of the shoulder coordinates. Fig. 8 shows the effect of the initial posture on maximum stride. Without the initial posture, the inverse kinematic solution of a foot trajectory when $\lambda = 60\ mm$ reaches singularity, as shown in Fig. 8 (a). However, as in Fig. 8 (b), the inverse kinematic solution of foot trajectory with the initial posture is smooth enough for the same stride. With the initial posture, the inverse kinematic solution of the foot trajectory reaches singularity when $\lambda = 75\ mm$ as shown in Fig. 8; this implies a 25% improvement in stride and consequently walking speed.

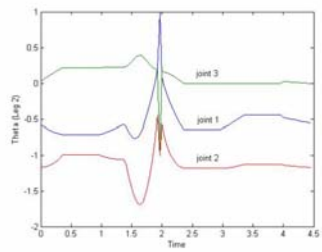

(a) Without the initial posture: $\lambda = 60\ mm$

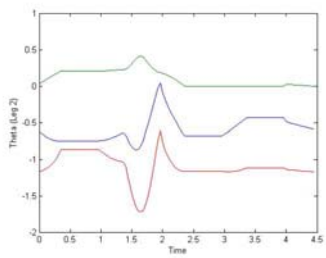

(b) With the initial posture: $\lambda = 60\ mm$

Fig. 8 Improvement of stride with the proper initial posture

3. Walking stabilization by centroid sway

In order to verify the effect by experiments, an inclinometer on the robot measured the body slope in the x and z axes during walking. Fig. 9 (a) is the inclinometer measurement without sway, and Fig. 9 (b) is the measurement with sway. The walking motion with sway is much more stable, as implied in the figure.

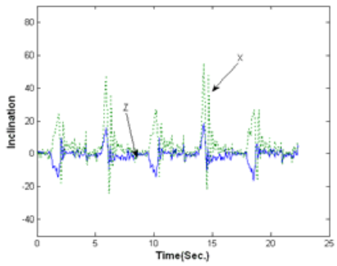

(a) Without centroid sway

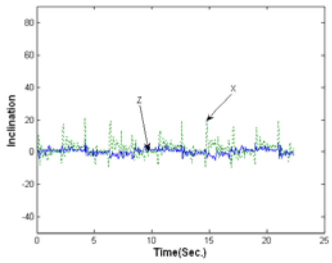

(b) With centroid sway

Fig. 9 x and z inclinometer data

4. Gait motion

The proposed gait planning algorithm was verified through experiments for several gaits. Due to space limitations, some snapshots of the forward and rotation gaits are presented only briefly in this paper.

• Forward gait: Fig. 10 shows the robot posture at the beginning and after one walking period of the forward gait. The robot posture at the beginning is the proper initial posture described in Section 3.4. Here, the walking period and walking distance were 4s and 65 mm respectively.

(a) Initial gait posture (b) After one walking period

Fig. 10 Forward straight gait

• Rotation gait: Fig. 11 shows the rotation gait with 15^o heading angle change command. After 6 steps, the robot changed its heading angle by 90^o as shown in Fig. 11 (b).

(a) Initial gait posture (b) After six walking periods

Fig. 11 Rotation gait

VI. CONCLUSION

Reliability and online characteristics are indispensable for the gait planning algorithm of a commercialized robot. In addition, gait planning should be compact and portable for an embedded controller.

In this study, which is based on systematic planning, a reliable gait control is proposed for the quadruped robot pet Genibo developed by DASA, Korea. The reliability of the proposed algorithm is ensured at two levels: trajectory planning and joint control. At the planning level, centroid sway is able to ensure walking stability for gait control. At the joint control level, sample-based interpolation is proposed to make the joint trajectories obtained at the planning level tractable for the small joint motor-controller of the miniaturized robot. Ground coordinate representation helps to integrate various gaits, and it is possible to maximize a stride by means of a proper initial posture that places all feet at appropriate positions, taking into account the admissible kinematic range in advance. Through experiments on the joint control and gait, it is possible to verify the performance of the proposed gait control algorithm.

ACKNOWLEDGEMENT

The authors would like to thank Suk-Hee Kang and researchers in Dasarobot co., Korea for their valuable advice and support in experiments of this paper.

REFERENCES

[1] Sony Corporation, Model information for ERS-7, OPEN-R SDK, 2004
[2] D. Choi et al., Intelligent Robot Pet Genibo, Korea Robotics Society Review 2008, 5(2), 4–11 (in Korean)
[3] S. Song et al., An Analytical Approach for Gait Study and Its Applications on Wave Gaits, The International Journal of Robotics Research 1987, 6(2), 60–71
[4] H. Hwang and Y. Youm, Steady Crawl Gait Generation Algorithm for Quadruped Robots, Advanced Robotics 2008, 22(13–14), 1539–1558
[5] B. Min, Analysis of Quadruped Crab Gait and its Application on Adaptive Gait Control, Ph.D. Thesis, KAIST, 1993
[6] Y. Lee et al., A Hierarchical Strategy for Planning Crab Gaits of a Quadruped Walking Robot, Robotica 1994, 12(1), 23–31
[7] G. Golubovic and Huosheng Hu, Parameter Optimization of an Evolutionary Algorithm for On–line Gait Generation of Quadruped Robots, Proceedings of the IEEE International Conference on Industrial Technology Dec. 2003, 1, 221–226
[8] J. Rebula et al., A Controller for the LittleDog Quadruped Walking on Rough Terrain, Proceedings of 2007 IEEE International Conference on Robotics and Automation, April 2007, 1467–1473

The development of the Omnidirectional Home Care Mobile Robot

Jie-Tong Zou[1] , Kuo L. Su [2] and Feng-Chun Chiang[3]

[1.] *Department of Aeronautical Engineering,National Formosa University, Taiwan*
(scott@nfu.edu.tw)

[2.] *Department of Electronical Engineering, National Yunlin University of Science and Technology, Taiwan*
(sukl@yuntech.edu.tw)

[3.] *Institute of Opto-Mechatronics and Materials,WuFeng Institute of Technology, Taiwan*
(q053751519@yahoo.com.tw)

***Abstract*:** Rapid progress of standard of living and health care resulted in the increase of aging population. More and more elderly people do not receive good care from their family or caregivers. Intelligent mobile robot combining sensing technologies and wireless communication technologies is very important in reducing the cost of medical resources.

The first objective of this research is to develop a service mobile robot for taking care of elderly people. The kinematic equations of the robot platforms will be developed in this research. The PC-based controller can control the mobile robot platform. This service mobile robot is equipped with "Indoor positioning system" and obstacle avoidanc e system. The indoor positioning system is used for rapid and precise positioning and guidance of the mobile robot. The obstacle avoidance system can detect static and dynamic obstacles.

***Keywords*:** Home care; intelligent mobile robot; Indoor Localization; remote control.

I. INTRODUCTION

In the last few years, intelligent robots were successfully fielded in hospitals [1], museums [2], and office buildings/department stores [3], where they perform cleaning services, deliver, educate, or entertain [4]. Robots have also been developed for guiding blind people, as well as robotic aids for the elderly.

Today, the number of elderly in need of care is increasing dramatically. As the baby-boomer generation approaches the retirement age, this number will increase significantly. Current living conditions for the majority of elderly people are already unsatisfactory, and situation will worsen in the future. [5]

Rapid progress of standard of living and health care resulted in the increase of aging population. More and more elderly people do not receive good care from their family or caregivers. Maybe the intelligent service robots can assist people in their daily living activities. Robotics aids for the elderly have been developed, but many of these robotics aids are mechanical aids. [6] [7] [8]. The intelligent service robot can assist elderly people with many tasks, such as remembering to take medicine or measure blood pressure on time.

The main objective of this research is to develop a service mobile robot for taking care of elderly people. This service mobile robot is equipped with "Indoor positioning system". The indoor positioning system is used for rapid and precise positioning and guidance of the mobile robot. Five reflective infrared sensors are placed around the robot for obstacle avoidance.

The wireless IP camera is placed on the top layer of this robot. Through the internet remote control system, the live image of the IP camera on the robot can be transferred to the remote client user. With this internet remote control system, the remote client user can monitor the elderly people or the home security condition. On the aid of this system, remote family member can control the robot and talk to the elderly. This intelligent robot also can deliver the medicine or remind to measure the blood pressure or blood sugar on time. We hope this intelligent robot can be a housekeeper or family guard to protect our elderly people or our family.The functions of the proposed robot are illustrated as follows:

1. Deliver medicine or food on time
2. Remind to measure and record the blood pressure or blood sugar of the elderly on time
3. Remind the elderly to do something important
4. Assist the elderly to stand or walk
5. Send a short message automatically under emergency condition
6. With the remote control system, remote family member can control the robot and talk to the elderly.

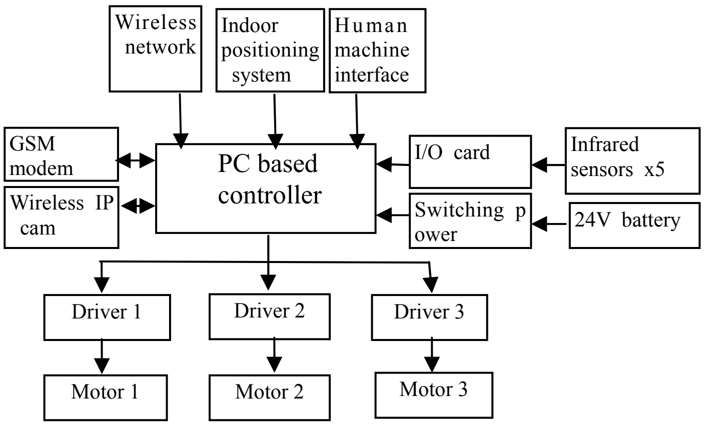

Fig.1. Hardware structure of the service mobile robot for taking care of elderly people.

Hardware structure of the service mobile robot for taking care of elderly people is shown in Fig. 1. A PC based controller was used to control three DC servo motors. The indoor positioning system was used for rapid and precise positioning and guidance of the mobile robot. Five reflective infrared sensors are connected to an I/O card for sensor data acquisition. The GSM modem can send a short message automatically under emergency condition. The live image of the wireless IP camera on the robot can be transferred to the remote client user. The subsystems of this robot are explained in the next section.

II. The Robot Mechanism

The proposed service mobile robot for taking care of elderly people is shown in Fig. 2. The main body of this robot is consisted with five layers of hexagonal aluminum alloy board. Many wheeled mobile robots are equipped with two differential driving wheels. Since these robots possess 2 degrees-of-freedom (DOFs), they can rotate about any point, but cannot perform holonomic motion including sideways motion[9]. To increase the mobility of this service robot, three omni-directional wheels driven by three DC servo motors are assembled on the robot platform (see Fig. 2). The omni-directional mobile robots can move in an arbitrary direction without changing the direction of the wheels.

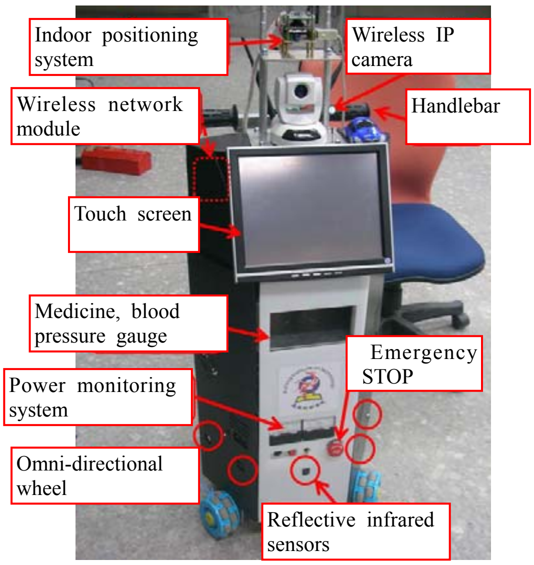

Fig.2.Structure of service mobile robot for taking care of elderly people.

The three-wheeled omni-directional mobile robots are capable of achieving 3 DOF motions by driving 3 independent actuators [10] [11], but they may have stability problem due to the triangular contact area with the ground, especially when traveling on a ramp with the high center of gravity owing to the payload they carry.

Fig. 3(a) is structures of the omni-directional wheel, Fig. 3(b) is the motor layout of the robot platform. The relationship of motor speed and robot moving speed is shown as:

$$V_1 = \omega_1 r = V_x + \omega_p R$$
$$V_2 = \omega_2 r = -0.5V_x + 0.867V_y + \omega_p R$$
$$V_3 = \omega_3 r = -0.5V_x - 0.867V_y + \omega_p R \qquad (1)$$

Where:

V_i=Velocity of wheel i
ω_i=rotation speed of motor i
ω_P= rotation speed of robot
r=radius of wheel
R=distance from wheel to center of the platform

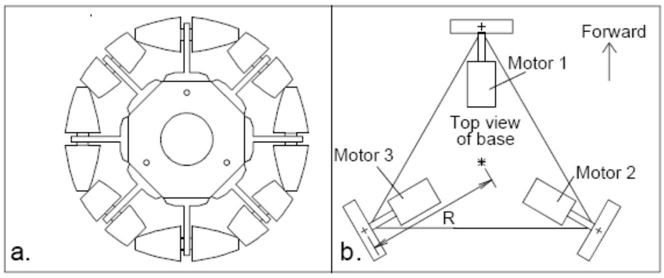

Fig.3. (a) Structure of Omni-directional wheel; (b) Motor layout of Robot platform

As shown in Fig. 4(a), 3D CAD software (SolidWork) was used to design the robot platform. An omni-directional wheel composed of passive rollers or balls was driven by a DC servo motor. Fig. 4(b) is the photo of the robot platform with three omni-directional wheels. The omni-directional robot platform can move in an arbitrary direction and can rotate about any point. The omni-directional robot platform can enhance the mobility of mobile robots.

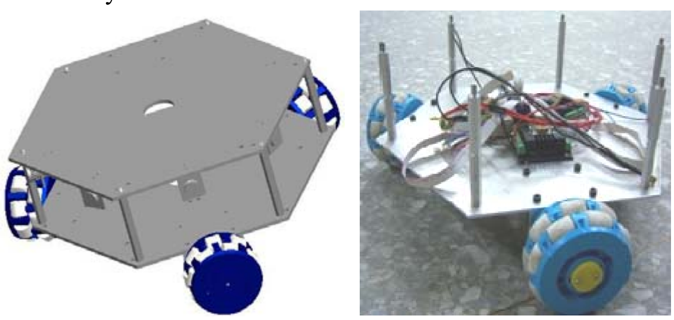

Fig.4. (a)3D CAD software was used to design the robot platform; (b) Photo of the robot platform with three omni-directional wheels

III. Indoor Localization System

Fig. 5. Indoor localization system (Hagisonic co.)

As shown in Fig. 5, Indoor localization system [12], which used IR passive landmark technology, was used in the proposed service mobile robot. The localization sensor module (see Fig. 6) can analyze infrared ray image reflected from a passive landmark with characteristic ID. The output of position and heading angle of a mobile robot is given with very precise resolution and high speed. The position repetition accuracy is less than 2cm; the heading angle accuracy is 1 degree.

Fig. 6. localization sensor module (Hagisonic co.)

IV. Human-machine interface (HMI)

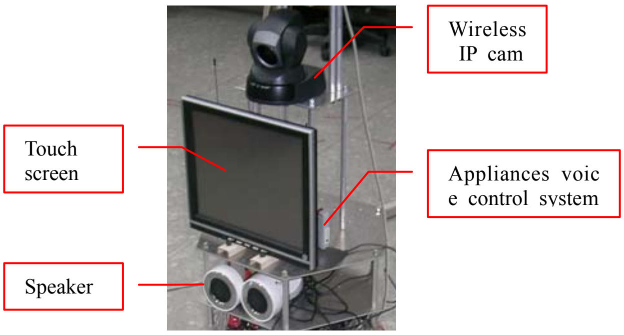

Fig. 7. Human-machine interface (HMI)

The human-machine interface (HMI) includes touch screen, speaker, and appliances voice control system. Touch screen can be regarded as input and display interface. Speaker can produce the voice of robot. Appliances voice control system can let users or the elderly to remote control the appliances by voice command.

V. Experimental Results

1. Path error test for the omni-directional robot platform.

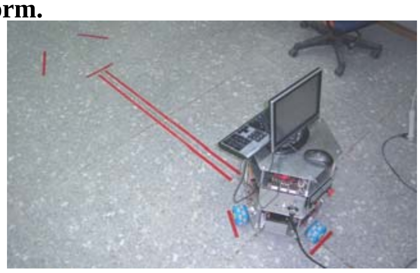

Fig.8. Straight Path error test for the omni-directional robot platform

The three-wheeled omni-directional mobile robots are capable of achieving 3 DOF motions by driving 3 independent actuators, but they may have stability problem due to the triangular contact area with the ground. In order to understand the stability of three-wheeled omni-directional mobile robot, we made some experiments to measure the straight path error of the mobile robot. As shown in Fig. 9, the three-wheeled omni-directional mobile robot moved along a 150cm straight path. A chalk was used to record the robot moving path. The transverse path error can be measured between robot moving path (path recorded by a chalk) and the preset red line. The experimental results are shown in Fig. 9(a)-9(c).

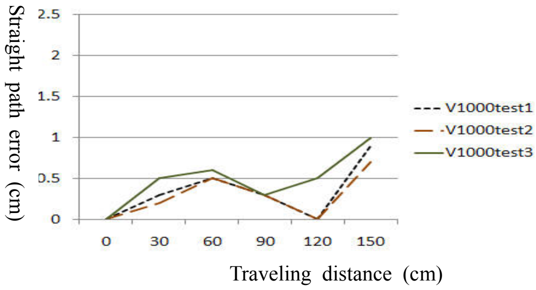

(a) Straight path error (cm) test, motor speed:V1000

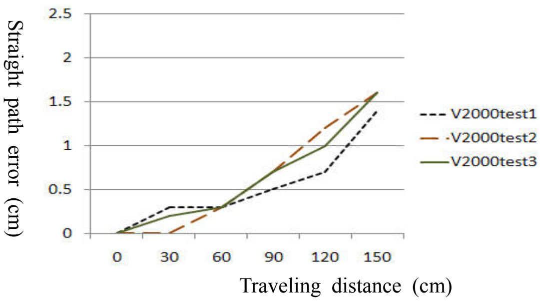

(b) Straight path error (cm) test, motor speed:V2000

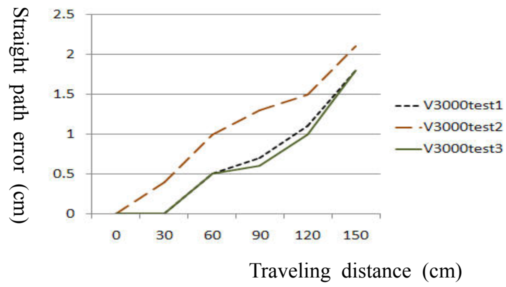

(c) Straight path error (cm) test, motor speed:V3000

Fig. 9.Straight path error with different motor speed

Table 1 Robot traveling speed (m/s) according to different motor speed

Motor speed(rpm)	Robot traveling speed(m/s)
V1000	0.0833
V2000	0.166
V3000	0.25

In Fig. 9(a)-9(c), V1000, V2000 and V3000 are the motor speed. The robot traveling speed (m/s) according to different motor speed is shown in Ta ble 1. From these experimental results, when the ro bot moves faster or farther, the straight line error will increase.

2. Test of moving distance after motor stop

The omni-directional mobile robot using omni-directional wheels composed of passive rollers or balls. As shown in Fig. 10, this experiment is to measure the moving distance after motor stop. The mobile robot moves along a straight line with different motor speed. From the experimental results in Fig. 11, when the robot moves faster, the inertia force will let the robot to move a longer distance after the motors stop. If the motor speed is under 1500 r.p.m., the robot moving distance approaches zero after motor stop.

Fig.10. Test of moving distance after motor stop fo r different motor speed

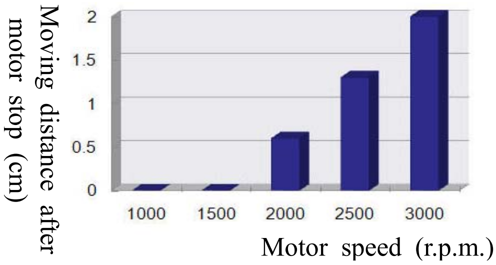

Fig.11. The moving distance after motor stop for di fferent motor speed

V. CONCLUSION

Today, the number of elderly in need of care is increasing dramatically. More and more elderly people do not receive good care from their family or caregivers. Maybe the intelligent service robots can assist people in their daily living activities.

The main objective of this research is to develop a service mobile robot for taking care of elderly people. This service mobile robot is equipped with "Indoor positioning system". The indoor positioning system is used for rapid and precise positioning and guidance of the mobile robot. Five reflective infrared sensors are placed around the robot for obstacle avoidance.

On the aid of the remote control system, remote family member can control the robot and talk to the elderly. This intelligent robot also can deliver the medicine or remind to measure the blood pressure or blood sugar on time. We hope this intelligent robot can be a housekeeper or family guard to protect our elderly people or our family.

In order to understand the stability of three-wheeled omni-directional mobile robot, we made some experiments to measure the straight path error of the mobile robot. From these experimental results, when the robot moves faster or farther, the straight line error will increase.

The omni-directional mobile robot using omni-directional wheels composed of passive rollers or balls. From the experimental results, when the robot moves faster, the inertia force will let the robot to move a longer distance after the motors stop. If the motor speed is under 1500 r.p.m., the robot moving distance approaches zero after motor stop.

REFERENCES

[1] King, S., and Weiman, C, "Helpmate autonomous mobile robot navigation system", Proceedings of the SPIE Conference on Mobile Robots, Vol. 2352, pp.190–198, 1990.

[2] Burgard, W.; Cremers, A.; Fox, D.; H¨ahnel, D.; Lakemeyer, G.;Schulz, D.; Steiner,W.; and Thrun, S. "Experiences with an interactive museum tour-guide robot", Artificial Intelligence,1999.

[3] Endres, H.; Feiten, W.; and Lawitzky, G., "Field test of a navigation system: Autonomous cleaning in supermarkets.", Proceedings of the 1998 IEEE International Conference on Robotics & Automation (ICRA 98),1998.

[4] Schraft, R., and Schmierer, G., "Serviceroboter", Springer verlag. In German,1998.

[5] Nicholas Roy, Gregory Baltus, Dieter Fox, Francine Gemperle, Jennifer Goetz, Tad Hirsch Dimitris Margaritis, Michael Montemerlo, Joelle Pineau, Jamie Schulte, Sebastian Thrun, "Towards Personal Service Robots for the Elderly", Workshop on Interactive Robots and Entertainment (WIRE 2000), 2000.

[6] Song, W.-K.; Lee, H.-Y.; Kim, J.-S.; Yoon, Y.-S.; and Bien, Z. Kares, "Intelligent rehabilitation robotic system for the disabled and the elderly. Proceedings of the 20th Inter. Conf. of the IEEE Engineering in Medicine and Biology Society, Vol. 5, pp. 2682–2685,1998.

[7] Dario, P.; Laschi, C.; and Guglielmelli, E., "Design and experiments on a personal robotic assistant.", Advanced Robotics 13(2) ,pp.153–69,1999.

[8] Takahashi, Y.; Kikuchi, Y.; T.Ibaraki; and Ogawa, S., "Robotic food feeder.", Proceedings of the *38th* International Conference of *SICE*, pp. 979–982,1999.

[9] Jae-Bok Song and Kyung-Seok Byun, "Design and Control of an OmnidirectionalMobile Robot with SteerableOmnidirectional Wheels", Mobile Robots, Moving Intelligence, pp. 576, 2006.

[10] Carlisle, B. "An Omnidirectional Mobile Robot", Development in Robotics, Kempston, pp.79-87, 1983.

[11] Pin, F. & Killough, S., "A New Family of Omni-directional and Holonomic Wheeled Platforms for Mobile Robot", IEEE Transactions on Robotics and Automation, Vol. 15,No. 6, pp. 978-989. 1999.

[12] http://www.hagisonic.com/

Path Planning of the Multiple Mobile Robot System

Sheng-Ven Shiau[1], Kuo-Lan Su[2], Chun-Chieh Wang[3], Jr-Hung Guo[1]

1. graduate school Engineering Science and technology, National Yunlin University of Science & Technology
2. Department of Electrical Engineering, National Yunlin University of Science & Technology, Taiwan
3. Department of Electronic Engineering Chienkuo Technology University, Taiwan
E-mail: g9610808@yuntech.edu.tw, sukl@yuntech.edu.tw

Abstract: We present the path planning techniques on the multiple mobile robot system. The mobile robot has the shape of cylinder and its diameter, height and weight is 8cm, 15cm and 1.5kg. The controller of the mobile robot is MCS-51 chip, and can acquire the detection signals from sensors through I/O pins, and receives the command from the supervised compute via wireless RF interface, and transmits the status of the mobile robots to the supervised computer via wireless RF interface. The mobile robot is module based system, and contains a controller module (including DC motor driver), an obstacle detection module, a voice module, a wireless RF module, an encoder module, and a compass detection module. We proposed the evaluation method to arrange the position of the multiple mobile robot system, and develop path planning interface on the supervised computer for the mobile robot system. In the experimental results, mobile robots can receive the command from the supervised computer, and move the next position according to the proposed method.

Keywords**:** path planning**,** mobile robot, compass

I. INTRODUCTION

With the robotic technologies development with each passing day, robot systems have been widely employed in many applications. Nowadays, robot systems have been applied in factory automation. Recently, more and more research takes interest in the robot which can help people in our daily life, such as service robot, office robot, security robot, and so on. In the future, we believe that robot will play an important role in our daily life.

In the past literatures, many experts research in the mobile robot. Some research addressed in developing target-tracking system of mobile robot [1,2,10], such as Hisato Kobayashi et al. proposed a method to detect human being by an autonomous mobile guard robot [3]. Yoichi Shimosasa et al. developed Autonomous Guard Robot [4] witch integrate the security and service system to an Autonomous Guard Robot, the robot can guide visitors in daytime and patrol in the night. D. A. Ciccimaro developed the autonomous security robot – "*ROBART III*" which equipped with the non-lethal-response weapon [5, 6]. Some researchers study path planning of the mobile robot [11].

The paper considers the problem of the multiple robot system working together. The multiple mobile robot system has more advantages than one single robot system [7]. First, the multiple mobile robots have the potential to finish some tasks faster than a single robot [8]. Furthermore, using several robots introduces redundancy. Multiple mobile robots therefore can be expected to be more fault tolerant than only one robot. Another advantage of multiple mobile robots is due to merging of overlapping information, which can help compensate for sensor uncertainty [9].

The paper is organized as follows: Section II describes the system architecture of the multiple mobile robot system, and explains the functions of the mobile robot. Section III explains the path planning method for the multiple robots on the user interfsce, and how to execute the formation exchange step by step. Section IV presents the experimental results on the formation exchange using the multiple mobile robot system. Section VI presents brief concluding remarks.

II. SYSTEM ARCHITECTURE

The system architecture of the multiple mobile robot system is shown in Fig 1. The system contains a supervised computer, a monitor, a wireless RF interface, remote supervised computer, a color CCD and some mobile robots. The supervised computer can transmits the command to control mobile robots, and receives the status of the mobile robots via wireless RF interface. They contain the orientation and displacement of mobile robots. Each robot is arranged an ID code. The supervised computer can transmits the ID code to the mobile robot, and transmits the orientation and position command to the mobile robot. The mobile robot can move the next position according the command from the supervised computer.

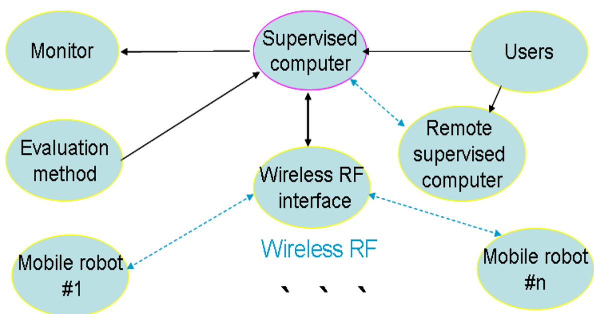

Fig. 1 The architecture of the multiple robot system

The mobile robot has the shape of cylinder, and it's equipped with a microchip (MCS-51) as the main controller, two DC motors, some sensor circuits, a voice driver module, an encoder module, switch input, three Li batteries and a wireless RS232 interface. In the input signals, the encoder module transmits the pulse signal to the controller, and program the displacement of the mobile robot. The reflective IR sensors to detect cross point of the grid plant, and decide the location of the mobile robot. The compass module can calculate the orientation of the mobile robot. The mobile robot can control two DC motors and voice module through I/O pins, and communicate with the supervised computer via wireless RF interface. The core of the RF module is microprocessor (AT89C2051), and communicates with the controller via series interface (RS232). Meanwhile, the mobile robot has four wheels to provide the capability of autonomous mobility. The block diagram of the mobile robot is shown in Fig. 2.

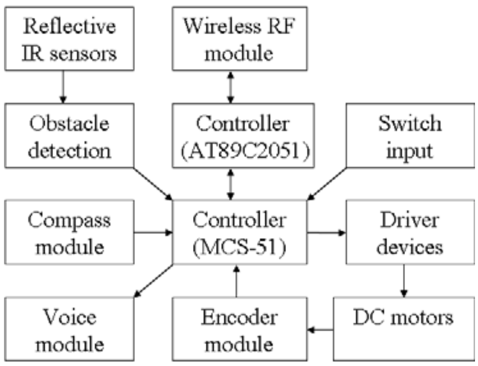

Fig. 2. The block diagram of the mobile robot

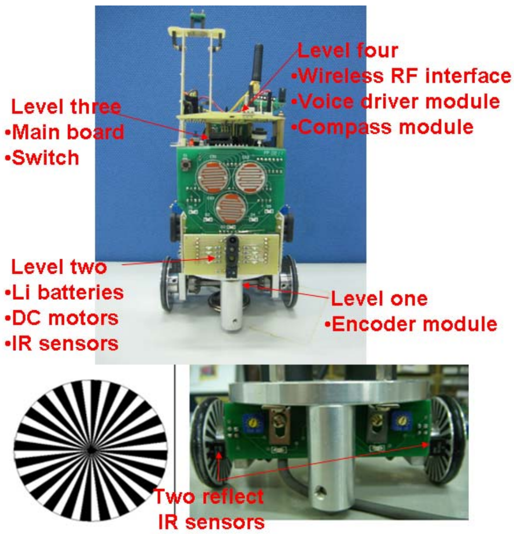

Fig. 3. The structure of the mobile robot

The structure of the mobile robot is shown in Fig. 3. It has some hardware circuits that are classified four levels in the mobile robot. The shape of each level is circle. The bottom of the mobile robot is level one, and the top is level four. The level one of the mobile robot is an encoder module. The module can calculate the displacement of the mobile robot using reflective IR sensors. We use two reflect IR sensors to calculate the pulse signals from the two wheels of the mobile robot. The power of the mobile robot is three Li batteries to be embedded in level two, and connects with parallel arrangement. The level has three obstacle detection circuits using IR sensors, and contains two DC motors to drive the mobile robot. The level three of the mobile robot has main board. The controller of the mobile robot can acquires the detection signal from sensors through I/O pins, and receives the status of the mobile robots via wireless RF interface. The controller of the mobile robot can transmits the detection results to the supervised computer via wireless RF interface. The switch input can turn on the power of the mobile robot, and selects power input to be Li batteries or adapter. The level four contains a wireless RF interface, a compass module and a voice driver module.

The bottom of the mobile robot is encoder module. The module can calculate the moving distance for the mobile robot. We plot the white line and black line on the wheel of the mobile robot, and use two reflect IR sensors to calculate the pulse signals from the two wheels of the mobile robot. We can set the pulse number for per revolution to be P , and the mobile robot move pulse number to be B . We can calculate the displacement D of the mobile robot using the equation

$$D = 4.25 \times \pi \frac{B}{P} \tag{1}$$

The diameter of the wheel is 4.25 cm.

III. USER INTERFACE

The user interface of the multiple mobile robot system is shown in Fig. 4. The interface has many parts. The label "A" is the communication protocol between the supervised computer and the mobile robots via wireless RF interface. The label "B" set the start position for the mobile robot. The label "C" set the goal position on the grid plate. The label "D" is the command data region by the user. The label "E" can set the information of the mobile robot. The label "F" displays the experimental results (success or failure) for the mobile robot. The label "G" can display the status for the mobile robot on real-time. The label "H" It can display the status of the mobile robot. It contains starting, searching success or failure. The label "I" can display the position on real-time and the final position for the mobile robot. The label "J" can display the orientation on real-time and the final orientation for the mobile robot. The label "K" displays the number of the success and failure for the mobile robot on the test.

The motion platform of the multiple mobile robot system is shown in Fig. 5. The platform is chessboard based rectangle. The arrangement of the platform is 7 grids on the horizontal direction, and is 9 grids on the vertical direction. The user can set the start position and goal position on the platform. The mobile robot can move on the platform from the start position to the goal position, and transmits the status (displacement and orientation) to the supervised computer via wireless RF interface. The mobile robot measures the displacement and orientation using the encoder module and the compass module. If the moving position of the mobile robot is over the goal position, and we define "failure" on the test. Otherwise the mobile robot moves to the goal position, and we can define "success" on the test. The mobile robot can decide the next orientation using random processing on the test.

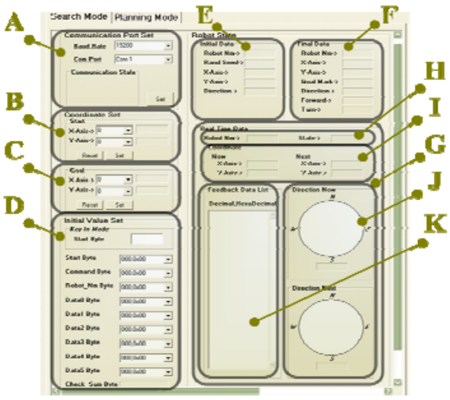

Fig. 4. The user interface of the multiple mobile robot system

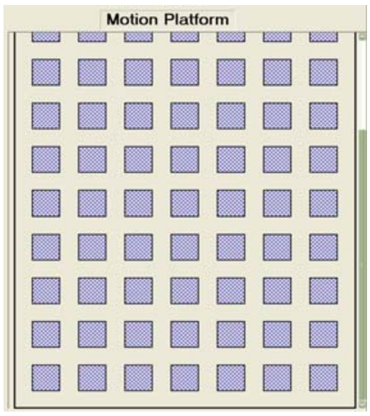

Fig. 5. The interface of the passive detection modules

IV. EXPERIMENTAL RESULT

We must test the accuracy of the mobile robot on the displacement and orientation. The displacement experimental results of the mobile robot is shown in Fig. . The start position of the mobile robot is presented in Fig. 6 (a). We set the displacement of the mobile robot is 10cm. The supervised computer can calculates the pulse number to be about 54, and transmits the command to the mobile robot. The mobile robot receives the pulse number from the encoder module move to the next position on the 54 pulse; the experiment result is shown in Fig. 6 (b). Then we set the displacement to be 30cm. we can compute the pulse number to be 162 according to the equation (1). The mobile robot can move forward on the 162 pulse from the encoder module. The experimental results are shown in Fig. 6 (c) and (d).

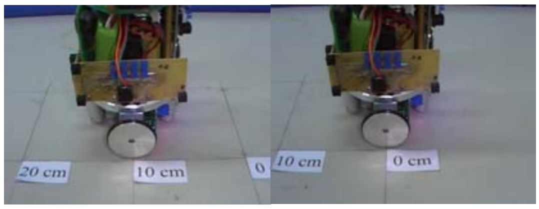

(a) Start position (b) Move to 10cm

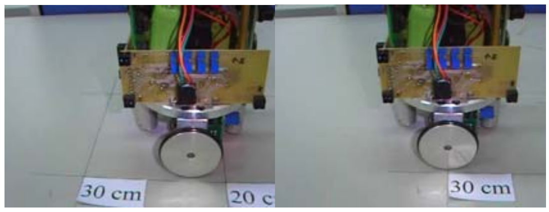

(c) Move to 30cm (continue) (d) Move to 30cm

Fig. 6. The displacement of the mobile robot

The orientation experimental results of the mobile robot are shown in Fig. 7. The start position of the mobile robot is presented in Fig. 7 (a). We set the orientation of the mobile robot is 45^0. The supervised computer can calculates the pulse number to be about 21 on the two driver wheel, and transmits the command to the mobile robot. The mobile robot receives the pulse number from the encoder module move to the next position on the 21 pulse; the right driver wheel is forward, and the left driver wheel is forward. The experiment result is shown in Fig. 7 (b). Then we set the orientation to be 270^0. The mobile robot can turn left 90^0 according to the command from the supervised computer. We can compute the pulse number to be 42 according to the equation (1). The mobile robot can move forward on the 42 pulse from the encoder module, and the left wheel can move backward 42 pulse. The experimental results are shown in Fig. 7 (c) and (d).

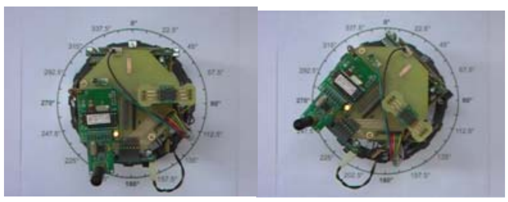

(a) Start position (b)Turn right 45^0

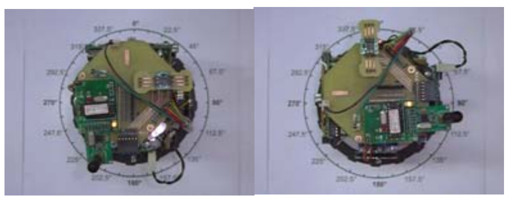

(c) Start position (d) Turn left 90^0

Fig. 7. The orientation of the mobile robot

We implement the formation change using the multiple mobile robot system. In the experiment results, we use four mobile robots to arrange on the four directions of the rectangle. The experimental scenario is shown in Fig 8 (a). The supervised computer orders the command to the four mobile robots. The robot #1 turns left, and moves one grid. The robot #2 turns right about, and move three grids. The robot #3 turns left, and moves two grids. The robot #4 turns left, and moves two grids. The experimental results are shown in Fig. 8 (b) and (c). Next the four robots turn right to move four grids (Fig 8 (d) and (e)). Next the four robots turn left, and move one grid (Fig. 8 (f) and (g)). Finally the robot #1 and #2 turn right, and the robot #3 turn left. The experimental results are shown in Fig. 8 (h). The programming processing is minimum displacement on the test by the four mobile robots.

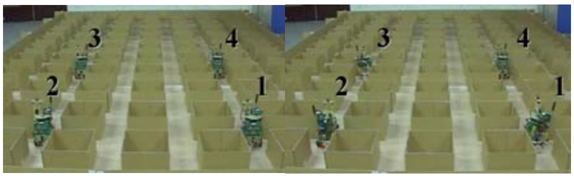

(a)Start position (b) First arrangement

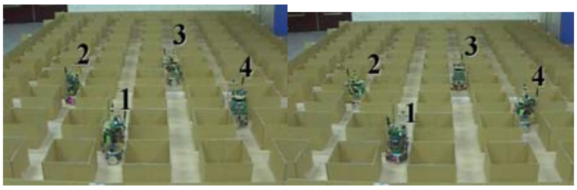

(c)Second arrangement (d) Third arrangement

(e) Forth arrangement (f) Fifth arrangement

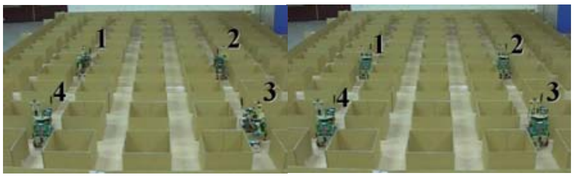

(g) Sixth arrangement (h) Final arrangement

Fig. 8. Formation change for multiple mobile robots

V. CONCLUSION

We have developed the path planning of the multiple mobile robot system. The system contains a supervised computer, a monitor, a wireless RF interface, remote supervised computer, a experimental plate and four mobile robots. The mobile robot has the shape of cylinder and its diameter, height and weight is 8cm, 15cm and 1.5kg, and executes the path planning using two interfaces. One is wireless RF interface, and the other is voice interface. The supervised computer can control multiple mobile robots, and receive the status of the multiple mobile robots via wireless RF interface. Users can program the motion trajectories on the supervised computer. The paper has been presented formation change using four mobile robots. In the future, we want to develop more applications of the multiple mobile robot system.

ACKNOWLEDGMENT

This work was supported by the project "The Development of Multiple Module Based Smart Robots," under Industrial Development Bureau Ministry of Economic Affair of Taiwan.

REFERENCE

[1] S. O. Lee, Y. J. Cho, *et al* (2000), A stable target-tracking control for unicycle mobile robots, The IEEE/RSJ International Conference on Intelligent Robots and Systems, (IROS 2000) , Vol.3 , pp.1822-1827.

[2] L. E. Parker and B. A. Emmons (1997), Cooperative multi-robot observation of multiple moving targets, The IEEE International Conference on Robotics and Automation,, vol.3, pp.2082-2089.

[3] H. Kobayashi and M. Yanagida (1995), Moving object detection by an autonomous guard robot, The 4th IEEE International Workshop on Robot and Human Communication, Tokyo, pp.323-326.

[4] Y. Shimosasa, J. Kanemoto, *et al* (2000), Some results of the test operation of a security service system with autonomous guard robot, The IEEE on Industrial Electronics Society, (IECON 2000), Vol.1, pp.405-409.

[5] Gilbreath, G. A., Ciccimaro, D. A. (2000), An Advanced Telereflexive Tactical Response Robot, Proceedings, Workshop 7: Vehicle Teleoperation Interfaces, IEEE International Conference on Robotics and Automation, ICRA2000, San Francisco, CA.

[6] Ciccimaro, D. A., H. R. Everett (1999), A Supervised Autonomous Security Response Robot, American Nuclear Society 8th International Topical Meeting on Robotics and Remote Systems (ANS'99), Pittsburgh, pp, 25-29.

[7] Y. Cao *et al*(1997), Cooperative mobile robotics: antecedents and directions, Autonomous Robots, Vol.4, No. 1, pp.7-27.

[8] D. Guzzoni et al (2006), Many Robots make short work, AI Mag., Vol. 18, No. 1, pp 55-64.

[9] W. Burgard, M. Moors *et al* (2005), Coordinated Multi-Robot Exploration, IEEE Transaction on Robotics, Vol. 21, No. 3, pp.376-386.

[10] M. J. Lee and G. H. Hwang (2008), Object tracking for mobile robot based on intelligent method, International journal on Artificial life and robotics, Vol. 13, No. 1, pp.359-363.

[11] Y. Y. Fu, C. J. Wu, *et al* (2008), A time-scaling method for near-time-optimal control of an omni-directional robot along specified paths, International journal on Artificial life and robotics, Vol. 13, No. 1, pp.350-354.

The Fifteenth International Symposium on Artificial Life and Robotics 2010 (AROB 15th '10),
B-Con Plaza, Beppu,Oita, Japan, February 4-6, 2010

Multi-level Multi-sensor Based Security System for Intelligent Home

Song-Hiang Chia[1,2], Kuo-Lan Su[3], Sheng-Ven Shiau[1], Ting-Li Chien[2]
1. graduate school Engineering Science and technology, National Yunlin University of Science & Technology
2. Department of Electronic Engineering, Wu-Feng Institute of Technology, Taiwan
3. Department of Electrical Engineering, National Yunlin University of Science & Technology, Taiwan
E-mail: g9610808@yuntech.edu.tw, sukl@yuntech.edu.tw

Abstract: The paper develops a multi-level multi-sensor based security system that has multiple interfaces to be applied in intelligent home. The security system contains four levels. There is passive detection level, active detection level, system supervised level and remote supervised level. The control unit of these passive modules is HOLTEK microchip. Each passive module has two variety interfaces (wireless RF and voice). These modules can use voice to alarm users for event condition, and transmit the real-time status and image signal to the active detection level and system supervised level via wireless RF interface. The active detection level can communicate with other level via wireless RF interface or wireless Internet. The remote supervised level, supervised level and active detection level can communicate with other level via wireless Internet. It can display status of these modules on the monitor. Finally, we present some experimental results using passive and active detection modules on the security system.

Keywords: multi-level multi-sensor**,** HOLTEK microchip, wireless RF interface, wireless Internet

I. INTRODUCTION

Intelligent buildings and home can provide safety, convenience and welfare for human living in the 21st century, and allow effective management of resource with minimum life-time costs at the same time. How to constructer a safety environment for human life? The most important role is security system. The hardware and software of the security system are complexity, and are not easy to maintain and repair. To increase their development and adaptability, the concept of the module-based security system (MBSS) has been studied in the intelligent building and home. We have developed some module based security modules for the intelligent. How to build up the communication protocol and user interface between the supervised computer and these security modules? It is very importance and difficult for researcher. The interface must be very easy to operate for users.

In the past literatures, many experts research in the security system. Wang and So [1] presented the history of development of building automation system (BAS). The structure of features of a modern BAS was introduced and future trends of BAS are discussed. Azegami and Fujiyoshi [2] described a systematic approach to intelligent building design. Kujuro and Yasuda [3] discussed the systems evolution in intelligent building. The quality of building services can be enhanced by updated information processing and communications functions of building automation systems. Finley et al. [4] presented a survey of intelligent building and reviews issues such as system perspective, subsystem services, and multi-tenant building. Chung and Fu expect to set up the standard of appliances and communication protocols, and propose a complete system architecture with integrate control kernel to construct an intelligent building system [5, 6].

The paper is organized as follows: section II describes the system structure of the multi-level multi-sensor based intelligent security system for intelligent home, and explains the relation of these levels, and contains devices of each level. The user interface of the intelligent security system is described in Section III. The section present functions of the hand-on controller of the system supervised level. Section IV presents the experimental results using these modules on the AC power detection and intruder detection. The brief concluding comments are described in Section V.

II. SYSTEM ARCHITECTURE

The system architecture of the multi-level multi-sensor based security system is shown in Fig 1. The system contains four levels. There is passive detection level, active detection level, system supervised level and remote supervised level. The passive detection level has wire and wireless security modules, wire and wireless appliance control modules and medical measurement modules. The active detection level has some remote platforms. Such as mobile robots, wheelchair…etc.. The system supervised level has supervised computer, mobile phone, wireless controller and hand-on controller. The communication medium is wireless RF interface and wireless Internet. The remote supervised level may be remote supervised computer, PDA and iPhone. The communication medium is wire/wireless Internet.

We develop the user interface using Visual Basic language for the security system. The system supervised level can control security modules and appliance control modules of the active detection level and passive detection level via wireless RF interface, and supervise the medical measurement modules via wireless RF interface. The remote supervised level can communicate with system supervised level, active detection level and passive detection level via wireless RF interface or wireless Internet. If the wireless Internet is broken, and the communication interface can use the wireless RF interface. Users can acquire detection results and image signals from system supervised level, active detection level or passive detection level.

In the architecture, there are many security detection modules and appliance control modules in the system. They are independent and autonomous, and can work concurrently. Each module of the security system can transmits the measurement values, parameter values and decision results to the active detection modules and the supervised computer via wireless RF interface (RS232). These modules can speech Chinese on real-time measured data using voice module. Users can reset the critical values of these modules from the user interface of the system supervised level or the remote supervised level via wireless RF interface or wireless Internet.

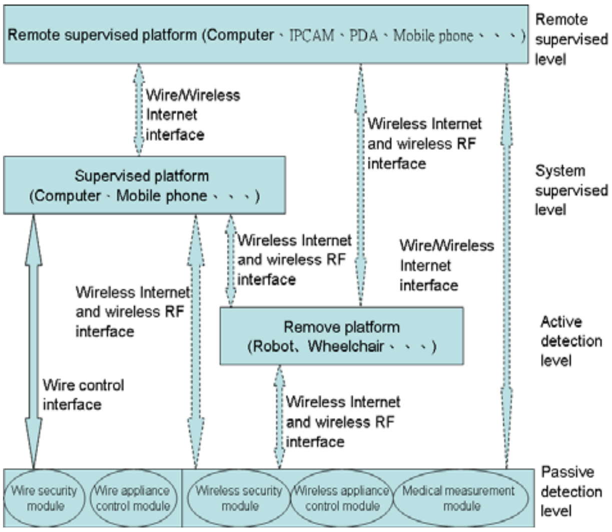

Fig. 1 The system architecture

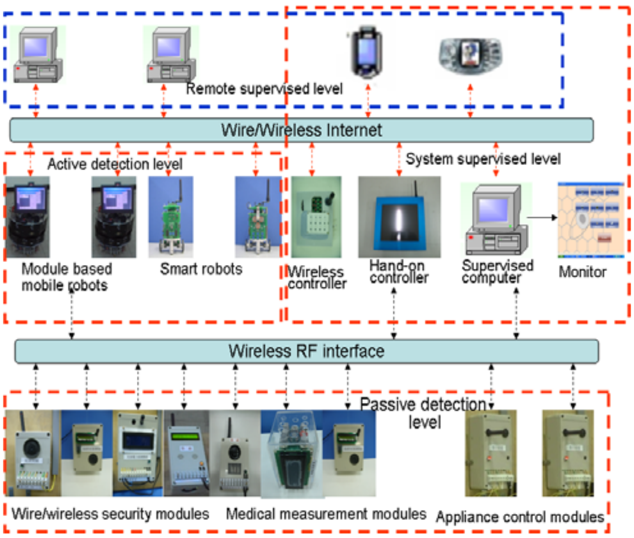

Fig. 2 The prototype of the security system

The controller of these modules is HOLTEK microprocessor. These modules of the passive detection module are classified three types. There are wire/wireless security modules, medical measurement modules and wire/wireless appliance control modules. The active detection level has some remove platform. The main device may be some intelligent mobile robots. We arrange an ID code in each module, and identify the module function by the ID. The prototype of the multi-level multi-sensor based security system is shown in Fig. 2. The security detection modules and appliance control modules of the passive detection level are developed in my laboratory [8]. The mobile robots have been designed in my laboratory, too [9]. In the paper we are interested in communication protocol of these levels for the security system.

III. USER INTERFACE

The user interface of the security system is shown in Fig. 3. The interface has four levels, too. There are wire/wireless passive detection modules and appliance control modules; mobile robot (1) (module based mobile robots), mobile robot (2) (smart robots), GSM interface, remote supervised interface and exit. The interface of the passive detection level is shown in Fig. 4. There are three regions in the supervised interface. This is the graphic supervised monitor for the intelligent security system in the region A. Users can move any modules (passive detection modules and appliance control modules) of the region B to the region using mouse. In the region C, users can program the output response for any security signal input. For example, if the fire condition, we can program alarm, and control appliance module to fight the fire, and control the module based mobile robots or smart robots move to the location. The supervised computer can transmit detection signals to the remote supervised computer and mobile phone via Internet or GSM modern.

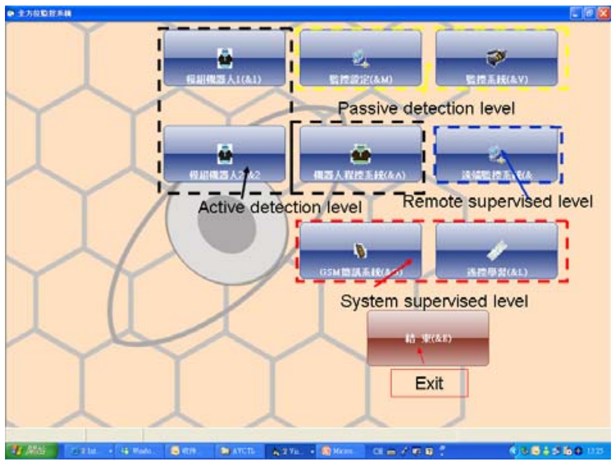

Fig. 3 The user interface of the security system

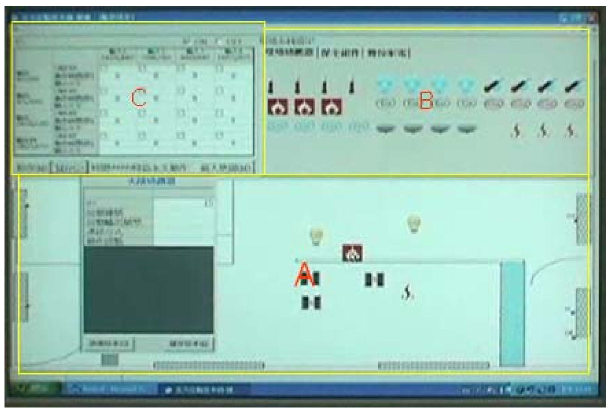

Fig. 4. The interface of the passive detection level

The user interface of the active detection level is shown in Fig. 8. The main role of the interface is mobile robots. The interface can control sixteen mobile robots simultaneously. There are three regions in the supervised interface. The user can program motion trajectory for each mobile robot in the region 1, and can program the motion status for sixteen mobile robots at the same time, and can program 300 motion statuses for each robot. The region 2 can display the status of mobile robots. It contains communication protocol and encoder status. We can know the motion trajectory of the mobile robot. The region 3 has many functions for the mobile robot system. There are loading and storage program file. The user can set the execute cycle for the programmed motion trajectory.

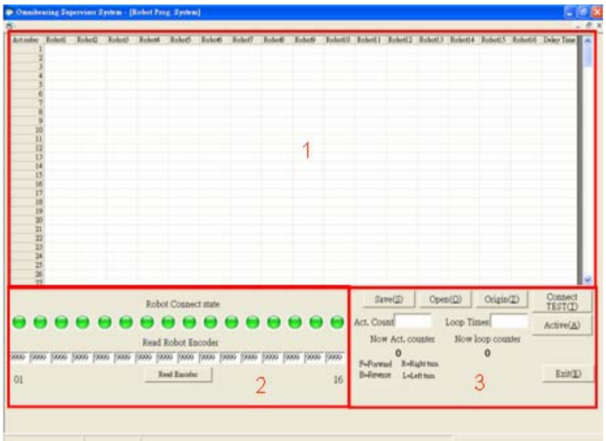

Fig. 5 The user interface of the active detection level

We design the hand-on controller using embedded system. The controller has a touch screen, a main board, a voice module, a wireless RF module and some devices. Users can touch the screen, and roll the screen to select the function on the hand-on controller. The controller can control security modules, appliance control modules and mobile robots on the passive detection level and the active detection level. The prototype of the hand-on controller is shown in Fig. 6. The hand-on controller can hang up the wall, too.

Fig. 6. The user interface of the hand-on controller

In the AC power security detection module, we use redundant management method to estimate the exact values on current and voltage for the security system [7]. The value of the measured parameter is obtained by the following equation at that sample time k, and the estimated value is

$$\hat{x}(k)=\frac{\sum_{i=1}^{l} m_i(k) I_i(k_i)}{\sum_{i=1}^{l} I_i(K)} \tag{1}$$

Where I_i is a weighted value for the each measurement value m_i at the given sample time k. So we can define Ii is

$$Ii=\sum_{j=1}^{l} f\left[\left|m_i(k)-m_j(k)\right| \le \left(b_i(k)+b_j(k)\right)\right] \quad i=1,2,\cdots l \tag{2}$$

$$f[*]=\begin{cases} 1, & if \quad * \quad is \quad true \\ 0, & if \quad * \quad is \quad false \end{cases} \tag{3}$$

The b_i is a threshold value for each measurement value m_i, and m_j is another measurement value.

IV. EXPERIMENTAL RESULT

In the passive detection modules, we use AC power detection module to detect power variety of the home. The power detection module can measure the exact current value using the proposed method, and display on the LCD panel to users, and transmit the detection results to the system supervised level (supervised computer and mobile phone) and the active detection level (mobile robots) via the wireless RF interface. The experimental results are shown in Fig. 7 (a).

(a)

(b)

Fig. 7 The experimental result for AC power detection module

The user can reset the critical power value (1600mA) of the AC power detection module on the user interface, and the initial critical value is 3000mA. The supervised computer of the system supervised level can transmit the reset power value to the module via wireless RF interface. Users can execute the function the on the remote client via wireless Internet. The experimental result is shown in Fig. 7 (b). Then we see the new critical value to display on the interface of the supervised computer.

Multi-level multi-sensor based security system can use passive detection modules and active detection modules to detect environment of the intelligent home. The dangerous event happens on the security system. The security modules of the passive detection level can transmits the signals to the active detection level and system supervised level. The active detection modules (mobile robots) can move to the event position to do double check, and deal with the event. The system supervised level can control the appliance control modules to deal with the dangerous event (fight the fire source), and transmits the status to the remote supervised level via wireless Internet.

Mobile robots of the active detection level can move autonomous according to environment using ultrasonic detection module and IR detection module (Fig. 8 (a)). Users can supervise mobile robots for forward, backward, turn right, turn left and stop using wireless controller, hand-on controller or supervised computer via wireless RF interface or wireless Internet. The security module finds out the intruder from the door. Mobile robots can receive the detection signal from passive detection modules via wireless RF interface, and move to the event location (Fig. 8 (b) and (c)). It can transmit the image signal and the real-time detection results to the supervised computer and the remote supervised computer. The user can control CCD device to catch the face of the intruder via wireless RF interface. The experimental result is shown in Fig. 8 (d).

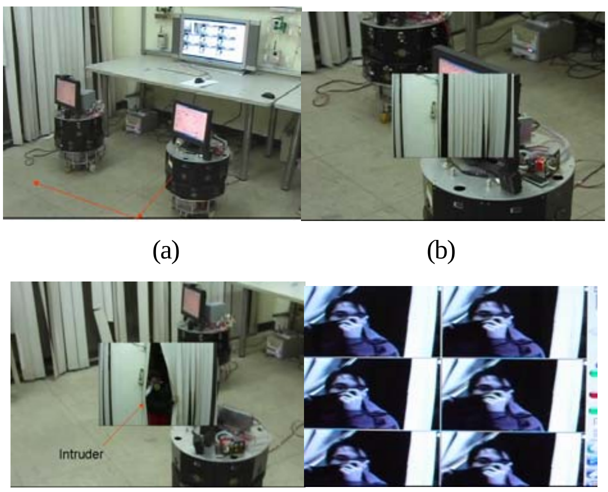

(a) (b)

(c) (d)

Fig. 8. Intruder experimental result using mobile robots

V. CONCLUSION

We have presented a a multi-level multi-sensor based security system that has multiple interfaces to be applied in intelligent home. The security system contains four levels. There is passive detection level, active detection level, system supervised level and remote supervised level. The controller of these modules is HOLTEK microchip. We want to develop multisensor fusion algorithms to enhance the detection results through these detection modules. In the AC power security detection module, we use redundant management method to estimates a exact power detection value for the security system. These security detection modules and appliance control modules can transmit signals to the system supervised level and action detection level. In the paper, we use the intruder event to implement the function of the multi-level multi-sensor based security system for intelligent home. The experimental results are very nice on the system. In the future, we want to increase some security detection modules, and extend the function of the user interface to present the perfect life for human.

ACKNOWLEDGMENT

This work was supported by the project "Design of an auto-recharging system intelligent Robot" under Ministry of Education of Taiwan, R. O. C. (98E-03-206).

·

REFERENCE

[1] C. W. Wang and A. T. P. So (1997), Building Automation In The Century, The 4-th International Conference on Advance on Advances in Power System Control, Operation Management, APCOM-97, Hong Kong, , pp.819-824.
[2] M. Azegami and H. Fujixoshi (1993), A systematic Approach to Intelligent Building Design, IEEE Communications Magazine, pp.46-48.
[3] A. Kujuro and H. Yasuda (1993), Systems Evolution in Intelligent Building, IEEE Communication Magazine, pp.22-26.
[4] Marion R. Finley, Jr. Ancilla Karajura *et al.* (1991), Survey of Intelligent Building Concepts, IEEE Communication Magazine, pp.18-20.
[5] W. Y. Chung, L. C. Fu et al. (2001), A Flexible, Hierarchical and Distributed Control Kernel Architecture for Rapid Resource Integration of Intelligent System, IEEE International Conference on Robotics Automation, Seoul, Korea, pp.1981-1987.
[6] L. C. Fu and T. J. Shih (2000), Holonic Supervisory Control and Data Acquisition Kernel for 21st Century Intelligent Building System", IEEE International Conference on Robotics and Automation, San Francisco CA, pp.2641-2646.
[7] Ren C. Luo, Kuo L. Su (2008), Multilevel Multisensor Based Intelligent Recharging System for Mobile Robot, IEEE Transaction on Industry Electronic. Vol.55, No.1, pp.270-279.
[8] Kuo-Lan Su, Sheng-Ven Shiau et al. (2009), Module Based Security System Applying in Intelligent Home, The Innovative Computing, Information and Control – Express Letters (ICIC-EL), Vol.3, No.4A, pp.1167-1172.
[9] Ting-Li Chein, Kuo L. Su et al. (2009), Intelligent Home-Automation Security System, International Journal of Automation Technology. Vol. 3, No. 2, pp.123-129,

Multisensor Fusion Based Gas Detection Module

Jr-Hom Guo[1], I-Chao Chien[2], Kuo-Lan Su[3], Chia-Ju Wu[3]

1. Graduate school Engineering Science and technology, National Yunlin University of Science & Technology
2. Department of Mechanical Engineering, National Central University,Taiwan
3. Department of Electrical Engineering, National Yunlin University of Science & Technology, Taiwan

Abstract: The paper develops a gas detection module for the intelligent home. The module uses many sensors to detect environment of the home and building. The gas sensors of the module have a NH3 sensor, an air pollution sensor, an alcohol sensor, a HS sensor, a smoke sensor, a CO sensor, a LPG sensor and a nature gas sensor, and can classify more than eight type gases using multisensor fusion algorithms. In the logical filter method, we can use AND or OR filter to be implemented in the gas detection module. Then we can calculate the system reliability of AND filter and OR filter, and classify the gas type in the environment. The controller of the gas detection module is HOLTEK microchip. The module can communicate with the supervised computer via wire interface or wireless RF interface, and caution the user by the voice module. Finally, we present some experimental results to measure unknown gas using the gas detection module on the security system of the intelligent building.

Keywords: intelligent home, multisensor fusion algorithms, logical filter method**.**

I. INTRODUCTION

An intelligent building system (IBS) is the integration of various services, and contains security system, building heating, ventilating and air-conditioning (HVAC) technologies, computer system, tele-communication and Internet. The most important role of the intelligent building is security system. How to build the security system? It is an important issue for the intelligent building. In the security system, redundant and complementally information results can enhance system reliability and certainty using multisensor fusion method, and use module based structure to make it easy to operation. To develop module based security devices is a important working for human life. In generally, it is most important to detect harmful gas in the security system of the home automation. We want to develop a intelligent gas detection module to decrease the dangerous event for intelligent building.

A gas detection module is an instrument comprising an array of chemical sensors to be combined in a board, and a pattern recognition system that is embedded in the controller to classify the gas [1]. The gas detection system plays an important role in the in many fields, e.g. environmental protection, production safety, food surveillance, intelligent transport system and life support system for manned spaceship [2,3,4]. To classify a single gas of the environment, a variety of pattern recognition technologies have been applied to the gas detection system. The most important ones are principlal component analysis (PCA), cluster analysis (CA). and discriminate function analysis (DFA) [5,6]. Meanwhile, quantitative data processing techniques such as multiple linear regression (MLR) and artificial networks (ANN_S) are also used to quantify the gas concentration [7].

The paper is organized as follows: section II describes the system structure of the gas detection system for home automation, and explains the functions of the gas detection module. Section III explains detection algorithms of the gas module, and presents the user interface of the gas detection system. Section IV presents the experimental results of the gas detection on three variety conditions using the module for the home security system. The brief concluding comments are described in Section V.

II. SYSTEM ARCHITECHTURE

The architecture of the gas detection system is shown in Fig. 1. The system contains a gas detection module, a master module, a supervised computer and a pair of wireless RF interface. The main element of the gas detection system is gas detection module. The module has eight gas sensors. There are a NH3 sensor, an air pollution sensor, an alcohol sensor, a HS sensor, a smoke sensor, a CO sensor, a LPG sensor and a nature gas sensor. The master module will convert the communication protocol from I2C to RS232, and transmits the signals to the supervised computer via wire interface, and transmits the signals to the supervised computer via wireless RF interface, too.

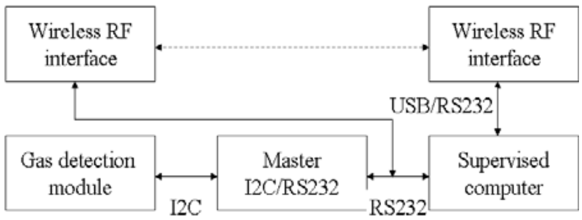

Fig. 1. The architecture of the gas detection system

In the gas detection module, we use many gas sensors that measure an unknown gas to be listed in Fig. 2. The HS133 and HS134 sensor elements have high sensitive, long life, reliable stability and good selectivity to low carbon monoxide concentration. The HS135 sensor element has long period stability and widely detecting scope. It should be suitable for detecting of smoke, SO2, CO2, isobutene, alcohol, etc. The sensor element HS129 can detect isobutene, propane, alcohol and hydrogen, and the resistance value changing will be cause by different gas concentration.

The sensor element HS130A can fast response and high sensitivity for alcohol, and the resistance value changing will be different base on different concentration alcohol. The sensing element of TGS826 is a metal oxide semiconductor which has low conductivity in clean air. In the presence of a detectable gas, the sensor's conductivity increase depending on the gas concentration in the air. The TGS826 has high sensitivity to ammonia gas.

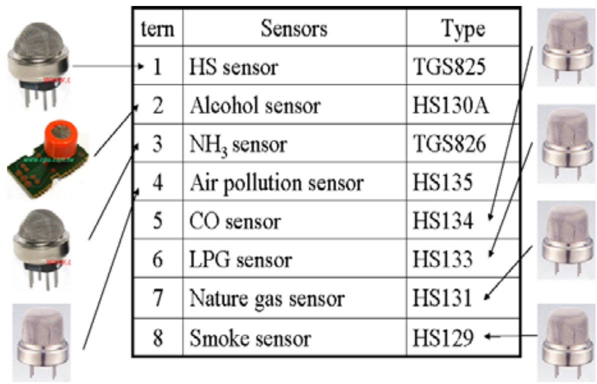

tem	Sensors	Type
1	HS sensor	TGS825
2	Alcohol sensor	HS130A
3	NH_3 sensor	TGS826
4	Air pollution sensor	HS135
5	CO sensor	HS134
6	LPG sensor	HS133
7	Nature gas sensor	HS131
8	Smoke sensor	HS129

Fig. 2. The sensor type of the gas detection module

Fig. 3 shows the basic structure of the gas detection module. Each sensor i of the gas detection module output s a measurement value x_i in the presence of an input unknown gas j. Where $i = 1,2,3,\ldots n$ and n denotes the number of the sensor in the array. Regard r_{ij} as the pre-processed response data. The patter recognition method combined with or without the knowledge database is used to execute the gas class prediction and component analysis, where y_i denotes the predicted gas output for the unknown gas.

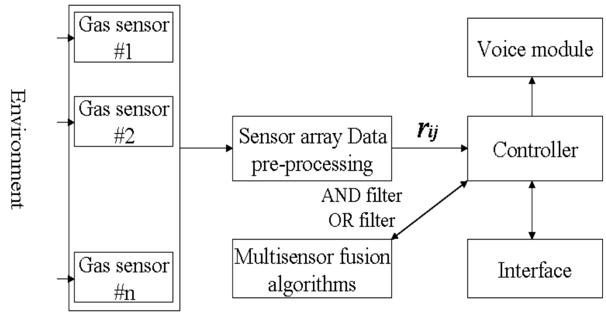

Fig. 3. The structure of the gas detection module

The prototype of the gas detection module is shown in Fig. 4. The gas detection module contains four levels and a fan. There is sensor level, driver level, control level and power level. The sensor level has eight gas sensors to be aligned in a board. The shape is shown in Fig. 5. Next level is pre-processing circuits for these gas sensors. The level has two boards, and the functions of the board are the same. The control level contains a HOLTEK microchip, a voice module and a wireless interface. The power level can convert AC power to DC power. The level provides DC power to each level. The fan can decrease the temperature of the gas detection module. It sucks wind from the sensor level of the module.

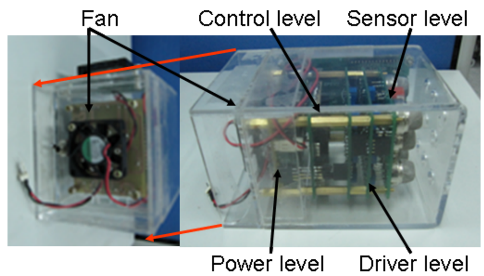

Fig. 4. The prototype of the gas detection module

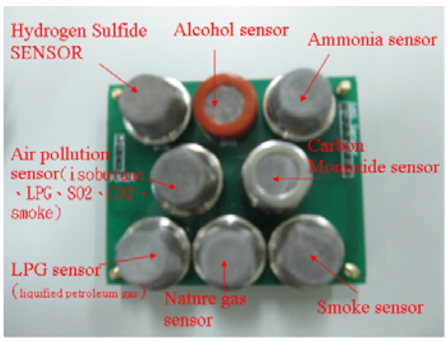

Fig. 5. The sensory arrangement of the module

III. DETECTION RULE

In the detection algorithms, we use logical filter method to classify the unknown gas in the module. In the logical filter method, we can use AND or OR filter on the gas detection module. Then we can calculate the system reliability of AND filter (R_S) and OR filter (R_P).

$$R_S = \prod_{i=1}^{n} R_i(t) \tag{1}$$

$$R_P = 1 - \prod_{i=1}^{n} \left[1 - R_i(t)\right] \tag{2}$$

R_i is the reliability of each sensor of the gas detection module. We can compare the reliability values using R_S and R_P for each unknown gas (CO, alcohol,… etc.), and decide which unknown gas to be found. How to implement the proposed method in the unknown gas? We measure the values (critical values) on the full concentration of the each sensor for any gas. We can define the critical values r_{ijf} , and calculate the value R_i for each sensor on the unknown gas.

$$R_i(t) = \frac{r_{ij}}{r_{ijf}} \tag{3}$$

For example, in the gas detection module, we can use sensor elements HS135, HS133, HS131 and HS129 to detect nature gas concentration of the environment, and compare these measurement values. We can use the logical filter method to decide the gas reliability to be over the critical value. In the other condition, we can use HS130A, TGS826 and HS133 sensors to detect alcohol concentration to be over the threshold using the same method, too.

The gas detection module interface of the supervised system is shown in Fig. 6. The user interface can acquire detection results from many detection modules, and display on the monitor of the supervised computer. The monitor has many regions to display the information from these detection modules. The upper of the left side can display fire signal (A1), power status (C3), environment measured value (A2), two axes compass signal and acceleration value (C1 and C2). The upper of the right side can display power measured value. The bottom of the left side can control the mobile robot forward, backward, turn right, turn left and stop. Users can speed up and slow down to the mobile robot (D1 and D2), too. The bottom of the right side can display the status of obstacle. It can display the two layer measured values for sixteen ultrasonic sensors (B2) and sixteen IR sensors (B1) [8]. In the paper, we are intered in the region A3. It can display the measurement concentration of the gas sensors, and classify the gas type using the proposed method on the bottom. The right side of the region A3 can display the reliability values for each detection gas.

Fig. 6. The architecture of the gas detection system

IV. EXPERIMENTAL RESULTS

We use the gas detection module to detect three variety gases. First the gas detection module detects the gas leakage of the building. The experimental result is shown in Fig. 7(a). we can see the concentration of these gas sensors #3, #6, #7 and #8 to be about 80%, 41%, 42% and 52%, and the consistence of these gas sensors #1, #2, #3 and #4 to be 0%. That is to say, the gas sensors #1, #2, #3 and #4 can not detect gas. The decision output display gas leakage using the proposed algorithm. The experimental result is shown in Fig. 7(b).

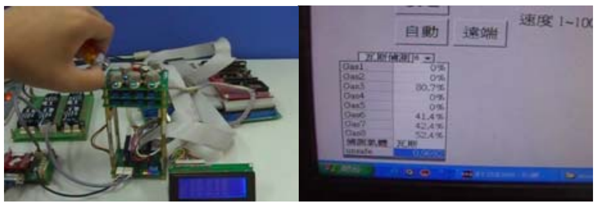

(a) Gas detection (b) User interface

Fig. 7. The experimental result of the gas detection

Then we use the gas detection module to detect another gas (alcohol). The experimental result is shown in Fig. 8(a). we can see the concentration of these gas sensors #2, #3 and #6 to be about 40%, 84% and 19%. and the concentration of these gas sensors #1, #4, #5, #7 and #8 to be 0%. That is to say, the gas sensors #1, #4, #5, #7 and #8 can not detect gas. The decision output display alcohol gas. The experimental result is shown in Fig. 8(b).

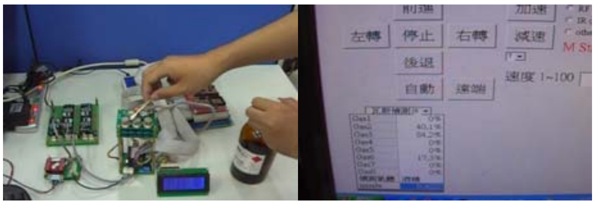

(a) Alcohol detection (b) User interface

Fig. 8. The experimental result of the alcohol detection

Finally, we use the gas detection module to detect CO gas. The experimental result is shown in Fig. 9(a). we can see the concentration of these gas sensors #2, #3, #5 and #6 to be about 26%, 68%, 89% and 13%, and the concentration of these gas sensors #1, #4, #7 and #8 to be 0%. That is to say, the gas sensors #1, #4, #7 and #8 can not detect CO gas. The decision output display gas leakage. The experimental result is shown in Fig. 9(b).

(a) CO detection (b) User interface

Fig. 9. The experimental result of the CO detection

VI. CONCLUSION

We have designed a gas detection module using eight chemical gas sensors for the security system of the intelligent building. The gas detection module can measure many gases using multisensor fusion algorithms, and can transmit the detection results to the supervised computer via wire/wireless interface. The controller of the gas detection module is HOLTEK microchip, and speaks the measurement status on real-time using voice module. In the experimental results, the module can detect three variety gases using multiple gas sensors. In the future, we want to develop multisensor fusion algorithms to detect more and more gas by the gas detection module, and revise the proposed algorithms to enhance the accuracy, and use the module to be applied in other fields. There are intelligent mobile robot, intelligent transport system and hospital.

ACKNOWLEDGMENT

This work was supported by the National Science Council of Taiwan, R. O. C. under Grand NSC 98-2622- E-224-030-CC3.

REFERENCES

[1] J. W. Gardner and P. N. Bartlet (1999), Electronic noses: Principles and Applications, Oxford University Press, UK.
[2] E. Scorsone, A. M. Pisanelli and K. C. Persaud(2006), Development of an electronic nose for fire detection, Sens. Actuators B, Vol. 116, pp.55-61.
[3] F. Sarry and M. Lumbreras (2000), Gas discrimination in an air-conditioned system, IEEE Transaction on Instr. Meas., Vol.49, No. 4, pp.809-812.
[4] K. Song, Q. Wang *et al* (2009), Design and implementation a real-time electronic nose system, International instrumentation and measurement technology conference.
[5] H. Yu, J. Wang *et al* (2008), Quality grade identification of green tea using E-nose by CA and ANN, LWT-Food Science and Technology, Vol. 41, pp.1268-1273.
[6] A. Bermak and S. B. Belhouari (2006), Bayesian learning using Gaussian process for gas identification, IEEE Transaction on Instr. Meas., Vol.55, No. 3, pp.787-792.
[7] H. Zhang, M. Chang et al (2008), Evaluation of peach quality indices using an electronic nose by MLR, QPST and BP network, Sens. Actuators B, Vol. 134, pp.332-338.
[8] Kuo-Lan Su, Sheng-Ven Shiau et al. (2009), Module Based Security System Applying in Intelligent Home, The Innovative Computing, Information and Control – Express Letters (ICIC-EL), Vol.3, No.4A, pp.1167-1172.

A Fast Parameters Estimation for Nonlinear Multi-regressions Based on Choquet Integral with Quantum-Behaved Particle Swarm Optimization

You-Min Jau[1], Chia-Ju Wu[2], Jin-Tsong Jeng[3]

1. Department of Electrical Engineering, National Yunlin University of Science & Technology, Taiwan
2. Department of Electrical Engineering, National Yunlin University of Science & Technology, Taiwan
3. Department of Computer Science & Information Engineering, National Formosa University, Taiwan

E-mail: g9510809@yuntech.edu.tw WUCJ@yuntech.edu.tw tsong@nfu.edu.tw

Abstract: In general, the inherent interaction among attributes must be considered circumspectly in the study of data mining and information fusion, a nonlinear model with nonlinear multi-regression model based on Choquet integral is suitable to deal with these problems. However, this nonlinear model is an over-determined systems and it is difficult to find the analytic solution. Hence, many researchers had proposed many algorithms; namely, genetic algorithm, neural network, particle swarm optimization, quantum-behaved particle swarm optimization (QPSO), to estimate parameters of this nonlinear model. In this study, an effective QPSO (EQPSO) algorithm which is used to estimate parameters of nonlinear multi-regression model was proposed. That is, the proposed EQPSO algorithm applied the concept of the genetic algorithm to the QPSO algorithm that can improve the convergent speed with premature phenomenon, stagnation and reducing the inference of the creative coefficient β in the QPSO algorithm. From the simulation results, the proposed EQPSO has the parameter estimation more precise and faster convergence speed than the genetic algorithm for the nonlinear multi-regression base on the Choquet integral.

Keywords: Choquet integral, Nonlinear multi-regression, QPSO, Mutation, Stagnation.

Ⅰ. Introduction

In data mining and information fusion, the most common aggregation tools are the weighted average method and the linear regression. These methods are all linear and must assumption that there is no interaction among attributes. However, in many practical problems, the inherent interaction among attributes must be considered circumspectly. Hence, a nonlinear multi-regression based on Choquet integral (NMRCI) with respect to non-additive measures has been proposed [1,3,4,11,15]. Liu et al [15] proposed Choquet integral's regression that derived from fuzzy support and deal with interaction among attributes based on the correlation in statistics. Wang et al [3-4] proposed a weighted NMRCI to deal with the data with some categorical attributes. It is more complex to estimate parameters of the nonlinear multi-regression. Hence, the non-weighted nonlinear multi-regression model [1] to deal with numerical attributes with the same dimension is adopted in this paper.

At present, there are some soft computing techniques [2-4] which can be used for determining regression parameters of the NMRCI. In this study, the modify particle swarm optimization with quantum behavior (QPSO) is proposed for the NMRCI. The QPSO [5] ensures the congregation of the particle swarm without losing the randomness. Particles can appear any position of the whole space which is searched in a certain probability. Because of the swift convergence speed of QPSO, when one particle finds a local optima state, the others will quickly converge to it. If particles cannot find any better state, the QPSO will take on the premature phenomenon. In order to depart from the local optima, some improvements have been proposed [6-9]. These improved algorithms try to change the state of the particles by the mutation mechanism and to get out of the local optima. But it is difficult to be realized, when the explicit distances between the best and the local optima state is difficult to determine. In this paper, a QPSO algorithm with elitism of genetic algorithm (GA), named EQPSO is proposed. From the results of experiment show that the proposed algorithm can improve the convergent speed and the global searching ability. This paper is organized as follows. In section Ⅱ, the nonlinear multi-regression model base on Choquet integral is introduced. In section Ⅲ PSO and QPSO theory will be presented. In Section Ⅳ, The EQPSO algorithm will be introduced in detail. Simulation results and comparisons are described in Section Ⅴ and the paper is concluded in Section Ⅵ.

Ⅱ. Nonlinear multi-regression model base on the Choquet integral

Let the data consist of k recorders (or observations) of input $X=\{x_1,x_2,\cdots x_n\}$ and output Y, denoted by $f_{j1}, f_{j2},\cdots f_{jn}, y_j$ and has a form as:

x_1	x_2	…	x_n	y
f_{11}	f_{12}	…	f_{1n}	y_1
f_{21}	f_{22}	…	f_{2n}	y_2
⋮	⋮		⋮	⋮
f_{k1}	f_{k2}	…	f_{kn}	y_k

where k is the number of observation and should take much large than n at 5 times of 2^n. Let X be a finite set of predictive attributes and Y be the objective attribute. In many real-world problems, the inherent interaction among predictive attributes must be considered circumspectly and the kind of interaction is essentially different from the correlation in statistics. Hence, the traditional linear multi-regression model will fail in these practical applications. In order to effectively describe the inherent interaction among predictive attributes, Wang and Klir [10,11] proposed a non-additive set function μ (named general measure) defined on the power set of predictive attributes *X,* i.e., $\mu: P(X) \to [0,1]$, which satisfy the conditions $\mu(\phi)=0$ and $\mu(X)=1$. When it deals with data mining and information fusion where data and information posses inherent interaction, it must adopt nonlinear integral with respect to the general measure. In general, the nonlinear integral has Sugeno integral, Wang integral, Choquet integral, etc [11]. The Choquet integral is the most frequent form and is defined as follows:

$$\int f d\mu = \int_{-\infty}^{0} [\mu(F_\alpha) - \mu(X)] d\alpha + \int_{0}^{\infty} \mu(F_\alpha) d\alpha, \quad (1)$$

where *f* is nonnegative function, and F_α is the α-cut set of function *f*. Because of *X* is finite, the Choquet integral can be express as:

$$\int f d\mu = \sum_{i=1}^{n} \left(f(x_i^*) - f(x_{i-1}^*) \right) \cdot \mu(\{x_i^*, x_{i+1}^*, \cdots, x_n^*\}), \quad (2)$$

where $\{x_i^*, x_{i+1}^*, \cdots, x_n^*\}$ is a permutation of $\{x_1, x_2, \cdots, x_n\}$ and $f(x_1^*) \le f(x_2^*) \le \cdots \le f(x_n^*)$, $f(x_0^*)=0$. Thus, *f* defined on *X* and the relation between predictive attributes *X* and objective attribute *Y* can be express as a nonlinear multi-regression model as follows:

$$y = c + q \cdot \int f d\mu + \varepsilon, \quad (3)$$

where *c*, *q* is a constant, $\int f d\mu$ is the Choquet integral of function *f* with respect to general measure μ, and $\varepsilon \sim N(0,\sigma^2)$ is a normally distributed random perturbation with zero mean and variance σ^2. In Eq. (3), the constant *c*, *q* and μ are called regression parameters. These regression parameters can be determined by minimizing the squared error [11]

$$e^2 = \sum_{j=1}^{k} \left(y_j - c - q \int f_j d\mu \right)^2. \quad (4)$$

However, it is an over-determined system and difficult to find an analytic solution of *c*, *q*, and μ. Hence, these parameters, *c* and *q*, can be estimated by the least square method.

Ⅲ. Particle Swarm Optimization (PSO) and Quantum Behavior PSO (QPSO)

From Eq. (3), to finds out a set of parameters satisfying the specific criteria is a heavy burden. Hence, a proper PSO algorithm can help to finish this work and it possesses an excellent ability of global search. In PSO, each particle keeps trajectory of its own position and velocity in the problem space. At the each iteration, the new positions and velocities of the particles are updated by the following two equations:

$$v_i(t+1) = v_i(t) + c_1 \cdot r_1 (p_i^{loc} - \varphi_i) + c_2 \cdot r_2 (p^{gol} - \varphi_i), \quad (5)$$

$$\varphi_i(t+1) = \varphi_i(t) + v_i(t+1), \quad (6)$$

where $\varphi_i = [\varphi_{i,1}, \varphi_{i,2} \cdots \varphi_{i,n}]$ and $v_i = [v_{i,1}, v_{i,2} \cdots v_{i,n}]$ are the position and the velocity of the i_{th} particle in the n-dimensional search space, respectively. $p_i^{loc} = [p_{i,1}^{loc}, p_{i,2}^{loc} \cdots p_{i,n}^{loc}]$ and $p^{gol} = [p_1^{gol}, p_2^{gol} \cdots p_n^{gol}]$ are the best position of the i_{th} particle and global best position found so far. i=1,2,$\cdots$*M*, *M* is the number of particle population, c_1 is called cognitive parameter, c_2 is called social parameter and r_1, r_2 are random numbers between [0,1]. Clerc and Kennedy [12] proved that if the upper bound of c_j*r_j is properly selected, the particle's position φ_i will converge to the center of potential field $pf^{cnt} = [pf_1^{cnt}, pf_2^{cnt} \cdots pf_n^{cnt}]$ (called equilibrium point), where pf_i^{cnt}, $i = 1,2\cdots,n$ is the coordinate of pf^{cnt} in i_{th} dimension, and is obtained by:

$$pf^{cnt}(i) = \frac{\left(r_1 \cdot p_i^{loc} + r_2 \cdot p^{gol} \right)}{\left(r_1 + r_2 \right)}, i = 1,2,\cdots,M. \quad (7)$$

Each particle moves around and careens toward pf^{cnt} with declining its kinetic energy to zero, like a retuning satellite orbiting the earth. Inspired by analysis of convergence of the classical PSO [5], an individual particle can be seen as moving in a Delta Potential Well which center is equilibrium point pf^{cnt} in search space, and the quantum mode of a particle is depicted by state of energy (or, called wave function) $\Psi(\vec{x},t)$ which follows the time-dependent Schrödinger equation:

$$i\hbar \frac{\partial}{\partial t} \Psi(\vec{x},t) = -\frac{\hbar}{2m} \nabla^2 \Psi(\vec{x},t) + V(\vec{x}) \Psi(\vec{x},t). \quad (8)$$

Sun et al [13] had showed the answer of Schrödinger equation for this model with time-independent in one-dimensional space as:

$$\varphi_{i+1} = pf^{cnt}(i) \pm \frac{L}{2} \cdot \ln(1/u), \quad (9)$$

where u is random number uniformly distribute on [0,1]. *L* is called "Creativity" or "Imagination" of particle. In order to avoid premature of the algorithm, Mainstream Thought Point is employed to evaluate parameter *L*. The Mainstream Thought Point or called Mean Best Position (*mbest*) and *L* are given as:

$$mbest = \left[\sum_{i=1}^{m} \frac{\varphi_{i,1}}{M}, \sum_{i=1}^{m} \frac{\varphi_{i,2}}{M}, \cdots, \sum_{i=1}^{m} \frac{\varphi_{i,n}}{M} \right], \quad (10)$$

$$L = 2 \cdot \beta \left| mbest - \varphi_i \right|, \quad (11)$$

where β is creative coefficient whose value will control the convergence speed of individual particle and the performance of the algorithm.

Ⅳ. An Efficient QPSO Algorithm

Huang et al [14] proposed an algorithm of improved QPSO (called IQPSO). Its basic concept is sharing the public information and variation by preserving the fore N elites at each generation. Though, this algorithm possesses some advances batter than the traditional PSO and QPSO and is more suitable for a complex nonlinear system, preventing premature, and improving the convergence speed, etc. But it still represents stagnating phenomenon in searching the global optimal solution, and is strongly influenced by the creative coefficient β and preserving number N. In order to improve this drawback, a modify algorithm EQPSO that combined the QPSO algorithm with the concept of GA to improve the IQPSO algorithm is proposed. In EQPSO, an index of stagnation (named *matu*) to monitor the convergence of particle's state is set. If the best value of p^{gol} is not updated over then ten generations that means the procedure getting into local minimum. In order to depart from this situation as soon as possible, EQPSO adopts the similar policy of elitism. That is, this procedure preserves the p^{gol} and sorts these collected parameters in each iteration. Once *matu*, the index of stagnation, reaches a specified value, the new particle swarm of next generation will be replaced by these collected parameters. The proposed EQPSO algorithm is as follow:

Step 1: Randomly initialize the particle swarm φ_i , $i = 1, 2, \ldots, M$ and evaluate their fitness value.

Step 2: Initialize p_i^{loc} with the best fitness value of i_{th} particle and p^{gol} with the best one of p_i^{loc}.

Step 3: Calculate the Mean Best Position ($mbest$) by Eq. (10).

Step 4: Calculate the center of potential field pf^{cnt} by Eq. (7).

Step 5: Randomly select the Eq. (12) with equal probability to update φ_i.

$$\varphi_i(t+1) = pf^{cnt}(i) \pm \beta \cdot \left\| \left(mbest - \varphi_i(t) \right) \right\| \cdot \ln(1/u), \quad (12)$$

Step 6: Evaluate the fitness value of $\varphi_i(t+1)$.

Step 7: By value calculated in step 6, sort $\varphi_i(t+1)$.

Step 8: Check whether the maximum iteration is reached or the termination criteria is satisfied. If yes, then go to step 14. If no, carry on next step.

Step 9: Check whether p_i^{loc} and p^{gol} should be updated. If p^{gol} is updated, then set matu = 0 and go back to step 3. If p^{gol} is not updated, then increase matu = 1 and go on next step.

Step 10: Check whether matu reaches 10 times M. If yes, let $\varphi(t+1) = p^{gol}$ and go back to step 3. If no, keep $\varphi(t+1)$ unchanged and go back to step 3.

Step 11: Check whether p_i^{loc} and p^{gol} should be updated and output results.

Ⅴ. Results and Comparisons

The simulations were conducted in the Matlab environment with Intel Core 2 Duo CPU P8400 and 4GB Ram. It has been successfully run for a number of examples.

Example 1: Let the regression parameters q=2.5, c=6, the dimension of predictive attribute is 4, $X = \{x_1, x_2, x_3, x_4\}$ and data size is 50 show in Table 1. The EQPSO and the GA algorithm are independently used with stop criteria $er \le 1e^{-3}$ and $er \le 1.5e^{-2}$, respectively. The average results are obtained as shown in Table 2. Besides, we also compare with PSO, QPSO, and IQPSO. In this example, the stop criteria $er \le 1e^{-2}$ usually cannot be achieved in running GA algorithm [1]. Hence, the stop criteria is released as $er \le 1.5e^{-2}$ for running GA algorithm. From Table 2, the proposed algorithm is superior to the GA, PSO, QPSO and IQPSO for the parameters of estimation in the NMRCI.

Ⅵ. Conclusions

The NMRCI can describe the multi-input single-output systems or multi-input multi-output systems and has been widely developed under the non-additive measures. Many researchers had proposed some algorithms such as GA, neural network, PSO and QPSO to estimate parameters of the NMRCI. In the study, we successfully combine the mutation concept of GA into the QPSO algorithm. From the results of simulation, the proposed algorithm is superior to the GA, PSO, QPSO and IQPSO for the parameters of estimation in the NMRCI.

Acknowledgments

This work was supported by the National Science Council of Taiwan, R. O. C. under Grand NSC98-2221-E-224-047.

References

[1] Wang Z, Leung KS, Wong ML, Fang J, Xu K (2000), Nonlinear nonnegative multi-regressions based on Choquet integrals. International Journal of Approximate Reasoning, Vol. 25, No. 2, pp. 71-87.

[2] Wang Z, Wang J (1999), A genetic algorithm for determining non additive set functions in information fusion. Fuzzy Sets System, Vol. 102, No. 3, pp. 463–469.

[3] Xu K, Wang Z, Wong ML, Leung KS (2001), Discover dependency pattern among attributes by using a new type of nonlinear multi-regression. International Journal of Intelligent Systems, Vol. 16, pp. 949-962.

[4] Wang Z, Guo H (2003), A new genetic algorithm for nonlinear multi-regressions based on generalized Choquet integrals. Proc. of Fuzz/IEEE, pp. 819-821.

[5] Sun J, Feng B, Xu WB (2004), Particle swarm optimization with particles having quantum behavior.

IEEE Congress on Evolutionary Computation, USA, pp. 325-331.

[6] Lin X, Feng B, Sun J (2008), Chaos quantum-behaved particle swarm optimization algorithm. Computer Engineering and Design, Vol. 29, No. 10, pp. 2610-2612.

[7] Ge HW, J WH (2007), Application of quantum-behaved PSO algorithm with mutation operator in system parameters identification. Computer Engineering and Applications, Vol. 43, No. 29, pp. 222-224.

[8] Wang Z, Feng B and Sun J (2008), Quantum-behaved particle swarm optimization with dimension mutation operator. Computer Engineering and Design, Vol. 29, No.6, pp. 1478-1481.

[9] Zhong W, Qian F, Xing J (2008), An improved theta-PSO algorithm with crossover and mutation. Proc. of the World Congress on Intelligent Control and Automation, pp. 5308-5312.

[10] Wang Z, Klir GJ (1992), Fuzzy Measure Theory, Plenum Press, New York.

[11] Wang Z, Klir GJ (2008), Generalized Measure Theory, Springer, New York.

[12] Clerc M and Kennedy J (2002), The particle swarm: explosion, stability, and convergence in a multi-dimensional complex space. IEEE Transactions on Evolutionary Computation, Vol. 6, No. 1, pp.68-73.

[13] Sun J, Feng B, Xu WB (2004), A global search strategy of quantum-behaved particle swarm optimization. Proc. of IEEE Conference on Cybernetics and Intelligent Systems, pp. 111-116.

[14] Huang Z, Wang Y, Yang C, Wu C (2009), A new improved quantum-behaved particle swarm optimization model. Proc. of the IEEE Conference on Industrial Electronics and Applications, pp. 1560–1564.

[15] Liu HC, Tu YC, Chen CC, Weng WS (2008), The Choquet integral with respect to λ measure based on γ support. Proce. of the International Conferences on Machine Learning and Cybernetics, Kuming, China.

Table 1: Predictive and object attributes for Example 1.

$f(x_1)$	$f(x_2)$	$f(x_3)$	$f(x_4)$	y
0.5	0.9	0.7	1.1	7.9750
0.5	1.3	0.3	0.2	7.0250
1.3	1.5	1.2	0.3	8.2375
1.7	0.7	0.5	0.3	7.7250
0.7	1.3	0.1	1.3	7.6750
1.5	0.8	1.5	1	9.0125
⋮	⋮	⋮	⋮	⋮
1.4	1	0.8	0.3	7.8750
0.5	0.8	1.5	1.7	9.2250
0.3	1.3	1.6	1	8.8250
1.2	1.5	1.6	1.7	9.8500
0.9	1	0.7	0.4	7.6500

Table 2: The average results of example 1, where MSE is minimum mean square error, iters is iterations.

	μ_{calc} GA	μ_{calc} PSO	μ_{calc} QPSO	μ_{calc} IQPSO	μ_{calc} EQPSO	μ_{org}		y_{calc} GA	y_{calc} PSO	y_{calc} QPSO	y_{calc} IQPSO	y_{calc} EQPSO	y_{org}
$\{x_1\}$	0.197	0.105	0.224	0.170	0.199	0.200	data(1)	7.963	8.030	8.023	8.028	7.975	7.975
$\{x_2\}$	0.103	0.036	0.065	0.083	0.099	0.100	data(2)	7.019	7.116	7.053	7.028	7.024	7.025
$\{x_1,x_2\}$	0.338	0.353	0.394	0.322	0.350	0.350	data(3)	8.274	8.069	8.210	8.263	8.240	8.238
$\{x_3\}$	0.384	0.333	0.263	0.238	0.398	0.400	data(4)	7.716	7.620	7.843	7.672	7.725	7.725
$\{x_1,x_3\}$	0.460	0.395	0.593	0.478	0.449	0.450	data(5)	7.657	7.777	7.650	7.759	7.676	7.675
$\{x_2,x_3\}$	0.498	0.348	0.287	0.509	0.499	0.500	data(6)	9.025	9.030	9.207	9.035	9.012	9.013
$\{x_1,x_2,x_3\}$	0.617	0.474	0.576	0.611	0.601	0.600	data(7)	7.904	8.004	8.021	7.885	7.926	7.925
$\{x_4\}$	0.282	0.177	0.280	0.349	0.298	0.300	⋮	⋮	⋮	⋮	⋮	⋮	⋮
$\{x_1,x_4\}$	0.458	0.459	0.419	0.378	0.449	0.450	data(44)	8.363	8.297	8.393	8.381	8.362	8.363
$\{x_2,x_4\}$	0.340	0.323	0.306	0.352	0.350	0.350	data(45)	7.037	6.986	6.979	7.027	7.024	7.025
$\{x_3,x_4\}$	0.602	0.577	0.589	0.634	0.600	0.600	data(46)	7.884	7.799	7.935	7.871	7.876	7.875
$\{x_1,x_2,x_4\}$	0.703	0.746	0.692	0.788	0.699	0.700	data(47)	9.235	9.235	9.248	9.398	9.224	9.225
$\{x_1,x_3,x_4\}$	0.893	0.990	0.951	0.887	0.900	0.900	data(48)	8.833	8.673	8.711	8.735	8.824	8.825
$\{x_2,x_3,x_4\}$	0.811	0.761	0.878	0.812	0.800	0.800	data(49)	9.864	9.764	9.864	9.867	9.851	9.850
X	1.000	1.000	1.000	1.000	1.000	1.000	data(50)	7.653	7.724	7.700	7.671	7.651	7.650

	Stop criteria	q	c	MSE	Elapse time (sec)
GA	0.015	2.51626	5.98430	0.014801	28.062
PSO	3000 iters	2.25588	6.33291	0.0957334	44.013
QPSO	3000 iters	2.39674	6.12287	0.0959836	43.785
IQPSO	3000 iters	2.43673	6.07210	0.0882585	86.308
EQPSO	0.001	2.50015	6.00107	0.0009860	8.847

Application of a Remote Image Surveillance System in a Robotic Weapon

Chun-Chieh Wang[1], Kuo-Hsien Hsia[2], Kuo-Lan Su [3], Yi-Chun Hsieh[4], and Chyun-Luen Lin[5]

[1,4,5]*Department of Electronic Engineering, Chienkuo Technology University*
No. 1, Chieh Shou N. Rd., Changhua City, Taiwan
(Tel : 886-4-7111111ext3350; Fax : 886-4-7111139)
(Email address: jasonccw@ctu.edu.tw)
[2] *Department of Management Information System, Far East University*
Tainan County, Taiwan
(Tel : 886-6-5979566ext7008; Fax : 886-6-5977600)
(Email address: loveyou90056@yahoo.com.tw)
[3] *Department of Electrical Engineering, National Yunlin University of Science & Technology, Yunlin County, Taiwan*
Yunlin County, Taiwan
(Tel : 886-5-5342601ext4249; Fax : 886-5-5312065)
(Email address: a829327@yahoo.com.tw)

Abstract: As one of the major steps toward fully intelligent autonomous robotic weapon, this paper works have accomplished in three major areas: (1) design of the surveillance system by AVR microcontroller, (2) implementation of the mechanism design, and (3) performance of the human machine interface surveillance system via LabVIEW graphical programming environment, such that the supervisor can control the vehicle by keyboard or genius mouse. In order to accomplish all these three achievements, there have been major additions and overhaul in both system software code and system circuit board developments. All these development including the developed algorithm, and hardware implementation are covered in this paper. The experimental results have shown the practicality of the AVR microcontroller, LabVIEW graphical programming environment, and the ZigBee wireless technology applied to robotic weapon.

Keywords: Robotic Weapon, LabVIEW, AVR Microcontroller, Remote scout robot.

I. INTRODUCTION

There are times when the rescue team is unable to enter the scene of the accident due to various shortcomings that might endanger the rescuers lives. In order to overcome these possible obstacles, a lot of researchers have built some various robots that can enter these dangerous sites in place of the rescuers. However, as regards HMI-guided control, few researchers use LabVIEW platform to delve into tracked robots. In 2001, Priya Olden et al. presented an open-loop motor speed control with LabVIEW [1]. In 2006, Prasanna Ballal et al. proposed a LabVIEW based test-bed with off-the-shelf components for research in mobile sensor networks [2].

Hence, we will extend the research in the past [3-7] to implement a weapon robot in this paper. The key feature is the application of an AVR microcontroller applied to design a controller so that all of the design functions can be implemented. Furthermore, the vehicle can be orientated by ZigBee based wireless system. Besides, we design the human machine interface surveillance system via LabVIEW graphical programming environment, such that the supervisor can control the weapon robot by keyboard/genius mouse.

To illustrate the effectiveness of the design, we plan an urban fight space as the scenario setting such that the robot can finish all functions. The experimental results validate the practicality of the AVR microcontroller, LabVIEW graphical programming environment, and the ZigBee wireless technology applied to weapon robots.

II. Self-Made Robotic Weapon

2.1 Mechanism of the Robot

Fig.1 is the vertical view for the platform of the weapon robot. Fig.2 shows the right side view. The structure contains two active wheels and one small assistant wheel. The specification of the robotic platform includes (1) the length is 41cm, (2) the width is 31cm, and (3) the height is 20cm. Fig.3 shows a MP5K electric BB gun. The self-made robotic weapon is shown in Fig.4. We put a MP5K electric BB gun on the platform of the robot and set one camera behind the sight of the gun. The specification of the robotic weapon includes (1) the length is 52cm, (2) the width is 31cm, and (3) the height is 34cm.

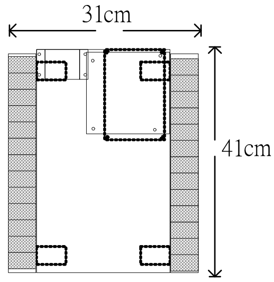

Fig.1. Vertical view of the platform

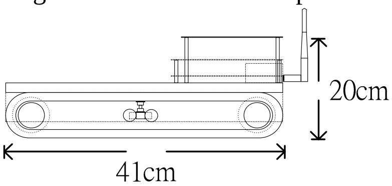

Fig.2. Right side view of the platform

Fig.3. MP5K electric BB gun

Fig.4. Robotic weapon

2.2 Remote Image Surveillance System

The procedures for the image transmission is shown in Fig.5. The system consists of an image receiver, a NI PXI/PIC-1411 board, a wireless camera, and a servo motor (see Fig.6-Fig.8) [7].

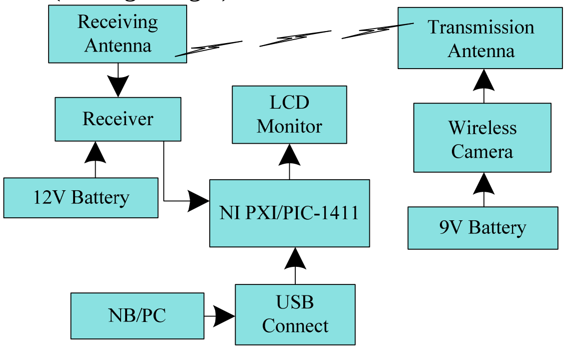

Fig.5. Procedures for the image transmission

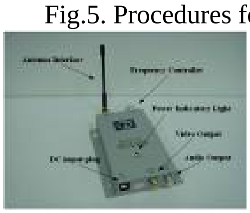

Fig.6. Image receiver

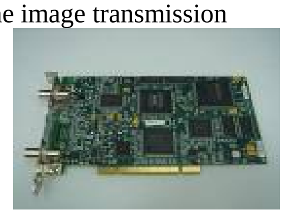

Fig.7. NI PXI/PIC-1411

Fig.8. Wireless camera

2.3 AVR microcontroller

Fig.9 shows the AVR32 microcontroller. The ATmega32 is a low-power CMOS 8-bit microcontroller based on the AVR enhanced RISC architecture. By executing powerful instructions in a single clock cycle, the ATmega32 achieves throughputs approaching 1 MIPS per MHz allowing the system designer to optimize power consumption versus processing speed.

Moreover, the main function of the CPU core is to ensure correct program execution. The CPU must therefore be able to access memories, perform calculations, control peripherals, and handle interrupts. Besides, the AVR architecture has two main memory spaces, the Data Memory and the Program Memory space. In addition, the ATmega32 features an EEPROM Memory for data storage. All three memory spaces are linear and regular.

Fig.9. AVR32 microcontroller

III. LabVIEW

LabVIEW（Laboratory Virtual Instrument Engineering Workbench） is an easy-to-use graphical development environment which allows users to rapidly develop applications for experiment, measurement and control. A complete system can be constructed very fast with hardware modules for data accomplishment, image processing, motion domination, or communication available from National Instruments (NI) [8]. Each application created in LabVIEW is referred to as a virtual instrument (VI). A VI consists of a user interface front panel and a block diagram. A VI can also be called from another VI, called a sub-VI. The standard LabVIEW package comes with various VIs in the form of libraries and drivers to permit program development rapidly [9].

In this paper, we use LabVIEW graphical programming to design a human machine interface surveillance system [3]. From the transmission of RS-232 and ZigBee modules, the command will be delivered to the controller, placed on the weapon robot so that the vehicle will be arrive at assigned place. The LabVIEW front panel is shown in Fig.10, where contains seven parts. Block 1 is the safety push-button. All of the functions can not be fulfilled if we don't put the button. Block 2 displays a keyboard/genius mouse switch device. We can choose the press-key or genius mouse to control the robot. Moreover, we can set the RS232 I/O port and baud rate by Block 3 and Block 4, respectively. Block 5 displays the character string when the keyboard is pressed. The ASCII code is shown in Block 6. Block 7 indicates the frame of controlling the order through the Genius mouse.

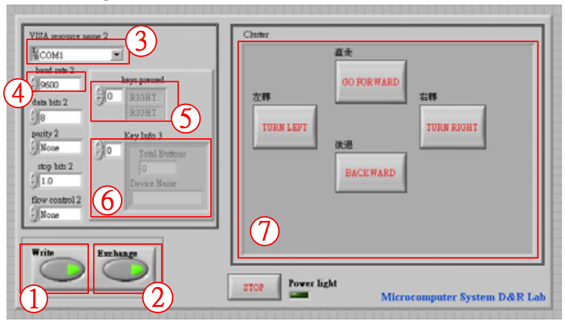

Fig.10. LabVIEW front panel

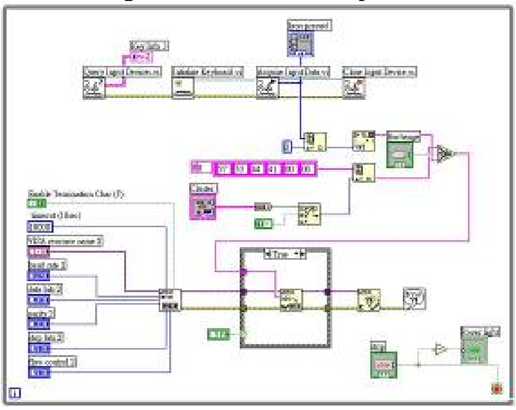

Fig.11. LabVIEW programming block diagram

IV. ZigBee Transparent–P2P Mode

ZigBee has been an intelligent digital protocol, operating at three frequencies, with the commonest one being at 2.4 GHz. At this operating frequency, data rates up to 250 kbit/s are claimed. This is a relatively low bandwidth, compared to other protocols such as Bluetooth. Moreover, the feature of ZigBee contains the robustness and simplicity of IEEE 802.15.4 standard, the versatility of ZigBee Compliance Platform, the low consumption and cost, and the standard-based short-range wireless networking.

In this paper, the ZigBee is developed for point-to-point transmission and area positioning. IP-Link 2220H, shown in Fig.12, provides a host of AT commands to allow easy configuration of key attributes of an IP-Link 2220 module. Users can use any terminal emulation utility or UART communication library on a particular host platform to issue these AT commands to IP-Link 2220.

Figure 13 shows the transparent point-to-point mode. The signal can be transmitted by connecting RS-232 series port and ZigBee transmitter such that the receiver can obtain it. Besides, a Tag (placed on the robot) transmits a continuous signal so that the node (placed on the scenario setting space), which is most close to the robot, can receive the signal and display on the monitor. Then, the supervisor will know the present position of the robot. [6]

Fig.12. IP-Link2220H

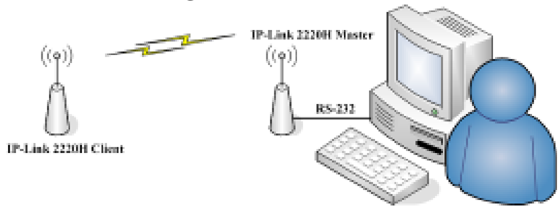

Fig.13. Transparent P2P Mode

V. EXPERIMENTAL RESULTS

For the scenario setting and the experimental test, we plan the indoor orientation diagram, shown in Fig.14. Fig.15 reveals the course that MP5K electric BB gun shot continuously. Fig.16 indicates the actual responses.

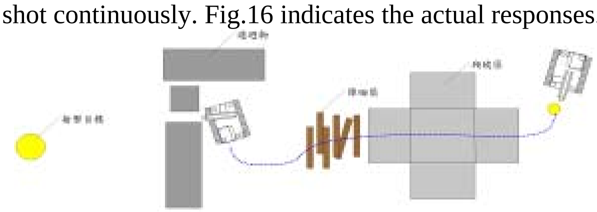

Fig.14. Indoor orientation diagram

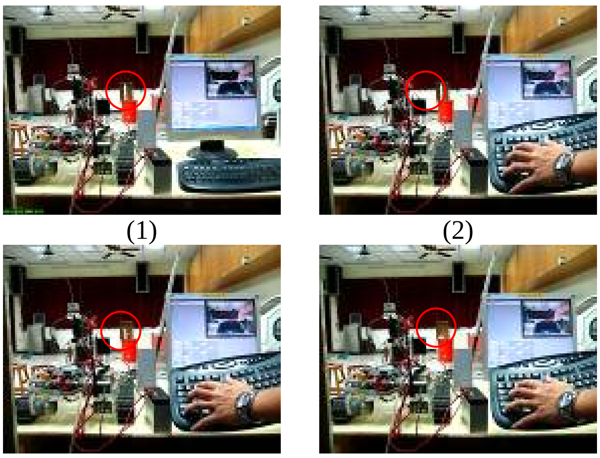

(1) (2)

(3) (4)

Fig.15. The course that BB gun shot continuously

(1) (2)

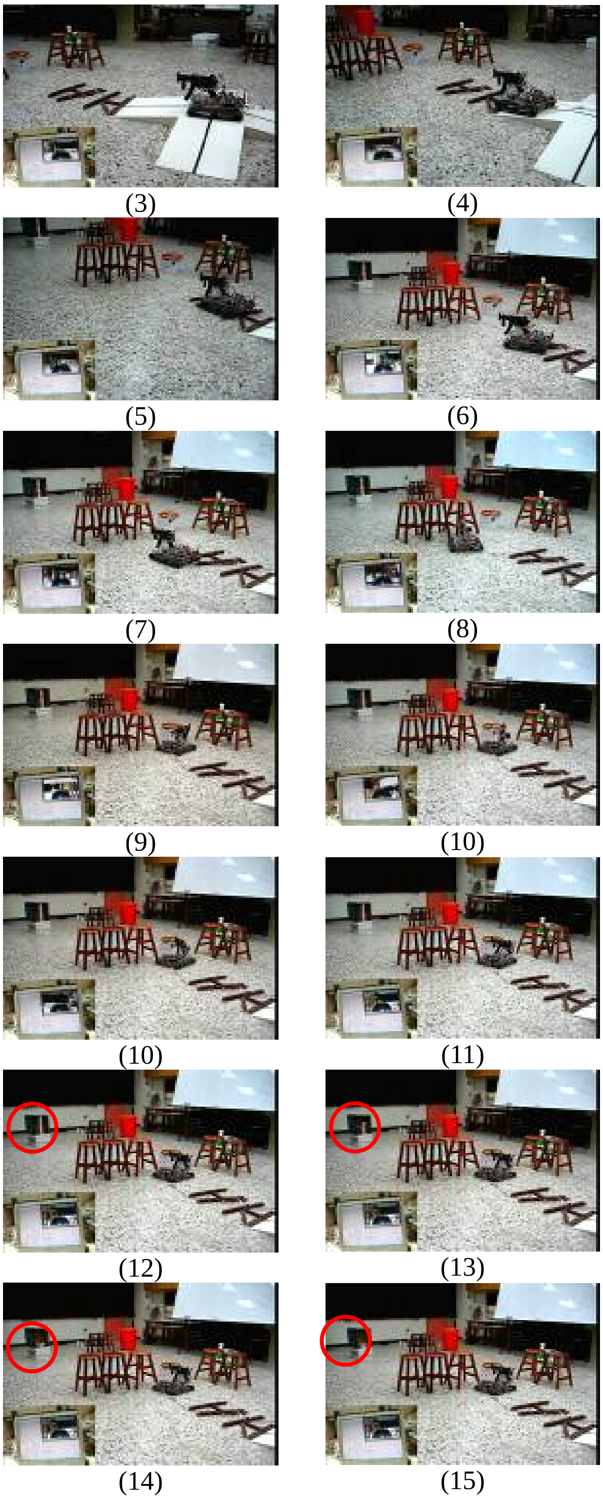

Fig.16. Actual responses

VI. CONCLUSION

In this paper, a weapon robot is implemented. Moreover, an AVR microcontroller is applied to design a controller so that all of the design functions can be implemented. Furthermore, the vehicle can be orientated by ZigBee based wireless system. Besides, we design the human machine interface surveillance system via LabVIEW graphical programming environment, such that the supervisor can control the weapon robot by keyboard/genius mouse.

The experimental results validate the practicality of the AVR microcontroller, LabVIEW graphical programming environment, and the ZigBee wireless technology applied to weapon robots.

REFERENCES

[1] Olden P., Robinson K., Tanner K., Wilson R., and Basher A.M.H. (2001), Open-loop motor speed control with LabVIEW, Proceedings of 2001 IEEE Southeast Conference, 259-262.

[2] Ballal P., Giordano V., Dang P., Gorthi S., Mireles J., and Lewis F. (2006), A LabVIEW based test-bed with off-the-shelf components for research in mobile sensor networks, Proceedings of the 2006 IEEE International Symposium on Intelligent Control, 112-118.

[3] Chun-Chieh Wang and Kuo-Lan Su (2009), Design and Implementation of Human Machine Interface Surveillance Systems for Tracked Robots, 14th International Symposium on Artificial Life and Robotics, 267-270.

[4] C.C. Wang and C.T. Shen (2008), Application of ZigBee Technology for Wheeled Mobile Robots, Proceedings of ICSSMET2008 International Conference on Safety & Security Management and Engineering Technology 2008, Nov. 28-29, WFC, Chiayi, Taiwan.

[5] C.C. Wang and C.T. Shen (2008), Implementation of Wireless Image Tracking for Wheeled Mobile Robots, 2008 International Conference on Innovative Computing, Information and Control（ICICIC 2008）, June 18-20, Dalian University, Dalian, China.

[6] C.C. Wang, F.Y. Huang, C.T. Shen, Y.Y. Chen, C.C. Jiang, C.L. Lin, and H.M. Chen (2008), Teleoperation System for Tracked Robots, 2008 Conference on Information Technology and Applications in Outlying Islands, NPU, Penghu, Taiwan, May 30-31, pp.474-478.

[7] C.C. Wang, C.T. Shen, J.S. Jhu, C.L. Lin, and H.M. Chen (2008), Human Machine Interface Surveillance Systems and Its Application to Tracked Robots, Proceedings of ICSSMET2008 International Conference on Safety & Security Management and Engineering Technology 2008, Nov. 28-29, WFC, Chiayi, Taiwan.

[8] National Instruments, www.ni.com.

[9] Mahdi Javer, Trevor W. Pearce, Mathieu Gibeault, and Mojtaba Ahmadi (2006), Profiling of the LabVIEW Development Environment and Real-Time Module, 2006 Canadian Conference on Electrical and Computer Engineering, 1296- 1299.

The Fifteenth International Symposium on Artificial Life and Robotics 2010 (AROB 15th '10),
B-Con Plaza, Beppu,Oita, Japan, February 4-6, 2010

Human Tracking with Variable Prediction Steps based on Kullback-Leibler Divergence

Noriko Takemura, Yutaka Nakamura, Yoshio Matsumoto and Hiroshi Ishiguro
Dept. of Adaptive Machine Systems, Graduate School of Engineering, Osaka University
2-1 Yamadaoka, Suita, Osaka 565-0871 Japan, *takemura.noriko@is.sys.es.osaka-u.ac.jp*

Abstract: This paper deals with a path planning problem for tracking humans in order to obtain detail information about human behavior and characteristics. In our method, path planning is performed based on Kullback-Leibler (KL) divergence between the predicted distribution of all human positions and the intensity of field of view of agents. The number of prediction steps is determined according to the consistency of the prediction. Experimental results show that when prediction of human movement is accurate, the long-term prediction is useful for the path planning. On the other hand, when prediction is inaccurate, long-term prediction might not be useful. Our path planning method works well even under changing circumstances by changing the number of the prediction length.
Keywords: path planning, human tracking, variable term prediction

I. INTRODUCTION

Visual surveillance methods have been intensively studied in order to ensure a security because it provides less stress to a tracked human, and most of these researches focus on improving the quality of position estimation by image processing technique [1] [2]. For a surveillance system, however, detail information such as human behavior and their characteristics are also important. Since high resolution images are necessary to obtain such information, visual sensors must be in close range to human. Mobile agents with visual sensors can be one of solutions to achieve this. In this research, we focus on a path planning for mobile agents to acquire detail information of tracked humans.

The human tracking system is often developed using a Kalman filter or a particle filter. Since these researches have only used one-step prediction of the human movement, the planned paths tend to be myopic one. In order to overcome this problem, it is useful to plan the path based on longer-term predictions in the future. Real-Time A* (RTA*) is a search algorithm for semi-optimal path planning, but it can be applied to a problem with given start and goal point. However, it was shown that long-term prediction make the performance of path planning improved.

Although an accurate prediction of human position improves performance of human tracking [3] [4], accurate long-term predictions are not always possible . For instance, long-term prediction becomes accurate if every humans move to a certain direction (Imagine a station at the morning and evening rush hours). In contrast, it becomes inaccurate if every human moves their own way like in a shopping moll or at an intersection without signals. When humans arrived at a cross over point, the prediction may become difficult because humans might interact with each other and therefore human movements might become complicated. As mentioned above, the accuracy of prediction varies with the situation, such as the day, the time and the location. In this research, we proposed a path planning method with varying prediction length according to changes in the environment to realize effective human tracking system.

II. HUMAN TRACKING TASK

In this research, the number of humans who independently walk in a surveillance area and the number of agents who track humans for obtaining humans' detail information were denoted by N_h and N_c. We assume that the position and velocity of each human can be measured by sensors embedded in the environment. This assumption would be satisfied by employing a recent research technique for human position tracking system using sensors embedded in the environment [5][6](See Fig.1). We also assume that no occlusions between humans and agents occur.

A set of planned paths of agents is evaluated based on following equation :

$$D = \frac{1}{N_t}\frac{1}{\sum_t N_{h\_in}(t)}\sum_t \sum_{i \in I(t)} \min_j ||\bar{\boldsymbol{\mu}}_{h\ i}(t) \quad \bar{\boldsymbol{\mu}}_{c\ j}(t)|| \quad (1)$$

where N_t is the number of time steps of the path planning task, $I(t)$ and $N_{h\_in}(t)$ are the set the of indexes of humans who exist in the surveillance area at time t and its element count. $\bar{\boldsymbol{\mu}}_{h\ i}$ and $\bar{\boldsymbol{\mu}}_{c\ j}$ are the position of the i-th human and the position of the j-th agent. Hereinafter $\min_j ||\bar{\boldsymbol{\mu}}_{h\ i}(t)$ $\bar{\boldsymbol{\mu}}_{c\ j}(t)||$ is called nearest neighbor distance (NND).

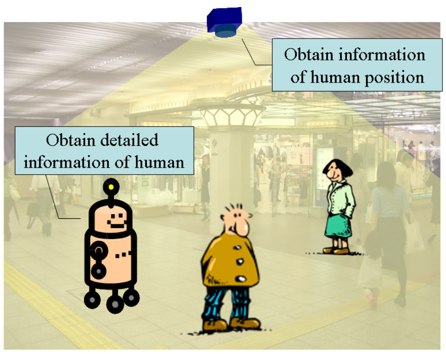

Fig. 1: Human tracking problem.

III. PATH PLANNING PROCEDURE

The predicted position of the i-th human at time $t +$ is approximated by a Gaussian whose center is $\boldsymbol{\mu}_{h\ i}(t + \ ;t)$

where t denotes the time to make the prediction. That is, the probability of the i-th human existing at $\boldsymbol{x}$ at time $t +$ is defined as:

$$H_i(\boldsymbol{x} \quad t + \quad ; t) = \frac{1}{2 \quad \sigma_h^2} \exp\left\{ \frac{||\boldsymbol{x} \quad \boldsymbol{\mu}_{h\ i}(t + \quad ; t)||^2}{2\sigma_h^2} \right\} \quad (2)$$

where $\sigma_{h\ i}$ is its variance.

The closer cameras are to a subject, the more detail information of the human can be obtained. In this research, we assume the distance between the camera and the human corresponds the amount of information of human behavior to be obtained, and the intensity of field of view (FOV) of the j-th camera is defined by a Gauss function :

$$C_j(\boldsymbol{\mu}_{c\ j}) = \frac{1}{2 \quad \sigma_c^2} \exp\left\{ \frac{||\boldsymbol{x} \quad \boldsymbol{\mu}_{c\ j}||^2}{2\sigma_c^2} \right\} \quad (3)$$

where $\boldsymbol{\mu}_{c\ j}$ is the position of the agent j and σ_c is size of FOV of cameras.

The predicted distribution of all humans' positions of all humans and the intensity of FOV of cameras at time $t +$ are calculated as follows :

$$H(t + \quad ; t) = \sum_{i=1}^{N_{h\_in}} H_i(\boldsymbol{\mu}_{h\ i}(t + \quad ; t) \quad \sigma_{h\ i}) \quad (4)$$

$$C(t + \quad ; t) = \sum_{j=1}^{N_c} C_j(\boldsymbol{\mu}_{c\ j}(t + \quad ; t) \quad \sigma_c) \quad (5)$$

In our method, the path is determined based on the Kullback-Leibler (KL) divergence between H and C, and the path which minimizes the KL divergence is obtained by a gradient method.

1 . Path Planning

The KL divergence between H and C at time $t +$ is calculated as :

$$KL(H(t + \quad ; t) \quad C(t + \quad ; t)) = \int_{\infty}^{\infty} H(t + \quad ; t) \log \frac{H(t + \quad ; t)}{C(t + \quad ; t)} d\boldsymbol{x} \quad (6)$$

We assume that the KL divergence at each time step is independent to the one at another time step and the multi step KL divergence can be calculated by the sum of single step KLs :

$$F(t) = \sum_{=1}^{T} \quad (t + \quad ; t) KL(H(t + \quad ; t) \quad C(t + \quad ; t)) \quad (7)$$

where is the weighting factor. By using movements of agents at every time steps $\boldsymbol{d} \equiv [\boldsymbol{d}(t+1;t)^\top \cdots \boldsymbol{d}(t + \quad ; t)^\top]^\top$, $\boldsymbol{\mu}_c(t + \quad ; t)$ can be calculated as:

$$\boldsymbol{\mu}_c(t + \quad ; t) = \bar{\boldsymbol{\mu}}_c(t) + \sum_{n=1} \boldsymbol{d}(t + n; t) \quad (8)$$

where $\boldsymbol{d}(t + n; t)$ is planned movements of agents at time $t + n$.

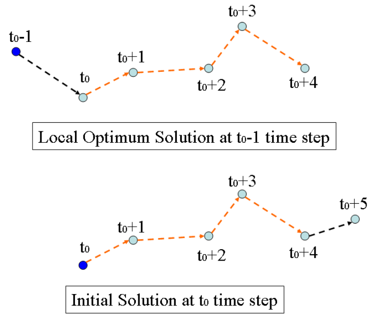

Fig. 2: Example of solutions. Orange dashed lines indicate the path which is able to be reused as initial solution at $t = t_0 + 1$ time step.

Since the maximum velocity of each agent is limited to V_{max}, the traveling distance for each agent is truncated when it becomes longer than V_{max} in the process of optimization based on the gradient method. That is, if $||\mathbf{d}^{(k+1)}(t + n; t)|| > V_{max} \quad n = 1 \ 2 \cdots \ T$, then $\mathbf{d}^{(k+1)}(t + n; t) := \frac{V_{max}}{||\mathbf{d}^{(k+1)}(t+n;t)||} \quad \mathbf{d}^{(k+1)}(t + n; t)$.

2 . Prediction Model of Human Motion

In order to calculate the prediction at each time step (equation (7)), a model of humans movement is necessary. For the simplicity, the motion of human is assumed to follow a fixed rule given in advance, for example, we use uniform linear motion, circular motion or zig-zag motion in our experiments. The performance of the prediction model would have large effect to the performance of human tracking [7], however, we focus on the number of the prediction steps in this research. If the predicted motion model is uniform linear motion model, the predicted position of human at time $t +$ can be calculated as :

$$\boldsymbol{\mu}_h(t + \quad ; t) = N(\bar{\boldsymbol{\mu}}_h(t) + \bar{\boldsymbol{v}}_h(t) \qquad \sigma_h) \quad (9)$$

where $\bar{\boldsymbol{\mu}}_h(t)$ and $\bar{\boldsymbol{v}}_h(t)$ are the position and the velocity of human at current time t.

3 . Generating an Initial Solution

Since the number of iterations in the gradient method depends on the distance between the initial solution and the suboptimal solution, it seems to be better that the initial solution is generated near by the optimal solution. In our method, the initial solution is generated as $\boldsymbol{d}^{(0)}(t + \quad ; t) = \bar{\boldsymbol{d}}(t + \quad ; t \quad 1)$, where $\bar{\boldsymbol{d}}(t + \quad ; t \quad 1)$ is the obtained solution at the previous time step. That is, the orange part of the path in Fig.2 is reused. Movements which were not dealt in the optimization at the previous time step are initialized to 0.

If the prediction is accurate, the longer prediction length makes the performance better but computational cost also becomes higher, because the dimensionality of $\boldsymbol{d}$ becomes large (curse of dimensionality). However, when the optimal solution at current time step is similar to that of the previous time step, the number of iterations would be reduced much, even if the prediction steps becomes large.

4 . Prediction Steps

Although path planning using accurate long-term prediction would be efficient, one using inaccurate long-term prediction might decrease performance of tracking in some

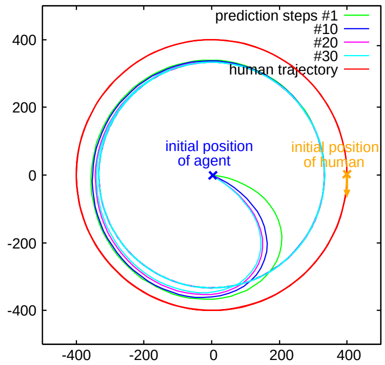

Fig. 3: Trajectories of human and agent in case of uniform circular motion

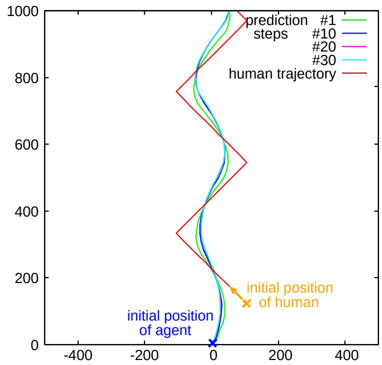

Fig. 4: Trajectories of human and agent in case of uniform zigzag movement

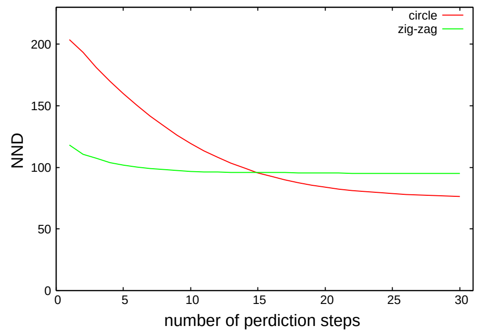

Fig. 5: NND between human and agent of each prediction step under static environment (refer to Fig. 3 and Fig. 4).

case. In our planning method, the number of prediction steps T is determined based on accuracy of the prediction. The probability that human moves following the prediction model until time $t+\ $ is calculated as:

$$P(t+\ ;t)=\prod(1\quad (t+\ ))\qquad(10)$$

where is the probability of human taking a motion different from the prediction model.

The weighting factor $(t+\ ;t)$ in equation (7) is calculated based on $P(t+\ ;t)$ as:

$$(t+\ ;t)=(1\quad (t))\quad (t+\quad 1;t\quad 1)\qquad(11)$$

where, $(t+1;t)=1$. When the $(t+\ ;t)$ becomes below a certain threshold, KL divergences after time $t+\ (\ >\ )$ are not used in the path planning procedure.

IV . SIMULATION EXPERIMENT

We conducted simulation experiments in a static environment where human movements do not change and those in a dynamic environment where human movements sometimes change. In these simulations, both the number of humans and that of agents are one.

1 . Tracking in Static Environments

In this case, the path planning was done by constant-term predictions $T = 1 \sim 30$. The length of each simulation was 200 time steps and the human motion models used in experiments are a circular motion model (Fig.3) and a zigzag motion model (turn $\pm 90^\circ$ every ten time steps)(Fig.4). The velocity of the human is 1 2 times faster than that of the agent.

Fig.3 and Fig.4 show the trajectories of the human and the agent. Red lines in the figures indicate the trajectory of the human and other lines show trajectories of the agents which are planned with constant prediction steps ($T = 1\ 10\ 20\ 30$). Fig.5 show NND between the human and the agent whose path planning was done with each prediction steps. According to Fig.3, 4 and 5, the longer-term prediction improve performance of the human tracking.

2 . Tracking in Dynamic Environment

The simulation experiment are conducted in the case of using zig-zag motion model with dynamically changing probability of human turning $\pm 90^\circ$ (Fig. 6). The total time step in this simulation was 200 and the probability of the turning are 0 3 at time step $t = 1 \sim 50\ 101 \sim 150$ (Mode1) and 0 05 at time step $t = 51 \sim 100\ 151 \sim 200$ (Mode 2). The ratio of velocity are same to the previous simulation. In this method, the uniform linear motion model is used as the motion prediction model. Ten sets of simulated human motion data are generated from this model. Fig. 6 shows an example of human trajectory in this case. Using these data sets, following three methods are compared.

Constant : The number of the prediction steps is constant ($T = 1 \sim 30$).

Variable : The number of the prediction steps is variable (proposed method)

Optimal : All human positions in the future was given in advance and used to calculate the path (upper bound).

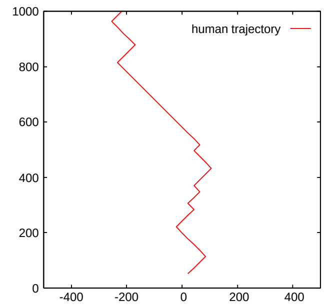

Fig. 6: Typical trajectory of human (unsteady zigzag movement)

A . Estimating probability of turning

In our method under the dynamic environment, the accuracy of prediction of human motion was calculated based on the probability of human turning. An online moving average of the turning probability of was used as , and was updated as:

$$(t)=0\ 7\quad (t\quad 1)+0\ 3\quad (t)\qquad(12)$$

$$(t)=\begin{cases}0 & \text{(go forward)}\\ 1 & \text{(turn)}\end{cases}\qquad(13)$$

B . Experimental results

Lines in Fig.7 shows the ten steps' moving average of the NND by each method. The comparison between *Constant*

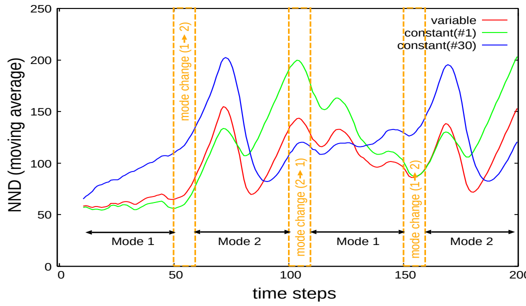

Fig. 7: Ten steps moving average of NND.

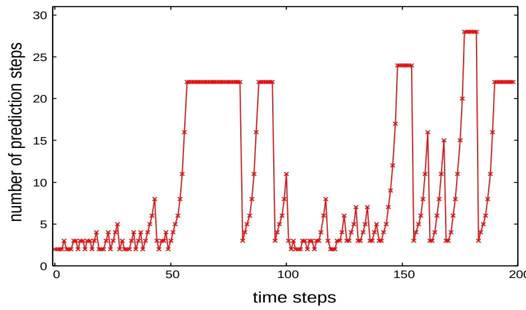

Fig. 8: Prediction steps of each time steps.

$(T = 1)$ and *Constant* $(T = 30)$ bear out that when the prediction was accurate (Mode 2), the path planning method with a long-term prediction (*Constant* $(T = 30)$) is efficient, on the other hand, when the prediction was inaccurate, the method with a short-term prediction (*Constant* $(T = 1)$) is efficient. The behavior by the *Variable* was similar to that of *Constant* $(T = 1)$ during Mode 1 and was similar to that of *Constant* $(T = 30)$ during Mode 2. Fig.8 shows the number of prediction steps of each time step. According to Fig.7 and 8, the number of prediction steps in *Variable* can be changed adequately based on the accuracy of the prediction.

Fig.9 shows the average NNDs of humans and agents against each data set (data ID = 1 $\sim$ 10). In Fig.9, the value for *Constant* shows the best value among NNDs by *Constant* with different prediction steps. The result of *Variable* was always better than that of *Constant*. Fig.10 shows an average NND of human and agents of *Constant* of each number of prediction steps. Red crosses indicate values for each dataset, and blue points indicate the average taken over ten data set. Green crosses plotted on the left side of the graph indicate average NND by *Variable*. The performance of *Variable* was better than that of *Constant*.

V. CONCLUSIONS

In this paper, we proposed a path planning method where the path planning was done based on the long-term prediction of human positions. In this method, the number of the prediction steps is varied according to the accuracy of the prediction because subsequent predictions would be similar (consistent) when the prediction is accurate. In a static situation, the performance of the human tracking becomes better by increasing the number of the prediction steps. On the other hand, in a dynamic situation, it is not necessarily the case that the long term prediction improve performance of the human tracking. In our method, the number of the prediction steps is adjusted according to the current situation, and the performance of the human tracking can be kept high in a changing environment.

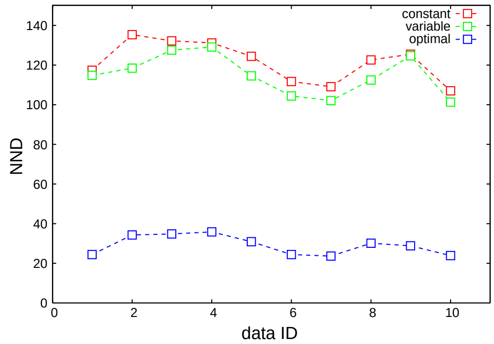

Fig. 9: NND between human and agent of each data set under dynamic environment.

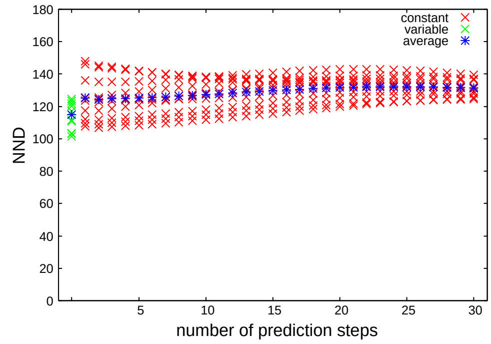

Fig. 10: NND between human and agent of each prediction step under dynamic environment.

VI. ACKNOWLEDGMENTS

This research was supported by "Special Coordination Funds for Promoting Science and Technology: Yuragi Project" of the Ministry of Education, Culture, Sports, Science and Technology, Japan.

References

[1] H. Buxton. Learning and understanding dynamic scene activity: a review. *Image Vision Comput.*, 21(1):125–136, 2003.

[2] C. Stauffer and W. E. L. Grimson. Learning patterns of activity using real-time tracking. *IEEE Trans. Pattern Anal. Mach. Intell.*, 22(8):747–757, 2000.

[3] B. Jung and G. Sukhatme. A generalized region-based approach for multi-target tracking in outdoor environments. In *Proceedings of the 2004 IEEE Int. Conf. on Robotics and Automation.*, pages 2189–2195, 2004.

[4] N. Takemura and J. Miura. View planning of multiple active cameras for tracking many persons based on multi-start local search. *Jouranl of the Robotics Society of Japan*, 25(8):82–89, 2007 (in Japanese).

[5] S. Khan and M. Shah. Tracking multiple occluding people by localizing on multiple scene planes. *IEEE Transactions of Pattern Analysis and Machine Intelligence*, 2008.

[6] K. F. MacDorman et al. Memory-based attention control for activity recognition at a subway station. *IEEE MultiMedia*, 14-2:38–49, 2007.

[7] A. Bruce and G. Gordon. Better motion prediction for people-tracking. In *In Proceedings of ICRA 2004*, 2004.

Optimal path planning with Holonomic mobile robot using localization vision sensors

Dong Seok Lee*, Chang Sup Kim*, Su Yong Kim*, Kil Soo Lee*, Hyung Gyu Park*, Yung Ho Koh**, Jong Il Bae***, Man Hyung Lee*

*School of Mechanical Engineering Pusan National University
(Tel : +82-51-510-1456; E-mail: dslee@pusan.ac.kr, changsup.kim@gmail.com, rocksy@pusan.ac.kr, melgibsoo@pusan.ac.kr, gyunious@pusan.ac.kr, mahlee@pusan.ac.kr)
**Futronic Co,. Ltd
(Tel : +82-51-931-5060; yhkoh@futronic.co.kr)
***Department of electrical Engineering, Pukyong National University
(Tel : +82-51-629-6306; jibae@pknu.ac.kr)

Abstract: Most of the present drive systems of the home service robots and the industrial robots use non-holonomic systems that function only when the robots are moving. For instance, the average vehicle can only be steered when driving so instant movement in all directions is not possible. And that is why the holonomic drive system is attracting attention. In this paper, we propose a holonomic system using three omni-direction wheels to enable instant movement in all directions. Also, IR-projector and vision sensors are proposed for autodrive robots to detect the robot's positioning. This system uses an infrared ray projector which processes the image reflected from the infrared reflector installed on the ceiling to detect the absolute position and direction angle of the robot in real time. Robot autodrive using vision sensors is also proposed.

Keyword - Holonomic, Non-holonomic, localization vision sensor, Optimal navigation, Omni-direction-wheel and Path-planning

I. INTRODUCTION

Industrial and technical applications of mobile robots are continuously gaining in importance. Mobile robots are already widely used for surveillance, inspection, and transportation tasks.

A further emerging market is that of mobile entertainment robots. The basic requirement for autonomous mobile robots is the ability to move through its operational area, avoiding hazards and obstacles, finding its way to the next location to perform its task.

These capabilities are known as localization and navigation. In order to know where to go, the robot must have an accurate knowledge of its current location. From here, the robot can navigate to the next position, using a great variety of sensors, external references, and algorithms.

The performance of a mobile robot is determined to a large extend by the tracking and localization algorithms, as well as its sensing capabilities. Research is continuously going on in this field, to improve the autonomous navigation capability of mobile robotic systems.

In order to test newly developed sensing, navigation and localization strategies, a universal mobile robotic base featuring omni-directional motion capability is designed, providing a flexible motion platform to test and improve developed algorithms and sensing systems.

In this paper, kinematics of omni-directional mobility will be derived. And then, navigation from the point on the reference path $P_p(i)$ to $P_p(i+1)$ via localization sensor will be shown.

II. Kinematics

The omniwheel powered base consists of three omniwheels, positioned at an angle α_i, relative to the local frame $[x_l, y_l]$. The center of this frame coincides with the center of gravity of the base and wheel 1 is located on the local axis (x_l), in other words: α_1 = 0, Fig. 1. The orientation of the base with respect to the global frame (x_g, y_g) is given by the global coordinates $[x, y, \theta]$. The relation between the global velocity of the platform $(\dot{x}, \dot{y}, \dot{\theta})$ and translational velocity v_i of wheel hub i can be obtained using the inverse kinematic equation of each wheel hub. The component of v_i in x_g direction, denoted as v_1x in Fig. 1, must be equal to $\dot{x}$, due to the fixed position of the hub relative to the center of the mass. For v_1y a similar relation can be derived. When the base rotates, the hub speed v_i needs to satisfy the condition $v_i = \theta \cdot R$, please note that r refers to the wheel radius, while R represents the distance from the center of the mass of the platform to the wheels along a radial path.

$$v_i = -\sin(\theta+\alpha_i)\dot{x} + \cos(\theta+\alpha_i)\dot{y} + R\dot{\theta} \qquad (1)$$

The translational velocity of the hub can be rewritten as a angular velocity $\dot{\phi}_i$ of the wheels using Eq. (2), resulting in Eq. (3)

$$v_i = r\dot{\phi}_i \qquad (2)$$

$$r\dot{\phi}_i = -\sin(\theta+\alpha_i)\dot{x} + \cos(\theta+\alpha_i)\dot{y} + R\dot{\theta} \qquad (3)$$

This can be transformed to matrix representation Eq. (4)

$$\underline{\dot{\phi}} = J_{inv}\underline{u} \qquad (4)$$

From Eq. (3) and Eq. (4) the inverse jacobian J_{inv} for the omniwheel powered base can be obtained, providing a direct relation between global velocities and angular velocities of the wheels.

$$\begin{bmatrix} \dot{\phi}_1 \\ \dot{\phi}_2 \\ \dot{\phi}_3 \end{bmatrix} = \frac{1}{r} \begin{bmatrix} -\sin(\theta) & \cos(\theta) & R \\ -\sin(\theta+\alpha_2) & \cos(\theta+\alpha_2) & R \\ -\sin(\theta+\alpha_3) & \cos(\theta+\alpha_3) & R \end{bmatrix} \begin{bmatrix} \dot{x} \\ \dot{y} \\ \dot{\theta} \end{bmatrix} \qquad (5)$$

In most cases, it is not convenient for users to steer a robot in global coordinates however. It is far more natural to think and steer in local coordinates. Fortunately, we can now simply convert global coordinates to local coordinates with the following equation.

$$\begin{bmatrix} \dot{x} \\ \dot{y} \\ \dot{\theta} \end{bmatrix} = \begin{bmatrix} \cos(\theta) & 0 & 0 \\ 0 & \cos(\theta) & 0 \\ 0 & 0 & 1 \end{bmatrix} \begin{bmatrix} \dot{x}_l \\ \dot{y}_l \\ \dot{\theta} \end{bmatrix} \qquad (6)$$

Substituting Eq. (6) in Eq. (5) leads to:

$$\begin{bmatrix} \dot{\phi}_1 \\ \dot{\phi}_2 \\ \dot{\phi}_3 \end{bmatrix} = \frac{1}{r} \begin{bmatrix} -\sin(\theta) & \cos(\theta) & R \\ -\sin(\theta+\alpha_2) & \cos(\theta+\alpha_2) & R \\ -\sin(\theta+\alpha_3) & \cos(\theta+\alpha_3) & R \end{bmatrix} \begin{bmatrix} \cos(\theta) & 0 & 0 \\ 0 & \cos(\theta) & 0 \\ 0 & 0 & 1 \end{bmatrix} \begin{bmatrix} \dot{x}_l \\ \dot{y}_l \\ \dot{\theta} \end{bmatrix} \qquad (7)$$

This matrix relation in the local frame can also be expanded to three separate equations for easy implementation in programming applications:

$$\begin{aligned} \dot{\phi}_1 &= (-\sin(\theta)\cos(\theta)\dot{x}_l + \cos^2(\theta)\dot{y}_l + R\dot{\theta})/r \\ \dot{\phi}_2 &= (-\sin(\theta+a_2)\cos(\theta)\dot{x}_l + \cos^2(\theta+a_2)\dot{y}_l + R\dot{\theta})/r \\ \dot{\phi}_3 &= (-\sin(\theta+a_3)\cos(\theta)\dot{x}_l + \cos^2(\theta+a_3)\dot{y}_l + R\dot{\theta})/r \end{aligned} \qquad (8)$$

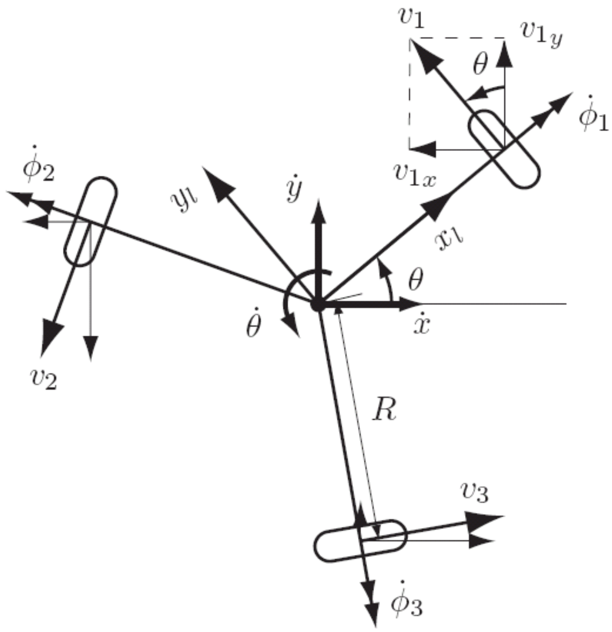

Fig 1. Kinematic diagram of the three wheel base

III. Localization Sensor

StarGazer is a localization sensor system for indoor localization of intelligent mobile robots. It analyzes infrared ray images which are reflected from a passive landmark with an independent ID. The output of position and heading angle of a robot is given with very precise resolution and high speed. It is seldomly affected by surroundings such as an infrared ray, a fluorescent light, and sunshine.

The sensor output data values are from the subsidiary's own protocol and communications used the RS232C output.

IV. CONTROLLER DESIGN

Design conditions of lateral controller of the omniwheel robot system are steady state error 2%, overshoot 5%, and rising time 1 second. The controller is designed by using system parameters.

The transfer function of PID controller is given by Eq. (9)

$$K(s) = K_P + \frac{K_I}{s} + K_D s \qquad (9)$$

V. EXPERIMENT

1. Experimental system

Experiments were conducted in order to verify that the omniwheel robot moves accurately along the reference path using the StarGazer sensor.

In Fig. 2, StarGazer is mounted on the robot's C.G so it can obtain the position information and orientation. The information of the localization is sent to a PC via Bluetooth and the PC executes its trajectory tracking control. So the robot moves along the reference path in a counterclockwise direction.

In Fig. 3, Landsmarks are located on the ceiling and they reflect infrared to the robot.

2 Reference path for the experiment

As seen in Fig. 5, the reference path is situated on a twenty target point track[5].

3. Navigation algorithm

Fig. 4 represents the unmanned navigation algorithm. Navigation algorithm is PTP(Point To Point) method. The robot moves from the point on the reference path $P_p(i)$ to $P_p(i+1)$. If the robot arrives at a target point, the system continuously determines the next target point. And if the distance error between current position and $P_p(i)$ is smaller than d_e, the system corrects the next target point $P_p(1)$ to $P_p(i+1)$. d_e is selected by the velocity of the robot and the error of the position measurement.

4. Experimental results

In this experiment, the position information of StarGazer sensor is measured using the consisted experimental system. Figures 4 ~ 8 represent the experimental results for other velocities and other controller gain. The faster the velocity of the system, the bigger the position error.

Range of position error is from 10cm to 20cm.

Fig. 2 Configuration of omni-directional system

Fig. 3 Total composition of the experimental system

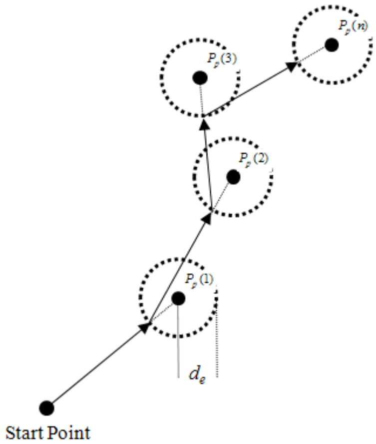

Fig. 4 Navigation algorithm

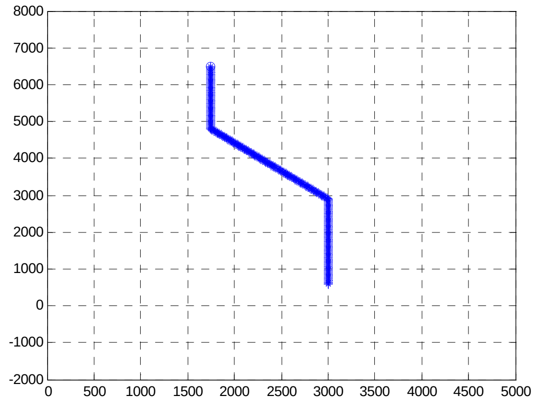

Fig. 5 Reference path

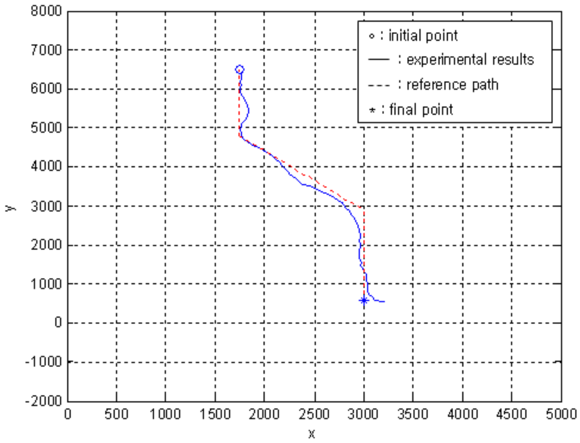

Fig. 6 Experimental result (0.25m/s)

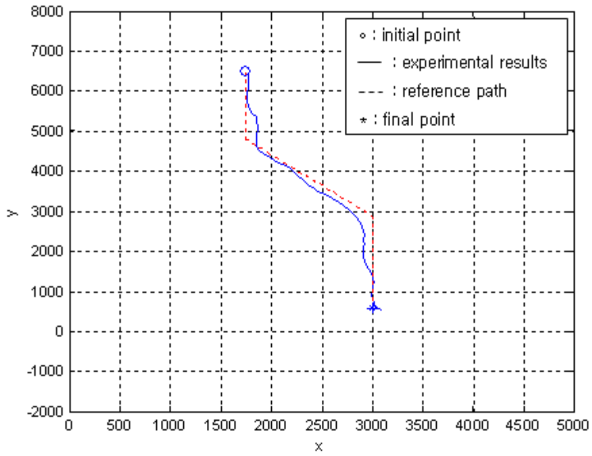

Fig. 7 Experimental result(0.3m/s)

VI. CONCLUSION

In this paper, the system model of an unmanned Holonomic-system robot is important to design parameter based controller in unmanned vehicle system. Using the subspace system identification method, we confirmed that the experimental model is very simple and accurate. It is important to design a controller that uses system parameters.

To minimize the modeling error, the system identification that uses system input-output data was used, and a PID controller was designed. To design the controller, the relation between the input and output is represented in state matrices.

The performance of the compensated system was satisfied based on the system identification.

Because modeling error of identification model is smaller than analytical model.

We will research the vehicle system identification with other dynamic and system conditions, for example, longitudinal control, nonlinear system, and MIMO system. And also, we will design a controller that is robust against system disturbance and parameter uncertainties.

VII. REFERENCES

[1] A. Ashmore and N. Barnes, "Omni-drive Robot Motion on Curved Paths: The Fastest Path between Two Points Is Not a Straight-Line", *AI 2002: Advances in Artificial Intelligence*, vol. 2557, pp. 225-236, 2002.

[2] T.A. Baede, "Motion control of an omnidirectional mobile robot", *Traineeship report DCT 2006*, Aug, 2006.

[3] Y. Liu, X. Wu, J. Zhu and J. Lew, "Omni-directional mobile robot controller design by trajectory linearization", in: *Proceedings of the American Control Conference*, vol. 4, pp. 3423-3428, June, 2003.

[4] Y. Liu, J. J. Zhu, R. L. Williams and J. Wu, "Omni-directional mobile robot controller based on trajectory lineariztion", *Robotics and Autonomous Systems*, vol. 56, pp. 461-479, May, 2008

[5] T.K. Nagy, P. Ganguly and R. D'Andrea, "Real-time trajectory generation for omnidirectional vehicles", in: *Proceedings of the American Control Conference*, vol. 1, pp. 286-291, 2002.

[6] K. Watanabe, "Control of an omnidirectional mobile robot", in: *Proceedings of 1998 Second International Conference on Knowledge-Based Intelligent Electronic Systems*, vol. 1, pp. 51-60, Apr, 1998.

[7] K. Watanabe, Y. Shiraishi, S.G. Tzafestas and J. Tang, "Feedback Control of an Omnidirectional Autonomous Platform for Mobile Service Robots", *Journal of Intelligent and Robotic System*, vol.22, no. 3-4, pp. 315-330, Nov, 1998.

[8] R.P.A. van Heandel, "Design of an omnidirectional universal mobile platform", *Internal report DCT 2005*, p. 117, 2005.

Efficient Robotic Memory Controller for long-term Planning

Hassab Elgaw Osman

Imaging Science and Engineering Lab, Tokyo Institute of Technology, Japan.
Email: osman@isl.titech.ac.jp

Abstract

This paper contributes on designing robotic memory controller for non-Markovian reinforcement tasks. Instead of holistic search for the whole memory contents, the controller adopts associated feature analysis to produce the most likely relevant action from previous experiences. Actor-Critic (AC) learning is used to adaptively tuning the control parameters, while on-line variant of Random Forest (RF) learner is used as memory-capable to approximate the policy of Actor and the value function of Critic. Learning capability is experimentally examined through non-Markovian cart-pole balancing task. The result shows that the proposed controller acquired complex behaviors such as balancing two poles simultaneously and displays long-term planning.

Keywords: non-Markovian, actor-critic, random forest, self-optimizing controller.

1 Introduction

As with the most real-world robot learning systems, the arising of perceptual aliasing, when the system has to scale up to a non-Markov setting or POMDP[1] renders conventional reinforcement learning (RL) methods impracticable, raising an interests in heuristic methods without world model (e.g., 'memory approach') that intrinsically and adaptively modifying the policy. In Memory-based systems the controller is unable to take optimal transitions unless it observed the past inputs, then the controller simultaneously solve the incomplete perception while maximizing discounted long-term reward. If a world model is available to the controller, it can easily calculate and update a *belief vector* $\vec{b_t} = \langle b_t(s_1), b_t(s_2), \cdots, b_t(s_N)\rangle$ over 'hidden states' at every time step t by taking into a account the history trace $h = o_1, o_2, \cdots, o_{t-1}, o_t$.

2 Our Approach

The process of memorizing and scaling up could be lengthy if traditional memory scheduling processes are to be used. In order to speed up learning process and improve the convergence rate, a RL-controller is modeled as scheduler for our proposed self-optimizing adaptive memory controller (Fig.1). Rather than holistic search for the whole memory contents the model adopt associated feature analysis to successively memorize a newly experience (state-action pair) as an action of past experience. Actor-Critic (AC) learning is used to adaptively tuning the control parameters, while on-line variant of random forests (RF) [1] learner is used as memory-capable function approximator coupled with Intrinsically Motivated Reinforcement Learning (IMRL) reward function to approximate the policy of *actor* and the value function of *critic*. At this point we would like to mention that M3 Computer Architecture Group at Cornell has proposed a similar work [2] to our current interest. They implement a RL-based memory controller with a different underlying RL implementation.

[1] basically, a POMDP is like an MDP but with observations (o) instead of direct state perception.

3 Controller Architecture

Fig.1 illustrates the general view of our memory controller based on heuristic memory approach for solving non-Markovian cart-pole balancing task and balancing two poles simultaneously. We briefly explain its components.

Past experiences. Sensory control inputs from environment would be stored at the next available empty memory location (chunk), or redundantly at several empty locations. In our memory implementation only the following parameters have to be specified by a designer: 1) The capacity of the memory, 2) A function which extracts features from its stored locations, 3) A predictor which provides relevant features of the current system state, and 4) A function which provides intrinsic rewards.

Feature predictor. Is utilized to produce associated feature for selective experience. This predictor was designed to predict multiple experiences in different situations. When the selective experience is predicted, the associated feature is converted to feature vector so the controller can handle it.

Features Map. The past experiences are mapped into multidimensional feature space using neighborhood component analysis, based on the Bellman error, or on the temporal difference (TD) error. In general this is done by choosing a set of features which approximate the states S of the system. A function approximator (FA) must map these features into a value function V^{π} for each state in the system. This generalizes learning over similar states and increases the speed of learning, but potentially introduces generalization error as the feature will not represent the state space exactly.

Memory access. The memory access scheduling is formulated as a RL agent whose goal is to learn automatically an optimal memory scheduling policy via interaction with the rest of the system. As can be seen in Fig.1 two scenarios are considered. In Fig.1a all the system parameters are *fully observable*, the agent can estimate V^{π} for each state and use its actions (past experiences). In Fig.1b the system is *partially observable* [3, 4], the agent does not know which state it is in due to sensor limitation, the agent updates its policy parameters directly. Since our system is modeled as non-Markovian (non-MDP) process decision depends on last state-action, and the state transitions $s_{t+1} = \delta(s_t, a_t)$ depend on arbitrary past state where the agent had visited. This transition is expressed by $Pr(s_t|s_{t-1}, a_{t-1}, s'_t, s''_t, \cdots)$, where s_{t-1}, a_{t-1} are the previous state and action, and t', t'' are arbitrary past time.

Learning behaviors from past experience. On each time step, a component of the TD learning algorithm, called the adaptive critic, is used to estimate the expected future reward of retaining various combinations of memory locations. The collection of memory locations show to have the highest accumulated rewards are more likely to be remembered. The amount of occasional intrinsic rewards received, a long with the estimates of the adaptive critic on this time step and on the previous time step, are used to compute the TD error–the change in expected future reward. This error signal also used to train the adaptive critic.

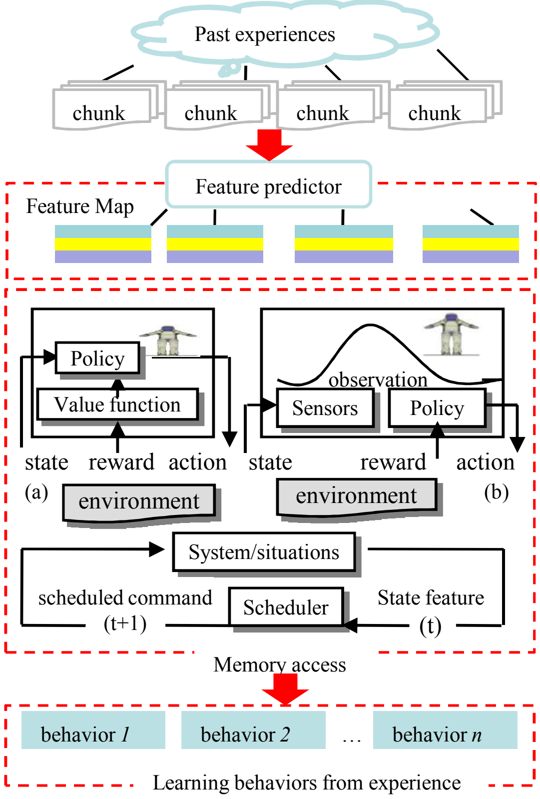

Figure 1: Architecture of self-optimizing memory controller. The controller utilizes associated feature analysis to memorize complete non-Markovian reinforcement task as an action of past experience.

4 Memory Capable FA

4.1 Actor-Critic Learning

Actor-critic (AC), a group of on-policy TD methods, separates the policy and the value function into independent memory structures. The policy structure, or *actor*, is used to decide which action to pick in each state. The estimate value function, or *adaptive critic*, determines whether the actions of the *actor* are to be rewarded or punished. The algorithms use these spare measures of performance to adopt an optimal behavior over time. The adaptive critic maps its current state event onto an estimate of whether it will be rewarded. The mapping is learned from the past experience. If $s+1$ is the situation that follows situation s in time, this expected future reward may be written as:

$$V(s) = \gamma^0 r(s) + \gamma^1 V(s+1) + \cdots + \gamma^n V(s+n) \quad (1)$$

The value of the current situation, $V(s)$, is the sum of all the rewards we will receive over the next n time steps. The rewards on each time step are "discounted" by factor, γ, in the range $[0, 1]$. Equation (1) can be rewritten in a recursive form:

$$V(s) = \gamma^0 r(s) + \gamma^1 V(s+1) = r(s) + \gamma V(s+1) \quad (2)$$

Obviously a value function estimates that fall far from this equality in considered inaccurate, and the error is estimated based on TD error:

$$\delta(s) = (r(s) + \gamma V(s+1) - V(s)) \tag{3}$$

Adopting these methods can save much computation for selecting optimal actions, due to utilizing separate memory for value function and policy.

4.2 AC in non-Markovian Domain

Due to non-Markovian characteristics, the controller infers the state of its environment from a sequence of observation it receives, learns an optimal action by detecting certain past events, that associated with its current perception.
In particular, at time t, the error of the critic is give by

$$E_c(t) = \frac{1}{2}([r(t) + \gamma J(t)] - J(t-1))^2 \tag{4}$$

while the error of the actor is

$$E_a(t) = \frac{1}{2}(J(t)] - R^*)^2 \tag{5}$$

where R^* is the optimal return, which is dependent on the problem definition. The expected return is expressed as the general cost function, $J(t)$, which is to be maximized by the controller. Specifically,

$$J(t) = r(t+1) + \gamma r(t+2) + \gamma^2 r(t+3) + \cdots \tag{6}$$

where $r(t)$ is the immediate reward and γ is the time-discounting factor $0 \leq \gamma \leq 1$.

4.3 RF Memory for Optimal Learning

On-line RF has the characteristics of a simple structure, strong global approximation ability and a quick and easy training [1]. It has been used with TD learning for building a hybrid function approximator [5, 6]. Here, in order to improve learning efficiency and to reduce the demand of storage space and to improve learning efficiency, the on-line RF approximator is structured in a way that both *actor* and *critic* can be embodied in one structure, subsequently, is used to approximate policy function of *actor* and the value function of *critic* simultaneously. That is, the actor and the critic can share the input and the basis functions structure of the RF. Let RF_{Appro} represent a hybrid approximator that combines actor and critic. Given a state $s(t)$ and action $a(t)$, RF_{Appro} is defined such that $RF_{Appro}(s(t), a(t)) = (J(t), a(t+1))$, where $J(t)$ is the estimated value of the given state-action pair, and $a(t+1)$ is the subsequent action to be taken by the controller. At the critic output the error is captured by TD error. However, at the action outputs the error is determined by the gradient of the estimated value $J(t+1)$ w.r.t the action $a(t+1)$ selected by the on-line RF at time t. Specifically,

$$\begin{aligned} e_a(t) &= \alpha \nabla_{a(t+1)J(t+1)} \\ &= \alpha \left(\frac{\partial J(t+1)}{\partial a_1(t+1)}, \cdots, \frac{\partial J(t+1)}{\partial a_d(t+1)} \right) \end{aligned} \tag{7}$$

where α is a scaling constant and d is the choices availabilities at action a. Accumulating the error for each choice of the selected action, the overall actor error is given be:

$$E_a(t) = \frac{1}{2}\left[\sum_{i=1}^{d} e_{ai}^2(t)\right] \tag{8}$$

where $e_{ai}(t)$ is the choice of the action error gradient $e_a(t)$. In finding the gradient of the estimated value $J(t+1)$ w.r.t the previously selected action $a(t+1)$, the direction of change in action, which will improve the expected return at time step $t+1$, is obtained. Thus by incrementally improving actions in this manner, an optimal policy can be achieved. $E(t) = E_c(t) + E_a(t)$ define the reduced error for the entire on-line forest.

5 Experiment and Results

The proposed controller brings a number of preferable properties for learning different behaviors. In this section, we investigate its learning capability through a task of cart-pole balancing problem, designed with non-Markovian settings.

5.1 Related work

The pole balancing algorithm has not been extensively modeled for non-MDP. Although a variation of Value and Policy Search (VAPS) algorithm [7] has been applied to this problem for the POMDP case [8], they have assumed that x and θ are completely observable. NeuroEvolution of Augmenting Topologies [9] and evolutionary computation [10], are another promising approaches where recurrent neural networks are used to solve a harder balancing of two poles of different lengths, in both markovian and non-Markovian settings.

5.2 Non-Markovian Pole Balancing

As illustrated in Fig.2A, Cart-Pole balancing involves a vertical pole with a point-mass at its upper end installed on a cart, with the goal of balancing the pole when the cart moves by applying horizontal forces to the cart, which must not stray too far from its initial position. The state description for the controller consists of four continuous state variables, the angle θ (radial), and the speed of the pole $\acute{\phi} = \delta x/\delta t$ plus the position x and speed of the cart $\acute{x} = \delta x/\delta t$. The two continuous actions set up for controller training and evaluation were RightForce (RF), (results in pushing the cart to the right), and LeftForce (LF), (results in pushing the cart left). At each time step t, the controller must only observe the θ and then takes appropriate action to balance the pole by learning from the past experience and the intrinsically rewards (Fig.2A). The optimal value function is shown in Fig.2B. A simulated sample run is shown in Fig.3. The controller could keep the pole balanced after about 4000 steps.

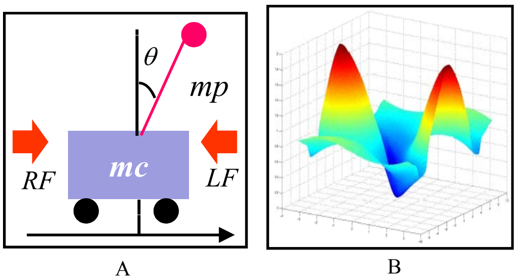

Figure 2: (A) Illustration of the non-Markov Cart-Pole balancing problem, where the angular velocity is not observing by the controller. (B) Optimal value function.

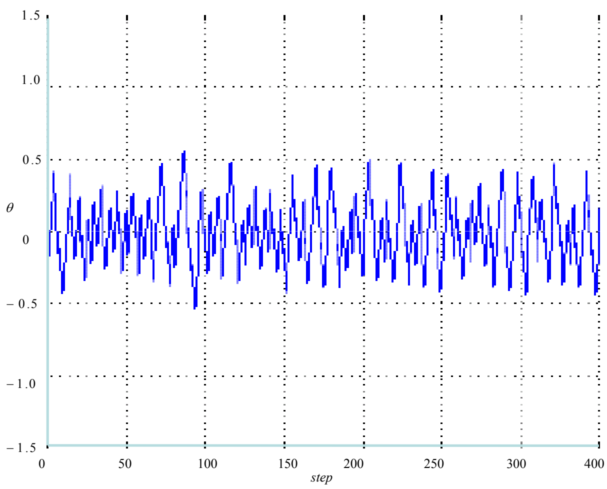

Figure 3: A sample learning for balancing the pole.

5.3 Non-Markovian 2-Pole Balancing

Then we moved to a harder setting of this problem, balancing two poles simultaneously. Each pole has its own position and angular velocity, θ_1 and $\dot{\theta}_1$ for the first pole and θ_2 and $\dot{\theta}_2$ for the second pole respectively. The controller must balance the two poles without velocity information. In order to assist the feasibility of our approach to balance two poles simultaneously we compared with state-of-the-art methods. Table 1 reports the performance of our controller compared with traditional value function-based methods (including SARSA-CMAC, SARSA-CABA, and VAPS) and policy search method (Q-MLP). Value function performance results are reported by [10], who used SARSA implementations by [11]. It shows that our controller takes the minimal evaluations to balance the poles. With regard to CPU time (reported in seconds) we slightly fall short to Q-MLP. However, it interesting to observe that none of the value function approaches could handle this task in within the set of steps due to the memory constraint. The result also indicates that our memory controller stand as a promising method in solving this benchmark more successful than the traditional RL techniques.

Table 1: Comparison of our result for balancing two carts simultaneously with state-of-the-art value function approaches and policy based methods.

	Method	Evaluation	time
V-function	SARSA-CMAC	Time Out	-
	SARSA-CABA	Time Out	-
	VAPS	Time Out	-
Policy	Q-MLP	10,582	153
Memory	Our	8,900	300

6 Conclusions

In this paper we provide evidences that the robot control system will benefit from the inclusion of a self-optimizing memory controller. Our model avoids manual 'hard coding' of behaviors, modeled the memory controller as a RL agent learning from past experience. Results based on non-Markov Cart-Pole balancing indicate that our model can memorize complete non-Markovian sequential tasks and is able to produce behaviors that make the controlled system to behave desirably in the future. One of our future plans is to overcome the limited capacity of memory. In our current design the number of "chunks" that can be used is quite limited. Another future plan will be in designing intelligent mechanism for memory updating, and to experiment with different applications such as visual and speech recognition, and robot navigation.

References

[1] Hassab Elgawi, O.: "Online Random Forests based on CorrFS and CorrBE," *In Proc.IEEE workshop on online classification*, CVPR, pp.1-7, 2008.

[2] Ipek, E., Mutlu, O., Martinez, J.F., and Caruana, R.: "Self-Optimizing Memory Control-

lers: A Reinforcement Learning Approach,". In *Intl. Symp. on Computer Architecture (ISCA)*, pp.39-50, 2008.

[3] Cassandra, A. R, Kaelbling, L. P, and Littman, M. L.: "Acting optimally in partially observable stochastic domains,". *Proc. Int'l. Conf on AAAI*, pp.1023-1028, 1994.

[4] Kaelbling, L, Littman, M and Cassandra, A.: "Planning and acting in partially observable stochastic domains,". *Artificial Intelligence*, 101:99-134, 1998.

[5] Hassab Elgawi, O.: "Architecture of behavior-based Function Approximator for Adaptive Control,". In *Proc. 15th Int'l. Conf on Neural Information Processing* ICONIP, LNCS 5507, pp.104-111, 2008.

[6] Hassab Elgawi, O.: "Random-TD Function Approximator," *Journal of Advanced Computational Intelligence and Intelligent Informatics* (JACIII), 13(2):155-161, 2009.

[7] Meuleau, N., Peshkin, L., Kim, K.-E., and Kaelbling, L. P.: "Learning finite-state controllers for partially observable environments,". In *Proc of the 15th Int'l Conf on Uncertainty in Artificial Intelligence*, pp.427-436, 1999.

[8] Peshkin, L., Meuleau, N., and Kaelbling, L. P.: "Learning policies with external memory,". In *Proc. of the 16th Int'l Conf on Machine Learning*, pp.307-314, I. Bratko and S. Dzeroski, Eds, 1999.

[9] Kenneth, O. S.: "Efficient evolution of neural networks through complexification,". Ph.D. Thesis; Department of Computer Sciences, The University of Texas at Austin. Technical Report AI-TR-04-314, 2004.

[10] Gomez. F.: "Robust non-linear control through neuroevolution,". Ph.D. Thesis; Department of Computer Sciences, The University of Texas at Austin. Technical Report AI-TR-03-303, 2004.

[11] Santamaria, J. C., Sutton, R. S., and Ram, A.: "Experiments with reinforcement learning in problems with continuous state and action spaces,". *Adaptive Behavior*, 6(2):163-218, 1998.

Appendix A: Pole-balancing learning parameters

Below are the equations and parameters used for cart-pole balancing experiments [10]

.1 Pole-balancing equations

The equations of motion for N unjoined poles balanced on a single cart are

$$\ddot{x} = \frac{F - \mu_c sgn(\dot{x}) + \sum_{i=1}^{N} \tilde{F}_i}{M + \sum_{i=1}^{N} \tilde{m}_i}$$

$$\ddot{\theta}_i = -\frac{3}{4l_i}(\ddot{x}\cos\theta_i + g\sin\theta_i + \frac{\mu_{pi}\dot{\theta}_i}{m_i l_i}),$$

where $\tilde{F}_i$ is the effective force from the i^{th} pole on the cart,

$$\tilde{F}_i = m_i l_i \dot{\theta}_i^2 \sin\theta_i + \frac{3}{4} m_i \cos\theta_i (\frac{\mu_{pi}\dot{\theta}_i}{m_i l_i} + g\sin\theta_i),$$

and $\tilde{m}_i$ is the effective mass of the i^{th} pole,

$$\tilde{m}_i = m_i(1 - \frac{3}{4}\cos^2\theta_i).$$

.2 Pole-balancing learning parameters

Table 2: Parameters for the single pole & double pole problem.

	Parameters for the single pole	
Sym	Description	Value
x	Position of cart on track	$[-2.4, 2.4]$m
θ	Angle of pole from vertical	$[-12, 12]$deg
F	Force applied to cart	-10.10N
l	Half length of pole	0.5m
M	Mass of cart	1.0kg
m	Mass of pole	0.1kg
	Parameters for double pole	Value
Sym	Description	Value
x	Position of cart on track	$[-2.4, 2.4]$m
θ	Angle of pole from vertical	$[-36, 36]$deg
F	Force applied to cart	-10.10N
l_i	Half length of i^{th} pole	$l_1 = 0.5$m
		$l_2 = 0.05$m
M	Mass of cart	1.0kg
m_i	Mass of i^{th} pole	$m_1 = 0.1$kg
		$m_2 = 0.01$kg
μ_c	friction coef on cart on track	0.0005
μ_p	friction coef if i^{th} pole's hinge	0.0005

Construction of the robot control system with use of pointing action and voice

Yuki TAKENAKA, Norihiro ABE, Yoshihiro TABUCHI
Kyusyu Institute of Technology
680-4 Kawazu, iizuka, Fukuoka 820-8502, Japan
Email: takenaka@sein.mse.kyutech.ac.jp

Hirokazu TAKI
Wakayama University
930 Sakaedani, Wakayama-shi
Wakayama 680-8510, Japan
Email: taki@sys.wakayama-u.ac.jp

Shoujie He
VuCOMP
Richardson, Texas, USA
Email: hesj@computer.org

*Abstract***:** This research is aiming at making the robot that can go to take an object designated by a user. We produce the robot control system that uses pointing action and voice. This system is composed of two systems. One system is the object instruction system that uses pointing action, another one is the object instruction system that uses voice. An approximate position of a designated object is recognized by the object instruction system that uses pointing, details of information on a designated object and an instruction operation correction are conveyed by the object instruction system that uses voice. A robot is able to be moved to a designated object by using this system.

Keywords: Robotics, Image Processing, Binocular Stereo, Pointing, Voice

I. INTRODUCTION

Recently, robots are expected to help people at a care facility because of labor scarcity. In this research, to develop the nursing mobile robot which every senior person can easily instruct to attain his/her requirement, the robot control system which is easily instructed with use of pointing action and voice is proposed. When a user tells a robot to carry an object to the user using pointing action and voice like " take it to me", the robot must move to the object and bring it near the user. The method calculates the location of an object designated by a user from the images which are acquired from network cameras installed on the robot. A robot figures out command from a user and object information with a voice recognition system. We control a robot with the pointing information and the voice information.

Not only elderly people but a lot of users can operate a robot easily with this system because it uses easy interface such as pointing action and voice.

II. SYSTEM CONFIGURATION

The system configuration is shown in Fig.1. The image acquired with network cameras on a robot is sent to PC using wireless LAN, and image processing calculates the position of a designed object. User's voice acquired with a headset which a user wears is sent to PC wirelessly, and the user's instruction is recognized, then a command corresponding to the given instruction is sent back to the robot.

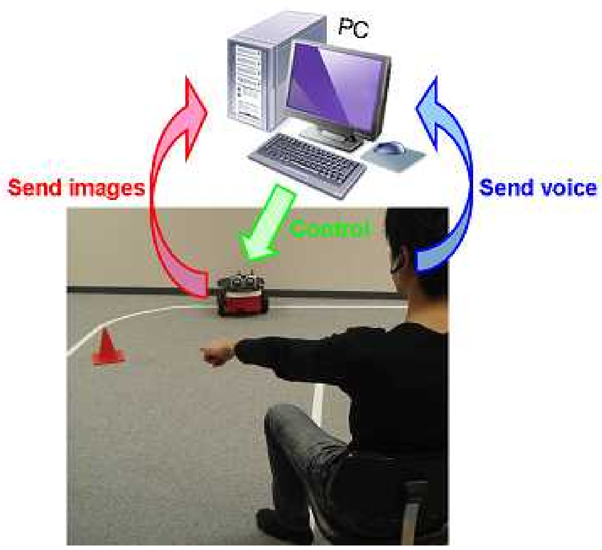

Fig.1. System configuration

III. THE OBJECT INDICATION USING POINTIG ACTION AND VOICE

When a user designates an object, a robot has to know the position of the object. It is not easy for a robot to calculate the precise location but the approximate one can be determined by referring to the direction of the user's hand if a little error is permitted. We propose the approach which makes a robot calculate the position of the object designated by the user and move to the position. There is, however, the possibility that a user erroneously designates a target by pointing action. When there are similar objects near the target one, the robot may not always succeeds in identifying the target. In the case, as a robot will probably move toward the different object from what the user intends, the user must give an advice using voice to the robot in order to make the robot change its behavior. User's voice captured with a headset is sent with a wireless LAN to the PC which is processing image data sent from a robot with another wireless LAN, and then the voice signals are translated into Japanese character strings with a voice recognition system. The strings are next segmented by referring to grammar rules and a dictionary including words registered beforehand into Japanese word sequence. A set of words available at present includes name, shape or color of objects, operation added to objects and demonstrative pronouns.

1. Image processing system

1.1. Get pointing information

As parts except for the arm are almost still when pointing action is performed, the arm can be detected by taking difference between consecutive two images. The arm vector is obtained as the line connecting two middle points of two narrow sides of the minimum rectangular which includes difference points.

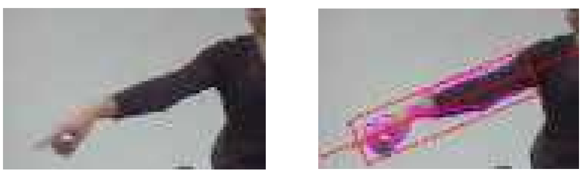

(a) Acquired image (b) Arm vector

Fig.2. Arm detector

Based on the binocular vision system, an arm vector can be obtained from right and left camera images as shown in Fig.2. It is possible to calculate in some measure the position of the designated object from the arm vector.

The binocular vision system is the method which has the position of an object in images calculated from right and left camera images by the use of the triangulation. Let the position of the object be P, the position of the object in left camera image be PL, the position of the object in right camera image be PR, the distance between cameras be d and the Focal distance be f as shown in Fig.3, then P is calculated by the following expression;

$$\begin{cases} X = \dfrac{dXL}{XL - XR} & \cdots(1) \\ Y = \dfrac{dYL}{XL - XR} & \cdots(2) \\ Z = \left(\dfrac{d}{XL - XR} - 1 \right) f & \cdots(3) \end{cases}$$

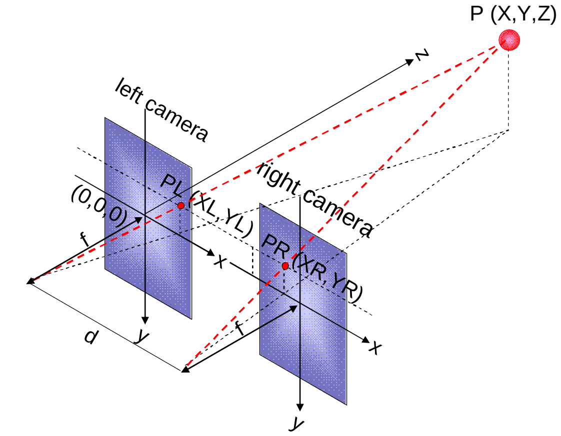

Fig.3. Binocular stereo

When the number of difference points is quite a few and the difference between consecutive numbers of difference points is negative as shown in Fig.4, pointing action is regarded as completed. Calculating a cross point between the ground and the arm vector obtained when pointing action completed will give the approximate position of the object designated by pointing action.

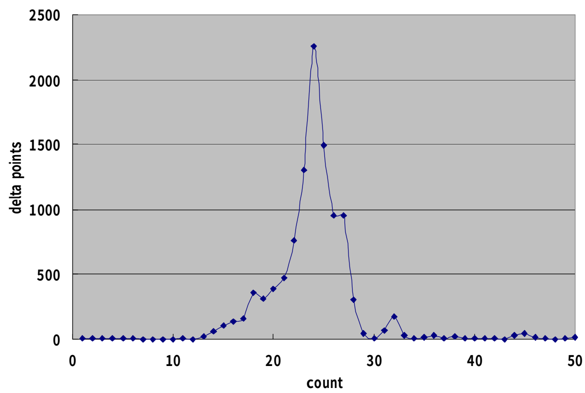

Fig.4. Change in number of difference points

When pointing action comes to an end, pointing information is obtained, and the robot will understand where to go. Fig.5 shows the execution result.

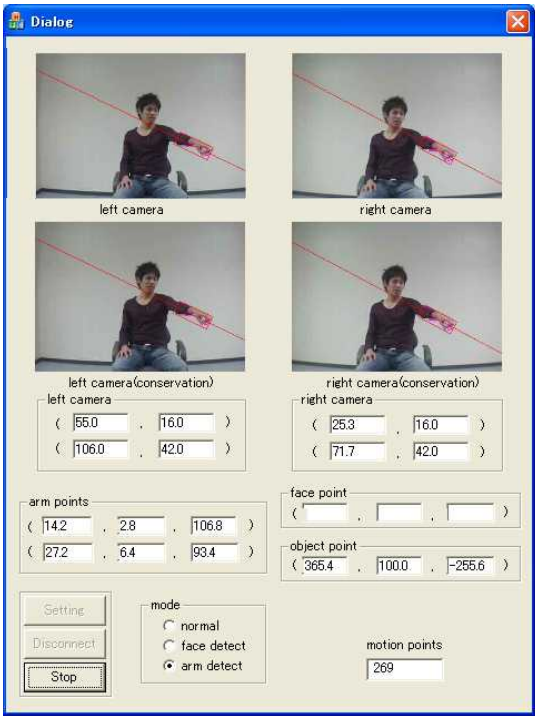

Fig.5. Excution result (Arm detection)

1.2. Motion correction by object correction

There is apparently some error in the calculated position of the designated object and it is clear that a robot cannot precisely reach the given goal. These facts make it difficult for a robot to reach the position of the designated object. Then additional information of the object must be given to the robot when a user finds the robot moving toward wrong place.

In the case, the user will utter words or phrases like 'stop' or 'go rightward' to interrupt the motion of the robot to make it notice its wrong behavior. When the robot is interrupted its action, it will stop moving and try to examine the user' utterance to decide what to do next. In the former case, it will need conversation with the user to know why the user interrupted its action, but this needs much complicate discourse analysis. On the other hand, in the latter case, it has only to change its posture using the method shown below.

As shown in Fig.6, the object location is recognized using right and left camera images, each position of the center of gravity is calculated and compared to judge the direction which the robot goes in. It is unnecessary to correct the behavior of a robot when the robot is facing toward the object. In contrast a robot must correct it heading when the robot is facing to the right or left of the object. In Fig.7, the target object deviates left by θ from front.

(a) Acquired image (b) Object recognition

Fig.6. Object detector

Let the distance from a robot to the object be Z, the distance between cameras be d, the Focal distance be f and the width of an image plane be width, then the θ is calculated by the following expression;

$$\theta = \tan^{-1}\left(\frac{width}{2f} - \frac{d\_r}{f} - \frac{d}{2Z}\right) \quad \cdots(4)$$

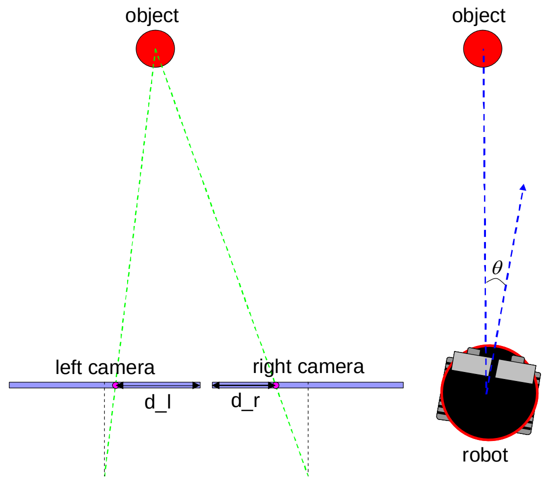

(a) Physical relationship

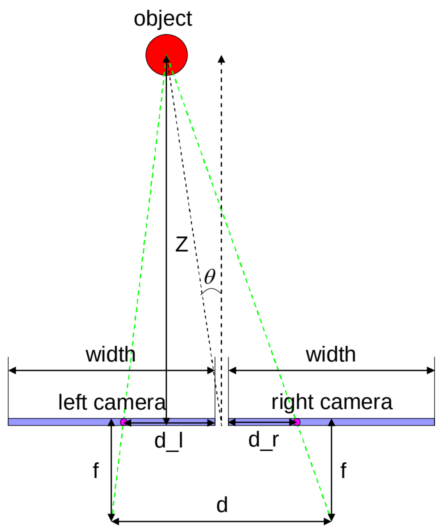

(b) Variable definition

Fig.7. Object recognition (d_l > d_r)

If the behavior of the robot must be corrected, then it will be led to near the position of the designated object. Fig.8 shows the execution result.

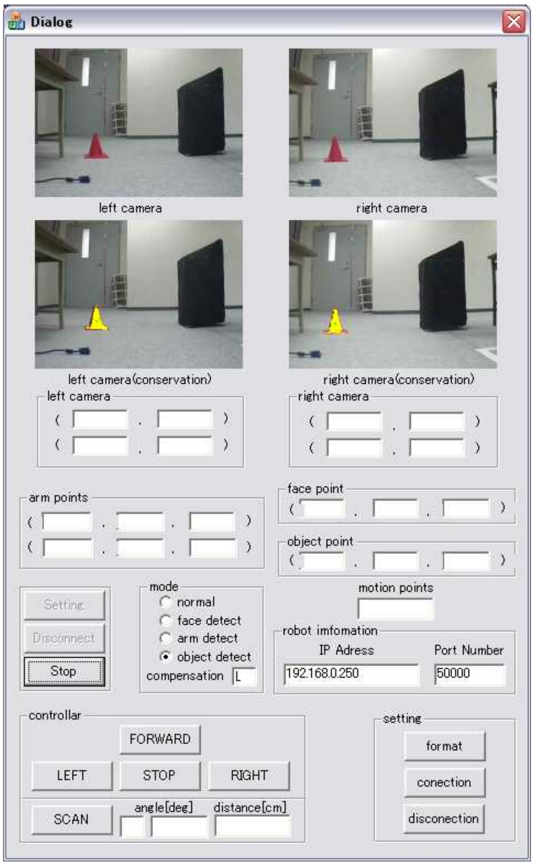

Fig.8.Excution result (Object recognition)

2. Voice recognition

We need two systems to communicate between a user and a robot. One is the system which enables a robot to recognize user's voice; the other is that which permits it to talk with a user. The former method uses Dragon Naturally Speaking 2005, the latter method uses Aques Talk. Fig.9 shows the execution result.

Fig.9.Excution result (Voice recognition)

IV. CONCLUSION

It is considered possible to calculate the position of an object which a user designates by pointing action an d voice. It is confirmed that the proposed method successfully makes a robot find the position of the designated object from pointing and voice information. Calculation results can contain errors, but they are considered to be within a tolerance as the behavior of a robot is corrected with object recognition and additional voice command from the user when it attains the task given by the user.

The design and implementation of an object indication system using pointing action and voice recognition system are nearly complete, but it must be verify whether a robot successfully attain the task in more complicated situation such as the case there are obstacles between the robot and object.

ACKNOWLEDGMENTS

We greatly appreciate the aid of the Grant-in-Aid for Scientific Research (S) and (A).

REFERENCES

[1] M. Inaba, S. Kagami, F. Kanehiro, Y.Hoshino, H. Inoue, Remote-Brained Robot Approach, International Journal of Robotics Research, Vol.19, No.10, pp.933-
Fig.8.Excution result (Object recognition)
954, 2000
[2] Yasuhiro Watanabe, Norihiro Abe, Kazuaki Tanaka, Hirokazu Taki, Tetsuya Yagi, Multimodal communication system allowing man and avatar to use voice and beck, 3rd International Conference on Information Technology and Applications(ICITA'2005), pp.161-166
[3] Hiroki Goto, Norihiro Abe, Kazuaki Tanaka, Yoshihiro Tabuchi, Hirokazu Taki, Shoujie He: Usage of Shared Memory for Multimodal Data Processing in an Outdoor Mobile Robot, proc. ISR (36th International Symposium on Robotics) (CD-ROM), 2005
[4] Moez Bellamine, Norihiro Abe, Kazuaki Tanaka, Hirokazu Taki :Remote Diagnosis System for Rotating Machinery Using Virtual Reality, IEICE Transactions,pp.895-903,2005
[5] Toshiaki Oomori, Norihiro Abe, Kazuaki Tanaka, Hirokazu TAKI, Shoujie HE: Concurrent development of Virtual Robots and Real Robots Based on Physical Low, IMEKO / IFAC / IFIP Workshop on Advanced Robot Systems and Virtual Reality.(CD-ROM), . 2005
[6] Norihiro Abe, Yoshihiro Tabuchi, Hirokazu Taki, Shoujie He " Synchronization between Audiovisual and Haptic Feeling for Constructing Edutainment Systems", international journal(Journal of Virtual Reality, accepted, 2006

The Fifteenth International Symposium on Artificial Life and Robotics 2010 (AROB 15th '10),
B-Con Plaza, Beppu,Oita, Japan, February 4-6, 2010

The water-tank test of novel underwater positioning system based on sensor networks

*Bin Fu, *Lian Lian, ** Feifei Zhang, ** Masanori Ito, * Wen tao Li
** State Key Laboratory of Ocean Engineerin, Shanghai Jiao Tong University, China*
*** Tokyo University of Marine Science and Technology, Japan*
(Tel: +86-21-62932610; Fax: +86-21-62933742)
(bfu@sjtu.edu.cn)

Abstract: To provide highly precise position information for autonomous navigation of AUV in large-scale area, we are developing one new underwater positioning system based on sensor networks. In this system, we set many standard stations on the sea surface and use GPS-sound positioning. To lower the cost of nodes and simplify signal processing, we have proposed a new method based on Sound Propagation Loss (SPL).This study discussed a new information integration method to solve the problems: (1) transmission path of sound may be blocked by some obstacle; (2) underwater nodes may get broken.

Key words: Underwater positioning system, Sound Propagation Loss, Sensor networks , Water-tank test.

I.INTRODUCTION

To provide highly precise position information for autonomous navigation in large-scale area, we are developing one new underwater positioning system based on sensors networks.

In this system, we set many standard stations on the sea surface and used GPS-sound positioning. The positioning precision of KGPS has become higher over the years，which assures that our standard station can be located. In this research, we have proposed a novel method based on Sound Propagation Loss (SPL) to lower the cost and simplify signal processing. To validate the SPL method, we have finished amounts of water-tank and sea tests. However, the major problem of this method comes from influences of background noise and reflected waves. [1][2] Moreover, in fact transmission path of sound may be blocked by some obstacle or underwater nodes may get broken, which results in great decrease of the positioning accuracy. To solve the problem, based on information communication between sensor network nodes, this paper proposed the information integration method of mean value method, and verified its performance in the water tank tests.

II.PRINCIPLE

1. Ranging

Based on acoustic wave energy attenuation, the system measures distance between transmitter and receiver. According to sonar equations, as we know Transmission voltage Tv [V], Propagation Loss PL [dB] can be obtained by measuring Receiving voltage Rv [V] as Eq. (1).

$$PL = 20\log(Tv)+Tx+Tg+Rx+Rg-20\log(Rv) \qquad (1)$$

Tx/Rx: Transmission/Receiving sensitivity [dB]

Tg/Rg: Transmission /Reception gain [dB]

Usually，Rv can be measured with FFT to the first non-reflective pulse of receiving wave and this method has a high accuracy. But when there are so many reflectors around, without receiving stationary non-reflective pulse, Rv can be estimated with FFT analysis of receiving energy. Though the measuring accuracy of this method is lower than the former, it can be used in long distance measurement. In accordance with measuring range and measuring environment, the two methods can be combined to use.

On the other hand, PL [dB] can be estimated the sum of diffusive loss log(R) and attrition loss αR as Eq.(2).

$$PL = 20\log(R) + \alpha R \quad (2)$$

R: propagation distance [m], got by solving Eq. (2).

α :attenuation coefficient, which is a constant when sound wave cycle and propagation environment are certain, and can be calculated according to empirical formula or measured in the experiments.

Various measuring environment and systems will bring systematic error in above methods. Therefore, the methods need to be corrected in the experiments.

2. Positioning

In this paper, we adopted the principle of LBL(Long Base Line), and only used ranging principle of propagation loss replacing the original transmission time positioning , as shown in Eq. (1).We took two-dimension positioning for example, as shown in Fig.1.

P (X_P, Y_P): sound source; T_{Dn} (X_{TDn}, Y_{TDn}): receiver;

Rn: the measured distance between TDn and P.

The Coordinate of false sound source P1 (X_{P1}, Y_{P1}) can be obtained by solving Eq. (3).

$$\begin{cases}(X_{TD1}-X_{P2})^2+(Y_{TD1}-Y_{P1})^2=R1^2 \\ (X_{TD2}-X_{P1})^2+(Y_{TD2}-Y_{P1})^2=R2^2\end{cases} \quad (3)$$

The coordinate of sound source (X_{Pn},Y_{Pn}) can be calculated with any two receiving signals.

The coordinate of sound source(X_P, Y_P) can be calculated as Eq. (4).with the mean value method.

$$\begin{cases}X_P = \sum X_{Pn} / N \\ Y_P = \sum Y_{Pn} / N\end{cases} \quad (4)$$

N: the number of receiving node.

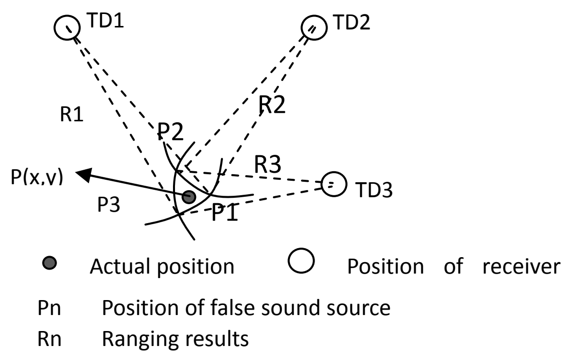

Fig.1. Ranging principle

Measuring accuracy increases with increase of number of effective node. In addition, blocking of obstacle or node fault can also cause a low accuracy.

Moreover, it is necessary to set up Voltage Threshold (VT) of receiving signal. When receiving signal of some node is less than VT, it is essential to stop using the data. On the contrary, the data can be brought into use. It can not only continuously update to use high accuracy node, but also eliminate the error messages caused by obstacle.

III. WATER TANK EXPERIMENTS

To guarantee the availability of ranging principle, we have completed the experiments in deepwater tank, as shown in Fig.2..

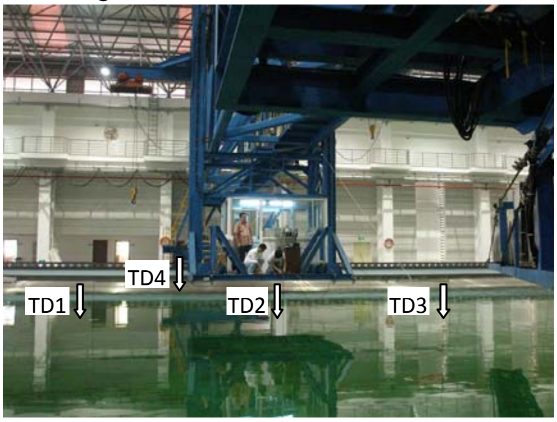

Fig.2. Experimental environment

Waveform of transmission signals is shown in Fig.3. The equipments include signal generator, power amplifier, signal acquisition unit, three hydrophones and transmitting transducer(20kHz-40kHz), see Fig.4..

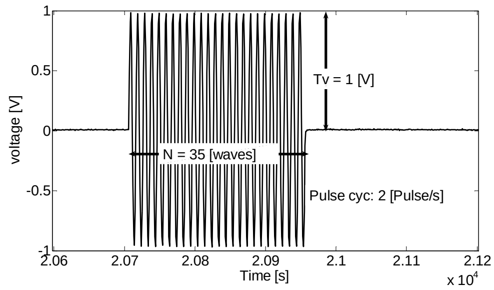

Fig.3. Waveform of transmission signals

(a) Measuring system

(b) Hydrophone (c) Transmitting transducer

Fig.4. Measuring system and sensors

1. Error correction method

We put sender and receiver vertically under water, and regulated its interval R from 1[m] to 6[m].We recorded Rv every 1[m], and got error correction coefficient compared with actual distance

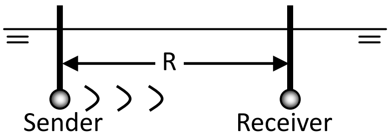

Fig.5. Error correction method

2. Positioning

Fig.6. shows three hydrophones is arranged along a straight line with the interval of 5[m]. We change the position of generator from P1 to P7, and separately record receiving signals of TD1-TD3 for 20 times. In data processing, we also analyze the position accuracy at different angles, discuss correction accuracy of mean value method and improve the accuracy by setting up VT

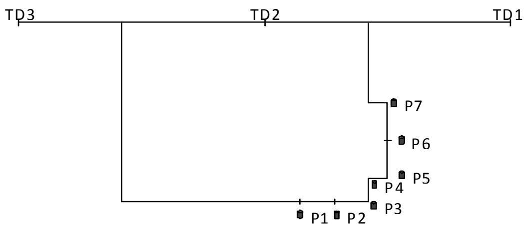

Fig.6. Sensor placement

IV. DATA PROCESSING

1. Error correction

Fig.7. shows a set of data in the experiments, where the background noise is about±0.04[V].

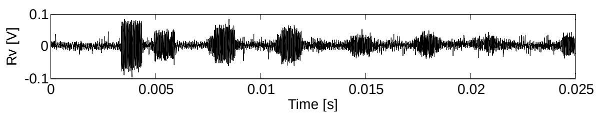

Fig.7. A set of data in the error correction experiments

Here, error was corrected with a linear method as Eq.(5).With the analysis of corrected data, we got the corrected parameter of each receiver, see Table1. Fig.8. shows the corrected results of measuring error of TD1.

$$R = aR' + b \quad (5)$$

R: truth value; R': measured value.

Table 1.The corrected parameter of every receiver

Number of receiver	a	b
TD1	1.077	0.333
TD2	1.078	-0.112
TD3	0.417	5.315

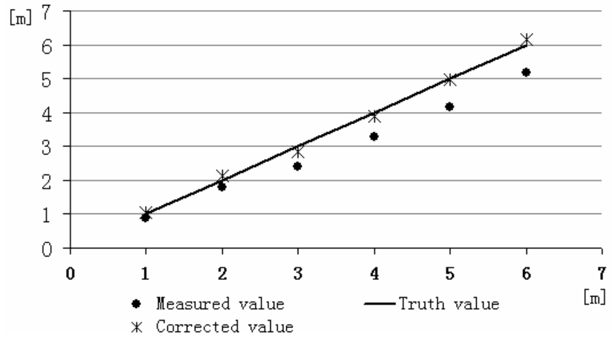

Fig.8. Corrected results of measuing error（TD1）

However, when several receivers are arranged on a small scale, they become reflectors each other, which results in decrease of accuracy. In fact, the accuracy is only ±0.5[m] in the positioning experiments.

2. Positioning with mean value method

As shown in Fig.9., we found that in front part of every set of data, neat direct waves can be received, so we can calculate the distance between sound source and receiver with the first method shown in II.PRINCIPLE.

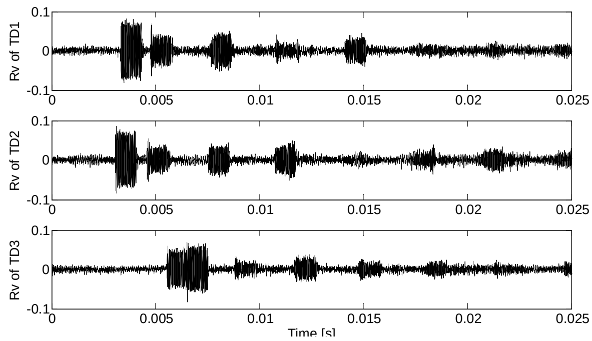

Fig.9. A set of data of sound source: P4

Fig.10. shows the comparison of positioning results(solid line) and truth value(broken line). The results demonstrate: (1) when the projection of sound source locates the position between two nodes, it can achieve high positioning accuracy, as shown in Fig.10 (a), (c). Therefore, when the projection of sound source leaves the position, it is so necessary to replace next node; (2) The nearer sound source located from node, the higher accuracy system can achieve, positioning accuracy in Fig.10(a) is better than in (c).This depends

on the character that dissociation energy is diluted by the increase of propagation distance. Consequently, it is necessary to set up voltage threshold of receiving signal. When receiving signal of some node is less than Voltage threshold, it is essential to stop using the data. On the contrary, the data can be brought into use; (3) In addition, it is found that through mean value method can make the accuracy of results more higher, see Fig.10.(d)., which has obvious compensation to Fig.10(c). In a similar way, we can introduce that the system can achieve much high accuracy through taking an average of multiple data when some node gets broken or is blocked by obstacle.

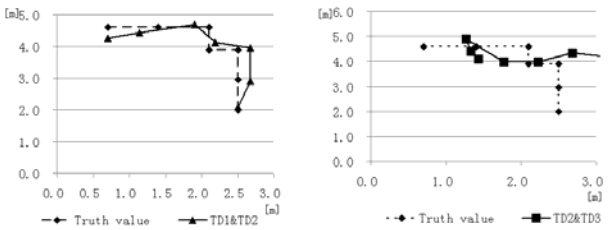

(a). Based on TD1&TD2 (b). Based on TD2&TD3

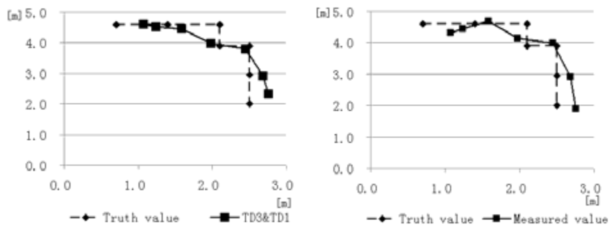

(c). Based on TD3&TD1 (d). Based on average value

Fig.10. Positioning results compared with truth value

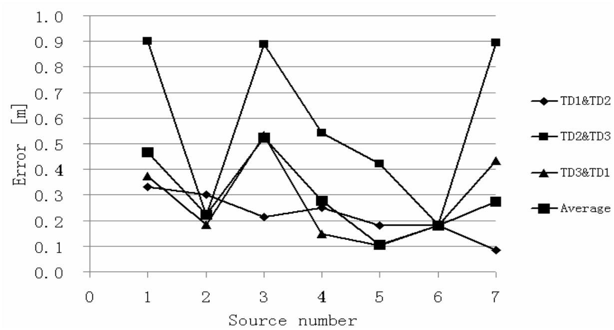

(a). The distance between measured value and truth value

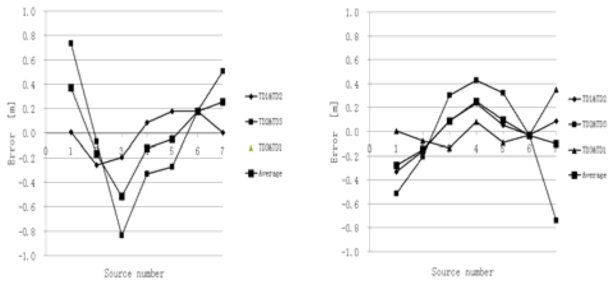

(b). Error at X axis (c). Error at Y axis.

Fig.11. Error analysis

3. The analysis of positioning error

The analysis of positioning error is shown in Fig.(11).. The results show: (1) The projection of sound source locates the position between two nodes, it can achieve the positioning accuracy about ±0.5[m] in accordance with measuring accuracy; (2) It can improve the positioning accuracy by mean value method.

V. CONCLUSTION

Based on the low-cost and easy-to-operate SPL ranging method proposed in the previous research and sensor networks positioning method which has the ability to communicate between nodes and extend positioning range, we have completed the first water tank positioning test successfully, and gave a new underwater positioning method. We also verified the basic characteristic and positioning accuracy of this method. In addition, we confirmed a positioning method based on average value, which possesses obvious corrective effect on the lower accuracy positioning signals.

In the future research of building sensor networks, we should consider the following things: (1)some way to judge the position relation between two nodes or node and sound source;(2) accuracy analysis of setting up threshold and prospective positioning;(3)the method of node replacement.

At last, the authors express their gratitude to Fan Lab. of SJTU and deepwater tank Lab. of SJTU.

REFERENCES

[1]. B. Fu, F. Zhang, M. Ito. et al (2009), Development of a new positioning system for underwater robot based on sensor network. J-AROB 14(1): 43-47.
[2]. B. Fu, F. Zhang, M. Ito. et al (2009), Development of a new underwater positioning system based on sensor network. J-AROB 13(1): 45-49.

The Fifteenth International Symposium on Artificial Life and Robotics 2010 (AROB 15th '10),
B-Con Plaza, Beppu,Oita, Japan, February 4-6, 2010

Countering Asymmetric Situations with Distributed Artificial Life and Robotics Approach

Peter Sapaty
Institute of Mathematical Machines and Systems, National Academy of Sciences
Glushkova Ave 42, 03187 Kiev, Ukraine, sapaty@immsp.kiev.ua

Masanori Sugisaka
Department of Mechanical and Electrical Engineering, Nippon Bunri University
1727 Oaza Itiki, Oita, 870-0397, Japan, ms@alife-robotics.co.jp

Abstract

A novel control model and technology, creating distributed virtual systems with artificial life features, is discussed. They become capable of runtime reshaping, adapting to unknown environments, and pursuing global goals. The approach is based on known holistic and gestalt principles, where the whole is first and parts are treated in the context of the whole. Distributed Scenario Language, DSL, the core of the approach, and its spatial interpretation in networked systems will be revealed. Mission scenarios in DSL, covering, integrating, tasking, and controlling distributed resources (robotic swarms including), can effectively fight world disasters and crises.

Keywords: irregular situations, integrity, overoperability, distributed scenario language, networked interpretation, smart structures, self-recovery, artificial life and robotics.

1 Introduction

The world dynamics is increasing due to global warming, numerous natural and manmade disasters, military conflicts, and international terrorism. New approaches to organization of distributed systems, especially for solving irregular and "asymmetric" problems, are needed [1]. The approach offered, symbolically called *overoperability*, allows us to create, modify, analyze, process, simulate, and manage any distributed systems by establishing advanced global control over them [2].

Within the overoperability philosophy, an integral mission scenario expressed in a special wave-like formalism (see Fig. 1*a*) is executed in a parallel manner by dynamically networked universal control modules U embedded into distributed worlds (Fig. 1*b*). This scenario, written in a special high-level Distributed Scenario language (DSL), can start from any unit and dynamically cover the whole system, setting its internal organization, and orienting behavior [2,3].

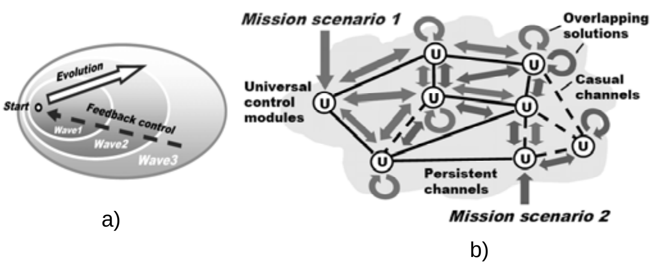

Figure 1. The overoperability paradigm.

During the scenario evolution, any operations can be accomplished in the distributed world, causing, if needed, movement of code and equipment and creation and maintenance of physical and virtual infrastructures supporting the missions. Different spatial scenarios can cooperate or compete in the networked space (as in Fig. 1*b*), allowing for effective distributed simulation of complex dynamic systems or their live management and control, with any combination of the two.

This paradigm has been extensively studied, discussed, and published elsewhere [4-6], and here we will be concentrating only on the latest updated version of DSL and its application for the creation of smart distributed structures, with their use in irregular situations.

2 DSL: The Scenario Language

DSL allows us to directly express semantics of problems to be solved in distributed worlds and, if needed, implicit or explicit system behavior to solve these problems.

2.1 DSL Key Features

The language operates with:

- Virtual World (VW), which is discrete and consists of nodes and links connecting the nodes.
- Continuous Physical World (PW), points in which are accessible by physical coordinates.
- Virtual-Physical World (VPW), as an extension of VW, where nodes additionally associate with coordinates in PW.

Other key DSL features include:

- A scenario in it develops as a transition between sets of progress points (*props*), as *parallel waves*.
- Starting from a prop, an action may result in one or more props (the resultant set of props may include the starting prop too).
- Each prop has a resulting value (which can be multiple) and a resulting state, being one of the four: *thru* (full success, also allowing us to proceed further), *done* (success with planned termination), *fail* (regular failure, with local termination), and *abort* (emergency failure, terminating the whole distributed process, associated with other props too).
- Different actions may evolve independently or interdependently from the same prop, forming altogether the resultant set of props.
- Actions may also spatially succeed each other, with new ones applied in parallel from all props reached by the preceding actions.

- Elementary operations can directly use local or remote values of props obtained from other actions (the latter including the whole scenarios).
- Elementary operations can result in open values that can be used by other operations in an expression or by the following operations in a sequence. They can also be directly assigned to local or remote variables (an access to which may invoke scenarios of any complexity).
- Any prop can associate with a node in VW or a position in PW, or both.
- Any number of props can be simultaneously linked with the same points of the worlds.
- Staying with world points (virtual, physical, combined) it is possible to access and update local data in them.
- DSL can be used as a universal programming language.

2.2 DSL Syntax and Main Constructs

DSL has a recursive syntax, which on top level may be expressed as follows (programs are called *waves*, braces show repetition, and vertical bar delimits alternatives):

wave → *phenomenon* | *rule* ({ *wave* , })
phenomenon → *constant* | *variable* | *special*
constant → *information* | *matter*
variable → *heritable* | *frontal* | *environmental* | *nodal*
rule → *movement* | *creation* | *elimination* | *echoing* | *fusion* | *verification* | *assignment* | *construction* | *advancing* | *branching* | *transference*| *timing* | *granting* | *type* | *usage*

The basic construct, *rule*, can represent any definition, action or decision, being for example:

- elementary arithmetic, string or logic operation;
- hop in a physical, virtual, or combined space;
- hierarchical fusion and return of (remote) data;
- distributed control, both sequential and parallel;
- a variety of special contexts for navigation in space, influencing operations and decisions;
- type or sense of a value, or its chosen usage, guiding automatic interpretation.

There are different types of variables in DSL:

- *Heritable variables* – these are starting in a prop and serving all subsequent props, which can share them in both read & write operations.
- *Frontal variables* – are an individual and exclusive prop's property (not shared with other props), being transferred between the consecutive props, and replicated if from a single prop a number of props emerge.
- *Environmental variables* – are accessing different elements of physical and virtual words when navigating them, also a variety of parameters of the internal world of DSL interpreter.
- *Nodal variables* – allow us to attach an individual temporary property to VW and VPW nodes; they can be accessed and shared by any props associated with these nodes.

These variables, especially when used together, allow us to create efficient spatial algorithms working *between* components of distributed systems rather than *in* them.

Elementary examples in DSL may look like follows.

- assignment of a sum of values to a variable: `assign(Result, add(27,33,55.6))`
- parallel hop into two given physical locations: `move(location(x5,y8), location(x1,y3))`
- creating isolated node `Peter` in a virtual space: `create(node(Peter))`
- extending the previous single-node network with a new link-node pair (`father of`, `Alex`): `hop(Peter); create(+fatherof, Alex))`

Traditional abbreviations of operations and delimiters can be used too, as in further examples throughout this text, to shorten the DSL programs.

3 Distributed DSL Interpreter

The DSL interpreter ([6], Fig. 2), with the following features, has been prototyped on different platforms.

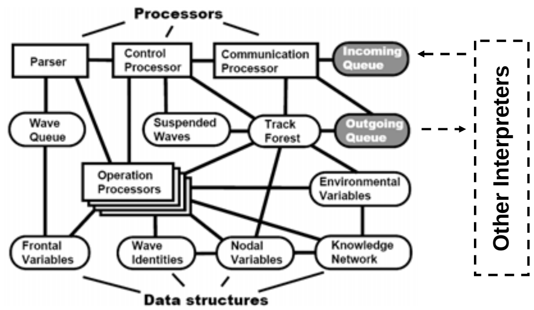

Figure 2. Organization of DSL interpreter.

- It consists of a number of specialized modules working in parallel and handling and sharing specific data structures supporting persistent virtual worlds and temporary hierarchical control mechanisms.
- The whole network of the interpreters can be mobile and open, changing at runtime the number of nodes and communication structure between them.
- The heart of the distributed interpreter is its *spatial track system*, with its parts kept in the Track Forest memory of local interpreters; these being logically interlinked with such parts in other interpreter copies, forming altogether *indivisible space coverage*. This allows for hierarchical command and control and remote data and code access, with high integrity of parallel distributed solutions.
- Copies of the interpreter can be concealed, say, in hostile systems, allowing us to impact them globally.

The dynamically crated track trees, spanning the systems in which DSL scenarios evolve, are used for supporting spatial variables and echoing and merging different types of control states and remote data, being self-optimized in the echo mode. They also route further waves to the positions in physical, virtual, or combined spaces reached by the previous waves, uniting them with the frontal variables delivered there by preceding waves.

4 Operating with Distributed Structures

Network creation. To create the virtual network of Fig. 3*a* in a distributed environment, and in a fully distributed way, the following DSL program will be sufficient (expressing the directed graph template of Fig. 3*b* based on depth-first spanning tree of the network, with all links named r, for simplicity):

```
create(hop(a); r#b; r#c; r##a,(r#d; r##b))
```

Starting with node a, it gradually self-evolves in a distributed space while creating the network topology needed (in the navigation mode shown in Fig. 1*b*).

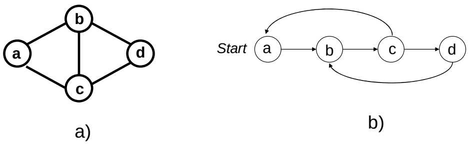

Figure 3. Distributed creation of a network structure.

Network modification. Another DSL scenario can make any modification of this network, also in a fully distributed and parallel way, say, substituting all existing triangles in the network with stars (naming additional central star nodes with combination of fringe node names), as in Fig. 4*a-b*:

```
hop(allnodes); F=C; twice(#; P>A; F&=C);
#; C==F:1; create(hop(unite(F)); r##F);
remove(##F)
```

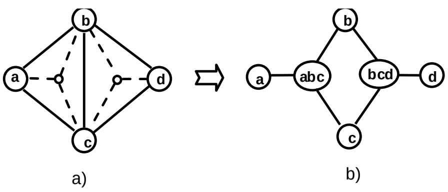

Figure 4. Distributed structure modification.

Network self-recovery. Applying another special DSL scenario to any network can make it capable of self-recovery after any indiscriminate damages of nodes and links, where missing elements can be restored by remaining neighboring nodes. The restored nodes can, in their turn, restore the other nodes (including the ones that restored them), and so on. A simplified example of such a program converting the whole network into a *self-regenerating live creature* may be as follows (the lost nodes a and d and links to them are restored by nodes b and c, as in Fig. 5*a-b*).

```
Fp={repeat(split(diff(Fi,(#; C))); Fn=V;
[or((direct#Fn; create(r##P)),
    (create(r#Fn); Fi=(#; C); run(Fp)))])};
hop(allnodes); Fi=(#; C); run(Fp)
```

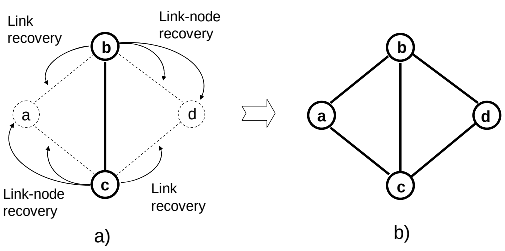

Figure 5. Distributed network self-recovery.

Distributed topology self-analysis. DSL allows us to directly analyze and process distributed topologies in a parallel way. For example, to find the weakest nodes in a network (like *articulation points*, Fig. 6*a*), which when removed split the network into disjoint parts, we only need the following program (resulting in articulation node d).

```
hop(allnodes); ID=C;
and((random(#); repeat(firstcome(#))),
    (firstcome(#)), out(C))
```

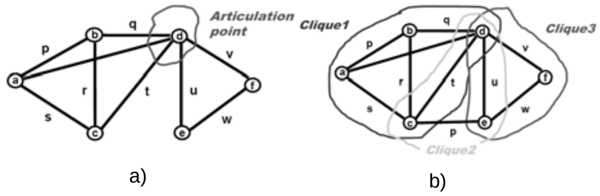

Figure 6. Distributed discovery of topological features.

Cliques (or fully connected sub-graphs of a graph, as in Fig. 6*b*), on the contrary, may be considered as strongest parts of a system. They can be found in parallel by the following program, resulting for the network in Fig. 6*b* in cliques: (a,b,c,d),(c,d,e),(d,e,f).

```
hop(allnodes); Fc=C;
repeat(#; notbelong(C, Fc);
 and(done(andparallel(#Fc)),
     or(done(B>C), Fc&=C))); out(Fc)
```

More on distributed topology operations are in [4,5].

5 Researched Applications

Overlaying the obtained integral virtual solutions onto networked hardware, which may be heterogeneous and open, allows us to work in the following modes:

- Simulation mode, where using computer networks for parallel simulation of large systems provides realistic results, both functional and behavioral.
- Live control mode, causing and guiding the needed hardware behavior in solving complex problems.
- Combined mode, where distributed simulation serves as intelligent look-ahead part of live control.

Collective Robotics. Installing the interpreter in mobile robots of different types (as in Fig. 7) allows us to organize effective group solutions (including any swarming) in distributed physical spaces.

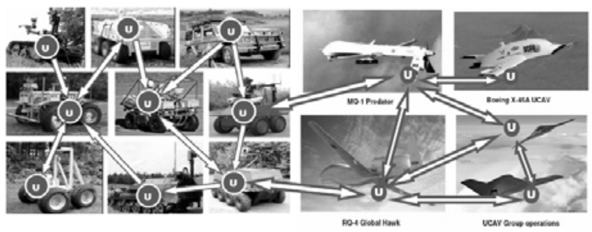

Figure 7. Grouping unmanned vehicles.

A simple example task here may be formulated as:

Go to physical locations of the disaster zone with coordinates (50.433, 30.633), (50.417, 30.490), and (50.467, 30.517). Evaluate damage in each location, find and transmit the maximum destruction value, together with exact coordinates of the corresponding location, to a management center.

The DSL program will be as follows:

```
transmit(maximum(move((50.433, 30.633),
  (50.417, 30.490), (50.467, 30.517));
  append(evaluate(destruction), WHERE)))
```

Details of automatic implementation of this scenario, as well as of many others, by different numbers of mobile robots and at different system levels are discussed in details elsewhere [7]. Under the technology developed, loose robotic swarming may be combined with strong hierarchical control to make quick global solutions and withstand unexpected situations.

Terrorism and Piracy Fight. No secret that mightiest world armies with classical organizations are often powerless against poorly armed terrorists and pirates, who are using flexible asymmetric tactics (see in Fig. 8 the 2009 world piracy map with possible information leakages, forming altogether a sophisticated distributed network). The ideology and technology discussed here can dynamically organize the whole world to withstand such activities, offering runtime spatial solutions--from global network search to managing unmanned swarms for asymmetric responses to asymmetric attacks [3].

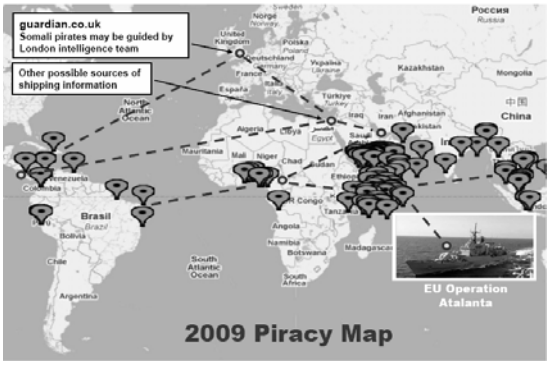

Figure 8. Global piracy fight.

Other applications. These are presented, discussed and published at numerous world events--from philosophy [8] to information technologies [1] to artificial life and robotics [9] to sensor networks [10] to crisis management [11] to defense [12-14]. Some of these researched applications are shown in Fig. 9.

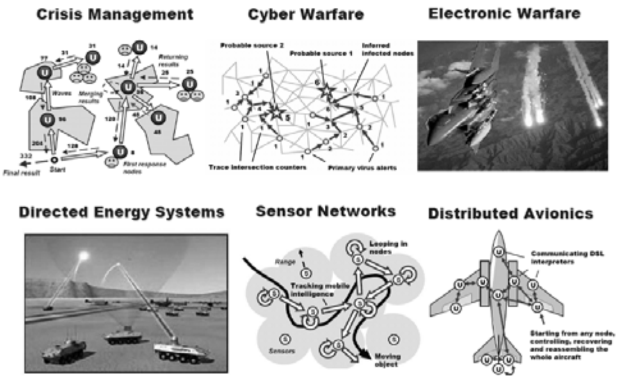

Figure 9. Other researched applications.

7 Conclusions

A distributed processing and control model and technology has been discussed, allowing us to obtain integral albeit fully distributed systems with artificial life features. These systems are capable of self-reshaping at runtime, changing networked structures, and adapting to unknown environments. The approach is based on holistic and gestalt philosophical principles, where the whole is first, greater than parts, and the parts are treated in the context of the whole rather than vice versa, as usual.

The approach, challenging conventional atomistic and agent-based philosophies in the system design and management, puts the artificial life concept, empowered with advanced distributed robotics, to the forefront of fight with numerous world disasters and crises.

Providing smooth transition from simulated to live solutions, with the watershed gradually shifting from the former to the latter, it can also support *a unified conversion from manned to fully unmanned advanced systems* within the same organizational concept.

Acknowledgments. Special thanks to the Alexander von Humboldt Foundation (AvH) in Germany and the Japanese Society for the Promotion of Science (JSPS) who supported (both morally and financially) these ideas, research, implementation, and related international cooperation throughout the years of their development.

References

[1] Sapaty, P. S., "Meeting the World Challenges: From Philosophy to Information Technology to Applications", Keynote lecture, Proc. 6th International Conference in Control, Automation and Robotics ICINCO 2009, Vol.1, Milan, Italy, IS-31--IS-43, 2009.

[2] Sapaty, P., "The Over-operability Organization of Distributed Dynamic Systems for Asymmetric Operations", Proc. IMA Conference on Mathematics in Defence, Farnborough, UK, 2009.

[3] Sapaty, P., "Gestalt-based Integrity of Distributed Networked Systems", SPIE Europe Security + Defence, bcc Berliner Congress Centre, Berlin Germany (2009).

[4] Sapaty, P. S., Mobile Processing in Distributed and Open Environments, John Wiley & Sons, 1999.

[5] Sapaty, P. S., Ruling Distributed Dynamic Worlds, John Wiley & Sons, New York, 2005.

[6] Sapaty, P., A distributed Processing System, European patent No. 0389655, European Patent Office, 1993.

[7] Sapaty, P. S., "Providing Spatial Integrity for Distributed Unmanned Systems", Proc. 6th International Conference in Control, Automation and Robotics ICINCO 2009. Milan, Italy, 2009.

[8] P. Sapaty, "Gestalt-Based Ideology and Technology for Spatial Control of Distributed Dynamic Systems", International Gestalt Theory Congress, 16th Scientific Convention of the GTA, University of Osnabrück, Germany, March 26 - 29, 2009.

[9] P. Sapaty, K.-D. Kuhnert, M. Sugisaka, R. Finkelstein, "Developing High-Level Management Facilities for Distributed Unmanned Systems", Proc. Fourteenth International Symposium on Artificial Life and Robotics (AROB 14th'09), B-Con Plaza, Beppu, Oita, Japan, Feb. 5-7, 2009.

[10] Sapaty, P., "Intelligent Management of Distributed Sensor Networks", In Sensors, and Command, Control, Communications, and Intelligence (C3I) Technologies for Homeland Security and Homeland Defense VI, Proc. of SPIE, Vol. 6538, 653812, 2007.

[11] Sapaty, P., Sugisaka, M., Finkelstein, R., Delgado-Frias, J., Mirenkov, N., "Advanced IT Support of Crisis Relief Missions", Journal of Emergency Management, Vol.4, No.4, 2006.

[12] Sapaty, P., Morozov, A., Sugisaka, M., "DEW in a Network Enabled Environment", Proc. International conference Directed Energy Weapons, Le Meridien Piccadilly, London, UK, 2007.

[13] Sapaty, P., "Grasping the Whole by Spatial Intelligence: A higher level for Distributed Avionics", Proc. International Conference Military Avionics 2008, Cafe Royal, London, UK, 2008.

[14] Sapaty, P., "Distributed Capability for Battlespace Dominance", In Electronic Warfare 2009 Conference & Exhibition, Novotel London West Hotel & Conference Center, London, 2009.

The Fifteenth International Symposium on Artificial Life and Robotics 2010 (AROB 15th '10),
B-Con Plaza, Beppu,Oita, Japan, February 4-6, 2010

Intelligent Classification of Bills by Neural Networks

Sigeru Omatu+ Michifumi Yoshioka+, and Hidekazu Yanagimoto+
+Osaka Prefecture University, Sakai, Osaka 599-8531, Japan
omatu@cs.osakafu-u.ac.jp

Abstract

For the pattern classification problems the neuro-pattern recognition which is the pattern recognition based on the neural network approach has been paid an attention since it can classify various patterns like human beings. In this paper, we adopt the learning vector quantization (LVQ) method to classify the various money. The reasons to use the LVQ are that it can process the unsupervised classification and treat many input data with small computational burdens. We will construct the LVQ network to classify the Italian Liras. Compared with a conventional pattern matching technique, which has been adopted as a classification method, the proposed method has shown excellent classification results.

1. Introduction

Bill money classification by transaction machines has been important to make progress the office automation [1]. Since sizes of bills are different according to kinds of bills, the measurement data of bills include various variations. Human being can classify the bills correctly even if they are suffered from those variations such as rotation and shift. But usual pattern recognition using a conventional transaction machine cannot give us the correct classification result under such cases since the basic method is a pattern matching principle. Furthermore, the conventional pattern matching method requires many template patterns for many kinds of bills, which takes much time and needs much experience [1].

Recently, neural networks which are based on the biological mechanism of human brain have been focussed since they have intelligent pattern recognition ability [2]. In this paper, we will apply the neural network approach to classify the bill money under various conditions by using transaction machines. The learning vector quatization (LVQ) has been used to classify the bills since it can treat high dimensional input and has simple learning structure [3]. The LVQ network adopted here has 64x15 units in the input layer and many units at the output layer. The bills are Italian Liras of 8 kinds, 1,000, 2,000, 5,000, 10,000, 50,000 (new), 50,000 (old), 100,000 (new), 100,000 (old) Liras with four directions A,B,C, and D where A and B mean the normal direction and the upside down direction and C and D mean the reverse version of A and B. The simulation results show that the proposed method can produce the excellent classification results.

2. Competitive Neural Networks

We will explain the competitive neural networks that are used to classify the bill money. The structure of a LVQ competitive network is shown in Fig. 1. The input for the LVQ is bill money data where an original image consists of 128x64 pixels and the input data to the network is compressed as 64x15 pixels to decrease the computational load. The output of the network consists of the Italian Liras of 8 kinds, 1,000, 2,000, 5,000, 10,000, 50,000 (new), 50,000 (old), 100,000 (new), 100,000 (old) Liras with four directions A,B,C, and D where A and B mean the normal direction and the upside down direction and C and D mean the reverse version of A and B.

In the input layer the original bill money data are applied and all the units at the input layer are connected to all the neurons at the output layer with connection weight W_{ij}. W_{ij} denotes the connection weight from the unit j in the input layer to unit i in the output layer. The output layer will output only one neuron which is called winner neuron. The winner neuron is selected as the neuron with the minimum distance between an input vector and its connection weight vector. The connection weights W_{ij} are set by the random number at the beginning. Here, we set the mean vector of the cluster plus small random number. Then the following learning algorithm of the connection weight vector is used.

LVQ algorithm

Step 1. Find the unit c at the output layer which has the minimum distance from the input data **x** (t)

$$\|\mathbf{x}(t) - \mathbf{W}_c\| = \min_i \|\mathbf{x}(t) - \mathbf{W}_i\|$$

where $\| \; \|$ denotes the Euclidean norm and t denotes the iteration time.

Step 2. If the input **x** (t) belongs to Category c, then

$$\mathbf{w}_c(t+1) = \mathbf{w}_c(t) + \alpha(t)(\mathbf{x}(t) - \mathbf{w}_c(t))$$

$$\mathbf{w}_i(t+1) = \mathbf{w}_i(t)\,,\ \ i \neq c$$

and if the input **x** (t) belongs to the other Category j (j$\neq$c), then

$$\mathbf{w}_c(t+1) = \mathbf{w}_c(t) - \alpha(t)(\mathbf{x}(t) - \mathbf{w}_c(t))$$

$$\mathbf{w}_i(t+1) = \mathbf{w}_i(t)\,,\ \ i \neq c$$

where $\alpha(t)$ is a positive function and denotes learning rate.

In the usual LVQ $\alpha(t)$ is given by

$$\alpha(t) = \alpha_0(1 - \frac{t}{T})$$

where (0<α_0<1) is a positive and T is a total number of learning iterations.

The above algorithm for selection of new weight vector $W_c(t+1)$ can be explained graphically as shown in Fig. 2 .

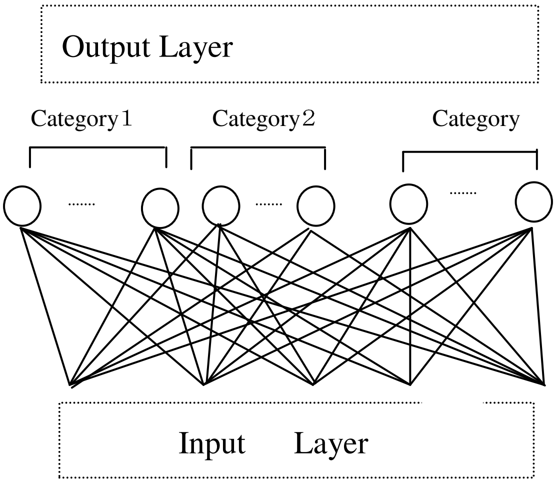

Fig. 1. Structure of the LVQ networks.

In the above LVQ algorithm, the learning rate $\alpha(t)$ plays an important role for convergence. To adjust the parameter, Kohonen has proposed an optimization method without proof as follows:

$$\alpha_c(t) = \frac{\alpha_c(t-1)}{1 + s(t-1)\alpha_c(t-1)}$$

where s(t) =1 if **x**(t) belongs to the same Category c and s(t)=-1 if **x**(t) does not belong to the same Category c. Here, $\alpha_c(t)$ denotes the learning rate for the pattern of Category C. In what follows, we will prove the above relation. From the learning rule of the LVQ, we have

$$\begin{aligned}\mathbf{w}_c(t+1) &= \mathbf{w}_c(t) + s(t)\alpha_c(t)(\mathbf{x}(t) - \mathbf{w}_c(t)) \\ &= (1 - s(t))\alpha_c(t)\mathbf{w}_c(t) + s(t)\alpha_c(t)\mathbf{x}(t)\end{aligned}$$

and

$$\begin{aligned}\mathbf{w}_c(t) &= \mathbf{w}_c(t-1) + s(t-1)\alpha_c(t-1) \\ &\quad (\mathbf{x}(t-1) - \mathbf{w}_c(t-1)) \\ &= (1 - s(t-1))\alpha_c(t-1)\mathbf{w}_c(t-1) \\ &\quad + s(t-1)\alpha_c(t-1)\mathbf{x}(t-1)\end{aligned}$$

Substituting the latter equation the former one, we have

$$\begin{aligned}\mathbf{w}_c(t+1) &= (1 - s(t)\alpha_c(t))(1 - s(t-1)\alpha_c(t-1))\mathbf{w}_c(t-1) \\ &+ s(t)\alpha_c(t)\mathbf{x}(t) + s(t-1)\alpha_c(t-1)(1 - s(t)\alpha_c(t))\mathbf{x}(t-1).\end{aligned}$$

We assume that the optimal rate adjusts the effect of x(t) and x(t-1) equally within the absolute value, that is,

$$\alpha_c(t) = (1 - s(t)\alpha_c(t))\alpha_c(t-1)\,.$$

Then we have

$$\alpha_c(t) = \frac{\alpha_c(t-1)}{1 + s(t-1)\alpha_c(t-1)}\,.$$

From the above equation, we can see that the value of $\alpha_c(t)$ become larger than 1 when s(t-1)= - 1, which may make the learning algorithm unstable. Thus, we must fix the $\alpha_c(t)$ to a boundary value α_0 when it becomes larger than 1.

$$\alpha_c(t+1) = \alpha_0 \quad \text{if} \quad \alpha_c(t+1) > 1\,.$$

Using the above OLVQ1 algorithm, we will classify the Italian bills in the following section.

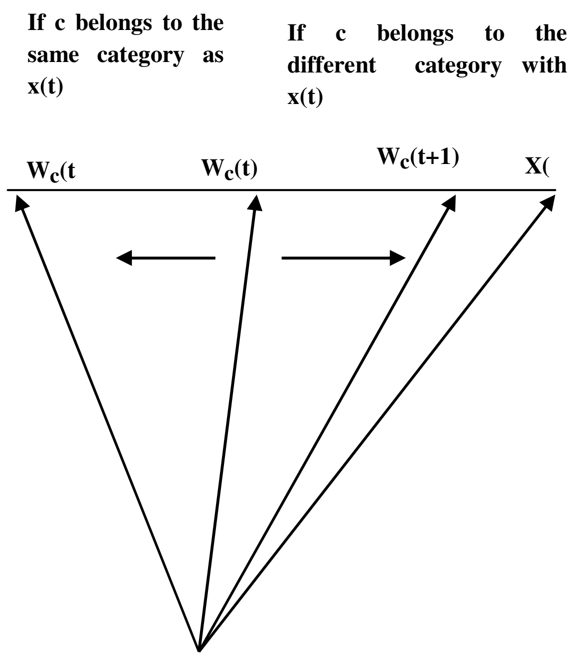

Fig.2. Principle of the LVQ algorithm where the right hand side shows the same category case of **x**(t) and Category c and the left hand side denotes the different category case.

3. Preprocessing Algorithm

The images obtained by transaction machine, there are variations such as rotation or shift. Therefore, we must adjust the images such that the variations may be reduced as much as possible by using the preprocessing. The flow char of the preprocessing procedure is illustrated in Figure 3. In this figure, the original image with 128x64 pixels are observed at the transaction machine in which rotation and shit are included. After correction of these effects, we select a suitable aria which show the bill image and compressed as the image with 64x15 pixels to the neural networks. Although the neural network of the LVQ type could process any order of the dimension of the input data, the small size is better to achieve the fast convergence result. Thus, we have selected the above size of the image.

4. Italian Lira Classification

The bills used here are Italian liras, which have 8 kinds such as 1,000 Liras, 2,000 Liras, 5,000 Liras, 10,000 Liras, new 50,000 Liras, old 50,000 Liras, new 100,000 Liras, and old 100,000 liras. Those Lira bills are used at the input of the transaction machine where four directions such as A, B, C, and D appear since normal direction, reverse direction, and their upside down directions occur at the input as shown in Fig.4. Thus, thirty-two bill images are one set of the classification pattern of the experiment.

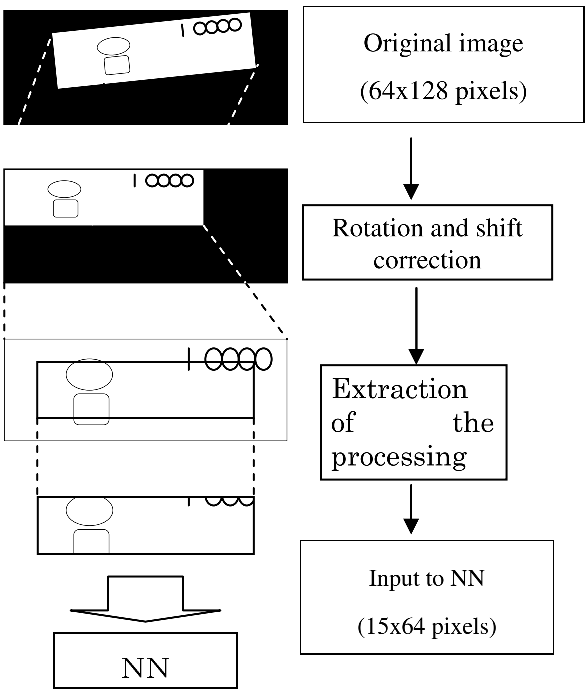

Fig. 3. Preprocessing algorithm.

Total number of data sets is 30 and 10 data sets are

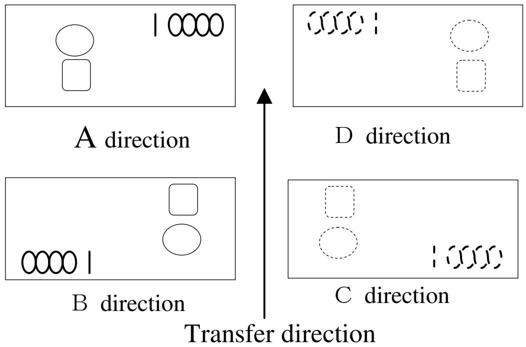

Fig. 4. Four directions of bill money.

used for training of the network and the remaining 20 data sets are used to test the network. In order to reduce the misclassification, we have set the threshold value d_θ such that if $d_c > d_\theta$, unit c is not fired. This means that if the minimum distance is not less than d_θ, the input data is not classified. The parameters of the neural network used here are as follows:
Number of units in the input layer=960
Number of units in the output layer in the initial state=32 where every 50 iterations the number has been adjusted.
Total learning time T=150, $\alpha_i(0) = 0.5$, $i = 1, \cdots M$
Initial values of the weight vectors=mean vectors for training patterns $d_\theta = \min_c (m_c + 4.5\sigma_c)$

After training the neural network, 20 data sets are tested how well the LVQ network could work. Tables 1 and 2 show those values at t=160. We can see the improvement by learning. Table 5 shows the number of the neuron units at t=160 which are determined by increasing them.

Table 1. Recognition rate (%) at t=160.

		Directions			
		A	B	C	D
Italian Liras	1,000	100	100	100	100
	2,000	100	100	100	100
	5,000	100	100	100	100
	10,000	100	100	100	100
	50,000(new)	100	100	100	100
	50,000(old)	100	100	95	95
	100,000(new)	100	100	90	100
	100,000(old)	100	100	95	90

From the original image data we can see that the difference between 50,000 Lira old and new is slight and the difference between old and new100, 000 Liras as shown in Figs. 5 and 6. Therefore, it is rather difficult to recognize them so perfectly. But in this case the misclassification like old and new bills within the same values is not serious. Thus, we have regarded this misclassification as the correct one. Furthermore, we have introduced the threshold value to prevent from making the misclassification. Thus, even if the minimum distance criterion results in the correct classification, we have decided these bells are unknown. Without threshold constraints, we could obtain 100% classification rate.

Table 2. Not fired rate (%) at t=160.

		Directions			
		A	B	C	D
Italian Liras	1,000	5	0	5	0
	2,000	0	10	25	25
	5,000	15	20	5	0
	10,000	10	0	0	5
	50,000(new)	5	0	0	0
	50,000(old)	0	5	0	0
	100,000(new)	0	0	0	0
	100,000(old)	0	5	0	0

5. Conclusions

We have proposed a new classification method of Italian Liras by using the OLVQ1 algorithm. The experimental results show the effectiveness of the proposed algorithm compared with the conventional pattern matching method.

References

[1] S. Fukuda, T. Kosaka, and S. Omatu: Bill Money Classification of Japanese Yen Using Time Series Data, Trans. Of IEE of Japan, Vol.115-C, No.3, pp.354-360, 9995(in Japanese).
[2] J. Dayhoff: Neural Network Architectures: An Introduction, International Thompson Computer Press, New York, 1990.
[3] T. Kohonen: Self-Organizing Maps, Springer, Berlin, 1997.

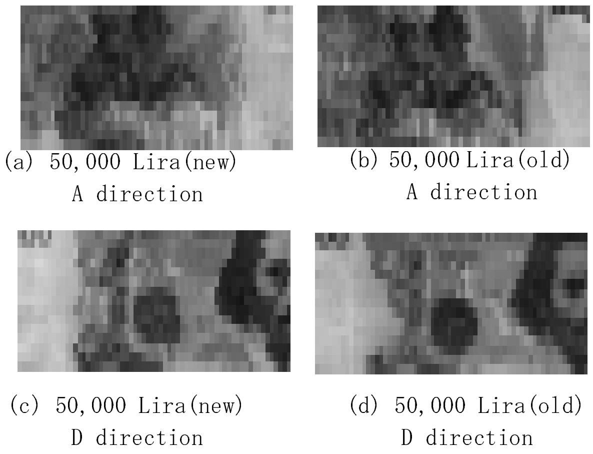

Fig. 5. New and old 50,000 Liras.

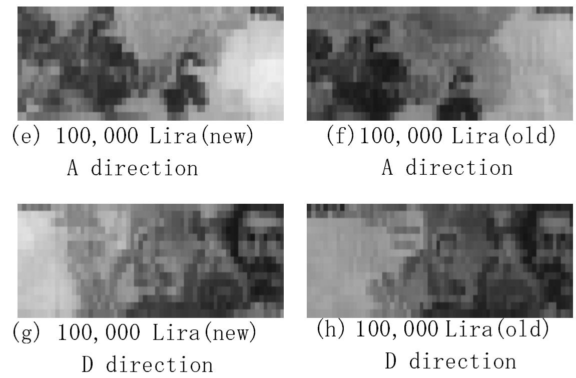

Fig.6. New and old 100,000 Liras.

Table 3. Number of units after learning.

		Directions			
		A	B	C	D
Italian Liras	1,000	2	2	2	2
	2,000	2	1	1	1
	5,000	1	1	1	1
	10,000	1	2	2	1
	50,000(new)	2	1	1	1
	50,000(old)	2	1	3	1
	100,000(new)	1	1	1	1
	100,000(old)	1	1	1	1

The Fifteenth International Symposium on Artificial Life and Robotics 2010 (AROB 15th '10),
B-Con Plaza, Beppu,Oita, Japan, February 4-6, 2010

Acoustic Signals Signal Separation by Independent Component Analysis

Sigeru Omatu, Michifumi Yoshioka, and Hidekazu Yanagimoto
Computer and Systems Sciences, Graduate School of Engineering,
Osaka Prefecture University, 1-1 Gakuen-cho, Sakai City, 599-8531
{omatu, yoshioka , hidekazu@cs.osakafu-u.ac.jp

Abstract

In this paper, a method of separating the acoustic signals of motors and gears of mechanical devices by using the independent component analysis (ICA) with band-pass filters is proposed. The frequency distribution of a recorded acoustic signal of the operating mechanical device can be divided into three fields, the low-frequency field, which corresponds to the frequency characteristics of the gear, the medium-frequency field, which is mixed with the frequency characteristics of the gear and the motor, and the high-frequency field, which corresponds to the frequency characteristics of the motor. Since only the medium-frequency components are the mixture of acoustic signals of gears and motors, the ICA with band-pass filters is expected to separate the acoustic signals of motors and gears more accurately than the conventional ICA. The simulation and experimental results show that the proposed method can separate the acoustic signals of motors and gears of mechanical devices successfully.

Keywords: ICA, Signal processing, Neural Networks

1 Introduction

In the quality evaluation of mechanical devices, it is important to separate the acoustic signals of motors and gears in order to identify the causes of failures. The ICA method, which is developed to solve the cocktail-party problem, can separate two independent acoustic signals from their mixtures by using the information measure of statistically independent properties [1]-[3]. However, many applications in practice denote that the ICA does not perform well in separation by using the observed acoustic signals directly [4]-[5]. In order to separate the independent acoustic signals correctly, additional data processing is necessary before applying the ICA.

By applying the fast fourier transform (FFT) to a recorded acoustic signal of the operating mechanical device, we observe that its frequency distribution can be divided into three fields, the low-frequency field, which corresponds to the frequency characteristics of the gear, the medium-frequency field, which is mixed with the frequency characteristics of the gear and the motor, and the high-frequency field, which corresponds to the frequency characteristics of the motor. Since the frequencies of a motor may be harmonics of the fundamental frequencies of a gear, which causes the independence assumption of the sources to fail and affects the separation accuracy. Therefore, the mixed acoustic signals with less frequency components are expected to be separated more accurately. In this paper, the ICA with band-pass filters is used to separate the acoustic signals of gears and motors. We first record the acoustic signals of the operating mechanical devices. By applying the band-pass filters, the respective components of low-frequency, medium-frequency and high-frequency can be obtained. Then the medium-frequency components are given to the ICA. After separation, the acoustic signals of gears and motors are recovered by adding the low-frequency and high-frequency components to the separated results, respectively. In this paper, the mixtures of two independent signals are also designed to simulate the separation process of acoustic signals of a gear and a motor. Both the simulation results and the experimental results show that the better separation results can be obtained by using the mixed medium-frequency field than using the whole frequency field.

2 Simulation Results

Suppose there are two independent signals s_1 and s_2, their frequency characteristics are illustrated in Figs. 1 and 2, respectively where f_1, f_2 and f_4 are constant and f_3 is variable.

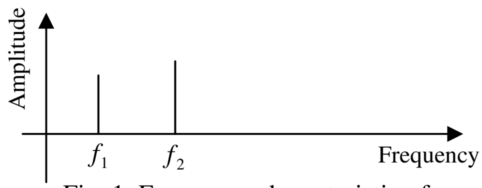

Fig. 1. Frequency characteristic of s_1.

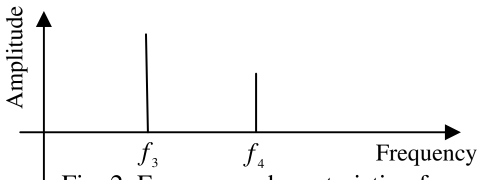

Fig. 2. Frequency characteristic of s_2.

If we use two microphones to record the acoustic signals, we have two observed signals $x_1(t) = a_{11}s_1 + a_{12}s_2$, $x_2(t) = a_{21}s_1 + a_{22}s_2$. We use the ICA to separate the two independent signals s_1 and s_2 from the observed signals. Table I shows the separation results where "Y" denotes that the independent signals s_1 and s_2 can be separated correctly and "N" denotes that they cannot be separated correctly. From Table I, it can be seen that sometimes we fail in separating the acoustic signals

s_1 and s_2 by using the observed signals x_1 and x_2 directly.

Table I. Separation results of observed signals (unit: Hz).

f_3	30	40	50	60	70	80	90	100	110
Y/N	Y	Y	Y	N	Y	Y	Y	N	Y
f_3	120	130	150	160	170	180	190	200	210
Y/N	N	Y	Y	Y	Y	N	Y	Y	Y
f_3	220	230	$f_1 = 20$, $f_2 = 140$, $f_4 = 240$						
Y/N	Y	Y							

However, after filtering the frequency components f_1 and f_4 with a band-pass filter, the frequency components f_2 and f_3 can be separated successfully by using the ICA. Thus, the original acoustic signals s_1 and s_2 can be obtained by adding the frequency components f_1 and f_4 to the separation results of the ICA, respectively. As an example, Figs. 3 and 4 show the frequency characteristics of separated signals s_1' and s_2' by using the ICA with band-pass filters, respectively where $f_3 = 100$ Hz. From these figures, it can be seen that the two acoustic signals of s_1 and s_2 are separated correctly.

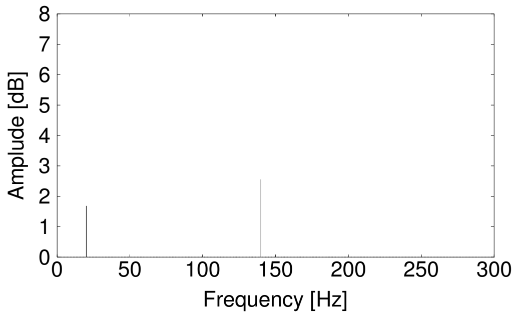

Fig. 3. Frequency characteristic of separated signal s_1' with band-pass filters.

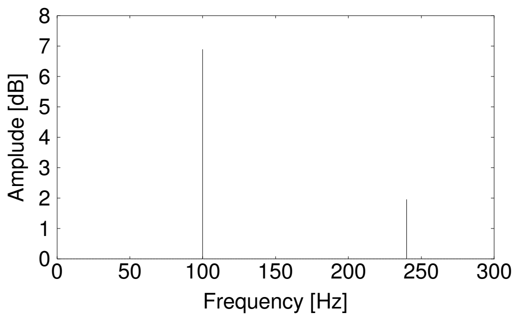

Fig. 4. Frequency characteristic of separated signal s_2' with band-pass filters.

Similarly, other unsuccessful separation experiments of Table I are redone by using the ICA with band-pass filters. The simulation results show that all the signals are separated successfully. And the separation experiments of mixed acoustic signals with multi-frequencies also show that the ICA with band-pass filters performs better than the conventional ICA in acoustic signals separation.

3 Experimental Results

According to the above simulation results, we separate the acoustic signals of motors and gears of mechanical devices by using the ICA with band-pass filters. The acoustic signals recording system is shown in Fig.5. Two microphones, which are held in different locations, are used to record the acoustic signals of operating mechanical devices. By applying the band-pass filters, we obtain the respective components of low-frequency, medium-frequency and high-frequency. Since only the medium-frequency components are the mixture of acoustic signals of gears and motors, we input the medium-frequency components to the ICA. Then the acoustic signals of gears and motors can be recovered by adding the low-frequency and high-frequency components to the separation results of the ICA, respectively.

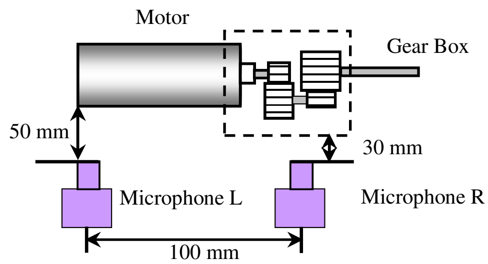

Fig. 5. The acoustic signals recording system.

An example of acoustic signals recorded by microphones L and R are shown in Figs. 6 and 7, respectively where the sampling rate is 8,000. Their frequency characteristics are shown in Figs. 8 and 9.

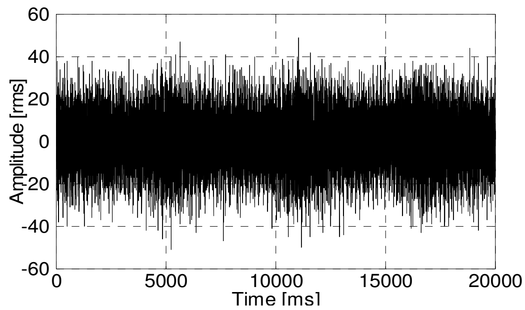

Fig. 6. Acoustic signal recorded by the left microphone.

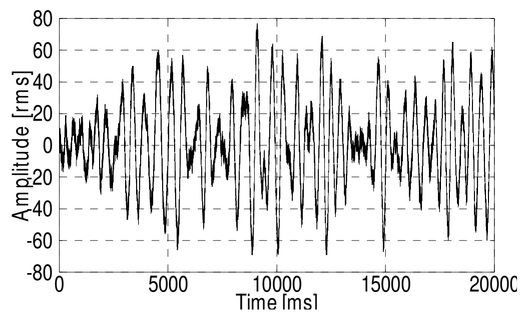

Fig. 7. Acoustic signal recorded by the right microphone.

Since the rotational speed of the motor is 3600 rpm and the rotor has 12 poles, the fundamental frequency of the motor is about 360 Hz. Similarly, since the gear ratio is

30:1, the fundamental frequency of the gear is about 12 Hz. Thus, it can be considered that the medium-frequency is the range of 300 to 2,000 Hz and the relevant band-pass filters are designed.

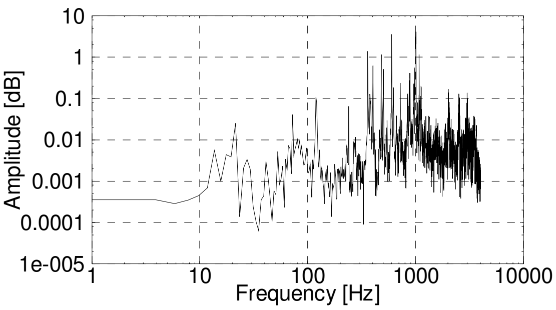

Fig. 8. Spectrum of acoustic signal of left microphone.

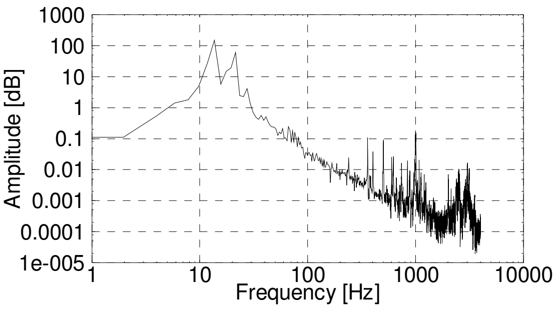

Fig. 9. Spectrum of acoustic signal of right microphone.

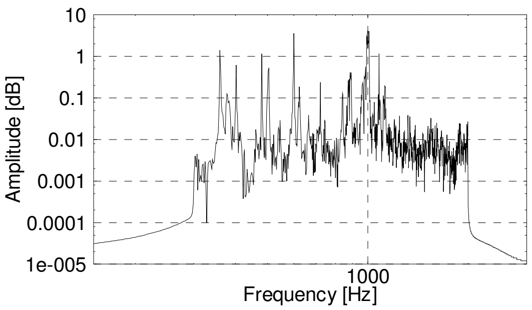

Fig. 10. Spectrum of Fig. 8 with a band-pass filter.

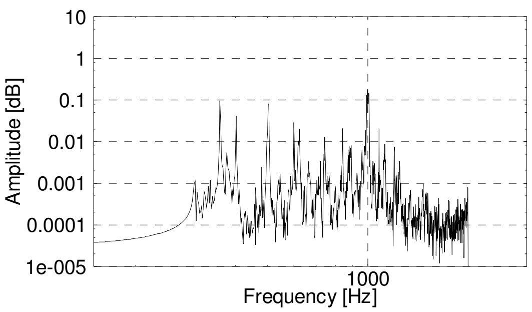

Fig. 11. Spectrum of Fig. 9 with a band-pass filter.

In Figs. 10 and 11, the medium-frequency fields of acoustic signals of left and right microphones with the band-pass filter are given respectively. The filtered signals are used as the input of the ICA. The spectra of the separated acoustic signals are shown in Figs. 12 and 13. Since a peak of amplitude nearby 1,000 Hz, which is about 3 times of the fundamental frequency of the motor, can be observed in Fig. 12, it is regarded that Figs. 12 and 13 show the medium-frequency fields of acoustic signals of the motor and the gear, respectively.

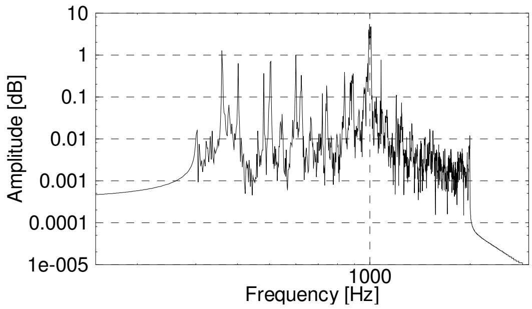

Fig. 12. Spectrum of the separated acoustic signal by using the ICA with a band-pass filter (motor).

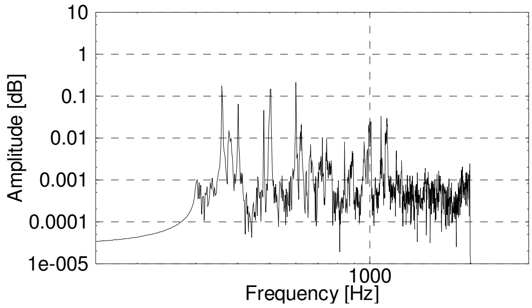

Fig. 13. Spectrum of the separated acoustic signal by using the ICA with a band filter-pass (gear).

To verify the effectiveness of our proposed method, we also give the separation results by applying the recorded acoustic signals of mechanical devices to the ICA directly. The frequency characteristics of the separated acoustic signal are shown in Figs. 14 (a) and 15 (a), and the medium-frequency characteristics are shown in Figs. 14 (b) and 15 (b). Comparing with Figs. 8 and 9, it can be concluded that Figs. 14 and 15 show the frequency characteristics of the motor and the gear, respectively.

From the above figures, it can be seen that the ICA with band-pass filters performs better than the conventional ICA in acoustic signals separation. The spectrum of Fig. 14 (b) is similar with the one of Fig. 15 (b), especially the peaks of amplitudes appeared in both figures, which are located in the multiple of fundamental frequency of the motor, denote that the separation results of acoustic signals of the motor and the gear are not good.

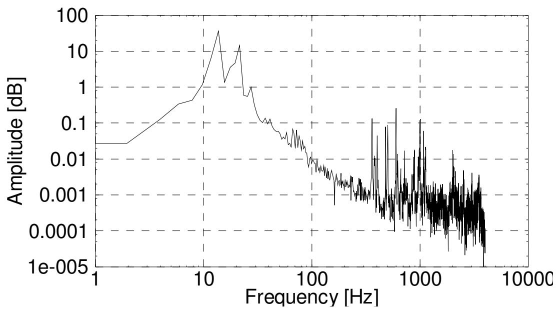

Fig. 14 (a). Frequency characteristics of the separated acoustic signal by using the ICA (motor).

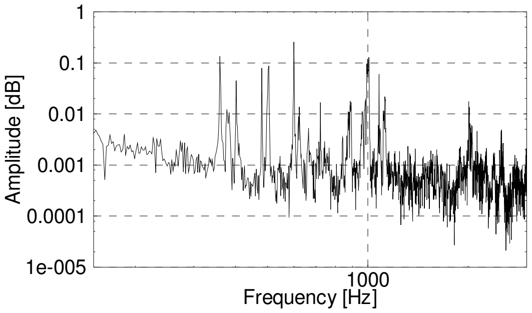

Fig. 14 (b). Medium-frequency characteristics of the separated acoustic signal by using the ICA (motor).

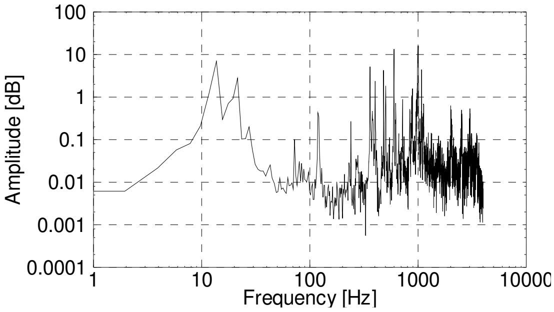

Fig. 15 (a). Frequency characteristics of the separated acoustic signal by using the ICA (gear).

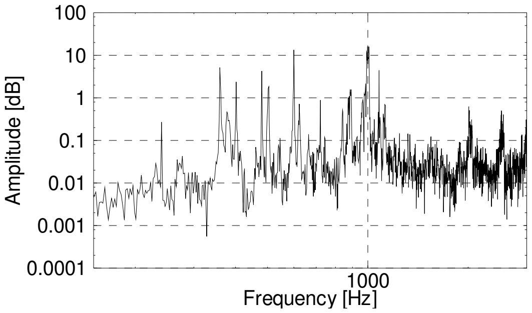

Fig. 15 (b). Medium-frequency characteristics of the separated acoustic signal by using the ICA (gear).

The acoustic signals of the gear and the motor are recovered by adding the low-frequency and high-frequency components to the separation results of Figs. 12 and 13, respectively. The spectra of recovered acoustic signals of the gear and the motor are shown in Figs. 16 and 17 where the amplitudes of medium-frequency are adjusted according to the amplitudes of low-frequency and high-frequency, respectively. Comparing with the above figures, it can be concluded that the separation results are reasonable. The separated acoustic signals of the gear and the motor are also checked by a technician, the sounds of the motor and the gear denote that the acoustic signals of the gear and the motor are separated successfully by using the ICA with band-pass filters.

6. Conclusion

In this paper, a method of separating the acoustic signals of gears and motors of mechanical devices by using the ICA with band-pass filter is proposed. The simulation results denote that the mixed acoustic signals with less frequency components can achieve better separation performance by using the ICA. Therefore, for those independent signals which are mixed only in medium-frequency field, the ICA with band-pass filters can separate the independent original signals more accurately than the conventional ICA. Using the proposed method, we have solved the acoustic signals separation problem of gears and motors of mechanical devices successfully.

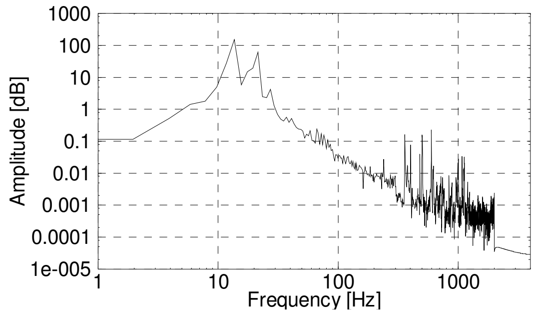

Fig. 16. Spectrum of recovered acoustic signal of the gear.

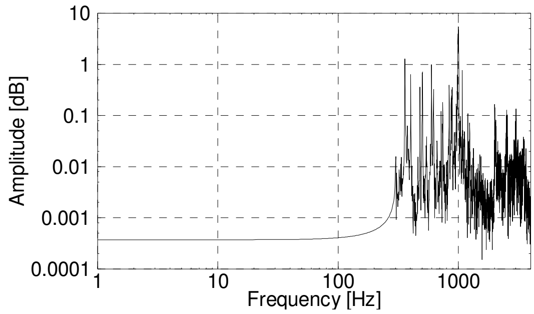

Fig. 17. Spectrum of recovered acoustic signal of the motor.

References

(1) A. Hyvarinen, J. Karhumen, and E. Oja, Independent Component Analysis, Wiley Publisher, New York, 2001.

(2) E.Bingham, and A. Hyvarinen, " A fast fixed-point algorithm for independent component analysis of complex valued signals," International Journal of Neural Systems, Vol. 10, No. 1, pp. 1-8, 2000.

(3) S. Hochreiter, and J. Schmidhuber, "LOCOCODE performs nonlinear ICA without knowing the number of sources," Proceedings of the First International Workshop on ICA and Signal Separation, Aussois, France, 1999, pp. 149-154.

(4) T. W. Lee, Independent Component Analysis: Theory and Applications, Kluwer Academic Publishers, Boston, 1998.

(5) A. Cichocki, and S. Amari, Adaptive Blind Signal and Image Processing: Learning Alogarithms and Applications, Wiley Publisher, New York, 2002.

The Land Cover Estimation with ALOS Satellite Image Using Neural-Network

Yuta Tsuchida Sigeru Omatu Michifumi Yoshioka
Computer and Systems Sciences Graduate School of Engineering
Osaka Prefecture University
Sakai, Osaka, 599-8531 Japan
tsuchida@cs.osakafu-u.ac.jp

Abstract

On May 12th 2008, large earthquake occurred in Sichuan, China. We analyze this disaster damage by using satellite images from ALOS, Japanese satellite. The land cover classi cation is operated by the image captured on AVNIR-2. The AVNIR-2 images can not be monitored frequently because of the cloud and solar irradiation, so near earthquake center area is covered by clouds. The goal of this paper is to classify land cover using PALSAR images. PALSAR can observe in 350km wide area independent on weather. The PALSAR is a single band sensor, and the inputs consist of many pixels by using nearest pixel values, and the supervisor signal is the estimated classes by AVNIR-2.
Keywords ALOS, PALSAR, AVNIR-2, the earthquake in Sichuan

1 INTRODUCTION

The large earthquake occurred on May 12th 2008 in Sichuan, China. This earthquake caused over 90 000 deaths, which had a magnitude 8. By the way, the satellite was launched for the land observation from Japan on 2006. This disaster damage is analyzed by using pre- and post-images, sent from PALSAR mounted on ALOS[1]. The PALSAR images are able to be observed a wide area ground shape however, it is di cult to gure out the land utilization with it because this sensor has only 1 band.

In this paper, we estimate the land cover classi cation with the image captured on AVNIR-2, mounted on the same satellite. Since AVNIR-2 has four bands sensor, the classi cation is easier than PALSAR.

In the cover classi cation from PALSAR, the classi cation result from AVNIR-2 is adopted as supervisor signal.

Now, there are two purposes of the classi cation from AVNIR-2. At rst, the raw AVNIR-2 data contains the many information. Therefor, the AVNIR-2 is classi ed to 8 classes to reduce it. Second, in the wide area PALSAR data, more sample data is included to enhance the classi cation accuracy.

In the classi cation with PALSAR, the number of the input layer has a problem, because the PALSAR has only one band sensor. We propose that the input signal employs not only one pixel but also near pixel values.

2 PALSAR IMAGE SUMMARY

PALSAR (Phased Array type L-band Synthetic Aperture Rader) is the active image sensor independent on weather. The center frequency is 1,270MHz (L band). The active sensor has advantages that these can observe the area covered with cloud in many season, or midnight, so the capture frequency is higher than passive e.g., optical sensor.

The ScanSAR mode was bought to need wide area because the detail position of the earthquake center was not able to be checked, though PALSAR is provided the three modes. The data has the following properties: band width is 14MHz, Polarization is HH, O -nadir angle is 27 1 , and spatial resolution is 100m[2]. The image size is 3 700 $\times$ 3 900 pixels, and the swath width is 370km. In an PALSAR image, the dark pixel depicts atness surface, e.g. water or airstrip, because the radar from satellite re ects in the opposite direction. On the other hand, the bright indicates the backscatter from the architectures in urban area. The mountain is expressed as contrast.

Figure 1 shows the PALSAR image in earthquake center. Being compared with Google maps, (1) in Figure 1 shows the Zipingpu dam, and (2) shows Guan Xian. Thus, PALSAR is suitable to survey the surface structure. Using this character, pre-image (in 2008/1/3) is compared with post-image (in 5/20) and checked on the damage refer from the Google maps, or the book[3].

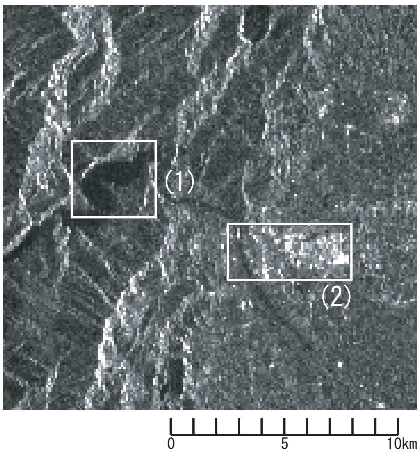

Figure 1: The data of the neighborhood of earthquake center (2008/5/20)

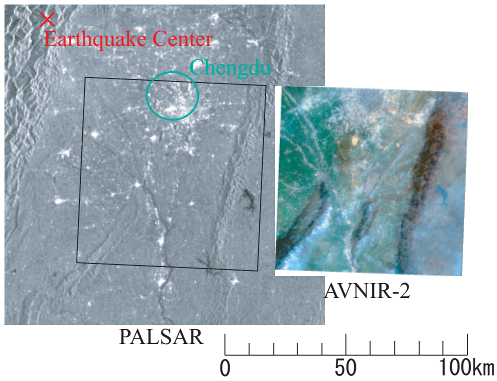

Figure 2: The image of AVNIR-2 and PALSAR. The square in PALSAR is position of AVNIR-2

3 AVNIR-2 IMAGE SUMMARY

AVNIR-2(Advanced Visible and Near Infrared Radiometer type 2) are the passive image sensor because the sun as light source a ects the image. This sensor can observe at 10m spatial resolution. The bands have three, and table 1 shows bands speci cation.

The bought data observes near Chengdu in 2007/3/31; the image size is 7 128 $\times$ 7 000 pixels, and swath width is 71 28km. Figure 2 shows the AVNIR-2 image and the PALSAR image.

Table 1: The Bands spec on AVNIR-2

Band1	0 42 m 0 50 m	Blue
Band2	0 52 m 0 60 m	Green
Band3	0 61 m 0 69 m	Red
Band4	0 76 m 0 89 m	Infra Red

AVNIR-2 has a shortage: It depends on weather, or night. Actually, the data near earthquake center can't be utilized due to cloud.

3.1 LAND COVER ESTIMATION USING AVNIR-2

The goal of this paper is to achieve the land cover classi cation using PALSAR in the area not observed by AVNIR-2. The land cover classi cation is estimated by using AVNIR-2. Then the classi cation is estimated with PALSAR. In the classi cation by using AVNIR-2, the neural-network, one of the supervised learning, is used, and then the supervisor signal is picked up manually.

Table 2 shows correspondence of class number and names. In pre-examination, the false classi cation exists in the edge of the river, "Along the river" is adopted. Figure 3 shows the structure of neural network. The input signals are 4 bands for a pixel. The raw data of AVNIR-2 have 8-bit wide and the signals range from 0 to 255, where in fact shows from 35 to 203. A threshold value x_0 has the center of the all bands luminance value: 84. There are 7 neurons in middle layer. There are 8 output signals as a classi cation. The learning coe cient is 0 003, and is 0 85. The supervisor data is set as 1 when it should be classi ed data in pixel, and the other are set as zeros.

Table 2: The classi cation type

No.	Class Name	Color
1	Sand	
2	Vegetation A	
3	Vegetation B	
4	Architecture	
5	Along the river	
6	Mountain	
7	Water	
8	Red Soil	

The learning employs 60 patterns in each class, summation is 480, and the test apples $40 * 8 = 320$ patterns. Table 3 shows the learning result, and Table 6 shows the test result. Any row means the average

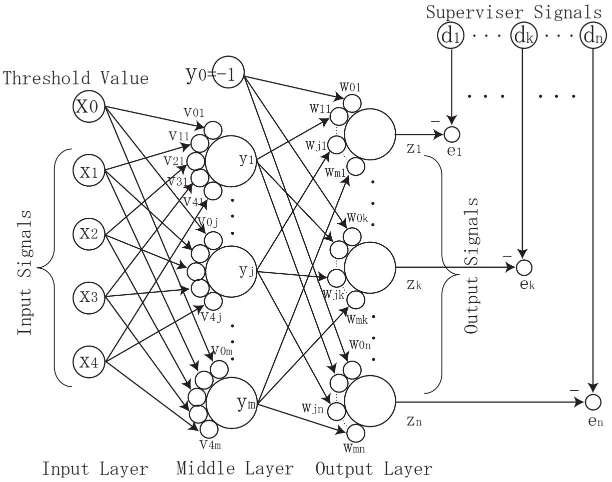

Figure 3: The structure of neural network

of output data for each supervised classes. Figure 4 shows the estimated result. Figure 4(a) is AVNIR-2 image, and (b) is the result. These tables explain how the classi cation has been achieved. For example, No.1: "Sand" and No.6: "Mountain" achieved. However No4: "Architecture" is misclassi ed as No.5: "Along the river" or No.7: "Water". The result is estimated by using all samples. However some areas covered with cloud make false recognition. Therefore, these areas are performed by the estimation using PALSAR.

Table 3: Learning result using AVNIR-2

	1	2	3	4	5	6	7	8
1	0.99	0.00	0.01	0.00	0.01	0.00	0.01	0.00
2	0.00	0.98	0.02	0.00	0.00	0.01	0.00	0.01
3	0.01	0.01	0.98	0.00	0.00	0.00	0.00	0.01
4	0.00	0.00	0.00	0.86	0.04	0.00	0.06	0.04
5	0.00	0.00	0.00	0.04	0.91	0.01	0.00	0.04
6	0.00	0.01	0.00	0.00	0.00	0.99	0.01	0.01
7	0.00	0.00	0.00	0.05	0.01	0.01	0.93	0.02
8	0.00	0.01	0.01	0.01	0.04	0.01	0.00	0.93

4 LAND COVER ESTIMATION USING PALSAR

The land cover estimation with PALSAR is performed by neural-network. We estimate it by using one pixel of PALSAR image input. However, the classi cation is di cult because of brightness distribution being biased. We consider to use the many pixels are adopted as an input of the neural network. The estimated result with AVNIR-2 is employed as supervisor signal and the axes and resolution are converted with a ne transform to PALSAR. The characteristic positions where these are common in PALSAR and AVNIR-2 were extracted, like river, lake or airport. Then the a ne coe cients are calculated with least-square method using these positions.

The PALSAR data was corrected with histogram equalization to reduce the bias. The input layer has $16(4 * 4)$, and the output is the same as AVNIR-2. The input value is divided by maximum to [0,1] and the threshold value x_0 is 1. In hidden layer, the 12 neurons are set. The pixel of PALSAR image is more narrow than it of AVNIR-2. The square of one pixel of PALSAR is similar to the square of 10×10 pixles of AVNIR-2. In these area of AVNIR-2, the many classes are contained, where maximum is 100, therefore mixed classes represent ratio. For example, in 10×10 pixels of AVNIR-2, when the 50 pixels is class No.1, the ratio of class No.1 is 0.5. The 16 pixels

Table 4: Test result using AVNIR-2

	1	2	3	4	5	6	7	8
1	0.97	0.00	0.01	0.00	0.02	0.00	0.01	0.00
2	0.00	0.96	0.02	0.00	0.00	0.01	0.00	0.01
3	0.01	0.02	0.98	0.00	0.00	0.00	0.00	0.01
4	0.00	0.00	0.00	0.83	0.14	0.00	0.05	0.02
5	0.00	0.00	0.00	0.07	0.79	0.01	0.00	0.09
6	0.00	0.01	0.00	0.00	0.00	0.98	0.01	0.01
7	0.00	0.00	0.00	0.08	0.01	0.01	0.90	0.01
8	0.00	0.03	0.00	0.00	0.18	0.00	0.00	0.78

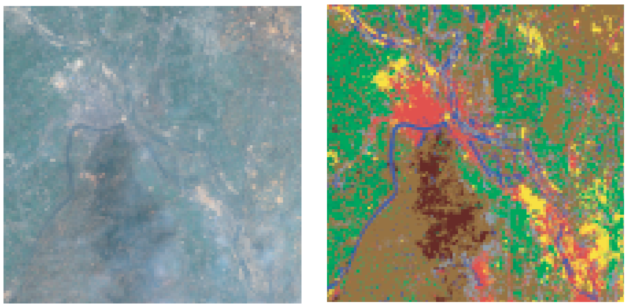

(a) AVNIR-2 Color image (b)Estimated result

Figure 4: The classi cation result using AVNIR-2

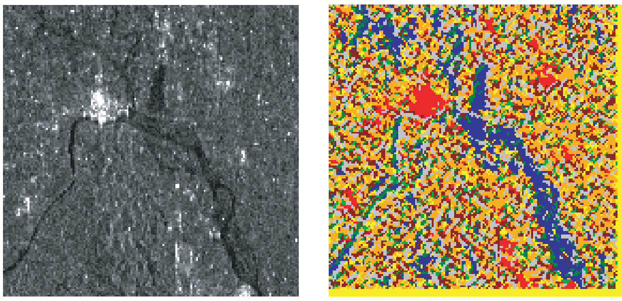

(a) PALSAR image (b)Estimated result

Figure 5: The classi cation result using PALSAR

of PALSAR contains 1600 pixels of AVNIR-2, therefor the ratio 60% correspond to the classes of 960 pixels in AVNIR-2. The ratio of classes estimated with AVNIR-2 are applied as the learning data. The output may not be enhanced near 1.

The sample data is picked over 60% for each class to get over 20 patterns . The learning data employs $10 * 8 = 80$ patterns. Table 5 shows learning result and Table 6 shows the test result. Some classes has positive reaction, though the tests have many false e.g.No4: "Architecture" and No.7: "Water" . The Figure 5 shows the estimated data, (a): PALSAR image and (b): estimated result. The Architecture or Water exists the same position on AVNIR-2.

Table 5: Learning result using PALSAR

	1	2	3	4	5	6	7	8
1	0.66	0.02	0.05	0.00	0.04	0.03	0.03	0.08
2	0.02	0.36	0.03	0.03	0.05	0.02	0.04	0.12
3	0.02	0.01	0.65	0.02	0.03	0.01	0.01	0.17
4	0.02	0.00	0.03	0.72	0.05	0.02	0.00	0.07
5	0.02	0.00	0.03	0.02	0.40	0.04	0.04	0.22
6	0.01	0.02	0.02	0.02	0.05	0.73	0.01	0.14
7	0.02	0.05	0.01	0.05	0.04	0.04	0.54	0.08
8	0.00	0.01	0.07	0.01	0.07	0.01	0.06	0.70

5 CONCLUSION

The PALSAR is single band radar and it is di cult to estimate land cover. However, the area or number of times is larger than the other optical sensor. The land cover estimation using PALSAR has many advantages. For example, the AVNIR-2 can not be observed from the cloud or midnight. However, the PALSAR is able to observe the data independent by on weather. Thus the PALSAR data is stocked larger than AVNIR-2. The ScanSAR mode has wide area and the cost per the area is lower. Actually, the cost of an AVNIR-2 data is the same as the PALSAR.

Table 6: Test result using PALSAR

	1	2	3	4	5	6	7	8
1	0.14	0.01	0.12	0.08	0.12	0.33	0.10	0.17
2	0.03	0.08	0.06	0.00	0.18	0.13	0.18	0.16
3	0.04	0.02	0.16	0.06	0.11	0.07	0.09	0.28
4	0.10	0.02	0.03	0.45	0.12	0.12	0.01	0.12
5	0.01	0.03	0.03	0.14	0.27	0.21	0.03	0.18
6	0.11	0.01	0.04	0.01	0.17	0.24	0.03	0.38
7	0.01	0.13	0.01	0.04	0.04	0.02	0.53	0.04
8	0.09	0.03	0.08	0.01	0.14	0.14	0.03	0.19

In this paper, the method to estimate the land cover with PALSAR is introduced. At rst, the classi cation with AVNIR-2 is estimated to pick the samples. As a result, the test data depicted acceptable result. This data is able to apply the land cover estimation with PALSAR.

The second, in the estimation with PALSAR, the many pixels in PALSAR image are employed as input layer. The estimated results with AVNIR-2 are applied as the learning data, where the ratio of classes are learned. As a result, some classes show reaction, though the many classi cation error occur.

The challenge for the future is that the number of input layer has to be adjusted. In PALSAR data, the single or 4 pixels cannot show the characteristic class. the many pixels are considered land cover. Then this result is applied for analyzing the earthquake damage.

COPYRIGHT OF SATELLITE IMAGES

A copyright in AVNIR-2 images are reserved by JAXA, and it in PALSAR images are reserved by METI, JAXA. These satellite images are distributed by RESTEC.

References

[1] Y.Tsuchida, S.Omatu and M.Yoshioka, "The land cover classi cation with PALSAR and AVNIR-2 image" IEEJ C convention, 2009 , GS11-7.

[2] RESTEC, "ALOS product and services", 2007 ,Japan.

[3] CAS , "Concise Atlas of the Wenchuan earthquake area" ,2008/1,Starmap pub ,China.

The Fifteenth International Symposium on Artificial Life and Robotics 2010 (AROB 15th '10),
B-Con Plaza, Beppu,Oita, Japan, February 4-6, 2010

The analysis of Japanese voice sound by using Real-Time Spectral Analysis

Hideto Nakatsuji *, Sigeru Omatu **
*Computer and Systems Sciences, Department of Engineering, Osaka Prefecture University, 1-1 Gakuen-cho, Nakaku, Sakai City, 599-8531
**Computer and Systems Sciences, Graduate School of Engineering, Osaka Prefecture University, 1-1 Gakuen-cho, Nakaku Sakai City, 599-8531
nakatuji@sig.cs.osakafu-u.ac.jp, omatu@cs.osakafu-u.ac.jp

Abstract

A voice signal processing requires a real-time processing. In consideration of the real-time processing, a new method which updates the spectrum by using an input data has been proposed. In this method, the analysis in time-frequency domain is executed as well as wavelet transform. Vowel /i/ and /e/ consist of fundamental, harmonics and high frequency waves. These high frequency waves determine the sound of /i/ and /e/. These high frequency waves might exist also in /a/ and /o/. In this paper, we analyze these high frequency waves by using new analyzing method, and we show the constitution of high frequency waves. Since a waveform of consonant does not repeat, the analysis can not be performed like the analysis of the high frequency wave of vowel. In consonant, we show the fluctuation of the spectrum for the time progress.

Keywords: Decomposition wave and reconstruction wave, Time-frequency domain

1 Introduction

In recent years, wavelet transform has attracted attention as an analysis in time-frequency domain. Here newly, a new analytical method with the same function as wavelet transform was presented by authors [2]-[4]. In this method, processing in search of spectrum is performed by using one input data. Since all processing are perfectly independent, complete parallel processing is possible, and so if parallel processing computer will be brought to realization, real-time processing is realized. We call this analytical method Real-Time Spectral Analysis Method. In Japanese, there are five vowels, and this is few in comparison with other language. Japanese vowel consists of fundamental, harmonics and high frequency waves. In Japanese vowel /i/ and /e/ , High frequency waves decide the sound /i/ and /e/. In Japanese vowel /a/ and /o/, it is not always true that the high frequency waves exist and high frequency waves do not decide the sound /a/ and /o/. High frequency waves are audible in each vowel sound. Here, by applying the method of decomposition and reconstruction of Real-Time Spectral Analysis to the Japanese vowel sound, the sound signal is decomposed to a fundamental, some harmonics and high frequency waves. By using these waves, we made experiment of hearing and we show how the vowel sound consists of these waves. In consonant, we show the fluctuation of the spectrum with time.

2 Analysis theory

The algorithm uses the inner products of multiple period sine, cosine waves (below referred to as cutting out waves)and a signal. T_s is the sampling interval. Let f_j denote the established frequency of the cutting out wave (angular frequency $\lambda_j = 2\pi f_j$). Here $j(=1,\cdots,n)$ is number of cutting out wave and n is the number of the cutting out waves. There are T periods (T is a natural number), here T is the number of periods. The length of the cutting out wave is $q_j(=T/f_j)$ and N_j denote the number of data included in the cutting out wave. Then the cutting out wave can be expressed as follows:

$$\begin{aligned}
&s_j(l) = \sin(\lambda_j l T_s) \quad c_j(l) = \cos(\lambda_j l T_s)\\
&s_j(-l) = -s_j(l) \qquad c_j(-l) = c_j(l)\\
&s_j(k+N_j) = s_j(k) \quad c_j(k+N_j) = c_j(k)\\
&k\text{ ; natural number} \quad l = 1,\cdots,N_j
\end{aligned} \tag{1}$$

Here we consider only sine waves as cutting out wave because the expansion for cosine waves is similar to the case of sine waves. A signal at time kT_s is $x(k)$. By using the signal which dated back to the past, the inner product of cutting out wave and signal at time kT_s can be written as follows:

$$Y_s^k(j) = \frac{2}{N_j}\sum_{l=1}^{N_j} x(k-l)s_j(l-k) \tag{2}$$

The inner product at time $(k+1)T_s$ is

$$\begin{aligned}
Y_s^{k+1}(j) &= \frac{2}{N_j}\sum_{l=1}^{N_j} x(k+1-l)s_j(l-k-1)\\
&= \frac{2}{N_j}x(k)s_j(-k) + Y_s^k(j) - \frac{2}{N_j}x(k-N_j)s_j(N_j-k)
\end{aligned} \tag{3}$$

From Eq.(3), the inner product at time $(k+1)T_s$ can be obtained by adding the product of the input data at time kT_s and the cutting out wave to the inner product at time kT_s, and subtracting the third term. Since the second and third term have already been calculated, the necessary calculation in Eq.(3) is a multiplication in the first term. If $k = N_j$, then third term on the right side of Eq.(3) is $s_j(0)$, but this can be found $s_j(N_j)$ by using Eq.(1). In the case of a cosine cutting out wave, the inner product $Y_c^k(j)$ is found using a similar way. By using these inner products, the following is calculated:

$$Y_{out}^{k}(j) = \sqrt{Y_s^{k}(j)^2 + Y_c^{k}(j)^2} \qquad (4)$$

The unit that outputs $Y_{out}^k(j)$ detects input signal components of certain frequency (close to the established frequency f_j), below, this unit is called an auditory cell, and $Y_{out}^k(j)$ is spectrum. Since there are two equations of inner product in an auditory cell, the multiplication number of times that is necessary for update of an inner product is twice. Since number of auditory cells is n, total multiplication number is $2n$. Auditory cells are independent each other, and two equations in an auditory cell are also independent. If parallel processing computer will be brought to realization, calculation number that need to calculates spectrums by Eq.(4) is 2 multiplications and one square root calculation. Even if number of auditory cells becomes large, the calculation number of times does not change. By using the inner products expressed by discrete system, we show below a procedure to get decomposition waves.

Step1 Calculate the inner products and $Y_s^k(j)$ and $Y_c^k(j)$ at time kT_s

Step2 multiply $Y_s^k(j), Y_c^k(j)$ by $-s_j(k), c_j$ and the following is calculated:

$$Y_{ss}^{k}(j) = -Y_s^{k}(j)s_j(k), \quad Y_{sc}^{k}(j) = Y_s^{k}(j)c_j(k)$$

$$Y_{cc}^{k}(j) = Y_c^{k}(j)c_j(k), \quad Y_{cs}^{k}(j) = -Y_c^{k}(j)s_j(k)$$

Step3 By using $Y_{ss}^k(j), Y_{sc}^k(j), Y_{cc}^k(j)$ and $Y_{cs}^k(j)$, The following is calculated:

$$Y_{cout}^{k}(j) = Y_{ss}^{k}(j) + Y_{cc}^{k}(j), \quad Y_{sout}^{k}(j) = Y_{sc}^{k}(j) - Y_{cs}^{k}(j)$$

Step4 Changing k into $k+1$, and returns to Step 1 and repeats below. $Y_{cout}^k(j)$ is the decomposition wave that appears on the auditory cell.

3 The analysis of Japanese vowel sound

I acquired the sound data of seven men. Sampling frequency is 44.1kHz, 16 bits, monaural. Number of periods T is 16, and constant. Now assume 261 auditory cells with the established frequency increasing from 100Hz to about 17kHz at a rate of about 2%.

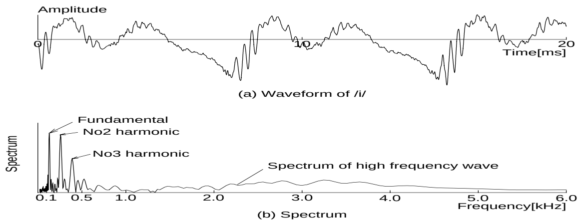

Fig. 1. Waveform and spectrum of /i/

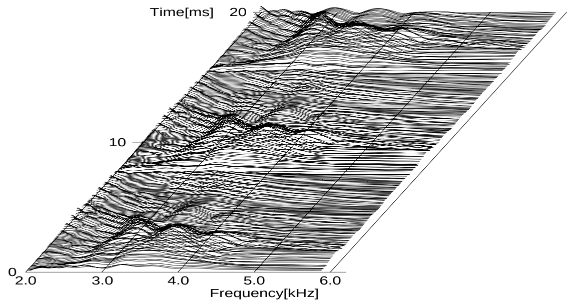

Fig. 2. Fluctuation of spectrum of high frequency wave with time

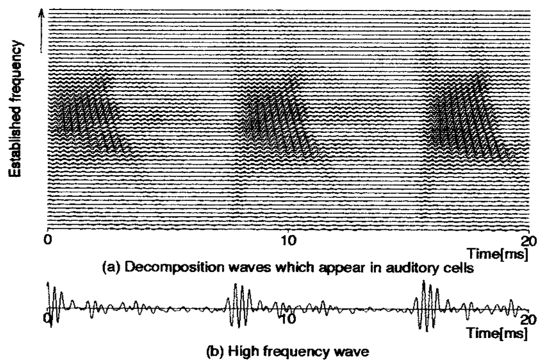

Fig. 3. Decomposition waves and high frequency wave

3.1 High frequency wave constituting a vowel sound

There are five vowels in Japanese, and the vowel generally consists of fundamental, harmonics and some high frequency waves. High frequency waves exist in higher frequency than 2kHz. The high frequency waves exist by all means in vowel /i/ and /e/. In addition, there are not the harmonics of higher frequency than 500Hz. A waveform and a spectrum of /i/ are showed in Fig.1. In Fig.1, there are fundamental, two harmonics and one high frequency wave. When the wave made by adding fundamental and harmonics is played back, we do not hear it with /i/, but the wave produced by adding high frequency wave to that wave is heard with /i/. When the high frequency wave only is played back, we hear that sound with /i/. In /i/, the existence of this wave decides /i/, and /e/ is similar to /i/. In /i/, the spectrum fluctuating with time is showed in Fig.2. In Fig.2, the spectrum repeats itself at fundamental frequency. The decomposition waves are calculated by the method shown with Section 2, and the decomposition waves is shown in Fig.3. In Fig.2 and Fig.3, time indicates until 20ms.

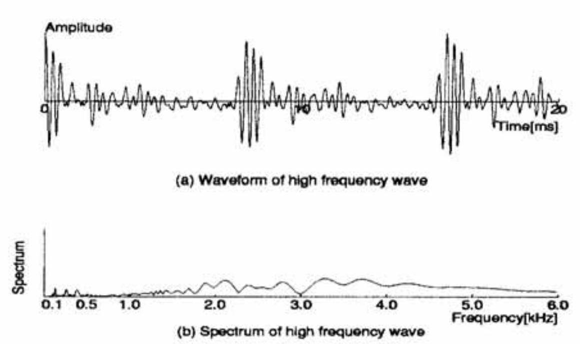

Fig. 4. Waveform and spectrum of high frequency wave

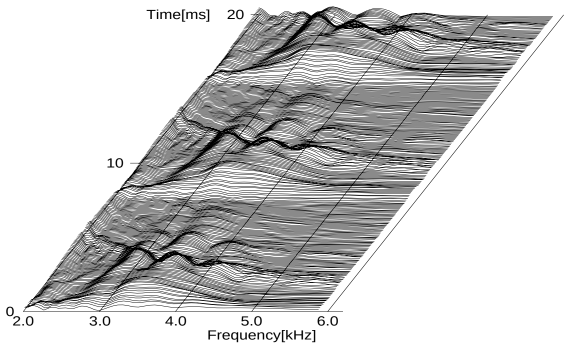

Fig. 5. Fluctuation of spectrum with time

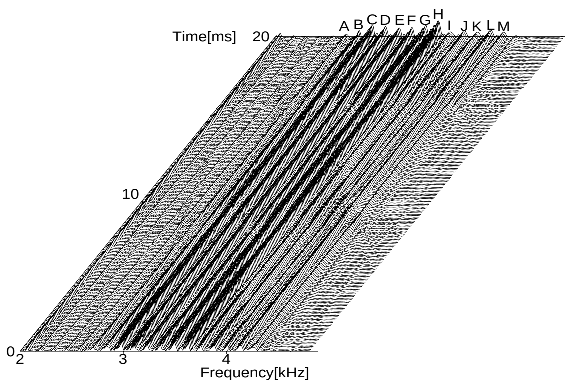

Fig. 6. Fluctuation of spectrum with time in case that T is 100

Fig.3(a) shows the decomposition waves of high frequency wave. In Fig.3(a), vertical axis is the established frequency, and in the upper part, frequency becomes high. Fig.3(b) is the wave that are made by adding all decomposition waves of high frequency, and this is the reconstruction wave of high frequency wave. When this wave is reproduced, we hear it with /i/. Fig.4 shows the spectrum obtained by analyzing this high frequency wave again. Fig.4(a) and Fig.3(b) are the same. Although fundamental and harmonics are small, they exist similarly in Fig.4(b), and high frequency wave exists too. Spectrum of this high frequency wave shows in Fig.5. Spectrum in Fig.5 is almost the same as spectrum in Fig.2. A high frequency wave corresponding to the spectrum in Fig.5 is made, and we hear it with /i/. In this way, the high frequency wave consists of fundamental, harmonics and high frequency wave, and this high frequency wave also

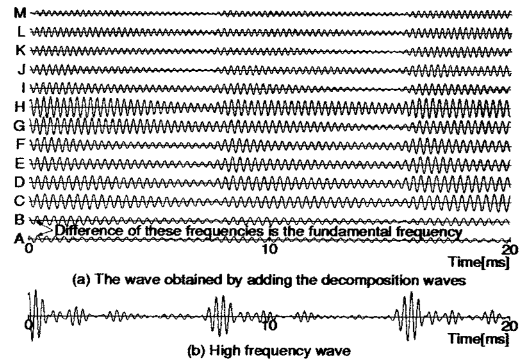

Fig. 7. Elements of high frequency wave and produced wave by adding those waves

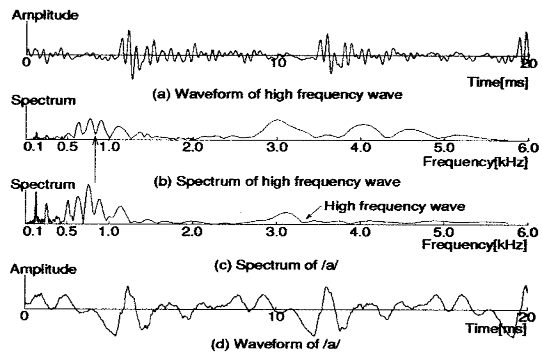

Fig. 8. waveform of /a/ and high frequency wave and that spectrums

consists of those waves.

3.2 The separation of the spectrum

By using number of periods T and the established frequency f, the length q of the cutting out wave is shown with T/f. The waves that length for $T+1$ periods and $T-1$ periods become q can not be detected by this auditory cells. The detection width of the auditory cell is designated as B. The following relationship $B = 2f/T$ or $Bf/T = 2$ is formed. That is, the area made from frequency width B and time length T/f becomes two and constant. When T is increased, B that shows the extension of the spectrum becomes small, and so it is possible to separate the spectrum that has extended in the direction of the frequency axis. In Fig.2, the spectrum repeats itself, and so we make T large and try separation of spectrum. Fluctuation of spectrum against the passage of time in case that T is 100 is shown in Fig.6. Fig.6 shows that a spectrum is separated into 13 from A to M. The decomposition waves from A to M and the wave made by adding all the decomposition waves is shown in Fig.7. Fig.7(a) is the decomposition waves, and Fig7.(b) is the reconstruction wave, and this wave is the high frequency wave. The frequency interval of the decomposition waves is fundamental frequency. Since this frequency interval is very smaller than 3kHz or 4kHz, when these waves are added, complicated large beat phenomenon occur. In this

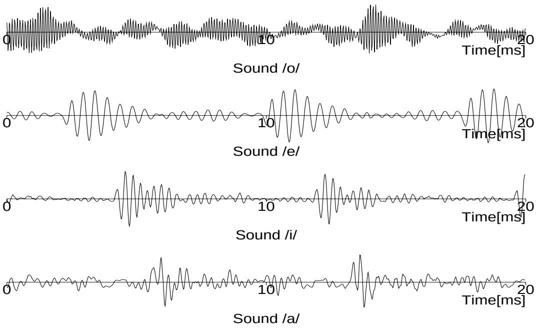

Fig. 9. Waveforms of high frequency waves of vowel /a/,/i/,/e/and/o/

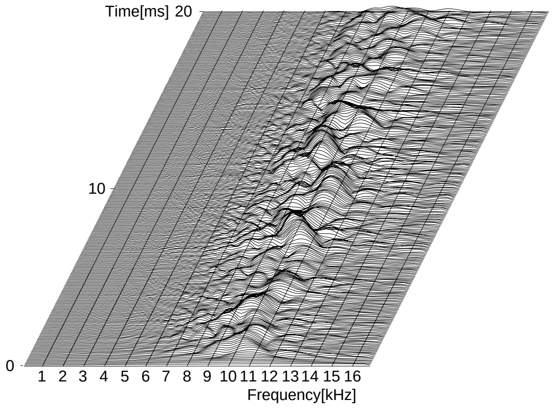

Fig.10. Fluctuation of spectrum of /s/of /sa/ with time

way, the high frequency wave becomes the wave which fluctuates largely. The spectrum in Fig.2 and in Fig.6 essentially the same. In /i/, one or more high frequency waves exist by all means, and we hear the wave with /i/. The existence of this wave determines /i/. Vowel /e/ is also similar to /i/. It is not always true that the high frequency waves exist in /a/ and /o/. In the case that the wave exists, we hear it with each vowel /a/ or /o/. A waveform of /a/ and that spectrum and high frequency wave and that spectrum are shown in Fig.8. In /a/, a wave produced by adding fundamental and harmonics is heard with /a/. Fig.8(c) is the spectrum of /a/ and Fig.8(b) is the spectrum of the high frequency wave, and in both spectrums, there are similar fundamental and harmonics, and so we hear high frequency wave with /a/. Vowel /o/ is also same as /a/. In Fig.6 and Fig.7, it was shown that the spectrum of high frequency wave was separated by enlarging T. This is the same also in /a/, /o/, and /e/. In /a/, high frequency wave exists in five persons among seven persons, and in /o/, high frequency wave exists in three persons among seven persons. In /u/, there are fundamental, harmonics and high frequency wave, but it is not always true that the high frequency waves exist. High frequency wave exists in four persons among seven persons. When high frequency wave is played pack, we do not hear it with /u/. It seems not to be decided how you hear it. Here we show the examples of high frequency waves in Japanese vowel /a/,/i/,/e/ and /o/ in Fig.9. Next, number of periods is 10, and the fluctuation of the spectrum of consonant /s/ in /sa/ with time is shown in Fig.10. In Fig.10, irregular concavo-convex shape appears around 10kHz. This is consonant. At 10kHz, the length of one period is 0.1ms. Since number of periods T is 10, the length of the cutting out wave (equivalent to window's width) is 1ms $(= 0.1ms \times 10)$. The length of the cutting out wave changes depending on the frequency. As a result, the spectrum which fluctuates with time can be expressed.

4. Conclusion

The vowel generally consists of fundamental, harmonics and high frequency wave. High frequency waves exist in /i/ and /e/ by all means, and the existence of this wave determines /i/, and /e/, but it is always true that the high frequency waves exist in /a/ and /o/. We hear the high frequency wave with each vowel. In /i/./e/,/a/ and /o/, since the spectrum of high frequency wave repeats itself, The spectrum is able to separate to some spectral components by enlarging T. Although the appearance is different in spectrum in case of small T and spectrum in case of large T, both of them are essentially same. Furthermore, the decomposition waves according to these spectral components are obtained, and the frequency interval of the decomposition waves is fundamental frequency. When these waves are added, complicated large beat phenomenon occur. In this way, the high frequency wave becomes the wave which fluctuates largely. In /u/, although the high frequency wave may exist also, it does not decide how you hear it. Since there is no repetition at a consonant, separation of a spectrum which was performed with the vowel cannot be performed. But the fluctuation of the spectrum against the passage of time can be shown. Here, we show the Japanese voice sound, but in other languages, it is expected that a different result will be obtained. For example, there are 5 vowel in Japanese, but in Korean, there are 10 vowell, and in addition, how about the consonant. I am very interested in these analysis and comparison

References

[1] O. Rioul and M. Vetterli, "Wavelet and Signal Processing," IEEE SP Magazine Vol.8, No4, pp.14-39 (1991).

[2] Nakatsuji, and S. Omatu, " Real-Time Spectrl Analysis," Electrical Engineering in Japan, Wiley InterScience , Vol. 161, No. 1, pp. 43-50, 2007

[3] H. Nakatsuji and S. Omatu, "Decomposition and reconsrtruction of signal in Real-time spectral analysis," Electrical Engineering in Japan, Wiley InterScience , Vol. 91, No.11, pp. 1123-1130, 2008

[4] H. Nakatsuji and S. Omatu, "Decomposition and reconsrtruction of signal in High-Speed Processing Method of Real-time spectral analysis," IEEJ Trans.EIS, Vol.128, No. 7, pp. 1168-1175, 2008 (in Japanese).

The Fifteenth International Symposium on Artificial Life and Robotics 2010 (AROB 15th '10),
B-Con Plaza, Beppu,Oita, Japan, February 4-6, 2010

Selection of parameters in design of Real-Time Spectral Analysis

Hideto Nakatsuji*, Sigeru Omatu**
*Computer and Systems Sciences, Department of Engineering, Osaka Prefecture University, 1-1 Gakuen-cho, Nakaku, Sakai City, 599-8531
**Computer and Systems Sciences, Graduate School of Engineering, Osaka Prefecture University, 1-1 Gakuen-cho, Nakaku Sakai City, 599-8531
nakatuji@sig.cs.osakafu-u.ac.jp, omatu@cs.osakafu-u.ac.jp

Abstract

A new analytical method with high speed processing in time-frequency domain was presented. In this method, sine and cosine wave with an established frequency, and with multiple periods are used, and we call these waves "cutting out wave". We call the frequency "established frequency", and call the number of periods of the cutting out wave "number of periods". The inner product of the cutting out wave and signal are calculated, and signal element with a frequency near the established frequency is detected. We call the unit that detects the signal element "auditory cell". There are many auditory cells, and those auditory cells have the established frequency which differs little by little. The design of this method is the arrangement of auditory cells. There are three parameters in the design, and these parameters are sampling frequency, number of periods and increasing rate of the established frequencies. In this paper, we show that selection of these parameters.

Keywords: Magnitude and phase characteristic, Time-frequency domain

1 Introduction

A new analytical method in time-frequency domain was presented by the authors [2]-[4]. In this method, processing in search of spectrum is performed by using one input data. Since all processing are perfectly independent, complete parallel processing is possible, and so if parallel processing computer will be brought to realization, real-time processing is realized. We call this analytical method Real-Time Spectral Analysis Method. In this method, sine and cosine waves for multiple periods with a certain frequency are used. We call these waves "cutting out wave" and call this frequency "established frequency", and call number of periods of the cutting out waves "number of periods". The inner product of the cutting out wave and signal are calculated, and a signal element with a frequency near the established frequency is detected. We call the unit that detects the signal element "auditory cell". There are many auditory cells, and those auditory cells have the established frequency which differs little by little. The design of this method is the arrangement of auditory cells. There are three parameters in the design, and these parameters are sampling frequency, number of periods and increasing rate of the established frequencies. In this paper, we show that selection of these parameters.

2 Analysis theory

2.1 Calculation of the decomposition wave in discrete system

The algorithm uses the inner products of the cutting out waves and signal. F_s is a sampling frequency and T_s is the sampling interval. f_j is the established frequency of the cutting out wave (angular frequency $\lambda_j = 2\pi f_j$). Here $j(=1,\cdots,n)$ is the cutting out wave number and n is the number of the cutting out waves. There are T periods (T is natural number) in the cutting out wave, here T is the number of periods. The length of the cutting out wave is $q_j(=T/f_j)$ and N_j denote the number of data included in the cutting out wave. Then the cutting out wave can be expressed as follows:

$$\begin{aligned} &s_j(l) = \sin(\lambda_j l T_s) \quad && c_j(l) = \cos(\lambda_j l T_s) \\ &s_j(-l) = -s_j(l) && c_j(-l) = c_j(l) \\ &s_j(k+N_j) = s_j(k) && c_j(k+N_j) = c_j(k) \\ &k\text{; natural number} && l = 1,\cdots,N_j \end{aligned} \tag{1}$$

Here we consider only sine waves as cutting out wave because the expansion for cosine waves is similar to the case of sine waves. A signal at time kT_s is $x(k)$. By using the signal which dated back to the past, the inner product of the cutting out wave and the signal at time kT_s can be written as follows:

$$Y_s^k(j) = \frac{2}{N_j}\sum_{l=1}^{N_j} x(k-l)s_j(l-k) \tag{2}$$

The inner product at time $(k+1)T_s$ is

$$\begin{aligned} Y_s^{k+1}(j) &= \frac{2}{N_j}\sum_{l=1}^{N_j} x(k+1-l)s_j(l-k-1) \\ &= \frac{2}{N_j}x(k)s_j(-k) + Y_s^k(j) - \frac{2}{N_j}x(k-N_j)s_j(N_j-k) \end{aligned} \tag{3}$$

From Eq.(3), the inner product at time $(k+1)T_s$ can be obtained by adding the product of the input data at time

kT_s and the cutting out wave to the inner product at time kT_s, and subtracting the third term. Since the second and third term have already been calculated, the necessary calculation in Eq.(3) is a multiplication in the first term. When it is $k = N_j$, third term on the right side of Eq.(3) is $s_j(0)$, but this can be found $s_j(N_j)$ by using Eq.(1). In the case of a cosine cutting out wave, the inner product $Y_c^k(j)$ is found using a similar way. By using these inner products, the following is calculated:

$$Y_{out}^k(j) = \sqrt{Y_s^k(j)^2 + Y_c^k(j)^2} \tag{4}$$

The unit that outputs $Y_{out}^k(j)$ detects a signal component of certain frequency (close to the established frequency f_j); below, this unit is called an auditory cell, and $Y_{out}^k(j)$ is spectrum. Since there are two equations of inner product in the auditory cell, the multiplication number of times that is necessary to update of an inner product is twice. Since number of auditory cells is n, total multiplication number is $2n$. Auditory cells are independent each other, and two equations are also independent. If parallel processing computer will be brought to realization, calculation number of times that need to calculates spectrums by Eq.(4) is 2 multiplications and one square root calculation. Even if number of auditory cells becomes large, the calculation number of times does not change. By using the inner products expressed by discrete system, we show below a procedure to get decomposition waves.

Step1 Calculate the inner products $Y_s^k(j)$ and $Y_c^k(j)$ at time kT_s

Step2 multiply $Y_s^k(j), Y_c^k(j)$ by $-s_j(k), c_j$ and the following is calculated:

$$Y_{ss}^k(j) = -Y_s^k(j)s_j(k), \quad Y_{cc}^k(j) = Y_c^k(j)c_j(k)$$

Step3 By using $Y_{ss}^k(j)$ and $Y_{cc}^k(j)$, the following is calculated:

$$Y_{cout}^k(j) = Y_{ss}^k(j) + Y_{cc}^k(j) \tag{5}$$

Step4 k is set to $k+1$, it returns to Step 1, and repeats below. $Y_{cout}^k(j)$ is the decomposition wave, and we call it "actual decomposition wave". The reconstruction wave is made by adding those decomposition waves, and we call this wave "actual reconstruction wave".

2.2 The signal detection range of the hearing cell

The established frequency is f and the length of the cutting out wave is q $(=T/f)$. The wave that length for $T+1$ and $T-1$ periods becomes q can not be detected by this auditory cell. The detection width of the auditory cell is designated as B. The following relationship $B = 2f/T$ or $Bf/T = 2$ is formed. That is, the area made from spectrum width B and time length T/f becomes two and constant.

2.3 Calculation of the decomposition wave in continuous system

Consider a signal that is a wave with angular frequency ω, magnitude A, and phase ϕ. The signal at time kT_s is shown as follows:

$$x(k-l) = A\sin(\omega(k-l)T_s) \tag{6}$$

Eq.(6) is substituted for Eq.(2), and by using $s_j(k)$ in Eq.(1), the inner product is expressed as follow:

$$\begin{aligned}\hat{Y}_s^k(j) &= -\frac{2}{N_j}\sum_{l=1}^{N_j}\sin(\omega(k-l)T_s+\phi)\sin(\lambda_j(k-l)T_s) \\ &= -\frac{2}{N_j}A\Bigg\{\cos(\phi)\sum_{l=1}^{N_j}\sin(\omega(k-l)T_s\sin(\lambda_j(k-l)T_s) \\ &\quad +\sin(\phi)\sum_{l=1}^{N_j}\cos(\omega(k-l)T_s)\sin(\lambda_j(k-l)T_s)\Bigg\}\end{aligned} \tag{7}$$

Writing $t = kT_s, \tau = lT_s, q_j = T/f_j$, the following is obtained by minimization of T_s:

$$\begin{aligned}\tilde{Y}_s(j,t) &= -\frac{2f_j}{T}A\cos(\phi)\int_0^{q_j}\sin(\omega(t-\tau))\sin(\lambda_j(t-\tau)) \\ &\quad -\frac{2f_j}{T}A\sin(\phi)\int_0^{q_j}\cos(\omega(t-\tau))\sin(\lambda_j(t-\tau))\end{aligned} \tag{8}$$

In the case of a cosine cutting out wave, the inner product $\tilde{Y}_c(j,t)$ is obtained by using similar way. The following is obtained by multiplying $\tilde{Y}_s(j,t)$ and $\tilde{Y}_c(j,t)$ by $-s_j(t)$ and $c_j(t)$.

$$\bar{Y}_{ss}(j,t) = -\tilde{Y}_s(j,t)s_j(t), \quad \bar{Y}_{cc}(j,t) = \tilde{Y}_c(j,t)c_j(t)$$

Here, $s_j(t) = \sin(\lambda_j t)$, $c_j(t) = \cos(\lambda_j t)$. Writing $\omega_j^+ = \omega - \lambda_j$, $\omega_j^- = \omega + \lambda_j$, and if we write

$$G_+(j) = \frac{2f_j}{T}\left\{\frac{1}{\omega_j^-}\sin(\frac{\omega_j^-}{2}q_j)\cos(\frac{\omega_j^-}{2}) + \frac{1}{\omega_j^+}\sin(\frac{\omega_j^+}{2}q_j)\cos(\frac{\omega_j^+}{2}q_j)\right\}$$

$$H_+(j) = \frac{2f_j}{T}\left\{\frac{1}{\omega_j^+}\sin^2(\frac{\omega_j^+}{2}q_j) + \frac{1}{\omega_j^-}\sin^2(\frac{\omega_j^-}{2}q_j)\right\}$$

Sum of two inner products is following:

$$\begin{aligned}Y_{out}^+(j,t) &= \bar{Y}_{ss}(j,t) + \bar{Y}_{cc}(j,t) \\ &= A\{G_+(j)\sin(\omega t+\phi) - H_+(j)\cos(\omega t+\phi)\}\end{aligned} \tag{9}$$

Furthermore, if we write

$$\Gamma_+(j) = \sqrt{G_+^2(j) + H_+^2(j)}, \quad \Psi_+(j) = \tan^{-1}(-H_+(j)/G_+(j))$$

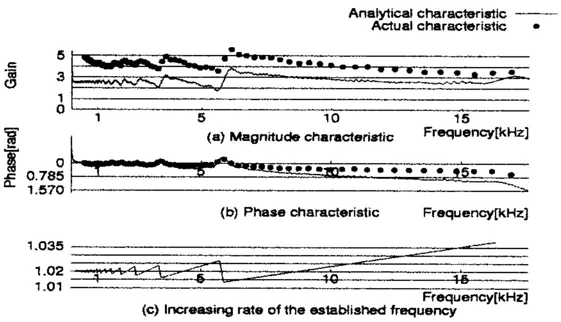

Fig. 1. Characteristic and increasing rate of the established frequency

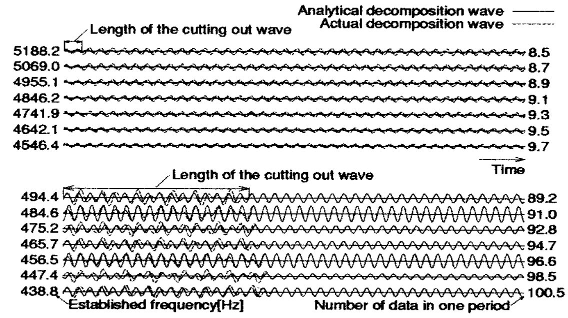

Fig. 2. Analytical decomposition waves and actual decomposition waves

Eq.(9) can be written as

$$Y_{out}^{+}(j,t) = A\Gamma_{+}(j)\sin(\omega t + \phi + \Psi_{+}(j)) \qquad (10)$$

Eq.(10) is the decomposition wave, and essentially equal to Eq.(5). We call $Y_{out}^{+}(j,t)$ "analytical decomposition wave".

3 Reconstruction of the signal

We call the wave made by adding decomposition waves in Eq.(10) "analytic reconstruction wave". It is written as

$$\hat{Y}_{out}(t) = A\left\{\sum_{j=1}^{n}(G_{+}(j))\sin(\omega t+\phi) - \sum_{j=1}^{n}(H_{+}(j)\cos(\omega t+\phi)\right\} \qquad (11)$$

Here, if we write

$$Z_G = \sum_{j=1}^{n} G_{+}(j), \qquad Z_H = \sum_{j=1}^{n} H_{+}(j)$$

$$\hat{r} = \sqrt{Z_G^2 + Z_H^2}, \qquad \hat{q} = \tan^{-1}(Z_H / Z_G)$$

Eq.(11) can be represented as

$$\hat{Y}_{out}(t) = A\hat{r}\sin(\omega t + \phi + \hat{q}) \qquad (12)$$

It should be noted that the frequency is not the established frequency but the signal frequency ω. Amplitude has changed by $\hat{r}$ times for amplitude of the signal, and Phase $\hat{q}$ has newly generated. We call $\hat{r}$ "analytical magnitude characteristic", and call $\hat{q}$ "analytical phase

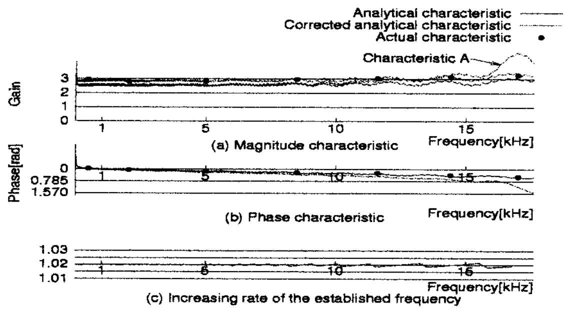

Fig. 3. Corrected actual characteristic and increasing rate of the established frequency

characteristic". Each characteristics based on the actual reconstruction wave are called "actual magnitude characteristic" and "actual phase characteristic". The conditions of reconstruction is as follow:

Magnitude characteristic; The magnitude ratio $\hat{r}$ is constant regardless of frequency.

Phase characteristic; The newly generated phases $\hat{q}$ are proportional to the frequency. This is linear-phase characteristic.

4 Selection of parameters in design

The characteristic to decide the precision of the reconstruction wave depends on three parameters, and those parameters are sampling frequency, the increasing rate of the established frequency and number of periods T. Below, selection of these parameters is shown.

4.1 Sampling frequency

When sampling frequency is 44.1kHz and number of periods T is 10, and the increasing rate μ of the established frequency is 1.02 (2%), the characteristic is shown in Fig.1. A solid line is the analytical characteristic and a mark ● is the actual characteristic. In Fig.1, there are two problems. First, actual reconstruction wave is essentially equal to analytic reconstruction wave, but both of them are different. Second, in Fig.1(c), the increasing rate μ changes like the saw, and according to it, the characteristics are also changing like a saw. At the beginning, we consider about the first problem. In the established frequency 5069Hz, number of data in one period of the cutting out wave becomes 8.7, and because the number of data is too small, the actual decomposition waves do not become approximation of the analytical decomposition waves. Because the both decomposition waves are different, the both reconstruction waves do not become the same. Both of the decomposition waves are shown in Fig.2. The number of the right side in Fig.2 is the number of data in one period of the cutting out wave, and at small number, both of the decomposition waves is different. When the number of data in one period of the cutting out wave is approaching 100, in order to increase the number of data in it, we make the sampli-

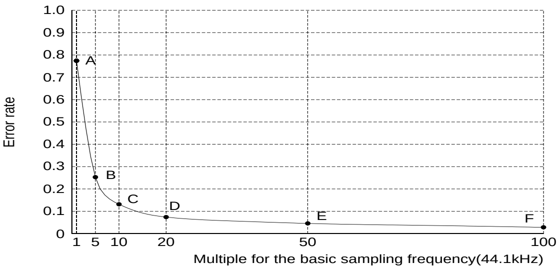

Fig. 4. Error rate between actual magnitude and analytical magnitude characteristic

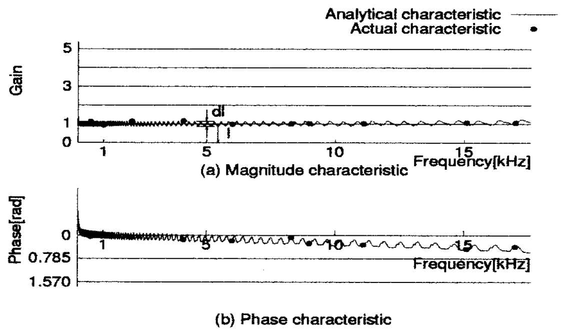

Fig. 5. Fluctuation of gain and phase in case that μ is 1.0527

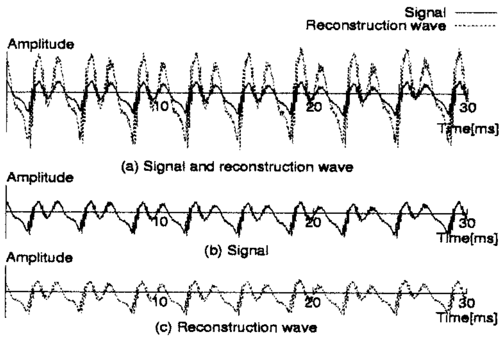

Fig. 6. The waveform of Japanese voices sound /i/ and reconstruction wave

ing frequency big. Here, at the established frequency of 333Hz, we make the sampling frequency 441kHz (10times), and the characteristic in that case is shown in Fig.3. Because the analytical range is designated until 17kHz, If auditory cells are set up by 17Hz, as A in Fig.3(a) shown, a big distortion will occurs. In order to ease this, auditory cells are set up to 25kHz. The actual characteristic is in good agreement with the analytical characteristic. The second problem is caused by the reason that it becomes impossible to maintain μ because the number of data in the cutting out wave decreases. However, because the number of data increases, this problem is improved, too. The error rate between actual and analytic magnitude characteristic for the increase of sampling frequency is shown in Fig.4. It is shown that the error rate decreases as the sampling frequency increases.

4.2 Increasing rate of the established frequency

Characteristic in case that μ is 1.0527 is shown in Fig.5. In the case, there are three auditory cells in B. Since number of auditory cell in B is small, each characteristic changes greatly like the wave. It is better for about ten auditory cells to exist in B. The number of data in B is designated as ν. T and μ are not determined independently but are decided by relationship of $2/T \quad \mu^{\nu}$.

4.2 Number of periods

It is impossible to make B which displays the spread of the spectrum and T which displays following characteristic small simultaneously. Although T should be decided by the situation of signal fluctuation, Usually it is good to make between 10 and 20.

5 The example of analysis using an voice signal

By using the auditory cells which become characteristic of Fig.3, the reconstruction wave of Japanese voice sound /i/ is shown in Fig.6. In Fig.6, the reconstruction wave with high approximation accuracy is obtained.

4. Conclusion

Approximation accuracy of the reconstruction wave when this analytical method is used is largely influenced by setting of the auditory cell. In the setting of the auditory cells, there are three parameters, a sampling frequency F_s and an increasing rate μ of the established frequency and the number of periods T. First, we decide T that decides follow efficiency. Next, we decide the sampling frequency F_s in consideration of the frequency range of the signal processing. Third, we decide increasing rate μ by using the relation of $2/T \quad \mu^{\nu}$. Here, it is better to decide that ν is about 10.

References

[1] C. K. Chui, Multivariate Splines, CBNS-NSF Series in Applied Math. #54, SIAM Publ, Philadelphia, 1988

[2] H. Nakatsuji, and S. Omatu, " Real-Time Spectrl Analysis," Electrical Engineering in Japan, Wiley InterScience , Vol. 161, No. 1, pp. 43-50, 2007

[3] H. Nakatsuji and S. Omatu, "Decomposition and reconsrtruction of signal in Real-time spectral analysis," Electrical Engineering in Japan, Wiley InterScience , Vol. 91, No.11, pp. 1123-1130, 2008

[4] H. Nakatsuji and S. Omatu, "Decomposition and reconsrtruction of signal in High-Speed Processing Method of Real-time spectral analysis," IEEJ Trans.EIS, Vol.128, No. 7, pp. 1168-1175, 2008 (in Japanese).

GA Simulation of Evolution of the Hierarchical Module Structure on Gene Networks

Shinji Nakashima* and Koji Kurata**

*Graduate School of Engineering and Science, University of the Ryukyus
**Faculty of Engineering, University of the Ryukyus
1 Senbaru, Nishihara, Okinawa. 903-0213
(Tel:098-895-8638 ; Fax:098-895-3636)
(shinji@mibai.tec.u-ryukyu.ac.jp)

Abstract: The animal body plan is controlled by the genetic networks of the hierarchical modular structure. For example, homeotic selector genes function at many levels in the regulatory hierarchy, so that homeotic mutations result in the transformation of one body segment into another, which is recognized by the misplaced development of structures that are normally present elsewhere in the embryo. The purpose of this research is to search for the mechanism of the evolution of such genetic networks. We modeled simplified genetic networks, and simulated the evolution of the genetic networks by GA. The simulation results show that the environmental perturbation possibly gave rise to the evolution of the hierarchical modular structure.

Keyword: Hierarchical Modular Structure, Genetic Networks, Genetic Algorithm, Evolution, Environmental perturbation

1 Introduction

The animal body plan is controlled by the genetic networks of the hierarchical modular structure. The homeotic selector genes function at multi levels in the regulatory hierarchy of the developmental genetic networks. Therefore, homeotic mutations result in the transformation of one body segment into another. For example, an *antennapedia* mutant, whose antennae are converted into leg structures caused by mutation in the *Antennapedia* gene [1–3]. Davidson and Erwin (2006, 2009) [4, 5] assumed the genetic networks that control the early development of animal embryos and proposed a hierarchical modular structure on genetic networks, which can be described by a hierarchy with four types of modules, *kernel, plug-ins, I/O switches* and *batteries*. The kernels are top components and the batteries are bottom components of hierarchy [5, 6]. If the genetic network were a nearly random network, any change to the network would result in drastic difference in the body plan because each gene may regulate or be regulated by several other genes, and the effects will spread out to the whole network [7].

The purpose of our research is to search for the mechanism of the evolution of such genetic networks of hierarchical modular structure. Why do genetic networks have hierarchical modular structure? We assumed one of the causes is the *environmental perturbation*, namely, the environmental perturbation is advantageous for hierarchical modular structure.

We modeled simplified genetic networks, and simulated the evolution of the genetic networks by GA. The simulation results show that the environmental perturbation possibly gave rise to the evolution of the hierarchical modular structure.

2 The model of genetic networks and phenotype

The various model of genetic networks [8–11] has been proposed, but these models are too complex for our simulation. Thus, we propose a simplified model of genetic networks. The model of a genetic network and phenotypic expression used for our simulation is similar to feedforward neural network with liner units, which is given as follows. A gene in our model can make other genes expressed. Then, those genes can also make other genes expressed. Fig.1 is a conceptual diagram of the model of genetic networks and phenotype. The genes are linearly-ordered and numbered. Let us call genes of larger (smaller) number as *lower* (*higher*) genes. We assume, for simplicity, a lower gene doesn't regulate a higher gene. Thus, the feedback is not considered in this model, and the generality of this model is restricted. But emergence of the hierarchical modular structure are expressible on this model. Therefore, the model is sufficient for the purpose or observation of evolution of the hierarchical modular structure. Each individual consists of genotype G and phenotype vector $\boldsymbol{p}$. The dimension of $\boldsymbol{p}$ is n_{p}, and G consists of n_{g} components. Gene g_i, the i-th component of G, is given by the following definition for

$i = 1\ 2 \quad n_{\mathrm{g}}$:

$$g_i = (x_i;\ \boldsymbol{\rho}_i\ \ \boldsymbol{\sigma}_i\ \ \boldsymbol{\gamma}_i) \tag{1}$$

$$\boldsymbol{\rho}_i = (\ \ _{1i}\ \ \ _{2i}\ \ \ \ \ _{i\ \ 1\ i}) \tag{2}$$

$$\boldsymbol{\sigma}_i = (\ \ _{i+1\ i}\ \ \ _{i+2\ i}\ \ \ \ \ _{n_{\mathrm{g}} i}) \tag{3}$$

$$\boldsymbol{\gamma}_i = (\ \ _{1i}\ \ \ _{2i}\ \ \ \ \ _{n_{\mathrm{p}} i}) \tag{4}$$

where $x_i (\geq 0)$ is an fi $\ _{ji}$ is a . The ampli cation coe cient x_i is the strength of in uence for the lower gene. the $\ _{ji}$ is the Boolean representation of the causal relation from the gene g_i to the phenotype p_j. $\ _{ij}$ and $\ _{ji}$ are Boolean to determine the in uence of gene g_j to gene g_i. For two genes g_i and g_j $(j < i)$, we suppose gene g_j makes gene g_i expressed only when $\ _{ij}\ \ _{ji} = 1$, so that the causal relation between g_i and g_j can change depending on the mutation in either of the two genes. And the expression level y_i of gene g_i is de ned as follows for $i = 1\ 2 \quad n_{\mathrm{g}}$:

$$y_i = x_i \sum_{j=1}^{i\ \ 1}\ \ _{ij}\ \ _{ji} y_j \quad y_1 = 1 \tag{5}$$

Note that $\ _{ij}$ belongs to g_j and $\ _{ji}$ belongs to g_i. g_1, which is the highest gene, is de ned as the trigger for the whole network, which exists only to make some other genes expressed, and so $y_1 = 1$, $\ _{i1} = 0 (i = 1\ 2 \quad n_{\mathrm{p}})$.

p_k is the component of phenotype vector $\boldsymbol{p}$, which is calculated shown as follows for $k = 1\ 2 \quad n_{\mathrm{p}}$:

$$p_k = \sum_{j=2}^{n_{\mathrm{g}}}\ \ _{kj} y_j \tag{6}$$

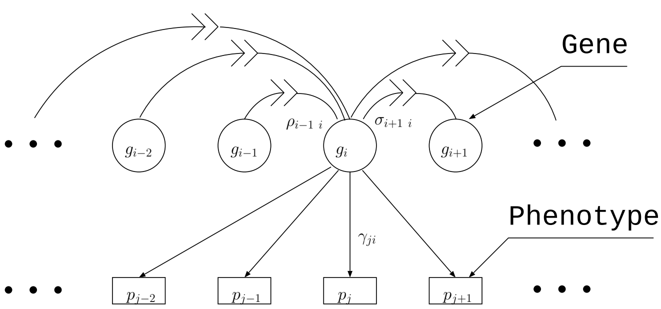

Fig. 1: Conceptual diagram of the model of genetic networks and phenotype

3 Method of individual's evolving

We applied genetic algorithm [12] (GA) to simulate the evolution of the genetic networks. Each genetic operations is given as follows.

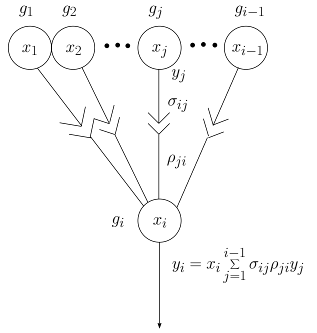

Fig. 2: Conceptual diagram of model of genetic networks

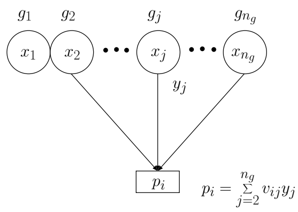

Fig. 3: Phenotype vector

Method of crossover
We apply the uniform crossover. Individual genes in the genotype are compared between two parents. The genes are swapped with a xed probability of 0.5.

Method of mutation
When the mutation of gene g_i occurs with a certain probability, Gaussian mutation occurs in ampli cation coe cient x_i, and then, the mutation in causal factors and coe cient $\ _{ji}$, $\ _{ji}$ and $\ _{ji}$ occurs in a certain probability.

Method of selection
We apply the elite preservation strategy.

The tness function f of an individual is de ned as follows:

$$f(\boldsymbol{t}; \boldsymbol{p}) = \quad ||\boldsymbol{t} \quad \boldsymbol{p}||^2 \tag{7}$$

where $\boldsymbol{p}$ is the phenotype vector of the individual and $\boldsymbol{t} = (t_1\ t_2 \quad t_{n_{\mathrm{p}}})$ is the best phenotype vector for a given environment, and we call $\boldsymbol{t}$.

4 Environmental perturbation and hierarchical modular structure

4.1 Environmental perturbation

The environmental perturbation is expressed by changing the target phenotype vector. For generation s, i-th component of the target phenotype vector is given as follows for $i = 1\ 2\quad n_{\mathrm{p}}$:

$$t_i(s) = \prod_{j=1}^{m} a_j(s)^{\ \ i}_{\ \ j} \quad (j = 1 \qquad m) \tag{8}$$

where $a_j(s)$ is an , which varies depending on generation s. Parameter $^{i}_{j}$ is the Boolean representation of the in uence of a_j to t_i. Let T_j be the set of components in uenced by environmental factor a_j. We call T_j a . For instance, a hand is useful only when the ngers are in good proportion. The environmental perturbation may require larger or smaller hands but the proportion of the ngers will remain the same. In this example, the sizes of the ngers are considered to form a functional module. Parameters $^{i}_{j}$ is set, so that the following relations hold: $T_j \subseteq T_k$ or $T_j \supseteq T_k$ or $T_j \cap T_k =$.

4.2 Hierarchical modular structure

The functional module in the components of phenotype vector $\boldsymbol{p}$ is the set P_j of components corresponding set T_j of target phenotype vector components. We say that gene g_i functional module P_j, when all the components in functional module P_j are changed at the same rate and all the other components stay unchanged by the mutation in ampli cation coe cient x_i of gene g_i. We say a genetic networks has when for any functional module there is one or more genes which regulate it.

5 Method of simulation

Each parameter was set as follows.

Table 1: The value of each parameter

Number of gene n_{g}	7
Dimension of phenotype vector n_{p}	5
Max generation	500000
Population size	800
O spring size	3200
Standard deviation in Gaussian mutation	0.15
Probability of mutation of each gene	0.08
Conditional probability that mutation of each causal coe cient of the gene occurs when mutation occurs in the gene	0.03

We prepared three environmental factors of $a_1(s)\ a_2(s)$, and $a_3(s)$. The environmental factors change respectively as shown in Fig.4, with the period of 306 generation.

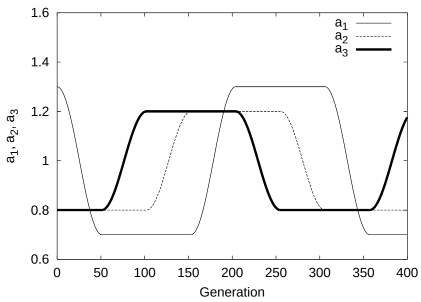

Fig. 4: Transition of the environmental factors

We put $^{1}_{1}\ ^{2}_{1},\ ^{3}_{1}\ ^{4}_{1},\ ^{5}_{1}\ ^{1}_{2},\ ^{2}_{2}\ ^{3}_{2},\ ^{4}_{3}\ ^{5}_{3}$ equal to 1 and the other equal to 0 in Eq. (8). Then Eq. (8) rewritten as:

$$t_1\ t_2\ t_3 = a_1(s)a_2(s) \tag{9}$$
$$t_4\ t_5 = a_1(s)a_3(s) \tag{10}$$

In this case, there were three function modules, $P_1 =\ p_1\ p_2\ p_3\ p_4\ p_5$, $P_2 =\ p_1\ p_2\ p_3$, and $P_3 =\ p_4\ p_5$.

6 Result of simulation

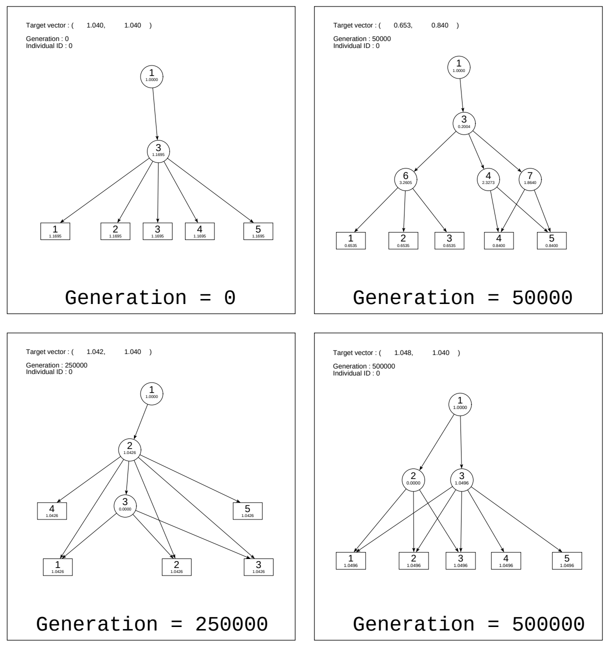

Fig. 5: Evolution of the genetic networks

Fig.5 represents the evolution of genetic networks. The circles represent genes, the rectangles phenotype components. The arrows the direction of the regulation of the gene(or phenotype). In each circle (rectangle) the gene (phenotype) number is displayed, under which the ampli cation coe cient (phenotype vector component) is. In this gure all the genes that have

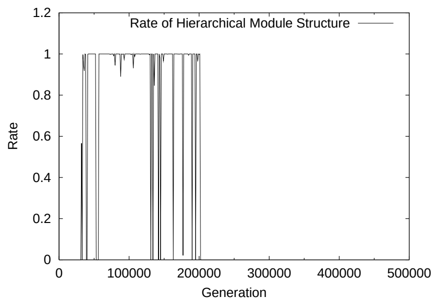

Fig. 6: The rate of the individuals which have the hierarchical modular structure

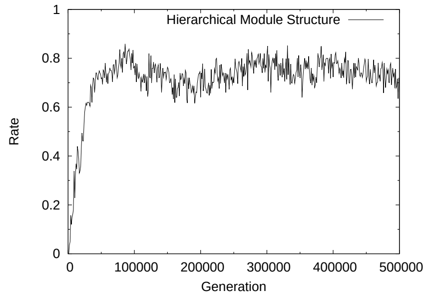

Fig. 7: The ensemble average of the rate of the individuals which have the hierarchical modular structure

no in uence on phenotype are omitted, for simplicity. The individual with the highest tness is displayed. Fig.6,7 are plots of the rate of individuals which have the hierarchical modular structure on genetic networks. Fig.6 is the result of the trial shown in Fig.5, and Fig.7 is an ensemble average of 50 trials.

7 Discussion

According to Fig.5, at generation 0 the ttest individual doesn't have hierarchical modular structure, but at generation 50,000 an individual with such structure appeared. However, the ttest in the generations 250,000 and 500,000 didn't show hierarchical modular structure. According to Fig.6, the genetic networks obtained the hierarchical modular structure at about the 40,000th generation. However, The structure collapsed after 200,000th generation.

In Fig.7, we can see that the genetic networks evolves to the hierarchical modular structure at the probability of about 70% at the 50,000th generation.

Our results indicates that the individual which have the genetic networks with the hierarchical modular structure are in an advantageous position in the environmental perturbation. If the genetic networks are without hierarchical modular structure, it needs simultaneous adaptive mutation in all genes in one functional module to follow the environmental perturbation. But such mutations are extremely rare.

8 Conclusion

We modeled the simpli ed genetic networks, de ned the hierarchical modular structure, and simulated the evolution by GA on the environmental perturbation. The simulation results show that the environmental perturbation possibly gave rise to the evolution of the hierarchical modular structure.

References

[1] Akam, M. (1987) The molecular basis for metameric pattern in the embryo. 101:1-22

[2] Ingham, P.W. (1988) The molecular genetics of embryonic pattern formation in 335:25-34

[3] Scott, M.P.; O'Farrell, P.H. (1986) Spatial programming of gene expression in early embryogenesis. 2:49-80

[4] Erwin, D.H., Davidson, E.H. (2009) The evolution of hierarchical gene regulatory networks. 10, 141-148

[5] Erwin, D.H., Davidson, E.H. (2006) Response to comment on "Gene Regulatory Networks and the Evolution of Animal Body Plans". 761c, 313

[6] He,J., Deem,M.W., Hierarchical evolution of animal body plans, (2009), doi: 10.1016/j.ydbio.2009.09.038

[7] Barabási, A.L, Zoltán, N.O. (2004) Network biology: understanding the cell's functional organization. 5,101-113

[8] Somogyi R, Sniegoski CA (1996) Modeling the complexity of genetic networks: understanding multigene and pleiotropic regulation. 1: pp45-63

[9] H. De Jong (2002) Modeling and Simulation of Genetic Regulatory Systems: A literature Review, 9, pp67-103

[10] H. De Jong, R. Lima (2005) Modeling the Dynamics of Genetic Regulatory Networks: Continuous and Discrete Approaches, 671, pp304-340

[11] Savageau, M.A. (1976) Biochemical Systems Analysis: a Study of Function and Design in Molecular Biology. Addison-Wesley, Reading, MA.

[12] Holland, J. (1975, 1992) Adaptation in Natural and Arti cial Systems, The University of Michigan, and MIT Press

Swing-up Control of the Acrobot Using Genetic Programming Considering an Actuator Dynamics

Ryo Fukushima* and Eiho Uezato**

*Graduate School of Engineering and Science, University of the Ryukyus
**Faculty of Engineering, University of the Ryukyus
1 Senbaru, Nishihara, Okinawa. 903-0213
(Tel:098-895-8638 ; Fax:098-895-3636)
(fukushima@mibai.tec.u-ryukyu.ac.jp)

Abstract: We present a control method for a three-degree-of-freedom (3-DOF) acrobot which is a model of a gymnast on a horizontal bar with three links, two active joints, and a passive joint. This robot is a non-holonomic and underactuated system, the swing-up control of the acrobot is therefore difficult. The active joints of the acrobot use the DC servomotor. We model the 3-DOF acrobot considering the dynamics of the DC servomotor. We propose a control method for the 3-DOF acrobot. First, swing-up control is performed by genetic programming (GP), and stabilizing control is handled by a linear quadratic regulator (LQR). GP can search widely for the optimum input for swing-up so that the acrobot is able to reach a near balancing point. The LQR is then switched on to stabilize the system. In the simulation results, the 3-DOF acrobot could swing-up to the desired position, and the proposed method could control the acrobot effectively.

Keyword: Underactuated robot, Nonlinear system, Genetic programming, Acrobot

1 Introduction

Underactuated robots, which have fewer number of actuators than that of degree-of-freedom, are difficult to design control laws. The development of control system design to the underactuated robots can save energy and reduce the cost and weight. Moreover, they are effective to work in space with no gravity or underwater with low gravity.

The acrobot [1] is one of underactuated robots, and has non-holonomic behavior. It is also known as the model of a gymnast on a horizontal bar. There have been many studies about 2-DOF acrobot[2][3][4]. In this paper, we discuss a control method for the 3-DOF acrobot with two active joints and a passive joint. The active joints are driven by DC servomotors. We model the 3-DOF acrobot considering the actuator dynamics in order to model a more realistic system.

We propose a control method for the 3-DOF acrobot where the swing-up stage is performed by GP and the balancing stage is handled by a linear quadratic regulator (LQR). GP is an approach which has been expanded from genetic algorithm (GA)[5], and it can search widely for the optimum input feedback function for the design of the acrobot control system, which is a difficult problem. Motion control using GP was discussed by Ogawa et al[6]. It is appropriate to use GP for such a difficult control problem as the acrobot.

2 Model of the acrobot

Figure 1 shows the model of the acrobot. m_i ($i = 1, 2, 3$) and I_i denote the mass and the moment of inertia, respectively; l_i and l_{ci} denote the length of the link and the distance to the center of mass. θ_i is the angle, and h_i is the height to the top of the link. Here, u_2 and u_3 are symbolized as input torques actuated the active joints.

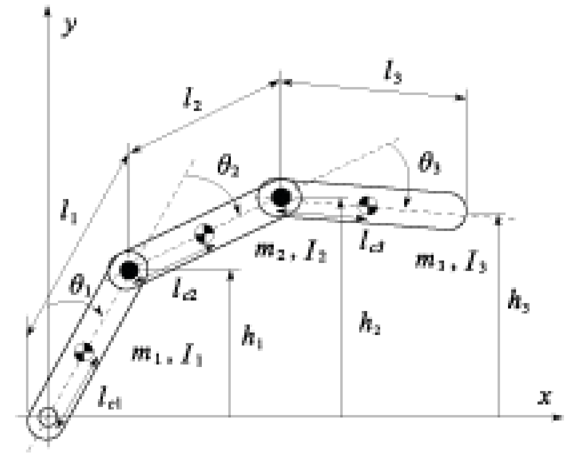

Fig. 1: Model of the acrobot

The equation of the motion of the acrobot system is

$$M(\theta)\ddot{\theta} + C(\theta\ \dot{\theta}) + G(\theta) = Hu \quad (1)$$

where

$$\theta = [\ \theta_1 \quad \theta_2 \quad \theta_3\ ]^T \qquad u = [\ u_2 \quad u_3\ ]^T$$

M is an inertial matrix, C is a coriolis term, G is a gravity term and H is constant matrix.

In this study, DC servomotors are applied as the actuators to drive the second and the third joints. We assume that the servomotors are provided with inner feedback loops to control the position angle, therefor, the actuator can be operated by giving a reference position angle. We model the actuator dynamics as

$$u = \begin{bmatrix} a_2\ddot{\theta}_2 \quad b_2\dot{\theta}_2 \quad c_2(\theta_2 \quad \theta_{a2}) \\ a_3\ddot{\theta}_3 \quad b_3\dot{\theta}_3 \quad c_3(\theta_3 \quad \theta_{a3}) \end{bmatrix} \quad (2)$$

where $\theta_a = [\ \theta_{a2} \quad \theta_{a3}\ ]^T$ represents reference of the position angle of the acrobot system, and a_i, b_i, c_i are constants including a parameters of the servomotor, for example a torque constant, a reduction ratio. From Eqs. 1 and 2, the equation of the motion of this system is

$$\{M(\theta) + \hat{A}\}\ddot{\theta} + C(\theta\ \dot{\theta}) + \hat{B}\dot{\theta} + G(\theta) + \hat{C}\theta = \hat{C}H\theta_a \quad (3)$$

where

$$\hat{A} = \mathrm{diag}(0 \quad {}_2 \quad {}_3) \qquad \hat{B} = \mathrm{diag}(0 \quad {}_2 \quad {}_3)$$
$$\hat{C} = \mathrm{diag}(0 \quad {}_2 \quad {}_3)$$

We regard the reference angle θ_a as new control input.

3 Control System

Figure 2 shows the block diagram for a closed-loop system. Suffix r represents the desired values. We define deviations as $e = \theta_r \quad \theta$, $\dot{e} = \dot{\theta}_r \quad \dot{\theta}$. The control goal is to swing the acrobot up to balancing point ($\theta_r = 0$, $\dot{\theta}_r = 0$). We propose a control method for the acrobot where swing-up stage is performed by GP and balancing stage is controlled by LQR.

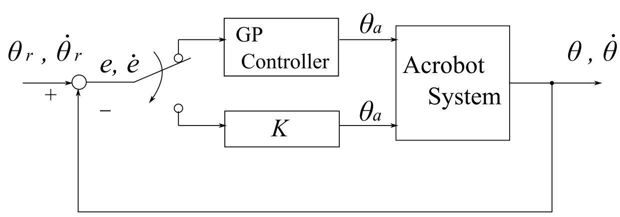

Fig. 2: Block diagram for the closed-loop system

3.1 Swing-up control using GP

GP is one of evolutionary approaches, which is the model of natural selection of genes. As evolution progresses, the individuals adapt to their given environment. In this study, GP searches for the optimum control input (feedback input function θ_a (e $\dot{e}$)) for swing-up. Each individual in GP represents tree structure which stands for a function. We operate the tree structure with genetic crossover and mutation so that the tree structure adapts to the given environment. The elements for the design of GP include the function nodes, the terminal nodes, fitness, parameters (crossover rate, mutation rate, population size), and a termination condition. We will get the desired feedback input function when the five elements are set effectively.

The calculation procedure is described below. First, set the number of generation G and the population size N. Generate an initial population, and evaluate the fitness of the population as shown below. Next, performs the crossover and mutation operations to the population with mutation rate , and generate a new population up to N , where is the crossover rate. Evaluate the population generated, and the individual with the highest fitness value is taken into the next generation. Repeat until generation reaches G. We adopt the most excellent individual as the input function of the control system.

The fitness function for evaluating the individuals is

$$E = \min_t \Big[w_1(l_1 \quad h_1)^2 + w_2(l_1 + l_2 \quad h_2)^2 + w_3(l_1 + l_2 + l_3 \quad h_3)^2 + w_4(\dot{\theta}_{r1} \quad \dot{\theta}_1)^2 + w_5(\dot{\theta}_{r2} \quad \dot{\theta}_2)^2 + w_6(\dot{\theta}_{r3} \quad \dot{\theta}_3)^2 \Big] \quad (4)$$

where t represents the time of the swing-up motion, t_f represents the finish time of the swing-up motion, and w_i represent the weight coefficients. The lower the fitness value, the closer the acrobot reaches to the desired position. The "min" in Eq. 4 is the minimum fitness value of each step from the range $0 < t \leq t_f$. Finally, this minimum fitness value is used for one individual only. Here, the first three terms in Eq. 4 are functions relating to the highest marks of each link. To consider the height of each link, the farthest distance from the balancing point causes the high fitness value. θ_2 and θ_3 are restricted to the range $3 \quad 4 < \theta_{2\ 3} < 3 \quad 4$ to limit the rotation of links 2 and 3. If θ_2 and θ_3 exceed the limited range while searching for the desired input function using GP, we add 10^6 to the fitness value of the individual as a penalty.

3.2 Stabilize control at balancing point

The stabilizing control uses a LQR at the near balancing point. If θ_i is sufficiently small ($\theta_i \approx 0$), we can use the approximations $\sin \theta_i \approx \theta_i$, $\cos \theta_i \approx 1$, and neglect $\dot{\theta}_i^{\,2}$. Thus, Eq. 3 is simplified to

$$\{\tilde{M} + \hat{A}\}\ddot{\theta} + \hat{B}\dot{\theta} + \tilde{G}\theta = \hat{C}H\theta_a \tag{5}$$

and we have eliminated C, which is the coriolis term, from Eq. 3. Here, the state variable defines $x = [\ \theta_1\ \theta_2\ \theta_3\ \dot{\theta}_1\ \dot{\theta}_2\ \dot{\theta}_3\ ]^T$, and Eq. 5 is

$$\dot{x} = Ax + B\theta_a \tag{6}$$

$$A = \begin{bmatrix} 0_{3\times3} & I_{3\times3} \\ \{\tilde{M} + \hat{A}\}^{\ 1}\tilde{G} & \{\tilde{M} + \hat{A}\}^{\ 1}\hat{B} \end{bmatrix}$$

$$B = \begin{bmatrix} 0_{3\times2} \\ \{\tilde{M} + \hat{A}\}^{\ 1}\hat{C}H \end{bmatrix}$$

4 Simulation

We carried out a simulation with a sampling time of 20[ms] and $t_f = 3\ 0$[s]. The initial values for the state variables were $[\ \theta_1\ \theta_2\ \theta_3\ \dot{\theta}_1\ \dot{\theta}_2\ \dot{\theta}_3\ ] = [\quad 0\ 0\ 0\ 0\ 0\ ]$, which is the hanging position of the acrobot on the bar. We set the terminal nodes as e, $\dot{e}$ and random real numbers from the range $[\ \ 10, 10]$. The function nodes are shown in Table 1. It is expected that the term tanh in the function node would get a better result by inhibiting the input angle. We searched for the individual (input function) which minimized E by a combination of the terminal nodes and the function nodes. Table 2 shows the parameters of GP, and Table 3 shows the parameters of the acrobot system.

The fitness function is very important for getting the optimum input angle. In particular, the setting of the weight coefficients of the fitness function strongly affects the results, but there is no effective way to determine the weight coefficients; those have to be decided by trial and error. First, we evaluate the position of the acrobot by considering the highest marks of each link. That is, the fitness value becomes lower near the balancing point and higher far away from the balancing point. In Eq. 4, the first three terms are the fitness value with the position of each link. It depends on the length of each link. We set the weight coefficients of the first three terms so that the fitness value of the position of each link becomes the value of the same scale. For this reason, the weight coefficients of the first three terms are $w_1 = 40$, $w_2 = 20$, $w_3 = 10$. Next, we evaluate the angular velocity of the acrobot by considering the reaction forces. Each link of the acrobot receives reaction forces from the next link. Thus, if we restrain the angular velocity of link 2, the angular velocities of links 1 and 3 will decrease with the decline of the angular velocity of link 2. As a result, the weight coefficients of the fitness function will be $w_1 = 40$, $w_2 = 20$, $w_3 = 10$, $w_4 = 1$, $w_5 = 10$, $w_6 = 1$.

We determine a switching time from swing-up control to stabilizing control as the time with the lowest fitness value in the simulation.

A criterion function of the LQR in shown as below. Using GNU Octave, the LQR controller was designed with weighting matrices

$$J = \int_0^{\infty} \left(x^T Q\ x + {\theta_a}^T R\ \theta_a \right) dt \tag{7}$$

$$Q = \mathrm{diag}(1\ 1\ 1\ 1\ 1\ 1)$$

$$R = \mathrm{diag}(10\ 10)$$

The state feedback controller is $\theta_a = \quad Kx$, where

$$K = \begin{bmatrix} 51\ 99 & 30\ 38 & 13\ 86 & 18\ 90 & 11\ 50 & 5\ 458 \\ 38\ 10 & 22\ 30 & 10\ 11 & 13\ 84 & 8\ 536 & 3\ 853 \end{bmatrix} \tag{8}$$

Table 1: Nodes of function

Function	Number of arg.	Description
+	2	arg.1 + arg.2
	2	arg.1 arg.2
	2	arg.1 arg.2
tanh	1	tanh(arg.1)

Table 2: Parameters of GP

Parameter	Value
Number of generation G	200
Population N	200
Mutation rate	0.60
Crossover rate	0.80

Table 3: Parameters of the acrobot

Parameter	Value	Parameter	Value
m_1 [kg]	0.5	l_{c1} [m]	0.25
m_2 [kg]	0.5	l_{c2} [m]	0.25
m_3 [kg]	1.0	l_{c3} [m]	0.50
l_1 [m]	0.5	I_1 [kgm^2]	0.010
l_2 [m]	0.5	I_2 [kgm^2]	0.010
l_3 [m]	1.0	I_3 [kgm^2]	0.083

5 Result and Discussion

Figure 3 shows the fitness value of the most excellent individual at each generation. As the generation proceeds, the fitness value decrease gradually.

Figure 4 shows successful simulation results for swing-up and balancing. θ_1, θ_2 and θ_3 converged on the balance point in about 5.0[s]. $\dot{\theta}_1$, $\dot{\theta}_2$, $\dot{\theta}_3$, θ_{a2} and θ_{a3} are

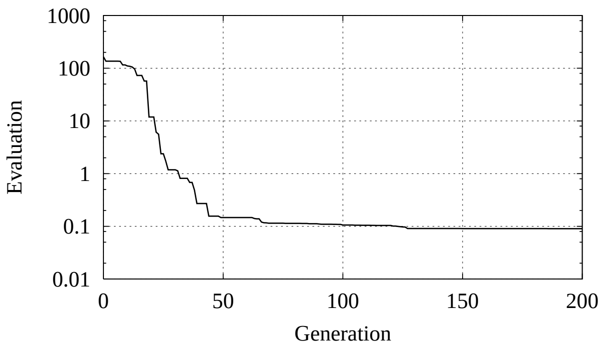

Fig. 3: Evaluation at each generation

similar results. The switching time from swing-up control to balance control is 2.88[s]. The acrobot reaches the balancing point quickly.

We obtained the optimum feedback input function using GP. The tree structure of θ_{a2} has 167 nodes and its depth is 45. The tree structure of θ_{a3} has 157 nodes and its depth is 36. The computer equipment in this study was Windows XP, Intel(R) Pentium(R) Dual CPU E2180 2.00GHz, and Java programming language was used. The computation time for the simulation was about 15 minutes per trial. The input functions are very complex because the depth and the number of nodes are large. Therefore, it is clear that performing swing-up control for a 3-DOF acrobot is very difficult.

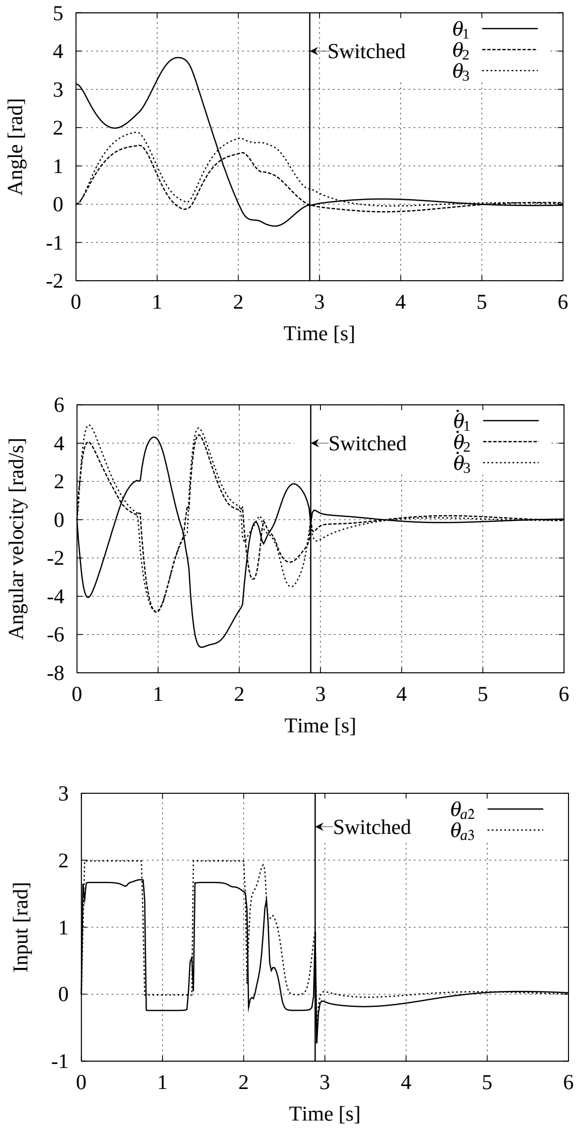

Fig. 4: Simulation results

6 Conclusion

We have proposed a control method for the 3-DOF acrobot.We modeled the acrobot considering the dynamics of the DC servomotor, which actuated the second and the third joints. GP searchers for a feedback input function, and we obtained the optimum control input using GP, but the input function is very complex. In the simulation results, the acrobot could swing-up to the desired position, and the proposed method could control the 3-DOF acrobot effectively. Further studies are needed in order to reduce the number of nodes, and real experiment should be carried out to verify the control method.

References

[1] M. W. Spong (1995), The Swing Up Control Problem For The Acrobot. IEEE Control System Magazine, Vol.15, No.2, pp.49–55

[2] K. Kawada, M. Obika and S. Fujisawa et al (2005), Creating Swing-Up Patterns of a Acrobot Using Evolutionary Computation. Proc. 2005 IEEE Int. Symposium on Computational Intelligence in Robotics and Automation, pp.261–266

[3] I. Matsumoto, K. Yoshida (2004), Swing–up and Stabilizing Control of the Acrobot. Transactions of the Institute of Systems, Control and Information Engineers, Vol.17, No.1, pp.17–25

[4] T.K. Nam, Y. Fukuhara and T, Mita et al (2002), Swing-up Control and Avoiding Singular Problem of an Acrobot System. Proc. SICE Ann. Conf. 2002 in Osaka (SICE2002), pp.2990–2995

[5] J. Koza (1992), Genetic Programming: On the Programming of Computers by Means of Natural Selection. MIT Press

[6] T. Ogawa, N. Oshiro and H. Kinjo (2008), Backward Movement Control with Two-Trailer Truck System Using Genetic Programming. Proc. of the 13th Int. Symposium on Artificial Life and Robotics, pp.597–600

The Fifteenth International Symposium on Artificial Life and Robotics 2010 (AROB 15th '10),
B-Con Plaza, Beppu,Oita, Japan, February 4-6, 2010

Neurocontrol for a Rotary Crane System with Disturbance

Kosuke Tamanoi*, Kunihiko Nakazono**, Hiroshi Kinjo**, and Kouhei Ohnishi***

*Graduate School of Engineering and Science, University of the Ryukyus
**Faculty of Engineering, University of the Ryukyus
1 Senbaru, Nishihara, Okinawa JAPAN 903-0213
tamanoi@mibai.tec.u-ryukyu.ac.jp
***Faculty of Science and Techonology, Keio University
3-14-1 Hiyoshi, Yokohama JAPAN 222-8522

Abstract: In this paper we propose a neurocontroller (NC) for suppression of load swing with disturbance in a crane system rotating around the vertical axis. As in a nonholonomic system, the classical control method using a static continuous state feedback law cannot stabilize the load swing. It is necessary to design a time-varying feedback controller or a discontinuous feedback controller. Previous research had been successful in constructing the suppression controller of the load swing with a single initial rotation angle when disturbance occurred. In this paper, the performance of the NC optimized by genetic algorithm will be examined with three initial rotation angles.

Keyword: rotary crane, genetic algorithm, neurocontroller, disturbance

1 Introduction

Rotary crane systems are generally operated using both the rotation angle and the lean angle in order to suppress a load swing. However, by restricting the motion of the jib to the rotation around the vertical axis alone, the system becomes a nonholonomic system. This results in a complex control problem and it is necessary to design time-varying feedback or discontinuous control methods. When operating this rotary crane system, the most important control purpose is to suppress a load swing on the reference position. Usually, techniques for suppressing the load swing depends on skillful operator's experiences [1]. Therefore, it may be necessary to develop automatic control crane systems.

Many control methods for load swing suppression in a rotary crane system have been presented [1]-[6]. However, most of these control methods require knowledge of difficult control theories [1] - [4]. In contrast, it is easy to apply a neurocontroller which has simple structure and generalization ability as a controller [5], [6]. A neurocontroller optimized by an evolutionary computation technique, such as a genetic algorithm, is substantially simpler to realize than conventional control methods. In this paper, we propose a neurocontroller (NC) optimized by a genetic algorithm(GA). In real environment, the load of the rotary crane system may swing due to disturbance. For example, there are gust of wind and constant wind. Therefore, it is necessary to consider the disturbance. We previously reported that when the rotary crane system starts movement from single initial rotation angle, it is able to use the NC to suppress the load swing to the reference position even if the load swings suddenly [6].

In this paper, we propose the NC which has optimal control performance even if rotary crane systems start movement from several initial rotation angles with disturbance.

2 Model of rotary crane system

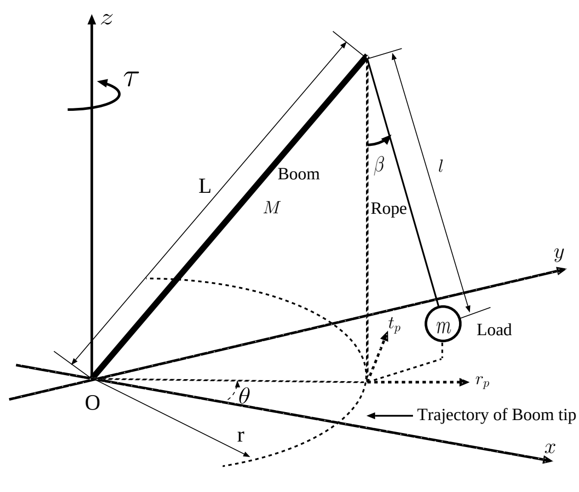

Fig. 1: Rotary crane system

Figure 1 shows the crane system rotating around the z axis. L is the jib arm length, m is the load mass, l is the wire length and r is the radius of rotation. θ is the rotation angle, α is angle of load lead, β is angle of load swing and τ is torque.

If the swing of the load is sufficiently small, we can consider the system in two-dimensional plane.

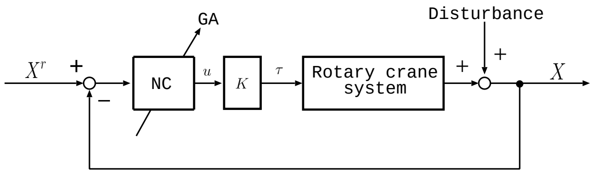

Fig. 2: Control system for rotary crane

Table 1: GA parameters

Parameter	Value/method
Initial parents NCs	100
Initial children NCs	50
Selection method	Ranking selection
Crossover	One-point crossover
Mutation rate	20%
Generation number	20000

Therefore, the dynamics and rotation movement of the system can approximately be described in terms of the following equations (1), (2) and (3)

$$\ddot{x} = \omega^2(r\cos\theta - x) \tag{1}$$

$$\ddot{y} = \omega^2(r\sin\theta - y) \tag{2}$$

$$\ddot{\theta} = Ku \tag{3}$$

where $\omega = \sqrt{g/l}$ is natural angular frequency. K is a constant value including the load mass and moment of inertia.

3 Control system for the rotary crane

3.1 Neurocontrol of the crane system

The control purposes to suppress the load swing movement from initial position (x_0, y_0), which is determined by several initial rotation angles, to the reference position (x^r, y^r) by rotating the jib arm. Figure 2 shows the control system using NC with GA. The state variable X and reference X^r are defined as follows :

$$X = [x, y, \theta, \dot{x}, \dot{y}, \dot{\theta}]^T \tag{4}$$

$$X^r = [x^r, y^r, \theta^r, \dot{x}^r, \dot{y}^r, \dot{\theta}^r]^T \tag{5}$$

The NC consists of three hierarchical layers with 6-12-1 structure. A linear function is used at the input layer and a sigmoid function is used for the hidden and the output layers. The NC receives the position error of the load, the velocity error, the rotation angle error, and the angular velocity error as inputs. And it outputs the control input u. Torque τ is calculated as the product of the control input u and constant value K.

This paper uses a simple GA as an optimization method for the NC. Table 1 shows the parameters of the GA. The performance of the NC is evaluated by a squared error function E which is defined with respect to the final state X^{end} and the reference X^r as following:

$$E = \sum_{p=1}^{P} (X^r - X_p^{end})^T Q (X^r - X_p^{end}) \tag{6}$$

Here, P is the number of initial rotation angles and Q is the unit matrix. In the GA evolutionary process, the connection weights of the NC are modified in order to minimize the error function E in Eq. (6)

3.2 Setting of disturbance condition

In general, the load of the system swings due to disturbance which is a gust of wind and a constant wind. In this paper, we assume the disturbance to be a gust of wind and we propose the NC which has optimal control performance even if the load swings suddenly. The disturbance is as follows: After t_{dis} second, the load position (x, y) suddenly moves to position $(x + \Delta x, y + \Delta y)$. The distance of disturbance Δx, Δy are determined by random numbers. Table 2 shows the parameters of the disturbance range and the times when it occurs.

Table 2: Parameters of disturbance

Parameters	Value
t_{dis} [s]	1.0 , 2.0 , 3.0 , 4.0
$(\Delta x, \Delta y)$ [m]	(0.05 , 0.05)

Table 3: Parameters and initial condition

Parameter	Value
Load mass : m [kg]	0.5
Rotation radius : r [m]	1.0
Length of wire : l [m]	2.0
Reference : X^r	(1,0,0,0,0,0)
Coefficient : K	5.0
Control time : T[s]	10.0
Initial rotation angle : θ_0 [deg]	90,120,150

4 Simulation results

Table 3 shows the parameters of the crane system and the initial conditions. The performance of the NC optimized by GA is verified using computer simulations. Runge-Kutta method is used for the system dynamic model, and sampling interval is 0.01 [s]. When the initial rotation angles are $\theta_0 = 90, 120, 150$ [deg], the evolutionary processes providing the best NCs are shown in Figure 3. Here, the position (x, y) of the load suddenly moves to $(x + \Delta x, y + \Delta y)$ at $t_{dis} = 1, 2, 3, 4$ [s]. The error function E decreases gradually until generation 20000. The result demonstrates that the GA evolutionary processes of the NCs is successful. Figure 5 shows the trajectory of the load mass in the $x - y$ plane and the movement of the rotary angle using the optimized NC with initial angles $\theta_0 = 120$ [deg], $t_{dis} = 3$ [s]. After t_{dis} second, the load is suddenly moved by disturbance, afterward, it converged and suppressed swing movement at the reference position. Figure 4 shows the movement of the rotary angle using the optimized NC with initial angles $\theta_0 = 90, 120, 150$ [deg], $t_{dis} = 3$ [s].

4.1 The performance of the NC

Next, to verify the performance of the NC, it is tested with different initial positions $(x_0, y_0) = (\cos\theta_0 + \delta_x\ , \sin\theta_0 + \delta_y)$ which are varied from the trained position (x_0, y_0) =($\cos\theta_0$, $\sin\theta_0$). In this test, rotary angles are $\theta_0 = 90, 120, 150$, and the changes of the initial position (δ_x, δ_y) are set by random numbers in the range $(\delta_x, \delta_y) = [-0.03, 0.03]$. The criterion for success in control is when the squared error E_1 less than 0.0001 which is defined as :

$$E_1 = (X^r - X_1^{end})^T Q (X^r - X_1^{end}) \tag{7}$$

Table 4 shows the successful rate of control performance for the system through 1000 trials. Overall, when the rotary angle θ_0 is 90 [deg], good result is obtained. It shows that the latter time when disturbance occurs, the more difficult to the control system. Figure 5 shows an example of control result. Here, even if the control system started from the initial position, the load is moved with very little swing oscillation and it is suppressed to the reference position. It can be seen that the optimized NC has good control performance and has generalization ability.

5 Conclusion

In this paper, we proposed a method to suppress the load swing movement from the initial positions, which is determined by three initial rotation angles, to the reference position by rotating the jib arm. As a result, simulations confirmed that the optimized NC by GA has good control performance. The NC suppress the load swing even if the load of the system is suddenly swung by disturbance, after the system started from several initial rotation angles. Moreover, to verify the performance of the NC, it is tested with different initial positions which are varied from the optimized position. We confirmed that the optimized NC has good control performance and has generalization ability.

Table 4: Success rate of control [%]

t_{dis} [s]	90[deg]	120[deg]	150[deg]
$t_{dis} = 1$	74.4	70.2	59.9
$t_{dis} = 2$	100.0	100.0	100.0
$t_{dis} = 3$	89.8	100.0	97.2
$t_{dis} = 4$	47.7	45.5	28.7

References

[1] M. Ohto and S. Yasunobu (1997), A Rotary Crane Control Method Based on a Skillful Operator 's Knowledge, Transaction of the Society of Instrument and Control Engineers, 33(9):923 - 929

[2] S. Yamazaki, T. Itoh, et al. (1979), Theoretical Consideration on a Control of Jib-Crane, Transaction of the Society of Instrument and Control Engineers, 15(6) : 826 - 832

[3] Y. Sakawa and Y. Shindo (1982), Optimal Control of Container Cranes, Automatica, 18(3)3 : 257 - 266

[4] R. Kondo (2006), Vibration Control of Rotary Crane via Two-Mode Switching Control (in Japanese), Journal of the Society of Instrument and Control Engineers, 45(7) : 632 - 637

[5] K. Nakazono, et al. (2009), Optimal Suppression Control of Load Swing with Disturbance for Rotary Crane System Using Neuro-controller, Artificial Life and Robotics 14th : 626 - 629

[6] K.Tamanoi, et al. (2009), Neuro Control of Load Swing for Rotary Crane System with Disturbance (in Japanese), Design & Systems Conference '09 : 109

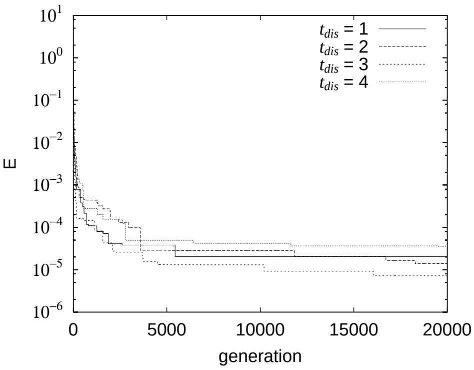

Fig. 3: Evolutionary processes

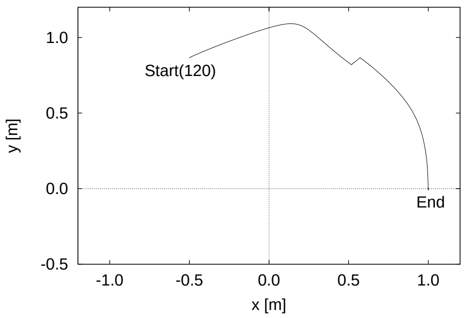

(a) Trajectory on x-y plane ($\theta_0 = 120$[deg])

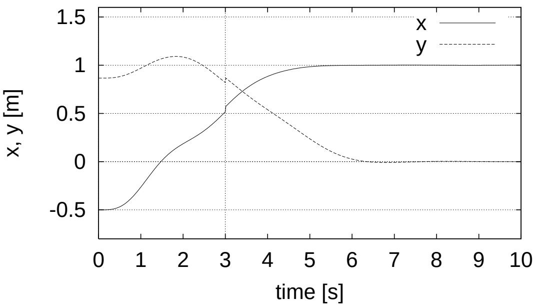

(b) Position x and y ($\theta_0 = 120$[deg])

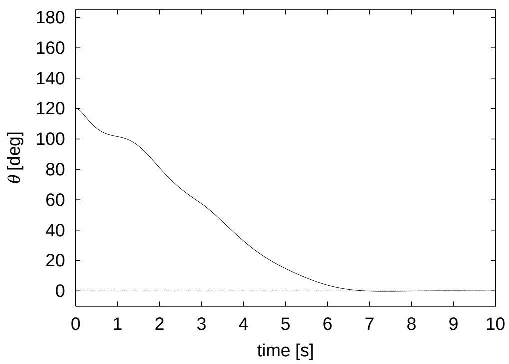

(c) Rotary angle θ ($\theta_0 = 120$[deg])

Fig. 4: Control results ($t_{dis} = 3$ [s])

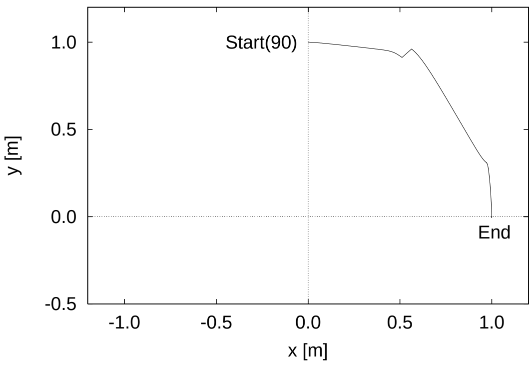

(a)Trajectory on x-y plane ($\theta_0 = 90$[deg])

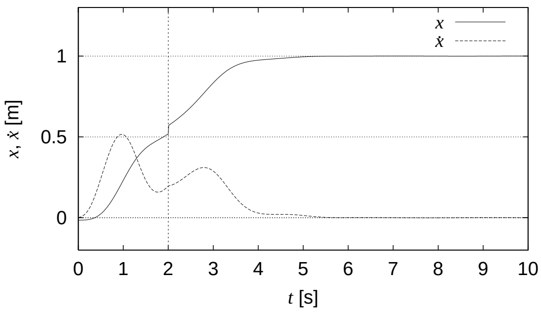

(b) Position x and velocity $\dot{x}$ ($\theta_0 = 90$[deg])

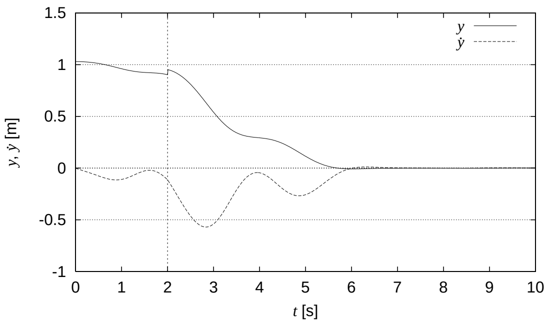

(c) Position y and velocity $\dot{y}$ ($\theta_0 = 90$[deg])

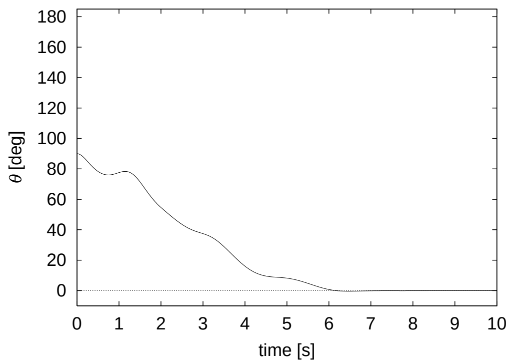

(d) Rotation angle θ ($\theta_0 = 90$[deg])

Fig. 5: Control results (t_{dis}=2, (δ_x, δ_y)=(-1.5 , 3.0))

The Fifteenth International Symposium on Artificial Life and Robotics 2010 (AROB 15th '10),
B-Con Plaza, Beppu,Oita, Japan, February 4-6, 2010

Particle Swarm Optimization with Genetic Recombination - A Hybrid Evolutionary Algorithm

Sam Chau Duong, Hiroshi Kinjo, Eiho Uezato
Faculty of Engineering, University of the Ryukyus
Senbaru 1, Nishihara, Okinawa 903-0213, Japan

Tetsuhiko Yamamoto
Tokushima Technology College
Itano-gun, Tokushima 779-0108, Japan

Abstract

This article presents a hybrid evolutionary algorithm (HEA) based on particle swarm optimization (PSO) and real-coded genetic algorithm (GA). In the HEA, PSO is used to update the solution and a genetic recombination operator is added to produce offspring individuals based on the parents that are selected in proportion to their relative fitness. Through the recombination, new offspring enter the population and the individuals with poor fitness are eliminated. The performance of the proposed hybrid algorithm is compared to those of the original PSO and GA and the impact of the recombination probability to the performance of the HEA is also analyzed. Various simulations of multivariable functions and neural network optimizations are carried out, showing that the proposed approach is superior over the canonical means.

Keywords: Hybrid evolutionary algorithm, Particle swam optimization, Genetic algorithm, Multivariable optimization, Neural network.

1 Introduction

Evolutionary algorithms have been emerged in the growing study and applied pervasively in various areas. Although their competence have been proved to be superior over the conventional methods, an experienced combination of operations (either full or partial) from different approaches may provide a more efficient performance. In fact, the hybridizations of evolutionary algorithms have been the focus of much research recently and they are considered as effective general-purpose tools for the goals of *exploration* and *exploitation* [1]. The hybrids of genetic algorithms (GAs) and particle swarm optimization (PSO) have become a popular and interesting framework with capability of handling several real world problems.

In general, evolutionary algorithms involve strong stochastic basic, they therefore require many generations to obtain good solution. In this article, a hybrid of PSO an real-coded GA is proposed, called the hybrid evolutionary algorithm (HEA). With the focus on the investigation of how quick an algorithm can find a solution, comparison between the proposed HEA and the canonical PSO and GA is carried out with small population size and generation.

The rest of this article is organized as follows. Section 2 is a background on the PSO and real-coded GA used in this study. In Section 3, the proposed hybrid algorithm is introduced. Simulations will be shown in Section 4, where the performance of the proposed method is investigated and compared to those of the canonical PSO and real-coded GA. The optimization problems of multivariable function are first considered. The neural network optimization for the exclusive-or (XOR) problem is then examined. Lastly, Section 5 is the discussion and conclusion of the study.

2 Brief Background on Particle Swarm Optimization and Genetic Algorithm

2.1 Particle Swarm Optimization

As one of the latest evolutionary optimization methods, PSO is a population-based stochastic approach which provides efficient performance with simple operators [2],[3].

Assume that the search space is D-dimensional, the n-th particle (solution) of the swarm is represented by a D-dimensional vector $X_n = [x_{n1}, x_{n2}, \cdots, x_{nD}]^{\mathrm{T}}$. The n-th particle's velocity is also a D-dimensional vector, denoted as $V_n = [v_{n1}, v_{n2}, \cdots, v_{nD}]^{\mathrm{T}}$. The best position of the n-th particle is $PB_n = [pb_{n1}, pb_{n2}, \cdots, pb_{nD}]^{\mathrm{T}}$ (the *local best*, the smallest objective value that the n-th particle has obtained so far), and the best position of the swarm is denoted as gb (the *global best*, the smallest objective value achieved by any particle in the population). After finding the two best values in the k-th iteration, the particle updates its velocity and position in the next iteration $(k+1)$ with following equations:

$$v_{nd}^{k+1} = \lambda v_{nd}^{k} + c_1 r_1 \left(pb_{nd}^{k} - x_{nd}^{k}\right) + c_2 r_2 \left(gb_{d}^{k} - x_{nd}^{k}\right) \quad (1)$$

$$x_{nd}^{k+1} = x_{nd}^{k} + v_{nd}^{k+1} \quad (2)$$

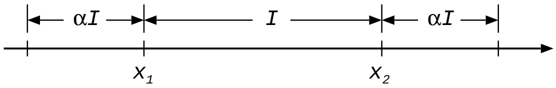

Figure 1: The BLX-α crossover

where $d = 1, 2, \cdots, D$; $n = 1, 2, \cdots, N$ (N is the swarm population size); $k = 1, 2, \cdots, K$ is the iteration (or generation) number; λ is the inertia weight; c_1 and c_2 are positive constants (in this study $c_1 = c_2$, which is usually used); r_1 and r_2 are random values in the range [0, 1].

2.2 Genetic Algorithms

Genetic Algorithms (GAs) are adaptive heuristic search techniques based on the ideas of natural selection and genetics. Generally, the main driving operators of GAs are selection, recombination via crossover, and mutation.

In this study, the recombination of a real-coded GA is used where offspring are produced by the so-called blend crossover (BLX-α) [4]. The BLX-α generates offspring by picking values on an interval that contains two parents and may extend equally on either side of the interval with a range determined based on a range parameter α (see Fig. 1).

3 A Hybrid of Particle Swarm Optimization and Genetic Algorithm

In this paper, a hybrid of PSO and GA is proposed, where the BLX-α crossover is used to produce offspring (M individuals). The operation of the proposed hybrid evolutionary algorithm (HEA) is shown in Fig. 2. In the figure, $(.)_b$ presents the local best value of an individual in PSO and x'_n is the new position of the individual (the updated position by Eqs. (1) and (2)). After being produced by the BLX-α recombination and being evaluated, the offspring x_{n+m} sets itself to be its local best value. A ranking procedure based on the fitness of each individual is performed for the pool of all parents and offspring, from which the individuals with poor fitness are eliminated to maintain a constant population. The individual with highest fitness is set to be the global best of the swarm.

The recombination with selection is the main difference of the HEA, GA compared to PSO. Suppose that the probability of offspring production is μ, the GA and the proposed HEA shall produce $M = \mu \times N$ offspring and also eliminate the same amount (the inferiors) to keep a constant population size of N at each generation. As a result, the number of individuals that is taken into the evaluation at each generation is $(1 + \mu) \times N$.

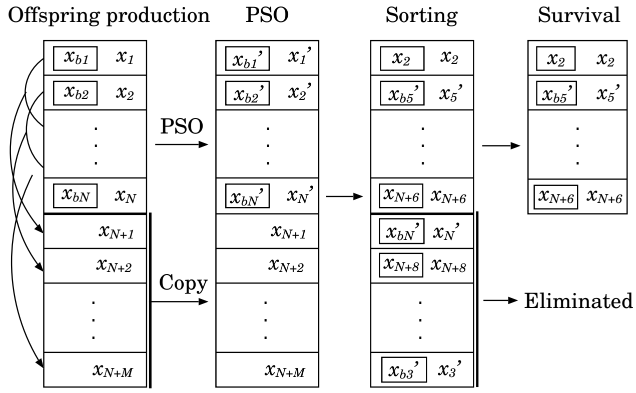

Figure 2: Process of the proposed hybrid algorithm

In the GA recombination, the Roulette wheel technique is used to select parents for reproduction in proportion to their relative fitness, which is defined as:

$$\text{Fitness} = \frac{1}{1 + E} \tag{3}$$

where E is the error between the obtained cost function value and the optimal cost function value (the optimal solution of the problem).

4 Numerical Simulations

4.1 Multivariable Function Optimization

4.1.1 Parameter and test design

In general, a high recombination probability results in a severe selection of several solutions and thus usually provides good performance of a competitive-selection based EA. Thus, in order to make a fair comparison with the PSO as well as to demonstrate the advantage of the proposed method, a small recombination probability is used, that is $\mu = 0.1$. Also, the generation number K is set to be small and the population size is between 10 and 40 (this range is often used in PSO).

Since evolutionary algorithms are highly dependent on the initial random weights, 100 replications of changing the initial population will be implemented. Also, while the algorithms search for optimal solution in hyperspace, the initial population are drawn randomly from a uniform distribution from the range $[-10.0, 10.0]$, which is intentionally set to be large enough to make the search problem more difficult. The performances of the algorithms are evaluated by the success rate and the mean cost function value. The success rate is the fraction of optimization runs in which an algorithm can achieve small enough error (*i.e.*, $E < E_{suc} = 10^{-4}$).

While using $c_1 = c_2 = 1.0$, which is found to be suitable for the problems being considered, we shall show only the best result (i.e., with highest success rate and/or

Table 1: Test functions

Function	Formula	Optimal solution	Sketch in 2D
F_1: Sphere	$f(x) = \sum_{i=1}^{D} x_i^2$	$F^* = 0, \quad x_i^* = 0$	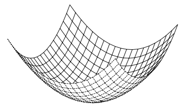
F_2: Rosenbroke	$f(x) = \sum_{i=1}^{D-1} \left(100 \left(x_{i+1} - x_i^2\right)^2 + (x_i - 1)^2\right)$	$F^* = 0, \quad x_i^* = 1$	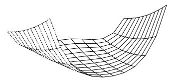
F_3: Rastrigin	$f(x) = \sum_{i=1}^{D} \left(x_i^2 - 10\cos(2\pi x_i) + 10\right)$	$F^* = 0, \quad x_i^* = 0$	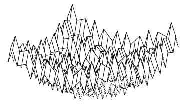
F_4: Griewank	$f(x) = \frac{1}{4000} \sum_{i=1}^{D} x_i^2 - \prod_{i=1}^{D} \cos\left(\frac{x_i}{\sqrt{i}}\right) + 1$	$F^* = 0, \quad x_i^* = 0$	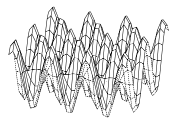

Table 2: Parameters resulting in the best performance of the algorithms for specific problems

Function	GA–α	PSO–λ	HEA–(α, λ)
$F1$	$\alpha = 1.0$	$\lambda = 0.2$	$\alpha = 0.9$, $\lambda = 0.4$
$F2$	$\alpha = 1.0$	$\lambda = 0.6$	$\alpha = 1.3$, $\lambda = 0.7$
$F3$	$\alpha = 1.6$	$\lambda = 0.5$	$\alpha = 1.0$, $\lambda = 0.4$
$F4$	$\alpha = 0.1$	$\lambda = 0.7$	$\alpha = 1.6$, $\lambda = 0.6$

smallest mean cost) of each algorithm for specific problem by tuning for the most suitable values of α in the GA, λ in the PSO, and (α, λ) in the HEA. Let us denote them as the BLX–α (or GA–α), PSO–λ, and HEA–(α, λ).

In this section the algorithms are investigated through the optimizations of four functions as shown in Table 1 with the dimension number of $D = 2$. In these functions optimizations, since the optimal solution is $F^* = 0$, we define $E = F$ where F is the value of the cost function obtained after a run of the algorithm.

4.1.2 Simulation result

Using the tuned parameters in Table 2, the results of optimizing the functions are shown in Table 3 for $K = 20$ and $K = 50$. It is clear that the HEA usually obtains higher success rates and lower averaged cost values.

4.2 Neural Network Optimization

4.2.1 Parameter and test design

This section presents the experiment of an NN optimization for the well-known exclusive-or problem (XOR) (see Table 4), which is known as a highly nonlinear multivariable optimization problem.

In the NN, a linear function $f(x) = x$ is kept for the input and output layers while activation for the hidden layer is a sigmoid function, which is:

$$f(x) = \frac{1}{1 + e^{-x}} \tag{4}$$

A 2-5-1 structured NN is utilized which results in a 15-variable optimization problem. The initial connection weights are drawn randomly from the range [-5.0, 5.0]. Performances of the algorithms are also evaluated through 100 iterations of changing the initial population. The error function is defined as

$$E = \sum_{p=1}^{4} (T_p - O_p)^2 \tag{5}$$

where T_p is the desired output or teacher signal, O_p is the obtained output value of NN for pattern p, and P is the number of patterns (for the XOR problem, $P = 4$).

4.2.2 Simulation result

Table 5 shows the simulation results of the NN optimization with $K = 50$ and $K = 100$ generations, using the GA–0.1, PSO–0.7, and HEA–$(0.6, 0.8)$. Again, the proposed HEA outperforms the PSO and GA.

5 Discussion and Conclusion

In this research, we have presented a novel hybrid evolutionary algorithm based on a PSO and a real-coded GA. The performance of the HEA is compared with those of the canonical approaches, showing a good performance of the proposed method regardless of the small values of the generation number, population size and the recombination probability μ.

In the tests the GA demonstrated a poor performance. This is due to the small values of generation, population size and the recombination probability μ as well as the fact that GAs are very sensitive to the initial population.

Table 3: Success rate [%] and mean cost value (**succ. rate**/mean cost) with $D = 2$, $K = 20, 50$

Func.	N	K	GA	PSO	HEA
F_1	10	20	**1**/10.96269	**68**/0.16374	**100**/0.0
		50	**1**/10.96269	**68**/0.16360	**100**/0.0
	20	20	**0**/0.75099	**99**/0.00077	**100**/0.0
		50	**2**/0.10052	**99**/0.00076	**100**/0.0
	30	20	**1**/0.49964	**100**/0.0	**100**/0.0
		50	**3**/0.08395	**100**/0.0	**100**/0.0
	40	20	**1**/0.21150	**100**/0.0	**100**/0.0
		50	**12**/0.01293	**100**/0.0	**100**/0.0
F_2	10	20	**0**/3006.9817	**1**/1.69848	**1**/1.51888
		50	**0**/3006.9817	**10**/1.26860	**8**/0.96206
	20	20	**0**/5.92721	**1**/0.46515	**2**/0.56743
		50	**0**/2.92093	**33**/0.21127	**35**/0.15171
	30	20	**0**/4.23923	**4**/0.24810	**4**/0.35501
		50	**0**/2.74650	**53**/0.06008	**63**/0.11816
	40	20	**0**/3.22764	**3**/0.03547	**14**/0.04609
		50	**2**/2.45530	**73**/0.00438	**92**/0.00057
F_3	10	20	**1**/88.29054	**5**/1.26160	**6**/1.81855
		50	**1**/88.29054	**36**/0.99607	**24**/1.63858
	20	20	**0**/30.36538	**10**/0.58992	**37**/0.81628
		50	**0**/11.55541	**54**/0.42886	**60**/0.43778
	30	20	**1**/31.93949	**18**/0.31230	**47**/0.49963
		50	**1**/13.60421	**81**/0.19661	**82**/0.28853
	40	20	**0**/18.76824	**29**/0.21593	**63**/0.39942
		50	**1**/5.64692	**90**/0.06410	**88**/0.13929
F_4	10	20	**1**/0.25129	**7**/0.01322	**18**/0.01153
		50	**1**/0.25129	**26**/0.01095	**27**/0.01047
	20	20	**0**/0.05075	**12**/0.00932	**15**/0.01206
		50	**0**/0.02451	**22**/0.00676	**20**/0.01193
	30	20	**1**/0.04892	**13**/0.00965	**19**/0.01083
		50	**1**/0.02640	**26**/0.00710	**27**/0.01070
	40	20	**0**/0.03243	**14**/0.00801	**35**/0.00779
		50	**1**/0.01320	**33**/0.00583	**38**/0.00649

Table 4: The XOR broblem

Pattern no.	Input		Desired output
p	x_1	x_2	T
1	0	0	0
2	0	1	1
3	1	0	1
4	1	1	0

At the beginning there is a strongly random and diverse population and the crossover tends to explore the search space wildly, therefore resulting in low success rates and several large-error individuals. The PSO appeared to rapidly converge during the beginning of the search, but around global optimum the search process becomes slow. Without a selection operator, individuals tend to follow the best one and get into a neighborhood of the optimum. This results in a low error in average but not so many solutions successfully found. In contrast, the proposed HEA could utilize the widespread search of the BLX at the beginning and the fine-tuning ability of the PSO when it gets near to the optimum. With a selection process to eliminate inferior individuals, the HEA thus balances between finding solution (successfully) and obtaining a low averaged cost, especially when K is small. There are some situations that the HEA is not much better or even worse than the PSO. This is apparently

Table 5: Success rate [%] and mean error (**succ. rate**/mean error) for the NN training with $K = 50, 100$

N	K	GA	PSO	HEA
10	50	**0**/51.09702	**0**/0.72811	**0**/0.89564
	100	**0**/51.09702	**1**/0.43889	**1**/0.38902
20	50	**0**/4.54599	**0**/0.41958	**0**/0.28397
	100	**0**/3.87397	**13**/0.14848	**24**/0.05066
30	50	**0**/4.36849	**0**/0.34127	**1**/0.25869
	100	**0**/2.82969	**23**/0.08107	**43**/0.03092
40	50	**0**/2.41389	**0**/0.21741	**2**/0.10718
	100	**0**/1.79364	**37**/0.05251	**69**/0.00970

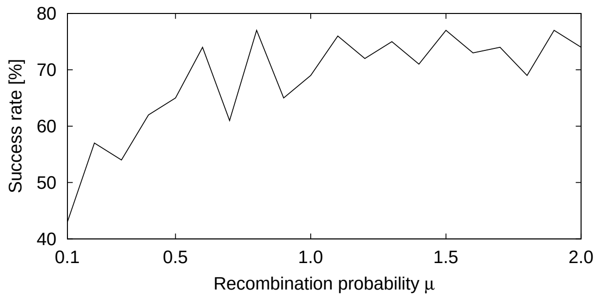

Figure 3: Performance vs. recombination probability μ in the HEA (in the case of the NN optimization by the HEA–$(0.6, 0.8)$ with $N = 30$, $K = 100$)

due to the low recombination probability μ used. The performance of the HEA can be improved when using higher value of μ. The impact of the recombination to its performance is shown in Fig. 3 for the NN optimization, for example. It appears that a high probability μ usually (but not always) provides better performance. For a particular problem, an optimal value of μ is able (and needed) to be determined.

In this study, although the proposed HEA could obtain good performance, it is necessary to validate the algorithm with more complex problems in future work.

References

[1] F. Grimaccia, M. Mussetta, R.E. Zich, "Genetical Swarm Optimization: Self-adaptive hybrid evolutionary algorithm for electromagnetics", *IEEE Trans. Antennas and Propagation* Vol.55, Iss.3, pp.781-785, 2007.

[2] J. Kennedy, R.C. Eberhart, "Particle swarm optimization", *Proc. of IEEE Intl. Conference on Neural Networks*, Piscataway, NJ. pp. 1942-1948, 1995.

[3] K.E. Parsopoulos, M.N. Vrahatis, "On the computation of all global minimizers through Particle swarm optimization", *IEEE Trans. on Evolutionary Computation*, Vol. 8, Iss. 3, pp. 211-224, 2004.

[4] L.J. Eshelman, D.J. Schaffer, "Real-coded genetic algorithms and interval-schemata", in L.D. Whitley (ed.) Foundations of genetic algorithms 2, Morgan Kaufmann, pp 187-202, 1993.

Why we talk?: Altruism and multilevel selection in the origin of language

Kana Sugiura Takaya Arita
Graduate School of Information Science, Nagoya University
Furo-cho, Chikusa-ku, Nagoya 464-8601, Japan
E-mail: kana@alife.cs.is.nagoya-u.ac.jp, arita@nagoya-u.jp

Abstract: Talking entails costs of production and time while some of the information sent to hearers will be of value to them in general. We believe that the matter of why we talk at all is a key question for the origin of language and the answer will shed some light on the mystery of human identity. This paper focuses on the altruism in communication and aims to demonstrate evolutionary scenarios based on multilevel selection. We constructed a computational model to examine these scenarios. The evolutionary experiments showed that in case of an unstructured population a linguistic system hardly emerged due to the dynamics between interpretable utterance that imposes a penalty and correct interpretation that yields a reward, which is similar to the prey-predator dynamics. However, in case of a multi-group population a linguistic system emerged owing to the multilevel selection among the groups. In addition, the probability of success in conversation was higher in a group with a severer environmental condition. This result supports the Bickerton's hypothesis based on the ecological gap between human ancestors and other ape species.

Keywords: language evolution, altruism, multilevel selection, artificial life.

1 Introduction

When we talk we usually transfer information to hearers. Talking entails costs of production and time although some of the information will be of value to hearers. Therefore, some explanation must be given if we admit that natural selection has shaped the human linguistic behavior. We believe that the matter of why we talk at all is a key question for the origin of language [1] and the answer will shed some light on the mystery of human identity.

This paper focuses on the altruism in communication and aims to demonstrate evolutionary scenarios based on multilevel selection [2]. Multilevel selection, a sophisticated version of group selection, refers to the idea that group-level selection and within-group individual-level selection are supposed to work simultaneously and thus alleles can spread in a population because of the benefits they bestow on groups regardless of the alleles' effect on the fitness of individuals within that group.

When considering the altruism in language, we should not neglect the difference between language and nonhuman communication systems (NCSs) [3]. Most signals in NCSs are designed not to communicate information but to confer fitness on the sender. Bickerton attributes this difference between language and NCSs to the ecological gap between human ancestors and other ape species. In short, the food-poor, predator-infested environments inhabited by protohumans placed a premium on cooperation, which might lead to the emergence of language based on altruism.

We construct a computational model to examine these scenarios. In the model, each agent has a word-meaning association matrix that explicitly stores the joint likelihood of the words and meanings. In conversation, if the receiver can successfully interpret the meaning of the sent word, the receiver receives a positive reward but the sender receives a negative reward. The matrix is evolved by the selection based on the total rewards. We conduct evolutionary experiments with unstructured and structured (multi-group) populations to investigate the effect of multilevel selection. Also, in multi-group setting, we examine the Bickerton's hypothesis by differentiating the penalties among groups.

2 Model

The population is composed of N agents and is divided into χ patches. The set of agents occupying a patch constitutes a group. Each agent has its own vocabulary represented as a Word-Meaning Association Matrix (WMAM), which is a likelihood $n \times m$ matrix that explicitly stores the joint likelihood of the n meanings and m words. The initial values of the elements are randomly set in the range of 0 to 1, and then normalized so that the sum of all elements is one.

Each agent plays one-to-one language game to send all meanings with every other member in its group in the game phase (Fig. 1). For a speaker, p_{ij}

$(= a_{ij}/\sum_{j=1}^{m} a_{ij})$ denotes the probability of using word j when sending meaning i, whereas for a hearer, q_{ij} $(= a_{ij}/\sum_{i=1}^{n} a_{ij})$ denotes the probability of interpreting it as meaning i when hearing word j. If conversation in the game is successful, in other words, the hearer can successfully interpret the meaning of the sent word, the hearer and speaker receive the payoff, α_i and β_i, respectively. The term $\sum_{j=1}^{m} p_{ij}^{(X)} q_{ij}^{(Y)}$ denotes the probability that speaker X will successfully send meaning i to hearer Y, and is then summed over all meanings, which will be the expected payoff for the agent X in one-to-one game as follows.

$$R_{L_{(X)},L_{(Y)}} = (1/2)\sum_{i=1}^{n}\sum_{j=1}^{m}(\alpha_i p_{ij}^{(X)} q_{ij}^{(Y)} + \beta_i p_{ij}^{(Y)} q_{ij}^{(X)}). \tag{1}$$

After the game phase, each agent decides whether to migrate to a randomly-chosen patch or not by using the migration function depending on its average payoff per game. The probability of migration for agent X, $E_{mig_{(X)}}$ is defined as $\rho \times (1 - \frac{R_{(X)} - R_{Min(x)}}{R_{Max(x)} - R_{Min(x)}})$, where ρ is the parameter of the function, $R_{(X)}$ is the payoff of the agent X, and $R_{Max(x)}$ and $R_{Min(x)}$ are the maximum and minimum payoffs in the group x to which the agent X belongs, respectively.

Next, a new population is generated by the roulette wheel selection according to the average payoff per game until the population size reaches N. The selection is performed on the whole population while the population structure is maintained during this phase, in other words, each offspring is generated in the same patch as their parents. Linear scaling modifies the payoff of each agent before the selection if the least one is negative. Then a normal random number (μ, σ) is added to each element of WMAM with a probability ω as mutation, after each WMAM is normalized. Finally, the agents chosen by the migration function perform migration.

A sequence of these phases is repeated 20000 times. We will focus on the evolutionary dynamics of the vocabulary by considering the frequency of the utterance of a word from a meaning or interpretation of a meaning from a word that can be measured quantitatively as a linguistic trait.

3 Experiments

The parameters common to all experiments were set as follows. The population size N was 100, and the numbers of meanings n and words m : were equally 3. The parameters controlling mutation $\omega = 0.001$, $\mu = 0$ and $\sigma = 0.05$. The payoffs of speaker's (α_i) and hearer's (β_i) for all meanings were -1 and 1.5, respectively. This setting makes the agents with the vocabulary by which to interpret correctly the meanings of the sent words and to send the words of which the

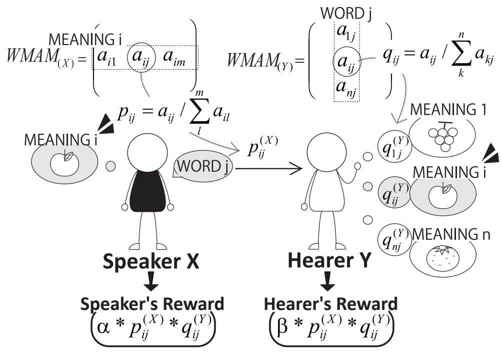

Figure 1: The language game: shows that speaker X talk about meaning i by using word j.

meanings the other agents cannot interpret correctly receive a high payoff. We shall investigate how a communication system evolves on the basis of altruism.

3.1 Unstructured population

First, we conducted the evolutionary experiments with one patch ($\chi = 1$) to grasp the basic dynamics of the communication system. Fig. 2 (top) shows the evolution of success rate in conversation. Starting from 1/3, it increased rapidly to around 0.4 within 30 generations, and then reached a peak of 0.58. After that, it gradually decreased and converged to approximately 1/3. One word was associated equally with all meanings in the converged communication system, in other words one word was used for expressing all meanings and the word was interpreted as each meaning with a probability 1/3.

Fig. 2 (bottom) shows the evolution of the six linguistic traits (expected frequencies in the population) concerning meaning 3. The trait responsible for mapping from meaning 3 to word 1 (M3W1, hereafter), M3W2 and M3W3 are expressed as "1", "2" and "3", respectively. Also, the trait responsible for mapping from word 1 to meaning 3 (W1M3, hereafter), W2M3 and W3M3 are expressed as "1' ", "2' " and "3' ", respectively. So, for example, if "1" = 1.0 and "1' " = 1.0 then success rate = 1.0 concerning meaning 3.

We see the repetition of rapid change in the dominant traits from this figure. There are at least three mechanisms that shaped this dynamics. 1) $M3W1 + M3W2 + M3W3 = 1$ by definition. Therefore, for example, M3W2 tends to decrease when M3W1 increased. 2) There is some correlation between the changes in the traits using the same words as they are based on the same elements in WMAM. 3) As conversation success gives speakers a penalty, increase in the traits responsible for interpreting a word as a meaning correctly makes decrease in a trait responsible for using the word for the meaning. Actually, we see in the graph a harmonic motion with a trait (e.g. W2M3) following another trait (e.g. M3W2), which can be seen in the classical Lotka–Volterra prey-predator model.

An increase in speaker's payoff should make it easier

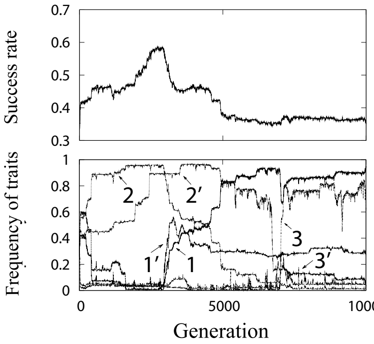

Figure 2: The success rate in conversation (top) and the frequencies of the linguistic traits concerning meaning 3 (bottom).

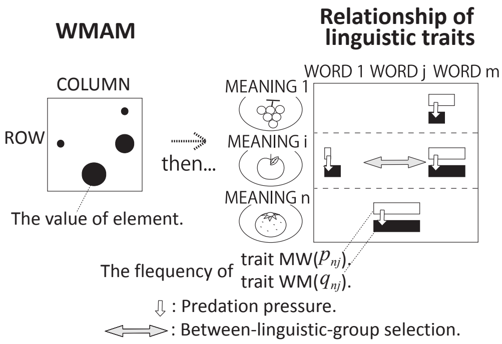

Figure 3: Multilevel selection for an implicit group.

to establish an ideal communication system in which one-to-one mapping between meanings and words. Additional experiments confirmed this tendency. It is worth noting that even the speaker's payoff was less than zero (e.g. -0.3), a high success rate (0.85) was achieved. The reason is, besides the above mechanism 2), supposed to be that agents that are the members of implicit groups in which successful conversations are held tend to gain higher payoff than the other agents who does not establish stable linguistic relations with other agents. This is a kind of multi-level selection based on the implicit linguistic groups (Fig. 3).

3.2 Structured population

Next, we examined the case with structured populations. We adopted random migration in which all agents migrate with a constant probability for comparison in addition to the method described in the previous section.

Fig. 4(a) shows the average success rate in conversation from 10000th to 20000th generations over 30 runs when varying the parameter of migration. It is shown that it was significantly greater than the one in the case of the unstructured population, especially when the number of the patch is more than 2. This suggests an effective linguistic system emerged in the structured population surely owing to multi-level selection. Also, we see that the weighted selection for poorer agents in migration works well when compared with the case with random migration (Fig. 4(b)) [4].

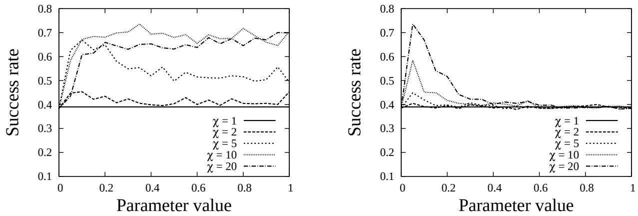

(a) Biased migration (b) Random migration

Figure 4: The success rate in conversation when ρ changed from 0.0 to 1.0 at intervals of 0.05. Each line corresponds to the number of patches (1, 2, 5, 10 and 20). The peak values of the lines are: (a) 0.39, 0.40, 0.49, 0.58 and 0.74, and (b) 0.39 0.45, 0.67, 0.74 and 0.70, respectively.

Here, we investigated the evolutionary scenario using the case in which the number of the patch was 5. The success rate in conversation averaged over the whole population fluctuated between 0.4 and 0.9. We found that the rate and the group size in each group were not converged but rather changing in a cyclic fashion. The mechanism can be explained as follows. As a general tendency, groups with a large conversation success rate have agents with high fitness in average. Therefore, the size of those groups tends to increase. However, at the same time, there is a tendency that agents who speaks and interprets correctly (*altruists*) have lower payoff than the agents who just interpret correctly (*free riders*). Therefore, when a group size becomes larger and larger, the average fitness has a tendency to decrease (Fig. 5).

It was also shown that extinction occurred frequently in a cyclic behavior of the group size. It is well known that the loss of variation could occur when a new population is established by a very small number of individuals (*founder effect*). This effect could accelerate the generation of cooperative groups in empty patches. Furthermore, agents from large groups tend to be consistent, in other words, speak a word for a meaning, and at the same time interpret the word as the meaning especially in the biased migration, which also facilitates the evolution of cooperation. This explanation based on multilevel selection and the founder effect is similar to the one we took in the context using the prisoner's dilemma model [4].

3.3 Effects of environmental variation

In short, nonhuman communication systems (NCSs) primarily benefit the speaker, while human language benefits the hearer. In this sense, the setup of the payoffs in the model is directed not to NCSs but

Number of patches	0	2	4	6	8	10
Success rate (biased migration)	0.509	0.518	0.523	0.525	0.525	0.527
Number of agents	41.6	24.3	15.2	10.8	8.3	6.9
Success rate (random migration)	0.437	0.441	0.442	0.445	0.447	0.449
Number of agents	75.9	7.6	4.9	4.4	4.3	4.8

Table 1: The success rate in conversation and the group size in each patch (averaged over generations and over 30 runs) with the parameters ρ=0.2 and θ=0.005 (biased migration) and ρ=0.05 and θ=0.02 (random migration).

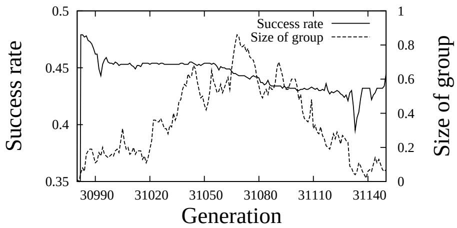

Figure 5: The conversation success rate and the population size in a group with ρ=0.1 (biased migration).

to language. We examined the effect of ecological difference on the emergence of a reliable communication system for which altruism is required, according to the discussion by Bickerton [3]. We represented the ecological gap simply as a difference in the default penalty for each patch. In this experiment, the average payoff of each agent in patch x was decreased by $x \times \theta$ as environmental severity ($0 \leq x \leq 10$).

From this experiment, we found a tendency that in severer patches the success rate was higher and the group size was smaller as the typical case in each setting is shown in Table 1. This tendency was slightly weaker when using random migration. Table 1 shows the differences in the success rate between group 0 and group 10 were 0.0179 (biased migration) and 0.0128 (random migration). The reason for this is supposed to be that severe environment requires cooperative communication and produces a larger founder effect caused by frequent extinction.

4 Conclusion

Altruistic traits that reduce the actors' fitness but increase the fitness of recipients of the act are selectively favored under positive assortment between cooperators and noncooperators [6]. Many researchers have reported that positive assortment is facilitated by such mechanisms as kin recognition, limited dispersal or behavioral bookkeeping.

This paper focused on the altruism concerning the traits responsible for speaking in the origin and evolution of vocabulary. Computational experiments showed that in an unstructured population a stable communication system hardly emerged and complex dynamics including prey-predator dynamics was observed. The experiments with a structured population demonstrated the key role of a realization of limited dispersal, that is multi-population accompanied with migration as environmental response, in the evolution of vocabulary. Also, the results supported Bickerton's claim on the significant role of ecological difference.

It should be noted that we observed that altruistic communication could evolve even in a single population. This derives from the fact that speakers tend to be correctly interpreted by the hearers having similar genetic information in this model (as both traits responsible for speaking and hearing share an identical association matrix and correlate each other) and very likely in general. We believe that this language-specific property facilitating positive assortment played a key role in the evolution of human identity.

Acknowledgements

We are grateful to R. Suzuki for fruitful discussions.

References

[1] T. C. Scott-Phillips, "The Social Evolution of Language and the Language of Social Evolution", *Evolutionary Psychology*, 5(4), 740-753, 2007.

[2] E. Sober and D. S. Wilson, *Unto Others, The Evolution and Psychology of Unselfish Behavior*, Harvard University Press, 1998.

[3] D. Bickerton, "Two neglected factors in language evolution", *The Evolution of Language*, World Scientific, 26-33, 2008.

[4] G. Ichinose and T. Arita, "The Role of Migration and Founder Effect for the Evolution of Cooperation in a Multilevel Selection Context", *Ecological Modelling*, 210(3), 221-230, 2008.

[5] M. A. Nowak, "Evolutionary biology of language", *Philosophical Transactions, Biological Sciences The Royal Society*, 355(1403), 1615-1622, 2000.

[6] D. S. Wilson, "Structured Demes and the Evolution of Group Advantageous Traits", *American Naturalist,* 111(977), 157-185, 1977.

A variety of competitive properties arises from STDP incorporating metaplastic regulation

S. Kubota[1], J. Rubin[2], T. Kitajima[3], and T. Nakamura[1]

[1]Department of Biomedical Information Engineering, Yamagata University
4-3-16 Jonan, Yonezawa, Yamagata, 992-8510, Japan
[2]Department of Mathematics, University of Pittsburgh
301 Thackeray Hall, Pittsburgh, PA 15260, USA
[3]Department of Bio-System Engineering, Yamagata University
4-3-16 Jonan, Yonezawa, Yamagata, 992-8510, Japan
(Tel : 81-238-26-3356; Fax : 81-238-26-3299)
(kubota@yz.yamagata-u.ac.jp)

Abstract: Spike-timing-dependent plasticity (STDP) induces competition among inputs, required for the construction of functional circuits, while maintaining the basic features of Hebbian plasticity. Here, we examine the competitive functi ons of STDP incorporating a metaplastic activity-dependent feedback (ADFB) mechanism, wherein higher postsynaptic activity suppresses LTP, in cases where a model neuron receives two groups of correlated inputs. We demonstrate that there are four distinct types of competitive properties depending on the relative input frequency between the different groups and the correlation time among the inputs within the same group: (1) competition with a bistable synaptic weight distribution (for identical frequency and brief correlation), (2) no competition (for identical frequency and prolonged correlation), (3) competition preferring strong input activity (for different frequencies and brief correlation), and (4) competition preferring weak input activity (for different frequencies and prolonged correlation). Our results suggest that ADFB regulation enables the modification of the Hebbian competition properties associated with STDP to increase its abilities to reflect the firing properties of input neurons.

Keywords**:** Plasticity, STDP, Synaptic competition, Neocortex.

I. INTRODUCTION

The development of functional neuronal connections depends on the competitive interaction between inputs [1]. In the presence of competition, the strengthening of some inputs causes the weakening of the others, thereby producing the input selectivity of neurons while maintaining the level of postsynaptic activity. A conventional view is that the consequence of competition is determined by the relative strength of input activities such that the synapses that are frequently activated are strengthened while those that are less frequently activated are suppressed. Such activity-dependent competition is consistent with Hebbian rule of plasticity, because the frequently-activated inputs will tend to produce strong postsynaptic discharge and therefore can be potentiated. However, recent observations suggest that some forms of neocortical plasticity cannot be explained by Hebbian competitive mechanisms: for example, in the adult rat, the active use of single whiskers for exploring new environment produces the contraction of the cortical representation of the inputs from the frequently-used whiskers [2]. The plasticity mechanism governing activity-dependent competition may be altered depending on the characteristics of inputs arising from the sensory stimuli [3].

The Hebbian-based competition has been suggested to emerge automatically through spike-timing-dependent plasticity (STDP) [4]. In STDP, the synapses that are activated slightly before and after the postsynaptic event is potentiated and depressed, respectively. Therefore, a group of temporally correlated inputs, which tends to arrive just before the postsynaptic spikes and can frequently contribute to evoking them, are selectively potentiated. However, our recent study [5] has revealed that when STDP is accompanied by metaplastic activity-dependent feedback (ADFB) modulation, wherein LTP is suppressed by the feedback of postsynaptic activity, the correlated inputs can be either potentiated or depressed depending on whether the correlation time is shorter or longer than a threshold, respectively. This finding suggests that the ADFB mechanism may serve to increase the ability of STDP to encode the firing statistics of inputs such that the resulting synaptic behavior can exhibit either Hebbian or anti-Hebbian property according to the correlation structure of input spikes [5].

In the present study, to further examine the impact of such switching in the plasticity mechanism on the activity-dependent competition, we examine the dynamics of synaptic population emerging through STDP incorporated with the ADFB mechanism. We construct a conductance-based pyramidal neuron model that receives inputs from two groups of plastic synapses, which are correlated within each group, and investigate the distribution of synaptic efficacies obtained by STDP. The results show that, depending on both the correlation time for the inputs within the same group and the relative activation frequency between the different groups, STDP can exhibit four types of competitive dynamics under ADFB modulation.

II. METHODS

1. Neuron model

We used a two-compartment neuron model consisting of a soma and a dendrite [5]. Both the compartments contain voltage-dependent sodium and potassium currents. A voltage-gated Ca^{2+} current and a Ca^{2+}-dependent potassium current are included in the dendritic compartment to reproduce firing rate adaptation exhibited in pyramidal neurons.

The neuron receives random inputs, generated by Poisson processes, from 4000 excitatory and 800 inhibitory synapses [5]. The excitatory inputs are comprised of AMPA- and NMDA-mediated currents, while the inhibitory inputs are mediated by GABA. To examine the correlation-based competition, we divided the excitatory synapses into two equally sized groups (2000 synapses each). We introduced independent correlations of equal magnitude to both of them by the method given by Song and Abbott [6]. The firing rate of the inputs within the same group has a correlation function that decays exponentially with a time constant τ_c (correlation time). The inhibitory synapses are activated by uncorrelated homogeneous Poisson processes. The mean firing rate for both the excitatory and inhibitory inputs are set to 3 Hz, unless otherwise stated. Considering a very low success rate (around 10%) of the synaptic transmission in central synapses [7], this input rate may approximately correspond to 30 Hz of firing frequency, which is within the physiological range of the sensory-evoked response of cortical neurons.

2. Synaptic weight modification

The synaptic weight modification by STDP acts on all the excitatory (AMPA) synapses. We define Δt = $t_{post} - t_{pre}$ to be the time lag between the pre- and postsynaptic action potentials. The weight change Δw induced by STDP is described as follows:

$$\Delta w = \begin{cases} A_+ \exp(-\Delta t/\tau_+), & \text{for } \Delta t > 0, \\ -A_- \exp(\Delta t/\tau_-), & \text{for } \Delta t < 0. \end{cases} \quad (1)$$

Here, A_+ (see below) and A_- (>0) represent the magnitude of LTP and LTD, respectively [5]. $\tau_+ = \tau_-$ = 20 ms are the parameters to decide the length of the temporal window of STDP. When a pre- or postsynaptic event occurs, the synaptic weights w are modified stepwise according to the additive rule of STDP. The weight changes caused by all the spike pairs are summed linearly. The upper bound of synaptic weights (w_{max}) is imposed to stabilize the learning dynamics.

Experimental findings suggest that LTP and LTD in STDP may depend on different signaling pathways: the activation of NMDARs for LTP and that of other signaling receptors (e.g., metabotropic glutamate receptors (mGluRs)) for LTD [8]. This may suggest that when higher postsynaptic activity facilitates Ca^{2+} entry through the voltage-gated Ca^{2+} channels, the Ca^{2+}-dependent desensitization of NMDARs will suppress LTP without affecting LTD. Additionally, functional NMDARs consist of obligatory NR1 subunits and modulatory NR2 subunits. The fact that Ca^{2+}-dependent desensitization occurs in NR2A- but not NR2B-containing NMDARs [9] implies that the expression pattern of NR2 subunits may regulate Ca^{2+}-dependent desensitization. To examine the effects of the subunit- and activity-dependent desensitization of NMDARs, we introduced the ADFB modulation of the magnitude of LTP proposed by ref. [5]:

$$A_+(t) = A_+^0 - k_{\max} \rho f_{post}(t). \quad (2)$$

Here, A_+^0 and $k_{\max}$ are positive parameters. $f_{post}(t)$ denotes the postsynaptic firing rate at time t. The parameter ρ is used to represent the expression pattern of distinct NMDAR subunits: ρ = 0 corresponds to the state where NMDARs are comprised of NR1 and NR2B subunits, whereas ρ = 1 denotes the state where the NMDARs contain many NR2A subunits. Therefore, in Eq. 2, the feedback effect is strengthened by the increased value of ρ, which corresponds to the enhanced expression of NR1/NR2A NMDARs exhibiting activity-dependent desensitization. The postsynaptic frequency was estimated by the equation $f_{post}(t)$ = $\int_0^\infty \lambda \exp(-\lambda\tau) S_{post}(t-\tau) d\tau$ by using the postsynaptic spike train $S_{post}(t)$ = $\sum_{t_{post}} \delta(t - t_{post})$.

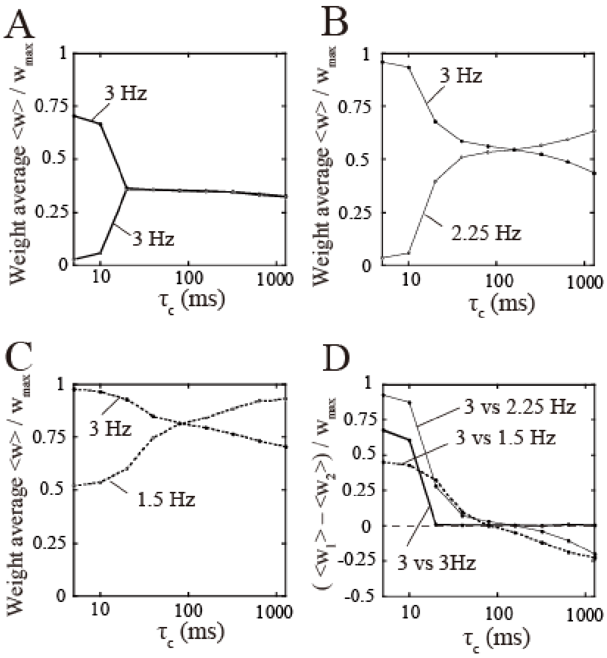

Fig.1. (A–C) The weight averages of the two input groups as function of τ_c at the equilibrium state. The mean input frequency of the two groups is the same (3Hz) in (A), whereas that of either one group is decreased by 25% in (B) or by 50% in (C). The input frequency for each group of synapses is shown in the labels. (D) The difference in the weight averages of two groups at the equilibrium state is plotted as function of τ_c for the three input cases corresponding to (A)-(C) by using the same line style.

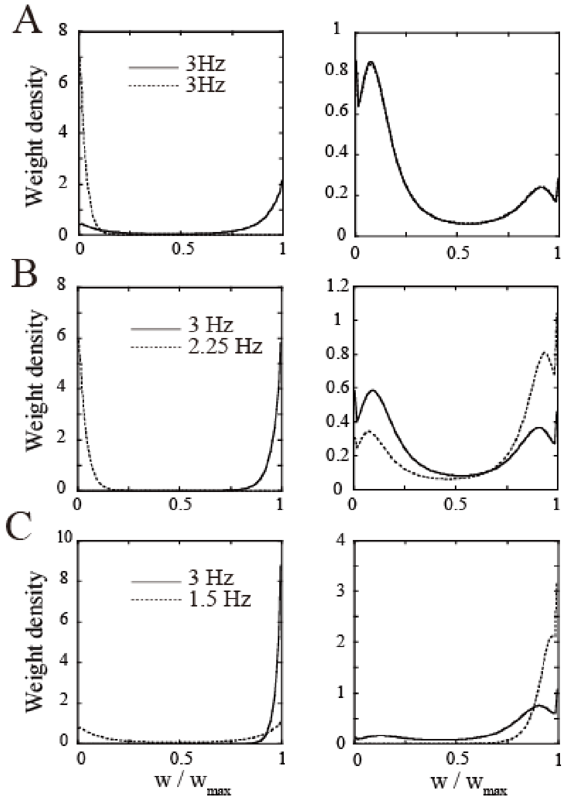

Fig.2. The steady-state weight distributions of the two synaptic groups are shown by the solid and dashed lines. Left and right columns show the cases for τ_c = 5 ms and τ_c = 1280 ms, respectively. The mean input frequencies for the two groups are the same in (A), whereas they are different in (B) and (C). The input rate for each group is shown in the legends. Since the weight distribution fluctuates even at the equilibrium, we have taken their temporal average over a sufficiently long period.

III. RESULTS

To examine how the competition by STDP depends on the input correlation properties, we examined the synaptic distribution at the equilibrium state by changing the correlation time τ_c, when the neuron receives two groups of correlated inputs (Figs. 1A and 1D). The figures show that when the correlation time is sufficiently short, the synaptic weights segregate into the two input groups with the one winning the competition suppressing the other. However, when the correlation time becomes prolonged ($\tau_c >$ 20 ms), the synaptic weights of both the groups converge to the same average strength, implying the absence of competitive interaction. This result is clarified by the steady-state weight distribution (Fig. 2A). The figure shows that for smaller τ_c, the final weight distribution is bimodal and the two groups converge to distinct distributions [6] (Fig. 2A, left). In contrast, for larger τ_c, the weight distributions of the two groups have the identical characteristic form that contains local peaks at the positions slightly apart from the boundaries (Fig. 2A, right). The competitive state obtained for smaller τ_c is bistable because the inputs are symmetric under exchange of the two groups, and therefore, which group becomes dominant at the present time can be determined by the past input activities [10]. The results here appear to be consistent with the previous result [5] that STDP exhibits Hebbian or anti-Hebbian property for smaller or larger τ_c values, respectively. For smaller τ_c, the Hebbian property of STDP can drive correlation-based competition as in the previous study [6]. In the presence of prolonged correlation, if either one group is potentiated more than the other, the potentiated group will tend to control the timing of the postsynaptic spiking. However, the activation of inputs with longer correlation time produces many post-pre timing spike pairs that cause LTD [4]. Thus, it would be difficult for the correlated group to be continuously potentiated in the presence of anti-Hebbian mechanism, in which a group of inputs having prolonged correlation tends to be strongly weakened [5].

Furthermore, when the mean input frequency for one group was decreased, the dominant group at the equilibrium state was reversed with changes in the correlation time (Figs. 1B–1D): the group activated by higher frequency inputs suppresses the other group at smaller τ_c, whereas the group activated by lower frequency inputs becomes dominant at larger τ_c. These changes are accompanied by the significant modification in the proportion of synapses within each group that accumulates near either the upper or lower boundary (Figs. 2B and 2C). These results imply that STDP functions to strengthen frequently and less-frequently activated inputs in the case of brief and prolonged correlation time, respectively, which may also be in line with the prediction by the switching from the Hebbian to anti-Hebbian plasticity through the increased correlation time [5].

IV. CONCLUSION

In this study, we have examined how an STDP model incorporated with the ADFB mechanism regulates competition between two groups of correlated inputs. The results have demonstrated that four distinct types of competitive properties emerge from STDP, depending on the relative difference in the frequencies with which the two groups generate inputs and the correlation time of the input activity within each group: (1) competition producing bistable synaptic pattern (for the same input frequencies and small correlation time); (2) no competition (for the same input frequencies and large correlation time); (3) the competition with a bias towards stronger input activity (for different input frequencies and small correlation time); and (4) the competition with a bias towards weaker input activity (for different input frequencies and large correlation time). Cases (1) and (3) can be expected from Hebbian plasticity, whereas (2) and (4) may result from anti-Hebbian plasticity, as mentioned above. A strong Hebbian learning has a non-democratic aspect since it will permit only a small number of frequently-activated inputs to acquire control of many postsynaptic neurons. Therefore, in biological systems, it would be useful to regulate the strength of Hebbian effects. The present findings suggest that ADFB regulation enables the modification of the Hebbian properties associated with STDP, which may be required for efficient central processing.

ACKNOWLEDGMENTS

This study is partially supported by Grant-in-Aid for Scientific Research (KAKENHI(19700281), Young Scientists (B)) from the Japanese government. S.K. is partially supported by the Program to Accelerate the Internationalization of University Education from the Japanese government and the International Research Training Program from Yamagata University.

REFERENCES

[1] Miller KD (1996), Synaptic economics: competition and cooperation in synaptic plasticity. Neuron 17: 371-374
[2] Polley DB, Chen-Bee CH, Frostig RD (1999), Two directions of plasticity in the sensory-deprived adult cortex. Neuron 24:623-627
[3] Feldman DE, Brecht M (2005), Map plasticity in somatosensory cortex. Science 310: 810-815
[4] Song S, Miller KD, Abbott LF (2000), Competitive Hebbian learning through spike-timing-dependent synaptic plasticity. Nature Neuroscience 3:919-926
[5] Kubota S, Rubin, J, Kitajima T (2009), Modulation of LTP/LTD balance in STDP by an activity-dependent feedback mechanism. Neural Networks 22:527-535
[6] Song S, Abbott LF (2001), Cortical development and remapping through spike timing-dependent plasticity. Neuron 32:339-350
[7] Hessler NA, Shrike AM, Mallnow R (1993), The probability of transmitter release at a mammalian central synapse. Nature 366:569-572
[8] Bender VA, Bender KJ, Brasier DJ et al. (2006), Two coincidence detectors for spike-timing-dependent plasticity in somatosensory cortex. Journal of Neuroscience 26:4166-4177
[9] Krupp JJ, Vissel B, Heinemann SF et al. (1996), Calcium-dependent inactivation of recombinant N-methyl-D-aspartate receptors is NR2 subunit specific. Molecular Pharmacology 50:1680-1688
[10] Kubota S, Kitajima T (submitted), Possible role of cooperative action of NMDA receptor and GABA function in developmental plasticity.

Automatic Estimation of Light Sleep Level during Short Nap

Bei Wang[1], Takenao Sugi[2], Xingyu Wang[1], Shuichiro Shirakawa[3], Masatoshi Nakamura[4]

[1]*Department of Automation, East China University of Science and Techonology, Shanghai, China*
[2]*Department of Electrical and Electronic Engineering, Saga University, Saga, Japan*
[3]*National Centre of Neurology and Psychiatry, Tokyo, Japan*
[4]*Research Institute of Systems Control, Institute for Advanced Research and Education, Saga University, Saga, Japan*
(Tel: 86-21-64253581; Fax: 86-21-64253386)
(wangbeish@gmail.com)

Abstract: Short nap is a good relaxation way when people feel sleepy and tired during the day time. An automatic light sleep level estimation technique was presented for short nap sleep evaluation. Parameters were extracted from the polysommnographic sleep record. Sleep stages of open eyes awake, close eyes awake, and stage 1 were determined automatically based on the conditional probability. The conditional probability indicated the possibility of occurrence of sleep stages during short nap. The light sleep level was estimated based on the continuous change of conditional probability of awake. The developed technique can be usable for comfortable short nap sleep control.

Keywords: light sleep level, short nap, conditional probability**.**

I. INTRODUCTION

Sleep is essential for the normal functioning of all the systems of our body. Sleep is fundamental for healthy, which is related to the circadian rhythms. Usually, sleep time or sleep/wake cycle is controlled by environmental factors and internal factors. Comfortable environment control has significant affect to ensure good sleep for human health.

Daytime prophylactic nap is an effective relaxation way which can avoid the decline of working efficiency and attention level [1]. This kind of short nap sleep has positive effects on performance level, while it also has negative effects as sleep inertia. The suitable latency of a short nap is suggested about 20 minutes to maintain the daytime arousal level [2]. However, the proper time of short nap is uncertain by various factors. The environment factors included the temperature, sound, etc. The internal factors were mainly the individual difference on mental and physical functions. Therefore, automatic control of short nap sleep time which can be adaptive to persons is necessary to be developed.

In this study, an automatic estimation technique for light sleep level during short nap was developed. The ultimate purpose is to control the sleep time for an effective short nap. The sleep stages of open eyes stage awake O(W), close eyes stage awake C(W) and stage 1 (S1) during short nap were determined automatically. The main method for sleep stage determination was based on the expert knowledge-based multi-valued decision making, which had been developed in our previous study [3]. The algorithm was modified in order to obtain the changing of conditional probability for sleep stages. The changing of conditional probability was adopted to estimate the light sleep level during short nap sleep.

II. METHOD

1. Data acquisition

The sleep data of five subjects were adopted for light sleep level analysis. The overnight sleep recording of two subjects was selected for training to obtain the parameter distribution for sleep stage discrimination. Another three were for testing to calculate the conditional probability which representing the possible occurrence of each sleep stage.

All of the sleep data were recorded based on the polysommnographic (PSG) measurement including four electroencephalogram (EEG), two electrooculargram (EOG) and one electromyogram (EMG). EEGs were recorded by using cup electrodes fixed to the scalp at points C3, C4, O1, and O2 with the reference of earlobe A1 and A2 according to the International 10-20 System [4]. EOG was recorded by using three cup electrodes which were pasted near the eyes to record the vertical and horizontal eye movements. Two cup electrodes were attached near chin to record the muscle activity of EMG.

2. Visual inspection

The continuous sleep data was divided into consecutive 30-second epoch. Sleep stages were inspected visually for each epoch by a qualified clinician (F. Kawana) in Toronomon Hospital.

The light sleep states were inspected mainly according to EEG characteristics [5]. SW was scored to open eyes awake O(W) and close eyes awake C(W) according to the alpha activity (8-13 Hz) in O1/A2 and O2/A1 channels. S1 was scored with low voltage slow wave activity of 2-7 Hz in C3/A2 and C4/A1. Eye movements were disappeared and muscle activities were depressed when vigilance level was gradually declined.

3. PSG parameters

The parameters for sleep stage determination were extracted from the periodograms of neurological signals of EEG, EOG and EMG. Table 1 showed the definition of three parameters. D_α was calculated in EEG channels as the ratio of the amount of alpha components (8-13Hz) to the amount of total frequency components (0.5-25Hz). A_{HF} was calculated in EEG channels as six times of the square root of the amount of high frequency components (25-35 Hz). S_{L-R} was calculated in EOG channels as the amount of eye movement. Those parameters were selected which can discriminate the parameter distribution among the sleep stages of O(W), C(W) and S1.

The parameter distributions were constructed for sleep stages. Cauchy distribution was adopted to estimate the parameter distribution, as

$$f(y\,|\,\zeta)=\frac{b}{\pi((y-a)^2+b^2)}, \tag{1}$$

Table 1. Parameter definition

	Definition
Duration [%]	$D_\alpha=\dfrac{S_\alpha}{S_T}\times 100\%$
Amplitude [μV]	$A_{HF}=6\sqrt{S_{HF}}$
Amount [μV^2]	S_{L-R}

**α*: 8-13 Hz, T: 0.5-25 Hz, HF: 25-35Hz, L-R: 2-10 Hz*

where y is parameter, ζ is sleep state, a and b are location and scale parameters of Cauchy distribution. a and b were determined by least square method applying to the histogram of parameters.

4. Conditional probability

The conditional probability was calculated based on the Bayes rule as,

$$P_{k|k}(\zeta^i)=\frac{f(y_k\,|\,\zeta^i)P_{k|k-1}(\zeta^i)}{\sum_{j=1}^{n} f(y_k\,|\,\zeta^j)P_{k|k-1}(\zeta_j)}, \tag{2}$$

where $P_{k|k-1}(\zeta^i)$ is the predicted probability, y_k is a parameter vector and $f(y_k|\zeta^i)$ is the joint probability density function of parameters in y_k for stage ζ^i .

The conditional probability of O(W), C(W) and S1 were calculated for every 5-second segment. The average value of each conditional probability among the six 5-second segments was adopted as the conditional probability for one 30-second epoch. The higher value between the conditional probabilities of stage O(W) and C(W) was adopted as the conditional probability of awake P_W. P_W was adopted to estimate the light sleep level during short nap sleep.

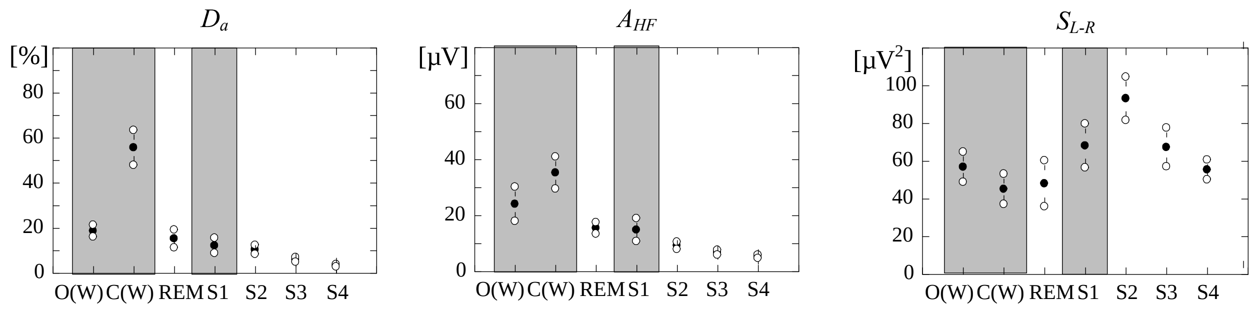

(a) Ratio of alpha components (8-13 Hz) calculated on O1/A2 and O2/A1 channels

(b) Amplitude of high frequency components (25-35 Hz) on C3/A2 and C4/A1 channels

(c) Amount of eye movement (2-10 Hz) on LOC/ROC channel

Fig.1. Probability density function of parameter for each sleep stage

III. RESULTS

1. Parameter distribution

The overnight sleep recordings of two subjects were utilized to obtain the parameter distribution. The probability density functions of Cauchy distribution for three parameters were given in Fig.1. The horizontal axis was stages and vertical axis was probability. The empty circle indicated the location parameter of Cauchy distribution while full circle the scale parameter of Cauchy distribution.

Since the training data were overnight sleep recording, the parameter distributions for all the sleep stages were illustrated, where W was stage awake, R was rapid eye movement stage, S1, S2, S3 and S4 were non-rapid eye movement of sleep stage 1, 2, 3 and 4, M was body movement. The darken parts represented the parameter distribution for O(W), C(W), and S1. The duration of alpha activity showed higher values for stage C(W). The amplitude of HF activity indicated C(W) and O(W) were separated from S1. The amount of eye movement of S1 was higher. The combination of those three parameters was utilized to calculate the conditional probability of each sleep stage for test subjects.

2. Light sleep level estimation

Another three subjects were utilized for testing. In Fig.2, the conditional probability of awake P_W was shown comparing with the visual inspection.

Fig.2 (a) showed the visual inspection by clinician. Fig.2 (b) showed the conditional probability of awake obtained by expert knowledge-based multi-valued decision making method. The horizontal axis was time. The vertical axis was sleep stages. The beginning 30 minutes of sleep data before falling to deep sleep were extracted from the whole recording. The conditional probability P_W was rather high when visual inspection was stage awake. P_W was decreased when stage awake changed to stage 1 and stage 2. When the body movement was inspected by clinician, the corresponding conditional probability P_W also has higher value. The darken parts showed that the changing of conditional probability was consistent with visual inspection. At the beginning of recording, the conditional probability slightly varied when visual inspection was kept to be stage awake.

The result of another two test subjects were shown in Fig.3 and Fig.4. The continuous changing of conditional probabilities P_W was given respectively.

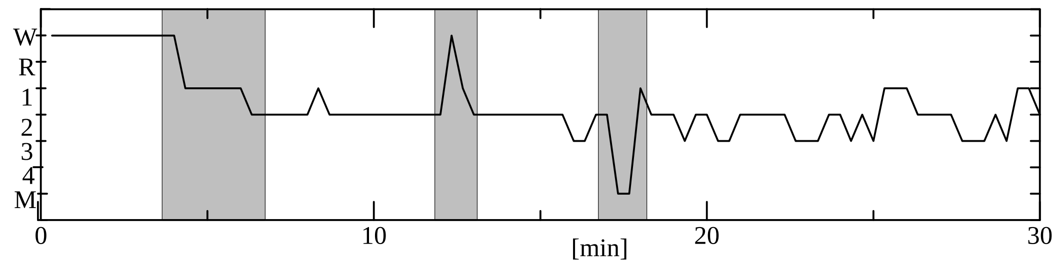

(a) Visual inspection by clinician

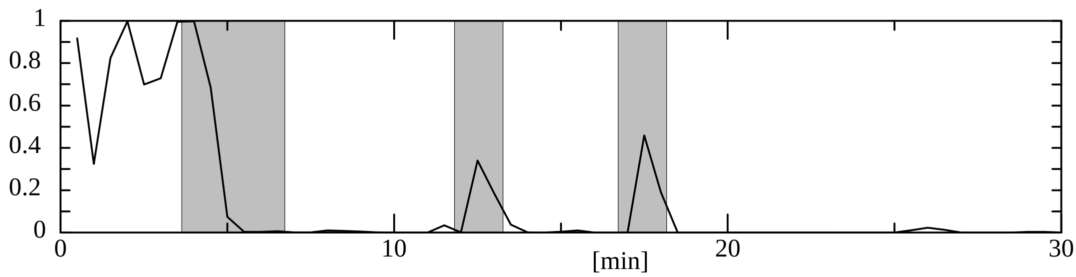

(b) Conditional probability of stage awake

Fig.2. Light sleep level estimation based on conditional probability by expert knowledge-based multi-valued decision making method for subject A.

Although the visual inspections were not given for these two subjects, the sleep stage changing can be estimated according to the continuous changing of conditional probability of stage awake P_W. The higher value indicated higher vigilance level which might be stage awake. The lower value indicated lower vigilance level where sleep was transited to stage 1 and stage 2.

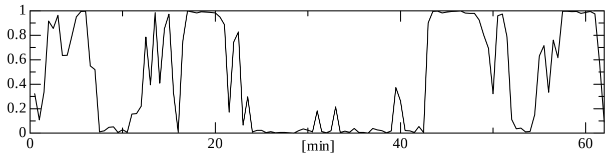

Fig.3. Light sleep level estimation for subject B.

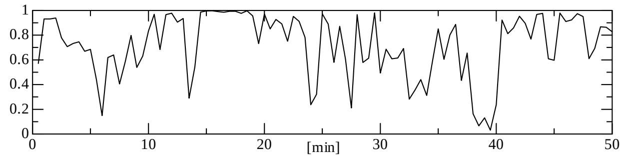

Fig.4. Light sleep level estimation for subject C.

IV. DISCUSSION

1. Light sleep level estimation

Adequate regulation of the sleep state is significant to ensure an effective short nap. During the short nap sleep, it is better to wake up from light sleep stage. The automatic sleep stage determination by expert knowledge-based multi-valued decision making method was effective for overnight sleep stage determination. It was also usable to obtain the continuous change of conditional probability.

In this study, the conditional probability of sleep stage was calculated continuously to indicate the light sleep level during short nap. The result showed that the conditional probability of awake is useful for light sleep level estimation. For further study, the relationship between light sleep level and conditional probability of all the sleep stages needs to be considered together to construct an effective parameter for light sleep level estimation in order to improve the accuracy.

2. Comfortable sleep circumstance control

The developed technique can be usable for comfortable sleep circumstance control especially to ensure an effective short nap. When conditional probability of awake was decreased, the sleep stage may be transited to light sleep stage 1 and stage 2.

Based on the light sleep level estimation result, subject can be waked gradually from light sleep by using proper environment controlling technique. Therefore, comfortable short nap sleep control can be realized.

V. CONCLUSION

Short nap sleep data was analyzed based on the expert knowledge-based multi-valued decision making method. The conditional probability of awake was utilized for light sleep level estimation during short nap. The developed technique can be usable for effective short nap control.

Acknowledgment

The authors are grateful to Dr. Fusae Kawana, Department of Clinical Physiology, Toranomon Hospital, Japan, for the technique help on sleep stage inspection. The authors also acknowledge Mr. Hiroaki Yoshiyama, graduate student of Department of Advanced System Control Engineering, Saga University, Japan, and Mrs Xiuyan Fu, graduate student of Department of Automation, East China University of Science and Technology, China, for their assistance on experiment and research works.

REFERENCES

[1] Hayashi M, Chikazawa Y, Hori T (2004), Short nap versus short rest: recuperative effects during VDT work. Ergonomics 47(14):1549-1560

[2] Hayashi M, Ito S and Hori T (1999), The effects of a 20-min nap at noon on sleepiness, performance and EEG activity. Int J Psychophysiol 32(2):173-180

[3] Wang B, Sugi T, Kawana F, Wang X and Nakamura M (2009), Expert knowledge-based automatic sleep stage determination by multi-valued decision making method. IEEJ transactions on Electronics, Information and Systems 129(4):614-619

[4] Jasper HH (1958), Ten-twenty electrode system of the international federation. Electroenceph Clin Neurophysiol 10:371-375

[5] Rechtschaffen A, Kales A (1968), A manual of standardized terminology, techniques and scoring system for sleep stages of human subjects. US Department of Health, Education and Welfare, National Institute of Health Publ. No. 204, Washington, 1968, 1-78

Evolving Behavior Sequences for a Humanoid Entertainment Robot

Wei-Po Lee Jih-Shiou Jong Tsung-Hsien Yang

Department of Information Management,
National Sun Yat-sen University, Taiwan

Abstract: One of the most important issues in developing entertainment robot is human-robot interaction, in which the robot is expected to learn new behaviors specified by the user. In this paper we present an imitation-based mechanism to support robot learning and use evolutionary computing to learn new behavior sequences. We also propose several advanced techniques at the task level and the computational level to evolve complex sequences. To evaluate our approach, we use it to evolve different behaviors for a humanoid robot. The results show the promise of our approach.

Keywords: Entertainment Robot, Humanoid Robot, programming-by- demonstration, Genetic Algorithm

I. INTRODUCTION

In recent years, entertainment robots have been considered the main trend of the next-generation electronic toys, and this type of robots has become an important application of intelligent autonomous robot [1][2]. Building fully autonomous artificial creatures with human-like intelligence is a long-term goal and it has not yet achieved at the present stage. However, with current technologies in computing and electronics, and new knowledge in ethology, neuroscience and cognition, it is now possible to create embodied prototypes of artificial living toys acting in this physical world.

One of the most important issues in developing entertainment robot is human-robot interaction, in which the robot is expected to learn new behaviors specified by the user. Entertainment robots are service robots to live with people, therefore we need to furthermore apply knowledge of biology and ethology to derive design principles for interaction and learning. Imitation is a powerful mechanism in social animals for learning and delivering new knowledge [3][4], and some researchers have proposed to endow a robot with such social-cognitive skills [5][6][7]. In this work, we choose to implement such a mechanism to provide a special kind of human-robot interaction.

In this paper we present an evolution-based approach to realize the imitation-based learning. In our work, the robot is shown how to perform the desired behavior first, and during the period of human demonstration, the behavior sequences are recorded and analyzed. Then the Genetic Algorithm is employed to evolve the behavior sequences: to determine how to rotate different motors on the robot's body parts to produce the same behaviors. To evaluate our approach, we use it to evolve different behaviors for a humanoid robot. As for complex behavior sequences, we propose some advanced techniques for performance enhancement, including the division of the overall behavior at the task level, and the exploitation of priori information and exploration of search space with an adaptive mutation at the computational level. The preliminary results and analyses show that our approach can successfully and effectively evolve behavior sequences for the robot.

II. EVOLVING BEHAVIOR SEQUENCES

1. System Overview

As mentioned above, this work aims to establish an imitation-based learning framework to evolve behavior sequences for a humanoid robot. Fig. 1 illustrates such a framework that mainly includes two parts for active learning and passive learning, respectively. The active part involves a gesture recognition procedure, which is to capture and record images of the demonstrator, and then extract the curve for further interpretation. If a match is found, the corresponding behavior module is retrieved and activated from the behavior library. The control code for generating the sequence is then sent to the robot. The library can be pre-constructed to include some behavior primitives as basic components, and is gradually expanded by the user during the human-robot interaction procedure.

The passive part is to build a new behavior that does not exist in the behavior library. Here the new behavior means a completely new sequence (if no sequences in the library matched any part of the newly demonstrated one) or a sub-sequence obtained from the demonstrated sequence (after the partially matched parts have been removed). Because this work focuses on the passive part of the demonstration-based learning framework, therefore we will concentrate on describing the development of our learning mechanism, in which a modified genetic algorithm is employed to evolve behavior sequences.

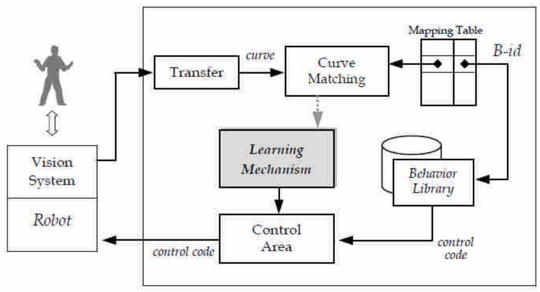

Fig. 1. The system overview.

2. Evolving Behavior Sequences

The first important step in evolutionary computation is to choose a proper representation for the individual. The goal here is to drive the motors of a humanoid robot to produce the same behavior sequences as that of the human demonstrator. We thus use a direct encoding scheme that takes the motors to be considered and their corresponding activities as gene pairs to constitute a chromosome. That is, a chromosome is a fixed length string that records a sequence of motor activities along time domain. The odd genes indicate the motor identifiers and the even genes are the motor rotating angles. To provide the robot a reasonable number of time steps to produce the target behavior sequence, the length of the chromosome is defined as the ratio of the estimated displacement of the behavior trajectory to the minimal motor speed.

As the behavior shown by the demonstrator may involve different body parts (for example, both hands in this work), the motors drive these parts can thus rotate independently at the same time. In such situations, the behavior trajectories of different parts can be built separately, in which only the motors driving the same part are used in the corresponding chromosome. However, in the above situations the synchronization problem between different body parts needs to be considered. For example, in Fig. 2, the demonstrator moved his right hand but halted the left hand (the x, y, z coordinates remain the same) in two short periods T_1 and T_2. Therefore, when the behavior sequences for the two hands are evolved separately, some motor genes with zero rotating angles (i.e., halting the motors) need to be inserted to the solution for the left hand to keep it synchronized with the right hand.

From the computational point of view, using motor genes with zero rotating angles will generate some redundant gene pairs and introduce extra difficulty in the evolutionary process, so we employ an alternative way to deal with the synchronization problem instead. In our method, sequences for different body parts are aligned and the halting periods are used to divide these sequences. For example, in Fig. 2 the two sequences for the right and the left hands are divided into four independent sub-sequences. Then the solutions are evolved separately for each sub-sequence and combined as the overall solution.

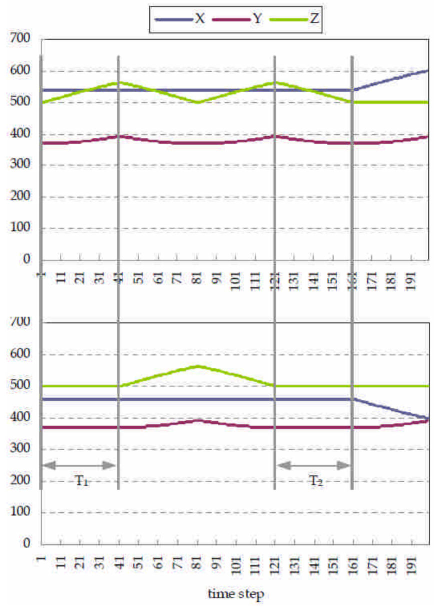

Fig. 2. An example of behavior sequence in which the upper (lower) part shows the x, y, and z coordinates of a tracking mark on the demonstrator's right (left) hand.

After the genetic representation has been defined, the next step is to evaluate individuals to determine their fitness for the creation of a new population. Here, the goal is to measure how the behavior sequence produced by the individual is close to the original sequence shown by the demonstrator. It is to accumulate the deviations derived from the motion effect of the motor activities described in a chromosome. If the target and actual positions for a tracking mark at time step t are $p(t)$ and $p'(t)$, respectively, the closeness of the target and actual sequences can be measured as:

$$closeness = \sum_{t=1}^{T} c(t) \quad \text{and}$$

$$c(t) = 1 \text{ if } d(t) < d_{thread}; \quad c(t) = 0 \text{ otherwise}$$

In the above equation, T is the number of time steps of the robot's performing the task; $d(t)$ means the distance between the target and actual positions at time t; and $c(t)$

indicates whether the actual sequence can approximate the target sequence at time *t*.

As the *closeness* measures the position difference of two sequences at discrete time points, it is thus possible to obtain two sequences with very similar closeness but have different motion trajectories. To distinguish among sequences precisely, a penalty term is introduced to estimate the differences of motion trajectories of the target and actual sequences as:

$$\sum_{1}^{T}[v_p(t)-v_p(t-1)]-\sum_{1}^{T}[v_{p'}(t)-v_{p'}(t-1)]$$

in which v is the velocity of the tracking mark (i.e., $v_p = |p(t) - p(t+1)|$ and $v_{p'} = |p'(t) - p'(t+1)|$). With the above two kinds of measurement, we then define the fitness function as their weighted sum:

$$fitness = closeness - \alpha \times penalty$$

Based on the above fitness function, the individuals can be evaluated and their performance can be determined. Then a certain selection scheme is used to choose parent individuals. In our implementation, the *tournament* selection scheme is employed to choose parents. Then, three genetic operators, *reproduction*, *crossover*, and *mutation*, are applied to create a new population for the next generation. As our representation includes two types of data (motor identifier and rotating angle), two kinds of crossover are used for the recombination of individuals: uniform crossover for motor genes and arithmetical crossover for rotating angles.

3 Evolving complex behavior sequences

After describing how an evolutionary framework is developed to learn new behavior sequences, this section presents how it is furthermore extended to evolve complex sequences from different points of view. Here the complex sequence means a sequence that needs specific skills to achieve; it is not necessarily a long sequence. The first way to evolve complex sequences is to reduce the complexity from the task level. That is, to take a divide-and-conquer technique to decompose a complex behavior sequence into several sub-sequences, evolve solutions for the sub-sequences and then combine them together for the complete sequence. Though this method provides a direct way to reduce task complexity by the division of original sequence, however, its corresponding disadvantages need to be seriously considered. For example, it is tedious for the user to deal with the large amount of tiny subsequences. Also it becomes difficult to attach suitable semantic interpretations for the tiny sequences and this is important to many service robot applications.

The other direction to encounter the complexity problem is to take a computational perspective to enhance the searching performance. Two methods have been developed in this work. The first method involves the exploitation of the priori knowledge in searching solution space. It is to retrieve some behaviors sequences, which are similar to but different from the target behavior, from the behavior library to the initial population. It is expected that with the guidance of these relatively good solutions, the evolutionary search can become more efficient and the target behavior can thus be obtained.

The other method is to develop an adaptive mutation scheme to maintain population diversity during the evolutionary process. It is to calculate the standard deviation of the fitness of all individuals at each generation (i.e., sd_i), and to record the maximum of the standard deviation from the first generation (i.e., *max-sd-so-far*). Then the ratio of current standard deviation to the maximum value is used to determine the mutation rate, which is the default mutation rate multiplies a factor of ($1 - sd_i/max\text{-}sd\text{-}so\text{-}far$). In this way, the population is guaranteed to include certain new individuals to main its diversity.

III. EXPERIMENT RESULTS

To assess the proposed methods, we used them to evolve different complex behavior sequences. In this work, we developed a simulator to generate the behavior sequences to be achieved and record the coordinates accordingly, to save the effort of human demonstration. In addition, to fit the hardware restrictions of the real robot used in this work, three motors, on the shoulder (pitching), elbow (rolling), and twist (rolling) joints, were used to drive each hand. Here, each motor was allowed to rotate within the range of +90 to –90 degrees. The behaviors evolved from simulation were transferred to a real humanoid robot for verification.

In the experiments, we pre-compiled three complex behavior sequences, as illustrated in Fig. 3 (due to the space limitation, only one behavior is shown), to evaluate the methods mentioned in section II.3 in evolving complex sequences. We also conducted a set of experiments that took the original framework to evolve the same tasks for performance comparison. The results without advanced techniques are shown in Fig. 4, in which no successful runs can be obtained.

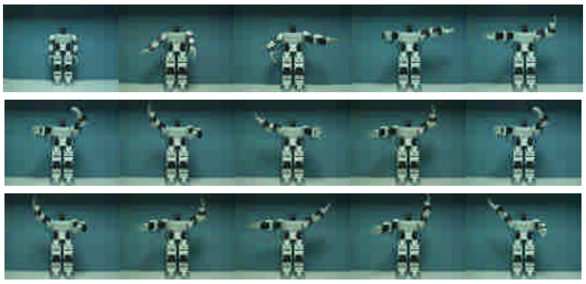

Fig. 3. One of the target behaviors.

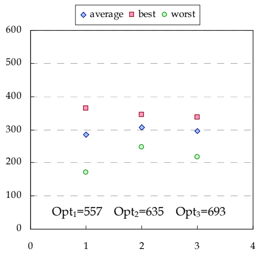

Fig. 4. The results for evolving behaviors with different population size (The *y*-axis means fitness value, and the indices 1, 2, and 3 in the *x*-axis represent experiments for three different behaviors, respectively).

1. Task decomposition

As described in section II.3, we can adopt the divide-and-conquer method to reduce task complexity, evolve partial solutions for subsequences, and then combine the partial solutions to obtain the final solution. To evaluate the performance of task decomposition, we divided the each of the tasks into two behavior subsequences, and then four subsequences (with approximately the same length), to examine the corresponding effect. In the experiments, ten independent runs were conducted for each of the divided subsequences. The population size is 1000, the crossover rate is 0.7 and the mutation is 0.003.

Fig. 5 lists the results of dividing the original tasks into different number of subsequences. As can be seen, initially all of the three complex behavior sequences cannot be evolved correctly. After each of the sequences was divided into two subsequences, the first behavior can be evolved successfully four times in the ten runs, and the third behavior, one time. We then furthermore divided them again into four subsequences and repeated the evolutionary runs again. As can be expected, the target tasks became more achievable after the division was performed again. But it should be noted that more and more tedious experimental runs will be needed if the task are divided iteratively. Also it will become difficult to attach semantic labels for the tiny sub-behaviors to be reused in other applications.

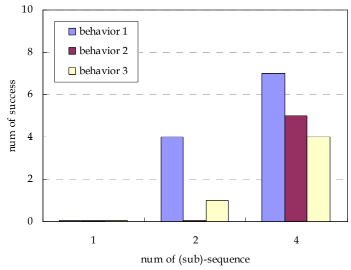

Fig. 5. The number of successful runs in evolving complex sequences by task decomposition.

2. Advanced evolutionary techniques

In addition to reducing complexity from the task level to evolve complex behaviors, we also investigate whether the priori information of a specific problem can be used to derive solutions in a more efficient manner. Here, the priori information means the similar behavior sequences already recorded previously in the behavior library. In this work, ten simple behaviors are pre-defined as primitive robot behaviors. To exploit the information already obtained, we measured the similarity between the target behavior and the ones recorded in the library, and then chose and inserted three most similar behaviors to the initial population in the evolutionary process.

Ten independent runs have been conducted for each of the tree tasks. In each run, a population of 1000 individuals was used, in which three of them were taken from the library as described above. Fig. 6(a) presents the results. It shows that in average the experiments with priori information have better performance than those without using information. However, we also noticed that with the guidance of priori information, the runs converged more quickly than those without using information. This feature caused evolutionary runs to lose population diversity and became premature. Consequently, we cannot obtain successful solutions.

To prevent the above premature situation, we have developed an operator of adaptive mutation to maintain population diversity. It is to introduce randomness of the population based on the standard deviation of the fitness of all individuals. In this set of experiments, the mutation rate of each generation was determined by the criteria described in section II.3. To observe the effect of adaptive mutation alone, we conducted ten runs for each of the three complex behaviors in which all other parameters were the same as the abovementioned methods. Fig. 6(b) summarizes the results. As can be seen, better results can be obtained, though there is no successful run obtained.

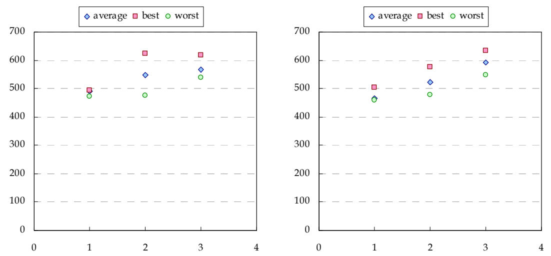

Fig. 6. The results of using priori information (a) and adaptive mutation (b) to evolve robot behaviors.

From the above two sets of experiments, it can be seen that using priori information or adaptive mutation can both improve search performance and evolve better solutions, but no perfect solutions can be obtained from all of the runs. Therefore, following the above experiments, we combine both strategies to conduct evolutionary runs (with the same parameter settings as before) in evolving complex behaviors. Fig. 7 summarizes the results, in which the numbers of successful runs for the three behaviors are now 5, 2, and 3, respectively. Fig. 8 shows how the fitness curves converged during the typical runs (for the behavior illustrated in Fig. 3). As can be seen clearly, by integrating two useful strategies to exploit all their advantages, perfect solutions can be evolved. It shows the success of our approach.

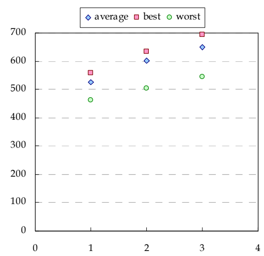

Fig. 7. The results of using both priori information and adaptive mutation.

IV. CONCLUSIONS

In this paper, we have indicated the importance of developing entertainment robots as an intelligent robot application. To realize the development of adaptive entertainment robot, an imitation-based learning mechanism has been constructed with which the user can teach the robot how to perform the expected behavior through demonstration. Here we use an evolutionary approach to support the imitation-based robot learning, and implement several advanced techniques at the task level and the computational level to evolve complex behavior sequences. The experimental results show that by the exploitation of priori information and the exploration of solution space with an adaptive mutation, the complex behavior sequences can be evolved successfully.

Based on the presented work, we are currently extending our approach to evolve robot behaviors with coordination of both hands and legs. Since this type of behaviors involves the balance of robot body, it becomes more difficult to achieve. We are investigating more advanced computational techniques to deal with the relevant problems. In addition, we plan to integrate an efficient vision system into the robot to acquire and analyze the demonstrator's behavior sequences in real time.

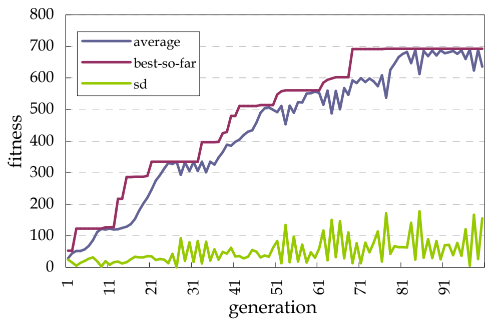

Fig. 8. The fitness curves of the typical run in evolving behaviors by both priori information and adaptive mutation.

REFERENCES

[1] Veloso MM (2002), Entertainment robotics. *Communication of the ACM*, 45, 59-63
[2] Fujita M (2004), On activating human communications with pet-type robot AIBO. *Proceedings of the IEEE*, 92, 1804-1813
[3] Rizzolatti G and Craighero L (2004), The mirror-neuron system. *Annual Review of Neuroscience* 27, 169-192
[4] Zentall TR (2006), Imitation: definitions, evidence, and mechanisms. *Animal Cognition* 9, 335-353
[5] Dantenhahn K (2007), Socially intelligent robots: dimensions of human-robot interaction. *Philosophical Trans. of the Royal Society B*, 362, 679-704
[6] Breazeal C (2002), *Designing Sociable Robots*, MIT Press, Bradford Book.

A guess for natural neural activity and a modification suggestion on the ANN

Y. G. Zhang
(The Institute of Systems Science, academia Sinica, Beijing, China, 100080)
Masanori Sugisaka
(The Bunri University, Oita, Japan)

ABSTRACT Based on the knowledge of brain and neural science, the author has a guess on the basic brain neural activity, that every stimulation from vision or other sensitive organs forms a micro-lighting in brain. The activity in brain neural organ, in fact, is a successive micro-lighting process. Also, the author suggest to modify the structure of Artificial Neural network(ANN), based on the guess above.

Key words: ANN, micro-lighting, brain neuralology

I. Introduction

In recent years, as the growing of interests on the research about artificial brain, people try to find some new type of model to describe the real activity in our brain, and aimed to lead a engineering model to develop artificial intelligent technology, in which the intelligence is more close the real process in our human brain. The authors think of that so far any intelligence appeared in the so-called "intelligent equivements" is not the true intelligence because they were given but not obtained. That means those intelligence are not evolutionary or not recognative by some sensing organs. So, trying to propose a mode to get information and then to transfer to knowledge is a valuable research direction. In addition, the present ANN model has some drawback, in fact, in every ANN all nodes in the same layer are connected to the all nodes in the next layer is not reasonable, in that case any ANN will can do only one job.

II. The guess----A micro--lighting for stimulate

We analyzed the real brain neural process, the fact is that the stimulate make the brain face have response only on some specific area, not the whole brain face. Also, it located the different area for the different type of stimulating, such as vision and listening. We could think of a neural network should be responded like the following: there are several coding type for the different stimulates, the coding form not very complicated as we thought; the coding form lead a micro-lighting which only active an area of the neural network.

Based on the knowledge and analysis above we try to guess a model for the real neural activity like that when a stimulate comes and active the network, a micro-lighting appear, it is stochastic and directed to a specific area of brain face, just like the real lightning in sky. (see fig.1)

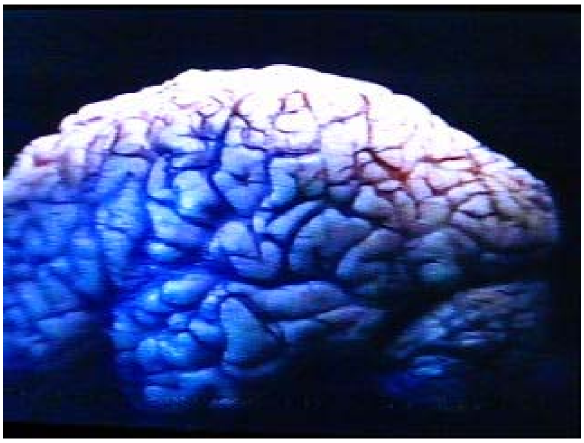

Simulation to the natural brain

Fig.1

This micro—lighting is a process in very short time. A primitive recognition process is a series of this kind of micro—lighting processes.

The micro—lighting is stochastic, but for a same recognition scheme has only small change and it will be fixed after repeating and training.

III. The suggestion on the ANN's modification

If you are interested in the guess and agree with us, we will propose a modification idea on the known Artificial Neural Network (ANN). There we suppose that some nodes which are located in several layers and the nodes in the same layer are connected to the all nodes in the next layer. See the Fig.2

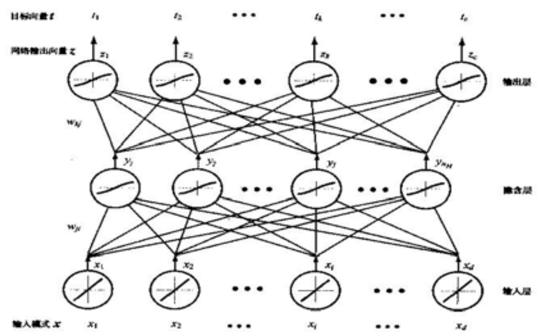

FIG.2

No doubt, the ANN is a very good model to simulate a learning process and have had many very successful researches. However, the assumption is not very natural. The problem is that what does the node means? In fact, the original thinking is to represent the contacted parts between the neural cells. These connections are the linkage between synapses and axons, these connections are only appeared in the neighbors of neural cells. These connections are nonlinear parts and can be simulated as a sigmoid or some other nonlinear function. It cannot be extended to the far neural cells. So, we suggest that these connections should restrict in the near nodes in a cells. So, we suggest that to change the connection type to that in Fig.3. (see Fig.3)

In fact, the fig.3 is a complicated electrical circket network. At the output terminal every end is a

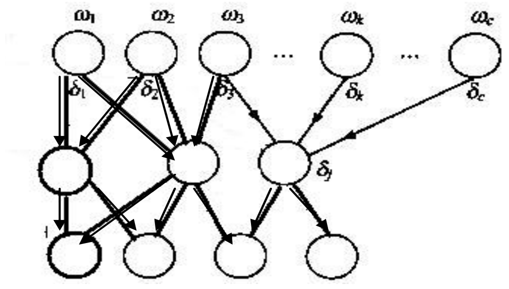

FIG.3

thermal unit and they are controlled by a threshold, if the voltage is high then the threshold it will be reactive and temperature get higher. We could define a state of the network by the set of all weights on the connections. In addition, the state of the network is essential, because it really storages information in the state.

IV. The open problems

While we proposed the model and the modification suggestion on ANN, it still has many questions to answer and more research works are needed.

1） How to define the input for this new type of ANN?

In another words, this question can be mentioned as that we need to give different coding form for vision, listening, and so on.

2) How to store the network state and to identify it? This will essential for recognition and to form a knowledge.

3) How to rebuild up the state? That means memory and recall function.

After resolve these problems this network will be really useful for building up an artificial brain. And it will be an intelligent chips.

REFERENCES

[1] Nils J.Nilsson, "Artificial Intelligence, A new Synthesis", Morgan Kaufmann Publishers, Inc. 1998

[2] Richard O. Dudas, Peter E. Hart, and David G. Stork, "Pattern Classification", 2nd Edition, John Wiley & Sons, 2001

[3] Y. G. Zhang, M. Sugisaka and L.Tang, "K(Knowledge)-net: Building up and its dynamics", Journal of ARTIFICIAL LIFE AND ROBOTICS", Vol.12, No.1-2, Springer(Tokyo), 2008

[4] Zhang, Y.G. and Sugisaka, M, "A mode to create artificial intelligence—From knowledge to intelligence", The proceedings of The nineth international symposium on artificial life and robotics (AROB'04), pp. I-28-31, 2004

Research on Automatic Text Summarization Based on Latent Semantic Indexing

Dongmei Ai[1, 2] , Yuchao Zhang[2] , Dezheng Zhang[2]

1 (School of Applied Science , University of Science and Technology Beijing, China)
2(School of Information Engineering, University of Science and Technology Beijing, China)

(Tel : 86-01-62332349; Fax : 86-01-62334071)
(aidongmei@sina.com)

Abstract: Automatic summarization is a common–concerned topic of computational linguistics and information science, the computer system of text summarization is considered as an effective means of processing information resources. In this paper, we propose an method of text summarization based on latent semantic indexing, which uses semantic indexing to calculate the sentence similarity. It improves the accuracy of sentence similarity calculation and subject delineation, and helps the generated abstracts universally cover the documents as well as reducing its redundancy. The effectiveness of the method is proved in the experimental results , compared to the traditional VSM-based method of automatic text summarization, the quality of generating abstracts was significantly improved.

Keywords : Latent Semantic Indexing ;vector space model; analysis of text structure; automatic text summary

I. INTRODUCTION

With the development of computer and information technology, especially the widely use of Internet, the amount of information available to the people increases rapidly. Facing such abundant information resources, it becomes more and more important for people to obtain useful information from them. Automatic Summarization is an effective tool to solve the above problem. It can significantly accelerate the speed of information filtering, and help readers get a basic understanding of the contents in related documents and find their necessary materials quickly and accurately [1].

In the traditional keyword-based Vector Space Model (VSM) [2], a document vector composed of m keywords $\mathrm{Di} = \{\mathrm{d1},\ \mathrm{d2},\ \ldots\ldots, \mathrm{dm}\}$ represents a document in the document set and it is the basis of text processing. The unstructured text can be represented in a form of vector, which makes a variety of mathematical processing be possible [3][4]. Its main advantage lies in that the process logic is simple and quick. However, VSM assumes that the relationship between words is independent (orthogonal assumption), which is difficult to be satisfied in the real environment. Generally, the words that appear in the text have a certain degree of correlation, which will impact the calculation results to some extent. Meanwhile, such kind of keyword-based text processing method is mainly based on word frequency information. The similarity between two texts is determined by the number of common words between them, thus making it hard to distinguish the semantic ambiguity of natural language. There exist a large number of synonyms and polysemant in the natural languages. The accurate representation of semantics not only depends on the proper use of vocabulary itself, but also on the contextual constraints on the meaning of the words. If ignoring the contextual constraints and only using isolated keywords to represent the content, it will surely impact the accuracy and completeness of text processing.

Latent Semantic Indexing (LSI) is a method used to achieve automatic knowledge extraction and representation. By performing statistical analysis of a large text set, it can extract the meaning of a word in the context. Technically, LSI is similar to VSM, as both of them use space vectors to represent texts. However, by using SVD decomposition to eliminate the impact of synonyms and polysemant, LSI improves the accuracy of post-processing. The basis of LSI is that, there exists a certain link between the words in the text, i.e., latent semantic structure. Such latent semantic structure is implicit in the pattern of word usage in the context. Therefore, when using statistical calculation method to analyze a large amount of texts to find such kind of latent semantic structure, we don't need deterministic semantic encoding. Simply by using the links of things in the context and representing words and texts with semantic

Supported by the National High-Tech Research and Development Plan of China under Grant No.2009AA01Z119 ; the National Natural Science Foundation of China under Grant No.60973065.

structure, we can eliminate the correlation between words and simplify the text vector.

In view of the above reasons, this paper will focus on the basic idea and features of LSI method, and propose LSI-based automatic text summarization method.

II. LSI Model

In the field of text processing, unstructured text can be formalized with the VSM model, thus making all kinds of mathematical processing be possible. However, the orthogonal assumption of mutual independence between words in the VSM model has obviously ignored the correlation between words in the natural languages. The text vector space composed of raw words will inevitably lead to the expansion of high-dimensional space and the inundation of text features.

To solve this problem, S. Deerwester proposed Latent Semantic Indexing (LSI) model [5] in 1990. Then, this model was widely used in many fields, such as information retrieval, text clustering, text filtering and others, and also has been improved continuously [6-9]. In this paper, we propose a method of text summarization based on LSI model.

LSI model first assumes that there exists certain latent semantic structure in the text, and then uses statistical methods to estimate such latent structure and project the text from the observed high-dimensional surface space (composed of raw words) to the low-dimensional latent semantic space (composed of concepts). In the way, it eliminates the impact of orthogonal independence assumption in the VSM, and determines the position of the text in the vector space more properly. In addition, while reducing the dimensionality of the text vector space, it still retains the semantic information of the original text to a large extent.

LSI uses the matrix Single Value Decomposition (SVD) method [10] in Linear Algebra to estimate the latent text vector matrix $\hat{X}$ from the text vector matrix X composed of original "word - document".

Mathematically, any t×d matrix with rank m can be decomposed as follows:

$$X = T_0 S_0 D_0^T \qquad (1)$$

In the above expression, T_0 and D_0^T are called the left singular vector and right singular vector respectively, which have orthogonal columns

$T_0^T T_0 = I, D_0^T D_0 = I$ ； S_0 is a diagonal matrix. $S_0 = diag(\lambda_1, \lambda_2, \ldots, \lambda_m)$, $\lambda_1 \geq \lambda_2 \geq \ldots \lambda_m \geq 0$ 。

By choosing proper value for k, we can satisfy the following inequality:

$$\sum_{i=1}^{k} \lambda_i \Big/ \sum_{j=1}^{m} \lambda_j \geq \theta \qquad (2)$$

In the inequality, θ is the threshold that contains the original information. By deleting the relevant rows and columns in S_0, we can obtain S; by deleting the relevant rows and columns in T_0 and D_0, we can have T and D. Then we perform multiplication operations over three matrixes, and obtain a new matrix $\hat{X}$. Using Similarity matrix $\hat{X}$ to replace the original matrix X, the new matrix with rank k is closest to the original matrix in the sense of least squares.

$$X \approx \hat{X} = TSD^T \qquad (3)$$

Fig.1 is the illustration of the singular value decomposition of the "word - document" matrix. The new "word - text" similarity matrix $\hat{X}$ obtained by SVD has the following two features compared with the original matrix X: (1) $\hat{X}$ ignores the smaller singular value, which is equivalent to the exclusion of the noise in the original matrix X. (2) Since the element in the original matrix X is the word's eigenvalue in the document and there exists sparse data problem in the matrix, the removal of items with smaller singular values is equivalent to smoothing X.

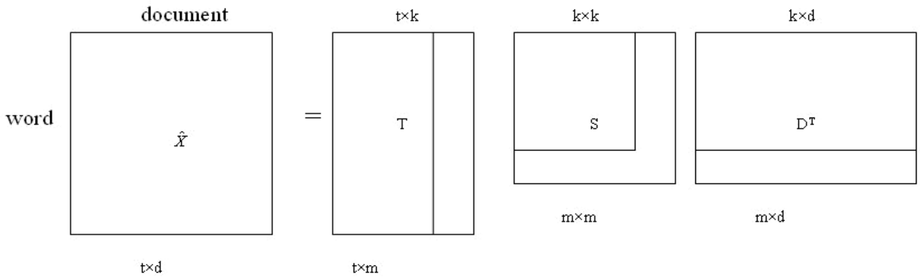

Fig.1. The illustration of SVD process

III. LSI-based Text Structure Analysis Method

The goal of text structure analysis is to automatically identify the boundary of paragraphs with independent meaning (meaning paragraphs) [11-12]. Generally, the meaning paragraph is greater than or equal to the natural paragraph and there is no clear boundary of meaning paragraphs as that of natural paragraphs. They are formed during the description of the article topic.

Note that, in fact, a meaning paragraph is composed of several successive text units (natural paragraphs or sentences). To support the ideas expressed in a meaning paragraph, the natural paragraphs (or sentences) contained in the same meaning paragraph often have great similarity in the choice of vocabulary as well as the term frequency. At the same time, considering that there exist "transform" sentences in the natural paragraphs of the article, we should select "sentences" as the text units to split the article from the perspective of subject delineation. Namely, we can process "sentences" as the above described "document" and construct the "word - sentence" matrix.

In view of these facts, we propose a LSI-based text structure analysis method in this section. By exploiting the similarity of adjacent text units in the LSI measure, we can determine the interval points with the lowest compact degree and thus complete the delineation of the document structure.

1. Calculation of Various Similarities

By using SVD, we can obtain the best approximation $\hat{X}$ of the "word - sentence" matrix of all the documents. With $\hat{X}$, it is easy to obtain the semantic relationship between words and sentences. In the latent semantic analysis, we mainly discuss three relationships, i.e., the relationship between words and sentences, the relationship between words and words, the relationship between sentences and sentences. Next, we will introduce the calculation method of these three relationships:

1) Distance between words and sentences

The similarity between sentences and words is $\hat{X}$ itself. The i-th row and the j-th column in $\hat{X}$ indicate the similarity degree between word i and sentence j.

2) Distance between words and words

When calculating the similarity degree between words, we need to perform "forward" multiplication on $\hat{X}$.

$\hat{X} * \hat{X}^T = T * S * D^T * D * S^T * T^T$,

$\because S$ is a diagonal matrix, $\therefore S = S^T$,

$\because D$ is an orthogonal matrix, $\therefore D * D^T = I$

Thus,

$$\hat{X} * \hat{X}^T = T * S * I * S * T^T = T * S^2 * T^T \qquad (4)$$

The i-th row and the j-th column in the matrix $\hat{X} * \hat{X}^T$ indicates the similarity between word i and word j.

3) Distance between sentences and sentences.

To calculate the similarity degree between sentences, we need to perform "reverse" multiplication on $\hat{X}$.

$\hat{X}^T * \hat{X} = D * S^T * T^T * T * S * D^T$

Same as above, $S = S^T, T * T^T = I$

Thus:

$$\hat{X}^T * \hat{X} = D * S^T * I * S * D^T = D * S^2 * D^T \quad (5)$$

The i-th row and the j-th column in the matrix $\hat{X}^T * \hat{X}$ indicates the similarity between sentence i and sentence j.

2.Calculation of Compact Degree

Suppose that the text D contains n sentences, k meaning paragraphs. Let H be the text meaning paragraph and s be the sentence. We have the following relationship:

$D = \{H_1 H_2 \cdots H_k\} = \{s_{i_1} \cdots s_{i_2 - 1}\}\{s_{i_2} \cdots s_{i_3 - 1}\} \cdots \{s_{i_k} \cdots s_{i_{k+1} - 1}\}$,in which $i_1 = 1 \le i_2 \le \cdots \le i_k \le i_{k+1} - 1 = n$. To facilitate the writing, the notations are simplified as s_i 、 s_{i+1} .

If taking the similarity degree between adjacent sentences in the text (i.e., $sim(s_i, s_{i+1})$) as the measure of compact degree, we can still reflect the consistency of the subject by using the similarity between adjacent sentences. Obviously, the splitting points of the text structure are naturally the interval points with a low similarity degree, which implies poor continuity in the context and can be taken as the candidates of delineation. Therefore, the interval points with low similarity are the objects that deserve more attention [14].

If regarding a text as a complete text vector space, we can use the sentences in the text as the basic processing unit and formalize it as a text vector. Assume that variable pair <s, w> means that the word w appears in

The sentences, $s \in S = \{s_1, s_2 \cdots, s_n\}$, $w \in W = \{w_1, w_2, \cdots, w_m\}$. We can use LSI model to construct the best approximation matrix $\hat{X}$ of the "word - sentence" matrix and calculate the similarity matrix between sentences and sentences (i.e., $\hat{X}^T * \hat{X}$). When extracting the related element in the similarity matrix, its value can be taken as the similarity degree between adjacent sentences (i.e., $sim(s_i, s_{i+1})$), as shown in Fig.2 A higher similarity degree means a higher compact degree in the context; otherwise, it means a lower compact degree in the context and implies the end of a subject.

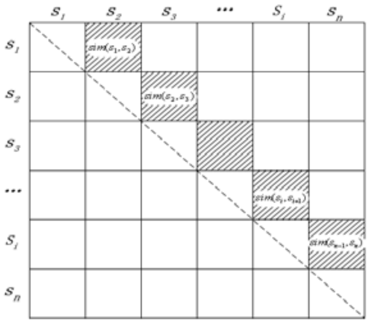

Fig.2. the illustration of the calculation of similarity degree between adjacent sentences.

3. Methods of Boundary Recognition

The objective of boundary recognition is to determine the candidate points of text delineation according to the compact degree between interval points. There are the following policies of boundary recognition [15]:

1) Threshold Method

Set a constant θ. If the similarity value between sentences satisfies $sim(s_i, s_j) < \theta$, we can think that s_i and s_{i+1} belong to different segments. The method is easy to implement and has a lower error ratio if choosing a proper θ.

2) Dynamic Constant Method

Although the threshold method is simple, the constant θ should be set manually and it is hard to provide the best value. Therefore, we can consider changing the value of θ dynamically according to the similarity degree between adjacent sentences. Suppose that the text to be split has n sentences, and then the similarity degree between adjacent sentences can be represented as:

$$SimTable = \{Sim_1, Sim_2, \cdots, Sim_i, \cdots, Sim_{n-1}\}$$

in which $Sim_i = sim(s_i, s_{i+1}), 1 \le i \le n-1$, Let,

$$avgSim = (Sim_1 + Sim_2 + \cdots + Sim_i + \cdots + Sim_{n-1})/(n-1) \qquad (6)$$

$$avgmSim = ((Sim_2 - Sim_1) + ... + (Sim_{n-1} - Sim_{n-1}))/(n-2) \qquad (7)$$

If $avgmSim \le sim(s_i, s_{i+1}) \le avgSim$, we can think that s_i 、 s_{i+1} belong to different pieces.

3) Local Minimum Method

Select the local minimum value $sim_{sim}(s_i, s_j)$ in the similarity table SimTable. Start from each local minimum value and move towards the left and the right to search the closet larger value Sim_l 、 Sim_r, and then use Equation (8) to calculate the relative depth:

$$d_{rel}(s_i, s_{i+1}) = (Sim_l + Sim_r)/(2 \times sim_{\min}(s_i, s_j)) - 1 \qquad (8)$$

Set a threshold value α. If the relative depth $d_{rel}(s_i, s_{i+1}) > \alpha$, s_i 、 s_{i+1} belong to different paragraphs. Our paper proposes to use the local minimum method to find the interval points of splitting text structure.

To summarize, our proposed LSI-based text structure analysis algorithm can be described as follows:

Step1： Construct the "word-sentence" matrix in the original text;

Step2： Use LSI model to decompose the original matrix and obtain the best approximation matrix $\hat{X}$ of the "word-sentence" matrix;

Step3： Calculate the similarity degree matrix between sentences and sentences, i.e., $\hat{X}^T * \hat{X}$. Extract the corresponding elements in the similarity degree matrix. The value can be taken as the similarity degree between adjacent sentences $sim(s_i, s_{i+1})$;

Step4： Use the boundary recognition method to find the interval points of splitting text structure and achieve the goal of text structure analysis.

IV. GENERATING SUMMARY

1.Calculation of Sentence Weight

The sentence weight is calculated after determining the subject. The equation to calculate the j-th sentence in the subject $H(i)$ (i.e., S_{ij}) is as follows:

$$I(S_{ij}) = \lambda_h \times \lambda_{pos} \times \sum_{k=1}^{n} sim(S_{ij}, S_{ik}) \qquad (9)$$

in which n is the number of sentences contained in the subject $H(i)$. It is the sum of similarity degree between this sentence and other sentences in the same subject and reflects the representation degree of the sentence for the belonging subject. The higher the value is, the more information of the subject the sentence contains, which implies a higher representation degree.

λ_h is the score determined by the number of prompting words contained in the sentence. Prompting words can be categorized into two types: ① Weight-added prompting words, which prompt that the sentence contains important contents, such as "in summary", "the main purpose of research", "this paper explores", "overall", "experiments show", etc. The sentences guided by such kinds of words should be given a positive weight to improve the sentence's importance; ② Weight-reduced prompting words, which indicate that the sentence doesn't contain important substantive content, such as "for example", "for instance", "take an example", "in other words", etc. For the sentences started with such words, we should reduce their weight to decrease its importance. This paper adopts the following empirical values:

$$\hat{C}(s_i) = \begin{cases} 0.5 & \text{Weight - added words} \\ 0 & \text{Others} \\ -0.5 & \text{Weight - reduced words} \end{cases} \qquad (10)$$

λ_{pos} is the score determined by the location of the sentence. The sentences that appear in the first paragraph or the last paragraph have a higher score. In the application of automatic text summarization system, the location feature is still very effective heuristic information. Our paper provides extra weights for the sentences in the special locations, such as the beginning paragraph, the ending paragraph, the paragraph after each sub-heading, the sentence at the beginning of a paragraph, the sentence at the end of a paragraph, to exhibit their importance. The location weight λ_{pos} of sentence s_i is defined as:

$$\lambda_{pos} = l_s(s_i) \times l_p(s_i), \qquad (11)$$

in which $l_s(s_i)$ is the weight tuning parameter of the location of s_i and $l_p(s_i)$ is the weight tuning parameter of the paragraph location of s_i.

Our proposed automatic text summarization method can use the following weight parameters, as shown in Table 1.

Table 1. Weight tuning parameters of paragraph location and sentence location

	First paragraph First sentence	First paragraph Other sentences	First paragraph Last sentence	Other paragraphs First sentence	Other paragraphs Other sentences	Other paragraphs Last sentence	Last paragraph First sentence	Last paragraph Other sentences	Last paragraph Last sentence
l_s	1.4	1.0	1.3	1.4	1.0	1.3	1.4	1.0	1.3
l_p	1.5	1.5	1.5	1.0	1.0	1.0	1.2	1.2	1.2

2. Extracting Sentences to Generate the Summary

In Summary, the LSI-based automatic text summarization algorithm proposed in this paper is as follows:

Step1: $N = [n(s,w)]_{m \times n}$; Construct the "word – sentence" matrix $N = [n(s,w)]_{m \times n}$ in the original text;

Step2:Use LSI model to decompose the original matrix and obtain the best approximation matrix $\hat{X}$ of the "word – sentence" matrix;

Step3: $sim(s_i, s_{i+1})$; Calculate the similarity degree matrix between sentences and sentences $\hat{X}^T * \hat{X}$. Extract the related elements in the similarity degree matrix and the value is taken as the similarity degree between adjacent sentences $sim(s_i, s_{i+1})$;

Step4: Use the boundary recognition method to find the interval points of splitting text structure and achieve the goal of text structure analysis and subject splitting.

Step5:Calculate the weight $I(S_{ij})$ of each sentence in the text;

Step6:First allocate the required summary length proportionally to each subject; then extract a comparable amount of summary sentences from each subject based on the ranking of sentence weights and generate the summary.

IV. EXPERIMENTAL RASULTS

To validate the effectiveness of our proposed Chinese automatic text summarization method, we build two Chinese automatic text summarization systems to conduct comparison experiments.

System I: the system uses our proposed automatic text summarization method;

System II: calculate the sentence similarity by constructing word-based VSM and then cluster the sentences with hierarchical clustering method. The sentence extraction method is the same as our proposed method.

Here, we use three measures – recall, precision, F-measure – to evaluate the text summarization system. Among them, recall refers to the ratio of correct recognition, and precision refers to the ratio of precise recognition. Their detailed expressions are as follows:

Recall = the number of sentences extracted by both the text summarization system and the expert / the number of sentences extracted by the expert

Precision = the number of sentences extracted by both the text summarization system and the expert / the number of sentences extracted by the text summarization system

To comprehensively evaluate the summary quality, we adopt a combined evaluation measure, i.e., F-measure.

$$F\_measure = \frac{2 \times P \times R}{P + R}$$

For example, in a given document, the summary length accounts for 15% of the whole document. If the number of sentences extracted by the system is 8, the number of sentences extracted by the expert is 12 and the number of common sentences is 5, we have:

Recall =5/12=0.417

Precision = 5/8=0.625

$$F\_measure = (0.417*0.625*2)/(0.417+0.625) = 0.5$$

In this paper, we randomly select 50 articles from the cor pus. We first obtain their standard summary by asking th e experts to manually label them, and then we use Syste m I and System II to conduct tests on them. We extract th e summary with a percentage of 10%、20%、25%、30% respectively and get the average precision, the avera ge recall, the average F-measure, as shown in Table 2.

It can be observed that, System I, which is built based on our method, has a higher value of recall, precision and F-measure than that of System II under different percentages of summary length. It implies that the summary generated by our method well balances the requirements of coverage and precision, and has a better quality.

Table 2.Comparison of precision, recall, F-measure of different systems (%)

Summary Percentage	Average Precision		Average Recall		Average F-measure	
	System I	System II	System I	System II	System I	System II
10%	41.81	41.40	22.94	21.33	27.50	25.60
20%	60.31	58.96	32.98	26.41	40.79	35.40
25%	61.56	58.49	40.96	29.91	46.87	37.61
30%	62.14	60.59	50.58	38.54	53.25	45.38

V. CONCLUSION

This paper proposed a LSI-based text summarization method. It exploits LSI to obtain the semantic structure of sentences and calculate the sentence similarity in the semantic space, and thus avoids the "bias" phenomenon caused by the word-based VSM. The experimental results show that the summary generated by our proposed method has better quality than that generated by the traditional VSM-based approach, and thus validate the effectiveness of our method.

The problems observed in the current experiments lie in the process of referencing relationship. Due to the use of statistical methods, it is hard to determine the referencing relationship in the context. It will affect the coherence and understandability of the sentences. This is also what we should improve in the next step when using semantic analysis method.

REFERENCES

[1] Tianshun Yao, Qianbo Zhu, Li Zhang(2002), Understanding Natural Languages Second Edition. Beiji ng: Tsinghua University Press

[2] Salton G, MeGill M J(1983), Introduction to modern Information Retrieval .New York: McGraw-Hill Book Company

[3] Eric W Brown, James P Callan, W Bruce Croft(1994), Fast Incremental ndexing for Fu11-Text Information Retrieval[C]. In: Proceedings of the 20th VLDB Conference Santiago, Chile:1-2

[4] Clifford A Lynch(1995),Networked Information Resource Discovery: An Overview of Current Issues. IEEE[J] .TOURNAL ON SELECTED AREAS IN COMMUNICATIONS,13 (8):1505-1522

[5] S. Deerwester, S. Dumais, G. Furnas, T(1990), Landauer and R. Harshman Indexing by Latent Semanti c Analysis[J]. Journal of the American Society for Inform ation Science, 41(6):391-407

[6] Chengqing Zong(2008), Statistical Natural Language Processing [M]. Beijing: Tsinghua University Press

[7] Jiantao Sun(2005), Dimension Reduction and Classification Method Research in Web Mining [D]. Beij ing: Tsinghua University

[8] Qiaozhu Mei, ChengXiang Zhai(2006), A Mixture Model for Contextual Text Mining[C]. In Proceedings of the 2006 ACM SIGKDD International Conference on Knowledge Discovery and Data Mining(KDD'06):649-655

[9] Yihong Gong, Xin Liu(2001), Generic Text Summarization Using Relevance Measure and Latent Semantic Analysis[C]. In Proceedings SIGIR2001:19-25

[10] Jen-Yuan Yeh, Hao-Ren Ke, and Wei-Pang Yang, (2002), Chinese Text Summarization Using a Trainable Summarizer and Latent Semantic Analysis[C]. Digital Libraries: People, Knowledge, and Technology: 5th International Conference on Asian Digital Libraries, ICADL 2002, Singapore, Proceedings: 76-87

[11] Hongfei Lin(2000), Text Structure Analysis Method Based on Concept [J]. Computer Research and Development, 37(3):324-328

[12] Xiongguan Wei(1997), Diagram-based Text Analysis Method [J]. Pattern Recognition and Artificial Intelligence, 10(2):112-117

[13] Zechner K, Lavie A(2001), Increasing the Coherence of Spoken Dialogue Summaries by Cross-Speaker Information Linking[C]. In Proceedings of the NAACL-01 Workshop on Automatic Summarization. Pittsburgh, PA: Association for Computational Linguistics:22-31

[14] Hearst, Marti A(1997), TextTiling: Segmenting Text into Multi-paragraph Subtopic Passages[J]. Computational Linguistics:33-64

[15] Jing Shi, Guozhong Dai(2007). Text Segmentation Based on PLSA Model [J]. Computer Research and Development, 44(2):242-248

Sensitivity improvement of automatic pulmonary nodules detection in chest X-ray CT images

Satoshi Shimoyama[1], Noriyasu Homma[2], Tadashi Ishibashi[1] and Makoto Yoshizawa[2]

[1] Tohoku University Graduate School of Medicine, 2-1 Seiryo-machi, Aoba-ku, Sendai, 980-8575 JAPAN
[2] Cyberscience Center, Tohoku University
[2] (Tel : 81-022-795-7130; Fax :81-022-263-9163)
(E-mail: simoyama@yoshizawa.ecei.tohoku.ac.jp)

Abstract: In this paper, we develop an automatic detection method of non-isolated pulmonary nodules as a part of computer-aided diagnosis (CAD) system for lung cancers in chest X-ray CT images. An essential core of the method is to separate non-isolated nodules from connecting structures like chest wall and blood vessels. The isolated nodules can be detected more easily by CAD syetems developed previously. To this end, we propose a binarization technique by using two thresholds as a preprocessing for nodule candidates. We evaluate the performance using the receiver operating characteristic (ROC) analysis in clinical chest CT images. The results suggest that detection ability of non-isolated nodules by the proposed method is superior to that by the conventional preprocessing methods.

Keywords: computer-aided diagnosis, lung nodule, X-ray CT, lung cancer, multiple thresholds.

I. INTRODUCTION

It is very important to detect cancers at an early stage. To this end, the X-ray computed tomography (CT) should be used because pulmonary nodules that are typical shadows of pathological changes of lung cancers and can be depicted more clearly compared to use of the chest X-ray examination [1-3]. This is true even the nodules are at early stages. A problem to use the CT is that radiologists have to diagnose at least more than 30 image slices per patient. Thus, some computer-aided diagnosis (CAD) systems have been proposed to help their diagnosis work. Some excellent results have been reported for isolated pulmonary nodules [4-6]. The previous methods are however inaccurate for non-isolated nodules connected to the chest walls and blood vessels, etc.

In this paper, as a preprocessing, we propose a novel binarization method for detection of non-isolated nodules. The core of this method is to use two thresholds in order to convert such non-isolated nodules into isolated ones. The effectiveness of the proposed method is verified by using to some clinical cases of lung cancer CT images.

II. AUTOMATIC NODULES DETECTION

1. Variable N-Quoit filter

The CAD system needs to detect suspicious lesions. It is used the variable N-Quoit filter for pulmonary nodules detection [4] in many CAD systems. Variable N-Quoit filter is based on mathematical morphological technique and formulated as

$$q(x,y) = f(x,y) - f(x,y) \oplus R(x_1,y_1) \tag{1}$$

$$\begin{aligned} & f(x,y) \oplus R(x_1,y_1) \\ & = \max_{(x_1,y_1)\in K_R} \{ f(x-x_1, y-y_1) + R(x_1,y_1) \} \end{aligned} \tag{2}$$

where (x,y) is the coordinate. f and q are pixel values of input and output images, respectively. $R(x_1,y_1)$ is a ring filter function at the target point (x,y). Then the ring filter R is defined by

$$R(x_1,y_1) = \begin{cases} 0, & r_1(x,y) < \sqrt{(x-x_1)^2 + (y-y_1)^2} \le r_2(x,y) \\ -\infty, & \text{otherwise} \end{cases} \tag{3}$$

The ring area K_R is defined by a set of coordinates (x,y) satisfying the condition $R(x_1,y_1) = 0$. r_1 and r_2 are internal ring radius and external ring radius, respectively. Here r_2 is set $r_2 = r_1 + 1$. Note that both r_1 and r_2 are as functions of the coordinate. The internal ring radius r_1 can be changed depended on the target nodule size, and this is a reason why the filter is called "variable" N-Quoit filter. To realize this adaptation, the following distance transformation may be used.

2. Distance transformation

Distance transformation is a process to acquire the minimum distance from background pixels (where any pixel value is 0) to each pixel that forms arbitrary target shape. This transformation is defined as

$$d(m,n) = \min_{k,l}(|m-k| + |n-l|) \tag{4}$$

where $d(m,n)$ is output of distance transformation, (m,n) is the coordinate of the arbitrary shape, and (k,l) is of background pixels. We compute this distance by four neighbors in this paper.

In this transformation, the target area must be distinguished from its background. This distinction can be generally done by a thresholding. It is, however, very difficult to determine the appropriate threshold because it is depended on individual and local properties of each image. In other words, optimal thresholds over a set of images are different from each other. In conventional method, due to this difficulty, detection ability of the filter may be affected badly, especially for non-isolated nodules. Indeed, non-isolated nodules are hardly detected by the N-Quoit filter because of the connecting structures. To overcome this problem, we will propose a new thresholding method in next section.

III. PROPOSED THRESHOLDING METHOD

Fig. 1(a) shows an example of a non-isolated nodule that cannot be detected by the conventional N-Quoit filter with the single thresholding technique. The fundamental idea of the proposed thresholding technique is to eliminate the effect of the connecting structures, the chest wall in this case, on the detection ability of the N-Quoit filter. To achieve this, we first consider the distribution property of the pixel value along the cross line A-A' over the undetectable nodule as shown in Fig. 1(a). Fig. 1(b) shows changes of pixel intensity as a function of the coordinates along the cross line A-A' shown in (a). From this figure, we can see that if we use double thresholdings instead of the conventional single one, we can separate the nodule area from both the lung and chest wall area. This process is defined as follows

$$I_{bi}(x,y) = \begin{cases} 1, & T_{low} < I(x,y) \le T_{high} \\ 0, & \text{otherwise} \end{cases} \quad (5)$$

where $I_{bi}(x,y)$ is output image, T_{low} and T_{high} are lower and higher thresholds, respectively. $I(x,y)$ is the pixel value of intput at the coordinate (x,y). The image acquired by this process is shown in Fig. 2(b), and the input image in Fig. 2(a). Two thresholds were set as following T_{low} = 100 and T_{high} = 200 in this study.

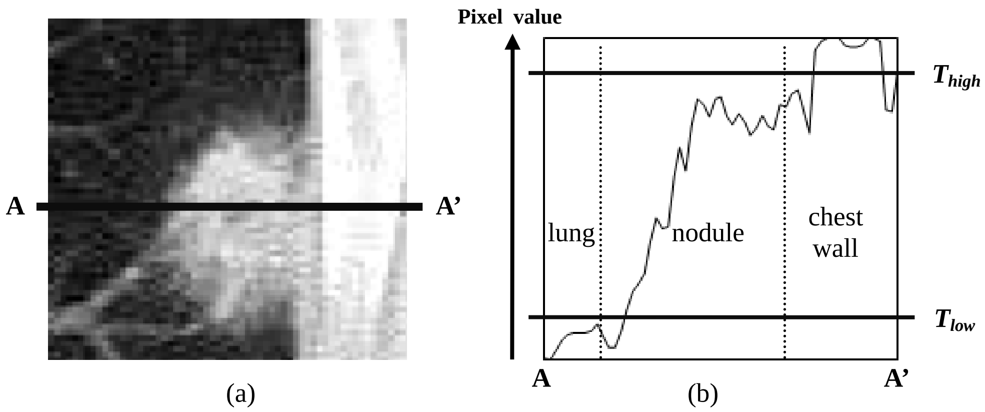

Fig. 1. (a) Example of a non-isolated nodule. (b) Changes of pixel intensity as a function of the coordinates along the cross line A-A' shown in (a).

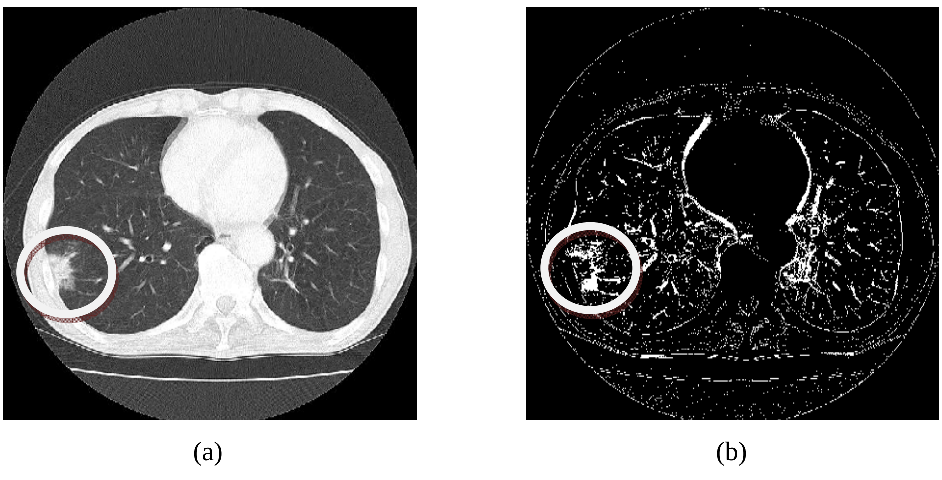

Fig. 2. (a) Original image has a non-isolated nodule in the white circle. (b) Binary image of the condition T_{low} = 100 and T_{high} = 200.

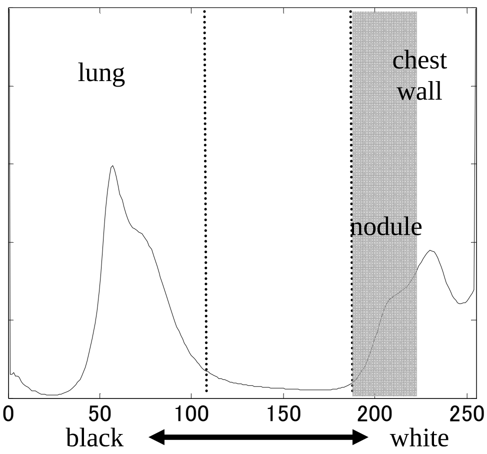

Fig. 3. Average of histogram of 169 chest CT images. Nodules may be included in gray area.

IV. RESULTS

We evaluated the performance of CAD system using receiver operating characteristic (ROC) analysis by changing the parameter of binarizing thresholds

Fig. 3 shows a histogram of 169 chest CT images, and pixel values of nodules are included in the gray area. Here, we need to discriminate nodules from lung and chest wall. We then choose thresholds so that intensities of nodules are greater than the lower threshold T_{low} and less than the higher one T_{high}. If T_{low} is chosen around 100, the lung and other structures will be divided. However, it is difficult to choose an appropriate value of T_{high} for discriminating chest wall from other structures as shown in Fig. 3. We thus evaluated the detection performance by using a range of T_{high} that cover the gray area: T_{high} = {190, 200, 210, 220}.

Conventional ROC curves were written as parameter of a threshold (corresponding T_{low} of our method). Then, for comparison, we used a set of parameter values of T_{low} = {90, 100, 110, 120, 130, 140, 150, 160, 170, 180, 190}.

Fig. 4(a) shows the ROC curve using the conventional single thresholding technique. While Figs. 4(b) and (c) show the ROC curves using proposed thresholding technique with T_{high} = 200, and 210, respectively. From the results, the best of true positive (TP) is approximately 0.6 in Fig. 4(a) while it is approximately 0.9 in Figs. 4(b) and (c). This result suggests that the proposed technique can be effective for improving the sensitivity of the detection.

There are, however, a larger number of false positive (FP) in Fig. 4(c) than in Fig. 4(b). This would be caused by isolated areas newly generated in the case that binarizing threshold T_{high} becomes approximately equal to pixel values of the chest wall. In other words, as T_{high} enlarges, the number of pseudo-isolated areas in chest wall increased. Note that the isolated areas in chest wall are not nodules but noises, and thus such areas make FP increase. Fig. 5 as expected from the

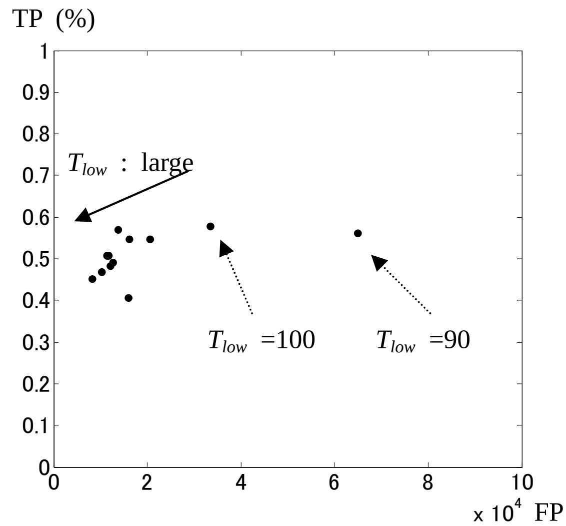

(a) Conventional method.

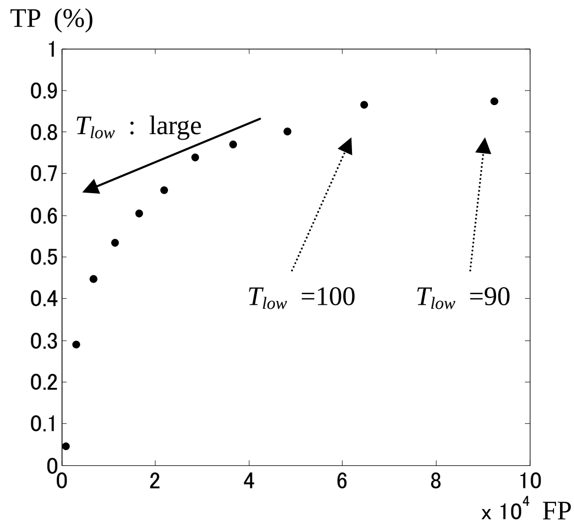

(b) ROC when T_{high} = 200.

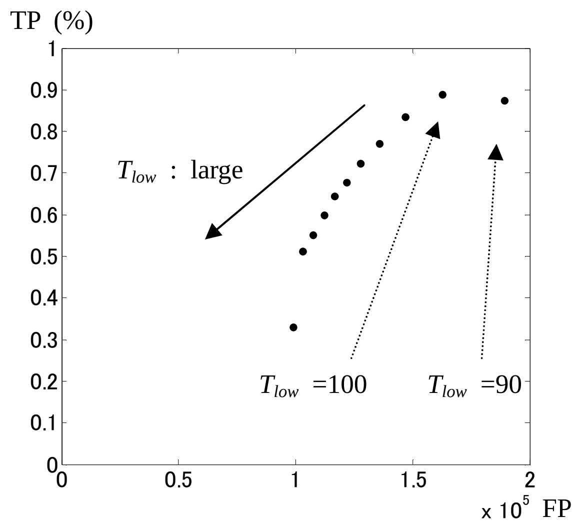

(c) ROC when T_{high} = 210.

Fig. 4. ROC curves

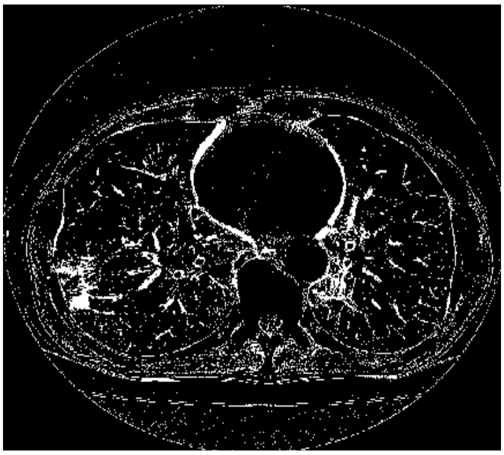

Fig. 5. Many pseudo-isolated areas have generated by an extra large threshold T_{high}. (T_{low} = 100 and T_{high} = 210).

result in Fig. 4(c), shows the binary image in case of T_{low} = 100 and T_{high} = 210. We can see that the number of noise points in Fig. 5 increase compared to Fig. 2(b). we used a smaller threshold than 200, such as T_{high} = 190, TP is getting worse. On the other hand, a larger threshold than 210, such as T_{high} = 220, the detection performance are almost same as for T_{high} = 210. (results area omitted.) From the results, The double thresholding method with T_{low} = 90 or 100 and T_{high} = 200 demonstrates the best performance in our date set.

V. CONCLUSION

In this paper, we proposed a novel preprocessing technique to improve detection sensitivity in CAD system. The technique is able to divide non-isolated nodules and connecting structures by using two thresholds. We have not conducted to decrease FP yet, but conventional effective methods [5] to do so can be incorporated into the proposed technique.

VI. ACKNOWLEDGMENTS

This work was partially supported by The Ministry of Education, Culture, Sports, Science and Technology under Grant-in-Aid for Scientific Research #19500413.

REFERENCES

[1] Takashi Iinuma, Yukio Tateno, Toru Matsumoto, et al. (1992), Preliminary Specification of X-ray CT for Lung Cancer Screening (LSCT) and its Evaluation on Risk-Cost-Effectiveness (in Japanese). Radiation Medicine 52(2): 182-190

[2] Yukio Tateno, Takashi Iinuma, Toru Matsumoto, et al. (1990), Development of the X-ray CT for lung cancer examination (in Japanese). New Medicine in Japan 17 (10):28-32

[3] Shinji Yamamoto, Ippei Tanaka and Masahiro Senda (1993), Image Processing for Computer Aided Diagnosis in the Lung Cancer Screening System by CT (LSCT) (in Japanese). IEICE TRANSACTIONS on Information and Systems J76-D2 (2): 250-260

[4] Tomoko Miwa, Junichi Kako, Shinji Yamamoto, et al. (1999), Automatic Detection of Lung Cancers in Chest CT images by the variable N-Quoit Filter. The transactions of the Institute of Electronics, Information and Communication Engineers J82-D-Ⅱ(2):178-187

[5] Noriyasu Homma, Kazunori Takei, and Tadashi Ishibashi (2008), Combinatorial Effect of Various Features Extraction on Computer Aided Detection of Pulmonary Nodules in X-ray CT Images. WSEAS Trans. Information Science and Applications 5(7):1127-1136

[6] Kazunori Takei, Noriyasu Homma, Tadashi Ishibashi, et al. (2008), Computer aided diagnosis for pulmonary nodules by extracting new shape features from X-ray CT images (in Japan). Japan Society for Fuzzy theory and Intelligent Informatics 20(1):108-116

A Time Variant Seasonal ARIMA Model for Lung Tumor Motion Prediction

K. Ichiji[1], M. Sakai[2], N. Homma[3], Y. Takai[4] and M. Yoshizawa[3]

[1] *Graduate School of Engineering, Tohoku University, 6-6-05 Aoba, Aoba-ku, Sendai 980-8579 JAPAN*
[2] *Center of Inform. Tech. Edu., Tohoku University, 41 Kawauchi, Aoba-ku, Sendai 980-8576 JAPAN*
[3] *Cyberscience Center, Tohoku University, 6-6-05 Aoba, Aoba-ku, Sendai 980-8579 JAPAN*
[4] *Tohoku University Graduate School of Medicine, 2-1 Seiryo-machi, Aoba-ku, Sendai 980-8575 JAPAN*
[1]*(Tel : 81-022-795-7130; Fax : 81-022-263-9163)*
[1]*(ichiji@yoshizawa.ecei.tohoku.ac.jp)*

Abstract: We propose a prediction method of lung tumor motion for real-time tumor following radiation therapy. An essential core of the method is a model building of time variant nature of the lung tumor motion. The method is based on a seasonal ARIMA model with an estimator of the time variant nature. The estimator provides the time variant period of the lung tumor motion by using a correlation analysis. The time variant SARIMA model can then predict complex lung motion by using the estimated period. The proposed method achieved highly accurate prediction of the average error 0.820$\pm$0.669[mm] at 0.5[sec] ahead prediction. This result is superior to other conventional methods at short- or mid-term prediction.

Keywords: Time series prediction, seasonal ARIMA, real time following radiation therapy, and lung tumor motion.

I. INTRODUCTION

To realize an effective radiation therapy, high power radiation dose must be given accurately to a limited area to enhance the effect of treatment and avoid irradiating to normal tissues to decrease adverse effects. Extracranial stereotactic radiation therapy (ESRT) is one of such advanced radiation therapy, and can irradiate accurate and sufficient dose to motionless tumor such as vesical tumor case [1]. However, lung tumor for example is not applicable target of the current ESRT because of its intra-fraction dynamic motion mainly due to the respiration.

One ideal way to give accurate and sufficient therapeutic dose to such dynamic tumor is real-time tumor-following radiation therapy (RTFT) [2]. RTFT can deliver dose to dynamic tumor continuously by moving the radiation sources or changing the shape of radiation area. For clinical use of RTFT, we need two technologies, i.e. real-time measurement technique of the tumor position and prediction technique of the tumor motion. X-ray fluoroscopy system will measure the position of the target in real-time. However, still we need to predict the position to compensate some time delays which is included in the radiotherapy instruments, such as control delay of radiation source and computational time for measurement of position and processing of time series.

Lung tumor moves mainly with patient's respiration and this motion is observed as a seasonal (i.e. cyclic) time series. There are many prediction methods for seasonal time series such as seasonal autoregressive integrated moving-average (SARIMA). However, the period of the lung tumor motion is time variant. Therefore, conventional SARIMA model is not applicable to this time series, because the SARIMA model assumes complete periodicity of the time series.

Homma *et al* developed a prediction system for lung tumor motion by using the SARIMA model [2,3]. This system converts the time variant period of target time series into a new time series with time invariant period, and achieved long-term prediction of the average error 1.05$\pm$0.99[mm] at 1[sec] ahead prediction [2].

In clinical use, we often need to predict short- or mid-term prediction at 0.1~0.5[sec] ahead. The desirable average error of short- or mid-term prediction is less than sub-millimeters. The prediction accuracy must then be more improved in such prediction.

In this paper, we propose a new prediction method of lung tumor motion for further improvement of the prediction accuracy. The basic idea of the method is to search more directly for reference points that are crucial for the prediction accuracy of the SARIMA model for the time variant seasonal time series. Simulation result by using clinical data will show that the accuracy of the

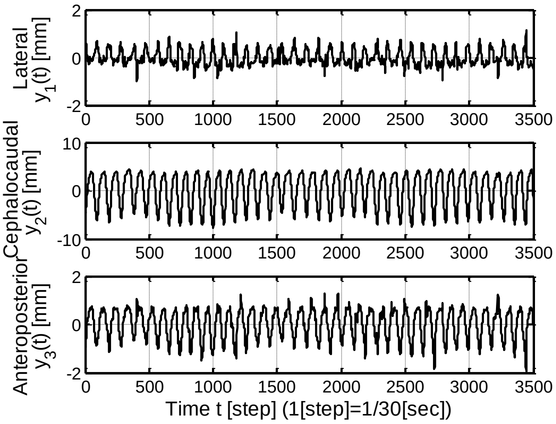

Fig.1. Three dimensional time series $\boldsymbol{Y}(t)$ of the lung tumor motion.

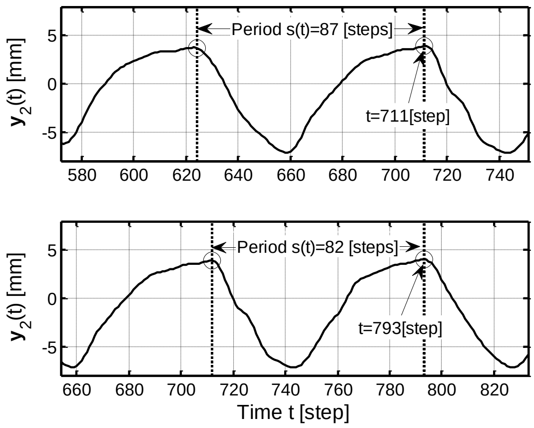

Fig.2. Two example of time variant periods as interval between peak and peak.

short- or mid-term prediction is improved by the proposed method.

II. TARGET TIME SERIES

In this study, we used a real data of lung tumor motion as target time series. We will show the time variant nature of the tumor motion.

1. Lung tumor motion

Three-dimensional time series of the motion of the marker implanted into the lung tumor was observed by a fluoroscopy system at Hokkaido University Hospital [4]. The sampling rate of time series was 30[Hz]. The time series was smoothed by using statistical filter and the Kalman filter for reduction of noise. In addition, the average value of the time series was removed.

The time series of lung tumor motion is expressed as follows.

$$\boldsymbol{Y}(t) = [\, \boldsymbol{y}_1(t),\ \boldsymbol{y}_2(t), \boldsymbol{y}_3(t)\,]. \quad (1)$$

where $\boldsymbol{y}_i(t)$, $i = 1,2,3$, are lateral, cephalocaudal, and anteroposterior coordinates of the target tumor at time t[step] (1[step] = 0.033[sec]), respectively. For simplify, we use a one dimensional time series as $\boldsymbol{y}(t) = \{y(t), y(t-1), y(t-2), \ldots, y(2), y(1)\}$ for explanation of prediction methods.

Fig.1 shows the time series of the lung tumor motion. The lung tumor motion is quasi cyclic due to patient's respiration and cardiac motion. Period of the cyclic motion is approximately 90[steps] (=3[sec]).

2. Period of the tumor motion

Period of the lung tumor motion changes with time evolution. For example, time intervals between peak and peak are time variant as shown in Fig.2 Peak to peak periods are 87[steps] at time t=711[step] and 82[steps] at time t=793[step] respectively.

There are many prediction methods for seasonal time series such as SARIMA model and Holt-Winters Seasonal [5]. However, they assume that cyclic period of their target time series is constant. Therefore, we need to modify those seasonal methods for accurate prediction of the lung tumor motion.

III. PREDICTION METHOD

The prediction method proposed in this paper is composed of a prediction model and a period estimator as shown in Fig.3. The period estimator provides the cyclic period of the tumor motion estimated at each time. Then the prediction model will generate predicted values by using the estimated periods.

1. Prediction model: Seasonal ARIMA model

The general SARIMA model can be given as follows.

$$\begin{aligned}\phi(B)\Phi(B^s)(1-B)^d(1-B^s)^D y(t) \\ = \theta(B)\Theta(B^s)e(t)\end{aligned} \quad (2)$$

$$\phi(z) = 1 - \phi_1 z - \phi_2 z^2 - \cdots - \phi_p z^p \quad (3)$$

$$\Phi(z) = 1 - \Phi_1 z - \Phi_2 z^2 - \cdots - \Phi_P z^P \quad (4)$$

$$\theta(z) = 1 + \theta_1 z + \theta_2 z^2 + \cdots + \theta_q z^q \quad (5)$$

$$\Theta(z) = 1 + \Theta_1 z + \Theta_2 z^2 + \cdots + \Theta_Q z^Q \quad (6)$$

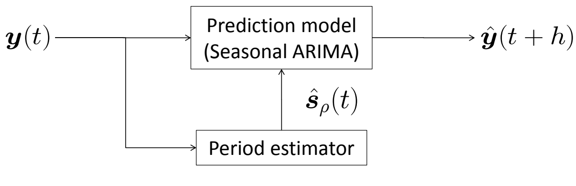

Fig.3. Schematic diagram of the proposed prediction system.

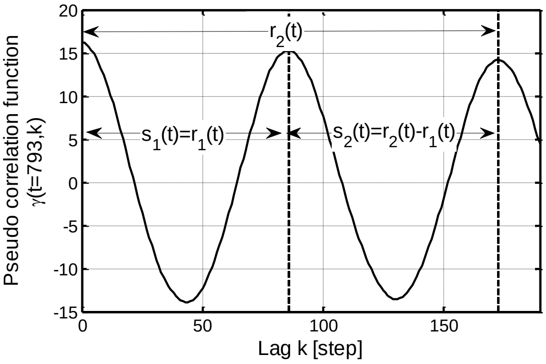

Fig.4. Pseudo correlation function $\gamma(t,k)$ at time t=793[step] and relationship between reference point $r_\rho(t)$ and estimated period $\hat{s}_\rho(t)$.

$$B^k x(t) = x(t-k) \tag{7}$$

where $e(t)$ is a Gaussian noise. Parameters d, D, p, P, q and Q imply differences, seasonal differences, autoregressive, seasonal autoregressive (SAR), moving average and seasonal moving average of the SARIMA model, respectively.

The SARIMA can express a wide range of time series by designing the parameters. In this study, we simplify the SARIMA model to avoid the over-fitting problem as $d = D = q = Q = p = 0$. The designed model is thus composed by SAR component only.

Then the prediction equation of the model can be expressed as follows.

$$\hat{y}(t+h) = \sum_{\rho=1}^{P} \Phi_\rho \cdot y(t-\rho \cdot s + h) \tag{8}$$

where $\hat{y}(t+h)$ is the prediction value at time $t+h$ of h[steps] forward. $\Phi_\rho, \rho = 1,2,\ldots,P$ are weight coefficients of SAR model, P is the order of SAR model and s is a constant period (time invariant). In this case, the prediction value is a function of the past values at the corresponding phase.

2. Period estimator by using correlation analysis

To predict a quasi cyclic time series using by SARIMA model, we need to know a period of the lung tumor motion. In the followings, we will show how to estimate the time variant period.

A. Correlation function

We used a kind of correlation analysis to estimate the period of the lung tumor motion.

The pseudo correlation function we used is calculated by using two subsets of time series, e.g.$\boldsymbol{y}_t = \{y(t), y(t-1), y(t-2), \ldots, y(t-w-1)\}$ and $\boldsymbol{y}_{t-k} = \{y(t-k), y(t-k-1), y(t-k-2), \ldots, y(t-k-w+1)\}$. Subset $\boldsymbol{y}_t$ is a time series within a window width w[steps] from past time $t-w-1$ to current time t and $\boldsymbol{y}_{t-k}$ is a k[steps] delayed subset time series. We used window length w=90[steps] in this study.

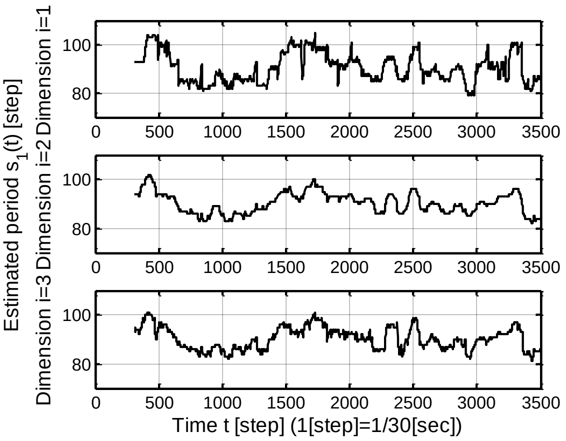

Fig.5. Time series of estimated period $\hat{s}_\rho(t)$ on each dimension i.

Then the pseudo correlation function as a function of time t and lag k will be given as follows.

$$\gamma(t,k) = \frac{1}{w}\sum_{j=0}^{w-1} y(t-j)\cdot y(t-k-j) \tag{9}$$

An example of the calculated correlation function at time t=793[step] is shown in Fig.4.

B. Estimation of time variant period

To estimate a period, we first search reference points as peak points of the correlation function as follows.

$$r_\rho(t) = \arg\max_{r_\rho(t-1)-l \le k \le r_\rho(t-1)+l} \gamma(t,k) \tag{10}$$

where l is the parameter to define the search area for the peak point.

The estimated period $\hat{s}_\rho(t)$ will then be able to calculate from the reference point $r_\rho(t)$ by using the following equation (Fig.4).

$$\hat{s}_\rho(t) = \begin{cases} r_\rho(t) - r_{\rho-1}(t), & \text{if } \rho > 1 \\ r_\rho(t), & \text{otherwise} \end{cases} \tag{11}$$

The initial value of the reference point is initialized by

$$r_\rho(1) = \rho \times \bar{s} \tag{12}$$

where $\bar{s}$ is the average value of the pre-estimated periods and is set $\bar{s}$=90[steps] in this study.

Fig.5 shows an example of the estimated period from the time series of the lung tumor motion.

3. Prediction model: Time variant Seasonal ARIMA model

We now propose a modified SARIMA model for time variant periodic time series by using the estimated period.

Modifying the equation (8), the prediction equation of the proposed SARIMA model can be given as follows.

$$\hat{y}(t+h) = \sum_{\rho=1}^{P} \Phi_\rho \cdot y(t - r_\rho(t) + h) \tag{13}$$

Note that there is no estimated period $\hat{s}_\rho(t)$ in equation (13). We can use reference point $r_\rho(t)$ instead of estimated period as $r_\rho(t) = \sum_{\rho=1}^{P} \hat{s}_\rho(t)$.

IV. RESULTS and DISCUSSIONS

We have evaluated prediction performance of the proposed method by comparing with these of conventional SARIMA and our previous SARIMA model [2]. For this evaluation, we used the clinical data of the lung tumor motion introduced in section 2 as test data. The parameters of the proposed method and the conventional methods were designed as P=2 and Φ_ρ=$1/P$.

We calculated a prediction error as the Euclidean distance between real and predicted positions as follows.

$$e(t+h,h) = \sqrt{\sum_{i=1}^{3} (\hat{y}_i(t+h) - y_i(t+h))^2} \tag{14}$$

Note that the prediction error $e(t+h,h)$ is a function of the prediction interval h.

Then mean absolute error (MAE) is calculated as prediction performance with the prediction interval h as follows.

$$\mathrm{MAE}(h) = \frac{1}{N}\sum_{n=1}^{N} e(n,h) \tag{15}$$

where $N = t_{\mathrm{end}} - t_{\mathrm{start}}$ =2500[steps] is time interval for this evaluation.

The evaluation results of the MAE and standard deviation (SD) of the error at h=15[steps] (0.5[sec]) are shown in Table 1. The proposed method demonstrated the least MAE and the least SD in comparison another methods. There is a difference of about 0.1[mm] against other methods on MAE. Fig.6 shows MAE as functions of the prediction interval h. As is clear from this figure, the prediction error of the proposed method is smaller than these of the other two SARIMA methods at any intervals $h \leq$30.

Table 1. The prediction performances of each prediction methods at 0.5[sec](h=15[step]) ahead.

Prediction method	MAE±SD[mm]
Conventional SARIMA[2]	0.9603±0.8775
Modified SARIMA[2]	0.9408±0.8239
Proposed SARIMA	**0.8204±0.6693**

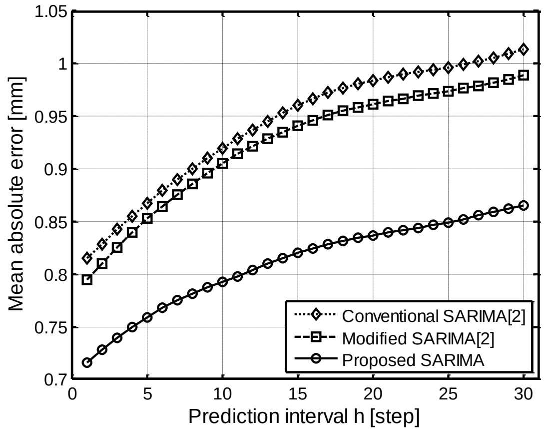

Fig.6. Comparison among three methods of mean absolute errors (MAE) as functions of the prediction interval h.

V. CONCLUSION

In this paper, we have developed a prediction method of time series for lung tumor motion. The proposed method is composed of the period estimator and the time variant SARIMA model. Simulation results showed the proposed method can achieve highly accurate prediction and has superiority against conventional methods in short- or mid-term prediction.

REFERENCES

[1] H. Ohnishi, T. Araki, T. Shirato, *et al*. (2004), Stereotactic hypofractionated high-doseirradiation for stage I non small cell lung carcinoma. Cancer 101(7):1623-1631

[2] N. Homma, M. Sakai, H. Endo, *et al*. (2009), A New Motion Management Method for Lung Tumor Tracking Radiation Therapy. IEEE WSEAS Transactions on Systems 8(4):471-480

[3] M. Sakai, N. Homma and Y. Takai. (2008), Respiratory motion prediction model of lung tumor for tracking radiation therapy. 51st the Japan Joint Automatic Control Conference 51.96-99 (in Japanese)

[4] Hokkaido University Hospital, Sapporo, Japan. http://www.huhp.hokudai.ac.jp/

[5] P.J. Brockwell and R.A. Davis (2002), Introduction to Time Series and Forecasting, 2nd edition, Springer Texts in Statistics, Springer

Pulse Transmission Time based on Temporal Difference in the Instantaneous Phase between Electrocardiogram and Photoplethysmogram Signals

M. Murakoshi[*1], M. Yoshizawa[*2], N. Sugita[*3], M. Abe[*2], N. Homma[*2], T. Yambe[*4], S. Nitta[*4]

[*1] *Graduate School of Biomedical Engineering, Tohoku University, Aoba 6-6-05, Aramaki, Aoba-ku, Sendai, Japan*
[*2] *Cyberscience Center, Tohoku University, Aoba 6-6-05, Aramaki, Aoba-ku, Sendai, Japan*
[*3] *Graduate School of Engineering, Tohoku University , Aoba 6-6-05, Aramaki, Aoba-ku, Sendai, Japan*
[*4] *Institute of Development, Aging and Cancer, Tohoku University, Seiryo-machi 4-1, Aoba, Senda, Japan*
(Tel : 81-22-795-7130; Fax : 81-22-263-9163)
(murakoshi@yoshizawa.ecei.tohoku.ac.jp)

Abstract: Analysis of the baroreflex characteristics is useful for the earlier detection of diseases such as hypertension. However, a continuous blood pressure signal must be measured with a comparatively-expensive device for this analysis. If information which has high correlation with the Mayer wave (0.05-0.15Hz) component of blood pressure can be obtained by an easy method, it will be possible to estimate the baroreflex characteristics in equipment for home healthcare and telemedicine systems. In this study, pulse transmission time (PTT), which is known to be correlated with blood pressure, was calculated by using not only a traditional method but also a new algorithm based on the temporal difference in the instantaneous phase between electrocardiogram and photoplethysmogram signals. Analysis of 94 healthy subjects' data showed that information which has a relatively high correlation with the Mayer wave component of blood pressure could be obtained from the two PTTs by selecting one of them on the basis of their powers in the Mayer wave-related band.

Keywords: blood pressure, pulse transmission time, instantaneous phase, photoplethysmogram, telemedicine

I. INTRODUCTION

Recently, not only the escalation of medical costs caused by rapid aging of the population, but also health disparities caused by a shortage of physicians are big problems in Japan. The utilization of information and communication technology (ICT) for medicine is one of methods to solve these problems because the number of Internet users reached 90.91 million, with a 75.3% diffusion rate in Japan [1]. In particular, telemedicine systems using ICT enable people living in small provincial towns to get advanced medical treatments. Furthermore, the telemedicine system may lead to the early detection of diseases if people can have clinical examinations frequently by using it. Using this system, a medical doctor can hear symptoms of diseases, check appearance of affected parts of the body and see data of electrocardiogram (ECG) and/or blood pressure of patients being somewhere away from him. However, more physiological information of the patient should be provided for accurate diagnosis.

In this study, we pay attention to the characteristics of the baroreflex system as new information used in the telemedicine system. The baroreflex system is the feedback control mechanism to attenuate the effect of perturbation in arterial blood pressure by changing heart rate and/or vascular resistance, and it is known that cardiovascular diseases such as hypertension are associated with malfunctions of this system [2]-[5].

However, to estimate the baroreflex characteristic (BRC), a continuous blood pressure signal must be measured with a comparatively-expensive device. This is making it difficult to use BRC-related indices in the telemedicine system. To solve this problem, we are trying to develop a method to estimate BRC without the measurement of the continuous blood pressure signal. In concrete terms, we calculate a physiological index reflecting BRC using pulse transmission time (PTT) which correlates with blood pressure [6] and can be measured with a compact and low-cost device. PTT is defined as the time interval between the time when a R-wave of ECG appeared and that when a pulse wave arrived at a peripheral point. Therefore, the accuracy of PTT depends on the method to detect the time when the pulse wave arrived at the position of a sensor. In most conventional methods, the time when the pulse wave begins to rise in photoplethysmogram (PPG) was used as the hitting time. However, these points observed in PPG are easily disturbed by noise and artifacts. In addition to this, the most appropriate method to detect the point of the hitting time has not been clear. So there are some methods to find the position of the arriving point [7]. Compared with this, we proposed a new method of calculating PTT based on the temporal difference in the instantaneous phase between ECG and PPG waves, and compared the proposed parameter with PTT obtained from the traditional method.

II. METHODS

1. Measurement

Ninety four healthy adults (69 males and 25 females; 23.4 ± 2.61 years) participated in this study. None of them was on cardiovascular medication. Informed consent was obtained from all the subjects before the experiment. They were instructed to sit on a chair and biological signals were measured for 5 minutes in the way hereinafter described.

ECG and PPG signals were measured from electrodes placed on the subject's chest and a photoplethysmographic sensor attached on the subject's finger, respectively. The continuous arterial blood pressure was measured non-invasively using a finger plethysmography (PORTAPRES Model-2; Finapres) or a tonometoric pressure sensor (Nihon Corin; JENTOW 7700). These signals were amplified and converted to digital data by a 16-bit A/D converter (MP100; BIOPAC System Inc.). The sampling frequency was 1 kHz.

2. Analysis

A. PTT obtained from the conventional method

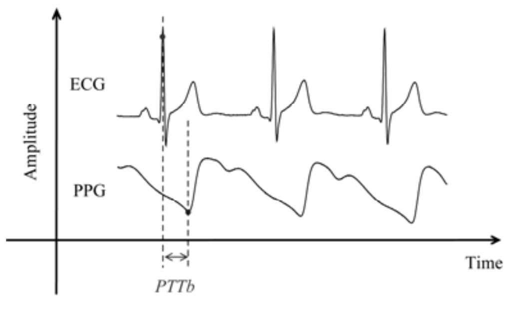

Fig.1. Definition of the pulse transmission time, *PTTb*, between ECG R-wave and the point at which PPG begins to rise

Figure 1 shows the definition of the pulse transmission time *PTTb* which is the time interval between the peak of ECG R-wave and the point at which PPG begins to rise.

B. PTT based on the temporal difference in the instantaneous phase between ECG and PPG signals

A biological signal $s(t)$ is given by

$$s(t) = \sum_k C_k \cos\theta_k(t) \qquad (1)$$

$$\theta_k(t) = k\omega_0 t + \psi_k + \phi_k(t) \qquad (2)$$

where ω_0 is a base angular frequency, C_k is a Fourier coefficient, ψ_k is an initial phase, and $\phi_k(t)$ is an instantaneous phase of the k-th harmonic wave. If k =1 and $t = t_m$ which is the time when a feature point (e.g. top point of ECG R-wave) appears at the m-th beat, eq. (2) is

$$\begin{aligned}\theta_1(t_m) &= \omega_0 t_m + \psi_1 + \phi_1(t_m) \\ &= 2m\pi \end{aligned} \qquad (3)$$

The time interval between two consecutive feature points at the m-th beat is given by

$$TI_m = \theta_1^{-1}(2m\pi) - \theta_1^{-1}\{2(m-1)\pi\} \qquad (4)$$

where $\theta_1^{-1}(n)$ is the inverse function of $\theta_1(t)$. Here, suppose that $s(t)$ is an ECG signal, TI_m means the R-R interval at the m-th beat. In a similar way, if $s(t)$ is a PPG signal, TI_m is the heartbeat interval at the m-th beat obtained from the PPG signal.

Next, PTT is considered as the time interval between a feature point of ECG and that of PPG at the same beat. So we defined the same phase temporal difference (*SPTD*) at the m-th beat as follows:

$$SPTD_m = \theta_{\mathrm{ECG}}^{-1}(2m\pi) - \theta_{\mathrm{PPG}}^{-1}(2m\pi) \qquad (5)$$

where $\theta_{\mathrm{ECG}}^{-1}(n)$ and $\theta_{\mathrm{PPG}}^{-1}(n)$ are the inverse function of $\theta_1(t)$ when $s(t)$ is ECG and that when $s(t)$ is PPG, respectively.

Figure 2 shows the flowchart of the calculation of *SPTD*. The base angular frequency ω_0 is obtained as the center frequency in the short-time Fourier transform of PPG signal. The time series of the instantaneous phase $\theta_{\mathrm{ECG}}(t)$ and $\theta_{\mathrm{PPG}}(t)$ are calculated using the Hilbert transform. The initial phase of $\theta_{\mathrm{PPG}}(t)$, ψ, is set to minimize the difference in the value of time average between *SPTD* and *PTTb*. Finally, the time series of *SPTD* is given by

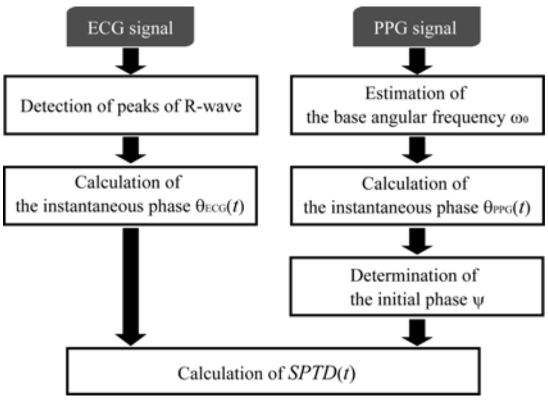

Fig.2. Flowchart of the calculation of *SPTD*

$$SPTD(t) = \theta_{\mathrm{PPG}}^{-1}\left[\theta_{\mathrm{ECG}}(t)\right] - t \tag{6}$$

In this study, the maximum cross-correlation coefficient $R_{\max}$ between PTT and the mean blood pressure (*MBP*) is defined as shown in Fig.3 to check the correlation between them in consideration of their lags. The values of $R_{\max}$ were calculated between -*PTTb* and *MBP* ($R_{PTTb\text{-}MBP}$), and between -*SPTD* and *MBP* ($R_{SPTD\text{-}MBP}$) whose frequency components were limited to the Mayer wave-related band (0.05-0.15Hz).

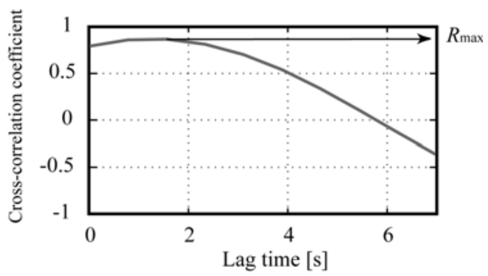

Fig.3. Definition of the maximum cross-correlation coefficient $R_{\max}$ between two parameters

III. RESULTS

Figure 4 shows changes in the Mayer wave component of *PTTb* and *SPTD* of a subject. As shown in this figure, the change in *SPTD* was roughly similar to that in *PTTb*. Fig.5 shows the scatter diagram for $R_{PTTb\text{-}MBP}$ and $R_{SPTD\text{-}MBP}$. In this figure, points above a diagonal line (dotted line) show data of subjects whose *SPTD* had a higher correlation with *MBP* than *PTTb*. This result indicates that it is possible to obtain the information which has higher correlation with blood pressure by using *SPTD* in addition to *PTTb*.

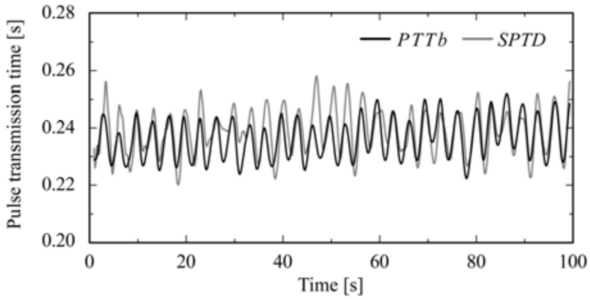

Fig.4. Changes in the Mayer wave component of *PTTb* and *SPTD* of a subject

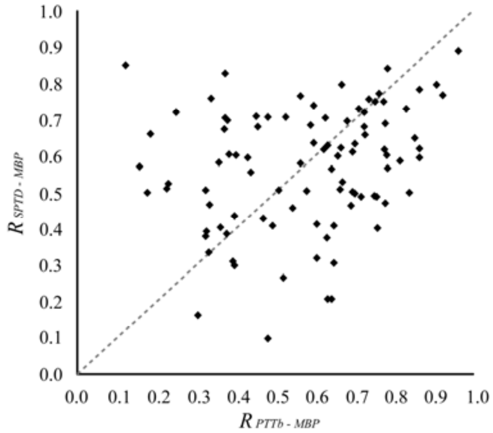

Fig.5. Scatter diagram for $R_{PTTb\text{-}MBP}$ and $R_{SPTD\text{-}MBP}$

Next, the power ratio (*PR*) of *SPTD* to *PTTb* in the Mayer wave-related band is defined as a criterion to determine whether *SPTD* should be used as the information of blood pressure instead of *PTTb* or not without the measurement of *MBP*. *PR* is given by

$$PR = \sqrt{\frac{P_{SPTD}}{P_{PTTb}}} \tag{7}$$

where P_{SPTD} and P_{PTTb} are the power of *SPTD* and that of *PTTb* in the Mayer wave-related band, respectively. Fig. 6 shows the scatter diagram for *PR* and the difference value of $R_{SPTD\text{-}MBP}$ and $R_{PTTb\text{-}MBP}$. This figure indicates that $R_{SPTD\text{-}MBP}$ was higher than $R_{PTTb\text{-}MBP}$ in most data whose *PR* is higher than 3. So we defined *PTTx* as follows:

$$PTT_x = \begin{cases} SPTD & \text{if } PR \geq 3 \\ PTTb & \text{otherwise} \end{cases} \tag{8}$$

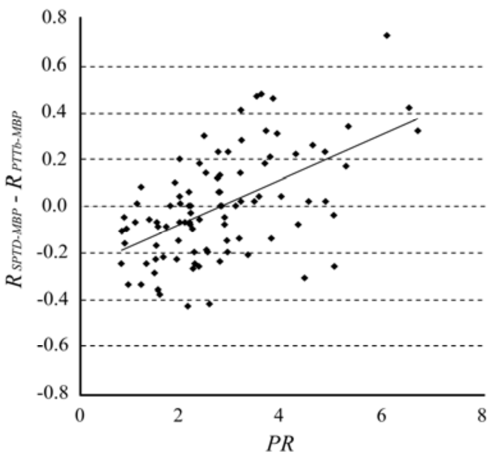

Fig.6. Scatter diagram for *PR* and the difference value of $R_{SPTD-MBP}$ and $R_{PTTb-MBP}$. *PR* is the power ratio of *SPTD* to *PTTb* in the Mayer wave-related band (0.05-0.15Hz)

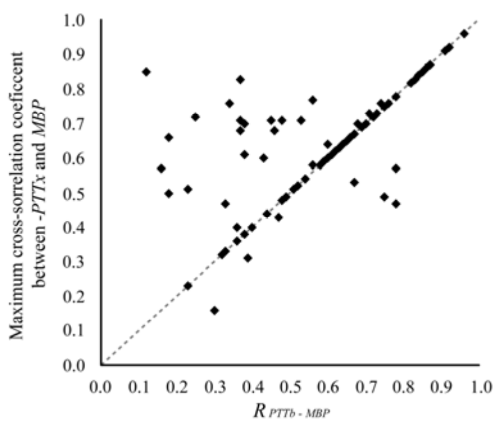

Fig.7. Scatter diagram for $R_{PTTb-MBP}$ and $R_{\max}$ between *-PTTx* and *MBP*. *PTTx* is selected from *PTTb* or *SPTD* based on *PR*

The scatter diagram for $R_{PTTb-MBP}$ and $R_{\max}$ between *-PTTx* and *MBP* is shown in Fig.7. This result shows that $R_{\max}$ of 25 subjects increased while that of 7 subjects decreased by using *SPTD* instead of *PTTb*.

The accuracy of detecting the position at which the pulse wave begins to rise is important for the estimation of *PTTb*. Thus disturbances in the PPG signal or decreased SN ratio at these points significantly reduces the accuracy of *PTTb*. On the other hand, *SPTD* is considered to be strong against short-term noise and artifacts in the PPG because the global pattern of waves was used for the estimation. The result of this study holds a possibility to obtain the blood pressure information in more accuracy by using *SPTD* in addition to *PTTb*.

IV. CONCLUSION

In this study, we focused on the pulse transmission time as a parameter which has information of blood pressure variability to estimate the baroreflex characteristics without the measurement of a continuous blood pressure signal. We proposed a parameter based on the temporal difference in the instantaneous phase between ECG and PPG signals. Analysis of the proposed parameter and the traditional pulse transmission time for 94 healthy subjects revealed that information which has a relatively high correlation with the Mayer wave component of blood pressure could be obtained by selecting one from the proposed or the conventional parameter based on the power of their Mayer wave components.

In future studies, an evaluation of baroreflex characteristic using the proposed parameter is needed. And a method to obtain the information which has higher relationship with the blood pressure variability should be developed by combining parameters other than *PTTb* and *SPTD*.

REFERENCES

[1] Communications Usage Trend Survey in 2008, The Ministry of Internal Affairs and Communications
[2] Guo GB and Abboud FM (1984), Impaired central mediation of the arterial baroreflex in chronic renal hypertension. Am J Physiol Heart Circ Physiol 246: H720-H727
[3] Guido G, Bianca MC, Gino S et al (1998), Baroreflex Control of Sympathetic Nerve Activity in Essential and Secondary Hypertension. Hypertension 31:68-72
[4] Parati G, Rienzo MD, Bertinieri G et al (1988), Evaluation of the baroreceptor-heart rate reflex by 24-hour intra- arterial blood pressure monitoring in humans. Hypertension 12:214-222
[5] Mancia G, Ludbrook J, Ferrari A et al (1978), Baroreceptor reflexes in human hypertension. Circulation Research 43:170-177
[6] Chen W, Kobayashi T, Ichikawa Y et al (2000), Continuous estimation of systolic blood pressure using the pulse arrival time and intermittent calibration. Medical and Biological Engineering and Computing 5(38): 569-574
[7] Kazanavicius E, Gircys R, Vrubliauskas A et al (2005), Mathematical Methods for Determining The Foot Point of The Arterial Pulse Wave and Evaluation of Proposed Methods. Info. Tech. Contl. 34(1): 29-36

Segmentation of Artery Areas on None-enhanced Fresh Blood Imaging Based on Dot Enhancement Filter and 3-D Region Growing Method

Akiyoshi Yamamoto, Takashi Nishizaki, Hyoungseop Kim, Joo Kooi Tan and Seiji Ishikawa

Kyushu Institute of Technology, 1-1 Sensui, Tobata, Kitakyushu 804-8550, Japan
(Tel : +81-93-884-3185; Fax : +81-93-861-1159)
(Email address: kim@cntl.kyutech.ac.jp)

Abstract: Peripheral arterial disease (PAD) is characterized by lower extremities arterial obstruction due to athe rosclerosis and manifests in lower extremities as intermittent claudicating, limb ischemia, or gangrene. The dia gnosis of the PAD using magnetic resonance imaging (MRI) equipment without contrast medium is available as a useful visual screening in clinical practice. In this paper, we propose a new method for segmentation of arterial images, which are obtained from non-contrast enhanced magnetic resonance angiography (MRA) based on dot enhancement filter and 3-D region growing methods, and satisfactory experimental results are obtained.

Keywords: PAD, non-enhanced MRA, dot enhancement filter, 3-D region growing methods

I. INTRODUCTION

Vascular diseases are among the most important public health problems and one of the leading causes of death in the worldwide. Furthermore peripheral arterial disease (PAD), one of the vascular diseases can result from atherosclerosis, inflammatory processes leading to stenosis, an embolism or thrombus formation, which causes either acute or chronic ischemia (lack of blood supply) in lower extremities, and the resulting PAD requires angioplasty or surgical bypass and may require amputation. Recently, because patients having the arteriosclerosis increase along with increasing patients of life-style related diseases, early detection and treatment for the PAD are vitally important [1].

In the diagnosis of the PAD, it is useful for detection of arteries to use computed tomography angiography (CTA) and magnetic resonance angiography (MRA). As for CTA, it can be acquired direct imaging of the arteries as an alternative to digital subtraction angiography (DSA). However, because of necessitating injecting contrast agent for diagnosing the arteries by multi-slice computed tomography (MSCT), it may be not necessarily safe examination. On the other hand, MRA is a very useful imaging technique which is obtained by magnetic resonance imaging (MRI), which has various advantages, for example, the ability to provide images blood flow signals without the need for contrast agent. In addition, a consideration for radiation exposure is not necessary for all patients. Especially, fresh blood imaging (FBI) method developed to image arteries in recent years may be useful to detect a variety of vascular diseases causes of the PAD [2-4]. The FBI is a non-enhanced MRA technique, which employs arterial signal difference between systole and diastole during a cardiac cycle, i.e., subtraction of the diastolic bright-blood arteries from the systolic black-blood arteries allowed visualization of the arteries by cancelling the veins. However, due to peristaltic movement of organs such as the intestine or the bladder, unnecessary background area may frequently develop on these MR images, and diagnoses of the vascular disease may be affected. Nevertheless, image processing techniques to resolve these issues have not been established.

The medical image processing and analysis technique to segment of vascular structures is one of the important tasks in computer vision and image processing field. Many researchers introduced 3-D and/or 2-D image processing techniques for visual screening not only in the medical field but also in the computer vision. Especially, in the field of handling a high resolution medical image, including CT, ultrasound image, and MRI, the 3-D image reconstruction process make burden to radiologists. Therefore, manual analysis for routine clinical use is impractical. In that point, they require a method for displaying the 3-D image and supporting a computer aided diagnosis (CAD) [5, 6]. Many CAD systems have been developed on the medical field to analyze the internal organs based on CT, and MRI etc [7, 8]. Unfortunately, most clinical routines still rely on manual operations. Automatic image processing techniques to detect the vessels on MR imaging are necessary.

A new development of a CAD system to visualize the results of extracted blood vessel area on non-enhanced fresh blood MR imaging based on a 3D-region growing method of tree structure theory and using feature value by selective enhancement filter will be presented in this paper.

II. MATERIALS AND METHODS

This section presents our proposed image preprocessing method for detecting the blood vessel region on MR images. These MR images, used in this paper are provided as DICOM (Digital Imaging and

Communication in Medicine) images, are achieved as the images which removed the vein region with use of FBI method . Fig. 1 gives an example of the original MR image obtained by the FBI method. A white area in Fig. 1 shows the blood vessel area. The outline of some image analyzing technique is shown below.

Moreover, the overall scheme of the image processing technique for extracting the region of blood vessels is illustrated in Fig. 2. The method consists of three main steps; extracting the initial enhanced points, acquisition of 3-D coordinate on the blood vessel regions, and displaying the blood vessel.

To segment the artery areas on MR imaging which is obtained non-enhanced FBI technique, some image processing techniques are introduced. In the first step, pre-processing technique such as smoothing and

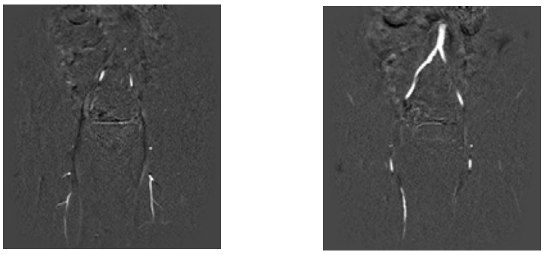

(a) (b)

Fig. 1 Examples of a successive MR image which is obtained by the FBI method.

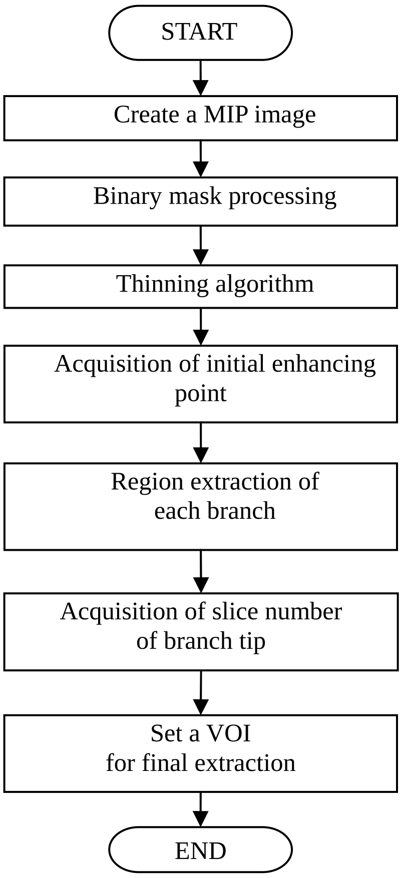

Fig. 2 Flow of procedure

binarization are performed to reduce image noise. In the second step, we make a maximum intensity projection (MIP) image from coronal plane to detect the initial artery areas on the FBI images. In the third step, we perform the thinning algorithms and selective enhancement filter (dot and line enhancement filter) on volume of interest (VOI) before adopting the 3-D region growing technique, finally a MIP image for diagnosis is made from these images extracted.

2.1 MIP

MIP is a method of adopting the maximum signal (pixel value) on the projective direction as a projection value. Fig. 3 shows the notion of MIP technique, which is introduced in our technique. In Fig. 3, (a) illustrates a coronal view, and (b) shows an axial view. In this study, first of all, the MR images obtained by using of FBI method are inputted as original image. Next, MIP image is reconstructed from the original image. At this time, three dimensional coordinates value of the area where have maximum pixel value on the viewpoint are saved.

2.2 Extracting the initial blood vessel regions

To extract the blood vessels area, binary mask processing (same threshold which has CT value of 3000 in all the cases) is done to all volume data in the first step of extracting a region of interest. Next, to decide starting point of region growing method, thinning algorithm is performed. The thinning algorithm is operation for extracting a central line of one pixel in width by making thinning the line width in a given figure. When a figure is used the thinning algorithm, because it is easy to analyze the shape and the relation of combination, the thinning algorithm is widely used.

The image including the noise obtained by thinning algorithm is also performed the thinning processing. In this study, to obtain only the blood vessel area, eight neighbor pixels are searched from the point of the blood vessels area, and by tracking the point which have these thinning pixel values, all of thinning parts except these points are reduced, we can obtain thinning images which are only the blood vessels parts. At this time, the highest point is made as the starting point, and this point has three dimensional coordinates which comes from the MIP image. As a result, the starting point of region growing method can be decided automatically.

2.3 3D-region growing method and tree structure

The region growing method is one of the important methods for segmentation on computer vision, medical imaging, and analyzing a video image field [9, 10]. It is applied to specify an accurate position of the blood vessel area, by performing the area expansion processing. When a good performance could not achieved for detecting the line segment, the successive blood vessel area appears as a discontinuous point of the line element on the MR image. It is because it could not correctly extract the peripheral vessel when it was

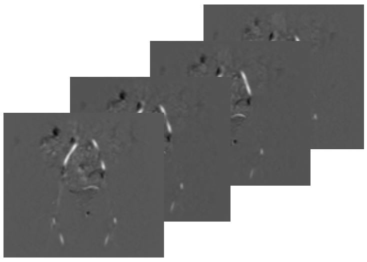

(a)

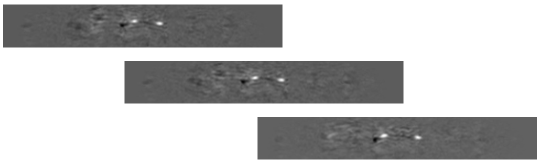

(b)

Fig. 3 MIP image which is obtained coronal plane from the MRI image

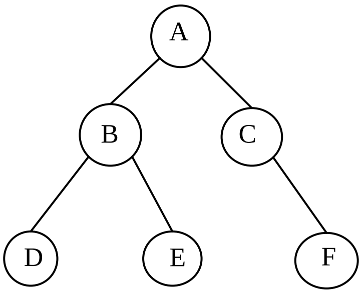

Fig.4 Tree structure

applied to binary imaging threshold processing. The resulting the extraction of the peripheral blood vessel area becomes difficult. To avoid this problem, in the first stage, we introduce a region growing method. Moreover, we assume that these blood vessels are exist some direction on the FBI images which having the tree structure shown in Fig. 4. These blood vessels are extracted in a slice of the images from the starting point on the region growing method. Next, three dimensional enhancement is done by extracting between successive slices. After enhancing process, labeling is done at a slice of the image, and divergence is understood A to B and C in Fig. 4. At this time, the threshold is changed by the labeled area of a blood vessel section. The blood vessel area is extracted by changing the threshold at each divergence B to D in Fig. 4. It returns to the previous divergence and the process is done to the branch that did not do the extraction process (D to B). At this time, the slice of branch tip (section of the peripheral blood vessel) can be obtained. The entire blood vessel area is extracted by repeating this processing (B to E, E to C and C to F).

2.4 Extracting the peripheral vessel

The thick blood vessel area can be extracted by the above mentioned technique. However, it is difficult to do the extracting process with a parameter when the top and bottom of the blood vessel are extracted. It is because the pixel value is resembled in the peripheral blood vessel area. To overcome this problem, we propose to set VOI in the second stage and to perform the 3D-region growing processing as the feature value which is applied dot and selective enhancement filter with selective enhancement filter to the thick blood vessel area [10]. As a result, when the over extraction is occurred, the influence can be decreased. Moreover, the processing time can be reduced by setting the area of interest, and limiting the range of processing. Thus the slice number of the peripheral blood vessel section is obtained in the first stage, and in the second stage, the range setting of VOI is specified from the slice and the center of gravity of the blood vessel section.

III. EXPERIMENTAL RESULTS

To detect blood vessel area, we applied automatically proposed method to MR image obtained by FBI method. Image size is 256 x 256 [pixels] and the image set consists of 50 to 100 slices images per case. Automatic extracting of the blood vessel area is performed by the discrimination analysis using the 3D-region growing method and the tree structure. The experimental results on processing for source images for 11 cases were shown with a good performance of extraction of blood vessel area. A result of the extraction processing is shown in Fig. 5. A MIP image from the coronal view is created from the original image as shown in Fig. 5 (a). In this Figure, the image noise of the bladder and the area where a high density value is indicated in other organs appear in the image beside the artery area to be extracted. A MIP image of detection result on initial artery area and final detection result are shown in Fig. 5 (b) and 5(c), respectively.

Overall the performance for these extraction results are evaluated by comparing some center lines on the original MIP image from the coronal and sagittal view which acquired by our proposed method with the correct data of blood vessel area indicated visually by a medical doctor. In particular, we assume that the true positive (TP) is the rate of crossover the extracted blood vessel area automatically to the correct data, and also the false positive (FP) is the rate of the over extraction area to the correct data. Moreover, the average recognition rate is acquired by the results applied to the true non-enhanced MR images of 11 cases with the proposed method. The result of the average recognition rate is shown in Table 1. Next, the result of the correspondence ratio for the assessment of performance is shown Table 2. Each equation of the TP, the FP and the correspondence ratio (*CR*) are shown in equation (1), (2) and (3), respectively.

$$TP = \frac{n\ (A \cap B)}{n\ (A)} \ * \ 100 \ [\%] \qquad (1)$$

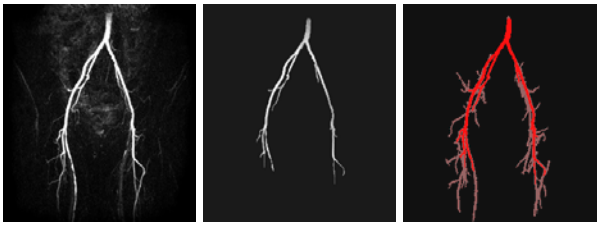

(a) (b) (c)

Fig.5 Extraction result

$$FP = \frac{n\ (C)}{n\ (B)} * 100[\%] \quad (2)$$

$$CR = \frac{n\ (A \cap B)}{n\ (A \cup B)} * 100[\%] \quad (3)$$

A, *B*, *C* and *n* in these parameters of each equations are shows the gold stand by radiologist, the extracted result, the over extraction and the number of pixels, respectively. In this study, the TP from the coronal view and the sagittal view are 82.95% and 92.1% in the average recognition rate are achieved, respectively.

Table 1 Result of average recognition rate of 11 cases

	TP (%)	FP (%)
Coronal	82.95	27.44
Sagittal	92.17	49.18

Table 2 Result of correspondence ratio of 11 cases

	Agreement rate (%)
Coronal	61.94
Sagittal	66.59

IV. DISCUSSION AND CONCLUSIONS

In this paper, we have developed a CAD system as an automatic extraction of blood vessel region to analyze non-enhanced MR image employing a FBI method in lower limbs area. In the extraction of the blood vessel area, a good performance was obtained by use of a 3-D coordinate value as the starting point from the MIP image with the thinning algorithm, the region growing method based on tree structure. In the assessment result of the precision of detecting in Table 1, a good performance has been obtained both the TP and the FP in the MIP image from the coronal view. On the other hand in the MIP image from the sagittal view, though the FP was slightly higher the value than one from the coronal view, a good performance was obtained with the TP was over 90%.

However, some cases including venous area on the original image may have mis-detections that the venous area as well as the arterial area is extracted, and for this reason, some improvements for extracting algorithm in the blood vessel area are required.

REFERENCES

[1] Conen D, Rexrode KM, Creager MA, Ridker PM, Pradhan AD.: "Metabolic syndrome, inflammation, and risk of symptomatic peripheral artery disease in women: a prospective study", Circulation, Vol.120, No.12, pp.1041-1047, 2009.

[2] Miyazaki M, Lee VS.: Nonenhanced MR Angiography, Radiology, 248, pp.20-43, 2008.

[3] K. Nakamura, A. Yamamoto, M. Miyazaki, S. Kawanami, Y. Shioya, Y. Matsufuji: "Clinical usefulness of non-contrast-enhanced MRDSA to evaluate hemodynamics of arterial diseases-initial experience-", Proc. International Society of Magnetic Resonance in Medicine, Vol.11, pp.1356, 2003.

[4] A. Yamamoto, K. Nakamura, M. Miyazaki, Y. Shioya, S. Kawanami, Y. Matsufuji: "Non-contrast-enhanced MRDSA of peripheral arteries using continuous acquisitions of ECG-Triggered 2D half-Fourier FSE within a cardiac cycle", Proc. International Society of Magnetic Resonance in Medicine, Vol.11, pp.1709, 2003.

[5] MacMahon H, Doi K, Chan HP, Giger ML, Katsuragawa S, Nakamori N: "Computer-aided diagnosis in chest radiology", J Thorac Imaging, Vol.5, No.1, pp.67-76, 1990.

[6] J. M. Fitzpatrick, D. L. G. Hill, Y. Shyr et al.: "Visual Assessment of the Accuracy of Retrospective Registration of MR and CT Images of the Brain", IEEE Trans. Med. Imaging, Vol.17, No. 4, pp.517-585, 1998.

[7] N. Ray, S.T. Acton, T.A. Altes et al.: "Merging parametric active counts within homogeneous image regions for MRI-based lung segmentation", IEEE Trans. Med. Imaging, Vol.22, No.2, pp.189-199, 2003.

[8] S. Busayarat, T. Zrimec: "Detection of bronchopulmonary segments on high-resolution CT preliminary results", IEEE International Symposium on Computer-Based Medical Systems, pp.199-204, 2007.

[9] J. Yi, J.B Ra: "A locally adaptive region growing algorithm for vascular segmentation", International Journal of Imaging Systems and Technology, Vol.13, No.4, pp.208-214, 2003.

[10] Li Q, Sone S, Doi K.: "Selective enhancement filters for nodules, vessels, and airway walls in two- and three-dimensional CT scans", Medical Physics, Vol.30, No.8, pp.2040-2051, 2003.

Construction of a sense of force feedback and vision for micro-objects

R.Uehara

Graduate School of Computer Science
and System Engineering
Kyushu Institute of Technology
680-4, Iizuka City, Fukuoka, Japan, 820-8502
uehara@mmcs.mse.kyutech.ac.jp

E.Hayashi

Department of Mechanical Information
Science and Technology
Kyushu Institute of Technology
680-4, Iizuka City, Fukuoka, Japan, 820-8502
haya@mse.kyutech.ac.jp

Abstract. The purpose of this research was to develop a combined sense system that uses both force feedback and visual feedback to determine the shape of the microscopic features of a microsample. It is thought that the efficiency of minute procedures would be improved if the operator were able to have a sense of force while using a manipulator. We used a cantilever to touch a minute object and obtain a reaction force from the degree of bending. We constructed a haptic device that gives a sense of that force to the operator, who can feel the force when a user touches the sample with a cantilever. In addition, when the haptic device is used in simulations, the user can feel a force as if he had touched the sample.

Key words: force feedback, haptic interface, simulation.

1. Introduction

Technologies that can accurately perform minute work are now being sought for both medical treatment and in the field of manufacturing semiconductors. Such minute work is improved by using micromanipulators, but their operation is difficult because the operator has no sense of force; he relies only on sight through a microscope. As a result, a person skilled in the use of this technology is needed for all minute work. It is thought that the efficiency of minute work would be improved if the operator were able to have a sense of force while using a manipulator.

This study describes the development of a more efficient system for minute operations. Our aim was to develop a system using not only the sense of sight through a microscope, but also a sense of force from the manipulator. For this fundamental research, a system was created to assess the reaction force when a minute sample was touched. A cantilever was used to touch the sample, and the reaction force was obtained from the degree to which the sample bent. In addition, we used a haptic device and amplified the force feedback from a minute sample of a virtual object.

2. System Structure

2-1. System Summary

The structure of the system is shown in Fig. 1a, and a schematic view is shown in Fig. 1b. This system consists of a microscope with an automatic x-y stage, a piezo stage, a feedback stage controller to control the x-y stage, a piezo stage controller, a haptic device for transmitting force feedback (Fig. 2), a cantilever (Fig. 3), and a PC via which the user can control and operate these components. The sample was fixed on the x-y stage by an injector (Fig. 4) and a holding pipette (Fig. 5). When the cantilever, which was fixed to the piezo stage, touched the sample, the operator could feel a force as if he had touched the sample using the haptic device. The resolution of the piezo stage is 1 nm. Table 1 gives the specifications of the injector, and Table 2 gives the specifications of the holding pipette.

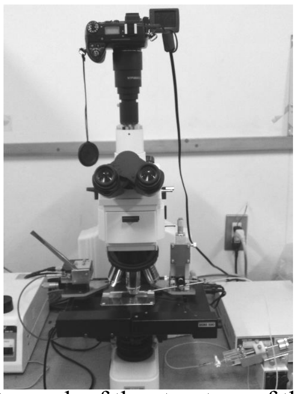

Fig. 1a. Photograph of the structure of the system.

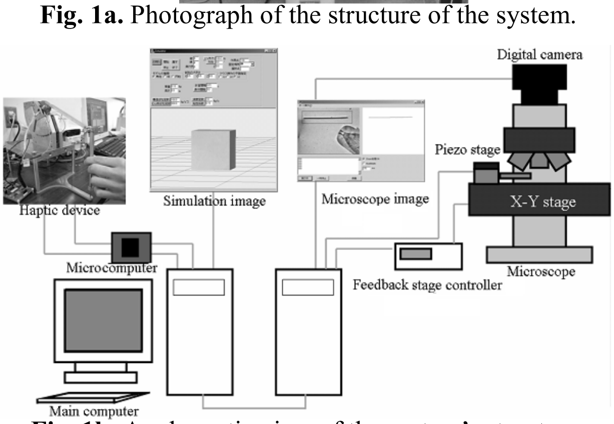

Fig. 1b. A schematic view of the system's structure.

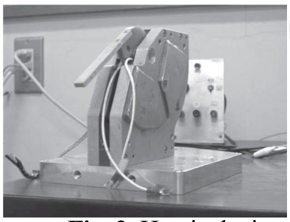

Fig. 2. Haptic device.

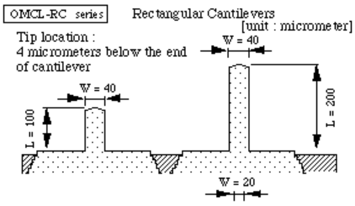

Fig. 3. Cantilever.

Fig. 4. Injector.

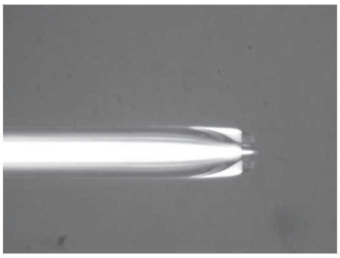

Fig. 5. Tip of holding pipette.

Table 1. Specifics of the injector.

Drive distance	40 mm
Braking distance	800 μ‖
Size	200×80×30 mm
Weight	2 kg

Table 2. Specifics of the holding pipette.

Length	60 mm
Inside diameter	13 μm

2-2. Haptic device

Figure 6 is a diagram of the haptic device. It consists primarily of a rotor, a laser, and a position-sensitive device (PSD). We installed a coil on the rotor with a polarity magnet, which generated electromagnetic induction by an electric current and a magnetic force. The angle of the rotor can be measured by the laser and the PSD. The rotor was able to follow any input waveform.

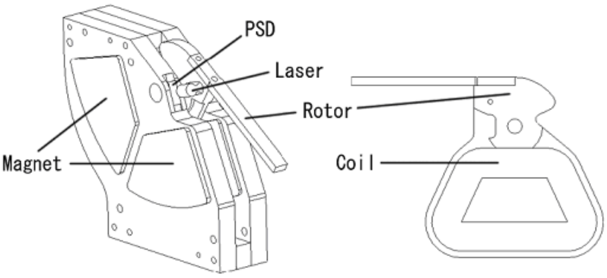

Fig. 6. Diagram of the haptic device.

It was necessary to control the actuator with a servomechanism on the actuator. Therefore, the system driving the actuator consisted of four actuators: a microcomputer, an inputting AD/DA port, an outputting microcomputer, and a PC outputting order value. The system controls the actuator during each part of the process. Figure 7 shows the structure of the haptic device.

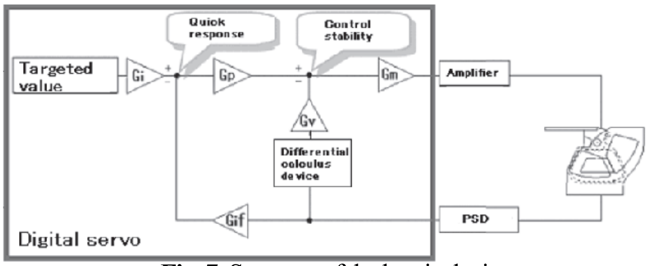

Fig. 7. Structure of the haptic device.

The actuator, which is structured by the PD control, is operated through a digital differential calculus device. A transfer function for the quadratic function system shown in Fig. 8 is provided for the actuator servo system. The role of each parameter of the control system is to adjust the total offset to a master in Gi/Gif, to regulate the item viscosity/resonance point in Gp/Gv, and to regulate the total gain in Gm. Table 3 is a list of the control parameters of the servomechanism system.

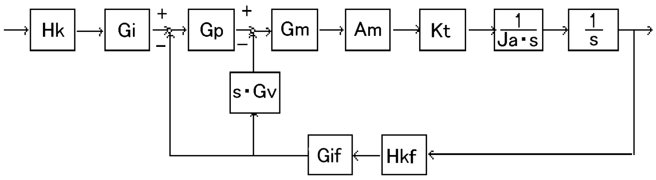

Fig. 8. Block diagram of the servomechanism system.

Table 3 Control parameters of the servomechanism system

Parameter	Reference	Unit
Gi	Controller Input Gain	1.0
Gif	Position Feedback Gain	1.0
Gp	Position Gain	1.0
Gv	Velocity Gain	0.0015
Gm	Manipulation Gain	1.0
Hk	Position Voltage Constant	18.531 V/rad
Hkf	Position Voltage Feedback Constant	18.531 V/rad
Am	Amplifier Constant	1.0 A/V
Kt	Torque Constant	2.768 Nm/A
Ja	Moment of Inertia	0.0002147 kg $\cdot m^2$

3. Measuring the antipower

The reaction force is used to calculate the force that is applied by the minute object. In this experiment, we touched the minute object with the cantilever shown in Fig. 3, and the reaction force was obtained from the degree of bend of the cantilever. The layout of the experiment is shown in Figs. 7

and 8, and the environment of the experiment is shown in Figs. 9 and 10. As a result of this experiment, we obtained the reaction force applied by the minute object.

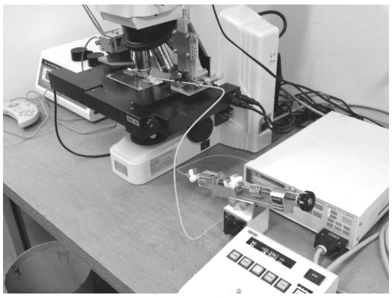

Fig. 9. Environment of the experiment.

Fig. 10. Environment of the experiment.

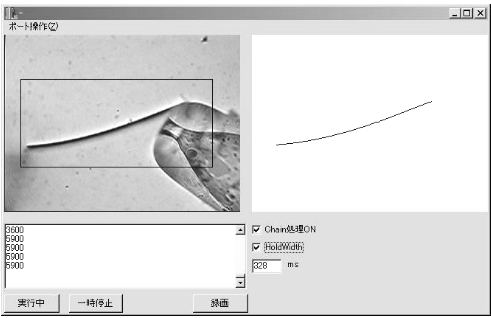

Fig. 11. Cantilever touching the tip of the holding pipette.

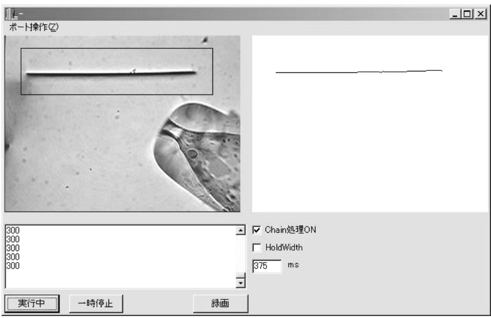

Fig. 12. The cantilever detection program.

Figure 11 shows the cantilever touching the tip of the holding pipette. The image processing speed of the cantilever was improved by the tracking process (Fig. 12). The bend of the cantilever is assumed to be linear-elastic so that Hooke's law may be applied. Then the restoring force F of the bend of the cantilever is given by

$$F = kx \qquad (1)$$

where x is the compression distance from the equilibrium position, and k is the spring constant.

4. Deforming the simulation of the sample

In this study, we aimed to build a working system using a microscope, a haptic device and a simulation. A fundamental element was the simulation of the deformation of a minute object. Figure 13 shows the graphical user interface (GUI) of the simulator. A graphic tool is created using OpenGL to draw the object and to choose the shape of the sample, for instance, a cube or sphere. A dynamic model of the sample consists of a spring-mass array of mass points in both the vertical and horizontal directions. An example of the arrangement of mass points is shown in Fig. 14. When a force was applied at a mass point, the simulation calculated the speed of all mass points that had been affected. The image is renewed after every ten calculations.

A spring is defined as having a size but no weight, and a mass point is defined as having a size, a weight and a rigid body. An arbitrary mass object can be placed on a spring on a bitmap (Fig. 15). In addition, a sample can be seen from various viewpoints, and the deformation of the sample, which is impossible to observe by microscope, can be checked. The shape of this object can be either a cube or a sphere, and any point may be selected as a fixed point or an operating point.

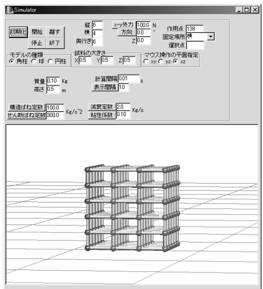

Fig. 13. Simulator.

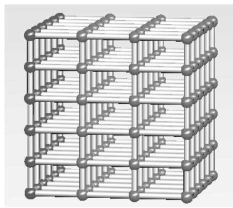

Fig. 14. Arrangement of mass points

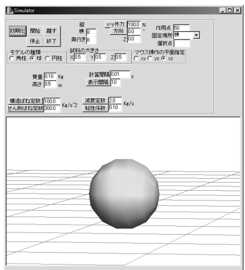

Fig. 15. Placing an arbitrary object on a bitmap.

The calculation method for the displacement of each mass point is based on Newton's equation of motion (Eq. 1) using the Euler method. A mass point is linked to an adjacent mass point at both ends of a spring. When the spring between the mass points is in the equilibrium position, the restoring force F is the sum of the elastic force of the construction spring and the shear spring, and the viscous force is given by

$$ma = \Sigma F \tag{2}$$

where m is mass and a is acceleration.

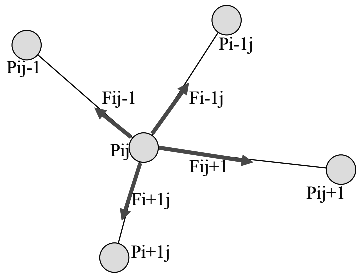

Fig. 16. Elasticity.

ΣF is sum of the elastic force of the construction spring and shear spring, the viscous force and the damping force. To obtain the restoring force F, the restoring force was divided into $F_{damping}$, F_{spring} and $F_{viscous}$. Equation 2 gives the following equations using the model shown in Fig. 16.

$$F_{spring} = \Sigma F_{ij} \tag{3}$$
$$F_{damping} = -C_d v_i \tag{4}$$
$$F_{viscous} = -C_v (v_i - v_j) \tag{5}$$
$$\Sigma F = F_{spring} + F_{damping} + F_{viscous} \tag{6}$$

where C_d is the damping factor, C_v is viscosity, and v_i and v_j are the velocities.

5. Conclusion

The present study evaluated whether the force feedback is amplified by touching a virtual object with a haptic device in a PC. We found that it is possible to amplify the reaction force, but were unable to create a large enough reaction force for a worker to feel its elasticity.

Future research should focus on building a system that allows a reaction force to be detected and shown more precisely. Such a system would make it possible to test smaller samples.

6. Acknowledgement

This research was supported in part by a Grant-in-Aid for Scientific Research, 2009 from the Ministry of Education, Science, Sports and Culture.

References

1. Li X, Zhang Z (2008) Probe-type microforce sensor for micro/nano experimental mechanics. Trans Tech Publications, Stafa-Zurich, Switzerland
2. Zhang J, Xi N, Li G, et al. (2006) Atomic force microscopy sensing using multiple modes. 2006 IEEE/RSJ International Conference on Intelligent Robots and Systems, Beijing, China, 9-15 October. IEEE, Piscataway, NJ
3. Hrouzek M (2005) Feedback control in an atomic force microscope used as a nano-manipulator. Acta Polytech Czech Tech Univ Prague 45(4):65-69
4. Ujihara R (2004) Developing the haptic device. Kyushu Institute of Technology
5. Yaacoub F, Hamam Y, Abche A (2008) Computer-based training system for simulating wrist arthroscopy. Université Paris-Est, ESIEE, Laboratoire A²SI, Cité Descartes, 93162 Noisy Le Grand, France. University of Balamand, Department of Electrical Engineering, P.O.Box 100, Tripoli Lebanon F'Satie – TUT, Private Bag X680, Pretoria 0001, South Africa. Proceedings of the 21st IEEE International Symposium on Computer-Based Medical Systems (CBMS 2008)
6. Tahmasebi AM, Taati B, Mobasser F, et al. (2005) Dynamic parameter identification and analysis of a PHANToM trade haptic device. School of Computing, Queen's University, Kingston, ON, Canada. Department of Electrical and Computer Engineering, Queen's University, Kingston, ON, Canada. 2005 IEEE International Conference on Control Applications (CCA) (IEEE Cat. No. 05CH37713)
7. Sonoda T (2006) Construction of super-micro sense of force feedback and visual for an elastic body. Kyushu Institute of Technology. Proceedings of the 12th International Symposium on Artificial Life and Robotics, Beppu, Oita, Japan, 2006
8. Miyamoto K (2007) Construction of super-micro sense of force feedback and visual for micro objects. Kyushu Institute of Technology. Proceedings of the 12th International Symposium on Artificial Life and Robotics, Beppu, Oita, Japan, 2007

A Real-time Face Detection and Recognition System for Mobile Robot in the Complex Background

Song Chen[1,2], Tao Zhang[1,2], Chengpu Zhang[1,2] and Yu Cheng[3]

[1]*Department of Automation, Tsinghua University, Beijing 100084, China*
(Tel: 86-10-6279-7710; Fax: 86-10-6278-6911)
(E-mail: chen-s03@mails.tsinghua.edu.cn)
[2]*Tsinghua National Laboratory for Information Science and Technology, Tsinghua University, Beijing 100084, China*
[3]*Department of Biomedical Engineering, Tsinghua University, Beijing 100084, China*

Abstract: The research presented in the paper focuses on a real-time face detection and recognition system applied to biped robot in the complex background. In the visual system, a multi-information method consisted of Adaboost algorithm and color information for face detection part is proposed and Embedded Hidden Markov Model (EHMM) is employed to recognize the detected faces. The system introduced in the paper improves the processing speed of detecting and recognizing faces in a frame with a suitable accuracy by integrating three rapid algorithms.

Keywords: face recognition, biped robot, complex background

I. INTRODUCTION

In the recent decades, the scope of applying mobile robots has been broadening with the development of robot technologies. The mobile robots can not only get used to the variety of terrestrial environments, but also are required to have more effective capability of interaction with users, for example, following the people's actions or communicating with people [1], which makes the ability of acquiring information by vision be more and more important to robots. Department of Automation, Tsinghua University has developed a biped robot used to research and integrate different robot technologies. The face recognition system introduced in the paper is developed for the robot to make it detect and recognize faces in the complex background.

The character of the system is real-time processing and adapting to uncontrolled indoor environments. For the purpose, a multi-information method consisted of Adaboost algorithm and color information, which are the fast face detection methods at present, for face detection part is proposed. In addition, Embedded Hidden Markov Model (EHMM) is presented using 2-DCT feature vector as the observation vector to recognize the detected faces. By setting the factors of EHMM, the processing speed and recognition rate of the system can be changed. Fig.1 illustrates the main procedure of the face recognition system.

In this paper, Section 2 presents the face detection algorithm, and EHMM algorithm for face recognition is explained in Section 3. In Section 4 the testing results of the whole system are explained in the uncontrolled indoor conditions. Finally, conclusions and future work are drawn in Section 5.

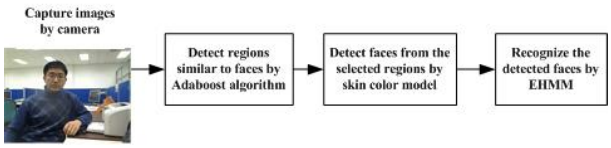

Fig.1. Flow of face detection and recognition

II. FACE DETECTION

The face detection section is integrated by Adaboost algorithm and skin color model method. Both approaches can process the images and video extremely rapidly.

1. Adaboost Algorithm

Adaboost algorithm was first proposed by Freund Y. and Schapire R.E. in 1996, which was an iterative and very important machine learning method [2]. On the basis, Viola, P. and Jones, M. proposed an improved machine learning approach, which could process the images extremely efficiently and achieve high detection rates, for visual objects detection [3][4].

Adaboost detector employs the extended set of Haar-like features which is proposed by Lienhart et al.

[5][6] to classify. Each feature is consisted of 2~3 rectangles to detect edge features, center-surround features and line features. Fig.2 describes the set of features. In order to compute the features rapidly, Viola P. introduced the integral image representation for images. The integral image at location (x, y) means the sum of the pixels above and to the left of (x, y), inclusive:

$$ii(x, y) = \sum_{x' \le x, y' \le y} i(x', y') \qquad (1)$$

where $ii(x, y)$ is the integral image and $i(x, y)$ is the original image.

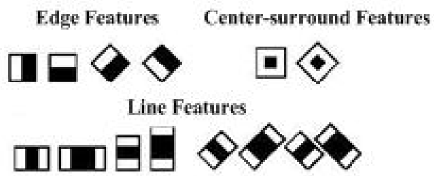

Fig.2. Haar-like features

With the feature set and a training set of positive and negative images, Adaboost algorithm is used to train strong classifiers and a cascade of classifiers is constructed to achieve increased detection performance while reducing computation time. The main procedure is below:

(1) Given example images $(x_1, y_2), \cdots, (x_n, y_n)$, and $y_i = 1, 0$ for negative and positive example respectively.

(2) Initialize weights $w_{1,i} = 1/2m, 1/2l$ for $y_i = 1, 0$ respectively, where *m* and *l* are number of negatives and positives respectively.

(3) For $t = 1, \cdots, T$:

a) Normalize the weights $w_{t,i} \leftarrow w_{t,i} / \sum_{j=1}^{n} w_{t,i}$, so that w_t is a probability distribution.

b) For each feature *j* train a classifier h_j which is restricted to using a single feature. The error is $\zeta_j = \sum_i w_i \left| h_j(x_i) - y_i \right|$.

c) Choose the classifier h_t with the lowest error.

d) Update the weights: $w_{t+1,i} = w_{t,i} \beta_t^{1-e_i}$, where $e_i = 0$ if example x_i is classified correctly, otherwise $e_i = 1, \beta_t = \zeta_t / (1 - \zeta_t)$.

(4) The final strong classifier is:

$$h(x) = \begin{cases} 1 \ \sum_{t=1}^{T} \alpha_t h_t(x) \ge (\sum_{t=1}^{T} \alpha_t)/2 \\ 0 \ otherwise \end{cases}, where\ \alpha_t = \log(1/\beta_t)$$

(5) Constructed the cascade of strong classifiers.

2. Skin Color Model

Human skin color has been used and proven to be an effective feature in face detection [7][8]. Several color spaces have been utilized to label pixels as skin including RGB, normalized RGB, HSV, YCrCb, YIQ, CIE XYZ and CIE LUV. The simplest and most effective model is YCrCb model, in which Y means luminance or gray value and Cr, Cb values are defined as skin tone pixels. YCrCb model is influenced little by illumination variations and the distribution of skin color pixels measured by Cr, Cb is very compact. In Fig.3 is shown the distribution according to the statistics of 200 images searched in the Internet.

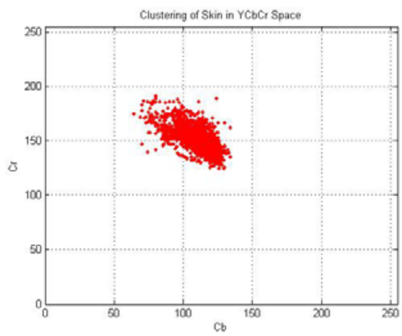

Fig.3. Distribution of skin color in YCrCb model

There are two methods to classify pixels. One is to construct the Gaussian Density Model based on the statistical data, and the other is to classify a pixel simply to have skin tone if its values (Cr, Cb) fall within a range, which is $133 < Cr < 173, 77 < Cb < 127$ concluded by experiments. Considering the detection rates and speed, the second method is employed in the paper. The skin color model is used to verify the regions detected by Adaboost algorithm. If the ratio of skin color pixels and total pixels is larger than the threshold, which is set as 0.355 got by experiments, the regions are considered as faces finally.

3. Face Detection Database

GTAV face database is used to test the effectiveness of face detection section in the paper. GTAV database includes a total of 44 persons with 27 pictures per person which correspond to different pose views (0º, ±30º, ±45º, ±60º, ±90º) under three different illuminations (environment or natural light, strong light source from an angle of 45º, and finally an almost frontal mid-strong light source). Furthermore, at least 10 more additional frontal view pictures are included with different occlusions and facial expression variations.

The resolution of the images is 240*320 with BMP format.

40 persons with 15 images per person with different illuminations and facial expressions are selected to detect, and the people's pose views are limited to 0º, ±30º. Two-thirds of the faces are used to train the cascade of classifiers. In Fig.4 is shown the examples of GTAV and Fig.5 describes the relevant detection results. The detector runs at 4.5 images per second and the detection rate is 97.5%.

Fig.4. Examples of GTAV

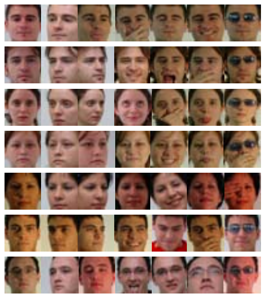

Fig.5. Detection results

III. FACE RECOGNITION

In the face recognition section, Embedded Hidden Markov Model abbreviated as EHMM is employed to recognize the faces detected. Lack of space, the section will just introduce the basic principle and program flow and references [9][10] are given a detailed mathematical derivation of HMM and EHMM.

Hidden Markov Model (HMM) is a set of statistical models used to characterize the statistical properties of a signal. HMM consists of five elements: (1) *N*, the number of states in the model; (2) *M*, the number of different observation symbols; (3) *A*, the state transition probability matrix; (4) *B*, the observation symbol probability matrix; (5) Π, the initial state distribution. With the factors, a HMM is defined as

$$\lambda = (A, B, \Pi) \qquad (2)$$

For faces of people, the significant facial regions (hair, forehead, eyes, nose, mouth and chin) come in a natural order from top to bottom regardless of the scale, illumination, rotation of faces. Each of these facial regions is assigned to a state in a left to right 1-demension continuous HMM. Then the observation vectors consist of a set of 2D DCT coefficients that are extracted from each region.

Thus, the HMM $\lambda = (A, B, \Pi)$ is initialized. The training data is uniformly segmented from top to bottom in $N = 5 \; or \; 6$ states and the observation vectors associated with each state are used to obtain initial estimates of the observation probability matrix B. The initial values for A and Π are set given the left to right structure of the face model.

EHMM is similar to HMM, but consists of s set of super states. Super states divide face into different regions which are hair, forehead, eyes, nose and mouth, from top to bottom. Each super state also consists of some states named embedded states. The faces are divided into some blocks both vertically and horizontally. 2D DCT features are extracted from the blocks as the observation vectors. EHMM utilizes more information of faces than HMM, so the recognition rate of EHMM is higher. In Fig.6 is described the face structure of EHMM while the program flow is shown in Fig.7.

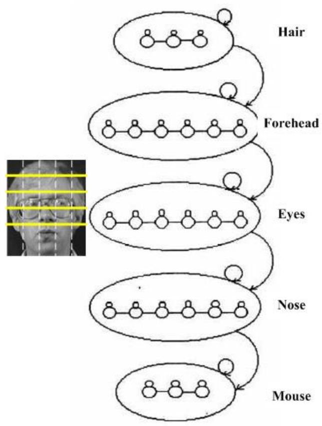

Fig.6. Face structure of EHMM

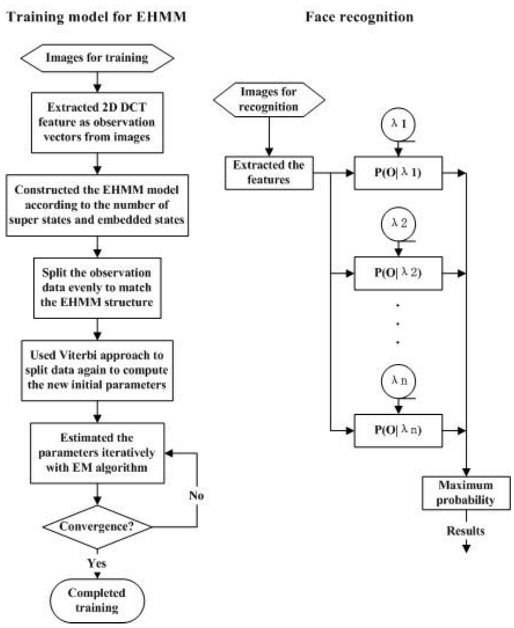

Fig.7. Program flow

ORL (Olivetti Research Ltd.) face database is employed to test the recognition section. ORL database consists of 40 persons with 10 pictures per person. Six pictures per person are used to train the EHMM while the other four images per person are recognized. The recognition results with parameters are shown in table 1.

Table 1. Recognition Results

	Super states number	Embedded states number	Recognition rate	Recognition speed
1	5	3,6,6,6,3	100%	4.1s/image
2	5	1,1,1,1,1	92%	1.3s/image

IV. EXPERIMENTS

The whole system is programmed based on OpenCV under the environment of VC 6.0. The CPU is Pentium Ⅳwith 3GHz frequency and 1.46G memory. The face detection and recognition results are also obtained under the computer's condition. Face database is established by taking photographs of 12 graduate students in the laboratory with 13 pictures per person, of which 8 pictures are used to construct the EHMM. The whole processing of detecting and recognizing a frame, which is 320×240, spends 1.4 seconds with the rapid recognition parameters and 4.2 seconds with the slow recognition parameters. In Fig.8 is described the experiment results, and the frame without yellow words means failure to recognize.

Fig.8. Experiment results

V. CONCLUSIONS

The paper introduces a face detection and recognition system developed for mobile robot to make it have the capability of interaction with people in the uncontrolled indoor environments. The face detection part consists of Adaboost algorithm and skin color model approach to detect faces in the complex background rapidly and efficiently. EHMM algorithm is employed to recognize the detected faces with high recognition rate. The integrated system spends 1.4s processing a frame. Future work will be directed on the improvement of EHMM to increase the recognition speed, and the system should be integrated with the mobile robot. The function of preventing the jitter of video caused by robot's moving also need to be developed.

REFERENCES

[1] E. GARCIA, M.A. JIMENEZ, P. GONZALEZ DE S ANTOS. The Evolution of Robotics Research. IEEE Robotics & Automation Magazine, 2007.3: 2-15.
[2] Freund Y., Schapire R.E. Experiments with a new boosting algorithm. Proceeding of the 13th International Conference on Machine Learning, 1996: 148-156.
[3] Viola, P., Jones, M. Rapid object detection using a boosted cascade of simple features. Computer Vision and Pattern Recognition, 2001: 511-518.
[4] Viola, P., Jones, M. Robust real-time face detection. ICCV, 2001.
[5] Lienhart, R., Maydt, J. An extended set of Haar-like features for rapid object detection. ICIP, 2002:900-903.
[6] Lienhart R., Kuranov A. Pisarevsky V, Empirical analysis of detection cascades of boosted classifiers for rapid object. Proceedings of the 25th Pattern Recognition Symposium, 2003: 297 -304.
[7] Ming-Hsuan Yang, David J. Kriegman, and Narendra Ahuja. Detecting Faces in Images: A Survey. IEEE Transactions on Pattern Analysis and Machine Intelligence, Vol. 24, No. 1, January 2002: 34-58.
[8] Jean-Christophe Terrillon, Mahdad N. Shirazi, Hideo Fukamachi, et al. Comparative Performance of Different Skin Chrominance Models and Chrominance Spaces for the Automatic Detection of Human Faces in Color Images. Automatic Face and Gesture Recognition, 2000.
[9] A. Nefian and M. H. H. III. Hidden Markov Models for face recognition. In ICASSP, Vol.5, 1998: 2721–2724.
[10] H. Othman and T. Aboulnasr. Low complexity 2-D Hidden Markov Model for face recognition. In IEEE Int. Symp. on Circuits and Systems, Vol.5, 2000: 33–36.

Biomimetic control architecture for robotic cooperative tasks

Nicu George Bizdoaca*, Hani Hamdan**, Daniela Coman*, Anca Petrisor*, Elvira Bizdoaca*

*University of Craiova, Mechatronics Department, Romania
**SUPELEC, Dept. Traitement du Signal et Systèmes Électroniques, France
(Tel : +0402514396999; Fax : +040251438488)
(nicu@robotics.ucv.ro, Hani.Hamdan@supelec.fr ,)

Abstract: The paper proposes control algorithms applied to MIROSOT robot league architecture. The MIROSOT league soccer game concept is fairly simple: two teams of robots, with tree/five robots per side which play football completely autonomously. The ball that the teams play with is an orange golf ball. Above the pitch is a machine vision camera running at 60 frames per second. This camera is linked back to a server which then calculates the positions and velocities of each of the robots and ball, from which it determines what each robot should be doing. These instructions are then communicated to the robots over a wireless link. In order to develop an efficient control strategy and architecture it has to use the strategy from the real human soccer game. Using software Simi Scout a suitable tactics analysis can be extract from the games. Analyzing the soccer game, a number of attributes are specified and are embedded at different levels. The specified levels are interconnected and the game analysis is processed for optimization. Using this information the robot program is adapted and the tests/games are experimented. The soccer robots software is composed by three parts; FindObjects () that determines the position of the robots and the target, My_Strategy () that defines the strategy to solve the player role and Send_Command () that sends out the commands for controlling the robot. Among these functions, FindObjects () is the function dealing with the vision program. The upper level is team strategy level witch distribute the players role. The results are commented and improved control architecture, based on practical results, is proposed.

Keywords: robotics, biomimetic approach, cooperative tasks.

I. INTRODUCTION

The nature's inventions have inspired researchers in developing effective algorithms, methods, materials, processes, structures, tools, mechanisms, and systems. Biomimetics is a new multidisciplinary domain that includes not only the uses of animal-like robots – biomimetic robots as tools for biologists studying animal behavior and as research frame for the study and evaluation of biological algorithms and applications of these algorithms in civil engineering, robotics, aeronautics. Multi-agent system has emerged as a subfield of AI and helps to understand and provide with theory and principles for constructing complex systems with multiple agents and their coordination/competition in dynamical environments. The robot soccer game is an interesting benchmark problem for the multi-agent systems.

Generally spoken in robot soccer regarding the division of labor between the components of a soccer team, namely between the host computer system and the autonomous mobile robots, three system configurations are defined: 1. Remote brainless system; 2. Robot-based system; 3. Vision-based system.

The vision-based system can be described as the step from the remote brainless to the robot based system, as some of the intelligence is transferred from the main computer to the single agents, but the control of the vision system and the strategic coordination still remain tasks of the host unit.

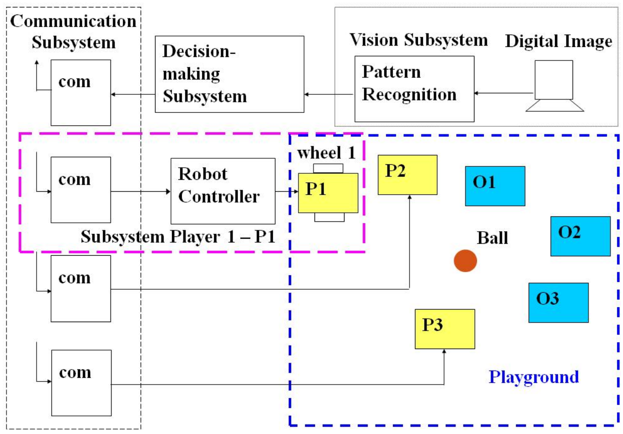

Fig. 1. Soccer robot architecture.

The Micro-Robot' World Cup Soccer Tournament (MiroSot) is the brainchild of Jong-Hwan Kim [1] of KAIST, Korea and was initiated in 1995. A mobile robot soccer team consists of up to three micro mobile robots. Two teams play soccer according to the rules similar in nature to the real soccer game. The Federation of International Robot Soccer Association (FIRA) has established these rules.

Above the field (at the height of approximately 2 m) an industrial camera is mounted.

The mechanical construction of the micro mobile robot is based on a duralumin frame, on which two DC motors with gear boxes and a controller board are mounted.

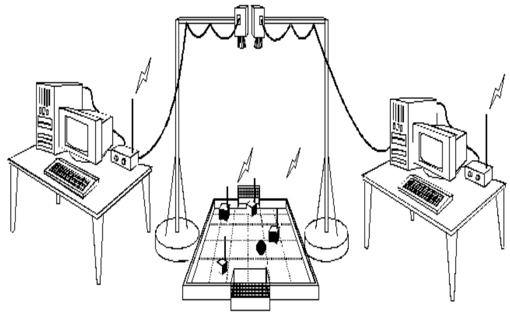

Fig. 2. Soccer robot system with the vision system, host computer and RF communication system.

Robot has two parallel wheels and in addition is suspended by two slipper elements mounted at the front and back part of the frame.

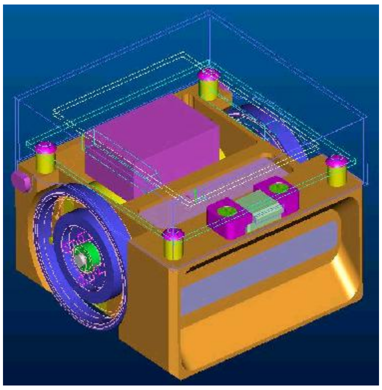

Fig. 3. The soccer robot CAD– Yujin Company

The basic features of the micro mobile robot are:

- dimensions: 7.5×7.5×7.5cm,
- weight with batteries: 0.43kg,
- maximum velocity: 1m/s,
- maximum acceleration: 0.75m/s

II. POLLING ROBOT SOCCER STRATEGY FROM THE REAL SOCCER GAME

The soccer robot game structure has 6 steps:

Step 1: Image acquisition and primary calculation (distance, velocity, relative angle calculation etc.)

Step 2: Decide which posture is suitable for player offensive or defensive.

Step 3: Determination of team strategy and player profile assignment.

Step 4: Determination of the target position.

Step 5: Path planning.

Step 6: Calculation of the wheels' moving direction, velocity and displacement.

In order to have a successful team the secret are: good player's profile, good team strategy.

The player profiles are:

- Attack
- Midfield
- Defender
- Goalkeeper

Using Simi Scout a real game is analyzed and the player profile is extracted (for this example is used Romania Columbia, 1994, soccer game, and for players profile, is used Romanian player profiles)

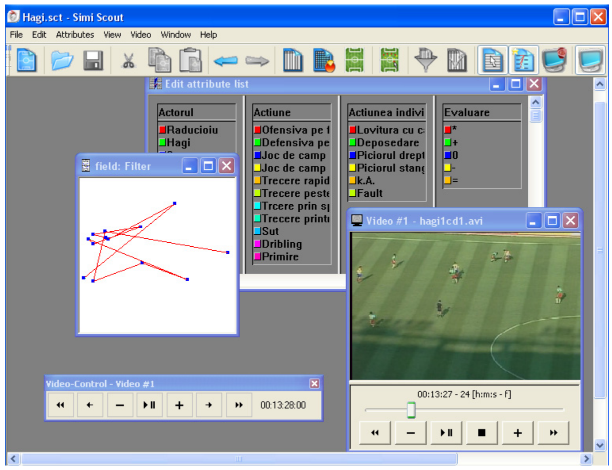

Fig. 4. SimiScout analise for soccer game Romania-Columbia

Using the real game information, the player situations can be extracted. Let's analyse , in detail, the strategy for **Attack player** [2]**.**

Assuming that the left half of the playground is the opponent side, it is reasonable that the attacking player must move to the right side of the ball as soon as possible.

The Petri net model [3] for the attacking soccer robot modeling the real situation, has been designed so that the topology to contain the following situations in which the attacking robot can be, as follows:

a) the attacking robot is behind the ball;
b) the attacking robot kicks the ball;
c) the attacking robot is in offside position;
d) the attacking robot is in contact with ball and the ball is situated behind the robot.

In state (a) the attacking robot is in a probable position to kick, in state (b) it is kicking the ball, in state (c) it is in front of ball, so should be careful to avoid the offside position, and in state (d) it is in contact with ball.

With these four states, the Petri-net for the attacking robot controller is formed. "Angle" is used to refer to the angle between the heading direction of the attacking robot and ball. "Distance" is used to refer to the distance between the attacking robot and ball in pixels. In state (a), the attacking robot is ordered to move to ball and kick it. In state (b), if "Angle" is above 45° , or "Distance" is more than 20 pixels, the attacking defense robot goes to state (a). In state (a), if the ball is on the right side of attacking robot (offside position), it should go to state (c). In state (b), if the attacking robot fails to kick the ball, the robot goes to state (c). In state (c), the attacking controller orders the robot to move sideways and it comes behind the ball without touching it and goes to state (a). In state (c), if "Distance" is below 10 pixels, the robot goes to state (d), so it should move away from the ball till "Distance" is above 20 pixels and then can get into state (c).

Analyzing the situations for Goalkeeper player, for Defender and for Midfield we can generalize the situations as:

p_1) the robot is behind the ball;

p_2) the robot kicks the ball in the opponent direction;

p_3) the robot is in unwanted position;

p_4) the robot is in contact with ball and the ball is situated behind the robot.

Using Simi Scout a set of attributes are assured. Statistically, after analyzing the all attributes proposed, only 7 are retained and become transition for our algorithm:

t_1 : tries to kick the ball, though it is not in a good position to kick,

t_2 : in front of the ball and at the following instant it is in a good position to kick,

t_3 : in front of the ball, and moving to an unwanted position,

t_4: in unwanted position and escaping from that,

t_5 : misses the ball, and is in front of the ball,

t_6 : in unwanted position, and then in contact with the ball and behind, and

t_7 : away from the ball and behind, but still in an unwanted position.

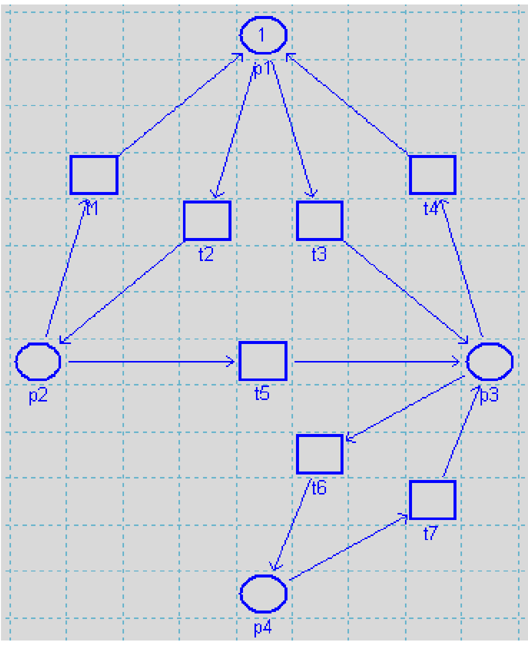

Fig. 5. Petri net model for the soccer robot

As every robot has the same strategy, the role for attack, defender, midfield or attack can be easily switched between the robots. The roll will be assigned dynamically, be image analyze.

A role assigned it is means that the intervention area of the robot is in:

- Attack Area
- Midfield Area
- Defense Area
- Goalkeeper Area

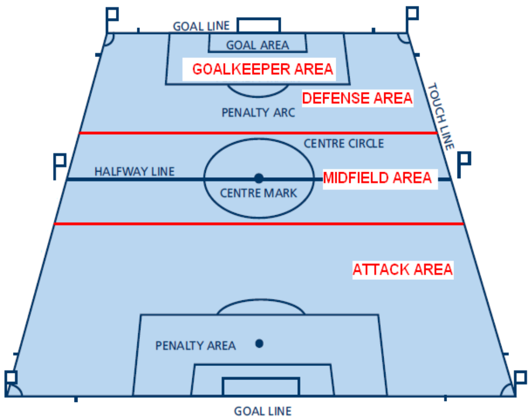

Fig. 6. Playfield division areas

The ball position will switch the team strategy.

The team strategy extracted (from Romania – Columbia 1994 - soccer game - using Simi Scout software) is:

- If the ball is in attack area then 2 player are attack player, and the nearest player to midfield area is midfield
- If the ball is in the midfield area, then 2 player are midfield player, and the nearest player to defense area is defender
- If the ball is in defense area, then 2 players are defense player, and the nearest player to goal area is goalkeeper.

III. NUMERICAL SIMULATION AND EXPERIMENTS

The results from the mathematical method of checking through the invariants method associated transitions and the corresponding positions after calculating the incidence matrix of the net have been validated through the simulations using Petri Net Toolbox in Mat lab environment.

It was validated in this way that the net topology, the evolution of (their dynamics), as well as structural and behavioral properties. The following two tables (Table 1- Global Statistics Places and Table 2 - Global Statistics Transitions) present the complete lists of global indices associated with the places and the transitions considered in the architecture of Petri net that modeling the controller for attacking robot.

Table 1. Global Statistics Places

Place Name	Arrival Sum	Arrival Rate	Arrival Dist.	Throughput Sum	Throughput Rate	Throughput Dist.	Waiting Time	Queue Length
p1	100	1	1	101	1.01	0.9901	0.9901	1
p2	51	0.51	1.9608	50	0.5	2	0	0
p3	149	1.49	0.67114	149	1.49	0.67114	0	0
p4	74	0.74	1.3514	74	0.74	1.3514	0	0

Also, the special options of Petri Net Toolbox, which confers a high capacity of analysis, has made possible a synthesis of this Petri net model which allows exploring the dependences of global performance indicators associated with the net positions/transitions on two "Design Parameters" (being considered places p_1 and p_4) for the various parameters of the simulation.

Table 2. Global Statistics Transitions

Transition Name	Service Sum	Service Rate	Service Dist.
t1	25	0.25	4
t2	51	0.51	1.9608
t3	50	0.5	2
t4	75	0.75	1.3333
t5	25	0.25	4
t6	74	0.74	1.3514
t7	74	0.74	1.3514

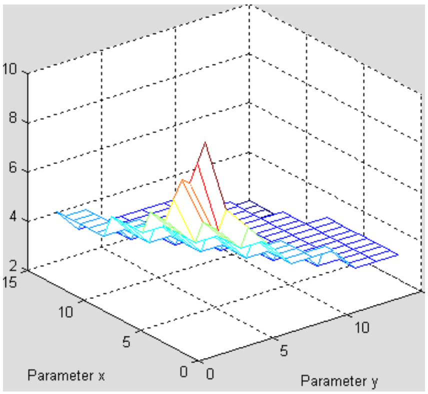

Fig. 7. Dependency of the Service Sum index associated t_2 transition

IV EXPERIMENTAL RESULTS

The experimental results obtained by applying the proposed method for the attacking robot are presented in snapshots Fig.8 and Fig.9. It is used three robots having the yellow team color, the ball having the orange color and the playing field with the color black.

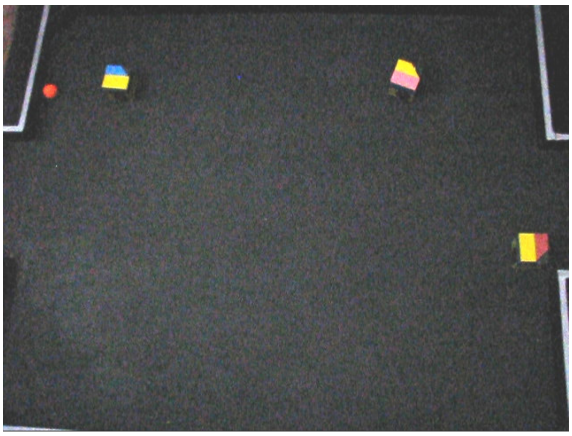

Fig. 8. The midfield robot become attack robot and goes to t_1 transition

The blue robot color is assigned as attacking robot and moves to the ball and then shoots it into the goal successfully.

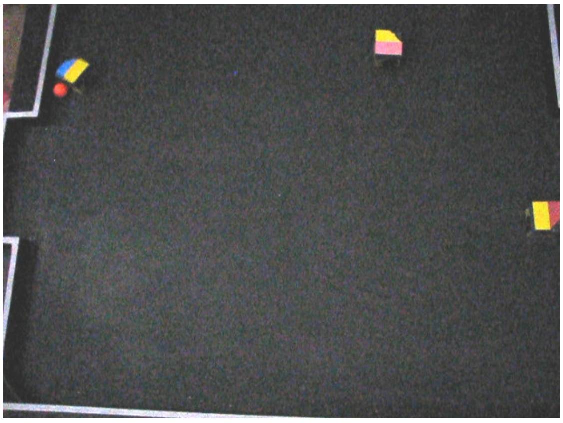

Fig. 9. The attack robot goes to t_2 transition

V CONCLUSION

The research proposes a biomimetic algorithm based on analyzing the real situation [4]. In this paper, a Petri net model is used for designing a low level controller for the soccer robots. The presented controller did not use the information of opponent team. A future development of this research will add the opponent predicted strategy and a more dynamical switching strategy. Using a single model robot controller offer advantages in terms of implementation, but the team strategy can be easily indentified by the opponent and annihilated. The Petri net model presented is implemented in MATLAB environment. The simulations studies was validated that the net topology, the evolution of (their dynamics), as well as structural and behavioral properties and was provided the global performance indices associated with the places and the transitions and also the whole set of global indices associated with all the nodes of the net. Finally, the feasibility of the proposed architecture is demonstrated by the experimental results.

ACKNOWLEDGMENTS

This report is part of the ROMANIAN NATIONAL UNIVERSITY RESEARCH COUNCIL (CNCSIS) contribution to the project PNCDI – II - 289/2008.

REFERENCES

[1] Kim J. H., Kim D.H., KimY.J., Seow K.T., Soccer Robotics, Springer-Verlag, 2004.
[2] Coman D., Using Petri Nets in the Soccer Robot Control Architecture, Annals of DAAAM for, 2008, pp. 295 – 296.
[3] Peterson J. L., Petri net theory and modelling of systems, Prentice-Hall Inc., 1981.
[4] Bîzdoacă N.G., Degertu S., Diaconu I. – Behavior based control for robotics demining – International Symposium on System Theory, SINTES 12, 20-22 octombrie 2005, ISBN 973-742-148-5, 973-742-152-3, pp. 249-254.

ANN Dexterous Robotics Hand Optimal Control Methodology Grasping and Manipulation Forces Optimization

Ebrahim Matter Al-Gallaf[1], Khaled Al Mutib[2] and Hani Hamdan[3]

[1]*College of Engineering, Box 13184, University of Bahrain, Kingdom of Bahrain*
[2]*College of Computer & Information Sciences, Box 51178, King Saud University, Kingdom of Saudi Arabia*
[3]*Dept. of Signal Processing and Electronic Systems, SUPELEC, 3 rue Joliot-Curie, 91192 Gif-sur-Yvette cedex, France*
ebrgallaf@eng.uob.bh, mutib@ccis.ksu.edu.sa, Hani.Hamdan@supelec.fr

Abstract: This article presents an efficient scheme for computing optimal grasping and manipulation forces for dexterous robotics hands. This is formulated as Quadratic Optimization problem formulation. Computation has been based on non-linear model of fingertips contacts and slips. In achieving grasping while in motion, hand inverse Jacobian is considered an important matrix to be computed, however, it is considered as highly intensive to be computed. Consequently, we investigate an efficient approach by using Artificial Neural Networks (ANN) for learning grasped optimal forces. ANN is used to learn the optimal contact forces relating hand joints torques to object result force. Results have indicated that ANN have reduced the computational time reasonable values, this is due to the ability to map nonlinear relations. Furthermore, results have revealed that ANN are capable of learning highly nonlinear relations relating distributed fingertips forces and the joints toques.

Keywords: Dexterous Manipulation, ANN Approximation, Optimal Forces**.**

I. INTRODUCTION

Kinematics and optimal distributed force control issues for Multi-fingered hands have been a theme for considerable research [1,2]. AI techniques have also been introduced by many researchers in areas of robotics control. ANN, for example, have been heavily employed in robotics technology such as robot arm visual control [3,4], kinematics of high degrees of freedom robot arm [5], furthermore, the study introduced by [6] in which they employ a real-time learning neural system in solving inverse kinematics, the research introduced by [6], in which they employ an artificial neural network for tracking and grasping a moving object observed by a six degrees of freedom robotics arm system. Maciejewski et. al. [7] introduced a methodology to reduce computational burdens based on Givens rotations. Research contributions in task space measure can also be found in [8], as static and dynamic manipulability ellipsoids have been used. An alternative employment of artificial neural networks has been the one presented by Wohlke, [9], here conception of control system was based on combination of a ANN for an adaptation of grasp parameters and a fuzzy logic for the correction of parameters values given to a conventional controller. [10] has proposed a Fuzzy-Neural system control system that learns specific hand-object mapping, without considering the issue of interaction forces among the fingers.

In this contexts, this manuscript rather glances at exerting optimal grasping forces while a grasped object is in motion. Jacobian hand inverse has been avoided to compute, as compared to other techniques which used other numerical algorithms to compute the inverse via the Singularity Robust Inverse. Mapping hand Jacobian inverse, i.e. joints space to fingertips optimal force distribution, to a set of ANN neurons interconnection weights facilitates a reduction of computational execution time. In addition, this gives an ability to add more training patterns that are valuable, particularly once a hand passes singularity.

II. DYNAMICS FORMULATION

Grasped object undergoes a motion, once fingertip forces are exerted, Fig. (1). Dynamic behavior of a grasp object is defined as time response of an object to change motion or force trajectories. It is quantitatively represented by natural frequencies and damping ratios of a grasp on each object frame degree of freedom. Defining a Cartesian based posture error of an object as $e \in \Re^{6\times1}$ as $e \cong u_d^c - u_a^c$. Entire object-hand contact system is described in terms of joint-space torques τ_h joint torques and Euler dynamics by :

$$\tau_h = \left(M_h J_h^{-1} X_h + T_{ex}\right) \tag{1}$$

$$T_{ex} = N_k + C_k + J_h^T\left(\phi_{cd} - Z_i \int_0^x \left(\phi_{cd} - \eta\lambda\right)\right)$$

$$X_h = \left(\Gamma^{+1}\Theta_a - J_h\,\Theta_k\right) \in \Re^{12\times1} \tag{2}$$

Control law stated in Equ. (1) depends on dexterous Hand inverse grip transform, Γ^{-1}. Computation of hand kinematics is not an easy task, specifically in real-time. Also inverting hand Jacobian matrix J_h^T, is complicated, due to fingers collectively to do movement. Fingertip force distribution depend on Γ^{-1} and J_h^T.

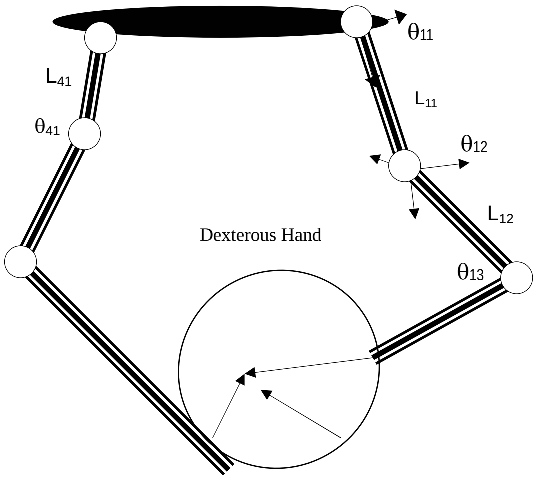

Fig. 1. Dexterous Manipulation.

III. OPTIMAL FINGERTIPS DISTRIBUTION

Fingertips forces and moments do yield a resultant force and moment acting on a grasped object. This is computed from eight vectors according to the following geometric vector-space relation :

$$f_{bi} = f_{oi} \quad (3)$$

$$m_{bi} = m_{oi} + f_{oi} \times r_{oi} \quad (4)$$

where r_{oi} defines a vector from an i^{th} contact location to object centre of gravity frame. For the case of no change from centre of each fingertip to the centre of the object (i.e. no fingertips slip), external forces f_e and moments m_e on a grasped object can be calculated (in terms of object results force F_b) from κ_{bi} and m_{bi} as :

$$F_b^T = \Gamma \kappa_{tip}^T \qquad \Gamma \in \Re^{6\times 24} \quad (5)$$

For frictional point contacts, general contact forces f_{tipi}, transmitted from fingertips to an object surface are filtered and reduced to three forces rather than a six-dimensional vector of forces f_{oi} and moments m_{oi}. Hence, contact force vector for the entire hand is expressed as :

$$\kappa_{tip}^T = \begin{bmatrix} \kappa_{tip1} & \kappa_{tip2} & \kappa_{tip3} & \kappa_{tip4} \end{bmatrix} \in \Re^{12\times 1} \quad (6)$$

According to Lee,, [8], fingertip force vector associated with an object dynamic F_b is defined by :

$$\kappa_{tip} = \left[\Gamma \Gamma^T\right]^{-1} \Gamma^T F_b + \eta\lambda \quad (7)$$

Equ. (7), represents a solution of a force distribution redundancy with possible adjustable force vector f_{hom} in such a way, a solution of f_{tip} must satisfy a contact cone and hand actuator's torque constraints. Once fingertips do not slip, (*i.e. firm grip at contact point*), few inequalities conditions must be satisfied. If the unknown contact force vectors onto the object are expressed at contact frame, hence with a contact normal (f_z^c) along the (z) direction and directed outward with a coefficient of friction (μ), the friction force cone constraints may be then expressed by $\sqrt{\left(\kappa^2{}_x + \kappa^2{}_y\right)} \le \mu\, \kappa_z$.

To contrast a newly adopted force optimisation algorithm with already used and previously presented methods, (i.e. algorithms for linearizing the nonlinear contact constraints and the simplex optimization), an optimal internal forces optimisation method is also investigated for a four-finger case. In finding a solution to force inequality formulation, an optimisation approach is used, as due to Nahon and Angeles whom they formulated quadratic objective function. Optimisation variables are the internal forces' magnitudes, which are used to determine the amount of stress on an object to be manipulated according to the following well know robotics hand linear equality and linear inequality constraints are thus defined by :

$$\begin{aligned} &\text{optimize} && \chi(\kappa_{tip}) \\ &\text{Subject to} && \Gamma\,\kappa_{tip} = F_b \\ & && \Psi\,\kappa_{tip} \le B \end{aligned} \quad (8)$$

Once a multi-fingered hand comes in a content with a grasped object The need for minimization of a grasp stress (or amount of squeeze) requires the minimization of the actuator torques τ_a. If the vector of all the actuator torques in the system is given by τ_a, then ½ $\left(\tau_a^T \tau_a\right)$ defines the actuator torque norm. Furthermore, the τ_a vector consists of two torques: the unconstrained torque τ_u and the torques needed to grasp the object given by $J_h^T \kappa_{tip}$:

$$\varphi(\kappa_{tip}) = ½\, \tau_a^T \tau_a \quad (9)$$

In this respect, we are computing f_{tipi} for a four multi-fingered robotics and fingertips, as this will be based on optimizations method, with a given constrains. After then, we shall generate large amount of training patterns to teach a four layers ANN structure. By this, we are designing a learned ANN for dexterous hand force optimization. In this respect, the main duty of a learned ANN system is to let teach a ANN the optimal distribution of fingertip forces to manipulate a grasped object. Optimal distribution are to be obtained using the classical optimization routines, as the system is formulated in terms of nonlinear optimization problem.

IV. ANN NONLINEAR APPROXIMATION

Four layers of fully connected neurons are thus used for approximating the nonlinear mapping function. That was done from a set of available examples called learning samples or training patterns. For the Hand-Object control system, the relation which we shall let the employed neural network to learn, Fig. (2), is defined in terms of some training patterns of object Cartesian posture u_a^c, rate of change of object posture Δu_a^c, and entire hand joints rate of change, $\Delta\Theta_{k-1}$ as expressed by :

$$\Delta\Theta_k = \beta\left(\kappa, \Delta u_a^c, u_a^c, \Delta\Theta_{k-1}\right) \qquad (10)$$

In (10), κ is the ANN function, changes in hand joints space ($\Delta\Theta_k$) is made a function of the neural network structural parameters in addition to grasped object motion parameters (Δu_a^c, u_a^c, $\Delta\Theta_{k-1}$). The focal purpose of neural network structure is to approximate the nonlinear mapping involving changes in hand joints to changes in the object position and optimal force distribution. Neural approximation of Equ (10) is used by hand Cartesian PID based controller, which indeed depends on nonlinear mapping between changes in hand joints to changes in the object position.

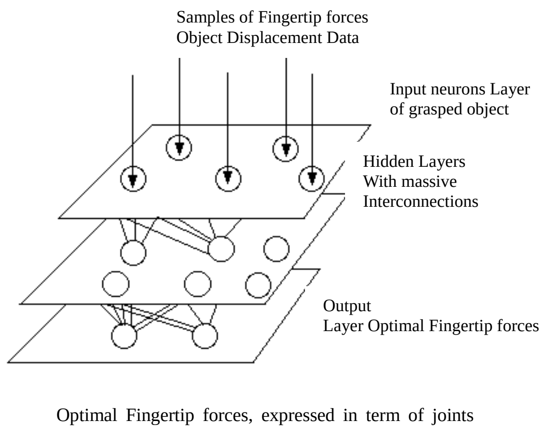

Fig. 2 . A four layers mapping ANN.

Inputs to the neural system are: desired Cartesian object forces u_a^c, changes in such Cartesian forces Δu_a^c, one step change in position of the entire joints in radians $\Delta\Theta_{k-1}$. Neural outputs are the required changes in joint forces for the entire hand $\Delta\Theta_k$. The desired object forces values are obtained in advanced by moving the object to the required position. Hence after, the neural network learns such a nonlinear relation between input and output patterns sufficiently, it shows a nonlinear map between the forces and orientation of the fingers and those of the object, which usually computed using hand Jacobian inverse.

V. TASK-SPACE SIMULATION

Dynamic simulation was done using kinematics and dynamics models for a four fingers hand. Object path of motion was defined. Learning patterns were generated via once the hand was to follow a pre-defined trajectory, while grasping. To illustrate aspects of computation, object Cartesian motion that passes the object through a (non-singular configuration) is employed. The task is to create 3-D sinusoidal object motion with no change in orientation. Articulated hand has been simulated, and hand dynamic motion simulation is presented in Fig. (3). The multi-layer neural network (for mapping object motion to hand joints toques) used in the simulation. The neural network does consist of 18 inputs, 12 outputs and 50 hidden units. These nets map the 18 inputs characterizing the object.

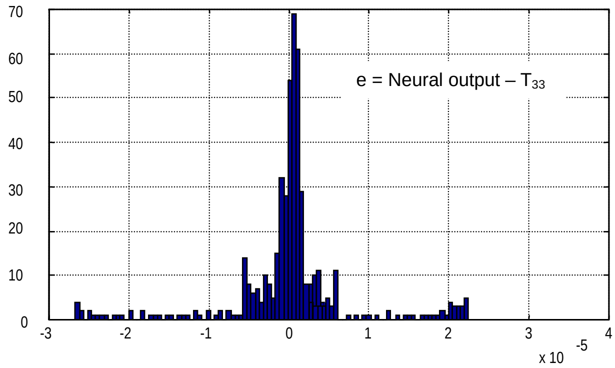

Fig. 3. Validating the neural hand controller : Training patterns and errors

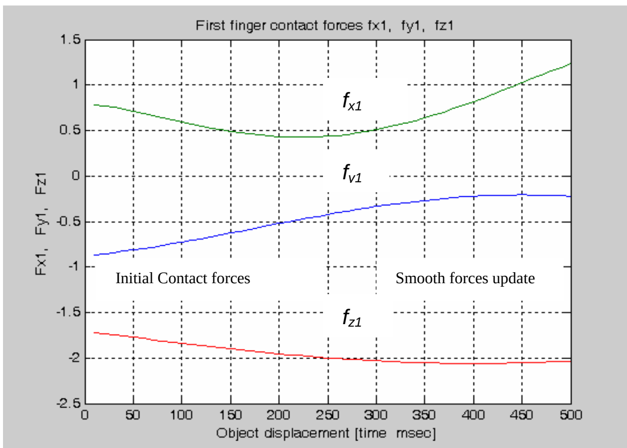

Fig. 4. Optimized fingertip contact forces.

To assess used control methodology, simulation of a constrained dynamics system has been initially achieved using both kinematics and dynamic models of an articulated robotics hand. The hand has been simulated with conventional inverse kinematics algorithms and optimal force distribution, where training patterns have been generated. Training patterns have been based on object Cartesian motion and associated joints displacement. The hand has been run for large number of trials to produce as large as possible of training patterns. The hand has been allowed to follow a pre-defined path over 5 sec. of manipulation time. In this sense, the associated patterns Δu_a^c, u_a^c, $\Delta\Theta_{k-1}$ are tabulated in the proper format to be suitable for the neural network training. The quantity of the training pattern was reaching a size of (500) for a single variable (e.g. Δu_a^c). Hence to validate the neural network ability to model the hand inverse kinematics, the error between a typical neural output node (e.g. θ_{33}) with the actual one has been computed and analyzed.

Execution process starts first with employing the trained ANN controller. Once grasped object position and orientation have been defined, the ANN, hence computes the associated hand joint torques by presenting the network with some patterns which were not included during the training process. Once the neural network presented with such pattern, it associates input patterns with trained joint displacement patterns. The ANN is employed in the hand controller for the calculation of joint displacement as required by the full controller already presented by (1). The employed ANN has proven it was able to reproduce a good mapping mechanism as compared to other full kinematics-based relations.

For instant, Fig. (3) shows training error associated with the object displacement by fingertips movements. Contrary to the method of internal forces optimisation, Fig. (4) shows distributed contact forces based on the use of nonlinear constraint optimisation of Equ (8) for training ANN. Contact forces do satisfy geometric, kinematics, and frictional constraints. It can be observed, distributed contact forces are symmetrical around the middle of the path. Normal forces along (z) axis direction are much greater than the two associated frictional forces by a factor determined by the type of material used at the fingertip-surface interaction. It is noticeable, how the employed optimisation technique has indeed computed the most suitable forces while satisfying all stated constraints.

It has been shown a computational methodology to compute an optimal set of fingertip forces, while updating the kinematics relation via an artificially learned neural network for multi-finger robot hands. Larger training patterns could result in longer hand training time and the possibility of not getting a convergence neural network.

VI. CONCLUSION

This article has presented a novel approach for computing both optimal set of fingertip forces distribution and an updating mechanism of the interrelated kinematics relations for dextrous robot hand. The problem has been quadraticlly formulated and structured, that was based on ANN, as to compute fingertip forces at object-fingertips contact. Computed forces are hence used in hand closed loop force control. Secondly, for achieving a manipulation task, the issue of the inverse kinematics for multi-fingered robot hand has been also considered. In this context, object motion is defined in a Cartesian based system, therefore differential Jacobian plays an important role in Cartesian object motion. Nonlinear relation between Cartesian object posture and hand joint-space settings, and control signals mapping were learned via four layers artificial neural networks trained for almost possible object displacement.

REFERENCES

[1] I. Yamano, and Takashi M., " Five-fingered Robot Hand using Ultrasonic Motors and Elastic Elements," Proceedings - IEEE International Conference on Robotics and Automation, vol. 2005, pp. 2673-2678, Barcelona, Spain 2005.
[2] Zhao, Jie, Li, Mu, Yan, Ji-Hong, Li, Ge, and Cao, Yu. , "Study on Algorithm of Dynamic Uncalibrated Eye-in-hand Visual Servoing system," Journal of Harbin Institute of Technology, vol. 14, no. 4, pp. 445-449, 2007.
[3] N. Xi, J. Tran, & K. Bejczy, " Intelligent Planning and Control for Multi-robot Coordination : An Event-Based Approach", IEEE Transactions on Robotics and Automation, 12(3), pp. 439-445, 1996.
[4] H. Hashimoto, T. Kubota, M. Kuduo & F. Harashima, "Self-organizing Visual Servo System Based on Neural Networks," IEEE Control Systems Magazine, pp. 31-36, 1992.
[5] Köker Rasit, Oz Cemil, Çakar Tank, and Ekiz Hüseyin" A Study of Neural Network Based Inverse Kinematics Solution for a Three-joint Robot, " Robotics and Autonomous Systems, vol. 49, no. 3-4, pp. 227-234, December 31, 2004.
[6] G. Schram, F. Linden, B. Krose & F. Groen, Visual Tracking of Moving Objects Using a Neural Network Controller, International Journal of Robotics and Autonomous Systems, (18), pp. 293-299, 1996.
[7] A. Maciejewski & C. Klein, "The Singular Value Decomposition: Computation and Applications to Robotics," International Journal of Robotics Research, vol. 8, no. 6, pp. 63-79, 1989.
[8] S. Lee, "Dual Redundant Arm Configuration Optimization with Task-Oriented Dual Manipulability," IEEE Transactions in Robotics and Automation, vol. 5, (1), 1989, pp. 78-97.
[9] G. Wohlke, "Neuro-Fuzzy Based System Architecture for the Intelligent Control of Multi-Finger Robot hands", Proceedings of the IEEE International Conference on Fuzzy Systems, ORLANDO, pp. 26-29, 1994.
[10] E. Al-Gallaf, "Neuro-Fuzzy Inverse Jacobian Mapping For Multi-Finger Robot Hand Control, International Journal of Intelligent & Robotic Systems, vol. 18, no.1, 2003.

Dense stereovision using mono-CCD color cameras

Hachem Halawana[1] and Hani Hamdan[2]

[1]*LAGIS, USTL, Bât. P2, Cité Scientifique, 59655 Villeneuve d'Ascq, France*
[2]*Dept. of Signal Processing and Electronic Systems, SUPELEC, 3 rue Joliot-Curie, 91192 Gif-sur-Yvette cedex, France*
Hachem.Halawana@ed.univ-lille1.fr, Hani.Hamdan@supelec.fr

Abstract: Most of the stereo algorithms were based only on the analysis of the luminance information. However with the advances in camera technology, in addition to the fact that color information can robustly improve matching, color stereovision gained more and more interest. Color stereovision setups are usually based on single-sensor cameras which provide Color Filter Array (CFA) images. In those, a single color component is sampled at each pixel rather than the three required ones (R, G, B). We show that standard demosaicing techniques, used to interpolate missing components, are not well adapted when the resulting color pixels are matched for estimating image disparities. In order to avoid this problem while exploiting color information, we propose a new matching cost designed for dense stereovision based on pairs of CFA images.

Keywords: Stereovision, demosaicing, matching cost.

I. INTRODUCTION

Dense stereo correspondence algorithms are based on measures of the similarity between image locations in a pair of stereo images. Typically, a matching cost is computed at each pixel of the left image for all the shifts in a predefined range, *i.e.* for a limited set of candidate pixels in the right image. Then, the candidate pixel which minimizes the cost is retained and its position yields the disparity. Matching costs assume that homologous pixels have almost the same component values, but they cope with limited radiometric changes and/or with noise. Common window-based matching costs include the sum of absolute or squared differences (SAD/SSD), normalized cross-correlation (NCC), and census transform [1]. Chambon et al have compared widely used stereo matching costs applied to gray level and color images [2]. They have shown that taking into account color information generally improves the performance of matching costs [3].

Color images can be acquired by two types of cameras: those including three sensors associated with beam splitters and color filters providing the so-called full-color images, and those including a single image sensor. Many recent digital cameras include a single-chip CCD (Charge Coupled Device) or CMOS (Complementary Metal Oxide Semiconductor) sensor, to increase the image size while reducing the device cost. The surface of such a sensor is covered with an array of small spectrally selective filters, arranged in an alternating pattern, so that each photo-sensitive element samples only one of the three color components Red (R), Green (G) or Blue (B). These single-sensor cameras actually provide a color filter array (CFA) image, where each pixel is characterized by a single color component. Fig. 1 shows the Bayer CFA image acquired by most of these cameras. To estimate the color vector $(R\ G\ B)^T$ at each pixel, one has to determine the levels of the two missing components. This process is commonly referred to as CFA demosaicing, and yields a color demosaiced image where each pixel is characterized by an estimated color vector [4] [5] [6].

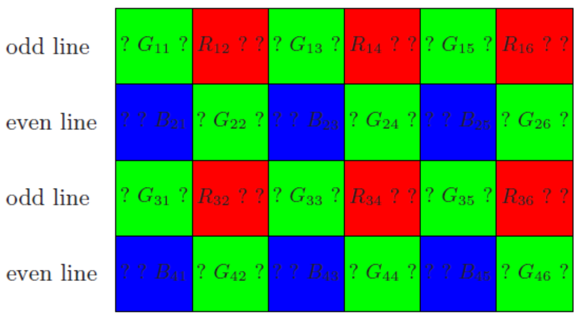

Fig. 1. Bayer CFA Filter.

Since the demosaicing methods intend to produce "perceptually satisfying" demosaiced images, they attempt to reduce the presence of color artifacts, such as false colors or zipper effects, by filtering the images [7]. So, some useful color texture information may be erased in the color demosaiced images. However, to match homologous pixels, window-based stereo matching costs need as much local texture information as possible. Thus, the quality of stereo matching on color demosaiced image pairs may suffer either from color artifacts or from the removal of color texture caused by demosaicing schemes.

In order to avoid this problem while exploiting color, we propose a new matching cost designed for stereovision based on color mono CCD cameras. In Section II, we briefly introduce dense color stereovision. The problem of demosaicing is discussed in Section III. Then, we propose in Section IV a new cost to deal with CFA image. Finally, experimental results are presented in Section V.

II. DENSE STEREOVISION

Stereovision schemes aim at computing a three dimensional representation of a scene observed by two cameras. Stereo correspondence of homologous pixels, *i.e.* pixels in the left and right images onto which the same physical point of the scene is projected, allows for 3D reconstruction. One of the key points of stereovision is to find these homologous pixels through stereo matching [4]. Sparse stereovision matching techniques match only the pixels marked on salient image features, such as lines or corners. Their performance depends on the quality of the primitive detection stage [2]. On the other hand, dense stereovision matching techniques search the homologous of every pixel.

When the geometry of the stereovision setup is precisely known, the images can be rectified. After rectification, epipolar lines correspond to horizontal lines in the images, and homologous pixels have the same vertical coordinate. Let us consider a pixel in a left image, called left pixel and denoted P_L with spatial coordinates (x_L, y_L). The spatial coordinates of its homologous pixel P_R in the line at the same vertical position of the right image are (x_R, y_L) (see Fig. 2). The disparity d, estimated at the left pixel P_L, is expressed as:

$$d(P_L) = x_L - x_R \tag{1}$$

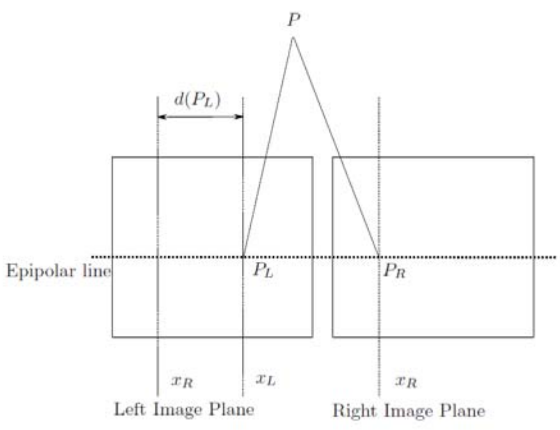

Fig. 2. Disparity between two homologous pixels.

The objective of the dense stereovision scheme is to estimate the disparity at each left pixel in order to produce the disparity map from which it is possible to reconstruct the 3D scene. For this purpose, it measures local similarity between the levels of the neighbors of the considered left pixel and the levels of the neighbors of each candidate right pixel thanks to correlation scores.

The sum of the absolute differences (SAD) between colors of neighboring pixels is one of the most widely used matching cost functions. The SAD score between the left pixel P_L with spatial coordinates (x_L, y_L) and a candidate pixel in the right image, with the s-shifted spatial coordinates $(x_L - s, y_L)$, is expressed as:

$$\begin{aligned} C(x_L, y_L, s) = \sum_{i=-w}^{w}\sum_{j=-w}^{w} & \left|R^L(x_L+i, y_L+j) - R^R(x_L+i-s, y_L+j-s)\right| \\ & + \left|G^L(x_L+i, y_L+j) - G^R(x_L+i-s, y_L+j-s)\right| \\ & + \left|B^L(x_L+i, y_L+j) - B^R(x_L+i-s, y_L+j-s)\right| \end{aligned} \tag{2}$$

where *R*, *G* and *B* are the color components of a pixel *P*, *s* is the spatial shift along the horizontal epipolar line, and *w* the half-width of a (*2w* +1)×(*2w* +1) correlation window.

SAD scores computed for different candidates, *i.e.* for different shifts *s*, are then compared. With respect to the *winner takes all (WTA)* method, the candidate pixel yielding the lowest SAD score is matched to the considered left pixel and the estimated disparity $\hat{d}(P_L)$ is given by:

$$\hat{d}(P_L) = \arg\min_s C(x_L, y_L, s) \tag{3}$$

III. DEMOSAICING AND COLOR STEREOVISION

In order to show the limits reached by applying SAD-based matching to a pair of color demosaiced images, we propose to consider Murs image pair available at http://www.irit.fr/~Benoit.Bocquillon and shown in Fig. 3.

For comparing SAD-based performance on full and demosaiced color images, we computed artificial left and right CFA images by removing two color components of each pixel according to the Bayer CFA (see Fig. 1). Then, the two missing color components were estimated by the Hamilton method [5] to produce demosaiced images. In those, each pixel *P* is characterized by an estimated three-dimensional color vector denoted $(R\ G\ B)^T$.

Hamilton method was selected since it reaches a good compromise between demosaicing quality and processing time [8].

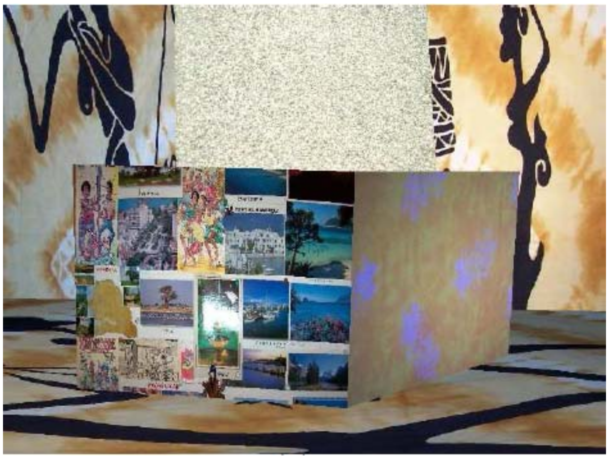

Fig. 3. Murs left image.

We matched all the pixels by computing color SAD scores on these two pairs of color stereo images. By comparing the estimated disparity $\hat{d}(P_L)$ and the ground truth disparity $d(P_L)$, we can estimate the percentage of correctly matched pixels, i.e. pixels for which the difference between the estimated and the ground truth disparities is lower than or equal to one pixel. Fig. 4 shows this percentage for full and demosaiced color image pairs as function of correlation window half-width w. It arises that, whatever window width, the percentage of correctly matched pixels for demosaiced color images is lower than for full color images. We notice that the difference of the correctly matched pixel percentages ranges between 2% and 4% although the demosaiced color Murs image seems to be visually identical to the full color one. This experimental result demonstrates that the demosaicing step degrades the quality of stereo matching. That led us to propose a SAD score specifically designed for CFA images.

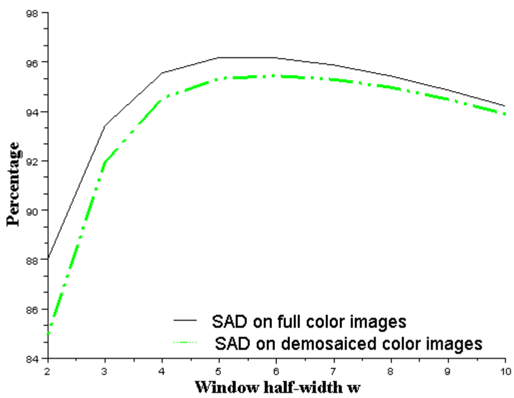

Fig. 4. Matching percentages on full and demosaiced color images.

IV. PARTIAL SAD COST

The main problem with CFA stereovision is that the available color components of homologous pixels in the left and the right images may be different. For example, let us examine Fig. 5 that shows a situation in which a physical space point P is projected onto a green pixel P_L in the left CFA image and onto a red pixel P_R in the right CFA image. A green (resp. red) pixel in a CFA image is characterized by only the green (resp. red) color component.

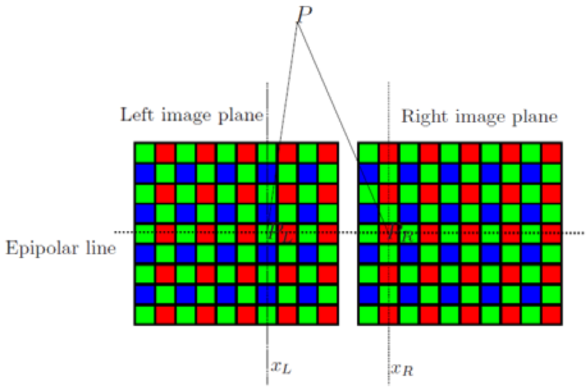

Fig. 5. CFA stereovision problem.

Therefore, one cannot assume that the green level, only available value for the left pixel, is equal to the red level of its homologous pixel in the right CFA image.

We use only the missing red or green level of each pixel located on an odd line, and only the missing blue or green level of each pixel located on an even line. Therefore, each pixel of an odd (resp. even) line is characterized only by its red (resp. blue) and green levels in the cost function. The missing color component is estimated by Hamilton's approach [5].

We propose to modify the SAD score of equation (2) to:

$$C(x_L,y_L,s)=\sum_{i=-w}^{w}\sum_{j=-w}^{w}\left|G^L(x_L+i,y_L+j)-G^R(x_L+i-s,y_L+j-s)\right| + \left|RB^L(x_L+i,y_L+j)-RB^R(x_L+i-s,y_L+j-s)\right| \quad (4)$$

where *RB* is the red color component in the odd lines and the blue color component in the even ones. We call this modified SAD score *partial SAD cost*.

V. RESULTS

In order to compare the quality of pixels matching, we apply the partial SAD coston the Murs demosaiced images. Fig. 6 shows the rates of correctly matched pixels obtained by applying SAD cost on the original full color images and the demosaiced color images, and partial SAD cost on the demosaiced images. We remark that our partial SAD costoutperforms the standard SAD cost applied to demosaiced color images. Obviously, our method does not reach the matching quality obtained on full color images even if the difference between these two rates decreases when the size of the correlation window increases. Furthermore, the processing time needed for demosaicing and for computing the partial SAD score is lower than that required by total demosaicing and SAD score computation since only one color component is estimated for each pixel and since the partial SAD cost takes into consideration two color components instead of three.

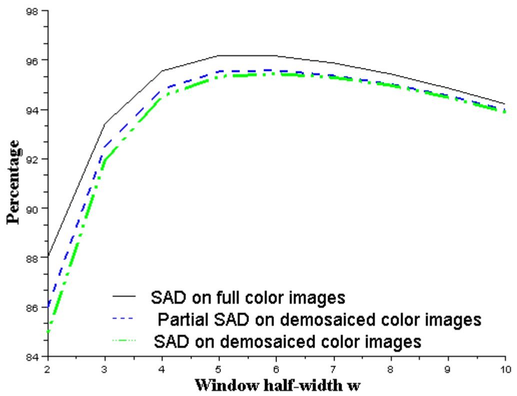

Fig. 6. Matching percentages of SAD applied on full and demosaiced color images and partial SAD applied on demosaiced color images.

VI. CONCLUSION

In this paper, we outlined that the demosaicing step can decrease the quality of pixels matching by considering images acquired by single-sensor color cameras.

We proposed a modified SAD cost, specifically designed to match pixels of stereo CFA demosaiced color images. We have experimentally shown that using partial cost instead of the standard one total demosaicing improves the disparity estimation results. Moreover, the proposed method is faster than the classical one.

We have assumed that the pair of CFA demosaiced images had been previously rectified so that assumptions on epipolar lines are satisfied. However, the rectification of CFA demosaiced images is an open problem.

REFERENCES

H. Hirschmuller and D. Scharstein. Evaluation of cost functions for stereo matching. In *IEEE Conference on Computer Vision and Pattern Recognition (CVPR'07)*, Minneapolis, USA, June 2007, pp. 1–8.

S. Chambon and A. Crouzil. Color stereo matching using correlation measures. In *SEE, editor, Proceedings of the First International Conference on Complex Systems Intelligence and Modern Technological Applications*, Cherbourg, France, september 2004, pp. 520–525.

E. Pinhasov, N. Shimkin, and Y. Zeevi. Optimal usage of color for disparity estimation in stereo vision. In *13th European Signal Processing Conference (EUSIPCO'05)*, Antalya, Turkey, september 2005.

S. Battiato, M. Guarnera, G. Messina, and V. Tomaselli. Recent patents on color demosaicing. *Recent Patents on Computer Science*, 1(3): 194–207, november 2008.

B. K. Gunturk, J. Glotzbach, Y. Altunbasak, R. W. Schafer, and R. M. Mersereau. Demosaicking: color filter array interpolation. *IEEE Signal Processing Magazine*, 22(1): 44–54, january 2005.

R. Lukac. *Single-Sensor Imaging: Methods and Applications for Digital Cameras*. CRC Press, 2008.

Y. Yang, O. Losson, and L. Duvieubourg. Quality evaluation of color demosaicing according to image resolution. In *Proceedings of the 3rd International Conference on Signal-Image Technology & Internet-based Systems (SITIS'07)*, Shanghai Jiaotong University, China, December 2007, pp. 640–646.

E. Pinhasov, N. Shimkin, and Y. Zeevi. Optimal usage of color for disparity estimation in stereo vision. In *13th European Signal Processing Conference (EUSIPCO'05)*, Antalya, Turkey, september 2005.

Intelligent OkiKoSenPBX1 Security Patrol Robot via Network and Map-Based Route Planning

Mbaïtiga Zacharie
Department of Media Information Engineering,
Okinawa National College of Technology, 905 Henoko, Nago, 905-2192, Okinawa, Japan

Abstract: With an increased demand for security and limited numbers of trained security personnel, some security mangers have a lot of ground to police and limited staff to cover it. To compensate for shortages of security staffs and to reduce the stress of security managers, we have developed an intelligent patrol robot system called OkiKoSenPBX1. The system integrates a variety of sensors to gather environmental information and to detect abnormal events including intruders. To tackle this problem, the route planning procedure is used. This route planning is based on determining a sequence of intermediary goal points or coordinates x and y composing the robot trajectory. A qualitative running experimental evaluation has been performed as a preliminary practical implementation, where a student playing the role of a guard man takes control of the camera pan and tilt functions remotely. The performance of the developed system was excellence hoping to leave security personnel hands-free for other important tasks. The developed system can also be put into practical use in public offices, manufacturing facilities or various construction sites-everywhere there's a need for advanced frontline security.

Keywords: Intelligent patrol robot, security robot, wireless network

1. INTRODUCTION

A robot is a machine designed to execute one or more tasks repeatedly, with speed and precision. There are different types of robots as there are tasks for them to perform. Security robots are protecting property and documenting facilities autonomously around the world. An important aspect of robotic security systems is surveillance of specified area. They provide surveillance on wheels and may be one of the security industry's best kept secret. The Naval Postgraduate School in Monterey, California first attempted the concept of a fully autonomous indoor security robot in the late 1970s. Other agencies including NASA and US Government of Defense were also working on implementation of robotics technology. One of the first robots was ROBARTI, which helped face a full gamut of technical challenges. Subsequent robots grew in capability and with the end of the cold war; the technology was made available for sale to private firms through Reagan-Bush government to industry privatization. After a decade continuous development, security robot keeps as an intensive research issue because of its ever-increasing application to different places and its economical and technological relevance. Interesting application can be seen in robot scanning areas to find explosive devices [1]. With an increased demand for security and limited numbers of trained security personnel, some security mangers are turning to robots to help get the job done. To assist security manager we have developed a security patrol robot. The system consists of an autonomous mobile robot that can move independently outside as well inside the facility to be patrolled via deployed wireless internet device to that area. Due to the robot contribution and costs saving, many researchers have done a lot of significant work on security robot whose some of them can be found in [2, 3]. These works mainly focus on target perception and identification, robot localization, terrain map updating. But here we are interested specifically in investigating a very critical and still open issue that is paramount for the success of these applications: The route planning. The main goal is to generate a very convenient trajectory that can follow by the robot so that it increases as much as possible the probability of finding the intruders or abnormal events inside the surveillance region.

2. ROBOT PLATFORM

The OkiKoSenPBX1 shown in Fig.1 originally developed for Humanoid (HR) Robot. Using this approach, high-level control of the robot is maintained by a remote and local PC/server communicating by a secure wireless link. Low-level functionality is managed by an onboard digital signal processor while computationally intensive operations are performed off board. The result is a robot that's lighter, draws less power, runs longer and is dramatically less expensive than a fully bundled or self-contained system. Moreover, since primary processing resides in a server, any hardware upgrades to the central unit are shared by all the robots it controls. With its integrated high bandwidth (54Mps) wireless fidelity (Wi-Fi 802.11G) module, the system can upload all sensors data to a PC or server at rate , in excess of 10Hz. Similarly, streaming audio and video (up to 30 fps) either for direct monitoring or for processing by high-level Artificial Intelligent schemes is a snap. Commands and instructions sent to the robot via the same wireless link also pass at rates exceeding 10Hz, providing real-time control and access.

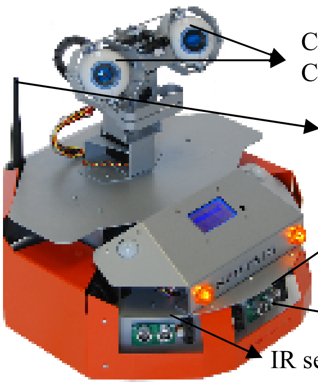

Fig.1: Robot with its equipped sensors

The OKiKoSenPBX1 includes all Wi-Robot development software components, enabling easy access to all data and information in a standard Microsoft Windows programming environment. Under the approach of using a separate PC for high-level control, there are no longer mobile system's processing power, memory and storage. For users of non-Windows operating systems OkiKoSenPBX1 can provide the raw communication protocol for direct integration with any other system or device.

3. ROBOT KINEMATICS

Robot considered in this study shown in Fig.2 is a differential motion with two degrees of freedom, composed by two active parallel and independent wheels, a third passive wheel with exclusively equilibrium function and proximity sensors capable of obstacles detection. The active wheels are independently controlled on velocity and sense of turning. Additionally the robot is equipped with specific sensors for detection and recognition of search objects or intruders. The robot model presents an interesting compromise between control simplicity and degrees of freedom that allow it to accomplish mobility requirements. Its motion is obtained by driving the active wheels. The resultant motion is described in terms of linear velocity v(t) and direction θ(t), representing on instantaneous linear motion of the medium point of the axis and a rotational motion or rotational velocity θ(t) of the robot over the same point.

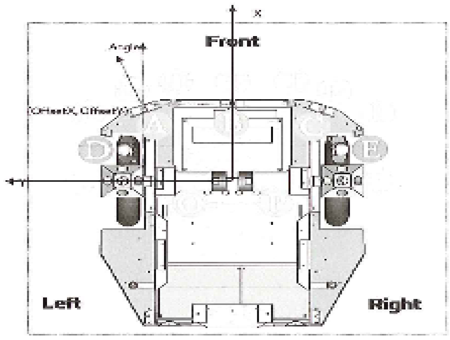

Fig.2: OkiKoSenPBX1 Robot sky view

The robot motion control is done by providing the wheels velocity $\omega_{left}(t)$ and$\omega_{right}(t)$, or equivalently the body linear and angular velocities v(t) and θ(t) called input or control variables. The mathematical model of the robot kinematics considers these two-input variables and three state variables: the robot position and orientation x(t), y(t) and θ(t), describe in the following equation:

$$\begin{bmatrix} \dot{x} \\ \dot{y} \\ \dot{\theta} \end{bmatrix} = \begin{bmatrix} \cos\theta & 0 \\ \sin\theta & 0 \\ 0 & 1 \end{bmatrix} = \begin{bmatrix} v \\ \omega \end{bmatrix} \qquad (1)$$

These equations constitute a non-holonomic dynamical system. The control of this system has been studied extensively by various research groups, and diverse solutions are available, for example in [4,5] .The motion control strategy adopted in this work involved a state feedback controller proposed in [6], which is an appropriate approach to produce a desired trajectory described by a sequence of coordinates $x_1(t)$, $y_1(t)$. This means that the route-planning task is given by a specialized robot module, independent of the motion control module that sets intermediate position lying on the requested path. The adopted control law considers the geometric situation, where the robot is placed at an arbitrary configuration, that is, the position x , y and orientation θ, and a desired position is defined by the robot route planner. In the robot reference frame X_RY_R, the configuration error vector is defined by $e = (\rho\varphi)^T$.

Where:

$$\left.\begin{matrix} \rho \\ \varphi \end{matrix}\right\} = \text{Target positions}$$

We defined the angle φ between the X_R axis of the body reference frame and the vector connecting the robot center and the desired position.

4. MAP-BASED ROUTE PLANNING

The planning procedure is based on determining a sequence of intermediary goal points or coordinates x and y that will compose the robot trajectory. The route-planning generator module uses an area-preserving map that is considered as a paradigm for area-preserving chaotic systems. This map, also called Taylor-Chirikov map [7]. It is a two-dimensional map which results from a periodic impulsive kicking of a rotor. This map was firstly proposed by Brian Taylor [8] and then independently obtained by Chirikov to describe the dynamic of magnetic field lines on the kicked rotor. The dynamic effect of this system is expressed mathematically through the map equations, given by:

$$\begin{aligned} \alpha_{n+1} &= \alpha_n + K \sin\beta_n \\ \beta_{n+1} &= \beta_n + \alpha_{n+1} \end{aligned} \qquad (2)$$

Where:
α = Periodic configuration variable or angular position
β = Momentum variable or angular speed

These map variables are both computed mod (2π). The map parameter K represents the strength of the nonlinear kick applied in the rotor mechanism. In its phase space and according to the value associated with the parameter K, it has stable and unstable periodic orbits, Kolmogorov-Arnold-Moser (KAM) surfaces, and chaotic regions. Depending on the nonlinear parameter K, the regions of regular motion and the regions of chaotic motion are complexly interwoven, but the chaotic regions are confined between KAM. As this parameter is increased, the KAM surfaces start to be destroyed, chaotic regions occupy increasingly large areas until, for a specific value of K, the last KAM is destroyed and the entire region of the phase space appears to be densely covered by a single chaotic orbit. Our route-planning generator module is implemented based on the map builder that presents this dynamics. Let us now show an example of how the map is used in the context of our route-planning generator module. By numerically simulating the map equations, we analyzed the properties of terrain covering considering the basic mission requirements for fast terrain scanning. We defined a terrain with different dimension in a normalized measurement unit. The map simulation begins with an arbitrary initial position, and considers the gain value K = 18. As the map equations simulation continues over and over, we noted in fact that, the necessary condition for the complete region to be patrolled is K > 18. The terrain covering can be judged through a performance index. This index is defined using a terrain division on square unit cells, and computing the visited cells percentage after the robot location planning.

5. CONTROL ARCHITECTURE

In our study wee associate a route-planning generator module with a closed-loop locomotion control module. At each step, the first one generates a position goal defined by its coordinates in the phase space. This position goal is provided to the second module, which drives the robot from its actual position to the desired one. When the robot arrives at the desired position, the route (path)-planning generator module is used again to give another position goal, which is subsequently provided to the second module. This sequence of action is repeated over and over again. The route-planning generator module is implemented by exploiting the dynamics of an area-preserving map in a chaotic regime. Different to a dissipative chaotic map, in which the chaotic evolution takes place on attractors, the chaotic region of an area-preserving map for specific parameter values extends practically over all of its phase spaces. For these parameter values, the entire phase space is covered by a single chaotic orbit. It is therefore possible to make an association between the physical regions that we wish to patrol with the phase space defined for the area-preserving map.

6. RESULTS AND DISCUSSION

The robot has three operating modes: Manual, Auto and Idle mode.

- In Manual mode, the robot relies on instructions from a remote user to navigate or controlled by mouse by first clicking the show control button in the control panel button on the left side of the program window. This will prompt navigation control panel. Alternatively the joystick shown in Fig.3 can be used to control the robot directly.
- In Auto mode the robot will wander its environment, using its build-in collision avoidance system to aid it from hitting any objects.
- In Idle mode the robot remains powered-on in a standby setting while minimizing power consumption.

To test our security robot patrolling approach, we have simulated the robot kinematic motion by starting with low speed, then automatically and gradually the robot adjusted its speed to reach the desired speed for the patrol mission.

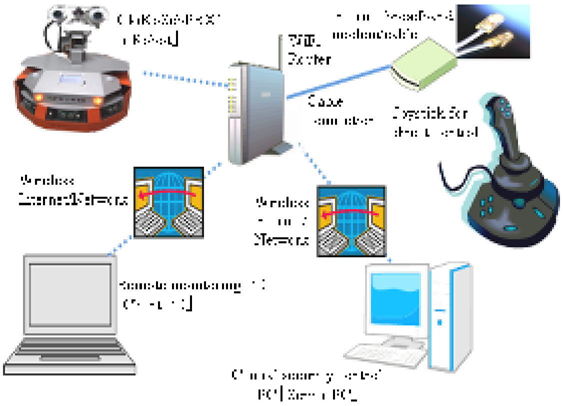

Fig. 3: Robot testing performance setup

Once the desired speed is reached it becomes constant throughout the patrol mission where it follows successfully the planned route and finished the first tour of the patrolling mission within the allocated patrol time set to 3 min (for the test purpose). The test has been repeated three times of which the robot did accomplish its mission successfully without colliding with any objects.

Next, to test the robot collision avoidance capability, two set of experiments have been done. The first test scenario consists of putting three chairs in the robot path then starts the robot from the remote monitoring computer. The robot has managed to get through the chairs and accomplished its patrol mission successfully again in the 3 min as expected. The second test consists of putting three chairs in the robot path as in the first test scenario and one big piece of wood just where the robot is expected to get out once avoiding these three chairs. The robot managed and gets through the three chairs, and once arrived in front of the wood it made a backward and changed direction without leaving its planned mission route, and then accomplished successfully its sixth mission with two seconds late. It was expected to finish it patrol mission in 3 min but instead of 3 min the robot arrived at the destination in 3 min and two seconds which is due probably to the backward. During the patrol mission through its two CCD cameras the robot sent a real-time video to the central security control computer, where a student like-guard took control of the camera pan and tilt-zoom functions remotely.

7. CONCLUSION AND FUTURE WORK

In this study, a map-based route planning for security patrol robot is presented. The approach of the proposed system consists of numerically simulate the map equations, and then analyzed the properties of the terrain covering considering the basic mission requirements for fast terrain patrolling. The system was verified in a real world experiment inside our College Campus Building. The performance validation test proves that the suggested system is able to accomplish its patrol mission successfully within the time required. The robot capability of avoiding any objects or obstacles has been also proven as the robot is able of making self-decision once faces an obstacle in front of it.

REFERENCES

[1] ROOKS, Brian, 2005. Robotics outside the Metals Industries. Industrial robot, vol.32, No.3, pp: 205-208.

[2] Everett. H.R and D.W Cage, 1999. From Laboratory to Warehouse: Security Robots Meet the Real World. The International Journal of Robotics Research, vol.18, No.7, pp: 760-768.

[3] F. Capezio, A. Sgorbissa and R. Zaccaria, 2005. GPS-based Localization for Surveillance UGV in outdoor areas. Proceedings of the 5th IEEE International Workshop on Robot Motion and Control, pp: 157-162

[4] Guangy Xu and Danwei Wang, 2000. Exponential Stabilization of Extended Chained Forms. Proceedings of the American Control Conference, pp: 3259-3263.

[5] Eric. Krotkov and John Blitch, 1999. The Defense Advanced Research Projects Agency (DARPA) Tactical Mobile Robotics Program. International Journal of Robotics Research, Vol. 18, No. 7, 769-776

[6] CANUDAS DE WITT C.; SØRDALEN O. J. 1992. Exponential Stabilization of Mobile Robots with Nonholonomic Constraints. IEEE Transaction on Automatic control, vol.37, No.11, pp: 1791-1797.

[7] J.D. Meiss, 1992. Symplectic maps, variational principles and transport. Review of Modern Physics, vol.64, No.3, pp: 795-848.

[8] B.V. Chirikov, 1979. A universal Instability of Many-Dimensional Oscillator Systems. Physics Reports, vol.54. No.5, pp: 263-379.

[9] S.O.Lee, Y.J.Cho, M.Hwang-Bo, B.J.You and S.R.Oh, 2000. A Stable target-tracking Control for Unicyle Mobile Robots. Proceedings of IEEE/RSJ International Conference on Intelligent Robot and Systems (IROS'00), vol.3, pp: 1822-1827.

[10] Johan Potgieter, Glen Brigth, Olaf Diegeland Sylvester tlale, 2002. Internet Control of a domestic Robot using a wireless Lan. Proceedings of 2002 Australian Conference on Robotics and Automation, pp: 212-215.

The Fifteenth International Symposium on Artificial Life and Robotics 2010 (AROB 15th '10),
B-Con Plaza, Beppu,Oita, Japan, February 4-6, 2010

Obstacle Arrangement Detection using Multichannel Ultrasonic Sonar for Indoor Mobile Robots

Kiyoshi OKUDA†, Masamichi MIYAKE†, Hiroyuki TAKAI†, and Keihachiro TACHIBANA††

† Graduate School of Information Sciences
Hiroshima City University
3-4-1 Ozuka-Higashi, Asa-Minami-Ku, Hiroshima, Japan
Tel: 082-830-1500, Fax: 082-830-1656.
{*okuda|miyake|takai*}*@sys.info.hiroshima-cu.ac.jp*

†† Graduate School of Computer Science
Osaka Gakuin University
2-36-1 Kishibe-Minami, Suita-city, Osaka, Japan
Tel: 06-6381-8434, Fax: 06-6382-4363
tatibana@ogu.ac.jp

Abstract: In the last several years, mobile robot systems that perform complicated tasks have been studied. To work in complicated environments, the robot has to avoid collisions with obstacles. Therefore the robot needs to detect the arrangement of any surrounding obstacles. We considered a simple distance estimation algorithm using ultrasonic sonar. Since the algorithm was able to estimate distance accurately, we also attempted stereo reception using two ultrasonic microphones. The stereo reception sonar was able to detect direction of obstacles. In order to make precise measurement, we attempted to use the signal coherence of ultrasonic waves. In order to install small system into mobile robots and to detect any surrounding obstacles, we designed a multi-channel sonar signal processing system using a high-performance embedded microcontroller. This paper describes our ideas for the distance estimation algorithm for ultrasonic sonar and a design for signal processing system using a high-performance microcontroller.

Keywords: Mobile robot, Ultrasonic sonar, Obstacle detection, Signal processing.

1. INTRODUCTION

In recent years, mobile robot systems that achieve complicated tasks such as repairing industrial facilities in hazardous environments have been studied. When robots work in these environments, the possibility of collisions with obstacles or other robots increase. In order to avoid collisions, each robot has to detect the arrangements of circumambient obstacles in the given workspace.

Ultrasonic sonar is one of the most popular obstacle detection systems for mobile robots. Ultrasonic sonar only measures the time period from the ultrasonic pulse emission to the reflected echo reception. This method is called time of flight (TOF) measurement. In an ideal situation, the distance to the reflective object L, is calculated from the time period t and the acoustic velocity V using Eq. (1). The parameter T is the temperature in degrees Celsius in this equation.

$$\begin{aligned} L &= V \times t / 2 \\ V &= 331.5 + 0.60714 \times T \end{aligned} \tag{1}$$

In a real situation, ultrasonic sonar receives many echo signals from different obstacles and needs to analyze these echoes, because it is difficult to detect the leading edge of the ultrasonic pulse. In conventional methods using ultrasonic sonar, the result not exact because its threshold decision mechanism has an incomplete theoretical background. Consequently, if the robot moves into another environment, the threshold value may be less accurate.

Therefore, we considered a distance estimation algorithm using a simple waveform analysis without thresholds [1, 2]. Since the proposed algorithm was able to estimate distances accurately in preparatory experiments, we attempted stereo reception using two ultrasonic microphones [3]. The stereo sonar not only measures distances but also detects the direction of reflective objects. In order to detect distance more accurately, we referred to the coherence of the ultrasonic wave. It is possible to accurately estimate distance if we analyze the receiving wave using coherence.

In order to detect the arrangement of circumambient obstacles, we considered multi-channel ultrasonic sonar that can capture more than two channels in parallel. Eight pairs of ultrasonic emitters and microphones were positioned on the circumference of the robot body facing outward. In order to capture signals, the sampling capability of the signal processing system needs more than twice the frequency of the ultrasonic signal because of the Nyquist-Shannon sampling theorem. We tried to attach implement multi-channel sonar systems onto the microcontrollers and install them onto small mobile robots for experiments.

2. TRUE DISTANCE ESTIMATION USING WAVEFORM ANALYSIS

Conventional ultrasonic sonar measures the time period from an ultrasonic pulse emission to the received echo that exceeds a threshold level. However, since the threshold level of this method has an incomplete theoretical background, the measurement result includes some inaccuracies. Therefore, this method is not appropriate for arrangement detection of circumambient obstacles and for an obstacle map creation. In order to detect the accurate arrangement of obstacles, we considered algorithms that measure distances without thresholds.

2.1 Basic concepts of true distance estimation

Fig. 1 shows a model of ultrasonic pulse reflection. Since an emitted ultrasonic pulse spreads to the corn of the beam to the beam width as shown in Fig. 1, the amplitude of the reflected signal is proportional to the temporal change in the size of the reflective cross section. Consequently, if the sonar measures a period of the echoes maximal amplitude of the echo, it measures the distance of maximum reflective cross section. Therefore, it does not indicate true distance.

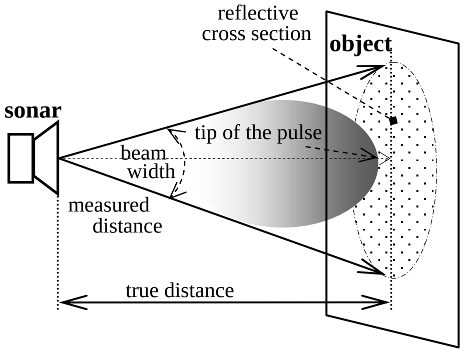

Fig. 1. A model of ultrasonic pulse reflection

The true distance is calculated by measuring the time period between an ultrasonic pulse emission and the tip of the return pulse reception. This is because the tip of the ultrasonic pulse hits and reflects off of the object first, and in turn the tip of the return pulse is received first. Therefore, the true distance is calculated using the received waveform.

2.2 True distance estimation without threshold

In order to estimate true distance, we considered a waveform analyzing algorithm. As previously mentioned we assumed that the amplitude of the reflected echo is proportional linearly to the temporal change in the size of the reflective cross section. We examined the algorithm which measures the arrival time at the tip of the reflected echo under this assumption.

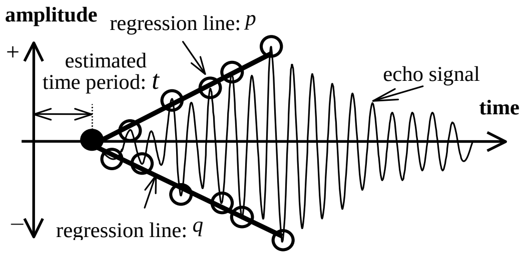

Fig. 2. A model of time period estimation algorithm

Fig. 2 shows a model of time period estimation algorithm. In Fig. 2, the horizontal axis is time and the vertical axis is amplitude. The regression lines p and q are computed based on the measured data sets using the least-square method. The time coordinates of the intersection of regression lines p and q shows the estimated time period t. The distance is calculated from the estimated time period t based on the acoustic velocity V using Eq. (1).

In addition, in order to detect distance more accurately, we refer to the coherence of the ultrasonic wave. We use a segment of continuous wave's interval as the transmitter pulse. We compare the received signal with the continuous wave that is used for generating the transmitter pulse.

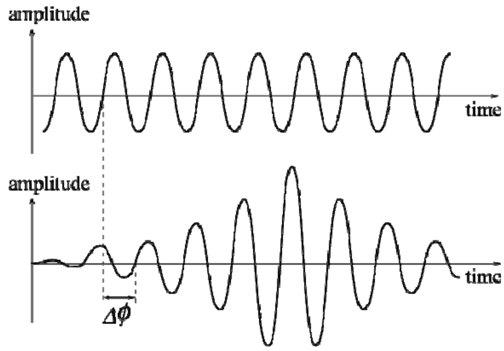

Fig. 3. A model of phase lag detection

Fig. 3 shows a model of phase lag detection. The upward wave pattern in the figure is the continuous source signal. The downward wave pattern is a model of the received signal. When we measured phase difference $\Delta\phi$ from the continuous source signal and the received signal, we considered the method of estimating the distance within less than one wavelength.

3. OBSTACLE ARRANGEMENT DETECTION USING STEREO SONAR

Because stereo sonar receives an echo using multiple microphones simultaneously, the reception time of each microphone of the same echo is different if the object is not in front of the microphones. Since the distance can be calculated using measurement of TOF of an ultrasonic pulse and the direction can be calculated using time difference of arrival (TDOA) of the echo, it is possible to indicate the position using the polar coordinates. Fig. 4 shows a model of stereo reception based on TDOA. In Fig. 4, S is an ultrasonic speaker at the center, and M_L, M_R are ultrasonic microphones on both sides. L is the shortest diffusion path between the emitter S and the reflective target T. L_L and L_R are the shortest return paths between the reflective target T and microphones Mx. The position of an object is calculated from L_L and L_R using Eq. (2).

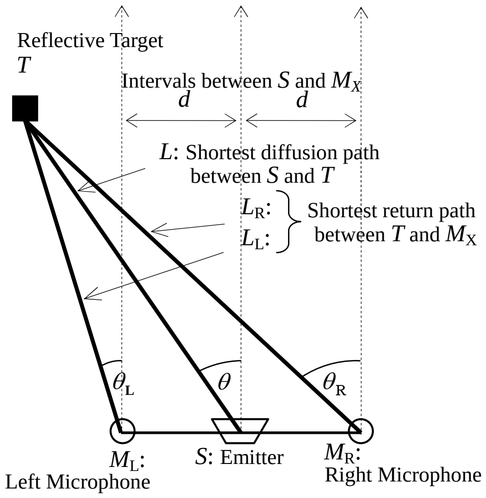

Fig. 4. A model of stereo reception based on TDOA

Value L_L and L_R, θ_L and θ_R alternate their position in this equation when an object is placed on the opposite side.

$$\theta_R = \arcsin\left(\frac{L_R^{\ 2} - L_L^{\ 2} + 4d^2}{4dL_R}\right)$$
$$\theta_L = \arccos\left(\frac{L_R \cos\theta_R}{L_L}\right) \tag{2}$$
$$\theta = \arctan\left(\frac{L_L \sin\theta_L + d}{L_L \cos\theta_L}\right) = \arctan\left(\frac{L_R \sin\theta_R - d}{L_R \cos\theta_R}\right)$$
$$L = \frac{L_L \cos\theta_L}{\cos\theta} = \frac{L_R \cos\theta_R}{\cos\theta}$$

4. A DESIGN OF ULTRASONIC SIGNAL PROCESSING SYSTEM

In order to detect obstacle locations from the ultrasonic echo, we considered the performance of the signal processing system. Table 1 shows the performance of well known embedded high-performance microcontrollers equipped with large size flash memory and static random access memory, high speed multi channel A/D converters and other interfaces.

Table. 1. Performance of embedded controllers

		H8/3069	ADuC7026
CPU	Frequency	25MHz	48MHz
Memory	Capacity	16MByte	512kByte
A/D converter	Channels	8ch	12ch
	Precision	10bit	12bit
	Speed	350ksps	1Msps

Ultrasonic sonar that emits a center frequency of 40 kHz is often used for mobile robot systems. The signal processing system needs a sampling capability that is more than twice the frequency of the signal because of the Nyquist-Shannon sampling theorem. If the integrated multi-channel A/D converters can capture more than 800k samples a second, it can capture 100k samples for 8 channels and process the ultrasonic echo. As seen table 1, ADuC7026 (Analog devices) is appropriate for our needs.

An external bus controller and a memory management unit are built on an FPGA. Fig. 5 shows the system block diagram.

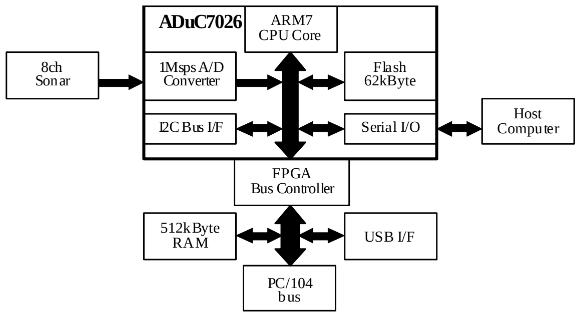

Fig. 5. Block diagram of signal processing system

5. PERFORMANCE CONFIRMATION OF MEASUREMENT ALGORITHMS

As previously mentioned, a true distance estimation algorithm using ultrasonic monaural sonar and an obstacle position detection algorithm using ultrasonic stereo sonar were proposed. A multi-channel signal processing system was also designed. We confirmed the measurement accuracy using the algorithms and the performance of the signal processing system in experiments.

5.1 Examination of A/D converter sampling frequency

In order to obtain ultrasonic wave information efficiently, A/D converter sampling frequencies were examined. We selected the 40kHz ultrasonic pulse. We tested five frequencies: 80ksps, 100ksps, 120ksps, 150ksps and 200ksps. We confirmed the measurement precision in stereo reception of the obstacle at the position of 50cm, 100cm, 150cm and 200cm at each frequency.

Table 2 shows the measurement error for sampling frequency. For sampling frequency more than 100ksps, any sampling frequency was almost the same error rate. Therefore, we adopted a frequency of 100ksps; as it required the least processing.

Table.2.Measurement error of sampling frequency

Target distance	Error distance				
	80ksps	100ksps	120ksps	150ksps	200ksps
500	-24.664	-16.330	-10.240	-17.212	-15.048
1000	-33.300	-21.671	-14.643	-27.085	-20.770
1500	-28.835	-23.967	-15.129	-26.950	-23.127
2000	-36.348	-19.503	-14.947	-29.342	-19.119
Average	-31.729	-20.007	-140042	-25.472	-19.821

Unit: Target distance (mm), Error distance (mm)

5.2 Obstacle position detection using stereo sonar

We examined the performance of ultrasonic stereo reception. In this experiment, ultrasonic transducers (Murata MA40B8R/S, Carrier frequency: 40kHz, Beam width: 50 degrees) were used. The received signals were amplified by a 40kHz tuned FET amplifiers.

Table 3 shows the experimental results derived from ultrasonic stereo sonar. In this table, the positional information is indicated by the distance and the direction, which can be measured using ultrasonic stereo sonar.

Table.3.Measurement results of ultrasonic stereo sonar

	Target 1		Target 2		Target 3	
	Distance	Angle	Distance	Angle	Distance	Angle
Theoretical	715.9	24.8L	1118.0	26.6R	1500.0	0.0
Trigger	701.2	21.6L	1094.4	26.4R	1502.5	2.4L
Error (Trig)	-14.7	-3.2	-23.7	-0.2	2.5	2.4
Burst	701.0	20.5L	1128.3	28.2R	1512.1	0.3L
Error (Burst)	-14.9	-4.2	10.3	1.7	12.2	0.3

Unit: Distance (mm), Angle (degree)

In table 3, the ultrasonic stereo sonar was able to measure distance at an error rate of approximately 2% or less and to measure angles at an error rate of approximately 4.2 or less in the experiments. In the results, the measurement accuracy of the obstacle positions measurement of the obstacle improved as the obstacle was positioned nearer to the center of the range of the stereo sonar.

In order to check the coherence of the received signal, we used a bigger sampling frequency than 100ksps. Our results showed that the coherence of the received signal was uniform.

6. CONCLUSION

We proposed a true distance estimation algorithm using ultrasonic monaural sonar and confirmed the accuracy of the algorithm. In the experiments, approximately error rate of 1% or smaller were achieved using the proposed algorithm.

We also considered an obstacle position estimation algorithm using ultrasonic stereo sonar and confirmed the accuracy of the algorithm. The ultrasonic stereo sonar was able to measure distance at approximately error rate of 2% or smaller and to measure angle at approximately error rate of 4.2 degrees or smaller in the experiments.

We proposed and designed a sonar signal processing system using ADuC7026 micro-controller. We adopted a frequency of 100ksps after testing other sampling frequency and their distance detection precision.

In future work, we will design printed circuit boards (PCBs) of the signal processing system. In order to install it onto small-scale mobile robots for experiments, it will be miniaturized to the PC/104 (90.17×95.89mm) size. When distance detection improves, the angle detection precision improves. Therefore we will try the improvement of distance measurement system that refers to coherence.

ACKNOWLEDGEMENT

This work is supported, in part, by the Sasagawa Scientific Research Grant from the Japan Science Society (No. 21-211).

REFERENCES

[1] J. Karashima, H. Takai and K. Tachibana (2006), A study on accuracy improvement of practical distance measurement using ultrasonic sonar (in Japanese), *Proceedings of the 11th student convention of kansai-section of IEICE*, p.16

[2] H. Takai, J. Mitsuoka, and K. Tachibana (2006), Feasibility study of Sensing Methods on Cooperative Localization for Team Operation of Multiple Mobile Robots, *The 3rd International Conference on Autonomous Robots and Agents (ICARA2006)*, pp.379-385

[3] M. Miyake, H. Takai and K. Tachibana (2009), Workspace mapping based on multi-sensor information fusion using heterogeneous onboard sensors, *Proceedings of the 14th International Symposium on Artificial Life and Robotics (AROB09)*, GS11-3

[4]H. R. Everett (1995), Sensors for Mobile Robots - Theory and Application-, A K Peters, Ltd.

[5]V. Kyrynyuk (2005), AN2291: Automotive - Ultrasonic Vehicle Parking Assistant with LIN 2.0 Interface, Cypress semiconductor

[6] H. Takai, K. Okuda, M. Miyake., et al. (2009) A Design of Onboard Multi-Channel Sonar Signal Processing System for Autonomous Mobile Robots, Proceedings of the ICCAS-SICE 2009, pp.5740-5744

A Collision Avoidance Achievement of Vehicle Warning System in Intersection via DSRC

C. W. Hsu, C. N. Liang, L. Y. Ke, H. Y. Huang, F. Y. Huang

Automotive Research & Testing Center
No.6, Lugong S. 7th Rd., Lugang Town, Changhua Country 50544, Taiwan (R.O.C.)
Tel : 886-4-7811222ext2351; Fax : 886-4-7811333
winsonhsu@artc.org.tw

Abstract: Many accidents were happened because of fast driving, habitual working overtime or tired spirit, moreover, more and more people are also interested in driving safety. This paper presents a solution to enhance intersection safety for adjacent vehicles driving using vehicular communication and developed algorithm. The developed system integrates dedicated short range communication (DSRC) and global position system (GPS) with embedded system into a delicate remote warning system. The proposed system has four mainly components, including positioning unit, communication unit, vehicular date unit and embedded platform in each vehicle. To transmit the vehicular information and broadcast vehicle position, DSRC communication technology is adopt as communication channel. The positioning unit is utilized to provide the position and heading information from commercial GPS module, and furthermore the vehicular data unit is used to receive the break signal, throttle signal, and other signals via controller area network (CAN) interface connected to each mechanism. The CAN module is based on the broadcast communication mechanism which is achieved by using a message oriented transmission protocol. These vehicular signals are held and processed by CAN module in operation platform. All of the communication, positioning and vehicular units are built with an embedded system using IXP processor in Linux operating system, and each unit is managed and processed by embedded platform. From position and vehicular information, this paper provided a conflict detection algorithm to do time separation and remote warning with error bubble consideration. The proposed system is carried out with theoretical algorithm and hardware integration, and the result shows collision avoidance applicability in intersection.

Keywords: Collision Avoidance, DSRC, CAN, GPS

I. INTRODUCTION

In recent years, the number of fatalities in traffic injuries is about nearly 43 thousands according to U.S. department of transportation (DoT) statistic data and the incapacity for work of over 3 consecutive days is about 3.2 million. In Taiwan, there are about four thousand body counts of each year in traffic incident. It is almost sixty percent accidents in intersection. To solve this kind of problem, such as intelligent transportation systems (ITS) and telematics concept, are the most popular method to implement at present traffic problems with the increase of people and vehicles all over the world. Telematics which contains telecommunication and informatics technologies is the most popular area which has many advanced concepts in assist systems in vehicular devices.

In the recent two decades, wireless communication had a tremendous growth in many applications. Cellular systems, infrared, Bluetooth and DSRC in wide area or local area communication have rapidly increased [1]. A general vehicular communication which depends on its coverage area can be classified into four categories: inter-vehicle, outer-vehicle, vehicle-to-infrastructure (V2I) and vehicle-to-vehicle (V2V). In outer-communication, mobile communication has presented its wide coverage, high reliability of data transmission in surveillance applications. The application of data reporting for surveillance or real time control is a rising demand where either GSM or GPRS services are available. However, mobile communication has a drawback in time delay about 1.0 sec in TCP mode or 0.8 sec in UDP mode. DSRC theoretically provides up to 1 km range and allows communications between vehicles moving up to 160 km/h. It also has low latency about 50 millisecond [2]. To meet a higher vehicle safety, DSRC which is a wireless communication protocol in the 5.9 GHz frequency band plays an important role of vehicular system.

GPS is a worldwide converge system that provides high accuracy position, any weather condition and has the advantage in faster positioning. Positioning accuracy and reliability is great concern to many users, and becomes a good engineering topic for study in depth. In this implementation, GPS module is taken to receive positioning data under driving.

This paper proposed a system configuration using an embedded system to operate as a control system to manipulate DSRC unit, CAN unit and GPS unit for collision avoidance. The test information is debugged and showed in the screen of laptop using well defined format, and the total lengths is about 8 bytes with its id in different devices.

II. SYSTEM DESCRIPTION

The system technology for collision avoidance warning system is designed with an integration of GPS and data transmitting through DSRC, as shown in Fig. 1. The information may display on the debugged screen to monitor other neighbor vehicles in remote time operation. The vehicular data of vehicle will be routed and broadcast to neighbor vehicles by short message protocol onto the internet via DSRC communication. A data fusion of collision avoidance warning system platform is built of the basic three parts, including GPS receiver, DSRC communication unit and CAN module. To fulfill the proposed anti-collision application, GPS data as well as vehicular data are processed in specific logic, digital formats and sent through DSRC module in controlled intervals.

In DSRC software, the network protocol is based on IEEE 802.11p standard under open system interconnection (OSI) model. This layer are ported from revising 802.11a, and other layers are followed the TCP/IP modes. In the network interface layer, the DSRC adopts the non-IP or IP base protocol to establish network connection without security or 1609.X.

In GPS module, the output adopts the NMEA-0183 standards as a format for interfacing marine electronic devices. The default communication parameters for NMEA output rate support fixed baud rate at 9600 bits/sec with 8 data bits, 1 stop bit, and no parity. The GPS fixed data is processed in one second period, including the acquisition of position, ground speed and heading.

In vehicular information, the break and throttle condition are transmitted to other vehicles by CAN acquisition. CAN is a serial, asynchronous, multi-master communication protocol for connecting electronic control modules, sensors and actuators in automotive and industrial applications. The CAN-based system is based on the broadcast communication mechanism which is achieved by using a message oriented transmission protocol and different id number.

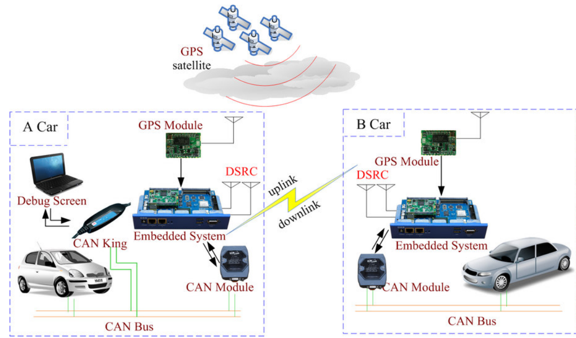

Fig. 1 System architecture

III. SYSTEM ALGORITHM

The onboard embedded system had mainly two tasks, including receiving neighboring vehicle's GPS data and calculating collision relation. The first task meant that the rover system would process the NMEA data and get the required data. The GPS fixed data (GPGGA) and GPRMC are adopted in this research, including the acquisition of position, ground speed and its course. Based on the acquired GPS data, the on-line display would be mapped into demonstrated map. The second task was collision detection which transforms vehicular coordinate frame from WGS-84 to north-east-down (NED) local navigation coordinate, and gets longitudinal and latitude collision times.

1. Geometry Analysis

Although GPS receiver supplies precision position under dependent performance, the output data of GPS receiver provides lower bandwidth and risks under interference and error. The error factor is considered by reason of GPS error uncertainty. As shown in Fig. 2, B is the ownership so it has an error bubble around it [3]. A is the intruder which drives near the vehicle B in any intersection. Their extrapolation lines have an intersection in the near future. A is positioned at (Λ_1,λ_1) in WGS-84 and travels with its speed V_A. B is positioned at (Λ_0,λ_0) and travels with its speed V_B.

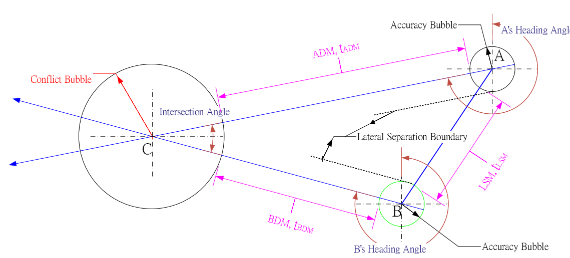

Fig.2. Geometry model of two conflicting objects

L_A and L_B are two line segments which predict future driving trajectory, and the driving distance is decided by initial position and heading. Through two forecasted extrapolation lines, any two vehicles on a planar motion can possibly extrapolate to an intersecting point C and can respectively decide the collision time which two vehicles arrive in point C. The predicted time (t) is an index which decides them whether approaching in the future. Generally speaking, two vehicles will cause conflict or collision when (Λ,λ,t) are all the same, as long as one of them is different, the dangerous condition can be avoided. The time must be observed whether being equal or not.

In conflict analysis, the rough calculation could calculate the relative distance first. If the relative distance is calculated under safe separation and maybe resulted of conflict collision, that needs delicate calculation and does three procedures which includes coordinate transform, geometry distance and collision time.

The first procedure is transformed from WGS-84 to ECEF and ECEF to NED frame using (1)-(2). The altitude (h) is given by GPGGA format from GPS receiver and the other parameters are eccentric (e) and semi-major axis (a). Equation (1) is result from the shape of the Earth which is an ellipsoid, not a true sphere. The following procedure is to take ownership as center and calculate relative position using (2).

$$\begin{bmatrix} x^E \\ y^E \\ z^E \end{bmatrix} = \begin{bmatrix} (N+h)\cos\Lambda\cos\lambda \\ (N+h)\cos\Lambda\sin\lambda \\ [N(1-e^2)+h]\sin\Lambda \end{bmatrix} \quad N = \frac{a}{\sqrt{1-e^2\sin^2\Lambda}} \tag{1}$$

$$\begin{bmatrix} x^N \\ y^E \\ z^D \end{bmatrix} = \begin{bmatrix} -C(\lambda_0)\cdot S(\Lambda_0) & -S(\lambda_0)\cdot S(\Lambda_0) & C(\Lambda_0) \\ -\sin(\lambda_0) & \sin(\lambda_0) & 0 \\ -C(\lambda_0)C(\Lambda_0) & -S(\lambda_0)C(\Lambda_0) & -S(\Lambda_0) \end{bmatrix} \times \begin{bmatrix} x_1^E - x_0^E \\ y_1^E - y_0^E \\ z_1^E - z_0^E \end{bmatrix} \tag{2}$$

Although the mathematical model usually adopts Cartesian coordinate, all of the angles are still referenced to NED coordinate. Fig. 2 only shows one kind of collision condition, but vehicle A maybe locates at different quadrant and has different heading angle result from geometry relationship. The collision conditions are discussed and suitable at any conflict area, and each possible case is listed in the following Table I(A) & I(B). In Table I, the global heading angle is (H_A,H_B) and local relative heading is (H_{AB},H_{BA}). The local relative heading (H_{AB}) takes B as center and could be given relative to North direction.

Table 1. Relative heading angle in Quad I&IV

	Case I	Case II	Case III	Case IV
∠A	2π -H_{BA}+H_A	H_{BA}-H_A	H_A-H_{BA}	H_A-H_{BA}
∠B	H_{AB}-H_B	H_B-H_{AB}	H_{AB}-H_B	2π +H_{AB}-H_B

Table 2. Relative heading angle in Quad II&III

	Case V	Case VI	Case VII	Case VIII
∠A	H_{BA}-H_A	H_A-H_{BA}	H_{BA}-H_A	2π -H_A+H_{BA}
∠B	2π -H_{AB}+H_B	H_{AB}-H_B	H_B-H_{AB}	H_B-H_{AB}

2. Collision Time Calculation

According to the pervious segment, the possible intersection is calculated and needs to forecast in time by considering the possible errors. This paper proposes a simplified computation that the possible ADM does plus and subtraction operations using (4) in vehicle A, moreover, the same concern is considered in own vehicle. The error is distributed over the circle whose magnitude of radius is changed by different GPS. One sigma error of commercial GPS is about 7 meters. In this paper, the circle error is known as the error intersecting bubble as shown in Fig.2. And it is also distributed over the driver response time whose magnitude is about 0.5 to 0.75 sec [4]

After the embedded processor calculates the ADM and BDM, both of regional collision times (t_{A1}, t_{A2}, t_{B1}, t_{B2}) are given by using (4). If the temporal separation between two vehicles is larger than zero, the time is no overlapping, it represents there is no significant intersection between them. It predicts there is no dangerous conflict in the near future, as shown in right Fig. 3. If $t_{A1\text{-}A2}$ occurs between the start of t_{B1} and the end of t_{B2}, the time range are overlapping in left Fig. 3. This represents a conflict or intersection. This condition can estimate that there will be an approaching incident in the near future, and then the collision time will be showed in the screen and given some sound by collision avoidance system.

After the coordinate is located in navigation frame in Eq.(2), the screen display needed to transform into vehicle coordinate, as shown in Fig. 4. And the transform matrix is Eq.(3). The right vector is NED position and H is the vehicle heading relative to earth pole. After the matrix multiplication, the left term in Eq.(3) is screen coordinate.

$$t_{A1} = (\mathrm{ADM} + \mathrm{error\ \ range}) / V_A, \quad t_{A2} = (\mathrm{ADM} - \mathrm{error\ \ range}) / V_A \tag{3}$$

$$\begin{bmatrix} B_x \\ B_y \end{bmatrix} = \begin{bmatrix} \cos(H) & -\sin(H) \\ \sin(H) & \cos(H) \end{bmatrix} \begin{bmatrix} E \\ N \end{bmatrix} \tag{4}$$

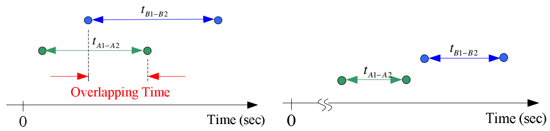

Fig. 3 A span overlapping time and opposite condition

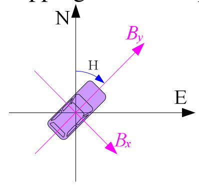

Fig. 4 Navigation coordinate to vehicle one

IV. SYSTEM IMPLEMENTATION

The test platform, as shown in Fig. 5, was used to implement the proposed on-line display system. Two vehicles were used to run on the ARTC roadway to verify the collision warning function; while two vehicles were followed on the road or driven to an intersection in order to easily verify system design in the verification. Under system design and implementation, vehicular data which connected to CAN interface was collected for scheduled tests. For test operations, DSRC module was used to do two-way data link communication. The embedded system used two DSRC modules to do data communication in control channel and service channel individually. The GPS receiver also outputted positioning data, and the positioning performance was well processed and mapped to demonstrated map.

Fig. 6 showed the on-line display test, where two vehicles were running on ARTC roadway. The test demonstrated the display system in a longer distance, and the driver drove along with preceding vehicle. Fig. 7 showed another test, where the driver drove into an intersection. Two cases offered an important awareness to the driver under test. The map reported neighbor vehicle positioning data about 1 second periodically, and broadcasted to other vehicle via DSRC. In these tests, the actual position of the vehicle was monitored and displayed on the screen. Although GPS error is inevitable, it is not a problem in this paper with error bubble consideration. The driver could easily see how other vehicle was presented in the digital ARTC map. The embedded processor predicted that there was possible danger in the near future. The display showed others position and speed signal of mapped vehicle that the operator could be fully aware of other vehicle situation under proposed system concept.

Fig. 5 System hardware and implementation

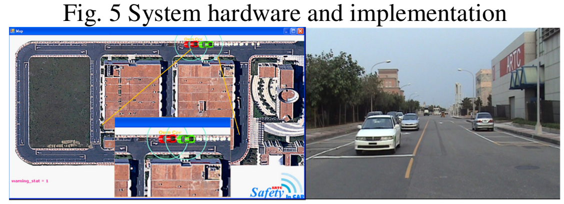

Fig. 6 Car following with safe distance (state=1)

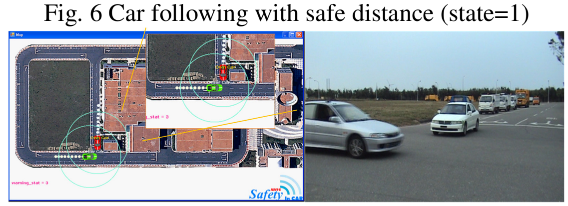

Fig. 7 Running into intersection (warning state=3)

VI. CONCLUSION

In this paper, the availability of on-line display system using GPS positioning is verified and the vehicle data is allowed on-line data exchange through DSRC module. The proposed warning system assists drivers to know current relationship to other vehicles through intersection and following tests with the situation awareness capability.

ACKNOWLEDGEMENT

This work is supported from Department of Industrial Technology, Ministry of Economic Affairs, Taiwan, R.O.C.

REFERENCES

[1] Jiang D, Taliwal V, Meier A (2006), Design of 5.9GHz-DSRC Based Vehicular Safety Communication, IEEE Transactions on Wireless Communications, Vol. 13, Issue: 5, pp. 36-43.
[2] Fernandes P, Nunes U (2007), Vehicle Communications : A Short Survey, IADIS Telecommunications, Networks and Systems, Lisbon, pp. 134-138.
[3] Lin CE, Hung SJ (2000), A Collision Avoidance Algorithm for Helicopter Flight Director and Surveillance System, AIAA Guidance, Navigation and Control Conference, Denver, AIAA-2000-4249.
[4] Muttart JW (2003), Development and Evaluation of Driver Response Time Predictors Based upon Meta Analysis, Society of Automotive Engineers, No. 2003-01-0885, pp. 1-21.

Autonomous Navigation System using Geographical Feature Elements Information for Navigation Mapping System

I. Zunaidi*, M. Rozailan*, MS Samsi*, N. Kato**

*TATi University College, Terengganu, Malaysia. **Mie University, Mie Prefecture Tsu City, Japan*

Abstract: A path-planning algorithm for an autonomous mobile robot using geographical information, under the condition that the robot moves in unknown environment. Image inputted by camera at every sampling time are analyzed and geographical elements are recognized, and the geographical information is embedded in environmental map. Then, the path is updated by integrating the exploited information and the prediction on unexploited environment. We used a sensor fusion method for improving the mobile robot dead reckoning accuracy. The experiment results, confirm the effectiveness of the proposed path-planning algorithm on the robot's reaching the goal successfully using geographical information are presented.

Key words: Path Planning, Autonomous Mobile, Geographical Information and Dead Reckoning

1. Introduction

In recent years, the working area of an autonomous mobile robot has not been limited to indoors only, but it has extended to the outdoors. Navigation systems are necessary when robots move autonomously and its have been studied for many years. Studies had begun from a basic research of *COM*, *Class*, *Bug*, etc., and in recent years some promising techniques have been proposed, for example, an autonomous action planning for the mobile robot that considered errors of an internal and external sensors together with the uncertainty of a map [(1)(2)(3)], an autonomous guidance that avoided wall-collision, by measuring distances to wall based on the detected edges [(4)], and a human-evading action planning system using GA [(5)].

Although many of these researches targeted obstacle avoidance, they didn't consider geographical feature elements that greatly influenced robot movement. If geographical environment consists of single flat element such as floor and asphalt, and if a robot were large-sized, it would not become crucial factor to be concerned whatever geographical feature elements are. However, if geographical environments are intensively changed, and if a robot is small-sized, we should take the geographical feature element into consideration. In this paper, we used encoder, accelerometer and gyro sensor data fusion with error model method for robot positioning. In this method, we use error model method where each sensor will measure the accumulated error to it's own position's [(6)(7)(8)]. The advantage of our propose method by considering feature elements, is that we also can reduce the accumulated errors of position and orientation. The another advantages are, for example, the decrease of damaging robot and the energy loss saving

Thus, in this research, we propose a path-planning algorithm using geographical feature information for the autonomous mobile robot to move in unknown environments.

2. Generation of environmental map

2·1 Evaluation values of geographical elements

When a robot generates an environmental map with geographical information, it is necessary to change into the appropriate information for the robot movement, rather than simply using a recognition result.

So, we use a technique of embedding the geographical feature information into an environmental map where the information is changed into an evaluation value representing the difficulty of moving for the robot. We call this value the geographical evaluation value.

Now, let's consider that "asphalt or concrete (AC)", "sand or soil (SS)", "gravel (GV)", and "grass (GR)" are regarded as elements on outdoors. The geographical evaluation value J to be embedded in the environmental map is given by

$$J = W_{AC}P_{AC} + W_{SS}P_{SS} + W_{GV}P_{GV} + W_{GR}P_{GR} \qquad (1)$$

where,

W_{LAND} : The weight coefficient that expresses the difficulty when the robot moving on a geographical feature element "LAND"

where

"LAND"$\in$ {"AC" , "SS" , "GV" , "GR" }

and

$$W_{AC} < W_{SS} < W_{GV} < W_{GR} \qquad (2)$$

are assumed.

P_{LAND} : The probability value of a point being geographical feature element "*LAND*", when camera taking image. ($0.0 \leqq P_{LAND} \leqq 1.0$)

2·2 Transformation from image coordinates to environmental map coordinates

A camera captures outdoor scene with WINDOWS DIB still-images of 240x340[pixel]. Sub images of the captured DIB images are classified into an outdoor element and, furthermore, the geographical evaluation values are allocated according to the elements. Next, the captured DIB still-images are transformed from image coordinates(Σ_I) to world coordinates(Σ_W), via camera coordinates(Σ_C), and robot coordinates(Σ_R), and the allocated geographical evaluation values are embedded in an environmental map.

The camera is set at 210[mm] in height, and with an angle of depression of 28[degree].

By performing coordinate transformation, the four-corner points on a DIB image is transformed into trapezoid area on Σ_R as shown in Fig.1. And, moreover, this trapezoid area is transformed to Σ_W.

We divide the transformed picture into 16x16 pieces, and update environmental maps by embedding geographical evaluation values in environmental maps.

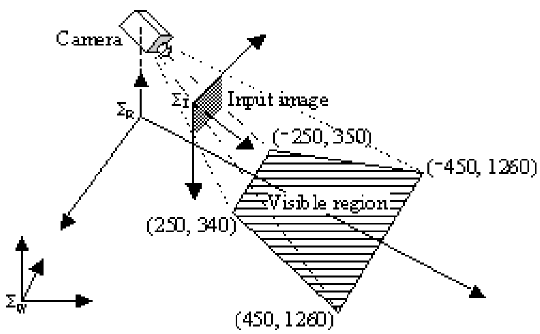

Fig.1 The flow of coordinates transformation and 4 trapezoid area points on Σ_R [mm]

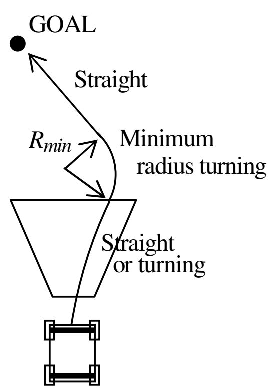

Fig.2 An example of the target path at "Approach to GOAL"

3. Path planning

3·1 Region definition

When using a CCD camera as a vision sensor, we find there is two kinds of areas exist. One is the area for which geographical elements can be recognized, and the other one is can not, because it is in the outside of visible area. Now, we define the former as the visible region (VR), and the latter as the unknown region (UR).

3·2 Generation of target path

As shown in Fig.2, the target path is that the robot performs turning or running straight in VR at first. And then in UR, the robot runs the shortest length path with minimum radius turning, and running straight aiming at GOAL directly.

However, when the distance from present representation point (central point of front wheel shaft) to GOAL the above is not far enough, mentioned target path is not necessarily successfully generated. Fig.3 shows two such cases. They are the case that GOAL exists in the area of the minimum turning radius in UR, and the other case that GOAL exists in VR. Therefore, we make a little change to generation of a target path in this case.

When L_{bor} shown is the distance from VR to GOAL

$$L_{bor} \geqq 2R_{min} \tag{3}$$

We define this case as "Approach to GOAL". Contrary to this, when L_{bor} satisfies

$$L_{bor} < 2R_{min} \tag{4}$$

We define this case as "Neighbor of GOAL".

where R_{min} : Minimum turning radius.

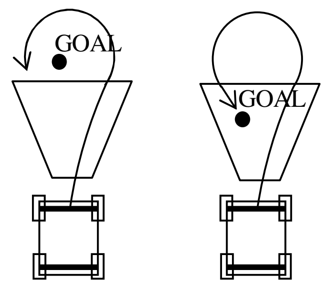

(a) GOAL exits inner of minimum radius turning

(b) GOAL exits at visible region

Fig.3 Examples of failing in reaching GOAL

3·3 Path planning at "Approach to GOAL"

The robot goes toward GOAL, searching the optimal path out of target pathes generated. Now, we consider a path evaluation value as a standard value for searching the optimal path. The path evaluation value expresses the grade of the difficulty of movement for a robot.

3·3·1 Calculation of path evaluation value in VR

The target path is generated by changing target angle α and control angle θ, as shown in Fig.4.

α : Target angle, which is defined as an angle between the Y_R axis and the line segment that connects the robot representation point and the target point being set in VR (P_{end}).

θ : Control angle, which is the steering angle of the robot.

The robot performs turning movement ($\alpha \neq \theta$) or straight movement ($\alpha = \theta$) in VR by changing α and θ.

When the robot moves in VR, the robot searches for the optimal path based on the geographical evaluation value.

When the robot moves, the geographical features should be examined only at the places that the robot's wheel steps on.

Therefore, the robot's shape should not be represented in a generally used shapes such as a circular and a rectangle, but in the two points, that is, the left and right wheel points.

It is considered that just the geographical feature, which the two points step on, should be taken into consideration.

Once a set of α and θ is given, the robot generates a target path in VR. Moving along the generated target path, the robot calculates the movement evaluation value at each of sampling step.

Movement evaluation value at a certain sampling step k, $J(k)$ is defined by

$$J(k) = K \times \frac{J_L(k) + J_R(k)}{2} \tag{5}$$

where

$J_L(k)$: Geographical evaluation value, on which robot's left wheel steps, at a sampling step k.

$J_R(k)$: Geographical evaluation value, on which robot's right wheel steps, at a sampling step k.

K : The weight coefficient used when right and left wheel step on different geographical feature elements.

As a result, path evaluation value in VR, J_v, by a set of α and θ is given by

$$J_v = \sum_{k=1}^{n} \left[L_{dev} \times \frac{J(k-1) + J(k)}{2} \right] \tag{6}$$

where

L_{dev} : Length of the path that the robot moves along in one sampling step as shown in Fig.8.

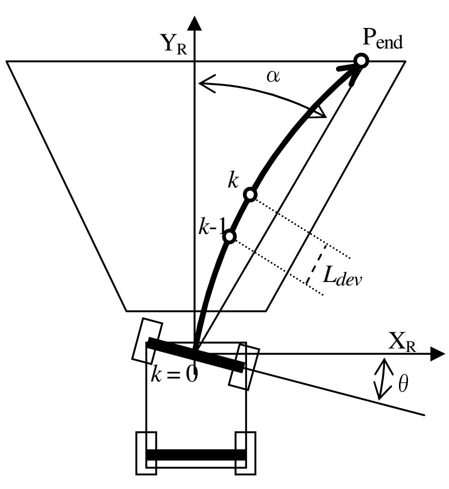

Fig.4 Target path at visible region GOAL

3·3·2 Path evaluation value in UR

In UR, the robot performs the shortest distance movement, the path of which is created by concatenating the minimum rotation radius movement with the straight movement to GOAL.

When the movement evaluation value at P_{end} is given as J_n, the path evaluation value in UR, J_u, is given by

$$J_u = \frac{J_n + J_G}{2} \times L_{unk} \tag{7}$$

J_G : Geographical evaluation value at GOAL (given)

L_{unk} : Estimated shortest length of the path, along which robot will run in UR.

4·3·3 Total path evaluation value

Finally, the total path evaluation value J_t is given by,

$$J_t = J_v + J_u \tag{8}$$

The robot repeats choosing the optimal course at every sampling time, for which a course evaluation value is the lowest, and moves toward GOAL.

3·3·4 Path planning at "Neighbor of GOAL"

At "Neighbor of GOAL", the target angle α is fixed toward GOAL direction from the robot position, and the control angle θ is changed one by one, and, thus, the target path is generated. Turning ($\alpha \neq \theta$) or running straight ($\alpha = \theta$).

Path evaluation value at Neighbor of GOAL is calculated by the same method that is used in Approach to GOAL.

4. Experiment

The experimental conditions are as follows.

・Width of robot wheel has 282[mm] by 220[mm] length.

・L_{dev} is 5.0[mm] length.

・The initial stage of environment is unknown and the GOAL is given.

Experimental results are shown in Fig.5 to Fig.7. In these figures, the brighter the graylevel is, the lower of the geographical evaluation value is. Contrary to this, the darker the graylevel is, the higher of the geographical evaluation value is. The geographical features recognition's also depend on the experiment time and weather condition, which the minute difference of graylevel contrast will affect to geographical evaluation value. But this is not effect to the essence result. Our experiments have conducted in clear weather condition. If the geographical evaluation value is same, we set priority to robot turn right. The white area shows the regions that haven't been capture by the camera. And all the area is unknown except the area captured by camera. The variable t represents sampling times that initiates from 0.

4·1 Far-ranging grass lies in depth direction

In Fig.5, START position is (0, 0)[mm], GOAL position is (0, 5000) [mm], rectangle Top-Left and Bottom-Right points of grassy field are (-1500, 4000) [mm] and (1500, 2000) [mm].

4·2 Narrowly-ranging grass lies in depth direction

In Fig.6, START position and GOAL position are same with Fig.10, rectangle Top-Left and Bottom-Right points of grassy field are (-1500, 2230) [mm] and (1500, 2000) [mm].

4·3 Asphalt road runs up as hook form

In Fig.7, START position is (0, 0) [mm], GOAL position is (-9000, 9000) [mm], asphalt field spreads as hook form.

5. Conclusion

The experimental results can conclude as below:

・Using the generated environmental map embedded geographical evaluation value, the robot was successfully reaches the GOAL.

・The robot passed through a grassy geography in the case that the grass area is narrowly ranging. Contrary to this, in the other case that the grassy area is far ranging, the robot escapes the grassy area.

・The robot will choose the optimal path based on the evaluation value and will give the advantage that can reduce the accumulated errors of position and orientation during traveling in that's path.

REFERENCES

[1] H.Noborio. "Several path Planning Algorithms of a Mobile Robot for an uncertain Workspace and Their Evaluation", Proc. of the IEEE Int. Work. Intel. Motion Control, vol.1, August 1990.

[2] V.Lumelsky, "Effect of Uncertainry on Continuous Path Planning for an Autonomous Vehicle", Proc. of the 23rd IEEE Conf. On Decision and Control, Las Vegas, Nevada, December 1984.

[3] T.Kanbara, "A Method of Planning Movement and Observation for a Mobile Robot Considering Uncertainties of Movement, Visual Sensing, and a Map", Transactions of the Japan Society of Mechanical Engineers, vol.65, no.629, 1999

[4] M.Yamada, "Autonomous Navigation of an Intelligent Vehicle Using 1-D Optical Flow", Transactions of the Japan Society of Mechanical Engineers, vol.64, no.617, 1998

[5] S.Tadokoro, "Generation of Avoidance Motion for Robots which Coexist and Cooperate with Human (2nd Report, Avoidance of Moving Obstacles for Mobile Robots)", Transactions of the Japan Society of Mechanical Engineers, vol.63, no.606, 1997

[6] Shoichi Maeyama, Akihisa Ohya, and Shin'ichi Yuta, "Robust Dead Reckoning System by Fusion of Odometry and Gyro for Mobile Robot Outdoor Navigation", Nihon Robot Journal., Vol.15, No. 8, pp.1180-1187(1997)

[7] Shoichi Maeyama, Nobuyuki Ishikawa and Shin'ichi Yuta, "Rule based filtering and fusion of odometry and gyroscope for a fail safe dead reckoning system of a mobile robot'', IEEE International Conference on Multisensor Fusion and Integration for Intelligence Systems,pp.541-548(1996.12)

[8] J. Borenstein and L. Feng, "Gyrodometry: A New Method for Combining Data from Gyros and Odometry in Mobile Robots", Proc. Of Int. Conference on Robotics and Automation, Vol.1, pp.423-428 (2001)

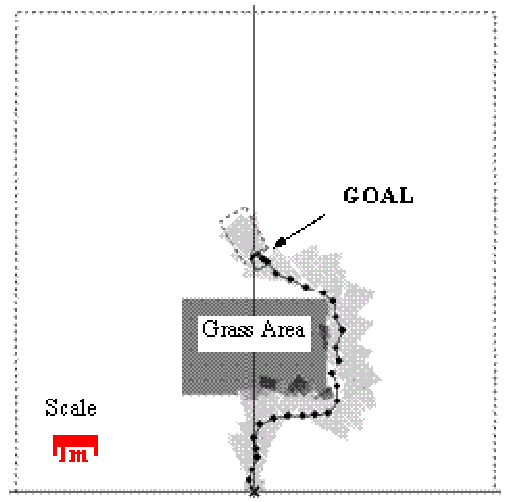

Fig.5 Experimental result in case of far-ranging grass lies in depth direction

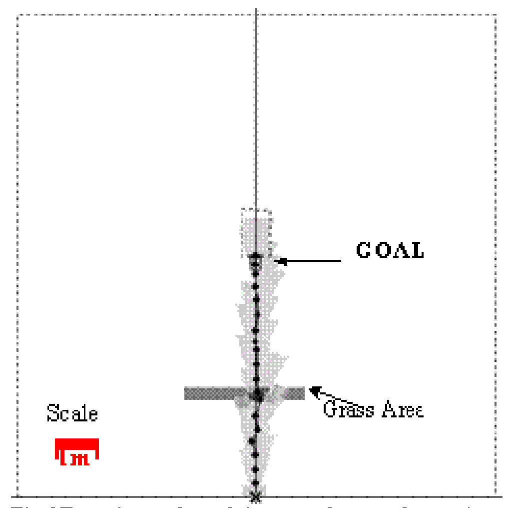

Fig.6 Experimental result in case of narrowly-ranging grass lies in depth direction

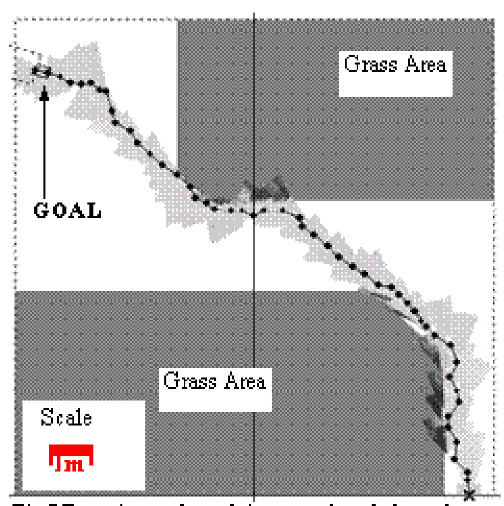

Fig.7 Experimental result in case of asphalt road runs up as hook form

The Fifteenth International Symposium on Artificial Life and Robotics 2010 (AROB 15th '10),
B-Con Plaza, Beppu,Oita, Japan, February 4-6, 2010

Visual attention model involving feature-based inhibition of return

Shinji Hotta, Shigeyuki Oba, and Shin Ishii

Graduate School of infomatics, Kyoto University, Gokasho, Uji, Kyoto 619-0011, Japan
(Tel : 0774-38-3938; Fax : 0774-38-3941)
(hotta-s@sys.i.kyoto-u.ac.jp)

Abstract: Visual attention tends to avoid locations where past visual attention has once focused. This phenomenon is called inhibition of return (IOR) and is known as one of important dynamic properties of visual attention. Recently, several studies have reported that IOR occurs not only on locations but also on visual features. In this study, we propose a visual attention model that involves the feature-based IOR by extending a recent model of `Saliency Map'. Our model is demonstrated by a computer simulation and its neuronal basis is also discussed.

Keywords: visual attention, feature-based IOR, saliency map

I. INTRODUCTION

Visual attention puts focus on a part of a large amount of visual information coming into human brain simultaneously so as to process the essential information intensively, because precise processing of whole information is impossible in a limited time.

Bottom-up visual saliency is a well-known factor that influences attentional control. Visual stimuli that stand out from their surroundings are said salient. The more salient a stimulus is, the more easily it deploys visual attention. Itti *et al*. formerly proposed a computational procedure that constracts saliency map in a way incorporating biological findings in the early visual system [1]. Although this procedure could reproduce locations of instantaneous bottom-up attention, dynamic properties of visual attention in the level of saliency maps were not considered sufficiently.

Inhibition of return (IOR) is an important dynamic property of visual attention [2]. Directions of visual attention tend to avoid locations on which past visual attention has once focused and eye movement does not return to the inhibited areas in a short while. This property allows us to find out desired things lying among many other salient objects in an efficient manner. Recently, E. Shin *et al*. reported that IOR occurs not only on locations but also on visual features [3]. Its mechanism, however, is not understood well.

In order to understand the mechanism underlying the feature-based IOR, in this study, we propose a new model of visual attention, which combines the saliency map and the feature-based IOR. A computer simulation was performed to know the basic character of our new model. Also its neural basis is discussed.

II. VISUAL ATTENTION MODEL

1. Saliency map

In the saliency map[1], visual saliency level of each spatial location in a current input image is calculated by a linear summation of multiple topographic feature maps which are obtained from the input image. Detail processes are as follows.

First, static color image is transformed to multi-scale images in a form of dyadic Gaussian Pyramids. The Gaussian Pyramid $P(\sigma)$, $\sigma=1,\ldots,8$, is a pile of natural images created by low-pass filtering and subsampling of the original input image P, where σ indicates the scale; P(0) is the original image and P(8) is an image reduced into 1/256 size.

Second, seven feature maps are extracted from the Gaussian Pyramid $P(\sigma)$; they are intensity map I, two color opponency maps R/G, B/Y, and four orientation maps with angles 0˚, 45˚, 90˚, 135˚.

Third, the difference between center and surround scale maps is computed for each of the seven feature maps. The difference between two different scales of a feature map highlights salient areas with respect to the feature, because those areas have different feature values from their surrounding areas; such a difference map is called a Center-Surround map.

Fourth, the Center-Surround difference maps are integrated over different scales and over different features in each modality. In each integration, summation of normalized maps of different scales and features over the modality is calculated, where the normalization operator N emphasizes such a map that involves single or small number of peak salient areas and degrades such a map that involves many peaks. As a result, three conspicuity maps $N(I)$, $N(C)$, and $N(O)$, corresponding to three modalities, intensity, color opponency, and orientations, respectively, are obtained.

Last, the three conspicuity maps are again normalized and linearly summed into the consequent saliency map,

$$S = \frac{1}{3}(N(I) + N(C) + N(O)).$$

2. Inhibition of return

In the procedure above, we obtain the saliency map $S_j(t)$ based on scale-integrated feature maps $F_{ij}(t)$ at time t=1,2,⋯, where i=1,…,N and j=1,…,M are indices of feature types and spatial locations in each map, respectively.

The location of attention $j^*(t)$ is determined such to maximize the current saliency $S_j(t)$ in the simplest model. In this simple model, however, the attention cannot be directed to second and third peaks on the same saliency map. Thus, the idea of IOR is proposed.

Using the IOR, we assume that location of visual attention is determined by the modulated saliency

$$MS_j(t) = IOR_j(t) S_j(t),$$

where $IOR_j(t)$ belongs to [0, 1] and denotes the strength of feature-based IOR at location j at time t, and the location of attention $j^*(t)$ is determined to maximize the modulated saliency $MS_j(t)$. The effect of IOR is determined based on the history of locations of focused attention, so that the dynamics of $IOR_j(t)$ is formulated as

$$\Delta M_j(t) = K_j(t) + \eta M_j(t),$$

where $M_j(t)=1-IOR_j(t)$, $\Delta M_j(t)= M_j(t+1)-M_j(t)$, and the constant η is a decaying coefficient. This expression means that the IOR effect is smoothed over the current and past instantaneous IOR. $K_j(t)$ is a map of inhibition at time t; location j is inhibited if $K_j(t)$=1 and not inhibited if $K_j(t)$=0.

We compare location-based IOR [1] and a newly proposed feature-based IOR. The difference between them is reflected in the map $K_j(t)$. In the location-based IOR [1], locations near $j^*(t)$ are inhibited after visiting $j^*(t)$ so that visual attention will not return to the area

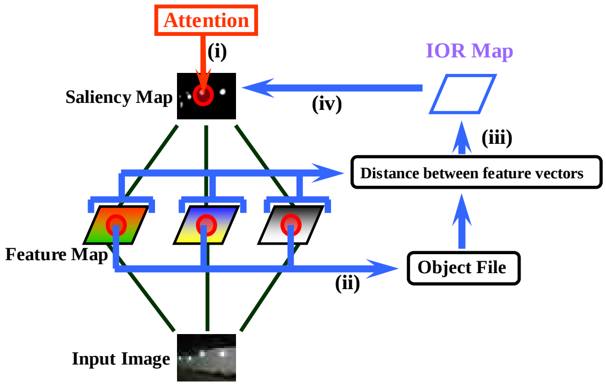

Fig.1. Proposed model.
(i)The location of focused attention is determined by the modulated saliency map. (ii)The feature vector of that location is taken into the object file module. (iii)The IOR map is created based on the Euclidian distance in the feature space. (iv)The modulated saliency map at the next time is calculated by the convolution of the saliency map and the IOR map. Attention is carried out according to the modulated saliency map.

around $j^*(t)$ in a short while. Namely, we set $K_j(t)$ =1 for all j such that

$$\| j^*(t) - j \| < \gamma$$

holds, where γ is a given constant and $\|\cdot\|$ is the Euclidean distance. In the proposed feature-based IOR, on the other hand, $K_j(t)$ is defined by means of the distance in the N-dimentional feature space so that $K_j(t)$=1 for all j such that

$$\| \mathbf{F}_{j^*(t)} - \mathbf{F}_j \| < \lambda$$

holds and $K_j(t)$=0 otherwise, where λ is a given constant, $\boldsymbol{F}_j = \{F_{1j}, \cdots, F_{Nj}\}$ is a feature vector at location j, and $\boldsymbol{F}_{j^*(t)}$ is a feature vector at the attended location $j^*(t)$.

III. RESULTS

We demonstrated the behaviors of the proposed feature-based IOR on several natural images, and two of them are shown in Fig. 2. In the left example image (A), there are five objects; four objects, D_1, D_2, D_3, D_4, are street lights which are significantly salient because of the high intensity, and have similar feature vectors to each other, while the target T_A is a fire hydrant whose saliency is high, but lower in total than those of the other four objects. In the right example image (B), there is a can, target T_B, within grasses. Some areas of the

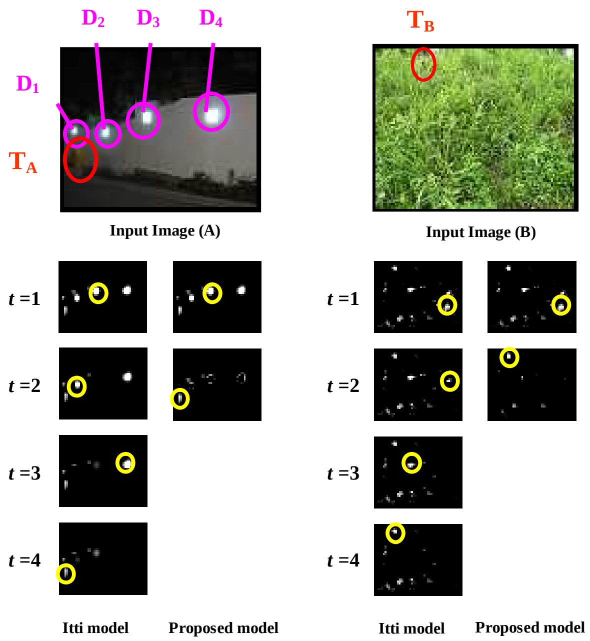

Fig. 2. Simulation results.
Two examples of natural images are shown in the top panels. In the panels below, the saliency maps with IOR convolved and the locations of focused attention (circles) at time t=1, 2, 3, 4 are shown. (Itti model) Itti *et al.*'s location-based IOR. (Proposed model) Our feature-based IOR.

grasses have high saliency because of the high intensity of green channel. The can has a different feature from grasses and its saliency is somewhat high, but lower than those of some grasses.

By the previous model based on location-based IOR, the attention focus tended to move between obstacles, the street lights in (A) or the grasses in (B), and to take long time to discover the target, T_A or T_B, respectively. By the proposed model based on feature-based IOR, on the other hand, attention rapidly moved onto the target. We also confirmed the efficient search ability based on the proposed feature-based IOR, through simulations using other natural images.

IV. DISCUSSION

We showed through computer simulations that the modulated saliency map with feature-based IOR leads to efficient search ever in cluttered situations. Thus we naturally think that the feature-based IOR is crucial for efficient visual search in human behaviors. In this section, we discuss neural mechanism underlying feature-based IOR.

In our model, feature-based inhibitory signals are assumed to be involved after calculating saliency map. This assumption is based on a biological finding by Shin *et al.*'s work on feature-based IOR [3]. They investigated modulation process in attentional control to generate distractor previewing effect (DPE) using an electrophysiological method. Repeating presentations of distractors composed of target-irrelevant features increases search time in subsequent visual search tasks, which is called DPE [4]. Shin *et al.* listed following four processing levels to generate the DPE; (a) preattentive perceptual processes, (b) preset attentional biases, (c) the ability to shift attention, and, (d) the weights to activate responses. They observed the event-related potential (ERP) corresponding to each processing level and achieved an evidence that DPE can directly affect (c) *the ability to shift attention toward the target*. This meant that IOR occurs on visual features. In the current study, we adopted their hypothesis in the proposed model by regarding processing level (a) as adaptation in feature maps, level (b) as weighting each feature map, and level (c) as determination of the location to be attended.

On the other hand, almost nothing has been known about neuronal basis of inhibitory signals applied on saliency map. In what follows, we discuss a possible mechanism that generates such signals in the neural system. The proposed model of modulated saliency map requires the following processes.

(I). Determine the attended location by the saliency map.
(II). Extract the feature vector in the attended location.
(III). Identify the areas whose feature vectors are similar to that of the attended location.
(IV). Provide inhibitional signals to the saliency map.

The saliency map (I) has been recognized as a plausible model of neural mechanism of visual attention control. In the visual pathway, especially early part, V1 [5], V4 [6] and so on, have been considered as neural bases of feature maps, because the retinotopic structure and simple visual features, such as color opponency and orientation, have been found in these areas. Treisman and Gerade had proposed the psychological notion `master map' which operates visual attention [7]. Koch *et al.* extended it to the saliency map in the computational viewpoint [8]. Recently, neural activities corresponding to the saliency are reported in V1 [9], the posterior parietal cortex [10], the frontal eye field [11], the superior colliculus [12], and so on.

For process (II), we assumed the `object file' module in the early visual system which memorizes the activities of feature neurons representing the feature vector at the attended location. `Feature Integration Theory' hypothesized that each feature information at the attended location is integrated into the object file, and transported to higher modules [7]. This theory may provide a mechanism to our idea.

Process (III) needs a `detector of synchronized firing neurons' module in the early visual system which detects population of firing neurons that are syncronized with those in the `object file module' indirectly. Based on such a synchronization mechanism, the detector specifies location j to be inhibited by matching feature vectors $\boldsymbol{F}_{j^*(t)}$ and $\boldsymbol{F}_j$. Since our feature-based IOR is represented as a weight value (Eq.(2)), it could be implemented by a probabilistic read-out, depending on $\| \boldsymbol{F}_{j^*(t)} - \boldsymbol{F}_j \|$.

In order for the processes (I), (II), and (III) to be linked to the process (IV), we assume five particular neural connctions between the modules; from `feature maps' to `object file', from `feature maps' and `object file' to `detector of synchronized firing neurons module', from `detector of synchronized firing neurons module' to `IOR signal generator module', and from `IOR signal generator module' to `the modulated saliency map'. In specific, the connection from V1 to the superior colliculus was found anatomically [13]. This connection suggests that the `detector of synchronized firing neurons module' in V1 can influence the IOR signals in the superior colliculus. Although the huge amount of anatomical data have suggested that the visual system is abundant in feedforward and feedback connections between various modules, further details of the implementation of the feature-based IOR is unclear.

V. Summary

We proposed a new model of visual attention involving the feature-based IOR which allows multiple salient objects to be inhibited when they have similar features. Simulation results showed that saliency of visually similar stimuli degenerated by the effect of the feature-based IOR, so that an efficient search for a target object was realized. We also discussed possible neural bases for the feature-based IOR.

REFERENCES

[1] Itti L, Koch C, Neibur E (1998), A Model of Saliency-Based Visual Attention for Rapid Scene Analysis. IEEE Transactions on Pattern Analysis and Machine Intelligence, 20, pp.1254-1259

[2] Posner MI, Cohen Y (1984), Components of Visual Orientating. Attention and Performance, 10, pp.531-556

[3] Shin E, Wan XI, Fabiani M, Gratton E, *et al.* (2008), Electrophysiological evidence of feature-based inhibition of focused attention across consecutive trials. Psychophysiology, 45, pp.804-811

[4] Goolsby BA, Grabowecky M, Suzuki S (2005), Adaptive modulation of color salience contingent upon global form coding and task relevance. Vision Research, 45, pp.901-930

[5] Knierim JJ, Van Essen DC (1992), Neuronal responses to static texture patterns in area V1 of the alert macaque monkey. Journal of Neurophysiology, 67, pp.961-980

[6] Schein SJ, Desimone R (1990), Spectral properties of V4 neurons in the macaque. The Journal of Neuroscience, 10, pp.3369-3389

[7] Treisman AM, Gerade G (1980), A Feature-Integration Theory of Attention. Cognitive Psychology, 12, pp.97-136

[8] Koch C, Ullman S (1985) Shifts in selective visual attention: towards the underlying neural circuitr. Human Neurobiology, 4, pp.219-227

[9] Lamme VA (1995), The neurophysiology of figure-ground segregation in primary visual cortex. The Journal of Neuroscience, 15, pp.1605-1615

[10] Gottlieb JP, Kusunoki M, Goldberg ME (1998), The representation of visual salience in the monkey parietal cortex. Nature, 391, pp.481-484

[11] Schall JD, Hanes DP, Thompsons KG, *et al.* (1995), Saccade target selection in frontal eye field of macaque: I. Visual and premovement activation. The Journal of Neuroscience, 15, pp.6905-6918

[12] McPeek RM, Keller EL (2002), Saccade target selection in the superior colliculus during a visual search task. Journal of Neurophysiology, 88, pp.2019-2034

[13] Lund JS, Lund RD, Hendrickson AE, *et al.* (1975), The origin of efferent pathways from the primary visual cortex, area 17, of the macaque monkey as shown by retrograde transport of horseradish peroxidase. The Journal of comparative neurology, 164, pp.287-304

Relation between impression of touch panels' coloration and operation

Makiba Sakamoto*, Hidetsugu Suto*, Masahiro Sawai**

*Graduate School of Engineering, Muroran Institute of Technology,
27-1 Mizumoto-cho, Muroran 050-8585, Japan
**Satellite Venture Business Laboratory, Muroran Institute of Technology,
27-1 Mizumoto-cho, Muroran 050-8585, Japan
(Tel : +81-143-46-5400; Fax :+81-143-46-5499)
(Email makiba@mail.svbl.muroran-it.ac.jp)

Abstract: The relationships between the color used in designs of a touch panel and operations on electronic devices are discussed. Experiments that investigate the effect of color in designs of touch panel interfaces on the operation and on impressions of users have been conducted. Subjects tried mental arithmetic tests on twelve screens which are used different color images. The following points: "time which passed during a task," "number of correct answers," "number of incorrect answers" and "number of timeouts" were measured and counted. After the tasks were administered, the subjects answered questionnaires about their impression of the displays' color design. The average numbers of correct answers was higher when using "cool-casual" than when using the other coloration. Furthermore, there was a positive correlation between the number of correct answers and preference for the displays' coloration. There are strong relationships between the coloration of interface and the speed and accuracy of operation. The results of the study lead us to expect that both the usability and accuracy of operations will be improved by considering the color designs of the touch panel interface.

Keywords: coloration, color design, touch panel, evaluation of impression of screens

I. INTRODUCTION

The use devices with touch panel interfaces such as ATM consoles, smart phones, and ticket vending machines has become increasingly widespread. Because these devices have no mechanical buttons, users need to understand how to operate them from the visual information displayed on the screen. Therefore, the users who have no experience using such interfaces cannot use them with a high degree of accuracy. Hence, it can be said that graphic design of the screen plays an important role in the usability of the electric devices.

We focus on the users' impressions of the coloration of touch panel devices. In particular, the relationship between the users' impressions and the operation are discussed. Experiments have been carried out to investigate the effects of the whole image of interface color on accurate and speed of operations. Moreover, the relation between impressions of touch panel and operation are analyzed on the basis of result of the experiment.

II. COROLATION AND OPERATION

Coloration, i.e. color scheme, is an important factor of design, and there are many laws of color harmony [1][2][3]. The authors focus on the effect of interface's colors on operators of an electronic device, and they already have conducted experiments which show that the accuracy and speed of operation change with the color of the buttons in the control panels. We found that the blue buttons were better than red ones in regard to accurateness and speed of operation[4]. The effects of images of combinations of the buttons in the control panels were also investigated, and we found that a "formal" image combination was better than the other ones.

Of course, the interfaces of electronic devices do not only consist of buttons, and operators look at all items on the screen even if they seem to be merely for decoration. Furthermore, ATM and multi-media information terminals usually have a coloration that is consistent with the corporate color. If the operations change with the coloration, the designers should consider the color design of the control panels.

III. EXPERIMENT

Experiments were done to investigate the relationship between operation and color image of the control panel. Subjects tried mental arithmetic tests (single-digit ones). The twelve interfaces were prepared. Each interface has a different color image. The twelve major patterns of coloration from the mixed image scale [5] were used. The Mixed Image Scale is an image map, which has two axes, "soft-hard" and "cool-warm," and colorations with words conveying the subjects' impression were arranged on the frame of reference. Using this image scale enables us to link coloration with impressions. We used twelve major descriptive phrases "casual," "cool-casual," "romantic," "modern," "elegant," "classic and dandy," "formal," "clear," "natural," "chic," "gorgeous," and "wild" in the experiments. The time that passed during a task, the correct and incorrect answers as well as the number of timeouts were measured or counted. After the tasks were completed, the subjects answered questionnaires about the color design of the screen by using the visual analogue scale (VAS) method [6].

1. Tasks in experiment

A snapshot of a screen of the computer program used in the experiments is shown in Fig. 1. One correct answer and two wrong answers are displayed under a problem. Subjects had to select the correct answer from three alternatives and touch one of three push panels. If a subject did not touch a panel in 1.5 sec., they were transferred to the next problem. Thirty different problems were given for a condition. The bottom of the program windows were decorated with different color patterns that varied with the condition of the experiments. The colors used in each condition are shown in Table 1. The background color of the window was pale gray (N8), and the background color of the push panels was white (N9.5). The characters' color in the window was dark gray (N3). These colors were decided by considering the visibility of the characters in the window. First, the subject practiced on a screen that had no colored decoration. They then tried tasks displayed on screens with the twelve conditions shown in Table 1. A two-minute break was given between each condition. During the break, the subject wore an eye mask to rest his/her eyes. The order of condition was changed for each subject to reduce the effects of order.

Table 1. Color patterns used for experiment

Conditions	Color paterns used for experiment				
Condition 1 casual	5R5/12	5PB4/10	10Y8/12		
Condition 2 cool-casual	6Y8/10	5B7/6	5PB6/8		
Condition 3 romantic	7.5R8/4	7.5Y9/6	2.5G8.5/2		
Condition 4 modern	6.25PB5.6/6	5B8/4	5B3/2		
Condition 5 elegant	10PB8/4	2.5RP8/4	2.5P6/6		
Condition 6 classic & dandy	10GY3/2	2.5Y6/8	2.5Y3/2		
Condition 7 fomal	5B4/4	7.5PB8/2	5PB2/2		
Condition 8 clear	10BG9/2	10Y9/0.5	10BG7/4		
Condition 9 natural	3RP8/4	5Y9.2/1	5P8/4		
Condition 10 chic	5PB6/4	5P6/2	5P7.5/0.5	5PB8/1	
Condition 11 gorgeous	5P2/1	3R4/12	5RP8/4	7R9.2/1	2.5P4/10
Condition 12 wild	N1	8YR5/8	10YR4/4		

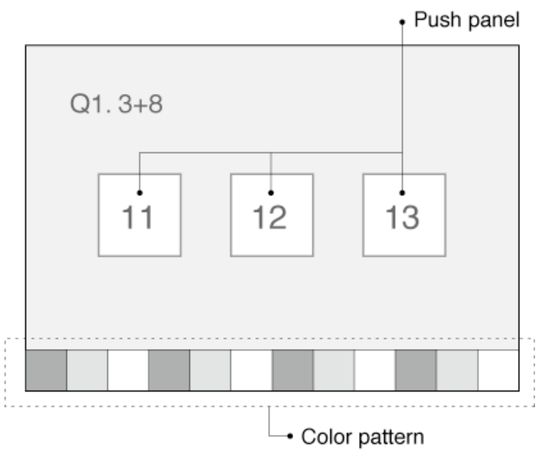

Fig. 1. Snapshot of screen displayed in computer program

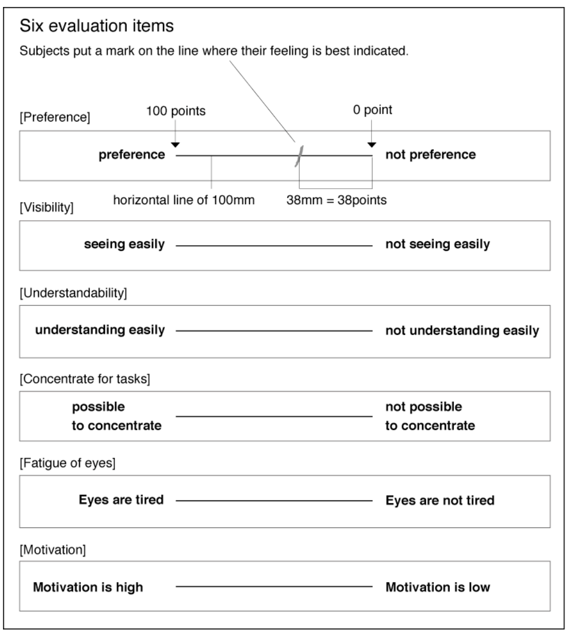

Fig. 2. Questionnaire sheet

The subjects were 24 mentally and physically healthy university students who were 22~25 years old.

2. Evaluation of screens

After the tasks, the subjects evaluated each screen, and the items which were evaluated were "preference," "visibility," "understandability," "enables concentration," "fatigue of eyes," and "motivation." The subjects used the visual analogue scale (VAS) method. An example of a questionnaire sheet used in the method is shown in Fig.2.

The VAS method is usually used in field of medicine to analyze a subject's statement regarding their psychological state. A horizontal straight line of 100 mm is drawn. Words that shows the item being evaluated and as well as its opposite are arranged on the right and left of the line. The subjects put a mark on the line where their feelings are most accurately expressed. In this process, the subjects evaluated each screen by marking a position on along a 100 mm line between two endpoints corresponding to a ward for each impression and the word's antonym. The ratio between the length of the negative item and the mark and length on the 100 mm show the value of the evaluation.

Six evaluation items in the questionnaire were shown at random for each subject, and the positions of the word and its antonym are also swapped at random. This was done to reduce order effects.

IV. RESULTS AND DISCUSSION

A graph of "measurement time" i.e., the average of time which passed during a task under each condition. There are significant differences between measurement times under condition 5, 6, 8, and 12 (P<0.01, Tukeys' multiple comparison test). A task took longest to complete under condition 12.

The number of correct answers under condition 2 was better than the number of correct answers under the other conditions, but there is not significant difference between the number of correct answers under the each condition. As a shown in Fig. 3 and Fig. 4, the measured time and number of correct answers were not necessarily connected. However under condition 2, the graphs show better results in both the time and the number of correct answers than under the other ones.

Averages of evaluation of "preference" on each screens used in the experiments are shown in Figure 5. The preference under condition 2 and 9 are better than the preference under the other conditions.

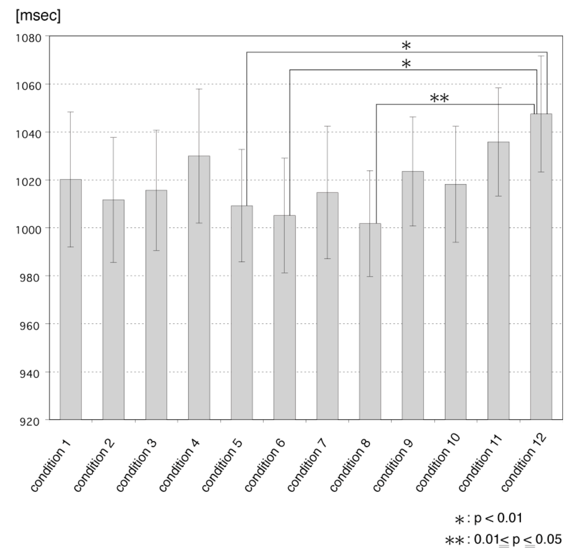

Fig. 3. Average time passed during tasks

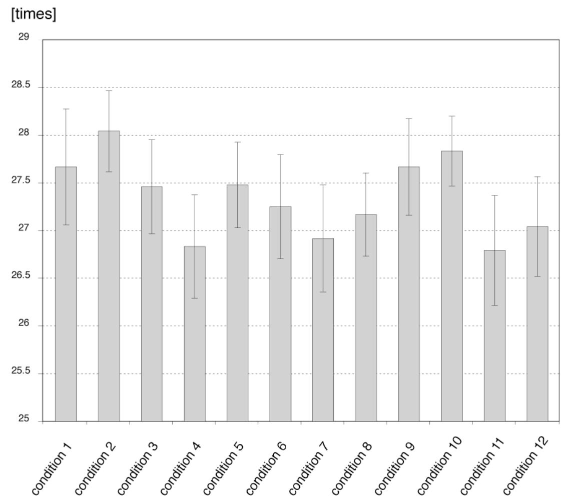

Fig. 4. Average number of correct answers

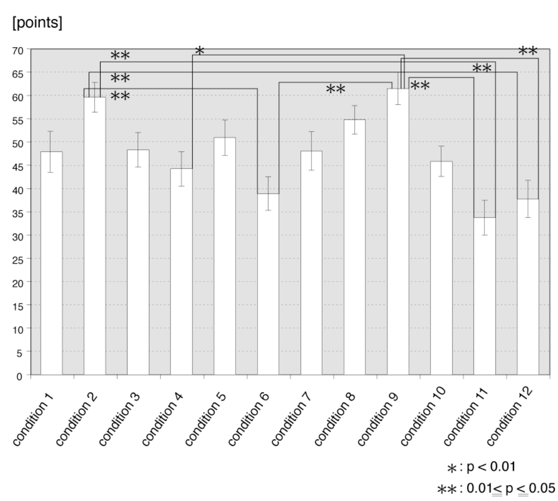

Fig. 5. Average of evaluation of "preference"

The correlations between results of operations and impressions of screens are shown in Table 2. There was positive correlation between number of correct answers and the preference. There was also positive correlation between the number of correct answers and the motivation. In addition, there was a negative correlation between the number of incorrect answers and preference of coloration, and the number of incorrect answers and the motivation.

V. CONCLUSION

We focused on the coloration and operation of a touch panel interface on electronic devices. Experiments were conducted to investigate relations between coloration and operation of touch panel screen.

The results of the experiments show that "cool-casual" is better than the other color images for the touch panels design in terms of speed and accuracy of operation. In addition, "classic & dandy" and "clear" are good for fast operation, but not good for accuracy.

On the other side, "gorgeous" and "wild" are not good for the panels in which accuracy of operations is important. Accordingly, we expect that the color images that are good for speed and accuracy of operation consist of a low-contrast bluish coloration as shown in Fig. 6 (A). Furthermore as shown in Fig. 6(B), the color images that do not improve speed and accuracy of operation consist of a high-contrast coloration, i.e., warmth and hardness.

Table 2. The result of no correlation authorization of data of the experiment

Data compared	Correlation coefficient r	p value
Number of correct answers · preference	0.65	0.0234
Number of incorrect answers · preference	- 0.61	0.0335
Number of incorrect answers · motivation	0.59	0.0438
Number of correct answers · motivation	- 0.66	0.0193
Preference · fatigue of eyes	0.68	0.01576
Preference · understandability	0.79	0.0022
Preference · visibility	0.83	0.0008
Preference · concentrate for tasks	0.75	0.0045

The result of this study are expected to be used to evaluate screens of electronic devices as well as the supporting system of interface designs. We plan to develop systems that are based on the results in which the choice of color improves the speed and accuracy of use.

ACKNOWLEDGMENTS

This work was supported by a Grand-in-Aid for Sc ientific Research by the JSPS (No. 20500220).

REFERENCES

[1] H.Mitsui (1996), Construction study of beauty, Chukoushinsyo Pub., (in Japanese)
[2] J.Murata (2002), Philosophy of Color, Iwanami Shoten Pub., (in Japanese)
[3] J.Nomura (2005), The secrets of Color, Bunsyun Bunko Pub., (in Japanese)
[4] H.Suto, N.Sakamoto, and M.Okita (2009), "Affect of color of interface on accuracy and speed of operations" Proc. 2009 International Conference on Biometrics and Kansei Engineering, pp.201-204
[5] S. Kobayashi (1987), A Book of Colors: Matching Colors, Combining Colors, Color Designing, Color Decration, Kodansha Amer Inc.,
[6] Y. Mikikazu (2009), "The Visual analogue scale is made my motto" JOHNS Vol.25 No.9 pp.1433-1435 TOKYO IGAKUSHA (in Japanese)

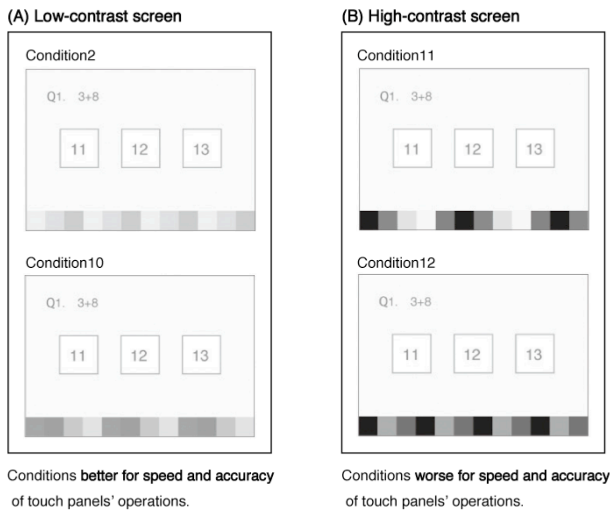

Fig. 6. Comparison between result of experiment and contrast of color images

Matrix diagonalization in the quantum anisotropic Kepler problem

Kazuhiro Kubo, Tokuzo Shimada
Department of physics, School of Science and Technology, Meiji University
1-1-1 Higashimita, Tama, Kawasaki, Kanagawa 214-8571

Abstract

In quantum chaos study, it is essential to study the statistical properties of energy levels of the system in order to unveil the quantum reflection of chaos. For this purpose we have to work out thousands of the energy levels. For the anisotropic Kepler problem a concrete method was devised by Wintgen et al. In this method a scaling parameter ϵ is introduced and the energy levels are calculated from the eigenvalues of a large size matrix at an in principle arbitrary choice of ϵ. However, in practice, the finite size effect caused by the truncation of the set of bases makes the matrix eigenvalues rather dependent on the value of ϵ. We propose a prescription which determines the most suitable choice of ϵ for a given matrix size and for given system parameters.

Keywords: quantum chaos, anisotropic Kepler problem, matrix diagonalization, level statistics.

1 Introduction

Nowadays systems which can be handled by experiments have reached nano-scale size and quantum theory analysis is required. However, most of these systems are classically non-integrable and the corresponding Schrödinger equation is not separable. Therefore one must rely on the numerical calculation to obtain approximate eigenvalues and various methods have been devised so far. It has been revealed that the statistics of the systems may be categorized into several distinct classes independent from the details of the systems. Only the symmetry property of the system is essential. For example, the nearest neighbour spacing distribution (NNSD) becomes Poisson when the system is integrable classically or the Wigner distribution when the system is chaotic. This is the way how the statistics of the quantum energy levels reflect the classical features of the system.

To this end it is desirable to explore a system which is suitable both for handling analytically in classical regime and computing the energy levels in the quantum regime. For this reason we focus our attention to the anisotropic Kepler problem (AKP). The AKP is a Kepler problem with the anisotropic mass tensor and it describes well the motion of the electron in a semiconductor. The classical theory of the AKP has been studied in detail in [1, 2] and it has been known that there is a one-to-one correspondence between an orbit and a binary sequence. In the quantum chaos study, the AKP was considered by Gutzwiller[3] which gave the foundation of the periodic orbit theory. The statistical approach are founded by Wigner, Mehta, Bohigas $\cdots$ and the numerical method is pioneered by Wintgen et al[4].

First detailed AKP energy level calculation was performed by Faulkner[5] and the lowest 27 levels are obtained with Rayleigh-Ritz method. However this is not sufficient because the level statistics require several thousands of levels in good accuracy. For this requirement a concrete and efficient method was devised by Wintgen et al[6]. In this method the energy levels are computed from the eigenvalues of a certain matrix which takes into account the scaling property of the AKP system and endowed with a scaling parameter ϵ. In principle this ϵ can be chosen arbitrary, but, in practice, the calculated energy levels rather depend on the choice of ϵ because only finite number of bases may be used. Therefore a good control of this behaviour is crucial to obtain the accurate energy levels.

We analyze the calculated energy levels and elucidate the systematics in them. We then propose a prescription how to obtain a large number of reliable energy levels by adjusting ϵ.

2 Scheme for calculations of the energy levels

The Hamiltonian of an electron in the three dimensional AKP is

$$H_0 = \frac{p_1^2 + p_2^2}{2m_\perp} + \frac{p_3^2}{2m_\parallel} - \frac{e^2}{\kappa\sqrt{q_1^2 + q_2^2 + q_3^2}} \tag{1}$$

with the dielectric constant κ and the electron charge e. Here $\vec{q} = (q_1, q_2, q_3)$ is the position of the electron in Cartesian coordinates and $\vec{p} = (p_1, p_2, p_3)$ is the conjugate momentum. The $m_\perp$, $m_\parallel$ are the diagonal elements of the electronic mass tensor with the anisotropy $m_\perp < m_\parallel$. We use the units $a_0 = \hbar^2\kappa/m_\perp e^2$, $E_R = m_\perp e^4/2\hbar^2\kappa^2$, $t_0 = \hbar^3\kappa^2/m_\perp e^4$ for length, energy, time, respectively. With following dimensionless quantities

$$(x, y, z) = \frac{\vec{q}}{a_0},\ (p_x, p_y, p_z) = \frac{\vec{p}}{m_\perp a_0/t_0},\ H = \frac{H_0}{E_R}, \tag{2}$$

eq. (1) is rewritten as

$$H = p_x^2 + p_y^2 + \gamma p_z^2 - 2/r. \tag{3}$$

Here $r = \sqrt{x^2 + y^2 + z^2}$ and $\gamma = m_\perp/m_\parallel < 1$ represents the mass anisotropy. For ordinary Kepler problem γ is unity and for the realistic cases 0.2079 (silicon), 0.05134 (germanium).

In case of $\gamma = 1$ the shapes of bounded trajectories in the position space are all elliptical and hence each motion is regular. As the value of γ decreases from unity the motion changes to the quasi-regular motion. When γ is smaller than γ_c 8 9, the motion becomes chaotic and complicated. Because the AKP has such a controlling parameter γ of the degree of chaos in the classical regime it serves as a vital model to examine how the chaos in the classical regime governs the behavior of the system in the quantum regime.

We recapitulate the scheme devised by Wintgen et al. It is an all order calculation and in this point surpasses the perturbation method. The Schrodinger equation is

$$[\ \triangle + (1 \quad \gamma)(\ ^2 \quad z^2) \quad 2\ r]\, \psi(r) = E\psi(r) \qquad (4)$$

For $\gamma \neq 1$ eq. (4) is not separable and we switch to a numerical way. For the bases, Sturumian functions in a spherical coordinates are de ned as

$$\begin{aligned} \langle r|n\ m\rangle &= \tfrac{1}{r}\phi_n(r;\lambda)Y_{\ m}(\theta\quad) \qquad (5)\\ \phi_n(r;\lambda) &= \sqrt{\tfrac{n!}{(2\ +n+1)!}}\,e^{\ \frac{r}{2}}(\lambda r)^{\ +1}L_n^{2\ +1}(\lambda r) \end{aligned}$$

Here n, , m are the radial, azimuthal, magnetic quantum numbers respectively and they are related to the principle quantum number n_p as $n_p = n + \ + 1$. The $Y_{\ m}(\theta\quad)$ are the spherical harmonics, $L_n^{\alpha}(x)$ are the generalized Laguerre functions which satisfy a di erential equation $xL'' + (\alpha + 1 \quad x)L' + nL = 0$. When $\lambda = 2\ n_p$, Sturumian functions are wave functions of hydrogen atom.

Using these bases the Schrodinger eq. (4) can be written as a matrix equation[6]:

$$\begin{aligned} \Big[\ \lambda(\overrightarrow{\triangle}) + (1 \quad \gamma)\lambda(\ ^2 \quad \overrightarrow{z^2}) \quad 2(1\ \overrightarrow{r})\Big]\,\psi \\ = (E\ \ \lambda)(\overrightarrow{\mathrm{Id}})\psi \end{aligned} \qquad (6)$$

Here $(1\ \overrightarrow{r}) = (\langle n'\ 'm'|1\ r|n\ m\rangle) = (\delta_{n\ n}\delta\quad\delta_{m\ m})$ is unit matrix. Other matrices have o diagonal elements which equal zero except for $' =$ or $' = \ + 2$; for instance elements of $(\overrightarrow{\mathrm{Id}})$ are

$$\begin{aligned} \langle n'\ 'm'|\mathrm{Id}|n\ m\rangle = (1\ \lambda)\delta\quad\delta_{m\ m}[2(n + \ + 1)\delta_{n\ n} \\ \sqrt{(n+1)(2\ + n + 2)}\delta_{n\ n+1}] \end{aligned} \qquad (7)$$

Because of a rotational symmetry about z axis the elements of matrix included in eq. (6) are all proportional to $\delta_{m\ m}$. By these properties eq. (6) is transformed to standard eigenvalue problem as

$$\begin{aligned} \overrightarrow{M}\psi &= (2\ \lambda)\psi \\ \overrightarrow{M} &= \quad(\overrightarrow{\triangle}) + (1 \quad \gamma)(\ ^2 \quad \overrightarrow{z^2}) + \epsilon(\overrightarrow{\mathrm{Id}}) \end{aligned} \qquad (8)$$

and $\epsilon = \quad E\ \lambda^2 < 0$. Here the matrix $\overrightarrow{M}$ is an $N \times N$ symmetric matrix. It is block diagonal in the sense that $' = \ + 2$ or and $m' = m$. Whole energy levels are obtained by putting together the levels which calculated from each sector. Hereafter we consider only the even and $m = 0$ sector. Then if we want eigenvalues for the states with the principle quantum number n_p up to N_p with this restriction the matrix size N must be $(N_p + 1)^2\ 4$. We should add that $\overrightarrow{M}$ is banded and sparse. By solving (8) for the eigenvalues $2\ \lambda_i$s $(i = 1 \qquad N)$ the energy levels are in turn determined as $E_i = \quad \epsilon\lambda_i^2$. Supposing that we choose another value for the parameter ϵ of the matrix $\overrightarrow{M}$, the eigenvalues $2\ \lambda_i$s will be accordingly changed and the physical energies will be kept invariant. However in practice the number of available bases is limited; we cannot help truncating the number of bases. Then the above ideal scaling becomes only approximate.

3 Results (The most suitable choice of ϵ)

As the truncation condition we adopt $N_p = 177$. The matrix size N of our sector is 7921. This is the largest size among all sectors. We present in Fig. 1 the results of diagonalizing eq. (8) for energy levels at various values of ϵ. The parameter γ is decreased through 18 panels from 0 9 down to 0 05. Instead of the energy levels E_is ($i = 1$ for ground state) we depict

$$f_i = \quad 1\ (4\sqrt{\gamma}E_i) \qquad i = 1\ 2 \qquad 7921 \qquad (9)$$

which are appropriately stretched so that $f_i = i$ and the average spacing $\delta f_i \quad f_{i+1} \quad f_i$ should be theoretically unity [1]. The curves of f_is are expected to be all parallel and their spacings are expected to be unity. However, at a glance one nds that the curves are all simultaneously deformed. Especially the deformation from the constant line is remarkable for small γ (extremely large spacing) and for small $|\epsilon|$ (anomalous accumulation of f_i curves). This dependence is not physical but an error which should be considered as the weak point of the matrix method. The remedy for this problem is our task discussed below.

Accordingly we have to select the part of calculated energy levels that we can trust. We propose a prescription to select 'good results' for each ϵ based on two criteria.

This concerns with the global property of levels. To check this, the whole $f_i(\epsilon)$s are divided into ensembles, $\mathcal{F}_n = \quad f_i(\epsilon)|200(n \quad 1) < i \quad 200n\ , (n = 1 \qquad 39)$, and the average of spacings $\langle\delta f_i\rangle_n$ is calculated for each ensemble $\mathcal{F}_n$ varying ϵ with inclement $\Delta\epsilon = 0\ 01$. In Fig. 1 we show the region on the $f \quad \epsilon$ plane where the deviation of $\langle\delta f_i\rangle_n$ from unity is 0.05 or less. It is connected and convex and we depict the boundary by a solid curve.

$(\gamma < 8\ 9)$ This concerns

[1]The cumulative mean density of levels of our sector should obey Thomas-Fermi formula[4],

$$N(E) = -1\ (4\sqrt{\ }E) \qquad (10)$$

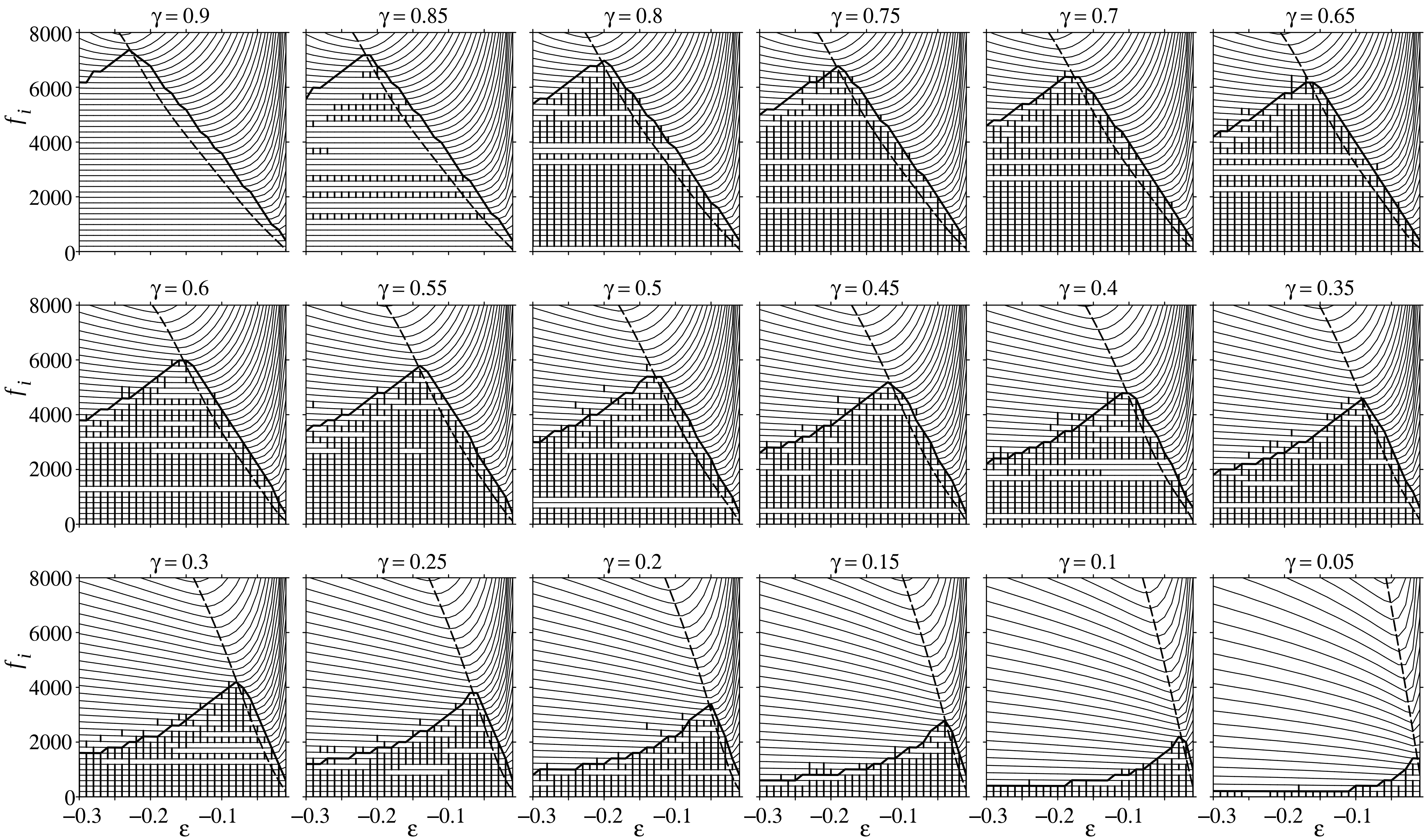

Fig. 1: Variation of $f_i =$ 1 $(4\sqrt{\gamma}E_i)$ with ϵ. N_p =177, $i = 1$ $N = 7921$, =even, m=0. Diagonalization is performed for each of $\epsilon =$ 0 01 0 02 0 3. Dashed curves connect the minimum points of f_i. Solid curve single out the region where the condition $|\langle \delta f_i \rangle_n$ 1$|$ 0 05 is satis ed(see text). In this region levels are reliable from the viewpoint of criterion A. Vertical lines show regions of $\langle (\delta f_i$ $\langle \delta f_i \rangle_n)^2 \rangle_n$ 0 3. In these regions levels are reliable from the viewpoint of criterion B. The regions allowed by critera A and B agree well.

with the local property of levels. Recall that in the region with $\gamma < 8\ 9$ the system is classically chaotic and hence the quantum levels must show repulsion. Here the NNSD is Wigner-like and the mean squared deviation (MSD) of level spacings is $4\ \pi\ \ 1\ \ \ 0\ 273$ for the ideal Wigner distribution. On the other hand for $\gamma > 8\ 9$ the distribution is expected to be Poisson and the MSD is unity. Based on this theoretical expectation we set a condition that MSD must be 0.3 or less with a tolerance of 10% in the regions with $\gamma < 8\ 9$. We indicate in Fig. 1 by vertical lines the regions where this condition is met. For $\gamma = 0\ 9(> 8\ 9)$ (the rst panel) there is naturally no region of repulsion. For other panels with $\gamma < 8\ 9$ the B allowed region remarkably agrees with the A allowed region. Fig. 1 succinctly shows this and strongly guarantees our prescription.

We list a few interesting observations in items.

(i) N_p is restricted by the computational ability. Thus one has to choose the best value of ϵ (ϵ_{max}) which gives the largest number of reliable levels. This ϵ_{max} can be read o from the crest of the convex curve in each panel of Fig.1. Now let us turn our eyes to the dashed curve. This connects the minimum points of $f_i(\epsilon)$ curves and hence the $f_i(\epsilon)$s below this curve at given ϵ are maximally compressed. Now if one follows this line downwards until one reaches the region allowed by the criterion A, remarkably one always meets the crest of the boundary curve. This is natural because at this time the compression reaches for the rst time to the extent $\langle \delta f_i \rangle_n \simeq 1$ and this implies the crest, at which the maximum number of $f_i(\epsilon)$s are contained below the curve.

(ii) Fig. 2 shows the relationship between γ and ϵ_{max}. Data points clearly follow a linear line well described by $\epsilon_{max} \simeq (\ \ 1\ \ 4)\gamma$.

(iii) Fig. 3 shows the ratio (R_{eff}) of the number of levels which satisfy the criteria at $\epsilon = \epsilon_{max}$ to number of whole levels N (=7921) is plotted as a function of γ. This relation is well described by $R_{eff} \simeq \sqrt{\gamma}$ with about 1% error for coe cient. From this we can estimate that the e ciency of determining reliable levels in the realistic cases of silicon or germanium is about 30% and 15% respectively.

These observations do not change even if we analyze smaller set of levels with $N_p = 75 (N = 1444)$ instead of $N_p = 177(7921)$. These regularities seem re ecting the e ect of truncating the set of bases.

4 Conclusions

In this article we have recapitulated the vital matrix method[4]. The relations between the calculated energy levels and the scaling parameter ϵ is elucidated in Fig. 1 and a prescription how to select suitable ϵ regions is presented. The best ϵ (ϵ_{max}) and the ratio of reliable levels (R_{eff}) are estimated for various γ and it is observed that they follow simple rules (Fig. 2, 3). The results in this article guarantee the reliability of the matrix method and provide us with a prescription

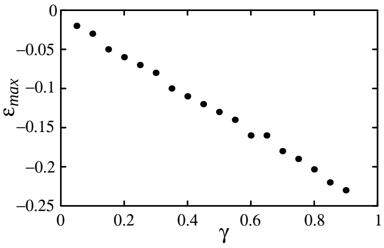

Fig. 2: The ϵ_{max} vs. γ.

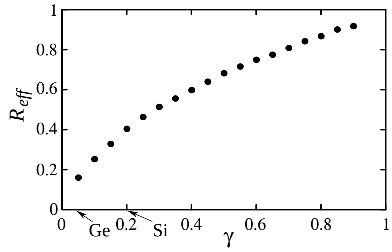

Fig. 3: Ratio of reliable levels vs. γ.

to increase the e ciency of the calculation.

Finally we comment on the subjects we are working with. Some random matrix model for an extended Gaussian orthogonal ensembles was constructed[7] and it was shown that the AKP may be treated within it. We are extensively studying this issue and will present elsewhere the relationship between γ values and the matrix-model temperatures. Armed by our prescription we will furthermore examine the multifractality of wave functions of the AKP.

References

[1] M. C. Gutzwiller, Bernoulli sequences and trajectories in the anisotropic Kepler problem, J. Math. Phys. **18**, 806-823 (1977). See also Kazuhiro Kubo and Tokuzo Shimada, Orbit systematics in anisotropic Kepler problem, Arti cial Life and Robotics **13**, 218-222, (2008).

[2] R. L. Devaney, Collision Orbits in the Anisotropic Kepler Problem, Inventiones. Math. **45**, 221-251 (1978).

[3] M. C. Gutzwiller, Periodic Orbits and Classical Quantization Conditions, J. Math. Phys. **12**, 343-358 (1971).

[4] D. Wintgen and H. Marxer, Level Statistics of a Quantized Cantori System, Phys. Rev. Lett. **60**, 971-974 (1988).

[5] R. A. Faulkner, Higher Donor Excited States for Prolate-Spheroid Conduction Bands: A Reevaluation of Silicon and Germanium, Phys. Rev. **184**, 713-721 (1969).

[6] D. Wintgen, H. Marxer, and J. S. Briggs, E -cient quantisation scheme for the anisotropic Kepler problem, J. Phys. **A 20**, L965-L968 (1987).

[7] A. M. Garcia-Garcia and J. J. M. Verbaarschot, Critical statistics in quantum chaos and Calogero-Sutherland model at nite temperature, Phys. Rev. **E 67**, 046104-1 - 46104-13 (2003).

Variable Step-size Affine Projection Algorithm Based on Excess Mean Square Error

Chang Hee Lee and PooGyeon Park

Electrical and Computer Engineering Division,
Pohang University of Science and Technology,
San 31, Hyojadong, Namgu, Pohang, Kyungbuk, 790-784, Korea
Tel: 82-54-279-5588; Fax: 82-54-279-2903
{eooe, ppg}@postech.ac.kr

Abstract

This paper proposes a computationally reduced method for the step-size update in the variable step-size affine projection algorithm (VSS-APA). Using the previous steady-state analysis and the estimated excess means square error, updating the step-size can be simplified while the advantage of VSS-APA is maintained.

keywords

Adaptive filters, affine projection algorithm, variable step-size

1 Introduction

Signal processing is one of the most important parts in the industrial applications. A useful operation could be control, data transmission, denoising, prediction, filtering and etc. [1]. It is also applicable to the sensor acquisition and the communication among each unit in robotics.

One of the widely used algorithms in this field is the normalized least mean square (NLMS) because of its simple implementation. However it has poor convergence speed for the colored input signal. To overcome this disadvantage, the affine projection algorithm (APA) was suggested by Ozeki and Umeda [2]. By whitening the input signal, the APA can achieve faster convergence speed than NLMS, while the steady-state error of the APA gets worse than that of the NLMS. Reducing step-sizes as time goes on may make the mean-square deviation (MSD) small, which help overcome the disadvantage. As well as, the previously suggested algorithms such as the variable step-size or the variable regularization algorithms can achieve both a fast convergence speed and low steady-state errors simultaneously [3, 4].

In this paper, we focus on the variable step-size APA (VSS-APA) suggested by Shin et al. [4]. Shin's VSS-APA shows good performance over the wide range of system orders, denoted by n, and the input signals, but the projection of the estimation error into the input regression space requires a large amount of computation and the resulting projection vector also has a big dimension (n by 1) that is used in the step-size adjustment at each iteration. As the system order increases, this issue becomes serious. To moderate this problem, this paper suggests an algorithm that estimates the excess mean square error (EMSE) instead of the projection vector. With a scalar value EMSE, a lot of computation is reduced including the projection operation.

To update the instant value of the step-sizes from the EMSE, we use the previous steady-state analysis of the APA. It is known that the steady-state errors are related to the step-size and the variance of the measurement noise in analysis. Moreover, when the step-size is large, it is also affected by the projection order. Since the expected EMSE can be calculated in the analysis for each step-size, the preferable step-size can be inversely obtained from the EMSE. Finally, the required computation gets remarkably reduced while the performance is still quite comparable for any possible input signals. The simulation results verify the performance of the proposed algorithm for various input signals and several system and projection orders.

2 Preliminary

In the APA to be analyzed, the input regression matrix and desired signal sequence is denoted by $\mathbf{U}_i$ and d_i, respectively at time $i \geq 0$. The recursion equation of estimated weight $\hat{\mathbf{w}}_i \in \mathcal{R}^{n\times 1}$ for an unknown weight vector $\mathbf{w}_o \in \mathcal{R}^{n\times 1}$ with the system order n and the projection order M is

$$\hat{\mathbf{w}}_{i+1} = \hat{\mathbf{w}}_i + \mu \mathbf{U}_i \left(\epsilon \mathbf{I} + \mathbf{U}_i^T \mathbf{U}_i\right)^{-1} \mathbf{e}_i, \quad (1)$$

where

$$\mathbf{U}_i = \begin{bmatrix} \mathbf{u}_i & \mathbf{u}_{i-1} & \cdots & \mathbf{u}_{i-M+1} \end{bmatrix} \in \mathcal{R}^{n\times M}, \quad (2)$$

$$\mathbf{u}_i = \begin{bmatrix} x_i & x_{i-1} & \cdots & x_{i-n+1} \end{bmatrix}^T \in \mathcal{R}^{n\times 1}, \quad (3)$$

$$\mathbf{e}_i = \mathbf{d}_i - \mathbf{U}_i^T \hat{\mathbf{w}}_i \in \mathcal{R}^{M\times 1} \quad (4)$$

$$\mathbf{d}_i = \begin{bmatrix} d_i & d_{i-1} & \cdots & d_{i-M+1} \end{bmatrix}^T \in \mathcal{R}^{M\times 1}, \quad (5)$$

ϵ is the regularization factor, and μ is the step-size. The desired vector from the linear model:

$$\mathbf{d}_i = \mathbf{U}_i^T \mathbf{w}_o + \mathbf{v}_i, \quad (6)$$

where $\mathbf{v}_i = \begin{bmatrix} v_i & v_{i-1} & \cdots & v_{i-M+1} \end{bmatrix}^T \in \mathcal{R}^{M\times 1}$ is additive measurement noise. Then, the error vector $\mathbf{e}_i$ rewritten as

$$\mathbf{e}_i = \mathbf{d}_i - \mathbf{U}_i^T \hat{\mathbf{w}}_i = \mathbf{U}_i^T \tilde{\mathbf{w}}_i + \mathbf{v}_i, \quad (7)$$

where $\tilde{\mathbf{w}}_i = \hat{\mathbf{w}}_i - \mathbf{w}_o$. The *a priori* error vector is denoted by $e_{a,i} = \mathbf{u}_i^T \hat{\mathbf{w}}_i$. The EMSE is defined by

$$\text{EMSE} \triangleq \lim_{i\to\infty} \text{E} \left|e_{a,i}\right|^2. \quad (8)$$

Since a small value of ϵ is assumed in this paper, we start from (22) in [5],

$$\text{EMSE} = \frac{\mu\sigma_v^2}{2-\mu} \frac{\text{Tr}\left(E[\mathbf{A}_i]\right)}{\text{Tr}\left(\mathbf{S}\cdot E[\mathbf{A}_i]\right)}, \quad (9)$$

where

$$\mathbf{A}_i = (\epsilon\mathbf{I} + \mathbf{U}_i^T\mathbf{U}_i)^{-1}\mathbf{U}_i^T\mathbf{U}_i(\epsilon\mathbf{I} + \mathbf{U}_i^T\mathbf{U}_i)^{-1} \quad (10)$$

and σ_v^2 is the variance of v_i. When μ is small, identity matrix $\mathbf{I} \in \mathcal{R}^{M\times M}$ can replace $\mathbf{S}$ in (9). Then

$$\text{EMSE} \simeq \frac{\mu\sigma_v^2}{2-\mu}. \quad (11)$$

When μ is large, $\mathbf{S} \simeq \mathbf{1}\cdot\mathbf{1}^T$ is substituted into (9). Since $\text{Tr}\left[\mathbf{R}_u\right] = \text{Tr}\left[\text{E}\left\{\mathbf{u}_i\mathbf{u}_i^T\right\}\right] = \text{E}\{\|\mathbf{u}_i\|^2\}$, in this case,

$$\text{EMSE} \simeq \frac{\mu\sigma_v^2}{2-\mu}\text{Tr}\left(\mathbf{R}_u\right)\text{E}\left\{\frac{M}{\|\mathbf{u}\|^2}\right\} \quad (12)$$

$$\simeq \frac{\mu\sigma_v^2 M \|\mathbf{u}_i\|^2}{2-\mu}\text{E}\left\{\frac{1}{\|\mathbf{u}\|^2}\right\}. \quad (13)$$

When $n \gg 1$, $\text{E}\{1/\|\mathbf{u}_i\|^2\} \simeq 1/\text{E}\{\|\mathbf{u}_i\|^2\}$, which results in

$$\text{EMSE} \simeq \frac{\mu\sigma_v^2 M}{2-\mu}. \quad (14)$$

3 Variable Step-size

In the previous section, theoretically EMSE is determined for both small and large step-sizes in the case of small ϵ. In this section, EMSE is estimated from the measured error. If v_i is assumed to be independent, identically distributed (i.i.d) and zero-mean, it is obtained that

$$\text{E}\{e_i\} = \text{E}\{e_{a,i} + v_i\} = \text{E}\{e_{a,i}\}. \quad (15)$$

The following time average ε_i of e_i is calculated by

$$\varepsilon_{i+1} = \alpha\varepsilon_i + (1+\alpha)e_i, \quad (16)$$

with a smoothing factor $\alpha = 1 - 1/(K)$, where K is a positive integer. When K is close to 1, $\varepsilon_i \simeq e_i$ and When $K \gg 1$, ε_i is close to $\text{E}\{e_{a,i}\}$. In the both cases,

$$\text{EMSE} = \text{E}\left|e_{a,i}\right|^2 \neq \left|\varepsilon_i\right|^2. \quad (17)$$

However, if we properly select the value of K so that $\varepsilon_i \simeq e_{a,i}$, it is reasonable that

$$\text{EMSE} \simeq |\varepsilon_i|^2. \quad (18)$$

Using the previous results (11) and (14), the following equation is possible:

$$\left|\varepsilon_i\right|^2 \simeq \frac{\mu\beta}{2-\mu}, \quad (19)$$

where

$$\beta = \begin{cases} \sigma_v^2 & \text{for small } \mu, \quad (20a) \\ M\sigma_v^2 & \text{for large } \mu. \quad (20b) \end{cases}$$

From (19), the step-size update equation is inversely obtained as follows:

$$\mu_i = \frac{2\left|\varepsilon_i\right|^2}{\beta + \left|\varepsilon_i\right|^2}. \quad (21)$$

Adjusting β in the run-time, depending on the state of the algorithm, is another issue for the performance improvement, which is out of the scope. Instead of varying β, the constant values are used in the following section. For the performance reason, upper bound 1 in μ is applied [6].

4 Simulations

We conduct several simulations to verify the proposed VSS-APA in a channel estimation scenario. The adaptive filters and the unknown channels are assumed

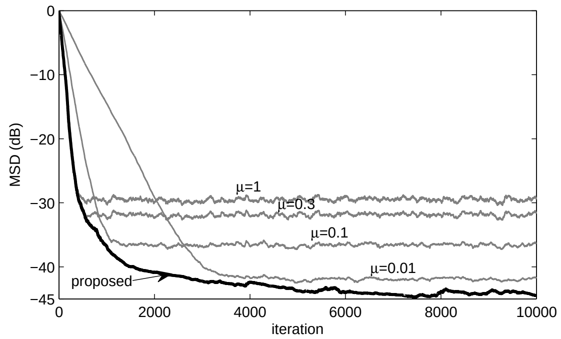

(a)

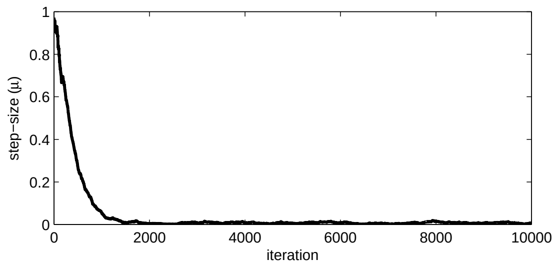

(b)

Figure 1: (a) MSD learning curves of the proposed VSS-APA and the standard APA with different step-sizes between 0.01 and 1 for a zero-mean white Gaussian input signal at $n = 64, M = 4$, SNR = 30 dB $\beta = \sigma_v^2$, and $K = 8$. (b) the corresponding variable step-size of the proposed VSS-APA.

to have the same length of taps in stationary environments. It is defined that SNR $= 10\log_{10}(\sigma_y^2/\sigma_v^2)$, where σ_y^2 is the variance of output signals. In this section, $n = 64$, $M = 4$, and SNR = 30 dB. The plots are the results of the ensemble average over 50 independent trials.

The first simulation is for verifying how closely the proposed algorithm follows the minimum route of the MSD of the each step-size. The input signal is a zero-mean white Gaussian with a unit variance. As shown in Fig. 1, the MSD learning curve of the proposed VSS-APA has fastest convergence rate that is almost equal to that of the standard APA with $\mu = 1$. It also shows the smaller steady-state error than that of the standard APA with $\mu = 0.01$. Fig. 1b shows how the step-size is varied according to the iteration. At the beginning, large step-sizes is used and after 2000 in the iteration, almost same small step-sizes are used.

The second simulation shows how the performance is affected by K. When $K = 1$, the proposed VSS-APA shows a poor performance in the convergence rate and the steady-state error. As K increases, the

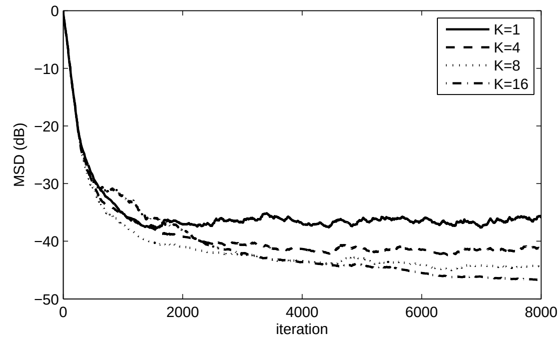

Figure 2: MSD learning curves of the proposed VSS-APA with different values of K at $n = 64$, $M = 4$, SNR = 30 dB, and $\beta = \sigma_v^2$.

convergence rate of the proposed VSS-APA get slower while the steady-state error get smaller, which mean the value K plays an important role in the performance of the proposed algorithm.

The third simulation shows how the performance is affected by β. When $\beta = \sigma_v^2$, the proposed VSS-APA

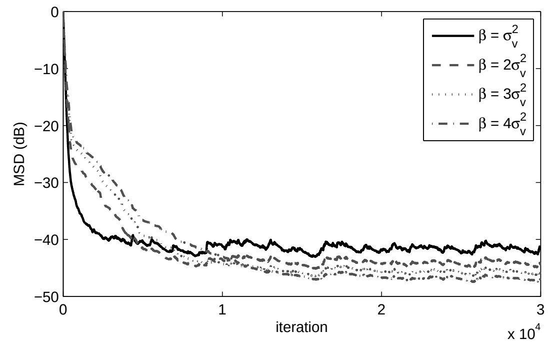

Figure 3: MSD learning curves of the proposed VSS-APA with different values of β at $n = 64$, $M = 4$, SNR = 30 dB, and $K = 4$.

shows apparently fastest convergence rate in Fig. 3 at the cost of larger steady-state error than those of others. It is verified that decreasing the value of β leads smaller steady-state errors.

The last two simulations are for performance comparisons to the previous results in the literature [3, 4]. Their tunning parameters are $\alpha = 0.9922$, $C = 1.875 \times 10^{-4}$ in Shin's VSS-APA and $\eta = 1$, $\delta = 0.06$ in Rey's VR-APA. Fig. 4 shows the MSD learning curves of the proposed VSS-APA, Shin's VSS-APA, and Rey's VR-APA when a zero-mean white Gaussian input signal excites the system. The proposed VSS-APA shows the comparable result.

Fig. 5 shows the MSD learning curves of the algorithms when an AR input signal excite the sys-

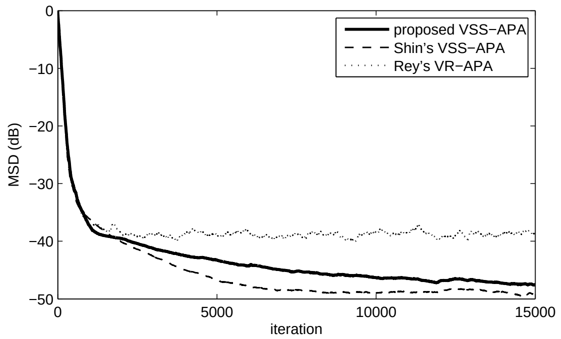

Figure 4: MSD learning curves of the proposed VSS-APA, Shin's VSS-APA and Rey's VR-APA excited by a zero-mean white Gaussian signal at $n = 64$, $M = 4$, SNR = 30 dB, $\beta = 2\sigma_v^2$, and $K = 8$.

tem. The AR input signal is generated by filtering a zero-mean white Gaussian signal through $G_1(z) = 1/(1 - 0.9z^{-1})$. In this case, the performance of the

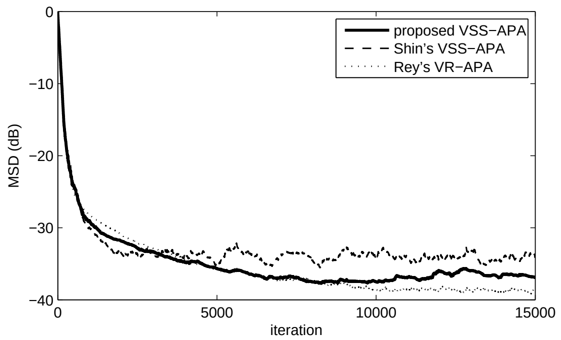

Figure 5: MSD learning curves of the proposed VSS-APA, Shin's VSS-APA and Rey's VR-APA excited by an AR signal at $n = 64$, $M = 4$ SNR = 30 dB, $\beta = \sigma_v^2$, and $K = 8$.

proposed VSS-APA is quite comparable to those of the others.

5 Conclusion

This paper proposed a simple way of updating the step-size using the EMSE. The EMSE was estimated from the measurement error and the step-size was inversely derived based on the previous steady-state analysis. As a result, the calculation needed for step-size update became significantly reduced compared to the previous VSS-APA, maintaining its advantage. The simulation results verified the performance of the proposed VSS-APA. It was also shown that additional parameter β led the trade-off between the convergence rate and the steady-state error in the performance.

Acknowledgements

This research was supported by WCU (World Class University) program through the Korea Science and Engineering Foundation funded by the Ministry of Education, Science and Technology (Project No. R31-2008-000-10100-0).

This research was supported by the MKE(The Ministry of Knowledge Economy), Korea, under the ITRC(Information Technology Research Center) support program supervised by the NIPA(National IT Industry Promotion Agency (N I PA-2009-C1090-0902-0004).

This research was supported by the Brain Korea 21 Project in 2009.

References

[1] Haykin, S. (2001) Adaptive Filter Theory, Prentice Hall, NJ 4th edition.

[2] Ozeki, K. and Umeda, T. (1984) *Electronics and communications in Japan* **67(5)**, 19–27.

[3] Rey, H., Vega, L. R., Tressens, S., and Benesty, J. (2007) *IEEE Transactions on Signal Processing* **55(5)**, 2096–2109.

[4] Shin, H. C., Sayed, A. H., and Song, W. J. (2004) *IEEE Signal Processing Letters* **11(2)**, 132–135.

[5] Shin, H. C. and Sayed, A. H. (2004) *IEEE Transactions on Signal Processing* **52(1)**, 90–102.

[6] Sankaran, S. G. and Beex, A. A. (2000) *IEEE Transactions on Signal Processing* **48(4)**, 1086–1096.

The Fifteenth International Symposium on Artificial Life and Robotics 2010 (AROB 15th '10),
B-Con Plaza, Beppu,Oita, Japan, February 4-6, 2010

Basic Research on a New Method for Underwater Localization Based on Machine Vision

Bin Fu, Wentao Li, Tong Ge, Lian Lian, Han Zhang
Ocean Engineering State Key Laboratory, Shanghai Jiao Tong University, Shanghai 200030
(Tel: 021-62933128, Fax: 021-62933742)
(bfu@sjtu.edu.c, wtli@sjtu.edu.cn)

Abstract: With the increasing needs for ocean investigation and new energy development, the application of autonomous underwater vehicle (AUV) has attracted more and more attention. Most of these attentions focus on the motion performance of AUV in large-scale operating environment. However, the observation for special underwater structure, as one important application of AUV, hasn't got enough research by our investigation. To realize the observation and operation of AUV around complex structures, we have developed one hovering AUV system, in which the issue of determining and control of horizontal x-y position becomes the bottleneck technique. To solve this problem, we introduce the machine vision into underwater application and verify its feasibility and basic characters.

Key Words: AUV, machine vision, underwater localization, light source, image processing

I. FOREWAORD

With the increasing needs for ocean investigation and new energy development, the application of autonomous underwater vehicle (AUV) has attracted more and more attention. Most of these attentions focus on the motion performance of AUV in large-scale operating environment.[1] However, the observation for special underwater structure, as one important application of AUV, hasn't got enough research. [2] To realize the observation and operation of AUV around complex structures, we developed one hovering AUV system, in which the issue of determining and control of horizontal x-y position becomes the bottleneck technique for keeping AUV's security and stability. The common acoustic positioning system owns very low accuracy because of big background noise and strong reflection wave in limited and closed space and the common INS (inertial navigation system) produces much bigger error because AUV has a low speed around obstacles. To solve the localization issue in complex unstructured environment, we propose one method of machine vision in underwater application. That is (1) to localize the object by camera mounted on AUV observing the light source array fitted on underwater object; (2) to localize AUV by camera mounted on mother-ship observing the light source array fitted on AUV.

However, it is necessary to consider the differences of propagation medium and object between in our application and in common application. Different attenuation coefficients, scatterings and background lights between underwater and on land may bring beneficial or harmful effect on image processing, Besides, the observation object in our research is underwater vehicle of low speed and various postures.

To be aimed at the above uncertainty, this paper verifies the feasibility of machine vision in underwater application and discusses basic performance of this method.

II. PRINCIPLE

1. System organization

This underwater vision system consists of light sources, camera, lens, image acquisition card and data processing computer. The light sources are placed in humid environment while other equipment in dry environment such as in compressive cabin or above water, as is shown in Fig.1. The light is projected on the camera's image sensor after multiple refractions The analog signal produced by image sensor are transformed into digital signal by image acquisition card and then processed in PC.

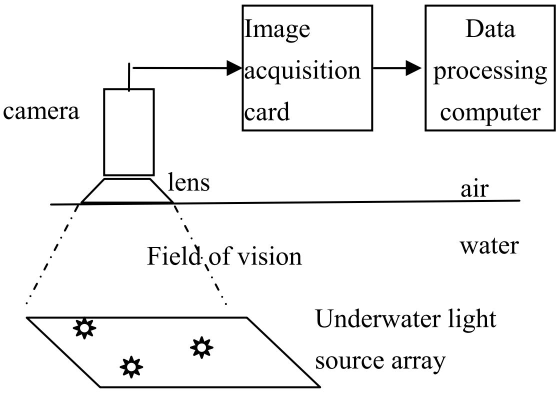

Fig.1. System organization

2. Image acquisition and processing

The first step is to capture and save one RGB image by camera. The second step is to transform the image into gray level image and de-noise by preset threshold value. The third step is to erode by preset erosion parameter. Final step is to compute the 2-D coordinates of the images of light sources in pixel reference frame (PRF) by searching algorithm.

3. Coordinate transformation

As the underwater vehicle is one object whose position and posture are both various in 3-D space, we need one array composed by at least 3 light source of fixed distance among them to localize them. PRF is shown in Fig.2. The origin O is in the top left corner, while the positive direction of x and y axis is respectively rightward and vertically downward. The points of a_1, a_2, a_3 are the images of each center of three light sources and the point of V is the image of their geometric center. The coordinates of V in global reference frame (GRF) are obtained sequentially by the following equations.

$$l_i=\sqrt{(x_{i+1}-x_i)^2+(y_{i+1}-y_i)^2}\ (i=1,2,3) \tag{1}$$

$$k_i=L_i/l_i \tag{2}$$

$$k=(k_1+k_2+k_3)/3 \tag{3}$$

$$(x'_i, y'_i)=(kx_i, ky_i) \tag{4}$$

$$\begin{cases} X_v=k*(x_1+x_2+x_3)/3 \\ Y_v=k*(y_1+y_2+y_3)/3 \end{cases} \tag{5}$$

Where (x_1, y_1), (x_2, y_2), (x_3, y_3) are coordinates in PRF of images of light sources. l_i and L_i (known) represent the distance among them respectively in PRF and GRF. k_i and k are respective calibration

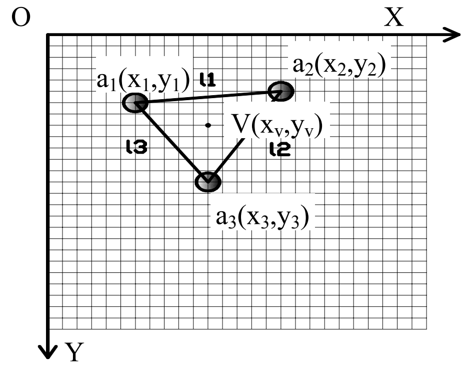

Fig.2. the images of light resources in PRF

coefficient and their average. (x'_i, y'_i) is the projection coordinate of every light source on the plane which is vertical to the optics axis of camera lens and V is located in and (x_v, y_v) is the coordinates of V in GRF.

III. WATER TANK TEST

The water tank test is taken in the Sate Key Laboratory in Shanghai Jiao Tong University. The radius and water depth of the columniform tank is 8 meters and 7meters respectively. The light sources are 3 LED of power of 0.2 [w]. The camera is watertight processed SS-880HO produced by SHEPER in UK and the lens is CCD image sensor of resolution of 576 pixels by 768 pixels. The final images are processed in Halcon, one developing environment for machine vision produced by MVtec Corp.

The vision system is shown in Fig.3. Three LED are fitted in equilateral triangle array on one black and nonreflecting panel placed underwater with its vertical normal. The camera is on the water surface and its optics axis is pointing down. The procedure to obtain the real value of light sources' coordinate is as follows. First measure the 2-D coordinates of the three LED and their geometric center in Microsoft Paint, then compute the respective calibration coefficients and their average, which is multiplied by coordinate of the geometric center.

The propagation distance of light may affect results of image processing by affecting its energy attenuation. To verify the effect of working distance (WD) on object recognition rate (ORR) and positioning accuracy (PA), we adjust WD from 2 to 6 meters with interval of 1 meter between the plane and

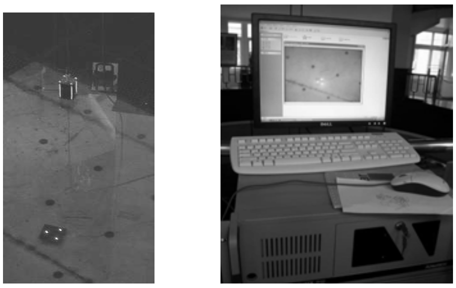

(a)underwater part (b) land part

Fig.3. vision system organization

camera lens.

The different horizonal positions of lignt source may induce the change of the angle of incidence (IA,the angle between line-of-sight of object and the optics axis of camera). To verify the effect of different IA on ORR and PA, we adjust the horizontal position respectively in the plane of 4[m] and 5[m] depth, as is shown in Fig.4.

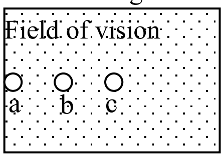

a: edge of field of vision

b: quarter of field of vision

c: center of field of vision

Fig.4. different positions of light source panel

On the other hand, de-noising threshold value and erosion value are respectively adjusted in the image processing algorithm to watch the variation of ORR.

IV. TEST RESULT AND ANALYSIS

1. The effect of WD

A. Effect on ORR

Table 1 shows the relationship between ORR and WD when the panel is at b in Fig.4. Set de-noising threshold value Th=10 and erosion value E=1. The ORR varies because the incident light energy (ILE) decreases with the increase of WD. ORR is higher than 30% at the distance of 2-6[m]and reaches the maximum at the distance of 4[m].

Table 1 the relationship between ORR and WD

WD [m]	2	3	4	5	6
ORR [%]	40	80	90	70	30

Fig.5 lists the processed images at different WD. One light source point is mistaken as two points for too much ILE at WD of 2[m] while no light source can be recognized at WD of 6[m] because they are cleared after eroding for too little ILE. We deduce the fundamental reason for such case is that erosion value doesn't match well with ILE. So we will adjust the variant in V part.

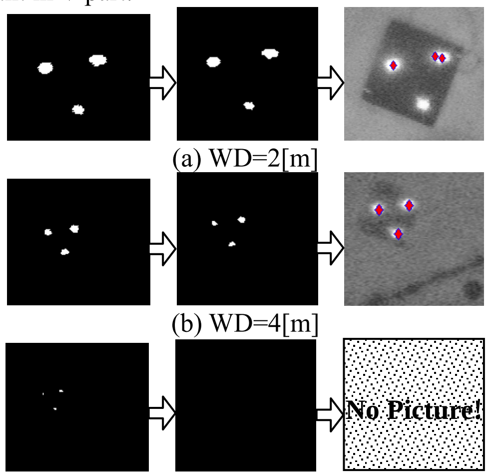

(a) WD=2[m]

(b) WD=4[m]

(c) WD=6[m]

Fig.5. processed images at different WD

B. Effect on PA

The relationship between PA and WD is shown in Table 2, which includes X error ΔX, Y error ΔY, distance error ΔD between measured value and real value of V's coordinates and system accuracy (SA, the ratio of size of field of vision to pixel numbers of CCD sensor) varying with WD. The data are obtained when the panel is at b and Th=10, E=1. Apparently PA varies nearly in direct proportion with SA.

Table 2 relationship between PA and SA

WD[m]	Error(cm)			Δ
	ΔX	ΔY	ΔD	
2	0.34	0.69	0.78	0.19
3	1.19	1.07	1.63	0.29
4	1.88	1.74	2.56	0.38
5	3.07	2.73	4.16	0.47

2. Effect of IA

A. Effect on ORR

Table 3 shows ORR value when IA varies at different points a, b and c. Set Th=15, E=1. ORR at b (IA is about 5 degrees) reaches highest while ORR at a and c are lower.

Table 3 relationship between ORR and IA

Depth[m]	a	b	c
4	40%	90%	60%
5	10%	80%	30%

Fig.6 shows the processed images when light source array is respectively placed at a, b and c of the plane in the depth of 4[m]. As is shown, the images of light sources get smaller with the decrease of IA (a→b→c) in the first column (de-noised images) while the images at b is bigger than that at a and c. There are two reasons: (1) When IA is big (at a), there are many flecks around images of light source cause by water medium scattering. These flecks will disappear after eroding so that the original images will become much smaller. (2) When IA is small (at c), although ILE is bigger, the images of light sources is very concentrative for the less effect of water scattering. In this case, the image may be cleared finally if being processed by the same erosion value. Based on above analysis, we suggest that the horizontal position of light source in field of vision should be one reference to figure out the image processing parameters.

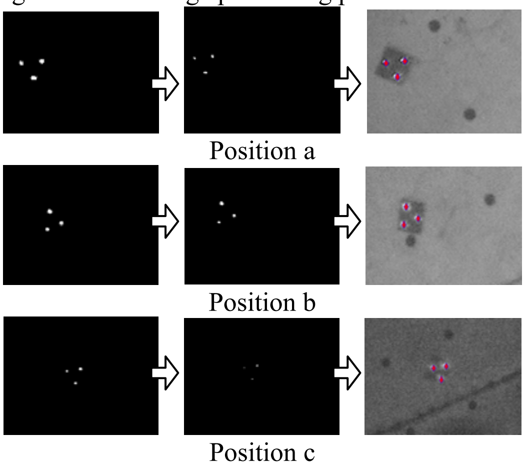

Fig.6. processed images in different incident angles

B. Effect on PA

Based on recognized image, we analyze IA's effect on PA. Table 4 shows the different PA at a, b, and c of the plane in depth of 4[m]. Apparently PA deteriorates with the increase of IA. So we conclude that WD increases with the increase of IA on the same horizontal plane, which finally affects PA.

Table 4 relationship between PA and IA

Position	Error(cm)			WD[m]
	ΔX	ΔY	ΔD	
a	0.86	2.32	2.47	4.11
b	1.34	1.28	1.85	4.02
c	1.26	0.73	1.45	4.00

V. OPTIMIZATION OF IMAGE PROCESSING PARAMETERS

As mentioned ahead, it is necessary to adjust Th and E to adapt different working conditions. This part compares the different ORR before and after optimizing the two parameters at WD of 2-5[m], as is shown in Fig.7. The optimized ORR reaches higher than 50%, which can meet the basic requirements for AUV's hovering and operating.

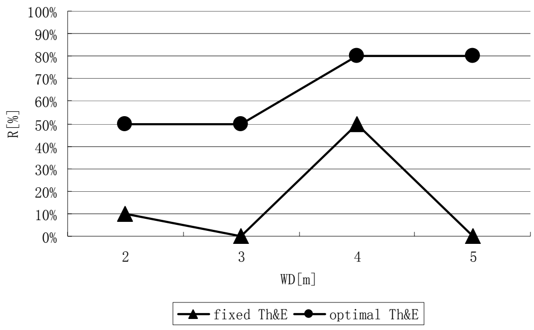

Fig.7. ORR before and after optimizing Th and E

In future, we can determine the optimized value of Th and E in different working conditions by experiment in advance and realize self-adaptive adjust of the two parameters in image processing algorithm by looking up preset tables.

VI. CONCLUSION

This paper introduces machine vision into underwater application and verifies its feasibility and basic characteristics by water tank test.

The test results show work distance and incident angle's material effect on object recognition rate and positioning accuracy and confirm the improvement of object recognition rate after optimizing the de-noising threshold value and erosion value. With the optimized parameters, object recognition rate can reach above 50% and positioning accuracy 2.5 centimeters in the work range, which can meet the requirement for AUV operating in limited and complex environment.

This research is sponsored by the fund for Hovering AUV program of Ocean Engineering State Key Laboratory.

REFERENCES

[1] J. YUH(2000), Design and Control of Autonomous Underwater Robots: A Survey. Autonomous Robots, 8(1):7-24(2000)

[2] Whitcomb, L.L. (2000), Underwater robotics: out of the research laboratory and into the field, International Conference on Robotics and Automation, 1(4):709-716(2000)

Basic Research on Underwater Laser Ranging and Speed-measuring

Bin Fu, Han Zhang, Tong Ge, Lian Lian, Wentao Li

State Key Laboratory of Ocean Engineering, Shanghai Jiao Tong University, China

(Tel: +86-21-62932610; Fax: +86-21-62933742)

(bfu@sjtu.edu.cn, zhanghan_121@163.com)

Abstract: This paper proposes one new method of calculating (1) the speed of AUV according to the distance measured by one laser range finder and (2) the angle between AUV head and the surface of underwater structure according to the different distances measured by two laser range finders. Besides discussing the selection of the laser type, this study tests computing speed, accuracy, range and other performance of underwater laser ranging method through a large number of experiments of simulating the process that the AUV gets close to and goes far away from the object in different postures. The results show that the accuracy for laser ranging has no major changes in the water medium. And the range of this method is affected by water quality, reflector materials, angle of reflection, etc.

Key words: Hovering AUV, Laser ranging, Underwater ranging.

I. INTRODUCTION

In recent years, Hovering AUV has been proposed out as a new concept of underwater vehicle. Its main feature is the capability of realizing the operation on a fixed point. Due to both of autonomous ability of traditional AUV and spatial mobility of ROV, it can be applied to the observation and operation around underwater structures. We have developed a hovering AUV and then found that in the process of getting close to target object, it is very hard for AUV to determine the distance and maintain a certain posture and distance relative to target object according to operational needs. One of the main technical difficulties in realizing autonomous control during that process lies in measuring the distance in a high accuracy. Previously, sonar is usually used to measure the distance between AUV and the objects. However, when the distance gets smaller, the accuracy of this method becomes poor, which not only affects operational efficiency but also creates possible risk of collision. This study proposes one new method of calculating (1) the speed of AUV according to the distance measured by one laser range finder and (2) the angle between AUV and underwater structure according to the different distances measured by two laser range finders.

Laser range finder is usually applied to measure the distance between two fixed points on land or the speed of cars. So far it has never been seen for underwater application in measuring the distance between moving objects and fixed objects. In water, because of smaller attenuation, acoustic wave has been applied extensively. And electromagnetic wave, due to maximum attenuation, had almost not been used in water. Owing to the attenuation coefficient between that of acoustic wave and electromagnetic wave, light wave can be applied within a limited range. In particular, owing to strong directivity and high measurement accuracy of laser, laser ranging and acoustic ranging can be used complementarily. [1][2]Nevertheless, the effect on measurement performance caused by aqueous medium or speed of AUV itself has not yet been verified either. Therefore, besides discussing the selection of the laser type, this study had a test of computing speed, accuracy, range and other performance of underwater laser ranging method through a large number of experiments of simulating the process that the underwater vehicle gets close to and goes far away from the object in different postures.

II. PRINCIPLE OF RANGING

1. Range finding

In this experiment, we adopt the ranging principle of laser range finder, which is calculating the distance l

[m] by measuring the propagation round-trip time between laser and target, as shown in Eq. (1).

$$l = t \times c \quad (1)$$

c=2.25×108 [m/s] is the propagation velocity of light in water. According to different principles of measuring propagation time, laser ranging method can be divided into phase difference method type and pulse method type. In underwater application, laser beam experiences three refraction processes: from air (laser transmitter) to glass (airproof glass) then to water, see Fig.1. It is difficult to correct the ranging error produced by phase change in the refraction process. Therefore, pulse method is used in this study and its basic ranging principle is shown in Fig.1. However, in the refraction process it will produce time loss ⊿t [s]. Then we assume that the distance of laser propagation in air and in water are l_0 [m] and l [m] respectively, so propagation processing time t[s] can be expressed as Eq. (2).

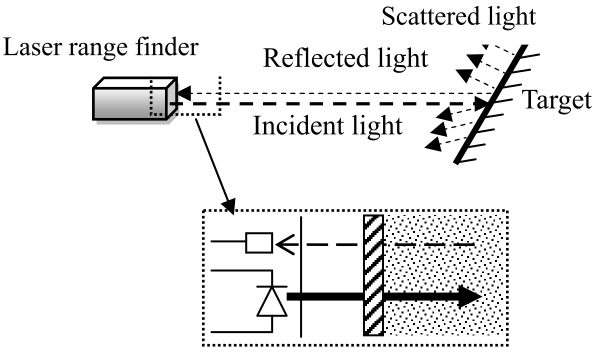

Fig.1. The principle of the ranging system

$$t = l_0 / c_0 + l / c_1 \quad (2)$$

$$c_1 = c_0 / n \quad (3)$$

c_0 and c_1 are the speed of light in air and in water respectively; n is the refractive index of media calculated through empirical equation Eq. (4)

$$n = 1.33333 + \frac{n_g - 1}{1 + \alpha t} \cdot \frac{P}{1013} \quad (4)$$

n_g is refractive index of media in standard condition; α [℃$^{-1}$] is expansion coefficient; t [℃] is temperature and P [hpa] is pressure.

We express the measuring distance as l'[m], see Eq. (5) , Ranging error as ⊿, see Eq. (6).

$$l' = tc_g \quad (5)$$

$$\Delta = l' - l = (l_0 / c_0 + l / c_1)c_g - l = l_0 / n_g + (c_g/c_1 - 1) \quad (6)$$

c_g is propagation velocity in aqueous medium under standard condition, l_0/n_g is constant error, measured by error correction experiment and $(c_g/c_1-1)l$ is error with the change of distance, corrected by the linear correction method.

2. Measuring angle and speed

Based on the ranging above, using two laser range finders of parallel arrangement we can separately measure the distance, and then calculate the angle between AUV and target as Eq. (7).

$$\tan\alpha = \frac{d}{|l_1 - l_2|} \quad (7)$$

α is the angle between centerline of laser and normal of target and d is the distance between two parallel laser beam.

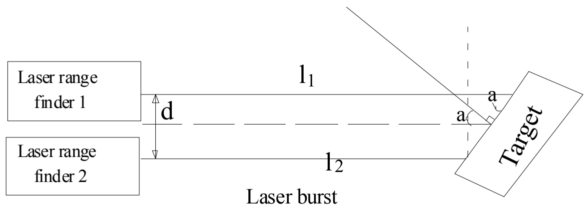

Fig.2. The principle of measuring angle

As shown in Fig.3, the target has moved from position a to position b in time T[s].By means of the cosine-theorem, we can give Eq. (8).

$$\bar{v} = \frac{\sqrt{l_a^2 + l_b^2 - 2l_a l_b \cos\alpha}}{t} \quad (8)$$

$\alpha = \beta_2 - \beta_1$ and $\bar{v}$ is average speed in time T.

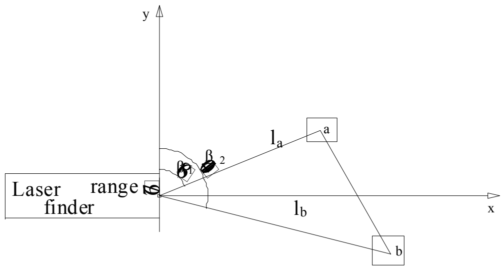

Fig.3. The principle of measuring average speed

However, when the underwater vehicle is moving, this method can only calculate the average speed for a period and can't tell the instantaneous speed at a given moment of time.

III. WATER TANK EXPERIMENTS

This experiment has been completed in underwater trial tank (depth:9[m],diameter:8[m]). We select and use pulsed laser range finder: DLE-B30 produced by DIMETIX Company. The measuring range of this instrument is 0.05-65[m] in air and its measurement error can reach up to ±5.0 [mm].

1. Experimental contents

A.Ranging accuracy and range

As shown in Fig.4, with vertical incidence to the reflector, laser range finder has recorded the data of 0-8[m] with the interval of 0.5 [m].

Fig.4. Ranging experiments

B.Effects of incidence angle

As shown in Fig.5., range and accuracy has been tested by regulating the angle between incident laser beam and normal line of reflection (incidence angle:0°, 30°,45°, 60°).

Fig.5. Regulation method of incidence angle

C.Continuous ranging

We designed that laser range finder was disposed vertically and went close or away from reflector, then collect data continuously.

D.Effects of water tightness processing

We investigated the variation of measurement range before and after water tightness processing.

2. Experimental results

A.Ranging accuracy and range

Measured value is compared with truth value in Fig. 6.. Error of this method becomes bigger with the increasing distance and is proportional to the distance. Its largest measured distance in water can rise to 5.5[m], which is about 1/11 in air.

B.Effects of incidence angle

With the increase of the incidence angle, measuring

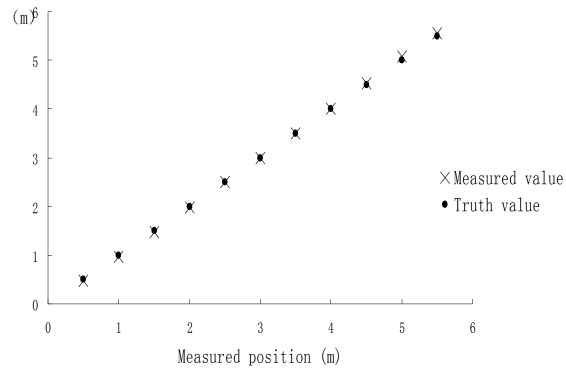

Fig.6. Ranging results compared with truth value

range changes greatly. As shown in Fig.7, range is about 2/3 of maximum measuring range at the angle of incidence of 30 degree and when the incidence angle is 60 degrees, range decreases to only 1/2 of maximum range. But position accuracy has no significant change.

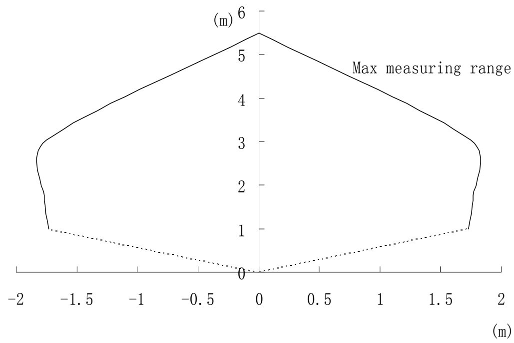

Fig.7. Relation between angle and range

C.Continuous ranging

Continuous ranging data has no marked change. Only with increasing distance, the time of data acquisition increases because of weaker reflected signal.

D.Effects of water tightness processing

It is proved by experiments that water tightness processing of laser lens will affect laser strength and then affect measuring range.

IV. ERROR CORRECTION

1. Error analysis

A. The speed of light error

As shown in Eq. (3), the speed of light in water is inversely proportional to refractive index affected by water pressure, water quality and water temperature, etc. Therefore, the variation of the speed of light in water will have an effect on the accuracy of ranging, and we call it "the speed of light error".

B. Instrumental error

The frequency of laser crystal oscillator is affected by environmental factors. In using laser range finder, ranging accuracy will be affected by the deviation between the actual frequency of modulated light and the standard frequency and its impact is proportional to the distance.

C. Time error

The time error has been fully discussed in II. Principle and can be modified with a method of linear error correction.

2. Correction method

Based on the error analysis，we proposed a method of linear error correction and got Eq. (9) on the relation of measured value and truth value.

$$y = kx+b \tag{9}$$

k and b are both affected by water temperature, water pressure, and water quality, etc. In this paper, by using a set of data at a 0 degree incidence angle, we got error correction coefficient: k=0.982, b=0.0488.

3. Corrected results

We can find corrected value is close to truth value, see Fig.10. Range error at different angles of incidence is separately shown Fig.11. (Forward direction of vertical axis: measured value is greater than truth value.)

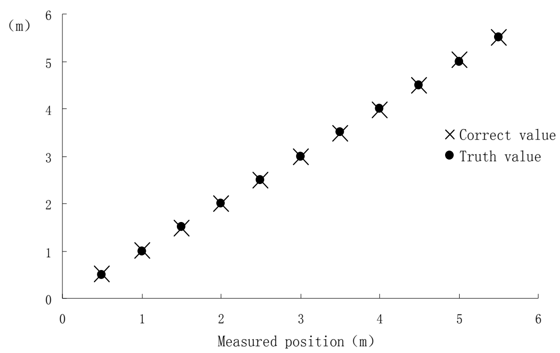

Fig.10. Ranging results after error correction compared with truth value

As the measured distance increases, the ranging accuracy has no significant change while errors are freely distributed on both sides of 0, see Fig.10.

As shown in Fig.11, we consider that the correction coefficient calculated at the angle of incidence of 0° can be applied at other degrees besides the accuracy of no significant change, about ±3[cm].

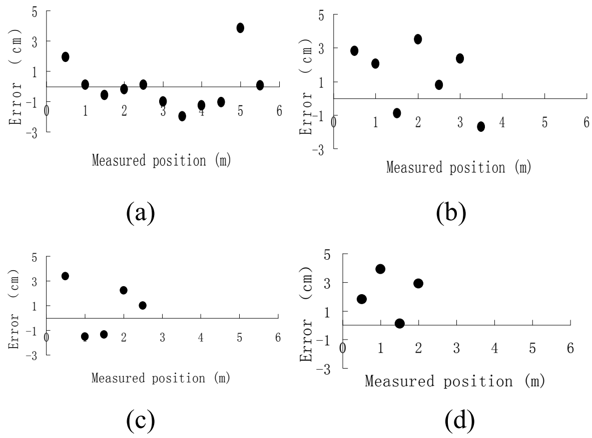

Fig.11. Range error at different incidence angle
(a) incidence angle:0° ; (b) incidence angle:30°
(c) incidence angle:45° ; (d) incidence angle:60°

V. CONCLUSION

This paper gave a method of underwater laser ranging based on the pulsed mode. With an analysis of experimental data, we have discussed the accuracy, range and other performance of this method and proposed an effective error correction method. The experiments confirmed the validity of this correction method. In future study, measuring range can be improved by selecting higher power laser or enhancing water tightness processing such as adopting optical glass airproof lens.

Underwater laser ranging can be used with acoustic ranging complementarily with high accuracy in continuous ranging at short distances. Besides application in hovering AUV at short distances, we will also consider it that the underwater laser ranging method is applied to underwater docking and other close ranging with high accuracy in the future research.

This study is sponsored by special fund program: Hovering AUV of State Key Lab. of Ocean Engineering.

REFERENCES

[1] Hsin-Hung Chen(2001), Variation reduction in quality of an optical triangulation system employed for underwater range finding. Ocean Engineering 29 (2002) 1871–1893

[2]Sakai.H,Akizono,J.,Yasumura,S.,etal.(1998),Underwater laser viewing system and its application. Proceeding of the 1998 International Symposium on Underwater Tec., pp. 161–167.

The Fifteenth International Symposium on Artificial Life and Robotics 2010 (AROB 15th '10),
B-Con Plaza, Beppu,Oita, Japan, February 4-6, 2010

Ultrasonic Sensor Based Navigation for a Mobile Robot Using Fuzzy Logic

Nguyen Huu Cong* and Sung-Hyun Han**

*Dept. of Mechanical System Engineering, Graduate School, Kyungnam University, Korea

**Division of Mechanical System and Automation Engineering, Kyungnam University, Korea

Address: 449 Wolyoung-dong, Masan, Gyeongsangnam-do, Korea, 631-701
(Tel : 82-55-249-2590)
(nhcong08@gmail.com)

Abstract: This paper proposes ultrasonic sensor-based navigation method which utilizes fuzzy logic and reinforcement learning for navigation of mobile robot in an unknown environment. It based on the combination of elementary behaviors has been developed. Most of these behaviors are achieved by means of fuzzy inference systems. The proposed navigator combines two types of obstacle avoidance behaviors, one for the convex obstacles and one for the concave ones. The use of fuzzy inference systems to generate the elementary behaviors is quite simple and natural. However, one can always fear that the rules deduced from a simple human expertise are more or less sub-optimal. This is why we have tried to obtain these rules automatically. A new navigation method using fuzzy logic and reinforcement learning is proposed in this paper.

Keywords: Robot navigation, ultrasonic sensor, fuzzy controller, local map.

I. INTRODUCTION

Various methods for controlling mobile robot systems have been developed which are generally classified into two categories: global planning and local control. The global path planning method includes configuration space method, potential field method, generalized Voronoi diagram, and graph search method. These methods have been carried out in off-line manner in completely known environments. However, these methods are not suitable for navigation in complex and dynamically changing environments where unknown obstacles may be located on a priori planned path. Thus, the sensor-based local path planning, so called obstacle avoidance, carried out in on-line manner is required in the navigation of mobile robots. Local path planning utilizes the information provided by sensors such as ultrasonic sensor, vision, laser range finder, proximity sensor and bumper switch. It is difficult to find the force coefficients influencing on the velocity and direction of mobile robots in cluttered environments which cannot be described as a mathematical model. In order to overcome the above problem, fuzzy logic and neural network approaches have been employed in navigation of mobile robot. A new navigation method using fuzzy logic and reinforcement learning is proposed in this paper. Whenever a mobile robot navigates in uncertain environment towards the goal position, avoidance behavior and goal-seeking behavior always conflict. The avoidance behavior is used to avoid the obstacles irrespective of the goal position, while the goal-seeking behavior is used to seek the goal position irrespective of obstacle location. It is necessary for a navigator to efficiently combine two behaviors. For this, two behaviors are independently designed by fuzzy logic and reinforcement learning and are combined by the action of a switching function according to situations around the mobile robot. The fuzzy logic is used to represent the mapping between the sensor input space and mobile robot action space. The correct mapping is found by reinforcement learning. Fuzzy rule bases are built by input and output fuzzy sets which quantize the sensor input space and the mobile robot action space, respectively.

II. OBSTACLE DETECTION AND LOCAL MAP

The mobile robot has three wheels; two driven wheels fixed at both sides of the mobile robot and one castor attached at the front and rear side of the robot. In this study, twelve ultrasonic sensors are mounted around of the mobile robot in middle layer for the detection of obstacles with various heights. Fig.1 shows the arrangement of the ultrasonic sensors marked as dots in the figure. The distances e_j $(j = 1, 2,...12)$ from the origin of the robot frame {R} to obstacles detected by the sensor s_j, can be defined as $e_j = \delta_j + R_r$. Here, R_r is the radius of the robot and the δ_j, is the range value measured by the sensor s_j. A local map is introduced to record the sensory information provided by the 12 ultrasonic sensors with respect to the mobile robot frame $\{R\}$. As shown in Fig.2, a sector map defined locally at the current mobile robot frame is introduced. Then, the obstacle position vector se'_j with respect to the frame $\{R\}'$ can be calculated by

$$Se_j' = \begin{bmatrix} \cos\delta\theta & \sin\delta\theta & 0 & -\sin\delta\theta/\rho_p \\ -\sin\delta\theta & \cos\delta\theta & 0 & (1-\cos\delta\theta)/\rho_p \\ 0 & 0 & 1 & 0 \\ 0 & 0 & 0 & 1 \end{bmatrix} \quad (1)$$

where se_j denotes the obstacle position vector defined at the frame $\{R\}$. Hence, when the mobile robot is located at a point $0'$. the distance value $se'_j = \| se'_j \|$ from the origin of the frame $\{R\}'$ to the obstacle and angle $s\varphi'$ can be calculated by Eq.(1) . Here, $\|.\|$ denotes Euclidean norm.

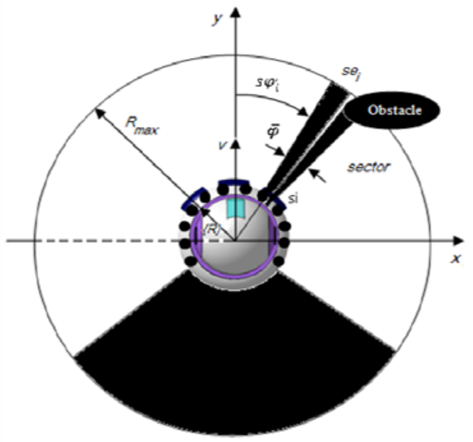

Fig. 1. The local map defined at the frame {R}

The local map defined at the frame $\{R\}'$ is newly constructed by using the previous local map defined at the frame $\{R\}$ as follows:

$$Se_n \leftarrow Se_j',\ n = INT(\frac{s\varphi_j'}{\bar{\varphi}}) + \frac{N}{2};\ j = 1,2,\dots, N \quad (2)$$

Where ← and INT denote the updating operation and integer operation, respectively. If the range values obtained by sensors when the mobile robot is located at a point O' are e_j = (j = 1,2 ,... 12) , the new local map is partially updated as follows :

se_j ← e_j, j = 1,2 .... 12. The maximum range of the sonar sensor is set to be $\delta_{max} = \delta_{max} - R_r$. Any return range which is larger than is ignored.

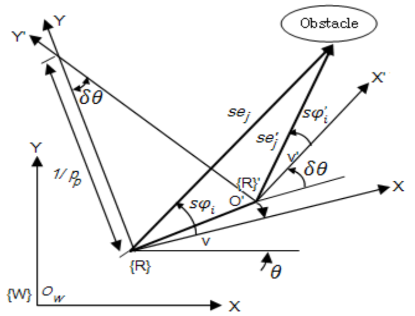

Fig. 2. The coordinate transformation for updating the local map

III. NAVIGATION OF MOBILE ROBOT

The primitive behaviors may be divided as follows: avoidance behavior and goal-seeking behavior. The output of a primitive behavior is defined by the vector

$$u(t) = (v(t), \Delta\theta(t))^T = (v(t), w(t), Tms)^T \quad (3)$$

where t and T_{ms} denote the time step and the sampling time, respectively. Here, T denotes the transpose and $\omega(t)$ denotes the angular velocity of the robot.

In order for the mobile robot to arrive at the goal position without colliding with obstacles, we must control the mobile robot motion in consideration of the obstacle position X_{oi}, = (x_{oi}, y_{oi}) , the mobile robot position $X = (x, y)$ and its heading angle θ with respect to the world coordinate frame $\{W\}$ shown in Fig.2.

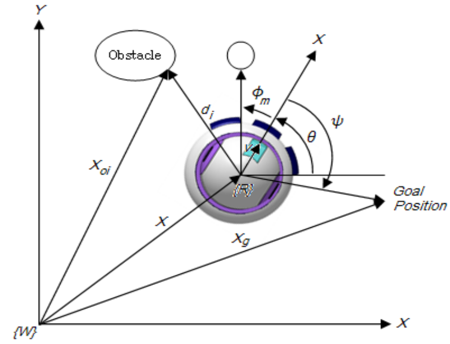

Fig. 3. The coordinate frames and control variables

In order to avoid the increase in the dimension of input space, the distance values d_i , (i = 1.2,3,4) are defined by

$$\begin{aligned} d_1 &= \min(se_1, se_2, se_3) \\ d_2 &= \min(se_4, se_5, se_6) \\ d_3 &= \min(se_7, se_8, se_9) \\ d_4 &= \min(se_{10}, se_{11}, se_{12}) \end{aligned} \quad (4)$$

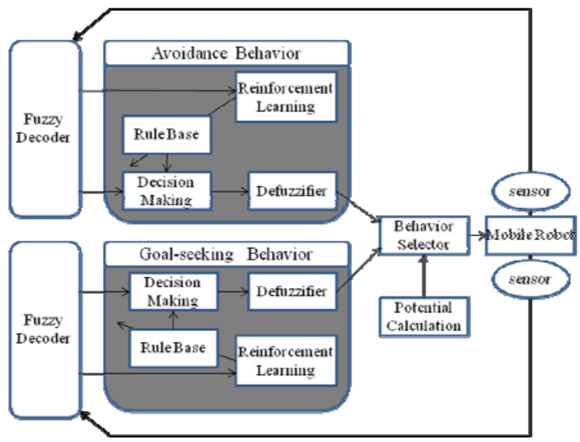

Fig. 4. The structure of the proposed navigator

The motion of mobile robot can be realized by the control of its heading velocity, v and incremental steering angle $\Delta\theta$. Thus, we choose the input variables for avoidance behavior as $d_i = \|X_{0i} - X\|, (i = 1,2, \cdots 4)$, and those for goal-seeking one as heading angle difference ψ and distance to goal, $z = \|X_g - X\|$. The output variables for two behaviors are chosen as the incremental steering angle, $\Delta\theta$ and velocity, v. The variable d_i is calculated by (Eq 4). The ψ is the angle between heading direction of the mobile robot and the direction of the goal position and the z is the distance from the current position, X = *(x,y)* to goal position, $X_g = (x_g, y_g)$.

A fuzzy operator converts the crisp input data, z into the linguistic values, $\tilde{z}$ considered as labels of fuzzy sets and is defined as

$\tilde{z} = fuzzifier(z)$

where fuzzifier denotes a fuzzification operator. From now on, tilde sign (~) representing the fuzzy set will be omitted for simplicity. The input linguistic variables $d_i(i = 1,2\cdots 4), \psi$ and z are expressed by linguistic values (VN, NR, FR), (NB, NM, NS, ZZ, PS, PM, PB) and (VN, NR, FR, VF), respectively. The output linguistic variables v and $\Delta\theta$ are expressed by the linguistic values with membership functions having the triangular shaped functions shown in Fig. 5. Their center positions are going to be determined by reinforcement learning method. The linguistic terms have the following meanings:

Table 1. Linguistic term meanings

VN: very near	NR: near
FR: far	VF: very far
NB: negative big	NM: negative medium
NS: negative small	ZZ: zero
PS: positive small	PM: positive medium
PB: positive big	

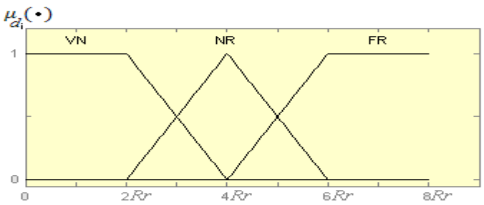

(a) The distance value of the *i*th sensor suit

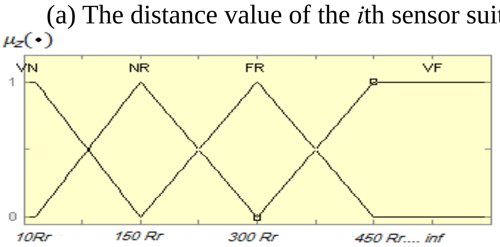

(b) The distance to goal position

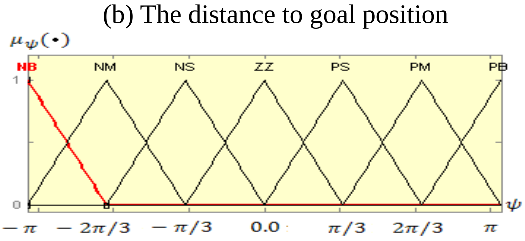

(c) The heading difference ψ

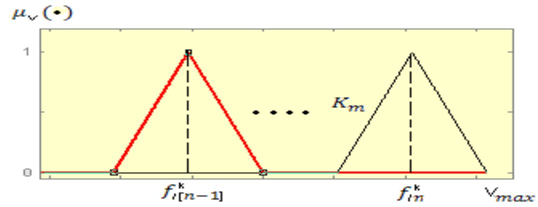

(d) The linear velocity of mobile robot for the k-th behavior

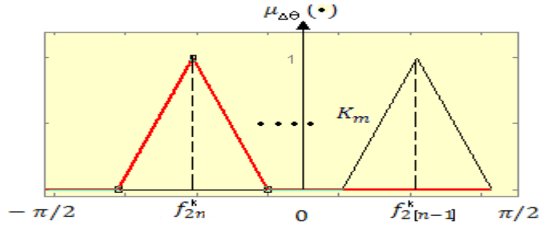

(e) The incremental steering angle for k-th behavior

Fig. 5. The membership functions of the input-output variables

Fuzzy subsets contain elements with degree of membership, while fuzzy membership function $\mu_z(\cdot)$ of fuzzy set, z assigns a real number between 0-1 to every element in the universe of discourse.

IV. SIMULATIONS AND EXPERIMENTAL RESULTS

1. Simulations

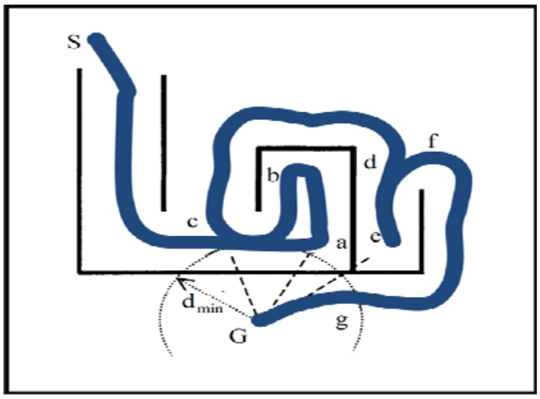

(a) Escape from loop type and dead-end type trap

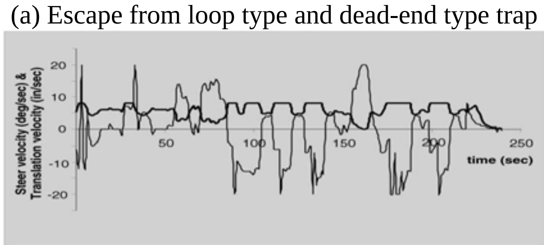

(b) Velocity (thick line) and steer velocity (thin line)

Fig. 6 Simulation for combining behaviors

Fig.6 is shown the simulation for combining behaviors. Once the rule bases for the two behaviors are completely built through reinforcement learning, the two behaviors will be combined so that the mobile robot arrives at the given goal position without colliding with obstacles. When the mobile robot navigates in a certain environment, one of these behaviors must be selected at each action step in order to accomplish its goal.

Fig. 6(a) shows the performance of the combining behaviors to escape from trap situations and go to goal. The robot first arrives by the wall-following behavior, and then enters a concave obstacle and leaves it under the avoidance of concave obstacle strategy. On the way, it encounters dead-end alleys, successfully recovers from them by avoidance behavior and eventually finds the goal under the goal-seeking behavior. The variation of the actual action decisions over time are shown in Fig. 6(b).

2. Experiment

The obstacle avoidance and goal-seeking experiments were performed in our laboratory.

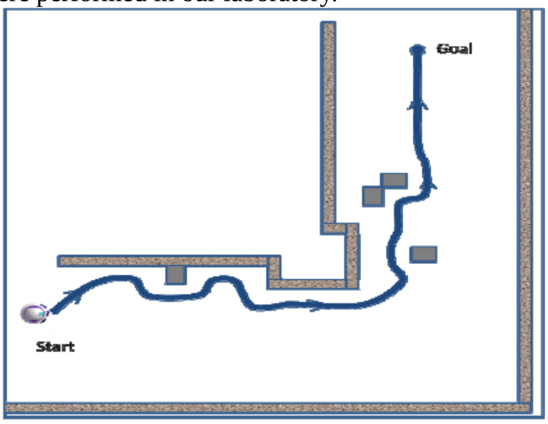

Fig. 7 Wall-following, obstacle avoidance, and goal-seeking experimental method

Fig. 8 shows the location of obstacles, the robot trajectory and its heading angle with respect to world coordinate frame when the robot travels from start position to goal position. If the robot encounters the

1. Wall-following 2. Wall-following

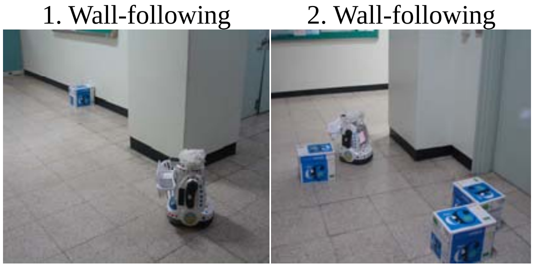

3. Goal-seeking 4. Obstacle avoidance

5. Obstacle avoidance 6. Goal-seeking

Fig. 8. Experiment for combining behaviors scene

obstacles, it avoids the obstacles by using the avoidance behavior. The behavior to be used at the present situation is selected by fuzzy decision maker. As can be seen from the figure, the robot can successfully navigate in unknown environments even if the environments are not used for constructing the rule bases of the behaviors in the simulations. This means that the robot can adapt to new environments.

V. CONCLUSION

We have proposed the navigation system capable of performing autonomous navigation in unknown environments. In order to evaluate the performance of the overall system, a number of experiments have been undertaken in various environments. The experimental results show that the mobile robot with the complete navigation system can arrive at the goal position according to the desire even if the wheel slip occurs. From the developed of navigation system, it was observed that the mobile robot can successfully arrive at the desired position through the unknown environments without colliding with obstacles.

REFERENCES

[1] O. Khatib, "Real-time obstacle avoidance for manipulators and mobile robots," Int. J. of Robotics Research, vol. 5, no. 1, pp. 90-98, Spring 1986.

[2] 0. Takahashi and R. J. Schilling, "Motion planning in a plane using generalized Voronoi diagrams," IEEE Trans. Robotics Automat., vol. 5, no. 2, pp. 143-150, 1989.

[3] H. R. Beom and H. S. Cho, "Path planning for mobile robot using skeleton of free space," in Proc. IFAC Symp. Informution Control Problems for Manufacturing (Toronto, Canada, May 25-28 1992). pp. 509-513.

[4] T. Lmano-ptrez and M. A. Wesley, "An algorithm for planning collision-free paths among the polyhedral obstacles," Communications of the ACM , vol. 22, no. 10, pp. 560-570, Oct. 1979.

[5] R. A. Brooks, "A robust layered control system for a mobile robot," IEEE Trans. Robotics Automation., vol. RA-2, no. 1, pp. 14-23, Mar. 1986.

The Fifteenth International Symposium on Artificial Life and Robotics 2010 (AROB 15th '10),
B-Con Plaza, Beppu,Oita, Japan, February 4-6, 2010

Robust Real-time Control of Autonomous Mobile Robot by Using Ultrasonic and Infrared sensors

Van-Quyet Nguyen, Shim-Byoung Kyun, and Sung-Hyun Han

Dept. of Mechanical System Engineering, Graduate School, Kyungnam University,
449 Wolyoung-dong, Masan, Gyeongsangnam-do, Korea, 631-701
(Tel: 82-55-249-2590; Fax: 82-55-249-2617)
(Email address: afi.quyet@gmail.com)

Abstract: This paper presents a new approach to obstacle avoidance for mobile robot in unknown or partially unknown environments. The method combines two navigation subsystems: low-level and high-level. The low-level subsystem takes part in the control of linear, angular velocities using a multivariable PI controller, and the nonlinear position control. The high-level subsystem uses ultrasonic and IR sensors to detect the unknown obstacle include static and dynamic obstacle. This approach provides both obstacle avoidance and target-following behaviors and uses only the local information for decision making for the next action. Also, we propose a new algorithm for the identification and solution of the local minima situation during the robot's traversal using the set of fuzzy rules. The system has been successfully demonstrated by simulations and experiments.

Keywords: Ultrasonic sensor, IR sensor, Autonomous mobile robot, Obstacle avoidance, Real-time control

I. INTRODUCTION

Autonomous robots are intelligent machines capable of performing tasks in the word by themselves, without explicit human control over their movements [1]. The autonomy implies that the robot is capable of reacting to static obstacles and unpredictable dynamic events. To achieve this level of robustness, methods need to be developed to provide solutions to localization, navigation, planning and control. The most difficulty of process is the real environment that robots are operated. It is unstructured environments and large uncertainties.

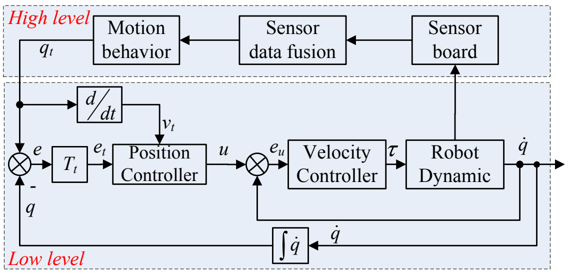

Fig. 1 Two-level control of Mobile robot

This paper proposes a new method of designing a robust autonomous mobile robot control system. This system provides the mobile robot that may navigate in a priority unknown indoor environment using sonar and IR sensor information. To achieve these requirements, the system is hierarchically organized into two distinct separated subsystems (Fig. 1) with arbitrary responsibility. A low-level includes both velocity controller and position controller. Velocity controller is developed using the standard PI multivariable control law, a dynamic model of a mobile robot and actuators. The position control law has to be nonlinear in order to ensure stability of the error, that is, its convergence to zero [2, 3, 4]. A high-level subsystem contains path planning and obstacle avoidance algorithms based on ultrasonic and IR sensors data as linguistic variables to design of fuzzy logic controller.

II. DAYNAMIC EQUATION MOTION OF MOBILE ROBOT

Consider a typical three-wheeled vehicle, two co-axial wheels provide both steering and power, while a single wheel is a passive caster shown in Fig. 2. The robot has two driving wheels mounted on the same axis and a free front wheel. The two driving wheels are independently driven by two actuators to achieve both transition and orientation. The position of the mobile robot in the world frame *XOY* can be defined by the position of the mass center of the mobile robot system, denoted by C, or alternatively by the position A, which is the center of the mobile robot gear, and θ the angle between the robot's body frame *xCy* and the world frame. The kinetic energy of the whole structure is given by the following equation:

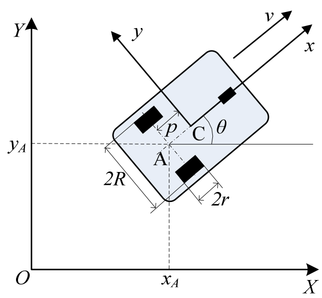

Fig. 2 A typical three-wheel vehicle.

$$T = T_t + T_r + T_m \tag{1}$$

where: T_t - the kinetic energy that is the consequence of pure translation of the entire vehicle, T_r - the kinetic energy of rotation of the vehicle in the *XOY* plane, T_m - the kinetic energy of rotation of the wheels and rotors of the DC motors. Total kinetic energy of the vehicle can be calculated in terms of $\dot{\theta}_R$ and $\dot{\theta}_L$:

$$T(\dot{\theta}_R,\dot{\theta}_L)=\left[\frac{mr^2}{8}+\frac{(I_A+mp^2)r^2}{8R^2}+\frac{I_0}{2}\right]\dot{\theta}_R + \left[\frac{mr^2}{8}+\frac{(I_A+mp^2)r^2}{8R^2}+\frac{I_0}{2}\right]\dot{\theta}_L + \left[\frac{mr^2}{4}+\frac{(I_A+mp^2)r^2}{4R^2}\right]\dot{\theta}_R\dot{\theta}_L \quad (2)$$

Now, the Lagrange equations are applied:

$$\frac{d}{dt}\left(\frac{\partial L}{\partial\dot{\theta}_R}\right)-\frac{\partial L}{\partial\dot{\theta}_R}=\tau_R-k\dot{\theta}_R$$
$$\frac{d}{dt}\left(\frac{\partial L}{\partial\dot{\theta}_L}\right)-\frac{\partial L}{\partial\dot{\theta}_L}=\tau_L-k\dot{\theta}_L \quad (3)$$

Here, τ_R and τ_L are right and left actuation torques, $k\dot{\theta}_R$ and $k\dot{\theta}_L$ are the viscous friction torques of right and left wheel-motor systems, respectively. Finally, the dynamic equations of motion can be expressed as:

$$\begin{bmatrix} M & N \\ N & M \end{bmatrix}\begin{bmatrix}\ddot{\theta}_R \\ \ddot{\theta}_L\end{bmatrix}=\begin{bmatrix}\tau_R-k\dot{\theta}_R \\ \tau_L-k\dot{\theta}_L\end{bmatrix} \quad (4)$$

where

$$M=\frac{mr^2}{4}+\frac{(I_A+mp^2)r^2}{4R^2}+I_0$$
$$N=\frac{mr^2}{4}-\frac{(I_A+mp^2)r^2}{4R^2} \quad (5)$$

III. DESIGNER OF SUBSYSTEM

In this section, we will describe detail about designing of each subsystem: low and high-level respectively. The function of this controller is to implement a mapping between the known information (e.g. reference position, velocity and sensor information) and the actuator commands designed to achieve the robot task. For a mobile robot, the controller design problem can be described as follows: given the reference position $q_t(t)$ and velocity $\dot{q}_t(t)$, design a control law for the actuator torques so that the mobile robot velocity may track a given reference control path with a given smooth velocity.

3.1. Position control

The trajectory tracking problem for a mobile robot is based on a virtual reference robot that has to be tracked (Fig. 3). The tracking position error between the reference robot and the actual robot can be expressed in the robot frame as:

$$e_t=\begin{bmatrix}e_1\\e_2\\e_3\end{bmatrix}=R_t\begin{bmatrix}e_x\\e_y\\e_\theta\end{bmatrix}=\begin{bmatrix}\cos\theta & \sin\theta & 0\\ -\sin\theta & \cos\theta & 0\\ 0 & 0 & 1\end{bmatrix}\begin{bmatrix}x_t-x\\y_t-y\\\theta_t-\theta\end{bmatrix} \quad (6)$$

The dynamics of the position error derived in (Eq. 6) is postulated as:

$$\dot{e}_1=\omega e_2+u_1$$
$$\dot{e}_2=-\omega e_1+v_t\sin e_3 \quad (7)$$
$$\dot{e}_3=u_2$$

where inputs u_1 and u_2 are new control inputs.

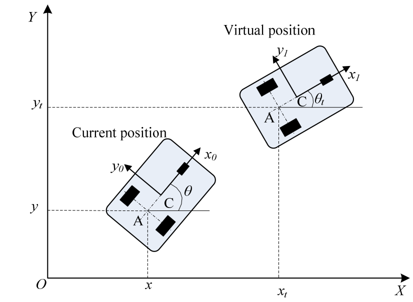

Fig. 3 Tracking of a virtual reference robot

In this paper, we propose the following control inputs in the velocity control loop:

$$u_1=v_t\cos e_3+\frac{k_1e_1}{\sqrt{k_4+e_1^2+e_2^2}}$$
$$u_2=\omega_t+\frac{k_2v_te_2}{\sqrt{k_5+e_1^2+e_2^2}}+\frac{k_3v_t\sin e_3}{\sqrt{k_6+e_3^2}} \quad (8)$$

where k_1, k_2, k_3, k_4, k_5 and k_6 are positive parameters.

3.2. Velocity control

The dynamics of the velocity controller is given by the following equations in the Laplace domain:

$$\tau(s)=\begin{bmatrix}\tau_R(s)\\\tau_L(s)\end{bmatrix}=\frac{1}{r}\begin{bmatrix}f_1(s) & f_2(s)\\ f_1(s) & -f_2(s)\end{bmatrix}\begin{bmatrix}e_v(s)\\e_\omega(s)\end{bmatrix} \quad (9)$$

where $e_v(s)$ is the linear velocity error and $e_\omega(s)$ is the angular velocity error. Transfer functions $f_j(s)$ are chosen to represent PI controllers:

$$f_1(s)=K_1\left(1+\frac{1}{T_{i1}s}\right)R$$
$$f_2(s)=K_2\left(1+\frac{1}{T_{i2}s}\right)R \quad (10)$$

After some transformations, Eq. 9 can express as:

$$\begin{bmatrix}\mu_1(s) & \mu_2(s)\\ \mu_1(s) & -\mu_2(s)\end{bmatrix}\begin{bmatrix}v(s)\\\omega(s)\end{bmatrix}=\begin{bmatrix}f_1(s) & f_2(s)\\ f_1(s) & -f_2(s)\end{bmatrix}\begin{bmatrix}u_1(s)\\u_2(s)\end{bmatrix} \quad (11)$$

where

$$\mu_1(s)=\frac{(M+N)s^2+(k+K_1T_{i1})s+K_1}{s}$$
$$\mu_2(s)=\frac{R(M-N)s^2+(Rk+K_2T_{i2})s+K_2}{s} \quad (12)$$

The following equations could be easily derived from (Eq. 11):

$$v(s)=\frac{f_1(s)}{\mu_1(s)}u_1(s)=F_1u_1(s)=\frac{K_1T_{i1}s+K_1}{(A+B)s^2+(k+K_1T_{i1})s+K_1}u_1(s)$$
$$\omega(s)=\frac{f_2(s)}{\mu_2(s)}u_2(s)=F_2u_2(s)=\frac{K_2T_{i2}s+K_2}{R(A-B)s^2+(Rk+K_2T_{i2})s+K_2}u_2(s) \quad (13)$$

It is obvious that transfer functions F_1 and F_2 are static with gains equal to "1", which completes the proof.

3.3. Design of hybrid position controller

It has been noticed that, during the preliminary simulations, at the beginning of tracking the control torques increase rapidly if the initial position of the reference robot does not belong to the straight line, determined with the robot and its initial orientation.

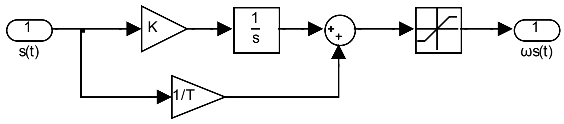

Fig. 4 Producing $\omega_s(t)$

For that purpose, the following control law, which provides velocity servo inputs, is proposed:

$$\begin{aligned} u_1^*(t) &= \beta(t)u_1(t) \\ u_2^*(t) &= \beta(t)u_2(t) + [1-\beta(t)]\omega_s(t) \end{aligned} \qquad (14)$$

Function $\omega_s(t)$ is generated as the output of the following system (Fig. 4). The input $s(t)$ is given by:

$$s(t) = \mathrm{sgn}\{atan2[e_y(t), e_x(t)] - \theta(t)\} \qquad (15)$$

The function $\beta(t)$ satisfies the following differential equation:

$$b_0 \frac{d^2\beta(t)}{dt^2} + b_1 \frac{d\beta(t)}{dt} + \beta(t) = \varepsilon(t) \qquad (16)$$

where $\varepsilon(t)$ is close to a step function and is given by:

$$\varepsilon(t) = \begin{cases} 1, & if\ \exists t_1 \in [0,t] : \theta(t_1) = atan2[e_y(t), e_x(t)] \\ 0, & \text{othewise} \end{cases} \qquad (17)$$

This way, the robot does not start tracking the virtual robot instantly; it first rotates around its own axis with an increasing angular velocity $\omega_s(t)$.

3.4. Sensory systems

3.4.1. Cooperation of Ultrasonic Sensors and IR Sensors

By overview of advantages and disadvantages of ultrasonic and IR sensor, we propose a method of combination two kind of these sensors. When K-RONI is planning to navigate in the surroundings, there are usually the static and dynamic obstacles stopping it from going to the given position. In order to make K-RONI avoid these uncertain obstacles successfully, the ultrasonic sensors and the IR sensors are used to detect if there exists obstacles simultaneously when K-RONI navigates in the real environment. If the distance between the obstacle and K-RONI is longer than 0.5m, the ultrasonic sensors are used to detect the obstacles; however the distance is shorter than 0.5m, the IR sensors are prior to be used.

For example, when K-RONI navigates in the environment, the ultrasonic sensors could detect the obstacle first with its long detection distance. And if this obstacle is static, the sensor can detect and avoid it continuously with safe distance. But this obstacle is dynamic, and it is close to K-RONI suddenly. This kind of unexpected behavior led the ultrasonic not to recognize this range information exactly. Finally, K-RONI used the IR sensors to execute the obstacle avoidance in order to go to the given position.

3.4.2. Obstacle avoidance behavior

The obstacle avoidance algorithm of K-RONI robot is emphasized the relation between IR and ultrasonic sensors. When the Sensor Fusion Model received the information of the IR and Ultrasonic sensors, they will be sent to the Robot Motion Behaviors. And the Robot Motion Behaviors will be divided into five conditions by using varied sensors modes when the K-RONI met different of obstacles in the navigating path (Fig. 5).

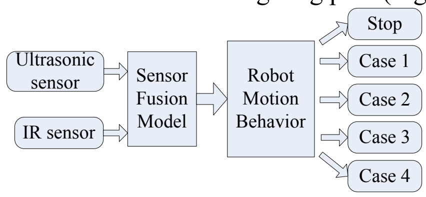

Fig. 5 Integration of IR and ultrasonic sensors for obstacle avoidance

There are two states to describe the situation which K-RONI run into obstacles as follow:

$\varepsilon \neq 0$: Ultrasonic sensor detected obstacle

$\gamma \neq 0$: IR sensors detected obstacle

- *Case 1: $\varepsilon = 0$, and $\gamma = 0$*: It means K-RONI is far away from the obstacles and moved toward the free-space areas when parameter ε and γ is zero.
- *Case 2: $\varepsilon \neq 0$, but $\gamma = 0$:* This case means the frontal Ultrasonic sensors have detected the obstacle in the navigating path. And the range information received is sent to motion commands. Robot can be avoided with long distance obstacle.
- *Case 3: $\varepsilon \neq 0$, and $\gamma \neq 0$*: Both Ultrasonic sensors and IR sensors take turns to be used for detecting the obstacles according to the distance from K-RONI to the obstacles. With the long-range detection and slow reaction rate of the Ultrasonic sensors, it is suitable for detecting the static obstacles. On the contrary, the short-range detection and fast reaction rate of the IR sensors is suitable for detecting the dynamic obstacles.
- *Case 4: $\varepsilon = 0$, but $\gamma \neq 0$:* IR sensors have detected the obstacles near K-RONI. The range information is sent to the motion agent starts to figure out the free-space areas after receiving the motion commands.

IV. SIMULATION & EXPERIMENTS

To show a usefulness of the proposed approach, a series of simulations and experiments has been conducted by using an arbitrarily constructed environment including static and dynamic obstacles. Almost simulations are performed in the MATLAB / SIMULINK software. In this paper, we used a mobile robot with the following parameters: M = 12 kg, I_A = 1 kg.m^2, r = 0.04 m, R = 0.250 m, p = 0.02 m and I_0 = 0.001 kg.m^2.

Fig. 6 and 7 are illustrated the errors of x, y axis, and orientation respectively. It also can be concluded that satisfactory tracking results are obtained using both control strategies. However, better tracking of the reference trajectory is achieved in the case of an ordinary controller, especially at the beginning of transient process.

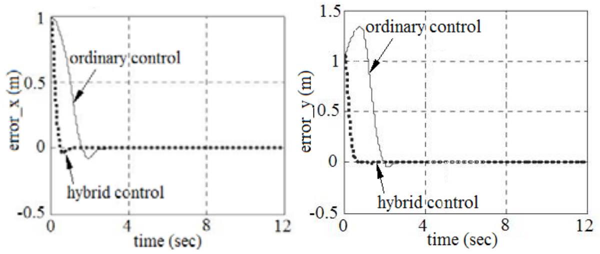

Fig. 6 x, y axis errors respectively

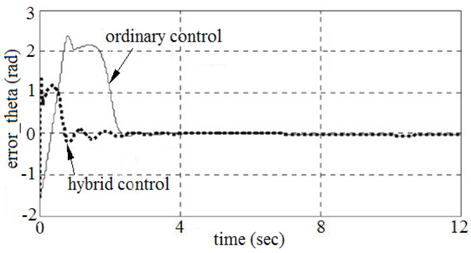

Fig. 7 Orientation error.

However, the hybrid controller ensures that much smaller values of the control input torques are needed to obtain the reference position and orientation trajectories shown in Fig. 8 and 9.

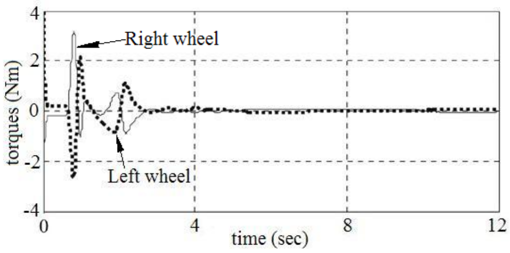

Fig. 8 Control torques – hybrid controller

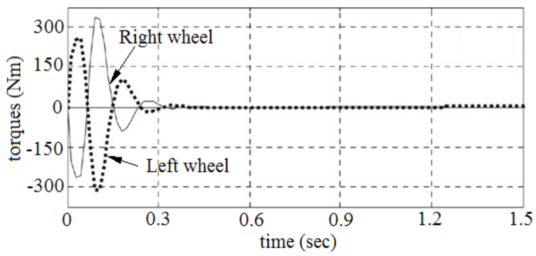

Fig. 9 Control torques – ordinary controller

Experimental results obtained in several different working scenarios are presented in Fig. 10. In all of the cases in which the target is surrounded by cluttered obstacles, which form the convex loop, the proposed algorithm helps the robot to find the target. The algorithm works very well in the case when a cluttered environment consists of walls in the form of long loops, which is always convex in order to current robot location.

V. CONCLUSION

Our approach presented a new mobile robot navigation strategy based on the computing technologies (such as fuzzy logic and other reasoning techniques) in an a priori unknown environment. Firstly, a dynamic model of a mobile robot with nonholonomic constraints is derived. The special feature of this model is that the main variables are the angular velocities of the wheels. Due to this approach, the impossibility of lateral motion is embedded into the model. In addition, such a model is easily simulated. The proposed navigation system consists of two control subsystems. Hence, a new approach is applied in robotics and approved by the results of simulation and experiments.

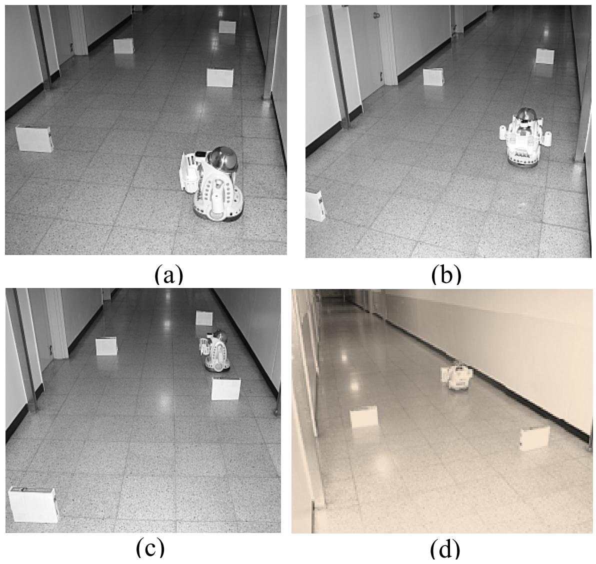

Fig. 10 **Experimental environment of K-RONI**

REFERENCES

[1] G.A. Bekey, Autonomous Robots: From Biological Inspiration to Implementation and Control, The MIT press, 2005.
[2] T. Hu, S.X. Yang, "Real-time motion control of a nonholonomic mobile robot with unknown dynamics", proc. of the Computational Kinematics Conf., Seoul, Korea, 2001.
[3] H.G. Tanner, K.J. Kyriakopoulos, "Backstepping for nonsmooth systems", Automatica No. 39, Vol. 5, pp. 1259–1265, 2003.
[4] P. Morin, C. Samson, "Application of backstepping techniques to time varying exponential stabilization of chained systems", European Journal of Control Vol. 3, No. 1, pp. 15–36, 1997.
[5] J. Hong, Y. Choi, and K. Park; "Mobile robot navigation using modified flexible vector field approach with laser range finder and IR sensor Control", ICCAS '07 International Conf., pp. 721 – 726, 2007
[6] M. Flynn, "Combining Sonar and Infrared Sensors for Mobile Robot Navigation", The International Journal of Robotics Research, Vol. 7, No. 6, pp. 5-14, 1988.
[7] J. L. Crowley, "World Modeling and Position Estimation for a Mobile Robot Using Ultrasonic Ranging", proc. of the 1989 IEEE International Conf. of Robotics and Automation, pp. 674-680, 1989.

Artificial Life Intelligent Contour Following Industrial Robot

MS Samsi*, I. Zunaidi*, M. Rozailan*, N Nagarajan ** , Y Sazali **

*TATi University College, Terengganu, Malaysia. **Universiti Malaysia Perlis

Abstract: Contour following is very important topic to be studied since the outcome of robot to follow contour automatically can simplify robot teaching process. Normal teaching to make robot capable of following contour is quite tedious and time consuming. It requires three points in order to model an arc. If the curve is quite complex it requires curve fitting of several points not to mentions teaching iterations in order to get correct overall curve path and speed. This research will empower industrial robot life artificially and can behave like intelligent entity whereby the industrial robot capable of self learning the curve and has the power to judge and discriminate the number of sampling points between simple curve and complex curve. Specifically this work will employ Fuzzy logic as a means to discriminate and to distribute the amount of sampling points adapted to the complexity of the curve. More points to approximate complex curve and less points to approximate simple curve. The impact of this research will transform the existing tedious manual training scenario of Industrial robot where the new robot will follow contour automatically while capturing points intelligently adapting to curve in order to be used later in repetitive playback process

Key words: Contour Tracking, Fuzzy Logic,.

1. Introduction

Robot is an essential added value tool in spray painting, arc welding and sealing application due to the complex nature of the process where the working condition is quite dangerous and undesirable to human being. In order to use robotics for such application two sequence of steps need to be considered, the programming phase and the playback phase. In the programming phase, teaching a group of points is required while for playback phase, the robot Tool Centre Point (TCP) will follow the taught points recorded previously. This programming phase especially for contour tracking application such as in arc welding, sealing and painting application is quite tedious and time consuming. For example, in order to track an arc, the robot programmer needs to manually use teaching box or teaching pendant to jog (powered motion) the robot Tool Centre Point to three points that enclosed an arc. For a complex contour, several series of three points must be taught, besides finding the optimum process parameter (voltage, current and electrode speed for arc welding application) related to those [(1) (2)(3)]. Next, the motion instruction, speed and type of termination that describes the closeness of zoning radial distance to the taught points needs also to be defined. The programmer must iterate the points and process parameters several times until the optimum combination are achieved. In comparison to assembly operation where the programmer just need to teach few points (approach, insert and depart points), contour tracking for painting, arc welding and sealing application requires a large number of points recorded and at the best location. After all the best program and process parameters are achieved for one sample part, the same quality is expected for the subsequent parts in a batch. This expectation alone poses difficult challenges to the industry since parts do vary dimensionally due to inaccuracy in manufacturing and joining operation. For example, in welding job such as gas-metal arc welding (GMAW) process the part expands dimensionally since the volume of molten material in the weld bead is proportional to the heat input[(4)(5)] . Furthermore, the current Flexible Manufacturing System concept requires different kind of parts variations for one production run. This means that a great number of robot programming is required to cater parts variations and uncertainties per production run compared to the old days

From these explanations, it can be justified that the effort to automate the robotics tedious teaching process in contour tracking application is really required in order to solve the abovementioned problems. Several actions will be studied in order to implement abovementioned task. First autonomous contour tracking algorithm for industrial robot is developed. Sweeping Radius Method will be used to implement this autonomous tracking[(1)(4)]. Second intelligence to the contour tracking algorithm developed previously will be increased by adding fuzzy logic algorithm to read the adjacent slope different and the local slope value for determining the sweeping radius distance and the number of sampling points, adapting to the curve . This algorithm will be tested on circular shape contour and the data will be presented in this paper The application of fuzzy logic control in robotics is to produce an intelligent robot with the ability of autonomous behavior and decision [(7)(8) (9)] .Fuzzy logic is a way of interfacing inherently analog processes, which move through a continuous range of values, to a digital computer, that likes to see things as well-defined discrete numeric values. They consist of an input stage, a processing stage, and an output stage. The input stage maps sensor or other inputs, to the appropriate membership functions. The processing stage invokes each appropriate rule and generates a result for each, then combines the results of the rules. Finally, the output stage converts the combined result back into a specific control output value[(9) (10)].

2. Generation of Autonomous Sweeping Radius Contour Tracking

2.1 TASK PLANNING FORMULATION

Users need to specify the contour length by recording the initial and final location of robot TCP (Tool Centre Point); smart sensors feed back and programming will guide the TCP to approximate the curve with a straight line segments that knot from points to points in three dimensional Cartesian XYZ plane. The measured knot points and segment slope will be stored in the database and will be used again and again in robot part program playback mode. Four degree of freedom SCARA ADEPT industrial robot will be used in this . The initial and final location of robot TCP will be recorded in joint coordinates and being transformed into world coordinate describing both orientation and position of the gripper Tool Centre Point refer to robot base world coordinate system as follow

$$P_{final} = P_{initial} T(N) \tag{1}$$

And after some manipulation

$$T(N) = (P_{initial})^{-1} P_{final} \tag{2}$$

Task planning matrices show the gross final tool position P_X , P_Y , P_Z and orientation yaw angle θ_Z which becomes

$$Px = n_A \bullet (p_B - p_A) \tag{3}$$

$$Py = s_A \bullet (p_B - p_A) \tag{4}$$

$$Pz = a_A \bullet (p_B - p_A) \tag{5}$$

$$\theta_Z = \tan^{-1}\left\{ \frac{\left[(n_A \bullet a_B).^2 + (s_A \bullet a_B)^2 \right]^{\frac{1}{2}}}{a_A \bullet a_B} \right\} \tag{6}$$

$$0 \le \theta \le \pi$$

which n_X , $s_{A,}a_A$ and θ_Z becomes input into next segment differential chord planning which will be discussed below. Modifying [(7)] Drive Transform Equation for four degree of freedom SCARA robot which only has yaw orientation angle, the chord segment relative path transformation drive transform is being simplified into one rotation matrices to orientate tool about *Z axis* and a straight line translation (one rotation about approach angle and another translation along tool axis) to achieve the motion between two consecutive Cartesian knot points. Motion from i to $i+1$ is related to drive transform as

$$T_4(i+1) = C_{Workobject} P_i D(i+1)({}^{tool}T_{i+1})^{-1} \tag{7}$$

is the input stored to the database and contain both tool position and orientation at any points which also becomes input to the inverse kinematics routine in order to get local coordinate of individual robot joint angles After some mathematical operation the position of consecutive knot points at beginning from i to end of segment $i+1$ is a function of drive transform as follow

$$D(i+1) = \begin{bmatrix} C(\theta) & 0 & S(\theta) & \delta_X \\ 0 & 1 & 0 & \delta_Y \\ -S(\theta) & 0 & C(\theta) & \delta_Z \\ 0 & 0 & 0 & 1 \end{bmatrix} \tag{8}$$

Total trajectory point generated at point N is as follow

$$P_N = \prod_{i=1}^{N-1} P_i D(i+1) \tag{9}$$

The related transformation at any point *N* which become input to inverse kinematics routine is

$$T_4(N) = \prod_{i=1}^{N} C_{Workobject} P_i D(i+1)({}^{tool}T_{i+1})^{-1} \tag{10}$$

Fig.1 Fuzzy Sweeping Radius with ADEPT SCARA Robot Implementation

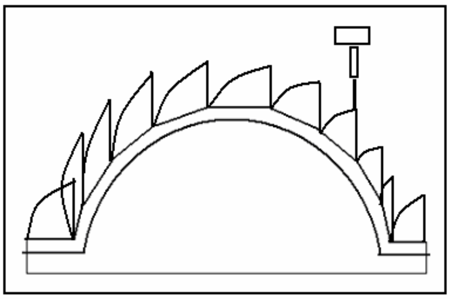

Fig.2 Fuzzy Sweeping Radius Movement

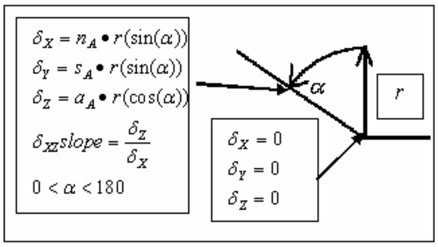

Fig.3 Important Parameter for Sweeping Radius

2·2 Sweeping Radius Contour Tracking

The objective of this research is to automate the incremental measuring motion utilizing the gross output of total positions and yaw orientation angles from task planning algorithm discussed before. Another important point is the slope gradient measurement at any knot points for correcting the optical sensor reflectance correction factor along the contour positive and negative slope gradient. The complex contour of any different gradient is being approximated by segment of chord distance r . The smaller the r value the higher the accuracy of contour shape being measured but at a higher computation cost (refers fig.1). The first pass of robot program is to measure the incremental position and slope along the contour gradient and store the positions recorded in the data base. The stored locations will be used again and again for playback purpose in subsequent passes (running a production part program).

2. Fuzzy Discriminator Development

The complexity of the curve can be represented by value of the slope differences and value of local slope. Fuzzy subprogram written in ADEPT SCARA robot V+ code will return the value of sweeping radius dr to the main program of sweeping radius method based upon curve complexities in real time(refer figure3). More sampling measurements points will be generated to complex curve and less sample on the flat simple curve. Three fuzzy sets of SMALL MEDIUM and BIG were used for each input to fire five output singletons of SMALL, MEDIUM, BIG, VERY BIG and MAXIMUM BIG giving a total of nine rules as follows;

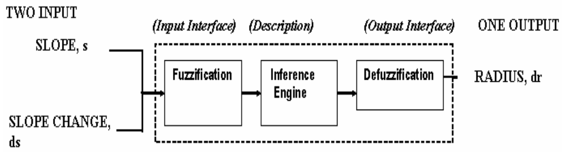

Fig.4 Two input one output Fuzzy Model

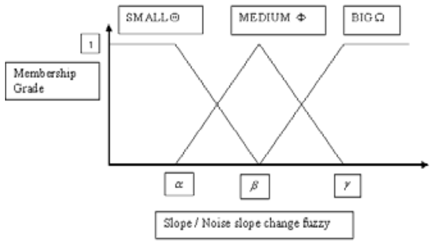

Fig.5. Input of Slope and Slope difference Fuzzy representation

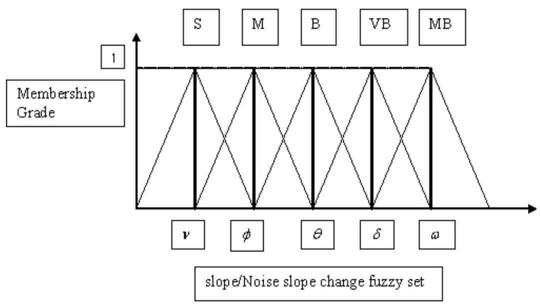

Fig.6. Singleton Output Sweeping Radius Sampler

Rule 1; IF u is B and du is S THEN dr is S

Rule 2; IF u is B and du is M THEN dr is M

Rule 3; IF u is B and du is B THEN dr is B

Rule 4; IF u is M and du is S THEN dr is M

Rule 5; IF u is M and du is M THEN dr is B

Rule 6; IF u is M and du is B THEN dr is VB

Rule 7; IF u is S and du is S THEN dr is B

Rule 8; IF u is S and du is M THEN dr is VB

Rule 9; IF u is S and du is B THEN dr is MB

Where :

$u =$ current local slope input, $du =$ slope error (noise slope changes)input, dr = radial sweeping parameter output, B: Big, M: Medium,S: Small, VB: Very big,MB: Maximum Big

The fuzzy output value then transformed to a crisp value using as defuzzification strategy the average of the impulses or average singletons. This method is considered as a special case of the average peak value (Lee, 1990), where the areas of output fuzzy set partitions by unity impulses centered at half support value of each set;

$$u = \frac{\sum_{i=1}^{n} w_i a_i \int_{w_i-\infty}^{w_i+\infty} \delta(w_i) dw}{\sum_{i=1}^{n} a_i}$$

3. Fuzzy Contour Tracking Result

The actual contour traced and the tracking error along contour, matching the semicircle geometry of radius 40 millimeter is plotted in figures 7 and 8. The safety margin of 0.1 to 2.5 millimeter is allowed at the beginning and near to the end of the semicircle object in order to avoid measuring the very high slope at those regions. The sweeping radius parameter is adjusted intelligently by this autonomous fuzzy contour tracking program dependent upon the contour slope and noise slope change. The total sample of 74 points were collected over 80 millimeter of horizontal measuring distance.

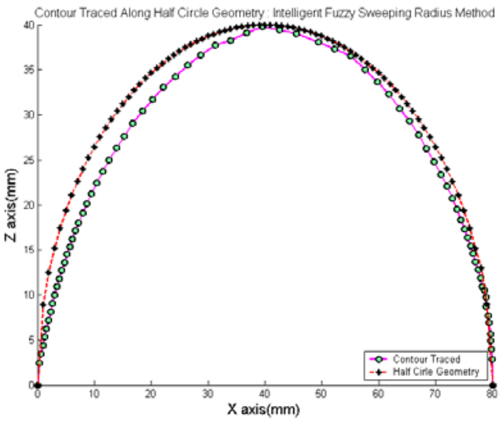

Fig.7.: Contour Traced along semicircle geometry with Intelligent Fuzzy Sweeping Radius Method.

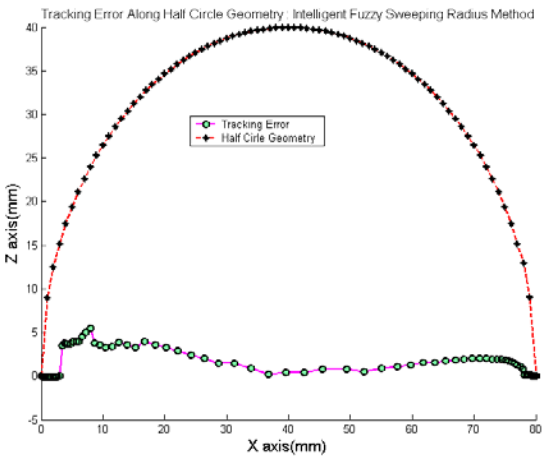

Fig 8 Tracking Error along semicircle geometry with Intelligent Fuzzy Sweeping Radius Method

4. Conclusion

This work demonstrate that :-

・The automation of tedious and time consuming robot contour tracking program is possible and feasible just by employing only one discrete optical sensor interface to ADEPT SCARA Robot.

・Fuzzy Logic can be programmed into industrial robot with the simplification on the output side by employing Sugeno Singleton output thus simplifying robot fuzzy programming.

・Using the Fuzzy Logic More samples is generated along infinity and high slope region curve and less samples approximating flat and low slope with less complexity

・Error is quite high in the high slope region especially in the positive slope portion. Negative slope portion posses less error in comparison to positive slope

・The higher the slope value the more error and more samples need to be generated in order to approximate and track a contour

REFERENCES

[1] Samsi MS and Nazim , "Autonomous and Intelligent Contour Tracking Industrial Robot", International Conference on Mechatronics, Proc ICOM Kuala Lumpur Malaysia, pp 78 – 86 May 2005.

[2] Prabuwono AS and Samsi MS "Autonomous contour tracking using staircase method for industrial robot", Proc. the 10th IEEE International Conference on Control, Automation, Robotics and Vision (ICARCV 2008), pp. 2272-2276, Hanoi, Vietnam, 2008.

[3] Prabuwono AS and Samsi MS "Dual sensor logic algorithm for contour following task: an application to Adept SCARA robot", International Journal of Computer Sciences and Engineering Systems, Vol. 3, No. 2, April 2009

[4] Adolfo Bauchspiessa,*, Sadek C. Absi Alfarob, Leszek A. Dobrzanski Predictive sensor guided robotic manipulators in automated welding cells, Journal of Materials Processing Technology,Vol. 9, pp. 13 to 19, 2001.

[5] Paul. R. P. 1979. *Manipulator Cartesian Path Control.* IEEE, Trans, System, Man, Cybernatics. Vol. 9 . pp.702-711.

[6] Paul. R. P. 1972. *Modeling, Trajectory Calculation, and servoing of a Computer Controlled Arm*. IEEE. Memo AIM-177. Stanford Artificial Intelligence Laboratory, Palo Alto California.

[7] T. Takagi and M. Sugeno. 1985. Fuzzy Identification of Systems and Its Applications to Modeling and Control. IEEE Transactions on Systems, Man and Cybernetics. Vol 15. pp. 116-132

[8] Zadeh, L.F.1968. Fuzzy Algorithms. Information and Control Journal. Vol 12, pp. 94-102.

[9] Zadeh, L.F.1972. Outline of a new approach to the analysis of complex system and decision processes . IEEE Tran. Systems Man Cybernet. Vol 3 pp. 28-44.

[10] Abu Mallouh, M. and Surgenor, B. (2008) "Force/Velocity Control of a Pneumatic Gantry Robot for Contour Tracking with Neural Network Compensation",

Real Time Traffic Signal Learning Control Using BPNN Based on Prediction for Probabilistic Distribution of Standing Vehicles

Chengyou Cui, Jisun Shin, Heehyol Lee

Graduate School of Information and Systems, Waseda University

2-7 Hibikino, Wakamatsu-ku, Kitakyushu, Fukuka, 808-0135, Japan

(tel:81-93-692-5164)

(cuichengyou@ruri.waseda.jp)

***Abstract*:** In this paper, a new method to predict the probabilistic distribution of traffic jam at crossroads and a traffic signal learning control system are proposed. First, the Dynamic Bayesian Network is used for build a forecasting model to predict the probabilistic distribution of vehicles for traffic jam during the each period of traffic signal. The adjusting algorithm of traffic signal control is applied to maintain the probability of a lower limit and ceiling of the standing vehicles to get the desired probabilistic distribution of the standing vehicles. In order to achieve the real time control, a learning control system based on the Back Propagation Neural Network is used. Finally, the effectiveness of the new traffic signal control system using the actual traffic data will be shown.

***Keywords*:** Traffic signal control, Bayesian Network, BP neural network, probabilistic distribution

Ⅰ INTRODUCTION

In recent years, the traffic congestion has become serious problem. The traffic volume continues to increase and the streets are congested with cars. The traffic signal control is the most-effective method to solve the problem.

In general terms, the traffic signal has three parameters that are cycle time, split, and offset. Traffic signal control method is selected on the complexity from the simple system that uses historical data to determine fixed timing plans, to the adaptive signal control, which optimizes timing plans for a network of signals according to traffic conditions in real time. As the adaptive signal control, the traffic forecasting has been known as a most important part. [1]

In this paper, the historical data and real time traffic flows of the adjacent to crossroads are used to predict the probabilistic distribution of standing vehicles. After that, the traffic signals are adjusted until to get desired probabilistic distribution of the standing vehicles. Finally, the BPNN model to establish the real time traffic signal learning control system is used.

Ⅱ FORECASTING MODEL

The Bayesian network is applied to build a forecasting model of the standing vehicles at crossroads. The Bayesian network is a directed and acyclic graphical model, and each node represents variables of the given problem. The relationship between each variable is evaluated quantitatively using the conditional probability. [2]

2.1 Bayesian network model of standing vehicles

Two crossroads are considered in this paper as shown in Fig.1.

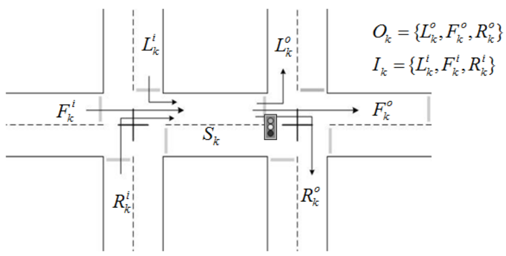

Fig.1 Crossroads

The random variables of the inflows *Ik*, and the outflows *Ok* and the standing vehicles *Sk* between crossroads have relationship as following: *Sk* = *S*(*k*-1)+*Ik*-*Ok*. And then, the Bayesian network model is built up using this relationship, and the random variables of the inflows and the outflows of each direction and the standing vehicles are represented as the nodes. The Bayesian network model is shown in Fig.2.

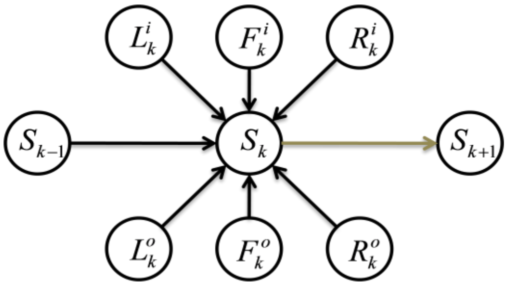

Fig.2 Bayesian network model of standing vehicles

The probabilistic distribution of the standing vehicles at *k th* cycle is obtained by summing over all values of the other variables as following,

$$P(S_k)=\sum_{S_{k-1}}\sum_{F_k^i}\sum_{R_k^i}\sum_{L_k^i}\sum_{F_k^o}\sum_{R_k^o}\sum_{L_k^o}P(S_k,S_{k-1},F_k^i,R_k^i,L_k^i,F_k^o,R_k^o,L_k^o) \tag{1}$$

With the chain rule, the joint probabilistic distribution is represented as the product of the conditional probability. And then, according to the d-separation, Eq.(1) can be represented as

$$P(S_k)=\sum_{S_{k-1}}\sum_{F_k^i}\sum_{R_k^i}\sum_{L_k^i}\sum_{F_k^o}\sum_{R_k^o}\sum_{L_k^o}P(S_{k-1}) \times P(F_k^i)P(R_k^i)P(L_k^i)P(F_k^o)P(R_k^o)P(L_k^o) \tag{2}$$

According to Eq.(2), the probabilistic distribution of the standing vehicles is predicted.

2.2 Procedure of prediction for probabilistic distribution of standing vehicles

In order to get the optimal traffic signals, the prediction of the probabilistic distributions of standing vehicles carried out three cycles before, because future probabilistic distribution of standing vehicles are necessary to adjust the traffic signals.

The procedure of the update for the priori probability and prediction for the probabilistic distribution of standing vehicles are illustrated in Fig.3. Firstly, the priori probability of each variable is updated by the previous data at *(k-1) th* cycle. Then, the probabilistic distribution of standing vehicles at *k th* cycle is predicted using Eq.(2). The future traffic densities are not measured, so the probabilities of the inflows and the outflows at *k th* cycle are assumed to be equal to those at *(k-1) th* cycle based the pre-timed signals. Next, the adjusting algorithm is applied to get the optimal traffic signals and it is used for update the priori probability of the outflows. The adjusting algorithm will be described at next session. Finally, at *k th* cycle the probabilistic distribution of standing vehicles is calculated to predict next cycles. The process of prediction at *(k+1) th* and *(k+2) th* cycles is the same as the *k th* cycle.

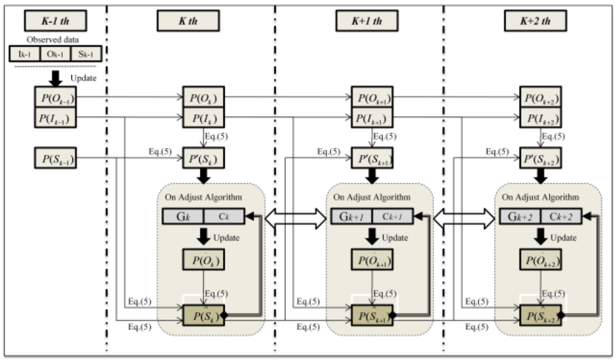

Fig.3 Procedure of prediction for standing vehicles

Ⅲ TRAFFIC SIGNAL CONTROL SYSTEM

The traffic signal control system has two parts: online and offline processing. In the online processing, BPNN is used for calculate the optimal traffic signals based on the result of the forecasting model for the prediction of standing vehicles. And then, the adjusting algorithm is applied to update the weight of BPNN model in offline processing. The Fig.4 shows the procedure of the traffic control system.

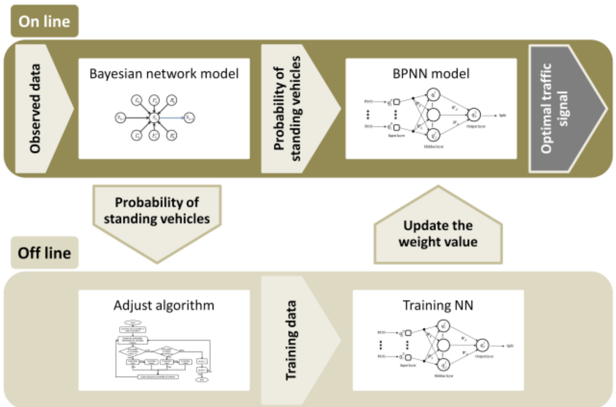

Fig. 4 Procedure of traffic signal control

3.1 Adjusting algorithm of traffic signals

The flowchart of the adjust algorithm is illustrated in Fig.5. The adjust procedure is followed.

Step1: Using observed data of *(k-1) th* cycle, update the priori probabilities of the inflows, the outflows, and the standing vehicles.

Step2: Predict the probabilistic distribution of the standing vehicles at *k th* cycle on pre-timed signal.

Step3: If the probability of over *Smax* of standing vehicles is bigger than a set value *a*, then extend the split or cycle time. And, if the probability of below *Smin* of standing vehicles is bigger than a set value *ß*, then shorten the split or cycle time. The *Smax* and *Smin* are obtained empirically.

Step4: Using new traffic signals, update the priori probability of the outflows.

Step5: Recalculate the probabilistic distribution of standing vehicles of *k t*h cycle.

Step6: If the adjustment of *k th* cycle is finished, go to next cycle.

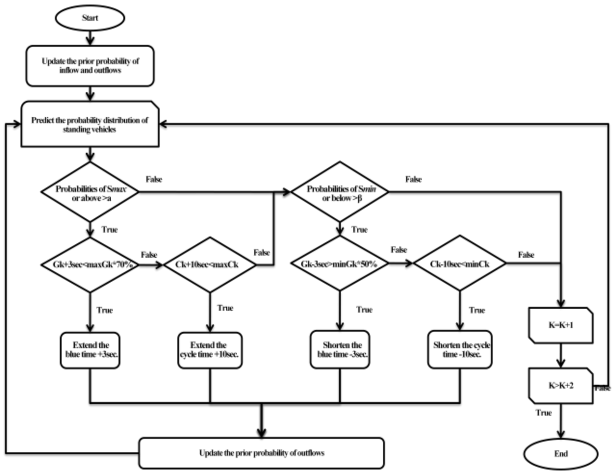

Fig.5 Flowchart of adjust algorithm

For the update of the prior probability for the outflows, the expected and it nearby values are increase and decrease the others.

3.2 Real time control system by BPNN model

The new traffic signal learning control by BPNN model is proposed for the real time control. The traffic signals are adjusted based the predicted and improved probabilistic distribution of the standing vehicles, which satisfy the condition of the probabilities for over Smax and over Smin. So that, the optimal traffic signals can be deduce using the pattern of its desirable probabilistic distribution of standing vehicles.

The BPNN model is powerful learning system, and it can be applied to pattern recognition. The BPNN is a multi-layers network that consists of the input layer, the hidden layer, and the output layer. And then, the BP algorithm can train a given feed-forward multilayer neural network for a given set of input patterns.

The BPNN model of the traffic signal control system is shown in Fig.6. The input values are the probabilities of standing vehicles, which probabilities are predicted by the Bayesian network model, and the output value are traffic signals.

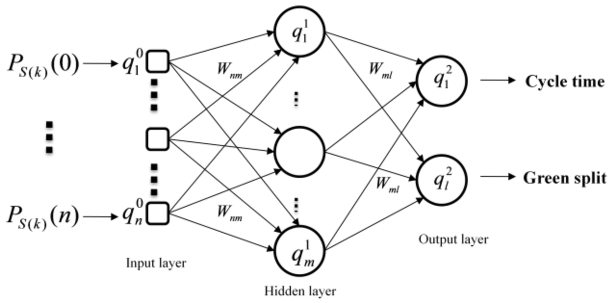

Fig.6 Structure of the BPNN

In this model, the number of the neurons are determined by the number of the input layer. The traffic signal is consisted of two parameters in this paper, green split and cycle time. So, 2 neuron in the output layer are set up. The number of the hidden layer can be calculated by empirical formula as following Eq.(3).

$$m = \sqrt{n \times l} \tag{3}$$

n= number of the neuron in the input layer
m =umber of the neuron in the hidden layer
l=number of the neuron in the output layer

Ⅳ SIMULATION

To prove the effectiveness of the proposed system, a simulation was carried out based on the actual data at Kitakyushu of Japan. The traffic signals of this crossroads have been adjusted by the pre-timed control: the cycle time is 150sec and split is 64% (green time is 96sec). There are 48 cycles actual data altogether, and 1*st* to 24*th* cycles are used as calculation of the initial priori probability of the inflows and the outflows, and the others are used to simulation.

4.1 Result of Adjusting algorithm

In the simulation, the set values of adjusting algorithm are shown in table1.

Tabel 1 Set value of adjusting algorithm

Cycle time	60-150 sec	Split	50-70%
Smax	75	*Smin*	40
a	20%	*ß*	15%

The result of traffic signals by the adjusting algorithm is shown in Fig.7. The new traffic signals obtained by the proposed method are compared with the pre-timed signals.

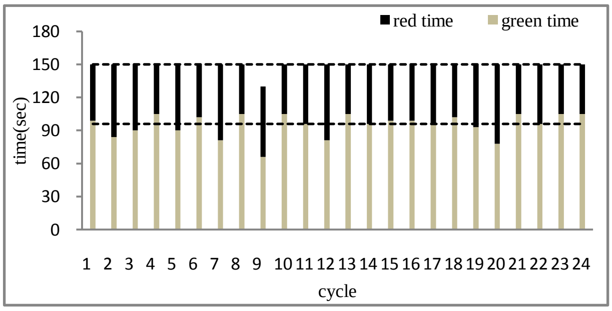

Fig.7 Adjusted Traffic signals

Fig.7 and Fig.8 show the result of standing vehicle at ecach cycle by the adjusted and pre-timed control in main road and mior road respectively.

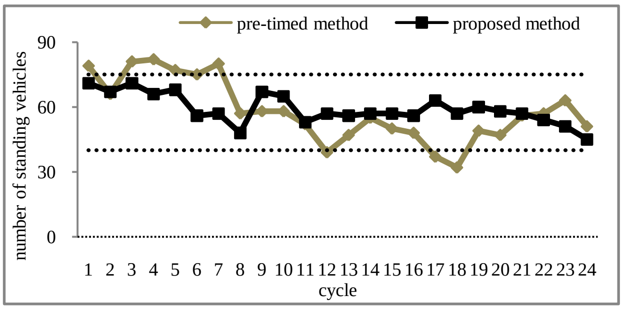

Fig.8 Number of standing vehicles in main road

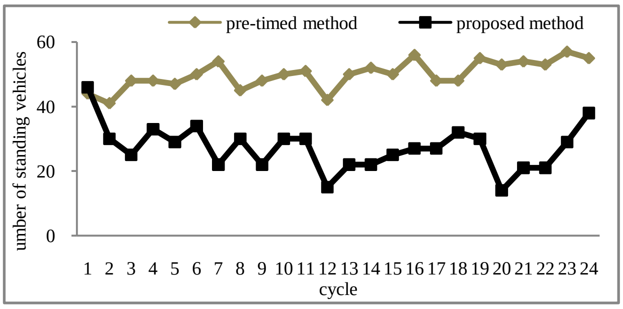

Fig.9 Number of standing vehicles in minor road

These figures show that the numbers of the standing vehicles are within the desired numbers from 40 to75 in main road, and the number of one is reduced markedly in minor road. The total number of the standing vehicles of the main and minor roads is shown in table 2. By the proposed adjusting algorithm the total number of the standing vehicles is decreased about 20% compared whit the pre-timed.

Table 2 Average number of standing vehicles

	Pre-timed method	Proposed method
Main road	58.2	59.0
Mior road	50.0	27.3
Total	108.2	86.3

4.2 Result of BPNN model

According to the Bayesian network model, the probabilities of standing vehicles over 100 are very small, so the number of neuron in the input layer is set up to 100 neurons, and the number of neuron in the hidden layer is set up to 14. The probabilistic distribution of standing vehicles from *1st* to *12th* cycles are used for tanning input pattern, and the result by the adjusting algorithm is used for target data, and then, *13th* to *24th* cycle are applied to obtain the new traffic signals.

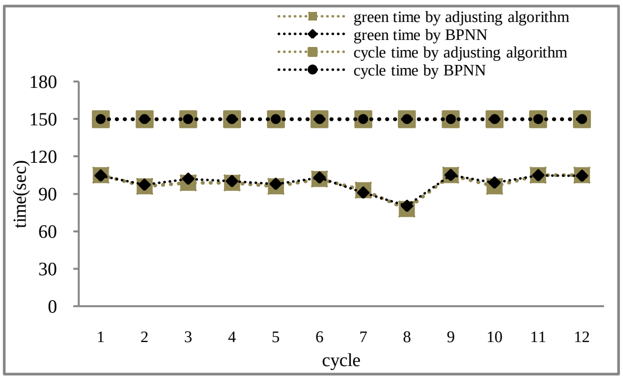

Fig.10 Traffic signals by adjust algorithm and BPNN

Fig.10 shows the traffic signals by BPNN model and by the adjusting algorithm. The result shows that the traffic signals by BPNN are close to the result by the adjusting algorithm and the average error of green time and cycle time is 1.3 sec and 0.1 sec respectively.

V CONCLUSIONS

In this paper, the real time learning traffic signal control system by BPNN based on the Bayesian network is proposed. Through the simulation using actual data, the effectiveness of the new signal control system is shown. The adjusting algorithm effectively calculates the optimal traffic signal to maintain the standing vehicles at main road, and then, the standing vehicles of minor road were also reduced.

REFERENCES

[1]Dipti Srinivasan; Min Chee Choy; Ruey Long Cheu (2006) Neural Networks for Real-Time Traffic Signal Control

[2] Richard E. Neapoltian (2003) Learning Bayesian Networks

[3] Kiyoshi Kawaguchi, Bess (2000) A Multithreaded Software Model for Back propagation Neural Network Applications

[4] Martin T.Hagan; Howark B.Demuth; Mark H,Beale(1995) Neural Network Design

[5]Japan Society of Traffic Engineers (2006) Manual on Traffic signal control (in Japanese)

The Fifteenth International Symposium on Artificial Life and Robotics 2010 (AROB 15th '10),
B-Con Plaza, Beppu,Oita, Japan, February 4-6, 2010

Advanced pipe inspection robot using rotating probe

Kentarou.Nishijima[1],Yixiang.Sun[2], Rupesh Kumar.Srivastava[3],Harutoshi.Ogai[1]and Bishakh.Bhattacharya[3]

[1]*Graduate school of Information, Production and Systems, Waseda University, Japan*
(Tel: +81-93-672-5147; Fax: +81-93-672-5147)
(E-mail: ogai@waseda.jp)
[2]*Department of Automation, Shanghai Jiao Tong University, China*
[3]*Department of Mechanical engineering, Indian Institute of Technology Kanpur, India*

Abstract: Recently many plants' pipes and drains became old and many robots to inspect these pipes were developed in the past. Wired robots were put to practical use, but they had a heavy power supply and a signal wire. Therefore, new inspection robots using wireless radio communication system are considered useful for long complex pipes and long distance pipes including straight, vertical and bend line. But sending wireless radio signals isn't practical because the properties of the radio wave are affected by the shape and material of the pipes. For these reasons, we measured the properties of wireless radio signal with steel pipes and ceramic pipes and we developed a practical wireless radio communication system. On the other hand, the Indian Institute of Technology Kanpur has researched a rotating probe using piezo element for inspecting the inside of pipes with a touch sensor system. This time, we developed and tested a new inspection robot that had integrated both the inspection system using wireless radio communication and image transmission developed by Waseda University and the inspection system using the rotating probe developed by the Indian Institute of Technology. In this experiment, we confirmed that we could drive the robot by wireless radio communication system in the inside test pipe and collect the image and some signals from the rotating probe.

Keywords: Pipe, Inspection robot, Wireless radio communication, Rotating probe

I. INTRODUCTION

Recently many plants became old, so steel pipes, ceramic pipes(earthenware pipes), concrete pipes and plastic pipes used for transportation of water and gas also became old. And, these pipes become cracked because of deterioration and corrosion. Many robots to inspect these pipes were developed in the past, but they had a heavy power supply and a signal wire. As a result, these wires caused problems with the movement of the robot. Therefore in this research, our purpose was to develop a flexible drain inspection robot using a wireless radio communication system. In 2005 and 2007, the radio communication properties inside the pipe were measured in an actual pipe and the appropriate radio frequency was analyzed. As a result, in steel pipe with a diameter of 30cm, the inside image information could be transferred by using radio communication system of 2.4GHz and 5.2GHz for a distance of about 100m. In an actual frequency test earthenware pipe with a diameter of 25cm and length of 20m, it was confirmed that the inside image could be transmitted using a radio frequency of 5.2GHz. On the other hand, the Indian Institute of Technology Kanpur has researched a rotating probe using piezo element for inspecting the inside of pipe with a touch sensor system. We developed the robot with this technique and report that the robot could inspect the inside of the pipe using the inside image information and the rotating probe data with touch sensor.

II. PIPE TRANSMISSION SYSTEM

2.1 Transmission Test in Steel Pipe

Experiment condition using a 10m steel pipe with a diameter of 30cm is shown in Fig.1. In the experiment, we emitted a wireless radio signal from the steel pipe inlet and it was measured in the steel pipe outlet. In the results, we could know the transmission loss in the steel pipe. Fig.2 and Fig.3 shows the transmission loss at different antenna positions respectively for 2.4GHz and 5.2GHz band. The transmission loss from transmitting antenna input to receiving antenna output is 14±6dB for 2.4GHz and 23±6dB for 5.2GHz band.

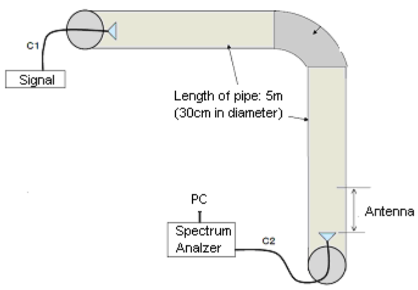

Fig.1. Wireless communication property measurement inside the steel pipe

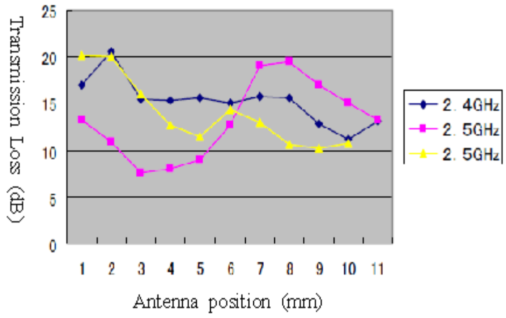

Fig.2. Transmission loss measured in steel pipe (2.4 GHz)

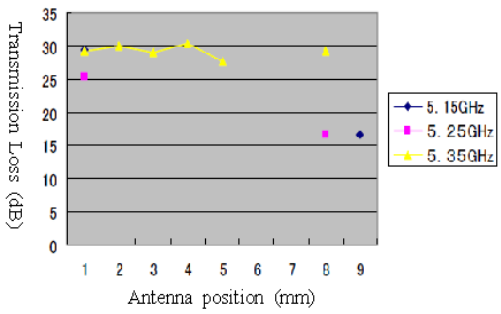

Fig.3. Transmission loss measured in steel pipe (5.2 GHz)

2.2 Transmission Test in Ceramic Pipe

Experiment condition using a 7m ceramic pipe with a diameter of 25cm is shown in Fig.4. This experiment inspected ceramic pipes using a similar method previously used for steel pipes. Transmission loss is 84±2.5dB for 2.4GHz and 52±1.5dB for 5.2GHz band. Fig.5 shows the relative electric field strength between ceramic pipe and free space. It is clear that 5.2GHz band has good performance in the ceramic pipe.

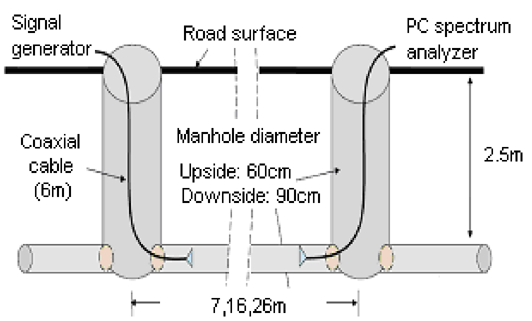

Fig.4. Wireless communication property measurement in the ceramic pipe

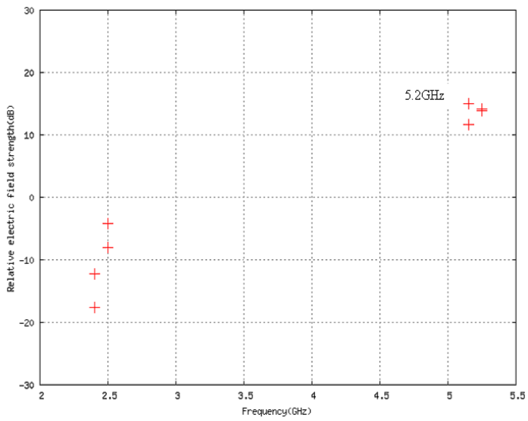

Fig.5. Wireless communication result in ceramic pipe

2.3 Transmission Test in Pipe using robot

Experiment condition using a 19m cleaned ceramic pipe with a diameter of 25cm and 30cm is shown in Fig.6. This experiment inspected transmission loss in ceramic pipes using previously tested robot and also inspected transmission loss in ground and space. And we clarified the relational equation between a pipe's diameter and the possible radio transmission distance in an earthenware pipe , as shown in Fig.7.

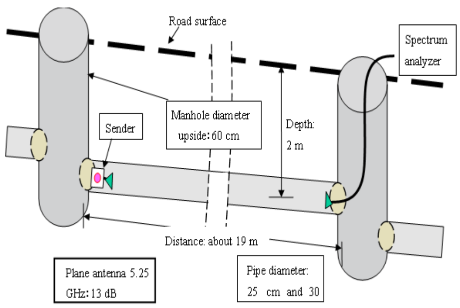

Fig.6. Transmission loss measurement system

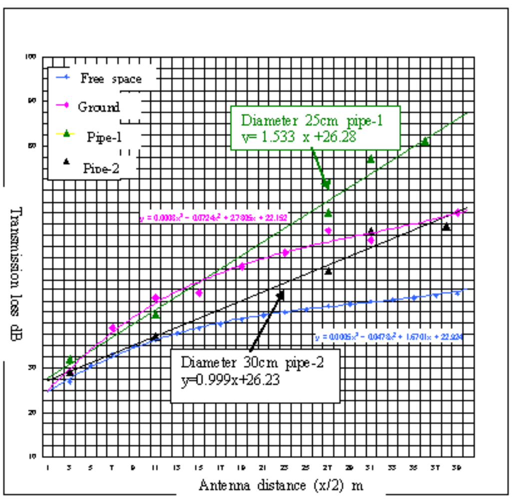

Fig.7. Transmission property

III. DEVELOPMENT OF ADVANCED INSPECTION ROBOT

From these results, we developed a drain pipe inspection robot equipped with practical wireless radio communication system. The robot was developed based on drain pipe inspection robot 'Mogurinko250' by Ishikawa Tekkousyo, as shown in Fig.8. This robot can be controlled by wireless radio communication in the inside pipe and can also transmit image information of the inside of the pipe in real time.

Specifications of this inspection robot:

- Size: length 370mm, width 180mm, height 160mm.
- Moving speed: 13.7m/min,
- Driving mode: double motor,
- Electric Power: rechargeable batteries 7.2V.
- Wireless frequency: apply to 2.4/5 GHz and Data transmission by 100 base-T Ethernet.
- USB Camera(300 thousand pixel)

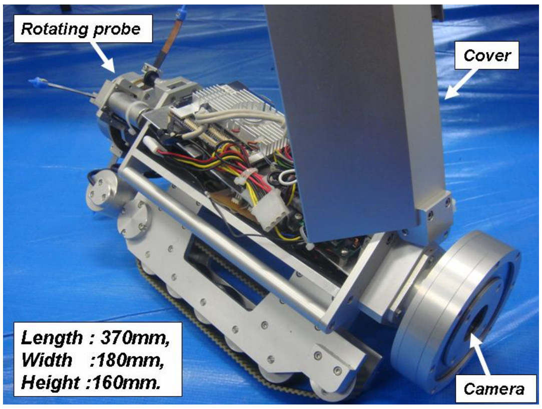

Fig.8. Inspection robot (Mogurinko)

IV. PIPE TOUCH SENSOR SYSTEM

4.1 Structure of Rotating Probe

The Indian Institute of Technology Kanpur has researched a rotating probe using piezo element for inspecting the inside of pipes with a touch sensor system. This time, a drain pipe inspection robot 'Mogurinko250' is equipped with this rotating probe and inspected the ceramic pipes. The four probes are equipped at the back of the robot. The rotating probe consisted of flexible steel and piezo film is positioned at the base of the probe. The steel strip can be used as cantilever. To control the cable of the rotating probe, a slipring was used, as shown in Fig.9.

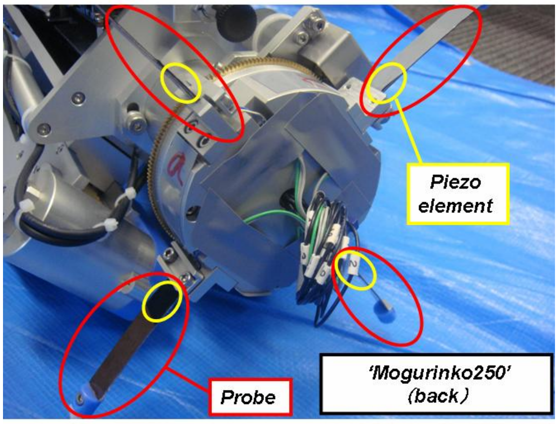

Fig.9. Rotating probe

4.2 Movement of Rotating Probe

When the rotating probe touched the defected area, the piezo film could detect the curve and change of the stress. This stress change of the piezo film can be measured as voltage change. Movement of rotating probe is shown Fig.10. First, four probes rotate and the probes approach the defect of the inside pipe. (Fig.10-①)Next, the probes start to touch the defect and its detected defect. (Fig.10-②,③) Afterward the probe moves away from the defect. (Fig.10-④)

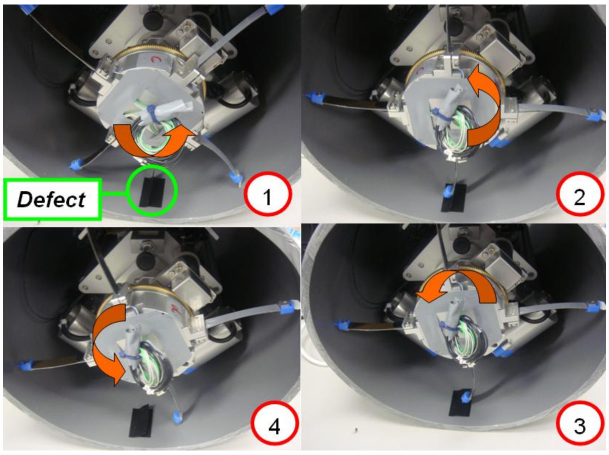

Fig.10. Movement of rotating probe

4.3 Rotating Probe Test in Vinyl Chloride Pipe

This experiment used a resting robot with a rotating probe in a clean vinyl chloride pipe with a 25cm diameter, as shown in Fig.11. Voltage change was measured in free rotation, and when the probe touched defects with heights and width of 5mm, 3mm and 1mm. The defects were made of slices of eraser.

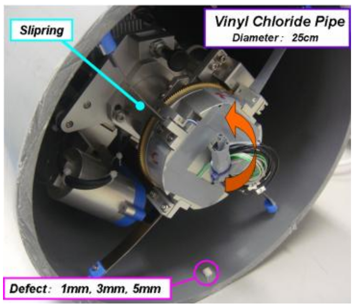

Fig.11. Voltage change measurement in the pipe

Detected voltage change was captured into the microcomputer by A/D converter. The main computer of the robot reads the data through serial transmission using the RS232C cable. The sampling cycle of the A/D converter is 0.01 seconds. These experimental results are shown in figure 12.

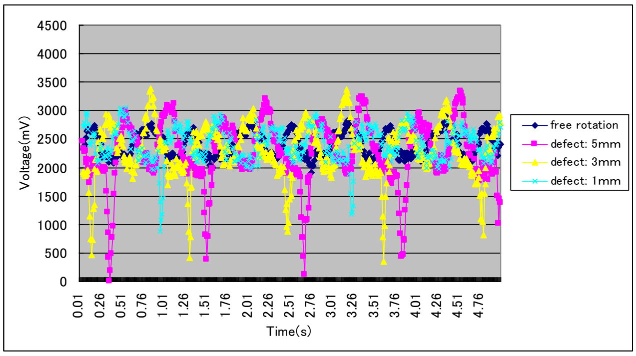

Fig.12. Voltage change using a resting robot

In this result, a probe could measure the defect of 5mm, 3mm and 1mm in the vinyl pipe. When a probe touched the defect, voltage showed a substantial decline. Therefore, we believe that four probes can be used to measure problems in inside pipes caused by corrosion, cracking and breakage. But, after a probe touched the defect, voltage change caused a strong rebound in the probe. For this reason we have to develop a probe using a harder substance.

4.4 Driving Test in Vinyl Chloride Pipe

Next, we carried out a test run with a robot equipped with a rotating probe. This experiment was used by a vinyl pipe, as shown in Fig.13.

Fig.13. Driving test

Fig.14 shows the relative voltage change by driving, and driving with a rotating probe in a vinyl chloride pipe.

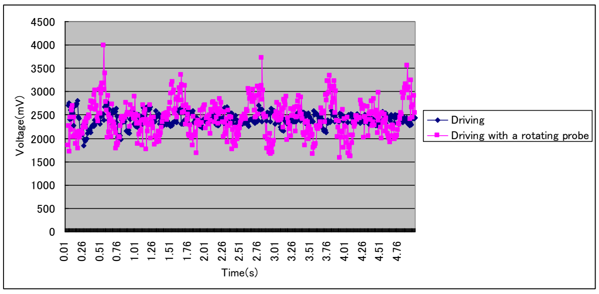

Fig.14. Voltage change in a driving robot

This results shows that the voltage change in driving with a rotating probe is greater than the change in driving with no rotating. This caused by vibration and small defects in the vinyl chloride pipe. In the future, we will try to improve the probe with no vibration and to inspect the real defect while driving.

V. CONCLUSION

In this paper, a rotating probe in vinyl chloride pipe was tested, and a new inspection robot system for drain pipe was developed. In future, we will analyze the image data and the probe data and research the best method for inspecting the defects and increasing the detection ability. In addition, we are going to do research on a smaller robot system and wireless radio communication system for small size's long drain pipe.

ACKNOWLEDGMENTS

We would like to thank ISHIKAWA IRON WORKS, who provides the inspection robot for this research.

REFERENCES

[1] Kosuke Wada (2007), Wireless Radio Communication System for Pipe Inspection Robot and Bridge Diagnosis Data. Waseda University, Master's thesis, pp. 9-11
[2] Harutoshi Ogai, Kosuke Wada, Katsumi Hirai, et al (2007), Wireless Radio Communication System for a Pipe Inspection Robot. ICASE Int'l Conf. 2007 (ICCAS 2007), Korea, pp.2616-2619, October 17-20
[3] Wei You, Dongmei Wu, Harutoshi Ogai, et al (2008), Wireless radio communication system for a pipe inspection robot. The 13th international Symposium on Artificial Life and Robotics, pp. 393-396, Jan. 31-Feb. 2
[4] Harutoshi. Ogai, Yichun. Yeh, Dongmei Wu, et al (2009), Pipe Inspection Robot using Wireless Communication System. The 14th International Symposium on Artificial Life and Robotics, pp. 59-62, February 5-7

The Fifteenth International Symposium on Artificial Life and Robotics 2010 (AROB 15th '10),
B-Con Plaza, Beppu,Oita, Japan, February 4-6, 2010

Quasi-ARX Neural Network and Its Application to Adaptive Control of Nonlinear Systems

Lan Wang, Yu Cheng and Jinglu Hu

Graduate School of Information, Production and Systems, Waseda University, Kitakyushu, Japans
(Tel : 81-93-692-5271; Fax : 81-093-692-5271)
(E-mail: wanglan@fuji.waseda.jp, chengyu0930@fuji.waseda.jp, jinglu@waseda.jp)

Abstract: This paper introduces a quasi-ARX neural network and discusses its application to adaptive control of nonlinear systems. A switching mechanism is employed to improve the performance of control system. An adaptive switching control of nonlinear system is established and some stability analysis of control system is shown. Simulations are given to show the effectiveness of the proposed method both on stability and accuracy.

Keywords: Nonlinear system, Quasi-ARX neural network, Adaptive control, Switching mechanism.

I. INTRODUCTION

Neural networks have been used to identify and control nonlinear dynamical systems because of its ability to approximate arbitrary map to any desired accuracy[1-4]. Some researchers have used neural networks directly to identify and control nonlinear systems[2, 5]. Many nonlinear ARX models based directly on neural networks also have been proposed. However, from a user's point of view, there are three major criticisms on those neural network models. One is that their parameters do not have useful interpretations. The second is that they do not have a friendly interface for controller design and system analysis[4]. The third one is that initialization and overfitting will lead to instability.

To solve these criticisms, a quasi-ARX neural network model has been proposed which embodied a macro-model part and a kernel part[3, 4]. The macro-model part is a user-friendly interface constructed using already known knowledge and the characteristic of network structure. In this paper, we will limit our discussion to a quasi-ARX approach. The linear ARX model has a various useful linearity properties which will solve the former criticisms. The kernel part is an ordinary neural network, which is used to parameterize the coefficients of macro-model. The quasi-ARX neural network is different from a nonlinear ARX model based directly on neural networks because of the linear characteristics and it also can be used to identify and control nonlinear systems accurately because of the nonlinear characteristics. In Ref.[4], we proposed an off-line control scheme based on the quasi-ARX neural network. We will discuss the adaptive control of nonlinear system in this paper.

Quasi-ARX neural network has two parts: the linear part and the nonlinear part. If the linear part would be used to ensure the nonlinear control stability and the nonlinear part would be utilized to improve the control accuracy, both stability and universal approximation capability will be realized. Motivated by the discussion, a switching law is established into the model based on the characteristic of quasi-ARX neural network structure in this paper. An adaptive switching control law is proposed for nonlinear dynamical systems and control system stability is proved.

The paper is organized as follows: In section 2, the considered system is given. In section 3, the quasi- ARX neural network model is introduced. Section 4 gives the parameters identification methods and the switching mechanism. Section 5 describes adaptive control system and analyzes the stability. Then, numerical simulations are carried out to show the effectiveness of the proposed modeling in Section 6. At last Section 7 gives some conclusions.

II. PROBLEM DESCRIPTION

Consider a single-input-single-output (SISO) black-box nonlinear system

$$y(t) = g(\varphi(t)) + v(t), \tag{1}$$

where $\varphi(t) = [y(t-1), ...y(t-n), u(t-d), ..., u(t-m-d+1)]^T$. $y(t)$ denotes the output at time t ($t = 1, 2, ...$), $u(t)$ the input, d the known integer time delay (Let d=1 in this paper, and other conditions can be got by the similar method.), $\varphi(t)$ the regression vector, and $v(t)$ the system disturbance. $g(\cdot)$ is a nonlinear function.

Assumption 1 (i) $g(\cdot)$ is a continuous function, and at $\varphi(t) = 0$ it is C^∞ continuous. (ii) the system is controllable, where a reasonable unknown controller may be expressed by $u(t) = \rho(\xi(t))$, where $\xi(t) = [y(t) \dots y(t-n)\ u(t-1) \dots u(t-m)\ y^*(t+1) \dots y^*(t+1-l)]^T$ ($y^*(t)$ denotes reference output). (iii) the system has a globally uniformly asymptotically stable zero dynamics.

III. QUASI-ARX NEURAL NETWORK MODEL

1. Regression Form Representation

Through Taylor expansion of function $g(\cdot)$ around the region $\varphi(t) = 0$

$$y(t) = g(0)+g'(0)\varphi(t)+\frac{1}{2}\varphi^T(t)g''(0)\varphi(t)+ ... +v(t). \tag{2}$$

Let

$$\theta(\varphi(t)) \quad = \quad \left(g'(0) + \frac{1}{2}\varphi^T(t)g''(0) + \cdots\right)^T$$

$$= [a_{1,t} \dots a_{n,t}\, b_{0,t} \dots b_{m-1,t}]^T$$

where the coefficients $a_{i,t} = a_i(\varphi(t))$ and $b_{i,t} = b_i(\varphi(t))$ are nonlinear functions of $\varphi(t)$. g(0)= 0 is assumed for simplicity. A regression form of the system (1) is described by (3):

$$y(t) = \varphi^T(t)\theta(\varphi(t)) + v(t). \quad (3)$$

Now, two polynomials $A(q^{-1}, \varphi(t))$ and $B(q^{-1}, \varphi(t))$ based on the coefficients $a_{i,t}$ and $b_{i,t}$ are defined by

$$\begin{aligned} A(q^{-1}, \varphi(t)) &= 1 - a_{1,t}q^{-1} - \dots - a_{n,t}q^{-n} \\ B(q^{-1}, \varphi(t)) &= b_{0,t} + \dots + b_{m-1,t}q^{-m+1} \end{aligned}$$

where q^{-1} is the backward shift operator, e.g. $q^{-1}u(t) = u(t-1)$.

A similar-linear ARX model is developed

$$A(q^{-1}, \varphi(t))y(t) = B(q^{-1}, \varphi(t))u(t-1) + v(t). \quad (4)$$

2. Weighted One-Step-Ahead Predicate

The theorem for a d-step prediction has been proved in Ref.[4]. When d=1, one-step predictor is given :

$$\hat{y}(t+1) = \alpha(q^{-1}, \phi(t))y(t) + \beta(q^{-1}, \phi(t))u(t) \quad (5)$$

where $\phi(t) = [y(t), ...y(t-n+1), u(t), ...u(t-m+1)]^T$. $\alpha(q^{-1}, \phi(t)) = \alpha_{0,t} + \dots + \alpha_{n-1,t}q^{-n-1}$ and $\beta(q^{-1}, \phi(t)) = \beta_{0,t} + \dots + \beta_{m-1,t}q^{-m+1}$.

The prediction model (5) is a general one that is nonlinear in the variable $u(t)$, because the coefficient $\alpha_{i,t}$ and $\beta_{i,t}$ are function of $\phi(t)$. With Assumption 1 (ii), the unknown $\rho(\cdot)$ replaces variable $u(t)$ in the coefficients $a_{i,t}$ and $b_{i,t}$

$$\begin{aligned} \alpha_{i,t} &= \alpha_i(\mathbf{x}(\varphi(t))) \simeq \alpha_i(\phi_\rho(t)) \triangleq \alpha_i(\xi(t)) \\ \beta_{i,t} &= \beta_i(\mathbf{x}(\varphi(t))) \simeq \beta_i(\phi_\rho(t)) \triangleq \beta_i(\xi(t)) \end{aligned}$$

where $\phi_\rho(t)$ is $\phi(t)$ whose element $u(t)$ is replaced by $\rho(\xi(t))$, that is, $\phi_\rho(t) = [y(t) \dots y(t-n+1)\ \rho(\xi(t))\ u(t-1) \dots u(t-m+1)]^T$. $\xi(t)$ has a form of

$$\begin{aligned} \xi(t) = [&y(t) \dots y(t-n+1)\ u(t-1) \dots \\ &u(t-m+1)\ y^*(t+1)]. \end{aligned}$$

We have a predictor expressed by:

$$\hat{y}(t+1) = \alpha(q^{-1}, \xi(t))y(t) + \beta(q^{-1}, \xi(t))u(t) \quad (6)$$

We finally express the predictor by

$$\hat{y}(t+1) = \Psi^T\Theta_\xi \quad (7)$$

where $\Psi(t) = [y(t) \dots y(t-n+1)\ u(t) \dots u(t-m+1)]$.

3. Incorporation of Neural Networks

Parameterizing Θ_ξ with a MIMO neural network, the quasi-ARX prediction model is expressed by

$$\hat{y}(t+1) = \Psi(t)^T(t)\mathcal{N}(\xi(t), \Omega) \quad (8)$$

where $\mathcal{N}(\cdot, \cdot)$ is a 3-layer neural network with n input nodes, M sigmoid hidden nodes and $n+1$ *linear* output nodes[1].

[1]The number of input node is $n = \dim(\xi(t)) = n_y + n_u$, the number of output node is equal to $\dim(\Phi(t)) = n+1$

Let us express the 3-layer neural network by

$$\mathcal{N}(\xi(t), \Omega) = W_2\Gamma(W_1\xi(t) + B) + \Theta \quad (9)$$

where $\Omega = \{W_1, W_2, B, \Theta\}$, $W_1 \in \mathcal{R}^{M\times n}$, $W_2 \in \mathcal{R}^{(n+1)\times M}$ are the weight matrices of the first and second layers, $B \in \mathcal{R}^{M\times 1}$ is the bias vector of hidden nodes, $\Theta_2 \in \mathcal{R}^{(n+1)\times 1}$ is the bias vector of output nodes, and Γ is the diagonal nonlinear operator with identical sigmoid elements σ (i.e., $\sigma(x) = \frac{1-e^{-x}}{1+e^{-x}}$). Then the quasi-ARX prediction model (9) is expressed in a form of

$$\hat{y}(t+1) = \Psi^T(t)\Theta + \Psi^T(t) \cdot W_2\Gamma(W_1\xi(t) + B). \quad (10)$$

The quasi-ARX neural networks prediction model consists of two parts: the first term of the right side of (10) is a linear ARX prediction model part, while the second term is a nonlinear part. Therefore, in the quasi-ARX prediction model the bias of output nodes Θ describes a linear approximation of the object system.

Assumption 2 (i) The linear parameters Θ lies in a compact region $\mathcal{B}$. (ii) The nonlinear term $\Psi^T(t) \cdot W_2\Gamma(W_1\xi(t) + B)$ is globally bounded, i.e. $\Psi^T(t) \cdot W_2\Gamma(W_1\xi(t) + B) \le \Delta$.

IV. PARAMETERS ESTIMATION AND SWITCHING CRITERION FUNCTION

1. Parameter Estimation

For the quasi-ARX model, the linear part parameter Θ is updated as:

$$\hat{\Theta}(t+1) = \hat{\Theta}(t) + \frac{a(t)\Psi(t)e_1(t)}{1 + \Psi(t)^T\Psi(t)} \quad (11)$$

$$a(t) = \begin{cases} 1 & \text{if } \ |e_1(t)| > 2\Delta \\ 0 & \text{otherwise} \end{cases} \quad (12)$$

where ε is a small positive constant. $e_1(t) = y(t+1) - \Psi(t)^T\hat{\Theta}(t)$.

For the quasi-ARX model, the nonlinear part error: $e_2(t) = y(t+1) - \Psi(t)^T\hat{\Theta}(t) - \Psi^T(t) \cdot W_2(t)\Gamma(W_1(t)\xi(t) + B(t))$. is chosen

The parameters Ω of the part combined with neural networks is adjusted by BP algorithm.

2. Switching Criterion Function

When the overfitting in the neural network part happens, nonlinear part will be turned off.

Now give the switching criterion function as in [7]:

$$\begin{aligned} J_i(t) = &\sum_{l=k}^{(t)} \frac{a_i(l)(\| e_i(l) \|^2 - 4\Delta^2)}{2(1 + a_i(l)\Psi(l-k)^TP_i(l-k-1)\Psi(l-k))} \\ &+ c * \sum_{l=t-N+1}^{t} (1 - a_i(l) \| e_i(l) \|^2) \end{aligned} \quad (13)$$

where N is an integer and $c \ge 0$ is a predefined constant.

By comparing $J_1(t)$ and $J_2(t)$, decides when the nonlinear part is abandoned. If $J_1(t) > J_2(t)$ the nonlinear part is chosen, else only use linear part to identify.

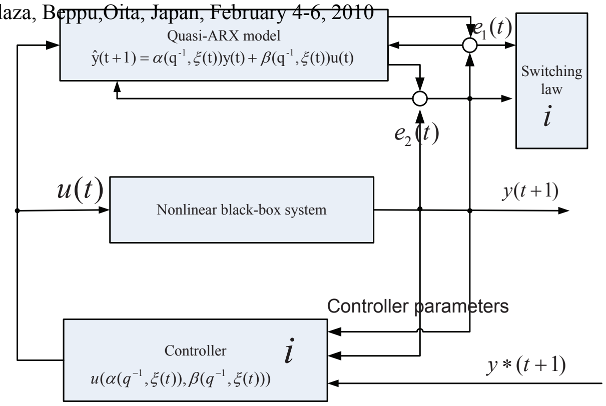

Fig. 1 A Switching control to nonlinear system based on linear model and quasi-ARX model

VI. CONTROLLER DESIGN AND STABILITY ANALYSIS

Consider a minimum variance control with the criterion function as follows:

$$M(t+1) = \left[\frac{1}{2}(y(t+1) - y^*(t+1))^2 + \frac{\lambda}{2}u(t)^2\right] \quad (14)$$

where λ is weighting factor for the control input.

The controller can obtain by solving:

$$\frac{\partial M(t+1)}{\partial u(t)} = 0 \quad (15)$$

Therefore, the proposed models can derive controller by solving (15):

$$u(t) = \frac{\beta_{0,t}}{\beta_{0,t}^2 + \lambda}((\beta_{0,t} - \beta(q^{-1}, \xi(t))q)u(t-1) + y^*(t+1) - \alpha(q^{-1}, \xi(t))y(t)). \quad (16)$$

where

$$[\beta(q^{-1}, \xi(t)); \alpha(q^{-1}, \xi(t))] = \quad (17)$$
$$\begin{cases} \Theta(t) & \text{if} \quad J_1(t) < J_2(t) \\ W_2(t)\Gamma(W_1(t)\xi(t) + B(t)) + \Theta(t) & \text{otherwise} \end{cases}$$

The proposed controller has three distinctive features:
(1) it is linear for the variables synthesized in control systems;
(2) its parameters have explicit meanings;
(3) it is one controller which have a switching algorithm.

Figure 1 shows the controller for unknown nonlinear systems. We can see that the identified model and controller model share their parameters.

Theorem For the system (1) with adaptive controller (13), all the input and output signals in the closed-loop system are bounded. Moreover, the tracking error of the system can converge on zero when a properly neural network is determined.

Proof: (i) Subtracting Θ_0 from both sides of (11), and gives:

$$\tilde{\Theta}(t+1) = \tilde{\Theta}(t) - \frac{a(t)\Psi(t)(\Psi(t)^T\tilde{\Theta}(t) - \omega(t))}{1 + \Psi(t)^T\Psi(t)} \quad (18)$$

where $\omega(t) = y(t+1) - \Psi(t)^T\Theta_1(t)$.

Consider the following functional:

$$V(t) = \|\tilde{\Theta}(t)\|^2. \quad (19)$$

Then, noting that a(t)=0 or 1, and combined with (11) and (12), we can get as in [6]:

$$V(t+1) \le V(t) + \frac{2a(t)\Delta^2}{1 + \Psi(t)^T\Psi(t)} - \frac{1}{2}\frac{a_1(t)e_1(t)^2}{1 + \Psi(t)^T\Psi(t)}. \quad (20)$$

In view of (20), {V(t)} is a nonincreasing sequence bounded below by zero. Moreover,

$$\lim_{N\to\infty} \sum_{t=1}^{N} \frac{a(t)(e_1(t)^2 - 4\Delta)}{2(1 + \Psi(t)^T\Psi(t))} < \infty, \quad (21)$$

and

$$\lim_{N\to\infty} \frac{a(t)(e_1(t)^2 - 4\Delta)}{2(1 + \Psi(t)^T\Psi(t))} \to 0. \quad (22)$$

Along with (iii) of Assumptions 1 similar to Ref.[7], $e_1(t)$ is bounded.

By (13) and (22), the second term of $J_1(t)$ is always bounded. $J_2(t)$ has two cases:

(i) $J_2(t)$ is bounded. so the model error $e(t)$ is bounded and satisfies (22).

(ii) $J_2(t)$ is unbounded. Since (1)$J_1(t)$ is bounded. So there exists a constant t_0 such that $J_1(t) < J_2(t), \ \forall t > t_0$. The model also has bounded error $e(t)$.

From above inequalities, the input and output of the closed-loop switching control system are bounded.

The linear model is always bounded. If a proper nonlinear model is chosen and the accurate parameters is adjusted, the nonlinear model error $e_2(t)$ can converge on zero. It also exists a constant T_0 satisfies $J_2(t) < J_1(t), \ \forall t > T_0$. Then the tracking error of model can converge on zero.

VII. CONTROL SIMULATIONS

Now consider a nonlinear system:

$$\begin{aligned} y(t) &= \frac{\exp(-y^2(t-2)) * y(t-1)}{1 + u^2(t-3) + y^2(t-2)} \\ &+ \frac{(0.5 * (u^2(t-2) + y^2(t-3))) * y(t-2)}{1 + u^2(t-2) + y^2(t-1)} \\ &+ \frac{\sin(u(t-1) * y(t-3)) * y(t-3)}{1 + u^2(t-1) + y^2(t-3)} \\ &+ \frac{\sin(u(t-1) * y(t-2)) * y(t-4)}{1 + u^2(t-2) + y^2(t-2)} \\ &+ u(t-1) \end{aligned} \quad (23)$$

The desired output in this example is a piecewise function.

$$y^*(t) = \begin{cases} 0.4493y^*(t-1) + 0.57r(t-1) \\ \qquad t \in [1,100] \cup [151,200] \\ 0.7\text{sign}(0.4493y^*(t-1) \\ \qquad +0.57r(t-1)) \\ \qquad t \in [101,150] \end{cases} \quad (24)$$

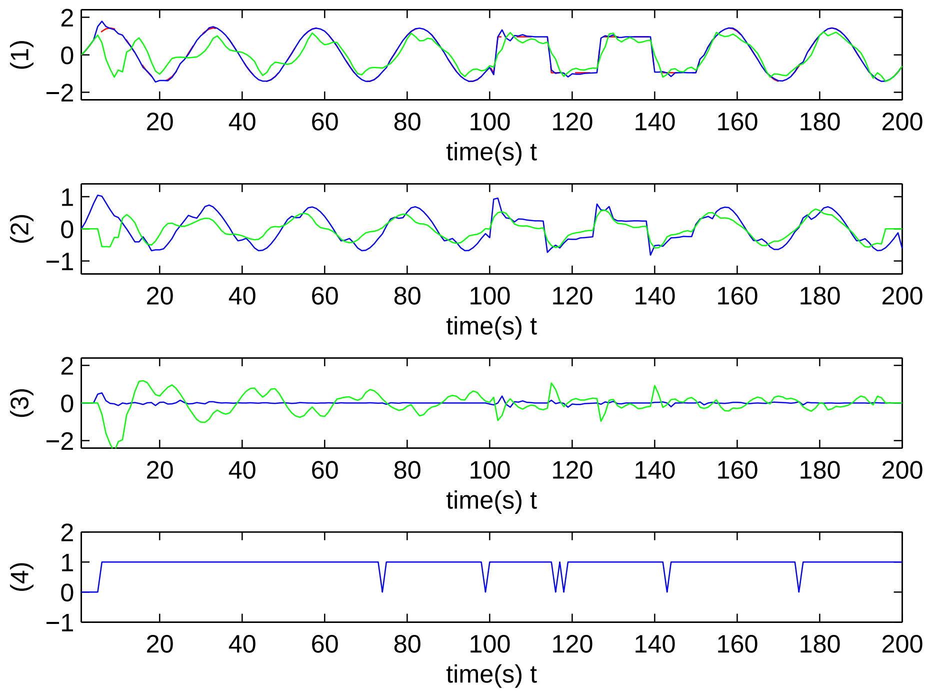

Fig. 2 switching control results of example 1

where $r(t) = 1.2 * \sin(2\pi t/25)$. At the nonlinear part, a neural network with one hidden layer and 20 hidden nodes as in Ref.[4] is used and other parameters satisfy m=4, n=3, c=1.2 and N=3. The quasi-ARX model can be trained off-line by the hierarchical training algorithm as in Ref.[4]. This model is used on-line as an identifier which is adjusted by BP algorithm. The linear part, m=4, n=3 which is adopted on-line by above section mentioned algorithm.

Figure 2 gives the results of example. In Fig.2(1), the red line is desired output, blue line proposed method control output and green pine linear control output. The Fig.2(2) gives the control input where blue and green denotes the proposed method control and linear control input. The errors are shown in Fig.2(3). The mean of linear control is -0.0364 and the variance is 0.2930. The mean of the proposed method control is 0.0035 and the variance is 0.0053. Therefore, our method is better than linear control. The switching sequence is presented which 1 is model with nonlinear part and 0 is model without nonlinear part in Fig.2(4).

VIII. CONCLUSION

In this paper, a new framework is established to adaptive control nonlinear system based on quasi-ARX neural network, and a switching algorithm is designed. Different from some relative researches which established more than two prediction models and made switching among so many corresponding controllers[7, 8], the proposed method is simpler and control-easier because of the compact and efficient structure of control system. Simulations are given to show the effectiveness of the proposed method both on stability and accuracy.

REFERENCES

[1] Hornik MK and White H(1989), Multilayer feedforward networks are universal approximators. Neural networks 2(1):359–366.

[2] Narendra K and Parthasarathy K(1990), Identification and control of dynamical systems using neural networks. IEEE Trans. on Neural Networks 1(1):4–27.

[3] Hu JL, Hirasawa K and Kumamaru K(1999), Adaptive predictor for control of nonlinear systems based on neurofuzzy models. Proc. of European Control Conference (ECC'99) (Karlsruhe) 8 1999.

[4] Hu JL and Hirasawa K (2004), A method for applying neural networks to control of nonlinear systems. Neural Information Processing: Research and Development. Springer 5:351–369.

[5] Chen F and Khalil H (1995), Adaptive control of a class of nonlinear discrete time systems using neural networks. IEEE Trans. on Automatic Control 40(5):791–801.

[6] Goodwin GC and Sin KS(1984), Adaptive Filtering Prediction and Control. Prentice-Hall, Inc..

[7] Chen L and Narendra KS(2001), Nonlinear adaptive control using neural networks and multiple models. Automatica 37:1245–1255.

[8] Fu Y and Chai T(2007), Nonlinear multivariable adaptive control using multiple models and neural networks. Automatica 43:1101–1110.

The Fifteenth International Symposium on Artificial Life and Robotics 2010 (AROB 15th '10),
B-Con Plaza, Beppu,Oita, Japan, February 4-6, 2010

Real-time Generation of Developed View for Drain Pipe Based on Web Camera Video

Zhicheng Wang, Harutoshi Ogai and Shigeyuki Takeno

The Graduate School of Information, Production and Systems, Waseda Univ.,
2-7 Hibikino, Wakamatsu-ku, Kitakyushu, Fukuoka, Japan
(Tel : 81-090-0650-2207; Fax : 81-093-692-5147)
(Email: edwardwang@toki.waseda.jp)

Abstract: A real-time algorithm for generating the interior developed view of a drain pipe based on video taken by a robot-inspector is presented. The objective is to increase the efficiency of examination and maintenance of a drain pipe, and make it possible to check the situation of the drain pipe with an easy view. The key idea of the paper is to identify the central point of the drain pipe automatically based on the video image and connect the images as a development map of the drain pipe in real time. We described the Hough transform method and the Least-Squares method for searching the centre of the drain pipe in detail.

Keywords: drain pipe, developed view, inspection system, real-time algorithm**.**

I. INTRODUCTION

With the increasing of the number of the drain pipes which have been over their lifetimes, the drain pipes are getting decrepit. On the other hand, the requirements of rebuilding the drain pipes and the laying of optical fiber in the sewer pipes are increasing. So in order to grasp the situation of the drain pipe exactly, the examination of the drain pipes is being more and more important.

In Japan, from 1982, we have used robot-inspectors with video cameras instead of human beings for small-bore drain pipes that we can not enter directly. Furthermore, in order to make the situation in the drain pipes to be easier to understand visually, systems which can generate the developed view of drain pipes have been produced and been put into practical use up to now.

But systems being used now usually create the unfolded view after the examination for the reason of time consuming. Because of this problem, we can not confirm the situation of the drain pipes during the investigation.

We are currently developing a remote system, designed to generate the developed map of a drain pipe in real-time and be advantaged of locating the center point of the pipe. The algorithm we presented this time use the computer vision library OpenCV and can automatically identify the centre points of different types of drain pipes. Therefore, it will be possible for us to check and record the developed view of the drain pipes during the investigation, and the accuracy and efficiency will be significantly improved. As a further purpose, we plan to develop an auto visual inspection system to recognize the defects based on this algorithm together will some auto detection algorithms.

In this paper, first we introduce the wireless inspection robot we used in our research briefly and describe the unfolding algorithm and the centre identification algorithm in detail. The real data taken by our robot will be introduced and used during the explanation.

II. HARDWARE ENVIRONMENT

The inspection robot we used in this research is developed together with the Technical Solutions Company ISHIKAWA IRON WORKS, shows in Fig.1.

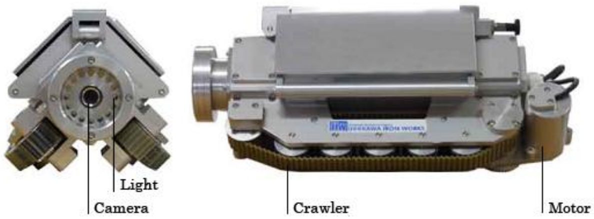

Fig.1. Structure of the inspection robot

The robot has the following specifications.

Table 1: Specifications of robot

Speed	:	13.7m per minute
Camera	:	44 mega pixels CCD
Drive system	:	Double motors eight-shaped crawlers
Power supply	:	Two 7.2 Volt batteries
Pipe diameter	:	200mm
Size	:	L355mm×W155mm× H150mm / 5.4Kg

Comparing with former inspection robots, the most significant feature is that it carries with wireless device. For that we can control and get the drain pipe image in the ground using a terminal computer instead of using cables like the former ones. This also makes it possible for us to do some processes for the real-time videos gotten through the wireless device.

In addition, we are also trying to improve this robot with other equipments to recognize defects. For example, a set of rotating detection arms is under studying now.

III. UNFOLDING ALGORITHM

Unfolding algorithm is the process to generate the developed view (also unfolded view) of the drain pipe. In order to make the developed map, the following processes should be executed, refer to Fig.2.

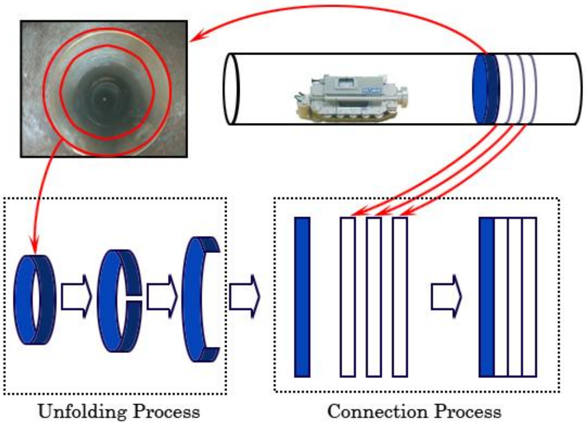

Fig.2. Processes for developed view

(a) Unfolding process: open out the circle image and lay it flat to a band one.
(b) Connection process: connect the unfolded images together from several frames to generate a developed map of the drain pipe.

Here we first introduce the unfolding algorithm.

It is easy for us to do this using the interpolation when we know the coordinate transformation between the original image and the unfolded one. Considering the process speed, here we use the bilinear interpolation to finish this work. The bilinear interpolation uses the nearly four pixels to estimate the object position.

We can see that the original image is the polar form of the unfolded image. So using the polar transformation based on a certain central point with some other calculations, we can get the coordinate relationship between them. It shows that the central point we used in the unfolding process is very important to assure the quality of the developed image. When the central point we used in the process is deviated from that of the drain pipe, the developed image will be distorted. For instance, the pipe-joint of the drain pipe will be a straight line in the developed image when we use the centre of the pipe. If the central point has been deviated, the pipe-joint will be a curve.

On the other hand, it is inevitable for the robot-inspector to have some shake due to the rough and uneven in surface which will cause the offset of the web camera and change the position of the central point of the drain pipe in the video image. For this reason, it is necessary for us to find the centre of the pipe from the image automatically.

In our algorithm, we use the combination of following two methods to finish this work.

IV. HOUGH TRANSFORM METHOD

The pipe-joints of the drain pipe can be obviously seen caused by the reflection of the light. Usually, the pipe-joints are almost of circular forms. So if we treat them as circles, we can use Hough transform to recognize them. Fig.3 shows the results by Hough transform we used in our algorithm.

Fig.3. Pipe-joints and Hough transform results

Hough transform is a feature extraction technique used in image analysis to find features of a shape in an image by voting procedure. In theory, the general Hough transform can be used on any kind of shapes, although the complexity of the transformation increase with the number of parameters needed to describe the shape. In practice, it is only generally used for finding straight lines or circles.

The Hough transform can be described as a transformation of a point in the x,y-plane to the parameter space. The parameter space is defined according to the shape of the object. For example, a circle can be described in the x,y-plane by:

$$r^2 = (x-a)^2 + (y-b)^2 \tag{1}$$

Where a and b are the center of the circle in the x and y direction respectively and where r is the radius.

The parameter space can now be spanned by (a, b, r). For each point on the desired circle, if we draw a circle with center in this point with the desired radius (For facilitate description, we suppose we know the radius while in fact we do not.), all the circles will pass through the center of the desired circle. If we use an accumulator to count all coordinates that the perimeter of the circles we drawn pass through, the maximum value will be the center we desired. When we do not know the radius, it is the same just change a 2-dimensional accumulator to a 3-dimensional one.

1. Pre-processing for Hough Transform

Although pipe-joints can present good objects for image processing, the video pictures were recorded under very difficult conditions, and there are three disadvantages inherent in these pipe-joint images:

- Low and uneven contrast around the pipe-joints due to poor illumination;
- A very dirty background owing to corrosion;
- A big gap because of residual effluent.

These features make it difficult to detect the pipe-joint boundaries. For this reason, we do the following pre-processing in our algorithm to increase the detection accuracy of the result.

(a) Gray-scale transformation
(b) Edge detection
(c) Dilatation and blurring

We do the gray-scale transformation to reduce the calculation amount, the edge detection process to find the edge of the pipe-joint and the dilatation and blurring to make the pipe-joint more visible and evident.

The advantage of Hough transform method is it can give an accuracy estimate of the central point although the pipe-joint is incomplete and with some noises. But for images without pipe-joints or the pipe-joints are unobvious, the Hough transform will be not applicable.

V. IMPROVED LEAST-SQUARES METHOD

Usually, the centers of the drain pipes are the darkest part in the pictures. The improved least-squares method is the method which we use the gray-scale data to find the minimum points of the x and y coordinates by least-squares method and to determine the central point.

By experiment, we find use a second degree curve (a parabola) to approximate the given set of data directly[2] can not give a satisfactory result. Therefore, we think of two improvements for this method in our algorithm.

The first improvement is to use a higher degree polynomial to approximate the given data set. Considering the computational complexity and consuming time, we use the least-squares 4^{th} degree polynomials to approximate the given set of gray-scale data in our research.

Another improvement introduced in our algorithm is using a variable scale of data set to perform the least-squares fitting. As for the influence by the lighting or the noises in the background of the image, the fitting result shows not very well. So we loop the fitting process with a new scale according to the darkest point found in the previous time. By experiment we found two cycles of the process can already give a satisfactory result for the centre estimation and do not cost much computation times. One example shows in Fig.4.

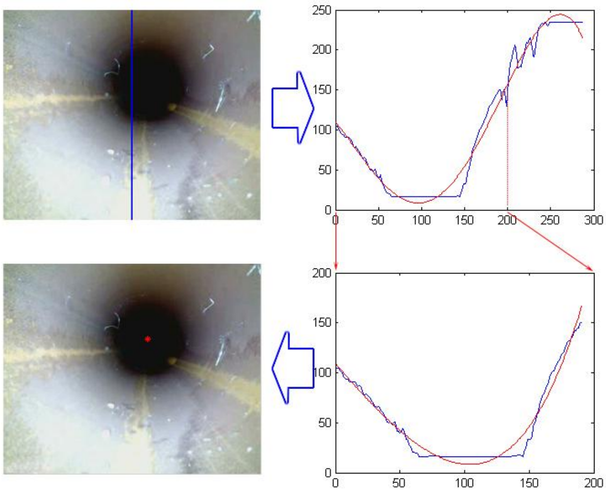

Fig.4. Improved least-squares method

The advantage of this method is it can be used in almost all kinds of drain pipes. But when the drain pipe is not very straight, the darkest point of the image may be different with the centre point of the drain pipe.

Considering the advantage and disadvantage of this two method, we apply the combination of them in our algorithm.

VI. CONNECTION

After getting the unfolded images of separate frames, we need to connect them to a developed map of the drain pipe. Usually, the splicing effect is affect by the speed of the robot-inspector, the diameter of the pipe, the width of the folded band image and the interval of the frames for which we do the unfolding process. It is difficult to determine a relationship of all these factors. But actually, the speed of the robot and the diameter of the drain pipe are constant, and the intervals of the frames can be determined by the real-time constraint. (As the more frequent we grab the frame for processing, the less processing time we will have to satisfy the real-time requirement.) We just need to determine the width of the folded band to finish the connection process.

Here, by experiment, with the speed of 13.7m per minute, the diameter of 200mm and the intervals of every three frames (we will discuss it later), a 5 pixels width of the folded band image can provide a better result. An example is given in Fig.5.

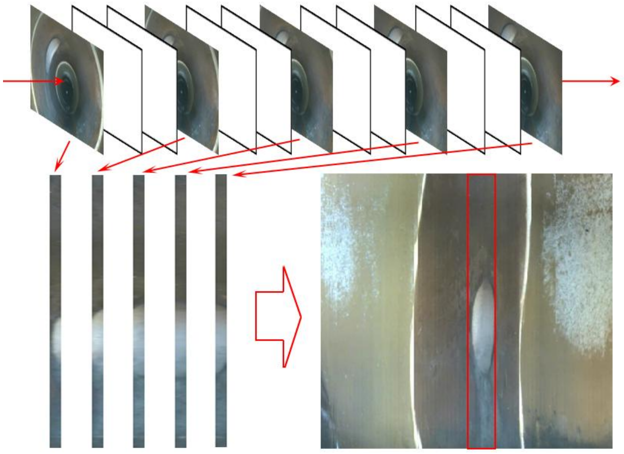

Fig.5. Example of connection

One problem here is that according to the different situation in the drain pipe, the identified central point maybe sometimes with a certain error. This will cause the developed map not be continuous. So in our algorithm, we check the deviation of the current central point with the previous one, and discard ones with too large deviations.

Then, let's discuss the real-time constraints. The following table shows the processing time's for our algorithm.

Table 2: Processing time

Operation environment	
CPU	2.10GHz × 2
Memory	1.00GB
Language	C++
Running time (per frame)	Hough*/LS**
Finding center	43.8ms / 17.1ms
Unfolding	28.1ms
Connection	1.5ms
All	73.5ms / 46.7ms

*Hough: Hough transform method

**LS: Improved Least-Squares method

For the video, usually it has the frame rate of 30fps (frame per second). One frame costs 33.3ms and three frames cost 100ms. As the process for one frame in our algorithm mostly cost 73.5ms, less than three frames' time, it is possible for our algorithm to be used in real-time process.

VII. CONCLUSION

In this paper, we have introduced an algorithm for generating the developed map of the drain pipe. The advantages of our algorithm are mainly in two parts.

First, it can identify the central point of the drain pipe automatically and accurately, by using the combination of Hough transform and Improved Least-Squares methods.

Second, it can be used in real-time detection, which makes it possible to confirm the situation of the drain pipes during the investigation.

One possible problem is that when the running situation of the drain pipe is so bad and makes the robot shake seriously, the connection result will be bad due to the rock of the video image.

As for the further research, based on this algorithm, we plan to develop an auto visual inspection system to recognize the defects together will some auto detection algorithms or some additional detectors. For example, by our algorithm, the pipe-joint will be near a straight line and be easier to be excepted from the defects than do it directly using the original video image.

REFERENCES

[1] Takayoshi OOSAKA, Kiichiro TouGOU and Shinji NUMAO(2005), The Development of a TV Inspection System with Panorama Sensor for Sewer Pipe(In Japan). *Nippon Koei technical forum*, Vol. 13, pp.77-82

[2] Hiroshi SAITO, Kinshi DATE and Tamotsu MOCHIDUKI(2003), The Development of Systems Concerned with Expansionary Image of Sewer Pipe(In Japan). *Nippon Koei technical forum*, Vol. 11, pp.101-107

[3] Kun XU, A.R LUXMOORE and T.DAVIES(1998), Sewer Pipe Deformation Assessment by Image Analysis of Video Surveys. *Pattern Recognition*, Vol. 31, No. 2, pp169-180

[4] Kikuhito KAWASUE, Shoji SAKAI and Terufumi WAKIYAMA(2008), Sewer Pipe Measurement Robot Using Parallel Laser Sheet(In Japan). *The Japan Society of Mechanical Engineers*, pp.90-97

The Fifteenth International Symposium on Artificial Life and Robotics 2010 (AROB 15th '10),
B-Con Plaza, Beppu,Oita, Japan, February 4-6, 2010

Revisited: Hebbian Postulate under Homeostatic Plasticity

Subha Fernando, Shuichi Matsuzaki, Yuichi Nakamura, Ashu Marasinghe

Nagaoka University of Technology, Nügata-ken, Nagaoka-shi, Kamitomioka-machi, 1603-1
(Tel: 81-258-47-9372; Fax: 81-258-47-9350)

(s085160@ics.nagaokaut.ac.jp)

Abstract: We propose a new method to model Hebbian Postulate with the intension of developing new learning algorithm based on it. The propose method integrate the Hebbian Postulate with Homeostatic Plasticity to avoid the node saturation of the conventional Hebbian based learning algorithms. Moreover the completely novel view of the brain as a network of agents with large number of constituent components, signal propagation within the network and complete elimination of weight components are main features that distinguish our method with the conventional approaches while making our model much closer to the biologically supported learning environment.

Keywords: Hebbian Postulate, Homeostatic Plasticity, Artificial Neural Network

I. INTRODUCTION

With the advancement of Information Technology, the world has being dreaming of imitating human cognitive system on machines. As an attempt of it, Artificial Neural Network, Fuzzy Logic, and Collective Intelligence are some of those technologies which have been evolved in mainly with this aspect. Artificial Neural Network is still considered as the main technology that reasonably imitates the human learning and memory formation. Artificial Neural Network has composed and evolved with many learning algorithms thereafter. Among many other learning rules, Hebbian learning rule is considered as the most effective learning rule that is supported by the biological findings. Hebbian learning rule is derived from the Hebbian Postulate which is based on the correlated activities of presynaptic neuron and postsynaptic neuron. In Hebbian Postulate, Hebb [1] says that "*When an axon of cell A is near enough to excite a cell B and repeatedly or persistently takes part in firing it, some growth process and metabolic change takes place in one or both cells such that A's efficiency, as the one of the cells firing B, is increased*".

It is very interesting to note that it has not been mentioned anything about what would happen when the cell A is not correlated with the cell B. One can argue that either it may decrease the correlated firing rate of the cell A and the cell B or there might be no significant changed to the current correlated firing rate of the cell A and the cell B when they become uncorrelated. The Hebbian learning algorithm is based on the first assumption and its basic mathematical formula is shown in "(1)".

$$\Delta w_{ij}(t) = \eta x_i x_j \qquad (1)$$

x_j is the output of the presynaptic neuron, x_i is the output of the postsynaptic neuron, η is the learning rate and w_{ij} is the strength of the connection between presynaptic neuron and postsynaptic neuron.

It can be seen that correlated input patterns will influence the neuron's weight and eventually produce the largest output. On the other hand weight strength of the uncorrelated neurons will tend to zero for uncorrelated input patterns. Either this unbounded increase of the strength of presynaptic and postsynaptic connectivity or the decrease of strength of the connectivity makes to lose the sensitivity of these neurons to external inputs. This issue is known as node saturation, and it can be seen in many Hebbian Postulate based learning algorithms, Williams and Noble [2]. To overcome this critical issue, many versions of Hebbian learning have been derived, some of those are Rate-based Hebbian learning, Spike based Hebbian learning, Gerstner and Kistler [3] and Differential Hebbian learning rule, Kosko [4]. Critical analysis on these learning algorithms, we can identify that they are based on six important factors, namely, locality, co-operativity, synaptic depression, boundedness, competition and long-term stability, Gerstner and Kistler [3]. The factor boundedness has been introduced mainly to eliminate this node saturation issue and it has been implemented as the concept of weight normalization. Basically it is an adjustment to weight components by a calculated parameter to bring it back a saturated node to unsaturated status, Williams H. and Noble[2], Abbott and Nelson [5], even though these updating significantly improve the signal propagation within the network, it has also damaged to the learning of the neural network and its performances, Williams H. and Noble [2], Williams [6]. Therefore, it is still a research challenge for researches to find appropriate learning algorithm based on Hebbian Postulate which is also supported by biological findings. In our article we propose a new approach to study Hebbian Postulate with the aim of developing more effective learning algorithm. Our study concentrate on the latter assumption that is there might be no significant changed (decreased) to the current correlated firing frequency of the cell A and cell B when they become uncorrelated. We propose to integrate Homeostatic Plasticity with the Hebbian Postulate instead of introducing weight normalization concept as a boundednes factor.

According to biologist while extremely large stimuli take neurons' firing frequency into very high firing frequency, extremely low stimuli may take neurons' into very low firing frequency, however as per biology, although fluctuations to external and internal stimuli are necessary for learning, it is also required to maintain the neuron's firing frequency in a feasible range. Homeostatic Plasticity is the mechanism that helps neurons to maintain their fluctuations in a feasible range, Turrigiano [7]. The significant feature of this process is it decreases the firing frequency of the neuron when it is extremely high and similarly it increases the firing frequency of neuron when its firing frequency is very low. This is supposed to be achieved through the change of neurons' electrical and, morphological properties and ionic concentrations. For an example, when a neuron is in high firing frequency, Homeostatic Plasticity closes down ca+2 ion channels to decrease the ca+2 ion concentration which in turn reduces the amount of neurotransmitter release and thereby the firing frequency of the neuron. On the other hand, when the neuron firing frequency is very low, it opens up ca+2 ion channels to increase the ca+2 ion concentrations in order to increase the amount of neurotransmitter release, Nicholls and Martin [8].

II. METHOD

We understand nervous system as a network of neurons; each neuron is an agent consists of a large number of constituent elements which work as synapses. A synapse can be either a transmitter or a receptor. A model neuron, in our study is shown in fig. 1. The propose model neuron enables synapses to have two dynamic statuses, either active or inactive. When a receptor receives a signal from a transmitter in another neuron, the receptor propagates the signal to a transmitter in the same neuron if the receptor is in an active status at the time of receiving. Similarly, a transmitter can transmit a signal to a receptor in other neuron, if the transmitter is in an active status at the time of signal transmitting. If the selected receptor or transmitter is in an inactive status at the time of receiving and transmitting respectively then the signal is dropped. Further, receptors in a neuron are grouped and number of receptor-groups within a neuron is equal to the number of neurons in the network -1. Number of receptors in a group may be different within a neuron and among neurons. Therefore, number of receptors and active number of receptors of a given connection are critical parameters that determine the strength of the connection between two neurons at a given time. These active and inactive statuses of constituent components are determined by an integrated process, which can be decomposed into two processes, synaptic computation and homeostatic plasticity. Our proposed network consists of 4 neurons because it has been proven that network with 4 neurons is capable enough to simulate learning effectively, Izquierdo-Torres and Harvey [9]. The network structure according to our approach is shown in fig 2. Receptors are grouped into three groups to establish the connection with other three neurons. For an example, if an active transmitter in neuron A wants to transmit a signal to a receptor in neuron B, then it selects a receptor from A-receptor group in neuron B.

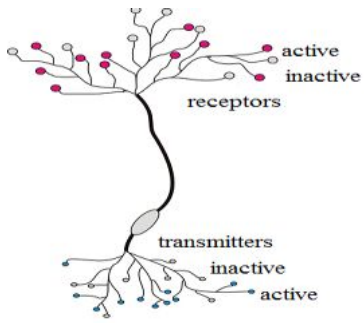

Fig. 1. A typical structure of a model neuron.

1. Signal Propagation within the Network

When a brief train of stimuli is applied to a pre-synaptic neuron, during the train, amplitude of the resulting pre-synaptic potential may either increase (called synaptic facilitation) or decease (synaptic depression). According to biologist, the amount of neurotransmitter release from pre-synaptic terminals is subject to these two relatively short-term modifications. At the facilitation, the amount of neurotransmitter release is very high and it decays along the time. This phenomenon can be easily explained using internal ca+2 ion concentration. Arrival of train of stimuli increases the amplitude of pres-synaptic potential which opens up ca+2 ion gates. The growth of internal ca+2 ions concentration increases the amount of neurotransmitter release, however, as time goes, the appearance of antagonized ions into pre-synaptic terminal such as magnesium, cadmium, nickel, etc reduces the internal ca+2 ions concentration. This decreases the amount of neurotransmitter release. Similarly, continuous stimulus may also reduce pre-synaptic potential which makes the amount of neurotransmitter release is minimal at the depression.

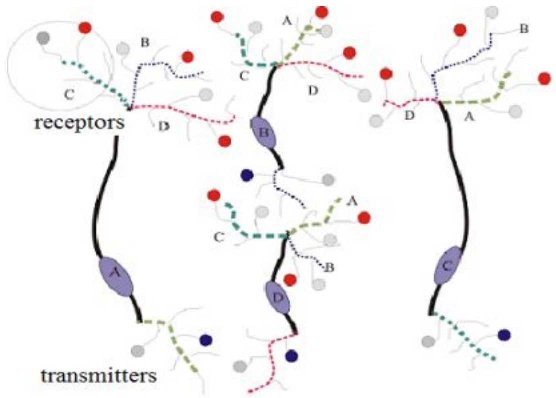

Fig.2. Structure of the network with four model neurons.

These two phenomena have been considered in the model proposed by Maass and Zador [10]. They have modeled the behavior of a synapse as a stochastic process with two finite statuses, i.e. R and F. This model is used in our approach to control signals propagation within the network. We map these two statuses, into active status and inactive status of our constituent components respectively. In their model, for each spike in spike train t, the output of a synapse consists of the sequence S(t) of those $t_i \in t$ on which neurotransmitters are released by S. Thus, $t \in S(t)$ becomes a stochastic process, computed by synapse S, with output sequence $q = q_1, q_2, q_3, ..., q_n \in \{R,F\}$. $P_s(t_i)$ defines, see "(2)", the probability that i^{th} spike in the pre-synaptic spike train $t = (t_1, t_2, .., t_k)$ triggers the release of a signal at time t of the synapse S. If $P_s(t_i) > 0$ then spike excites synapse and releases the neurotransmitters, so the output is R, otherwise the output is F. Non-negative functions C(t) and V(t), defined in "(3)" and "(5)" model facilitation and depression. Function C(s) in "(4)", models the response of C(t) to a pre-synaptic spike that had reached to the synapse S at t-s. Moreover function V(s) in "(6)" models the response of V (t) to a proceeding release of the synapse S at time t-s $\leq$ t. Whilst non-negative parameters α, τ_c and τ_v model the magnitude of the signal and decay constants of facilitation and depression respectively. C_0 and V_0 model the parameters for facilitation and depression at the equilibrium. So that, C_0 is the internal ca+2 ions concentration at the equilibrium and V_0 is the maximum amount of neurotransmitters can be released by a synapse.

$$P_s(t_i) = 1 - \exp(-C(t_i) * V(t_i)) \qquad (2)$$

$$C(t) = C_0 + \sum_{t_i < t} C(t - t_i) \qquad (3)$$

$$C(s) = \alpha.\exp(-s/\tau_c) \qquad (4)$$

$$V(t) = \max(0, V_0 - \sum_{t_i < t \, \mathrm{and} \, t_i \in S(t)} V(t - t_i)) \qquad (5)$$

$$V(s) = \exp(-s/\tau_v) \qquad (6)$$

This stochastic process has been developed and tested only for a one synapse, but in our research it is applied into thousands of individual synapses. Therefore, we modified the model by introducing a θ as a threshold value, if $P_s(t_i) > \theta$ then spike excites synapse, so the output becomes R otherwise it is F. This threshold value is determined in the training phase under homoeostatic plasticity process.

2. Homeostatic Plasticity

Each model neuron has got four threshold values. One threshold value is for transmitters and other three threshold values are for three receptor-groups. These threshold values are determined to ensure the stability of the network within a particular range. So that, when firing rate of a neuron increases, it also increases the threshold values of the relevant groups to derive the network towards stability. Similarly, when the firing rate of a neuron is very low, it decreases threshold values of the relevant groups, in order to increase the firing frequency of the neuron. Let RIJ is J-receptor-group of I-neuron. For an example, RAC is the C-receptor-group of the A-neuron. XAC is the output of the RAC receptor-group. TI is the transmitter group of I-neuron and OI is the output of the transmitter group of I-neuron. For an example, TA is the transmitters in neuron A and OA is the output of the transmitter group of neuron A, see fig. 3.

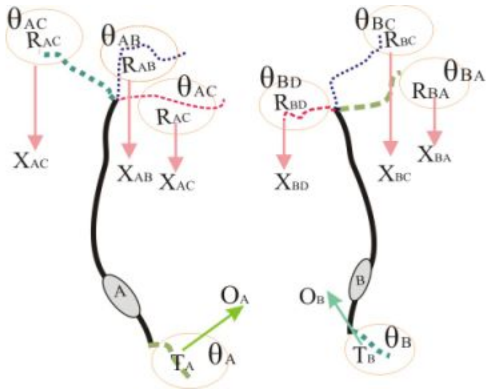

Fig..3. Signal transmission among neurons.

θI is the threshold value for the transmitters in neuron I. θIJ is the threshold value for the J-receptor-group of the I-neuron. We define θI as in "(7)". Instance of "(7)" is shown in "(8)". The output of IJ-receptor-group, XIJ, can be expressed in terms of active receptors in the IJ-group as define in "(9)". Similarly, OI can be defined in terms of active transmitters in I-neuron as shown in "(10)". f(.) is the threshold calculation function, defined in "(11)".

$$\theta_I = f(O_I * [X_{IJ_1} + X_{IJ2} + X_{IJ3}]) \qquad (7)$$

$$\theta_B = f(O_B * [X_{BA} + X_{BC} + X_{BD}]) \qquad (8)$$

$$X_{IJ} = \frac{Act.Re\,cp.in\,R_{IJ}}{Re\,cp.in\,R_{IJ}} \qquad (9)$$

$$O_I = \frac{Act.Trans.in\ T_I}{Trans.in\,T_I} \qquad (10)$$

$$f(x) = 1/(1+\exp(-x)) \qquad (11)$$

Similarly, we calculate threshold values for each receptor-group, θIJ, in terms of active number of constituent components in relevant neurons, as defined in "(12)". Calculated threshold values are then use as constant values in the testing phase.

$$\theta_{IJ} = f(\frac{X_{IJ}}{O_J}) \qquad (12)$$

III. DISCUSSION

In our study instead of defining weight component to represent synaptic efficacy we define small programmable computational units which change their statuses, active and inactive, according to the amount of signal processing. These programmable units are attached to the neurons which are defined as agents and their communication enable through the message passing which in turn represents the internal and external signals to the network. Thus number of active computational units defines the strength of the connectivity between presynaptic and postsynaptic neurons at a given time. The active and inactive statuses of these small programmable units are subjected to the Homeostatic plasticity process and Zador and Mass approach. The most significant feature of our method is no initialization of weight components but the introduction of threshold increment process to the training phase. Bipolar status of constituent components at the site of neurotransmitter release, i.e. R or F, and integration of Homeostatic plasticity as a stability supportive mechanism and the complete elimination of weight components are other significant features that distinguish our method from others while making us much closer to the biological findings than existing learning environments in Artificial Neural Network.

REFERENCES

[1] Hebb D.O (1949), The Organization of Behavior, New York: Wiley
[2] Williams H. and Noble J. (2007), Homeostatic plasticity improves signal propagation in continuous time recurrent neural networks, Biosystem 87 (2-3) pp 252-259
[3] Gerstner W and Kistler W.M (2002), Mathematical Formulations of Hebbian Learning, Biological Cybernetics, Special Issue on Hebb in Perspective.
[4] Kosko A (1986), Differential Hebbian learning, in Proceeding of American Institute of Physics, 151 (1), pp-277-282.
[5] Abbott L .F and Nelson S. B (2000), Synaptic Plasticity: taming the beast, Nature 3, pp 1178-1183.
[6] Williams H (2005), Homeostatic plasticity improves continuous-time recurrent neural network as a behavioral substrate, Adaptive Motions in Animals and Machine, pp 161-163
[7] Turrigiano GG (1999), Homeostatic plasticity in neural networks: the more things change, the more they stay the same, Trends in Neuroscience 22, pp-221-227
[8] Nicholls J.G, Martin A.R (2001), Wallace B.G. and Fuchs, P.A., "From Neuron to Brain", Sinauer Associates, Inc, USA
[9] Izquierdo-Torres E. and Harvey I (2007), Hebbian Learning using Fixed Weight Evolved Dynamical 'Neural' Networks, in the Proceedings of the First IEEE Symposium on Artificial Life. Hawaii: IEEE Press.
[10] Maass W. and Zador A. M (1998), Dynamic Stochastic Synapses as Computational Units, MIT Press.

Memory Capacity and Information Capacity of the Sparsely Encoded Associative Memory with Replacing Units

Ryota Miyata*, Shinnosuke Muta**, and Koji Kurata**

*Graduate School of Engineering and Science, University of the Ryukyus
**Faculty of Engineering, University of the Ryukyus
*,**1 Senbaru, Nishihara, Okinawa JAPAN 903-0213
miyata@mibai.tec.u-ryukyu.ac.jp

Abstract: We introduce sparse encoding into the autoassociative memory model with replacing units. We search by computer simulation the optimal number of replacing units in two terms; the memory capacity and the information capacity of the network. We show that the optimal number of replacing units to maximize the memory capacity and the information capacity decreases as the firing ratio decreases, and that the difference of the memory capacity between sparse encoding and non-sparse encoding becomes small as the number of replacing units increases.

Keyword: autoassociative memory, sparse encoding, catastrophic forgetting, rebirth neuron, memory capacity, information capacity

1 Introduction

The associative memory model is one of neural network models made by imitating the form of memory in human brain, and consists of neurons and synapses.

Properties of an associative memory model largely depend on how items are encoded in pattern vectors to be stored. When most of the components of encoded patterns are 0 and only a small ratio of the components are 1, the encoding scheme is said to be sparse. Rolls(1987) observed that sparse encoding was realized in the hippocampus, and he proposed an associative memory model of the hippocampus[1]. Amari(1989) gave a mathematical analysis of associative memory models with sparse encoding[2]. He proved that the memory capacity (the maximum number of patterns to be stored in the network in the form of its equilibria) and the information capacity (the total amount of information stored) of the sparsely encoded associative memory model are much larger than the ordinary non-sparse encoding scheme. Moreover, he proved that the sparsely encoded associative memory model had a large basin of attraction around each memorized pattern, when and only when an activity (the number of excited components) control mechanism is attached to it.

If the number of memorized patterns surpasses the memory capacity, the network cannot recall any memorized pattern due to the overloading[3]. This phenomenon is called catastrophic forgetting.

Eriksson et al.(1998) discovered newborn neurons in the hippocampus, where the associative memory was considered to be realized[4]. Date and Kurata(2008) reported that the network, in which a fixed number of units are replaced by newborn ones while the model learns one pattern, can keep up memorized patterns studied recently without catastrophic forgetting[5]. They showed that the optimal number of replacing units to maximize the memory capacity is about 3, and that it is independent of the network size. Komatsu et al.(2009) analyzed the associative memory model with replacing units by utilizing statistical mechanics[6]. They showed that replacing 3.2 or more units could make the network avoid catastrophic forgetting and that replacing 6.9 units is optimal to maximize the memory capacity. The difference between the results of Date and Kurata(2008) and that of Komatsu et al.(2009) is due to the order of selection of units to be replaced. While Date and Kurata(2008) set units replaced in a fixed order repeatedly, Komatsu et al.(2009) set units replaced randomly with a certain probability.

Now we introduce sparse encoding into the associative memory model with replacing units. We search the optimal number of replacing units to maximize the memory capacity and the information capacity of the model by using computer simulation. The replacing order is the same as Date and Kurata(2008). We treat in the present paper only an autoassociative memory model, which recalls a memorized pattern from its noisy version. We show that the optimal number of replacing units decreases as the firing ratio decreases, and that increase of the number of replacing units reduces the difference of the memory capacity between sparse encoding and non-sparse encoding, but then makes the information capacity of sparse encoding smaller than that of non-sparse encoding.

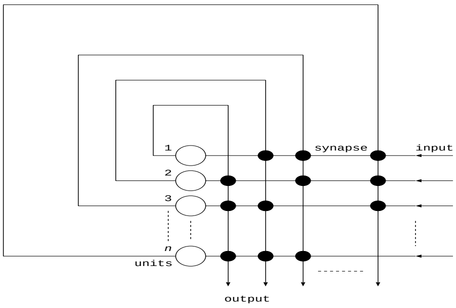

Fig. 1: The autoassociative memory model. The units are interconnected by the network of synapses with the synaptic strength w_{ij} from unit j to unit i. Each unit i has two states, $x_i = \pm 1$.

2 Associative memory model

Let us consider a neural nework of n mutually connected formal neurons. We assume that all the neurons work synchronously at discrete-times $t = 1, 2, \cdots$. The associative memory model consists of memorizing process and recall process.

2.1 Memorizing process

The autoassociative memory model is a network whose connection weight matrix $W = \{w_{ij}\}$ is determined by

$$w_{ij} = \sum_{\mu=1}^{m} s_i{}^{(\mu)} s_j{}^{(\mu)}, \tag{1}$$

from m patterns $\boldsymbol{s}^{(\mu)} = (s_1{}^{(\mu)}, s_2{}^{(\mu)}, \cdots, s_n{}^{(\mu)})^{\mathrm{T}}, \mu = 1, 2, \cdots, m$, to be stored, where $s_i^{(\mu)}$ is the i-th component of $\boldsymbol{s}^{(\mu)}$. w_{ij} is the weight of connection from the j-th neuron to the i-th neuron and it is, therefore, symmetric. Regardless of this definition, w_{ii} is assumed to 0. This learning process is local; the increment for connection w_{ij} does not depend on the global structure of the state or past memories, but only on $s_i{}^{(\mu)}$ and $s_j{}^{(\mu)}$. It is fast, and does not need to learn each memory repeatedly.

This network now functions as an associative memory. For example, if started from an initial state which somewhat resembles state $\boldsymbol{s}^{(1)}$ and which resembles other $\boldsymbol{s}^{(\mu)} (\mu \neq 1)$ very little, the state will evolve to the state $\boldsymbol{s}^{(1)}$. The state $\boldsymbol{s}^{(1)}$ is evocable memory, and the system correctly reconstructs an entire memory from any initial partial information, as long as the partial information is sufficient to identify a single memory. Detailed properties of the collective operation of this network have been studied extensively[3].

2.2 Recall process

Let $\boldsymbol{x}(t) = (x_1(t), x_2(t), \cdots, x_n(t))^{\mathrm{T}}$ be a vector whose component $x_i(t)$ denotes the output of the i-th neuron. This vector is called the state vector of the network.

In our network of the associative memory model (Fig.1), each unit i has two states, and is described by variable $x_i(t) = \pm 1$. The instantaneous state of the system of n units can be thought of as an n-dimensional vector having components $x_i(t)$. The units are interconnected by a network synapses, with a synaptic strength w_{ij} from unit$j$ to unit i. The instantaneous output to unit i is

$$x_i(t+1) = \mathrm{sgn}(\sum_{j=1}^{n} w_{ij} x_j(t)), \tag{2}$$

where $x_j(t)$ is the present state ± 1 of unit j. This equation defines the state transition of the network from the state $x_i(t)$ at discrete-time t to the next state $x_i(t{+}1)$. The function $\mathrm{sgn}(u)$ denotes the unit signum function,

$$\mathrm{sgn}(u) = \begin{cases} 1, & u > 0, \\ -1, & u \leq 0. \end{cases} \tag{3}$$

A neuron is excited when a weighted sum of its inputs exceeds 0. A neuron emits output 1 when it is excited, and its output is -1 when it is not excited.

The state of the system changes in time; each unit i readjusts its state, setting $x_i(t) = \pm 1$ according to whether $\sum_{j=1}^{n} w_{ij} x_j(t)$, the input to i at this moment, is greater or less than 0. This algorithm defines the time evolution of the state of the system. For any symmetric connection matrix $\{w_{ij}\} : w_{ji}$, there are stable states of the network of units. Starting from any arbitrary initial state, the system reaches a stable state and cease to evolve.

2.3 Catastrophic forgetting

There is a critical memory capacity in the conventional associative memory model. The memory capacity for one-half coded random memories is given by Amit et al.(1985) as about $0.138n$, where n is the number of units[3]. If the number of memorized patterns surpasses the memory capacity, the network cannot recall any memorized patterns due to the overloading[3]. This phenomenon is called catastrophic forgetting. Fig.2 shows catastrophic forgetting; the network which consists of $n = 1000$ neurons could recall all the memorized patterns for $\mu < 140$, but at $\mu = 140$, forgetting started, and no memorized pattern could be recalled correctly after $\mu = 200$, i.e., the network could not recall even the most recent memory.

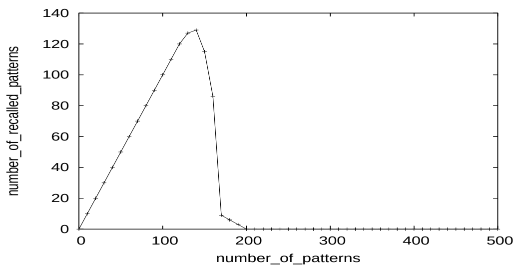

Fig. 2: Catastrophic forgetting on the conventional autoassociative memory model with 1000 neurons.

If the dynamics of weight connections of the network have decay or saturation, the catastrophic forgetting does not occur, and the network can keep recent memories[7]. But, as yet, there is no conclusive experimental evidence for the existence of such a system in human brain.

3 Rebirth neuron and the modeling; replacing units

Eriksson et al.(1998) discovered newborn neurons in the hippocampus, where the associative memory was considered to be realized[4]. Date and Kurata(2008) reported that the one-half coded associative memory network, in which a fixed number of units were replaced by newborn ones while learning one pattern, could keep up memory patterns studied recently without catastrophic forgetting[5]. This corresponds to resetting the connection weights $w_{ij} = w_{ji} = 0, j = 1, 2, \cdots, n$, for replaced neurons i. Units were replaced from the oldest one first, i.e., they were always replaced in the same order.

4 Sparse encoding

We consider the case where patterns to be stored are generated independently and randomly under the condition that they have a fixed activity. The encoding that the number of active components in $\boldsymbol{s}^{(\mu)}$ is negligibly small compared to n is said to be sparse. $\boldsymbol{s}^{(\mu)}$ are independent random vectors subject to a common probability distribution. More precisely, $\boldsymbol{s}^{(\mu)}$ are generated in such a manner that, $nq, (0 \leq q \leq 1)$ components, randomly chosen among n components, take $1 - q$ and all the other components are put equal to $-q$.

Amari(1989) proved that the memory capacity C_{M} of the associative memory model increases as encoding sparser[2]. One pattern to be stored has an average information content $H(q)$ with the occurence probability q as below

$$H(q) = -q \log_2 q - (1 - q) \log_2 (1 - q). \qquad (4)$$

So, one sparsely encoded pattern $\boldsymbol{s}^{(\mu)}$ includes a smaller amount of information than non-sparse encoding case. However, Amari(1989) proved that the total amount of information stored in the network, or the information capacity increases as encoding is sparser[2]. This is due to the increase of the memory capacity in the sparse encoding case.

Here, We define the information capacity C_{I} of the network as below,

$$C_{\mathrm{I}} = H(q) C_{\mathrm{M}}. \qquad (5)$$

5 Simulation

5.1 Settings

Simulations were carried out on a computer for $n = 1000$ and 2000 by varying the number R of replacing units and the firing ratio q to maximize the memory capacity and the information capacity.

We applied equation(1) with replacing units to memorizing process. For simplicity, we assume that the total number of neurons does not change over time. Every time the network memorizes a new pattern, R neurons die and the same number of neurons are born. The number m of memorized patterns depends on the number R of replacing units as below,

$$m = \frac{n}{R}. \qquad (6)$$

We also used a non-integer value for R. In this case, we define the number $r(t)$ of replacing units at t as below,

$$r(t) = \mathrm{int}(R(t + 1)) - \mathrm{int}(Rt), \qquad (7)$$

where $\mathrm{int}(x)$ is the function which truncates a number after the decimal point. We used the memorized patterns for the initial states in recall process. Since the firing ratio calcurated with equation(3) couldn't keep the constant value q, the top nq neurons in descending order of the sum of weighted inputs were let to fire. The proximity of the state $\boldsymbol{s}^{(\mu)}$ of the memorized pattern and the state $\boldsymbol{x}^{(\mu)}$ of the recalled pattern was measured by the direction cosine

$$\cos\theta = \frac{\boldsymbol{s}^{(\mu)} \cdot \boldsymbol{x}^{(\mu)}}{\|\boldsymbol{s}^{(\mu)}\| \|\boldsymbol{x}^{(\mu)}\|}, \quad \mu = 1, 2, \cdots, m. \qquad (8)$$

We counted the number of successfully recalled memories in which the proximity was larger than 0.8. Because the system has the finite state transitions, the state is always supposed to reach an equilibrium or a periodical solution, and the period is known to be no more than 2. Here we assume that the system is forced to stop when the present state equals the second to last one in recall process.

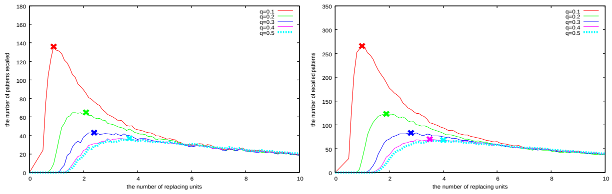

(a)$n = 1000$ (b)$n = 2000$

Fig. 3: The results of simulation to maximize the memory capacity. The horizontal axes are the number R of replacing units. The vertical axes are the memory capacity C_{M}. The 5 points represent the each optimal number in the firing ratio q from 0.1 to 0.5.

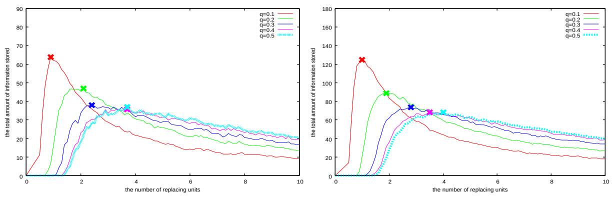

(a)$n = 1000$ (b)$n = 2000$

Fig. 4: The results of simulation to maximize the information capacity. The horizontal axes are the number R of replacing units. The vertical axes are the information capacity C_{I}. The 5 points represent the each optimal number in the firing ratio q from 0.1 to 0.5.

5.2 Results

Fig.3 shows that the sparsely encoded associative memory model with a small number of replacing units for $R < 4$ had a larger memory capacity than the non-sparsely encoded one, i.e., $q = 0.5$, but there was little difference of the memory capacity between sparse encoding and non-sparse encoding after $R \approx 6$. It turned out that the optimal R to maximize the memory capacity decreased as the firing ratio decreased; $R \approx 1$ for $q = 0.1$, $R \approx 2$ for $q = 0.2$, $R \approx 2.6$ for $q = 0.3$, $R \approx 3.7$ for $q = 0.4$ or $q = 0.5$. As shown in Fig.3(a), $n = 1000$, and (b), $n = 2000$, the optimal R seemed to be independent of the size of the network.

Fig.4 shows that the sparsely encoded associative memory model with a small number before $R \approx 2$ had also a larger information capacity than the non-sparsely encoded one, but, after $R \approx 6$, the information capacity of sparse encoding became smaller than that of non-sparse encoding. It turned out that the optimal R to maximize the information capacity decreased as the firing ratio decreased, and it was about the same number as to maximize memory capacity. As shown in Fig.4(a) and (b), the optimal R also seemed to be independent of the size of the network.

6 Conclusion

We introduced sparse encoding into the associative memory model with replacing units. We reported the optimal number of replacing units to maximize the memory capacity and the information capacity of the model by using computer simulation. The sparsely encoded associative memory model with a small number of replaced units has also a larger memory capacity and a larger information capacity than the non-sparsely encoded one. We showed that the optimal number of replacing units decreases as the firing ratio decreases, and that increase of the number of replacing units reduces the difference of the memory capacity between sparse encoding and non-sparse encoding, but then makes the information capacity of sparse encoding smaller than that of non-sparse encoding. We also found that the optimal number of replaced units was independent of the size of the network.

References

[1] Rolls, E. T. (1987), Information representation, processing, and storage in the brain: Analysis at the single neuron level. In J.-P. Changeux & M. Konishi(Eds.). *The neural and molecular bases of learning* 503-539

[2] Amari, S. (1989), Characteristics of sparsely encoded associative memory. *Neural Networks* 2:451-457

[3] Amit, D. J., Gutfreud, H., & Sompolinsky, H. (1985), Spin-glass models of neural networks. *Physical Review* A2:1007-1018

[4] Eriksson, P. S., Perfilieva, E., Bjork-Eriksson, T., Alborn, A. M. , Nordborg, C., Peterson, D. A., & Gage, F. H. (1998), Neurogenesis in the adult human hippocampus. *Nat. Med.* 4(11):1313-7.

[5] Date, A., & Kurata, K. (2008), On the distribution of posterior probability in bayesian inference with a large number of observations. *Artificial Life and Robotics* 12:291-294

[6] Komatsu, Y., Aonishi, T., & Kurata, K. (2009), Statistical mechanics of the Hopfield model with replacing units (in Japanese). *IEICE technical report. Neurocomputing* 108(383):49-54

[7] Okada, M., Mimura, K., & Kurata, K. (1994), Associative memory with forgetting process -Analysis by statistical neurodynamics (in Japanese). *IEICE D-II* J77-D-II:1178-1180

The Fifteenth International Symposium on Artificial Life and Robotics 2010 (AROB 15th '10),
B-Con Plaza, Beppu,Oita, Japan, February 4-6, 2010

A Study on Q-learning Considering Negative Rewards

Takayasu FUCHIDA Kathy Thi Aung
Atsushi SAKURAGI
Graduate School of Science and Engineering, Kagoshima University
1-21-40 Kohrimoto Kagoshima-city, 890-0065 Japan
Email: fuchda@ibe.kagoshima-u.ac.jp

Abstract: In the reinforcement learning system, the agent obtains positive reward such like 1 when it achieves own goal. Positive rewards are propagated around the goal area and the agent gradually becomes to success to reach his goal. If you want to avoid some situations such like dangerous places or poison items, you might want to give negative reward to the agent. But conventional Q-learning, negative rewards are not propagated more than one state. In this paper, we propose a new way to propagate negative rewards. This is very simple and efficient technique for Q-learning. At last, we show the results of computer simulations and the effectiveness of proposed method.

Keywords: reinforcement learning, Q-learning, negative rewards

I INTRODUCTION

Reinforcement learning (RL) methods are powerful and hopeful way to control the agents like an autonomous robot [1], [2]. In the RL, a Q-learning is the very popular way to construct the intelligence about the given environments [3].

Normally, a state which is the goal for the agent gives the reward 1 to the agent, and other states will give the reward 0 to the agent. When we want to show that a state which is bad for the agent, we would want to give the reward -1 to the agent. But in the normal Q-learning, only the maximum Q-value in the next state must be selected even if a negative Q-value would exist. So if a state has a negative Q-value which absolute value is maximum value, the positive Q-value will be selected and negative Q-value is not propagated. When we could use the negative reward in order to indicate the bad state for the agent, the agent would possibly avoid the states such like this.

Reinforcement learning using reward and punishment was proposed by OKADA in 2000 [4] but in this paper experimental results were not shown.

In this paper, we propose a new learning method in which the negative Q-value can be propagated, and show the effectiveness of this method. The reason that the negative Q-value is not propagated is that the learning equation of normal Q-learning method uses the maximum value of the next state. So we changed the term of the equation from selecting the maximum value of next state to using the absolute value of Q-values.

As the results of computer simulations, we illustrate that the propagation of the negative Q-values forces the agent to avoid the bad states and go to the goal effectively.

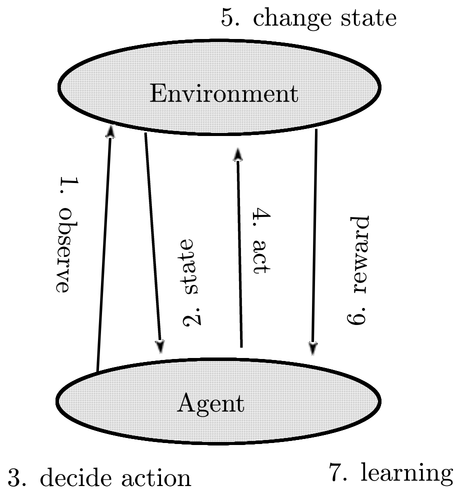

Figure 1: Interactions of RL

II REINFORCEMENT LEARNING

Figure 1 illustrates the interactions of the reinforcement learning. In the reinforcement learning, first, the agent observes the environment and obtains the state. The agent decides the next action using the state and do it to the environment. The environment is influenced by that action and changes their own state. After changing the state, the environment returns the reward to the agent. Finally, the agent learns with received reward.

During the learning period, this process is repeated and the agent accumulates the knowledge about its circumstances as the value of Q.

1 Q-learning

In the Q-learning, the worth of selecting an action in the specified state is quite important. The Q-value is the expected value of returns which is the discounted sum of the rewards the agent received, and is used as the worth of action and state pair.

On the general Q-learning, every action and state pair have own Q-value. These values are initialized to small random numbers and gradually change toward the optimal values through the learning.

At the time t, the agent observe the state s_t and executes the action a_t. As the result, the agent obtained the reward r_t, and finally the state of environment turned into s_{t+1}, then the Q-value $Q(s_t, a_t)$ is updated as following equation (1).

$$\begin{aligned} Q(s_t, a_t) \quad \leftarrow \quad & Q(s_t, a_t) \\ & +\alpha \left(r_t + \gamma \max_a Q(s_{t+1}, a) - Q(s_t, a_t) \right) \end{aligned} \tag{1}$$

In this equation, α is the learning factor and γ is the discount factor.

2 Deciding action

The agent selects next action which has highest Q-value. The action which has large Q-value is considered as the good way to achieve the goal. But selecting highest Q-value continually decreases the opportunities to find better way. Therefore the agent sometimes selects next action randomly. This random selection is useful for exploring the state space and finding the new better way which has not been found yet.

3 Propagation of worth

In the equation (1), the term $\max_a Q(s_{t+1}, a)$ selects the highest value of next state s_{t+1}. This term has an role to spread the worth of Q-value.

Generally, in the reinforcement learning, the agent acts many times before it reaches to the goal. Excepting the goal state, other states usually give the reward $r_t = 0$ to the agent. So the update equation becomes as (2).

$$\begin{aligned} Q(s_t, a_t) \quad \leftarrow \quad & Q(s_t, a_t) \\ & +\alpha \left(\gamma \max_a Q(s_{t+1}, a) - Q(s_t, a_t) \right) \\ = \quad & (1-\alpha) Q(s_t, a_t) + \alpha\gamma \max_a Q(s_{t+1}, a) \end{aligned} \tag{2}$$

This means that Q-value gradually decreases and is added the discounted maximum value of next state.

For example, if the state s_1 had large Q-value and the state s_2 was the previous state that could move to s_1 with one action. The agent staying the state s_2, without random action, must selects an action which leads it to the state s_1 and This means that the worth of s_1 is propagated to s_2.

In this way, the worth of goal area is propagated step by step into the whole state space and the agent will become to be able to reach to goal efficiently.

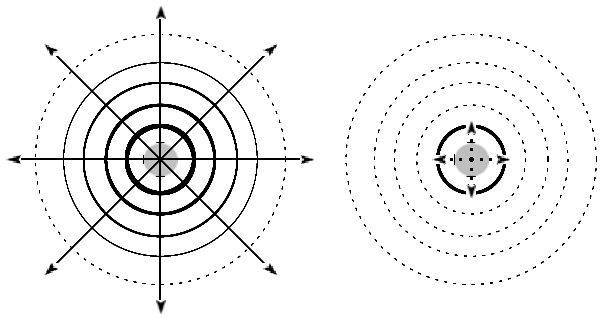

(a) positive worth (b) negative worth

Figure 2: Propagation of worth on conventional Q-learning

III PROPOSED METHOD

1 Problem in conventional way

If the objective of the agent would be only reaching the goal, it was enough just to put the positive reward in the state space. But if you want the agent to avoid the obstacles and to reach the goal, you might be want to put some negative rewards in the state space. The negative reward represents the bad result and is to be avoided by the agent. Because of the agent acts in order to increase the sum of rewards, the states which have negative rewards are not suitable for the agent.

But in the conventional Q-learning, the positive worth can be propagated around the goal area but the negative worth can not be propagated. This is because you select the highest Q-value of next state s_{t+1} in the equation (1).

Figure 2 illustrates the situations of spreading positive and negative worth. The center points of these tow figures are the states giving their own rewards. The positive worth will be propagated around the reward state like fig.2-(a), but the negative worth will not be propagated more than one movement length like fig.2-(b).

2 Propagation of negative worth

In the case that some negative reward states exist, it is better that the negative worth is also propagated. If the negative worth would not be propagated, the agent could not notice that the dangerous state was approaching to him until the danger was close to just next to him. If the negative worth would be propagated, the agent might become to be able to avoid the dangerous zone in early time.

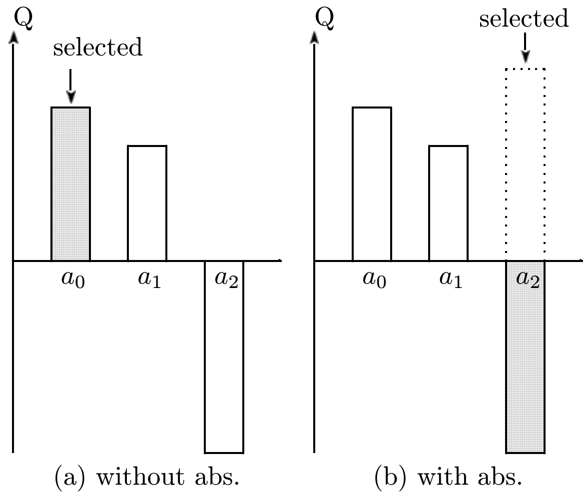

Figure 3: The difference of eqn.(1) and (3)

In this paper, we propose a new learning method to be able to propagate the negative worth. The learning equation is shown in (3).

$$\begin{cases} p = \arg\max_a |Q(s_{t+1}, a)| \\ Q(s_t, a_t) \;\leftarrow\; Q(s_t, a_t) \\ \qquad\qquad +\alpha\left(r_t + \gamma Q(s_{t+1}, p) - Q(s_t, a_t)\right) \end{cases} \tag{3}$$

In this equation, p is the argument of action index which has the largest absolute Q-value in next state s_{t+1}.

Figure 3 illustrates the difference of equation (1) and (3). In this example, 3 actions a_1, a_2 and a_3 can be selected in 1 state. For equation (1), the action a_1 which has largest Q-value is selected, but for equation (3), even though the largest Q-value is a_1, the action a_3 is selected because a_3 has largest absolute Q-value. In the actual learning, absolute value is not used.

Therefore, if the state has large negative Q-value, the negative worth is propagated around this state.

IV COMPUTER SIMULATIONS

In order to confirm the efficiency of proposed method, we experiments several computer simulations.

1 Problem

The problem treated here is as follows.

A bug moves in the closed 2 dimensional world. This bug is an agent in this model. We call this world "bait world", because several bait areas for the bug are put on this world. The bug eats the bait when he enters into the bait area. There are two kinds of bait. One is very good taste for the bug and gives positive reward to him, and the other is very bad and

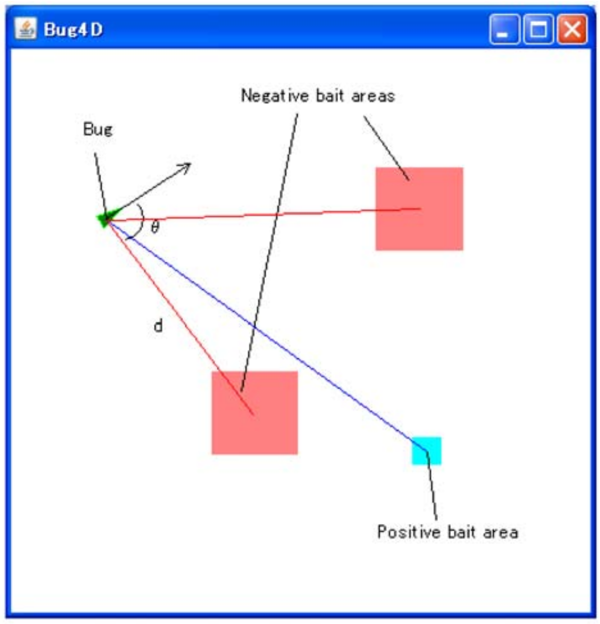

Figure 4: Image of experiments

negative reward is given. The objective of the bug is to eat as mush as baits during a specific period.

Figure 4 illustrates an image of "bait world". In this figure, the bug is represented as a triangle and the arrow of that triangle shows the direction of the bug. A large rectangular area is represented a negative bait area and a small one is positive area.

The agent observes angle and distance to each area. In the case of fig.4, since the number of bait area is 3, the agent observes 6 parameters. These 6 parameters construct the 6 dimensional state space.

The actions of the agent are 1:go straight 2:turn left and 3:turn right.

If the agent eat a bait, the position of the agent is randomly changed in the world.

2 Simulation conditions

In the simulations, "one turn" means a cycle of reinforcement learning — from an observation of the agent to an update of the Q-value. 100,000 turns make "one period". We executed 200 periods in "one experiment". we count the number of bait that the agent has eaten during one period.

Q-values are initialized to small random numbers. Positive reward is 1 and negative reward is -1. Other state gives reward 0.

Learning rate $\alpha = 0.1$ and discount factor $\gamma = 0.9$.

3 Results

We done following two types of simulation experiments.

exp1 1 positive area and 1 negative area are placed in the bait world.

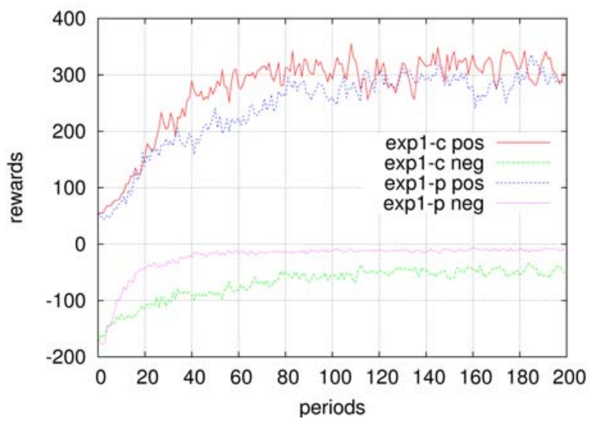

Figure 5: Result of 1 positive and 1 negative

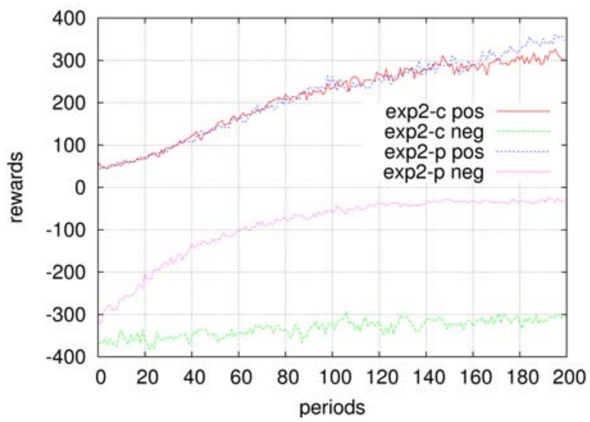

Figure 6: Result of 1 positive and 2 negatives

exp2 1 positive area and 2 negative areas are placed in the bait world.

Each experiment is done for 5 times and the results are averaged.

Figure 5 shows the result of exp1. "exp1-c" shows the conventional learning method and "exp1-p" shows the proposed method.

From this graph, the positive rewards are almost same on conventional method and proposed method, but the negative rewards are different. The number of negative rewards using proposed method is less than the one using conventional method. This means that proposed method is efficient for avoiding the bad situations and reaching to good goal.

Figure 6 show the result of exp2. In this case, the number of negative area is more than exp1. So the probability to trap the bad area is larger than exp1. From this result, you realize that the proposed method is much more efficient for avoiding the unworthy situations.

V CONCLUSION

1 Conclusion

In this paper, we proposed a new learning method which can propagate the worth of negative and showed that this method can useful for avoiding that unsuitable situations. Since this method works to propagate the negative worth around the bad state, the agent can be able to know the dangerous item at the far point of such negative areas.

And also this method is very simple way. The idea of this method is to use the absolute value of next state. By using absolute value when we select the next Q-value in learning, if the state has large negative value, it become to be able to propagate the negative worth.

The results of computer simulations, it is shown that this proposed method is very efficient for avoiding the bad situations.

2 Future works

In our experiments, the result of negative rewards have been improved but the positive one is not so much. This reason may be that in order to avoid the bad area, the agent went a long way to reach the positive goal.

Over spreading of negative worth often causes a wasteful action for the agent. To avoid this, we may have to control adaptively the discount factor γ. In this simulation, we use the constant number for γ.

References

[1] Richard S. Sutton and Andrew G. Barto, "Reinforcement Learning — An Introduction —", The MIT Press, 1998

[2] Leslie P. Kaelbling, Michael L. Littman and Andrew W. Moore, "Reinforcement Learning: A Survey", Journal of Artificial Intelligence Research 4 pp.237-285, 1996

[3] Soushi YAMADA, Takeshi OHASHI, Takichi YOSHIDA and Toshiaki EJIMA, "Research about Reinforcement Learning for Autonomic Robot in Multi-Agent Environment", IPSJ Kyushu Conference 2B-2 pp.177-186, 1998

[4] Hiroyuki OKADA, Hiroshi YAMAKAWA and Takashi OMORI, "Reinforcement Learning by Reward and Punishment", Technical Report of IEICE, NC99-100 pp.55-62 March 2000

Intelligent Agent Construction Using the Attentive Characteristic Patterns of Chaotic Neural Networks

M. Obayashi*, T. Kuremoto*, and K. Kobayashi*

*Graduate School of Science and Engineering, Yamaguchi University
2-16-2 Tokiwadai, Ube, Yamaguchi, 755-8611, Japan
(Tel : +81-836-85-9518, Fax : +81-836-85-9501)
(Email : {m.obayas, wu, koba}@yamaguchi-u.ac.jp)

***Abstract*: Human learns incidents by own actions and reflects them on the subsequent action as own experiences. These experiences are memorized in his brain and recollected if necessary. This research incorporates such an intelligent information processing mechanism, and applies it to an autonomous agent. In the proposed system, reinforcement Q-learning method is used for learning. Auto-associative chaotic neural network is also used as mutual associative memory system. However agent cannot retrieve some stored patterns exactly, in the case of too many stored patterns and strong correlation among them. To solve this problem, we propose to use kinds of attentive parameters and attentive characteristic patterns. The attentive characteristic pattern is a part of the stored patterns. When robots concentrate their attention on the specific part of the stored pattern, i.e., the attentive characteristic pattern, whole stored patterns are retrieved easily and completely. Finally, the effectiveness of this proposed method is verified through the simulation applied to the plural maze-searching problems.**

Keywords: Intelligent, Attentive parameter, Chaotic neural network, Mutual associative memory system

I. INTRODUCTION

Recently, use of robots has been considered in various fields. Such robots which behave near to humans, namely intelligent robots have been required and have attracted attention of many researchers. As a part of things which are required for the robots, experience, learning, memory and their use etc. need to be considered.

In our previous work we proposed a method [1] to realize these functions of the intelligent robots mentioned above, that is, by reinforcement learning algorithm for learning function [2] and chaotic neural networks for memorization and association [3][4]. It is important that robots can memorize their experiences and remember them quickly and exactly and behave making use of them. However in our work there is a problem, i.e., agent could not retrieve some stored patterns exactly, because of too many stored patterns and strong correlation among them.

As a way to solve this problem, in this paper we propose to use kinds of attentive parameters and attentive characteristic patterns. The attentive characteristic pattern is a part of the stored patterns. When robots concentrate their attention on the specific part of the stored pattern, i.e., the attentive characteristic pattern, whole stored patterns are retrieved easily and completely. The attentive parameter is a scalar value and corresponds to its attentive characteristic pattern and is defined for every stored pattern.

To be specific, the agent calculates the degree of similarity, i.e., the value of attentive parameter, between a specific attentive characteristic pattern and each retrieval pattern in the chaotic neural network. After that the agent changes the maximum attentive parameter value among them to 1.0, meanwhile, others to 0.0. Therefore the chaotic neural network can represent the whole pattern including the specific attentive characteristic pattern quickly and exactly.

As another issue, there is a so-called aliasing problem that agents regard the two different overall states as the same because of partially observable ability of sensors of agents. One way to solve this problem is to make use of the past history of the agent's behaviors. However it is difficult for the agent to retain its whole past history because of the memory capacity. Therefore we propose to retain the parity information of them less required capacity than whole information of history. Finally we show that our proposed methods are effective through computer simulations of the optimal path searching problem in mazes.

II. ASSOCIATIVE CHAOTIC NEURAL NETWORK

Chaotic Neural Network (CNN) is constructed with chaotic neuron models that have refractory and continuous output value. Its useful usage is as associative memory network named ACNN [3][4]. Here are the dynamics of ACNN.

$$s_i(t+1) = f(y_i(t+1) + z_i(t+1)) \qquad (1)$$

$$y_i(t+1) = k_r \cdot y_i(t) - \alpha \cdot s_i(t) + a_i \qquad (2)$$

$$z_i(t+1) = k_f \cdot z_i(t) + \sum_{j=1}^{n} \omega_{ij} s_j(t) \qquad (3)$$

where $s_i(t)$: output value of ith neuron at time t, n: numbers of input, ω_{ij}: synapse from ith neuron to jth neuron, $y_i(t)$: internal state of ith neuron at time t, $z_i(t)$: internal state of ith neuron as to reciprocal action, a_i : threshold of ith neuron, k_r, k_f : damping coefficient, α : constant.

An input-output function $f(\cdot)$ to be used with CNN is described as follows,

$$f(t) = \frac{1-\exp(-t/\varepsilon)}{1+\exp(-t/\varepsilon)}, \tag{4}$$

where ε is a positive constant. Threshold for binary representation is set to 0.5 for all neurons.

For example, in the case of ACNN, patterns stored into the ACNN are set as follows,

$$\omega_{ij} = \frac{1}{P}\sum_{p=1}^{P}(2x_i^p - 1)(2x_j^p - 1), \tag{5}$$

x_i^p : ith element of pth stored pattern (0 or 1), P : a number of stored patterns.

Fig. 2 shows the example of behaviors of the chaotic neural network consists of $n = 100$ neurons (10 times 10) with 4 memory patterns and the network as shown in Fig. 1. We find that the stored patterns in the CNN are appearing through patterns of the output chaotically. Table 2 shows the parameters used in this CNN.

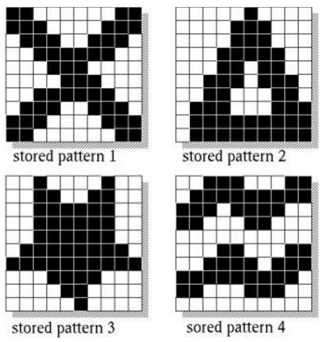

Fig. 1 Stored patterns in CNN

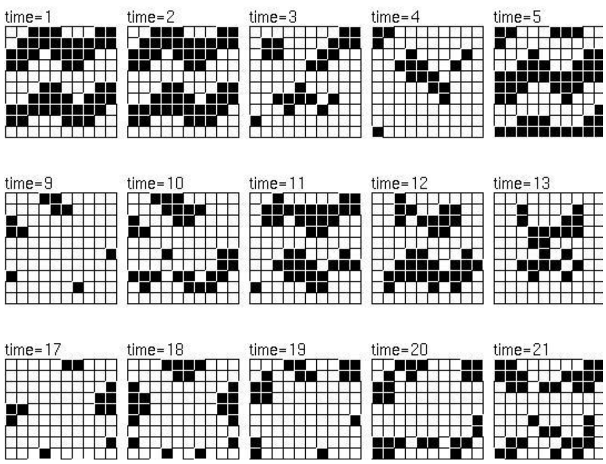

Fig. 2 Behavior of the CNN

Table 1 Parameters used in the computer simulation

k_f	k_f	a_i	α	ε
0.20	0.90	2.0	10.0	0.015

III. MUTUAL ASSOCIATIVE CHAOTIC NEURAL NETWORK

In this section, we consider the CNN as memory system of the agent, i.e. we explain the way to use the auto-associative CNN as a mutual-associative CNN (MACNN). The structure of both CNNs is same except the meaning of the synaptic weights. In the MCNN, it consists of environmental inputs (I) and their corresponding actions (O) and other neurons with random values to weaken the correlation among each stored patterns (M) (see Fig. 3). After learning of the optimal actions and input-output patterns are stored into the MACNN, when the agent moves in the environment, agent gets the information from environments and set the input information (I) to MACNN as the initial state, the action corresponding to input information (O) are retrieved. The agent executes the action. However, as the stored patterns increase, it becomes difficult to retrieve the desired patterns because of their strong correlations. Therefore, to solve this problem, we propose the method with using the attentive parameters.

$$W\{=\omega_{ij}\} = \begin{bmatrix} I^1 \\ M^1 \\ O^1 \end{bmatrix}\begin{bmatrix} I^{1T} & M^{1T} & O^{1T} \end{bmatrix} + \cdots + \begin{bmatrix} I^P \\ M^P \\ O^P \end{bmatrix}\begin{bmatrix} I^{PT} & M^{PT} & O^{PT} \end{bmatrix} \tag{6}$$

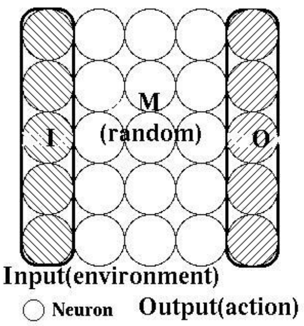

Fig. 3 Image of Mutual Associative CNN

IV. ATTENTIVE PARAMETERS

1. *Attentive parameter*

The synaptic weights are set as follows,

$$\omega_{ij} = \frac{1}{P}\sum_{p=1}^{P}\lambda_p(t)\cdot(2x_i^p - 1)(2x_j^p - 1), \tag{7}$$

where $\lambda_p(t)$: attentive parameter of $p\,th$ stored pattern $x_i^p (= [I^{pT}\ M^{pT}\ O^{pT}]^T)$ at time t. The $\lambda_p(t)$ is restricted as follows,

$$\begin{cases} 0 \le \lambda_p(t) \le 1 \\ \sum_{p=1}^{P} \lambda_p(t) = 1 \end{cases} \quad (8)$$

2. *Calculation of values of attentive parameters*

In MACNN, the part of the stored pattern is set as the characteristic. An example of two stored patterns and characteristic 20 bits during operation at time t are shown in Fig. 4(a)(b), respectively. The values of attentive parameters of the stored pattern $\lambda_p(t)\ (p=1,2)$ are as follows,

$$\lambda_1(t) = \frac{9/20}{9/20 + 17/20} = 9/26$$
$$\lambda_2(t) = \frac{17/20}{9/20 + 17/20} = 17/26 \quad (9)$$

Thus, attentive parameter gives the similarity of the output pattern for the $p\,th$ stored patterns.

3. *Operation of the MACNN*

The attentive parameter is used as follows.

Step1: The values of each attentive parameter of stored patterns are calculated like Eq. (9).

Step2: The number of stored pattern which has max value of attentive parameter is decided by

$$k = \arg\max_i \lambda_i(t).$$

Step3: If $\lambda_k(t) > \theta_{th}$, then

$$\lambda_k(t) = 1.0, \lambda_i(t) = 0.0\ (i \ne k)$$

else nothing is done.

Step4: Go to the next MACNN operation.

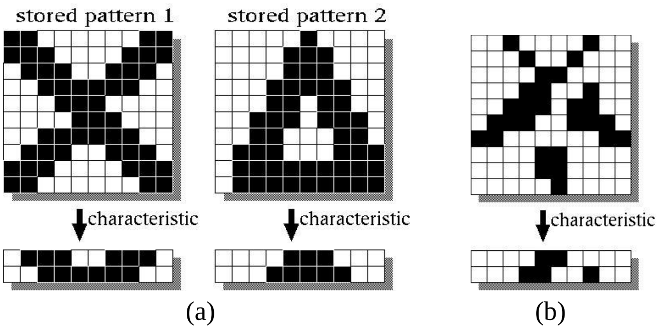

Fig.4 (a) Example of two stored patterns, (b) the characteristic bits at time t during operation

V. STORED PATTERNS WITH PARITY BIT

The agent is often faced with aliasing problem, i.e. there is often that agent is mistaken certain different environments as same environment because of the lack of its sensor ability. In this paper, we solve this problem by making use of past information, i.e. adding parity bits to the stored patterns of state-action pairs. This is the less memory required method than storing of all information used before.

VI. REINFORCEMENT LEARNING

In this paper, agent uses the Q-learning method to learn the optimal action, as follows,

$$Q(s,a) = Q(s,a) + \alpha\{r + \gamma \max_{a'} Q(s',a') - Q(s,a)\}, \quad (10)$$

where s : state, a : action, s' : next state, a' : next action, r : reward. α, γ : positive constant.

The agent action is selected using the next probability,

$$B(a \mid s) = \frac{\exp(Q(s,a)/T)}{\sum_{b \in A} \exp(Q(s,b)/T)}, \quad (11)$$

where $B(a \mid s)$ is probability of action a under the state s, T is positive constant called temperature parameter.

VII. ALGORITYM

Our proposed method is organized as follows,

1) Learning of the optimal action using the Q-leaning with the parity bits in section V and VI.
1) Constructing the synaptic weights with attentive parameters (Eq. (6)-(7)) in section III and IV using the results of learning.
2) Agent moves step by step in the maze making use of MACNN with Eq. (1)-(4) in section II.

VIII. COMPUTER SIMULATION

In this section, our proposed method, MACNN with attentive parameters and parity bits, are simulated to confirm their effectiveness through the optimal path searching of maze problems in Fig. 6. Fig. 5 shows the sensor range of the agent. Table 1 shows the action and its code taken by the agent. The agent always moves keeping the attitude that its front of head is always upward of the paper and take one action shown in Table 2.

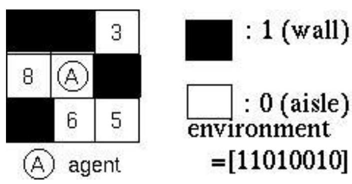

Fig.5 The sensor range of the agent

Table 2 The action of the agent and its code

action	up-left	up	up-right	right	down-right	down	down-left	left
code	0100	0000	0101	0011	0110	0001	0111	0010

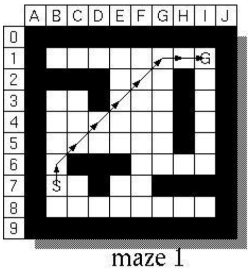

maze 1

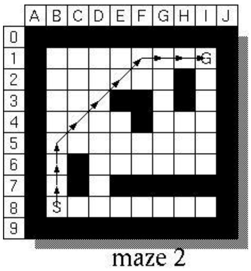

maze 2

maze 2

coord.	env.	act.
(8,B)	10101111	up
(7,B)	10110011	up
(6,B)	10011011	up
(5,B)	10001011	up-right
(4,C)	00000000	up-right
(3,D)	00010000	up-right
(2,E)	00001100	up-right
(1,F)	11100000	right
(1,G)	11101000	right
(1,H)	11100100	right

maze 1

coord.	env.	act.
(7,B)	10100011	up
(6,B)	10010011	up-right
(5,C)	00001100	up-right
(4,D)	01000000	up-right
(3,E)	10000001	right
(3,F)	00000000	up-right
(2,G)	10100011	up-right
(1,H)	11100100	right

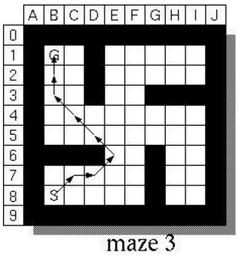

maze 3

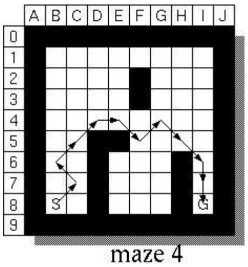

maze 4

maze 4

coord.	env.	act.
(8,B)	10001111	up-right
(7,C)	001110000	up-left
(6,B)	10000011	up-right
(5,C)	00011000	up-right
(4,D)	00001100	right
(4,E)	00100110	down-right
(5,F)	00000001	up-right
(4,G)	10000000	down-right
(5,H)	00000100	down-right
(6,I)	00111011	down
(7,I)	10111011	down

maze 3

coord.	env.	act.
(8,B)	10001111	up-right
(7,C)	11100000	up
(7,D)	11000000	up-right
(6,E)	00000001	up-left
(5,D)	00000110	up-left
(4,C)	00100000	up-left
(3,B)	10000011	up
(2,B)	10000011	up

maze 5

coord.	env.	act.
(8,B)	10001111	up-right
(7,C)	00100000	up-left
(6,B)	10100011	up
(5,B)	10010011	up-right
(4,C)	11001100	up-right
(3,D)	00000001	up-left
(2,C)	00000110	up-left

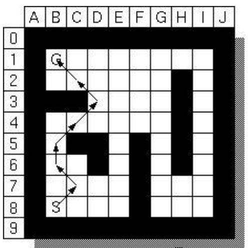

maze 5

Fig. 6 Mazes and its optimal path used in the simu.

At first 5 mazes in Fig. 6 are solved using Q-Learning and their optimal paths are also drawn in each maze by lines with arrows. The coordinate, environment and its corresponding to action of each maze are also shown in Fig. 6. Next these pairs of environments and actions of five mazes are stored in CNNs using form of Eq. (7). Showing in Fig.6, there are 44 patterns to store in the MACNN, and 6 of them are aliasing cases, i.e., some environments are same but each optimal action is different, as following cases,

$$(5,C)_1 \text{ and } (4,D)_4,\ (2,E)_2 \text{ and } (4,D)_4,\ (6,E)_3 \text{ and } (5,F)_4$$
$$(3,D)_5 \text{ and } (5,F)_4,\ (3,A)_3 \text{ and } (6,A)_4,\ (2,A)_3 \text{ and } (6,A)_4$$

where (a,b), c in $(a,b)_c$ mean coordinates and the number of mazes, respectively.

1. *Simulation results only with attentive characteristic without parity bits*

In this case, in maze 1 and 2 agent could get the goal within 10 and 12 steps making use of the attentive parameters though there are aliasing (5,C) and (2,C), respectively. In maze 3 and 5, agent could get the goal when the agent select the action as learning chaotically, but it could not get the goal within the predefined trial number when the agent select the other actions. In maze 4, The agent could not get the goal because of aliasing at $(3,B)_3$ and $(6,B)_4$,$(4,D)_4$ and $(5,F)_4$.

2. *Simulation results with attentive characteristic and parity bits*

In this case, the agent could get the goal in all mazes because that the agent could discriminate the appropriate action through the past 4 step parity bits and attentive parameters to recollect the exact patterns.

VII. CONCLUSION

We proposed the method to use kinds of attentive parameters and attentive characteristic patterns to solve the problem recollecting the false pattern and proposed using the parity bits required less memory to solve the aliasing problem.

REFERENCES

[1] Obayashi, M. and Narita, K. and Kuremoto, T. and Kobayashi, K., A Reinforcement Learning System with Chaotic Neural Networks-Based Adaptive Hierarchical Memory Structure for Autonomous Robots, Proceeding of International Conference on Control, Automation, and Systems, pp.69-74 (2008)
[2] R.S. Sutton, A.G. Barto, Reinforcement Learning, The MIT Press (1998)
[3] Aihara, K. and Takabe, T. and Toyoda, M., Chaotic Neural Networks, Physics Letters A, pp.333-340 (1990)
[4] Adachi, K., Tanabe, T., Associative Dynamics in Chaotic Neural Networks, Neural Networks, Vol.10, pp.83-98 (1997)

The Fifteenth International Symposium on Artificial Life and Robotics 2010 (AROB 15th '10),
B-Con Plaza, Beppu,Oita, Japan, February 4-6, 2010

An Effective Image Transmission Method in ZigBee System for Intruder Detection Systems

Seon-Ki Hwang*, Sang-Gu Lee**

Dept. of Computer Engineering. Hannam University, Korea
(Tel : 82-42-629-7551)
hwangsae7@naver.com, sglee@hnu.kr***

Abstract: The characteristics of ZigBee System are highly reliable, highly secure, able to use very lower power, cost effective, and an open global standard. In this paper, we implement an intruder detection system using image transmission techniques based on ZigBee networking. The proposed system is composed of many sensor modules of infrared, temperature, humidity and illumination, together with RFID reader and camera modules. Image transmission is performed only in the emergency environment such as intruder detection in order to reduce overhead in the routing transmission. This system will be applied to low-cost image-based ZigBee product and will provide good security, user convenience and easy use.

Keywords: ZigBee, RFID, Image transmission, Intruder detection system

I. INTRODUCTION

The characteristics of ZigBee System are highly reliable, highly secure, able to use very lower power, cost effective, and an open global standard. While most wireless applications are getting to go faster, ZigBee aims for low data rate and low power. So many ZigBee applications can be fitted on even 8-bit microcontrollers as like ATmega128. In this paper, we will propose an intruder detection system using image transmission based on ZigBee IEEE 802.15.4 protocol. The proposed system is composed of ATmega128 based ZigBee motes, many sensors to detect an intruder and to catch hold of indoor environment, and camera modules. This system provides user convenience and effectiveness.

The organization of this paper is as followings. In Chapter 2, Organization of the proposed system is covered. Experimentation and results are discussed in Chapter 3. And finally, Chapter 4 draws a conclusion.

II. ORGANIZATION OF THE PROPOSED SYSTEM

In the proposed system, we use ZigbeX motes and 13.56 MHz RFID tags and reader, many sensors including infrared sensor and camera modules. Each ZigbeX mote has ATmega128L microcontroller, CC2420 RF chip, and many sensors including temperature, humidity, and antenna module.

Figure 1 shows the entire organization of the proposed system. Mote 1 is a sink node that receives sensed data from other motes in RF communication and transfer data to main PC in serial communication. Mote 2 and 3 are installed on the floor and received the sensed data from motes from 4 to 9 through RF communication. In the mote 4, RFID reader is installed in order to identify visitors. In the mote 5, camera module C328 is added to acquire image information in the limited situation as like intruder detection and a fire occurring. Motes from 6 to 9 detect the temperature, humidity, illumination, and infrared sensing, and transfer data to main PC in RF communication via mote 1.

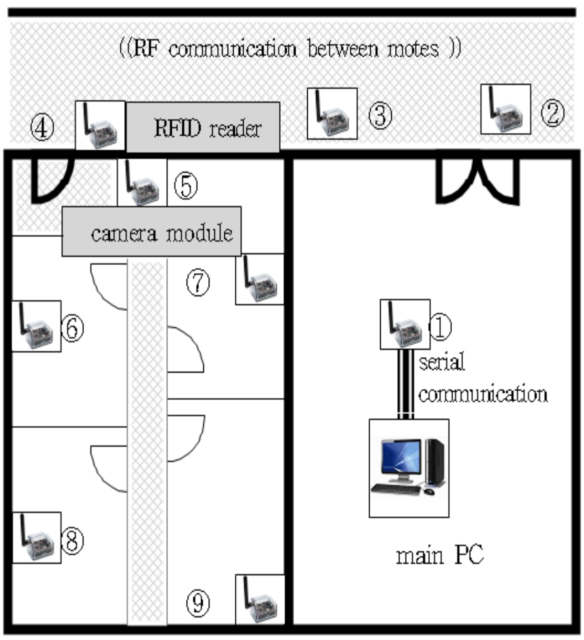

Fig.1. Organization of the entire system

In the proposed system, we can monitor a situation of environment using camera module in the limited situations. Originally, ZigBee system was developed for low data rate and low power consuming. Image transmission needs much data to transfer between motes. In this paper, therefore, we take the efficiency of image data transmission into fall account. ZigBee system uses 20~250kbps in speed, so it is not good for image in real-time, however, it is much efficient for monitoring on the unit of several minutes interval. In the proposed system, the camera module has image Codec inside and provides 160 * 128 pixel size image, and JPEG file. Camera module uses compressed data so that the system has not much overhead in image transmission.

Figure 2 shows the number of image frames per one minute in one node. We can know from this figure that the proposed system can receive about 18.5 frames in 20 minutes. In this figure, red line represents the average number of frames.

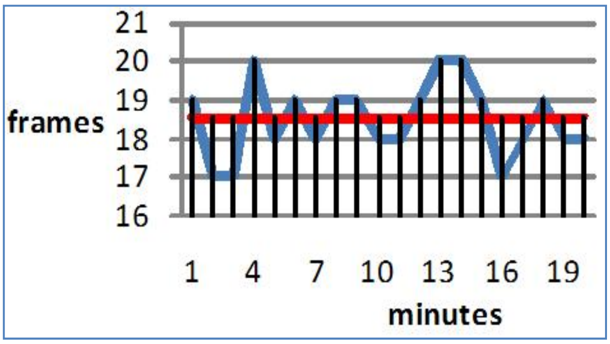

Fig.2. Number of Frames in minutes

III. EXPERIMENTAION AND RESULT

In this paper, we implemented a main operation program using Visual C++ MFC environment. For ZigBee environment, TinyOS is used for mesh networking and operating written in a language called NesC. In the NesC, all sensors are treated as objects.

Table 1 shows a sensed packet sample data in this system.

Table 1. Packet samples

7E 42 7D 5E 0 6A 7A 20 1 0 0 0 FE FF FE FF FF 0 0 0 1 AA A 5 3C 6 0 9F 0 0 7E
7E 42 7D 5E 0 6A 7A 20 1 0 0 0 FE FF FE FF FF 0 0 0 1 0 0 3A 0 FF D8 FF E0 0 11 4A 46 49 46 0 1 2 3 4 5 6 7 8 9 A FF DB 0 43 0 10 C C E C A 10 E E E 12 12 10 14 18 28 1A 18 16 16 18 32 24 26 1E 28 3A 34 3E 3C 3A 34 10 0 40 0 0 7E
7E 42 7D 5E 0 6A 7A 20 1 0 0 0 FE FF FE FF FF 0 0 0 1 1 0 3A 0 38 38 40 48 5C 4E 40 44 58 46 38 38 50 6E 52 58 60 62 68 68 68 3E 4E 72 7A 70 64 78 5C 66 68 64 FF DB 0 43 1 12 12 12 16 16 16 30 1A 1A 30 64 42 38 42 64 64 64 64 64 64 64 29 0 34 0 0 7E
. . .
7E 42 7D 5E 0 6A 7A 20 1 0 0 0 FE FF FE FF FF 0 0 0 1 7 0 3A 0 A B FF C4 0 B5 11 0 2 1 2 4 4 3 4 7 5 4 4 0 1 2 77 0 1 2 3 11 4 5 21 31 6 12 41 51 7 61 71 13 22 32 81 8 14 42 91 A1 B1 C1 9 23 33 52 F0 15 62 72 EA 0 8 0 0 7E

In Table 1, each part of one sensed packet is as like Table 2.

Table 2. Packet analysis

7E 42 7D 5E 0 7A 7A 20 3 0 0 0 FE FF FE FF CC 0 0 0 1A 0 36 0 8A 1 9C 0 0 0 0 0 0 0 0 0 0 0 0 0 0 2 7E

For Table 2, packet explanation is shown in the Table 3.

Table 3. Packet explanation

Data	Analysis
7E	Start byte
42	Packet type
7D 5E 0	Serial communication address
7A	Type (image or sensor)
7A	Group ID
20	Data length (16 byte)
3 0	Source node address
0 0	Destination node address
FE FF	Multi-hop communication
FE FF	Multi-hop communication
CC 0 0 0	Packet number
1A 0	Temperature
36 0	Humidity
8A 1	Illumination
9C 0	Infrared ray
0 0 0 0	Null
0 0 0 0	Null
0 0 0 0	Null
0 2	CRC check byte
7E	Last byte

Data (little-endian)	Calculation (big-endian)
1A 0	16*1+10 = 26
36 0	3*16+6 = 54
8A 1	16^2*1+16*8+10 = 394
9C 0	16*9+12 = 156

Figure 3 shows an acquired image through ZigBee networking in the proposed system.

Fig.3. Acquired image in the proposed system

Figure 4 shows the operation window of the proposed system. In this, there are many display items of command box, several sensor's data, visitors identification, moving routes, information of serial communication, and received packets.

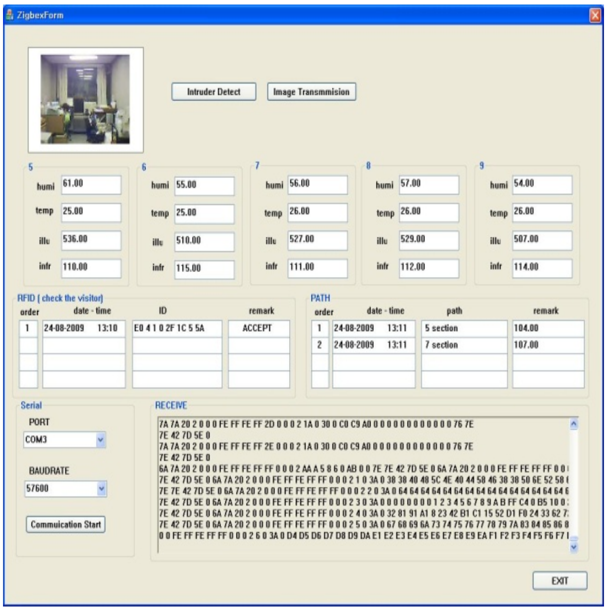

Fig.4. Operation window of the proposed system

VI. CONCLUSION

In this paper, have implemented an intruder detection system using image transmission based on ZigBee/IEEE 802.15.4 networking on emergency environment. Image data that are divided by 4 blocks are transferred in RF communication between nodes, therefore RF communication overhead are reduced.

The proposed system has major function such as

(1) Identification of image on emergency environment using user commands,
(2) Identification of real-time temperature, humidity, illumination, and infrared sensing data,
(3) Identification of visitors using RFID,
(4) and, identification of emergence on main PC.

In the future study, we will develop a more effective image transmission method without degradation of ZigBee performance.

ACKNOWLEDGEMENT

This work was supported by Security Engineering Research Center, granted by the Korea Ministry of Knowledge Economy.

REFERENCES

[1] Zhao and Guibas, Wireless sensor network, Morgan Kaufmann, 2004.
[2] Drew Gislason, ZIGBEE Wireless Networking, Newnes, 2008.
[3] Eady, Hands-On ZigBee, Newnes, 2007.
[4] Philip Levis, David Gay, "TinyOS Programming", Cambridge University Press, 2009.
[5] Mc. Andrew, An Introduction to Digital Image Processing with Matlab, Course Technology Ptr, Mar. 2004.
[6] ZigbeX, http://hanback.co.kr

A color-based particle filter for multiple objects tracking in outdoor environment

Budi Sugandi, Hyoungseop Kim, Joo Kooi Tan and Seiji Ishikawa
Graduate School of Engineering, Kyushu Institute of Technology
1-1 Sensui, Tobata, Kitakyushu, Fukuoka, Japan
Tel : +81-93-884-3185; Fax :+ 81-93-861-1159
budi@kimlab.cntl.kyutech.ac.jp

Abstract: Tracking of multiple objects is more challenging than tracking a single object. Some problems arise in multiple object tracking that do not exist in single object tracking such as objects occlusion, appearing new object and disappearing already existed object, updating the occluded object, etc. In this paper, we present an approach to handle multiple objects tracking in the presence of occlusions, background clutter and appearance change. The occlusion is handled considering the predicted trajectories of the objects based on a dynamic model and likelihood measures. We propose also a target-model update conditions, ensuring the proper tracking multiple objects. The proposed method is implemented in the probabilistic framework such as particle filter in conjunction with a color feature. The particle filter has proven very successful for non-linear and non-Gaussian estimation problems. It approximates a posterior probability density of the state such as the object position by using samples or particles, where each state is denoted as the hypothetical state of the tracked object and its weight. The observation likelihood of the objects is modeled based on color histogram. The sample weight is measured based on Bhattacharya coefficient that measures the similarity between each sample's histogram with a specified target model. The algorithm can track the multiple objects in the present of occlusion and noise successfully. Some experimental results show the effectiveness of our method to track the multiple objects.

Keywords: particle filter, color feature, multiple objects, occlusion.

I. INTRODUCTION

The increasing interest in visual tracking is motivated by a huge number of promising applications that can now be tackled in real-time applications. These applications include performance analysis, surveillance, video-indexing, smart interfaces, teleconferencing and video compression. However, tracking objects can be extremely complex and time-consuming especially when it is done in outdoor environments. Here, we can mention some problems of object tracking in outdoor environments such as fake-motion background, illumination changes, shadows and presence of clutter. Some problems are also taken into account concerning whether a single or multiple objects should be tracked. Because the multiple objects tracking has more challenging problem due to the presence of objects occlusion, objects appearing and disappearing or appearance changes.

Traditionally, the tracking problem is formulated by Ristic et al. [1] as a sequential recursive estimation that is having an estimate of the probability distribution of the target in the previous frame and estimates the target distribution in the new frame using all available prior knowledge and the new information brought by the new frame. The state-space formalism where the current tracked object properties are described in an unknown state vector updated by noisy measurements is very well adapted to model the tracking. One of the methods of the sequential estimation is Kalman filter [2] which is dealing with target tracking in the probabilistic framework. But it cannot resolve the tracking problem when the model is nonlinear and non-Gaussian. The extended Kalman filter [2] can deal to this problem, but still has a problem when the nonlinearity and non-Gaussian cannot be approximated accurately.

Recently, particle filter, a numerical method that allows to find an approximate solution to the sequential estimation [3] has been proven very successful for nonlinear and non-Gaussian estimation problems [4-6]. It approximates a posterior probability density of the state such as the object position by using samples which are called particles. As for one of the particle filters, the Condensation algorithm was introduced by M. Isard et al. [4]. This algorithm has been typically used for tracking problems of moving object contours. For another particle filter, Monte Carlo filter was introduced by Kitagawa [5] and Bayesian bootstrap filter was introduced by Gordon et al. [6].

Although particle filters have been widely used in recent years, they have important drawbacks [7]. One of them is sampling impoverishment that is samples are spread around several modes pointing out the different hypotheses in the state space, but most of them may be spurious. Especially in the multiple objects tracking, the objects with higher likelihood may monopolize the samples set and objects whose samples exhibit lower likelihood have higher probability of being lost. Besides that, the multiple target tracking has another problem with occlusion, appearance change and background clutter.

In recent years, many improvements have been introduced, but there is still much ground to cover. Different approaches have been taken in order to overcome these facts. Nummiaro et al. [8] used a particle filter based on color histograms features. Histograms are robust to partial occlusions and rotations but no shape analysis is taken into account. Moreover, no multiple-target tracking is considered and complete occlusions are not handled. Perez et al. [9] proposed also a particle filter based on color histogram. They introduced interesting extension in multiple-part modeling, incorporation of background information and multiple targets tracking. Nevertheless, it requires an extremely large number of samples, since one sample contains information about the state of all targets, dramatically increasing the state dimensionality. Further, no appearance model updating is performed, what usually leads to target loss in dynamic scenes. Comaniciu et al. [10] proposed to use mean shift in order to track non-rigid object. His work has real time capabilities. However, the problem for object tracking with color occurs when the region around the object is cluttered and illumination is change. In this way, a color feature based tracking does not provide reliable performance because it fails to fully model the target especially when occlusion occurs. In another work, Comaniciu et al. [11] approach relied on gradient-based optimization and color-based histograms. In this case, no dynamic model is used therefore no occlusion can be predicted. Deutscher et al. [12] presented an interesting approach called annealing particle filter which aims to reduce the required number of samples, however, it could be inappropriate in a cluttered environment. They combine edge and intensity measures but they focused on motion analysis, and thus, no occlusion handling is explored. Some effort have been done in contour tracking [13] although it may be inappropriate, if used as the only cue, in crowded scenarios because of multiple occlusions.

Another issue of the multiple target tracking is the management of multiple tracks caused by newly appearing targets and the disappearance of already existing targets. Some of them rely on hybrid sequential state estimation. In [14], the state vector denoting all the existing targets is augmented by a discrete random variable which represents the number of existing objects in a video sequence. The particle filter developed in [15] has multiple models for the object motion, and comprises an additional discrete state component, denoting which of the motion models is active. The Bayesian Multiple-Blob Tracker (BraMBLe) [16] presented a multiple persons tracking system based on statistical appearance models. The multiple blob tracking is managed by incorporating the number of objects present in the state vector and state vector is augmented as in [14] when a new object enters the scene.

In this paper, we propose to solve some tracking problems related to the difficulties described above, such as multiple objects tracking with unknown dynamics in presence of background clutter and strong noise and in the presence of occlusion.

The remaining of this paper is organized as following. In section 2, we describe a probabilistic tracking framework. Section 3 describes the multiple objects tracking. Section 4 presents some experimental results and finally section 5 is the conclusion of the paper.

II. PROBABILISTIC TRACKING FRAMEWORK

Since the tracking problem is formulated by sequential recursive estimation, a probabilistic framework is commonly used. The computation of the expected state $\mathbf{x}_k$ given all observations to data $\mathbf{z}_{1:k}$ is called filtering. Under certain assumptions, the posterior probability distribution function (pdf) $p\left(\mathbf{x}_k \middle| \mathbf{z}_{1:k}\right)$ can be calculated through recursive estimation,

$$p\left(\mathbf{x}_k \middle| \mathbf{z}_{1:k}\right) \propto \underbrace{\underbrace{p\left(\mathbf{z}_k \middle| \mathbf{x}_k\right)}_{\text{likelihood}}}_{\text{updating}} \underbrace{\int \underbrace{p\left(\mathbf{x}_k \middle| \mathbf{x}_{k-1}\right)}_{\text{trans. model}} \underbrace{p\left(\mathbf{x}_{k-1} \middle| \mathbf{z}_{1:k-1}\right)}_{\text{prev. post}} dx_{k-1}}_{\text{prediction}} . \quad (1)$$

The pdf is projected forward according to the transition model to make a prediction. Then, it is updated in agreement with the new observation $\mathbf{z}_k$. When no assumptions are taken about the involved distributions, this problem is overcome by simulating N random samples from the posterior pdf, $\{\mathbf{x}_k^i; i = 1:N\}$. This approach is called particle filters [4-6].

In Bayesian sequential estimation, the filtering distribution can be computed according to the two step recursions, prediction and update step. The prediction step follows from marginalization and updated step is obtained through observation model. This recursion requires the specification of a dynamic model describing the state evolution, $p(\mathbf{x}_k|\mathbf{x}_{k-1})$ and a model that gives the likelihood of any state in the light of the current observation, $p(\mathbf{z}_k|\mathbf{x}_k)$. The recursion is initialized with some distribution for the initial state $p(x_0)$.

The basic idea behind the particle filter is very simple. Starting with a weighted set of samples at k-1 $\{\mathbf{x}_{k-1}^i, \pi_{k-1}^i; i = 1:N\}$ approximately distributed according to $p(\mathbf{x}_{k-1}|\mathbf{z}_{1:k-1})$, new samples are generated from a suitable proposal distribution, which may depend on the previous state and the new measurements. To maintain a consistent sample, the new importance weights are set to

$$\pi_k^i = \pi_{k-1}^i \frac{p\left(\mathbf{z}_k \middle| \mathbf{x}_k^i\right) p\left(\mathbf{x}_k^i \middle| \mathbf{x}_{k-1}^i\right)}{q\left(\mathbf{x}_k \middle| \mathbf{x}_{1:k-1}, \mathbf{z}_{1:k}\right)} . \quad (2)$$

The new particle set is re-sampled using normalized weights $\bar{\pi}_k^i$ as probabilities. This sample set represents the posterior at time k, $p(\mathbf{x}_k|\mathbf{z}_{1:k})$. Then, the expectations can be approximated as

$$E\,p(\mathbf{x}_k|\mathbf{z}_{1:k}) \cong \sum_{i=1}^{N} \bar{\pi}_k^i \hat{\mathbf{x}}_k^i \,. \tag{3}$$

This implementation of the approach corresponds to the bootstrap filter as proposed in [6].

III. MULTIPLE OBJECTS TRACKING

In this paper, we proposed an algorithm based on particle filtering in conjunction with color feature. The motion of the central point of a bounding box is modeled using first-order dynamics model.

The state of the object is defined as $\mathbf{s}_k = (\mathbf{x}_k, \dot{\mathbf{x}}_k, \mathbf{w}_k, \dot{\mathbf{w}}_k, \mathbf{A}_k)$ where the components are position, speed, bounding-box size, bounding-box scale and pixel appearance, respectively. Each object associates one specific appearance model to the corresponding samples, allowing multiple objects tracking. The observations $\mathbf{z}_k$ is given by input images $\mathbf{I}_k$.

3.1. System Flow Diagram

In this paper, we want to apply a particle filter in a color model-based framework to track multiple objects in outdoor environment. Initially, the samples are drawn randomly for the first frame. The sample prediction is performed based on a system model. The weight calculation is performed based on histogram distance computed using Bhattacharya coefficient. The estimate is performed based on the sample's weight. Then resampling is performed for the next sample iteration. Target model is updated to ensure the proper tracking multiple objects. The overall working flow diagram is shown in Figure 1.

3.2 Tracking Model

We consider the motion of an object as the discrete time 2-dimensional (2D) motion with constant velocity.

The state vector at a time step k is denoted by $\mathbf{s}_k$, including position, speed, size and bounding box scale of each sample and is predicted according to

$$\begin{aligned}
\hat{\mathbf{x}}_k &= \mathbf{x}_{k-1} + \dot{\mathbf{x}}_{k-1}\Delta t + \xi_{\mathbf{x}}\,,\\
\hat{\dot{\mathbf{x}}}_k &= \dot{\mathbf{x}}_{k-1} + \xi_{\dot{\mathbf{x}}}\,,\\
\hat{\mathbf{w}}_k &= \mathbf{w}_{k-1} + \dot{\mathbf{w}}_{k-i}\Delta t + \xi_{\mathbf{w}}\,,\\
\hat{\dot{\mathbf{w}}}_k &= \dot{\mathbf{w}}_{k-1} + \xi_{\dot{\mathbf{w}}}\,.
\end{aligned} \tag{4}$$

The random vectors $\xi_{\mathbf{x}}, \xi_{\dot{\mathbf{x}}}, \xi_{\mathbf{w}}, \xi_{\dot{\mathbf{w}}}$ provide the system with a diversity of hypotheses.

3.3. Likelihood Function

The likelihood function computes the pdf of image features given the state. The target appearance can be represented by means of color histograms. Histograms are broadly used to represented human appearance, since they are claimed to be less sensitive than color templates to rotations in depth, the camera point of view, non-rigid targets, and partial occlusions.

To achieve robustness against mixed color, rotation and variant illumination condition, we focus on weighted color histograms to represent the target model. In this paper, the color histogram is used as the discretized color distribution. The histograms are calculated from the function $h(\boldsymbol{x}_i)$ that assign the color at location $\boldsymbol{x}_i$ to the corresponding bin. Following [8-10], we do not use the entire image as a measurement, but rather we compute the color histogram inside the image region that is specified by the state vector.

To increase the reliability of the target model, smaller weight are assigned to the pixels that are further away from region center by employing a weighting function

$$g(r) = \begin{cases} 1 - r^2 & r < 1 \\ 0 & otherwise \end{cases}, \tag{5}$$

here, r is the distance from the center of the region.

The color histogram $p_{\boldsymbol{y}} = \{p_{\boldsymbol{y}}^{(u)}\}u = 1,\dots,m$ at location $\boldsymbol{y}$ is calculated as

$$p_{\boldsymbol{y}}^{(u)} = f \sum_{j=1}^{I} g\left(\frac{\|\boldsymbol{y} - \boldsymbol{x}_j\|}{a}\right)\delta\left[h(\boldsymbol{x}_j) - u\right], \tag{6}$$

here respectively, I is the number of pixels in the region, $\boldsymbol{x}_j$ is the position of pixels in the region, δ is the Kronecker delta function, a is the normalization factor, and f is the scaling factor defined as

$$f = \frac{1}{\sum_{i=1}^{I} g\left(\frac{\|\boldsymbol{y} - \boldsymbol{x}_i\|}{a}\right)}, \tag{7}$$

to ensures that $\sum_{u=1}^{m} p_{\boldsymbol{y}}^{(u)} = 1$.

The similarity between two color histograms $\boldsymbol{p} = \left\{p^{(u)}\right\}u = 1,\dots,m$ and $\boldsymbol{q} = \left\{q^{(u)}\right\}u = 1,\dots,m$ is measured using Bhattacharyya distance defined as

$$d = \sqrt{1 - \rho[\boldsymbol{p},\boldsymbol{q}]}\,, \tag{8}$$

where

$$\rho[\boldsymbol{p},\boldsymbol{q}] = \sum_{u=1}^{m} \sqrt{p^{(u)} q^{(u)}}\,. \tag{9}$$

From this equation, the larger ρ shows the more similar the distributions. For two identical histograms we obtain $\rho = 1$, indicating a perfect match.

The weight $\pi^{(i)}$ of i-th state $\boldsymbol{x}^{(i)}$ is calculated as

$$\begin{aligned}
\pi^{(i)} &= \frac{1}{\sqrt{2\pi\sigma}} \exp\left(-\frac{d^2}{2\sigma^2}\right)\\
&= \frac{1}{\sqrt{2\pi\sigma}} \exp\left(-\frac{\left(1 - \rho\left[\boldsymbol{p}\left(\boldsymbol{x}^{(i)}\right), \boldsymbol{q}\right]\right)}{2\sigma^2}\right)
\end{aligned}. \tag{10}$$

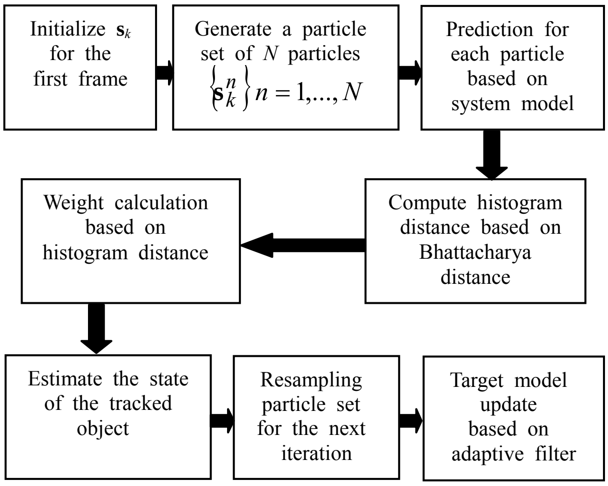

Fig. 1. Particle filter implementation flow

Where $\boldsymbol{p}(\boldsymbol{x}^{(i)})$ and $\boldsymbol{q}$ are the color histogram of sample and target, respectively. From this equation, we can see that small Bhattacharya distance corresponds to large weight. During resample step of particle filter, samples with a high weight may be chosen several times leading to identical copies, while others with relatively low weights may be ignored.

3.4 Weight Normalization

In a multiple targets tracking scenario, those targets whose samples exhibit lower likelihood are more likely to be lost, since the probability of propagating one mode is proportional to the cumulative weights of its samples. In order to avoid one target absorbing other target samples, we proposed to normalize the weights as

$$\bar{\pi}_k^{i,l} = \frac{\pi_k^{i,l}}{\sum_{i=1,j=l}^{N} \pi_k^{i,j}} \frac{1}{L}, \tag{11}$$

here L is the number of tracked targets. Each weight is normalized according to the total weight of the target's samples. Thus, all targets have the same probability of being propagated, since the addition of the weights of each target samples sums $1/L$.

3.5 State Estimation

The k-target estimates are computed according to

$$\begin{aligned}
\mathbf{x}_k &= (1-\alpha_{\mathbf{x}})(\mathbf{x}_{k-1} + \dot{\mathbf{x}}_{k-1}\Delta t) + \alpha_{\mathbf{x}}\left(L\sum_{i=1}^{N} \bar{\pi}_k^i \hat{\mathbf{x}}_k^i\right) \\
\dot{\mathbf{x}}_k &= (1-\alpha_{\dot{\mathbf{x}}})\dot{\mathbf{x}}_{k-1} + \alpha_{\dot{\mathbf{x}}}\left(\frac{\mathbf{x}_k - \mathbf{x}_{k-1}}{\Delta t}\right) \\
\mathbf{w}_k &= (1-\alpha_{\mathbf{w}})\mathbf{w}_{k-1} + \alpha_{\mathbf{w}}\left(L\sum_{i=1}^{N} \bar{\pi}_k^i \hat{\mathbf{w}}_k^i\right) \\
\dot{\mathbf{w}}_k &= (1-\alpha_{\dot{\mathbf{w}}})\dot{\mathbf{w}}_{k-1} + \alpha_{\dot{\mathbf{w}}}\left(\frac{\mathbf{w}_k - w_{k-1}}{\Delta t}\right)
\end{aligned} \tag{12}$$

where $\alpha_{\mathbf{x}}, \alpha_{\dot{\mathbf{x}}}, \alpha_{\mathbf{w}}, \alpha_{\dot{\mathbf{w}}} \in [0,1]$ denote the adaptation rates.

3.6 Target update

The target appearance must also be updated. However, this is a sensitive task. The target models are only updated when two conditions hold: (i) the target is not occluded and (ii) the likelihood of the estimated target's state suggests that the estimate is sufficiently reliable. In this case, they are updated using an adaptive filter

$$\mathbf{q}_k = (1-\alpha_{\mathbf{q}})\mathbf{q}_{k-1} + \alpha_{\mathbf{q}}\mathbf{p}_{est}, \tag{13}$$

where $\alpha_{\mathbf{q}} \in [0,\ 1]$ is the learning rate that contribute to the updated histogram and $\mathbf{p}_{est}$ is histogram of the estimated state, respectively. In order to determine when the estimate is reliable, the likelihood of the current estimate is computed, π_{est}. The appearance is then updated when this value is higher than an indicator of the expected likelihood value and is calculated following an adaptive rule

$$\lambda_k = (1-\alpha_u)\lambda_{k-1} + \alpha_u \pi_{est}, \tag{14}$$

here λ_k is expected likelihood, $\alpha_u \in [0,\ 1]$ is the learning rate and π_{est} is estimated likelihood, respectively. This value indicates that the object has to be well matched to the model histogram before the update is applied.

3.7 Occlusion Handling

Occlusions can cause a failure in the tracking multiple objects. They may cause inaccurate in estimation and updating of the position and size of the tracked object. Thus, the target's estimated position would be shifted and its size should be adapted to the area that the target can be seen or not occluded. Moreover, the appearance model may be updated with completely wrong values which would cause target loss in few frames. The situation during complete occlusion could be even worst since the likelihood of the occluded target would be meaningless, the resampling phase would propagate the wrong random samples and quickly cause the loosing of the object. Therefore, a proper handling of occlusions is crucial.

In this paper, occlusions are predicted according to the dynamic models by using the predicted distance between the objects such as,

$$(\mathbf{x}_{m,k}^i - \mathbf{x}_{n,k}^i)^2 + (\mathbf{y}_{m,k}^i - \mathbf{y}_{n,k}^i)^2 < R^2 \tag{15}$$

here x_m, y_m, x_n and y_n are the sample position of each object and R is a threshold, respectively. When the predicted distance exceeds a certain threshold, the object is pointed out as occluded object. Subsequently, by exploring the maximum sample likelihoods and comparing them with recent historical values, we can conclude which object is being occluded. When the occlusion is detected, the object status turns into occluded object. This status involves several changes in the normal development of the process. First of all, the adaptation rates $\alpha_{\mathbf{x}}, \alpha_{\dot{\mathbf{x}}}, \alpha_{\mathbf{w}}, \alpha_{\dot{\mathbf{w}}}$ are set to zero and the target estimated speed is kept constant and the position is updated only according to its speed. In addition, no size or appearance adaptation is performed. Finally, those samples belonging to the occluded target are not resampled according to their weights since they are meaningless but they are just propagated. As a result samples spread around the target, because of the uncertainty predictions terms. The other object samples are normally resampled but they cannot be assigned to the occluded target. When the occlusion is no longer predicted or sample likelihood exceeds the value of previous likelihood of the occlusion object, the object status turns into not occluded, which immediately implies the samples to be resampled again. In addition, position and speed are again updated.

IV. EXPERIMENTAL RESULT

In order to evaluate our proposed method, we have done the experiments to track the multiple objects in the presence of occlusion and background clutter in outdoor environment. The experiments are implemented on Pentium IV with 2.53 GHz CPU and 512 MB RAM. The resolution of each frame is 320×240 pixels image. The color histogram is calculated in RGB space with 8×8×8 bins.

Figure 2 and 3 show the experimental results of the tracking objects. The small circle shows the estimated position of the tracking objects and the square shows the region of the tracked object used in color histogram.

On the first experiment, we try to track the objects when they move on the opposite direction and merge in the middle of the scene. The tracking performance is shown in Figure 2. Firstly, the first object appears on the left side of scene and the second object appears afterward on the right side. After several frames, the first object occludes the second object in the middle of the scene. Occlusion is correctly detected by avoiding resampling of samples of the occluded object and appearance models updating. The occluded object is successfully tracked as shown in frame #123, #127 and #133. The object is also tracked successfully although the full occlusion is occurred (frame #127). The system successfully recovers the object from occlusion (frame #137). After the occlusion is no longer occurred, each object is normally resampled and the appearance is update again. On both conditions (occlusion and not occlusion), we successfully update the appearance models when reliable measures are obtained.

On the second experiment, the objects have same moving direction and merge in the middle of the scene. The second object moves faster than the first one. On this experiment the occlusion status takes longer time (from frame #190 to frame #300). The occlusion is detected in the frame #190. At that time, the samples of the occluded object are not resampled but they are just propagated. The first complete occlusion is occurred on frame #220. The second object is still in the status of occlusion after several frames (frame #240 ~ frame #265). The second complete occlusion then occurs on frame #285 as the second object change the motion direction to the left side of scene. The system successfully recovers the second object from occlusion (frame #315). After the occlusion is no longer occurred, each object is normally resampled and the appearance is update again. On both conditions (occlusion and not occlusion), we successfully update the appearance models when reliable measures are obtained. Figure 3 shows the tracking performance of our method.

V. CONCLUSION

This paper presented a new method to track multiple objects employing color-based particle filter. The robust color likelihood is used to properly evaluate samples associated to target which present high appearance variability. We rely on Bhattacharya coefficient between target and sample histogram to perform this task. Model updating is carried to update the object in the presence of appearance change. The multiple objects tracking cause several problems such as occlusion. These problems can be tackled by redefining the weight normalization, prediction based on the dynamical model and likelihood measures. The performance of the tracking algorithm was tested by experiments. From the results, the algorithm can successfully track multiple objects moving in the presence of occlusion, background clutter and appearance change.

It should point out that although the experimental data used in this paper only contain close to linear motion model, there is no inherent difficulty for the proposed method to handle nonlinear motion model. This is because that the particle filter framework is generally not constrained to linear motion model. Furthermore, the performance of the multiple objects tracking can be improved in several ways such as adding the background modeling information [9] in the calculation of likelihood, detection of appearing objects and disappearing already existed object using hybrid particle filter [13] and so on. Taking them into consideration could lead to some improvement. These are remaining for our future works.

REFERENCES

[1] Ristic B, Arulampalam S and Gordon N (2004), Beyond the Kalman filter: particle filters for tracking applications, Artech House.

[2] Arulampalam S, Maskell S, Gordon N and Clapp T (2002), A tutorial on particle Filters for on-Line nonlinear/non-Gaussian Bayesian tracking", IEEE Trans. on Signal Processing, 2002, pp. 174-188.

[3] Doucet A, Freitas J, Gordon N (2001), Sequential Monte Carlo methods in practice, Springer, New York.

[4] Isard M and Blake A (1998), Condensation: Conditional density propagation for visual tracking, Int J of Computer Vision, 29(1): 5-28.

[5] Kitagawa G (1996), Monte Carlo filter and smoother for non-Gaussian nonlinear state space models, J of Comput and Graph Stat 5(1):1-25.

[6] Gordon N, Salmon D and Smith A (1993), Novel approach to nonlinear/non-Gaussian Bayesian state estimation, IEE Proceeding on Radar and Signal Processing, 140(2):107-113.

[7] King O and Forsyth D (2000), How does Condensation behave with a finite number of samples, Proceedings of 6th European Conference on Computer Vision, Dublin, Ireland, pp 695-709.

[8] Nummiaro K, Koller E, Gool L (2002), An adaptive color-based particle filter, Image and Vision Comput, 25(1): 99-110.

[9] Perez P, Hue C, Vermaak J and Gangnet M (2002), "Color-based probabilistic tracking", Proceedings of the 7th European Conference on Computer Vision, London, pp. 661-675.

[10] Comaniciu D, Ramesh V, and Meer P (2000), Real-time tracking of non-rigid objects using mean shift, Proceedings of the IEEE Conference on Comp Vision and Pattern Recog, pp 142–149.

[11] Comaniciu D, Ramesh V, and Meer P (2003), Kernel-based object tracking. IEEE Trans. on Pattern Analysis and Machine Intelligence, 25(5):564-577.

[12] Deutscher J and Reid I (2005). Articulated body motion capture by stochastic search, Int J of Computer Vision, 61(2):185-205.

[13] MacCormick J and Blake A (1999). A probabilistic exclusion principle for tracking multiple objects, Proceedings of the Int Conference on Computer Vision, pp 572-578.

[14] Czyz J, Ristic B, and Macq B (2007), A particle filter for joint detection and tracking of color objects, Image and Vision Comput, 25(8): 1271-1281.

[15] Isard M and. Blake A (1998), A mixed-state condensation tracker with automatic model-switching, Proceedings of Int. Conference on Comp Vision, pp. 107-112.

[16] Isard M and MacCormick J (2001), Bramble: a Bayesian multiple blob tracker, Proceedings of Int. Conference on Comp Vision, pp. 34-41.

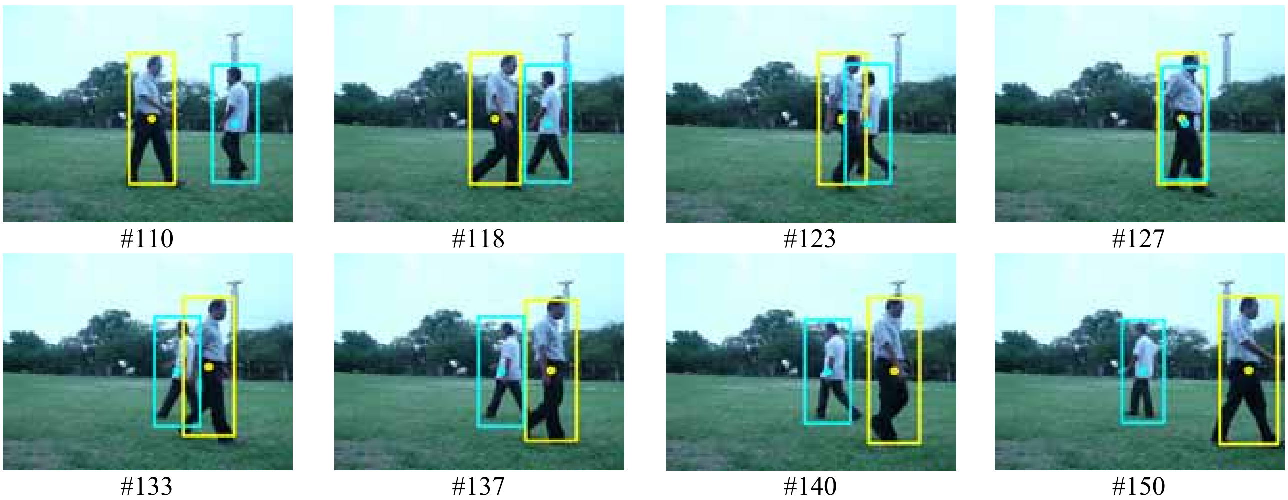

Fig.2. Two objects move in opposite direction and occlude in the middle of scene

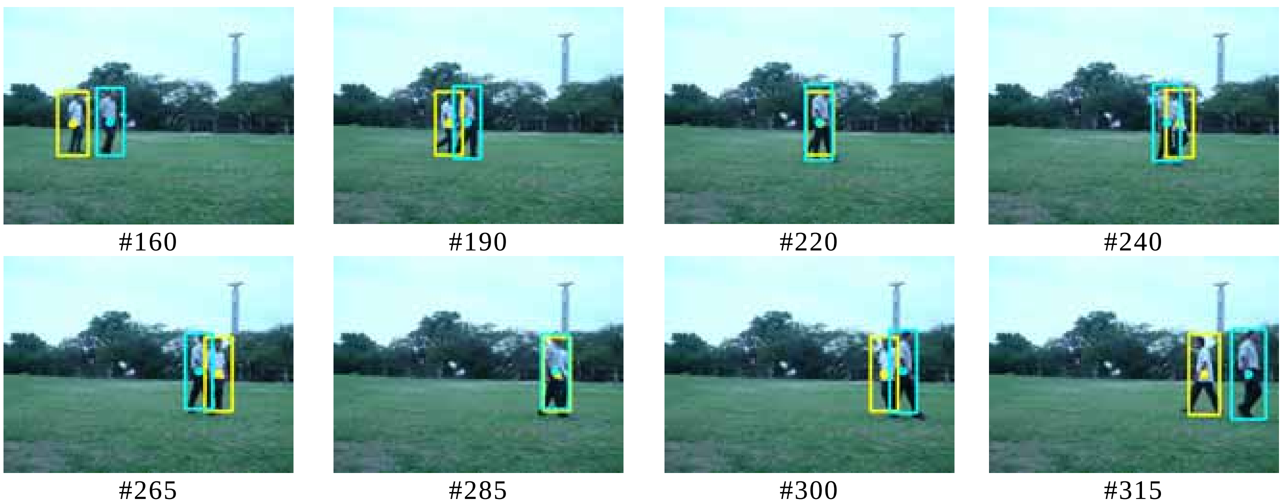

Fig.3. Two objects move in the same direction and occlude in the middle of scene

The Fifteenth International Symposium on Artificial Life and Robotics 2010 (AROB 15th '10),
B-Con Plaza, Beppu,Oita, Japan, February 4-6, 2010

A Study of Dimension Reduction of Gabor Features from Different Facial Expressions

Rosdiyana Samad and Hideyuki Sawada

Department of Intelligent Mechanical Systems Engineering, Faculty of Engineering, Kagawa University, 2217-20 Hayashi-cho, Takamatsu, Kagawa, 761-0396, Japan.
Tel: +81-(0)87-864-2324 Fax: +81-(0)87-864-2369
s09d501@stmail.eng.kagawa-u.ac.jp, sawada@eng.kagawa-u.ac.jp

***Abstract*:** Facial expressions are an important channel of nonverbal communication. Currently, many facial expression analysis or recognition systems have been proposed. In this paper, a study of dimension reduction of Gabor features from different facial expressions is presented. Principle Component Analysis (PCA) is used as dimension reduction method. The experiment is conducted by using samples of face image for eight subjects. There are six facial expressions; anger, fear, happy, neutral, sadness and surprise are used in this study. In this experiment, we use different poses and head postures of each subject. Experiment results demonstrated the reduced dimensions of Gabor features could be effectively used in the next processing for recognizing facial expressions.

Keywords: **facial expression, Gabor features, dimension reduction, PCA.**

I. INTRODUCTION

Nowadays, computer-based applications become more sophisticated and are increasingly involved in our daily life. Human-computer interface is one of the outcomes that have been developed to fulfill human needs in facilitating some task. Over the last decade, face detection and facial expression recognition have become an active research area that finds potential applications for human-computer interfaces, talking heads, image retrieval and human emotion analysis [1]. In recent years, numerous algorithms for face detection and facial expression recognition have been proposed.

Moore and Bowden [2] wrote in their literature review, the earliest work on facial expression recognition was introduced by Ekman, and it was called Facial Action Coding System (FACS). FACS provided a prototype of the basic human expressions and allowed researchers to study facial expressions based on anatomical analysis of facial movement. In other research, Ma and Khorasani [3] applied two-dimensional discrete cosine transform (DCT) over the entire face image to extract the facial feature, and developed one-hidden-layer feed forward neural network to recognize the facial expressions. Littlewort et al. [4] proposed a method to extract the dynamics of facial expression automatically from video. In this study, Gabor energy filter was used in feature extraction technique and then three different classifiers were used to classify the facial expressions into 7 classes (neutral, anger, disgust, fear, joy, sadness, surprise). These three classifiers were AdaBoost, Supervised Vector Machine (SVM) and Linear Discriminant Analysis (LDA). At the end of this experiment, they had examined the performance of the classifier.

Deng et al. [5] proposed a facial expression recognition system based on local Gabor filter banks with the selected part of frequency and orientation parameters. Two stages of feature compression method were employed to select and compress the Gabor features. First stage was PCA and then followed by LDA. The recognition of facial expression was done by applying minimum distance classifier. Loh, Wong & Wong [6] developed an e-learning system that used facial expression recognition. They also applied Gabor wavelet for facial feature extraction and back propagation neural network for the classification.

In this paper, a study of dimension reduction of Gabor features from different expressions is presented. We selected 6 facial expressions in this work, which are sadness, happy, anger, fear, surprise and neutral.

II. METHODOLOGY

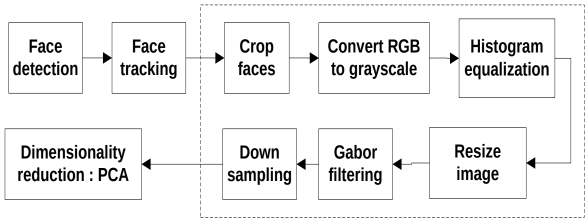

Fig.1. Block diagram of the proposed method.

Figure 1 shows the block diagram of our work. In this paper we briefly present a face detection method, and then explain in detail the facial feature extraction technique.

1. Face detection & tracking

Haar-like features and AdaBoost algorithm were used in the face detection phase. This technique was introduced by Paul Viola and Micheal Jones[7], and then was improved by Reiner Lienhart[8]. Following the algorithms, face tracking technique was added which enabled the face detector to track the moving face. This technique is called Camshift, otherwise known as Continuously Adaptive Mean Shift. At this stage, we used 700 positive samples (patch of human face) and 437 negative samples (background images or non-face) to train AdaBoost algorithm.

2. Pre-processing & facial feature extraction

In this experiment we used images from eight subjects that were selected from FEEDTUM [9] database. Multiple images of six facial expressions with different poses and head postures were taken from each subject. Total number of sample images was 943.

Firstly, at the pre-processing stage we cropped the face images manually in order to remove the background information and have only face details. Figure 2 shows samples of face image that were used in this study.

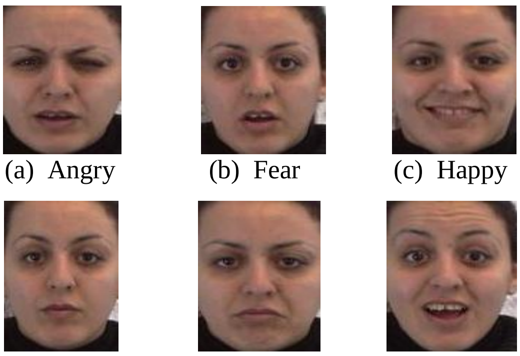

(a) Angry (b) Fear (c) Happy
(d) Neutral (e) Sadness (f) Surprise

Fig.2. Image samples for different facial expressions.

Fig.3. Output image of histogram equalization.

At the beginning, all sample images were in RGB and then we converted them into grayscale. The grayscale images outcome from the conversion were poor because of lacking contrast; thus we employed the histogram equalization on the images. As a result, the images were enhanced and the face detail was improved. Figure 3 shows the output image of histogram equalization.

The Gabor filter represents the properties of spatial localization, orientation selectivity and spatial frequency selectivity. The Gabor filter can be defined as:

$$\psi(z) = \frac{k_{u,v}^2}{\sigma^2} \exp\left(-\frac{k_{u,v}^2 z^2}{2\sigma^2}\right)\left[\exp\left(ik_{u,v}z\right) - \exp\left(-\frac{\sigma^2}{2}\right)\right] \quad (1)$$

where z = (x,y), u and v define the orientation and scale of the Gabor wavelets, respectively [10]. $k_{u,v}$ is defined as follows:

$$k_{u,v} = k_v e^{i\Phi} \quad , \qquad (2)$$

where $k_v=k_{max}/f^v$ and $\Phi u = \pi u/8$. k_{max} is the maximum frequency, and f is the spacing factor between kernels in the frequency domain.

In this experiment we applied Gabor filter with one scale (v=1) and one orientation (u= 4), with the parameters $\sigma = 2\pi$, $k_{max} = \pi/2$ and $f=\sqrt{2}$. The Gabor representation of an image, which is called the Gabor image, is produced from the convolution of the image with the Gabor kernels as defined by Eq.(1). For each image pixel, it produces two Gabor parts: the real part and the imaginary part. Subsequently, these two parts were transformed into two kinds of Gabor features: magnitude and phase. In this study we used magnitude features to represent the facial Gabor features. Figure 4 shows the Gabor magnitude responses for each expression (anger, fear, happy, neutral, sadness and surprise) derived from the images shown in Figure 2.

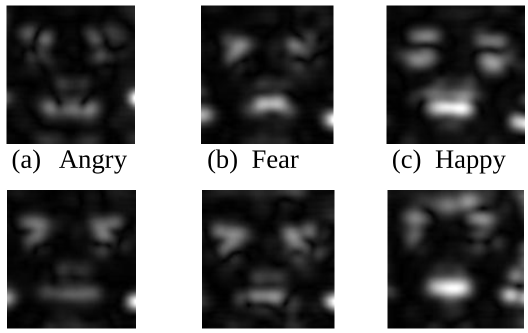

(a) Angry (b) Fear (c) Happy
(d) Neutral (e) Sadness (f) Surprise

Fig.4. Gabor magnitude responses for different facial expressions.

The Gabor image size was 120x120 pixels, which produced 14,400 feature vectors. The numbers of the features were too many therefore we needed to reduce the image size so the number of features would be smaller. To get the smaller size of images we performed Gaussian pyramid down sampling [10]. This method reduced the size of an image by a factor of 2. The down sampling method performs a Gaussian smooth using 5x5 Gaussian kernel and then removes every other line from an image. The image result obtained from the down sampling was 60x60 pixels. The output images still large, and again, we downsized the images into 30 x 30 pixels so that we could have only 900 features.

3. Dimensionality reduction

As mentioned in the previous section, the final output image size was 30x30 pixels that produced 900x1 feature vectors. We used these feature vectors as input data to the Principle Component Analysis (PCA). PCA is a way of identifying patterns in data and expressing the data in such a way as to highlight their similarities and differences [11]. The other main advantage of PCA, it is able to reduce the number of dimensions without much loss of information. Besides, PCA is a powerful tool for analyzing high dimension data, since graphical representation for high dimension data is not available. In this paper, we used PCA to reduce the number of feature vectors so it also will cut down the computation time for the classification in the next stage.

At this stage, we subtracted the mean from each of the data. The mean subtracted is the average across each dimension, then the covariance matrix was calculated. After that, eigenvectors and eigenvalues were calculated based on covariance matrix that has been computed before. Next, we selected 20 most significant eigenvalues to get the eigenvectors. Finally, the eigenvectors were projected onto subspace.

III. EXPERIMENTAL RESULTS & DISCUSSION

In this study, Gabor filter with horizontal orientation was selected because it produced discriminative Gabor features better than other orientations. In addition, by using only one orientation it helped to reduce the computational complexity of Gabor features extraction. As a result, facial features, such as eyes, nose, mouth and wrinkles at each expression (as shown at Fig. 4) would give different appearance. The variability in the underlying Gabor magnitude response of facial images corresponds to differences among different facial expressions. In the PCA, the eigenvector indicates the direction in which the data greatly distributed. The direction of maximum separation is called the first component of a dataset. We plotted the first, second and third component of dataset and it shows the separation of the data.

From the observation of the scatter plots, the facial expression data for each subject were grouped with one another but some of them were slightly overlapped with the different group of expressions. It shows data in the tight cluster have least variability while data from separated cluster have the greatest variability (as shown at Fig. 5(a)). From the results, we found that our data were separated into each type of facial expression. Facial expressions data for subject number 5, 6 and 7 had slightly scattered and overlapped. At these figures, the overlapped data were the expressions of sadness and neutral. This is because the sadness and neutral expressions for the subject is nearly similar which is shown in Figure 6.

IV. CONCLUSION

In this paper, a study of features extraction by using Gabor filter and dimension reduction by PCA is carried out. The PCA was used to downsize the big number of Gabor features. The purpose of the dimension reduction is not only to cut down the dimension, but also to reduce the computational time. Fast processing time will give advantage to the next process which is the classification of different facial expressions that we will develop later. Results obtained from the scatter plots show that facial expression data were grouped with one another according to the type of expressions. From the detailed analysis of data plots, the compressed Gabor features could be effectively used in the next processing for recognizing facial expressions.

REFERENCES

[1] Fasel B and Luettin J (2003), Automatic facial expression analysis - a survey. Pattern Recognition Vol.36, pp. 259-275
[2] Moore S and Bowden R (2007), Automatic facial expression recognition using boosted discriminatory classifiers. Computer Science Vol. 4778, pp.71-83
[3] Ma L & Khorasani K (2004), Facial expression recognition using constructive feed forward neural network. IEEE Trans. on Systems, Man & Cybernetics Vol. 34, pp.1588-1595
[4] Littlewort G et al (2004), Dynamics of facial expression extracted automatically from video. Proc. of Computer Vision and Pattern Recognition Workshop, pp. 80-90.
[5] Deng H B et al (2005), A new facial expression recognition method based on local Gabor filter bank and PCA plus LDA. Information Technology Vol. 11, pp. 86-96
[6] Loh, Wong & Wong (2006), Facial expression recognition for e-learning system using Gabor wavelet & neural network. Proc. of 6th IEEE Int. Conf. on Advanced Learning Technology, pp. 523-525
[7] Viola P & Jones M (2001), Rapid object detection using a boosted cascade of simple features. Computer Vision and Pattern Recognition Vol.1, pp.511-518
[8] Lienhart R & Maydt J (2002), An extended set of haar-like features for rapid object detection. Proc. of IEEE Int. Conf. on Image Processing, pp.900-903
[9]Facial Expressions & Emotion Database Technische Universitat Munchen (FEEDTUM) http://www.mmk.ei.tum.de/~waf/fgnet/feedtum.html
[10] Lee TS (1996), Image representation using 2D Gabor wavelets. IEEE Trans. On Pattern Analysis & Machine Intelligent Vol.18, pp. 959-971
[11] Smith LI (2002), A tutorial on principle component analysis. Cornell University USA, pp.2-2

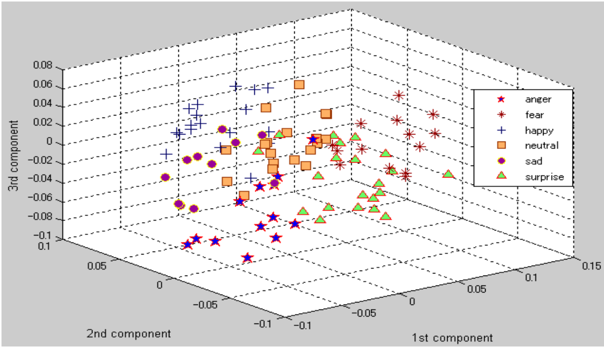

(a) Subject no.

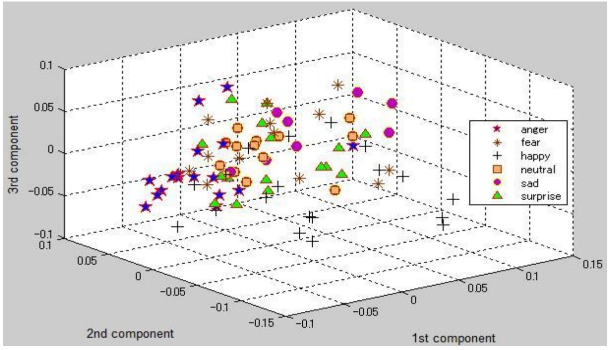

(d) Subject no. 5

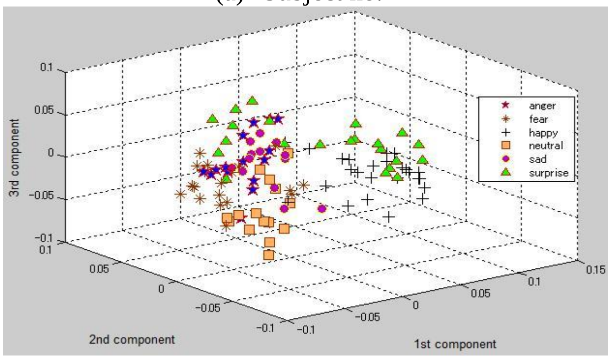

(b) Subject no. 2

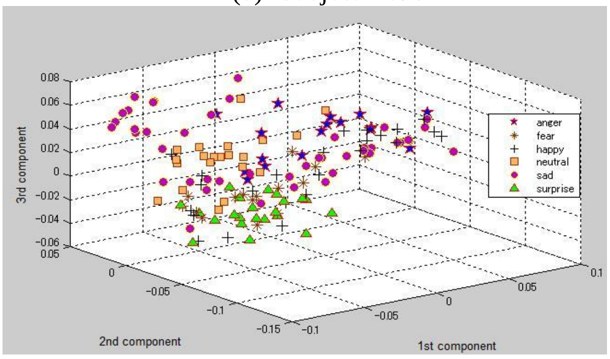

(e) Subject no. 6

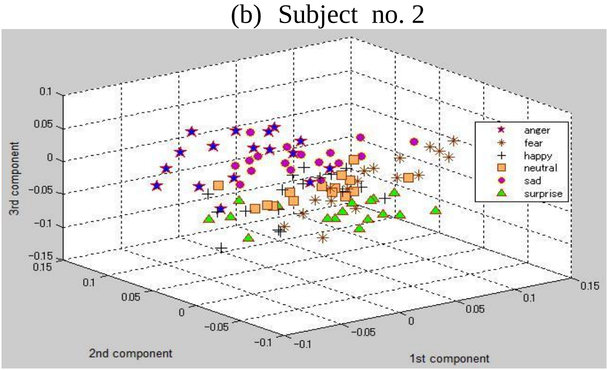

(c) Subject no. 3

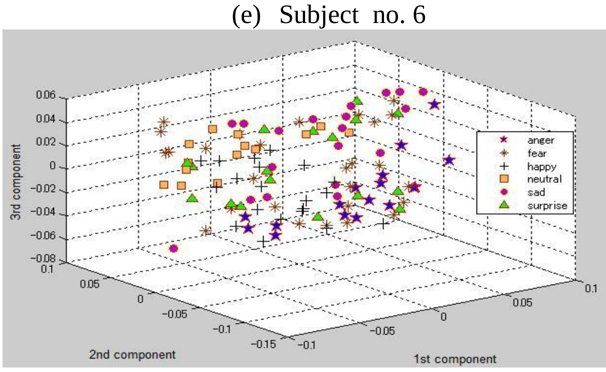

(f) Subject no. 7

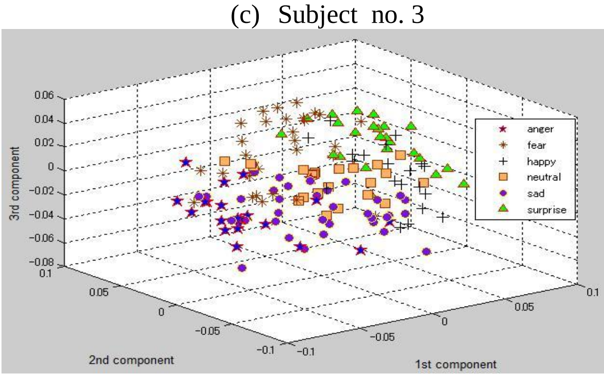

(d) Subject no. 4

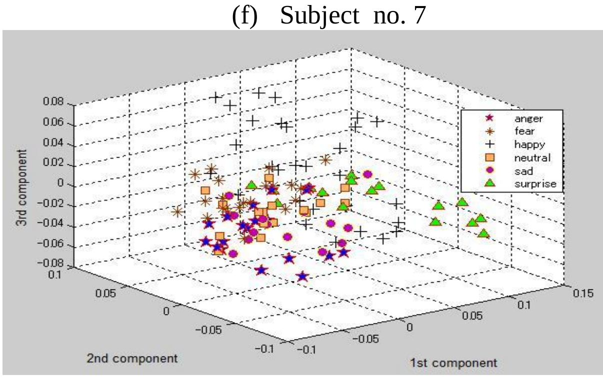

(h) Subject no. 8

Fig. 5 3D Plots of facial expression data from 8 subjects.

Fig.6. Facial expressions of sadness and neutral that seemed almost the same.

Interactive musical editing system to support human errors and offer personal preferences for an automatic piano

- A method for searching for similar phrases using DP matching and for inferring performance expression with the best alignment of DP matching –

Kenichi Koga *Eiji Hayashi*
Department of Mechanical Information Science and Technology
Faculty of Computer Science and Systems Engineering, Kyushu Institute of Technology
680-4, Kawazu, Iizuka-City, Fukuoka Prefecture, Japan

Abstract: We have developed a system that allows a piano to perform automatically. In order to play music in the manner of a live pianist, we must add expression to the piano's performance. In the case of piano music, there are often 1000 or more notes in the score of even a short piece of music, requiring that an editor spend a huge amount of time to accurately simulate the emotionally expressive performance of a highly skilled pianist. Therefore, we have developed an interactive musical editing system that utilizes a database to edit music more efficiently. We have analyzed MIDI data regarding the performances of highly skilled pianists in order to observe the stylistic tendencies of their performances. Our result showed that phrases having similar patterns in the same composition were performed in similar styles. Therefore, we developed a system that searches for similar phrases throughout a musical score and evaluates the style of the performance. The method of searching for similar phrases uses DP (Dynamic Programming) matching, and it evaluates performance expression based on the best alignment of DP matching.

Keywords: automatic piano, knowledge database, computer music, DP matching

I. INTRODUCTION

We have developed a performance system for an automatic piano. In this system, 90 actuators are installed on the 88 keys and the 2 pedals of a grand piano. These actuators operate key strokes and execute pedaling on the piano. (See Figure 1)

Reproducing music with the piano is similar in some ways to reproducing music on the computer. Essentially, variations in tempo, dynamics, and so on are needed to arrange the respective tones in the desired way. However, in the case of piano music, there are 1000 or more notes in a score of even a short piece of music, and for this reason an editor must spend an enormous amount of time working with an arrangement in order to simulate the expressions of an actual performance. Therefore, in this research, we have developed an interactive musical editing system to edit music more efficiently [1].

We have analyzed MIDI data from the performances of highly skilled pianists in order to observe the stylistic tendencies of their performances. Out results showed that phrases having similar patterns in the same composition were performed in similar styles. Moreover, we found that the pattern of notes in a score sometimes influences the expression of a piece of music..

In this research we developed a system that searches for similar phrases throughout a musical score and evaluates the style of a performance. We propose a method that uses DP matching as a way to search for similar phrases. This system converts notes into character strings. In addition, the system runs DP matching using character strings and calculates the degree of disagreement between these strings. We use these calculations as an index to determine whether the strings resemble each other. Moreover, we designed a method for evaluating the performance expression based on similar phrases as found by DP matching.

In this paper, we describe the results of searching for similar phrases using DP matching and evaluating performance expression.

Figure 1: View of the automatic piano

II. Musical Editing Support System

2.1 System Architecture

The structure of the system is shown in Figure 2.1. The user edits music via the user's interface on a computer display. The user can also access a database that has musical grammar, the user's preferences, and so on. As a result, editorial work is reduced and efficient editing becomes possible.

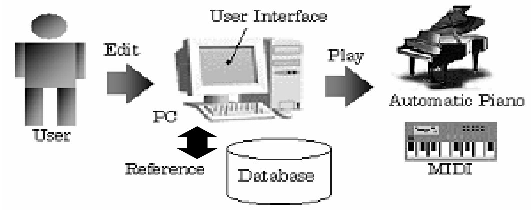

Figure 2.1 Structure of the editing system

2.2 Format of Performance Information

The parameters of performance information are shown in Tables 1 and 2. The automatic piano that we have developed uses a music data structure that is similar to MIDI. We defined performance information, dividing it into two categories: the notes and the pedals. The note information is comprised of the six parameters involved in producing a tone: "Key (note)", "Velo (velocity)", "Gate", "Step", "Bar", and "Time". "Velo" is the dynamics, given by the value of 1 ~ 127. "Gate" is the duration of the note in milliseconds. "Step" is the interval of time between notes, and it also exhibits tempo. "Bar" is the vertical line placed on the staff to divide the music into measures.

The pedal information is comprised of four parameters: "Key (indicating the kind of pedal: "Damper" or "Shifting")", "Velo (the pedaling quantity)", "Time (the duration for which the pedal is applied)", and "Bar".

2.3 Editing Support Process with Database

Our system can automatically apply a rough performance expression using a Musical Rules Database and Score Database. (See Figure 2.2)

In addition, the system has Preference Database, wh ich stores the editing characteristic of the user.

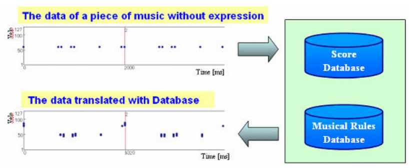

Figure 2.2: Automatic translation with database

2.3.1 Musical Rules Database

This database contains the architecture of musical grammar necessary to interpret symbols in musical notation. It is composed of five tables containing "Dynamics marks", "Articulation marks", "Symbol of Changing Dynamics or Changing Tempo (symbol that affects the speed of a note or the increase or decrease of the volume)", "Time signature", and "Tempo marks".

Analyzing a music symbol according to its usage allows efficient information processing by the system.

2.3.2 Score Database

This database has symbols including notes, time signature, rests and so on in standard musical notation. Symbols were pulled together in order of bars, and bar symbols are arranged in time series. Performance expression in itself is only information such as pitch, strength, and length and concerns only the enumeration of a sound. Because the identification of each sound is difficult, editing of the performance expression is difficult. By adding the Score Database's information to performance expression, we can connect each note. In doing so, it becomes easy to edit each phrase.

This database consists of three tables, the "Element table" (showing the position of the note and the composition of the chord), the "Symbol table" (showing the position of the music symbol) and the "Same table" (showing the position of the repetition of the phrase).

The Element table contains the field "Note Value". Data in this field indicates the type of note, e.g., a quarter note, a triplet, and so on. "Note Value" is expressed by three hexadecimal numbers, which are shown in Figure 2.3.

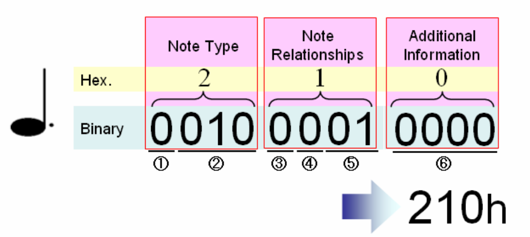

① Note or Rest (0: Note, 1: Rest)
② Note Value (000: A whole note, 001: A half note …etc)
③ Tie (If the note has a tie then this number is 1.)
④ Ornament
(If the note has an ornament then this number is 1.)
⑤ The number of dots
(Exceptionally, if it is "11" then the note is tuplet.)
⑥ Additional Information
The number of tuplets. (Triplets: 0011)
The type of an ornament. (Trill: 0101) etc…

Figure 2.3: Note Value

III. Searching for Similar Phrases

As a result of the analysis, it was found that phrases of the same pattern existing in the same tune are performed in a similar expression. This time, we used DP matching to search for similar phrases.

3.1 DP matching

a) DP matching

DP matching is a technique used well in the field of speech recognition, bioinformatics and so on. It has a feature that can calculate similarity between two words that are different in a number of characters from each other.

In Figure 3.1, the route of minimum cost in each point is taken, and the route with the lowest cost is assumed finally to be an optimal path. The cost at that time is defined as the distance between patterns. In this system, this distance is handled as a threshold to judge whether the phrases are similar to each other.

For example, if the cost moves up or to the right, then it is increased by 1. If it moves to the upper right, then it does not increase. Also, if the characters do not correspond in each point, then the cost is increased by 5.

$$g(i,j) = \min\begin{Bmatrix} g(i-1,j) \\ g(i,j) \\ g(i,j-1) \end{Bmatrix} + d(i,j)$$

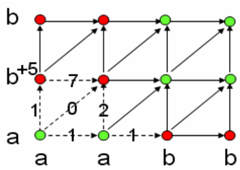

Figure 3.1 DP matching

b) Best alignment of DP matching

The best alignment of DP matching is what enables it to express the best correspondence between notes. Figure 3.2 shows the best alignment from Figure 3.1. This relation is not used because of the searching processing but instead is used because of the inference processing.

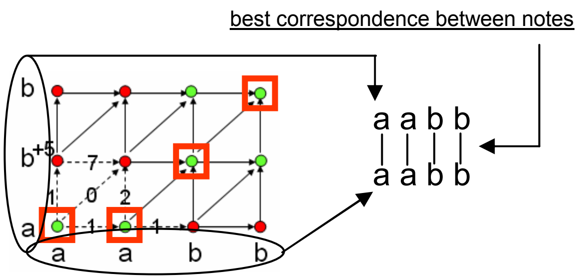

Figure 3.2 Best alignment of DP matching

3.2 Searching with DP matching

In this passage, we describe a method of searching with DP matching. We had to convert a musical score into character strings (a Note Pattern) before searching for similar phrases. This process is explained below.

3.2.1 Note Pattern

Our system converts a score into a Note Pattern using Note Values (See Passage 2.3) in order to perform DP matching. Of the three columns of Note Values, we used the two columns on the left. The system replaces numbers in the second column with letters of the alphabet (from G) because a letter, being a different notation than that used in the first column, allows the expression of one note with two columns. An example of a Note Pattern conversion is shown in Figure 3.3.

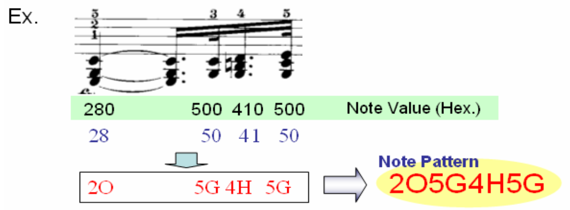

Figure 3.3 Example of Note Pattern

3.2.2 The Method of Searching

The flow of the similar phrase search is shown in Figure 3.4.

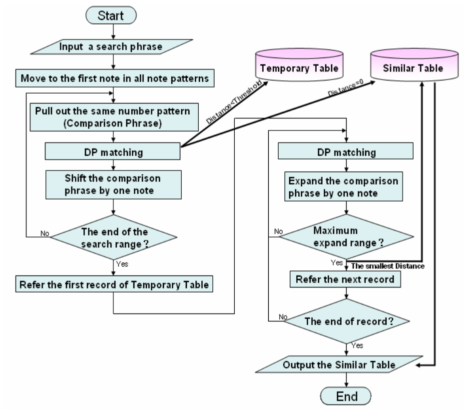

Figure 3.4 The flow of the similar phrase search
(Search range and expand range are set beforehand.)

Essentially, two rounds of search processing are performed. The first processing round narrows down the points to those having a resemblance in all search ranges. A pattern with the same number as the search phrase is pulled out, and the distance between two patterns is calculated using DP matching. If they are in complete accord (distance = 0), then the phrase is stored in the Similar Table. If the distance is lower than the threshold, then the phrase is stored in the Temporary Table. In the second round of processing, DP matching is performed again using the phrases in the Temporary Table while increasing the number of characters. In other words, the system looks for the most similar phrases in the surrounding phrases. The threshold of this system has been decided by trial and error.

VI. Phrase Expression System of Evaluations

The similar phrases derived by the search method described in Chapter 3 are evaluated with regard to the performance expressions of the search phrases.

3.3 Method of evaluating phrase expressions

The method of evaluating performance expression, which uses the best alignment in DP matching, enables it to express the best correspondence between notes. The best alignment in DP matching gives us points of agreement and disagreement.

Our evaluation method to determine the disagreement points is as follows. A correspondence between note patterns is revealed when the distance is minimized in DP matching. Next, the ratio of Velo to the previous sound is calculated for each sound in the searching phrases. The Velo of associated phrases is determined using a ratio R_i so that the ratio of the Velo is shown in the expression:

$$R_i = \frac{V_{i+1}}{V_i}$$

V is the Velo of each searching phrase, and W is the Velo of similar phrase as calculated in R.

$$W_{i+1} = W_i \times R_i$$

Thus, the Velo of a similar phrase is determined. The value of Time uses the value determined by Automatic translation (see Passage 2.3).

3.4 Searching & Inference Result

The result of the searches and inferences using this system is shown in Figure 4. The phrase in the seventh bar of Beethoven's Sonata No. 23 in a performance by Gerhard Oppitz was inferred from the first bar . The figure shows that the basis for this result is that the distance = 33 between the two phrases. The inferred phrase was similar to the performance expression of the searched phrase.

In addition, even the phrase which distance leaves, we understand that the reasoning that resembled closely to some extent is made.

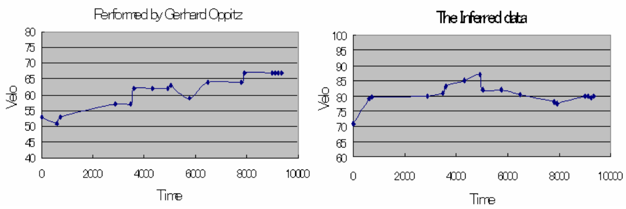

Distance 33

Figure 4 Searching and Inference Results

V. CONCLUSION

We designed methods of searching for similar phrases and evaluating performance expressions using DP matching and combined these functions into a single system.

In the similar phrase search, the system was able to find similar phrases using DP matching in a short time, and it was even possible to find phrases whose resemblance might not be immediately apparent.

In evaluating performance expressions, the system could make the best associations between phrases by DP matching of search results.

The performance expression of some similar phrases that exist in a tune can be inferred at the same time using this system. We believe that this system can increase work efficiency by its automatic editing without sacrificing quality, in contrast to editing a piece by hand from the beginning.

In this study, we were able to perform only similar phrase searches and evaluations of performance expressions in the same piece of music. In the future we will perform evaluations with different pieces of music and will evaluate the existing system. In addition, it will be necessary to consider the music sign in these evaluations

REFERENCES

[1] Hayashi, E. et al, "Behavior of piano-action in a grand piano.I", Journal of acoustical Society of America, Vol.105, pp.3534-3544, 1999.

[2] Hayashi, E et al, "Interactive musical editing system for supporting human errors and offering personal preferences for an automatic piano", Proc. of the 7th International Symposium on Artificial Life and Robotics, Vol.2, pp 513-516, 2002.

[3] Hikisaka, Y., Hayashi, E., et al, "Interactive musical editing system for supporting human error and offering personal preferences for an automatic piano –Method of searching for similar phrases with DP matching and inferring performance expression-", Proc. of the 12th International Symposium on Artificial Life and Robotics, GS4-3, 2007.

A Corpora-based Detection of Stylistic Inconsistencies of Text in the Targeted Subgenre

Kiyota Hashimoto*, Kazuhiro Takeuchi**, Hideaki Ando**

Osaka Prefecture Univ.: 1-1, Gakuen-cho, Naka-ku, Sakai, 599-8531, Japan*
*Osaka Electro-Communication Univ**., 18-8, Hatsu-machi, Neyagawa, 572-8530, Japan*
(Tel : 81-72-252-1161; Fax : 81-72-254-99441)
(hash@lc.osakafu-u.ac.jp)

Abstract: The authors are currently on the way to develop a couple of educational applications for learners to improve their utterance/writing skills with a particular reference to stylistic coherence: a visual aid for teachers and learners to detect style inconsistencies with advice on improvements, an evaluation aid for teachers to grade learners' writings. In this paper, as a foundational data accumulation and analyses for them, we propose a method using multi-corpora comparison to correctly extract expressions not suited to a particular subgenre intended.

Keywords: computational stylistics, writing support, expression classification, visualization, educational tool

I. INTRODUCTION

Any kind of text expressions, from human utterances and writings to robotic utterances and text generations, require stylistic consistency suited to the targeted genres and the author's communicative purposes. Particularly in the educational field, automatic error detection and proof-reading tools are effective for students to learn how to write good essays. However, most of these tools including grammar and style checkers implemented in commercial word processing software ignore genre/subgenre differences and thus the user do not know whether the expressions that are pointed out as bad or wrong are indeed bad or wrong for the targeted genre/subgenre. So alternative method for detecting undesirable expressions for the targeted genre/subgenre is required.

II. GENRE AND STYLISTIC CONSISTENCY

Any text is classified into a genre. A genre is a set of criteria for a category of text, usually according to its topic and its way of publication. Thus, a text may be categorized as in the genre of biology according to its topic, or as a newspaper article because it is published in a newspaper. A genre is further divided into subgenres, part of which is sometimes regarded as linguistic register, mainly according to narrative aspects. How to narrate, or style, is highly related to the targeted audience and the author's communicative purpose of the text, and stylistic consistency is required in a text, though deliberate inconsistencies bring extra literary effects.

Stylistic consistency constitutes the use of suitable words, grammatical expressions, syntactic word orders and complexities, average sentence length, and information flow, though not limited to them. Several studies have tackled with style; particularly it has long been pointed out that basic stylistic consistency is held by the restrictive use of functional expressions particularly in the case of Japanese and other languages that have a rich variety of stylistic grammar forms.

a. Kore-wa hon-desu.
   this book be-pres.
   This is a book.
b. Kore-wa hon-da.

Both 'desu' and 'da' are auxiliary copular verbs and the difference is up to politeness, which in turn should be determined according to the targeted audience and the author's communicative purpose. So the mixed use of 'desu' and 'wa' causes undesirable stylistic inconsistency and thus should be avoided.

However, finer-grained observations of various kinds of human texts have found that a text genre traditionally considered to hold one single style should be decomposed into several different styles according to their subtle differences of the targeted audience and the author's communicative purposes. For example, we can easily distinguish a newspaper article and a newspaper editorial, or a textbook for graduate students and one for undergraduate or high school students, not just in terms of their contents but in terms of their style, though few of us can always make clear our criteria for this kind of distinction. Style has been studied mainly in the field of linguistics, literature, and education (for example, [1], [2]) but most of them are based on subjective, aesthetic judgments, and the finer-grained distinction of subgenres requires more objective, corpora-based analysis. From this viewpoint, in order to develop educational tools for better utterances and texts, it is necessary to first develop computational tools for detecting and evaluating stylistic inconsistencies.

III. STYLISTIC FEATURE EXTRACTION AND STYLISTIC VISUALIZATION

Stylistic consistency does not only depend on the inner consistency in the text, but also on the appropriate choice of style for the textual purpose. In other words, the targeted audience and the author's communicative purpose determine the desirable style; then the author, with his/her limited reading experiences, tries to use as many appropriate stylistic features as possible and tries not to use inappropriate stylistic features. Very often the author, particularly the learning one, makes mistakes on the choice of appropriate expressions partly because the stylistic distinction is subtle and often unconscious, partly because the author unconsciously relies on his/her judgments that comes from the most accustomed style, informal speech style, and partly because every one of us speaks and writes a number of different texts each of which has its own style and tends to rely on his/her intuition which only tells them that a particular stylistic feature may not suit the purpose.

With these in mind, we first construct a set of textual corpora that consists of two or more subgenres and extract stylistic features of each subgenre. This set roughly corresponds to our reading experiences but the larger size is naturally expected to contribute to a better detection of stylistic features. For the first approximation, let us consider that stylistic features of a subgenre are based on the preferable and unused expressions for the subgenre. The definition of 'expression' may vary, but we should note that a large number of words, including misspelled ones, are found unregistered in the dictionaries that any taggers use, that our current target language, Japanese, has still some serious problems in tokenization, and, most importantly, that the mere frequency of a word or a phrase without regard to its context does not reflect the precise tendency of the use of the word in a subgenre because a word usually has more than one meaning and usage, each of which are differently preferred or avoided in different subgenres. So here, we tentatively define an expression as an n-gram character string. The n-gram character extraction is a simple way of extracting expressions, but successfully contains contextual information when n is large enough, though too large n naturally causes too many low frequencies. The determination of the proper (range of) n is a heuristic issue, and we first adopt the range of n as two to four, partly because most of the Japanese words consist of one or two characters.

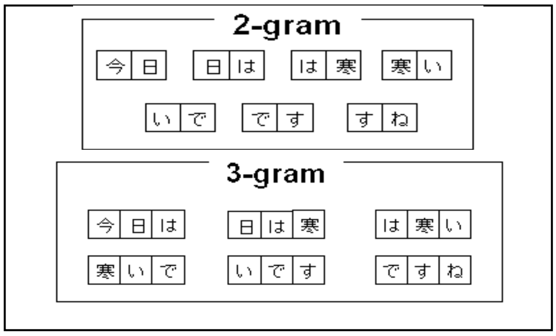

Fig.1. n-gram sample expressions in a Japanese equivalent of 'It is cold today'

As sample contrastive data, we use a dumped file of Japanese Wikipedia [3] and a sample of 2ch BBS (http://www.2ch.net/).

Data	Number of characters
Wikipedia	161,223,892
2ch	108,031,243

Table 1. Data set

The frequency of each expression in Wikipedia and 2ch classifies the expressions roughly in three classes: (a) expressions frequently used in Wikipedia but not frequently used in 2ch, (b) expression frequently used in both data, and (c) expressions not frequently used in Wikipedia but frequently used in 2ch. This classification means that the class (b) consists of rather neutral expressions, but the class (a) and (c) are to be considered to be stylistic features for Wikipedia and 2ch, respectively. The scatter diagram of 2- to 4-gram expressions is shown in Fig.2.

With this kind of scatter diagram, each expression, or stylistic feature, can be graded according to its distance from the catercorner([4]). Let a function gr(e) be defined as follows:

For a given expression e, the grade function gr (e) of Wikipedia-preferred expressions is
gr (e) = c dis (e)
where dis (e) is the distance from the catercorner,
and c = 1 if e is plotted below the catercorner
c = 0 if e is plotted on the catercorner
c = -1 if e is plotted above the catercorner.

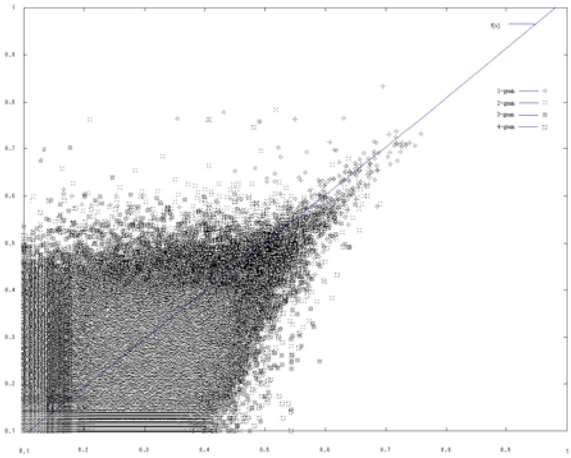

Fig.2 Scatter Diagram of 2- to 4-gram expression (X: frequencies in Wikipedia, Y: frequencies in 2ch)

Then, a given text T can be analyzed using gr (e) for every expression in T in terms of the resemblance with Wikipedia or 2ch.

We made an expression database $\Sigma(e)$ consisting of gr (e) of all the expressions in the Wikipedia and 2ch corpora we used. Then every expression that appears in a given text T is graded using $\Sigma(e)$, with which we obtain a sequence of gr (e) of T. A sample visualization of a student’ essay is shown in Fig. 3.

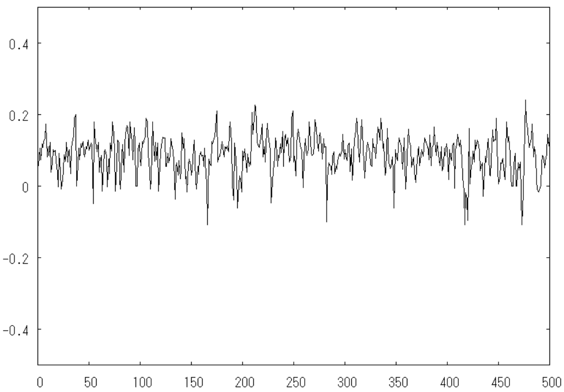

Fig. 3 Resemblance Visualization

As shown in Fig. 3, the overall tendency of the student’s essay used for this analysis resembles more to Wikipedia than to 2ch, but still it contains lots of expressions that are avoided in Wikipedia or preferred in 2ch. In other words, if we have a model set of corpora, one of which represents the targeted subgenre, any text can be graded and visualized with the function gr (e), and this type of visualization, though more improvements are necessary for practical use, can be used to visually point out expressions that may be avoided for the targeted subgenre.

IV. IMPROVEMENTS

In the previous section, we proposed a rather simple approach to evaluate a text in term of its appropriate style for the targeted subgenre by comparing its expressions with a model set of corpora, and visualized the result. In order to apply this method to an educational tool, at least two problems are to be solved. First, the method only uses the frequency of expression to judge whether a given expression is preferable or not for the targeted subgenre, but there should be different reasons for each expression being judged unfavorable: some may contain spelling errors, some grammatical errors, and others undesirable choice of words or phrases. Second, the visualization like Figure 3 is redundant for educational purposes, since what is important is to point out unfavorable expression for the targeted subgenre, and the grade differences among preferable expressions make little sense because the value of gr (e) near zero means that the expression tends to be used neutrally among corpora.

For dealing with the first problem, an additional method detecting serious errors is required. As for the determination of the serious errors, we manually observed a set of students’ essays and picked up the following five frequent serious errors that should be detected:

(a) Spelling errors
(b) Inappropriate choice of case particles
(c) Nouns with inappropriate modifiers
(d) Inappropriate letter choice in nouns
(mischoices among hiragana, katakana, and kanji)
(e) ordering errors of phrases (*bunsetsu* in Japanese)

Then we prepared an artificial set of data in which five types of errors pointed above were mechanically added. With this data set, we tested two error detection models for Japanese optical character reading ([5], [6]), and made experiments for evaluating these two models and tuning parameters. One model ([5]) focuses on the contextual allegation and detects the maximum inappropriateness. The other model ([6]) employs *m*th Order Markov Model to detect the lowest probability of transitions of a given string x_i following the prior *m* strings using the following equation:

$$P(x_i \mid x_{i-m}, x_{i-m+1}, \cdots, x_{i-1}) \equiv \frac{O(x_{i-m}, x_{i-m+1}, \cdots, x_{i-1}, x_i)}{O(x_{i-m}, x_{i-m+1}, \cdots, x_{i-1})}$$

Neither models can detect all the errors of (a) to (e) but tuning up the parameters with the artificial set of data improved the detection rate.

As for the second problem, it is desirable to visualize only the appearances of undesirable expressions effectively, but at the same time, visualizing the sequence of the raw value of gr (*e*) as in Figure 3 should be smoothed. For these purpose, we propose a function score (x, w) for smooth visualization of the appearances of undesirable expressions for the targeted subgenre:

$$\text{score}(x, w) = -\sum_{e \in n\text{-gram}(x, x+w)} b(e)$$

where b (e) = 0 when dis (e) – α >0

= (dis (e) – α)^2 when dis (e) – α <0

α is a heuristically determined coefficient.

n-gram (x, x+w) is a function that returns the set of n-gram expressions included from x-th to w-th strings.

With this function, the result visualization of the same student's essay used for Figure 3 is as follows:

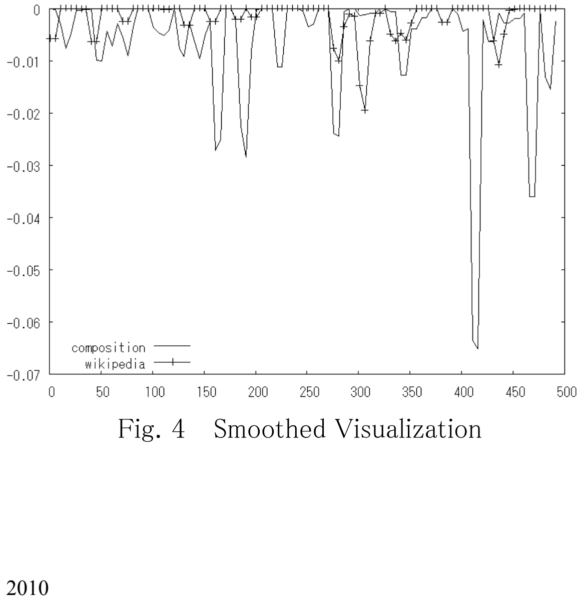

Fig. 4 Smoothed Visualization

With these improvements, we are currently implementing a pilot application for enabling teachers and students to easily detect expressions that are to be revised or improved in an essay.

V. CONCLUSION

In this paper, as a foundational data accumulation and analyses for them for the purpose of developing educational tools for improving stylistic aspects of writing skills, we proposed a method using multi-corpora comparison to correctly extract expressions not suited to a particular subgenre intended, and developed an experimental visualization for teachers and students. Much has to be done towards a practically effective tool, but any advanced tool to help teachers and students to detect undesirable expression should be conscious of stylistic differences among subgenres and our proposed methods are foundationally effective.

REFERENCES

[1] Strunk Jr., W. and E.B. White (2000^4) *The Elements of Style*, Longman.
[2] Williams, J.M. (2008) *Style: The Basics of Clarity and Grace*, Longman.
[3] Japanese Wikipedia dumped file http://download.wikimedia.org/jawiki/20071013/jawiki-20071013-pages-articles.xml.bz2
[4] Masao Uchiyama and Kiyomi Chujo (2007) Linking Word Distribution to Technical Vocabulary, Technical Report B, College of Industrial Technology, Nihon Univ. Vol.40 pp.13-21.
[5] Masaki Murata, Hitoshi Isahara (2002) Automatic Detection of Mis-Spelled Japanese Expressions Using a New Method for Automatic Extraction of Negative Examples Based on Positive Examples, IEICE Transactions on Information and Systems, E85-D(9) pp.14165-1424.
[6] Tetsuo Araki, et al, (2000) A Method for Detecting and Correcting of Characters Wrongly Substituted, Deleted, or Inserted in Japanese Strings Using *m*th-Order Markov Model, The Transactions of the Institute of Electronics, Information and Communication Engineers, D-II J83-D-II(6) pp.1516-1528.

Emotion Inspired Mechanism in the intelligent system

JeongYon Shim

Div. of GS, Computer Science, Kangnam University, Kugal Dong 111, KiHeung Gu, YongIn Si, KyeongKi Do, Korea
(Tel : +82-31-280-3736; E-mail: mariashim@kangnam.ac.kr)

Abstract: In this paper, for designing more sophisticate Emotional process considering the personality Emotional Inspired mechanism in the intelligent system is studied. We propose the mechanism for implementing the connection between knowledge and emotion, personality and emotional reaction process. Also personally different emotional reaction mechanism about the same external emotional stimulus is designed and tested with virtual memory.

Keywords: Emotional Reaction, Type matching Selection, Thought thread, personality

1. INTRODUCTION

Why does a human being have a different emotional reaction to the same stimulus individually? This is not a solvable problem but it is guessed that the main reason is caused by personality and current emotion. The personality is the own property which the individual person has. It is thought that the personality is formed by inherent characteristics and acquired characteristics. The acquired characteristics mean the obtained knowledge and experience. Human being percepts the things on the basis of neural network in the brain which is obtained by learning and experience. That is to percept and process the things in the own viewpoint.

Recently as one way of implementing Human-Computer-Interface the research on emotion has started in the engineering part for implementing more human friendly computer system. However the main problem of Emotional process is that it is difficult to formalize the emotional factor because its characteristic is too personal and subjective. In order to overcome this shortcoming, the personality should be quantified as concrete as possible and designed sophisticatedly. Suppose that the personality depends on the structure, contents and type of neural network in the brain, we should investigate these factors. Every person has his own type and receives the matching typed knowledge and makes the structure of memory. According to the research of Neuro-Science, it is known that there are two pathways in the process of memorization. One is a pathway to memorize the knowledge including the Emotional state and the other is a pathway to store the knowledge without emotional factor. In the brain hippocampus takes part in the main memorizing process and amygdaloid nucleus plays an important role of emotional process. In the first pathway, both of hippocampus and amygdaloid nucleus are working but in the second pathway only hippocampus takes part in the memorizing process. It is known that the knowledge including the emotion lasts longer. Nobody can deny the fact that the emotion has much effects on the memorizing process, reasoning, and decision making process.

The main issue is how to design and implement the emotional state which has much personal tendency. Fortunately we can find some clues from the brain function. First key is to make the emotion state quantified, second is to connect emotion factor to knowledge and third is to qualify the type to the knowledge.

In this paper,considering the above three points of view Emotion inspired system is designed for making more sophisticate intelligent system. The emotional reaction mechanism is proposed and its experimental results are investigated.

2. THE DESIGN OF EMOTION, KNOWLEDGE AND TYPE MATCHING

2.1 Emotional factor

Many studies on the Emotional modeling have been made for these decades, for example, valance-arousal-plane of Emotion space based on Russells circomplex model of affects[4], The Tellegen-Watson-Clark model of mood[5],OCC model[6]. The most popular example of this is the Ortony, Clore and Collins(OCC) model. The OCC model divides a character's concerns in an environment into goals(disired states of the world), standards (ideas about how people should act) and preference(likes and dislikes).

In this study,we differentiate moods and Emotions on the basis of three criteria: like, excited and stable. Emotion state is represented by three dimensional space as following figure 1. The emotion state is specified as the degree of three factors.

Emotional State E_i=(a degree of 'like', a degree of 'excited', a degree of 'stable') where the degrees of three factors have values of [-1.0,+1.0].

For example, the six emotional states can be expressed by the following space. The value of degree is not fixed and can have a variation depending on the situation.

happy=(+1.0,+0.8,+1.0)
surprise=(0.0, +1.0, -1.0)
sad=(-1.0,-1.0,-0.5)
fear=(-1.0,+1.0,-1.0)
disgust=(-1.0,+0.5,-0.5)
interest=(+1.0,+0.5,+0.8)

2.2 The knowledge network design

We designed knowledge network as a structure of memory for efficient processing. The knowledge network consists of knowledge nodes and their associative rela-

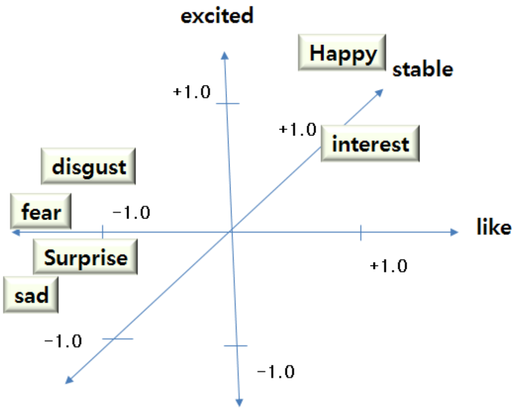

Fig. 1 Emotion space

tions[1]. It is represented as a form of

$\langle$K-node$_i$, R_{ij},$K-node_j$ $\rangle$

where $K-node_i$ is the name of knowledge node and R_{ij} is connection strength between two knowledge nodes. R_{ij} is calculated by equation (1).

$$R_{ij}=P(K-node_i \mid K-node_j) \quad (1)$$

Knowledge node is an basic atom composing the Knowledge Network. It contains 'ID','Type(T)','Self Energy(S)','Retained Emotional Energy(E)' attributes which can identify itself. Knowledge node is represented as a form of 'struct'.

struct k-node$_i\langle ID, T, S, E\rangle$

Type,T,represents its own property of knowledge which is base factor for the personality and Self Energy,S,is used for the forgetting or incarnation mechanism. The term of Retained Emotional Energy,E, is used for processing the emotional part. Emotional energy has a value between -1.0 and +1.0. The value 0.0 means that emotional energy is in the neutral state. The explanation about this emotional factor will be described in the next section in detail.

2.3 Type Matching Selection

Type is defined as a factor representing the property of a thing and is classified to five types, M,F,E,K and S. These five types can be flexibly designed for the application area. We also defined Type matching rule. Type matching rule is used for selecting the knowledge from master Knowledge Network. There are two types of matching relations,Attracting Relation and Rejecting Relation[1].

Attraction Relation	Attracting degree d_i
M $\oplus\gg$ F	d_1=0.5
F $\oplus\gg$ E	d_2=0.5
E $\oplus\gg$ K	d_3=0.5
K $\oplus\gg$ S	d_4=0.5
S $\oplus\gg$ M	d_5=0.5

Rejecting Relation	Rejecting degree d_i
M $\ominus\gg$ E	d_1=-0.5
E $\ominus\gg$ S	d_2=-0.5
S $\ominus\gg$ F	d_3=-0.5
F $\ominus\gg$ K	d_4=-0.5
K $\ominus\gg$ M	d_5=-0.5

The matching rule 'M $\oplus\gg$(0.5) F' means that M type helps F type with attracting degree 0.5. The value d_s of 'M $\oplus\gg(d_s)$ S' is derived from 'M $\oplus\gg$(0.5) F $\oplus\gg$(0.5) E $\oplus\gg$(0.5) K $\oplus\gg$(0.5) S'. The attracting degree of multiple relation is calculated by the following equation(2).

$$d_s=\begin{cases} \prod_{i=1}^{n}(-1)^{n+1}d_i & \text{if } Type_i \neq \text{Type}_j \\ 1 & \text{otherwise} \end{cases} \quad (2)$$

If the value of d_s is positive, it is attracting relation. Otherwise, the minus value means rejecting relation.

3. THE DESIGN OF EMOTION INSPIRED SYSTEM

3.1 The Emotional process

As described in the previous section, the knowledge network consists of ID, Type,Self Energy and Retained Emotional Energy. In the process of structuring the memory,the system acquires the knowledge including the emotional factor. There are two pathways to receive the learning data for constructing the knowledge network. One is to get the knowledge including the emotion factor and the other is to receive only knowledge. In the first case including the emotional factor, the value of emotional Energy is represented as a vector form as follows.

$E_i=(E_x, E_y, E_z)$,
where E_x is 'like' term, E_y is 'excited' term and E_z is 'stable' term.

In the second case, the value of Emotional energy is E_i =(0.0, 0.0, 0.0)

The learning structure and mechanism are described in the paper[1,2,7] in detail. In this section we 'll explain the mechnism focusing on the emotional reaction by the personal perspective and emotional state. For deciding the reaction emotional state, three factors of input emotional stimulus,E_s, and the emotional energy of retrieved Thougth thread, E_i^M, are considered.

The figure 2 shows the Emotional reacting process. when the emotional stimulus, E_s, comes into the system, the system receives the stimulus knowledge and its type together and starts the emotional reaction process. First of all, the system extracts the related Thought threads from the Emotion inspired knowledge network using Type Matching Selection mechanism. Through this extracting mechanism, several Thought threads can be

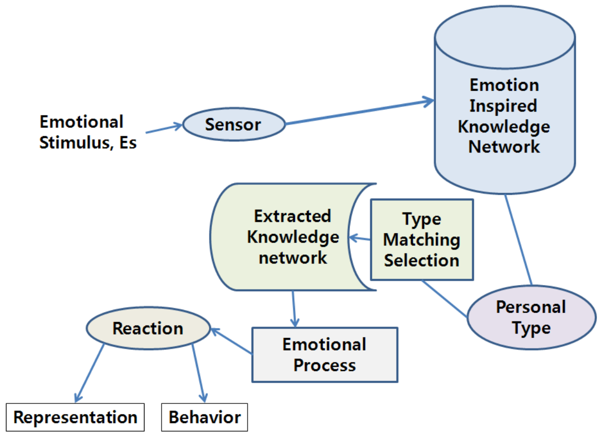

Fig. 2 Emotional reacting process

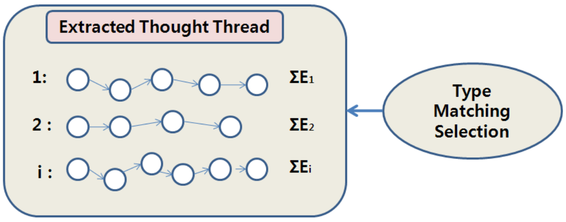

Fig. 3 Extracted Knowledge Network :Thought thread

retrieved. As shown in Figure 3, the related Thought threads are extracted by Type Matching Selection mechanism. In this step the system should select one Thought thread for reaction and Decision making. For emotional process, the system evaluates the mean value of the emotional energy in the extracted Thought threads. The mean value of Thought thread,E_i^M, can be calculated as following equation.

$$\begin{aligned} E_i^M &= (E_{ix}^M, E_{iy}^M, E_{iz}^M) \\ &= \left(\frac{\Sigma_{i=1}^n E_{ix}}{n}, \frac{\Sigma_{i=1}^n E_{iy}}{n}, \frac{\Sigma_{i=1}^n E_{iz}}{n}\right) \end{aligned} \quad (3)$$

After calculating the mean value of emotional energy in the retrieved Thought thread, one Thought thread matched with stimulus emotional stateshould be selected. Suppose that the stimulus emotional state is E_s=(E_{sx},E_{sy},E_{sz}), the choosing rule is as following equation(4).

$$T = \sqrt{(E_{sx} - E_{ix}^M)^2 + (E_{sy} - E_{iy}^M)^2 + (E_{sz} - E_{iz}^M)^2} \quad (4)$$

$$p = argmin_i T \quad (5)$$

From this calculation, the Thought thread,p, is selected. The final emotional state,E_f is calculated by equation (6).

$$E_f = (E_{fx}, E_{fy}, E_{fz}) \quad (6)$$

$$E_{fx} = \begin{cases} E_{sx} + E_{px} & \text{if } -1 <= E_{sx} + E_{px} <= 1 \\ 1 & \text{if } x > 1 \\ -1 & \text{otherwise} \end{cases} \quad (7)$$

$$E_{fy} = \begin{cases} E_{sy} + E_{py} & \text{if } -1 <= E_{sy} + E_{py} <= 1 \\ 1 & \text{if } x > 1 \\ -1 & \text{otherwise} \end{cases} \quad (8)$$

$$E_{fz} = \begin{cases} E_{sz} + E_{px} & \text{if } -1 <= E_{sz} + E_{pz} <= 1 \\ 1 & \text{if } x > 1 \\ -1 & \text{otherwise} \end{cases} \quad (9)$$

3.2 Emotional Reaction Algorithm

Based on the the calculation of Emotional state in the previous section, Emotional Reaction process is performed by following algorithm.

Algorithm 1 : Emotional Reaction Process

STEP1 input Type T, Emotional stimulus E_s;
STEP2 Type Matching selection;
STEP3 i=1;
STEP4 while(queue != Empty) do
begin
Calculate the mean value of Emotional state, E_i^M
end
STEP5 Select Thought thread p;
STEP6 Calculate reaction Emotion;
STEP7 Interpretation;
STEP8 : Stop.

4. EXPERIMENTS

In this experiment, we tested the emotional reaction process with the virtual memory which consists of 15 knowledge nodes as shown in Figure 4. Input condition is set that the Type of input data is 'M' and input stimulus comes variously. Figure 5 shows the four extracted Thought threads about Type 'M' by Type maching selection. In this step, the mean values of emotional states in the Thought threads were calculated. As shown in Figure 6, the emotional distance between 5 incoming emotional stimulus and the mean value of emotional state of Thought thread. As a result of experiment, the closest Thought thread was selected and reacted. From the data in Figure 7, we can check that when the incoming input stimuli is E_1(-1.0,-1.0,-1.0) Thought thread4 is selected and its reaction value is also (-1.0,-1.0-1.0). In the case of E_3(0.0,0.0,0.0), Thought thread3 is choosed and it reacts as (0.18,0.40,0.35). It means that there is no emotonal stimulus but the emotional state stored in memory is represented. This experiments have a meaning that this mechanism consniders not only external emotional stimulus but also internal emotional state stored in the memory.

	E_x	E_y	E_z
E_1	1.0	1,0	0.9
E_2	0.8	0.9	0.7
E_3	0.5	0.5	0.3
E_4	0.2	0.0	0.1
E_5	0.6	0.7	1.0
E_6	0.8	0.9	1.0
E_7	0.3	0.3	0.3
E_8	-0.1	-0.2	-0.5
E_9	0.1	0.1	0.0
E_{10}	0.4	0.5	0.7
E_{11}	-1.0	-1.0	-1.0
E_{12}	-0.8	-0.7	-1.0
E_{13}	-0.7	-0.8	-0.5

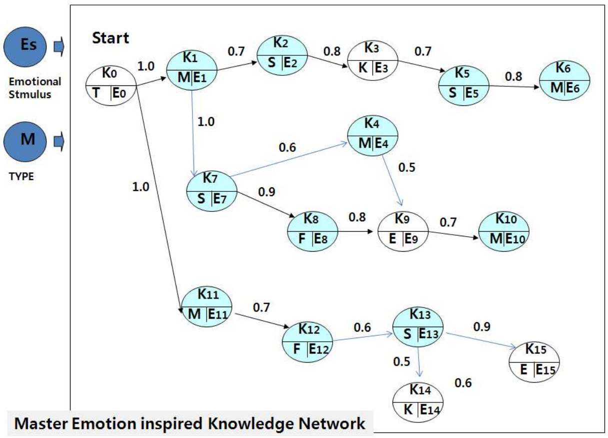

Fig. 4 Master Emotion inspired Knowledge Network

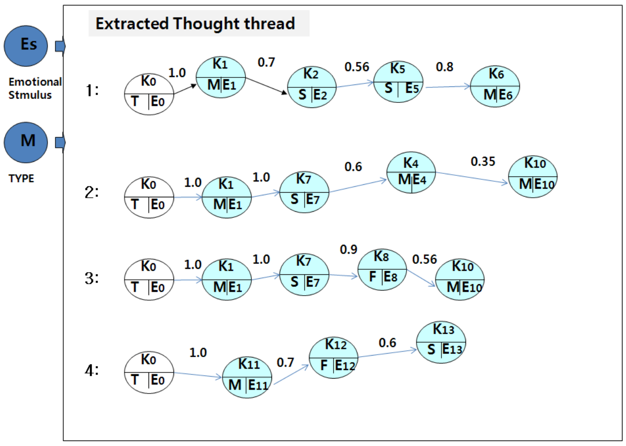

Fig. 5 Extracted Thought threads

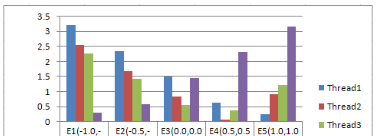

	E1(-1.0,-1.0,-1.0)	E2(-0.5,-0.5,-0.5)	E3(0.0,0.0,0.0)	E4(0.5,0.5,0.5)	E5(1.0,1.0,1.0)
Thread1	3.219569	2.353853	1.488498	0.625	0.256174
Thread2	2.55502	1.68912	0.823483	0.055902	0.910014
Thread3	2.272251	1.410009	0.559576	0.371652	1.209597
Thread4	0.289252	0.576773	1.442798	2.308824	3.174849

Fig. 6 Emotional distance

Emotional Stimulus	Selected Thread	Emotional Reaction
E1(-1.0,-1.0,-1.0)	Thread4	(-1.00 ,-1.00, -1.00)
E2(-0.5,-0.5,-0.5)	Thread4	(-1.00, -1.00, -1.00)
E3(0.0,0.0,0.0)	Thread3	(0.18, 0.40. 0.35)
E4(0.5,0.5,0.5)	Thread2	(0.98, 0.95, 1.00)
E5(1.0,1.0,1.0)	Thread1	(1.00, 1.00, 1.00)

Fig. 7 Emotional Reaction

5. CONCLUSION

In this paper, Emotional Inspired mechanism in the intelligent system was studied. We designed the mechanism for implementing the connection between knowledge and emotion, personality and emotional reaction process. Also personally different emotional reaction mechanism about the same external emotional stimulus was designed and tested with virtual memory. As a result, it shows the successful testing results. This strategy can be usefully applied to design and construct more sophisticate Intelligent System.

REFERENCES

[1] JeongYon Shim, **A Design of Brain Sensory Ensemble Structure for Intelligent system** ICCAS2008.

[2] JeongYon Shim, **Personal Knowledge Network Reconfiguration Based on Brain like function using Self Type Matching Strategy** IDEAL, volumn 5326, Springer,2008.

[3] Jean-Marc Fellous, Michael A. Arbib, **Who needs Emotions?** Oxford University press,2005.

[4] Russell, and B.S.Peterson, **The circumplex model of affect: An intergrative approach to affective neuroscience, cognitive development, and psychopathology** Development and Psychopathology, 17(03),715-734,(2005).

[5] A. Tellegen, D.Watson and L.Clark **On the dimensional and hierarchical structure of affect** 1999, Psychological Science.

[6] A. Ortony, G.L. Clore, and A. Collins, **The Cognitive Structure of Emotions** Cambidge Univ. Press,1988.

[7] JeongYon Shim, **Knowledge Network Management System with medicine Self Repairing strategy** ICES2007,LNCS4684,pp119-128,Springer Verlag,Berlin Heidelberg2007.

[8] JeongYon Shim, **The design of Self Internal Entropy Balancing System with Incarnation process** LSMS2007,LNCS4688,pp55-62,Springer Verlag,Berlin Heidelberg2007.

[9] E. Bruce Goldstein, **Sensation and Perception** Fifth edition,Brooks/Cole Publishing Company,1999.

[10] Michael A. Arbib, Jeffrey S. Grethe, **Computing the brain : A guide to Neuroinformatics** Academic Press,2001.

The Fifteenth International Symposium on Artificial Life and Robotics 2010 (AROB 15th '10),
B-Con Plaza, Beppu,Oita, Japan, February 4-6, 2010

Object Recognition Algorithm using Vocabulary Tree and Pre-Matching Array

Ho-Yong Seo and Ju-Jang Lee

Department of Electrical Engineering and Computer Science
Korea Advanced Institute of Science and Technology (KAIST)
Daejeon, Republic of Korea
(Tel : 82-42-350-8032; Fax : 82-42-350-5432)
(E-mail: hyseo@kaist.ac.kr)

Abstract: Vocabulary Tree algorithm builds a tree structure by performing the off-line learning method using the large number of training image datasets. After constructing, we can retrieve a query image class very quickly by searching the tree structure. Because of the great improvement for computation time reduction, this algorithm comes into the spotlight recently.

In this paper, we suggest a method which improves the classification accuracy via searching our tree with multiple times per one test data. The information which given by pre-matching array determines how the tree is visited. Taking our new algorithm, we can reduce miss-classification rate considerably. On the other hand, losses from computation time and memory allocation are negligible.

Keywords: Vocabulary Tree, Pre-Matching Array, Object Recognition

I. INTRODUCTION

Object recognition field which is a one of central parts in computer vision, deals with the method that determines the unknown class of test image from given training image datasets.

When constructing training image datasets from a large number of images, we can't use whole image pixel information for computation time and memory allocation problems. Recently, the method, so called keypoint based feature extraction technique, is widely used for making training data values. One of SIFT, SURF, MSER, CenSurE and the others is used for each proper design goal. These techniques use some meaningful pixels which appear more frequently than other pixels when image information such as scale, orientation, illumination is changed. Using above feature extraction technique, we can get D-dimensional vector for each keypoint. These vectors are used for our training image datasets [1].

When Object recognition based on above feature extraction methods performs learning process, we can categorize object recognition by which learning method is used among various kind of method such as offline learning, online learning, supervised learning and unsupervised learning.

Offline learning is done before test input is coming. In other words, when test step is on progress, there isn't additional learning. On the other hand, online learning performs learning step and test step simultaneously. Supervised learning is used when we know all classes of training image. Otherwise, we can use unsupervised learning to categorize all images [2].

The most general method used for object recognition is machine learning techniques such as support vector machine(SVM), kernel machine, expectation-maximization(EM) and their variations [2]. These techniques assume that the labels of our training image datasets are already known. In other words, supervised learning case is popular for object recognition field.

But vocabulary tree case, which is mainly referred by our paper, uses K-means clustering and tree structured vocabulary. The former allow us using unlabeled training datasets easily [3], and the latter give less computation time with respect to other method which doesn't use tree structure. And, the retrieval performance is about 70~80% [4].

In this paper, we tried to get more accurate retrieval performance than that of previous vocabulary tree case. Once the tree is constructed, when performing test process through this tree, we are just required very short computation time. So, we try to search tree structure in multiple times per one test image for the object of improvement of performance. Because we use tree structure, multiple time searching doesn't need too much additional calculation time. Also, by adding simple array so called pre-matching array, we can do multiple tree searching process efficiently just using few additional memory space.

II. REVIEW OF VOCABULARY TREE

1. Characteristics

Using vocabulary tree(VT) is usable whether training datasets have label or not. VT always categorize class of test data very quickly with reasonable performance.

At training step, we construct a tree using K-means clustering which is one of popular methods in unsupervised learning. At test step, we try to search that tree, then our computation time is expressed with $O(KLD)$ where K is branch factor of tree, L is depth of tree and D is input vector dimensions as described Fig.1 [4].

2. Implementation

A. Training Step

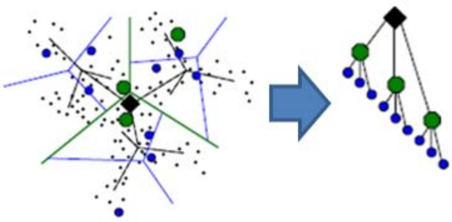

Fig.1 Tree construction Process when K=3,L=2 [4]

Step1. Using one of keypoint feature extraction algorithm, extract all feature D-dimensional vectors from all training image sets.
Step2. Define some constant K. And, categorize features for K-children node using K-means clustering based on all feature vectors within current node.
Step3. Define tree depth constant L. Repeat Step 2 until arrives at leaf-node.
Step4. At each leaf node, save number of training image numbers(N_i) within ith node.
Step5. Save the number of feature vectors(n_i) for each image within ith leaf node. Repeat for all images within ith leaf node.

B. Test Step

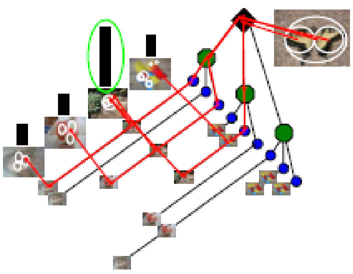

Fig.2 Testing Process concept [4]. Minimum scoring described as maximum counting.

Step1. Extract all feature vectors from test image.
Step2. Start at root node.
Step3. For each feature vector, compute Euclidean distance with this vector and K-means vector.
Step4. Go child node which give smallest distance number. Repeat until arrive at leaf node.
Step5. Repeat Step 3-4 for all feature vectors from test image.
Step6. Count and save the number of feature vectors(m_i) within ith leaf node. Repeat for all leaf node.
Step7. For each training image, calculate score s as follows.

$$w_i = \ln \frac{N}{N_i} \tag{1}$$

where N is total number of training image.

$$\begin{aligned} q_i &= n_i w_i \\ d_i &= m_i w_i \end{aligned} \tag{2}$$

$$s = \left\| \frac{q}{\|q\|} - \frac{d}{\|d\|} \right\|_2^2 = 2 - 2 \sum_{i | q_i \neq 0, d_i \neq 0} q_i d_i \tag{3}$$

Step8. For all training image, find minimum score. And, return image index information which give minimum score value as Fig.2.

These all steps are progressed by referring [4].

III. PRE-MATCHING ARRAY

1. Characteristics

If we change the index returning method that retrieve not only one image but also multiple images, then we expect that test process give correct classification for all images returned. But, as we mentioned, average retrieval performance is about 70~80%, in other words, not perfect.

So, we suggest pre-matching array for the object of improvement of retrieval performance, maintaining fast computation time as possible using VT structure.

2. Definition

Pre-matching array contains retrieved training image indexes with high scored sequence from one test image. So, array size(N_p) determines how many images we consider.

And regarding each saved training image as new test image, we can search tree structure again and get another result image indexes.

Next, among these all result image indexes, we have to extract image indexes regard as same class with our test image. This process is performed by using new variable defined R .

Here, R is defined as the number of count that calculated from all result image indexes. So, from $N_p(N_p - 1) \times 1$ vector R , we can get best image index what we want to extract. When using training image as test image, we have to eliminate first resulting image index because first index is always that of training image itself.

3. Implementation

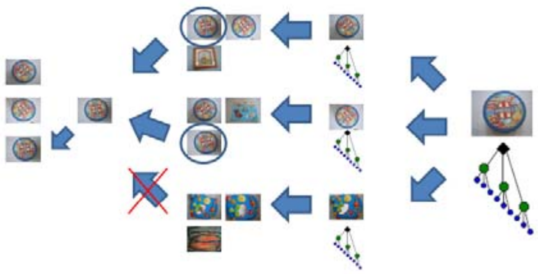

Fig.3 Correction of miss-classification by using pre-matching array

Step1. Construct VT using training image dataset.
Step2. From putting test image into VT, get N_p number of training image indexes which has best score sequentially.
Step3. For all selected training images, put those images into VT, get $N_p\left(N_p-1\right)$ number of result image indexes except of first result image index for each selected training image.
Step4. Count for each result image index, and save that result at R.
Step5. Return one result image index which has best R count and replace lowest counted training image index as our selected image index as Fig.3.

IV. EXPERIMENT & RESULT

1. Parameter Setting

Among wide variety of keypoint feature extraction method, we select SURF algorithm for the object of fast calculation via filter scaling method [1]. We utilized SURF inside OpenCV library.

When performing tree construction process, we have to determine K and L. As referred from [4], to get reasonable performance, we select K=10 and L=6.

Next, we have to determine training image contents and numbers. As Fig.4, we select same training images with [4]. Four images exist for each one specific object.

Fig.4. Part of our training image dataset [4].
Total number of training images is 1000, in other words, 250 objects. Our purpose is relative comparison with previous VT and our pre-matching array algorithm, for simplicity, number of training images is fixed.

2. Result

A. Basic training image dataset case

Using above training image dataset, we extract feature vectors from SURF, construct tree and classifying randomly selected test images. Our result values are tree construction time, test time, and performance for all randomly selected test images.

Table 1. parameter variation for Np when fixed training image dataset is used.

	Construction time	Test time
0(VT)	356.8sec	39.3sec
1	356.9sec	40.8sec
2	355.3sec	40.3sec
3	352.8sec	41.5sec
4	357.7sec	41.5sec
5	358.0sec	41.3sec
6	360.2sec	42.2sec
7	356.1sec	42.7sec
8	355.6sec	43.6sec
9	358.3sec	42.9sec

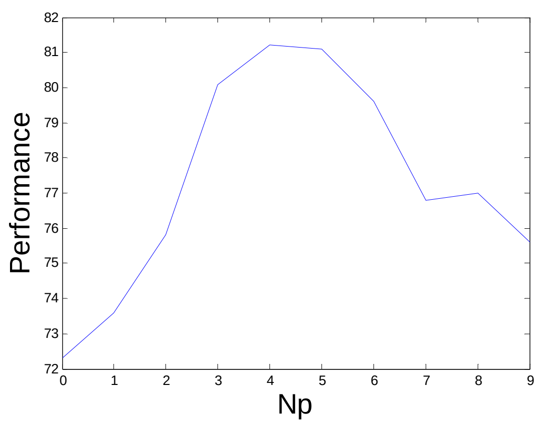

Fig.5. Performance graph when fixed training image dataset is used.(Best at Np=4)

As we expected, computation times for both construction and test case are slightly increase with respect to that of basic VT case. But, those increment value is negligible.

And, when Np=4, best performance is returned and this value is much better than that of basic VT case. Best performance is taken when Np equals 4. Because we use training images which have equally 4-images for each one class, Np=4 give us best performance.

B. Random selected training image dataset case

To verify generalization which means our algorithm is robust for changing training image datasets. So, in this step, we select randomly 1000 images regardless of equal number of class for equal number of image groups.

Our result is as follows.

Table 2. parameter variation for Np when randomized training image dataset is used.

	Construction time	Test time
0(VT)	358.3sec	40.6sec
1	358.1sec	40.9sec
2	357.7sec	40.5sec
3	359.8sec	41.1sec
4	362.3sec	41.0sec
5	366.8sec	40.3sec
6	361.5sec	49.9sec
7	353.7sec	40.2sec
8	361.1sec	42.5sec
9	359.6sec	41.8sec

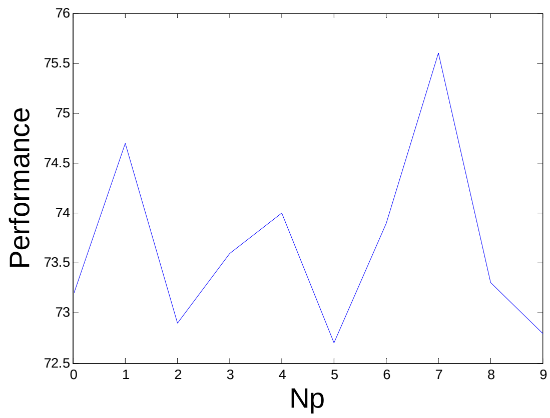

Fig.5. Performance graph when randomized training image dataset is used.

If our data is selected randomly, the Np value which give us best performance can be changed. Also, Our best performance value is decreased. Np = 5 case give us worse than that of basic VT tree case. For generalization, the method that determines good Np value have to be studied later.

Of course, computation time is very close to constant.

V. CONCLUSION

Combining vocabulary tree and pre-matching array, we can get considerably improved retrieval performance with compensating additional small memory allocation and computation time. The tree structure gives us almost same calculation time. And, just additional $N_p\left(N_p - 1\right)\times 1$ memory allocation is needed. Our algorithm can be applied for auto categorization for unlabeled digital camera pictures or unlabeled image at web search engine which requires high accuracy for retrieval task.

If the number of images in one class is varying greatly, in other words, when we use random unlabeled image, another N_p selection method have to be introduced. We tried this problem later for generalization.

VI. ACKNOWLEDGEMENT

Authors are gratefully acknowledging the financial support by Agency for Defence Development and by UTRC(Unmanned Technology Research Center), Korea Advanced Institute of Science and Technology.

REFERENCES

[1] Herbert Bay, Tinne Tuytelaars, and Luc Van Gool (2006), Speeded-Up Robust Features(SURF). Springer 3951 : 404-417
[2] Christopher M.Bishop(2006), Pattern Recognition and Machine Learning. Springer : 1-4
[3] J.Sivic , A.Zisserman(2003), Video Google : A Text Retrieval Approach to Object Matching in Videos. Citeseer 2: 1470-1477
[4] D.Nister, H.Stewenius(2006), Scalable Recognition with a Vocabulary Tree. Citeseer 5

The Fifteenth International Symposium on Artificial Life and Robotics 2010 (AROB 15th '10),
B-Con Plaza, Beppu,Oita, Japan, February 4-6, 2010

Memory Association and Reaction by Conditioning Mechanism

JeongYon Shim

Div. of GS, Computer Science, Kangnam University, San 6-2, Kugal Dong, KiHeung Gu, YongIn Si, KyeongKi Do, Korea (Tel : +82-31-280-3736; E-mail: mariashim@kangnam.ac.kr)

Abstract: As an interest in researching brain is growing for recent years, the researches into intelligence, mind, sensory and memory based on the brain function is getting activated. focusing on conditioning among the brain functions,we designed the strategy of memory association and reaction process. First of all, the functions of amygdala in the brain is investigate and applied to design the intelligent system. We developed memory association system considering 'conditioning'. DTAM(Dynamic Thinking Association Map)was designed for implementing 'conditioning' function. It is applied to the virtual memory and tested with sample data.

Keywords: Conditioning,Thinking chain extraction, Data selection, knowledge network

1. INTRODUCTION

Human brain has evolved for several million years and has a most optimum functions for surviving in the dynamic complex environment. That is, the brain is a final intelligent product which is adaptable in the dynamic situation.

Many of innovations introduced in the field of technology by the scientific and information revolutions set the stage for a qualitative change in the base of human society. We are standing on the dramatically changing point where human society and computer world overlap. In this situation, the importance of implementing more human friendly computer system is getting high and more convenient Human-Computer-Interface(HCI) is required. The strategy of adopting human brain functions has a strong point in two perspectives. One is that human brain is most outstanding problem solver in the circumstance enclosing the human society. Human brain is not only intelligent but also adaptable in data learning, memorizing, reasoning and memory recalling process. The other is that it has an effective communication tools and process. Recently many studies on the brain science has been made and applied to many engineering parts for making more intelligent and efficient systems.

In this paper, focusing on conditioning among the brain functions,we designed the strategy of memory association and reaction process. First of all, the functions of amygdala in the brain is investigate and applied to design the intelligent system. We developed memory association system considering 'conditioning'. DTAM(Dynamic Thinking Association Map)was designed for implementing 'conditioning' function. It is applied to the virtual memory and tested with sample data.

2. CONDITIONING AND HUMAN AMYGDALA

Since Pavlov(1927), it has been known that an initially stimulus, a conditioned stimulus(CS), can acquire affective properties upon repeated temporal pairings with a biologically significant event, unconditioned stimulus(US)[1]. As the CS-US relation is learned, innate physiological and behavioral responses come under the control of CS. Research from several laboratories combined in the 1980s to paint a relatively simple and clear picture of the neuroanatomy of fear conditioning[2,11,12,13,14]. In this studies, the CS and US are typically an audible tone and foot shock, and the responses measured include freezing. It is thought that fear conditioning is mediated by the transmission about the CS and US to a small almond-shaped area which is called 'Amygdala'. Amygdala is a group of nuclei located deep within the medial temporal lobes of the brain in complex vertebrates, including humans. Shown in research to perform a primary role in the processing and memory of emotional reactions, the amygdalae are considered part of the limbic system

The control of fear reactions is made by way of output projections from the Amygdala to behavioral autonomic, and endocrine response control systems located in a collection of nuclei, altogether referred to as the 'brain stem'. In addition to expressing fear responses to the CS, rats exhibit these when returned to the chamber in which the tone and shock were paired or a chamber in which shocks occur alone. It is called 'Contextual fear conditioning' where context refers to various visual and olfactory aspects of the chamber, and requires both the Amygdala and hippocampus, a brain structure know to enable long-term memories. Conditioning can be mediated by US inputs to the Amygdala from either thalamic or cortical area.

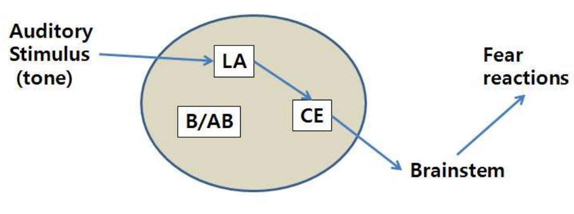

Fig. 1 Initial

As shown in figure 1, Conditioning to a tone involves projections from the auditory system to the lateral nucleus of the amygdala (LA) from LA to the central nucleus of the amygdala(CE). In contrast in figure 2, conditioning to the apparatus and other contextual cues present

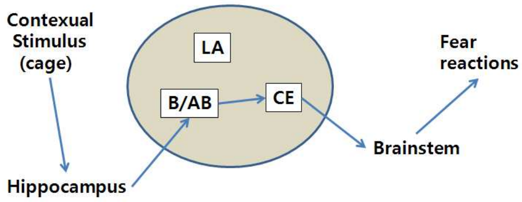

Fig. 2 Conditioning

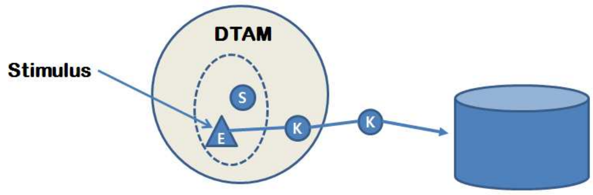

Fig. 5 Stimulus :E

when the conditioned stimulus and unconditioned stimulus are paired involves the representation of the context by the hippocampus and the communication between the hippocampus and basal(B) and accessory basal(AB) nuclei of the amygdala, which in turn project to CE. As for tone conditioning, CE controls the expression of the response.

3. MEMORY ASSOCIATION AND REACTION BY CONDITIONING PROCESS

3.1 The design of DTAM

Adopting the function of amygdala Dynamic Thinking Association Map(DTAM) composed by conditioned learning process is designed. Also based on the formed Dynamic Thinking Association Map the system extracts the related knowledge fragments from the Knowledge Network.

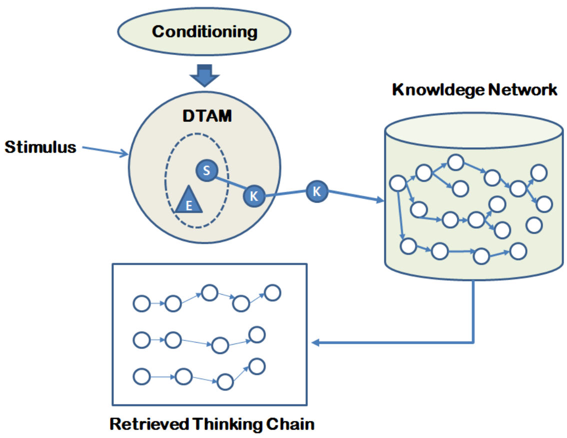

Fig. 3 Dynamic Thinking Association Map

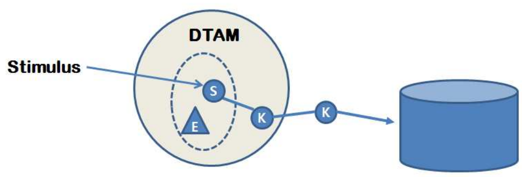

Fig. 4 Stimulus : S

As shown in figure 3, two nodes in DTAM are associated by conditioning mechanism. The associative relation between S and E node is gained by conditioning. After conditioning process, S-E pair shows the associative reaction. Especially in memory recalling process,the conditioned associative relation effects on the knowledge extraction. In the initial states, node E has no relation with the retrieved thinking chains connected to node S. But after conditioning mechanism, only stimulus of E can retrieve the thinking chains related to node S.

3.2 Hierarchical Memory Construction with Knowledge Networks

The knowledge network which construct memory consists of knowledge nodes and their associative relation. We design the knowledge network as a base of memory for the efficient reasoning and extracting process. And it also has a strong point that it is easy to express the conceptual dependence in the knowledge.

The basic unit of knowledge network consists of two nodes and their connected relations as following figure 6.

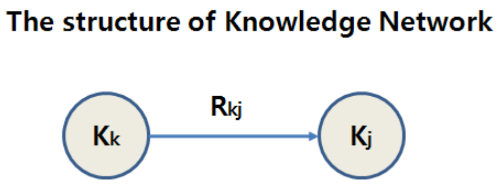

Fig. 6 The basic frame of knowledge network node and knowledge network

Knowledge node, K_j represents jth knowledge node. One knowledge node is connected to the other knowledge nodes with relational strengths. Relational strength, R_{jk},represents association degree between two nodes. The knowledge network is stored in the memory in a form of knowledge associative list[3].

$$R^i_{jk} = P(K^i_k | K^i_j) \tag{1}$$

3.3 Conditioning Mechanism in DTAM

In this system, DTAM(Dynamic Thinking Association Map) is designed for implementing Conditioned Reaction. Conceptual thinking association makes DTAM by repeated process of conditioned learning. As a Thinking activity is repeated, the new conceptual association is created and its Thinking relational strength gets high. Thinking Relational strength,T_{qs}, is calculated by equation (2).

$$T_{qs} = \frac{\sum C_{qs}}{\sum n_q + \sum n_s} \tag{2}$$

where C_{qs} is a number of Conceptual thinking association between knowledge node K_{pq} and K_{rs} and n_q, n_s is the referred number of knowledge node K_{pq} and K_{rs} respectively .

Given Firing threshold,θ, associative activating status,a_i, is determined by equation(3).

$$a_i = \begin{cases} 1 & \text{if } T_{qs} > \theta \\ 0 & \text{otherwise} \end{cases} \tag{3}$$

3.4 Thinking chain extraction from Knowledge Network using DTAM

Using Conditioning Thinking association on DTAM, the system extracts Thinking chains from Knowledge Network. If the activation status is on, the system finds the related knowledge node and from these nodes it starts to extract the connected knowledge fragments from the knowledge associative list. The knowledge fragments extracting algorithm is as follows:

Algorithm 1 : Knowledge Fragments Extraction

** Search DTAM*
STEP1 : If(activate status = on)
STEP2 : Put the related nodes to queue;
STEP3 : while(queue != Empty) do
begin
Take out node.
** Extract the related Knowledge Fragments from knowledge associative list.*
STEP4 : Search the matched knowledge node with the Keyword in knowledge associative list.
STEP5 : while(found != true) do
begin
Attach the extracted knowledge network to the starting node;
node = node-next;
end
end
STEP6 : Output the concatenated knowledge Fragments.
STEP7 : Stop.

If there are branches in knowledge network, several paths of knowledge fragments are extracted. We define this knowledge fragment as Thinking chain. For the decision making process, the efficient selection process is needed for choosing the best matching knowledge path. The selection process has two steps: First step is filtering the path by the threshold of Relational strength. In this step the connected path which has the relational strength greater than threshold value. The next step is to select the best matching path by Maximum Likelihood method.

$$K_B = argmax_v P(v) \prod_i P(K_i|v) \tag{4}$$

4. EXPERIMENTS

We apply Conditioning process to the example of virtual memory as following Figure 7. In the example, there is no conceptual relation between K_1 and E node in the initial state, but the new association in DTAM was made by Conditioning process. As shown in figure 8, when input data stimulates E node in the initial state,there is no reaction because there are no related knowledge node to node E. But in the case of DTAM=active, E-K1 pair is formed and K1 node is activated. Then the system starts to extract the connected knowledge nodes with node K1.

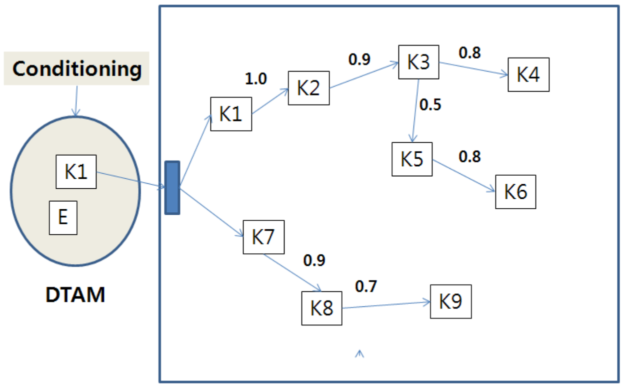

Fig. 7 Example of virtual memory:Initial state

K_1	1.0	K_2
K_2	0.9	K_3
K_3	0.8	K_4
K_4	1.0	Null
K_3	0.5	K_5
K_5	0.8	K_6
K_6	1.0	Null
K_7	0.9	K_8
K_8	0.7	K_9
K_9	1.0	Null

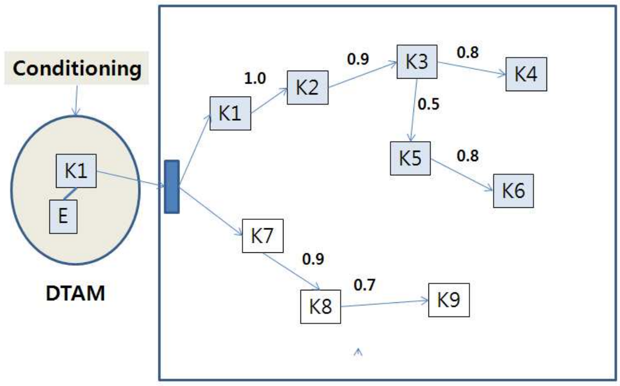

Fig. 8 The activation of Knowledge Network: After conditioning

In the experiments, the new creating process of Thinking Chain and DTAM made by conditioned Learning module was shown. The conditioning mechanism can be usefully used for reasoning process, conceptual dependency and data extraction. Like a main function of amygdala in human brain, the concept of knowledge association including emotional factor can be designed and implemented naturally in the future work. This system also can be applied to construct core brain like frame of Intelligent System.

```
Conditioning test...
DTAM? N
STIMULUS?E
DTAM = not active

No Reaction.

Conditioning test...
DTAM? Y
STIMULUS?E
DTAM = active

Knowledge extraction...

K1 1.0 K2 0.9 K3 0.8 K4 1.0 NULL
K1 1.0 K2 0.9 K3 0.5 K5 0.8 K6 1.0 NULL
```

Fig. 9 DTAM test

5. CONCLUSION

As a Thinking Association system by conditioning mechanism, DTAM was designed for representing internal conceptual association. Based on DTAM the system extracts the related thinking chains from the Knowledge network. The knowledge extracting process is made in various ways of level extraction by threshold. It means that this system can control the depth of Knowledge extraction by threshold values. As a results of experiments, we could find that the extracted knowledge fragments were successfully obtained in the different conditions. This system can be applied to construct core brain like frame of Intelligent System.

REFERENCES

[1] Jean-Marc Fellous, Michael A. Arbib, **Who needs Emotions?** Oxford University press,2005.

[2] LeDoux,J.E., **Brain mechanisms of emotion and emotional learning** Current Opinion in neurobiology,2,191-197,1992.

[3] JeongYon Shim, **Knowledge Network Management System with medicine Self Repairing strategy** ICES2007,LNCS4684,pp119-128,Springer Verlag,Berlin Heidelberg2007.

[4] JeongYon Shim, **The design of Self Internal Entropy Balancing System with Incarnation process** LSMS2007,LNCS4688,pp55-62,Springer Verlag,Berlin Heidelberg2007.

[5] JeongYon Shim, **Intelligent capsule Design for the multi functional aspects** LSMS2007,LNCS4688,pp719-725,Springer Verlag,Berlin Heidelberg2007.

[6] E. Bruce Goldstein, **Sensation and Perception** Fifth edition,Brooks/Cole Publishing Company,1999.

[7] Michael A. Arbib, Jeffrey S. Grethe, **Computing the brain : A guide to Neuroinformatics** Academic Press,2001.

[8] Ning Zhong, Jiming Liu, **Intelligent Technologies for Information Analysis** Springer,2004.

[9] Paol Giudici, **Applied Data Mining : Statistical Method for Bussiness and Industry** Wiley 2003.

[10] Daniel L. Schacter, Elaine Scarry, **Memory, Brain, and Belief** Harvard University Press, Cambridge, Massachusetts, London/2000.

[11] Luc De Raedt Arno Siebes, **Principles of Data Mining and Knowledge Discovery** Springer 2001.

[12] Ian Cloete and Kacek M. Zurada, **Knowledge Based Neuro Computing** MIT press 2000.

[13] Canteras,N.S., Swanson, L.W. **Projection of the ventral subiculum to the amygdala, septum, and hypothalamus: A PHAL anterograde tract-tracing study in the rat.** Journal of Comparative Neurology,1992.

[14] Kim,J.J,Fenselow,M.S. **Modality-specific retrograde amnesia of fear** Science,256,675-677, 1992.

[15] Maren,S.,Aharonov,G., Fenselow, M.S. **Neurotoxic lesions of the doesal hippocampus and pavlovian fear conditioning in rats** Behavioural Brain Research,1997.

[16] Phillips,R.G, LeDoux, J. E, **Differential contribution of the amygdala and hippocampus to cued and contextual fear conditioning** Behavioural Neuro Science,1992.

Application of Neuro-Fuzzy PID Controller for Post Chlorine Process

Ho-Hyun Lee[1], Chang-Mok Oh[2], Ju-Jang Lee[2], An-Kyu Lee[3], and Dong-Hoon Lee[3]

[1]*Robotics Program, Korea Advanced Institute of Science and Technology, Daejeon, Korea*
(Tel : +82-42-350-8032; E-mail: lhh72@kaist.ac.kr)
[2]*Electrical Engineering and Computer Science, Korea Advanced Institute of Science and Technology, Daejeon, Korea*
(Tel : +82-42-350-5432; E-mail: cmoh@kaist.ac.kr , jjlee@ee.kaist.ac.kr)
[3]*Cheoung-choung Regional Head Office, Korea Water Resources Corporation, Daejeon, Korea*
(Tel : +82-41-629-4224; E-mail: finger@kwater.or.kr , dhhero@kwater.or.kr)

Abstract: Drinking water can be contaminated by microorganisms which can be re-grown in case of not controlling chlorine concentration well in water treatment plant (hereafter WTP). It can be harmful to public health. Most WTPs have used chlorine as disinfectant. It can be used in pre-chlorination, post-chlorination and re-chlorination. In post-chlorination, it is injected after filtration to keep residual chlorine from being contaminated by microorganisms. Post-chlorine process without re-chlorination is directly serviced to citizens. If the concentration is low, drinking water can be contaminated by bacterial re-growth. On the other hand, the high chlorine can lead to customer complaints about taste and odor. Therefore, it is necessary to predict chlorine decay in clear well to maintain desired chlorine levels. In this paper, it is shown that artificial neuro-fuzzy inference system could be used to model chlorine decay in the process and control residual chlorine better than present controller, in which cascade control is considered to compensate the error in the output.

Keywords: Post-chlorination, Neuro-Fuzzy inference system, Chlorine decay

I. INTRODUCTION

A major objective of drinking water treatment is to provide microbiologically safe drinking water. Water contaminated by microorganisms can be a major risk to public health. Chlorine is the most commonly used disinfectant due to its ease of application and monitoring, its low cost and its effectiveness in killing bacteria [1–3].

Usually, chlorine dosing rate is determined by operator by monitoring input and output chlorine rate in WTP. However, it is hard to concentrate on the process all day long among many processes and the rate is usually fixed, which doesn't guarantee the output chlorine to be as we wish. Therefore, it is necessary to predict the proper rate based on reliable data to ensure pleasant drinking water.

The simplest model for chlorine decay is the first order decay model in which the chlorine concentration is assumed to decay exponentially [4–6] and for a given initial concentration and temperature, the first order model can provide a fair approximation. The difficult problems are to decide the decay constant and carry out many experiments that can vary with the quality of the source water, the water temperature, the Reynolds number and the material properties. These kinds of works are based on a high level of knowledge of the chlorination process. First order decay with respect to chlorine [7] :

$$dC/dt = -kC \text{ or } C_t = C_0 \exp(-kt) \qquad (1)$$

Where k is the first order decay constant.

As an alternative, statistical models can be used. Unlike first order decay model, it is not necessary to decide the constant and take experiment. Instead, it requires much reliable data stored in a database to predict residual chlorine. The development of statistically based models for disinfection control purposes is proper in cases where parameter estimation within the process-based model is imprecise or difficult to obtain [8] or where the data required for the development of first order models are not available. This data driven method doesn't require a prior knowledge of chemistry and mathematics related to residual chlorine [9]. It is very important to find related variables to predict residual concentration well. Most WTPs are computerized to monitor and control their processes and then to accumulate huge amounts of data in hard disk drives. These large amounts of data can be used to analyze chlorine decay and to determine proper injection rate. The following figure demonstrates water treatment plant and detailed post-chlorination process.

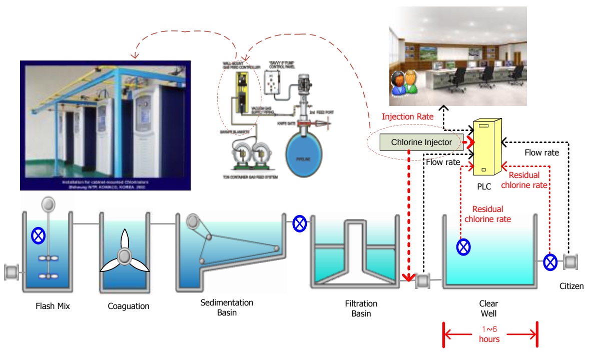

Fig. 1. Conventional Water Treatment Process

II. CASE STUDY

1. Object WTP

The case study considers chlorine decay and residuals in the Cheonan WTP, Cheonan, Korea. This treatment has a capacity of 414,000 m^3/day and has served citizens living in North Cheoung-cheong province since December, 2003.

2. Research Procedure

The most important item in controlling post-chlorine is to model travel time as accurately as possible and to know the decay according to time. If chlorine decay is predicted, it is easy for the controller to decide desired input chlorine. In the following figure, design procedure is introduced.

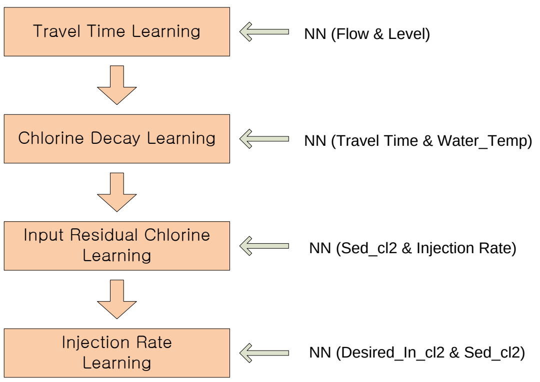

Fig. 2. Design Procedure

3. Comparison of Learning Algorithm

There are many learning algorithms which can predict output according to states. Applied algorithm is selected considering error and easy implementation. Test result is as follows:

Table 1 Comparison of Learning Algorithm

	NN(BP)		ANFIS		LR		SVR	
APE (%)	Trn.	Chk.	Trn.	Chk.	Trn.	Chk.	Trn.	Chk.
	7.24	8.35	7.84	8.13	8.15	8.79	8.59	8.41

As a result, neural network (back propagation) has the best result only in training data but its check data isn't best. It appears slightly over fitted. ANFIS has better result in training data compared to LR and SVR, and its check data has the best result. Also, ANFIS with fuzzy C-means clustering can reduce the number of rules which make implementation easier. Thus, ANFIS is selected as modeling algorithm for the process.

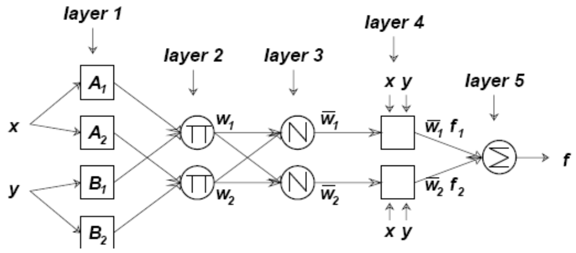

Fig. 3. ANFIS Structure

Layer 1 : Create fuzzy set with proper function

$$O_i^1 = \mu A_i(x) \tag{2}$$

$$\mu A_i(x) = 1/\left\{1 + \left(\frac{x-c_i}{a_i}\right)^{2b_i}\right\} \tag{3}$$

Layer 2: Multiply the incoming signals and send the product out.

$$w_i = \mu A_i(x) \times \mu B_i(y), i = 1, 2 \tag{4}$$

Layer 3: Normalize the weight

$$\bar{w}_i = \frac{w_i}{w_1 + w_2} \tag{5}$$

Layer 4: Compute the result of each node

$$O_i^4 = \bar{w}_i\,(p_i x + q_i y + r_i) \tag{6}$$

Layer 5: Compute the overall output as the summation of all incoming signals

$$O_i^5 = \text{overall output} = \sum_i \bar{w}_i \times f_i = \frac{\sum_i w_i \times f_i}{\sum_i w_i} \tag{7}$$

The premise $[a_i, b_i, c_i]$ and the consequent parameters $[p_i, q_i, r_i]$ can be chosen to minimize the following sum of squared error by least square estimate [10].

$$\boldsymbol{E} = \sum_{m=1}^{N} (\mathbf{T_m} - \mathbf{O_m})^2 \tag{8}$$

III. RESULTS

1. Simulation

The following figure is the proposed structure to model and control post-chlorination process.

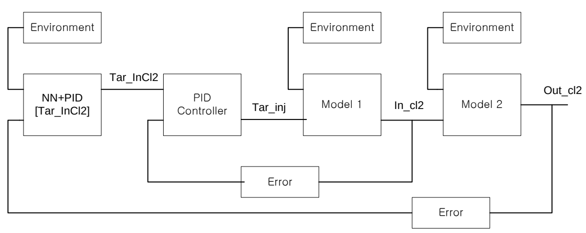

Fig. 4. Modeling and Controller

At first, its variables are chosen by the use of correlation coefficient and prominent component analysis. All of modeling is based on neuro-fuzzy inference system. If the system gives desired input according to states, PID controller try to get rid of its error. Other PID controller is used for cascade control, because this process has very long delay time. The result of simulation is as follow.

A. Modeling

- Estimate of travel time

Table 2 Error according to Selected Variables

Variables	APE
Level, Out_flow, Travel Time(n-1)	9.1%
Level, Out_flow, Level_dot	9.2%
Level, Out_flow, Out_flow_dot	9.6%
Level, Fil_flow, Out_flow	8.1%

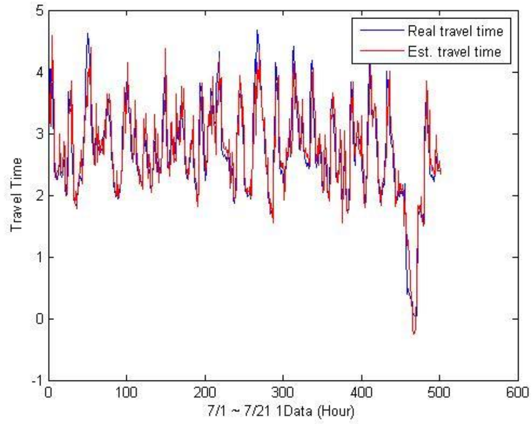

Fig. 5. Estimate Result of Travel Time

- Estimate of Out_cl2

Table 3 Error according to Selected Variables

Variables	APE
In_cl2, Travel time	2.21%
In_cl2, Travel time, Water temp	2.16%

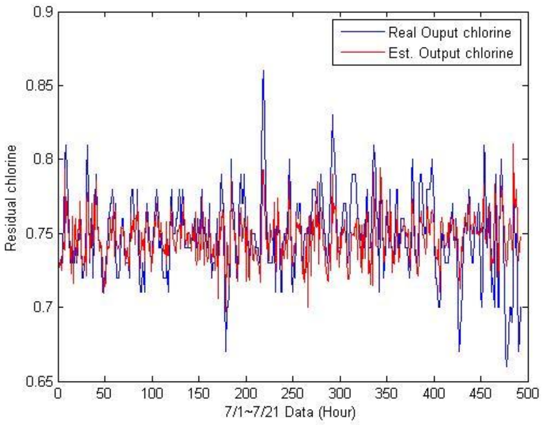

Fig. 6. Estimate Result of Output Chlorine

B. Controller

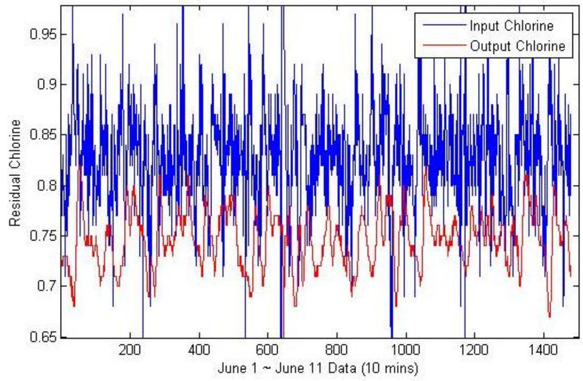

Fig. 7 Old Controller

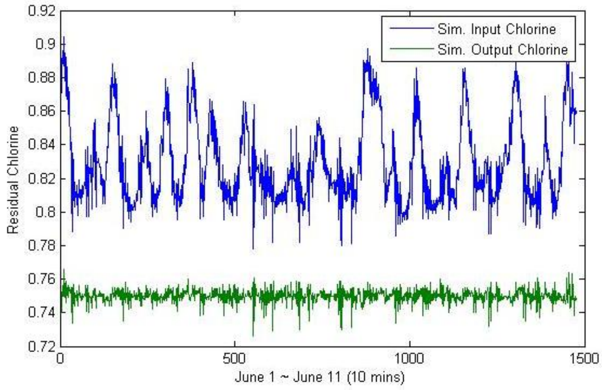

Fig. 8. New NF+PID Controller

Table 4 Comparison of Controller

Old Controller		New Controller	
Mean	STDEV	Mean	STDEV
0.746	0.0286	0.75	0.0038

C. Simulation result

Given the above figures, the output chlorine by old controller varies from 0.66mg/L to 0.82mg/L but new controller ranges from 0.723mg/L to 0.766mg/L. The major difference is whether travel time is fixed or not. While input of old controller is not changed a lot, neuro-fuzzy system helps to calculate the desired input chlorine in real time. Additionally, PID controller would help to keep the desired output chlorine by controlling the offset.

2. Experiment

Control input given by neuro-fuzzy system was given from Sep 18 11:40 to Sep 19 01:00. Its output result would be affected 3 hours later owing to its delay at that time. Then, its real result is from Sep 18 14:40 to Sep 19 04:00. Before new input was given, sedimentation chlorine became fixed not to affect the output, and delay time became shorter from 30 to 5 minutes to get quick feedback. The experiment could be divided into 3 sections, which are before experiment, during experiment and after experiment.

- Before experiment : Delay time =30min, Gain=0.5, Sedimentation chlorine considered.
- During experiment: New input by neuro-fuzzy, Delay time =5min, Gain=0.5, Sedimentation chlorine not considered.
- After experiment: Delay time =5min, Gain=0.5, Sedimentation chlorine considered.

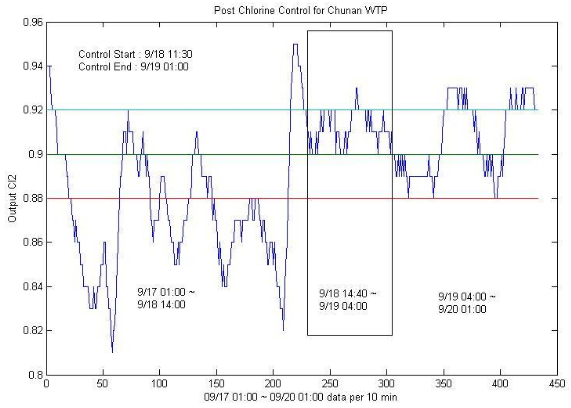

Fig. 9 Experiment result

Table 5 Experiment Result

Before Exp.		During Exp.		After Exp.	
Mean	STDEV	Mean	STDEV	Mean	STDEV
0.875	0.029	0.912	0.008	0.907	0.016

A. Experiment result

In the "before experiment" section, its outputs are deviated because it doesn't consider travel time and sedimentation chlorine. In "During experiment," new desired input chlorine is set according to its travel time and most output data are located from 0.90 to 0.92mg/L. It looks well controlled. Besides, the mean of "during experiment" has an error from its desired output 0.9mg/L. The result is that training data set is considered until August 23th and its environment is changed a little. To compensate for this, the following equation would be applied to desired input chlorine as a bias.

$$Bias = 1/\mathrm{n}\sum_{i=1}^{n} (Des\_Out\_cl2_i - Out\_cl2_i) \quad (9)$$

Output chlorine rates are expected to move around its desired output.

IV. CONCLUSION

Present chlorine controller doesn't consider travel time in real time until now, which usually relies on operator's experience. It is supposed to be difficult to change it in real time. Here, travel time is calculated by neuro-fuzzy inference system. Even though it has some errors, output chlorine becomes much better than before. Its boundary becomes much shorter. It is expected to help to drink water with more pleasant characteristics.

REFERENCES

[1] V.K. Chambers, J.D. Creasey, J.S. Joy, Modeling free and total chlorine decay in potable water distribution-systems, Journal of Water Supply Research and Technology—Aqua 44 (2) (1995) 60–69.
[2] F. Hua, J.R. West, R.A. Barker, C.F. Forster, Modeling of chlorine decay in municipal water supplies, Water Research 33 (12) (1999) 2735–2746.
[3] L. Kiene, W. Lu, Y. Levi, Relative importance of the phenomena responsible for chlorine decay in drinking water distribution systems, Water Science and Technology 38 (6) (1998) 219–227.
[4] Jadas-HeÂ cart A., Morer A., Stitou A. and Bouillot P.(1992) The chlorine demand of a treated water. WaterRes. 26, 1073-1084.
[5] Zhang G.R., Kiene L., Wable O., Chan U.S. and Duguet J.P. (1992) Modelling of chlorine residual in the water distribution network of Macao. Environ. Technol. 13, 937-946.
[6] Rossman L.A., Clark R.M. and Grayman W.M. (1994) Modeling chlorine residual in drinking water distribution systems. J. Environ. Eng. 120, 803-820.
[7] N.B. Hallam, J.R. West, C.F. Foster, J.C Powell, I. Spencer : The decay of chlorine associated with the pipe wall in water distribution system, Water Research 36(2002) 3479-3488.
[8] M.J. Rodriguez, J.R. West, J. Powell, J.B. Serodes, Application of two approaches to model chlorine residuals in Severn Trent Water Ltd(STW) distribution systems, Water Science and Technology 36 (5) (1997) 317–324.
[9] J.B. Serodes, M.J. Rodriguez, A. Ponton, Chlorcastc : A methodology for developing decision-making tools for chlorine disinfection control, Environmental Modelling & Software 16 (1) (2001) 53–62.
[10] Jyh-Shing Roger Jang, Chuen-Tsai Sun and Eiji Mizutani. "A Computational Approach to Learning and Machine Intelligence. Prentice-Hall, 1997.

The Fifteenth International Symposium on Artificial Life and Robotics 2010 (AROB 15th '10),
B-Con Plaza, Beppu,Oita, Japan, February 4-6, 2010

Face image make up system by using ε-filter

M. Yoshioka, S. Omatu and H. Yanagimoto
Osaka Pref. Univ., Sakai, Osaka 599-8531, Japan

Abstract

Recently, it becomes easy for consumers to make up face images in photographs for special events through the spread of digital cameras and photo editing tools. However, it is still difficult to make up spots and wrinkles naturally. In order to solve these problems, many artificial make up systems have been proposed. One of these methods using filter has good performance. However, this method requires many parameter tunings for achieving good performance. In order to improve these points, we have developed auto parameter tuning system by using templates. As the result of simulations, it is proved that the proposed method has good performance with auto tuned parameters.

1 Introduction

In late years, it becomes easy for consumers who are not familiar with optical equipments and image editing on computers to make up face images in photographs for special events through the spread of easy-to-use digital cameras and photo editing tools. However, it is still difficult to clean up spots and wrinkles without artificiality because the excess face image smoothing breaks natural face texture. In order to solve these problems, many artificial make up systems based on signal processing methods have been proposed. One of these methods using -filters [1, 2, 3] and its filter banks [4] has good performance. However, this method requires many parameter optimization for achieving good performance. Therefore, it is not easy for users unfamiliar with signal processing technology to obtain good quality images. In order to improve these points, we have developed auto parameter tuning system by using ellipse templates for spots and line segments for wrinkles. As the result of simulations, it is proved that the proposed method has good performance with automatically optimized parameters.

2 Traditional method

In order to develop face image make up system, many methods have been proposed. In this paper, we have adopted the method using - filter as the basis. In this method, input face images are separated into some signal components in frequency domain and the components which include wrinkles and spots are eliminated. The overview about the -filter and its filter bank are as follows.

2.1 -filter

The -filter is one of nonlinear filters, which is defined by following equations.

$$y(n) = x(n) + \sum_{i=\ N}^{N} a_i F(x(n+i) \quad x(n)) \tag{1}$$

$$F(x) = \begin{cases} x & \le x \le \\ 0 & other \end{cases} \tag{2}$$

where, $x(n)$, $y(n)$ are input and output signals, a_i are filter coefficients whose summation becomes 1, $2N+1$ is corresponding to the filter window size. By using this filter in the image processing, noise in the image is removed with preserving edges.

2.2 -filter bank

The filter bank [5] for face image make up system is composed of the above filters(Fig.1). The filter bank divides input signals into some components(Fig.2). In this figure, $_1$, $_2$, and $_3$ are the parameters used in the filter E_1, E_2 and E_3 respectively , and f_1 and f_2 are correspoinding to the window sizes used in the filter E_0 and E_1. In the divided components, the signal y_3 which has middle frequecy and small amplitude and y_4 which has high frequeny and middle amplitude mainly contain spots and wrinkles respectively. By eliminating these two components and combining remaining components, the clean face image is obtained without wrinkles and spots.

The Fifteenth International Symposium on Artificial Life and Robotics 2010 (AROB 15th '10),
B-Con Plaza, Beppu,Oita, Japan, February 4-6, 2010

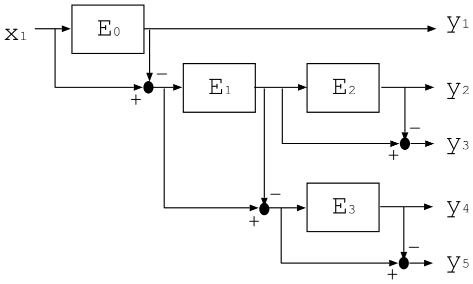

Figure 1: -filter bank

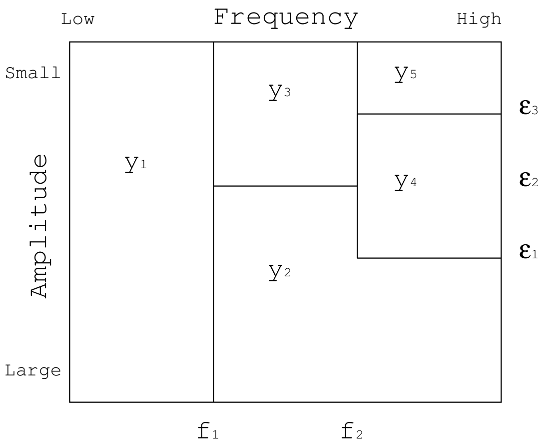

Figure 2: Separated Components

2.3 Examples

The result image where wrinkles and spots are eliminated from the original image shown in Fig.3 by the filter bank mentioned above is shown in Fig.4. The result image shows that the spot beneath the eye in the original image clearly disappears. Fig.5,6 show extracted components y_3, y_4 respectively.

2.4 Difficulty in traditional method

The effectiveness of face image make up system using -filter is obvious from the above example. However, there is the difficulty to put in practice because the filter bank has many parameters to be optimized for achieving best performance. These parameters are N_1, N_2, $_1$, $_2$ and $_3$. The parameter N_1 and $_2$ are corresponding to spot regions, and N_1, $_1$ and $_3$ are corresponding to wrinkle regions respectively. In the above example, these parameters are manually optimized. However, it is not easy for users who are not familiar with -filter to optimize those. In order to overcome this point, we have proposed the automatic parameter optimization as mentioned in following section.

Figure 3: Face image 1.

Figure 4: Simulation result 1(Manual).

3 Proposed method

In order to solve the parameter optimization problem in the traditional method, we propose new method for automatic parameter optimization. Our proposed method is composed of two parts. As the first part, we propose the parameter optimization corresponding to spot regions and the second part is the method for wrinkle regions.

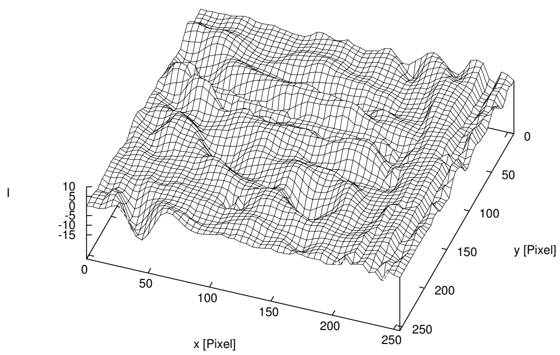

Figure 5: Component y3.

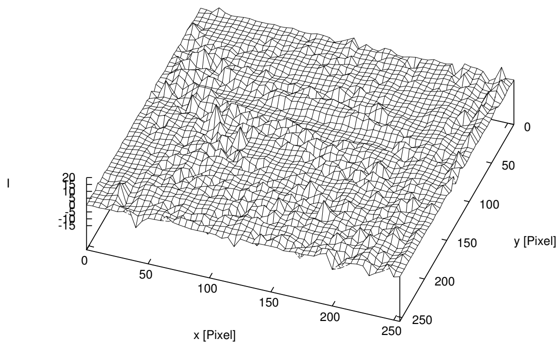

Figure 6: Component y4.

3.1 Spot region

Spot regions, for example shown in Fig.3, are approximated by ellipses defined by the equation 3.

$$E = \sum_{x\ y \in S_1} (I(x\ y) \quad (a(x \quad x_1)^2 + b(x \quad x_1)(y \quad y_1) + c(y \quad y_1)^2 + d))^2 \qquad (3)$$

where $I(x\ y)$ denotes the intensity of face image at point (x,y), a,b,c,d denote ellipse parameters, the region S_1 denotes spot respectively. As result of this approximation, the parameter N_1 and $_2$ are determined as the diameter of the ellipse and the intensity difference between the center and the edge of ellipse. In this method, the approximate position of the ellipse is required for efficient fitting. Therefore, users need to select the spots which should be cleaned up. This additional procedure is cumbersome for users. However, the completele automation in the face image make up is impractical because the spots which shoud be cleaned up are variant depending on the users and their situations. This is also applicable in the next wrinkle elimination.

Table 1: Filter parameters.

Sim No.	N_1	N_2	$_1$	$_2$	$_3$
1(Manual)	31	7	25	20	7
1(Auto)	50	10	14	26	7
2	42	6	6	23	3

3.2 Wrinkle region

As the second part of our proposed method, the parameters N_2, $_1$, $_3$ corresponding to wrinkles are determined. Wrinkles are approximated by line segments which are determined by users' giving start and end points. Along the approximated line segment, the face image has the valley of intensity which is the wrinkle. Along this line segment, image intensities are accumulated and the averages of intensities on the opposite side of the valley are used to reduce noise influence, and the accumulated intensity histogram becomes the monotonically increasing function from the bottom of intensity to the outer side. For example, the intensity histogram of the wrinkle beneath the left eye in the face image 1 (Fig.3) is shown in Fig.7. By using the intensity difference between the first peak and bottom in the above function, and the width of valley, $_1$ and N_2 are determined respectively. Finally, $_3$ is set at the half of $_1$ empirically.

4 Simulation

In order to confirm effectiveness of our proposed method, the method is applied to sample face images shown in Fig.3,9. Result images are shown in Fig.8,10 and optimized parameters are shown in Table 1. Simulation results show effectiveness of our proposed method. In order to remove remaining spots in Fig.10, finer segmentation in frequency domain is needed to eliminate signal components which include only spots by adding more -filters to the filter bank.

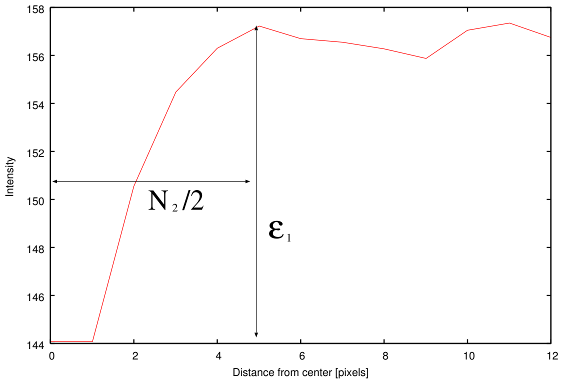

Figure 7: Intensity histogram.

Figure 8: Simulation result 1.

5 Conclusions

We have proposed the face image make up system using -filter and their parameters optimization. Simulation results show the effectiveness of our proposed method. As the future work, we consider about finer segmentation of input face images in frequency domain for strict spots and wrinkles elimination.

Figure 9: Face image 2.

Figure 10: Simulation result 2.

References

[1] K.Arakawa, H.Watabe and Y.Arakawa, "Nonlinear digital filter for beautifying facial images," J.Three Dimensional Images, vol.13, no.3, pp.41-46, Sept., 1999.

[2] H. Watanabe, K. Arakawa, and Y. Arakawa, "Nonlinear inverse filter using -filter and its application to image restoration," IEICE Trans., vol.E83-A, no.2, pp.283-290, Feb. 2000.

[3] K. Arakawa, K. Matsuura, H. Watanabe, and Y. Arakawa, "A method of noise reduction for speech signals using component separating -filters," IEICE Trans., vol.J85-A, no.10, pp.1059-1069, Oct. 2002.

[4] M.Vetterli and C.Herley, "Wavelts and filter banks: Theory and design," IEEE Trnas. Signal Process., vol.40, no.9, pp.2207-2232, 1992.

[5] P.P.Vaidyanathan, "Multirate Systems and Filter Banks," Prentice-Hall, Englewood Cliffs, 1993.

The Fifteenth International Symposium on Artificial Life and Robotics 2010 (AROB 15th '10),
B-Con Plaza, Beppu,Oita, Japan, February 4-6, 2010

Image Segmentation Using Probability Density Estimation

Kouki Imgauma, Michifumi Yoshioka, Shigeru Omatu and Hidekazu Yanagimoto
Computer and Systems Sciences, Graduate School of Engineering,
Osaka Prefecture University, 1-1 Gakuen-cho, Sakai City, 599-8531
imaguma@cs.osakafu-u.ac.jp

Abstract

The image recognition is an important technology for analyzing the content from the image data. As the basic process, it is necessary to do image segmentation for the image recognition. Human-beings unconsciously does this process, but it is difficult for the computer. To improve the accuracy of the image recognition, an optimal region segmentation technique is needed. In this paper, we propose a new region segmentation technique. To reflect human-beings' sensory perception, we use the HSI color space. And we consider the HSI histograms to be the probability density function. We approximate the probability density function by using the HSI histogram and kernel density estimation for clustering. At last, we superimpose those results and obtain the final output. As the result of the simulation, the effectiveness of our proposed method is confirmed.

Keywords: Image Segmentation, HSI color space, kernel density estimation

1 Introduction

In recent years, a huge amount of image data has been accumulated in the computer by a rapid spread of the digital camera and the Internet. There are systems which retrieve the images according to the keyword from image database. To search an image data by keyword, the correspondence of between the keyword and the image data have to be correct. Human-beings can add proper information to image data. However, for enormous image data, the work is difficult only by human power. Thus, the technology of the image recognition with the computer is necessary.

The image recognition system extracts the outline of the objects to separate from background, and analyzes what the object is. Human-beings unconsciously does this process. However, it is difficult and complex for the computer. Therefore, to improve the accuracy of the image recognition, an optimal region segmentation technique is important. The recognition system equal to by human-beings is preferable. Therefore, to obtain optimal region segmentation, human-like quality is requested.

Here, we introduce some clustering methods of the region segmentation. K-means algorithm is a famous clustering method. However, there is a problem that it is necessary to give a number of clusters and center values of initial clusters beforehand. Then we can not automatically obtain the optimal number of clusters. By using ISODATA method, we can decide an effective number of clusters automatically within the range from half to twice of selected number of clusters. However, to use this method, we have to decide not only initial clusters but also many parameters beforehand.

In this paper, we propose a new image segmentation technique for solving these problems. We expect that the optimal image segmentation can be obtained by reflecting human-beings' sensory perception to the computer. To use human-beings' sensory perception, we converted the RGB color space into the HSI color space. In considering the probability density function of HSI histograms, we find characteristics of the image. The probability density function is approximated by using the HSI histogram and the kernel density estimation. We divide the cluster of hue, saturation and intensity based on the probability density function. And we superimpose three division result, we can obtain the final output. As a result of the comparison with the conventional method, the effectiveness of the proposal method is confirmed. The comparison image is an result by the method[1]. The image which we used is the global standard images

2 Image segmentation method

This chapter introduces the process of the proposal method for image segmentation. We write down about a flow of the proposal method here.

Step.1: Convert the RGB color space to the HSI color space.
Step.2: By using kernel density estimation, get smooth approximation of the probability

density function.

Step.3: Get borders of characteristic from each histogram and divide regions.

Step.4: Superimpose divided regions.

Step.5: Reduce some small regions and obtain the final output.

In the following descriptions, we introduce the details of each step.

Figure 1: Input image "**Pepper** "

2.1 The HSI color space

K-means method is used as clustering technique for the image segmentation. In many case this method uses the RBG color space. But when we judge the difference of similar colors, we do not always accord with Euclid distance of the colors. We adopt the HSI color space. The HSI color space is near to human-beings' sensory perception. We adopt the HSI6 pyramid color model in conversion equation from the RBG color space[2] to the HSI color space.

$$I = \max(r, g, b) \tag{1}$$

$$S = \frac{I - \min(r, g, b)}{I} \tag{2}$$

$$H = \begin{cases} 60(1 + b - g) & \cdots \quad (if \quad r = I) \\ 60(3 + r - b) & \cdots \quad (if \quad g = I) \\ 60(5 + g - r) & \cdots \quad (if \quad b = I) \end{cases} \tag{3}$$

where r, g, and b are the normalized values of R, G and B. The range of the each H, S and I becomes $0 \leq H \leq 360$, $0 \leq S \leq 1.0$ and $0 \leq I \leq 1.0$ respectively. The HSI color space has high independence nature of each attribute in comparison with RGB color space. The following figures are histograms of saturation and hue.

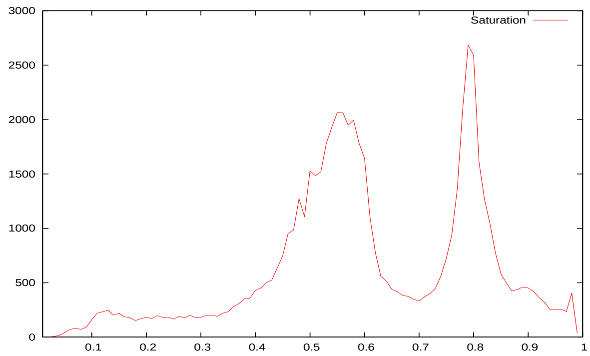

Figure 3: Saturation histogram

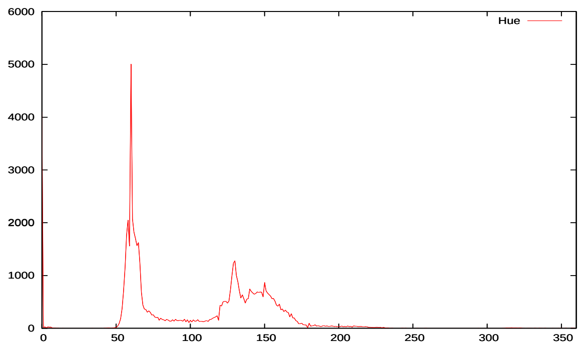

Figure 4: Hue histogram

2.2 Kernel Density Estimation

Like **Figure 3**, obtained histograms have a lot of ups and downs. When we consider such histograms in the probability density function, it is difficult to find the optimal border of clusters. To find the optimal border of clusters and to approximate the probability density function, we use kernel density estimation. This technique performs an approximation of the probability density function by the following equation from obtained data.

$$p(x) = \frac{1}{2nh} \sum_{i=1}^{n} K\left(\frac{x - x_i}{h}\right) \tag{4}$$

where $p(x)$, n, h and K are the probability density function, data, band width and kernel function respectively. To get more smooth approximation, we use the variable kernel density estimation. This technique uses neighboring density of each data point to obtain a smooth approximation. Thus, this technique uses a different value for band width corresponding to each data point. In the following, we show the equations of the band width and the probability density function finding again.

$$h_i = \frac{c}{\sqrt{p(x_i)}} \tag{5}$$

$$\tilde{p}(x) = \frac{1}{2n}\sum_{i=1}^{n}\frac{1}{h_i}K\left(\frac{x-x_i}{h_i}\right) \tag{6}$$

where $\tilde{p}(x)$ is the new probability density function. Here, h=2, c=1. The histogram of hue is extreme in comparison with the histograms of saturation and intensity. Thus, this work applies to only saturation and intensity.

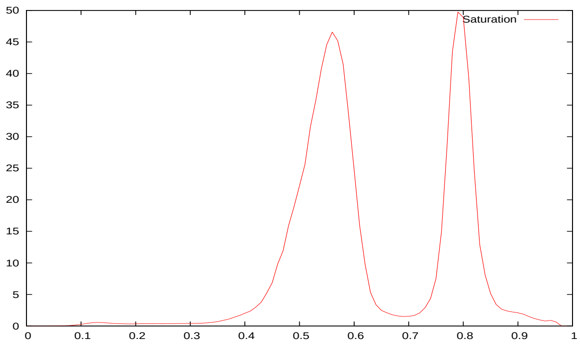

Figure 5: Saturation histogram after kernel density estimation

2.3 Clustering

With each probability density function of obtained hue, saturation and intensity, we divide there regions by using the mode method. This technique is expressed by following inequalities.

$$z_1 < t < z_2 \tag{7}$$

$$\frac{p(t)}{\min\{p(z_1), p(z_2)\}} < \theta_1 \tag{8}$$

where z_1, z_2 are peaks of the histograms. t is a border of clusters. Here, threshold θ_1 is set 0.5. When t is set in the deepest valley between two peaks and holds above inequalities, t is judged as a border.

2.4 Merge region

To obtain the final output, we superimpose results of hue, saturation and intensity. We compare a certain two points and gather it up to one region if they belong to the same cluster in hue, saturation and intensity. If even one is a different cluster among three attributes, it is judged as a different cluster.

2.5 Reduction of small region

We reduce some small region from the obtain region. At first we calculate the mean value of saturation and intensity of every region. We compare each mean value by Euclid distance. If it is smaller than 0.05, we go to the next step. At last, the results of cluster in hue are the same cluster, we superimpose the two regions.

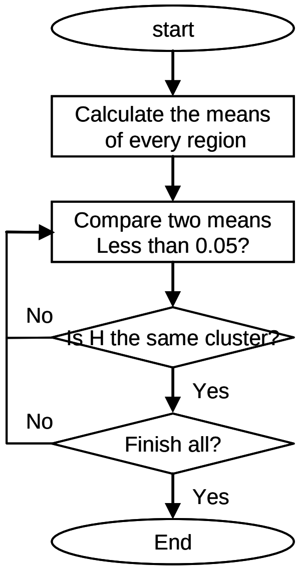

Figure 6: Flow chart of reduction method

4. Results

Figure 7 is a result by the method[1], and **Figure** 8 is a result by the proposal method. As can be seen, proposal method has less number of small regions than conventional method. In the same way, we simulated it about image "Parrots". In comparison with Figure 10, Figure 11 has a clear outline.

Figure 7: Output image by the conventional method

Figure 8: Output image by the proposal method

Figure 9: Input image "Parrots"

Figure 10: Output image by the conventional method

Figure 11: Output image by the proposal method

5 Conclusion

We performed image segmentation which was near to human-beings' sensory perception. In simulation of the image "Pepper", the proposal method reduces some small regions in the object. In simulation of the image "Parrots", the proposal method (see Figure 11) reduces some small regions of the part of the leaf. However, small regions increase in the part of the feather. In the future work, we will try to reduce of small regions more. And the examination of the threshold in mode method is necessary.

Reference

[1] D. Comaniciu and P. Meer, "Mean Shift: A Robust Approach toward Feature Space Abalysis," IEEE Transactions on pattern analysis and machine intelligence, Vol. 24, No. 5, pp. 603-609, 2002

[2] M. Takagi and H. Shimoda, "A Handbook of Image Analysis [Revised Edition]," pp. 1187-1196, University of Tokyo Press, 2004

Particle Swarm Optimization with a Modified Sigmoid Function for Gene Selection from Gene Expression Data

M.S. Mohamad[1,2] S. Omatu[1] S. Deris[2] and M. Yoshioka[1]

[1]*Department of Computer Science and Intelligent Systems, Graduate School of Engineering,*
Osaka Prefecture University, Sakai, Osaka 599-8531, Japan
(Tel : 81-72-254-9278; Fax : 81-72-257-1788)
(mohd.saberi@sig.cs.osakafu-u.ac.jp; omatu@cs.osakafu-u.ac.jp; yoshioka@cs.osakafu-u.ac.jp)

[2]*Department of Software Engineering, Faculty of Computer Science and Information Systems,*
Universiti Teknologi Malaysia, 81310 Skudai, Johore, Malaysia
(Tel : 60-7-553-7784; Fax : 60-7-556-5044)
(safaai@utm.my)

Abstract: In order to select a small subset of informative genes from gene expression data for cancer classification, recently, many researchers are analyzing gene expression data using various computational intelligence methods. However, due to the small number of samples compared to the huge number of genes (high-dimension), irrelevant genes, and noisy genes, many of the computational methods face difficulties to select the small subset. Thus, we propose an enhancement of binary particle swarm optimization to select a small subset of informative genes that is relevant for classifying cancer samples more accurately. In this proposed method, three approaches have been introduced to increase the probability of bits in particle's positions to be zero. By performing experiments on two gene expression data sets, we have found that the performance of the proposed method is superior to previous related works, including the conventional version of binary particle swarm optimization (BPSO) in terms of classification accuracy and the number of selected genes. The proposed method also produces lower running times compared to BPSO.

Keywords: Binary particle swarm optimization, Gene selection, Gene expression data, Cancer classification.

I. INTRODUCTION

Recent advances in microarrays technology allow scientists to measure the expression levels of thousands of genes simultaneously in biological organisms and have made it possible to create databases of cancerous tissues. It finally produces gene expression data that contain useful information of genomic, diagnostic, and prognostic for researchers [1]. Thus, there is a need to select informative genes that contribute to a cancerous state. However, the gene selection process poses a major challenge because of the following characteristics of gene expression data: the huge number of genes compared to the small number of samples (high-dimensional data), irrelevant genes, and noisy data. To overcome this challenge, a gene selection method is usually used to select a subset of informative genes that maximizes classifier's ability to classify samples more accurately [2]. The advantages of gene selection has been reported in Mohamad *et al*. [2].

Recently, several gene selection methods based on particle swarm optimization (PSO) have been proposed to select informative genes from gene expression data [3],[4],[5]. PSO is a new optimization technique proposed by Kennedy and Eberhart [6]. It is motivated from the simulation of social behavior of organisms such as bird flocking and fish schooling. Shen *et al*. [3] have proposed a hybrid of PSO and tabu search approaches for gene selection. However, the results obtained by using the hybrid method are less meaningful since the application of tabu approaches in PSO is unable to search a near-optimal solution in search spaces. Next, an improved binary PSO have been proposed by Chuang *et al*. [4]. This approach produced 100% classification accuracy in many data sets, but it used a high number of selected genes (large gene subset) to achieve the high accuracy. It uses the high number because of the global best particle is reset to zero position when its fitness values do not change after three consecutive iterations. After that, Li *et al*. [5] have introduced a hybrid of PSO and genetic algorithms (GA) for the same purpose. Unfortunately, the accuracy result is still not high and many genes are selected for cancer classification since there are no direct probability relations between GA and PSO. Generally, the PSO-based methods [3],[4],[5] are intractable to efficiently produce a small (near-optimal) subset of informative genes for high classification accuracy. This is mainly because the total number of genes in gene expression data is too large (high-dimensional data).

Therefore, we propose an enhancement of binary PSO (EPSO) to select a small (near-optimal) subset of informative genes that is most relevant for classifying cancer classes more accurately. In order to test the effectiveness of our proposed method, we apply EPSO to two gene expression data sets, including binary-classes and multi-classes data sets.

II. METHODS

2.1. The Conventional Version of Binary PSO (BPSO)

BPSO is initialized with a population of particles. At each iteration, all particles move in a problem space to find the optimal solution. A particle represents a potential solution in an *n*-dimensional space [7]. Each particle has position and velocity vectors for directing its movement. The position vector and velocity vector of the *i*th particle in the *n*-dimension can be represented as $X_i = (x_i^1, x_i^2, ..., x_i^n)$ and $V_i = (v_i^1, v_i^2, ..., v_i^n)$, respectively, where $x_i^d \in \{0,1\}$; *i*=1,2,..*m* (*m* is the total number of particles); and *d*=1,2,..*n* (*n* is the dimension of data). v_i^d is a real number for the *d*-th dimension of the particle *i*, where the maximum v_i^d, $V_{\max} = (1/3) \times n$.

In gene selection, the vector of particle positions is represented by a binary bit string of length *n*, where *n* is the total number of genes. Each position vector (X_i) denotes a gene subset. If the value of the bit is 1, it means that the corresponding gene is selected. Otherwise, the value of 0 means that the corresponding gene is not selected. Each particle in the *t*-th iteration updates its own position and velocity according to the following equations:

$$v_i^d(t+1) = w(t) \times v_i^d(t) + c_1 r_1^d(t) \times (pbest_i^d(t) - x_i^d(t)) + c_2 r_2^d(t) \times (gbest^d(t) - x_i^d(t)) \quad (1)$$

$$Sig(v_i^d(t+1)) = \frac{1}{1+e^{-v_i^d(t+1)}} \quad (2)$$

if $Sig(v_i^d(t+1)) > r_3^d(t)$, then $x_i^d(t+1) = 1$;

else $x_i^d(t+1) = 0$ (3)

where c_1 and c_2 are the acceleration constants in the interval [0,2]. $r_1^d(t), r_2^d(t), r_3^d(t) \sim U(0,1)$ are random values in the range [0,1] that sampled from a uniform distribution. $Pbest_i(t) = (pbest_i^1(t), pbest_i^2(t), ..., pbest_i^n(t))$ and $Gbest(t) = (gbest^1(t), gbest^2(t), ..., gbest^n(t))$ represent the best previous position of the *i*th particle and the global best position of the swarm (all particles), respectively. They are assessed base on a fitness function. $Sig(v_i^d(t+1))$ is a sigmoid function where $Sig(v_i^d(t+1)) \in [0,1]$. $w(t)$ is an inertia weight.

2.2. An Enhancement of Binary PSO (EPSO)

In this article, we propose EPSO for selecting a near-optimal (small) subset of genes. It is proposed to overcome the limitations of BPSO and previous PSO-based methods [3],[4],[5]. EPSO in our work differs from BPSO and the PSO-based methods on three parts: 1) we introduce a scalar quantity that called particles' speed (s); 2) we propose a rule for updating $x_i^d(t+1)$; 3) we modify the existing sigmoid function, whereas BPSO and the PSO-based methods have used the original rule (Eq. 3) and the standard sigmoid function (Eq.2), and no particles' speed implementation. The particles' speed, rule, and sigmoid function are introduced in order to:

- increase the probability of $x_i^d(t+1) = 0$ $(P(x_i^d(t+1) = 0))$.
- reduce the probability of $x_i^d(t+1) = 1$ $(P(x_i^d(t+1) = 1))$.

The increased and decreased probability values cause a small number of genes are selected and grouped into a gene subset. $x_i^d(t+1) = 1$ means that the corresponding gene is selected. Otherwise, $x_i^d(t+1) = 0$ represents that the corresponding gene is not selected.

The particles' speed, rule, and sigmoid function are proposed as follows:

$$s_i(t+1) = w(t) \times s_i(t) + c_1 r_1(t) \times dist(Pbest_i(t) - X_i(t)) + c_2 r_2(t) \times dist(Gbest(t) - X_i(t)) \quad (4)$$

$$Sig(s_i(t+1)) = \frac{1}{1+e^{-5s_i(t+1)}} \quad (5)$$

subject to $s_i(t+1) \geq 0$

if $Sig(s_i(t+1)) > r_3^d(t)$, then $x_i^d(t+1) = 0$;

else $x_i^d(t+1) = 1$ (6)

where $s_i(t+1)$ represents the speed of the particle *i* for the *t*+1 iteration, whereas in BPSO and previous PSO-based methods (Eq. 1, Eq. 2, and Eq. 3), $v_i^d(t+1)$ represents a single element of a particle velocity vector for the particle *i*. In EPSO, Eq. 4, Eq. 5, and Eq. 6 are used to replace Eq. 1, Eq. 2, and Eq. 3, respectively. $s_i(t+1)$ is the rate at which the particle *i* changes its position. The most important property of $s_i(t+1)$ is $s_i(t+1) \geq 0$. Hence, $s_i(t+1)$ is used instead of

$v_i^d(t+1)$ so that its positive value can increase $P(x_i^d(t+1)=0)$. In Mohamad *et al*. [8], there is an explanation on how to calculate the distance between two positions of two particles, e.g., $dist(Gbest(t)-X_i(t))$ in Eq. 4.

Equations (4-6) and $s_i(t) \geq 0$ increase $P(x_i^d(t)=0)$ because the minimum value for $P(x_i^d(t)=0)$ is 0.5 when $s_i(t)=0$ $(\min P(x_i^d(t)=0) \geq 0.5)$. Meanwhile, they decrease the maximum value for $P(x_i^d(t)=1)$ to 0.5 $(\max P(x_i^d(t)=1) \leq 0.5)$. Therefore, if $s_i(t)>0$, then $P(x_i^d(t)=0) >> 0.5$ and $P(x_i^d(t)=1) << 0.5$. For example, the calculations for $P(x_i^d(t)=0)$ and $P(x_i^d(t)=1)$ are shown as follows:

if $s_i(t)=1$, then $P(x_i^d(t)=0)=0.993307$ and $P(x_i^d(t)=1)=1-P(x_i^d(t)=0)=0.006693$.

if $s_i(t)=2$, then $P(x_i^d(t)=0)=0.999955$ and $P(x_i^d(t)=1)=1-P(x_i^d(t)=0)=0.000045$.

A. Fitness functions

The fitness value of a particle (a gene subset) is calculated as follows:

$$fitness(X_i)=w_1 \times A(X_i)+(w_2 \times (n-R(X_i))/n) \qquad (7)$$

in which $A(X_i) \in [0,1]$ is leave-one-out-cross-validation (LOOCV) classification accuracy that uses the only genes in a gene subset (X_i). This accuracy is provided by support vector machine classifiers (SVM). $R(X_i)$ is the number of selected genes in X_i. n is the total number of genes for each sample. w_1 and w_2 are two priority weights corresponding to the importance of accuracy and the number of selected genes, respectively, where $w_1 \in [0.1, 0.9]$ and $w_2 = 1-w_1$.

III. EXPERIMENTS

3.1. Data Sets and Experimental Setup

Two real microarrays data sets are used to evaluate EPSO and BPSO: leukemia cancer and mixed-lineage leukemia (MLL) data sets. The leukemia data set contains the expression levels of 7,129 genes and can be obtained at http://www.broad.mit.edu/cgi-bin/cancer/datasets.cgi. It has two cancer classes: acute lymphoblastic leukemia (ALL) and acute myeloid leukemia (AML). In this data set, bone marrow and blood samples were taken from 72. There are also 72 samples in the MLL cancer data. It has three tumor classes (MLL, ALL, and AML) and can be obtained at http://www.broad.mit.edu/cgi-bin/cancer/datasets.cgi.

In order to avoid selection bias, the implementation of LOOCV is in exactly the same way as did by Chuang *et al*. [4] where the only one cross-validation cycle (outer loop), namely LOOCV is used.

3.2. Experimental Results

Based on the standard deviation of classification accuracy in Table 1, results that produced by EPSO were consistent on all data sets. Interestingly, all runs have achieved 100% LOOCV accuracy with less than 71 selected genes on the Leukemia data set. Over 97% classification accuracies have been obtained on the MLL data set. This means that EPSO has efficiently selected and produced a near-optimal gene subset from high-dimensional data (gene expression data).

According to the Table 2, overall, it is worthwhile to mention that the classification accuracy of EPSO are superior to BPSO in terms of the best, average, and standard deviation results on all the data sets. Moreover, EPSO also produces a smaller number of genes compared to BPSO. The running times of EPSO are lower than BPSO in all the data sets. EPSO can reduce its running times because of the following reasons:

For an objective comparison, we compare our work with previous related works that used PSO-based methods in their proposed methods [3],[4],[5]. It is shown in Table 3. For the leukemia data set, the averages of classification accuracies of our work were higher than the previous works. Our work also have resulted the smaller averages of the number of selected genes on all the data sets compared to the previous works.

Table 1. Experimental results for each run using PSO

Run#	Leukemia #Acc (%)	Leukemia #Selected Genes	MLL #Acc (%)	MLL #Selected Genes
1	100	55	100	131
2	100	65	100	123
3	100	65	100	117
4	100	70	100	113
5	100	51	100	116
6	100	62	100	109
7	100	58	100	116
8	100	61	100	114
9	100	63	100	111
10	100	67	100	111
Average ± S.D.	100 ± 0	61.70 ± 5.72	100 ± 0	116.10 ± 6.56

Note: The result of the best subsets is shown in the shaded cells. It is selected based on the following priority criteria: 1) the highest classification accuracy; 2) the smallest number of selected genes; 3) the lowest running time. #Acc and S.D. denote the classification accuracy and the standard deviation, respectively, whereas #Selected Genes and Run# represent the number of selected genes and a run number, respectively. #Time stands for running time.

Table 2. Comparative experimental results of EPSO and BPSO

Data	Method / Evaluation	EPSO Best	EPSO #Ave	EPSO S.D	BPSO Best	BPSO #Ave	BPSO S.D
Leukemia	#Acc (%)	100	100	0	98.61	98.61	0
	#Genes	51	61.70	5.72	3488	3528.75	26.83
	#Time	7.52	7.46	0.67	261.34	261.41	0.18
MLL	#Acc (%)	100	100	0	95.83	95.83	0
	#Genes	109	116.10	6.56	6101	6153.1	31.62
	#Time	13.51	13.83	0.18	236.759	239.00	1.34

Note: The best result of each data set is shown in the shaded cells. It is selected based on the following priority criteria: 1) the highest classification accuracy; 2) the smallest number of selected genes; 3) the lowest running time.

Table 3. A comparison between our method (EPSO) and previous PSO-based methods

Data	Method / Evaluation	EPSO	IBPSO [4]	PSOTS [3]	PSOGA [5]
Leukemia	#Acc (%)	(100)	100	(98.61)	(95.10)
	#Genes	(61.70)	1034	(7)	(21)
MLL	#Acc (%)	(100)	100	-	-
	#Genes	(116.10)	1292	-	-

Note: The result of the best subsets is shown in the shaded cells. It is selected based on the following priority criteria: 1) the highest classification accuracy; 2) the smallest number of selected genes. '-' means that a result is not reported in the previous related work. A result in '( )' denotes an average result.
IBPSO = An improved binary PSO. PSOGA = A hybrid of PSO and GA. PSOTS = A hybrid of PSO and tabu search.

The latest previous work also came up with the similar LOOCV results (100%) to ours on the Leukemia data sets but they used many genes obtain the same results [4]. Moreover, they could not have statistically meaningful conclusions because their experimental results were obtained by only one independent run on each data set, and not based on average results. The average results are important since their proposed method is a stochastic approach. Additionally, in their approach, the global best particles' position is reset to zero position when its fitness values do not change after three successive iterations.

According to Tables 1-3, EPSO is reliable for gene selection since it has produced the near-optimal solution from gene expression data. This is due to the proposed particles' speed, the introduced rule, and the modified sigmoid function increase the probability $x_i^d(t+1)=0$ $(P(x_i^d(t+1)=0))$. This high probability causes the selection of a small number of informative genes and finally produces a near-optimal subset (a small subset of informative genes with high classification accuracy) for cancer classification. The particles' speed is introduced to provide the rate at which a particle changes its position, whereas the rule is proposed to update particle's positions. The sigmoid function is modified for increasing the probability of bits in particle's positions to be zero.

IV. CONCLUSION

In this paper, EPSO has been proposed for gene selection on two gene expression data sets. Overall, based on the experimental results, the performance of EPSO was superior to BPSO and PSO-based methods that proposed by previous related works in terms of classification accuracy, the number of selected genes, and running times. EPSO was excellent because the probability $x_i^d(t+1)=0$ has been increased. For future works, a modified representation of particle's positions in PSO will be proposed to reduce the number of genes subsets in solution spaces.

REFERENCES

[1] Knudsen S (2002) A biologist's guide to analysis of DNA microarray data. New York: John Wiley & Sons.

[2] Mohamad MS, Omatu S, Yoshioka M, Deris S (2009) A cyclic hybrid method to select a smaller subset of informative genes for cancer classification. Int J Innovative Comput, Inf, Control 5(8):2189–2202.

[3] Shen Q, Shi WM, Kong W (2008) Hybrid particle swarm optimization and tabu search approach for selecting genes for tumor classification using gene expression data. Comput Biol Chem 32:53–60.

[4] Chuang LY, Chang HW, Tu CJ, Yang CH (2008) Improved binary PSO for feature selection using gene expression data. Comput Biol Chem 32:29–38.

[5] Li S, Wu X, Tan M (2008) Gene selection using hybrid particle swarm optimization and genetic algorithm. Soft Comput 12:1039–1048.

[6] Kennedy J, Eberhart R (1995) Particle swarm optimization. Proc 1995 IEEE Int Conf Neural Networks 4:1942-1948.

[7] Kennedy J, Eberhart R (1997) A discrete binary version of the particle swarm algorithm. Proc 1997 IEEE Int Con Systs, Man, Cybernetics 5:4104–4108.

[8] Mohamad MS, Omatu S, Deris S, Yoshioka M, (2009) Particle swarm optimization for gene selection in classifying cancer classes. Int J Artif Life Robotics 14(1):16–19.

Informative Gene for Cancer Classification by Using Particle Swarm Optimization

M.S. Mohamad[1,2] S. Omatu[1] S. Deris[2] and M. Yoshioka[1]

[1]*Department of Computer Science and Intelligent Systems, Graduate School of Engineering,*
Osaka Prefecture University, Sakai, Osaka 599-8531, Japan
(Tel : 81-72-254-9278; Fax : 81-72-257-1788)
(mohd.saberi@sig.cs.osakafu-u.ac.jp; omatu@cs.osakafu-u.ac.jp; yoshioka@cs.osakafu-u.ac.jp)

[2]*Department of Software Engineering, Faculty of Computer Science and Information Systems,*
Universiti Teknologi Malaysia, 81310 Skudai, Johore, Malaysia
(Tel : 60-7-553-7784; Fax : 60-7-556-5044)
(safaai@utm.my)

Abstract: Microarrays technology offers the ability to measure the expression levels of thousands of genes simultaneously in biological organisms. Gene expression data that produced by the technology are expected to be of significant help in the development of efficient cancer diagnoses and classification platforms. The main problem that needs to be addressed is the selection of a small subset of genes from the thousands of genes in the data that contributes to a cancer disease. Therefore, this article proposes particle swarm optimization (PSO) with the constraint of particle's velocities to select a near-optimal (small) subset of informative genes that is relevant for cancer classification. The performance of the proposed method was evaluated by two well-known gene expression data sets and obtained encouraging results as compared with the standard version of binary PSO.

Keywords: Binary particle swarm optimization, Gene selection, Gene expression data, Optimization.

I. INTRODUCTION

Advances in microarray technology allow scientists to measure the expression levels of thousands of genes simultaneously in biological organisms and have made it possible to create databases of cancerous tissues. It finally produces gene expression data that contain useful information of genomic, diagnostic, and prognostic for researchers [1]. Thus, there is a need to select informative genes that contribute to a cancerous state [2]. However, the gene selection process poses a major challenge because of the following characteristics of the data: the huge number of genes compared to the small number of samples (high-dimensional data), irrelevant genes, and noisy data. To overcome this challenge, a gene selection method is used to select a subset of informative genes that maximizes classifier's ability to classify samples more accurately [3]. In computational intelligence domains, gene selection is called feature selection.

Recently, several gene selection methods based on particle swarm optimization (PSO) have been proposed to select informative genes from gene expression data [4],[5]. PSO is a new evolutionary technique proposed by Kennedy and Eberhart [6]. Shen *et al*. [4] have proposed a hybrid of PSO and tabu search approaches for gene selection. However, the results obtained by using the hybrid method are less meaningful since the application of tabu approaches in PSO is unable to search a near-optimal solution in search spaces. Next, Li *et al*. [5] have introduced a hybrid of PSO and genetic algorithms (GA) for the same purpose. Unfortunately, the accuracy result is still not high and many genes are selected for cancer classification since there are no direct probability relations between GA and PSO. Generally, the PSO-based methods are intractable to efficiently produce a small (near-optimal) subset of informative genes for high classification accuracy [4],[5]. This is mainly because the total number of genes in gene expression data is too large (high-dimensional data).

The diagnostic goal is to develop a medical procedure based on the least number of possible genes that needed to detect diseases. Thus, we introduce an enhancement of binary PSO based on the proposed constraint and rule (CPSO) to select a small (near-optimal) subset of informative genes that is most relevant for the cancer classification. The small subset means that it contains the small number of selected genes. In order to test the effectiveness of our proposed method, we apply CPSO to two gene expression data sets.

II. THE STANDARD VERSION OF BINARY PSO (BPSO)

BPSO is initialized with a population of particles. At each iteration, all particles move in a problem space to find the optimal solution. A particle represents a potential solution in an *n*-dimensional space [7]. Each particle has position and velocity vectors for directing its movement. The position vector and velocity vector of the *i*th particle in the *n*-dimension can be represented as $X_i = (x_i^1, x_i^2, ..., x_i^n)$ and $V_i = (v_i^1, v_i^2, ..., v_i^n)$, respectively, where $x_i^d \in \{0,1\}$; *i*=1,2,..*m* (*m* is the total number of particles); and *d*=1,2,..*n* (*n* is the dimension of data). v_i^d is a real number for the *d*-th dimension of the particle *i*, where the maximum v_i^d, $V_{\max} = (1/3) \times n$.

In gene selection, the vector of particle positions is represented by a binary bit string of length *n*, where *n* is the total number of genes. Each position vector (X_i) denotes a gene subset. If the value of the bit is 1, it means that the corresponding gene is selected. Otherwise, the value of 0 means that the corresponding gene is not selected. Each particle in the *t*-th iteration updates its own position and velocity according to the following equations:

$$v_i^d(t+1) = w(t) \times v_i^d(t) + c_1 r_1^d(t) \times (pbest_i^d(t) - x_i^d(t)) + c_2 r_2^d(t) \times (gbest^d(t) - x_i^d(t)) \quad (1)$$

$$Sig(v_i^d(t+1)) = \frac{1}{1+e^{-v_i^d(t+1)}} \quad (2)$$

$$\text{if } Sig(v_i^d(t+1)) > r_3^d(t), \text{ then } x_i^d(t+1) = 1; \text{ else } x_i^d(t+1) = 0 \quad (3)$$

where c_1 and c_2 are the acceleration constants in the interval [0,2]. $r_1^d(t), r_2^d(t), r_3^d(t) \sim U(0,1)$ are random values in the range [0,1] that sampled from a uniform distribution. $Pbest_i(t) = (pbest_i^1(t), pbest_i^2(t), ..., pbest_i^n(t))$ and $Gbest(t) = (gbest^1(t), gbest^2(t), ..., gbest^n(t))$ represent the best previous position of the *i*th particle and the global best position of the swarm (all particles), respectively. They are assessed base on a fitness function. $Sig(v_i^d(t+1))$ is a sigmoid function where $Sig(v_i^d(t+1)) \in [0,1]$. $w(t)$ is an inertia weight.

III. AN IMPROVEMENT OF BINARY PSO BASED ON THE CONSTRAINT OF PARTICLE'S VELOCITIES (CPSO)

We propose CPSO for selecting a near-optimal (small) subset of genes. It is proposed to overcome the limitations of BPSO and previous PSO-based methods [4],[5]. CPSO in our work differs from BPSO and the PSO-based methods on two parts: 1) we propose the constraint of elements of particle velocity vectors; 2) we introduce a rule for updating $x_i^d(t+1)$, whereas BPSO and the PSO-based methods have used the original rule (Eq. 3) and no constraint of elements of particle velocity vectors. The constraint and rule are introduced in order to:

- increase the probability of $x_i^d(t+1) = 0$ $(P(x_i^d(t+1) = 0))$.
- reduce the probability of $x_i^d(t+1) = 1$ $(P(x_i^d(t+1) = 1))$.

The increased and decreased probability values cause a small number of genes are selected and grouped into a gene subset. $x_i^d(t+1) = 1$ means that the corresponding gene is selected. Otherwise, $x_i^d(t+1) = 0$ represents that the corresponding gene is not selected. The constraint of elements of particle velocity vectors and the rule are proposed as follows:

$$Sig(v_i^d(t+1)) = \frac{1}{1+e^{-v_i^d(t+1)}} \quad (4)$$

subject to $v_i^d(t+1) \geq 0$

$$\text{if } Sig(v_i^d(t+1)) > r_3^d(t), \text{ then } x_i^d(t+1) = 0; \text{ else } x_i^d(t+1) = 1 \quad (5)$$

The constraint of elements of particle velocity vectors and the rule increase $P(x_i^d(t) = 0)$ because the minimum value for $P(x_i^d(t) = 0)$ is 0.5 when $v_i^d(t) = 0$ $(\min P(x_i^d(t) = 0) \geq 0.5)$. Meanwhile, they decrease the maximum value for $P(x_i^d(t) = 1)$ to 0.5 $(\max P(x_i^d(t) = 1) \leq 0.5)$. Therefore, if $v_i^d(t) > 0$, then $P(x_i^d(t) = 0) >> 0.5$ and $P(x_i^d(t) = 1) << 0.5$. For example, the calculations for $P(x_i^d(t) = 0)$ and $P(x_i^d(t) = 1)$ are shown as follows:

if $v_i^d(t) = 1$, then $P(x_i^d(t) = 0) = 0.73$ and $P(x_i^d(t) = 1) = 1 - P(x_i^d(t) = 0) = 0.27$.

if $v_i^d(t) = 2$, then $P(x_i^d(t) = 0) = 0.88$ and $P(x_i^d(t) = 1) = 1 - P(x_i^d(t) = 0) = 0.12$.

The fitness value of a particle (a gene subset) is calculated as follows:

$$fitness(X_i) = w_1 \times A(X_i) + (w_2 \times (n - R(X_i))/n) \quad (6)$$

in which $A(X_i) \in [0,1]$ is leave-one-out-cross-validation (LOOCV) classification accuracy that uses the only genes in a gene subset (X_i). This accuracy is provided by support vector machine classifiers (SVM). $R(X_i)$ is the number of selected genes in X_i. *n* is the total number of genes for each sample. w_1 and w_2 are two priority weights corresponding to the importance of accuracy and the number of selected genes, respectively, where $w_1 \in [0.1, 0.9]$ and $w_2 = 1 - w_1$.

IV. EXPERIMENTS

4.1. Data Sets and Experimental Setup

The gene expression data sets used in this study are summarized in Table 1. Experimental results that produced by CPSO are compared with an experimental method (BPSO) for objective comparisons. Additionally, the latest PSO-based methods from previous related works are also considered for comparison with CPSO [4],[5]. Firstly, we applied the gain ratio technique for pre-processing in order to pre-select 500-top-ranked genes. These genes are then used by CPSO and BPSO. Next, SVM is used to measure LOOCV accuracy on gene subsets that produced by CPSO and BPSO. For LOOCV, one sample in the training set is withheld and the remaining samples are used for building a classifier to classify the class of the withheld sample. By cycling through all the samples, we can get cumulative accuracy rates for classification accuracy of methods. In this research, LOOCV is used for measuring classification accuracy due to the small number of samples in gene expression data. Several experiments are independently conducted 10 times on each data set using CPSO and BPSO. Next, an average result of the 10 independent runs is obtained. High LOOCV accuracy, the small number of selected genes, and low running time are needed to obtain an excellent performance.

Table 1: The summary of gene expression data sets.

Data Sets	Number of Samples	Number of Genes	Number of Classes
Leukemia	72	7,129	2
Colon	62	2,000	2

Note:
DB = database.
DB Leukemia: http://www.broad.mit.edu/cgi-bin/cancer/datasets.cgi
DB Colon: http://microarray.princeton.edu/oncology/affydata/index.html

4.2. Experimental Results

Based on the standard deviation of classification accuracies in Table 2, results that produced by CPSO were almost consistent on all data sets. Interestingly, all runs have achieved over 98% LOOCV accuracy with less than 12 selected genes on the leukemia data set. Moreover, at least 88% classification accuracies have been obtained on the colon data set.

Table 2. Experimental results for each run using CPSO

Run no.	Leukemia data set		Colon data set	
	#Acc (%)	No. selected genes	#Acc (%)	No. selected genes
1	100	10	90.32	4
2	100	5	90.32	6
3	100	3	88.71	28
4	98.61	9	91.94	10
5	98.61	9	88.71	8
6	100	31	88.71	8
7	98.61	11	88.71	7
8	98.61	10	88.71	7
9	98.61	8	88.71	5
10	98.61	9	88.71	130
Average ± S.D.	99.17 ± 0.72	10.50 ± 7.61	89.36 ± 1.13	21.30 ± 38.80

Note: The results of the best subsets are shown in the shaded cells. A near-optimal subset that produces the highest classification accuracy with the smallest number of genes is selected as the best subset. #Acc and S.D. denote the classification accuracy and the standard deviation, respectively.

For an objective comparison, CPSO is compared with BPSO. According to the Table 3, it is worthwhile to mention that the classification accuracy and the number of selected genes of CPSO are superior to BPSO in terms of the best, average, and standard deviation results on all the data sets. CPSO also produces smaller numbers of genes and lower running times compared to BPSO on all the data sets. CPSO can reduce its running times because of the following reasons:

- CPSO selects the smaller number of genes compared to BPSO.
- The computation of SVM is fast because it uses the small number of features (genes) that selected by CPSO for classification process.

We also compare our work with previous related works that used PSO-based methods in their proposed methods [4],[5]. It is shown in Table 4. For all the data sets, the averages of the number of selected genes of our work were smaller than the previous works [4],[5]. Our work also have resulted the higher averages of classification accuracies on the leukemia data set compared to the previous works. However, experimental results produced by Shen *et al*. were better than our work on the colon data sets [4]. Running time between CPSO and the previous works cannot be compared because it was not reported in their articles.

Table 3. Comparative experimental results of CPSO and BPSO

Data	Method / Evaluation	CPSO			BPSO		
		Best	#Ave	S.D	Best	#Ave	S.D
Leukemia	#Acc (%)	100	99.17	0.72	98.61	98.61	0
	#Genes	3	10.50	7.16	216	224.70	5.23
	#Time	5.26	6.13	1.44	13.86	13.94	0.03
Colon	#Acc (%)	91.94	89.36	1.13	87.10	86.94	0.51
	#Gene	10	21.30	38.80	214	231	10.19
	#Time	8.78	9.26	0.70	30.58	30.63	0.27

Note: The best result of each data set is shown in the shaded cells. It is selected based on the following priority criteria: 1) the highest classification accuracy; 2) the smallest number of selected genes; 3) the lowest running time.

Table 4. A comparison between our method (CPSO) and previous PSO-based methods

Data	Method / Evaluation	CPSO	PSOTS [4]	PSOGA [5]
Leukemia	#Acc (%)	(99.17)	(98.61)	(95.10)
	#Genes	(10.50)	(7)	(21)
Colon	#Acc (%)	(89.36)	(93.55)	(88.7)
	#Genes	(21.30)	(8)	(16.8)

Note: The result of the best subsets is shown in the shaded cells. It is selected based on the following priority criteria: 1) the highest classification accuracy; 2) the smallest number of selected genes. A result in '( )' denotes an average result.
IBPSO = An improved binary PSO.
PSOGA = A hybrid of PSO and GA.
PSOTS = A hybrid of PSO and tabu search.

V. CONCLUSION

Overall, based on the experimental results, the performance of CPSO was superior to BPSO and previous PSO-based methods in terms of classification accuracy and the number of selected genes. CPSO was excellent because the probability $x_i^d(t+1)=0$ has been increased by the proposed constraint of elements of particle velocity vectors and the introduced rule. The constraint and rule have been proposed in order to yield a near-optimal subset of genes for better cancer classification. CPSO also obtains lower running times because it selects the small number of genes compared to BPSO. For future works, a statistical test will be applied on CPSO in order to test its reliability.

REFERENCES

[1] Knudsen S (2002) A biologist's guide to analysis of DNA microarray data. New York: John Wiley & Sons.

[2] Mohamad MS, Omatu S, Deris S, Misman MF, Yoshioka M (2009) Selecting informative genes from gene expression data by using hybrid methods for cancer classification. Int J Artif Life Robotics 13(2):414-417.

[3] Mohamad MS, Omatu S, Yoshioka M, Deris S (2009) A cyclic hybrid method to select a smaller subset of informative genes for cancer classification. Int J Innovative Comput, Inf, Control 5(8):2189–2202.

[4] Shen Q, Shi WM, Kong W (2008) Hybrid particle swarm optimization and tabu search approach for selecting genes for tumor classification using gene expression data. Comput Biol Chem 32:53–60.

[5] Li S, Wu X, Tan M (2008) Gene selection using hybrid particle swarm optimization and genetic algorithm. Soft Comput 12:1039–1048.

[6] Kennedy J, Eberhart R (1995) Particle swarm optimization. Proc 1995 IEEE Int Conf Neural Networks 4:1942-1948.

[7] Kennedy J, Eberhart R (1997) A discrete binary version of the particle swarm algorithm. Proc 1997 IEEE Int Con Systs, Man, Cybernetics 5:4104–4108.

RADON TRANSFORM FOR FACE RECOGNITION

Jamal Ahmad Dargham, Ali Chekima, Ervin Moung (University Malaysia Sabah), S. Omatu (Osaka Prefecture University, Japan)

Abstract

Face recognition is an important biometric because of its potential applications in many fields, such as access control, surveillance, and human-computer interface. In this paper, an investigation of the effect of the step size for both the angle and vector of the Radon transform on the performance of a face recognition system based on Principal Component Analysis (PCA) and Euclidean distance is carried out. It was found out the change of either the vector or the angle step size affects the performance of the system. However, the best equal error rate is achieved when the step size for both angle and vector is set to 1.

1. Introduction

Over the past two decades face recognition has received considerable interest as it is a widely accepted biometric because of its potential applications in many fields, such as access control, surveillance, human-computer interface, and so on. Several methods are available to extract and represent the facial features. One of the widely used representations of the face region is Eigenfaces [1], which are based on principal component analysis (PCA). The goal of the Eigenface method is to linearly project the image space to a feature space of a lower dimension.

Chunming et al. [2] proposed a face recognition method called Statistical PCA. The improved PCA algorithm is used to compute the eigenvectors and eigenvalues of the face. Then, Bayesian rule is used to design the classification rule. The experimental result shows that the method introduced has the advantages of simple computation and high recognition rate up to 95.08%.

Jamikaliza et al. [3] presented a face recognition system based on Eigenfaces as feature extractor and Fuzzy ArtMap (FAM) neural network as classifier. The motivation of using FAM as a classifier is due to its unique solution to the stability-plasticity dilemma, where it has the ability to preserve previously learned knowledge and the potential to adapt to new patterns indefinitely. They reported recognition rate of 97.22% using local dataset and 98% using ORL dataset.

Jadhao and Holambe [4] described a new technique for face recognition which uses Radon transform and Fourier transform to derive the directional spatial frequency features. The Radon transform is used for the line integral of features and the DFT is used to enhance the features. They used FERET and ORL databases and achieved recognition rates 99.133% and 97.33%, respectively.

Dabbah et al [5] presented a novel method to face biometric. They proposed randomized Radon signature (RRS) to overcome the natural limitations of biometric. They used the Eigenface algorithm for evaluation. The results have shown 81.99% accuracy.

1.1 Radon transform

The Radon transform is one of the techniques used to detect features within an image. The Radon transform defined as:

$$R(\theta,\rho) = \int_{\infty}^{\infty} A(\rho cos\theta - sin\theta, \rho sin\theta + scos\theta)ds \qquad (1)$$

where S is defined as an integral line in the image and ρ is defined as the distance of the line from the origin and θ is the angel from the horizontal as shown in Figure 1.

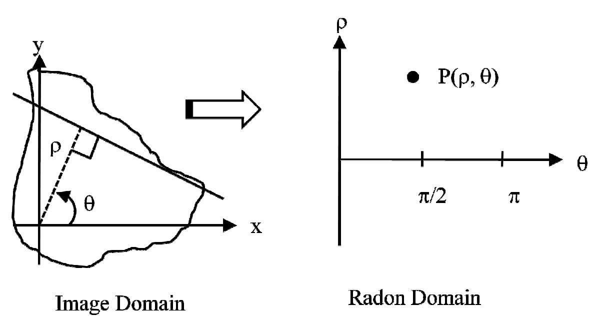

Figure 1. Image domain and Radon domain [7].

The Radon transform is a mapping from the Cartesian rectangular coordinate (x, y) to a distance and angel (ρ, θ) also known as the polar coordinate [6, 7].

2. Face databases

2. Face databases

A total of 500 images with frontal face of a person were selected from the FERET database. They represent 200 different individuals. 100 individuals are used for training & testing, and the other 100 different individuals are used for testing only. All the 500 selected FERET images were cropped to get only the desired face part of a person (from forehead to the chin). All images have been adjusted so that both eyes of an individual are aligned in the same horizontal line.

2.1 Training database

Each of the 100 persons in the training and testing database (Known Database) has four images. Up to three images will be used for training and 1 image will be used for testing. Figure 2 shows an example of training and testing database. The four images are of the same person. The three images on the left will be used for training while the image on the right will be used for testing. Thus, three training databases were created. These are (i) one image per person (1p1i), (ii) two images per person (1p2i), and (iii) three images per person (1p3i). Figure 3 shows a sample image of each of these databases.

(a) (b)

Figure 2. An example of the known database.

(a) (b) (c)

Figure 3. Examples of the training databases (a) 1p1i, (b) 1p2i, (c) 1p3i.

2.2 Testing database

Two testing databases were created. The first database, known test database, has 100 images of the 100 persons in the training database. This database will be used to test the recall capability of the face recognition system. The second database, unknown test database, has also 100 images of 100 different persons. This database will be used to test the rejection capability of the system.

3. Results and discussion

3.1 System block diagram

Figure 4 shows the block diagram of the system. The system has training and a testing stage. The Radon transform will be applied on the image to compute its 2-D projection image along angles varying from 0 to 180°. The result of the projection is the sum of the intensities of the pixels in each direction. All the projections of the image are concatenated to form 1-D radon transform's vector. The 1-D radon transform's vectors for all training images are computed. PCA is then applied on the collection of 1-D radon transform's vector to produce a low-dimensional features vector.

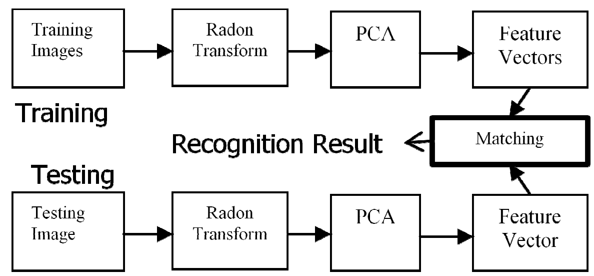

Figure 4. Block diagram of the system

For the classification task, the Euclidean distance measure is used. If the Euclidean distance between test image y and image x in the training database d(x,y) is smaller than a given threshold t then images y and x are assumed to be of the same person. The threshold t is the largest Euclidean distance between any two face images in the training database, divided by a threshold tuning value (Tcpara) as given in Equation 1.

$$t = \frac{[\, max\, \{\|\Omega j - \Omega k\|\}\,]}{Tcpara} \qquad (1)$$

where j, k = 1, 2 … M. M is the total number of training images, and Ω is the reduced dimension images.

To measure the performance of the system, several performance metrics are used. These are:

- For Recall
  - ***Correct Classification***. If a test image $\mathbf{y_i}$ is correctly matched to an image $\mathbf{x_i}$ of the same person in the training database.
  - ***False Acceptance.*** If test image $\mathbf{y_i}$ is incorrectly matched with image $\mathbf{x_j}$, where ***i*** and ***j*** are not the same person
  - ***False Rejection.*** If image $\mathbf{y_i}$ is of a person ***i*** in the training database but rejected by the system.
- For Reject
  - ***Correct Classification***. If $\mathbf{y_i}$, from the unknown test database is rejected by the program

- ***False Acceptance***. If image $\mathbf{y_i}$ is accepted by the program.

3.2 Setting the Threshold Tuning Parameter

The value of the threshold tuning parameter can be used to tune the performance of the system to have either high correct recall with high false acceptance rate for application such as boarder monitoring or high correct rejection rate for unknown persons for application such as access control. For this work, the threshold tuning parameter was set so that the system has equal correct recall rate and correct rejection rate. Figure 5 shows the correct recall and rejection rates for different values of the threshold tuning parameter when the number of images per person used for training is (i) one image per person (ii) two images per person and (iii) three images per person. As can be seen from Figure 5, the equal error rate (EER) for 1p1i is 58%, 84.5% when using 1p2i, and 89% when using 1p3i training database. The value of the threshold tuning parameter (Tcpara) that gives an equal error rate depends on the number of images per person used for training. For the training database 1p3i it is 4.34. This value will be used on all subsequent investigation

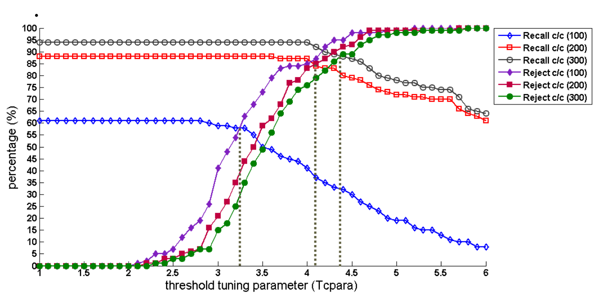

Figure 5. The effect of the threshold tuning parameter on the correct classification

3.3 The effect of the angle θ step size

We have investigated the effect of changing the angle step size on the performance of the system. The angle step size was increased by 1(default), 2, 3, …,10. As can be seen from Figure 6, the correct recall rate is constant for all step sizes of the angle. However, the correct reject rate is different for different values of step size but on average is decreasing. The highest equal error rate of 89% is achieved when the angle step size of 1.

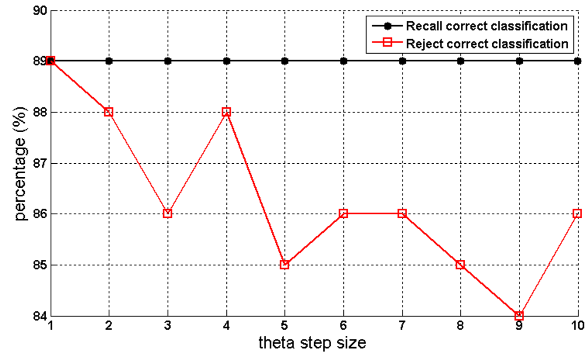

Figure 6. The effect of the angle θ step size on correct classification

3.4 The effect of the vector ρ step size

We have also investigated the effect of changing the vector (ρ) step size on the performance of the system. The vector step size was increased by 1(default), 2, 3, …,10. As can be seen from Figure 7, for step size of 3 and below the correct recall rate is higher that the correct rejection rate. However, for step size larger than 3 the reverse is true. Thus, in general the correct recall and reject rates tend to change in opposite directions as the step size increase. The step size that gives the highest equal error rate of 89% is still 1.

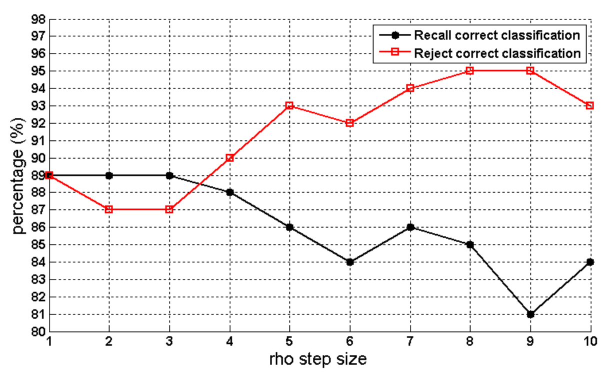

Figure 7. The effect of the vector ρ step size on correct classification

3.5 The effect of the vector and angle step sizes

We have also investigated the effect of changing both the vector (ρ) step size and the angle step size on the performance of the system. The vector and angle step sizes were increased by 1(default), 2, 3, …,10. As can be seen from Figure 8(a), for any value of the step size greater than 1 for the angle θ, the correct recall rate, on average, increases as the step size for the vector ρ increases. On the other hand, the correct reject decreases as the as the step size for the vector ρ increases as can be seen in Figure 8(b). Thus, it is possible to use step sizes of ρ and θ to select the required performance of the system. For example, the combination of step size 1 for the angle θ and step size 8 for the vector ρ gives a correct recall rate of 86% and a correct reject rate of 95%.

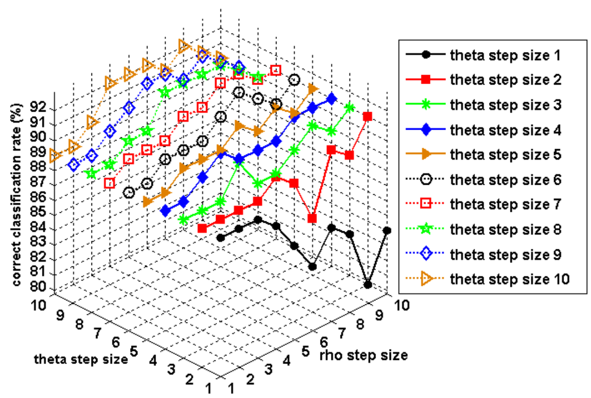

a. Correct recall rate

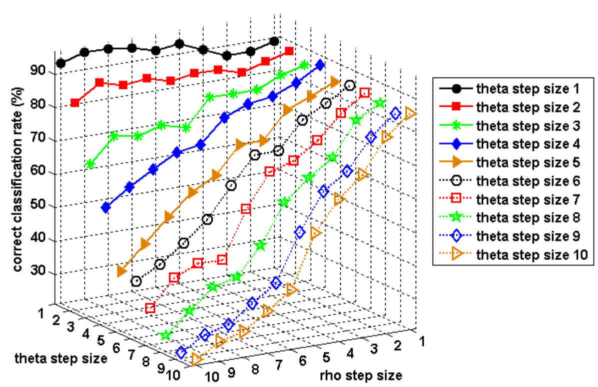

b. Correct reject rate

Figure 8. The effect of changing both the angle θ and vector ρ step size on (a) the correct recall and (b) correct reject rates

4. Conclusion

In this paper, an investigation of the effect of the step size for both the angle and vector of the Radon transform on the performance of a face recognition system based on Principal Component Analysis (PCA) and Euclidean distance is carried out. It was found out that changing either the angle θ step size or the vector ρ step size affect the performance of the system. Thus, these can be used to tune the performance of the system in addition to the Euclidean distance tuning parameter. The work carried out so far was on an image size of 60 by 60 pixels, thus, we intend to investigate the effect of having larger image sizes.

5. References

[1] M. Turk and A. Pentland, "Eigenfaces for Recognition," Journal of Cognitive Neuroscience, Volume 3, No. 1, Page(s):71-86, 1991.

[2] Li Chunming, Diao Yanhua, Ma Hongtao, and Li Yushan; A Statistical PCA Method for Face Recognition; Intelligent Information Technology Application, 2008. IITA 2008. Second International Symposium on Volume 3, 20-22 Dec. 2008 Page(s):376 – 380.

[3] Karim Jamikaliza Abdul, Yusof Rubiyah, and Khalid Marzuki; Investigate the Performance of Fuzzy Artmap Classifier for Face Recognition System; Signal Image Technology and Internet Based Systems, 2008. SITIS '08. IEEE International Conference on November 30 2008-Dec. 3 2008 Page(s):254 – 259.

[4] Jadhao, Dattatray V.; Holambe, Raghunath S.; "Feature Extraction and Dimensionality Reduction Using Radon and Fourier Transforms with Application to Face Recognition":, Conference on Computational Intelligence and Multimedia Applications, 2007. International Conference on, Volume 2, 13-15 Dec. 2007 Page(s):254 - 260

[5] Dabbah, M.A.; Dlay,S.S.; Woo,W.L.;2008 "Randomized Radon Signature for face biometric verification", Image Processing, 2008. ICIP 2008. 15th IEEE International Conference on, Page(s):273 - 276

[6] Carsten Høilund, "The Radon Transform"; Aalborg University, Vision, Graphics and Interactive Systems (VGIS), November 12, 2007.

[7] http://idlastro.gsfc.nasa.gov/idl_html_help/RADON.html

The Fifteenth International Symposium on Artificial Life and Robotics 2010 (AROB 15th '10),
B-Con Plaza, Beppu,Oita, Japan, February 4-6, 2010

A Dynamically Reconfigurable Processor for the H.264/AVC Image Prediction

Y. Hayakawa and A. Kanasugi

Graduate School of Engineering, Tokyo Denki University
2-2 Kanda Nishiki-cho, Chiyoda-ku, Tokyo, 101-8457 Japan
(Tel: 03-5280-3705; Fax: 03-5280-3565)
(Email address: 09kme40@ms.dendai.ac.jp, kanasugi@eee.dendai.ac.jp)

Abstract: H.264/AVC provides high video quality at substantially low bit rates. It is useful for a save and transfer of video images by robot cameras. However, the computational complexity of H.264/AVC is very high. A high-speed general-purpose processor is necessary to process H.264/AVC. However, it is difficult to use such a processor for a portable device. Therefore, an application specific processor is necessary. Dynamic reconfiguration can expand virtually circuit area in limited chip area. Thus, this paper proposes a dynamically reconfigurable processor for the H.264/AVC image prediction. H.264/AVC contains intra and inter prediction process. Intra and inter prediction processes are not used at the same time. The proposed dynamically reconfigurable processor reconfigures those circuits. Proposed processor was designed and synthesized. As a result, LUTs (look up tables) were reduced to 93%, flip flops were reduced to 94%, and maximum delay was about the same.

Keywords: H.264/AVC, dynamically reconfiguration, inter prediction, intra prediction

I. INTRODUCTION

H.264/AVC is the latest video compression standard[1]. H.264/AVC provides high video quality at substantially low bit rates. It is useful for a save and transfer of video images by robot cameras. However, the computational complexity of H.264/AVC is very high[2]. The video resolution is proportional to the frame rate of application. Furthermore, video resolution increases every year. A high-speed general-purpose processor is necessary to process H.264/AVC. However, it is difficult to use such a processor for a portable device. Therefore an application specific processor is necessary.

H.264/AVC contains intra and inter prediction process, deblocking filter process, quantization process, integer discrete cosine transform process, encoding process, decoding process, inverse quantization process, and inverse integer discrete cosine transform process. Intra and inter prediction processes are not used at the same time. Intra and inter prediction process circuits are implemented independently by the general decoder.

Dynamic reconfiguration can expand virtually circuit area in limited chip area. Although reconfiguration requires temporary stop of circuit in a few milliseconds, dynamic reconfiguration changes circuit construction during operation without stopping circuit. Therefore, we can design circuit of many functions in small circuit[3-4].

Therefore, this paper proposes a dynamically reconfigurable processor for the H.264/AVC main profile image prediction.

II. H.264/AVC MAIN PROFILE INTRA AND INTER PREDICTION

H.264/AVC contains intra and inter prediction process, deblocking filter process, quantization process, integer discrete cosine transform process, encoding process, decoding process, inverse quantization process, and inverse integer discrete cosine transform process. Intra and inter prediction processes are not used at the same time by the general decoder. Intra prediction process uses neighboring samples for N by N block (for example 4 by 4, 16 by 16, etc). Inter prediction process uses reference picture (namely, before and after current picture). Intra and inter prediction process circuits are implemented independently.

1. Inter prediction process

Most inter prediction process is sample interpolation process. Luminance (luma) sample interpolation process and chrominance (chroma) sample interpolation process are different. Although luma sample interpolation process calculates quarter samples using 6-tap filter, chroma sample interpolation process calculates 1/8 samples. Luma sample interpolation process needs 448 times addition for a 4 by 4 block. Chroma sample interpolation process needs 96 times addition for a 2 by

2 block. Figure 1 shows luma sample interpolation circuit.

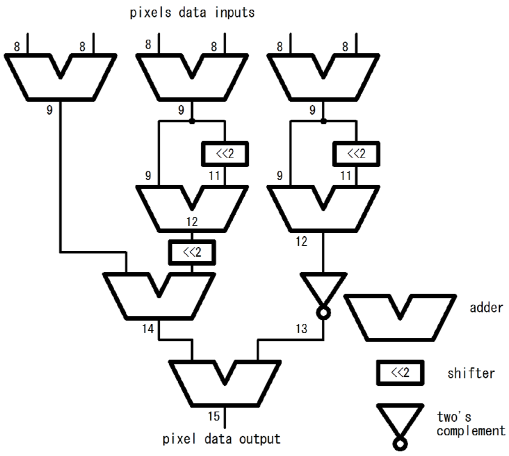

Fig. 1 Luma sample interpolation circuit

The 6-tap filter for luma sample interpolation process calculates as follows.

$$\begin{cases} p_{t1}=A-5B+20C+20D-5E+F & (1) \\ \quad A\sim E\text{: 8 bit integer samples} & \\ p_1=\mathrm{Clip}((p_{t1}+16)/32) & (2) \end{cases}$$

$$\begin{cases} p_{t2}=G-5H+20I+20J-5K+L & (3) \\ \quad G\sim L\text{: 15 bit filtered samples } (p_{t1}) & \\ p_2=\mathrm{Clip}((p_{t2}+512)/1024) & (4) \end{cases}$$

$$\mathrm{Clip}(p)=\begin{cases} 0, & p<0 \\ p, & 0\le p\le 255 \\ 255, & p>255 \end{cases} \quad (5)$$

Chroma sample interpolation process for one sample calculates as follows.

$$\begin{cases} p_{t3}=O\cdot(8-x)(8-y)+P\cdot(x)(8-y)+Q\cdot(8-x)(y)+R\cdot(x)(y) & (6) \\ \quad O\sim R\text{: 8 bit integer samples} & \\ p_3=\mathrm{Clip}((p_{t3}+32)/64) & (7) \end{cases}$$

2. Intra prediction process

Intra prediction process uses top and left neighbor samples. Intra prediction process consists of luma intra prediction process for a 4 by 4 block, luma intra prediction process for a 16 by 16 block, and chroma intra prediction process for an 8 by 8 block. Luma intra prediction process for a 4 by 4 block contains three calculations as indicated by the following.

16 times sum of 2 values.

16 times sum of 4 values.

A sum of 8 values.

Luma intra prediction process for a 16 by 16 block contains two calculations as indicated by the following.

A sum of 32 values.

$$\begin{cases} p[x,y]= & \\ \quad \mathrm{Clip}((a+b\cdot(x-7)+c\cdot(y-7)+16)>>5), & \\ \quad \text{with } x,y=0,1,\ldots,15 & (8) \\ a=16\,(p[-1,15]+p[15,-1]) & (9) \\ b=(5H+32)>>6 & (10) \\ c=(5V+32)>>6 & (11) \\ H=\sum_{x'=0}^{7}(x'+1)(p[8+x',-1]-p[6+x',-1]) & (12) \\ V=\sum_{y'=0}^{7}(y'+1)(p[-1,8+y']-p[-1,6+y']) & (13) \end{cases}$$

Chroma intra prediction process contains two calculations as indicated by the following.

A sum of 8 values.

$$\begin{cases} p[x,y]= & \\ \quad \mathrm{Clip}((a+b\cdot(x-3)+c\cdot(y-3)+16)>>5), & \\ \quad \text{with } x,y=0,1,\ldots,7 & (14) \\ a=16\,(p[-1,7]+p[7,-1]) & (15) \\ b=(34H+32)>>6 & (16) \\ c=(34V+32)>>6 & (17) \\ H=\sum_{x'=0}^{3}(x'+1)(p[4+x',-1]-p[2+x',-1]) & (18) \\ V=\sum_{y'=0}^{3}(y'+1)(p[-1,4+y']-p[-1,2+y']) & (19) \end{cases}$$

III. PROPOSED PROCESSOR

Intra and inter prediction process circuits are implemented independently by general decoder. In this paper, circuit area was reduced by dynamically reconfiguration for these circuits. The proposed circuit is based on 13 luma sample interpolation process, because this process is the largest. This process consists of 91 adders. The connections of adders are reconfigured by the multiplexers. Some circuits did not incorporate, because circuit areas increase. These 70 adders were reduced by reconfiguration.

The proposed dynamically reconfigurable processor reconfigures luma sample interpolation process, chroma sample interpolation process, luma intra prediction process, and chroma intra prediction process. Luma intra prediction process has 13 modes. Chroma intra prediction process has 4 modes. This processer calculates luma sample interpolation process for a 4 by 4 block in 19 clock cycles. This processer calculates chroma sample interpolation process for a 2 by 2 block in 2 clock cycles. This processer calculates luma intra prediction process for a 4 by 4 block in 4 clock cycles at the maximum. This processer calculates luma intra prediction process for a 16 by 16 block in 66 clock cycles at the maximum. This processer calculates chroma intra prediction process for an 8 by 8 block in 18 clock cycles at the maximum.

Proposed circuit has 13 blocks. The connections of those blocks and adders are reconfigured by the multiplexers. Those 13 blocks were numbered. Six blocks are almost the same type (No.6~12). Figure 2 shows block diagram of those circuits. Figure 3 shows block diagram of three blocks (No.0, 1, and 2). Those blocks are used for luma sample interpolation process, luma intra prediction process, and chroma intra prediction process. For example, luma intra prediction process for a 16 by 16 block uses shaded adders. Those adders calculate H in (12). Figure 4 shows block diagram of three blocks (No.3, 4, and 5). Those blocks are almost the same as the previous description blocks (No.0, 1, and 2). However, those can calculate p in (8). Those blocks are used for luma sample interpolation process, luma intra prediction process, and chroma intra prediction process. For example, luma intra prediction process for a 16 by 16 block uses shaded adders. Those adders calculate p in (8). Nine blocks (No.0~8) have 6 by 8 bits inputs at the minimum. However, 4 blocks (No.9~12) have 6 by 15 bit inputs at the minimum. Because, processor have to calculate p_{t2} in (3). In addition, those blocks (No.9~12) calculate p_{t1} in (1).

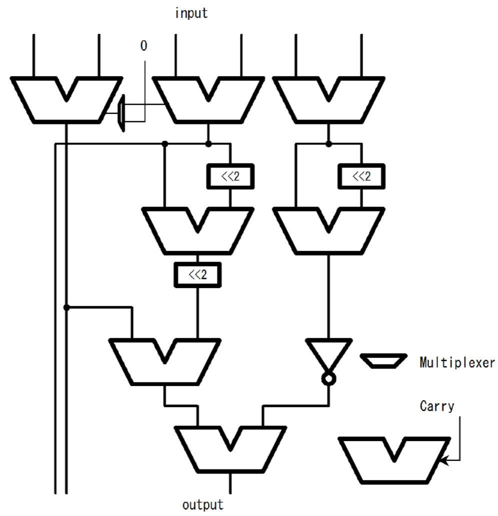

Fig. 2 The block diagram of one block (No.6 ~12)

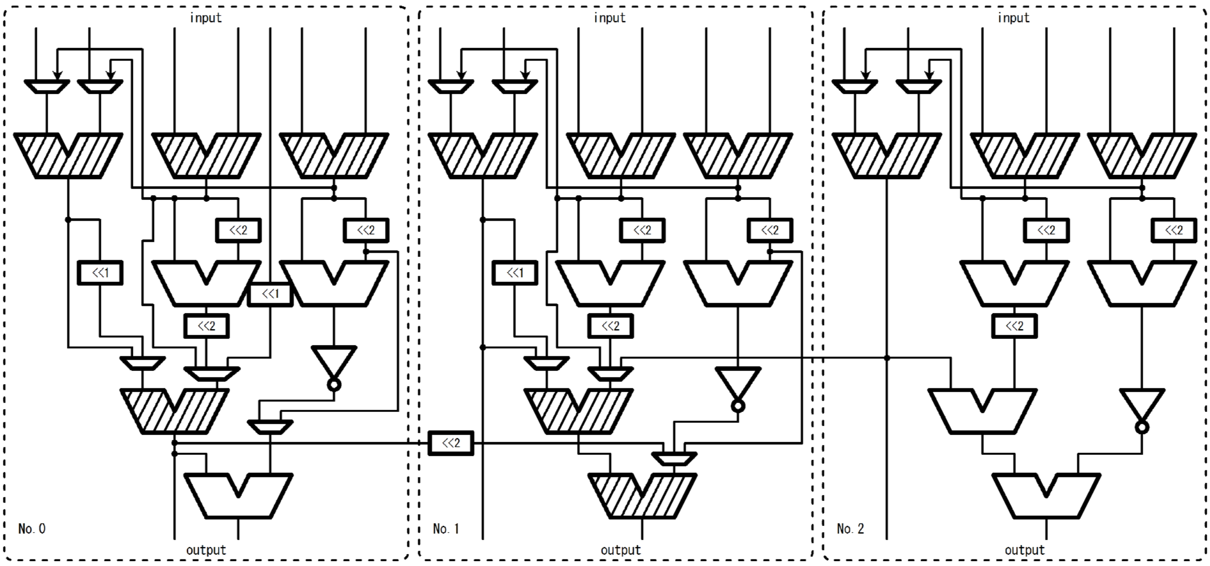

Fig. 3 The block diagram of three blocks (No.0, 1, and 2)

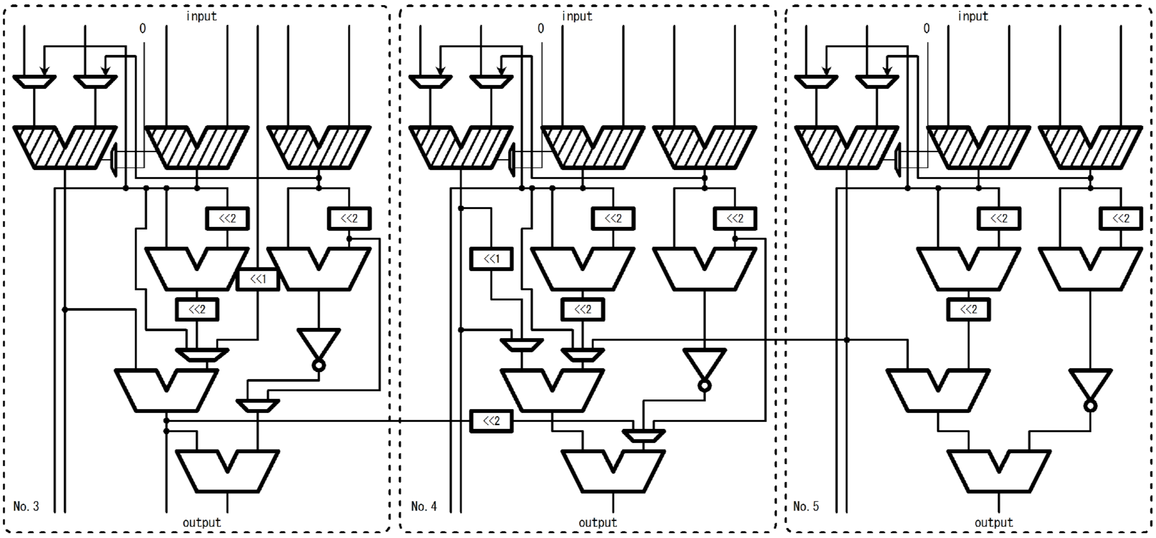

Fig. 4 The block diagram of three blocks (No.3, 4, and 5)

Reconfigurations of 13 blocks and connection of 13 blocks are controlled by control unit. The inputs of control unit are samples data, mode (luma intra prediction process, luma intra prediction process for a 16 by 16 block, and so on) select signals, and so on. Calculation results are output four pixels (32 bits) at a time.

IV. EVALUATION

The dynamically reconfigurable prediction circuit for H.264/AVC decoding was synthesized using Xilinx ISE 11.1 CAD software. The target FPGA (Field Programmable Gate Array) is Virtex-5 of Xilinx Corp. (XC5VLX50T). The result was compared with a circuit without dynamically reconfiguration. These circuits can calculate in the same clock cycles. Table 1 summarizes the logic synthesis results. As a result, LUTs (look up tables) were reduced to 93%, flip flops were reduced to 94%, and maximum delay was about the same.

Table 1. Processor synthesis results

	LUTs	Flip flops	Delay[ns]
Proposed	4181	1608	11.678
General	4508	1705	11.878
Rate	0.927	0.943	0.983

V. CONCLUSION

This paper proposed a dynamically reconfigurable processor for the H.264/AVC image prediction. The proposed processor contains 13 blocks. The proposed processor reconfigures luma sample interpolation process, chroma sample interpolation process, and intra prediction process. Seventy adders were reduced by reconfiguration. The proposed processor was designed and synthesized. The result was compared with a circuit without dynamically reconfiguration. As a result, LUTs (look up tables) were reduced to 93%, flip flops were reduced to 94%, and maximum delay was about the same.

ACKNOWLEDGEMENTS

This work was supported by Tokyo Denki University Science Promotion Fund (Q09J-01).

REFERENCES

[1] ITU-T Recommendation H.264 (2005), Advanced Video Coding for Generic Audiovisual Service

[2] S. Chien, Y. Huang, C. Chen, H. Chen, and L. Chen (2005), Hardware architecturedesign of video compression for multimedia communication systems, IEEE Commun. Mag., vol. 43, no. 8, pp. 123–132

[3] T. Sato, H. Watanabe and K. Shiba (2005), Implementation of dynamically reconfigurable processor DAPDNA-2, VLSI Design, Automation and Test, 2005 IEEE VLSI-TSA International Symposium, pp. 323-324

[4] T. Sugawara, K. Ide and T. Sato (2004), Dynamically Reconfigurable Processor Implemented with IP Flex's DAPDNA Technology, IEICE Trans. Inf. & Syst., D, E87 (8), pp. 1997-2003

The Fifteenth International Symposium on Artificial Life and Robotics 2010 (AROB 15th '10),
B-Con Plaza, Beppu,Oita, Japan, February 4-6, 2010

X-ray Computed Tomography using Material-Class Modeling by Markov Random Field Energy Minimization

Wataru Fukuda, Shin-ichi Maeda, Atsunori Kanemura, and Shin Ishii

Graduate School of Informatics, Kyoto University
Kyoto 611-0011, Japan
fukuda,ichi,atsu-kan,ishii @sys.i.kyoto-u.ac.jp

Abstract: We develop a new statistical reconstruction method for X-ray computed tomography. We utilize the knowledge that the human body is composed of a finite number of material kinds and CT values depend on the material classes. The problem is formulated in the framework of maximum a posterior (MAP) estimation and tomographic image and material classes are simultaneously estimated. To minimize the MAP objective function, we use an expansion algorithm which is a variant of graph cuts.

Keywords: Computed tomography, image reconstruction, metal artifact reduction

I. INTRODUCTION

Computed tomography (CT) is an important medical imaging technology, and a number of CT algorithms for reconstructing tomographic image from a series of X-ray projections have been developed [1–6]. One of the difficulties of CT techniques stems form the requirement for the reducing X-ray exposure in order to avoid overdoes of radiation. However, such limitation on the X-ray exposure would make the observed data noisy or make the amount of the observed data insufficient. Thus, the classical filtered back projection (FBP) and maximum likelihood (ML) solutions become ill-conditioned and unstable. We resolve this ill-poseness by introducing suitable prior knowledge that regularizes the ML solution. As the prior knowledge, we assume that X-ray attenuation coefficients depend on the material classes and the human body is composed of a finite number of material classes; they include soft tissue (fat), normal tissue (muscle), and born.

Another difficulty of CT techniques is metal artifact. It is known that the presence of high density objects such as metal prostheses and dental fillings cause streak or star artifacts when the FBP algorithm is applied [1, 3, 5]. The most popular approach to metal artifact reduction (MAR) is the projection completion method [1]. Although this approach is effective for MAR by detecting and interpolating the metal regions in the sinogram, information from the projections passing through metal may be lost. Even worse, it is not easy to determine the metal regions, especially when two or more metals are inserted. We tackle this MAR problem by a statistical approach, in which we introduce a material class of implanted metal.

Although there are studies that assume the material-class-dependent X-ray attenuation [3–5], most of them estimate the tomographic image and the material classes in a separate manner. Since the estimation of reconstructed image and the material classes are closely related, such separate estimation may deteriorate the reconstruction performance. Therefore, simultaneous estimation for a tomographic image and material classes in term of a consistent cost function is desired. One of such solutions was proposed in [6], which was based on Bayesian inference. Their model consists of the prior probability of the X-ray attenuation coefficients and the likelihood that describes the observation process given X-ray attenuation coefficients. However, due to the high-dimensionality and nonlinear dependency of random variables, they use a simple model and approximation method. In this study, we consider to use a more realistic observation model and a suitable prior distribution. The tomographic image and material classes are estimated by maximum a posteriori (MAP) estimation. Especially, a variant of the graph cut algorithms called an expansion algorithm [7–9] is used for an efficient and accurate MAP estimation.

II. ALGORITHM

Suppose we have T projections $\mathcal{D} = \ \mathbf{y}^{(1)} \quad \mathbf{y}^{(T)}$ and the tth projection is represented by $\mathbf{y}^{(t)} = \ y_1^{(t)} \quad y_I^{(t)}$, where $y_i^{(t)}$ denotes the number of photons sensed at detector i when projected from a certain direction $^{(t)}$. Our aim is to reconstruct a tomographic image represented by a J-dimensional vector $\mathbf{x} = \ x_1 \quad x_J$ obtained by raster scanning the attenuation coefficients.

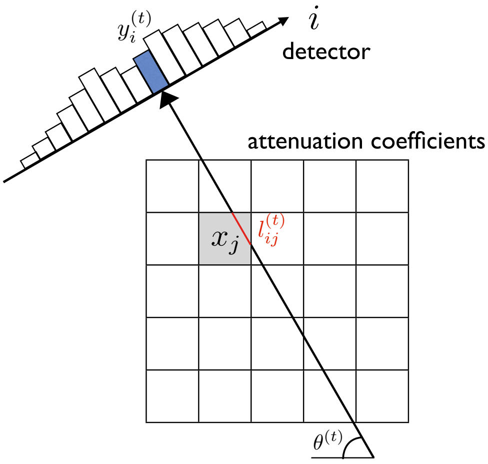

Figure 1: Geometry of CT. x_j is the attenuation coefficient at pixel j, and $l_{ij}^{(t)}$ is the intersection length at pixel j when projected from the direction $^{(t)}$ to the detector i.

1. Observation Model

The data acquisition model is written by

$$\hat{y}_i^{(t)} = b_i^{(t)} \exp \quad \sum_{j=1}^{J} l_{ij}^{(t)} x_j \tag{1}$$

Here, $\hat{y}_i^{(t)}$ denotes the expected number of detected photons, $b_i^{(t)}$ is the number of photons that would be detected in the absence of any absorber, and $l_{ij}^{(t)}$ is the effective intersection length of projection i with pixel j when projected from the direction $^{(t)}$. Fig. 1 illustrates the data acquisition process.

The main source of the fluctuation in the observation is assumed to be arisen from a quantum nature of X-ray photons [2–4]. We represent the fluctuation by an independent Poisson distribution over the measurements:

$$p(\mathcal{D}|\mathbf{x}) = \prod_{t=1}^{T}\prod_{i=1}^{I} p(y_i^{(t)}|\mathbf{x}) = \prod_{t=1}^{T}\prod_{i=1}^{I} \frac{\hat{y}_i^{(t)y_i^{(t)}} e \quad y_i^{(t)}}{y_i^{(t)}!} \tag{2}$$

2. Conditional Prior

We incorporate some *a priori* knowledge in reconstruction of tomographic image. We assume that each element of $\mathbf{x}$ is classified into different material classes: air, soft tissue, normal tissue, bone, and implanted metal. We denote the number of classes by K (here, $K = 5$). Thus, the prior $p(\mathbf{x})$ is represented via variables $\mathbf{z} = \quad \mathbf{z}_1 \qquad \mathbf{z}_J$:

$$p(\mathbf{x}) = p(\mathbf{x}|\mathbf{z})p(\mathbf{z}) = \prod_{j=1}^{J} p(x_j|\mathbf{z}_j)p(\mathbf{z}_j) \tag{3}$$

Input : Observation $\mathcal{D}$
Output : Estimate of CT value $\hat{\mathbf{x}}$

1 : **until** Convergence criterion is satisfied **do**
2 : Update x_j to minimize (9) by SCG method
3 : Update $\mathbf{z}_j$ to minimize (10) by graph cuts
4 : $\hat{\mathbf{x}}$ $\quad _j$

Figure 2: Proposed algorithm for CT reconstruction.

where $\mathbf{z}_j$ is a K-dimensional binary random vector whose kth element $z_{jk} \in \quad 0 \ 1$ is 1 when the pixel j belongs to the kth material class and other elements z_{jk} are 0. Since each pixel belongs to a single material class, $\sum_k z_{jk} = 1$ is satisfied.

When the material class is given, the attenuation coefficients $\mathbf{x}$ are assumed to obey a Gaussian distribution:

$$p(x_j|\mathbf{z}_j) = \prod_{k=1}^{K} \mathcal{N}(x_j| \quad _k \ r_k^2)^{z_{jk}} \tag{4}$$

where $_k$ and r_k^2 denote the mean and the variance of the Gaussian distribution, respectively, and r_k^2 was determined irrelevant to the material class (Table 1).

Although the class-wise means $_k$ should be calibrated in advance, this task would not be required for every subject because the values of $_k$ are expected not to vary significantly. Variations of $_k$ due to the unreliability of the CT scanner or the fluctuation of the CT values over different individuals, different organs, or different tissues are assumed to be captured by the randomness of Gaussian distribution, whose uncertainty is controlled by its variance r_k^2.

3. Prior for Class

We give the prior of the material class as the following Boltzmann distribution:

$$p(\mathbf{z}) = \frac{1}{Z} \exp \quad E(\mathbf{z}) \tag{5}$$

where Z is a normalizing constant and the energy is defined by

$$E(\mathbf{z}) = \quad \sum_{k=1}^{K} \quad J_k^{\text{self}} \sum_{j=1}^{J} z_{jk} + J_k^{\text{inter}} \sum_{j=1}^{J} \sum_{s\in \ (j)} z_{jk}z_{sk}) \tag{6}$$

Here, (j) represents the set of pixels adjacent to pixel j, and J^{self} and J^{inter} are nonnegative constants that control the characteristics of the class prior. The Boltzmann distribution takes a high probability when energy $E(\mathbf{z})$ is low. Therefore, the first term of the energy function represents the relative proportion of each material: large J^{self} promotes $z_{jk} = 1$. The second term defines the degree of correlation between neighboring pixels within the material, so as to control the spatial continuity.

Table 1: Parameter settings.

k: material	$_k$	r_k^2 (in §1)	J_k^{self} (in §1)	J^{inter} (in §1)	r_k^2 (in §2)	J_k^{self} (in §2)	J^{inter} (in §2)
1: air	0 000	$10\ ^{6}$	6	30	$10\ ^{6}$	0	50
2: soft tissue	0 018	$10\ ^{6}$	8	30	$10\ ^{6}$	20	50
3: normal tissue	0 022	$10\ ^{6}$	5	30	$10\ ^{6}$	10	50
4: bone	0 050	$10\ ^{6}$	10	30	$10\ ^{6}$	10	50
5: metal	0 120				$10\ ^{6}$	20	50

4. MAP Estimation

According to the Bayes theorem, the posterior distribution for $\mathbf{x}$ and $\mathbf{z}$ is proportional to the product of the prior distribution and likelihood function:

$$p(\mathbf{x}\ \mathbf{z}|\mathcal{D}) \propto p(\mathcal{D}|\mathbf{x})p(\mathbf{x}|\mathbf{z})p(\mathbf{z}) \tag{7}$$

We determine the variable $\mathbf{x}$ and $\mathbf{z}$ by maximizing the posterior probability. Taking the negative logarithm of (7), we can find the solution as a minimizer of the following objective function:

$$L(\mathbf{x}\ \mathbf{z}) = \quad \ln p(\mathcal{D}|\mathbf{x}) \quad \ln p(\mathbf{x}|\mathbf{z}) \quad \ln p(\mathbf{z}) \tag{8}$$

Since the simultaneous optimization for continuous variable $\mathbf{x}$ and discrete variable $\mathbf{z}$ is intractable, we iteratively update each component of the objective function:

$$\mathbf{x}^* = \arg\min_{\mathbf{x}} L(\mathbf{x}\ \mathbf{z}^*) \tag{9}$$

$$\mathbf{z}^* = \arg\min_{\mathbf{z}} L(\mathbf{x}^*\ \mathbf{z}) \tag{10}$$

Here, $\mathbf{x}^*$ is updated using the scaled conjugate gradient algorithm (SCG) and the $\mathbf{z}^*$ is updated by an expansion algorithm, which is a variant of graph cuts [7–9]. The algorithm is terminated when the relative change of $\mathbf{x}$'s norm is smaller than a predetermined threshold $10\ ^{5}$.

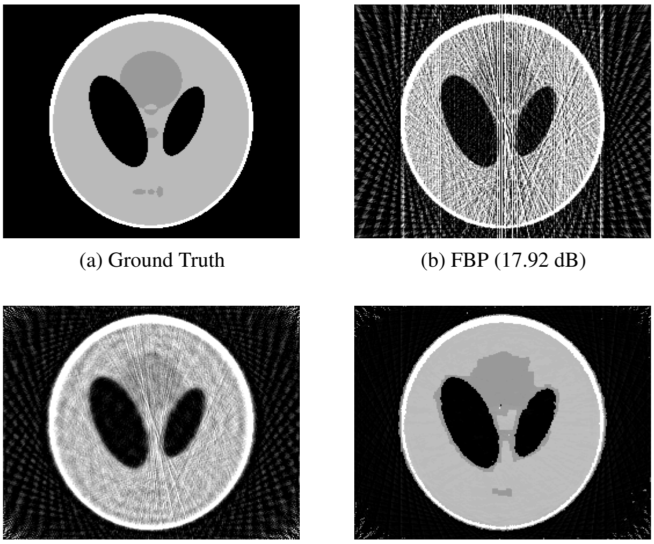

(a) Ground Truth (b) FBP (17.92 dB)

(c) ML (20.96 dB) (d) Proposed (22.58 dB)

Figure 3: Phantom without metal. The window used is [500 500] HU so that the corresponding x_j values are within [0 01, 0 03].

III. EXPERIMENTAL RESULTS

We tested our method by reconstructing phantom images in two severe situations. In the first experiment, the phantom did not include metal, but the number of projections was severely restricted. This setting was prepared to see the reconstruction performance when X-ray exposure was minimized. In the second experiment, metal was inserted into the phantom. This setting was to see how metal artifacts could be reduced by our method.

An attenuation coefficient x can be transformed into the Hounsfield unit (HU) by the following transformation: $1000(x \quad x_0)\ x_0$, where x_0 $(= \ 0\ 02)$ is the attenuation coefficient of water (H_2O).

1. Phantom Data Without Metal

A phantom was created as shown in Fig. 3(a) (471×353 mm ellipse). Parallel beam acquisition was simulated using 367 detectors and 32 projection angles over 180 . The blank scan value b_i was set to 10^5. Images of size 256×256 pixels were reconstructed. The following three different approaches were compared: filtered back projection (FBP), maximum likelihood (ML) [2], and our proposed method. The model parameters were fixed at hand-tuned values: $r_k^2 = 10\ ^{6}$, $J^{\text{inter}} = 30$, $J_1^{\text{self}} = 6$, $J_2^{\text{self}} = 8$, $J_3^{\text{self}} = 5$, $J_4^{\text{self}} = 10$ (Table 1).

The estimation results are shown in Fig. 3. The panels show (a) the ground truth image, reconstructed images by (b) FBP, (c) ML, and (d) the proposed method. The performances were measured by peak signal-to-noise ratio (PSNR), which is shown at the bottom of each panel. The PSNR of our algorithm (22.58 dB) is higher than those by the existing algorithms. The reconstruction results of FBP and ML are very noisy due to the limited number of projections. However, our result is smooth thanks to the prior incorporating the knowledge of material classes knowledge.

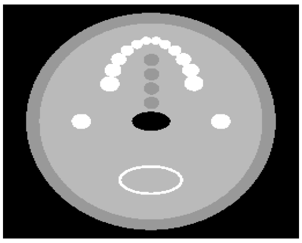

(a) Ground Truth

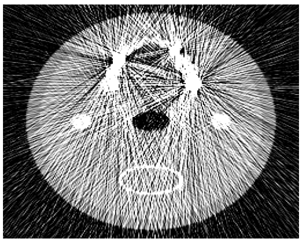

(b) FBP (24.29 dB)

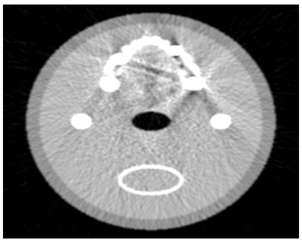

(c) PCLIS (30.36 dB)

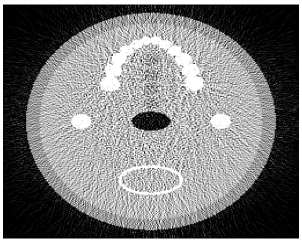

(d) ML (28.25 dB)

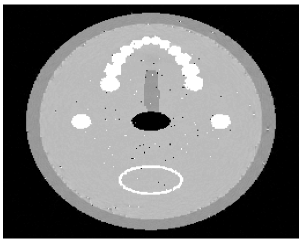

(e) Proposed (34.27 dB)

Figure 4: Phantom without metal. The window used is [500 500] HU so that the corresponding x_j values are within [0 01, 0 03].

2. Phantom Data With Metal Inserted

A head phantom (ellipse 472×436 mm) shown in Fig. 4 was created for the experiment with metal inserted; it includes three dental fillings (three disks with diameters 18, 19, and 23 mm) made of metal. Parallel beam acquisition was simulated using 185 detectors and 1791 projection angles over 180 . The blank scan value b_i was set to 10^5. The size of reconstructed images was 256×256 pixels.

Reconstruction was performed by FBP, ML, the projection completion method based on linear interpolation in the sinogram (PCLIS) [1], and our proposed method. The model parameters were set at hand-tuned values: $r_k^2 = 10\ ^{6}$, $J^{\text{inter}} = 50$, $J_1^{\text{self}} = 0$, $J_2^{\text{self}} = 20$, $J_3^{\text{self}} = 10$, $J_4^{\text{self}} = 10$, $J_5^{\text{self}} = 20$ (Table 1).

The reconstruction results are shown in Fig. 4. The panels show (a) the ground truth, reconstructed images by (b) FBP, (c) PCLIS, (d) ML, and (e) the proposed method. The corresponding PSNR is shown at the bottom of each panel. Our algorithm achieved the highest PSNR (34.27 dB) in the algorithms we compared. Good smoothing within each region was obtained by our method.

IV. CONCLUSION

In this article, we have proposed a new CT reconstruction method based on a statistical approach. The key point of our method was the introduction of the material class which allows the existence of extremely high-dense objects such as metal. Our new method enabled significant reduction of the metal artifacts compared to the existing algorithms. Furthermore, it showed better performance when the metal was not inserted but the signal-to-noise ratio was low due to the limited number of projections. Besides our material class model is beneficial for improving the reconstruction image quality, it would be helpful to detect the tumor and to identify anatomical structures owing to our material class segmentation based on CT values, even in the existence of metal.

REFERENCES

[1] W. A. Kalender, R. Hebel, and J. Ebersberger, "Reduction of CT artifacts caused by metallic implants," in *Radiology*, Aug. 1987, vol. 164, pp. 576–577.

[2] J. Nuyts, B. D. Man, P. Dupont, M. Defrise, P. Suetens, and L. Mortelmans, "Iterative reconstruction for helical CT: a simulation study," *Phys. Med. Bio.*, vol. 43, pp. 729–737, 1998.

[3] C. Lemmens, D. Faul, and J. Nuyts, "Suppression of metal artifacts in CT using a reconstruction procedure that combines MAP and projection completion medical imaging," *IEEE Trans. Med. Imaging*, vol. 28, no. 2, pp. 250–260, Feb. 2009.

[4] I. T. Hsiao, A. Rangarajan, and G. Gindi, "Joint-MAP Bayesian tomographic reconstruction with a gamma-mixture prior," *IEEE Trans. Image Process.*, vol. 11, pp. 1466–1477, 2002.

[5] M. Bal and L. Spies, "Metal artifact reduction in CT using tissue-class modeling and adaptive prefiltering," *Med. Phys.*, vol. 33, no. 8, pp. 2582–2859, 2006.

[6] A. Mohammad-Djafari, "Gauss-Markov-Potts priors for images in computer tomography resulting to jonit optimal reconstruction and segmentation," *Int. J. Tomogr. Stat.*, vol. 11, pp. 76–92, 2008.

[7] Y. Boykov, O. Veksler, and R. Zabih, "Efficient approximate energy minimization via graph cuts," *IEEE Trans. Pattern Anal. Mach. Intell.*, vol. 20, no. 12, pp. 1222–1239, Nov. 2001.

[8] Y. Boykov and V. Kolmogorov, "An experimental comparison of min-cut/max-flow algorithms for energy minimization in vision," *IEEE Trans. Pattern Anal. Mach. Intell.*, vol. 26, no. 9, pp. 1124–1137, Sept. 2004.

[9] V. Kolmogorov and R. Zabih, "What energy functions can be minimized via graph cuts?," *IEEE Trans. Pattern Anal. Mach. Intell.*, vol. 26, no. 2, pp. 147–159, Feb. 2004.

Implementation of TFT Inspection System Using The Stream Processor

Bum Yong Park , Chang Hee Lee, and PooGyeon Park

Electrical and Computer Engineering Division
Pohang University of Science and Technology Pohang, Kyungbuk, 790-784, Korea
(Tel : 82-54-279-5588; Fax : 82-54-279-2903)
(merongyong@postech.ac.kr, eooe@postech.ac.kr, ppg@postech.ac.kr)

Abstract: Recently, computational power of parallel processor is strong enough to be used in many applications. Following these trends, we adapted the stream processor for thin film transistor liquid crystal displays (TFT-LCD) inspection. In this paper, we explain various defects on TFT-LCD and describe the implementation of the inspection system on the stream processor and CPU respectively. The components and behavioral properties of the inspection system are also explained. Then, we compare the performance of the systems equipped with the stream processor and CPU using the inspection algorithm that utilizes the repeated characteristics of the TFT-LCD. It will be shown that this algorithm is easy to implement on the stream processor. Finally, the experiment results show the successful transition from the traditional CPU-based system to the stream processor based system in the TFT-LCD inspection.

Keywords: Thin Film Transistor (TFT), Inspection System, Stream Processor, Parallel Processing, Liquid Crystal Displays (LCD)

I. INTRODUCTION

The TFT-LCD is widely used in many electronic devices. As its manufacturing industry requires faster production speed with higher yield, a more accurate and faster inspection instrument is crucial. Since early 1990's, practical LCD inspection methods have been proposed [1]. Most of the early methods require physical contact on LCD panel, which results in slow inspection speed and complex production line. Recently, many inspection systems begin to use digital images captured by the charge coupled devices (CCD) or the complementary metal oxide semiconductor (CMOS) devices. Since these devices make non-contact inspection system possible, a fast and efficient inspection has been expected to be realized. However, the higher resolution and faster inspection speed, the huge amount of data needs to be processed.

The TFT-LCD has repeated patterns around the whole panel. Therefore, the inspection algorithms can utilize its repeated pattern [2]. Simple computation is repeated through the inspection, processing a huge amount of data. However, traditional serial processing using the central processing unit (CPU) is very inefficient for this application. As a solution of realizing the parallel processing, digital signal processors (DSP), application specific integrated circuits (ASIC) or field-programmable gate array (FPGA) connected in parallel have been solutions in the embedded system at extremely high costs. Moreover, their solutions have difficulties in modifying the algorithm.

In this paper, we adapt the stream processor of Stream Processor Inc. (SPI) against the previous solutions because of the parallel architecture inside a single chip and high programmability with C-like programming langue, called StreamC, at an affordable cost. The stream programming model exposes the parallelism and locality inherence in the application, and the SPI processor design and software development tools can easily exploit this parallelism and locality in hardware. Because of these advantages, it is possible to use it in many applications. The vision inspection is a good example of performance enhancement.

The paper is organized as follows. Section II explains defects on various TFT-LCD. Section III represents the algorithm used for the inspection and the performance comparisons. Section IV explains the implementation of the inspection systems on a stream processor. Section V shows simulation results and the improvement of the inspection speed of the system based on stream processor. Finally, section VI is conclusion.

II. DEFFECTS ON TFT-LCD

Defects on the TFT-LCD cause visual failure and electrical failure. Visual failure on TFT-LCD is classified into two parts: macro and micro-defects [3]. Macro-defects include "MURA", "SIMI" and "ZURE". "MURA" means unevenness of color. "SIMI" means a clack on TFT-LCD. ZURA means misalignment of TFT-LCD. They are generally large size and can be detected human's eye. Micro-defects include scratches, fingerprints, particles and pinholes. They are very small size and can be hardly found human's eye.

The proposed method in this paper focuses on macro-defects. Although macro-defects are large size, some defects cannot be founded by the visual system of human. Human inspector slows down the processing speed. So, as mentioned before, we used vision inspection system.

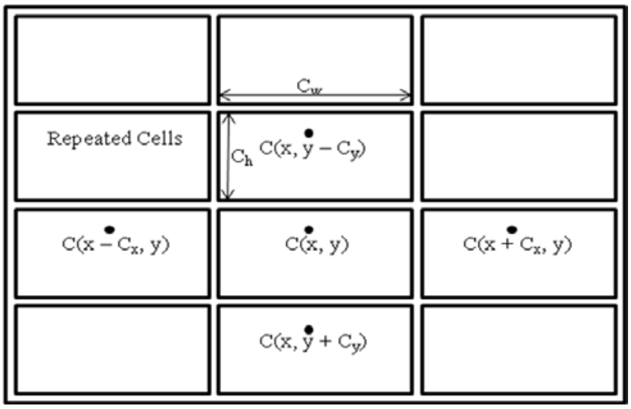

Fig.1. Repeated cells and variables on TFT-LCD

III. INSPECTION ALGORITHM

The following equations describe the basic decision scheme [4]. Fig. 1 shows repeated pattern on TFT-LCD and variables used in this algorithm. One pixel has a value of image data of 8 bit. The main equations of proposed algorithm are the followings.

$$D_U(x,y)=\begin{cases}|c(x,y)-c(x,y-C_h)| & if\ y>C_h,\\ |c(x,y)-c(x,y+2C_h)| & if\ y<C_h,\end{cases}\quad (1)$$

$$D_D(x,y)=\begin{cases}|c(x,y)-c(x,y+C_h)| & if\ y<H-C_h,\\ |c(x,y)-c(x,y-2C_h)| & if\ y>H-C_h,\end{cases}\quad (2)$$

$$D_L(x,y)=\begin{cases}|c(x,y)-c(x-C_x,y)| & if\ x>C_w,\\ |c(x,y)-c(x+2C_x,y)| & if\ x<C_w,\end{cases}\quad (3)$$

$$D_R(x,y)=\begin{cases}|c(x,y)-c(x+C_x,y)| & if\ x<W-C_w,\\ |c(x,y)-c(x-2C_x,y)| & if\ x>W-C_w,\end{cases}\quad (4)$$

$$O(x,y)=\begin{cases}0 & if\ \min(D_U,D_D)\le T,\\ 1 & if\ \min(D_U,D_D)\ge T,\end{cases}\quad (5)$$

$$O(x,y)=\begin{cases}0 & if\ \min(D_R,D_L)\le T,\\ 1 & if\ \min(D_R,D_L)\ge T,\end{cases}\quad (6)$$

$$O(x,y)=\begin{cases}0 & if\ \min(D_U,D_D,D_R,D_L)\le T,\\ 1 & if\ \min(D_U,D_D,D_R,D_L)\ge T,\end{cases}\quad (7)$$

$$T=\begin{cases}T_L & if\ c(x,y)\le S\\ T_H & if\ c(x,y)>S\end{cases}\quad (8)$$

where
a) W is positive integer value of horizontal width.
b) H is positive integer value of vertical height.
c) c(x,y) is integer value of intensity at position (x,y) ranging from 0 to 255.
d) C_w is constant integer of horizontal length of repeated cell patterns.
e) C_h is constant integer of vertical length of repeated cell patterns.
f) $D_U(x,y)$, $D_D(x,y)$, $D_L(x,y)$ and $D_R(x,y)$ are differences of values of pixels.
g) T is positive constant integer of threshold to decide whether the target pixel is defective or not.
h) O(x,y) is the inspection result of pixel at (x,y). The value 1 means defective pixel and 0 means normal pixel.
i) T is decided by S which is a standard of value of pixel.

These are three equations (5), (6) and (7) in output value, O(x,y). When horizontal width, W is not longer than three times of that of cell, $3C_w$, equation (5) is used. When vertical height, H is not longer than three times of that of cell, $3C_h$, equation (6) is used. Threshold, T differs by value of pixel. Since defects are represented to black, T should be small when the value of pixel is small.

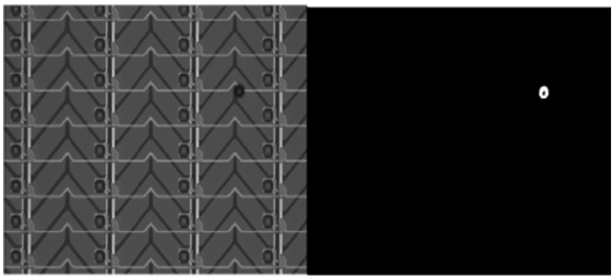

Fig.2. Tested image with defective pixels and resultant image.

IV. IMPLEMENTATION

The system consists of several CCD or CMOS sensors and stream processors. Most parts of the inspection algorithm run on the stream processor in a parallel manner.

A stream processor contains a general purpose unit (GPU) for data handling and control, a data parallel unit (DPU) for compute-intensive inner loop computations, and peripheral units that perform device i/o. The stream processor GPU contains two MIPS processors: System MIPS handles user interface and device i/o, while DSP MIPS handles communication with the DPU.

Implementation of algorithm on stream processor is simple. Input image data from CCD sensors are transferred to stream processor. One pixel line of image data is loaded to one lane which is process unit in DPU. Since the stream processor used this system have 16 lanes, once 16 pixel lines of image data are loaded to DPU. Values of pixels that loaded in DPU are calculated by DPU using the proposed algorithm.

V. RESULT

We used 2 different size of images, (1024, 720), (1024, 1000) pixel^2. Testing was done with previously acquired images. Fig. 2 shows one of tested images with the resolution (1024, 720) pixel^2 and has defective pixels to

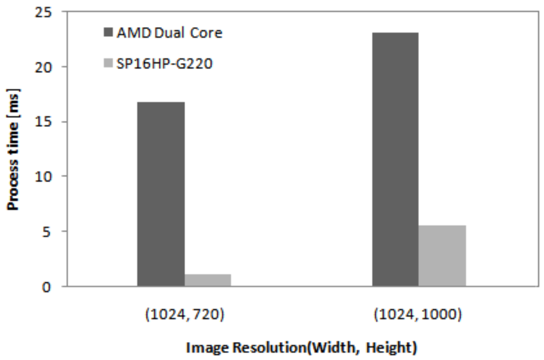

Fig.3. Comparison of the processing time by stream processor and CPU

show the inspection result more clearly. It is made by converting 0 to 255 and 1 to 0 from the results of equations (5) to visualize it.

Fig. 3 shows the comparison of processing speeds. Process time by stream processor contains the image data transmission from flash memory in system MIPS to memory in DPU. It shows superior speed enhancement of stream processor about 10 times better though it contains the transmission time. It also shows that processing time of a large image size is fast.

VI. CONCLUSION

We have presented implementation of a TFT-LCD inspection algorithm and its performance with stream processor and CPU. The TFT-LCD inspection algorithm is simple operation but it is applied to a huge size of data. So it requires parallel processing. Stream processor is one of the most proper devices that can increase processing speed. Also it is used for embedded system. The experimental results show how much its performance can be improved. As a future work, we consider that implementations of more sophisticate algorithm and the optimization of stream processor architectures.

ACKNOWLEDGMENT

This research was supported by WCU (World Class University) program through the Korea Science and Engineering Foundation funded by the Ministry of Education, Science and Technology (Project No. R31-2008-000-10100-0).

This research was supported by the MKE(The Ministry of Knowledge Economy), Korea, under the ITRC(Information Technology Research Center) support program supervised by the NIPA(National IT Industry Promotion Agency (N I PA-2009-C1090-0902-0004)

This research was supported by the Brain Korea 21 Project in 2009.

REFERENCES

[1] S. M. Sokolov and A. S. Treskunov, Automatic vision system for final test of liquid crystal displays, IEEE International Conference on Robotics and Automation, ser. Proceedings of the 1992 IEEE International Conference on Robotics and Automation, vol. 2. Nice, Fr: Publ by IEEE, 1992, pp. 1578–1582.

[2] D. M. Tsai and C. Y. Hsieh, Automated surface inspection for directional
Textures, Image and Vision Computing, vol. 18, no. 1, pp. 49–62, 1999.

[3] K. Nakashima, Hybrid inspection system for lcd color filter panels, Conference Record - IEEE Instrumentation and Measurement Technology Conference, vol. 2, pp. 689–692, 1994.

[4] Chang Hee Lee, Changki Jeong, Moonsoo Chang and PoogGyeon Park, Implementation of TFT Inspection System using the Common Unified Device Architecture (CUDA) on Modern Graphics Hardware, Control, Automation, Robotics and Vision, 2008. ICARCV 2008. 10th International Conference, pp.1899-1902.

Study on the Crack Detection of Bridges Based on Digital Image Processing

Jiwu Wang Guoqi Zhang Mingcheng E

Department of Mechanical Engineering, Beijing Jiaotong University, Beijing, China
Email: jwwang@bjtu.edu.cn, 07121735@bjtu.edu.cn, emch@bjtu.edu.cn

Abstract: It is necessary to carry on the inspection of the bridge after more and more bridges are built. In view of present inspection techniques, we try to explore to inspect the bridge by machine vision. Considering the practical complex working conditions, such as lighting conditions, interference of the shadows of the trees or cables, it is difficult to realize the reliable crack extraction. In this paper, we try to solve those problems with various algorithms. Some initial good results were obtained. The further research will be carried on soon.

Keywords: Crack detection, Machine vision, Image processing**.**

I. INTRODUCTION

In the bridge inspection, more and more attention is paid on the crack detection. Compared with other defects, the crack is important to determine whether the bridge will be maintained or not. Although a crack is the defect on the surface of a bridge, we will find the internal stress indirectly based on the length, width and depth of the crack on its surface.

Now people can only inspect the bridge manually in most cases. We check the cracks for each building by human being's eye or using telescope. In order to get the dimensions of each crack, they have to measure it with some tools. However, in some cases, such as the high bridge, or the bridge is not easy to reach, they have to use some telescope or special equipments. Even if we can get some results, the high accuracy is difficult to be satisfied. On the other hand, we have to consider the cost, safety and efficiency, etc.

In view of present inspection methods, it is necessary to develop some methods to detect the cracks automatically. Machine vision is a good solution. In the machine vision, it captures the images by the CCD camera; with the special image processing technique, the target object (such as the crack) is extracted; the dimensions of the target will be calculated. That is, machine vision works like human beings. It tries to help people to perform some tasks where people are not appropriate to reach.

It is different from the laboratory conditions or indoor environments, where the influence is generally controlled. But in the outside, the background is various. It makes the crack extraction more difficult. That means we have to use the compound methods to extract the cracks, moreover, we have to consider the recognition method to separate the cracks from other objects. At the same time, we will also need to consider the speed of the image processing in the real applications.

Till now, various defects' detection is developed with the machine vision. But for the crack detection, we have to consider the practical working environments, such as lighting conditions. At the same time, we also need to consider the interference by the shadow of the cables or trees etc. In this paper, based on some images of the cracks, we explored the methods to extract the cracks.

In the following sections, we will give more details explanations about each topic. Moreover, we will also provide some crack extraction results by our image processing methods.

II. IMAGE PROCESSING

After we get the image from the CCD video camera, we will detect the cracks in that image based on corresponding algorithms. Automatic crack detection is highly desirable for efficiency and objectivity of crack assessment. However, generally it is difficult to extract cracks automatically from noisy bridge surfaces. Cracks in the images obtained from the practical workspace are contaminated by noises such as oil paint, scratch, cables and so on. Besides, the light condition, focal distance seriously effected the images' quality. Thence a satisfied result cannot be obtained only with several common algorithms of the image processing.

Based on the analysis of the characteristics of images contained bridge cracks this article proposed some special image processing algorithms to obtain the cracks’ area, length and width. Besides, one software using MATLAB language was developed. The processed result showed that the software was suitable for the crack detection of bridge surface.

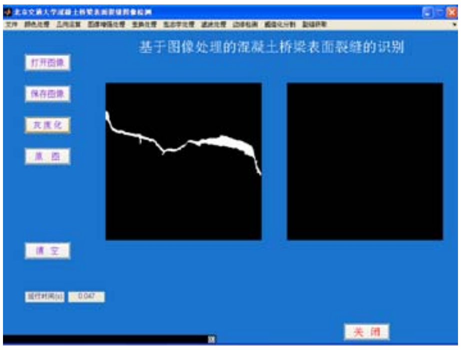

Fig.1. Interface of the software

Now we take one sample image as an example. The image processing will be explained as followings.

1. Graying

The RGB image shown in Fig.2 was obtained by the CCD camera. Normally, in order to accelerate the images' processing speed, the RGB image can be transformed to gray one shown in Fig.3 which contains the necessary information to meet the following process.

Fig.2. Original Image

Fig.3. Gray image

2. Image enhancement

The principal objective of enhancement is to process an image so that the result is more suitable than the original image for a special application. Image enhancement approaches fall into two broad categories: spatial domain methods and frequency domain methods. In this paper, the gray level transformation, fourier transformation, wavelet transformation were applied to enhance the gray images.

Fig.4. Result after enhancing image.

3. Threshold

The simplest segmentation algorithm is to threshold the image. The threshold operation is defined by:

$$S = \{(r,c) \in R \mid g_{\min} \le f_{r,c} \le g_{\max}\}$$

This paper applies the Basic Global Thresholding, Otsu and customized thresholding algorithm in order to divide an image into several parts according to the pixels' different gray value.

Global Threshold

Global Threshold is based on visual inspection of the histogram. The following algorithm can be used to obtain T automatically:

1) Select an initial estimate for T.
2) Segment the image using T. This will produce two groups of pixels: G_1 consisting of all pixels with gray level values>T and G_2 consisting of pixels with values <=T.
3) Compute the average gtray level values μ_1 and μ_2 for the pixels in regions G_1 and G_2.
4) Compute a new threshold value:

$$T = \frac{1}{2}(\mu_1 + \mu_2)$$

5) Repeat steps 2 through 4 until the difference in T in successive iterations is smaller than a predefined parameter T_0.

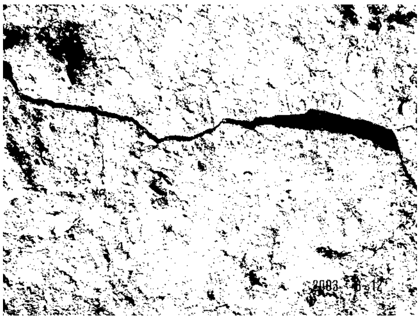

Fig.5. Result of global thresholding from Fig.4.

Otsu thresholding

It is considered to be an adaptive thresholding method. An image is divided into parts of background and object. The more inter-class variance provided, the more difference between the background and object. If a part of object area was mistaken to background, the difference will be reduced, and vice versa.

An image: I(X,Y),size:M×N.

$$W_0 = N_0 / M * N$$
$$W_1 = N_1 / M * N$$
$$N_0 + N_1 = M * N$$
$$W_0 + W_1 = 1$$
$$\mu = W_0 \times \mu_0 + W_1 \times \mu_1$$
$$g = W_0 \times (\mu_0 - \mu)\hat{}2 + W_1 \times (\mu_1 - \mu)\hat{}2$$

In the formulations above, N_0 represents the number of object pixels. N_1 represents the number of background pixels. μ_0 represents the average value of the object area. μ_1 represents the average value of the background area. μ represents the average gray value of the global image. g represents the inter-class variance. We can utilize the traversal method to find the largest threshold value T. The result is shown in Fig.6.

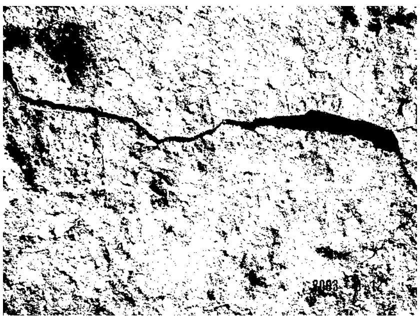

Fig.6. Result of OTSU

Customized threshold

By virtue of Matlab language, we can compare the images under the different threshold value between 0 and 255. Fig.5 shows the threshold image under the value 110.

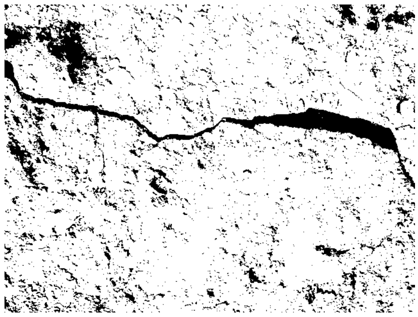

Fig.7. Result of customized threshold image

Fig.8. Result of filtering image

4. Filtering

In this paper, we utilize the median filtering method to filter the segmentation image shown in Fig.8.

5. Feature extracting

In the images with rather single background, in general the connected area of crack is larger than other feature's and the length is longer than other feature's, too.

1) Invert the background' color to black and the object' color to white. Result is shown in Fig.9.
2) Mark the region in the image obtained after filtering.
3) Compute all regions' area, length, round-degree, compare them separately. And then, get the label number N with the minimum round-degree, but its area and length are both the maximum value among those regions.
4) Keep the pixels' value 1 in the region N, and set the value of remaining region's pixels 0. The final result is shown in Fig.10.

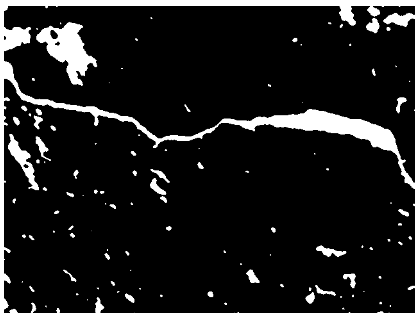

Fig.9. Result of inverting image

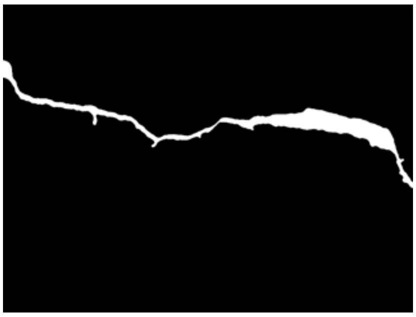

Fig.10. Final result

In the end, after the five steps above, we receive the processed image only with the crack feature. At the same time, the crack's area, length and width have been computed.

III. CONCLUSION

In this paper, we carry on the initial study on the crack detection based on the image processing technique. Some results are obtained. Next step, we will test with more samples, and consider the influence of the lighting conditions etc.

REFERENCES

[1] M.Sugisaka, Wang Xin and J. Lee, "Artificial brain f or a mobile vehicle", Applied mathematics and computa tion, Vol. 111, 2000.
[2] Jiwu Wang, M.Sugisaka, "Study on a color based target detection technique", Proc. of the seventh Int. Symp. On artificial life and robotics (AROB 7th'02), Beppu, Oita, Japan. 16-18 January, 2002.
[3] Cathy-Ann Radix, Andrey Loukianov, Masanori Sugisaka, "Evaluating motion on the alife robot prototype", Proceedings of the 32nd ISR (International Symposium on Robotics), 19-21 April 2001.
[4] Ulrich Nehmzow, Carl Owen, "Robot navigation in the real world: experiments with Manchester's Fortytwo in unmodified, large environments", Robotics and autonomous systems, Vol. 33, 2000.
[5] F.El-Khaly, M.A.Sid-Ahmed, "Machine recognition of optically captured machine printed Arabic text", Pattern recognition, vol. 23, No. 11, 1990.
[6] Alireza Khotanzad, Yaw Hua Hong, "Rotation invariant image recognition using feature selected via a systematic method", Pattern recognition, Vol. 23, No. 10, 1990.
[7] S.O.Belkasim, M.Shridhar and M.Ahmadi, "Pattern recognition with moment invariants: a comparative study and new results", Pattern recognition, Vol. 24, No. 12, 1991.
[8] Jiwu Wang, M.Sugisaka, "Improve digit recognition capability of backpropagation neural networks by Enhancing image preprocessing technique", Proceedings of International Conference on Control, Automation and Systems, Cheju University, Jeju, Korea, October 17-21, 2001.
[9] Jiwu Wang, M.Sugisaka, "Study on calibration of stereo cameras for a mobile robot prototype", Proc. of the seventh Int. Symp. On artificial life and robotics (AROB 7th'02), Beppu, Oita, Japan. 16-18 January, 2002.
[10] Seth Hutchinson, Gregory D.Hager, Peter I.Corke, "A tutorial on visual servo control", IEEE Transactions on Robotics and Automation, Vol. 12, No. 5, October 1996.
[11] Peter I.Corke, Malcolm C.Good, "Dynamic effects un visual closed-loop systems", IEEE Transactions on Robotics and Automation, Vol. 12, No. 5, October 1996.

Adaptive Image Filtering for Tracking Control of Robots

Di Cao[1], Yingmin Jia[1], Junping Du[2]

1. The Seventh Research Division, Beihang University(BUAA), Beijing 100191, P.R.China
2. Beijing Key Laboratory of Intelligent Telecommunications Software and Multimedia,
Beijing University of Posts and Telecommunications, Beijing 100876, P.R.China
(dic_2003@yahoo.com.cn, ymjia@buaa.edu.cn, junpingd@bupt.edu.cn)

Abstract: In this paper, a new adaptive image filtering scheme is first proposed based on color and pixel features, in which a compensation algorithm for the background difference of global illumination, and the H/S Model based adaptive image filtering algorithm are developed respectively. Then a tracking control strategy of robots is given, and the corresponding experimental results are provided to demonstrate the effectiveness of the proposed scheme.

Keywords: *Image Processing, Adaptive Filtering, Visual Tracking, Mobile Robots*

I. Introduction

Recently, the adaptive image filtering problem has attracted a great deal of attention in many fields such as robotics, signal processing, pattern recognition, control engineering, etc.. Image filtering is a set of techniques used to enhance or restore images, including image smoothing, sharpening, blurring, edge detection, mean removal and embossing. At present, some valuable adaptive filters have been proposed, whose fundamental issues includes temporal averaging [1] and median filtering. The Wiener filter is not adequate for removing speckle since it is designed mainly for additive noise suppression. To address the multiplicative nature of speckle noise, Jain developed an approach by which the multiplicative noise can be turned into additive noise by taking the logarithm of the image [2]. Kuan considered a multiplicative speckle model and designed a linear filter based on the minimum mean-square error criterion when the scene and the detected intensities are Gaussian distribution [3]. Sadjadi and Bannour proposed a two-dimensional Kalman filter, which is in a Markov field satisfying autoregressive model [4]. The Model-Based Diagnosis(MBD) technique [5] is essentially a Maximum Aposteriori Probability(MAP) filter, which was developed based on modeling textured areas.

In reality, there exist a variety of local image feature-dependent adaptive filtering strategies, including local image statistics filtering [6], adaptive neighborhood averaging which uses piecewise approximation of uniform regions [7], least-squares error filtering [8], gradient inverse-weighted filtering [9], multiple-model filtering, local shape-based template-matched adaptive filtering, and gradient-controlled anisotropic diffusive filtering [10-13]. Whitaker and Pizer [14] presented a multi-scale nonlinear diffusive filtering approach in which diffusion is controlled under a time varying scale parameter. Weickert [15] proposed an anisotropic, nonlinear diffusion process that uses both modulus as well as direction of gradients. De Grandi presented a wavelet multi-resolution representation to provide a unified framework for signal approximation, filtering and classification [16].

With this background, we investigate an adaptive image filtering based on color and pixel features, and apply it to the tracking control of mobile robots. To this end, we first present an algorithm to compensate the background difference for global illumination. Then, we propose the H/S Model and the adaptive image filtering algorithm.

II. Main Results

The task of adaptive image filtering is to recognize target in the image acquired by the camera. The general flowchart of the algorithm is shown in Fig. 1. There, we can see clearly that the input to the algorithm is raw image from the camera, and the output is tracking control strategy of robots. Adaptive image filtering consists of three core aspects, i.e., illumination compensation algorithm, adaptive image filtering algorithm based on H/S model and tracking control strategy of robots. These are described in detail below.

A. Illumination Compensation Algorithm

The algorithm is used to compensate the background difference for global illumination, which can be completed by five steps.

Step 1 Initialization: Monitor the change of attribute values of the reference points. Determine the initial thresholds of the image of environment. The initial thresholds are (H_0, S_0). Let $\triangle H = 0, \triangle S = 0$, where $\triangle H$ is the change in hue and $\triangle S$ is the change in saturation.

Step 2 Filtering: Perform 5×5 median filtering on the resulted image.

Step 3 Reference points P_i sampling: Obtain the values of reference points, and calculate hue mean value

μ_{REFH} and saturation mean value μ_{REFS} of reference points.

$$\mu_{REF} = [\mu_{REFH}, \mu_{REFS}] \quad (1)$$

Then, calculate the standard deviation σ_{REF}.

$$\sigma_{REF} = [\sigma_{REFH}, \sigma_{REFS}] \quad (2)$$

Step 4 Standard deviation analysis: if $\sigma_{REF} > \sigma_T$, then calculate $\triangle H$ and $\triangle S$:

$$[\triangle H, \triangle S] = \mu_{REF} - \mu'_{REF} \quad (3)$$

The thresholds are calculated as follows:

$$\begin{aligned} H_{TH} &= H_0 + \triangle H \\ S_{TH} &= S_0 + \triangle S \end{aligned} \quad (4)$$

The new thresholds (H_{TH}, S_{TH}) are used in the next operation.

Step 5 Update image: For each pixel on position(x,y) of the reference points, compute the change of attribute values.

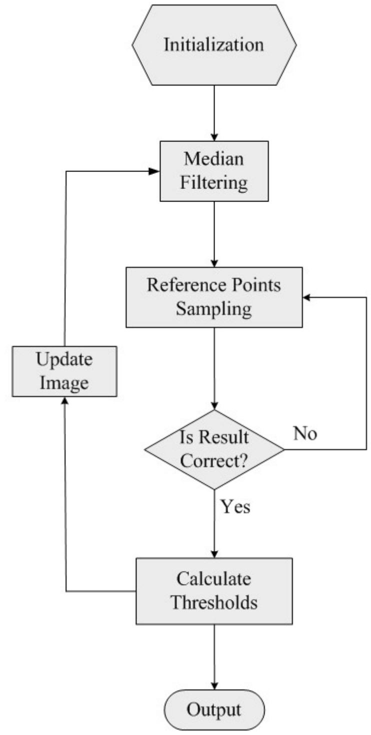

Fig.2. Illumination Compensation Method

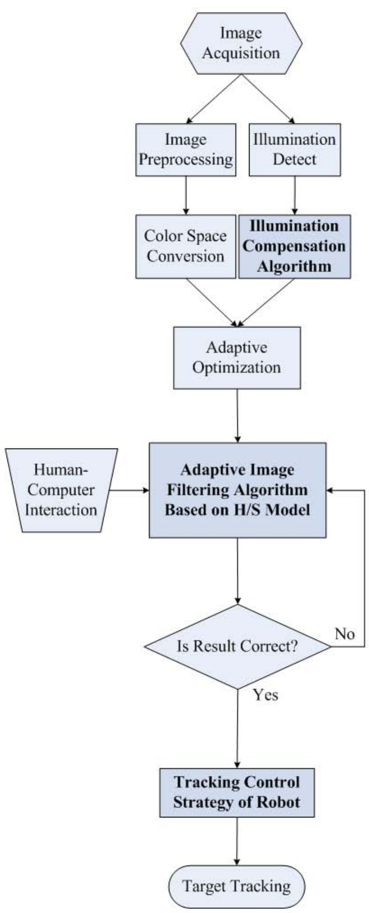

Fig.1. General Flow Chart of the Algorithm

B. Adaptive Image Filtering Algorithm Based on H/S Model

The algorithm is designed to set the thresholds of images adaptively. The thresholds will be calculated in HSI color spaces [17]. The calculation is important to subsequent operations. The next step is to select the target that is recognized during initialization of image. And the initial values of thresholds are determined by means of off-line learning. We propose the H/S Model based on which the adaptive image filtering algorithm is formulated as follows:

Step 1: For each pixel in the image:

$$D_i = [R_i, G_i, B_i] \quad (5)$$

Most color grading systems use HSI rather than RGB values to specify color preferences because it is based on human-distinguishable hues and a more intuitive representation than RGB. Due to the geometric discontinuity of color space it is difficult to set or adjust color grade boundaries using hue values alone. It can be overcome by including the intensity component from the HSI color space in the computations [18]. Therefore, we convert the input RGB image to the HSI color space.

$$\begin{aligned} H_i &= \{\theta_i \mid if B_i \le Gi \ ; \ 360 - \theta_i \mid if B_i > Gi\} \\ S_i &= 1 - \frac{3}{R_i + G_i + B_i} \min(R_i, G_i, B_i) \\ I_i &= \frac{1}{3}(R_i + G_i + B_i) \end{aligned} \quad (6)$$

where

$$\theta_i = \cos^{-1} \frac{(R_i - G_i) + (R_i + B_i)}{[(R_i - G_i)^2 + (R_i - B_i)(G_i - B_i)]^{\frac{1}{2}}} \quad (7)$$

And the value of $\min(R_i, G_i, B_i)$ denotes the minimum among of red, green and blue components of the image.

Step 2: Calculate color histogram of image and use it as its color feature. Then we divide image data into blocks and calculate the mean value (H_{Ki}, S_{Ki}) of each block that can be described by the normalized method [19] on both hue and saturation.

$$\begin{aligned} \triangledown Q &= (\triangledown Q_x, \triangledown Q_y) \\ \triangledown Q_x &= \| \partial_x H_{Ki}, \partial_x S_{Ki} \| \\ \triangledown Q_y &= \| \partial_y H_{Ki}, \partial_y S_{Ki} \| \end{aligned} \quad (8)$$

Note that

$$\begin{aligned} V_k &= [V_{kx}, V_{ky}], U_k = [U_{kx}, U_{ky}] \\ V_{kx} &= \partial_x H_{Ki} / \partial x \\ V_{ky} &= \partial_y H_{Ki} / \partial y \\ U_{kx} &= \partial_x S_{Ki} / \partial x \\ U_{ky} &= \partial_y S_{Ki} / \partial y \end{aligned} \quad (9)$$

Step 3: Establishing the H/S Model:

$$F_i = \Sigma_{j=1}^{n} \lambda_j P_j (n = 1, 2, 3, 4) \quad (10)$$

where

$$P_j = \begin{cases} V_k & j = 1 \\ U_k & j = 2 \\ H_{ki} & j = 3 \\ S_{ki} & j = 4 \end{cases}$$

λ_j is a weighted value, according to the contributions of the values of P_j. And F_i is confidence coefficient

$$\gamma_i = \begin{cases} 0 & F_i = [0, \alpha_1) \\ \varphi F_i & F_i = [\alpha_1, \alpha_2] \\ 1 & F_i = (\alpha_2, 1] \end{cases} \quad (11)$$

The value of γ_i denotes the output result of filtering.

C. Tracking Control Strategy of Robots

After adaptive image filtering, the moving object can be recognized in image. The motion vector of the object is calculated in image coordinate system. The coordinates of the moving object can be obtained by means of calculating the center vector G_c on image plane[20].

$$\Gamma_i = G_c K_i \quad (12)$$

where, Γ_i represents the position of object in the image coordinate system. K_i is the coefficient matrix of the image.

We can calculate the coordinates of the moving object relative to image.

$$\Gamma_R = M_i^r \Gamma_i N_R \quad (13)$$

$$N_R = G_i N_R^i \quad (14)$$

where, M_i^r is the coordinate conversion matrix. Γ_R represents position and angle parameters of the moving object relative to the mobile robot. Further, we can calculate the motion vector of the mobile robot.

III. Experiments and Results

The system architecture includes a camera, which is fixed up on the top of a lab mobile robot. The video frames are 320×240 pixels in size, and were recorded at 25 frames per second. The host computer was a PC/104 embedded industry controll computer, with an 850MHz Pentium processor and 512MB of 266MHz RAM. The entire tracking system was implemented using C++ under Microsoft Windows XP, with no platform specific optimizations.

In the experiment, the mobile robot begins to track the object, when the object starts to move. As shown in Figure 3, the horizontal and vertical axes in the figure stand for time and the error of robot tracking respectively. It shows that the error of robot tracking decreases along with time. We believe that the robot and the target move synchronously when the tracking error is less than 5 pixels.

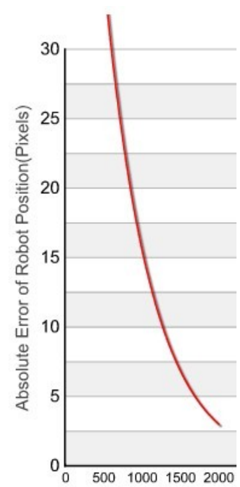

Fig.3. Robot Tracking Process

Fig.4 shows absolute error of robot position changing with time. The horizontal and vertical axes in the figure stand for time and absolute error of robot position respectively. It is known that the error of robot position can be constrained below 15 pixels.

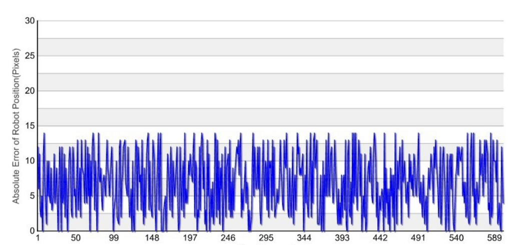

Fig.4. Absolute Error of Robot Position

IV. Conclusions

In this paper, we have proposed an adaptive image filtering approach based on color and pixel features, and applied it to solve the problem of tracking control of mobile robots. Experimental results show that the proposed approach is robust with high recognition rate and can find a wide application. Although discussion is done only within the indoor environment, and it is also possible to be used for outdoor environment, which is currently under consideration.

V. Acknowledgements

This work was supported by the National Natural Science Foundation of China (Grant Nos. 60727002, 60774003, 60921001, 90916024), the National 973 Program (No.2005CB321902), and the COSTIND (No. A2120061303).

References

[1] J. W. Goodman(1976), Some fundamental properties of speckle, J. Opt. Soc. Amer., vol. 66, pp. 1145-1150, Nov. 1976.

[2] A. K. Jain(1989), Fundamental of Digital Image Processing. Englewood Cliffs, NJ: Prentice-Hall, 1989.

[3] D. T. Kuan, A. A. Sawchuk, T. C. Strand, P. Chavel(1985), Adaptive noise smoothing filter for images with signal-dependent noise, IEEE Trans. Pattern Anal. Mach. Intell., vol. PAMI-7, no. 2, pp. 165-177, Feb. 1985.

[4] M. R. Azimi-Sadjadi, S. Bannour(2000), Two-dimensional adaptive block Kalman filtering of SAR imagery, IEEE Trans. Geosci. Remote Sens., vol. 29, no. 5, pp. 742-753, Sep. 1991. M.Walessa and M. Datcu, "Model-based despeckling and information extraction from SAR images," IEEE Trans. Geosci. Remote Sens., vol. 38, no. 9, pp. 2258-2269, Sep. 2000.

[5] M.Walessa, M. Datcu(2000), Model-based despeckling and information extraction from SAR images, IEEE Trans. Geosci. Remote Sens., vol. 38, no. 9, pp. 2258-2269, Sep. 2000.

[6] H. Xie, L. E. Pierce, F. T. Ulaby(2002), SAR speckle reduction using wavelet denoising and Markov random field modeling, IEEE Trans. Geosci. Remote Sens., vol. 40, no. 10, pp. 2196-2212, Oct. 2002.

[7] A. Achim, P. Tsakalides, A. Bezerianos(2003), SAR image denoising via Bayesianwavelet shrinkage based on heavy-tailed modeling, IEEE Trans. Geosci. Remote Sens., vol. 41, no. 8, pp. 1773-1784, Aug. 2003.

[8] S. Foucher, G. Farage, G. B. Bni(2006), SAR Image Filtering Based on the Stationary Contourlet Transform, IGARSS, Denver, pp. 4021-4024, Jul. 2006

[9] H. Chen, Q. Gao(2005), "Efficient Image Region and Shape Detection by Perceptual Contour Grouping", in Proc. of IEEE International Conf. on Mechatronics and Automation, Vol. 2, 2005, pp. 793-798

[10] D. Manolakis, C. Siracusa, G. Shaw(2001), Hyperspectral subpixel target detection using the linear mixing model: Analysis of hyperspectral image data, IEEE Trans. Geosci. Remote Sens., vol. 39, no. 7, pp. 1392-1409, Jul. 2001.

[11] Y.-C. Chang, B.-K. Shyu, C.-Y. Cho et al(2000), Adaptive postprocessing for region-based fractal image compression, in Proc. Data Compression Conf., 2000, p. 549.

[12] Y. Dong, S. Xu(2007), A New Directional Weighted Median Filter for Removal of Random-Valued Impulse Noise, IEEE Signal Processing Letters, Vol. 14, pp. 193-196, Mar. 2007.

[13] A. S. Awad, H. Man(2008), High performance detection filter for impulse noise removal in images, Electronics Letters, Vol. 44, pp.192-194, Jan. 2008.

[14] T.-C. Lin, P.-T. Yu(2006), Thresholding noise-free ordered mean filter based on Dempster-Shafer theory for image restoration, IEEE Trans. on Circuits and Systems, Vol. 53, No. 5, pp. 1057-1064, May 2006.

[15] I. Aizenberg, C. Butakoff(2004), Effective impulse detector based on rank order criteria, IEEE Signal Processing Letters, Vol. 11, Issue 3, pp. 363-366, Mar. 2004.

[16] G. De Grandi, D. Hoekman, J.-S. Lee, D. Schuler, T. Ainsworth(2004), A Wavelet multiresolution technique for polarimetric texture analysis and segmentation of SAR images, Proc. IGARSS, Vol. 1, Sept. 2004.

[17] Olivier D. Faugeras, Zhengyou Zhang(2003), Calibration of Mobile Robot with Application to Visual Navigation [J]. Intelligent Robots and Systems. 2003.

[18] Dorin Comaniciu, Visvanathan Ramesh(2003), Kernel Based Object Tracking [J]. IEEE transactions on pattern analysis and machine intelligence. Vol 25, No 5, May 2003

[19] Gulcin Caner, A.Murat Tekalp(2006), Local Image Registration by Adaptive Filtering [J]. IEEE Transactions on image processing. Vol 15, No.10, October 2006

[20] Heeyoul Choi, Sookjeong Kim, Seungjin Choi(2005), Trust-Region Learning for ICA. Digital Object Identifier. Vol 5, 2005

Non-Fragile Control for Trajectory Tracking of Mobile Robots with Time-Delay

Na Ni[1], Yingmin Jia[1] and Junping Du[2]

1. Department of Systems and Control, Beihang University (BUAA), Beijing 100191, P.R.China
2. Beijing Key Laboratory of Intelligent Telecommunications Software and Multimedia,
Beijing University of Posts and Telecommunications, Beijing 100876, P.R.China
(andyou_1211@163.com, ymjia@buaa.edu.cn and junpingd@bupt.edu.cn)

Abstract: This paper is devoted to the problem of non-fragile controller design for the trajectory tracking of mobile robots. Firstly, the model of the mobile robots is exactly linearized via non-linear state feedback and proper coordinate transformation under certain conditions. Secondly, the time-delay is added to the linearized model and the non-fragile controller is designed for the trajectory tracking by employing linear matrix inequalities (LMIs) approach. Finally, simulation examples are included to illustrate the effectiveness of the proposed controller.

Keywords: Mobile Robots; Non-Fragile Control; Trajectory Tracking; Time-Delay; LMIs

I. INTRODUCTION

The mobile robot can be regarded as an effective extension of man's motor ability, and therefore it is sure to be indispensable in the course of recognition and exploration of the world. For example, to achieve the trajectory tracking, the nonlinear and nonholonomic motion of the mobile robot must be considered. Oriolo et al [1]. showed that dynamic feedback linearization was an efficient design the tool to solve trajectory tracking problem. Wang et al [2]. proposed novel, asymptotical, nonlinear adaptive trajectory tracking control laws based on Lyapunov stability theory. Dixon et al [3]. developed a velocity field for the constrained mobile robot trajectory, and formulated a differentiable controller for global asymptotic velocity field tracking. In [4], an adaptive controller for trajectory tracking was developed based on the learning ability of wavelet network(WN). In [5], the fuzzy control solution was introduced to resolve the robustness of mobile robot trajectory tracking problem. Liu et al [6]. used an artificial potential field to navigate the mobile robot in a novel simple adaptive tracking controller. To avoid premature convergence and trapping into local minimum, a chaos genetic algorithm based on population high-efficiency mutation (CGAPM) was presented in [7]. And a novel vector field control method based on nonlinear control algorithm was proposed for the mobile robots in [8].

On the other hand, it is well known that the time-delay usually occurs in the practical plants. Its existence may affect the stability of the system seriously and the dynamic performance of the system. Similarly, it is important for the tracking control of mobile robots to consider the time-delay effect, however it has been attracting little attention.

Further, we know that the mobile robot is driven by the DC motor. The designed control strategies need to be digitized in order to realize control goal. In this process, the small change of the control parameters exists and may cause control failure, or even destroy the system. L.H.Keel et al [9]. indicated that the traditional controller design method like optimal control and robust control only lead to fragile controller. That means that small offset of controller gain coefficient will be likely to damage the stability of the closed-loop system and degrade the performance. This requires that the designed controller gain coefficient should have sufficient adjustable redundancy or non-fragility in order to meet different performance requirements.

In this paper, we design a non-fragile controller by using LMI approach for the mobile robots with time-delay. The paper is organized as follows. In Section 2, the equation of a nonholonomic mobile robot is linearized via state feedback and the model of the mobile robots with time-delay is introduced based on the linearized model. The non-fragile trajectory tracking controller is designed in Section 3. And finally, the effectiveness of designed controller is verified by the simulation in Section 4.

II. PROBLEM FORMULATION AND PRELIMINARIES

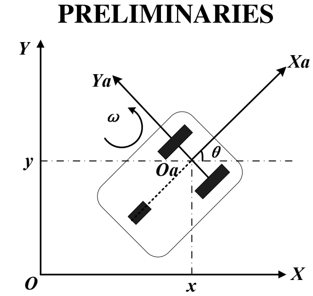

Fig. 1 The planar graph of a mobile robot

In Fig. 1, XOY is the world coordinate system, $X_aO_aY_a$ is the coordinate system fixed the mobile robot body ,Oa is the center of the axle of two driving wheels, (x,y) indicates the coordinate of the robot in world coordinate system and θ is the angle of moving direction (right angle to the wheel axis). v is the linear velocity of the robot and ω is its angular velocity.

Suppose that the wheels of the mobile robot rotate without slipping, the constraint can be denoted by

$$\dot{x}sin\theta - \dot{y}cos\theta = 0. \tag{1}$$

Then the equation of the mobile robot with two independently driving wheels can be obtained

$$\begin{aligned} \dot{x} &= vcos\theta \\ \dot{y} &= vsin\theta \\ \dot{\theta} &= \omega \end{aligned} \tag{2}$$

Introduce an auxiliary variable $\dot{v} = a$, and let

$$X = [x_1 \;\; x_2 \;\; x_3 \;\; x_4]^T = [x \;\; y \;\; \theta \;\; v]^T,$$

$$Y = [y_1 \;\; y_2]^T = [x \;\; y]^T,\ u = \begin{bmatrix} a & \omega \end{bmatrix}.$$

Then the system (2) can be transformed to the following form:

$$\begin{aligned} \dot{X} &= f(X) + g(X)u \\ Y &= h(X) \end{aligned} \tag{3}$$

where

$$f(X) = \begin{bmatrix} x_4cosx_3 \\ x_4sinx_3 \\ 0 \\ 0 \end{bmatrix},\ g(X) = \begin{bmatrix} 0 & 0 \\ 0 & 0 \\ 0 & 1 \\ 1 & 0 \end{bmatrix},$$

$$h(X) = \begin{bmatrix} 1 & 0 & 0 & 0 \\ 0 & 1 & 0 & 0 \end{bmatrix} \mathrm{X}$$

Setting

$$\xi(t) = [y_1 \; L_f y_1 \; y_2 \; L_f y_2]^T = [x_1 \; x_4cosx_3 \; x_2 \; x_4sinx_3]^T$$

and $u(t) = [acosx_3 - \omega x_4 sinx_3 \quad asinx_3 + \omega x_4 cosx_3]$, the system (3) becomes:

$$\begin{aligned} \dot{\xi}(t) &= \begin{bmatrix} 0 & 1 & 0 & 0 \\ 0 & 0 & 0 & 0 \\ 0 & 0 & 0 & 1 \\ 0 & 0 & 0 & 0 \end{bmatrix} \xi(t) + \begin{bmatrix} 0 & 0 \\ 1 & 0 \\ 0 & 0 \\ 0 & 1 \end{bmatrix} u(t) \\ &= \tilde{A}\xi(t) + \tilde{B}u(t) \\ Y(t) &= \begin{bmatrix} y_1 \\ y_2 \end{bmatrix} = \begin{bmatrix} 1 & 0 & 0 & 0 \\ 0 & 0 & 1 & 0 \end{bmatrix} \xi(t) = \tilde{C}\xi(t) \end{aligned} \tag{4}$$

Now, introducing time-delay in mobile robots, we have:

$$\begin{aligned} \dot{\xi}(t) &= \tilde{A}\xi(t) + A_\tau \xi(t-\tau) + \tilde{B}u(t) \\ Y(t) &= \tilde{C}\xi(t) \end{aligned} \tag{5}$$

where τ is constant time-delay. Consider the non-fragile controller:

$$u(t) = (K + \Delta K)\xi(t) \tag{6}$$

where K is the state feedback controller; $\Delta K = E\Delta(t)F$ is the additive gain perturbation of the controller with E,F the real matrices of known appropriate dimension, $\Delta(t)$ Lebesgue measurable matrix and $\Delta^T(t)\Delta(t) \le I$.

Combining the system (5) and controller (6) yields the following closes-loop system:

$$\begin{aligned} \dot{\xi}(t) &= [\tilde{A} + \tilde{B}(K + \Delta K)]\xi(t) + A_\tau \xi(t-\tau) \\ Y(t) &= \tilde{C}\xi(t) \end{aligned} \tag{7}$$

The objective of this paper is to design a non-fragile controller (6) such that the closed-loop system (7) is asymptotically stable.

Lemma 1: [10] Let E,F be the real matrices of appropriate dimensions, and $\Delta(t)$ be time-varying matrix with $\Delta^T(t)\Delta(t) \le I$. Then, for any scalar $\varepsilon > 0$, we have

$$E\Delta(t)F + F^T\Delta^T(t)E^T \le \varepsilon EE^T + \varepsilon^{-1}F^TF.$$

Lemma 2: [11] Let $M > 0, L, Q > 0$ be matrices of appropriate dimension. Then

$$M + L^TQ^{-1}L < 0$$

if and only if $\begin{bmatrix} M & L^T \\ L & -Q \end{bmatrix} < 0$ or $\begin{bmatrix} -Q & L \\ L^T & M \end{bmatrix} < 0.$

III. NON-FRAGILE CONTROLLER DESIGN

The following theorem gives the necessary and sufficient condition for existence of non-fragile state feedback controller for system (5) when the controller has additive gain perturbation.

Theorem 1: Given positive scalar τ, the system (7) is asymptotically stable if there exist scalar $\varepsilon > 0$, matrices $P > 0, Q > 0$ and R, such that the following linear matrix inequalities hold.

$$\begin{bmatrix} S + S^T & \varepsilon\tilde{B}E & A_\tau Q^{-1} & P^{-1} & P^{-1}F^T \\ * & -\varepsilon I & 0 & 0 & 0 \\ * & * & -Q^{-1} & 0 & 0 \\ * & * & * & -Q^{-1} & 0 \\ * & * & * & * & -\varepsilon I \end{bmatrix} < 0 \tag{8}$$

where $S = \tilde{A}P^{-1} + \tilde{B}R$, $*$ expresses the corresponding symmetric terms. And further, the state feedback controller may be taken as $K = RP$.

Proof: For the system (7), define a common Lyapunov function candidate

$$V = \xi^T(t)P\xi(t) + \int_{t-\tau}^{t} \xi^T(s)Q\xi(s)ds \tag{9}$$

where P,Q are solutions of equation (8).

$$\begin{aligned} \dot{V} &= \begin{bmatrix} \xi(t) \\ \xi(t-\tau) \end{bmatrix}^T \begin{bmatrix} P\hat{A} + \hat{A}^TP + Q & PA_\tau \\ A_\tau^TP & -Q \end{bmatrix} \begin{bmatrix} \xi(t) \\ \xi(t-\tau) \end{bmatrix} \\ &= \begin{bmatrix} \xi(t) \\ \xi(t-\tau) \end{bmatrix}^T M \begin{bmatrix} \xi(t) \\ \xi(t-\tau) \end{bmatrix} \end{aligned} \tag{10}$$

where $\hat{A} = \tilde{A} + \tilde{B}(K + \Delta K) = \tilde{A} + \tilde{B}(K + E\Delta(t)F)$, $M = \begin{bmatrix} P\hat{A} + \hat{A}^TP + Q & PA_\tau \\ A_\tau^TP & -Q \end{bmatrix}$. If $M < 0$, then the system (7) is asymptotically stable.

Pre- and post- multiplying M by diagonal matrix $\begin{bmatrix} P^{-1} & 0 \\ 0 & I \end{bmatrix}$ and its transpose respectively, and let $R = KP^{-1}$, we can obtain

$$\begin{aligned} & \begin{bmatrix} P^{-1} & 0 \\ 0 & I \end{bmatrix} M \begin{bmatrix} P^{-1} & 0 \\ 0 & I \end{bmatrix} \\ = & \begin{bmatrix} \hat{A}P^{-1} + P^{-1}\hat{A}^T + P^{-1}QP^{-1} & A_\tau \\ A_\tau^T & -P^{-1}QP^{-1} \end{bmatrix} \\ = & \begin{bmatrix} S + S^T + \hat{B} + \hat{B}^T + P^{-1}QP^{-1} & A_\tau \\ A_\tau^T & -Q \end{bmatrix} \\ < & \ 0 \end{aligned} \tag{11}$$

where $S = \tilde{A}P^{-1} + \tilde{B}R$ and $\hat{B} = \tilde{B}E\Delta(t)FP^{-1}$. According to Lemma 2, we obtain

$$\begin{bmatrix} S + S^T + \hat{B} + \hat{B}^T & A_\tau & P^{-1}Q \\ A_\tau^T & -Q & 0 \\ QP^{-1} & 0 & -Q \end{bmatrix} < 0 \tag{12}$$

Rewrite the above equation

$$\begin{bmatrix} S + S^T & A_\tau & P^{-1}Q \\ A_\tau^T & -Q & 0 \\ QP^{-1} & 0 & -Q \end{bmatrix} + \Sigma_1\Delta(t)\Sigma_2 + (\Sigma_1\Delta(t)\Sigma_2)^T < 0 \tag{13}$$

where $\Sigma_1 = \begin{bmatrix} \tilde{B}E & 0 & 0 & 0 \end{bmatrix}^T, \Sigma_2 = \begin{bmatrix} FP^{-1} & 0 & 0 & 0 \end{bmatrix}$. Then, from the Lemma 1, if there exists scalar $\varepsilon > 0$, we have

$$\begin{bmatrix} S + S^T & A_\tau & P^{-1}Q \\ A_\tau^T & -Q & 0 \\ QP^{-1} & 0 & -Q \end{bmatrix} + \varepsilon\Sigma_1\Sigma_1^T + \varepsilon^{-1}\Sigma_2^T\Sigma_2 < 0 \tag{14}$$

Note that Lemma 2 again, we have

$$\begin{bmatrix} S + S^T & \varepsilon\tilde{B}E & A_\tau & P^{-1}Q & P^{-1}F^T \\ * & -\varepsilon I & 0 & 0 & 0 \\ * & * & -Q & 0 & 0 \\ * & * & * & -Q & 0 \\ * & * & * & * & -\varepsilon I \end{bmatrix} < 0 \tag{15}$$

Pre- and post-multiplying (15) by diagonal matrix $diag(I, I, Q^{-1}, Q^{-1}, I)$ and its transpose respectively, the upper formula can be expressed by the following

$$\begin{bmatrix} S + S^T & \varepsilon\tilde{B}E & A_\tau Q^{-1} & P^{-1} & P^{-1}F^T \\ * & -\varepsilon I & 0 & 0 & 0 \\ * & * & -Q^{-1} & 0 & 0 \\ * & * & * & -Q^{-1} & 0 \\ * & * & * & * & -\varepsilon I \end{bmatrix} < 0 \tag{16}$$

And the state feedback controller is $K = RP$. This completes the proof. ■

Obviously, if $\Delta(t) = 0$, Theorem 1 degenerates to the normal state feedback control.

Now applying the designed controller K in Theorem 1 to the mobile robots (5), we obtain

$$u(t) = K\xi = \begin{bmatrix} acos\theta - \omega vsin\theta \\ asin\theta + \omega vcos\theta \end{bmatrix}.$$

IV. NUMERICAL EXAMPLES

Consider the systems (5)-(7) with

$$A_\tau = \begin{bmatrix} 0.01 & 0 & 0 & 0 \\ 0 & 0 & 0 & 0 \\ 0 & 0 & 0.02 & 0 \\ 0 & 0 & 0 & 0 \end{bmatrix}, \tau = 0.2,$$

$$E = \begin{bmatrix} 1 & 0 \\ 0 & 1 \end{bmatrix}, F = \begin{bmatrix} 0.5 & 0.5 & 0.5 & 0.5 \\ 0.5 & 0.5 & 0.5 & 0.5 \end{bmatrix}$$

$$\Delta_1 = -I = \begin{bmatrix} -1 & 0 \\ 0 & -1 \end{bmatrix}, \Delta_2 = I = \begin{bmatrix} 1 & 0 \\ 0 & 1 \end{bmatrix}.$$

From Theorem 1, we get the non-fragile controller by employing the LMI Toolbox in MATLAB

$$K_{nf} = \begin{bmatrix} -4.4453 & -4.8047 & -1.4766 & -1.5234 \\ -1.4766 & -1.5234 & -4.4453 & -4.8047 \end{bmatrix}$$

and the normal state feedback controller is

$$K_{normal} = \begin{bmatrix} -2.9687 & -3.2813 & 0 & 0 \\ 0 & 0 & -2.9687 & -3.2813 \end{bmatrix}.$$

When the two controllers exist the perturbation Δ_1, they all can make the system stable, see Fig.2 and Fig.3. Using the normal control with the perturbation Δ_2, the system becomes unstable (see Fig.4), while the non-fragile controller with the perturbation Δ_2 still makes the system stable (see Fig.5).

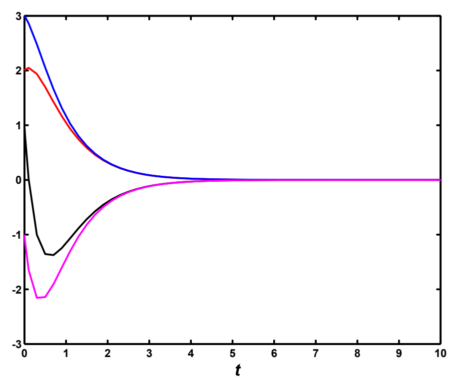

Fig.2 The control effect of the normal controller with Δ_1

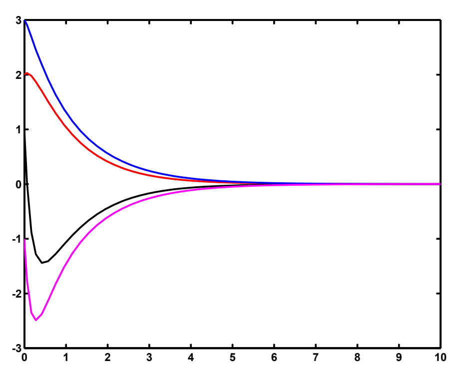

Fig.3 The control effect of the non-fragile controller with Δ_1

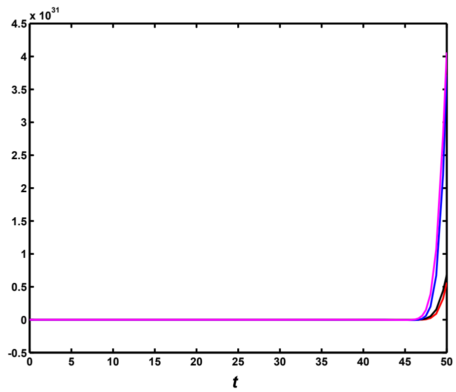

Fig.4 The control effect of the normal controller with Δ_2

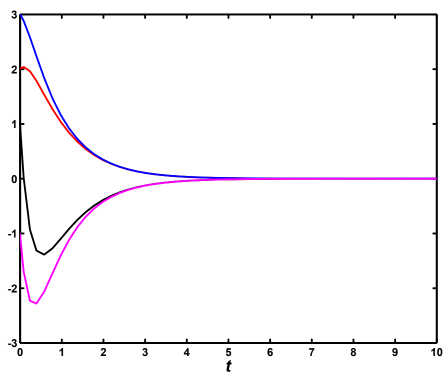

Fig.5 The control effect of the non-fragile controller with Δ_2

Next, we apply the designed non-fragile controller K to the trajectory tracking of the mobile robot system. We hope the mobile robot to make the circular motion:

$$x_d(t) = 0.5cos(0.01t), y_d(t) = 0.5sin(0.01t), \theta_d(t) = t.$$

Fig.6 is the mobile robot motion trajectory using the non-fragile controller on the $x-y$ plane. We can see that the trajectory can converge to the expected trajectory quickly.

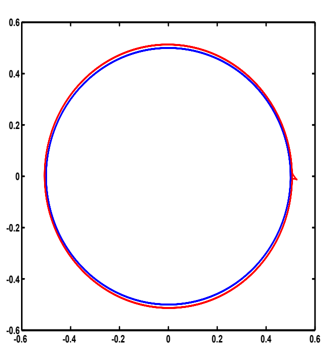

Fig.6 The mobile robot motion trajectory

V. CONCLUSIONS

In this paper, we have introduced non-fragile control to the mobile robots with time-delay for the first time. After exactly linearizing the model of the mobile robots via non-linear state feedback and proper coordinate transformation under certain conditions, we give the model of mobile robots with time-delay. Based on which, the non-fragile controller with the additive gain perturbation is designed in order to make the mobile robots asymptomatically stable. Finally, the proposed non-fragile controller is used to the mobile robots trajectory tracking control. Simulation results show that the designed non-fragile controller has strong robustness to controller gain perturbations which guarantee the fast response and superior control effect.

VI. ACKNOWLEDGMENTS

This work is supported by the National Natural Science Foundation of China (Grant Nos. 60727002, 60774003, 60921001, 90916024), the National 973 Program (No. 2005CB321902), and the COSTIND (No. A2120061303).

REFERENCES

[1] Oriolo G, Luca AD and Vendittelli M(2002), WMR control via dynamic feedback linearization: design, implementation and experimental validation. IEEE Transactions on Control Systems Technology: 835-852

[2] Wang TY and Tsai CC(2004), Adaptive trajectory tracking control of a wheeled mobile robot via Lyapunov techniques. The 30th Annual Conference of the IEEE Industrial Electronics Society: 389-394

[3] Dixon WE, Galluzo T, and Hu G et al.(2005), Adaptive velocity field control of a wheeled mobile robot. Fifth International Workshop on Robot Motion and Control: 145-150

[4] Purwar S, Gupta N and Kar IN(2007), Trajectory tracking control of mobile robots using wavelet networks. 22nd IEEE International Symposium on Intelligent Control Part of IEEE Multi-conference on Systems and Control Singapore: 550-555

[5] Zhu FC, and Dai J(2008), An optimized fuzzy trajectory tracking control of mobile robots. 2008 Chinese Control and Decision Conference: 2156-2161

[6] Liu ZY, Jing RH, and Ding XQ et al.(2008), Trajectory tracking control of wheeled mobile robots based on the artificial potential field. Fourth International Conference on Natural Computation: 382-387

[7] Chen NJ, Wang SA, and Di HY et al.(2009), An improved chaos genetic algorithm and its application in parameter optimization for robot control system. ICIEA: 1940-1945

[8] Kwon JW, Kim CJ and Chwa DY(2009), Vector field trajectory tracking control for wheeled mobile robots. ICIT: 1-6

[9] Keel LH, and Bhattacharyya SP (1997), Robust, fragile or optimal. IEEE Transactions on Automatic Control 42(8): 1098-1105

[10] Li L and Jia Y (2009). Non-fragile dynamic output feedback control for linear systems with time-varying delay. IET control theory & applications 3(8): 995-1005

[11] Zhao CY (2008), Non-fragile generalized H_2 control for linear time-delay systems. Natural sciences journal of Harbn normal university 24(4): 40-43

Experimental Comparison among Three Typical Data-Driven Control Algorithms

Shangtai Jin, Yongqiang Li, Yuanming Zhu, Jiangen Hao, Zhongsheng Hou

Advanced Control Systems Lab, Beijing Jiaotong University, Beijing, China
(Tel : 010-51688617)
(Email address shtjin@bjtu.edu.cn, zhshhou@bjtu.edu.cn)

Abstract: The differences, similarities and insights of three typical data-driven control algorithms, model free adaptive control (MFAC), iterative feedback tuning (IFT) and virtual reference feedback tuning (VRFT), are briefly discussed, and these differences, similarities and insights are certified through a series of experiments on the three-tank water system in our university lab.

Keywords: data-driven control, model-free adaptive control, iterative feedback tuning, virtual reference feedback tuning**.**

I. INTRODUCTION

Data-driven control methods focus on finding controller, merely using input/output data of the control system. Up to now, there exist a few data-driven control methods [1], such as iterative learning control (ILC), unfalsified control (UC), virtual reference feedback tuning (VRFT), iterative feedback tuning (IFT), model free adaptive control (MFAC), etc. In order to enhance their applications and make a clearly understanding the drawbacks and advantages of these data-driven control methods in practice, three typical data-driven control algorithms (MFAC, IFT and VRFT) are briefly discussed and the differences, similarities and insights of these methods are certified through a series of experiments.

The rest of this paper is organized as follows. In section 2, three typical data-driven control methods are brief discussed. In section 3, a series of experiments are given to demonstrate the correctness of the discussion in section 2. The conclusions are drawn in section 4.

II. Three Typical Data Driven Control Methods

1. Model-Free Adaptive Control

Model-free adaptive control method was proposed for a class of general SISO nonlinear discrete time systems by Hou [2]. Instead of identifying a, more or less, known global nonlinear model of the plant, an equivalent dynamical linearization time varying model are built along the dynamic operation points of the controlled plant using a novel concept called pseudo-partial derivative (PPD), which is estimated merely using the I/O data of the controlled plant. The dynamic linearization method includes the compacted form dynamic linearization (CFDL), the partial form dynamic linearization (PFDL), and the full form dynamical linearization (FFDL).

In detail, the MFAC approach can be described by the following steps: (a) Choose one dynamic linearization method, such as, CFDL. (b) Design the MFAC algorithm based on the selection in step 1, which includes a PPD updating law, a control input learning law, and a reset algorithm. (c) If the system output error is 0, then the control input remains value of the previous time instant, otherwise go to Step d. (d) Estimate the time varying parameter PPD merely using the on-line I/O data. (e) Update the control input using the PPD estimate values iteratively. (f) Repeat from step c.

Compared with other adaptive control schemes, the MFAC method is a data-driven control approach, and has several attractive properties, which make it suitable for many practical control tasks. First, the MFAC algorithm just depends on the real time measurement data of the controlled system. Secondly, the MFAC algorithm does not require any external testing signals and any training process they are necessary for the neural networks based nonlinear adaptive control and can be called a less expensive and lower cost controller. Thirdly, the MFAC algorithm is simple and easily implemented with minimum computational burden, and has strong robustness. Fourthly, under some assumptions, the convergence and stability of the presented MFAC methods can be guaranteed with rigorous mathematic analysis [1, 3-4]. Fifthly, the results of the MFAC for SISO nonlinear discrete-time systems have its corresponding extended ones for the MISO, and MIMO nonlinear systems. Finally, MFAC has been successfully implemented in many practical fields, such as, the chemical industry [5-6], the linear motor control, the injection modelling process [7], the PH value control [8], and so on.

2. Virtual Reference Feedback Tuning

The VRFT method was proposed by Guardabassi and Savaresi [9], which is a "one-shot" direct data-based controller design method. The procedure of VRFT can be summarized as follows: (a) Collect a batch of input/output data coming from the plant, (b) Calculate the virtual error signal, the virtual input of controller, (c) Calculate the virtual output of controller, (d) Use the batch of virtual input/output data of controller, to identify the optimal controller parameters using. Till now, a few applications of VRFT could be found in reference [10-12].

3. Iterative Feedback Tuning

The IFT method was proposed by Hjalmarsson [13], which considers the controller design as a parameter optimization problem. The procedure of VRFT can be summarized as follows: (a) Perform a normal experiment on the closed loop controlled system with the reference signal and collect N measurements of the output signal $y^{(1)}(\boldsymbol{\theta}_i)$ of the plant, (b) Perform a gradient experiment on the closed loop controlled system with the reference signal $r - y^{(1)}(\boldsymbol{\theta}_i)$ and collect N measurements of the output of the plant which can be expressed as $y^{(2)}(\boldsymbol{\theta}_i)$, (c) Take $\frac{\partial \hat{y}}{\partial \boldsymbol{\theta}}(\boldsymbol{\theta}_i) = \frac{1}{\mathrm{C}(\boldsymbol{\theta}_i)} \frac{\partial \mathrm{C}}{\partial \boldsymbol{\theta}}(\boldsymbol{\theta}_i) y^{(2)}(\boldsymbol{\theta}_i)$ as gradient approximation, (d) Estimate the controller parameters using the gradient approximation. Till now, a few applications of IFT could be found in reference [14-15].

Table 1 The characteristics of three data-driven control methods

Method	MFAC	VRFT	IFT
Controlled Plant	General nonlinear plant	Linear time invariant plant	Linear time invariant plant
feature	● Adaptive control of the plant whose parameters and structure may be time-varying ● Low computational costs ● Online	● Parameters tuning method for the controller whose structure is given ● "One-shot" method using a batch of input/output data of the plant ● Offline	● Parameters tuning method for the controller whose structure is given ● Iterative method, for each iterative using two batches of input/output data of the plant ● Offline
Factors affecting performance	● Control input length constant of linearization	● The structure of the controller ● The quantity of the batch of data	● The structure of the controller ● The quantity of the batch of data ● The initial value of parameters of the controller
Assumptions	● Generalized Lipschitz	● Structure of the controller needs to be given ● Reference model is invertible, and cannot be 1	● Structure of the controller needs to be given ● All signals of the loop remain bounded throughout the iterations
Others	● A series of dynamical linearization methods ● A series of methods for design controller ● Extended to MIMO plant ● Having BIBO stability proof ● Modularized design	● Extended to nonlinear plant ● Extended to MIMO plant	● Extended to nonlinear plant ● Extended to MIMO plant

4. Characteristics of Three Methods

The characteristics of three typical data-driven control methods are summarized as table 1.

III. EXPERIMENT

The control performance of MFAC [5], IFT [12] and VRFT [18] has been evaluated on an equipment of Three Tank Water System, which is manufactured and provided by Tianhuang Technology Company in China.

The sampling time is adopted 1s and the simulation time is 400s. The set point of T3 is 5cm. The initial condition of system is $u(0) = 0$, $y_1(0) = 0$, $y_2(0) = 0$, $y_3(0) = 0$, where u denotes the flow rate of upper tank, and y_1, y_2, y_3 denote the liquid-level of upper, middle and lower tank, respectively. The parameters of three data-driven control methods, experimental conditions and parameter tuning results are shown in table 2.

The performance of MFAC method is shown in Fig.1. From Fig.1 we can see that the MFAC with L = 5 gave better control performance. However, larger L will lead to more parameters which should be adjusted online, resulting in increasing the online computation. In addition, MFAC is an adaptive control method, thus there are few restrictions on the sampled data.

The performance of VRFT method is shown in Fig.2. From Fig.2 we can see that larger quantity of data will lead to better control performance for the same controller order, while higher order of controller will lead to better control performance for the same quantity of data. However, offline computation will increase with the growth of controller order and quantity of data. Moreover, the experiment time depends on the quantity of data.

Table.2 experimental conditions and parameter tuning results

Scenario	Control algorithm	Controller order	Quantity of data	Iterative time	Initial parameters of controller	Final parameter of controller
1	MFAC	L=3	On-line	0	$\hat{\Phi}(0)=[0.5\quad 0\quad 0]^T$ $\rho=1,\lambda=1,\eta=1,\mu=1$	$\hat{\Phi}(k)$ is estimated by on-line I/O data $\rho=1,\lambda=1,\eta=1,\mu=1$
2	MFAC	L=5	On-line	0	$\hat{\Phi}(0)=[0.5\quad 0\quad 0\quad 0\quad 0]^T$ $\rho=1,\lambda=1,\eta=1,\mu=1$	$\hat{\Phi}(k)$ is estimated by on-line I/O data $\rho=1,\lambda=1,\eta=1,\mu=1$
3	IFT	I=3	400	5	$K_1=7.5, K_2=-8, K_3=1$	$K_1=9.561, K_2=-11.682, K_3=2.648$
4	IFT	I=3	200	5	$K_1=7.5, K_2=-8, K_3=1$	$K_1=13.431, K_2=$ -18.973, $K_3=6.066$
5	IFT	I=5	400	5	$K_1=7.5, K_2=-8, K_3=1$ $K_4=0, K_5=0$	$K_1=8.62, K_2=-8.92, K_3=0.555, K_4=-0.585, K_5=0.85$
6	IFT	I=5	200	5	$K_1=7.5, K_2=-8, K_3=1$ $K_4=0, K_5=0$	$K_1=11.56, K_2=-12.699, K_3=0.453, K_4=-0.133, K_5=1.342$
7	VRFT	I=3	400	"one shot"	$K_1=7.5, K_2=-8, K_3=1$	$K_1=10.99, K_2=-11.45, K_3=0.6728$
8	VRFT	I=3	200	"one shot"	$K_1=7.5, K_2=-8, K_3=1$	$K_1=12.19, K_2=-12.49, K_3=0.61$
9	VRFT	I=5	400	"one shot"	$K_1=7.5, K_2=-8, K_3=1$ $K_4=0, K_5=0$	$K_1=12.04, K_2=-11.78, K_3=-2.045, K_4=0.747, K_5=1.365$
10	VRFT	I=5	200	"one shot"	$K_1=7.5, K_2=-8, K_3=1$ $K_4=0, K_5=0$	$K_1=14.04, K_2=-13.08, K_3=-3.801, K_4=0.84, K_5=2.526$

The performance of IFT method is shown in Fig.3. From Fig.3 we can see that after iterative optimization of controller parameters, the performance of controlled system is not improved significantly in four scenarios. The reason may lie in that the step size γ is not selected suitably, and after 5 iterations controller parameters have not converged to the optimal values. It is worth to point out that the experiment for IFT method is very time-consuming, so only five iterations are taken in this paper.

To compare the performance of three methods, choosing the best parameters for each algorithm, make liquid-level of lower tank achieve the reference level, when k=250s, close the inlet valve of upper tank and open the inlet valve of lower tank. Because of omitting two tanks, the order and delay time of plant will become smaller. The performances of three algorithms are shown in Fig.4. From Fig.4 we can see that during the first 250s, the performance MFAC and VRFT is satisfactory, but the performance of IFT is not satisfactory because the controller parameters have not converged to the optimal values. After time 250s, the system structure and parameters changed, and the performance of MFAC is best because the PPD vector parameter $\hat{\Phi}(k)$ of MFAC is updated by on-line I/O data of plant.

VI. CONCLUSION

Through above theoretical analysis and experimental comparison, we obtain the conclusion of this paper as follows: (a) The MFAC method uses the on-line I/O data of controlled plant only. The MFAC mechanism does not require any external testing signals and any training process. The MFAC scheme is simple and can be easily implemented, and has minimum computational burden and strong robustness. (b) The optimal parameters of the VRFT controller are obtained by an optimization procedure using a batch of off-line I/O data. The control performance depends on the controller structure, reference model, and quantity of collected I/O data. However, in practice, it is hard to select the appropriate reference model and controller structure. The VRFT scheme has compromised computational burden. (c) The IFT method is based on an iterative tuning of the controller parameter vector along the gradient direction of some control criterion. In each iteration, the controller parameters of IFT method are updated by using off-line I/O data from two experiments. The performance of IFT depends on the initial controller, and quantity of collected I/O data, step-size. The basic requirement of parameters convergence is that all signals of the loop remain bounded throughout the iterations, it is implies that the controller in each iteration must be stable. (d) In the last experiment, the performance of MFAC is best because the PPD vector parameter $\hat{\Phi}(k)$ of MFAC is updated by on-line I/O data of plant. While the performance VRFT and IFT is not satisfactory because they are off-line controller parameters tuning method, and can not deal with the time-varying plant.

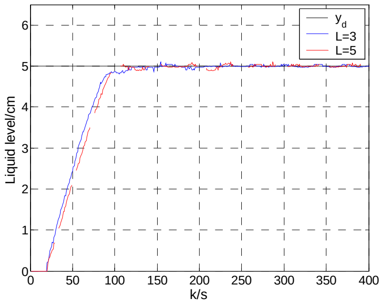

Fig. 1 The control performance of MFAC

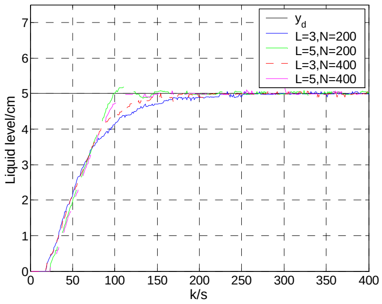

Fig. 2 The control performance of VRFT

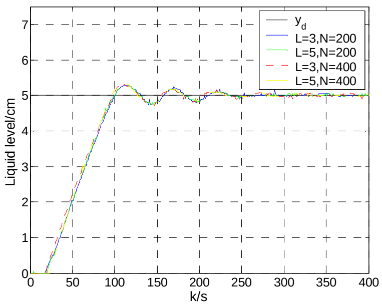

Fig. 3 The control performance of IFT

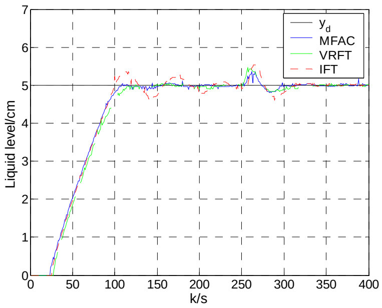

Fig. 4 The comparison among three methods

REFERENCES

[1] Hou ZS, and Xu JX (2009), On data-driven control theory: the state of the art and perspective, ACTA Automatica Sinica, Special Issue on data-based control, decision, scheduling, and fault diagnostics, 35(6), 650-667.

[2] Hou ZS (1994), The parameter identification, adaptive control and model free learning adaptive control for nonlinear systems, Ph. D thesis, Northeastern University, China (In Chinese).

[3] Hou ZS, and Huang WH (1997), The model-free learning adaptive control of a class of SISO nonlinear systems. In: Proceedings of the American Control Conference. Albuquerque, USA, 343-344.

[4] Hou ZS (1999), Non-Parametric Model and its Adaptive Control Theory. Science press, Beijing (in Chinese).

[5] Coelho LDS, Coelho AAR (2009) Model-free adaptive control optimization using a chaotic particle swarm approach, Chaos, Solitons and Fractals, 41: 2001-2009.

[6] Coelho LDS, Marcelo WP, Rodrigo RS, Coelho AAR (2010), Model-free adaptive control design using evolutionary-neural compensator, Expert Systems with Applications, 37: 499-508.

[7] Tan KK, et al (2001), Adaptive Predictive Control of a Class of SISO Nonlinear Systems. Dynamics and Control, 11(2): 151-174.

[8] Zhang B, and Zhang WD (2006), Adaptive predictive functional control of a class of nonlinear systems. ISA Transactions, 45(2): 175-83.

[9] Guardabassi GO, and Savaresi SM (2000), Virtual reference direct design method: an off-line approach to data-based control system design, IEEE Transactions on Automatic Control, 45(5): 954-959.

[10] Previdi F, Ferrarin M, Savaresi SM, and Bittanti M (2005), Closed-loop control of FES supported standing up and sitting down using Virtual Reference Feedback Tuning. Control Engineering Practice, 13(9): 1173-1182.

[11] Previdi F, Schauer T, Savaresi SM, and Hunt KJ (2004), Data-driven control design for neuroprotheses: a virtual reference feedback tuning (VRFT) approach, IEEE Transactions on Control Systems Technology, 12(1): 176-182.

[12] Yabui S, Yubai K, and Hirai J (2007), Direct design of switching control system by VRFT -application to vertical-type one-link arm, In: Proceedings of the 2007 SICE Annual Conference, Kagawa, Japan: SICE, 120-123.

[13] Hjalmarsson H, Gunnarsson S, and Gevers M (1994), A convergent iterative restricted complexity control design scheme, In: Proceedings of the 33rd IEEE Conference on Decision and Control, Orlando, USA: IEEE, 1735-1740.

[14] Hjalmarsson H, Gevers M, Gunnarsson S, and Lequin O (1998), Iterative feedback tuning: theory and applications, IEEE Control Systems Magazine, 18(4): 26-41.

[15] Hjalmarsson H (2002), Iterative feedback tuning-an overview, International Journal of Adaptive Control and Signal Processing, 16(5): 373-395.

Adaptive Identification and Prediction Control for Time Delay Nonlinear Systems Based on Neural Networks

Jing Na and Xuemei Ren

School of Automation, Beijing Institute of Technology, Beijing, 100081, P.R.China
(Tel: 86-10-68914506; Fax: 86-10-68412863)
(Email: najing@163.com; *xmren@bit.edu.cn*)

Abstract: This paper presents the identification, prediction and control design for nonlinear strict-feedback systems with an input time-delay. The system is firstly transformed into a normal form by defining new state variables. A dynamical identification with a neural network (NN) is proposed to estimate the system states. The predictive NN weights are obtained without iterative calculations and utilized in constructing the adaptive predictor. Feedback control design using the predictive states is finally studied. Simulations are included to validate the effectiveness of the proposed method.

***Keywords*:** Time-delay systems, state observer, nonlinear predictor, neural networks

I. INTRODUCTION

The control design for systems with input time-delay has been widely studied, e.g. [1-5] and references therein. For linear systems, the Smith predictor [1], sliding mode control [2] and dead time compensator [3] have been validated theoretically and practically. To deal with unknown nonlinearities, neural controllers were proposed in [4] and [5] for nonlinear time-delay systems. However, the employed local linearization methodologies are inapplicable to the system, where the delay is intrinsic in the plant (e.g. fluid control, temperature control). Tan and Cauwenberghe established one-step-ahead [6] and d-step-ahead [7] predictors for nonlinear systems using neural networks. Lu and Tsai [8] proposed a neural generalized predictive control for process system. Nevertheless, these predictors mainly focus on the discrete systems, and iterative prediction calculations are required within the sample interval resulting in significant computation costs.

In this paper, we study the neural predictor and control design for strict-feedback time-delay systems without the backstepping design. The system is firstly transformed into a normal form as in [10]. A neural network is then utilized in a dynamical identification to estimate the system states, and the NN weights and their derivative can be obtained. Predictive NN weights are deduced via Taylor series expansion and used to establish the state predictor. A feedback control with the predictive states is finally constructed to achieve the tracking. The closed-loop system is guaranteed to be bounded. Compared to other NN-based predictors, the off-line learning phase, the past system information and iterative calculations are all avoided to reduce the computation costs.

II. PROBLEM STATEMENT

Consider a class of nonlinear systems with an input time-delay as

$$\begin{cases} \dot{x}_i(t) = f_i(\bar{x}_i) + g_i x_{i+1}(t), \ \ 1 \le i \le n-1 \\ \dot{x}_n(t) = f_n(x) + g_n u(t-\tau) \\ y(t) = x_1(t) \end{cases} \tag{1}$$

where $\bar{x}_i = [x_1, x_2 \cdots x_i]^T \in \mathbb{R}^i, i = 1, \cdots n$, $x = [x_1, x_2 \cdots x_n]^T \in \mathbb{R}^n$, $y(t) \in \mathbb{R}$ and $u(t) \in \mathbb{R}$ are state variables, the output and input, respectively; $f_i(\bullet), i = 1, \cdots n$ are unknown but smooth nonlinear functions, $g_i, i = 1, \cdots n$ are known constant gains, and τ is a constant input delay.

The objective of this paper is to find a control $u(t)$, such that the output $y(t)$ tracks a desired trajectory $y_d(t)$. Inspired by [10], we can transform system (1) into a normal form by redefining the state variables as

$$\begin{cases} z_1 = x_1 \\ z_i = \dot{z}_{i-1}, i = 2, \cdots, n \end{cases} \tag{2}$$

Then we have $z_2 = \dot{z}_1 = f_1(x_1) + g_1 x_2$ and

$$\begin{aligned} \dot{z}_2 = \ddot{z}_1 &= \frac{\partial f_1(x_1)}{\partial x_1}\left(f_1(x_1) + g_1 x_2 \right) + g_1 \left(f_2(\bar{x}_2) + g_2 x_3 \right) \\ &= \alpha_2(\bar{x}_2) + \beta_2 x_3 \end{aligned} \tag{3}$$

where $\alpha_2(\bar{x}_2) = \left(\partial f_1(x_1) / \partial x_1\right)\left(f_1(x_1) + g_1 x_2 \right) + g_1 f_2(\bar{x}_2)$ is an unknown function and $\beta_2 = g_1 g_2$ is a known constant.

Similar to (3), for $i = 3, \cdots, n-1$, we can obtain that

$$\begin{aligned} \dot{z}_i = \ddot{z}_{i-1} &= \frac{\partial \alpha_{i-1}(\bar{x}_{i-1})}{\partial \bar{x}_{i-1}} \dot{\bar{x}}_{i-1} + \beta_{i-1} \dot{x}_i \\ &= \alpha_i(\bar{x}_i) + \beta_i x_{i+1} \end{aligned} \tag{4}$$

where $\alpha_i(\bar{x}_i) = \sum_{j=1}^{i-1} \partial \alpha_{i-1}(\bar{x}_{i-1}) / \partial x_j \left(f_j(\bar{x}_j) + g_1 x_{j+1} \right) + \beta_{i-1} f_i(\bar{x}_i)$ is unknown, and $\beta_i = \beta_{i-1} g_i = \prod_{j=1}^{i} g_j$ is a known constant.

Finally, for $i = n$, we have

$$\begin{aligned} \dot{z}_n = \ddot{z}_{n-1} &= \frac{\partial \alpha_{n-1}(\bar{x}_{n-1})}{\partial \bar{x}_{n-1}} \dot{\bar{x}}_{n-1} + \beta_{n-1} \dot{x}_n \\ &= \alpha_n(x) + \beta_n u(t-\tau) \end{aligned} \tag{5}$$

where $\alpha_n(x_n) = \sum_{j=1}^{n-1} \partial \alpha_{n-1}(\bar{x}_{n-1}) / \partial \bar{x}_{n-1} \left(f_j(\bar{x}_j) + g_j x_{j+1} \right) + \beta_{n-1} f_n(x)$

This work is supported by National Natural Science Foundation of China under grant No. 60974046.

is an unknown function and $\beta_n = \beta_{n-1} g_n = \prod_{j=1}^{n} g_j$ is a known constant.

From (2)~(5), we can rewrite system (1) as

$$\begin{cases} \dot{z}_i = z_{i+1}, & i = 1, \cdots, n-1 \\ \dot{z}_n = \alpha_n(x) + \beta_n u(t-\tau) \\ y = z_1 \end{cases} \quad (6)$$

As can be seen, by transforming the strict-feedback system (1) into the normal form (6) with the output $y = z_1 = x_1$, the backstepping design can be avoided. However, the newly defined states $z_i, i = 2, \cdots, n$ are unavailable since the function $\alpha_n(x)$ is unknown.

A linear parameter neural network (LPNN) [4-5] can approximate a nonlinear function on a compact set Ω as

$$Q(Z) = W^{*T}\Phi(Z) + \varepsilon, \quad \forall Z \in \Omega \subset \mathbb{R}^n \quad (7)$$

with bounded weights $W^* = [w_1^*, w_2^* \cdots w_L^*]^T \in \mathbb{R}^L$ and error $\varepsilon \in \mathbb{R}$, i.e. $\|W^*\| \le W_N$, $|\varepsilon| \le \varepsilon_N^*$. $\Phi(Z) = [\Phi_1(Z), \cdots \Phi_L(Z)]^T \in \mathbb{R}^L$ is a vector with $\Phi_k(\boldsymbol{Z})$ being a sigmoid function.

III. CONTROL DESIGN

A. Identification with Neural Network

For system (6), the following identification model is developed to estimate the states $z_i, i = 2, \cdots, n$:

$$\begin{cases} \dot{\hat{z}}_i = \hat{z}_{i+1}, & i = 1, \cdots, n-1 \\ \dot{\hat{z}}_n = -\sum_{i=1}^{n} a_i \hat{z}_i + \hat{W}(t)\Phi(x(t)) + \beta_n u(t-\tau) \\ \hat{y} = \hat{z}_1 \end{cases} \quad (8)$$

where $\hat{z}_i, i = 1, \cdots, n$ are the estimation of z_i; the vector $\hat{W} = [\hat{w}_1, \hat{w}_2 \cdots \hat{w}_L]^T \in \mathbb{R}^L$ is the NN weights given by

$$\dot{\hat{W}}(t) = F\left(\tilde{y}(t)\Phi(x(t)) - k_e \hat{W}(t)\right) \quad (9)$$

with the parameters $F = F^T > 0$, $k_e > 0$, and $\tilde{y} = y - \hat{y}$ is the output measurement error.

We can select appropriate positive parameters $a_1, \cdots a_n$ such that following matrix A is Hurwitz

$$A = \begin{bmatrix} 0 & 1 & 0 & \cdots & 0 \\ & \ddots & \ddots & & \vdots \\ \vdots & & \ddots & \ddots & 0 \\ & & & 0 & 1 \\ -a_1 & -a_2 & \cdots & \cdots & -a_n \end{bmatrix} \in \mathbb{R}^{n\times n}, B = \begin{bmatrix} 0 \\ 0 \\ \vdots \\ 0 \\ 1 \end{bmatrix} \in \mathbb{R}^n, C = \begin{bmatrix} 1 \\ 0 \\ \vdots \\ 0 \\ 0 \end{bmatrix} \in \mathbb{R}^n.$$

and $A^T P + PA = -Q$ and $PB = C$ hold for symmetric positive definite matrices P and Q.

Define the identification error as $\tilde{x}(t) = z(t) - \hat{z}(t)$, the NN weight error as $\tilde{W} = W^* - \hat{W}$, and apply the NN approximation (7) on the unknown nonlinear function $\varphi(x) = \alpha_n(x) + \sum_{i=1}^{n} a_i z_i(t)$, then we can get the error equation from (6) and (8) as

$$\begin{cases} \dot{\tilde{x}}(t) = A\tilde{x}(t) + B\tilde{W}^T(t)\Phi(x(t)) + B\varepsilon \\ \tilde{y} = C\tilde{x}(t) \end{cases} \quad (10)$$

B. Adaptive Predictor

In identification (8), the NN weights $\hat{w}_i(t); i = 1, \cdots n$ contain the time-varying system information. Therefore, the following adaptive predictor can be proposed:

$$\begin{cases} \dot{x}_{pi}(t+\tau) = x_{p(i+1)}(t+\tau), & i = 1, \cdots, n-1 \\ \dot{x}_{pn}(t+\tau) = -\sum_{i=1}^{n} a_i x_{pi}(t+\tau) + \hat{W}^T(t+\tau)\Phi(x_p(t+\tau)) + \beta_n u(t) \\ y_p(t+\tau) = C^T x_p(t+\tau) \end{cases}$$
$$(11)$$

where $x_p(t+\tau) = [x_{p1}(t+\tau), x_{p2}(t+\tau) \cdots x_{pn}(t+\tau)]^T \in \mathbb{R}^n$, $y_p(t+\tau) \in \mathbb{R}$ are the predictions of future states and the output, and $\hat{W}(t+\tau) \in \mathbb{R}^L$ denotes the predictive NN weights, which can be given as

$$\hat{W}(t+\tau) = \hat{W}(t) + \tau \dot{\hat{W}}(t) \quad (12)$$

Define the prediction error as $\tilde{x}_p(t) = z(t+\tau) - x_p(t+\tau)$, then from predictor (11) and system (6), one can obtain

$$\begin{aligned} \dot{\tilde{x}}_p(t) = A\tilde{x}_p(t) + B[W^{*T}(t+\tau)\Phi(x(t+\tau)) \\ -\hat{W}^T(t+\tau)\Phi(x_p(t+\tau))] + B\varepsilon \end{aligned} \quad (13)$$

C. Control Design

Denote $x_d(t) = [y_d, \dot{y}_d, \cdots y_d^{(n-1)}]^T$ as the reference trajectory, then the control error and the filtered error between $x_p(t+\tau)$ and $x_d(t)$ can be given as

$$E(t) = x_p(t+\tau) - x_d(t), \quad \delta(t) = [\bar{\lambda}^T \quad 1]E(t) \quad (14)$$

with $\bar{\lambda} = [\lambda_1, \lambda_2 \cdots \lambda_{n-1}]^T$ an appropriate vector, such that $s^{n-1} + \lambda_{n-1}s^{n-2} + \cdots \lambda_1$ is Hurwitz.

We can design the feedback control $u(t)$ as

$$\begin{aligned} u(t) = \frac{1}{\beta_n}\Big\{ -k_r\delta(t) + y_d^{(n)}(t) - [0 \quad \bar{\lambda}^T]E(t) \\ + \sum_{i=1}^{n} a_i x_{pi}(t+\tau) - \hat{W}^T(t+\tau)\Phi(x_p(t+\tau)) \Big\} \end{aligned} \quad (15)$$

where $k_r > 0$ is a positive control parameter.

Remark 1. During each sample interval, the NN weights $\hat{W}(t)$ and $\dot{\hat{W}}(t)$ in the identification (8) are obtained according to (9). Then $\hat{W}(t)$ and $\dot{\hat{W}}(t)$ are utilized in the predictor (11) to obtain the predictive weights $\hat{W}(t+\tau)$. Finally, the predictive states $x_p(t+\tau)$ and the term $\hat{W}^T(t+\tau)\Phi(x_p(t+\tau))$ are employed in the controller (15) to deduce the control $u(t)$.

D. Stability Analysis

We have the following results:

Theorem 1. Consider the time-delay system (1) with the identification (8), the predictor (11) and the controller (15), then all signals in the closed-loop system are bounded. Moreover, the tracking error $\vartheta(t)=x(t+\tau)-x_d(t)$ is also bounded.

Proof: It is known that the NN basis function $\Phi(x)$ is bounded, i.e. $\|\Phi(x)\|\le\Phi_M$ and $\|\Phi(x)-\Phi(x_p)\|\le\Phi_X$ with positive constants $\Phi_M\ge 0$, $\Phi_X\ge 0$. We first select a Lyapunov function as $V_1=\frac{1}{2}\hat{W}^T F^{-1}\hat{W}$, then the derivative of V_1 along (9) can be given as

$$\begin{aligned}\dot{V}_1=\hat{W}^T F^{-1}\dot{\hat{W}}&=\tilde{y}\hat{W}^T\Phi(x)-k_e\hat{W}^T\hat{W}\\ &\le-\|\hat{W}\|(k_e\|\hat{W}\|-\lambda_M(C)\Phi_M\|\tilde{x}\|)\end{aligned}\tag{16}$$

Then according to Lyapunov theorem, it is known that $\hat{W}$ is bounded by $\|\hat{W}\|\le\lambda_M(C)\Phi_M\|\tilde{x}\|/k_e$.

Furthermore, from (9) and (12), we get

$$\begin{aligned}\|\dot{\hat{W}}\|&\le\lambda_M(C)\lambda_M(F)\Phi_M\|\tilde{x}\|+k_e\lambda_M(F)\|\hat{W}\|\\ &\le 2\lambda_M(C)\lambda_M(F)\Phi_M\|\tilde{x}\|\end{aligned}\tag{17}$$

and

$$\begin{aligned}&\|\hat{W}(t+\tau)\|\le\|\hat{W}\|+\tau\|\dot{\hat{W}}\|\\ &\qquad\le[\lambda_M(C)\Phi_M/k_e+2\tau\lambda_M(C)\lambda_M(F)\Phi_M]\|\tilde{x}\|\end{aligned}\tag{18}$$

Then select the Lyapunov function as

$$V=V_2+V_3=\frac{1}{2}\tilde{x}_p^T P\tilde{x}_p+\frac{1}{2}\tilde{x}^T P\tilde{x}+\frac{1}{2}\tilde{W}^T F^{-1}\tilde{W}+\frac{1}{2}\delta^2\tag{19}$$

Differentiating $V_2=\frac{1}{2}\tilde{x}_p^T P\tilde{x}_p+\frac{1}{2}\tilde{x}^T P\tilde{x}+\frac{1}{2}\tilde{W}^T F^{-1}\tilde{W}$ along (9), (10) and (13), it follows

$$\begin{aligned}\dot{V}_2=&-\frac{1}{2}\tilde{x}_p^T Q\tilde{x}_p+\tilde{x}_p^T PB\{W^{*T}(t+\tau)\Phi(x(t+\tau))\\ &-\hat{W}^T(t+\tau)\Phi(x_p(t+\tau))\}+\tilde{x}_p^T PB\varepsilon-\frac{1}{2}\tilde{x}^T Q\tilde{x}\\ &+\tilde{x}^T PB\tilde{W}^T\Phi(x)+\tilde{x}^T PB\varepsilon+\tilde{W}^T F^{-1}F(-\tilde{y}\Phi(x)+k_e\hat{W})\end{aligned}\tag{20}$$

From (18), we can get

$$\begin{aligned}&\|W^{*T}(t+\tau)\Phi(x(t+\tau)-\hat{W}^T(t+\tau)\Phi(x_p(t+\tau))\ \|\\ &=\|\tilde{W}^T(t+\tau)\Phi(x(t+\tau))+\hat{W}^T(t+\tau)[\Phi(x(t+\tau))-\Phi(x_p(t+\tau))]\|\\ &\le\Phi_M W_N+(\Phi_X+\Phi_M)\|\hat{W}(t+\tau)\|\le C_1+C_2\|\tilde{x}\|\end{aligned}\tag{21}$$

where $C_1=\Phi_M W_N$, $C_2=[2\tau\lambda_M(C)\lambda_M(F)\Phi_M+\lambda_M(C)\Phi_M/k_e](\Phi_X+\Phi_M)$ are positive constants.

Moreover, consider $\tilde{W}^T\hat{W}=\tilde{W}^T(W^*-\tilde{W})\le-\frac{1}{2}\|\tilde{W}\|^2+\frac{1}{2}W_N^2$ and $ab\le(a^2+k^2b^2)/2k$ with $k>0$, we have

$$\begin{aligned}\dot{V}_2\le&-\frac{1}{2}[\lambda_m(Q)-\frac{1}{k}-\lambda_M(P)C_2]\|\tilde{x}_p\|^2+\frac{k}{2}[\lambda_M(P)(C_1+\varepsilon_N)]^2\\ &-\frac{1}{2}[\lambda_m(Q)-\frac{1}{k}-\lambda_M(P)C_2]\|\tilde{x}\|^2+\frac{k}{2}[\lambda_M(P)\varepsilon_N]^2-\frac{1}{2}k_e\|\tilde{W}\|^2+\frac{1}{2}k_eW_N^2\end{aligned}\tag{22}$$

On the other hand, taking the time derivative of $V_3=\delta^2/2$ along (14) and (15), it can yield

$$\dot{V}_3=\delta\dot{\delta}\le-k_r\delta^2\tag{23}$$

Then from (22) and (23), it can be deduced that

$$\dot{V}=\dot{V}_2+\dot{V}_3\le-\overline{\beta}\overline{V}+D\tag{24}$$

where $D=[k\lambda_M^2(P)(C_1^2+2\varepsilon_N C_1+2\varepsilon_N^2)+k_eW_N^2]/2$ and $\overline{\beta}=\min\{(\lambda_m(Q)-1/k-\lambda_M(P)C_2)/\lambda_M(P),\ k_e/\lambda_M(F^{-1}),2k_r\}$.

According to Lyapunov theorem, the filtered error δ, the identification error $\tilde{x}$, the prediction error $\tilde{x}_p$ and the NN weight error $\tilde{W}$ are all bounded. Furthermore, the control error E is also bounded according to (14). Thus, the boundedness of NN weights $\hat{W}(t)$, $\dot{\hat{W}}(t)$, $\hat{W}(t+\tau)$ and system states $\hat{x}(t)$, $x_p(t+\tau)$ are guaranteed. Consequently, the control $u(t)$ in (15) is also bounded.

Finally, the tracking error between the system states $x(t+\tau)$ and the reference trajectory $x_d(t)$ is

$$\begin{aligned}\vartheta(t)=x(t+\tau)-x_d(t)&=x(t+\tau)-x_p(t+\tau)\\ &+x_p(t+\tau)-x_d(t)=\tilde{x}_p(t)+E(t)\end{aligned}\tag{25}$$

then we know $\lim_{t\to\infty}\|\vartheta(t)\|=\lim_{t\to\infty}\|\tilde{x}_p(t)+E(t)\|\le\lim_{t\to\infty}\|\tilde{x}_p\|+\lim_{t\to\infty}\|E\|$, which implies that the closed-loop tracking error $\vartheta(t)$ is also bounded. □

IV. SIMULATION

Example 1: Consider the following nonlinear system

$$\begin{cases}\dot{x}_1(t)=x_2(t)+0.5x_1^2(t)\\ \dot{x}_2(t)=0.2(1-x_1^2(t))x_2(t)-x_1(t)\sin(x_2(t))+u(t-\tau)\\ y(t)=x_1(t)\end{cases}\tag{26}$$

The reference signal is specified as $y_d(t)=\sin(0.2\pi t)$. The simulation parameters are set as $a_1=6$; $a_2=1$, $\lambda_1=1$, $k_r=1$, $\Phi(x)=2/(1+e^{-0.5x})+3$, $F=diag(20,\cdots,20)$ and $k_e=5$. The initial conditions are $x_i(0)=\hat{x}_i(0)=x_{pi}(0)=0$ and $\hat{W}(0)=[0,\cdots,0]^T$.

The tracking response of the controlled system with a time-delay $\tau=0.3$ s is depicted in Fig.1. The top figure is the system output $y(t)$ and the reference $y_d(t)$. The profile of system states $x_1(t)$, $x_2(t)$ and the control signal $u(t)$ are provided in the middle and the bottom. As can be seen, the control and system states are all bounded. Moreover, the satisfactory tracking performance is achieved since the effect of input time-delay and unknown nonlinearities can be compensated effectively by the proposed method.

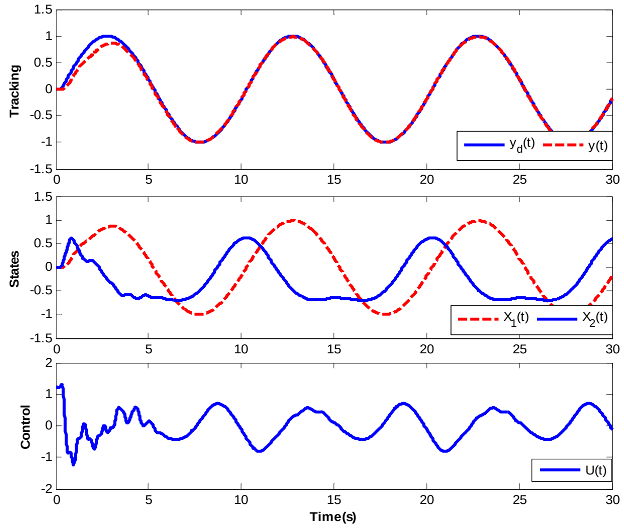

Fig.1 Control performance

Example 2: To further verify the proposed method, the following system as in [11] is utilized without the state delay term

$$\begin{cases} \dot{x}_1 = x_2 \\ \dot{x}_2 = -3x_1 - 2x_2 + 0.5x_1\sin(x_2) + \sin(60\pi t) + u(t-\tau) \\ y = x_1 \end{cases} \quad (27)$$

In this example, the reference signal is selected as $y_d(t) = 0$. The initial system conditions are chosen as $x_1(0) = -1.6; x_2(0) = 1$. In simulation, the parameters are specified as $a_1 = 3$; $a_2 = 2$, $\lambda_1 = 10$, $k_r = 10$, and the parameters of NN identification and predictor are given as $\Phi(x) = 2/(1+e^{-0.1x}) - 0.5$, $F = diag(0.2,\cdots,0.2)$, $k_e = 5$. The initial conditions are chosen as $\hat{x}_i(0) = x_{pi}(0) = 0$ and $\hat{W}(0) = [0,\cdots,0]^T$.

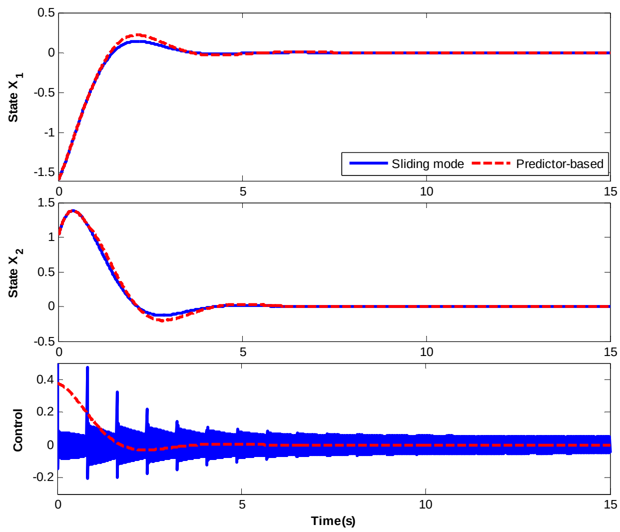

Fig.2 Comparative control performance

For comparison, the sliding model control presented in [11] is also provided. The system states under different controllers and the corresponding control signals are depicted in Fig.2. It is shown that both the sliding mode control and the proposed predictor-based control can guarantee the convergence of system states. However, the control signal of the predictor-based method is smoother than that of the sliding mode scheme.

V. CONCLUSION

A novel neural adaptive nonlinear state predictor is developed in this paper. The predictive NN weights can be obtained from the NN weights in the identification via Taylor series expansion. The proposed identification, prediction and control schemes can be implemented online without recursive calculations such that the computational costs can be reduced. Moreover, strict-feedback systems are transformed into a class of normal systems such that the backstepping design can be avoided in the control design.

REFERENCES

[1] Z. J. Palmor and M. Blau (1994), An auto-tuner for Smith dead time compensator, *Int. J. Contr.*, 60(1):117-135.

[2] Y. Q. Xia and Y. M. Jia (2003), Robust sliding-mode control for uncertain time-delay systems: an LMI approach, *IEEE Trans. Automat. Contr.*, 48(6):1086-1092.

[3] J. E. Normey-Rico and E. F. Camacho (2007), *Control of Dead-time Process*, Springer, Berlin.

[4] J. Q. Huang and F. L. Lewis (2003), Neural-network predictive control for nonlinear dynamic systems with time delay, *IEEE Trans. Neural Netw.*, 14(2):377 - 389.

[5] J. Na, X. M. Ren and H. Huang (2008), Time-delay positive feedback control for nonlinear time-delay systems with neural network compensation, *ACTA Automat. Sin.*, 34(9):1196-1203.

[6] Y. H. Tan and A.V. Cauwenberghe (1996), Nonlinear one-step-ahead control using neural networks: control strategy and stability design, *Automatica*, 32(12):1701-1706.

[7] Y. H. Tan and A.V. Cauwenberghe (1999), Neural-network-based d-step-ahead predictors for nonlinear systems with time delay, *Eng. Appl. Artif. Intel.*, 12:21- 35.

[8] C. H. Lu and C. C. Tsai (2007), Generalized predictive control using recurrent fuzzy neural networks for industrial processes, *J. Proc. Contr.*, 17(1):83-92.

[9] J. Na, X. M. Ren, Q. Chen, J. P. Xu and Y. Gao (2008), Adaptive Neural Network State Predictor for Nonlinear Time-delay Systems, *Proc. of the 27th Chinese Contr. Conf.* , Kunming,Yunnan, China, pp.638-643.

[10] J. H. Park, S.H. Kim and C.J. Moon (2009), Adaptive neural control for strict-feedback nonlinear systems without backstepping, *IEEE Trans Neural Netw.,* 20(7):1204-1209.

[11] Y. H. Roh and J. H. Oh (2000), Sliding mode control with uncertainty adaptation for uncertain input-delay systems, *Int. J. Contr.*, 73(13):1255-1260.

Behavior Based Autonomous Navigation System for Mobile Robots

Maki K. Habib
Mechanical Engineering Department, School of Sciences and Engineering,
The American University in Cairo, Egypt
maki@ieee.org

Abstract- **Mechanized and roobotized solutions properly sized with suitably modularized structure and well adapted to local conditions of minefields can greatly improve the safety of personnel as well as efficiency and flexibility. Such flexible machines with some level of decision-making capabilities can speed the clearance process when used in combination with other mine detection. A population of lightweight, robust, adaptable, low-cost, and multi operational mode robots that can integrate high speed mine detection and deactivation system is a clear answer to the problem of demining vast condemned areas. They will work together under close supervision of a monitoring station. The robot has three levels of control: Local scan, navigation (GPS and odometry) and collective behavior through radio coordination. Ground pressure of the developed robot is low enough not to make the mine explode. Pemex-B has to scan a large area, and assure the coverage of every part of it.**

I. INTRODUCTION

The major effect of landmines is to deny access to land and its resources, affect rebuilding process, causing deprivation and social problems among the affected populations. In addition the medical, social, economic, and environmental consequences are immense [1-4, 6-8]. The international Committee of the Red Cross estimates that the casualty rate from mines currently exceeds 26,000 people every year [5]. Unlike a bomb or artillery shell that explodes when it approaches or hits its target, a landmine is a blind weapon that lies dormant until a person, vehicle, or animal triggers its firing mechanism. Mines are prominent weapons because they are simple devices, so effective, yet so inexpensive, readily manufactured anywhere, easy to lay and yet so difficult and dangerous to find and destroy [1-4, 6-8]. Landmine technology ranges from very simple to high technology devices. There are many different varieties of mines produced by many countries worldwide that can be categorized in the following groups: landmines (anti-tanks (AT) and vehicles, antipersonnel (AP)) and sea-mines. In addition to mines, areas of ongoing or former conflict are contaminated with unexploded ordnance (UXO): grenades, mortar and artillery shells, bombs, rockets, and cluster bombs [5]. Modern AP mines are fabricated from sophisticated non-metallic materials and incorporate advance electronics. According to the United Nation there is a need to have at least 99.6% clearance success rate [7]. The amount of time it takes to clear an area is less important than the safety of the clearance personnel.

Humanitarian demining aims at locating and neutralizing of all landmines, UXO and booby traps in order to make infected areas available for human activities and development, and to allow people to use their land without fear. It should be performed efficiently, reliably and as safely and as rapidly as possible while keeping cost to the minimum. Engineers and other scientists can and should help in accelerating the speed of demining, lowering its cost and reducing the deminers' risks, by providing adequate, i.e. really usable in the field and cost-effective tools, sensors and platforms. Most people in the mine clearance community would be delighted if their work could be performed remotely or, even better, robotically. The task for a robot is to detect mines, mark them and eventually destroy them. Generally robots should improve quality of tasks performed by humans, and release human beings from working in hazardous environment, i.e., reduce the role of the human on the actual mine field.

Realistic environment is covered with vegetation of various sizes, containing rocks, holes, roots and other different sized obstacles, steep slopes and trenches. All those obstacles will have different properties and negotiability according to the size of the robot. Accordingly, the open question is: Is it effective to build one huge robot that will be powerful enough to destroy or go across the obstacles, or bunch of small-sized robots? Robots could increase productivity, saving in cost and could improve the safety of the mine detection operations and its targets by keeping the deminer of AP mines out of physical contacts with mines. The detection capability of landmines under all conditions with near 100% probability is dictated by the sensor(s) while the complete coverage of a defined area is the responsibility of the robot.

Demining robots solution can be as, modular components that can convert any mine clearing vehicle to a remote-controlled device, prodding tools connected to a robotic arm, multi modes mobile robot platforms (Teleoperated, Semi-autonomous and Autonomous), etc. with arrays of sensors and area mine clearance devices.

There exist different approaches to develop and use robots for demining. Proposals have been initiated to adapt available robot mechanisms and functionalities, to design and develop new robots, and then some of these robots were used in a team to enable parallel tasks. The navigation problem of a demining robot has some similarities with that of service robots [9, 10]. Obstacles avoidance while following a predefined trajectory is a general problem for planetary rovers [11, 12]. Much work has been performed on path planning which is not relevant to this application, because the robot is semi-autonomous and has to follow precise trajectories it defines only partly by itself. Coordination of the work of several robots is also simplified by a central monitor station allocating the task to every robot, and reassigning the work according to the observed situation. The control architecture is also simplified by a limited number of obstacle sensors, and by the possibility to better sense the obstacles with motion control, in order to obtain more precise information on their shape. Vision is powerful but is not yet, considered for economical reasons. Reliability and robustness of the control system is very important for that application [13]. This paper presents the general architecture of the Pemex-B robot, and some preliminary navigational software. Tests are conducted on a reduced size model using Khepera processor, sensors, and positioning system.

II. Development of the Demining Robot

The conceptual principles of Pemex-B structure include a robot with two large wheels robot built to investigate cross-country navigation and to evaluate sensors for the detection of AP mines. The sensors (for obstacle and mine detection) are located inside a hemisphere at the front side of the robot that acts as the third contact point on the ground surface (Fig. 1). In addition, the hemisphere can act as a shield to protect the sensor from dust and other environmental effect. The size of the robot will depend on the type of the terrain. Wheels of one or two meters in diameter may be adequate for most situations; scaling up will not significantly increase weight and cost. Local material resources, such as bamboos, gunny bags, etc. can be used for building up the wheels. The motors, accumulators and control electronics are packaged in a solid box to protect them from any possible explosion. This type of technology can be employed for marking the position of located mines and eventually destroy or neutralize them. Wheels are slanted in order to increase the stability with the same size and weight for the central part like a wheelchair for sports; it may also improve mobility below trees.

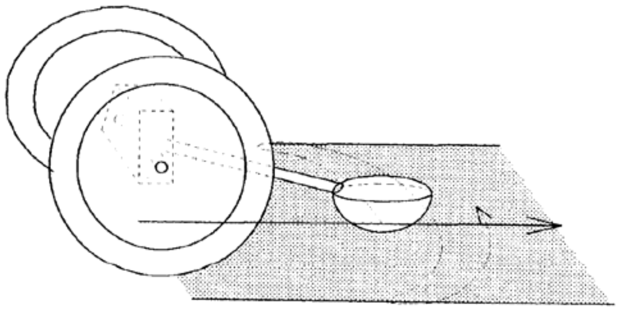

Figure 1: The structure principle of Pemex-B.

There is no problem due to the hemisphere rubbing on the ground: when the effort increases, the couple on the wheels reduces the apparent weight of the hemisphere, hence the friction. Of course odometry is less reliable due to the torque increase on the wheels, which creates skid. Experience shows that this effect is negligible on dry terrains. If the sensor is inside the head of the Pemex-B robot, its position may be given by the odometry of the wheels. Due to the slippering of the wheels, a repositioning mechanism must be used (laser, ultrasounds, precise GPS). In case of an expected explosion of a mine, the sphere will be blown up by the explosion and may get less damage by describing half a circle in the air around the wheels rather than by resisting the explosion.

The small-scale prototype robot Pemex-BS is one of the main objectives of first development stage. Khepera [14] consists of several printed circuit boards having 6cm in diameter and it has been installed on the top of scaled down hemisphere after removing its wheels while keeping its motor drives (Fig.2.a). The motors, the power supply, the metal detector and the tag distributor are installed on the main board. Larger sized motors and batteries have been installed in the central block between the wheels. The infrared distance sensors are used for obstacle detection and they are able to detect objects/obstacles within short-range (2-6cm) and are far to provide reliable range information on the obstacles. In addition, the robot has radio communication, compass and gyroscope modules. Figure 2.a shows the block-diagram of the hardware modules associated with Pemex-B. Nevertheless, this has the advantage of stimulating the development of robust algorithms. For demonstration purposes, a metal sensor is installed inside the sphere, and a motor driven distributor of color tags is used to mark the ground when hidden metallic objects are found. The laser positioning consists of a laser and a rotating mirror, both fixed on the ceiling above Khepera. The precision of the positioning system is 8mm (5% of the wheel base) and 5 degree for the angle, which corresponds to what can be obtained from a military GPS on the final Pemex.

The Pemex-BS model robot is shown in Fig.2.b. The length of the robot is 10 inches and wheel diameter is 5 inches for each. With 4 AA-sized batteries, the robot runs for 1 hour. During algorithm, programming and testing development, the robot is powered through a cable that also carries a serial line for downloading programs and providing in return sensor data to the workstation. Programs are written in C and Labview is frequently used for testing interactive modules [14]. Pemex-BS was successfully tested using experimental laboratory setup.

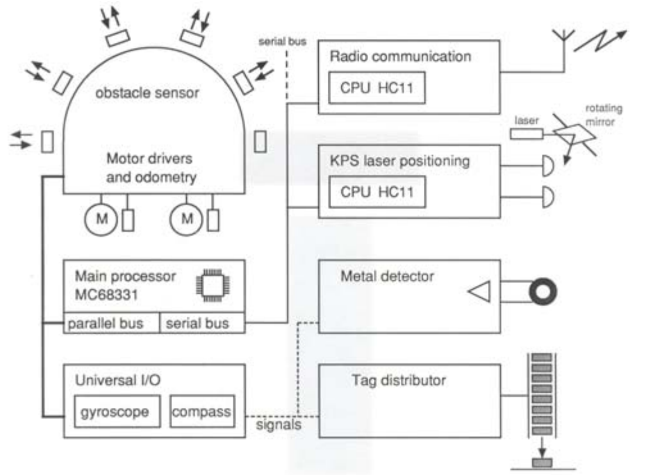

(a) The block-diagram of the hardware modules of Pemex-BS.

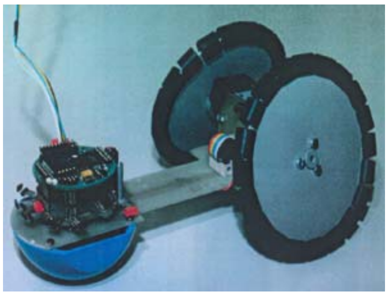

(b) Pemex-BS with its Khepera control boards.

Figure 2: Pemex-BS model robot

During the second stage a larger robot model called Pemex-BE has been built [8]**.** The total weight of this robot is less than 16 kg (exerts a maximum force of 6 kg on the ground). This robot can climb 30 degree slopes and stairs that the robot might face in destroyed urban areas, and it floats on the water, propelled by paddles, and can be carried as hand luggage. It is powered by rechargeable batteries which provide 60 minutes of autonomy. The locomotion of Pemex-BE is based on two mountain-bike wheels driven by 90W DC motors from Maxon with 1:72 reductors (Fig. 3) aiming to give to the robot a maximum speed of about 6 km/h with excellent cross-country capabilities. The on-board 68331 microprocessor permits autonomous or teleoperated navigation. Infrared and ultrasonic sensors are used to detect obstacles. In relation to the mine detection capabilities that are intended to be integrated with the robot, an AP mine sensor has been evaluated that is based on a combination of a metal detector (MD) and ground-penetrating radar (GPR). The ERA radar was selected and different metal detectors brands. The sensor was tested in the laboratory under controlled conditions with the ultimate objective of conducting tests on a real minefield

Figure 3: Pemex-BE in different environments

III. BEHAVIOR BASED NAVIGATION SYSTEM

For the developed demining robot, simple fixed priority layered behavior based navigational architecture will be adequate.. A sector of land is assigned to the robot with width, depth, starting position and orientation as a reference location. This location is specified at the utmost left of the sector and toward the cleared road or pathway. Each sector is divided into lanes. The width of each lane is equal to the arc of the zigzag fine movement to the left and right sides of the robot. The search for mines is conducted lane by lane and from left to right within the assigned sector.

Pemex-BE robot behavior depends on a list of typical situations stored in memory and analyzed by a simple fuzzy algorithm. Figure 4 shows the architecture of the developed navigation system for Pemex-BE robot. The highest layer of the navigation system is a task oriented navigational layer. This layer represents a collection of high-level behaviors, which guide the robot through roughly predefined trajectory pattern to guarantee scanning coverage of the assigned sector by the robot. Environmental constraints, such as obstacles or narrow paths, etc. should through appropriate sensors, trigger lower level set of behaviors that are responsible for obstacle avoidance and stability maintenance for coverage purposes. Deviations from predefined search path caused by natural environmental influences should be recorded using suitable grid based mapping techniques. At the end of the mission, checked and skipped area should be clearly marked using incrementally built digital mapping of the terrain, together with the detected and marked mine targets. The robot can adaptively selects a suitable search pattern while negotiating the terrain, or the search pattern can be decided by a higher level of control (like a supervisory controller) using digital model of the terrain.

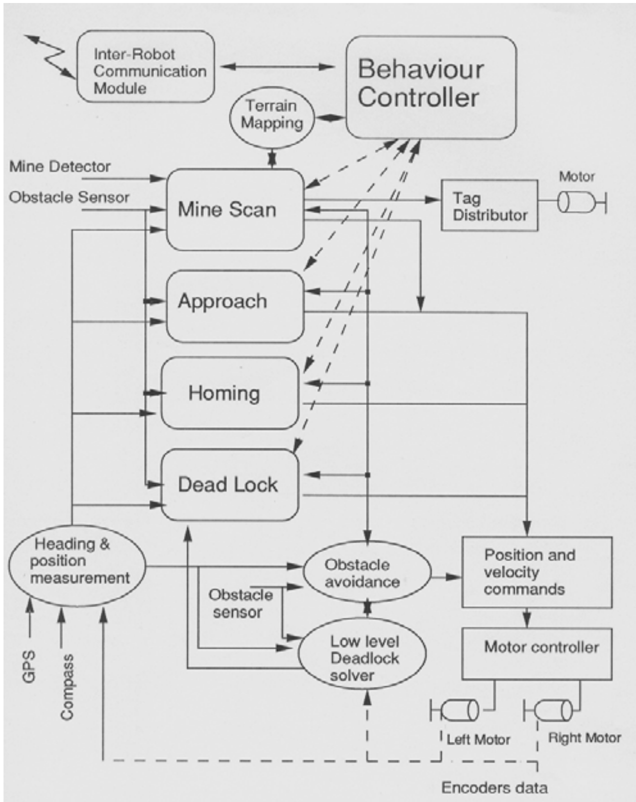

Figure 4: The developed navigation system for Pemex-BE

The Pemex-BE robot has the following core functionalities:

1. Initialize itself, perform self-check, and declare its readiness to execute a set of specified mission to a higher level of control,
2. Receive an allocated task from a higher level of control that describes a sector of land within a minefield in terms of width, depth, and the global reference starting point, i.e., enables the robot to know about the boundaries of the sector to be explored. In addition, the robot plans for its own S-

path to assure proper search coverage with sufficient overlaps while considering all possible navigational errors. Furthermore, the trajectory planner starts its work by dividing the allocated sector into lanes,

3. Search the assigned sector using the set of behaviors available at the task oriented navigational layer. The following set of behaviors are executed as needed during the searching process for mines (see Fig. 4):

   a) Approach

   This phase is described by the "Approach" behavior that aims to move the robot on a safe terrain in order to reach the stated global reference starting point of the assigned sector while avoiding any possible obstacles along the way.

   b) Mine Search

   The essential function of this behavioral phase is to generate a fine zigzag movement that is suitable to search a lane by lane completely while utilizing efficiently the effective range of the mine detector. The fine zigzag movement enables the robot to achieve a reliable search for mines and to detect any possible obstacle within any lane the robot is negotiating at the time. Since the robot is scanning a width larger than the wheel-base, obstacles may force the robot to reduce the scanning width, without the necessity to modify the trajectory as long as the available width is still larger than the wheel-base. Otherwise, the obstacle has to be avoided, and in this case the scanning amplitude on the opposite side may be reduced, because it overlaps the adjacent lane. During the mine search, behaviors from a lower layer may be triggered for avoiding and tracing the boundary of any obstacle blocking the searching process (Mine search).

   c) Homing

   When the robot complete the search/scan of the allocated sector, it returns to the mission lunching area using only the information available about the previously explored land within the sector (already mapped terrain), and moving backward at a faster speed using course zigzag movement.

   c) Dead Lock

   This behavior is executed when one of the navigational behaviors reports that it cannot exit a deadlock situation using robot's own resources. In this case, the navigational layer triggers a higher level of deadlock solver behavior. If this also fails in solving the deadlock, this behavior reports to a higher level control through the behavioral module to help guiding the robot to go out of the deadlock.

4. Lower navigational layer that includes a set of behaviors, such as, Obstacle avoidance, Mine tagging and reporting, Deadlock solver, power supply monitoring, etc.

5. Communicate through the inter-robot communication module to exchange information with other robots, and also to exchange information with a higher level control to report its activities and receiving further instructions about the task. The robot may send information about:

   a) Any detected mine with its coordinate for mapping purpose and following up,
   b) Detected deadlocks that can't be solved by robot's own resources.
   c) Ask for help and request for needed resources.

   The robots use the following communication strategies to support these activities:

   i. Communication with nearby robots (single or group of robot broadcasting);
   ii. Communication with a higher level of control (in a polling or a demand based broadcasting)

IV. CONCLUSIONS

Research into individual, mine-seeking robots is still in the development stages. In addition, robotized solutions are yet too expensive to be used for humanitarian demining operations in economically poor countries. In their current status, they need to have flexible mechanisms integrated with different type of sensors to support their autonomous navigation. In order to make these systems adaptable to various situations and type of goals to be pursued, it is necessary to dynamically select behaviors and to change their respective priority to make the system behave appropriately according to the situations it encounters in the real world.

REFERENCES

[1] T.J. O'Malley, "Seek and Destroy - Clearing Mined Land", Armada International, 1993, pp 6-15.
[2] C. King, "Mine Clearance in the Real World", SusDem97: International Workshop on Sustainable Humanitarian Demining, Zagreb, 1997, pp. S2.1-8.
[3] P.M. Blagden, "Summary of UN demining", Symposium on Anti-Personnel Mines, Montreux, April 1993, CICR/ICRC, pp 117-123.
[4] M. K., Habib, "Mine Detection and Sensing Technologies: New Development Potentials in the Context of Humanitarian Demining", 2001 IEEE IECON'2001, USA, 2001, pp. 1612-1621.
[5] International Committee of Red Cross, "Antipersonnel Mines-Friends or Foe?", Geneva, Ref. 0654, 1996.
[6] M. K., Habib," Mine Clearance Techniques and Technologies for Effective Humanitarian Demining", International Journal of Mine Action, Vol.6, No.1, 2002.
[7] M. K. Habib, "Machine Assisted Humanitarian Demining Mechanization and Robotization", International Field and Service Robots'2001, Finland, pp. 153-160.
[8] J.-D. Nicoud and M.K. Habib, "PEmex-B Autonomous Demining Robots: Perception and Navigation Strategies", IROS'95, Pittsburgh, Aug. 1995, pp. 419-424.
[9] P., Burkhanpurkar, "Design of Commercial Autonomous Service Robots" , 25th ISIR, 1993, pp. 267-272.
[10] H. R. Everett, et. al., "Coordinated Control of Multiple Security Robots", SPIE on Mobile Robots,, Vol. 2058, 1993, pp. 292-305.
[11] C., Gourley, R1. Trivedi, "Sensor Based Obstacle Avoidance and Mapping for Fast Mobile Robots", IEEE Robotics an Automation Conference, 1994,
[12] Y., Koren, and J. Borenstein, "Potential Field Method and their Inherent Limitations for Mobile Robot Navigation", IEEE Robotics an Automation Conference, 1991, pp 1398-1404
[13] C., Ferrell, "Robust and Adaptive Locomotion Control of an Autonomous Hexapod", PerAc'94 from Perception to Action, IEEE CS Press, 1994, pp 66-77
[14] F., Mondada et al, "Mobile robot miniaturization: A tool for investigation in control algorithms", ISER' 93, Kyoto, Oct 1993.

The Optical FBG Contact Force Measurement System for the Haptic Feedback of Minimal Invasive Surgery Robot

Ho-seok Song, Jung-wook Suh, Young-ik Yoo, and Jung-ju Lee*

**Mechanical Engineering Department, KAIST, Guseong-dong, Yuseong-gu, Daejeon, Republic of Korea*
(Tel : 82-42-350-3033; Fax : 82-42-350-3210)
(leejungju@kaist.ac.kr)

Abstract: Haptic feedback plays a very important role in medical surgery, but it is difficult to provide haptic information in MIS (minimally invasive surgery) or MIRS (minimally invasive robotic surgery). Recently, many sensors are being developed for MIS or MIRS, but they have some obstacles such as size limit and sterilizability in their application to real situations of medical surgery. Optical fiber sensors are one of the most suitable sensors for this environment. Especially, optical fiber Bragg grating (FBG) sensor is not influenced by intensity of light source. In this paper, we would like to present the initial results of study on the application of the FBG sensor to measure reflected forces in MIRS environments and then suggest the possibility of successful application to the MIRS systems.

Keywords: MIS (minimally invasive surgery), FBG (fiber Bragg grating), Laparoscopy

I. INTRODUCTION

Minimally invasive surgery (MIS) is a broad term to describe all kinds of surgery to minimize injury to the patient. MIS including laparoscopic surgery lessens pain, the need for post-surgical pain medication, scarring, and the likelihood of incisional complications. But there is a constraint of the degree of freedom (DoF) because bar of tools are inserted through ports of incision points. The surgical tools lose 2 DoF because of these ports of incision points and the surgeon can no longer approach tissue from an arbitrary angle. As a result, the surgeon feel more tired than when performing open surgery. In addition, haptic feelings are also impaired because of the long and thin bar of surgical tools. Recently, MIRS (minimally invasive robotic surgery), such as Da Vinci^{TM} has been introduced to solve motion constraint problems in MIS. MIRS uses a telemanipulation system that consists of a master console and a slave manipulator. As a consequence, dexterity of tool and tissue manipulation has been considerably augmented.

However, it is still difficult to provide haptic information in MIS or MIS. Tactile information allows discrimination of the different consistencies of tissue. The surgeon can feel the hardness or tension of tissues, measure the variation of their properties, and evaluate anatomical structures. Also, force-feedback information allows determination of the force applied to the tissue of the patient without damaging the tissue. But up-to-date commercialized MIRS systems are still missing haptic information.

In the previous research, there has been some effort to measure and reproduce haptic information using electric devices [1], [2], [3]. However, electric systems need many connection wires and packaging to shield against electromagnetic interference (EMI). A sterilization method is also should be considered. Peirs et al [4]. have developed a micro force sensor using three optical fibers to measure 3-axis forces for above reasons. However, this system is negatively influenced by fluctuation of the light source.

We decided to use optical fiber Bragg grating (FBG) sensors to solve these problems. Because optical FBG sensor can be used as a kind of wavelength filter, this FBG sensor is not affected by intensity of light but by wavelength of reflected light. Thus, in this paper we suggest an optical FBG system for the safe MIRS. Using 4-bendable beams aligned with the longitudinal axis of the shaft, this system can be used to directly measure the 3-axial forces applied on the surgical tool-tip. These 4-beams are placed at 4-quarters of the external circumference of the shaft, i.e. two couples of two beams facing each other are placed at 180degrees. The fiber Bragg grating (FBG) is used to measure the strains exerted on the 4-beams. This optical FBG sensor system would be effective for the surgeon to perform surgery much faster and more safely.

II. MECHANICAL DESIGN OF THE MANIPULATOR

In this research, the human arm-like manipulator for the MIS that we have developed is used [5]. Some researchers have reported that the development of either mechanical or electromechanical teleoperators, which enable surgeons to move a MIS system in a manner analogous to an open instrument, could potentially reduce the time of current laparoscopic procedures by at least 15%.

Our MIRS system has 7 DoF by adding an elbow-like joint in order to mimic the motion of a human arm; however, one of its rotational motions in the shoulder has been replaced with a translational motion. The proximal part corresponding to a human's shoulder adopts a double parallelogram that has a remote center to avoid the constraint of the ports of incision point. The surgical tool inserted into the abdomen has an elbow joint and roll-pitch-yaw joints to change the orientation of the tooltip. The surgical tool can be attached to the proximal portion of the surgical manipulator in order to exchange various kinds of tools. A cable-pulley mechanism is used to mechanize the surgical tool; the tension control device is designed for holding the tension of the wire.

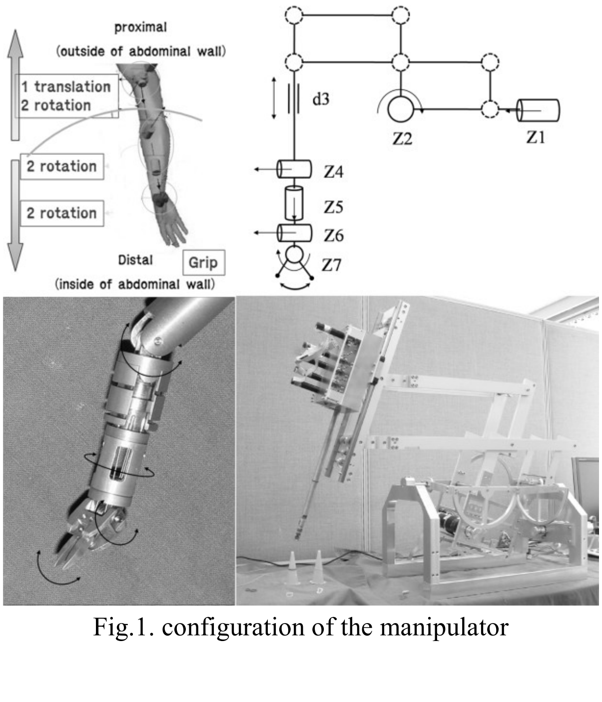

Fig.1. configuration of the manipulator

III. DESIGN OF OPTICAL FBG SENSOR AND MEASURING METHOD

1. Design of Flexure

There are two kinds of forces that are applicable in the surgical situation; 1) the force applied on the tool-tip, 2) The force applied inside forceps i.e. grip force. We have designed a loadcell with FBG sensors to measure the former type of the force. The loadcell can measure 1-axial force and 2-moments. In order for the sensor to measure the 3-axial forces on the tool-tip, the following assumptions are employed.

1) Wires driving wrist joint don't slip and elongate.
2) Sensor is affected by only F_{zs}, M_{xs} and M_{ys}
3) 3 moments were not applied on the tool-tip
4) 3 axial forces always act on the midpoint between the ends of the forceps.

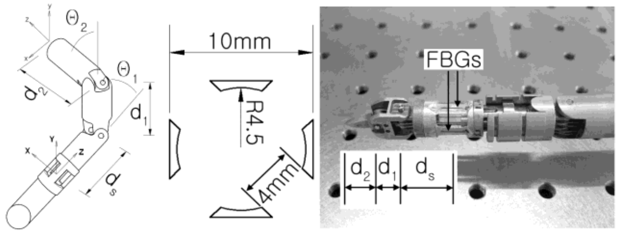

Fig.2. Sensor kinematics, cross section of sensor and developed sensor

F_{zs} is the force of z-axis applied on the sensor, and M_{xs} and M_{ys} are 2 moments of x,y-axes applied on the sensor. F_x, F_y, and F_z are the forces applied on the tooltip. If the wrist joint rotates θ_1 about x-axis and θ_2 about y-axis, then the forces and moments matrix applied on the middle of the sensor can be obtained. (Fig 2)

Because the organs inside abdominal wall act like passive devices, Moments applied on the tooltip are negligible. Then we could calculate the relation between the forces applied on the tooltip and the forces and the moments induced at the sensor by it.

$$\begin{bmatrix} F_Z \\ M_X \\ M_Y \end{bmatrix} = \begin{bmatrix} -C_1S_2 & -S_1 & C_1C_2 \\ S_1S_2d_s & -C_1d_s - d_1 - d_2C_2 & -S_1C_2d_s \\ C_1C_2d_1 + C_1d_2 + C_2d_s & S_1S_2d_2 & C_1S_2d_1 + S_2d_s \end{bmatrix} \begin{bmatrix} F_x \\ F_y \\ F_z \end{bmatrix} \quad (1)$$

d_1, d_2, and d_s are already known variables as shown in Fig.2. And θ_1 and θ_2 can be calculated by encoder signal. Hence, we can derive F_x, F_y, and F_z from F_{zs}, M_{xs}, and M_{ys} by using linear algebra. Using shift of central wavelengths of the reflected signal by optical FBGs, we can obtain ε_{33} (strain to the z-axis) of the four beams constituting the sensor: ε_1, ε_2, ε_3 and ε_4. We can derive F_{zs}, M_{xs}, and M_{ys} from ε_4, ε_2, ε_3 and ε_4 using Euler's beam theory. The axial force is able to be measured by means of simultaneous compressions or extensions of 4-beams. The moments of the loadcell are also measured by means of compressions and extensions of 4-beams. In this case, when one beam is applied by compression, another beam standing opposite is applied by extension. Therefore, we can calculate the force applied on the center of the loadcell reversely by using these relationships.

$$\begin{bmatrix} \varepsilon_1 \\ \varepsilon_2 \\ \varepsilon_3 \\ \varepsilon_4 \end{bmatrix} = \frac{1}{E} \begin{bmatrix} 1/A & C/I & 0 \\ 1/A & -C/I & 0 \\ 1/A & 0 & C/I \\ 1/A & 0 & -C/I \end{bmatrix} \begin{bmatrix} F_{zs} \\ M_{xs} \\ M_{ys} \end{bmatrix} \tag{2}$$

E, A, C, I are Young's modulus, the area of sensor's cross section, the largest distance from the neutral surface, and moment of inertia respectively.

2. Measuring Method

In this research, there are 6 FBGs to measure the strains. Among them, 2 FBGs located outside the abdominal wall are used to compensate for temperature or characteristics of fiber Fabry-Perot (FFP) filter. The other 4 FBGs are used to measure the force on the tooltip. Light from a broadband source is input into a 1x4 coupler via a circulator, and the light reflected by the FBGs is directed via a circulator to a tunable FFP filter, which is swept in wavelength by a control voltage used to adjust the mirror spacing. The magnitude of the spectral light is measured by photo diode (PD). In order to increase stability, a low pass filter is used during data acquisition process and a Gaussian line-fitting algorithm is applied for peak detection [6]. The measured peak location shifts are compensated with two reference FBGs and translated into strains. Finally, forces are calculated by using the strains and the above equations.

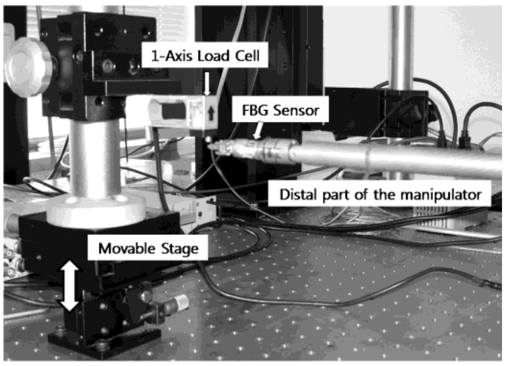

Fig.3. Experimental Setup

IV. FORCE MEASURING TEST FOR SYSTEM VERIFICATION

In order to determine the amount of force precisely, the force on the manipulator was given by a load cell. As shown in Fig.3, the manipulator is fixed on the table and the load cell is mounted on a vertical stage to apply force on the manipulator in a particular direction (x or y). If the force is applied from the x(or y)-direction, there will theoretically be only the force of the x(or y)-axis. However, some cross-talk was induced for several reasons. To measure the cross-talk, constant force in a particular direction is applied and the measured force from FBG sensor is recorded in real time. After a certain period of time, the value converged to a certain value and the proportion of the values was found. Using this value, we were able to construct a calibration matrix.

$$\text{Calibration Matrix} = \begin{bmatrix} -3.083 & -0.666 \\ 0.333 & 5.333 \end{bmatrix}$$

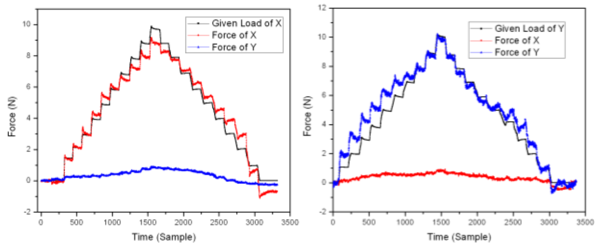

Fig.4. Real time observation of x and y-axis force

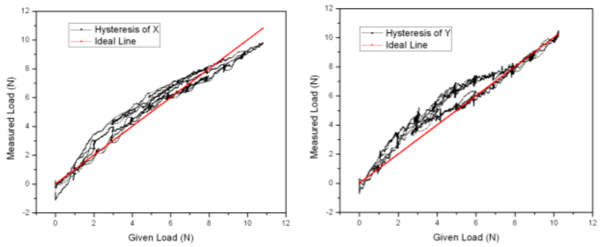

Fig.5. Hysteresis curve of x and y-axis force

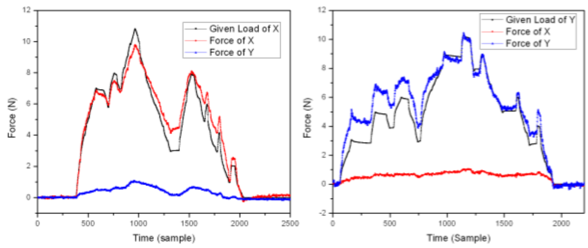

Fig.6. Random history measure of x and y-axis force

For the performance test, the forces are exerted from zero to nearly 10N and removed gradually. Each force was maintained for about twenty seconds and then we went on the next step. Measured forces are shown in Fig.4. Cross-talk was significantly reduced but still a small portion is remained. Fig.5 shows the relationship between the given forces and the measured forces. Hysteresis occurred on both the x and the y-axis. In the case of x-axis, measured load followed ideal line until 7N. Over 7N, stiff increment of estimated load was occurred. In the case of y-axis, there is no stiff increment of load, but estimated load strayed from the ideal line a little earlier. It is considered to be occurred by complicate structure of manipulator. Compliances induced by joints, driving wires and miss-align of joints make error. Additionally, frictions on the movable joints seem to make a hysteresis. Fig.6 shows real-time measurement histories of randomly applied load. Even though these measured reflect forces are not highly accurate, however we can recognize a collision or have the amount of force applied on the tool-tip approximately. Thus this force measuring system can help a surgeon operate safe surgery within a safe zone of applied force.

Originally, the optical FBG sensor system was designed for measuring 3-axis forces. However, at this time, the force of the Z-axis was excluded for lack of consistency induced by drift effect of the FFP filter system. In continuous work, we are looking for a method that is not influenced by the characteristics of the FFP filter system. At that time, the force of the Z-axis will be added.

V. CONCLUSION

We developed an optical FBG force sensor system for the application to minimally invasive surgery (MIS). The FBG sensor has many advantages compared with traditional electrical or optical sensors. It is sterilizable in an autoclave, flexible, and immune to water and EMI. It has simple wire connections compared to an electronic sensor, has a small diameter, and isn't influenced by light intensity. Therefore, the FBG sensor is one of the most suitable sensors for minimally invasive surgery. The test results show that the force sensor can be operated until over 10N but we need some more continuous effort to obtain high accuracy of measured forces. However, the most important fact is to warn the surgeon not to exceed the safe zone of applied forces rather than absolute accuracy of measured forces. Therefore this system which is equipped with optical FBG sensor is very useful and effective to warn of the breakage of a suturing thread or an unexpected collision. Hysteresis and unexpected cross-talk can be reduced with advanced system of ongoing work in near future.

Additionally, In order to verify usefulness of FBG sensor system, the test of tele-operation using haptic device like a Phantom will also be performed.

ACKNOWLEDGEMENT

This work was supported by the Korea Science and Engineering Foundation (KOSEF) grant funded by the Korea government (MEST) (No. 2009-0063570)

REFERENCES

[1] Ulrich Seibold, Bernhard Kuebler, and Gerd Hirzingger (2005), Prototype of Instrument for Minimally Invasive Surgery with 6-Axis Force Sensing Capability, ICRA 2005, 498-503.
[2] P. Valdastri, K. Harada, A. Menciassi, L. Beccai, C. Stefanini, M. Fujie, and P. Dario (2006), Integration of a Miniaturised Triaxial Force Sensor in a Minimally Invasive Surgical Tool, IEEE Transactions on Biomedical Engineering, 53(11).
[3] Mamoru Mitsuishi, Naohiko Sugita, and Phongsaen Pitakwatchara (2007), Force-Feedback Augmentation Modes in the Laparoscopic Minimally Invasive Telesurgical System, IEEE/ASME Transactions on Mechatronics, 12(4).
[4] J. Peirs, J. Clijnen, D. Reynaerts, H. V. Brussel, P. Herijgers, B. Corteville, ans S. Boone (2004), A micro optical force sensor for force feedback during minimally invasive robotic surgery, Sensor Actuat A-Phys, 115, 447-55.
[5] Ho-seok Song, Ki-young Kim and Jung-ju Lee (2006), Development of a 5 DoF dexterous manipulator executable inside abdomen for Minimally Invasive Surgery, Assistive Robotics and Mechatronics, 7(4).
[6] H. W. Lee and Minho Song (2005), FBG interrogation with a scanning Fabry-Perot filter and Gaussian line-fitting algorithm, IEEE LEOS Annual Meeting, Sydney, Australia, Oct.

The Fifteenth International Symposium on Artificial Life and Robotics 2010 (AROB 15th '10),
B-Con Plaza, Beppu,Oita, Japan, February 4-6, 2010

Impedance Model Force Control Using a Neural Network-Based Effective Stiffness Estimator

F. Nagata, T. Mizobuchi
Tokyo University of Science, Yamaguchi
Sanyo-Onoda, Japan

T. Hase, Z. Haga
R&D Center, Meiho Co. Ltd.
Nogata, Japan

K. Watanabe
Okayama University
Okayama, Japan

Maki K. Habib
American University in Cairo
Cairo, Egypt

Abstract

In manufacturing industries of metallic molds, various NC machine tools are used. We have already proposed a desktop NC machine tool with compliance control capability to automatically cope with the finishing process of LED lens molds. The NC machine tool has an ability to control the polishing force acting between an abrasive tool and a workpiece. The force control method is called impedance model force control. The most effective gain is the desired damping of the impedance model. Ideally, the desired damping is calculated from the critical damping condition in consideration of the effective stiffness in force control system. However, there exists a problem that the effective stiffness of the NC machine tool has undesirable nonlinearity. The nonlinearity gives bad influences to the force control stability. In this paper, a fine tuning method of the desired damping is considered by using neural networks. The neural networks acquire the nonlinearity of effective stiffness. The promise is evaluated through an experiment.

1 Introduction

Up to now, many kinds of robot systems for polishing and deburring have been developed in various manufacturing fields. In manufacturing process of small metallic molds such as LED lens molds, 3D CAD/CAM system and NC machining center are used generally and widely, and these have drastically rationalized the design and manufacturing process. However, the finishing process after the machining process has been hardly automated yet, because the target mold has several concave areas to be polished in almost all cases. That means the target mold is not axis-symmetric, so that conventional effective polishing systems, which can deal with only axis-symmetric workpiece, can not be applied. Accordingly, such axis-asymmetric lens molds are polished by skilled workers in related industrial fields.

To automate the finishing process of metallic molds, we have already proposed the polishing robot for PET bottle blow molds [1] and desktop NC machine tool for LED lens molds. The control strategy for these two types of systems is almost common. A ball-end abrasive tool attached to the arm tip is controlled by the CAD/CAM-based position/force controller. The force controller used is called the impedance model force controller, in which the desired damping is tuned to be in critical damping condition. The desired damping is one of the impedance parameters and has a large influence on force control stability. The critical damping condition is calculated with the effective stiffness that includes the characteristics of the robot or NC machine tool itself, force sensor, abrasive tool, jig, floor and so on. However, there exist undesirable nonlinearities in the effective stiffness.

In this paper, an impedance model force control using neural networks is proposed to deal with the nonlinear effective stiffness. In advance, the nonlinearity is examined by a simple static position and force measurement. The effectiveness stiffness is easily obtained by the measurement. The desired damping in impedance model force control law is statically calculated from the critical damping condition of the force control system. The neural networks learn the relation between the contact force and effective stiffness, so that the desired damping can be dynamically generated according to the contact force. The effectiveness and promise are demonstrated through an experiment using the desktop NC machine tool.

2 Desktop NC machine tool

Figure 1 shows the developed desktop NC machine tool consisting of three single-axis robots with position resolution of 1 m. The size of the robot is 850 645 700 mm. The single-axis robot is a position control device ISPA with high-precision resolution provided by IAI Corp., which is composed of a base, linear guide, ball-screw, AC servo motor. The effective strokes in x-, y- and z-directions are 400, 300 and 100 mm, respectively. The tool axis is designed to be parallel to z-axis. A small wood stick tool is fixed to the tip through a 3-DOF compact force sensor. To regulate the rotation, a servo spindle is located parallel to the tool axis.

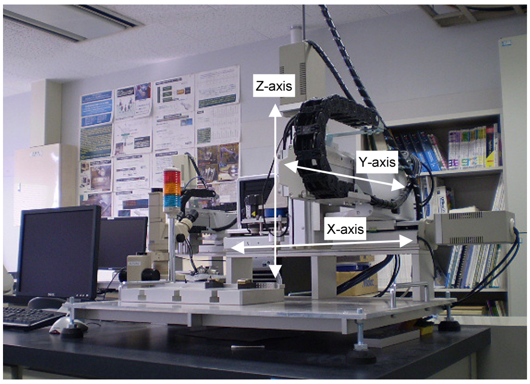

Figure 1: Proposed NC machine tool.

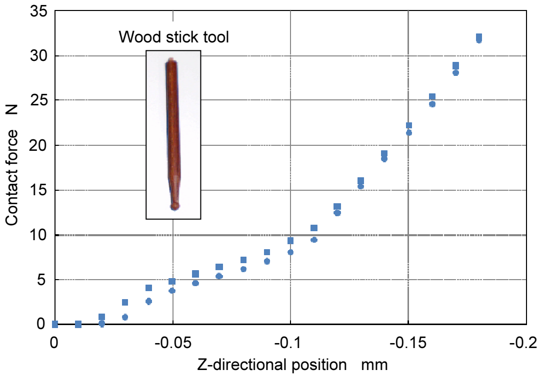

Figure 2: Static relation between position and force.

2.1 Measurement of effective stiffness

In this subsection, effective stiffness, valid position resolution of Cartesian-based servo system and resultant force resolution are evaluated through a simple static position/force measurement. The effective stiffness means the total stiffness including the characteristics composed of the single axis robot, force sensor, attachment, wood stick tool, workpiece, jig and floor.

Figure 2 shows the relation obtained by a simple contact experiment. The quantity of the position is the z-directional component at the tip of a wood stick tool. The quantity of force is yielded by contacting the tool tip with a workpiece and measured by the force sensor. The graph drawn with squares in Fig. 2 shows the relation the position and contact force in press motion. After the press motion, the tool tip was away from the workpiece once, and returned to the position again where 32 N had been obtained. After that, the tool tip was unpressed every 0.01 mm. The graph drawn in circles in Fig. 2 shows the relation of the position and contact force of this case. It is observed that small backlash exists. Also, the force is about 32 N when the position of the tool tip is 0.18 mm, so that the effective stiffness within the range can be estimated with 177.7 N/mm.

2.2 Learning of effective stiffness

The force control method used is called the impedance model force control. When the force controller is applied, the desired damping should be suitably tuned according to the effective stiffness. Since unstable phenomena such as overshoot and non-contact state tend to appear in force control system with the increase of the effective stiffness, the desired damping has to be given larger values. A systematic tuning method for the desired damping was already proposed in consideration of the critical damping condition in force control system. The calculation of the critical damping condition requires the effective stiffness of force control system. Figure 3 shows the nonlinear variations of effective stiffness in press and unpress motions obtained from Fig. 2.

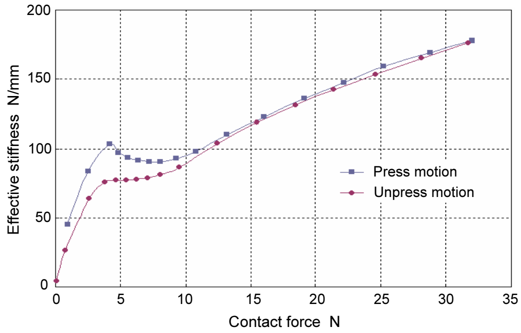

Figure 3: Effective stiffness of the NC machine tool.

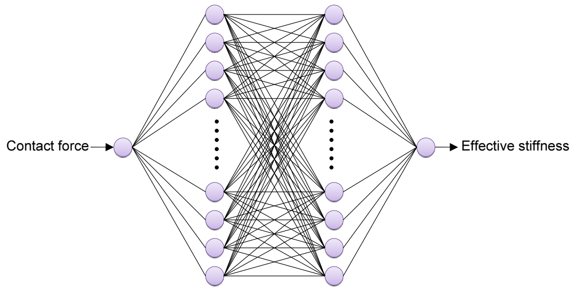

Figure 4: Neural network for acquiring nonlinearities.

In this subsection, in order to consider the nonlinearity, a neural network is employed as shown in Fig. 4. Hereafter, the neural network is called NN. Two NNs are learned for the press and unpress motions, respectively. The NN consists of an input layer, two hidden layers and an output layer. Each layer has one, thirty and one units, respectively. Note that the output layer does not have an activated function, i.e., sigmoid function. Therefore, the NN directly yields an estimated effective stiffness from the calculation of weighted sum. The NN acquires the relation between the contact force and the effective stiffness shown in Fig. 3 by the back propagation algorithm. Teaching patterns are given in the order from left to right on horizontal axis in Fig. 3.

Figures 5 and 6 show the learning results of the press and unpress motion, respectively. It is recognized that the learnings are successfully conducted with the increase of the trial times. The learned NNs are called NN-based effective stiffness estimator.

3 Design of controller

3.1 CAD/CAM-based controller

Figure 7 shows the block diagram of the CAD/CAM-based control system used in the NC machine tool. The tip of abrasive tool is controlled the

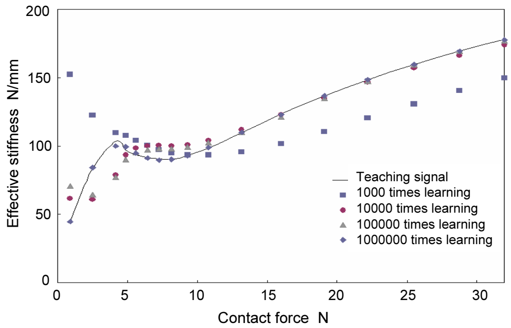

Figure 5: Learning result in press motion.

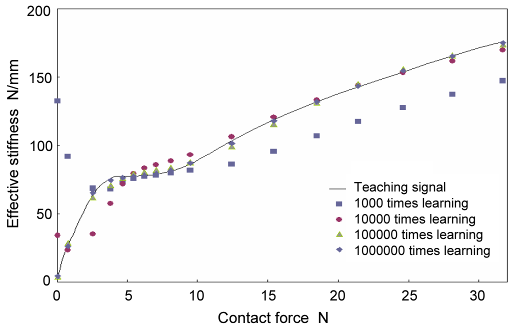

Figure 6: Learning result in unpress motion.

translational velocity ${}^W\boldsymbol{v}(k) \in \Re^{3\times 1}$ given by

$$ {}^W\boldsymbol{v}(k) = {}^W\boldsymbol{v}_t(k) + {}^W\boldsymbol{v}_n(k) + {}^W\boldsymbol{v}_p(k) \tag{1} $$

where k denotes the discrete time and ^{W} means a work coordinate system. First of all, ${}^W\boldsymbol{v}_t(k)$ is the manipulated variable generated from the feedforward control law based on cutter location data called CL data. ${}^W\boldsymbol{v}_t(k)$ is the tangential velocity along curved surface and written by

$$ {}^W\boldsymbol{v}_t(k) = v_{tangent}(k)\frac{{}^W\boldsymbol{t}(k)}{\|{}^W\boldsymbol{t}(k)\|} \tag{2} $$

where $v_{tangent}(k)$ is a velocity scalar generated from the fuzzy feed rate generator. The fuzzy feed rate generator yields suitable feed rate norms according to surface curvatures. ${}^W\boldsymbol{t}(k)$ is the tangential vector obtained by analyzing the CL data [1].

${}^W\boldsymbol{v}_n(k)$ is the manipulated variable generated from the force feedback control law. ${}^W\boldsymbol{v}_n(k)$ is the normal velocity at the contact point and written by

$$ {}^W\boldsymbol{v}_n(k) = v_{normal}(k){}^W\boldsymbol{o}_d(k) \tag{3} $$

where ${}^W\boldsymbol{o}_d(k)$ is the normalized normal vector calculated using the direction components of CL data. The scalar $v_{normal}(k)$ representing the norm of the normal velocity is the output of the impedance model force control law, which is calculated by

$$ \begin{aligned} v_{normal}(k) &= v_{normal}(k \quad 1)\, e^{\ \frac{B_d}{M_d}\ t} \\ &\quad + \Big(e^{\ \frac{B_d}{M_d}\ t} \quad 1\Big)\frac{K_f}{B_d}E_f(k) \end{aligned} \tag{4} $$

where K_f is the force feedback gain, impedance parameters M_d and B_d are the desired inertia and damping coefficients, respectively. t is the sampling time.

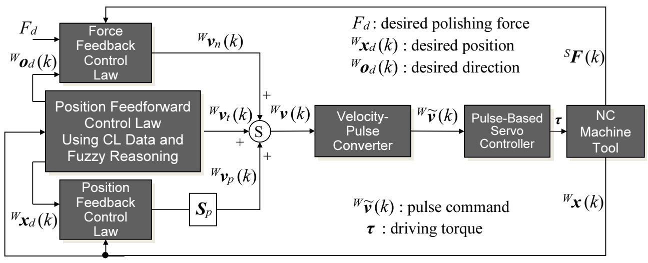

Figure 7: Block diagram of control system.

Also, $E_f(k)$ is the force error between the desired polishing force F_d and norm of force ${}^S\boldsymbol{F}(k) \in \Re^3$ measured by the force sensor, which is given by

$$ E_f(k) = F_d \quad \|{}^S\boldsymbol{F}(k)\| \tag{5} $$

where superscript ^{S} represents the sensor coordinate system. Further, we consider another velocity ${}^W\boldsymbol{v}_p(k)$ for regular position control in spiral direction. ${}^W\boldsymbol{v}_p(k)$ is the manipulated variable yielded by a position feedback control law represented by

$$ {}^W\boldsymbol{v}_p(k) = \boldsymbol{S}_p\Big\{\boldsymbol{K}_p\boldsymbol{E}_p(k) + \boldsymbol{K}_i\sum_{n=1}^{k}\boldsymbol{E}_p(n)\Big\} \tag{6} $$

where $\boldsymbol{E}_p(k) = {}^W\boldsymbol{x}_d(k) \quad {}^W\boldsymbol{x}(k)$ is the position error. The desired position ${}^W\boldsymbol{x}_d(k)$ is calculated using CL data. $\boldsymbol{K}_p = \mathrm{diag}(K_{px}\ K_{py}\ K_{pz})$ and $\boldsymbol{K}_i = \mathrm{diag}(K_{ix}\ K_{iy}\ K_{iz})$ are proportional and integral gains for position feedback control. Switch matrix $\boldsymbol{S}_p = \mathrm{diag}(S_x\ S_y\ S_z)$ makes the weak coupling control to the direction of force control active or inactive. If an element of $\boldsymbol{S}_p$ is set to 1, then the weak coupling control in the corresponding direction becomes active. Due to the weak coupling control, it is simultaneously realized that stable polishing force control and regular profiling control along a spiral path.

${}^W\boldsymbol{v}_n(k)$, ${}^W\boldsymbol{v}_t(k)$ and ${}^W\boldsymbol{v}_p(k)$ comprise ${}^W\boldsymbol{v}(k)$. Further, the velocity pulse converter transforms the fine manipulated value in velocity into the pulse command given by an integer, which can be outputted to the pulse-based servo controller. The velocity pulse converter for the pulse-based servo controller is located after the position/force controller as shown in Fig. 7.

3.2 NN-based effective stiffness estimator

Figure 8 shows the detailed block diagram of the force feedback control law illustrated in Fig. 7. Figure 9 also shows the detailed block diagram of the NN-based effective stiffness estimator illustrated in Fig. 8. The two NNs in Fig. 9 are switched by the sign of

$$ \|{}^S\boldsymbol{F}(k)\| = \|{}^S\boldsymbol{F}(k)\| \quad \|{}^S\boldsymbol{F}(k \quad 1)\| \tag{7} $$

If $\|{}^S\boldsymbol{F}(k)\| > 0$, then NN learned with the teaching patterns in press motion is selected. Also, if $\|{}^S\boldsymbol{F}(k)\| < 0$, then NN learned with the teaching patterns in unpress motion is used. For example, when the desired polishing force F_d is set to 10 N, the points

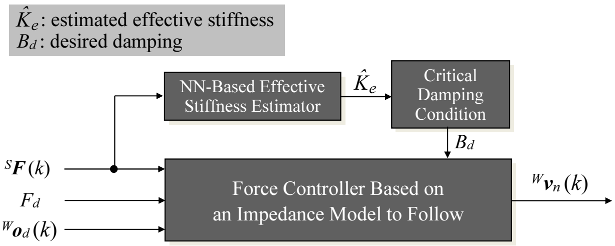

Figure 8: Feedback control law shown in Fig. 7.

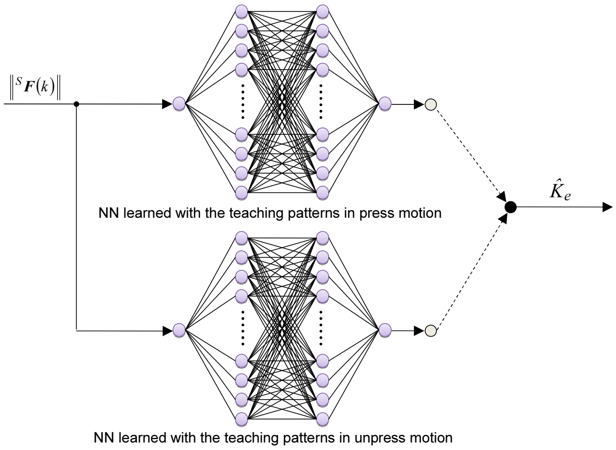

Figure 9: NN-based effective stiffness estimator.

of 10 N in Figs. 5 and 6 become the operating points. The NN-based effective stiffness estimator generates time-varying effective stiffness $\hat{K}_e$ around the operating points. In the next subsection, critical damping condition in force control system generates the desired damping for stable force control.

3.3 Tuning of desired damping

When the polishing force is controlled, the characteristics of force control system can be varied according to the combination of impedance parameters such as desired mass and damping. In order to increase the force control stability the desired damping, which has much influence on force control stability, should be tuned suitably. Here, a tuning method of desired damping is proposed by using the effective stiffness of the NC machine tool. Eq. (4) is derived from the following impedance model.

$$M_d(\ddot{x} \quad \ddot{x}_d) + B_d(\dot{x} \quad \dot{x}_d) = K_f(F \quad F_d) \tag{8}$$

where $\ddot{x}$, $\dot{x}$ and F are the acceleration, velocity and force scalars in the direction of force control, respectively. $\ddot{x}_d$, $\dot{x}_d$ and F_d are the desired acceleration, velocity and force, respectively. When the force control is active, $\ddot{x}_d$ and $\dot{x}_d$ are set to zero. It is assumed that F is the external force given by an environment and is model as

$$F = \quad B_m\dot{x} \quad K_m x \tag{9}$$

where B_m and K_m are the viscosity and stiffness coefficients of the environment, respectively. Eqs. (8) and (9) lead to the following characteristics equation.

$$s^2 + \frac{B_d + K_f B_m}{M_d}s + \frac{K_f K_m}{M_d} = 0 \tag{10}$$

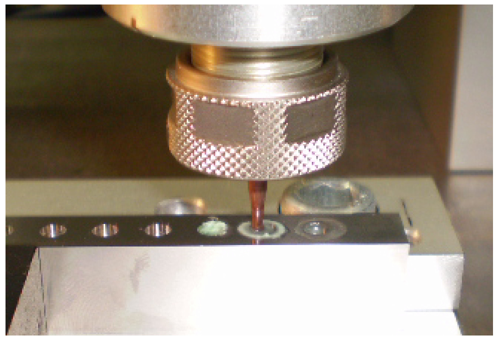

Figure 10: Finishing scene by using the wood stick tool and diamond lapping paste.

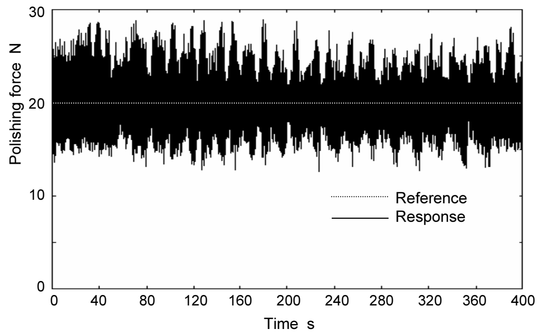

Figure 11: Control result of polishing force $\|{}^{S}\boldsymbol{F}(k)\|$.

By solving Eq. (10) with the critical damping condition, the desired damping can be given by

$$B_d = 2\sqrt{M_d K_f K_m} \quad K_f B_m \tag{11}$$

4 Experiment

In this section, the proposed system is applied to the finishing of an LED lens mold. The small ball-end tool lathed from a wood stick is used, whose tip diameter is 1 mm. A spiral path for finishing is generated along the small curved surface by using a CAD/CAM. Figure 10 shows the finishing scene, where a special oil including the diamond lapping paste is poured. In this case, the polishing force was successfully controlled around 20 N as shown in Fig. 11 in spite of oscillations caused by tool rotation of 400 rpm.

5 Conclusions

An impedance model force control using neural networks has been proposed to deal with the nonlinear effective stiffness of a desktop NC machine tool. The neural networks learned the nonlinear relation between the contact force and effective stiffness, so that the desired damping could be dynamically generated according to the contact force. The effectiveness and promise of the proposed method were demonstrated by a finishing experiment of an LED lens mold.

References

[1] F. Nagata, T. Hase, Z. Haga, M. Omoto and K. Watanabe, "CAD/CAM-based position/force controller for a mold polishing robot," , vol. 17, no. 4–5, pp. 207–216, 2007.

The Fifteenth International Symposium on Artificial Life and Robotics 2010 (AROB 15th '10),
B-Con Plaza, Beppu,Oita, Japan, February 4-6, 2010

Fuzzy Sliding Mode Control for Under-Actuated System with Mismatched Uncertainties

Seung-Yong Shin and Ju-Jang Lee

Department of Electrical Engineering and Computer Science
Korea Advanced Institute of Science and Technology (KAIST)
Tel: 82-42-350-8032; Fax: 82-350-5432
Email: Sngyong-shin@kaist.ac.kr

Abstract: This paper presents a robust fuzzy sliding mode controller. The methodology of sliding mode control provides an easy way to control under-actuated nonlinear systems with uncertainties. The structure of sliding surface is designed as follows. First, decouple the entire system into second-order systems such that each subsystem has a separate control target expressed in terms of a sliding surface. Second, from sliding surface of subsystems, organize the main sliding surface system. Third, generates a control input for main sliding surface to make whole subsystems moving toward their sliding surface. A fuzzy controller is used for obtaining smooth boundary layer of sliding surface. Finally presented fuzzy sliding mode controller is used to control under-actuated nonlinear system and confirms the validity of the proposed approach and its robustness for uncertainties.

Keyword: Robust controller, Sliding mode controller, Fuzzy controller

I. INTRODUCTION

There are needs for machines which have missions in extremely harsh situations that human can never stand. A robust controller is studied to withstand those kinds of situations. The sliding mode control is a powerful and robust nonlinear feedback control method. It has been developed and applied to feedback control systems for last three decades. The sliding mode controller is insensitive to internal parameter variation and external disturbances when system is on sliding surface. [1], [2]

Mechanical systems with fewer number of control inputs than the number of degree of freedom which should be controlled are called under actuated systems. These systems can be found in industry areas easily. However, their unexpected properties such as nonlinearity and coupling effect make design procedure difficult. In this paper inverted double pendulum will be considered as an example of a class of under-actuated systems. [1], [3]

In this paper, the under-actuated system is controlled using decoupled sliding mode controller. With proposed controller, the system can be controlled simple fuzzy controller which has an equivalent expression of a classical sliding mode control with a boundary layer. It is possible to remove high frequency switching (chattering phenomena) by introducing our fuzzy controller.

This paper is organized as follows. In section II, the design of decoupled controller motivated by [1] is presented. Section III shows design of fuzzy controller is equivalent to boundary layer sliding mode controller [4]. In section IV, the proposed controller is used to control double inverted pendulums. Conclusions are in the last section.

II. DECOUPLED SLIDING MODE CONTROL

Consider an under-actuated nonlinear system as follows:

$$\begin{aligned}
\dot{x}_1(t) &= x_2(t) \\
\dot{x}_2(t) &= f_1(\mathbf{x}) + b_1(\mathbf{x})u(t) + d_1(t) \\
\dot{x}_3(t) &= x_4(t) \\
\dot{x}_4(t) &= f_2(\mathbf{x}) + b_2(\mathbf{x})u(t) + d_2(t) \\
\dot{x}_5(t) &= x_6(t) \\
\dot{x}_6(t) &= f_3(\mathbf{x}) + b_3(\mathbf{x})u(t) + d_3(t)
\end{aligned} \tag{1}$$

Where $\mathbf{x} = [x_1(t), x_2(t), x_3(t), x_4(t)]$ are the state variables; $f_1(\mathbf{x}), f_2(\mathbf{x}), b_1(\mathbf{x})$, and $b_2(\mathbf{x})$ are bounded nominal nonlinear functions; $u(t)$ is the control input; and $d_1(t)$ and $d_2(t)$ are the lumped disturbances, which include the system uncertainties and external disturbances; and assume they are bounded by some positive constants ε_i $(i = 1,\ 2)$ This system can be considered as two subsystems with second-order canonical form.

Define a pair of sliding surfaces as

$$s_1 = c_1 x_1 + x_2 \tag{2}$$

$$s_2 = c_2 x_3 + x_4 \tag{3}$$

$$s_3 = c_3 x_5 + x_6 \tag{4}$$

where c_1, c_2, c_3 are positive constants. From (1) time derivatives of (2), (3) and (4) are obtained as

$$\dot{s}_1 = c_1\dot{x}_1 + \dot{x}_2 = c_1 x_2 + f_1(\mathbf{x}) + b_1(\mathbf{x})u(t) + d_1(t) \tag{5}$$

$$\dot{s}_2 = c_2\dot{x}_3 + \dot{x}_4 = c_2 x_4 + f_2(\mathbf{x}) + b_2(\mathbf{x})u(t) + d_2(t) \tag{6}$$

$$\dot{s}_3 = c_3\dot{x}_5 + \dot{x}_6 = c_3x_6 + f_3(\mathbf{x}) + b_3(\mathbf{x})u(t) + d_3(t). \quad (7)$$

Assuming the lumped disturbance in (4) is ignored, i.e., $d_1(t) = 0$ by the condition of sliding mode $\dot{s}_1 = 0$, an equivalent control law can be obtained as

$$u_{eq} = \frac{-c_1x_2 - f_1(\mathbf{x})}{b_1} \quad (8)$$

However, this control only considers the control of subsystem defined by (x_1, x_2) while disregard lumped disturbance and control of (x_3, x_4) and (x_5, x_6) subsystems.

To solve problem stated above, define a hierarchical coupled sliding surface and its derivative as

$$S = s_1 - \eta_2 s_2 - \eta_2 s_3 \quad (9)$$

$$\begin{aligned}\dot{S} &= \dot{s}_1 - \eta_2\dot{s}_2 - \eta_3\dot{s}_3 \\ &= c_1x_2 + f_1(\mathrm{x}) + b_1(\mathrm{x})u(t) + d(t) - \eta_2\dot{\bar{s}}_2 - \eta_3\dot{\bar{s}}_3\end{aligned} \quad (10)$$

where η_2 and η_3 are positive constants and referred to as coupling factor, $d(t)$ is total uncertainty in $\dot{S}$ i.e., $d(t) = d_1(t) + d_2(t) + d_3(t)$ and $\dot{\bar{s}}_i$ $(i = 2,3)$ are same as (6) and (7) with removing each disturbance $d_2(t)$, $d_3(t)$. These η_2 and η_3 are important parameters which will play a main role for the interaction among sliding surfaces s_1, s_2, and s_3 which are shown in Fig. 1.

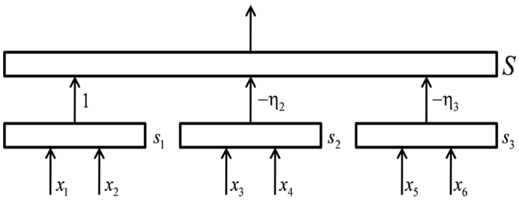

Fig.1. Structure of hierarchical sliding surfaces

The total control input is defined as

$$u = u_{eq} + u_{sw} \quad (11)$$

where u_{eq} is given in (6), and u_{sw} is switching control term to deal with the lumped disturbance and interactive coupling influence.

Consider a Lyapunov function

$$V = \frac{1}{2}S^2. \quad (12)$$

From Lyapunov theorem if $\dot{V}$ is negative definite, the system trajectory will be driven and attracted toward the sliding surface and remain sliding on it until the origin is reached asymptotically.

From (9), (10), and (11) the Lyapunov stability condition can be derived as follows:

$$\begin{aligned}\dot{V} &= S\dot{S} \\ &= S[c_1x_2 + f_1 + b_1u + d_1 - \eta_2\dot{s}_2 - \eta_3\dot{s}_3] \\ &= S[c_1x_2 + f_1 + b_1(u_{eq} + u_{sw}) + d - \eta_2\dot{s}_2 - \eta_3\dot{s}_3] \\ &= S[b_1u_{sw} + d - \eta_2\dot{s}_2 - \eta_3\dot{s}_3]\end{aligned} \quad (13)$$

Choose u_{sw} as follows:

$$u_{sw} = \frac{-\varepsilon\,\mathrm{sgn}(S) - \eta_2\dot{s}_2 - \eta_3\dot{s}_3}{b_1} \quad (14)$$

where $\mathrm{sgn}(\bullet)$ is a sign function and ε is positive number whose value is larger than supremum of total uncertainty d.

Then (13) becomes

$$\begin{aligned}\dot{V} &= -\varepsilon\,\mathrm{sgn}(S)S + d_1S \\ &\le -(\varepsilon - d_{1\max})|S| \\ &\le -\delta\end{aligned} \quad (15)$$

where δ is positive number.

In summary, the control law is given as

$$u = \frac{-c_1x_2 - f_1(\mathrm{x}) - \eta_2\dot{s}_2 - \eta_3\dot{s}_3 - \varepsilon\,\mathrm{sgn}(S)}{b_1} \quad (16)$$

III. FUZZY SLIDING MODE CONTROL

In this section, we propose the fuzzy controller for sliding surface boundary layer. It can be shown a particular fuzzy controller is an extension of an SMC with a boundary layer [4]. Through decoupling sliding mode control, it can be easily implemented using simple fuzzy rules.

Suppose the fuzzy controller is constructed from the following IF-THEN rules.

R^1 : if s is NB, then u_f is BIGGER

R^2 : if s is NM, then u_f is BIG

R^3 : if s is ZR, then u_f is MEDIUM

R^4 : if s is PM, then u_f is SMALL

R^5 : if s is PB, then u_f is SMALLER

where NB is negative big, NM is negative medium, ZR is zero, PM is positive medium, PB is positive big.

Let X and Y be the input and output space of fuzzy rules. For any arbitrary fuzzy set $\tilde{F}$ in X, each rule R^i can determine a fuzzy set $\tilde{F}_x \circ R^i$ in Y. Use sup-min compositional rule of inference with condition that $\tilde{F}_x$

is fuzzy singleton. Then

$$\begin{aligned}\mu_{\tilde{F}_x \circ R^i}(\mu_f) &= \min[\mu_{\tilde{F}_s^i}(\alpha), \mu_{\tilde{F}_{\mu_f}^i}(\alpha)] \\ \mu_{\tilde{F}_{\mu_f}^d}(\mu_f) &= \max[\mu_{\tilde{F}_x \circ R^1}(\mu_f), \ldots, \mu_{\tilde{F}_x \circ R^5}(\mu_f)]\end{aligned} \tag{17}$$

The crisp output is obtained by center-of-area defuzzifier

$$u_c = \frac{\int u_f \cdot \mu_{\tilde{F}_{u_f}^d}(u_f) du_f}{\int \mu_{\tilde{F}_{u_f}^d}(u_f) du_f} \tag{18}$$

Then u_c has the following form:

$$u_c = \tilde{u} - K_f f_{fuzzy}(s) \tag{19}$$

where

$$f_{fuzzy}(x) = \begin{cases} -1 & \text{if } x < -1 \\ -\frac{1}{2}\frac{(2x+3)(3x+1)}{4x^2+6x+1} & \text{if } -1 \le x < -1/2 \\ -\frac{1}{2}\frac{x(2x+3)}{4x^2+2x-1} & \text{if } -1 \le x < -1/2 \\ \frac{1}{2}\frac{x(2x-3)}{4x^2-2x-1} & \text{if } 0 \le x < 1/2 \\ \frac{1}{2}\frac{(2x-3)(3x-1)}{4x^2-6x+1} & \text{if } 1/2 \le x < 1 \\ 1 & \text{if } x \ge 1 \end{cases}$$

This controller has a nearly same property of boundary layer sliding mode controller with boundary width 1 as shown in Fig. 2

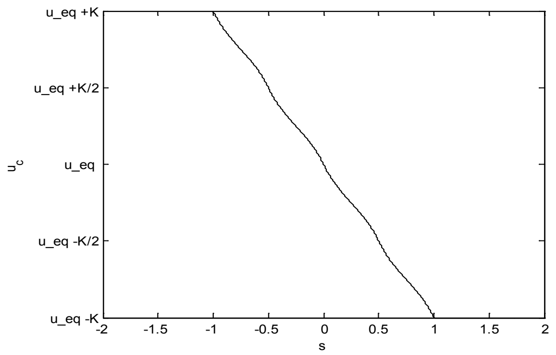

Fig.2 Result of fuzzy controller

The controller shown in (16) will have high frequency switching (chattering phenomena) near the sliding surface due to $\operatorname{sgn}(\bullet)$ function. These rapid changes of input can be avoided by introducing boundary layer method. The fuzzy controller (19) has same form of sliding mode controller (16). By replacing sign function $\operatorname{sgn}(\bullet)$ with $f_{fuzzy}(s)$, we can easily obtain a boundary layer and we can remove chattering phenomena.

IV. SIMULATION RESULT

In this section, we shall show that proposed method is applicable to double inverted pendulums system which is typical example of a nonlinear under-actuated system. The structure of the system is illustrated in Fig. 3.

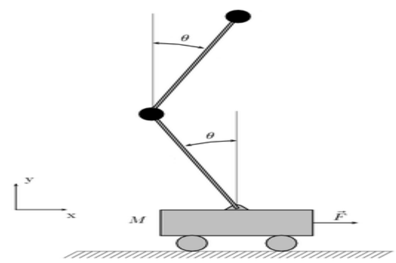

Fig. 3 Structure of double inverted pendulums

The system's dynamics can be represented as

$$\begin{aligned}\dot{x}_1 &= x_2 \\ \dot{x}_2 &= f_1 + b_1 u + d_1 \\ \dot{x}_3 &= x_4 \\ \dot{x}_4 &= f_2 + b_2 u + d_2 \\ \dot{x}_5 &= x_6 \\ \dot{x}_6 &= f_3 + b_3 u + d_3\end{aligned} \tag{20}$$

where $x_1 = \theta_1$ is angle of lower pole with respect to the vertical axis, $x_2 = \dot{\theta}_1$ is angular velocity of lower pole with respect to the vertical axis; $x_3 = \theta_2$ is angle of upper pole with respect to the vertical axis, $x_4 = \dot{\theta}_2$ is angular velocity of upper pole with respect to the vertical axis; $x_5 = x$ is the position of cart, $x_6 = \dot{x}$ is velocity of cart; u is control input, and f_i, b_i is given in [3] and d_i is the mismatched uncertain term whose bound is known.

For simulation, the system parameter are chosen as the cart mass $M = 1kg$, lower pole mass $m_1 = 1kg$, upper pole mass $m_2 = 1kg$, the lower pole length $l_1 = 1m$, the upper pole length $l_2 = 1m$ the gravitational acceleration $g = 9.81 m \cdot s^{-2}$ and $d_i = 0.0872\rho$ where ρ is a random number whose range is $(-1,1)$ and the total mismatched uncertainty d is bounded by 0.3, i.e., $|d| \le 0.3$.

The parameters for presented fuzzy sliding mode controller are selected as sliding surface parameter $c_1 = 6$, $c_2 = 0.4$, $c_3 = 0.15$ and interaction parameter $\eta_2 = 0.016$, $\eta_3 = 0.676$, $\varepsilon = 5$ after trial and error. The initial values are:

$\theta_1 = \pi/6$, $\dot{\theta}_1 = 0$, $\theta_2 = \pi/18$, $\dot{\theta}_2 = \pi/18$, $x = 0$, $\dot{x} = 0$.

Our control objective is making the system from the initial state $(\pi/6, 0, \pi/18, 0, 0, 0)$ to the desired states $(0,0,0,0,0,0)$. Fig. 4 and Fig. 5 show the simulation result.

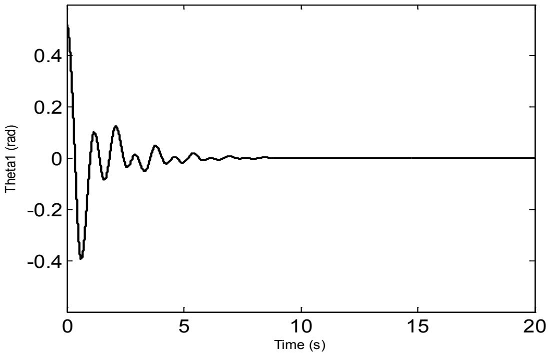

Fig. 4(a) Angle of lower pole

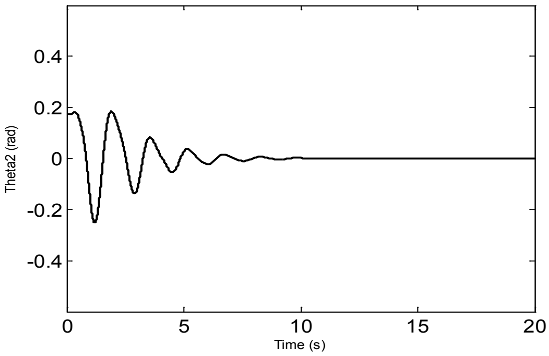

Fig. 4(b) Angle of upper pole

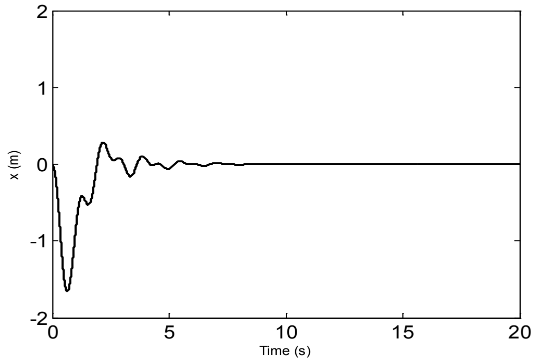

Fig. 4(c) Cart position

Fig. 4(a) and Fig. 4(b) show the proposed controller can make the double inverted pendulums upright. Fig. 4(c) shows the cart position is well controlled as well.

Fig. 5 shows control effort for moving cart. As the graph shows, the presented controller alleviate chattering problem effectively. Furthermore, the figure shows that presented method use relatively small control force.

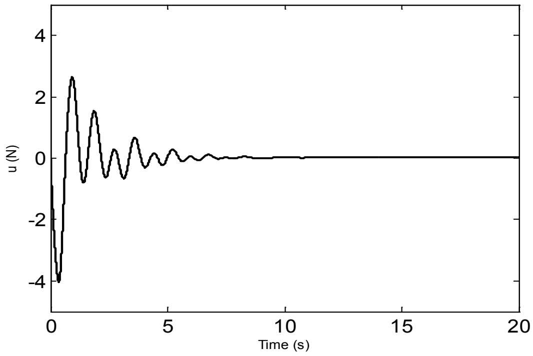

Fig. 5 control force

V. CONCLUSION

Fuzzy sliding mode controller has been proposed for a class of under-actuated systems. By introducing hierarchical switching scheme, it is possible to decouple the whole system into subsystems which has canonical form. The advantage of this approach is that the control law is determined by lyapunov function, so this approach can guarantee the system stability. By decoupling sliding surface, fuzzy rule based controller design can be easily obtained. A fuzzy controller is used for obtaining smooth boundary of sliding surface. It is shown that chattering problem can be solved using fuzzy scheme. Proposed method is well applied to double inverted pendulum which is typical example of highly nonlinear under-actuated system.

VII. ACKNOWLEDGMENT

Authors are gratefully acknowledging the financial support by Agency for Defence Development and by UTRC(Unmanned Technology Research Center), Korea Advanced Institute of Science and Technology.

References

[1]D. Qian, J. Yi and D. Zhao (2007) "Robust Control Using Sliding Mode for a Class of Under-Actuated Systems with Mismatched Uncertainties," *IEEE International Conference on Robotics and Automation* 1449-1454

[2]C. W. Tao, J. S. Taur and M. L. Chan (2004) "Adaptive Fuzzy Terminal Sliding Mode Controller for Linear Systems With Mismatched Time-Varying uncertainties," *IEEE Trans. System, Man, and Cybernetics* 34(1):255-262

[3]J.C. Lo and Y.H. Kuo (1998) "Decoupled Fuzzy Sliding-Mode Control," *IEEE Trans. Fuzzy Systems* 6(3): 426-435

[4]C. M. Lin and Y. J. Mon (2005) "Decoupling Control by Hierarchical Fuzzy Sliding-Mode Controller," *IEEE Trans. Control systems technology* 13(4):593-598

A study of Embedded Community Network System in Home automation

Chun-Liang Chen1, Pi-Yu Chen2 and Der-An Wang3

1. Dept. of Electronic Engineering, Nan Kai University of Technology , Taiwan
2.Graduate Institute of Electrical Engineering &Computer Science, Nan Kai University of Technology, Taiwan
3. Dept. of Mechanical Engineering, Nan Kai University of Technology , Taiwan
(Tel : 886-49-256-3489ext3367; Fax : 886-49-256-9834)
(junchen@nkut.edu.tw)

Abstract: This paper presents home automation in community network with embedded system. The system includes home security monitor and home energy monitor. Home security monitor uses sensors and micro switches to monitor home status; home energy monitor adopts Hall sensor to oversee household energy consumption and control the power consumption of home appliances, Furthermore, use embedded database to record, energy consumption. Besides, the system use Shortest Paths and Topological Sort of power dispatch module. Data is transmitted to computers, mobile phones, or other devices connected to Internet. The system integrates every node subsystem and is constructed on net framework by using Common Gateway Interface (CGI) and Cell Spitting.

Keywords: Embedded Data Base, Common Gateway Interface (CGI)

I. INTRODUCTION

Currently, most households install grille as a basic home security. However, grille may hinder rescuing in accident. By implementing the home monitoring automation system, one can ensure community safety with other residences in the neighborhood. With regard to increasing population and declining energy reserves, it is important to discuss how to efficiently use electricity. The power supply system of Taiwan Power Company does not provide for customer, so the user is unable to know how to use electricity efficiently. Presently many home appliances are advocated to be energy efficient and can reduce pollution; therefore, the researchers also use the energy monitoring function of this system to calculate electricity consumption per household so as to optimize this action research cycle [1] (Fig. 1). The system is able to tell which appliances consume more energy, so users can manage to save energy. This Home To Automate In Community is mainly established by the use of a basic community framework (Fig. 2).

II. SYSTEM DESCRIPTION

1. System Framework

The system used Intel XScale PXA270 ARM10 development platform as its central processing unit, and it then ports SQLite database to the platform. ARM is powerful and fast, so the researchers test inputs of peripheral equipments of two separate systems.[2] These two systems are home security monitor and home power monitor, and they are later integrated into two major functions of one single system. Each single node subsystem (Fig. 3) composes a comprehensive safety monitoring system (Fig. 4), and the system is then processed by a remote server and connected through network to form the Home To Aytomate In Community (Fig. 5).

2. Platform

This system mainly uses ARM development platform module to complete various tasks. The ARM development platform module adopts Intel XScale PXA270 (Fig. 6) as its central processing unit. The purpose of this research is to port database into the embedded platform for application; therefore, the researchers choose module with larger memory capacity as the development platform. [3]

3. DataBase

It is usually a must for a database to be able to process large amounts of data. However, if the data is fixed in content and does not have a lot of amounts, or the database will only be used on one single computer and not by multiple users, it is not necessary to establish a particular database system. Users can merely adopt embedded database such as SQLite[4].

4. Software framework(Fig.7)

- Web Service AP：To make a Web Service with CGI that user can use and control in Web Browser.
- GUI AP：The interface of ARM with Touch panel
- Data Picking up：Read message in Hall Sensor.
- Device Drivers：to link with peripheral device.
    (1). Anti-theft I/O：Monitoring switch whether on/off.
    (2). Power Monitor I/O：to control the relay of power loop relay.

5 Boa Web Server

uClinux has three major web servers: htpd, thttpd, and Boa. Httpd is the simplest web server. It has fewer functions and does not support any certifications or CGI. Both thttpd and Boa support certifications and CGI and areequipped with more functions. To realize dynamic Web technology, the researchers choose Boa Web Server, which supports CGI and is suitable to be embedded into the system. Boa is a single-task, open-source, and highly capable http server. uClinux has already included source codes of Boa. One needs only some setups and modifications to use Boa under uClinux. There are by far four techniques for choice regarding the implementation of dynamic web page: CGI(Common Gateway Interface), ASP(Active XServer Page), PHP(Personal Home Page), and JSP(Java Server Page). However, to make dynamic web page under uClinux, only CGI is applicable since uClinux does not support ASP or PHP. The picture (Fig.8) shows the procedure of establishing Boa.[5]

6. Common Gateway Interface (CGI)

Common Gateway Interface (CGI)(Fig.9) can connect network host and browser to allow data storage. CGI can complete the said action, and it is a general interface instead of a particular program. CGI program can be compiled using several programming languages. Based on various operating platform, the most common programming languages for CGI are C, C++, Perl, PHP, TCL, JAVA, VB, etc. Functions such as message boards, discussion forums, visitor counters, online voting, electronic cards, online visitors, ect. all belong to CGI. An intercommunication channel is an environment variable. HTTP can convey data in <FORM> to CGI via STDIN; and CGI can use STDOUT to return outputs to HTTP and show them on browser. The second communication channel offered by CGI is method=get. It uses environment variable to transmit data. The capacity of environment variable is limited, so when conveyance of large amount of data is needed, the space for storing environment variable may be insufficient, causing data incompletion or CGI implementation failure. Method=post utilizes I/O redirection to allow CGI to communicate directly with browser via STDIN and STDOUT, solving the shortcoming of method=get.

7.Cell Spitting

There are many kinds of coding algorithms to carry out in genetics, the methods we used of cell Spitting as follows .Fig. 10 and Fig. 11 show the Cell spitting.[6]:

(1).Select one initial vectorial Xi from training the vector quantity =[Xi1 Xi2 Xi3 Xip], uses this to be initial produce vector quantity m piece from for the initial for yards of vector quantity [V1 V2 Vm], among them Vj =[Vj1 Vj2 Vj3 Vjp], i =j = m, v jk =xjk =Xij+(2* i-m-1) *δ.

(2).By m an initial yard vectorial V1 V2 Vm central point, hive off other training vector quantity, calculate group of central points again, get other m a new central point.

(3).This m is a new central point, will all split into m vectors, and hive off again, calculates the new central point. The movement that split can sustain, split once, number of group with m. It is awfully quick and long. Repeat the step described above, until reach the size of coding set u.

III. System Implementation

The system consists of two parts: home security monitor(Fig.12) and home energy monitor.(Fig.13) Both parts can operate independently, but all records are stored in a common database. The records are sorted with database page format to avoid data disorder. Home security monitor allows users to control anti-theft switch through network, and it records when the switch is turned on. Once the anti-theft switch is activated, the system alarms to owners, neighbors, or security contactors. The home power monitor is also based on net framework, and users can also switch on or off home appliances through network while there is no one at home; on the other hand, they can also turn on before returning home. The timer function allows appliances to be activated at the same time, and it helps reduces electricity fees.

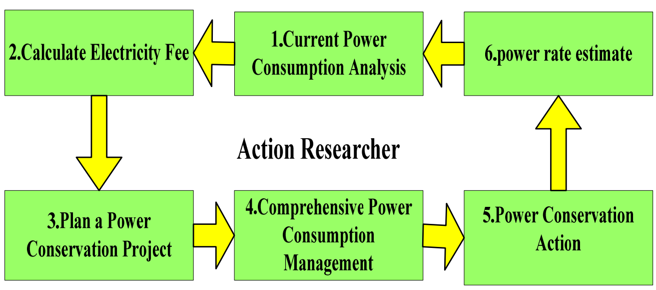

IV. FIGURES

Fig. 1 Power Consumption Analytical Cycle

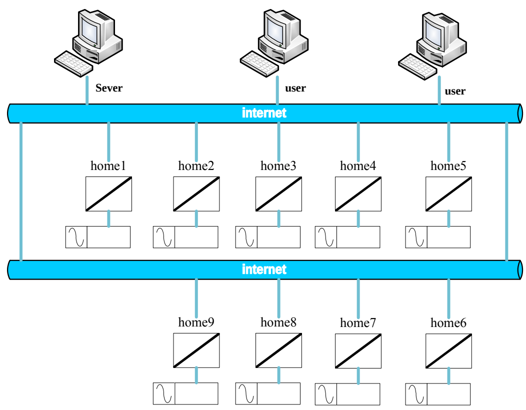

Fig. 2 Basic Community Framework

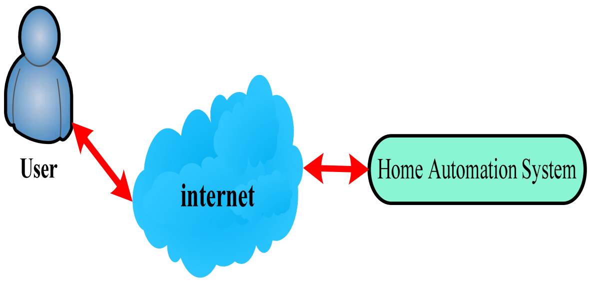

Fig. 3 Single Node Subsystem

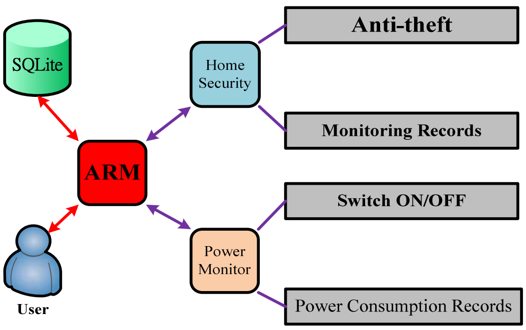

Fig. 4 Embedded Safety Monitoring System

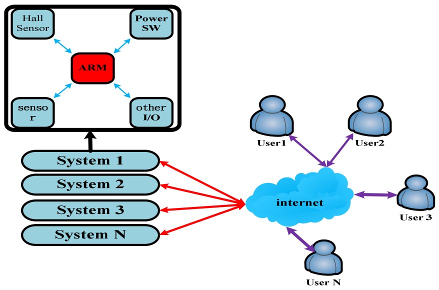

Fig.5 Home Automation In Community

Fig. 6 Intel XScale PXA270 Module

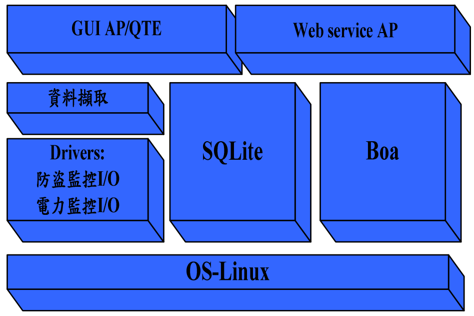

Fig. 7 Software framework

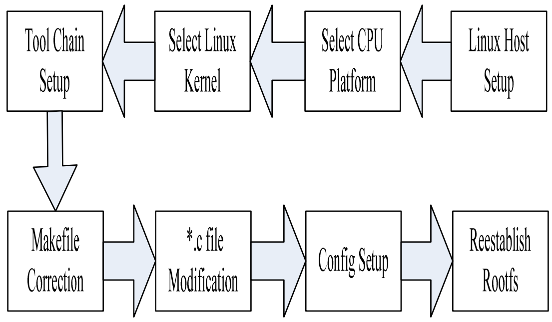

Fig. 8 Procedure of Establishing Boa

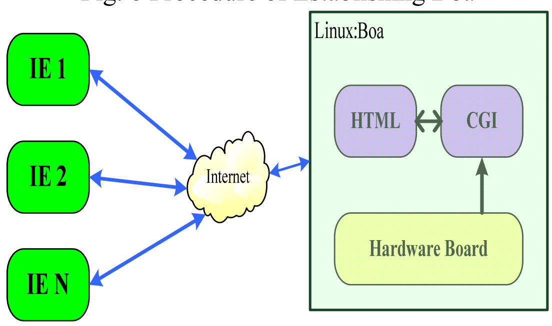

Fig.9 CGI Framwork

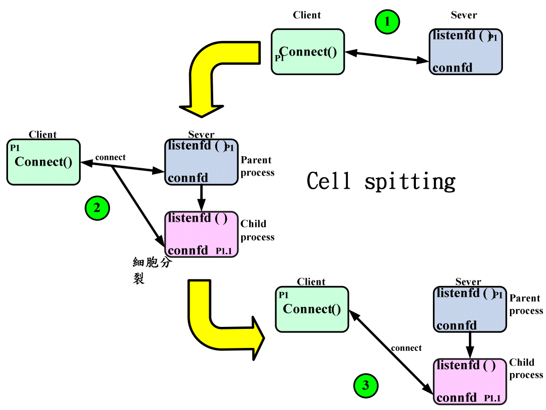

Fig.10 Socket using Cell spitting

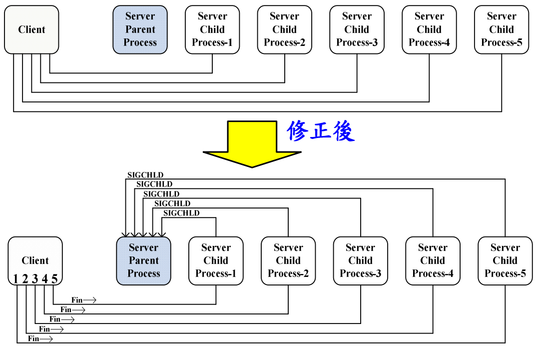

Fig.11 Socket using Modified Cell spitting

System Information for Server										
User Name	Enable	SW1_Name	SW1_State	SW2_Name	SW2_State	SW3_Name	SW3_State	SW4_Name	SW4_State
tony1	1	door-1	1	windows-1	0	door-2	1	windows-2	0
tony2	0	door-1	0	door-2	0	image	0	windows-2	0
tony3	0	safe	0	image	0	windows-1	0	windows-2	0
tony4	1	door-2	1	safe	1	image	0	door-1	0
tony5	1	windows-1	1	windows-2	1	safe	1	door-1	1
tony6	0	windows-2	0	door-2	0	safe	0	door-1	0

Fig. 12 Home Security Monitor

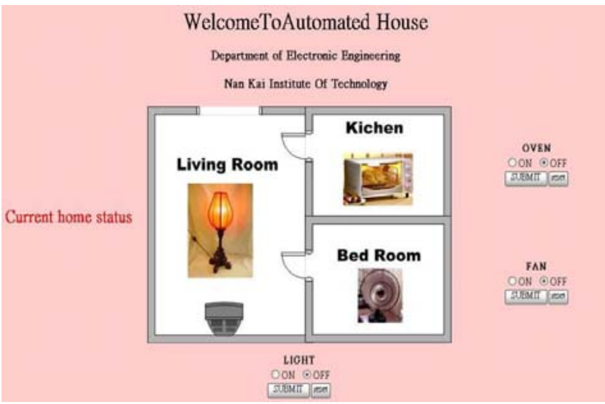

Fig. 13 Home Power Monitor

V. CONCLUSION

The system in this research has been established and tested. Its home power monitor oversees and manages each circuit. Power consumption and on/off time is recorded separately in database, allowing users to adjust power saving project based on the data. Another high power consumption source is from appliances (lights, fans, etc.) not switched off in rooms with no one. Such issue is also improved by using this system since it can determine if there is anyone in a room by reading related sensors. If there is no human activity in a room for a time period, the system will switch off appliances in it. For home security monitor, the researchers have completed basic sensor testing such as reed switch and infrared sensor. The result shows the system can detect when sensors are activated and indicate it on web pages so that users can easily control home security. Users will still be notified of sensor activation by short messages even if they are not at home. They can also accurately record when and which sensors are activated. This system has been established and reached expected goals after testing; therefore, it can be used in home automation system in the future.

REFERENCES

[1]B.T. Hou (2005), The Design and Implementation of A Microarray Data Analysis Tool Using Embedded Database(in Taiwan). 85-90.
[2]C.A. Yu (2006), , Implementation of ARM-9 Based Wireless Internet Radio, (in Taiwan). 45-48.
[3]C. T. Lin(2005), Home-Agent Systems On ARM9 Develop Platform(in Taiwan). 32-35.
[4] Industrial Development Bureau Ministry of Economic Affairs：http://support.oss.org.tw
[5]C.L. Chen[1], Y. H. Chiang[2],D.Y. Wong[3] [2008],Embedded Community Network System of Security Monitor,, The 3rd Intelligent Living Conference (in Taiwan).
[6]Hu, Y. C. and Chang, C. C.(1999),A progressive Codebook Training Algorithm for Image Vector Quantization, Proceeding of the Fifth sia-Pacific Conference on Communications and Fourth Optoelectronics and Communications Conference(APCC/OECC 99'), Beijing, China,vol. 2 , pp.936-939,

A novel coding method for genetic algorithms based on redundant binary number

A. Murayama and A. Kanasugi

Graduate School of Engineering, Tokyo Denki University
2-2 Kanda-Nishiki-cho, Chiyoda-ku, Tokyo, 101-8457 Japan
(Tel: 03-5280-3705; Fax: 03-5280-3565)
(Email address: 09kme47@ms.dendai.ac.jp, kanasugi@eee.dendai.ac.jp)

Abstract: This paper proposes a novel GA which switches the expression of solution from redundant binary number to usual binary number. Furthermore, a GA which switches the expression from Gray code to usual binary number is compared. Gray code is a binary numeral system where two successive values differ in only one bit. In this paper, comparison of performance among five GA (binary number, redundant binary number, Gray code, switching from redundant binary number to binary number, switching from Gray code to binary number) were illustrated. The performance were evaluated by solving some equations. It is confirmed that the proposed GA was effective for improvement of error rate.

Keywords: Genetic Algorithm, Redundant binary number, Gray code.

I. INTRODUCTION

Genetic algorithm (GA) is one of optimization algorithm that is based on an idea for evolution of life [1]. GA can solve various problems such as combination optimization problem, machine learning, and so on.

This paper proposes a novel GA based on redundant binary number, though general GA expresses chromosomes in binary number. The performance comparisons were simulated by solving some equations. It was confirmed that the proposed GA was effective for improvement of error rate.

II. PROPOSED METHOD

In this paper, GA is based on redundant binary number. The advantage with redundant binary number is variety of expression for optimized solution. From this advantage, we can expect that improvement in searching speed and decrease of error rate. The redundant binary number uses values '0', '1' and '-1'. We assume that '0' sets "00" or "11", '1' sets "01", '-1' sets "10". The procedure of GA based on redundant binary number is almost the same as conventional GA. However, when GA based on redundant binary number evaluates individual, it is necessary to decode from redundant binary number to binary number. In this paper, as a decoding method, we separate chromosomes into odd number bit and even number bit. Then we subtract even number bit from odd number bit.

This paper proposes a novel GA based on redundant binary number [2]. The proposed GA can avoid suboptimal by variety of expression pattern with redundant binary number, in the first-half generation. Then the GA can search in detail with binary number in the second-half generation.

In addition, number of bits for the solution expression doubles in redundant binary number compared with usual binary number. Therefore, number of individuals can be doubled by switching the construction from redundant binary number to binary number in the second-half generation.

Furthermore, a GA which is realized by switching the expression from Gray code to usual binary number is compared.

III. EXPERIMENTS

Comparison among five GA (binary number, redundant binary number, Gray code, switching from redundant binary number to binary number, switching from Gray code to binary number) were simulated. The performance of each GA was evaluated by solving following three functions [3].

1) Rosenbrock function

$$f_1(x) = \sum_{i=1}^{9} \left[100 \times \left(x_{i+1} - x_i^2\right)^2 + \left(x_i - 1\right)^2 \right] \quad (1)$$

2) Weighted sphere function

$$f_2(x) = \sum_{i=1}^{10} \left(10000 - x_i^2\right) \quad (2)$$

3) Schwefel function

$$f_3(x) = -\sum_{i=1}^{5} x_i \ sin \sqrt{|x_1|} \qquad (3)$$

$f_1(x)$ has dependence among variables and it is unimodal function.

$f_2(x)$ doesn't have dependence among variables and it is unimodal function.

$f_3(x)$ doesn't have dependence among variables and it is multimodal function. The parameters of GA are summarized in table 1. However, number of population for redundant binary number becomes the half of the parameter.

Table 1. GA parameters

Function	(1)	(2)	(3)
Generation	300	200	500
Population	128		
Selection	Roulette		
Crossover	One Point		
Crossover Rate	0.99		
Mutation Rate	0.01		

All GA program are implemented in C language. The error rates of three functions are shown in figure 1, 2 and 3, respectively. Each result is the average of 1000 times of simulation. In these figures, 'B' means binary number, 'G' means Gray code, "G2" means switching from Gray code to binary number, 'R' means redundant binary number, and "R2" means switching from redundant binary number to binary number.

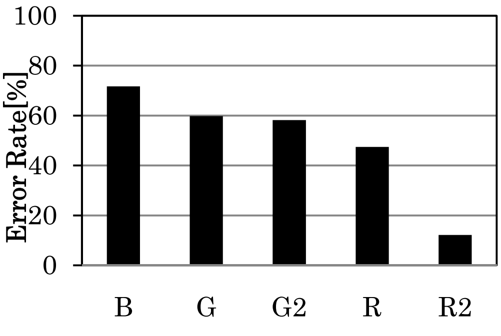

Fig.1. Error rate of $f_1(x)$

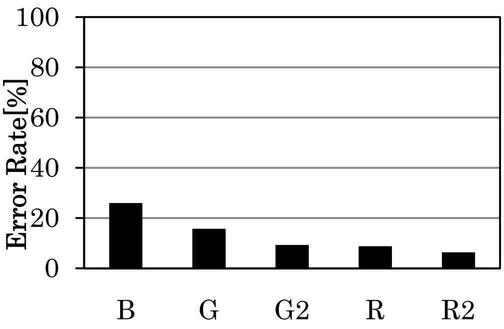

Fig.2. Error rate of $f_2(x)$

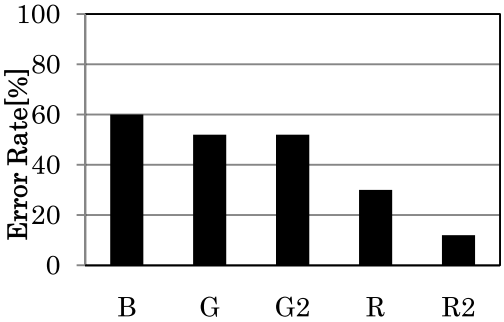

Fig.3. Error rate of $f_3(x)$

In figure 1, solutions tend to converge in the suboptimal solution by strong dependence among variables. However, GA with redundancy binary number tend to avoid suboptimal solution by variety of chromosomes expression and gets the optimal solution. In figure 2, though error rate didn't have much difference, GA with redundant binary number showed good results. Similarly, in figure 3, the proposed GA gave good results.

From these results, it was confirmed that proposed GA was effective for improvement of error rate.

IV. CONCLUSION

In this paper, we proposed a novel coding method for genetic algorithms based on redundant binary number. As the novel code increases the variety of chromosomes expression, the proposed GA is effective to escape from local optimum solution.

It was confirmed that proposed GA was effective for improvement of error rate by three test function.

REFERENCES

[1] L. Davis ed. (1991), Handbook of Genetic Algorithms, Van Nostrand Reinhold

[2] A. Tsukahara and A. Kanasugi (2009), Genetic Algorithm with Dynamic Variable Number of Individuals and Accuracy International Journal of Control, Automation, and Systems, vol. 7, no.1: 1-6

[3] X. Yao, Y. Liu, and G. M. Lin (1999), Evolutionary programming made faster, IEEE Trans. Evol. Comput., vol. 3, no. 2: 82–102

The Fifteenth International Symposium on Artificial Life and Robotics 2010 (AROB 15th '10),
B-Con Plaza, Beppu,Oita, Japan, February 4-6, 2010

THE OPTIMAL COMBINATION OF DITHER MATRIX BY USING GENETIC ALGORITHM

Tsuneyasu Kato and Ken-ichi Tanaka

School of Science and Technology ,Meiji Univ.

1-1-1,Higashi-Mita,Tama,Kawasaki,Kanagawa 214-8571 Japan

E-mail:ce91022@isc.meiji.ac.jp

Abstract: In this study, optimal combination of dither matrix is searched on a viewpoint of image quality with Genetic Algorithm(GA). At first, the combination of matrix is selected at random. The method of Crossover is interchanging positions of two individuals from element no.0 to element no. X. No. X is selected at random. And the type of selecting individuals is the tournament. The criterion of comparing data is cost E that is the evaluation value of gray level. And it is addition of cost Em and cost Ec. Individuals that have small cost E are prior carried over. The cost E of Bayer dither is 102.846. The cost E of GA is 102.826. It is clear that the result of GA is more super than Bayer dither on a viewpoint of image quality.

Keywords: GA, dither matrix, optimal combination, cost E, Tournament, One-pointed Crossover

I. INTRODUCTION

Nowadays, dither matrix which is four rows and four columns is used by newspaper, color photocopier and so on. The famous dither matrices are used in many situations. For example, Bayer method is one of famous methods. However, the study that these famous methods are really optimal combinations by viewpoint of optimization for combinations is not found. In this study, the matrix that has better evaluated value than existence matrices is searched for to enhance image quality. Its optimal combination is searched by GA.

II. ALGORITHM OF USING GA

In this study, individuals are themselves. Elements of individuals are threshold level of gray level from 0 to 255. The threshold levels are Equation.1. “I[x]” is position x of the matrix. "i” is numerical number from 0 to 15. The numeral numbers of elements of Table 1 are “i” of equation (1).

The same number is not set in the same individual. GA is to convert grouping and to search what combination of elements is the optimal combination. In this study, the operation of GA which Toshiharu[1] shows is as below.

(1) The matrices which have elements set in at random are prepared
(2) Set up solution of cost function E. Cost function E is the addition of cost Em and cost Ec. Cost Em is evaluated value of gray level. Cost Ec is Evaluated value of contrast. Equation of cost function E is as below.
(3) The individuals of next generation are decided by using the tournament method.
(4) Selecting two individuals and doing single point Crossover.
(5) Two elements of the individual which is selected at random are exchanged.
(6) Running over from (2) to (5) until the numbers of generations reach the generation number.

The number of individual is 200, the number of generation is 40, the probability of shakeout is 0.1 and the probability of mutation evolution is 0.01.

Single point Crossover is exchanging the position of elemental number from 0 to X of individual. The position of elemental number X is selected at random.

If the same elements are in the same individual, empty number of element sets one of duplicative element.

III. RESULT

The evaluated values of using GA and Bayer method which is the famous method are as below.

Fig.1 Em=6.7611,Ec=126.7910,E=102.7850

Fig.2 Em=6.8215,Ec=126.8531,E=102.8468

The lower cost E is, the matrix is optimal. Result of using GA is better than Bayer method. Ken-ichi [2] shows that the best of coefficients of cost Em and Ec are 0.2 and 0.8.

Because one pointed Crossover is more optimal than other methods, it is imagined that the sort of last individual of generation tends to live to be exchanging elements in group better than separately.

Even if generation numbers are over 40, the evaluated value is not good any more. As a result, it is assumable that the matrix of table1 is the optimal combination by the point of view of gray level.

IV. FIGURES/TABLES

1. Figures

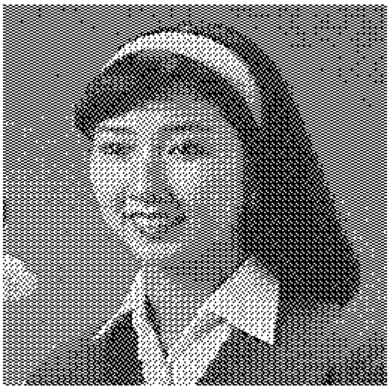

Fig1. The image using dither matrix searched by GA.

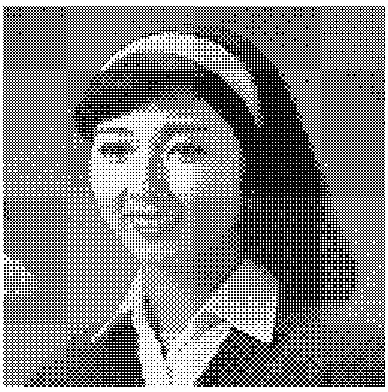

Fig2. The image using dither matrix of Bayer method.

2.Table

Table1. The matrix of using GA

7	11	0	8
3	13	6	15
9	2	10	4
12	5	14	1

3.Equation

I[x]= (2xi+1)x8 (1)

E=0.2xEm+0.8xEc (2)

x:times

IV. CONCLUSION

This matrix is gotten good evaluated value in color images. Therefore, if the optimal matrix is found by using GA, it will be used for many images.

In this study, parameters that are the individual number, the probability of mutation evolution and so on, are checked by hand. Therefore, it is unclear that these parameters are really optimal numerical number. For solving this problem, these parameters are become elements of GA. GA that has these elements is capable to search matrix that has better evaluated value than Figure1.

REFERENCES

[1] Toshiharu N (2002), Evolutionary Image Processing Publication Shoukoudou Inc.

[2] Ken-ichi T(2007), Color Images Halftoning Using Simulated Annealing. Publication The Journal of The Institute of Image Information and Television Engineers Vol.61, No.6, pp828-834.

The Fifteenth International Symposium on Artificial Life and Robotics 2010 (AROB 15th '10),
B-Con Plaza, Beppu,Oita, Japan, February 4-6, 2010

Improved Algorithm for Solving the Maximal Clique Problem with DNA Computing

H. Aoyagi [#1], N. Rajaee[#1] and O. Ono [#1]

[#] *Department of Electronic and Bioinformatics, Meiji University,*
1-1-1 Higashimita, Tamaku, Kawasaki, Kanagawa, 214-8571 Japan

(Tel : 044-934-7377; Fax : 044-934-7289)
[1] *(ee77082, nrajaee, ono)@isc.meiji.ac.jp*

Abstract: In this paper, we improve an algorithm proposed by Q. Ouyang to solve a maximal clique problem. While we can determine the size of the largest clique by sorting the length of the DNA strands in Q. Ouyang proposal, we cannot determine the exact vertices involved in the maximal clique. Thus in our improved algorithm, the exact vertices for each clique can be derived straightforwardly from the read-out in the gel electrophoresis process.

Keywords: DNA computing, the maximal clique problem, the parallel overlap assembly

I. INTRODUCTION

DNA computing which uses bio-molecules as a basis for computation is thought one day to be able to outperform electronic computers in computing complex combinatorial problems such as NP hard. Since then, many proposals to solve NP hard problems with DNA computing have been published including an algorithm proposed by Q. Ouyang [1] for solving a maximal clique problem (MCP) in 1997. The MCP is encoded in DNA sequences by assigning a binary number to each possible clique in the graph as the data structure. A bit set to 1 represents a vertex in a clique and a bit set to 0 represents a vertex out of the clique. Therefore for a graph with N vertices, the complete set of possible cliques is ensemble into an N digit binary numbers. The data structure is then designed in the form of double stranded DNA (dsDNA) and restriction enzyme sites are embedded for each bit value = 1. These restriction enzyme sites provide a "cutting" reaction to the enzymes and were not amplified during PCR. Reading the size of the largest clique is then based on the shortest length of the elongated DNA strands.

In our work, we improve the algorithm proposed by Q. Ouyang for better qualitative results of the computation. While we can determine the size of the largest clique by sorting the length of the DNA strands in Q. Ouyang proposal, we cannot determine the exact vertices involved in the maximal clique. Thus in our improved algorithm, the exact vertices for each clique can be derived straightforwardly from the read-out in the gel electrophoresis process.

II. THE MAXIMAL CLIQUE PROBLEM

A complete graph is a simple graph in which every pair of distinct vertices is connected by an edge. The MCP is to find a maximum size complete sub-graph, a maximal clique, from a given graph. The MCP is proven to be an NP-hard problem, and is difficult to solve efficiently.

III. ALGORITHM

We discuss an algorithm to solve the MCP by showing the graph example in Fig.1. Consider a graph with eight vertices, sixteen edges and three maximal cliques. Fig.3 shows an adjacency matrix of the given graph. The complementary graph (Fig.4) contains all edges missing in the original graph.

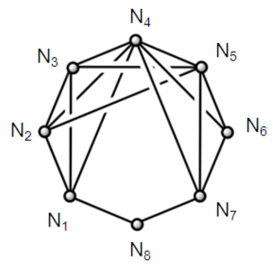

Fig.1. The graph of our example

Showing the connection of the node N_1

		N_1	N_2	N_3	N_4	N_5	N_6	N_7	N_8
Tube N1	N_1	1	1	1	1	0	0	0	1
Tube N2	N_2	1	1	1	1	1	0	0	0
Tube N3	N_3	1	1	1	1	1	0	0	0
Tube N4	N_4	1	1	1	1	1	1	1	0
Tube N5	N_5	0	1	1	1	1	1	1	0
Tube N6	N_6	0	0	0	1	1	1	1	0
Tube N7	N_7	0	0	0	1	1	1	1	1
Tube N8	N_8	1	0	0	0	0	0	1	1

Fig.2. Adjacency matrix for the graph

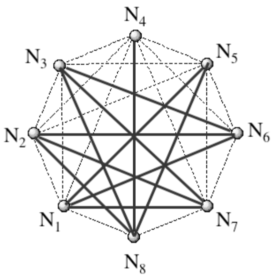

Fig.3. The complementary graph

The new algorithm consists of the following six steps.

Step 1 Cording (DNA sequence Generator)

First, we construct the sequence for value N_i and position E_i as described in Fig.1. There are eight value sections (N_1 - N_8) and its position (E_1 - E_9). The position sequences are used for connecting each node N_i (i=0,…,8). The eight value sections are set sandwiched between nine positions. Each combined oligonucleotide consists of two position motifs, $E_{i+1}N_iE_i$ for odd i, $\overline{E_{i+1}N_iE_i}$ for even i, where the bar shows the complementary sequence and the value of N_i can be either 1 or 0. In this experiment, we designed the DNA sequences in the form of ssDNA. We set E_i = 10 bp, N_i = 0 bp (if the value = 1) and N_i =15 bp (if the value = 0). The sequence of vertices are constructed from restriction enzyme (RE) sites for each bit value = 1.

Step 2 Merge (Parallel Overlap Assembly)

We produce a pool containing all possible solution with eight tubes T1-T8. Following Fig.2, we add combined ENE DNA sequences including nodes N_i^1 showing value 1 and all nodes N_i^0 showing value 0 into each tube. By performing POA, the DNA sequences for a position are annealed to the complementary sequence for the other DNA sequences and the combinations of $N_1N_2N_3N_4N_5N_6$, a pool containing possible solution, is generated.

Step 3 Cutting (Restriction Enzyme)

Contents of T1-T8 are digested with each RE (RE1-RE8) to eliminate illegally connected edges (Fig. 3) in each test tube.

Step 4 Amplify (Polymerase Chain Reaction)

Amplify only strands with E_0 and $\overline{E_9}$ for each tube by supplying primers E_0 and $\overline{E_9}$.

Step 5 Extract (Gel Electrophoresis)

The clique of the largest size is represented by the shortest DNA length. From gel electrophoresis process, extract only the shortest band 150bp (clique size = 4) for T1-T8 and separate into tubes T1'-T8'. Add RE1-RE8 into tubes T1'-T8' and observe the band lengths.

Step 6 Identify

The experiment result is observed by performing gel electrophoresis. Each vertex involved in individual cliques can be identified separately by the clustering of lengths for the vertices. From the result, you can find the vertices (1,2,3,4), (2,3,4,5), and (4,5,6,7) form the maximal cliques with size = 4.

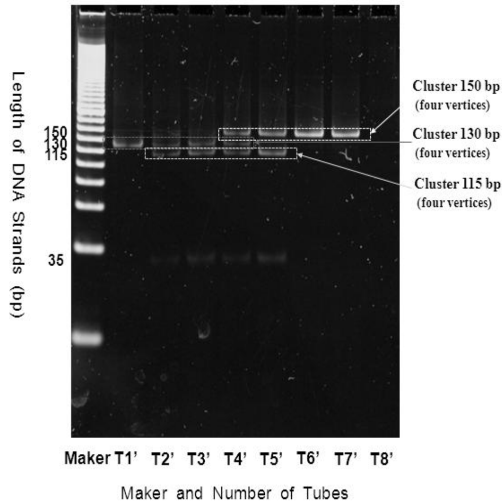

Fig.4. Gel Electrophoresis

VI. CONCLUSION

The experiment was carried out using basic bio-molecular tools as used such as parallel overlap assembly, polymerase chain reaction (PCR) and gel electrophoresis process. A major difference in our proposal is the inclusion of Step 6. In the original algorithm by Q. Ouyang, separate vertices involved in a clique were confirmed using molecular cloning technique which is time and resources inefficient. Using our algorithm the size of each clique can be determined by its DNA strand length and each vertex involved in individual cliques can be identified separately.

REFERENCES

[1] Q. Ouyang, P. D. Kaplan, S. Liu et al. (1997), DNA Solution of the Maximal Clique Problem, Science 278: 466-449
[2] I. Kim, D. J. Jeng, and J. Watada (2006), Redesigning Subgroups in a Personnel Network Based on DNA Computing, International Journal of Innovative Computing, Information and control 4:885-896

Difference of 3-back task performance due to three levels of arousal

M. H. Choi[a], J. S. Choi[a], B. C. Min[b], G. R. Tack[a] and S. C. Chung[a*]

[a]*Department of Biomedical Engineering, Research Institute of Biomedical Engineering, College of Biomedical & Health Science, Konkuk University, Chungju, South Korea*
[b]*Department of Industrial & Management Engineering, Hanbat National University, Daejeon, South Korea*
(Tel : 81-43-840-3759; Fax : 81-43-851-0620; E-mail : scchung@kku.ac.kr)

Abstract: The purpose of this study was to investigate how three levels of arousal affect performance of a 3-back task. Ten university male (25.7 ±1.5 years) and ten female (age 24.5 ±1.8 years) students participated in this experiment. Using pictures selected from a group test, three levels of arousal (arousal, neutral, and relaxed emotions) were induced. Each subject was run through the procedure three times, once for each arousal level. The procedure consisted of six phases for each arousal condition; Rest 1 (2 min), Picture 1 (2 min), 3-back Task 1 (2 min), Picture 2 (2 min), 3-back Task 2 (2 min), and Rest 2 (2 min). Skin conductance level (SCL) of electrothermal activity was also measured during all phases of the experiment. The accuracy rate of 3-back task performance was the highest at a neutral emotional state. Based on the results, it could be inferred that arousal emotion, induced by stimuli unrelated to cognitive tasks, decreases the ability to perform cognitive tasks.

Keywords: Arousal level, 3-back task, cognition ability**.**

I. INTRODUCTION

Recent studies showed that one axis of two-dimensional space (pleasantness-unpleasantness) might influence on cognitive processing abilities such as memory. People memorized pictures which induced negative (unpleasantness) emotion better than pictures which induced neutral emotions [1].

Some studies reported that emotional arousal influences on information processing [2, 3]. The emotional arousal controls consolidation of memory [4]. Using emotional Stroop task, subjects at high level of anxiety took longer reaction time to report the color names of threat words than those of non-threat words [5]. The results indicate that emotional arousal level might affect human being's cognitive ability.

This study examined how the arousal axis of human emotion affects cognitive performance ability by using three levels of arousal induced by emotional pictures and appropriate cognitive task measuring immediate memory. After inducing each level of arousal, it was observed how these arousal states influenced the accuracy of a 3-back task. To check whether the proper arousal level was achieved by using emotion inducing pictures, skin conductance level (SCL) of electrothermal activity was measured and subjective evaluation was performed after experiment.

II. METHODS

Ten healthy male (25.7 ± 1.5 years old) and ten healthy female (24.5 ± 1.8 years old) university students participated in the study.

Biopac MP30 and acqknowledge 3.5 (Biopac System, Inc. USA) were used to measure the SCL from the index and middle fingers on the left hand (sampling rate: 500 samples/sec).

The experiment consisted of three runs of a 3-back cognition test. The procedure consisted of six phases for each arousal condition; Rest 1 (2 min), Picture 1 (presenting emotion arousing photos for 2 min), 3-back Task 1 (2 min), Picture 2 (presenting emotion arousing photos for 2 min), 3-back Task 2 (2 min), and Rest 2 (2 min).

During 3-back Task 1 & 2 phases, a total of 80 alphabetical characters were presented and total correct answer was 20. The subject was asked to press the answer button if the currently presented character was same to the third previous presented character. The pictures and 3-back tasks were presented using SuperLab 1.07 (Cedrus Co. San Pedro, USA).

SCL of each subject was normalized by the Rest 1 value after calculating the average value of each phase. To investigate if there was any statistical difference under the three arousal levels and between each phase of SCL, two-way repeated measures ANOVA was employed with arousal level and phase as independent variables. The accuracy rate on the 3-back test was calculated. Significance in the differences in accuracy rate based on arousal levels were determined using one-way repeated measures ANOVA.

III. RESULTS

As shown in Figure 1, the mean SCL at each phase was the greatest during presentation of the arousal pictures, then neutral and relaxed pictures in order. Two-way repeated measures ANOVA showed a significant difference in the arousal level ($F=4.393$, $df=2$, $p=0.019$) and phase ($F=9.493$, $df=4$, $p<0.001$).

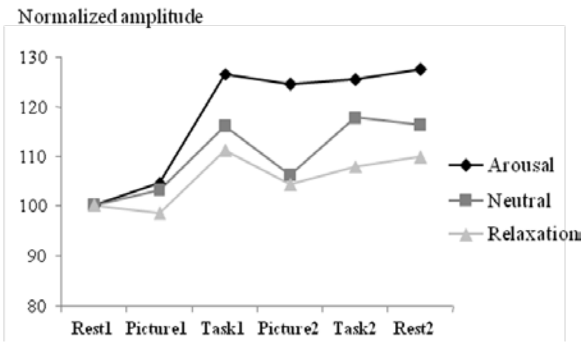

Fig.1. The normalized amplitude of SCL in each phase by 3 types of emotion induced pictures

As shown in Figure 2, the accuracy rate of the 3-back task was the highest when presented with neutral pictures (78.0 ± 16.4 [%]), then relaxed pictures (74.0 ± 15.7 [%]), and then arousal pictures (70.3 ± 14.4 [%]), in order ($F=4.938$, $df=2$, $p=0.012$).

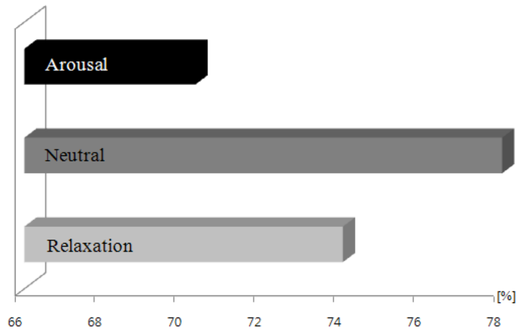

Fig.2. The accuracy rate by 3 types of emotion

IV. DISCUSSION

This study investigated the effect of arousal level on the performance of a 3-back task.

Physiological stimulation especially had a negative effect on information processing of succeeding input [6], and it was reported that the increase in physiological stimulus had a negative effect on cognitive processing [7]. From these studies, it could be inferred that the increase in the physiologically arousal state, which is irrespective of cognitive processing, had a negative effect on information processing of succeeding input. From this, it would be expected that the ability of performing a 3-back task would decrease, as shown in this study.

It was well known that cognitive processing activated the sympathetic nervous system [8]. Inducing a relaxed state of this study can activate the parasympathetic nervous system, and by disturbing the concentration for a given task, it can be expected that the ability to perform a given task decreases.

Preceding studies about the valence axis showed that people could remember much more items when emotion is accompanied, whether or not the memory was related with tasks [1, 9]. This study on the arousal (arousal/relaxation) axis showed that the memory ability without emotion was higher. Therefore, it is necessary to clarify how the human emotional state affects cognitive processing ability by considering both axes of human emotion at the same time.

ACKNOWLEDGEMENT

This research project was supported by the Korea Sport Promotion Foundation from Ministry of Culture, Sports and Tourism.

REFERENCES

[1] Kensinger EA, Garoff-Eaton RJ, Schacter DL (2006), Memory for specific visual details can be enhanced by negative arousing content. J Mem Lang 54: 99–112
[2] Heuer F, Reisberg D (1992). Emotion, arousal, and memory for detail. In: Christianson, The handbook of emotion and memory: research and theory. Hillsdale, NJ: Erlbaum, 151-180
[3] Revelle W, Loftus DA (1992), The implications of arousal effects for the study of affect and memory. In: Christianson, The handbook of emotion and memory: research and theory. Hillsdale, NJ: Erlbaum, 113-149
[4] LaBar KS, Phelps EA (1998), Arousal-mediated memory consoldiation: role of the medial temporal lobe in humans. Psychol Sci 9: 490-493
[5] Mogg K, Mathews A, Weinman J (1989), Selective processing of threat cues in anxiety states: a replication. Behav Res Ther 27: 317-323
[6] Bower GH (1991), Mood congruity of social judgments. Emotion and social judgments. Pergamon Press, Oxford, 31-53
[7] Pennebaker JW (1989), Confession, inhibition, and disease. Advances in experimental social psychology. Academic Press 22: 211-244
[8] Chung SC, Lee B, Tack GR, et al., (2008), Physiological mechanism underlying the improvement in visuospatial performance due to 30% oxygen inhalation. Appl Ergon 39: 166-170
[9] Kensinger EA (2007), Negative emotion enhances memory accuracy: behavioral and neuroimaging evidence. Psychol Sci 16: 213-218

Detection of Human Respiration Based on Measurement of Current Generated by Electrostatic Induction

K. Kurita

Department of Electrical Engineering and Information Science, Kochi National College of Technology, Nankokushi, Monobe-otsu 200-1, Kochi, Japan 783-8508
(Tel : 81-888-64-5547; Fax : 81-888-64-5547)
(kurita@ee.kochi-ct.ac.jp)

Abstract: In this study, we developed an effective technique for measuring human respiration using a noncontact and nonattached electrode. The technique requires measurement of the current generated due to the difference in capacitance between a given electrode and the human body. The subpicoampere electrostatic induction current flowing through the electrode when placed a few centimeters from the subject is detected. We propose an occurrence model for the electrostatic induction current generated by the change in the capacitance caused by the movement of the body surface while taking a breath. This model effectively describes the behavior of the current flowing through the measurement electrode.

Keywords: Noncontact measurement, Respiration rate, Current measurement, Human heartbeat

I. INTRODUCTION

Obstructive sleep apnea syndrome (OSAS) affects many people, frequently as an asymptomatic, undiagnosed condition, and is associated with increased morbidity and mortality. Conventional diagnosis requires overnight monitoring in a specially equipped sleep laboratory. Furthermore, the conventional thermocouple method used for detecting human respiration requires insertion of a sensor directly into the nose. The inconvenience of overnight polysomnography has led to a need for more easily implemented techniques for detecting respiration using nonattached probes. Recently, researchers investigating noncontact respiration monitoring have been trying to create easier-to-use techniques for diagnosis and measurement of breathing rate. For example, Yama [1] proposed capacity-coupled electrodes, Jong [2] attempted the use of phase detection radar, Tanaka [3] suggested a pressure sensor, and Aoki [4] relied on near-infrared light pattern projection.

We think that among the above, the most effective technique is the use of a capacity-coupled electrode. The capacitance measured is between the human body and an electrode that is isolated from human body by a dielectric such as cloth. In the conventional capacity-coupled electrode method, the voltage on the electrode is measured against the body surface. An isolated electrode must be attached to the human body because of the low permittivity of the air between the body and electrode. However, if we can monitor the respiration rate or other parameters without the use of an attached electrode, the method will find wide application in medical practice.

In this study, we developed an effective technique for measuring human respiration using a noncontact and nonattached electrode. The technique requires measurement of the current generated due to the difference in capacitance between a given electrode and the human body. The subpicoampere electrostatic induction current flowing through the electrode when placed a few centimeters from the subject is detected. It is necessary to emphasize that the method for the detection of the electrostatic induction current is different from the conventional method described in the previous paragraph.

Furthermore, we propose an occurrence model for the electrostatic induction current generated by the change in the capacitance caused by the movement of the body surface while taking a breath. This model effectively describes the behavior of the electrostatic induction current flowing through the measurement electrode.

II. PRINCIPLE

It is well known that the human body is electrically charged at all times [5–10]. Let us assume that for a subject sitting on a chair, there are two highly resistive objects between the subject's body and the surface of the floor, as shown in Fig. 1. One layer is the sole of the subject's footwear (C_s) and the other is the chair (C_c). The capacitance of the feet relative to the ground is the sum of the capacitances $C_s + C_c$ and that of the floor surface C_f. In addition, C_o is the capacitance of the rest of the subject's body relative to neighboring objects on the floor. We assume that the human body is a good conductor. Therefore, the potential U_B of the body on the chair can be expressed as follows:

$$U_B = Q_B /(\frac{(C_S + C_c)C_f}{C_S + C_c + C_f} + C_O)\,, \tag{1}$$

where Q_B is the instantaneous charge of the human body.

The induced charge Q on the measurement electrode placed at distance d from the subject's body can be expressed as follows:

$$Q = C(U_B - V)\,, \tag{2}$$

where C represents the capacitance between the human body and the measurement electrode, and V is the potential of the measurement electrode.

When the subject moves his/her abdomen during respiration such that it is almost perpendicular to the electrode, the capacitance C can be expressed as follows:

$$C \propto \frac{\varepsilon_a S}{x}\,, \tag{3}$$

where S represents the area of the electrode, x represents the distance between the subject's abdomen and the electrode, and ε_a represents the permittivity of air. Using the above equations, we can express the induced current I flowing through the measurement electrode as follows:

$$I = \frac{dQ}{dt} = U_B \frac{dC}{dt} \propto -U_B \frac{\varepsilon_a S}{x^2} v\,, \tag{4}$$

where v represents the velocity of the body surface.

Equation (4) describes the electrostatic induction current resulting from the motion of the subject's abdomen toward the electrode. The current generated is approximately proportional to the velocity of the movement of the subject's abdomen. Therefore, we can conclude that under perfect noncontact conditions, it is possible to measure the electrostatic induction current generated due to the movement of the abdomen by the respiration.

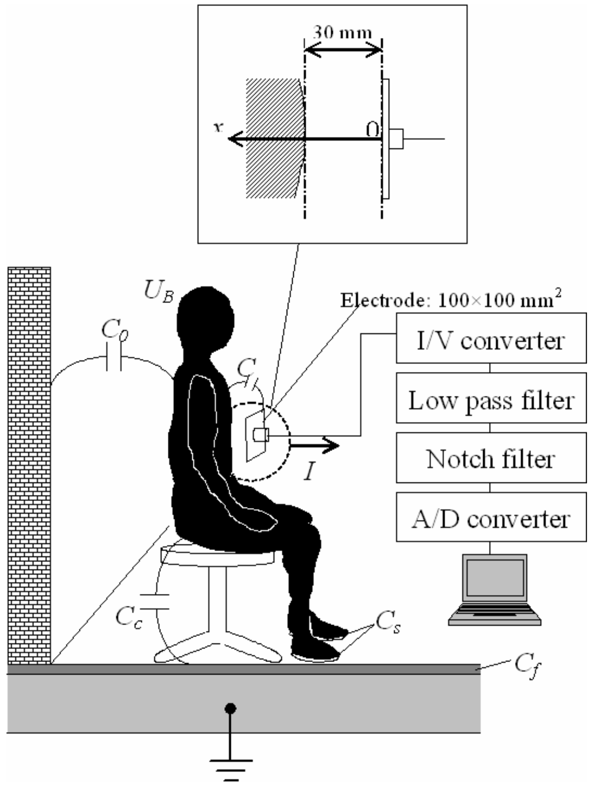

Fig.1. Schematic of the measurement system for measuring the electrostatic induction current

III. EXPERIMENTAL

A schematic of the measurement system for measuring the electrostatic induction current generated by human respiration is shown in Fig. 1. The electrostatic induction current flowing through an electrode placed 30 mm from the subject's abdomen was converted into a voltage by an I–V converter comprising an operational amplifier. The conversion ratio was 15 V/pA because the electric current was on the subpicoampere level. In addition, the induction currents generated by commercial power sources were present in the form of noise. Therefore, a filtering system with a cutoff frequency of 20 Hz was used. The analog signals were subsequently converted into digital signals by an analog-to-digital (A/D) converter. The data were acquired at a sampling frequency of 100 or 250 Hz and stored on a personal computer. The measurement electrode was square in shape with a side length of 10 cm.

During the experiment, the subject was asked to sit comfortably in a chair. Further, the movement of subject's abdomen surface was tracked by a wireless accelerometer attached to the subject's navel. The acceleration of the subject's abdomen with respect to the electrode and the electrostatic induction current were all measured simultaneously. The acceleration data were acquired at a sampling frequency of 200 Hz and stored on a personal computer. The obtained acceleration data were converted by numerical integral into velocity data for the subject's abdomen with respect to the electrode.

IV. RESULTS AND DISCUSSIONS

The upper panel in Fig. 2 shows a waveform of the current generated by human respiration for subject A with a sampling frequency of 100 Hz. Periodical components with a period of approximately 4.2 s are observed in the resulting waveform.

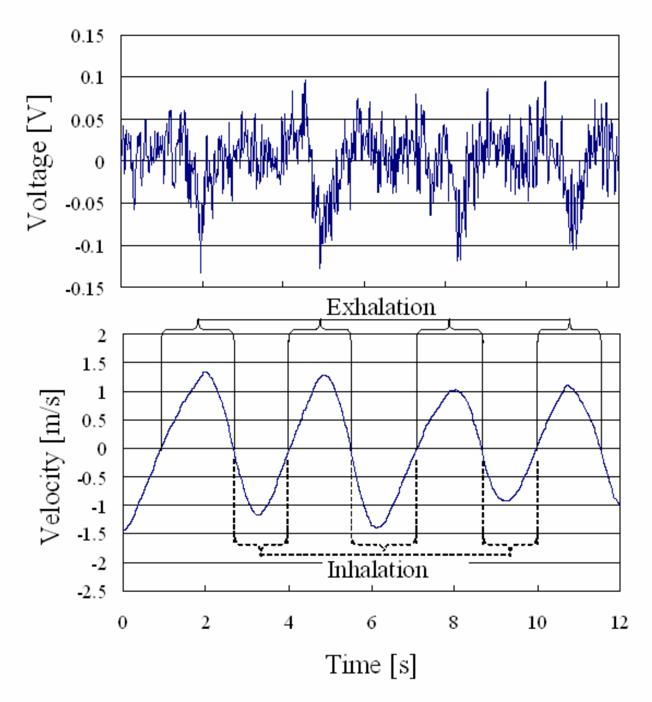

Fig. 2. Waveform of electrostatic induction current (upper panel) and of the velocity of the subject's abdomen (lower panel) generated by human respiration for subject A

The lower panel shows the waveform of the velocity of the subject's abdomen with respect to the electrode. As predicted by Eq. (4), movement of the subject's body surface toward the electrode resulted in an increase in I, whereas movement of the subject's body surface away from the electrode resulted in a decrease. The regions indicating exhalation and inhalation are indicated by the solid and broken lines, respectively. Therefore, we can conclude that Eq. (4) effectively describes the behavior of the waveform of I.

Figure 3 shows the waveform of the current generated by human respiration for subject B with a sampling frequency of 250 Hz. Periodical components with a period of approximately 4.2 s are observed here as well. Figure 4 shows a magnified version of a part of the waveform in Fig. 3. Periodical components with a period of approximately 0.9 s are observed in Fig. 4. At this point, the origin of the short-period components is still unclear. They may originate from the human heartbeat because the observed signal has a similar cycle.

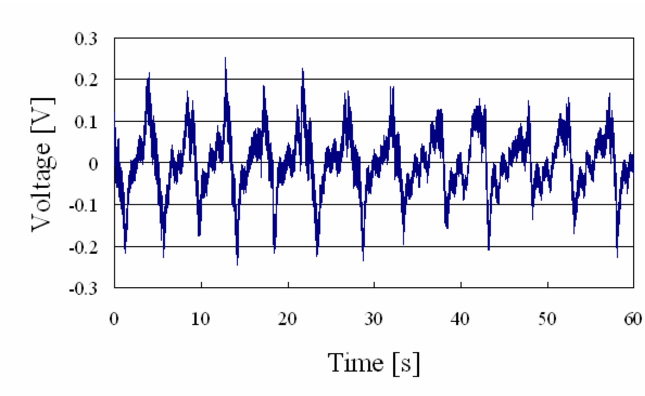

Fig. 3. Waveform of electrostatic induction current generated by human respiration for subject B with a sampling frequency of 250 Hz

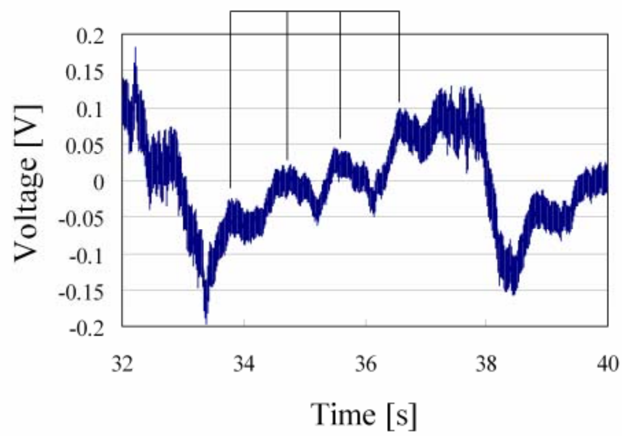

Fig.4. Magnified waveform of electrostatic induction current generated by human respiration for subject B with a sampling frequency of 250 Hz

The obtained waveforms for subjects A and B have a periodical component due to human respiration. It was observed that the intensity of the electrostatic induction current was inversely proportional to the square of the distance between the electrode and the body surface, and was proportional to the velocity of the body surface. The proposed technique showed good measurement reproducibility.

V. CONCLUSION

In this study, we developed an effective technique for measuring human respiration using a noncontact and nonattached electrode. The technique requires measurement of the current generated due to the difference in capacitance between a given electrode and the human body. The subpicoampere electrostatic induction current flowing through the electrode when placed a few centimeters from the subject is detected.

Furthermore, we propose an occurrence model for the electrostatic induction current generated by the change in the capacitance caused by the movement of the body surface while taking a breath. This model effectively describes the behavior of the electrostatic induction current flowing through the measurement electrode.

In the magnified waveform, periodical components with a period of approximately 0.9 s are observed. They may originate from the human heartbeat, because the observed signal has a similar cycle. The proposed technique showed good measurement reproducibility.

REFERENCES

[1] Yama Y and Ueno A (2009), Unrestrained facile measurement of narrow-band ECG and respiratory variation in infants with a capacitive sheet-type sensor (in Japanese), Transactions of Japanese Society for Medical and Biological Engineering, Vol. 47, No. 1, pp. 42–50, Feb. 2009.

[2] Jong HJ, et al (2007), Measurement of human heartbeat and respiration signals using phase detection radar, Review of Scientific Instruments, Vol. 78, No. 10, pp. 104703–104703-3

[3] Tanaka S, et al (2007), Clinical evaluation of a fully automated physiological monitoring system for providing support on the medical care (in Japanese), IEICE Technical Report, MBE2007-13, pp. 49–52

[4] Aoki H, et al (2009), Basic study on noncontact respiration measurement under pedaling motion with upright bicycle ergometer, WACBE World Congress on Bioengineering 2009, pp. 193

[5] Amoruso V, et al (2000), An improved model of man for ESD application, *Journal of Electrostatics*, Vol. 49, pp. 225–244

[6] Ohsawa A (2001), Electrostatic characterization of antistatic floors using an equivalent circuit model, *Journal of Electrostatics*, Vol. 51–52, pp. 625–631

[7] Fujiwara O, et al (1990), Electrification properties of human body by walking, *The Transactions of the IEICE*, Vol. 73, No. 6, pp. 876–878

[8] Fujiwara O (1992), New approaches for measurement of static electricity toward preventing ESD, *IEICE Trans. Commun.*, Vol. E75-B, No. 3, pp. 131–140

[9] Fujiwara O, et al (1998), An analysis of charged floor potential using electromagnetic field theory, *Electron. Commun. Japan*, Vol. 81, pp. 28–35

[10] Ficker T (2006), Electrification of human body by walking, *Journal of Electrostatics*, Vol. 64, pp. 10–16

Authentication of the reconstructed image from computer-generated hologram: synthesized by Complex Hadamard Transform.

Fumiya Inaba, Norihiro Fujii, Ken-ichi Tanaka
School of Science and Technology, Meiji University
1-1-1 Higasi-Mita, Tama, Kawasaki-City, Kanagawa 214-8571, Japan; Tel: +81-44-934-7326; Fax: +81-44-934-7326
E-mail: ce81009@isc.meiji.ac.jp, ce91055@isc.meiji.ac.jp, tanaken@isc.meiji.ac.jp

Abstract: Computer-Generated Hologram (CGH) has been targeting the application areas such as a reconstruction three-dimensional image, optical information processing, optical memory and scanner. The reconstructed image of CGH includes noise caused by quantization error when synthesis a hologram. Therefore, authentication of the reconstructed image by using computer is difficult. Fourier Transform (FT) is a normal way when synthesis and reconstruction CGH. This study proposes a method using Complex Hadamard Transform (CHT). CHT is used only addition and subtraction. And CHT eliminates the need for multiplication operations. In this study, CHT is compared with FT at the points of the detection accuracy. The possibility of adaptation to authentication of the reconstructed image calculated by CGH, in the case of this proposal using for calculation method, are examined. Phase-Only Correlation (POC) is adopted as a correlation method. As a result, the correlation value is better than that of the past. However, bad value appeared in several points. But, the impact of identification could reduce by choosing the optimal combination of correlation. Therefore, there is a good possibility that the adaptation to authentication, in the case of this proposal using for calculation method.
Keywords: Computer-Generated Hologram (CGH), Complex Hadamard Transform (CHT), authentication

I. INTRODUCTION

This study is about a type of steganography or digital watermarking.[1] CGH has been targeting the application areas such as a reconstruction three-dimensional image, optical information processing, optical memory and scanner.[2] The reconstructed image of CGH includes noise caused by quantization error when synthesis a hologram. Therefore, authentication of the reconstructed image by using computer is difficult.

This study proposes a method using CHT. CHT is a function of the basis for the conversion functions required by the Hadamard Matrix, using only addition and subtraction. In this study, CHT is compared with FT at the points of the detection accuracy. The possibility of adaptation to authentication of the reconstructed image calculated by CGH, in the case of this proposal using for calculation method, are examined.POC is adopted as a correlation method.

II. EXPERIMENT

1. How to create sample images for experiment

i. What is "Complex Hadamard Transform (CHT)"

Hadamard transform is the orthogonal transformation. Processing can be performed by the sum of the product of Hadamard matrix and the input data.[3] *"F"* is output. *"n"* is the number of rows or columns. *"f"* is input.

$$F = \frac{1}{\sqrt{n}} Hf \tag{1}$$

The basis of this transformation is a Hadamard matrix. As the following equation which represents an example of a Hadamard matrix.

$$H = \begin{bmatrix} 1 & 1 \\ 1 & -1 \end{bmatrix} \tag{2}$$

This matrix is only represented by real number. Complex Hadamard transform is used to complex Hadamard matrix. Complex Hadamard matrix is using the real and imaginary parts. As the following equation which represents an example of a Complex Hadamard matrix.

$$H = \begin{bmatrix} 1 & i \\ -i & -1 \end{bmatrix} \tag{3}$$

Two-dimensional Complex Hadamard transform, as in the case of two-dimensional Fourier transform, first horizontally, second vertically are in the process.

ii. Sample images

256 × 256 pixels on the image of the black, starting at the top left of the image of the alphabet A ~ Z of the one who created the characters are written in white letters. Image files are created with 256 colors bitmap format. This image as original image, used to convert those who applied. Each images shown in Fig.1, Fig.2 and Fig.3.

2. Experiment

Correlation values of images are measured in the following combination of image groups. Correlation values in type 1 and type 2 are measured with a combination of brute force.

Table 1.Combination of image groups

	Type 1	Type 2
1	Original image	Reconstructed image from CGH made by FT
2	Original image	Reconstructed image from CGH made by CHT
3	Reconstructed image from CGH made by FT	Reconstructed image from CGH made by FT
4	Reconstructed image from CGH made by CHT	Reconstructed image from CGH made by CHT
5	Original image	Original image

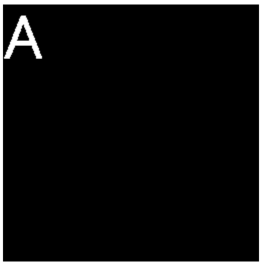

Fig.1.Original image (A)

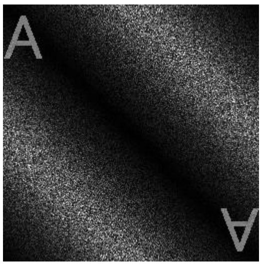

Fig.2.Reconstructed image from CGH made by FT (A)

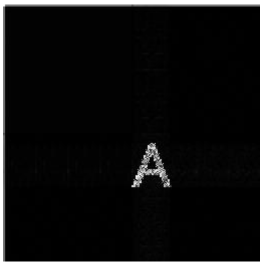

Fig.3.Reconstructed image from CGH made by CHT (A)

III. RESULTS AND CONSIDERATION

The threshold is set to identify "self" and "other". Threshold is set as the value shall be uniform in each of the correlation. Threshold is set between "autocorrelation" value (maximum value) and the next highest correlation value. The width between maximum value and the next highest correlation value should be broad as possible. The next highest correlation values were as follows.

In the experiment No.1 and No.2, maximum values which a state of "autocorrelation" are not in 1.0. Therefore, in the process of dividing the value of each element in that series the maximum value of the series (normalization process) are done.

Table 2.Combination of image groups and correlation value

	Type 1	Type 2	The next highest correlation value
1	Original image	Reconstructed image from CGH made by FT	0.8070969482
2	Original image	Reconstructed image from CGH made by CHT	0.9895463015
3	Reconstructed image from CGH made by FT	Reconstructed image from CGH made by FT	0.0342630240
4	Reconstructed image from CGH made by CHT	Reconstructed image from CGH made by CHT	0.2378456832
5	Original image	Original image	0.5634082960

In the experiment No.2, the width between maximum value and the next highest correlation value is about 0.01045. This width is very narrow. Set of threshold is difficult.

Meanwhile, result of experiment No.3 is the best value. And, result of experiment No.4 is the next best value.

In the experiment No.4, the width has been reduced to 79% of the width of experiment No.3. But, threshold setting is easily if the width of this level can be secured. This result is better than the result of experiment No.5.

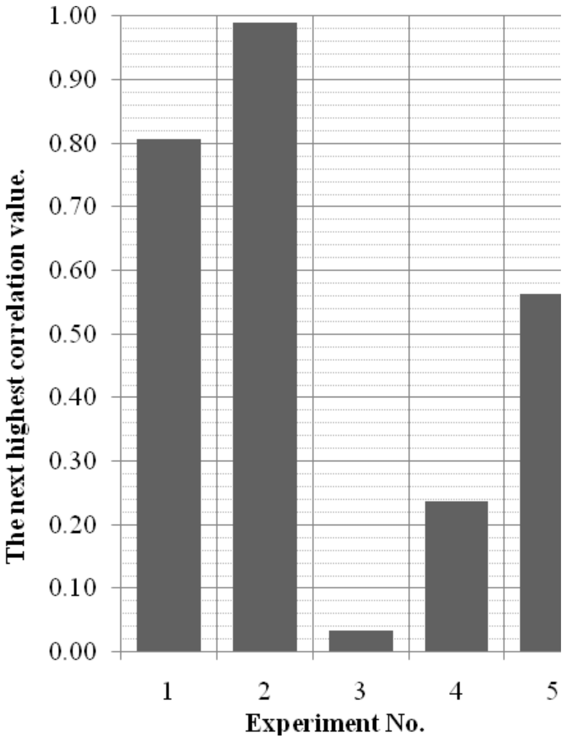

Fig.4. Combination of image groups and correlation value

VI. CONCLUSION

Reconstructed image from CGH made by CHT is compared with reconstructed image from CGH made by FT at the points of the detection accuracy with correlation value. Need to choose the optimal combination of correlation, it is possible to identify self and others using the image correlation value.

Using a combination of autocorrelation can be obtained. Good results are obtained using these combinations.

Therefore, there is a good possibility that the adaptation to authentication, in the case of this proposal using for calculation method.

REFERENCES

[1]N.Komatsu, K.Tanaka (2004), Digital-watermarking technology, The Institute of Image Electronics Engineers of JAPAN (in Japanese).

[2]T.Yatagai, (2004), Optical Computing, Kyoritu Shuppan Ltd (in Japanese).

[3]Z.Kiyasu (1983), The Hadamard matrix and its application, IEICE (in Japanese).

The Fifteenth International Symposium on Artificial Life and Robotics 2010 (AROB 15th '10),
B-Con Plaza, Beppu,Oita, Japan, February 4-6, 2010

Feature Extraction Method using Laser Range Finder for SLAM

Taerim Kim, Sungyoung Jung, Jungmin Kim, and Sungshin Kim

School of Electrical Engineering, Pusan National University,
Jangjeon-dong, Geumjeong-gu, Busan, 609-735, Republic of Korea
(Tel : 82-51-510-2367; Fax : 82-51-513-0212)
(Email : {rimkt, pleiades0223, kjm16, sskim}@pusan.ac.kr)

Abstract: In this paper, we propose the feature extraction method from laser range finder data using angle histogram algorithm. Most people commonly know that laser range finder has relatively accurate performance. But noises were existed in experimental result that a few points appeared empty space. We proposed noise reduction method using angle histogram algorithm that accumulated repeatedly counted points in each angle. Laser range finder data with reduced noise is used for the feature extraction method. We find feature point using that one line lies cross at right angles to another line. And we tested simulation of SLAM using the feature extraction.
+

Keywords: Feature Extraction, SLAM, Laser Range Finder, Mobile robot, Angle histogram, EKF

I. INTRODUCTION

Recently, there is popular research field of robot such as application for army, home and education, etc. Among various kinds of robots, mobile robot is particularly actively researched. For autonomous movement of robot, it is important to localization and environmental recognition (Related research is called simultaneous localization and mapping). It can know using odometry from various sensors (sonar, infrared, laser, vision. etc.). One of sensors is laser range finder that it becomes popular in mobile robot[1]. Because it provides dense and more accurate range measurements, it has good range distance and resolution. For example, laser range finder has been used in localization, map building, collision avoidance. We also use laser range finder for feature extraction[2, 3]. We can know how to accurately match sensed data against information in a priori map through feature extraction.

This paper proposed feature extraction method for SLAM. First, we tested to use laser range finder and propose laser range finder noise reduction method using angle histogram[4]. And we tested feature extraction from laser range finder data by SLAM simulation.

II. LASER RANGE FINDER NOISE

We use laser range finder (LMS200) for SLAM for the reason that laser range finder is relatively more accurate than others. LMS200 can measure every 1 degree and maximum distance is 8m. But experimental result is that laser range finder data included irregular white noise as shown in Fig. 1. Therefore, laser range finder data is used selective data in 4m for precise feature point and need to precede noise reduction.

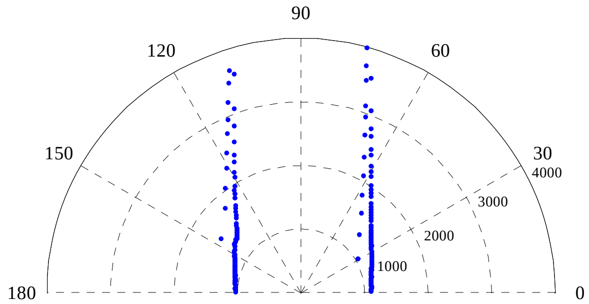

Fig.1. Measurement laser range finder

III. NOISE REDUCTION USING ANGLE HISTOGRAM

We propose angle histogram for irregular noise reduction of laser range finder. In this paper, Because our object is indoors environment SLAM, we assumed according to :

1. Noise of laser range finder data is irregular and unpredictable white noise.
2. General indoors environment consists of a hallway, wall, corner, door, etc. and can be described straight lines.
3. Angle of continuous data has regular in indoors environment which consists of straight lines.

If we use these assumptions, then noise reduction is possible to use angle histogram. First, for angle histogram, we convert cylindrical coordinates to rectangular coordinates because of laser range finder data have cylindrical coordinates.

$$x(i) = x_k + r_x \times (\theta_k + i - 90)$$
$$y(i) = y_k + r_y \times (\theta_k + i - 90) \qquad (\, i = 0, 1, 2, \cdots, 180) \qquad (1)$$

where (x_k, y_k, θ_k) denote a position of robot. And every angle of continuous points is calculated in (2).

$$T(i) = \mathrm{atan}\left(\frac{x(i) - x(i-1)}{y(i) - y(i-1)}\right) \qquad (\, i = 0, 1, 2, \cdots, 180) \qquad (2)$$

We made angle histogram using calculated angles and extracted that magnitude is over 15 percent. Therefore, we can reduce white noise and remained data is possible to describe straight line. We confirmed noise reduction using angle histogram as shown in Fig. 2.

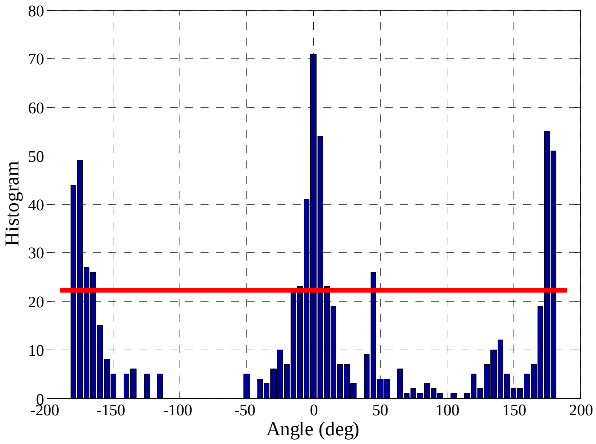

(a) Angle histogram

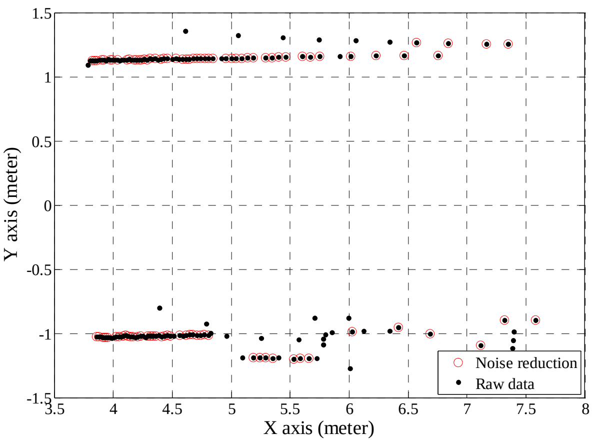

(b) Apply angle histogram to laser range finder data

Fig.2. Noise reduction using angle histogram

IV. FEATURE EXTRACTION METHOD

This paper is limited to 2D indoors environment and target performing SLAM. We used only laser range finder so that just obtained little information. So we selected clearly distinguishable feature points such as corners of hallway, wall, and door. In advance, we assumed according to :

1. A hallway is generally made straight lines and has irregularly door, stair, locker, etc.
2. The corner is generally made a rectangular line in a hallway.
3. Distance of between the walls is minimum 1.5m.
4. Ground is flat so that measurement error of laser range finder is none.

When feature extract under assumption, we can think two direction of mobile robot such as forward and backward. First, forward searching is that mobile robot look between the walls of corner. Second, backward searching is that mobile robot look one side of a wall and don't look opposite side of a wall.

1. Forward searching

Forward searching is that we select right and left points of regular distance from based point. Using points make straight line and we can judge feature by whether two lines is rectangular.

Right and left points is selected far 300, 600, 900, 1200mm from based point and L_{pt}, R_{pt} is defined (3) , (4). We need to calculate angle from based point for judgment whether feature using selected points like (5), and (6). And we tested proposed forward searching as shown in Fig. 3.

$$L_{pt} = \left[\begin{bmatrix} x_{lpt} \\ y_{lpt} \end{bmatrix}_{300} \begin{bmatrix} x_{lpt} \\ y_{lpt} \end{bmatrix}_{600} \begin{bmatrix} x_{lpt} \\ y_{lpt} \end{bmatrix}_{900} \begin{bmatrix} x_{lpt} \\ y_{lpt} \end{bmatrix}_{1200} \right] \qquad (3)$$

$$R_{pt} = \left[\begin{bmatrix} x_{rpt} \\ y_{rpt} \end{bmatrix}_{300} \begin{bmatrix} x_{rpt} \\ y_{rpt} \end{bmatrix}_{600} \begin{bmatrix} x_{rpt} \\ y_{rpt} \end{bmatrix}_{900} \begin{bmatrix} x_{rpt} \\ y_{rpt} \end{bmatrix}_{1200} \right] \qquad (4)$$

$$Slope_L = \begin{bmatrix} \mathrm{atan}(y_{lpt} - y_{idx}, x_{lpt} - x_{idx})\,|_{300} \\ \mathrm{atan}(y_{lpt} - y_{idx}, x_{lpt} - x_{idx})\,|_{600} \\ \mathrm{atan}(y_{lpt} - y_{idx}, x_{lpt} - x_{idx})\,|_{900} \\ \mathrm{atan}(y_{lpt} - y_{idx}, x_{lpt} - x_{idx})\,|_{1200} \end{bmatrix}^T \qquad (5)$$

$$Slope_R = \begin{bmatrix} \mathrm{atan}(y_{rpt} - y_{idx}, x_{rpt} - x_{idx})\,|_{300} \\ \mathrm{atan}(y_{rpt} - y_{idx}, x_{rpt} - x_{idx})\,|_{600} \\ \mathrm{atan}(y_{rpt} - y_{idx}, x_{rpt} - x_{idx})\,|_{900} \\ \mathrm{atan}(y_{rpt} - y_{idx}, x_{rpt} - x_{idx})\,|_{1200} \end{bmatrix}^T \qquad (6)$$

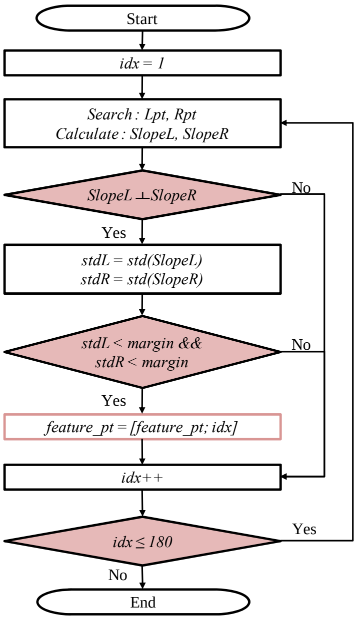

Fig.3. Forward searching algorithm

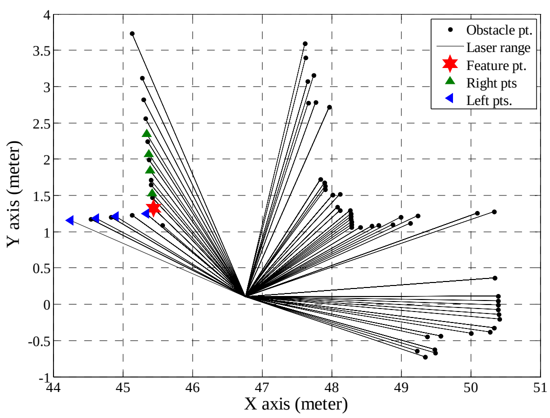

Fig.4. Feature extraction using forward searching

2. Backward searching

We can judge a corner by confirming distance between continuous points because of that mobile robot looks only one side of a wall. Backward searching algorithm is expressed to use flow chart as shown in Fig. 5. Because mobile robot don't look opposite side of a wall, between continuous points could have a far distance over 1.5m. But laser range finder data is used under 4m and over data is defined infinite as mentioned section 1. So, we judge that based point and next point have whether a finite value or infinite value. If two points have a finite value and distance between two points is over 1.5m, then feature is defined near point of two points with robot as shown in Fig.6.(a). In the other case, if two points have infinite value and distance between next point and robot is less than difference between max distance 4m and 1.5m, then feature is defined next point as shown in Fig.6.(b).

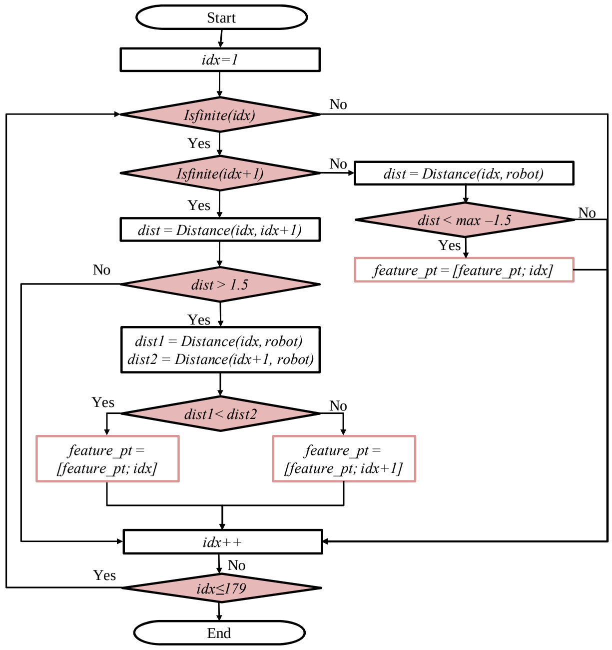

Fig.5. Backward searching algorithm

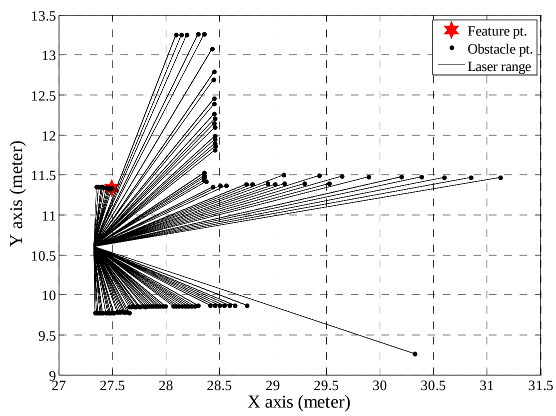

(a) Feature extraction (finite)

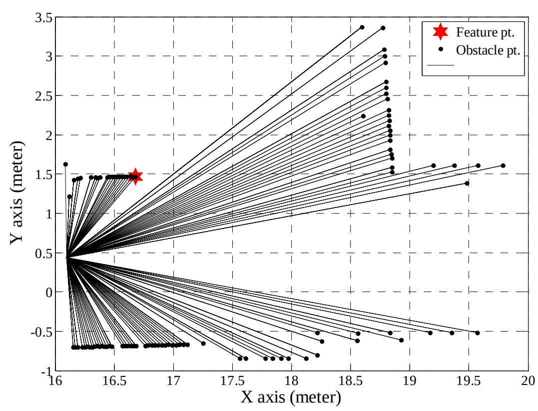

(b) Feature extraction (infinite)

Fig.6. Feature extraction using backward searching

V. SLAM

We tested feature extraction using laser range finder by SLAM simulation. SLAM used extended kalman filter for estimation of posterior distribution of feature and robot's position[5]. We used mobile robot in Fig. and simulation result is good performance as shown in Fig.

(a) Mobile robot

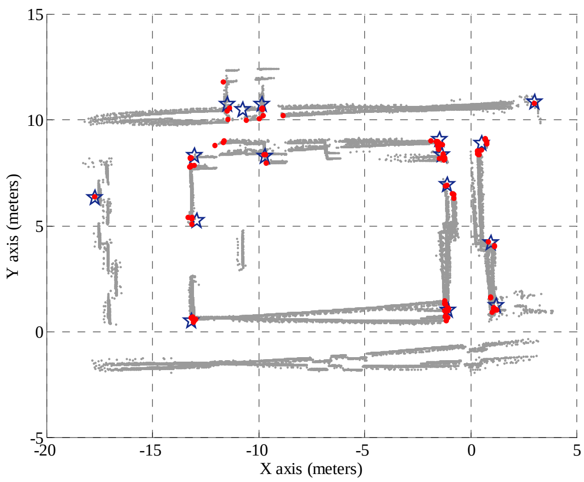

(b) EKF-SLAM using feature extraction

Fig.7. Feature extraction using forward searching

VI. CONCLUSION

This paper proposed feature extraction method using laser range finder for SLAM. We tested laser range finder and confirmed that data is included irregular white noise. For noise reduction, we used angle histogram and experimental result is shown reduced noise. And we extracted feature using reduced noise data. We proposed feature extraction method that two ways are forward and backward searching. Because a hallway generally consists of straight lines, feature is defined corners. Using proposed method, SLAM simulation result is confirmed good performance of localization and robust repeatedly many continuous data.

Because proposed method is developed under assumption that SLAM execute indoors environment, then has many assumptions and restrictions. So, there remains to be more studied feature extraction in outdoors environment for SLAM.

Acknowledgment This work was supported (Pusan National University Specialized Environment Navigation/ Localization Robot Technology Research Center) by Ministry of Knowledge Economy under Human Resources Development Program for Convergence Robot Specialists.

REFERENCES

[1] Viet Nguyen, Agostino Martinelli, Nicola Tomatis, Roland Siegwart (2005), A Comparison of Line Extraction Algorithms using 2D Laser Rangefinder for Indoor Mobile Robotics. Intelligent Robots and Systems. 1929-1934

[2] I. Tena Ruiz, Y. Petillot, D. M. Lane, C. Salson (2001), Feature Extraction and Data Association for AUV Concurrent Mapping and Localisation. International Conference on Robotics & Automation. 3:2785-2790

[3] Kai Oliver Arras, Roland Y. Siegwart. (1997) Using histogram correlation to create consistent laser scan maps. Proceedings of SPIE. 3210:42-53

[4] Rofer.T. (2002), Using histogram correlation to create consistent laser scan maps. Intelligent Robots and Systems. 1:625-630

[5] J. Weingarten, R. Siegwart (2005), EKF-based 3D SLAM for Structured Environment Reconstruction. Intelligent Robots and Systems. 3834-3839

A case study of discussion classes in mathematics education

(Research for the improvement of mathematics education)

Hyang Joo Rhee

Dept. of Mathematics, College of Natural Science, Duksung Womens University, Seoul,Korea
(Tel : 82-2-901-8505; Fax : 82-2-901-8321)
(rhj@duksung.ac.kr)

***Abstract*:** Modern society demands leaders who are trained with competence to not only approach knowledge but also create new knowledge by comprehensively understanding and applying it, and a leader with character and commitment to share one's ideas with others and be able to accept criticisms. In response to these societal changes, universities are increasingly adopting 'small group discussion-based' classes with an attempt to develop and strengthen communication skills through reading, writing and speaking. This paper seeks to introduce a case of a math lecture, where discussion-based class was applied to mathematical education, requiring practical problem-solving through an argumentative thought process.

Key words: Discussion-based class, General mathematics

I. INTRODUCTION

Recently, there has been an increased interest amongst universities in increasing the number of students studying science in response to the phenomenon of students evading science and engineering fields. Each university is analyzing programs in various perspectives, generating interest in the field of scientific technology in education fields and running programs at different levels to spread the culture of science. There are number of reasons for this.

One of them is the humanization education for a holistic education, related to character education. Our education has been criticized for being a memorization-intensive education focused at university entrance exams. As a result, it led to a shortcoming of character education such as logical thinking, creativity development and leadership qualities, showing a low academic achievement rate. In fact, there has been a rise in the percentage of students who dislike mathematics and the mathematical ability of our elementary, middle, secondary and post-secondary school students have declined. In the Achievement Test conducted by the Japan Science Foundation in 2004 for the high-school and university students in science fields for the four countries of South Korea, Japan, China and Singapore, Korean university students scored the lowest, with the exception of Singapore.

Universities today focus on character education and value education to cultivate global leaders who can freely analyze and criticize specialized knowledge from interdisciplinary studies. In this vein, an emphasis is given to discussion-based classes where students can develop analytical skills, widen their horizon through the group and establish a proper worldview.

The University which the author belongs to selects twelve books from social sciences and natural sciences and twelve books from literary fields for the first year students and ask them to read one book per week. After reading a book a week, students must take a class entitled 'Reading and Expression' for two semesters, where they debate in small groups for the discussion topics distributed earlier in the semester. This course was established as a mandatory elective course called 'The Reading Plan' in 1969 and has continued for the past forty years. In this paper, cases of discussion-based lectures for mathematical education, with math-related books from the reading list, including '*A World Made Of Mathematics*' and '*Chaos*' will be introduced. In the main section, the methodology for running a discussion-based class and the response from students will be outlined, and search for the future direction for application and improvement.

II. Mathematics found in real life

Mathematics has a more inclusive meaning beyond math education. Behind every day issues such as weather forecast, sports, music, arts, the nature and culture which we live in, such as computers, world of animals and plants, various career paths, love and marriage, mathematics is alive. However, the students' sentiments towards mathematics are recognized as a means of passively acquiring absolute knowledge.

Keith Devlin, in his introduction, asserts: "This is not a typical 'math book' that people often talk about. From the outset, it was not written with the goal of teaching techniques for solving math questions. Therefore, the readers will not be able to learn very much about that kind of 'math' through this book or find mathematical formula or complicated practice questions anywhere in this book. Instead, you will find that mathematics is very different than how you thought of it before. And you will find out for sure that mathematics, often slightly deceptive its appearance, plays a very important role in almost all aspects of our daily lives. If there is anybody who thinks that math has nothing to with our daily lives, this book is for that kind of person."

To encourage a discussion class with a math-related book, it is absolutely necessary to first remove pre-conceptions about math. As a result of education focused on university entrance exams, students automatically think of symbols, numbers, formula and problem solving when they hear the word "math." Therefore, for the first discussion topic, encourage students to discuss the definition of math provided by Keith Devlin in the *World Made of Mathematics* from their own perspectives. By introducing cases of mathematical cases found in the nature, such as 'how did the leopard prints in leopards get created,' or 'the mathematical symphony resounding in the fourth dimension,' or 'Fight against virus with a knot,' encourage students to naturally come up with their own definition.

The author explains that the mathematical principles and the curriculum taught at school are merely the tools necessary for doing the 'real' math, and defines mathematics as a "scholarship about an effort to better understand ourselves and the world in which we live in." Moreover, he emphasizes that it is not that the world is mathematical, but that mathematics provides a powerful tool for us to examine the world. In his own words, "Mathematics provides a method of understanding the world, that is, a way of bringing the world into our minds."

By comparing the author's view on mathematics and their own interpretations, it would be an effective way of teaching students that mathematics that they traditionally perceived as a difficult problem solving is actually something that can be easily discovered and which co-exists with us in our day to day interactions.

Even though it is not visible to the eyes, our body is composed of over a 100 trillion cells. The cell is a basic functional and structural unit of all living creatures and is critical for our body's survival. Even though mathematics is not very visible to our eyes, from everything that happens in our world under the sun to the events that happen beyond the sun, mathematics exists everywhere. Therefore, the world cannot be understood without mathematics. Hence, mathematics can be defined as something akin to the cells. From this aspect, amongst the definitions provided by the author, the one that states "mathematics is transparent so it is not visible to the user's eyes, but the basis of everything we do is mathematics," best expresses a perspective for examining mathematics.

In conclusion, by presenting their own definition of mathematics, students will be able to naturally express their preconceptions about mathematics. Moving away from a consciousness that mathematics is a difficult and boring subject that brings headaches when they think of symbols and calculations, students will be empowered to find interest and enthusiasm towards mathematics.

The second topic is the question about mathematics that can be found in reality. Discussion classes may pose a burden for students that they must read one book for each week and give a daunting impression about the discussion culture which they are not familiar with. Therefore, one cannot help but ponder upon the method of running the discussion to improve the class satisfaction rate. Mathematics found in real life asks students to research media releases, internet data and newspapers, so that they may share a wide breadth of information and perspective, as well as create a spontaneous opportunity to get involved in the discussion, in order to generate an active discussion. Examples of presentations include:

1) $1:\sqrt{2}$ of A4 sized paper: aesthetics of economic efficiency
2) Soju glass and Soju bottle 1:7.5: marketing strategy
3) Barcodes: a combination of black sticks and white blanks
4) The boundary between a long leg and short leg: the golden rate
5) Why a hive is a hexagon and a tile is a square
6) Hidden mathematical principle behind the seven musical scale
7) Probability in our life, lottery
8) Beautiful fractal found after repetition
9) Fibonacci sequence found in a pine cone
10) Efficiency of 21 teeth of a saw found in a bottle cap

As well, there are cases such as why the manhole covers are shapes of constant width, the mathematical principle behind breathalyzer, and cicada's wisdom for living in prime number cycles. Through mathematics found in real life, students will be able to establish the concept of 'mathematics'. By applying them in our lives and understanding them, students will understand that mathematics is much more than just numbers and formulas, and that mathematics helps us to better understand the world of nature.

III. Mathematics is an analysis and categorization of all possible patterns.

"Mathematics is an analysis and categorization of all possible patterns." The term 'pattern' should be interpreted in a broad sense. In another words, pattern can be defined as something inclusive, from the regularity of forms that are visibly identified to the regularity of invisible things that are only recognized through our hearts."

In the natural world, there is some degree of regularity. For instance, when the temperatures go down in autumn, the trees create a separate layer in the leafstalk to bring down the leaves. Also, to survive in a dry climate and coldness, they move the water and nutrients saved in branches and stalks to the roots. The phenomenon of how the trees that barely preserved themselves as if they were dead pumps up water in the spring; or the phenomenon of how different parts of our body functions actively to the environment in spring, when the daytime for the biorhythm of our body extends and the temperature difference between day and night varies greatly; or the phenomenon of how the birds recognize the black and yellow ties surrounding the hornets, are cases of how all living things with life recognize patterns.

Furthermore, the nature and the society are filled with confusing patterns. Yet, today's physics has proven the fact that even the most complicated patterns can be written in an equation with just a few variables, and that it is possible to predict some parts. To recognize that mathematics is a science of patterns, define and discuss examples of a fractal in our body and nature as the third topic of the book, <<*Chaos*>>. Some examples for presentation include:

1) Crystallized shape of snow: Koch's snowflake curve
2) Lightening which appears to be irregular
3) Stock Market, regularity within irregularity
4) A field of study using fractal - Statistics
5) Similarity of the blood vessel structure stemming from the heart
6) Repetitive quality of brain wrinkles/ surface area of the lung
7) Fractal found in plants (leaves of brackens, broccoli and water stratum of leaves)
8) Computer graphic art created by applying the fractal formula
9) The Universe & I
10) The spirit and chaos of oriental philosophy

Rather than delivering objective knowledge in a discussion class, an experience to encounter mathematics that appears to have very little in common with reality, as a play, naturally changes the image. Fractal cards were made using the origami papers and knives. Simple patterns using self-resemblance looks most beautiful and you may experience how the simple patterns of geometry is the most efficient structure accepted by the nature. The patterns and relations studied by mathematicians are seen in all parts of the nature. Some examples include the symmetrical patterns of flowers, various types of complicated patterns found in knots, patterns of dots on the external skin of leopards, voting patterns of certain population group, patterns found in a dice play or roulette game, relationships between the words that make up a sentence, the pattern of sounds we recognize in a music, and many more. As such, it is evident that we live within the nature surrounded by patterns and develop close relations with mathematics in our lives, before we even realize it.

IV. We are able to see the invisible through mathematics

Mathematics enables us to see things that are not visible to the eye. If you let go of something in your hand, it falls down. This is because of the force of gravity. However, 'gravity' is just a name given to the cause. The name itself does not help very much in understanding the real cause. And that cause is not even visible to the eye. The correct answer is Newton's equation of movement from the 17th century.

Newton's mathematics made it possible to see the force that was not visible to the eye. That force is the reason why the earth can continue to revolve around the sun and an apple falls down from a tree. Furthermore, the equation that Daniel Bernoulli discovered in the early 18th century made visible the invisible power of making an airplane fly in the air. Two thousand years before a spacecraft took a photograph of the earth, Greek mathematician Eratosthenes demonstrated the fact that the earth is circular using mathematics. We use mathematics to see the invisible things. Ranging from the origins of the universe to the bottom of the sea, from the pattern of coincidental events to the application into the inner mind of humans, we would not be able to understand our world without mathematics.

Logical thinking is an act which distinguishes humans as advanced living creatures. Through the training of critical and rational thinking, human beings are able to arrive at a more logical mental world. For the training of invisible logical thinking, an advertisement called 'the beauty of 30 seconds' was used. To emphasize the strengths of the product, the advertisement skips some parts of the preposition. If the advertisements are carefully examined from a critical perspective, it is possible to discover how the first impression from the advertisement and the outcome of the advertisement are unclear and explained in a distorted way. Look at the following advertisements and think about how the first impression from each advertisement and the meaning of the advertisement are different.

1) An automobile advertisement where a driver is speeding up in a curved road of a highway with no other cars in traffic
2) An advertisement of a long-distance phone company that says "You can save more money by talking longer."
3) "Get a 50% discount if you live in the same house." – only when the years of membership for the family members totals up to more than 40 years
4) A beverage company which advertises the recognition gained from the Association of Korean Oriental Medicine – the period for recognition is only one year
5) Apartment advertisement which runs, "This is the first time I'm bringing him to my home," or "This is the

first time I'm going to meet her parents."
6) Female-priority loan company's advertisement which screams "No interest for 30 days!"

Training of critical thinking through these advertisements is not simply about understanding the meaning of advertisements and assessing whether they are reasonable. It is a training to comprehensively restructure one's experiences to understand the advertisement, and subsequently, think critically and creatively. In another words, it is a process of changing one self. After assessing what is true or false, you will no longer be the same person that you were before.

V. CONCLUSION

With the 7th Education Curriculum applied to all grades in elementary, middle and high-schools since 2004, the curriculum for mathematics set the goal of extending 'Mathematical Power' which can create self-directed intellectual value, along with problem-solving skills and all sorts of advanced thinking capability. It seeks to promote creative thinking ability, critical thinking ability, problem-solving skill, reasoning ability, communication ability, confidence about mathematics, positive attitude, and relevance of mathematics to other related field of study and realization of the utility of mathematics. Towards that goal, appropriate study contents, increasing classes focusing on the learner's activity and education for each step and level.

However, the mathematics curriculum has not yet escaped from a teacher-focused, cramming method of teaching, and passive and standardized type of problem solving persists. This type of learning is showing limitation in giving a real mathematical perspective to students or cultivating creative and productive problem solving skills. This paper introduced a case as a solution to this problem, by suggesting thoughtful mathematics and discussion-based mathematical education. Further research is in order to select appropriate texts for discussion-based mathematical education, development of discussion topics and for the use and assessment of instructors and teaching aids.

REFERENCES

[1] Mi-Suk Jeong(2007), Education Of Reading, Discussion And Writing Based On Critical Thinking, Research, Institute for Liberal Arts Education , Vol. 1, No.2, pp. 119-134.

[2] Seung-Hyeon Choi (2004), *State of Mathematical Education Curriculum and Plans for Improvement & Plans for Improving the Education Curriculum*, Seoul: Korea Institute for Curriculum Evaluation.

[3] Jae-Seung Jeong (2003), *Science Concert*, East Asia.

[4] Keith Devline, Gi-Yong Seok (2003), A World Made of Mathematics, École Libre.

[5] James Gleick, Bae-Sik Park & Ha-Wun Sung (1993), Chaos, Dongmunsa.

[6] American Classical Foundation, Teaching Reading Discussion, Duksung University Press, 1965.

The Fifteenth International Symposium on Artificial Life and Robotics 2010 (AROB 15th '10),
B-Con Plaza, Beppu,Oita, Japan, February 4-6, 2010

An Izhikevich type silicon neuron circuit

Y. Nagamatsu† K. Aihara†, ‡ T. Kohno†, ‡

† *Graduate School of Engineering The University of Tokyo, 7-3-1 Hongo, Bunkyo-ku, Tokyo 113-8656, Japan*
‡ *Institute of Industrial Science, The University of Tokyo, 4-6-1 Komaba, Meguro-ku, Tokyo 153-8505, Japan*
(Tel : +81-3-5452-6693; Fax : +81-3-5452-6694)
(nagamatsu@sat.t.u-tokyo.ac.jp)

Abstract: The Izhikevich model is 2-variable differential equations of a qualitative neuron model. In spite of its simple mathematical structure, it can produce a variety of firing patterns because of its nonlinearity, including jump of state in the equations. When we construct spiking neural networks, we need simple circuitry that can produce rich dynamics because more dynamical patterns are thought to give the higher probability of complex information processing. In our research, we aim to design an Izhikevich-type simple silicon neuron circuit by reproducing the mathematical structure in the original model using analog electronic circuit. It is operated in the subthreshold region of Metal-Oxide-Semiconductor Field-Effect Transistors (MOSFETs) for low energy consumption in the Complementary Metal-Oxide-Semiconductor Very Large Scale Integration circuit (CMOS VLSI) technology.

Keywords: Silicon neuron, Izhikevich model, mathematical structure-based method, subthreshold.

I Introduction

Silicon neuron is designed to mimic electrophysiological functions of neurons. Some of silicon neurons are intended to be utilized as an element of artificial spiking neural networks that process complex information in the same manner as the human brain.

There are several approaches to design silicon neurons in the analog electronic circuit. One of them is to reproduce significant neuronal behaviors, the phenomenological method in other words [1]. Another is the conductance-based method which tries to solve the models of ionic conductances in neurons by analog electronic circuits [2].

Recently, Kohno proposed a new approach [3–5], a mathematical-structure-based method, where we re-construct the mathematical structures in the differential equations of neuron models. By applying mathematical techniques, we can design a silicon neuron with simpler circuitry while keeping the neuronal dynamics.

There have been proposed variety types of silicon neurons. Generally, simple silicon neurons can produce only several types of spike patterns whereas complex ones can variety of patterns because the latter reproduces more realistic dynamics in the neurons. Simple silicon neurons are mainly applied to large-scale networks because they need large number of silicon neurons as the element. On the other hand, complex silicon neurons are applied to hybrid systems because they behave very close to the neurons. To construct large-scale spiking neural networks, we need simple silicon neurons that have rich dynamics because recent neuroscientific researches are finding that it is crucial in the information processing in the nerve system.

Izhikevich proposed a simple qualitative neuron model [6, 7], which is able to produce 20 kinds of firing patterns. Though the mathematical structure in the Izhikevich model is very simple, it has nonlinearity, including jump of the state, which makes it possible to produce various firing patterns.

In our research, we aim to design an Izhikevich-type silicon neuron circuit by reconstructing the mathematical structure in the Izhikevich model into a simple circuitry using an analog electronic circuit. We designed a silicon neuron circuit composed of MOSFETs operated under the subthreshold condition for low energy consumption in VLSI. The power supply voltage is 3 3V, Vdd=1 65V and Vss= 1 65V.

II Izhikevich model

The Izhikevich model is 2-variable differential equations that have nonlinearity including jump of state when the membrane potential excesses 30mV :

$$\frac{dv}{dt} = 0\ 04v^2 + 5v \quad 140 + I \tag{1}$$

$$\frac{du}{dt} = a(bv \quad u) \tag{2}$$

$$\text{if} \quad v = 30\text{mV} \quad \text{then} \quad v \leftarrow c \quad u \leftarrow u + d$$

where v is membrane potential and u is an internal variable. This model contains 4 parameters and we can realize various dynamics by setting them up appropriately. Parameter c is the membrane voltage after the jump of state and d is increase amount of u when v is reset. Tunability of dynamics in the Izhikevich model mainly depends on these two parameters.

In the Izhikevich model, parameter b represents the slope of the u-nullcline (Fig. 1(a)), which is difficult to control when this model is implemented in an electrical circuit. To avoid this problem, we control the positional relation between the v- and the u-nullclines instead of b

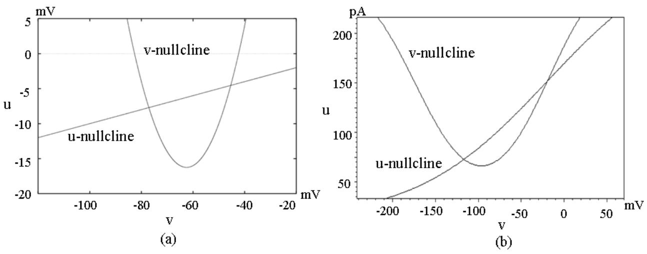

Fig. 1: The phase plane of the Izhikevich model. (a) the original model's phase plane. (b) reconstructed phase plane by utilizing the characteristic curve of differential pair circuits.

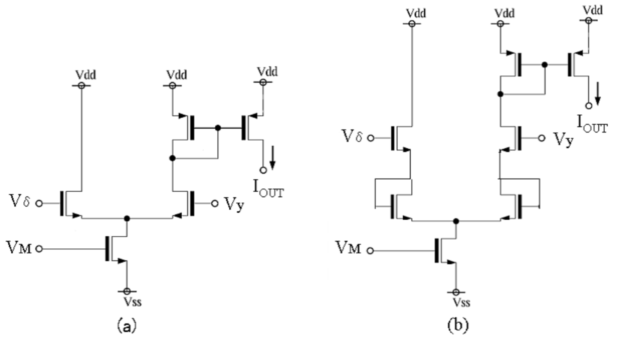

Fig. 2: Schematics of the differential pair circuitries utilized for the composition of the v- and the u-nullclines. M, δ in Eqs. (3) and (4) are applied at the nodes labelled V_M and V_δ.

This allows us to tune the mathematical structure in our silicon neuron model in the same manner as in the original model. We adopted a new parameter I_{bias}, a bias current into the membrane potential, which is responsible to the positional relation.

III Mathematical method

We applied the mathematical design method proposed by Kohno [3–5] to design an Izhikevich-type silicon neuron model. In this method, we reproduce the mathematical structures in differential equations of neuronal models using output characteristic curves of simple analog electronic circuitries. One of the advantages in this method is that we do not need to exactly copy the equations in the original model. The geometrical features of the nullclines and their positional relationship are reproduced, which allows us to copy the dynamics in the original model by a simple circuitry.

We utilize the sigmoidal curves that are output characteristics of differential pair circuitries to reproduce the geometrical features of the nullclines in the Izhikevich model. The characteristic curves of these differential pair circuits Fig. 2 (a) and (b) are represented in Eqs. (3) and (4), respectively.

$$I_{\text{OUT}} = M \frac{1}{1+exp(\quad \kappa(y \quad \delta) \;\; U_T)} \tag{3}$$

$$I_{\text{OUT}} = M \frac{1}{1+exp(\quad \kappa(y \quad \delta) \;\; 2U_T)} \tag{4}$$

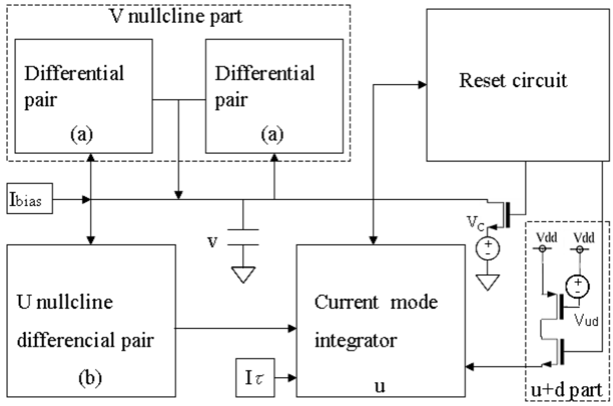

Fig. 3: Brief overview of designated circuit

where κ represents the capacitive coupling ratio and U_T is the thermal voltage.

Utilizing these sigmoidal curves, we are able to reconstruct the topological relationships of the Izhikevich model's nullclines (Fig. 1(b)). The v-nullcline in our silicon neuron model is produced by connecting a couple of symmetrical sigmoidal curves. The u-nullcline in the Izhikevich model is linear, which is substituted by a sigmoidal curve.

The v-nullcline of our silicon neuron model is produced by the differential pair circuit shown in Fig. 2(a), and the u-nullcline is by the circuit in Fig. 2(b)

IV Designed circuit

An overviewed diagram of our silicon neuron circuit is shown in Fig. 3. Our circuit consists of the v-nullcline, the u-nullcline, a current-mode integrator, reset circuit, and the u+d module.

1. Current-mode integrator

In our silicon neuron circuit, variable u is represented by an amount of a current. We utilized current-mode integrator to integrate u, which corresponds to the differential equation (2). Figure 4 shows the current-mode integrator circuit designed to operate in the subthreshold region.

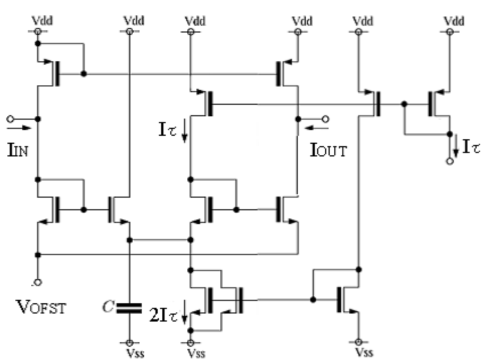

Fig. 4: The schematic of the current-mode integrator. The time constant of Eq. (5) depends on the capacitance and the bias current I_τ. We can tune the time constant by tuning I_τ externally. V_{OFST} is a bias voltage.

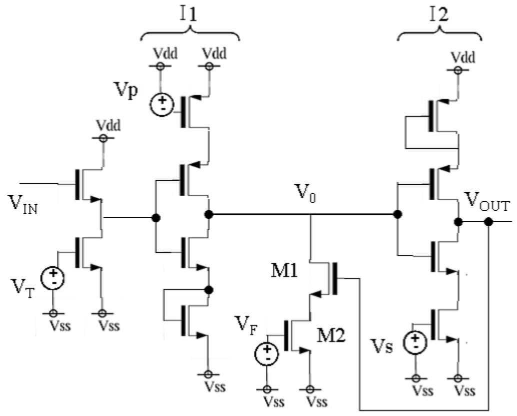

Fig. 5: The schematic of reset circuit. V_T, V_P, V_F and V_S are bias voltages. V_T, V_P and V_F are applied to switch output voltage V_{OUT} high when the input voltage excesses 30mV. M1 and M2 give a positive feedback voltage to inverter I2.

This circuit integrates the input current I_{IN} as follows:

$$\frac{dI_{OUT}}{dt} = \frac{I_\tau}{CU_T}(I_{IN} \quad I_{OUT}) \tag{5}$$

where I_{OUT} and C are the output current and the capacitance in the circuit, respectively. The time constant of the integrator corresponds to the parameter a in the model, which is decided by I_τ. In this circuit, current I_{OUT} is dependent on the voltage of the capacitor. We use this property of the current-mode integrator in the u+d module.

2. reset circuit

In the Izhikevich model, when the membrane potential excesses 30mV, v jumps to potential c and u increases by d. To realize an Izhikevich-type silicon neuron circuit, we have to equip this kind of discontinuity. The circuit for this property is shown in Fig. 5. We refer to it as the reset circuit.

The reset circuit is composed of a source follower, two inverters I1 and I2 and transistor M1 and M2 that give a positive feedback voltage to I2. Node Vo is protected from being shorted to Vss by M2. This function realizes the precipitous response and low power consumption.

3. Parameter control of Izhikevich-type silicon neuron

To realize stable and simple parameter tuning, we focus on I_{bias} and the circuit parameters correspond to a and c in the original model. The v-nullcline is displaced vertically by I_{bias}. We can control the stability of equilibrium points by tuning this parameter (see Fig. 6(a)).

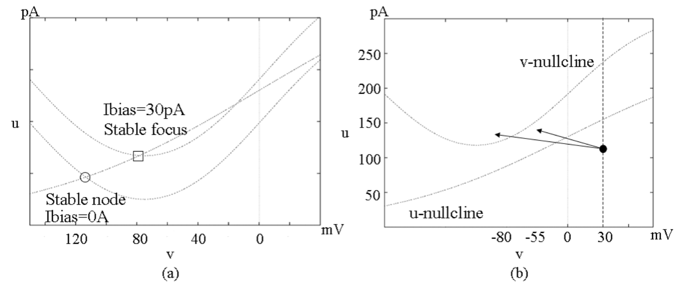

Fig. 6: Parameter control of our Izhikevich-type silicon neuron. (a) The stability of equilibrium points can be controlled by I_{bias}. When I_{bias} is 0A, the equilibrium point is a stable node and when I_{bias} is 30pA, it is a stable focus. (b) Controlling the jumping dynamics by parameter c. When parameter c is 85mV, the state comes inside of the v-nullcline after the first jump, but it is the outside of it when c is 55mV.

4. u+d module

In section IV.1, we mentioned that u depends on the voltage of the capacitance in the current-mode integrator circuit. If we increase this voltage externally, the voltage of u is increased just after the reset circuit performs its function.

The circuit of the u+d module injects current I_P into the capacitor dependent on the reset circuit. Equation (5) is modified as follows if we incorporate the effect of I_P into the integrator circuit.

$$\frac{dI_{OUT}}{dt} = \frac{I_\tau}{CU_T} \; I_{IN} \quad I_{OUT} + I_P exp(\frac{V_C \quad V_{OFF}}{U_T}) \tag{6}$$

where V_C is voltage of the capacitor and V_{OFF} is offset voltage in the current mode integrator. It is not easy to control the exact magnitude of increase in u because the V_C in Eq. (6) changes dynamically while the current-mode integrator is operating. In the Izhikevich model, many firing patterns depend on whether the jumped state is inside the v-nullcline or not. The jumping dynamics is controlled by the parameter c as shown in Fig. 6(b). For example, to produce bursting dynamics, we set c around 55mV where is usually outside of the v-nullcline until the state takes few jumps.

We fix the amount of injection current by setting Vud to 100mV to reduce the number of the parameters to be controlled. By the effect of the leak current in the u+d module, the u-nullcline is displaced to the direction of the u-axis by a few tens of pA in the phase plane.

V Simulation

We simulated our silicon neuron circuit using HSPICE software with the technology library of TSMC .35 μ mixed signal process. Figure 7 shows the results of the simulation. We could successfully produce 17 firing patterns reported in the Izhikevich model by our simplified parameter tuning sheme.

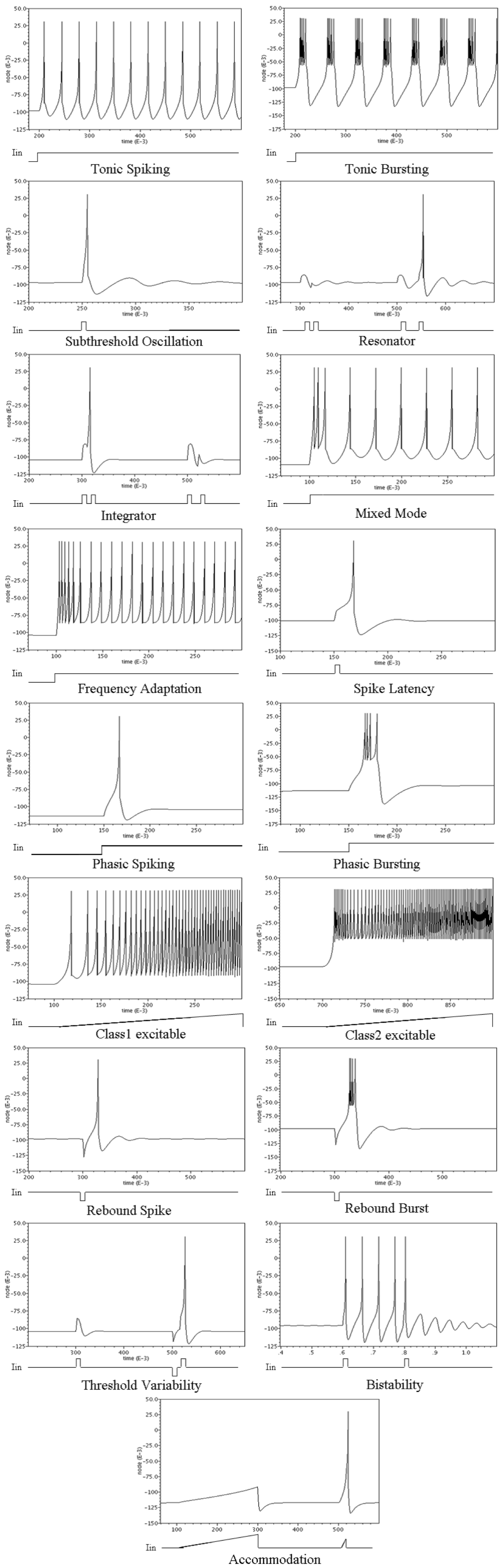

Fig. 7: Produced firing patterns

VI Conclusion

We proposed a simple implementation of an Izhikevich-type silicon neuron. The total number of transistors is 44. In the Izhikevich model, 4 parameters have to be tuned to realize all of the intended firing patterns. By noticing the mathematical structure in the model, we could output these patterns by tuning only 3 parameters. In addition, parameters b can be positive or negative in the original model, but we succeeded to output 17 patterns out of 20 by only positive b. This allows us to reduce the total number of transistors by eliminating extra circuits. In the remaining three patterns, however, parameter a or d is negative, to realize which in the silicon neuron circuit we have to add another circuit blocks. This will be addressed in our future works.

Our circuit is designed to operate with very small power consumption, about 15nW in average.

Acknowledgements

The study was partially supported by a Grant-in-Aid for Young Scientists (A) 19680015 from the Ministry of Education, Culture, Sports, Science, and Technology, the Japanese Government.

References

[1] G. Indiveri, A low-power adaptive integrate-and-fire neuron circuit, Circuits and System, 2003. ISCAS'3. Procedings of the 2003 International Symposium, Vol. 4, pp. 820-823

[2] M. F. Simoni, G. S. Cymbalyuk, and M. E. Sorensen, A Multiconductance Silicon Neuron With Biologically Matched Dynamics, IEEE TRANSACTIONS ON BIOMEDICAL ENGINEERING, Vol.51, No.2, 2004

[3] T. Kohno, K. Aihara, A Design Method for Analog and Digital Silicon Neurons -Mathematical-Model-Based Method-, AIP Conference Proceedings, 2008

[4] T. Kohno, K. Aihara, A MOSFET-Based Model of a Class 2 Nerve Membrane, IEEE TRANSACTIONS ON NEURAL NETWORKS, Vol. 16, No. 3, MAY 2005

[5] T. Kohno, K. Aihara, A simple aVLSI burst silicon neuron circuit, Nonlinear Theory and its Applications, 2008

[6] E. M. Izhikevich, Simple Model of Spiking Neurons, IEEE TRANSACTIONS ON NEURAL NETWORKS, Vol. 14, No. 6, NOVEMBER 2003

[7] E. M. Izhikevich, Which Model to Use for Cortical Spiking Neurons?, IEEE TRANSACTIONS ON NEURAL NETWORKS, Vol. 15, No. 5 SEPTEMBER 2004

A digital spiking silicon neural network

T. Nakayama*,**, Y. Katori**, K. Aihara**, and T. Kohno**

* Graduate School of Engineering The University of Tokyo 7-3-1 Hongo, Bunkyo-ku, Tokyo 113-8656, Japan
**Institute of Industrial Science, The University of Tokyo 4-6-1 Komaba, Meguro-ku, Tokyo 153-8505, Japan
(Tel : +81-3-5452-6693; Fax : +81-3-5452-6694)
(keanu505@sat.t.u-tokyo.ac.jp)

Abstract: A silicon neuron is an electrical circuit that replicates the electrophysiological phenomena of biological neural system. Despite most of conventional spiking silicon neuron models are designed for analog circuit technology, we proposed, in the previous study, a digital spiking silicon neuron (DSSN), which is optimally designed for digital circuit technology. The DSSN model was based on a mathematical-modeling point of view and successfully produced three types of neural excitability with fewer hardware resources. In addition to the DSSN, we propose here a digital silicon synapse that mimics the elemental features of a chemical synapse and underlies the construction of a silicon neural network. We built a fully-connected digital silicon neural network with the digital silicon synapses and demonstrate synchronization and phase-locking in neural activities in a hardware description language (HDL) simulation.

Keywords: silicon neural network, digital synaptic circuit

I. INTRODUCTION

The silicon neural network is an electrical circuit that mimics electrophysiological properties and functions of biological neural systems. Such neural system attracts much attention due to not only clinical objectives but also engineering purposes, and their parallel structure and robustness might bring high scalability and adaptability in information processing. Silicon neural networks with these features are applicable to, for example, a real-time simulator of complicated nerve systems [1], a hybrid system of biological and silicon neurons for the purpose of verification of a neuron model [2], and brain machine interfaces.

In the present study, we focused on designing the silicon spiking neural network with DSSNs and the silicon synapses. Spikes (or action potentials) are thought to be a main carrier of information in neural systems and are generated when a neuron receives inputs from other neurons and its membrane potential reaches the threshold. Once a spike is generated, the spike travels to other neurons and yields current on their membrane via excitatory or inhibitory synapses. These synaptic interactions lead variety of neural dynamics. For example, in mutually connected neurons with excitatory synapses, their neural activities tend to be synchronized. Synchronized neural activities are widely observed in biological systems and are supposed to play crucial roles e.g. in cardiac pacemaker cells [3] and in motor controls [4]. Those dynamical features of spiking neural network might bring variety of engineering applications.

In designing the silicon neural network, selection of a proper model is a key issue. One possible approach of neural modeling is to focus on the detail of neurons' structure, for example, multi-compartmental models of neurons based on dynamics of various kinds of ionic channels and dendritic tree structure. Such physiologically realistic neuron models might produce the detail of the neural activity. However, implementations of those models require vast hardware and power resources, and when trying to operate the neural system it can be hard to analyze their behaviors. Another approach is to simplify the neuron model and to optimize them to a target device maintaining the core features of activity of the original neuron. The DSSN model proposed in our previous study is based on this requirement and on mathematical modeling point of view. The DSSN model exhibits rich dynamical behavior and allows us to realize a silicon neural network with fewer hardware resources.

In this paper, we report a digital synaptic circuit with same design principal as that of the DSSN model and a digital silicon neural network with the synaptic circuit. In the following sections, dynamical properties of the DSSN are briefly reviewed. Then, models of synaptic circuits and the neural network are explained. In the result section, phase-locking phenomena of neural activities in the network are demonstrated. In the final section, conclusions, discussions for the result, and our future works are remarked.

II. MODEL AND METHOD

In this study, we used the DSSN model as an element of the neural network, which is optimally designed for digital circuit technology [5] and is described by the following equations:

$$\frac{dv}{dt} = \frac{\phi}{\tau}(f(v) - n + I_0 + I_{stim}) \;, \tag{1}$$

$$\frac{dn}{dt} = \frac{1}{\tau}(g(v) - n) \;, \tag{2}$$

$$f(v) \equiv \begin{cases} a_n(v + b_n)^2 - c_n & (v < 0) \\ -a_p(v - b_p)^2 + c_p & (v \geq 0) \end{cases} \;, \tag{3}$$

$$g(v) \equiv \begin{cases} k_n(v - p_n)^2 + q_n & (v < r) \\ k_p(v - p_p)^2 + q_p & (v \geq r) \end{cases} \;, \tag{4}$$

where variables v and n respectively represent the membrane potential and an activity of slow ionic channels. Parameters a_x, b_x, c_x, k_x, p_x, q_x (for x=n and p), and r determine dynamical properties of the neuron. Φ and τ are parameters that specify the time constant. I_0 is a constant bias current. I_{stim} is the sum of currents given by other neurons. See reference [5] for the parameter values.

This neuron model is designed so that they can be implemented on limited resource of digital arithmetic circuits while maintaining the qualitative structure of their dynamical system. The structure of the dynamical system can be depicted on the phase-plane plots and the bifurcation diagrams (Fig. 1(a)-(c)). Those plots show structures of dynamics in two different types of neuron models: Class I and II excitability. This classification is based on difference on the frequency-input relationship of a neuron as depicted in Fig. 1(d). A neuron with Class I excitability begins to fire gradually at arbitrarily low frequency as the sustained stimulus current is increased. In Class II excitability, on the other hand, a neuron starts to fire at non-zero frequency. Differences of those excitabilities can be clear with the phase plane and the bifurcation diagrams. In the former, the structure of the dynamical systems are characterized with nullclines, which are sets of points satisfying $\dot{v} = 0$ or $\dot{n} = 0$, called the v- and the n-nullclines respectively. Intersections of these nullclines represent equilibriums whose stabilities are determined by the eigen value analyses. As the magnitude of the input increases, the v-nullcline moves upward in Fig. 1(a) and the position and presence of intersections can be changed as in Fig. 1(b) and (c). In the case of a Class I neuron, the qualitative change in the dynamical system is induced by a saddle-node on invariant circle bifurcation. In a Class II neuron, this is by the Hopf bifurcation.

In order to construct a silicon neural network with DSSNs, we have developed a digital silicon synapse. We used a synaptic model which is analogue to elemental features of activities in biological synapses. The activity of the model synapse is triggered by an arrival of a spike and decays exponentially toward zero [7]. The synaptic model used in this paper is described by

$$\frac{ds}{dt} = -\frac{1}{\tau_s}s + (s_{peak} - s)\delta(t - t_s) \;, \tag{5}$$

where s is a synaptic activity, parameter s_{peak} = 2 is the peak value of synaptic activity, τ_s= 3.2ms is the decay

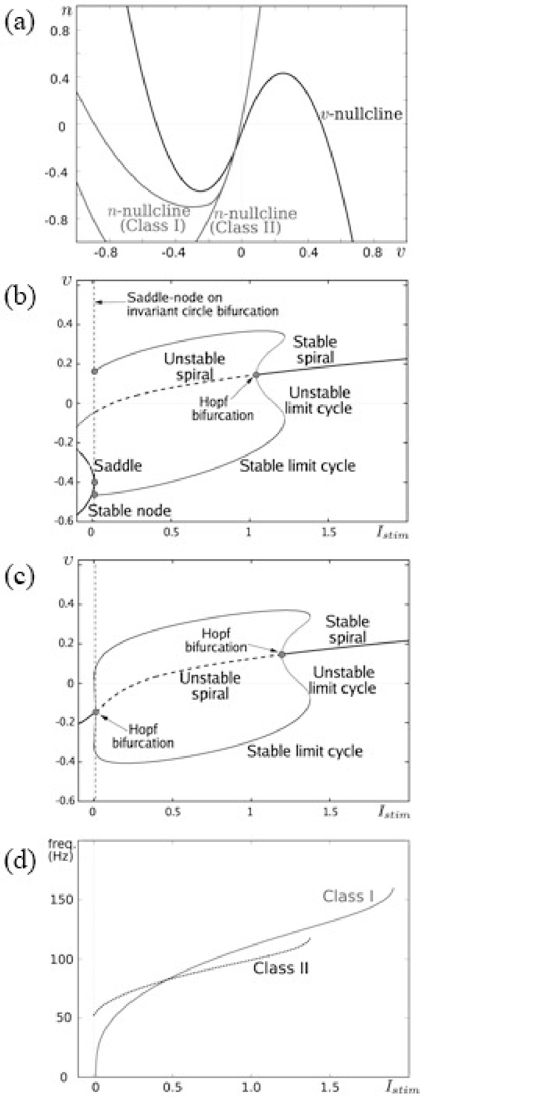

Fig. 1. Analyses of Class I and II neurons in our DSSN model. (a) The v-n phase plane. (b), (c) Bifurcation diagrams of Class I and II neurons, respectively. (d) Frequency-input relationship of Class I and II neurons. These figures are cited from [5][6].

time constant of synaptic activity, t_s is the time when the presynaptic neuron emits a spike. δ is Dirac's delta function. The second term in the right-hand side of Eq. (5) represents reset of synaptic activity.

Although, a single neuron sends spikes to multiple neurons and generates synaptic currents on their membranes, we assumed that the time series of the synaptic currents are common among these synapses except for their amplitude. In other words, the synaptic currents are given by a product of the synaptic activity and a weight value that corresponds to efficiency of each synapse (Fig. 2).

Figure 3 shows the block diagram of the single spiking neuron circuit and the corresponding synaptic circuit. Three variables in this model, v, n, and s are stored in register circuits (boxes of the right side in Fig. 3) and are updated with difference equations that are derived from Eqs. (1), (2), and (5). Differences are calculated according to the stored values of the variables and the external input (boxes of the left side in Fig. 3) and these differences are summed with the current states of variables in adders (middle in Fig. 3). The summed values are read out by the variable registers simultaneously at the rising edge of the clock signal. The variable that represents the synaptic activity is reset to their peak value when the sign bit of variable v is switched from 1 to 0, namely, when the membrane potential go through the threshold v=0 from below to above.

As to the network, we constructed a fully-connected network in which all neurons have connections for all other neurons including themselves. In this study, we built a neural network that consists of three silicon neurons connected each other via the silicon synapses of unique weight value w.

In this digital silicon neural network, the variables in above equations are represented by two's complement representation and the size of the circuit is crucially depended on the selection of their bit width. We tried several values for the bit width and found that 19 bit is sufficient to attain accurate integration to operate the silicon neural network appropriately. Furthermore, several parameter values in above models

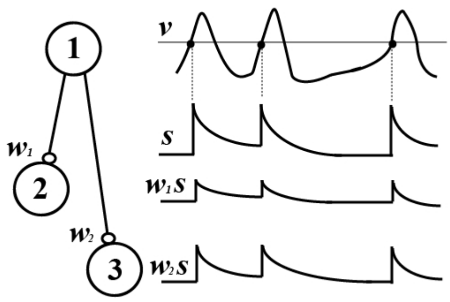

Fig. 2. Schematics of synaptic activity. v represents the membrane potential of neuron 1. s represents a synaptic activity. w_1 and w_2 represent weights of synapses from neuron 1 to neuron 2, and to neuron 3, respectively.

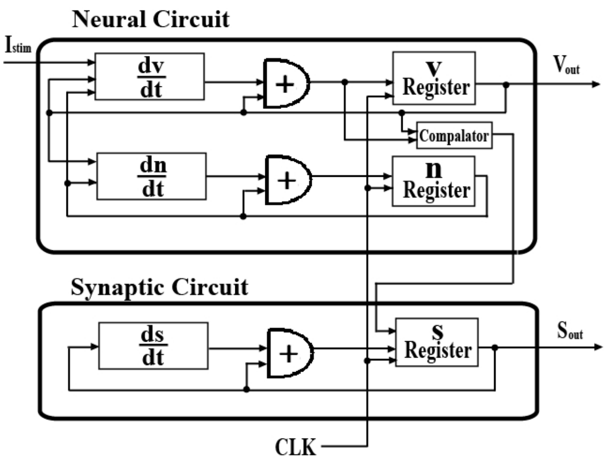

Fig. 3. Block diagram of a single neuron circuit and a synaptic circuit. I_{stim} is the external input. V_{out} is the output of membrane potential. S_{out} is the synaptic activity.

are selected from m th power of two (m is supposed to be an integer number) so that the multiplier circuits can be replaced by bit shifters. This replacement leads remarkable reduction in hardware resource requirement and less latency. In the calculating process of division of τ, bit shift operation is also utilized. We simulated this spiking silicon neural network with a HDL simulator software (Modelsim Xilinx Edition-III). In the following HDL simulation, we set the bit width of variables to be 19 bits.

III. RESULT

We confirmed that the individual spiking silicon neurons show both of Class I and II excitabilities in HDL simulation (Fig. 4). In the Class I mode, our silicon neuron begins to fire at very low frequency and their frequency is gradually increased by an increase in the input magnitude. In the case of the Class II mode, as the input magnitude increased, their frequency suddenly increases just above a threshold and then they increases relatively slowly in the above threshold. In relation to synaptic activity, as the membrane potential exceeds the threshold, synaptic activities are triggered and decayed exponentially.

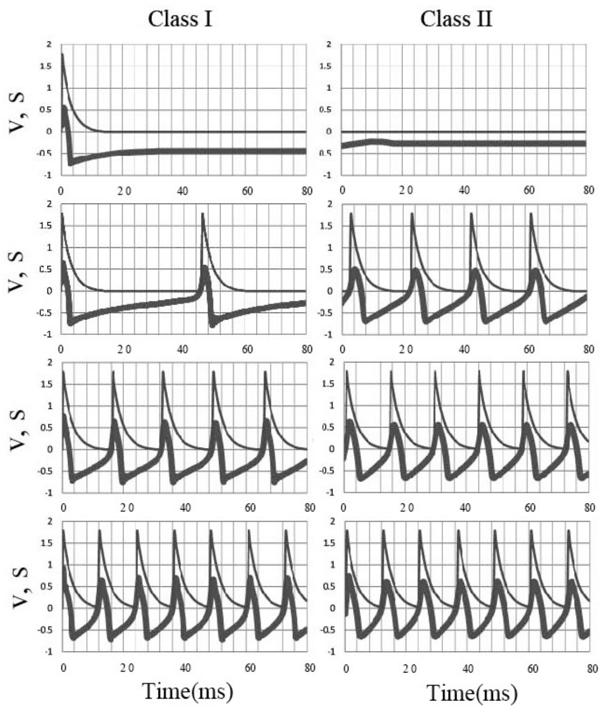

Fig. 4. HDL simulation of our silicon neuron circuit. The vertical axes represent the magnitude of v and s, and these figures show time series from 0 to 80ms. A synaptic activity is indicated by thin curve. The membrane potential is represented by bold curves. The left column is Class I neuron. The right one is Class II neuron. In sequence from top figures, I_{stim}= –0.25, 0.0156, 0.5, 1. Note that in this simulation, the frequencies of v at the values of each I_{stim} about both Class I and II are different from those of Fig. 1(d). However, the qualitative characteristic of Class I and II corresponds to that of Fig. 1(d).

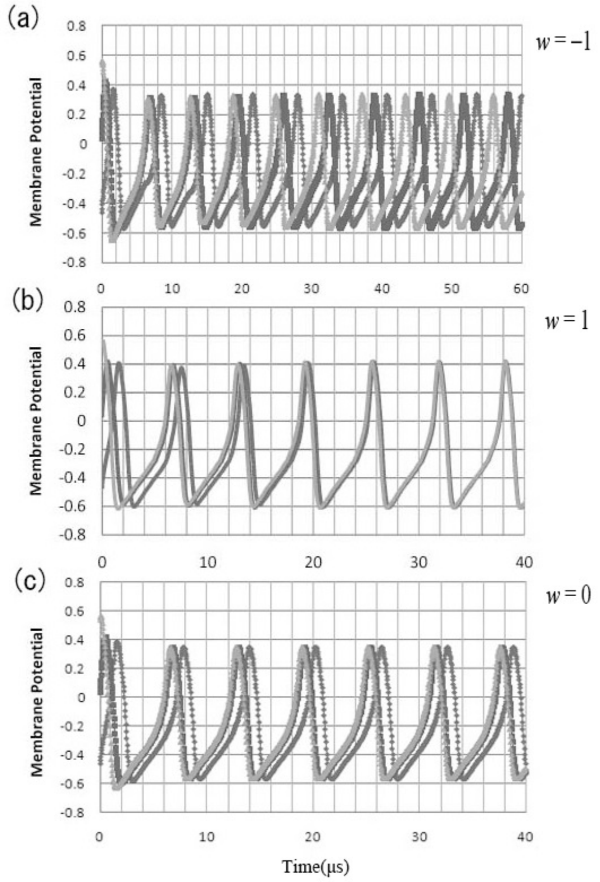

Fig. 5. Responses on the digital silicon neural network. The vertical axes represent the magnitude of v. (a) An anti-phase locking. (b) Synchronization. (c) Response without interactions.

As shown in Fig. 5, the spiking silicon neural network shows synchronization and phase-locking phenomena in their activity. We performed simulation for the cases of the inhibitory, excitatory, and neutral synaptic connections. In this simulation, the Class I neurons are implemented. In the model, interaction with inhibitory synapses leads an anti-phase locking (Fig. 5(a)) and excitatory interactions bring the synchronized activities (Fig. 5(b)). These well-ordered collective behaviors cannot be observed without any interactions (Fig. 5(c)).

IV. DISCUSSION AND CONCLUSION

In this paper, we proposed a digital silicon neural network and confirmed, in HDL simulations, that individual neurons show two different classes of excitability and their activities trigger synaptic activities, and that the fully-connected neural network shows synchronization and phase-locking phenomena due to the interaction via the synaptic connection.

In our silicon neural network, several spatio-temporal patterns are realized by changing the connectivity among the network. Application of this phenomenon involves, for example, a control of multi-channel actuators. As the future works, we will implement the silicon neural network in a field programmable gate array (FPGA) and evaluate their performances in such applications. Furthermore, to implement learning ability or flexible plastic features in the silicon neural network, a synaptic plasticity circuit is required. We will develop the plasticity circuit based on the same design principal as used in the present research.

ACKNOWLEDGEMENTS

This study was partially supported by a Grant-in-Aid for Challenging Exploratory Research 21650069 from the Ministry of Education, Culture, Sports, Science, and Technology, the Japanese Government.

REFERENCES

[1] S. Renaud-Le Masson, G. Le Masson, and L. Alvado, et al (2004), A neural simulation system based on biologically realistic electronic neurons, Information Sciences, Vol. 161, pp.57-69.
[2] G. Le Masson, S. Renaud-Le Masson, and D. Debay, and et al (2002), Feedback inhibition controls spike transfer in hybrid thalamic circuits, Nature, Vol. 417, No. 6891,pp. 854-858.
[3] Renato E. Mirollo and Steven H. Strogatz (1990), Synchronization of pulse-coupled biological oscillators, Society for Industrial and Applied Mathematics. Vol. 50, No 6, pp.1645-1662
[4] Yuichi Katori, Eric J. Lang, Miho Onizuka, Mitsuo Kawato, and Kazuyuki Aihara (2010), Quantitative Modeling of Spatio-temporal Dynamics of Inferior Olive Neurons with a Simple Conductance-based Model, International Journal of Bifurcation and Chaos. Vol. 20 (3), (in press).
[5] Kohno T and Aihara K (2007), Digital Spiking Silicon Neuron: Concept and Behaviors in GJ-coupled Network, Proc. Int. Symp. Artificial Life and Robotics 2007.
[6] Kohno T and Aihara K (2008), A Design Method for Analog and Digital Silicon Neurons –Mathematical-Model-Based Method- . AIP Conf. Proc. Vol 1028,pp,113-128.
[7] W. Gerstner and W. Kistler (2002), Spiking Neuron Models. CAMBRIDGE UNIVERSITY PRESS, pp.93-102.

The Fifteenth International Symposium on Artificial Life and Robotics 2010 (AROB 15th '10),
B-Con Plaza, Beppu,Oita, Japan, February 4-6, 2010

Failure of pseudo-periodic surrogates

Masanori Shiro, Yoshito Hirata and Kazuyuki Aihara
Institute of Industrial Science, the University of Tokyo
4-6-1 KOMABA MEGURO-KU, TOKYO 153-8505, JAPAN
{shiro, yoshito, aihara}@sat.t.u-tokyo.ac.jp

Abstract: A surrogate test is a method for revealing properties of time series data. To judge whether or not a pseudo-periodic time series has deterministic properties beyond the pseudo-periodicity, some methods to generate surrogate data have been proposed. Luo's test is one of such methods. In this report, Luo's test and its problem will be discussed. On that test, surrogate datasets are produced by adding the original data to their time-shift. So, the pseudo-periodicity of the time series will be presumably preserved, but fine structure related to the determinism is destroyed. The test gives correct results for many ordinary data. However, Luo's test also provides wrong results for certain time series, for example, time series of Rössler chaos and phase-shifted sinusoidal waves. To overcome this problem, we propose an alternative method based on the Poincaré section.
Keywords: surrogate test, time series, pseudo-periodicity, Luo's test, Poincaré section, deterministic chaos.

1. Introduction

A surrogate test is hypothesis testing which is often used for revealing properties of the time series data. To show that the time series has a certain property, one often chooses a null-hypothesis. Then, one generates surrogate datasets that are randomized so that they preserve the properties of the null-hypothesis. Then, the original dataset and its surrogate datasets are compared by using a test statistic. If the test statistic for the original dataset is out of the range specified with the surrogate datasets, then the null-hypothesis is rejected. Otherwise, it cannot be rejected.

Many methods to generate surrogate data have been proposed. For example, random-shuffled surrogates [1] test the serial dependence, while iterative amplitude adjusted Fourier transform surrogates [2] test the nonlinearity of time series.

To judge whether or not a pseudo-periodic time series has deterministic properties beyond the pseudo-periodicity, some methods to generate surrogate data have been proposed. For example, Small's test [3] is well-known. Luo's test [4] is another of such methods. In this report, the test of Luo and its problem will be shown.

2. Tested data and results

On the test of Luo, surrogate datasets are produced by adding the original data to their time-shift. So, the pseudo-periodicity of the time series will be presumably preserved, but fine structure related to the determinism is destroyed.

The test gives correct results for many ordinary data. However, Luo's test also provides wrong results for certain time series, for example, time series of Rössler chaos and phase-shifted sinusoidal waves. We will show that in what follows.

In the Fig. 1, a tested time series, which is the Rössler attractor, is shown. The original data have 15000 points which were generated by Eq. (1). The initial values were $x_0 = y_0 = z_0 = 1$, the sampling rate was 0.05 unit times, and the first 1000 points were discarded.

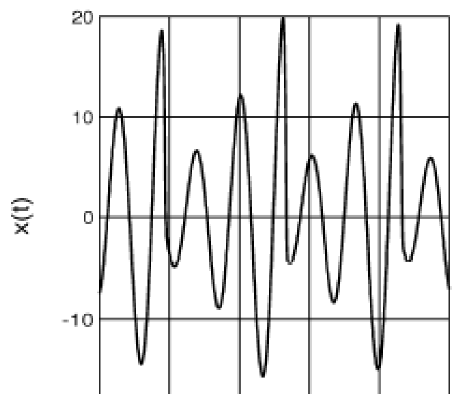

Fig. 1: Time series of Rössler attractor generated by Eq.(1).

$$\begin{cases} \frac{dx}{dt} = -y - z \\ \frac{dy}{dt} = x + 0.15y \\ \frac{dz}{dt} = 0.2 + z(x - 10) \end{cases} \quad \cdots(1)$$

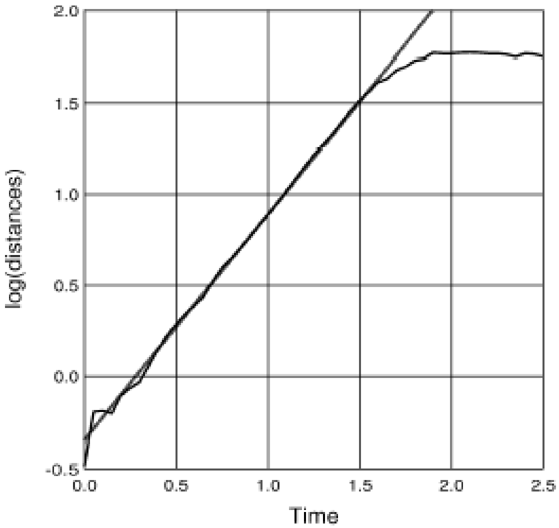

Fig. 2: Exponential increase of distances on Rössler attractor.

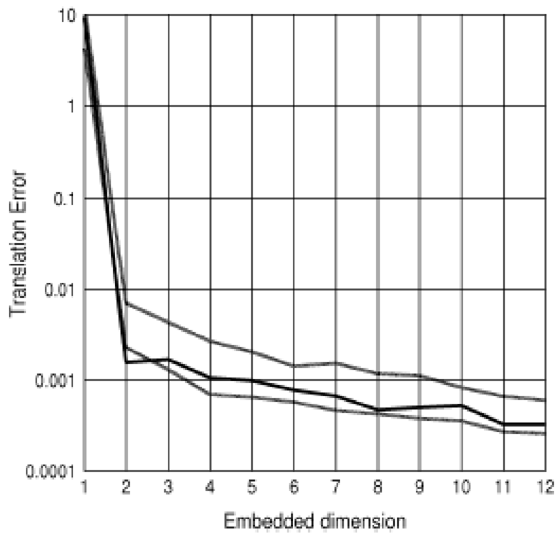

Fig. 3: Results of Luo's test on Rössler attractor.

On the certain parameters, the Rössler attractor behaves as non-chaotic time series. Therefore, we confirmed that the tested time series generated from the above equations show the positive Lyapunov exponent by using Kantz's method [5]. The increase of distances between a point and neighborhood points on the delay coordinates, is shown in Fig. 2. The Lyapunov exponent of the data is calculated by the slope of the scaling region in the logarithmic plot. The Fig. 2 shows that the exponent is 1.24, or a positive value. Our tested dataset is likely to be of deterministic chaos.

The 39 surrogate datasets were produced by Luo's method from the above dataset. We compared the original dataset and its surrogates by Wayland's method [6]. In this method, neighboring points $x_{n_i(t)}$ ($i = 1, 2, \cdots, k$) are chosen for each selected point x_t ($t \in T \subset \{1, 2, \cdots, N\}$) in a time series $\{x_t : t = 1, 2, \cdots, N\}$, where n_i is the time index for the i-th nearest point for x_t and we set $n_0(t) = t$. As the second step, for each selected point x_t ($t \in T$), we calculate the translation errors $v_i(t) = x_{n_i(t)+1} - x_{n_i(t)}$ and their average $v(t) = \frac{1}{k+1}\sum_{i=0}^{k} v_i(t)$. As for the third step, we calculate the normalized mean difference between the translation errors and their average, i.e., $e(t) = \frac{1}{k+1}\sum_{i=0}^{k} \frac{\|v_i(t)-v(t)\|^2}{\|v(t)\|^2}$. The statistic we use is the median of $\{e(t) : t \in T\}$.

The results are shown in Fig. 3. In the figure, a thick line which shows the test statistic for the original dataset is inside of the two broken lines which show the upper and lower values for the test statistic obtained from the surrogate datasets. The results of Luo's test mean that *the chaotic data have no deterministic property beyond the pseudo-periodicity*, which should not be correct.

As another example, we applied the same method to a phase-shifted sinusoidal wave. The original data which were generated by Eq. (2) are shown in Fig. 4, in which $\eta(t)$ is a random value chosen for each t from the range of $[-0.1, 0.1]$ uniformly. The data represent a noisy periodic orbit with pseudo-periodicity.

$$\begin{cases} x(t) = \sin\theta(t) \\ \theta(t+1) = \theta(t) + \omega + \eta(t) \\ \eta(t) \in [-0.1, 0.1] \end{cases} \quad \cdots(2)$$

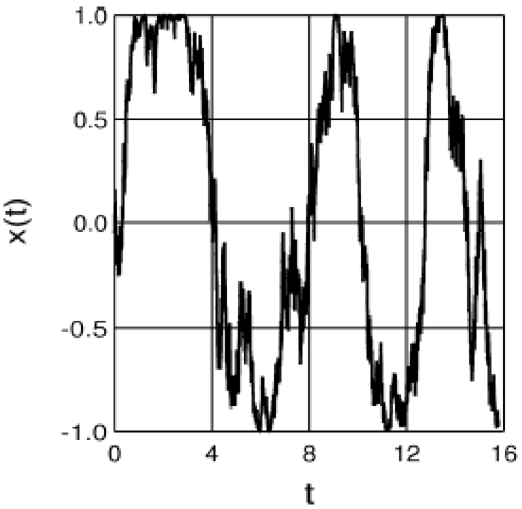

Fig. 4: Phase-shifted sinusoidal wave

The 39 surrogate datasets were also prepared by using Luo's method, and the test statistic for each surrogate was obtained. The results shown in Fig. 5 imply that the dataset has determinism beyond pseudo-periodicity, which should be wrong too.

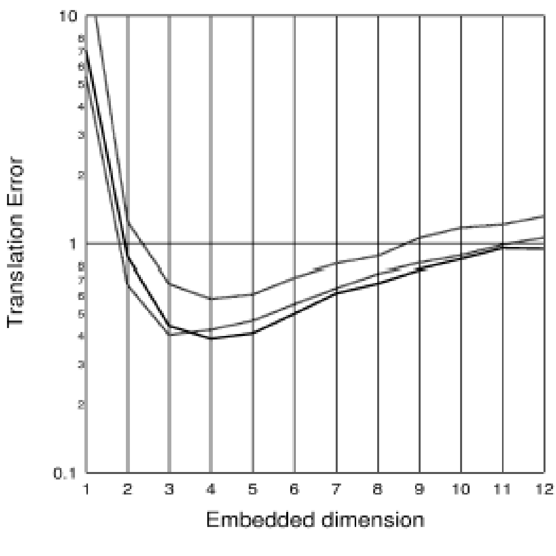

Fig. 5: Results of Luo's test on phase-shifted sinusoidal waves.

3. Proposal method

So far, we found that Luo's method does not classify phase-shifted pseudo-periodicity data correctly. To overcome this weak point, we propose an alternative method based on the Poincaré section.

If a time series has the determinism beyond the pseudo-periodicity, some structures should be found on the Poincaré section. Therefore, by comparing the original data with its random shuffle surrogates on the Poincaré section, one will be able to judge whether or not time series has fine deterministic properties beyond the pseudo-periodicity.

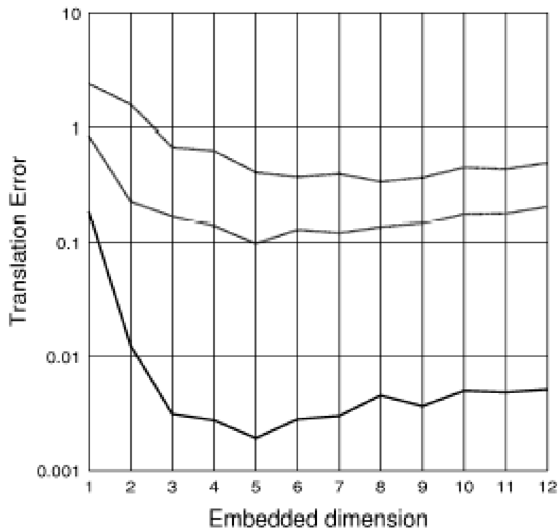

Fig. 6: Results of random shuffle surrogate on the Poincaré section (Rössler chaos).

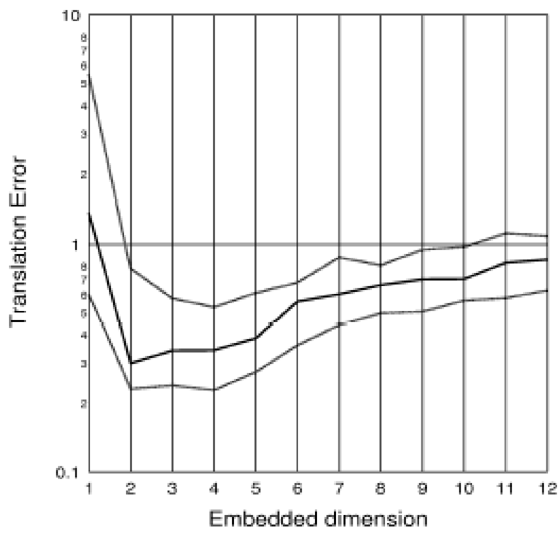

Fig. 7: Results of random shuffle surrogate on the Poincaré section (phase-shifted sinusoidal wave).

We applied the method based on the Poincaré section to the datasets of the Rössler chaos and phase-shifted sinusoidal waves. The results are plotted in Figs. 6 and 7, respectively. Because we found serial dependence on the Poincaré section of the Rössler attractor, but not on the Poincaré section of the phase-shifted sinusoidal waves, we confirmed that this method provides correct results on the tested datasets.

4. Conclusion

We examined the performance of Luo's test for generating pseudo-periodic surrogates and found that it sometimes provides wrong results for "phase-shifted" pseudo-periodicity data. Therefore, we proposed an alternative method that tests serial dependence on a Poincaré section. We showed that the proposed method provides consistent results on the tested datasets.

References

[1] J. A. Scheinkman and B. LeBaron, *J. Business* **62**, 311 (1989).

[2] T. Schreiber and A. Schmitz, *Phys. Rev. Lett.* **77**, 635(1996).

[3] M. Small, D. Yu, and R. G. Harrison, *Phys. Rev. Lett.* **87**, 188101 (2001).

[4] X. Luo, T. Nakamura, and M. Small, *Phys. Rev. E* **71**, 026230 (2005).

[5] H. Kantz, *Phys. Lett. A* **185**, 77 (1994).

[6] R. Wayland, B. Bromley, D. Dickett, and A. Passamante, *Phys. Rev. Lett.* **70**, 580 (1993).

Acknowledgment

This study is partially supported by Grant-in-Aid No. 17022012 for Scientific Research on Priority Areas System study on higher-order brain functions from the Ministry of Education, Culture, Sports, Science and Technology of Japan.

Estimation of excess entropy from spike trains

H. Motoyoshi*, Y. Katori**, and H. Suzuki*'**

** Graduate School of Information Science and Technology, The University of Tokyo,
7-3-1 Hongo, Bunkyo-ku, Tokyo 113-8656, Japan
** Institute of Industrial Science, The University of Tokyo,
4-6-1 Komaba, Meguro-ku, Tokyo 153-8505, Japan*

(motoyoshi@sat.t.u-tokyo.ac.jp)

Abstract: Entropy rate is widely used for analysis of neural data as a measure for randomness of spike trains. In addition, its convergent process also contains information on spike trains' structures or patterns. Therefore, it can be expected to be a measure for certain aspects of spike trains. In this paper, we investigate applicability of excess entropy to neural spike train data by numerical simulations of gamma process. We show that even when the spike train is not so long, the estimated excess entropy correctly reflects the shape parameter of the gamma process.

Keywords: Excess entropy, spike trains, gamma distribution, entropy rate

I. Introduction

In neural systems, spikes are thought to be a main carrier of information and are necessary to transmits e.g. sensory information and motor commands. Information representation and transmission in the neural systems are crucial issues in neuroscience. For example, in inferior olive (IO) system, prominently low firing rates of spikes of IO neurons are supposed to transmit error signals in motor control and their detailed information coding is still controversial. In order to quantify the information flow in neural system, statistical and information theoretical approaches are often used. One of the major approaches quantifying information flow is to measure the entropy rate. In addition to entropy rate, excess entropy was proposed by Clutchfield and Feldman [1]. Excess entropy captures a different element that is related with structure from entropy rate that expresses randomness. It can be a useful tool for analyzing spike trains. Excess entropy has been investigated by various researchers. Effective measure complexity proposed by Grassberger [2] is the same as excess entropy. Predictive information proposed by Bialek et al. [3] is similar to the excess entropy. However, estimating excess entropy has some problems. Excess entropy needs infinite length sample by definition. In practice, these measures need to be estimated from finite length sample. Considering fluctuation of sample data set, estimated value of the excess entropy should be corrected [4]. In the case of spike train data observed from neurons, distributions of inter-spike intervals (ISI) are known to be well approximated by the exponential distribution (Poisson process) or the gamma distribution [5]. Since the gamma distribution has two parameters: shape and scale parameters, ISI distributions of physiological data are better approximated by the gamma distribution than the exponential distribution. Here, we assume that ISI distribution follows the gamma distribution and we apply information theoretical measures to spike trains generated from gamma process.

In this paper, first, we review two information theoretic measures: entropy rate and excess entropy. Second, we review a correction method for estimated value from finite sample. Third, we apply information theoretic measures with the correction to spike trains generated from the gamma process. Finally, a brief conclusion is remarked.

II. Information theoretic measures

Estimation of excess entropy and entropy rate is based on Shannon entropy that intuitively represents randomness or uncertainty. Let X be a random variable taking value x in a finite set χ. Then Shannon entropy of the random variable X is defined by

$$H(X) = -\sum_{x\in\chi} p(x)\log_2 p(x) \,. \qquad (1)$$

Entropy of a string of random variables $X^L = X_1 ... X_L$ is defined as

$$H(X^L) = -\sum_{x^L\in\chi^L} p(x^L)\log_2 p(x^L), \qquad (2)$$

where $p(x^L) = p(x_1,...x_L)$ is joint probability. Then uncertainty or average amount of information per symbol is given by

$$h(L) = H(X^L)/L. \tag{3}$$

The entropy rate h is defined by $h(L)$ in the limit as L goes to infinity as follows:

$$h = \lim_{L\to\infty} h(L). \tag{4}$$

As the length L increases, $h(L)$ decreases and approaches to the entropy rate h (Fig. 1(b)). To quantify its convergence, the excess entropy E is defined by

$$E = \sum_{L=1}^{\infty} h(L) - h. \tag{5}$$

The system appears more random than it is when the length L is small. Excess entropy tells us how much additional information about the configuration is required to reveal the actual randomness h.

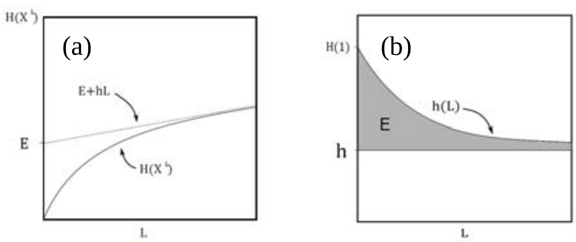

Fig.1. Image of excess entropy in relation with (a) entropy growth and (b) convergence of entropy rate.

Another definition of the excess entropy using mutual information allows us to understand meaning and nature of the excess entropy:

$$E = I(\overleftarrow{X}, \overrightarrow{X}) = H[\overrightarrow{X}] - H[\overrightarrow{X} \mid \overleftarrow{X}], \tag{6}$$

where $\overleftarrow{X} = ...X_{-3}X_{-2}X_{-1}$ and $\overrightarrow{X} = X_0X_1X_2$ are the left and the right part of infinite chain of random variables $\overleftrightarrow{X}$. This formulation suggests that excess entropy captures how much information on the half part of chain affects the other side. That is, excess entropy measures memory, predictability or correlation.

III. Estimation from finite length data set

To estimate the entropy rate h from a finite sequence of length N, we first need to estimate the probabilities $p(x_1,...x_L)$ from the finite sequence. A naive estimation of $p(x_1,...x_L)$ is given by

$$\hat{p}(x_1,...x_L) = \frac{n_{x_1,...x_L}}{N}, \tag{7}$$

where $n_{x_1,...x_L}$ is the number of occurrences of the word $x_1,...x_L$. By substituting Eq. (7) into Eq. (2), we obtain an estimated value of the entropy rate as follows:

$$\hat{h} = \lim_{L\to\infty} \frac{\hat{H}(X^L)}{L}. \tag{8}$$

However, this estimation tends to underestimates the true value. This can be understood by considering an expectation value of $\hat{H}(X^L)$ [4].

$$\begin{aligned}\left\langle \hat{H}(X^L) \right\rangle &= \left\langle -\sum_{x^L\in\chi^L} \frac{n_{x_1,...,x_L}}{N} \log \frac{n_{x_1,...,x_L}}{N} \right\rangle \\ &\le \left\langle -\sum_{x^L\in\chi^L} \frac{n_{x_1,...,x_L}}{N} \log p(x_1,...,x_L) \right\rangle \\ &= -\sum_{x^L\in\chi^L} \frac{\left\langle n_{x_1,...,x_L} \right\rangle}{N} \log p(x_1,...,x_L) = H(X^L).\end{aligned} \tag{9}$$

Figure 2(a) shows the result of estimation with finite length sample of sequence generated by the logistic map. It indicates that $\hat{H}(X^L) \approx \hat{h}L$ in the realm of good statistic and that $\hat{H}(X^L) \approx \log N$ in the realm of bad statistics [6]. Accuracy of the estimation depends not only on the fluctuation of the sample but also on the sample length.

A correction of the estimated value was given by Schürmann and Grassberger [4]:

$$\tilde{H}(X^L) = \sum_{j=1}^{M} \frac{n_j}{N}\left(\log N - \psi(n_j) - \frac{(-1)^{n_j}}{n_j+1} \right), \tag{10}$$

where M is the number of distinct words of length L that occurs in the given sequence, n_j is the number of occurrence of the jth word, and $\psi(x)$ is the logarithmic derivative of gamma function.

We apply the correction described in Eq. (10) to estimate the entropy of the logistic map. Figure 2(b) indicates that the estimation of the entropy of the logistic map is significantly improved with this correction. However, the entropy rate should be evaluated within the realm of good statistics.

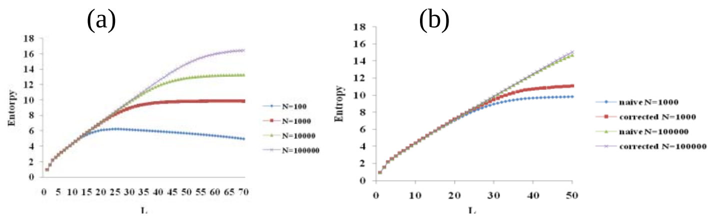

Fig. 2. Estimated entropy of the logistic map (a) without the correction and (b) with the correction.

IV. Application to Gamma process

In this section, we consider applicability of estimation of the excess entropy of spike trains with numerical simulations. Spike trains are often assumed to be generated from a point process. Here, we suppose that ISIs t follow the gamma distribution whose probability density function is given by

$$f(t;\kappa,\lambda) = \frac{\lambda^{\kappa}}{\Gamma(\kappa)} t^{\kappa-1} e^{-\lambda t}, \qquad (11)$$

where κ is a shape parameter and λ is a scale parameter. Figure 3 shows an example of probability density function of Gamma distribution.

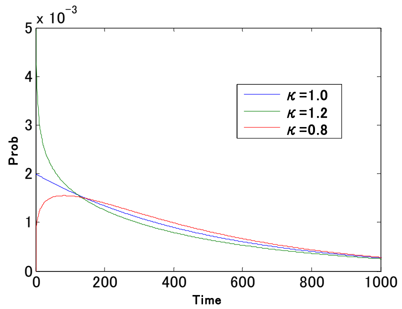

Fig. 3. Gamma distribution

The excess entropy can capture structural differences in ISI distribution from complete random process, like the Poisson process. This property of the excess entropy can be confirmed with the gamma distribution. The gamma distribution with κ=1 is equivalent to the Poisson distribution. As shown in Fig. 4, the difference of the shape parameter κ from 1 is considered to represent differences between the gamma distribution and the exponential distribution. Furthermore, the excess entropy E takes the minimum value E= 0 when κ=1 (Poisson process). This can be understood by considering discrete time Markov process:

$$p(x_L \mid \{x_{1\le i\le L-1}\}) = p(x_L \mid x_{L-1}). \qquad (12)$$

The excess entropy of this process is written as

$$E = \sum_{\{x_i\}} p(\vec{x}) \log \frac{p(x_L \mid x_{L-1})}{p(x_L)}. \qquad (13)$$

Since discrete-time Poisson process is a Bernoulli process, the excess entropy E takes zero for the gamma process with $\kappa = 1$. If κ moves away from 1, spike trains have time correlations and the excess entropy increases (Fig. 4).

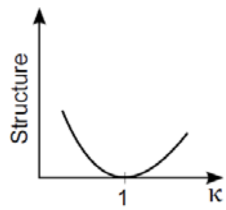

Fig. 4. Dependency of excess entropy on κ

Here, we apply information theoretic measures to spike trains generated from the gamma process. As in Fig. 5, spike train is discretized into bins and is analyzed as symbolic sequences of 0's and 1's.

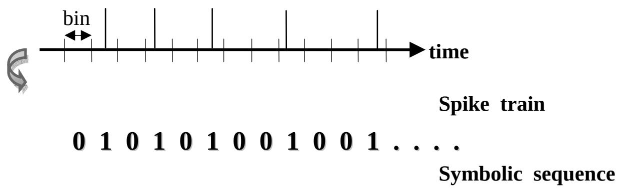

Fig. 5. Discretization of spike trains

For comparison with numerical estimation of excess entropy, we show information gain induced from Gamma distribution [7-8]. The information gain is Kullback-Leibler (KL) distance between gamma distribution and exponential distribution written as

$$\begin{aligned} G &= KL(f_g, f_e) \\ &= 1-\kappa-\log\Gamma(\kappa)+\log\kappa+(\kappa-1)\psi(\kappa)_{[bit/spike]} \\ &= \frac{\lambda}{\kappa}(1-\kappa-\log\Gamma(\kappa)+\log\kappa+(\kappa-1)\psi(\kappa)),_{[bit/time]} \end{aligned} \qquad (14)$$

where f_g is density function of gamma distribution and f_e is density function of exponential distribution. Note that we consider continuous distribution for easy calculation. This quantity also represents structural information stored in spike trains. The information gain G takes the minimum value (zero) at κ=1 (Fig. 6(a)) and this corresponds to characteristics of the excess entropy. The estimated excess entropy E is concave up around

$\kappa=1$ and has good agreement with characteristics of the information gain G. This corresponds to the above theoretical consideration and suggests that the excess entropy measures structural information (Fig. 6(b,c)).

Our method is applicable for analyses of practical neuronal data. In practical neuronal data, length of data is usually limited. As shown in section II, estimation of the entropy rate requires much long data; we hence consider estimation from experimentally practicable length of data. Figure 6(d) shows the result of estimation of the excess entropy with different length of data. As the data length gets shorter, the precision of estimation becomes worse, but its shape of curve is roughly preserved.

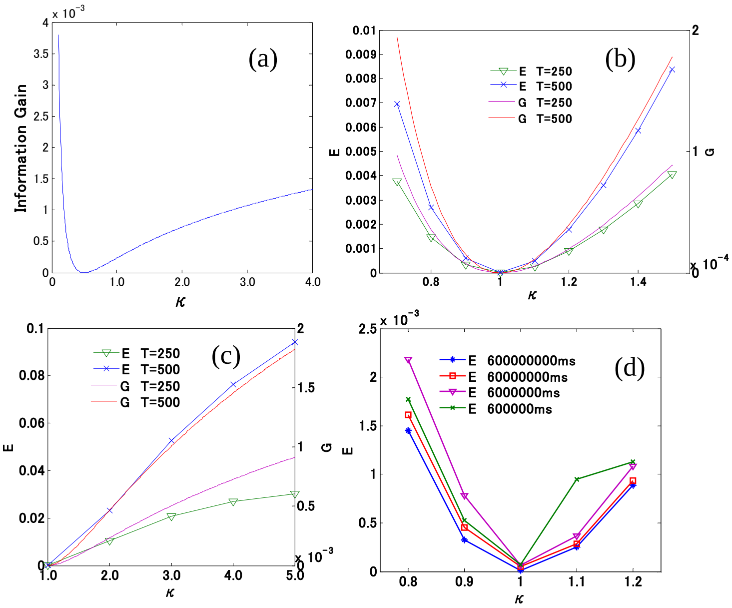

Fig.6 Estimation of the excess entropy of the gamma process and the corresponding information gain. (a) Information gain at $T=\kappa/\lambda=500$. (b,c) Result of estimation of excess entropy (Sample length: $6.0\times10^{8} ms$, bin size: $10 ms$) G are fit to the scale of E. (d) Result of estimation from finite length samples.

V. Conclusion

We showed that the excess entropy can be used as a measure for capturing spike trains' structure.

In practice, there seems to be problems since infinite length sample are theoretically needed for the estimation of the excess entropy. Considering convergence, excess entropy needs much long sample. However, numerical estimation shows that we can detect structural difference from short sample to some extent.

Theoretically, excess entropy is an effective measure for spike trains like Gamma process, since spike trains have correlation or structure inside. Spike trains have more than randomness. Excess entropy captures spike trains' structure.

Also, excess entropy is a measure similar to information gain. Excess entropy directly uses spike trains and preserves structure. On the other hand, the approach to spike trains by using information gain cannot detect structural elements beyond ISI distribution. Excess entropy can detect higher order structure above ISI distribution such as temporal coding. Thus, excess entropy can be expected to be an effective measure for spike trains.

References

[1] Feldman DP, McTague CS, and Crutchfield JP. (2008), The Organization of Intrinsic Computation: Complexity-Entropy Diagrams and the Diversity of Natural Information Processing. Chaos. Vol.18, No.4: 59-73.

[2] Grassberger P. (1986) Toward a quantitative theory of self-generated complexity. Int. J. Theor. Phys. 25:907-928.

[3] Bialek W, Nemenman I, Tishby N. (2001) Predictability, Complexity, and Learning. Neural Computation. Vol.13, No.11:2409-2463.

[4] Schürmann T and Grassberger P. (1996) Entropy Estimation of Symbol Sequences. Chaos. Vol.6, No.3:414-427.

[5] Fujiwara K and Suzuki H. (2009) Evaluation of Analysis Methods on Neural Spike Trains using Stochastic Models (in Japanese). SEISANKENKYU. Vol.61, No.2:122-124.

[6]Herzel H, Schmitt A and Ebeling W. (1994) Finite sample effects in sequence analysis. Chaos, Solitons, and Fractals. Vol.4:97-113.

[7] Daley DJ and Vere-Jones D. (2005). An introduction to the theory of point processes, Volume 2. Springer.

[8] Kostal L and Lansky P. (2006). Similarity of interspike interval distributions and information gain in a stationary neuronal firing. Biol. Cybern. Vol.94:157–167.

Synchronized brain activity changes related to perceptual alternations

Koji Iwayama[1,2], Kohske Takahashi[3,4], Katsumi Watanabe[2,3,5,6],
Yoshito Hirata[7], Kazuyuki Aihara[1,7], Hideyuki Suzuki[1,7]

[1]Graduate School of Information Science and Technology,
The University of Tokyo, Tokyo 113-8656, Japan
[2]Hokuriku Innovation Cluster for Health Science, Ishikawa 920-0981, Japan
[3]Research Center for Advanced Science and Technology,
University of Tokyo 153-8904, Japan
[4]JSPS Research Fellow, Japan
[5]Japan Science and Technology Agency, Japan
[6]Japan Advanced Institute of Science and Technology, Japan
[7]Institute of Industrial Science, The University of Tokyo, Tokyo 153-8505, Japan
(Tel : +81-3-5452-6693; Fax : +81-3-5452-6694)
(Email: koji@sat.t.u-tokyo.ac.jp)

Abstract: When we look at ambiguous figures, perception spontaneously changes from one to the other (perceptual alternation). We measured the brain activity from subjects who observed the Necker cube, one of the most famous ambiguous figures, using magnetoencephalography (MEG). To identify the brain activity inducing perceptual alternation, we propose a novel change-point detection method using spectral clustering to recurrence plots, and apply to measured data. Synchronized activity changes were detected at parietal channels.

Keywords:Perceptual Alternation, Magnetoencephalography, Recurrence Plot, Spectral Clustering

I Introduction

Ambiguous figures are figures which allow multiple perceptions. When we look at ambiguous figures, perception spontaneously changes from one to the other. This phenomena is called "perceptual alternation". Because consciousness alternates without any stimulus changes, perceptual alternations are thought to be related to perceptual consciousness.

When perceptual alternations occur, brain activity should change in some way. To detect changes of brain activity, we propose a novel change-point detection method that divides "recurrence plots", which visualize time series, by a graph partitioning method "spectral clustering" and apply it to signals measured by magnetoencephalography (MEG). Synchronized changes are detected by the proposed method in the parietal area.

II Experiment

Subjects observed the Necker cube (fig. 1) which is the famous ambiguous figure for 60sec, and pressed a button by the right hand when perception changed. We measured the brain activity using MEG with 160 channels. The sampling rate is 1000Hz.

Some MEG signals measured from parietal channels are shown in fig. 2. Our purpose is to detect changes of brain activities related to perceptual alternations from these signals.

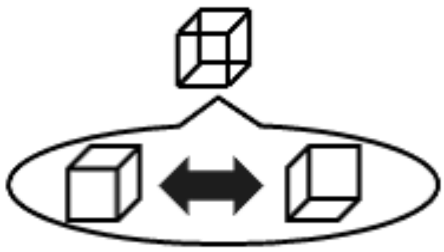

Figure 1: Necker cube (top) and its two perceptions (bottom).

III Method

1 Reconstruction of the state space

Generally, we cannot observe all of variables of dynamical systems. Therefore, it is necessary to reconstruct the state space of the system from observed time series. It is known that the delay coordinate,

$$\mathbf{x}(t) = (s(t), s(t+\tau), \ldots, s(t+(m-1)\tau)),$$

becomes an embedding of the attractor of the dynamical system with the dimension d when $m > 2d$[1]. Here τ is the delay and m is the embedding dimension.

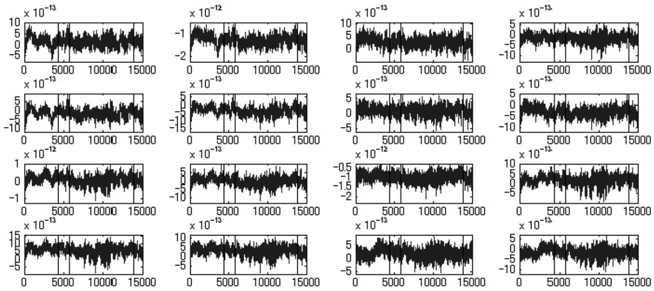

(a) Left parietal channels.

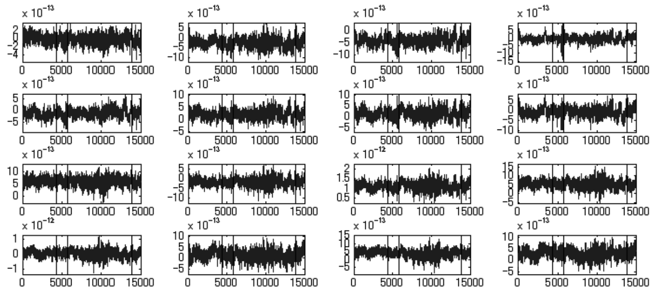

(b) Right parietal channels.

Figure 2: Measured signals from left parietal channels (a) and right parietal channels (b). The time when a subject pressed a button is indicated by black vertical lines. Horizontal axes represent time(ms).

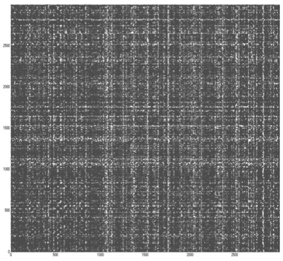

(a) White noise.

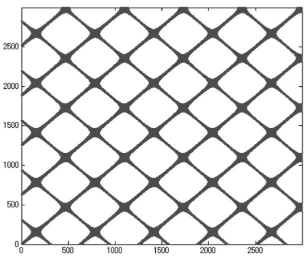

(b) Sine wave.

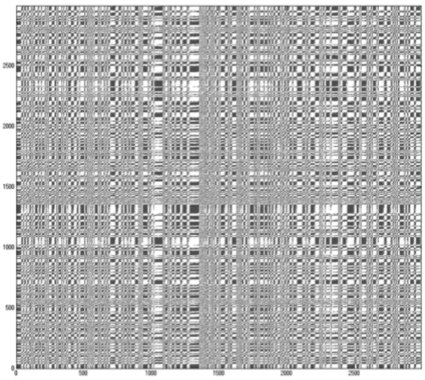

(c) Lorenz equation.

Figure 3: Examples of recurrence plots.

2 Recurrence plots

Recurrence plots[2] visualize time series as two dimensional plots whose horizontal and vertical axes correspond to time. The recurrence plot of a time series $\{s(t)\}$ is defined by using the delay coordinates as follows:

$$\mathbf{R}(r)_{i,j} = \begin{cases} 1, & (\|\mathbf{x}(i) - \mathbf{x}(j)\| \leq r), \\ 0, & (\|\mathbf{x}(i) - \mathbf{x}(j)\| > r), \end{cases} \tag{1}$$

where r is the threshold. Recurrence plots visualize various features of time series. Examples of recurrence plots are shown in fig. 3. Fig. 3(a) is the recurrence plot of white noise. In recurrence plots of stochastic data, points are distributed randomly. Recurrence plots of periodic data like a sine wave have lines parallel to the diagonal line (fig. 3(b)). Recurrence plots of chaotic data are complex but not random. Fig. 3(c) is the recurrence plot of the Lorenz equation.

3 Spectral clustering

Spectral clustering partitions a graph to disjoint sets that minimize a certain cost function. We used "normalized cut"[3] as the cost function. When we partition a graph $(\mathbf{V}, \mathbf{E})$ to subgraphs $(\mathbf{A}, \mathbf{E_a})$ and $(\mathbf{B}, \mathbf{E_b})$, a normalized cut is defined as follows:

$$\begin{aligned} NCut(\mathbf{A}, \mathbf{B}) &= \frac{\sum_{u \in \mathbf{A}, v \in \mathbf{B}} \mathbf{W}(u,v)}{\sum_{u \in \mathbf{A}, t \in \mathbf{V}} \mathbf{W}(u,t)} \\ &\quad + \frac{\sum_{u \in \mathbf{A}, v \in \mathbf{B}} \mathbf{W}(u,v)}{\sum_{u \in \mathbf{B}, t \in \mathbf{V}} \mathbf{W}(u,t)}, \end{aligned} \tag{2}$$

where $\mathbf{W}$ is the adjacency matrix whose element $\mathbf{W}(u,v)$ is the weight of the edge between the vertex u and v. Minimizing the normalized cut is equivalent to minimizing the Rayligh quotient:

$$\frac{\mathbf{y}^{\mathbf{T}}(\mathbf{D} - \mathbf{W})\mathbf{y}}{\mathbf{y}^{\mathbf{T}}\mathbf{D}\mathbf{y}},$$

$$\mathbf{y}_i = \begin{cases} 1, & (v_i \in \mathbf{A}), \\ 0, & (v_i \in \mathbf{B}). \end{cases}$$

If $\mathbf{y}$ is relaxed to one that takes real values, we can minimize the normalized cut by solving the eigenvalue system:

$$\mathbf{D}^{-\frac{1}{2}}(\mathbf{D} - \mathbf{W})\mathbf{D}^{-\frac{1}{2}}\mathbf{z} = \lambda \mathbf{z}, \tag{3}$$

where $\mathbf{D}$ is the diagonal matrix whose diagonal elements are degrees of vertices and $\mathbf{z} = \mathbf{D}^{1/2}\mathbf{y}$. Because the matrix $\mathbf{D}^{-1/2}(\mathbf{D} - \mathbf{W})\mathbf{D}^{-1/2}$ is the symmetric positive semidefinite matrix, the minimum eigenvalue is 0 and the corresponding eigenvector is the vector whose all elemtents are the same value. This corresponds to the trivial partition $\mathbf{A} = \mathbf{V}, \mathbf{B} = \phi$ or $\mathbf{A} = \phi, \mathbf{B} = \mathbf{V}$. Hence, when $\mathbf{z}_1$ is the eigenvector corresponding to the second smallest eigenvalue, $\mathbf{y} = \mathbf{D}^{-1/2}\mathbf{z}_1$ is the partition minimizing the normalized cut. If $\mathbf{y}_i > 0$, $v_i \in \mathbf{A}$, otherwise $v_i \in \mathbf{B}$.

4 Proposed method

We regard recurrence plots $\mathbf{R}$ as adjacency matrices $\mathbf{W}$, and apply spectral clustering. If t and $t+1$ are included in different subgraphs, we detect the time t as the change-point. Because the order of rows and columns of the adjacency matrix is meaningless, permutation of those have no effect to the result of spectral clustering. However, rows and columns in the recurrence plot are in the temporal order, and hence rows and columns cannot be permutated. Therefore, application of spectral clustering to recurrence plots discards the temporal information. To avoid this problem, we generate a new matrix by adding edges between vertices i and j when time i and j are sufficiently close.

$$\hat{\mathbf{R}}_{i,j} = \begin{cases} 1, & |i-j| \le n, \\ \mathbf{R}_{i,j}, & |i-j| > n. \end{cases} \tag{4}$$

We apply spectral clustering to this matrix. This matrix was used in the study of reconstructing time series from recurrence plots[4].

IV Result

We analyzed signals measured from 64 channels located at left parietal, right parietal, left occipital, and right occipital areas. To avoid artifacts, we extracted 8 components from 16 signals measured from each area by blind source separation using ICALAB toolbox[5][6]. We applied the proposed method to the extracted components. We used embedding dimension $m = 25$, delay $\tau = 1$, and $n = 70$. Thresholds of recurrence plots were determined to fix recurrence rate (probability that we find a point in a recurrence plot) to be 0.0015. Eigenvectors obtained by the spectral clustering to matrices $\hat{\mathbf{R}}$ are shown in fig. 4.

For example, positive (negative) components in the eigenvectors can be interpreted as corresponding to one perception, and absolute values of the components can be interpreted as strengths of perception (fig. 5). Then, eigenvectors are considered as a sequence of perceptual states.

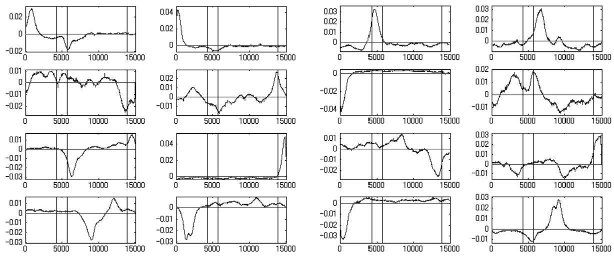

(a) Left parietal area (b) Right parietal ares

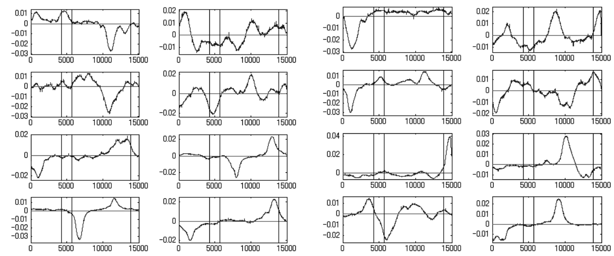

(c) Left occipital area (d) Right occipital area

Figure 4: Eigenvectors obtained by spectral clustering. The time when a subject pressed a button is indicated by black vertical lines. Horizontal axes represent time(ms).

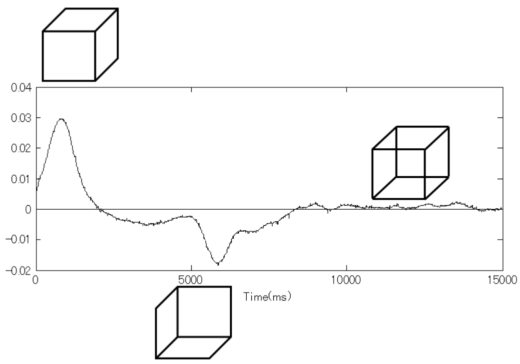

Figure 5: The eigenvector and percptual state.

To investigate synchronaization of changes of brain activities when perceptual alternations occur, we calculated cross-correlation functions of these eigenvectors. The peaks of absolute value represents degree of synchronization and the delay of peaks represents the delay of changes of brain activity. Peaks of absolute value and delay are shwon in fig. 6. In the left and right parietal areas, changes of many components are highly correlated (fig. 6(a)). These results imply that changes of brain activities in these area are synchronized. Moreover, right parietal changes procede left parietal changes(fig. 6(b)).

V Conclusion

We proposed the novel change-point detection method in which spectral clustering is applied to recurrence plots. We applied the proposed method to signals measured by MEG from subjects observing the Necker cube. Changes of brain activities related to perceptual alternations are detected by the proposed method. Cross-correlation functions of eigenvectors obtained by the proposed method indicate that brain activities were highly correlated in parietal area, and the right parietal activity precedes the left parietal acitivity. These results imply that changes of brain activities in the parietal area are related to perceptual alternations and the right parietal activities change earlier than the left parietal acitivities when perceptual alternations occur.

Acknowledgements

This work was partially supported by Hokuriku Innovation Cluster for Health Science. The researches of Y.H. and H.S. were also partially supported by A Grant in Aid No. 21700249 and No. 18686011, respectively, from the Japanese Ministry of Education, Culture, Sports, Science and Technology. K.W. was supported by Japan Science and Technology Agency.

References

[1] F. Takens (1981), "Detecting strange attractors in turbulence", in: Dynamical Systems and Turbulence, Lecture Notes in Mathematics, Vol. 898, pp. 366-381.

[2] J.-P. Eckmann, S. O. Kamphorst, and D. Ruelle (1987), "Recurrence plots of dynamical systems", Europhys. Lett., Vol. 4, No. 9, pp. 973-977.

[3] J. Shi and J. Malik (2000), "Normalized cuts and image segmentation", IEEE Trans. Pattern Analysis and Machine Intelligence, Vol. 22, No. 8, pp. 888-905.

[4] M. Tanio, Y. Hirata, and H. Suzuki (2009), "Reconstruction of driving forces through recurrence plots", Phys. Lett. A, Vol. 373, pp. 2031-2040.

[5] A. Cichocki, S. Amari, K. Siwek, et al., "ICALAB Toolboxes", http://www.bsp.brain.riken.jp/ICALAB.

[6] A. Cichocki and S. Amari (2003), "Adaptive Blind Signal and Image Processing: Learning Algorithms and Applications", Wiley.

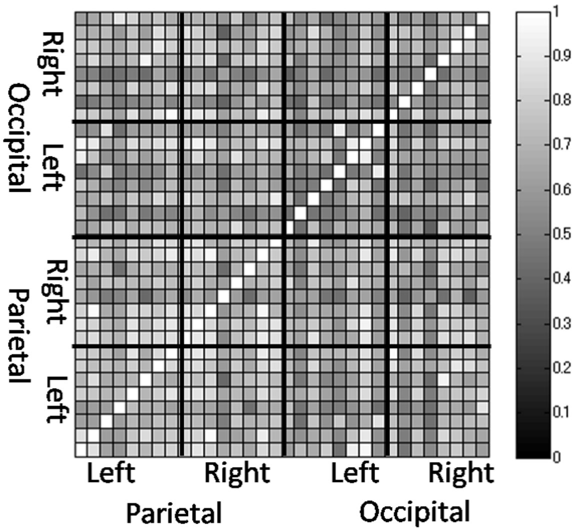

(a) Peaks of absolute values of cross-correlation functions

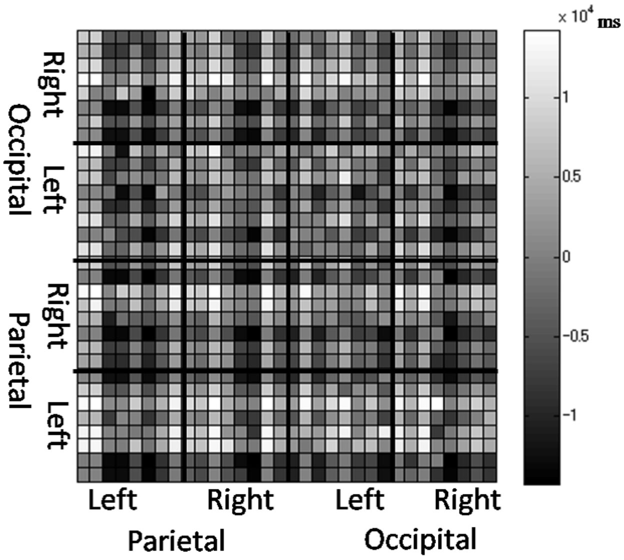

(b) Delay of cross-correlation functions

Figure 6: Peaks of absolute values and delay of cross-correlated functions calculated from eigenvectors obtained by spectral clustering.

Structural Change Point Detection by Sequential Probability Ratio Test and Chow Test

*Tetsuo Hattori, *Katsunori Takeda, **Izumi Tetsuya, ***Hiromichi Kawano

**Graduate School of Engineering, Kagawa University / 2217-20 Hayashi, Takamatsu City, Kagawa 761-0396, Japan*
***Micro Technica Co., Ltd., / Yamagami BLD. 3-12-2 Higashi-ikebukuro, Toshima-ku, Tokyo 170-0013, Japan*
**** NTT Advanced Technology s, / Musashino-shi Nakamachi 19-18, Tokyo 180-0006, Japan*
(Tel : 81-87-864-2221; Fax : 81-87-864-2262)
(hattori@eng.kagawa-u.ac.jp)

Abstract: Time series analysis is used in various fields. The problem of predicting time series can be classified into three. The first problem is how to make a prediction model, that adequately represents the characteristics of the past time series data. The second problem is how to correctly and promptly detect the structural change, when the estimated prediction model does not meet the data. The third problem is how to quickly find the new prediction model after the change. This paper focuses on the second problem and proposes a method based on a probability ratio test. This paper also shows some experimental results comparing with a conventional method, Chow test, and presents the effectiveness.

Keywords: Time series analysis, sequential probability ratio test (SPRT), Chow Test

I. INTRODUCTION

Time series analysis is used in various fields such as not only in economics but also in pattern recognition, where the analysis is used for contour (or shape) analysis and sound signal processing, etc.

The problem of time series can be classified into three types, in a practical sense. The first problem is how to generate a prediction model that adequately represents the characteristics of the early time series data. For this purpose, various kinds of model such as Box-Jenkins method [1], and Kalman Filter [2], neuro network [3], fuzzy model [4], Chaos model [5] have been proposed. Also, model selection criteria have been proposed such as AIC [6], Cp [7], CV [8] and CMV [9]. The second problem is how to detect the structural change of the time series, as soon and correctly as possible, when the estimated prediction model does not meet the real data. The third problem is, after the change detection, how to quickly estimate the time series model again.

This paper focuses on the second problem and proposes a novel method, that is based on a sequential probability ratio test (SPRT)[10], [11], for quick detection of the structural change point in time series. And, this paper also describes the features of the method from numerical experimentation results and also shows its effectiveness in comparison with the Chow Test [12].

II. Structural change point detection

For the early structural change detection problem, we propose an application of Sequential Probability Ratio Test (SPRT) that has been mainly used in the field of quality control.

1. SPRT

The SPRT is used for testing a null hypothesis H_0 (e.g. the quality is under pre-specified limit 1%) against hypothesis H_1 (e.g. the quality is over pre-specified limit 1%). And it is defined as follows:

At each stage of successive events $Z_1, Z_2, \cdots Z_i$ that are respectively corresponding to observed time series data, the probability ratio λ_i is computed.

$$\lambda_i = \frac{P(Z_1 \mid \mathbf{H}_1) \cdot P(Z_2 \mid \mathbf{H}_1) \cdots P(Z_i \mid \mathbf{H}_1)}{P(Z_1 \mid \mathbf{H}_0) \cdot P(Z_2 \mid \mathbf{H}_0) \cdots P(Z_i \mid \mathbf{H}_0)} \quad (1)$$

where $P(Z \mid H_0)$ denotes the distribution of Z when H_0 is true and $P(Z \mid H_1)$ denotes the distribution of Z when H_1 is true.

Two positive constants C_1 and C_2 ($C_1 < C_2$) are chosen. If $C_1 < \lambda_i < C_2$, the experiment is continued by taking an additional observation. If $C_2 < \lambda_i$, the process is terminated with the rejection of H_0 (acceptance of H_1). If $\lambda_i < C_1$, the process is terminated with the acceptance of H_0.

$$C_1 = \frac{\beta}{1-\alpha} \quad C_2 = \frac{1-\beta}{\alpha} \tag{2}$$

where α means type I error (reject a true null hypothesis), and β means type II error (accept a null hypothesis as true one when it is actually false).

2. Application to change point detection

For simplicity, we describe our proposed method for structural change detection of time series, by taking an example. We assume that the time series is generated in the following equation as a function of time t.

$$y_t = \beta_1 \cdot t + \beta_0 + \varepsilon \tag{3}$$

where $\varepsilon \approx N(0,\sigma^2)$, i.e., the error ε is a random variable subject to the Normal Distribution with the average 0 and the variation σ^2.

Then we also assume that the structural change occurred at the time point tc* (what we call change point), involving the change of equation coefficients β_1, β_0. Concretely speaking, such data is generated by the following equations.

$$y_t = \beta_{11} \cdot t + \beta_{10} + \varepsilon \quad (t \le tc^*) \tag{4}$$

$$y_t = \beta_{21} \cdot t + \beta_{20} + \varepsilon \quad (tc \le t^*) \tag{5}$$

where tc* is called a change point in the structural change.

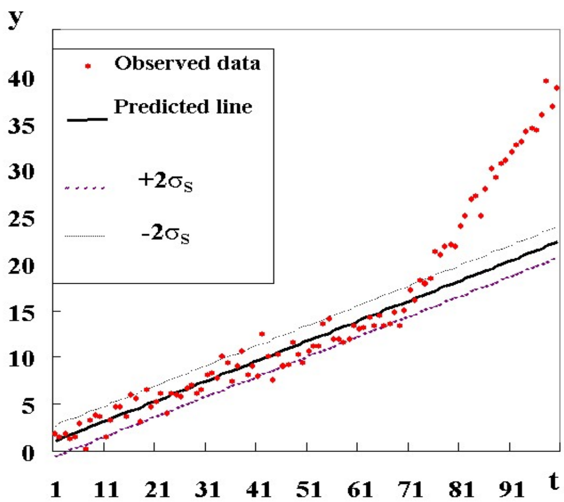

Fig.1. Example of time series data where the change point tc* =70.

In Fig.1, a time series data based on the above Equations (4) and (5) is plotted, where $\beta_{11} = 0.2$, $\beta_{10} = 1.0$, $\beta_{21} = 0.8$, $\beta_{20} = -41.0$, and tc* =70, $\varepsilon \approx N(0,1)$. Moreover, σ_S means the standard deviation of error between early-observed data $\{y_t \mid 1 \le t \le 40\}$ and the predicted line obtained from the early data.

The concrete procedure of structural change detection is as follows:

Step1: Make a prediction expression and set the tolerance band (***a***) (e.g. ***a***=**2**σ_S) that means permissible error margin between the predicted data and the observed one.

Step2 : Set up the null hypothesis H_0 and alternative hypothesis H_1.

H_0: Change has not occurred yet.

H_1: Change has occurred.

Set the values α, β and compute C_1 and C_2, according to Equation (2). Initialize i = 0, $\lambda_0 = 1$.

Remark:

The statement of the null hypothesis H_0, "Change has not occurred yet.", means in statistical sense. It means that the generation probability for the data to go out from the tolerance band is less than (or equal to) θ_0 (for instance, 1%). Similarly, the statement of the alternative hypothesis H_1, "Change has occurred." means that the generation probability for the data to go out from the tolerance band is greater than (or equal to) θ_1 (for instance, 99%). Additionally, we suppose that θ_1 is considerably greater than θ_0.

Step3: Incrementing i (i = i+1), observe the following data y_i. Evaluate the error $|\varepsilon_i|$ between the data y_i and the predicted value from the aforementioned prediction expression.

Step4: Judge as to whether the data y_i goes in the tolerance band or not, i.e., the ε_i is less than (or equal to) the permissible error margin or not. If it is Yes, then set $\lambda_i = 1$ and return to Step3. Otherwise, advance to Step5.

Step5: Calculate the probability ratio λ_i, using the following Equation (6) that is equivalent to Equation (1)

$$\lambda_i = \lambda_{i-1} \frac{P(\varepsilon_i \mid \mathbf{H}_1)}{P(\varepsilon_i \mid \mathbf{H}_0)} \tag{6}$$

where, if the data y_i goes in the tolerance band, $P(\varepsilon_i |H_0) = \theta_0$ and $P(\varepsilon_i |H_1) = \theta_1$, otherwise, $P(\varepsilon_i |H_0) = (1-\theta_0)$ and $P(\varepsilon_i |H_1) = (1-\theta_1)$.

Step6: Execution of testing.

(i) If the ratio λ_i is greater than C_2 (= $(1-\beta)/\alpha$), dismiss the null hypothesis H_0, and adopt the alternative hypothesis H_1, and then End.

(ii) Otherwise, if the ratio λ_i is less than C_1 (= $\beta/(1-\alpha)$), adopt the null hypothesis H_0, and dismiss the alternative hypothesis H_1, and then set $\lambda_i = 1$ and return to Step3.

(iii) Otherwise (in the case where $C_1 \le \lambda_i \le C_2$), advance to Step7.

Step7: Observe the following data y_i incrementing i. Evaluate the error $|\ \varepsilon_i\ |$ and judge whether the data y_i goes in the tolerance band, or not. Then, return to Step5 (calculation of the ratio λ_i).

III. Experimentation in comparison with Chow Test

We have experimented with the proposed method for both artificial and real time series data, in comparison with the well-known Chow Test [12]. Those artificial time series data are generated based on aforementioned Equations (4) and (5). In this section, we show the experimental results.

1. Chow Test

The well known Chow Test checks the significant differences among residuals for three Regression Lines, where regression Line 1 obtained from the data before a change point tc, Line 2 from the data after tc, and Line 3 from the whole data so far, by setting up hypothesis of change point at each point in the whole data. Fig.2 shows the conceptual image of Chow Test.

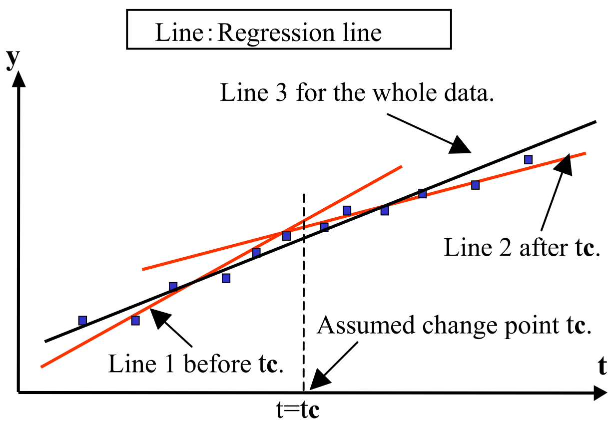

Fig.2. Chow Test in the situation where a hypothesis is set up that the structural change has occurred at t=tc.

2. Experimentation

The experimental results from artificially generated time series data are illustrated in Fig.3-6, where the standard deviation σ of error ε and so on in the generated data are varied and horizontal axis shows observing time t (detection operation has started from t=41). The vertical axis shows the detected change point tc, whose value is the average of experimentation results for 100 sets of generated time series data where the true change point is tc*=70. Fig.3-6 show that Chow Test outputs the change point at the time when every data is observed after t=40. This means that Chow Test cannot detect the change point properly. And, the time point when Chow Test can work well is long late enough after the true change occurs.

On the other hand, the proposed method detects the change points a, b, c, where each of them correspond to different parameter values of θ_0, θ_1 that are used in the SPRT as **a**:(θ_0=0.1, θ_1=0.9), **b**:(θ_0=0.2, θ_1=0.8), and **c**:(θ_0=0.3, θ_1=0.7).

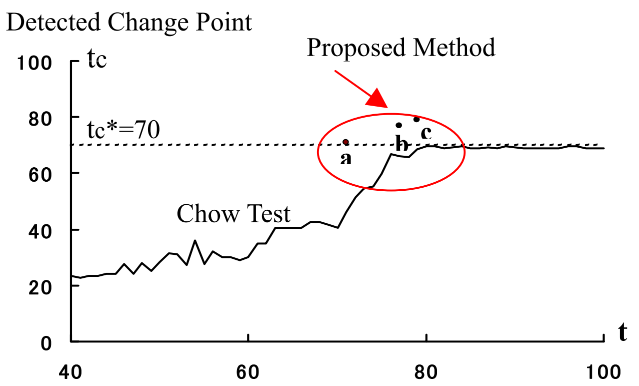

Fig.3. Relation between the observing time and detected change point. (β_{11}=0.2, β_{21}=0.4, σ=0.5. Detection operat ion starts at t=41.)

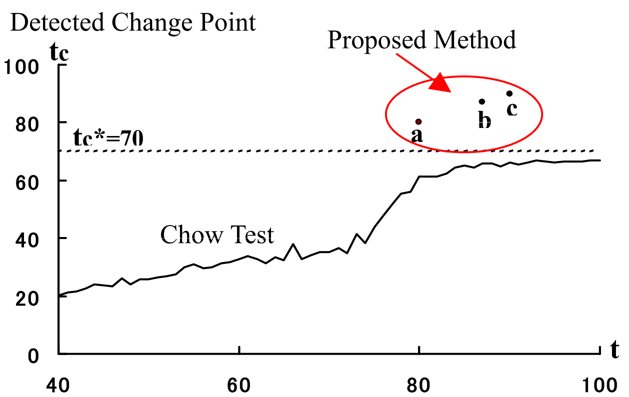

Fig.4. Relation between the observing time t and detecte d change point tc. (β_{11}=0.2, β_{21}=0.4, σ=1.0. Detection operation starts at t=41.)

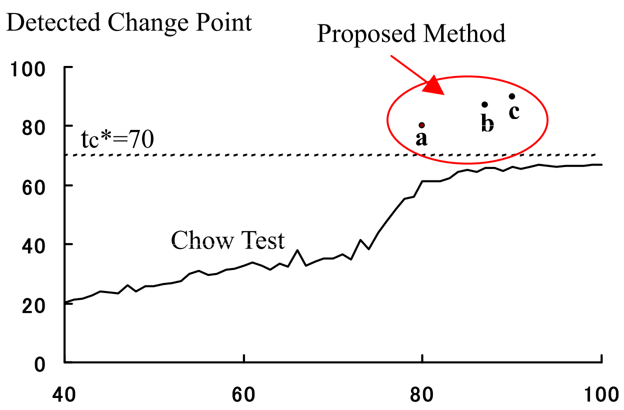

Fig.5. Relation between the observing time and detected change point. (β_{11}=0.2, β_{21}=0.4, σ=1.5. Detection operation starts at t=41.)

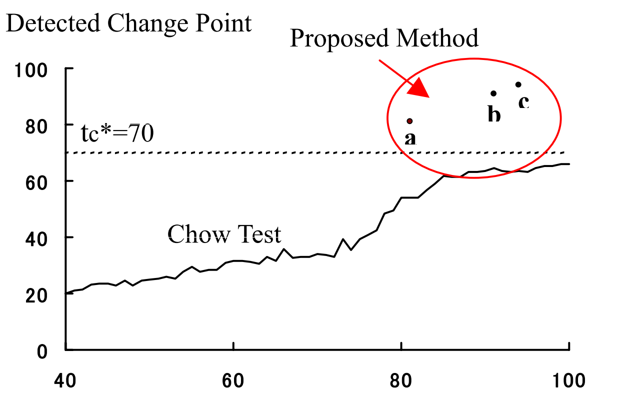

Fig.6. Relation between the observing time and detected change point. (β_{11}=0.2, β_{21}=0.3, σ=1.5. Detection operation starts at t=41.)

IV. CONCLUSION

We have proposed a sequential probability ratio test for structural change point detection of time series data. We have presented the algorithm and procedure how to apply a probability ratio test to change detection problem. Based on numerical experimentation results, we have found the effectiveness of SPRT in comparison with Chow Test, as follows:

It can quickly and accurately detect the structural change point when a forecasting model cannot forecast the time series.

It can detect correctly the structural change point even when the trend in time series changes little (Chow test can not detect the change point when the trend changes little).

Moreover the SPRT is effective in the sense as follows. (1)Differently from the Chow Test, it does not need to set the change point in a priori. (2)Unlike the Bay's method, it does not need to give the distribution of time series data. (3) It can early detect the structural change point by sequential processing. (4) It is a meta-level method so that we can apply it to any prediction model.

REFERENCES

[1]C.G.E.P.Box and G.M.Jenkins (1976), Time Series Analysis: Forecasting and Control, Prentice Hall.
[2] Peter J. Brockwell, Richard A. Davis (2003), Introduction to Time Series and Forecasting, Springer; 2nd edition.
[3] Robert J. Jannarone (1997), Concurrent Learning and Information Processing: A Neuro-Computing System That Learns During Monitoring, Forecasting, and Control, Kluwer Academic Pub.
[4] George Bojadziev, Maria Bojadziev (2007), Fuzzy Logic for Business, Finance, and Management (Advances in Fuzzy Systems -Applications and Theory), World Scientific Pub Co. Inc..
[5] H. Tong (1995), Chaos and Forecasting (Nonlinear Time Series and Chaos, Vol 2), World Scientific Pub Co. Inc..
[6]Akaike,H.(1973), Information theory and an extension of the maximum likehood principle, Proc. 2nd International Symposium on Information Theory, Akademia Kiado, budapest, pp.269-281.
[7]Mallows, C.L. (1973), Some remarks of Cp, Technometrics, Vol.15, No.4, pp.661-675.
[8] Allen,D.M. (1971), Mean squqre error of prediction as a criterion of selecting variables, Technometrics, Vol.13, pp.469-475.
[9] Hjorth,U. (1982), Model selection and forward validation, J. Statist., Vol.9, pp.95-105.
[10] A. Wald (1947), Sequential Analysis, John Wiley & Sons.
[11]Hiromichi Kawano, Tetsuo Hattori, Ken Nishimatsu (2008), Structural Change Point Detection Method of Time Series Using Sequential Probability Ratio Test－Comparison with Chow Test in the ability of early detection－(in Japanese), IEEJ Trans. EIS, Vol.128, No.4, pp.583-592.
[12] Chow,G.C. (1960), Tests of Equality Between Sets of Coefficients in Two Linear Regressions, Econometrica, Vol.28, No.3.

Extended SPRT for Structural Change Detection of Time Series Based on Multiple Regression Model

*Katsunori Takeda, *Tetsuo Hattori, **Izumi Tetsuya, ***Hiromichi Kawano

**Graduate School of Engineering, Kagawa University / 2217-20 Hayashi, Takamatsu City, Kagawa 761-0396, Japan*
***Micro Technica Co., Ltd., / Yamagami BLD. 3-12-2 Higashi-ikebukuro, Toshima-ku, Tokyo 170-0013, Japan*
**** NTT Advanced Technology s, / Musashino-shi Nakamachi 19-18, Tokyo 180-0006, Japan*
(Tel : 81-87-864-2221; Fax : 81-87-864-2262)
(hattori@eng.kagawa-u.ac.jp)

***Abstract*:** It is important to quickly detect the structural change of time series as a trigger to remodel the forecasting model. The well-known Chow Test has been used as a standard method for the change detection, especially in economics. On the other hand, we have proposed the application of sequential probability ratio test (SPRT) for the change detection of single regression modeled time series data. In this paper, we show experimental results by SPRT and Chow Test when applying to time series data that are based on multiple regression models. And we clarify the effectiveness of the SPRT comparing with the Chow Test, in the sense of ability of early and correct change detection and computational complexity. Moreover, we extend the definition of the detected structural change point in the SPRT method, and show the improvement of the change detection accuracy.

***Keywords*:** Time series analysis, multiple linear regression, sequential probability ratio test (SPRT), Chow Test

I. INTRODUCTION

There are three types of problems in time series analysis([1],[2]): (i)The first is how to generate a prediction model that adequately represents the characteristics of the early time series data. (ii)The second is how to detect the structural change of the time series, as immediately and correctly as possible, when the estimated prediction model does not meet the real data ([3],[4]), (iii)The third is, after the change detection, how to quickly estimate the time series model again.

For the second problem, we have proposed an application of a sequential probability ratio test (SPRT) ([5],[6])that has been mainly used in the field of quality control, and have presented the experimental results in comparison with Chow Test that is well-known standard method for such structural change detection of time series data [7].

Our experimentation has been done just by using single regression model [6] and has shown that the SPRT is more effective than Chow Test. However, multiple regression models are more generally used for time series data analysis than single regression one.

In this paper, we examine by experimentation if the SPRT surpasses Chow Test as well in the change detection of multiple regression model based data. And also, we show the extended SPRT for more accurate estimation of the change point.

II. SPRT AND CHOW TEST

1. SPRT

The sequential probability ratio test (SPRT) is used for testing a null hypothesis H_0 (e.g. the quality is under pre-specified limit 1%) against hypothesis H_1 (e.g. the quality is over pre-specified limit 1%). And it is defined as follows:

Let $Z_1, Z_2, \cdots Z_i$ be respectively observed time series data at each stage of successive events, the probability ratio λ_i is computed as follows.

$$\lambda_i = \frac{P(Z_1 \mid \mathbf{H}_1) \cdot P(Z_2 \mid \mathbf{H}_1) \cdots P(Z_i \mid \mathbf{H}_1)}{P(Z_1 \mid \mathbf{H}_0) \cdot P(Z_2 \mid \mathbf{H}_0) \cdots P(Z_i \mid \mathbf{H}_0)} \quad (1)$$

where $P(Z \mid H_0)$ denotes the distribution of Z if H_0 is true, and similarly, $P(Z \mid H_1)$ denotes the distribution of Z if H_1 is true.

Two positive constants C_1 and C_2 ($C_1 < C_2$) are chosen. If $C_1 < \lambda_i < C_2$, the experiment is continued by taking an additional observation. If $C_2 < \lambda_i$, the process is terminated with the rejection of H_0 (acceptance of H_1). If $\lambda_i < C_1$, then terminate this process with the acceptance of H_0.

$$C_1 = \frac{\beta}{1-\alpha}, \quad C_2 = \frac{1-\beta}{\alpha} \quad (2)$$

where α means type I error (reject a true null hypothesi s), and β means type II error (accept a null hypothesis as true one when it is actually false).

2. Procedure of SPRT

The concrete procedure of structural change detection is as follows (see Fig. 1):

Step1: Make a prediction expression and set the tolerance band (***a***) (e.g. $\boldsymbol{a}=2\sigma_S$) that means permissible error margin between the predicted data and the observed one. (σ_S denotes a standard deviation in learning sample data at early stage.)

Step2 : Set up the null hypothesis H_0 and alternative hypothesis H_1.

H_0 : Change has not occurred yet.

H_1 : Change has occurred.

Set the values α, β and compute C_1 and C_2, according to Equation (2). Initialize i = 0, $\lambda_0 = 1$.

Step3: Incrementing i (i = i+1), observe the following data y_i. Evaluate the error $|\varepsilon_i|$ between the data y_i and the predicted value from the aforementioned prediction expression.

Step4: Judge as to whether the data y_i goes in the tolerance band or not, i.e., the ε_i is less than (or equal to) the permissible error margin or not. If it is Yes, then set $\lambda_i = 1$ and return to Step3. Otherwise, advance to Step5.

Step5: Calculate the probability ratio λ_i, using the following Equation (3) that is equivalent to Equation (1).

$$\lambda_i = \lambda_{i-1} \frac{P(\varepsilon_i \mid \mathbf{H}_1)}{P(\varepsilon_i \mid \mathbf{H}_0)} \qquad (3)$$

where, if the data y_i goes in the tolerance band, $(P(\varepsilon_i|H_0), P(\varepsilon_i|H_1)) = (\theta_0, \theta_1)$, otherwise, $(P(\varepsilon_i|H_0), P(\varepsilon_i|H_1)) = ((1-\theta_0), (1-\theta_1))$.

Step6: Execution of testing.

(i) If the ratio λ_i is greater than C_2 (= $(1-\beta)/\alpha$), dismiss the null hypothesis H_0, and adopt the alternative hypothesis H_1, and then End.

(ii) Otherwise, if the ratio λ_i is less than C_1 (= $\beta/(1-\alpha)$), adopt the null hypothesis H_0, and dismiss the alternative hypothesis H_1, and then set $\lambda_i = 1$ and return to Step3.

(iii) Otherwise (in the case where $C_1 \le \lambda_i \le C_2$), advance to Step7.

Step7: Observe the following data y_i incrementing i. Evaluate the error $|\varepsilon_i|$ and judge whether the data y_i goes in the tolerance band, or not. Then, return to Step5 (calculation of the ratio λ_i).

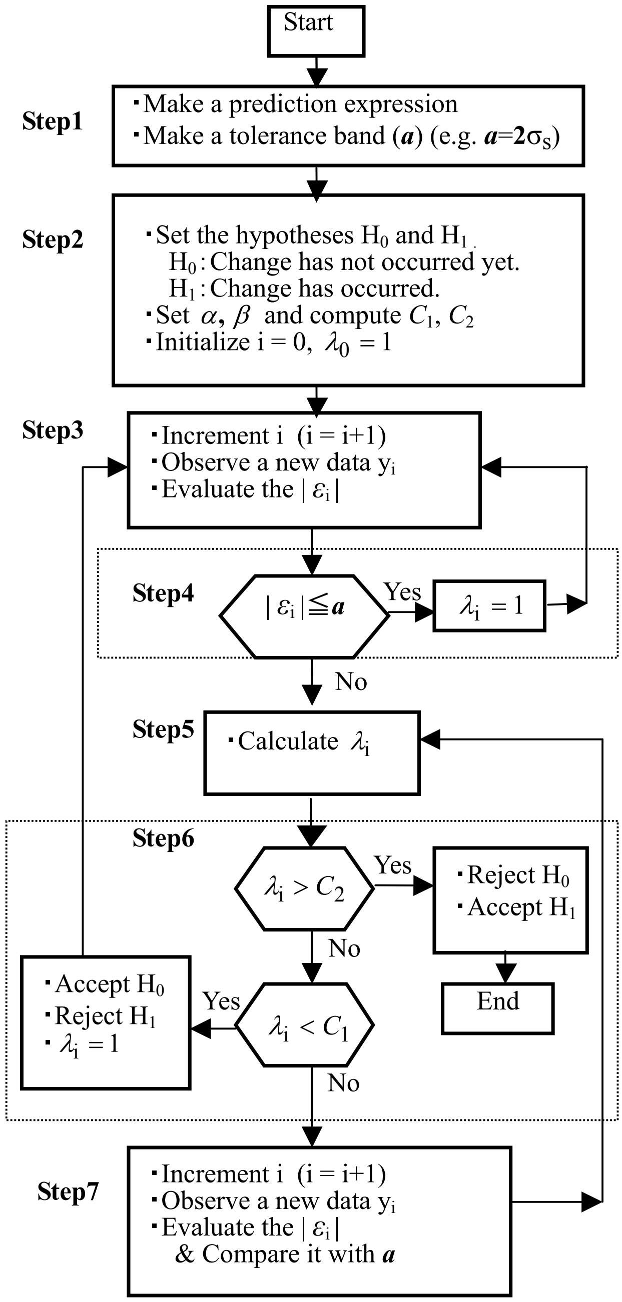

Fig.1. Flow of SPRT structural change point detection.

3. Chow Test

The well known Chow Test checks if there are significant differences or not, among residuals for three Regression Lines, where regression Line 1 obtained from the data before a change point tc, Line 2 from the data after tc, and Line 3 from the whole data so far, by setting up hypothesis of change point at each point in the whole data. Fig.2 shows the conceptual image of Chow Test.

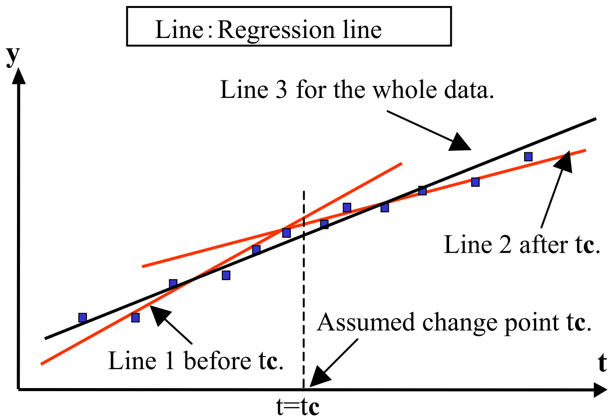

Fig.2. Chow Test in the situation where a hypothesis is set up that the structural change has occurred at t=tc.

III. EXPERIMENTATION

In our experimentation for time series data based on multiple linear regression model, the data is generated by the following equations.

$$y = a_{11}x_1 + a_{12}x_2 + b + \varepsilon \qquad (t \le t_c^*) \qquad (4)$$

$$y = a_{21}x_1 + a_{22}x_2 + b + \varepsilon \qquad (t_c^* \le t) \qquad (5)$$

where ε~N(0,σ^2), i.e., the error ε is subject to the Normal Distribution with the average 0 and the variation σ^2, and tc* means the change point. In addition, we have set tc*=70.

We have experimented with SPRT and Chow Test for the artificial data based on the above equations (4) and (5). The concrete values of parameters are shown in Table 1. Fig.3 shows an example of the graph of generated time series data by the above equations. Fig.4 shows the situation of change point detections.

The one of the results is illustrated in Fig.5, where horizontal axis shows observing time t (detection operation has started from t=41). The vertical axis shows the detected change point tc, whose value is the average of experimentation results for 200 sets of generated time series data where the real change point tc*=70.

From Fig.5, we can see that Chow Test outputs the change point at the time when every data is observed after t=40. This means that Chow Test cannot detect the change point properly. And, the time point when Chow Test can work well is long late enough after the real change occurs.

On the other hand, the SPRT detects the change as points cases **a**, **b**, **c**, each corresponding to different parameter values of $\boldsymbol{\theta_0}$, $\boldsymbol{\theta_1}$ that are used in the SPRT.

Table 1. Parameters for generating time series data.

Equation (4) (time t=1,2,…,69)	Equation (5) (time t=70,71,…,100)	σ
$y = 2x_1 + 3x_2 + 10$	$y = 3x_1 + 3x_2 + 10$	5

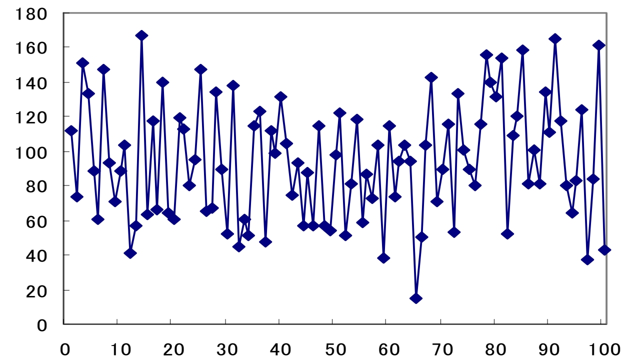

Fig.3. An example of time series data based on multiple linear regression model. Change is occurred at tc=70.

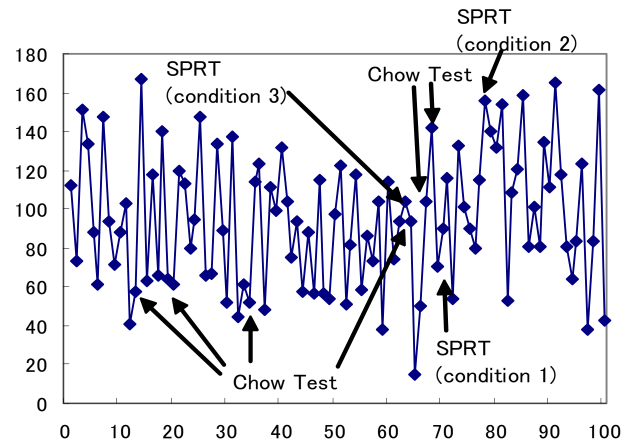

Fig.4. Example of situation of change point detections by SPRT and Chow Test, where tc*=70, and detection operation has started from t=41.

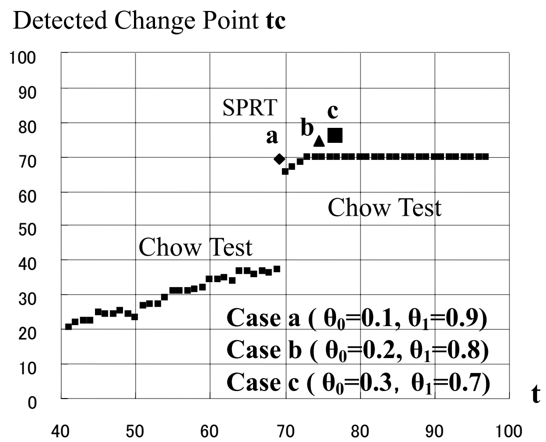

Fig.5. Relation between the observing time t and detected change point tc, where tc*=70, and detection operation has started from t=41.

IV. EXTENDED CHANGE POINT BY SPRT

The SPRT detects a change point at the time when the probabilistic ratio λ_i is greater than C_2 (=(1-β)/α). Then, the detected change point equals to the terminated time point and its detection tends to be delayed from true change point. Thus in this section, we extend the definition of detected change point by SPRT. As such extension, we adopt the number tc-***M*** where tc is ordinary aforementioned change point and ***M*** is the number of times when the observed data continuously goes of tolerance zone until the ratio $\lambda_i > C_2$ The number ***M*** can be obtained from the equation (6).

$$\left(\frac{\theta_1}{\theta_0}\right)^M > C_2 \left(= \frac{1-\beta}{\alpha}\right) \tag{6}$$

Then we have the following equation using Gauss notation. So, the value of ***M*** depends on the parameters (see Table 2). That is, ***M***=2 (case **a),** ***M***=3 (case **b),** ***M***=4 (case **c).**

$$M = \left\lceil \log_{\frac{\theta_1}{\theta_0}} \frac{1-\beta}{\alpha} \right\rceil \tag{7}$$

Table 2. Parameter values in SPRT and ***M***.

α	β	θ_0	θ_1	M
0.05	0.05	0.1	0.9	2
		0.2	0.8	3
		0.3	0.7	4

Applying the extended definition, we obtain the improvement of hitting percentage in the sense that the detected change point justly equals the true change point. It means pinpoint hitting percentage. Table 3 shows the resultant percentage when using the old definition of detected change point. On the other hand, Table 4 shows the resultant one when using extended definition.

Table 3. Frequency of change point detection and percentage of true change point (TCP) detection.

Case	Time Series Point					Percentage of TCP detection
	70	71	72	73	74	
a	7	141	4	12	1	0.35%
b	1	7	105	5	12	0.05%
c	1	1	5	98	2	0.05%

Table 4. Detected change point frequency and percentage of true change point (TCP) detection.

Case	Time Series Point					Percentage of TCP detection
	70	71	72	73	74	
a	7	141	4	12	1	74.90%
b	1	7	105	5	12	56.50%
c	1	1	5	98	2	50.10%

From those experimental results, we can understand that, if we adopt the interval [tc-***M***, tc] as existing range of true change point, the hitting percentage will considerably increase.

V. CONCLUSION

We have presented and evaluated the experimental results of the structural change detection by SPRT and Chow Test for ongoing time series data that is based on multiple linear regression model. From the results, we consider that SPRT will be more effective in the sense of early detection, accuracy, and computational cost. And also, we are sure that the extended definition of the detected change point is promising and that it would bring about more accurate detection.

REFERENCES

[1] C.G.E.P.Box and G.M.Jenkins (1976), Time Series Analysis:Forecasting and Control, Prentice Hall.
[2] Peter J. Brockwell and Richard A. Davis (2003), Introduction to Time Series and Forecasting, Springer; 2nd edition.
[3]C.Han, P.k.Willet and D.A.Abraham (1999), Some methods to evaluate the performance of Page's test as used to detect transient signals, IEEE Trans. Signal processing, Vol.47, No.8, pp.2112-2127.
[4] S.D.Blostein (1991), Quickest detection of a time-varying change in distribution, IEEE Trans. Information Theory, Vol.37, No.4, pp.1116-1122.
[5] A. Wald (1947), Sequential Analysis, John Wiley & Sons.
[6]Hiromichi Kawano, Tetsuo Hattori, Ken Nishimatsu (2008), Structural Change Point Detection Method of Time Series Using Sequential Probability Ratio Test－Comparison with Chow Test in the ability of early detection－(in Japanese), IEEJ Trans. EIS, Vol.128，No.4，pp.583-592.
[7]Chow,G.C. (1960), Tests of Equality Between Sets of Coefficients in Two Linear Regressions, Econometrica, Vol.28, No.3, pp.591-605.

Application of SPRT to Image Data Sequence for Remote Monitoring System

*Katsunori Takeda, *Tetsuo Hattori, **Izumi Tetsuya, ***Hiromichi Kawano, ****Shinichi Masuda

**Graduate School of Engineering, Kagawa University / 2217-20 Hayashi, Takamatsu City, Kagawa 761-0396, Japan*
***Micro Technica Co., Ltd., / Yamagami BLD. 3-12-2 Higashi-ikebukuro, Toshima-ku, Tokyo 170-0013, Japan*
**** NTT Advanced Technology s, / Musashino-shi Nakamachi 19-18, Tokyo 180-0006, Japan*
*****C Micro Co., Ltd., 269-1 Hayashi-Cho, Takamatsu City, Kagawa 761-0396, Japan*
(*Tel : 81-87-864-2221; Fax : 81-87-864-2262, hattori@eng.kagawa-u.ac.jp*)

Abstract: Recently, remote monitoring camera systems are widely used for security. In such systems, we need an important function that it automatically detects the some change of the scenes from monitoring cameras. Generally, in wireless remote monitoring camera systems, the scene images are transmitted as compressed data (e.g., JPEG file), because of the wireless channel capacity. This paper shows the automated detection of the change point for the time series data of compressed JPEG file quantity (Kbytes) from monitoring camera, applying sequential probabilistic ratio test (SPRT) and Chow Test that is well known as a standard method for structural change detection of time series data.

***Keywords*:** Remote monitoring camera system, sequential probability ratio test (SPRT), security

I. INTRODUCTION

Remote monitoring camera systems are widely used for security in recent society (Masuda et al [1]). Because information quantity of images from monitoring cameras is very massive, we need a function in such camera system that automatically detects the some change in the image sequence. Thus, it is better that the method adopted in the function can simply detect the change as promptly and correctly as possible, for quick security action.

Here, we note that, in general, wireless remote monitoring camera systems send the scene images as compressed data (e.g., JPEG file), because of limit of the wireless channel capacity. In addition, if some movement happens in the ordinal images, the quantity of the JPEG image file differs from those of ordinal images.

In this paper, we show a method for the automated change point detection in time series data of JPEG file quantity (Kbytes), using sequential probabilistic ratio test (SPRT) (Wald [2], Kawano et al [3]). Moreover, we show its effectiveness in comparison with Chow Test (Chow [4]) that is well known as a standard method for structural change detection of time series data.

II. CHANGE DETECTION USING SPRT

For the change detection problem, we propose an application of Sequential Probability Ratio Test (SPRT) that has been mainly used in the field of quality control.

1. SPRT

The SPRT is used for testing a null hypothesis H_0 (e.g. the quality is under pre-specified limit 1%) against hypothesis H_1 (e.g. the quality is over pre-specified limit 1%). In addition, it is defined as follows:.

At each stage of successive events $Z_1, Z_2, \cdots Z_i$ that are respectively corresponding to observed time series data, the probability ratio λ_i is computed.

$$\lambda_i = \frac{P(Z_1 \mid \mathbf{H}_1) \cdot P(Z_2 \mid \mathbf{H}_1) \cdots P(Z_i \mid \mathbf{H}_1)}{P(Z_1 \mid \mathbf{H}_0) \cdot P(Z_2 \mid \mathbf{H}_0) \cdots P(Z_i \mid \mathbf{H}_0)} \quad (1)$$

where $P(Z \mid H_0)$ denotes the distribution of Z when H_0 is true and $P(Z \mid H_1)$ denotes the distribution of Z when H_1 is true.

Two positive constants C_1 and C_2 ($C_1 < C_2$) are chosen. If $C_1 < \lambda_i < C_2$, the experiment is continued by taking an additional observation. If $C_2 < \lambda_i$, the process is terminated with the rejection of H_0 (acceptance of H_1). If $\lambda_i < C_1$, the process is terminated with the acceptance of H_0.

$$C_1 = \frac{\beta}{1-\alpha} \qquad C_2 = \frac{1-\beta}{\alpha} \quad (2)$$

where α means type I error (reject a true null hypothesis), and β means type II error (accept a null hypothesis as true one when it is actually false).

2. Procedure

The concrete procedure of structural change detection is as follows (see an example of time series data in Fig.1).

Step1: Make a prediction expression and set the tolerance band (***a***) (e.g. ***a***=2σ_S) that means permissible error margin between the predicted data and the observed one.

Step2 : Set up the null hypothesis H_0 and alternative hypothesis H_1.

H_0: Change has not occurred yet.

H_1: Change has occurred.

Set the values α, β and compute C_1 and C_2, according to Equation (2). Initialize i = 0, $\lambda_0 = 1$.

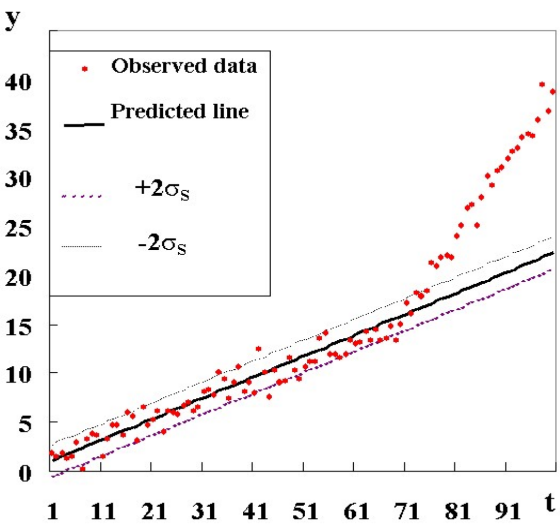

Fig.1. Example of time series data where the change point tc* =70.

Remark: The statement of the null hypothesis H_0, "Change has not occurred yet.", means in statistical sense. It means that the generation probability for the data to go out from the tolerance band is less than (or equal to) θ_0 (for instance, 1%). Similarly, the statement of the alternative hypothesis H_1, "Change has occurred." means that the generation probability for the data to go out from the tolerance band is greater than (or equal to) θ_1 (for instance, 99%). Additionally, we suppose that θ_1 is considerably greater than θ_0.

Step3: Incrementing i (i = i+1), observe the following data y_i. Evaluate the error $|\varepsilon_i|$ between the data y_i and the predicted value from the aforementioned prediction expression.

Step4: Judge as to whether the data y_i goes in the tolerance band or not, i.e., the ε_i is less than (or equal to) the permissible error margin or not. If it is Yes, then set $\lambda_i = 1$ and return to Step3. Otherwise, advance to Step5.

Step5: Calculate the probability ratio λ_i, using the following Equation (3) that is equivalent to Equation (1)

$$\lambda_i = \lambda_{i-1} \frac{P(\varepsilon_i \mid \mathbf{H}_1)}{P(\varepsilon_i \mid \mathbf{H}_0)} \tag{3}$$

where, if the data y_i goes in the tolerance band, $P(\varepsilon_i |H_0) = \theta_0$ and $P(\varepsilon_i |H_1) = \theta_1$, otherwise, $P(\varepsilon_i |H_0) = (1-\theta_0)$ and $P(\varepsilon_i |H_1) = (1-\theta_1)$.

Step6: Execution of testing.

(i) If the ratio λ_i is greater than C_2 (= $(1-\beta)/\alpha$), dismiss the null hypothesis H_0, and adopt the alternative hypothesis H_1, and then End.

(ii) Otherwise, if the ratio λ_i is less than C_1 (= $\beta/(1-\alpha)$), adopt the null hypothesis H_0, and dismiss the alternative hypothesis H_1, and then set $\lambda_i = 1$ and return to Step3.

(iii) Otherwise (in the case where $C_1 \le \lambda_i \le C_2$), advance to Step7.

Step7: Observe the following data y_i incrementing i. Evaluate the error $|\varepsilon_i|$ and judge whether the data y_i goes in the tolerance band, or not. Then, return to Step5 (calculation of the ratio λ_i).

III. APPLICATION TO IMAGE SEQUENCE

As a simple automated change detection method of the scenes from a monitoring camera, we apply the SPRT method to the time series data of compressed JPEG file quantity (Kbyte).

Fig.2 and Fig.3 show two sets of images when a person has moved at low speed and high speed, respectively, in front of a bookshelf. Fig.4 and Fig.5 show two graphs on time series data of JPEG file volumes, corresponding to Fig.2 and Fig.3, respectively.

We assume that change point is the time point when the some change happens, that is, when some person appears in the image data. The SPRT can detect the change point quickly from the sequence of image data. We show experimental results of change detection using two tests (SPRT and Chow Test) and discuss those effectiveness.

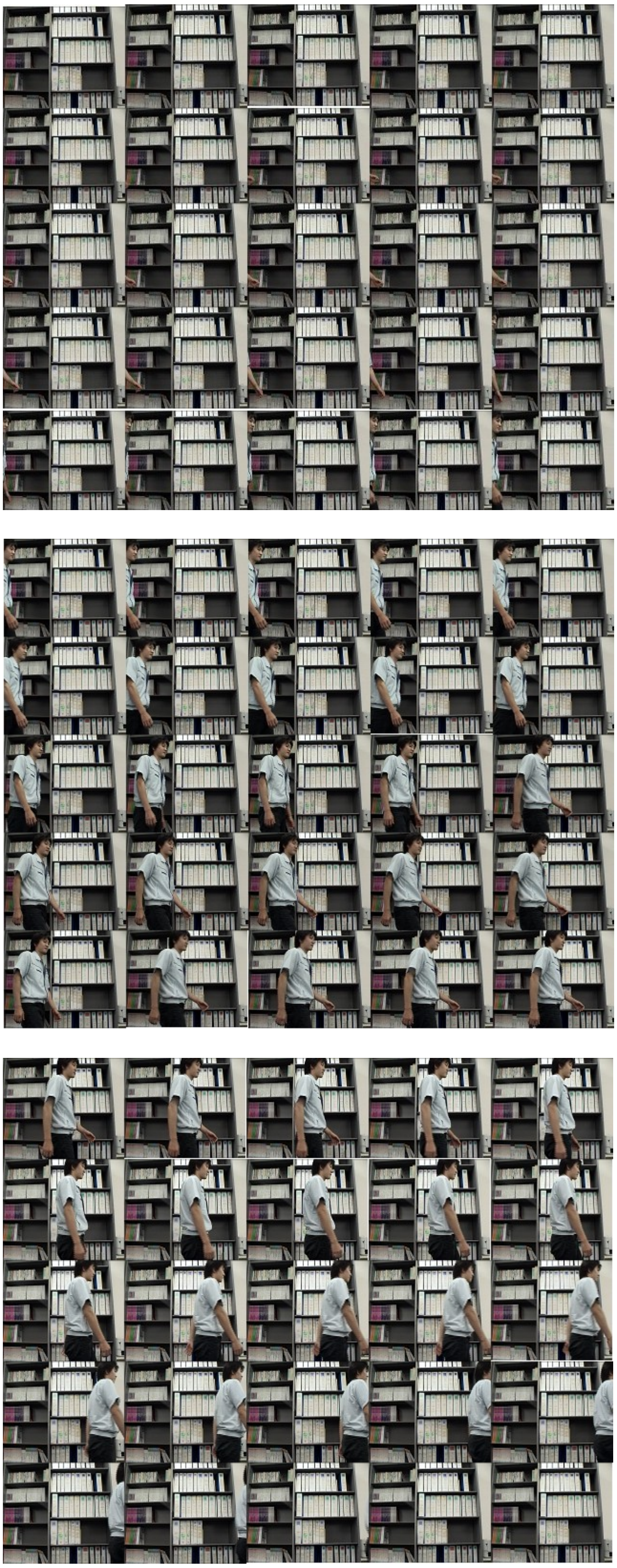

Fig.2. Example of images where someone passes by at low speed (Time is counted from upper left to lower right.)

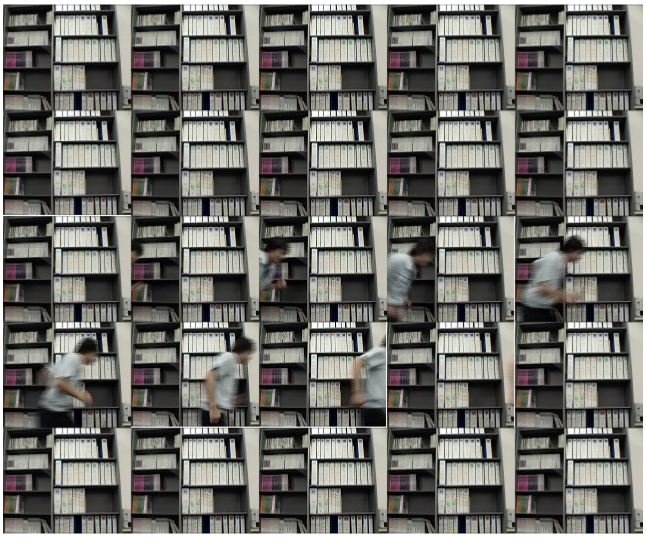

Fig.3. Example of images where someone passes at high speed. (Time is counted from upper left to lower right.)

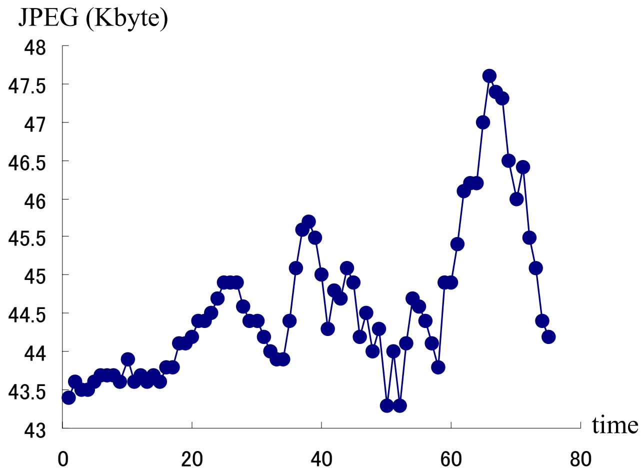

Fig.4. Total time series of image data, i.e., sequence of JPEG file volumes in Fig.2.

The results of change detection by the two Tests (SPRT and Chow Test) are shown in the graphs in Fig.6 and Fig.7, respectively, where the SPRT detects change points in the case of condition 1(θ_0=0.9, θ_1=0.1), and condition 2 (θ_0=0.87, θ_1=0.13), and condition 3(θ_0=0.8, θ_1=0.2).) The number of samples in the stage of learning and analysis, where samples are used for concretely deciding prediction model (regression line), is seven in both cases of low speed and high-speed passing-by movement and in both tests.

From the results in both cases of low speed and high-speed passing-by movement, we find that the SPRT can detect the change quickly and correctly after the change happens. Moreover, the SPRT method is simple and takes very low computational cost (i.e., necessary time and memory storage for computation). On the contrary, the Chow Test tends to make a mistake in the early stage after the change happens, and to takes long time for correct change detection. In addition, the computational cost is considerably high. Then, we consider that the performance of SPRT is very effective in comparison with Chow Test, even if the time series data of sequence of JPEG file volumes is fluctuated by lighting and so on.

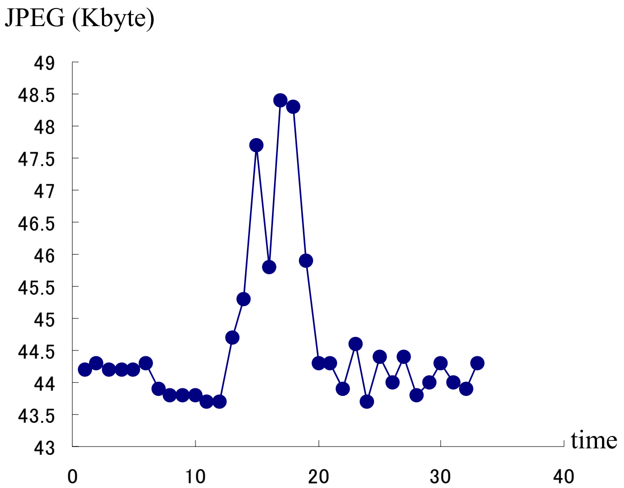

Fig.5. Total time series of image data, i.e., sequence of JPEG file volumes in Fig.3.

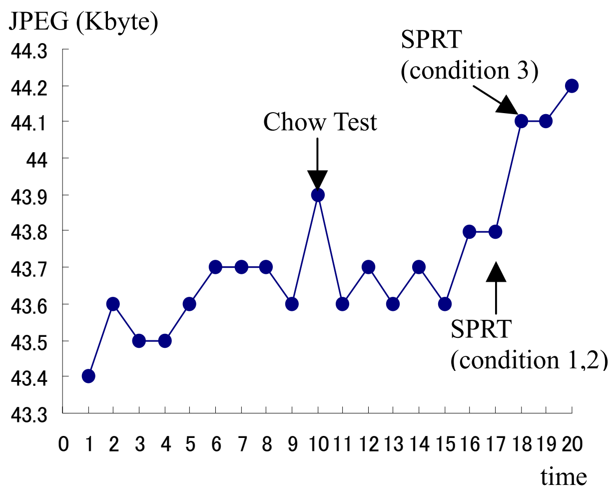

Fig.6. Change point detection (low speed passing-by movement in Fig.2) using SPRT and Chow Test. (condition 1 means (θ_0=0.9,θ_1=0.1), condition 2 is (θ_0=0.87,θ_1=0.13), and condition 3 is (θ_0=0.8,θ_1=0.2).)

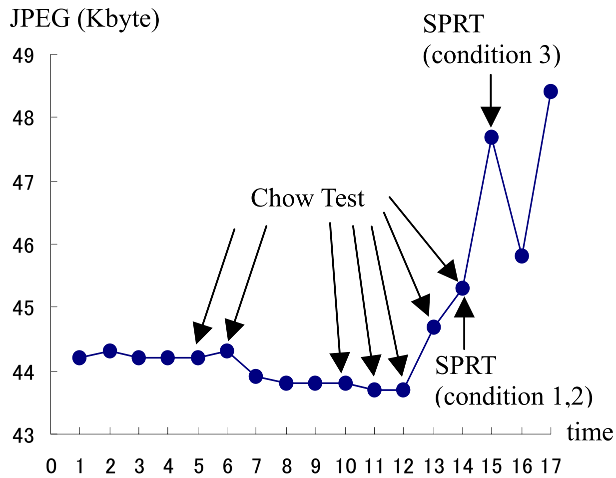

Fig.7. Change point detection (high speed passing-by movement in Fig.3) using SPRT and Chow Test. (condition 1 means (θ_0=0.9,θ_1=0.1), condition 2 is (θ_0=0.87,θ_1=0.13), and condition 3 is (θ_0=0.8,θ_1=0.2).)

IV. CONCLUSION

For security, remote monitoring camera systems are widely used. Because of channel capacity limitedness and of burdensome work for watching, it is desirable to reduce the number of transmission images. For this purpose, we have proposed a sequential probability ratio test (SPRT) for change detection of sequence of JPEG file volumes. Also, we have shown its effectiveness in comparison with Chow Test, based on experimental results.

REFERENCES

[1]Shinichi Masuda, Tetsuo Hattori (2007), Development of a Wireless Remote Monitoring System Utilizing Multiple Wireless Sensors (in Japanese), IEEJ Trans. IA, Vol.127, No.6, pp.610-617.

[2] A. Wald(1947), Sequential Analysis, John Wiley & Sons.

[3]Hiromichi Kawano, Tetsuo Hattori, Ken Nishimatsu (2008), Structural Change Point Detection Method of Time Series Using Sequential Probability Ratio Test－Comparison with Chow Test in the ability of early detection－(in Japanese), IEEJ Trans. EIS, Vol.128, No.4, pp.583-592.

[4]Chow,G.C. (1960), Tests of Equality Between Sets of Coefficients in Two Linear Regressions, Econometrica, Vol.28, No.3, pp.591-605.

Early Structural Change Detection as an Optimal Stopping Problem (I) --- Formulation Using Dynamic Programming with Action Cost ----

*Tetsuo Hattori, *Katsunori Takeda, **Izumi Tetsuya, ***Hiromichi Kawano

**Graduate School of Engineering, Kagawa University / 2217-20 Hayashi, Takamatsu City, Kagawa 761-0396, Japan*
*** Micro TechnicaCo., Ltd./ Yamagami BLD. 3-12-2 Higashi-ikebukuro, Toshima-ku, Tokyo 170-0013, Japan*
**** NTT Advanced Technology / Musashino-shi Nakamachi 19-18, Tokyo 180-0006, Japan*
(Tel : 81087-864-2221; Fax : 81-087-864-2262)
(hattori@eng.kagawa-u.ac.jp)

Abstract: Even if an appropriate prediction expression and/or model are constructed to fit a time series, the model gradually begins to fail the prediction of the time series from some time point. In such case, it will be important not only to quickly detect the failing situation but also to renew the prediction model after the detection as soon as possible. In this paper, we formulate the structural change detection in time series as an optimal stopping problem, using the concept of DP (Dynamic Programming). The cost function is defined as the sum of a loss cost by failing and an action cost after the detection. And we present propose the optimal solution and the correctness by numerical calculation. Also we clarify the effectiveness by a numerical experimentation.

Keywords: time series, structural change, optimal stopping problem

I. INTRODUCTION

Change point detection (CPD) problem in time series is to find that a structure of generating data has changed at some time point by some cause. We consider that the problem is very important and that it can be applied to a wide range of application fields [1]. The processing method for the CPD problem is roughly divided into two types: one is batch processing that checks all generated data in the past and another is sequential processing that checks if the structure has changed or not at every new data generation.

As the former representative method, Chow test is well known and is often used in econometrics [2]. It does a statistical test by setting the hypothesis that the change has occurred at time t. As the latter representative method, there are Bayes' method [2],[3] CUSUM, etc., [4] based on sequential probability ratio test.

In practical situation, we have to consider not only that a loss cost is involved with prediction error, but also that an action to be taken after the change detection will need a cost. Conversely, the CPD is necessary in order to judge when to take the action. Under such situations, we must consider the trade-off between loss by the degradation and cost for the quality reformation. However, as far as the authors can know, no such conventional CPD method considering the action cost has been proposed, in spite of the fact that such method is very useful at practical level.

In this paper, we propose a new and practical method based on an evaluation function of loss cost. And we formulate the CPD problem as an optimal stopping problem using the concept of DP (Dynamic Programming) and give the optimum solution by numerical calculation the formulation. We consider that our method is effective in the sense as follows.

1) Differently from the Chow test, it does not need to set the change point in a priori.

2) Unlike the Bayes' method, it does not need to give the generation distribution of time series data.

3) It minimizes the evaluation function that sums up the loss involved with prediction error and action cost to be taken after the change detection.

Also in this paper, we show the effectiveness of our method by numerical experimentation

II. FORMULATION AS OPTIMAL STOPPING PROBLEM

1. Evaluation function

We formulate the CPD problem as an optimal stopping one based on DP with an evaluation function that sums up the cost involved by prediction error and action cost to be taken after the change detection.

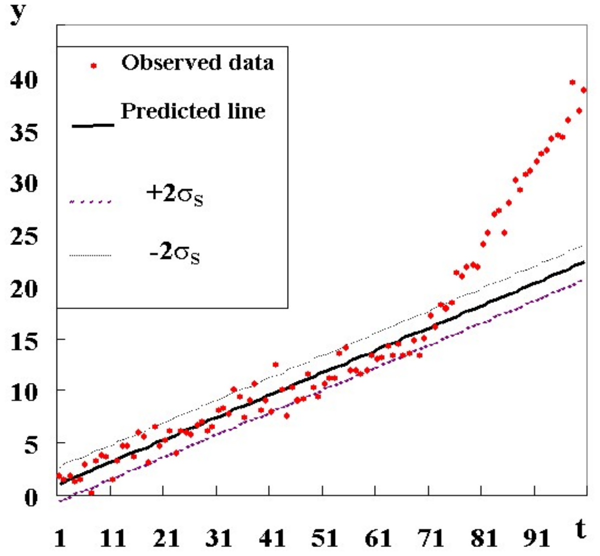

Fig.1. Example of time series data where the true change point tc* =70.

For example, a prediction expression is given in the following equation as a function of time t, where y_t, β_1, β_0, ε mean the function value, two constant coefficients, and error term, respectively.

$$y_t = \beta_1 \cdot t + \beta_0 + \varepsilon \quad (1)$$

The error term ε is given as a random variable of the normal distribution of variance σ^2 and average of 0, i.e., $\varepsilon \sim N(0, \sigma^2)$. A time series data based on the Equation (1) is shown in Fig.1, that is generated by making normal random numbers of average 0 and variance 1 for ε, and by setting $\beta_1=0.2$, $\beta_0=1$ for the time t=1,2,…,70, and $\beta_1=0.8$, $\beta_0=-41$ for the time after t=71. The tolerant error interval or tolerance zone between two broken lines as shown in Fig. 1 is decided using the first time series data from t=1 to t=20.

In Fig.1, we think of two situations: one is the situation that the observed data goes out from the tolerance zone, and another the situation that the observed data goes in the zone. We call the former situation "failing" (or "not hitting") and the latter "hitting". We assume that the structure changes when the failing occurs for continuing *N* times.

The evaluation function is given by (2) as the sum of two kinds of cost: the damage caused by the failing (i.e., failing loss) and action cost to be taken after the change detection.

Total_cost=cost(*A*)+cost(*n*) (2)

where cost(*n*) is the sum of the loss by continuing *n* times failing before the structural change detection, and cost(*A*) denotes the cost involved by the action after the change detection. Then we have to find the number of *N* that minimizes the expectation value of Total_cost, assuming that the structural change occurs randomly.

2. Structural change model

We can assume that the structural change is Poisson occurrence of average λ, and that, once the change has occurred during the observing period, the structure does not go back to the previous one. The reason why we set such a model is that we focus on the detection of the first structural change in the sequential processing (or sequential test). The concept of the structural change model is shown in Fig. 2.

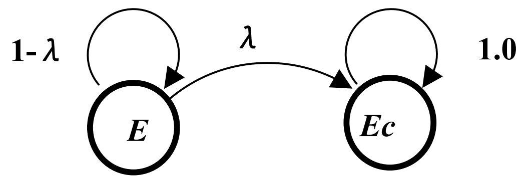

Fig.2. Structural change model.

Moreover, we introduce a more detailed model. Let *R* be the probability of the failing when the structure is unchanged. Let *R*c be the probability of the failing when the structure change occurred. We consider that *R*c is greater than *R*, i.e., *R*c>*R*. The detailed model for the State *E*c and *E* are illustrated as similar probabilistic finite state automatons in Fig.3 and Fig.4, respectively.

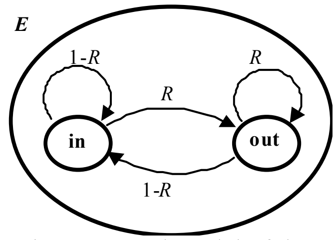

Fig.3. Internal model of the State *E*.

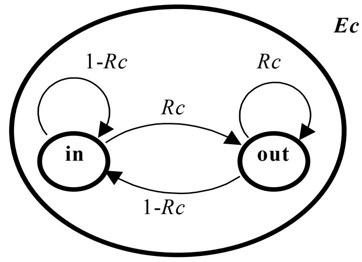

Fig.4. Internal model of the State *E*c.

3. Definition

Let the cost(n) be $a \cdot n$ as a linear function for n, where a is the loss caused by the failing in one time. And for simplicity, let C and A denote the Total_cost and cost (A), respectively. Then, the evaluation function in (2) is denoted as the following equation (3).

$$C = A + a \cdot n \tag{3}$$

We recursively define a function $EC(n,N)$ to obtain the optimum number of times n that minimizes the expectation value of the evaluation function of Equation (3), using the concept of DP (Dynamic Programming). Let N be the optimum number. Let the function $EC(n,N)$ be the expectation value of the evaluation function at the time when the failing has occurred in continuing n times, where n is less than or equal to N, i.e., $0 \le n \le N$.

Thus the function is recursively defined as follows.

$$(\text{if} \quad n = N) \quad EC(n,N) = A + a \cdot N \tag{4}$$

$$(\text{if} \quad n < N) \quad EC(n,N) = P(\bar{S}_{n+1} \mid S_n) \cdot a \cdot n + (1 - P(\bar{S}_{n+1} \mid S_n)) EC(n+1,N) \tag{5}$$

where S_n means the state of failing in continuing n times, $\bar{S}_{n+1}$ the state of hitting at the (n+1) th observed data, and $P(\bar{S}_{n+1} \mid S_n)$ means the conditional probability that the state $\bar{S}_{n+1}$ occurs after the state S_n.

The first term in the right-hand side (RHS) of Equation (4) indicates the expectation value of the evaluation function at the time when hitting happens at the (n+1)th data after the continuing n times failing. The second term in the RHS of Equation (5) indicates the expectation value of the evaluation function for the time when failing happens at the (n+1)th data after continuing n times failing.

Then, from the definition of the function $EC(n,N)$, the goal is to find the N that minimizes $EC(0,N)$, because the N is the same as n that minimizes the expectation value of the evaluation function of (4).

4. Minimization of the evaluation function

The analytical solution N that minimizes $EC(0,N)$ can be deduced. The strict proof needs many pages, then we show numerical solution.

The function $EC(0,N)$ is defined by recursive expressions (4) and (5), then $EC(0,N)$ can be computed by recursively. In the process of this computation, $P(\bar{S}_{n+1} \mid S_n)$ can be calculated as follows.

Let E_{cn} be the event that the structural change occurs once during the period of observation in continuing n times. Let $P(E_{cn} \mid S_n)$ be the conditional probability that the E_{cn} happens under the condition that failing has already occurred for continuing n times. Based on the model in Fig.3 and Fig.4,

$$P(\bar{S}_{n+1} \mid S_n) = (1-R)(1-P(E_{cn} \mid S_n)) + (1-R_c)P(E_{cn} \mid S_n) \tag{6}$$

Let E be the event that there is no structural change. According to the Bayes' theorem $P(E_{cn} \mid S_n)$ can be represented as (7).

$$P(E_{cn} \mid S_n) = \frac{P(S_n \mid E_{cn})P(E_{cn})}{P(S_n \mid E_{cn})P(E_{cn}) + P(S_n \mid E)P(E)} = \frac{\sum_{i=0}^{n-1} (1-\lambda)^i R^i \lambda R_c^{n-i}}{\sum_{i=0}^{n-1} (1-\lambda)^i R^i \lambda R_c^{n-i} + (1-\lambda)^n R^n} \tag{7}$$

The procedure to calculate $EC(0,N)$ is shown in Fig.5.

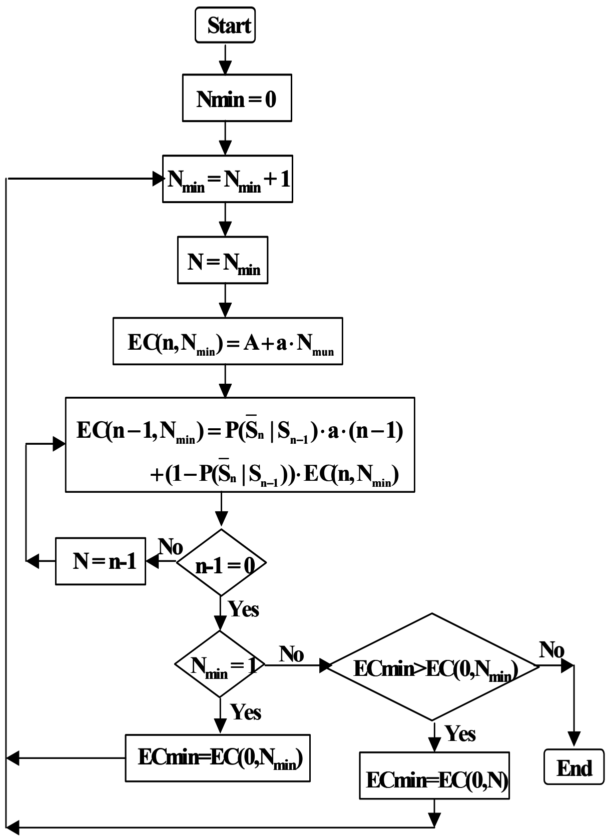

Fig.5. The procedure to calculate N that minimizes $EC(0,N)$ according to the recursive definition.

III. EXPERIMENTATION

In this section, we make a comparison between the proposed method and Chow Test using the time series data shown in Fig.1.

1. Outline of experimentation

Step1: Generate the time series data (Fig.1) based on the Equation (1), by making normal random numbers of average 0 and variance $\sigma^2 = 1$ for ε, and by setting β_1=0.2, β_0=1 for the time t=1,2,…,70, and β_1=b, β_0=(0.2-b)71+1, for the time after t=71.

Step2: Make prediction expression, using a sequence of data at the time t=1…40, from the above generated time series.

Step3: Decide the tolerant zone.

Step4: Based on the proposed method, measure the number of times when the observed data goes out from the tolerance zone for observation data after the time at k+1, and detect the structural change point.

Step5: Perform the above things repeatedly by M times, and calculate the average of the structural change point.

2. Experimental condition

(i)Tolerant zone: $\pm 2\sigma$ of the distribution on error ε.

(ii)The trend β_1 (=b) for the time after t=71:b=0.4.

(iii)Parameter value of the evaluation function:
λ=0.01, and $\boldsymbol{A/a}$=10,15.

(iv)Repetition times: M=100.

(v)Significance level for testing the hypothesis:
α=0.05 (in case of Chow Test)

3. Results

Results are illustrated in Fig.6 where horizontal axis shows observing time t (observation is started after t=40). The vertical axis in left hand shows an averaged time point of detected change point, where the average is taken from 100 times experimentation. The proposed method detects the change point based on the beforehand calculated value N that minimizes $EC(0,N)$.

Although the detection of the change point depends on the value of $\boldsymbol{A/a}$, we expect that the change point will be detected around the time at t=70, because the structure of the time series is changed at t=70. We have verified that the results by the proposed method meet our intuition very well.

However, Fig.6 shows that Chow Test decides the change point almost every time when data is observed, and detecting change point varies every time when new data is observed. This means Chow Test cannot correctly detect change point around the time of true change point.

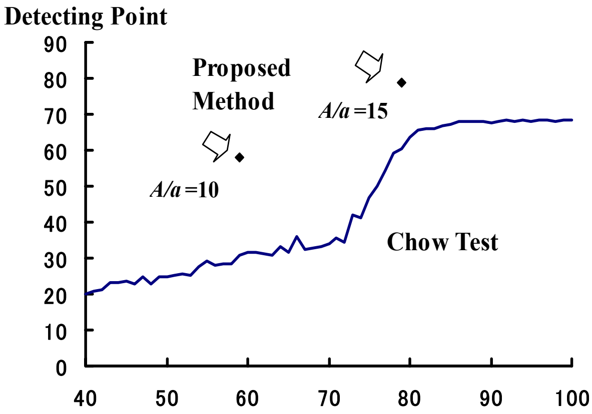

Fig. 6. Change point detection by the proposed method and Chow Test.

IV. CONCLUSION

We have proposed a sequential processing method for structural change point detection of time series data, and have presented a formulation as an optimal stopping problem using the concept of DP. We have defined an evaluation function with an action cost, recursively. In addition, we have revealed the optimum solution by numerical computation and also have shown some experimentation results, where the results meet our intuition and well detect the structural change point in artificially generated time series data. We also have shown that the method is more effective than Chow Test.

We consider that method is effective, especially in the sense that it can quickly detect the change point without a priori knowledge of probabilistic distribution and that it can be applied to arbitrary prediction model, because it is a meta-level one.

REFERENCES

[1] R.Jana and S.Dey (2000), Change detection in Teletraffic Models, IEEE Trans. Signal Processing, vol.48, No.3, pp.846-853.
[2] Chow,G.C. (1960), Tests of Equality Between Sets of Coefficients in Two Linear Regressions, Econometrica, Vol.28, No.3, pp.591-605.
[3] S.MacDougall, A.K. Nandi and R.Chapman (1998), Multisolution and hybrid Bayesian algorithms for automatic detection of change points, Proc. of IEEE Visual Image Signal Processing, vol.145, No.4, pp.280-286.
[4]E.S.Page (1954), Continuous inspection schemes, Biometrika, Vol.41, pp.100-115.

Early Structural Change Detection as an Optimal Stopping Problem (II) --- Solution Theorem and its Proof Using Reduction to Absurdity ----

*Hiromichi Kawano, **Tetsuo Hattori, **Katsunori Takeda, ***Izumi Tetsuya

**NTT Advanced Technology / Musashino-shi Nakamachi 19-18, Tokyo 180-0006, Japan*
***Graduate School of Engineering, Kagawa University / 2217-20 Hayashi, Takamatsu City, Kagawa 761-0396, Japan*
****Micro TechnicaCo., Ltd./ Yamagami BLD. 3-12-2 Higashi-ikebukuro, Toshima-ku, Tokyo 170-0013, Japan*
(Tel : 81-087-864-2221; Fax : 81-087-864-2262)
(hattori@eng.kagawa-u.ac.jp)

Abstract: Change point detection (CPD) problem in time series is to find that a structure of generating data has changed at some time point by some cause. We formulated the structural change detection in time series as an optimal stopping problem using the concept of DP (Dynamic Programming) and presented the optimal solution and the correctness by numerical calculation. In this paper, we present the solution theorem and its proof using reduction to absurdity.

Keywords: time series data, structural change point detection, optimal stopping problem

I. INTRODUCTION

Change point detection (CPD) problem in time series is to find that a structure of generating data has changed at some time point by some cause. In the literature [1],[2], we have proposed a new and practical method based on an evaluation function of loss cost. In addition, we have formulated the CPD problem as an optimal stopping problem and have given the algorithm for the optimum solution and also have presented the effectiveness using numerical experimental results.

In this paper, we show the solution theorem and its proof using reduction to absurdity.

II. FORMULATION

1. Definition of Function

Let the cost(n) be an as a linear function for n, where a is the loss caused by the failing (i.e., missing the forecast, or fail in prediction) in one time. And for simplicity, let C and A denote the Total cost and cost (A), respectively. Then, the evaluation function is denoted as the following Equation (1).

$$C=A+a\cdot n \tag{1}$$

We introduce a function $EC(n,N)$ to obtain the optimum number of times n that minimizes the expectation value of C, using the concept of DP. Let N be the optimum number. Let the function $EC(n,N)$ be the evaluation function at the time when the failing has occurred in continuing n times ($n \le N$). Then the function can be defined in the following form.

$$(\text{if } n=N)\quad EC(n,N)=A+a\cdot N \tag{2}$$

$$(\text{if } n<N)\quad EC(n,N)=P(\bar{S}_{n+1}\mid S_n)\cdot a\cdot n + (1-P(\bar{S}_{n+1}\mid S_n))EC(n+1,N) \tag{3}$$

where S_n is the state of failing in continuing n times, $\bar{S}_{n+1}$ is the state of unfailing (or hitting) for the (n+1)-th time observed data, and $P(\bar{S}_{n+1}\mid S_n)$ means the conditional probability that the state $\bar{S}_{n+1}$ occurs after the state S_n.

Then, from the definition of the function $EC(n,N)$, the goal is to find the N that minimizes $EC(0,N)$, because the N is the same as n that minimizes the expectation of the evaluation function of (1).

2. Minimization of the Evaluation Function

For the aforementioned $EC(0,N)$, the following theorem holds and gives the n that minimizes the expectation value of the evaluation function of (1).

A. Theorem

The N that minimizes $EC(0,N)$ is given as the largest number n that satisfies the following Inequality (4).

$$a<(A+a)\cdot P(\bar{S}_n\mid S_{n-1}) \tag{4}$$

where the number N+1 can also be the optimum one that minimizes $EC(0,N)$, i.e., $EC(0,N) = EC(0,N+1)$, only if $a=(A+a)\cdot P(\bar{S}_{N+1}\mid S_N)$.

Proof.

We derive a contradiction with two assumptions under a premise as follows.

Premise: a number N' is the largest number n that satisfies the Inequality (4).

Assumption 1:

There exists a number N'' such that

$$N''<N' \text{ and } EC(0,N'')<EC(0,N').$$

Assumption 2:

There exists a number N'' such that

$$N'<N'' \text{ and } EC(0,N')>EC(0,N'').$$

We give the proof of this theorem by three steps. At Step 1, we prove fundamental lemmas: Lemma 1-1 and Lemma 1-2. At Step 2, we prove two lemmas: Lemma 2-1, and Lemma 2-2. Using those lemmas, we show that the above Assumption 1 contradicts the Premise. Similarly, at Step 3, we show that the Assumption 2 contradicts the Premise, using two lemmas: Lemma 3-1 and Lemma 3-2, which are proved in Appendix.

B. Step 1

Lemma 1-1.

Let E_{cn} be the event that the structural change occurs once during the period of observation in continuing *n* times. Let $P(E_{cn} \mid S_n)$ be the conditional probability that the E_{cn} happens under the condition that failing occurs in continuing *n* times.

$P(E_{cn} \mid S_n)$ is an increase function for *n*.

Proof.

We derive some useful equations for this proof.

The event E_{cn} is given in (5).

$$E_{cn} = \bigcup_{i=0}^{n-1}\left(E^i \cap E_c^{n-i}\right) \tag{5}$$

where *E* is the event that there is no structural change, E_c is the event that the structural change occurred, and E^n is defined as $E^n = \bigcap_{i=1}^{n} E^i$.

The probability of the event E_{cn} defined in (5) is given as follows.

$$P(E_{cn}) = P\left(\bigcup_{i=0}^{n-1}\left(E^i \cap E_c^{n-i}\right)\right) = \sum_{i-0}^{n-1} P\left(E^i \cap E_c^{n-i}\right)$$

$$= \sum_{i=0}^{n-1}(1-\lambda)^i \lambda \tag{6}$$

λ **:** Probability of the structural change occurrence. The joint event of E_{cn} and S_n, and its probability are given by (7) and (8), respectively. Let *R* be the probability of the failing when the structure is unchanged. Let *Rc* be the probability of the failing when the structural change occurred.

$$S_n \cap E_{cn} = S_n \cap \left(\bigcup_{i=0}^{n-1}\left(E^i \cap E_c^{n-i}\right)\right) \tag{7}$$

$$P\left(S_n \cap E_{cn}\right) = \sum_{i=0}^{n-1}(1-\lambda)^i R^i \lambda R_c^{n-i} \tag{8}$$

Therefore, using (6) and (8), we have

$$P(S_n \mid E_{cn}) = \frac{P(S_n \cap E_{cn})}{P(E_{cn})}$$

$$= \frac{\sum_{i=0}^{n-1}(1-\lambda)^i R^i \lambda R_c^{n-i}}{\sum_{i=0}^{n-1}(1-\lambda)^i \lambda} \tag{9}$$

According to the Bayes' theorem, the posterior probability $P(E_{cn} \mid S_n)$ is given by the following (10).

$$P(E_{cn} \mid S_n) = \frac{P(S_n \cap E_{cn})}{P(S_n \cap E_{cn}) \cup P(S_n \cap E^n)}$$

$$= \frac{\sum_{i=0}^{n-1}(1-\lambda)^i R^i \lambda R_c^{n-i}}{\sum_{i=0}^{n-1}(1-\lambda)^i R^i \lambda R_c^{n-i} + (1-\lambda)^n R^n}$$

$$= \frac{1}{1 + \dfrac{(1-\lambda)^n R^n}{\sum_{i=0}^{n-1}(1-\lambda)^i R^i \lambda R_c^{n-i}}} = \frac{1}{1 + D(n)} \tag{10}$$

where $D(n) = \dfrac{(1-\lambda)^n R^n}{\sum_{i=0}^{n-1}(1-\lambda)^i R^i \lambda R_c^{n-i}}$.

The $D(n)$ is also expressed as the following (11).

$$D(n) = \frac{(1-\lambda)^n \left(\dfrac{R}{R_c}\right)^n}{\lambda \sum_{i=0}^{n-1}(1-\lambda)^i \left(\dfrac{R}{R_c}\right)^i} = \frac{\mathbf{X}^n}{\lambda \sum_{i=0}^{n-1}\mathbf{X}^i}$$

$$= \frac{1}{\lambda\left(\dfrac{1}{\mathbf{X}^n} + \dfrac{1}{\mathbf{X}^{n-1}} + \cdots + \dfrac{1}{\mathbf{X}}\right)} \tag{11}$$

where $\mathbf{X} = (1-\lambda)\dfrac{R}{R_c}$.

Since $0 \le \lambda < 1$, $0 < 1-\lambda \le 1$, and $R_c > R$, then $0 < X < 1$. So, the $D(n)$ becomes a monotonous decrease for *n*. Therefore, the probability $P(E_{cn} \mid S_n)$ of (10) is a monotonous increase function for *n*.

Lemma 1-1 is proved.

Remark: Lemma 1-1 indicates that, if the number of times of the failing *n* increases, the probability that the structural change has occurred increases. This meets our intuition clearly.

Lemma 1-2.

The conditional probability $P(\overline{S}_{n+1} \mid S_n)$ is a decrease function for *n*.

Proof.

We have

$$P(\bar{S}_{n+1} \mid S_n) = (1-R)(1-P(E_{cn} \mid S_n)) + (1-R_c)P(E_{cn} \mid S_n) \quad (12)$$

The first term in the RHS of (12) shows the probability that the hitting occurs for the (n+1)-th time observed data when the structure is unchanged. The second term shows the probability that the hitting occurs for the (n+1)-th time observed data when the structure changed. From (12), we have

$$P(\bar{S}_{n+1} \mid S_n) = 1 - R + P(E_{cn} \mid S_n)(R - R_c) \quad (13)$$

By Lemma 1-1, $P(E_{cn} \mid S_n)$ is an increase function, and $R < R_c$, therefore, $P(\bar{S}_{n+1} \mid S_n)$ is a decrease function for n. (The decreasing situation by the numerical computing is shown in Fig.1.)

Lemma 1-2 is proved.

Remark: Lemma 1-2 indicates that, if the number of times of continuous failing increases, the probability of the hitting for the next observed data after those continuous failing decreases. This is intuitively clear, because, by Lemma 1-1, the probability of the structural change increases if the number of times of the continuous failing increases.

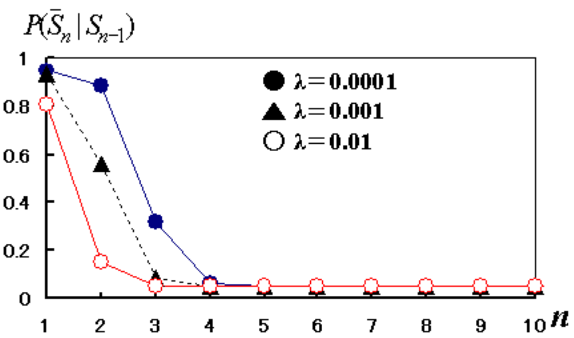

Fig.1. The probability $P(\bar{S}_n \mid S_{n-1})$ for three kinds of λ (Occurrence probability of structural change) in the case of Rc =0.95.

C. Step 2

We derive a contradiction for proving the Theorem using the following Lemma 2-1 and Lemma 2-2, where the notation is the same as aforementioned.

Lemma 2-1.

If $N'' < N'$, then $EC(N'', N') < EC(N'', N'')$

Proof.

Since $N'' < N'$, we can represent N'' as $N'' = N' - m$, where $m = 1,,, N'$. Then we have the equivalent inequality to this lemma as follows.

$$EC(N'-m, N') < EC(N'-m, N'-m) \quad (14)$$

We prove the Inequality (14) by mathematical induction on m.

(i) If $m=1$, applying the Equation (3) to the left hand side (LHS) of Inequality (14), we have

$$EC(N'-1, N') = P(\bar{S}_{N'} \mid S_{N'-1}) \cdot a(N'-1)$$
$$+ (1 - P(\bar{S}_{N'} \mid S_{N'-1})) \cdot EC(N', N')$$
$$= P(\bar{S}_{N'} \mid S_{N'-1}) \cdot a(N'-1)$$
$$+ (1 - P(\bar{S}_{N'} \mid S_{N'-1})) \cdot (A + a \cdot N')$$
$$= A + aN' - (A+a) \cdot P(\bar{S}_{N'} \mid S_{N'-1}) \quad (15)$$

By the Premise,

$$(A+a)P(\bar{S}_{N'} \mid S_{N'-1}) > a \quad (16)$$

Therefore, next inequality holds on the RHS of (15).

$$A + aN' - (A+a) \cdot P(\bar{S}_{N'} \mid S_{N'-1}) < A + aN' - a$$
$$= A + a(N'-1)$$

Then we have,

$$A + aN' - (A+a) \cdot P(\bar{S}_{N'} \mid S_{N'-1}) < EC(N'-1, N'-1) \quad (17)$$

This proves the Inequality (14) for m=1.

(ii) Assume that the Inequality (14) holds for $m = k$. In case of $m = k+1$, applying Equation (3) to the LHS of the Inequality (14), we have,

$$EC(N'-k-1, N') = P(\bar{S}_{N'-k} \mid S_{N'-k-1}) \cdot a \cdot (N'-k-1)$$
$$+ (1 - P(\bar{S}_{N'-k} \mid S_{N'-k-1})) \cdot EC(N'-k, N') \quad (18)$$

By the assumption for $m = k$, the next inequality holds.

$$EC(N'-k, N') < EC(N'-k, N'-k).$$

Therefore, for the RHS of (18), we have

$$P(\bar{S}_{N'-k} \mid S_{N'-k-1}) \cdot a \cdot (N'-k-1)$$
$$+ (1 - P(\bar{S}_{N'-k} \mid S_{N'-k-1})) \cdot EC(N'-k, N')$$
$$< P(\bar{S}_{N'-k} \mid S_{N'-k-1}) \cdot a \cdot (N'-k-1)$$
$$+ (1 - P(\bar{S}_{N'-k} \mid S_{N'-k-1})) \cdot EC(N'-k, N'-k) \quad (19)$$

Applying Equation (2) to the RHS of (19), we have

$$P(\bar{S}_{N'-k} \mid S_{N'-k-1}) \cdot a \cdot (N'-k-1)$$
$$+ (1 - P(\bar{S}_{N'-k} \mid S_{N'-k-1})) \cdot (A + a \cdot (N'-k))$$
$$= A + a \cdot (N'-k) - (a+A) \cdot P(\bar{S}_{N'-k} \mid S_{N'-k-1}) \quad (20)$$

By Lemma 1-2, $P(\bar{S}_n \mid S_{n-1})$ is a decrease function for n and by the Premise for N', we have

$$(A+a)P(\bar{S}_{N'-k} \mid S_{N'-k-1}) > (A+a)P(\bar{S}_{N'} \mid S_{N'-1})$$
$$> a$$

Therefore, next inequality is obtained for the RHS of (20).

$$A + a \cdot (N'-k) - (a+A) \cdot P(\bar{S}_{N'-k} \mid S_{N'-k-1})$$
$$< A + a \cdot (N'-k) - a \quad (21)$$

By Equation (2), the RHS of (21) is equal to
$EC(N'-k-1, N'-k-1)$.

Thus, we have the following (22), and this implies that Inequality (14) holds for the case $m=k+1$.

$$EC(N'-k-1, N') < EC(N'-k-1, N'-k-1) \quad (22)$$

This proves the Lemma 2-1.

Lemma 2-2

If $N'' < N'$, then, for m ($0 < m \le N''$),

$$EC(N''-m, N') < EC(N''-m, N'') \quad (23)$$

Proof.

We prove this by mathematical induction for *m*.

(i) First, for *m*=1, we prove the following inequality.

$$EC(N''-1, N') < EC(N''-1, N'') \quad (24)$$

Applying Equation (3) to the LHS of the Inequality (24), we have

$$EC(N''-1, N') = P(\bar{S}_{N''} \mid S_{N''-1}) \cdot a \cdot (N''-1)$$
$$+ (1 - P(\bar{S}_{N''} \mid S_{N''-1})) \cdot EC(N'', N') \quad (25)$$

By applying Lemma 2-1 to the RHS of (25), the following inequality is obtained.

$$EC(N''-1, N') < P(\bar{S}_{N''} \mid S_{N''-1}) \cdot a \cdot (N''-1)$$
$$+ (1 - P(\bar{S}_{N''} \mid S_{N''-1})) \cdot EC(N'', N'') \quad (26)$$

Applying the Equation (3) to the RHS of Inequality (24), $EC(N''-1, N'')$ is equal to the RHS of (26). Then, the Inequality (24) holds, and this establishes the Lemma 2-2 for $m=1$.

(ii) Assuming that the Lemma 2-2 holds for $m=k$, we prove it for the case of $m=k+1$. The LHS of Inequality (23) is expressed as (27) using Equation (3).

$$EC(N''-k-1, N')$$
$$= P(\bar{S}_{N''-k} \mid S_{N''-k-1}) \cdot a \cdot (N''-k-1)$$
$$+ (1 - P(\bar{S}_{N''-k} \mid S_{N''-k-1})) \cdot EC(N''-k, N') \quad (27)$$

Here, recalling the assumption that, for $m=k$,

$$EC(N''-k, N') < EC(N''-k, N'')$$

We can obtain the following inequality from (27).

$$EC(N''-k-1, N')$$
$$< P(\bar{S}_{N''-k} \mid S_{N''-k-1}) \cdot a \cdot (N''-k-1)$$
$$+ (1 - P(\bar{S}_{N''-k} \mid S_{N''-k-1})) \cdot EC(N''-k, N'') \quad (28)$$

The RHS of Inequality (23) for $m=k+1$,
$EC(N''-k-1, N'')$ is equal to the RHS of (28), by Equation (3). Therefore, we have

$$EC(N''-k-1, N') < EC(N''-k-1, N'') \quad (29)$$

This completes the proof of the Lemma 2-2.

By putting $m = N''$ in the Lemma 2-2, we have
$EC(0, N') < EC(0, N'')$ in case of $N'' < N'$.
This inequality contradicts the Assumption 1: There exists a number N'' such that $N'' < N'$ and $EC(0, N'') < EC(0, N')$.

D. Step 3

Similarly to the Step 2, the following Lemma 3-1 and Lemma 3-2 hold, as described in subsequent Appendix.

Lemma 3-1.

If $N' < N''$, then $EC(N', N'') \ge EC(N', N')$,
Where the equality holds only if $N'' = N'+1$ and $a = (A+a) \cdot P(\bar{S}_{N'+1} \mid S_{N'})$.

Lemma 3-2.

If $N' < N''$, then, for m ($0 < m \le N'$)

$$EC(N'-m, N'') \ge EC(N'-m, N'),$$

where the equality holds only if $N'' = N'+1$ and $a = (A+a) \cdot P(\bar{S}_{N'+1} \mid S_{N'})$.

By putting $m = N'$ in the Lemma 3-2, we have $EC(0, N'') \ge EC(0, N')$ in case of $N' < N''$.
This contradicts Assumption 2: There exists a number N'' such that $N' < N''$ and $EC(0, N') > EC(0, N'')$.

After all, $EC(0, N') \le EC(0, N'')$ ($N'' < N'$ or $N' < N''$), where the equality holds only if $N'' = N'+1$ and $a = (A+a) \cdot P(\bar{S}_{N'+1} \mid S_{N'})$.

It means that N' minimizes $EC(0, N)$. And, when $a = (A+a) \cdot P(\bar{S}_{N'+1} \mid S_{N'})$, $N'+1$ also minimizes $EC(0, N)$, i.e., $EC(0, N') = EC(0, N'+1)$.

This completes the proof of Theorem. Fig.2 shows that the relation between the expectation *EC*(0,*N*) and *N*.

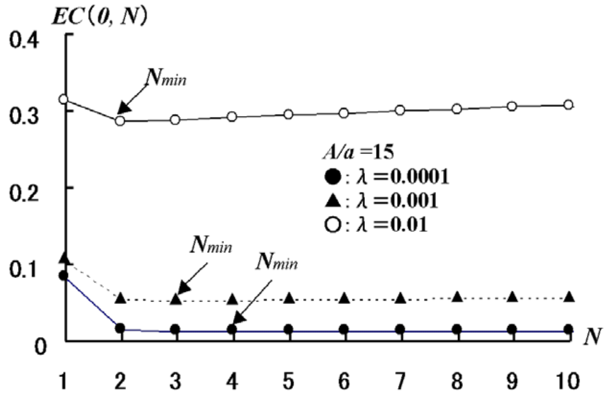

Fig.2. The expectation *EC*(0,*N*) and *N* with the ratio of ***A***/***a*** fixed (***A***=1.5, ***a*** =0.1) and varying λ. N_{min} means the optimum number that minimizes *EC*(0,*N*).

III. CONCLUSION

We have proposed a sequential processing method for structural change detection of time series data as an optimal stopping problem with a cost evaluation function. We have presented the solution theorem and its proof using reduction to absurdity.

Appendix

Proof of Lemma 3-1 and Lemma 3-2

A1. Lemma 3-1

If $N' < N''$, then $EC(N', N'') \geq EC(N', N')$,

Where the equality holds only if $N'' = N'+1$ and if $a = (A + a) \cdot P(\bar{S}_{N'+1} \mid S_{N'})$.

Proof.

Since $N' < N''$, we can let $N'' = N'+m$ (m: natural number), and we have $EC(N', N'+m) \geq EC(N', N')$.

We prove this by mathematical induction for m.

(i) For m=1, we prove that

$$EC(N', N'+1) \geq EC(N', N') \qquad \text{(a1)}$$

By applying the Equation (3) to the LHS of (a1), we have

$$EC(N', N'+1) = P(\bar{S}_{N'+1} \mid S_{N'}) \cdot a \cdot N' + (1 - P(\bar{S}_{N'+1} \mid S_{N'})) \cdot EC(N'+1, N'+1)$$

$$= P(\bar{S}_{N'+1} \mid S_{N'}) \cdot a \cdot N' + (1 - P(\bar{S}_{N'+1} \mid S_{N'})) \cdot (A + a \cdot (N'+1))$$

$$= A + a \cdot (N'+1) - (A + a) \cdot P(\bar{S}_{N'+1} \mid S_{N'}) \qquad \text{(a2)}$$

By the Premise that N' is the largest number n that satisfies $a < (A + a) \cdot P(\bar{S}_n \mid S_{n-1})$, and by the fact that $P(\bar{S}_n \mid S_{n-1})$ decreases for n, we have

$a \geq (A + a) \cdot P(\bar{S}_{N'+1} \mid S_{N'})$ for $N'+1$.

Then,

$$EC(N', N'+1) = A + a \cdot (N'+1) - (A + a) \cdot P(\bar{S}_{N'+1} \mid S_{N'})$$

$$\geq A + a \cdot (N'+1) - a = A + a \cdot N' = EC(N', N').$$

This implies that (a1) holds.

We can see that the equality in (a1) holds only if $(A + a) \cdot P(\bar{S}_{N'+1} \mid S_{N'}) = a$, otherwise,

$EC(N', N'+1) > EC(N', N')$.

However,

even if $EC(N', N'+1) = EC(N', N')$, i.e.,

if $(A + a) \cdot P(\bar{S}_{N'+1} \mid S_{N'}) = a$,

it holds that $(A + a) \cdot P(\bar{S}_{N'+2} \mid S_{N'+1}) < a \qquad$ (a3)

because the probability $P(\bar{S}_{n+1} \mid S_n)$ decreases for n.

Here, we prove the following Proposition.

Proposition.

$$EC(N', N'+2) > EC(N', N') \qquad \text{(a4)}$$

Even if $EC(N', N'+1) = EC(N', N')$.

Proof.

Using the Equation (3),

$$EC(N', N'+2) = P(\bar{S}_{N'+1} \mid S_{N'}) \cdot a \cdot N' + (1 - P(\bar{S}_{N'+1} \mid S_{N'})) \cdot EC(N'+1, N'+2) \qquad \text{(a5)}$$

By applying the Equation (3) to $EC(N'+1, N'+2)$ in (a5), we have

$$EC(N'+1, N'+2) = P(\bar{S}_{N'+2} \mid S_{N'+1}) \cdot a \cdot (N'+1) + (1 - P(\bar{S}_{N'+2} \mid S_{N'+1})) \cdot EC(N'+2, N'+2)$$

$$= P(\bar{S}_{N'+2} \mid S_{N'+1}) \cdot a \cdot (N'+1) + (1 - P(\bar{S}_{N'+2} \mid S_{N'+1})) \cdot (A + a \cdot (N'+2))$$

$$= A + a \cdot (N'+2) - (A + a) \cdot P(\bar{S}_{N'+2} \mid S_{N'+1}) \qquad \text{(a6)}$$

Using (a3), (a6) and the Equation (2), we have

$EC(N'+1, N'+2) > A + a \cdot (N'+1) = EC(N'+1, N'+1)$.

Thus, $EC(N'+1, N'+2) > EC(N'+1, N'+1) \qquad$ (a7)

Moreover, using (a5), (a7) and the Equation (3),

$$EC(N', N'+2) > P(\bar{S}_{N'+1} \mid S_{N'}) \cdot a \cdot N' + (1 - P(\bar{S}_{N'+1} \mid S_{N'})) \cdot EC(N'+1, N'+1)$$

$$= EC(N', N'+1)$$

Then, using (a1) that we have already proved, we obtain $EC(N', N'+2) > EC(N', N')$.

Thus we have proved the above Proposition.

(ii) Accordingly, we can assume that

$EC(N', N'+k) > EC(N', N')$ for $m = k$ (>1).

And, we go on to prove that, for $m = k + 1$,

$EC(N', N'+k+1) > EC(N', N')$ holds.

By applying Equation (3) to the above LHS, we have

$$EC(N', N'+k+1) = P(\bar{S}_{N'+1} \mid S_{N'}) \cdot a \cdot N'$$

$$(1 - P(\bar{S}_{N'+1} \mid S_{N'})) \cdot EC(N'+1, N'+k+1) \qquad \text{(a8)}$$

Let $\alpha = P(\bar{S}_{N'+1} \mid S_{N'}) \cdot a \cdot N'$, $\beta = (1 - P(\bar{S}_{N'+1} \mid S_{N'}))$,

then we have $0 \leq \alpha < 1$, $0 < \beta \leq 1$, and

$$EC(N', N'+k) = \alpha + \beta \cdot EC(N'+1, N'+k)$$

$$EC(N', N'+k+1) = \alpha + \beta \cdot EC(N'+1, N'+k+1) \qquad \text{(a9)}$$

Thus, $EC(N', N'+k+1) > EC(N', N'+k)$ holds if and only if $EC(N'+1, N'+k+1) > EC(N'+1, N'+k)$.

Similarly,

$EC(N'+1, N'+k+1) > EC(N'+1, N'+k)$ if and only if

$EC(N'+2, N'+k+1) > EC(N'+2, N'+k)$.

Consequently, we have the following equivalent relation.

$EC(N', N'+k+1) > EC(N', N'+k)$ if and only if

$EC(N'+k, N'+k+1) > EC(N'+k, N'+k) \qquad$ (a10)

By applying the Equation (2) and (3) to the LHS of (a10), we have

$$EC(N'+k, N'+k+1) = P(\bar{S}_{N'+k+1} \mid S_{N'+k}) \cdot a \cdot (N'+k)$$
$$+ (1 - P(\bar{S}_{N'+k+1} \mid S_{N'+k})) \cdot EC(N'+k+1, N'+k+1)$$
$$= P(\bar{S}_{N'+k+1} \mid S_{N'+k}) \cdot \{a \cdot (N'+k) - (A + a \cdot (N'+k+1)\}$$
$$+ A + a \cdot (N'+k+1)$$
$$= A + a \cdot (N'+k+1) - (A+a) \cdot P(\bar{S}_{N'+k+1} \mid S_{N'+k}) \quad \text{(a11)}$$

Since $(A+a) \cdot P(\bar{S}_{N'+k+1} \mid S_{N'+k}) < a$, and by the Equation (2), we have

The last RHS of (a11) $> A + a \cdot (N'+k+1) - a$

$$= A + a \cdot (N'+k) = EC(N'+k, N'+k) \quad \text{(a12)}$$

Thus, it establishes the Inequality (a10), i.e., $EC(N'+k, N'+k+1) > EC(N'+k, N'+k)$.

Since this inequality is equivalent to the following $EC(N', N'+k+1) > EC(N', N'+k)$,

and by the assumption of induction for $m = k$, $EC(N', N'+k) > EC(N', N')$, we have $EC(N', N'+k+1) > EC(N', N')$.

This completes the proof of Lemma 3-1.

A2. Lemma 3-2

If $N' < N''$, then for m ($0 < m \le N'$),

$$EC(N'-m, N'') \ge EC(N'-m, N') \quad \text{(b1)}$$

where the equality holds only if $N'' = N'+1$ and $a = (A+a) \cdot P(\bar{S}_{N'+1} \mid S_{N'})$.

Proof.

We prove this by mathematical induction for m.

(i) If $m = 1$, applying the Equation (3) to the LHS of (b1), we have

$$EC(N'-1, N'') = P(\bar{S}_{N'} \mid S_{N'-1}) \cdot a \cdot (N'-1)$$
$$+ (1 - P(\bar{S}_{N'} \mid S_{N'-1})) \cdot EC(N', N'') \quad \text{(b2)}$$

Using the Lemma 3-1, we have

$$EC(N'-1, N'') \ge P(\bar{S}_{N'} \mid S_{N'-1}) \cdot a \cdot (N'-1)$$
$$+ (1 - P(\bar{S}_{N'} \mid S_{N'-1})) \cdot EC(N', N') \quad \text{(b3)}$$

where the equality holds only if $N'' = N+1$ and $(A+a) \cdot P(\bar{S}_{N'+1} \mid S_{N'}) = a$.

By the Equation (3), the RHS of (b3) equals to $EC(N'-1, N')$. Thus we have

$$EC(N'-1, N'') \ge EC(N'-1, N') \quad \text{(b4)}$$

This establishes the Lemma 3-2 for $m = 1$, where the equality holds only if $N'' = N+1$ and $(A+a) \cdot P(\bar{S}_{N'+1} \mid S_{N'}) = a$.

(ii) Assuming that Lemma 3-2 holds for $m = k$, we prove it for $m = k+1$. By applying the Equation (3) to the LHS of (b1), we have

$$EC(N'-k-1, N'')$$
$$= P(\bar{S}_{N'-k} \mid S_{N'-k-1}) \cdot a \cdot (N'-k-1)$$
$$+ (1 - P(\bar{S}_{N'-k} \mid S_{N'-k-1})) \cdot EC(N'-k, N'') \quad \text{(b5)}$$

By the above assumption,

$$EC(N'-k, N'') \ge EC(N'-k, N').$$

Then, from (b5), we have

$$EC(N'-k-1, N'')$$
$$\ge P(\bar{S}_{N'-k} \mid S_{N'-k-1}) \cdot a \cdot (N'-k-1)$$
$$+ (1 - P(\bar{S}_{N'-k} \mid S_{N'-k-1})) \cdot EC(N'-k, N') \quad \text{(b6)}$$

By the Equation (3), the RHS of (b6) equals to $EC(N'-k-1, N')$. Thus we have

$$EC(N'-k-1, N'') \ge EC(N'-k-1, N').$$

This establishes the Lemma 3-2 for $m = k+1$, where the equality holds only if $N'' = N+1$ and $(A+a) \cdot P(\bar{S}_{N'+1} \mid S_{N'}) = a$.

The proof of Lemma 3-2 is completed.

REFERENCES

[1] Hiromichi Kawano, et al (2004), Structural Change Detection in Time Series Based on DP with Action Cost, Proc. of IEEE ISCIT2004, pp.114-119.

[2] Tetsuo Hattori, et al (2010), Early Structural Change Detection as an Optimal Stopping Problem (I), AROB 15th '10.

The Fifteenth International Symposium on Artificial Life and Robotics 2010 (AROB 15th '10),
B-Con Plaza, Beppu,Oita, Japan, February 4-6, 2010

Autonomous Load-Balancing Data Transmission Scheme to Multiple Sinks for Long-Term Operation of Wireless Sensor Networks

Kakeru Matsumoto†, Akihide Utani‡, and Hisao Yamamoto‡

†*Graduate School of Engineering, Tokyo City University*
‡*Faculty of Knowledge Engineering, Tokyo City University*
1-28-1, Tamazutsumi, Setagaya, Tokyo 158-8557, Japan
{autani; yamahisa}@tcu.ac.jp

Abstract: There is growing expectation for wireless sensor networks as a means of realizing various applications, such as natural environmental monitoring, object tracking, and environmental control in residential spaces or plants. In wireless sensor networks, hundreds or thousands of micro-sensor nodes with such resource limitation as battery capacity, memory, CPU, and communication capacity are placed in an observation area and used to gather sensor information of environments. Therefore, a routing algorithm or a data gathering scheme saving and balancing energy consumption of each node is needed to prolong the lifetime of wireless sensor networks. This paper proposes a new data transmission scheme for the long-term operation of wireless sensor networks. By using the proposed scheme, autonomous load-balancing data transmissions to multiple sinks are actualized. We evaluate the proposed scheme using computer simulations and discuss its development potential. In simulation experiments, the performance of the proposed scheme is compared with those of the existing ones to verify its effectiveness.

Keywords: Wireless Sensor Networks, Multiple Sinks, Data Gathering, Autonomous Load-Balancing.

I. INTRODUCTION

Wireless sensor networks have a wide range of applications, such as natural environmental monitoring, object tracking, and environmental control in residential spaces or plants [1]. In wireless sensor networks, hundreds or thousands of sensor nodes, which are generally compact and inexpensive, are placed in a large-scale observation area and sensor information of each node is gathered to a sink node by inter-node wireless multi-hop communication. Each node consists of a sensing function to measure the status (temperature, humidity, motion, etc.) of an observation point or object, a limited information processing function, and a simplified wireless communication function, and generally operates on a resource of a limited power-supply capacity such as a battery. Therefore, a routing algorithm or a data gathering scheme capable of meeting the following requirements is needed to prolong the lifetime of wireless sensor networks.

1. Efficiency of data gathering
2. Balance on communication load among nodes
3. Adaptability to network topology changes

Clustering-based data gathering scheme [2] and synchronization-based data gathering scheme [3] are under study as communication protocols for the long-term operation of wireless sensor networks, but not all the above requirements are satisfied.

Recently, ant-based routing algorithms have attracted attentions as the algorithms that satisfy the above three requirements [4]. In ant-based routing algorithms, the routing table of each node is generated and updated by applying a process in which ants build routes between their nest and feed by chemical substances (pheromones). The advanced ant-based routing algorithm of [5] is an efficient route-learning algorithm, which shares route information between control messages (ants). In contrast to the conventional ant-based routing algorithms, this algorithm can suppress the communication load of sensor nodes and adapt itself to network topology changes. However, this does not positively ease the communication load concentration to specific nodes that are the source of problems on the long-term operation of wireless sensor networks. Intensive data transmission to specific nodes brings on concentrated energy consumption of them and causes them to break away from the network early. This makes long-term observation by wireless sensor networks difficult.

In wireless sensor networks, the communication load is generally concentrated on sensor nodes around a sink node during the operation process of wireless sensor networks. In case sensor nodes are not placed evenly in a large-scale observation area, the communication load is concentrated on sensor nodes placed in an area of low node density. To solve this node load concentration problem, data gathering scheme for wireless sensor networks with multiple sinks has been proposed [6]. Each node, in this scheme, sends sensing data to the nearest sink node. In comparison with the case of one sink-wireless sensor networks, the communication load on sensor nodes around a sink node is reduced. In each node, however, the destination (sink) node is not selected autonomously and adaptively.

This paper proposes a new data transmission scheme that adaptively reduces the load on load-concentrated nodes and facilitates the long-term operation of wireless sensor networks. The proposed scheme is an autonomous load-balancing data transmission scheme devised by considering the application environment of wireless sensor networks as a typical example of complex systems where the adaptive adjustment of the entire system is realized from the local interactions of components of the system. In the proposed scheme, the load of each node is autonomously balanced. The routing table of each node is composed of the pheromone value of every neighbor node. Each node determines a relay node of sensing data from the pheromone value updated by considering the residual energy of neighbor nodes. Consequently, the destination sink node and the data transmission route to the sink node are determined.

The rest of this paper is organized as follows. In Section II, the proposed scheme is first detailed, and its novelty and superiority are described. In Section III, the results of simulation experiments are reported, and the effectiveness of the proposed scheme is demonstrated by comparing the performance of it with those of the existing ones. Finally, the paper closes with conclusions and ideas for further study in Section IV.

II. PROPOSED SCHEME

Wireless sensor networks are generally used to observe and monitor the status of an object area. At a set sink node, it is expected that the gathering of sensing data from sensor nodes placed in a large-scale object area can be performed. For actual sensor network service, recently, it has been considered to introduce multiple sink nodes in wireless sensor networks [6]. In wireless sensor networks with multiple sinks, the sensing data is allowed to gather at any of the available sink nodes. The proposed scheme is a new data transmission scheme based on this assumption, which can be expected to produce a remarkable effect in multiple sink-wireless sensor networks.

1. Construction of Data Gathering Environment

In each node, its sensing data is not transmitted to a specified destination sink node. By repetitive data transmission that is dependent on the pheromone value of every neighbor node in the routing table of each node, the data gathering at any of the available sink nodes is consequently completed. Each sink node has a pheromone value named a "value to self", which is not updated by transmitting a control packet and receiving a data packet. In the proposed scheme, this pheromone value is dispersed from each sink node to each sensor node in the initial state. In each sensor node, the pheromone value is stored in its routing table as an index to evaluate the value of a neighbor node as the relay destination.

In the initial state of a wireless sensor network, each sink node locally broadcasts a control packet composed of its own ID and "value to self". On receiving this control packet, each sensor node performs the following processing and locally broadcasts a new control packet.

1. A node (l) that has received the control packet stores the received pheromone value in the source field of the routing table first, where "value to self" is stored in case that the source is a sink node.
2. As a piece of information included in a new control packet, next, node (l) computes its own pheromone value (v_l) from the greatest pheromone value ($vmax$) in the routing table as follows:

$$v_l = vmax \times dr_{hop} \qquad (0 < dr_{hop} < 1) \qquad (1)$$

where dr_{hop} is the pheromone value attenuation factor accompanying the hop. Then, a new control packet composed of a node ID (l) and this computed value (v_l) is locally broadcast.

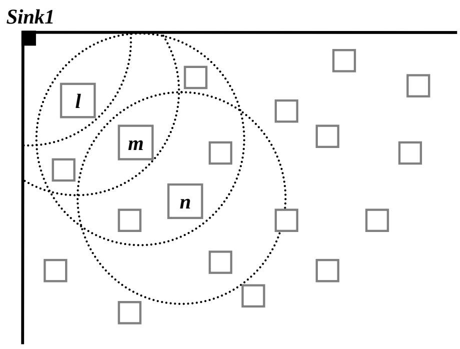

node l routing table

Next Hop		
SN*1*	NH*m*	···
100	*25*	···

node m routing table

Next Hop		
NH*l*	NH*n*	···
50	*12.5*	···

node n routing table

Next Hop		
NH*m*	···	···
25	···	···

Fig.1. Pheromone dispersion from a sink node

The Fifteenth International Symposium on Artificial Life and Robotics 2010 (AROB 15th '10),
B-Con Plaza, Beppu,Oita, Japan, February 4-6, 2010

In Figure 1, an example of pheromone dispersion is shown when "value to self" of the sink node is 100 and the attenuation factor (dr_{hop}) is 0.5. By executing the above processing at appropriate time intervals at each node, "value to self" of the sink node is efficiently dispersed to surrounding nodes with attenuating.

2. Data Transmission and Pheromone Value Update

For data packet transmission, each node selects a node with the greatest pheromone value from the neighbor nodes as a relay node and transmits the data packet to this selected node. In case that more than one node share the greatest pheromone value, however, a relay node is determined from them at random.

To realize load-balancing data transmission by considering residual node energy, a data packet in the proposed scheme includes a pheromone value updated as follows:

$$v_l = vmax \times dr_{hop} \times dr_{lec} \quad (0 < dr_{hop} < 1) \qquad (2)$$

$$dr_{lec} = E'_l / E \qquad (3)$$

The above (2) and (3) are the pheromone update equations of a node (l), where E_l' and E represent the residual energy of node (l) and the battery capacity of each node, respectively.

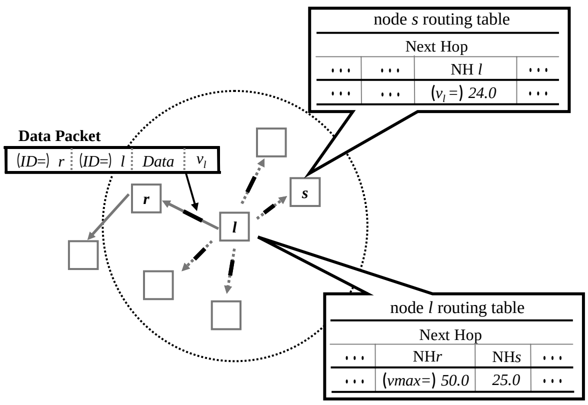

Fig.2. Data transmission and pheromone value update

In the proposed scheme, a data packet addressed to a node of the greatest pheromone value is intercepted by all neighbor nodes. This data packet includes the pheromone value of the source node updated with the residual energy taken into consideration. Each node that has intercepted this packet stores the value in the routing table and updates the pheromone value of the source node. In Figure 2, an example on the transmission of a data packet addressed to a node of the greatest pheromone value and its accompanying pheromone value update is shown. In this example, node (l) refers to its own routing table and transmits a data packet addressed to node (r), which has the greatest pheromone value. When this data packet is intercepted, each neighbor node around node (l) stores the updated pheromone value (v_l) computed by the above equations (2) and (3) in the NHl field of the routing table.

The proposed scheme requires the construction of a data gathering environment in the initial state of wireless sensor networks, but needs no special communication for network control. In the proposed scheme, each node adds a pheromone value updated by considering the residual energy to a data packet at data transmission. At the data transmission process, each neighbor node intercepts this data packet and updates the pheromone value of the source node in the routing table. This simple mechanism alone achieves autonomously adaptive load-balancing data transmission using multiple routes and sink nodes. The lifetime of wireless sensor networks can be extended by reducing the communication load for network control and solving the node load concentration problem.

III. SIMULATION EXPERIMENT

Through simulation experiments, the performance of the proposed scheme is investigated in detail to verify its effectiveness.

1. Conditions of Simulations

In a wireless sensor network consisting of many sensor nodes placed in a wide range, only sensor nodes that detected abnormal values or obtained specific information were assumed to transmit the measurement data. The conditions of simulation, which were used in the experiments performed, are shown in Table 1. In the simulation area, sensor nodes are arranged at random. Two sink nodes are placed on the two corners of this area. In Figure 3, the network configuration is illustrated.

In the experiments performed, the pheromone value attenuation factor accompanying hop (dr_{hop}) and the "value to self" of each sink node were set to 0.5 and 100.0, respectively. The sizes of data packet and control packet were set to 18 bytes and 6 bytes, respectively. The battery capacity (E) of each node was set to 0.5 J.

In the experimental results reported, the proposed scheme is evaluated through the comparison with the existing ones of [4]-[6]. On the schemes of [4]-[6], the simulation settings that were used in [7] and produced good results in a preliminary investigation were adopted for the comparison with the proposed scheme.

Table 1. Conditions of simulations

Simulation size	*2,400 m × 2,400 m*
The number of sensor nodes	*1,000*
Range of radio wave	*150 m*
The number of sink nodes	*2*

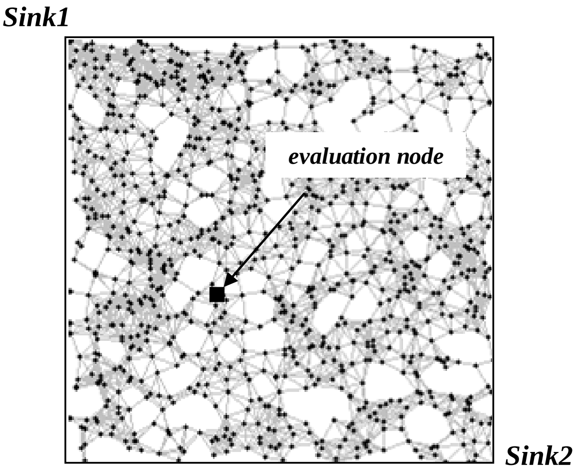

Fig.3. Multiple sink-wireless sensor network

2. Experimental Results

As the first experiment, it was assumed that the evaluation node marked in Figure 3 detected an abnormal value and transmitted a data packet periodically. The routes used by applying the proposed scheme are shown in Figure 4. Of the 2,000 data packet transmissions from the evaluation node, the routes illustrated in (1) were used in the first 300 transmissions, those of (2) 1 to 1,000 transmissions, and those of (3) in a total of 2,000 transmissions. From (1)-(3) in Figure 4, the autonomous switching of destination sink nodes and routes to each sink node can be confirmed. Since the proposed scheme is not a data transmission one specifying address, autonomous load-balancing data transmissions to two sink nodes using multiple routes are enabled. The node load can be improved and balanced by applying the proposed scheme.

Next, it was assumed that data packets were periodically transmitted from a total of 20 sensor nodes to sink nodes. In Figure 5, the transition of the delivery ratio on the number of total transmissions from a total of 20 nodes randomly selected to sink nodes is shown and the lifetime of the multiple sink-wireless sensor network used in this experiment is compared. In this figure, two existing schemes based on ant-based routing algorithms of [4] and [5] are denoted as *MUAA* and *AAR*, respectively. The existing scheme of [6], which is a data gathering one for multiple sink-wireless sensor networks, is denoted as *NS*. The result of Figure 5 verifies that the proposed scheme is substantially advantageous for the long-term operation of wireless sensor networks.

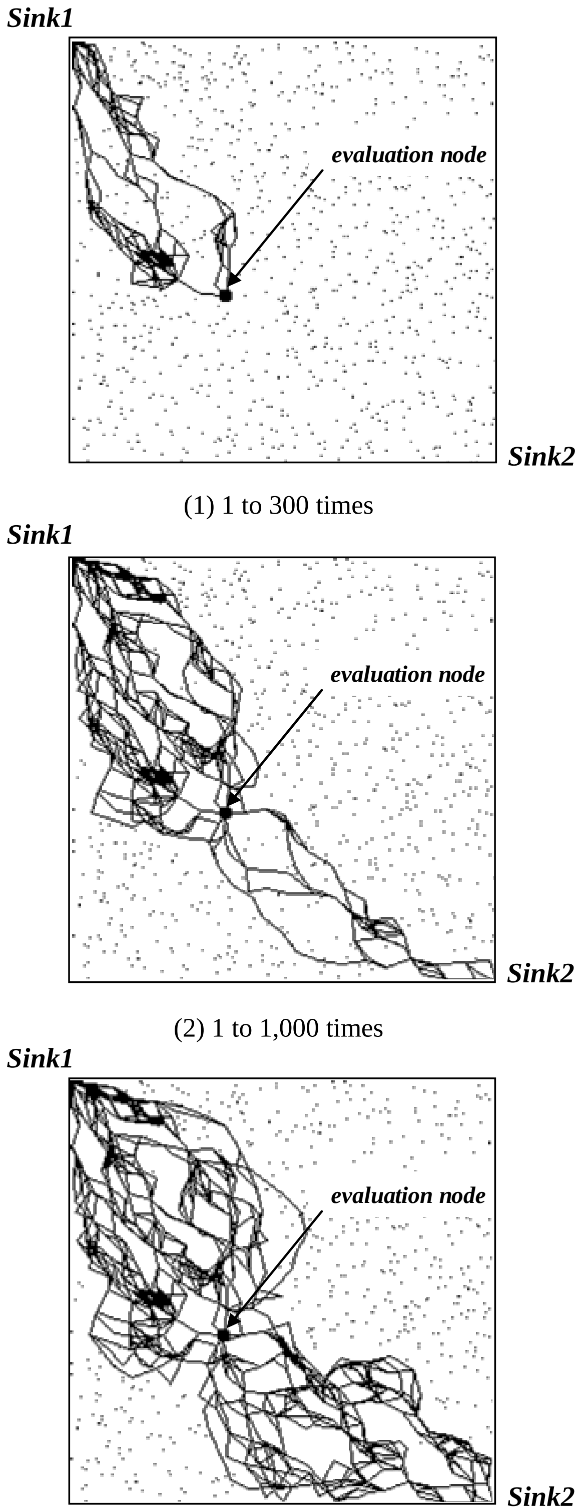

(3) 1 to 2,000 times

Fig.4. Routes used by applying the proposed scheme

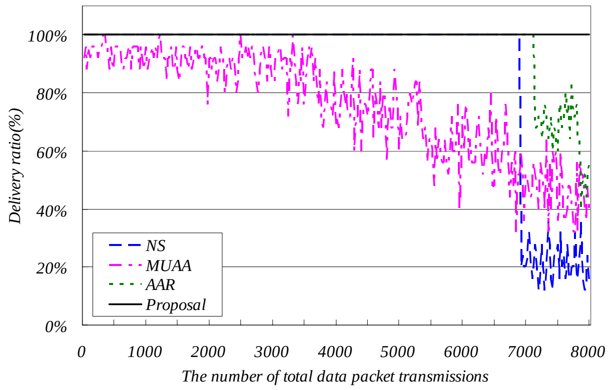

Fig.5. Transition of delivery ratio

IV. CONCLUSIONS

In this paper, a data transmission scheme that adaptively reduces the load on load-concentrated nodes and facilitates the long-term operation of wireless sensor networks, which is an autonomous load-balancing data transmission one devised by considering the application environment of wireless sensor networks to be a typical example of complex systems, has been proposed. In the experiments, the performance of the proposed scheme was compared with those of the existing ones. Experimental results indicate that the proposed scheme is superior to the existing ones and has the development potential as a promising one from the viewpoint of the long-term operation of wireless sensor networks. Future works include evaluation on the parameter introduced in the proposed scheme in detail and verification of its effectiveness to various network environments.

REFERENCES

[1] Akyildiz I, Su W, Sankarasubramaniam Y, and Cayirci E (2002), Wireless sensor networks: A survey. Computer Networks Journal 38(4):393-422
[2] Dasgupta K, Kalpakis K, and Namjoshi P (2003), An efficient clustering-based heuristic for data gathering and aggregation in sensor networks. Proc. IEEE Wireless Commun. and Net. Conf. (WCNC), pp.16-20
[3] Nakano H, Utani A, Miyauchi A, and Yamamoto H (2009), Data gathering scheme using chaotic pulse-coupled neural networks for wireless sensor networks. IEICE Trans. Funds. E92-A(2):459-466
[4] Ohtaki Y, Wakamiya N, Murata M, and Imase M (2006), Scalable and efficient ant-based routing algorithm for ad-hoc networks. IEICE Trans. Commun. E89-B(4):1231-1238
[5] Utani A, Orito E, Kumamoto A, and Yamamoto H (2008), An advanced ant-based routing algorithm for large scale mobile ad-hoc sensor networks. Trans. SICE 44(4):351-360
[6] Oyman EI and Ersoy C (2004), Multiple sink network design problem in large scale wireless sensor networks. Proc. Int. Conf. on Commun. (ICC)
[7] Orito E, Utani A, and Yamamoto H (2009), Load-balanced and reduced data transmission scheme for wireless sensor networks with multiple sinks. IEICE Technical Report 108(447):13-16

The Fifteenth International Symposium on Artificial Life and Robotics 2010 (AROB 15th '10),
B-Con Plaza, Beppu,Oita, Japan, February 4-6, 2010

Robust Ride Comfort Control of vehicles without Measurements of Tire Deflection

Katsuhiro Okumura , Masahiro Oya and Hideki Wada

Fukuoka Industrial Technology Center, 3-6-1 Norimatsu, Yahatanishi-ku, Kitakyushu-shi, Fukuoka, Japan
(Tel: +81-93-691-0260; Fax: +81-93-691-0252) (E-mail: kokumura@fitc.pref.fukuoka.jp)
Department of Mechanical and Control Engineering, Kyushu Institute of Technology
1-1 Sensui-cho, Tobata-ku, Kitakyushu-shi, Fukuoka, Japan
Shin-Nippon Nondestructive Inspection Co., Japan, 4-10-13, Ibori, Kokurakita-ku, Kitakyushu-shi, Fukuoka, Japan

Abstract: In this paper, a robust ride comfort control scheme for vehicles is proposed in which the measurements of the tire deflections are not required. The controller has good property that we can specify a location where the ride comfort becomes best. To achieve this end, an estimator for the tire deflections and the road disturbances is proposed. Next, a combined ideal vehicle is designed. In the ideal vehicle, the location where ride comfort becomes best can be moved by setting only one design parameter. Finally, to force the real vehicle track the motion of the combined ideal vehicle, a robust tracking controller is designed.

Keywords: Vehicle, Ride comfort, Active suspension, Robust Tracking Control, Ideal Model

I. INTRODUCTION

Recently, in order to achieve good ride and good handling qualities, a large amount of control schemes using active suspensions have been proposed in [1]-[10]. In the case of realizing the best ride comfort at every location on a vehicle body, it must be required that the vertical acceleration and the angular acceleration of the vehicle body must be controlled so as to be zero. Then, some serious problems arise. For example, the suspension stroke may over an admitted range and the handling qualities may become worse. Therefore, in conventional schemes [1]-[10], the active suspensions are controlled so that the suspension strokes lie within an admitted range and the handling quality does not become worse. As a result, the ride comfort becomes best at only one specified location on the vehicle body. In case when the specified location has to be moved, the conventional active suspension controllers require a trial and error method, and then, too much time is spent to redesign an active suspension controller.

To struggle with the problem stated above, the authors have proposed schemes [11] [13]. In vehicle systems using the active suspension controllers proposed in [11]-[13], there exist good properties as follows: 1) The ride comfort at a specified location becomes best, 2) The best location can be easily moved by setting only one design parameter without redesigning a different suspension controller. However, in the proposed schemes [11]-[13], it is assumed that the tire deflections can be measured. Since the road surfaces are uneven, using non-contact sensors such as laser position sensors, it is difficult to measure the tire deflections with high accuracy.

In this paper, to overcome the problem stated above, a robust ride comfort control scheme is proposed. In the proposed controller, active suspensions are used as actuators and the measurements of tire deflections are not required. To realize good ride comfort without using the measurements of the tire deflections, we propose estimation methods for the tire deflections and the accelerations of road disturbances. The road disturbances imply the displacement of road surfaces. Using the estimate of the accelerations of road disturbances, we can design a combined ideal vehicle proposed in [13], and then, a robust tracking controller can be also designed so that the real vehicle track the motion of the combined ideal vehicle. At last, numerical simulations are carried out to demonstrate of the proposed robust active suspension controller.

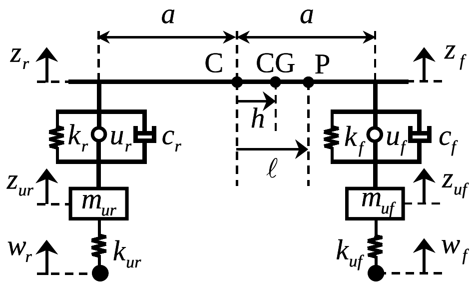

Fig. 1. Two wheels model.

II. VEHICLE MODEL

The two wheels model is shown in Fig. 1. The explanation of parameters is shown in Table 1. It is assumed that the pitching angle $\theta(t)$ is small, and then, the dynamic equation of vehicles is given as follows [7].

$$\left.\begin{aligned}
&\ddot{\boldsymbol{x}}_z(t) = \boldsymbol{d}(t) \quad H^{\ 1}\ddot{\boldsymbol{w}}(t)\\
&\ddot{\boldsymbol{x}}_u(t) = \quad K_u\boldsymbol{x}_u(t) \quad M_u^{\ 1}\boldsymbol{f}(t) \quad \ddot{\boldsymbol{w}}(t)\\
&\boldsymbol{x}_z(t) = H^{\ 1}[z_f(t) \quad w_f(t)\ z_r(t) \quad w_r(t)]^T\\
&\boldsymbol{x}_u(t) = [z_{uf}(t) \quad w_f(t)\ z_{ur}(t) \quad w_r(t)]^T\\
&\boldsymbol{d}(t) = M^{\ 1}H^T\boldsymbol{f}(t)\\
&\boldsymbol{f}(t) = [f_f(t)\ \ f_r(t)]^T\\
&\qquad = \quad C\dot{\boldsymbol{x}}_s(t) \quad K\boldsymbol{x}_s(t) + \boldsymbol{u}(t)
\end{aligned}\right\} \quad (1)$$

Table 1 Notation of vehicle model.

C CG	center and center of gravity of vehicle body
z_{cg} θ	vertical displacement at CG and pitching
z_f z_r	vertical displacement of vehicle body at positions on front and rear wheel axle
z_{uf} z_{ur}	vertical displacement of front and rear unsprung mass
w_f w_r	vertical displacement of road disturbance added to front and rear wheel
v	longitudinal velocity of vehicle
m i_c	sprung mass and moment of inertia of vehicle body
a	half of vehicle body length
h	distances from C to CG and from C to P
m_{uf} m_{ur}	front and rear unsprung mass
k_f k_r	front and rear suspension stiffness
c_f c_r	front and rear suspension damping rate
k_{uf} k_{ur}	front and rear tire spring stiffness
f_f f_r	front and rear force added to sprung mass
u_f u_r	front and rear active suspension control force

$$\left.\begin{array}{l} \boldsymbol{x}_s(t) = H\boldsymbol{x}_z(t) \quad \boldsymbol{x}_u(t) \\ \boldsymbol{u}(t) = [u_f(t)\ \ u_r(t)]^T \quad \boldsymbol{w}(t) = [w_f(t)\ \ w_r(t)]^T \\ M = (T_h^T)\ {}^1\mathrm{diag}[m\ \ i_c]T_h\ {}^1 \\ M_u = \mathrm{diag}[m_{uf}\ \ m_{ur}] \ \ K = \mathrm{diag}[k_f\ \ k_r] \\ C = \mathrm{diag}[c_f\ \ c_r] \ \ K_u = M_u\ {}^1\mathrm{diag}[k_{uf}\ \ k_{ur}] \\ T_h = I_2 \quad Dh \ \ H = \left[\begin{array}{cc} 1 & a \\ 1 & a \end{array}\right] \ \ D = \left[\begin{array}{cc} 0 & 1 \\ 0 & 0 \end{array}\right] \end{array}\right\}(2)$$

The control objective is to develop an active suspension controller so that the vertical acceleration at any specified location on the vehicle body can be reduced to a small value easily. To meet the objective, the following assumptions are made for actual vehicles considered here.

A1 The accelerations $\ddot{z}_f(t)$, $\ddot{z}_r(t)$, $\ddot{z}_{uf}(t)$ and $\ddot{z}_{ur}(t)$ are measured.

A2 The force $\boldsymbol{f}(t) = [f_f(t)\ \ f_r(t)]^T$ added to the sprung mass are measured.

A3 Suspension displacement $\boldsymbol{x}_s(t)$ and its velocity $\dot{\boldsymbol{x}}_s(t)$ are measured.

A4 Vehicle parameters are known except for the length a, the front and the rear tire stiffness k_{uf} k_{ur} and the tire mass m_{uf} m_{ur}.

A5 The second and third derivation of the road disturbance $\boldsymbol{w}(t)$ are bounded.

III. ESTIMATE OF STATE VARIBLES AND ROAD DISTURBANCE

Fig. 2 shows the configuration of the vehicle system proposed in [13]. The combined ideal model shown in Fig. 2 has good properties. Namely, 1) The ride comfort at a specified location becomes best, 2) The best location can be easily moved by setting only one design parameter without redesigning the combined ideal vehicle. If the real vehicle can track the motion of the designed combined ideal vehicle, the control objective can be achieved. The tracking controller in Fig. 2 is designed so that the real vehicle can track the motion of the combined ideal vehicle. To achieve control objective, the signals of road disturbance $\ddot{\boldsymbol{w}}(t)$ and state variables $\boldsymbol{x}_z(t)$, $\dot{\boldsymbol{x}}_z(t)$, $\boldsymbol{x}_u(t)$, $\dot{\boldsymbol{x}}_u(t)$ $\boldsymbol{d}(t)$ are required. According to assumptions, it can be seen that the following signals are available.

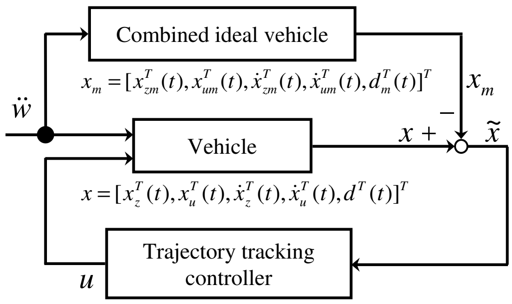

Fig. 2 Configuration of active suspension control system.

$$\left.\begin{array}{l} \ddot{\boldsymbol{x}}_s(t) = [\ddot{z}_f(t)\ \ \ddot{z}_r(t)]^T \quad [\ddot{z}_{uf}(t)\ \ \ddot{z}_{ur}(t)]^T \\ H\boldsymbol{d}(t) = [\ddot{z}_f(t)\ \ \ddot{z}_r(t)]^T \end{array}\right\}(3)$$

Moreover, it is easy from (1), (2) to ascertain that the following signals are also available.

$$\left.\begin{array}{l} \boldsymbol{p}_1(t) = K_u\ {}^1 \quad \ddot{\boldsymbol{x}}_s(t) \quad (H\boldsymbol{d}(t) + M_u\ {}^1\boldsymbol{f}(t)) \\ \qquad = \boldsymbol{x}_u(t) \\ \boldsymbol{p}_2(t) = \boldsymbol{x}_s(t) + \boldsymbol{p}_1(t) = H\boldsymbol{x}_z(t) \end{array}\right\}(4)$$

Since the signal $\dot{\boldsymbol{x}}_s(t)$ is available, if an estimator for $\dot{\boldsymbol{x}}_z(t)$ is developed, then, the signal $\dot{\boldsymbol{x}}_u(t)$ becomes also available. Therefore, we will develop an estimator for $\dot{\boldsymbol{x}}_z(t)$ and $\ddot{\boldsymbol{w}}(t)$. Let's consider the new state $\boldsymbol{\eta}(t) = [H\dot{\boldsymbol{x}}_z(t))^T\ \ \ddot{\boldsymbol{w}}(t)^T]^T$. Then, we have

$$\left.\begin{array}{l} \dot{\boldsymbol{\eta}}(t) = A\ \ \boldsymbol{\eta}(t) + \boldsymbol{q}_w(t) \\ A\ \ = \left[\begin{array}{cc} O_2 & I_2 \\ O_2 & O_2 \end{array}\right] \ \ \boldsymbol{q}_w(t) = [0\ 0\ (\boldsymbol{w}(t)^{(3)})^T]^T \end{array}\right\}(5)$$

where O_n I_n denote n n zero matrix and n n unit matrix. Based on the relation (5), the estimator for the state $\boldsymbol{\eta}(t)$ is proposed as

$$\left.\begin{array}{l} \widehat{\boldsymbol{\eta}}(t) = (2\ \ C \quad 3\ \ {}^2B\ \ )\boldsymbol{p}_2(t) + \boldsymbol{\zeta}(t) \\ \dot{\boldsymbol{\zeta}}(t) = A\ \ \widehat{\boldsymbol{\eta}}(t) \quad (2\ \ C \quad 3\ \ {}^2B\ \ )C^T\widehat{\boldsymbol{\eta}}(t) \\ \boldsymbol{\zeta}(0) = \quad (2\ \ C \quad 3\ \ {}^2B\ \ )\boldsymbol{p}_2(0) \\ B\ \ = [O_2\ I_2]^T \quad C\ \ = [I_2\ O_2]^T \end{array}\right\}(6)$$

where is a positive deign parameter introduced to improve performance of the proposed estimator. Defending the estimated error $\widetilde{\boldsymbol{\eta}}(t)$ as

$$\widetilde{\boldsymbol{\eta}}(t) = \left[\begin{array}{cc} I_2 & O_2 \\ O_2 & {}^1I_2 \end{array}\right](\boldsymbol{\eta}(t) \quad \widehat{\boldsymbol{\eta}}(t)) \qquad (7)$$

and differentiating the first equation in (6), we obtain the following the error equation.

$$\dot{\widetilde{\boldsymbol{\eta}}}(t) = \quad A_E\widetilde{\boldsymbol{\eta}}(t) + \quad {}^1\boldsymbol{q}_w(t) \ \ A_E = \left[\begin{array}{cc} 2I_2 & I_2 \\ 3I_2 & O_2 \end{array}\right](8)$$

Table 2 Nominal values of parameters.

m	781	kg	i_c	990	kgm^2
h	0.04	m	a	1.38	m
k_f	27160	N m	k_r	29420	N m
c_f	4000	Ns m	c_r	2500	Ns m
m_{uf}	69	kg	m_{ur}	96	kg
k_{uf}	229000	N m	k_{ur}	255000	N m

For the proposed estimator, the following theorem holds

Theorem 1: For estimated errors $C^T\widetilde{\boldsymbol{\eta}}(t)$ and $B^T\widetilde{\boldsymbol{\eta}}(t)$, there exist bounded positive constants $^-_{Ei}$ $i = 1\ 2$ independent of the design parameter such that

$$\|C^T\widetilde{\boldsymbol{\eta}}(t)|^2 \le {}^-_{E1} \quad {}^4 \quad \| \quad B^T\widetilde{\boldsymbol{\eta}}(t)\|^2 \le {}^-_{E2} \quad {}^2 \tag{9}$$

Proof of Theorem1: Since the system matrix A_E is asymptotically stable, Lyapnov equation

$$A_E^T P + P A_E = \quad 2I_4 \tag{10}$$

has the positive definite matrix solution P. Then, differentiating the positive definite function $V(t) = \widetilde{\boldsymbol{\eta}}(t)^T P \widetilde{\boldsymbol{\eta}}(t)$, we have

$$\dot{V}(t) \le \quad \frac{}{{}_{\max}[P]} V(t) + \quad {}^3 \quad {}_w \tag{11}$$

where $_w$ is a positive constant value independent of the design parameter . Using the relation above, the inequalities in (9) can be derived.

It can be concluded from theorem 1 that estimated errors decrease as the design parameter increases. In case when the design parameter is set to be large enough, we can obtain the signals $\ddot{\boldsymbol{w}}(t)$ and $H\dot{\boldsymbol{x}}_z(t)$ with enough accuracy. Then, the signal $H\dot{\boldsymbol{x}}_z(t) \quad \dot{\boldsymbol{x}}_s(t) = \dot{\boldsymbol{x}}_u(t)$ becomes also available.

To demonstrate of the usefulness of the proposed estimator, numerical simulations are carrying out. Values of vehicle parameters are shown in Table 2. The vehicle velocity is set as $v = 100 \quad 1000 \ 3600[\mathrm{m\ s}]$. Fig. 3 (a) shows the road disturbance $w_f(t) = w_r(t \quad L)$ $L = 2a \ v$ and Fig. 3 (b) shows the disturbance $w_{nd1}(t)$ added to the measurement of $\boldsymbol{c}^T\boldsymbol{d}(t)$ $\boldsymbol{c} = [1 \ \ 0]^T$. It is assumed that the disturbance $w_{nd1}(t)$ appears due to measurement accuracy of acceleration sensors and the maximum measurement error is 0 1m/s ^{2}.

At first, in case of using measurements without disturbances, we show responses of the velocity $y_z(t) = \boldsymbol{c}^T C \ \boldsymbol{\eta}(t)$, the road disturbance $y_w(t) = \boldsymbol{c}^T B \ \boldsymbol{\eta}(t)$, the estimated errors $\widetilde{y}_z(t) = \boldsymbol{c}^T C \ \widetilde{\boldsymbol{\eta}}(t)$ and $\widetilde{y}_w(t) = \ \boldsymbol{c}^T B \ \widetilde{\boldsymbol{\eta}}(t)$ in Fig. 4. As shown in Fig. 4, the estimated errors become small as the design parameter increases. Next, in the case of using measurements with disturbances, we show responses of the estimated errors $\widetilde{y}_z(t)$ and $\widetilde{y}_w(t)$ in Fig. 5. In this case, the design parameter is set as $= 2000$ and similar disturbances shown in Fig. 3 (b) are added in all measurements of acceleration sensors and force sensors. As shown in Fig. 5, also in the case of using measurements with disturbances, it is seen that estimated errors do not become large and available estimated signals can be obtained.

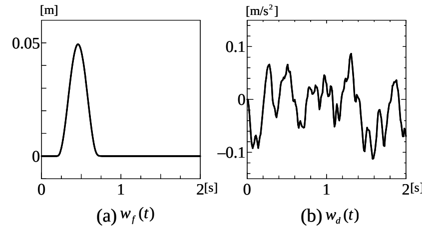

Fig. 3 Road disturbance $w_f(t)$ and disturbance $w_{nd1}(t)$ added to measurement $\boldsymbol{c}^T\boldsymbol{d}$.

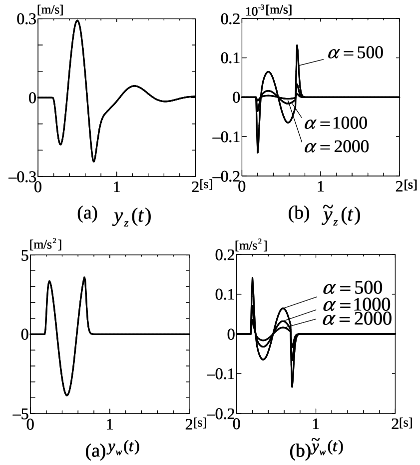

Fig. 4. Responses of $y_z(t)$, $y_w(t)$ and $\widetilde{y}_z(t)$, $\widetilde{y}_w(t)$.

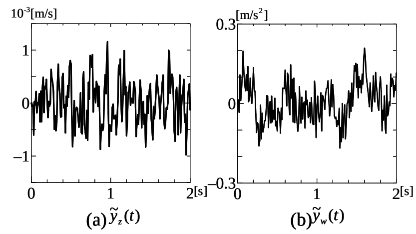

Fig. 5 Responses of $\widetilde{y}_z(t)$, $\widetilde{y}_w(t)$ in the presence of measurement disturbances.

IV. TRACKING CONTROLLER

Fig. 6 shows the vehicle system using estimates proposed in the previous section. The stability and good tracking performance of the vehicle system can be shown by using the similar manner stated in [13].

V. NUMERICAL SIMULATION RESULTS

The numerical simulation results are shown to confirm usefulness of the proposed robust active suspension controller. The values shown in Table 2 are used as nominal values for vehicle parameters, and the vehicle velocity is set as $v = 100 \quad 1000 \ 3600\mathrm{m\ s}$. The combined ideal vehicle designed in [13] is used. The design parameters are set as $= 2000$ $\gamma = 100$. The design parameter γ is the feed back gain introduced in [13] to force the actual vehicle track the motion of the combined ideal vehicle. Fig. 7 shows the maximum gain curves of the nominal vehicle controlled so that the real vehicle can track the motion of the combined ideal vehicle. The thin lines show the maximum gain curves of the controlled nominal vehicle, the

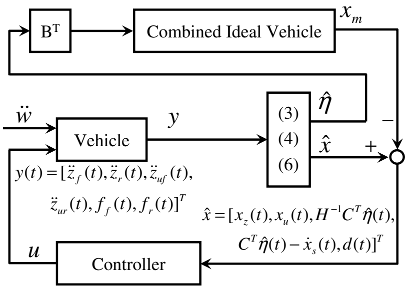

Fig. 6 Configuration of the vehicle system using estimates.

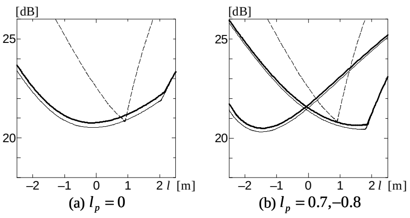

Fig. 7 Maximum gain curves of the controlled nominal vehicle.

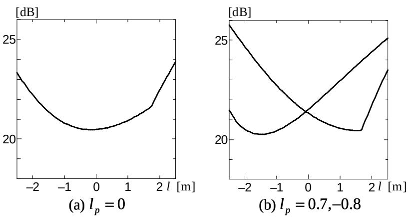

Fig. 8. Maximum gain curves for variations of $K\ C$.

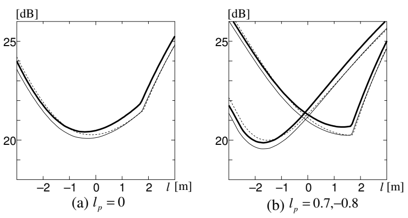

Fig. 9. Maximum gain curves for variations of M.

thick lines show the maximum gain curves of the combined ideal vehicle, and the dashed lines show the nominal vehicle without control. It is seen from Fig. 7 that the maximum gain curves are mostly same between the combined ideal vehicle and the controlled nominal vehicle. It is also seen that the location where the ride comfort becomes best can be easily moved by setting only one design parameter $\ _p$. The design parameter $\ _p$ is introduce to move the location where the ride comfort becomes best in the combined vehicle model proposed in [13].

Fig. 8 shows the maximum gain curves of the controlled vehicle with the parameter uncertainties $(K\ C) = (\overline{K}\ \overline{C})\ (0\ 8\overline{K}\ 0\ 8\overline{C})\ (1\ 2\overline{K}\ 1\ 2\overline{C})$. The thick lines show the maximum gain curves of the controlled nominal vehicles, and the thin lines show the maximum gain curves of the controlled vehicle with parameter uncertainties. There is no difference for variations of $K\ C$.

Fig. 9 shows the maximum gain curves of the controlled vehicle with the parameter uncertainties $(m\ i_c\ h) = (\overline{m}\ \bar{i}_c\ \overline{h})\ (0\ 8\overline{m}\ 0\ 8\bar{i}_c\ \overline{h} + 0\ 3)\ (1\ 2\overline{m}\ 1\ 2\bar{i}_c\ \overline{h} + 0\ 3)$. The thick lines, dashed lines, and thin lines show the each results with the parameter$(m\ i_c\ h) = (\overline{m}\ \bar{i}_c\ \overline{h})\ (0\ 8\overline{m}\ 0\ 8\bar{i}_c\ \overline{h} + 0\ 3)\ (1\ 2\overline{m}\ 1\ 2\bar{i}_c\ \overline{h} + 0\ 3)$. It can be seen that some differences appear between the controlled vehicle with uncertainties and the controlled nominal vehicle but small enough.

VI. CONCLUSION

We have proposed the active suspension control scheme in which tire deflections are not required. The proposed suspension controller has a good property that the location where the ride comfort becomes best can be easily moved by setting only one design parameter $\ _p$. It has been shown by carrying out numerical simulations that ride comfort becomes best at the specified location even if there are uncertainties in the suspension stiffness k_f, k_r, damping rate c_f, c_r, the sprung mass and the moment of inertia $m\ i_c$ and the distance h from C to CG.

REFERENCES

[1] D. Hrovat, Survey of Advanced Suspension Developments and Related Optimal Control Application, *Automatica*, Vol.33-10, pp.1781-1817, (1997).

[2] A.G. Thompson and B.R. Davis, RMS values for control force, suspension stroke and tire deflection in an active suspension, *Vehicle System Dynamics*, Vol. 34, pp. 143-150, (2000).

[3] A.G. Thompson and C.E.M. Pearce, Performance index for a preview active suspension applied to a quarter-car model, *Vehicle System Dynamics*, Vol. 35, No. 1, pp. 55-66, (2001).

[4] A.G. Thompson and C.E.M Pearce, Direct computation of the performance index for an optimally controlled active suspension with preview applied to a half-car model, *Vehicle System Dynamics*, Vol. 35, No. 2, pp. 121-137, (2001).

[5] L. Wenger and F. Borrelli, The application of constrained optimal control to active automotive suspensions, *Proceedings of IEEE Conference on Decision and Control*, pp. 881-886, (2002).

[6] L. Zuo and S.A. Nayfeh, Structured H_2 optimization of vehicle suspensions based on multi-wheel models, *Vehicle System Dynamics*, Vol. 40, No. 5, pp. 351-371, (2003).

[7] J.-S. Lin and C.-J. Huang, Nonlinear backstepping active suspension design applied to a half-car model, *Vehicle System Dynamics*, Vol. 42, No. 6, pp. 373-393, (2004).

[8] H. Chen and C.W. Scherer, An LMI based model predictive control scheme with guaranteed H_∞ performance and its application to active suspension, *Proceedings of the American Control Conference*, pp.1487-1492, (2004).

[9] H. Chen and K.-H. Guo, Constrained H_∞ control of active suspensions: An LMI approach', *IEEE Trans. Control System Technology*, Vol. 13, No. 3, pp. 412-421, (2005).

[10] H. Nishimura and N. Takahashi, Active Vibration Control for Suspension by Consideration Its Stroke Limitation, *Journal of System Design and Dynamics*, Vol.1, No.2, pp.138-146, (2007).

[11] M. Oya, H. Harada, Y. Araki, An Active Suspension Controller Achieving the Best Ride Comfort at Any Specified Location on A Vehicle, *Journal of System Design and Dynamicss*, pp.245-256, (2007).

[12] H. Okuda, Y. Tsuchida, M. Oya, Q. Wang, and K. Okumura, Robust Active Suspension Controller Achieving Good Ride Comfort, Proc. of SICE Annual Conference 2007, September 17-20, Kagawa, Japan, pp. 1305-1310, (2007).

[13] M. Oya, Y. Tsuchida, Q. Wang, Y. Taira, Adaptive Active Suspension Controller Achieving the Best Ride Comfort at Any Specified Location on Vehicles with Parameter Uncertainties, *International Journal of Advanced Mechatronic Systems*, Vol. 1, No. 2, pp. 125-136, (2008).

Specification and real-time control of robotic manufacturing systems based on concurrent process modeling

G. Yasuda

Nagasaki Institute of Applied Science, Nagasaki 851-0193, JAPAN
(Tel : 81-95-838-5184; Fax : 81-95-830-2091)
(YASUDA_Genichi@NiAS.ac.jp)

Abstract: The paper deals with a systematic method of specification and real-time control for robotic manufacturing systems based on concurrent process modeling. The large scale and complex manufacturing systems have a hierarchical structure where a system is composed several lines with some stations and each station also has several machines and so on. In such a hierarchical structure, the controllers are geographically distributed according to their physical structure. So it is desirable to realize the hierarchical and distributed control. In this paper, the task specification of discrete event manufacturing processes is represented using a global Petri net. Then it is decomposed and distributed into the machine controllers, which are coordinated through communication between the coordinator and machine controllers so that the decomposed transitions fire at the same time. Implementation of a real-time distributed control system is described for an example robotic manufacturing system. The demonstrations show that the proposed system can be used as an effective tool for consistent modeling and control of large and complex manufacturing systems.

Keywords: Robotic manufacturing systems, specification, real-time control, concurrent process modeling, Petri nets.

I. INTRODUCTION

Recently, based on the rapid development of the computer technology, the factory automation systems have been becoming larger and more complex. The system architecture has shifted to distributed and parallel processing from centralized processing in order to reduce the development cost and to improve the reliability. In the field of factory automation systems, a demand for the automatic control has diversified and the control logic has become extremely complicated. This is because the combinative complexity of the control requirement, which comes from the non-deterministic features of event driven systems such as manufacturing control systems, is inevitable. To deal with the complexity, a new methodology on control system design based on the concept of event driven system is necessary. However, appropriate representation methods and analysis methods for control mechanism have not sufficiently been established.

Programming paradigm modeled by a network, such as Petri net, has been considered to be useful, because the network model can describe the execution order of parallel/sequential processes directly without ambiguity. The Petri net is excellent in expression and analysis of the dynamic behavior of event driven systems, because it can model the system that consists of simultaneous process elements that interfere to each other. The programming technique makes it possible to realize systematic and high-level description of system specification. Therefore, it has been applied to a variety of system developments such as real-time systems, production systems, communication systems, and so on.

However, in case of factory automation systems, the network model becomes complicated and it lacks for the readability and comprehensibility. Besides, only specification analysis stage has been supported, and the support for the control software coding stage is insufficient [1]. Therefore, the flexibility and expandability are not satisfactory in order to deal with the specification change of the system.

Due to its complexity, a large and complex manufacturing system is commonly structured into a hierarchy. A coarsely grained hierarchy of abstraction levels is made up of the followings: planning, scheduling, coordination, and local control. Each level operates on a certain time horizon, on a certain view of the manufacturing system. At the upper level, the time horizon is long and the global system is considered. In the hierarchy, each lower level is a disaggregation of the upper one (factory, shop, cell, station, machine, etc) and on the other hand more details are taken into account (products, parts, operations, steps, etc). Progressively, real-time constraints are introduced and at the bottom of the hierarchy (local control) they are very hard and all the emergency procedures are implemented at this level.

Thus the manufacturing system handles complicated tasks by dividing a task hierarchically in this structure, which is expected to be effective in managing cooperation tasks executed by great many machines or robots. Conventional Petri net based control systems were implemented based on an overall system model. Since in the large and complex systems, the controllers are geographically distributed according to their physical (hardware) structure, it is desirable to realize the hierarchical and distributed control.

The hierarchical and distributed control for large and complex discrete event manufacturing systems has not been implemented so far. If it can be realized by Petri nets, the modeling, simulation and control of large and complex discrete event manufacturing systems can be consistently realized by Petri nets. In this paper, the author presents a methodology for hierarchical and distributed control of large and complex robotic manufacturing systems using extended Petri nets, to construct the control system where the cooperation of each controller is implemented so that the behavior of the overall system is not deteriorated and the task specification is completely satisfied.

II. PETRI NET BASED SPECIFICATION OF MANUFACTURING SYSTEMS

Discrete event systems such as robotic manufacturing systems have the properties of asynchronism, ordering, concurrency and conflict, so that unsafeness and deadlock will be apt to occur in the systems. The Petri net is one of the effective means to represent such systems. For applying it to the design, analysis, and control of the systems the guarantee of safeness and the notation of input/output of signals from/to machines should be required. A kind of graph deduced from the Petri net was proposed so as to satisfy the above requirements [2].

The extended Petri net consists of the following six elements: place, transition, directed arc, token, gate arc, output signal arc. A place represents a condition of a system element or action. A transition represents an event of the system. A directed arc connects a place to a transition, and its direction shows the input and output relation between them. Places and transitions are alternately connected using directed arcs. The number of directed arcs connected with places or transitions is not restricted. A token is placed in a place to indicate that the condition corresponding to the place is holding.

A gate arc connects a transition with a signal source, and depending on the signal, it either permits or inhibits the occurrence of the event which corresponds to the connected transition. Gate arcs are classified as permissive or inhibitive, and internal or external. An output signal arc sends the signal from a place to an external machine. A transition is enabled if and only if it satisfies all the following conditions:

(1) It does not have any output place filled with a token.
(2) It does not have any empty input place.
(3) It does not have any internal permissive arc signaling 0.
(4) It does not have any internal inhibitive arc signaling 1.

An enabled transition may fire when it does not have any external permissive arc signaling 0 nor any external inhibitive arc signaling 1. The firing of a transition removes tokens from all its input places and put a token in each output place connected to it. The assignment of tokens into the places of a Petri net is called marking and it represents the system state. In any initial marking, there must not exist more than one token in a place. According to these rules, the number of tokens in a place never exceeds one, thus, the Petri net is essentially a safe graph. If a place has two or more input transitions or output transitions, these transitions may be in conflict for firing. When two or more transitions are firable only one transition should fire using some arbitration rule.

The proposed procedure of modeling and decomposition of robotic manufacturing systems are shown as follows. A global, conceptual Petri net model is first chosen which describes the aggregate manufacturing process. At the conceptual level each task specification is represented as a place of the Petri net as shown, where the activity of each equipment is also represented as a place.

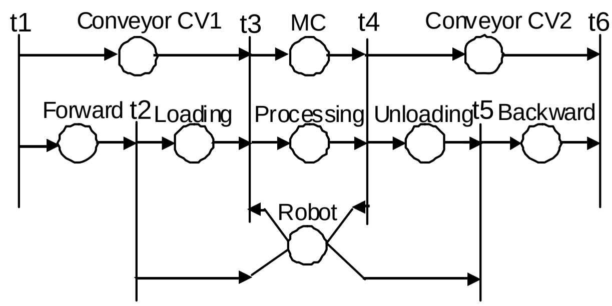

Fig.1 Petri net representation of example system at the conceptual level

A typical example system at the subsystem coordination level in the factory automation system concerns a robot loading and unloading a machining tool with input and output conveyors, and its Petri net representation at the conceptual level is shown in Fig.1.

Based on the hierarchical approach, the Petri net is translated into detailed subnets by stepwise refinements from the highest system control level to the lowest machine control level. At each step of detailed specification, some parts of the Petri net, transitions or places, are substituted by a subnet in a manner, which maintains the structural properties. The detailed Petri net representation of the loading operation in the example system is shown in Fig.2. Loading a workpiece to the machining center necessitates the cooperative or synchronized activities among the conveyor CV1, the machining center, and the robot. Similarly, unloading a workpiece from the machining center, necessitates the cooperative or synchronized activities among the conveyor CV2, the machining center, and the robot.

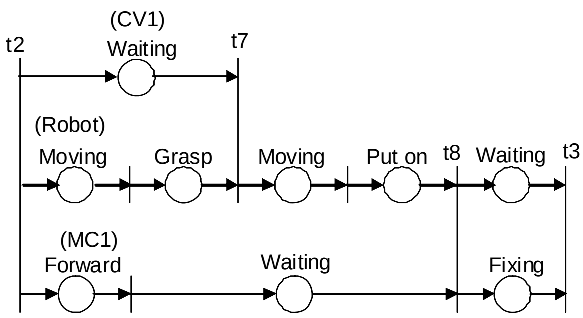

Fig.2 Detailed Petri net representation of loading operation

Unit operations in the detailed Petri net representation concern the real-time control of machines, devices, etc. They interact directly with the sensors and actuators. When a token enters a place that represents a unit operation, the hardware controller defined by the controller code is informed to execute a determined subtask with a determined data that are both defined by the place parameters. From these places, output signal arcs are connected to the machines, and external gate arcs from the machines are connected to the transitions of the Petri net when needed, for example, to synchronize and coordinate operations. The general form of Petri net representation at the local control level is shown in Fig.3.

From the viewpoint of real-time control, controlling a process consists in driving its devices from a state to another one. In discrete event system control domain, several steps are necessary for each evolution of the process: first, the control system sends a request to the process actuators, second the external machine sends an acknowledge, third the process evolves according to the request and, at the end of the evolution, returns an execution report to the control system, and the control system updates the states of the control models according to the report; then it is ready to send another request. This outline points out that, each time the control system sends a request to the process, it must wait for the associated report. Thus the token should not be moved until the operation, shown by each place, is finished, even if the marking satisfies the ignition condition.

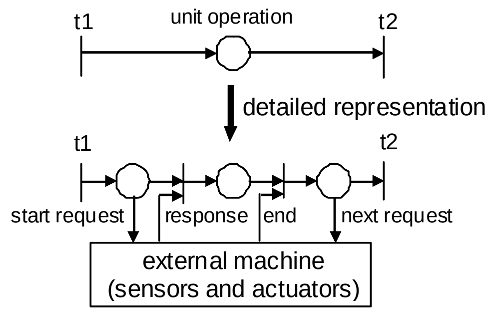

Fig.3 Detailed Petri net representation at the local control level

III. DECOMPOSITION AND COORDINATION

It is natural to implement a hierarchical and distributed control system, where one controller is allocated to each control layer or block. For the manufacturing system, an example structure of hierarchical and distributed control is composed of one station controller and three machine controllers. The detailed Petri net is decomposed into subnets, which are executed by each machine controller.

In the decomposition procedure, a transition may be divided and distributed into different machine controllers. Decomposed transitions are called global transitions (t2, t7, t8, t3 in Fig.2) and other transitions are called local transitions. By the Petri net model, the state of the discrete event system is represented as the marking of tokens, and firing of any transition brings about change to the next state. So the firing condition and marking before decomposition should be the same as those after decomposition. From the logical formulation of firability condition and marking before and after decomposition, it is proved that the firability condition of the original transition is equal to AND operation of firability conditions of decomposed transitions [3]. In case that a transition in conflict with other transitions is decomposed, these transitions should be coordinated by the station controller.

The Petri net based control structure with introduction of coordinator is shown in Fig.4. The control software is distributed into the station controller and machine controllers. The station controller is composed of the Petri net based controller and the coordinator. The conceptual Petri net model is allocated to the Petri net based controller for management of the overall system. The detailed Petri net models are allocated to the Petri net based controllers in the machine controllers. The control of the overall system is achieved by coordinating these Petri net based controllers such that decomposed transitions fire at the same time and the task specification is completely satisfied. System coordination is performed through communication between the coordinator in the station controller and the Petri net based controllers in the machine controllers.

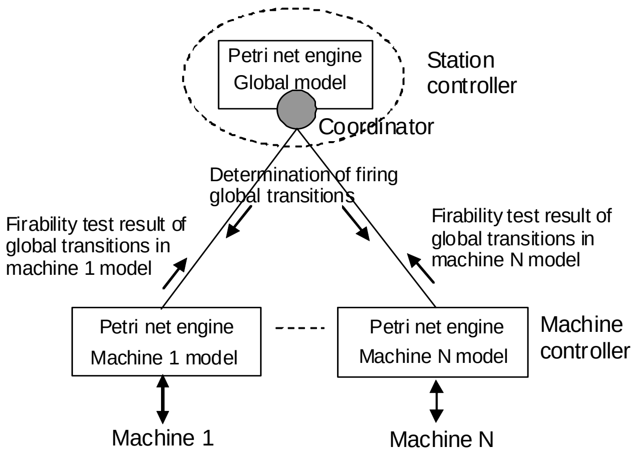

Fig.4 Petri net based control structure with coordinator

IV. PETRI NET MODEL BASED CONTROL EXPERIMENTS

From the fact that the control of a system represented by a Petri net can be realized directly by executing the corresponding Petri net as the control algorithm, a Petri net based controller was developed with a microprocessor. Also software was developed on a common PC to support synthesis, simulation, and debugging of Petri nets and to load the program into the controller. The names of global transitions and their conflict relations are loaded into the coordinator in the station controller. The connection structure of a decomposed Petri net model and conflict relations among local transitions are loaded into the Petri net based controller in a machine controller. Petri net simulation is performed by scanning these structural data in a tabular form. Using them, a control system was implemented for an experimental system, and their effectiveness was confirmed by executing tasks specified.

V. CONCLUSIONS

A methodology to construct hierarchical and distributed control systems, which correspond to the structure of manufacturing systems, has been presented. The controllers are arranged according to the hierarchical and distributed nature of the manufacturing system. The control software does not use the overall detailed system model, and the decomposed Petri net model in each machine controller is not so large and easily manageable.

Multilevel hierarchical and distributed control for large and complex manufacturing systems can be also constructed such that the control system structure corresponds to the hierarchical and distributed structure of the general manufacturing system. The overall system is consistently controlled, such that a coordinator in a layer coordinates one-level lower Petri net based controllers and is coordinated by the one-level upper coordinator.

The Petri net model includes the control algorithm; control is executed in order that the behavior of the Petri net model is in correspondence with that of the real system. Thus modeling, simulation and control of large and complex manufacturing systems can be performed consistently using Petri nets.

REFERENCES

[1] Desrochers, A. D. and Al-Jaar, R. Y., (1995) Applications of Petri Nets in Manufacturing Systems: Modeling, Control and Performance Analysis, IEEE Press
[2] Hasegawa, K., Takahashi, K., and Miyagi, P. E., (1988) Application of the Mark Flow Graph to represent discrete event production systems and system control, Trans. of SICE, 24, 69-75
[3] Yasuda, G., (2009) Implementation of distributed cooperative control for industrial robot systems using Petri nets, Preprints of the 9th IFAC Symposium on Robot Control (SYROCO '09), 433-438

Learning algorithm of the revised RBF network and its application to the media art system

Chihiro Kondo[1] and Tadashi Kondo[2]

[1]*Graduate School of Media Design, Keio Univ., 4-1-1 Hiyosi, Kouhokuku, Yokohama 223-8521, Japan*
[2] *Graduate School of Health Sciences, The Univ. of Tokushima, 3-18-15 Kuramoto-cho, Tokushima 770-8509 Japan*
(*E-mail: kondo@medsci.tokushima-u.ac.jp*)

Abstract: In this study, a revised radial basis function (RBF) network is proposed and applied to the identification problems of the nonlinear system and the media art system. In the revised RBF network, the structural parameters such as means and variances of the radial basis functions in the neurons are determined automatically and so revised RBF network can be easily applied to the practical complex problems such as the media art system. The media art system outputs the art expressions such as the sound and graphics using the artificial sensibility surfaces that are identified using the revised RBF network.
Keywords: neural network, radial basis function, media art system, nonlinear system identification

I. INTRODUCTION

In this study, a revised radial basis function (RBF) network is proposed and applied to the identification problems of the nonlinear system and the media art system. In the conventional RBF network [1]-[3], the structural parameters such as means and variances of the radial basis functions in the neurons are not determined automatically and so it is needed to repeat the RBF network calculations many times changing these structural parameter values. In this study, a revised RBF network algorithm in which these structural parameters are automatically determined so as to fit the characteristics of the training data, is proposed and it is shown that the revised RBF network is accurate and easy to apply to practical complex problem because the structural parameters are automatically determined.

II. RBF NETWORK AND ITS LEARNING ALGORITHM

In this study, a revised RBF network is proposed and applied to the nonlinear system and the media art system. The revised RBF network had a 3-layered architecture with the input, hidden and output layers. Architecture of the revised RBF neural network is shown in Fig.1. In this figure, x shows the input variable and ϕ shows the output variable and h shows the radial basis function. In the revised RBF neural network, the structural parameters, which are means and variances of the radial basis functions in the neurons, are calculated automatically using the training data. The revised RBF neural network is organized as follows:

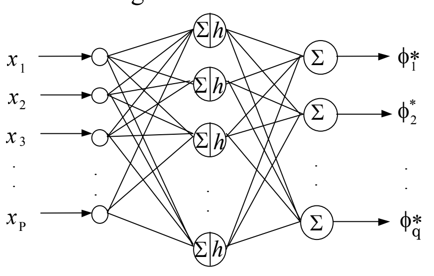

Fig.1 Architecture of the revised RBF network (1)

(1)Input layer

$$u_i=x_i \quad (i = 1,2,\ldots,p) \tag{1}$$

Here, x_i is input variable and p is the number of input variables and u_i is the output variable of the input layer.

(2)Hidden layer

In the hidden layer, the output (h_j) of the RBF neuron is calculated by the following equation:

$$h_j = \exp(-z_j^2) \quad (j = 1,2,\ldots,g) \tag{2}$$

z_j is estimated using the regression analysis [4] for the training data by the following equations.

$$z_j=a_0+a_1 d_j \tag{3}$$

$$d_j = \|u - c\| \tag{4}$$

Here, a_j (j=0,1) are the regression coefficients and estimated using stepwise regression analysis for the training data, and d_j are the distance between the training data points (u) and the center (c) of the neuron which is the mean of the radial basis function.

In the conventional RBF network, the value z_j is described as follows,

$$z_j = \frac{d_j}{v_j} \tag{5}$$

Here, v_j is a variance of the j-th radial basis function. Equation (3) is described as follows,

$$z_j = \frac{d_j + \dfrac{a_0}{a_1}}{\dfrac{1}{a_1}} \tag{6}$$

Comparing Eq.(5) and (6), we see that v equals $1/a_1$, and a_0/a_1 is a correct value for d_j. In this algorithm, The variance v and the mean c of the radial basis function are determined so as to fit characteristics of the training data in the revised RBF network.

(3)Output layer

$$\phi_i^*(x) = \sum_{j=1}^{g} w_{i,j} h_j(u) \quad (i=1,2,\ldots,q) \tag{7}$$

Here, $w_{i,j}$ (i=1,2,…,q; j=1,2,…,g) are the weights of the neural network and q is the number of neurons in the output layer and $\phi_i^*(x)$ (i=1,2,…,q) are the outputs of the neural network.

Weights $w_{i,j}$ (i=1,2,…,q; j=1,2,…,g) are estimated using multiple regression analysis [4] as follows:

$$\underline{w}_i(n) = (H^T(n)H(n) + \Lambda)^{-1} H^T(n)\underline{\phi}_i(n)$$
$$= P(n)H^T(n)\underline{\phi}_i(n) \qquad (i=1,2,\ldots,q) \qquad (8)$$

Here,

$$\underline{w}_i(n)^T = (w_{i,1,} w_{i,2,} ..., w_{i,g}) \quad (i=1,2,\ldots,q) \qquad (9)$$
$$H^T = [\underline{h}(1), \underline{h}(2), ..., \underline{h}(n)] \qquad (10)$$
$$\underline{h}^T(k) = (h_1(k), h_2(k), \ldots, h_g(k)) \quad (k=1,2,\ldots,n) \qquad (11)$$
$$\underline{\phi}_i^T(n) = (\phi_i(1), \phi_i(2), ..., \phi_i(n)) \quad (i=1,2,\ldots,q) \qquad (12)$$

n is the number of training data. Λ is a diagonal matrix.

In the revised RBF network, the structural parameters such as means and variances of the radial basis functions in the neurons are automatically determined from the training data using the following procedures. The number of neurons in the hidden layer was set to the number of the training data and the centers (means) of the radial basis functions are located at the training data points. Means are determined at the training data points. Variances are estimated using the regression analysis [4] of the training data to fit the characteristics of the training data. Using these procedures, the structural parameters such as means and variances of the radial basis functions, are automatically determined from the training data.

When the (n+1)-th additional new training data ($\phi_i(n+1)$, $\underline{x}^T(n+1)$) are obtained, we can update the values of the weights using the following equations.

$$\underline{w}_i(n+1) = \underline{w}_i(n) + P(n+1)\underline{h}(n+1)e_{n+1} \qquad (13)$$
$$e_{n+1} = \phi_i(n+1) - \underline{h}^T(n+1)\underline{w}(n) \qquad (14)$$
$$P(n+1) = P(n) - \frac{P(n)\underline{h}(n+1)\underline{h}^T(n+1)P(n)}{1 + \underline{h}^T(n+1)P(n)\underline{h}(n+1)} \qquad (15)$$
$$\underline{x}^T(k) = (x_1(k), x_2(k), ..., x_p(k)) \quad (k=1,2,\ldots,n+1) \qquad (16)$$

III. APPLICATION TO THE NONLINEAR SYSTEM IDENTIFICATION

Nonlinear system is assumed to be described by the following equations:

$$\phi_1 = (1.0+2.0x_1^2+3.0x_1x_2+4.0x_2^2+5.0exp(x_1x_2x_3))^3 \qquad (17)$$
$$\phi_2 = (1.0+2.0x_1+3.0x_1^2x_2+4.0x_2^2+5.0exp(x_1x_2x_3))^3 \qquad (18)$$
$$\phi_3 = (1.0+2.0x_1^2+3.0x_1x_2^2+4.0x_2+5.0exp(x_1x_2x_3))^3 \qquad (19)$$

Here, ϕ_i is the i-th output variable and $x_1 \sim x_3$ are input variables. Neural network is organized by ten training data. Ten other data are used to check prediction and generalization ability. Identification results of revised RBF network are compared with those of the conventional RBF network and the conventional sigmoid function neural network.

1. Identification results of the revised RBF network.

Identification results of the revised RBF network are shown as follows:

The neural network was developed as a three layered architecture. Three input variables were used in input layer and ten neurons were used in hidden layer and these neurons were located at the training data points. Weights of neural network, the values of variances and means of the radial basis functions were estimated by regression analysis.

Estimation accuracy was evaluated by the following equation:

$$J_1 = \frac{1}{10}\sum_{k=1}^{10}\left|\phi_i(k) - \phi_i^*(k)\right| \qquad (20)$$

where $\phi_i(k)$ (i=1,2,3; k=1,2,···,10) are actual values and $\phi_i^*(k)$ (i=1,2,3; k=1,2,···,10) are estimated values by the revised RBF network. $\phi_i(k)$ (i=1,2,3; k =1,2,···,10) were used to organize revised RBF network. Value of J_1 is shown in Table1.

Prediction accuracy was evaluated by using the following equation:

$$J_2 = \frac{1}{10}\sum_{k=11}^{20}\left|\phi_i(k) - \phi_i^*(k)\right| \qquad (21)$$

where $\phi_i(k)$ (i=1,2,3; k=11,12,···,20) are actual values and $\phi_i^*(k)$ (i=1,2,3; k=11,12,···,20) are predicted values by revised RBF network. $\phi_i(k)$ (i=1,2,3; k =11,12,···,20) were not used to organize revised RBF network and were used to check generalization ability. Value of J_2 is shown in Table1. Estimated and predicted values of $\phi_1(k)$ by the revised RBF network are shown in Fig.2.

Table 1 Estimation and prediction accuracy

	J1	J2
ϕ1	0.013697	0.043621
ϕ2	0.013731	0.040899
ϕ3	0.012484	0.037977

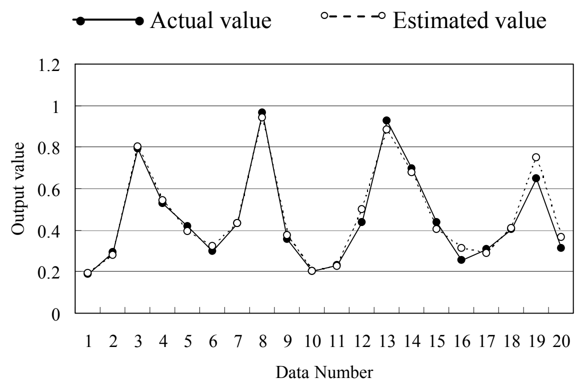

Fig.2 Estimated and predicted values ϕ_1

2. Identification results of the conventional RBF network.

Identification results of the conventional RBF network are shown as follows:

The neural network was also developed as a three layered architecture. Three input variables were used in input layer and ten neurons were used in hidden layer and these neurons were located at the training data points. Weights of neural network were estimated by regression analysis. The values of variances of the radial basis functions were set to 1.0. Estimation accuracy was evaluated by Eq. (20) and value of J_1 is shown in Table2. Prediction accuracy was evaluated by Eq.(21) and value of J_2 is shown in Table2.

Table 2 Estimation and prediction accuracy of the conventional RBF network

	J1	J2
ϕ1	0.066868	0.072537
ϕ2	0.063003	0.068088
ϕ3	0.049768	0.055042

3. Identification results of the conventional sigmoid function neural network trained using back propagation algorithm

Identification results obtained by the conventional neural network trained using back propagation algorithm are shown as follows:

In conventional multilayered neural network, the neural network was developed as a three layered architecture. Three input variables were used in input layer and four neurons were used in hidden layer. Weights of neural network were estimated by back propagation algorithm. Initial values of the weights were set to random values. The learning calculations of the weights were iterated at 100,000 times. Estimation accuracy was evaluated by Eq.(20) and value of J_1 is shown in Table3. Prediction accuracy was evaluated by Eq.(21) and value of J_2 is shown in Table3.

Table 3 Estimation and prediction accuracy of the conventional sigmoid function neural network

	J1	J2
ϕ1	0.069191	0.064316
ϕ2	0.060103	0.060559
ϕ3	0.050405	0.047165

4. Comparison of the identified results.

Identification results of revised RBF network were compared with those of the conventional RBF network and the conventional sigmoid function neural network trained using the back propagation algorithm. From these identification results, both estimation and prediction errors (J_1 and J_2) of revised RBF network are smaller than those of the conventional RBF network and the conventional sigmoid function neural network. Estimated and predicted values of ϕ by revised RBF network are accurate and the estimation and prediction errors of the revised RBF network are decreased remarkably. From these results, we can see that revised RBF network algorithm is an accurate identification method for the nonlinear system.

VI. APPLICATION TO THE MRDIA ART SYSTEM

The revised RBF network is applied to the media art system and generates the artificial sensibility in the media art system. The artificial sensibility simulates the human sensibility in the computer and outputs the art expressions using the sound and graphics.

1. Architecture of the media art system.

The architecture of the media art system is shown in Fig.3. Input signals are inputted from the sensors and these input signals from sensors are transmitted to the computer using Gainer, which is an I/O module to control actuators such as LED and motors. Input signals can be also inputted from display using a mouse. In the computer, first, the signals, which have been transmitted from Gainer or the display, are received with the processing [5], which is programming software for the production of computer art that specializes in visual expression and interaction. The revised RBF network is programmed by processing software and generates the artificial sensibility. The artificial sensibility selects the output signals according to the input signals and generates output patterns to express the art using sound and graphics.

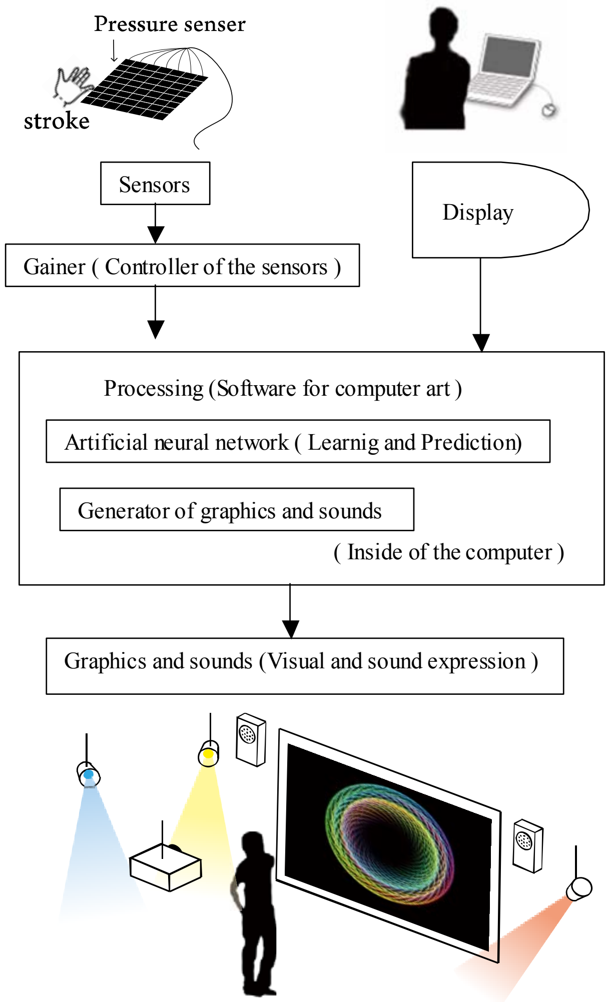

Fig. 3 Architecture of the media art system

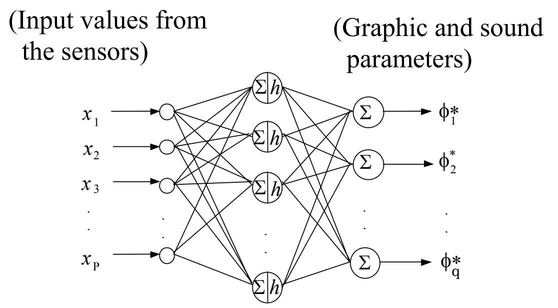

Fig.4 Architecture of the revised RBF network (2)

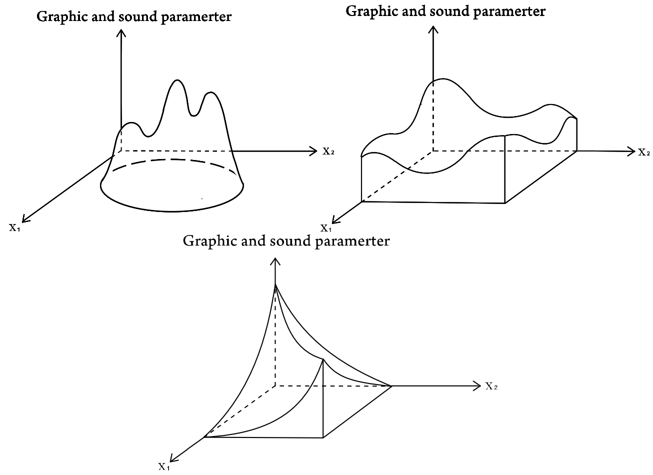

Fig.5 Identification of artificial sensibility surface using the revised RBF network

2. Identification of artificial sensibility surfaces using the revised RBF network.

The revised RBF network generates the artificial sensibility in the computer. In this study, the input signals are inputted from the sensors and the display. Figure 4 shows the architecture of the RBF network with p input variables obtained from the sensors and the display. Output variables of the neural network are the graphic and sound parameters such as colors of Red, Green and Blue, speed of the graphic drawing, positions of the graphics, kinds of the sound and so on. The revised RBF network identifies the artificial sensibility surfaces using the learning procedures of the neural network. In Fig.5, the examples of the artificial sensibility surfaces identified using the revised RBF network are shown. The learning data (teacher signals) for each graphical parameter are obtained through the interaction between man and the computer using the man-computer communications and the revised RBF network identifies the artificial sensibility surface using the obtained learning data. The revised RBF network can identify various kinds of the artificial sensibility surfaces accurately using the data which are obtained through the interaction between man and the computer using the man-computer communications.

3. Generation of graphics using the identified artificial sensibility surface and modification of the graphics using the man-computer communications.

The computer generated the graphics using identified artificial sensibility surface of each graphical parameter. Here, we input signals from the display and person moved the mouse and the computer read the mouse pointer positions. The revised RBF network output the graphical parameters and the new graphics were generated using the graphical parameters that were output from the revised RBF network. These processes were repeated until the processing software system was stopped. If the desirable graphics for the person are not obtained, the artificial sensibility surfaces can be modified by the additional learning procedures of the revised RBF network using Eq.(13), (14) and (15). The additional learning data were obtained through the interaction between man and the computer using the men-computer communications. We show the examples of the graphics in Fig.6 which were generated and output from the media art system. These generated graphics are changed according to the mouse pointer positions on the display.

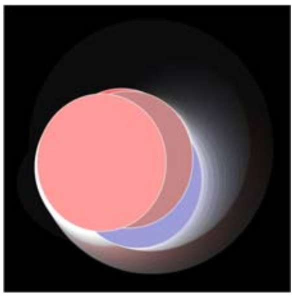

(a)

(b)

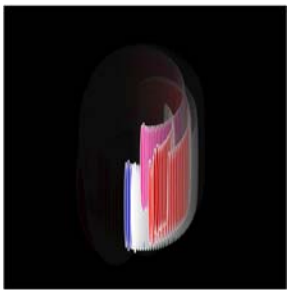

(c)

(d)

Fig.6 Output images from the media art system

V. CONCLUSION

In this paper, a revised RBF network algorithm was proposed. In this algorithm, the structural parameters such as means and variances of the radial basis functions in the neurons are automatically determined so as to fit the characteristics of the training data and so we can easily apply this algorithm to practical complex problems. This algorithm was applied to the identification problems of the nonlinear system and the media art system and it was shown that revised RBF network algorithm was a useful method for the nonlinear system identification and media art system.

REFERENCES

[1] J.Moody and C.J.Darken (1989), Fast learning in networks of locally-tuned processing units, *Neural Computation*, Vol.1, pp.281-294.

[2] T.Kudo, T.Kondo, M.Nakagawa and J.Ueno (2009), Medical image recognition of the white and gray matters of the brain by radial basis function (RBF) neural network, *Proceedings of the 40-th ISCIE international symposium on stochastic sytems theory and its applications*, pp.259-263.

[3] T.Kondo, A.S.Pamdya, and H.Nagashino (2007), GMDH-type neural network algorithm with a feedback loop for structural identification of RBF neural network, *International Journal of Knowledge-based and Intelligent Engineering Systems,* Vol.11 pp.157-168.

[4] N.R.Draper and H.Smith (1981), *Applied Regression Analysis*, John Wiley and Sons, New York.

[5] C.Reas and B.Fry (2007), Processing, A programming Handbook for Visual Designers and Artists, The MIT Press, London.

Feedback GMDH-type neural network algorithm and its application to medical image analysis of cancer of the liver.

Chihiro Kondo[1], Tadashi Kondo[2] and Junji Ueno[3]

[1]Graduate School of Media Design, Keio Univ., 4-1-1 Hiyosi, Kouhokuku, Yokohama 223-8521, Japan
[2,3] Graduate School of Health Sciences, The Univ. of Tokushima, 3-18-15 Kuramoto-cho, Tokushima 770-8509 Japan
([2]E-mail: kondo@medsci.tokushima-u.ac.jp)

Abstract: A revised Group Method of Data Handling (GMDH)-type neural network algorithm for medical image recognition is proposed and is applied to the medical image analysis of cancer of the liver. The revised GMDH-type neural network algorithm has a feedback loop and can identify the characteristics of the medical images accurately using feedback loop calculations. In this algorithm, the polynomial type and the radial basis function (RBF) type neurons are used for organizing the neural network architecture. The optimum neural network architecture fitting the complexity of the medical images is automatically organized so as to minimize the prediction error criterion defined as Prediction Sum of Squares (PSS).

Keywords: Neural network, GMDH, Medical image recognition.

I. INTRODUCTION

The conventional GMDH-type neural network algorithms were proposed in our early works [1],[2]. In this paper, a revised GMDH-type neural network algorithm for medical image recognition is proposed and is applied to the medical image analysis of cancer of the liver. The revised GMDH-type neural network algorithm has a feedback loop and can identify the characteristics of the medical images accurately using feedback loop calculations. In this algorithm, the polynomial type and the radial basis function (RBF) type neurons are used for organizing the neural network architecture. A lot of complex nonlinear combinations of the input variables fitting the complexity of the medical images are generated using the polynomial type neurons and only useful combinations of the input variables are selected for organizing the neural network architecture. In the output layer, the RBF type neuron is used for organizing the neural network.

The revised GMDH-type neural network algorithm proposed in this study is applied to medical image analysis of cancer of the liver. The neural network architecture that fits the complexity of the medical images is automatically organized by the revised GMDH-type neural network algorithm so as to minimize the prediction error criterion defined as PSS [3] using the heuristic self-organization method [4],[5]. Heuristic self-organization method is a kind of the evolutional computation and can organize the optimum neural network architecture so as to minimize the prediction errors. The outlines of the liver are recognized using the neural network organized by the revised GMDH-type neural network algorithm and the regions of cancer of the liver are extracted. The results are compared with those obtained using the conventional neural network trained using the back propagation method. It is shown that the revised GMDH-type neural network algorithm is useful for the medical image analysis of cancer of the liver and it is very easy to apply the practical complex problem because the optimum neural network architecture is automatically organized so as to minimize the prediction error criterion PSS.

II. REVISED GMDH-TYPE NEURAL NETWORK ALGORITHM

In the conventional GMDH-type neural network [2], many kinds of neuron architectures such as the sigmoid function type, the RBF type and polynomial type neuron architectures are used for organizing neural network to fit the complexity of the nonlinear system. The optimum neuron architectures fitting the complexity of the nonlinear system are automatically selected by using the PSS [3]. Therefore, many kinds of nonlinear systems can be automatically identified by using the conventional GMDH-type neural network.

In the revised GMDH-type neural network, many kinds of nonlinear combinations of the input variables are generated by using the polynomial type neurons and only useful nonlinear combinations of the input variables are selected. Optimum neural network architectures are organized by using selected useful combinations of the input variables.

The revised GMDH-type neural network is shown in Fig.1. Here, nonlinear function g_i is described by the following Kolmogorov-Gabor polynomial:

$$g_i(x_1,x_2,\cdots,x_p)= a_0+\sum_i a_i x_i+\sum_i\sum_j a_{ij}x_i x_j+\cdots \tag{1}$$

This nonlinear function is automatically organized by using the second type neuron of the conventional GMDH-type neural network which is a polynomial type neuron.

The architecture of the revised GMDH-type neural network is produced as follows:

1. First loop calculation

First, all data are set to the training data. In this algorithm, it is not necessary to separate the original data into the training and test sets because PSS can be used for organizing the neural network architectures.

(1) Input layer

$u_j = x_j \quad (j=1,2,\cdots,p)$ (2)

where x_j (j=1,2,···,p) are the input variables of the system, and p is the number of input variables. In the input layer, input variables are set to the output variables.

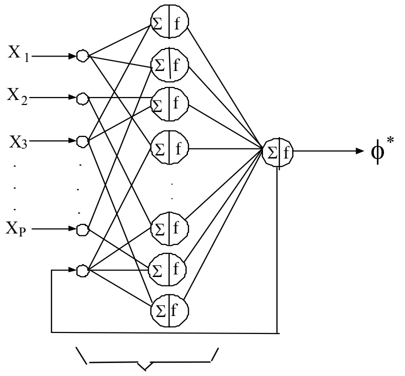

$g_i\,(x_1, x_2, \cdots, x_p)$

Output layer:

Σ: (Nonlinear function)

$z = \sum w_i\, g_i\,(x_1, x_2, \cdots, x_p)$

f : (Nonlinear function)

$\phi^* = \exp(-z^2)$

Fig.1 Architecture of revised GMDH-type neural network

(2) Hidden layer

All combinations of two variables (u_i,u_j) are generated. For each combination, the neuron architecture is described by the following equations:

Σ: (Nonlinear function)

$$z_k = w_1u_i + w_2u_j + w_3u_iu_j + w_4u_i^2 + w_5u_j^2 + w_6u_i^3 + w_7u_i^2u_j + w_8u_iu_j^2 + w_9u_j^3 - w_0\theta_1 \quad (3)$$

f : (Linear function)

$$y_k = z_k \quad (4)$$

where θ_1 =1 and w_i (i=0,1,2,···,9) are weights between the input and hidden layer. This neuron is equal to the second type neuron of the conventional GMDH-type neural network. The weights w_i (i=0,1,2,···,9) are estimated by using the multiple regression analysis [6]. This procedure is as follows:

First, the values of z^{**} are calculated by using the following equation:

$$z^{**} = (-\log_e(\phi'))^{1/2} \quad (5)$$

where ϕ' is the normalized output variable whose values are between 0 and 1. ϕ' is calculated using following equation.

$$\phi' = \frac{\phi - \phi_{\min}}{|\phi_{\max} - \phi_{\min}|} \quad (6)$$

Here, ϕ_{max} is the maximum value of the output variable (ϕ), and ϕ_{min} is the minimum value of ϕ. Then the weights w_i (i=0,1,2,···,9) are estimated by using the stepwise regression analysis [6] which selects useful input variables by using the PSS[3]. Therefore, only useful variables in Eq.(3) are selected and neuron architecture are organized by these selected useful variables.

PSS is described by the following equation:

$$PSS = \sum_{\alpha=1}^{n} \left\{ \frac{z_\alpha^{**} - z_{k\alpha}}{1 - \underline{u}_\alpha^T (U^T U)^{-1} \underline{u}_\alpha} \right\}^2 \quad (7)$$

where

$$z_{k\alpha} = w_1u_{i\alpha} + w_2u_{j\alpha} + w_3u_{i\alpha}u_{j\alpha} + w_4u_{i\alpha}^2 + w_5u_{j\alpha}^2 + w_6u_{i\alpha}^3 + w_7u_{i\alpha}^2u_{j\alpha} + w_8u_{i\alpha}u_{j\alpha}^2 + w_9u_{j\alpha}^3 - w_0\theta_1, \quad \alpha=1,2,\ldots,n \quad (8)$$

$$\underline{u}_\alpha^T = [1,\ u_{i\alpha},\ u_{j\alpha},\ u_{i\alpha}u_{j\alpha},\ u_{i\alpha}^2,\ u_{j\alpha}^2], \quad \alpha=1,2,\ldots,n \quad (9)$$

$$U^T = [\ \underline{u}_1,\ \underline{u}_2,\ \ldots,\ \underline{u}_n\ ] \quad (10)$$

$z_{k\alpha}$ is the α-th estimated value obtained by the multiple regression analysis of all the data. PSS criterion does not contain the statistical assumption in the regression model.

From these generated neurons, L neurons which minimize the PSS are selected. The output values (y_i) of L selected neurons are set to the input values (u_i) of the neuron in the output layer.

$$u_i = y_i \quad (i=1,2,\ldots,L) \quad (11)$$

(3) Output layer

The inputs (u_i) of the neuron in the output layer are combined by the following linear function.

$$z = w_0 + \sum_{i=1}^{L} w_i u_i \quad (12)$$

The useful intermediate variables (u_i) are selected by using the stepwise regression analysis in which PSS is used as the variable selection criterion. Then, the estimated output values (z) is used as the feedback value and it is combined with the input variables in the next loop calculation.

2. Second and subsequent loop calculations

First, the estimated output value (z) is combined with the input variables and all combinations between the estimated output value (z) and the input variables are generated. The same calculation as the first feedback loop is carried out for each combination. When PSS value of the linear function in (12) does not decrease, the loop calculation is terminated. The output values of the neural network (ϕ^*) are calculated from z as follows:

$$\phi^* = \exp(-z^2) \quad (13)$$

So, in the last feedback loop, the neuron architecture becomes as follows:

Σ: (Nonlinear function)

$$z = w_0 + \sum_{i=1}^{L} w_i u_i \quad (14)$$

f : (Nonlinear function)

$$\phi^* = \exp(-z^2) \quad (15)$$

By using these procedures, the revised GMDH-type neural network can be organized.

III. APPLICATION TO THE MEDICAL IMAGE ANALYSIS OF CANCER OF THE LIVER

In this study, the regions of cancer of the liver were recognized and extracted automatically by using the revised GMDH-type neural network. Multi-detector row CT (MDCT) images of the liver are used in this study. In the recognition procedure, the revised GMDH-type neural network is organized to recognize the liver regions and then the regions of cancer of the liver are extracted.

1. Extraction of the candidate image regions of the cancer of the liver.

A liver image shown in Fig. 2 was used for organizing the revised GMDH-type neural network. The statistics of the image densities and x and y coordinates in the neighboring regions, the N×N pixel regions, were used as the image features. Only five parameters namely, mean, standard deviation, variance and x and y coordinates were selected as the useful input variables. The output value of the neural network was zero or one. When N×N pixel region was contained in the region of the liver, the neural network set the pixel value at the center of the N×N pixel region to one and this pixel was shown as the white point. The neural networks were organized when the values of N were from 3 to 15. It was determined that when N was equal to 7, the neural network architecture had the smallest recognition error. Five useful neurons were selected in each hidden layer. Figure 3 shows the variation of PSS values in the layers. The calculation of the revised GMDH-type neural network was terminated in the sixth feedback loop. The PSS value in the first feedback loop was not small but the PSS value was decreased gradually through the feedback loops and the small PSS vale was obtained in the sixth layer. The revised GMDH-type neural network outputs the liver image (Fig.4) and the first post-processing analysis of the liver image was carried out. In the first post-processing of the output image, the small isolated regions were eliminated and the outlines of the liver regions were expanded outside by N/2 pixels. Figure 5 shows the output image after the first post-processing. The output image after the first post-processing was overlapped to the original image (Fig.2) in order to check the accuracy of the image recognition as shown in Fig.6. The recognized liver regions are accurate. The regions of the liver were extracted from the original image using the output image. Figure 7 shows the extracted image of the liver. The second post-processing such as the closing was carried out and the region of the liver which contained the abnormal regions was obtained as shown in Fig.8. Figure 9 shows the extracted image of the liver. The candidate image regions of cancer of the liver were extracted from Fig.9 using Fig.7 and shown in Fig.10. The recognition results were compared with those of the conventional sigmoid function neural network trained using the back propagation method.

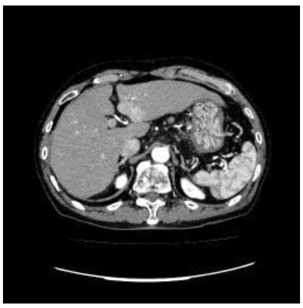

Fig.2 Original image

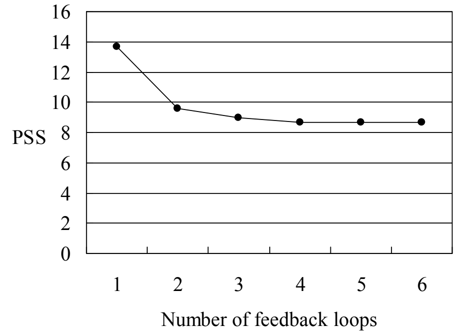

Fig.3 Variation of PSS in the revised GMDH-type neural network

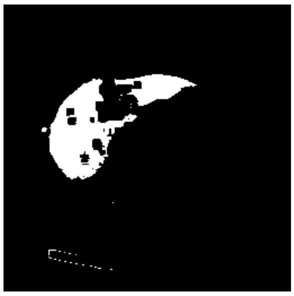

Fig.4 Output image of the neural network

Fig.5 Output image after the first post-processing

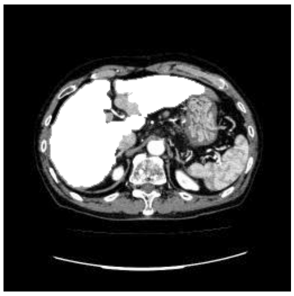

Fig.6 Overlapped image

Fig.7 Extracted image (1)

Fig.8 Output image after the second post-processing

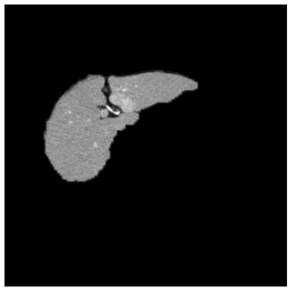

Fig.9 Extracted image (2)

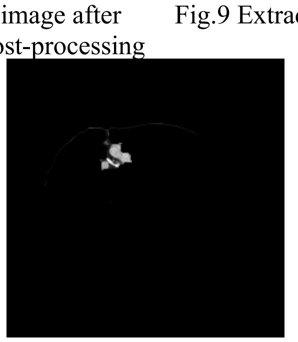

Fig.10 The candidate image regions of cancer of the liver

2. Recognition results of the conventional neural network trained using the back propagation algorithm

A conventional neural network trained using the back propagation algorithm was applied to the same recognition problem and the recognition results were compared with the results obtained using the revised GMDH-type algorithm. The conventional neural network had a three layered architecture, which was constructed using the input, hidden and output layers, and the same five input variables, which were mean, standard deviation, variance, x and y cordinates, were used in the input layer. Weights of the neural network were estimated using the back propagation algorithm and initial values of the weights were set to random values. The learning calculations of the weights were iterated changing structural parameters such as the number of neurons in the hidden layer and the initial values of the weights. The output images, when the numbers of neurons in the hidden layer (m) are 3, 5 and 7, are shown in Fig.11. These images contain more regions which are not part of the liver and the outlines of the liver are not extracted with required clarity compared with the output images obtained using the GMDH-type neural network algorithm, which is shown in Fig.4. Note that, in case of the conventional neural network, we obtain many different output images for various structural parameters of the neural network and many iterative calculations of the back propagation are needed for various structural parameters in order to find more accurate neural network architecture. In case of the revised GMDH-type neural network, the optimum neural network architecture is automatically organized so as to minimize prediction error criterion PSS using heuristic self-organization method [4],[5] and many iterative calculations for various structural parameters are not needed because all structural parameters are automatically determined.

V. CONCLUSION

In this paper, the revised GMDH-type neural network algorithm was applied to the medical image analysis of cancer of the liver and the results of the revised GMDH-type neural network were compared with those of the conventional sigmoid function neural network trained using the back propagation algorithm. Structural parameters such as the number of feedback loops, the number of neurons in hidden layers and useful input variables are automatically selected to minimize prediction error criterion defined as PSS. In the case of the conventional neural network, we obtain many different output images for various structural parameters of the neural network and many iterative calculations of the back propagation are needed for various structural parameters in order to find more accurate neural network architecture.

In this paper, the revised GMDH-type neural network algorithm was applied to the medical image analysis of cancer of the liver and it was shown that the revised GMDH-type neural network algorithm was a useful method for the medical image analysis of cancer of the liver because the neural network architecture is automatically organized so as to minimize the prediction error criterion defined as PSS.

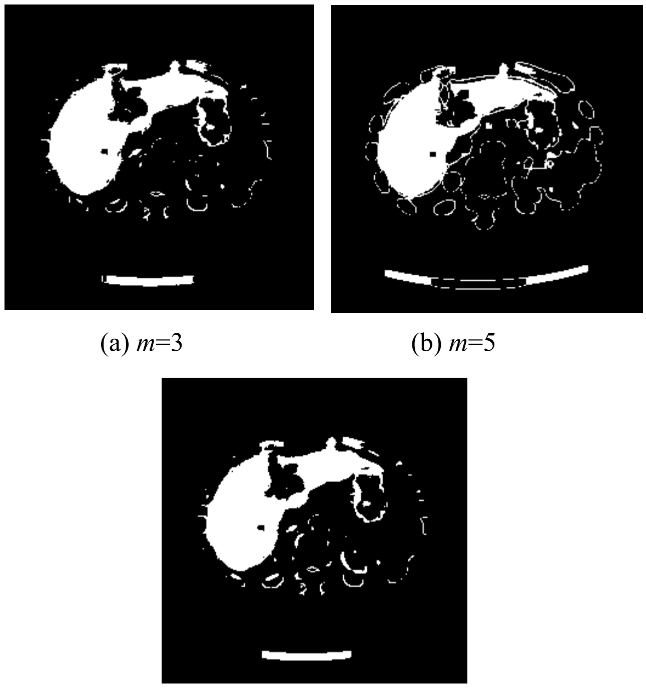

(a) m=3 (b) m=5

(c) m=7

Fig.11 Output images of the conventional sigmoid function neural network

Acknowledgment This work was supported by (JSPS) KAKENHI 21560428.

REFERENCES

[1] Kondo T. and J.Ueno (2008), Multi-layered GMDH-type neural network self-selecting optimum neural network architecture and its application to 3-dimensional medical image recognition of blood vessels, *International Journal of innovative computing, information and control*, Vo.4,No.1, pp.175-187.

[2]. Kondo T.(1998), GMDH neural network algorithm using the heuristic self-organization method and its application to the pattern identification problem, *Proc. of the 37th SICE Annual Conference*, pp.1143-1148.

[3] Tamura H. and T.Kondo (1980), Heuristics free group method of data handling algorithm of generating optimum partial polynomials with application to air pollution prediction, *Int. J. System Sci.,* Vol.11, No.9, pp.1095-1111.

[4] Farlow S.J. ed. (1984), *Self-organizing methods in modeling, GMDH-type algorithm*, Marcel Dekker, Inc., New York.

[5] Ivakhnenko A.G. (1970), Heuristic self-organization in problems of engineering cybernetics, *Automatica*, Vol.6, No.2, pp.207-219.

[6] Draper N.R. and Smith H. (1981), *Applied Regression Analysis*, John Wiley and Sons, New York.

Improvement of a Neural Network Based Motion Generator with Bimanual Coordination for Upper Limb Prosthesis

E. Inohira and H. Yokoi

Kyushu Institute of Technology, 2-4 Hibikino, Kitakyushu, Fukuoka, Japan
(Tel : 81-93-695-6050; Fax : 81-93-695-6050)
({inohira,yokoi}@life.kyutech.ac.jp)

Abstract: We propose to redesign a neural network used as a motion generator with bimanual coordination for upper limb prosthesis in order to improve its learning capability. We assumed that a wearer of the prosthesis is a unilateral amputee. In our previous work, we have proposed a prosthesis control system using a neural network that learns bimanual coordination in advance in order to smoothly implement motion with both hands. However, the previous proposed system has a problem that a neural network cannot generate desire coordina ted motion in special cases. The reason is that a desire posture of the prosthesis is generated from only a cu rrent posture of the healthy arm regardless of a current posture of the prosthesis. We propose to use both a healthy arm's posture and prosthesis' posture as neural network input in order to solve this problem. In this p aper, we showed that a single neural network whose input is current posture of both arms can learn relation of coordinated motions of holding a box with different size and the newly proposed system can generate desi red motions of the prosthesis for such coordinated motions through computer simulation.

Keywords: Upper limb prosthesis, Motion generation, Bimanual coordination, Neural network.

I. INTRODUCTION

We focus on upper limb prostheses for above-elbow amputees. We targeted at a unilateral amputee. Upper limb prostheses are classified into several types in terms of control mechanism. In a myoelectric prosthesis, each joint is controlled by surface myoelectric signals, which are generated from muscles when a human moves it. Utah Arm [1] is a typical myoelectric prosthesis. A wearer can operate a myoelectric prosthesis according to its intention through myoelectric signals. However, operating a myoelectric prosthesis is hard for an above-elbow amputee because it elbow is lost and its remaining muscles are few.

Then we have focused on coordinated motions of both arms to increase an above-elbow amputee's quality of life (QOL). Our basic idea is that an intelligent prosthesis moves according to a healthy arm's motion and facilitates tasks with both arms such as holding a box with both arms. We have proposed a prosthesis control system using a neural network that learns bimanual coordination in advance in our previous work [2]. The trained neural network generates desired posture of the prosthesis from current posture of the healthy arm at each sampling time. A training dataset of the neural network is prepared from healthy volunteer's motion through a motion capture system. We have shown that a neural network can learn a relation of five kinds of coordinated motions such as lifting up a box and turning a steering wheel with both hands. A trained neural network can generate desired prosthesis' motion for healthy arm's motion with different speed from the training dataset due to its generalization capability.

However, the previous proposed system has a problem that a neural network cannot generate desire coordinated motion in special cases. For instance, when a wearer holds a box with both hands, relation of posture of both arms depends on size of the box. It means that desire posture of the prosthesis for the same posture of the healthy arm is determined by size of the box. A single neural network whose input is current posture of the healthy arm cannot learn relation of coordinated motions of holding a box with different size simultaneously. The reason is that the same desire posture of the prosthesis is generated from the same posture of the healthy arm in the single neural network.

We propose to use both a healthy arm's posture and prosthesis' posture as neural network input in order to solve this problem. In the previous proposed system, current posture of the prosthesis is ignored when the desired posture of the prosthesis is generated. On the other hand, in the newly proposed system, desired posture of the prosthesis is generated from current posture of both the prosthesis and the healthy arm. In this paper, we showed that a single neural network whose input is current posture of both arms can learn relation of coordinated motions of holding a box with different size and the newly proposed system can generate desired motions of the prosthesis for such coordinated motions through computer simulation. We also showed experimental results using the previous proposed system, which cannot learn those coordinated motions properly for comparison.

II. MOTION GENERATOR

1. Prosthesis control system

We propose a new prosthesis control system using coordinated motion of both arms as shown in Fig.1. This system is composed of a motion capture system, a motion generator and a prosthesis controller. The motion capture system measures rotation angles of the healthy arms' joints. The motion generation system generates the desired posture of the prosthesis from the current posture of the healthy arm and the prosthesis. These postures are represented in rotation angles of each arm's joints. The controller drives actuators of the prosthesis according to the desired posture.

The motion generator is implemented by using a neural network. The motion generator needs to learn a relation between primitively coordinated motions of both arms before an amputee wears the prosthesis. Motion of a healthy man is used for the training of the motion generator.

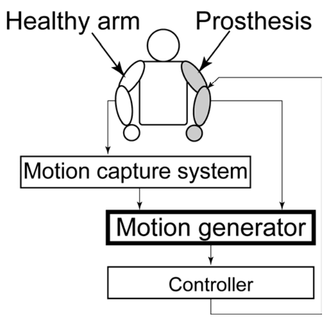

Fig.1. The proposed prosthesis control system

2. Redesign of the motion generator

A difference between the newly proposed system and our previous proposed system [2] is input of the motion generator. Inputs of the newly proposed motion generator are the current posture of the healthy arm and the current posture of the prosthesis as shown in Fig.2. On the other hand, inputs of the newly proposed motion generator are the current posture of the healthy arm and the current posture of the prosthesis as shown in Fig.2. As mentioned in Section I, the previous motion generator cannot generate desire coordinated motion in special cases. An example of the special cases is shown in Fig.4. There are the two movement patterns in which the initial posture of the healthy arm is the same. The previous motion generator cannot learn the two movement patterns simultaneously. The reason is that the two different postures of the prosthesis cannot be generated from the same posture of the healthy arm. Thus the previous proposed motion generator can learn only either Case 1 or Case 2 in Fig.4. It means that the previous motion generator can learn only a coordinated motion of holding a box in either Case 1 or Case 2. To solve this problem, the current posture of the prosthesis is needed in motion generation as shown in Fig.2.

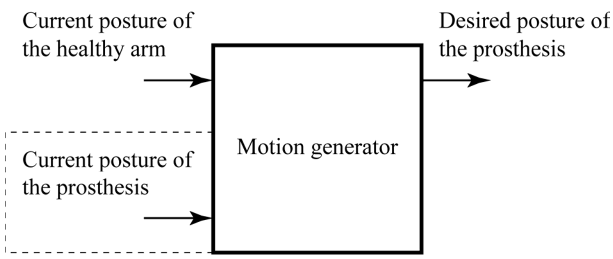

Fig.2. The newly proposed motion generator

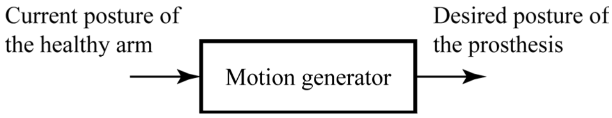

Fig.3. The newly proposed motion generator

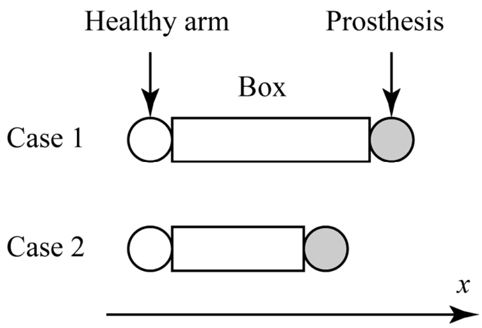

Fig.4. An example of the special relationship of the both arm

III. EXPERIMENT

1. Experimental setup

We compared the two motion generator by using a training dataset including the special cases as shown in Fig.4. The training dataset of the two motion generator was prepared through a kinematics model of both arms rather than a motion capture system because accurate postures of both arms should be given. A posture of the healthy arm is represented by the seven rotation angles; the three rotation angles of the shoulder, the single rotation angle of the elbow and the three rotation angles of the wrist.

In this paper, we targeted at the special cases. We simplified the experiments as much as possible. Rotation angles of the wrist were always set to be zero. Data length of movement patterns was possibly reduced. Training dataset was generated from movements of moving a box. The 9 kinds of movement patterns were made from the 3 different speed and width of both arms under the condition where the movement of the healthy arm is always the same. Fig.5 shows input data of the training dataset. The solid line in Fig.5 is a rotation angle of the healthy arm. The dashed line in Fig.5 is a rotation angle of the prosthesis. In Fig.5, the 9 kinds of movement patterns were a series signal.

We used the 4-layer neural networks as motion generators. In the previous motion generator, a 7-x-y-7 networks was used. In the previous motion generator, a 7-x-y-7 networks was used. The number x and y of neurons in hidden layers was determined through optical design proposed in [3]. It means that best performance of the previous motion generator and the newly proposed motion generator was evaluated.

We showed the experimental results in Fig.6 and 7. Fig.6 shows that the newly proposed motion generator can successfully generate the desired posture of the prosthesis for all the 9 kinds of movement patterns. On the other hands, Fig.5 shows that the previous motion generator cannot generate the desired posture of the prosthesis. The reason is that the movements of the healthy arm are the same and those of the prosthesis are different. That is, a neural network cannot generate different outputs from the same inputs. These experimental results showed that the newly proposed motion generate worked successfully in the special case under the condition where patterns of the same movements of the healthy arm and the different movements of the prosthesis was included in the training dataset.

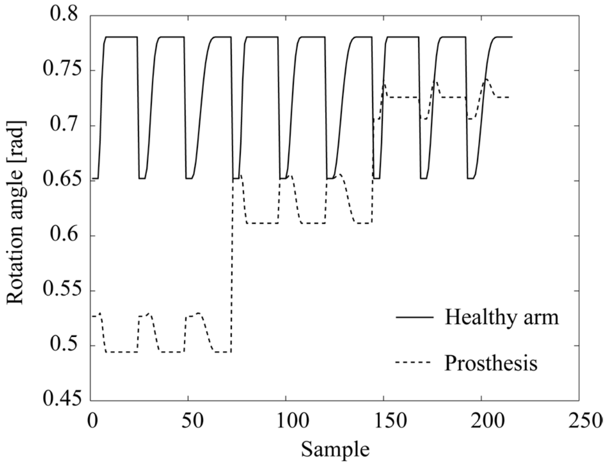

Fig.5. Input data given to motion generators

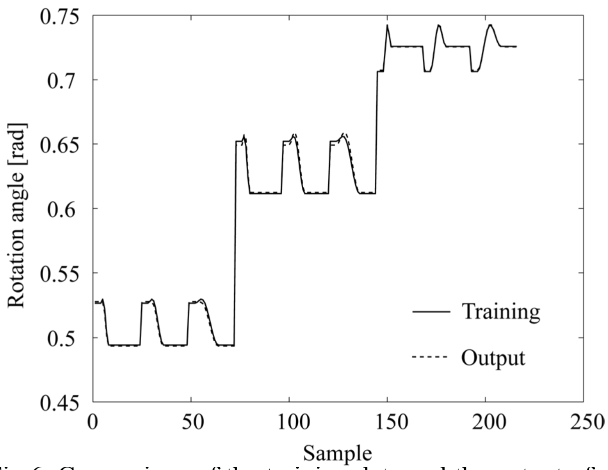

Fig.6. Comparison of the training data and the output of the newly proposed motion generator

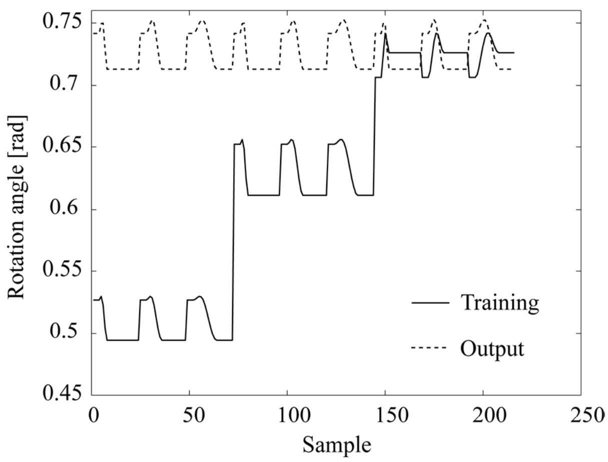

Fig.7. Comparison of the training data and the output of the previous motion generator

IV. DISCUSSION

From the results of Fig.6, the newly proposed motion generator can generate desired posture of the prosthesis even in the special cases. The reason is that current posture of the prosthesis is given to the motion generator.

Desire posture of the prosthesis is a future posture by one sampling time. The current posture and the desire posture of the prosthesis are very near. Thus it is expected that the newly proposed motion generator can generate the desired motion more accurately than the previous one because the current posture of the prosthesis is available.

VI. CONCLUSION

This paper proposed the motion generator using both a healthy arm's posture and prosthesis' posture as its input. We demonstrated that the newly proposed motion generator can generate desired posture of the prosthesis under the special case.

In the future work, performance of the newly proposed motion generate will be evaluated by using practical movement patterns.

REFERENCES

[1] Jacobsen SC, Knutti DF, Johnson RT and et al (1982), Development of the Utah artificial arm, IEEE Trans on Bio Eng, 29(4):249-269

[2] Inohira E and Yokoi H (2008), Generalization capability of neural networks for generation of coordinated motion of a hybrid prosthesis with a healthy arm, Intl J of innovative computing, information and control, 4(2): 471-483

[3] Inohira E and Yokoi H (2007), An optimal design method for artificial neural networks by using the Design of Experiments, J of Advanced Computational Intelligence and Intelligent informatics, 11(6): 593-599

The Fifteenth International Symposium on Artificial Life and Robotics 2010 (AROB 15th '10),
B-Con Plaza, Beppu,Oita, Japan, February 4-6, 2010

Midpoint-Validation Algorithm for Support Vector Machine Classification

Hiroki Tamura, Shingo Yamashita and Koichi Tanno

Faculty of Engineering, University of Miyazaki
1-1 Gakuken kibanadai-nishi, Miyazaki-shi, 889-2192 Japan
(htamura @ cc.miyazaki-u.ac.jp)

Abstract: In this paper, we propose midpoint-validation algorithm for Support Vector Machine, which improves the generalization of support vector machine so that midpoint-validation error is minimized. We compare its performance with the other paper techniques of support vector machine and also tested our proposed method on fifth benchmark problems. The results obtained from the simulation shows the effectiveness of the proposed method.

Keywords: Support Vector Machine; Midpoint-Validation; Pattern Classification Problem

1. Introduction

Support vector machine (abbr. SVM) proposed by Vapnik [1] is one of the most influential and powerful tools for solving classification[2-6]. The main concept is based on the formation of a Lagrange multiplier equation combining both objective terms and constraints. The most attractive notions are the idea of the large margin and kernel. It has produced a remarkable performance in a number of difficult learning tasks without requiring prior knowledge and with guarantee on its generalization behavior dues to the method of structural risk minimization.

A number of improved SVM have been proposed to improve the generalization. Weston [8] proposed an algorithm to leverage the Universum by maximizing the number of observed contradictions, and showed experimentally that this approach delivers accuracy improvements over using labeled data alone. Raicharoen [12] proposed the learning algorithms that do not need any kernel functions to map the input vectors into a linearly separable feature space. The separability is based on the critical Support vectors essential to determine the locations of all separating hyperplanes. A separating hyperplane is placed in the middle of the line connecting two support vectors, one from each class, and it is also orthogonal to this line.

We proposed a midpoint-validation method which improves the generalization of neural network (Tamura & Tanno, Oct. 2008[9]). This method creates midpoint data in input space, and calculates criteria using the midpoint data and previous training data. We stop training as soon as the criteria is higher than it was the last time it was checked. Further, we proposed the adjustment method of SVM from the result obtained from the SVM that used the midpoint data (Tamura & Tanno, Jul. 2008[10]). This method is adjusted for threshold value in order for the output of the midpoint data to be set to nearly 0. This technique had better results than SVM, Multilayer Perceptron using midpoint-validation method or cross-validation method.

In this paper, we propose midpoint-validation algorithm, which improves the generalization of SVM so that midpoint-validation error is minimized. This idea applies midpoint-validation method to learning algorithm of SVM and has the new rules of adjustment method. We compare performance of midpoint-validation algorithm with those of the SVM, *soft margin* SVM, SVM using midpoint-validation method and tested our proposed method on fifth benchmark problems. The simulation results carried out shows the effectiveness of the midpoint-validation algorithm.

The rest of this paper is organized into six sections. Section 2 reviews the concept of original SVM algorithm. Section 3 introduces Midpoint-Validation Method for SVM about paper [10]. Section 4 presents our proposed midpoint-validation algorithm for SVM. Section 5 provides the experimental results performed with several benchmark data and compares them with the others'. Section 6 concludes the paper.

2. Review of SVM

The SVM is a mechanical learning system that uses a hypothesis space of linear functions in a high dimensional feature space. Assume the training sample $S=((\mathbf{x}_1,y_1),....(\mathbf{x}_N,y_N))$ consisting of vectors $\mathbf{x}_i \in R$ with i=1,..., N , and each vector $\mathbf{x}_i$ belongs to either of the two classes. Thus it is given a label $y_i \in \{-1,1\}$. The pair of $(\mathbf{w},b)$ defines a separating hyper-plane of equation as follows:

$$(\mathbf{w},\mathbf{x})+b=0 \qquad (1)$$

However, Eq.(1) can possibly separate any part of the feature space, therefore one needs to establish an optimal separating hyper-plane (abbr. OSH) that divides ***S*** leaving all. The points of the same class are accumulated on the same side while maximizing the margin which is the distance of the closest point of ***S***. The closest vector $\mathbf{x}_i$ is called support vector and the OSH($\mathbf{w}'$,b') can be determined by solving an optimization problem. The solution of this optimization problem is given by the saddle point of the Lagrangian.

Maximize margin $\frac{1}{2}(\mathbf{w},\mathbf{w})$

Subject to $y_i((\mathbf{w}\cdot\mathbf{x}_i)+b)\geq 1$ (2)

To solve the case of nonlinear decision surfaces, the OSH is carried out by nonlinearly transforming a set of original feature vectors $\mathbf{x}_i$ into a high-dimensional feature space by mapping $\mathbf{\Phi}$: $\mathbf{x}_i \rightarrow \mathbf{z}_i$ and then performing the linear separation. However, it requires an enormous computation of inner products ($\mathbf{\Phi}(\mathbf{x}) \cdot \mathbf{\Phi}(\mathbf{x}_i)$) in the high-dimensional feature space. Therefore, using a Kernel function which satisfies the Mercer's theorem significantly reduces the calculations to solve the nonlinear problems. In this paper, we used the Gaussian kernel given in Eq.(3) as the kernel function while the SVM decision function $g(\mathbf{x})$ and output of SVM are as given in Eq.(4), (5).

$$K(\mathbf{x},\mathbf{x}_j)=\exp\left(\frac{-\|\mathbf{x}-\mathbf{x}_j\|^2}{2\sigma^2}\right) \quad (3)$$

$$g(\mathbf{x})=\sum_{i=1}^{N} w_i K(\mathbf{x}_i,\mathbf{x})+b \quad (4)$$

$$O=sign(g(\mathbf{x})) \quad (5)$$

3. Midpoint-Validation Method [10]

3.1 Creation of Midpoint Data

Step 1: A training data (x_i) that belongs to group ***D0*** is selected accordingly.
Step 2: A training data (x_j) that has nearest distance in group ***D1*** is selected.
Step 3: A training data (x_i*) that has nearest distance in groups ***D0*** is also selected.
Step 4: Go to Step 5 when training data (x_i*) and training data (x_i) are the same.
Else to Step 2 and (i^*) is substituted for (i).
Step 5: A midpoint of training data (x_i) and (x_j) is decided as the new midpoint data (x_k^{new}).

Fig 1. Flow of Midpoint Data Creation Algorithm

Midpoint data are created from the existing known training data which has different teacher signal. The midpoint data created is midpoint of the known training data and it is expected that by doing so, the generalization would improve. As for the teacher signal, it is assumed to have two classes (-1or 1). Training data groups that belongs to each teacher signal is assumed to be ***D0*** and ***D1***.The creation process of the midpoint data from training data groups ***D0*** is stated as Fig 1.

This processing is done by all training data, and midpoint data is created. Midpoints data (*x, y*) are made up from Step1 to Step5.

3.2 Midpoint-validation method for SVM

Step 1: SVM is created by the known training data.
Step 2: Create the midpoint data using Midpoint data creation algorithm.
Step 3: The output value of SVM of the midpoint data and training data are computed.
Step 4: The value of B is computed according to Eq.(8).
Step 5: The output of the proposed SVM is also computed according to Eq.(6) and Eq.(7).

Fig 2. Flow of Midpoint-Validation Method for SVM

We introduce the adjustment method of SVM from the result obtained from the SVM that used the midpoint data created with Section 3.1. First, SVM is created using known training data. Next, the output value of SVM of the midpoint data and training data are computed. It is assumed that the desired output of SVM by the midpoint data is a value as nearly 0. Therefore, we assume that the midpoint data is near to the classifier line. Then, B from Eq.(6) is adjusted so that the SVM output of the midpoint data may become close to 0. The method is shown in Eq.(8), where M is number of midpoint data.

$$h(\mathbf{x})=g(\mathbf{x})+B \quad (6)$$

$$O=sign(h(\mathbf{x})) \quad (7)$$

$$B=-\frac{1}{M}\sum_{m=1}^{M} g(\mathbf{x}_m) \quad (8)$$

Therefore, SVM is adjusted in order for the output of the midpoint data to be set to nearly 0. We call this technique midpoint-validation method for SVM. The flow of this method is shown in Fig 2.

Midpoint-validation method is applicable to all the techniques of SVM and it is also easy since only one value of parameter B has to be computed.

4. Midpoint-Validation Algorithm

The published paper [10] showed that it was effective to use midpoint data in input space. The method of paper [10] is only adjusted for parameter B in order for the output of the midpoint data to be set to nearly 0. But parameter $\boldsymbol{w}$ were not adjusting. Then, our proposed new method used midpoint data to learning algorithm of SVM.

We propose midpoint-validation algorithm for SVM, which improves the generalization of SVM so that midpoint-validation error in input space is minimized. Eq.(9) is objective function of midpoint-validation error.

$$E = \frac{1}{M} \left| \sum_{m=1}^{M} \mathbf{w} \cdot \mathbf{x}_m + b \right| \tag{9}$$

Eq.(9) of midpoint-validation error is computed simultaneously. Furthermore, the state of SVM in case midpoint-validation error is the minimum is saved for use model. When midpoint-validation error is 1.0 or more, our proposed technique judges that deviation is large than margin of SVM and midpoint-validation method [10] is applied. We call this technique midpoint-validation algorithm for SVM. The flow of midpoint-validation algorithm is shown as below.

Step 1: Create the midpoint data using
Midpoint data creation algorithm.
Step 2: Learning Algorithm of original SVM.
And midpoint-validation error (Eq.(9))
is computed.
Step 3: The state of SVM (in case midpoint-validation
error is the minimum) is saved.
Step 4: **If** Training error less than ***e1***.
: Learning Algorithm stop and go to **Step 5**.
Else : go to **Step2**.
Step 5: **If** Midpoint-validation error lager than ***1.0***.
: Adjusting parameter B using
midpoint-validation method

Fig 3. Midpoint-Validation Algorithm for SVM

Improvement in generalization capability is more expectable by abolishing the deviation of the classifier line in input space by this proposed method using midpoint-validation error.

5. Simulations

In order to test the effectiveness of the midpoint-validation algorithm, we compared its performance with those of the original SVM (from our simulation results using Eq.(4) and Eq.(5)), SVM using midpoint-validation method [10] and tested our proposed method on several benchmark problems. We also applied it to a realistic 'real-world' problem. The data set was created by Johns Hopkins University and obtained from the database [7]. In this paper, we tested on several benchmark problems of Ionosphere, Pima Diabetes, Wisconsin breast cancer (Wisconsin), Sonar and Liver Disorders. We performed only one time using the proposed method. All experiments are the same conditions as database [7] in terms of separating the training data and test data. In this simulation, we used ***e1*** was *1e-6*.

We performed 10 trials (The value of Gaussian kernel parameter σ of different 10) with each method and the simulation results are shown in Table 1. The number of training data vectors, number of test data vectors and the dimensions of the data vectors are set to *n1* be, *n2* and *d* respectively. These three values of *n1, n2* and *d* used in our experiments are shown in Table 1. And, M is number of midpoint data. The results of SVM using midpoint-validation algorithm are better than SVM in fifth benchmark problems. The midpoint-validation algorithm almost has improved SVM in this simulation results. Although midpoint-validation algorithm is almost the same as midpoint-validation method, midpoint-validation algorithm has better results in the conditions of good parameters.

The comparison between SVM using midpoint-validation algorithm and other paper technique are summarized in Table 1. We compare its performance with those of *soft margin* SVM from software LIBSVM [11] (*C*-SVC). The other SVM experimental results are obtained from the published papers [12]. The results show that the proposed method has the best performance in two benchmark problems. But published paper [12] results showed the best performance in Sonar problem and Liver Disorders, where as in other problems the proposed method has better or same results. The method of paper [12] resembles our proposed method by creating a kernel using midpoint data. From Table 1, our proposed method and paper [12] technique have a speciality and a non-speciality by problem.

Table 1. Simulation Results (Testing Correctness [%]).
* t-test (significance level of 5%) had statistical significance than SVM

Dataset ($n1,n2 \times d$)	**SVM**		***C*-SVC[11]**	**CSVM[12]**	**SVM+MV[10]**		**Proposed Method**	
	Ave	**Best**	**-**	**-**	**Ave**	**Best**	**Ave**	**Best**
Ionosphere (200,151 × 34) M=15	88.7	97.4	**98.0**	92.7	89.8	97.4	87.2	**98.0**
Pima Diabetes (576,192 × 8) M=79	77.5	77.6	81.3	**82.3**	80.1*	81.3	80.6*	81.7
Wisconsin (342,341 × 9) M=12	91.7	97.1	**98.8**	-	98.5*	98.5	98.4*	**98.8**
Sonar (104,104 × 60) M=9	92.1	93.3	87.5	**98.1**	92.3	93.3	91.9	93.3
Liver Disorders (230, 115 × 6) M=30	63.3	63.5	51.3	**81.4**	77.0*	77.4	77.2*	78.3

6. Conclusions

SVM performs the large margin in the feature space. However, many experiment results showed that the boundary line created by SVM has deviation in input space. The deviation of SVM is considered to have been generated under the influence of kernel function parameter. Moreover, it is thought that "overfitting" was caused in SVM. Therefore, we think that the adjusting method gives SVM the improvement result in many problems by using the new function made by using the middle point data. The new function is one standard of fine-tuning to finality.

In this paper, we proposed a midpoint-validation algorithm which could be utilized to improve the generalization of SVM. The simulation results on some benchmark problems showed that proposed method be able to find the best performance in the two benchmark problems. The midpoint-validation algorithm had improved the deviation of the output of SVM by kernel function using midpoint data and also simpler than the previous SVM algorithm. Moreover, we think that the proposed method has eased the condition of the labyrinthian problem by using the average value of midpoint data outputs for Eq.(8), (9).

How to select more optimal parameter of proposed method can be further studied.

References

[1]C. Cortes and V.N. Vapnik, "Support Vector Networks", Machine Learning, 20(3), pp. 273-297, 1995.

[2]C.J.C. Burges, "A Tutorial on Support Vector Machines for Pattern Recognition", Data Mining and Knowledge Discovery, vol.2,no. 2, 1998.

[3]T. Joachims, "Making Large-Scale Support Vector Machine Learning Practical", in Advances in Kernel Methods: Support Vector Learning, Shoelkopf, B.,Burges, C., Smola, A., eds., pp. 169-184, 1999.

[4]O.L. Mangasarian and D.R. Musicant, "Active support vector machines", Technical Report 00-04, Data Mining Institute, Computer Sciences Department, University of Wisconsin, madison,Wisconsin, April 2000.

[5]O.L. Mangasarian and D.R. Musicant, "Lagrange Support Vector Machines", Journal of Machine Learning Research Vol. 1, pp. 161-177, 2001.

[6]L.Prechelt, ``Automatic Early Stopping Using Cross Validation Quantifying the Criteria '', Neural Networks Vol, 11 No.4 , pp. 761-767, 1998.

[7]C.L. Blake, C.J Merz, UCI Repository of machine learning databases,
http://www.ics.uci.edu/~mlearn/MLRepository.html,
University of California, Department of Information and Computer Science, Irvine, CA, 1998.

[8]J. Weston, R. Collobert, F. Sinz, L. Bottou, V. Vapnik "Inference with the Universum", Proc of ICML'2006, Pittsburgh, USA, 2006.

[9]H.Tamura and K.Tanno, "Midpoint-Validation Method of Neural Networks for Pattern Classification Problems", International Journal of Innovative Computing, Information and Control, Vol.4, No.10 pp.2475-2482. 2008.

[10]H.Tamura and K.Tanno, "Midpoint-Validation Method for Support Vector Machine Classification", IEICE Trans. on Information and Systems Vol.E91-D No.7 pp.2095-2098. 2008.

[11]LIBSVM: http://www.csie.ntu.edu.tw/~cjlin/libsvm/
Chang and Lin 2001.

[12] T.Raicharoen, T. C.Lursinsap, "Critical support vector machine without kernel function", Proceedings of ICONIP '02, vol.5, pp.2532-2536, 2002.

An analog-digital circuit for sound localization based on the biological auditory system

Takanori Tomibe and Kimihiro Nishio

Tsuyama National College of Technology, 624-1, Numa, Tsuyama, Okayama, Japan, 708-8509
(Tel: 81-868-24-8266; Fax: 81-868-24-8219)
(T. Tomibe: e-t-t@tsuyama-ct.ac.jp)
(K. Nishio: nishio@tsuyama-ct.ac.jp)

***Abstract*:** In this study, we proposed the analog-digital circuit for sound localization based on the biological auditory system. The proposed circuit is constructed with the delay line and the comparator. The delay line was constructed with the simple analog circuits of current mode. The NOR circuit was used as the comparator. The current mode delay line was evaluated by the simulation program with integrated circuit emphasis (SPICE). The test circuit was fabricated by discrete metal oxide semiconductor (MOS) transistors on the breadboard. The result with SPICE and the measured results of the test circuit showed that the time for transmitting the signal of the current mode delay line becomes short when the sound of the target is large. When the sound of target is small, the time for transmitting the signal became long. The proposed circuit for sound localization was evaluated by SPICE. The result with SPICE showed that the circuit can generate the signal for detecting the position of the sound of the target. We can realize novel target tracking system by applying the novel circuit based on the biological auditory system to the previous proposed tracking system based on the biological vision system.

Keywords: sound localization, auditory system, tracking system, analog circuit, digital circuit,

I. INTRODUCTION

It is necessary for robotics vision, monitoring system and collision avoidance system to capture quickly the target in the center of the visual field. However, it is difficult for the typical systems using only vision system since the system can not detect the target when the target is not projected on the visual area. Both the vision system and the auditory system exist in the brain of the animal. The animal can capture the target in the center of the visual area by using auditory system which can process the sound information of the target and detects the position of the sound, even if the target is not projected on the visual area.

Recently, many researchers proposed and fabricated the simple circuit for target tracking system based on the biological vision system [1]-[3]. Since the circuits were proposed by mimicluing only the vision system, the system could not track the target when the target was not projected on the photodiode array which is input part. And the system could not track the target in the lightless situation since the dynamic range against light intensity of the circuit was small. If the circuit based on the vision system is connected with the circuit based on the auditory system, it is able to track the target in various situations. However, there are no simple circuits based on the auditory system.

L. A. Jeffress proposed the model for sound localization based on the biological auditory system [4]. The model is constructed with the delay line and the comparator.

In this study, we proposed the simple analog-digital circuit for sound localization based on the model by Jeffress. We tried to propose the simple analog circuit for delay line. We call the delay line the current mode delay line. The NOR circuit was used as the comparator. The results with the simulation program with integrated circuit emphasis (SPICE) and the measured result of the test circuit fabricated by discrete metal oxide semiconductor (MOS) transistors on the breadboard showed that the current mode delay line can operate normally. The results with SPICE showed that the proposed circuit can generate the signal for detecting the position of the sound of the target.

II. SOUND LOCALIZATION MODEL

Figure 1 shows the model for sound localization proposed by Jeffress [3]. The model is constructed with the delay line constructed with the delay neuron D and the comparator C. I_{right} and I_{left} are input signal generated by the right ear and the left ear, respectively. When the sound of the target is large, I_{right} and I_{left} become large. Inversely, I_{right} and I_{left} are small when the sound of the target is small. I_{right} is input to the delay line (right). I_{left} is input to the delay line (left). I_{right} transmits the delay line (right) from D_n to D_1. I_{left} transmits the delay line (left) from D_1 to D_n. Therefore, delay neurons output the signal sequentially. When I_{right} (I_{left}) is large, the delay time t_{delay} for transmitting the delay line (delay time) is short. When I_{right} (I_{left}) is small, the time t_{delay} is large. The delay times of the delay line right and left are t_{dright} and t_{dleft}, respectively. The comparator inputs the output signals of delay neurons. When both delay neurons output the signal, the comparator outputs the signal. The model can detect the position of the sound by detecting the position of the comparator which outputs the signal firstly.

When the sound of the target is located in the center of the model, I_{right} is equal to I_{left}. Then, the comparator located in the center outputs the signal, since t_{dright} is equal to t_{dleft}. When the sound of the target is located in the right of the model, I_{right} is larger than I_{left}. Then, the comparator located in the left outputs the signal since t_{dright} is shorter than t_{dleft}. When the sound of the target is located in the left of model, I_{right} is smaller than I_{left}. Then, the comparator located in the right outputs the signal. Thus, the model has the function of the sound localization. As shown in Fig. 1, we call the cell constructed with two delay neurons and one comparator the Unit.

Ⅲ. SOUND LOCALIZATION CIRCUIT

The unit circuit of the delay line is shown in Fig. 2.

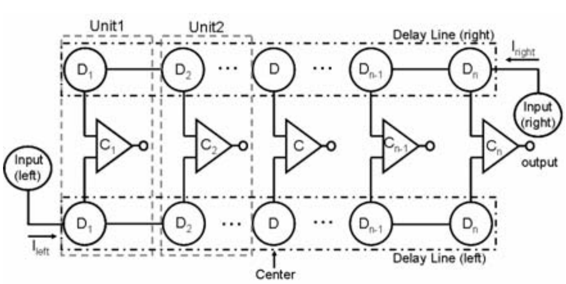

Fig.1. The model for sound localization by Jeffress.

Since the unit circuit is operated by the current mode, we call the delay line constructed with the unit circuits the current mode delay line.

The unit circuit is constructed with 9 MOS transistors and 1 capacitor. The unit circuit corresponds to the delay neuron in Fig. 1. I_{in} is the input current. I_{in} corresponds to I_{left} in Fig. 1, when the unit circuit is used as D_1 of the delay line (left). It is assumed that I_{in} (I_{right} and I_{left}) is the signal generated by the microphone. When the sound of the target is large and small, I_{in} is large and small, respectively.

I_{in} flows into the integration circuit constructed with the capacitor C_n and the nMOS transistor M_{n1}. The voltage V_C is represented by

$$V_C = \frac{I_{\text{in}}}{C_n} t_d + V_0 \tag{1}$$

V_0 is the constant voltage, and V_0 is equal to 0 V. The t_d is equal to the delay time. The voltage V_{SW} is represented by

$$V_{SW} \cong \frac{V_{DD} - V_{th}}{V_C + (V_{DD} - V_{th})} V_{DD} \tag{2}$$

V_{th} is the constant voltage. When V_C is smaller than V_{DD}-V_{th}, V_{SW} is about the supply voltage V_{DD}. Then, the output current I_{out} is 0 since the pMOS transistor M_{p1} as the switch turns off. When V_C is larger than V_{DD}-V_{th}, V_{SW} is about 0. Then, I_{out} becomes I_{in} since M_{p1} turns on. I_{out} is transmitted to the neighbouring unit circuit, and I_{out} is used as the input current of the neighbouring circuit.

When I_{in} is large, the delay time t_d is short. When I_{in} is large, I_{out} is early equal to I_{in} since the delay time t_d which is the time for increasing V_C is short, as shown in eq. (1). When I_{in} is small, I_{out} is slowly equal to I_{in} because t_d is long. Thus, the proposed circuit in Fig. 2 can be used as the delay neuron.

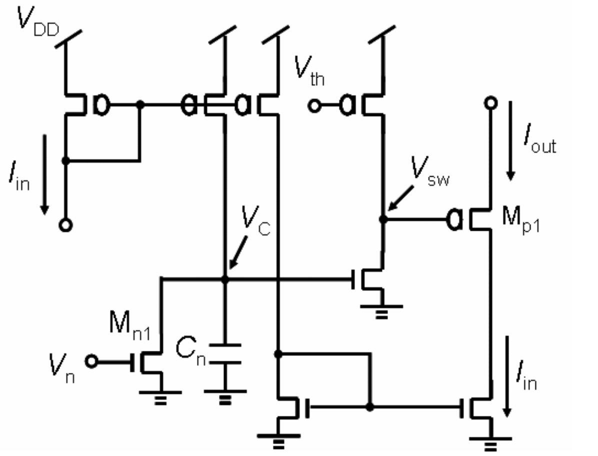

Fig.2. The unit circuit of the current mode delay line.

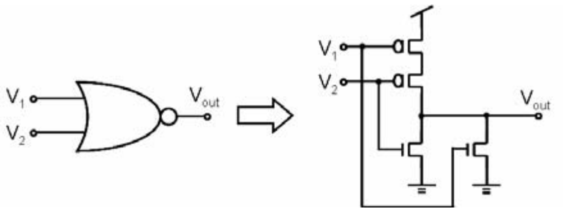

Fig. 3. The structure of the NOR circuit.

The NOR circuit was used as the comparator in Fig.1. The NOR circuit is shown in Fig. 3. The circuit is constructed with 4 MOS transistors. V_1 and V_2 is input voltage. V_{SW} of unit circuit used to the delay line (right) is connected with the terminal of V_1. V_{SW} of unit circuit used to the delay line (left) is connected with the terminal of V_2. V_{SW} became 0 when the signal is transmitted to the unit circuit. The circuit outputs the supply voltage V_{DD} in the only case that V_1 and V_2 are 0. By detecting the position of the comparator which outputs firstly V_{DD}, the proposed circuit can detect the position of the sound of the target.

Ⅳ. SIMULATION AND EXPERIMENTAL RESULT

We investigated the proposed unit circuit in Fig. 2 by using SPICE. In all simulations, the model parameter of 1.5 μm CMOS process was provided. The channel length and channel width of all MOS transistors was 3.0 μm and 4.5 μm, respectively. C_n was set to 100 pF. V_{DD} was set to 5 V. V_{th} was set to 4.25 V. V_n was set to 0 V.

Figure 4(a) shows output current I_{out} when the input current I_{in} is 10 nA. The unit circuit outputted I_{out} after about 10 msec. The delay time was about 10 msec. Figure 4(b) shows the output current I_{out} when the input current I_{in} is 50 nA. The unit circuit outputted I_{out} after about 1 msec. The delay time was about 1 msec. Thus, the delay time became short when the I_{in} became large.

The current mode delay line constructed with 5 proposed unit circuits was evaluated by SPICE. Figure 5 shows the simulation results. I_{in} is the input current of the first unit circuit. I_{out} is the output current of the 5th unit circuit. I_{in} was set to 10 nA. After about 18 msec, the 5th unit circuit output I_{out}. The delay time was 18 msec. We understand that the current mode delay line can transmit the signal.

In order to investigate the current mode delay line, the test circuit was fabricated on the breadboard by using discrete MOS transistors (nMOS: 2SK1398, pMOS: 2SJ184, NEC). Figure 6 shows the photograph of the fabricated test circuit and the experimental equipment. The current mode delay line was constructed with 3 unit circuits in Fig. 2. V_{DD} was set to 5 V. V_{th} was set to 3.3 V. V_{in} was set to 1.4 V and V_n was set to 0 V.

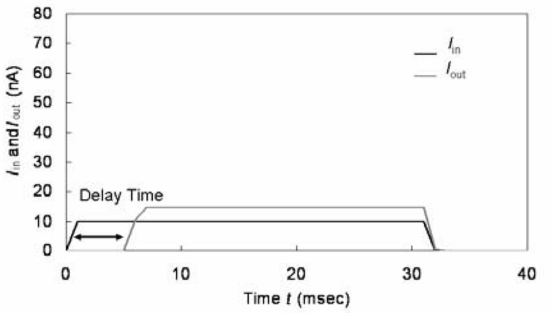

(a)

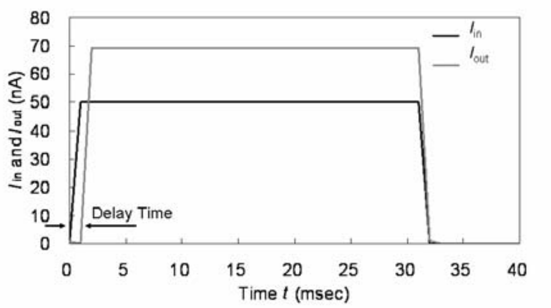

(b)

Fig. 4. The simulation result of the unit circuit. (a) The result when I_{in} is 10 nA. (b) The result when I_{in} is 50 nA.

Figure 7 shows the measured results of the test circuit of the current mode delay line. Each V_{SW} in Fig. 2 is shown in Fig. 7. When V_{SW} becomes 0, the signal is transmitted to the unit circuit. The results in Fig. 7 showed that the test circuit can transmit the signal.

The proposed circuit for sound localization was evaluated by SPICE. 20 unit circuits were arranged in one-dimensionally. The construction is equal to that in Fig. 1. Figure 8(a) shows the output voltages of comparators when the input current I_{right} was equal to

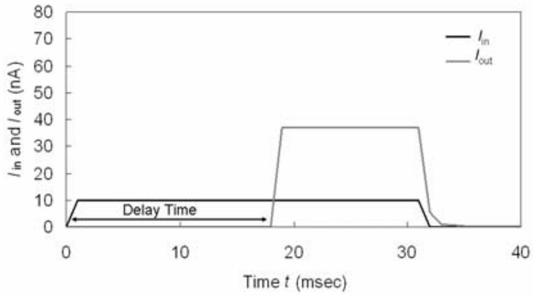

Fig. 5. The simulation result of the delay line.

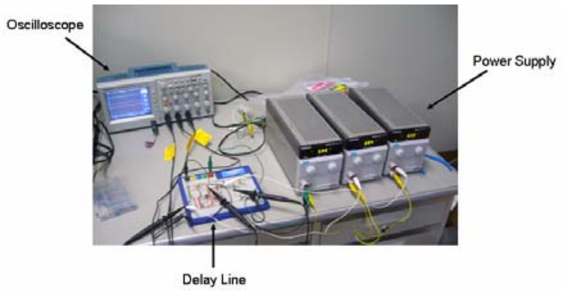

Fig. 6. The photograph of the fabricated test circuit and experimental.

the input current I_{left}. Then, the sound of the target was located in the center. I_{right} and I_{left} were set to 20 nA. The comparators of Unit10 and Unit11 located in the center firstly outputs the voltage.

Figure 8(b) shows the output voltage of comparators when I_{left} is smaller than I_{right}. Then, the sound of the target was located in the right side. I_{right} was set to 25 nA. I_{left} was set to 20 nA. The comparator of Unit3 located in the left side firstly output the voltage. The result with SPICE showed that the proposed circuit has the function of the sound localization.

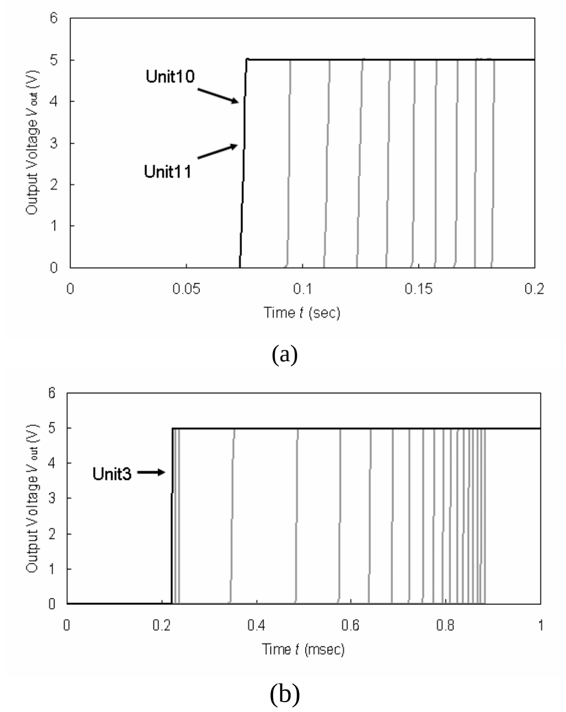

Fig. 8. The simulation result of the circuit for sound localization. (a) Output voltages when the sound of the target was located in the center. (b) Output voltages when the sound of the target was located in the right side.

VI. CONCLUSION

In this study, we proposed the analog-digital circuit for sound localization based on the biological auditory system. The proposed circuit is constructed with the current mode delay line and the comparator. The NOR circuit was used as the comparator. The current mode delay line was evaluated by SPICE. The test circuit of the delay line was fabricated by discrete MOS transistors on the breadboard. The result with SPICE and the measured results of the test circuit showed that the delay time becomes short when the sound of the target is large. When the sound of target is small, the delay time became long. The result with SPICE showed that the proposed circuit can generate the signal for detecting the position of the sound of the target. We can realize novel target tracking system by applying the novel circuit based on the biological auditory system to the previous proposed tracking system based on the biological vision system.

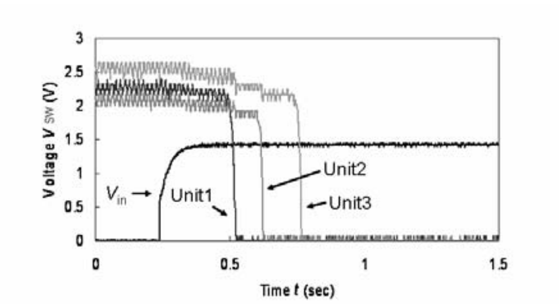

Fig. 7. Measured result of the test circuit of the current mode delay line.

REFERENCES

[1] A. Moini, Vision Chips, Kluwer Academic, Norwell, MA, 1999.

[2] K. Nishio and K. Matsuzaka, "Target Tracking System Using Analog Circuit for Motion Detection", *Proc. of 2008 IEEE Int. Conf. on Mechatronics and Automation*, TC3-5, 2008.

[3] K. Nishio and K. Matsuzaka, "Target Tracking System Using Analog Motion Detection Circuit Based on Biological Vision system", *For East Journal Electronics and Communications*, Vol.3 111-124, 2009.

[4] L. A. Jeffress, "A Place Theory of Sound Localization", *J. Comp. Physiol. Phychol.* 41, 35-39, 1948.

The Fifteenth International Symposium on Artificial Life and Robotics 2010 (AROB 15th '10),
B-Con Plaza, Beppu,Oita, Japan, February 4-6, 2010

Artificial Neural Networks Paddy Field Classifier using Spatiotemporal Remote Sensing Data

Takashi Yamaguchi*, Kazuya Kishida*, Eiji Nunohiro*, Jong Geol Park**, Kenneth J. Mackin*,
Keitaro Hara**, Kotaro Matsushita**, and Ippei Harada**

** Department of Information Systems, Tokyo University of Information Sciences,
4-1Onaridai, Wakaba-ku, Chiba, 265-8501 Japan*
*** Department of Environmental Information, Tokyo University of Information Science,
4-1Onaridai, Wakaba-ku, Chiba, 265-8501 Japan*
(Tel/Fax: 81-43-236-1329)
(tyamagu@edu.tuis.ac.jp)

Abstract: Monitoring changes in paddy field area is important since rice is staple food, and paddy agriculture is a major cropping system in Asia. For monitoring change in land surface, various applications using different satellites were researched in the field of remote sensing. However monitoring paddy field area with remote sensing is difficult due to the temporal change in land surface, and difference of spatiotemporal characteristics in countries and regions. In this paper, we applied artificial neural network to classify paddy field areas using moderate resolution sensor data that includes spatiotemporal information. Our aim is to automatically generate a paddy field classifier in order to create localized classifiers for each country and region.

Keywords: artificial neural network, classification, Remote sensing, MODIS.

I. INTRODUCTION

Monitoring changes in paddy field area is important since rice is staple food and paddy agriculture is a major cropping system in Asia. For monitoring change in land surface, many satellites were launched and its applications were researched in the field of remote sensing.

Monitoring paddy field area with remote sensing is difficult because a paddy has an annual cycle that can be classified into three main periods [1]: (1) the flooding and rice transplanting period, when the land surface is observed as water; (2) the growing period, when increasing vegetation index was observed; (3) the fallow period, when land surface is observed as soil. For monitoring change in land cover, moderate resolution remote sensing is effective because of the high frequency of these satellites to scan the same area.

In the past research for paddy field area estimation using remote sensing, decision trees or stochastic analysis based methods using spatiotemporal information were proposed [1] [2]. On the other hand, it is difficult to apply the same models for different countries and regions. In this paper we applied artificial neural network to classify paddy field area using moderate resolution remote sensing data in order to automatically generate the classifier.

II. METHOD

Multi-Layered Perceptron

Multi-layered perceptron (MLP) is a type of artificial neural network (ANN) that can approximate complex function by machine learning. In this research, we used MLP shown as Fig. 1 in order to learn a classification function of paddy field area from the MODIS data set.

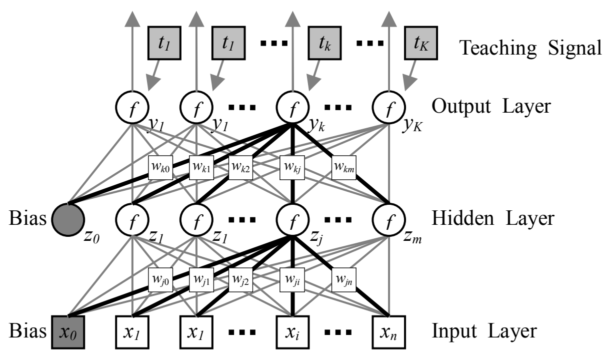

Fig 1. MLP Network Structure

MLP consists of 3 layers: input layer with *n* neurons and a bias neuron, hidden layer with *m* neurons and a bias neuron, and output layer with *K* neurons. Each neuron is connected with every neuron in the next layer, and each connection has a weight value. When an input signal $x = \{x_1,x_2,\ldots x_n\}$ is given, jth output signal z_j of hidden layer's neuron and kth output signal y_k of output layer's neuron are calculated by following expressions:

$$z_j = f\left(\sum_{i=0}^{n} w_{ji} x_i\right), \quad (1)$$

$$y_k = f\left(\sum_{j=0}^{m} w_{kj} z_j\right), \quad (2)$$

where $i = 0, 1, 2 \ldots, n$; $j = 0, 1, 2 \ldots, m$; $k = 0, 1, 2 \ldots, K$; f is the activation function, and z_0 and x_0 are bias neurons. Bias neuron always output 1.0 to next layer's neurons. For activation function, Sigmoid function was used.

MLP modifies each weight value using back propagation (BP) training [3]. Let be $x^p = \{x_1^p, x_2^p, \ldots x_n^p\}$, $p = 1, 2, \ldots, N$ is pth input signal, and $t^p = \{t_1^p, t_2^p, \ldots t_K^p\}$ is pth teaching signal. The teaching signal is true output signal that correspond to pth input signal x^p where projection function can be defined as follow

$$t_p = g(x_p). \quad (3)$$

When pth training pattern $\{x^p, t^p\}$ is given, BP training modifies weights for minimizing mean square error E defined as following expression

$$E = \frac{1}{N}\sum_{p=1}^{N}\left\|t^p - y^p\right\|^2. \quad (4)$$

At the training step in BP training, the weight modification $\Delta w_{ji}(s)$ and $\Delta w_{kj}(s)$ are defined as follows:

$$\Delta w_{ji}(s) = -\lambda \cdot \frac{\partial E}{\partial w_{ji}} + \mu \cdot \Delta w_{ji}(s-1), \quad (5),$$

$$\Delta w_{kj}(s) = -\lambda \frac{\partial E}{\partial w_{kj}} + \mu \cdot \Delta w_{kj}(s-1), \quad (6)$$

where λ is a learning rate, and μ is a momentum rate. Each weight is commonly initialized by random value. As a result of training, MLP learns a function $g(x)$ by modifying weight values.

In this research, MLP was used as 2 class classifier such that classifies positive or negative (1 or 0) for paddy field class. However MLP output is continuous value, so that it is necessary to decide positive or negative from the continuous output value. In this experiment, pth final output was defined by following function.

$$Output^p = \begin{cases} positive & if \quad y^p > \theta \\ negative & otherwize \end{cases}. \quad (7)$$

where θ is predefined threshold value.

MLP learning result is unstable from the initialization problem that MLP learning falls into different local minima by the initial weight values. For resolving unstableness, combination with ensemble learning and MLP is commonly used. Ensemble Learning is a method for improving the stability of machine learning algorithms by using multiple learners. For ensemble method, bagging method was used [4]. bagging is a typical ensemble method that aggregates multiple training results. For aggregating, voting was used, as this is commonly used in bagging for classifier. Let $L(x)$ be an aggregated learner, $L_s(x)$ be a multiple weak learner where $s = 1, 2, \ldots, r$; and $c = 1, 2, \ldots, C$ be class label. A robust learner $L(x)$ is defined by following expression.

$$L(x) = \arg\max_{c} \left|\{s; L_s(x) = c\}\right|. \quad (8)$$

Each learner is trained by using bootstrap samples [5]. Let T be training data set, training data subset $T_s \in T$ for sth learner is constructed by using random sample.

III. EXPERIMENT

1. Paddy Field Area Estimation using Moderate Resolution Remote Sensing

For this paper, we used MODIS (Moderate Resolution Imaging Spectoradiometer) data collected at Tokyo University of Information Sciences TUIS, Japan. TUIS receives satellite MODIS data over eastern Asia, and provides this data for open research use.

Fig. 2 shows NDVI (Normalized Difference Vegetation Index) maps for north region of Kyushu, Japan in 3 different months (A, January; B, June; C, September) derived from 1-month composite MODIS sensor data. NDVI is a vegetation index defined by bands 1 and 2 (visible red and near infra-red).

D of Fig. 2 shows the land-truth data provided by the Japanese Ministry of Land, Infrastructure, Transport and Tourism (JMLIT). The red colored pixels show that the paddy area ratio is larger than other land-use types in the corresponding 500m x 500m area. The land-truth data is provided in vector data format, so the data was converted into raster format of 500m scale pixel data (1 pixel = 500m x 500m resolution) in order to use the data as the solution set.

From these maps, it can be seen that paddy field areas' vegetation changes in period of time. However, it is difficult to extract a generalized rule for paddy classification from this spatiotemporal information. Because annual cycle of a paddy is different in each countries and region, the changes in spatiotemporal information are different in each region. Our aim is to automatically generate a paddy classifier using artificial neural network and spatiotemporal MODIS sensor data shown as D of Fig. 2.

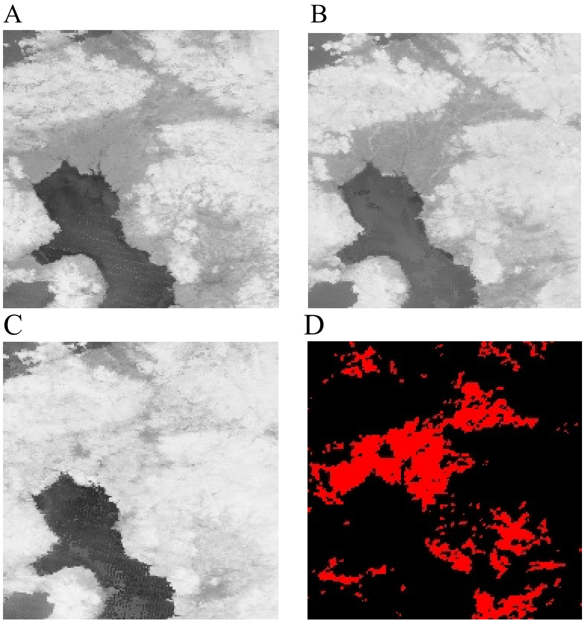

Fig 2 NDVI maps and land-truth data for north region of Kyushu, Japan

2. MLP Paddy Field Classifier

In previous our research, we evaluate MLP paddy field classifier using spatiotemporal MODIS band 1 and band 2 (red and infra red) data [6]. From this result, proposed MLP paddy field classifier could not yield sufficient accuracy for practical use. For improving classification accuracy, we investigate using 3 bands as input signals.

In the paddy field annual cycle, the features of paddy fields are vegetation, soil and water index. For vegetation index, NDVI was commonly used. NDVI is defined as follow.

$$NDVI = (RED - NIR)/(RED + NIR), \quad (9)$$

where RED is visible red reflectance, and NIR is near infra-red reflectance.

Similarly, for indices of soil and water, NDSI (Normalized Difference Soil Index) and NDWI (Normalized Difference Water Index) was proposed by W. Takeuchi and Y. Yasuoka [7]. NDSI and NDWI are defined as follows

$$NDSI = (SWIR - NIR)/(SWIR + NIR), \quad (10)$$

$$NDWI = (RED - SWIR)/(RED + SWIR), \quad (11)$$

where $SWIR$ is short wave infra-red reflectance. Short wave infra-red reflectance is corresponds to band 6 data in MODIS data set. Considering NDSI and NDWI, we additionally used band 6 data.

In this paper, we prepared 4 different MLP Paddy field Classifier model shown in Table 1 for the evaluating improvement of accuracy using band 6 data. The differences of each model are input size n and hidden size m.

In 3 bands models, 1 month part of input signals consists of band 1, band 2, and band 6. In 2 bands models, 1 month part of input signals consists of band 1 and band 2. In 3 months models, input signals consist of bands data of January, June and September (2 or 3 x 3 inputs). This 3 months correspond to 3 periods of the paddy annual cycle. In 11 months models, input signals consist of bands data of January to November per 1-month (2 or 3 x 11 inputs). The band data of each month was derived from 1-month composite MODIS sensor data of 500m resolution.

For teaching signal, land-truth data was used. This value is paddy or non-paddy (1 or 0), it were derived from digital national land information provided by the JMLIT. The parameters of MLP were defined by prior experiment.

Table 1. MLP parameters for the paddy classifier using MODIS sensor data.

	Parameters					
	n	m	K	λ	μ	θ
3 bands 3 months	9	9	1	0.25	0.05	0.3
3 bands 11 months	33	33	1	0.25	0.05	0.3
2 bands 3 months	6	6	1	0.25	0.05	0.3
2 bands 11 months	22	22	1	0.25	0.05	0.3

n: input size, m: hidden size, K: output size,
λ: learning rate, μ: momentum rate, θ: output threshold

3. Experimental Result

In this experiment, we evaluated classification accuracy by using proposed paddy classifier. For evaluating classification accuracy, MODIS data was divided into 2 disjoint sub set, training data set and test data set, by using random sampling from the north region of Kyushu, Japan shown in Fig. 1. The number of test data set was 10% of the number of training data set. Table 2 shows classification accuracy of the proposed paddy classifier.

Table 2 shows the comparison of classification accuracy. It can be confirmed that 3 bands 11 month model yielded best total classification rate. In addition, 3 bands models yielded better result compared with 2 bands models in total and paddy classification rate. This result shows the effectiveness of using band 6 data in MLP paddy field classifier.

On the other hand, in the classification rate for paddy field, 3 months models were tend to yield better result than 11 months models. This tendency was similar to previous our research. It is expected that this accuracy reduction was caused by increasing input size. Considering automatically generating paddy classifier, it is necessary to investigate feature selection methods because the annual cycle changes when the target region is changed.

Table 2. The comparison of classification accuracy in proposed paddy classifier.

	Correctly Classification Rate		
	Total	Paddy	Non-Paddy
3 bands 3 months	0.879	0.746	0.908
3 bands 11 months	0.908	0.714	0.953
2 bands 3 months	0.873	0.719	0.908
2 bands 11 months	0.876	0.707	0.915

IV. CONCLUSION

In this paper, we proposed MLP paddy field classifier using spatiotemporal MODIS band 1, band 2 and band 6 data in order to automatically generate a classifier. From the computer simulation, we confirmed that the improvement of classification accuracy by additionally using band 6 data. This result shows the effectiveness of using band 6 data in MLP paddy field classifier. In addition the proposed paddy field classifier yielded 0.908 classification rate. Considering that 0.95 or more accuracy is necessity for practical use, it can be concluded that proposed MLP paddy field classifier yields good result.

In this experiment, we confirmed that error was occurred when convert into raster format from vector format for create land-truth data. It is expected that accuracy can be improved by the reducing this error. In addition, we plan to compare with other paddy classifier based on decision tree method, and other machine learning methods.

REFERENCES

[1] T. Le Toan, F. Ribbes, L. Wang, et al (1997), Rice crop mapping and monitoring using ERS-1 data based on experiment and modeling results. IEEE Transactions on Geoscience and Remote Sensing, 1, 41-56

[2] X. Xiao, S. Boles, S. Frolking, C. Li, et al (2006), Mapping paddy rice agriculture in south and southeast Asia using multi-temporal MODIS images. Remote Sensing of Environment, 100, 95-113

[3] D. E. Rumelhart, G. E. Hinton, R. J. Williams (1986) Learning representations by back-propagating Errors. Nature, vol. 323, pp. 533-536

[4] L. Breiman, (1996) Bagging Predictors. Machine Learning, 24(2), 123-140

[5] B. Efron, R. Tibshirani (1993), "An Introduction to the Bootstrap". Chapman and Hall.

[6] Takashi Yamaguchi, Eiji Nunohiro, Jong Geol Park (2009) Application of Artificial Neural Network for Land Cover Classification using Spatiotemporal Information, 5th International Conference on Information,

[7] W.Takeuchi, Y. Yasuoka (2004), Development of normalized vegetation, soil and water indices derived from satellite remote sensing data, Journal of the Japan Society of Photogrammetry and Remote Sensing, Vol. 43, No. 6, pp. 7-19 (in Japanese).

Transformation of neural network weight trajectories on 2D plane for learning type neural network direct controller

Takayuki Yamada
Department of Computer and Information Sciences
Faculty of Engineering
Ibaraki University
4-12-1 Nakanarusawa, Hitachi, Ibaraki, 316-8511, Japan

Abstract: Through the simulation of tracking method of neural network weight change on 2D plane, we noticed that it was hard for untrained users to observe the neural network weight performance on 2D plane in some cases. To overcome this problem, this paper applied a transformation of the neural network weight trajectories on 2D plane to the learning type neural network direct controller. The simulation results confirmed that if the trajectory of the neural network weight change on 2D plane had the simple structure, we could easily determine whether the leaning of the neural network was terminated. However, if it had more complex structure, we could not determine. The proposed transformation of the neural network weight trajectories to one dimensional values was useful for such cases

Keywords: Neural network, Controller, Learning, Adaptive

I. INTRODUCTION

Many studies have been undertaken in order to apply both the flexibility and the learning capability of neural networks to control systems. Although many neural network controllers have been proposed, we still have to tune several parameters of neural networks in order to obtain a better neural network learning performance in practical applications. A tracking method of neural network weight change has been proposed for better parameter tuning of the neural network controllers. This tuning method derives a weight vector from whole neural network weights. We can calculate an angle between this weight vector and a standard vector. The neural network weight change can be directly drawn on 2D plane by the use of the norm of the weight vector and the above angle. Drawn trajectories on 2D plane are not affected by the plant dynamics in comparison with the observation of the squared error between the neural network output and the plant output.

We have applied our tracking method to several types of the neural network controllers and confirmed its usefulness.[1][2 [3][4] However, we noticed through the simulation that it was hard for untrained users to observe the neural network weight performance on 2D plane in some cases. To overcome this problem, this paper proposes a transformation of the trajectories on 2D plane to one dimensional values. This transformation is to observe the velocity of weight change on 2D plane or its components. That is, when this velocity is almost zero, we can easily determine that the neural network learning is terminated in comparison with the observation of only neural network weight trajectories on 2D plane. The basic idea of this transformation was introduced by one example of the application to the learning type feedforward feedback neural network controller in my previous paper.[4] However, in order to obtain more accurate examination, we should apply it to more simple neural network controller.

Thus, this paper applies a transformation of the neural network weight trajectories on 2D plane to the learning type neural network direct controller and examines details of its performance. The reason of the choice of the direct controller is that this type controller has simplest structure and we can eliminate the effect of the feedback loop. Simulation results introduce the cases such that it is hard for untrained users to observe the neural network weight performance on 2D plan. Next, we confirm that our transformation of the neural network weight trajectories is useful for these cases.

II. TRACKING METHOD OF NEURAL NETWORK WEIGHT CHANGE

This section briefly explains the tracking method of the neural network weight change. This tracking method is applied to the learning type neural network direct controller for the SISO plant. Here, an output layer of the neural network has one neuron, the weights between the output layer and a hidden layer can be expressed as a vector ω and the weights between the hidden layer and the input layer can be expressed as a matrix W. For simplicity, the neuron number of the input layer is equal to that of the hidden layer. That is, the weight matrix W is a square matrix. The tracking method uses the following steps.

(Tracking method of neural network weight change)

(1) We can derive one weight vector Γ from the neural network weight vector ω and weight matrix W as follows:

$$\Gamma^T = [\omega_1 \cdots \omega_n \; W_{11} \cdots W_{1n} W_{21} \cdots W_{2n} \cdots W_{n1} \cdots W_{nn}] \qquad (1)$$

where n is the neuron number both the input layer and the hidden layer.

(2)We must define a standard vector Γ_0. Any vector which is of same order as that of the weight vector Γ, can be selected as the standard vector. For example, the weight vectors derived from the initial neural network weights, the final neural network weights and so on.

(3) We can calculate an inner product of the weight vector Γ and the standard vector Γ_0 because these vectors are of the same order. We can also calculate the angle between the weight vector Γ and the standard vector Γ_0 as follows:

$$X = |\Gamma| \cos\theta, \quad Y = |\Gamma| \sin\theta \qquad (2)$$

$$\theta = \cos^{-1}\left(\frac{<\Gamma_0 \cdot \Gamma>}{|\Gamma_0| \cdot |\Gamma|}\right) \qquad (3)$$

where $<\Gamma_0 \cdot \Gamma>$ is the inner product between the vector Γ_0 and the vector Γ, and $|\Gamma|$ is the norm of the vector Γ.

(4) We can draw a new weight performance on the 2D plane by the use of X and Y in equations (2) and (3).

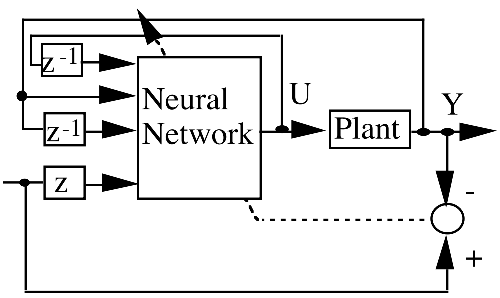

Fig.1 Block diagram of neural network direct controller for second order discrete time plant.

III. SIMULATION

This paper applies the tracking method of the neural network weight change to the learning type neural network direct controller. The simulated plant is follows:

$$Y(k) = - a_1 Y(k-1) - a_2 Y(k-2) + U(k-1) + bU(k-2) - a_3 Y(k-3) + C_{non} Y^2(k-1) \qquad (4)$$

where Y(k) is the plant output, U(k) is the plant input, k is the sampling number, a_1, a_2 and b are the plant parameters, a_3 is the parasite term, and C_{non} is a nonlinear term. For this simulation, a_1=-1.3, a_2=0.3, b=0.7, a_3=-0.03 and C_{non}=0.2 are selected. The rectangular wave is also selected as the desired value Yd. The output error ε and the cost function J are defined as follows:

$$\varepsilon(k) = Yd(k) - Y(k) \qquad (5)$$

$$J(p) = \frac{1}{2} \sum_{k=1}^{\rho} \varepsilon^2(k) \qquad (6)$$

where p is the trial number and ρ is the sampling number within one trial period.

For this simulated plant, the neuron number n in both the input and the hidden layers is 4. The neural network input vector I is defined as the following equation.

$$I^T(k) = [Y_d(k+1) \; Y(k) \; Y(k-1) \; U(k-1)] \qquad (7)$$

We select the following sigmoid function f(x) as the input-output relation of the hidden layer neuron.

$$f(x) = \frac{X_g\{1-\exp(-4x/X_g)\}}{2\{1+\exp(-4x/X_g)\}} \qquad (8)$$

where Xg is the parameter which defines the sigmoid function shape. The neural network output U(k) is composed as follows:

$$U(k) = \omega^T(p) f\{W(p) I(k)\} \qquad (9)$$

The block diagram of the learning type neural network direct controller is shown in Fig.1. The learning rule of this neural network controller is designed so as to minimize the cost function J. When we apply the δ rule to this learning rule, it is expressed as

$$W_{ij}(p+1) = W_{ij}(p) + \eta \sum_{k=1}^{\rho} [\varepsilon(k)\omega_i(p) I_j(k-1) f'\{\sum_{j=1}^{n} W_{ij}(p) I_j(k-1)\}] \qquad (10)$$

$$\omega_i(p+1) = \omega_i(p) + \eta f [\sum_{j=1}^{n} \{W_{ij}(p) \sum_{k=1}^{\rho} (\varepsilon(k) I_j(k-1))\}] \qquad (11)$$

where η is the parameter to determine the neural network learning speed. We select the weight vector derived from the initial neural network weights as the standard vector Γ_0 of the equations (2) and (3)

In order to realize the easier expression of the neural network weight performance for untrained users, this paper proposes a transformation of the trajectories on 2D plane to one dimensional values as follows:

$$Vwx(p) = X(p+1) - X(p) \qquad (12)$$

$$Vwy\ (p) = Y(p+1) - Y(p) \tag{13}$$

$$Vw\ (p) = \sqrt{(Vwx\ (p))^2 + (Vwy\ (p))^2} \tag{14}$$

As shown in eq.(14), Vw in eq.(14) is the velocity of neural network weight change on 2D plane. Vwx and Vwy show the X and Y components of the velocity Vw respectively That is, when the velocity Vw is almost zero or both its X and Y components Vwx and Vwy are almost zero, we can easily determine that the neural network learning is terminated. Eqs.(12)-(13) is our proposed method.

Fig.2 shows the example 1 of the trajectory of the neural network weight change on 2D plane. It can be drawn through the use of eqs.(2) and (3). It has the simple structure and we can easily observe that the neural network weights convergence as shown here. Figs.3 and 4 show the example 2 of the trajectory of the neural network weight change on 2D plane and its expansion respectively. This example of the trajectory has more complex structure and it is difficult to observe the neural network weight performance on 2D plane. If we can expand the example 2 as shown in fig.4, we can observe the fine structure of the neural network weight performance, but this work requires big effort for the untrained users.

Fig.5 shows the velocity Vw of the neural network weight change on 2D plan for example 2. As shown here, Vw has the simple structure and the untrained users can easily determine whether the learning of the neural network is terminated or not. Vw is similar to the cost funtion J, but they are different because the cost function is affected by the plant dynamics. We can not observe the large vibration of the neural network weight change on 2D plane through the use of Vw. If this information is important for some applications, Vwx and Vwy in eqs.(12) and (13) are useful.

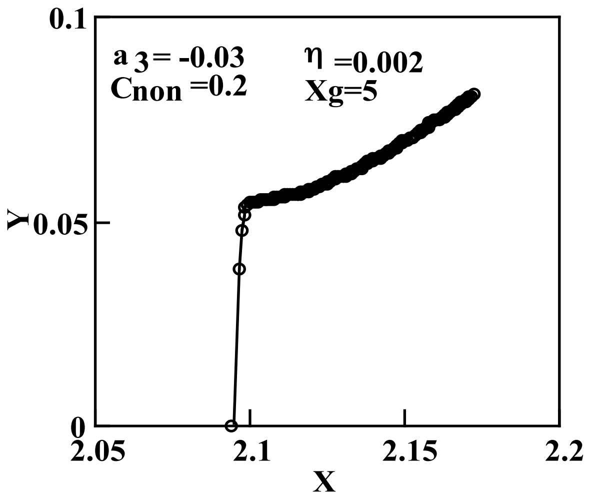

Fig.2 Example 1 of trajectory of neural network weight change.

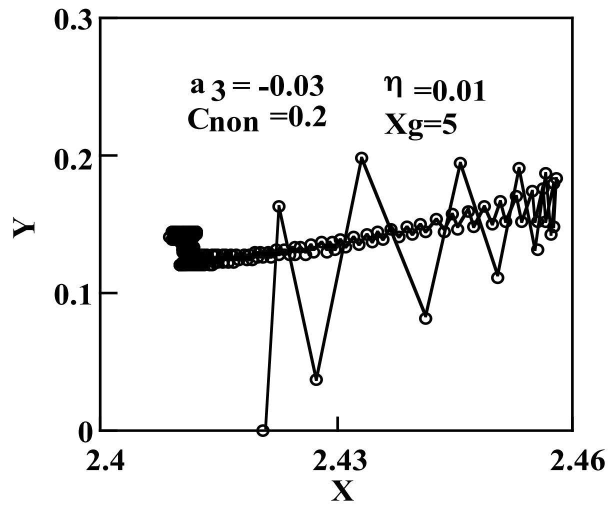

Fig.3 Example 2 of trajectory of neural network weight change.

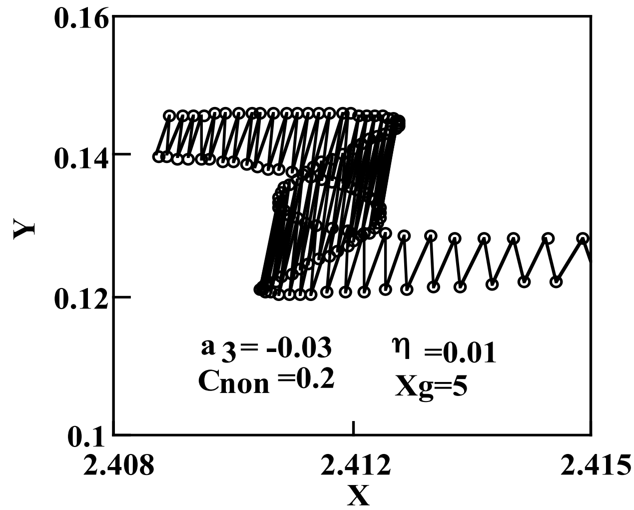

Fig.4 Expansion of example 2.

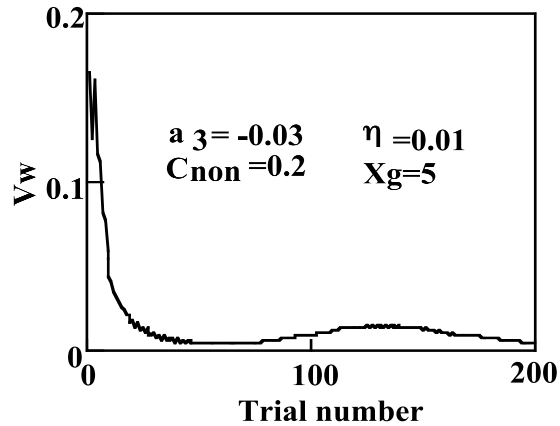

Fig.5 Vw for example 2.

Figs.6 and 7 show Vwx and Vwy for example 2 respectively. As shown in these figures, we can observe the vibration of the neural network weight change and we can easily determine whether the learning of the neural network is terminated or not. Fig.8 shows the example 3 of the trajectory of the neural network weight change on 2D plane. It is another example which has more complex structure. However, Vw, Vwx and Vwy are also useful for this more complex structure.

IV. CONCLUSION

This paper applied the transformation of the neural network weight trajectories on 2D plane to the learning type neural network direct controller and the simulation results examine details of its performance. They confirmed that if the trajectory of the neural network weight change on 2D plane had the simple structure, we could easily determine whether the leaning of the neural network was terminated. However, if it had more complex structure, we could not determine. The transformation of the neural network weight trajectories to one dimensional values was useful for such cases. This is because these one dimensional values have simple structure and the untrained users can easily observe the neural network weight performance through the use of these values.

ACKNOWLEDGMENT

The author wishes to express his thanks to Mr.Taka-aki Kuji graduated student, Ibaraki University, for his programming and simulation.

REFERENCES

[1] Takayuki Yamada, "Remarks on tracking method of neural network weight change for learning type neural network direct controller", Proceedings of AROB 10th '05 (The Tenth International Symposium on Artificial Life and Robotics 2005), pp.624-627(2005)

[2] Takayuki Yamada, "Remarks on tracking method of neural network weight change for adaptive type neural network direct controller", Proceedings of AROB 11th '06 (The Eleventh International Symposium on Artificial Life and Robotics 2006), GS19-3 (2006)

[3]Takayuki Yamada, "Remarks on tracking method of neural network weight change for adaptive type neural network feedforward feedback controller", Proceeding of AROB13th '08 (The Thirteenth International Symposium on Artificial Life and Robotics), pp.559-562(2008)

[4] Takayuki Yamada, "Remarks on tracking method of neural network weight change for learning type neural network feedforward feedback controller", Proceeding of AROB14th '09 (The Fourteenth International Symposium on Artificial Life and Robotics), pp.389-392(2009)

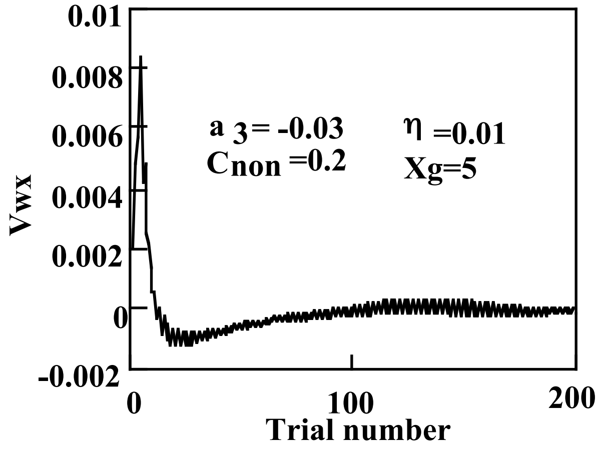

Fig.6 Vwx for example 2.

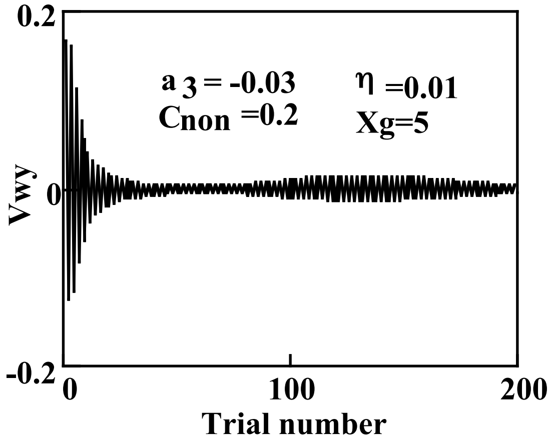

Fig.7 Vwy for example 2.

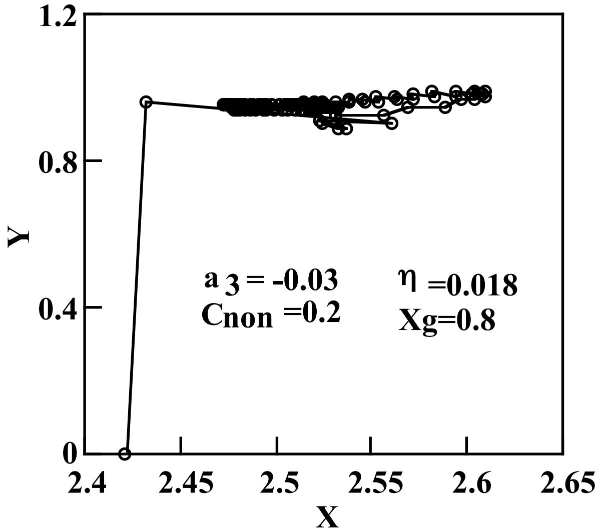

Fig.8 Example 3 of trajectory of neural network weight change.

The Fifteenth International Symposium on Artificial Life and Robotics 2010 (AROB 15th '10),
B-Con Plaza, Beppu,Oita, Japan, February 4-6, 2010

Study upon Cooperative Optimization Problem between Two Humans by Mutual Tracking

Yoshikatsu Hayashi[A], Yurie Tamura [B], Fumihiko Ishida [C], Ken Sugawara [B], Yasuji Sawada[A]

A Tohoku Institute of Technology, 35-1, Kasumi-cho, Taihaku-ku, Sendai, Miyagi, 982-8577, Japan
B Tohoku Gakuin University, 2-1-1 Tenjinzawam Izumi, Sendai 981-3193 Japan
C Toyama National College of Technology, 13, Hongo-cho, Toyama-shi, Toyama-ken, 939-8630, Japan
(Tel : 81-22-721-2035; Fax : 81-22-721-2035)
(hayashi@natural-science.or.jp)

Abstract:
Verbal communication is essential for human society. Nonverbal communication, on the other hand, is more widely used not only by human but also other kind of animals. Predictive function is important for human and other animals to adapt for the constantly changing environment and to communicate smoothly with other members of the society. The "real time" response cannot be realized without this function by humans and other animals which is not equipped with the fast response system of milliseconds. In our study, we investigate how human overcome the inevitable time delay and generate synchronized motion, based on the mutual tracking experiment.

Keywords: Nonverbal communication, Mutual tracking, Prediction mechanism.

I. INTRODUCTION

Verbal communication is essential for human society. Nonverbal communication, on the other hand, is more widely used not only by human but also other kind of animals, and the content of information is estimated even larger than the verbal communication. Among the non-verbal communication mutual motion is the simplest and easiest to study experimentally and analytically.

Predictive function is important for human and other animals to adapt for the constantly changing environment and to communicate smoothly with other members of the society [1]. The "real time" response cannot be realized without this function by humans and other animals which are not equipped with the fast response system of milliseconds which modern robots easily achieve.

In order to reveal the prediction mechanism, we carried out an intermittently-visual tracking experiment where a circular orbit is segmented into the target-visual and target-invisible regions [2]. Main results found in this research were following. Recognition of a time step, obtained from the environmental stimuli, is necessary for the predictive function. The period of the rhythm in the brain obtained from environmental stimuli is shortened more than 10 percent. The shortening of the period of the rhythm in the brain accelerates the hand motion as soon as the visual information is cut-off, and causes precedence of the hand motion to the target motion.

Proactive response is widely observed in the human life, such as in driving a car in a curved road [3]. Proactive control to move the hands preceding the target is realized by over-predicting and over-compensating the delay.

From an engineering point of view, it is also important to improve cooperative process in Man-Machine interaction system. We first have to investigate the cooperation mechanism between humans. Kon and Miyake [4] used synchronization cooperation tapping task to reveal timing control mechanism between two subjects. They made an experiment that has Cross-Feedback system between sound and tapping of tow subjects. Tap onset times and relative position between two tap-onset intervals were analyzed. They clarified that similarity and difference of temporal development of correlation of rhythm and error between two onset.

In our study, we investigate how human overcome the inevitable time delay and generate synchronized motion, based on the mutual tracking experiment.

II. EXPERIMENTAL METHOD

1. Hand-tracking experiment

Hand-tracking experiment is a paradigm to trace a moving object to reveal a mechanism of visual motion control based on perception of position and velocity. Six male and female subjects (20 to 33 years old) participated in the present hand-tracking experiments. A subject was seated at 50 cm in front of a computer screen and was asked to trace a moving visual target (a red closed circle of 6 mm diameter) as accurately as possible by the motion of a cursor (a blue closed circle of 6 mm diameter) in the screen produced by hand motion through a mechanical computer mouse.

The subject is asked to follow the programmed target for 10 seconds in order to keep the tracer velocity in the mutual tracking experiments, and after 10 seconds the target is switched to the tracer of other person. This mutual tracking lasts for 40 seconds, and 10 trials are recorded to calculate an average value in each experimental condition.

To reveal the mechanism of the feed-forward control, we performed intermittent-blind experiments in which we regulated the region where target was shown in a circular orbit.

2. Intermittent-blind tracking experiment

The subject first follows the moving target, and when the target disappears, subject has to follow the circle line in a process of guessing target velocity and position. The circular orbit was constructed by two target-hidden regions as shown in Fig.1 (each 30%, at the top and the bottom). Target frequency was set to 0.1 Hz, 0.3 Hz, and 0.5 Hz. The velocity of two tracers was sampled every 0.02 second and the correlation function was calculated.

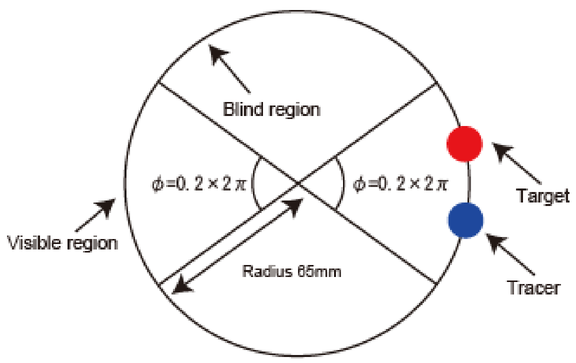

Fig.1. An example of intermittent-blind experiment with two visible belt (20%) and blind belt (30%).

III. RESULTS AND DISCUSSION

1. Communication frequency

There is a difference in velocity between programmed target and the tracer velocity in the mutual tracking experiments. We call the latter velocity communication frequency. First, we examine the communication frequency as a function of the programmed frequency. As shown in Fig. 2, the communication frequency is always less that the programmed frequency. This is considered to be due to corrective movement for the relative phase difference.

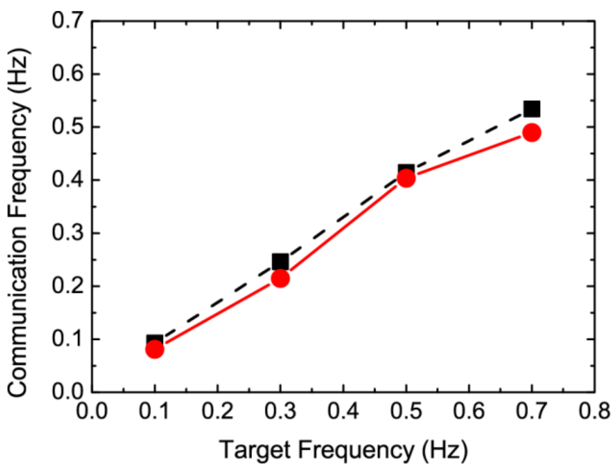

Fig.2. Communication frequency as a function of target frequency in mutual tracking experiment. Solid line represents the fully visible experiment and dashed line represents the intermittent-blind experiment.

2. Mutual correlation function

Fig. 3 shows the correlation function of tracer velocity of two subjects. Concave shape was found around the time delay zero, and correlation coefficient had two peaks around the time delay zero, which are located at the delay time of +0.5 second and -0.5 second. We found that the each subject increases or decreases the velocity of his or her tracer in accordance with other person's movement. However, this corrective motion is accompanied by the time delay of 0.5 second. The subject is asked to trace the target as accurately as possible, however, due to the time delay of visual-motor system in human, human performs the reactive control with time delay.

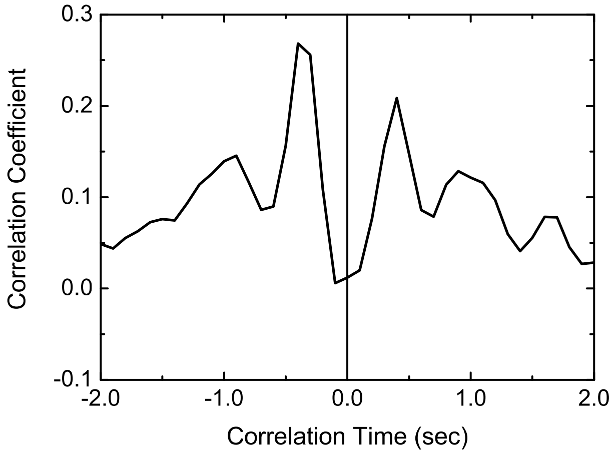

Fig.3. Mutual velocity correlation function in fully visible experiment. The target frequency is 0.1 Hz.

In the case of intermittent-blind experiments, the correlation function shows no time delay since there is a peak at time delay zero as shown in Fig. 4, i.e., subjects trace each other in synchronized manner with no time delay. The subject has to predict the position and velocity of target in the blind region. And in visible region, the subject can adjust the relative position. When the prediction mechanism works, synchronized control appears. There are other two peaks at 1.25 second and -1.25 second. Those peaks appear periodically at every 1.25 second, which means that there is a rhythmic component in hand motion.

Our finding is that the cut-off of the visual information induces the rhythmic component in hand motion, and this rhythmic component is shared mutually with no phase delay. We have introduced the region where the visual information is cut-off. Even though this is artificial effect in the experimental set-up, in our daily communication, we do not always pay attention to every movement of words of the other person, rather pay attention intermittently. When we feel as if we could communicate deeply, we have a feeling that we share the rhythm of conversation.

Our results suggest that in verbal or none-verbal communication, prediction mechanism produces the rhythm in brain, intermittently suppressing the sequence of information. Even though time-delay is inevitable in visual-motor or other sense of human, human has the prediction mechanism in which rhythmic component is shared mutually, and mutual motion works in the synchronized manner without time delay.

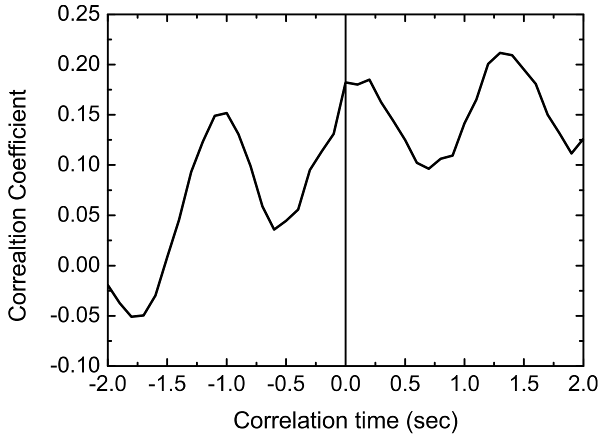

Fig.4. Mutual velocity correlation function in intermittent-blind experiment with two visible belt (20%) and blind belt (30%). The target frequency is 0.5 Hz.

IV. FUTURE STUDY

It is important to apply the basic knowledge to contribute to our society. After we reveal the mechanism of communication between two persons, we are going to develop an interface between human and robot. Thus, we plan to develop rehabilitation implement in which human and robot can work in the synchronized manner.

REFERENCES

[1] F. Ishida and Y. Sawada, Human hand moves proactively to the external stimulus, An evolutional strategy for minimizing transient error, Physical Review Letters, 96, 168105, (2004).
[2] Y. Hayashi, Y. Tamura, K. Sase, K. Sugawara and Y. Sawada, Intermittently-visual tracking experiments reveals the roles of error-correction and predictive mechanisms in human visual motor control system, Journal of control, measurement, and system integration, submitted.
[3] Y. Takachi, K. Muraoka, Y. Sawada, and H. Ohta, Older drivers' behavior in a curve -Analysis using a driving simulator-, The Japanese Journal of Ergonomics, 44, 165-170 (2008).
[4] H. Kon and Y. Miyake, An Analysis and Modeling of Mutual Synchronization Process in Cooperative Tapping, Journal of Human Interface, 7, 477-486, (2005).

A Study on The Behavior of A Few Ant Workers

Ken Sugawara[1], Mai Yuki[1], Yoshikatsu Hayashi[2], Tomonori Kikuchi[3], Kazuki Tsuji[3]

1) Tohoku Gakuin University 2-1-1, Tenjinzawa, Izumi-ku, Sendai, Miyagi, 981-3193, Japan
2) Tohoku Institute of Technology, 35-1, Kasumi-cho,Taihaku-ku, Sendai, Miyagi, 982-8577, Japan
3) University of the Ryukyus, 1 Senbaru, Nishihara-cho, Nakagami-gun, Okinawa 903-0213, Japan
(Tel : 81-22-773-3306; Fax : 81-22-773-3306)
(Email:sugawara@cs.tohoku-gakuin.ac.jp)

Abstract: It is well-known that social insects such as ants show interesting collective behaviors. To expand understanding of collective behaviors of ants, we focused on ants, Diacamma sp, and analyzed the behavior of a few individuals. We placed a few ant workers in hemisphere without a nest, food, the queen, and the trajectory of them is recorded. As a result, we found following characteristics: 1. Activity of individuals increases and decreases periodically in anti-phase. 2. Spontaneous meeting process is observed between two ants and it may cause an anti-phase synchronization.

Keywords: *Diacamma sp*, behavior of a few ants, anti-phase synchronization

I. INTRODUCTION

Many social insects have some interesting characteristics and show organized group behaviors. Especially, ants' colonies are highly organized and exhibit number of remarkable behaviors. Their colonies consist of numerous individuals and engage in nest construction/maintenance, taking care of eggs, defending, foraging and so on by well-organized division of labor. These collective behaviors do not require a special individual that controls the behavior of the entire group. Hereditarily homogeneous individuals achieve these collective behaviors by interacting with each other through direct sight or chemical materials, such as pheromones.

Many researchers have been investigating behaviors of ants[1-3] and lots of interesting results have reported. However, not so large number of researches have treated single or some ants' behaviors[4,5]. We consider that the essential point of the collective behavior greatly depends on the local interaction of a few ants, and that the observation of group behavior in a small scale provides some significant knowledge. This means, in other words, the knowledge of the relationship between the colony-level behaviors and the individual level behaviors is not enough at this stage.

Through the observation of one or more ants' behavior, we aim to describe their behavior by simple model. Modeling is one of the most effective approaches to confirm and understand the individual-level behaviors and colony-level behaviors. We aim to describe ants' behavior as the dynamics of interacting self-driven particles. By treating ants' behaviors from physical viewpoint, we aim to construct a universal model of ants' behaviors.

This kind of approach is considered to be very attractive not only for biologist and scientist but also for engineers. In robotics, especially, many researchers have investigated multi-robot systems, and some of them were inspired by such biological systems and analyzed their performance using real robot systems[6-8]. If we can construct the abstract model of ants' behaviors, it is considered to be helpful for developing useful multi-robot system.

II. METHOD

In this paper, we treat the behavior of Diacamma sp. Diacamma sp is a large ponerine ant, which live in Okinawa and several islands in Japan. Average size of the worker is about 10mm length, and their colony comprises 20 to 400 workers.

In order to analyze the ant worker's behaviors, two ants are randomly picked up and placed in acrylic hemisphere (30cm in diameter) field in our experiment. The hemisphere is covered by a transparent acrylic board during the experiment. CCD camera is equipped at the top of the experimental equipment, which size is 40cm x 40cm x 90cm height. Trajectory of the ant in hemisphere is recorded (Fig.1) and we analyze the trajectory of ants as a function of time.

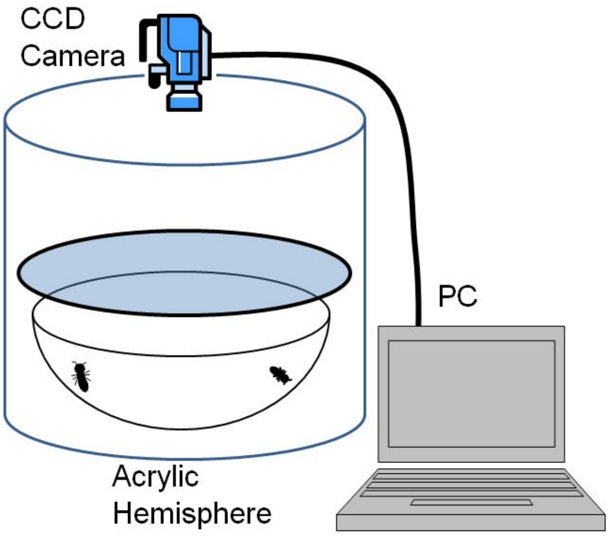

Fig.1: Experimental set up: Trajectory of ants placed in hemisphere is recorded from above.

III. RESULTS

We analyzed two ants' behavior. As same as the case of single ant, we made some trials using some individuals under the same condition. We discuss the feature using some typical results.

1. Trajectory

Fig.2 shows the trajectory of two ants overlapped in one picture. Green circle denotes the place where the distance of two ants is less than one body length, which is regarded as a meeting spot of two ants. High density spot of trajectories overlaps with meeting spot of two ants. It can be concluded that two ants meet at the certain position.

2. Velocity

Typical time series of each ant's velocity is shown in Fig.3. Individual activity is same as the case of single ant, i.e. the ant walks actively in the first 60 - 100 minutes, and after that, the movement gradually decreases and eventually becomes inactive at 100 minutes. After 100 minutes, they repeat active and inactive role. Even when two ants are in the experimental field, each ant has some rhythmic component in its activity.

3. Power spectrum of the velocity

The spectrum of their velocities is shown in Fig.4. We can see a peak at 0.064 /min, i.e. approximately 16-minute periodicity in each ant.

From the analysis of power spectrum, we know both ants have the same frequency component.

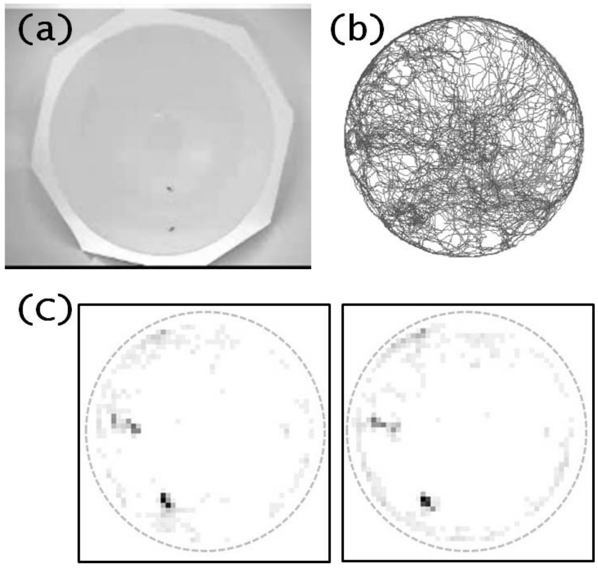

Fig.2: (a) A snapshot of experimental field. (b) Overlapped trajectories of two ants. Some high density area can be seen. (c) Existing rate of ant A (left) and ant B (right) in the field. The rate is expressed the darkness.

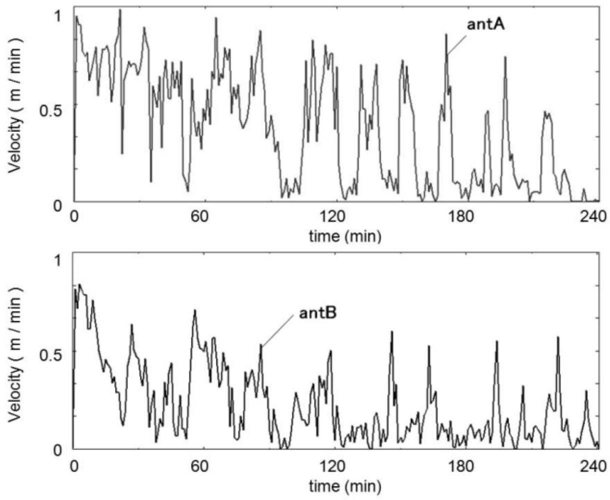

Fig.3: Time series of two ants' velocity. After 100 minutes, they repeat active and inactive role.

Next, we focus on the phase of their active-inactive repetition. Do they oscillate in the same phase or antiphase? For simple analysis, we binarize their activity based on the average velocity, and calculate $d = A - B + 2AB$, in which the activity of ant A and ant B is denoted as $A=\{0,1\}$, $B=\{0,1\}$. Here we show two examples in Fig.5.

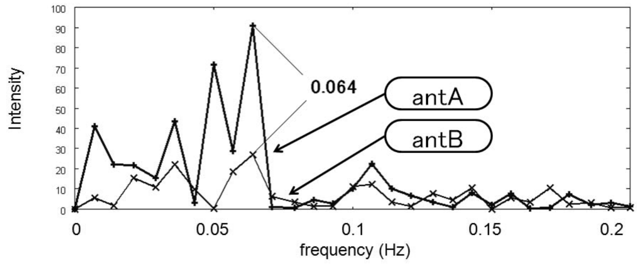

Fig.4: Power spectrum of two ants' velocity.

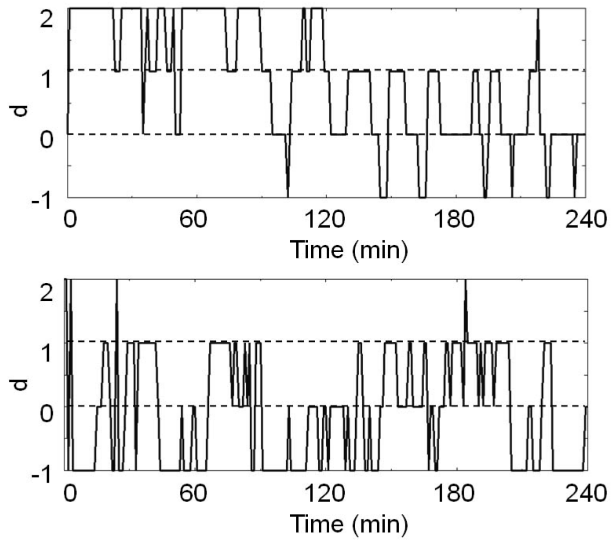

Fig.5: Two examples of two ants' active-inactive phase.

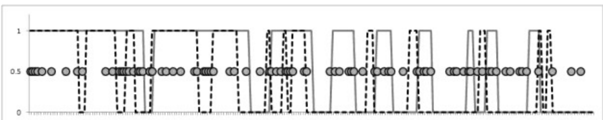

Fig.6: Binarized behavior of two ants (lines) and the moment they have a physical contact (plot).

Discussion and conclusion

In Fig.5, we can see the repetition of 1 and -1 in both cases. It means active-inactive behavior of ant A and ant B is alternately turned on and off in antiphase. In addition, spontaneous physical contact process is also observed between two ants as shown in Fig.6. These results imply that the contact process may cause the anti-phase synchronization.

In order to shed light on the collective behavior of ants, we analyzed the behavior of a few ant workers. From this bottom-up approach, we conclude following points;

1. Spontaneous contact process is observed between two ants.
2. Periodic behavior of two ants synchronizes in anti-phase.
3. It is considered that the contact process causes the anti-phase synchronization.

REFERENCES

[1] Holldobler B, Wilson EO (1990), The Ants. Harvard University Press.
[2] Holldobler B, Wilson EO (1995), Journey to the Ants: A Story of Scientific Exploration, Harvard University Press.
[3] Gordon D (2000), Ants at Work, W W Norton & Co Inc.
[4] Bonabeau E, Theraulaz G, Dorigo M (1999), Swarm Intelligence: From Natural to Artificial Systems. Oxford Univ Press.
[5] Krieger MJB, Billeter JB and Keller L (2000), Ant-like task allocation and recruitment in cooperative robots. Nature 406:992-995.
[6] Balch T, Parker LE (2002), Robot Teams: From Diversity to Polymorphism. A K Peters Ltd.
[7] Cole BJ (1992), Short-term activity cycles in ants. Behav. Ecol. Sociobiol. 31:181-187.
[8] Cole BJ, Cheshire D (1996), Mobile Cellular Automata Models of Ant Behavior. Am. Naturalist 148: 1-15.
[9] Uchikawa T, Sugawara K, Kikuchi T, Tsuji K, Hayakawa Y(2007), Time-series analysis of ant behavior and its modeling, IEICE tech. report. Nonlinear problems. Vol.106, No.573, 20070226:27-30. (in Japanese)
[1] Casti JL (1995), Bell curves and monkey languages. Complexity 1:12-15
[2] Tsuchiya K (1995), Model dynamics and function of a complex system (in Japanese). Control inf 39(1):29-34

The Fifteenth International Symposium on Artificial Life and Robotics 2010 (AROB 15th '10),
B-Con Plaza, Beppu,Oita, Japan, February 4-6, 2010

Estimation of Average Hitting Time in Genetic Algorithms by Markov Chain

QingLian Ma, Yu-an Zhang, Makoto Sakamoto, Hiroshi Furutani
Faculty of Engineering, University of Miyazaki
Miyazaki City 889-2192 Japan

Abstract

The hitting time T is an important topic in the theory of Genetic Algorithms (GAs). In this paper, we develop a new approach to estimate the mean first hitting time of optimum solution in GA. We consider the success probability S of GA on the multiplicative landscape and study the relation between S and T by Markov chain. The success probability S is defined as that there is at least one optimum solution in a population at the stationary distribution. We performed numerical experiments with and without crossover, and found that crossover accelerates the speed of evolution. The mean first hitting time becomes very short when crossover is included in GA calculation.

1 Introduction

Recently, there have been many theoretical attempts for obtaining the mean first hitting time of optimum solution(s) in Evolutionary Computation [1]. Researchers consider this quantity is very important measure for the evaluation of applied methods. Among these studies, the analysis adopting Markov chain model is most promising one. However, there should be done a lot of attempts to obtain more quantitative results. In this paper, we develop a new approach to estimate the mean first hitting time of optimum solution T in Genetic Algorithm (GA) on the multiplicative landscape.

First, we define the success probability of GA S as the one that there is at least one optimum solution in a population at the stationary distribution [2]. We have developed a method to calculate the success probability by using Markov chain as the function of the string length L. In this approach, we assume that the population is in linkage equilibrium through the effect of crossover, and the population is fully represented by the distribution of the first order schema. The frequency distribution of the first order schema can be obtained by using Wright-Fisher model, which also adopts the Markov chain changing with generation t. The analytical expression of the transition matrix P can be obtained for the GA on the multiplicative landscape, and we calculate the distribution of the first order schema $\mu(t)$. The success probability S is given by using this distribution $\mu(t)$ at the stationary stage of Markov chain.

Next, we use this S for the estimator of the mean first hitting time T with the relation $T = 1/S$. The rationale of this equation is that there are populations containing the optimum solution with probability approximately given by $1/S$, and the mean first hitting time is also given by $1/S$.

In this study, we performed numerical experiments with and without crossover, and found that crossover accelerates the speed of evolution. The mean first hitting time becomes very short when crossover is included in GA calculation. We will discuss the mechanism of this phenomenon.

2 Model and Methods

2.1 Model

We studied the GA on the multiplicative landscape with selection, crossover and mutation. The analysis of GA evolution was done by using Markov chain theory.

An individual is represented by a binary string of fixed length L. The genotype is given by the integer i, and $i(k)$ is the kth bit of the binary string. Thus there are $n = 2^L$ genotypes. $N_i(t)$ represents the frequency of the ith genotype at generation t, and $x_i(t)$ its relative frequency. The population size N is assumed to be time-independent.

If a population is in linkage equilibrium, the distribution of individuals depends only on the frequencies of the first order schema[3]. Therefore, the relative frequency x_i is represented by

$$x_i = \prod_{k=1}^{L} h_{i(k)}, \tag{1}$$

where $h_{i(k)}$ is the frequency of the first order schema corresponding to $i(k)$. This decomposition enables us to treat the population by using the schema theory [2].

We study the evolution of the GA on the multiplicative landscape. The fitness function is

$$f_i = \prod_{k=1}^{L} \{1 + s\, i(k)\}, \tag{2}$$

where s is a parameter representing selection strength.

2.2 Markov Chains

We consider a population having two alleles A and a. We assume that the A genes have selective advantage $1+s$ while a genes have selective advantage unity. The number of A genes in any generation is a Markovian variable with the transition matrix P give by

$$P_{ij} = P(j|i) = \binom{N}{j} a^j \, (1-a)^{N-j}, \tag{3}$$

$$a = \frac{(1+s)\, i}{(1+s)\, i + N - i}. \tag{4}$$

The matrix element P_{ij} is the probability that the number of A individuals selected at the $t+1$ th generation is j, given that the number of A individuals in the t th generation is i. To take into account the effect of mutation with mutation rate p_m, we replace a by b in equation (3)

$$b = (1 - 2p_m)a + p_m, \tag{5}$$

and we have

$$P(j|i) = \binom{N}{j} b^j \, (1-b)^{N-j}. \tag{6}$$

The evolution of GA population is given by

$$\mu_j(t+1) = \sum_{i=0}^{N} \mu_i(t)\, P_{ij}, \tag{7}$$

where $\mu_i(t)$ is the probability that there are i A individuals in the population. The stationary distribution π is given by

$$\lim_{t\to\infty} \mu(t) = \pi. \tag{8}$$

2.3 Calculation of success probability

In the following, we give a short description for calculating the success probability S [4]. We call the $(\ell \le L)$ bit string of $< 1, 1, \ldots, 1, 1 >$ as the partial optimum solution. The random number X_ℓ represents the number of partial optimum solution of length ℓ in the population. The probability that there are j units of optimum solution is $S_j^{(\ell)} = \Pr\{X_\ell = j\}$. We can get the success probability S

$$S = \sum_{j=1}^{N} S_j^{(L)}. \tag{9}$$

To obtain S, we have to calculate $S_j^{(\ell)}$, and this is done by iteration. The initial condition is

$$S_j^{(1)} = \pi_j, \quad (0 \le j \le N). \tag{10}$$

The transition probability from j units of partial optimum solution of length $\ell - 1$ to j units of optimum solution of length ℓ is

$$Q_{i,j}^{(\ell)} = \Pr\{X_\ell = j | X_{\ell-1} = i\}.$$

The transition probability $Q_{i,j}^{(\ell)}$ can be calculated by using the distribution of the first order schema π. If $j > i$, $Q_{i,j}^{(\ell)} = 0$. For $j \le i$, we have

$$Q_{i,j}^{(\ell)} = \sum_{m=j}^{N-i+j} \binom{N}{m}^{-1} \binom{i}{j} \binom{N-i}{m-j} \pi_m. \tag{11}$$

Here $\binom{0}{0} = 1$. The probability $S_j^{(\ell)}$ of having j units of ℓ- bit partial optimum solution can be calculated by

$$S_j^{(\ell)} = \sum_{i=0}^{N} S_i^{(\ell-1)}\, Q_{i,j}^{(\ell)}. \tag{12}$$

3 Results

In this paper, we study the relation between success probability S and the mean first hitting time T by experiment. We performed numerical calculations of GA with roulette wheel selection on the multiplicative landscape. Population size $N = 50$ and string length $L = 20$, selection strength with $s = 0.04$. Crossover was done with the uniform crossover of crossover rate p_c. We used mutation rates p_m from 0.02 to 0.09 and compared their results. The initial value of the first order schema was $h_1 = 1/2$. The calculations were performed repeatedly, and results were averaged over 10000 runs.

Figure 1 shows the distribution of generations finding optimum solution with crossover.

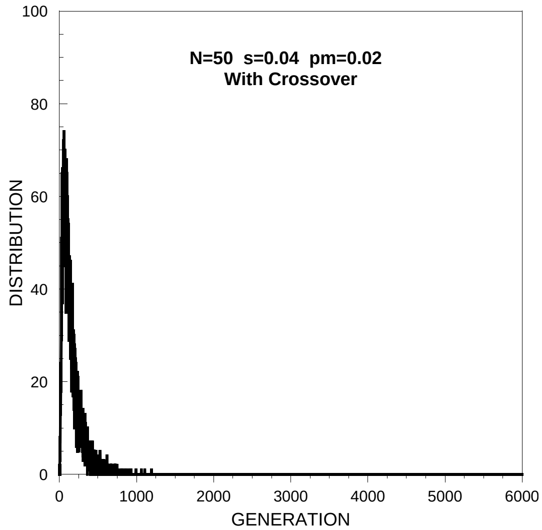

Figure 1: Distribution of generations finding optimum solution with crossover. Population size $N = 50$ and selection strength $s = 0.04$.

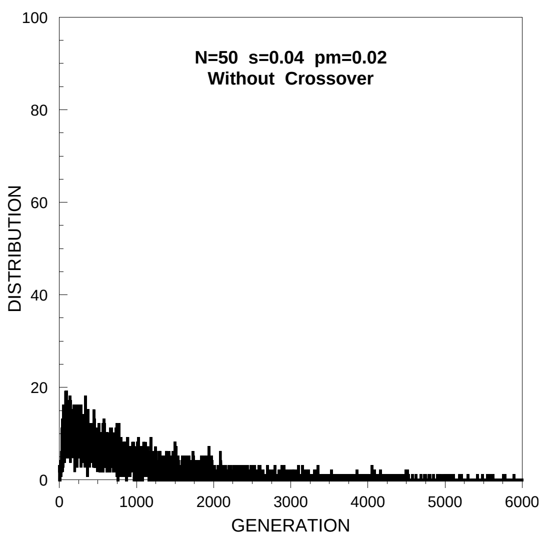

Figure 2: Distribution of generations finding optimum solution without crossover. $N = 50$ and $s = 0.04$.

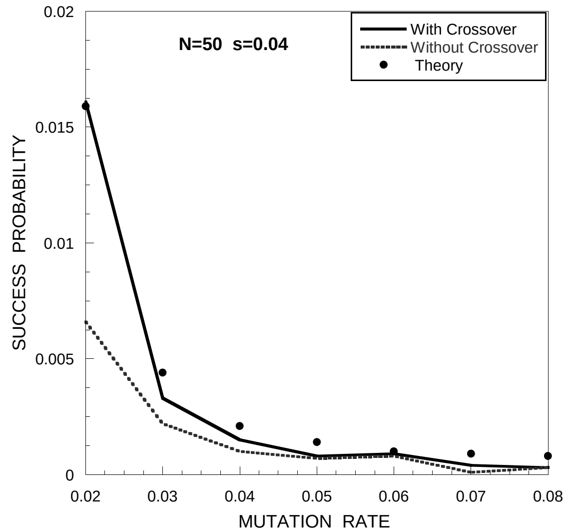

Figure 3: p_m-dependence of success probability S with $N = 50$ and $s = 0.04$. Crossover rate are $p_c = 1, 0$. The horizontal axis represents mutation rate p_m.

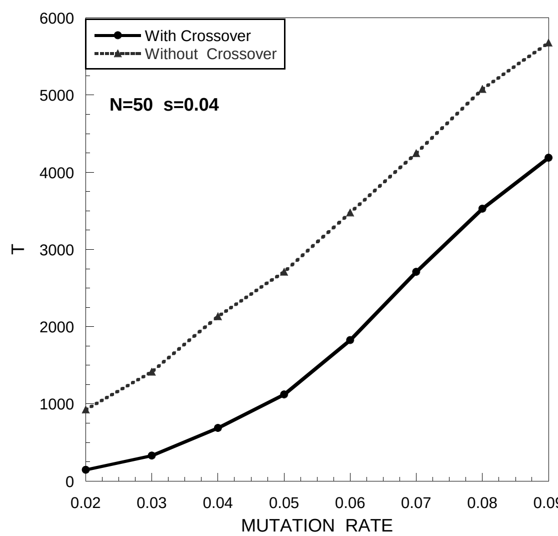

Figure 4: p_m-dependence of T with $N = 50$ and $s = 0.04$. Crossover rate are $p_c = 1, 0$. The horizontal axis represents mutation rate p_m.

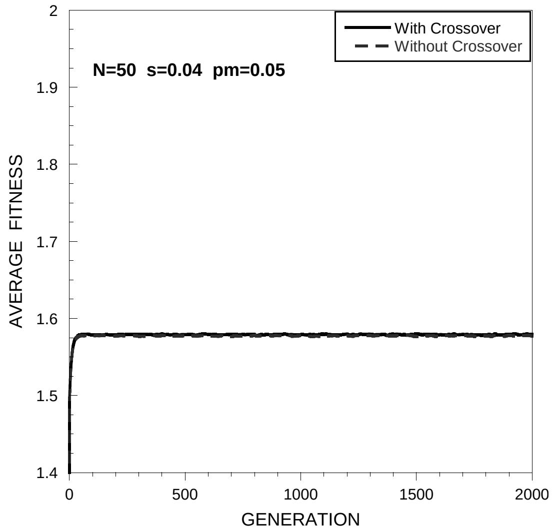

Figure 5: Average fitness $\bar{f}(t)$ with $N = 50$ and $s = 0.04$. Mutation rate $p_m = 0.05$ and crossover rate are $p_c = 1, 0$. The horizontal axis represents generation.

Figure 2 shows the distribution of generations finding optimum solution without crossover by using the same parameter with Fig(1). By comparing Figs.1 and 2, we can obtain that the convergence of optumun solution distribution with crossover is earlier than that of without crossover.

Figure 3 shows p_m-dependence of success probability S with $N = 50$ and $s = 0.04$. ($\bullet$) is theoretical value from equation (12). As show in this figure, the effect of crossover on success probability is small when mutation rate is larger.

Figure 4 shows p_m-dependence of T. T without crossover is larger than that of with crossover. Figs.3 and 4 also shows the relation of T and $1/S$ with and without crossover. Where $p_m = 0.05$, when $p_c = 1$, $S = 0.0008$ and $T = 1121$, when $p_c = 0$, $S = 0.0007$ and $T = 2710$. From these date, we can obtain the conclusion as follows. With crossover, $T = 1/S$. Without crossover, $T > 1/S$.

Figure 5 shows the convergence of average fitness is almost equal with and without crossover when p_m is large.

4 Summary

In numerical calculation, we found that our method reproduces the distribution of the first order schema, and our predicted success probabilities agree quite well with calculated ones. We also found that in the case of crossover rate $p_c = 1$, the proposed estimator shows the good agreement with calculated T. In the case of no crossover, though the calculated success probabilities are almost the same as those calculated with crossover, the calculated T is larger than $1/S$. For example at string length $L = 20$, T without crossover is about two times larger than T, which means crossover accelerates the speed of evolution in GA.

References

[1] J. He and X. Yao: Towards an Analytical Framework for Analysing the Computation time of Evolutionary Algorithms *Artificial Intelligence*, Vol.145, 59–97 (2003).

[2] H. Furutani, Y. Zhang and M.Sakamoto: Study of the Distribution of Optimum Solution in Genetic Algorithm by Markov Chains, *Transactions on Mathematical Modeling and its Applications (TOM)*, to be published.

[3] Y. Zhang, M.Sakamoto, H. Furutani: Effects of Population Size and Mutation Rate on Results of Genetic Algorithm, *Proceedings of Third International Conference on Natural Computation*, Vol.3, (2008) 70–75.

[4] Y. Zhang, Q. Ma, M.Sakamoto and H. Furutani: Effect of Mutation to Distribution of Optimum Solution in Genetic Algorithm, *Proceedings of Fourth International Workshop on Natural Computation (IWNC 2009)*, 345–352 (2009).

The Fifteenth International Symposium on Artificial Life and Robotics 2010 (AROB 15th '10),
B-Con Plaza, Beppu,Oita, Japan, February 4-6, 2010

Quest for Genetic Information Hidden behind Disorder in DNA Sequences

Yuka KOYAMA[1)], Kentaro NISHIMUTA[1)],
Kunihito YAMAMORI[1)], Moritoshi YASUNAGA[2)], Ikuo YOSHIHARA[1)]

[1)]1-1, Gakuen Kibanadai-nishi, Miyazaki, 889-2192, Japan, University of Miyazaki
(Tel : +81-985-58-7384; Fax : +81-985-58-7384)
(Email address : { koyama, yamamori, yoshiha }@taurus.cs.miyazaki-u.ac.jp)

[2)]1-1-1, Tennoudai, Tsukuba, Ibaraki, 305-8573, Jaban
Graduate School of Systems and Information, Engineering,
University of Tsukuba

***Abstract*:** Most of conventional base sequences are analyzed by order of base sequences, for example, pattern matching. Pattern matching compares unknown base sequences with that of known gene to find similar patterns and to identify gene information. We try to search for hidden information in DNA sequences without pattern matching. We focus on disorder of base sequences, because disorder analysis is available, if we do not know particular function of genes. We use the exponent α of $1/f^{\alpha}$ fluctuation and self-information as indices of disorder. Our experimental data are ribosomal protein of eukaryotic species. The exponent α is calculated for three kinds of data, i.e. whole base sequences, base sequences in exon or intron. The average of α in exon regions are smaller than that in intron regions. It suggests that exon regions are somewhat more ordered than intron regions. SOM is used to look for similarity of species by self-information which is calculated for codons of base sequences. SOM shows that self-information is usable for a classification of species.

Keywords: DNA, 1/f, fluctuation, self-information, entropy, SOM

I. INTRODUCTION

DNA of organisms involves various genetic information to form themselves, which has been inherited from generation to generation.

Recent years, it has been active to analyze DNA sequences for finding organic evolution. Pattern matching is widely used to find similar patterns in a pair of base sequences and to identify function and evolutionary relationships.

We notice using disorder of base sequences instead of order to reveal hidden genetic information. Disorder analysis is available, even if we do not know meaningful patterns in advance. We focus on $1/f^{\alpha}$ fluctuation of chaos theory and self-information to extract hidden information buried in disorder of base sequences.

Takushi and Miyagi [1-3] researched $1/f^{\alpha}$ fluctuation of bacteriophage φ-X174 and suggested that several fractal group correlations exist in a sub-sequences and whole sequences. They examine whether specific expression of genes can be found. We aim at finding hidden information in DNA sequences of many species.

Information theory is introduced by Shannon can play a major role in analyzing features and characteristics of sequences, if DNA sequences carry the information over generations. Since information entropy and self-information are measure of the uncertainty associated with a random variable. They are treated as an amount of characteristic of DNA sequence.

II. DISORDER ANALYISIS BY $1/f^{\alpha}$ FLUCTUATION

1. $1/f^{\alpha}$ Fluctuation

" $1/f$ fluctuation", strictly speaking " $1/f^{\alpha}$ fluctuation" is observed in natural phenomena such as flame of candle, the breeze and the classical music etc. We try to use α as an index of disorder. It is said in musical sphere that α of classical music is 0.5-1.75 and that of rock music is 0.01-1.0[4]. α is probably depending on kinds of music. We use analogy to explain disorder of base sequences by α .

2. Calculation of exponent α

The exponent α of $1/f^{\alpha}$ fluctuation of base sequences is calculated by the following procedure.

Step1. Numerical expression of DNA sequences

DNA sequences consist of four kinds of bases; A (Adenine), C (Cytosine), G (Guanine), and T (Thymine). It is necessary to convert all bases into numerical values before Fourier transform. Bases are converted into complex numbers, which are located almost on four apexes of a square.

$$\begin{aligned}
&\mathrm{A}\cdots(1+r_1)+(1+r_2)i\\
&\mathrm{G}\cdots(-1+r_3)+(1+r_4)i\\
&\mathrm{C}\cdots(1+r_5)+(-1+r_6)i\\
&\mathrm{T}\cdots(-1+r_7)+(-1+r_8)i \qquad r_n\in(-0.01,0.01)
\end{aligned}$$

Step2. Discrete Fourier Transform (DFT)

DFT is employed for Fourier Transform of discrete data. Power spectrum S_f is calculated by Eq.(2), where $f_n(n=0,1,\cdots,N-1)$ are base sequences expressed by complex number mentioned above.

$$F_k=\sum_{n=0}^{N-1} f_n e^{-i\frac{2\pi kn}{N}}\ (k=0,1,\cdots,N-1). \qquad (1)$$

$$S_f=|F_k|^2. \qquad (2)$$

Step3. Calculation of α

α is a gradient in low-frequency range of the power spectra (Fig.1). The gradient is calculated by linear regression.

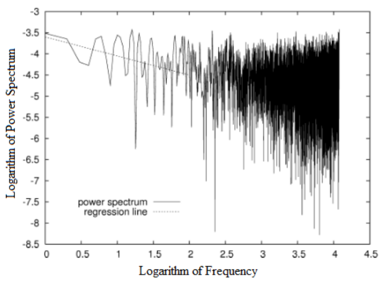

Fig.1. Power spectrum and regression line

3. Experiments

A. Experimental Conditions

We use ribosomal protein data of eukaryotic species for experiments. Table.1 shows the names of the eukaryotic species and their abbreviation (abbr.). The kinds of the ribosomal proteins are as follows;

RPS2 RPS5 RPS7 RPS8 RPS9 RPS12
RPL5 RPL8 RPL9 RPL26 RPL32 RPLP0

These data have been released on Ribosomal Protein Gene Database: (RPG) by Frontier Science Research Center, University of Miyazaki [5]. We calculated α for exon regions, intron regions and whole regions including exon and intron for all the data. Base sequences involving no less than 50 bases are used.

Table.1. Eukaryotic species

name of species	abbr.
H.sapiens	Hs
M.musculus	Mm
A.ganbiae	Ag
C.elegans	Ce
P.falciparum	Pf
M.grisea	Mg

B. Results

Fig.2-a, Fig.2-b and Fig.2-c show the average α of exon, intron and whole regions. Fig.2-a and Fig.2-b show that average of α in exon regions are smaller than that in intron regions in all species. In the field of music, α of rock music are smaller than that of classical music. We assume rock musics correspond to exon and classical musics correspond to intron. Rock music is stormy sounds whereas classical music is comparatively calm sounds. Exon regions may involve partly distinguished sub-sequences. Exons are made for protein–coding transcripts, but introns are not. The experiments suggest that exon regions probably have more particular base sequences than intron regions.

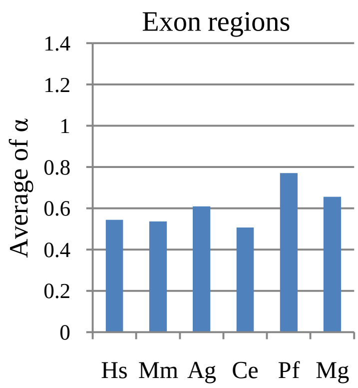

Fig.2-a. Average α for exon regions

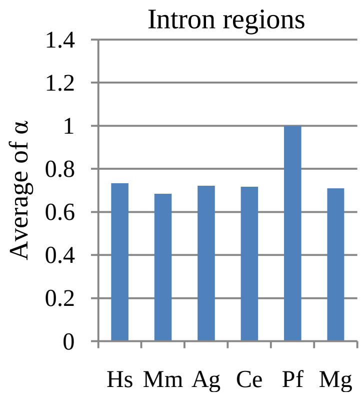

Fig.2-b. Average α for intron regions

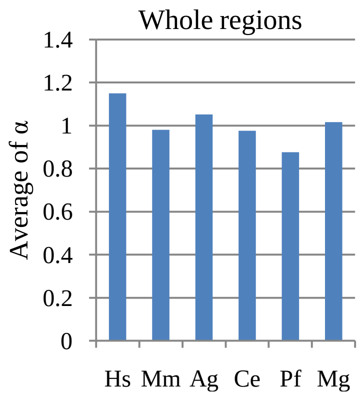

Fig.2-c. Average α for whole regions

III. DISORDER ANALIYSIS BY INFORMATION ENTROPY AND SOM

1. Information entropy

Information entropy of base sequences is assumed to be a measure of characteristic of species. Information entropy is defined as follows. DNA sequences X is composed of four kinds of bases {A, G, C, T}. The complete event system (X, P) of X is determined by the occurrence probability $P(X)$ for each event $X(\mathrm{A}), X(\mathrm{G}), X(\mathrm{C}), X(\mathrm{T})$.

$$\begin{pmatrix} X \\ P \end{pmatrix} = \begin{pmatrix} \mathrm{A} & \mathrm{G} & \mathrm{C} & \mathrm{T} \\ P(\mathrm{A}) & P(\mathrm{G}) & P(\mathrm{C}) & P(\mathrm{T}) \end{pmatrix}.$$

Self-information is defined by the probability $P(X)$,

$$I(P(X)) = -\log_2 P(X). \qquad (3)$$

Information entropy $H(P(X))$ is an expected value of self-information $I(P(X))$, i.e. $H(P(X)) = -P(X)\log_2 P(X)$.

Because $\{X_i\}$ corresponds to A, G, C, T, $H(P(X_i))$ becomes as follows,

$$H(P(x_1), P(x_2), \cdots, P(x_n)) = -\sum_{i=0}^{n} P(x_i)\log_2 P(x_i). \qquad (4)$$

The number of occurrence is $64=4^3$, because codon is triplet of 4 kinds of bases. When we analyze the base sequences from the view point of codon.

Fig.3. is information entropy of codon in whole regions. The figure does not show clear difference in six species. An additional approach is required.

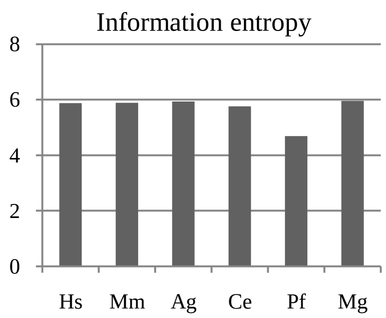

Fig.3. Information entropy of codon

2. Positional self-information

Sub-sequence is a part of base sequences cut out with a given number of bases and depends on the position of the base sequences (Fig.4). An additional approach is to calculate self-information for codons of sub-sequences, that varies from the beginning of the base sequence to the end (Fig.5).

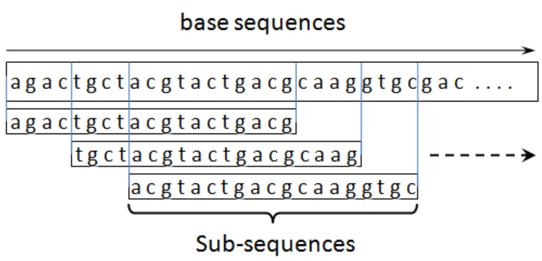

Fig.4. Shifting of cut-out position

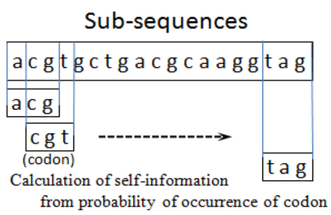

Fig.5. Shifting of codon

3. Self-organizing map (SOM)

Self-organizing map (SOM) proposed by Kohonen [6] is an unsupervised-leaning neural network which is used for clustering and visualization. SOM is also an algorithm to map high dimensional data to two dimensional space, to visualize buried structure in high dimensional space on two understandable dimensional maps.

We use SOM to distinguish species by self-information. The number of elements of input vectors to SOM is 64, corresponding to variety of codons.

4. Experiments

A. Experimental Conditions

Experimental data are the same as used by $1/f^{\alpha}$ fluctuation. Parameters of SOM in experiments are as follows; map-size is 30×30, and iteration of learning is 100.

Table.3 shows the number of training samples and correspondence symbols of species on the map in Fig.6. Lengths of sub-sequences are same for all samples i.e. 2048 bases.

Table.3. Correspondence list for SOM

name of species	#s of training samples (RPL32)	symbol
H.sapiens	234	H
M.musculus	188	M
A.ganbiae	119	A
C.elegans	68	C
P.falciparum	65	P
M.grisea	81	m
Total	755	

B. Results and discussion

Fig.6 shows all the species are classified. We change the length of the sub-sequence from 64 bases to 2048 bases. The experiments show the longer, the better. In case of 2048 bases, all the species are successfully clarified shown in Fig.6.

VII. CONCLUSION

We try to search for hidden information in DNA sequences with disorder of DNA sequences, because this method is available, even if characteristic pattern is unknown. We use ribosomal proteins of eukaryotic species and investigate the exponent α of $1/f^{\alpha}$ fluctuation and self-information as indices of disorder.

The exponent α is calculated for exon regions, intron regions and whole regions. The average of α in exon regions are smaller than that in intron regions. It suggests that exon regions are somewhat more ordered than intron regions.

SOM successfully distinguishes species with self-information for codons of sub-sequences in the whole region.

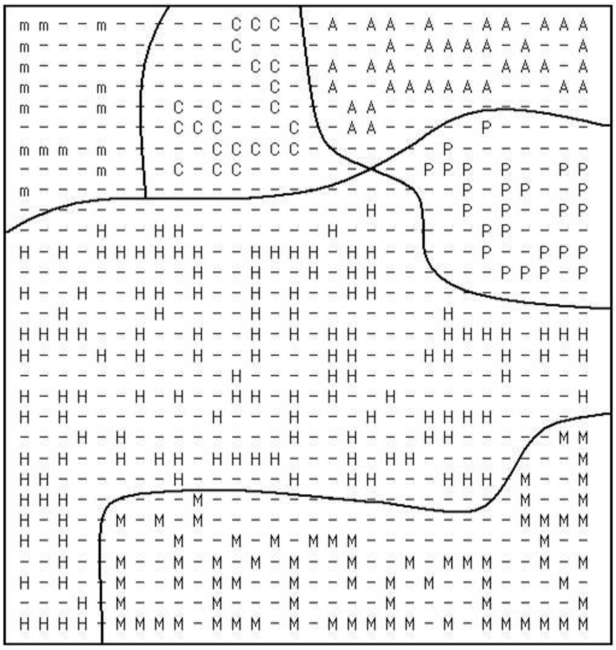

Fig.6. SOM of RPL32

REFERENCES

[1] Takushi E and Miyagi H (2000), Fractal Packing of the DNA Sequence of Bacteriophage φ-X174 (in Japanese). Bull. Fac. Sci. Univ. Ryukyus, 70:43-46

[2] Takushi E and Miyagi H (2001), Fractal Packing of the DNA Sequence of Bacteriophage φ-X174 (II). Bull. Fac. Sci. Univ. Ryukyus, 71:21-23

[3] Takushi E and Miyagi H (2001), Fractal Packing of the DNA Sequence of Bacteriophage φ-X174 (III). Bull. Fac. Sci. Univ. Ryukyus, 72:43-47

[4] 1/f of music; http://bodysonic.cc/1fyuragi.htm

[5] RPG; http://ribosome.med.miyazaki-u.ac.jp/

[6] Kohonen T (2005), Self-Organizing Maps (Translated in to Japanese by Tokutaka et.al.). Springer-Verlag Tokyo.

Development of A Novel Crossover of Hybrid Genetic Algorithms for Large-scale Traveling Salesman Problems

Masafumi KURODA[1], Kunihito YAMAMORI[1], Masaharu MUNETOMO[2], Moritoshi YASUNAGA[3], Ikuo YOSHIHARA[1]

[1] 1-1, Gakuen Kibanadai-nishi, Miyazaki, 889-2192, Japan, University of Miyazaki
(Tel : +81-985-58-7384; Fax : +81-985-58-7384)
(Email address : {kuroda, yamamori, yoshiha}@taurus.cs.miyazaki-u.ac.jp)

[2] Information Initiative Center, Hokkaido University
[3] Graduate School of Systems and Information Engineering, University of Tsukuba

Abstract: In this paper, we propose a novel crossover operator for solving the traveling salesman problem (TSP) with a Hybrid Genetic Algorithm (HGA) involving Lin-Kernighan (LK) heuristic for local search. We call the crossover operator Sub-tour Recombination Crossover (SRX) which divides each tour of the parents into many sub-tours under some rules and reconnects sub-tours from both the parents so as to construct a new tour of TSP. The method is evaluated from the viewpoint of tour quality and CPU time for ten well-known benchmarks e.g. dj38, qa194 … ch71009.tsp in the TSP website of Georgia Institute of Technology. We compare SRX with the conventional crossover operators; variant of the Maximal Preservative Crossover operator (MPX3), variant of the Greedy Sub-tour Crossover operator (GSX2) and variant of the Edge Recombination Crossover operator (ERX6), and show that the SRX succeeded in finding better solution and running faster than the conventional methods.

Keywords: Traveling Salesman Problem, Hybrid Genetic Algorithm, Lin-Kernighan, Crossover

I. INTRODUCTION

The traveling salesman problem (TSP) is one of the most widely studied problems in combinatorial optimization. Given a collection of cities and the cost of travel between each pair of cities, the TSP is to find the cheapest way of visiting all the cities only once and returning to the starting city. The TSP is NP-hard and very difficult to find true optimal solutions of large-scale instances. We will target instances of over 10^6 cities. We employ technique of a hybrid genetic algorithms (HGAs) combining GAs with Lin-Kernighan (LK) [1] heuristic for local search. The key of the method is a new crossover operator fitting to LK.

It is believed that to inherit long sub-tours from parents to offspring is important in order to avoid breeding a bad offspring. For example, in conventional crossovers, the Maximal Preservative Crossover (MPX) by Mühlenbein et al. and the Greedy Sub-tour Crossover (GSX) by Sengoku and Yoshihara inherit long sub-tours from both the parents to offspring [2][3]. The Edge Recombination Crossover (ERX) by Whitley et al. inherits many edges from both the parents to offspring [4]. Therefore the ERX inherits long sub-tours from them to offspring. But we believe that it is not always advantageous to inherit long sub-tours from both the parents to offspring when using heuristic. Because long sub-tours inherited from parents to offspring have already been improved by heuristic, there is almost no room to be improved by heuristic. However, if sub-tours are too short, they do not inherit parents' character well. Therefore, there must be an appropriate length of sub-tours cut out from the parents. We assume that length of sub-tours should be changed according to the problem size of the TSP. The preliminary experiments show that the best length of sub-tours is around $\sqrt{N}$ (N; number of cities).

We develop a novel crossover operator of HGA employing LK heuristic for local search. We call it Sub-tour Recombination Crossover (SRX) which divides each tour of the parents into many sub-tours that are limited by maximum tour length K, and reconnects sub-tours from both the parents so as to construct a new tour of TSP. We compare SRX with the conventional crossover operators; variant of the MPX operator (MPX3 [6]), variant of the GSX operator (GSX2 [7]) and variant of the ERX operator (ERX6 [8]). We used well-known 10 benchmarks with sizes from 38 to 71,009 cities in the TSP website of Georgia Institute of Technology. We evaluate the SRX from the viewpoint of tour quality and CPU time.

II. HYBRID GENETIC ALGORITHM

Fig.1 shows the flow chart of our HGA. In the step "*Initialization*", we use Quick-Boruvka method for constructing initial tours [9]. The Quick-Boruvka is slightly modified so as to add randomness for producing diversity in the initial population of HGA.

The step "*LK heuristic*" and the step "*Crossover*" are described in detail later. The step "*Selection*" selects individuals according to the ranking of tour lengths. Mutation is not used in this paper.

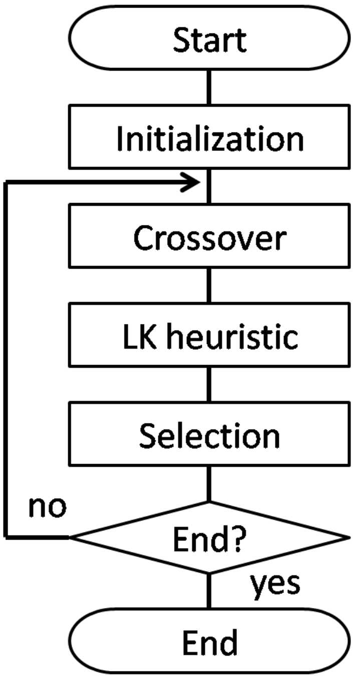

Fig.1. The Flow Chart of HGA

1. Lin-Kernighan Heuristic

Like many other HGA methods for TSPs [10][11], we also use the LK heuristic, because it is widely recognized as powerful local search heuristic for TSPs.

Our LK heuristic uses 8-quadrant nearest neighbors for two-dimensional TSPs, and the search depth is imposed a maximum value of 25. In addition, our LK implementation uses technique of "don't look bits", technique of "distance caching" and data structure of "two-level tree segment list" [6].

2. Chromosome Representation

Tours are represented by so-called *path representation*. For example, a tour "1-2-5-3-4-1" is represented by (12534) by path representation. If a city *i* appears in the *j*th position of the list, city *i* is the *j*th visit.

3. Crossover

The proposed crossover SRX divides each tour of both the parents into many sub-tours that are limited by maximum tour length *K*, and reconnects sub-tours from both the parents so as to construct tour of TSP. The details of the SRX are as follows.

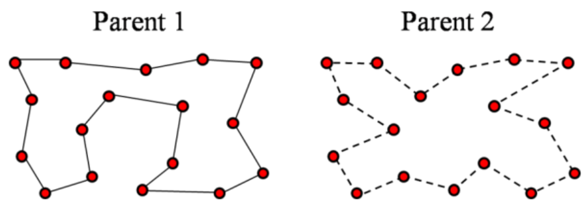

Fig.2. An Example of Parents

Step1

A starting city is selected at random. A sub-tour from parent 1 is extended from the starting city to both directions until the length of the sub-tour is *K*. But if a candidate city to be selected is already copied from the parents, the extension is terminated. (Fig.3)

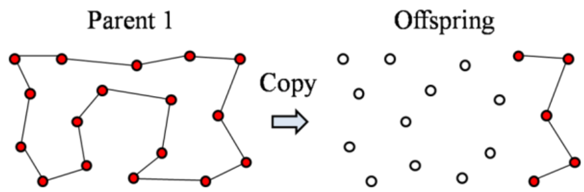

Fig.3. An Example of a Sub-tour Copied from Parent 1 (assume $K = 4$)

Step2

A city is randomly selected as a starting city. A sub-tour from parent 2 is extended to both directions from the starting city until the extension is terminated as Step1. (Fig.4)

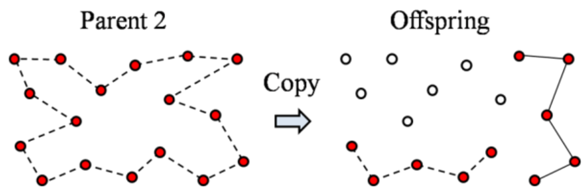

Fig.4. An Example of a Sub-tour Copied from Parent 2 (assume $K = 4$)

Step3

Repeating Step1 and Step2 until all the cities are copied from the parents to offspring. (Fig.5)

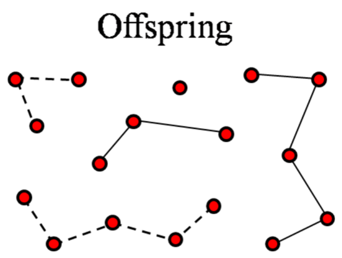

Fig.5. An Example of Sub-tours Copied from both the Parents

Step4

A pair of end cities belonging to different sub-tours are connected so as to makeup a new TSP tour.

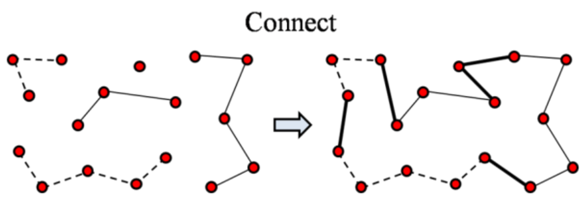

Fig.6. An Example of Offspring Produced by Connecting Sub-tours

III. EXPERIMENTS AND DISCUSSIONS

Benchmark tests evaluate the effectiveness of the SRX. We compare the SRX with the three conventional crossovers; MPX3, GSX2 and ERX6. We used ten benchmarks with sizes from 38 to 71,009 cities taken from the TSP website of Georgia Institute of Technology. Ten time experiments are executed for each benchmark.

We evaluate it from the viewpoint of tour quality and CPU time. The tour quality is measured as gap from the optimum or known best tour if optimum is unknown. In this case study, optima of two instances (bm33708, ch71009) are unknown. *Quality* is defined by the following equation:

$$quality = \frac{tour\_length - optimum}{optimum} \times 100(\%)$$

The program code is written in the C++ language and compiled by GNU g++ compiler (version 2.95) with "-O2" optimizing option. The LK algorithm is programmed by referring CONCORD code [12].

The HGA parameters are set as follows according to preliminary experiments. The population size is 30, maximum generation is 10000, and SRX parameter K is $\sqrt{N}$ (N; number of cities).

The HGA is executed on cluster in our Lab. (2.8-GHz Xeon, 6.0 GHz memory, CentOS 5.2).

Experimental results of five larger benchmarks are given in Table 1 and Fig.7. In table 1, number in the instance name is a size of the problem. The bold type shows the best value of each benchmark.

Table 1. Results of Comparison Experiments of Four Crossovers for Large-scale TSPs.

Instance	Crossover	Ave. Quality (%)	Ave. CPU Time (s)
it16862	SRX	**0.173**	**96336.6**
	MPX3	1.235	116145.2
	GSX2	1.566	125236.0
	ERX6	1.117	107793.8
vm22775	SRX	**0.204**	**166895.4**
	MPX3	1.217	227173.2
	GSX2	1.781	238013.4
	ERX6	1.006	236780.6
sw24978	SRX	**0.239**	**155305.0**
	MPX3	1.431	195722.0
	GSX2	1.570	210031.8
	ERX6	1.120	183382.8
bm33708	SRX	**0.274**	**209373.2**
	MPX3	1.320	279107.4
	GSX2	1.632	303155.8
	ERX6	1.162	269690.8
ch71009	SRX	**0.253**	**379655.6**
	MPX3	1.148	604409.4
	GSX2	1.402	723723.0
	ERX6	0.946	682159.6

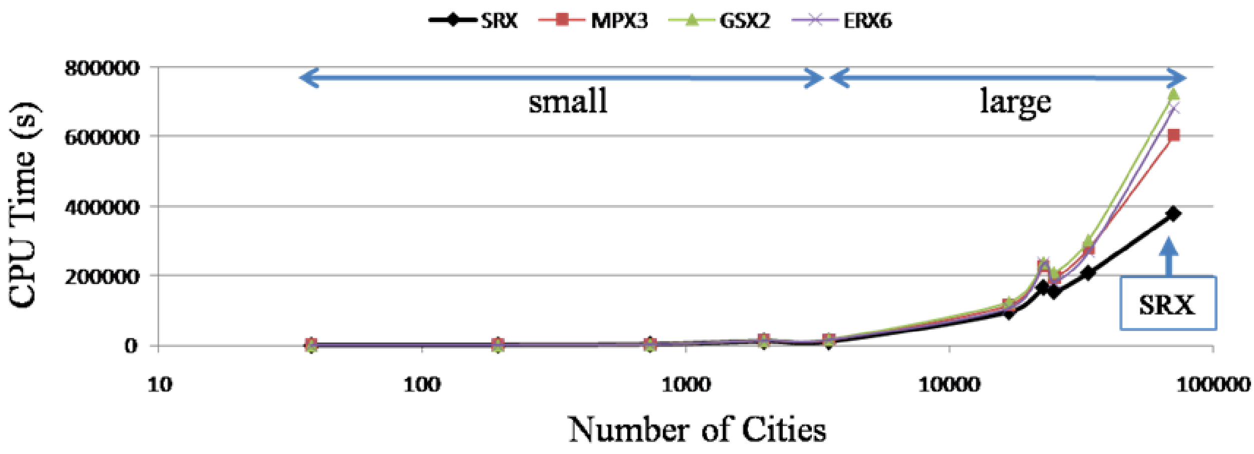

Fig.7. Comparison CPU times of Four Crossovers for Large-scale TSPs

In all benchmarks, the SRX succeeded in finding better solution and running faster than the conventional crossovers.

IV. CONCLUSIONS

We propose a novel crossover operator named SRX of HGA with LK heuristic for large-scale TSPs. Employing ten benchmarks, we compare the SRX to three conventional crossovers (MPX3, GSX2, ERX6) from the viewpoint of tour quality and CPU time. For all benchmarks, the SRX gives best solution compared with other crossovers, and is faster than them.

We intend to parallelize HGA to solve more large-scale TSPs.

ACKNOWLEDGEMENT

This research is partly supported by the collaborative research program 2009, information initiative center, Hokkaido university.

REFERENCES

[1] S. Lin and B. Kernighan (1973), An Effective Heuristic Algorithm for the Traveling Salesman Problem, Operations Research 21(2): 498-516

[2] H. Mühlenbein and M. Gorges-Schleuter and O. Krämer (1988), Evolution Algorithms in Combinatorial Optimization, Parallel Computing, North-Holland 7: 65-85

[3] H. Sengoku and I. Yoshihara (1998), A Fast TSP Solver Using GA on JAVA, Proc. of the 3rd Int. Symp. on Artificial Life and Robotics (AROB-3): 283-288

[4] D. Whitley and T. Starkweather and D. Fuquay (1989), Scheduling Problems and Traveling Salesman: The Genetic Edge Recombination Operator, Proc. Of the 3rd ICGA: 133-140

[5] National TSPs
http://www.tsp.gatech.edu/world/countries.html

[6] H. D. Nguyen (2004), Hybrid Genetic Algorithms for Combinatorial Optimization Problems, Ph. D. dissertation Univ. of Miyazaki

[7] H. D. Nguyen and I. Yoshihara and K. Yamamori and M. Yasunaga (2002), Greedy Genetic Algorithms for Symmetric and Asymmetric TSPs, IPSJ Tech. Report SIG-MPS 43(SIG10): 165-175

[8] H. D. Nguyen and I. Yoshihara and M. Yasunaga (2000), Modified Edge Recombination Operators of Genetic Algorithms for the Traveling Salesman Problem, Proc. Of the 3rd Asia-Pacific Conf. on Simul. Evol. and Learn. SEAL 2000: 2815-2820

[9] D. Applegate and W. Cook and A. Rohe (2003), Chained Lin-Kernighan for Large Traveling Salesman Problems, INFORMS J. of Computing 15(1): 82-92

[10] R. Baraglia and J. I. Hidalgo and R. Perego (2001), A Hybrid Heuristic for the Traveling Salesman Problems, IEEE Trans. EC 5(6): 613-622

[11] N. D. Nguyen and I. Yoshihara and K.Yamamori and M. Yasunaga (2007), Implementation of an Effective Hybrid GA for Large-Scale Traveling Salesman Problems, IEEE Trans. SMC 37(1): 92-99

[12] Concorde TSP Solver
http://www.tsp.gatech.edu/concorde/

Signal Integrity Improvement Method and Its Robustness Evaluation for VLSI and VLSI-packaging

Masami Ishiguro †, Hiroshi Nakayama †, Yuki Shimauchi †, Noriyuki Aibe †, Yoshiki Yamaguchi †,

Ikuo Yoshihara ‡, Moritoshi Yasunaga †

† *Graduate School of Systems and Information Engineering, University of Tsukuba*
Tsukuba ,Ibaraki 305-8573, JAPAN
‡ *Factory of engineering, University of Miyazaki*
Miyazaki, Miyazaki 889-2192, JAPAN
masami@islab.cs.tsukuba.ac.jp

Abstract: Recently, GHz frequency signal is required to be propagated in the PCB (printed circuit board) with low distortions. And the higher frequency-signal of 10 GHz or more will be also required to be propagated with low distortion in the VLSI in the future. The signal-propagation with low distortion, however, is getting difficult more and more as the frequency increases.

In order to solve this problem and to ensure the signal integrity, we have proposed a novel transmission line called "Segmental transmission Line (STL)" already. In the STL, a transmission line is divided into multiple segments of individual characteristic impedance. The multiple segments are designed to fix the waveform distortion on the transmission line by solving a combinatorial explosion problem using the genetic algorithms.

In our previous paper, we have shown effectiveness of the STL designed to GHz-clock-signal on the computer simulations. And, we have fabricated two scale-up STL prototypes for clock-signal using real PCBs.

In this paper, we input random-signal changing its frequency to the scale-up STL prototype designed to 150MHz clock-signal. And, we show that the STL has high robustness to the random-signals and the frequency fluctuation, which indicates generality of the STL technique.

Keywords: Signal Integrity, Transmission Line, Random Signal, Genetic Algorithms

Ⅰ. INTRODUCTION

Signals of GHz frequency, the wavelengths of which are less than 15cm and are shorter than the PCB, are terribly distorted at the impedance mismatching points in the PCB traces. And this problem will also occur in the VLSIs in the future at the frequency more than 10 GHz.

They have used conventional impedance-matching techniques [1][2] to fix the distorted waveforms. These techniques works well up to hundreds MHz, but will not work well at more than GHz.

In order to overcome this problem and ensure the signal integrity we have proposed a novel transmission line called "Segmental Transmission Line (STL)" [3] .

In the STL, a transmission line is divided into multiple segments of individual characteristic impedance. In this structure, noises are generated purposely at the segments boundaries to cancel the target noises, which occur due to the impedance mismatching between the transmission line and the devices connected to the transmission line. We have shown the effectiveness of the STL to GHz-clock signals on the computer simulation already. Furthermore, we have fabricated two scale-up STL prototypes designed to clock-signals using real PCBs [4][5]. In the scale-up prototypes, the STL for GHz-frequency is designed to be measured in the MHz-frequency domain by lengthening the wire or trace length in proportion to the ratio between the GHz and MHz.

The robustness of the STL designed to the clock-signals, however, has not been evaluated yet in terms of random-signal and frequency-fluctuation, and the purpose of this paper is to evaluate the robustness using the scale-up prototypes. We thus input random-signals to the scale-up STL prototype designed to 150MHz-clock-signal changing the random-signal-frequency and measure the distortion of the waveforms to evaluate the robustness.

Ⅱ. SEGMENTAL TRANSMISSION LINE

The idea of STL is completely different from the conventional methods such as [1][2], in which the impedance mismatching points are tried to be fixed.

In the STL, we use noises that are generated purposely a t segment boundaries to cancel the target noises, which are reflection and transmission-waves that occur due to the impedance mismatching bet ween the transmission line and device-inputs connected to the transmission line. And the target noises are the sources of the waveform distortion at the point where the device-inputs are connected to the transmission line.

To generate these noises purposely, a transmission line is divided into multiple segments of individual characteristic impedance, which can be implemented with adjustment of segment-widths.

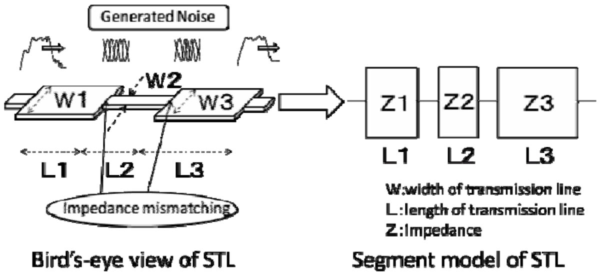

Figure 1: Overview of STL

Figure 1: shows an overview of the STL and its segment-model.

In the STL, it is necessary to obtain the best combination of segment-widths and segment-lengths. It is however next to impossible to find the best combination because of the combinatorial explosion.

For example, 10 widths and 100 lengths for each of 10 segments results in the combination of $(10*100)^{10} = 1.0*10^{30}$. We thus use the genetic algorithms [6] to solve the combinatorial explosion problem and to find semi-optimized combination quickly.

In the GA coding, the chromosome consists of two kinds of loci i.e., one is for the segment-width and the other is for the segment-length. Each chromosome thus represents each STL of multiples segments of individual characteristic impedances and individual lengths. Figure 2 shows the STL design system named STL-Designer, which is composed of a newly developed GA calculation-loop specialized for the STL and the circuit simulator SPICE.

And in the fitness evaluation, each chromosome is translated to the transmission-line net-list for the circuit simulator SPICE and the waveform, which is the result from the simulator, is evaluated compared with the ideal waveform as shown in Fig. 3 . The STL prototypes are fabricated based on the design results from the STL-Designer

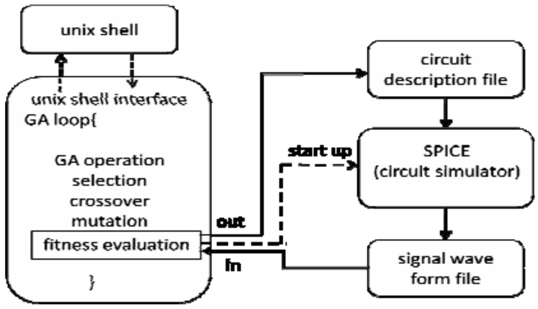

Figure 2: STL design system

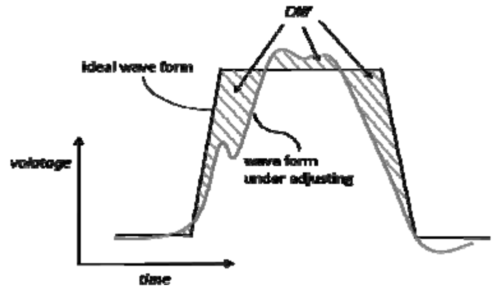

Figure3: Difference between the wave form under adjusting and the ideal wave form

Ⅲ. 150MHz SCALE-UP STL PROTOTYPE

Figure 4 shows the circuit-diagram of the scale-up STL prototype for 150MHz clock-signal [5]. The transmission line of 1m long is divided into 15 segments. Two capacitors of 24pF each represent two device-inputs, e.g., VLSI inputs connected to the transmission line.

Figure 5 shows a distorted waveform observed in the conventional transmission line (left) and a improved waveform observed in the STL prototype (right) at 150MHz clock-signal.

The logical margin is improved to about 0.8 – 1.0[V] in the STL while it in the distorted wave is reduced to about 0.5 – 0.5[V] in the conventional transmission line.

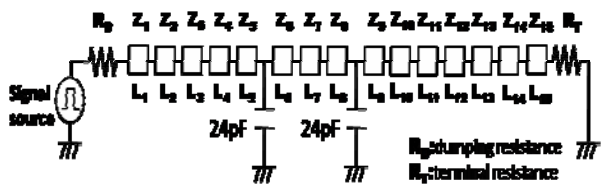

Figure 4: Circuit-diagram of the scale-up STL Prototype for 150MHz clock-signal

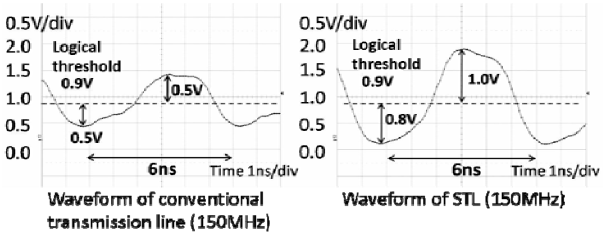

Figure 5: Waveforms at 150MHz clock-signal

Ⅳ. ROBUSTNESS EVALUATION

In this paper, we evaluate the robustness of the 150 MHz scale-up STL prototype designed for clock signal to the random-signal-input and base-clock frequency-fluctuation. We input the random signals generated from 150 MHz base-clock, and we also change the base-clock frequency from 150 MHz.

1. Signal-Generation and Measurement

We made a pseudorandom number generation circuit by using the linear feedback shift register (LFSR), which is one of the famous random number-generation methods.

The LFSR mainly consists of a n-bit shift-register circuit and an exclusive-OR of a feed-back-loop from the shift-register, which generates random cycle length of 2^{n-1}.

In this paper, we used a 7-bit LFSR of 127-bit random-cycle-length as shown in Fig. 6 . We implemented it onto the FPGA in the Virtex5-ML505-board provided by Xilinx Co. and used it as the random-signal-generator.

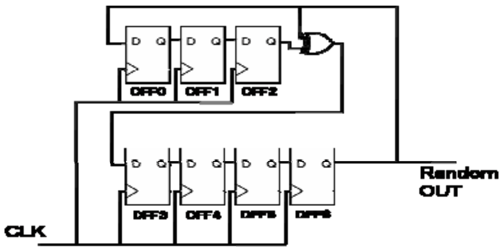

Figure 6: 7bit linear feedback shift register

In the measurements, waveforms are probed with a probe from a digital sampling oscilloscope of 2 GHz band-width and 10

GS/s sample-rate contacted t-o the trace in the prototype.

2. Eye-pattern measurement

Signal integrity of the random signals is usually evaluated in the eye-pattern, or eye-diagram, in which waveforms are overwritten at the clock-frequency interval period (e.g., inverse of the frequency). Its name comes from the fact that the observed patterns look like human-eye, and the eye opens more clearly as the waveform distortion decreases.

In this paper, we define the quality of the signal with the eye-height at 1/4 clock-period after the starting point of the signal switching and with the eye-width at the threshold voltage.

3. Robustness to random-signal

Figure 7 shows eye-patterns to 150MHz random-signal-input observed in the conventional transmission-line (left) and in the STL (right).

In the conventional transmission-line, the eye-height at 1.65 ns (1/4 clock-period) from the switching point is 0.2 [V]. On the other hand, it in the STL is improved to 0.55 [V], which is larger than it in the conventional one by 2.75 times. The eye-width of 2.1 [ns] ns in the conventional transmission line is also improved to 2.6 [ns], which is longer than it in the conventional one by 1.23 times (results are summarized in Tab. 1).

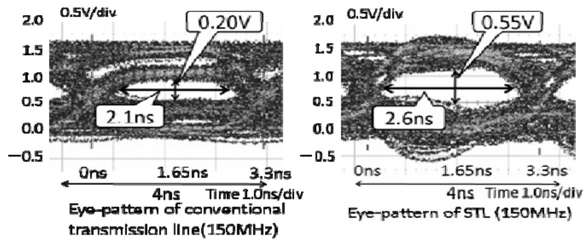

Figure 7: Eye-patterns to 150MHz random-signal

Table 1: Signal integrity improvement at 150 MHz random-signal

	Conventional Transmission Line	STL	Improvement Ratio
Eye-height	0.2[V]	0.55[V]	2.75
Eye-width	2.1[ns]	2.6[ns]	1.23

4. Robustness to Frequency-fluctuation

We change the base-clock-frequency from 150 MHz to 130MHz, 140MHz, 160MHz, and 170MHz in the above experiments. Eye-patterns observed at 130 MHz and 170 MHz are shown in Figs. 8 and 9, respectively, and the signal-integrity-improvements measured at the same points as in the previous section are summarized in Tabs. 2 and 3, respectively.

High robustness in the eye-height, the improvement-ratio of which is 2.25, is still maintained even at 130 MHz. An eye-height improvement-ratio of 1.50, which is not so high as at 150MHz and 130MHz, is also observed at 170 MHz. On the contrary, remarkable improvement is not observed in the eye-width.

In the measurements in this paper, we clearly showed that the STL designed to clock-signal waveform had high robustness to the random-signals and the frequency fluctuation. The results thus indicate generality of the STL technique.

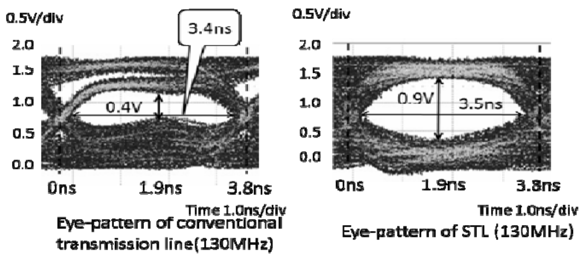

Figure 8: Eye-patterns to 130MHz random-signal

Table 2: Signal integrity improvement at 130 MHz random-signal

	Conventional Transmission Line	STL	Improvement Ratio
Eye-height	0.4[V]	0.9[V]	2.25
Eye-width	3.4[ns]	3.5[ns]	1.03

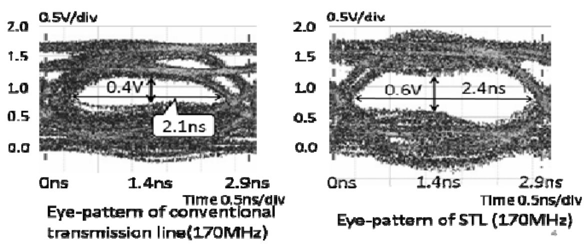

Figure 9: Eye-patterns to 170MHz random-signal

Table 3: Signal integrity improvement at 170 MHz random-signal

	Conventional Transmission Line	STL	Improvement ratio
Eye-height	0.4[V]	0.6[V]	1.50
Eye-width	2.1[ns]	2.4[ns]	1.14

Ⅴ. CONCLUSIONS and FURTHER WORK

We carried out the random and frequency-fluctuated signal-injection-tests to the STL scale-up prototype designed at 150MHz clock-signal. The measured eye-patterns showed high improvement ratio from 1.50 to 2.75 in the eye-height and small ones in the eye-width. The results as a whole indicate high robustness of the signal-integrity improvement-capability in the STL against the random and frequency-fluctuated signals.

The reason of the high robustness, however, is not cleared yet. We will analyze its mechanism in terms of the impulse-response in the frequency domain.

Ⅵ. ACKNOWLEDGMENTS

This research is partly supported by 2009 Scientific Research B (No. 21360178) in Japan Grand-in-Aid for Scientific Research.

REFERENCES

[1] Naono,N., Nakamura,Y., Details on High-speed Digital System Design.", NikkeiBP INc., 2001.
[2] Taguchi.M, "High-speed, small-amplitude I/O interface circuit for memory bus appli-cation" , IEICE Trans. Electron., vol.E77-C, no.12, pp.1944-1950, Dec. 1994.
[3] Yasunaga,M., Yoshihara,I., The Segmental Transmission Line and Its Design Methodology :Line Trace Ensuring High Signal Integrity in VLSI Mounting Boards", The transactions of the Institute of Electronics, Information and Communication Engineers. D-I, vol.J88-D-I, no.5, pp.915-929, May. 2005.
[4] Nakayama,H.,, Yasunaga,M., Yamaguchi,Y., Yoshihara,I, Koizumi,N., "Experimental Verification of Improved Signal Integrity Using the Segmental Transmission Line", The 70th National Convention of Information Processing Society of Japan, 1pp.9-10, tsukuba, Mar. 2008.
[5] Nakayama,H., Shimauchi,Y., Aibe,N., Yoshihara, I., Yamaguchi,Y., Yasunaga,M., "AHigh-Signal-Integrity transmission-Line for High Speed VLSI Packaging: Its proposal and PrototypeEvaluation", DA Symposium 2009, pp.187-192.
[6] Melanie,M., Iba,H., "AN INTRODUCTION TO GENETIC ALGORITHMS", Tokyo Denki University Press, 1997.

The Fifteenth International Symposium on Artificial Life and Robotics 2010 (AROB 15th '10),
B-Con Plaza, Beppu,Oita, Japan, February 4-6, 2010

Onto-biology: clarifying also the spatiotemporal structure

K. Naitoh
Waseda University, Faculty of Science and Engineering, 3-4-1 Ookubo, Shinjuku, Tokyo, 169-8555 Japan
(Tel : 81-3-5286-3265)
(Email address:k-naitoh@waseda.jp)

Abstract: A protocol describing the origins and evolutions of life is outlined, based on the seven principles of information, topology, function, diversity, discontinuity, temporal cycle, and metabolic conservatibity. This is derived based on the nonequilibrium quantum chemistry on time-dependent electron clouds: the general mobilization of thermo-fluid dynamics, stochastic mechanics, traditional quantum mechanics, chemistry, and mathematics as warp and the biologies related to molecular biology, morphogenesis, bioinformatics, origin of life, and medicine as weft. This also reveals the procedure to generate left-right asymmetric liver and symmetric kidneys and also the standard clock common to stem-cell cycle and circadian clock.

Keywords: Protocol, Seven principles, Life, Origin, Evolution

I. INTRODUCTION

Frontiers [1,2] showed how to generate amino acids and nucleic acids artificially. Yanagawa et al. artificially generated something like a cell membrane in a high-pressure chamber. [3] Ricardo and Szostak wrote a comprehensive review of recent studies on artificial production of elementary components. [4]

The polymerase chain reaction (PCR) is widely used to replicate DNA sequences in vitro, using an enzyme called DNA polymerase and nTP as elements. [5] This may be the first milestone toward achieving artificial replication of life. However, in PCR, the enzyme is not replicated automatically, though the DNA sequence is. A closed cycle of chemical reactions, which is a hyper-cycle like that shown by Eigen et al. [6], is not achieved in PCR.

Joyce and Orgel [7] demonstrated that various RNA polymers can be generated randomly without enzymes. Instead of enzymes, metal, such as magnesium ions, is necessary for catalyzing the synthesis of RNA polymers. In this system, a metallic catalyzer may deteriorate, because metal is not regenerated. Synthesis based on metal is also prebiotic because of the noncyclic reactions.

Thus, researchers have still not found a definite way and principle for generating the minimum hyper-cycle capable of replicating both information and functional molecules. The road to an artificial cell may be long. We still do not know the design diagram of life over billions of years.

The design diagram of life should be outlined based on the seven key principles of (I) information, (II) topology (structure), (III) function, (IV) diversity, (V) discontinuity, (VI) temporal cycle, and (VII) metabolic conservativity. Our previous reports [8-16] show the principles on (I), (III), (V), and (VI).

Although traditional quantum mechanics yields the static state of the electron cloud, the cyto-fluid dynamic theory [8, 9, 10] for (I) and (III) describes the time-evolution process of the unstable cloud, which can be non-equilibrium quantum chemistry. Some mysteries on biological information and function are clarified by the theory. Our previous studies on (V) and (VI) [12, 15, 16] reveal some temporal aspects. Thus, in the following sections, we will show the bio-principles on (II), (IV), and (VII).

II. TOPOLOGY

It is well known that the electron cloud is not spherical around an atom heavier than helium (He). Thus, non-spherically electron cloud induces string-like and ring-like molecules in amino acids and nitrogenous bases, without spherical connections of carbons. Nitrogenous bases without a spherical electron cloud generate string-like DNA and RNA. This is an essential principle of chemistry.

The string-like connections of non-spherical particles can be also seen in cells. Here, let us separate cell aggregation into two parts: the internal side around the center of the aggregation and the external side close to the surface. External cells close to the surface move relatively easily, because one part of the cell is free without any connection to other cells. However, internal cells often receive forces from many directions due to the presence of other cells, making it relatively difficult for them to move relative to the origin on the earth. Thus, inner cells deform relatively easily without any translational motion. [10,12,15] This deformation brings the discrepancy from a complete sphere, i.e., its scabrous shape, which induces a string-like connection of deformed cells, although parcels with less deformation connect as a spherical aggregation or a spherical surface aggregation in two- or three-dimensional space (Fig. 1). It should be stressed that there will also be three sub-types of strings: straight strings, rings, and bifurcation strings of deformed cells (Fig. 2). One of these three types of strings will be chosen based on the cell deformation rates and the types of molecules lying between cells such as cell adhesion molecules (CAMs), morphogens, and extracellular matrix (ECM).

Then, an aggregation of long strings (straight strings, rings, and bifurcation strings) will be close to the next larger sphere like yarn waste because of their flexibility. Repeats of strings and spheres are natural, because we can see the repeats in several levels of living beings.
It is no wonder that spherical biological cells such as bacteria include string-like DNA and also connections of spherical cells become a string-like shape such as intestine and blood vessel again.

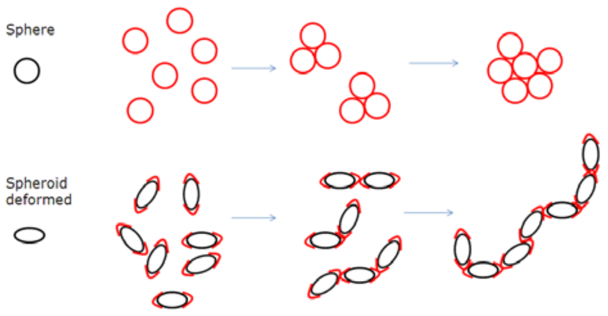

Fig. 1. Two types of aggregations. Upper: sphere, lower: string

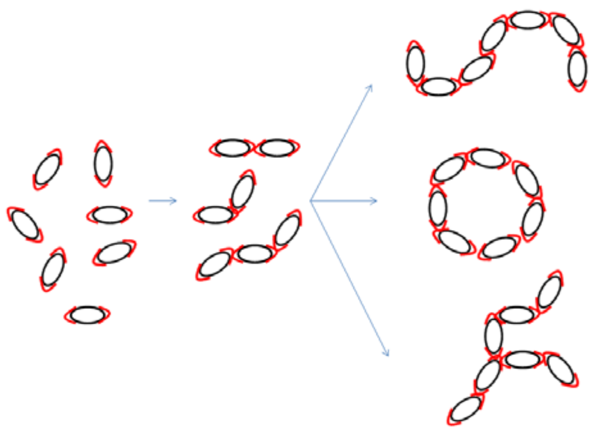

Fig. 2. Three types of strings. a: string, b: ring, c: bifurcation string

The representative length of a string is relatively longer than that of a sphere or a surface, when the weight of the string is equal to that of the sphere. This is because the diameter of the sphere is proportional to the cubic root of the string length (Fig. 3). This leads to compression buckling of the string inside the sphere: the conclusion that the string must bend inside the sphere. A representative example of this is the intestines inside the human body.

Blood vessels resemble the string type at first glance. Thus, the heart and liver, representing two parts connected to blood vessels, are distorted due to the buckling effect, leading to the left-right asymmetric distribution. However, the other parts of blood vessels are left-right symmetric, because vessels bifurcated at a lot of points in a tree structure are mathematically close to a three-dimensional dense sphere.

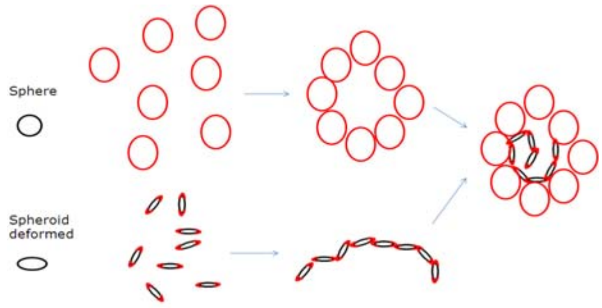

Fig. 3. Buckling of a string inside a sphere.

II. Diversity

The molecular weights of the twenty types of amino acids show a threefold variation between 240 of cysteine as the maximum and 75 of glycine as the minimum, although that of purines and pyrimidines among nitrogenous bases varies by only about 1.5 times. The frequency ratios of hydrophilic and hydrophobic amino acids in proteins are also more stochastic than those of purines and pyrimidines in nucleic acids. Although there are only five main types of nitrogenous bases in living beings, there are many types of proteins. How is this variety determined?

Information carriers such as DNA are relatively deterministic, because accurate conservation of information is necessary. It is stressed that accurate conservation of information is achieved by the relatively hard structure of DNA. Thus, DNA maintains a certain spiral shape having a fixed width and pitch. In contrast, functional molecules such as proteins and RNA provide a variety of functions for several environmental changes. This variety of functions comes from the flexible shapes of the molecules.

This concept of "hard deterministic" and "soft stochastic" can be validated by the stochastic determinism, representing new dynamics, at the triple point of the Boltzmann, Langevin, and Schrodinger equations. [17,18]

First, let us recall the cyto-fluid dynamic theory derived from continuum mechanics [8,9,10], which describes the motions of deformation and translation for a flexible parcel consisting of a nitrogenous base and water molecules surrounding the base. (See Eq. 1a.) We must rethink whether the parcel can be a continuum or not. It is apparent that the parcel is not a continuum, because it is on a very small scale. Larger windows for averaging in continuum mechanics cannot resolve the phenomenon in principle. The scale for averaging, i.e., the minimum scale representing the phenomenon, will be between the atomic scale and the size of the base, because the spatial distribution of the deformation rate in the parcel should be analyzed. Let us define this minimum scale representing the phenomenon as the stochastic determinism window (SDW). When this SDW is used for averaging, the density and also the other physical variables have indeterminacy because of molecular discontinuity. Then, the stochastic governing equation having indeterminacy (Eq. 1b) shows a slightly vague solution for the phenomenon. This indeterminacy also implies that variations of molecular sizes are possible in a limited range.

$$d^2x/dt^2=(e-1)(dx/dt)^2+(e^3-3)x+q(t) \tag{1a}$$

$$d^2x/dt^2=(e-1)(dx/dt)^2+(e^3-3)x+q(t)+\varepsilon(t) \tag{1b}$$

where the parameters e, q(t), and ε(t) denote the size ratio of the two parcels connected under equilibrium conditions, the time-dependent force generated by the other connected parcel, and random fluctuation due to indeterminacy, respectively. [17,18]

The quantum mechanics of the Schrodinger equation is based on an indeterminacy principle. The presence of electrons is given in a certain area, not at a deterministic point. This vague viewpoint with indeterminacy shows an outline of a possible solution. We can obtain the value solution in exchange for abandoning the determinant solution. Although this stochastic determinism for biomolecules is based on a governing equation different from that for the Schrodinger equation, a weak indeterminacy lying at the triple point of the Boltzmann, Lanvevin, and Schrodinger equations leads to new findings underlying living beings, when we also use the quasi-stability concept of life.

An important point of the indeterminacy principle is generally that the level of indeterminacy determined by the averaging window size implies the level of variety in natural phenomena.

Hard systems such as DNA will experience less deformation, leading to a relatively larger stochastic determinism window, i.e., a larger representative scale. On the other hand, soft molecules such as RNA and proteins will have large curvature (severe bending) locally, which leads to the necessity of a smaller SDW. As a result, the difference in SDWs produces manifold variety.

VII. Metabolic conservation

We must consider the five components necessary for a living cell: (Group 1) a DNA group including genes, (Group 2) an RNA group, (Group 3) molecules for the cell wall, (Group 4) a protein group including enzymes, and (Group 5) a lipid group.

Let us consider the relation between these five molecular groups and the five types of nTPs (ATP, GTP, CTP, TTP, UTP). ATP is used as the main energy carrier for the five molecular groups, while UTP, GTP, and CTP are also employed for generating polysaccharides of the cell wall, proteins, and lipids, respectively. It is also known that DNA uses A, T, G, and C as components, while RNA employs A, U, G, and C as components.

Thus, the reaction scheme for the five groups (cell wall, proteins, lipids, DNA, and RNA) per generation is described by Eq. (4), by using [A], [U], [G], [C], and [T] for adenine, uracil, guanine, cytosine, and thymine.

$$\begin{aligned}
&[\text{Cellwall}] \leftarrow m_1[A]+n_1[U] \\
&[\text{Protein}] \leftarrow m_2[A]+n_2[G] \\
&[\text{Lipid}] \leftarrow m_3[A]+n_3[C] \\
&[\text{DNA}] \leftarrow \{(1-\alpha)([A]+[T])+\alpha([G]+[C])+2k_1[A]\}\omega \\
&[\text{RNA}] \leftarrow \{(1-\beta)\{[A]+[U]\}+\beta\{[G]+[C]\}+k_2[A]\}\omega
\end{aligned} \tag{4}$$

where $\alpha, \beta,\ m_i, n_i,\ k_i,$ and ω denote the rate of GC pairs inside DNA, the rate of GC pairs inside RNA, the rate of A as the energy supplier for generating the cell wall, proteins, and lipids, the rates of U, G, and C as the energy suppliers for generating the cell wall, proteins, and lipids, the consumption rate of A as the energy supplier for generating DNA and RNA, and the number of loci in nucleic acids, respectively.

The consumption rate of purines during a cell division will be on the order of that of pyrimidines. This constraint and Eq. 4 lead to the relation

$$(2k_1+k_2)\omega+(m_1+m_2+m_3) \approx n_1+n_3-n_2$$

which yields some interesting results. The increases in k_i, i.e., the acceleration of DNA replication, leads to a decrease in GTP, thus reducing n_2. The natural tradeoff between nucleic acid generation by ATP and protein generation by GTP is seen in Eq. 4. The five frameworks (cell wall, protein, lipid, DNA, RNA) do not increase at the same time. Guanine functions as the switch for changing the phases of DNA replication and protein generation.

The alternating generation of DNA and protein also leads to the spatial asymmetry of molecular distributions, although the simultaneous generation of DNA and protein will induce a symmetric distribution. This spatial asymmetry also causes cell deformation.

IV. CONCLUSION

Thought experiments based on data pertaining to life lead to the conclusion that life can be tentatively defined as the object controlled by all of the seven principles mentioned above. The prebiotic self-replication systems without cell walls do not represent life, because they only involve four principles of (I), (II), (III), and (I V). More than seven principles or detailed algorithms within the seven explained here may be necessary to produce an artificial cell in vitro. The present protocol shows the minimum scenario.

REFERENCES

[1]Miller SL (1953), A production of amino acids under

possible primitive earth conditions. Science, 117: 528-529.
[2]Oro J and Kimball AP (1961), Synthesis of Purines Under Possible Primitive Earth Conditions. I. Adenine from Hydrogen Cyanide, Arch. Biochem. Biophys. 94: 217–227.
[3]Yanagawa H (1991) How Life Originated. TBS Britannica. 1-466.
[4]Ricardo A and J.W. Szostak JW (2009) Origin of Life on Earth. Scientific American.
[5]Mullis KB (1990), The unusual origins of the polymerase chain reaction. Sci. Am. 262: 56-65.
[6]Eigen M (1992), Steps toward Life, Oxford University Press, pp. 1-173.
[7]Joyce GF and Orgel LE (1986), Non-enzymic template-directed synthesis on RNA random copolymers: poly (C,G) templates. J. of Molecular Biology, 188: 433-441.
[8]Naitoh K (2001) Cyto-fluid Dynamic Theory, Japan Journal of Industrial and Applied Mathematics, **18-**1: 75-105.
[9]Naitoh K (2005), Basic pattern underlying life, NIKKEI SCIENCE, Vol. 6: 58-65. (in Japanese)
[10]Naitoh K (2008), Stochastic Determinism underlying Life, Artificial Life and Robotics, Springer, **13,** 10-17.
[11] Naitoh K (2008), Inevitability of nTP: Information-energy carriers, Artificial Life and Robotics, Springer, 13: 81-83.
[12]Naitoh K (2008), Onto-biology: Inevitability of Five Bases and Twenty Amino-acids, Proc. of 13th Int. Conf. on BioMedial Engineering, (ICBME), Singapore. Springer-Verlag.
[13]Naitoh K (2008), Fluid Dynamics underlying Morphogenesis, Proc. of 13th Int. Sym. on Artificial Life and Robotics.
[14]Naitoh K (2008), Engine for cerebral development, Artificial Life Robotics, Springer, **13:** 18-21.
[15]Naitoh K (2008), Physics underlying Topobiology, Proc. of 13th Int. Conf. on BioMedial Engineering, (ICBME), Singapore. Springer-Verlag.
[16]Naitoh K (2009), Onto-biology, Proceedings of 2009 Chemical, Biologhical, Environmental Engineering, (CBEE2009).
[17]Naitoh K (2008, Y. Nakagawa, and H. Shimiya, Stochastic determinism approach for simulating the transition points in internal flows with various inlet disturbances. Computational Fluid Dynamics 2008, Springer-Verlag.
[18]Naitoh K (2009), Stochastic determinism. Proceedings of the Annual Meeting of JSIAM, 2009. (Also in H. Simiya and K. Naitoh, Space-Time Structure around the Transition Point in Channel Flow Revealed by the Stochastic Determinism. Proc. of 6th International Symposium on Turbulence and Shear Flow Phenomena (TSFP6), Korea (2009).)
[19]Losick R and Desplan C (2008), Stochasticity and Cell Fate, Science, 320: 65-68.

Morphogenetic-cycle Model: clarifying several stages of embryo, brain, lung, and heart

A. Suzuki and K. Naitoh
Waseda University, Faculty of Science and Engineering, 3-4-1 Ookubo, Shinjuku, Tokyo, 169-8555 Japan
(Tel : 81-3-5286-3265)
(Email address:k-naitoh@waseda.jp)

Abstract: Development processes of multi-cellular systems have attracted attention for a long time. The macroscopic model having six categories of molecules shows that the antagonism between the negative controllers and the positive replication factors induces bifurcations in stem and pluripotent cells at rhythmic intervals comprising about 6-7 cell divisions. Our theoretical model for the morphogenetic process shows that this cycle of 6-7 cell divisions, i.e., branching time between periodic bifurcation events, corresponds to the emergence timings of early developing stage, the nervous system, the respiratory system, and the circulatory system.

Keywords: Morphogenesis, Organs, Cell division

I. INTRODUCTION

Development processes of multi-cellular systems have attracted attention for a long time. [1,4,8,9]

Development processes of multi-cellular systems can be examined separately from two viewpoints of space and time. In this report, we especially examine the temporal aspects.

The deterministic differential equation model of six variables [2], which is extended from the minimum hypercycle model describing the smallest self-reproduction system [3], shows the oscillations of molecular densities due to the negative enzyme system and the gene group in the minimum hyper-cycle, which has the cycle of about six or seven-fold beats of fundamental clock.

Next, we examined in detail about the timing when organs of human beings and mouse are formed. An important point is that the six or seven-beat cycle calculated by the model corresponds to the actual emergence timing of several stages of embryo and organs.

II. MORPHOGENETIC CYCLE [2,3]

1. Minimum hyper-cycle [3]

All of the molecules are classified into some categories, based on their representative physical characteristics.

At least two types of molecular categories (enzyme systems), which are for replicating gene groups and enzyme systems, are necessary for achieving a closed reaction cycle. Examples of the former and latter are DNA-replicase and ribosome protein, respectively. This leads to the conclusion that two types of gene groups are also inevitable and serve to code the two enzyme systems. The core cycle for self-replication can be modeled by these four molecular categories, two gene groups and two enzyme systems (Categories D1: Gene group 1 that codes enzyme system R1 for DNA production, D2: Gene group 2 that codes enzyme system R2 for enzyme production, R1: Enzyme system 1 for DNA production, and R2: Enzyme system 2 for enzyme production). [3]

Here, Di and Ri for i = 1 and 2 also denote the density of each molecular category. We assume that the production rate of a category due to the reaction of categories Dj and Rj is restricted by the smaller one of Dj and Rj.

Then, Eq. 1 can describe the densities of four categories averaged over all the cells at generation *N*.

$$D_i^{N+1} - D_i^N = \alpha_{ij} D_i^N \otimes R_j^N \,, i = 1,2 \,, j = 1,2 \qquad (1)$$

where $D_i \otimes R_j$ and α_{ij} denote min(*Di*,*Rj*) and a constant, respectively.

This system of D1, D2, R1, and R2, the 4-cylinder engine for life, can replicate each other.

2. Six-variable differential equation [2]

The negative enzyme system and its gene group (D3: Gene group 3 that codes protein system R3 for suppressing D2 gene expressions, and R3: Protein system 3 for suppressing D2 gene expressions) are then incorporated into the minimum hyper-cycle, because the morphogenetic process of multi-cellar systems in mammals must include negative controllers such as Oct-4 and SOX2 for producing tissues and organs. [4, 5, 6]

Only the protein system generated in Category R3, a negative controller, attaches to the positive gene group D2**.** Thus, the production rate of R2 can be re-written in the form of min (D2-R3, R2).

Then, the densities of six categories averaged over all the cells at generation *N* are described by the following equations.

$$D_i^{N+1} - D_i^N = \alpha_{i1} D_i^N \otimes R_1^N , i = 1,2,3 \quad (2)$$

$$R_1^{N+1} - R_1^N = \alpha_{12} D_1^N \otimes R_2^N$$
$$R_2^{N+1} - R_2^N = \alpha_{22} \delta(D_2^N - R_3^N) \otimes R_2^N \quad (3)$$
$$R_3^{N+1} - R_3^N = \alpha_{32} D_3^N \otimes R_2^N$$

where $D_i \otimes R_j$ denotes min(*Di,Rj*) for i=1-3 and j=1-3, and also where $\delta(x)$ denotes the larger one of x or 0, i.e., max (*x*, 0). (Here, the constant α_{i1} includes the influences of many types of molecules in the category and the molecule movements on reaction probability. There is an important constraint, i.e., the densities of D1, D2, and D3 are identical, because the three gene groups 1, 2, and 3 are in one set of DNA in each generation. Thus, α_{i1} for D1, D2, and D3 is a set having the identical value of 1.0. Initial densities of D1, D2, D3, R1, R2, and R3 are set to be 1.0, respectively.)

Let us denote the number of cell divisions after the mother cell generation as N. Generation N is less than 50, because an adult human body can be generated by about 50 cell divisions from a fertilized egg. Accordingly, the number of cells at generation N is defined as P(N). There are many types of cells among P(N) such as somatic and stem cells. A cell must have one set of DNA. Thus, the number of cells, P(N), is equal to D_i^N .

Broadly speaking, computational results obtained by Eqs. (2) and (3) show nearly exponential or hyperbolic increases of Di and Ri. Then, the antagonism between the negative controller R3 and the positive factors R1 and R2 induces bifurcation events at rhythmic intervals constituting about 6-7 divisions although the intervals are slightly chaotic and the vibrational amplitude is attenuated. It is stressed that this cycle of 6-7 divisions, i.e., branching time between periodic bifurcation events, corresponds to the emergence timings of blastocysts, germ layers, tissues, and organs, which can be observed for about every 6-7 cell divisions. (Figs. 1 and 2)

(a)

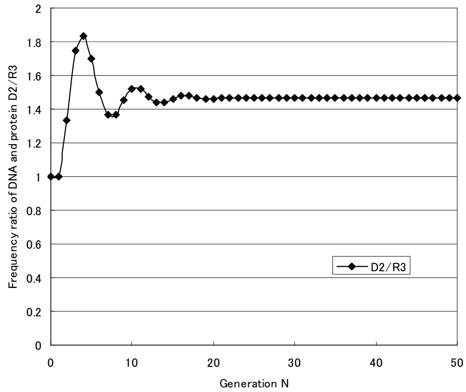

(b)

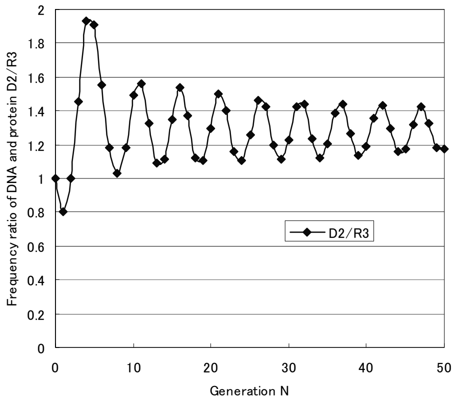

Fig.1. Time histories of D2/R3 during 50 generations of the morphogenetic process. (a) α_{i2} =1.0 and (b) α_{i2} =1.5

The flexible shapes of transcription factors may give the parameters of α_{i2} various values. However, it is stressed that three system parameters, α_{i2}, have less influence on the time cycle of bifurcations. The cycle of about 6-7 divisions is stable. (Fig. 1b) [2]

The condition of D2/R3 > 1.0 means that a part of D2 is not covered by R3. This implies that several types of proteins in D2 emerge and also several types of somatic cells are produced to make organs and tissues. The condition of D2/R3 < 1.0 means that D2 is completely blocked by redundant R3, which implies stem or iPS cells. This oscillation of D2/R3, which implies the amount of D2 uncovered by protein group R3, will lead to the changes in the gene combination for expressions. This corresponds to the fact that iPS cells can be reprogrammed by the presence of much Oct-4.

III. MORPHOGENETIC PROCESS

1. Human beings

The morphogenetic process of human beings began with the fertilization. We examine the date when each of the organs is formed. (Fig.2)

At first, we examine the early stage of the morphogenetic process, from a fertilized egg to germ layers. (Fig.3) A fertilized egg becomes blastocysts with 4 or 5 days, diploblastics with 8 or 9 days, germ layers with 15 or 16 days. Cell cycle of human beings is about 16–24 hours. Thus we can consider that embryos undergo cell division about once a day. However, the first cleavage needs about 24 hours, and the following each division before moluras needs about 12 hours. Thus, it takes 6 or 7 times of cell divisions between a fertilized egg and blastocysts, 4 or 5 times of cell divisions between blastocysts and diploblastics, and 7 or 8 times of cell divisions between diploblastics and germ layers. According to these results, we can see that important structures are formed by around 6-7 times cell divisions in the early stage of the morphogenetic process.

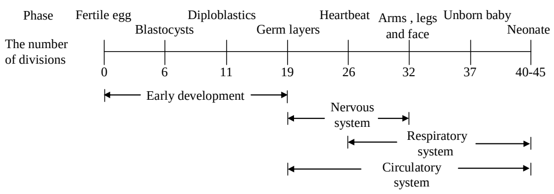

Fig.2. Simple overview of the morphogenetic process of human beings.

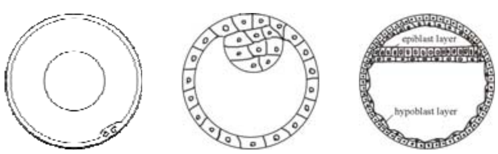

a b c

Fig.3. Morphogenetic process of early development.
(a: fertile egg, b: blastocysts, c: diploblastics) [7, 8]

Secondly, we examine the nervous system. (Fig.4) Neural plate is formed on the 18th day. After that, neural plate develops into neural tube on the 22nd or 23rd day, into primary brain vesicle on the 27th or 28th day, and into secondary brain vesicle on the 31st–33rd day. Because of this, we can suppose that neural plate undergoes 4 or 5 times of cell divisions before forming neural tube, neural tube undergoes 5 or 6 of times cell divisions before forming primary brain vesicle, primary brain vesicle undergoes 4-6 times of cell divisions before forming secondary brain vesicle. According to these results, we can see that important structures are formed by about 6 times cell divisions in the nervous system. [9]

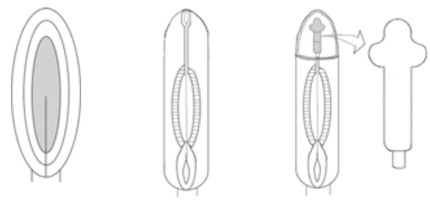

a b c

Fig.4. Morphogenetic process of the nervous system.
(a: neural plate, b: neural tube, c: primary brain vesicle) [7, 8]

Next, we will see about the respiratory system. (Fig.5) At the beginning of the respiratory system, lung bud is differentiated from foregut on the 24th-26th day. After that, lung bud develops into trachea and primary bronchus on the 29th or 30th day, into secondary bronchus on the 34th or 35th day, and into tertiary bronchus on the 41st or 42nd day. Thus, we can conclude that lung bud undergoes 4-6 times of cell divisions before forming trachea and primary bronchus, primary bronchus undergoes 5 or 6 times of cell divisions before forming secondary bronchus, secondary bronchus undergoes 7 or 8 times of cell divisions before forming tertiary bronchus. Therefore, we can see that important structures are formed by around 6-7 times of cell divisions in the respiratory system.

a b c

Fig.5. Morphogenetic process of the respiratory system.
(a: lung bud, b: trachea and primary bronchus, c: secondary bronchus) [7, 8]

Finally, let us see the circulatory system. [7, 8] At the beginning of the circulatory system, cardiogenic cord is formed on the 17th-19th day, and cardiogenic cord develops into cardiac tube on the 22nd or 23rd day. After that, common atrium is formed on the 26th or 27th day. Bilobed atrium is formed on the 30th or 31st day, while 3-chamberd heart is formd on the 34th or 35th day. The 4-chamberd heart is formed on the 48th or 49th day. Thus, we can suppose that cardiogenic cord undergoes 4-6 times of cell divisions before forming cardiac tube, cardiac tube undergoes 4 or 5 times of cell divisions before forming common atrium, common atrium undergoes 4 or 5 times of cell divisions before forming bilobed atrium, bilobed atrium undergoes 4 or 5 times of cell divisions before forming 3-chamberd heart, 3-chamberd heart undergoes 14 or 15 times of cell divisions before forming 4-chamberd heart. Therefore, we can see that some structures are formed by about 4-6 cell divisions between cardiogenic cord and 3-chamberd heart, although 3-chamberd heart and 4-chamberd heart are not formed by the cycle.

From the above investigations, we can show that most of the morphogenetic cycles of these four organs correspond to the result of section II, about 6-7 cell divisions.

2. Mouse

We also investigate about the morphogenetic process of mouse. At the morphogenetic process of mouse, blastocysts are formed on the 3rd or 4th day, germ layers and neural plate are formed on the 8th or 9th day, and neural tube is formed on the 11th or 12th day. (The emergence timings corresponding for human beings are the 4th or 5th day for blastocysts, the 15th and 16th day for germ layers, the 18th day for neural plate, and the 22nd or 23rd day for neural tube.) Then, the cell cycle of mouse is approximately half of human beings. Thus, the morphogenetic cycle, 6-7 cell divisions, will apply to the early stages of both human beings and mouse.

We should examine the later stages of the morphogenetic processes of both species further, in order to confirm the similarity.

IV. CONCLUSION

Equations 2 and 3 of the sixvariable differential equation shows the morphogenetic cycle of six-seven fold beats of cell divisions.

The experimental data on morphogenetic processes of human beings and mouse shows the possibility that important organs of mammals are formed by every 6-7 times of cell divisions.

REFERENCES

[1] Nishikawa S(Ed) (2008), Ultimate Stem Cell, Newton 6: 12-55
[2] Naitoh K (2009), Physics underling Topobiology: Space-time Structure underlying the Morphogenetic Process.
[3] Naitoh K (2008), Stochastic determinism underlying life, to be published in Artificial Life and Robotics **13** [selected from among Proceedings of 1st European Workshop of Artificial life and Robotics, 2007]
[4] Edelman G (1988), Topobiolog*y*, pp1-371(Basic Books Inc., New York)
[5] Niwa HJ, Miyazake, Smith A (2000), Quantitative expression of Oct3/4 defines differentiation, dedifferentiation, or self-renewal of ES Cells. Nature Genetics **24**: 372-376
[6] Takahashi K, Yamanaka S (2006), Induction of Pluripotent Stem Cells from Mouse Embryonic and Adult Fibroblast Cultures by Defined Factors, *Cell* **126**: 663-676
[7] T.W.Sadler, Ph.D. (2006), Langman's Medical Embryology. Medical Science International
[8] Keith L.Moore,M.Sc., Ph.D., F.I.A.C, (1988), The Developing human; Clinically Oriented Embryology. Ishiyaku Publishers, Inc.
[9] Mark F. Bear, Barry W. Connors, Michel A. Paradiso (2007), Neuroscience: Exploring the brain. Nishimurashoten 144-152

Inner-asymmetry and Outer symmetry underlying life

K. Ogata and K. Naitoh

Waseda University, Faculty of Science and Engineering, 3-4-1 Ookubo, Shinjuku, Tokyo, 169-8555 Japan
(Tel : 81-3-5286-3265)
(Email address: k-naitoh@waseda.jp)

***Abstract*:** Fusion of symmetry and asymmetry can be observed in biological molecules and cells. For example, the frequencies of purines and pyrimidines in double-strand DNA in a symmetric ratio of 1:1, while the asymmetric density ratios of purines and pyrimidines in RNA are between 1:1 and approximately 2:3.Size ratios of cells are also in the symbiotic fusion of symmetry and asymmetry. The cyto-fluid dynamic theory and onto-biology reported previously (Naitoh, 2001 & 2008) clarify the physics on the inevitability of symmetry and asymmetry underlying life. An important point is relatively inner cells among a colony divide into asymmetric ones, while outer cells on the colony surface proliferate symmetrically with an identical size. In this report, we examined the concept of inner-asymmetry and outer-symmetry by experiments.
***Keywords*: Asymmetry, Cyto-fluid dynamics, Cell divisions, Nitrogenous base.**

I. INTRODUCTION

Nitrogenous bases which construct DNA and RNA are classified into purines and pyrimidines. The frequency and size ratio of purines and pyrimidines are around 2:3.

Then the symbiotic concept of symmetry and asymmetry is a key for understanding the spatial structures in living organisms. Naitoh has shown the model based on a continuum pheroid particle (parcel) to reveal the physics underlying the fusion of inner-asymmetry and outer-symmetry: the fact that inner cells divide into different size of cells, while outer ones differentiate with an identical size. [1, 2, 3]

In the reports [1, 2, 3], the equation describing cell deformation is obtained by assuming that flow inside the parcel is potential flow, while the state outside it is empty. The present study shows that the model equation is also valid for the opposite situation: the liquid flow outside the parcel and nothing inside the parcel and also that the inner-asymmetry and outer-symmetry also occur for the situation of inner empty.

Then, we examined the concept of inner-asymmetry and outer-symmetry further by experimental observations of division processes of yeast (Saccharomyces cerevisiae).

II. CYTO-FLUID DYNAMICS THEORY

1. Assumption

A.Original Model [1, 2, 3]

Here,we will consider two nitrogenous base, such as the pair of a purine and a pyrimidine, connected by hydrogenbonds in a large quantity of water. Owing to

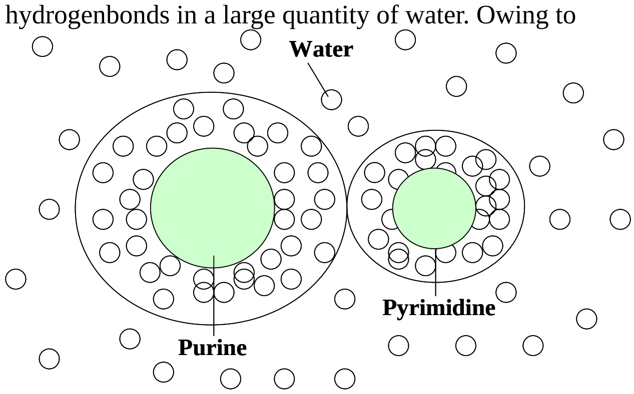

Fig.1. Hydrogen-bonded connection of purine and pyrimidine surrounded by water molecules

the influence of the nitrogenous bases, water molecules around the bases have different densities and arrays from those far away. Thus, we divide the water into two regions by drawing a boundary around bases. We assume that each nitrogenous base and the water molecules inside the boundary act as a flexible continuum spheroid particle (parcel), in which the flow is irrotational (Fig.1) Further, we assume that the spheroid particle size is proportional to the size of each nitrogenous base.

The internal flow is incompressible and irrotational flow. Then, the velocity potential ϕ for the internal flow is [3]

$$\Delta\phi = \frac{\partial^2\phi}{\partial x^2} + \frac{\partial^2\phi}{\partial r^2} = 0 \qquad (1)$$

where x, r denote the cylindrical coordinates.

Then, it satisfies the condition

$$\begin{aligned} &0 \le (x - X_s + a)^2 / a^2 + r^2 / b^2 \le 1 \\ &X_s - 2a \le x \le X_s, 0 \le |r| \le b \end{aligned} \tag{2}$$

where X_s denote the surface position related to the absolute origin [3]. Variables a and b denote the radii in the single spheroid parcel. This equation represents inside of the parcel.

The assumptions of potential flow and spheroid droplet necessarily lead to Eq. 3 on the velocity v

$$\begin{aligned} &v_x \equiv \partial\phi / \partial x = A(x - X_s + a) + d(X_s - a) / dt \\ &v_r \equiv \partial\phi / \partial r = -Ar / 2 \end{aligned} \tag{3}$$

where A is a function of time t. [3, 4] The terms of $A(x - X_s + a)$ and $-Ar/2$ representing the velocities observed at the center of gravity. The term of $d(X_s - a)/dt$ evaluate the translation motion of the parcel center of gravity. [3]

By using Eqs. (2) and (3), we show two-dimensional velocity distribution in a flexible spheroid. (Fig.2)

B. A New Model

In the cyto-fluid dynamic theory Naitoh, [1,2,3] the flow outside the flexible continuum particle is a vacuum. Here, we will derive the governing equation ofr the opposite state: inner empty. (Fig.3).

The external flow is also incompressible and irrotational flow. Then, the velocity potential ϕ' for the external is

$$\Delta\phi' = \frac{\partial^2\phi'}{\partial X^2} + \frac{\partial^2\phi'}{\partial R^2} = 0 \tag{4}$$

where X, R denote the cylindrical coordinates.

Then, X, R can be represented by using x, r (original coordinates). (See Eqs. 5 and 6.)

$$X = \frac{a^2}{x - X_s + a} \cos^2(\arctan(\frac{r}{x - X_s + a} \cdot \frac{a}{b})) + X_s - a \tag{5}$$

$$R = \frac{b^2}{r} \sin^2(\arctan(\frac{r}{x - X_s + a} \cdot \frac{a}{b})) \tag{6}$$

Then, the flow outside the spheroid parcel satisfies the condition of Eq. 7.

$$\begin{aligned} &1 \le (X - X_s + a)^2 / a^2 + R^2 / b^2 \le \infty \\ &0 \le |X| \le \infty, 0 \le |R| \le \infty \end{aligned} \tag{7}$$

The assumption of potential flow outside the parcel necessarily leads to Eq. 8 for the velocities v.

$$\begin{aligned} &v_X \equiv \partial\phi / \partial X = A(X - X_s + a) + d(X_s - a) / dt \\ &v_R \equiv \partial\phi / \partial R = -AR / 2 \end{aligned} \tag{8}$$

Equations (7) and (8) show the two-dimensional flow velocity distribution in Fig.4.

Equations 4 and 8 imply that the governing equation is also applicable for all the cases where inner density differs from that of outer area, even if both inner and outer regions are not empty.

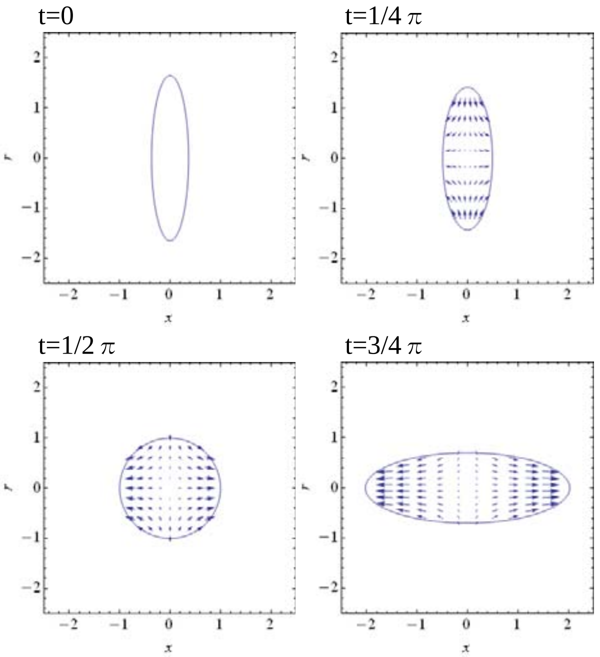

Fig.2. Velocity distribution of the parcel inside (Flow velocity satisfies the following conditions.
($A = \sin t$, $a = e^{-\cos t}$, $b = e^{-\sin t/2}$, $X_s = a$)

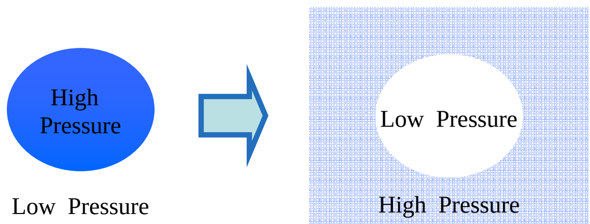

Fig. 3. The condition changed in the model

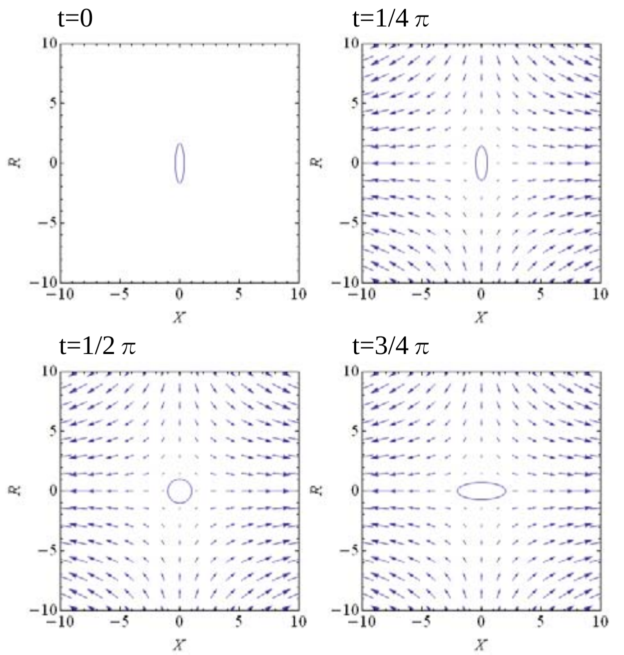

Fig.4. Velocity distribution of the parcel outside.
($A = \sin t$, $a = e^{-\cos t}$, $b = e^{-\sin t/2}$, $X_s = a$)

2. Size of Parcel

Based on these assumptions in Section II.1, we derive the common deterministic momentum equation describing particle deformation. [1,2,3] When a small disturbance is given for two connected flexible particles, the dimensionless deformation ζ of each particle, dependent on dimensioless time τ, can be described as

$$d^2\zeta/d^2\tau = (e-1)(d\zeta/d\tau)^2 + (e^3-3)\zeta + q(\tau) \qquad (9)$$

where parameter e and term $q(\tau)$ denote the size ratio of the two particles connected at the equilibrium condition and the time-dependent force generated by the other connected particle, respectively. Equation 9 can be applied for all the cases where density varies between inner and outer regions, when we want to know the quasi-stable ratio of e.

When the particles are spheres at the equilibrium condition, ζ is zero. A symmetric ratio of 1.0 makes the first term on the right-hand side of the equation zero, while an asymmetric ratio of $\sqrt[3]{3}$ around 1.5 makes the second term zero. The deformation speed is smaller for e=1.0 and $\sqrt[3]{3}$ than for the other values of e.

Life is relatively quasi-stable when the size ratio of hydrogen-bonded nitrogenous bases takes the values of 1.0 and $\sqrt[3]{3}$ around 1.5.

The present quasi-stability maintains the hydrogen-bonded pairs of two identical bases and of purine-pyrimidine pairs over a period of time at the initial stage just after the small disturbance affects the pairs. (Pairs of two identical bases can often be seen in RNA, while purine-pyrimidine pairs are numerous in RNA and DNA.)

It is stressed that the flow inside the flexible continuum particle is potential flow, i.e., irrotaional flow, because impulsive disturbances generate potential flow at the start of deformation motions. (It is well known that an impulsive start produces irrotational flow, which also satisfies the Navier-Stokes equations.) [1,2,3]

III. SPATIAL STRUCTURE OF CELL [1]

The cyto-fluid dynamic theory [1,2 3] also clarifies the relation between small deformation and asymmetric division for the aggregation of cells such as those in a colony, because a cell is also a flexible continuum spheroid particle.

Let us separate cell aggregation into two parts, the internal side around the center of the aggregation and the external side close to the surface. External cells close to the surface move relatively easily under the influence of inhomogeneous force, because one part of the cell is free without any connection to other cells. However, internal cells often receive homogenous forces from many directions due to the presence of other cells, making it relatively difficult for them to move relative to the origin on the earth. Thus, inner cells deform relatively easily. (Fig.5) As a result, the inner and outer cells determine whether cell divisions are asymmetric or symmetric, respectively. [1,2]

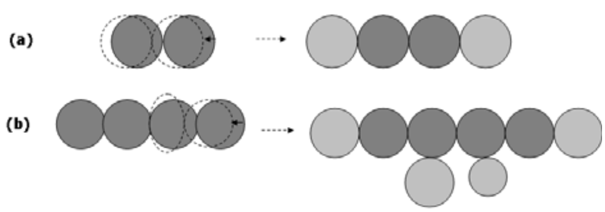

Fig. 5. Division pattern related to neighboring states of cells.

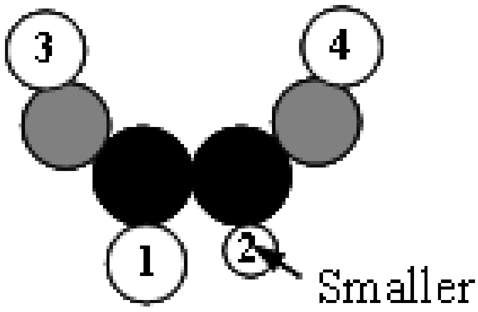

Fig. 6. Cell division process of Saccharomyces cerevisiae.

Let us examine the cell division process of yeast (Saccharomyces cerevisiae), because symmetric and asymmetric size ratios are also observed at the cell level of microorganisms. We cultivated Saccharomyces cerevisiae at a constant temperature of 37 degrees Celsius on a warm plate and observed continuously under a microscope until eight cells were formed. Figure 6 shows that internal mother cells (black) generate child cells in asymmetric division, while external mother cells (gray) produce symmetric ones. Figure 7 shows the relation of the size ratio of inner cells (1/2) and that of outer ones (3/4). Inner cells divide into more asymmetric size ratios, while most of outer cells are close to symmetric ones.

IV. CONCLUSION

The cyto-fluid dynamic theory is extended for a wide range of density variations between inner and outer regions of parcels.

Asymmetric and symmetric size ratios are also observed at the cell level of microorganisms. For example, internal mother cells generate child cells in asymmetric division, while external mother cells produce relatively symmetric ones in Saccharomyces cerevisiae.

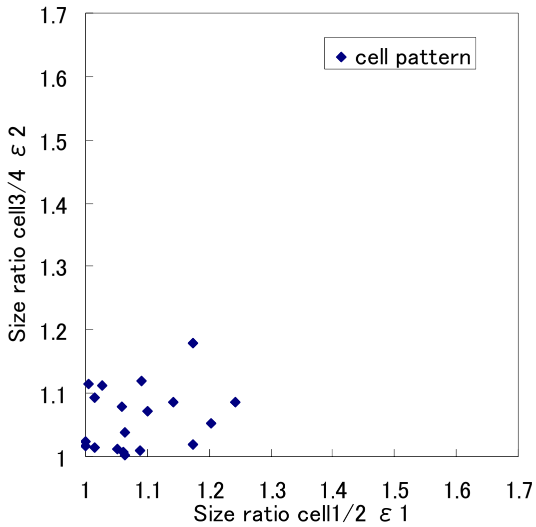

Fig.7. Relation between the size ratios between inner cell 1/2 and outer cell 3/4

REFERENCES

[1] Naitoh K, (2009) Physics underling Topobiology: Space-time Structure underlying the Morphogenetic Process, IFMBE Proceedings Vol.23.

[2] Naitoh K, (2008) Stochastic determinism underlying life: systematic theory for assisiting the sythesis of artificial cells and new medicines, Artif Life Robots (2008) 13:10-17

[3] Naitoh K, (2001) Cyto-fluid Dynamic Theory, the JAPAN JOURNAL OF INDUSTRIAL AND APPLIED MATHEMATICS Vol.18. No.1, pp. 75-105.

[4] Brazier-Smith, P.R., (1971) The stability of a water drop oscillating with finite amplitude in an electoric field, J. of Fluid Mechanics, Vol.50, part3.

[5] Kataoka K and Ioi T, (1993) Fundamental of Mechanical Vibration, CORONA PUBLISHING (in Japanese)

Entrainment of a circadian clock *in vitro*

Hiroshi Ito[1], Takuya Yoshida[2], Yoriko Murayama[2], Masato Nakajima[2] and Takao Kondo[2]

[1]*Academic Production, Ochanomizu University, 2-1-1, Ohtsuka, Bunkyo, Tokyo, Japan*
[2]*Graduate school of Science, Nagoya University, Furocho, Chikusa, Nagoya, Japan*
(TEL: +81-3-5978-5067; E-mail:ito.hiroshi@ocha.ac.jp)

Abstract: Circadian rhythms are the physiological oscillations with about 24 h periods that have period stability under various circumstances. While gene regulatory feedback loop has been proposed for the model of the origin of the circadian oscillation, my colleagues and I had proposed an alternative model. The cyanobacterial circadian clock can be reconstituted in vitro only by mixing the three clock proteins, KaiA, KaiB, and KaiC, with ATP. Namely, the ratio of phosphorylated KaiC oscillates every 24 h in the mixture. This simple biochemical reaction shows self-sustained oscillation like Belosov-Zhabotinsky reaction. Thus, KaiC phosphorylation rhythm can be core oscillator producing cyanobacterial circadian clock. In this paper, I will discuss entrainment of the "in vitro clock" by temperature cycles.

Keywords: Circadian clock, Cyanobacteria, Entrainment, in vitro clock, KaiC phosphorylation

I. INTRODUCTION

Circadian rhythms are the physiological oscillations with about 24 h periods; it can organize behavior to match the alternating day/night environment. All circadian clocks share three prominent characteristics. First, clocks generate self-sustained oscillations under constant conditions with ~24 hour period. Second, unlike typical biochemical processes, the period of circadian clocks is robust against environmental changes, such as temperature conditions or nutrient in medium. Third, circadian clocks can be entrained to external time cues derived from day/night alternation.

Cyanobacteria, a kind of prokaryote, is one of extensively studied model organism. Before 2005, transcription/translation feedback loop system had been proposed for the model of the origin of cyanobacterial circadian oscillation [1]. The mechanism was also proposed as a clock mechanism of the other model organisms, e.g. mammalian, fishes, flies and plants. However, we recently succeeded in reconstitution of minimal circadian oscillator without transcriptional processes. We incubated the three recombinant Kai proteins (KaiA, KaiB, KaiC) in vitro (in a test tube) with ATP at 30 ºC. Surprisingly, a self-sustained oscillation of KaiC phosphorylation with a 24 hours period was observed [2]. In other words, the ratio of phosphorylated KaiC to total KaiC autonomously oscillated. Furthermore, period of the oscillation was compensated under a variety of ambient temperature. Thus, the first and second characteristics of the in vitro clock had been already shown. In this paper, we will focus on the last property, entrainment of the in vitro clock.

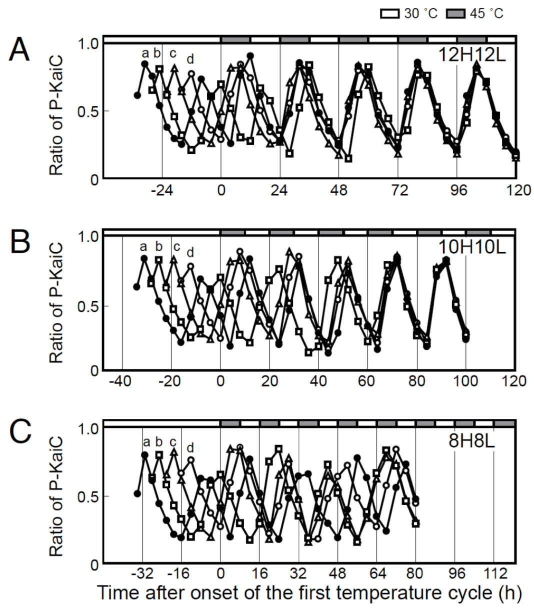

Fig.1 Temperature entrainment of *in vitro* clock

II. TEMPERATURE ENTRAINMENT OF IN VITRO OSCILLATOR

Daily alteration of both light and temperature are the main time cues that can entrain the circadian clocks. Here, we chose temperature cycles as an external cue because any Kai proteins are not concerned as photoreceptors. If a self-sustained rhythm is entrained by an external cycles, the period of the rhythm should adjust to the external cycle and the peak of the rhythm should be locked at a unique phase of the external cycle. To test whether the in vitro KaiC phosphorylation rhythm could be entrained by a temperature cycle, we prepared four mixtures of Kai proteins at 6 hours intervals. Under constant conditions (30 °C), the rhythm persisted with a period of 23.1 ± 0.23 h (n=4), maintaining the phase angle differences determined by the time of mixing. Next, we exposed the four mixtures to temperature cycles of 12 h at 45 °C and 12 h at 30 °C (12H12L). As depicted in Fig. 1A, the peaks of the four KaiC phosphorylation rhythms were locked at the same phase and the periods of the four mixtures were extended to 24 h (23.9 ± 0.22 h, n=4). As shown in Fig. 1B, the 10H10L regimen also entrained the rhythm, as the period approached 20 h (19.9 ± 0.24 h, n=4) after the 4th cycle. In contrast, under 8H8L temperature cycles, the interval between peaks changed from cycle to cycle (18.4 to 24.4 h) and the peaks did not come together (Fig. 1C). Thus, in vitro clock could be entrained by 12H12L and 10H10L temperature cycles, but not by an 8H8L cycle.

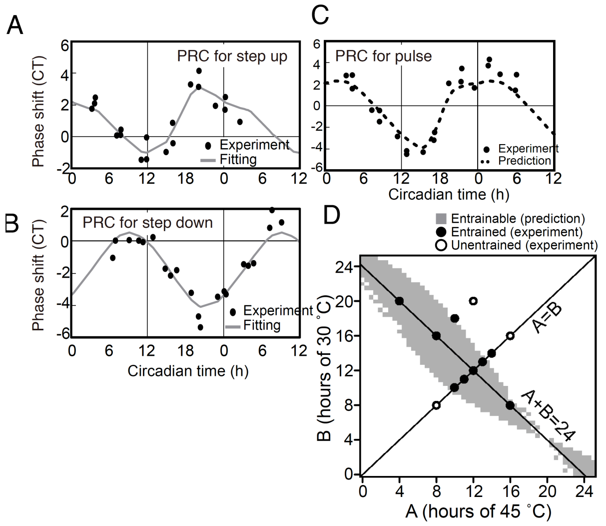

Fig.2 Phase Response curve (PRC) and Range of entrainment

III. PHASE RESPONSE AND RANGE OF ENTRAINMENT

Next we considered how the proteins sense the temperature cycles and adjust to them. We hypothesized that the temperature entrainment of in vitro rhythm might be due to discontinuous jumps in phase caused by temperature steps. To examine this possibility, we analyzed the effects of temperature shifts from 30 to 45 ^{o}C (step-up) and 30 to 45^{o}C (step-down) on the rhythm. As shown in Fig. 2AB, the rhythm was shifted by temperature step stimulus. Step-up and step-down tends to make the rhythm advanced and delayed, respectively.

If the rhythm can sense the step temperature stimulation, phase shifting by temperature pulse is assumed to be the sum of phase shifts caused by step-up and step-down. If a phase shift by temperature step-up is completed before step-down, the phase shift $\Delta(\phi)$ of the high-temperature pulse at phase ϕ is calculated by the following equation:

$$\Delta(\phi) = f(\phi) + g\left(\phi + f(\phi) + 24A/\tau\right) \qquad (1)$$

where $f(\phi)$ and $g(\phi)$ respectively represent phase shift by step-up and step-down. We examined actual phase shifting by administering 4 h pulses at various times. Fig. 2C depicts phase shifts caused by 21 different temperature pulses ranging across the circadian cycle. On the other hand, we calculated phase shifting by 4 h high temperature pulses using equation (1) and overlaid the results with the observed phase shifts. As shown in Fig. 2C, the predicted PRC correlated well with the experimental results, suggesting that our hypothesis works in this biochemical oscillator.

Furthermore, we predicted a range of entrainment by cycles of various fractions of high and low temperature. When stable entrainment is attained under a cycle of A h at high temperature and B h at low temperature, equation (2) should be satisfied with a specific phase of ϕ_s (phase of onset of high temperature in entrained status), because under entrained conditions, the difference in free-running period of the rhythm and external cycle length should be compensated by two phase shifts accompanied by a temperature cycle.

$$\tau - (A+B) = \left(f(\phi_S) + g\left(\phi_S + f(\phi_S) + 24A/\tau\right)\right)\cdot(\tau/24) \qquad (2)$$

As shown in Fig. 2D, most of the temperature cycles that entrained the rhythm (closed circle) fell within the predicted range of entrainment. On the other hand, protocols that failed to entrain the rhythm (open circle) fell outside the range.

Temperature entrainment of circadian rhythms has been studied in many organisms as far. An extensive study of the eclosion rhythm of *Drosophila* demonstrated that temperature entrainment could be similarly ascribed to phase shifting by discontinuous temperature changes. Entrainment induced by discontinuous phase jump may be a common principle for temperature entrainment, because temperature can shift the phase of the rhythm but fails to alter period length due to temperature compensation of period.

REFERENCES

[1] Ishiura M (1998), Expression of a gene cluster kaiABC as a circadian feedback process in cyanobacteria. Science 281:1519-1523
[2] Nakajima M (2005), Reconstitution of circadian oscillation of cyanobacterial KaiC phosphorylation in vitro Science 308:414-415

Delay, Noise and Resonance: Human balancing and temporal non-locality

Toru Ohira

Sony Computer Science Laboratories, Inc.
3-14-13 Higashigotanda, Shinagawa, Tokyo 141-0022
(Tel : 81-3-5448-438-0; Fax : 81-3-5448-4273)
(ohira@csl.sony.co.jp)

Abstract: We would like to present here a rather peculiar observation during human stick balancing at his fingertip. It is observed that the balancing time improves when the subject moves objects with the other hand. This is particularly so for many subjects with medium skill of stick balancing. Based on this example, we would like to consider how this seemingly simple task is composed of intricate mixtures of feedback delay, fluctuations, and predictions. We will present some simple models of dynamics in which these factors lead to complex behaviors. It is inferred, from these examples, that the concept of "non-locality" could possibly play an important role in characterizing biological and physiological systems.

Keywords: Delay, Noise, Resonance, Balance Control, Non-locality

I. INTRODUCTION

Stick balancing in upright position is a topic which has been investigated much in mechanics and control theories. Human stick balancing on his fingertip appears as a very simple task. It is, however, rather intricate combination of physiological feedback delays, predictions under the influence of fluctuations. In particular, we have found that if one moves objects with the other hand, balancing of sticks becomes easier. This rather unexpected effect indicates that human stick balancing could be far different from the ones studied in control engineering. From this effect, we would like to discuss if the concept of "non-locality" could play an important role in describing biological and physiological systems.

II. STICK BALANCING

Let us describe the experiment of human stick balancing. A subject is asked to sit on a chair and balance on his fingertip a wooden stick of about half a meter length. In the original experiment done by Milton and Cabrera[1-3], they measured the time duration of balancing a stick before its fall as well as tracking the motions of the top of the stick and the fingertip. They found that the motion of the stick shows small amplitude fluctuations with intermittent large movements. Our experiment is to add in an extra fluctuations or rhythmic movements on this basic experimental paradigm[4-6]. The motivation to introduce such external fluctuations comes from inference to the effect of stochastic resonance (Fig 1), which we shall describe briefly in the next section.

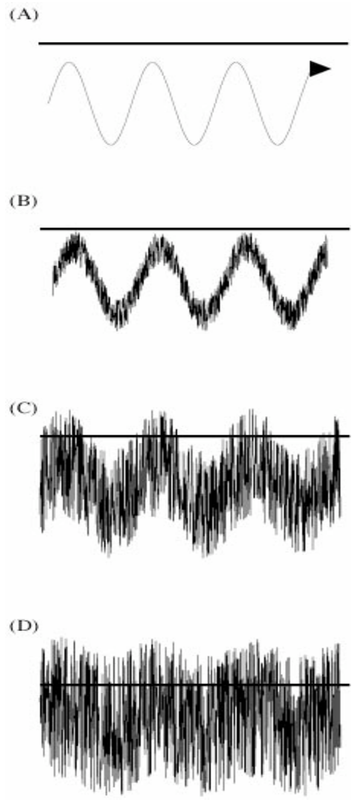

Fig.1. Schematic view of Stochastic Resonance. (A) a sub-threshold incoming oscillatory signals. (B) Small amplitude noise added, but still undetectable. (C) Appropriate amplitude noise added, the signal is now detectable and reflecting some nature of underling oscillatory signals. (D) Too large amplitude noise added, detectable but incoming signals characteristics are lost.

III. STOCHASTIC RESONANCE

Normally, noise or fluctuations are considered as an obstacle to information processing systems. However, in nature, there appear to exist examples that noise has a beneficial effect through a resonance like effect. These systems are investigated under the name of "Stochastic resonance"[7-9]. One representative example is the detection of sub-threshold oscillating signals with added noise of appropriate strength (Fig.1). Other types of mechanisms have been also investigated, leading to variety of applications[10-15]. This concept of beneficial effect of fluctuations motivated us to consider it in the context of stick balancing.

IV. STICK BALANCING WITH FLUCTUATIONS

Based on the inference from stick balancing, we have added fluctuations in various ways during human stick balancing. The original idea was to shake a bottle of water with the other hand (Fig. 2). Then, we have tried subjects to stand on a vibrating platform. On both schemes, we have found the following.

(1) It takes a bit of practice to balance a stick with added fluctuations.

(2) However, for people with medium level of skill in the stick balancing, added fluctuation leads to longer balancing time.

(3) For those people with poor or very good skills, added fluctuations did not help or acted as a disturbances in balancing.

Fig.2. A subject moving an object while balancing a stick

Typically, the improvement in balancing time with added fluctuations ranged from 20 to 50 percent.

Our current hypothesis on this effect is as follows. We tend to view ourselves like a machine which could control the stick very fast with our visual feedback and predictions of its motion. However, in reality this control is highly unstable, and due to our physiological delay, our control ability is not fast enough or accurate enough to keep stick balancing, if we rely too much on our feedback loop. Thus, it is constructive to cut this reliance on the feedback control loop occasionally. The added fluctuations help in this cutting of the control loop at appropriate levels.

We should note that there is a mathematical study on so-called "wait and act" controls[16-18] which are proved to be effective in the presence of delay in the feedback control loop. It requires a further investigation to see if the added fluctuations in the human stick balancing task relates to the framework of such controls.

V. NON-LOCALITY IN BIOLOGICAL SYSTEMS

Another issue which emerged from our experiment is the question if the concept of "non-locality" could be important in characterizing biological and physiological systems. Moving an object with the one hand, at first sight, would have nothing to do with the balancing of the stick on the other hand. At least, it goes outside of the traditional thinking of engineering. Also, delay could be considered as non-locality[19,20] on the time axis in the sense the system's behavior is not only decided by its current state, but also depends on a separated temporal point in the past. So, even in this seemingly simple task of stick balancing may involve various factors in both spatial and temporal non-localities. In physics, the concept has been puzzling separating classical and quantum physics and still much effort is underway to understand its nature. It could be also true that the concept of "non-locality", though probably different from that of physics, may serve to characterize biological or physiological systems.

VI. CONCLUSION

In this paper, we have introduced our observation that added fluctuations help in human stick balancing controls. It may be considered as another example of

Stochastic Resonances. Also, we inferred that concept of non-locality in both space and time may be important in biological systems, which requires more explorations.

ACKNOWLEGEMENTS

I would like to thank Prof. J G. Milton and Dr. J. L. Cabrera for their collaboration with stick balancing experiments. Thanks also go to Mr. Shigeru Tajima and Dr. Y. Tonosaki for their constructions of stick balancing machines and discussions of engineering control systems. This work was in part supported by National Science Foundation of the United States of America (Grant 0617072).

REFERENCES

[1] Cabrera, JL and Milton, JG (2002)
On-Off Intermittency in a Human Balancing Task
Physical Review Letters 89: 158702

[2] Cabrera, JL and Milton, JG (2004)
Human stick balancing: Tuning Lévy flights to improve balance control
Chaos 14: 691

[3] Cabrera, JL and Milton, JG (2004)
Stick balancing: On-off intermittency and survival times
Nonlinear Studies 11: 305

[4] Cabrera, JL et. al. (2004)
State-dependent Noise and Human Balance Control
Fluctuation Noise Letters 4: L107

[5] Hosaka, T et. al. (2006)
Balancing with Noise and Delay
Progress of Theoretical Physics, Suppl. 161: 314

[6] Milton J et. al. (2009)
Balancing with Vibration: A Prelude for "Drift and Act" Balance Control
PLos One, 0007427

[7] Wiesenfeld K and Moss F (1995)
Stochastic resonance and the benefits of noise: from ice ages to crayfish and SQUIDs
Nature 373: 33

[8] Bulsara AR and Gammaitoni L (1996)
Tuning in to noise
Physics Today 49: 39

[9] Gammaitoni L et. al. (1998)
Stochastic resonance
Rev. Mod. Phys. 70: 223

[10] McNamara B et. al. (1988)
Observation of Stochastic Resonance in a Ring Laser
Phys. Rev. Lett. 60: 2626

[11] Longtin A et. al. (1991)
Time-interval sequences in bistable systems and the noise-induced transmission of information by sensory neurons
Phys. Rev. Lett. 67: 656

[12] Collins JJ et. al. (1995)
Stochastic resonance without tuning
Nature 376: 236

[13] Ohira T and Sato Y (1999)
Resonance with Noise and Delay
Physical Review Letters 82: 2811

[14] Chapeau-Blondeau F (2003)
Stochastic resonance for an optimal detector with phase noise
Sign. Process. 83: 665

[15] Lee I et. al. (2003)
Nanosignal Processing: Stochastic Resonance in Carbon Nanotubes That Detect Subthreshold Signals
Nano Letters 3: 1683

[16] Flugge--Lotz, I
Discontinuous and optimal control (1968)
(McGraw--Hill, New York)

[17] Insperger, T (2006)
Act-and-wait concept for time-continuous control systems with feedback delay
IEEE Trans. Control Sys. Tech. 14: 974

[18]Insperger T and Stepan G (2007)
Act-and-wait control concept for discrete-time systems with feedback delay
IET control theory & applications 1:33:553-557

[19] Ohira T (2009)
Temporal Stochasticity and Non-locality
Journal of Statistical Mechanics P01032

[20] Ohira T (2007)
Stochasticity and Non-locality of Time
Physica A 379: 483

The Fifteenth International Symposium on Artificial Life and Robotics 2010 (AROB 15th '10),
B-Con Plaza, Beppu,Oita, Japan, February 4-6, 2010

Robots' Action Control of Autonomous Decentralized FMS by Remorse Mind

Hidehiko Yamamoto[1], Keisuke Ikebuchi[2], Takayoshi Yamada[3]

[1]*Department of Human and Information Systems, Gifu University, Japan*
(yam-h@gifu-u.ac.jp)
[2]*Graduate School of Engineering, Gifu University, Japan*
(n3128002@edu.gifu-u.ac.jp)
[3] *Department of Human and Information Systems , Gifu University, Japan*
(yamat@gifu-u.ac.jp)

***Abstract*:** This paper describes the control of moving robots in an autonomous decentralized flexible manufacturing system (FMS) by "changes in the mind" of the moving robots. In an autonomous decentralized FMS, many moving robots are operating, and path interference problems occurred. It is very difficult to grasp the innumerable path interference situations that really occur. Therefore, to avoid these unexpected situations flexibly, we used mind model. In this way, we could solve path interference problems. However, the previous mind model we proposed had problems while taking evasive action. Robots having the previous proposed mind model are inefficient in solving path interference problems. Therefore, we propose a new mind model that can allow robots to avoid path interference efficiently.

Keywords: Robot moving collision, FMS, AGV, Path interference, Mind

I. INTRODUCTION

Today, a robot's actions is made by determined control rules. Robots cannot do anything without determined controls. Therefore, robots needed to be adaptable and designed for all situations.

In this paper, the human mind is used as a model to solve this circumstance. Humans can cope with many situations and can modify their action by thinking for themselves. If we can provide a humanlike mind to robots, they will be able to perform complicated operations and will be able to adapt to every situation. In this research, we propose a mind model that allows robots to act flexibly.

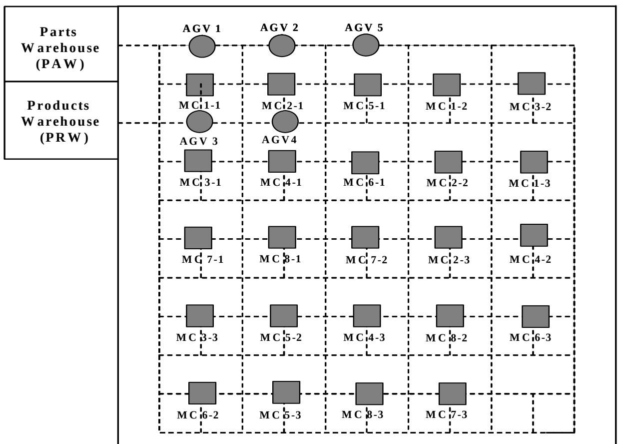

Fig.1 Autonomous decentralized FMS

II. AD-FMS

1. AD-FMS

In this paper, we adopt Autonomous Decentralized Flexible Manufacturing System (AD-FMS), an autonomous distributed system, as the production system of a virtual factory.

Figure.1 shows the AD-FMS model. In the AD-FMS, many moving robots called Automated Guided Vehicles (AGVs) are in use. AGVs carry parts and the completed product to the warehouse and a machining center (MC) [1].

2. Problems of AGV moving control

In the AD-FMS, path interference problems occur when many AGVs are in operation. There is an existing method we developed called Algorithm Avoid AGVs (AAA) which avoids these interference problems by knowledge exchange [2]-[4]. Even with this method, it is very difficult to identify the innumerable path interference situations that really occur. Therefore, to avoid these unexpected situations flexibly, we use the mind model.

III. REMORSE MIND

1. Element of mind

We proposed that the mind model is not static but changes ambiguously. The mind model is the combination of three elements: Stimulation Vector, Unit and Load.

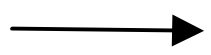

Fig.2 Stimulation vector

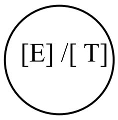

Fig.3 Unit

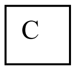

Fig.4 Load

The function of the Stimulation Vector shown in Fig.2 is to link the Unit and the Load. If the stimulation signal is sent to the Stimulation Vector, the stimulation signal is sent to either the Unit or Load to indicate the arrow direction.

Figure.3 shows the schematic figure of the Unit with the variables Excited Degree [E] and threshold value [T]. [E] of Unit A is shown as A[E]. Below, Unit A is shown as just A. Similarly, [T] of A is shown as A[T]. The increase or decrease of [E] depends on the value of stimulation. If [E] exceeds [T], [E] is decreased to [T] and its Unit will send an output stimulation signal in the direction of the Stimulation Vector arrow. In this way, the Unit function will receive an input stimulation signal and send an output stimulation signal. When [E] and [T] are equal, the Unit state is called "Excited". Meanwhile, when [E] is lower than [T], the Unit is said to be in a "Calm" state. These two states can be changed and the change corresponds to a mind change.

The Load shown in Fig.4 has one numerical value plus or minus called the control value. The Stimulation Vector links the Load with the Unit. If a stimulation signal is sent to the Load, [E] of the Unit is added or reduced by Control Value of the Load.

2. Basic mind model

Figure.5 shows the basic model of AGV that consists of three Stimulation Vectors, two Units (A,B), and a Load α with random negative numerical values.

Figure.6 shows the work of the basic mind model. In AD-FMS environment, AGVs can determine each other's positions by exchanging their information[4]-[5].When one AGV-1 gets closer to the other AGV, the possibility for the path interference is input into the mind of A. Subsequently, the mind outputs one of the two actions by the two states of its A, Calm and Excited.

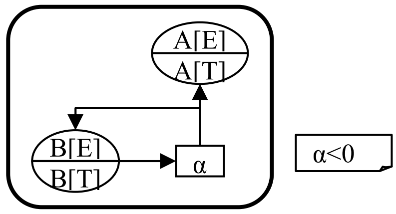

Fig.5 Basic mind model of AGVs

We call the mind with state A Calm as arrogant and that of state A Exited as modest.

When the arrogant AGV and the modest AGV gets closer, the arrogant AGV forces itself ahead, while simultaneously, the modest AGV clears the path so that the arrogant AGV can pass.

When the two arrogant AGVs get closer and path interference occurs, AGVs stimulate their individual mind by sending A the signal to increase A[E]. A gets Excited when A[E] equals A[T]. As a result, one of the AGVs becomes modest and both AGVs can avoid path interference.

In contrast, when the two modest AGVs get closer and try to mutually concede the path, AGVs stimulate their individual minds by sending B the signal to increase B[E]. B gets Excited when B[E] equals B[T] and sends a signal to α. Load α sends a stimulation to Units A and B to decrease A[E] and B[E] by random integers from 1 to A[T] and from 1 to B[T]. As a result, Unit A becomes Calm and the AGV with its Unit A becomes arrogant.

In this way, as for Unit A, the state of A changes (Excited ⇔ Calm) by path interference or mutual concessions. This change corresponds to a mind change. The mind whose state of A is Calm behaves like an arrogant AGV and the mind whose state of A is Excited behaves like a modest AGV.

When many AGVs get closer, AGVs avoid path interference by repeating the mind change.

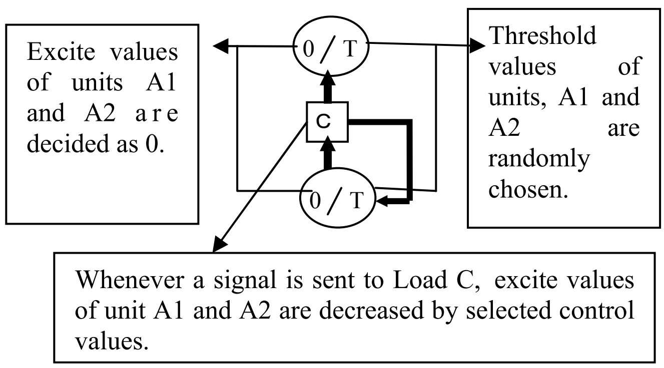

Fig.6 Work of basic mind model

3. Problems of a basic mind model

The number of path interferences is reduced to 0 by the mind we developed before [5]. However, the basic mind model has other problems when taking evasive action.

We know that the number of bad evasions is the same as the number of a good evasions. This means that AGVs with a basic mind inefficiently avoid path interference inefficiently. Table.1 shows the number of the both evasive actions.

Table.1 Date of evasion

Good evasion	Bad evasion
33	32

Good evasion means that the AGV that is far from the goal gives way to the AGV that is close to the goal.

Bad evasion means that the AGV that is close to the goal gives way to the AGV that is far from the goal.

Thus, we focus on AGVs evasive actions. We propose the new mind model that can increase the number of good evasions.

4. Remorse mind

Figure.7 shows the new mind model. We call it the "remorse mind". We propose that this remorse mind can control the tendency of mind change by estimating its own situation. We call this action "Remorse" like human remorse.

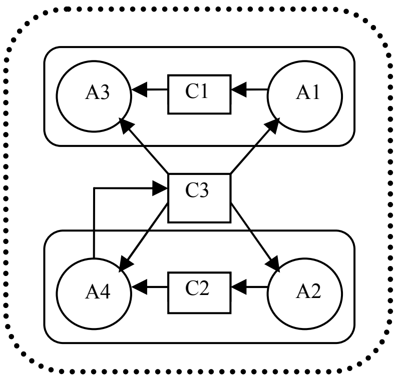

Fig.7 Model of remorse mind

5. Constructive features of remorse mind

We will explain constructive features of the remorse mind, which has three Loads and four Units. The control value of one Load is minus. The others are plus. Figure.8 shows the structure of the remorse mind. We show that the remorse mind consists of the structure of a basic mind model, which is defined as a core structure that a certain structure has the same structure inside.

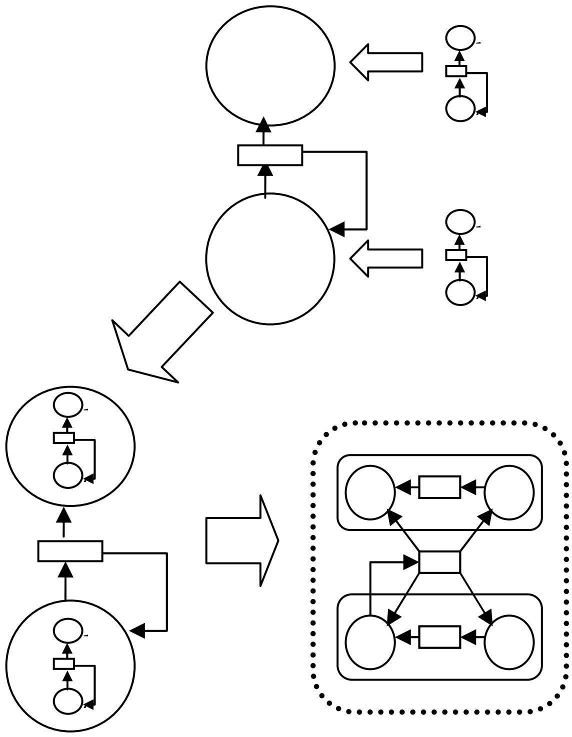

Fig.8 Structure of remorse mind

6. Functional features of remorse mind

AGVs with a remorse mind can evaluate their own situation by referring to their distance to the Goal. AGVs always have information on both their current position and the goal. This information is always being refreshed. AGVs can calculate the distance to the goal based on this information.

AGVs with remorse mind can control the control value [X] and [Y] by the distance to the goal point. If AGVs get closer to the goal, the remorse mind tends to become arrogant. Then, [X] becomes higher than [Y]. If AGVs are far from the goal, the remorse mind tends to become modest (Fig.9). Then, [Y] becomes higher than [X]. Figure.10 shows the remorse mind that tends to be arrogant.

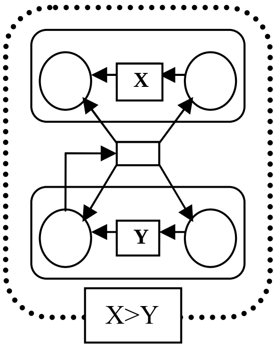

Fig.9 Tend to be modest

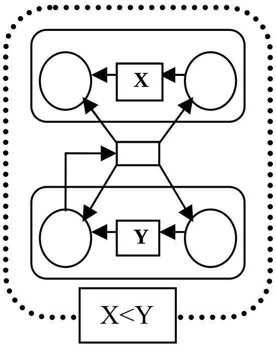

Fig.10 Tend to be arrogant

IV. SIMULATION EXPERIMENTS

In this paper, we applied the remorse mind to AGVs in an AD-FMS that was computer modeled and on which production simulations were performed.

In addition, to compare the conditions of the remorse mind with the condition of the basic mind model, the simulations of the basic mind model were performed.

Figure.11 shows the layout of the AD-FMS factory.

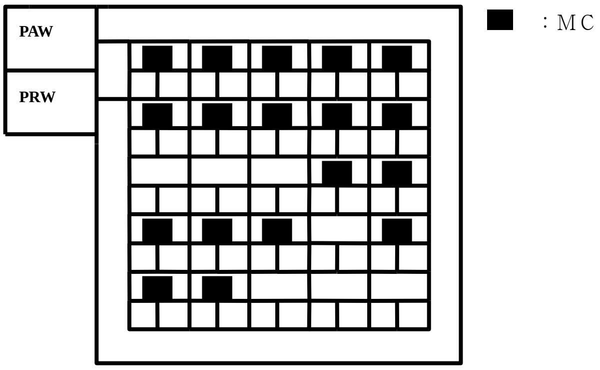

Fig.11 Layout of simulation

V. SIMULATION RESULTS

Table.2 shows the simulations results (the volume of production, average efficiency of machining centers, and the number of good and bad evasions).

The results shown in Table.2 reveal that the number of good evasions is increased and the number of bad evasions is decreased significantly. Therefore, one can say that AGVs that have the remorse mind can efficiently avoid path interferences rather than AGVs that have the basic mind model..

Table.2 The Simulation Results

	Outputs	Average Efficiency	Good evasion	Bad evasion
Basic mind	266	29.9	33	32
Remorse mind	268	30.0	42	5

Both the volumes of production and the average efficiency of machining centers of the remorse mind were better than those of the basic mind model.

VI. CONCLUSIONS

In this paper, we proposed the remorse mind model of AGVs that can efficiently avoid path interference situations better than the basic mind model. Comparing the proposed remorse mind model with the basic mind model, we were able to obtain better results that reduced the number of bad avoids by 15.6%.

REFERENCES

[1] H.Yamamoto and E.Marui(2003), Intelligent Real-time Production Control To Realize Autonomous Decentralized FMS, Proceedings of International Conference on Industrial Engineering and Production Management

[2] H.Yamamoto and R.Bin Ramli(2006), Real-time Decision Making of Agents to Realize Decentralized Autonomous FMS by Anticipation, International Journal of Computer Science and Network Security, VOL.6 No.12, pp.7-17

[3] H.Yamamoto and E.Marui(2001), Decentralized Autonomous FMS Control by Hypothetical Reasoning including Discrete Simulator, The Fourteenth Internationl Conference on Industrial & Engineering Applications of Artificial Intelligence & Expert Systems (IEA/AIE-2001), Lecture Notes in the Computer Science/Lecture Notes in Artificial Intelligence series. Springer-Verlag, pp.571-581

[4] H.Yamamoto(2000), AGV's Actions Decision by Reasoning to Anticipate Future in Decentralized Autonomous FMS, CD-ROM Proceedings of 2000 Japan-USA Symposium on Flexible Automation, ASME

[5] H.Ymamoto and S.Kato(2007), AGV Action Control of Autonomous Decentralized FMS by Fickleness, Proceedings of the 4th International Conference on Leading Edge Manufacturing in 21st Century (LEM21), Fukuoka, pp.923-928

The Fifteenth International Symposium on Artificial Life and Robotics 2010 (AROB 15th '10),
B-Con Plaza, Beppu,Oita, Japan, February 4-6, 2010

Improvement of a Software Estimate Efficiency Centered PSP Practice Support System Using Multiagent Techniques

Daisuke Yamaguchi[1], Ayahiko Niimi[2] and Muneo Takahashi[1]

1:Toin University of Yokohama, 1614 Kurogane-cho, Aoba-ku, Yokohama, JAPAN
2:Future University-Hakodate, 116-2 Kamedanakano-cho, Hakodate, Hokkaido, JAPAN
yamaguti@intlab.toin.ac.jp

***Abstract*: In this paper, we propose the PSP Practice Support System necessary to efficiently of estimative capabilities of software. This system can transmit programming to specific human among many software processes using a Multiagent technology. The system is also synthesized to do parallel and cooperative proposing internally. Applying the proposed method to a personal process-removing task, a flexible programming for quality of software. Software developments depend on information, which is possible to collection of personal process. Agent planning has get use working data on user action and other communication. Therefore collection of all user data is necessary for agent learning. Agent studies the best transmission programming, planning and quality according to the makes planning in the personal process.**

Keywords: Multi-Agent System, Personal Software Process, Software Engineering, Artificial Intelligence

I. INTRODUCTION

An agent is a computational entity such as a software program or a robot, and can be viewed as perceiving and acting upon its environment. This agent is autonomous in that its behavior at least partially depends on its own experience.

Multiagent systems have the capacity to play an important role in developing and analyzing models and theories of interactivity in human societies. Humans interact in various ways and at many levels: for instance, they observe and model one another, they request and provide information, they observe and model one another, they request and provide information, they negotiate and discuss, they develop shared views of their environment, they detect as terms, committees, and economies. Many interactive processes among humans are still poorly understood, although they are an integrated part of our everyday life. Multiagent technologies enable us to explore their sociological and psychological foundations.

PSP support system is built using this. Moreover, We think that the data inputted can acquire software development process by sorting out using a user action record table.

In this paper, the PSP system of programming is built and the analysis data of Multiagents learning method. Generally, software process data is complicated, and when building a support system using such data including some action time, the calculation with expression is difficult in many cases. Then, the PSP systems configuration from a data pattern is effective using the Machine Learning who is excellent in pattern recognition to such a problem.

Furthermore, in order to treat effectively the error included in data, a Rough Neural Network is formed using the extended type Rough Neuron defined from Rough Aggregate Theory. Moreover, change of the diagnostic accuracy by using Genetic Programming to changing the number and combination of the data inputted is seen. Back Propagation generally used in a Neural Network is used for study of a network.

The data of the prostates cancer offered by the medical institution and a renal cancer was used for verification of a system.

II. Intelligent Agents and Multiagent System

Artificial Intelligence (AI) has made great strides in computational problem solving using explicitly represented knowledge extracted from the task. If we continue to use explicitly represented knowledge exclusively for computational problem solving, we may never computationally accomplish a level of problem solving performance equal to humans. From this idea, the paper describes the development of a multiagent system that can be used to support the assessment of design performance in the cellular automata model.

Agents represent objects or people with their own behavior, and take the structure of cellular automata lattice.

Intelligent agents and multiagent systems are one of the most important emerging technologies in computer science today [1]. The advent of multiagent systems has brought together many disciplines in an effort to build distributed, intelligent, and robust applications. They have given us a new way to look at distributed systems and provided a path to more robust intelligent applications.

Multiagent systems deal with coordinating intelligent behavior among a collection of autonomous agents. Emphasis is placed on how the agents coordinate their knowledge, goals, skills, and plans jointly to take action or to solve problems. Constructing the multiagent systems is difficult [2,3]. They have all the problems of traditional distributed and concurrent systems plus the additional difficulties that arise from flexibility requirements and sophisticated interactions.

III. Personal Software Process

The Personal Software Process (PSP) is a self-improvement process that helps you to control, manage, and improve the way you work. It is a structured framework of forms, guidelines, and procedures for developing software [4]. Properly used, the PSP provides the data you need to make and meet commitments, and it makes the routine elements of your job more predictable and efficient.

The PSP's sole purpose is to help you improve your software engineering skills. It is a powerful tool that you can use in many ways. For example, it will help you manage your work, assess your talents, and build your skills. It can help you to make better plans, to precisely track your performance, and to measure the quality of your products. Whether you design programs, develop requirements, write documentation, or maintain existing software, the PSP can help you to do better work.

Rather than using one approach for every job, you need an array of tools and methods and the practiced skills to use them properly. The PSP provides the data and analysis techniques you need to determine which technologies and methods work best for you.

The PSP also provides a framework for understanding why you make errors and how best to find, fix, and prevent them. You can determine the quality of your reviews, the defect types you typically miss, and the quality methods that are most effective for you.

After you have practiced the exercises in this book, you will be able to decide what methods to use and when to use them. You will also know how to define, measure, and analyze your own process. Then, as you gain experience, you can enhance your process to take advantage of any newly developed tools and methods.

The PSP is not a magical answer to all of your software engineering problems, but it can help you identify where and how you can improve. However, you must make the improvements yourself.

PSP write several program using the evolving process shown Figure 1.

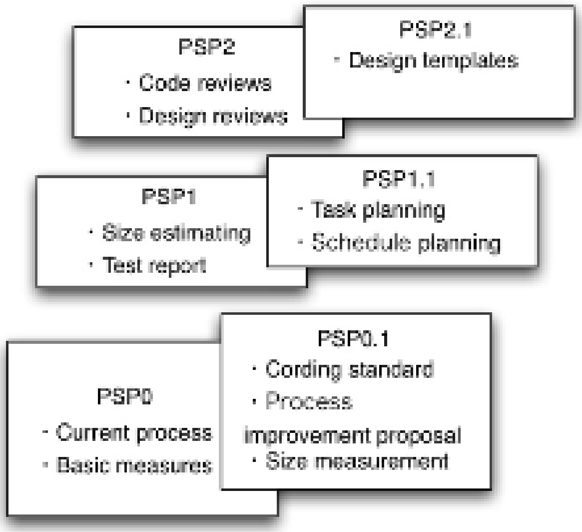

Fig.1. PSP Process Evolution

PSP0 and PSP0.1 hierarchy include introduces process discipline and measurement. PSP1 and PSP1.1 hierarchy include introduces estimating and planning. PSP2 and PSP2.1 hierarchy include Introduces quality management and design. Team Software Process exists over the PSP hierarchies.

IV. The PSP Practice support system using Multiagent

In this section, we study combined as it occurs in genetic Techniques into agent learner. We used as a tool for searching wide and complex solution space in Intelligent Agent learns data. Intelligent agent using complex techniques of related research. Multiagent is state in a filed shown Figure 2.

Figure 2 depicts the Agent Communication Module and shared Information Data. The Agent make filed in order to share information data from Agent communication filed. These fields include other Learner kept in Intelligent Agent shown Figure 3.

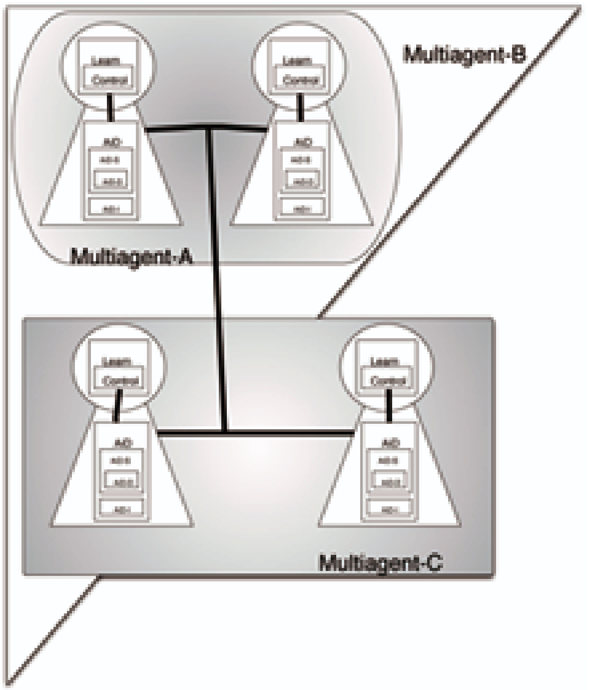

Fig.2. Support System Communication of Multiagent

Figure shows the Agent between communication modules in other communicate method. In this case, Intelligent Agent supports the PSP time and size measures record to user manipulation data. Intelligent Agent Controller selects Agent Information Data Share (AiD-S) or Agent Information Data Delivery (AiD-D).

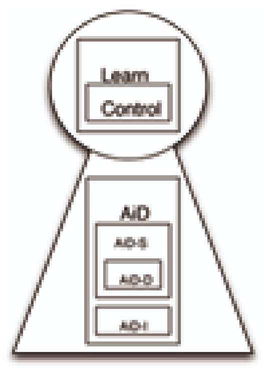

Fig.3. The Configuration of Agent Module

Other Learner support anything AI techniques of input data. Intelligent Agent has made combined these techniques into the Machine Learning. Machine Learning include same function of standard algorithm using user analyses data. These techniques supported by analysis data in time sheet that retrieval of start and end point.

Table 1 shows the PSP record form Time Measures and Size Measures [4].

Table 1. The scale of Program size categories

	Plan	Results	Accumulation
Base			
Added			
Modified			
Deleted			
New and changed			
Re-used			
New Re-used			
Total			

In the PSP, engineers use the time recording log to measure the time spent in each process phase. In this log, they note the time they started working on a task, the time when they stopped the task, and any interruption time. For example, an interruption would be a phone call, a brief break, or someone interrupting to ask a question. By tracking time precisely, engineers track the effort actually spent on the project tasks. Since interruption time is essentially random, ignoring these times would add a large random error into the time data and reduce estimating accuracy.

Since the time it takes to develop a product is largely determined by the size of that product, when using the PSP, engineers first estimate the sizes of the products they plan to develop. Then, when they are done, they measure the sizes of the products they produced. This provides the engineers with the size data they need to make accurate size estimates. However, for these data to be useful, the size measure must correlate with the development time for the product. While a line of code (LOC) is the principal PSP size measure, any size measure can be used that provides a reasonable correlation between development time and product size. It should also permit automated measurement of actual product size.

So, This any measure record to support agent consider with using this Agent Learner expanded of PSP support. A person engaging in a person who experienced PSP and software development for many years is not very worried about a form record-keeping work.

Record keeping is vague, and what is performed of a person pressed by a work still increases. Necessity to perform automatically is important in a soldier, remission of an activity and process assay to record an activity precisely.

Therefore I record all activities, and a support system shares the documentary information, and Intelligent Agent examines to whether be content which documentary information to shows personal characteristic of difference with another person.

V. Improvement of Software Estimate Efficiency Centered Multiagent

In this section, explain improvement of Software Estimate used to Multiagent internal Agent Learner for Intelligent Agent. Multiagent connect in other Intelligent Agents. Hence, those Intelligent Agent put the Agent Learner on necessary thoughts in Multiagent.

1. Software Estimate Design of Agent Learner

The Software Design Estimate kept in Intelligent Agent. Figure 4 shows the Agent internal Data, PSP database and user logs connection modules in other communication method. In this case, Intelligent Agent supports the PSP time and size (LOC: Line of Code) measures record to user manipulation data. Intelligent Agent used to learning Control on internal database for AiD.

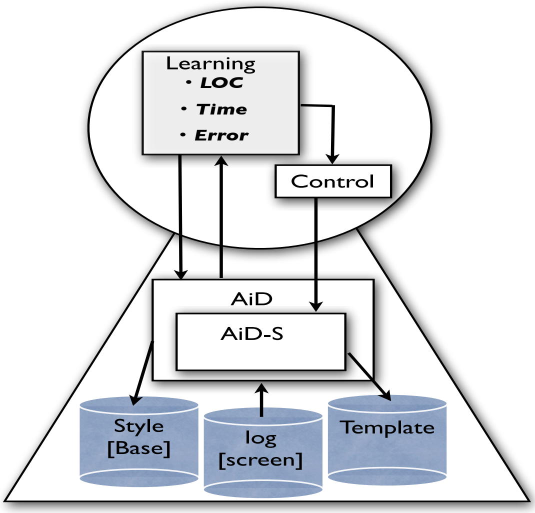

Fig.4. The AiD Data transferred from Agent Learner to action logs

2. The Estimating Probe Method of Agent Software Design

The Probe Method guides user in using historical data to make estimates. With estimated proxy size E, Intelligent Agent can calculate the projected program size P and did total estimate development time. The parameters β_0 and β_1 are used in the following equation to calculate projected added modified size:

$$\text{Projected Added and Modified } Size(P) = \beta_0 + \beta_1 * \mathrm{E} \qquad (1)$$

When two sets of data are strongly related, Intelligent Agent can use the linear regression method to represent that relationship. This means that linear regression is often appropriate. The parameters β_0 and β_1 are calculated from user historical data.

VI. CONCLUSION

In this research we build Multiagent complex system sensing user working data. We were able to searching user experience data. We create agent learner data in user working analyses system.

For future works, we will consider methods quick running of agent learner in communication data and user experience data. We try to delete user missing work date filter on experience data. We consider to that delete missing work filter on experience data.

Future versions of this model will aim to show how the system in communication response in a more natural, unscripted scenario, involving multiple parts in addition to other forms of process and contingency.

REFERENCES

[1] Weiss, G. (1999), Multiagent Systems, A Modern Approach to Distributed Artificial Intelligence, the MIT Press
[2] Abul, O., Polat, F., and Alhajj, R. (2000), Multiagent Reinforcement Learning Using Function Approximation, IEEE Transaction on systems, man, and cybernetics-part c: application and reviews, Vol. 30, No. 4, pp. 485-497.
[3] Khosla, R., and Dillon, T. (1997), Engineering Intelligent Hybrid Multi-Agent Systems, Kluwer Academic Publishers
[4] Watts S. Humphrey (2005), PSP - A Self Improvement Process for Software Engineers, Addison-Wesley

A Communication Protocol Based on IR-Space Division Transceivers for Mobile Robots

Tetsuo ABE†, Hiroyuki TAKAI†, and Keihachiro TACHIBANA††

† *Graduate School of Information Sciences*
Hiroshima City University
3-4-1 Ozuka-Higashi, Asa-Minami-Ku, Hiroshima, Japan
Tel: 082-830-1500, Fax: 082-830-1656.
{*abe*|*takai*}*@sys.info.hiroshima-cu.ac.jp*

†† *Graduate School of Computer Science*
Osaka Gakuin University
2-36-1 Kishibe-Minami, Suita-city, Osaka, Japan
Tel: 06-6381-8434, Fax: 06-6382-4363
tatibana@ogu.ac.jp

Abstract: In this paper, we propose MAC protocols based on our designed Infrared-Space Division Transceiver (IR-SDT) for mobile robots. The IR-SDT has 8 communication modules, so it can communicate with maximally 8 other nodes simultaneously. The number of parallel multiple accesses will be improved by using this transceiver and the protocol specialized for it._In addition, we consider situations in which a packet collision occurs, and propose a protocol that resolves communication-conflictions using signal collision-detection function of IR-SDT. Finally we consider the performance of these protocols, and discuss the influence of signal collision-detection accuracy.

Keywords: mobile robot, MAC protocol, directional communication, SDMA, CDMA/CD on wireless

I. INTRODUCTION

Cooperation by autonomous mobile robots that designed for the purpose of rescue or information collection in disaster areas, exploration in unknown environments has been studied [1][2]. Robots have to exchange information of task progress or report their position each other in order to execute tasks smoothly. Therefore the study about communication networks for mobile robots has been an important theme. Especially over the past decade, this field has become more popular since wireless LAN technology became cheaper.

Broadly divided into 2 specifications as follows are required for communication networks of autonomous mobile robots.

- *Decentralized autonomy*

Autonomous mobile robots have to construct their communication networks by themselves. It is because they basically perform in unknown environments that do not have communication infrastructures. Furthermore, important functions in the system must be decentralized to be fault tolerant.

- *Scalability*

These networks have to keep high performance when the number of robots in the system is large, i.e., in the tens or hundreds. Therefore it is not realistic to prorate limited channels among each robot, like FDM.

These 2 requirements are conflicting, so reconciling them has been a main issue. Using an intensive central station is suitable to manage communications of a lot of robots. However a system that depends on only one station is unreliable.

We proposed a space division transceiver using infrared LEDs and photodiodes up to now in order to realize networks that satisfy these requests. In this paper, we propose a space division MAC protocol specialized for this transceiver. In addition we also look at situations in which signal collision occurs based on the spatial arrangement of robots, and propose a protocol that resolves communication-conflictions. We think we can realize spatially efficient networks using these protocols.

This paper is constructed as follows. In section II, we will give features and issues of several related works, and introduce our designed IR-SDT in section III. In section IV, we will describe the detail of proposed protocols, and mention these performances in section V. Finally we will conclude this paper and mention future work in section VI.

II. RELATED WORKS

Several single channel type-distributed MAC protocols for the wireless communication among mobile robots have been proposed.

1. AR-TDMA [3]

AR-TDMA is a MAC protocol specialized for the cooperative transport by mobile robot team. Robots take the role of leader or follower, and the leader manages the time slot for time-division communication.

In the paper, there is an important premise. If packet collision occurred when the followers are bidding for slot reservation, then the leader will detects the collision by measuring the change in the signal level. However it is difficult since the change in the signal level is related to the distance from a peer on wireless communications. The accuracy of the collision detection is not considered in the simulation of this protocol, but the factor can influence the system performance.

2. CSMA/CD-W [4]

CSMA/CD-W is a random access MAC protocol for communications among robots that provides the function of signal collision-detection on wireless medium, and is based on CSMA/CD. In this protocol, sender nodes sense the carrier state immediately after transmitting to detect simultaneous sending from other nodes. If a sender detects other's simultaneous sending, then it is recognized as a collision, and the sender informs others that. By the scheme, the overhead that caused by a receiver node requesting the retransmission can be reduced when a collision occurs.

However it is the same as CSMA/CD in that senders retransmit after random back-off when collision occurs. Therefore performance will drop when the number of robots in the system increases.

III. OUR PREVIOUS WORKS

The spatial efficiency of wireless communication will improve by using infrared rays that have strong directionality as the carrier, instead of radio waves that diffuse every direction. It is reported that the directional antenna can provide approximately 5 times of the number of parallel communication links, compared with omni-directional antenna in wireless mesh networks [5]. We focused on this advantage, and designed Infrared-Space Division Transceiver (IR-SDT) for the communication among mobile robots [6]. The overhead view of IR-SDT is illustrated in Fig.1.

This equipment consists of 8 communication modules that are placed on the board facing outward. Each module has a photodiode that can detect AOA (angle of arrival) of signals, and an infrared LED, so it can receive and transmit infrared rays. In addition, they are separated by physical barriers, so the reception angle of each module is limited to 60 [deg]. Moreover it prevents disruption of links by setting overlapped areas.

Therefore this equipment can receive several signal rays from different angles simultaneously, and also can transmit signals to a particular direction or omni-directionally. However, notice that it cannot simultaneously send and receive since the LED rays that are emitted when transmitting will diffuse, reflect, and interfere with their own receiver. Therefore it is the same as general antenna in that can perform half duplex communications.

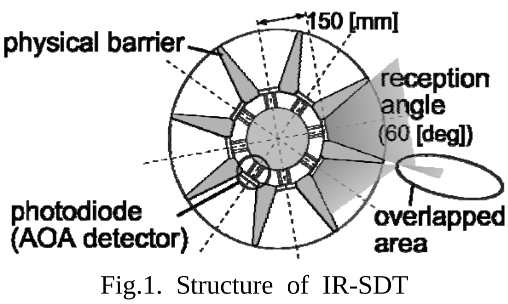

Fig.1. Structure of IR-SDT

Furthermore, the function of AOA detection is important. We use a commercial AOA detecting device (HAMAMATSU, S6560), which outputs the AOA θ as the ratio of electric currents $c\theta$, as shown in Fig.2. By using it, robots can accurately estimate the angle of the peer; and also if 2 or more signal rays enter into a same module, it can be detected as a collision from the fluctuation of the output as shown in Fig.3.

In the next section, protocols that provide the p arallel connection and collision resolution using thes e features will be proposed.

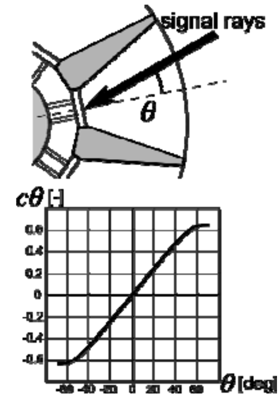

Fig.2. Specification of AOA detector

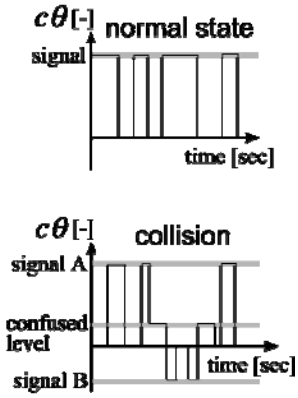

Fig.3. Response for a collision

IV. PROPOSAL

1. Simultaneous Multiple Access Protocol

First, we will describe the protocol for the nodes that make simultaneous multiple access links autonomously in a network. As shown in Fig.4, we implement 4 nodes: S, D, n_1, n_2 on the plane, and they can receive each other's signals. They have unique node-ID, and modules of them IR-SDT also have module-ID. Now node S wants to send message to D, then the steps that follow are executed.

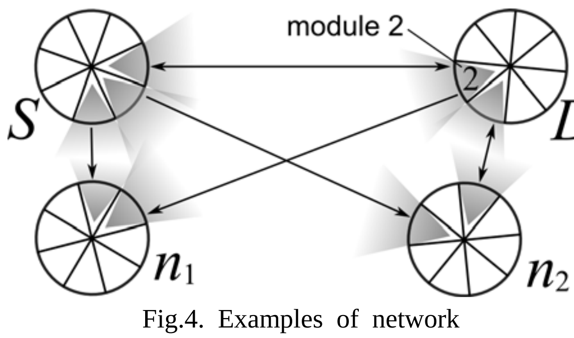

Fig.4. Examples of network

i) S broadcasts a RTS (Request To Send) that specifies the node ID of D. Then it is expressed as "RTS(S, D)" as the RTS from S to D.

ii) n_1 and n_2 wait for constant time t_{waitCTS}, and D returns a CTS (Clear To Send) to S. Then that CTS is only transmitted from the module that is used for communication (in this example, module 2), so it is expressed as CTS(D, 2, S) as the CTS from module 5 of D to S.

iii) S receives the CTS and starts to send a message MSG(S, D) to D. Then if other nodes did not receive the CTS, they are allowed to send signals to D; because then they are not facing with module 2 of D. In this case, n_1 is prohibited to send signals to D, but n_2 is allowed to do it. In addition, D returns an ACK (Acknowledgement) with packet-ID to S by receiving constant number *p* of message packets, while receiving the message.

iv) D emits RF (Reception was Finished) from module 2 to release it when receiving the message is finished. Here, it is RF(2).

The sequence chart of above steps is illustrated in Fig.5. By using this method, D can receive messages from other nodes in parallel while ensuring the link for receiving the message from S.

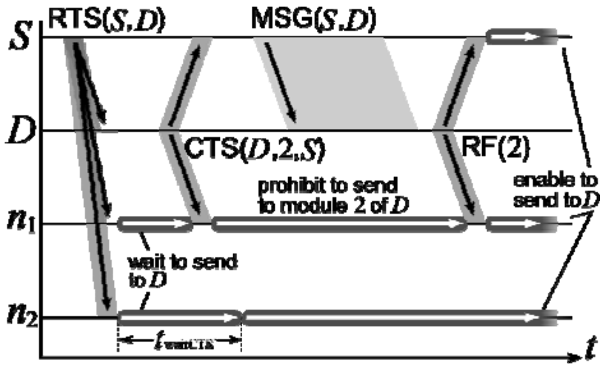

Fig.5. Simultaneous Multiple Access Protocol

2. Collision Detection and Resolution Protocol

In a network consist of IR-SDT, if 2 or more signal rays are received by a same communication module, then these bit patterns are broken and they cannot be decoded. We call this status as collision. Situations that collision occurs can be existed as follow 2 patterns.

A. *Simultaneous RTS broadcasting*
2 or more nodes broadcast RTS at the same time, and they are received by a same module of some node

B. *Interruption by a node that did not listen to RTS/CTS*
While S is sending a message to D, a node that did not listen to RTS/CTS among node S and D moves near D and broadcasts a RTS, and the RTS is received by busy module of D.

We will describe a protocol that detects such collisions and retransmit signals smoothly. For example, we use a network consists of 3 nodes: S_1, S_2 and D on the plane, as shown in Fig.6.

Then we consider situation A and explain an countermeasure for it. The sequence chart of the scheme is illustrated in Fig.7.

A-i) S_1 and S_2 broadcast RTS at the same time. (Then they cannot listen to each other's RTS, since IR-SDT communication is half duplex.)

A-ii) These RTS are received by module 5 of D and collide. D detects the collision, and transmits Collision Notification (CN) from module 5. This CN contains the node-ID, module-ID and the status information when collision occurs. In this example, node-ID is D, module-ID is 5 and status is idling, so the packet is expressed as CN(D, 5, IDLE).

A-iii) S_1 and S_2 receive the CN. In this example, S_1 wants to send a message to D, so S_1 waits a random time and retransmits a RTS only to D. Instead, S_2 wants to send a message to other node, so S_2 waits a constant time for a CTS from desired node. After that, if the CTS is not received, S_2 broadcasts a RTS again, except to the direction of D.

By using this method, conditions in which random back off is inserted can be significantly reduced.

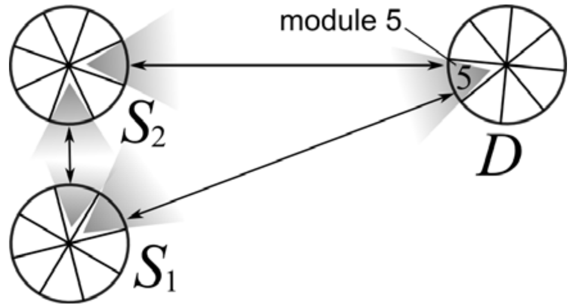

Fig.6. Examples of network

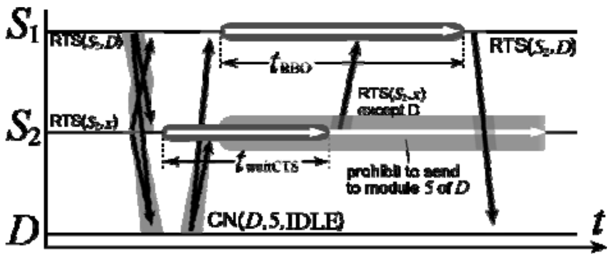

Fig.7. Collision Detection and Resolution Protocol in situation A

Next, let us consider situation B and give a response procedure. Its sequence chart is illustrated in Fig.8.

B-i) When S_1 is sending a message to D, S_2 that could not listen to signals from S_1 or D approaches them, and broadcasts a RTS.

B-ii) The RTS is received by module 5 of D and collide with the message from S_1. Then D transmits CN. This CN is expressed as CN(D, 5, BUSY) because D is receiving a message from S_1.

B-iii) S_2 receives the CN, then if S_2 wants to send a message to D, waits until module 5 of D is released.

B-iv) S_1 retransmits message packets that were not sent successfully.

Owing to this method, S_2 can immediately notice that its own signal was caused by collision.

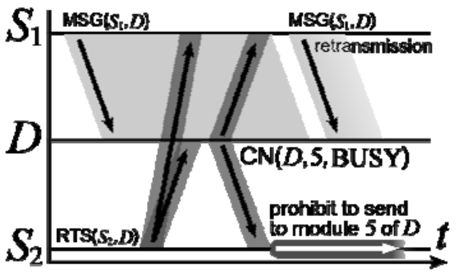

Fig.8. Collision Detection and Resolution Protocol in situation B

V. ABOUT PERFORMANCES

In this section, we discuss about performances of above proposed protocols.

1. Simultaneous Multiple Access Protocol

By the method, every communication module of IR-SDT is used independently, so the maximum number of simultaneous connection links can be 8. However, it cannot reasonably be assumed that all adjacent nodes are at the position where interference does not occur, so the effective value is considered to be lower than it.

In addition, if the time period t_{waitCTS} that waiting for transmission until CTS is too short, then a collision can occur. Instead, if it is too long, it can be an overhead. Therefore we have to investigate the optimal value of the parameter.

2. Collision Detection and Resolution Protocol

About the method, we first consider situations that collisions occur.

Situation A can occur in a network based on CSMA/CA using omni-directional antenna, and the probability can be also considered equal to that. However, diffusion area of signals is limited after step A-3, so nodes can retransmit signals with a low collision probability.

In contrast, situation B only can occur in directional communications, because S_2 refrains from transmission in the environment using omni-directional antenna since then S_2 can listen to messages from S_1. However in directional communications, S_2 refrains from transmission if it received an ACK from D. Therefore the probability depends on the frequency of ACK $1/p$ and the velocity of robots. Thus we also have to set the parameter p to the optimal value.

Moreover, we will discuss about the function of signal collision detection of IR-SDT. If incident angles of collided signal rays are very close, then the fluctuation of the AOA detector's output is small, so it cannot be recognized as a collision. Then the Collision Detection and Resolution Protocol does not work. Therefore the minimum difference of incident angles θ_{lim} that allows a collision to be detected is an important constant for the system.

VI. CONCLUSION

In this paper, we proposed a communication-equipment and MAC protocols based on it for autonomous mobile robots, and discussed about their performances. We will quantitatively evaluate them by numerical simulations to confirm their efficiency. In addition, we have to derive analytically optimal values of parameters as previously mentioned. Furthermore the critical value of incident angle's difference θ_{lim} is also should be obtained by actual experiments.

ACKNOWLIDGEMENT

This work was supported, in part, by the research promotion grant of the Telecommunications Advancement Foundation.

REFERENCES

[1] Kawai K., Nakazawa A., Kiyokawa K., et al. (2005), Development of a Control System of a Mobile Robot for 3D Reconstruction of a Disaster Area (in Japanese), *Technical report of IEICE Multimedia and virtual environment* 105(256) pp.13-18

[2] Sugiyama H., Tsujioka T. and Murata M. (2005), Victim detection system consists of networked mobile robots (in Japanese), *Transactions of Information Processing Society of Japan* 46(7) pp.1777-1788

[3] Arai J., Koyama A., and Barolli L. (2005), Performance Evaluation of an Adaptive Medium Access Control Protocol for Robot Communication in Autonomous Distributed Systems (in Japanese), *Transactions of Information Processing Society of Japan* Vol.46 No.11 pp.2676-2686

[4] Wang J., Premvuti S. and Tabbara A. (1995), A wireless media access protocol (CSMA/CD-W) for mobile robot based distributed robotic systems, *Robotics and Automation, 1995. Proceedings., 1995 IEEE International Conference on* vol.3 pp.2561-2566

[5] Furuhi, T. and Ohira, T. (2002), Efficacy Consideration on Directional Antennas in Wireless Ad-hoc Networks (in Japanese), *The transactions of the Institute of Electronics, Information and Communication Engineers. B* J85-B(12) pp.2223-2233

[6] Ueda T., Takai H. and Tachibana K. (2001), An Investigation of Space-Division Infrared Communication System (in Japanese), *Technical report of IEICE, ITS* 100(576) pp.7-12

Intelligent Network Surveillance System based on Ontology

Soomi Yang

Department of Internet Information Engineering
The University of Suwon, Gyeongi-do, 445-743, Korea
(Tel : 82-01-7446-6242; Fax : 82-31-229-8138)
(E-mail: smyang@suwon.ac.kr)

Abstract: For the surveillance of the area consisting in an integrated framework of networked RFID sensors, CCTVs and smart cameras, we made wide area surveillance systems which provide collaborations between distributed agents having heterogeneous data from various sources. In our intelligent network surveillance system, each of agents has autonomy and collaborates and does reasoning based on distributed knowledge bases.

Keywords: Network surveillance system, Physical security, Agent, Context ontology**.**

I. INTRODUCTION

This paper describes an on-going work aimed at designing and deploying a system for the surveillance and monitoring of province area containing about 15 cities. Our project is also aiming to be included in the construction of the ubiquitous city. We made the design of architecture for the surveillance of the area consisting in an integrated framework of networked RFID sensors, CCTVs and smart cameras. Wide area surveillance system should provide collaborations between distributed agents having heterogeneous data from various sources. We are developing an intelligent network surveillance system in which each of agents has autonomy and collaborates. Various data such as video, feature data including biometrics, event alarms are come from many kinds of input devices such as smart cameras, RFID sensors. They may be in fixed location or put on robot for some dangerous situation. Although agents are ordered by geographic area hierarchy, they have their own knowledge base and inference engine issuing queries independently.

II. SYSTEM ARCHITECTURE

We have developed system architecture for deploying a network of agents that focus on collaboratively analyzing data came from various sources. This architecture includes that the execution of the elementary tasks are distributed and independently executed with a certain degree of autonomy and/or mobility. It views each of agents as a knowledge processing engine that is to be applied to process data and make some decision. The knowledge base architecture presented in Figure 1 has hierarchy according to administrative divisions. R represents the set of knowledge bases including facts, rules and context ontologies related to raw data extracted from the CCTV, Smart Camera and RFID. It includes ontology representing physical and logical raw entities and associations among them. W_0 through W_n represents the set of knowledge bases including facts, rules and context ontologies related to wanted data covering from small area to large area.

In our network surveillance system, many kinds of

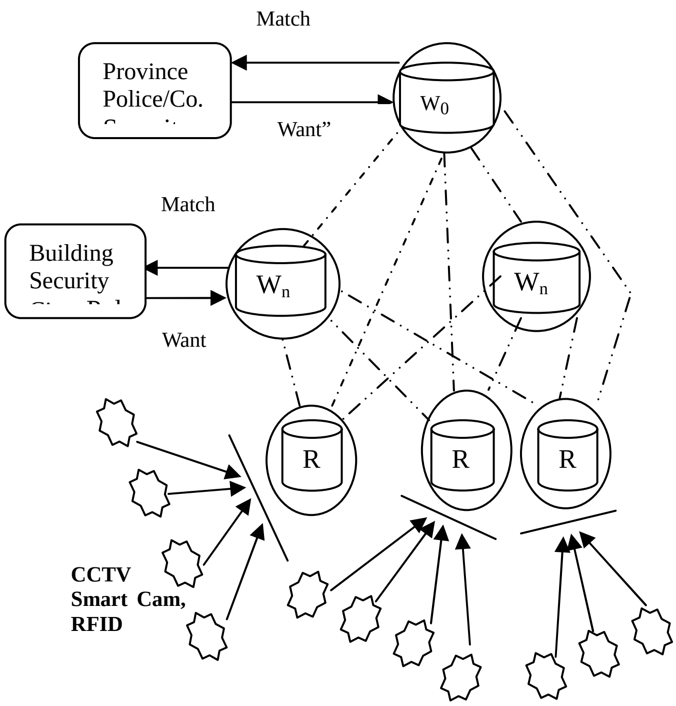

Fig.1. Knowledge base Architecture

input devices are interconnected through Internet and their collected and/or recognized data form a web of surveillance data. We want to make agent's data representation which is not only human process-able but also machine process-able. We would like to extend the current wide area surveillance system to a web of data and allow for agents to exploit the data directly each other with complete independence to their administrative hierarchy. A web of data needs to be augmented for intelligent inference and activity decision by inquiring additional required data to any other agents through common APIs.

III. KNOWLEDGE-BASED SURVEILLANCE

Making a complex decision is an essential task in networked surveillance systems. We show simplified application scenarios in Figure 2 for the cases detection during real time and detection by request. Extraction system, detection system and filter system make use of semantic information contained in the R and W knowledge base. For the collaboration between distributed agents, data should be uniquely identifiable and we should allow data to link to each other and classify the data to convey some meaning. Furthermore we should use standards for all these.

Semantic web is a collection of standard technologies to realize a web of data to be arranged, liked, classified and uniquely identifiable. Classification is achieved through ontologies and uniqueness is achieved through URIs. Our network surveillance application can be thought of semantic web. Building a semantic web application for network surveillance provides several advantages such as many distributed data sources, decentralized semi-structured images, knowledge base, distributed inference, open systems.

We build a knowledge base to elaborate an inference engine such that it will return different decisions for each different context intelligently. For making better and intelligent decisions we develop huge background data, rules, ontologies and structure them with an annotation label to the links. Inference engines make use of those data. Every search event return related data including still picture, video, feature data, event alarm that are ranked from top to bottom. Our system constructs area profile ontology for each agent by observing events occurrence in the area. For example some sound may indicate burglar alarm in some area. However the same sound might be a school bell in

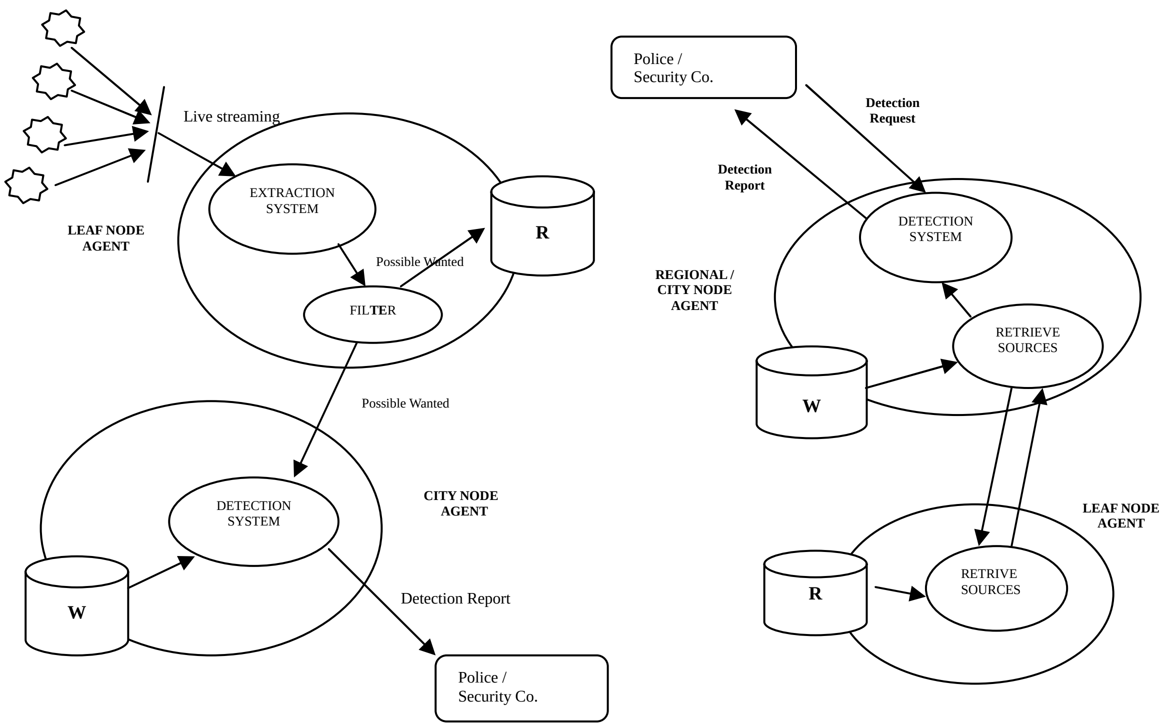

(a) Detection during real-time (b) Detection by request

Fig.2.Application Scenarios

another area. Area profile ontology is further used for reordering query results. Although the training phase needs some set up cost, it helps the agents learn the behaviors in the area and for better inference results.

IV. WEB INTERFACE

For the availability of small, power-aware, and high-performance camera nodes, amounts of available video data grow. However transmitting video data in affordable rate consumes large amounts of network bandwidth. Developing interactive systems for efficiently querying this data about specific events has become a significant need in surveillance. Such a system should be able to bridge the gap between the high-level users' queries and raw data within leaf node agents. This can be achieved by providing the powerful user interface for submitting queries, providing a mapping from the query into a set of filters that can utilize the feature data provided by other agents to infer high-level semantics, and then displaying the results in such a way the user can reformulate the further in-depth query and use the search results to foster new search inputs. We develop common APIs for each agent for standardized interface between agents and for the public web services. It forms an interactive system for querying surveillance data about events.

The surveillance system manager can control the state of the system via a graphical interface that shows an up-to-date, high-level representation of the system status. We can manage agents through a graphical user interface that supports the monitoring and deployment phases. The user authentication is performed and the configuration can be changed according to the privileges.

U-City Security System web interface has been Implemented and some example pages are shown in Figure 3. Figure 3 (a) shows member list. When we click a member it shows further information including location and privileges. Figure 3 (b) shows statistics graph representing trend and comparison visually. It also gives table with precise number data. In Figure 3 (c), it shows a regular user interface. On the top left side of the screen, the system officer can see the list of surveillance servers in its domain. By clicking specific item, live video from designated server can be seen in the popup window. On the bottom left side of the screen, the system officer can choose other surveillance area under the user access control. On the top right side of the screen, the system officer can see the list of alarming locations. By clicking some specific alarm, stored video or the real-time view of the site can be seen.

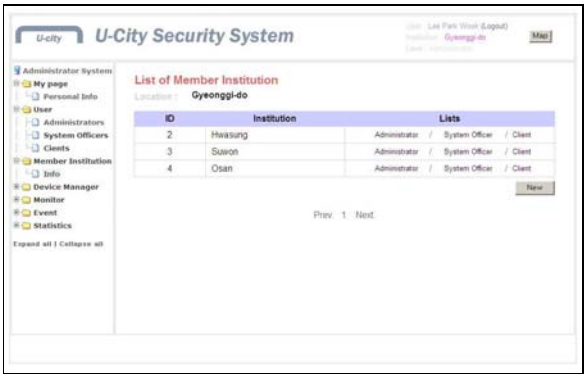

(a) Member inquiry

(b) Statistics graph

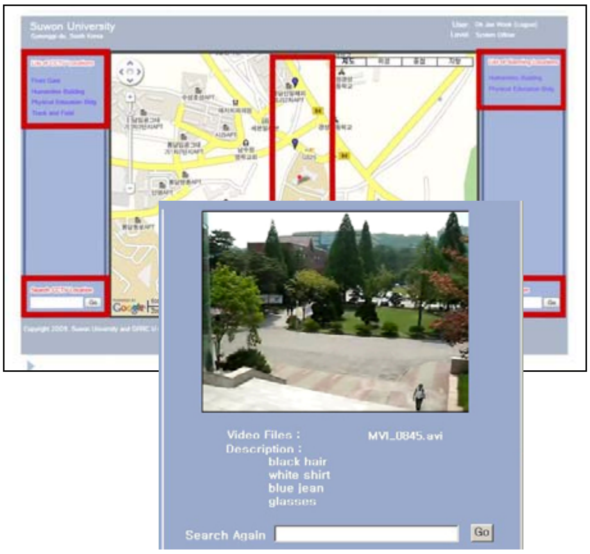

(c) Location mapping and video inquiry

Fig.3. U-City Security System

Depend on the characteristics of the event we can see various types of result data. On the bottom right side of the screen, stored video can be searched through typed keywords. Through the center pop-up search form, we can elaborate the search options. Some of our ongoing work is provision of more customizable graphical user interface for specifying user-defined policies and distributed user access control using attribute certificates which is defined in PMI[9].

V. RELATED WORKS

Networked surveillance systems can be used in many applications requiring images from multiple data sources to be combined in order to interpret the scene and understand the situation[1] such as disease surveillance[2]. For a wide area physical security surveillance, monitoring systems are connected and communicate [3,4,5]. However they do not adopt artificial intelligence technique. To ease the mergence between heterogeneous data, effort for the standardization for physical security is done by PSIA(Physical Security Interoperability Alliance) that defines, recommends, and promoting standards for IP-enabled security products[6]. There are few of surveillance systems adopting ontology-driven technologies. [7] introduces artificial intelligence techniques only for the interpretation of objects. [8] uses ontology but does not build agents for web of data.

VI. CONCLUSION

In this paper we introduce for wide area security service we connect the regional surveillance systems utilizing the preprocessing of smart cameras and sensor systems. Local region servers act as an intelligent agents doing more intelligent induction with more knowledge. Knowledge base includes facts, rules and context ontologies. Analysis for large areas generally requires combining information from several data source agents or other several region agents. The synergy between the agents allows obtaining more high level, enhanced and intelligent decision.

Our goal is building cooperative intelligent agents. Multi-agent systems have proven to be a powerful technology for building distributed applications. We see our system making a complex decision which is an essential task in networked surveillance systems.

ACKNOWLEDGEMENT

This work was supported by the GRRC program of Gyeonggi province. [GGA0801-45700, Center for U-city Security and Surveillance Technology]

REFERENCES

[1] A. Sankaranarayanan, A. Veeraraghavan, and R. Chellappa(2008), Object Detection, Tracking and Recognition for Multiple Smart Camaras, Proceedings of the IEEE, vol. 96, no. 10, pp. 1606-1624
[2] Hsin-Min Lu, Daniel Zeng, Lea Trujillo, Ken Komatsu and Hsinchun Chen(2008), Ontology-enhanced automatic chief complaint classification for syndromic surveillance, Journal of Biomedical Informatics, vol. 41, issue 2, pp. 340-356
[3] N. Siebel and S. Mybank(2004), The Advisor Visual Surveillance System, 2000, Applications of Computer Vision, pp. 103-111
[4] M. Shah, O. javed, and K. Shafique(2007), Automated visual surveillance in realistic scenarios, IEEE Multimedia, vol. 14, no. 1, pp.30-39
[5] D. Lymberopoulos, T. Teixeira, and A. Savvides(2008), Macroscopic Human Behavior Interpretation Using Distributed Imager and Other Sensors, Proceedings of the IEEE, Vol. 96, No. 10, pp. 1657-1677
[6] PSIA (Physical Security Interoperability Alliance Specification Package Q12009, http://www.psiaalliance.org
[7] R. Martinez-Tomas, M. Rincon, M. Bachiller and J. Mira(2008), On the correspondence between objects and events for the diagnosis of situations in visual surveillance tasks, Pattern Recognition Letters, vol. 29, Issue 8, pp. 1117-1135
[8] Roberto Vezzani and Rita Cucchiara(2008), ViSOR: Video Surveillance On-line Repository for annotation retrieval, IEEE International Conference on Multimedia and Expo, pp.1281-1284
[9] ISO/IEC 9594-8, Information Technology Open Systems Interconnection-The Directory: Public-Key and Attribute Certificate Frameworks, ITU-T Recommendation X.509 . 2005

A Multi-Agent-Based Approach for Furniture Arrangement

Satoshi Ono Takayuki Oshige Shigeru Nakayama

Department of Information Science and Biomedical Engineering,
Graduate School of Science and Engineering, Kagoshima University
1-21-40, Korimoto, Kagoshima, 890-0065 Japan
ono@ibe.kagoshima-u.ac.jp, k6180136@kadai.jp, shignaka@ibe.kagoshima-u.ac.jp

Abstract

This paper proposes a furniture arrangement method based on a multi-agent approach for interior coordination. In the proposed model, each furniture item acts as an agent, interacts with an environment and other agents, and moves to where it wants to go. Consequently, all furniture items reach well-coordinated placement. Agent movement of the proposed method is inspired by particle movement in particle swarm optimization algorithms, that is, agent's velocity is calculated from linear summation of vectors to avoid constraint violation, to harmonize with other agents, and so on. A simple example shows that the proposed method can make well-coordinated furniture arrangement from randomized positions.

1 Introduction

Interior coordination is a task involving the careful selection and placement of materials, fittings, furniture, and furnishings. Most of Japanese apartments and houses are sold or lent without any furniture and furnishings. Inhabitants must therefore buy furniture items such as a dining table, chairs, sofas, desks, beds, living boards, refrigerator, and so on, and arrange their placements whether they like it or not.

For those who wish to coordinate their privately-owned houses and apartments to the highest and most sophisticated standards it will most-likely involve the employment of an interior design specialist with whom a great deal of time is spent in communicating personal preferences, taste and style in order for the designer to be able to make and offer their best selections. With the rise in peoples purchasing wealth and expectations there is a greater demand for coordinated interior designing. To reduce the cost of design and enable more people to enjoy the benefits of personalized custom interior coordination, customers will consider not only the enlistment of an expensive interior designer but another reasonable independent way which can be done if the customers supply their own room requirements and user computer systems to provide the design coordination for them.

In this paper we focus on furniture placement of interior coordination, and propose a furniture arrangement method based on multi-agent system (MAS)[1, 2, 3]. An agent corresponds to a furniture item, sees the whole room, and decides which direction to go; consequently each furniture item thinks and moves autonomously. Agents negotiate with one another when a conflict occurs between them. Well-coordinated furniture arrangement is conducted by agents (furniture items) moving to their favorite positions.

We also develop a system for a non-design-professional resident to coordinated furniture arrangement. The system uses three dimensional graphics of furniture items which are sold on the actual market, so a user can recognize outputs of the proposed method at a glance and can judge whether the derived furniture arrangement is in harmony and functionable.

2 The proposed algorithm

2.1 Overview

The proposed model is a kind of homogeneous communicating multi-agent system[2, 3]. An agent corresponds to a furniture item, and an environment corresponds to a room involving floor, wall, ceiling, and fittings such as doors and windows. The agent knows its and other all agents' positions in the room as if using a camera mounted on the ceiling, investigates whether it violates constraints, and autonomously decides which direction to move. This model is therefore similar to Small Size robot League, one of the RoboCup Soccer League divisions [4].

Each agent moves to satisfy constraints concerning with itself only, and negotiates with other agent when they compete in a violation. As a consequence

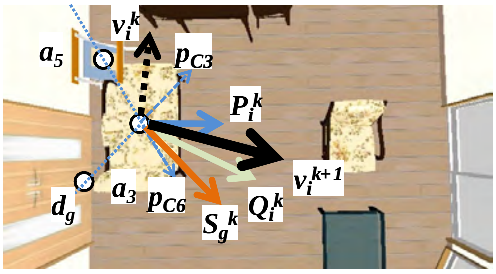

Figure 1: Example of velocity calculation.

of agents' independent-minded movements, the furniture items reached to well-coordinated arrangement.

At this stage, the proposed model allows furniture items to overlap during the process of arrangement, although it's impossible for real furniture to overlap each other in an the real world. Real furniture items cannot move along agents trail obtained from the proposed model's simulation, but the resulting furniture arrangement is valuable even in the real world.

2.2 Agent movement

Planning method in each agent is inspired from Particle Swarm Optimization[5, 6]. Furniture item's position and velocity are basically updated by simple equations involving linear summation of elemental vectors by the following equations:

$$\boldsymbol{v}_i^{k+1} = w\boldsymbol{v}_i^k + \boldsymbol{P}_i^k + \boldsymbol{Q}_i^k + \boldsymbol{S}_g^k \tag{1}$$

$$\boldsymbol{x}_i^{k+1} = \boldsymbol{x}_i^k + \boldsymbol{v}_i^{k+1} \tag{2}$$

$\boldsymbol{v}_i^k$ and $\boldsymbol{x}_i^k$ are velocity and the center position of furniture (agent) i at step k. $\boldsymbol{P}_i^k$, $\boldsymbol{Q}_i^k$, and $\boldsymbol{S}_g^k$ are vectors calculated from violation resolution rules, negotiation results, and group coordination. w is an inertia weight.

The process flow is outlined as follows:

[Step 1] The agent checks all constraints as described in Section 2.3.

[Step 2] The agent looks for a vector $\boldsymbol{P}_i^k$ indicating a direction to resolve violations based on resolution rules corresponding to constraints.

$$\boldsymbol{P}_i^k = \sum_{m=1}^{N_i^V} {}_m c_m^P r_m^P \boldsymbol{p}_m^k \tag{3}$$

N_i^V is the number of violations agent i commits, $\boldsymbol{p}_m^k$ is a vector calculated from a rule to resolve a violation m, c_m^P is a weight parameter, and r_m^P is a random real number from 0 through 1. $_m$ is 1 when violation m is of a unary constraint, or when violation m is of a binary constraint and agent i loses precedence by negotiation. Otherwise $_m$ is 0. When violating a binary constraint, $\boldsymbol{p}_m^k$ is calculated after negotiation in **step 3**.

[Step 3] The agent negotiates with other agents when they are competing, i.e. violating a binary constraint. Negotiation is conducted by comparing agents' priority. The agent with lower priority level must break away from the agent with higher priority.

[Step 4] The agent calculates $\boldsymbol{Q}_i^k$ to coordinate other agents in the same group by the following equation:

$$\boldsymbol{Q}_i^k = \sum_{j \in N_g} {}_{i\,j} c_j^Q r_j^Q \boldsymbol{q}_{i\,j}^k \tag{4}$$

$\boldsymbol{q}_{i\,j}^k$ is calculated by two ways; if agent i and j are close and their distance is longer than the threshold T_l, then $\boldsymbol{q}_{i\,j}^k = \boldsymbol{x}_j^k \quad \boldsymbol{x}_i^k$, or $\boldsymbol{q}_{i\,j}^k$ turns into one of vectors to align themselves, side by side, face to face, L-shape, and so on. c_j^Q is a weight parameter, and r_j^Q is a random real number from 0 through 1. S_g is a set of agents in group g to which agent i belongs, and $_{i\,j}$ is 1 when the distance between agents i and j is less than threshold T_c, otherwise $_{i\,j} = 0$.

The agent also figures on a relationship between groups, and moves to keep adequate distance by calculating the following vector $\boldsymbol{S}_g^k$:

$$\boldsymbol{S}_g^k = \sum_h \gamma_h c_h^S r_h^S \boldsymbol{s}_{g\,h}^k \tag{5}$$

γ_h is 1 when the distance between the center positions of group g (to which agent i belongs) and group h is less than the threshold T_g. $\boldsymbol{s}_{g\,h}^k$ is calculated from center positions $\boldsymbol{g}_g^k$ and $\boldsymbol{g}_h^k$ of group g and h,

$$\boldsymbol{s}_{g\,h}^k = \boldsymbol{g}_g^k \quad \boldsymbol{g}_h^k \tag{6}$$

c_h^S is a weight parameter, and r_h^S is a random real number from 0 through 1.

[Step 5] The agent calculates its velocity by equation (1). Inertia weight w is set to higher value when the simulation starts, and decreases at a fixed rate.

[Step 6] The agent moves to its new positions by equation (2).

Fig. 1 shows an example of velocity calculation of agent a_3. a_3 is in front of a door and overlap with

Table 1: Constraints and resolution rules.

Constraint no.	Constraint	Type	Rule no.	Rule	Priority weight o_m
C_1	A furniture item must be in a room.	Unary	R_1	Move toward the center of the room.	$2(n \quad 1)$
C_2	At least 800mm width space must be free in front of functional faces of a furniture	Unary	R_2	Move toward the room's center.	—
C_3	No furniture item must be placed in front of a door.	Unary	R_3	leave the door's front.	$1\ 5(n \quad 1)$
C_4	No furniture item must be placed in front of a window.	Unary	R_4	leave the window's front.	$1\ 5(n \quad 1)$
C_5	A furniture item whose hight exceeds 1,000mm must be placed with its back against a wall.	Unary	R_5	Move toward the wall behind the item.	$n \quad 1$
C_6	Furniture items must not overlap each other.	Binary	R_6	Negotiate with each other	—
C_7	The same furniture items next to each other must look to the same direction.	Binary	R_7	Negotiate with each other.	—
C_8	At least 800mm width space must be free in front of functional faces of a furniture.	Binary	R_8	Negotiate with each other.	—
C_9	A table must not stand behind a sofa.	Binary	R_9	Negotiate with each other.	—

Figure 2: Screenshot of the implemented system.

other agent a_5, and violates C_3 and C_6. Vector $\boldsymbol{p}^k_{C_3}$ to resolve the former violation is $(\boldsymbol{x_{a_3}} \quad \boldsymbol{d}^g)$ where $\boldsymbol{d}^g$ indicates the center position of the door. Assuming that agents a_3 and a_5 have the priority level of 2 and 9, agent a_3 must depart from agent a_5, and $\boldsymbol{p}^k_{C_6}$ is calculated as $(\boldsymbol{x_{a_3}} \quad \boldsymbol{x_{a_5}})$. $\boldsymbol{P}^k_i$ is therefore calculated by adding $\boldsymbol{p}_{C_3}$ and $\boldsymbol{p}_{C_6}$. Because there are some furniture items belonging to the same group, vector $\boldsymbol{Q}^k_i$ is calculated to come close other sofa and low table. Dining table and chairs belongs to other group, Vector $\boldsymbol{S}^k_g$ therefore arises to step away. Finally, vector $\boldsymbol{V}^{k+1}_i$ is calculated by adding vectors $\boldsymbol{P}^k_i$, $\boldsymbol{Q}^k_i$, and $\boldsymbol{S}^k_g$.

2.3 Constraints

Constraints are provisions for a feasible furniture arrangement[7, 8]. Unary constraint is a condition between an agent and the environment, and binary one is a condition between agents. The proposed model involves nine constraints as shown in Table 1, and a simulation stops when all constraints are satisfied.

2.4 negotiation and priority

Negotiation is conducted by comparing furniture items' priority; the item having lower priority must deviate from the item having higher priority. Priority pri^k_i of agent i is calculated by the following equation.

$$pri^k_i = pri^0_i + \sum_m o_m + u_i + r^{pri}_i \tag{7}$$

pri^0_i is an initial priority level defined by its furniture items static attributes; taller and larger furniture items have higher priority level. o_m is a dynamic element calculated by constraint violation m as shown in Table 1, and u_i is another additional element by user operation, respectively. r^{pri}_i is a random number.

2.5 Furniture group

In the proposed method, furniture items comprise a group based on their functional height. Functional height means the height at which inhabitants use the furniture items; they use the item with standing or sitting on a floor, a low chair like a sofa, or a high chair like a dining chair.

- H_{floor}**:** Furnitures such as floor cushions and low tables have this function height H_{floor}. Inhabitants use the furnitures with sitting on the floor.
- H^{low}_{seat}**:** Furnitures such as sofas, low tables, and television boards have this function height H^{low}_{seat}. Inhabitants use them with sitting on sofas.
- H^{high}_{seat}**:** Furnitures such as chairs, dining tables and desks have this function height H^{high}_{seat}. Inhabitants use them with sitting on chairs.

(a) Step 1. (b) Step 500. (c) Step 1,000. (d) Step 2,000. (e) Step 3,055.

Figure 3: Example search progress.

H_{stand}: Furnitures such as dining boards have this function height H_{stand}. Inhabitants use them with standing.

Furniture items with the same functional height gather in a group.

3 Output examples

Fig. 2 shows a screenshot of the resulting system consisting of three-dimensional viewer, two-dimensional floor plan viewer, and agent status window. Fig. 3 shows a sample transition to coordinate a furniture arrangement with a room involving an irregular rectangle floor shape and windows on South and East sides. An item circumscribed with a translucent rectangle violates one or more than one constraints.

At the earlier stage of the simulation, furniture items such as sofas and a center table belonging the same group roughly moves to cluster together. And all items drift from place to place till about step 2,000. As the simulation progresses, the group in which items have the functional height H_{seat}^{low} moves nearby the windows, and the dining table and chairs move to the back of the room.

4 Conclusions

Proposed in this paper is a multi-agent-based model for furniture arrangement, in which its agent movements are inspired by particle swarm optimization.

It is our future work to make a model in which furniture items' collision is prohibited. The improved model will allow to utilizing not only derived furniture positions but furniture trails, which is a plan to change the furniture arrangement[9].

Acknowledgements

We would like to thank TIS Inc. for supporting this research.

References

[1] E. H. Durfee and J. S. Rosenschein, "Distributed problem solving and multiagent systems: Comparisons and examples," , 1994, pp. 94–104.

[2] M. Wooldridge and N. R. Jennings, "Intelligent agents: Theory and practice," , vol. 10, no. 2, pp. 115–152, 1995.

[3] P. Stone and M. M. Veloso, "Multiagent systems: A survey from a machine learning perspective," , vol. 8, no. 3, pp. 345–383, 2000.

[4] H. Kitano, M. Asada, Y. Kuniyoshi, I. Noda, and E. Osawa, "Robocup: The robot world cup initiative," , 1995.

[5] J. Kennedy and R. Eberhart, "Particle swarm optimization," , vol. 4, 1995, pp. 1942–1948.

[6] J. Kennedy, R. C. Eberhart, and Y. Shi, Morgan Kaufmann, 2001.

[7] S. Ono, T. Izumi, A. Fujiyama, C. J. Ashley, and S. Nakayama, "Interior coordination using case-based reasoning and constraint satisfaction paradigm," , 2004, pp. 1066–1071.

[8] T. Izumi, S. Ono, and S. Nakayama, "Case- and constraint-based interior design system," , vol. 19, no. 7, pp. 293–295, 2006.

[9] S. Ono, Y. Hamada, S. Yamamoto, K. Mizuno, and S. Nishihara, "Rearrangement of floor layouts based on constraint satisfaction," , 2001, pp. 2759–2764.

The Fifteenth International Symposium on Artificial Life and Robotics 2010 (AROB 15th '10),
B-Con Plaza, Beppu,Oita, Japan, February 4-6, 2010

Design of robotic arm's action to imitate the mechanism of an animal's consciousness

Takahiro Yamasaki Eiji Hayashi

Department of Mechanical Information Science and Technology
Faculty of Computer Science and Systems Engineering, Kyushu Institute of Technology
680-4, Kawazu, Iizuka-City, Fukuoka Prefecture, Japan
(Tel: 0948-29-7793)
(yamasaki@mmcs.mse.kyutech.ac.jp)

Abstract: We are attempting to develop a system so that a user is able to let robots perform an intellectual action that has a healing and friendly feeling. Based on the development process of the actions and consciousness of animals[1], we constructed a structure model which connects consciousness and action hierarchically, built a valuation function for action selection, and developed software to control the action of a robot. This software is called Consciousness-Based Architecture (CBA). With it, our aim is to connect a user and robot as closely as possible and to allow smooth communications between them by developing an emotional system that takes notice of consciousness.

In our system, the robotic arm's finger is outfitted with a small Web camera, which allows the arm to recognize external information so that the robot can select various actions that comply with certain factors in the outside environment. Furthermore, by using the actuator of the robotic arm, the system we have built provides a correspondence between the robot's internal states, such as the degree of rotation angle, and the outside temperature. In the present study, a motivation model which considers the outside environment and the internal states has been built into the CBA, and the behavior of the robotic arm has been verified.

Keywords: CBA, The consciousness of the robot, Motivation, Tiredness, Outside environment, Internal state

I. Introduction

At the present time, not only industrial robots but also non-industrial robots are being quickly developed. The non-industrial robot is called a service robot and is of various types: a business robot, a research robot, a welfare robot, and a domestic robot, to mention some. The necessary thing in the development of these robots is user affinity, such as the healing possibilities that are facilitated by making a robot's appearance similar to that of a living being and by adding sociability to a robot. In order to provide ways to prevent users from becoming bored and also to create a sense of closeness or affinity that could give a healing quality to a user, we have paid attention to how animals (such as dogs and cats) by their existence in real space fulfill these functions for people.

In order to copy the consciousness of an animal, we modeled our generating locus by paying attention to dopamine, a substance in a brain which manages an animal's actions. By regarding this as a robot's motivation, the robot is given a way to make action choices.

The service robot is defined as "the machine which can acquire external information by itself, can determine self-action, and has the purpose of substituting for people, providing the support and cooperation that people would provide." To fulfill these functions, the robotic arm's finger is outfitted with a small Web camera, allowing the arm to recognize external information so that the robot can select various actions in compliance with the outside environment by changing the amount of dopamine released. Moreover, a behavioral selection process that is more intellectual considers the outside environment. In addition, an internal state for the robot becomes possible through the construction of a system which changes the amount of dopamine released. Through the actuator on the robotic arm that is able to change its angle rate, the system can regulate the robot's internal states (with regard to such things as the degree of the turning angle and the temperature). As a result, the robotic arm can express "Tiredness" and "Stress" just like living creatures.

In the present study, we verified the behavior of a robot arm according to a motivation model that considers both the outside environment and internal states.

II. System structure

Fig. 1 shows the appearance of the robot arm, and Fig. 2 shows its degree of freedom. The robot arm has 7 levels of flexibility {shoulder (Joint1, Joint2), elbow (Joint3, Joint4), wrist (Joint5, Joint6), and finger (Joint7)} at its full length of 450 [mm]. The hand part has 3 fingers with one flexibility; the weight of a main part is about 0.8 kg. A small CCD camera, equipped at the tip of a robot arm, can recognize an external situation. The web camera and the robot arm's actuator are controlled by USB communication.

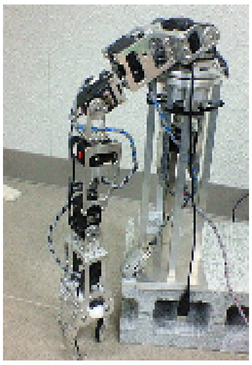

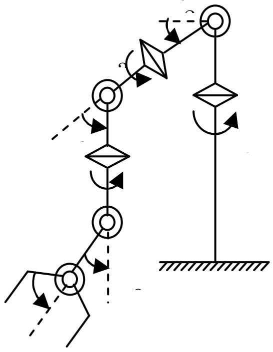

Fig. 1 robot arm　　Fig. 2 degree of robot arm

III. Consciousness-Based Architecture

Fig. 3 shows a diagram of the hierarchical structure model called CBA (Consciousness-based Architecture) that relates consciousness to behavior hierarchically. The characteristic of this model is that the consciousness and behavior fields are built separately. In a dynamic environment, the CBA determines the consciousness level for the environment that the robot is most strongly considering, and the robot then selects a behavior corresponding to the consciousness level and performs this behavior. This model is characterized by the consciousness level reaching an upper level so that the robot can select advanced behaviors when a certain behavior corresponding to a particular consciousness level is discouraged by the external environment. In addition, from an upper level behavior, the robot can choose a low-level behavior. The mechanism of this model allows the robot at its pleasure to select the most comfortable behavior among the low-level behaviors in such a way that the robot aims for certain goals.

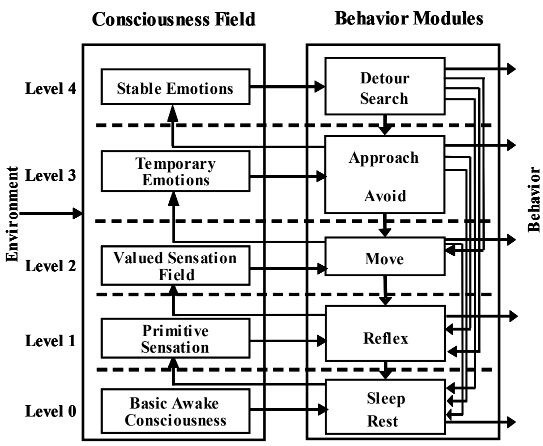

Fig. 3 Consciousness-Based Architecture (CBA)

IV. Flowchart

The flowchart of this system is shown in Fig. 4, and the details of each item are given below.

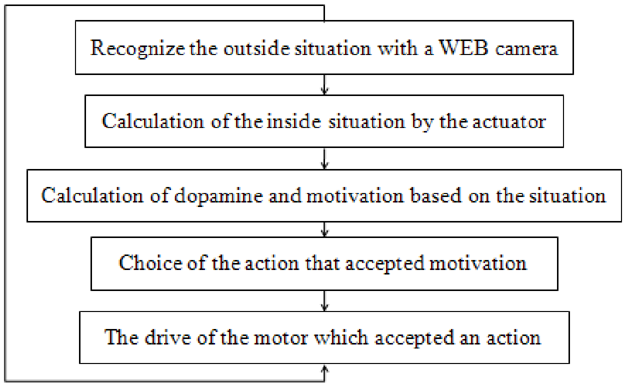

Fig. 4 Flowchart of this system

1. Recognize the outside situation with a Web camera

In this research, we simplify the picture acquired from the Web camera to three kinds, such as green, blue, and other colors We also perform labeling processing so that green and blue are recognized to be qualities of variety-entertainment objects For example, the system may dislike a blue ball and instead like a green ball, which then becomes the favorite. The ability to like something are thus set into the robot arm so that as a result of a labeling process both favorite and disagreeable things can be recognized by the size and form of variety-entertainments objects .

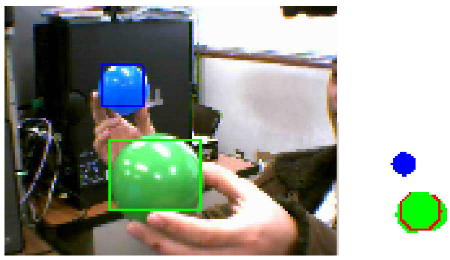

Fig. 5 A former image and a labeling image

2. Calculation of the inside situation by the actuator

The actuator currently used for a robot arm is a DX-117. In operation, this actuator can feed back position, speed, temperature, and other characteristics. Therefore, in real time, you can ask for the temperature and the degree of the rotation angle, and have these reflected by the action of a robot arm, which by its movements indicates a rise in heat or the change in an angle. In relating these values, a robot can be made to express "Tiredness" for example.

3. Calculation of dopamine and motivation based on the situation

When a man and an animal take action, changes occur in the dopamine in the brain. The dopamine generating locus is regarded as a robot's motivation model, and the generating locus was copied using the control model. A control model is shown below. In the graph, changes in ω_n, ζ and T as an example are shown in the following figure.

Rising $y'' + 2\omega_n \zeta y' + \omega_n^2 y - \omega_n^2 u_{(t)} = 0$ · ·(1)

Decaying $y = e^{-t/T}$ · ·(2)

ω_n: natural angular frequency : earliness of a rising

ζ : braking rate : height of the peak of a rising

T : time constant : attenuation performance

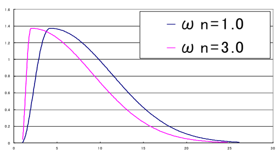

(a) change ω_n

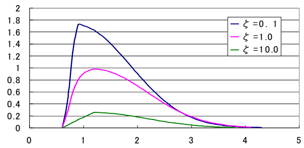

(b) change ζ

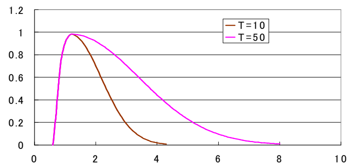

(c) change T

Fig. 6 Motivation model

Based on this, a control model is created, and dopamine is generated with reference to a favorite thing or a disagreeable thing.

ω_n, ζ and T are determined by the outside environment and the internal state. Moreover, they are defined by asking for the total generated dopamine and calculating the secondary delay response in such a way that the total is considered as the input into a robot's motivation.

4. Choice of the action that accepted motivation

The action level was set up by dividing a robot's motivation by a fixed value. In this way, the action which can be chosen according to an action level was limited.

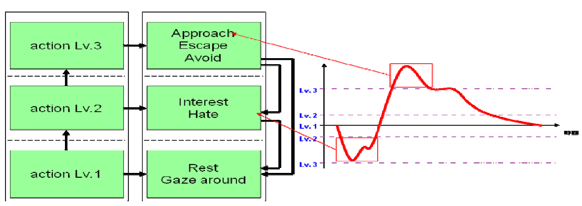

Fig. 7 Choice of the action that accepted motivation

5. The drive of the motor which accepted an action

The robot arm is divided into the shoulder, the elbow, and the wrist, and is driven by giving each control over a finger.

V. Expression of tiredness

A robot arm has the feature that its actions change not only as a result of the outside environment but also internal states. Therefore, it becomes possible to make a robot express tiredness. First, the concept of tiredness is explained. Although various aspects of the factor of tiredness have been considered, the factor of tiredness has not been solved yet. We tried to express tiredness by paying attention to the accumulation of lactic acid. Fig. 8 shows a transition in the lactic acid value at the time of movement, while Fig. 9 shows a transition at the time of the end of the movement.

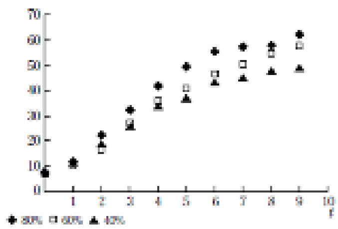

Fig. 8 Transition of the lactic acid value at the time of movement

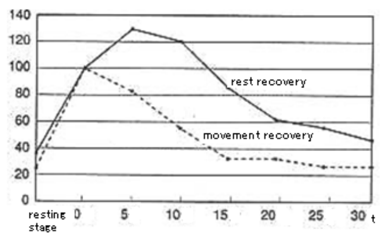

Fig. 9 Transition of the lactic acid value at the time of the end of movement

The speed of a motor and the parameter of motivation were changed by using the graph above. In such a way, the system tried to express tiredness.

Tiredness can be classified into two categories: whole body tiredness and partial tiredness. Whole body tiredness concerns tiredness from moving the whole body greatly and is caused mainly by jogging movements and aerobic workouts. Partial tiredness concerns tiredness of small muscle groups in the hand, shoulder, etc. It is the tiredness which mainly begins in the shoulder and the waist when lifting something. Therefore, whole body tiredness is computed from the internal temperature and the total amount of rotations and is expressed by changing motor speeds and a motivation parameter. By contrast, partial tiredness is computed from the rotation moment of each motor and is expressed by changes to posture positions.

VI. Verification experiment

In order to verify the expression of tiredness, the system verified both whole body and partial tiredness.

1. Whole body tiredness

Since whole body tiredness is defined as tiredness depending on the internal temperature or the total amount of rotations, we investigated each numerical value at the time of operating a robot arm for 5 minutes. Fig. 10 shows the internal temperature; Fig. 11 shows the amount of rotations.

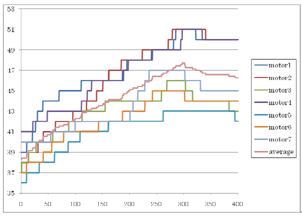

Fig. 10 Internal temperature

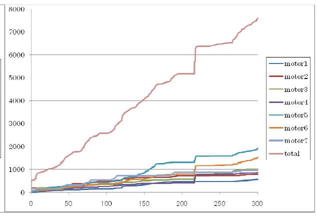

Fig. 11 the amount of rotations

Since the temperature change was lost from the beginning to the end in Fig. 10, it turned out that it is difficult to express tiredness. Moreover, although the value of Fig. 11 was remarkable, since tiredness was related also to the driven time, computations were carried out using the amount of integration and the amount of rotations. Fig.12 shows the integration value of the amount of rotations.

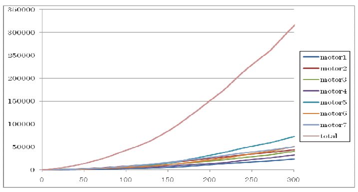

Fig. 12 The integration value of the amount of rotations

In order to express whole body tiredness using Fig. 12, motor speed and a motivation parameter were changed.

2. Partial tiredness

Since partial tiredness is defined as tiredness depending on rotation movements, calculation of the rotation moment was attempted. However, since calculation of the rotation moment did not meet the deadline, only posture change is described. By setting a threshold value as the computed rotation moment, the robot arm can change from usual to light tiredness or from light tiredness to tiredness. Fig. 13 shows the posture change: (a) usual, (b) light tiredness, and (c) tiredness. In Fig. 13(a), an object is followed using all the motors. However, in Fig. 13(b), the object was followed using the motor of an elbow and a wrist, while the motor of the shoulder was stopped. Furthermore, in Fig. 13(c), the object was followed using the motor of only a wrist, while the motor of the shoulder and an elbow were stopped.

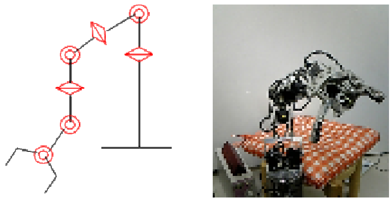

(a) Usual

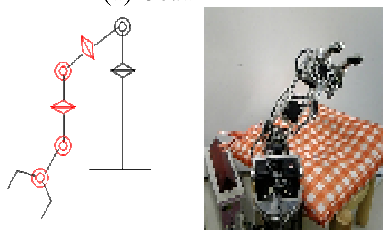

(b) Light tiredness

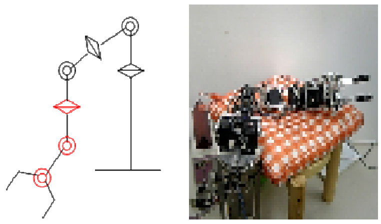

(c) Tiredness

Fig. 13 Posture change

VII. Conclusion

In this paper, we designed the action of the robot arm so that it reflected both the outside environment and an internal state. It is thought that the development of a new action selection based on tiredness would give a user greater affinity. Since at this time we have advanced to a division of tiredness into two categories, we should express tiredness from now on so as to unify the two measures of tiredness.

VIII. Acknowledgement

This research was partially supported by the Ministry of Education and Science,
Sports and Culture, Grant-in-Aid for Scientific Research, 2009.

IX. References

[1]Tran Duc Thao, "Phenomenology and Dialectical Materialism," Godo-shuppan CO., LTD. 1989

[2]Motoki Shimono, Eiji Hayashi, Design of robotic behavior that imitates animal consciousness, proceedings of the 13th international symposium on artificial life and robotics, Beppu, Oita, Japan, 2008

Development of an autonomous-drive personal robot (Self-position correcting by door recognition)

Seiki Matsuura *Eiji Hayashi*
Department of Mechanical Information Science and Technology
Faculty of Computer Science and Systems Engineering, Kyushu Institute of Technology
680-4, Kawazu, Iizuka-City, Fukuoka Prefecture, Japan

Abstract : We are attempting to develop an autonomous personal robot that has the ability to perform practical tasks in a human living environment by using information derived from sensors and a knowledge database. When a robot is made to function in a human environment, the issue of safety must be considered in regard to its autonomous movements. Thus, robots absolutely require systems that can recognize the external world and maintain correct driving control. We have thus developed a navigation system for an autonomous robot. The system requires only image data captured by an ocellus CCD camera. In this study, we focused on developing the necessary self-position recognition that that would allow the robot to move precisely. We limited the environment in which it drove to a corridor. In this system, the robot presumes the position of a door from the image offered by an ocellus CCD camera. Next, it moves to the presumed position and a door is checked. If a door is discovered, the robot calculates the distance between the door and a robot. The calculation result is compared with a map, and the self-position is recognized. This system allows the robot to operate safely and correctly.

KeyWords : Personal robot, Autonomous driving, Ocellus camera

Ⅰ. Introduction

Currently, autonomous self-driving robots are expected to provide various services within humans' living environments. Such robotic technology is already seeing practical use in industry. Thus far, however, the robots used in industry simply carry out the motions indicated by humans. Therefore, we are developing an autonomous personal robot with the ability to perform practical tasks in a human living environment by using information derived from sensors and a knowledge database.

Our robot has a drive mechanism consisting of two front wheels and one back wheel. The front wheels are attached to a motor that independently operates the wheels on either side, while the back wheel is a passive castor wheel. This method has the advantage that a far smaller turn can be negotiated than, for instance, when using a steering system that turns the wheel of a passenger car. DC servo motors are used for the robot's drive mechanism, and position control and speed control are achieved by the drive mechanism's control system. An installed wireless LAN can provide a remote control for humans. All devices are controlled by a PC, and lead batteries supply the electric power.

The navigation system uses only an ocellus CCD camera and processes the image information displayed by that camera. In this study, we focused on developing the necessary self-position recognition that would allow the robot to move precisely. We limited the environment that it drove in to a corridor. A human being in a corridor recognizes his own rough movement distance and current position by placements such as a door, a window, and a fire hydrant. Therefore, to allow our robot to drive correctly, we have registered a map of the life space with the robot beforehand and developed a system in which the robot's self-position is determined by its recognition of a door as the standard marker of its position by means of a CCD camera. In the system, when a thing like a door is reflected at the end of the picture of a passage, the domain is checked with a camera. The system then determined whether the domain is a door. If it is a door, the distance to the door will be calculated and the self-position will be recognized as compared with a map.

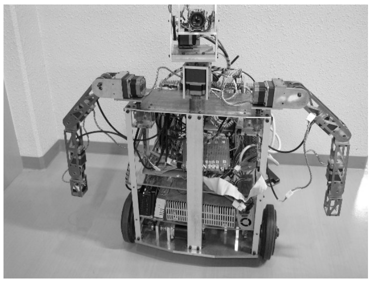

Fig.1. Robot appearance

The map of the life space can prevent the robot from colliding with walls, a door, and other obstacles. One pixel in its map represents a true distance of 5 cm, and the robot moves with the map as a standard. The map of the life space utilized in the present study is shown in Fig. 2.

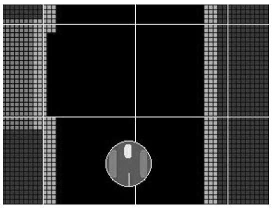

Fig. 2. Map of life space

Ⅱ. A self-position recognition system

This system extracts a straight line ingredient from an image provided from the ocellus CCD camera and distinguishes the door from information about the color of a domain that is surrounded by a straight line.

This system's flowchart is shown in Fig. 3.

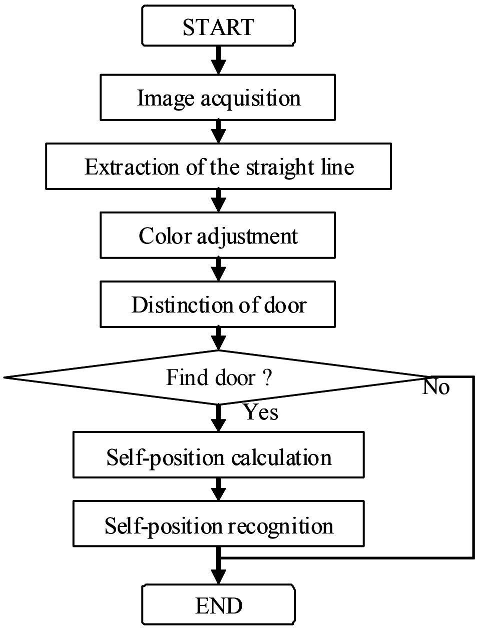

Fig. 3. System flowchart

1. Image acquisition

The image acquired from the ocellus CCD camera has a size of 320×240 pixels and is a 24-bit color image in the RGB form.

2. Extraction of the straight line

The system performs Hough transform processing of the acquired image in order to extract straight lines and circles from points that lie scattered on the image. The extraction of the straight lines is intended to distinguish the boundary lines between the door and wall and between the floor and wall.

This system first performs an edge extraction to determine the border of each domain. The edge extraction detects a discontinuity in the color density by the use of a differential calculus filter. I consider that detected discontinuous ingredients represent the border of a door and the wall or the floor. With a Hough transform, the system converts these ingredients into a straight line that divides the domains. A chart of the extraction of a straight line is shown in Fig. 4.

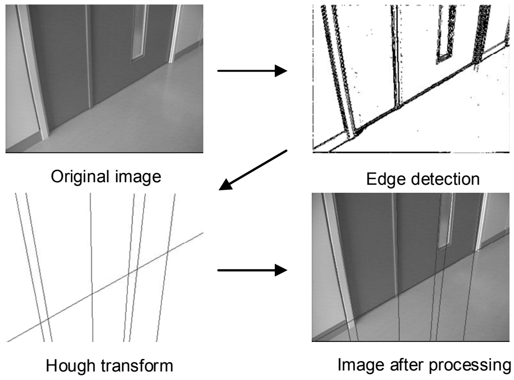

Fig. 4. Extraction of a straight line

3. Color adjustment

When there is no big difference between the color of a door and the wall in a living environment, the system performs a color revision. This is a method to increase contrasts by expanding the distribution in a histogram showing the brightness of the image.

It is easy to increase the distinction when there are slight color differences between a door and the wall by performing this processing. The results of this process are shown in Fig. 4 and Table 1.

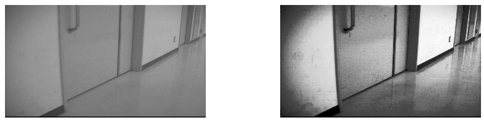

(a) Before adjustment (b) After adjustment

Fig. 4 Results of color adjustment

Table 1. Results of color adjustment

	Before adjustment			After adjustment		
	R	G	B	R	G	B
Wall	138	137	136	152	160	158
Door	139	132	129	157	141	132

4. Distinction of door

By extracting a straight line, the system distinguishes the domain of a door from an image divided into plural domains. I consider a line straight when its lurch is within 0 to 0.9 of the boundary line of a wall and the floor. In addition, the door is considered to be a domain on this straight line, and the average of the pixel values is calculated in the upper part of each domain . As a result, when the domain satisfies a condition set by every working environment, the system distinguishes the domain from a door. To calculate the distance to a door, the system takes a point at the intersection between the door and the domain that is distinguished from a door. It then considers two points in the outside the both ends of the door most, and records them.

5. Self-position calculation

・Calculation of the camera's pan angle

This process calculates the pan angle of the camera so that it can distinguish a door. As with distinguishing the door, I consider a straight line that declines the most to be the boundary line between the wall and the floor. From this line, the system acquires two points as suitable coordinates, and the degree of leaning is calculated.

・Calculation of the distance to the door

From the above, with the points at both ends of the door that the system recorded for door identification and from the angle of pan of the camera calculated as described above, the system calculates the distance between the robot and the edge of the door based on its movement direction and also the shortest distance to the wall.

When the system is not able to detect a door, it calculates only the distance to the wall.

6. Self-position recognition

The system compares the distance between the robot and the edge of the door based on its movement direction and the distance between the robot and the wall based on the angle of the pan of the camera, which it calculated with a map and which allowed it to revise its self-position. It is supposed that the door on the map is the door that it detected according to its movement distance and has been provided from the encoder and the initial position of the robot.

It does not perform a revision for the movement distance when it is unable to detect a door.

The results of the self-position revision on the map are shown in Fig. 5.

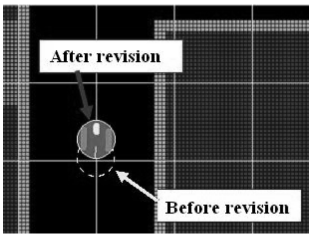

Fig. 5 Self-position revision

Ⅲ. Door-position presumption system

This system detects a domain like a door from camera pictures obtained on-going in a passage. In addition, it calculates the distance to the domain. The timing which checks a door is determined from the calculated distance.

This system is shown in Fig. 6.

1. Shading

This processing rectifies the drop in luminosity of the corner of a camera picture. The characteristics of this drop in luminosity of a camera are investigated beforehand, and the results are reflected in the camera picture.

2. Extraction of the straight line

In this processing, the Hough transform is performed like Ⅱ-2. The edge of the passage is then extracted, and the picture is divided into a wall and a floor. In this system, in order to observe the wall, the floor portion is deleted.

3. Color adjustment

In this processing, the color adjustment is performed like Ⅱ-3.

4. Labeling

Label processing is carried out to acquire a number that is peculiar to each existing connection ingredient in an image and that can be used to classify pixels. In this system, domains other than a wall are extracted from a color.

5. Door presumption

In this processing, a domain with an area more than defined value is presumed to be a door. In addition, it is assumed that a domain that is under a picture most is the nearest. The coordinates of the nearest domain are recorded.

6. Distance calculation

The distance to a thing like a door is calculated based on the coordinates recorded by □-5. The timing which checks a door is determined from this calculated distance.

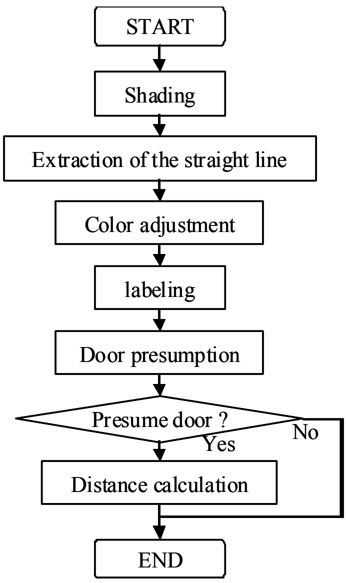

Fig.6 Door position presumption system

Ⅳ. Driving plan

The system uses a map of the life space. Figure 7 shows the driving algorithm. At first, a goal is set up on the map, and a path-finding system searches for a course to arrive at it. Next, the robot starts its movement after having made a driving plan from the course. As the robot runs along the course plan, it constantly repeats the door-position presumption. When the domain that can be presumed to be a door is discovered, a self-position recognition is performed based on the presumed position. The door position presumption is then continuously repeated, and the robot continues toward the goal.

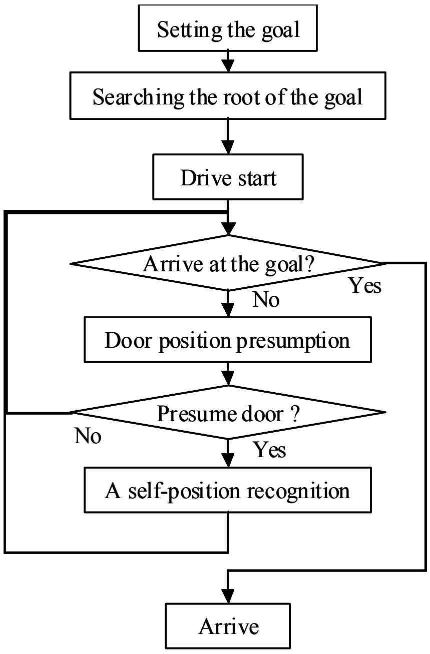

Fig.7 Driving algorithm

Ⅴ. System evaluation experiment

1. Experiment procedure

In order to check the recognition accuracy of this system and to determine the time needed to perform the door-position presumption process, the system evaluation experiment was conducted.

In this experiment, the height of the ocellus CCD camera was set at 87.5 cm from the floor. The robot's migration length was set to 850 cm. The start point was set to 650 cm from the door. The robot's movement speed was 0.5 m/s.

In order to determine the recognition error, the experiment was carried out in an environment that would not easily produce errors. The robot performed the movements and revisions ten times under the conditions described above.

2. Experiment results

The experiment results are shown in Table 2. The average error was 9.6 cm, and the greatest error was 11.7 cm. The average time required for the door-position presumption process was 314 ms.

The error for the system was below the dangerous domain set for the map. This error was an approximately 2-pixel error on the map, suggesting that sufficient revision is possible.

The robot moves 15 cm in 314 ms. The width of the door is between 120 and 150 cm. It is therefore considered that there is little chance of overlooking a door in the door-position presumption system.

Table 2. Experiment results

Average error(cm)	Greatest error(cm)
9.6	11.7

Ⅵ. Conclusions

The average error for this system was found to be 9.6 cm. This is a minute error on a map with regard to the standards of movement. It may therefore be said that the system provides sufficient recognition of the living environment.

It is difficult with this system to recognize doors that are in close proximity to one another. And when an attempt is being made to recognize such doors, other processes cannot be carried out in the meantime. It is therefore considered that the addition of an interval which checks a door is required.

In addition, in the door-position presumption system, other items such as a fire extinguisher may be incorrectly identified as a door domain. It is therefore considered that the conditions for distinguishing the domain of a door from other objects must be added to the system.

References

[1] D.J. Kriegman, E. Triendl, and T.O. Binford(1989), Stereo Vision and Navigation in Buildings for Mobile Robots. IEEE Trans. on Robotics and Automation, vol.5, no.6: pp.792-803

[2] Thorsten Belker and Dirk Schulz (2002), Local Action Planning for Mobile Robot Collision Avoidance. IEEE/RSJ International Conference on Intelligent Robots and Systems '02 IROS: pp. 601–606, 2002.

[3] Hiroshi Mizoguchi, Eiji Hayashi, Development of an obstacle recognition system for autonomous robots in indoor environment, proceedings of the 12th international symposium on artificial life and robotics, Vol1.12th, pp.348, Beppu, Oita, Japan, 2007

[4] Tomoyuki Kinoshita, Eiji Hayashi, Development of distance recognition using an ocellus camera for an autonomous personal robot, proceedings of the 13th international symposium on artificial life and robotics, Vol1.13th, Beppu, Oita, Japan, 2008

A user recognition system using a stemma camera

Seiichi Tanaka **Eiji Hayashi**
Department of Mechanical Information Science and Technology
Faculty of Computer Science and Systems Engineering, Kyushu Institute of Technology
680-4, Kawazu, Iizuka-City, Fukuoka Prefecture, Japan
(0948-29-7793)
(tanaka@mmcs.mse.kyutech.ac.jp)

Abstract: Communication between a person and a robot is necessary for the robot to be able to function in a human living environment in such a way as to be helpful to the humans. A human being needs to send a command to a robot without having to use exclusive equipment, and this requires that the robot recognize the human being. For this purpose, I have developed in this study a system for recognizing a user whose images appear in a CCD camera. The purpose of this system is to enable a robot to recognize the position of a user with a stemma camera image.

This system detects a moving object from an image provided by the stemma of a CCD camera and estimates a search domain. Using color and form information, it judges whether a human being exists in a camera image. In addition, using the zoom function of the camera and an obtained detailed image, it detects the position of the eyes and nose. It also detects features around obtained portions of an image. Finally, it identifies a user by comparing the features with information in a database.

Keywords**:** Robotics, Image processing

1 Introduction

Due to the insufficient number of workers in Japan's low-birthrate society, autonomous self-driving robots will be called upon to provide various services in human living environments. Robots are currently used in industry, where they simply perform a given motion previously made by humans. However, such robots are less useful for tasks in the home. We are developing an autonomous personal robot with the ability to perform practical tasks in a human living environment by using information derived from sensors and a knowledge database.

Our robot has a drive mechanism composed of two front wheels and two back wheels. The two front wheels are attached to a motor, which operates them independently, while the back wheels are castor wheels. DC servo motors are used for the robot's drive mechanism, and position control and speed control are achieved by means of a control system for the drive mechanism. One CCD camera is installed on the head of the robot. It can be rotated to some sides (90 degrees in the top direction, 65 degrees to lower degrees, 90 degrees in the right direction, and 90 degrees in the left direction) by two DC motors. This camera contains approximately 300,000 pixels. All devices are controlled by a personal computer, and electric power is supplied by lead batteries.

To work, the robot needs to receive a command from the human. The robot can be easily sent instructions from devices such as remote controls, personal computers and so on. However, because this step is inconvenient, I developed a system which can recognize a user who appears in camera images.

This system detects a moving object from an image provided by the stemma of a CCD camera and estimates a search domain. Using color and form information, it judges whether a human being exists in a camera image. In addition, it obtains a detailed image of a face using the zoom function of the camera, detecting the position of the eyes and nose from an obtained detailed image. It also detects features around obtained portions of an image. Finally, it identifies a user by comparing the features with information in a database.

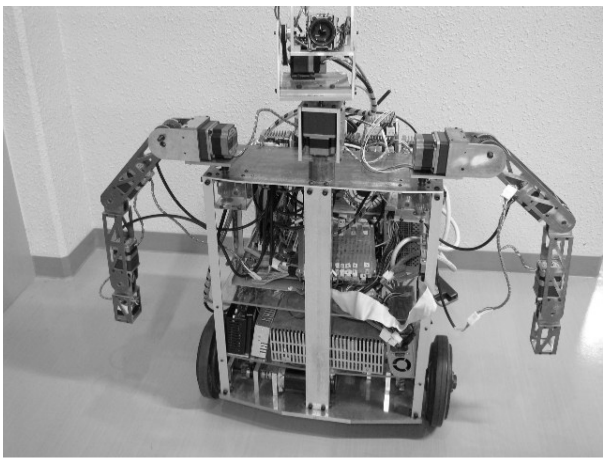

Fig. 1 Robot appearance

2 A user recognition system

2.1 Outline of the system

From an image provided by a CCD stemma camera, the system detects a moving object and carries out a search in its data domain. It pays attention to the shape and color of the object and determines whether it is a non-human object or a human being. In addition, it determines the position of a human face and whether it is a human being from the color, size, and position of the face that it detected. Finally, it takes a zoom picture of the face and determines its features from the obtained expanded image.

2.2 Method for a user recognition system

Here in Section 2, we explain the method for obstacle detection. The flow for a user recognition system is shown in Fig. 2.

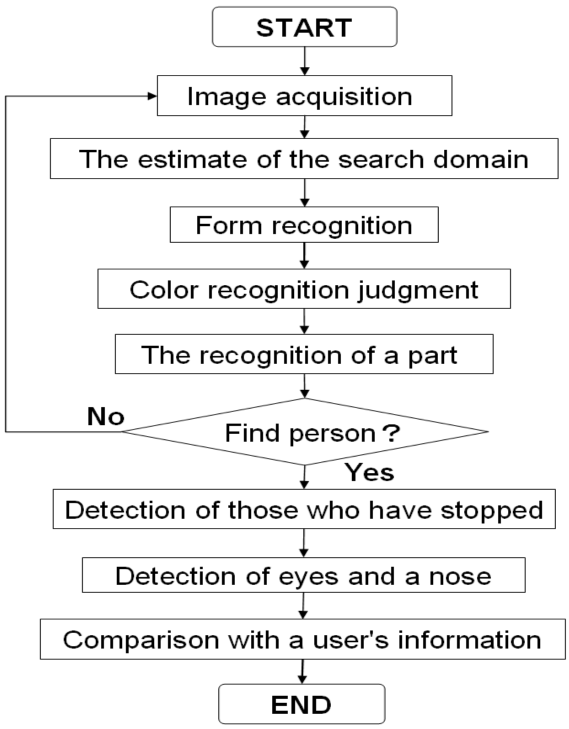

Fig. 2 System flow

Ⅰ. Image Acquisition

The image obtained by the CCD camera is read into a PC in the robot.

Ⅱ. The estimate of the search domain

This process estimates the domain where a human being is from information provided by the difference between frames.

ⅰ.The detection of the difference between frames

This system uses the difference between frames to extract certain objects moving within the camera's view. Because the system is not easily affected by changes in the background, it can resist the effects of such changes. First, our robot acquires an image from the camera and saves it. Next, it acquires a succession of images and compares them with the first image. When differences in the RGB color model exceed a threshold, the system determines whether a significant difference has appeared. An image made from differences between frames is shown in Fig. 3.

ⅱ. The detection of the maximum height

This system detects the maximum height Y of each X point in the image from the differential image which it acquired from the differences between the frames. The image from these detections is shown in Fig. 4.

ⅲ. Average

This system makes a smooth graph by creating an average by 40 pixels of the values of the height Y which it detected at the maximum. It does this because the position sensing of the domain is difficult only at the maximum height Y. The image of the average values is shown in Fig. 5.

ⅳ. The detection of the search domain

From the graph, the system detects the part which is at the top and estimates the position of a human being. Next, it scans from a person's position and detects the point below the top or the point that is lower than 1/3 from the height of the person's position. I assume that a part surrounded by points is a search domain.

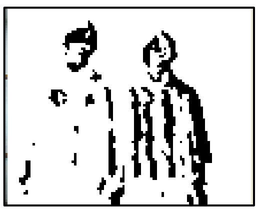

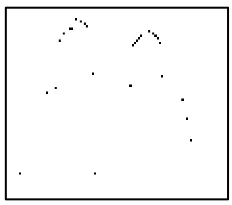

Fig. 3 For a difference Fig. 4 Height at the maximum

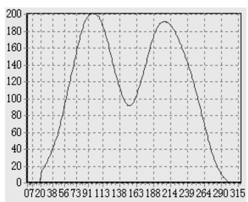

Fig. 5 The graph of the average

Ⅲ. Form recognition by template matching

When this system begins its operation, it reads the template that imitates the head of a person. The outline acquired in the previous process is compared with the template. The size of the template changes according to the size of the search range. Generally, this process requires a great deal of calculation time. Real time operation is achieved by reducing the number of comparisons. When the matching rate is higher than the threshold and reaches its maximum, the position is output as the position of a human face.

Ⅳ. Confirmation by using color information

An image is difficult to identify using only conventional processing. The system has to definitely confirm that the image is that of a human being. Thus, skin color is used to ultimately determine this, using the template matching process to decide the identity and position of the human image. In this case, color information processing uses the HSV color model.

Ⅴ.The recognition of a part piled up

HSV converts the lower domain that this system took as a human face. Then it detects the part of the external color. It makes a histogram of external color pixels for the X and Y coordinates and then judges the position of the face from the histogram. The image which is detected as an external color part is shown in Fig. 6, and the image of the histogram is shown in Fig. 7.

When our system performs these processes and determines that the head of a person is in view, it outputs the position information.

Fig.6 External color extraction

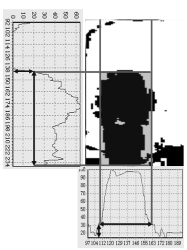

Fig.7 Histogram

Ⅵ. Detection of those who have stopped

In order to detect a human being who tries to take a robot and communication, the human being who is not moving within the picture is distinguished from the human being who is detected. At this time the system detects the human being who has previously appeared in the processing and whose face has not changed its position in the image.

The system zooms on that position in order to acquire information from a detailed image of the face. The image which is detected as that of the stop person is shown in Fig. 8, and the zoom image is shown in Fig. 9.

Fig. 8 Stop person

Fig. 9 The zoom image

Ⅶ. Detection of the part of a face

In order to judge a user, the eyes and nose in a face are recognized. Therefore, the frequency of a certain angle in the image is detected. The detected image at a frequency of 90 degrees is shown in Fig. 10.

The system creates a histogram from the features at the detected frequencies and specifies the eyes and a nose as the features that are detected as a result of the histogram. The image of the detection of eyes and a nose is shown in Fig. 11.

Fig.10 90 degrees

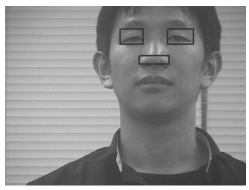

Fig.11 the detection of the part

Ⅷ. Comparison with a user's information

This system judges a user using two processings. First, the position of the detected eyes and nose is compared with the information in a database. Next, it averages the frequency component of each angle. Then it matches these averages with the template of the eyes in a database. The image of detection with the frequency component of each angle is shown in Fig. 12.

Fig. 12 The frequency component of each angle

2.3 Experiment

We performed the following experiment to evaluate the performance of this system for user recognition using a stemma camera.

We have recognized those who are not a user and a user using this system.

The system has recognized users registered by the database. However, when the zoom function of a camera was not appropriate, the system made incorrect detections. When a not user is recognized, It may have been rarely recognized as the user.

The image of user recognition is shown in Fig. 13. The image of not user recognition is shown in Fig. 14.

Fig. 13 User

Fig. 14 Not user

3. Conclusions

We have proposed a system, composed of a stemma camera and intended for use in a indoor environment, that extracts a user's position from a field of view. This system constitutes the beginning for communication between a robot and a human being. Experimental results show that a user can be detected with high probability. However, there was a case in which the system could not successfully search for the user because of various factors. Therefore we propose raising the recognition accuracy by making a nose and a mouth consistent. For these reasons, we believe that the present system requires further improvement. Our next subject of study will be to develop a system that makes possible the recognition of a user's gesture.

References

[1] Takuma Umeno, Eiji Hayashi, Development of an au tonomous personal robot "The visual processing system for autonomous driving," proceedings of the 10th intern ational symposium on artificial life and robotics、Vol.10th, pp. 44, Beppu, Oita, Japan, 2005

[2]Yoshitaka Hane, Eiji Hayashi, User-recognition system for an autonomous robot in human living environments, proceedings of The twelfth international symposium on artificial life and robotics、Vol.12th,pp. 72-75, Beppu, Oita, Japan, 2007

[3]Toshifumi Uewaki, Eiji Hayashi, Development of an autonomous mobile system for an autonomous robot in an indoor environment, proceedings of The twelfth international symposium on artificial life and robotics、Vol.12th, pp. 52-55, Beppu, Oita, Japan, 2007

[4]K. Belloulata and J. Konrad, Fractal Image compression with region-based functionality, *IEEE Transactions on Image Processing*11 (2002) , p. 351

Design of robotic behavior that imitates animal consciousness -Development of Method for Pursuing or Escaping from an Object-

Kouichirou Kurogi Eiji Hayashi

Department of Mechanical Information Science and Technology
Faculty of Computer Science and Systems Engineering, Kyushu Institute of Technology
680-4, Kawazu, Iizuka-City, Fukuoka Prefecture, Japan

***Abstract*:** In this research, in order to aim at "user affinity," a trial to give a robot "consciousness" like a person or an animal is performed. User affinity here includes the function of providing healing, being easy to be with or providing a sense of closeness to a user, or not being boring to a user. Our "the discovery mechanism model of consciousness and action" was built as a trial intending to provide "consciousness" first. For it, we developed a software architecture whereby the system controls the action of an artificial animal based on this model. This architecture is called Consciousness-based Architecture (CBA). Moreover, our newly built "motivation model" is based on the assumption that a certain motive exists in action of an animal; this gives a robot the motive of action. The dopamine generating mechanism of an animal is modeled and included in the the robot arm, thus combining the CBA and the motivation model. Book research has determined how a robot's motivation is affected by a change in the dopamine amount in emergencies. In addition, a system for pursuing a missing object was built.

***Keywords*:** CBA, consciousness of the robot, Motivation of the robot

I. INTRODUCTION

In recent years, the development of non-industrial robots in such fields as medical care and welfare and for life in general has flourished. The function of these robots requires not only the basic functions of robots, such as a high level of intellectual activity, but also the function of user compatibility or affinity so that a user can feel close to the robot as a result of its appearance and behavior. User compatibility includes being able to easily use a robot, not getting tired from this use, and easily developing a sense of closeness with it; it also indicates the function of receiving healing from the use of a robot.

However, although a robot may achieve user compatibility by genuinely modeling a face, it is far more difficult to achieve user compatibility by behavior and actions. User compatibility in this case entails ease of use, non-fatiguing control, robot "friendliness" (i.e., sympathetic use), and human-like capricious behavior. The attempt to give robots "consciousness" such as that identified in humans and animals is a part of these requirements.

In our laboratory, we studied an animal's adjustment to its environment in an attempt to emulate its behavior. We constructed a hierarchical structure model in which consciousness and behavior were related. In regard to this, we developed a software architecture we call Consciousness-based Architecture (CBA). We also made a program to imitate a state with dopamine as the motivation of the robots and included it in CBA. The CBA introduces an evaluation function for behavior selection and controls the robot's behavior.

In the present study, we developed a robotic arm that has six degrees of freedom, with the aim of providing the robot with the ability to autonomously adjust to a target position. Fig. 1 shows an overview of the robotic arm. The robotic arm that we used has a hand consisting of three fingers in which a small monocular Web camera is installed. A landmark object is detected in the image acquired by the Web camera, enabling the robot to perform holding and carrying tasks. In an autonomous action experiment, CBA was applied to a robot arm and its behavior then inspected.

In addition, a system that pursues and escapes from an object was built.

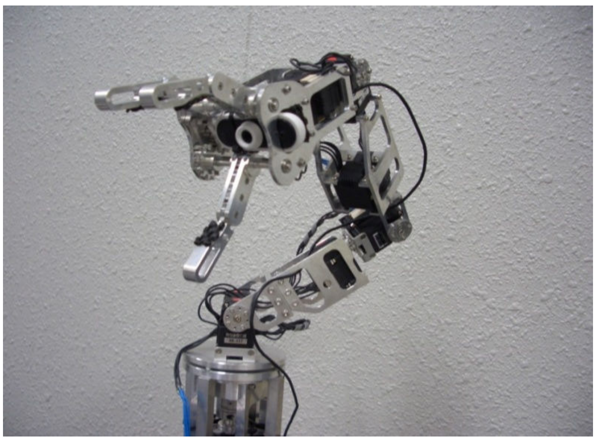

Fig. 1. Overview of Robotics arm

II. SYSTEM STRUCTURE

Fig. 2 shows an arrangement plan of the degree of freedom of the robotic arm. Figs. 2- and 3 show a configuration diagram of the experimental system. The robotic arm manufactured by the Kihara Iron Works is 450 millimeters long and has 6 degrees of freedom. The robotic hand part of the robotic arm has 3 fingers and 1 degree of freedom. Additionally, there is a small Web camera in the robotic hand.

We applied the Dynamixel DX-117 manufactured by ROBOTIS CO., LTD. as the actuator of each joint of the robotic arm. The DX-117 provides a motor, decelerator, and angular sensor unit. This actuator is able to perform position control by providing the robot with a target angle, torque limit, speed limit, and so on. Its transmission method is RS485. Hard wiring can simplify the system by connecting a daisy chain to each actuator used as a joint of the robotic arm.

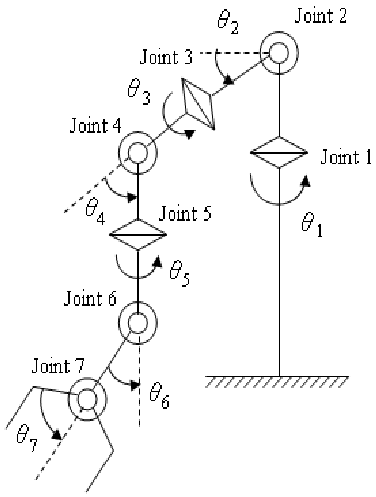

Fig. 2. Arrangement chart of degree of freedom

III. AUTONOMOUS BEHAVIOR

1. The motivation of the robot

Most robots are pleasing to people because of their unique movements. However, because the action choices of robots are too mechanical, those that will resemble human beings and animals are needed to actualize user compatibility. Therefore, at first we considered human actions.

Actions of an animal, including a human being, can be represented in a flow chart by such as "Recognition → Comprehension → Motivation → Action". By contrast, actions of a robot show a simple flow such as "Recognition (Comprehension) → Action".

We considered this simple flow to be one of the causes of "the mechanical action choices of the robot". Therefore, in this study, we incorporated the concept of "the motive" in a robot, and aimed at an action choice that resembled that of a human being or an animal.

2. Imitation of the outbreak mechanism of dopamine

Dopamine is a hormone-like substance in the brain that is related to motivation. When animals, including human beings, take some actions, dopamine is secreted in the brain.

Our laboratory thought that more biologic action choice would be enabled if the outbreak mechanism of motivation by dopamine could be reproduced in a robot.

As a result, a generating model of the dopamine was developed. Fig. 3 shows such a model that expresses a change in the quantity of dopamine outbreak.

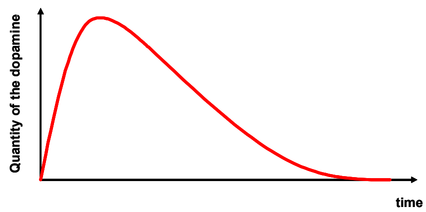

Fig. 3. Traces from outbreak of the dopamine to extinction

Our purpose was for the control model that combined "a second order system" with "a first order system" to output a trace that would show in the figure . First, we used a second order step response for the start of the dopamine. After having arrived at the peak value, we used a primary delay reply that assumed a peak value input. The system expresses a trace of various amounts of dopamine by setting the natural frequency ωn, damping ratio ζ, and time constant Tc of the variable appropriately included in this control model. In this study, we view a trace of this dopamine as the motivation of the robots and will call this function a "Motivation model" in future. Fig. 4 shows the Motivation model

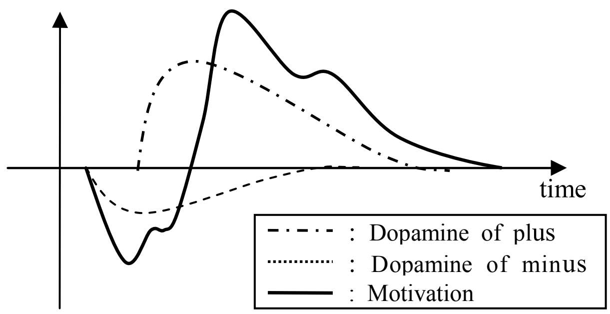

Fig. 4. Motivation model

4. Consciousness architecture (CBA)

Fig. 5 shows a diagram of a hierarchical structure model called CBA (Consciousness-based Architecture) which relates consciousness to behavior. The characteristic of this model is that a consciousness field and a behavior field are built separately. In a dynamic environment, this model relates the consciousness level to the environment that a robot must strongly consider, and the robot then selects a behavior corresponding to that consciousness level and performs the behavior. This model is characterized by the consciousness level reaching an upper level at which the robot can select an advanced behavior when certain behaviors corresponding to the consciousness level are discouraged by the external environment.

Additionally, the robot expressing an upper level behavior can choose a lower level behavior. The mechanism of this model is that it selects the most comfortable behavior within the lower level behaviors at pleasure, so that the robot aims for goals.

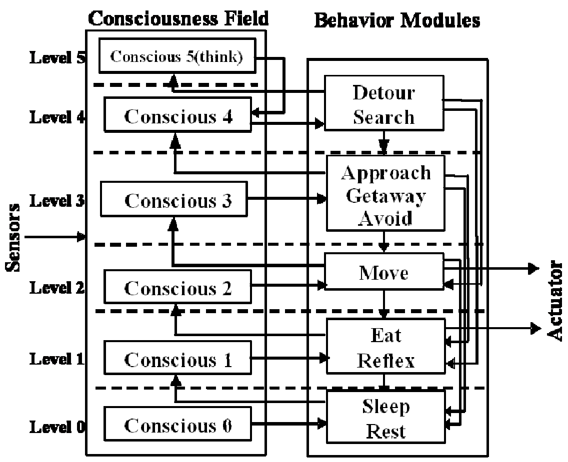

Fig. 5. Consciousness-based Architecture (CBA)

6. Situation recognition with a Web camera

We make a labeling image from an image of a web camera installed in the robot hand. which is divided into green, blue, and flesh colors We divided colors into lumps and determined the shape, size, and center at a gravity position. From this information and the posture of the robot arm, the robot could recognize a position and the distance of a colored object.

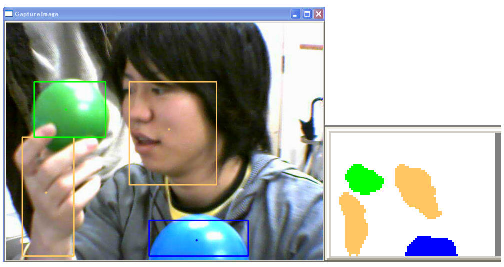

Fig. 6. A Web camera image and a labeling image

IV. System of Object pursuit and escape

It has been possible for a robot as it has been developed until now to pursue a favorable object if it is in the visual angle, and also for it to escape from a disagreeable object. However, an animal and a human being get interested regardless of a favorite thing or a disagreeable thing. Therefore, our laboratory developed the system which pursues an object. In this system, robot pursues the object which moved to outside of the robot's visual angle from the inside of the robot's visual angle, and the object which passed through the inside of the robot's visual angle. In addition, the "main system" shows the robot's entire system developed until now.

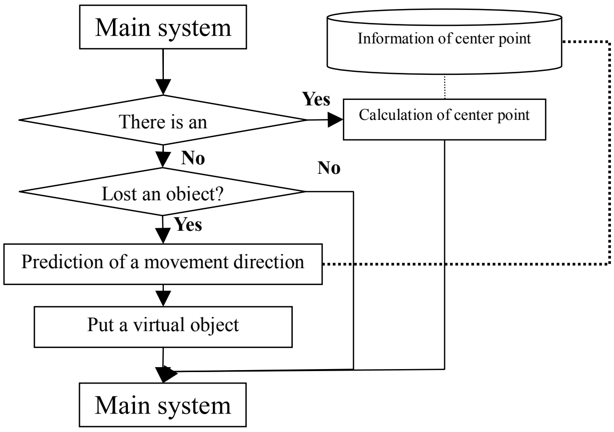

Fig. 7 Flow chart

2. Calculation of the objective central point

At the time of a situation recognition by a Web camera, the maximums and minimums of object's x- and y-coordinates which have been recognized are acquired from the picture to which labeling processing is performed. In order to recognize only the central point of the attentional object, in the object recognized with the WEB camera, a small thing does not obtain the central point of an object as what is not. From the maximum and minimum values of x and y which were acquired, the object was enclosed with a quadrangle and the middle point of an diagonal line of the quadrangle was made into the objective central point. In addition, the system memorizes the central point for three frames.

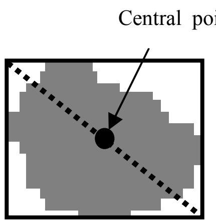

Fig. 8. Central point

3. The objective move direction prediction

The move direction is predicted only when an object is missed at the time of situation recognition. A picture is divided into eight domains in order to predict the move direction. It uses the domain and decides which direction an object moved to. A domain is shown in Fig. 9.

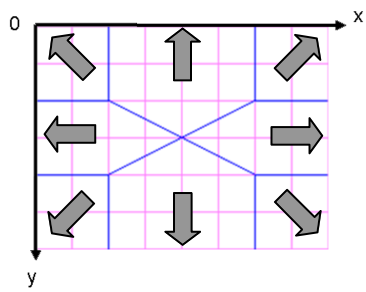

Fig. 9. A division domain and the prediction direction

4. Virtual object creation

The virtual object corresponding to the move direction of the predicted object is created in the visual angle. Since it is possible to pursue the object within the visual angle, a virtual object will be created and it will run after a real object by running after the virtual object.

Ⅴ. INSPECTION OF AUTONOMOUS BEHAVIOR

We applied the motivation model and CBA for a robot arm which we showed in Chapter III, and we inspected the autonomous behavior.

1. Condition setting

The built object pursuit system was incorporated, and the experiment for the robot arm in operation was conducted.

・When a green object (favorite thing) is moved out of the visual angle from the inside of the visual angle.

・When a blue object (disagreeable thing) is moved out of the visual angle from the inside of the visual angle.

Action of a robot arm is shown in Figs. 10 and 11.

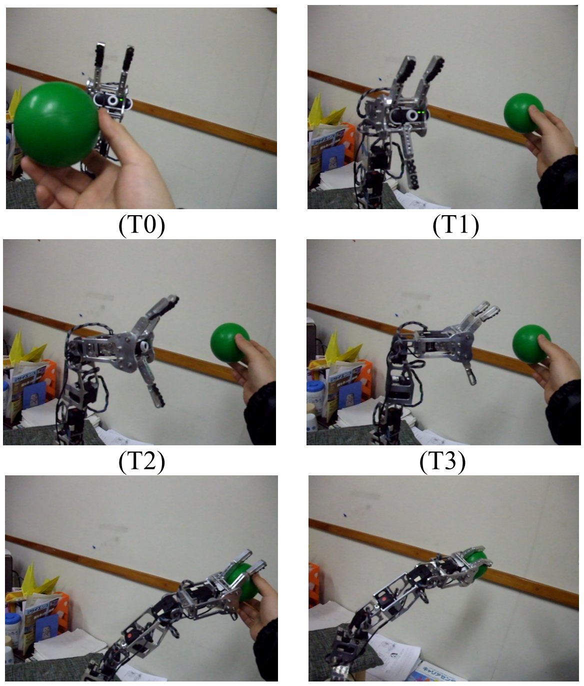

(T0) (T1) (T2) (T3) (T4) (T5)

Fig. 10 Behavior of the robot arm

If a green object is moved from the (T0) position to (T1), the system will recognize that the green object passed inside of the robot's visual angle. At this time, the robot arm judges which direction an object moved to. Then, although pursued to the (T2) position, since the green object had not been recognized, it is pursued to the (T3) position. Furthermore, since the green object has been recognized, robot held the object (T5).

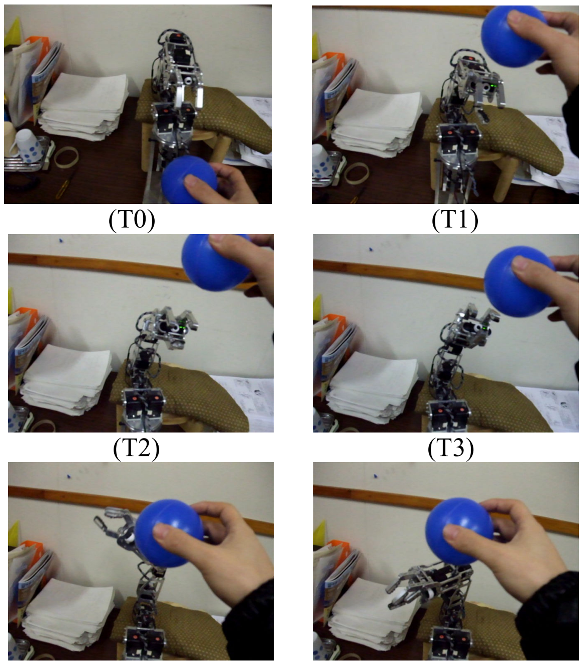

(T0) (T1) (T2) (T3) (T4) (T5)

Fig. 11 Behavior of the robot arm

If a green object is moved from the (T0) position to (T1), the system will recognize that the green object passed the robot arm in the visual angle. At this time, it is being judged like the green object to which the robot arm moved. Then, although pursued to the (T2) position, since the green object had not been recognized, it is pursued to the (T3) position. At (T3), since the green object had been recognized (T4), the operation which the robot dislikes, as shown in (T5), was performed.

VI. CONCLUSION

In this research, We built the system of method for pursuing or escaping from an Object. Pursuing an object which moved to outside of the visual angle from the inside of a visual angle has been checked in an experiment by placing a virtual object according to the direction of movement

VII. Acknowledgement

This research was partially supported by the Ministry of Education, Science, Sports and Culture, Grant-in-Aid for Scientific Research, 2009.

VIII. REFERENCES

[1] Motoki Shimono, Eiji Hayashi, Design of robotic behavior that imitates animal consciousness (AROB 13th ' 08)、Oita, Japan, 2008

Recognition and Movement in Artificial Environment with Bipedal Robot

Naohiro OHTSU, Norihiro ABE, Kazuaki TANAKA, Yoshihiro TABUCHI

Kyusyu Institute of Technology

680-4 Kawazu, iizuka, Fukuoka 820-8502, Japan

Email:ohtsu@sein.mse.kyutech.ac.jp

Abstract: However well we control a bipedal robot in walking, images gotten by the cameras are tilted by left or right swing and small bumps. This complicates recognition of environment by using cameras in walking, and the robot can't move smoothly. Introducing a bipedal robot is to make it possible for both a human and the robot which have the same embodiment to make collaboration by making both take the same behavior as far as possible which is difficult to attain with other types of robots such as a wheel driven robot. Under the artificial environment mainly consisting of vertical and horizontal lines, images must be corrected by detecting the tilt angle of them using Hough Transformation, which detects nearly-vertical lines from artificial environment. As a result, a robot successfully recognizes the environment with a stereo vision using images obtained by correcting tilted ones.

Keywords: Bipedal Robot, Image Processing, Tilt, Correction.

I. INTRODUCTION

In recent years, high-performance and excellent bipedal robots have been developed to support humans. Many of the robots recognize environment with cameras because the robots can acquire much information easily. Although the robots can get much information, even now the robots can't recognize around smoothly. The robots stop in front of obstacles, and then move again. One of the reasons is that recognition of the environment with cameras mounted on the robot is very difficult. However well we control the robots in walking, images gotten with the cameras are tilted by left or right swing and small bumps. This complicates recognition of the environment because it is too difficult to apply general image processing methods to such tilted images directly. Thus, the robots can't get any precise information from the images (distance between a robot and obstacles, and their shapes, etc) easily.

As a result, a robot can't move smoothly. This makes it difficult to make a human cooperate with it. Therefore, a method for correcting the tilted images is required.

One of ideas to correct the images is to use sensors which can detect a physical tilt angle. By using these sensors, a robot can correct the images by rotating them at the angle. However, the precision of the angle depends on mechanical characteristic of the sensors, and the acquisition of sensor values must be synchronized with that of images. Thus, usage of sensors is not suitable for the current purpose because the camera used is of not external but internal synchronization.

In our research, a bipedal robot is equipped with stereo cameras on its head, and images are corrected using a tilt angle detected from them directly with Hough Transformation based on the fact that it moves in artificial environment.

II. BIPEDAL ROBOT

In our research, a bipedal robot as shown in Fig.1 is used to examine whether it can over stride or go up on and down an obstacle safely.

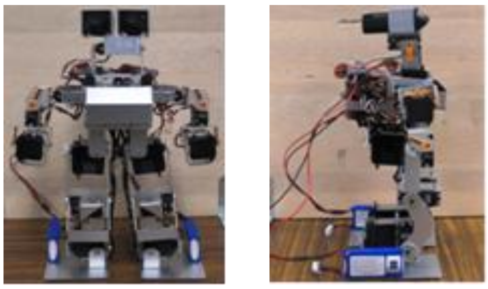

[a] Front View [b] Side View

Fig.1 Bipedal Robot

The specifications of the robot are shown in Table.1.

Table.1 Specifications of the Robot

Size	W240×D140×H345mm(at stand up right)
Weight	1720g (not contain the batteries)
Degrees of Freedom	20 (Head:2 Arm:6 Leg:12)

III. SYSTEM CONFIGRATION

The system configuration constructed for this research is shown in Fig.2.

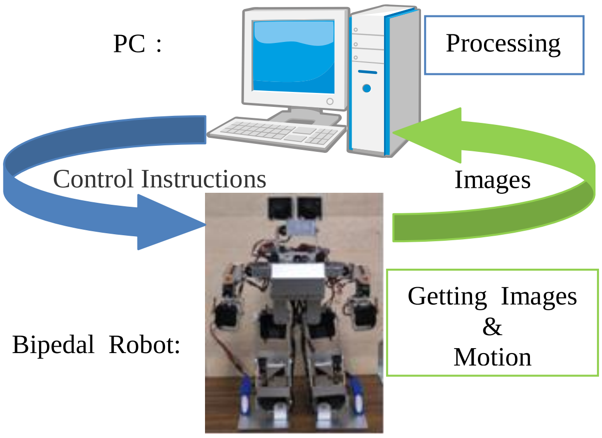

Fig.2 System Configuration

In this system, images captured with cameras are sent to PC and commands to a robot are sent through wireless communication.

IV. LENS DISTORTION

A distorted image as shown in Fig.3[a] is captured with a camera mounted on a robot.

[a] Before Correction

[b] After Correction
Fig.3 Lens Distortion

This distortion can be calibrated with an image processing method. As a result, the image as shown in Fig.3[b] is obtained.

V. IMAGE PROCESSING

1. Methods for Correcting Tilted Images

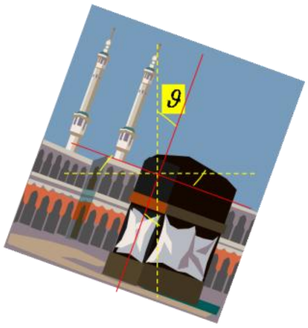

[a] Before Correction

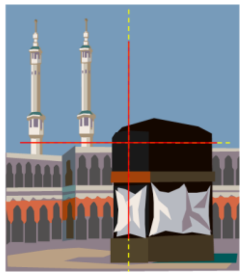

[b] After Correction
Fig.4 Image Blurring

Even when a robot walks on a flat plane, images acquired are tilted as shown in Fig.4[a]. Calculating the tile angle and rotating images as shown in Fig.4[b] by the angle makes it easy to measure the distance to obstacles with an ordinal stereo vision.

Artificial environment includes many static structures of which edges are vertical or horizontal lines. Of course, there are other lines constituting other objects, but the length of them is less than that of vertical lines of walls or doors.

In Fig.4[a], if lines corresponding to the vertical or horizontal lines constituting the artificial environment can be detected, the tilt angle can be found.

In other words, as the longest nearly-vertical line in an image corresponds to a real vertical line of a static artificial structure, detecting it gives the tilt angel.

The number of points on the line, its gradient and the length of a perpendicular on the line from the origin are enough to find the line. They are easily determined with Hough Transformation.

2. Hough Transformation

Using a derivative operator, a sequence of points on an edge shown in Fig.5[a] are detected.

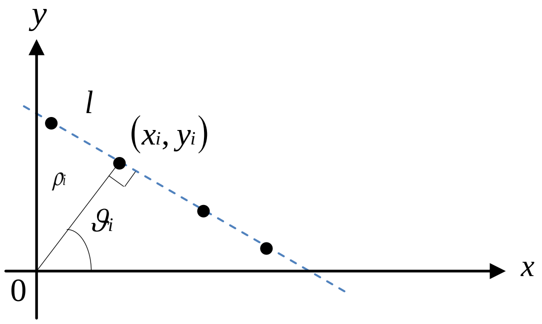

[a] xy Image Space

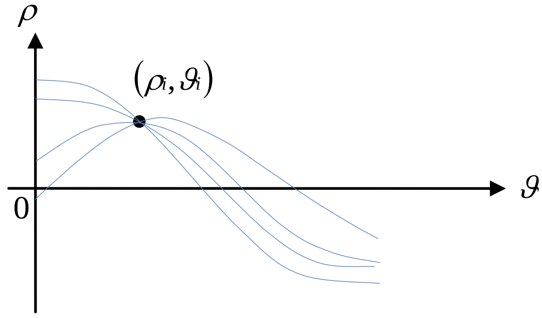

[b] $\rho\vartheta$ Parametric Space

Fig.5 Mapping to $\rho\vartheta$ Parametric Space

Here, each point (x_i, y_i) on a line as shown in Fig.5[a], can be mapped to one sinusoidal wave on a $\rho\vartheta$ parametric space shown in Fig.5[b] which is expressed by equation.(1) when ϑ_i is changed at a regular interval.

$$\begin{aligned}\rho_i &= x_i \cos \vartheta_i + y_i \sin \vartheta_i \\ &= A \sin(\vartheta_i + \alpha)\end{aligned} \tag{1}$$

ρ_i : the length of a perpendicular on the line

ϑ_i : a gradient angle of a perpendicular
$(0 \le \vartheta_i < \pi)$

$$A = \sqrt{x_i^{\,2} + y_i^{\,2}}\ , \alpha = \cos^{-1}(y_i / A)$$

The $\rho\vartheta$ parametric space is composed of a set of small cells, and a counter value of each cell is added by one every time the point with the same (ρ_i, ϑ_i) is found. This processing is called voting.

As a result, the result as shown in Fig.5[b] is obtained after voting against the all points.

Based on the above theory, length of each detected lines is calculated as follow. Length of each line is expressed as a voting number because the number is relative to the length.

Each line detected has a unique (ρ_i, ϑ_i) as a parameter, ϑ_i corresponds to the gradient of the line.

Based on experiment conducted using the robot, 30 degrees is set as the maximum angle of inclination. To detect only lines of which gradient is within the limit, as cells beyond the permissible rage are not taken into count, time needed for performing Hough Transformation is expected to be reduced than the conventional one, but at present it is not implemented.

VI. DETECTION OF THE LONGEST LINE AND THE TILT ANGLE

Here the result obtained with Hough Transformation is shown.

[a] Detection of the Longest Line

[b] Detection of the Tilt Angle

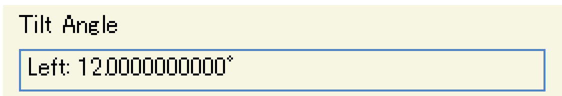

[c] Values of Tilted Angle in the [b]
Fig.6 Detection of the Tilt Angle

Fig.6[a] shows the longest line in the given image, Fig.6[b] shows the image in which the longest line is successfully detected when a robot leans toward right about 12 degrees from a vertical line. The tilt angle is shown in Fig.6[c].

Finally, Fig.7 shows the image obtained by rotating the image shown in Fig.6[b].

Fig.7 Corrected Image

At present, there are cases where Hough Transformation detects not a real but false line as shown in Fig.8, because a long edge of a display is accidentally the longest near-vertical line.

Fig.8 Image of False Detection

The reason is that the system regards an edge of a display as vertical line because it is within 30 degrees. This happens because position of the camera is low and at quite a near location relative to the display. As the height of a robot is low, such an accidental case will often happen.

Therefore, the false detection must be avoided using following methods. Even if a real vertical edge of a wall or column is occluded by objects near a camera, the line will be detectable by searching the upper part of the image, unless the camera is too close to the objects. Usually a robot should not approach but avoid an object unless it must grasp the object. Therefore, it is thought possible to avoid false detection by only detecting vertical lines from the upper part of an image (In our research, we try to detect the lines from the upper quarter part as shown in Fig.9).

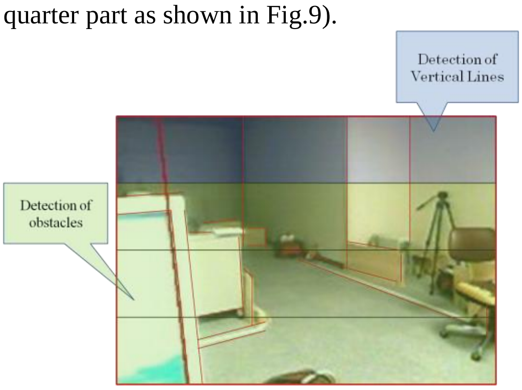

Fig.9 Avoiding False Detection and
Detection of the Obstacles

In addition to this, it is thought that edges of obstacles tend to be in the lower part of the image and edges of polyhedral objects like furniture or equipments are orthogonal with vertical lines (see Fig.9). These facts allow Hough Transformation to find polyhedral obstacles from the lower region of the image. Of course, it is impossible to detect edges of other obstacles, but any artificial objects include straight edges except for a solid sphere, such edges will useful to obstacle recognition.

By subtracting all line segments from edges extracted with a derivative operator, other types of edges can be extracted. Consequently, straight edges and the rest edges are separately available to calculate distance information with a stereo vision method.

We try to avoid false detection and detect of the obstacles with these methods.

Exploiting multi core PC makes it possible to implement image processing using parallel computation.

Further, application of GPU should be also tried to make much faster computation possible than that of CPU.

REFERENCES

[1] Okutomi M, Ozawa S, Shimizu M, Hori O, Ejiri M, Kitamoto A, Goto M, Saito H, Sato Y, Chiba N, Naoi S, Ninomiya T, Fujiyoshi H, Miyahara K, Morisaki K, Yamanouchi Y (2004), Digital image processing (in Japanese). pp.211-214
[2] Forsyth DA, Ponce J (2003), Computer Vision: a Modern Approach.
[3] Nara Institute of Science and Technology OpenCV Programming Book Creative Team (2007), OpenCV Programming Book (in Japanese).
[4] Yasuda K, Kobayashi S, Iiduka H, Abe T, Aoyagi S (2007), Parallel Programming for Multi-Core CPU (in Japanese).
[5] Minami Sato, Yoshihiro Tabuchi, Norihiro Abe, Hirokazu Taki, Shoujie He: "An Autonomously Moving Robot Using Network Cameras", International Symposium on Artificial Life and Robotics (AROB 2008).
[6] Akihiro Fujiwara, Norihiro Abe, Yoshihiro Tabuchi, Hirokazu Taki, Shoujie He: "Control of Autonomous Mobile Robot with Laser Sensor and Image Processing Approach", WMSCI2009.

The Fifteenth International Symposium on Artificial Life and Robotics 2010 (AROB 15th '10),
B-Con Plaza, Beppu,Oita, Japan, February 4-6, 2010

Estimation of other's sensor patterns based on motion imitation and communication –Identification of symbolization strategy for sensor by comparative evaluation questions–

*Keisuke OKUNO and Tetsunari INAMURA

***Abstract*— Estimation of user's sensorimotor patterns by motion observation enables robots to achieve user friendly supporting tasks. In previous works, we proposed a non user specific method to estimate other's sensorimotor patterns by a projection function between other's and self's sensorimotor experiences. Estimation errors derived from differences in body conditions were corrected by queries for sensory patterns. However, other's strategies how to symbolize for sensory patterns were not discussed. Thus, in this paper, we propose comparative evaluation queries for motions for this matter. With the method, the estimation for the other's torque patterns converged after a few queries with successful identifications. Feasible applications of the proposed method are not restricted only for the identification, but can estimate continuous sensory patterns that cannot be expressed by symbol representations.**

I. INTRODUCTION

One of the hard problems of intelligent robots which work in daily life environment is to understand user's intention. To understand user's intention, many methods have been proposed. For instance, observation of user's activity using video camera and rooms with sensor embedded floor with a use of RFID tags are proposed. However, estimation of inner states, such as whether a user would like to be assisted, is not easy to be estimated by these methods. It requires estimation of sensorimotor patterns of the user; it is an important basic technology for the purpose.

Several methods have been proposed to estimate tensional force on muscles with observation of a human's motion patterns by utilizing motion capture system and electromyography with detailed musculo-skeletal model of human's whole body[1][2]. Other methods using measurement devices of brain activities, such as fMRI, PET and EEG, have been also developed to estiamte what motor command a subject is trying to attempt. However, these methods require preparation of user specific musculo-skeletal model or avaraged brain activites in advance. In addition, these approaches cannot deal well with real environment where many users are expected to use in turn. Thus, we are interested in a flexible method that can estimate the sensorimotor patterns even in such real environment.

We propose an approach to estimate other's sensor patterns by a projection function between other's and self's sensorimotor experiences, in order to estimate sensorimotor patterns of the other's without predefined user specific model. By motion imitation with the projection function, the self could observe the other's sensorimotor patterns as if the self experienced that of the other's. Human beings, in daily life, are thought to estimate the other's sensorimotor patterns using the other's simulated experience by the projection function. This is called simulation theory[3], and this way, human beings could make the estimation flexibly.

This approach will work well if the self and the other have identical body conditions. However, it is natural that the conditions are different; estimation errors thus arises from the difference when the self makes the estimation based on the projection function between the sensorimotor experiences.

We have proposed a method[4] to clear this errors when using the approach of projection function, by communication and the mimesis model[5]. The general steps is outlined as follows.

1) The self and the other perform shared motions. From the motion patterns, the self estimates the other's sensory patterns using the mimesis model.
2) The both convert the sensory patterns to an expression call symbol-index, then exchange the expressions by communication.
3) The self uses the communication result in order to detect difference in the sensory patterns, then, modifies the mimesis model to have a better estimation of the other's sensory patterns.

a few repetition of these three steps resulted in a successful estimation of other's sensory patterns with 10%-20% errors[4].

However, there was a remaining problem, a symbolization strategy how to convert sensory patterns into the symbol-index was given for sake of simplicity. Intrinsically, the strategy is supposed to be unknown and it should change dynamically according to circumstances. Thus, it is required to estimate the unobservable symbolization strategy of the other. It is possible to estimate the strategy by the method in the previous work[4] if sets of motions and queries are prepared properly. However, it would require as same or more number of queries as of the strategy candidates. It is because the communication method used was a *open question* and there are almost infinite number of choices for the answers. When interactions between robots and humans

Keisuke OKUNO: The Graduate University for Advanced Studies (SOKENDAI) Japan, k-okuno@nii.ac.jp
Tetsunari INAMURA: National Institute of Informatics (NII) Japan, Assoc. Prof., inamura@nii.ac.jp

are considered, it is better to limit the number of queries from the robot to the human and to reduce the possible choice of the answers. In other words, using *closed question* suits well for human robot interaction.

Thus, in this paper we propose a method, *comparative evaluation queries with motoins*, in order to have less amount of queries. In this method, the other was asked to perform two kinds of motions and answer which motion was heavier, or observed larger torque on joints. Expressing the comparison of the torque as an answer makes the method *closed question*. The *comparative evaluation queries with motoins* is used in the framework of the previous work[4] in order to estimate the intrinsically unknown symbolization strategy how to convert sensory patterns into the symbol-index.

In the second section, the mimesis model's properties and functions are explained followed by an explanation of the method in the previous work[4]. In the third section, the new method is explained. In the fourth section, an experiment using robots as an application of the proposing method will be explained and discussed. In the fifth section we finish the paper with conclusion.

II. Mimesis Model

A. General Properties

It is an engineering model of mirror neuron system[6][7][3]. The mirror neurons fire both when the subject observes a specific behavior and when the subject acts in the same manner. Findings in brain physiology suggestes that it describes relationship of the self and the other. Relationship between the mirro neurons and simulation theory[3] are also discussed.

The mimesis model abstracts sensory patterns $\boldsymbol{S}$ and motion patterns $\boldsymbol{M}$ of humans and humanoid robots. The abstracted representations called *proto-symbol* are calculated using Hidden Markov Models. A geometric space called *proto-symbol space* (PSS) is defined so that it expresses relationship of the proto-symbols as distances among static points x in the space. When a set of motor patterns $\boldsymbol{M}$ and sensory patterns $\boldsymbol{S}$ is defined as $\boldsymbol{O} = \ \boldsymbol{M}\ \boldsymbol{S}$, and a database of sensorimotor patterns is defined as $D = \ \boldsymbol{O}_1 \quad \boldsymbol{O}_n$, the PSS is represented by $P = F_{build}(D)$, where F_{build} is a function to construct the PSS from D. The distances between xs in the space are defined by both using Kullback-Leibler Divergence[8] to calculate distances between HMMs that correspond to the similarities of sensorimotor patterns, and using multi-dimensional scaling method[9].

B. Functions

The mimesis model offers following functions by utilizing the PSS. F_{recog}; a function to recognize sensorimotor patterns as a static point x in PSS, F_{gen}; a function to generate sensorimotor patterns from a x, an imitation function that outputs imitated sensorimotor patterns, and F_{assoc}; an association function that associates a partial sensorimotor patterns with a whole sensorimotor patterns even when only partial information is observed. Motion patterns can be also interpolated and extrapolated by creating internal/external dividing points of two proto-symbols in the PSS to define novel motion patterns[10]. In this way, the mimesis model can recognize and generate even unknown sensorimotion patterns, which are not in the database D.

C. Estimation of Sensorimotor Patterns

We realized the concept, which is an estimation of other's sensorimotor patterns by projection function between sensorimotor experiences of the self and the other, by using the mimesis model. We proposed a method with *open question* type communication to estimate the other's sensorimotor patterns in more precise manner, even if the body conditions are different in the slef and the other[4]. The outline of this process explained as follows and is depicted in Fig.1.

1) As an initial state, the self sets the other's inference model $\hat{P}_{other}$ based on own experience $D_{other} = \ \boldsymbol{S}_{self}\ \boldsymbol{M}_{self}$.
2) The self constructs $\hat{P}_{other}$ with $\hat{D}_{other} = \ \hat{\boldsymbol{S}}_{other}\ \boldsymbol{M}_{other}$ using F_{build}.
3) The other executes the shared motion $\boldsymbol{M}$ and observes corresponding $\boldsymbol{S}_{other}$. The self obtains $\hat{\boldsymbol{S}}_{other}$ from $\boldsymbol{M}_{other}$ using F_{assoc}.
4) Both the self and the other converts $\hat{\boldsymbol{S}}_{other}\ \boldsymbol{S}_{other}$ into symbol-indexes $k_{self}\ k_{other}$ respectively using a discretization function $F_{symbolize}$,
$$k_{self} = F_{symbolize}(\hat{\boldsymbol{S}}_{other}) \tag{1}$$
$$k_{other} = F_{symbolize}(\boldsymbol{S}_{other}) \tag{2}$$
The symbol-indexs are integers corresponding to strength of the sensor $\boldsymbol{S}$s.
5) The self modifies the $\hat{\boldsymbol{S}}_{other}$ in the $\hat{D}_{other}$ according to the result of exchange of the symbols k_{self} and k_{other}.
$$\hat{\boldsymbol{S}}\ _{other} = \frac{k_{other}}{k_{self}} \hat{\boldsymbol{S}}_{other} \tag{3}$$
6) The self reconstructs $\hat{P}_{other}$ with the newly modified $\hat{D}\ _{other} = \ \boldsymbol{M_{other}}\ \hat{\boldsymbol{S}}\ _{other}$,
$$\hat{P}_{other} = F_{build}(\hat{D}\ _{other}) \tag{4}$$

Steps through 3 to 6 are considered as single conversation set. The self adaptively acquires $\hat{P}_{other}$ with repetition of the conversation sets.

The remaining problem in the work[4] is that $F_{symbolize}$ was given. Intrinsically, the $F_{symbolize}$ is supposed to be unknown and it might change dynamically according to circumstances. In the next section, a method to estimate the other's $F_{symbolize}$ will be explained.

III. Comparative Evaluation Queries with Motions

In this section, we propose a communication method using *comparative evaluation queries with motions* in order the self to estimate other's symbolization strategy $F_{symbolize}$ how to convert sensory patterns to symbol-index. Choices of answers for the *comparative evaluation queries with motions*

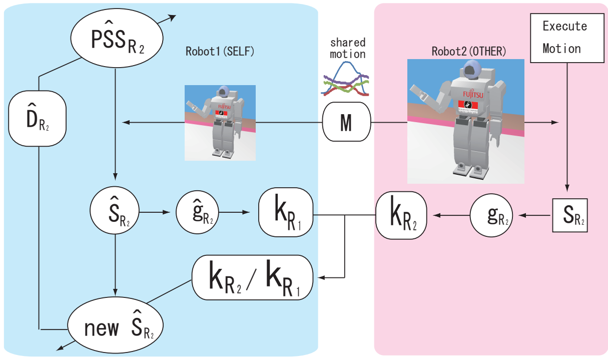

Fig. 1. Adaptive acquisition flow diagram of the other's proto-symbol space by open question

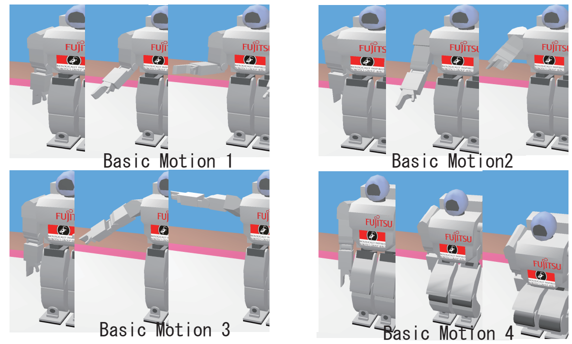

Fig. 2. Basic shared motion patterns for constructing PSS

are finite. For example, the answer could be either "yes" and "no". When the self attempts to estimate the other's $F_{symbolize}$, the self prepares more than two shared motion patterns. These motion patterns are designed specifically for the estimation of other's $F_{symbolize}$. The query of the *comparative evaluation queries with motions* is to ask for relative relationship of the observed sensory patterns for the motions. For example, an answer would be "Motion 1 is heavier". When there is an association function between sensorimotor patterns of the self and the other, this method can be applied to estimate continuous sensory patterns even if that cannot be expressed by symbol representation. The self can estimate the other's $\hat{F}_{symbolize}$ by following steps.

1) According to the identification target $F_{symbolize}$, the self prepares motion patterns $\boldsymbol{M}_i(i = 1\ \ 2)$.
2) The other imitates each $\boldsymbol{M}_i$ and observes corresponding sensory patterns $\boldsymbol{S}_i$.
3) The other converts $\boldsymbol{S}_i$ into scalar value g_i using conversion function $F_{symbolize}$.

$$g_i = F_{symbolize}(\boldsymbol{S}_i) \qquad (5)$$

4) The other replies with a symbol-index K that tells the magnitude relation of the $g_1\ \ g_2$.

$$K = F_{comp}(g_1\ \ g_2) \qquad (6)$$

That is, K is either "M_1 is heavier"('>'), "M_2 is heavier"('<') or "same"('equal').

5) The self identifies the other's $F_{symbolize}$ based on the replied symbol-index K.

If necessary, the self prepares a new set of motion patterns and repeats the steps above till identifies the $F_{symbolize}$.

IV. Application

For a validation of the proposing method *comparative evaluation queries with motions*, in this section, an application is introduced and an experiment is explained. The experiment of the application to solve a remaining problem in the previous work[4] is conducted. It is that the self estimates the other's symbolization strategy $F_{symbolize}$ that is unknown.

A. Conditions

The experiment involved two virtual humanoid robots HOAP-2 in a simulator environment. R_1 weighted 2 4[kg] as the self and R_2 weighted 4 8[kg] as the other were used. The masses were unknown to each others. Only symmetrical motions were used in the experiment, and considered joint angles are that of the right elbow, right shoulder's roll and pitch rotation and the right knee $\boldsymbol{\theta} = [\ _1\ \ _2\ \ _3\ \ _4]$. Considered joint torques were consisted of observed torques of the same joints $\boldsymbol{\tau} = [\ _1\ \ _2\ \ _3\ \ _4]$ respectively. The self prepared database $D_{R_1} = \ \boldsymbol{\tau}\ \boldsymbol{\theta}$ with four basic motions(Fig.2) for constructing proto-symbol space P_{R_1}.

As an association function F_{assoc} from $\boldsymbol{\theta}$ to $\boldsymbol{\tau}$, the R_2 observed the torque patterns $\boldsymbol{\tau}$ on the joints when R_2 performed the motions $\boldsymbol{\theta}$. In the experiment, we deal with estimation of $F_{symbolize}$ by R_1 identifying the conversion rule F_{conv} (Eq.(5)). It is because $F_{symbolize}$ is a composite function of F_{div} and F_{conv}, where the F_{div} divides input g into d equal segments and assigns symbol-index k based on TableI. This time the F_{div} was fixed and known to the self. As a discussion will be made in the section 6, estimation of the unknown F_{div} using the proposing method is possible and left for a future work.

TABLE I
RELATION BETWEEN SYMBOL INDEX AND VOCABULARY

k	d=3	d=5	d=7
1	light	light	very light
2	normal	bit light	light
3	heavy	normal	bit light
4	-	bit heavy	normal
5	-	heavy	bit heavy
6	-	-	heavy
7	-	-	very heavy

In this paper, following four conversion rules $f_i(i = 1\ \ \ 4)$ were prepared as candidates for the F_{conv} that converts joint torques($\boldsymbol{\tau}$) to an intermediate scalar value g.

- Average of all the torque patterns

$$f_1(\boldsymbol{\tau}) = \frac{\sum_j^J \frac{\int \ _j(t)dt}{T}}{J} \qquad (7)$$

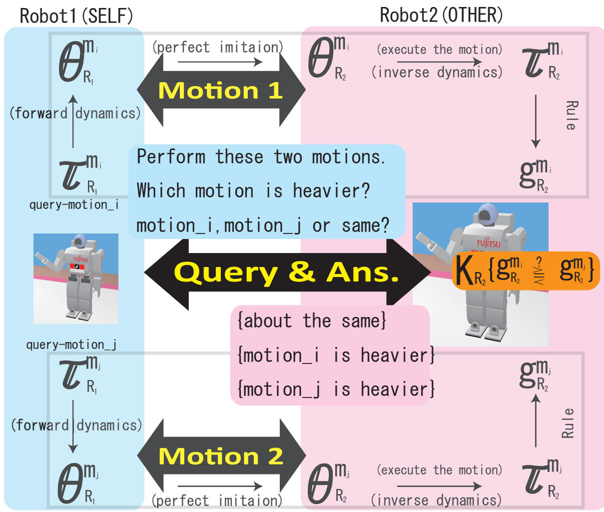

Fig. 3. Diagram of "comparative evaluation queries with motions"

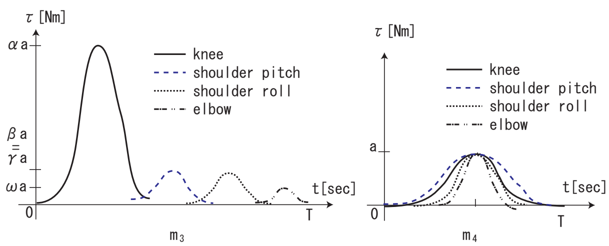

Fig. 4. Motion3 and Motion4 for the query2

- Sum of maximum values of each joint torques

$$f_2(\boldsymbol{\tau}) = \sum_{j}^{J}(\max_{t} \quad _j(t) \quad) \tag{8}$$

- Maximum value of composed joint torque patterns.

$$f_3(\boldsymbol{\tau}) = \max_{t} \sum_{j}^{J} \quad _j(t) \tag{9}$$

- Maximum value of maximum of each joint torques

$$f_4(\boldsymbol{\tau}) = \max_{j} \ \max_{t} \quad _j(t) \tag{10}$$

where T was the time period of $\boldsymbol{\tau}$. In this paper $J = 4$ was used.

B. Method

We explain how to design motion patterns and what queries makes the identification effectively. The flow of procedures is depicted in Fig.3. Two queries were prepared for the identification of the F_{conv}.

1) At first, R_1 makes query1 to identify whether $\hat{F}_{conv} = f_1$ or not. At query1, the R_1 uses two motions $m_1 \ m_2$ to execute query procedure explained in the section 3. R_2 imitates the motions($i = 1 \ j = 2$ in Fig.3). In order to identify whether $F_{conv} = f_1$, the m_1 and m_2 are designed so that maximum torques are differents but average torques over the same time period are the same.
2) The R_1 identifies $\hat{F}_{conv}$ based on the R_2's reply K. If $K =' \quad . \quad ,'$ then identifies as $\hat{F}_{conv} = f_1$, otherwise makes the next *comparative evaluation queries with motions*, and proceeds to query2.
3) The R_1 uses two motions m_3 and m_4(Fig.4) to execute query procedure explained in the section 3. At the query2, m_3 and m_4 were designed to identify the $\hat{F}_{conv}$ from $f_2 \ f_3 \ f_4$ at a time. The m_4(Fig.4) is a motion that the four joints bend and then stretch simultaneously, and the maximum torque are taken at the same time at the same value a. The m_3(Fig.4) is a motion that starts with a bending and stretching movement on the knee (a squat), followed by an up-and-down movement of the pitch rotation on the shoulder, followed by an up-and-down movement of the roll rotation on the shoulder, and ended with a bending and stretching of the elbow joint. The maximum values of each joint torque of the m_3 are $(\ a \ \ a \ \ a \ \ a)$. Constants a are required to meet the following conditions for the identification of the F_{conv}.

$$a < \quad < 4a \tag{11}$$

$$4a = \quad + \quad + \quad + \tag{12}$$

$$0 < \tag{13}$$

In this paper, $(\qquad) = (3\ 0a \ \ 0\ 4a \ \ 0\ 4a \ \ 0\ 2a) \ \ a = 0\ 5$ were used.
4) The R_1 identifies $\hat{F}_{conv}$ based on the R_2's reply K. If $K =' \quad . \quad ,'$ then $\hat{F}_{conv} = f_2$, if $K =' >'$ then $\hat{F}_{conv} = f_4$, If $K =' <'$ then $\hat{F}_{conv} = f_3$.

It is assumed that the R_2 made perfect imitation of m_i performed by R_1, also assumed that the same conversion rule F_{conv} was applied to all the joints regardless of motion patterns.

C. Evaluation

In this paper, both R_1 and R_2 had identical body structures and mass density distribution with different amount of masses. The assumption that the R_2 imitates the motions of R_1 perfectly was taken. These conditions and assumptoin results in 100% successful identification of the conversion rule F_{conv}

To show the importance of identification of the F_{conv}, R_2's joint torques were estimated both with a successful identification of the F_{conv} and with an incorrect identification. 10 kinds of unknown motions $\boldsymbol{M'}_i (i = 1 \quad 10)$, which were different from the four basic motions, were introduced for the evaluation. These unknown motions consisted of arbitrary movement of the 4 joints. An error e between estimated torque $\hat{g}$ and the real g were defined as follows, using both known and unknown motions.

$$e = \frac{1}{N}\sum_{i}^{N}\frac{|\hat{g}_i \quad g_i|}{g_i} \tag{14}$$

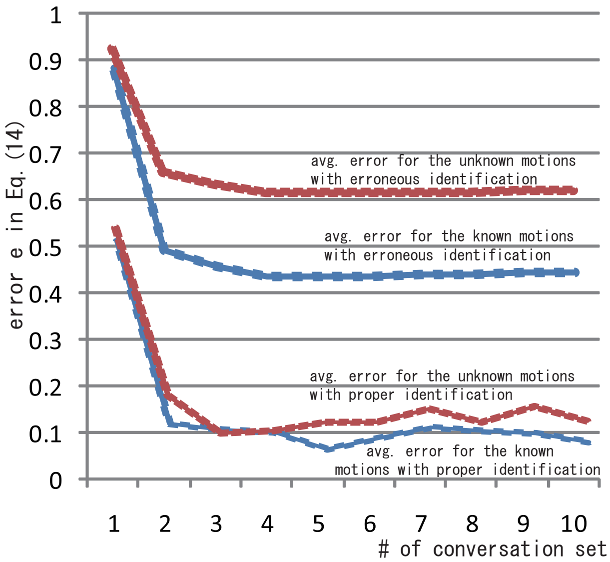

Fig. 5. Estimation results of torques of known and unknown motions when both successful and erroneous strategy identification when $d = 5$ and $F_{conv} = f_4$. The horizontal axis is number of conversation sets explained in section 2, and the vertical axis is the error e.

N was the number of motion patterns used for the evaluation. Experiment results when N=10 were shown in Fig.5. It shows, after a few set of conversation, that estimation of the other's torque can be achieved with approximately 10% error even if the motions are unknown. It also shows that errors are 45 60% for torque estimation when the identification of the $\hat{F}_{conv}$ failed.

The *comparative evaluation queries with motions* can estimate 3^N kinds of symbolization strategies by making qeuries with motions N times. This efficiency is important when the human robot interaction is considered, that is, the human can use the system without complex and large amount of preparation.

V. Conclusion

In this paper, we proposed a estimation method by *comparative evaluation queries with motions*. This enables robots to estimate 3^N kinds of symbolization strategies, how to convert torque patterns to symbol-indexes, by making queries with motions N times. The method consists of making queries with motions about unobservable sensory patterns, based on simulated other's experience that is calculated by projection function between experience of the self and the other. We think that the method is a fundamental interaction method for estimating other's unobservable inner information, such as sensory patterns.

This method is also thought to be useful to deal with the *correspondence problem*[11][12][13]. The *correspondence problem* is generally considered as a problem that deal with correspondence relationship between body parts of the self and the other. However, using the *query with motions*, it is possible not only to deal with motions, which can be shared between the self and the other, but also to deal with a new problem how to map between the self's sensory patterns and the other's unobservable sensory patterns.

In addition, with *comparative evaluation queries with motions*, it is possible to estimate continuous sensory pattern even when that cannot be expressed by symbol representations. The comparative evaluation of sensory patterns is an objective measure and the result is accurate, even when an estimation target sensor is other's unobservable one. Taking advantage of these properties, the proposed method can be applied, for instance, to estimate F_{div} defined at Table I and weight coefficient for each joints in Eq.(7)-Eq.(10).

Future works include estimation of the other's sensory patterns with the other's imperfect imitation, training method how to correct the other's imperfect imitation, estimation of information that cannot be expressed by scalar value such as line of sight and tactile information, estimations with different density distribution of the masses, and estimations with different DoF configuration of body structures.

References

[1] Gentiane Venture, Katsu Yamane, and Yoshihiko Nakamura. Identification of human musculo-tendon subject specific dynamics using musculo-skeletal computations and non linear least square. In *Proc. of the IEEE/RAS-EMBS International Conference on Biomedical Robotics and Biomechatronics*, pp. 211–216, 2006.

[2] Gentiane Venture, Katsu Yamane, and Yoshihiko Nakamura. In-vivo estimation of the human elbow joint dynamics during passive movements using musculo-skeletal model computations. In *Proc. of the IEEE/RAS-EMBS International Conference on Biomedical Robotics and Biomechatronics*, pp. 205–210, 2006.

[3] Vittorio Gallese and Alvin Goldman. Mirror neurons and the simulation theory of mind-reading. *Trends in Cognitive Sciences*, Vol. 2, No. 12, pp. 493–501, 1998.

[4] Tetsunari Inamura and Keisuke Okuno. Estimation of other's sensory patterns based on dialogue and shared motion experiences. In *International Conference on Humanoid Robots*, pp. 617–623, 2009.

[5] Tetsunari Inamura, Hiroaki Tanie, and Yoshihiko Nakamura. From stochastic motion generation and recognition to geometric symbol development and manipulation. In *International Conference on Humanoid Robots*, 2003. (CD-ROM).

[6] Giacomo Rizzolatti and Michael Arbib Language within our grasp. *Trends in NeuroScience*, Vol. 21, pp. 188–194, 1998.

[7] Merlin Donald. *Mimesis and the Executive Suite: missing links in language evolution*, chapter 4, pp. 44–67. Approaches to the Evolution of language: social and cognitive bases, Cambridge University Press, j. hurford and m. kennedy and c. knight edition, 1998.

[8] Solomon Kullback. *Information Theory and Statistics*. Wiley, 1959.

[9] Susan Schiffman. *Introduction to Multidimensional Scaling: Theory, Methods, and Applications*. Academic Press, 1981.

[10] Tetsunari Inamura and Tomohiro Shibata. Geometric proto-symbol manipulation towards language-based motion pattern synthesis and recognition. In *Proc. of Int'l Conf. on Intelligent Robots and Systems*, pp. 334–339, 2008.

[11] Aris Alissandrakis, Chrystopher L. Nehaniv, and Kerstin Dautenhahn. Imitation with alice: Learning to imitate corresponding actions across dissimilar embodiments. *IEEE Transactions on System, Man and Cybernetics -Part A: Sysmtes and Humans*, Vol. 32, No. 4, pp. 482 – 496, 2002.

[12] Verena Hafner and Frederic Kaplan. Interpersonal maps and the body correspondence problem. In *In Proceedings of the Third International Symposium on Imitation in Animals and Artifacts: Social Intelligence and Interaction in Animals, Robots and Agents*, pp. 48 – 53, 2005.

[13] Christopher Nehaniv and Kerstin Dautenhahn. *The correspondence problem. In Imitation in Animals and Artifacts*. MIT Press, 2002.

The Fifteenth International Symposium on Artificial Life and Robotics 2010 (AROB 15th '10),
B-Con Plaza, Beppu,Oita, Japan, February 4-6, 2010

A Walking Gait Generation Using Stance-leg Actuation

Xiaoyue Zhang[2] and Mingguo Zhao[1,2]

1. State Key Laboratory of Robotics and System (HIT)
2. Dept. of Automation, Tsinghua Univ. Beijing, P. R. China
(Tel : 86-10-6279-5448; Fax : 86-10-6278-6911)
(zhangxy08@mails.tsinghua.edu.cn)

Abstract: We study a simple two-link model based on Passive Dynamic Walking which can walk on the level ground. It is powered by extending and shortening the telescopic stance-leg. Through the simulation of an easy equivalent instantaneous model, we find that the stance-leg actuation is a way to compensate for the lost energy at the collision. It has stable cyclic walking gait. Besides, the model has mechanical energy feedback.

Keywords: stance-leg actuation, passive dynamic walking, powered walking, mechanical energy.

I. INTRODUCTION

In the early 1990s, McGeer pioneered Passive Dynamic Walking (PDW) robots that can walk down on shallow slopes without actuation and control [1]. This passive robot has a gait which is very natural and energy-efficient. The PDW concept shows us that walking can be sustained only by gravity. These passive robots must walk on a slope which provides a source of energy to compensate for the lost energy at the inelastic collision with floor. However, it is impossible to restore energy by gravity on level ground. So it is important for a robot to restore the lost kinetic energy through other approaches.

When McGeer proposed the PDW, he also put forward some ways to make passive walkers walk on level ground with active sources which have been realized by the followers [2]. These applications compensate for the lost energy with either kinetic energy or potential energy. Recently, Asano and Luo *et al* propose a parametric excitation approach which is a principle to increase the amplitude of vibration by swinging [3]. They demonstrate that the mechanical energy compensation is a good way to achieve energy-efficient and high-speed gait. The Robots lab in Automation Department in Tsinghua University introduced the "virtual slope walking" that compensates for lost energy through extending the stance leg and shortening the swing leg.

In this paper, we propose another way to compensate for the lost energy with mechanical energy. The model we discuss here has telescopic actuators on the legs. The system's energy is increased through up-and-down motion of the mass in the hip by the stance leg's extension and shortening. It is hard to study the model analytically when the leg's length is in the course of changing. But through numerical simulations we can find an equivalent place in the middle of the process of extension where the leg extends instantaneously. So does in the process of shortening. Then we can study this equivalent model which is easy to analyse under the conservation of angular of momentum.

This paper is organized as follows. In section Ⅱ, the model with telescopic legs and its parameters are introduced. In Section III, the walking map is presented using Lagrange Equation. In section IV, we find an easy equivalent model. In section V, the analysis of this equivalent model is conducted to clarify the existence of the fixed point and its stability. Finally, in section VI, we study the mechanical energy of this model.

II. THE MODEL

The model in this paper is a simplified model with only one mass *m* in the hip and two massless telescopic legs connected to the hip. As shown in Fig. 1(a). The other parameters and the whole walking step are shown in the Fig. 1(b). θ is clockwise angle of the stance leg with respect to the vertical, ω is the angular velocity of the stance leg and φ_0 is the counter clockwise inter-leg angle. A step starts when the prior swing leg has just made contact with the ground and the prior stance leg is ready to leave the ground. At this instant both legs have equal length r_s. The new stance leg begins to swing freely. When it gets to a key position where we have $\theta=\theta_{II}$, it begins to extend until its length is equals to r_e. We take this instant as another key position where $\theta=\theta_{III}$. Here we define leg length ratio $\beta= r_s / r_e$. Note that the velocity along the direction of the leg is zero in these two positions. After its length reaches the maximum value r_e, it begins to shorten to r_s at the key position where $\theta=\theta_{IV}$. The velocity along the direction of leg is also zero here. Finally, it swings freely until it strikes the floor, namely the instant V. Here we consider the collision as an inelastic one (no slip and no bounce). After the collision, the swing leg sticks to the ground and the stance leg is about to leave the ground. The transformation of the two legs is the end of one walking step.

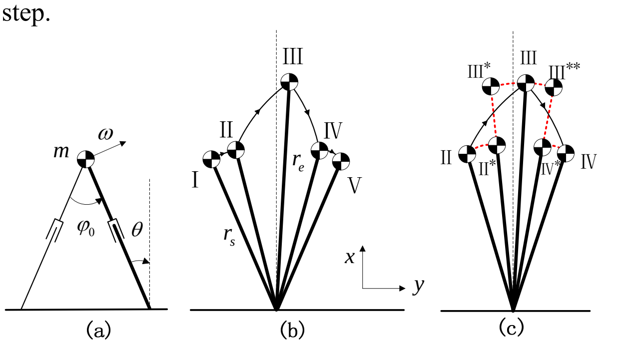

Fig.1. Model and key instants in one walking step

III. THE WALKING MAP

A walking step in the model is considered as a Poincare map or stride function [1], which consists of the dynamic function in swing phases and the strike function at collision. We choose the instant after collision as the Poincare section. Limit cycles are the fixed points of the walking map.

1. Dynamic Equations

In order to obtain the dynamic equations, we create a coordinates where the x-axis is along horizontal direction and y-axis is along the vertical direction with the origin in the stance foot contact point. In this system, the zero potential energy plane is the horizontal plane on the ground.

According to the Lagrange Equation, we have the dynamic equation in free swing phases I to II, IV to V.

$$\ddot{\theta}(t)=\frac{g}{r_s}\sin\theta(t) \tag{1}$$

We rescale time by $\tau=\sqrt{g/r_e}\,t$, (1) is rewritten as

$$\ddot{\theta}(\tau)=\frac{1}{\beta}\sin\theta(\tau) \tag{2}$$

Using the Lagrange Equation, we can also obtain the dynamic equation in the stance leg extension and shortening phase II to IV. Notice that the length r(τ) is a variable parameter when in the process of extension and shortening.

$$\ddot{\theta}(\tau)=\frac{r_e\sin\theta(\tau)}{r(\tau)}-\frac{2}{r(\tau)}\dot{r}(\tau)\dot{\theta}(\tau) \tag{3}$$

2. Transition in Inelastic Collision

In the collision, the geometric condition is met.

$$\theta_{\mathrm{I}}(n+1)=-(\varphi_0-\theta_{\mathrm{V}}(n)) \tag{4}$$

We assume the collision occurs instantaneously and there is no double support. According to the conservation of angular momentum, the new stance leg angular velocity is determined by

$$\omega_{\mathrm{I}}(n+1)=\omega_{\mathrm{V}}(n)\cos(\varphi_0) \tag{5}$$

(2) to (5) are the walking map **f** of this model. Note that the Poincare section is at the beginning of a step, and the walking map **f** maps the states in one section to the states in the next section.

IV. THE EQUIVALENT MODEL

1. Model Description

Because it is difficult to study the extension and shortening process analytically, we find an equivalent model which extends and shortens instantaneously. This equivalent model is shown in Fig. 1(c).

In this equivalent model, the stance leg extends from r_s to r_e instantaneously at the position where $\theta^*_{II}=\theta^*_{III}$ and then shortens instantaneously at the position where $\theta^{**}_{III}=\theta^*_{IV}$. So we have the conservation of angular momentum about the stance foot contact point, which leads to a discontinuous change in the angular velocity of the stance leg. From II* to III*, we have

$$\omega^*_{\mathrm{III}}=\beta^2\omega^*_{\mathrm{II}} \tag{6}$$

Similar to the process II* to III*, we can obtain the relationship between III** and IV*.

$$\omega^*_{\mathrm{IV}}=\frac{1}{\beta^2}\omega^{**}_{\mathrm{III}} \tag{7}$$

The equivalence we consider here is from the mechanical energy's point of view. In such a definition of equivalence, we must make sure the mechanical energy in instant II* equals to the mechanical energy in instant II and the mechanical energy in instant III* equals to that of instant III. The same goes for the shortening process. Here we only discuss how to get the position II* according to II and III, which can be applied to the position IV*.

From the mechanical energy equality, we have the following two equations:

$$\frac{1}{2}\omega_{\mathrm{II}}^2\beta+\cos\theta_{\mathrm{II}}=\frac{1}{2}\omega^{*2}_{\mathrm{II}}\beta+\cos\theta^*_{\mathrm{II}} \tag{8}$$

$$\frac{1}{2}\omega_{\mathrm{III}}^2+\cos\theta_{\mathrm{III}}=\frac{1}{2}\omega^{*2}_{\mathrm{III}}+\cos\theta^*_{\mathrm{III}} \tag{9}$$

Note that the kinetic energy has been rescaled by the dimensionless time τ.

From (6), (8) and (9), the instantaneously extension angle θ^*_{II} can be represented as:

$$\theta_{II}^{*} = \arccos\left(\frac{\frac{1}{2}\left(\omega_{III}^{2} - \beta^{4}\omega_{II}^{2}\right) + \cos\theta_{III} - \beta^{3}\cos\theta_{II}}{1-\beta^{3}}\right) \quad (10)$$

Using the same method, we can also get θ^*_{IV}.

$$\theta_{IV}^{*} = \arccos\left(\frac{\frac{1}{2}\left(\omega_{IV}^{2} - \beta^{4}\omega_{III}^{2}\right) + \cos\theta_{IV} - \beta^{3}\cos\theta_{III}}{1-\beta^{3}}\right) \quad (11)$$

The free swing phases and the collision rules are the same in these two models.

2. The Equivalent Walking Map

In the equivalent model, the walking step can be divided as: free swing phase with leg length r_s from I to II^*, instantaneously extension phase from II^* to III^*, free swing phase with leg length r_e from III^* to III^{**}, instantaneously shortening phase from III^{**} to IV^*, and free swing phase with leg length r_s from IV^* to V.

The dynamic function from III^* to III^{**} is

$$\ddot{\theta}(\tau) = \sin\theta(\tau) \quad (12)$$

So (2), (6), (7) and (12) are the walking map in this equivalent model.

According to this function, the simulation results are shown in Fig. 2. The red dotted line is the limit cycle of the equivalent model in Fig. 1(c) while the black solid line is the limit cycle of the model in Fig. 1(b). These two limit cycles are the same expect in the extension and shortening phases, so we can say that these two models' extension and shortening have the equivalent effect.

V. ANALYSIS OF EQUIVALENT MODEL

1. Finding Fixed Point

In order to find the cyclic gait of this model, we need to find the fixed point of the walking map. The fixed point is an initial state which maps to itself in the Poincare section. The state in this model is the stance leg angle θ_I and stance leg rate ω_I. Since θ is a constant that depends on the inter-leg angle φ_0 in the instant after collision, there leaves only one state variable ω_I in Poincare section.

In free swing phases, we have the mechanical energy conservation as follows:

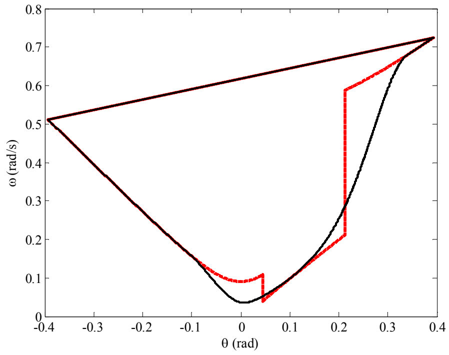

Fig.2. Limit cycles in phase space

$$\begin{cases} E_{I} = E_{II} = E_{II}^{*} \\ E_{III}^{*} = E_{III}^{**} \\ E_{IV}^{*} = E_{IV} = E_{V} \end{cases} \quad (13)$$

Together with the discontinuous changes of stance leg angular velocity in instantaneous extension, shortening and collision, we can obtain

$$\omega_I^2(n+1) = f(\omega_I^2(n)) \quad (14)$$
$$= \cos^2\varphi_0\omega_I^2(n) + \frac{2\cos^2\varphi_0(1-\beta^3)}{\beta^4}[\cos\theta_{II}^*(n) - \cos\theta_{IV}^*(n)]$$

To make it easy to analyse the fixed point, we take a new state variable $q = \omega_I^2$ into consideration, then according to the definition of a fixed point

$$q^f = f(q^f) \quad (15)$$

We have the analytical expression of fixed point.

$$q^f = \frac{2\cos^2\varphi_0(1-\beta^3)[\cos\theta_{II}^* - \cos\theta_{IV}^*]}{\beta^4(1-\cos^2\varphi_0)} \quad (16)$$

Once we have the expression of fixed point, we can calculate it with the parameters' values of the model. So the equivalent model is much easier to study.

2. Stability of Fixed Point

A. Local Stability

Once we have obtained a fixed point, we would like to know whether it is stable or not. The stable fixed point is what we want. The eigenvalues of the Jacobian matrix of the walking map can determine the local stability of the fixed point. If all eigenvalues are inside the unit cycle, which means a small disturbance will decay over time, then the fixed point is asymptotical stable, else if there is one eigenvalue outside the unit cycle, the fixed point is unstable.

From the analytical expression of fixed point (14), we can calculate the eigenvalue of Jacobian matrix.

$$\lambda = \frac{\partial f}{\partial q^f} = \cos^2\varphi_0 \quad (17)$$

According to (5), we have $\cos\varphi_0 < 1$, so the fixed point is asymptotical stable. This can be confirmed by the simulation results, as shown in Fig. 3. It shows that an initial state near fixed point will always converge to the fixed point after several cycles. But this initial state cannot be too far away from the fixed point.

B. Global Stability

However, the eigenvalun of Jacobian matrix can only reflect the local stability. Wisse *et al* propose the basin of attraction to analyze the global stability [4]. The basin of attraction is an area where the initial states can lead to a stable walking instead of falling. Fig. 4 shows the basin of attraction with respect to different β.

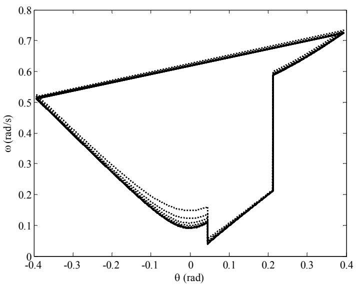

Fig.3. The convergence towards limit cycle

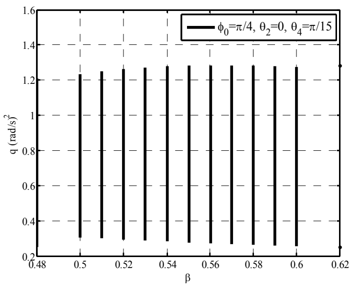

Fig.4. Basin of attraction

VI. MECHANICAL ENERGY

The model's total mechanical energy is the sum of kinetic energy and potential energy. It can be given by

$$E_i(n) = \frac{1}{2} m\dot{\theta}_i(t)^2 r_i^2 + mgr_i \cos\theta_i \tag{18}$$

Note that the time has been rescaled and leg length *r* is different in different phases.

We have energy conservation during free swing phases. That is (13). The energy changes during the instantaneously extension, instantaneously shortening and collision. For a fixed point, the complementary energy E_c is equal to the lost energy E_r. We know the energy is lost during collision, so it must be increased from instant II^* to instant IV^*. They can be expressed as

$$E_c = E_{IV}^* - E_{II}^* \tag{19}$$

According to the relationships about stance leg's angle, angular velocity and energy, we can obtain

$$E_c = mgr_e[\cos\theta_{II}^* - \cos\theta_{IV}^*](\frac{1-\beta^3}{\beta^2}) \tag{20}$$

$$E_r = mgr_e[\frac{1}{2}\beta^2(1-\cos^2\varphi_0)\omega_I^2 + (\cos\theta_{II}^* - \cos\theta_{IV}^*)(\frac{1-\beta^3}{\beta^2})(1-\cos^2\varphi_0)] \tag{21}$$

From (20), we can see that the complementary energy only depends on the θ^*_{II}, θ^*_{IV}, β and r_e. These parameters are constant in the model, so the complementary energy is the same for different initial state. The lost energy depends on not only the above parameters, but also on the initial state ω^2_I. This means that there exists feedback in this model. When the initial state is larger than fixed point, the lost energy is larger than the complementary energy which makes the initial state in the next step smaller. Finally it will converge to the fixed point when the lost energy is equal to the complementary energy. When the initial state is smaller than fixed point, it will converge to the fixed point because the lost energy is smaller than the complementary energy. The energy feedback can also illustrate that the fixed point is stable.

VII. CONCLUSION

This paper has proposed a powered bipedal model walking on level ground. It has been proven that a passive dynamic walking model can walk down on a shallow slope without actuation or control because of the lost energy is recovered from the descent of center of mass. From this point of view, we study the up-and-down motion of the hip mass on stance-leg actuation. The simulation results of the model and its equivalent model show that there exist stable periodical gait. When the model has appropriate structure parameters, the complementary energy is a constant, which means there exist energy feedback.

REFERENCES

[1] McGeer, Passive Dynamic Walking. The Int. J. of Robotics Research, 1990, 9(2):62-68

[2] McGeer T, Stability and Control of Two-Dimensional Bipedal Walking. Technical Report CSS-IS TR 88-01, 1998, Simon Fraser University

[3] Asano F, Luo Z.W, Energy-Efficient and High-Speed Dynamic Biped Locomotion Based on Principle of Parametric Excitation . IEEE Transactions on Robotics, December 2008 24(6):1289-1301

[4] Schwab A, Wisse M, Basin of attraction of the simplest walking model. The Int. Conf. Noise and Vibration,2001,1-9

Sampled-data models for affine nonlinear systems using a fractional-order hold and their zero dynamics

Masatoshi Nishi and Mitsuaki Ishitobi
Department of Mechanical Systems Engineering
Kumamoto University, Kumamoto 860-8555
E-mail: 085d9203@st.kumamoto-u.ac.jp

Abstract: One of the approaches to sampled-data controller design for nonlinear continuous-time systems consists of obtaining an appropriate model and then proceeding to design a controller for the model. Hence, it is important to derive a good approximate sampled-data model because the exact sampled-data model for nonlinear systems is often unavailable to the controller designers. Recently, Yuz and Goodwin have proposed a more accurate model than the simple Euler model in the case of a zero-order hold. This paper derives a sampled-data model for nonlinear systems using a fractional-order hold, and analyzes the zero dynamics of the sampled-data model.
keywords: Nonlinear systems, sampled-data models, zero dynamics, fractional-order hold.

I. INTRODUCTION

Real systems are usually modeled by using laws of physics and are consequently described by ordinary differential equation models. However, we typically interact with these systems by digital devices that utilize sampled data. Thus, the study of sampled-data control systems has become an important issue in control fields.

When dealing with sampled-data models for nonlinear systems, the exact sampled-data model is often unavailable to the controller designers [1]. Then, the accuracy of the approximate sampled-data model has proven to be a key issue in the context of control design, where a controller designed to stabilize an approximate model may fail to stabilize the exact discrete-time model [2].

Recently, Yuz and Goodwin have proposed a more accurate model than the simple Euler model [3]. The resulting model includes extra zero dynamics corresponding to the relative degree of the continuous-time nonlinear system. Such extra zero dynamics are called sampling zero dynamics. It is shown that they are unstable when the relative degree of a continuous-time nonlinear plant is greater than or equal to two. Thus, the closed-loop system becomes unstable when a discrete-time controller design method based on the assumption of the stability of the zero dynamics is applied [5], [6].

In the linear case, the properties of the sampling zeros corresponding to the sampling zero dynamics for nonlinear systems have been discussed in many papers [4], [7]-[13]. Some of the previous studies show that when the relative degree of a continuous-time plant is two, use of a fractional-order hold instead of a zero-order hold overcomes the problem above [8], [9], [13]. Hence it is natural to raise a question how the results of the linear case with the fractional-order hold can be extended to nonlinear systems.

This paper derives a sampled-data model for nonlinear systems using a fractional-order hold, and analyzes the zero dynamics of the sampled-data model to show a condition which assures the stability of the sampling zero dynamics of the model.

II. SAMPLED-DATA MODELS WITH FROH

Consider a class of the following single-input single-output nth-order nonlinear system with the uniform relative degree $r(\leq n)$ which is expressed in its so-called normal form [14], [15]

$$\left\{\begin{array}{rcl} \dot{\boldsymbol{\xi}} & = & \begin{bmatrix} \mathbf{0}_{r-1} & I_{r-1} \\ 0 & \mathbf{0}_{r-1}^T \end{bmatrix} \boldsymbol{\xi} \\ & & + \begin{bmatrix} \mathbf{0}_{r-1} \\ 1 \end{bmatrix} (b(\boldsymbol{\xi},\ \boldsymbol{\eta}) + a(\boldsymbol{\xi},\ \boldsymbol{\eta})u) \\ \dot{\boldsymbol{\eta}} & = & \boldsymbol{c}(\boldsymbol{\xi},\ \boldsymbol{\eta}) \\ y & = & \xi_1 \end{array}\right. \tag{1}$$

$$\boldsymbol{\xi} = \begin{bmatrix} \xi_1 \\ \vdots \\ \xi_r \end{bmatrix}, \boldsymbol{\eta} = \begin{bmatrix} \eta_{r+1} \\ \vdots \\ \eta_n \end{bmatrix}, \boldsymbol{c} = \begin{bmatrix} c_{r+1}(\boldsymbol{\xi},\ \boldsymbol{\eta}) \\ \vdots \\ c_n(\boldsymbol{\xi},\ \boldsymbol{\eta}) \end{bmatrix}$$

where $a(\boldsymbol{\xi},\ \boldsymbol{\eta}) \neq 0$, $b(\mathbf{0}, \mathbf{0}) = 0$ and $\boldsymbol{c}(\mathbf{0}, \mathbf{0}) = \mathbf{0}$.

We are interested in the sampled-data model for the nonlinear system (1) when the input is generated by a fractional-order hold (FROH); i.e.,

$$u(t) = u(kT) + \beta \cdot \frac{u(kT) - u((k-1)T)}{T}(t - kT), \quad kT \leq t < (k+1)T, \quad k = 0,\ 1, \cdots \tag{2}$$

where β is a real design parameter and T is a sampling period. The signal reconstruction of a fractional-order hold is shown in Fig. 1 [8], [9], [13].

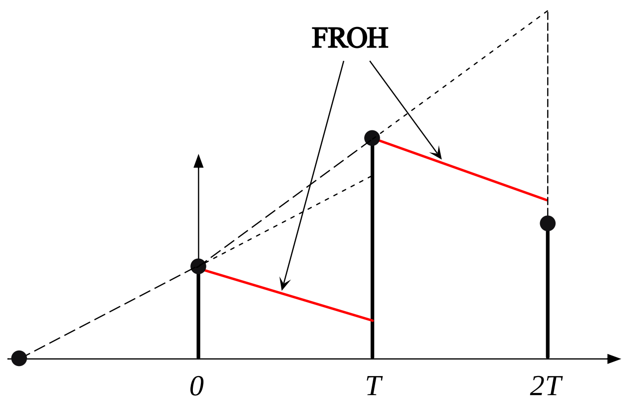

Fig. 1: The signal reconstruction of a fractional-order hold with $\beta = -0.5$.

The sampled-data model for (1) is derived below. First, note that

$$\dot{u}(t) = \beta \cdot \frac{u(kT) - u((k-1)T)}{T}, \quad \ddot{u}(t) = 0 \tag{3}$$

then, one can obtain for sufficiently small sampling periods that

$$\left\{ \begin{array}{rcl} \dot{y} & = & \dot{\xi}_1 = \xi_2 \\ & \vdots & \\ y^{(r-1)} & = & \dot{\xi}_{r-1} = \xi_r \\ y^{(r)} & = & b + au \\ y^{(r+1)} & = & \dot{b} + \dot{a}u + a\dot{u} \\ & = & \dot{b} + \dot{a}u + a\beta \cdot \dfrac{u(kT) - u((k-1)T)}{T} \\ & \approx & a\beta \cdot \dfrac{u(kT) - u((k-1)T)}{T} \end{array} \right. \tag{4}$$

The final approximation result of $y^{(r+1)}$ is derived from the fact that the third term with β is dominant in the second equation for a sufficiently small T.

Applying the Taylor's expansion formula to $y^{(i)}((k+1)T)$ and using (4) yield

$$\begin{aligned} \xi_{i+1,k+1} &= y_{k+1}^{(i)} \\ &\approx y_k^{(i)} + Ty_k^{(i+1)} + \frac{T^2}{2}y_k^{(i+2)} + \\ &\quad \cdots + \frac{T^{r-i}}{(r-i)!}y_k^{(r)} + \frac{T^{r-i+1}}{(r-i+1)!}y_k^{(r+1)} \\ &\approx \xi_{i+1,k} + T\xi_{i+2,k} + \frac{T^2}{2}\xi_{i+3,k} + \cdots \\ &\quad + \frac{T^{r-i}}{(r-i)!}(b_k + a_k u_k) \\ &\quad + \frac{T^{r-i}}{(r-i+1)!}\{a_k\beta(u_k - u_{k-1})\} \\ &\quad\quad i = 0, \cdots, r-1 \end{aligned} \tag{5}$$

where

$$b_k \equiv b(\boldsymbol{\xi}_k,\ \boldsymbol{\eta}_k),\ a_k \equiv a(\boldsymbol{\xi}_k,\ \boldsymbol{\eta}_k) \tag{6}$$

and, the subscripts k and $k+1$ denote the time instants kT and $(k+1)T$, respectively.

Hence, a sampled-data model for (1) is obtained as follows.

$$\boldsymbol{\xi}_{k+1} = F_{\beta,k}\boldsymbol{\xi}_k + \boldsymbol{g}_{\beta,k}u_k + \boldsymbol{h}_k \tag{7}$$

$$\boldsymbol{\eta}_{k+1} = \boldsymbol{\eta}_k + T\boldsymbol{c}(\boldsymbol{\xi}_k,\ \boldsymbol{\eta}_k) \tag{8}$$

$$y_k = \xi_{1,k} \tag{9}$$

where

$$\boldsymbol{\xi}_k = [\ \xi_{1,k}\ \cdots\ \xi_{r,k}\ u_{k-1}]^T$$

$$F_{\beta,k} = \begin{bmatrix} 1 & T & \frac{T^2}{2!} & \cdots & \frac{T^{r-1}}{(r-1)!} & -\frac{T^r}{(r+1)!}\beta a_k \\ 0 & 1 & T & \cdots & \frac{T^{r-2}}{(r-2)!} & -\frac{T^{r-1}}{r!}\beta a_k \\ \vdots & \vdots & \vdots & & \vdots & \vdots \\ 0 & 0 & 0 & \cdots & 1 & -\frac{T}{2!}\beta a_k \\ 0 & 0 & 0 & \cdots & 0 & 0 \end{bmatrix}$$

$$\boldsymbol{g}_{\beta,k} = \begin{bmatrix} \frac{T^r}{r!}a_k + \frac{T^r}{(r+1)!}\beta a_k \\ \frac{T^{r-1}}{(r-1)!}a_k + \frac{T^{r-1}}{r!}\beta a_k \\ \vdots \\ Ta_k + \frac{T}{2!}\beta a_k \\ 1 \end{bmatrix}, \ \boldsymbol{h}_k = \begin{bmatrix} \frac{T^r}{r!}b_k \\ \frac{T^{r-1}}{(r-1)!}b_k \\ \vdots \\ Tb_k \\ 0 \end{bmatrix}$$

The local truncation error between the true system output and the output of the sampled-data model is of order T^{r+1} which implies that the accuracy of the obtained sampled-data model is the same order as that by Yuz and Goodwin's model [3].

III. SAMPLING ZERO DYNAMICS OF THE SAMPLED-DATA MODELS

In this section, we obtain the sampling zero dynamics of the sampled-data model (7)-(9). First, substituting $y_{k+1} = y_k = 0$ into (7) and (8) yields

$$\begin{aligned} \begin{bmatrix} \bar{\boldsymbol{\xi}}_{k+1} \\ 0 \end{bmatrix} &= M \begin{bmatrix} \bar{\boldsymbol{\xi}}_k \\ u_k \end{bmatrix} + \boldsymbol{l} \qquad (10) \\ \boldsymbol{\eta}_{k+1} &= \boldsymbol{\eta}_k + T\boldsymbol{c}(0,\ \bar{\boldsymbol{\xi}}_k,\ \boldsymbol{\eta}_k) \qquad (11) \end{aligned}$$

where

$$\bar{\xi}_k = \begin{bmatrix} \xi_{2,k} & \cdots & \xi_{r,k} & u_{k-1} \end{bmatrix}^T$$

$$M = \begin{bmatrix} M_{11} & \boldsymbol{m}_{12} \\ \boldsymbol{m}_{21}^T & m_{22} \end{bmatrix}$$

$$M_{11} = \begin{bmatrix} 1 & T & \frac{T^2}{2!} & \cdots & \frac{T^{r-2}}{(r-2)!} & -\frac{T^{r-1}}{r!}\beta a_{k0} \\ 0 & 1 & T & \cdots & \frac{T^{r-3}}{(r-3)!} & -\frac{T^{r-2}}{(r-1)!}\beta a_{k0} \\ \vdots & & & \ddots & & \vdots \\ 0 & & \cdots & 0 & 1 & -\frac{T}{2!}\beta a_{k0} \\ 0 & & \cdots & & 0 & 0 \end{bmatrix}$$

$$\boldsymbol{m}_{12} = \begin{bmatrix} \left(\frac{T^{r-1}}{(r-1)!} + \frac{T^{r-1}}{r!}\beta\right) a_{k0} \\ \left(\frac{T^{r-2}}{(r-2)!} + \frac{T^{r-2}}{(r-1)!}\beta\right) a_{k0} \\ \vdots \\ \left(T + \frac{T}{2!}\beta\right) a_{k0} \\ 1 \end{bmatrix}$$

$$\boldsymbol{m}_{21} = \begin{bmatrix} T & \frac{T^2}{2} & \cdots & \frac{T^{r-1}}{(r-1)!} & -\frac{T^r}{(r+1)!}\beta a_{k0} \end{bmatrix}^T$$

$$m_{22} = \left(\frac{T^r}{r!} + \frac{T^r}{(r+1)!}\beta\right) a_{k0}$$

$$\boldsymbol{l} = \begin{bmatrix} \frac{T^{r-1}}{(r-1)!}b_{k0} & \cdots & Tb_{k0} & 0 & \frac{T^r}{r!}b_{k0} \end{bmatrix}^T$$

and, a_{k0} and b_{k0} are defined as a_k and b_k, respectively, with $y = 0$. Deleting u_k in (10) leads to the following sampling zero dynamics for sufficiently small sampling periods

$$\bar{\boldsymbol{\xi}}_{k+1} = M_r \bar{\boldsymbol{\xi}}_k \qquad (12)$$

where

$$\begin{aligned} M_r &= \begin{bmatrix} m_{1,1} & \cdots & m_{1,r} \\ \vdots & \ddots & \vdots \\ m_{r,1} & \cdots & m_{r,r} \end{bmatrix} \\ m_{i,j} &= T^{j-i}\left\{\frac{1}{(j-i)!} - \frac{\gamma_i}{j!}\right\} \\ &\quad i \le j,\ i = 1,\ \cdots,\ r-1,\ j = 1,\ \cdots,\ r-1 \\ m_{i,j} &= -T^{j-i}\frac{\gamma_i}{j!} \\ &\quad i > j,\ i = 1,\ \cdots,\ r-1,\ j = 1,\ \cdots,\ r-1 \\ m_{i,r} &= T^{r-i}\left\{-\frac{1}{(r+1-i)!} + \frac{\gamma_i}{(r+1)!}\right\}\beta a_{k0} \\ &\quad i = 1,\ \cdots,\ r-1 \\ m_{r,j} &= -\frac{1}{T^{r-j}}\frac{\gamma_r}{j!a_{k0}},\ j = 1,\ \cdots,\ r-1 \\ m_{r,r} &= \frac{\beta}{(r+1)+\beta} \\ \gamma_i &= \frac{\frac{(r+1)!}{(r-i)!} + \frac{(r+1)!}{(r+1-i)!}}{(r+1)+\beta},\ i = 1,\ \cdots,\ r-1 \\ \gamma_r &= \frac{(r+1)!}{(r+1)+\beta} \end{aligned}$$

The matrices M_r are listed below for a few values of r.

$$M_1 = \frac{\beta}{2+\beta} \qquad (13)$$

$$M_2 = \begin{bmatrix} \frac{-3-2\beta}{3+\beta} & -\frac{T}{6+2\beta}a_{k0}\beta \\ -\frac{1}{T}\frac{6}{(3+\beta)a_{k0}} & \frac{\beta}{3+\beta} \end{bmatrix} \qquad (14)$$

$$M_3 = \begin{bmatrix} -\frac{8+3\beta}{4+\beta} & -T\frac{2+\beta}{4+\beta} & \frac{T^2\beta a_{k0}}{3!(4+\beta)} \\ -\frac{1}{T}\frac{24+12\beta}{(4+\beta)} & -\frac{8+5\beta}{4+\beta} & \frac{T\beta a_{k0}}{2!(4+\beta)} \\ -\frac{4!}{T^2(4+\beta)a_{k0}} & -\frac{4!}{T(8+2\beta)a_{k0}} & \frac{\beta}{4+\beta} \end{bmatrix} \qquad (15)$$

As a result, the sampling zero dynamics of the sampled-data model with FROH have the following properties.

Properties 1: Consider the sampled-data model with FROH for a continuous-time system (1) with relative degree r.

Case (i) $r = 1$. The sampling zero dynamics are stable if

$$-1 < \beta \tag{16}$$

Case (ii) $r = 2$. Assume that the term $a(0,\ \dot{y},\ \cdots,\ y^{(r-1)},\ \boldsymbol{\eta})$ is constant. The sampling zero dynamics are stable if

$$-1 < \beta < 0 \tag{17}$$

Case (iii) $r = 3$. The sampling zero dynamics are unstable.

Remark 1: It is easy to see that Properities 1 are similar to the results of the linear case [13].

Remark 2: On the controlled Van der Pol system with relative degree two, the closed-loop system becomes unstable when Yuz and Goodwin's model is used for design of feedback controller which requires the stability of the zero dynamics [6]. However, from the Properties 1 (ii), on such a case, the resulting feedback control system is stable when FROH with $-1 < \beta < 0$ is used for a hold.

IV. CONCLUSION

This paper derives a sampled-data model and analyzes its zero dynamics for nonlinear systems in the case of a fractional-order hold. The resulting model has an advantage to the Yuz and Goodwin's model with respect to the stability of the sampling zero dynamics when the relative degree of a continuous-time nonlinear plant is two.

References

[1] D. S. Laila, D. Nešić and A. Astolfi: Sampled-data control of nonlinear systems, *Advanced Topics in Control Systems Theory, LNCIS 328*, A. Loría *et al.* (Eds.), Springer-Verlag London Limited, pp.91–137, 2006.

[2] D. Nešić and A. Teel: A framework for stabilization of nonlinear sampled-data systems based on their approximate discrete-time models, *IEEE Trans. on Automatic Control*, Vo.49, No.7, pp.1103–1122, 2004.

[3] J. I. Yuz and G. C. Goodwin: On sampled-data models for nonlinear systems, *IEEE Trans. on Automatic Control*, Vo.50, No.10, pp.1477–1489, 2005.

[4] K. J. Åström, P. Hagander and J. Sternby: Zeros of sampled systems, *Automatica*, Vol. 20, No. 1, pp. 31-38, 1983.

[5] M. Ishitobi, M. Nishi and S. Kunimatsu: Stability of zero dynamics of sampled-data nonlinear systems, *Proc. of the 17th IFAC World Congress*, pp.5969–5973, 2008.

[6] M. Nishi, S. Kunimatsu, M. Ishitobi and T. Wada: On sampled-data models for nonlinear systems with relative degree two, *Proc. of the 3rd Int. Symp. on Advanced Control of Industrial Processes*, pp.272–276, 2008.

[7] T. Hagiwara, T. Yuasa and M. Araki: Stability of the limiting zeros of sampled-data systems with zero- and first-order holds, *Int. J. Control*, Vol.58, No.6, pp.1325–1346, 1993.

[8] K. M. Passino and P. J. Antsaklis: Inverse stable sampled low-pass systems, *Int. J. Control*, Vol.47, No.6, pp.1905–1913, 1988.

[9] M. Ishitobi: Stability of zeros of sampled system with fractional order hold, *IEE Proc.-Control Theory and Applications*, Vol.143, No.3, pp.296–300, 1996.

[10] Y. Hayakawa, S. Hosoe and M. Ito: On the limiting zeros of sampled multivariable systems, *Syst. Contr. Lett.*, Vol. 2, No. 5, pp. 292–300, 1983.

[11] S. R. Weller: Limiting zeros of decouplable MIMO systems, *IEEE Trans. on Automatic Control*, Vol. AC-44, No. 1, pp. 129–134, 1999.

[12] M. Ishitobi: A stability condition of zeros of sampled multivariable systems, *IEEE Trans. on Automatic Control*, Vol.45, No.2, pp.295–299, 2000.

[13] M. Ishitobi: Properties of zeros of a discrete-time system with fractional order hold, *Proc. of the 35th IEEE Conference on Decision and Control*, pp.4339–4344, 1996.

[14] A. Isidori: *Nonlinear Control Systems*, 3rd ed. New York: Springer Verlag, 1995.

[15] H. Khalil: *Nonlinear Systems*, 3rd ed., Upper Saddle River, NJ: Prentice-Hall, 2002.

The Fifteenth International Symposium on Artificial Life and Robotics 2010 (AROB 15th '10),
B-Con Plaza, Beppu,Oita, Japan, February 4-6, 2010

Development of 6DOF Force Feedback System with Pneumatic Parallel Mechanism

Yasunobu HITAKA*, Yoshito TANAKA**, Yutaka TANAKA** and Junko ISII*

** Kitakyushu National College of Technology*
Tel : +81-93-964-7244
Email hitaka@kct.ac.jp

*** Hosei University*

Abstract: In this paper, it is presented the development of a new type force feedback system. It is based on a 6-DOF Stewart parallel mechanism[1] which has six pneumatic actuated cylinders. The thrust force of each cylinder is controlled by PWM control for the solenoid valve and it is actualized by PIC controller. When the pneumatic actuator is controlled, it must be considered the influence on the compressibility of air. For this problem, we guarantee the control characteristics by the effect of the accumulator. It is confirmed that the thrust force of the cylinder can be applied to the pneumatic parallel mechanism, and is presented the experimental result of force control for vertical direction.

Keywords: stewart type parallel mechanism, six degree of freedom, PWM control

I. INTRODUCTION

For the patients afflicted with paralysis, the rehabilitation aid by the physical therapist is necessary. In recent years, the number of the paralyzed patients is increasing due to some reasons, like the adult disease, traffic accident and aging, and the shortage of the physical therapist becomes a new social problem. Thus, it is required the rehabilitation support technology. Corresponding to the patients with various paralysis symptoms, it is necessary for the rehabilitation equipment to support the multiple degree of freedom movement[2] [3].

We note the Stewart type parallel mechanism and consider applying it to the rehabilitation equipment for the wrist or hand paralysis. This mechanism achieves six degree of freedom motion and has two characteristics that are high power and high rigidity. Therefore, it is useful for the wrist or hand rehabilitation equipment. The multiple motion of this mechanism can be achieved by the coordinated telescopic motion of six actuated cylinders. The power source of the cylinder is hydraulic pressure, pneumatic or servomotor. We choose the pneumatic cylinder since this actuator has a flexible characteristics due to the compaction property of the air and therefore it actualizes friendly and soft rehabilitation aid for the patients.

In this paper, it is presented the development of the force feedback system which generates the feedback force through the pneumatic parallel mechanism. This system will be a base technology of the rehabilitation equipment for the wrist or hand paralysis. The pneumatic parallel mechanism is designed by 3DCAD and made a prototype model. Control of the thrust force of each pneumatic cylinder is actualized by PWM control for the solenoid valve. The PIC is used to the controller for the PWM control. When the pneumatic actuator is controlled, it must be considered the influence on the compressibility of air. For this problem, the control characteristics are guaranteed by the effect of the accumulator.

This paper consists of six sections. This section is introduction. Next section shows the configuration of the force feedback system. In 3rd section, the design of the parallel mechanism and the developed prototype model are presented.

The detail of force control of the pneumatic cylinder is denoted in section 4. In section 5, the result of the force control experiment for unit cylinder is presented. And then, for the parallel mechanism which has the six cylinders, the experimental results for vertical direction motion are presented

Ⅱ. SYSTEM CONFIGURATION

Figure 1 shows the configuration of the force feedback system. It mainly consists of the pneumatic parallel mechanism and the personal computer. As shown in Fig.2, there is a gripper on the platform of the pneumatic parallel mechanism and it can be moved in 6-DOF direction by hand. Each cylinders of the parallel mechanism has a position detector detects the cylinder length. The PC calculates the attitude of the parallel mechanism by solving the direct kinematics of the parallel mechanism with the data of each cylinder length. With the calculation result, the PC draws a simple moving object which shows the harmonic motion with the parallel mechanism in the virtual working space on the display.

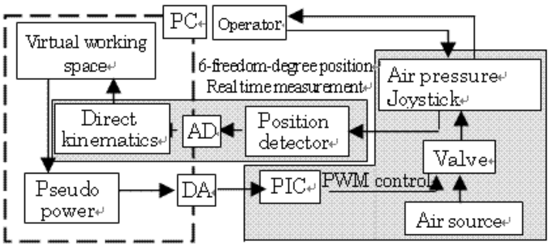

Fig.1. Configuration of force feedback system

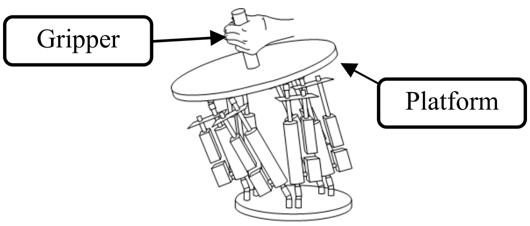

Fig.2: Pneumatic parallel mechanism with gripper on the platform

When the moving object in the virtual space contacts some kind of obstacle as shown in Fig.3, PC calculates the virtual reaction force and sends the control signals to the six PIC controllers, respectively. Each PIC controller controls two solenoid valves on one air cylinder of the parallel mechanism by PWM. The one solenoid valve is used for the pushing force of the cylinder and the other is for the pulling force. The resultant force of six cylinders is equivalent to the virtual reaction force. Then, the operator feels the reaction force generated in the virtual space at his hand.

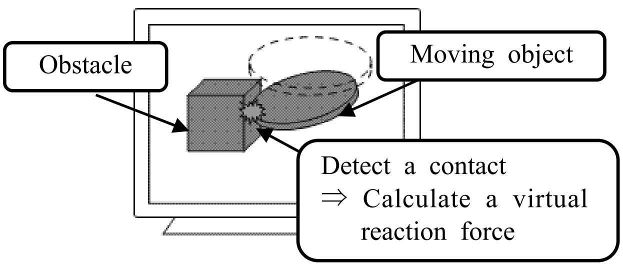

Fig.3: Contact the obstacle in a virtual space

Ⅲ. PROTOTYPE MODEL OF PNEUMATIC PARALLEL MECHANISM

In this section, a prototype model of the pneumatic parallel mechanism for the use of the force feedback system is presented. The left figure in Fig.4 is the 3D CAD design image of the prototype model. This mechanism has 6-DOF motion, namely, translational motion along x-axis (surge motion), y-axis (sway motion) and z-axis (heave motion), and rotational motion about x-axis (roll motion), y-axis (pitch motion) and z-axis (yaw motion). The right figure of Fig.4 is the overall view of the prototype model and Fig.5 is close up of one of the pneumatic cylinders. It has a position detector and two solenoid valves. The bottom end of cylinder is connected to the bottom base by a universal joint. The upper end of cylinder is connected to the platform by a spherical magnetic joint. The reason of using the magnetic joint for upper joint is that if unexpected huge force acts on gripper, the platform uncouples from the upper joints and therefore the destruction of the parallel mechanism is averted.

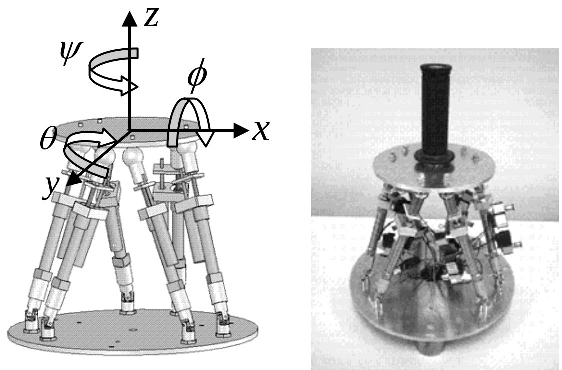

Fig.4: CAD image and overall view of Prototype model

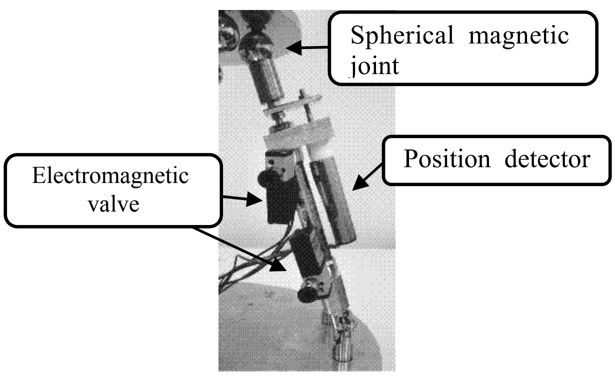

Fig.5: Close up of the pneumatic cylinder

Ⅳ. FORCE CONTROL OF PNEUMATIC CYLINDERS

The force control of each pneumatic cylinder of the prototype model is actualized by regulating the supplied airflow. The airflow is regulated by PWM control for the solenoid valve. As shown in Fig.6, the PWM (Pulse Width Modulation) is a modulation method that is tuning ON time for the pulse wave at a constant cycle by changing the modulation rate. Where, let τ denotes the modulation rate, T denotes one constant cycle and T_{on} denotes ON time in T, τ is described as

$$\tau = \frac{T_{on}}{T}.$$

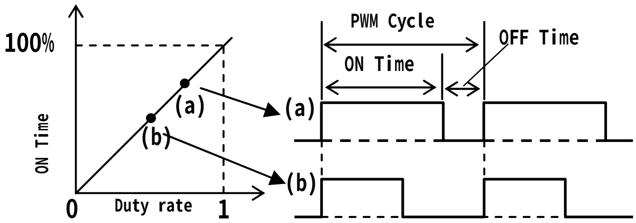

Fig.6: PWM wave and Duty rate

By the PWM signal, opening-closing time of the solenoid valve is tuned, and thereby supplied airflow for pneumatic cylinder is regulated. Figure 7(a) and (b) show turn-on and off of three-way solenoid valve, respectively.

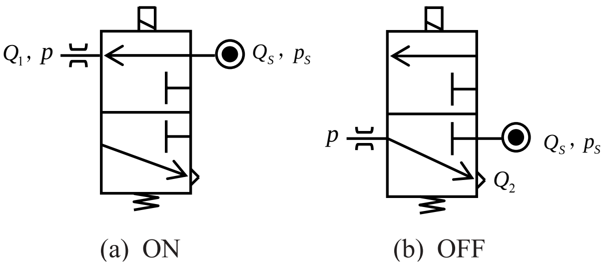

Fig.7: Three way solenoid valve

Figure 8 is the circuit of the force control of the pneumatic cylinders. The duty rate τ decided by PC is converted to analog signal (voltage) through the DA convertor. The analog signal is input into PIC controller. The PIC generates PWM signal and sends it to two solenoid valves. The one valve is used for the pushing force of the cylinder and the other is for the pulling force. The relation between the average control pressure and the modulation rate τ of PWM is written as

$$p = p_s \frac{\tau^2}{\tau^2 + (1-\tau)^2}, \tag{1}$$

where, sign p_s is supply pressure. From Eq. (1), thrust force F of the cylinder is given by

$$F = \eta A p_s \frac{\tau^2}{\tau^2 + (1-\tau)^2} \tag{2}$$

where, A is an area of the pushing side or pulling side of the cylinder, and η is a load factor.

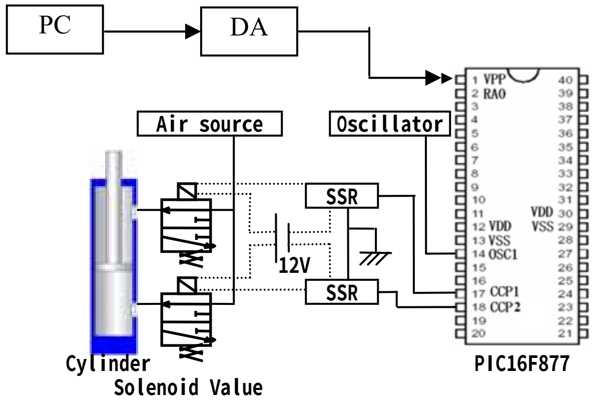

Fig.8: Control Circuit

Ⅴ.EXPERIMENTAL RESULTS

In this section, the experimental results of force control of the prototype of pneumatic parallel mechanism are presented. At first, the average control pressure for the change in the modulation rate τ of PWM is measured. Figure 9 is the overview of the experiment and Fig.10 shows the result where the supply pressure is adjusted to 0.15MPa and the pipe length between the solenoid valve and the manometer sets 50mm.

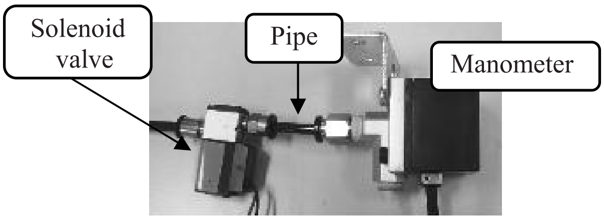

Fig.9: Measurement of air pressure

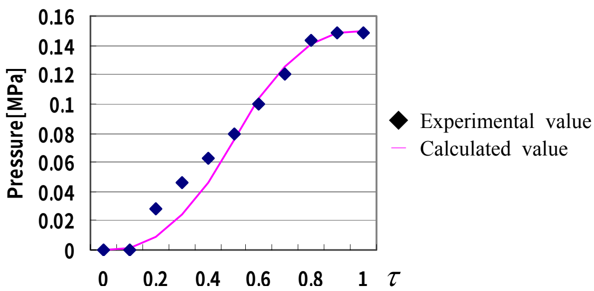

Fig.10: Pressure (pipe length 50mm)

It shows the difference between the measurements and predictions by Eq.(1). For the result, we try to improve the control performance by using the effect of the accumulator. Figure 11 is the result where the pipe length between the solenoid valve and the manometer set 500mm to increase the accumulator. As shown in Fig.11, the control performance is improved, and therefore it was known that when the volume between the solenoid valve and the cylinder is small, the compressibility of air influences the pressure characteristic. And it is understood that the force characteristic is depend on the capacity of the accumulator.

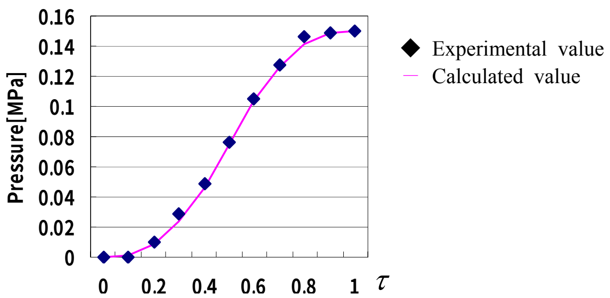

Fig.11: Pressure (pipe length 500mm)

Next, the experimental results of force control of the pneumatic mechanism are shown. Figure.12 is over view of the experiment. The force sensor (0～100N) consists of the strain gauge, and the force in z-direction is measured. The force generation of the parallel mechanism for z-direction is that the same modulation rate is given for solenoid valves of six cylinders.

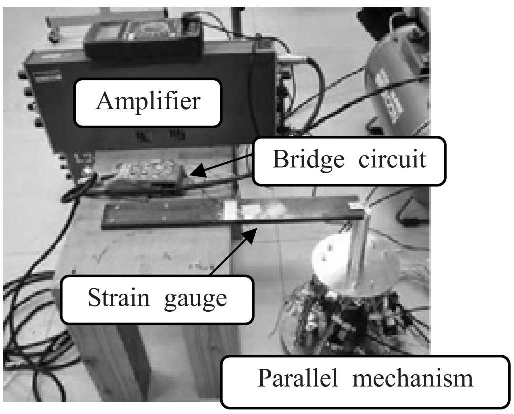

Fig.12: Experiments with the parallel mechanism

Figure 13 shows the results of experiment. Where the posture is adjusted to be neutral position (cylinder expansion and contraction 15mm) and the supply pressure is 0.15Mpa. The calculated value is summation of each thrust force of 6 cylinders in vertical direction obtained thrust from Eq.(2). The prediction agrees well with the measurements, and it is known that z-axis force control is possible. A force of approximate 60N is generated when the supply pressure is 0.15Mpa, and it is understood the enough force experienced by man is generated.

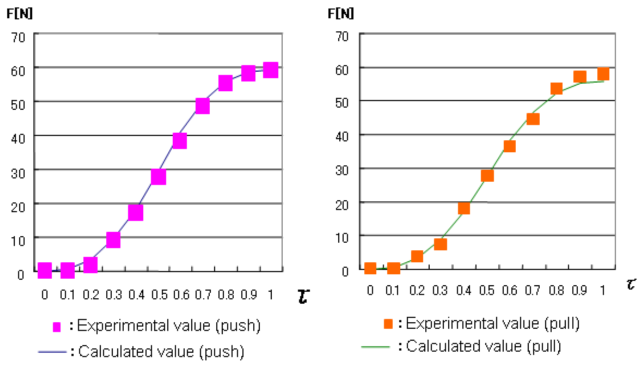

Fig.13: Force control of parallel mechanism

Ⅵ. CONCLUSION

The prototype model of pneumatic parallel mechanism for use of the force feedback system has been developed, and the 6-DOF force control was achieved. The conclusion is shown below.

(1) The compressibility of air can be compensated with accumulator, and the control characteristic of the thrust force of the cylinder has been improved.

(2) The pneumatic 6-DOF parallel mechanism was developed. The push and pull force control in z-axis was evaluated by the experiment, and it was confirmed that the force control by the PWM control was possible.

References

[1] Stewart, D., A Platform with 6 degrees of freedom, Proc. Inst. Mech. Eng., Vol.180, Part I, No.15, pp.371-386, 1965-66.

[2] Lung-Wen Tsai, Robot Analysis, John Wiley & Sons, Inc.1999, pp116

[3] Takaiwa, M., Noritsugu, T., Development of Human-Robot Haptic Interface Using Pneumatic Parallel Manipulator, Proc. 4th JHPS Int. Symp. on Fluid Power, pp.181-186, 1999.

A study of Guaranteed Cost Control of the Manipulator with Passive Revolute Joint

J. Hara, N. Takahashi, J. Kato, O. Sato and M. Kono

Faculty of Engineering, University of Miyazaki
1-1 Gakuenkibanadai-Nishi, Miyazaki, 889-2192, JAPAN
Tel & Fax : +81-985-58-7419
ntaka@cs.miyazaki-u.ac.jp

Abstract : In this paper, we consider a robust control problem of a two link RR manipulator with uncertainty in the joint angle which is caused by several factors. The first purpose is to derive an uncertain LTI system of a two link RR manipulator which includes uncertainty in a rotational angle of each joint. The uncertainty is expressed in a system structure matrix in an explicit form. For this uncertain system, we apply guaranteed cost control. At last, we show the effectiveness of our method by a numerical example.
Keywords: Robust control, Guaranteed cost control, Structured uncertainty, Two link RR manipulator

I. Introduction

In practice, the effect of an uncertainty is a considerable problem. Such an uncertainty is caused by a measurement error, noise in the signal, secular distortion of the device, etc. and makes degradation of the performance index. One of an approach to deal with the influence of uncertainty is to include these effects in the form of the LTI system by a structured uncertainty. By using this uncertain system, it is able to design the robust control system. S.S.Chang and T.K.C.Peng proposed a new robust control method which called the guaranteed cost control [1]. This method guarantees the existence of an upper bound of an uncertainty in the performance index. Yamamoto et al. showed a deviation method for the structured uncertainty that is caused by the higher order terms of the Taylor series expansion [2]. N. Takahashi et al. showed a generalization of the guaranteed cost control problem [3]. Kono et al. extended this problem to the case with cross-term in the performance index [4]. Sato et al. considered the object throwing motion problem that by the manipulator with a passive revolute joint [5]. Takahashi et al. extended the guaranteed cost control problem to the case with an uncertainty in an output matrix [6] and introduced an uncertainty in the angle of a car inverted pendulum system [7]. In this paper, we will introduce two uncertainties in a joint angle of the manipulator system and will apply the guaranteed cost control to our uncertain LTI system. Through the numerical example, we will show the effectiveness of our method. In section II, we will show the formulation of the uncertain LTI system of a two link RR manipulator with a passive revolute joint. And we will apply the guaranteed cost control to the uncertain LTI system to design a robust stable system. In section III, we will give a numerical example to show the effectiveness of our proposed method. At last, we will give a conclusion in section IV.

II. Formulation of uncertain system

In this section, we will give a formulation of the uncertain LTI system of a two link RR manipulator and apply the guaranteed cost control to this uncertain system. The link 1 is connected to the base with a rotational joint 1 and the link 2 is connected to another end point of the link 1 with a rotational joint 2. Each joints and arms have physical parameters illustrated in table 1.

Table.1: Parameters of the Manipulator

Parameters	**Meaning** [unit]
θ_i	Angle of the Joint [rad]
m_i	Mass of the Arm [kg]
I_i	Inertia moment of the Arm [kg $\cdot$ m^2]
l_i	Length of the Arm [m]
l_{Gi}	Distance from the joint to the center of gravity of the Arm [m]
g	Gravity [m/sec^2]
τ_i	Input torque to the joint [N$\cdot$ m]

It is well know that the equation of the motion of a two link RR manipulator is expressed as following nonlinear differential equation.

$$H(\boldsymbol{\theta})\ddot{\boldsymbol{\theta}} + \boldsymbol{h}(\boldsymbol{\theta}, \dot{\boldsymbol{\theta}}) + \boldsymbol{g}(\boldsymbol{\theta}) = \boldsymbol{\tau} \tag{1}$$

where

$$\boldsymbol{\theta} = \begin{bmatrix} \theta_1 \\ \theta_2 \end{bmatrix}, \boldsymbol{\tau} = \begin{bmatrix} \tau_1 \\ \tau_2 \end{bmatrix} \tag{2}$$

Inertia term $H(\boldsymbol{\theta})$ is

$$\begin{aligned} &H(\boldsymbol{\theta}) \\ &= \left[\begin{array}{c} I_1 + m_1 l_{G1}^2 + I_2 + m_2(l_1^2 + l_{G2}^2 + 2 l_1 l_{G2} c_2) \\ I_2 + m_2(l_{G2}^2 + l_1 l_{G2} c_2) \end{array} \right. \\ &\qquad \left. \begin{array}{c} I_2 + m_2(l_{G2}^2 + l_1 l_{G2} c_2) \\ I_2 + m_2 l_{G2}^2 \end{array} \right] \end{aligned} \tag{3}$$

Nonlinear term $\boldsymbol{h}(\boldsymbol{\theta})$ is

$$\boldsymbol{h}(\boldsymbol{\theta}, \dot{\boldsymbol{\theta}}) = \begin{bmatrix} -m_2 l_1 l_{G2}(\dot{\theta}_2^2 + \dot{\theta}_1 \dot{\theta}_2) s_2 \\ -m_2 l_1 l_{G2} \dot{\theta}_1 \dot{\theta}_2 s_2 \end{bmatrix} \tag{4}$$

Gravity term $\boldsymbol{g}(\boldsymbol{\theta})$ is

$$\begin{aligned} \boldsymbol{g}(\boldsymbol{\theta}) &= \begin{bmatrix} -m_1 g l_{G1} s_1 - m_2 g(l_1 s_1 + l_{G2} s_{12}) \\ -m_2 g l_{G2} s_{12} \end{bmatrix} \\ &= \begin{bmatrix} g_1(\boldsymbol{\theta}) \\ g_2(\boldsymbol{\theta}) \end{bmatrix} \end{aligned} \tag{5}$$

where we denote $\sin(\theta_1 + \theta_2) = s_{12}$ and $\cos(\theta_1 + \theta_2) = c_{12}$. If we assume that $\dot{\theta}_1$ and $\dot{\theta}_2$ takes very small value, thus $\dot{\theta}_2^2, \dot{\theta}_1 \dot{\theta}_2 \to 0$ and the nonlinear term becomes $\boldsymbol{h}(\boldsymbol{\theta}, \dot{\boldsymbol{\theta}}) = \boldsymbol{0}$. From Eq. (1), we have

$$H(\boldsymbol{\theta})\ddot{\boldsymbol{\theta}} + \boldsymbol{g}(\boldsymbol{\theta}) = \boldsymbol{\tau} \tag{6}$$

By multiplying from the left by $H(\boldsymbol{\theta})^{-1}$, we get

$$\ddot{\boldsymbol{\theta}} = -H(\boldsymbol{\theta})^{-1}\boldsymbol{g}(\boldsymbol{\theta}) + H(\boldsymbol{\theta})^{-1}\boldsymbol{\tau} \tag{7}$$

Here we define

$$H(\boldsymbol{\theta}) = \begin{bmatrix} h_{11} & h_{12} \\ h_{12} & h_{22} \end{bmatrix}$$

Then, we have

$$H(\boldsymbol{\theta})^{-1} = \frac{1}{h_D} \begin{bmatrix} h_{22} & -h_{12} \\ -h_{12} & h_{11} \end{bmatrix}$$

$$h_D = h_{11} h_{22} - h_{12}^2$$

and

$$\begin{aligned} \ddot{\boldsymbol{\theta}}(t) &= \frac{1}{h_D} \begin{bmatrix} -h_{22} g_1(\boldsymbol{\theta}) + h_{12} g_2(\boldsymbol{\theta}) \\ h_{12} g_1(\boldsymbol{\theta}) - h_{11} g_2(\boldsymbol{\theta}) \end{bmatrix} \\ &\quad + \frac{1}{h_D} \begin{bmatrix} h_{22} & -h_{12} \\ -h_{12} & h_{11} \end{bmatrix} \begin{bmatrix} \tau_1 \\ \tau_2 \end{bmatrix} \end{aligned} \tag{8}$$

We consider that the rotational angle of joint 1 $\theta_1(t)$ and joint 2 $\theta_2(t)$ include uncertainties $\Delta\theta_1$ and $\Delta\theta_2$, respectively.

$$\theta_1(t) = \theta_1^*(t) + \Delta\theta_1 \tag{9}$$
$$\theta_2(t) = \theta_2^*(t) + \Delta\theta_2 \tag{10}$$

where $\theta_1^*(t)$ and $\theta_2^*(t)$ denote nominal angle of joints. Let us assume that $\Delta\theta_1$ and $\Delta\theta_2$ are very small values, then

$$\begin{aligned} \sin\Delta\theta_1 &\to 0 \\ \sin\Delta\theta_2 &\to 0 \\ \cos\Delta\theta_1 &\to \Delta c_1 \\ \cos\Delta\theta_2 &\to \Delta c_2 \end{aligned}$$

Thus, we have

$$\begin{aligned} \sin(\theta_1(t)) &= \sin(\theta_1^*(t))\Delta c_1 + \cos(\theta^*(t)) \\ &= \Delta c_1 \sin(\theta_1^*(t)) \end{aligned} \tag{11}$$
$$\begin{aligned} \cos(\theta_1(t)) &= \cos(\theta_1^*(t))\Delta c_1 - \sin(\theta_1^*(t)) \\ &= \Delta c_1 \cos(\theta_1^*(t)) \end{aligned} \tag{12}$$

Next, we apply a same operation to $\theta_2(t)$,

$$\sin(\theta_2(t)) = \Delta c_2 \sin(\theta_2^*(t)) \tag{13}$$
$$\cos(\theta_2(t)) = \Delta c_2 \cos(\theta_2^*(t)) \tag{14}$$

Moreover, about $\theta_1(t) + \theta_2(t)$,

$$\begin{aligned} &\sin(\theta_1(t) + \theta_2(t)) \\ &= \sin(\theta_1(t))\cos(\theta_2(t)) + \cos(\theta_1(t))\sin(\theta_2(t)) \\ &= \Delta c_1 \Delta c_2 \sin(\theta_1^*(t))\cos(\theta_2^*(t)) \\ &\quad + \Delta c_1 \Delta c_2 \cos(\theta_1^*(t))\sin(\theta_2^*(t)) \end{aligned} \tag{15}$$

Taking a first-order of the Taylor expansion around $\theta_1^*(t) = 0$ and $\theta_2^*(t) = 0$, we can approximate Eqs. (11)-(15) as follows [7]

$$\begin{aligned} \sin(\theta_1(t)) &\approx \Delta c_1 \theta_1^*(t) \\ \cos(\theta_1(t)) &\approx \Delta c_1 \\ \sin(\theta_2(t)) &\approx \Delta c_2 \theta_2^*(t) \\ \cos(\theta_2(t)) &\approx \Delta c_2 \\ \sin(\theta_1(t) + \theta_2(t)) &\approx \Delta c_1 \Delta c_2 (\theta_1^*(t) + \theta_2^*(t)) \end{aligned}$$

In vertue of the above results, the first row element of term in the left-hand side of Eq. (8) becomes

$$-h_{22} g_1(\boldsymbol{\theta}) + h_{12} g_2(\boldsymbol{\theta}) = \bar{h}_{11}\theta_1^* + \bar{h}_{12}\theta_2^* \tag{16}$$

where

$$\begin{aligned} \bar{h}_{11} &= \Delta c_1 g(h_{22}(m_1 l_{G1} + m_2 l_1) \\ &\quad + \Delta c_2 m_2 l_{G2}(h_{22} - h_{12})) \end{aligned} \tag{17}$$
$$\bar{h}_{12} = \Delta c_1 \Delta c_2 m_2 g l_{G2}(h_{22} - h_{12}) \tag{18}$$

The second row element of term in the left-hand side of Eq. (8) becomes

$$h_{12} g_1(\boldsymbol{\theta}) - h_{11} g_2(\boldsymbol{\theta}) = \bar{h}_{21}\theta_1^* + \bar{h}_{22}\theta_2^* \tag{19}$$

where

$$\bar{h}_{21} = \Delta c_1(-h_{12}g(m_1 l_{G1} + m_2 l_1) + \Delta c_2 m_2 g l_{G2}(h_{11} - h_{12})) \quad (20)$$

$$\bar{h}_{22} = \Delta c_1 \Delta c_2 m_2 g l_{G2}(h_{11} - h_{12}) \quad (21)$$

h_{11}, h_{12} and h_{22} are given as follows

$$\begin{aligned} h_{11} &= I_1 + m_1 l_{G1}^2 \\ &\quad + I_2 + m_2(l_1^2 + l_{G2}^2 + \Delta c_2 2 l_1 l_{G2}) \\ h_{12} &= I_2 + m_2(l_{G2}^2 + \Delta c_2 l_1 l_{G2}) \\ h_{22} &= I_2 + m_2 l_{G2}^2 \end{aligned}$$

Thus we can transform Eq. (8) to following form

$$\begin{aligned} \ddot{\boldsymbol{\theta}}(t) &= \frac{1}{h_D}\begin{bmatrix} \bar{h}_{11} & \bar{h}_{12} \\ \bar{h}_{21} & \bar{h}_{22} \end{bmatrix}\boldsymbol{\theta}(t) \\ &\quad + \frac{1}{h_D}\begin{bmatrix} h_{22} & -h_{12} \\ -h_{12} & h_{22} \end{bmatrix}\boldsymbol{\tau} \end{aligned} \quad (22)$$

Let us define a state vector $\boldsymbol{x}(t)$ and an input vector $\boldsymbol{u}(t)$ are

$$\boldsymbol{x}(t) = \begin{bmatrix} \theta_1^*(t) \\ \dot{\theta}_1^*(t) \\ \theta_2^*(t) \\ \dot{\theta}_2^*(t) \end{bmatrix}, \boldsymbol{u}(t) = \begin{bmatrix} u_1(t) \\ u_2(t) \end{bmatrix}$$

Consequently, we obtain a following uncertain LTI system.

$$\dot{\boldsymbol{x}}(t) = A(\xi)\boldsymbol{x}(t) + B(\zeta)\boldsymbol{u}(t) \quad (23)$$

where, an input matrix $A(\xi)$ and an output matrix $B(\zeta)$ are

$$A(\xi) = \begin{bmatrix} 0 & 1 & 0 & 0 \\ \bar{h}_{11}/h_D & 0 & \bar{h}_{12}/h_D & 0 \\ 0 & 0 & 0 & 1 \\ \bar{h}_{21}/h_D & 0 & \bar{h}_{22}/h_D & 0 \end{bmatrix}$$

$$B(\zeta) = \begin{bmatrix} 0 & 0 \\ h_{22}/h_D & -h_{12}/h_D \\ 0 & 0 \\ -h_{12}/h_D & h_{22}/h_D \end{bmatrix}$$

Here we consider that the system matrices are consisted of deterministic elements A_0, B_0 and uncertain elements $\Delta A, \Delta B$.

$$A(\xi) = A_0 + \Delta A \quad (24)$$

$$B(\zeta) = B_0 + \Delta B \quad (25)$$

From $A(\xi)$ and $B(\zeta)$, we can obtain deterministic elements A_0 and B_0 as $(\Delta\theta_1, \Delta\theta_2) = (0, 0)$. A_1 and B_1 are obtained in the condition of $(\Delta\theta_1, \Delta\theta_2) = (max_1, 0)$ and A_2 and B_2 are obtained in the condition of $(\Delta\theta_1, \Delta\theta_2) = (0, max_2)$. Where max_i is a maximum uncertainty of the rotational angle in the joint i. The structured uncertain elements ΔA and ΔB are

$$\Delta A = \sum_{i=1}^{p} \xi_i A_i, \ |\xi_i| \le 1$$

$$\Delta B = \sum_{j=1}^{p} \zeta_j B_j, \ |\zeta_j| \le 1$$

where $p = 1, 2$. ξ_i, ζ_j and A_i, B_j denote the scale and structure of an uncertainty in the system, respectively.

For the uncertain LTI system (23), we apply the guaranteed cost control. The perfoemance index fuction to be minimized is

$$J = \int_0^\infty (\boldsymbol{x}^{\mathrm{T}}(t)Q\boldsymbol{x}(t) + \boldsymbol{u}^{\mathrm{T}}(t)R\boldsymbol{u}(t))dt \quad (26)$$

The stoctastic algebraic Riccati equation based on the eugenvalue upper bound is

$$A_0^{\mathrm{T}}P + PA_0 - PB_0R^{-1}B_0^{\mathrm{T}}P + Q + U_E = \mathbf{O} \quad (27)$$

Upper bound matrix U_E is

$$\begin{aligned} &U_E(\Delta A(\xi), \Delta B(\zeta), P, R) \\ &= \sum_{i=1}^{p} L_i|\Lambda_i|L_i^{\mathrm{T}} + \sum_{j=1}^{p} M_i|\Gamma_i|M_i^{\mathrm{T}} \end{aligned} \quad (28)$$

where $|\cdot|$ denotes the matrix which has absolute value of each elements. L_i, M_i, Λ_i and Γ_i are

$$L_i^{\mathrm{T}}(PA_i + A_i^{\mathrm{T}}P)L_i = \Lambda_i \quad (29)$$

$$M_i^{\mathrm{T}}P(B_iR^{-1}B_0^{\mathrm{T}} + B_0R^{-1}B_i^{\mathrm{T}})PM_i = \Gamma_i \quad (30)$$

where Λ_i and Γ_i are diagonal matrices which have eigenvalues on the diagonal elements. L_i and M_i are orthogonal matrices which constructed from the corresponding orthogonal vectors. From the solution P of Eq. (27), we obtain the feedback gain matrix F as

$$F = -R^{-1}B_0^{\mathrm{T}}P \quad (31)$$

The closed-loop system that the feedback gain is F to be a robust stable system.

III. Numerical example

In this section, we will show the numerical example. Here we consider that the joint 2 is passive, thus the input matrix $B(\zeta)$ becomes

$$B(\zeta) = \begin{bmatrix} 0 \\ h_{22}/h_D \\ 0 \\ -h_{12}/h_D \end{bmatrix}$$

The weighting matrices are $Q = \mathrm{diag}(1, 1, 1, 1)$ and $R = 1$. The initial value is $\boldsymbol{\theta}(0) = [\ 0.1 \ \ 0.0 \ \ -0.05 \ \ 0.0\ ]$. The uncertainty is $\Delta\theta_1 = \Delta\theta_2 = 0.08$. The values of the physical paratemers are illustrated as in table 2.

Table 2: Parameters

parameter	value	parameter	value
m_1	1	m_2	1
I_1	0.03	I_2	0.03
l_1	0.3	l_2	0.3
l_{G1}	0.15	l_{G2}	0.15
g	9.8		

For this system, we design the closed-loop system by using two method, linear quadratic regulator (LQR) and guaranteed cost control (GCC). The simulation enviroment is MATLAB and SIMULINK. The LQR problem is solved by the `lqr` in the control system toolbox and the GCC problem is solved by the Euler method algorithm of our coded m-file. Figure 1 illustrates the trajectory of the joints angle θ_1 and θ_2 of both simulation results.

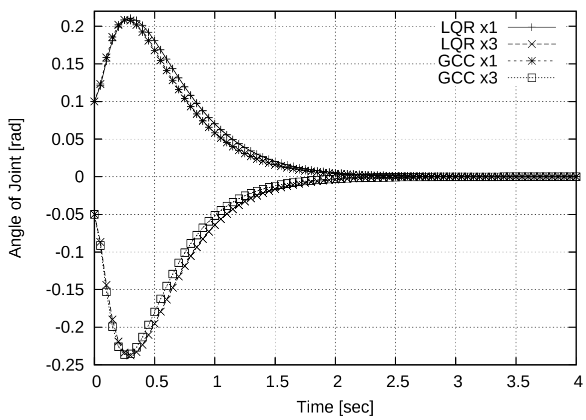

Fig.1 : Simulation Results

The solution of the algebraic Riccati equation P_{LQR} and feedback gain F_{LQR} are (ordinary method)

$$P_{LQR} = \begin{bmatrix} 309.6216 & 80.0140 & 250.8530 & 45.7467 \\ 80.0140 & 20.8360 & 65.4442 & 11.9295 \\ 250.8530 & 65.4442 & 210.2729 & 37.8890 \\ 45.7467 & 11.9295 & 37.8890 & 6.9139 \end{bmatrix}$$

and

$$F_{LQR} = [-47.5721 - 12.6897 - 47.3509 - 8.7623]$$

The eigenvalues of the closed-loop system are

$$(-23.0041, -2.8177, -4.3278 \pm 0.7210i)$$

The solution of the SARE (27) P_{GCC} and feedback gain F_{GCC} are (proposed method)

$$P_{GCC} = \begin{bmatrix} 384.4634 & 99.3605 & 304.8125 & 56.5752 \\ 99.3605 & 25.8774 & 79.3563 & 14.7504 \\ 304.8125 & 79.3563 & 250.4025 & 45.7241 \\ 56.5752 & 14.7504 & 45.7241 & 8.4955 \end{bmatrix}$$

and

$$F_{GCC} = [-54.9208 - 14.5893 - 53.4964 - 9.8803]$$

The eigenvalues of the closed-loop system are

$$(-23.6828, -2.8569, -4.8189 \pm 0.1002i)$$

From the figure 1, we can recognize that our proposed method have designed a robust stable system.

IV. Conclusion

In this paper, we showed the formulation of a uncertain LTI system of a two link RR manipulator with uncertainty in the rotational angle of joints. For this system, we applied the guaranteed cost control to obtain the robust stable system and showed that the simulational result. Future study is to apply the observer to this system.

References

[1] S. Chang and T. Peng (1972), Adaptive Guaranteed Cost Control of System with Uncertain Parameters, IEEE Transactions on AC, 17(4):474-473

[2] S. Yamamoto, Q. Shen and H. Kimura (1993), Quadratic Stabilization for a class of Uncertain Linear Systems and its Application to a Magnetic Levitation system, Transactions of the Society of Instrument and Control Engineers, 29:334-339

[3] N. Takahashi, M. Kono, K. Hiranuma and O. Sato (2000), Generalization of Guaranteed Cost Control, Transactions of the Japan Society of Mechanical Engineers (Series C), 66(645):1531-1536

[4] M. Kono, N. Takahashi, O. Sato and A. Sato (2002), Generalization of Guaranteed Cost Control - Extension to the case with Cross Terms, Proceedings of the SICE Annual Conference 2002, 542-545

[5] A. Sato, O. Sato, N. Takahashi and M. Kono (2008), A Study of Manipulator with Passive Revolute Joint, Artificial Life and Robotics, 13:31-35

[6] N. Takahashi, M. Kono and O. Sato (2009), Guaranteed Cost Control of the Uncertain System with Parameter Variations in an Output Matrix, Proceedings of the 1st Japan-Korea Joint Symposium on Dynamics & Control, 139-142

[7] N. Takahashi, O. Sato and M. Kono (2009), Robust Control Method for the Inverted Pendulum System with Structured Uncertainty Caused by Measurement Error, Artificial Life and Robotics, 14 (To Appear)

The Fifteenth International Symposium on Artificial Life and Robotics 2010 (AROB 15th '10),
B-Con Plaza, Beppu,Oita, Japan, February 4-6, 2010

Analysis of Manipulator in Consideration of Relative Motion between Tray and Object

Asaji SATO[1] , Osamu SATO[2] , Nobuya TAKAHASHI[2] , Akira UEKUBO[2] and Michio KONO[2]

[1]*Dept. of Mechanical Engineering, Miyakonojo National college of Technology, Miyakonojo 885-8567, Japan.*
[2]*Dept. of Computer Science and Systems Engineering, Faculty of Engineering, University of Miyazaki, Miyazaki 889-219, Japan.*

Abstract: In this paper, equations of motion of a manipulator, whose mechanism has a tray installed by passive revolute joint, are derived in consideration of characteristics of driving source. Considering the relative motion between the tray and object, trajectories of velocity for saving energy are calculated by iterative dynamic programming. And, the dynamic characteristics of manipulator controlled based on the trajectory for saving energy are analyzed theoretically.

Keywords: Manipulator, Trajectory, Dynamic Programming, DC Motor, Minimum Energy, Passive joint.

1 Introduction

For the purpose of enlarging the work space, it is necessary for studying the optimal control of the manipulator whose mechanism has a passive joint. In a previous report [1], a casting manipulator is introduced, and it has large work space compared with its simple mechanism. But, the consideration of energy consumption is not enough. In horizontal plane, obstacle avoidance motion planning for a three-axis planar manipulator with a passive joint is investigated [2]. But, energy consumption is not considered.

In previous report by the authors [3][4], trajectories for saving energy of manipulator, whose mechanism has two active joints, were easily calculated by iterative dynamic programming. And, dynamic characteristics of the system were analyzed.

In this paper, equations of motion of a manipulator, whose mechanism has a passive revolute joint, are derived in consideration of the characteristics of DC servomotors, and a performance criterion for saving energy is defined in consideration of energy consumption of the driving source. When the manipulator is operated in a vertical plane, the system is highly non-linear due to gravity, and an analytical solution can not be found. Then, a numerical approach is necessary. Considering the relative motion between the tray and the object, the trajectories of velocity for energy saving are calculated by iterative dynamic programming. The dynamic characteristics of manipulator controlled based on above mentioned trajectory are analyzed theoretically and investigated experimentally.

2 Modeling of manipulator with passive joint

The dynamic equations of the manipulator with four degrees of freedom as shown in Figure 1, which is able to move in a vertical plane, are as follows.

$$\begin{bmatrix} A_{11} & A_{12} & A_{13} & A_{14} \\ A_{21} & A_{22} & A_{23} & A_{24} \\ A_{31} & A_{32} & A_{33} & A_{34} \\ A_{41} & A_{42} & A_{43} & A_{44} \end{bmatrix} \begin{bmatrix} \ddot{\theta}_1 \\ \ddot{\theta}_2 \\ \ddot{\theta}_3 \\ \ddot{\theta}_4 \end{bmatrix} = \begin{bmatrix} \tau_1 - \tau_2 + A_{15} \\ \tau_2 - \tau_3 + A_{25} \\ \tau_3 - \tau_4 + A_{35} \\ \tau_4 + A_{45} \end{bmatrix} \quad (1)$$

where

$A_{11}=a_1+a_6C_2+a_8C_{23}+a_9C_{234}$, $A_{12}=a_6C_2+a_8C_{23}+a_9C_{234}$,
$A_{13}=a_8C_{23}+a_9C_{234}$, $A_{14}=a_9C_{234}$, $A_{21}=a_2+a_6C_2+a_7C_3+a_{10}C_{34}$,
$A_{22}=a_2+a_7C_3+a_{10}C_{34}$, $A_{23}=a_7C_3+a_{10}C_{34}$, $A_{24}=a_{10}C_{34}$,
$A_{31}=a_3+a_7C_3+a_8C_{23}+a_{11}C_4$, $A_{32}=a_3+a_7C_3+a_{11}C_4$,
$A_{33}=a_3+a_{11}C_4$, $A_{34}=-a_5+a_{11}C_4$, $A_{43}=a_4+a_{11}C_4$, $A_{44}=a_4+a_5$,
$A_{41}=a_4+a_9C_{234}+a_{10}C_{34}+a_{11}C_4$, $A_{42}=a_4+a_{10}C_{34}+a_{11}C_4$,
$A_{15}=a_6(\dot{\theta}_1+\dot{\theta}_2)^2S_2+a_8(\dot{\theta}_1+\dot{\theta}_2+\dot{\theta}_3)^2S_{23}+a_9(\dot{\theta}_1+\dot{\theta}_2+\dot{\theta}_3+\dot{\theta}_4)^2S_{234}-a_{12}C_1$,
$A_{25}=-a_6\dot{\theta}_1^2S_2+a_7(\dot{\theta}_1+\dot{\theta}_2+\dot{\theta}_3)^2S_3+a_{10}(\dot{\theta}_1+\dot{\theta}_2+\dot{\theta}_3+\dot{\theta}_4)^2S_{34}-a_{13}C_{12}$,
$A_{35}=-a_7(\dot{\theta}_1+\dot{\theta}_2)^2S_3-a_8\dot{\theta}_1^2S_{23}+a_{11}(\dot{\theta}_1+\dot{\theta}_2+\dot{\theta}_3+\dot{\theta}_4)^2S_4-a_{14}C_{123}$,
$A_{45}=-a_9\dot{\theta}_1^2S_{234}-a_{10}(\dot{\theta}_1+\dot{\theta}_2)^2S_{34}-a_{11}(\dot{\theta}_1+\dot{\theta}_2+\dot{\theta}_3)^2S_4-a_{15}C_{1234}$,

$a_1=I_{G1}+m_1r_1^2+(m_2+m_3+m_4)l_1^2$, $a_2=I_{G2}+m_2r_2^2+(m_3+m_4)l_2^2$,
$a_3=I_{G3}+m_3r_3^2+m_4r_3'^2$, $a_4=m_4r_4^2$, $a_5=I_{Gb}\left(r_4^2/r_b^2\right)$,
$a_6=\{m_2r_2+(m_3+m_4)l_2\}l_1$, $a_7=(m_3r_3+m_4r_3')l_2$, $a_8=(m_3r_3+m_4r_3')l_1$,
$a_9=m_4l_1r_4$, $a_{10}=m_4l_2r_4$, $a_{11}=m_4r_3'r_4$, $a_{12}=(m_1r_1+m_2l_1+m_3l_1+m_4l_1)g$,
$a_{13}=(m_2r_2+m_3l_2+m_4l_2)g$, $a_{14}=(m_3r_3+m_4r_3')g$, $a_{15}=m_4gr_4$,

$C_j=\cos\theta_j$, $S_j=\sin\theta_j$, $C_{jk}=\cos(\theta_j+\theta_k)$, $S_{jk}=\sin(\theta_j+\theta_k)$,
$C_{jkn}=\cos(\theta_j+\theta_k+\theta_n)$, $S_{jkn}=\sin(\theta_j+\theta_k+\theta_n)$,
$C_{jknp}=\cos(\theta_j+\theta_k+\theta_n+\theta_p)$, $S_{jknp}=\sin(\theta_j+\theta_k+\theta_n+\theta_p)$,
$(j=1\sim4, k=1\sim4, n=1\sim4, p=1\sim4)$

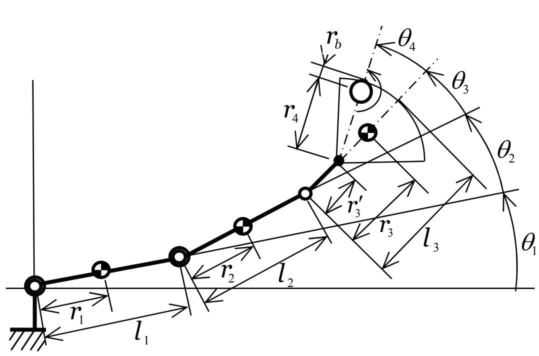

Fig.1 Mechanism of manipulator

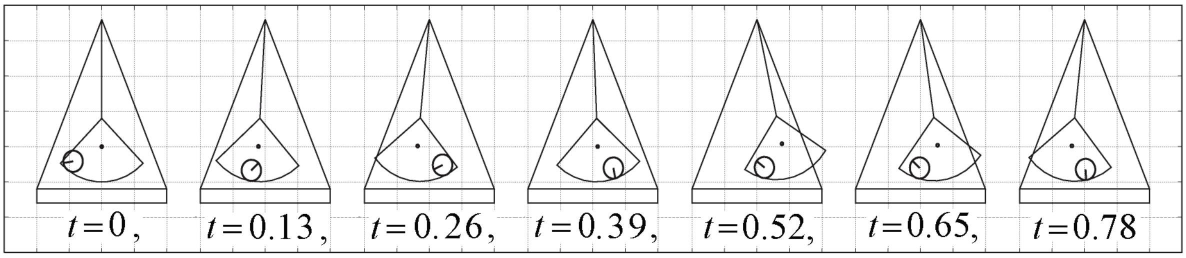

(a) Simulation of pendulum movement about the tray and the object

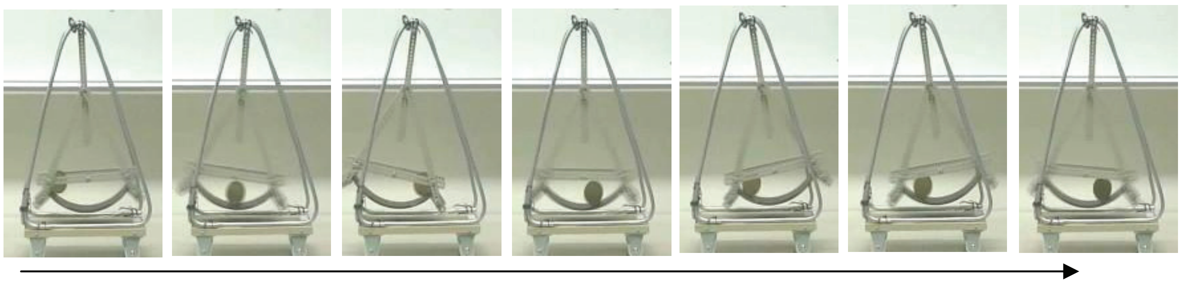

(b) Experimental results of pendulum movement (every 0.13 s)

Fig.2 Pendulum movement about the tray and the object

And, the relation between $\dot{\phi}$ and $\dot{\theta}_4$ is

$$r_b\dot{\phi} = -r_4\dot{\theta}_4 \quad . \tag{2}$$

($\dot{\phi}$; rotational speed of the object)

The kinetic energy of the mechanism is

$$\begin{aligned} K =& \frac{a_1}{2}\dot{\theta}_1^2 + \frac{a_2}{2}(\dot{\theta}_1+\dot{\theta}_2)^2 + \frac{a_3}{2}(\dot{\theta}_1+\dot{\theta}_2+\dot{\theta}_3)^2 \\ &+ \frac{a_4}{2}(\dot{\theta}_1+\dot{\theta}_2+\dot{\theta}_3+\dot{\theta}_4)^2 + \frac{a_5}{2}\dot{\theta}_4^2 \\ &+ a_6\dot{\theta}_1(\dot{\theta}_1+\dot{\theta}_2)C_2 + a_7(\dot{\theta}_1+\dot{\theta}_2)(\dot{\theta}_1+\dot{\theta}_2+\dot{\theta}_3)C_3 \\ &+ a_8\dot{\theta}_1(\dot{\theta}_1+\dot{\theta}_2+\dot{\theta}_3)C_{23} + a_9\dot{\theta}_1(\dot{\theta}_1+\dot{\theta}_2+\dot{\theta}_3+\dot{\theta}_4)C_{234} \\ &+ a_{10}(\dot{\theta}_1+\dot{\theta}_2)(\dot{\theta}_1+\dot{\theta}_2+\dot{\theta}_3+\dot{\theta}_4)C_{34} \\ &+ a_{11}(\dot{\theta}_1+\dot{\theta}_2+\dot{\theta}_3)(\dot{\theta}_1+\dot{\theta}_2+\dot{\theta}_3+\dot{\theta}_4)C_4 \quad , \end{aligned} \tag{3}$$

and potential energy of the mechanism is

$$U = a_{12}S_1 + a_{13}S_{12} + a_{14}S_{123} + a_{15}S_{234} \quad . \tag{4}$$

The applied voltage of the servomotor is

$$e_j = b_{1j}\dot{\theta}_j + b_{2j}\ddot{\theta}_j + b_{3j}\tau_j + b_{3j}\tau_{fj}\,\mathrm{sign}(\dot{\theta}_j) \quad , \tag{5}$$

where

$b_{1j} = k_{vj} + (R_{aj}/k_{tj})D_{mj}$, $b_{2j} = (R_{aj}/k_{tj})I_m$, $b_{3j} = R_{aj}/k_{tj}$,

i_{aj} : electric current of the armature ,

R_{aj} : resistance of armature ,

I_{mj} : moment of inertia of armature,

D_{mj} : coefficient of viscous damping .

Then, the electric current is

$$i_{aj} = (e_j - k_{vj}\dot{\theta}_j)/R_{aj} \; . \tag{6}$$

And, the consumed energy is

$$E = \sum_{j=1}^{3} \int (e_j \cdot i_{aj})dt \; . \tag{7}$$

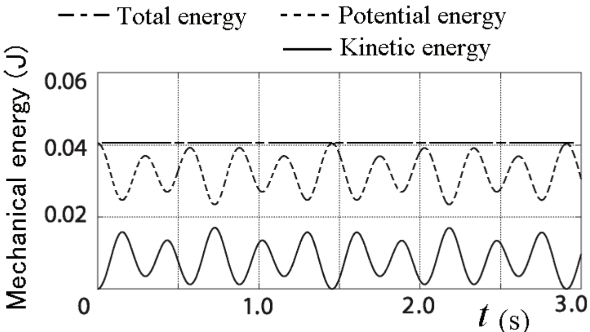

Fig.3 Mechanical energy of pendulum movement

3 Simulation of the pendulum movement

Under the condition that joint 1 and 2 are fixed, simulations of the system are shown in Fig.2 and 3. We shall take the parameters of the system as $m_3 = 0.109, m_4 = 0.122(\mathrm{kg}), r_4 = 0.075, r_b = 0.015(\mathrm{m})$. And, initial conditions are $\theta_{3i} = -(\pi/2)$, $\theta_{4i} = -(\pi/5)$, $\dot{\theta}_{3i} = \dot{\theta}_{4i} = 0$. Figure 2 shows the motion of the system like a pendulum movement, and Figure 3 shows the response about the conservation of mechanical energy of the pendulum movement.

4 Simulation of the manipulator

We shall take the parameters of the system as shown in Table 1.

Figure 4 shows a flow chart for iterative dynamic programming method. In frame (A), the trajectory for saving energy is searched by dynamic programming [3]. In frame (B), the searching region is shifted to minimize the consumed energy, and width of the region is changed smaller.

Figure 5 shows the trajectory for searching, and initial trajectory for searching is expressed as

$$\dot{\theta}_j = \dot{\theta}_{ij} + \left(\frac{\dot{\theta}_{fj} - \dot{\theta}_{ij}}{t_f}\right)t + \frac{\pi}{2}\left(\frac{\theta_{fj} - \theta_{ij}}{t_f} - \frac{\dot{\theta}_{fj} + \dot{\theta}_{ij}}{2}\right)\sin\left(\frac{\pi t}{t_f}\right). \quad (8)$$

The tray and the object are shown in Figure 6. Considering the relative motion between the tray and the object, the performance criterion is changed as

$$E' = \sum_{j=1}^{3} \int_0^T (e_j \cdot i_{aj})\ dt + k\{|\theta_4| - (\lambda/2)\} \quad . \quad (9)$$

A response of the manipulator from the initial position ($\theta_{1i} = -\pi/4$, $\theta_{2i} = -\pi/4$, $\theta_{3i} = 0$, $\dot{\theta}_{1i} = 0$, $\dot{\theta}_{2i} = \dot{\theta}_{3i} = 0$) to the release position ($\theta_{1f} = 13\pi/36$, $\theta_{2f} = -7\pi/36$, $\theta_{3f} = -7\pi/24$, $\dot{\theta}_{1f} = 13.9$ rad/s, $\dot{\theta}_{2f} = -1.1$ rad/s) is shown in Figure 7, under the condition that working time $t_f = 0.8$ (s). In this case, joint 3 is passive, and joint 1, 2 are actuated. In order to prevent the object falling from the tray at turning point 2, and not to prevent the object releasing from the tray at point 3, the center of gravity of the tray is adjusted in consideration of the analysis about the relative motion between the object and the tray.

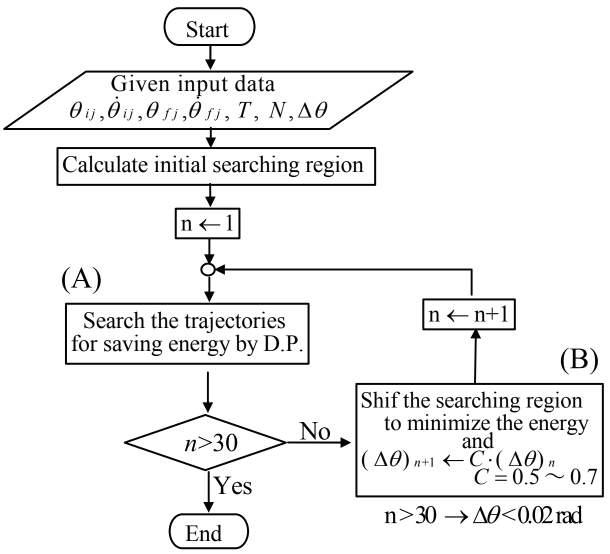

Fig.4 Flow chart for simulation

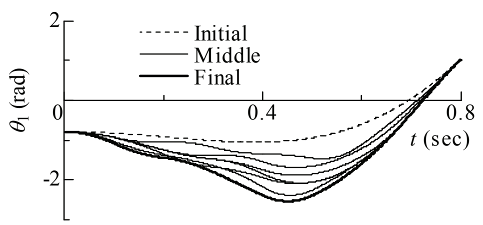

Fig.5 Trajectory for searching

Table 1 Parameters of the manipulator

Parameter	Value	Parameter	Value
l_1 (m)	0.080	I_{G1} (kgm^2)	1.7×10^{-5}
l_2 (m)	0.115	I_{G2} (kgm^2)	8.4×10^{-5}
l_3 (m)	0.015	I_{G3} (kgm^2)	1.2×10^{-6}
r_1 (m)	0.044	I_{Gb} (kgm^2)	4.8×10^{-7}
r_2 (m)	0.078	k_{t1},k_{t2} (Nm/A)	0.046
r_3 (m)	0.028	k_{v1},k_{v2} (Vs/rad)	0.046
r_3' (m)	0.000	D_{m1},D_{m2}(Nms/rad)	7.9×10^{-5}
r_4 (m)	0.005	τ_{f1}, τ_{f2} (Nm)	0.0013
r_b (m)	0.010	R_{a1}, R_{a2} (Ω)	3.5
m_1 (kg)	0.020	m_3 (kg)	0.018
m_2 (kg)	0.047	m_4 (kg)	0.012

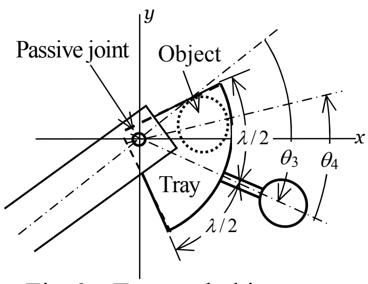

Fig.6 Tray and object

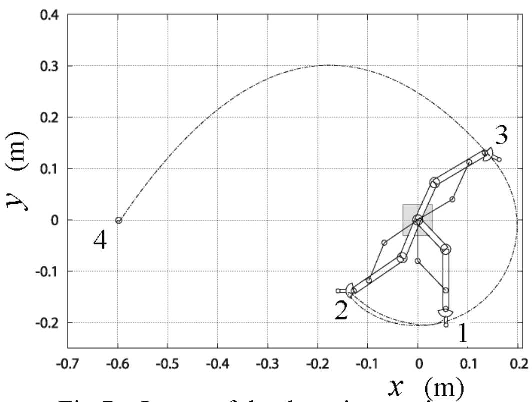

Fig.7 Locus of the throwing motion

5 Experimental results

In this section, the results of fundamental experiment are shown to examine the effectiveness of modeling for the simulations.

Figure 8(a) shows the experimental results of the manipulator in throwing motion, under the same condition as Fig.7. This apparatus is used in previous report by the authors [4]. A mechanism of manipulator is a closed type and a tray (link 3) is connected to link 2 by a passive revolute joint. Under the condition that the torque of joint 3 is zero, the angular acceleration of joint 1 and 2 are given in iterative dynamic programming method, and the acceleration of link 3 and torques of joint 1, 2 are calculated simultaneously. The parameters of the system are shown in Table 1. The motors 1 and 2 (rated 24 V, 60W) are on the frame, and sampling time of the control is 0.002 [s]. The feedback gain for angular displacement is 50[V/rad], and the feedback gain for angular velocity is 0.5[Vs/rad].

Figure 8(b) shows the theoretical results which is similar to the experimental one.

Figure 9 (a) and (b) show the experimental response of angular velocity of the motor which are calculated by angular displacement measured by rotary encoder. And, Figure (c) shows the angular displacement of the tray. From initial position to release position, the theoretical results (broken line) are similar to the experimental results (solid line). From these results, it is considered that modeling for simulation is effective.

From experimental results, it is clear that the holding and releasing of the object are possible by analyzing the relative motion between the object and the tray.

6 Conclusions

The results obtained in this paper are summarized as follows.

(1) It is considered that the holding and releasing of the object is possible by analyzing the relative motion between the object and the tray.

(2) From experimental results, it is considered that modeling for simulation is effective.

References

[1] H.Arisumi, K.Yokoi, T.Kotoku et al (2002), Casting manipulation (Experiments of swing and gripper throwing control), International Journal of JSME, Vol.45, No.1 C, 267-274.

[2] N. Shiroma, K.M.Lynch, H.Arai and K.Tanie (2000), Motion planning for a three-axis planar manipulator with a passive revolute joint, Journal of JSME (in Japanese), Vol.66, No.642, 545-552.

[3] A.Sato, O.Sato, N.Takahashi and M.Kono (2006), Trajectory for saving energy of direct-drive manipulator in throwing motion, Artif Life Robotics, 11:61-66

[4] A.Sato, O.Sato, N.Takahashi and M.Kono (2008), A study of manipulator with passive revolute joint, Artif Life Robotics, 13: 31-35

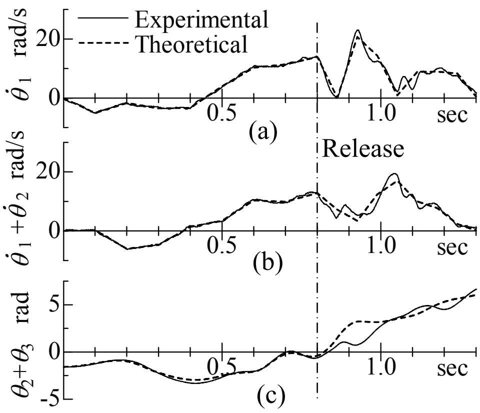

Fig.9 Experimental results

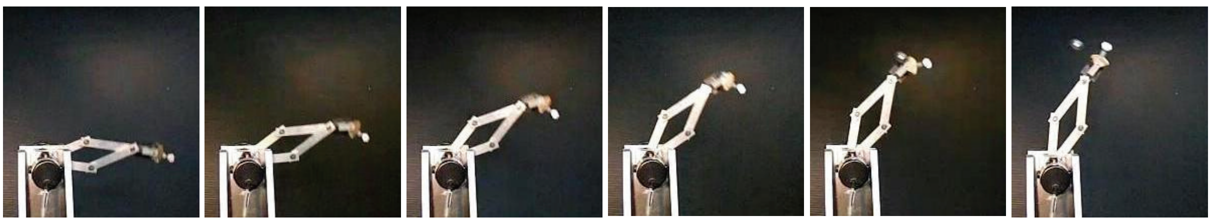

(a) Experimental results

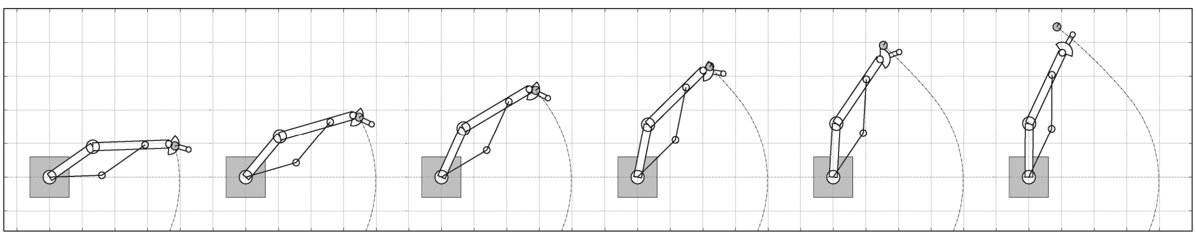

(b) Theoretical results

Fig.8 Throwing motion of the manipulator

Parallel Turing Machines on Four-Dimensional Input Tapes

Takao Ito[1], Makoto Sakamoto[2], Ayumi Taniue[2], Tomoya Matsukawa[2],
Yasuo Uchida[1], Hiroshi Furutani[2], and Michio Kono[2]

[1] Dept. of Business Administration, Ube National College of Technology, Ube 755-8555, JAPAN
[2] Dept. of Computer Science and Systems Engineering, University of Miyazaki, Miyazaki 889-2192, JAPAN

Abstract

A parallel Turing machine (PTM) proposed by Wiedermann is a set of identical usual sequential Turing machines (STM's) cooperating on two common tapes storage tape and input tape. On the other hand, due to the advances in many application areas such as motion picture processing, computer animation, virtual reality systems, and so forth, it has become increasingly apparent that the study of four-dimensional pattern has been of crucial importance. Thus, we think that the study of four-dimensional automata as a computational model of four-dimensional pattern processing has also been meaningful. In this paper, we propose a four-dimensional parallel Turing machine (4-PTM), and investigate its some properties, based on hardware complexity.

Key Words: computational complexity, four-dimensional automaton, hardware-bounded computation, parallel Turing machine, space constructibility

1 Introduction

Informally, a parallel Turing machine (PTM) is a set of identical sequential Turing machines (STM's) cooperating on two common tapes storage tape and input tape [6]. Moreover, STM's which represent the individual processors of the parallel computer can multiply themselves in the course of computation. In [6] it is shown, for example, that every PTM can be simulated by an STM in polynomial time, and that the PTM cannot be simulated by any sequential Turing machine in linear space.

In [1,2], two- or three-dimensional version of PTM was investigated. On the other hand, due to the advances in many application areas such as motion picture processing, computer animation, and so forth, it has become increasingly apparent that the study of four-dimensional pattern processing has been of crucial importance. Thus, we think that the study of four-dimensional automata as a computational model of four-dimensional pattern processing has also been meaningful. During the past about seven years, automata on a four-dimensional tape have been proposed and several properties of such automata have been obtained . In this paper, we propose a four-dimensional parallel Turing machine (4-PTM), and investigate its some properties. Especially, we deal with a hardware-bounded 4-PTM, a variant of the 4-PTM, which each side-length of each input tape is equivalent.

2 Preliminaries

Definition 2.1. Let Σ be a finite set of symbols, a over Σ is a four-dimensional rectangular array of elements of Σ. The set of all four-dimensional tapes over Σ is denoted by $\Sigma^{(4)}$. Given a tape $x \in \Sigma^{(4)}$, for each integer j $(1 \leq j \leq 4)$, we let $l_j(x)$ be the length of x along the jth axis. The set of all $x \in \Sigma^{(4)}$ with $l_1(x) = n_1$,$l_2(x) = n_2$,$l_3(x)$=n_3 and $l_4(x)$=n_4 is denoted by $\Sigma^{(n_1\ n_2\ n_3\ n_4)}$. When $1 \leq i_j \leq l_j(x)$ for each j $(1 \leq j \leq 4)$, let $x(i_1\ i_2\ i_3\ i_4)$ denote the symbol in x with coordinates $(i_1\ i_2\ i_3\ i_4)$. Furthermore, we define

$$x[(i_1\ i_2\ i_3\ i_4),(i_1'\ i_2'\ i_3'\ i_4')],$$

only when $1 \leq i_j \leq i_j' \leq l_j(x)$ for each integer j $(1 \leq j \leq 4)$, as the four-dimensional input tape y satisfying the following conditions:

(1) for each j $(1 \leq j \leq 4)$, $l_j(y) = i_j' \quad i_j + 1$;

(2) for each r_1, r_2, r_3, r_4 $(1 \leq r_1 \leq l_1(y)$, $1 \leq r_2 \leq l_2(y)$, $1 \leq r_3 \leq l_3(y)$, $1 \leq r_4 \leq l_4(y))$, $y\ (r_1,r_2,r_3,r_4) = x\ (r_1+i_1\text{-}1,\ r_2+i_2\text{-}1,\ r_3+i_3\text{-}1,\ r_4+i_4\text{-}1)$. (We call $x[(i_1\ i_2\ i_3\ i_4),(i_1'\ i_2'\ i_3'\ i_4')]$ the $[(i_1\ i_2\ i_3\ i_4),(i_1',i_2'\ i_3'\ i_4')]$- of x.)

Definition 2.2. (denoted by 4-PTM) is a 10-tuple $M = (Q, E, U, q_s, q_0, \Sigma, \ , F, \ _n, \ _f)$, where

(1) $Q = E \cup U \cup \ q_0$ is a finite set of ;

(2) E is a finite set of [illegible];

(3) U is a finite set of [illegible];

(4) q_s is the [illegible];

(5) $q_0 \in Q - q_s$ is the [illegible];

(6) Σ is a finite [illegible] ($\# \in \Sigma$ is the [illegible]);

(7) is a finite [illegible] containing the special [illegible] symbol B;

(8) $F \quad Q \quad q_s$ is the set of [illegible];

(9) $_n$: $E \quad (\Sigma \cup \#) \rightarrow 2^{(Q \; \{q_s\}) \times (\; \{B\}) \times D_{in} \times D_s}$ (where $D_{in} =$ east, west, south, north, up, down, future, past, no move and $D_s =$ left, right, no move) is a [illegible]; and

(10) $_f : U \quad (\Sigma \cup \#) \quad \rightarrow \cup_{1 \leq k \leq \infty} ((Q \quad q_s) \; (\quad B) \quad D_{in} \quad D_s)$ is a [illegible] with the restriction that for each $q \in U$, each $a \in \Sigma \cup \#$, and each $A \in$, if $(q \; a \; A) = ((p_1 \; c_1 \; d_{11} \; d_{21}), (p_2 \; c_2 \; d_{12} \; d_{22}), \quad , (p_k \; c_k \; d_{1k} \; d_{2k}))$, then $c_1 = c_2 = \quad = c_k$.

As shown in Figure.1, M has a read-only four-dimensional rectangular input tape with boundary symbols "#'s", and one semi-infinite storage tape (extended to the right), initially filled with the blank symbols. Furthermore, M has infinite processors, $P_1 \; P_2$, each of which has its input head and storage-tape head. M starts in the situation that (1) the processors P_1 is in the initial state q_0 with its input head on the upper northwestmost corner of the first cube of the input tape and with its storage-tape head on the leftmost cell of the storage tape, and (2) each of other processors is in the quiescent state q_s with its input head on the upper northwestmost corner of the first cube of the input tape and with its storage-tape head on the leftmost cell of the storage tape.

[illegible] (denoted by $SV4$-PTM) is a 3-PTM, input heads of whose processors cannot move in the past direction. In this paper, we are concerned with three-dimensional parallel Turing machines, which each side-length of each input tape is equivalent. Let $L : \mathbf{N} \rightarrow \mathbf{N}$ and $H : \mathbf{N} \rightarrow \mathbf{N}$ be functions. A 4-PTM ($SV4$-PTM) M is called $L(n)$ [illegible] if for any $n \quad 1$ and for any input tape x with $l_1(x) = l_2(x) = l_3(x) = l_4(x) = n$, M on x uses at most $L(n)$ cells of the storage tape, and M is $H(n)$ [illegible] if for any $n \quad 1$ and for any input tape x with $l_1(x) = l_2(x) = l_3(x) = l_4(x) = n$, M on x activates at most $H(n)$ processors. We use the following notations:

· $D4$-$PTM(L(n) \; H(n))$: the class of sets of four-dimensional tapes accepted by $L(n)$ space-bounded and $H(n)$ hardware-bounded deterministic 4-PTM's.

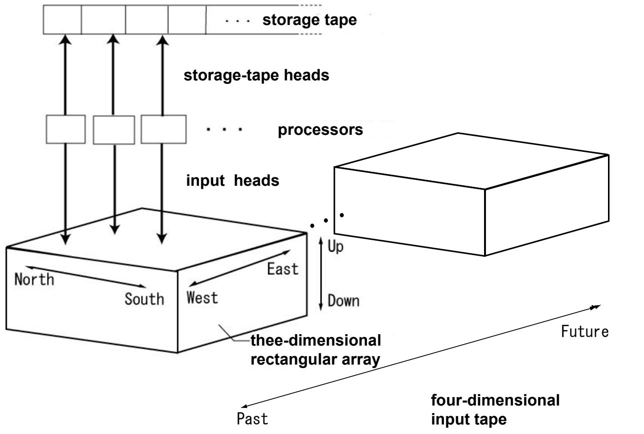

Figure 1: Three-dimensional parallel Turing machine.

· $N4$-$PTM(L(n) \; H(n))$: the class of sets of four-dimensional tapes accepted by $L(n)$ space-bounded and $H(n)$ hardware-bounded nondeterministic 4-PTM's.

· $DSV4$-$PTM(L(n) \; H(n))$: the class of sets of four-dimensional tapes accepted by $L(n)$ space-bounded and $H(n)$ hardware-bounded deterministic $SV4$-PTM's.

· $NSV4$-$PTM(L(n) \; H(n))$: the class of sets of four-dimensional tapes accepted by $L(n)$ space-bounded and $H(n)$ hardware-bounded nondeterministic $SV4$-PTM's.

3 Main Results

This section mainly investigates accepting powers of $SV4$-PTM's, based on hardware complexity.

A function $L : \mathbf{N} \rightarrow \mathbf{N}$ is [illegible] by a k [illegible] if there is a k head one-dimensional deterministic Turing machine [5] M such that for any $n \quad 1$ and any input word x of length n, M on x marks off exactly $L(n)$ cells of the storage tape and halts. (In this case, we say that M [illegible] the function L.)

Theorem 3.1. Let $H : \mathbf{N} \rightarrow \mathbf{N}$ [illegible] (1), (2), and (3), where $k \quad 1$ [illegible]:

(1) H [illegible]

[illegible] ;

(2) $\exists_{n_0} \in \mathbf{N}, \forall_n \quad n_0\ [H(n) \quad k]$;

(3) $\frac{H(n)}{2} \leq \frac{n}{2}(n \leq 2)$.

[illegible] $H' : \mathbf{N} \rightarrow \mathbf{N}$ [illegible] $L : \mathbf{N} \rightarrow \mathbf{N}$ be functions which satisfy the following (4) and (5):

(4) $\exists_{n_0} \in \mathbf{N}, \forall_n \quad n_0\ [\ \frac{H\ (n)}{2} \ \leq\ \frac{H(n)}{2}\ ]$;

(5) max $\quad H'(n)^2\ \frac{H(n)}{2}\ log\, n$,

$H'(n)^2\ \frac{H(n)}{2}\ log\, L(n)$,

$L(n)H'(n)\ \frac{H(n)}{2} \quad = o(n)$.

[illegible]

$DSV4\text{-}PTM(H(n),H(n)) \qquad NSV4\text{-}PTM(L(n), H'(n)) \neq \quad .$

Proof: Let $T(H)$ be the following set depending on the function H in the theorem:

$T(H) = \quad x \in \ 0\ 1\ ^{(4)} \mid \exists_n \quad 2\ \frac{H(n)}{2}\ [l_1(x){=}l_2(x) {=}l_3(x){=}l_4(x){=}n\ \&\ \forall_i(1 \leq i \leq\ \frac{H(n)}{2}\ )$ [the ith cube of x is identical with the $(2\ \frac{H(n)}{2}\ +1 \quad$ i)th cube of x]] .

To prove the theorem, we show that $T(H) \in DSV4\text{-}PTM\ (H(n)\ H(n)) \qquad NSV4\text{-}PTM\ (L(n)\ H(n))$. $T(H)$ is accepted by an $H(n)$ space-bounded and $H(n)$ hardware-bounded $DSV4\text{-}PTM$ M which acts as follows. Suppose that an input tape x with $l_1(x) = l_2(x) = l_3(x) = l_4(x) = n$ is presented to M. Let M_1 be a k head one-dimensional deterministic Turing machine which constructs the function H. By simulating the action of M_1 on the first cube of x, the first k processors $P_1\ P_2 \qquad P_k$ of M mark off exactly $H(n)$ cells of the storage tape.

After this, each processor $P_i(2 \leq i \leq k)$ positions its storage-tape head on the ith cell (from the left) of the storage tape, and processor P activates processors $P_{k+1}\ P_{k+2} \qquad P_{H(n)}$ in such a way that for each j $(k + 1 \leq j \leq H(n))$, the storage-tape head of P_j is positioned on the jth cell (from the left) of the storage tape. Then P_1 positions the input head at the northwestmost corner of the $(2\ \frac{H(n)}{2}\ + 2 \quad H(n))$th cube of x, which for each i $(2 \leq i \leq H(n))$, P_i positions the input head on the northwestmost corner of the $(H(n) \quad i + 1)$th cube of x. And P_1 systematically traverses the $(2\ \frac{H(n)}{2}\ +2 \quad H(n))$th cube, , the $2\ \frac{H(n)}{2}$ th cube (from the first plane to the last plane in each cube, from the first column to the last column in each plane, and from the first row to the last row in each column), and compares these cubes with the $(H(n) \quad 1)$th cubes, …, the first cubes, respectively, by using the information from $P_2\ P_3 \qquad P_{H(n)}$.

These input heads are then positioned at the northwestmost end of the $H(n)$th cube of x. The same procedure is used inductively to verify that $H(n)$th cube through the $(2\ \frac{H(n)}{2}\ + 1 \quad H(n))$th cube has a desired form.

Next, we show that $T(H) \in NSV4\text{-}PTM\ (L(n), H'(n))$. Suppose to the contrary that there is an $NSV4\text{-}PTM\ (L(n),H'(n))$ M' accepting $T(H)$. Let s and t be the numbers of states of the finite control of each processor and storage tape symbols of M', respectively. For large $n \quad 2\ \frac{H(n)}{2}$, let

$V(n) = \quad x \in \ 0\ 1\ ^{(4)} \mid l_1(x) = l_2(x) = l_3(x) = l_4(x) = n\ \&\ \forall_i\ (1 \leq i \leq\ \frac{H(n)}{2}\ )$ [the ith cube of x is identical with the $(2\ \frac{H(n)}{2}\ + 1 \quad i)$th plane of x] & $[(1\ 1\ 1\ 2\ \frac{H(n)}{2}\ + 1),\ (n\ n\ n\ n)] \in \ 0\ ^{(4)}$.

Below, we consider the computation of M' on input tapes in $V(n)$. Clearly, each tape x in $V(n)$ is in $T(H)$, and so x is accepted by M'.

A configuration of M' is an infinite-tuple (, $((h_1\ k_1\ j_1\ i_1)\ q_1\ r_1)$, $((h_2\ k_2\ j_2\ i_2)\ q_2\ r_2)$, ..., $((h_m\ k_m\ j_m\ i_m),\ q_m,\ r_m), \ldots)$ where is the nonblank contents of the storage tape of M', and for each $m \quad 1$, $(h_m\ k_m\ j_m\ i_m)$, q_m and r_m are the input head position, the state of the finite control and the position of storage-tape head of the mth processor of M', respectively. The type of a configuration $C{=}(\ ,\ ((h_1\ k_1\ j_1\ i_1)\ q_1\ r_1),\ ((h_2\ k_2\ j_2\ i_2)\ q_2\ r_2), ..., ((h_m\ k_m\ j_m\ i_m),\ q_m,\ r_m), \ldots)$, denoted by $Type(C)$, is an infinite-tuple $([i_1] \quad [i_m] \quad)$, where for each $m \quad 1$,

$$[i_m] = \begin{cases} i_m & \text{if } i_m \leq \frac{H(n)}{2} \\ 2\ \frac{H(n)}{2} & otherwise \end{cases}$$

Let $c_1(x)$, $c_2(x)$, ..., $c_{l_x}(x)$ be the sequence of configurations of M' during an (arbitrary selected) accepting computation of M' on a tape x in $V(n)$. Here l_x is the length of this computation. Let $d_1(x)\ d_2(x) \qquad d_{l\ x}(x)$ be the subsequence obtained by selecting $c_1(x)$ and all subsequent $c_i(x)$'s such that $Type(c_i(x)) \neq Type(c_{i+1}(x))$. We call $d_1(x)\ d_2(x) \qquad d_{l\ x}(x)$ the pattern of x. Let $p(n)$ be the number of possible pattern of M' on x in $V(n)$. Since $L'_x \leq H'(n)(2\ \frac{H(n)}{2} \quad 1) + 1 \equiv Q(x)$ (note that M' uses at most $H'(n)$ processors when it reads tapes in $V(n)$), we get the following inequality:

$p(x) \quad \leq \quad ((s(n\ +\ 1)(n\ +\ 1)(n\ +\ 1)(n\ + 1)L(n))^{H\ (m)t^{L(n)}})^{Q(n)}$.

Now we classify the tapes in $V(n)$ according to their patterns. There must exist a pattern $\hat{d}_1\ \hat{d}_2 \qquad \hat{d}_l$ which corresponds to a set $S(n)$ of at least $2^{n\times n\times n\times(\frac{H(n)}{2})}$ / $p(n)$ tapes in $V(n)$. Since $\frac{H\ (n)}{2} \leq \frac{H(n)}{2}$ (from condition (4) in the theorem), the same observation as in the proof of Theorem 3 in [3] reveals that for any computation of M' on an $x \in V(n)$, there exists an index i

such that the ith cube of x and the $(2\ \frac{H(n)}{2}\ +1\quad i)$th cube of x are never being read simultaneously.

Let i_0 be such a value for the pattern $\hat{d}_1\ \hat{d}_2\quad \hat{d}_l$. we now define a binary relation E on tapes in $S(n)$ as follows: For each u and v in $S(n)$, let

${}_uE_v \Leftrightarrow \forall_i(\in\ i_0\ i_0\ i_0\ 2\ \frac{H(n)}{2}\ +1\quad i_0)$ [ith cubes of u and v are identical].

Obviously the relation E is an equivalence relation, and there are $q(n) = 2^{n^3((\frac{H(n)}{2})\quad 1)}$ E-equivalence classes of tapes in $S(n)$. From condition (5) in the theorem, we can easily show that $|S(n)| > q(n)$ for large n. Therefore, there exist two different tapes in $S(n)$ which belong to the same equivalence class. Let x and y be such two different tapes in $S(n)$. And let z be the tape obtained from x by replacing the $(2\ \frac{H(n)}{2}\ +1\quad i_0)$th cube with the $(2\ \frac{H(n)}{2}\ +1\quad i_0)$th cube of y. By an argument similar to that in the proof of theorem 1 in [7], it can be shown that there is an accepting computation of M' on z. Consequently, z must be accepted by M'. This contradicts the fact z is not in $T(H)$. □

We consider the following functions:

$\cdot\ log^{(1)}n = \begin{cases} 0 & (n=0) \\ \lceil logn \rceil & (n\quad 1), \end{cases}$

and for each $r\quad 1$,

$\cdot\ log^{(r+1)}n = log^{(1)}(log^{(r)}n)$.

It is shown in [4] that the function $log^{(k)}n$ $(k\quad 1)$ are fully space-constructible by three head one-dimensional deterministic Turing machines. A similar result is provided about the four dimensions. From this fact and Theorem 3.1, we have:

Corollary 3.1. $k\quad 3$,
$DSV4\text{-}PTM\quad (log^{(k)}n\ log^{(k)}n)\qquad NSV4\text{-}PTM\ (log^{(k)}n,\ log^{(k+1)}n) \neq\ $.

Corollary 3.2. $X \in\ D\ N$ and each $k\quad 3$,
$XSV4\text{-}PTM\quad (log^{(k)}n\ log^{(k+1)}n)\qquad XSV4\text{-}PTM\ (log^{(k)}n\ log^{(k)}n)$.

Letting $H(n) = k+1$ (where k is a positive integer), $H'(n) = k$, and $L(n) = o(n)$ in Theorem 3.1, we have :
$DSV4\text{-}PTM\ (k+1\ k+1)\quad NSV4\text{-}PTM\ (0(n)\ k) \neq\ $.

From this and from the obvious fact that

$DSV4\text{-}PTM\ (k+1\ k+1) = DSV4\text{-}PTM(1\ k+1)$,

we have the following corollary.

Corollary 3.3. $k\quad 1$,
$DSV4\text{-}PTM\ (1\ k+1)\quad NSV4\text{-}PTM\ (o(n)\ k) \neq\ $.

4 Conclusion

This paper investigated fundamental properties of four-dimensional parallel Turing machines with bounded number of processors. We conclude the paper by giving several open problems.

(1) What is a relationship between the accepting powers of $SV4\text{-}PTM$'s and 4-PTM's?

(2) What is a hierarchy of the accepting powers of $SV4\text{-}PTM$'s, based on the hardware complexity depending on the side-length of input tapes?

References

[1] T. Ito, "Synchronized alternation and parallelism for three-dimensional automata", , 2008.

[2] K. Okinaka, K. Inoue, A. Ito,and Y. Wang, "A note on hardware-bounded parallel Turing machines", , pp. 90-100, 2002.

[3] A. L. Rosenberg, "On multihead finite automata", , Vol. 10, pp. 388-394, 1996.

[4] M. Sakamoto, K. Inoue, and I. Takanami, "Three-dimensionally fully space constructible functions", , E77-D(6), pp. 723-725, 1994.

[5] S. Sakurayama, K. Inoue, I. Takanami, H. Taniguchi, and H. Matsuno, "A note on multi-head on-line Turing machines", , Vol.3, No.2, pp.183-192, 1983.

[6] J. Wiedermann, "Parallel Turing machines", , 1984.

[7] A. C. Yao and R. L. Rivest, "k+1 heads are better than k", , Vol.25, No.2, pp.337-340, 1978.

The Fifteenth International Symposium on Artificial Life and Robotics 2010 (AROB 15th '10),
B-Con Plaza, Beppu,Oita, Japan, February 4-6, 2010

Some Properties of Four-Dimensional Parallel Turing Machines

Yasuo UCHIDA[1], Makoto SAKAMOTO[2], Ayumi TANIUE[2], Ryuju KATAMUNE[2],
Takao ITO[1], Hiroshi FURUTANI[2], and Michio KONO[2]

[1] Dept. of Business Administration, Ube National College of Technology, Ube 755-8555, JAPAN
[2] Dept. of Computer Science and Systems Engineering, University of Miyazaki, Miyazaki 889-2192, JAPAN

Abstract

Informally, a parallel Turing machine (PTM) proposed by Wiedermann is a set of identical usual sequential Turing machines (STM's) cooperating on two common tapes   storage tape and input tape. Moreover, STM's which represent the individual processors of the parallel computer can multiply themselves in the course of computation. On the other hand, during the past about seven years, automata on a four-dimensional tape have been proposed as computational models of four-dimensional pattern processing and several properties of such automata have been obtained. In [1], we proposed a four-dimensional parallel Turing machine (4-PTM), and dealt with a hardware-bounded 4-PTM, which each side-length of each input tape is equivalent. We believe that this machine is useful in measuring the parallel computational complexity of three-dimensional images. In this paper, we continue the study of 3-PTM, which each side-length of each input tape is equivalent, and investigate some accepting powers of it.

Key Words: computational complexity, four-dimensional automaton, hardware-bounded computation, nondeterminism, parallel Turing machine

1 Introduction

A parallel Turing machine (PTM) is a set of identical sequential Turing machines (STM's) cooperating on two common tapes   storage tape and input tape [8]. Moreover, STM's which represent the individual processors of the parallel computer can multiply themselves in the course of computation. In [8] it is shown, for example, that every PTM can be simulated by an STM in polynomial time, and that the PTM cannot be simulated by any sequential Turing machine in linear space.

In [2,4,6,7], two- or three-dimensional version of PTM was investigated. On the other hand, due to the advances in many application areas such as moving image processing, computer animation, and so on, it has become increasingly apparent that the study of four-dimensional pattern processing has been of crucial importance. Thus, we think that the study of four-dimensional automata as a computational model of four-dimensional pattern processing has also been meaningful. From this viewpoint, we first introduced four-dimensional automata [3,5]. In [1], we proposed a four-dimensional parallel Turing machine (4-PTM), and investigated its some properties. Especially, we dealt with a hardware-bounded 4-PTM, a variant of the 4-PTM, which each side-length of each input tape is equivalent. The hardware-bounded 4-PTM is a 4-PTM, the number of whose processors is bounded by a constant or variable depending on the size of inputs. The investigation of hardware-bounded 4-PTM's is more useful than that of 4-PTM's from the practical point of view. In this paper, we continue the study of 4-PTM [1], and investigate some accepting powers of its parallel computational model, which each side-length of each input tape is equivalent.

2 Preliminaries

Definition 2.1. Let Σ be a finite set of symbols, a [illegible] over Σ is a four-dimensional rectangular array of elements of Σ. The set of all four-dimensional tapes over Σ is denoted by $\Sigma^{(4)}$. Given a tape $x \in \Sigma^{(4)}$, for each integer j $(1 \leq j \leq 4)$, we let $l_j(x)$ be the length of x along the jth axis. The set of all $x \in \Sigma^{(4)}$ with $l_1(x) = n_1$, $l_2(x) = n_2$, $l_3(x)=n_3$ and $l_4(x)=n_4$ is denoted by $\Sigma^{(n_1\ n_2\ n_3\ n_4)}$. When $1 \leq i_j \leq l_j(x)$ for each j $(1 \leq j \leq 4)$, let $x(i_1\ i_2\ i_3\ i_4)$ denote the symbol in x with coordinates $(i_1\ i_2\ i_3\ i_4)$. Furthermore, we define

$$x[(i_1\ i_2\ i_3\ i_4),(i'_1\ i'_2\ i'_3\ i'_4)],$$

only when $1 \leq i_j \leq i'_j \leq l_j(x)$ for each integer j $(1 \leq j \leq 4)$, as the four-dimensional input tape y satisfying the following conditions:

(1) for each j $(1 \leq j \leq 4)$, $l_j(y) = i'_j \quad i_j + 1$;

(2) for each r_1, r_2, r_3, r_4 $(1 \leq r_1 \leq l_1(y)$, $1 \leq r_2 \leq l_2(y)$, $1 \leq r_3 \leq l_3(y)$, $1 \leq r_4 \leq l_4(y))$, y $(r_1,r_2,r_3,r_4) = x$ $(r_1+i_1\text{-}1,\ r_2+i_2\text{-}1,\ r_3+i_3\text{-}1,\ r_4+i_4\text{-}1)$. (We call $x[(i_1\ i_2\ i_3,\ i_4),(i'_1\ i'_2\ i'_3\ i'_4)]$ the $[(i_1\ i_2\ i_3\ i_4),(i'_1,i'_2\ i'_3\ i'_4)]$-[illegible] of x.)

Definition 2.2. [illegible] (denoted by 4-PTM) is a 10-tuple $M = (Q$, E, U, q_s, q_0, Σ, Γ, F, $\ _n$, $\ _f)$, where

(1) $Q = E \cup U \cup \ q_0$ is a finite set of [illegible];

(2) E is a finite set of [illegible];

(3) U is a finite set of [illegible];

(4) q_s is the [illegible];

(5) $q_0 \in Q$ - q_s is the [illegible];

(6) Σ is a finite [illegible] ($\# \in \Sigma$ is the [illegible]);

(7) Γ is a finite [illegible] containing the special [illegible] symbol B;

(8) $F \quad Q \quad q_s$ is the set of [illegible];

(9) $\ _n$: $E \quad (\Sigma \cup \ \# \ ) \quad \Gamma \to 2^{(Q\ \{q_s\})\times(\Gamma\ \{B\})\times D_{in}\times D_s}$ (where $D_{in} =$ east, west, south, north, up, down, future, past, no move and $D_s =$ left, right, no move) is a [illegible]; and

(10) $\ _f$: $U \quad (\Sigma \cup \ \# \ ) \quad \Gamma \to \cup_{1\leq k\leq\infty}$ $((Q \ q_s\ ) \quad (\Gamma \quad B\ ) \quad D_{in} \quad D_s)$ is a [illegible] with the restriction that for each $q \in U$, each $a \in \Sigma \cup \ \#$, and each $A \in \Gamma$, if $(q\ a\ A) = ((p_1\ c_1\ d_{11}\ d_{21}), (p_2\ c_2\ d_{12}\ d_{22}), \quad , (p_k\ c_k\ d_{1k}\ d_{2k}))$, then $c_1 = c_2 = \quad = c_k$.

As shown in Figure 1, M has a read-only four-dimensional rectangular input tape with boundary symbols "#'s", and one semi-infinite storage tape (extended to the right), initially filled with the blank symbols. Furthermore, M has infinite processors, $P_1\ P_2 \quad$, each of which has its input head and storage-tape head. M starts in the situation that (1) the processors P_1 is in the initial state q_0 with its input head on the upper northwestmost corner of the first cube of the input tape and with its storage-tape head on the leftmost cell of the storage tape, and (2) each of other processors is in the quiescent state q_s with its input head on the upper northwestmost corner of the first cube of the input tape and with its storage-tape head on the leftmost cell of the storage tape.

[illegible] (denoted by $SV4$-PTM) is a 4-PTM, input heads of whose processors cannot move in the past

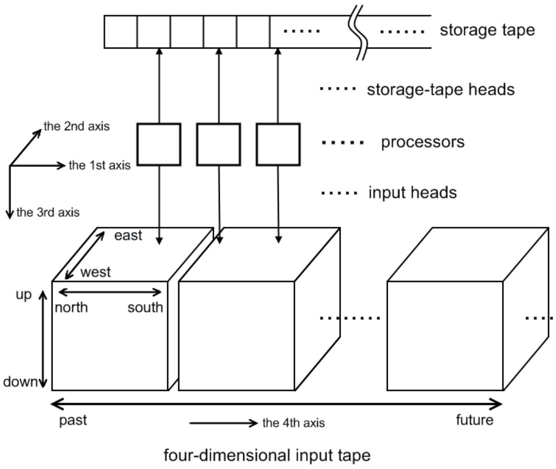

Figure 1: Four-dimensional parallel Turing machine.

direction. In this paper, we are concerned with three-dimensional parallel Turing machines, which each side-length of each input tape is equivalent. Let $L : \mathbf{N} \to \mathbf{N}$ and $H : \mathbf{N} \to \mathbf{N}$ be functions. A 4-PTM ($SV4$-PTM) M is called $L(n)$ [illegible] if for any $n \quad 1$ and for any input tape x with $l_1(x) = l_2(x) = l_3(x) = l_4(x) = n$, M on x uses at most $L(n)$ cells of the storage tape, and M is $H(n)$ [illegible] if for any $n \quad 1$ and for any input tape x with $l_1(x) = l_2(x) = l_3(x) = l_4(x) = n$, M on x activates at most $H(n)$ processors. We use the following notations:

$D4$-$PTM(L(n)\ H(n))$: the class of sets of cubic tapes accepted by $L(n)$ space-bounded and $H(n)$ hardware-bounded deterministic 4-PTM's

$N4$-$PTM(L(n)\ H(n))$: the class of sets of cubic tapes accepted by $L(n)$ space-bounded and $H(n)$ hardware-bounded nondeterministic 4-PTM's

$DSV4$-$PTM(L(n)\ H(n))$: the class of sets of cubic tapes accepted by $L(n)$ space-bounded and $H(n)$ hardware-bounded deterministic $SV4$-PTM's

$NSV4$-$PTM(L(n)\ H(n))$: the class of sets of cubic tapes accepted by $L(n)$ space-bounded and $H(n)$ hardware-bounded nondeterministic $SV4$-PTM's

3 Seven-Way versus Eight-Way

This section investigates a relationship between the accepting powers of $SV4$-PTM's and 4-PTM's.

Theorem 3.1. $H : \mathbf{N} \rightarrow \mathbf{N}$ $\frac{H(n)}{2} < \frac{n}{2}(n \quad 2)$. *, Let* $L : \mathbf{N} \rightarrow \mathbf{N}$ *and* $H' : \mathbf{N} \rightarrow \mathbf{N}$
(1) $\exists n_0 \in \mathbf{N}, \forall n \quad n_0$ [$\frac{H(n)}{2} \leq \frac{H(n)}{2}$], *and*
(2) $max \quad H'(n)^2 \frac{H(n)}{2} \log n,$
$H'(n)^2 \frac{H(n)}{2} \log L(n),$
$L(n)H'(n) \frac{H(n)}{2} = o(n).$
Then,

$D4$-PTM(1,2) $\quad NSV4$-$PTM(L(n) \ H'(n)) \neq$.

Proof: Let $T_1 = \ x \in \ 0 \ 1 \ 2 \ ^{(4)}|\exists n \quad 3[l_1(x) = l_2(x) = l_3(x) = l_4(x) = n$ & there exists an odd number i $(3 \leq i \leq n)$ such that
(i) $x[(1\ 1\ 1\ 1)\ (n\ n\ n\ i \quad 1)] \in \ 0\ 1\ ^{(4)}$,
(ii) $x[(1\ 1\ 1\ i)\ (n\ n\ n\ n)] \in \ 2\ ^{(4)}$, and
(iii)$\forall j(1 \leq j \leq i \quad 1)$ [the jth cube of x is identical with the (i-j)th cube of x]] .

It is easily seen that $T_1 \in D4$-PTM(1,2). On the other hand, by using the idea as in the proof of Theorem 3.1 in [1], we can show that $\mathrm{T}_1 \in NSV4$-$PTM(L(n) \ H'(n))$ for any $L(n)$ and any $H'(n)$ in the theorem. The proof is obtained by replacing $V(n)$ (in the proof of Theorem 3.1 in [1]) with $T_1(n)$, where for large $n \quad 2 \ \frac{H(n)}{2} + 1$, let

$$\begin{gathered} T_1(n) = \ x \in \ 0\ 1\ 2\ ^{(4)}| \\ l_1(x) = l_2(x) = l_3(x) = l_4(x) = n \ \& \\ x[(1\ 1\ 1\ 1)\ (n\ n\ n\ 2\ \frac{H(n)}{2}\ )] \in \ 0\ 1\ ^{(4)} \& \\ x[(1\ 1\ 1\ 2\ \frac{H(n)}{2} + 1)\ (n\ n\ n\ n)] \in \ 2\ ^{(4)} \& \\ \forall i(1 \leq i \leq \ \frac{H(n)}{2}\ )[\text{the } i\text{th cube of } x \text{ is} \\ \text{identical with the } (2\ \frac{H(n)}{2} + 1 \quad i)\text{th cube of } x] \ . \end{gathered}$$

□

Corollary 3.1. $k \quad 1$,

$D4$-PTM(1,2) $\quad NSV4$-$PTM(o(n) \ k) \neq$.

Letting $H(n) = \lceil n^{\frac{1}{4}} \rceil \ L(n) = 1$, and $H'(n) = \lceil n^{\frac{1}{5}} \rceil$ ($\lceil r \rceil$ means the smallest integer greater than or equal to r.) in Theorem 3.1, we also have

Corollary 3.2.

$D4$-PTM(1,2) $\quad NSV4$-$PTM(1, \lceil n^{\frac{1}{5}} \rceil) \neq$.

4 Determinism versus Nondeterminism

This section investigates a relationship between the accepting powers of deterministic and nondeterministic seven-way 4-PTM's.

Theorem 4.1. *Let* H,L, *and* H' 3.1. *Then,*

$NSV4$-PTM(1,2) $\quad DSV4$-$PTM(L(n) \ H'(n)) \neq$.

Proof: Let $T_2 = \ x \in \ 0\ 1\ 2\ ^{(4)}|\exists n = 2m+1 \quad 3[l_1(x) = l_2(x) = l_3(x) = l_4(x) = n$ & (there exists an integer i $(3 \leq i \leq n)$ such that
(i) $x[(1\ 1\ 1\ i)\ (n\ n\ n\ n)] \in \ 2\ ^{(4)}$,
(ii) $\forall j(1 \leq j \leq i \quad 1)$ $[w_j = x[(1\ 1\ 1\ j)\ (m\ n\ n\ j)] \in \ 0\ 1\ ^{(4)}$ & $x[(m+1\ 1\ 1\ j)\ (m+1\ n\ n\ j)] \in \ 2\ ^{(4)}$ & $w'_j = x[(m+2\ 1\ 1\ j)\ (n\ n\ n\ j)] \in \ 0\ 1\ ^{(4)}]$,
(iii) $\exists k\ \exists l\ (1 \leq k < l \leq i \quad 1)$ $[w_k = x[(1\ 1\ 1\ k)\ (m\ n\ n\ k)] \in \ 0\ 1\ ^{(4)}$ &
$x[(m+1\ 1\ 1\ k)\ (m+1\ n\ n\ k)] \in \ 2\ ^{(4)}$ &
$w'_k = x[(m+2\ 1\ 1\ k)\ (n\ n\ n\ k)] \in \ 0\ 1\ ^{(4)}$ &
$w_l = x[(1\ 1\ 1\ l)\ (m\ n\ n\ l)] \in \ 0\ 1\ ^{(4)}$ &
$x[(m+1\ 1\ 1\ l)\ (m+1\ n\ n\ l)] \in \ 2\ ^{(4)}$ &
$w'_l = x[(m+2\ 1\ 1\ l)\ (n\ n\ n\ l)] \in \ 0\ 1\ ^{(4)}$ &
$w_k = w_l$ & $w'_k \neq w'_l])$.

That is, each cube consists of a w_j and a w'_j. A tape x is in T_2 iff there is a pair of cubes (of x) with the same tag field but different value fields and the bottom cubes of x consist of 2's. Clearly $T_2 \in NSV4$-PTM(1,2).

We below show that $T_2 \in DSV4$-$PTM(L(n) \ H'(n))$. We just present the main idea here and leave the details to the reader, as they are quite similar to those of the proof of Theorem 3.1 in [1]. For each integer $n = 2m+1 \quad 2\ \frac{H(n)}{2} + 1$, let

$T_2(n) = \ x \in T_2|l_1(x)=l_2(x)=l_3(x)=l_4(x)=n$ &
$\forall j(1 \leq j \leq 2\ \frac{H(n)}{2}\ )$[($\mathrm{w}_j$ consists of the former continuous a 1's and the latter continuous $m(2m+1)(2m+1)$ a 0's by scanning w_j systematically from the first plane to the $(2m+1)$th plane in w_j, from the first column to the $(2m+1)$th column in a plane and from the first row to the mth row in a column) (a = min $j,\ 2\ \frac{H(n)}{2} + 1 \quad j$) and $w'_j = \ 0\ 1\ ^{m(2m+1)(2m+1)}$] & $x[(1,1,1,2\ \frac{H(n)}{2} + 1),(n\ n\ n\ n)] \in \ 2\ ^{(4)}$.

As in the proof of Theorem 3.1 in [1], there can be constructed a tape in $T_2(n)$ which M will reject, using the fact that there are many words having this tag structure such that the jth cube and the $(2\ \frac{H(n)}{2} + 1 \quad j)$th cube are identical for $1 \leq j \leq \frac{H(n)}{2}$ (and thus not in T_2). □

Letting $H(n)=\lceil n^{\frac{1}{4}} \rceil$, $L(n)=1$, and $H'(n)=\lceil n^{\frac{1}{5}} \rceil$ in Theorem 4.1, we have

Corollary4.1

$NSV4\text{-}PTM(1,2)$ [illegible] $DSV4\text{-}PTM(1$ [illegible] $\lceil n^{\frac{1}{5}} \rceil) \neq$ [illegible].

5 Conclusion

This paper investigated some accepting powers of four-dimensional parallel Turing machines, which each side-length of each input tape is equivalent. We conclude the paper by giving some open problems.

(1) What is a hierarchy of the accepting powers of 4-PTM's or $SV4\text{-}PTM$'s, based on the hardware complexity depending on the input length?

(2) What is a relationship between the accepting powers of deterministic and nondeterministic 4-PTM's with bounded hardware?

(3) For any k [illegible] 1,

$D4\text{-}PTM(1$ [illegible] $k+1)$ [illegible] $N4\text{-}PTM(o(logn)$ [illegible] $k) \neq$ [illegible] ?

References

[1] T.Ito, M.Sakamoto, Y.Nagamizu, K.Iihoshi, N.Tomozoe, H.Furutani, and M.Kono, "Four-dimensional parallel Turing machines", [illegible], 2010, to appear.

[2] T.Ito, "Synchronized alternation and parallelism for three-dimensional automata", [illegible], 2008.

[3] H.Okabe, S.Taniguchi, T.Makino, S.Nogami, Y.Nakama, M.Sakamoto, and K.Inoue, "Computation for motion image processing by 4-dimensional alternating Turing machines", [illegible], pp. 241-246, 2003.

[4] K.Okinaka, K.Inoue, A.Ito, and Y.Wang, "A note on hardware-bounded parallel Turing machines", [illegible], pp. 90-100, 2002.

[5] M.Sakamoto, H.Okabe, and K.Inoue, "Some properties of four-dimensional finite automata", [illegible], p.351, 2002.

[6] M.Sakamoto, T.Ito, H.Furutani, and M.Kono, "Some accepting powers of three-dimensional parallel Turing machines", [illegible], Vol.13, No.1, pp.27-30, 2008.

[7] M.Sakamoto, N.Tomozoe, H.Furutani, M.Kono, T.Ito, Y.Uchida, and H.Okabe, "A survey of automata on three-dimensional input tapes", [illegible], Issue10, Vol.7, pp.1638-1647, 2008.

[8] J.Wiedermann, "Parallel Turing machines", [illegible], 1984.

The Fifteenth International Symposium on Artificial Life and Robotics 2010 (AROB 15th '10),
B-Con Plaza, Beppu,Oita, Japan, February 4-6, 2010

Adaptation of Robot Perception on Fuzzy Linguistic Information by Evaluating Vocal Cues for Controlling a Robot Manipulator

A.G.B.P. Jayasekara
Dept of Advanced Systems Control Engineering
Saga University
1 Honjo machi, Saga 840-8502, Japan.
buddhika@ieee.org

Keigo Watanabe
Dept of Intelligent Mechanical Systems
Okayama University
3-1-1 Tsushima-naka, Kita-ku
Okayama 700-8530, Japan.
watanabe@sys.okayama-u.ac.jp

Kazuo Kiguchi and Kiyotaka Izumi
Dept of Advanced Systems Control Engineering
Saga University
1 Honjo machi, Saga 840-8502, Japan.
{kiguchi,izumi}@me.saga-u.ac.jp

Abstract

This paper proposes a method for adapting robot's perception on fuzzy linguistic information by evaluating vocal cues. Robot's perception on fuzzy linguistic information such as "very little" depends on the environmental arrangement and the user's expectations. Therefore robot's perception on the corresponding environment is modified by acquiring user's perception through vocal cues. Fuzzy linguistic information related to primitive movements are evaluated by a behavior evaluation network (BEN). Vocal cue evaluation system (VCES) is utilized to evaluate the vocal cues for modifying the BEN. The proposed system is implemented by a PA-10 robot manipulator.

1 Introduction

Voice communication is a better option among the other alternatives for human-robot interaction. Ability of the robot companion to understand the uncertain information is crucial for effective human-robot interaction. A successful human-friendly robot equipped with human-like voice communication capabilities will be able to help disabled people, to assist the aged people, to help in complex tasks such as surgery, etc. [1].

In Pulasinghe et al. [2], robot control by using information-rich voice commands such as "move a very little forward" has been studied. Generally, the voice commands, which include fuzzy linguistic information are referred as fuzzy voice commands (FVCs) [3]. The quantitative assessment for such information depends on the environmental conditions and the user's expectations. The main limitation of the abovementioned methods is that the system of understanding and quantifying the fuzzy linguistic information in voice commands is predetermined. Normally, humans possess a natural ability of adapting to other humans and artifacts. The mutual adaptation is important in acquiring the information that included in the voice commands in human-human communications [4].

Therefore this paper proposes a method for interpreting fuzzy linguistic information by adapting the robot's perception based on user's perception on corresponding environment. Here, the user's perception is acquired based on vocal cues. The system overview is discussed in section 2. Next section 3 discusses the adaptation process of the robot's perception based on vocal cues. Finally, summary is presented.

2 System Overview

We have proposed a method to understand FVCs by evaluating fuzzy linguistic information based on user's guidance. Functional overview of the proposed method is shown in Fig. 1. Vocal cues and FVCs are fed into the VCES and the BEN respectively. Here, end-effector movements of a manipulator are considered as the primitive behaviors for the proposed system. The BEN is utilized to evaluate the primitive behaviors and implemented by using a fuzzy-neural network. The VCES is introduced to evaluate the vocal cues. If the user command is a vocal cue, the BEN is adapted based on the assessment of the movement error e. If the user command is an FVC, the corresponding primitive behavior is activated and fuzzy

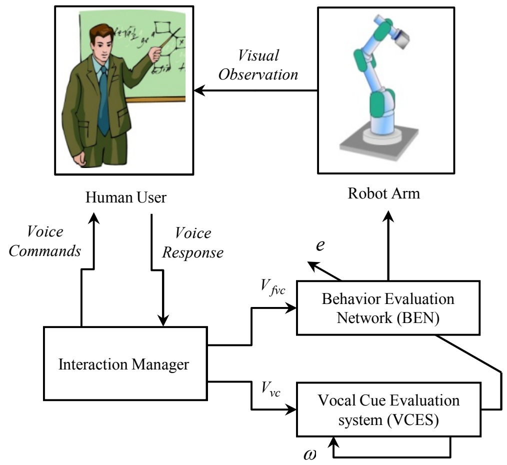

Figure 1: Functional overview of the proposed system.

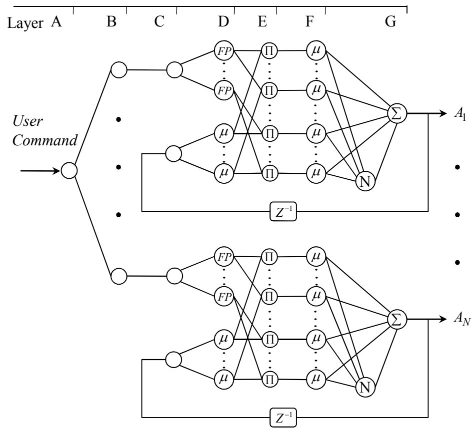

Figure 2: Fuzzy-neural network for the BEN.

Table 1: Fuzzy voice motion commands

Action groups	Actions	Modification
G1	Move forward Move backward	very little little (medium) far
G2	Move left Move right	
G3	Move up Move down	

linguistic information is evaluated by the BEN. In addition, the user's willingness to change the robot's perception is identified as a parameter that is capable of improving the adaptation process by acquiring the information related to repetition of vocal cues. After the adaptation phase, the system can be used to navigate the tip of the robot manipulator by using FVCs.

3 Adaptation of Robot Perception

A quantitative assessment for a fuzzy linguistic term such as " little" highly depends on the environmental conditions. Therefore, it is proposed to acquire the user's desire through vocal cues for adapting the robot's perception toward the user's perception.

3.1 Behavior Evaluation Network

Fuzzy implications in FVCs are interpreted by the BEN. The corresponding primitive movement is identified based on the action and the action modification phrases. Fuzzy linguistic terms are evaluated and quantified based on the previous output of the corresponding action. The proposed structure is shown in Fig. 2. The available actions are grouped into three action groups by considering the similarity of movements and shown in Table 1. Separate behavior evaluation sections are proposed for each action group in the BEN [5].

Layer A transmits the user commands directly to the next layer. Layer B acts as an action selection layer. Layer C consists of two types of nodes; one is a command node to pass the fuzzy predicate included in the user command and the other is a node to acquire the previous value of the corresponding action. Layer D acts as the fuzzification layer of the fuzzy-neural network. Layer F links the fuzzy antecedent part to the consequent part. Any node $t$of kth action represents a triangular membership function with center $a_t^k \in [(a_t^k)_L \ \ (a_t^k)_H]$ and width $b_t^k \in [(b_t^k)_L \ \ (b_t^k)_H]$ where $t = 1 \quad T$. The nodes in the final layer generate the output and act as the defuzzification layer. Then the output can be formulated based on the sum-product composition for Mamdani fuzzy system [6]:

$$A_k = \frac{\sum_{t=1}^{T} u_t^k a_t^k b_t^k}{\sum_{t=1}^{T} u_t^k b_t^k} \tag{1}$$

The initial membership functions for the previous movement and the new movement are defined by assuming the uniform distribution over the universe of discourse. Here, the membership function for the previous distance and the new distance are used to initialize the corresponding parameters of the layer D and layer G respectively. The connection weights of the layer G are adjusted by applying the backpropergation algorithm in the training phase based on the movement error.

3.2 Vocal Cue Evaluation System

The VCES is introduced to evaluate the vocal cues for assessing the movement error e. A vocal cue includes user's directives to modify the robot behaviors. VCES is realized by using a fuzzy inference system. The fuzzy linguistic information in the vocal cue is interpreted by assuming that the behavior change depends on the robot movement observed by the user. Therefore, the observed robot movement and the vocal cue are considered as the inputs of the fuzzy inference system. The evaluated error is the output. The user feedback consists of a set of command components (i.e. "Too Large," "Slightly Large," "Good," "Slightly Small," and "Too Small") that are considered as singleton membership functions.

3.3 Adaptation of Behavior Evaluation Network

The BEN is adapted toward the environmental conditions based on the user's guidance. In the training phase, the BEN is adapted based on the movement error that is calculated by the VCES. The training process is continued by considering a selected set of tasks until the user feels a satisfactory level of robot's movements. Satisfactory level of the user toward the robot's movements for kth action group $\ _k \in [0\ 1]$ is defined by

$$\ _k = \frac{N_G^k}{N_T^k} \tag{2}$$

where, N_G^k is the number of user feedback "Good" in robot's movements of action group k from number of total vocal cues N_T^k, which is from recent previous movements.

User's willingness to change the robot's perception is identified as a parameter that can extract the user's motivation to change an assessment for a particular fuzzy linguistic term by considering a series of vocal cues. Therefore the user's willingness to change the robot's perception for ath fuzzy predicate in kth action group is defined by

$$\ _a^k = (1 \quad _k) \sum_{m=1}^{N_T^k} \ _m \tag{3}$$

Here, the component for user's willingness to change the robot's perception from the vocal cue related to mth previous movement is $\ _m$.

Aadaptation of the BEN is implemented by training the parameters of the membership functions for new distance corresponding to the parameters of the layer G. The membership parameter training corresponding to the network weight training for the tth node and its neighboring nodes of kth action at the $(\ +1)$th time step are given by

$$a_t^k(\ +1) = \begin{cases} a_t^k(\ ) + \ e_1^k u_t^k & \text{if } a_t^k(\ +1) \\ & \in [(a_t^k)_L\ (a_t^k)_H] \\ a_t^k(\ ) & \text{otherwise} \end{cases} \tag{4}$$

$$b_t^k(\ +1) = \begin{cases} b_t^k(\ ) + \ e_2^k u_t^k & \text{if } b_t^k(\ +1) \\ & \in [(b_t^k)_L\ (b_t^k)_H] \\ b_t^k(\ ) & \text{otherwise} \end{cases} \tag{5}$$

here, represents the learning rate. e_1^k and e_2^k are modified values of movement error e, which is decided by the VCES based on the vocal cues and calculated by

$$e_i^k = \ _i(1 + |\ _a^k|) f_k e \quad i = 1\ 2 \tag{6}$$

$\ _1$ and $\ _2$, where $0 < \ _1\ \ _2 \leq 5$, are defined to match the corresponding ranges. $\ _a^k$ is the user's willingness to change the robot's perception for ath fuzzy predicate in kth action group. The excitatory function f_k for kth action group is defined accordingly.

4 Summary

A set of tasks, which consists of sequences of primitive movements were used in the adaptation phase. The proposed system was implemented based on 7-DOF PA-10 robot manipulator. The end-effector movements of the robot manipulator were used as the primitive behaviors. The parameters related to the adaptation of the BEN were chosen as $\ = 0\ 1$, $\ _1 = 1\ 5$, and $\ _2 = 4\ 5$ experimentally.

The adaptation process was continued until the user satisfied with the robot's movements. The user's satisfaction was identified based on a satisfactory limit of 90% (i.e. for all $\ _k = 0\ 9$ where $k = 1\ 2\ 3$). Variation of the satisfactory levels of action group G2 by considering the user's willingness to change the robot's behavior and without considering it are shown in Fig. 3. The final set of parameters for the membership functions of new distance are shown in Table 2. The universe of discourse of the membership functions for previous distance is also adjusted accordingly.

According to the results, the manipulator movements for the user commands containing fuzzy linguistic terms "very little" and " little" were reduced in all the action groups. The evaluated values of the user commands containing fuzzy linguistic terms "medium" and "far" were increased in the movements

Table 2: The final set of parameters for membership functions of new distance after the adaptation

Action group	Parameters of the membership function for new distance [mm]								
	VVS	VS	S	B	VB	VVB	F	VF	VVF
	a_1	a_2	a_3	a_4	a_5	a_6	a_7	a_8	a_9
(Initial)	25.00	25.00	25.00	25.00	25.00	25.00	25.00	25.00	25.00
G1	16.88	28.34	34.07	47.08	71.11	84.32	87.21	82.67	39.70
G2	19.06	36.05	37.03	48.41	68.67	97.33	130.14	115.12	73.16
G3	17.08	33.12	29.25	23.26	25.66	35.08	41.49	45.81	23.97
	b_1	b_2	b_3	b_4	b_5	b_6	b_7	b_8	b_9
(Initial)	0.00	25.00	50.00	75.00	100.00	125.00	150.00	175.00	200.00
G1	0.00	11.41	25.36	70.62	132.42	177.99	208.07	227.01	247.86
G2	0.00	11.23	29.80	72.61	128.76	197.49	272.46	308.52	349.25
G3	0.00	10.81	19.37	34.88	62.99	101.62	135.74	156.92	179.72

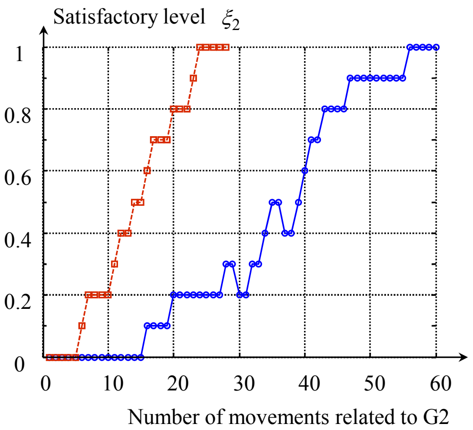

Figure 3: Variation of satisfactory level with number of movements for action group G2. The Variation without considering the user's willingness and with considering the user's willingness are represented by blue continuous line and Red dotted line respectively.

of action group G1 and G2 and reduced in the movements of action group G3. This particular result implies that the robot movements for FVCs were performed as expected by the user according to the contextual information. The user's capability of using voice commands including fuzzy linguistic information for coarse and fine movements is also enhanced. The number of voice commands required to complete a particular task was reduced. In addition, the possibility of occurring overshoots also minimized. Finally, the adaptation of the system based on the environment improved the overall usability of the system.

References

[1] P. Menzel and F. D'Aluisio, , The MIT Press, England, 2000.

[2] K. Pulasinghe, K. Watanabe, K. Izumi, and K. Kiguchi, "A modular fuzzy-neuro controller driven by spoken language commands," , vol. 34, pp. 293–302, 2004.

[3] C. Jayawardena, K. Watanabe, and K. Izumi, "Posture control of robot manipulators with fuzzy voice commands using a fuzzy coach-player system," , vol. 21, pp. 293–328, 2007.

[4] Y. Mohammad and T. Nishida, "Human adaptation to a miniature robot: Precursors of mutual adaptation," in , Munich, Germany, Aug. 2008, pp. 124–129.

[5] A.G.B.P. Jayasekara, K. Watanabe, and K. Izumi, "Evaluating fuzzy voice commands by internal rehearsal for controlling a robot manipulator," in , Fukuoka, Japan, Aug. 2009, pp. 3130-3135.

[6] C.T. Lin and C.S.G. Lee, "Reinforcement structure/parameter learning for neural-network-based fuzzy logic control systems," , vol. 2, pp. 46–63, 1994.

Stick-Slip Motion Control for an Orthogonal-Type Robot

F. Nagata, T. Mizobuchi, S. Tani
Tokyo University of Science, Yamaguchi
Sanyo-Onoda, Japan

T. Hase, Z. Haga
R&D Center, Meiho Co. Ltd.
Nogata, Japan

K. Watanabe
Okayama University
Okayama, Japan

Maki K. Habib
American University in Cairo
Cairo, Egypt

Abstract

In this paper, a new desktop orthogonal-type robot, which has abilities of compliant motion and stick-slip motion, is presented for lapping small metallic molds with curved surface. The robot consists of three single-axis devices with a high position resolution of 1 m. A thin wood stick tool is attached to the tip of the z-axis. The tool tip has a small ball-end shape. In order to improve the lapping performance, a small stick-slip motion control is considered in the control system. The small stick-slip motion is orthogonally generated to the direction of the tool's moving direction. The effectiveness of the stick-slip motion control is examined through an actual lapping test of an LED lens mold with a diameter of 4 mm.

1 Introduction

In manufacturing process of small lens molds such as an LED lens and pickup lens, 3D CAD/CAM systems and NC machining centers are used generally, and these advanced systems have rationalized the design and manufacturing process. However, the finishing process called the lapping after machining process has been hardly automated yet, because an LED lens mold has plural small concave areas to be finished. That means the target mold is not axis-symmetric. Almost conventional effective polishing systems can deal with axis-symmetric workpieces but cannot be applied to such an LED lens mold. In other words, no effective finishing systems have been successfully developed for axis-asymmetric LED lens molds. For example, Tsai et al. developed a mold polishing robot [1] and its path planning technique [2], however, the applicability to small axis-asymmetric LED lens molds was not described. Also, we could not find out other previous literature concerning the finishing of axis-asymmetric LED lens molds. Actually, axis-asymmetric LED lens molds are manually finished by skilled workers in almost all cases.

In this paper, a new desktop orthogonal-type robot, which has abilities of compliant motion and stick-slip motion, is first presented for lapping small metallic molds with curved surface. The robot consists of three single-axis devices with a high position resolution of 1 m. A thin wood stick tool is attached to the tip of the z-axis. The tool tip has a small ball-end shape. The control system is composed of a force feedback loop, position feedback loop and position feedforward loop. The force feedback loop controls the polishing force consisting of tool contact force and kinetic friction forces. The position feedback loop controls the position in pick feed direction, e.g., z-direction. The position feedforward loop leads the tool tip along a desired trajectory called cutter location data (CL data). The CL data are generated from the main-processor of a CAM system. The proposed robot has realized a compliant motion required for the surface following control along a spiral path.

In order to improve the finishing performance, a small stick-slip motion control strategy is further added to the control system. The small stick-slip motion is orthogonally generated to the direction of the tool's moving direction. Generally, the stick-slip motion is an undesirable phenomenon and should be eliminated in precision machineries [3, 4]. However, the proposed robot employs a small stick-slip motion to improve the lapping quality. The effectiveness of the robot with the ability of stick-slip motion is examined through an actual lapping test of an LED lens mold with a diameter of 4 mm. It is expected due to the abilities of compliant motion and stick-slip motion that the undesirable small cusps can be uniformly removed and the robot has an effectiveness to achieve a higher quality surface like a mirror finishing.

2 Desktop Orthogonal-Type Robot

Figure 1 shows the developed desktop orthogonal-type robot consisting of three single-axis devices with position resolution of 1 m. The size is 850 645 700 mm. The single-axis device is a position control robot ISPA with high-precision resolution provided by IAI Corp., which is composed of a base, linear guide, ball-screw, AC servo motor. The effective strokes in x-, y- and z-directions are 400, 300 and 100 mm, respectively. The tool axis is designed to be parallel to z-axis of the robot. A wood stick tool is fixed to the tip through a 3-DOF compact force sensor. To regulate the rotation, a servo spindle is located parallel to the tool axis. The position resolution and force resolu-

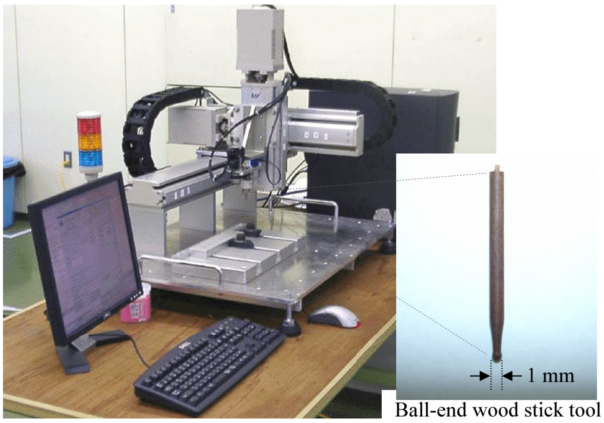

Figure 1: Proposed desktop orthogonal-type robot with compliance control capability.

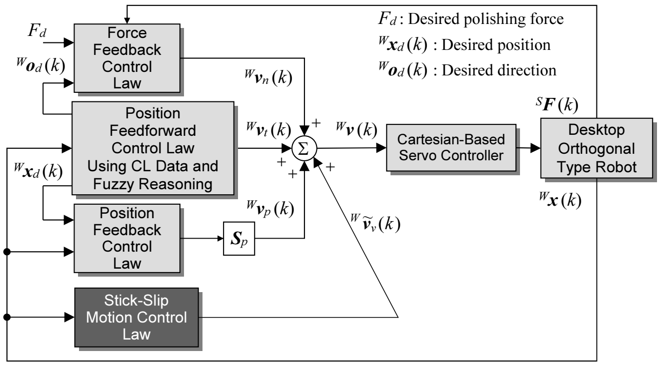

Figure 2: Position/force controller with stick-slip motion control method.

tion, and effective stiffness at the tool tip were examined through a simple contact experiment, so that the force resolution of 0.178 N was obtained due to the position resolution of 1 m. Therefore, the effective stiffness can be estimated about 178 N/mm.

3 Basic Position/Force Control

The basic lapping strategy is conducted along a continuous spiral path while performing a stable polishing force [5]. In this section, the control system is briefly explained. The tool tip is controlled by the translational velocity ${}^W\boldsymbol{v}(k) = [{}^Wv_x(k)\ {}^Wv_y(k)\ {}^Wv_z(k)]^T$ given by

$$ {}^W\boldsymbol{v}(k) = {}^W\boldsymbol{v}_t(k) + {}^W\boldsymbol{v}_n(k) + {}^W\boldsymbol{v}_p(k) \tag{1} $$

where k denotes the discrete time; superscript ^{W} denotes the work coordinate system. Note that the control system easily realized 1 msec sampling time by using the Windows multimedia timer. It is assumed that the polishing force is the resultant force of the contact force and kinetic friction forces, and is obtained as the resultant force of x-, y- and z-directional force sensor measurements. Figure 2 shows the proposed position/force controller with the stick-slip motion control. First of all, ${}^W\boldsymbol{v}_t(k)$ is the manipulated variable generated from the feedforward control law based on cutter location data called the CL data. ${}^W\boldsymbol{v}_t(k)$ is the tangential velocity and written by

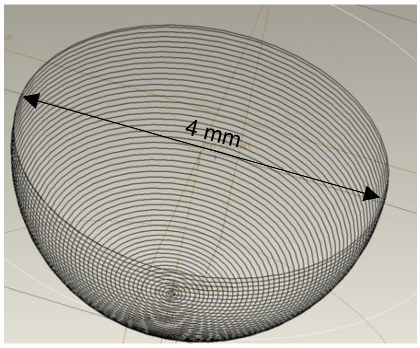

Figure 3: Spiral path generated by using the main-processor of the CAM, which is used for the desired trajectory of the wood stick tool.

$$ {}^W\boldsymbol{v}_t(k) = v_{tangent}(k)\frac{{}^W\boldsymbol{t}(k)}{\left\|{}^W\boldsymbol{t}(k)\right\|} \tag{2} $$

where $v_{tangent}(k)$ is a velocity scalar. ${}^W\boldsymbol{t}(k)$ is the tangential vector calculated by the CL data. Also, ${}^W\boldsymbol{v}_n(k)$ is the manipulated variable generated from the force feedback control law. ${}^W\boldsymbol{v}_n(k)$ is the normal velocity and written by

$$ {}^W\boldsymbol{v}_n(k) = v_{normal}(k){}^W\boldsymbol{o}_d(k) \tag{3} $$

where ${}^W\boldsymbol{o}_d(k)$ is the normalized normal direction vector calculated by using the CL data. The scalar $v_{normal}(k)$ representing the normal velocity is the output of the impedance model following force control law [5] given by

$$ v_{normal}(k) = v_{normal}(k \quad 1)e^{\ \frac{B_d}{M_d}\ \ t} + \left(e^{\ \frac{B_d}{M_d}\ \ t} \quad 1\right)\frac{K_f}{B_d}E_f(k) \tag{4} $$

where K_f is the force feedback gain, and impedance parameters M_d and B_d are the desired mass and damping coefficients, respectively. t is the sampling time. Also, $E_f(k)$ is the error between the desired polishing force F_d and norm of force ${}^S\boldsymbol{F}(k) \in \Re^3$ measured by the force sensor, which is written by

$$ E_f(k) = F_d \quad \|{}^S\boldsymbol{F}(k)\| \tag{5} $$

where superscript ^{S} represents the sensor coordinate system. Further, ${}^W\boldsymbol{v}_p(k)$ is the manipulated variable yielded by a position feedback control law given by

$$ {}^W\boldsymbol{v}_p(k) = \boldsymbol{S}_p\left\{\boldsymbol{K}_p\boldsymbol{E}_p(k) + \boldsymbol{K}_i\sum_{n=1}^{k}\boldsymbol{E}_p(n)\right\} \tag{6} $$

where the switch matrix $\boldsymbol{S}_p = \mathrm{diag}(S_x\ S_y\ S_z)$ makes the weak coupling control to the force control active or inactive in each direction; $\boldsymbol{E}_p(k) = {}^W\boldsymbol{x}_d(k) \quad {}^W\boldsymbol{x}(k)$ is the position error. The desired position ${}^W\boldsymbol{x}_d(k)$ is calculated by using CL data. $\boldsymbol{K}_p = \mathrm{diag}(K_{px}\ K_{py}\ K_{pz})$ and $\boldsymbol{K}_i = \mathrm{diag}(K_{ix}\ K_{iy}\ K_{iz})$ are proportional and integral gains for position feedback control. Due to the weak coupling control, it is simultaneously realized that stable polishing force control and profiling control along a spiral path.

Next, the proposed system is applied to the finishing of an LED lens mold. Figure 3 shows the spiral

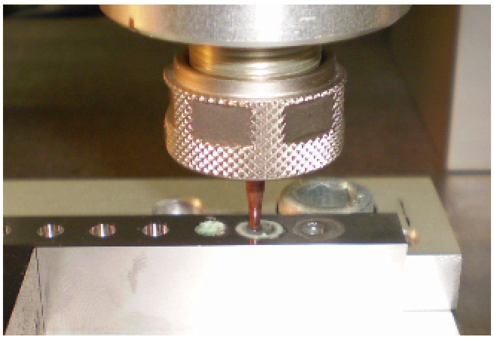

Figure 4: Lapping scene by using the proposed robot, in which a special oil including diamond lapping paste is poured.

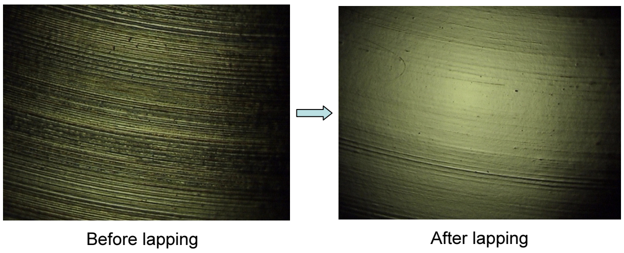

Figure 5: Finished surface before and after the lapping process.

path generated from the main-processor of the CAM, which is used in the lapping experiment. The spiral path has position and orientation components. Figure 4 shows the lapping scene of the LED lens mold, where a special oil including the diamond lapping paste is poured. In this case, a small ball-end tool lathed from a wood stick is used, whose tip diameter is 1 mm. Figure 5 shows large scale photos of the surfaces before and after the lapping process. It is observed that the undesirable cusps still remain on the surface of concaved area.

4 Stick-Slip Motion Control

In this section, the effectiveness of the tool's stick-slip motion is evaluated to improve the surface quality. Generally, the stick-slip motion is an undesirable phenomenon and should be eliminated in various precise machine tools. However, the proposed orthogonal-type robot employs a small stick-slip motion not only to improve the finishing quality but also to skillfully emphasize the polishing energy. Figure 6 shows a simple image of the stick-slip motion seen like small vibrations. The stick-slip motion is given along curved surface and also to orthogonal directions of tool's profiling velocity ${}^W\boldsymbol{v}_t(k)$. Here, how to generate small stick-slip motion vectors is explained in detail by using Fig. 7. In Fig. 7, point O is the origin in work coordinate system, where the tool tip initially contacts the workpiece. Point P is the current contact point. ${}^W\boldsymbol{x}(k)$ is the position vector given by ${}^W\boldsymbol{x}(k) = [{}^Wx(k)\ {}^Wy(k)\ {}^Wz(k)]^T$ viewed from O; ${}^W\boldsymbol{o}_d$ is the normalized normal vector at the

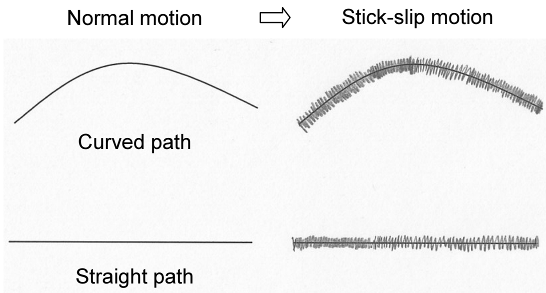

Figure 6: Image of the small stick-slip motion.

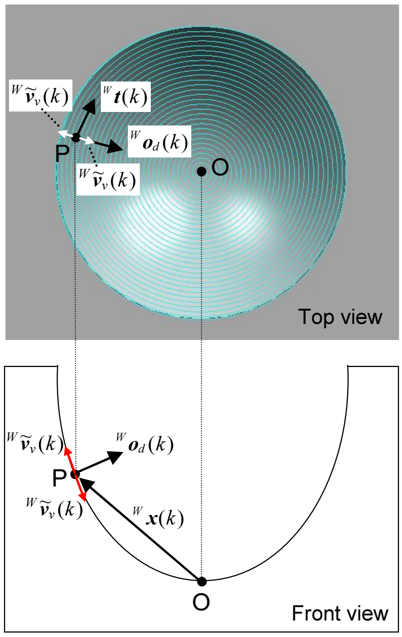

Figure 7: Calculation of stick-slip motion vector

point P given by ${}^W\boldsymbol{o}_d = [{}^Wo_{dx}(k)\ {}^Wo_{dy}(k)\ {}^Wo_{dz}(k)]$; ${}^W\boldsymbol{t}(k) = [{}^Wt_x(k)\ {}^Wt_y(k)\ {}^Wt_z(k)]^T$ is the tangential vector at the point P. Here, it is assumed that ${}^W\boldsymbol{v}_v(k) = [{}^Wv_{vx}(k)\ {}^Wv_{vy}(k)\ {}^Wv_{vz}(k)]^T$ is a small stick-slip vector to be calculated.

In this example, the tool approaches to the workpiece with a low speed and follow the spiral path after contacting the point O. Because ${}^W\boldsymbol{v}_v(k)$ is perpendicular to ${}^W\boldsymbol{o}_d(k)$, the following relation is obtained.

$$
{}^Wv_{vx}(k)\ {}^Wo_{dx}(k) + {}^Wv_{vy}(k)\ {}^Wo_{dy}(k) + {}^Wv_{vz}(k)\ {}^Wo_{dz}(k) = 0 \qquad (7)
$$

Also, ${}^W\boldsymbol{v}_v(k)$ and ${}^W\boldsymbol{t}(k)$ are orthogonal each other, so that

$$
{}^Wv_{vx}(k)\ {}^Wt_x(k) + {}^Wv_{vy}(k)\ {}^Wt_y(k) + {}^Wv_{vz}(k)\ {}^Wt_z(k) = 0 \qquad (8)
$$

Further, ${}^W\boldsymbol{v}_v(k)$ is located in a plane which includes both ${}^W\boldsymbol{o}_d(k)$ and ${}^W\boldsymbol{x}(k)$, so that the components of ${}^W\boldsymbol{v}_v(k)$ are represented by

$$
{}^Wv_{vx}(k) = i\ {}^Wo_{dx}(k) + j\ {}^Wx(k) \qquad (9)
$$

$$ {}^{W}v_{vy}(k) = i\ {}^{W}o_{dy}(k) + j\ {}^{W}y(k) \quad (10) $$
$$ {}^{W}v_{vz}(k) = i\ {}^{W}o_{dz}(k) + j\ {}^{W}z(k) \quad (11) $$

where i and j are real numbers. By solving the Eqs. (7), (8), (9), (10) and (11), ${}^{W}v_{vx}(k)$, ${}^{W}v_{vy}(k)$ and ${}^{W}v_{vz}(k)$ can be obtained. Here, however, a simpler calculation is considered. First of all, substituting Eqs. (9), (10) and (11) into Eq. (7) and considering $\|{}^{W}\boldsymbol{o}_d(k)\|$=1 lead to

$$ i = \quad j\ {}^{W}o_{dx}(k)\ {}^{W}x(k) + {}^{W}o_{dy}(k)\ {}^{W}y(k) + {}^{W}o_{dz}(k)\ {}^{W}z(k) \quad (12) $$

Accordingly, by giving Eq. (12) into Eqs. (9), (10) and (11), the following equations are obtained.

$$ {}^{W}v_{vx}(k) = j\ {}^{W}x(k) \quad ({}^{W}o_{dx}(k)\ {}^{W}x(k) + {}^{W}o_{dy}(k)\ {}^{W}y(k) + {}^{W}o_{dz}(k)\ {}^{W}z(k))\ {}^{W}o_{dx}(k) \quad (13) $$
$$ {}^{W}v_{vy}(k) = j\ {}^{W}y(k) \quad ({}^{W}o_{dx}(k)\ {}^{W}x(k) + {}^{W}o_{dy}(k)\ {}^{W}y(k) + {}^{W}o_{dz}(k)\ {}^{W}z(k))\ {}^{W}o_{dy}(k) \quad (14) $$
$$ {}^{W}v_{vz}(k) = j\ {}^{W}z(k) \quad ({}^{W}o_{dx}(k)\ {}^{W}x(k) + {}^{W}o_{dy}(k)\ {}^{W}y(k) + {}^{W}o_{dz}(k)\ {}^{W}z(k))\ {}^{W}o_{dz}(k) \quad (15) $$

Because both ${}^{W}\boldsymbol{o}_d(k)$ and ${}^{W}\boldsymbol{x}(k)$ are known, ${}^{W}\boldsymbol{v}_v(k)$ can be normalized as $\boldsymbol{v}_v(k)\ \ \|\boldsymbol{v}_v(k)\|$. Further, by using a scalar K_v and a sign SIGN(k), the stick-slip motion vector is finally obtained as

$$ {}^{W}\tilde{\boldsymbol{v}}_v(k) = \mathrm{SIGN}(k)\ K_v\ \frac{\boldsymbol{v}_v(k)}{\|\boldsymbol{v}_v(k)\|} \quad (16) $$

where SIGN(k) is given by

$$ \mathrm{SIGN}(k) = \begin{cases} 1 & \text{if } k = \text{odd number} \\ \ \ 1 & \text{otherwise} \end{cases} \quad (17) $$

${}^{W}\tilde{\boldsymbol{v}}_v(k)$ is a velocity vector to yield another polishing energy, and which is given to the tool alternatively changing the direction every sampling period. The stick-slip motion control is simply added as shown in Fig. 2. As can be seen from Eqs. (2) and (3), the directions of ${}^{W}\boldsymbol{v}_t(k)$ and ${}^{W}\boldsymbol{v}_n(k)$ are the same ones of ${}^{W}\boldsymbol{t}(k)$ and ${}^{W}\boldsymbol{o}_d(k)$, respectively. Also, ${}^{W}\boldsymbol{v}_p(k)$ is generated in the direction of z-axis called the spiral direction.

Next, the effectiveness of the stick-slip motion control is examined through a same lapping experiment conducted in the previous section. Figure 8 shows the large scale photo of the LED lens mold after the lapping process by using the proposed stick-slip motion control. It is observed that the undesirable remained cusps can be removed uniformly. It has been confirmed from the result that the proposed finishing strategy by using the stick-slip motion control has a significant effectiveness to achieve a higher quality surface.

5 Conclusions

The final goal of this study is the development of a novel orthogonal-type robot with compliance controllability that can be applied to from the cusp mark removing process to the finishing process for mirror-like surface of LED lens molds. In this paper, a desktop orthogonal-type robot was first designed by combining three single-axis devices. The position resolution and force resolution, and effective stiffness are 1 m, 0.178 N and 178 N/mm, respectively. Next, a basic position/force controller with compliance controllability was proposed for the lapping task of LED lens molds, in which position control, force control or their weak coupling control can be selected independently. Further, a stick-slip motion control for a wood stick tool was developed to finely improve the finishing quality. The proposed desktop orthogonal-type robot using the stick-slip motion control was applied to a lapping experiment of an LED lens mold, so that the high performance and promise were successfully confirmed. In future work, we plan to consider other potential applications using the robot.

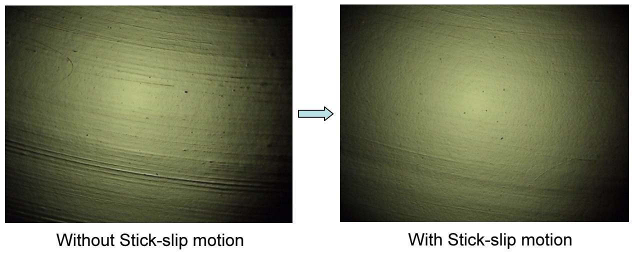

Figure 8: Large scale photos without and with by using the proposed stick-slip motion.

References

[1] M. J. Tsai, J. L. Chang and J. F. Haung, "Development of an Automatic Mold Polishing System," , pp. 3517–3522, Taipei, Taiwan, 2003.

[2] M. J. Tsai, J. J. Fang and J. L. Chang, "Robotic Path Planning for an Automatic Mold Polishing System, , vol. 19, no. 2, pp. 81–89, 2004.

[3] O. Bilkay and O. Anlagan, "Computer Simulation of Stick-Slip Motion in Machine Tool Slideways," , vol. 37, no. 4, pp. 347–351, 2004.

[4] X. Mei, M. Tsutsumi, T. Tao and N. Sun, "Study on the Compensation of Error by Stick-Slip for High-Precision Table," & , vol. 44, no. 5, pp. 503–510, 2004.

[5] F. Nagata, T. Hase, Z. Haga, M. Omoto and K. Watanabe, "CAD/CAM-Based Position/Force Controller for a Mold Polishing Robot," , vol. 17, no. 4–5, pp. 207–216, 2007.

Modeling an Autonomous Underwater Vehicle with Four-Thrusters

Zainah Md. Zain, Keigo Watanabe, Tomomi Danjo, Kiyotaka Izumi†, and Isaku Nagai

Division of Industrial Innovation Sciences,
Graduate School of Natural Science and Technology, Okayama University
3-1-1 Tsushima-naka, Kita-ku, Okayama 700-8530, Japan
Tel & Fax: +81-86-251-8064
E-mail: zainah@usm.sys.okayama-u.ac.jp, {watanabe, in}@sys.okayama-u.ac.jp
† Department of Advanced Systems Control Engineering,
Graduate School of Science and Engineering, Saga University
1-Honjomachi, Saga 840-8502, Japan
Tel: +81-952-28-8696, Fax: +81-952-28-8587
E-mail: izumi@me.saga-u.ac.jp

Abstract: In order to reduce the drag forces against a stream for an X4-autonomous underwater vehicle (AUV), a new type of hull shape is considered with an ellipsoid body. The associated dynamical model is derived by using a Lagrangian mechanics, as well as taking account of the effect of added mass and inertia.

Keywords: AUV, underactuated control system, nonholonomic systems, kinematic model, dynamical model.

I. INTRODUCTION

Generally, underwater vehicles can be divided into three, namely, manned submersibles, remotely operated vehicles (ROVs) and autonomous underwater vehicles (AUVs). The latter two are mostly utilized in the oil and gas industries, and for scientific and military applications. AUVs have great importance in underwater tasks due to its ability to navigate in abyssal zones without necessitating a tether that limits the range and maneuverability of the vehicle. Note however that their autonomy property directly affects the design of control system. That is, it requires advanced controllers and specific control schemes for achieving given tasks.

Most of AUVs have six degrees-of-freedom (DOFs) in motion. The vehicle of interest here falls into the class of underactuated AUVs because it has fewer actuators than the DOFs in motion. Many control systems for underwater vehicles have been designed up to now [1], [2] under the restrictions of cost, weight and complexity, keeping some reliability advantages. The vehicle is also a nonlinear system: all equations of motion of the system include highly coupled terms. Some equations of the motion of the system appear as a second-order nonholonomic constraints, and they cannot be integrated to obtain the position. Therefore, such underwater vehicles pertain to nonholonomic systems. Control of nonholonomic systems poses a difficult problem requiring a special control approach depending on the nature of the mechanical system, as stated in Arslan et al. [3].

An X4-AUV with a spherical hull shape was studied by Okamura [4], in which it makes only use of four thrusters to control the vehicle without using any steering rudders, falls into the class of underactuated AUVs and has nonholonomic features. The consideration of nonholomic systems is an interesting study from a theoretical standpoint because, as pointed out in the earlier works of Brockett, they cannot be asymptotically stabilized to a fixed point in the configuration space using continuously differentiable, time-invariant and state feedback control laws. In this paper, to overcome the demerit that in the former X4-AUV studied in [4] the drag forces against a stream are relatively higher than other AUVs, a new type of hull shape is proposed for the X4-AUV with an ellipsoid body that mostly closes to a streamlined shape and has the durability over pressure like a sphere. The ideal streamlined hull shape is known to minimize the drag forces acting on the hull while the X4-AUV is cruising. The corresponding X4-AUV kinematic and dynamic models are also presented here. When the X4-AUV moves underwater, additional forces and moment coefficients are added to account for the effective mass of the fluid that surrounds the robot, which causes an excessive acceleration of the robot, compared to the case where there is no any added mass and moment of inertia.

II. MODEL OVERVIEW

1. Former X4-AUV

The X4-AUV with a spherical hull shape is our former type of AUV. It has four thrusters to control the position and attitude changes in the motion [4]. It is categorized in underactuated AUVs and also has nonholonomic features. As shown in Fig. 1, the arrows around the thrusters indicate the rotational direction of the thrusters. The rotational angles consist of roll, pitch and yaw angles commonly used in guidance and navigation.

2. Proposed X4-AUV

The proposed X4-AUV is shown in Fig. 2. Previous work on X4-AUV suggests some limitations on the shape of the vehicle due to the hydrodynamics. A well thought out hull design for an AUV can improve the performances and efficiency of the vehicle. The body length will generally decrease the pressure drag by making the

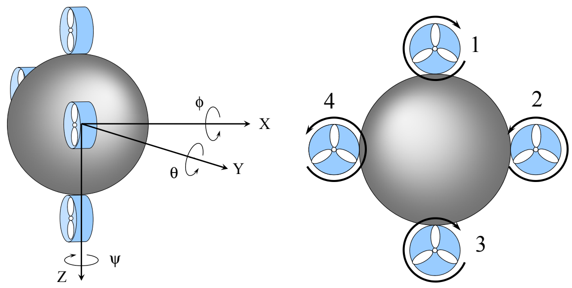

(a) Side view (b) Front view

Fig. 1. Conventional X4-AUV

body more slender. A general ratio for an ellipsoid is length over diameter, l_E/d_E. This is the slenderness ratio of the body, whose values are in the range between five and ten. A typical value for ellipsoids is five. The induced lift on the ellipsoids having high slenderness ratios ($l_E/d_E \geq 5$) is about 90 percent of the induced lift on the infinite cylinder, as reported by Zlotnick and Samuel [5]. In the design of a new X4-AUV, the goal was to make vehicle slenderness with a ratio of 5. Therefore, parameters r_1, r_2 and r_3 that are the lengths of the semi axes of the ellipsoidal vehicle are reduced to r_2= $5r$ and $r_2 = r_3 = r$.

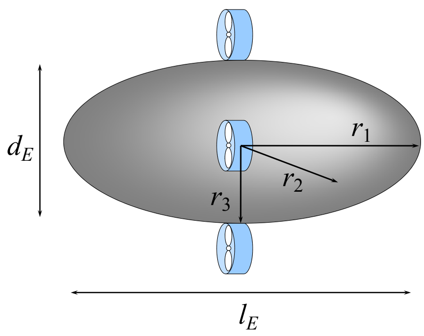

Fig. 2. Coordinate systems

III. MODEL DERIVATION

1. Definition of Coordinate Systems

In order to describe the motion of the underwater vehicle, a special reference frame must be established. There have two coordinate systems: i.e., inertial coordinate system (or fixed coordinate system) and motion coordinate system (or body-fixed coordinate system). The coordinate frame {E} is composed of the orthogonal axes {E$_x$, E$_y$, E$_z$} and is called as an inertial frame. This frame is commonly placed at a fixed place on Earth. The axes E$_x$ and E$_y$ form a horizontal plane and E$_z$ has the direction of the gravity field. The body fixed frame {B} is composed of the orthogonal axes {X, Y, Z} and attached to the vehicle. The body axes, two of which coincide with principle axes of inertia of the vehicles, are defined in Fossen [6] as follows:

X is the longitudinal axis (directed from aft to fore)
Y is the transverse axis (directed to starboard)
Z is the normal axis (directed from top to bottom)

Figure 3 shows the coordinate systems of AUV, which consist of a right-hand inertial frame {E} in which the downward vertical direction is to be positive and right-hand body frame {B}.

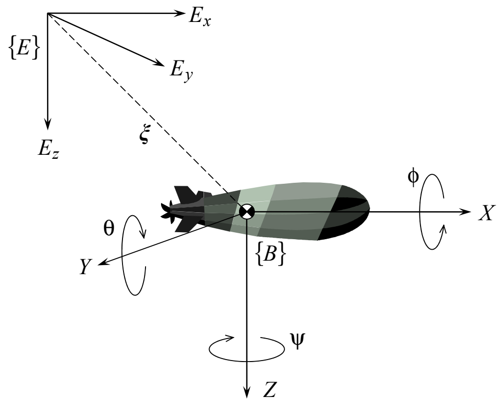

Fig. 3. Frames of X4-AUV

Letting $\boldsymbol{\xi} = [x \quad y \quad z]^T$ denote the mass center of the body in the inertial frame, defining the rotational angles of X-, Y- and Z-axis as $\boldsymbol{\eta} = [\phi \quad \theta \quad \psi]^T$, the rotational matrix R from the body frame {B} to the inertial frame {E} can be reduced to:

$$R = \begin{bmatrix} c\theta c\psi & s\phi s\theta c\psi - c\phi s\psi & c\phi s\theta c\psi + s\phi s\psi \\ c\theta s\psi & s\phi s\theta s\psi + c\phi c\psi & c\phi s\theta s\psi - s\phi c\psi \\ -s\theta & s\phi c\theta & c\phi c\theta \end{bmatrix} \tag{1}$$

where $c\alpha$ denotes $\cos\alpha$ and $s\alpha$ is $\sin\alpha$.

2. Mass and Inertia Matrix

A phenomenon that affects underwater vehicles is added mass. When a body moves underwater, the immediate surrounding fluid is accelerated along with the body. This affects the dynamics of the vehicle in such a way that the force required to accelerate in the water can be modeled as an added mass. Added mass is a fairly significant effect and is related to the mass and inertial values of the vehicle. M is a mass matrix of the body, J is an inertia matrix of the body, m_b is a mass of the vehicle, J_b is an inertia matrix of the vehicle and I is a 3×3 identity matrix. From the characteristics of added mass, M and J can be written as

$$M = \text{diag}(m_1, m_2, m_3) = m_b I + M_f \tag{2}$$
$$J = \text{diag}(I_x, I_y, I_z) = J_b + J_f \tag{3}$$

Here, the added mass matrix M_f and the added inertia matrix J_f are defined by

$$M_f = \text{diag}(\bar{A}, \bar{B}, \bar{C}) \tag{4}$$
$$J_f = \text{diag}(\bar{P}, \bar{Q}, \bar{R}) \tag{5}$$

The added mass and inertia can be determined by the following relations [8].

$$\begin{aligned}\bar{A} &= \frac{\alpha}{2-\alpha}\rho V \\ \bar{B} &= \frac{\beta}{2-\beta}\rho V \\ \bar{C} &= \frac{\gamma}{2-\gamma}\rho V\end{aligned} \tag{6}$$

$$\begin{aligned}\bar{P} &= \frac{1}{5}\frac{(r_2^2-r_3^2)(\gamma-\beta)}{2(r_2^2-r_3^2)+(r_2^2+r_3^2)(\beta-\gamma)}\rho V \\ \bar{Q} &= \frac{1}{5}\frac{(r_3^2-r_1^2)(\alpha-\gamma)}{2(r_3^2-r_1^2)+(r_3^2+r_1^2)(\gamma-\alpha)}\rho V \\ \bar{R} &= \frac{1}{5}\frac{(r_1^2-r_2^2)(\beta-\alpha)}{2(r_1^2-r_2^2)+(r_1^2+r_2^2)(\alpha-\beta)}\rho V\end{aligned} \tag{7}$$

where r_i $(i = 1, 2, 3)$ is a semi axis of the ellipsoid body along each axis, $V = (4/3)\pi r_1 r_2 r_3$ is a volume of the vehicle and ρ is a density of the fluid. Additionally, the α, β and γ are defined by

$$\alpha = r_1 r_2 r_3 \int_0^\infty \frac{d\lambda}{(r_1^2+\lambda)\Delta} \tag{8}$$

$$\beta = r_1 r_2 r_3 \int_0^\infty \frac{d\lambda}{(r_2^2+\lambda)\Delta} \tag{9}$$

$$\gamma = r_1 r_2 r_3 \int_0^\infty \frac{d\lambda}{(r_3^2+\lambda)\Delta} \tag{10}$$

$$\Delta = \sqrt{(r_1^2+\lambda)(r_2^2+\lambda)(r_3^2+\lambda)} \tag{11}$$

where λ is the eccentricity of the Y-Z axis cutting plane for the ellipsoid body, in which the formula is given in [7]. From equations (4)–(11), the components of M_f and J_f are reduced to

$$\begin{aligned}\bar{A} &\approx 0.0591\rho V = 3.94\pi r^3 \\ \bar{B} = \bar{C} &\approx 0.894\rho V = 5.96\pi r^3 \\ \bar{P} &= 0 \\ \bar{Q} = \bar{R} &\approx 3.640\rho V = 24.3\pi r^3\end{aligned}$$

3. Dynamic Model

This section describes the dynamic model of the X4-AUV depicted in Fig. 2 by using a Lagrangian method. Assume that the body remains in a neutral buoyancy state at which the gravity and the buoyancy are balanced. We can first obtain the following kinetic energy formula,

$$T = T_{trans} + T_{rot} \tag{12}$$

where T_{trans} and T_{rot} are the translational kinetic energy and the rotational kinetic energy, which are given by

$$T_{trans} = \frac{1}{2}\dot{\boldsymbol{\xi}}^T M \dot{\boldsymbol{\xi}} \tag{13}$$

$$T_{rot} = \frac{1}{2}\dot{\boldsymbol{\eta}}^T J \dot{\boldsymbol{\eta}} \tag{14}$$

so that the kinetic energy can be rewritten in terms of M and J such that

$$T = \frac{1}{2}\dot{\boldsymbol{\xi}}^T M \dot{\boldsymbol{\xi}} + \frac{1}{2}\dot{\boldsymbol{\eta}}^T J \dot{\boldsymbol{\eta}} \tag{15}$$

From the assumption of the balance between buoyancy and the gravity, the potential energy, U is reduced to

$$U = 0 \tag{16}$$

Taking a generalized coordinate as $\boldsymbol{q} = [\boldsymbol{\xi}^T \quad \boldsymbol{\eta}^T]^T$, the Lagrangian L satisfies the following equations:

$$L = T - U \tag{17}$$

$$\frac{d}{dt}\left(\frac{\partial L}{\partial \dot{q}}\right) - \frac{\partial L}{\partial q} = F \tag{18}$$

From equations (15) and (16), it follows that

$$L = \frac{1}{2}(\dot{\xi}^T M \dot{\xi} + \dot{\eta}^T J \dot{\eta}) \tag{19}$$

Noting the representation of Lagrangian in (19), each derivative (or partial derivative) in (18) can be reduced to

$$\frac{\partial L}{\partial \dot{\boldsymbol{q}}} = M\dot{\boldsymbol{\xi}} + J\dot{\boldsymbol{\eta}} \tag{20}$$

$$\frac{d}{dt}\left(\frac{\partial L}{\partial \dot{\boldsymbol{q}}}\right) = \begin{bmatrix} M\ddot{\boldsymbol{\xi}} \\ J\ddot{\boldsymbol{\eta}} + \dot{J}\dot{\boldsymbol{\eta}} \end{bmatrix} \tag{21}$$

$$\frac{\partial L}{\partial \boldsymbol{q}} = \frac{1}{2}\begin{bmatrix} 0 \\ \frac{\partial}{\partial \boldsymbol{\eta}}(\dot{\boldsymbol{\eta}} J \dot{\boldsymbol{\eta}}) \end{bmatrix} \tag{22}$$

The equations of motion of X4-AUV due to Lagrangian mechanics become

$$\begin{bmatrix} M\ddot{\boldsymbol{\xi}} \\ J\ddot{\boldsymbol{\eta}} + \dot{J}\dot{\boldsymbol{\eta}} \end{bmatrix} - \begin{bmatrix} 0 \\ \frac{1}{2}\frac{\partial}{\partial \boldsymbol{\eta}}(\dot{\boldsymbol{\eta}} J \dot{\boldsymbol{\eta}}) \end{bmatrix} = F \tag{23}$$

where the generalized force F is given by

$$F = \begin{bmatrix} F_\xi \\ \boldsymbol{\tau} \end{bmatrix} \tag{24}$$

$$\boldsymbol{\tau} = \begin{bmatrix} \tau_\phi & \tau_\theta & \tau_\psi \end{bmatrix}^T \tag{25}$$

Here, F_ξ and $\boldsymbol{\tau}$ are the translational force and the rotational torque for the AUV.

Letting u_1 be an input to control X-directional translational motion for the AUV and f_i be a thrust generated by each thruster. Then, u_1 is defined by

$$u_1 = f_1 + f_2 + f_3 + f_4 \tag{26}$$

Introducing the unit vector $\boldsymbol{e}_X$ for the X-direction at the body frame, the corresponding translational force F_ξ is reduced to

$$\begin{aligned} F_\xi &= R\boldsymbol{e}_X u_1 \\ &= \begin{bmatrix} \cos\theta\cos\psi \\ \cos\theta\sin\psi \\ -\sin\theta \end{bmatrix}[f_1 + f_2 + f_3 + f] \end{aligned} \tag{27}$$

Defining the torque generated by each motor as τ_{Mi}, the moment around each axis at the body frame is given by

$$\tau_\phi = \sum_{i=1}^{4}\tau_{Mi} \tag{28}$$

$$\tau_\theta = (f_1 - f_3)l \tag{29}$$

$$\tau_\psi = (f_2 - f_4)l \tag{30}$$

where l denotes the distance between the center of gravity of the body and each thruster. The equations of motion are divided into the translational motion and the rotational motion, respectively,

$$M\ddot{\boldsymbol{\xi}} = F_\xi = \begin{bmatrix} \cos\theta\cos\psi \\ \cos\theta\sin\psi \\ -\sin\theta \end{bmatrix} [f_1 + f_2 + f_3 + f] \tag{31}$$

$$J\ddot{\boldsymbol{\eta}} + (\dot{J}\dot{\boldsymbol{\eta}} - \frac{1}{2}\frac{\partial}{\partial\boldsymbol{\eta}}(\dot{\boldsymbol{\eta}}^T J\dot{\boldsymbol{\eta}}) = \boldsymbol{\tau} = \begin{bmatrix} \sum_{i=1}^{4} \tau_{Mi} \\ (f_1 - f_3)l \\ (f_2 - f_4)l \end{bmatrix} \tag{32}$$

Here, the second term of left-hand side in the equation of rotational motion (32) is related to the Coriolis term in general equations of motion, and equal to the following equation that represents the Coriolis torque and the gyro torque:

$$\boldsymbol{\omega} \times J\boldsymbol{\omega} + \sum_{i=1}^{4} J_t(\boldsymbol{\omega} \times \boldsymbol{e}_X)\omega_i \tag{33}$$

where $\boldsymbol{\omega} = [\dot{\phi} \quad \dot{\theta} \quad \dot{\psi}]^T$, J_t is a moment of inertia for the thruster, ω_i is a rotational speed for the thruster i. Since $\boldsymbol{\omega}\times$ is a skew symmetric matrix, it follows that

$$\boldsymbol{\omega} \times J\boldsymbol{\omega} = \begin{bmatrix} -\dot{\theta}\dot{\psi}(I_y - I_z) \\ -\dot{\theta}\dot{\psi}(I_z - I_x) \\ -\dot{\theta}\dot{\psi}(I_x - I_y) \end{bmatrix} \tag{34}$$

$$\boldsymbol{\omega} \times \boldsymbol{e}_X = \begin{bmatrix} 0 \\ \dot{\psi} \\ -\dot{\theta} \end{bmatrix} \tag{35}$$

From the above results, equation (32) can be rewritten as

$$J\ddot{\boldsymbol{\eta}} + \begin{bmatrix} -\dot{\theta}\dot{\psi}(I_y - I_z) \\ -\dot{\theta}\dot{\psi}(I_z - I_x) \\ -\dot{\theta}\dot{\psi}(I_x - I_y) \end{bmatrix} + J_t \begin{bmatrix} 0 \\ \dot{\psi} \\ -\dot{\theta} \end{bmatrix} [\omega_2 + \omega_4 - \omega_1 - \omega_3] = \begin{bmatrix} \sum_{i=1}^{4} \tau_{Mi} \\ (f_1 - f_3)l \\ (f_2 - f_4)l \end{bmatrix} \tag{36}$$

Thus, the final dynamical model for the X4-AUV can be summarized by

$$m_1\ddot{x} = \cos\theta\cos\psi\, u_1 \tag{37}$$
$$m_2\ddot{y} = \cos\theta\sin\psi\, u_1 \tag{38}$$
$$m_3\ddot{z} = -\sin\theta\, u_1 \tag{39}$$
$$I_x\ddot{\phi} = \dot{\theta}\dot{\psi}(I_y - I_z) + u_2 \tag{40}$$
$$I_y\ddot{\theta} = \dot{\phi}\dot{\psi}(I_z - I_x) - J_t\dot{\psi}\Omega + lu_3 \tag{41}$$
$$I_z\ddot{\psi} = \dot{\phi}\dot{\theta}(I_x - I_y) - J_t\dot{\theta}\Omega + lu_4 \tag{42}$$

Here, the values of m_1, m_2, m_3, I_x, I_y, and I_z are defined as in Section 3.2. u_1, u_2, u_3, and u_4 are the control inputs for the translational (X-axis) motion, the roll (ϕ-axis) motion, pitch (θ-axis) motion, and yaw (ψ-axis) motion, respectively. Additionally, letting b be a thruster factor, d be a drag factor such as $\tau_{Mi} = d\omega_i^2$, it is found that Ω, u_1, u_2, u_3, and u_4 are described by

$$\begin{aligned} \Omega &= \omega_2 + \omega_4 - \omega_1 - \omega_3 \\ u_1 &= f_1 + f_2 + f_3 + f_4 \\ &= b(\omega_1^2 + \omega_2^2 + \omega_3^2 + \omega_4^2) \\ u_2 &= d(-\omega_2^2 - \omega_4^2 + \omega_1^2 + \omega_3^3) \\ u_3 &= f_1 - f_3 = b(\omega_1^2 - \omega_3^2) \\ u_4 &= f_2 - f_4 = b(\omega_2^2 - \omega_4^2) \end{aligned}$$

IV. CONCLUSION

In this paper, for an autonomous underwater vehicle (AUV), called "X4-AUV," a new type of hull shape has been proposed to reduce the drag forces against a stream. After taking account of added mass and inertia for this new type of hull shape considered here, the equations of motion for the X4-AUV were derived by using a Lagrangian mechanics. For the future work, any time-varying or switching control approach should be applied to the present X4-AUV to realize an underactuated control system.

REFERENCES

[1] Yuh J (2000), Design and control of autonomous underwater robots: A survey. Autonomous Robots, 8(1): 7–24
[2] Watanabe K and Izumi K (2008), Skilful control for underactuated robot systems: From the ground to the air and underwater. Proc. of the 2nd International Conference on Underwater System Technology: Theory and Applications 2008 (USYS '08), Bali, Indonesia, Paper ID 39
[3] Arslan MS, Fukushima N, Hagiwara I (2007), Optimal control of an underwater vehicle with single actuator. Proc. of Symposium on Underwater Technology and Workshop on Scientific Use of Submarine Cables and Related Technologies, pp. 581–587
[4] Okamura K (2009), Position and attitude control for an autonomous underwater robot using a manifold theory. Master Thesis, Saga University
[5] Zlotnick M and Samuel WR (1953), A simplified mathematical model for calculating aerodynamic loading and downwash for midwing of arbitrary plan form. NACA RM L52J27a
[6] Fossen TI (1994), Guidance and Control of Ocean Vehicles. John Wiley & Sons Ltd.
[7] Eccentricity of an ellipse, available online at: http://www.mathwarehouse.com/ellipse/eccentricity-of-ellipse.php
[8] Leonardo NE (1997), Stability of a bottom-heavy underwater vehicle. Automatica 33(1): 331–346

The Fifteenth International Symposium on Artificial Life and Robotics 2010 (AROB 15th '10),
B-Con Plaza, Beppu,Oita, Japan, February 4-6, 2010

The Number of Unscented Transformations and the Effect of Noise Estimates in an Unscented Kalman Filtering Problem

Saifudin bin Razali, Keigo Watanabe, Shoichi Maeyama, and Kiyotaka Izumi†

Division of Industrial Innovation Sciences,
Graduate School of Natural Science and Technology, Okayama University
3-1-1 Tsushima-naka, Kita-ku, Okayama 700-8530, Japan
Tel & Fax: +81-86-251-8064
E-mail: saifudin@usm.sys.okayama-u.ac.jp, {watanabe, maeyama}@sys.okayama-u.ac.jp
† Department of Advanced Systems Control Engineering,
Graduate School of Science and Engineering, Saga University
1-Honjomachi, Saga 840-8502, Japan
Tel: +81-952-28-8696, Fax: +81-952-28-8587
E-mail: izumi@me.saga-u.ac.jp

Abstract: The unscented transformation is known as a technique to firstly generate a set of $2n + 1$ sigma points and their weights, and secondly to propagate each sigma point value through a nonlinear function, where n denotes the dimension of the random state variable. Note however that there are two cases in a discrete-time filtering problem: one is the case where such a transformation is applied two times to the nonlinear model function and the nonlinear measurement function separately by using different mean and covariance, whereas the other is the case where such a transformation is basically applied to the nonlinear model function and the same sigma point values are only propagated to the nonlinear measurement function. So, we here examine the performance difference between them in a particular estimation problem. In addition, it is sometimes to encounter the case where for an unscented Kalman filter, the original state is augmented with other system and measurement noises simultaneously as if the original state and measurement noises are included in nonlinear functions, even though they are actually to be additive to each model function. Therefore, we further check how much the performance improvement or degradation is, compared to the case where there is no inconsistency in the model assumptions.

Keywords: Nonlinear system, Unscented transformation, Sigma point.

I. INTRODUCTION

The nonlinear filtering problem has been extensively studied and various methods are provided in literature. Among them, the most useful ones are the Extended Kalman Filter (EKF), the Ensemble Kalman Filter (EnKF), the Unscented Kalman Filter (UKF), and the Particle Filter (PF). Historically, the EKF is still the most widely adopted approach to solve the nonlinear estimation problem. It is based on the assumption that the nonlinear system dynamics can be accurately modeled by a first-order Taylor series expansion as shown by van de Merwe [1]. The EnKF introduced by Evensen [2] is a reduced rank filter which propagates the states through nonlinearity and updates a relatively small ensemble of samples from which an assumed Gaussian distribution captures the main characteristics in the uncertainty. The PF also uses a sampling approach to estimate the higher order moments of the posterior probability distribution by propagating and updating a number of particles, but without assuming Gaussian statistics as explained by Arulampalam et al. [3]. The UKF, which is a derivative-free alternative to EKF, overcomes the differentiation problem by using a deterministic sampling approach demonstrated by Julier and Uhlmann [4] and Wan and van der Merwe [5].

The state distribution is represented using a minimal set of carefully chosen sample points, called sigma points. This technique is used to linearize a nonlinear function of a random variable through a linear regression between n points drawn from the prior distribution of the random variable. Since we are considering the spread of the random variable during linearization, the technique tends to be more accurate than Taylor series linearization used in the EKF, particularly in the presence of strong nonlinearities as proved by van de Merwe [1]. The $2n+1$ sigma points, are chosen based on a square-root decomposition of the prior covariance, where n is the state dimension. These sigma points are propagated through the true nonlinear function, without approximation, and then a weighted mean and covariance is taken. This approach results in approximations that are accurate to the third order (Taylor series expansion) for Gaussian inputs for all nonlinearities. For non-Gaussian inputs, approximations are accurate to at least the second-order as mentioned by Julier and Uhlmann [4], whereas the linearization approach of the EKF results only in first order accuracy.

However, there are two cases in a discrete-time filtering problem: one is the case where such a transformation is applied two times to the nonlinear model function and the nonlinear measurement function separately by using different mean and covariance, whereas the other is the case where such a transformation is basically applied to the nonlinear model function and the same sigma point values are only propagated to the nonlinear measurement function. This paper examines the performance difference between them in a particular estimation problem. In addition, it is sometimes to encounter the case where for an unscented Kalman filter, the original state is augmented with other system and measurement noises simultaneously as if the original state and measurement noises are included in nonlinear functions, even though they are actually to be additive to each model function. Therefore, we further check how much the performance improvement or degradation is, compared to the case where there is no inconsistency in the model assumptions.

The structure of this paper as follows: In Section II we describe the problem statement for applying a difference set of sigma points of Kalman Filter to propagate nonlinear model function and update nonlinear measurement function. An example is presented in Section III, in which the effect of a different set of sigma points applied to nonlinear model and measurement functions is discussed. The paper is concluded in Section IV.

II. UNSCENTED KALMAN FILTER

The basic framework for the UKF involves the estimation of the state for discrete-time nonlinear dynamic system:

$$x_{k+1} = f(x_k, u_k) + w_k \tag{1}$$

$$y_k = h(x_k, u_k) + v_k \tag{2}$$

where x_k represents the n-dimensional unobserved state of the system, u_k is a known exogenous input, and y_k is the m-dimensional observed measurement signal. The system noise is represented by w_k and the observation noise is given by v_k, where these noises are uncorrelated each other, but with their covariances Q_k and R_k, respectively. The standard UKF implementation uses the following weight definitions of $\{w^{(i)}\}$, where $w_0^{(m)} = \frac{\lambda}{\lambda+n}$, $w_0^{(c)} = w_0^{(m)} + (1-\alpha^2+\beta)$ and $w_i^{(c)} = w_i^{(m)} = \frac{1}{2(n+\lambda)}$. $\lambda = \alpha^2 + (n+\kappa) - n$ and $\gamma = \sqrt{n+\lambda}$ are scaling factors. The constant α determines the spread of the sigma points around its mean and is usually set ranging from $10^{-4} \leq \alpha \leq 1$. κ is a secondary scaling parameter (set to 0 for state estimation). The β is used to incorporate prior knowledge of the distribution of x_k and $\beta = 2$ for Gaussian distributions.

We now evaluate this nonlinear system using two different approaches of transformation of sigma point. In the first case, the transformation of sigma points is applied two times to the nonlinear model function and the nonlinear measurement function separately by using different mean and covariance, whereas the other is the case where such a transformation is basically applied to the nonlinear model function and the same sigma point values are only propagated to the nonlinear measurement function. In addition, we investigate the case where for an unscented Kalman filter, the original state is augmented with other system and measurement noises simultaneously as if the original state and measurement noises are included in nonlinear functions, even though they are actually to be additive to each model function.

1. Two times transformation of sigma points

In this case, generated sigma points are propagated two times through a nonlinear model function as well as nonlinear measurement function, respectively. The algorithm for this case can be summarized as Table 1.

Table I. UKF algorithm with two-times transformation of sigma points

$$\chi_{k-1} = [\hat{x}_{k-1} \cdots \hat{x}_{k-1}] + \gamma[0 \quad \sqrt{P_{x_{k-1}}} \quad -\sqrt{P_{x_{k-1}}}] \tag{3}$$

$$\chi^*_{i,k} = f(\chi_{i,k-1}, u_{k-1}) \tag{4}$$

$$\hat{x}_k^- = \sum_{i=0}^{2n} w_i^{(m)} \chi^*_{i,k} \tag{5}$$

$$P_{x_k}^- = Q_{k-1} + \sum_{i=0}^{2n} w_i^{(c)} (\chi^*_{i,k} - \hat{x}_k^-)(\chi^*_{i,k} - \hat{x}_k^-)^T \tag{6}$$

$$\chi_k^- = [\hat{x}_k^- \cdots \hat{x}_k^-] + \gamma[0 \quad \sqrt{P_{x_k}^-} \quad -\sqrt{P_{x_k}^-}] \tag{7}$$

$$\mathcal{Y}_{i,k} = h(\chi_{i,k}^-, u_k) \tag{8}$$

$$\hat{y}_k^- = \sum_{i=0}^{2n} w_i^{(m)} \mathcal{Y}_{i,k} \tag{9}$$

$$P_{\hat{y}_k} = R_k + \sum_{i=0}^{2n} w_i^{(c)} (\mathcal{Y}_{i,k} - \hat{y}_k^-)(\mathcal{Y}_{i,k} - \hat{y}_k^-)^T \tag{10}$$

$$P_{x_k y_k} = \sum_{i=0}^{2n} w_i^{(c)} (\chi_{i,k}^- - \hat{x}_k^-)(\mathcal{Y}_{i,k} - \hat{y}_k^-)^T \tag{11}$$

$$K_k = P_{x_k y_k} P_{\hat{y}_k}^{-1} \tag{12}$$

$$\hat{x}_k = \hat{x}_k^- + K_k(y_k - \hat{y}_k^-) \tag{13}$$

$$P_{x_k} = P_{x_k}^- - K_k P_{\hat{y}_k} K_k^T \tag{14}$$

2. Single transformation of sigma points

In this case, generated same sigma points are propagated through a nonlinear model function as well as nonlinear measurement function [8]. The algorithm of this case can be described as Table 2.

Table 2. UKF algorithm with single transformation of sigma points

$$\chi_{k-1} = [\hat{x}_{k-1} \cdots \hat{x}_{k-1}] + \gamma[0 \quad \sqrt{P_{x_{k-1}}} \quad -\sqrt{P_{x_{k-1}}}] \tag{15}$$

$$\chi_{i,k} = f(\chi_{i,k-1}, u_{k-1}) \tag{16}$$

$$\hat{x}_k^- = \sum_{i=0}^{2n} w_i^{(m)} \chi_{i,k} \tag{17}$$

$$P_{x_k}^- = Q_{k-1} + \sum_{i=0}^{2n} w_i^{(c)} (\chi_{i,k} - \hat{x}_k^-)(\chi_{i,k} - \hat{x}_k^-)^T \quad (18)$$

$$\mathcal{Y}_{i,k} = h(\chi_{i,k}, u_k) \quad (19)$$

$$\hat{y}_k^- = \sum_{i=0}^{2n} w_i^{(m)} \mathcal{Y}_{i,k} \quad (20)$$

$$P_{\hat{y}_k} = R_k + \sum_{i=0}^{2n} w_i^{(c)} (\mathcal{Y}_{i,k} - \hat{y}_k^-)(\mathcal{Y}_{i,k} - \hat{y}_k^-)^T \quad (21)$$

$$P_{x_k y_k} = \sum_{i=0}^{2n} w_i^{(c)} (\chi_{i,k} - \hat{x}_k^-)(\mathcal{Y}_{i,k} - \hat{y}_k^-)^T \quad (22)$$

$$K_k = P_{x_k y_k} P_{\hat{y}_k}^{-1} \quad (23)$$

$$\hat{x}_k = \hat{x}_k^- + K_k (y_k - \hat{y}_k^-) \quad (24)$$

$$P_{x_k} = P_{x_k}^- - K_k P_{\hat{y}_k} K_k^T \quad (25)$$

3. State augmented case

In this section, we investigate the effect when the original state is augmented with other system and measurement noises simultaneously [9] as if the original state and measurement noises are included in nonlinear functions, even though they are actually to be additive to each model function. Note however that a single set of generated sigma points are used to evaluate the result. The algorithm can be summarized as in Table 3.

Table 3. UKF algorithm with an augmented state vector

$$x_k^a = \begin{bmatrix} x_k^T & w_k^T & v_k^T \end{bmatrix}^T, \; P_{x_k}^a = \mathrm{diag}\,(P_{x_k}, Q_k, R_k) \quad (26)$$

$$\chi_{k-1}^a = [\hat{x}_{k-1}^a \cdots \hat{x}_{k-1}^a] + \gamma [0 \quad \sqrt{P_{x_{k-1}}^a} \quad -\sqrt{P_{x_{k-1}}^a}] \quad (27)$$

$$\chi_{i,k}^x = f(\chi_{i,k-1}^x, u_{k-1}) + \chi_{i,k-1}^w \quad (28)$$

$$\hat{x}_k^- = \sum_{i=0}^{2L} w_i^{(m)} \chi_{i,k}^x \quad (29)$$

$$P_{x_k}^- = \sum_{i=0}^{2L} w_i^{(c)} (\chi_{i,k}^x - \hat{x}_k^-)(\chi_{i,k}^x - \hat{x}_k^-)^T \quad (30)$$

$$\mathcal{Y}_{i,k} = h(\chi_{i,k}^x, u_k) + \chi_{i,k-1}^v \quad (31)$$

$$\hat{y}_k^- = \sum_{i=0}^{2L} w_i^{(m)} \mathcal{Y}_{i,k} \quad (32)$$

$$P_{\hat{y}_k} = \sum_{i=0}^{2L} w_i^{(c)} (\mathcal{Y}_{i,k} - \hat{y}_k^-)(\mathcal{Y}_{i,k} - \hat{y}_k^-)^T \quad (33)$$

$$P_{x_k y_k} = \sum_{i=0}^{2L} w_i^{(c)} (\chi_{i,k}^x - \hat{x}_k^-)(\mathcal{Y}_{i,k} - \hat{y}_k^-)^T \quad (34)$$

$$K_k = P_{x_k y_k} P_{\hat{y}_k}^{-1} \quad (35)$$

$$\hat{x}_k = \hat{x}_k^- + K_k (y_k - \hat{y}_k^-) \quad (36)$$

$$P_{x_k} = P_{x_k}^- - K_k P_{\hat{y}_k} K_k^T \quad (37)$$

Note here that L denotes $2n + m$, $\chi_{i,k-1}^x$, $\chi_{i,k-1}^w$, and $\chi_{i,k-1}^v$ denote the i-th column of χ_{k-1}^x, χ_{k-1}^w, and χ_{k-1}^v which are also the components of $\chi_{k-1}^a = [(\chi_{k-1}^x)^T \quad (\chi_{k-1}^w)^T \quad (\chi_{k-1}^v)^T]^T$. Note also that n in the weights appearing in the former algorithms should be replaced by L for the present algorithm.

III. AN EXAMPLE APPLICATION

In this section we consider the problem that a vehicle enters the atmosphere at high altitude and at a very high speed. The position of the body is to be tracked by a radar which accurately measures range and bearing. This type of problem has been identified by Mehra [10], Austin and Leondes [11] and Athans et al. [12] as being particularly stressful for filters and trackers because of the strong nonlinearities exhibited by the forces which act on the vehicle. There are three types of forces which act: i.e., (1) the most dominant is aerodynamic drag, which is a function of vehicle speed and has a substantial nonlinear variation in altitude; (2) gravity force which accelerates the vehicle towards the centre of the earth; and (3) random buffeting force terms. The effect of these forces gives a trajectory of the form that initially the trajectory is almost ballistic but as the density of the atmosphere increases, drag effects become important and the vehicle rapidly decelerates until its motion is almost vertical. The tracking problem is made more difficult by the fact that the drag properties of the vehicle might be only very crudely known.

This tracking system should be able to track an object which experiences a set of complicated, highly nonlinear forces. These depend on the current position and velocity of the vehicle as well as on certain characteristics which are not known precisely. The filter's state space consists of the position of the body (x_1 and x_2), its velocity (x_3 and x_4) and a parameter of its aerodynamic properties (x_5). The vehicle state dynamics are

$$\begin{aligned} \dot{x}_2(k) &= x_4(k) \\ \dot{x}_2(k) &= x_4(k) \\ \dot{x}_3(k) &= D(k)\, x_3(k) + G(k)\, x_1(k) + v_1(k) \\ \dot{x}_4(k) &= D(k)\, x_4(k) + G(k)\, x_2(k) + v_2(k) \\ \dot{x}_5(k) &= x_3(k) \end{aligned} \quad (38)$$

where $D(k)$ is the drag-related force term, $G(k)$ is the gravity-related force term and $v(k)$ are the process noise terms. Defining $R(k) = \sqrt{x_1^2(k) + x_2^2(k)}$ as the distance from the center of the Earth and $V(k) = \sqrt{x_3^2(k) + x_4^2(k)}$ as absolute vehicle speed then the drag and gravitational terms are $D(k) = -\beta(k) \exp\left\{\frac{R_0 - R(k)}{H_0}\right\} V(k)$, $G(k) = -\frac{G m_0}{r^3(k)}$ and $\beta(k) = \beta_0 \exp x_5(k)$.

For this example, the parameter values are $\beta_0 = -0.59783$, $H_0 = 13.406$, $Gm_0 = 3.9860 \times 10^5$ and

$R_0 = 6374$ and reflect typical environmental and vehicle characteristics. The parameterization of the ballistic coefficient, $\beta(k)$, reflects the uncertainty in vehicle characteristics. β_0 is the ballistic coefficient of a typical vehicle and it is scaled by $\exp x_5(k)$ to ensure that its value is always positive. This is vital for filter stability. The motion of the vehicle is measured by a radar which is located at (x_r, y_r). It is able to measure range r and bearing θ at a frequency of 10Hz, where

$$r_r(k) = \sqrt{(x_1(k) - x_r)^2 + (x_2(k) - y_r)^2} + w_1(k) \tag{39}$$

$$\theta(k) = \tan^{-1}\left[\frac{x_2(k) - y_r}{x_1(k) - x_r}\right] + w_2(k) \tag{40}$$

$w_1(k)$and $w_2(k)$ are zero mean uncorrelated noise processes with variances of 1 m and 17 mrad respectively. The high update rate and extreme accuracy of the sensor means that a large quantity of extremely high quality data is available for the filter. The true initial conditions for the vehicle are

$$x(0) = \begin{pmatrix} 6500.4 \\ 349.14 \\ -1.8093 \\ -6.7967 \\ 0.6932 \end{pmatrix},$$

$$P(0) = \text{diag}(10^{-6}, 10^{-6}, 10^{-6}, 10^{-6}, 0)$$

In other words, the vehicle's coefficient is twice the nominal coefficient.

The vehicle is buffeted by random accelerations,

$$Q(k) = \text{diag}(2.4046 \times 10^{-5}, 2.4046 \times 10^{-5}, 0)$$

The initial conditions assumed by the filter are,

$$x(0) = \begin{pmatrix} 6500.4 \\ 349.14 \\ -1.8093 \\ -6.7967 \\ 0 \end{pmatrix},$$

$$P(0) = \text{diag}(10^{-6}, 10^{-6}, 10^{-6}, 10^{-6}, 1)$$

The filter uses the nominal initial condition and, to offset for the uncertainty, the variance on this initial estimate is 1. Both filters were implemented in discrete time and observations were taken at a frequency of 10 Hz, but the integration step was set to be 50 ms which meant that two predictions were made per update.

IV. CONCLUSION

In this paper, we have examined three cases related to sigma points of unscented transformation of nonlinear model and measurement functions. In the first case, the sigma points are applied two times to the nonlinear model and measurement functions separately by using different mean and covariance. In the second case, the transformation is once applied to the nonlinear model function and the same sigma point values are only propagated to the nonlinear measurement function. Lastly, the performance of an unscented Kalman filter was further evaluated for the case where the original state is augmented with other system and measurement noises simultaneously as if the original state and measurement noises are included in nonlinear functions, even though they are actually to be additive to each model function.

REFERENCES

[1] van der Merwe R (2004), Sigma point Kalman filter for probabilistic inference in dynamic state-space models. PhD Thesis, Oregon Health & Science University, Portland

[2] Evensen G (2003), The ensemble Kalman filter: Theoretical formulation and practical implementation. Ocean Dynamics, 53: 343–367

[3] Arulampalam MS, Maskell S, Gordon N, and Clapp T (2002), A tutorial on particle filters for online nonlinear/non-Gaussian Bayesian tracking. IEEE Trans. on Signal Processing, 50(2), 174–188

[4] Julier SJ and Uhlmann JK (2004), Unscented filtering and nonlinear estimation. Proceedings of the IEEE, 92(3): 401–422

[5] Wan E and van der Merwe R (2001), The Unscented Kalman Filter. Wiley Publishing

[6] Terejanu G, Singh T and Scott PD (2007), Unscented Kalman filter/smoother for a CBRN puff-based dispersion model. Proc. of the 10th Int. Conf. on Information Fusion, Quebec City, Quebec, July 9–12

[7] Sarkka S (2010), Continuous-time and continuous-discrete-time unscented Rauch-Tung-Striebel smoothers. Signal Processing, 90: 225–235

[8] Lefebvre T, Bruyninckx H, and De Schutter J (2002), Comment on "A new method for the nonlinear transformation of means and covariances in filters and estimators," IEEE Trans. Automatic Control, AC-47(8): 1406–1408

[9] Wang X and Zhang H (2007), A UPF-UKF framework for SLAM. Proc. of IEEE Int. Conf. on Robotics and Automation, pp. 1664–1669

[10] Mehra RK (1971). A comparison of several nonlinear filters for reentry vehicle tracking. IEEE Trans. on Automatic Control, AC-16(4): 307–319

[11] Austin JW and Leondes CT (1981), Statistically linearized estimation of reentry trajectories. IEEE Trans. on Aerospace and Electronic Systems, AES-17(1): 54–61

[12] Athans M, Wishner RP and Bertolini A (1968), Suboptimal state estimation for continuous-time nonlinear systems from discrete noisy measurements. IEEE Trans. on Automatic Control, AC-13(6): 504–518

Research on Movements in Formation of Multiple Mobile Robots

Tatsuya Kato, Shoichi Maeyama, and Keigo Watanabe

Department of Intelligent Mechanical Systems,
Davison of Industrial Innovation Sciences,
Graduate School of Natural Science and Technology, Okayama University,
3-1-1 Tsushima-naka, Kita-ku, Okayama 700-8530, Japan
Tel & Fax: +81-86-251-8064
E-mail: t.kato@usm.sys.okayama-u.ac.jp, {maeyama, watanabe}@sys.okayama-u.ac.jp

Abstract: Multi-robot systems are expected to improve the ability of processing tasks, a work efficiency, and an extendability of a robot system by cooperating each other. However, using multiple robots complicates its control system. As one of the associated problems, robot movements are picked up. Since a robot formation is useful to transfer multiple robots to their destinations effectively, many studies have been performed. This paper describes a method, which is called "IET method," for forming a formation with multiple robots. The method can specify the position of each robot in a group and change the shape of a formation. Note that each robot is assumed to have different ability and identified each other. Alternatively, the method needs a system that obtains the ID and relative position of the robots. We describe how to construct the measurement system using wireless communication and ultrasonic sound, and evaluate it through some simulation experiments.

Keywords: Multi-robot system, Formation, Robot identification, Measurement of relative position.

I. INTRODUCTION

Multi-robot systems are expected to improve the ability of processing tasks, a work efficiency, and an extendability of a robot system by cooperating each other. Note however that using multiple robots complicates its control system. When transferring multiple robots simultaneously, it is difficult to move them to their destination smoothly due to the fact that any robot is an obstacle for other robots, and vice versa. Since a robot formation is useful to transfer multiple robots to their destinations effectively, many studies have been performed up to now.

In [1], the size of virtual robots that has not been considered yet is reflected on simulations, and the line and circle formations are formed while avoiding obstacles. In [2], line, polygon and circle formations are realized in simulations by adjusting its own position, while referring to the positions of the furthest robot and closest robot. The reference [3] aims to use robots as macrosensors, in which the distributed in a space by using the concept of a virtual spring mesh. In these research, since similar or homogeneous robots have the same ability in function, it is not concerned that any robots go anywhere in the formation. It should be noted, however, that in multi-robot systems, robots that have different ability in function should cooperate to accomplish some complicated tasks each other. In such a case, it is necessary to deploy the robots at each desired position where their ability is demonstrated enough. For example, a robot that has the ability to recognize the environment or to remove obstacles should be placed at the most outer part of the swarm.

There are some studies for using heterogeneous robots. Jakob and Maja [4] propose a method for forming a formation with some identified robots. Its key idea is to set that every robot in the group positions itself relative to a designated neighbor robot (i.e., its friend). In their paper, the time required for forming a desired formation or changing a formation to another one was evaluated through several experiments with some real robots. Balch and Arkin [5] propose a method for forming "line," "column," "diamond," and "wedge." However, it is behavior-based control, so the reconfiguration of parameter values needs to decide own behaviors. Therefore, it is not easy to change any current robot formation to other one.

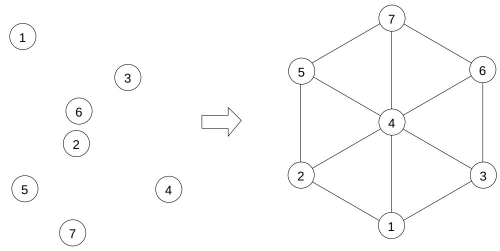

Fig. 1. A formation with a specified position

In this paper, we propose a formation method for a multi-robot system, which can specify the position of each robot in a group and can change easily the shape of a formation. Note however that each robot is assumed to have different ability each other, and the developed method is here called "IET (Imaginary Equilateral Triangle) method."

Alternatively, the method needs a system that obtain the ID and relative position of robots. We describe here how to construct the measurement system using wireless communication and ultrasonic sound, and evaluate it through some simulation experiments.

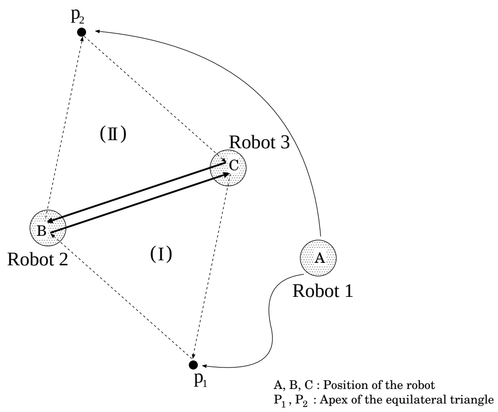

Fig. 2. Apexes for forming an IET

II. FORMING OF A FORMATION WITH IET METHOD

First, assume that the shape of formation is composed of a combination of some equilateral triangles (Fig. 1). According to this assumption, robots can form several formations by changing the combination of the triangles. Especially, it is easy to add or exclude a robot to the existing formation of robots. In order to realize a formation, it is essential to form an equilateral triangle with three robots. Therefore, we propose an IET method to form an equilateral triangle with robots.

1. IET Method

Consider the case where there exist three robots as shown in Fig. 2. If Robot 2 and Robot 3 do not move anymore, then Robot 1 has to move to P_1 or P_2 to form an equilateral triangle. Here, the points P_1 and P_2 are the apexes of equilateral triangles whose base is just to be BC (or CB). As a triangle BCP_1 or BCP_2, an equilateral triangle imagined by using the position of other two robots is called IET.

Since there are two possible IETs for one base, a rule for determining one candidate is set as follows:

- Two reference robots and the associated order are given to every robot.
- An IET fabricates the triangle clockwise according to the reference order of robots.

If Robot 1 is given Robot 2 $\rightarrow$ Robot 3 as the reference robots, the destination of Robot 1 is just P_1, whereas Robot 3 $\rightarrow$ Robot 2 are given, the destination is reduced to P_2.

For a case where all the robots move, the fundamental view is the same as the former case. When the initial distribution of three robots is shown as Fig. 3(a), every robot images each IET at each initial position (Fig. 3(b)) and moves toward to the apex of each IET (Fig. 3(c)). Fig. 3(d) shows the state of three robots after consuming a few steps from Fig. 3(c). It can be expected that the group form of three robots approaches an equilateral triangle by spending more time steps. Thus, three robots

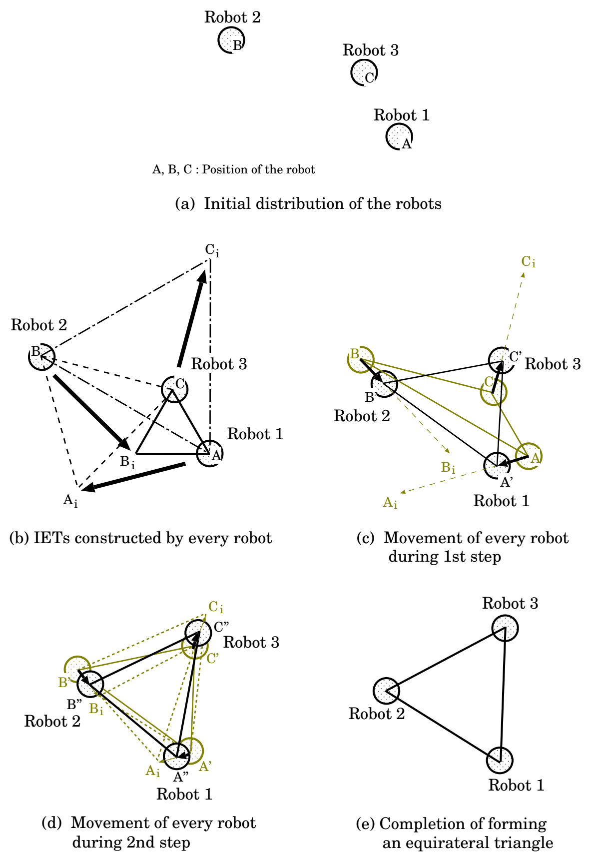

Fig. 3. Formation of an equilateral triangle

can form an equilateral triangle formation by respectively moving toward the apex of an IET.

When forming a formation by multiple robots, each robot forms an equilateral triangle with given reference robots to form a desired formation by setting reference robots suitably as shown in Fig. 4. Fig. 5 shows a simulation result.

III. OBTAINING ID AND POSITIONS

The IET method needs a system which can obtain the ID and relative positions of robots in a team to realize a formation by using real robots. Thus, we propose a system with wireless communication and ultrasonic sound. As shown in Fig. 6, three ultrasonic sensors are equipped to a measuring robot (Robot 1), whereas a ultrasonic transmitter is equipped to other robots (Robot 2, Robot 3). Note that every robot has a wireless communication ability. The positions of ultrasonic sensors are apexes of an equilateral triangle whose centroid matches the center point of the robot. As an example of detecting the ID and position of a robot, we describe a situation where Robot 2 is the object to be measured.

1) *Request of measurements*
Robot 2 sends own ID to other members by wireless communication (broadcast). This sending is a cue to begin the measurement of relative position of the robot. Until the measurement is completed,

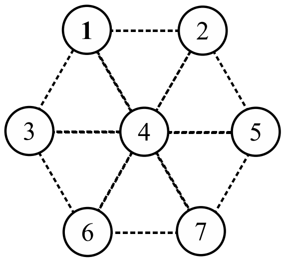

Table of reference robots

Robot's ID	Order of reference robots
1	2 -> 4
2	4 -> 1
3	1 -> 4
4	1 -> 2
5	4 -> 2
6	3 -> 4
7	4 -> 5

Fig. 4. Hexagonal formation

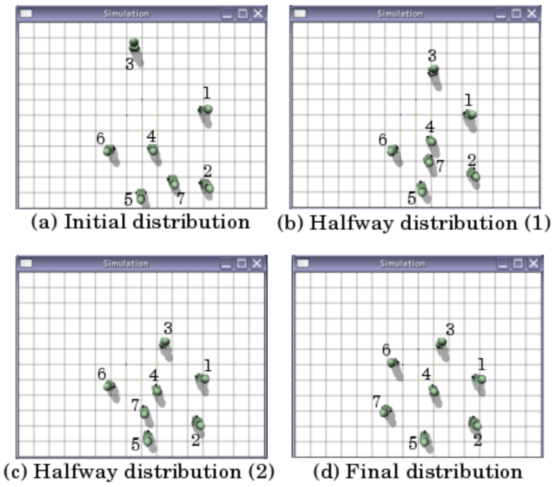

Fig. 5. Simulation of forming the shape of a hexagon

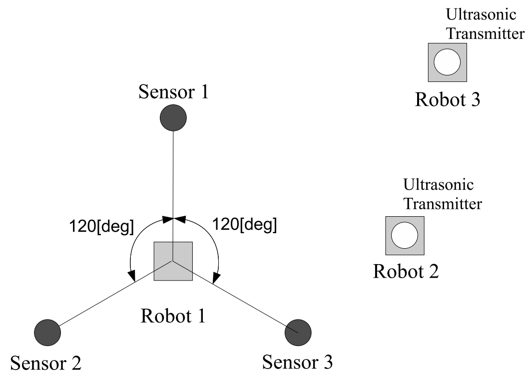

Fig. 6. System of measuring a robot's ID and its relative position

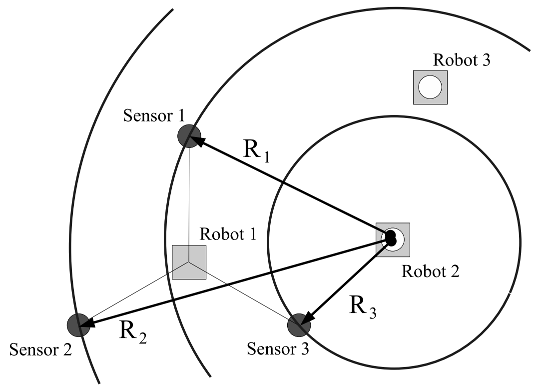

Fig. 7. Receiving an ultrasonic wave and calculating distances between sensors and robot 2

other robots can't send both wireless signal and ultrasonic sound.

2) *Transmitting an ultrasonic sound*
Robot 2 transmits an ultrasonic sound omnidirectionally, simultaneously with the transmission of own ID.
3) *Receiving the wireless signal and ultrasonic sound*
Assuming that the wireless signal can approximately arrive at robot 1 with 0 [s], the distance between the sensor and the Robot 2 can be calculated with a counted time, which is the time until the ultrasonic sound arrives after receiving the wireless signal (Fig. 7).
4) *Estimation of relative position*
The relative position of Robot 2 (x_2, y_2) is estimated by figuring out the coordinate point where three circles whose radius is the distance to Robot 2 cross.

IV. SIMULATION EXPERIMENTS

In this section, we evaluate the accuracy of estimation of a relative position of a robot through two simulation experiments. Fig. 9 shows the experimental environment. Robot 1 is a measuring robot, and the origin of the coordinate is defined as the center of Robot 1, where the x-directional coordinate is just to be a line connected with the origin and Sensor 1. Although Robot 1 estimates the position of Robot 2 (x_2, y_2) based on the distance between sensors and Robot 2, the measured value includes noise up to $\pm$ 1 [%]. The accuracy of estimation is evaluated for cases where the distance between sensors, L, or the distance between robots, D, changes independently.

Additionally, the sound speed is 340 [m/s], and standard deviations are calculated with 100 times of measurement result per one plotting.

1. Experiment 1: Distance between sensors

In this experiment, the impact of the distance between sensors, L, on the estimation accuracy is evaluated when L changes from 0.1 [m] to 0.5 [m]. Here, the position of Robot 2 is (x_2, y_2) = (3.0 [m], 3.0 [m]): in other words, L = 4.243 [m] and θ = 45 [deg]. Fig. 10 shows a result of the simulation experiment. The result indicates a great impact of the distance between sensors on the estimation accuracy.

2. Experiment 2: Distance between robots

In this experiment, the impact of the distance between robots, D, on the estimation accuracy is evaluated, when D changes from 1.0 [m] to 10.0 [m], under the fixed values of $L = 0.3$ [m] and $\theta = 45$ [deg]. Fig. 11 is the result of the simulation experiment. The standard deviation increases exponentially with the distance between

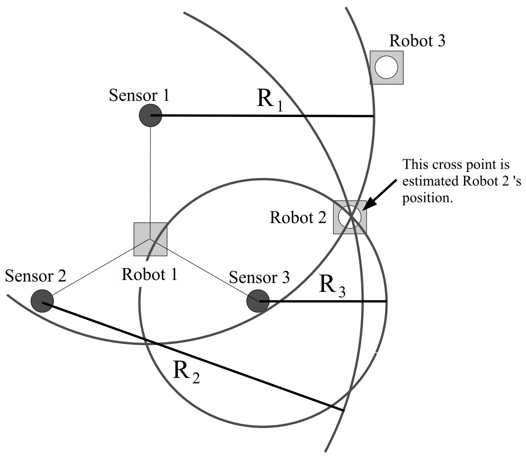

Fig. 8. Estimation of the position of robot 2

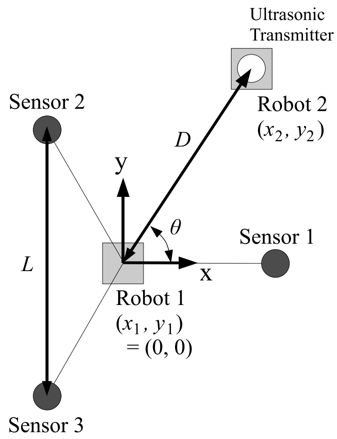

Fig. 9. Symbol of simulation parameters

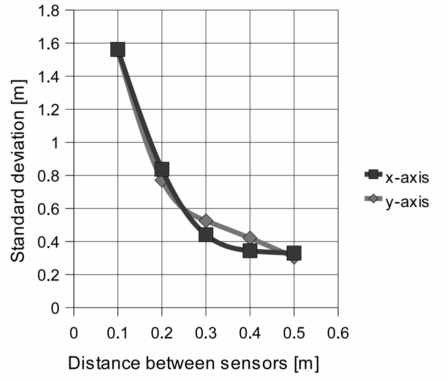

Fig. 10. Relationship between an estimation accuracy and a distance between sensors

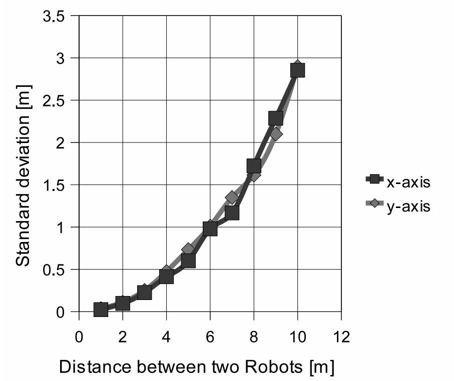

Fig. 11. Relationship between an estimation accuracy and a distance between two robots

robots. Although the accuracy of ultrasonic sensors is ± 1, the accuracy of the proposed estimation method is inferior to is when a certain boundary is crossed, and it is not reliable if the distance exceeds the boundary extremely. The result shows that the system can ensure the accuracy equivalent to ultrasonic sensors ($\pm$ 1 [%]) up to about 5 [m] range, where the distance between sensors L = 0.3 [m].

V. CONSIDERATION

Although a longer distance between sensors allow us to obtain more accurate estimation of relative position, the size of the system is about 0.3 [m] from the view-points of the robot size to be fabricated. Thus, from the result of experiment 2, the system needs the estimation distance up to 5 [mm] to ensure the accuracy equivalent to ultrasonic sensors ($\pm$ 1 [%]). However, instead of using reflected ultrasonic sound, a sound transmitted from the object robot is measured directly. It is expected to obtain the better accuracy of measuring distance than any general measurement system with ultrasonic sound. Since the accuracy of measuring distance gives a big impact to the estimation accuracy of relative position of the robot, an improvement of the accuracy of measuring distance may give us a better estimation result.

VI. CONCLUSIONS

In this paper, we have explained the IET method and proposed the system which can obtain ID and a relative position of a robot simultaneously. The proposal system was tested in simulation experiments which examine the impacts of the distance between sensors or robots on the estimation accuracy. In the future, we need to construct and test the system in a real experiment.

REFERENCES

[1] Yun X, Alptekin G, and Albayrak O (1997), Line and circle formation of distributed physical mobile robots. Journal of Robotic Systems, 14(2): 63–76
[2] Sugihara K and Suzuki I (1996), Distributed algorithms for formation of geometric patterns with many mobile robots. Journal of Robotic Systems, 13(3): 127–139
[3] Shucker B and Bennett JK (2006), Scalable control of distributed robotic macrosensors. Distributed Autonomous Robotic Systems (DARS), pp. 379–388
[4] Fredslund J and Mataric MJ (2002), A general algorithm for robot formations using local sensing and minimal communication. IEEE Trans. on Robotics and Automation, 18(5): 837–846
[5] Balch T and Arkin RC (1998), Behavior-based formation control for multi robot teams. IEEE Trans. on Robotics and Automation, 14(6): 926–939

Development of variable stiffness joint drive module and experimental results of joint angle control

J. Kobayashi*, K. Okumura, Y. Watanabe, and N. Suzuki

*Kyushu Institute of Technology, Kawazu 680-4, Iizuka, Fukuoka, 820-8502, Japan
(Tel : +81-948-29-7747; Fax :+ 81-948-29-7709)
(Email jkoba@ces.kyutech.ac.jp)

Abstract: Two prototypes of variable stiffness joint drive module imitating a human joint structure are presented in this paper. A human joint is driven by a pair of flexor and extensor muscles that work antagonistically. The stiffness of the joint is adjusted by their co-contraction. Such a structure was given to the joint drive module so that it could achieve a variable stiffness property. The joint is driven by two wires with nonlinear springs. Thanks to the nonlinearity of the springs, the stiffness of the joint can be adjustable by quasi-co-contraction of the wires. With the first prototype, the stiffness adjustability of the joint was empirically confirmed. Regarding joint angle control, a three-layered PID control algorithm was implemented in the second prototype, and it was verified that the control algorithm worked properly.

Keywords: Variable Stiffness, Antagonistic Wire-Driven Mechanism, Joint Angle Control.

I. INTRODUCTION

Most robotic joints are usually driven by electric motors through gear trains. Since typical electric motors have high speed and low torque characteristics that are inappropriate for robotic systems, gear trains with high reduction ratio are used as a driving torque transmission mechanism. The gear trains convert the undesirable characteristics into the appropriate ones for robotic systems, low speed and high torque. In addition, robotic joints with higher gear ratio are stiffer, and it was common knowledge that stiffer joints were indispensable for precise position control. However, Pratt et al. have suggested that actuators with elasticity provide a lot of benefits for robots executing natural tasks because animals use elasticity for a variety of purposes [1].

For instance, human beings change stiffness of their joints depending on a given task, unlike traditional robotic joints. They can easily do a task involving an impulsive force, in which robots with gear trains are weak, by adjusting the stiffness of their joints.

A human joint is basically driven by a pair of flexor and extensor muscles. These muscles are also called agonist and antagonist respectively. The drive mechanism of a human joint is briefly explained as follows. The difference of tensional forces of the agonist and antagonist works as a driving torque to rotate a joint. When both of the muscles generate a larger tensional force, which is called co-contraction, the stiffness of the joint comes to be higher.

A robot will be able to obtain human-like motions if it has variable stiffness joints, and the soft and refined human-like motions will probably broaden the range of application of the robot. In addition, since upcoming robots are expected to work in a living environment together with people, the high stiffness of the joints is an issue to resolve in terms of safety, and the variable stiffness joints could be one of the possible solutions.

In order to provide the human-like characteristic for robots, we have developed a joint drive module imitating the human joint structure. In the drive module, a joint is antagonistically driven by two wires, and each of the wires is taken up by an electric motor. The wire is connected to the electric motor through a nonlinear spring. The stiffness of the nonlinear spring depends on the change in length of the spring. Utilizing the nonlinearity, the developed joint drive module realizes variable stiffness of the joint like a human joint.

In this paper, two prototypes of variable stiffness joint drive module that we developed are presented and some experimental results are shown. Using the first prototype, the variable stiffness characteristic was confirmed. The second prototype was used to verify that a joint angle control algorithm worked properly.

II. VARIABLE STIFFNESS JOINT DRIVE MODULE

This section outlines the variable stiffness joint drive module that we are developing, and describes nonlinear springs, which is a key component of the module.

Fig. 1 shows a concept diagram of the variable stiffness joint drive module. The joint is antagonistically driven by two wires, which works like agonist and antagonist. There is a wire take-up mechanism including two electric motors in the module box. The electric motors reel in and out the wires that are connected to the joint through nonlinear springs.

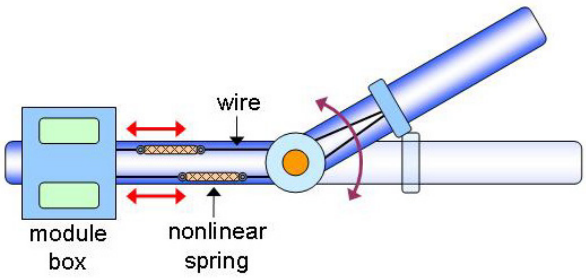

Fig.1. Concept Diagram of Variable Stiffness Joint Drive Module

The nonlinear springs give a desired characteristic, variable stiffness joint, to the joint drive module. Hooke's law does not work for nonlinear springs. The more a nonlinear spring stretches, the higher its stiffness goes. Utilizing this characteristic of nonlinear springs, you can change the stiffness of the joint. For instance, if both of the motors reel in the two wires extremely, the stiffness of the joint will be high because of the tightly stretched nonlinear springs.

For nonlinear springs, several kinds of nonlinear springs have been proposed. Bigge et al., for example, have designed an electric actuator called a programmable spring that can emulate complex multimodal spring damping systems [2]. Shirai et al. have devised a nonlinear spring called Stiffness Adjustable Tendon (SAT) [3]. We have chosen the SAT for our joint drive module because of its simple structure. Moreover, necessary materials for the SAT, silicon rods and woven sleeves, are ease of availability. Therefore, you can make the SAT quickly and easily. Fig. 2 shows the SAT we made.

III. FIRST PROTOTYPE

We have developed two prototypes of the variable stiffness joint drive module. This section describes the first prototype shown in Fig. 3.

Fig. 4 shows the block diagram of the first prototype. As stated in the previous section, the two wires to rotate the joint are reeled in and out by the wire take-up mechanism. The two electric motors in the wire take-up mechanism are powered by the driver board (RoboPlus HIBIKINO). The microcontroller unit (MCU) (Atmel, AVR, ATmega168) counts pulses from the optical encoder that measures the angle of the joint. The driver board and the microcontroller communicate with a PC via RS-232C serial communication. An operator of the first prototype module gets the value of the joint angle and sends a command to the driver board through a user interface program running on the PC.

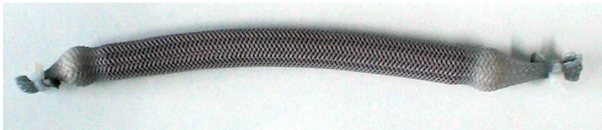

Fig.2. Stiffness Adjustable Tendon (SAT) [3]

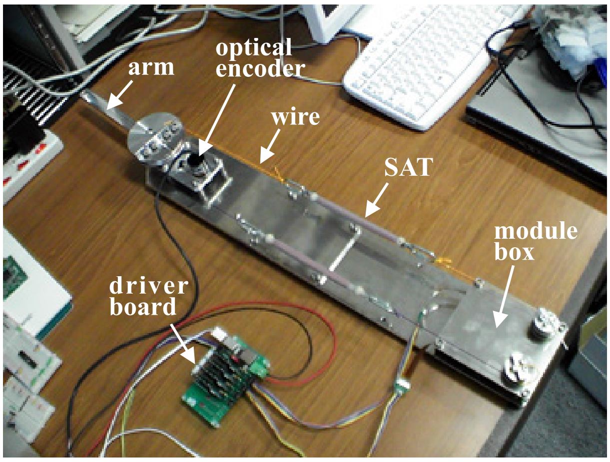

Fig.3. First Prototype of Variable Stiffness Joint Drive Module

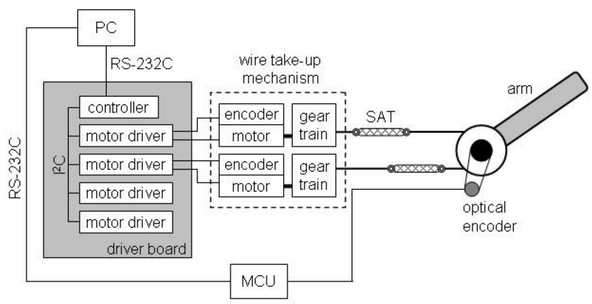

Fig.4. Block Diagram of First Prototype

Fig. 5 shows the wire take-up mechanism. Just as the name suggests, this mechanism takes up the two wires to rotate the joint and/or to change the stiffness. The wire is wound onto a bobbin driven by the electric motor through a worm gear train. The worm gear train prevents the wire from loosening abruptly when turning the power of the motors off. The gear ratio is 4080.

Fig.5. Wire Take-up Mechanism

The driver board has four motor drivers communicating each other with Inter-Integrated Circuit (I^2C) protocol, and exchange data with the PC via RS-232C serial communication. Because a joint drive module needs to exchange data with other ones as they work together in a robotic system, the communication system is suitable for the joint drive module, but the motor drivers have a problem that their maximum output current capacity is not enough. Due to the problem, we had to choose small electric motors (Maxon, RE13, 1.5W) with an optical encoder for the wire take-up mechanism of the first prototype. Consequently, the motion rate of the first prototype is very slow.

However, with the first prototype, we could carry out experiments to confirm the adjustability of the joint stiffness. In the experiments, the tip of the arm of the first prototype was pulled by an external force until the angle of the joint reaches a specified angle, and the amount of the external force was measured by a digital push pull force gauge.

Fig. 6 shows the experimental results. The x-axis indicates a displacement of the joint angle, and the y-axis indicates an external joint torque calculated from the measured amount of the external force and the length of the arm. In the legend of the graph, the symbol 'L' and 'R' indicate the initial length of the two SATs. According to the characteristic of the SAT, it turns stiffer as it is stretched more. The slope of the plots in the graph expresses the stiffness of the joint. From the experimental results, it was confirmed that the stiffness of the joint was adjustable by changing the length of the SATs in the first prototype of the variable stiffness joint drive module.

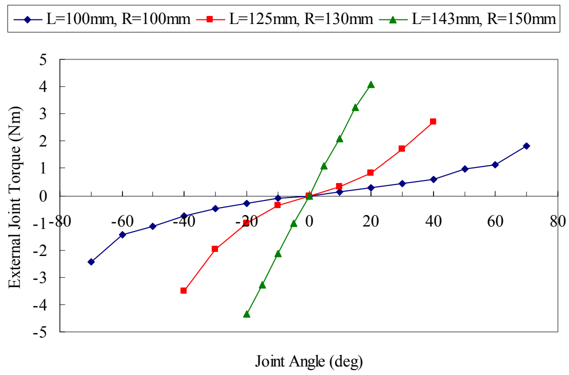

Fig.6. Joint Stiffness of First Prototype

IV. SECOND PROTOTYPE

As we developed the second prototype shown in Fig. 7, some changes in the electric motors, the motor drivers as well as the mechanical structure have been accomplished. To speed up the motion rate of the joint, more powerful electric motors (Maxon, RE25 GB, 20W) and motor drivers (DimensionEngineering, SyRen 25A regenerative motor driver) with higher output current capacity were adopted.

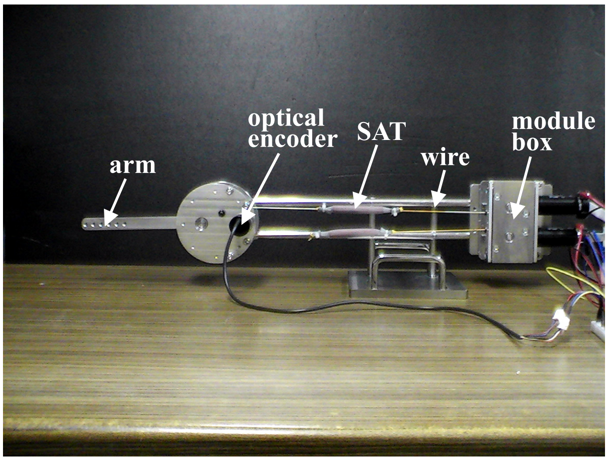

Fig.7. Second Prototype of Variable Stiffness Joint Drive Module

Fig. 8 shows the block diagram of the second prototype. The MCU (Renesas Technology, SH7145F) counts pulses from the optical encoders of the electric motors and the joint, and calculates commands to the motor drivers for joint angle control. The MCU counts the encoder pulses every 15.6 μs, and the sampling period for control is 20 ms.

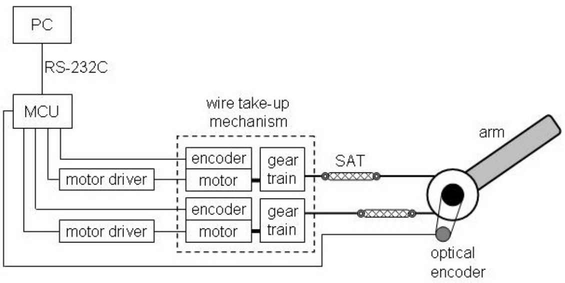

Fig.8. Block Diagram of Second Prototype

As for joint angle control method, we tentatively implemented a three-layered PID control algorithm. The rate and angle of rotation of the electric motors in the take-up mechanism are controlled in two lower control layers, and the highest control layer works for positioning the joint angle. Fig. 9, Fig. 10, and Fig. 11 show the result of a control experiment.

Concerning the joint angle control, the experimental results showed that the joint angle control worked properly; however, it has a problem that the highest control layer relating to positioning the joint angle spoils the intrinsic stiffness of the nonlinear springs. It is preferable that angle control and stiffness control are separable, but the feedback loop for the joint angle control strongly influences the stiffness of the joint.

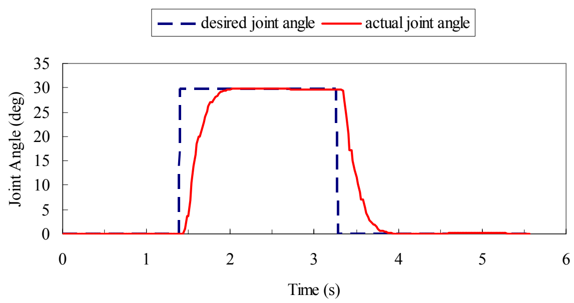

Fig.9. Joint Angle Control Result

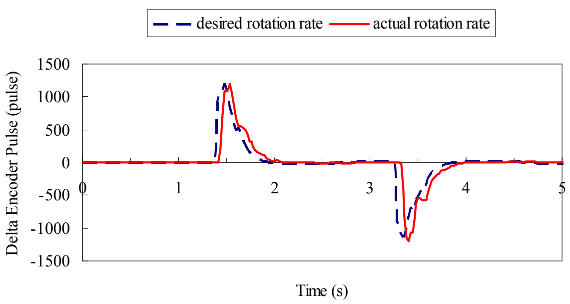

Fig.10. Motor Rotation Rate Control Result

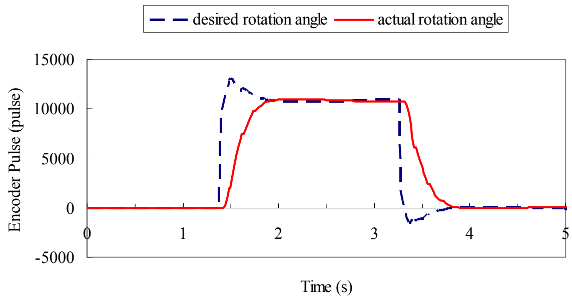

Fig.11. Motor Rotation Angle Control Result

For a human elbow joint, Kistemaker et al. have focused on the equilibrium point (EP) theory and addressed the similar issue about stiffness [4]. They have investigated an open-loop EP, which is achieved without the aid of feedback. Therefore, we will tackle our problem from their perspective.

V. CONCLUSIONS

Two prototypes of the variable stiffness joint drive module were presented in this paper. In the experiment with the first prototype, it was confirmed that the stiffness of the joint was adjustable by changing the length of the SATs. Moreover, the joint angle control was implemented in the second prototype, and it was verified that it worked properly. However, it was left as a future work to separate the intrinsic stiffness of the nonlinear spring from the reflexive stiffness that results from the joint angle feedback.

ACKNOWLEDGEMENTS

This work is funded by the Iizuka Research & Development Organization. We would like to thank Prof. Tatsuya Shirai for his suggestions about the SAT.

REFERENCES

[1] Pratt GA and Williamson MM (1995), Series Elastic Actuators. Proc. of the IEEE/RSJ International Conference on Intelligent Robots and Systems:399-406
[2] Bigge B and Harvey IR (2007), Programmable Spring: Developing Actuators with Programmable Compliance for Autonomous Robots. Robotics and Autonomous Systems 55(9):728-734
[3] Shirai T, Tanaka N, and Tomioka T (2003), Mechanism and Characteristic of Non-Linear Spring SAT (in Japanese). Proc. of the 21st annual conference of the robotics society of Japan:1C25
[4] Kistemaker DA, Soest AJV, and Bobbert MF (2007), A model of open-loop control of equilibrium position and stiffness of the human elbow joint. Biological Cybernetics 96:341-350

The Fifteenth International Symposium on Artificial Life and Robotics 2010 (AROB 15th '10),
B-Con Plaza, Beppu,Oita, Japan, February 4-6, 2010

Digital RAC with Disturbance Observer for Underwater Vehicle-Manipulator Systems

Shinichi Sagara Takashi Yatoh Tomoaki Shimozawa
Department of Control Engineering, Kyushu Institute of Technology
Tobata, Kitakyushu 804-8550, Japan
E-mail: sagara@cntl.kyutech.ac.jp

Abstract

Most of control methods of Underwater Vehicle-Manipulator Systems (UVMS) are based on the computed torque method that is used for underwater robotic vehicles. We have proposed a Resolved Acceleration Control (RAC) method for UVMS. In this paper, we propose a disturbance compensation control method for both vehicle and manipulator based on the RAC method. Experimental results using an underwater robot with vertical planar 2-link manipulator show that the proposed control method has good control performance.

1 Introduction

Most of the control methods of Underwater Vehicle-Manipulator Systems (UVMS) [1–5] are based on the computed torque method that is used for Underwater Robotic Vehicles [6]. Since the computed torque method only uses joint-space errors, the control performance of the end-effector of the manipulator depends on the vehicle control performance. Therefore, if the acceleration and velocity relations between the end-effector and joints are inaccurate or the control performance of the vehicle is not better, good control performance of the end-effector cannot be obtained.

We have proposed a Resolved Acceleration Control (RAC) method with position and velocity feedbacks both of the vehicle and the end-effector [7]. In general, added mass, added moment of inertia and drag coefficient are used constant value that depends on the shape of the robots. Our proposed method described above can reduce the influence of hydrodynamic force by position and velocity feedbacks. Moreover, to obtain higher control performance, we have proposed a disturbance compensation control method based on the RAC method [8]. In this control method, the influence of hydrodynamic force with respect to the vehicle is treated as a disturbance.

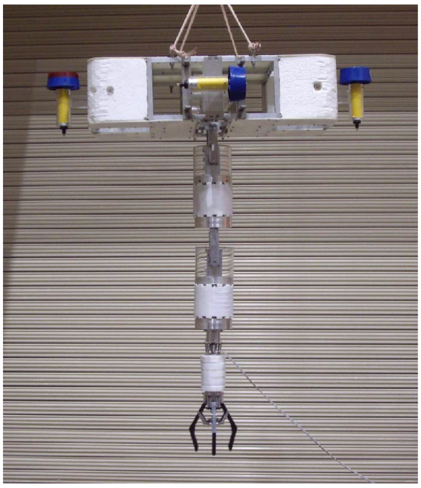

Fig. 1 2-link underwater robot

In this paper, we propose a disturbance compensation control method for both vehicle and manipulator. To verify the effectiveness of the digital RAC method with disturbance observer, experiments using an underwater robot with vertical planar 2-link manipulator shown in Fig. 1 are performed. From the experimental results, we show that the proposed control method has good control performance.

2 Modeling [7]

The UVMS model used in this paper is shown in Fig. 2. It has a robot base (vehicle) and an n-DOF manipulator. Symbols are defined as follows:

n : number of joint
Σ_I : inertial coordinate frame
Σ_i : link i coordinate frame ($i = 0, 1, 2, \cdots, n$; link 0 means vehicle)
${}^I\boldsymbol{R}_i$: coordinate transformation matrix from Σ_i to Σ_I
$\boldsymbol{p}_e$: position vector of end-effector
$\boldsymbol{p}_i$: position vector of origin of Σ_i

$\boldsymbol{r}_i$: position vector of gravity center of link i
ϕ_i : relative angle of joint i
$\boldsymbol{\psi}_0$: roll-pitch-yaw attitude vector of Σ_0
$\boldsymbol{\psi}_e$: roll-pitch-yaw attitude vector of end-effector
$\boldsymbol{\omega}_0$: angular velocity vector of Σ_0
$\boldsymbol{\omega}_e$: angular velocity vector of end-effector
$\boldsymbol{\phi}$: relative joint angle vector ($= [\phi_1,\ \cdots,\ \phi_n]^T$)
$\boldsymbol{k}_i$: unit vector indicating a rotational axis of joint i
m_i : mass of link i
$\boldsymbol{M}_{a_i}$: added mass matrix of link i
$\boldsymbol{I}_i$: inertia tensor of link i
$\boldsymbol{I}_{a_i}$: added inertia tensor of link i
$\boldsymbol{x}_0$: position and attitude vector of Σ_0 ($= [\boldsymbol{r}_0^T,\ \boldsymbol{\psi}_0^T]^T$)
$\boldsymbol{x}_e$: position and attitude vector of end-effector ($= [\boldsymbol{p}_e^T,\ \boldsymbol{\psi}_e^T]^T$)
$\boldsymbol{v}_0$: linear and angular vector of Σ_0 ($= [\dot{\boldsymbol{r}}_0^T,\ \boldsymbol{\omega}_0^T]^T$)
$\boldsymbol{v}_e$: linear and angular vector of end-effector ($= [\dot{\boldsymbol{p}}_e^T,\ \boldsymbol{\omega}_e^T]^T$)
$\boldsymbol{E}_j$: $j \times j$ unit matrix

The tilde operator stands for a cross product such that $\tilde{\boldsymbol{r}}\boldsymbol{a} = \boldsymbol{r} \times \boldsymbol{a}$. All position and velocity vectors are defined with respect to Σ_I

First, for the model shown in Fig. 2 the following kinematic and momentum equations can be obtained:

$$\boldsymbol{v}_e = \boldsymbol{A}\boldsymbol{v}_0 + \boldsymbol{B}\dot{\boldsymbol{\phi}}, \tag{1}$$

$$\boldsymbol{s} = [\boldsymbol{\eta}^T,\ \boldsymbol{\mu}^T]^T = \boldsymbol{C}\boldsymbol{v}_0 + \boldsymbol{D}\dot{\boldsymbol{\phi}} \tag{2}$$

where

$$\boldsymbol{A} = \begin{bmatrix} \boldsymbol{E}_3 & -(\tilde{\boldsymbol{p}}_r - \tilde{\boldsymbol{r}}_0) \\ \boldsymbol{0} & \boldsymbol{E}_3 \end{bmatrix}, \quad \boldsymbol{B} = [\boldsymbol{b}_1\ \boldsymbol{b}_2\ \cdots\ \boldsymbol{b}_n],$$

$$\boldsymbol{C} = \begin{bmatrix} \sum_{i=0}^{n} \boldsymbol{M}_{T_i} & -\sum_{i=1}^{n} \boldsymbol{M}_{T_i}\tilde{\boldsymbol{r}}_{0i} \\ \sum_{i=0}^{n} \tilde{\boldsymbol{r}}_{0i}\boldsymbol{M}_{T_i} & \sum_{i=0}^{n} \{\boldsymbol{I}_{T_i} - \tilde{\boldsymbol{r}}_{0i}\boldsymbol{M}_{T_i}\tilde{\boldsymbol{r}}_{0i}\} \end{bmatrix},$$

$$\boldsymbol{D} = \begin{bmatrix} \boldsymbol{d}_{11} & \boldsymbol{d}_{11} & \cdots & \boldsymbol{d}_{1n} \\ \boldsymbol{d}_{21} & \boldsymbol{d}_{21} & \cdots & \boldsymbol{d}_{2n} \end{bmatrix},$$

$$\boldsymbol{b}_i = \left[\{\tilde{\boldsymbol{k}}_i(\boldsymbol{p}_r - \boldsymbol{p}_i)\}^T \quad \boldsymbol{k}_i^T\right]^T, \ \boldsymbol{r}_{0i} = \boldsymbol{r}_i - \boldsymbol{r}_0,$$

$$\boldsymbol{d}_{1i} = \sum_{j=i}^{n} \boldsymbol{M}_{T_i}\tilde{\boldsymbol{k}}_i(\boldsymbol{r}_j - \boldsymbol{p}_i),$$

$$\boldsymbol{d}_{2i} = \sum_{j=i}^{n} \boldsymbol{I}_{T_j}\boldsymbol{k}_i + \tilde{\boldsymbol{r}}_{0j}\boldsymbol{M}_{T_j}\tilde{\boldsymbol{k}}_i(\boldsymbol{r}_j - \boldsymbol{p}_i)$$

and, $\boldsymbol{\eta}$ and $\boldsymbol{\mu}$ are a linear and an angular momentum of the robot.

Next, to obtain the dynamic equation of UVMS, hydrodynamic the drag and lift forces are necessary.

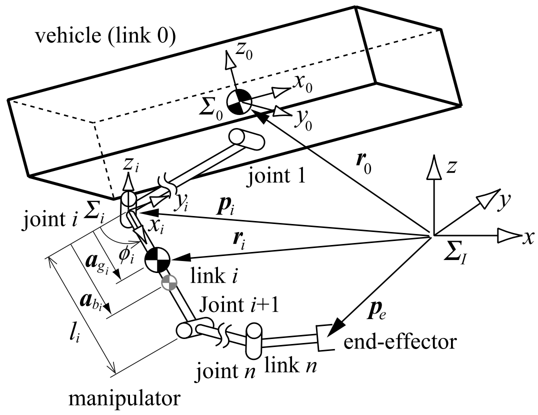

Fig. 2 n-link underwater robot model

The drag force and moment of joint i can be generally represented as follows [9]:

$$\boldsymbol{f}_{d_i} = \frac{\rho}{2} C_{D_i} D_i {}^I\boldsymbol{R}_i \int_0^{l_i} ||\boldsymbol{w}_i||\boldsymbol{w}_i dx_i, \tag{3}$$

$$\boldsymbol{t}_{d_i} = \frac{\rho}{2} C_{D_i} D_i {}^I\boldsymbol{R}_i \int_0^{l_i} \hat{\boldsymbol{x}}_i \times ||\boldsymbol{w}_i||\boldsymbol{w}_i dx_i \tag{4}$$

where

$$\boldsymbol{w}_i = \begin{bmatrix} 0 & \boldsymbol{0} \\ \boldsymbol{0} & \boldsymbol{E}_2 \end{bmatrix} {}^i\boldsymbol{R}_I\left(\dot{\boldsymbol{r}}_i + \tilde{\boldsymbol{\omega}}_i\hat{\boldsymbol{x}}_i\right), \quad \hat{\boldsymbol{x}}_i = \begin{bmatrix} x_i & 0 & 0 \end{bmatrix}^T.$$

and ρ is the fluid density, C_{d_i} is the drag coefficient of link i, D_i is the width of link i, l_i is the length of link i,

In the similar manner, the gravitational and buoyant forces acting link i are described as follows:

$$\boldsymbol{f}_{g_i} = (\rho V_i - m_i)\boldsymbol{g}, \tag{5}$$

$$\boldsymbol{t}_{g_i} = (\tilde{\boldsymbol{a}}_{b_i}\rho V_i - \tilde{\boldsymbol{a}}_{g_i} m_i)\boldsymbol{g} \tag{6}$$

where $\boldsymbol{a}_{g_i}$ is the position vector from joint i to gravity center of link i, $\boldsymbol{a}_{b_i}$ is the position vector from joint i to buoyancy center of link i, V_i is the volume of link i, $\boldsymbol{g}$ is the gravitational acceleration vector.

Considering the hydrodynamic forces described above and using the Newton-Euler formulation, the following equation of motion can be obtained [5]:

$$\boldsymbol{M}(\boldsymbol{q})\dot{\boldsymbol{\zeta}} + \boldsymbol{b}_C(\boldsymbol{q},\ \boldsymbol{\zeta}) + \boldsymbol{f} = \boldsymbol{u} \tag{7}$$

where $\boldsymbol{q} = [\boldsymbol{x}_0^T,\ \boldsymbol{\phi}^T]^T$ and $\boldsymbol{\zeta} = [\dot{\boldsymbol{v}}_0^T,\ \dot{\boldsymbol{\phi}}^T]^T$, $\boldsymbol{M}$ is the inertia matrix including the added mass $\boldsymbol{M}_{a_i}$ and inertia $\boldsymbol{I}_{a_i}$, $\boldsymbol{b}_C$ is the vector of Coliolis and centrifugal forces, $\boldsymbol{f}$ is the vector consisting of the drag, gravitational and buoyant forces and moments, $\boldsymbol{u} = [\boldsymbol{f}_0^T,\ \boldsymbol{\tau}_0^T, \boldsymbol{\tau}_m^T]^T$, $\boldsymbol{f}_0$ and $\boldsymbol{\tau}_0$ are the force and torque vectors of vehicle, $\boldsymbol{\tau}_m$ is the joint torque vector of manipulator.

Furthermore, the relationship between $\boldsymbol{\omega}_*$ and $\dot{\boldsymbol{\psi}}_* = [\psi_{r_*},\ \psi_{p_*},\ \psi_{y_*}]^T$ $(* = 0,\ e)$ is described as

$$\boldsymbol{\omega}_* = \boldsymbol{S}_{\boldsymbol{\psi}_*}\dot{\boldsymbol{\psi}}_* \tag{8}$$

where

$$\boldsymbol{S}_{\boldsymbol{\psi}_*} = \begin{bmatrix} \cos\psi_{p_*}\cos\psi_{y_*} & -\sin\psi_{y_*} & 0 \\ \cos\psi_{p_*}\sin\psi_{y_*} & \cos\psi_{y_*} & 0 \\ \sin\psi_{p_*} & 0 & 1 \end{bmatrix}.$$

Thus the relationship between $\dot{\boldsymbol{q}}$ and $\dot{\boldsymbol{\zeta}}$ is described as

$$\dot{\boldsymbol{\zeta}} = \boldsymbol{S}_q\dot{\boldsymbol{q}} \tag{9}$$

where $\boldsymbol{S}_q = \text{blockdiag}\{\boldsymbol{S}_{v\boldsymbol{\psi}_0},\ \boldsymbol{E}_n\}$ and $\boldsymbol{S}_{v\boldsymbol{\psi}_*} = \text{blockdiag}\{\boldsymbol{E}_3,\ \boldsymbol{S}_{\boldsymbol{\psi}_*}\}$ $(* = 0,\ e)$.

3 Configuration of Control System

3.1 Digital RAC [7]

Differentiating Eqs. (1) and (2) with respect to time, the following equation can be obtained:

$$\boldsymbol{W}(t)\boldsymbol{\alpha}(t) = \boldsymbol{\beta}(t) + \boldsymbol{\gamma}(t) - \dot{\boldsymbol{W}}(t)\boldsymbol{\zeta}(t) \tag{10}$$

where

$$\boldsymbol{W} = \begin{bmatrix} \boldsymbol{C}+\boldsymbol{E}_6 & \boldsymbol{D} \\ \boldsymbol{A} & \boldsymbol{B} \end{bmatrix},\quad \boldsymbol{\alpha} = \dot{\boldsymbol{\zeta}},\quad \boldsymbol{\beta} = \begin{bmatrix} \dot{\boldsymbol{v}}_0 \\ \dot{\boldsymbol{v}}_e \end{bmatrix},\quad \gamma = \begin{bmatrix} \dot{\boldsymbol{s}} \\ \boldsymbol{0} \end{bmatrix}$$

and $\dot{\boldsymbol{s}}$ is the external force, including hydrodynamic force and thrust of the thruster which act on the base.

Discretizing Eq. (10) by a sampling period T, and applying $\boldsymbol{\beta}(k)$ and $\dot{\boldsymbol{W}}(k)$ to the backward Euler approximation, we have

$$\begin{aligned} \boldsymbol{W}(k)\boldsymbol{\alpha}(k-1) = \frac{1}{T}\,[&\boldsymbol{v}(k) - \boldsymbol{v}(k-1) + T\boldsymbol{\gamma}(k) \\ &- \{\boldsymbol{W}(k) - \boldsymbol{W}(k-1)\}\boldsymbol{\zeta}(k)] \end{aligned} \tag{11}$$

where $\boldsymbol{v} = [\boldsymbol{v}_0^T\ \boldsymbol{v}_e^T]^T$. Note that a computational time delay is introduced into Eq. (11), and the discrete time kT is abbreviated to k.

For Eq. (11), the desired acceleration and velocity are defined as follows:

$$\begin{aligned} \boldsymbol{\alpha}_d(k) = \frac{1}{T}\boldsymbol{W}^{\sharp}(k)\,[&\boldsymbol{v}_d(k+1) - \boldsymbol{v}_d(k) \\ &+ \boldsymbol{\Lambda}\boldsymbol{e}_v(k) + T\boldsymbol{\gamma}(k)], \end{aligned} \tag{12}$$

$$\boldsymbol{\nu}_d(k) = \frac{\boldsymbol{S}_{0e}}{T}\left\{\boldsymbol{x}_d(k) - \boldsymbol{x}_d(k-1) + \boldsymbol{\Gamma}\boldsymbol{e}_x(k-1)\right\} \tag{13}$$

where $\boldsymbol{e}_v(k) = \boldsymbol{v}_d(k) - \boldsymbol{v}(k)$, $\boldsymbol{e}_x(k) = \boldsymbol{x}_d(k) - \boldsymbol{x}(k)$, $\boldsymbol{S}_{0e} = \text{blockdiag}\{\boldsymbol{S}_{\nu\psi_0},\ \boldsymbol{S}_{\nu\psi_e}\}$, and $\boldsymbol{W}^{\sharp}$ is the pseudoinverse of $\boldsymbol{W}$, i.e. $\boldsymbol{W}^{\sharp} = \boldsymbol{W}^T(\boldsymbol{W}\boldsymbol{W}^T)^{-1}$, $\boldsymbol{x}_d$ is the desired value of $\boldsymbol{x} = [\boldsymbol{x}_0^T,\ \boldsymbol{x}_e^T]^T$, $\boldsymbol{\Lambda} = \text{diag}\{\lambda_i\}$ and $\boldsymbol{\Gamma} = \text{diag}\{\gamma_i\}$ $(i = 1, \cdots, 12)$ are the velocity and the position feedback gain matrices.

From Eqs. (11), (12) and (13), if λ_i and γ_i are selected to satisfy $0 < \lambda_i < 1$ and $0 < \gamma_i < 1$, respectively, and the convergence of the acceleration error, $\boldsymbol{e}_\alpha(k) = \boldsymbol{\alpha}_d(k) - \boldsymbol{\alpha}(k)$, tends to zero as k tends to infinity, then the convergence of $\boldsymbol{e}_\nu(k)$ and $\boldsymbol{e}_x(k)$ to zero as k tends to infinity can be ensured.

3.2 Disturbance compensation

From the viewpoint of underwater robot control, parameters and coefficients of hydrodynamic models are generally used as constant values that depends on the shape of the robots [6]. Here, to obtain higher control performance, the influence of hydrodynamic modeling error is treated as a disturbance and a disturbance compensation method is introduced.

The nominal model of $\boldsymbol{M}$ in Eq. (7) is defined as $\bar{\boldsymbol{M}}$. In $\bar{\boldsymbol{M}}$ the added mass and moment of inertia and the drag coefficient are constant. Furthermore, the following force is similarly defined:

$$\boldsymbol{f}_t = \bar{\boldsymbol{b}}_C(\boldsymbol{q},\ \boldsymbol{\zeta}) + \bar{\boldsymbol{f}} \tag{14}$$

where $\bar{\boldsymbol{b}}_C$ and $\bar{\boldsymbol{f}}$ are nominal of $\boldsymbol{b}_C$ and $\boldsymbol{f}$, respectively.

When the modeling error with respect to the hydrodynamic force regards the disturbance, the following estimated value can be obtained:

$$\hat{\boldsymbol{f}}_E = F(s)\left(\boldsymbol{u} - \bar{\boldsymbol{M}}\boldsymbol{\alpha}_d - \boldsymbol{f}_t\right) \tag{15}$$

where $F(s) = 1/(T_f s + 1)$ is a low pass filter with a time constant T_f.

Using Eqs. (14) and (15) we have the following control input of the robot:

$$\boldsymbol{u} = \bar{\boldsymbol{M}}\boldsymbol{\alpha}_d + \boldsymbol{f}_t + \hat{\boldsymbol{f}}_E \tag{16}$$

The configuration of the disturbance compensation is shown in Fig. 3(a). In Fig. 3(a) $\boldsymbol{f}_L$ is the external force. Furthermore, for the digital control system, Fig. 3(a) can be descretized to Fig. 3(b) [10] where $h = e^{-T_f/T}$.

4 Experiments

In this section, experiments of catching an object using the robot shown in Fig. 1 are done to verify the effectiveness of the proposed control method. Physical parameters of the robot are shown in Table 1.

Fig. 4 shows a configuration of an experimental system. A robot has a 2-DOF manipulator with joints that are actively rotated by torque-control-type

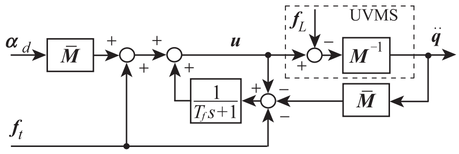

(a) analog

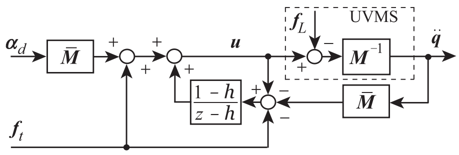

(b) digital

Fig. 3 Disturbance compensation

Table 1 Physical parameters of underwater robot

	Base	Link 1	Link 2
Mass [kg]	20.82	4.65	5.29
Moment of inertia [kg m^2]	1.33	0.075	0.26
Link length (x axis) [m]	0.2	0.35	0.64
Link length (z axis) [m]	0.81	-	-
Link width [m]	0.42	0.13	0.13
Added mass(x) [kg]	72.7	0.35	0.35
Added mass(z) [kg]	6.28	3.31	3.92
Added moment of inertia [kg m^2]	1.05	0.06	0.076
Drag coefficient(x)	1.2	0	0
Drag coefficient(z)	1.2	1.0	1.0

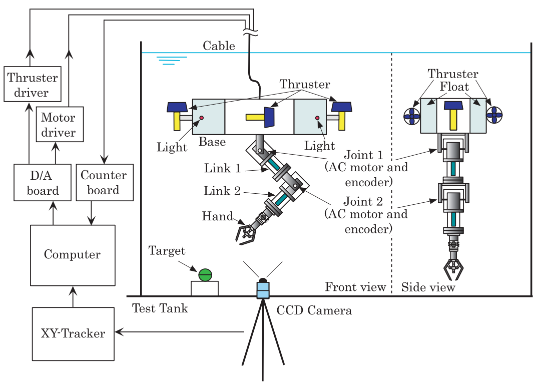

Fig. 4 Configuration of underwater robot system

servo actuators consisting of AC servo motors and incremental-type encoders. Four 40[W] thrusters are attached to the vertical and horizontal direction on the robot base to provide propulsion for controlling the position and attitude angle of the base.

Experiments are carried out under the following condition. The object is a ball that is 0.4[kg] in weight and 0.085[m] in diameter. The sampling period is $T = 1/60$[s], the time constant of the low-pass filter is $T_f = 1$[s] for the base and $T_f = 0.2$[s] for the manipulator. The feedback gains are $\mathbf{\Lambda} = \mathrm{diag}\{0.01,\ 0.01,\ 0.03,\ 0.02,\ 0.02\}$ and $\mathbf{\Gamma} = \mathrm{diag}\{0.02,\ 0.02,\ 0.06,\ 0.005,\ 0.005\}$. Furthermore, the initial relative joint angles are $\phi_0 = -\pi/2$[rad], $\phi_1 = \pi/3$[rad] and $\phi_2 = -7\pi/18$[rad].

The desired position and attitude of the robot base is set up to the initial values. On the other hand, the desired position of the end-effector is set up the following procedure:

Action 1: Moving along a straight path from the initial position to the target.

Action 2: Catching the object keeping the position.

Action 3: Lifting up the object along the straight path.

The experimental results without and with the disturbance compensation are shown in Figs. 5 and 6, respectively. From Fig. 5, we can be seen that the robot cannot lift up the object because of the change of the physical parameter of the manipulator including the object. On the other hand, from Fig. 6, it can be seen that the base position and attitude errors become small values and the manipulator can lift up the object by using the disturbance compensation. Therefore, the control performance can be improved by using the disturbance compensation.

5 Conclusion

In this paper, we proposed a disturbance compensation control method for UVMS based on the RAC method. The experimental results showed the effectiveness of the proposed method.

References

[1] H. Maheshi *et al.*, "A Coordinated Control of an Underwater Vehicle and Robotic Manipulator", *J. Robotic Systems*, Vol. 8, No. 3, pp. 339 – 370, 1991.

[2] T. W. McLain *et al.*, "Experiments in the Coordinated Control of an Underwater Arm/Vehicle System", *Autonomous Robots 3*, Kluwer Academic Publishers, pp. 213 – 232, 1996.

[3] G. Antonelli *et al.*, "Tracking Control for Underwater Vehicle-Manipulator Systems with Velocity Estimation", *IEEE J. Oceanic Eng.*, Vol. 25, No. 3, pp. 399 – 413, 2000.

[4] N. Sarkar and T. K. Podder, "Coordinated Motion Planning and Control of Autonomous Underwater Vehicle-Manipulator Systems Subject to Drag Optimization", *IEEE J. Oceanic Eng.*, Vol. 26, No. 2, pp. 228 – 239, 2001.

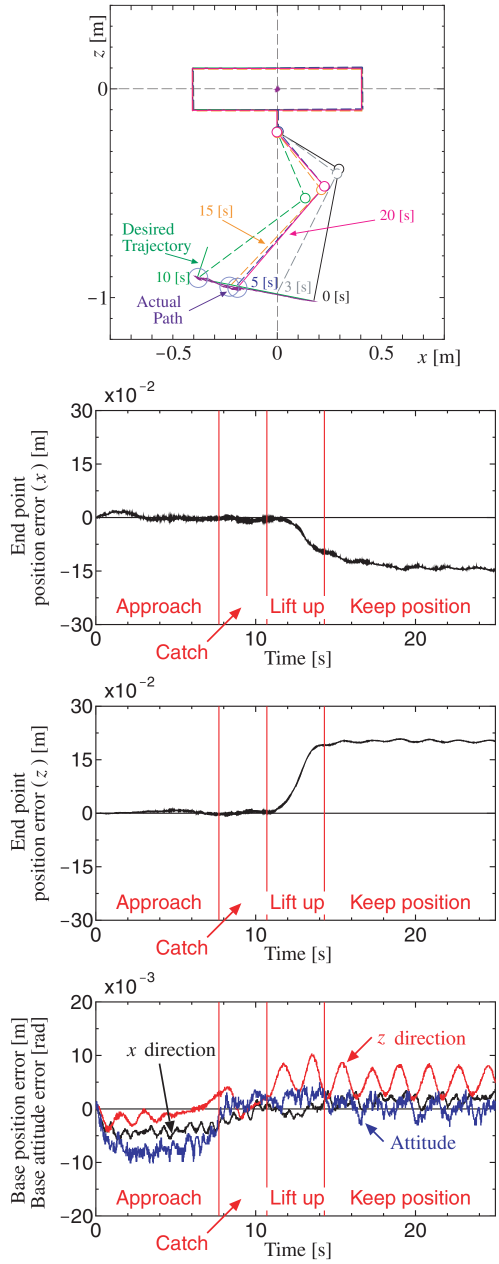

Fig. 5 Experimental result without compensation

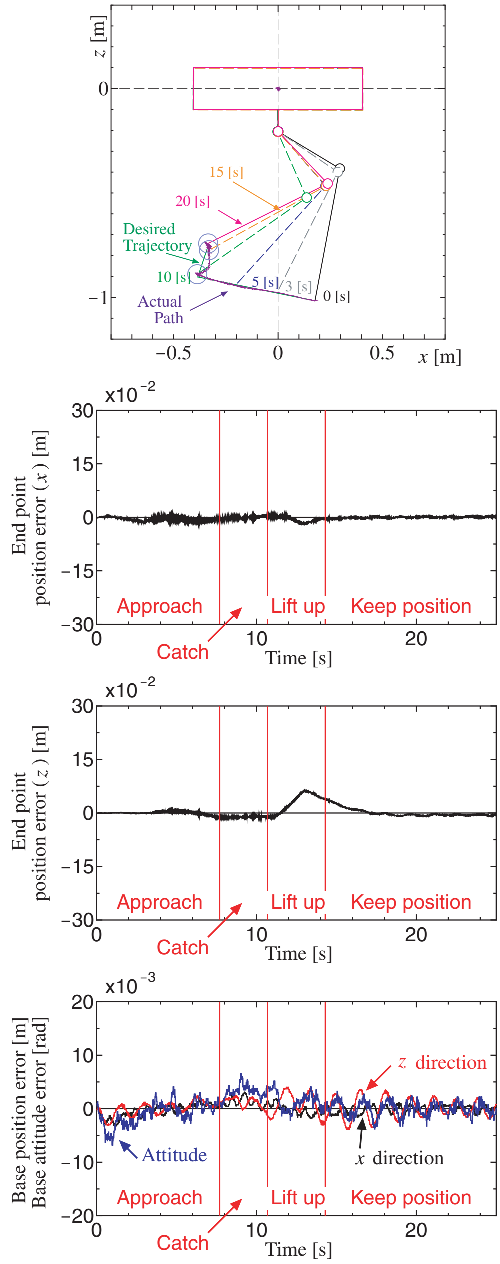

Fig. 6 Experimental result with compensation

[5] G. Antonelli, *Underwater Robotics*, Springer, pp. 1194–1206, 2003.
[6] T. I. Fossen, *Guidance and Control of Ocean Vehicles*, John Wiley & Sons, pp. 431–452, 1995.
[7] S. Sagara *et al.*, "Digital RAC for Underwater Vehicle-Manipulator Systems Considering Singular Configuration", *J. Artificial Life and Robotics*, Vol. 10, No. 2, pp. 106 – 111, 2006.
[8] T. Yatoh and S. Sagara, "Digital Type Disturbance Compensation Control of Underwater Vehicle-Manipulator Systems", *Proc. OCEANS'08 MTS/IEEE Kobe-Techno-Ocean'08*, Paper No. 071109-002, 2008.
[9] B. Lévesque and M. J. Richard, "Dynamic Analysis of a Manipulator in a Fluid Environment", *Int. J. Robot. Res.*, Vol. 13, No. 3, pp. 221 – 231, 1994.
[10] I. Godler, H. Honda and K. Ohnishi, "Design Guidelines for Disturbance Observer's Filter in Discrete Time", *Proc. 7th Int. Workshop on Advanced Motion Control*, pp. 390 – 395, 2002.

Development of an autonomous-drive personal robot "An object recognition system using image processing and an LRS"

Yasushi Kibe Eiji Hayashi
Department of Mechanical Information Science and Technology
Faculty of Computer Science and Systems Engineering, Kyushu Institute of Technology
680-4, Kawazu, Iizuka-City, Fukuoka Prefecture, Japan

Abstract: We are developing an autonomous personal robot able to perform practical tasks in a human environment based on information derived from camera images and an LRS (a laser range sensor). In the robot's adjustment to a human environment, it is very important that it be able to identify objects. If an object cannot be identified, the robot cannot hold or transport the object. For this reason, we have developed an object recognition system that allows a robot to identify an object and acquire exact location information about the object. This object recognition system is composed of both an object recognition processing part and a location information acquisition processing part. At first, the object recognition processing part searches for the object based on the shape and color of the object, image information that the user specifies. Next, the location information about the searched object is acquired by the location information acquisition processing part, which comes from LRS. Here we explain the algorithm used to acquire the location information of an object. In addition, as an evaluation of our system, we describe the results of an experiment in which location information for an object is acquired.

Keywords: Personal robot, monocular camera, Image processing, LRS, Object recognition

1. Introduction

In the near future, autonomous self-driving robots are expected to provide various services in human living environments. For this to occur, the robots will need to gain a grasp of the drive environment. Therefore, systems to provide environmental recognition based on image information are being widely studied. However, it is very difficult to determine the exact position of an object from image information only. For that reason, we are developing an autonomous personal robot able to perform practical tasks in a human environment based on information derived from camera images and an LRS (a laser range sensor), which is used to acquire two-dimensional distance information.

This object recognition system is composed an object recognition processing part and a location information acquisition processing part, both of which are based on a sensor using a monocular camera and an LRS. An object is identified by using range information obtained from LRS in addition to the processing of the image information provided by the camera. At first, the object recognition processing part searches for the object that a user specified in terms of its shape and color, characteristics based on image information from the monocular camera. Next, location information concerning the searched object is acquired by the location information acquisition processing part, which uses LRS. The range information which LRS obtains is converted from its irradiation point and measurement distance into three dimensional coordinates. However, the LRS measurement regarding the object position cannot be understood only from the data. Therefore, the measurement part of LRS is matched to the camera image, and whether it is correct data about the object's position is then judged. In addition, this system acquires the location information from two places within the object area, thus preventing false detection. The robot can do a holding operation for the object according to this object location information.

2. System for robot

Our robot has a drive mechanism consisting of two front and two back wheels. The front wheels are attached to a motor that operates the wheels on either side independently, while the back wheels function as castor wheels. This method has the advantage of allowing a small turning radius. In addition, to acquire image information, a single CCD camera with approximately 300,000 pixels and an LRS, to acquire range information, are installed on the head of the robot and can be rotated to all sides by two motors. DC servo motors are used for the robot's drive mechanism, and position and speed control are achieved by the control system of the drive mechanism. The robot also has two arms and hands equipped with sensors, which enable it to respond to the various demands of humans. Finally, an installed wireless LAN can provide remote control for humans. All devices are controlled by a PC, and lead batteries supply the robot's electric power.

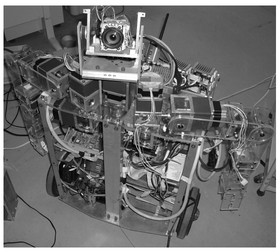

Fig. 1 Our developed robot

3. Object-recognition system

3.1 Outline of the system

We developed an object-recognition system for robots that can acquire the object position with image information captured by a monocular CCD camera and range information obtained by LRS. This system can acquire the object position on the assumption, for example, that the object is put on a desk. The system then acquires the location information of the object by using LRS with the recognized object.

3.2 Method for object-recognition

In this section, we explain the method for object-recognition. The flow for the object-recognition is shown in Fig. 2.

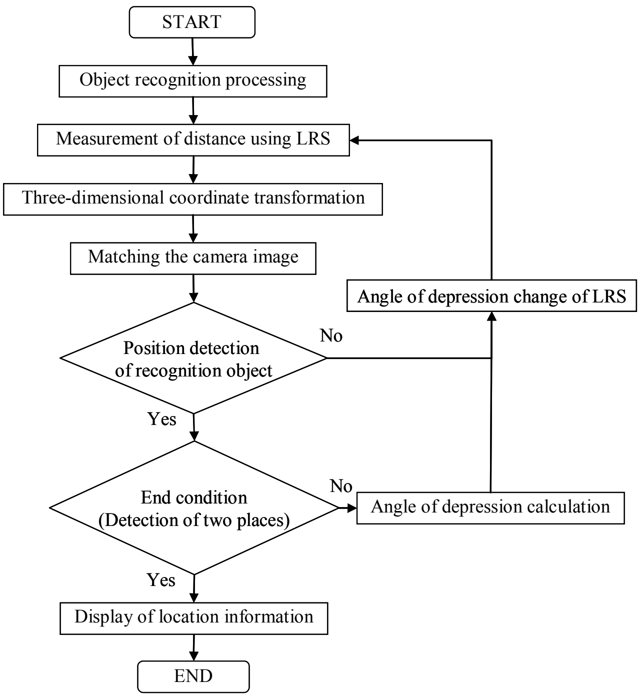

Fig. 2 System flow

Ⅰ. Object recognition processing part

This processing part can search for objects with image information captured by a monocular CCD camera. The system then searches for the object with the shape and color of the object registered by the database. This processing part notes the shape and color of the object and then step by step narrows down the objects. Fig. 3 shows an example of the results of the object-recognition processing.

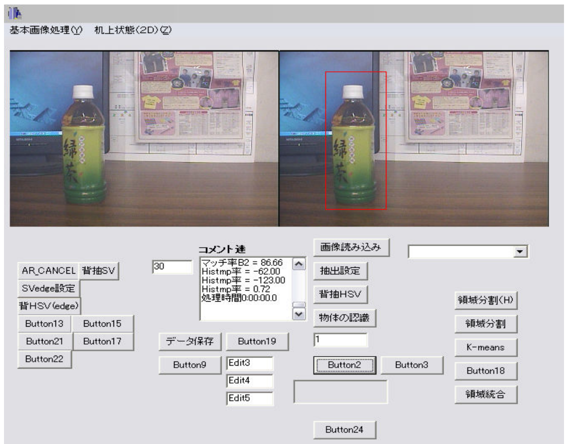

Fig. 3 Object-recognition processing

Ⅱ. Measurement of distance using an LRS

LRS is a noncontact laser measurement system and is made by HOKUYO AUTOMATIC CO., Ltd., for use in this study. The maximum detection distance of this LRS is 4m. Moreover, a horizontal plane space is scanned by 270° at intervals of about 0.36° (360°/1024), and the distance and the direction of the detection body are detected. However, this LRS requires the time of 100msec for a single scanning. Therefore, a reduction in the distance acquisition time was enabled by using LRS only for the material part recognized with the monocular camera in this study. Fig. 4 shows the externals of the LRS.

Fig. 4 Scanning laser range sensor

LRS acquires range information on the object recognized in the object recognition processing. LRS is fixed to the robot head, and moves with the camera.

Fig. 5 shows the situation in which the range information is acquired.

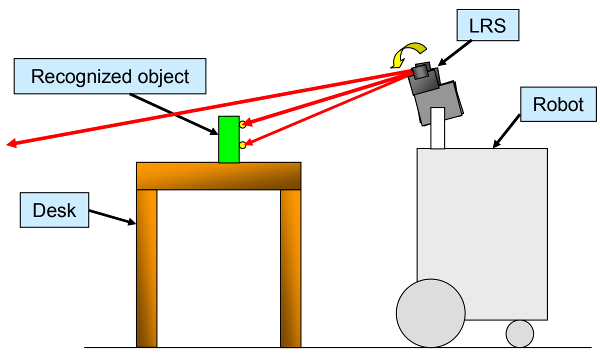

Fig. 5 Position information acquisition situation

The Fifteenth International Symposium on Artificial Life and Robotics 2010 (AROB 15th '10),
B-Con Plaza, Beppu,Oita, Japan, February 4-6, 2010

Ⅲ. Three-dimensional coordinate transformation

The range data of LRS is range information from the irradiation point to the measurement point of LRS. Therefore, this range data is converted into a three-dimensional coordinate. This conversion is derived in the provided data on the distance data and the horizontal and perpendicular angles.

Ⅳ. Matching the camera image

The system successfully matched the LRS data to the camera image by integrating the camera image with the LRS data. First, a perspective projection face with the same aspect ratio as a camera image was set. The system converted the data into three-dimensional coordinates, as explained above. Then the system matched the perspective projection face with a camera image. Therefore, the LRS data was matched with the camera image. Fig. 6 shows an example of matching the LRS data to the camera image.

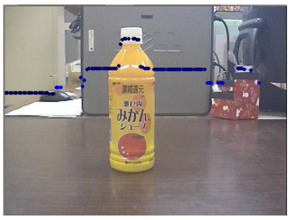

Fig. 6 Matching the camera image

Ⅴ. Position detection of recognition object

Whether the LRS data describes the location information of the object is judged. This involves determining which position of the camera image, provides the measurement point for LRS to detect the object. It can be determined that the object can be measured if the object area recognized in the object recognition processing corresponds to the image coordinates of the LRS measurement point. This system acquires a three-dimensional coordinate in the vicinity of the center of the object as location information when the LRS measurement point is in the part that is in the below 60% of the object. However, when the LRS measurement point is not in this area, LRS must be inclined. The location information acquisition judgment is repeated with the distance information acquisition using LRS through a three-dimensional coordinate transformation and matching to the camera image. In addition, to prevent false detection and to provide good, accurate detection, data acquisition is done in two places in the area (the upper part and the lower part). Fig. 7 shows an example in which location information acquisition is done for the first time and where the measurement point of LRS changes the angle of depression of LRS because it cannot acquire the location information at the time of points A and B. In this case, however, the location information could be acquired at point C. Fig. 9 shows an example of an inclining LRS after Fig. 8 where the location information was acquired a second time at point D.

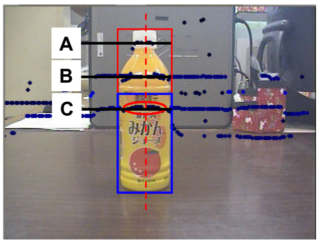

Fig. 7 First location information acquisition

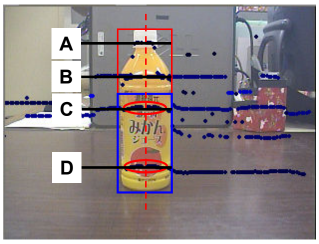

Fig. 8 Second location information acquisition

The location information in two places in the area (the upper part and the lower part) could be acquired in this processing. Fig. 9 shows an example where the LRS data of the image is acquired at two places.

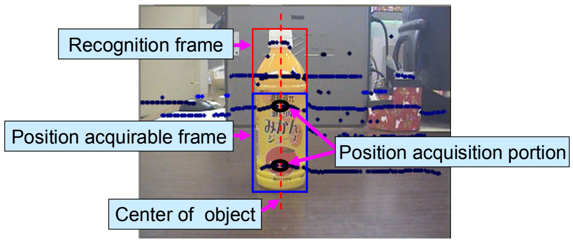

Fig. 9 Object location information acquisition

Ⅵ. Angle of depression calculation method

The part where the system seeks to acquire location information of the object is at two places in the area (the upper part and the lower part). After the first location information is acquired in the upper part of the area, the angle of depression of LRS is calculated according to this information. If the distance of the object and the robot can be found, the angle of depression can be calculated from the image information by a geometrical calculation.

Ⅶ. Display of location information

When the location information of the recognition object in two places can be acquired through acquisition of the range data using LRS, the three-dimensional coordinate transformation, and the determination of matching between the camera image and the location information, final location information on the object is displayed in two places. Because it is preferable that the acquired positional data reflect the exact position of the object, a part in the center of the object in two places is acquired as object location information. The calculation of final location information for the object involves computing the average of the location information in two places for x and z coordinates. Y coordinates use the first value acquired in the upper part of the object by LRS because the purpose of this system is to hold the object. A part near the center of the object was displayed as the y coordinate value.

4. Experiment

4.1 Method of experiment

We performed the following experiment to evaluate the performance of this system in acquiring the location information of an object for which it searches by object recognition processing. Two kinds of objects were put on a desk, and the actual measurement value was compared with the acquisition value for various positions. As a result, an error caused by the acquisition of the location information was measured. The angle of depression of the camera was set at 10°. Figs. 10 and 11 show the experimental environment when the object were a PET bottle and a can, respectively. The experimental location was a placement on the desk in the laboratory that has a single color. It was measured 12 times in each measurement place.

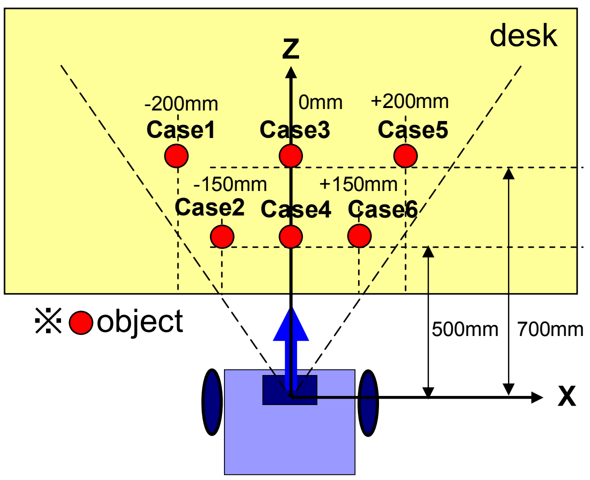

Fig. 10 Experiment environment of PET bottle

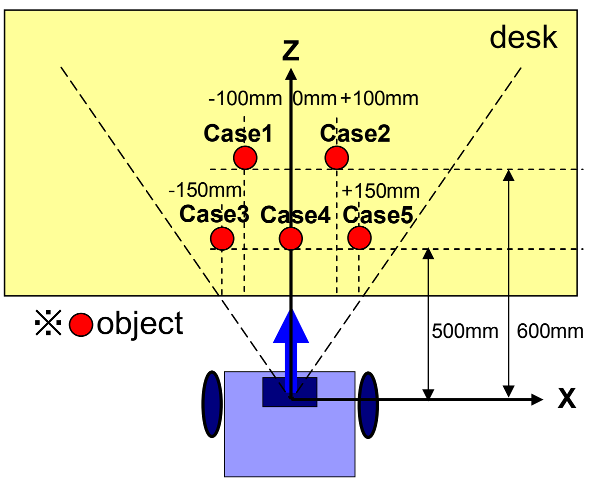

Fig. 11 Experiment environment of can

4.2 Result of experiment

Table 1 shows an average error and the maximum error by the actual measurement value and the acquisition value at each object position when the object is a PET bottle. Table 2 shows the same when the object is a can.

Table 1 Location information of PET bottle

	Actual measurement [mm]			Average error (Maximum error) [mm]		
	X	Y	Z	X	Y	Z
Case1	−200	793	700	1.583 (2.0)	0.583 (1.0)	0.583 (2.0)
Case2	−150	800	500	0.667 (2.0)	1.167 (2.0)	1.167 (2.0)
Case3	0	793	700	0.917 (2.0)	0.167 (1.0)	1.500 (3.0)
Case4	0	800	500	0.500 (3.0)	0.250 (1.0)	1.000 (3.0)
Case5	200	793	700	1.250 (2.0)	0.417 (1.0)	1.250 (2.0)
Case6	150	800	500	0.417 (1.0)	0.750 (2.0)	0.917 (3.0)

Table 2 Location information of can

	Actual measurement [mm]			Average error (Maximum error) [mm]		
	X	Y	Z	X	Y	Z
Case1	−100	742	600	1.250 (2.0)	0.417 (1.0)	0.750 (2.0)
Case2	100	742	600	0.917 (1.0)	0.750 (1.0)	1.250 (3.0)
Case3	−150	753	500	1.500 (3.0)	1.167 (2.0)	1.333 (3.0)
Case4	0	753	500	0.167 (1.0)	0.417 (1.0)	0.833 (2.0)
Case5	150	753	500	0.750 (2.0)	0.417 (1.0)	1.083 (2.0)

For both objects, we could confirm that there was no problem in the accuracy of the acquired location information, even when the object was at each position. Moreover, the result of measurements for the two kinds of objects showed the maximum error of each coordinate was within 3mm, and the error of the distance to the object was less than 1% . It is thought that this result is sufficient considering that the holding operation of the object was done based on acquired information.

5. Conclusions

We proposed a system for acquiring exact location information of an object by using image processing and LRS. This object recognition system acquires the location information of a recognition object by integrating range data obtained by LRS and image processing results recognized by the shape and color of the object. In an assessment experiment with the system, the object location information with very good accuracy could be acquired even when the can or a small object was recognized by the object recognition processing.

Our next subject of study will be the development of a program to acquire object location in formations other than those of a recognition object. The reason is that the final purpose of our robot development involves developing the best way for it to hold an object.

Path planning algorithm using the values clustered by k-means

Won-Seok Kang[1], Seung-Hyun Lee, Berdakh Abibullaev, Jin-Wook Kim and Jinung An

DGIST, Room 401, 4rd Floor, Daegu Technopark Venture 1 Plant, 75 Gongdanbuk2gil, Dalseo-gu, Daegu, 704-230, Korea

(Tel : 82-53-430-8500; Fax : 82-53-430-8476)

(wskang@dgist.ac.kr[1])

Abstract: Path planning has been studied focusing on finding the shortest paths or smallest movements. The previous methods, however, are not suitable for stable movements on real environments in which various dynamic obstacles exist. In this paper, we suggest a path planning algorithm that makes the movement of an autonomous robot easier in a dynamic environment. Our focus is based on finding optimal movements for mobile robot to keep going on a stable situation but not on finding shortest paths or smallest movements. The proposed algorithm is based on GA and uses k-means cluster analysis algorithm to recognize the much more information of obstacles distribution in real-life space. Simulation results confirmed to have better performance and stability of the proposed algorithm. In order to validate our results, we compared with a previous algorithm based on grid maps-based algorithm for static obstacles and dynamic obstacles environment.

Keywords: Path Planning, GA, Clustering and static/dynamic obstacles

I. INTRODUCTION

Path planning is a navigation problem that mobile robots should find optimal movements to reach the destination position from the start point. It has been one of the complex problems on NP-Complete or NP-Hard domains that must have been solved for autonomous robots. Many researchers have studied for decades to construct robots that are capable of moving around autonomously.

Path planning is divided into the hierarchical maps-based and the grid maps-based[1]. The hierarchical maps-based method has an advantage of faster path planning because robot has simplified map data structures and can easily understand them. Thereupon the robot can't recognize the detailed information in working environments. On the other hand, the grid maps-based may have the detailed information with the grid resolution on entire map, however the problem is the usage of much operating memory. In this paper, we focused on the grid-maps based approach to represent much more information that is helpful to autonomous robots in a dynamic real environment. The method is based on such a A*[1], potential field[1] and the Genetic Algorithm(GA).

Recently, many autonomous robot researches have approached on evolutionary computing by employing GA, ACS (Ant Colony System) to solve the heuristic optimal problem for path planning. The researches based on evolutionary computing have mainly used the GA[3][4][5][6].

In [3], it was suggested that a path planning operated with the chromosome structure have sufficient information, such as movement direction and so on. Though, its drawback of static chromosome size is that it has not been applied in dynamic space information. In [5][6], authors suggested the knowledge-based path planning that the chromosome of path routes could be dynamically resizable and that could be operated with the modified GA operators with the additional operators for faster processing than traditional GA. There are no approaches for various dynamic obstacles. Also, there is limitation for the real-life space application. In other study [7][8], it was suggested that ACSs can be applied to find shortest paths using pheromone that ants lay on for moving paths. They also focused on finding shortest paths and with no consideration of dynamic obstacles like Fig. 1.

Fig.1. Motivation of this paper

As it was mentioned above, most of the researches still focused on finding shortest paths or smallest movements as be shown in Fig. 1. Besides the previous methods may be limited for mobile robots to avoid the various dynamic obstacles and make a stable path route in real-life space.

Clustering method is one of data-mining techniques. Clustering is a set of methodologies for automatic classification of samples into a number of groups using a measure of association, so that the samples in one group are similar and samples belonging to different groups are not similar. Owing to the features of clustering, if it is adopted into path planning, it can be utilized for recognizing a workspace of a mobile robot while it is operating. It also reduces searching space and is helpful to find out optimal paths with more detailed information[2].

We suggest a path planning algorithm that makes the movement of an autonomous robot easier in a dynamic environment. We focus on finding optimal movements for mobile robot to keep going, on a stable situation but not on finding shortest paths or smallest movements. The proposed algorithm is based on GA and uses k-means of cluster analysis to recognize the much more information of obstacles distribution in real-life space. Simulation results confirmed to have better performance and stability of the proposed algorithm. The obtained results is validated and compared with previously proposed algorithms which are based on grid maps algorithm for static obstacles and dynamic obstacles environment.

The rest of this paper is organized as follows: Section 2 describes an overview of k-means as one of clustering analysis and building clustered information, included into the chromosome structure, for the proposed algorithm. We explain the proposed path planning algorithm in Section 3. Section 4 presents the experimental results for static and dynamic environment that is similar to the layout of official room to show efficiency of the proposed algorithm. Finally, section 5 concludes the paper.

II. MAP REPRESENTATION

In this section, we describe the k-means as non-hierarchical clustering one to make groups using similarity among scattered data. We also see how one can build grouping information, included into the chromosome structure, when computed into the level of GA processing. Subsection A briefly presents the k-means algorithm. Subsection B presents how to build combined groups with the same similarity.

A. *k-means clustering*

k-means (MacQueen, 1967) is one of the simplest unsupervised learning algorithms that solve the well-known clustering problem. The procedure follows a simple and easy way to classify a given data set through a certain number of clusters (assume k clusters) fixed a priori. The main idea is to define k centroids, one for each cluster **Error! Reference source not found.**. As an example the basic algorithm is as follows:

Set $D = \{ (x_i, y_i) \mid x_i \in N, y_i \in N\}$

Step 1) For k point, Select the initial centroid point(x,y) of Set D randomly and set a new group(k) where k is a random value.

Step 2) For all unsigned point, calculate the distance between one point and all k's centroid point and assign one point into the closest centroid group(any k). After assigned, recalculate the centroid point for any k .

Step 3) Iterate the Step 2 until not assigned newly any one point into other groups

B. *Map representation using k-means*

Fig. 2 shows the map where a mobile robot moves around. As you see Fig. 2, we divide the map into the grid unit cells of *X* x *Y* matrix. Let C_{xy} be the set of the cells. Also C_{xy} includes various values such as the points of Cells, the center point of Cells, the obstacles-occupied density of the grid unit and the mean density of the *k* centroid for the grid unit. The detailed attributes is shown in table I. Let C^{d}_{xy} be the density of the grid cell and $C^{k\_centroid\_d}_{k}$ be the mean density of the *k* centroid for the grid cell. Then we can describe these equations as below:

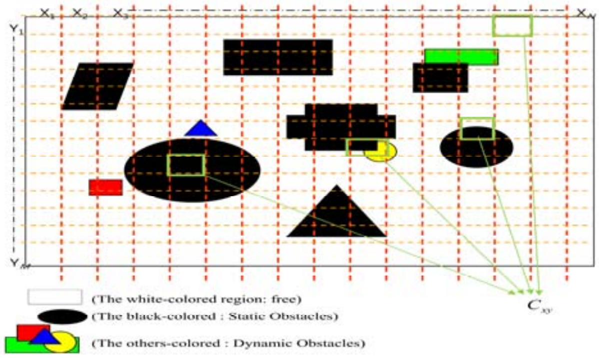

Fig.2. Grid-based representation for a work-space

$$C^{d}_{xy} = \frac{Number\ of\ \text{(the bright colored pixels)}}{Number\ of\ \text{(all of pixels)}}$$

, where *x* and *y* is index value of cells.

$$\mathrm{C}_k^{k\_centroid\_d} = \frac{\text{Sum of the density of all } \mathrm{C}_{xy}}{Count\ of \text{ all } \mathrm{C}_{xy} \text{ allocateed in } k \text{ centorid)}}$$

, where k is a constant index of centroids.

First, we calculate all C_{xy}^{d} for each cell to represent a map using k-means algorithm and then $\mathrm{C}_{k}^{k\_centroid\_d}$ is calculated by using k-means algorithm. The calculated clustering **values** hold on the constructed data structure until all path planning procedures have been completed.

Fig. 3 shows the represented maps using k-means algorithm with the distance vector equation (1) which is modified from Euclidean distance.

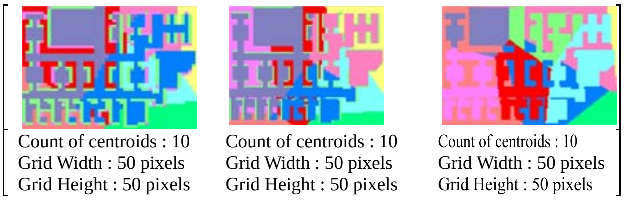

Fig. 3. Examples of represented map using *k*-means

The Function is defined as

$$\mathrm{D}(\mathrm{C}_i, \mathrm{C}_j) = |\mathrm{C}_i^d - \mathrm{C}_j^d| + \frac{\sqrt{(C_{i,x} - C_{j,x}) + (C_{i,y} - C_{j,y})}}{\beta} \quad \text{-------- (1)}$$

where β is a constant to scale the distance value down.

III. Path Planning Algorithm

A. *Outline of whole processing procedure*

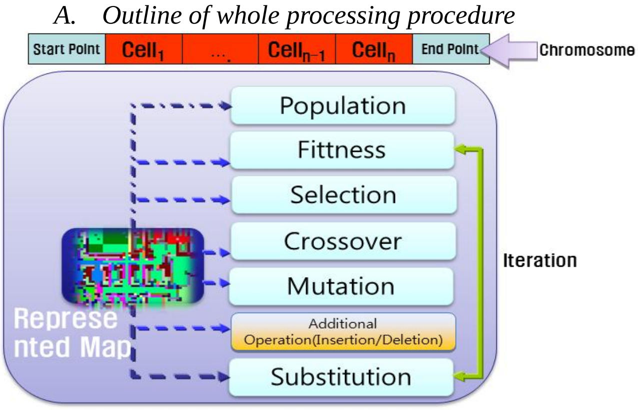

Fig.4. Whole scheme of the proposed algorithm

The entire scheme of the proposed algorithm is given in Fig. 4. The distribution information of static/dynamic obstacles is constructed as the initial step. In the next step, some random populations are generated subsequently fitness procedure is processed using the equation to find the optimal paths. The equation is explained in subsection C. In the Selection Operation, we use the tournament method proposed in the previous studies. In the next step, The Crossover Operation is processed to make better population generations than the pre-generated. The Mutation Operation is achieved to explore the low-rate searching spaces. The Additional Operations, which are the Insertion and the Deletion, are processed to smooth the chromosome and to cut them into the cycled paths off. In the final step, the proposed algorithm substitutes the old generation populations with the new generations which is done by this paper's GA. The scheme iterates until the best optimal paths are found out.

B. *Chromosome*

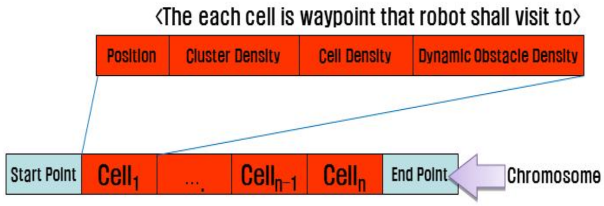

Fig.5. Chromosome structure

As mentioned above, each chromosome consists of various fields like Fig. 5. The first's cells mean a start location and the last's cells mean a destination location. The remained cells are random location to explore the optimal paths. Each cell of a chromosome is composed by selection, mutation, insertion and deletion operation and it has the information of cell's map point, density of static/dynamic obstacles of k-means index value and its mean density.

C. *Fitness Operation*

Fitness function which is defined in conventional GA is an important thing to find the best optimal path. In this paper, we made a fitness function as in the equation (2) in order to calculate cluster information to apply to GA. The fitness function is defined as

$$\left(\sum_{i=1}^{ch\_s} FC_i\right) \times \alpha + \sum_{i=0}^{ch\_s-1} E(C_i, C_{i+1})$$
$$+ \sum_{i=0}^{ch\_s-1} \left[|C_i^{k\_means\_d} - C_{i+1}^{k\_means\_d}| + |C_i^d - C_{i+1}^d| + \frac{\sqrt{(C_{i,x}^d - C_{i+1,x}^d)^2 + (C_{i,y}^d - C_{i+1,y}^d)^2}}{\beta} \right] \quad \text{------------ (2)}$$

Where *ch_s* is array size of the chromosome, *k_mean_d* is mean value of obstacles density's distribution on a cluster, α is a constant value to scale fitness values up with infeasible paths, *FC* is the number of infeasible paths, β is a constant to scale fitness values down.

IV. Experimental Results

To confirm the better performance and stability of the proposed algorithm, we compared with a previously studied methods based on grid maps-based algorithm for static obstacles as well as for dynamic obstacles environment. The algorithm has been developed using CxImage Open Library as the image processing tool and Visual Studio 2008 as the development toolkit on Windows system family.

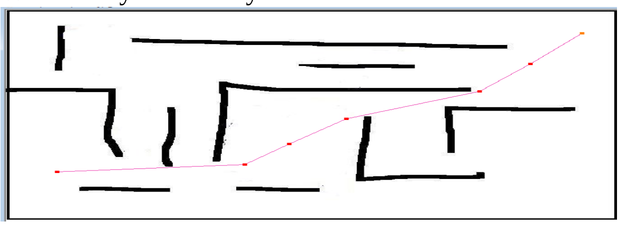

(a) Map resolution : 674x461x24b, Path finding result without dynamic obstacles

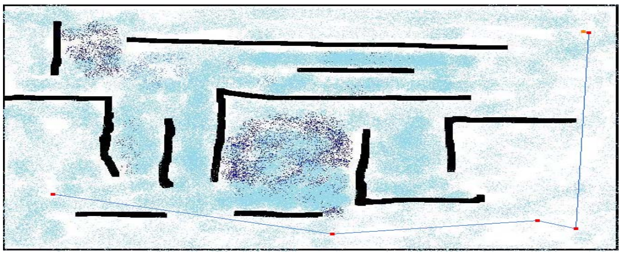

(b) Map resolution : 674x461x24b, Path finding result with distributions of dynamic obstacles

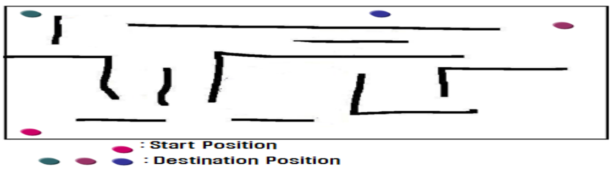

(c) The pink-colored point : start position and the violet-colored point : destination position

Fig.6. Comparison of path planning results between non-dynamic obstacles space and dynamic obstacles space

Fig. 6 shows the comparative result when the proposed algorithm is processed with and without dynamic obstacles. The results demonstrate that the optimal and stable path can be achieved in the environment with various dynamic obstacles. Certainly, one can confirm that the proposed algorithm has better performance than the previous grid-based approach(A*) in the space with static obstacles as Fig.7 and Fig. 8 show.

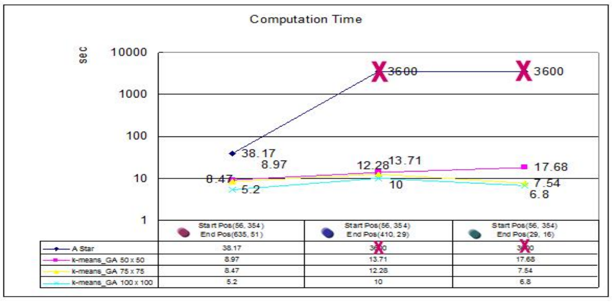

Fig.7. Comparison of processing speed with A^*

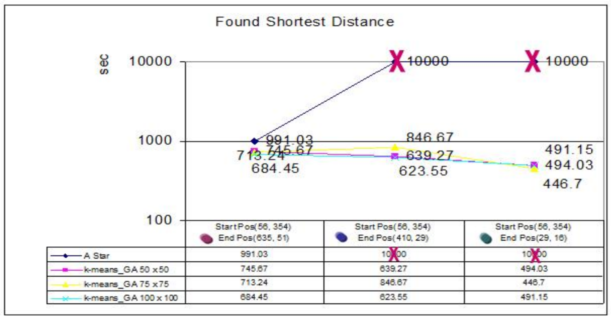

Fig.8. Comparison of found shotest path with A^*

V. CONCLUSION

As the result of simulation, the proposed algorithm produces to process the optimal path by the order of routes having much less obstacles distribution with the clustered information when is compared with the previous grid-based approach.

ACKNOWLEDGEMENTS

This work was supported by the Daegu Gyeongbuk Institute of Science and Technology(DGIST) and funded by Ministry of Education, Science and Technology(MEST).

REFERENCES

[1] ROBIN R. MURPHY, "Introduction to AI Robotics", The MIT Press.
[2] Mehmed Kantardzic, "Data Mining: Concepts, Models, Methods, and Algorithms", ISBN:0471228524, John Wiley & Sons, 2003.
[3] Kamran H. Sedighi, Kaveh Ashenayi, Theodore W. Manikas, et al., "Autonomous Local Path Planning for a Mobile Robot Using a Genetic Algorithm", pp.1338~1345, IEEE, 2004.
[4] O. Castillo and L. Trujillo, "MULTIPLE OBJECTIVE OPTIMIZATION GENETIC ALGORITHMS FOR PATH PLANNING IN AUTOMOUS MOBILE ROBOTS", pp.48~63, International Journal of Computers, Systems and Signals, Vol.6, No.1, 2005.
[5] Yanrong Hu and et al, "A Knowledge Based Genetic Algorithm for Path Planning in Unstructured Mobile Robot Environments", pp.767~772, ICRB 2004, IEEE.
[6] Xuanzi Hu and Cunxi Xie, "Niche Genetic Algorithm for Robot Path Planning", ICNC 2007, IEEE.
[7] Marco Dorigo and Luca Maria Gambardella, "Ant Colony System: A Cooperative Learning Approach to the Traveling Salesman Problem", IEEE Trans. On Evolutionary Computation, Vol.1,No.1,April, 1997, pp.53-66.
[8] Ying-Tung Hsiao, Cheng-Long Chuang and Cheng-Chih Chien, "Ant Colony Optimization for Best Path Planning", International Symposium on Communications and Information Technologies 2004.

The Fifteenth International Symposium on Artificial Life and Robotics 2010 (AROB 15th '10),
B-Con Plaza, Beppu,Oita, Japan, February 4-6, 2010

Homing Navigation with Image Matching Approach

Jiwon Lee and DaeEun Kim

Biological Cybernetics, School of Electrical & Electronic Engineering
Yonsei University
Seoul, 120-749, Corea (South Korea)
(Tel : 82-2-2123-5879; Fax : 82-2-393-4010)
(E-mail: daeeun@yonsei.ac.kr)

Abstract: Many studies have tried to develop more accurate and highly sophisticate vision-based navigation algorithm. Simple and efficient navigation has been considered to save computation time and spatial memory. Bio-inspired navigation methods follow the navigation model of insects or animals, and it is believed that their mechanism use the image matching between the home snapshot image and the current snapshot image to determine the homing direction without any other information. This kind of simple navigation approach can be applied to robotic navigation. In this paper, we show the potential of the image matching approach for homing navigation

Keywords: visual navigation, image matching, bio-inspired robotics

I. INTRODUCTION

Extensive researches have been conducted on visual navigation. Many studies have tried to develop more accurate and highly sophisticate vision-based navigation algorithm. Yet simple and efficient algorithms are required for real application of navigation. Bio-inspired approaches to model animal behaviours are plausible ideas to find efficient navigation methods.

Many animals and insects are known to be able to return home by using the vision-based navigation system. Many animals including gerbils, hamsters, rats and pigeons use landmarks to find the location of their nest place.

The honeybee is a representative insect to use landmark navigation. Anderson argued that honeybees do not recognize the entire environment in great details, but use the configuration of surrounding objects roughly by dividing the visual environment into some sectors [1]. It means that honeybees show the visual environment as an overall configuration of landmarks. Anderson suggested a distribution model based on the concept of sectors to support the real experiments of honeybees.

According to the landmark navigation proposed by Cartwright and Collett [2], honeybees remember a snapshot near the nest and compare the current image with the home snapshot. Comparing the two images, the insect decides the homeward direction at any spot and ultimately approaches home. This image matching model becomes a basis of many insect navigation algorithms afterwards. Among them, we focus on the image matching algorithm established by Franz et al. [3].
They use the equidistance assumption that all landmarks are in the same distance and calculate the estimation of image displacements for every possible movement (direction). The image displacements produce a new snapshot image from the current image. The homing agent can choose the direction with the best matching score between the home snapshot and estimated snapshot. Franz et al. showed that the homing strategy is adequate for the robot navigation [3,4].

Standing on the basis of snapshot model, we have proposed a new method for robotic home navigation which is named *Sector-based image matching method* [5]. The method use the estimation process shown in Franz et al.'s approach with the equidistance assumption and the division of the image found in Anderson's model. The landmark position and the number of landmarks in a given sector can be considered as the image information and so pixel-by-pixel comparison in the Franz et al.'s approach is replaced by sector-by-sector comparison.

We compared the performance with Franz's image matching method. It has shown hat it is more efficient to return home in some regions than the image matching method in computer simulation. In this paper, we show experiments of a robotic navigation through the sector-based matching method, and discussed the performance and application for a robot.

II. METHOD

1. Pixel-based Image Matching

According to Franz et al.'s method, the visual information about surroundings is represented as a binary array of image. The binary 1 indicates the existence of landmark in a specific angle and binary 0 no landmark. We assume that the visual environment is taken as an omnidirectional camera information. A continuous part of binary values is a measure of the size of the landmark. Franz et al. suggested an estimation process for the next moving directions. For each directon, the information of surrounding landmarks can be converted to a new array of binary values – see Figure 1, if we know the location of landmarks. Here, they assume that all landmarks are in the same distance, which simplifies the calculation of the new image.

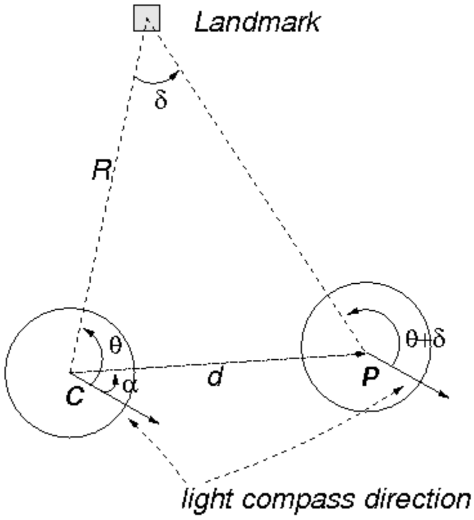

Figure 1. Visual displacements with a landmark (reprinted from [6])

The estimation image for each moving direction forms a virtual image from the current snapshot image. The image is compared with the snapshot image near the nest. The home snapshot is also recorded as a binary array of image. Here, the dot product between the two images to be compared produces the image matching level. The higher level means closer to the nest. If an agent chooses the moving direction with the best matching level, it has more chance to approach home. Surprisingly, this simple mechanism works well for the environment with surrounding landmarks.

2. Sector-based Image Matching

The concept of sector information is an index about how to recognize the visual environment. The whole image is divided into several sectors. For instance, if a robot recognizes the visual environment with five sectors, the range of each sector is 72 degrees of angular space in visual image. Each sector keeps the information of the landmarks which belong to the sector, for example, the number of landmarks and the landmark sizes. Visual environment is not recorded as pixel information, but as sector information.

The sector-based encoding uses two components, occupancy and landmark size difference. The occupancy is to check whether at least one landmark exists in each sector or does not. If a landmark is in a sector, the occupancy of the sector is set to 1 and otherwise, set to 0. The landmark size difference is how much the apparent landmark sizes are different at the nest and at an arbitrary point. It is equivalent to the distance difference of landmarks. The robot does not have to know the accurate size of individual landmarks as long as it knows how much a sector is filled with landmarks. If there are several landmarks in a sector, then the average size should be considered by checking how many landmarks are found and how much the landmarks fill the sector space.

Here, we also use the equidistance assumption that all landmarks have the same distances from each robot, the robot can easily calculate the distance from the landmark according to its size.

The matching score is calculated with the two factors, the occupancy and landmark size difference between the two snapshot images. One image is from the nest place and the other is from the current robot position.

Matching score = occupancy * (1-α*size difference)

where α is the scaling factor to normalize the size difference into [0,1]. The higher matching score indicates the more similar images.

Considering both the occupancy and the size difference in the matching score allows the robot to recognize its relative position with respect to its surroundings.

III. EXPERIMENTS

We tested the sector-based approach with simulation and robotic experiments. For a mobile robot, we used the Roomba cleaning robot and a laptop computer was mounted on the robot to control the motor actions. Also an omnidirectional camera (designed by Seunghun Baek in our lab) consisting of webcam and a metallic sphere was stacked on the top of the robot to take omnidirectional snapshot images.

We used red-colored cylindrical objects for landmarks. The omnidirectional image is converted into the panoramic image and the robotic system initially processes to find red-colored landmarks with a given color threshold, and the angular resolution is 1 degree and so the red-colored side is marked 1 in the binary array with a size of 360.

We pick up a set of test points in an arena and calculate the home vectors based on the sector-based approach. Without compass, the system needs to check all possible head directions as well as the moving directions. To reduce the time complexity, we use 72 head directions and 72 moving directions. The number of moving directions is related to the angular resolution of possible movements for the best matching score. We assume that all landmarks are in the same distance of 100 cm. The moving distance from the current position, the number of head directions, and the number of moving directions can vary. Two different numbers of head directions, 6 and 36 were tested. The moving distance is 10 cm, and 72 moving directions. Here, we used four sectors for the whole image. The result is shown in Figure 2. The number of head directions influences the vector map. More possible head directions have better performance for homing navigation.

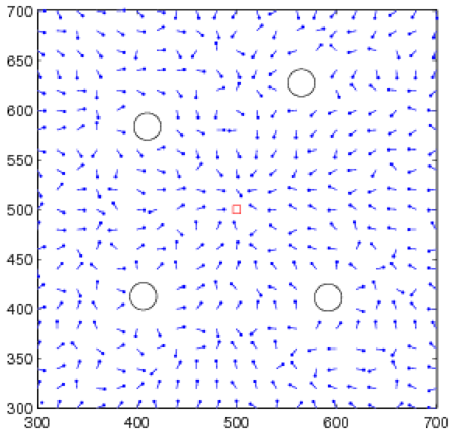

(a)

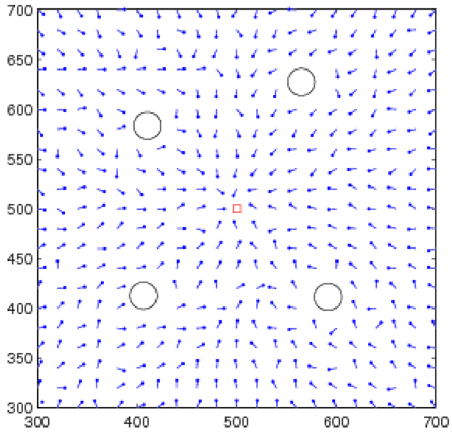

(b)

Figure 2. Vector map with sector-based approach (dot direction: moving direction with the best matching score) (a) 6 head directions (b) 36 head directions (center point (500,500): home) (reprinted from [7])

We simulated the robot trajectory for any arbitrary position outside the landmarks and the robot can reach home successfully – see Figure 3. The pixel-based approach suggested by Franz et al. [3] shows that the agent can return home with high probability inside the landmarks, but it has difficulty in returning home inside the landmarks. In contrast, the sector-based approach shows effective homing navigation for any spot, if the rate of moving distance over the landmark distance is appropriately chosen.

With a similar environment, we tested the robotic navigation with sector-based approach. It shows similar performance to the simulation. Sometimes noise influences the homing direction, but generally the homing direction is very close to that in simulation results. Figure 4 shows the robot can return home with the sector-based approach regardless of different home positions.

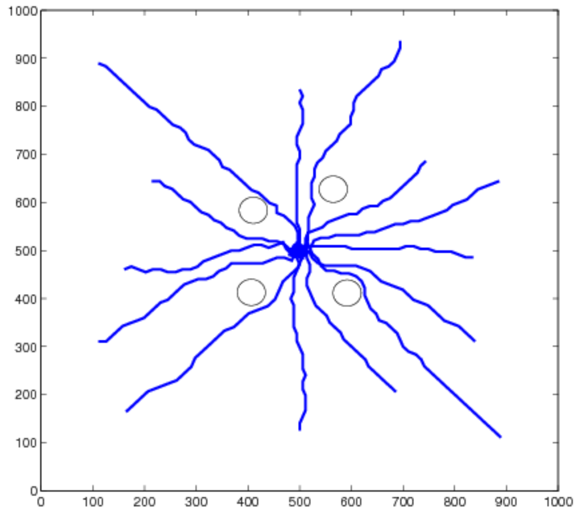

Figure 3. Trajectory map (reprinted from [8])

IV. DISCUSSION

The snapshot image is taken with an omnidirectional camera and the image covers landmarks for all the directions. The snapshot image is divided into several sectors. Each sector checks the landmark information inside the zone. We investigate several variations of sector-based approaches by overlapping the sector zones, increasing the number of sectors, or changing the size of sectors. Especially overlapping the sectors with an appropriate number of sectors may be more robust in noisy environments.

In this paper, we show that the sector-based image matching approach is a simple and efficient algorithm for a robot's navigation system based on visual landmarks. If the landmark navigation is combined with path integration mechanism, the agent can return home even for the area far from the nest. We can apply the path integration at far distance and use the image matching method at close distance. The sector-based algorithm reduces the time complexity by simple comparison of snapshot images, and also can efficiently find the way back home at a far distance or even under low resolutions of vision if the view of landmarks is available.

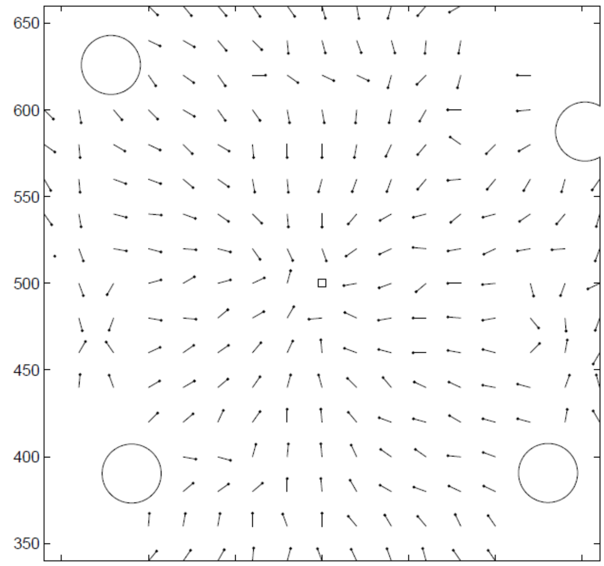

(a)

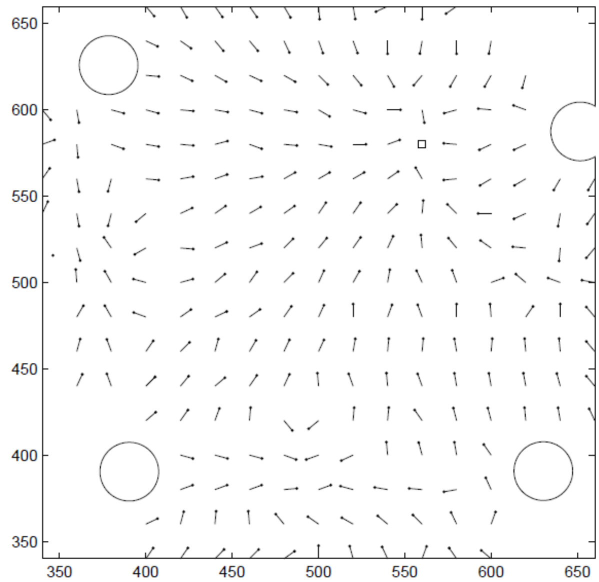

(b)

Figure 4. Vector map with robotic test over two different home positions (a) home (500,500) (b) home (560, 580) (reprinted from [8])

V. CONCLUSION

The image matching process records the snapshot image near the nest place, and compares the current snapshot image with the nest snapshot. Each snapshot image is divided into several sectors, and each sector encodes the landmark occupancy and landmark size. Then a pair of snapshot images are compared each other sector by sector. This suggested approach is more effective and efficient than the pixel-by-pixel image matching method. With the approach, a mobile robot can return home accurately with several landmarks, if it remembers the snapshot image near the nest.

VI. ACKNOWLEDGMENTS

This research was supported by the MKE (The Ministry of Knowledge Economy), Korea, under the ITRC (Information Technology Research Center) support program supervised by the NIPA (National IT Industry Promotion Agency) (NIPA-2009-C1090-0902-0007)

REFERENCE

[1] Anderson, A. (1977). A model for landmark learning in the honey-bee. *Journal of Comparative Physiology A: Neuroethology, Sensory, Neural, and Behavioral Physiology*, 114(3):335–355.
[2] Cartwright, B. and Collett, T. (1983). Landmark learning in bees. *Journal of Comparative Physiology A: Neuroethology, Sensory, Neural, and Behavioral Physiology*,151(4):521–543.
[3] Franz, M., Schoelkopf, B., Mallot, H., and B¨ulthoff, H. (1998). Where did I take that snapshot? Scene-based homing by image matching. *Biological Cybernetics*, 79(3):191–202.
[4] Franz, M. and Mallot, H. (2000). Biomimetic robot navigation. *Robotics and Autonomous Systems*, 30(1-2):133–154.
[5] Lee, J. and Kim, D. (2009). Landmark navigation using sector-based image matching. In *Proceedings of the 10th European Conference on Artificial Life*, Budapest,Hungary.
[6] Cho, H. and Kim, D. (2009) A neural model of landmark navigation in the Fiddler Crab *Uca lactea*, Proceedings of European Symp. on Artificial Neural Networks, pp. 355-360
[7] Lee, J. and Kim, D. (2010). Sector-based image matching method (*in preparation*). *Connection Science*.
[8] Lee, J. and Kim, D. (2009). A Sector-based Image Matching Approach to Visual Navigation, Master Thesis, Yonsei University

Online-based Therapeutic Services for Individuals who are searching for new challenges in life

Ji Hyang, Lim1, Hyo Woon Yoon2

[1] *dept of art therapy, Daegu cyber university, KOREA*
[2] *Neuroscience Research Institute, Gachon university of medicine and science, KOREA*

Abstract: The aim of the present study is to describe the social interests and practical progress, which related with therapeutic services for the individuals, who are searching new challenges in life. In order to achieve this goal, the database from the national statistic institute was cited, especially in the field of social welfare related with children, adolescents and family life. In addition, some examples from DCU are presented for educating expertise in this field for reporting practical progress. The interests as well as the inquiries of demand due to therapeutic service are significantly increasing in last few years. This phenomenon is probably based on some factors such as family relation changes, increased portion of small families etc and unexpected social problems as a consequence. Among them the care of juvenile population in the unstable family relations should be treated with priority. Thus, the large number of expertise is necessary for counseling / making therapeutic service of such population. DCU tries to establish special program for educating expertise in the field of therapeutic services currently. For example, DCU provides Interdisciplinary approach, Transregional approach, and International collaboration etc in order to satisfy nationwide necessity of therapeutic service expertise education. Even though this program is not fully completed, the special program of DCU is a big positive example to fulfill social interests in terms of therapeutic services as well as Life Long & Higher Education.

Keywords: art therapy, online-based, therapeutic services, new challenges in life

I. INTRODUCTION

The online based whole life education system is becoming more meaningful especially in the time of information. Reeducating to adapt such social phenomenon seems to be necessary.

Park (200) defined the 20 C as social safety net era, whereas the 21 C is social risk management era. The target population in the era of social safety net is the small portion of whole population, who are coming from social weak class. However, the risk in 21C is valid for the whole population. Thus, risk management is necessary. For example, the job security is comparably weaker, the employees should train themselves for confronting / overcoming unexpected problems. Also, the network of social risk management is necessary.

One of best examples to avoid high risks from this viewpoint is the lifetime learning and most realizable tool for this is the e-learning. E-learning is not limited spatially or temporally, thus the sharing of information is possible (Park, 200)

The lifetime learning is based on each individuals' willingness to learn / self-directed learning capacity. This doesn't mean alone the collecting / perceiving of existing knowledge, but this must be related with the capacity to create / treat new information.

The e-learning based lifetime learning includes such factors, so that this should be one of representative tool for preparing newly coming 21C era of risk management network. The e-learning also provides lots of contents, which covers various expertise fields.

The social problems in 21 C is detailed and diverse. However, it is regarded that melting point of problems is lying in the family. The individual definition or understanding about family should be newly formulated.

In order to solve these problems, individual based therapeutic service is recommended. To effectively provide this service, the understanding current social problems and predictions of future problems should be simultaneously done.

For this purpose the database from the national statistic institute was cited, especially in the field of social welfare related with children, adolescents and family life. This might help to understand the newly coming social problems in 21 C. Thus, the necessity of therapeutic service is also emerging. In addition, some examples from DCU are presented for educating expertise in this field

II. Materials and Methods

The increasing demand of therapeutic services

Some subdivisions were done to effectively understand / organize the change of family relation for better therapeutic services to adolescents / children currently.

1. The change of family relations
2. The future of social welfare services
3. Cases of special-care needed children and their social environment
4. Details of juvenile counseling
5. Types of inner family violence

III. Results and Discussion

Examples of specific programs for educating the expertise for therapeutic services at DCU

Following examples are presented for educating expertise in the field of the therapeutic services at online education institute. These projects are undergoing at DCU currently.

1. Interdisciplinary approach- Collaboration of departments such as playing, art, language therapy as well as social welfare, consulting psychology, special pedagogy.
2. Trans regional approach- Establishing domestic collaboration network due to practice and clinical aims
3. International collaboration-Integrating close relationship with foreign institutes and universities
4. The program consists of theoretical as well as practical, clinical lectures in the form of seminars and workshops.

1.Interdisciplinary approach

For educating expertise of therapeutic service it is important to consider how the similar disciplines are connected. Following examples demonstrate the detailed know-how of interdisplinary work due to e-learning.

Collaboration with many disciplines

The collaboration of many departments is meaningful especially in the viewpoint of e-leaning's self-directed education. Effective e-learning should therefore include effective curriculum to achieve effective learning results (Woo, 2006). DCU provide some remarkable examples, especially in credit acquisition.

<Interdisplinary program due to credit sharing>

1.Handout of certificate signed by university president after graduate from the major

2Acquisition of certificate by achieving credits in non-majors.

3.Expertise training by minors

4.Certificate of non-major through double- major system

Such open learning system is in line with the idea of the expertise of therapeutic service.

< Interdisplinary program besides credit sharing >

1.For sharing all expertise information regular off-line meetings were planned. It should be done across all students and alumni. The information is for example job opportunity etc.

2.The meeting is recorded as a movie clip and uploaded in the web in order to share this with member, who could not attend the meeting..

3.Seminars in form of tele-conference are also planned to expand the chance to have a direct contact with the teaching personnel.

4. The professional experience is shared with the students by the alumni.

2. Trans regional approach

For educating therapeutic services expertise the relationship with other local organization is necessary.

The sister institutes with DCU can obtain following benefits.

1Facilitated scholarship if the members of institute want to enter DCU

2.Obtaining students personnel in form of vo1untarily participation

3.Supporting many kinds of collaboration

4. Obtaining professional advice

3. International collaboration

In form of developmental aid, the countries, which have already good e-learning system, should have good relations with the developmental countries. This e-learning sharing started from 1980s. But the ingredients of this sharing are changed. The e-learning university system was worldwide challenge projects, therefore there are institutes, which successfully achieved such jobs and also institutes, which did not reach that goal.. The most remarkable difference between success and failure is lying on the sharing of on-line and off-line systems. The successful institutes are for example, open university in England, University of Phenix and nova southerwestern university in US. The examples of success story is presented next.

<Off-line relations>

MOU in form of sister institutes or inviting distinguished scholars were main stream for this purpose

1.Evidence-based Therapy for Children·Adolescents with EBD, March 2009

2. Developmental aid

<Distance learning/ on-line relations>

Supervision service for clinical work by university or departments

1. Supervision of students abroad

Distance learning clinical supversion

2. Collaboration with distinguished scholar groups.

On-line communication is very advantageous, since this method allows sharing information, planning new research works with foreign partners without time delay etc.

USA and Australia, for example, have already e-learning program worldwide due to intensive development of number of contents. This is also valid for therapeutic service. They provide not only therapy program by e-learning, but also examples of experience of professionals by doing on-line seminars and so on. One can obtain on-line lecture related with the appliance of US doctoral licence or German engineering seminar. On the basis of high quality and time /space limit free accessibility of these on-line lectures, the number of persons, who are willing to visit the lecture are continuously increasing despite the high costs.

4. Education program

A main purpose of on-line university is to support / provide the method, which can facilitate the self-directed education to the lecture attendees. Differently to the off-line, real lecture, the program of on-line lecture should be more compact, i.e. lots of animation presentation during the lecture.

The big challenge of on-line lecture is the keeping attention during the seminar of participants. The program should help the participants to concentrate lecture. Simply speaking, the lecture must be interesting.

Csikszentmihaly(1990) suggest nine components of such concentration / attention during on-line lecture.

.

1.Controlling the lecture difficulty and the level of participants' knowledge
2.Should show clear goals
3.Clear Feedback
4.Perception and doing must be non-separated
5.Concentration on current work
6. Feeling of possibility that one can control his environment and himself during lecture
7.Should not be conscious to themselves
8.Time flow should be differently perceived
9. One must be capable of enjoying such flows

.

The experience of such concentration has positive influence on self-estimation, learning time, and success rate of learning achievement (Csikszentmihaly, 1993, Hektner, 1996). Therefore, self-directed learning based e-learning program must include some components. Even though there are many research works for increasing the effectiveness of learning currently, the program for educating therapeutic service expertise should be differently approached. Following suggestions will be presented for making better on-line lecture program in terms of therapeutic service.

In terms of searching effective model of education related with the development of self-directed learning, the concentration to the lecture is not only important for understanding the ingredients, but also meaningful for the participants, because this is one of key components by doing therapeutic service. US reports from clinical psychology society (1947) indicate following 15 characters of therapy expertise.

1.Capablity as a therapist
2.Creativity and rich resources
3.Curiosity
4.Interest to human beings
5.Intuition to themselves
6.Sensitivity to complex motivation
7.Patience
8.Ability to have good relations with other social partner
9.Continuity and hardness to the pressure
10.Responsibility
11..wit
12.Ability for self-control
13.Clear view to ethical apects
14diverse cultural backgrounds
15.Understanding clinical psychology

The commonality between the experience of concentration and ability as a therapist is healthy self-estimation. The experience of concentration affects positively to the self-estimation, because healthy self-estimation is very important to become a good therapist. In addition, the joy of concentration makes the learning interesting. The wit rich therapist can enjoy his therapy time with the patients. The patients are in most cases lack of self-value-estimation and therefore it is very important for them to increase such feelings. The therapist should respect himself for doing this job.

Increasing this feeling by doing feedback in e-learning system based on artificial intelligence from the patients / clients is the main purpose of the therapy. Such system called as Carnegie Learning (2005) is widely used in US; approx. 150,000 middle school boys and girls use this system. This type of on-level-upgraded e-learning system can be exported to other countries.

The on-line university does not have such AI based tutor system yet, they are trying to develop similar system by doing LMS and LCMS. DCU also has special program for this. The lecture consists of theory, practice, clinical work, and supervision, which related with the credit acquisition. The self study consists of seminar, workshop and case study etc.

.

1.Course with the credit acquisition

This course consists of theory, practice, clinical work, and supervision. Theoretical work is available in 100% on-line. Clinical work is based on the application after completing video lecture. After learning some cases through videos some practices should be done. This includes self-report and reports about other persons. Voluntarily work in any social welfare organization should help such learning. Overall, the clinical work includes meta-cognition, controlling motivation and behavior.

The student should be able to setup goals and plan whole procedure. The lecture of planning, controlling includes such facts (Chung, 2008). The student can with the help of LMS service can control his own plan, learning progress in weekly base. In addition, he can also successfully achieve the lectures.

Other important fact, the feedback between student and teacher can be easily done by using LMS system. The web-blogs includes Q&A etc and this will help simultaneous interaction for both parties.

The student can ask help to his teaching personnel actively and this of course includes progress controlling. .

This might be helpful for the future job opportunity for the students.

The supervision service also aimed to educate good therapeutic service expertise. Supervision can be accompanied with advice of the field experts.

2.Self study (non-credit)
Semianar
Workshop
Case study
Voluntary work

Non credit self study provides free to the students and alumni. This study includes identical ingredients to credit one and this is available for both on and off line. The students in DCU are distributed all country area even abroad, thus the regular seminars, Seminar, workshop, case study, voluntary work are organized by the university administration.

IV.Conclusions

The present work demonstrates the growing social interest in terms of online therapeutic service in Korea. The existing literature data and governmental statistics were cited as a social /environmental background. DCU as one of the online education organization is now trying to setup special program for educating expertise of therapeutic service.

REFERENCES

Chung, a,k, (2008) development of a mobile platform(mobile embeded in lms) to support self-regulated learning. Dept of educational technology the graduate school of education ewha women's university

Csikszentmihalyi M, Csikszentmihalyi IS.(1993) Family influences on the development of giftedness. Ciba Found Symp. 178:187-200;

Jeong, s.(2006) implementation of dialogue-based feedback system to improve flow learning in e-learning environment. major in computer education graduate school of korea national university of education chung-buk, korea

Kim. J (2005). Investigating the quality control of cyber universities. Dankuk University press.

Kim, H. (2007). For establishing competitive distance university due to e-learning.

Na, I and Im, C(2005). Investigating of analysis of effectiveness by cyber education: examples from foreign countries. Korean Institute for education information.

Park, S et al. (2007). Making long life education. Reports from Korean institute for job development.

Tiesel, J.W.(1994). Capturing family dynamics: The reliability and validity of FACESⅣ. Unpublished doctoral dissertation. St. Paul, MN: Family Social Science. University of Minnesota

Woo, Y (2006) a study on the self-directed learning management system. Dept.of information engineering the graduate school of sungkyunkwan university

National Institute of statistics (1970-2005). Distributionof family form. Total reports from poulation

National Institute of statistics (2007). Future based social welfare service.

Korean Ministry of Health and Social Welfare (1999-2008). Current situation of special care need children. Dtabase from each local government.

Korean Ministry of Health and Social Welfare (1999-2008). Different types of child care. Database from each local government

Korean Ministry of Health and Social Welfare (1999-2008). Descriptive statistics about juvenile counseling nationwide

Korean Ministry of Health and Social Welfare (1999-2008). Current status of counseling needed adolescents nationwide. Korean Institute of Juvenile Conseling.

Ministry of Woman(2002-2008). The number of counseling supporting family violence. A statistical approach.

The Design of GHG(Greenhouse Gas) Reduction Control System

Yong-sik Choi, Sang-kyun Cha, Kyeong-jae Cheon, Hwan-chul Kim

Comesta, Inc. #714 Gwanpyoung-Dong, Yusung-Gu, Daejeon, 305-509, Korea.

(Tel : +82-42-863-5259: Fax : +82-42-863-5258)
(nmaster@comesta.com, skcha@comesta.com, kjcheon@comesta.com, hkim@comesta.com)

Abstract: In this era, the GHG(Green House Gas) is regarded as a very important issue of world wide economics. After declaring United Nations Framework Convention on Climate Change, world wide economy environment needs GHG Reduction, changes accelerative by Emission Trading System, and etc. After 2012 when Kyoto Protocol is Finished, New System is established by international agreement. And no matter what the system is, The range of countries have a duty for reducing GHG will be widened gradually. Therefore, the effort for reducing GHG must be necessary and we have to prepare for new trade barrier called the environment regulation for GHG . This paper shows the design of GHG Reduction Control System based on smart metering that can reduce GHG in the manner of dynamic management and planning for the progress of production. Also, we propose the simulation environment that can verify and validate the required functionalities of GHG Reduction Control System

Keywords: Greenhouse Gas. Reduction**.**

I. INTRODUCTION

Kyoto protocol is a main motive which created and developed the present carbon market by Kyoto mechanism, and etc. However, Kyoto protocol is finished by 2012. so, the appearance of carbon market to come changes by the result of international negotiation.

According to fourth Assesement Report IPCC presents in 2007, the emission of whole world's GHG is 49 billion tons that increase about 20 billion tons more than 1997's 28.7 billion tons. Also, the level of GHG in earth's atmosphere is estimated about 455 ppm in 2005. and the carbon dioxide's level of it is about 379 ppm that increase about 100 ppm more than 280 ppm in 1750 before industrialization. If we want to stabilize the level of carbon dioxide at this level, we have to reduce emission of carbon dioxide about 50~85% as of 2000.

As we can see fourth Assesement Report of IPCC and etc for emission of carbon dioxide. In 'Post 2012' system, in order to reduce the damage of climate change by global warming, the reducing goal of Advanced countries include USA must be strengthen more and developing coutries' reducing effort for GHG also must be added According to Human Development Report which UNDP presents in 2007, in order to prevent the average temperature of earth from growing 2℃, the level of carbon dioxide in atmosphere must be stabilized at 450 ppm following of IPCC's fourth Assesement Report, for this, we have to reduce the emission of GHG 50% as of 1990 till 2050. Therefore, the report is pointing to need not only the effort of advanced countries but also the effort of developing countries'.

The specific form of carbon market is decided by the end of 2009 which ongoing international negotiation for 'Post 2012' is finished. Depending on the outcome of negotiations, carbon market will have two situations. The first is made international agreement which Annex I countries includes USA agrees the reduce of respectable scale. The second is not made an international agreement. so, the reducing goal of each countries is decided by depending on their situation. In any situation, carbon market will be widened, and it is inevitable assignment that reduce GHG

This paper shows the design of GHG Reduction Control System based on smart metering that can reduce GHG in the manner of dynamic management and planning for the progress of production because of corresponding to international flow. Also, we propose the simulation environment that can verify and validate the required functionalities of GHG Reduction Control System

II. Simulation Environment

GHG Reduction Control System proposed and designed in this paper is in Carbon Management System based on Smart Metering which Daedeok Innopolis is a supervisor of project. The outlines of Carbon Management System based on Smart Metering is shown as [Fig 1].

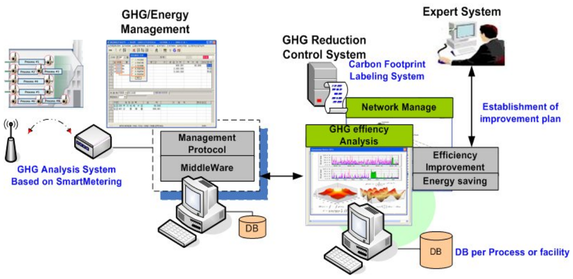

Fig 1. outline diagram of Carbon Management System based on Smart Metering

Carbon Management System based on Smart Metering is divided into two, measurement and analysis system based on Smart Metering and GHG Reduction Control System. Measurement and analysis system based on Smart Metering receives the consumption of electronic power which is measured by process via Zigbee interface, analyzes carbon footprint, and transmits analysis information of carbon footprint to GHG Reduction Control System. GHG Reduction Control System receives analysis information of carbon footprint, establishes statistics information, visualizes it, and presents interfaces that can let operators make a plan for reducing GHG.

Carbon Management System based on Smart Metering chose one facility and will have an test after implementation is finished. So, Before Testing, in order to verify and validate the required functionalities of GHG Reduction Control System, simulation environment that simulate Carbon Management System based on Smart Metering is established. Organization of simulation environment is show as [Fig 2].

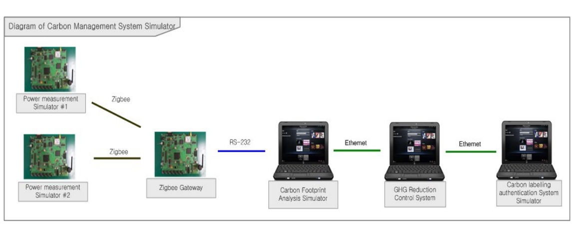

Fig 2. Organization diagram of simulation environment

Simulation environment is made up of three boards for communicating and three notebooks based Windows platform. Three boards and one notebook takes a role as measurement and analysis system, one notebook takes a role as GHG Reduction Control System, and last one takes a role as a Carbon Labeling Authentication System. Carbon Labeling Authentication System receives carbon labeling information from GHG Reduction System.

Two boards simulate smart meter of electronic power and transmit information of electronic power's consumption via Zigbee interface. One board takes a role as Zigbee gateway, receives the information, and transmits to notebook which generates carbon footprint information via RS232. Carbon footprint information is transmitted to notebook which takes a role as GHG Reduction Control System. The notebook generates carbon labeling information from analysis information of carbon footprint and transmits to notebook which takes a role as Carbon Labeling Authentication System.

III. GHG Reduction Control System

GHG Reduction Control System takes two primary roles. The first is exchanging the information with measurement and analysis system, generating carbon labeling authentication information and transmitting it to Carbon Labeling Authentication System. The second is establishing statistics information, visualizing it, and making a plan for reducing GHG. The outline of functionalities is shown as [Fig 3]

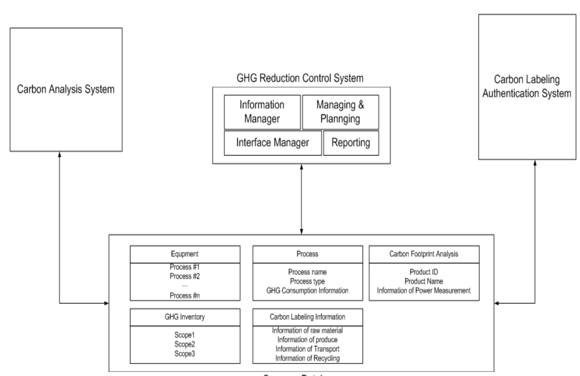

Fig 3. Outline diagram of GHG Reduction Control System

All the systems in Carbon Management System based on Smart Metering share the necessary information by Common database. All the system have their own databases, but they read the information to need, and write the information to be transmitted

1. Information managing

This functionality is Managing Information which will be transmitted to and received from. Information doesn't means only carbon footprint information, carbon labeling information, and GHG Inventory but also equipment, process, and product information. So, let GHG Reduction Control System have a scalability that can manage a number of equipment.

2. Managing and Planning

GHG Reduction Control System presents visualization of statistics information for GHG. Also, let operator can establish the plan of reducing GHG and progress by them.

3. Carbon Labeling Authentication Information

Carbon Labeling is the system that labels product with the emission of GHG which adds the emission whole level of product from raw material, to discard. Carbon Management System based on Smart Metering only measure electronic power. So, GHG Reduction Control System reads the necessary information from GHG Inventory except receiving from measurement and analysis system, and generates carbon labeling authentication information

IV. Conclusion

GHG Reduction Control System in this paper is designed as a part of Carbon Management System based on Smart Metering. Carbon Management System based on Smart Metering presents the functionality which measures the consumption of electronic power by Smart Metering by process, and makes a plan for reducing GHG by analysis information of carbon footprint that smart meter generates accurately more. its goal is growing efficiency of The Environment Management System

GHG Reduction Control System takes a role that manage carbon footprint information and GHG inventory and etc. and makes a plan for reducing GHG so that will correspond to the environment regulation to come.

In order to firm up operational ability and the scalability which can manage a number of facilities, Additional Experiment for minimizing access chances to common database of [Fig 3] is needed. Because, present design makes all the systems use one common database. So, have to find out more suitable data modeling by analyzing the quantity and the property of data and traffic that each equipment generates.

REFERENCES

[1] IPCC (2007), Climate Change 2007 : Synthesis Report
[2] UNDP (2008), Human Development Report 2007/2008
[3] ISO (2006), ISO 14040 – Environmental management : Life Cycle Assessment
[4] ISO (2006), ISO 14064 – an emerging standard on Greenhouse Gas accounting and verification.
[5] BSI British Standard, The PAS 2050

The Fifteenth International Symposium on Artificial Life and Robotics 2010 (AROB 15th '10),
B-Con Plaza, Beppu,Oita, Japan, February 4-6, 2010

Design of LCL filter for renewable energy sources using Bacterial Foraging Optimization

Jae Hoon Cho[1] ,Dong Hwa Kim[2], Young Dal Kim[2] and Jang Seok Kim[2]

[1]Chungbuk National University, 410 Seongbong-Ro, Heungduk-Gu, Cheongju Chungbuk, Korea
[2]Hanbat National University, San 16-1, DuckMyoung-Dong, Yuseong-Gu, Daejeon, Korea
(Tel : 82-42-821-1712, 82-42-821-1170)
(Email: jhcho@hanbat.ac.kr, kimdh@hanbat.ac.kr)

Abstract: As the traditional resources have become rare, renewable energy sources are developing quickly. The grid connected renewable sources is one of the most importance problem in smart grid fields. To reduce harmonic in this grid, many filter techniques have been developed. Compared traditional L filter, a LCL filter is more effective on reducing harmonic distortion at switch frequency. So, it is important to choose the LCL filter parameters to achieve good filtering effect. In this paper, a design method of LCL filter by bacterial foraging optimization is proposed. Simulation result and calculate data are provided to prove that the proposed method is more effective and simple than traditional methods.

Keywords: Renewable energy sources, Smart grid, LCL filter Bacterial foraging optimization**.**

I. INTRODUCTION

Voltage-source PWM method has many advantages such as bidirectional power flow, controllable power factor and sinusoidal input current. A PWM converter with higher switching frequency will result in smaller LC filter size. However, switching frequency is generally limited in high power applications. As an alternative solution, LCL filter is more attractive for two reasons: [1]

- It has better attenuation than LC filter given the similar size.
- LCL filter provides inductive output at the grid interconnection point to prevent inrush current compared to LC filter.

In 2005, Marco Liserre presented a step by step design method to design the LCL filter [2]. But the method is complicated.

Recently, artificial intelligence has become a popular search technique used in computing to find exact or approximate solutions to optimization and search problems. There are many kinds of artificial intelligence and Genetic Algorithm (GA) is used mostly[3]. Genetic algorithms are a particular class of evolutionary algorithms the use techniques inspired by evolutionary biology such as inheritance, mutation, selection, and crossover [4]. It becomes successful because of its concise arithmetic describing. On the other hand, as natural selection tends to eliminate animals with poor foraging strategies through methods for locating, handling, and ingesting food and favor the propagation of genes of those animals that have successful foraging strategies. Based on this conception, Passino proposed an optimization technique known as the Bacterial Foraging Optimization (BFO). The BFO mimicking biological bacterial food-searching behavior has been applied in the field of optimization. Optimization methods inspired by bacteria can be categorized based on the chemotaxis algorithm and bacterial foraging algorithm. The chemotaxis algorithm was proposed for analogy to the way bacteria to react chemoattractants in concentration gradients. The bacterial foraging algorithm is based on bacterial chemotaxis, reproduction and elimination-dispersal events and has been variously applied to some problems such as optimal control design [5], harmonic estimation [6], transmission loss reduction [7], active power filter synthesis[8], and learning of artificial neural networks [9]. This paper presents a new design method of LCL filter using bacterial foraging optimization.

II. SIMPLIFIED DESIGN PRINCIPLE OF LCL FILTER

The Three-phase Voltage Source PWM converter with LCL filter is shown in Fig.1. The filter has three unknowns, L_1,C_f and L_2. In the following, three considerations that lead to three equations for determining the three unknowns will be discussed.

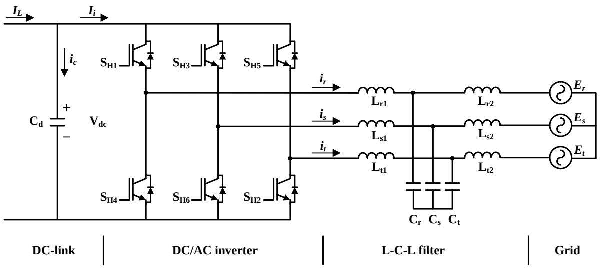

Fig.1. Topology of three phase VSC with LCL filter

The traditional design method can be calculated by following equations[4].

$$L_1 = \frac{V_g}{2\sqrt{6} f_s i_{ripple,peak}} \quad (1)$$

$$C_f \leq 0.05 C_b \quad (2)$$

$$C_b = \frac{1}{(\omega_n Z_b)} \quad (3)$$

$$Z_b = \frac{V_{gLL}^2}{P_n} \quad (4)$$

V_g is the RMS value of grid voltage, f_s is inverter switching frequency, is the base capacitance, Z_b is base impedance, V_{gLL} is grid line voltage and P_n is inverter rated power.

$$C_f = 0.025 C_b \quad (5)$$

The grid side inductance of LCL filter L_2 is computed as follow.

$$L_2 = 0.8 L_1 \quad (6)$$

III. BACTERIAL FORAGING OPTIMIZATION

Search and optimal foraging of animals can be used for solving engineering problems. To perform a social foraging, an animal needs communication capabilities and it gains advantages to exploit essentially the sensing capabilities of the group, so that the group can gang-up on larger prey, individuals can obtain protection from predators while in a group [10].

1. Optimization Function for the Bacterial foraging

For applying the bacterial foraging to optimization problem, conventional BFO was described as following [11].

In the minimal problem, the main goal of the BFO based algorithm is to find the minimum of $J(\theta), \theta \in R^p$ not the gradient $\nabla J(\theta)$. Here, θ is the position of a bacterium, and $J(\theta)$ denotes an attractant-repellant profile. That is, where nutrients and noxious substances are located, $J(\theta) < 0$, $J(\theta) = 0$, $J(\theta) > 0$ represent the presence of nutrients, neutral medium, and noxious substances, respectively. On the other hand, the population of bacteria can be defined by

$$P(j,k,l) = \{\theta^i(j,k,l) \mid i = 1, 2, \cdots, S\} \quad (5)$$

where $\theta^i(i,j,k)$ represents the position of each member in the population of the S bacteria at the jth chemotactic step, kth reproduction step, and lth elimination-dispersal event. Let $J(i,j,k,l)$ denote the cost at the location of the ith bacterium $\theta^i(i,j,k) \in R^p$ and the bacterial position after the next chemotactic step can be represented by

$$\theta^i(j+1,k,l) = \theta^i(j,k,l) + C(i)\phi(j) \quad (7)$$

where $C(i) > 0$ is the size of the step taken in the random direction specified by the tumble. If the cost $J(i, j+1, k, l)$ at $\theta^i(j+1,k,l)$ is better than at $\theta^i(j,k,l)$, then another chemotactic step of size $C(i)$ in this same direction will be taken and repeated up to a maximum number of steps N_s which is the length of the lifetime of the bacteria as long as it continues to reduce the cost.

During the process of chemotactic, the bacterium which has searched the optimal position tries to provide an attractant or repellent signal for the swarm behaviors of a group. Function $J_{cc}^i(\phi)$, $i = 1, 2, \ldots, N$, to model the cell-to-cell attractant and a repellant effect is represented by

$$J_{cc}(\theta, P(j,k,l)) = \sum_{i=1}^{S} J_{cc}^i(\theta, \theta^i(j,k,l))$$

$$= \sum_{i=1}^{S}\left[-d_{attract}\exp\left(-\omega_{attract}\sum_{m=1}^{p}(\theta_m - \theta_m^i)^2\right)\right]$$

$$+\sum_{i=1}^{S}\left[-h_{repellant}\exp\left(-\omega_{repellant}\sum_{i=1}^{p}(\theta_m - \theta_m^i)^2\right)\right] \quad (8)$$

where $\theta = [\theta_1,\ldots,\theta_p]^T$ is a point on the optimization domain, θ_m^i is the mth component of the ith bacterium position, $d_{attract}$ is the depth of the attractant released by the cell, $\omega_{attract}$ is a measure of the width of the attractant signal, $h_{repellant} = d_{attract}$ is the height of the repellant effect magnitude, and $\omega_{repellant}$ is a measure of the width of the repellant. Therefore, the final cost at the location of the ith bacterium $\theta^i(i,j,k) \in R^p$ reflecting the effect of an attractant and repellant can be defined by

$$J(i,k,k,l) + J_{cc}(\theta, P) \tag{9}$$

After chemotactic steps, a reproduction step is taken. The bacteria with the highest J values (low fitness cost) die and the other bacteria having lower values J (high fitness cost) split into two bacteria, which are placed at the same location, and then elimination-dispersal events is carried out. In these events, each bacterium in the population is subjected to elimination-dispersal with probability. Here, it is noted that each bacterium has the same predefined probability of elimination-dispersal events.

2. Design of LCL filter parameters by Bacterial foraging optimization.

In this paper, the structure of bacterial position is presented as follows.

$$X = [L_1 \; L_2 \; C_f] \tag{10}$$

This paper uses harmonic attenuation rate which is defined is equation (11) as the fitness function. To achieve good filter effort, a low harmonic attenuation rate is required

$$\frac{i_g(h_{sw})}{i(h_{sw})} = \frac{z_{LC}^2}{\left|\omega_{res}^2 - \omega_{sw}^2\right|} \tag{11}$$

$$\omega_{res}^2 = \frac{L_T z_{LC}^2}{L_1}, \quad L_T = L_1 + L_2, \quad z_{LC} = \frac{1}{L_2 C_f}$$

$$\omega_{sw}^2 = (2\pi f_{sw})$$

VI. SIMULATION RESULTS

This paper uses MATLAB/SIMULINK to simulate photovoltaic(PV) generation systems. Table1 and Table 2 show simulation parameters for PV and Bacterial foraging optimization. Table 3 shows simulation results by the traditional method and BFO.

Table 1. Simulation parameters

Parameter	Values
Inverter Power (P_n)	100kW
Utility line (V_{gLL})	600V
Utility frequency(f_n)	60Hz
Switching frequency (f_{sw})	4.5kHz
DC rated voltage (V_{dc})	1225V
Current(i)	96A (rms)

Table 2. Simulation parameters for BFO

	Parameter	Value
S	The initial bacteria population size for BPO	300
N_c	Chemotactic steps	
N_{re}	The number of reproduction steps	
N_{ed}	The number of elimination-dispersal events	
P_{ed}	Elimination-dispersal with probability,	
C	The step size for a swimming bacteria	

Table 3. Simulation results

Methods	L_1	L_2	C_f	fitness(F)
Traditional method	1.1mH	0.3mH	13.24uF	0.085
BFO	2.32mH	1.03mH	14.24uF	0.035

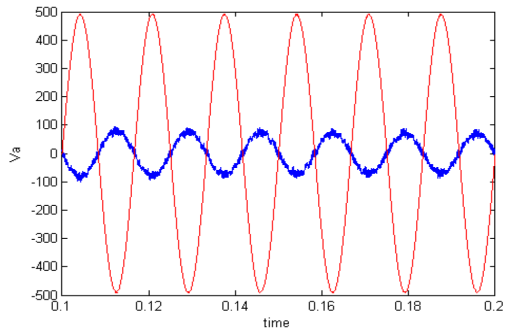

Fig.2. Converter current and voltage by traditional method

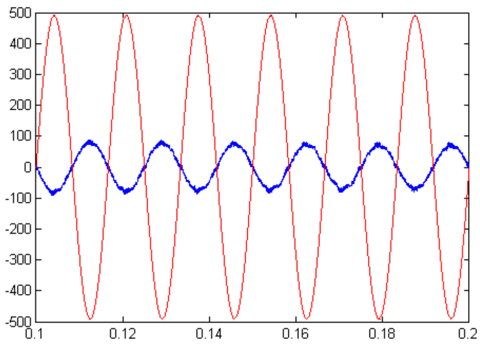

Fig.3. Converter current and voltage by Bacterial Foraging Optimization

Fig. 2 shows converter current and voltage by traditional method and Fig. 3 shows converter current and voltage by BFO. Table 3 and Fig. 3 show that the proposed method is better than traditional method

VI. CONCLUSION

As the traditional resources have become rare, renewable energy sources are developing quickly. The grid connected renewable sources is one of the most importance problem in smart grid fields. To reduce harmonic in this grid, many filter techniques have been developed. In this paper, a design method of LCL filter by bacterial foraging optimization is proposed. Simulation result and calculate data are provided to prove that the proposed method is more effective and simple than traditional methods.

ACKNOWLEDGEMENTS

The work developed in this paper has been supported by the DAEDEOK INNOPLIS ("R&D Hub Cluster project").

REFERENCES

[1]Wang, T.C.Y. Zhihong Ye Gautam Sinha Xiaoming Yuan(2003), Output filter design for a grid-interconnected three-phase inverter. Power Electronics Specialist Conference :779-784.

[2] M. Liserre, F. Blaabjerg, S. Hansen (2005), Design and Control of an LCL-filter based Three-phase Active Rectifier. IEEE Trans. Industry Applications : 1281-1291.

[3]Z. Wang, D. Cui(2004), Optimization Design Based on Genetic Algorithm for Rectifier. Trans. Of China Electrotechnical Society[J] 19(5): 7-9.

[4]Wei Sun, Zhe Chen and Xiaojie Wu(2009), Intellignet Optimize Design of LCL filter for Three-Phase Voltage-Source PWM Rectifier. IPEMC 2009 : 970-974:

[5]D. Kim, A. Abraham, and J. Cho(2007),A hybrid genetic algorithm and bacterial foraging approach for global optimization," Information Sciences(177) :3918-3937

[6]S. Mishra(2005), A hybrid least square-fuzzy bacterial foraging strategy for harmonic estimation," IEEE Transactions on Evolutionary Computation(9): 61-73

[7]M. Tripathy, S. Mishra, L. Lai, and Q. Zhang, "Transmission loss reduction based on facts and bacteria foraging algorithm," Lecture Notes in Computer Science, vol. 4193, p. 222, 2006.

[8]S. Mishra and C. Bhende(2007), Bacterial foraging technique-based optimized active power filter for load compensation. IEEE Transactions on Power Delivery(22) : 457-465.

[9]J.H. Cho, M.G Chun, and D.J Lee(2007), Parameter Optimization of Extreme Learning Machine Using Bacterial Foraging Algorithm. International Symposium on Advanced Intelligent Systems : 742-747.

[10]W. O'brien, H. Browman, and B. Evans, "Search strategies of foraging animals," *American Scientist*, vol. 78, pp. 152-160, 1990.

[11]K. Passino, Biomimicry of bacterial foraging for distributed optimization andcontrol. *IEEE Control Systems Magazine*(22): 52-67..

Semantic Query Processing Based on SQL

Hyun-Chang Lee

Division of Information and e-Commerce, WonKwang Univ., Institute of Information and Science
344-2 Sinyoun-dong, Iksan, Jeonbuk, 570-749, Korea
(Tel : 82-63-850-6260; Fax : 82-63-850-7302)
(hclglory@wku.ac.kr)

Abstract: According to the development of ubiquitous technology, the concept of ontology is widely used in the fields such as telematics and intelligent robots that require information processes for context. Web-based ontology languages like RDF/S and OWL represent resources in the web to a type of triple (subject, predicate, object). However, the use of languages is restrictive. Therefore, in this paper, we propose an OWL context relational model and semantic query processing mechanism based on SQL.

Keywords: SQL, semantic query, query processing.

I. INTRODUCTION

Ontologies are special forms of conceptual models whose primary role is not to serve documentation but to be machine interpretable and that capture the knowledge of a particular domain as computational artifacts based on principles of knowledge representation in information system. In various application contexts, and within different communities, ontologies have been explored from different points of view. The dominating definition of ontology is the following one, "an ontology is a formal explicit specification of a shared conceptualization of a domain of interest", by Gruber[1]. In addition, ontology concept is widely used in the fields of semantic web application, home networking, telematics, intelligent robot that require the processing of context awareness.

The definition of ontology captures several characteristics of ontology as a specification of domain knowledge, namely the aspects of formality, explicitness, being shared, conceptuality and domain-specificity. The principle constituents of ontology are concepts, relations and instances [2].

Concepts represent the ontological categories and classes of objects that are relevant in the domain of interest. The concepts and relations in an ontology can be intuitively grasped by humans, as they correspond to the elements in our mental model. An ontology tries to cover as many situations as possible that can potentially occur [3]. Relations semantically connect concepts, as well as instances, specifying their interrelations. Instances represent the named and identifiable concrete objects in the domain of interest. The most prominent insights have been published in [4] and are summarized in figure 1.

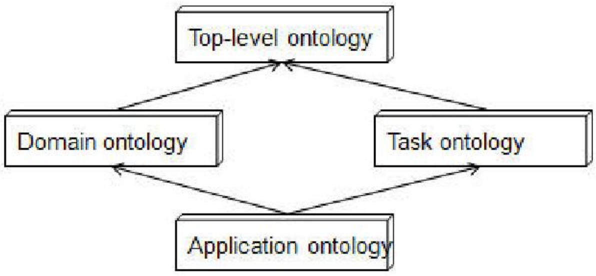

Fig.1. Types of ontologies

Top-level ontologies attempt to describe very abstract and general concepts that can be shared across many domains and applications. Prominent examples for top-level ontologies are DOLCE and SUMO [5,6]. The types of domain ontologies and task ontologies capture the knowledge within a specific domain of discourse, such as medicine or geography, or the knowledge about a particular task, such as diagnosis or configuration. Application ontologies provide the specific vocabulary required to describe a certain task enactment in a particular application context.

Owing to context-awareness systems provided by semantic web technology, most of applications accept the international standards because those have to serve the context awareness services [7]. As for an international standard, there are two types of standards: one is OWL that is a kind of web ontology language. The other is web service that enables to interoperate among software modules. [8] shows methodologies to store and manage ontology documents based on RDF/S to process context-awareness efficiently. In this paper, we propose a relational query process model based on OWL web ontology language.

The rest of this paper is organized as follows. Part 2 begins the discussion on related work. In part 3, it describes the semantic query processing models. And finally, part 4 is the conclusion.

II. RELATED WORKS

There are web based ontology languages such as RDF/S and OWL provided by W3C. In this paper, it is describing about query processes related to the above languages [9,10,11] and extended[12]. RDF has a triple form for framework consisting of subject, predicate and object as a description of resource. That documentation can be shown in form of graphs to be readable from machine. At that time, subject and object are shown as an oval and as a box respectively. The predicate is shown as an arc.

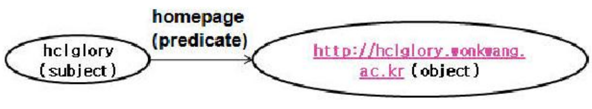

Fig.2. Graphical statement for RDF

As a semantic query language for RDF which is made by W3C, RDQL provides a similar type of the conventional SQL query model for relation database. The following table 1 shows syntax for RDQL briefly. An example for the syntax is in figure 3.

Table 1. The illustration of RDQL syntax

Keyword	Description
SELECT	Variables returned as result
FROM	URI for documentation to query
WHERE	Triples to query Variables for querying Patterns : ({subject|?var} {predicate|?var} {object|?var}) Enable Boolean operations
USING	Prefix to URI

Jena, Sesame, Parka and Tap are known for semantic information management system [13,14,15]. In case of Jena, it is an open source and operates on JAVA framework to build applications. It also provides JAVA API to store and manage documentations of OWL, RDF, RDFS and DAML+OIL[16], and RDQL for query language of ontology data.

III. SEMANTIC QUERY PROCESSING

In this section, we consider the steps for semantic query process and conversions.

First, the representative query language for relational database refers to SQL. The type of fundamental retrieve formula for SQL is "SELECT <field name> FROM <table name> WHERE <condition>;". Moreover, an example for conversion RDF into SQL statement to process semantic query language is shown in figure 3.

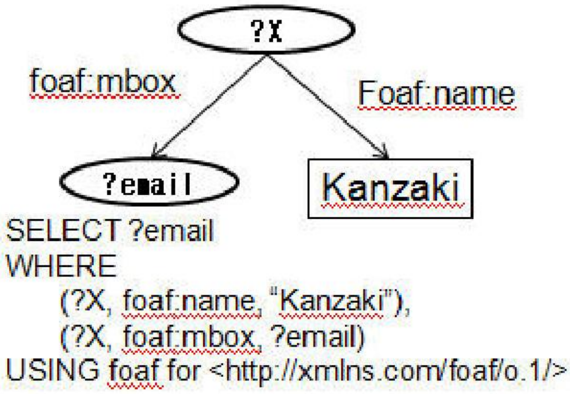

Fig.3. Graphical statement and SQL for RDF data retrieve

In figure 3, the query of graphical statement means that name(foaf:name) is Kanzaki and it has a node for email address(foaf:mbox). Nodes, such as "?X" and "?email", begin with character "?". These nodes play a role in variables that represent what nodes find in searching. In case of RDF, the meaning of graph is products of triples. Therefore, we do not use "AND" operator in triples of "WHERE" clause.

If we make a SQL statement using a theorem to convert variable name into field name, the statement is that "SELECT email FROM addressbook WHERE name = 'Kanzaki'". Therefore, we propose the following theorem as an algorithm to convert graphical RDF into SQL statement.

Lemma1. Let T be a set of triples consisting of RDF graph. T = { t_1, t_2, …, t_n }. Let S be a set of SQL statements. S= { s_1, s_2, …, s_n}. Each element of T can be converted to SQL statements in the following figure 4. For instance, t_1 is s_1, t_2 is s_2 etc.

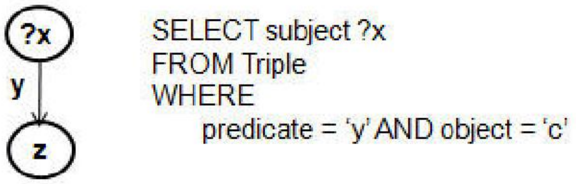

Fig.4. SQL query conversion in single triple

Lemma2. In multiple triples, literal operations are first processed.

For example, one of literals in figure 3 is "Kanzaki". Therefore, the node named "Kanzaki" is first computed and then an email address with foaf:mbox of that node is retrieved.

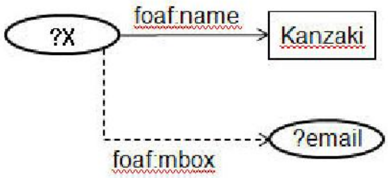

Fig.5. Order of literal and nodes

Lemma3. Graph having multiple triples, i.e., the case of a subject with several properties is joined with operation "Inner Join".

For example, in figure 5, if each node and literal is kind of nodes, then they are sharing the subject. In addition, in figure 6, a node (?X) has two other nodes (z, y). As for 'z' and 'y' nodes, they have same parent node. Then, we can make two SQL statements with same subject using key.

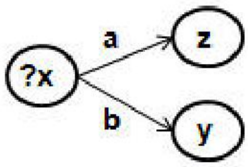

Fig.6. Multiple triples

Lemma4. If an object of a node in a triple is a subject of another node, then add property element to the node belonging to object.

Fig.7. Multiple level nodes

The node (y) has a role in a value as an object and subject. Therefore, in that case of the node, we can make a SQL statement using the key in inner SQL statement.

Until now, we considered the model to convert graphical RDF model to SQL statement based on lemmas.

IV. CONCLUSION

The paper addresses the issues converting graphical RDF to SQL statements. The algorithm is used for applying to the ubiquitous technology requiring information processes for context.

Recently, owing to the development of web technology, web-based ontology languages like RDF/S and OWL are emerged. Those languages represent resources in the web to a type of triple which is consisting of subject, predicate and object. However, the use of languages is restrictive. Therefore, we have proposed and addressed the issues converting to SQL statements. First, we have briefly considered the representative query language for relational database. Next, we have shown the results as an example to convert RDF into SQL statement. To do those works, we have suggested several lemmas.

As a further works, we are investigating effective methods for converting RDF into SQL by taking an experience using data.

REFERENCES

[1] T. Gruber. A Translation Approach to Portable Ontologies. Knowledge Acquisition, 5(2):199-220, 1993.
[2] S. Grimm, R. Volz. Semantics At Work Ontology Management – Tools and Techniques, FZI Forshungszentrum Informatik an der Universitat Karlsruhe(TH), 2007.
[3] N. Guarino. Formal Ontology and Information Systems, Preface. In N. Guarino, editor, Proceedings of the 1st International Conference on Formal Ontologies in Information Systems, FOIS-98, Trento, Italy, pages 3-15. IOS Press, 1998.
[4] N. Guarino. Semantic Matching: Formal Ontological Distinctions for Information Organization, Extraction, and Integration. In M. Pazienza, editor, Information Extraction: A Multidisciplinary Approach to an Emerging Information Technology, number 1299 in LNCS, pages 139-170. Springer-Verlag, 1997.
[5] A. Gangemi, N. Guarino, C. Masolo, A. Oltramari, and L. Schneider. Sweetening Ontologies with DOLCE.

In EKAW-02: Proceedings of the 13th International Conference on Knowledge Engineering and Knowledge Management. Ontologies and the Semantic Web, pages 166-181. Springer-Verlag, 2002

[6] I. Niles and A. Pease. Towards a Standard Upper Ontology. In C. Welty and B. Smith, editors, Proceedings of the 2nd International Conference on Formal Ontology in Information Systems (FOIS-2001), 2001.

[7] Z. X. Pan and J. Heflin: DLDB: Extending relational databases to support semantic web queries, Workshop on Practical and Scalable Web Systems, pp. 109-113, 2003.

[8] J. Broekstra, A. Kampman, F. van Harmelen: Sesame: A Generic Architecture for Storing and Querying RDF and RDF Schema. In The Semantic Web-ISWC 2002, volume 2342 of Lecture Notes in Computer Science, pp. 54-68, 2002. http://openrdf.org/

[9] Dave beckett and et al.: RDF/XML Syntax Specification (Revised), W3C Recommendation 10 February 2004. http://www.w3.org/TR/rdfsyntax-grammer/.

[10] Dan Brickely, R.V. Guha and et al.: RDF Vocabulary Description 1.0: RDF Schema, W3C Recommendation 10 February 2004. http://www.w3.org/TR/rdf-schema/.

[11]Deborah L. McGuinness, Frank van Harmelen: OWL Web Ontology Language Overview W3C Recommendation. Feb 2004. http://www.w3.org/TR/owlfeatures

[12] H.S.Kim, J.H.Son, SQL-based Semantic Query Processing in the OWL-aware Relational Model. In the Journal of KIISE Vol35. Pp44-53. Feb 2008.

[13] Jeremy Carrol, Brian McBride: The Jena Semantic Web Toolkit. HP-Labs, Bristor, 2001. http://jena.sourceforge.net/

[14] J. Broekstra, A. Kampman, F. van Harmelen: Sesame: A Generic Architecture for Storing and Querying RDF and RDF Schema. In The Semantic Web-ISWC 2002, volume 2342 of Lecture Notes in Computer Science, pp. 54-68, 2002. http://openrdf.org/

[15] Kilian Stoffel, Merwyn Taylor, James handler: Efficient management of very large ontologies. Proc. 14th Nat'l Conference AAAI, AAAI press, pp. 442-227, 1997.

[16] Ian Horrocks, Frank van Harmelen and et al.: DAML+OIL (March 2001). http://www.daml.org/2001/03/daml+oil-index.html.

Detection of volume data of aortic tissues based on three dimensional domain growing

T. Tokuyasu, T. Shuto, K. Yufu*, N. Abe**, S. Kanao, A. Marui***, M. Komeda

* Oita National College of Technology/Mechanical Engineering, Oita, Japan
** Kyushu Institute of Technology/Mechanical Information Science, Fukuoka, Japan
*** Kyoto University/Cardiovascular Surgery, Kyoto, Japan
****Nagoya Heart Center, Aichi, Japan
(Tel&FAX 81-97-552-7403) (E-mail: tokuyasu@oita-ct.ac.jp)

Abstract: In general, three dimensional computed tomography (CT) is used in diagnosis of a patient suffering from aneurysm. This medical imaging technique can clearly show the region of blood flow by using contrast agent. Cardiovascular surgeons construct three dimensional volume model based on patient CT data in order to make a surgical plan before surgery. Effective information to diagnosis patient's condition is contained in the computed tomography image, however it does not produce sufficient information for surgical planning. There is a lack of information about aneurysm tissue, so that it makes it difficult to derive a safe surgical plan. In order to overcome this problem, a diagnosis support system is highly required by the co-author cardiac surgeons. In this paper, we built an algorithm to automatically generate a volume model from patient's CT images. This paper presents our image processing methods to extract volume data from patient's CT data, and some volume rendering results are shown in this paper.

Keywords: *Virtual reality, Image processing, Computer aided system, and Surgical planning.*

1. **Introduction**

For a patient suffering from aneurysm, cardiovascular surgeons displace the diseased artery with artificial vessel according to a surgical plan made by the patient thoracic CT image. Aneurysm often occurs at distant arch aorta part, and then the operation becomes difficult because surgeons have to perform coronary surgery against the arteries connecting to the brachial region and brain by using a heart lung machine before the operation. Important thing of this surgery is to arrive at the aneurysm and ensure the surgical field with a small invasion. And then cardiac surgeons carefully make a surgical plan that determines how to approach to the diseased part and how to replace the diseased artery with artificial vessel by dereferencing to the three dimensional reconstructed model composed of patient CT image.

Computed tomography, especially the one taken by using contrast agent, is commonly used in a diagnosis of patient's aorta condition, where an image is drawn with gray scale as shown in Fig. 1. White areas show bone and vessel. The reason why the vessel region is shown with white color is that the contrast agent flow in vessel and it is reflected on CT image. Meanwhile, contrast agent does not sink in tissue of aorta. As a result, the outer wall cannot be detected clearly from CT image as well as inner region of aneurysm. In aneurysm, thrombus prevents inflow of blood so it is not also shown in CT image. Due to the mentioned reasons, CT image for diagnosis is hard to make surgeons know the statement of aneurysm before patient thoracic incision in operation room. Additionally, because of them, it sometimes happens that the surgical plan is forced to be changed during operation. In the case of the mentioned scene, skilled surgeon breaks through but the operation time and patient physical load are increased.

Against the current situation of cardiovascular field, the co-authors of cardiac surgeon highly require a diagnosis support system for patient's aneurysm that enables the surgeons to see the accurate figure of aneurysm from any view point. In this paper we have built an algorithm that can automatically extract inner region of vessel and reconstruct it as three dimensional model on a computer display. Additionally, we try to extract not only inner region but also outer wall, aorta tissue. This algorithm and some volume rendering results are drawn in the following sections.

Fig. 1 Original computed tomography image

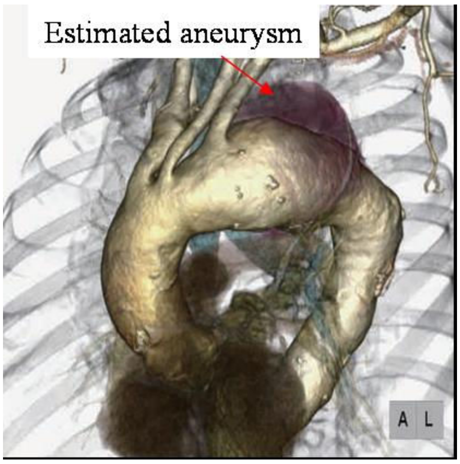

Fig. 2 Estimated aneurysm

2. Current situation

Fig. 2 shows the images generated by the combination of masking images. Masking is a filtering method, where three dimensional organ we'd like to obtain from patient image can be take out by varied the settings of threshold. This figure is composed of the following masking organ, bronchus, bone, and coronary veins. Surgeons use this composed image to estimate the statement of aneurysm before surgery. This masking procedures are manually performed by radiation technicians. In the field of radiology, to make it rapid and accurate to perform the mentioned processes is one of the problem to be solved.

In order to support doctor's diagnosis with patient medical image, lots of techniques for medical image processing are developed and reported. Kitasaka [1] proposed an extraction method for bronchus from patient 3DCT image. They applied region growing to inner volume of bronchus of CT image and sterically reconstructed the extracted volume data on a computer display. Qi Zhang [2] presented a real-time beating heart model by using high performance graphical board, where patient thoracic multidetector CT image are sterically-constructed and continuously switched in order to show a beating motion. Do-Yeon[3] used 3D region growing to extract carotid artery for automatic generation of navigation path. According to earlier studies, region growing is one of effective methods to extract artery. Then, we have adopted this method to recognize the region of aneurysm and extract its volume data from patient 3DCT image.

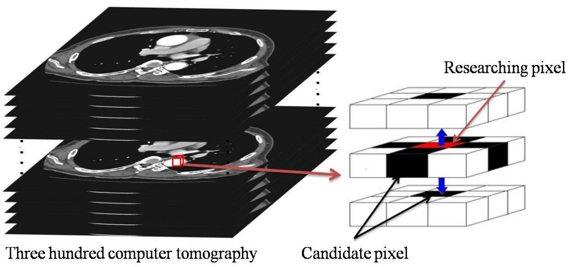

Fig. 3 Schematic diagram of region growing method

3. Method

3.1 Pre-processing

A total number 788 of computed tomography images from patient's thoracic part had been taken. And, consecutive images of 300 image data including the main artery are chosen from the original data set.

As mentioned above, region growing method is an effective extraction method against three dimensional medical images. This method explores the pixel which indicates a part of the target organ by using conditional equations such as threshold and other significant data. In this study, region growing algorithm searches around six pixels as shown in Fig. 3 under the condition of threshold. Depending on the value of threshold, the number of volume data extracted by region growing changes. In this study, we firstly applied region growing in the centre pixel of vessel of the lowest CT image. Selecting the start point for region growing is only one procedure we have to do manually to use our system.

Fig. 4 shows the image taken as the result of region growing, where a white region is region passed the threshold. The higher the threshold increases, the lower the number of volume data passed. Therefore, the setting of threshold has an impact on post-processed image and computation time. We experimentally decide threshold to clearly detect the cross section of vessel.

OpenGL Volumizer that is high level graphics library for volume rendering API is employed in this study. Fig. 5 shows a result of volume rendering taken by applying region growing to the original CT image,

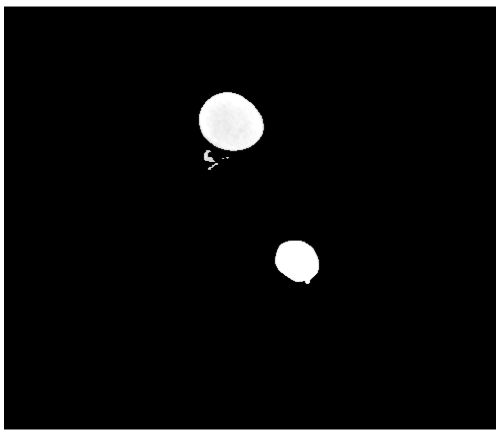

Fig. 4 Result of region growing method

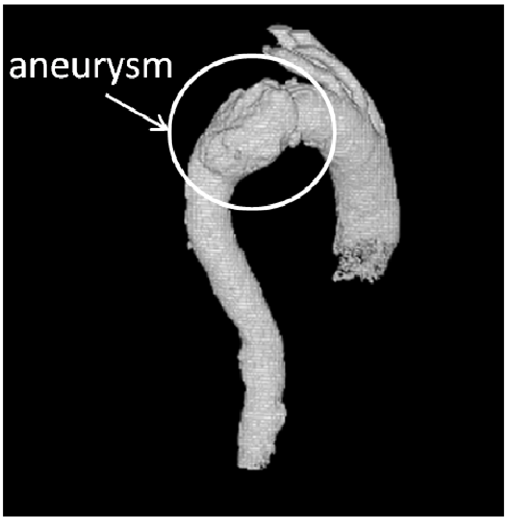

Fig. 5 Result of volume rendering for CT image data

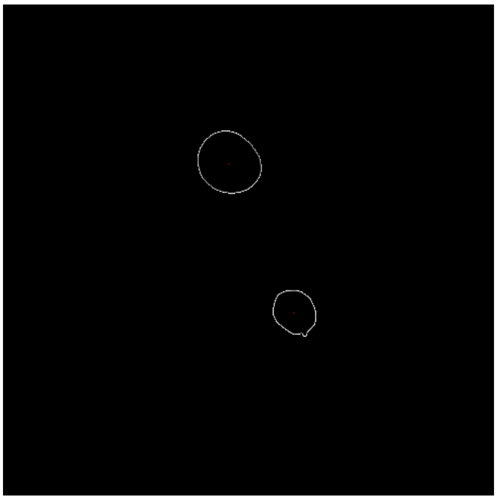

Fig. 6 Result of detect edge

where we can distinguish a part of aneurysm around arch part, and other vessels derived from heart are also remained in the result.

3.2 Extraction aortic outer wall

To render inner region of aorta as three dimensional model is succeeded, but not only aneurysm but also outer wall tissue of aorta is not visualized. The reason why this result, region growing we applied had extracted only high contrast pixels by judging with the threshold. This means that conventional use of region growing is not able to completely detect the region of aorta and aneurysm.

So, we try to apply the following processes to overcome the mentioned problems. First, labelling process excludes the regions in respect to little arteries from figure 3, after this labelling process the cross sections of the arch aorta are clearly shown. Second, Laplacian filtering, described in equation (1), is applied to detect the edge line of aortic cross section. Fig. 6 shows the result of edging process.

$$\nabla^2 f(x,y) = \frac{\partial^2 f(x,y)}{\partial x^2} + \frac{\partial^2 f(x,y)}{\partial y^2} \tag{1}$$

Fig. 7 shows a cross section of vessel. The blue line shows the edge of inner wall and the red line is the edge of outer wall that we have to automatically detect from patient's CT image. We use region growing again, here it judges the pixel along with the edge of the inner section as shown in Fig. 6. The condition of this application of region growing, a threshold and the distance between the center of cross section and the pixel that is subjected to be processed. In Fig. 7, a radius of inner wall is shown as r(θ), and a radius of outer wall is shown with R(θ).*P*(*x*, *y)* is a value of brightness of the coordinate point that is subjected to be processed by region growing. The square of inner region is easily derived by accumulating total number of white color pixels. It is shown as S. If the pixel has a brightness higher than the threshold and its distance from the center point of inner section is less than r(θ) + R(θ), then this pixel is judged as a part of tissue of vessel and/or aneurysm, where R(θ) is derived with equation (3).

$$r(\theta) = \sqrt{\frac{S}{\pi}} \tag{2}$$

$$R(\theta) = \text{const} \times r(\theta) \tag{3}$$

After implementations the mentioned processes, the cross sectional images including a part of outside wall issue as shown in Fig. 8.

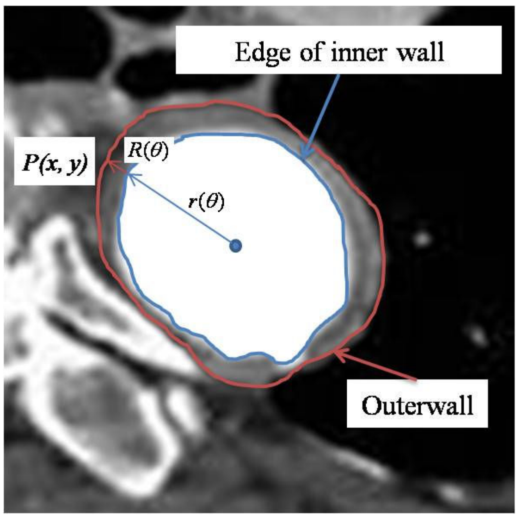

Fig. 7 Scheme of a cross section of vessel

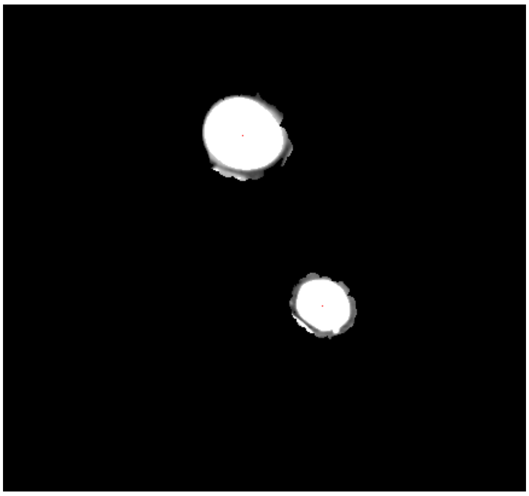

Fig. 8 Result of the second region growing method along to the edge

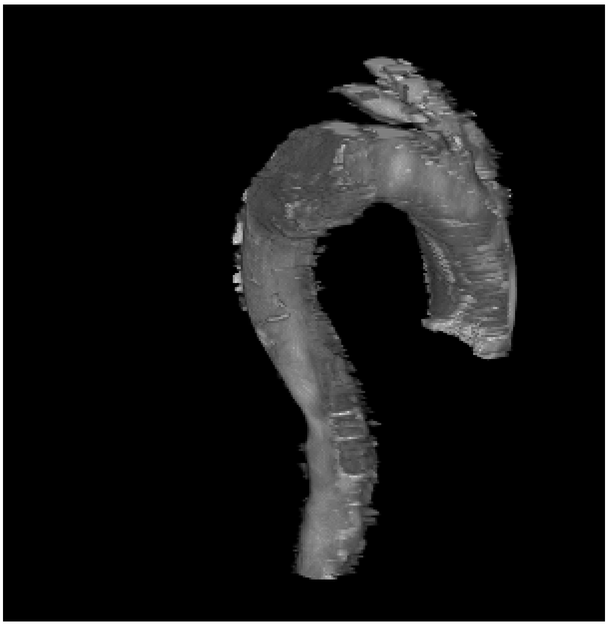

Fig. 9 Volume rendering result executed against the second region growing method

Fig. 9 shows a volume rendering result through OpenGL Volumizer, where approximately 1480000 volume data constructs this volume model. The inner model shown in Fig. 5 is composed of approximately 900000 volume data. The increased volume data is for the volume data of outside tissue of aorta. However, there is a lack of outside of aneurysm at arch part, and we can find this volume model is not smoothly composed. Because of them, the conditions of region growing were not enough to detect accurately the tissue of aorta.

4. Discussion

Due to difficulty to let computer recognize the tissue of aorta, cardiovascular surgeons cannot accurately know the shape of aneurysm of patient. So, the surgeons expect the development of diagnosis support system for patient aneurysm before surgery.

In order to recognize the region of aortic tissue from patient's thoracic CT data, a method of region growing is applied two times. First use succeeded to detect the inner region of aorta that reflected with high contrast. And after edge processing against inner region of aorta, second region growing is applied along with the edge. However, this method extracted a part of the outer tissue of aorta.

In order to extract all pixels of outer tissue, we have to firstly detect the edge of outer tissue of vessel and aneurysm based on the skill of doctor's interpretation of radiogram. Recently some report applies Fuzzy inference to image processing. By optimizing Fuzzy set, membership function and so on, some reports have succeeded to extract the edge of object from image such as fruits, vegetables, and signal plates. Application of Fuzzy inference has possibility to complete our purpose [5]. If the edge of outer wall and/or the region of aneurysm can be detected, region growing has possibilities to extract the most of pixels of aneurysm.

References

[1] T. Kitasaka et al. Extraction of bronchus regions from 3D chest X-ray, International Congress Series 1256 (2003) 240-245.

[2] Qi Zhang et al, Dynamic real-time 4D cardiac MDCT image display using GPU-accelerated volume rendering, Computerized Medical Imaging and Graphics 33 (2009) 461–476.

[3] Do-Yeon et al, Automatic navigation path generation based on two-phase adaptive region-growing algorithm for virtual angioscopy, Medical Engineering & Physics 28 (2006) 339–347.

[4] S.Watanabe et al., A Method for Automated traction of Liver Regions from Multi-Phase Abdominal X-ray CT Images Based on Region Growing, Journal of Computer Aided Diagnosis of Medical Images, Vol. 7 No. 4-4, pp. 1-7.

[5] M. Terao et al., Automated Extraction of the Endorrhachis from MR Lumbar Images based on Fuzzy ROI Representation, IEICE technical report, 101(580) pp. 43-48.

Autonomous Walking with use of Quadruped Virtual Robot

Kouki MIYOSHI, Norihiro ABE, Yoshihiro TABUCHI
Kyusyu Institute of Technology
680-4 Kawazu, iizuka, Fukuoka 820-8502, Japan
Email:miyosi@sein.mse.kyutech.ac.jp

Hirokazu TAKI
Wakayama University
930 Sakaedani, Wakayama-shi
Wakayama 680-8510, Japan
Email: taki@sys.wakayama-u.ac.jp

Shoujie He
VuCOMP
Richardson, Texas, USA
Email: hesj@computer.org

Abstract: In the development of a robot, it needs much cost and time to verify a robot's motion with use of real machinery. Especially it is difficult to validate a robot's behavior at the unsafe place. Then developers have paid attention to virtual debugging system. It makes verification of a machine's behavior makes more efficient and easy by using a program validated in VR space.

In this research, we have a virtual robot walk on a road autonomously with the images which are captured by cameras on the virtual robot.
Keywords: *VR, Virtual Robots, Virtual Space*

1. INTRODUCTION

In recent years, many robots have been developed. It is easily to expect that a robot becomes a member of the general public in the near future. But the development of robots takes much cost and time. One of the reasons is to validate with real machinery in real space. If a real robot should be damaged, it will force us to pay much time and expense for fixing the robot. This will increase necessary expense and the length of a period for robot development, so no one deploys any robots in dangerous environment for fear of damage owing to violent fall or collision.

Then a virtual debugging system has gotten attention [1][2][3]. Developers are allowed to design the same machinery as the real one in VR space, and to verify the robot motion by using it. It saves speed of developments by verifying whether the virtual robot works well or not in the virtual debugging system. Additionally, developers enable to create various testing environments and test the robot's behavior on these environments.

In this research, we make a virtual four legged robot built in virtual space based on physics, and have it move autonomously. By analyzing images captured with two cameras installed on the four legged robot, we have it track a line and walk on a road by using the algorithm that tracks a line.

2. Construction of Virtual Reality Space

In the simulation, it is necessary to construct the virtual reality space based on a physical rule because of making virtual environment close to real one as far as possible [4]. So we use the rigid physics calculation library, Vortex (developed by CMLabs Simulations, Inc [5][6].) to build the virtual reality space. The Vortex provides the function that creates fundamental objects like plane, box, corn, sphere, and cylinder. We enable to use a constant restraint between objects as a joint. We are able to combine different basic objects to create a composite object. Combination of composite objects and joints enables to express a complex object like robot and car.

3. Expression of Virtual Robot

In this research, servomotors of virtual quadruped robot are expressed with a hinge joint between solids two boxes and two rectangular as shown in Fig.1 [7].

(a) Hinge joint (b) Servomotor
Fig.1. A Virtual Servomotor

A virtual quadruped robot consists of 13 composite objects and 12 hinges. Each part of body, shoulders, upper legs, and lower legs is composed of boxes and cylinders. These parts are linked with a hinge joint. Fig.2 shows an appearance of robot.

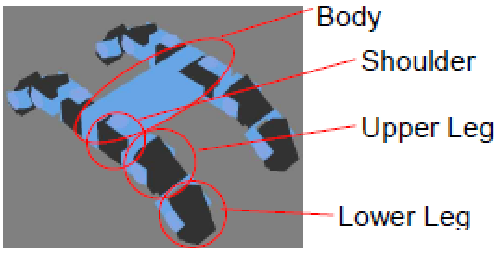

Fig.2. Quadruped Robot

4. Autonomous Walk

4.1. Image Buffer

In this research, images of the environment that robot sees are used to control the robot, but the position of the image buffer is not provided with Vortex but with Open GL. On the other hand, both Open GL and Vortex manage any rigid object with the transformational matrix, then the robot can acquire its transformational matrix from the result of image processing and infer it location based on the images observed with two virtual cameras.

4.2. Virtual Gradient Sensor

Images captured with cameras will decline (shown as Fig.3) because the four-legged robot declines when it goes ahead. So in addition to cameras, a virtual gradient sensor is installed on the robot. The images are rotated by the angle detected with a gradient sensor to make images processing easy.

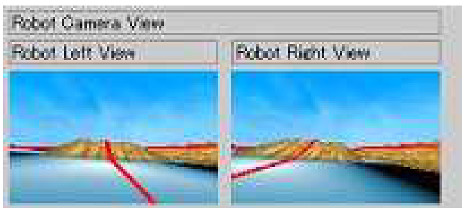

Fig.3. Images from two virtual cameras

A virtual gradient sensor calculates the gradient angle of camera. The gradient θ is represented as the expression (1) by using two coordinates (x_1, y_1) and (x_2, y_2) shown in fig.4.

$$\theta = \sin^{-1}\left(\frac{x_1 - x_2}{\sqrt{(x_1 - x_2)^2 + (y_1 - y_2)^2}}\right) \qquad (1)$$

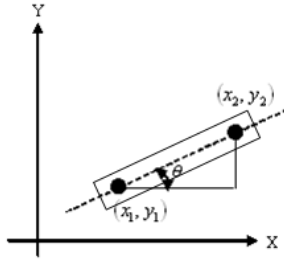

Fig.4. The Virtual Gradient Sensor

4.3. Autonomous walk along a line

Before correcting an image captured with a virtual camera, the image is binaried and linearly expanded. The binalization makes tracking a line easier and the linear expansion prevents a line from being segmented when the image is rotated.

There may be several lines except for the line the robot should trace in the captured image as shown in fig.5, when the robot walk along the line. After rotating images, system searches a line from a point close to the robot in the image to find the line the robot should follow.

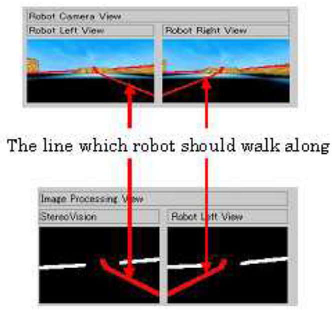

Fig.5. Extracting Line the Robot should Follow

To make a walking command, the left image is used as a base image. The first step is to find a red pixel that is a part of red line from the left image. The second step is to find the rod pixel that has same y-coordinate value as one of the red point found in left image from the right image as shown in Fig.6. This process is run over until a red point is found in the both images. The average number of x-coordinate of the right and the left images decides that the robot is on line or deviates from side to side.

If the robot is on the line, the average x-coordinate is equal to the half size of the image width. If the robot deviates to the right side, the average x-coordinate will be less than the half size of the image width. On the other hand, in case the robot deviates to the left side, the x-coordinate will be more than the half size of the image width (shown as Fig.6). Even if a robot is going straight, as it will shake from side to side, the x-coordinate dose not precisely coincide to the half size of the image width. So the decision of whether the robot is on the line or not is relaxed. If a robot is judged to be on the left side, it will be given a command to move to the right direction, and vice versa.

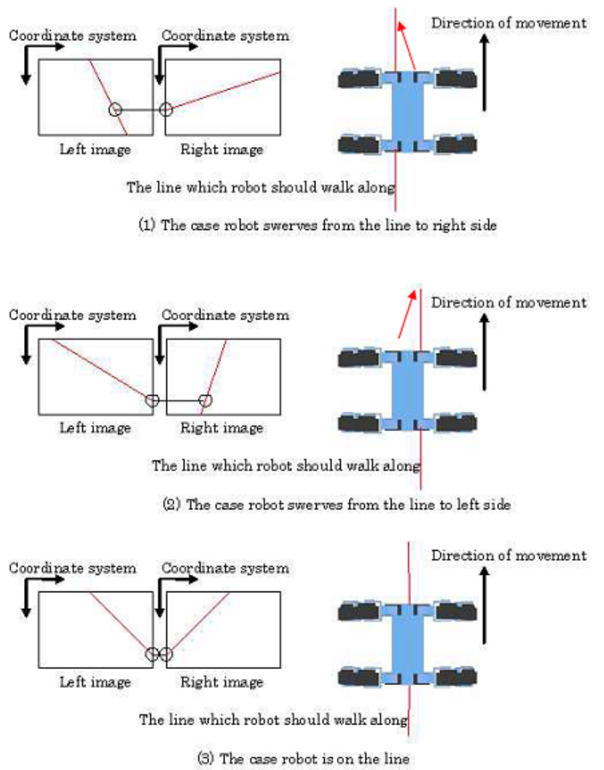

Fig.6. The Decision of a Walk Order

The robot must turnaround only when a draft exceeds a threshold value, because four legged robot always slips during a walk to some extent from side to side. If the line is found in just one of images, say right one, it must turn to the left because it is on the right of the line to track.

4.4. Autonomous walk on a road

When the robot walks on a road, system calculates an imaginary center line passing through the center between two white lines (shown as Fig.7) white lines which are the edges of the road. The robot follows the line with the algorithm shown above.

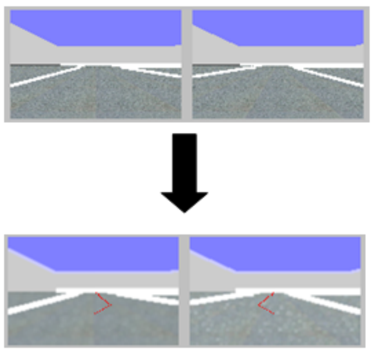

Fig.7.Plot the Imaginary Center Line

Finding a branch is necessary to correspond to a road that has branches. A white line on a road on which there is a branch is disconnected, for example, as shown in Fig.8 (a), in which there is a corner toward left, at the two points marked with arrows a white line is disconnected. If there is no branch at all, a white line remains as it is as shown in Fig 8 (b).

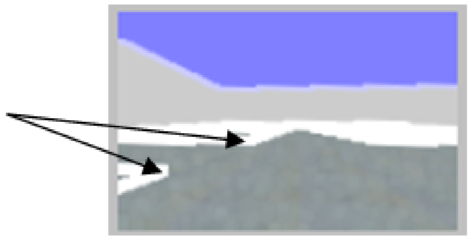

(a) A road with divergence

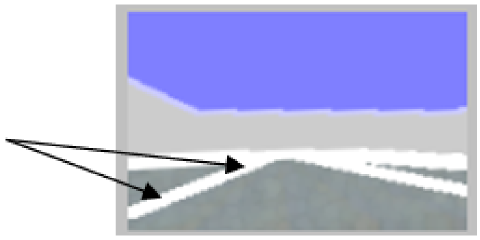

(b) A road without divergence

Fig.8. Branch Point on White Line

Detection of a branch point is done based on the fact me ntioned above. Which direction a branching road extend s to is determined by finding portions where a white line is disconnected. As the robot is always swaying toward right or left while walking, disconnection on a white li ne is not always observable from the robot, that is, even if it has been observed at the previous frame, it may not be observable at the current frame but it may be observe d again at the next frame. This will cause the robot to mi sunderstand there are two disconnection on the same wh ite line.

It is necessary to give a map to a robot in advance because it must determine the route leading it to the goal from the start. The map exploited by a robot is a topological one without distance information. This map allows a robot to infer its current location with respect to branching points. Assuming that distance between two successive branches on a white line is enough long, it is considered that such intermittent observation of disconnection means that the robot staying in a branch observes the same branch repeatedly. Consequently, if a robot encounters the sequence as shown in Fig.9, it can recognize that there is one branch in the interval B and D respectively, where 1 corresponds to the discovery of one disconnection.

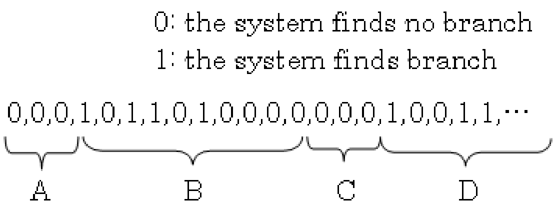

Fig.9 Determine Whether the Robot is at Branch Point

As s robot is subject to non holonomic constraints, it does neither move sideways nor turn without translation. This means that a robot must be given a reparatory of trajectories in the same way as a car-like non holonomic robot. At present, a robot is not given such a reparatory but it must generate a trajectory to turn a corner being close at hand using a distance measurement with a stereo vision. There are, however, the cases it goes over a white line at a corner if it curves to near right angle. To avoid this problem, a bird's eye view of the region observed by the robot using a stereo vision is necessary to guide the robot behavior.

First, correspondence between a right and left image is calculated for each edge of white lines based on an edge based stereo vision. Next, correlation based on the correspondence between pixels successfully corresponded is calculated, then based on the result three dimensional coordinates of points are obtained. A robot judges where to start rotation to turn a corner being close at hand.

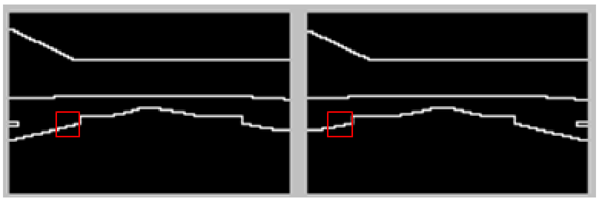

(a) Edge Images

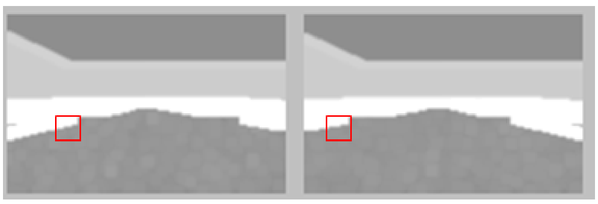

(b) Gray Scale Images

Fig.10 Corresponding Point of Stereo Vision

5. Conclusions and Future Work

This research's aim is to make a virtual robot autonomously walk in the Virtual space and we successfully implement simulation. Now the robot is able to walk autonomously along without a branch. In the case that the road has diverging, system finds the branch point and detects how many branch points the robot passed.

Now, except for up hills or down hills, the system successfully simulates the behavior of a robot on a flat plane with a constant homogeneous friction coefficient. Next we would like to simulate the behavior on rolled ground with variable friction coefficients. To have a robot walk autonomously along a road with several forks, the robot must locate itself refereeing to the map information calculated using given start and goal points to the robot. The robot must recalculate the route, if the robot judges it impossible to go ahead in motion for the reason that the road is occupied with obstacles or the road is too narrow for the robot to go through.

6. Acknowledgment

We greatly appreciate the aid of the Grant-in-Aid for Scientific Research (S) and (A).

7. Reference

[1] Yi PAN, Norihiro Abe, AND Kazuaki Tanaka (2003): The Virtual Debugging System for Embedded Software Development, *SCI2003*, 78-84.
[2] Yi Pan, Norihiro ABE, Kazuaki Tanaka (2003): The Virtual Debugging System for Embedded Software Development, *VRAI2003*.
[3] Yi Pan, Norihiro Abe, Kazuaki Tanaka, Hirokazu Taki (2004): The Virtual Debugging System for Developing Embedded Software Using Virtual Machinery. *Embedded and Ubiquitous Computing, International Conference (EUC 2004),* Aizu, Japan, 85-95.
[4] Norihiro Abe, Yoshinori Takamura, Kazuaki Tanaka, Hirokazu Taki (2003): Construction Of Physics Simulation Environment for Education Using Vortex, In *proceedings of the SCI2003*, 301- 307.
[5] VORTEX Developer Guide, CMLabs Simulation, Inc, 2002
[6] VORTEX Viewer Developer Guide, CMLabs Simulation, Inc, 2001
[7] Toshiaki Oomori, Norihiro Abe, Kazuaki Tanaka, Hirokazu TAKI, Shoujie HE (2005): Concurrent development of Virtual Robots and Real Robots Based on Physical Low, *IMEKO / IFAC / IFIP Workshop on Advanced Robot Systems and Virtual Reality. ISMCR2005*.

Construction of the head model for the operation simulation system targets the brain aneurysm

Toshihide Miyagi, Norihiro Abe
Kyushu Institute of Technology
680-4 Kawazu, Iizuka, Fukuoka 820-8502, Japan
(Email: miyagi@sein.mse.kyutech.ac.jp)

Yoshimasa Kinoshita
Munakata Suikokai General Hospital, Japan

Tatsushi Tokuyasu
OitaNational College of Technology, Japan

Hirokazu Taki
Wakayama University
930 Sakaedani, Wakayama-shi, Wakayama

Shoujie He
VuCOMP, USA

Abstract: In this paper, we propose a system that is necessary for an operation simulation system targeting a brain aneurysm. In traditional clinical training, the doctor has acquired medical skills through experiences of medical operation. But, these training contain some problems that are security and burden to a patient. And so, as a new approach for the medical training, researches of the operation simulation system using Virtual Reality are worked. So, we aim a development of operation simulation system targeting a brain aneurysm, we construct the necessary function for this system such as a detection of blood vessel and brain aneurysm and construction of head model use at simulation.

Keywords: Virtual Reality, Operation simulation, Brain aneurysm, Image processing

I. INTRODUCTION

In traditional clinical training, the doctor has acquired medical skills through experiences of medical operation. But, these training contain some problems that are security and burden to a patient. And so, as a new approach for the medical training, researches of the operation simulation system using Virtual Reality are considered promising.. As a back ground, points that human body is possible to rebuild from high resolution image obtained by CT or MRI, and advancement of computer's processing speed, are adduced. Especially, the purpose of this research is development of the simulation system which targets brain aneurysm that is occurred at inside of blood vessel of the head. The purposes of this research are the detection of the operation target, and modeling the head including the operation target.

Advantages of this system are possible visualizing the position of target and to increase the reality by using actually patient's image data.

In this paper, the methods are shown which detect blood vessel and brain aneurysm, and construct the head model used when the medical operation is conducted not to have aneurysm burst away.

This research is conducted based on our experience on both diagnosis of lug cancer or structural analysis of tracheole from CT images [1][2], how to cut a virtual surface model [3] or a virtual voxel model [4] with a scalpel, and simulation of medical manipulation ICSI using a deformable surface model [5].

II. Detection of the blood vessel

First, we mention about the detection method of blood vessel. When we want to detect the brain aneurysm, it is postulated that blood vessel is detected. Images that we use are MRA, so the brightness value of the artery is higher than else parts. Then, we apply the growing region method to image and decide as blood vessel when the brightness value of the part that is near blood vessel is higher than threshold value. The threshold value is decided based on the experience.

And, the start point of this process is setup by following method; raster scanning the image and picking up the point that brightness value is higher than threshold as a start point.

Fig. 1 shown the how to growing the region when this process.

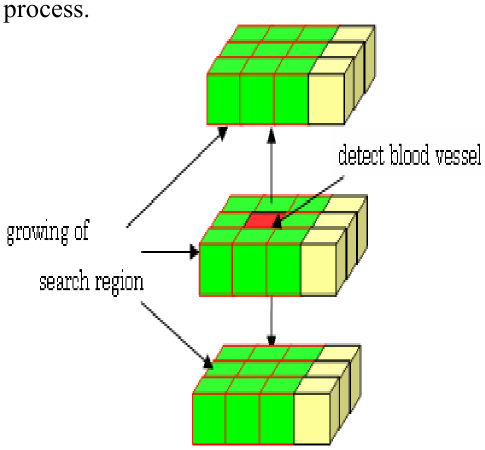

Fig.1. The region growing for detect blood vessel

III. Detection of the brain aneurysm

If it is possible to make the location of a brain aneurysm clear in advance before training or diagnosis, it will help not only a trainee confirm a target but also a doctor determine if medical operation is needed or not.

In this system, the detection method of the brain aneurysm is based on facts that a brain aneurysm is a lump (1) and it occurs near the divergent point between blood vessels (2).

First, we focused the fact 1 and examine the expanse appearance of the local area of the blood vessel by apply the region growing method to the blood vessel that is detected by the method shown in chapter 2. And, we detect the part that the expansion area is larger than else area as a brain aneurysm.

But, this method comprehends the mis-detection, so we apply the fact 2 to detection method; when the area A and B are detected by the method based on the fact 1, we examine the distance from the bifurcation to point A and B. If the distance is near compare with the set up value, this point is detected as a brain aneurysm. This method is shown in Fig. 2.

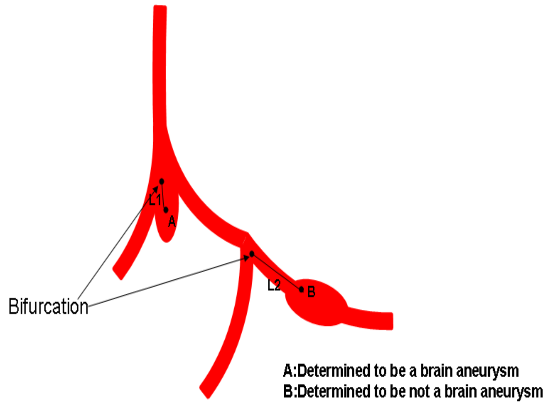

Fig. 2. Detection with the bifurcation distance

IV. Construction of the head model using a CT images

When we simulate an operation, construction of the head model to be operated is needed.

In this system, the head model is restored based on CT images taken from a patient who will be receive medical operation. This allows the operation simulation that meets each patient's medical condition.

In this system, three types of CT images shown below are used.

1, Image extracting only bone
2. Image extracting both bone and artery
3. Image extracting all bone, artery and vein

It seems apparent to obtain artery and vein region can be extracted with difference operation from these images,

$$\text{artery} = \text{Image2} - \text{image1} \qquad (1)$$

$$\text{vein} = \text{Image3} - \text{image2} \qquad (2)$$

As shown method above, we extract the artery and vein. Additionally, we extract the bone using the growing region method explained in section 2.

V. Execution result

In this chapter, we show detection result of blood vessel, detection result of brain aneurysm and construction result of head model based on CT images.

Detection result of blood vessel and brain aneurysm are shown the result applied to 4 MRA images. Construction result of head model is shown the result applied to CT image.

1. Detection result of the blood vessel

In this section, we show the detection result of blood vessel. Fig. 3 shows original image and Fig. 4 shows detection result.

As shown in Fig. 4, it is confirmed the detection is successfully.

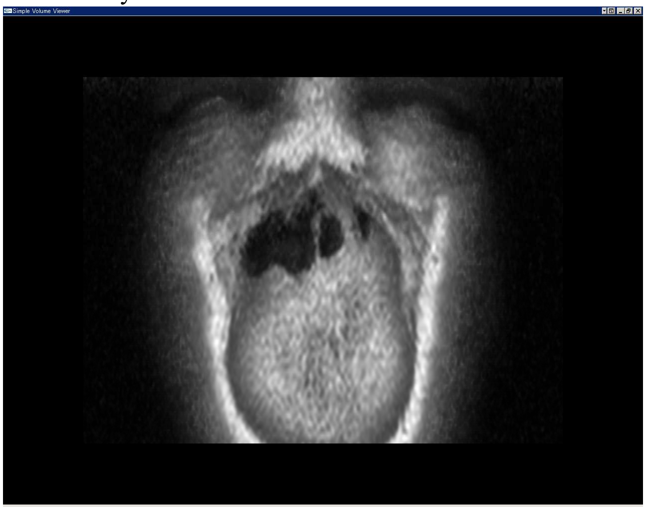

Fig. 3. An original image

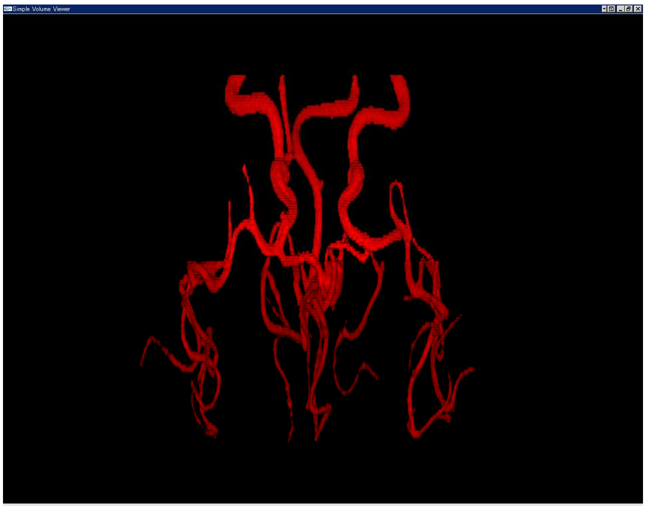

Fig. 4. Detected result of a blood vessel

2. Detection result of brain aneurysm

Next, we show the detection result that is detected by the proposed method in Fig. 5. The yellow part is shown the candidate part that is detected as brain aneurysm.

Table 1 shows result that the one uses only the fact 1 and the other uses the fact 1 and fact2. Table 1 shows each one is possible to detect the brain aneurysm, additionally, it is possible to decrease a false positive using the fact 2 about 48[nodules/case].

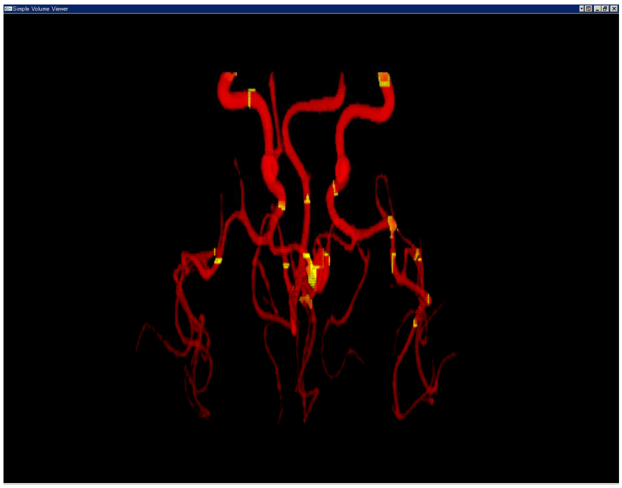

Fig. 5 Detection result of brain aneurysm

Table 1 Detection result of brain aneurysm

	True positive	False Positive [nodules/case]
Not use distance	100%(4/4)	82.25
Use distance	100%(4/4)	36.25

3. Construction result of head model

In this section, we show the construction result of head model using CT images. In fig.5, the white, red and blue region correspond to bone, artery and vein, respectively..

As shown in Fig. 5, artery and vein region are detected to a certain degree, but artifacts or leakages are found, so the improvement is needed.

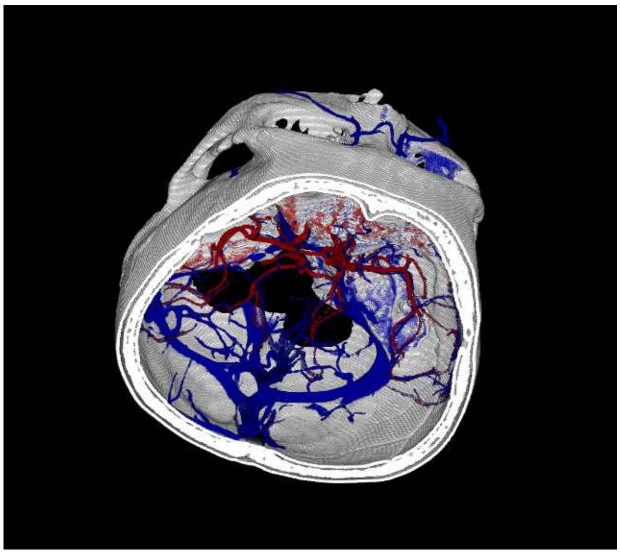

Fig. 6. Constructed head model

VI. Conclusion

In this article, functions necessary for the system to be used for medical training, detection of both blood vessel and brain aneurysm are shown, Then how to construct a head model which will be expected to help trainees experience virtual medical operation is shown. At present, it is not perfect owing to misdetection of critical parts inevitable for the operation necessary to pinch a brain aneurism.

In a future, it is necessary to simulate the process in which an aneurism is pinched with a clip. .In this problem, reducing calculation time taken to simulate object deformation is one of major challenge in our work. As the resolution of this problem, parallel computation with GPU is under construction.

VII. Acknowledgement

We greatly appreciate the aid of the Grant-in-Aid for Scientific Research (S) and (A).

REFERENCE

[1] Tetsuya Sato, Norihiro Abe, Yoshimasa Kinoshita, Shoujie He (2006): *Toward Developing Multiple Organs and Diseases Diagnosing Intellectual System referring to Knowledge Base and CT Images*, accepted, CBMS 2006(19th IEEE International Symposium on Computer-Based Medical Systems), 359-364.

[2] Tetsuya Sato, Norihiro Abe, Yoshimasa Kinoshita, Shoujie He (2007): *Toward the Developmentof an Intelligent System for the Diagnosis of Multiple Organs and Diseases*, The Second International Conference on Complex Medical Engineering-CME2007, 703-710.

[3] Koichi Yamamoto, Kazuaki Tanaka, Norihiro Abe, Yoshimasa Kinosita, Akira Yokota (1999): *Cutting operation of virtual object and it application to medical simulation*, ICAT'99, 161-165.

[4] D. Tokumoti, N. Abe, K. Tanaka, H. Taki, Y. Kinoshita (2004): *Cutting of the Voxel ModelUsing a Haptic Feedback Device*, Conference on Systemics, Cybernetics and Informatics (SCI), Orlando, Florida.

[5] Ryutarou Mizokami, Norihiro Abe, Yoshimasa Kinoshita, Shoujie He (2007): *Simulation of ICSI Procedure Using Virtual Haptic Feedback Model*", The Second International Conference on Complex Medical Engineering-CME2007, 176-181.

The construction of remote communication system between haptic-devices

Yasutaka UCHIDA, Norihiro ABE

Kyushu Institute of Technology, 680-4, Kawazu, Iizuka-shi, Fukuoka, 820-8502, JAPAN
(Tel : 81-948-29-7776)
(uchida@sein.mse.kyutech.ac.jp)

Yoshimasa KINOSHITA

Munakata Suikokai General Hospital
341-1, Kamisaigou, Fukutsu-shi, Fukuoka, 811-3298, JAPAN
(Tel : 81-940-34-3111)

Tatsushi TOKUYASU

Oita National College of Technology
1666, Oaza-maki, Oita-shi, Oita, 870-0152 JAPAN
(Tel :81-97-522-6072)

Hirokazu TAKI

Wakayama University
930, Sakaedani, Wakayama 640-8510, JAPAN
(Tel:81-73-457-8126)

Shoujie He

VuCOMP
1231 West Campbell Road Richardson, TX 75080 U.S.A
(Tel :1-888-266-7462)

***Abstract*:** Recent years, advances in medical technology are remarkable. With the development, many lives being difficult to save are saved and burden reduction to patients is realized. Further growth will be expected in future. As there are a few cases which need the latest medical technologies, it is difficult for doctors to acquire experience to cope with such cases. But the human life must be respected, so they are not permitted to practice the operations for a real patient. At present, they must learn by experiences such as lectures, reference books, the teach wares of past successful examples and the operation practices with experienced professors.
This research purpose is construction of the operation simulation system which allows learners to experience the medical specialist's manipulation of a knife and a scissor in operation and makes it possible to reproduce the real operation.

Keywords: PHANTOM**,** Haptic-feedback device, Communication, Skype

I. INTRODUCTION

Recent years, advances in medical technology are remarkable. With the development, many lives being difficult to save are saved and burden reduction to patients is realized. Further growth will be expected in the future.

On the other hand, the quantities of learning required to doctors and young trainees increase to cope with medical technique which progress every day. From this aspect, their burdens grow bigger and bigger. This phenomenon is thought as one of the factors that candidates for doctors decrease.

As there are a few cases which need the latest medical technologies, it is difficult for doctors to acquire experience to cope with such cases. But the human life must be respected, so they are not permitted to practice the operations for a real patient. At present, they must learn by experiences such as lectures, reference books, the teach wares of past successful examples and the operation practices with experienced professors.

In these methods, the true experience is limited and the technical acquisition takes time. So the construction of the operation simulation system with reality is hurried to solve this problem.

So, this research purpose is construction of the operation simulation system which allows learners to experience the medical specialist's manipulation of a knife and a scissor in operation and makes it possible to reproduce the real operation.

II. SYSTEM STRUCTURE

Fig.1 shows the system structure in this research. The operator uses PHANTOM, and manipulates the operation on the virtual space. (PHANTOM is haptic-feedback device.) The computer is connected with this PHANTOM in a special line.

Next, we prepare a similar another device. It is necessary to transmit data between two spots to enable the operation training in the remote place. OpenGL was used for drawing of the operation of PHANTOM. Microsoft Visual C++ is used for the display and operation by a virtual space. As the system configuration, it is the above.

We develop this communication system, go over about the efficiency of the communication, and make a suggestion.

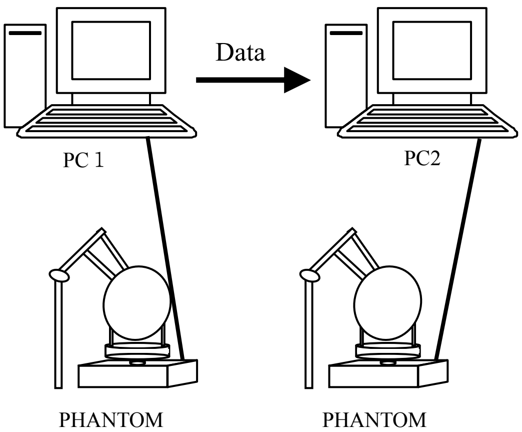

Fig.1 System structure

1. PHANTOM

PHANTOM is a three dimensional haptic feedback device. The user uses it, and sense of force interaction of high accuracy can be realized. PHANTOM can not only visual information, but also re-create realistic the sense of touch that is one of senses to which expressions are abundant most in three dimensional object and dynamic interaction.

Another feature, it loads the positional sensor of at least three degree of freedom.

In addition, it loads the force feedback mechanism of at least three degree of freedom by torque control that used direct current motor. The update rate is also very high, and it is possible to process it by about 1000Hz. So it can re-create a more detail, more exact model. Fig.2 shows actual PHANTOM.

Fig.2 PHANTOM Premium 1.5

2. Skype communication

Skype is Internet communication service. It uses technology of PSP. As for Skype merit, a telephone steady in a low-speed line and firewall is possible. And, security is secured because data is encrypted. The other party's online can be easily distinguished. All in all, it is used telephone service and messenger. It applied it to the data communication in this research.

3. Open GL

Open GL is programming interface for 3D graphics. It is possible to operate at the very high speed, and to draw in 3D highly accurate image.

III. DATA COMMUNICATION

Fig.3 shows the application that we develop. OpenGL is used at the left of application for drawing of PHANTOM point that the user operates.

As a method of operation

1. Selection of other party user's ID
2. Selection of sender side or receiver side
3. Selection of UDP communication or TCP communication

The communication can begin by completing this procedure. The communication is confirmed; when the user starts the transmission of data, they can check the data-coordinates of present PHANTOM point, force to hang to PHANTOM, image compressibility and image update time.

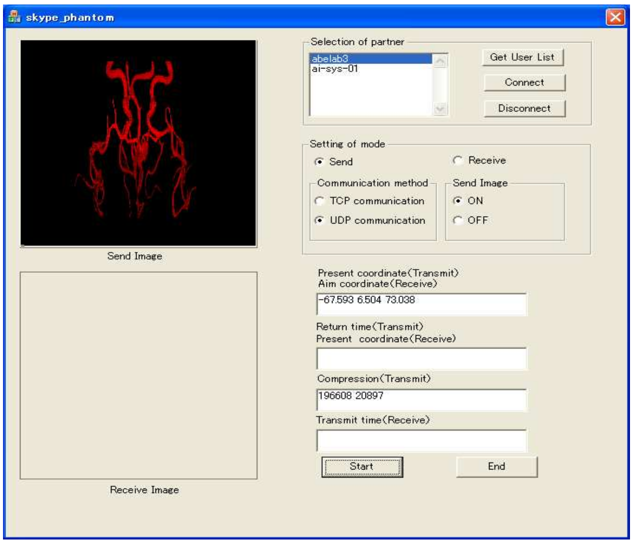

Fig.3. Operation screen

IV. DATA COMMUNICATION

The communicated data is PHANTOM's coordinate data, force data and image data in the research. The communication environment is in LAN in the laboratory.

1. PHANTOM coordinate data

The coordinate data is the numerical data in each direction of x, y and z to be able to treat PHANTOM. We compare the data update time of the UDP communication with that of TCP communication by Skype communication.

As a result, the data up data time of the UDP communication is shorter than that of TCP communication. As this factor, UDP communication is doesn't confirm the arrival of data on the receiver side, and the sender side keeps sending data one after another. When the data come off and the lack of one, the data is sent again to transmit data surely in the TCP communication. So it takes time to communicate.

2. Image data

The volume of image data is very large compared with that of coordinate data and the time needed to send ima ge data is also long. This makes a use feel unnatural be cause images are not synchronized with the haptic sensati on. Consequently, the compressed image data must be se nt and then restored at the destination.

Fig4 shows this idea.

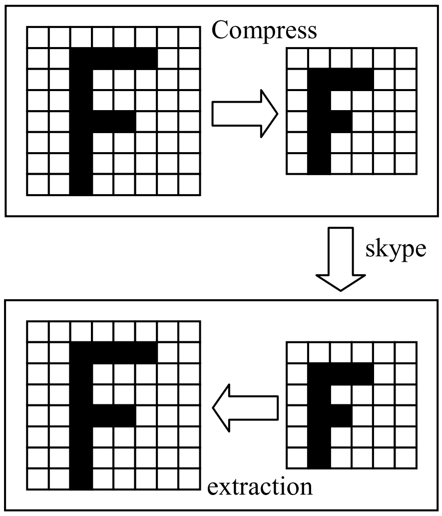

Fig.4. Idea of image compression

For 4 types of image data as shown in Table 1, the upd ate rate of each image at destination are examined, and t he influence which the compression rate gives the update rate are also measured, as shown in the same table.

When the compression rate is 100%, the update rate in creases along with the decrease of resolution, and the up date rate for the images of 100×100 is almost same as t hat for the 50×50 image.

When the compression rate is 80%, the same trend is ob served as that of 100% compression. The update rates of all images except for the 500X500 image are almost sa me.

When the compression rate is 50%, the same update r ates are obtained for both 100×100 and 50×50 images bu t the rates decrease for 500×500 and 300×300 images. It seems that when an image is too large, the time taken i n compressing the image is more than that taken in trans mitting it.

Table1 Result of image data communication

ms

		Compressibility		
		100%	80%	50%
Resolution	500×500	47	32	200
	300×300	31	16	100
	100×100	16	15	16
	50×50	15	15	15

It is difficult to improve the efficiency of image data t ransmission with method mentioned above. To reduce the time required, it seems effective to reduce the size of th e image to be sent but too small image is useless.

Another solution is to use more efficient computer co nsisting of 4 CPU; after dividing an image into 4 region s and by allocating each region to each CPU using APL provided with OpenMP, the efficient compression of an image is attained. Unfortunately, the computational efficie ncy is not quadruple but twice of the original one becaus e it takes time to divide the original image into 4 region s.

In a medical application with use of haptic device, it is considered that a visual point is not changed often but the tissue added operation with medical tools such as a scalpel or clamp is locally deformed. This implies that the image observed from a view point will not change globally. Consequently, the region except for the deformed portion remains intact; the difference between successive two images can be exploited. Of cause, a deformed part varies along with the movement of a medical tool, difference between successive two deformed regions. The detailed method is now under construction.

V. CONCLUSION

In this research, we develop communication system using the haptic-feedback device PHANTOM and Skype communication.

We develop a virtual space on the computer, and the user operates PHANTOM while watching the virtual space. This virtual space is developed by OpenGL and Microsoft Visual C++. The communication data is the coordinate data and the image data.

At a result, because coordinate data is the numerical data, the early communication was comparatively possible. But, the capacity of the image data is larger, and it takes time to communicate. We develop the data compression method and improve the performance of the computer, and try the efficiency improvement of the transmission rate. So, we were able to obtain the result of corresponding.

Problems to be solved include followings:

A method to calculate collision detection between a medical tool and tissue

A method to simulate deformation process along with calculating haptic reactive force

How to make both image and reaction force synchronized at the destination to give a remote trainee the high reality of medical operation.

ACKNOWLEDGMENT

We greatly appreciate the aid of the Grant-in-Aid for Scientific Research (S) and (A).

REFERENCE

Study on communcation system between haptic device(2009), Yasutaka UCHIDA, Norihiro ABE, Yoshimasa KINOSHITA Hirokazu TAKI, Tatsushi TOKUYASU, Shoujie He, AROB 2009

Construction of Virtual Dense Elastic Object from Medical Image Data and Deformation with Haptic Device

Hiroshi TAKADA, Norihiro ABE

Kyushu Institute of Technology, 680-4 Kawazu, Iizuka-shi, Fukuoka, 820-8502, JAPAN
(Tel: 81-948-29-7776)
(takada@sein.mse.kyutech.ac.jp)
(abe@mse.kyutech.ac.jp)

Yoshimasa KINOSITA

Munakata Suikokai General Hospital
341-1, Kamisaigou, Fukutsu-shi, Fukuoka, 811-3298, JAPAN

Tatsushi TOKUYASU

Oita National College of Technology
1666, Oaza-maki, Oita-shi, Oita, 870-0152, JAPAN

Hirokazu TAKI

Wakayama University
930, Sakaedani, Wakayama 640-8510, JAPAN

Shoujie He

VuCOMP
1231 West Campbell Road Richardson, TX 75080, USA

Abstract: In recent years, there have been various problems in medical treatments, of which human error by the surgeon in an operation. Therefore, the simulation of a medical operation with a sense of reality, as in a real operation, is required. Our objective in this research is to construct the training system of a medical operation which gives the haptic sense of operation, and an inexperienced surgeon can try operation again and again to improve his skill by using the system. We construct a virtual dense elastic object which considers inner tissue from medical image data such as computed tomography (CT) or magnetic resonance imaging (MRI), and we use a spring-mass model to represent the movement of elastic deformation. Haptic sense which is generated from a deformation of the object is given to an operator with haptic device in this system. In this paper, we study a real time rendering and real time deformation which is needed in surgical simulation.

Keywords: Virtual Reality, Surgical Simulation, Haptic Device, Deformation

I. INTRODUCTION

In recent years, there have been various problems in medical treatments, of which human error by the surgeon in an operation is one of the most serious problems. The major cause is considered to be the surgeon's lack of experience. A great deal of experience is necessary in medical operations, and tactile or haptic sensations, such as a manual sensation, become important in order to prevent mistakes. However, it is impossible to use a real human body to practice a medical operation. Therefore, the simulation of a medical operation with a sense of reality, as in a real operation, is required.

We have studied cutting during an operation using the surface model (Koichi [1]), the deformation of the surface model (Ryuichirou [2]), and synchronization between audiovisual and haptic feelings (Yoshihiro [3]) in previous research in our laboratory in order to construct the training system of a medical operation.

In this research, we approach the construction of the training system for a medical operation by creating a virtual human organ model which is deformable, and deforming the model with a haptic device called PHANToM. The data for the human organ were obtained from medical image data such as computed tomography (CT) or magnetic resonance imaging (MRI) to express the patient's organs. Real time rendering and deformation inevitable in surgical simulation are shown in detail.

II. SYSTEM CONFIGURATION

As shown in Fig.1, this system consists of two PCs connected with SCRAMNet+: one PC (PC1) renders a virtual dense elastic object with Open GL and also calculates the deforming process of the object, and the other (PC2) operates PHANToM and calculates the haptic feedback given to the operator through PHANToM. In this way, the process of calculation is able to distribute. A flowchart of the entire process is shown in Fig. 2. Information of PHANToM is shared between PC1 and PC2 through high speed network SCRAMNET to make it possible both for an operator to deform an organ with PHANToM at PC1 and to simulate corresponding deforming process at PC2.

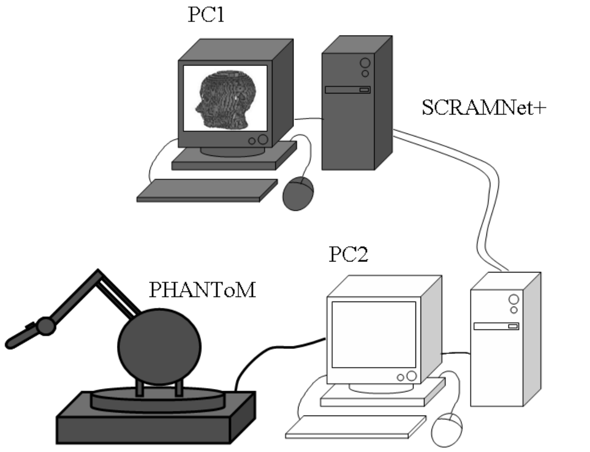

Fig.1 System configuration

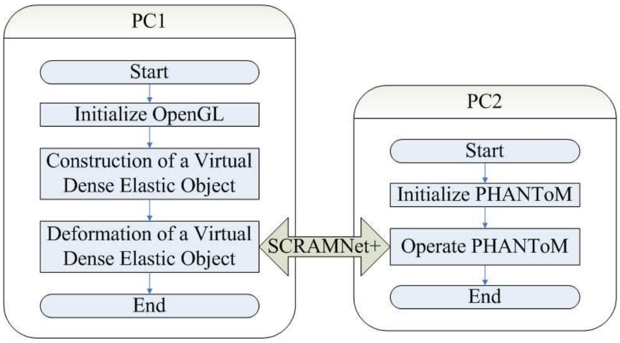

Fig.2 Flowchart of entire process

III CONSTRUCTION OF A VIRTUAL DENSE ELASTIC OBJECT

In the surgical simulation which needs the cutting or deforming operation, not only surface information of the object but also the inner one of the tissue must be considered. Therefore, a virtual dense elastic object is constructed in order to create a virtual human organ model reflecting deformable inner tissue of the organ.

1. Creation of the loading data

We use medical image data such as CT or MRI to express any human organs. In order to create the CT or MRI data in a new format, which can be loaded into our system, we used the OpenGL Volumizer. The new format data include size of partition number of voxel of the original medical image data and the RGBA value of each voxel.

2. Creation of a virtual dense elastic object

As shown in Fig.3, at first, rigid voxels are obtained by dividing the area where the model is to be created. The data loaded in our system consist of both voxels corresponding to the substance and those corresponding to the vacancy. Not to waste the memory and for saving the rendering time, only the former remain as real data but the latter are deleted. Position and the connection of the each voxel are stored in the memory to keep the shape of the object. Then, voxels are divided into tetrahedrons to make them deformable. Finally, we set RGBA value as color information to each tetrahedron from the data which we create.

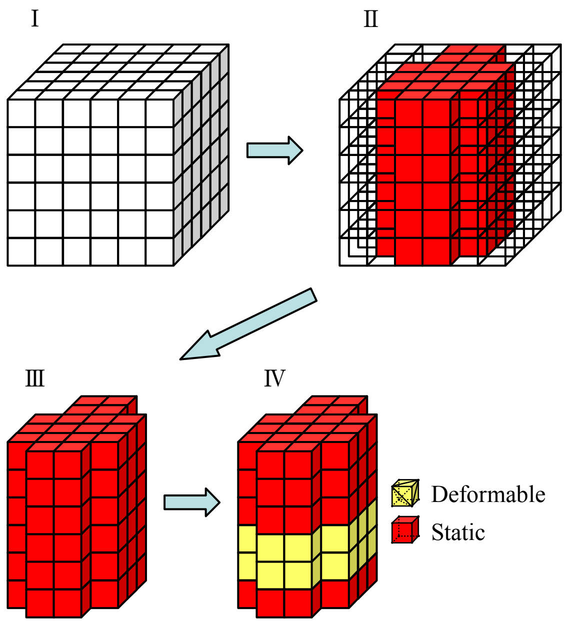

Ⅰ. Divide creating area into voxel
Ⅱ. Load the data
Ⅲ. Delete not necessary voxel
Ⅳ. Divide deformable area into tetrahedron

Fig.3 Construction of a virtual dense elastic object

3. Spring-mass model

A spring–mass model is a model which is a set of mass-less springs with a point mass. As shown in Fig.4, a spring-mass model is given to each tetrahedron in order to realize deformation based on mechanics (Koichi [4]). We replace each side of a tetrahedron by a spring and damper, and each vertex of a tetrahedron by a point mass. When vertex moves, a spring force is generated from the displacement between connected vertices and the object deform elastically. Here by using a damper, we apply a damping which is proportional to the velocity of the vertex to the force.

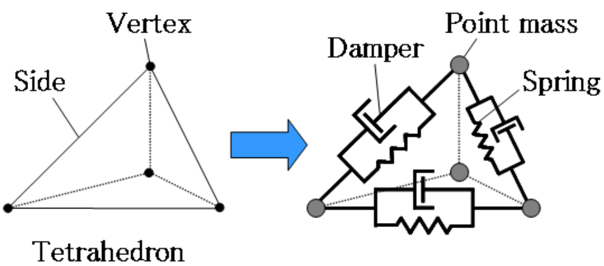

Fig.4 Spring-mass model

4. High performance of rendering process

We set an RGBA value for each tetrahedron as color information to render a virtual dense elastic object.

In order to increase the resolution of the object, we have to divide the object into a lot of tetrahedrons. If partition number of voxels increases, the number of tetrahedrons also increases and the process of rendering all tetrahedrons results in a bad performance. Therefore, we render only the visible part of the object from the user's viewpoint in order to improve the performance. The inner object is invisible to the user, so it is not necessary for it to be rendered. We make a rendering list of visible tetrahedrons, and we obtain a high performance in the rendering process by using that list. In order to judge whether a voxel is visible or not, we check the surrounding of the voxel. As shown in Fig.5, if a voxel is covered with voxels which has color information, the voxel is inner object and it will be invisible. If there is at least one voxel which do not have the color information around the voxel, the voxel is surface of the object and it will be visible.

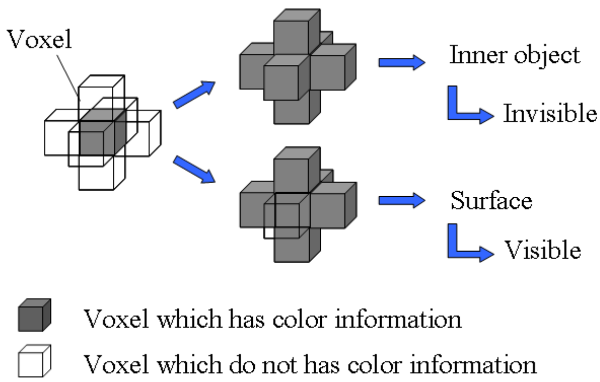

Fig.5 Judging visible or not

IV. DEFORMATION OF A VIRTUAL DENSE ELASTIC OBJECT

Tetrahedrons share their vertices, and if the vertices move, the tetrahedrons deform. Therefore, we can represent the deformation process of a virtual dense elastic object as the movement of the vertices. A medical tool which deforms the object is represented as a rigid stick, and it is controlled with PHANToM. Information such as position, acceleration, and force are stored on each vertex. Each force acting on a vertex can be obtained from the velocity and the displacement between vertices connected with the springs and the dampers, and it can express as an equation (1).

$$F_i = \sum \left(\frac{l_{ij}}{|l_{ij}|} k_{ij} \left(|l_{ij}| - |l_{0ij}| \right) + c_{ij} v_{ij} \right) \tag{1}$$

$$l_{ij} = x_i - x_j$$

F_i is force of point mass i, x_i is position of point mass i, x_j is position of point mass j, k_{ij} is constant of a spring between point mass i and j, v_{ij} is relative velocity of point mass i and j, c_{ij} is coefficient of viscosity of a damper between point mass i and j. Then compute the motion equation to obtain each position of the vertex using the force. The Euler method is used to solve the dynamic characteristics of the spring–mass model using Hook's law and a motion equation. Then the information stored on each vertex adjacent to the vertex that moved is recomputed and the entire object will deform. The deformation effect passes to the operator through the PHANToM.

1. Multipoint collision detection

Collision between the medical tool and the object is detected at vertices of tetrahedrons, so multipoint collision detection is needed to implement the collision with a rigid stick used as the medical tool. As shown in Fig.6, the medical tool and the vertex are express as a vector to detect collision. Collision is detected by calculating the cross-product and length of the vector. We label the edge of the medical tool *AB*, and the vertex C. Then we can express the vector *AB*, *AC*, and *BC* as $\vec{D}$, $\vec{E}$ and $\vec{F}$ respectively. A collision is detected when *C* is on the segment *AB*. It is possible to judge whether *C* is on the line *AB* or not by checking whether or not $\vec{D}$ and $\vec{E}$ are parallel using a cross product of the vector. A normal vector can be obtained from a cross product. If the result of the normal vector is zero, then $\vec{D}$ and $\vec{E}$ are parallel, that is to say *C* is on the line *AB*. Next, if *C* is on the line *AB*, we check the length of $\vec{E}$ and $\vec{F}$, and if they are less than or equal to length of medical tool, *C* is on the segment *AB*. The length of the medical tool is the length of $\vec{D}$. Multipoint collision detection is implemented by adding the vertex which collides with the medical tool to the list of collided vertex.

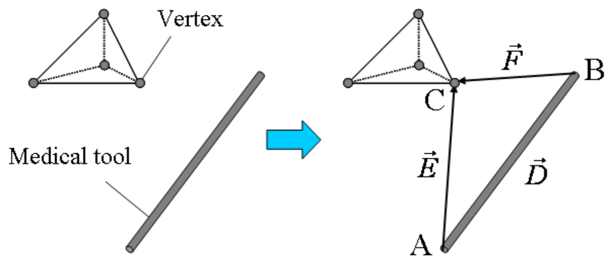

Fig.6 Multipoint collision detection

2. High performance of deforming process

If partition number of tetrahedrons increases to improve the resolution, the number of vertices to calculate also increases. The process of deforming the object requires high computational power when we calculate all part of the object. In a real medical operation, the target tissue is only a portion of the whole organ. This time, in order to reduce the computational load of deforming process, we select a portion of the object as a deformable object. In order to select a portion which deform, we mark the target when we create the loading data. Then change around the area where the target exists into deformable area. Deform not all part of the object, but select deformable area and deform only the area to reduce the computational load.

V. EXECUTION RESULT

A virtual dense elastic object restored from CT is shown in Fig. 7, where the partition number of voxels is (256, 256, 77). The entrails appear as shown in Fig. 7 if the threshold amount is changed. This fact shows that a virtual dense elastic object is successfully implemented.

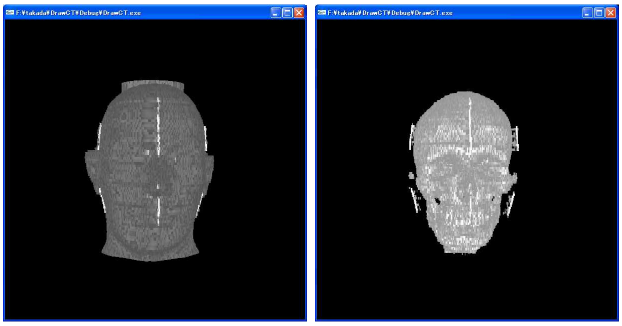

Fig.7 Rendering head data

Fig.8 shows the deformation of the virtual dense elastic object. This time, the MRI data of blood vessel of brain on which aneurysm occurred is used as the virtual human organ object. The partition number of voxels is (336, 336, 140). 10 voxels around the gravity center of the aneurysm are transformed into deformable area and they are deformed by operating PHANToM. In this case, we confirmed that the blood vessel is deformed with a medical tool and the adequate haptic feedback is returned to operator's hand.

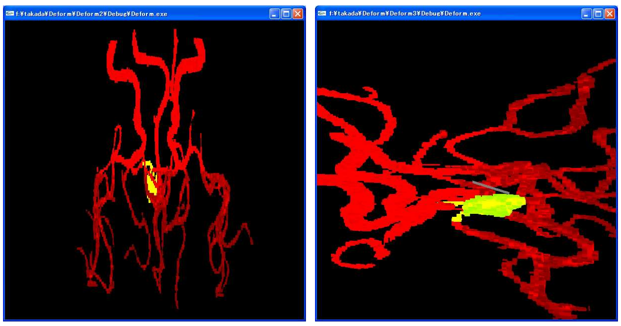

Fig.8 Deforming blood vessel data

VI. CONCLUSION

We have constructed a system of rendering a virtual dense elastic object obtained from medical image data such as CT or MRI data, and expressing deformation of the tissue in order to achieve the development of the training system for a medical operation.

This time, in order to render and deform in a real time, we render only the visible part of a virtual dense elastic object from the user's viewpoint, and deform only the deformable part which is selected by a user. However, there is a limit of partition number of voxels to process in real time and more improvement of performance is demanded. In a real medical operation, deforming part is not only the tissue of the target but also the route to access the target must be deformed. We are now studying how to accelerate the deforming process by using the parallel processing such as OpenMP or GPU to improve the performance of deforming process. In this research, we also confirmed the force obtained from computing the amount of deformation. However, we need the real haptic feeling as in a real operation in the surgical simulation. In the future, we would like to give the operator a real haptic feeling.

ACKNOWLEDGMENTS

We greatly appreciate the aid of the Grant-in-Aid for Scientific Research (S) and (A).

REFERENCES

[1] Koichi Y, Kazuaki T, Norihiro A, et al., "Cutting operation of virtual object and it application to medical simulation", **ICAT'99,** 1999, pp.161-165.
[2] Ryuichirou M, Norihiro A, Yoshimasa K, et al., "Simulation of ICSI Procedure Using Virtual Haptic Feedback Model", **CME2007** 2007, pp.176-181.
[3] Yoshihiro T, Norihiro A, Hirokazu T, et al., "Synchronization between Audiovisual and Haptic Feeling for Constructing Edutainment Systems", **Journal of Virtual Reality,** Vol.12, No.1, 2008, pp.27-36.
[4] Koichi S, **Introductory Book of Making Dynamic Animation with OpenGL,** Tokyo: Morikita Publishing Co, 2006

The Fifteenth International Symposium on Artificial Life and Robotics 2010 (AROB 15th '10),
B-Con Plaza, Beppu,Oita, Japan, February 4-6, 2010

Stability Analysis of 3D Grasps by Considering Curvatures and Torsions of Contact Geometry

Takayoshi Yamada[1], Toshiya Taki[2], Manabu Yamada[2], Yasuyuki Funahashi[3], and Hidehiko Yamamoto[1]

1: Gifu University, 1-1, Yanagido, Gifu, 501-1193, Japan
(Tel: 81-58-293-2515; Fax: 81-58-293-2491; Email: yamat@gifu-u.ac.jp)
2: Nagoya Institute of Technology, Gokiso, Showa, Nagoya 466-8555, Japan
3: Chukyo University, 101 Tokodachi, Kaizu-cho, Toyota, Aichi 470-0393, Japan

Abstract: This paper analyzes 3-dimensional static grasp stability taking into account of contact geometry (metric tensor, curvature, and torsion). Grasp stiffness matrices are derived by replacing each finger with a 3-dimensional spring model. The stability is evaluated by eigenvalues and eigenvectors of the matrices. Any friction condition is considered at each contact point. That is, rolling contact occurs at friction contact point, and sliding contact occurs at frictionless contact point.

Keywords: Grasp stability, 3D spring model, frictionless grasp, frictional grasp, curvature, torsion.

I. INTRODUCTION

Magicians and jugglers perform dexterous and fine manipulation of multiple objects by their own hands. Multi-finger robotic hands also have potential ability executing the manipulation, because the hands have been developed and improved on the basis of human hands.

Stability is the tendency of a system to return to an equilibrium state when the system is displaced from this state. Yamada et al. [1][2][3] explored static grasp stability of single object and multiple objects. Arimoto and Yoshida [4] discussed dynamic stability by considering spring-mass-damper systems. In these analyses, curvature effect at contact point was considered.

To improve the dexterity of the hands, effect of contact surface geometry (metric tensor, curvature, and torsion) is analyzed in static grasp stability of single object in three dimensions. This analysis is formulated from the viewpoint of potential energy method.

II. PROBLEM FORMULATION

As shown in Fig. 1(a), we suppose that an n-fingers robot hand grasp an arbitrary shaped object in three dimensions. We analyze stability of the grasp.

1. Assumptions

For simplicity of discussions, the following conditions are assumed.

(A1) Both an object and fingers are rigid bodies.

(A2) The contact between two bodies is of single contact.

(A3) Initial grasp configuration is in wrench (force and moment) equilibrium.

(A4) Infinitesimal configuration displacement of an object occurs due to external disturbance.

(A5) The relationship between finger configuration displacement and reaction force is replaced with a three-dimensional orthogonal spring model.

In Assumption (A5), the spring stiffness is denoted by $K_i = \mathrm{diag}[k_{xi}, k_{yi}, k_{zi}] \in \Re^{3\times 3}$, where subscript i means finger number. Direction of the stiffness is fixed along the axes of fingertip coordinate frame. In Assumption (A3), the spring is compressed at initial configuration and generates initial fingertip force $\boldsymbol{f}_i = K_i \boldsymbol{x}_{fi0}$.

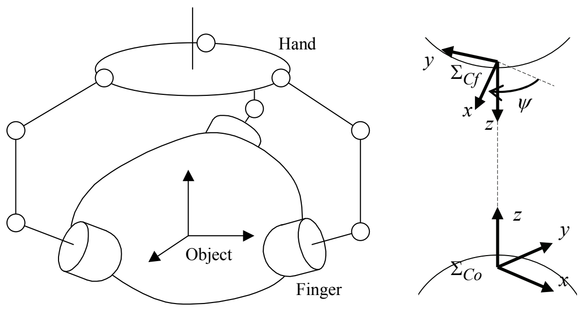

(a) (b)

Fig. 1. An object grasped by a multi-fingers hand, and torsion between contact coordinate frames.

2. Symbols

The following coordinates and notations are used.

Σ_{bo} : Initial object coordinate frame.

Σ_o : Displaced object coordinate frame.

Σ_{Lo} : Local coordinate frame at contact point on the object surface.

Σ_{Co} : Contact coordinate frame on the object surface.

Σ_{bf} : Initial finger coordinate frame.

Σ_f : Displaced finger coordinate frame.

Σ_{Lf} : Local coordinate frame at contact point on the finger surface.

Σ_{Cf} : Contact coordinate frame on the finger surface.

$\boldsymbol{\varepsilon}_o \in \Re^6$: Configuration (position and orientation) displacement of the grasped object.

$\boldsymbol{\varepsilon}_f \in \Re^6$: Configuration (position and orientation) displacement of the finger.

$$\boldsymbol{\varepsilon} := [\boldsymbol{x}^T, \boldsymbol{\xi}^T]^T = [x, y, z, \xi, \eta, \zeta]^T \tag{1}$$

$\boldsymbol{\alpha}_o \in \Re^2$: Displacement parameter of contact point on the object surface.

$\boldsymbol{\alpha}_f \in \Re^2$: Displacement parameter of contact point on the finger surface.

$\psi \in \Re$: Torsion between two objects (Fig.1(b)).

${}^aT_b \in \Re^{4\times4}$: Homogeneous matrix expressing configuration of Σ_a in Σ_b.

$$ {}^aT_b = \left[\begin{array}{c|c} {}^aR_b & {}^a\boldsymbol{p}_b \\ \hline 0 & 1 \end{array}\right] \tag{2}$$

Symbols ${}^a\boldsymbol{p}_b$ and ${}^aR_b$ are position vector and rotation matrix. The other homogeneous matrices are similarly defined.

3. Contact Geometry

To derive contact frame velocity on the surfaces, we use contact surface geometry (metric tensor M_C, curvature K_C, and torsion T_C)[5]. Configuration of contact coordinate frame Σ_C in local coordinate frame Σ_L is depend on contact displacement parameter $\boldsymbol{\alpha}$. Hence, body velocity of Σ_c with respect to Σ_L is obtained as

$$\begin{aligned} \hat{V}_{L,C}(t) &:= [{}^LT_C(t)]^{-1}[{}^L\dot{T}_C(t)] \\ &= \left[\begin{array}{cc|c|c} 0 & -T_CM_C\dot{\boldsymbol{\alpha}} & K_CM_C\dot{\boldsymbol{\alpha}} & M_C\dot{\boldsymbol{\alpha}} \\ T_CM_C\dot{\boldsymbol{\alpha}} & 0 & & 0 \\ \hline \multicolumn{2}{c|}{-(K_CM_C\dot{\boldsymbol{\alpha}})^T} & 0 & \\ \hline \multicolumn{3}{c|}{0} & 0 \end{array}\right] \end{aligned} \tag{3}$$

The symbols ${}^LT_C$, M_C, K_C, T_C, $\boldsymbol{\alpha}$ mean ${}^{Lo}T_{Co}$, M_{Co}, K_{Co}, T_{Co}, $\boldsymbol{\alpha}_o$ in case of object surface, and mean ${}^{Lf}T_{Cf}$, M_{Cf}, K_{Cf}, T_{Cf}, $\boldsymbol{\alpha}_f$ in case of finger surface.

III. FINGER POSITION DISPLACEMENT

In this section, we omit subscripts of the number of finger for simple description. Finger configuration displacement ${}^{bf}T_f$ is derived by the following homogeneous matrix:

$$\begin{aligned} {}^{bf}T_f(\boldsymbol{\varepsilon}_f) =& [{}^{bf}T_{bo}][{}^{bo}T_o(\boldsymbol{\varepsilon}_o)][{}^oT_{Lo}][{}^{Lo}T_{Co}(\boldsymbol{\alpha}_o)] \\ &\times[{}^{Co}T_{Cf}(\psi)][{}^{Lf}T_{Cf}(\boldsymbol{\alpha}_f)]^{-1}[{}^fT_{Lf}]^{-1} \end{aligned} \tag{4}$$

Hence, finger position displacement $\boldsymbol{x}_f \in \Re^3$ and finger orientation displacement ${}^{bf}R_f \in \Re^{3\times3}$ is derived by the following form:

$$\boldsymbol{x}_f = [I_3, 0_{3\times1}][{}^{bf}T_f(\boldsymbol{\varepsilon}_f)]\begin{bmatrix} 0_{3\times1} \\ 1 \end{bmatrix} \tag{5}$$

$${}^{bf}R_f(\boldsymbol{\xi}_f) = [I_3, 0_{3\times1}][{}^{bf}T_f(\boldsymbol{\varepsilon}_f)]\begin{bmatrix} I_3 \\ 0_{1\times3} \end{bmatrix} \tag{6}$$

From (4) and (5), finger position displacement depends on displacements $\boldsymbol{\varepsilon}_o$ and $\boldsymbol{\alpha} := [\boldsymbol{\alpha}_o^T, \psi, \boldsymbol{\alpha}_f^T]^T \in \Re^5$.

$$\boldsymbol{x}_f = \boldsymbol{x}_f(\boldsymbol{\varepsilon}_o, \boldsymbol{\alpha}). \tag{7}$$

IV. GRASP STABILITY

1. Potential Energy of the Grasp

From Assumption (A5), potential energy stored in the i-th finger spring is obtained by

$$\begin{aligned} &U_i(\boldsymbol{\varepsilon}_o, \boldsymbol{\alpha}_i) \\ &= \tfrac{1}{2}\{\boldsymbol{x}_{fi0} + \boldsymbol{x}_{fi}(\boldsymbol{\varepsilon}_o, \boldsymbol{\alpha}_i)\}^T K_i \{\boldsymbol{x}_{fi0} + \boldsymbol{x}_{fi}(\boldsymbol{\varepsilon}_o, \boldsymbol{\alpha}_i)\} \end{aligned} \tag{8}$$

Parameter $\boldsymbol{\alpha}_i$ depends on both object configuration $\boldsymbol{\varepsilon}_o$ and contact friction condition, because each finger is replaced by 3D spring model.

$$\boldsymbol{\alpha}_i = \boldsymbol{\alpha}_i^{fc}(\boldsymbol{\varepsilon}_o) \tag{9}$$

This constraint is formulated in the following subsections. Hence, the potential energy is written as

$$U_i^{fc}(\boldsymbol{\varepsilon}_o) := U_i(\boldsymbol{\varepsilon}_o, \boldsymbol{\alpha}_i^{fc}(\boldsymbol{\varepsilon}_o)) \tag{10}$$

Total potential energy of the grasp is given by

$$U(\boldsymbol{\varepsilon}_o) = \sum_{i=1}^{n} U_i^{fc}(\boldsymbol{\varepsilon}_o) \tag{11}$$

From Appendix, gradient G and hessian H of the grasp are calculated by

$$G_i^{fc} := \left.\frac{\partial U_i^{fc}(\boldsymbol{\varepsilon}_o)}{\partial \boldsymbol{\varepsilon}_o}\right|_0 = [I_6, Q_i^{fc}]G_i \in \Re^6 \tag{12}$$

$$\begin{aligned} H_i^{fc} &:= \left.\frac{\partial^2 U_i^{fc}(\boldsymbol{\varepsilon})}{\partial \boldsymbol{\varepsilon}_o \partial \boldsymbol{\varepsilon}_o^T}\right|_0 \\ &= [I_6, Q_i^{fc}]H_i\begin{bmatrix} I_6 \\ [Q_i^{fc}]^T \end{bmatrix} + \left.\frac{\partial^2 (U_{i,\alpha}^T \boldsymbol{\alpha}_i^{fc})}{\partial \boldsymbol{\varepsilon}_o \partial \boldsymbol{\varepsilon}_o^T}\right|_0 \in \Re^{6\times6} \end{aligned} \tag{13}$$

where

$$G_i := \begin{bmatrix} U_{i,\varepsilon} \\ U_{i,\alpha} \end{bmatrix} \in \Re^{11}, \quad H_i := \begin{bmatrix} U_{i,\varepsilon\varepsilon} & U_{i,\varepsilon\alpha} \\ U_{i,\alpha\varepsilon} & U_{i,\alpha\alpha} \end{bmatrix} \in \Re^{11\times 11},$$

$$U_{i,\varepsilon} := \left.\frac{\partial U_i(\boldsymbol{\varepsilon}_o,\boldsymbol{\alpha}_i)}{\partial \boldsymbol{\varepsilon}_o}\right|_0, \quad U_{i,\alpha} := \left.\frac{\partial U_i(\boldsymbol{\varepsilon}_o,\boldsymbol{\alpha}_i)}{\partial \boldsymbol{\alpha}_i}\right|_0,$$

$$U_{i,\varepsilon\varepsilon} := \left.\frac{\partial^2 U_i(\boldsymbol{\varepsilon}_o,\boldsymbol{\alpha}_i)}{\partial \boldsymbol{\varepsilon}_o \partial \boldsymbol{\varepsilon}_o^T}\right|_0, \quad U_{i,\varepsilon\alpha} := \left.\frac{\partial^2 U_i(\boldsymbol{\varepsilon}_o,\boldsymbol{\alpha}_i)}{\partial \boldsymbol{\varepsilon}_o \partial \boldsymbol{\alpha}_i^T}\right|_0,$$

$$U_{i,\alpha\varepsilon} := \left.\frac{\partial^2 U_i(\boldsymbol{\varepsilon}_o,\boldsymbol{\alpha}_i)}{\partial \boldsymbol{\alpha}_i \partial \boldsymbol{\varepsilon}_o^T}\right|_0, \quad U_{i,\alpha\alpha} := \left.\frac{\partial^2 U_i(\boldsymbol{\varepsilon}_o,\boldsymbol{\alpha}_i)}{\partial \boldsymbol{\alpha}_i \partial \boldsymbol{\alpha}_i^T}\right|_0,$$

$$Q_i^{fc} := \left.\frac{\partial (\boldsymbol{\alpha}_i^{fc})^T}{\partial \boldsymbol{\varepsilon}_o}\right|_0 \in \Re^{6\times 5}. \tag{14}$$

Because vector G_i and matrix H_i are independent of contact friction, these terms are calculated using (4), (5), and (8). But matrix Q_i^{fc} is dependent of contact friction condition. To obtain hessian H_i^{fc}, we derive Q_i^{fc} in the following sections.

2. Frictionless Contact

In case of frictionless contact, a body slides on other bodies' surface. If once object configuration moves due to external disturbance, finger moves on the object surface. If each finger motion is stable, finger position moves to local minimum of its potential energy. In this case, we can write displacement parameters $\boldsymbol{\alpha}_o$ and ψ as functions of $\boldsymbol{\alpha}_f$. Hence, we have the following constraint:

$$\boldsymbol{h}^T = \frac{\partial U(\boldsymbol{\varepsilon}_o,\boldsymbol{\alpha}(\boldsymbol{\alpha}_f))}{\partial \boldsymbol{\alpha}_f^T} = \frac{\partial U(\boldsymbol{\varepsilon}_o,\boldsymbol{\alpha})}{\partial \boldsymbol{\alpha}^T} A_f = 0 \tag{15}$$

where

$$A_f := \begin{bmatrix} \left[[{}^{Lf}R_{Lo}] \begin{bmatrix} \Omega K_{Co} \\ T_{Co} \end{bmatrix} M_{Co}, \boldsymbol{u}_3 \right]^{-1} \begin{bmatrix} \Omega K_{Cf} \\ T_{Cf} \end{bmatrix} M_{Cf} \\ I_2 \end{bmatrix}, \in \Re^{5\times 2}$$

$$\Omega := \begin{bmatrix} 0 & -1 \\ 1 & 0 \end{bmatrix} \in \Re^{2\times 2}, \quad \boldsymbol{u}_3 := [0,0,1]^T \in \Re^3 \tag{16}$$

Derivative of (15) is calculated as

$$\frac{\partial \boldsymbol{h}^T}{\partial \boldsymbol{\varepsilon}_o} = \left[I_3, \frac{\partial \boldsymbol{\alpha}^T}{\partial \boldsymbol{\varepsilon}_o} \right] \begin{bmatrix} \dfrac{\partial^2 U(\boldsymbol{\varepsilon}_o,\boldsymbol{\alpha})}{\partial \boldsymbol{\varepsilon}_o \partial \boldsymbol{\alpha}^T} \\ \dfrac{\partial^2 U(\boldsymbol{\varepsilon}_o,\boldsymbol{\alpha})}{\partial \boldsymbol{\alpha} \partial \boldsymbol{\alpha}^T} \end{bmatrix} [A_f] = 0 \tag{17}$$

We require other three constraints, because two constraints exist in (15) and five constraints exist in (9). From Assumption (A5), hence, we use the following finger orientation constraint ($\xi_f = 0$):

$${}^{bf}R_f(\boldsymbol{\varepsilon}_o,\boldsymbol{\alpha}) = I_3 \tag{18}$$

From (17) and (18), Q^{fc} is obtained as

$$Q^{fs} := -\left[\begin{array}{c|c} \dfrac{0}{[{}^{bf}R_{bo}]^T} & U_{\varepsilon\alpha} A_f \end{array} \right] \times \left[\begin{array}{c|c} M_{Co} \begin{bmatrix} \Omega K_{Co} \\ T_{Co} \end{bmatrix}^T [{}^{bf}R_{Lo}]^T & \\ \hline \boldsymbol{u}_3^T [{}^{bf}R_{Lf}]^T & U_{\varepsilon\varepsilon} A_f \\ \hline -M_{Cf} \begin{bmatrix} \Omega K_{Cf} \\ T_{Cf} \end{bmatrix}^T [{}^{bf}R_{Lf}]^T & \end{array} \right]^{-1} \in \Re^{6\times 5} \tag{19}$$

where superscript "*fs*" means finger sliding. And we have

$$\left.\frac{\partial^2 (U_{i,\alpha}^T \boldsymbol{\alpha}_i^{fs})}{\partial \boldsymbol{\varepsilon}_o \partial \boldsymbol{\varepsilon}_o^T}\right|_0 = 0 \tag{20}$$

Hence, stiffness matrix of frictionless contact finger is given by

$$H_i^{fs} = [I_6, Q_i^{fs}] \begin{bmatrix} U_{i,\varepsilon\varepsilon} & U_{i,\varepsilon\alpha} \\ U_{i,\alpha\varepsilon} & U_{i.\alpha\alpha} \end{bmatrix} \begin{bmatrix} I_6 \\ [Q_i^{fs}]^T \end{bmatrix} \tag{21}$$

3. Frictional Contact

In case of frictional contact, a body rolls on other bodies' surface. In this case, relative velocity of two bodies at contact point becomes zero.

$$V_{Co,Cf}^b(t) = 0 \tag{22}$$

From (18) and (21), we have

$$Q^{fr} := -\begin{bmatrix} 0_{3\times 2} & 0_{3\times 3} \\ 0_{3\times 2} & [{}^{bf}R_{bo}]^T \end{bmatrix} \times \left[\begin{array}{c|c} M_{Co} R_\psi(\psi_0) & M_{Co} \begin{bmatrix} \Omega K_{Co} \\ T_{Co} \end{bmatrix}^T [{}^{bf}R_{Lo}]^T \\ \hline 0_{1\times 2} & \boldsymbol{u}_3^T [{}^{bf}R_{Lf}]^T \\ \hline -M_{Cf} & -M_{Cf} \begin{bmatrix} \Omega K_{Cf} \\ T_{Cf} \end{bmatrix}^T [{}^{bf}R_{Lf}]^T \end{array} \right]^{-1}, \in \Re^{6\times 5}$$

$$R_\psi(\psi_0) := \begin{bmatrix} \cos\psi_0 & \sin\psi_0 \\ \sin\psi_0 & -\cos\psi_0 \end{bmatrix} \tag{23}$$

where superscript "*fr*" means finger rolling and ψ_0 is initial torsion between the object and the finger. And we have

$$\left.\frac{\partial^2(U_{i,\alpha}^T \boldsymbol{\alpha}_i^{fr})}{\partial \boldsymbol{\varepsilon}_o \partial \boldsymbol{\varepsilon}_o^T}\right|_0 = 0 \tag{24}$$

Hence, stiffness matrix of friction contact finger is given by

$$H_i^{fr} = [I_6, Q_i^{fr}] \begin{bmatrix} U_{i,\varepsilon\varepsilon} & U_{i,\varepsilon\alpha} \\ U_{i,\alpha\varepsilon} & U_{i.\alpha\alpha} \end{bmatrix} \begin{bmatrix} I_6 \\ [Q_i^{fr}]^T \end{bmatrix} \tag{25}$$

3. Grasp Stiffness Matrix

Grasp stiffness matrix is obtained by summation of stiffness matrix of each finger.

$$H = \sum_{i=1}^{n} H_i^{fc} \in \Re^{6\times 6} \tag{26}$$

where friction condition "*fc*" stands for "*fs*" or "*fr*". This condition is assigned depending on each finger friction condition.

V. CONCLUSIONS

This paper has analyzed static stability of three-dimensional grasp of single object from viewpoints of potential energy. And we have the following contributions: (1) Grasp stability is analyzed considering the torsion in addition to the curvature of an object's and fingers' surfaces. (2) In case of frictionless contact, each finger motion is treated as sliding on the object. (3) In case of frictional contact, each finger motion is treated as rolling on the object. (4) Stiffness matrices of mixed friction condition grasps are derived.

The following contributions are omitted due to lack of pages. We can calculate eigenvalues and eigenvectors of the derived matrices. Grasp stability is quantitatively evaluated by using the eigenvalues. Moreover, stable and unstable directions of object displacement are derived. Effectiveness of our proposed method is verified through numerical examples.

Our analyses of frictionless contact are applicable to the following cases: (1) Small friction objects are grasped. For examples, a cube of ice or a cake of soap is grasped. (2) Friction property is unknown before grasping, but object shape is acquired with image sensor.

Our method is applicable to optimization problem for grasp position design and fixture position design.

In our projected work, we will attack grasping multiple objects, consideration of finger rotation, and so on.

This work was financially supported by Grant-in-Aid for Scientific Research (c), Japan, No. 20560237.

REFERENCES

[1] T. Yamada, T. Koishikura, Y. Mizuno, N. Mimura, Y. Funahashi (2003), Stability Analysis of 3D Grasps by A Multifingered Hand (in Japanese), Trans. of JSME, 69(670): 127-134.
[2] T. Yamada, T. Ooba, T. Yamamoto, N. Mimura, Y. Funahashi (2006), Grasp Stability Analysis of Two Objects in Two Dimensions (in Japanese), Trans. of JSME, 72(714), 178-185.
[3] T. Yamada, S. Yamanaka, M. Yamada, Y. Funahashi, H. Yamamoto (2009), Grasp Stability Analysis of Multiple Planar Objects, Proc. of ROBIO2009, to be appeared.
[4] S. Arimoto and M. Yoshida (2008), Modeling and Control of Three-Dimensional Grasping by a Pair of Robot Fingers, SICE Journal of Control, Measurement, and System Integration, 1(1), 2-11.
[5] M. Murray, Z. Li, S. S. Sastry (1994), A Mathematical Introduction to Robotic Manipulation, CRC Press.

APPENDIX

Total potential energy of the grasp is denoted by $U(\boldsymbol{\varepsilon})$, where $\boldsymbol{\varepsilon}$ stands for independent displacement parameters of the grasp. The grasp is stable if and only if $U(\boldsymbol{\varepsilon})$ is local minimum at $\boldsymbol{\varepsilon} = 0$ (initial configuration). Taylor expansion of $U(\boldsymbol{\varepsilon})$ is written as

$$U(\boldsymbol{\varepsilon}) = U(0) + \boldsymbol{\varepsilon}^T G + \boldsymbol{\varepsilon}^T H \boldsymbol{\varepsilon} + \cdots \tag{27}$$

where G and H are the gradient and the hessian, respectively.

$$G := \left.\frac{\partial U}{\partial \boldsymbol{\varepsilon}}\right|_0, \quad H := \left.\frac{\partial^2 U}{\partial \boldsymbol{\varepsilon} \partial \boldsymbol{\varepsilon}^T}\right|_0 \tag{28}$$

Hence, the grasp is stable if the following two conditions are satisfied.

(C1) $G = 0$.

(C2) H is positive definite.

Condition (C1) is satisfied by Assumption (A3). Hence, the grasp stability can be evaluated by Condition (C2).

Therefore, this paper derives independent parameter $\boldsymbol{\varepsilon}$, potential energy $U(\boldsymbol{\varepsilon})$, and hessian *H*. In this paper, the hessian is called as a grasp stiffness matrix, because the grasp system is replaced with spring model.

The Fifteenth International Symposium on Artificial Life and Robotics 2010 (AROB 15th '10),
B-Con Plaza, Beppu,Oita, Japan, February 4-6, 2010

Real time interpolation of haptic information using case base

Takayuki Toki[1], Hirokazu Taki[2], Hirokazu Miura[2], Noriyuki Matsuda[2], Masato Soga[2], and Norihiro Abe[3]

[1]*Graduate School of Systems Engineering, Wakayama University, 930, Sakaedani, Wakayama-shi, Wakayama*
(Email s101064@center.wakayama-u.ac.jp)
[2]*Faculty of Systems Engineering, Wakayama University*
[3]*School of Computer Science and Systems Engineering, Kyushu Institute of Technology*

Abstract: This paper has described a real time interpolation technology for haptic information using case base. To share haptic data in multiple points, we must send complete haptic data. However, in the transmission line, packet loss and noise are occurred sometimes. In this situation, users don't sense correct force. We developed new interpolation method for haptic sense data without conventional mathematical approach. We can interpolate haptic information lag and loss using case-based approach. In our method, the system selects a suitable case and reconfigures it to fit the error.

Keywords: haptic, interpolation, case base, haptic interface.

I. INTRODUCTION

Recently, image data and sound data can transport efficiently by reason of development of transmission technology as QoS[1]. But, transmission technology of haptic data still has many problems. One of problem is that packet loss and noise are occurred sometimes in the transmission line. Even if image and sound data has a few noises, we can understand. But, in case of haptic data, the noise struck us as incongruous.

Linear interpolation method and Lagrange interpolation method are general mathematical interpolation method[2],[3]. They are effective method in linear situation. In other case, the method cannot interpolate correctly.

We propose that a real time interpolation technology for haptic information using case base. The purpose of our system is to provide the high quality haptic information transfer system which interpolates packet loss and noise on the data.

II. Interpolate system for haptic information

In this study, we use PHANToM Omni (Sensable Technologies) as a haptic interface device. Our system can interpolate the data for haptic data of the PHANToM.

1. The outline of interpolation method

The Fig.1 shows the outline of a multimedia communication environment. Each terminal has a haptic device. The sender sends haptic data to the receiver. The image and sound data can be transferred by Qos Technology. This target area of this research, haptic data communication environment, is shown in the broken line circle area of the figure 1. The system interpolates packet loss or noise for the haptic data and controls the receiver haptic device according to interpolated data.

At first, the system has gathered haptic data for haptic cases, and constructed the haptic case base. Next, the system compares them and the element of the case base, and checks error of them. After this process, the system controls the PHANToM force according to the interpolation.

We assume that the first 3 points of the input data are correct.

2. Composition of case base

The each case in the case base is represented in the text format. A set of data consists of the three dimensional position(X,Y,Z). An each line of the text file represents these positions.

We prepared the following case data for evaluation of our method. To evaluate the interpolation, the case data are generated by the linear function or quadratic function. These data are in the target virtual space. The case data are fragments of the haptic data, so the start positions and the finish positions of each data are not same.

3. Case Search

The system searches similar cases from the case base to repair the original data. To decide the similarity of cases, the system measures the distance between the input haptic data and case by each coordinate(X,Y,Z). The system memorizes these distances into the local memory array for each coordinate(X,Y,Z). The system

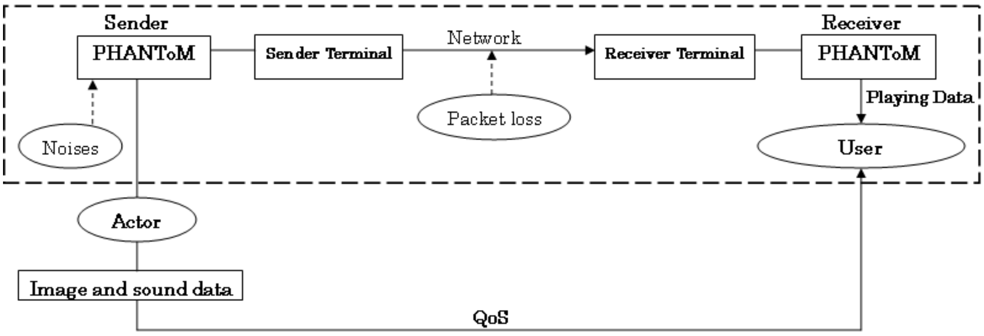

Fig.1 The outline of a multimedia communication

calculated the same distance data for each case when the case base was build. After the system compares cases and the input haptic data, it selects the cases which distances are same more than 3. This selection criteria is based on the assume that the first 3 points of the input data are correct.

4. Offset cancellation

The system uses the translation of axes for offset cancellation. For example, if the offset of the X-axis is 2.0, all x position values of the input data are increased 2.0 points from original data of the similar case. This means that the x values are translated to the position which is shifted positively by adding 2.0. Even if cases are translated, relative distances between cases and the haptic data are not changed. This translation makes no effect for the motion of the stylus of the haptic device. The system doesn't treat the offset cancellation as data error, so it doesn't repair the following complex process.

But it is possible that the haptic data include both offset and errors. In this case, the system memorizes the offset and the similar case. When the system decides that the data include errors, it translates offset cancellation and repairs the errors. As a result, the system can repair data which include both offset and error, and control the haptic device according to the repair data.

5. Haptic data Interpolation

The system selects the similar case and compares the input haptic data and the case. If there are some different points, the system repairs the original data according to the case. We assume that the case is correct. If there are errors in the haptic data, the system repairs or interpolates them. After all interpolation process were finished, the system controls the haptic device using the interpolated data.

In this study, there are two error types which are data alteration and data loss. Therefore, the system must solve these errors. We explain the detail of our repair method and interpolation.

At first, the alteration error is treated as follows.

① The system checks errors and finds alteration error.
② It searches the difference between the similar case and the input data.
③ It replaces the alteration of the input data referring to the case.

The Fig.2 shows the alteration correction process. The system compares the series of the input data at upper part of the Fig.2 with the case at lower part of the Fig.2. In the Fig.2, the third position of the case is "C", but same position of the input data is "X". The system copies "C" of the case to the third position of the input data. After all interpolation methods were finished, the system replays the input data to control the haptic device.

Next, the loss error is treated as follows.

① The system checks errors and finds data loss.
② It searches the difference between the similar case and the input data.
③ It interpolates for the position of data loss.

The Fig.3 shows the interpolation process for data loss. If the data order of the case is "A,B,C,D", and the data order of the input data is "A,B,D", the system finds the data loss for "C". In the second step, the system refers the correspondence position of the case. In the third step, it inserts the data "C" between the data "B" and the data "D" of the input data.

If the control data of the haptic device is increased by this method, the system controls the device according to increased data. If the last positioning data for the haptic device is lacked, the system interpolates the last position into the input data instead of the data loss. There are some differences between the input haptic data and the case. The first data or the last data of these two data are always not same.

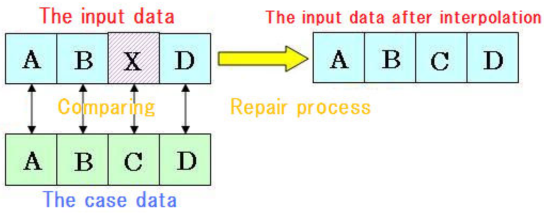

Fig.2. The alteration correction process

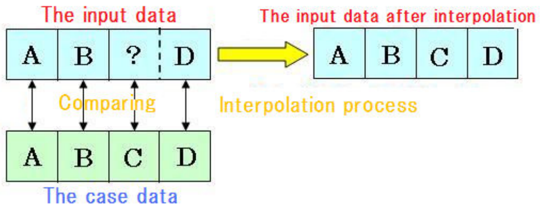

Fig.3. The interpolation process

6. Haptic device control according to the interpolated data

After the interpolation process is finished, the system sends the haptic data into the haptic device. The control process for the haptic device is shown as follows.

① The system calculates distance between the current position of the haptic device's stylus and the next destination of it, and multiplies its distance and a spring constant K to make haptic force. The system calculates them for each three axes, and gives this force to the haptic device.

② The system controls the device to move it to the next destination.

③ It repeats the process ① and ② until the device arrives at the next position.

④ If the device arrives at the next position, it reads the next destination from the input data, and sets up the next position.

⑤ It repeats the process between process ① and process ④ until the device arrives at final position.

III. EXPERIMENTATION

To evaluate the system, we assume that there are alterations and data losses of the haptic data in the linear function and the quadratic function. We made three examples for each functions. There are two kinds of the input data that include alteration and data loss. We also prepared the third type data that include these two errors and offset shifted error. We evaluated the interpolation functions for each data. Some evaluation examples include several errors. The offset errors are given *independent on each axis.

We also measured the execution time for all interpolation process to evaluate real-time performance.

IV. THE EXPERIMENTAL RESULT AND CONSIDERATION

We report the experimental results of the test input data in the linear function and the quadratic function.

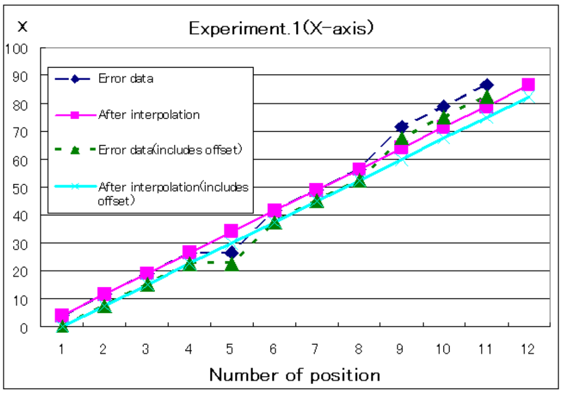

Fig.4. X-axis

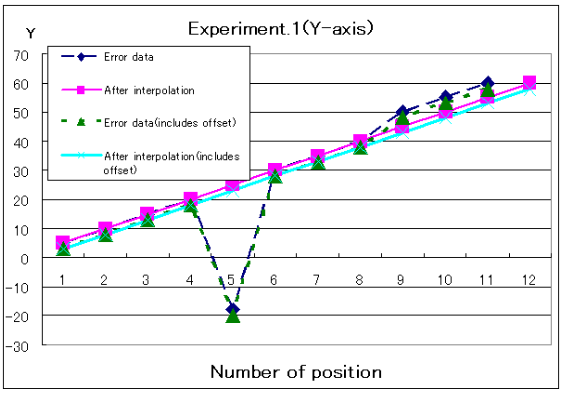

Fig.5. Y-axis

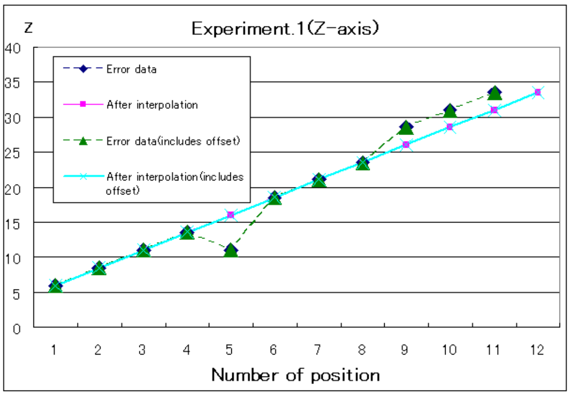

Fig.6. Z-axis

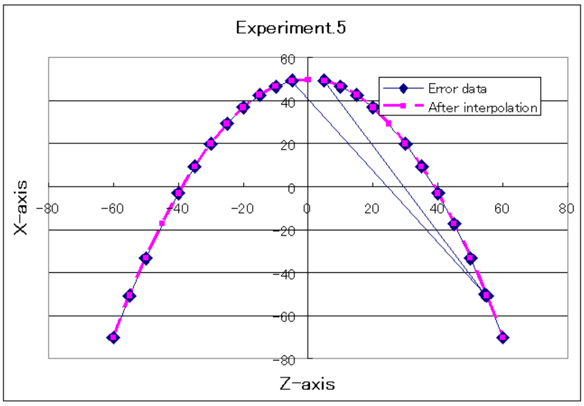

Fig.7. The quadratic function

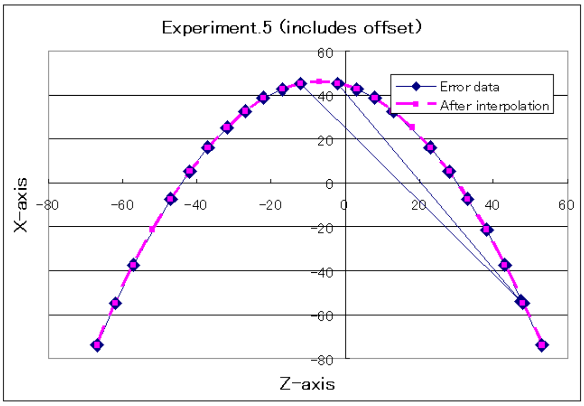

Fig.8. The quadratic function includes offset

The Fig.4, the Fig.5 and the Fig.6 show the experimental interpolation results of each axis for the input data in the linear function. They show the linear line correctly that system executed interpolation process or repairing process. We also confirmed the translation function for offsets of X-axis and Y-axis. The value of offset X-axis is -4.0 and the value of offset Y-axis is -2.0.

The Fig.7 and the Fig.8 are the experimental results in case of the quadratic function. They show the relation between Z-axis and X-axis. The value of Y-axis is fixed at 20. In this case, the offset of X-axis is -4.0 and the offset of Z-axis is -7.0.

In the experiment-1, there are errors that the alteration error is at fifth position, and the data loss error is excited between the eighth and the ninth position. In the experiment of the data in the linear function, each data is at regular interval which is equal to the interval between positions. The system can check the error to find an irregular interval. If there is no offset in the input haptic data, the system executes the translation process only. The Fig.6 shows non offset case. The offset of Z-axis is 0.0 .

In the experiment-5, it is difficult to calculate position simply like the experiment-1 because the distance between positions isn't always constant. In this study, the system can execute this process correctly under the condition that first 3 points of the input data are correct. In the Fig.7 and the Fig.8, we confirmed that the system executes all processes correctly.

We measured the execution time required for the repairing and the interpolation process. As a result, the execution time is measured less than 1 m seconds. The human don't feel a delay less than 1 m seconds, because there is 1 m seconds delay that is from touching an object to sense it in the human neurons[4].

V. CONCLUSION

The purpose of this study is interpolation of error haptic data at network communication. We evaluated out interpolate method to apply the data in the linear and quadratic functions for these experiments. But we don't study more complex cases, for example, as the cubic function. In this study, the system can execute this process correctly under the condition that first 3 points of the input data are correct. But if the 3 points are not correct, the system can't treat the data. Therefore, the issues are to improve our method that combines the fragment of the case data to new cases to suit the exception case. In the next development, we will try to transmit the haptic data using the communication system like Skype, and we will improve our method for this communication.

We greatly appreciate the aid of the Grant-in-Aid for Scientific Research (A)"(No.18200008).

REFERENCES

[1] Toda I (2001), A detailed explanation technology of network QoS (in Japanese), Ohmsha.
[2] Kawamura T (2005), Linear Algebra & numerical analysis (in Japanese), Asakurashoten.
[3] Kawasaki H (1993), The fundamentals of numerical analysis by C&FORTRAN (in Japanese), Kyoritsushuppan.
[4] M. R. Bennett, P. M. S. Hacker (2003), Philosophical Foundations of Neuroscience. Wiley-Blackwell.
[5] Uchida Y, Abe N, Tanaka K (2007), Construction of the remote communication system with the haptic-feedback device (in Japanese). Proceedings of the virtual reality society of Japan Vol.13, No.3A5-2.

The Fifteenth International Symposium on Artificial Life and Robotics 2010 (AROB 15th '10),
B-Con Plaza, Beppu,Oita, Japan, February 4-6, 2010

Recovery Technique from Classified Errors in Skill-Based Manipulation

Akira Nakamura and Yoshihiro Kawai

Intelligent Systems Research Institute
National Institute of Advanced Industrial Science and Technology (AIST)
Central 2, 1-1-1 Umezono, Tsukuba, Ibaraki, 305-8568 Japan
a-nakamura@aist.go.jp, y.kawai@aist.go.jp

Abstract: Dexterous manipulation is an important function for working robots. Manipulator tasks such as assembly and disassembly can generally be divided into several motion primitives. We call such motion primitives "skills" and explain how most manipulator tasks can be composed of sequences of these skills. We are currently planning to construct a maintenance robot for household electrical appliances. We considered hierarchizing the manipulation tasks since the maintenance of such appliances has become more complex than ever before. Additionally, we considered grouping errors into several classes according to their estimated causes. The reliability of the task achievement increases with the classification of errors. This paper contributes to the achievement of these concepts by showing our restoration technique for each class of error. The technique is described with the concrete examples.

Key words: manipulation skill, maintenance task, error recovery

1. Introduction

For manipulation robots to be useful in several fields, it is necessary for robots to achieve various tasks using special techniques. By analyzing human motions in tasks such as assembly and disassembly, we found that movements consisted of several significant motion primitives. We have called these "skills" and have shown that most of the tasks of a manipulator can be composed of sequences of skills [1]–[4].

We have researched maintenance robots working in various factories and power plants. In future research, we will consider manipulation robots used for the maintenance of household electrical appliances and consumer electronics. At present, we are working toward producing a prototype of a maintenance robot for system components and personal computers (Fig. 1). Maintenance requires the use of many manipulation skills, and the composition of the tasks is complex. However, stratification of tasks makes development more manageable.

Manipulation tasks with skills are performed in theory by sequences of visual sensing, geometric modeling, planning and execution. In an ideal environment, the tasks are achieved without any errors occurring. In actual manipulation, however, errors often occur for various reasons. Various approaches for error recovery have been reported [5]–[8]. However, few methods for realistic error recovery have been proposed for the various errors that could actually occur during maintenance tasks. We have described our concept of error classification and process flow with error recovery in the task hierarchy. Errors are grouped into several classes according to their estimated causes. In this paper, we describe our restoration technique for each class of error. Error recovery can be performed effectively using the detailed restoration sequences.

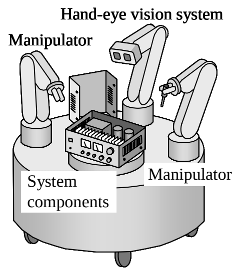

Fig. 1 Maintenance robot for audio-visual system components

The next section explains manipulation skills and the stratification of manipulation tasks. The classification of errors and error recovery in the task hierarchy are shown in section 3. The restoration sequences in each class of error are detailed in section 4.

2. Stratification of Tasks

This section explains our concept of skills and stratification of tasks. See References [1], [2] for more details.

2.1. Manipulation Skills

We analyzed human motions in such tasks as assembly and disassembly and found that the movements consisted of several significant motion primitives. We call motion primitives "skills" [1], [2]. We considered three fundamental skills: move-to-touch, rotate-to-level and rotate-to-insert, which play an important part in such tasks. A specific task is composed of sequences of skill primitives such as these three skills. Moreover, many skills such as rotate-to-bite and rotate-to-loosen skills in screwdriver tasks can be defined based on slightly changed versions of these three fundamental skills [3], [4].

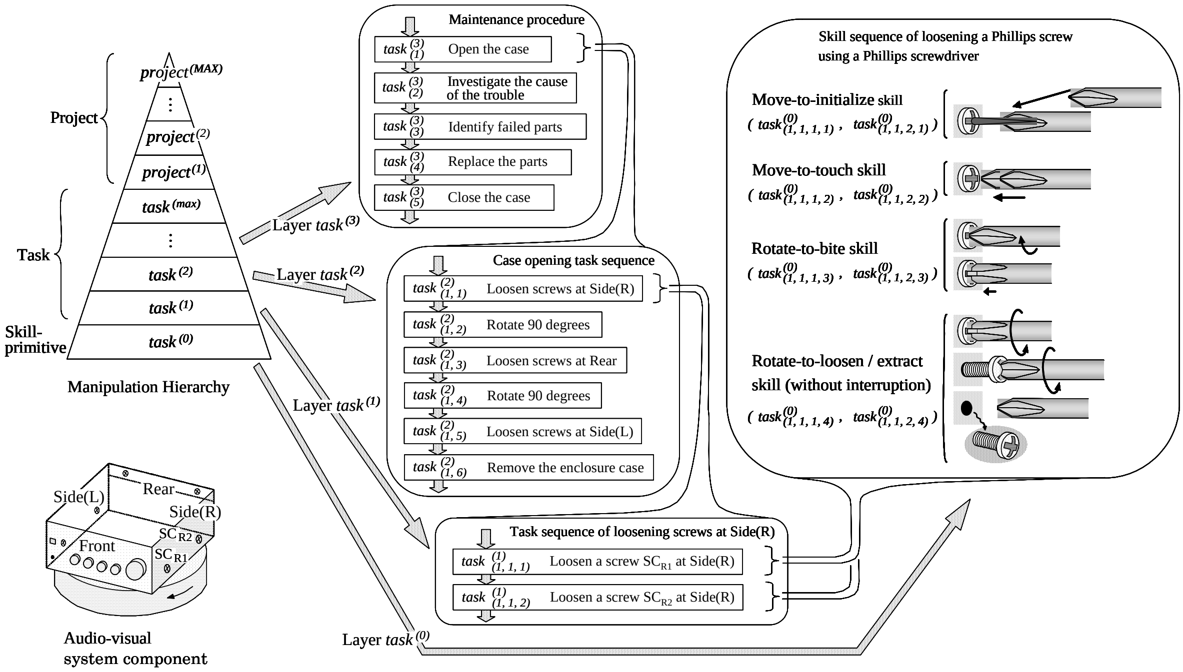

Fig. 2 Task of opening the case of an audio-visual system component

2.2. Stratification of Tasks

Figure 2 shows a hierarchy of manipulation tasks using the repair of system components in consumer audio-visual equipment as an example [4]. If we ignore the servo layer, the *skill* layer, which consists of elements such as move-to-touch and rotate-to-bite skills, is located in the lowest layer called the $task^{(0)}$ layer. Each skill is performed by the processes of visual sensing, geometric modeling, planning and execution. One tier above the $task^{(0)}$ layer is called the $task^{(1)}$ layer. Similarly, $task^{(i+1)}$ is composed of sequences of $task^{(i)}$ elements. The top layer, where the error recovery loop is closed, is called $task^{(max)}$ and one tier above $task^{(max)}$ is called the *project* layer. The *project* layer might also be hierarchized, but we will not discuss this here.

3. Error Recovery in Stratified Tasks

In an ideal environment, tasks are achieved without any errors occurring. In actual manipulation, however, errors often do occur from various causes. Our concept of error classification and process flow with error recovery in the task hierarchy are described in this section. See References [4] for more details.

3.1. Classification of Errors

The causes of failures can be attributable to several kinds of errors. We group the error states into several classes according to the possible causes as follows. The classes of errors are described in detail in Reference [4].

・Execution error.
・Planning error
・Modeling error
・Sensing error

Merely restoring the causes of these errors does not always solve the problem. It may be necessary to return to a previous step when the working environment is greatly changed by the error.

3.2. Error Recovery based on Classification

A generalized process flow of stratified tasks that takes error recovery into account has been shown in [4]. Figure 3 is an illustration of the central portion of Fig. 10 in [4]. At the confirmation step in each skill primitive $task^{(0)}_{(i0)}$, an automatic process or a human operator judges whether the result is correct or a failure. Error recovery is performed using the following error classification. To simplify the explanation in this paper, we have not considered returning to the layer above the $task^{(2)}_{(i1)}$ layer.

Class 1: When the error is judged to be an execution error, $task^{(1)}_{(i1)}$ is executed again without a correction in the parameters.

Class 2: When the error is judged to be a planning error, $task^{(1)}_{(i1)}$ is executed again with a change in the planning parameters .

Class 3: When the error is judged to be a modeling error, $task^{(1)}_{(i1)}$ is executed again with a change in the modeling parameters.

Class 4 (= Class $T^{(1)}$) : When the error is judged to be a sensing error, $task^{(1)}_{(i1)}$ is executed again with a change in the sensing parameters.

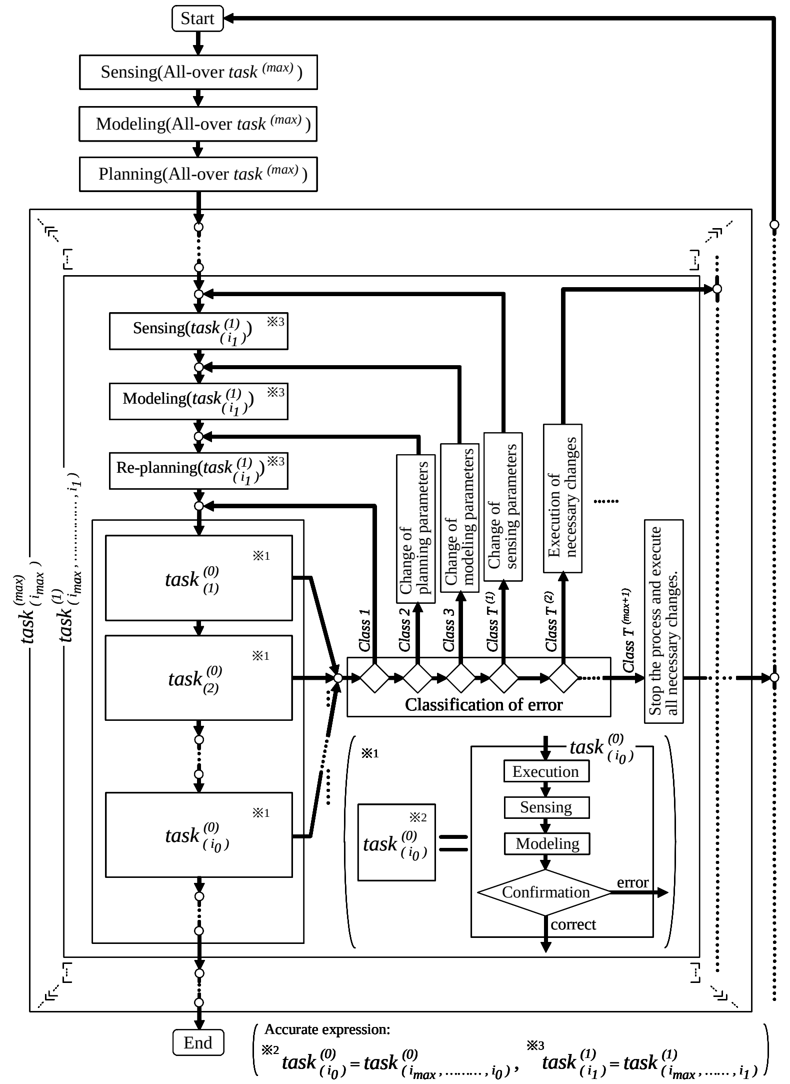

Fig. 3 Process flow with error recovery

4. Recovery from Classified Errors

We will explain the technique based on concrete examples using the maintenance robots.

(1) Class 1

This is a mechanical error caused in the manipulator mechanism such as a gear backlash. If the error happened by accident, the possibility of recovery succeeding is large if the robot retries repeatedly. It moves to Class 2 or more, if the task will not succeed no matter how many tries are repeated.

(2) Class 2

This is an error caused by inaccurate parameter values in planning. The process changes according to the kind of parameter with the wrong value. The following are typical: a) When passing planning parameters are inapposite, it is necessary to derive a correct initial position and orientation and a moving path by correcting the parameters. For example, Figure 4 shows the correction of the initial region of a screwdriver by revising the angle of the vertex of the control uncertainty cone. Additionally, this case includes correction of the path by various causes such as avoiding obstacles. b) When the threshold to judge the state is inappropriate, correction must be done. For example, the threshold of the contact force value is revised if the detection of the contact condition is not achieved properly. c) When the task of manipulation doesn't advance properly, the values of power or torque must be changed. For example, the rotating torque is increased, if the screwdriver inserted in the screw doesn't rotate.

It moves to Class 3 or more, if the task will not recover properly even if a correction is done.

(3) Class 3

This is an error caused by differences in the real object and the geometric model in the software. The following two kinds of errors are considered: a) When the real object and the geometric model in the software are different, the correction must be done. For example, Figure 5 shows that the size or the type of a screw has been correctly changed.

b) When the tool grasped by the manipulator and the geometric model in the software are different, the correction of the tool model must be done.

(4) Class 4

This is an error occurring during visual sensing. This error happens by causes such as inaccurate calibration of the vision system and incorrect relationships of the coordinate systems of the object and tool. Figure 6 shows the correction of the relationships of the coordinate systems of the object and tool.

(5) Additional Task

Additional tasks are necessary in some cases to perform the corrections of Class 2, 3 and 4 errors (Fig. 7). For example, additional geometry modeling of the working environment may be necessary in Class 2 a), and additional geometry modeling of the object and the tool may be necessary in Class 3 a) and 3 b), respectively. And additional geometry modeling of the working environment and calibration of the vision system may be necessary in Class 4. Furthermore, a task for changing the grasped tool might be needed in Class 3 b).

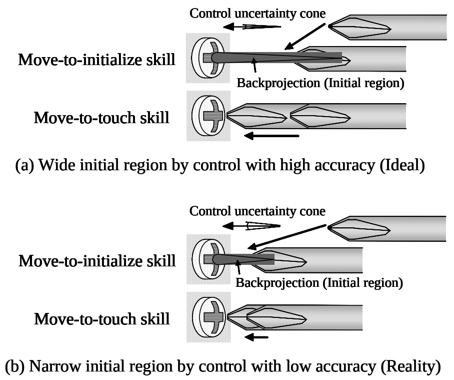

Fig. 4 Influence of control accuracy on planning

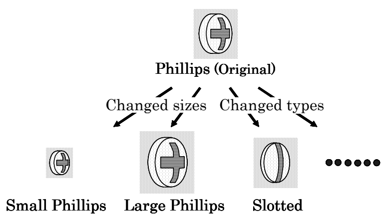

Fig. 5 Changed Models

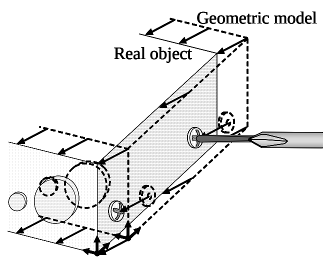

Fig. 6 Correction of position and orientation of geometric models of objects

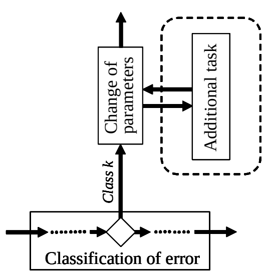

Fig. 7 Additional task

5. Conclusions

In recent years, dependability has been a topic in robotics research. It is necessary to increase the reliability of the maintenance robots that work on household appliances. Therefore, as error recovery technique is important, we considered a method of error recovery that uses the concepts of both task stratification and error classification. In this paper, we have described our restoration technique in detail for each class of error. The capability to recover from errors has been improved.

In the future, we will further research optimum adjustment methods for the various parameters used in error recovery and a fully automatic method to confirm achievement of tasks composed of skills. We will attempt to apply our technique to actual maintenance robots.

References

[1] Hasegawa T, Suehiro T, Takase K (1992), A model-based manipulation system with skill-based execution. IEEE Trans Robotics Autom 8(5):535-544

[2] Nakamura A, Ogasawara T, Suehiro T, Tsukune H (1996), Skill-based backprojection for fine motion planning, Proceedings of the IEEE/RSJ International Conference on Intelligent Robots and Systems (IROS '96), Osaka, Japan, Nov 4-8, 1996, pp.526-533

[3] Nakamura A, Ogasawara T, Kitagaki K, Suehiro T (2001), Using robust and simplified geometric models in skill-based manipulation, Proceedings of the IEEE/RSJ International Conference on Intelligent Robots and Systems (IROS 2001), Hawaii, USA, Oct 29-Nov 3, 2001, pp.138-145

[4] Nakamura A, Kotoku T (2009), Systematization of Error Recovery in Skill-Based Manipulation, Proceedings of the 14th International Symposium on Artificial Life and Robotics (AROB 14th '09), Oita, Japan, Feb 5-7, 2009, pp.610-613.

[5] Donald BR (1989), Error detection and recovery in robotics. Springer-Verlag, Berlin Heidelberg New York, pp.1-256

[6] Visinsky ML, Walker ID, Cavallaro JR (1993), Layered dynamic fault detection and tolerance for robots, Proceedings of the IEEE International Conference on Robotics and Automation (ICRA '93), Georgia, USA, May 2-6, 1993, vol.2, pp.180-187

[7] Seabra Lopes L, Camarinha-Matos LM (1995), A machine learning approach to error detection and recovery in assembly, Proceedings of the IEEE/RSJ International Conference on Intelligent Robots and Systems (IROS '95), Pennsylvania, USA, Aug 5-9, 1995, vol.3, pp.197-203

[8] Yamazaki K, Tomono M, Tsubouchi T, Yuta S (2006), Motion planning for a mobile manipulator based on joint motions for error recovery, Proceedings of the IEEE/RSJ International Conference on Intelligent Robots and Systems (IROS 2006), Beijing, China, Oct 9-15, 2006, pp.7-12

Development of an inheritance assist system for experienced operation skill by using a haptic function of PHANToM

T. Tokuyasu, K. Yufu, T. Shuto*, N. Abe**, A. Marui***

* Oita National College of Technology/Mechanical Engineering, Oita, Japan
** Kyushu Institute of Technology/Mechanical Information Science, Fukuoka, Japan
*** Kyoto University/Cardiovascular Surgery, Kyoto, Japan
(Tel&FAX 81-97-552-7403) (E-mail: tokuyasu@oita-ct.ac.jp)

Abstract: Recently, various kinds of medical issues have been reported such as lacks of doctors and/or nurses, medical mistakes, and escalation of medical costs. On the other hand, medical quality and doctor's skill are required to be enhanced. Then, virtual surgical simulator has been developed and used in inexperienced doctors' training. However virtual training simulators provide the training opportunities for doctors to practice cutting and/or sewing against virtual organ by them. In order to maintain and enhance medical quality the experience doctors had constructed, it is required to provide an environment where inexperienced doctors can learn the skills of experienced doctors. This study proposes a training factor that helps to take over experienced operation skills to inexperienced doctors. In order to make this training factor, we have to develop a skill recording system that can store the operation data as supervised data, and and reproduce the stored data on a surgical simulator. A trainee intuitively learns the other doctor's skill. In this paper, a recording system based on a haptic device is presented. Some experimental results where a subject tries to manipulate a mock surgical forceps according to the supervised data are discussed.

Keywords: *Virtual reality, Mechanical modelling, Surgical simulator, and Computer aided system.*

1. Introduction

Both surgical skills and medical expertises of experienced doctors have to be taken over next generation. It has been reported that the number of doctor is gradually decreasing, meanwhile the number of cases of diagnosis errors and treatment failures have been increasing. Against them, inexperienced doctor and residences have been required to have high quality medical treatment skills and accurate diagnostic skills. Recently, surgical simulator or surgical planning assist system have been developed based on collaboration of between virtual reality technique and haptic technologies[1][2][3]. Most of the reported surgical simulator enables doctors to practice the skills of cutting and sewing virtual organs. In this virtual environment trainees can practice surgical skills without concerns about the patient's physical load and surgical risks. The effect of training simulator increases by operation is infrequent. For example, considering a case of that patient's vitality level is low and/or significant preparation for operation is essential and so on, experienced doctors perform the operation and inexperienced doctors devote to assist the operating surgeon. Therefore surgical opportunities for inexperienced doctors are not enough as the operation skills needed in operation are more difficult. Then a training simulator including a training factor that enables to teach various experienced skills to trainee has some possibilities to become one of solutions for the current medical issues.

This study aims to construct a training factor that enables trainee to intuitively learn the skills of experienced doctors and to apply this factor to a simple operation technique. In this paper, some fundamental studies about recording operation data as supervised data and the effect of reproducing the supervised data on training on a surgical simulator. A simple surgical knife operation is subjected in our fundamental research. Ideas of recording function and reproducing function are described in the following sections, and experimental results for this simple operation are discussed.

2. Concepts

Considering doctors' manipulation of forceps for patient's organ during operation, the doctors operate the forceps according to not only visual information but also force information of operation target. Not only for doctors, we are doing same things even in our daily life, for example window cleaning. We wipe out the window by using a dust cloth, where we make visual feedback and force feedback in ourselves and control our hand force against the dust on the window by obeying these feedback loops.

When a doctor cuts the body surface by using a knife forceps depending on the previously determined surgical plan, he/she controls both of forceps's position, posture, force, and moment. In other words, cutting operation is performed by the feelings of organ's stiffness, elasticity, and viscosity transmitted via the forceps to doctor's fingertip. Then a lack of force feedback functions for tele-robot surgical system, for example Da Vinch, Zeus, etc., is assumed as one of the significant problems of tele robotics surgical system [5]. Doctors wear globes in operation. Their tactile sensibility is prevented by wearing globes but they can recognize the differences of organs' elasticises. For example, cardiovascular surgeons determine the region of left ventricular by the basis of feelings of cardiac muscle palpation [4].

3. Method

In this chapter, two basic functions of our system are presented. A recording function by the basis of function of a haptic device PHANToM Premium is firstly described, where operation data will be stored in the computer memory as a supervised data. Next is a reproducing function. This function is composed of a haptic control function of PHANToM Premium. The system structure we have developed is composed of a PC and HANToM Premium. The PC is running on Windows XP and its development environment is Visual C++ 2005.

3.1 Recording function

PHANToM Premium is one of commercially available haptic devices. It can detect its end effecter's position and posture in three dimension. Force feedback function is effect on the three axis direction, where Fx, Fy, and Fz are controllable. We employ this haptic device as human interface in order to record operation data in this study, where a pen type end effecter is used as a mock device of knife forceps. Then time variation data of forceps is recorded, where $x(t)$, $y(t)$, and $z(t)$ are stored in the computer memory.

3.2 Reproducting function

The recorded data, $x_r(t)$, $y_r(t)$, and $z_r(t)$, based on the recording function is used as supervised data for trainee, and is used the target data of force control of PHANTom. This force control assists the operation of trainee.

In the force control system of PHANToM, HD library can make PHANToM output force by the settings of parameters in the programming code. Its control frequency is approximately 1000Hz, complete real-time processing might be prevented due to process for graphical application or resident programs of Windows Operation System. A simple PID control method is employed in this system. Equation (1) is a control low for force control in respect to x-axis direction.

Each axis direction's control low are established as well as equation (1), where; Fx shows output force, K_p, K_d, K_i are proportional, differential, and integral feedback gains respectively. x_r is a variable of target coordinate and x is for current x-axis coordinate variable. We are coding this PID control low with empirically adjusting each feedback gains.

$$F_x = K_p(x_r - x) + K_d(-\dot{x}) + Ki\int (x_r - x)dt \qquad (1)$$

3.3 Virtual organ model

As mentioned above, a doctor operates a surgical forceps depending on the feelings of patient's organ, so a virtual organ based on a dynamic model has to be build.

Co-author who is cardiovasuclar surgeon desires an application of this study for cardiovascular surgical field. Therefore, a virtual aorta model has been developed in our laboratory [6]. However, rigorous simulation model for aorta is not requested in our current step. So, a cylindrical dynamic model imitating shape of aorta has been constructed.

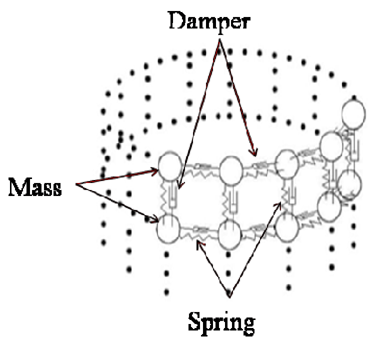

Fig. 1 A scheme of the cylindrical dynamic model based on spring network system

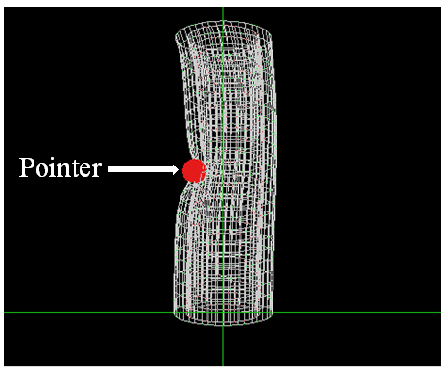

Fig. 2 A graphical model of the bilayed dynamic model

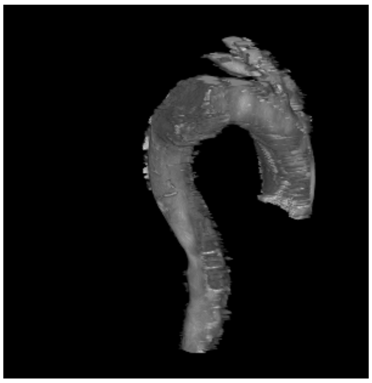

Fig. 3 A volume model of patient's aorta rendered with OpenGL Volumizer

Fig. 1 shows a schematic diagram of the cylindrical dynamic model based on mass-spring network model. Because aortic tissue construct both inner wall and outer wall, so two cylindrical dynamic models are arranged as like as a bilayer film. All of mass of these two layers are connected with springs and dampers in order to make this virtual model have aortal thickness. Fig. 2 is a graphical model of the virtual organ used in this study. This is drawn by using OpenGL. The accurate shape of aorta is going to be interpolated with patient three dimensional computer tomography data. The co-author has been tried to extract the volume data of aorta from patient's computer tomography.

Fig. 3 is a volume model, where OpenGL Volumizer rendered this graphical model by the basis of the volume data derived a patient's computer tomography data. We would like to extract three dimensional coordinates of aorta from this model in future.

4. Experiment

4.1 Recording experiment

As mentioned above, a simple knife operation is used as a basic operation in this study. Then, the three

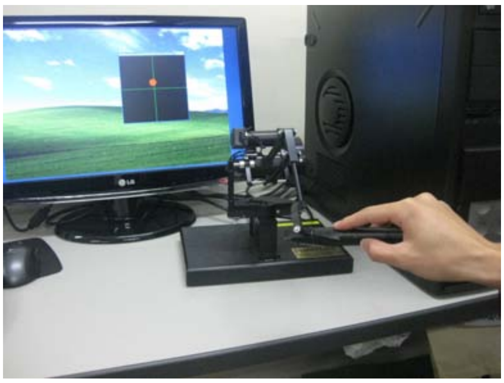

Fig. 4 Experimental scene of operating PHANToM Premium A

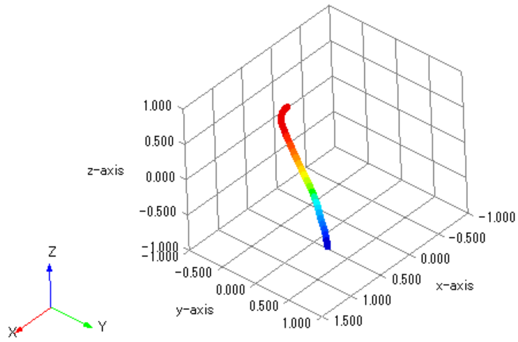

(a) line

Fig. 5 Recorded supervised data

dimensional coordinates of the edge of PHANToM end-effecter are stored in the computer memory and are saved in a file. This paper introduced a virtual organ model in section 3.3, however this experiment uses no virtual organ model. Because we have to mount a function that judges the contact between the surface of cylindrical dynamic model and a pointer which is controlled by the trainee via PHANoM in order to use our dynamic model as a virtual organ model. Fig. 4 shows a scene of experiment for recording operation data, where a laboratory student performed like that a doctor cut an organ with knife forceps. The obtained data are shown in Fig. 5 by using Graph-R. The data starts at red color and moves to blue color.

4.2 Reproducing experiment

In this experiment, we implemented experiments under two different conditions. The first condition is that the computer gives subjects only visual information. The supervised data is drawn as a point moving according to the recorded data. Total four subjects tried to trace the supervised data. After five times trials, we evaluate the experimental data by using mean square method.

Next condition is that both visual information and force information are given. The force information is just a force assist instructed from the force control of PHANToM.

5. Result and discussion

The experimental results implemented under the first condition are shown in Table 1. And the experimental results for the second condition are shown in Table 2. Each table are indicating the evaluation results based on applying mean square method to between the supervised data and subject's operation data. All subject tried five times under same experimental condition. These results clearly show most subjects were getting skilful by the

Table 1 Experimental result for the first condition

	Subject A			Subject B			Subject C			Subject D		
Exp. I	x	y	z	x	y	z	x	y	z	x	y	z
1	30.38	30.72	55.54	42.40	113.18	137.54	52.36	140.90	15.36	17.64	364.57	1028.12
2	13.04	26.43	30.07	13.93	8.21	200.49	2.44	106.34	390.42	109.96	727.46	1512.75
3	20.30	21.05	26.04	23.93	155.13	263.00	19.09	77.25	445.77	5.72	233.63	1410.12
4	16.91	5.57	42.72	23.28	105.81	249.94	36.32	180.63	495.83	10.85	93.78	143.24
5	8.31	17.01	99.54	15.68	58.84	198.50	45.29	70.59	783.55	10.90	14.14	20.75

Table 2 Experimental result for the second condition

	Subject A			Subject B			Subject C			Subject D		
Exp. II	x	y	z	x	y	z	x	y	z	x	y	z
1	5.44	0.84	28.63	7.97	1.23	86.93	133.82	80.08	179.61	5.72	14.90	6.91
2	0.48	6.45	61.17	9.59	15.15	20.23	59.57	101.29	218.50	8.60	8.60	6.39
3	5.28	25.23	64.50	4.10	5.07	53.52	56.18	99.13	264.14	5.18	5.18	1.89
4	1.31	10.57	68.95	3.36	7.06	26.01	31.10	135.73	346.60	10.19	10.19	1.57
5	3.03	8.40	48.38	3.78	5.46	19.41	36.37	148.51	399.47	2.07	2.07	1.60

number of times progress regardless of conditions. And the results of experiment II are entirely better than that of experiment I due to assistance of force control.

Because it was difficult to create a sense of depth in the virtual environment, most of subjects were not able to get good result in respect to z-axis against the other axis direction. Realistic shape of forceps is necessary to make the virtual training environment more practice. Then, the evaluation criterion about posture of forceps can be added. In this experiment we adopted a simple operation like a doctor cuts the body surface as the supervised data. To make it possible to apply the reproducing function for other operation skill such as sewing a blood vessel, not only a virtual forceps model but also torque control function of a haptic device is requested. Constructions of a virtual forceps model and the contact model between the virtual forceps model and the dynamic model are our future work.

6. Conclusions

This paper described the technical factors of new training factor that helps to inherit the surgical skills of experienced doctors to inexperienced doctors and/or residents. Though the supervised data was a simple operation and there were no dynamic model in experimental environment, the results under the second condition showed the force assist function has an effect for operation training.

For the next step, we firstly improve the virtual environment where a virtual forceps model will be built and the dynamic model will be added. In order to embed the dynamic model, realistics of virtual model makes the training sysmte more plastic. So we are planning to apply OpenGL Volumizer to volume rendering the vitual organ model. Then, the computation speed and imaging speed of GPGPU would be helpful. The integration of the development environments for the haptic device, OpenGL Volumizer, and GPGPU are neccesary.

References

[1] Roger W. Webster, Dean I. Zimmerman, Betty J. Mohler, Michael G. Melkonian, Randy S. Haluck, A Prototype Haptic Suturing Simulator, Medicine Meets Virtual Reality 2001, pp567 - 569.

[2] Bro-Nielsen M, Helfrick D, Glass B, Zeng X, Connacher H. VR simulation of abdominal trauma surgery. Stud Health Technol Inform 1998;50:117-23.

[3] Derek T. Woodrum, Pamela B. Andreatta, Rajani K. Yellamanchilli, Lauren Feryus, Paul G. Gauger, and Rebeca M. Minter, Construct validity of the LapSim laparoscopic surgical simulator, The American Journal of Surgery 191 (2006) pp. 28-32.

[4] Tatsushi Tokuyasu, Akito Ichiya, Tadashi Kitamura, Gen'ichi Sakaguchi, and Masashi Komeda, Development of a simulation system with a haptic device for cardiac muscle palpation, Proceedings of Computer Assisted Radiology and Surgery, 2005 1:p.539.

[5] Y Yamauchi, Is force-feedback effective on surgical assist devices? : Perception of elasticity through forceps, Journal of Japan Society of Computer Aided Surgery, 8(3) pp.270-271.

[6] Tatsushi Tokuyasu, Takashi Shuto, Kenji Yufu, Toshihide Miyagi, Yasutaka, Uchida, Hiroshi Takada, Hironori Abe, Akira Marui, Shotaro Kaneo, and Masashi Komeda, Establishment of A Deformable Aorta Model based on Patient's Chest CT Data, The proceedings of, the Fourth International Conference on Innovative Computing, Information and Control, 2009,(ICICIC2009) (To Appear)

Automatic Detection of Pedestrians from Stereo Camera Images

Kazuki Inumaru*1, Joo Kooi Tan*1, Seiji Ishikawa*1 and Takashi Morie*2

Department of Mechanical and Control Engineering, Kyushu Institute of Technology[*1]
Department of Brain Science and Engineering, Kyushu Institute of Technology[*2]
{inumaru, etheltan ,ishikawa}@ss10.cntl.kyutech.ac.jp[*1], *morie@brain.kyutech.ac.jp*[*2]

Abstract: we propose a technique for detecting pedestrians employing stereo camera images based on probabilistic voting. From a disparity map, each pixel on the image is voted on a depth map employing a 2-D Gaussian distribution. The region having a peak value of the vote is chosen as the foot of an object. The object is specified by a rectangle on the right image, which is referred to as a region of interest (ROI). This ROI is described by HOG features and it is judged by SVM if it contains a person. With the ROI containing a person, Kalman filter is applied to track the person through successive image frames. Performance of the detection of persons was evaluated employing a ground truth data. The rate of detected persons to the ground truth data, called a recall rate, was 80 %. This is a satisfactory result.

Keywords: Stereo cameras, Pedestrians detection, HOG, Kalman filter.

1. INTRODUCTION

In recent years, intelligence of a car has been advancing, and advanced safe technologies to support driving of a driver using an in-vehicle camera have become much important. Several methods have been put into practical use for controlling a vehicle such as recognizing traffic lanes from a camera, detecting obstacles by radar, etc. In particular, to realize a safe traffic society, various studies and technology development have been enthusiastically performed aiming at protection of pedestrians. As the pedestrian detection method from in-vehicle camera images, Gavrila[1] proposed a matching method employing a hierarchical template of the shape of a pedestrian. But it has a problem that it must perform the matching repeatedly at a rough position on the image. Uchimura [2] uses U-V-disparity and it applies Gabor Filter to an object region to obtain its features and distinguishes them by Support Vector Machine. However, the object detection in the complicated background such as a downtown seems difficult. Other than the use of in-vehicle cameras, Zhao & Thorpe [3] realize pedestrian recognition by a neural network. However, the precision of recognition with this technique is not enough for practical use.

In this paper, we propose a pedestrian detection method using a stereo camera system. Similar technique [1-3] has already been suggested, but our study differs from them in that, after the detection of pedestrians, it aims at judging the degree of risk with each pedestrian and informs a driver in the order of the degree. In this particular paper, however, we concentrate on pedestrian detection: We propose a pedestrian detection method employing a stereo camera system and a voting using Gaussian distribution.

In the following, we present the proposed technique and show experimental results with discussion.

2. PROPOSED TECHNIQUE

2.1 Parallel Stereo Cameras

In this study, we employ a parallel stereo camera system. The two cameras are of the same height with each other. Let us denote the camera lens coordinate system of the left camera and the right camera by O_l-$X_lY_lZ_l$ and O_r-$X_rY_rZ_r$, respectively. The light axes coincide with the Z_l axis and the Z_r axis, respectively, and the X_l axis and the X_r axis are collinear horizontally. A pair of arbitrary corresponding points on the left image and on the right image receives epipolar constraint. In case of parallel stereo, the constraint becomes a horizontal line and we only have to search a partner point on the horizontal constraint line. Let us denote a point on the left image by (u_l,v_l) and its corresponding point by (u_r,v_r) on the right image. Then disparity d is calculated by

$$d = u_l - u_r \,. \qquad (1)$$

The relation between the image coordinate system and camera lens coordinate system O-XYZ is given by

$$\begin{aligned} X &= b(u_r - c_u)/d \\ Y &= b(v_r - c_v)/d \\ Z &= bf/d. \end{aligned} \qquad (2)$$

Here f is a focal length and b is a base line length.

2.2 Corresponding Stereo Images

In correspondence point search between two images, we use the technique proposed by Franke & Joos [4]. It performs the correspondence search employing initially a low resolution image, then higher resolution images. This results in the reduction of computational cost to a large extent.

Let us define the right image as a base image and the left image as a reference image. In the first place, Sobel filtering and binarization is applied to the base image to obtain the edge image of the original. By the employment of the pyramidal representation of an image, lower resolution images are produced with the base, reference and the edge image of the base image. Correspondence is searched on the low resolution edge images first. If a pixel on an edge is found on the edge image, its corresponding pixel is specified on the lower resolution base image and its partner is searched on the lower resolution reference image. Normalized correlation is employed for the search, since it is robust to illumination change. Once a corresponding pair of pixels is found, the pixel and its 3-neighbor pixels, i.e., the next column pixel of the same row, the next row pixel of the same column and the next column pixel of the next row, on the higher resolution base image are examined correspondence with the higher resolution reference image. The image coordinate of a corresponding point is computed to the sub-pixel order by use of parabola fitting. This procedure is repeated in turn to higher resolution images to obtain the final solution. **Fig. 1** shows a disparity map of a road image.

2.3 Object Detection

2.3.1 Depth map

Employing the distance information provided from the disparity image, the 3-D position of the object is specified on the real space, from which the region of the object is identified on the right (base) image. Let us fix the *Y* coordinate to a certain constant, e.g., *Y*=0. The *XZ* plane is then a voting plane which is separated into unit cells. All the pixels on the edge image of the base image receive transform by Eq.(2) and voted on the cells.

2.3.2 2-D Gaussian distribution

The cell where a vertical object exists has a large number of votes. This is, however, not the case in a practical situation, since a longer distance will contain larger errors in parallel stereo. To overcome this difficulty, instead of voting '1' on a certain cell, the voting is done by a 2-D Gaussian distribution whose center is the voted cell.

(a) (b)

Fig.1. Deriving a disparity map: (a) The base (the right) image is given and (b) the depth image is computed from the disparity.

It converts arbitrary point $p(ur, vr; d)$ in provided disparity image into point $\mu(u_r, 0, Z_r)$ in the *uZ* plane. Here *uZ* plane is a two-dimensional plane owning horizontal direction *u* of the image on depth direction *Z*, the cross axle in a vertical axis. It converts *d* into Z_r by Eq (2) and v_r is 0, for all pixels *p* with the same disparity. We vote on the *u*Z plane with the probability value of the 2-D normal distribution at a provided point $\mu(u_r, 0, Z_r)$. The 2-D Gaussian distribution is defined by

$$f_v(u,Z;\boldsymbol{\mu},\Sigma)=\frac{1}{2\pi|\Sigma|^{1/2}}\exp\left\{-\frac{1}{2}\left(\mathbf{U}^T\Sigma^{-1}\mathbf{U}\right)\right\} \quad (3)$$

$$\boldsymbol{\mu}=\begin{pmatrix}\mu_u\\ \mu_z\end{pmatrix}=\begin{pmatrix}u_r\\ Z_r\end{pmatrix},\quad \mathbf{U}=\left(u-\mu_u,\quad Z-\mu_z\right),\quad \Sigma=\begin{pmatrix}\sigma_u & 0\\ 0 & \sigma_z\end{pmatrix}$$

After all voting, we convert the *u* axial direction into the *X*-axis direction employing Eq (2). The *uZ* plane is converted into an *XZ* plane by this procedure and this yields a depth map.

2.3. 3 Evaluating cell regions and occupation rate

We take a region called a cell region composed of 3×3 cells and evaluate an occupation rate of the cell region. *The occupation rate* is defined as the average of the voted values over the 9 cells. *A depth image* is an image showing the voted values of the cell regions having the occupation rate larger than a threshold. A binarized depth image is called *a grid image*. The depth image receives labeling and clustering and the weighted centroid of each labeled region is calculated on the depth image. The image giving the locations of the centroids is called *a centroid image*. See **Fig. 2** for examples of these images.

2.3. 4 Region of interest

The equation of the road is given by

$$aX + bY + cZ + 1 = 0. \quad (4)$$

Here, *a*, *b*, *c* are road parameters and calculated in

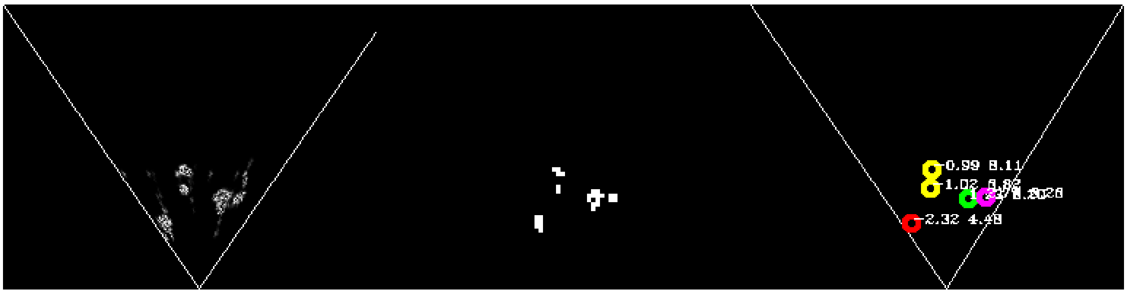

(a) (b) (c)

Fig.2. Employed maps: (a) Depth map, (b) grid map, and (c) centroid map.

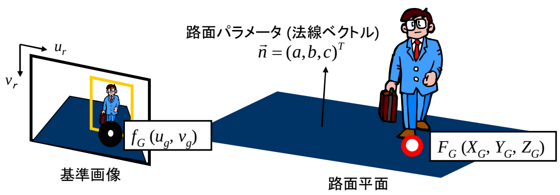

Fig. 3. Diagram of a region of interest.

advance. Using $G(X_G, 0, Z_G)$ and Eq(3), a contact point $P_G(X_G, Y_G, Z_G)$ between the road and the object is identified. Y_G is given by

$$Y_G = \frac{-1}{b}\left(aX_G + cZ_G + 1\right). \tag{5}$$

Once $P_G(X_G, Y_G, Z_G)$ is identified, it is converted by Eq. (2) reversely and the object and its grounding point $p_G\ (u_g, v_g)$ is identified so that it may be put on the image of the road. The Region of Interest is expressed with a rectangle, and its size is given by

$$\begin{aligned} Height &= sf / Z_G \\ Width &= Height / 2 \end{aligned} \tag{6}$$

Here s is a scale factor and the aspect ratio is fixed to 2:1. **Fig 3** shows a diagram of the ROI.

2.4 Pedestrians Recognition and Tracking

The HOG feature [5] is calculated within the ROI in the frame and the region is judged whether or not it contains a human by the employment of the support vector machine (SVM).

From the position recognized as a pedestrian, we employ Kalman Filter [6] to track it in successive frames.

3. EXPERIMENTAL RESULTS

Experimental results using the proposed method are shown in this section. In experiment 1 (Exp1-1), a stereo camera system is fixed and it take images of the scene where pedestrians pass in front of the cameras, and the scene (Exp1-2) where pedestrians moved around to various orientations. In experiment 2 (Exp2), pedestrians in a zebra crossing are captured images from a moving stereo camera system.

The proposed method was applied to these videos. **Fig.4** shows the results of Exp1-2 and Exp2. Red boxes show the ROIs judged as containing a human, whereas a blue box is the ROI judged as not containing a human. The result of tracking is depicted by respective colors. The size of the processed images is 320*240 pixels. The employed PC is Intel Core2 (CPU:2.39GHz, memory: 4GB).

4. DISCUSSION

4.1 Evaluation Criteria

We consider that not only the result of the detection but also the range of an ROI containing a pedestrian should be evaluated. A detected ROI is therefore compared to ground truth data. It is evaluated what extent of an ROI is included in a ground truth data and, in the same way, what extent of a ground truth data is detected. For this purpose, we define two indices called *cover* and *overlap* given by the following equations.

$$\begin{aligned} Cover &= \frac{GT \cap OA}{GT} \\ Overlap &= \frac{GT \cap OA}{OA} \end{aligned} \tag{7}$$

Here GT is the area of a ground truth region and OA is that of a detected ROI. If each value exceeds 0.5, it is judged as detected exactly. **Fig.5** shows a conception diagram of the cover and the overlap.

4.2 Evaluation Results

If we denote the number of all the employed GT data by A, the ratio of the number of correctly detected GT data to A is called *Recall* and is defined by

$$Recall = TP / A. \tag{8}$$

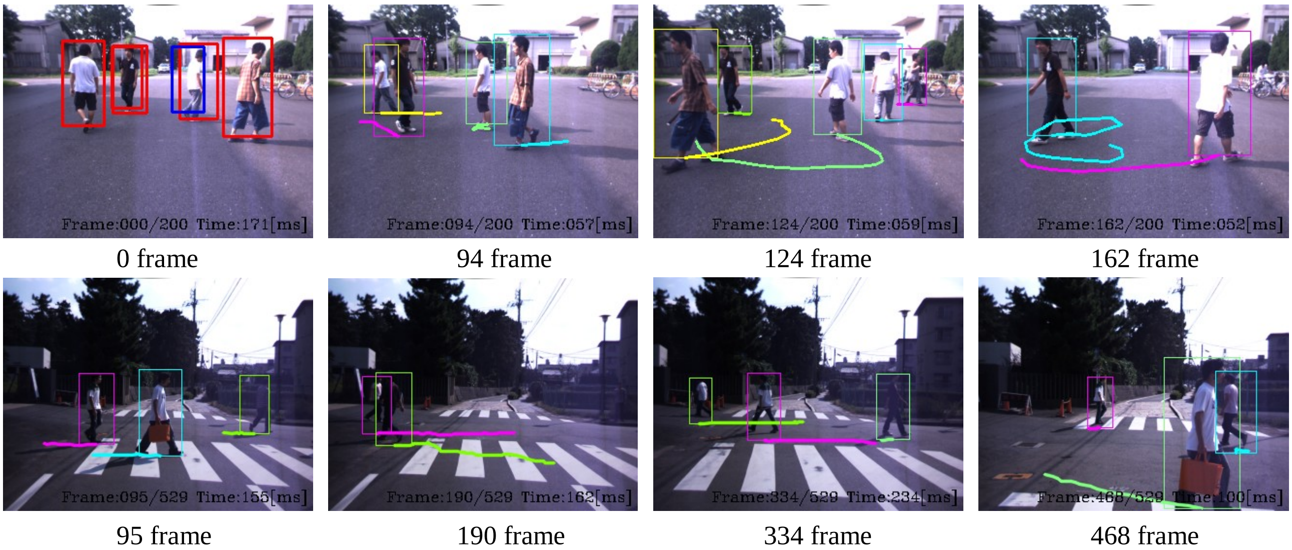

Fig. 4. Experimental results: Pedestrians detection and tracking; a fixed camera case (the upper row) and a mobile camera case (the lower row).

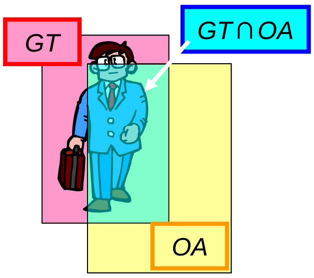

Fig. 5. Diagram of the cover and the overlap.

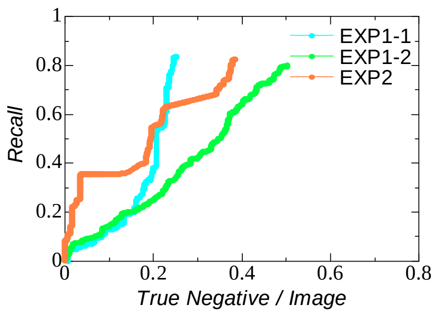

Fig. 6. An evaluation graph.

Here *TP* means true positive. **Fig.6** shows a graph which indicates the relation between the *Recall* values and *TN* values with respect to every experiment. Average processing time with each experiment is 50.5, 61.7 and 150 [ms/frame], respectively.

5. CONCLUSIONS

This paper proposed a method of detecting a pedestrian from a video image taken from a stereo camera system. In order to extract an object from an image, voting of distances of the points detected on the image was done by the employment of a 2-D Gaussian distribution. The detected object region was represented by HOG features and it was judged if the region contains a human by SVM. Experimental results showed satisfactory performance of the method.

The degree of danger with various human activities will be defined and recognized in the next step of this study. To raise the precision of the disparity map and detecting multiple people also remain for further study.

REFERENCES

[1] D. M. Gavrila: "Pedestrian detection form a moving vehicle", *Proc. European Conf. on Computer Vision*, vol.2, pp.37- 49, 2000.

[2] K. Matsushima, H. Zhencheng, K. Uchimura: "Pedestrian recognition using stereo sensor", Information Processing Society, Research report, pp.49-54, 2006.

[3] L. Zhao, C. E. Thorpe: "Stereo and neural network based pedestrian detection", *IEEE Transactions on Intelligent Transportation System*, Vol.1, No.3, pp.148-154, 2000.

[4] U. Franke, A. Joos: "Real time stereo vision for urban traffic scene understanding", *Proc. IEEE Intelligent Vehicles Symposium* 2000.

[5] N. Dalal, B. Triggs: "Histgrams of oriented gradients for human detection", *Proc. of IEEE Computer Vision and Pattern Recognition*, pp. 886-893, 2005.

[6] G. Welch, G. Bishop:"An Introduction to the Kalman Filter", Technical Report TR95-041, University of North Carolina at Chapel Hill, 1995.

Human Behavior Analysis with Optical Flow and Median-filtered Temporal Motion Segmentation Method

Md. Atiqur Rahman Ahad, J.K. tan, H. Kim and S. Ishikawa

Department of Control Engineering, Kyushu Institute of Technology,
Kitakyushu, Tobata, Sensui-cho 1-1, T-804-8550, Japan,
(Tel : 81-93-884-3183; Fax : 81-93-884-3183)
(Email: atiqahad@yahoo.com)

Abstract: We focus on human activity analysis so that an intelligent system (e.g., a robot) can easily understand some important activities and help thereby. Hence we present an improved method for activity analysis, called Median-filtered Temporal Motion Segmentation (MfTMS) method, which can segment and understand motion temporally from the video sequence. It is based on the computation of optical flow and thereafter split it into four different channels. Later median filtering is applied and we produce four motion-history templates based on the directional motion vectors. Based on the total pixel volumes on these history templates and their related variations, various directions of the action primitives are segmented temporally. We conduct experimentations both indoor and outdoor environments and achieved sound performance. This segmentation method can assist an intelligent system or a robot to understand activities and take decisions afterwards. It is a simple but robust approach.

Keywords: Motion segmentation, behavior understanding, DMHI, optical flow, MfTMS**.**

I. INTRODUCTION

Motion understanding and behavior analysis are important research areas in computer vision arena with various important applications [1-2]. In this paper, we attempt to understand and segment human behavior based on the concept of our Directional Motion History Image (DMHI) method [3], which is based on four channels of optical flow. There are various action segmentation approaches. For temporal motion segmentation approach, Kahol et al [4] focused on developing a gesture segmentation system based on HMM states. Yuan et al [5] presented a method for detecting motion regions in video sequences observed by a moving camera, in the presence of strong parallax due to static 3D structures. Ref. [6] proposed a method to divide all the motion data into segmental motions based on breaking points. After segmentation, all the data are classified into clusters, called basic motion. Ihara et al. [7] proposed a gesture-description model based on synthesizing fundamental gestures. They developed a gesture semantics database based on 'fundamental gestures', which are defined on some set of meaningful actions. Inspired by the natural language processing, an approach for automatically segmenting sequences of natural activities into atomic sections and clustering them is proposed [8]. Ref. [9] segmented video based on the connections between certain low level and computationally simple features; and high level, semantically meaningful features.

Ref. [10] proposed methods for motion patterns of humanoid robots observed as a continuous flow using pattern correlations and associative memory. Ref. [11] proposed approaches that have a more similar connotation with our approach: to segment behaviors into distinct behaviors. Ref. [12] proposed a scheme based on the basic movement transition graph for extracting motion beats from given rhythmic motion data. Similarly, [13] developed a method that automatically detect the musical rhythm and segment the original motion to classify to the primitive motions.

Section II presents the method. Next in Section III, experimental results and analyses are presented. Finally, we conclude the paper in Section IV.

II. THE MfTMS METHOD

Based on the directional motion history evaluation, we can temporally segment a motion sequence into its action primitives [3,14]. Fig. 1 shows the system flow diagram of the MfTMS method.

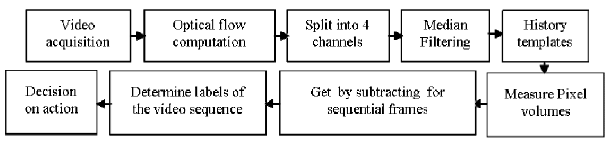

Fig. 1 System flow diagram of MfTMS method.

We calculate the directional motion *history* templates based on the DMHI [3] in order to develop the Median-filtered Temporal Motion Segmentation (MfTMS) method. The MfTMS is the technique for the intermediate interpretation of complex motion into four directions, namely, right, left, up and down. In this method, extracted features are created from pixel-wise optical flow method. We compute the optical flow vector directly from consecutive frames. Then it is split into two scalar fields corresponding to the horizontal and vertical components of the flow. Later, these components are half-wave rectified into four separate channels. We exploit the median filter to filter out the noise, so that the noise remains on the boundary of the object. Based on the four directions, four separate optical flow motion history templates (i.e., summation of optical flow on a sliding temporal window for each pixel) are created after deriving the four optical flow components. After having the motion templates for a complex action or activity, we calculate the volume of pixel values ($\nu_t \in \{\nu_t^{x+}, \nu_t^{x-}, \nu_t^{y+}, \nu_t^{y-}\}$) after summing up the motion templates' brightness levels. For consecutive frames, it is defined by,

$$\nu_t^{\ell} = \sum_{x=1}^{M} \sum_{y=1}^{N} H_\tau^{\ell}(x,y,t) \tag{1}$$

Here, ℓ is a label (which can be one of the four directions based on $\ell \in \{up, down, left, right\}$) of the segmented motion after some threshold values (to determine the starting point for a motion above Θ_α and to determine the stop of motion at Θ_β) as shown:

$$\Delta_t^{\ell} = \nu_t^{\ell} - \nu_{t-k}^{\ell} \tag{2}$$

$$\ell = \begin{cases} \ell & if \quad \Delta_t^{\ell} > \Theta_\alpha \\ \Phi & if \quad \Delta_t^{\ell} < \Theta_\beta \end{cases} \tag{3}$$

Here, Δ_t^{ℓ} is the difference between two *volume* of pixel values (ν_τ) for two frames. Variable k is the frame number, where the value of k might be 1 or more. When k=1, then we are calculating consecutive two frames in the video sequences. These four different labels are identified. When the difference Δ_{t+k}^{ℓ} is more than a starting threshold value Θ_α, we can decide the label of the segmented motion. But when the Δ_t^{ℓ} reduces to $\Theta_\beta > \Delta_t^{\ell}$, we can say that there is no motion or the motion is no longer present (Φ). We choose Θ_α and Θ_β empirically.

So the total pixel volumes obtained by the summation of the motion histories over the pixel neighborhood, decides the direction of the action. Therefore, based on this mechanism from the motion history templates, we can easily segment a complex motion sequence into four directions. Note that in this case, based on the relationships of total pixel volumes for four directions and individual pixel volume in one direction, the system sets the ν_τ to zero, considering no change in that direction. In this way, the system can perform consistently. Figures below illustrate this concept as we find that when an action has finished in one direction, the variation of pixel volumes sets back to zero, and in some cases, increases instantly from zero to some values to denote the action.

III. EXPERIMENTAL RESULTS

We demonstrated two experiments. Fig. 2 shows 'sit-down' and 'stand-up' sequences in indoor. One person sits down, then stands up and repeats the actions in indoor with various speeds. If we employ consecutive frames for analysis, k=1 as in Fig. 3 and Fig. 5(a). The ground truth is presented with the segmentation result.

Fig. 2. Sequences for sit-down and stand-up actions

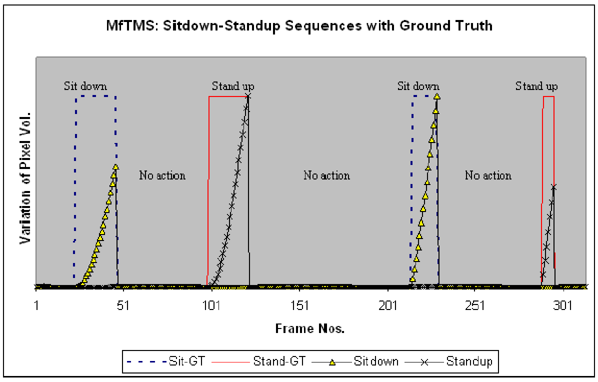

Fig. 3. Results of segmentation for actions of Fig. 2

The output is shown with the ground-truth data (GT as unit step-pulse-shaped representations) for better evaluation, where the abscissa represents 'Frames numbers' and the ordinate stands for 'Variation of pixel volumes'. From Fig. 3, we note that the action primitive extraction and identification are done accurately. After first sitting down and stand-up, we find some small spikes which can be considered as noise. We manually checked the original action sequences frame by frame and the corresponding experimented output. We also consider an experiment in outdoor and cluttered environment having textured road-marks and static but complex background. In this experiment, one person walks on the zebra-crossing from one side of the road to other side. He walks to left and back to right.

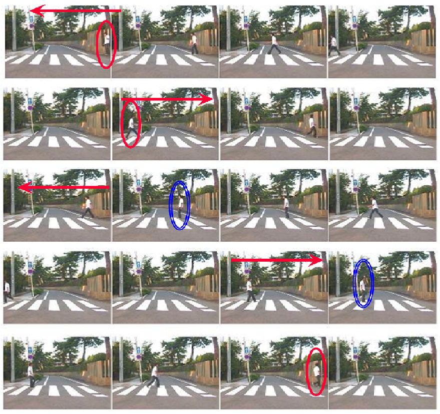

Fig. 4. Sequences of outdoor experiment

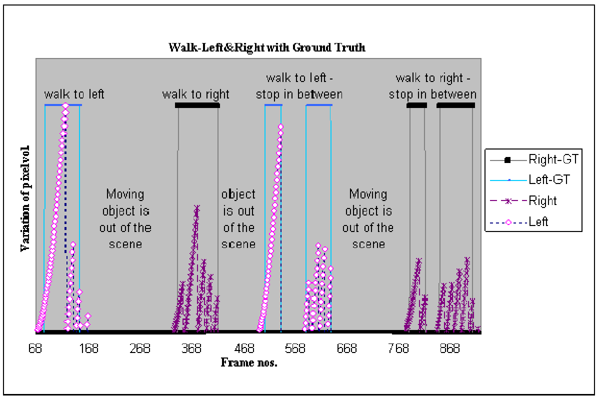

(a) Outdoor experiment of 'walk to left, walk to right, then again walk to left, stop for a while, then left'. Next the motion for walk-stop-walk to right. Ground truth (GT) depicts the segmentation as excellent.

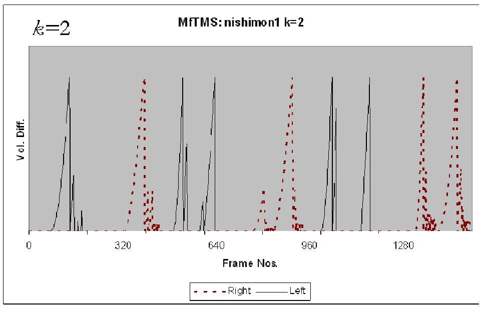

(b) Same result with k=2 to reduce the noisy patterns and to produce better output.

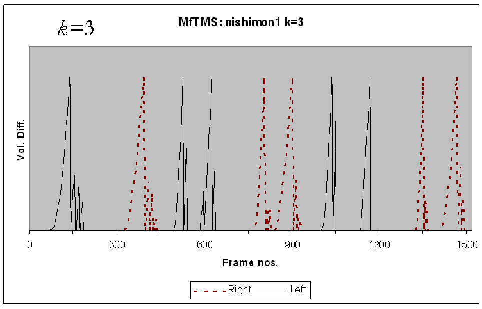

(c) Same result with k=3.

Fig. 5. Experimental results for outdoor experiment

Then again come to the scene as walking to left with sudden stop for a while and does the same in right direction. So we tried to identify the action primitives using the MfTMS method. Fig. 4 shows some sequences where a person is in motion – to left, right or out of the scene. Fig. 5 demonstrates the result of segmentation and identification. The output shows satisfactory resemblance for this long video sequence. Around frame no. 568, we notice a sudden stop ('no motion') for a while and then again the start of motion. Similarly, after 820 frames, we can observe this 'no motion' part (i.e., sudden stop while walking towards right). In this graph, we notice more than one steep curves under one action (e.g., for 'walk to left' action, we see three major steeps). As explained above, the system reduces the volume of pixel values (V_τ) to zero based on the relationship of total pixel volumes of four directions. This is not tricky as in between there is no other motion directions and these curves are just adjacent to another to cover one block of action based on that direction. However, another finding depicts (Fig. 5(b)) that introduction of different values of k can reduce the noisy patterns and provide better output. From Fig. 5(b)~(c), it is evident that by the introduction of k as 2 and 3, the noisy spikes are less.

However, as the frame nos. in between are a few and no other actions, we consider the entire block as one single action primitive. For example, from frames around frame no. 70 till 'walk to left' part (Fig. 5(a)), we note two other almost consecutive step-pulses to denote 'walk to left'. Similarly, we can get the block of one action for walk to right and so on. These clearly separate the actions in different directions and this information can easily aid an intelligence system or robot to identify a sequential or continuous activities. We manually evaluated the video data to analyze the reasons for this nature of output in this case. We manually checked the possible *start* frame and *stop* frame for each action primitives from original video for both activities, and the experimental results. Except in one cases for both, we find that the start and stop for each action primitive is the same or differed by less than five frames on average. In the second 'Sitting' action, the ending lingered for more frames in the experiment, and for the first 'Walk to Left' action, the experimental results show early stop of walking. We think that noise in optical flow seems responsible for this disarray after the evaluation of frames and output. Moreover, due to the outdoor environment, change in illumination, variable speed of walking, cluttered background, textured road-marks, the computed optical flow has varied and hence the final output has some variations like setting to zero values back and forth.

We have tried with few other activities (e.g., walking and fall-down on the floor, walking towards the camera or off the camera along its optical axis) and have found satisfactory and promising results. In this manner, a robot can annotate a complex motion and take the appropriate decision as per the situation. For example, if a robot finds one person walking and suddenly stops and then sitting down on the floor or ground in a park or rehabilitation center and thereafter no motion, then it can sense that the person is sick or need some help immediately. Based on this, the robot can help the person and send a signal or message to the appropriate operator to initiate assistance. It is clear from these Figures that changes in activity can be detected, and the system is able to determine what kind of motion is performed. It produces the action information based on the action itself, hence timing issue is not a problem. However, four optical flow vectors is a concern, as sometimes, it incorporates some noise that presumes some motion components though there is originally no motion in that specific direction.

IV. CONCLUSION

We presented a simple but robust Median-filtered Temporal Motion Segmentation (MfTMS) method, based on the directional motion *history* templates. This process can separate a complex motion sequence into four directions promptly. In this method, we do not need to calculate feature vectors or we do not require any classification method or recognition scheme. Therefore, this segmentation process is simple and thus it is fast, too. As shown in the experimental results, the MfTMS can accurately determine the directions, which can lead a robot to better decision. This method can be employed for other application areas too.

One of the key issues concerning to this method is related to the proper correlation between previous state and the current movement. Employing Hidden Markov Model may improve the system with increasing complexity. Moreover, the presence of noise due to optical flow errors (e.g., low-textured people) limits the performance, which is inherently related to the computation of optical flow. Proper choice of optical flow or a new robust mechanism to deal in calculating the optical flow vectors are very crucial to improve the system. In future, one may consider magnitude and orientation of optical flow for a patch (e.g., patch of 5x5 pixels) and then run RANSAC to ignore outliers and consider the dominant parts of optical flow. We hope that this way can minimize noises and hence can improve the four-directed motion history templates.

REFERENCES

[1] Ahad MAR, Tan J, Kim S, Ishikawa S (2008), Human activity recognition: various paradigms, Int. Conf. Control, Automation and Systems 1896-1901
[2] Ahad MAR, Tan J, Kim S, Ishikawa S (2009), Human activity analysis: concentrating on motion history image and its variants, Int. Conf. ICASS-SICE
[3] Ahad MAR, Tan J, Kim S, Ishikawa S (2009), Temporal motion recognition and segmentation approach, Int. J. of Imaging Systems & Technology 19:91-99
[4] Kahol K, Tripathi P, Panchanathan S (2006), Documenting motion sequences with a personalized annotation system, J. of Multimedia 13:37-45
[5] Yuan C, Medioni G, Kang J, Cohen I (2007), Detecting motion regions in the presence of a strong parallax from a moving camera by multiview geometric constraints, IEEE Trans. on PAMI 29:1627-1641
[6] Osaki R, Shimada M, Uehara K (1999), Extraction of primitive motion for human motion recognition, Int. Conf. on Discovery Science 1721:12 pages
[7] Ihara M, Watanabe N, Nishimura K (1999), A gesture description model based on synthesizing fundamental gestures, IEEE SouthEastCon 47-52
[8] Wang T, Shum H, Xu Y, Zheng N (2001), Unsupervised analysis of human gestures, IEEE Pacific Rim Conf. on Multimedia 174-181
[9] Peker K, Alatan A, Akansu A, Low-level motion activity features for semantic characterization of video, IEEE Conf. on Multimedia and Expo 801-804
[10] Kadone H, Nakamura Y (2006), Segmentation, memorization, recognition and abstraction of humanoid motions based on correlations and associative memory, IEEE-RAS Int. Conf. on Humanoid Robots 1-6
[11] Barbic J, Safonova A, Pan J, Faloutsos C, Hodgins J, Pollard N (2004), Segmenting motion capture data into distinct behaviors, Graphics Interface 185-194
[12] Kim T, Park S, Shin S (2003), Rhythmic-motion synthesis based on motion-beat analysis, ACM Trans. Graphics 22:392-401
[13] Shiratori T, Nakazawa A, Ikeuchi K (2004), Detecting dance motion structure through music analysis, IEEE Conf. Automatic Face and Gesture Recognition 857-862
[14] Ahad MAR, Uemura H, Tan J, Kim S, Ishikawa S (2008), A simple real-time approach for action separation into action primitives, Int. Workshop on Tracking Humans for the Evaluation of Their Motion in Image Sequences, 69-78

The Fifteenth International Symposium on Artificial Life and Robotics 2010 (AROB 15th '10),
B-Con Plaza, Beppu,Oita, Japan, February 4-6, 2010

A Method Using Same Light Sensor for Detecting Multiple Events on Window in Home Intruding Crime

Akira Yamawaki, Takayuki Katakami, Yuhki Kitazono, Seiichi Serikawa

Kyushu Institute of Technology, 1-1, Sensui, Tobata, Kitakyushu, 804-8550, Japan
(Tel: 81-93-884-3255; Fax: 81-93-884-3214)
(yama@ecs.kyutech.ac.jp)

Abstract: Combining robots with many sensor nodes on the sensor network is important to improve the home security. From view of the cost of such system, it is desired that each sensor node is very cheap. The three events to the window and the key occurring when a thief attempts to intrude into the house are detected by the different sensors conventionally. This paper proposes a method detecting the three events by using the simple light-sensor consisting of an infrared LED and a photodiode. In the experiments, the light sensor shows the characteristic tendencies that can detect each event. This fact indicates that our proposal can realize a sensor node more efficiently instead of using different sensors.

Keywords: Light-sensor, detecting method, sensor node, multiple events, home security

I. INTRODUCTION

Combining robots with many sensor nodes on the sensor network is important to improve the home security [1][2]. From view of the cost of such system, it is desired that each sensor node is very cheap and small.

For the home intruding crime, three events mainly occur on the window [3]. First one is that the window is shocked. Next one is that the window is opened. Final one is that the key is opened. Traditionally, these three events are detected by using multiple sensors. For example, the magnetic sensor detects the window opened and the key opened [4]. The impact sensor detects the shock to the window [4].

This paper proposes new method that uses the same light sensor detecting three events mentioned above. By using the same light sensor, the cost buying many same sensors would be lower than buying the fewer number of different sensors. The light sensor is constructed by the trivial components which are an infrared LED and a photodiode. They are very cheap and can be obtained easily because many makers distribute them with the same characteristic.

The rest of this paper is organized as follows. Section II shows an organization of the sensor node that employs our method using the simple light-sensors. Also, how to detect the three events by our method is described. Section III performs the preliminary experiments to confirm whether the light sensor shows the characteristic tendencies that can detect each event or not. Finally, Section IV concludes our paper.

II. Proposed Detecting Method

1. Sensor Node Organization

Fig. 1 (a) shows a sensor node that employs our proposed detecting method using the light sensor. The

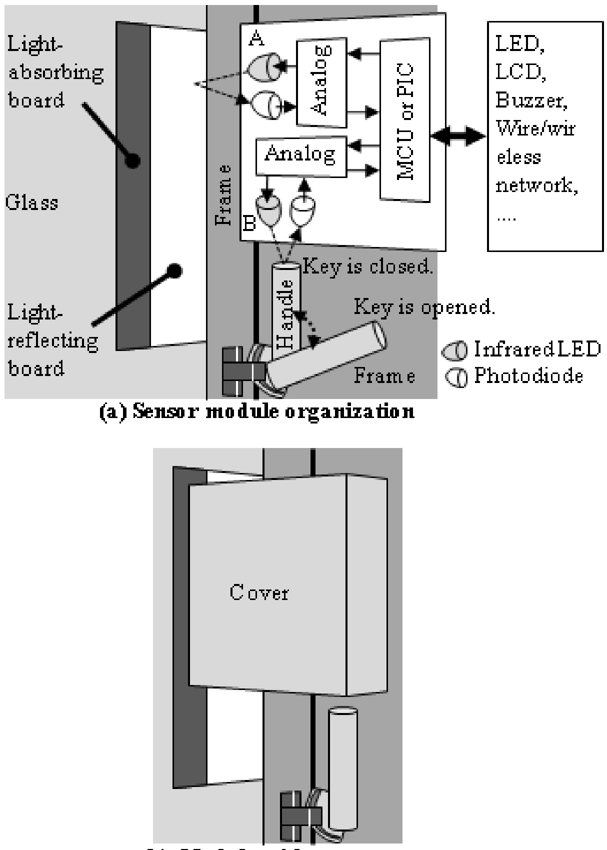

(a) Sensor module organization

(b) Module with cover

Fig. 1 Sensor Node Organization

proposed method uses two light-sensors (light-sensor A and light-sensor B) and two boards attached to the window as shown in Fig. 1 (a).

In the light-sensor, the infrared LED irradiates a material and the photodiode detects the infrared light which is reflected by the material. The light-reflecting board and the light-absorbing board are attached to the

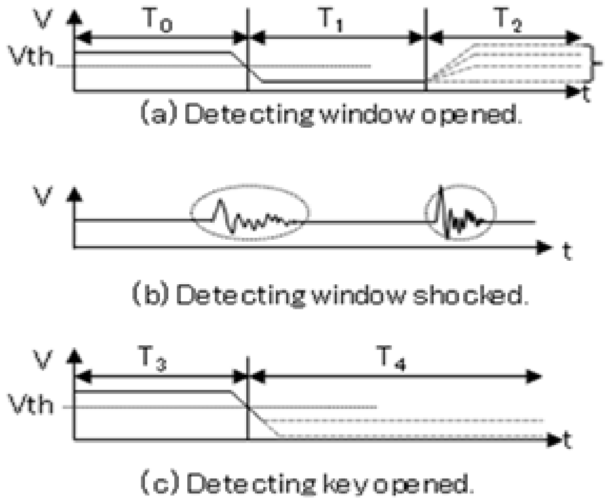

Fig. 2 Detecting Method

window as shown in Fig. 1 (a). The light-sensor A irradiates the light-reflecting board when the window is closed. Thus, when the window is opened, the infrared light irradiated by the light-sensor A crosses the light-absorbing board. The light-sensor B irradiates the light-reflecting board when the window is closed. The other irradiates the top of the handle of the key when the key is closed. The size of the two boards is enough large to hide the sensor node from the outside light as shown in Fig. 1 (b). In addition, the cover wrapping the sensor node is used to obstruct the outside light as much as possible.

In the sensor node, the output voltage of the photo diode passes through the analog circuits like an amplifie r, a filter circuit, and an A/D converter. The output vol tage that has passed the analog circuits is processed by the microcontroller. Then, the microcontroller d rives some devices like the buzzer, LED and so on for alert. You can connect this sensor node to a s ensor wire/wireless network to realize more intellige nt security system.

2. Detecting Method

When the closed window is opened, the output voltage of the light-sensor A will change like Fig. 2 (a). The T0 means the period of which the window is closed and the light-sensor A irradiates the light-reflecting board. The T1 means the period of which the window is being opened and the light-sensor is crossing the light-absorbing board. The T2 indicates the period of which the window has been opened and the light-sensor A irradiates the outside through the window. The change of the output voltage from T0 to T1 can detect the window opened. In T2, the output voltage of the light-sensor A may be uncertain according to the outside situation like the weather and the time (day or night). Thus, we prepare the T1 by using the light-absorbing board to make the drop of the output voltage clear.

When the closed window is shocked, the window

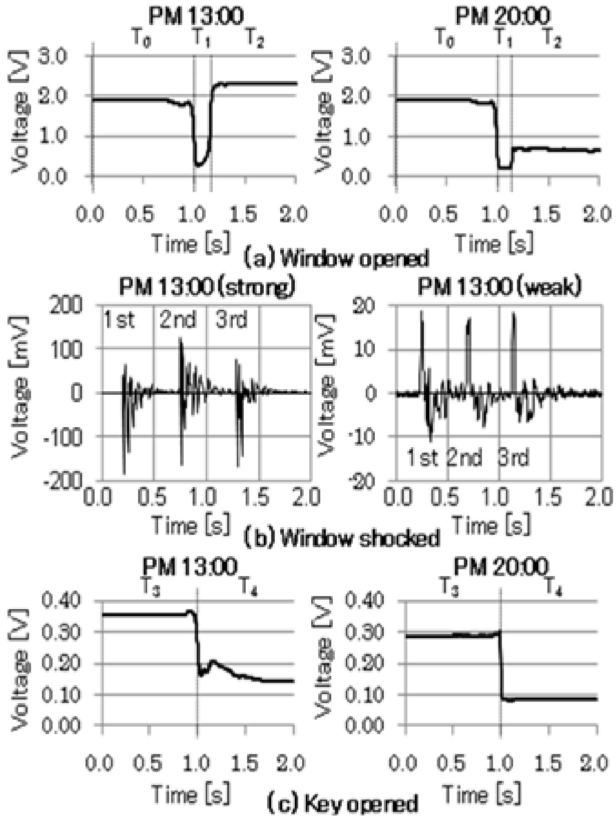

Fig. 3 Experimental Result

would wave [5]. By waving, the distance between the light-sensor A and the light-reflecting board will change. Consequently, since the amount of the reflected light varies, the output voltage of the light-sensor A changes as shown in Fig. 2 (b). Compared with the co nstant voltage without the shock, the window shock ed can be detected by the differences of the output voltage.

When the closed key is opened, the output voltage of the light-sensor B will change like Fig. 2 (c). The T3 means the period of which the key is closed. The T4 means the period of which the key has been opened. Compared with the period of which the key is closed, the distance between the light-sensor B and the handle of the key becomes longer. Thus, the output voltage of the T2 is smaller than that of the T1. By using this drop, the key opened can be detected.

III. Experimental Result and Discussion

1. Experimental Environment

To confirm that proposed method can really detect the three events in the house intruding crime, we have developed a prototype.

In the prototype, we have used the TLN110 of the infrared LED and the TPS611 of the photodiode. The light-reflecting board is a corrugated paper whose surface is shiny white. The light-absorbing board is constructed on the same corrugated paper by painting its edge black.

The prototype is set to the southern window in the lab room. We have set the distance between the light-sensor A and the light-reflecting board to about 0.8cm. T The distance between the light-sensor B and the top of the handle of the closed key has been set to about 1.5cm.

We have made a cover by the corrugated paper and painted the inside of the cover black. The chink between the cover and the light-reflecting board is about 0.2cm. The chink between the cover and the handle of the closed key is about 1.0cm.

We have measured at 8:00am, 13:00pm, 17:00pm, and 20:00pm in sunny day. For the case shocking the window, we have extracted only the differences to the c onstant voltage, removing the DC by the capacitor.

2. Result and Discussion

A. Window Opened

Fig. 3 (a) shows a part of the results of which we have opened the window 10 times. The output voltages of the light-sensor A when the window is closed are 1.97V to 2.03V. In contrast, the output voltages when the light sensor A crosses the light-absorbing board are decreased until 0.19V to 0.26V. This fact indicates that the window opened can be detected by using this difference.

B. Window Shocked

Fig. 3 (b) shows a part of the results of which we have shocked the window 10 times at each time. Most thieves break the window around the key when intruding to the house. Thus, we have shocked around the key from outside the window. The shocked area is within about 20cm radius from the key.

As shown in Fig.3 (b), you can see the clear differences of the output voltage between two cases. For example, when the window is not shocked, the peak-to-peak voltages of the light-sensor B are lower than 0.5mV. In contrast, when the window is shocked, they are 12 mV to 310mV. Thus, the shock to the window can be detected by using the differences to the constant voltage.

C. Key Opened

Fig. 3 (c) shows a part of the results of which we have opened the key 10 times. The output voltages of the light-sensor B are 0.29V to 0.37V when the key is closed. In contrast, they are 0.08V to 0.14V when the key is opened. By using this voltage drop, the key opened can be detected.

IV. Conclusion

We have proposed the detection method of three events to the window and the key in the intruding crime using the simple light sensor. Through the preliminary experiment, it has been confirmed that the simple light-sensor can detect three events actually as expected. This fact indicates that our proposal can realize a sensor node more efficiently instead of using different sensors.

As future work, for putting our method to practical use, we will decide the threshold voltages and signal processing methods, giving stimulus corresponding to the real crime to the window.

REFERENCES

[1] Kim YG, Kim HK, Yoon SH, Lee SG, and Lee KD (2006), Home Security Robot based on Sensor Network. Proc. of SICE-ICASE International Joint Conference, pp. 5977-5982.

[2] Ueno Y, Kawasaki Y, and Oshima R (2007), A bout Security Measures of Fittings for Plural Means of the Invasion Crime (Part1): The Security Perfor mance and Cost of Windows (in Japanese). Summar ies of Technical Papers of Annual Meeting Architec tural Institute of Japan, pp.749-750.

[3] Mitsuhashi K and Torimiya N (2002), Home Security System "BBee" (in Japanese). Annual design review of Japanese Society for the Science of Design, 8 (8), pp.26-29.

[4] Mizuki N, Aratani S, Hidenori O, and Takayama K (2003), Experimental Study of Glass Strength against Shock Wave Loading: Stress Generation of Float Glass Plates (in Japanese), Journal of the Ceramic Society of Japan, 111 (1297), pp.674-679.

A Learning Control of Unused Energy Power Generation

Satomi Shikasho, Ji-Sun Shin, ChengYou Cui, Hee-Hyol Lee

Graduate School of Information Production and Systems, Waseda University
2-7 Hibikino, Wakamatsu0ku, Kitakyushu, Fukuoka 808-0135, Japan
(Email address: 44081024ips@toki.waseda.jp)

Abstract: In recent years, the new clean energy without dependence on the fossil fuel is required. The control system of the power generation using low temperature gap is designed to keep the speed of the steam turbine in real environment. This system includes nonlinearity and the characteristics of the system change in real environment with the aged deterioration. The evaporator, the condenser, and the turbine systems are modeled, and the PID control with the ability of learning based on BP neural network is designed.

Keywords**:** Learning control, BP Neural Network, Power generator, Low thermal gap, Evaporator, Turbine

I. INTRODUCTION

The clean energy exits in the natural world, and this energy does not emit exhaust gas when it used. The clean energy is widely used for wind energies, solar power and so on, whereas there is some clean energy that has not been used yet such as hot spring heat or exhaust heat of factories. The power generation with these unused clean energies can obtain small heat capacity from heat sources and low thermal efficiency because these power generations scatter the utilizable energies so widely. The temperature gap of unused energy is low as 20℃ to 30℃. In contrast, the temperature gap of the thermal power generation is 500℃ and the temperature gap of the nuclear power generation is 200℃. The heat efficiency is also low as well as 3% to 4%, while the thermal power generation is 40%. Moreover, these heat sources are scattered and the scale of these heat sources is small. Therefore it is necessary to establish a control method that is suitable for the power generation capacity and scale.

This paper deals with the performance improvement of the power generation using low temperature gap in the steady state. This power generation system is composed by Water/ Ammonia fluid as working fluid. This paper set up a heat exchanger model and a turbine model. The control of turbine parts is difficult, because the turbine parts include nonlinear factor. Also this paper confirms usefulness and practicability about BPNN PID-controller through simulations.

II. POWER GENERATION USING LOW TEMPERATURE GAP

The main component of the power generation system using low temperature gap with closed cycle is constructed by heat exchanger (evaporator, condenser), turbine and pump. This working fluid is liquid and carried to the evaporator by the pump. Then it is boiled and becomes steam in the evaporator by hot water. While steam of working fluid passes through the turbine, this system can generate electric power by rotating the turbine blade shaft. The working fluid that passed through the turbine is cooled with cold water in condenser, and becomes liquid again. The structure of the power generation system is illustrated in Fig.1.

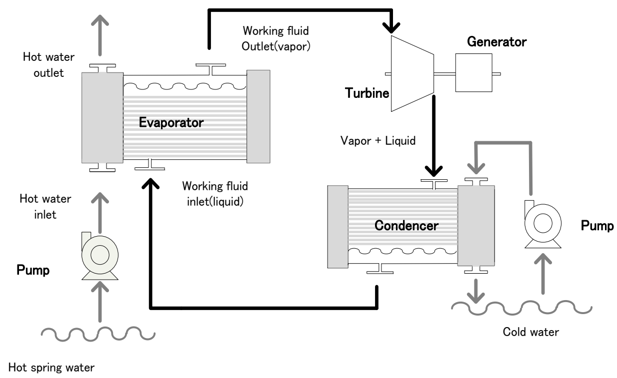

Fig.1 Closed cycle power generation system

2.1 Evaporator Model

The evaporator is shell-and-tube type is shown in Fig.2. The liquid of working fluid is carried to the evaporator tank by pump soaking the heat exchanger tube. Hot water circulates in the heat exchanger tube, and then, the working fluid is steam.

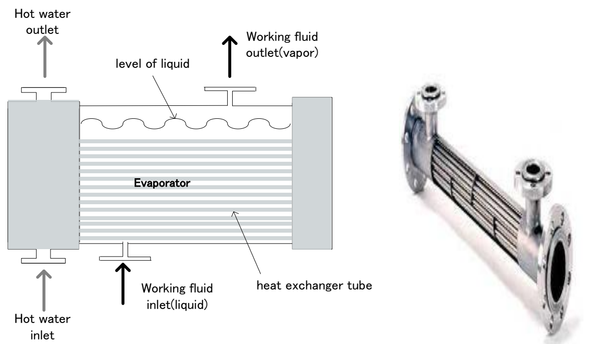

Fig.2 Structure of evaporator

Assumptions of Modeling:
- When the working fluid flows into the evaporator, it is preheated the saturation temperature to liquid phase state.
- The heat exchanger tubes are soaked by the working fluid.
- No consider radiation heat on the entire evaporator.

The steam pressure equations are as follows. [1]

$$H(s) = \frac{1-exp\,(\tau s)}{\tau s} \quad (1)$$

The steam flow of evaporator outlet response is $\Delta Q(s)$, the change in temperature of the hot water to the inlet is $\Delta\theta_h(s)$, and the change of flow for the hot water is $\Delta G_h(s)$.

$$\Delta Q(s) = \{Z_1 \quad Z_2\}\begin{Bmatrix}\Delta\theta_h(s)\\ \Delta G_h(s)\end{Bmatrix} \quad (2)$$

Here,

$$Z_1(s) = \frac{K_1(1-e^{-\tau s})}{\tau s(1+T_c s)(1+T_h s)} \quad (3)$$

$$Z_2(s) = \frac{K_2(1-e^{-\tau s})}{\tau s(1+T_c s)} \quad (4)$$

T_c, T_h are staying time constant, K_1 K_2 are constant value, τ is system constant value.

2.2 Turbine Model

The turbine is composed of the steam control valve and rotor blade, as shown in Fig.3. The steam is piped from the evaporator into the turbine blade through the steam control valve. The steam control valve adjusts steam flow to turbine blade.

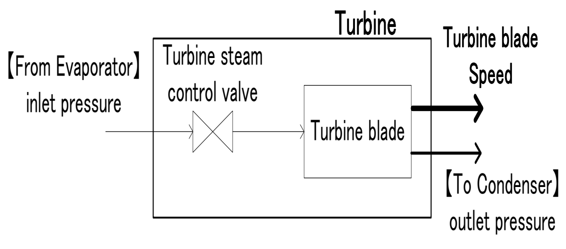

Fig.3 Turbine system

Turbine systems equations are as follows [2]:

Working fluid steam control valve:

$$\frac{dx_1}{dt} = K_3\frac{v}{v_{max}},\ 0 \le x_1 \le 1 \quad (5)$$

Working fluid steam mass rate:

$$\mu_T = \frac{x_1}{M_E}\left(\phi_E{}^2 - \phi_T{}^2\right)^{1/2} \quad (6)$$

Turbine blade speed :

$$\frac{dv}{dt} = \frac{1}{\tau_T}\left[\frac{\phi_E-\phi_T}{\phi_E-\overline{\phi}_T}\frac{\mu_T}{v\overline{\mu_T}} - (1-\varepsilon)\frac{1}{v} - \varepsilon v^2\right] \quad (7)$$

v_{max} : max speed of turbine blade
K_3 : gain
M_E : constant
ϕ_E : evaporator outlet vapor pressure
ϕ_T : turbine outlet vapor pressure
τ_T : system constant
ε : electric load
: desired value

III. Back Propagate Neural Network

The BPNN is a multi-layers network that consists of the input layer, the hidden layer, and the output layer. The standard structure is shown in Fig.4.

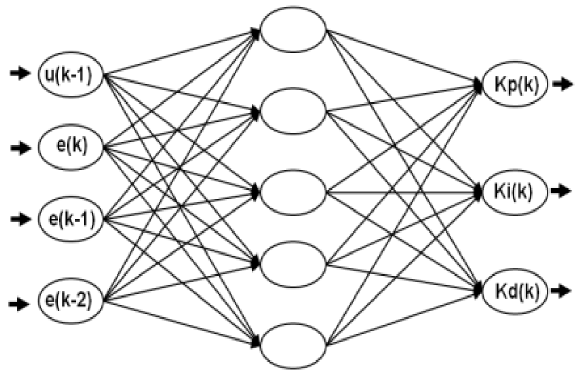

Fig.4 Structure of BP network

BP algorithm step.

Firstly, the actual output of BPNN will obtain from the actual outputs as Eq. (8). It is forward progress.

$$a^{k+1} = f^{k+1}(w^{k+1}\cdot a^k + b^k) \qquad k = 0,1,\dots,m-1 \quad (8)$$

a: output of each layer
w: weight value
b: bias value
m: number of layer

Secondly, the error will be generated at the output layer by comparing between the actual output and the target output. The error function at output layer is defined as

$$E_p = \frac{1}{2}\sum_{k=1}^{m}(T_k - A_k)^2 \quad (9)$$

T_k : reference output
A_k : actual output

The total error function of neural network is shown in Eq. (10).

$$E = \sum_{k=1}^{P} E_p \quad (10)$$

P: total numbers of pattern

Thirdly, the gradient descent method is utilized to calculate the weights of network and adjusts the weights of interconnections to minimize the output error. The gradient descent algorithm adopts the weights according to the gradient error, which is given by Eq. (11).

$$\Delta W_{ij} = -\eta \times \frac{\partial E}{\partial W_{ij}} \quad (11)$$

η: Learning rate

The general form of ∂E/ ∂W is expressed as following Eq. (12).

$$\frac{\partial E}{\partial W_{ij}} = -\delta_j^n \times A_i^{n-1} \quad (12)$$

A: output value of each layer
W: connective weight
δ: error signal
n: layer number of BP network

Substituting Eq. (11) into Eq. (12), the gradient error is expressed as

$$\Delta W_{ij} = \eta \times \delta_j^n \times A_i^{n-1} \qquad (13)$$

ΔW adjusts the weight values between the input layer nodes the output layer nodes from output layer to the input layer. According to these adjustments, the error will decrease until the small set point.

IV. PID parameters with BP NN

BP Neural Network PID control system has structure as depicted in Fig.5. In this PID controller, the connection between the output and the input is given by Eq. (16). BPNN block in Fig.5 shows the structure of NN.

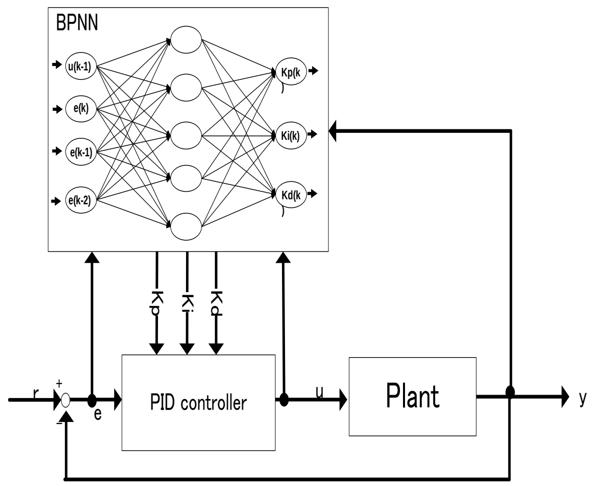

Fig.5 Structure of BP network System

Algorithm:
Step1 Initialization
Neural Network parameters, W_{kj}, W_{kj}, η, α.
k: outputs unit number
j : middle unit number
i :Input unit number
Step2 Load
Plant input $u(t)$, output $y(t+1)$.
Step3 Calculate Neural Network output

$$O_j = f(net_k),\ net_j = \sum_{i-0}^{M} W_{ji}\, O_i,$$

$$f(x) = \frac{1}{1+exp\,(-x)} \qquad (14)$$

$$O_k = net_k,$$

$$net_k = \sum_{i-0}^{N} W_{kj}\, O_j \quad k = 1,2,3 \qquad (15)$$

Step4 Calculate the PID parameter

$$u(n) = u(t-1) + K_p\big(e(t) - e(t-1)\big) + K_i e(t) + K_d\big(e(t) - 2e(t-1) + e(t-2)\big) \qquad (16)$$

Next, calculate *y(t+1)* from *u(t)*.
Step5 Calculate and evaluate error

$$e(t+1) = r(t+1) - y(t+1) \qquad (17)$$

$$E(t+1) = \frac{1}{2} e(t+1)^2 \qquad (18)$$

Step6 Calculate normalized error

$$\delta_k = e(t+1)J(n)\frac{\partial u(t)}{\partial O_k} \quad k = 1,2,3$$

$$\delta_j = \sum_{k=1}^{3} \delta_k W_{kj}\, O_j\big(1 - O_j\big)$$

$$j = 1,2,\dots,5,\ i = 1,2,\dots,4 \qquad (19)$$

Step7 Update weight value

$$W_{ji}(t+1) = W_{ji}(t) + \eta\delta_k O_i + \alpha\Delta W_{ji}(t) \qquad (20)$$

$$W_{kj}(t+1) = W_{kj}(t) + \eta\delta_k O_j + \alpha\Delta W_{kj}(t) \qquad (21)$$

V. SIMULATION

BPNN has 3 layers: input layer, middle layer, output layer. There are 4 units in the input layer, 5 units in the middle layer, and 3 units in the output layer. Learning rate is α=0.25, and inertia coefficient is η=0.005.

5.1 Evaporator outlet pressure control

The block diagram of control system for the evaporator outlet pressure is illustrated in Fig.6. The manipulate variable is the hot water flow to the evaporator, and the controlled output is the outlet pressure of the evaporator. The simulate result of the outlet pressure in shown in Fig.7.

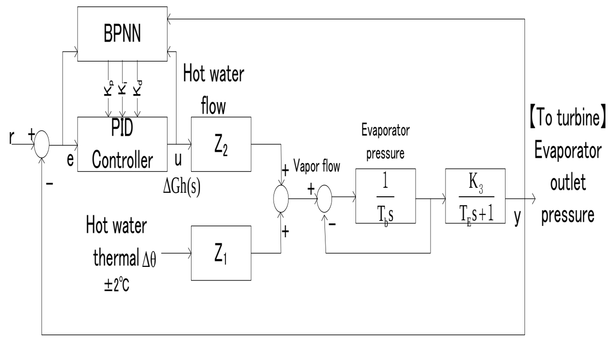

Fig.6 Evaporator block diagram

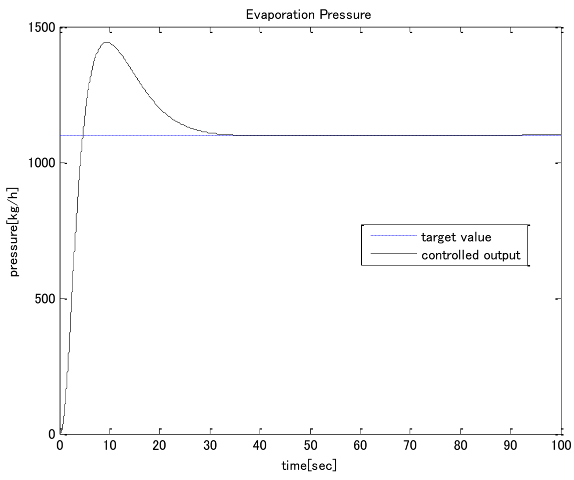

Fig.7 Result of the evaporator outlet Pressure

5.2Turbine blade speed control

The block diagram of the turbine blade speed control system is illustrated in Fig.8. The manipulated variable is the steam control valve, and the controlled output in the turbine blade speed. The simulation result is shown in Fig.9.

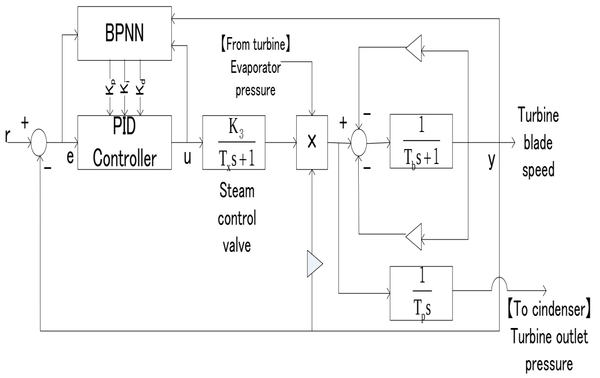

Fig.8 Turbine block diagram

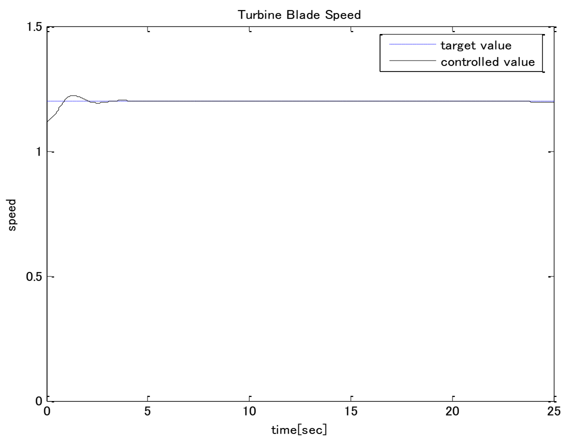

Fig.9 Control performance of
Turbine Blade Speed

The turbine has complicated nonlinear factor, however BPNN PID controller is adjusted.

VI. CONCLUSION

The control systems of the power generation using low temperature gap were designed in this paper. The models of the evaporator and the steam turbine system were deduced, and PID controller with BP Neural Network was designed to keep the turbine blade speed to be constant.

REFERENCES

[1]Hashizume T, Kawai S, Machiyama T (1981) Experimental Studies on the Dynamic Characteristics of Evaporator in the L. B. M. Turbine System. Japan Society of Mechanical Engineers, C, 47(421), pp.1161-1168

[2]OWENS W. L.,(1982) OTEC Plant Response and Control Analysis, ASME, Jour. of Solar Energy Engine, 104, pp.208-215

[3] Jitsuhara S, Nakamura M, Ikegami Y, et al (1994) Controller Design for Vapor Temperatures of OTEC Plant Based on Reduced Order Model, The Society of Instrument and Control Engineers, 30(9) pp.1060-1068

[4] Fujinaka T, Omatu S (2006) Self-Tuning of PID Parameters with Neural Networks(<Special Issue>Parameters Tuning in PID Control), Systems, control and information 50(12) pp.453-458

Design Optimization of Switched Reluctance Motor Torque Controller in Electric Vehicles

Yueying Zhu[1], Guifan Zhao[1], Dafang Wang[1], Dongyu Yang[1], and Takao Ito[2]

1 School of Automobile Engineering, Harbin Institute of Technology, Weihai 264209, Shandong Province, China
(Tel : 86-631-567-2276; Fax : 86-631-568-7523)
(hityueying929@163.com, zgf7071@163.com)

2 Dept. of Business Administration, Ube National College of Technology, Yamaguchi, Japan
(Tel : 81-836-35-7115; Fax : 81-836-35-7115)
(ito@ube-k.ac.jp)

Abstract: The drive performance of Switched Reluctance Motor (SRM) used for electric vehicles is one of the important issues for improving the stability and comfortable operation of the vehicle. This paper introduces a study of design optimization of the SRM torque controller. The purposes of the SRM nonlinear dynamic model established with the MATLAB/Simulink are to reduce the torque ripple and increase the average torque. The torque ripple and average torque, as functions of turn-off angles and rotor speed, are developed by simulation in this paper. The optimized torque controller is designed based on the changeable turn-off angles. The simulation results show that the proposed optimization of the torque controller has strong impact on the improvement of the torque ripple and the average torque.

Keywords: Electric vehicle, switched reluctance motor, torque control, optimization, computer simulation.

I. INTRODUCTION

We have to find the way to save our energies and protect our environment for the energies short. The development of the electric vehicles (EV) will contribute to save our energies and realize the zero emission in automobile industry.

Compared to other motors, the switched reluctance motor (SRM) used in the EV has some advantages, such as simple structure, low cost and flexible control, etc [1-3]. Therefore, the SRM has lately drawn considerable attention in the automobile drive system. However, the SRM suffers from a major drawback for its torque ripple which is harmful to the motor and the vehicle drive system [1, 4]. In order to obtain good drive performance of the EV, it is very significant to design a high torque controller for reducing the torque ripple and increasing the average torque of the SRM.

There are two ways to control the torque of the SRM as a whole now. One is to optimize and control the torque in changing phase condition, such as hysteresis current control [5], PWM voltage control [6] and direct instantaneous torque control [1,7,8]. The other is to control the torque by using modern intelligent control strategy, such as fuzzy logic control [9], sliding mode control [10] and artificial neural network control [11, 12]. With the development of control strategies, SRM has a good improvement in reducing the torque ripple.

The main contribution of this paper is to design a torque controller used in the EV and optimize it for reducing the torque ripple and increasing the average torque. Compared with the fixed turn-off angle controller, the optimized controller has great advantage to reduce the torque ripple and increase the average torque.

This paper is organized as follows. Section 2 introduces the main structure and characteristics of the SRM. The nonlinear dynamic model of the SRM using the MATLAB/Simulink is built under hysteresis current control strategy. In Section 3, the torque ripple and average torque as functions of turn-off angles and rotor speed are obtained by simulation. In order to reduce the torque ripple and increase average torque, the optimized controller based on turn-off angles and rotor speed is proposed in Section 4. In Section 5, the simulation results are presented, and the performance of the optimized controller is also discussed.

II. SRM NONLINEAR MODEL

1. The Structure of the 8/6 SRM

There are four parts for the SRM drive system, SRM, converter, controller and detection sensor. An 8/6 SRM matching with the four phase asymmetrical converter is chosen in this paper. Obviously the asymmetrical converter can manage the phase singly by controlling the switches and reduce the torque ripple by overlapping appropriately between on-going and off-going phase. In addition, the driving range is very important for electric vehicle, which can be extended by using this converter because of the ability of energy recovery. That is the reason why this converter is chosen.

2. Mathematical Model of SRM

The flux linkage in each phase can be calculated with phase voltage across the winding by Faraday's law as Eq. (1).

$$\psi_k(i,\theta) = \int (u_k - R_k i_k)dt \qquad (1)$$

where ψ_k is the phase flux linkage, u_k is the phase voltage, R_k is the electrical resistance of the winding, i_k is the phase current, θ is the angle of rotor.

The magnetic torque generated by the SRM is obtained by co-energy in the magnetic circuit using Eq. (2).

$$T_e(i,\theta) = \frac{\partial}{\partial\theta}W'(i,\theta) = \frac{\partial}{\partial\theta}\int_0^i \psi(i,\theta)di \qquad (2)$$

where T_e is the magnetic torque generated by the motor, $W'(i, \theta)$ is the co-energy.

The torque and load mechanical dynamic is presented in Eq. (3) based on mechanical principle.

$$T_e(i,\theta) = J\frac{d\omega}{dt} + B\omega + T_L \qquad (3)$$

where J is the inertia of the SRM system, B is the total friction coefficient, ω is the angular velocity of the rotor, T_L is the load torque.

The average torque is very important for the dynamic output of motor. As a four phase SRM, the average torque is determined using Eq. (4).

$$T_a = \frac{12}{\pi}\int_0^{\pi/3} T_e(i,\theta)d\theta \qquad (4)$$

The SRM suffers from a major disadvantage which is the torque ripple. The ripple affects not only the SRM dynamic performance, but also increases the inside noise and reduces the driving stability when the SRM is used to electric vehicle. So it is greatly significant for the vehicle to minimize the torque ripple. Literature [13] defines the motor ripple coefficient as Eq. (5).

$$T_r = \frac{T_{\max} - T_{\min}}{T_a} \qquad (5)$$

where T_r is the SRM torque ripple coefficient, $T_{\max}$ is the torque maximum value, $T_{\min}$ is the torque minimum value.

3. Implementing Flux and Torque in Simulink

The magnetization characteristic is basal for evaluating the SRM dynamic performance. And the flux linkage as a function of the current and turn-on angle is very important for establishing the nonlinear model of SRM. So the function $\psi(i, \theta)$ is needed to obtained before founding the SRM model in the MATLAB /Simulink environment.

There are many approaches found in literatures to determine the SRM magnetization characteristic, such as using mathematical model [14, 15], establishing neural network model [16, 17], making experiment and analyzing by finite element method (FEM) [18]. An 8 kW 8/6 SRM is chosen in this paper and the experimental data which is SRM phase fluxes relating to phase currents and rotor angles is obtained from FEM.

The flux data $\psi(i, \theta)$ at different currents i and rotor angles θ can be changed to the function $i(\psi, \theta)$ which is the phase current as a function of the flux and rotor angle. The Lookup Table among the phase current, rotor angle and flux which is presented in Fig.1 is established using the function $i(\psi, \theta)$ in Simulink environment, and the corresponding current value will be obtained when the flux and rotor angle value input to the Lookup Table.

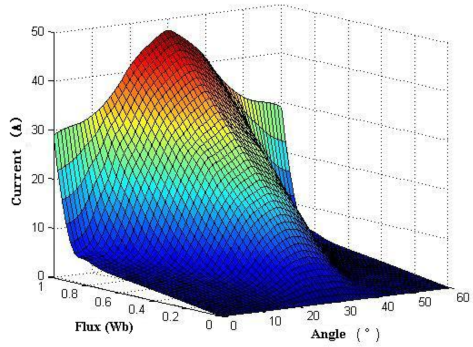

Fig.1. Lookup table of current versus flux and rotor angle.

The phase torque can be calculated using Eq. (2) when the inputs are phase currents and rotor angles. In order to improve the execution speed of the simulation system, the phase torque function $T(i, \theta)$ is pre-calculated and stored in a Lookup Table as shown in Fig.2. With the phase current and rotor angle as inputs, the Lookup Table produces the corresponding torque value.

4. Modeling the SRM Drive

With the phase voltage and the rotor angle as inputs and the phase current and total torque as the outputs, the SRM model is established with the MATLAB/Simulink in terms of the Eq. (1) and the two Lookup Tables.

The power converter model which is required to commutate the SRM phases is determined as asymmetrical converter. The motor and load mechanical dynamic model is governed by Eq. (3) and the hysteresis current controller model is established to avoid higher current which is harmful to the system. Fig.3 shows a Simulink diagram presenting a model of the current controlled SRM drive described above.

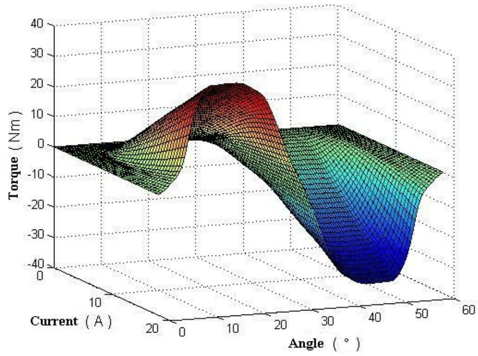

Fig.2. Lookup table of torque versus current and rotor angle.

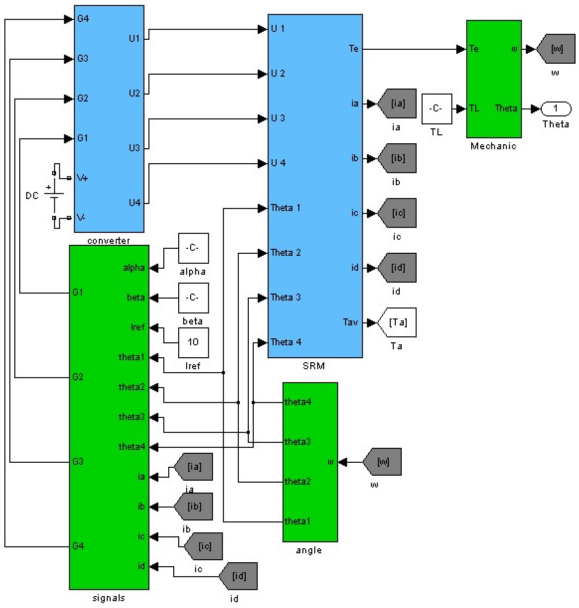

Fig.3. Simulink diagram of the 8/6 SRM drive.

III. SIMULATION OF SRM DRIVE

The SRM considered in the paper 8/6 motor with the following parameters, rated voltage U is 150V, reference current I_{ref} is 10A, armature resistance R is 1.3Ω, moment of inertia is J is 0.0013kg.m^2, and rated speed n is 300rad/s.

The purpose of the simulation is to obtain the SRM torque characteristic over the phase current and speed when the turn-off angles vary in appropriate ranges. With the simulation for the torque characteristic, the torque and torque ripple as functions of turn-off angles and output speed are obtained. According to the SRM rated speed is 300rad/s, so the speed will vary from 0-3300 rpm by steps of 300 rpm. With simple consideration and analyses, the changeable range of turn-off angles is 20°-30° and the turn-on angle is fixed on 0°.

In order to obtain the intuitionist numerical relation among torque ripple, speed and turn-off angle, the torque ripple data in simulation is presented in the form of 3-D surface chart as shown in Fig.4. The turn-off angle value which minimizes the torque ripple in given speed can be obtained by the simulation data and the function relation between optimizing turn-off angle and speed $\theta_{op}=f(\omega)$ is determined to achieve the optimization torque controller.

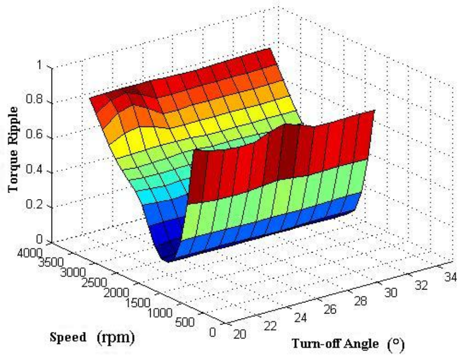

Fig.4. Torque ripples vs. speeds and turn-off angles.

IV. DESIGN OPTIMIZATION TORQUE CONTROLLER

It is very significant to select appropriate turn-off angles in SRM drive for improving dynamic performance of the motor and good drive performance of the EV as the turn-off angle value of SRM drive directly affect the average torque and torque ripple of the motor.

In this paper, the optimizing turn-off angles in different speeds is selected in the objective of reducing torque ripple and increasing average torque based on the torque function and torque ripple function established in Section 3. And the function relation between optimizing turn-off angle and speed $\theta_{op}=f(\omega)$ is determined by fitting data from simulation as shown in Fig.5.

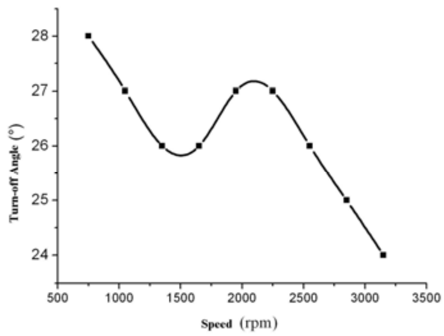

Fig.5. Turn-off angles versus speeds.

The variable turn-off angle model which is changing with the speed is established using the curve described in Fig.5. The model is imported to the simulation system using a Lookup Table in MATLAB/Simulink environment.

IV. SIMULATION RESULTS AND ANALYSIS

The simulation of 8 kW 8/6 SRM drive selected in this paper is carried on based on the SRM nonlinear dynamic model described above. With the fixed turn-on angle α=0°, the variable turn-off angle founded in Section 4 and fixed turn-off angle θ=25° are determined respectively to the SRM drive model. And the voltage U is 150V, the reference current I_{ref} is 10A.

The torque ripple and optimizing one can be obtained respectively by giving a steady speed to the SRM by simulation, which can be directly compared the two results from normal torque controller and optimization torque controller. The optimizing torque ripple and average torque performance are improved seen intuitively from Fig.6 which shows the normal average torque and optimizing one when the speed is about 2000rpm.

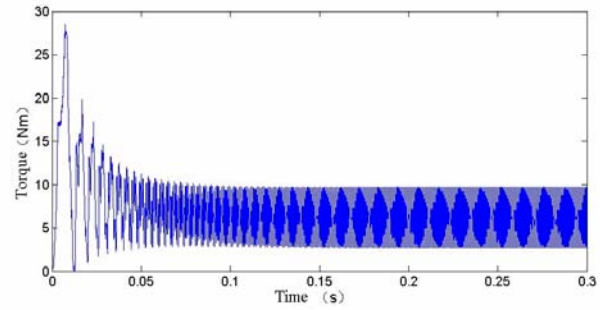

(a) Normal torque.

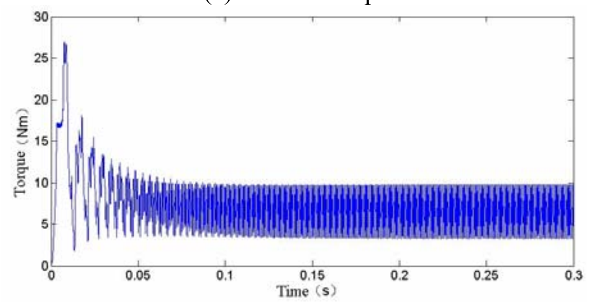

(b) Optimizing torque.

Fig.6. Total torque when speed is 2000rpm.

In order to present an easier comparison between the two drive systems, the SRM torque ripple coefficient data in different speeds from simulation results is described in the form of curve as shown in Fig.7 where the black square curve and the red round one respectively denote normal and optimizing results.

By comparing results from the two drive systems, the torque ripple reduces about 16.95% from 0.59 to 0.49 when the speed is imposed 375rpm. With the imposed speed 2300rpm, the optimizing torque ripple reduces 13.61% from 0.955 to 0.825 comparing with the normal ripple, and reduces 7.69% from 0.65 to 0.60.

In addition, it can be seen by comparing the results that the reduction effect of SRM torque ripple is very obvious as the SRM drive operating at low or high speed and the maximum reduction value can achieve 16.95%. While the reduction value falls a little when the drive runs at medium speed, and the value keeps around 7.7%.

When we reduce the torque ripple, the impact to average torque will directly determine the effect of the optimization controller designed in this paper as the purpose of optimization controller is to reduce the torque ripple without decreasing the average torque. In order to show an easier comparison, the SRM average torque data in different speeds from simulation results is described in the form of curve as shown in Fig.8 where the black square curve and the red round one respectively denote normal and optimizing results.

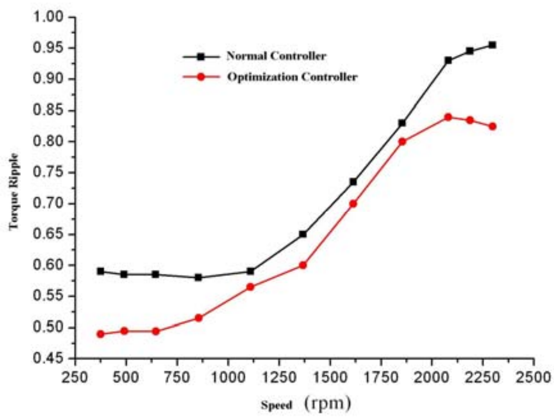

Fig.7. Comparison of the torque ripple.

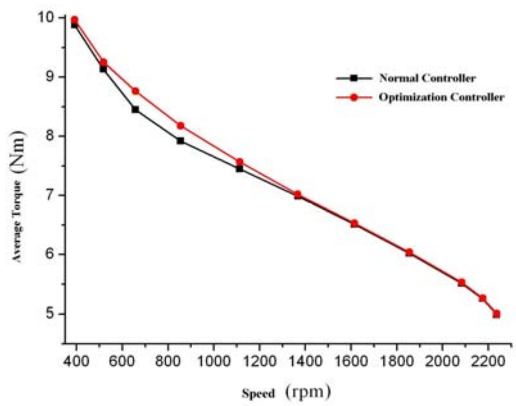

Fig.8. Comparison of the torque.

By comparing, the average torque is also improved at low and medium speed. It increases about 3.2% when the speed ranges from 500rpm to 1200rpm and about 1.0% at low speed. At high speed, there isn't a notable factor of two between the average torque curves.

In total, the power performance and driving stability of the EV will be improved greatly as the optimization controller can greatly reduce torque ripple over a wide speed range and appreciably increase average torque at low and medium speed.

VI. CONCLUSION

Considering the SRM flux linkage characteristic, a nonlinear dynamic model is established for 8 kW 8/6 SRM used in electric vehicles in this paper. With the hysteresis current control strategy, the optimization torque controller is designed based on the variable turn-off angle.

By the simulation on dynamic model established in the MATLAB/Simulink environment according to the SRM flux linkage characteristic, the torque ripple and average torque as functions of turn-off angles and speeds are determined using the simulation results. In order to reduce the torque ripple and increase the torque, the optimizing turn-off angles as a function of speed is obtained to achieve the optimization controller. Then the optimization torque controller is designed based on the variable turn-off angle.

The simulation results show that the nonlinear dynamic model of SRM established in this paper is good at robustness and dynamic performance, and the optimization torque controller based on the variable turn-off angle can effectively reduce the torque ripple and increase the ripple. Meanwhile the simulation results have a good reference value for designing EV and improving the performance.

REFERENCES

[1] Sun Jianbo, Zhan Qionghua, Wang Shuanghong, et al (2008), Control strategy of switched reluctance motor to restrain vibration acoustic noise and torque ripple. Proceedings of the CSEE 28(12):134-138
[2] A.M. Omekanda (2003), A new technique for multidimensional performance optimization of switched reluctance motors for vehicle propulsion. IEEE Transactions on Industry Applications 39(3): 672-676
[3] K.M. Rahman, S.E. Schulz (2002), High performance fully digital switched reluctance motor controller for vehicle propulsion. IEEE Transactions on Industry Applications 38(4): 1062-1071
[4] Nihat Inanc, Veysel Ozbulur (2003), Torque ripple minimization of a switched reluctance motor by using continuous sliding mode control technique. Electric Power Systems Research 66: 241-251
[5] Wang Xudong, Wang Xilian, Wang Yan (2000), Current chopping with double amplitude for switched reluctance control. Proceedings of the CSEE 20(4): 83-86
[6] Husain I, Ehsani M (1996), Torque ripple minimization in switched reluctance motor drives by PWM current control. IEEE Transactions on Power Electronics 11(1): 83-88
[7] Cheok A D, Hoon P H (2000), A new torque control method for switched reluctance motor drives. IEEE IECON, Nagoya, Japan
[8] Inderka R B, De Doncker R WAA (2003), DICT-direct instantaneous torque control of switched reluctance drives. IEEE Transactions on Industry Applications39 (4): 1046-1051
[9] Zhang Jingjun, Zhang Haijun, Gao Ruizhen (2008), Fuzzy compensation control for switched reluctance motor system based on finite element model. IEEE Southeast Con., pp.480-484
[10] Roy A. Mccann, Mohammad S. Islam, Iqbal Husain (2001), Application of a sliding mode observer for position and speed estimation in switched reluctance motor drives. IEEE Transactions on Industry Applications 37(1): 51-58
[11] Kucuk Fuat, Goto Hiroki, Guo Haijiao, et al (2007), Artificial neural networks and inductance vector based sensorless torque estimation in switched reluctance motor drive. Proceeding of International Conference on Electrical Machines and Systems, pp.503-507
[12] Xia Changliang, Chen Ziran, Li Bin (2006), Instantaneous torque control of switched reluctance motors based on RBF neural network. Proceedings of the CSEE 26(19): 127-132
[13] Wu Jianhua (2000), Design and Application of the SRM (in Chinese). Mechanism Industry Press.
[14] Zhang Le, Zhou Bo, Fang Sichen (2006), Research on the double salient electromagnetic generator based on three dimensional nonlinear inductance model. Proceedings of the CSEE 26(23): 126-131
[15] Si Liyun, Lin Hui, Liu Zhen (2007), Modeling of switched reluctance motors based on LS-SVM. Proceedings of the CSEE 27(6): 26-30
[16] Zheng Hongtao, Cai Jiling, Jiang Jingping (2001), Nonlinear modeling of switched reluctance motor based on variable structure fuzzy-neural networks. Transactions of China Electrotechnical Society 16(6): 1-6
[17] Cai Yan, Xu Zhenlin, Gao Chao (2006), Simulation of SRD based on neural net nonlinear model. Transactions of China Electrotechnical Society 21(8): 1-6
[18] R.B. Inderka, R.W.A.A. De Doncker (2003), High dynamic direct average torque control for switched reluctance drives. IEEE Transactions on Industry Applications 39(4): 1040-1045

The Fifteenth International Symposium on Artificial Life and Robotics 2010 (AROB 15th '10),
B-Con Plaza, Beppu,Oita, Japan, February 4-6, 2010

An improvement of MSEPF for visual tracking

Yuki Nakagama, Masahiro Yokomichi
University of Miyazaki, 1-1,Gakuenkibanadainishi,Miyazaki,Miyazaki,Japan
(0985-58-7420)
(tge813u@student.miyazaki-u.ac.jp)

Abstract: Recently, many approaches on applying particle filter to visual tracking problem have been proposed. However, it is hard to implement it to the real-time system because it requires a lot of computation and resources in order to achieve higher accuracy. As a method for reduce the computation time, Shan and coworkers proposed combining particle filter and Mean-Shift in order to keep the accuracy with small number of particles. In their approach, the state of each particle moves to the point in the window with the highest likelihood value. It is known that the accuracy of estimation depends on the size of the window, but the larger window size make the computation slower. In this paper, the authors propose method for exploring the highest likelihood more quickly by means of random sampling. Moreover, our approach defines likelihood in terms of not only color cue but also motion cue for higher-accuracy object tracking. The effectiveness of the proposed method is evaluated by real image sequence experiments.

Keywords: Particle filter; Real-time visual tracking; MSEPF

I. Introduction

Visual tracking is one of the important researches in the autonomous mobile robot. Visual tracking requires high-accuracy tracking and real-time processing. To achieve high accuracy tracking, many approaches have been studied. . Particle filter is one of the robust tracking approaches in visual tracking, which has recently been developed. It performs a random search guided by a stochastic motion model to obtain an estimate of the posterior distribution describing the object's configuration. However, it is known that the degeneracy is one of the difficult problems inherent in particle filter. Degeneration problem is a phenomenon of the tracking accuracy's decreasing because most particles may have very low likelihood. One of approaches that deal with it is to use very large number of particles, but it is hard to implement it to real-time systems because it requires a lot of computation times and resources. Shan and coworkers proposed combining particle filter and Mean-Shift (MSEPF) in order to keep the accuracy with small number of particles. In their approach, the state of each particle moves to the point in the window with the highest likelihood value. In general, MSEPF overcomes the degeneration problem because each particle has higher likelihood. In addition, the accuracy of estimation depends on the size of the window, but the larger window size makes the computation slower.

In this paper, we propose a method for exploring the highest likelihood more quickly by means of random sampling. Using random sampling in Mean-Shift, computing time will be considerably reduced keeping accuracy. When total of likelihoods is less than threshold, particles do relocation using extended reset method. Moreover, likelihood function is also modified such that the computing time reduces. In general, visual tracking uses only color cue to define the likelihood function. In the proposed approach, the likelihood function is defined in terms of not only color cue but also motion cue for higher-accuracy object tracking.

II. The Mean Shift Embedded Particle Filter

1. Particle Filter

Particle filter is model estimation technique based on simulation. A continuous state vector of a target object at time step t is denoted by x_t. Dynamic model is assumed to be represented as a temporal Markov chain:

$$p(\mathbf{x}_t \mid \mathbf{x}_1,\ldots,\mathbf{x}_t) = p(\mathbf{x}_t \mid \mathbf{x}_{t-1}), \quad (1)$$

and

$$p(\mathbf{z}_1,\ldots,\mathbf{z}_t \mid \mathbf{x}_1,\ldots,\mathbf{x}_t) = \prod_{i=1}^{t} p(\mathbf{z}_i \mid \mathbf{x}_i). \quad (2)$$

Particle filter aims to estimate the sequence of hidden parameters $\mathbf{x}_t$ based only on the observed data $\{\mathbf{z}_1,\ldots,\mathbf{z}_t\}$. According to the Bayes rule, the prior density is then given by

$$p(\mathbf{x}_t \mid \mathbf{z}_1,\ldots,\mathbf{z}_{t-1}) = \int p(\mathbf{x}_t \mid \mathbf{x}_{t-1}) p(\mathbf{x}_{t-1} \mid \mathbf{z}_1,\ldots,\mathbf{z}_{t-1}) dx_{t-1} \quad (3)$$

and posterior is given by

$$p(\mathbf{x}_t \mid \mathbf{z}_1,\ldots,\mathbf{z}_t) = k_t p(\mathbf{z}_t \mid \mathbf{x}_t) p(\mathbf{x}_t \mid \mathbf{z}_1,\ldots,\mathbf{z}_{t-1}), \quad (4)$$

where k_t is the normalization term.

In the particle filter, by using a set of samples and the corresponding weights $\{(\mathbf{s}_t^n,\pi_t^n\}_{n=1}^N$ at time step t (where N is the number of particles), the posterior is approximated as

$$p(\mathbf{x}_t \mid \mathbf{z}_{1,\ldots},\mathbf{z}_t) \approx \sum_{n=1}^{N} \pi_t^n \delta(\mathbf{x}_t - \mathbf{s}_t^n) \quad (5)$$

where $\delta(\mathbf{x}_t - \mathbf{s}_t^n)$ is the Dirac's delta function. Then, the prior is approximated as

$$p(\mathbf{x}_t \mid \mathbf{z}_{1,\ldots},\mathbf{z}_{t-1}) \approx \sum_{n=1}^{N} \pi_{t-1}^n p(\mathbf{x}_t \mid \mathbf{s}_{t-1}^n). \quad (6)$$

The weights π_t^n is determined such $\pi_t^n \propto p(\mathbf{z}_t \mid \mathbf{x}_t^n)$, $\sum_{n=1}^{N} \pi_t^n = 1$. If a sufficiently large number of particles can be prepared, Eq. (5) and (6) are accurate. In reality, however, using an infinite number of particles is not allowed, especially for real-time processing.

2. Mean-Shift

The mean shift algorithm is a non-parametric technique that climbs the gradient of a probability distribution to find the nearest dominant mode (peak). In the search window, the mean position of the target object is computed and the search window is centered at that position. The mean position can be obtained as follows,

$$x_c = \frac{M_{10}}{M_{00}}, y_c = \frac{M_{01}}{M_{00}}, \tag{7}$$

where

$$M_{00} = \sum_x \sum_y I(x, y),$$

$$M_{10} = \sum_x \sum_y xI(x, y),$$

$$M_{01} = \sum_x \sum_y yI(x, y).$$

Here, (x_c, y_c), $I(x, y)$ denote the mean search window position, pixel (probability) in the position (x, y) in the image. Position of the target object is tracked by iterating this mean position calculation until shift length converges.

3. MSEPF

MSEPF is novel algorithm that incorporates Mean-Shift into particle filter. In MSEPF, Mean-Shift analysis is applied to each particle based on observation density, after each particle was measured by likelihood function. MSEPF can keep the accuracy using fewer particles because particles converge to the local maximum. Therefore, MSEPF can reduce particles than particle filter. Figure1 shows a graphical representation of the MSEPF. It is known that the accuracy of estimation depends on the size of the window. However, the larger window size requires additional computation time.

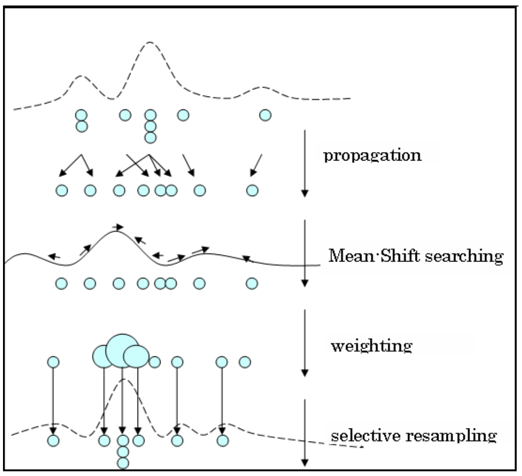

Fig.1. a graphical representation of MSEPF

III. An improvement of MSEPF and the observation model

1. An improvement of MSEPF

As described in the previous section, the accuracy of estimation depends on the size of the window, but the larger window size requires additional computation time. As pointed out by Yang and Duraiswami [3], the computational complexity of traditional Mean-Shift tracking is quadratic in the number of samples, making real-time performance difficult. To deal with their problem, it was proposed new algorithm using random sampling in Mean-Shift. In addition, particle filter embedded it. The approach can define more complex likelihood function because the computational complexity is considerably reduced. To summarize, algorithm of proposed MSEPF was outlined in Fig.2.

Given particle set $S_{t-1} = \{s_{t-1}^i, \pi_{t-1}^i \mid i = i, \cdots N\}$ at time $t-1$, perfume the following step:

1. Propagation: propagate each particle by dynamic mo del to obtain the sample set $\tilde{S}_t$
2. Mean-Shift searching: apply Mean-Shift that used random sampling to each particle
3. Weighting: weight each particle using likelihood functio n
4. Resampling: obtain new particles S_t
5. Estimate: obtain estimate state using ohtsu's method [4]

Fig.2 An iteration step of proposed MSEPF

2. Dynamic model

The state transition model characterizes the motion change between frames. In a visual tracking problem, it is ideal to have an exact motion model governing the kinematics of the object. In practice, however, it is hard to get at accurate state transition model. Moreover, object motion is irregular movement. Therefore, our approach approximates state transition model by simple model

$$\begin{aligned} x_t &= x_{t-1} + w_x \\ y_t &= y_{t-1} + w_y \end{aligned} \tag{8}$$

where w_x and w_y are each uniform pseudorandom number.

3 Likelihood function

Particle filter requires a likelihood function of the target object. In general, visual tracking apply color cue to likelihood function. Our approach uses not only color cue but also motion cue. Our approach takes the statistic of chromatins of target object in advance. Here, likelihood of color cue $\pi_c(x, y)$ at x is defined as

$$\pi_c = \frac{1}{2\pi\sigma_r} e^{-\frac{(\mu_r - R(x,y))}{\sigma_r^2}} + \frac{1}{2\pi\sigma_g} e^{-\frac{(\mu_g - G(x,y))}{\sigma_g^2}} + \frac{1}{2\pi\sigma_b} e^{-\frac{(\mu_b - B(x,y))}{\sigma_b^2}} \quad . \qquad (9)$$

Here, μ_r , μ_g , μ_b , σ_r , σ_g and σ_b are red, green, and blue components of color saturation of mean or variance, respectively. In addition, $R(x, y)$, $G(x, y)$ and $B(x, y)$ are defined

$$R(x, y) = \frac{r(x, y)}{r(x, y) + g(x, y) + b(x, y)}$$

$$G(x, y) = \frac{g(x, y)}{r(x, y) + g(x, y) + b(x, y)}$$

$$B(x, y) = \frac{b(x, y)}{r(x, y) + g(x, y) + b(x, y)} ,$$

where $r(x, y)$, $g(x, y)$ and $b(x, y)$ are respectively intensity in the position (x, y) .

Next, likelihood used motion cue was outlined below. First, edge images were extracted from real image sequences. Second, only moving object were extracted using emporal differecing. If particles exist near edge, likelihood of samples are defined

$$\pi(x, y) = k\pi_c$$

where, k is invariable ($k \geq 1{,}0$). If it does not exist, there are defined

$$\pi(x, y) = \pi_c .$$

Figure.3 shows a graphical representation of the likelihood function.

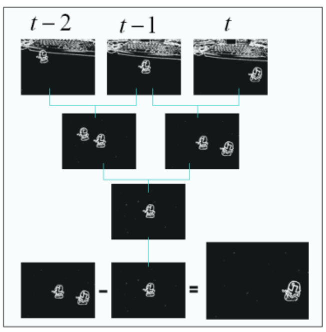

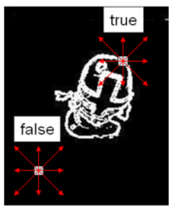

$$\pi = \begin{cases} K\ \pi_c & (TRUE) \\ \pi_c & (FALSE) \end{cases}$$

$$K > 1.0$$

Fig.3. a graphical representation of our likelihood function

IV. Experiment

Aim of this section is evaluate proposed MSEPF. To illustrate the differences between conventional MSEPF and proposed MSEPF, same sequences ware applied. These video sequences are captured at 14 frames per second in a usual office environment with background clutters. The resolution of each image is 240×180 pixels, window size in Mean-Shift are 4 patterns of 5×5 pixels, 10×10 pixels, 15×15 pixels and 20×20 pixels. The numbers of samples change 5, 10, 20, 50, and 100 in our approach. The numbers of particles are 100 in all algorithms.

Figure.4 shows that computation time and tracking accuracy of conventional MSEPF and our MSEPF. Experimental results demonstrate that our algorithm outperforms conventional MSEPF. It understands that computing time greatly decreases as the number of samples increases. When window size is 20×20 pixels, conventional MSEPF spent 103 ms on average for each frame. Our proposed MSEPF of samples 10 when window size is 20×20 pixels, spent 33 ms on average for each frame, it is about one-third. Moreover, this experiment obtained the surprising result proposed MSEPF requires only very few samples. High accuracy tracking as equal as conventional MSEPF can be achieved with 10 less or equal random samples.

In addition, next experiment was performed to evaluate likelihood function. As discussed in preceding section, likelihood function was applied color cue and motion cue to. Some tracking results of two trackers are shorn Fig.5. In this experiment, computation speeds of each tracker are almost equal. As it can be seen in Fig.5 (a), tracker that uses likelihood function only of color cue tracks motionless object that is similar color of target object. The trackers with our proposed likelihood can track as shown in Figure.5 (b). This likelihood function will be able to track more effective and robust tracking than observation model only of color cue because likelihood make high when particle exist near motion object. Table.1 shows that tracking results of conventional MSEPF with likelihood function based on only color cue and our proposed MSEPF with likelihood function based on our observation model. Computing speed of each tracker is almost equal. Despite almost equal computation speed, our proposed method is dramatically highly accurate tracking than conventional method.

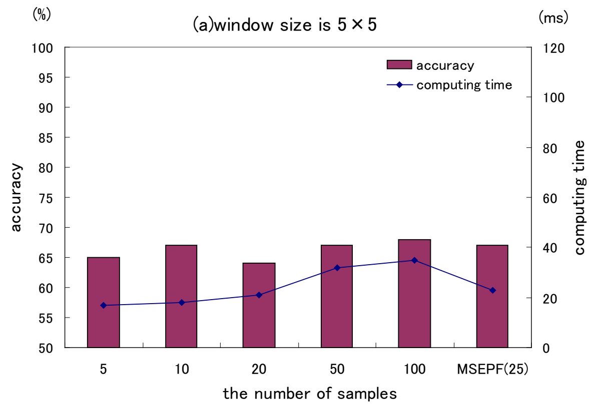

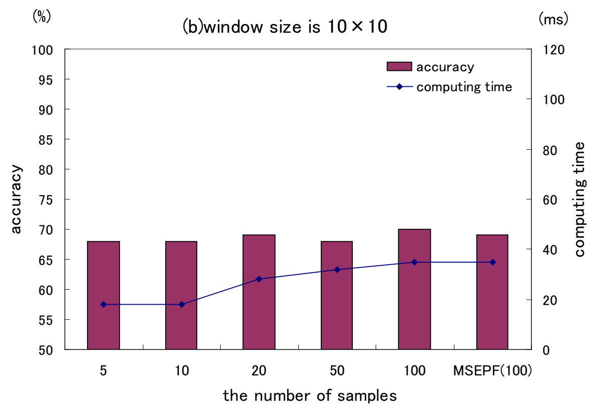

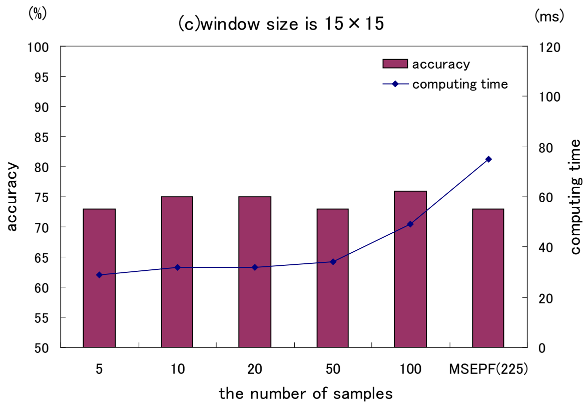

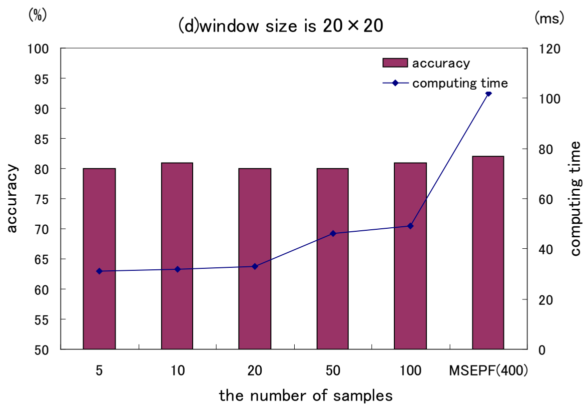

Fig.4. Computation time and tracking accuracy of conventional MSEPF and proposed MSEPF. (a), (b), (c), and (d) are window size of 5×5 pixels, 10×10 pixels, 15×15pixels and 20×20 pixels.

(a) Tracking using likelihood function based on only color cue.

(b) Tracking using likelihood function based on color and motion

Figure.5 Tracking using observation based on color and motion cues and based on color and motion cues. The frames 250, 260, and 270 are shown.

Table.1. tracking results of conventional MSEPF with likelihood function based on only color cue and our proposed MSEPF with likelihood function based on color and motion cue.

	accuracy	computing time
Conventional MSEPF	59.3%	36ms
Proposed MSEPF	75.1%	32ms

V. Conclusion

This article presented about improvement of MSEPF for visual tracking. Mean shift that used random sampling embedded particle filter can quickly track than conventional MSEPF. Using as few as even 10 random samples, our proposed MSEPF is almost equal to conventional MSEPF. Using color and motion cues in likelihood function our method can track accurately and robustly than observation model only of color cue. By incorporating accurate dynamic model, the performance of tracking will be improved greatly. We will apply EM algorithm to learn dynamic model, in our future work.

REFERENCES

[1] Caifeng Shan, et al.(2004), Real Time Hand Tracking by Combining Particle Filtering and Mean Shift, Automatic Faces and Gesture Recognition:669-674
[2]Ryuichi Ueda, at el. (2005), Recovery Methods for Fatal Estimation Errors on Monte Carlo Localization. JERC 23(4):466-473
[3] Changjiang Yang, et al. (2005), Efficient Mean-Shift Tracking via a New Similarity Measure(1):176-183
[4] N. Otsu (1995), Discriminant and Latest Squares Threshold
Selecton. *Proc of 4IJPCPR* 1978, pp 592-596.
[5] G. Kitagawa (1996), Monte Carlo filter and smoother for non-Gaussian nonlinear state space models, Journal of Computational and Graphical Statistics 5(1):1–25.
[6] T. Bando et al (2006), Switching particle filters for efficient visual tracking, Robotics and Autonomous Systems 54:873–884

A System for Synchronizing Nods of a CG Character and a Human Using Thermal Image Processing and Moving Average Model

R. Kato[1], Y. Yoshitomi[1], T. Asada[2], and M. Tabuse[1]

1: Div. of Environmental Sciences Graduate School of Life and Environmental Sciences Kyoto Prefectural University
2: Dept. of Environmental Information Graduate School of Human Environment Science Kyoto Prefectural University
1&2: 1-5 Nakaragi-cho Shimogamo Sakyo-ku Kyoto 606-8522 JAPAN
r_kato@mei.kpu.ac.jp, yoshitomi@kpu.ac.jp, t_asada@aoi.kpu.ac.jp, tabuse@kpu.ac.jp

Abstract: The purpose of the present study is to develop a system for communication between a human and a CG character for making him or her more peaceful and cheerful. The nonverbal communication using such as a facial expression, a nod, and a hand gesture is very important for reciprocal communication between humans. In the present study, an image registered by infrared rays which describes the thermal distribution of the face and neck has been used for developing a system for communication between a human and a CG character. In the present system, the CG character can synchronize its nod with a person's nod by predicting his or her nod angle. The measured feature parameter is inputted to a fuzzy algorithm system to obtain the nod angle of a person in front of an infrared ray camera, and then the Moving Average model is used for predicting the nod angle of the person. The average error of the nod angle obtained by the present system has been estimated as about $5°$. The CG character nods its head, not only when a human nods his or her head, but also when a human shakes his or her head left or right.

Keywords: Thermal image processing, nod, Fuzzy algorithm, AIC and Moving Average model.

I. INTRODUCTION

The nonverbal communication using such as a facial expression, a nod, and a hand gesture is very important for reciprocal communication between humans. These nonverbal communications are effective for expressing mutual consciousness. The realization of suitable communication between a human and a computer will help the developments of a computer itself, networking, a robot, and a computer system which can encourage a person living alone. In aging society, for example, Japan, something to talk to would be helpful for a person living alone and advanced in years to live peacefully.

The embodied communication technologies have been developed using the relationship between the speech and the nod [1]–[4]. On the other hands, several investigations for head gesture recognition have been reported [5]-[9]. In our daily lives, it is relatively difficult to take visual information on a person's head movement into account for synchronizing the nod of a CG character, compared to audio information on it. The main reason of the difficulty is that nuances of shade, reflection, and local darkness influence considerably the accuracy of head gesture recognition through the inevitable change of gray levels.

In the present study, in order to avoid the difficulty, an image registered by infrared rays (IR) which describes the thermal distribution of a face and neck has been used for developing a method for synchronizing nods of a human and a CG character.

II. THERMAL IMAGE ACQUISITION

The principle of thermal image generation comes from the well-known law by Stefan and Boltzmann, which is expressed by $W = \varepsilon\sigma T^4$, where W is radiant emittance (W/cm^2), ε is emissivity, σ is Stefan-Boltzmann constant (=5.6705×10^{-12}W/cm^{2}K^4), T is Temperature (K).

For human skin, ε is estimated at 0.98 to 0.99 [10], [11]. In the present study, however, the approximate value of 1 was used as ε for human skin. The values of ε for almost all substances are lower than that for human skin [10]. Accordingly, the human face and neck are easily extracted in the scene when the range of skin temperature is selected for producing the thermal image, using the value of 1 for ε [12], [13]. Fig.1 shows examples of male face and neck images by visible ray and IR. We can get a thermal face and neck image without lighting even at night. In principle, the temperature measurement by IR does not depend on skin color [11], darkness, or lighting condition, resulting in that the face, neck and their characteristics are easily extracted from the surrounding area on the thermal image.

III. BASIC PROCESSING FLOW

Fig.2 shows the flow chart of our method. We beforehand make the fuzzy rules between the ratio (hereinafter referred as the *nod*) of horizontal length to

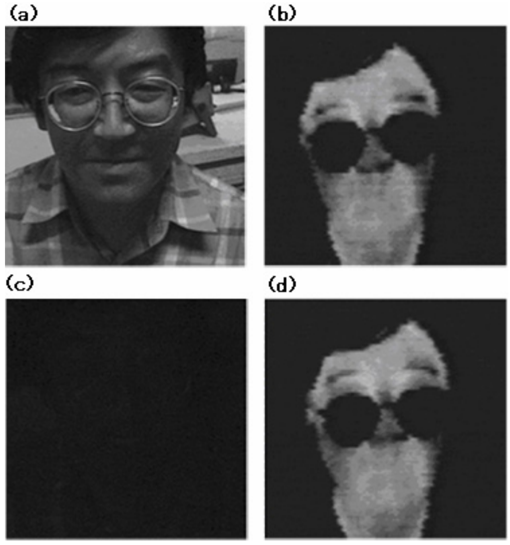

Fig. 1. Examples of face and neck image at night ; (a) visible ray with lighting, (b) IR with lighting, (c) visible ray without lighting, (d) IR without lighting [14]

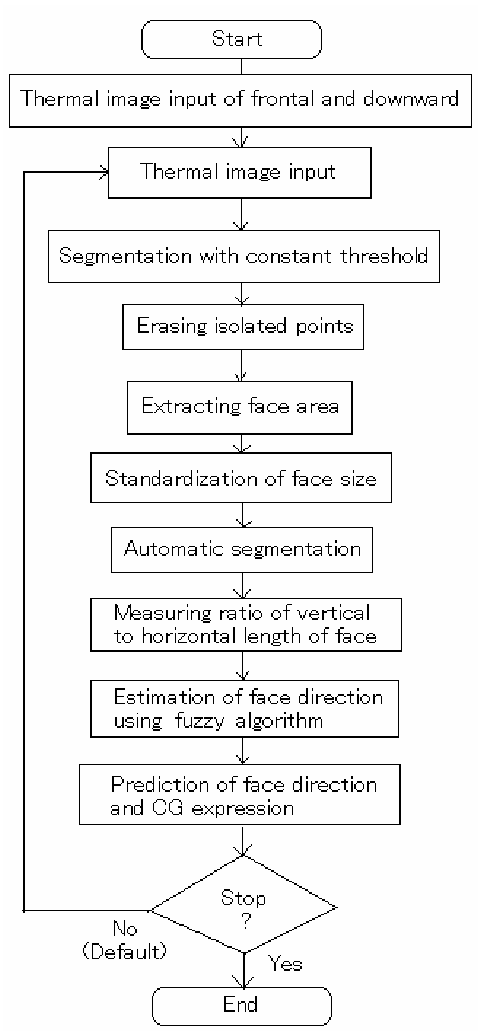

Fig. 2. Flow chart of our method

vertical length of face region on the thermal image and the face direction vector (hereinafter referred as $\boldsymbol{n}$) having the norm of 1. For making the rules, we prepare a thermal image for measuring the *nod*, while we use a motion capture system for measuring $\boldsymbol{n}$. Using the fuzzy algorithm and an input of the *nod*, $\boldsymbol{n}$ is outputted as three estimated values of elements of the vector. $\boldsymbol{n}$ is used for expressing the nod of a CG character. We explain the fuzzy algorithm and the process for measuring $\boldsymbol{n}$ in the Section IV.

At first, we get a pair of thermal images for the frontal and downward face directions for a subject to normalize the value of the *nod* as 1 in the case of frontal direction, and to transform the value of the *nod* of the subject to that of a typical subject. We explain the normalization and the transformation for the value of the *nod* in the Subsections IV(2) and VII(5), respectively. As a preprocessing for measuring the *nod*, a segmentation with a constant threshold, an erase of the isolated points, an extraction of the face area, a standardization of the size of face, and an automatic segmentation [15] are performed for a thermal image. Then, the *nod* is measured. For predicting the nod of a human, we use the Moving Average (MA) model. We explain the process for the prediction of the nod of the human in the Section V.

IV. FUZZY ALGORITHM FOR FACE DIRECTION ESTIMATION

1. Parameters used for fuzzy rules

Fig.3 shows a three-dimensional coordinate system used in the present study. $\boldsymbol{n} = (0,0,1)$ corresponds to the face direction when the face is frontal. Fig.4 demonstrates how to measure $\boldsymbol{n}$ using a motion capture system. For making the fuzzy rules and evaluating the accuracy of nod angle obtained by our method, three markers are attached on a subject's jaw, and both temples as shown in Fig. 4 (left figure) demonstrating an experiment scene where we place an IR camera and a computer monitor in front of the subject. We also place separately two cameras, which are not seen in Fig. 4 (left figure), of the motion capture system on the two diagonal positions from the frontal direction of the subject. With use of coordinates of three markers, $\boldsymbol{n} = (\alpha, \beta, \gamma)$ is determined by geometric calculation. The three elements of $\boldsymbol{n}$ are used as parameters of consequent in the fuzzy rules.

Fig.5 demonstrates face's downward rotation. The *nod* used as a parameter of antecedent in the fuzzy rules is measured as the ratio of vertical length to horizontal length of face. For eliminating the influence of hair style and throat region on the binary image to the utmost, the area having the horizontal pixels less than a threshold which is experimentally decided is ignored in measuring the vertical length of face, and the area having the vertical pixels less than another threshold which is also experimentally decided is ignored in measuring the horizontal length of face.

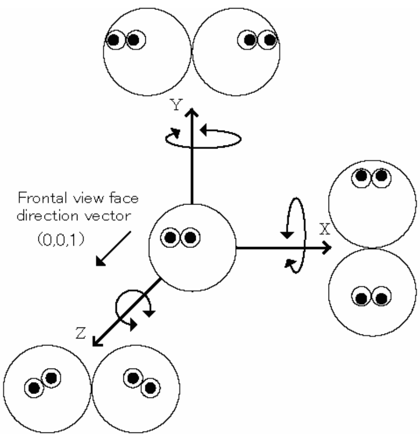

Fig. 3. Three-dimensional coordinate system

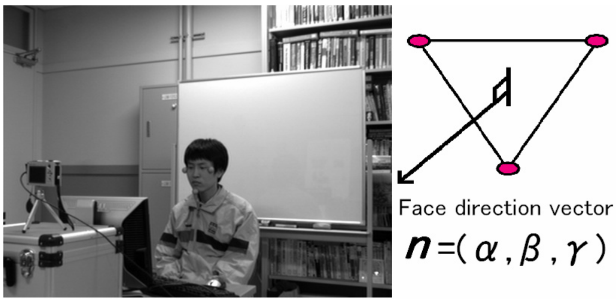

Fig. 4. Face direction vector ***n***
Left: face image with three markers to be measured their coordinates,
Right: way for making a face direction vector ***n***

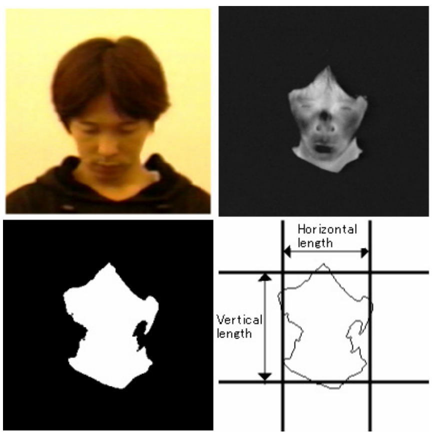

Fig. 5. Downward rotation [16]
Upper & left: visible image, Upper & right: thermal image, Lower & left: binary image, Lower & right: schematic diagram for explaining parameter *nod*

2. Fuzzy rules and algorithm

The fuzzy rules are described in (1). The fuzzy algorithm is described in (2)-(5).

$$\text{If } X = A_i \text{ then } Y_1 = B_{i1}, Y_2 = B_{i2}, Y_3 = B_{i3}, \quad (i = 1, 2, 3) \tag{1}$$

$$\mu^*_{B_{ij}}(Y_j) = W_i \mu_{B_{ij}}(Y_j), (i = 1, 2, 3, \;\; j = 1, 2, 3) \tag{2}$$

$$W_i = \mu_{A_i}(X^*), \;\; (i = 1, 2, 3) \tag{3}$$

$$B^0_j = \bigcup_{i=1}^{3} B^*_{ij}, \;\; (j = 1, 2, 3) \tag{4}$$

$$Y^*_j = \frac{\int \mu_{B^0_j}(Y_j) Y_j dY_j}{\int \mu_{B^0_j}(Y_j) dY_j}, (j = 1, 2, 3), \tag{5}$$

where X denotes a parameter of antecedent, Y_1, Y_2, Y_3 denote parameters of consequent, A_i, B_{i1}, B_{i2}, B_{i3} denote the corresponding fuzzy labels for X, Y_1, Y_2, Y_3, respectively, W_i denotes a fitness value of i th rule to the input of X^*. Y^*_j denotes an output for Y_j. The integral in (5) is performed in the whole range of Y_j. In the present study, X=*nod*, $Y_1=\alpha$, $Y_2=\beta$, $Y_3=\gamma$ .We use three fuzzy rules described as 'frontal', 'rather downward', and 'downward'.

Fig.6 shows a schematic diagram of membership functions used for both antecedent and consequent. C_i denotes a fuzzy label of antecedent or consequent, for example, A_3. Z corresponds to a variable of antecedent or consequent, for example, X. For determining each actual shape of membership function, we use the measured values for the corresponding parameter. In the case of C_2, the corresponding measured value is neither a maximum nor minimum value among three measured values. In the case of C_1 and C_3, the corresponding measured values are minimum and maximum among three measured values, respectively. In the case of C_2, whose shape of membership function is a triangle, its membership function has a maximum value of 1 at the corresponding measured value and a minimum value of 0 at the corresponding measured values for C_1 and C_3. In the case of C_1, its membership function has a maximum value of 1 at its corresponding measured value or less and decreases linearly to a minimum value of 0 at the measured value for C_2. In the case of C_3, its membership function has a maximum value of 1 at the corresponding measured value or more and decreases linearly to a minimum value of 0 at the measured value for C_2. As each measured value, we use an average for six persons.

In addition, the value of *nod* is normalized by dividing by the value in the case of 'frontal'. We use a fuzzy algorithm for outputting ***n*** with three fuzzy rules and the value of the *nod* as an input. For integrating outputs from all rules, we use (4) and (5).

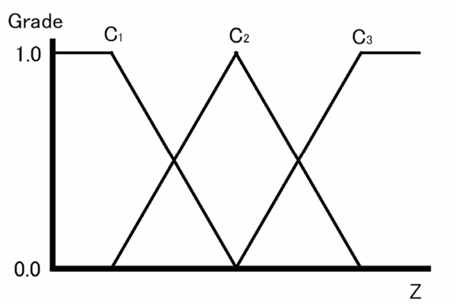

Fig. 6. Membership functions

3.Nod angle calculation

(6) defines a nod angle θ (°) which is calculated with γ.

$$\theta = 57.3\cos^{-1}\gamma \tag{6}$$

In the present study, θ is positive in case of downward rotation.

V. PREDICTION OF NOD ANGLE

For predicting the nod angle of a subject, we use the MA model expressed by (7).

$$\hat{\theta}(i) = \sum_{j=1}^{J} a(j)\theta(i-j), \tag{7}$$

where $\hat{\theta}(i)$ is a predicted value for $\theta(i)$, $a(j)$ is a coefficient for prediction, and J is a dimension for prediction. J is decided with Akaike's Information Criterion (AIC) expressed by (8).

$$AIC = n\ln S + 2p, \tag{8}$$

where n is the number of data, S is the summation of squared error, and p is the number of parameters. J is decided as p which gives the minimum value of AIC.

VI. FACE DIRECTION EXPRESSION USING CG

We use Virtual Reality Modeling Language (VRML) and Java for expressing a CG character. Fig.7 shows examples of CG expression of nod.

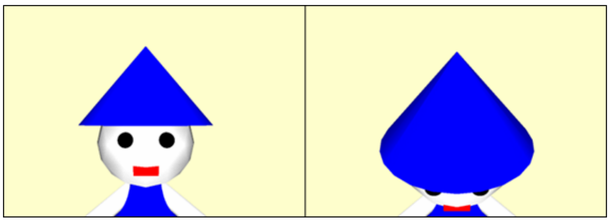

Fig. 7. CG expression of nod. Left: frontal view, Right: nod by 30 degree

VII.EXPERIMENT AND DISCUSSION

1. Experimental environment

The thermal image produced by a Thermal Video System (Thermo Shot F30) (NEC Avio Infrared Technologies Co., Ltd.) was transformed into a digital signal by an A/D converter (ADVC-300)(Thomson Canopus) and were input into a computer with an IEEE1394 interface board (1394-PCI3/DV6)(I・O Data Device). We used a computer (DELL Optiplex 745) (CPU: Intel Core 2 Duo 6600 2.4 GHz, a main memory: 2 GB, and OS: Windows XP (Microsoft)). We used Visual C++6.0 (Microsoft) and Java 2 SDK Standard Edition version 1.3, VRML2.0 for programming. A thermal image to be processed in a computer had a spatial resolution of 240×160 pixels and 8 bits gray levels at each pixel. We used Radish (Library) as a motion capture system for measuring the position of markers attached on the subject' face. We also used a computer, Dell Dimension 8300 (CPU: Pentium IV 3.2 GHz, main memory: 2.0 GB, OS: Windows XP), for performing the motion capture by Radish. Fig.8 shows a monitor screen of computer at experiment.

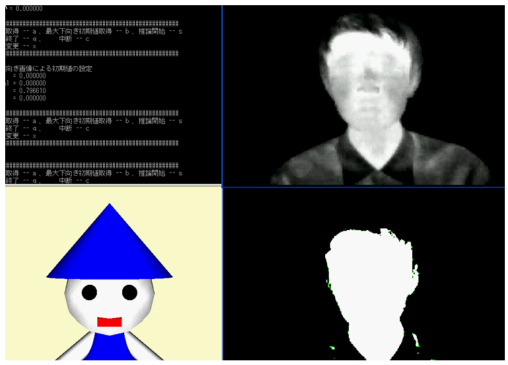

Fig. 8. Monitor screen of computer at experiment. Upper & left: expression on command prompt, Upper & right: thermal image, Lower & left: CG, Lower & right: binary image

2. Measurement of parameters used for fuzzy labels and treatment for input out of range decided by fuzzy labels

We obtained each fuzzy label as an average value for four male (A, B, C, D) and two female (E, F) subjects. Table 1 shows the fuzzy labels for each rule.

Table 1. Fuzzy labels for each rule

Rule \ Variable	*nod*	α	β	γ
1 (frontal)	1.000	0.000	0.000	1.000
2 (rather downward)	0.908	0.027	0.147	0.989
3 (downward)	0.750	0.042	0.379	0.925

We got the nod angle θ using the output of γ, obtained by fuzzy algorithm, and (6). Because we use membership functions whose shapes are described in

Fig. 6, the output of γ is within the range of maximum and minimum obtained from three rules. When we got *nod* of 1.000 or above, the output by fuzzy algorithm was $\gamma = 1.000$. When we got *nod* of 0.750 or under, the output by fuzzy algorithm was $\gamma = 0.925$. For overcome the above problem, when the input of *nod* was under 0.750, we used a linear equation decided experimentally for getting the nod angle θ from *nod* having the value of 0.750 or under.

3. Approximation to nod angle θ obtained by motion capture system

Since we used the fuzzy labels shown in Table 1, the nod angle θ inevitably had errors for an individual subject. For predicting a nod angle of subject as precisely as possible, we approximated the nod angle θ to that obtained by the motion capture system, using a linear graph approximation method. For one male subject (G), we got the linear graph described in Fig.9 and used the relation for predicting his nod angle.

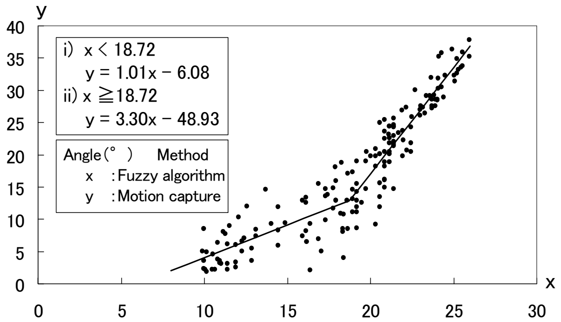

Fig. 9. Line graph approximation of nod angle from output using fuzzy algorithm

4. Prediction of nod angle θ of subject using MA model

According to (7) and (8), we got for the subject G the value of 23 as J which gave the minimum value of AIC when J is used for p, as shown in Fig.10. Then, we got (9) for predicting the nod of subject G.

$$\begin{aligned}\hat{\theta}(i) = {} & 1.39\hat{\theta}(i-1) - 0.19\theta(i-2) - 0.24\theta(i-3) \\ & -0.11\theta(i-4) + 0.053\theta(i-5) + 0.032\theta(i-6) \\ & -0.043\theta(i-7) - 0.028\theta(i-8) + 0.024\theta(i-11) \\ & +0.03\theta(i-10) + 0.12\theta(i-11) - 0.15\theta(i-12) \\ & -0.005\theta(i-13) + 0.0073\theta(i-14) + 0.11\theta(i-15) \\ & +0.031\theta(i-16) - 0.14\theta(i-17) - 0.041\theta(i-18) \\ & +0.18\theta(i-19) - 0.056\theta(i-20) + 0.052\theta(i-21) \\ & -0.18\theta(i-22) - 0.14\theta(i-23)\end{aligned} \tag{9}$$

We did not have the value of $\theta(i-1)$ at the timing position of $i-1$ because it took about 0.13 s for getting $\theta(i-1)$. Accordingly, we used $\hat{\theta}(i-1)$ instead of $\theta(i-1)$ as described in (9). Fig.11 shows the accuracy of predicted nod angle for the subject G using (9) made beforehand with data for subject G at the previous experiment. The average error on predicted nod angle was $5.1°$. For a CG expression, the nod angle is transformed to 0 when $\hat{\theta}(i)$ is negative.

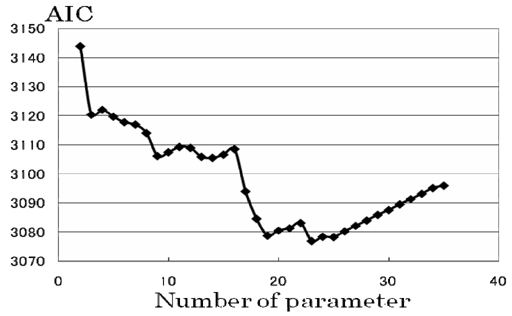

Fig. 10. AIC

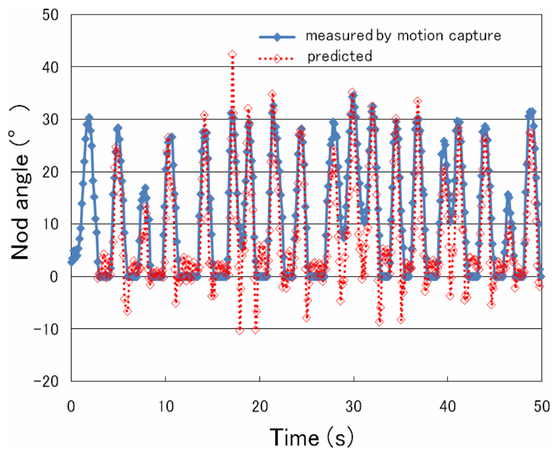

Fig. 11. Accuracy of predicted nod angle

5. Application to other subjects

We use the line graph approximation, as shown in Fig.9, for getting nod angle from the output of fuzzy algorithm. The line graph obtained for the subject G may not be appropriate for other subjects. However, it is time-consuming to get the line graph for each subject using a motion capture system. For overcoming this problem, when we use our system for another subject, we approximately transform the value of nod for another subject to that for the subject G, using a linear equation decided experimentally with two pairs of nod values of the subject G and another subject in cases of frontal and downward, followed by the same way as that for the subject G for getting the predicted nod angle.

For two male subjects (H and I), we used the above method for getting the predicted nod angle. The average errors for the subjects H and I on predicted nod angle were $4.4°$ and $5.5°$ respectively. The difference between the errors for the subject G and for the subjects H and I was within $1.0°$. This result shows that the method using the line graph approximation of nod angle made for a typical subject (G) and the transformation of nod value from another subject to the typical subject is useful.

6. Future targets

The appearance of CG character gave a great influence on the impression of a user. It is necessary to improve the appearance of CG character so that it could give good impression to a user. In addition, a target of not only appearance but also movement of a CG character depends on the usage of the system. As the usage of future system, we assume an agent for an answer-phone using a computer and a virtual friend for a person living alone. In the present system, the movement of CG character is just nod. We will add other movements besides nodding, according to the usage.

We adopt the fuzzy algorithm for estimating $\boldsymbol{n}$ from the *nod*, because it is easy to improve its accuracy by adjusting the rules, the membership functions, and the way for integrating the outputs from rules for an input. In the present study, we propose a method for synthesizing nods of a CG character and a human. At the next stage, we will investigate the suitable embodied communication between a human and a CG character. The flexibility of fuzzy algorithm will help us to extend the present method to the next version.

Furthermore, we will compare the present method with the embodied communication technologies using the relationship between the speech and the nod [1]–[4]. Then, we will investigate a new technology for communicating a human and a CG character or a robot with use of human's speech besides his or her head gesture.

VIII. CONCLUSIONS

We have developed a method for communication between a human and a CG character by exploiting thermal image processing. The CG character can synchronize its nod with a human's nod by predicting his or her nod angle. The measured feature parameter is inputted to fuzzy algorithm system to estimate the nod angle of the person in front of the infrared ray camera, then we use the MA model for predicting the nod of person. The average error of the nod angle obtained by the present system was estimated at about 5°. The CG character itself gave a great influence on the impression of user. Therefore we need to improve the CG character considering the usage of the system and the individual user.

REFERENCES

[1] Watanabe T, and Yuuki N (1989), A voice reaction system with a visualized response equivalent nodding. Advances in Human Factors/Ergonomics, 12A:396-403

[2] Watanabe T, Okubo M, and Ogawa H (2000), An embodied interaction robots system based on speech. J. Robotics and Mechatronics, 12(2):126-134

[3] Watanabe T, Danbara R, and Okubo M (2002), InterActor: speech-driven embodied interactive actor. Poc. of 11th IEEE Int. Workshop on Robot and Human Interactive Communication, 430-435

[4] Watanabe T, Okubo M, Nakashige M, and Danbara R (2004), InterActor: speech driven embodied interactive actor. Int. J. Human-Computer Interaction, 17(1):43-58

[5] Zelinsky A, and Heinzmann J (1998), A novel visual interface for human-robot communication. Advanced Robotics, 11(8):827-852

[6] Choi HI, and Rhee PK (1999), Head gesture recognition using HMMs. Expert Systems with Applications, 17(3):213-221

[7] Nonaka H (2003), Communication interface with eye-gaze and head gesture using successive DP matching and fuzzy inference. J. Intelligent Information Systems, 21(2):105-112

[8] Lin CS, Ho CW, Chang KC, Hung SS, Shei HJ, and Yehd MS (2006), A novel device for head gesture measurement system in combination with eye-controlled human-machine interface. Optics and Lasers in Engineering, 44(6):597-614

[9] Jia P, Hu HH, Lu T, and Yuan K (2007), Head gesture recognition for hands-free control of an intelligent wheelchair. Industrial Robot -An Int. Journal, 34(1):60-68

[10] Kuno H (1994), Infrared Rays Engineering (in Japanese). Tokyo, IEICE, 22

[11] Kuno H (1994), Infrared Rays Engineering(in Japanese). Tokyo, IEICE, 45

[12] Yoshitomi Y, Kimura S, Hira E, and Tomita S (1996), Facial expression recognition using infrared rays image processing. Proc. of the Annual Convention IPS Japan, 2:339-340

[13] Yoshitomi Y, Kimura S, Hira E, and Tomita S (1997), Facial expression recognition using thermal image processing. IPSJ SIG Notes, CVIM103-3, 17-24

[14] Yoshitomi Y, Miyawaki N, Tomita S, and Kimura S (1997), Facial expression recognition using thermal image processing and neural network. Proc. of 6th IEEE Int. Workshop on Robot and Human Communication, 380-385

[15] Yoshitomi Y, and Tanijiri T (2002), A machine for automatic segmentation of image and its method (in Japanese). Japan patent application 2002-344185

[16] Yoshitomi Y, Tsuchiya A, and Tomita S (1998), Face recognition using dynamic thermal image processing. Proc. of 7th IEEE Int. Workshop on Robot and Human Communication, 443-448

Quadruped walking with parallel link legs

Takumi Yaginuma*, Takasi Takesima*, Etsurou Shimizu*, Masanori Ito* and Junnichiro Tahara**

*Tokyo University of Marine Science and Technology,
2-1-6 Etchujima,Koto-ku,Tokyo,135-8533,Japan
(Tel:+81-3-5245-7426;Fax:+81-3-5245-7426)
(d062011@kaiyodai.ac.jp ,t062035@kaiyodai.ac.jp, shimizu@kaiyodai.ac.jp, itom@kaiyodai.ac.jp)
and
**Japan Agency for Marine-Earth Science and Technology
2-15 Natsushima-cho, Yokosuka 237-0061 Japan
(Tel:+81-46-867-9391,Fax:+81-46-867-9375)
(tahara@jamstec.go.jp)

Abstract: We are proposing an underwater robot for the work. In this study, we designed the robot, which has body of rectangular plane and 4 legs at each corner. The leg is consisted with parallel mechanism of 2or3 cylinders, and the end of each cylinder is attached on the robot body with free rotational joint and the end of both piston rods are connected with pin joint. 2 cylinder leg's motion is restricted in forward or backward direction but 3 cylinder leg can move any direction. We are studying the control scheme of walking for this robot, which is putting mind especially on smooth and steady movement without rolling, pitching, yawing or heaving motion and keeping the body horizontally. We confirmed the validity of control scheme with simulation and experiments.

Keywords: Underwater working robot, walking, parallel link

I. INTRODUCTION

In late years, importance of the marine technical use increases widely in the world. As deep sea is very severe environment for human, we usually use an underwater robot instead of human. In many years, the underwater robot was used for exploration, so the mainstream of research and development to the robot was for exploration. And the resources in the sea floor, such as petroleum or mines, were cleared from the results of exploration. Now, it is thought that the underwater working robot which has special functions such as maintenance, management or setting on sea floor of observation machinery is necessary. We thought that it was desirable to give robots the function changing their form suitably for work environment and work kinds to get high work performance, and suggested the mechanism design of the robot and the conformity method to environment and the work kinds. In this paper, we refer to the moving mechanism and control of the robot. As well known, robot faces to big reactive force when it is working and it should move stably, carrying heavy goods. We thought a quadruped walking robot which has parallel mechanism for the leg structure is adequate, and confirmed the basic performances keeping prescribed posture and smooth movement by using the experiment and simulation, and expanded the walking condition to uneven terrain surface and to soft surface like mud or sand.

II. LEG STRUCTURE

1. Correspondence to Underwater Work

Depending on a difference of working environment, the structure and control method for underwater robot has big difference to a land robot at the points such as buoyancy, load mass, waterproofing, the power supply etc. Therefore, we proposed the concept that under water robot equipping multi-arms and legs should change the role adequately for stability of posture and effectiveness of work, and showed the judging algorithm in AROB13th (2008). In this study, we show the detail of quadruped moving mechanism and walking control as the most fundamental system to realize the concept.

2. Parallel mechanism

When the robot works in the water, the load to each joint becomes small because the main body weight decreases with buoyancy. But it has a reactive force depending on a work motion and resistance force to the body with fluid. For this reason the posture control becomes difficult to underwater work robot. And leg has important role for stable work. Giving high power to leg comes to size up and weight up of the robot under using conventional serial mechanism. Therefore we decided to adopt the parallel mechanism as shown in Fig. 1, which is keeping objective enough functions for work, and preventing upsizing and weight up of leg.

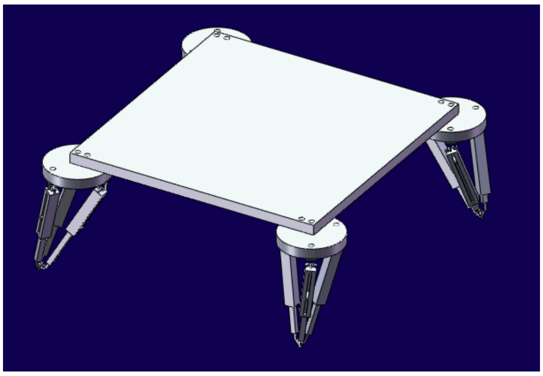

Fig.1. Underwater working robot (parallel link)

The parallel mechanism is constructed with parallely arranged links, base plate and end plate. Themovable space is smaller than serial link mechanism with mechanical restriction, but it can move more quickly and precisely, because it can move any direction with one action and the position error does not pile up. It also has higher rigidity because it can distribute the load to each link. Considering those characteristics, we can get a stronger and more active leg when we apply parallel mechanism to the leg. Moreover, it will bring the improvement of ability such as payload, smoothness of walking or acceptability to the change of situation such as posture in work environment or reactive force with a working motion.

In this study, we decided to use a parallel mechanism as shown Fig. 2. This leg is consisted with 3(three) sliders and the end of piston are connected with universal joints.

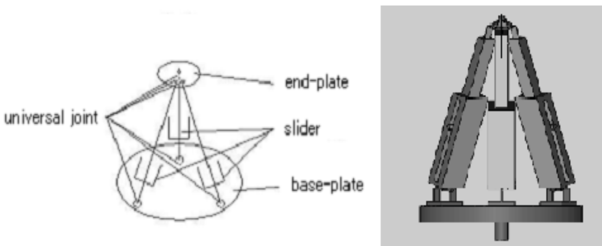

Fig.2. Leg of parallel mechanism

When we constitute one leg with three cylinders, we can define the movable range on the flat plane walking with the slide length of the slider and distance between the attached position of the slider to baseplate. In this study, when quadruped robot walks, we move the leg not to interfere each other. Then we designed the robot that has square shape body and at each corner leg mechanism consisted with circular plate and three (3) sliders attached. The sliders are attached to the plate at the top of right-angled isosceles triangle as shown in Fig. 3.

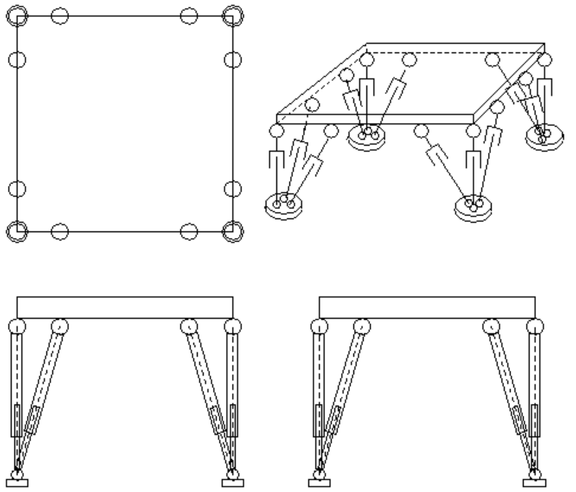

Fig.3. Joint design

One of the reasons of this design is that this arrangement is able to draw a large trajectory of foot and it guarantees the stability of body with putting the center of gravity of the robot into inside of the figure which landing foots draw. Second is that the side view as shown in Fig. 3 is same, so it can easily switchover control mode when it changes the walk direction on the work. In addition, as shown later in this paper, when we consider that the robot walks forward, backward or side direction mainly, only two sliders are used in Fig. 3 design and all sliders are used in Fig. 2 design. So, we are thinking that Fig. 3 type is advantageous from the view point of control or reliability than Fig. 2 type. As walking, we will hereinafter describe in detail.

III. WALKING

1. Concept

In this study, we assumed constant speed walking with keeping horizontal posture of body plane on a horizontal flat ground as a basic walk. These conditions are basic motion for the robot when he carries everything and not realized yet.

We will describe here the advantage of this walking.

- The main body of robot is stable
- The accuracy of work is improved because sensor or actuator is released from vibration or noise with stable robot motion.
- The influence on load deteriorates and accidents such as collapse, damage or fall of carrying material effectively prevent.

- In case of remote control, it becomes easy with reducing additional subtraction speed or vibration of the main body.
- The control system is designed for working part and moving part independently.

2. Walking Pattern

We will expand this walk to undulating land, a slant place, a step in future as well as level ground. When we compare the operation range of the robot with 3 slider type and 2 slider type, only side or oblique walk is impossible for 2 slider type and those walk are not so often appear in actual walk, and control become easy to 2 slider type. Therefore we are thinking that 2 slider type robot is more practical than 3 slider type.

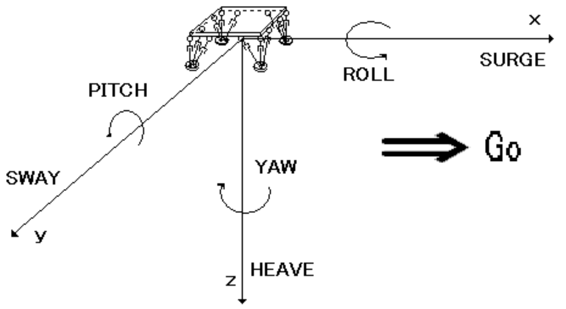

Fig.4. Body-fix

Here we show the walking pattern for straight walking with constant speed, keeping horizontal posture and constant height on a flat horizontal ground. The walking motion can separate following 3 modes.

- Walking start mode···
  ①Float and move front left leg ahead
  ②Another supporting legs move the body to go ahead
- Walking (cruise) mode···
  ①After landing front left leg, float front right leg and another legs move the body.
  ②After front right leg landing, float aft left leg and then aft right leg. Continue this sequence.
- Walking stop mode···
  ①Move supporting legs to get vertical condition when stop order given.
  ②Land the floating leg to get vertical condition。

The pattern is shown in Fig. 5.

To make walking control easy, we adopted pattern control that moves leg with predetermined pattern and change or correct the pattern if necessary. The algorithm of the walk pattern change is going to use action judgment algorithm based on suggestion as the IF-THEN method that was introduced in AROB13th (2008)[1]. About the motion of leg such as landing-backward moving-floating-forward moving, we set some basic patterns so that a walk of constant speed, horizontal posture and constant height can perform smoothly.

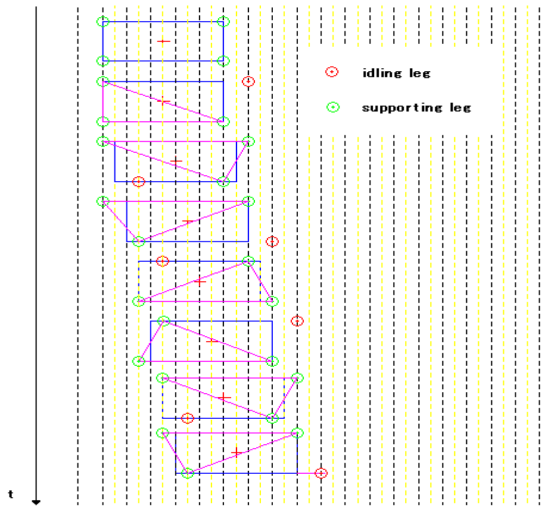

Fig.5. Example of walking pattern of 2 slider type

3. Walking Control

Walking motion of this robot includes many kinds such as Straight walk (forward or backward), Curving walk (right or left), Turning (right or left) and Climbing or descending slope or step. We must establish control algorithm for every walking. Here we introduce basic control system depending on pattern method

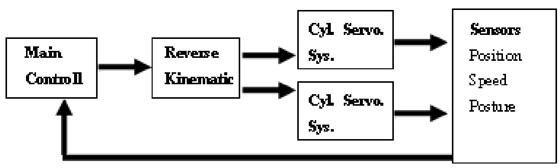

Fig. 6 Control System

IV. EXPERIMENT

Simulation

At first we confirmed the performance with simulation. Here we built 3-D model with Solid Works and gave each slider of each leg mentioned pattern of motion. As shown in Fig. 6, we could get expected results of constant speed, horizontal posture and constant height.

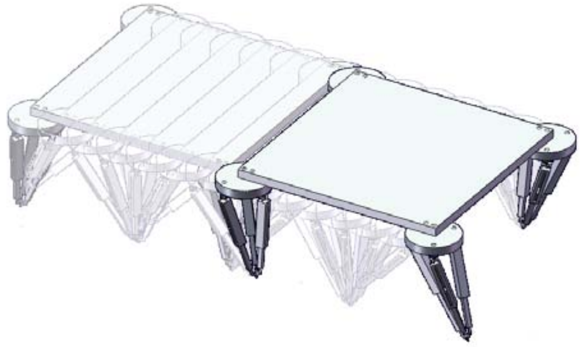

Fig. 7 Simulation Results

Experiment

2.1 Experiment System

In this experiment, we install a device for 1 that we constituted by two electric cylinders to show in Fig. 6 on a surface plate in form to do a joint as ankle on the top and build a system moving this by Matlab-Simulink and confirm a cylinder control system for walking. We show the specifications of the electric cylinder to use for this experiment in Table 1.

Table.1 Experiment system

Control system	: MatLab (simulink)
Electric cylinder	: YAMAHA YMS45
Cylinder stroke	: 20cm
Thrust force	: 2-6kg
Driver	: YAMAHA SR1-X

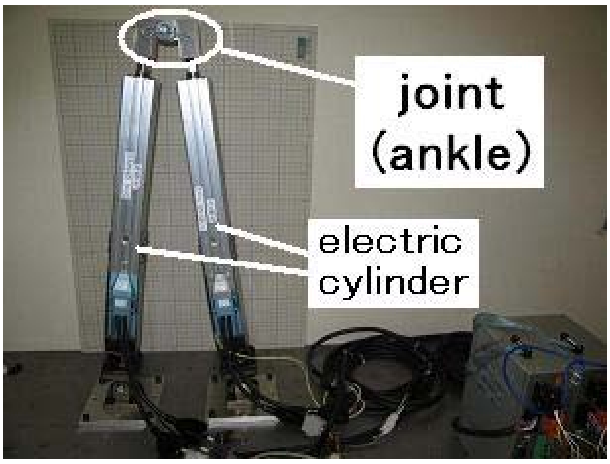

Fig.8 Experimental equipment

2.2 Control Method

In this system, we built the control system to realize the motion shown in Fig. 9. Each cylinder was controlled with the reference length decided from reverse kinematics depending on the trajectory and moving speed. This motion control program is shown in Fig. 10.

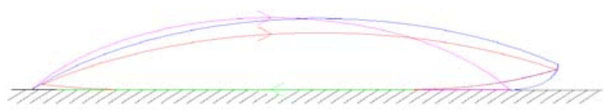

Fig.9 Example of trajectory pattern of foot

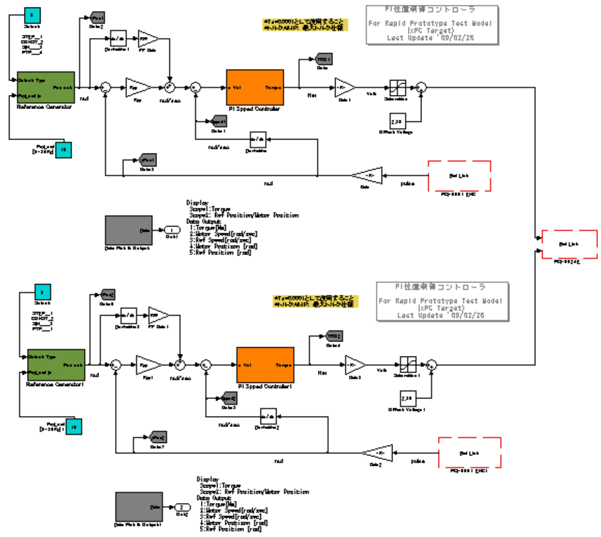

Fig.10 Control system

3. Experimental Results

We would like to report those results on the symposium as much as possible.

V. CONCLUSION

We proposed the walking robot having 4 legs with the parallel mechanism as underwater work use and examined the motion performance.

It showed enough possibility about the basic walking with simulation, and it is on the confirmation with experiment now.

Those results suggest us that this type of robot has a higher performance than conventional type and we would like to develop the system to higher level of applications.

REFERENCES

[1] Yaginuma T(2008),Study of autonomouous work control for multiple limbs under water robot. AROB13th734-738

[2] Okawa Y(2007),Introduction to model base development for mechanical design (in Japanese), Omusya.

The Fifteenth International Symposium on Artificial Life and Robotics 2010 (AROB 15th '10),
B-Con Plaza, Beppu,Oita, Japan, February 4-6, 2010

Development of under water use humanoid robot

Yunyi Li, Eturo Shimizu, Masanori Ito

Tokyo University of Marine Science and Technology
2-1-6,Ecchujima,Koto-ku,Tokyo,Japan
(Tele: 03-5245-7300-8756Fax: 03-5245-7300-8756)

(iamliyunyi2000@yahoo.co.jp, shimizu@e.kaiyodai.ac.jp, itom@kaiyodai.ac.jp,)

Abstract: In this research, we have developed a swimming robot with flutter kick of two legs, which can swim freely both on the surface of water and in the water, and established the control method for all kinds of motion of this robot, such as straight swimming, turning, down going or up going. Furthermore, with optimizing the three-dimensional action of underwater robot, we can expect improvement of the performance of underwater robot for complex work.

Keywords: Humanoid, Underwater Robot,

I. INTRODUCTION

With the development of science and technology, robot has been experienced surprising rapid advancement. Particularly, the research on humanoid robot becomes very high level and its motion is improving day by day. The authors think that the humanoid type underwater robot is convenient for underwater works as on the ground. The underwater environment is so dangerous for human, that many kinds of robot have been extensively used for underwater work, such as underwater resources exploration, oceanographic mapping, undersea wreckage salvage, ocean engineering survey, dam security inspection, and so on. However, there has been no underwater robot which can take the place of the diver by now. Considering those situation, the authors are putting the focus on developing Underwater Humanoid Robot.

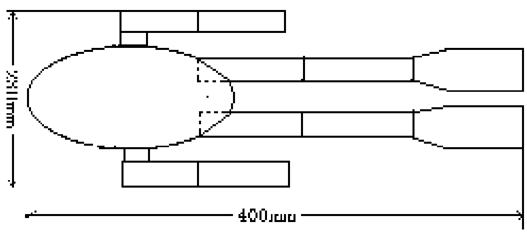

Fig.1 Image of Underwater Humanoid Robot

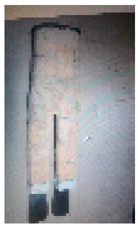

Humanoid-1

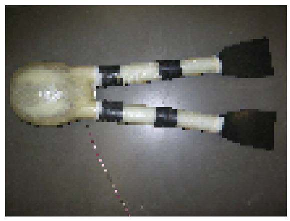

Humanoid-2

Humanoid-3

Fig.2 Example of Underwater Humanoid Robot

II.DESIGN OF ROBOT

As illustrated in Fig.1, the propulsive structure treated here is a free-swimming humanoid robot. It is composed of three parts: a body with two arms and two legs. Each of the legs is composed of two links and one oscillating fin. The robot is wearing a waterproof suit on the body. And it is designed to get neutral buoyancy also.

The neutral buoyancy is the condition that the gravity equal to buoyancy. And the center of buoyancy and gravity are arranged to be collinear along the body z-ax

Fig. 2 shows prototypes of radio-controlled underwater humanoid robot. They have been developed in our laboratory. The mechanical device used in this paper is humanoid-3. The body of the robot is wrapped with gum. In the body, following devices are installed in a water shielded package. 1)Microcontroller board: Motion Greator for TTL and PS/2 Bluetooth controller, 2)Communication devices: Parani ESD-200 Bluetooth Serial Adapter, 3)Arm servo motors, 4)Batteries and 5)Underwater camera. The total weight is approximately 1.5 kg. And the length is 400mm. We can control the swim of robot with wireless communication. Its speed is adjusted with frequency and amplitude of oscillating signal, and its turning motion is controlled with arm motion.

III.MOTION ANALYSIS

In this section, the authors built the dynamic model on the basis of undulated fins and the drag model in fluid mechanics. The dynamic model of undulated fins can make clear the relation between the forces/moments and propulsive wave parameters, geometric parameters as well as swimming velocity. We can study about the motion of the robot, control method and efficiency of propulsion. This dynamic model for undulated fin has been validated with experimental tests in thrust, and propulsive velocity of the underwater robot.

1. Basic motion of straight swimming

When the robot is swimming on a straight course, the desired motion can be expressed as

$$\mathrm{f}(\mathrm{x},\mathrm{t})=\left(c_1\frac{x}{l}+c_2\left(\frac{x}{l}\right)^2\right)sin\left(k\frac{x}{l}+\varpi t\right)l \qquad (1)$$

where f is transverse displacement of the body, x is displacement along the main axis. t is time, k is body wave number, ϖ is body wave frequency, l is length of the robot.

2. Thrust force

To simulate the dynamics of the swimming, we simply considered a equation of thrust force with flutter kick.

$$p=\rho s\,cos[\alpha_0\,cos(2\pi ft-\phi)]\,c$$
$$\left\{h_0 2\pi f\,sin(2\pi ft)-tan\left[\alpha\,cos(2\pi ft-\varphi)\right]\frac{2fh_0}{s'_t}\right\}$$
$$2h_0\pi\,sin(2\pi t) \qquad (2)$$

$$s'_t=\frac{fh}{2v}$$

where p is thrust force, ρ is density of fluid, α_0 is the maximum attack angle, f is the frequency, v is velocity of robot, φ is phase difference and c is coefficient of interference between two legs. As the influences of the interference of flutter kick is very complex, we use the approximation and calculate under ideal condition in this paper.

3. Resistance force

We assume the shape of body is not plate but an ellipsoid, then the resistance force on the body is assumed to be generated in the usual steady flow. Under this assumption, the resistance force becomes as follows

$$R=\frac{1}{2}c_D\alpha\rho Sv^2 \qquad (3)$$

where v is velocity of the body, c_D is resistance coefficients, α is attack angle, s is projected area of body and arms in the x-y plane.

4. Dynamic equation of straight swimming

When robot is swimming in the water, buoyancy is equal to gravity of robot. Then the equation of dynamics can be written as

$$m\frac{dv}{dt}=p-R \qquad (4)$$

where m is mass of the robot.

IV. CONTROL

1. Turning control

When the robot is required to turn uniformly with given angular velocity w and turning diameter D, a centripetal force F and a turning moment T should be offered as

$$F = \frac{1}{2} m \omega^2 D \tag{5}$$

$$T = \frac{1}{4} m \frac{d\omega}{dt} D^2 \tag{6}$$

If we set the robot arms making angle between body as θ, we can get the centripetal force from thrust force and resistance force. It makes possible to change direction and continuous direction change becomes turning. Confirming the motion, we applied data table looking up control method, which is determining θ from data table between θ and w.

2. Speed control

From the equation (2) (3) (4), we can get the relationship between velocity and frequency of flutter kick. Then with changing flattering frequency, we can get a desired swimming speed, As a note, the phase difference φ is set at 80°, because it is evaluated that we can get the best thrust force.

V. SIMULATION

In order to evaluate the applicability and capabilities of humanoid robot, we made simulations study with using developed model. From Fig.3 to Fig.6 we will show the results of simulation for swimming start mode as an example. The condition for simulation is shown in Table 1.

Table 1 Condition of Simulation

Dimension of Robot:
Body Width ;23cm, Body Length;40cm
Body Depth; 11cm, Leg Length;20cm
Fin Size; 10cm*6cm
Weight; 1.5kg
Frequency of Leg Motion; 2Hz

The coefficients of resistance of the body were calculated with approximating the body as ellipsoid and arms as columns.

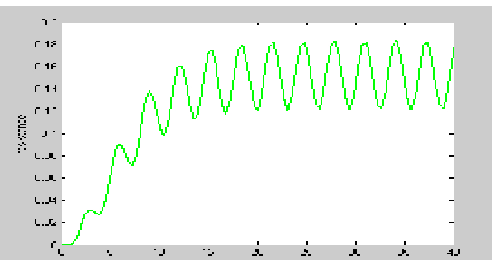

Fig.3 Resistance

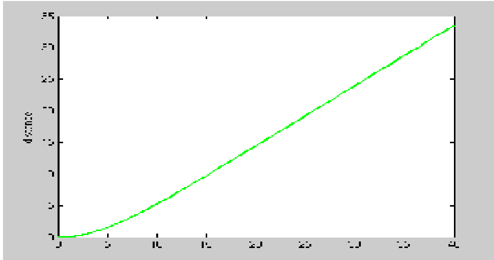

Fig.4 Moved Distance

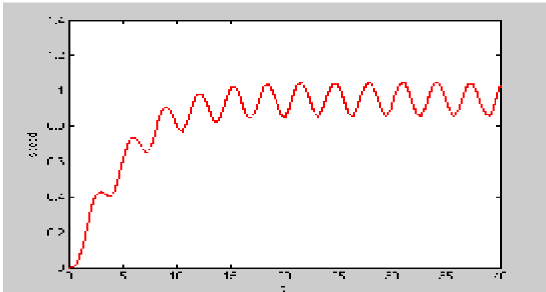

Fig.5 Moving Speed

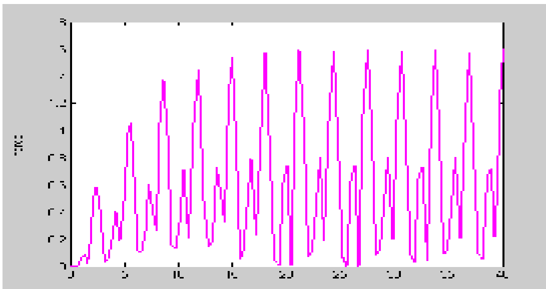

Fig.6 Thrust Force

VI. EXPERIMENT

For the confirmation of the simulation results and further study, we made experiments with actual robot.

1. Experiment system

In this experiment, we used a high performance humanoid robot as a base machine and covered it with waterproof suit. It can be controlled with game controller remotely or with program autonomously. It equips an underwater camera on a body. The photograph of shown in Fig.7. This robot was tested in the water tank of 2m × 2m × 1m (length × width × height) in our laboratory. Fig. 8 shows the shape of the tank.

Table 2 Specification of Humanoid Robot

Servo motor: ROBOTIS Dynamixel AX-12+
Number of AXIS:10
Computer: Motion Greator for TTL(Atmel ATMEGA128)
Wireless: Parani ESD-200 Bluetooth Serial Adapter
Controller: PS/2 Bluetooth controller

Base robot Controller Waterproof suit

Fig. 7 Robot System for Experiment

Fig.8 Water Tank

2. Experiment Resuluts

We would like to report those results on the symposiun as much as possible.

VI. CONCLUSION

Here we proposed a humanoid type underwater robot. Through the basic study, we are thinking that this type of robot has higher performance than conventional underwater robot and can accomplish higher level of work instead of diver. In this paper, we introduced mainly the propulsion system, such as principal, the structural design or control algorithms to generate appropriate thrust force. This mechanism has a disadvantage that the flutter kick of both leg interfere each other. We found the method to decrease the influence and to satisfy manipulation requirements. This propulsion system can also generate turning moment, upward going moment or downward going moment adding thrust force with selecting angular velocity of fluttering and center angle of fluttering. And with integrating basic control to cooperated control, we can realize free posture control and get various kind of motion.

REFERENCES

[1] Colgate J E , Lynch KM(2004), Mechanics and Control of Swimming .A Review [J] . IEEE J . Oceanic Eng,29 (3) :660 - 673.
[2] YAMAMOTO I, TERADA Y(1995)Propulsion system with flexible / rigid oscillating fin [J]. IEEE Journal of Ocean Engineering 20 (1): 23-30.

Improvement of Underwater Vehicle Remote Control Environment with Parallel Link Operation Base

Kimiyo Inabe, Etsurou Shimizu, Masanori Ito and Junnichiro Tahara

Tokyo University of Marine Science and Technology,
2-1-6 Etchujima,Koto-ku,Tokyo,135-8533,Japan
(Tel:+81-3-5245-7426;Fax:+81-3-5245-7426)
(inabe@giga.ocn.ne.jp, shimizu@kaiyodai.ac.jp, itom@kaiyodai.ac.jp)
and
Japan Agency for Marine-Earth Science and Technology
2-15 Natsushima-cho, Yokosuka 237-0061 Japan
(Tel:+81-46-867-9412,Fax:+81-46-867-9375)
(tahara@jamstec.go.jp)

Abstract: This research is connected with ROV's remote control, and is carried out to solve ROV's operator's severe seasickness caused by disagreement between mother ship's motion and the image including ROV's motion from underwater vehicle expressed at the station.

Keywords: ROV, Remote Control, Seasickness.

I. INTRODUCTION

Now, there are two types of underwater vehicle, that is, manned and uninhabited type.

Former is superior in activeness and function, for an operator and a researcher ride together, but because of lack of safety, latter is the mainstream. This includes ROV which needs remote control by man, and AUV which chooses movement by itself.

ROV doesn't need complicated control because of human handling and can be observed with real time processing, viewing images which has high resolving power, be manipulated. And electric power is provided from mother ships, and it is free from limitation of time, but it's range of action is limited by length of cable.

On the other hand, it is still hard to make AUV carry out minute work with manipulator and hand.

This research is connected with ROV's remote control, and carried to solve ROV's operator's severe seasickness caused by disagreement between mother ship's motion and the image including ROV's motion from underwater vehicle expressed at the station .

The principle of the research is to make environment as if an operator rides on the underwater vehicle with getting rid of ship's motion and unite with motion of underwater vehicle,

To recreate this situation in laboratory by a Stewart type parallel link system, as an operation base, and show him(or her) the image which was taken on the vehicle, we measured the level of seasickness. And then, we moved the parallel link with same motion to the vehicle.

On these experiments, we compared the level of seasickness. we can develop the system which reproduces a vibration of underwater vehicle separated from that of a ship, including a series of handling and indication ,as new remote control environment of underwater vehicle.

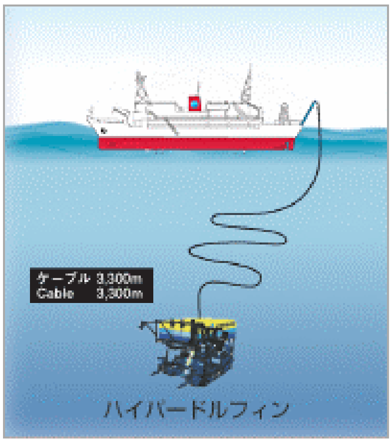

Fig.1 Remote Control of Underwater Vehicle

Fig.2 Station for Remote Control on Mother Ship

II. Environment of Remote Control

As an example, we show the rolling and pitching motion of Shioji-maru in Fig. 3, which is the training ship of our university. Under those motions, operator moves underwater vehicle with watching monitor display. we calculate the length of six legsof the parallel link operation base from the angles of roll and pitch changing every time, and reproduce the motion of the ship by their expand and contracting.

At first, I can't help operating by appointing length of six legs changing every second by signals from AD/DA converter,but in the future I want to master to operate automatically by retrieving Excel's Data in C language program.

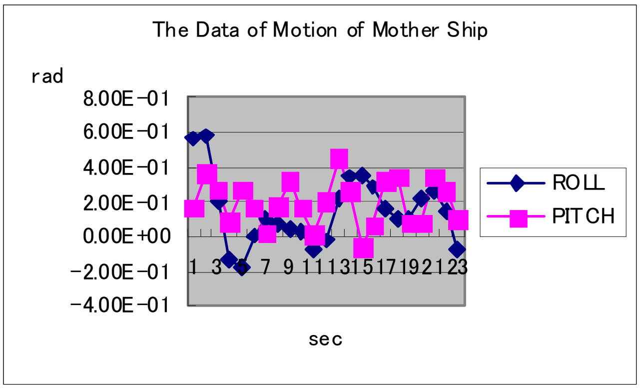

Fig.3 Motion of Mother Ship

III. IMPROVED OPEATION SYSTEM

1. BASIC CONCEPT

This research is carried out to solve seasickness caused by disagreement between motion of mother ship and that of an image seen through underwater camera, which has long been significant problem among ROV's operators.

The main purpose of this research is to make situation as if an operator rides underwater vehicle by getting rid of ship's motion and fitting that of underwater vehicle.

2. SYSTEM CONSTRUCTION

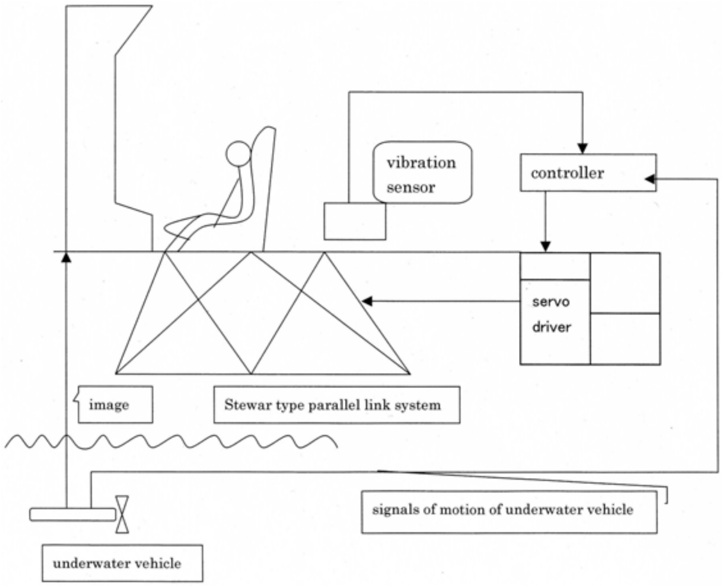

Fig. 4 New Operation System

Stewart type parallel link operation system which has six legs moved by oil pressure.
Monitor and underwater camera
AD/DA converter which change from analog signal into digital one, or from digital to analog.

IV. CONFIRMATION OF THE EFFECT

1. Outline of Experiments

In this experiment, we reproduce motion of the mother ship by Stewart type parallel link system, and ask a subject to sit on it, show him(or her) the image added the motion of the vehicle apart from the mother ship, and measure the level of sea sickness. After getting rid of motion of the ship, and reproduce that of the underwater vehicle, we show the subject the same image, and compare the level of seasickness.

2. Equipments of Experiment

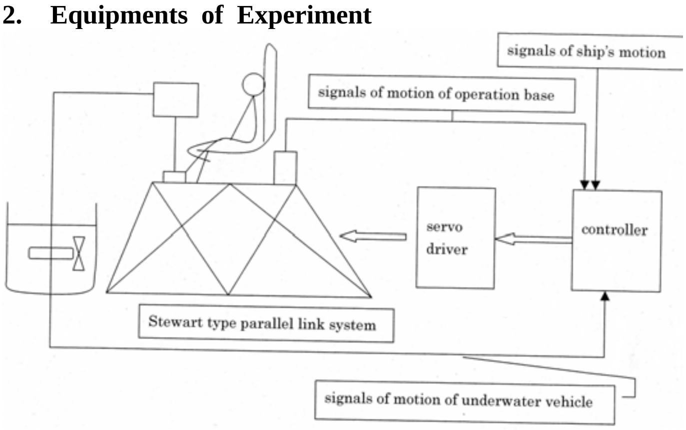

Fig.5 Outline of Experimental System

Fig.6 Experimental System

3. Control System

We calculate length of the six legs by means of Back-function-Theory, that is, make the operation base move contrary to motion of the ship.
In other words, we need equations to invalidate the following one.

3.1 Control Algorithm

The length of six legs of the operation base

L1=sqrt((H+0.866*R*sin(b)+0.5*R*sin(c))*(H+0.866*R *sin(b)+0.5*R*sin(c))+(r*r-r*R+R*R))……(1)

L2=sqrt((H-0.866*R*sin(b)+0.5*R*sin(c))*(H-0.866*R*sin(b)+0.5*R*sin(c))+(r*r-r*R+R*R))……(2)

L3=sqrt((H-0.866*R*sin(b)+0.5*R*sin(c))*(H-0.866*R*sin(b)+0.5*R*sin(c))+(r*r-1.25*r*R+R*R))……(3)

L4=sqrt((H-R*sin(c))*(H-R*sin(c))+(r*r-r*R+R*R) …(4)

L5= sqrt((H-R*sin(c))*(H-R*sin(c))+(r*r-r*R+R*R) …(5)

L6=sqrt((H+0.866*R*sin(b)+0.5*R*sin(c))*(H+0.866*R*sin(b)+0.5*R*sin(c))+(r*r-1.25*r*R+R*R)) …(6)

L1～L6 : the length of Leg1～Leg6
r:the radius of the base plate
R:the radius of the platform
H:the hight of the operation base

4. RESULT OF THE EXPERIMENT

4.1 Seasickness Level Evaluation

We will use the following four-grade-evaluation.

Grade0:Don't feel seasickness at all.
Grade1:Feel slight discomfort, but can live as usual
Grade2:Feel discomfort, and hard to work.
Grade3:Feel severe discomfort, nausea, can't work

4.2 Comparison with Conventional System and Improved System

We will compare the two type of system, that is conventional and suggested system(improved one). Former is carried out under the recreated motion of mother ship, and latter is after getting rid of the previous motion and make modification as the motion of the underwater vehicle.

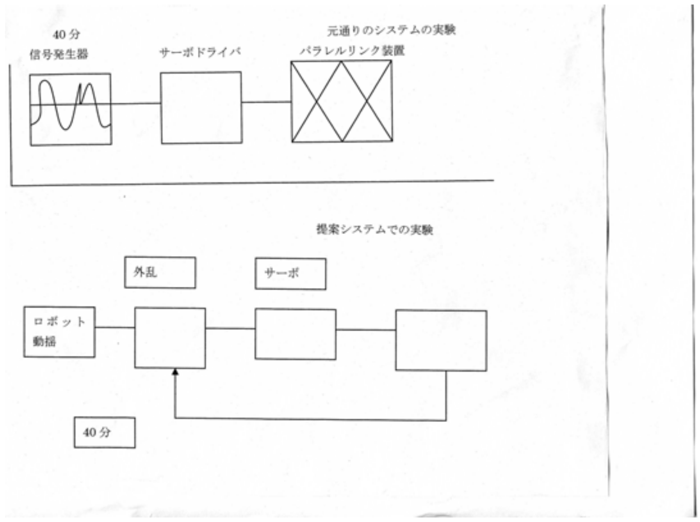

We suppose that the user can't operate more than 30 minutes because of the difference between the motion of the vehicle and the ship, before getting rid of motion of the ship. But after it, he(or she) can operate much more longer.

V. CONCLUSION

I want to make sure result of the experiment is true as a subject

REFERENCES

[1]Suzuki.M Research about artificial horizontal support for ships.
[2]HaniwaN Research about control of Stewart parallel link system operated by oil pressure.
[3]InoueD Development ob device for pursuing satellite using parallel link system

Spinning Control of Basketball with Robot Fingers

Yuuki Ohtake, Masanori Ito, Feifei Zhang

Tokyo University of Marine Science and Technology
Etchujima2-1-6, Koto-ku, Tokyo
(Tel :03-5245-7426)
(itom@kaiyodai.ac.jp)

Abstract: In this paper, we consider dexterous manipulation by robot hand through spinning control of basketba ll. We investigate a spinning basketball, and propose that control process for keep up spinning basketball on f ingertip. This problem is to control manipulating a dynamic object under equilibrium grasp. We analyze the m otion characteristic of a ball that spinning at high speed and its on a fingertip, and propose the control metho d to prevent the ball from dropping by the feedback control. And, we verified the effectiveness of this metho d by the simulation.

Keywords: Amusement robot, Ball-spinning trick, Dexterous manipulation, Equilibrium grasp

I. Introduction

A robot hand has dexterous fingers is important element for intelligence humanoid robot. So, many robotics researcher studies robot hands possible humanlike dexterous work. However, it is not easy to achieve it by robot hand because dexterity of human hand. When manipulating the object, which is constrained from the hand in the form that is called force-closure and form-closure[1] in the many researches manipulation that using robot hand. At this time, the object is constrained by fingers of an enough number, and grasped by an appropriate finger force. When the manipulation object is dynamic, it is preferable to reduce the contact point with the object.

In the researches about dexterous manipulation that using robot finger and hand, there are Pen spinning by Ishihara and others[2], Dish spinning by Kajiwara and others[3], and Rolling based manipulation by Harada and others[4]. In [2], Ishihara and others have achieved a dynamic pen spinning using multifingered hand by feedback system. In [3], Kajiwara and others have achieved a dish spinning by robot with the open-loop control. And in [4], Harada and others achieved the manipulation of a object on the robot hand by the trajectory planning of the manipulation object. This like, the research on a dexterous manipulation with the robot hand is done by various approaches. However, there is no research, manipulating a dynamic object by the feedback system under equilibrium grasp yet. And so, we chose spinning control of basketball as a dynamic model that achieved such a control, and achievement by the robot was tried.

This is like basketball player plays spinning a ball on own fingertip. But, we were not able to find the document that had been described how to spin a basketball on fingertip. Then, first of all, we analyze the mechanism of ball spinning, and show the condition to manipulate the ball with stability. And, we propose control techniques to achieve spinning a ball by robot hand, and show the effectiveness by the simulation.

II. Spinning Ball Dynamics

When the fingertip catches the rotation axis of a ball, and the ball rotates at high speed, the ball does a steady rotation by the gyroscopic effect. Therefore, as one means because of no drop of the ball from fingertip, there is a method of beating the side of ball by hand when spin velocity slow down and torque the ball. But, we don't think about control to add torque a ball, because we focus attention on control the fingertip has a ball in this paper. In this instance, we think about control methods because of no drop of a spinning ball on fingertips by adding appropriate power to the ball by movement of the robot hand against inclination and movement of a spinning ball. We dynamically explain how to control the robot hand when the inclination of a spinning ball grows.

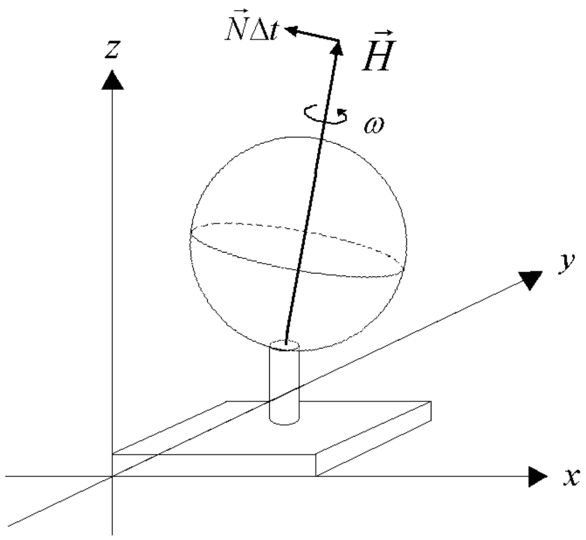

Fig.1 Control of Spinning Ball

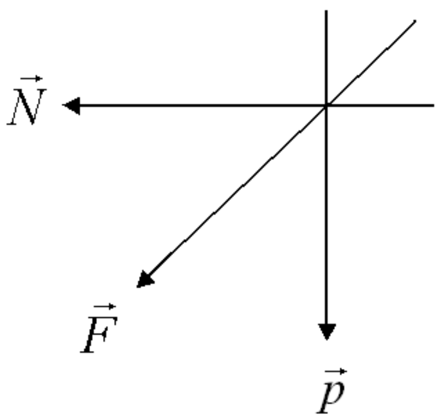

Fig.2 Relation of Vector

The $\vec{H}$ angular momentum vector of the ball that has inclined turns on the diagonal like Fig.1.

It is necessary to control this $\vec{H}$ to be suitable for a vertical direction to keep a steady rotation of ball. So, the following expressions are given,

$$\Delta\vec{H} = \vec{N}\Delta t \qquad (1)$$

At this moment, $\vec{H}$ is a variation in the angular momentum vector, and $\vec{N}$ is force moment. In a word, it has to add force moment $\vec{N}$ for this $\vec{H}$ to be suitable for a vertical direction. At this time, the problem to which direction to add force $\vec{F}$ is caused. Here, we assume position vector that to force point from gravity of ball is $\vec{p}$, as follows,

$$\vec{N} = \vec{p} \times \vec{F} \qquad (2)$$

At this time, the direction of three vectors is a relation of Fig.2. As a result, it is understood in which direction the robot hand should be moved for the inclination of the ball.

III. Control Model

In this section, we show the control model and planning of the robot hand for spinning control of ball, based on the spinning ball dynamics described in the foregoing section.

At the first, we show the model of the spinning control of ball in Fig.3. There is a cylindrical robot finger on the base where it can move on the x-y plane, and a ball on it. (x_p, y_p, z_p) is barycentric coordinate of robot finger, and (x_b, y_b, z_b) is barycentric coordinate of the ball. This robot finger is assumed to have the elasticity of rubber. When man has basketball by the fingertip, the fingertip that touches the bowl is transformed according to the shape of the ball. The fingertip becomes shape near the form of a cylinder rather than the oval, and the finger and the ball are in the state of surface contact.

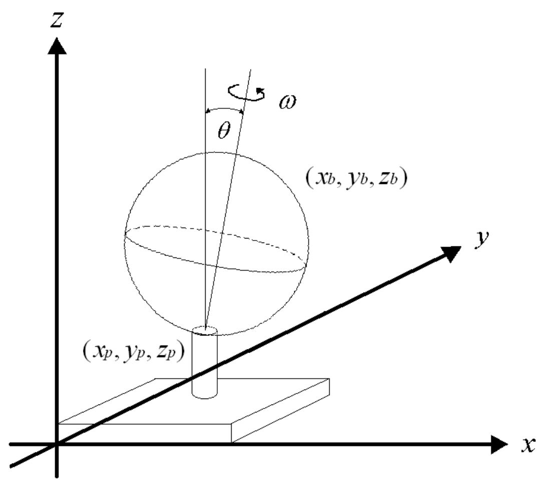

Fig.3 Control Model

We control the inclination and the barycentric position of the ball by the PID control. At this time, the state that spins with stability is not necessarily $\theta = 0$ in the spinning ball by movement characteristic. Therefore, it rather becomes unstable in the control planning that aims at deviation is 0.

Then, we set the following control rules. A downward moment from the center of gravity of the ball is shown in Fig.4. When this downward moment indicates the fingertip, the inclination is gradual. But when it indicates the outside of fingertip, the inclination of the ball increases at a dash. Then,

$$\theta \geq k_r \frac{180r}{R\pi} \quad (0 < k_r \leq 1) \tag{3}$$

to respond in this case, we did the control planning.

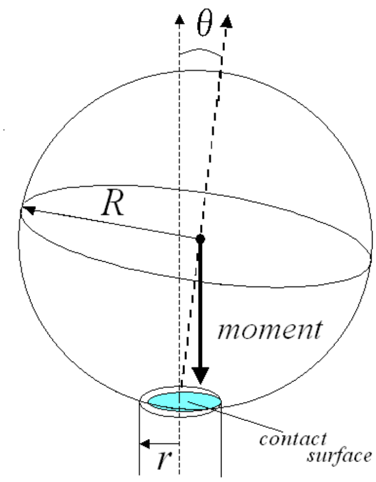

Fig.4 Moment of Ball

IV. Simulation

The result of the simulation is shown about the spinning ball model described in the foregoing section. Fig.5. is verification animation that we are used ODE and made, and Fig.6-8. is the result graph.

We set the parameter of the start of the simulati on at $\omega = 20rad/s$ (counterclockwise-rotation), $(x_p, y_p) = (x_b, y_b) = (0,0)$, $k_r = 0.5$.

In Fig.6, the angular velocity and the inclination of the ball are shown. And, x,y constituent of barycentric coordinate of robot finger in Fig.7, x,y constituent of barycentric coordinate of ball in Fig.8 is shown respectively. These graphs are shown that spinning speed of the ball fell at time, the robot hand is controlled without dropping the ball from the fingertip to the inclination of the spinning ball.

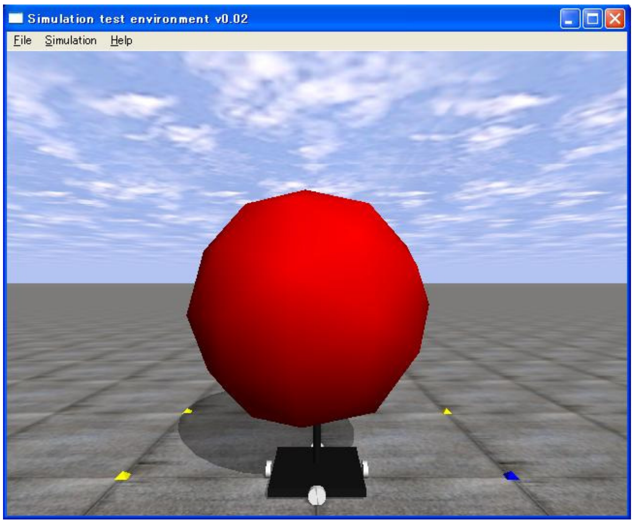

Fig.5 Animation by ODE

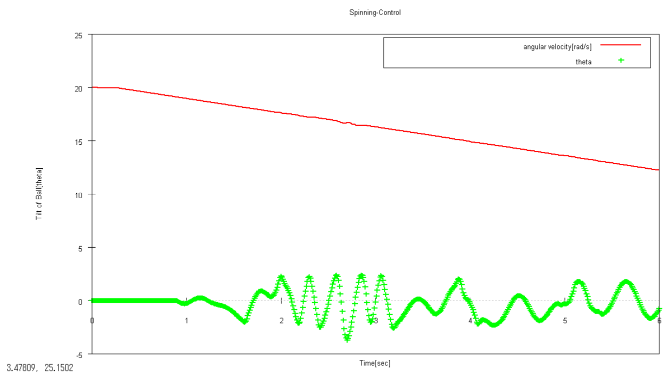

Fig.6 Angular Velocity and Inclination of Ball

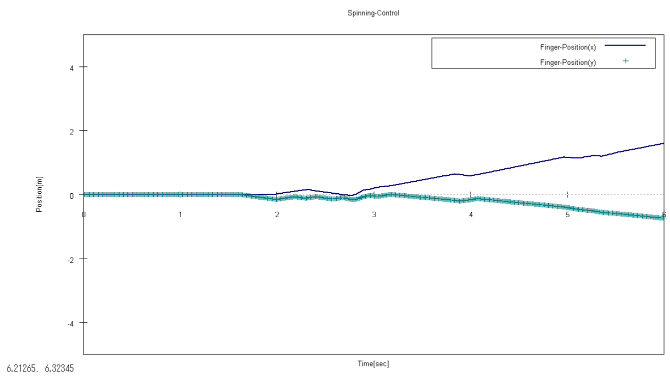

Fig.7 Excursion of Barycentric Coordinate of Finger

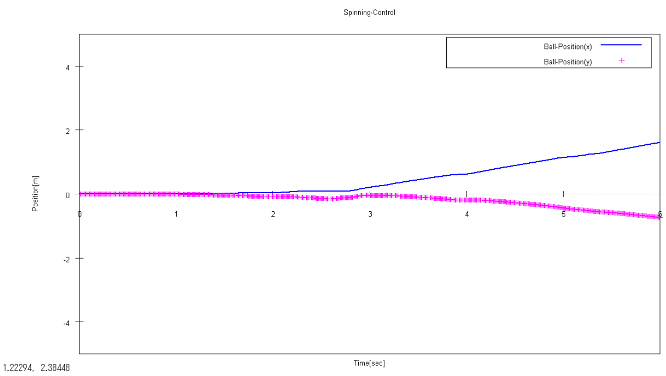

Fig.8 Excursion of Barycentric Coordinate of Ball

V. Conclusion

In this paper, we proposed control method of robot finger that manipulated a spinning ball as one example of dexterous manipulation by the robot hand, and verified by the simulation, and the effectiveness was shown. Consequently, we clarified whether to control the robot hand of the ball spinning that had not been discussed up to now like any. We can expect the achievement of the robot hand to be able to do a quick, appropriate correspondence by manipulating the movement of grasped object with the robot hand by the feedback control with stability. We plan to verify it by the real machine experiment in the future. But, we thought that it is a problem how to detect the inclination and the position of the ball changed at high speed for that accurately. In this time, we handled only the manipulation control of the spinning ball, we would like to think also about the control that gives the spinning force to the ball when the rotational speed of the ball descend in next time. Moreover, we thought that it is a problem that should also examine control method that think about the control of the vertical direction though we thought only about the control of horizontal direction this time.

References

[1] Shinichi H, Hidefumi W (2005), Handling Technology, Corona Publishing CO., LTD. pp.71-88

[2] Tatsuya I, Akio N, Masatoshi I, and Makoto S (2006),Dynamic Pen Spinning Using a high-speed Multifingered Hand with High-speed Tactile Sensor. 2006 IEEE RAS International Conference on Humanoid Robots. Proceedings, pp.258-263

[3] Hidekazu K, Yukio H, Toshihiko M, and Takeshi T (1998), Dynamics of a Dish-Spinning Trick and Its Realization by Robot, International Journal of Robotics Research, Vol.16, No.4, pp.483-490, 1998

[4] Kensuke H, Taiga K, and Makoto K (2002), Rolling Based Manipulation under Gravitational Equilibrium, International Journal of Robotics Research, Vol.20, No.2, pp.164-172, 2002

[5] Kousei D (2007), Robot Simulation, Morikita Publishing Co., Ltd.

[6] Hiroshi T (2006), Basic of Multi Body Dynamics, Tokyo Denki University Press.

AUTHORS INDEX

Notation of session name:PT: Plenary Talk, IT: Invited Talk,
OS: Organized Session, GS: General Session, PS: Poster Session
Note: **33/**90 = (page no. in Technical Paper Index) / (page no. in Abstracts)

エム・イーシステム株式会社			〒　８７９－１５０６ 大分県速見郡日出町９７１－５
ＴＥＬ	０９７７－７２－７７１６	ＵＲＬ	http://www.me-system.co.jp
ＦＡＸ	０９７７－７２－８７７１	Ｅ-mail	info@me-system.co.jp

自動組立機・自動検査装置・画像処理装置の設計製作

E&C
ENERGY & COMMUNICATION

OITA GAS

5-25 KITA-MATOGAHAMA
BEPPU-CITY OITA
JAPAN 874-0928

PHONE 0977-24-2111